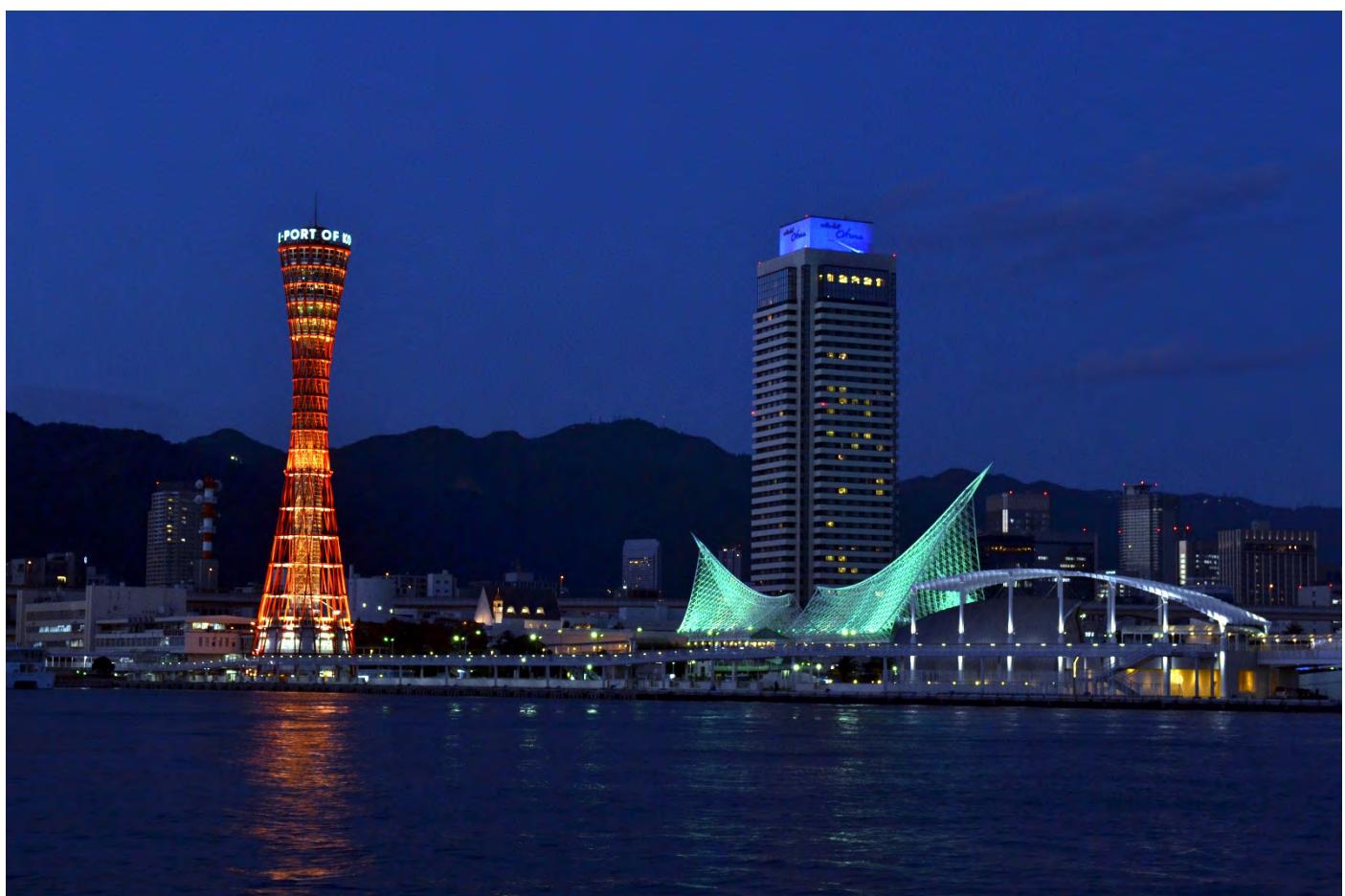


IUS IEEE International Ultrasonics Symposium
Including Short Courses
2018 October 22 -25, 2018
Portopia Hotel, Kobe, Japan



ABSTRACT BOOK



IEEE ULTRASONICS, FERROELECTRICS,
AND FREQUENCY CONTROL SOCIETY



1A - Cardiac Elasticity

Topaz (400)

Tuesday, October 23, 10:30 am - 12:00 pm

Chair **Guy Cloutier**
University of Montreal Hospital

1A-1

10:30 AM Analyzing the shear wave mechanics in cardiac shear wave elastography using finite element simulations

Annette Caenen¹, Mathieu Pernot², Mathias Peirlinck¹, Luc Mertens³, Patrick Segers¹

¹*IBiTech-bioMMedia, Ghent University, Ghent, Belgium*, ²*Institut Langevin, ESPCI Paris, PSL Research University, CNRS UMR 7587, INSERM U979, paris, France*, ³*Hospital for Sick Children, University of Toronto, ON, Canada*

Background, Motivation, and Objective

Acoustic radiation force (ARF) based shear wave elastography (SWE) has the potential to differentiate normal from pathological tissue based on tissue stiffness. However, its fundamental working principles are challenged in the cardiac setting because of the heart's complex material properties, dynamic loading and boundaries. Therefore, we built a finite element (FE) simulation environment incorporating a realistic orthotropic material law in combination with mechanical loading to investigate the performance of cardiac SWE. Furthermore, this model allows to theoretically evaluate the effect of myocardial fibrosis on shear wave characteristics.

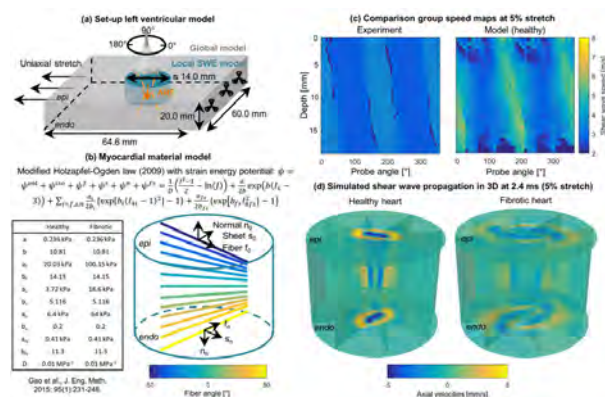
Statement of Contribution/Methods

The FE model in Abaqus was set up to mimic earlier SWE experiments in the left ventricular (LV) free wall of ex vivo porcine hearts (Caenen et al., IEEE IUS 2017), i.e. a rectangular slab of LV tissue as shown in fig. a. A modified Holzapfel-Ogden law (2009) was implemented to describe the material mechanical response in fiber (f), sheet (s) and sheet-normal (n) direction of the heart (fig. b), with fiber orientation varying linearly from -50° (epi) to 50° (endo). Material constants for healthy and fibrotic myocardial tissue were taken from literature (fig. b).

The model composed of two steps. First, a uniaxial global stretch (5-10-15%) was applied to the global model in the LV circumferential direction. Second, shear waves were excited in the local model by applying a body force (fig. a), derived from the acoustic pressures simulated in Field II using experimental push parameters.

Results/Discussion

The group speed map of the healthy heart simulation showed realistic results compared to that of the experiment (fig. c), despite the use of literature-based parameters. The location of the simulated shear wave front in the healthy heart varied across tissue thickness (left panel of fig. d). This is clearly visible in the epi- and endocardial surface, demonstrating ellipsoidal shear wave propagation in different directions. This shear wave directionality corresponds with the predefined fiber orientation (fig. b). Modeling myocardial fibrosis increased the propagation speed and altered the wave pattern drastically in the virtual SWE acquisition (right panel of fig. d), providing insights into the sensitivity of SWE in detecting changes in myocardial material characteristics.



- 10:45 AM Validation of 2D non-rigid image registration to assess regional myocardial strain in a clinical setting**
Bidisha Chakraborty¹, João Pedrosa¹, Oana Mirea¹, Monica Dobrovie¹, Brecht Heyde¹, Jens-Uwe Voigt¹, Jan D'hooge¹
¹*Cardiovascular Sciences, KU Leuven, Leuven, Belgium*

Background, Motivation, and Objective

Myocardial deformation imaging based on speckle tracking echocardiography (STE) allows to assess regional myocardial function. Commercial STE solutions are based on optical flow although 2D non-rigid image registration (NRIR) of B-mode images has been proposed as a – potentially more robust - alternative. To date, NRIR has been validated *in-silico* and *in-vitro* but systematic *in-vivo* evaluation is lacking. The aim of this study was therefore to investigate the potential of NRIR in assessing regional strain in clinical images.

Statement of Contribution/Methods

B-mode images (apical views, frame rate ~60 Hz) from the inter-vendor variability study on STE standardization were made available (i.e. 40 patients with previous infarction using 7 commercial systems) [1]. In addition, segmental strains were available from 8 commercial STE solutions as well as the regional findings of the correlative delayed enhancement CMR studies [1].

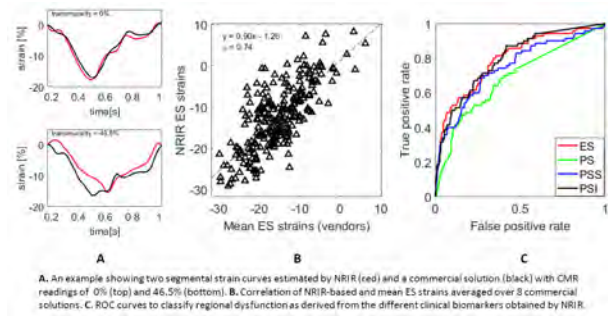
Inter-frame displacement was estimated on the B-mode images using NRIR (i.e. displacement model: tensor product cubic B-splines; similarity: sum of squared differences; regularizer: bending energy). Next, an endocardial border defined by a semi-automatic segmentation tool was divided into 6 segments in order to compute segmental strain curves from which clinical biomarkers such as end-systolic (ES), peak-systolic (PS), post-systolic (PSS) strain as well as post-systolic strain index (PSI) were extracted.

To quantify performance, the mean ES strains averaged over the 8 commercial solutions were correlated to NRIR-based strains using the Pearson's correlation coefficient (CC). In addition, as in [1], receiver operating characteristics (ROC) and area under the curve (AUC) for the detection of scarred segments were computed using the CMR data as a reference assuming that a segment with >75% delayed enhancement is scarred.

Results/Discussion

The CC of the ES strain was 0.74 ($p<0.01$). The mean estimated ES strain for the non-scared vs. scarred segments was -13.9 % and -5.7 % respectively ($p<0.01$) while the AUC for ES, PS, PSS and PSI were 0.79, 0.69, 0.75 and 0.80 respectively; values comparable to those reported in [1]. In conclusion, NRIR-based regional strain estimation in the clinical setting is feasible and provides competitive performance to commercially available solutions based on optical flow.

[1] Mirea et al., JACCI, 2018, 11, 25-34



11:00 AM 4D mechanical wave velocity mapping using Clutter Filter Wave Imaging. Healthy subjects versus Patients**Sebastien Salles¹, Lasse Lovstakken¹, Torvald Espeland¹, SveinArne Aase², Asbjorn Stoylen¹, Hans Torp¹**¹*Department of Circulation and Medical Imaging, and CIUS, NTNU, Trondheim, Norway, ²GE Vingmed Ultrasound, Norway***Background, Motivation, and Objective**

Myocardial fibrosis is recognized as a physio-pathologic substrate of several cardiovascular diseases. Knowing that fibrosis leads to increased myocardial stiffness, elastography techniques, e.g. shear wave imaging, has shown potential for detection of fibrotic tissue. In this work, a specific mechanical wave (MW) produced by natural cardiac events at the late peak diastolic 'a' is described, and its propagation along the left ventricle (LV) wall is mapped using 4D high frame rate imaging for both healthy subjects and sick patients.

Statement of Contribution/Methods

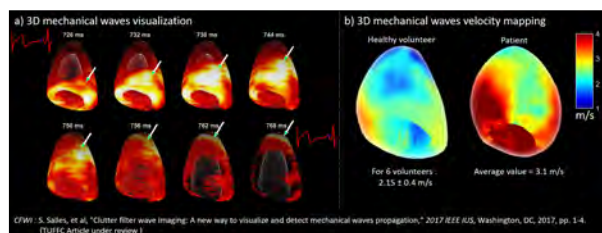
A 4D high frame rate imaging setup was implemented on a locally modified GE Vivid E95 with the 4V matrix array, by transmitting 20 planes waves to cover a sector of 60x60°, resulting in 820 volumes/s when stitching over 4 cardiac cycles. Sequentially, 2 cardiac cycles were used to acquire a high-quality 3D B-mode images for segmentation of a 3D LV model. Five healthy volunteers and 2 sick patients were investigated over 6 cardiac cycles for each subject.

The MW were detected using clutter filter wave imaging (CFWI) with further developments, including improved MW velocity (MWv) estimation and a fully automatic 3D mapping process. Several 2D spatiotemporal maps are extracted along each arch of the 3D volume from the AV plane to the Apex by assuming a uniform direction of propagation. The local MWv were estimated using piecewise linear regression of the wave front maxima, where the MW time of flight was quantized monotonically.

Results/Discussion

a) shows the 3D propagation of the MW occurring at late peak diastolic 'a' over a time interval of 42ms. We observed that the 'a' wave propagate from the AV-plane to the apex in a uniform longitudinal direction, and in the entire myocardium. b) shows the 3D MWv mapping results for one healthy volunteer and one patient. The global average MWv estimated for the healthy volunteers was $2.15 \pm 0.4 \text{ m.s}^{-1}$, while 3.1 and 2.4 m.s^{-1} for the two sick patients (aortic stenosis). Locally we observed that the estimated MWv was found higher in the base area than in the apex area, for most subjects. More patients and MRI comparison will be presented to confirm or not the presence of fibrotic tissue in patients locally.

This work demonstrates the feasibility to map and estimate 4D left ventricle MW for healthy voluntaries and patients, providing a pathway to for full 3D elasticity mapping of the LV using ultrasound



CFWI - S. Salles, et al. "Clutter Filter wave imaging: A new way to visualize and detect mechanical waves propagation," 2017 IEEE ICIS, Washington, DC, 2017, pp. 1-4
[DOI:10.1109/ICIS.2017.8027441]

11:15 AM

In vivo estimation of myocardial mechanical wave propagation in the fetusSolveig Fadnes^{1,2}, Sébastien Salles^{1,2}, Eva Tegnander^{3,4}, Siri Ann Nyrnes^{1,5}, Lasse Lovstakken^{1,2}¹*Department of Circulation and Medical Imaging, NTNU, Norway*, ²*Centre for Innovative Ultrasound Solutions (CIUS), Norway*, ³*Department of Clinical and Molecular Medicine, NTNU, Norway*, ⁴*National Center for Fetal Medicine, St. Olavs University Hospital, Norway*, ⁵*Department of Pediatrics, St. Olavs University Hospital, Norway***Background, Motivation, and Objective**

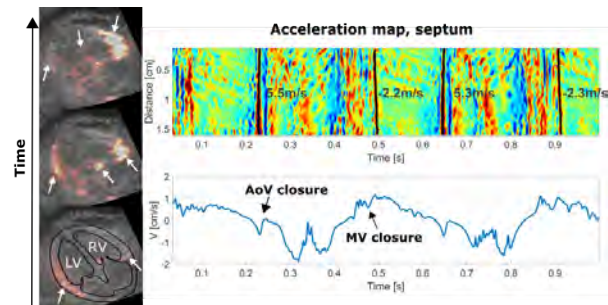
Maturation of the fetal cardiac muscle during pregnancy imply changes in elasticity and contractility. Previous research on fetal cardiac wall properties is largely based on animal studies and histology. Mechanical wave mapping using ultrafast ultrasound imaging makes it possible, for the first time, to investigate the myocardial stiffness of the developing human heart *in utero*. If feasible, the method has potential to increase pathophysiological knowledge of the normal and abnormal fetal heart, and contribute in difficult decision-making i.e in conditions where one is questioning the degree of endocardial fibroelastosis. We present initial results of fetal mechanical wave imaging at gestational week 28 in a healthy fetus.

Statement of Contribution/Methods

A continuous diverging wave acquisition (single source, $f_0 = 2.97$ MHz, $\text{fps} = \text{PRF} = 3$ kHz) was implemented on a Verasonics Vantage system (Verasonics, Inc., USA) for a curvilinear array (C5-2v) and approved for fetal imaging. Channel data (1 s, 2.5 heart cycles) were stored and beamformed offline. The Clutter Filter Wave Imaging method (Salles 2017) was used to estimate the mechanical wave propagation velocity. The spatiotemporal map was extracted by taking the time gradient of the clutter filtered (3rd order Butterworth, high-pass cut-off = 2.6 cm/s) IQ data along the left and right ventricle free walls and septum. The wave propagation velocity was estimated with linear regression of the maxima of the wave slope in the longitudinal direction.

Results/Discussion

Reproducible mechanical wave propagation velocities for two cardiac cycles of a healthy fetus (week 28) is shown in the Fig. To the left, the mechanical wave propagation up the cardiac walls is visualized in red. The upper panel to the right shows the acceleration map for the septum with the calculated propagation velocities after aortic (Ao) and mitral valve (MV) closure. The bottom panel shows the tissue Doppler curve from the septum (close to the MV plane). Compared to the septum, higher propagation velocities were observed for the LV free wall after AoV and MV closure (approx. 6.5 m/s and -4 m/s). For RV, the propagation velocities were similar to the velocities in the septum. The initial results are promising, however, to investigate clinical value and feasibility of the method, more data from healthy fetuses at different gestational ages is being analyzed.



11:30 AM 4D cardiac ultrafast imaging of natural mechanical waves: towards quantitative elastography of the human ventricle

Victor Finel¹, Clément Papadacci¹, Emmanuel Cohen², Mickaël Tanter², Mathieu Pernot²

¹*Institut Langevin, INSERM U979, ESPCI, CNRS UMR 7587, ART, France*, ²*Institut Langevin, ESPCI Paris, PSL Research University, CNRS UMR 7587, INSERM U979, Paris, France*

Background, Motivation, and Objective

Many heart diseases are associated with heart stiffening [1], but up to date, there is no method to quantify cardiac elasticity in the clinic. Natural mechanical waves induced by mechanical events such as the closing of valves can provide information on the ventricular stiffness [2]. In this study, a method was developed to assess 3D left ventricle stiffness mapping during systole and diastole in human using 4D cardiac ultrafast imaging of natural wave speeds induced by both aortic valve closure and atrial contraction.

Statement of Contribution/Methods

A 3MHz matrix array probe (1024 elements, 0.3mm pitch) connected to a 1024 channel ultrasound scanner was positioned by a cardiologist on the apical four chambers view centered on the left ventricle of N=3 healthy volunteers. Diverging waves were emitted at 1800Hz during an entire cardiac cycle. Electrocardiogram (ECG) was co-registered. Inter-volume axial displacements were computed using 1D cross-correlation on demodulated IQ volumes. Two 3D time-of-flight maps of natural waves induced by aortic valve closure and atrial contraction were computed using a correlation algorithm on time windows selected using the ECG. 3D distance maps from the wave sources were computed with a fast marching algorithm to derive the 3D speed maps.

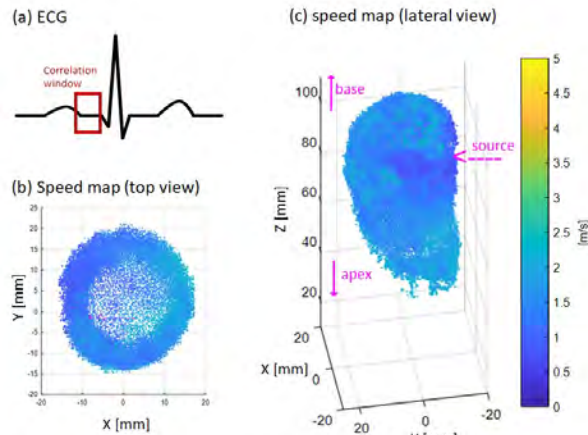
Results/Discussion

Natural wave induced by aortic valve closure and atrial contraction were successfully observed in the left ventricle. For each volunteer, 3D speed maps were derived during systole and diastole. The waves had an average speed of 4.1+-0.5m/s for aortic valve closure and 1.4+-0.1 m/s for atrial contraction. Frequencies of waves were within the range 50-100 Hz.

4D cardiac ultrafast imaging of natural mechanical waves enabled the quantification of the local wave speeds in entire volumes. Systolic and diastolic assessments showed stiffness differences. This method could potentially become a major tool to evaluate cardiac stiffness in clinic for various cardiomyopathy diagnosis.

[1] S A Glantz and W W Parmley, "Factors which affect the diastolic pressure-volume curve," *Circulation Research*, 1978;42:171-180

[2] H. Kanai, "Propagation of spontaneously actuated pulsive vibration in human heart wall and in vivo viscoelasticity estimation," *IEEE Trans. Ultrason. Ferroelectr. Freq. Control*, vol. 52, no. 11, pp. 1931–1942, Nov. 2005.



Figure(1). Example of result obtained on one volunteer during diastole.

(a): Time window used for correlation.

(b),(c): Top view and side view of speed map.

11:45 AM

Ultrafast ultrasound imaging grants alternate methods for assessing diaphragm function.

Damien Bachasson¹, Martin Dres², Marie-Cécile Nierat², Jonne Doorduin³, Jean-Luc Gennisson⁴, Jean-Yves Hogrel¹, Thomas Similowski²

¹Institute of Myology, France, ²Neurophysiologie Respiratoire Expérimentale et Clinique / INSERM / APHP, France,

³Radboud University Medical Center, Netherlands, ⁴IR4M / CNRS / UPSUD / CEA, Orsay, France

Background, Motivation, and Objective

Gold standard methods for assessing diaphragm contractility involves the recording of transdiaphragmatic pressure (Pdi) or electromyographic response (EMGdi) gathered during ventilatory tasks or in response to electrical stimulation. Pdi computation requires the measurement of esophageal and gastric pressures using internal balloons introduced by the nose. Both Pdi and EMGdi are indirect measures of diaphragm contractility. Ultrafast shear wave elastography (SWE) has been shown to provide reliable estimates of force output in locomotor muscles [1]. Ultrafast plane wave imaging (PWI) enables very high frame rate and allows capturing and gauge very short stimulated muscle contractions (~100 ms) [2]. The aim of this project was to investigate the potential of SWE and PWI for gauging diaphragm contractility during ventilatory tasks (experiment 1) and during electrical stimulation (experiment 2), respectively.

Statement of Contribution/Methods

14 volunteers were studied using an ultrafast ultrasound scanner (Aixplorer, Supersonic Imagine, France). During experiment 1, participants performed a stepwise inspiratory loading protocol from 0 to 50% of maximal inspiratory pressure during closed-airways maneuvers and during ventilation against external elastic loads. Pdi was monitored with balloons into the body and shear modulus of the diaphragm (SMdi) was measured in the lower intercostal area. Repeated measures correlation (R) were used to ascertain overall relationships between Pdi and SMdi, respectively. During experiment 2, unilateral transcutaneous electrical phrenic nerve stimulation (PNS) and cervical magnetic stimulation (CMS) were triggered by the Aixplorer to acquire a 500-ms movie of the stimulated diaphragm at 5000 Hz. Displacement of the diaphragm was inferred from axial tissue velocity profiles. By cross-correlation algorithm, diaphragm displacement was estimated for high and low stimulation intensities and compared to Pdi and EMGdi evoked by PNS and CMS, respectively.

Results/Discussion

In experiment 1, during closed-airways maneuvers, mean Pdi was linearly related to mean SMdi ($R=0.82$, 95% CIs [0.77, 0.87], $p<0.001$). During inspiratory-loaded ventilation, Pdi (range: 1.26-125 cmH²O) swing correlated to maximal SMdi (range: 7.5-90.0 kPa) with $R=0.69$ (95% CIs [0.66, 0.73], $p<0.001$). In experiment 2, displacement evoked at low and high intensities were significantly different using both PNS and CMS (0.45 +/- 0.14 mm versus 1.38 +/- 0.58 mm and 0.40 +/- 0.29 mm versus 0.58 +/- 0.20 mm, respectively). These results emphasize the potential of SWE and PWI as noninvasive and specific approaches to assess diaphragm contractility during ventilation and artificially evoked responses.

References: [1] Hug, Exercise and Sport Sciences Reviews 2015 [2] Deffieux, IEEE-UFFC 2008

1B - Advances in Clinical Ultrasound

Topaz (400)

Tuesday, October 23, 1:30 pm - 3:00 pm

Chair **Yoshifumi Saito**
Tohoku University

1B-1 _____

1:30 PM Viscoelasticity Measurement in the Liver Using Dispersion Imaging of Shear Wave US Elastography
Fuminori Moriyasu¹
¹*Sanno Hospital*

Background, Motivation, and Objective

Statement of Contribution/Methods

Results/Discussion

2:00 PM Echocardiographic Particle Image Velocimetry in Heart Diseases

Haruhiko Abe¹

¹Osaka National Hospital

Background, Motivation, and Objective

Statement of Contribution/Methods

Results/Discussion

2:30 PM Novel Non-Shelled Nanobubbles as a New Ultrasound Imaging and Drug Delivery Tool

Katsuro Tachibana¹

¹Fukuoka University

Background, Motivation, and Objective

Statement of Contribution/Methods

Results/Discussion

1C - Cardiac and Cerebrovascular Imaging

Topaz (400)

Tuesday, October 23, 4:00 pm - 5:30 pm

Chair **Damien Garcia**
CREATIS

1C-1

4:00 PM

Instantaneous Volumetric Flow Rate Measurement Using High-Frame-Rate Ultrasound

Billy Y. S. Yiu¹, Adrian J. Y. Chee¹, Alfred C. H. Yu¹

¹Schlegel-UW Research Institute for Aging, University of Waterloo, Waterloo, ON, Canada

Background, Motivation, and Objective

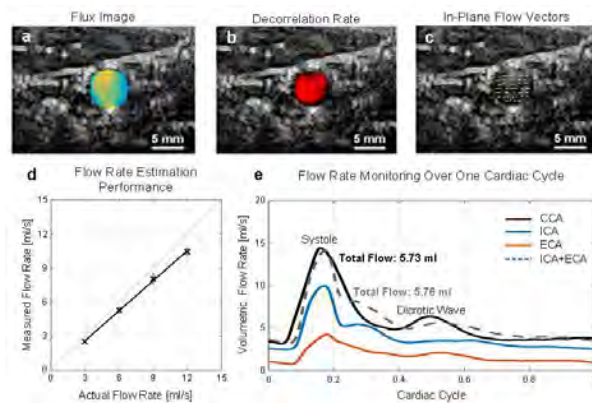
Vascular dementia is a consequence of chronic cerebral hypoperfusion, a condition describing reduced brain-blood supply. Its diagnosis requires quantification of brain-blood flow. In principle, volumetric blood flow rate can be measured by estimating the flow flux over a cross luminal area. Although merits of diagnostic ultrasound to measure flow velocities are well established, flow measurements are only limited to in-plane flow. Here, we present a framework to perform time-resolved quantification of instantaneous volume flow rate by measuring the flow flux over the arterial lumen.

Statement of Contribution/Methods

Flux (in Y direction; see Fig. a) is estimated by subtracting the in-plane (X & Z) velocities from the total flow velocities in all three directions (X, Y & Z). Specifically, the total flow velocities are measured from the speckle decorrelation due to blood cells moving away from a region of interest, i.e. the rate of decorrelation is defined by the blood flow rate. The decorrelation rate (Fig. b) is derived as the standard deviation of a correlation curve computed using normalized cross-correlation and Gaussian-fitted along slow-time. Meanwhile, in-plane velocities (Fig. c) were derived using our multi-angle vector Doppler technique (T-UFFC, 2016; 63; 1733-1744). Implemented on a SonixTouch scanner with an L14-5 array, full-view images were first acquired using unsteered plane wave firings (5-cycle 5 MHz pulse; 10 kHz PRF). For validation, measurements were verified on a straight tube under different flow rates (3 - 12 ml/s). To demonstrate the efficacy of our framework, *in vivo* study was conducted on a 25-year-old subject to match the flow rate in the common carotid artery to its two bifurcation branches.

Results/Discussion

Estimated flow rate against its true value was plotted in fig. d, indicating a 13% underestimation for the measured ranges. In fig. e, we plotted the volumetric flow measured in the CCA, ICA and ECA branches. On the assertion that instantaneous flow in the CCA is the summation of flow in ECA and ICA branches, we compared the sum of the two outlet branches to the CCA. The flow rate for both matches well, with discrepancy in the total volume flow over the 1 s being less than 0.5%. These results show that our framework is capable of profiling time-varying volumetric flow. This may render new insights in cerebral hypoperfusion diagnostics.



4:15 PM

Volume flow estimation in valvular jets using 3D high frame rate ultrasound**Jørgen Avdal^{1,2}, Alfonso Rodriguez-Molares^{1,2}, Erik Andreas Rye Berg^{1,2,3}, Hans Torp^{1,2}**¹*Department of Circulation and Medical Imaging, NTNU, Norway*, ²*Centre for Innovative Ultrasound Solutions (CIUS), Norway*, ³*Heart Clinic, St. Olavs Hospital, Norway***Background, Motivation, and Objective**

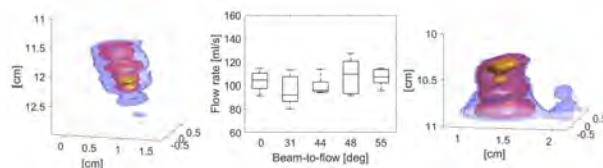
Valvular regurgitation is backflow of blood through a leaky heart valve, and is a prevalent condition (estimated 1-2 % of population). Following the increased volume load, the heart may enlarge, potentially leading to heart failure. Because of the lack of widely reliable quantitative predictors of outcome, assessment of valvular insufficiency is currently based on several indices, leading to prolonged examination times and increased interobserver variability. Reliable estimates of regurgitant flow volume or orifice size would significantly improve this assessment. In this work, we aim to develop a flow volume estimator for jet flow from 3D high frame rate recordings of the jet. The estimator should be accurate for a large range of clinically relevant beam-to-flow angles, orifice sizes and flow volumes, and feasible to implement and use on a clinical scanner.

Statement of Contribution/Methods

The performance of the estimator is assessed using computer simulations and a jet flow phantom with replaceable valves. The 3D high frame rate acquisition is implemented on a modified GE E95 scanner. After acquisition and beamforming, spectral Doppler estimates are calculated, and used to estimate the maximum velocity present, for each voxel in a region of interest. The data are then filtered to isolate the signal from the highest velocities, and a vena contracta cross-section normal to the beam direction is found using a power threshold. The flow volume estimate is produced by integration over the power spectrum and over the vena contracta cross-section.

Results/Discussion

The left panel shows a 3D rendering of a stationary jet in the flow phantom with orifice diameter 3 mm. Spatial points with velocities above 40%, 60% and 80% of maximum are color coded in blue, red and yellow, respectively. The middle panel shows flow rate estimates from the same jet, insonated from 5 different beam-to-flow angles. Bars show 25th and 75th percentiles, whereas whiskers show maximum and minimum values from 30 flow rate estimates, each calculated from a temporal window of 25 ms. The right panel shows the corresponding 3D rendering of jet from a pilot patient with mitral regurgitation, with total volume flow during systole estimated to be 32 ml. The preliminary results indicate consistency of the estimator for different beam-to-flow angles, and feasibility of the method *in vivo*.



4:30 PM Next-generation echocardiography – opportunities and challenges

Lasse Løvstakken¹

¹*NTNU, Norway*

Background, Motivation, and Objective

Abstract

Echocardiography is going through a technology-enabled revolution. With the availability of real-time channel data acquisition and software beamforming, new opportunities for improved image quality, more accurate quantification, and higher frame rates in 2D and 3D cardiac imaging has emerged. For instance, by exploiting new flexibility in the channel data domain combined with increased processing capabilities, improved spatial and contrast resolution can be achieved using dynamic transmit focusing, and through more advanced adaptive and coherence-based beamforming approaches. Further, by utilizing wide transmit beams and parallel beamforming improved quantification based on ultrafast imaging has shown promise, including high-frame-rate deformation imaging and elastography, and angle-independent blood flow imaging.

In this talk, fundamental clinical and technical imaging challenges in cardiac imaging will be presented, and current clinical state of the art imaging technology will be demonstrated. This is the foundation for the next-generation cardiac imaging, which will need to demonstrate both clinical feasibility and ease-of-use. Relevant discussion topics include the inherent trade-offs between frame rate, penetration and image quality, as well as the importance of 2nd harmonic imaging for state-of-the-art echocardiography. Attention is given to both 2D and 3D imaging, and the most recent cardiac imaging technology proposed from the ultrasound community will be presented.

Biography

Lasse Løvstakken is a Professor at the Department of Circulation and Medical Imaging, at the Norwegian University of Science and Technology (NTNU), in Trondheim, Norway. His research efforts are focused towards medical ultrasound imaging, with interests in image formation, signal processing, machine learning, and visualization. Clinical applications are mainly in cardiovascular disease. He has published > 50 papers and is coinventor of 2 patents in the field of medical ultrasound imaging, and has supervised 5 PhD students to completion. His main contributions have been dedicated to the development and application of improved methods for blood flow imaging using ultrasound. He is recipient of the Young Research Talent grant from the Norwegian Research Council, and a member of the NTNU Outstanding Academic Fellows program. He serves as a member of the technical program committee for the IEEE International Ultrasonics Symposium.

Statement of Contribution/Methods

1

Results/Discussion

2

5:00 PM Ultrafast Doppler Observation in Rat Stroke Model --- Comparison with High Field Magnetic Resonance Imaging

Yu-Chieh Kao^{1,2}, Bao-Yu Hsieh³

¹Research Center of Translational Imaging, Taipei Medical University, Taiwan, ²Department of Radiology, School of Medicine, Taipei Medical University, Taiwan, ³Department of Biomedical Imaging and Radiological Science, China Medical University, Taiwan

Background, Motivation, and Objective

Stroke is the leading cause of death or disability in adults due to a sudden interruption in the blood supply of the brain tissue. Cerebral tissue fate after stroke is determined by the restoration of blood flow. Hemodynamic observation is, thus, motivated to access related cerebral blood flow (CBF) changes of stroke. Ultrafast Doppler imaging is a quantitative vasculature imaging to map hemodynamics in preclinical small animal brains. In this study, the ultrafast Doppler images of stroke lesions were compared with T₂-weighted (T2w) and susceptibility weighted imaging (SWI) from high field MRI, the gold standard neuroimaging for stroke brains, to show the validation/complementary information to further understand the mechanism of strokes.

Statement of Contribution/Methods

Ultrafast Doppler imaging was acquired in rats underwent permanent occlusion of the right middle carotid artery (MCAo). The skull on top of the brain was removed by craniotomy. For ultrafast Doppler imaging, a 18-MHz linear array transducer and a programmable ultrasonic system (Prodigy, S-Sharp, Taiwan) was used in this study. 5-angle compounding images at 1kHz was conducted for imaging acquisition. The processing is based on the ultrafast Doppler imaging technique followed a spatio-temporal filter, a singular value decomposition (SVD), was applied. 96 compounding images were acquired for Doppler estimation. SWI and T₂-weighted images was performed on a Bruker 7 T PharmaScan. Finally, the ultrafast Doppler image was manually coregistered on the SWI images.

Results/Discussion

The cerebral vasculature denoted by ultrafast Doppler image represented the similar patterns in SWI. Significant flow change after stroke was observed in the ultrafast Doppler image. In contrast to the limited flow signal in the infarct lesion, the enhanced flow signal (arrows) close to the stroke lesion may imply the vascular remodeling in the peri-infarct regions. Apparent higher flow signal was observed in the left cortex (arrowheads) compared with the right cortex, suggesting the flow compensation in the contra-lesional hemisphere after stroke. Ultrafast Doppler not only provides structural information about cerebral vasculature but accesses perfusion status after ischemic stroke. Combining ultrafast Doppler and MRI may serve as a powerful tool to understand the cerebral vascular flow change after stroke.

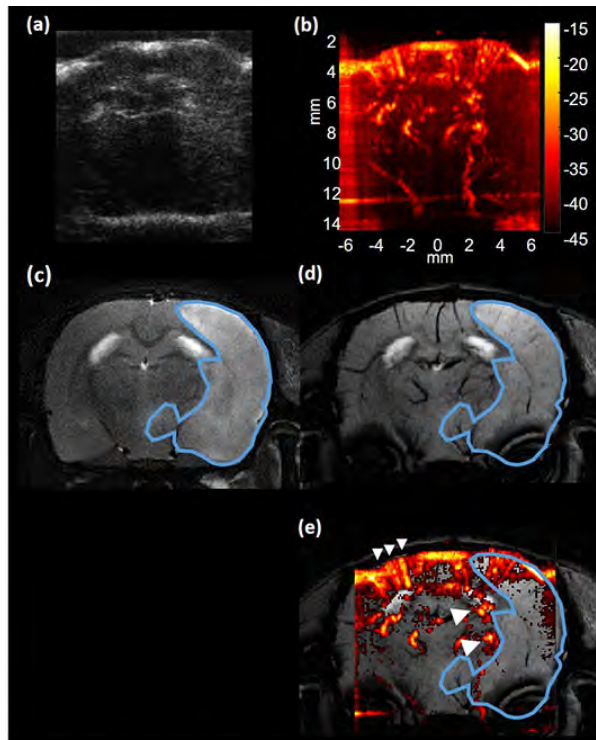


Fig. 1. a) Conventional ultrasound B-mode image, b) ultrafast Doppler image, c) MRI T2w image with the contour of infarct lesion, d) SWI image and e) fusion images (ultrafast Doppler+SWI) of rat's stroke brain.

5:15 PM

The continuous cardiac thick-slice acquisition - for simultaneous flow and tissue motion estimation**Morten Wigen^{1,2}, Sebastien Salles^{1,2}, Asbjorn Stolyen^{1,2}, Lasse Lovstakken^{1,2}**¹*Department of Circulation and Medical Imaging, NTNU, Norway, ²Centre for Innovative Ultrasound Solutions (CIUS), Norway***Background, Motivation, and Objective**

Both established and new cardiac ultrasound measurements rely on high frame rates to capture rapid cardiac events. Today, multiple acquisitions are made, e.g. Bmode, CFI, TVI, M-modes, PW spectra, etc., to gather all information. A multi-purpose continuous acquisition scheme is here proposed, enabling retrospective calculation of most information used in cardiac imaging at ultrahigh frame rates (UHFR). This enables the calculation of combined indices commonly used, as well as new information such as vector-velocity imaging, pressure gradients and mechanical wave mapping from one recording.

Statement of Contribution/Methods

A locally modified GE E95 system with a 4V-D matrix array transducer was used for plane wave transmission, each covering a sector of ~10x10 degrees and beamformed with 12x10 MLAs in azimuth and elevation direction in real-time. 5-6 transmits were needed to cover the full width of a left ventricle. A continuous acquisition at full PRF (4kHz) was thus obtained by using one transmit direction per heartbeat, with retrospective ECG-stitching over 5-6 heart cycles to reconstruct the images. Sequentially, two heartbeats were used for conventional high-quality B-mode. A real-time CFI display was available during recording. The UHFRdata was further stored as raw IQ signals, and filtered to extract tissue and blood signals, respectively. Derived measurements such as pressure gradients and mechanical wave mapping was further calculated from CFI and the CFWI method (Salles 2017). Vector velocity estimation was done using speckle tracking.

Results/Discussion

Fig. 1 shows examples of different modalities produced from a single recording. Due to the ultrahigh frame rate (4kHz), M-modes and spectral information could be obtained from any position with full quantitative information. With the 3D slice recorded, vector velocity estimation can also provide out-of-plane velocity estimates, with potential opportunities for improved volume flow and through-plane flow estimation. With the continuous acquisition, improved clutter filtering can further be achieved. The proposed setup also has a potential for investigation of flow/tissue interaction, by investigating (near-)simultaneous mechanical wave mapping, UHFRstrain imaging, and flow and vortex propagation characteristics. The main limitation is the need for a stable heart rate during recording.

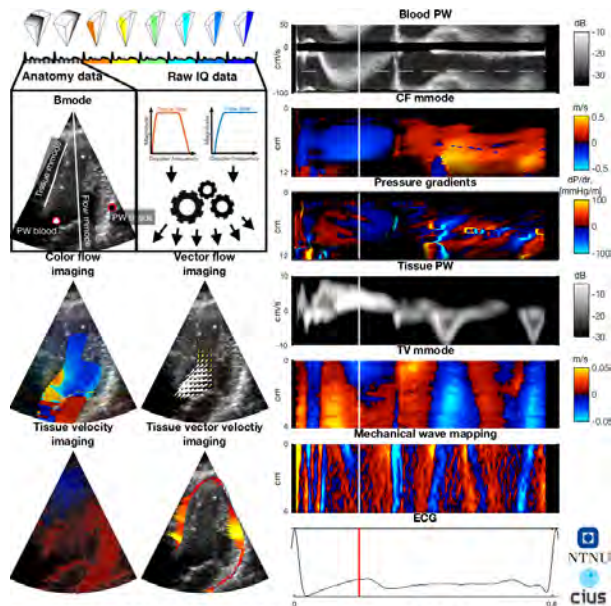


Figure 1. Top left: Bmode and ultrahigh frame rate data acquired by ECG-gating and stored for postprocessing. Bottom left: examples of image data produced from the acquired data. Right column: PW Doppler spectra and mmodes extracted from arbitrary positions in the image retrospectively.

2A - Spotlight Session: Photo-acoustics

Diamond (300)

Tuesday, October 23, 10:30 am - 12:00 pm

Chair **Koen W.A. van Dongen**
TU Delft

2A-1

10:30 AM Ultrasound-guided photoacoustics: from basic science tool to clinically-viable functional and molecular imaging
Stanislav Emelianov¹

¹*Georgia Institute of Technology and Emory University School of Medicine*

Background, Motivation, and Objective

Ultrasound-guided photoacoustics (USPA) is a high-resolution, high-sensitivity, depth-resolved, multi-scale imaging technique based on a synergistic combination of what seems to be drastically different energy sources: light and sound. Augmented with targeted imaging contrast nanoagents, this technique is capable of simultaneous visualization of structural, functional, and molecular/cellular properties of tissue. This presentation, via examples, will offer a few insights into how the USPA imaging can change both fundamental medical science and the clinical management of diseases. Several biomedical and clinical applications including microscopic and macroscopic imaging of pathology, cell and particle tracking, cancer detection and diagnosis, and molecular therapy will be presented. The desired characteristics of the devices and design of nanoconstructs with specific physicochemical properties will be discussed. Finally, current challenges and concerns associated with clinical translation of USPA imaging will be presented, and possible solutions will be discussed.

Biosketch

Dr. Stanislav Emelianov is a Joseph M. Pettit Endowed Chair, Georgia Research Alliance Eminent Scholar, and Professor of Electrical & Computer Engineering and Biomedical Engineering at the Georgia Institute of Technology. He is also appointed at the Emory University School of Medicine, where he is affiliated with Winship Cancer Institute, Department of Radiology, and other clinical units. Furthermore, Dr. Emelianov is Director of the Ultrasound Imaging and Therapeutics Research Laboratory at the Georgia Institute of Technology focused on the translation of diagnostic imaging & therapeutic instrumentation, and nanobiotechnology for clinical applications.

Throughout his career, Dr. Emelianov has been devoted to the development of advanced imaging methods capable of detecting and diagnosing cancer and other pathologies, assisting treatment planning, and enhancing image-guided therapy and monitoring of the treatment outcome. He is specifically interested in intelligent biomedical imaging and sensing ranging from molecular imaging to small animal imaging to clinical applications. Furthermore, Dr. Emelianov develops approaches for image-guided molecular therapy and therapeutic applications of ultrasound and electromagnetic energy. Finally, nanobiotechnology plays a critical role in his research. In the course of his work, Dr. Emelianov has pioneered several ultrasound-based imaging techniques, including shear wave elasticity imaging and molecular photoacoustic imaging. Overall, projects in Dr. Emelianov's laboratory, which focuses on cancer and other diseases, range from molecular imaging to functional imaging and tissue differentiation, from drug delivery and release to image-guided surgery and intervention.

Statement of Contribution/Methods

1

Results/Discussion

2

11:00 AM **Quantitative GHz ultrasonic imaging of biological cells and transparent structures**
Oliver B. Wright¹
¹*Replace*

Background, Motivation, and Objective

Picosecond ultrasonics has been recently applied to characterize single cells after decades of being used to investigate the mechanical properties of metals and semiconductors on sub-micron scales. This technique monitors GHz Brillouin oscillations in the time domain, allowing acoustic properties—sound velocity and ultrasonic attenuation—for the nucleus and vacuole of animal or vegetal cells to be measured. In addition, cell density, compressibility and adhesion, as well as mechanical properties of cell walls have been studied.

In the talk we present the experiments on the 3D imaging of mammalian cell properties using picosecond ultrasonics with sub-micron spatial resolution.[1] A 830-nm pump beam consisting of a train of ultrashort optical pulses is focused at normal incidence to a ~1 micron spot on the film from the substrate side, heating the Ti film from underneath. A picosecond ultrasonic pulse then traverses the cells. These ultrasonic pulses are monitored by a 415-nm probe beam, focused to a ~0.5 micron spot size to the same point and controlled by a delay line that provides temporal scanning. By this method we obtain three-dimensional images with ~0.5 micron lateral resolution.

We also introduce a new technique that can provide quantitative imaging of both the sound velocity and refractive index independently. This work should lead to a new means for non-invasive investigations of internal cellular structure as well as being applicable to the evaluation of inorganic transparent structures.

[1] S. Danworaphong, et al., Appl. Phys. Lett. 106, 163701-1-4 (2015)

Statement of Contribution/Methods

1

Results/Discussion

2

11:30 AM **Compressed Sensing in Photoacoustic Tomography**

Markus Haltmeier¹

¹*Universität Innsbruck*

Background, Motivation, and Objective

Increasing the imaging speed is a central aim in photoacoustic (PA) tomography. This issue is especially important in the case of sequential scanning approaches as applied for most existing optical detection schemes. In this talk we address this issue using techniques of compressed sensing. We demonstrate, that the number of measurements can significantly be reduced by allowing general linear measurements instead of point-wise pressure values. A main requirement in compressed sensing is the sparsity of the unknowns to be recovered. For that purpose, we develop the concept of sparsifying temporal transforms for PA tomography. To efficiently exploit the induced sparsity, we develop a two-stage reconstruction framework as well as a direct algorithm that jointly recovers the initial and the modified sparse source. Reconstruction results with simulated as well as experimental data are given.

Statement of Contribution/Methods

1

Results/Discussion

2

2B - Photoacoustic Contrast and Theranostic Agents

Diamond (300)

Tuesday, October 23, 1:30 pm - 3:00 pm

Chair **Roger Zemp**
University of Alberta

2B-1

1:30 PM **Plasmonic gold nanoparticles for combined photoacoustic imaging and photothermal therapy using a pulsed laser**

Oscar Knights¹, David Cowell², Steven Freear², James R. McLaughlan³

¹School of Electronic & Electrical Engineering, University of Leeds, Leeds, United Kingdom, ²University of Leeds, Leeds, United Kingdom, ³University of Leeds, United Kingdom

Background, Motivation, and Objective

Gold nanorods (AuNRs) show potential for use in cancer diagnostics and therapeutics such as photoacoustic imaging (PAI) and plasmonic photothermal therapy (PPTT). Generally in PPTT, continuous wave (CW) lasers are used to destroy cancerous tissue through bulk heating. However, in order to add a diagnostic component through PAI, a pulsed wave (PW) laser is needed. If PPTT can be achieved using PW lasers then combined theranostic applications with the same laser system is possible. Additionally, AuNRs can be many different sizes but exhibit equivalent surface plasmon resonances (SPRs) so the size may be significant in the efficacy of these modalities. These techniques could be applied in lung cancer and combined with endobronchial ultrasound to provide a treatment to one of the deadliest forms of cancer.

Statement of Contribution/Methods

A tuneable 7 ns PW laser was used to irradiate AuNR solutions at their specific SPRs ($811 \pm 2\text{nm}$, $803 \pm 2\text{nm}$, $790 \pm 2\text{nm}$, & $841 \pm 2\text{nm}$) across a fluence range of $1\text{-}40\text{mJcm}^{-2}$ to determine AuNR melting thresholds. The photoacoustic (PA) emissions from AuNRs with four different lateral widths (10, 25, 40 and 50 nm) across a range of equivalent concentrations were measured (Fig. 1a), and their PA emission amplitudes calculated via a technique similar to that used for PA image reconstruction. The Hilbert transform was applied to the PA signals (Fig. 1a) before integrating across the waveform to obtain an amplitude. These same four AuNR sizes were then used for PPTT in a lung cancer cell line (A549), irradiated for 5 min with the same PW laser (fluence below the melting threshold) as well as a CW laser (2 Wcm^{-2}).

Results/Discussion

The maximum PA amplitude for each AuNR size was measured at 5 concentrations (Fig. 1b). The results indicate that larger AuNRs produce stronger PA signals but are more prone to melting (Fig. 1c) compared with the smallest AuNRs (10nm), suggesting that AuNR size has a significant effect on PA response. The PPTT efficacy of the four AuNR sizes on an A549 cell line was determined and the temperature profile monitored via a thermal imaging camera (Fig. 1c & 1d). These results suggest that a PW laser can achieve increased cell death without bulk heating (Fig. 1f), leading to a highly selective approach for cancer treatment. Once determined, PA imaging of a lung-mimicking phantom containing AuNRs will be obtained using the Ultrasound Array Research Platform.

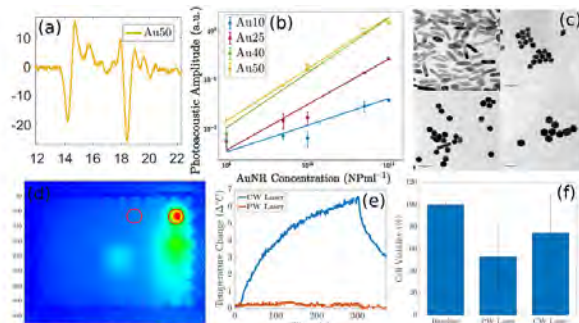


Figure 1. a) Example measured photoacoustic signal, b) photoacoustic response of AuNRs from a concentration of $1 \times 10^9 \text{ NPmL}^{-1}$ to $1 \times 10^{11} \text{ NPmL}^{-1}$ at a fixed laser fluence for four sized AuNRs (Au10 = 10nm, Au25 = 25nm, Au40 = 40nm, Au50 = 50nm lateral width). c) TEM analysis confirming melting of AuNRs at high laser fluences. d) Thermal imaging snapshot of 96-well plate during PPTT. Red circles show CW and PW laser irradiation targets; e) Temperature profile of PW and CW laser irradiation for 5min, and f) cell viability of A549 cells after laser irradiation.

1:45 PM

In vivo Photoacoustic, ¹⁹F MR and fluorescent imaging of clinically-applicable perfluorocarbon-loaded nanoparticles

Khalid Daoudi¹, Edyta Swider², Alexander Staal², Olga Koshkina², Koen van Riessen², Eric van Dinther², I. Jolanda M. de Vries², Managla Srinivas², Chris de Korte¹

¹Radiology and Nuclear Medicine, Radboud university medical center, Nijmegen, Netherlands, ²Department of Tumor Immunology, Radboud university medical center, Nijmegen, Netherlands

Background, Motivation, and Objective

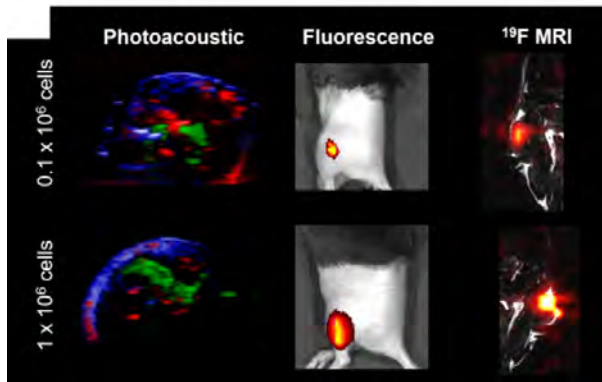
Several endogenous chromophores are exploited by photoacoustic molecular imaging, however, these chromophores provide access to a limited range of biological processes. The use of exogenous agents, therefore, could unlock the understanding of disease processes and provide signal at depths not possible with natural chromophores. Here, we report on a multimodal polymeric nanoparticle (NPs) agent that has been recently approved for a clinical trial for in vivo cell tracking of cell therapies. We investigate its optical properties and its use for in-vivo lymph node detection and cell imaging with a multimodal approach using photoacoustic (PA), fluorine magnetic resonance (¹⁹F MRI), and fluorescence (FL) imaging.

Statement of Contribution/Methods

Poly(lactic-co-glycolic acid) NPs encapsulating perfluoro-15-crown-5 ether (PFCE) and ICG were prepared using single emulsion solvent evaporation method. In-vitro and in-vivo imaging of NPs were performed using high frequency US and PA Vevo LAZR 2100 imaging system equipped with Nd:YAG laser irradiating from 680 to 970 nm (FUJIFILM VisualSonics Inc. Canada). Wild-type C57BL/6J female mice were used for in-vivo imaging, by injecting NPs in thigh muscle or in footpad and imaging popliteal lymph node after 30 min and 4h post-injection. Cell imaging was performed on immature monocyte-derived human dendritic cells (moDCs) labeled with NPs upon injection in the thigh muscle. NP's signal was extracted using spectral imaging and unmixing algorithm and results were validated using ¹⁹F MRI (11.7T MRI, Biospec, Ettlingen, Germany) and FL (IVIS LUMINA).

Results/Discussion

Our results show that NPs can be detected both in vitro and in vivo using PAI. Upon footpad injection of free NPs, we observed an increase in PA signal in popliteal lymph node over time reflecting a progressive accumulation of NPs. Primary human dendritic cells as little as 0.1×10^6 cells could be detected in vivo using PA spectroscopy. The results were validated by FL and MRI (see figure). This result shows that PLGA-PFCE-ICG NPs can be potentially used as non-invasive labels for cell tracking and lymph node detection, as they do not show any toxicity after cell loading and are stable even with long incubation times with the cells which makes them attractive for use as in vivo cell tracers in cellular therapies. We are currently producing these NPs at GMP grade for human use.



2:00 PM

Ultrasound and Photoacoustic Imaging to Aid Design, Optimization, and Validation of Pathogen-like Particle Vaccines

Kelsey Kubelick¹, Pallab Pradhan¹, Krishnedu Roy¹, Stanislav Emelianov^{1,2}

¹Wallace H. Coulter Department of Biomedical Engineering, Georgia Institute of Technology & Emory University, Atlanta, GA, United States, ²School of Electrical and Computer Engineering, Georgia Institute of Technology, Atlanta, GA, United States

Background, Motivation, and Objective

Particulate vaccines, termed pathogen-like particles (PLPs), are of interest to stimulate a more robust, durable immune response. High resolution intravitral two-photon imaging can be used to study PLP mechanism of action, transport, and immune response *in vivo*, but limited imaging depth requires an invasive, specialized surgical procedure. Photoacoustics (PA) – imaging of optical properties at ultrasound (US) penetration depth and resolution, is an excellent alternative. We developed a US/PA imaging method that allows longitudinal monitoring of PLP transport and provides critical spatiotemporal information to optimize PLP properties and more effectively design these particulate vaccines.

Statement of Contribution/Methods

PLPs, composed of poly(lactide-co-glycolic acid), were synthesized using a double emulsion and loaded with PA dyes, dye750 and dye950, absorbing at 750 and 950 nm, respectively. Dynamic light scattering (DLS) and UV-vis-NIR spectrophotometry was used to confirm PLP size and dye encapsulation. PLPs were imaged in phantoms (8% gelatin/0.2% silica) using a US/PA imaging system (Vivo LAZR, 20 MHz transducer, 680-970 nm). For *in vivo* studies, a 50 μ l PLP solution was subcutaneously injected near the mammary fat pad of BALB/c mice. Spectroscopic US/PA images of the inguinal lymph node were acquired *in vivo* up to 24 hours post-injection. Data was post-processed in MATLAB.

Results/Discussion

Micro- and nano-PLPs had approximately 1 μ m or 300 nm diameter, respectively (Fig. 1A). UV-vis-NIR confirmed encapsulation of dye (Fig. 1B). US/PA phantom images showed that 0.0195 mg/ml of micro- and nano-PLPs could be detected, proving feasibility of *in vivo* imaging. Spectroscopic US/PA imaging detected nano-PLPs at the periphery of the lymph node by 2 hours post-injection. Nano-PLPs accumulated at the lymph node and surrounding vasculature for 24 hours *in vivo* (Fig. 1C). Spatiotemporal distribution of PLPs indicates passive drainage rather than cellular transport. Results provide critical information to redesign PLPs to achieve the intended immune response. In the future, nano- and micro-PLPs will be injected simultaneously (Fig. 1D) to target different immune cell types and stimulate a robust response. The tool developed here can be used for high-throughput tracking studies with multiplex PA imaging of color-coded PLPs to aid vaccine development.

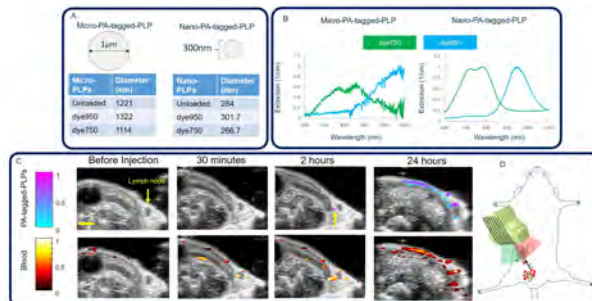


Figure 1. DLS/PA and UV-vis results (B) indicate successful synthesis of micro- and nano-PLPs loaded with PA dyes. *In vivo* US/PA imaging and spectroscopic analysis distinguished nano-PLPs from blood (C). Prior to injection, no PLPs were detected, proving algorithm accuracy and sensitivity to small concentrations of PLPs at early time points. Changes in blood flow were also observed. In future studies, nano- and micro-PLPs labeled with distinct PA dyes will be co-injected and imaged to determine how to combine types of PLPs to stimulate a robust immune response (D). Scale bar=20 μ m.

2:15 PM

A feasibility study of targeted nanoparticle-based photoacoustic imaging of ex vivo endoscopic mucosal resection tissue from Barrett's esophagus patients

Han Ho Jeon^{1,2}, Sam Liang Lim¹, Yi Qiu¹, Juan Chen¹, Corwyn Rowsell³, C. Felipe Roa⁴, Nancy Basset⁵, Maria Cirocco⁵, Catherine Streutker³, Norman Marcon⁵, Brian C. Wilson^{1,4}, Gang Zheng^{4,6}, F. Stuart Foster^{4,7}, Christine Demore^{4,7}

¹Princess Margaret Cancer Centre, University Health Network, Toronto, ON, Canada, ²Gastroenterology, Ilsan Hospital, Goyang, Korea, Republic of, ³Pathology, St. Michael's Hospital, Toronto, ON, Canada, ⁴Medical Biophysics, University of Toronto, Toronto, ON, Canada, ⁵Gastroenterology, St. Michael's Hospital, Toronto, ON, Canada, ⁶University Health Network, Toronto, ON, Canada, ⁷Sunnybrook Research Institute, Toronto, ON, Canada

Background, Motivation, and Objective

Esophageal cancer is one of the leading causes of death in the world. Diagnosis and complete resection of dysplasia or cancer at its early stages in patients with Barrett's esophagus (BE) can decrease the mortality rate and reduce health care cost. The current gold standard for diagnosis is to take multiple biopsies under endoscopy guidance, but is limited by biopsy sampling that misses foci of disease. So, there is a clinical need for an imaging method to easily identify dysplasia or early esophageal adenocarcinoma in BE. In this paper we explore whether photoacoustic (PA) imaging augmented with molecular targeted contrast agents may be able to identify cancer cells and aid biopsy guidance. EGFR, a receptor protein expressed on the luminal surface of the esophageal mucosa, is overexpressed during the histologic progression in BE and therefore may be a suitable target for PA imaging. We investigate, in an ex vivo study, whether EGFR-targeted organic porphysome nanoparticles (EGFR-PS) can be used as PA contrast agents to identify dysplasia and adenocarcinoma in patients undergoing endoscopic mucosal resection (EMR) for known dysplasia.

Statement of Contribution/Methods

EMRs were performed using a Duette suction device (Cook Medical, Bloomington, IN) then tissue bathed for 15 min in EGFR-PS (1ml, 100 uM), followed by rinsing with PBS. Registered volumetric B-mode ultrasound and PA scans (at 680, 750, and 850 nm laser wavelength) were acquired of 14 EMR specimens using a commercial PA system (Veo LAZR, Visualsonics, Toronto). Tissue were then sliced and fixed in formalin for histology with hematoxylin and eosin (H&E) staining. Digitized whole sections of each EMR specimen were segmented and color-coded by expert pathologist. Histopathology slices were co-registered with the closest corresponding ultrasound and PA images.

Results/Discussion

After soaking in EGFR-PS, normal mucosa showed minimal photoacoustic signal, whereas the dysplasia or adenocarcinoma, as identified in histology, was clearly visible, with up to 11-fold higher photoacoustic signal compared to the normal mucosa (Fig. 1A). Our results indicate the initial feasibility of EGFR-targeted PA contrast agents to bind to dysplasia or adenocarcinoma on esophageal tissue, and be observed with PA imaging. These are promising results that point towards improved biopsy guidance during endoscopy.

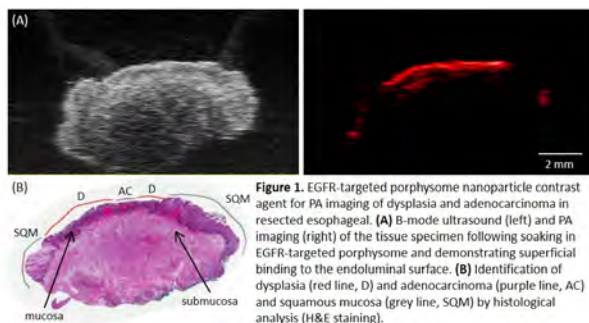


Figure 1. EGFR-targeted porphysome nanoparticle contrast agent for PA imaging of dysplasia and adenocarcinoma in resected esophageal. **(A)** B-mode ultrasound (left) and PA imaging (right) of the tissue specimen following soaking in EGFR-targeted porphysome and demonstrating superficial binding to the endoluminal surface. **(B)** Identification of dysplasia (red line, D) and adenocarcinoma (purple line, AC) and squamous mucosa (grey line, SQM) by histological analysis (H&E staining).

2:30 PM

Sono-Photoacoustic Vaporization of Polypyrrole coated Perfluorocarbon Droplets for Clot Lysis**David Li^{1,2}, Kacper Lachowski¹, Ivan Pelivanov², Thomas Matula³, Matthew O'Donnell⁴, Lilo Pozzo⁴**¹*Department of Chemical Engineering, University of Washington, Seattle, WA, United States*, ²*Department of Bioengineering, University of Washington, Seattle, WA, United States*, ³*Center of Industrial and Medical Ultrasound, University of Washington, Seattle, WA, United States*, ⁴*University of Washington, Seattle, WA, United States***Background, Motivation, and Objective**

Theranostic strategies to destroy clots using photoacoustic (PA) imaging in combination with photothermal heating or cavitation have previously been demonstrated. However, poor light penetration into tissue has restricted photoacoustic theranostic applications to superficial sites. Phase-change contrast agents (PCCAs) can be effective alternatives to conventional dye or particle based PA contrast agents. The threshold-based vaporization of PCCAs and large displacements generated from vaporizing nanodroplets to form microbubbles enables PCCAs to be effective theranostic agents. However, PA thresholds for vaporizing droplets still require a minimum optical fluence of 10 mJ/cm^2 , making them unsuitable for deep tissue imaging and therapy

Statement of Contribution/Methods

Sono-photoacoustic imaging is a non-linear imaging modality using simultaneous optical and acoustic activation of PCCAs. Using combined optical and acoustic sources to initiate vaporization, greater penetration depths can be achieved than by either source alone at optical fluences and acoustic pressures within FDA and ANSI limits. In this study, sono-photoacoustic vaporization of targeted polypyrrole coated liquid perfluorocarbon core agents for clot lysis is presented.

Results/Discussion

Using the ouzo method to spontaneously nucleate the droplet in solution, agents can be easily synthesized with diameters $<200 \text{ nm}$, making them well suited for extravascular imaging and theranostics. These agents have been shown to have no adverse effects on cell viability and can be functionalized for targeted delivery. Preliminary studies on sono-photoacoustic clot lysis show that agents can penetrate into fibrin clots (Figure 1). Once delivered, sono-photoacoustic cavitation of the agents can be used to disrupt the fibrin clot to restore blood flow.

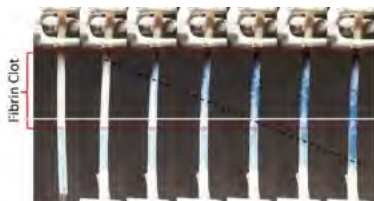


Figure 1: A fibrin clot (between dotted red line) was synthesized in a 5mm diameter thin walled plastic tube. A bolus injection of 0.05ml PPy emulsions was made and infused at 3ml/hour. The front of the PPy emulsion bolus is indicated using the black dotted line. The PPy emulsions can easily penetrate the clot when background flow was present.

2:45 PM

Nanobubble Facilitated Optoporation and Ultra High Frequency Photoacoustic Imaging of BT-474 Breast Cancer Cells in Vitro

Filip Bodera^{1,2}, Michael Moore^{1,2}, Yanjie Wang^{1,2}, Agata Exner^{3,4}, Michael Kolios^{1,2}

¹*Physics, Ryerson University, Toronto, Canada*, ²*Institute for Biomedical Engineering, Science and Technology, Li Ka Shing Knowledge Institute, Keenan Research Centre, St. Michael's Hospital, Toronto, ON, Canada*, ³*Department of Radiology, Case Western Reserve University, Cleveland, OH, United States*, ⁴*Department of Biomedical Engineering, Case Western Reserve University, Cleveland, OH, United States*

Background, Motivation, and Objective

Permeabilization of the cell membrane for enhanced drug and DNA plasmid delivery can be achieved through techniques such as sonoporation, electroporation, and microinjection. An alternative technique is optoporation, which uses tightly focused laser pulses to selectively porate individual cells *in vitro*. Localized cell damage/modification has been demonstrated using light absorbing nanoparticles heated with short laser pulses. Here we use targeted nanobubbles (NB) stained with Sudan Black B (SBB) and fluorescent dye DiO as agents for the dual purpose of enhancing optoporation and as contrast agents for photoacoustic (PA) imaging.

Statement of Contribution/Methods

Nanobubbles were fabricated according to our previous work [1]. SBB and DiO were added to the lipid solution prior to NB fabrication. NBs were targeted with Herceptin and were added to each petri dish of BT-474 cells and incubated for 2 hours before PA imaging. After incubation, fluorescence microscopy (Ex 480 nm/Em 517 nm) was used to confirm the presence of NBs on the cell membrane. The cells were rinsed 3x then exposed to propidium iodide (PI) in DMEM media.

A PA microscope (SASAM, Kibero GmbH) was equipped with a 400 MHz US transducer and a 532 nm laser (4 kHz pulse repetition rate, 330 ps pulse duration) focused through a 10X objective. The focal spots of the transducer and laser were co-aligned. A portion of the laser beam was directed to a joulemeter for pulse energy measurement. NB loaded cells were scanned through the laser focal spot in a raster pattern with a step size of 1 μ m and 10x signal averaging.

Results/Discussion

Fig 1a shows a Representative RF-line of the PA signal generated by the SBB dyed NBs within a cell. PI is membrane impermeable in healthy cells; however fluorescence was detected in the NB loaded cells as early as 7 minutes after scanning, indicating successful cell poration. No PA signals or PI fluorescence was detected in cells devoid of NBs. The PI intensity within the cell increased as a function of time (Fig 1b-d); with the rate of increase in a given cell dependent on the incident pulse energy (Fig 1e). The intracellular uptake and high SNR PA signal suggest that these SBB dyed NBs can be used both to facilitate single cell optoporation and be used as PA contrast agents.

[1] Y. Gao et al. Nanomedicine: Nanotechnology, Biology, and Medicine, 13 (2017) 2159-2168

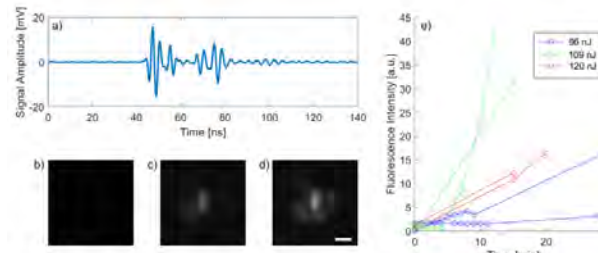


Fig 1: a) representative RF line from cell loaded with SBB dyed NBs. b – d) PI fluorescence images of the same group of cells at 1, 15, and 20 minutes post scan, respectively. e) PI fluorescence uptake as a function of time after laser exposure. The scale bar is 20 μ m.

2C - Technical Advances in Photoacoustic Imaging

Diamond (300)

Tuesday, October 23, 4:00 pm - 5:30 pm

Chair **Muyinatu Bell**
Johns Hopkins University

2C-1

4:00 PM Sparsity-Based Super-Resolution for Photoacoustic Tomography with a Ring Array Transducer

David Egolf¹, Quinn M. Barber², Roger Zemp²

¹University of Alberta, Edmonton, AB, Canada, ²University of Alberta, Canada

Background, Motivation, and Objective

Using high frequency linear array transducers, we have previously shown that incorporating sparsity constraints in the image reconstruction allows photoacoustic resolution to be improved beyond the standard limited-view limit [Egolf et al. 2018]. We now seek to test the hypothesis that sparsity-based reconstruction (SBR) can enable super-resolution photoacoustic tomography using a ring array, beating the half-wavelength diffraction limit and minimizing unwanted background signal.

Statement of Contribution/Methods

SBR forms images by seeking to express channel data sinograms as a superposition of approximate point-responses through optimizing a weighted sum of the accuracy of the approximation and the sparsity of the estimated image. To characterize the resolution obtainable by SBR, we used a 5 MHz ring array to image two crossed wires (18 μm diameter) in water. We measured resolving power as the separation between the wires at the last cross section where the wires were resolved. The separation between the wires on each cross section was determined using *a priori* information about wire trajectory geometry. Finally, the resolving power obtained by SBR was compared to that obtained by universal back-projection (UBP), a standard photoacoustic beamforming algorithm.

Results/Discussion

Initial results suggest SBR obtains a resolving power of roughly 135 μm , improving on the roughly 210 μm resolution obtained by UBP. Note that the SBR resolution obtained is at least comparable to the half-wavelength diffraction-limited resolution of 145 μm for this transducer. In addition, the images reconstructed with sparsity constraints enjoyed a lower level of undesired background signal. The C-scans below were formed by maximum amplitude projection of Gaussian-smoothed B-scan images, each of which were images of the two wires in cross section, followed by upsampling. The increase in resolution may have application to areas such as contrast agent tracking, imaging of sparse neuron activation, and imaging of microvasculature surrounding cancerous tumors. Ongoing work is exploring the generalization of SBR to less sparse settings and in deep scattering media.

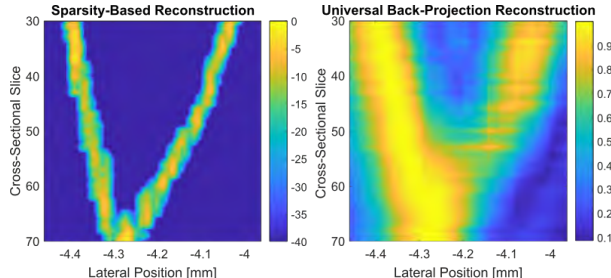


Fig.1. Experimental photoacoustic tomography volumetric images of wire phantoms projected as C-scans formed using sparsity-based reconstruction (left) and universal back-projection reconstruction (right).

4:15 PM

Sparsity-based optimization of the initial pressure distribution using a linear array transducer in photoacoustic imaging

Ruibo Shang¹, Geoffrey Luke¹, Richard Archibald², Anne Gelb³

¹Thayer School of Engineering, Dartmouth College, Hanover, NH, United States, ²Computational and Applied Mathematics Group, Oak Ridge National Laboratory, Oak Ridge, TN, United States, ³Department of Mathematics, Dartmouth College, Hanover, NH, United States

Background, Motivation, and Objective

Photoacoustic imaging (PA) is an emerging imaging technique for many clinical applications. One of the challenges posed by clinical translation is that, imaging systems will rely on a finite-aperture transducer rather than a full tomography system. This results in imaging artifacts arising from an underdetermined reconstruction of the initial pressure distribution (IPD). Furthermore, clinical applications often require deep imaging resulting in a low signal-to-noise ratio (SNR) for the acquired signal because of strong light attenuation in tissue. Conventional approaches to reconstruct the IPD such as back-projection (BP) do not adequately suppress the artifacts and noise. Here we propose a sparsity-based optimization approach to suppress noise and artifacts without compromising image quality.

Statement of Contribution/Methods

We build a mathematical forward model mapping the IPD to the acquired radio-frequency (RF) data and formulate it into a matrix multiplication model $\mathbf{y} = \boldsymbol{\psi}\mathbf{x}$, where \mathbf{x} is the IPD to be reconstructed, \mathbf{y} is the RF data and $\boldsymbol{\psi}$ is the forward model matrix mapping \mathbf{x} to \mathbf{y} . Then, we propose to solve the following sparsity-based optimization problem using two-step iterative shrinkage/thresholding (TwIST) algorithm,

$$\mathbf{x} = \operatorname{argmin}_{\mathbf{x}} \frac{1}{2}\|\mathbf{y} - \boldsymbol{\psi}\mathbf{x}\|_2^2 + \lambda\|\boldsymbol{\Phi}\mathbf{x}\|_1$$

where $\boldsymbol{\Phi}$ is the sparse operator on \mathbf{x} (here $\boldsymbol{\Phi}$ is chosen to be the identity matrix or total variation (TV) operator with the knowledge that IPD is usually sparse in spatial or TV domains), and λ is the regularization parameter (RP).

Results/Discussion

Both simulations and experiments were conducted for IPD reconstruction. K-Wave toolbox was used for simulations on point objects, Shepp-Logan and blood vessel phantoms. All the simulations showed that TwIST outperformed the BP, frequency-domain reconstruction and K-Wave developed iteration method in terms of artifacts and noise reduction. Experiments were conducted with the phantom in Fig. 1(a). For comparison, the full width at half maximum (FWHM) of the left peaks in Fig. 1 (e) and (f) was calculated. TwIST outperformed BP with a 25% improvement of the resolution. Besides, TwIST outperformed BP in noise reduction in terms of SNR of the reconstructed images for varying number of averaged frames and RPs from Fig. 1(g). In conclusion, our proposed method addresses the low SNR and finite-aperture issues in PA imaging and is promising for future clinical applications.

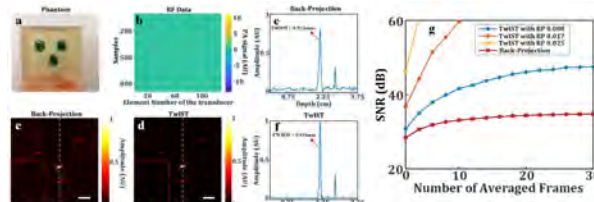


Figure 1 Image reconstructions of the phantom with back-projection and TwIST respectively. (a) The phantom prepared using gelatin from porcine skin and indocyanine green (ICG) dye. (b) 30 averaged RF data acquisitions of the phantom (the phantom was illuminated with 7-ns laser pulses ($t = 770$ nm) from a laser system (Fluence Mobile HE, Optoelek Inc.) and the PA signal from the optically absorbing ICG was simultaneously acquired by the linear array ultrasound transducer (L11-4s, Verasonics) with the pitch size of 0.5mm and the sampling frequency at 22.7MHz. The acoustic response of the imaging system was estimated experimentally by measuring the RF data of the PA signal at the center of a single image. (c) Reconstruction of the phantom using back-projection. (d) Reconstruction of the phantom using TwIST. (e) The profile along the white dotted line in (c) where the FWHM of the left peak is 0.81mm. (f) The profile along the white dotted line in (d) where the FWHM of the left peak is 0.61mm. (g) The plot of SNR with respect to varying number of averaged frames for back-projection and TwIST with 3 RPs respectively with the signal region chosen to be the cyan solid rectangular region and the background region chosen to be the red dotted rectangular region in (c) and (d) respectively. The scale bar is 5mm.

4:30 PM

Structured acousto-optic imaging with ultrafast ultrasonic plane waves

Jean-Luc Gennisson¹, Jean Baptiste Laudereau², Maïmouna Bocoum², Clément Dupuy², Jean-Michel Tualle³, François Ramaz²

¹IR4M / CNRS / UPSUD / CEA, Orsay, France, ²Institut Langevin / ESPCI / CNRS / INSERM, France, ³Laboratoire de physique des lasers / UPXIII / CNRS, France

Background, Motivation, and Objective

Acousto-optic (AO) imaging consists in mapping at cm depths the local intensity of light which propagates through a scattering medium by “tagging” the photons with a few-cycle ultrasound (US) in the MHz range. Although, AO showed promising *ex vivo* results [1, 2], current AO sequences based on focused US pulses are still too slow for *in vivo* imaging. AO using US plane waves (PW) to tag photons was then demonstrated as a faster imaging modality, at the cost of loss in lateral resolution [4]. Here a new type of AO sequences is proposed based on structured US plane waves (US-SPW) with subapertures and tomographic reconstruction that allows to retrieve lateral resolution and keep a high acquisition framerate.

Statement of Contribution/Methods

We have developed an AO imaging system based on wavefront adaptive holography detection of photons [3] coupled with an ultrafast US scanner driving a linear array @6 MHz (Aixplorer, Supersonic Imagine, France) allowing to measure AO signal on a photodiode with a good SNR [3]. Light absorbing inclusions were embedded within optically scattering phantoms (scattering coef. 10 cm^{-1} mimicking biological tissues) and illuminated @ 783nm. AO images were reconstructed from three different sequences presented in fig1. In step a) classical focused US were used. In step b) US-PW were used and reconstruction was performed by filtered backprojection of the AO signal as described in [4]. In step c), US-SPW were emitted 4 times with an ordered lateral shift (x-axis). After summation of the 4 acquisitions, in the Fourier space, the lateral Fourier component of the object is retrieved giving access to the lateral resolution over US-PW.

Results/Discussion

In the 3 sequences the number of US pulses and acquisition times are respectively: a) 192000, 20s, b) 41000, 4s and, c) 164000, 16s. As previously demonstrated [4], the SNR obtained with US-PW is higher than for focused pulses, thus allowing to decrease the number of averaging by a factor of 50. At equivalent SNR, the PW sequence lasts 0.82s [4] and the US-SPW sequence lasts 3.24s both at 100 μs firing rate with an adequate lateral resolution. Thanks to a high SNR, this last technique is suitable for real-time AO imaging, which is required by various application such as live oxygenation of blood level.

References

- [1] Laudereau, J. Biophoton. 2014 [2] Bocoum, Opt. Lett. 2018 [3] Farahi, Opt. Lett. 2010 [4] Laudereau, Opt. Exp. 2016

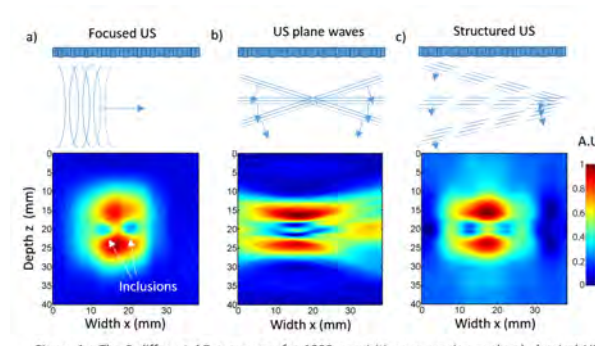


Figure 1 : The 3 different AO sequences for 1000 acquisitions averaging each: a) classical US focused AO sequences (192 lines), b) US-PW emitted with different propagation angles (-20° to 20°, 1° step), c) US-SPW emitted with subapertures for 4 different lateral position and different propagation angles (-20° to 20°, 1° step).

4:45 PM

Alternative elasticity measurement in deep tissue using strain-photoacoustic imagingGuan Xu¹, Yunhao Zhu¹, Laura Johnson¹, Jonathan Rubin¹, Jie Yuan², Xueding Wang¹, Peter Higgins¹¹*University of Michigan, United States*, ²*Nanjing University, China, People's Republic of***Background, Motivation, and Objective**

Tissue elasticity, defined as the ratio between the stress exerted onto a tissue volume and the corresponding strain, is a biomarker of many diseases. Ultrasound (US) Speckle tracking has been used to quantify strain in biological tissues. However, the stress in deep tissue is difficult to measure. With the hypothesis that the blood vessel collapsing is a reflection of the external pressure exerted to its surrounding tissue, the correlation between the photoacoustic (PA) signal changes and the strain could provide an estimation of the elasticity of deep tissue.

Statement of Contribution/Methods

A mathematical model describing the correlation between the PA signal changes and the strain in tissue was established. The model was examined using a PA-US parallel imaging system with the probe connected to a mechanical compression system with real time pressure monitoring (Fig. 1). The strain caused by the compression was measured using US speckle tracking. Rabbit ears were initially examined *in vivo* as they have rich vasculatures and the soft bone in the ears minimally deforms under pressure. Such model provides an opportunity to directly observe the correlation between the PA signal changes and the external stress without the interference of the tissue strain. Animal models of inflammatory and fibrotic intestinal strictures with confirmed difference in elasticity were also examined *in vivo*.

Results/Discussion

Fig. 1 shows strong correlation ($r>0.9$) between the PA signal changes and the pressure exerted on the 10 rabbit ears. Fig. 2 shows that the strain-PA correlations demonstrated significant differences between the inflammatory and fibrotic intestinal strictures in rats *in vivo*. The proposed strain-PA approach could be a quantitative measurement of the elasticity of deep tissue *in vivo*.

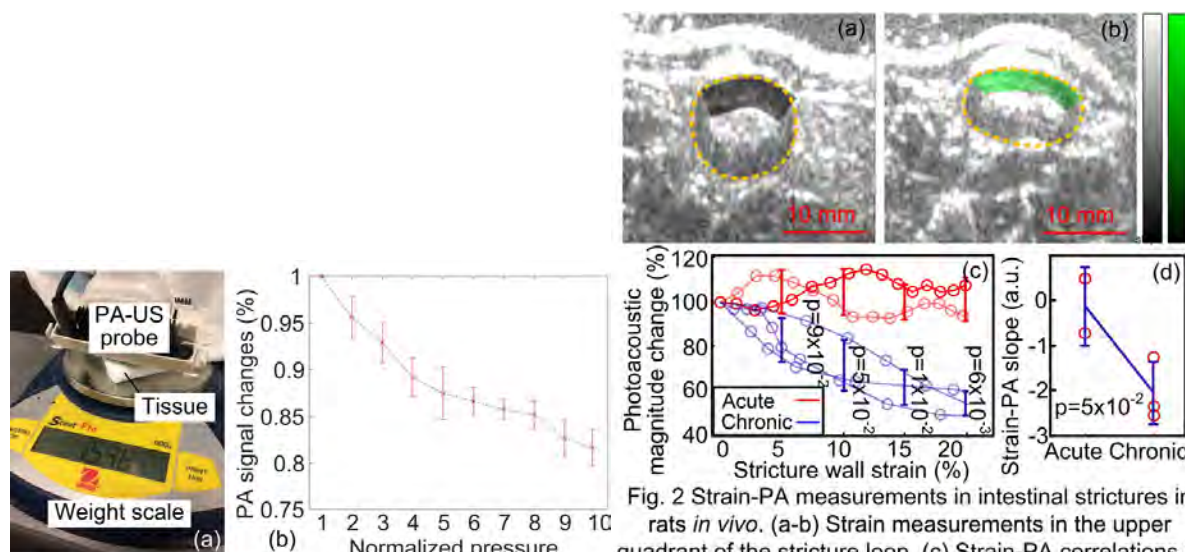


Fig. 1 (a) Experiment setup and (b) The PA-pressure correlation in rabbit ear *in vivo*

Fig. 2 Strain-PA measurements in intestinal strictures in rats *in vivo*. (a-b) Strain measurements in the upper quadrant of the stricture loop. (c) Strain-PA correlations in 2 inflammatory and 3 fibrotic intestinal strictures. (d) Statistics of the descending trends of the two groups in (c).

5:00 PM Portable LED-based photoacoustic and ultrasound imaging system for guiding minimally invasive procedures with peripheral tissue targets

Mithun Kuniyil Ajith Singh¹, Wenfeng Xia^{2,3}, Efthymios Maneas^{2,3}, Naoto Sato⁴, Yusuke Shigeta⁴, Toshitaka Agano⁴, Sébastien Ourselin^{2,5}, Simeon J. West⁶, Adrien Desjardins^{2,3}

¹Research and Business Development Division, PreXion Corporation, Rotterdam, Netherlands, ²Department of Medical Physics and Biomedical Engineering, University College London, United Kingdom, ³Wellcome / EPSRC Centre for Interventional and Surgical Sciences, University College London, United Kingdom, ⁴Research and Development Division, PreXion Corporation, Tokyo, Japan, ⁵Centre for Medical Imaging Computing, University College London, United Kingdom, ⁶Department of Anaesthesia, University College Hospital, London, United Kingdom

Background, Motivation, and Objective

Photoacoustic (PA) imaging holds potential in guiding minimally invasive procedures, but clinical translation of this technology has often been hindered by bulky and expensive excitation sources. In this work, the potential of a portable, dual-mode LED-based PA and US imaging system to guide minimally invasive procedures is investigated.

Statement of Contribution/Methods

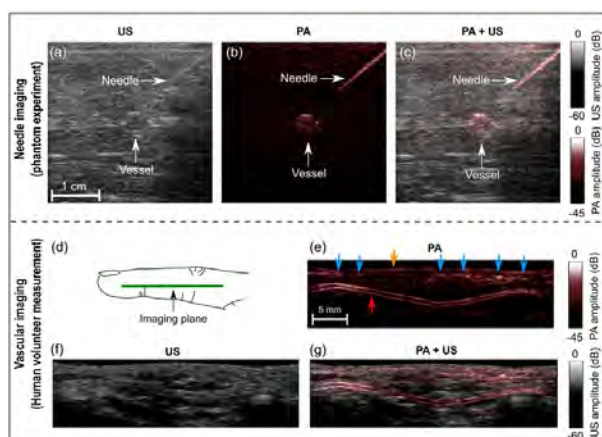
The system (AcousticX, PreXion Corp, Tokyo, Japan) comprises a linear array US probe with center frequency of 9 MHz; PA excitation light was provided by two LED arrays (wavelength: 850 nm, pulse width: 70 ns, pulse energy: 200 μ J/pulse/array) placed on both sides of the US probe. This system provides interleaved PA and US imaging at a frame rate of 30 Hz. Two experiments were performed to investigate the potential of the system to guide minimally invasive procedures. In the first, PA/US imaging was performed during needle insertions (14-gauge, Terumo, Surrey, UK) towards a blood vessel mimicking gel wax phantom (BVP), which was embedded in chicken breast tissue. In the second experiment, micro-vasculature of a human finger *in vivo* was imaged. In addition, the imaging depth and spatial resolution were measured using phantoms.

Results/Discussion

With needle insertions towards the BVP, both the needle and the BVP were clearly visualized in the PA images (Fig 1b). PA imaging enabled needle visualization with signal-to-noise ratios that were 1.2 to 2.2 times higher than those obtained with US imaging, over insertion angles of 26 to 51 degrees. The BVP could be visualized with PA imaging at a depth up to 3.8 cm into chicken breast tissue. The average axial and lateral resolution of the system were 0.22 mm and 0.46 mm, respectively.

With finger imaging, prominent PA signals were visible from a double-layered subsurface structure (red arrow), and pulsations that were apparent in the real-time image display indicated that this structure was arterial (Fig 1e). The skin surface (yellow arrow) and several superficial veins (blue arrows) were also visible in the PA image.

With the capability of providing real-time visualization of clinical metal needles and tissue targets, the LED-based PA/US system could be useful for guiding minimally invasive procedures in many clinical contexts. The results indicate that this system has strong clinical translation potential in non-invasive PA imaging.



5:15 PM

Characterizing non-resolvable tissue structures in photoacoustic imagingEno Hysi^{1,2}, Muhamnad N. Fadhel^{1,2}, Michael Moore^{1,2}, Jason Zalev^{1,2}, Eric Strohm^{3,4}, Michael Kolios^{1,2}¹*Physics, Ryerson University, Toronto, ON, Canada*, ²*Institute for Biomedical Engineering, Science and Technology, Toronto, ON, Canada*,³*Mechanical and Industrial Engineering, University of Toronto, Toronto, ON, Canada*,⁴*Translational Biology and Engineering Program, Ted Rogers Centre for Heart Research, University of Toronto, ON, Canada***Background, Motivation, and Objective**

In ultrasound (US) and photoacoustic (PA) imaging, speckle can be used to characterize the morphological properties of underlying tissue. It arises from the spatiotemporal superposition of pressure waves backscattered/emitted from scatterers/absorbers. Here, we examine the physical and mathematical formulation of PA speckle in US resolution PA imaging using numerical simulations and experimental validation to extract information about sub-resolution absorbers.

Statement of Contribution/Methods

Simulations: Forty numerical phantoms were constructed using spherical absorbers with various sizes and concentrations. The PA signals were computed from wave equation solutions using Green's function. The transducer modeled was a 21 MHz linear array probe. Fully developed PA speckle was evaluated using Rayleigh envelope statistics and the Nakagami scale Ω parameter was computed. Radiofrequency spectroscopy was performed between 9-33 MHz. The spectral slope (SS) and midband fit (MBF) were calculated for bead sizes ranging from 5 to 100 μm and number densities from 64 to 128/mm³.

Experiments: Four PA imaging systems (5 to 400 MHz) were used to image phantoms containing black polystyrene beads. For the 40 MHz transducer, the effect of absorber size on the SS was tested using 3.5 and 15 μm beads. The PA speckle size was measured using the autocovariance function to determine if it behaves similar to US speckle.

Results/Discussion

PA speckle was ubiquitous to all images as shown in Fig. 1a, with $\text{SNR} = 1.91$ in cases of fully developed speckle. Just like in US imaging, experimental speckle size estimates for all phantoms (absorber size 200 nm to 250 μm) were within 8.5% of the system spatial resolution (Fig. 1b). Envelope statistics (Fig. 1c) and radiofrequency spectroscopy (Fig. 1d) contain information on absorber size and concentration. Specifically, the Nakagami Ω parameter increases 36x with number density and 100x when doubling size (Fig. 1c). Increasing absorber concentration by 2x increases the MBF by 25 dB size. The PS SS decreases with size and remains unchanged beyond 30 μm , suggesting a "ka" dependence, similar to that of US imaging. These findings show that PA images containing speckle encode information about absorber morphology with potential applications in monitoring changes in vessel size during vascular targeted cancer therapies.

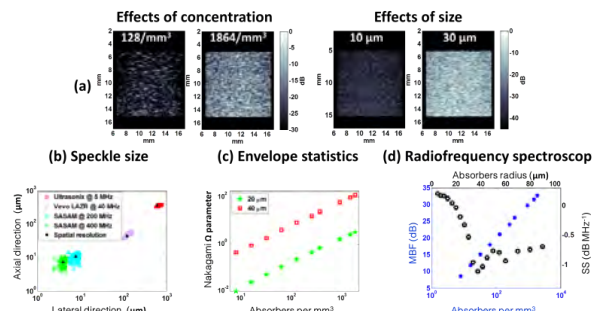


Fig. 1: (a) PA B-mode images from spherical absorbers at 21 MHz for varying concentration and size.
(b) PA speckle size and its comparison to the spatial resolution of each imaging systems used.
(c) Nakagami Ω fit parameter and (d) PA MBF and SS as a function of absorber size and concentration.

3A - Hemodynamics: Estimation and Visualization

Emerald (280)

Tuesday, October 23, 10:30 am - 12:00 pm

Chair **Kai Thomenius**
Massachusetts Institute of Technology

3A-1

- 10:30 AM Simultaneous measurement of stimulus and response in Flow Mediated Dilation: a pilot clinical study**
Alessandro Ramalli^{1,2}, Kunihiko Aizawa³, Angela C. Shore³, Carmela Morizzo⁴, Carlo Palombo⁴, Matteo Lenge⁵, Piero Tortoli²
¹*Lab. on Cardiovascular Imaging & Dynamics, Dept. of Cardiovascular Sciences, KU Leuven, Leuven, Belgium*,
²*Department of Information Engineering, University of Florence, Florence, Italy*, ³*Diabetes and Vascular Medicine Research Centre, NIHR Exeter Clinical Research Facility, University of Exeter Medical School, Exeter, United Kingdom*, ⁴*Department of Surgical, Medical, Molecular Pathology and Critical Care Medicine, University of Pisa, Pisa, Italy*, ⁵*Pediatric Neurosurgery Unit, Children's Hospital Meyer, University of Florence, Florence, Italy*

Background, Motivation, and Objective

The Flow Mediated Dilation (FMD) technique, despite its recognized validity in the assessment of the endothelial function by ultrasound, is still not widely used in clinical practice. A complete FMD exam requires estimating both the instantaneous brachial artery wall shear stress (stimulus) and diameter change (response) for 10 minutes, while blood flow is restricted by a cuff and then suddenly released. Technical, practical and methodological challenges have been faced in order to make feasible a two-center pilot clinical FMD study based on the ULA-OP research scanner. In this work, we present the results of such a study, with a partial correlation analysis on magnitude, time-course and kinetic parameters of measured wall shear rate (WSR) and diameter (D) trends.

Statement of Contribution/Methods

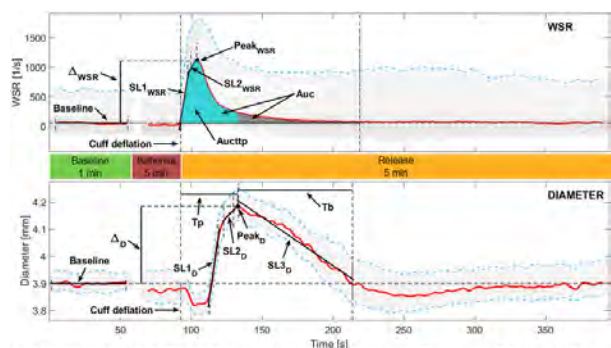
An upgrade of the ULA-OP research scanner permits the display and acquisition of B-mode and Multigate Spectral Doppler (MSD) data simultaneously and continuously for up to 15 minutes. A processing platform was developed to extract: WSR values, estimated from the velocity profiles associated to the MSD data; D values, measured by an edge detection algorithm applied to B-mode data. WSR and D time-trends were further processed to extract magnitude, kinetics and time-course parameters, as sketched in the figure.

35 young (20-40-yo) healthy individuals were recruited in Exeter and Pisa hospitals for this study.

Results/Discussion

The measured D trends reveal that: the first increasing slope ($SL1_D$) was associated ($r=0.417, p=0.014$) with the brachial artery vasodilatory response (Δ_D); both the first and second ($SL2_D$) increasing slopes were inversely associated ($r=-0.381, p=0.026$ and $r=-0.461, p=0.041$ respectively) with the time-to-peak interval (T_p); the deceleration slope ($SL3_D$) was positively associated ($r=0.356, p=0.042$) with the time to return to baseline (T_b). The absolute WSR increase (Δ_{WSR}) was positively associated to Δ_D ($r=0.41, p=0.021$); the WSR area under the curve (Auc) until its return to baseline was the strongest predictor of Δ_D in response to hyperemia ($r=0.46, p=0.008$). In contrast, kinetics parameters of D were not directly associated with WSR kinetics parameters.

Our observations show that a direct and accurate estimation of WSR stimulus by MSD is imperative to understand brachial artery vasodilatory response to reactive hyperemia.



A schematic description of WSR and diameter parameters obtained from FMD. Top: peak (light blue) and mean (red) values of WSR. Bottom: variations in diameter (light blue) and mean (red) diameter of the brachial artery.

10:45 AM

Laterally-dependent velocity estimation bias in plane wave Doppler ultrasoundLuxi Wei^{1,2}, Thanasis Loupas³, Peter N. Burns^{1,2}¹*Medical Biophysics, University of Toronto, Toronto, ON, Canada*, ²*Sunnybrook Research Institute, Toronto, ON, Canada*, ³*Philips Ultrasound, Bothell, WA, United States***Background, Motivation, and Objective**

Doppler ultrasound blood velocimetry is used to diagnose and monitor vascular disease, as well as to obtain quantitative volume flow estimates. Ultrafast plane wave Doppler has attracted interest because of its ability to provide rapid simultaneous colour and spectral Doppler measurements across the entire field of view [1]. However, here we report a substantial laterally-dependent velocity bias in both spectral Doppler (Fig 1a) and colour Doppler (Fig 1b) using plane waves compared to conventional focused beams. We further demonstrate that this bias is due to asymmetrical geometric spectral broadening and propose a correction algorithm.

Statement of Contribution/Methods

Experiments were performed using a Supersonic Aixplorer (L10-2 transducer, 38mm aperture) and a Verasonics Vantage 128 (L12-5 transducer, 38mm aperture), on a wall-less vessel of 6.6 mm diameter within 3% agar. Steady flow of blood mimicking fluid at 350 cm³/min was imaged using planar non-steered and steered beams with a constant Doppler angle of 78–80 degrees. Aixplorer spectral Doppler measurements were obtained using both focus and plane wave modes at 5–6 locations across the field of view, and mean velocities were estimated using on-cart velocity estimation tools. Verasonics measurements were obtained using channel data and off-line beam-forming with a 24° acceptance angle, followed by step-initialized IIR filtering and the Kasai estimator on 100-pulse ensembles. Velocity bias correction was performed by calculating the effective Doppler angle considering the acceptance angle at each pixel combined with a weighting factor based on the directivity function of each transducer element.

Results/Discussion

As can be seen from Figures 1a and 1b, velocity bias is symmetrical relative to the aperture center and reached 40% for non-steered plane waves, whereas for steered plane waves it is asymmetrical and reached higher values. Analysis indicates that the cause of the velocity bias is location-dependent geometric spectral broadening, due to the position and size of the receive aperture. The proposed correction scheme accounts for synthetic aperture position, width and directional sensitivity. For steered and non-steered cases, the bias is corrected to less than 5% and 10% respectively over more than 90% of the aperture (Fig 1b).

[1] J Bercoff *et al*, IEEE Trans UFFC, vol 58, pp 134-147, 2011.

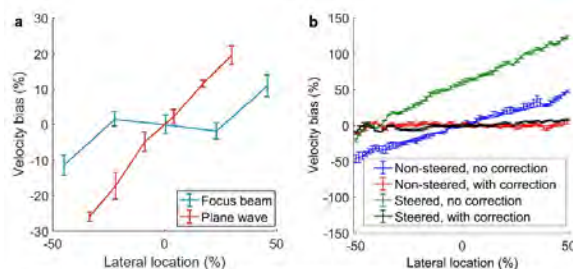


Figure 1: a) Focus beam and plane wave non-steered spectral Doppler mean velocity bias on the Supersonic Aixplorer system at 4 cm depth ($n = 5$). b) Plane wave colour Doppler velocity bias on the Verasonics system before and after correction at 4 cm depth ($n = 5$). Percentage bias is relative to the mean velocity at the center of the receive aperture.

11:00 AM

Real-Time Flow Visualization through Locally Activated Nanodroplets and High Frame Rate ImagingMatthieu Toulemonde¹, Ge Zhang¹, Mengxing Tang¹, Robert Eckersley²¹*Department of Bioengineering, Imperial College London, United Kingdom*, ²*Department of Biomedical Engineering, King's College London, London, United Kingdom***Background, Motivation, and Objective**

Blood flow visualisation and quantification with microbubble (MB) contrast agents using High-Frame-Rate (HFR) ultrasound has recently been investigated [C.H. Leow, UMB 2018]. However the technics proposed have no real-time flow feedback because of the high concentration of MB or computational cost. More recently, nanodroplet contrast agents have been investigated as an alternative to MB, due to their smaller size, longer half-life. In addition, they provide potential for spatiotemporal control of their activation. However, their potential use as a flow indicator has not been fully explored. The aim of this work is to demonstrate the feasibility of real-time flow pattern visualization in a realistic carotid bifurcation phantom using HFR ultrasound acquisition using locally activated nanodroplets.

Statement of Contribution/Methods

A PVA carotid bifurcation phantom connected to a pulsatile pump (80 beats/min – 0.25 ml/min) was used in an open water circuit (2.5L/37°C) with 2.5mL of decafluorobutane (DFB) nanodroplets. A 5 mm nanodroplet activation area at 25 mm depth was chosen on the side of the phantom, before the bifurcation. The nanodroplets were activated with a focused wave (10-cycle, 4MHz) [G. Zhang, IUS 2017] and imaged with an 11 HFR angles compounded diverging transmission (1-cycle, 4MHz, 1000Hz). Maximum intensity projection (MIP) of 75 consecutive compounded images was performed before log compression.

Results/Discussion

The figure shows MIP frames before and after the activation of nanodroplets. The following flow patterns are visible after activation: (at 0.028s) splitting of the activated nanodroplets, (at 0.168s) a vortex with reverse flow near the carotid wall and (at 0.723s) fast flow. Then most of the activated nanodroplets have been washout after 1s and the acquisition can be repeated. These patterns are visible in real-time due to the high contrast between the water and the activated nanodroplets. In this work, we showed that locally activated DFB nanodroplets present an opportunity to introduce indicator into flow non-invasively and visualize flow patterns with a high temporal resolution.

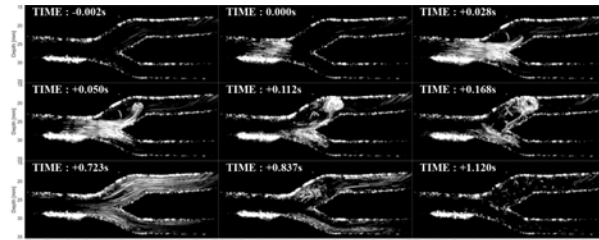


Figure: HFR B-Mode acquisition before and after nanodroplets activation in a PVA bifurcation phantom. The following flow patterns are visible after activation: (0.028s) splitting of the activated nanodroplets at the bifurcation, (0.168s) a vortex with reverse flow near the wall and (0.723s) a fast flow. All activated nanodroplets have been washout after 1s. Each frame corresponds to the maximum intensity projection of 75 consecutive compounded images and displayed with a 15 dB dynamic range.

11:15 AM Time-Resolved Wall Shear Rate Mapping: Spatiotemporal Profiling of a Key Hemodynamic Factor Related to Atherosclerosis

Chung Kit Ho¹, Billy Y. S. Yiu¹, Adrian J. Y. Chee¹, Alfred C. H. Yu¹¹Schlegel-UW Research Institute for Aging, University of Waterloo, Waterloo, ON, Canada**Background, Motivation, and Objective**

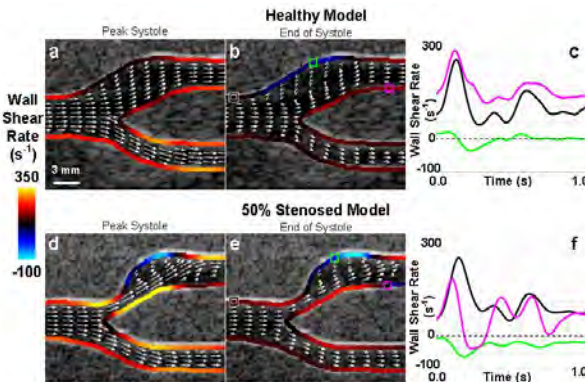
Wall shear rate (WSR) is known to be strongly associated with plaque formation and stroke risk. The temporal dynamics of this hemodynamic factor may be estimated using Doppler ultrasound at a single site. However, tracking WSR dynamics over multiple vessel wall positions in a full image view has not been convincingly demonstrated. Here, we propose a new non-invasive WSR mapping technique that makes use of high-frame-rate ultrasound principles to track the spatiotemporal evolution of WSR in an artery segment.

Statement of Contribution/Methods

Our new WSR mapping method is built upon three key principles: 1) high-frame-rate flow vector estimation; 2) dynamic wall tracking; 3) velocity gradient estimation via 2D spatial derivative. In brief, after acquiring high-frame-rate ultrasound data using plane wave excitation, a set of flow vector maps was generated using our multi-angle vector Doppler estimator (T-UFFC, 2016; 63: 1733-1744). Next, flow region was identified from a semi-automated dynamic wall tracker (MAUI, Hedgehog Medical), and the vectors were regularized using a penalized least squares method (CSDA, 2010; 54: 1167-1178). Subsequently, spatial velocity gradients of the vector map were derived using a Sobel filter. The WSR was finally computed by projecting the velocity gradient tensors onto the normal vectors of the walls. Our framework was demonstrated on two bifurcation models (healthy and 50% stenosed) with pulsatile flow (8 ml/s systolic). Data was acquired using SonixTouch with L14-5 probe (3Tx-3Rx plane wave; 5 MHz 3-cycle pulse; 10 kHz PRF).

Results/Discussion

Frames depicting peak and end systole were rendered in Fig. a, b, d & e. WSR at selected positions (note colored boxes) were plotted in Fig. c & f. In the bulb of the healthy model, WSR oscillates at a low magnitude about zero (Fig. c green line). This observation agrees with the association of the bulb region with plaque development due to low WSR. Drawing insights from the diseased model, increased WSR at the stenosed ICA inlet can be attributed to the formation of flow jet during peak systole. However, as the flow jet dissipates, WSR at the ICA distal wall dipped promptly to a negative WSR (Fig. f magenta line), suggesting flow reversal after peak systole. These results show that our framework is capable of profiling spatiotemporal WSR dynamics, which could provide new insights in atherosclerosis diagnostics



11:30 AM In vivo wall shear stress and blood flow mapping using native blood speckle or contrast enhanced echo particle image velocimetry and plane wave imagingKai Riemer¹, Ethan Rowland¹, Chee Hau Leow¹, Mengxing Tang¹, Peter D. Weinberg¹¹*Bioengineering, Imperial College London, London, United Kingdom***Background, Motivation, and Objective**

A wide range of cardiovascular diseases manifest themselves with abnormalities in blood flow and wall shear stress (WSS). Contrast-enhanced echo particle image velocimetry (echo-PIV) can be used to assess the spatiotemporally varying magnitude of near wall flow and WSS accurately *in vitro* [1]. However, the need for contrast agent might limit clinical applications. Recently, the efficacy of high frame rate speckle echo-PIV has been demonstrated *in vivo* for cardiac blood flow imaging [2]. In this study we demonstrate that ultrafast echo-PIV can be used *in vivo* for WSS mapping and we will compare near-wall tracking capabilities using microbubble (MB) or native blood speckle (NBS).

Statement of Contribution/Methods

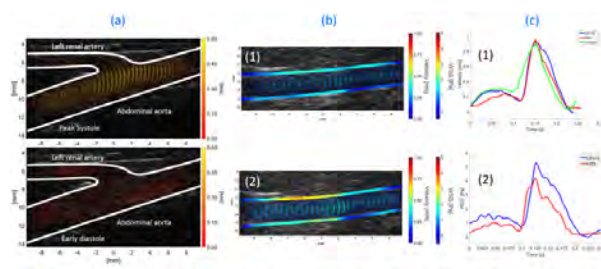
A Verasonics Vantage 64 LE research ultrasound system with a L11-4v broadband probe was used to image the abdominal aorta of a male New Zealand White rabbit. Images were acquired with either a B-Mode or a PI transmit sequence with a PRF between 1500-7500Hz. Up to five plane waves with angles spanning 12° were transmitted. The transmit frequency was between 3-5MHz or 6-10MHz for PI and B-Mode respectively; MI was between 0.05-0.3. In addition, microbubbles were injected as a bolus (6-25µl/kg) via the marginal ear vein. Vessel tracking was semi-automated using a cross-correlation method. Post-acquisition a sliding window SVD clutter filter was applied.

Results/Discussion

Extraction of blood or microbubble signal was improved substantially by the sliding window SVD clutter filter. Tracking of NBS or CEUS delivered slightly different results for velocity and WSS and NBS gave lower SNR ratios. Vessel tracking was more robust for B-Mode acquisitions than for PI but equally accurate for MB and NBS. Differences between MB and NBS can be attributed to non-parallel acquisition, initial uncertainties in wall location and out-of-plane motion. We demonstrate that both MB or NBS can be used for WSS and velocity mapping *in vivo*.

[1] Leow et al. Ultrasound Med. Biol., no. I, 2017

[2] Takahashi, Jpn. J. Appl. Phys., vol. 53, no.7 SPEC. ISSUE, 2014



(a) Complex flow field in the abdominal aorta of a NZW white rabbit at different phases of the cardiac cycle. Wall shear stress and velocity using microbubbles (b1) and native blood speckle (b2). Velocity (c1) and WSS (c2) waveform averaged over three cycles.

11:45 AM

Clinical evaluation of wall shear stress by ultrafast vector flow imaging in carotid atherosclerotic stenosis

Guillaume Goudot¹, Olivier Pedreira¹, Jonathan Porée¹, Lina Khider², Jean-Marc Alsac³, Pierre Julia³, Tristan Mirault², Mickaël Tanter¹, Emmanuel Messas², Mathieu Pernot⁴

¹Institut Langevin, INSERM U979, Paris, France, ²PARCC INSERM U970, Paris, France, ³Vascular Surgery, APHP, Paris, France, ⁴Institut Langevin, INSERM U979, Paris, France

Background, Motivation, and Objective

Carotid plaque vulnerability assessment is an important factor in guiding the decision to perform carotid endarterectomy in case of asymptomatic stenosis. Ultrafast Ultrasound Imaging (UUI) offers the possibility of evaluating local flow velocities over an entire 2D image, allowing access to velocity measurements in contact with the arterial wall and to measure the wall shear stress (WSS). Our objective was to evaluate the feasibility of WSS measurement in a prospective series of patients with carotid stenosis.

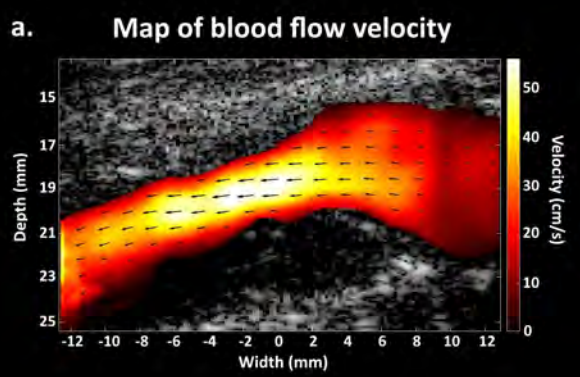
Statement of Contribution/Methods

For this study, a linear probe was used (SL10-2, 7.5 MHz, SuperSonic Imagine[®]). UUI acquisitions last 600 ms, started at the foot of the QRS, with 3 tilted plane waves transmits (-10; 0; 10°) for an effective frame rate of 5000Hz. We evaluated the flow velocity in 5 areas of the carotid wall: common carotid artery (1), plaque ascent (2), plaque peak (3), plaque descent (4), internal carotid artery (5) (see Figure 1.b). The WSS was computed with the vector field speed using the following formula, $WSS = \mu \cdot \delta_n \cdot v$ with v the blood velocity, n the normal vector to the vessel wall and μ , the blood viscosity, calculated from the haematocrit value for each patient. Shear stress measurement method was validated using a laminar flow phantom with laminar flow and known viscosity.

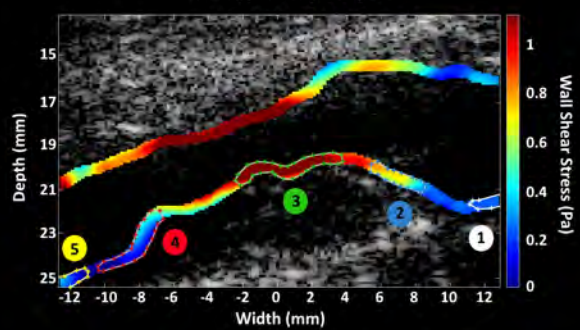
Results/Discussion

48 patients were included in this study. Among them, 25 patients (mean age: 72±5 years), had suitable images of carotid plaque analysis, as a longitudinal visualization of the whole plaque was necessary to perform the measurements of WSS. The mean percentage of stenosis was 75±12% (NASCET). The maximal WSS was variable along the carotid plaque with a progressive increase to a maximum value at the peak (2.12 ± 1.27 Pa). The post-stenotic descent zone has the lowest shear stress (0.57 ± 0.39 Pa), lower than the WSS values in the healthy zone (1.02 ± 0.36 Pa for the common carotid and 0.68 ± 0.39 Pa for the internal carotid artery) (see Figure 1.c).

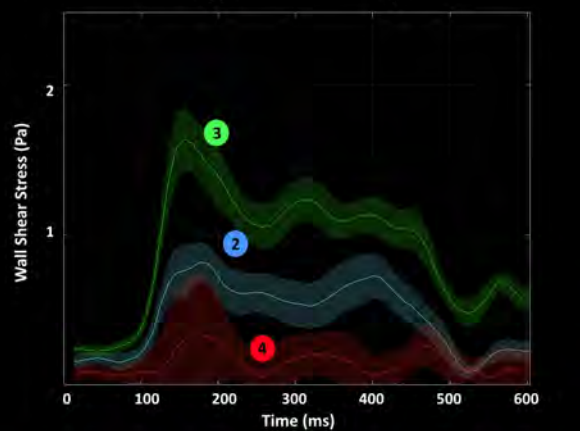
This method allowed the local and direct evaluation of the plaque's wall shear stress. Unlike the global evaluation of speed using conventional Doppler, these measurements make it possible to better characterize the haemodynamic conditions to better identify areas of vulnerability. Correlation between WSS values and histological vulnerability analysis is currently on going.



b. Maximum of Wall Shear Stress (WSS) along the plaque



c. Wall Shear Stress (WSS) variation during the cardiac cycle



3B - Tips and Tricks for Doppler and Contrast Imaging

Emerald (280)

Tuesday, October 23, 1:30 pm - 3:00 pm

Chair **Svetoslav Nikolov**
BK Ultrasound

3B-1

1:30 PM

Higher order singular value decomposition for high contrast microvascular imaging

Chee Hau Leow¹, Marta Braga², Nigel L. Bush³, Antonio Stanziola¹, Anant Shah³, Javier Hernández-Gil^{2,4}, Nicholas J. Long^{2,4}, Eric O. Aboagye², Jeffrey Bamber³, Mengxing Tang¹

¹*Department of Bioengineering, Imperial College London, United Kingdom, ²Department of Surgery & Cancer, Imperial College London, United Kingdom, ³Joint Department of Physics and Cancer Research UK Cancer Imaging Centre, Institute of Cancer Research, United Kingdom, ⁴Department of Chemistry, Imperial College London, United Kingdom*

Background, Motivation, and Objective

Spatio-temporal clutter filtering using singular value decomposition (SVD) has demonstrated superior performance in microvascular imaging when coupled with high-frame rate data acquisition. However, matrix SVD only deals with 2D matrices and therefore higher-order tensors such as 2D+t or 3D+t ultrasound images need to be unwrapped to a 2D matrix before the decomposition. In this study, we proposed a tissue-clutter filtering technique using higher order SVD (HOSVD) and compare its performance with state-of-the-art SVD clutter filtering techniques.

Statement of Contribution/Methods

High frame rate (500Hz, 7 compounding) 2D CEUS images of a Balb-c mouse kidney were acquired using a linear probe (L22-14v, 18MHz centre frequency) attached to a Verasonics Vantage™. Without unwrapping the 4D matrix, HOSVD was performed on the 4D matrix, resulting in a core tensor and four eigen-matrices (depth, channel, angle, and temporal eigenvectors). Clutter and noise filtering was performed by selecting the bases which best separated the clutter, contrast signal, and noise in all of the eigen-matrices.

Results/Discussion

Figure 1 shows examples of lag-1 autocorrelation-imaged kidney vasculature after clutter filtering with 4 different filtering techniques. The contrast to tissue ratios, quantified from the green (contrast) and white (tissue) boxes, are 11.6, 14.1, 14.0, and 14.3dB for the SVD, BSVD, HOSVD and BHOSVD, respectively. BHOSVD outperformed all the other spatio-temporal filters. Global HOSVD performed better than the global SVD, although it suppressed smaller vessels when compared to BSVD and BHOSVD, as indicated by the magnified image on the top left of all images. In conclusion, we have presented a clutter filtering technique for microvascular imaging using HOSVD and compared its performance with that of the state-of-the-art SVD filter

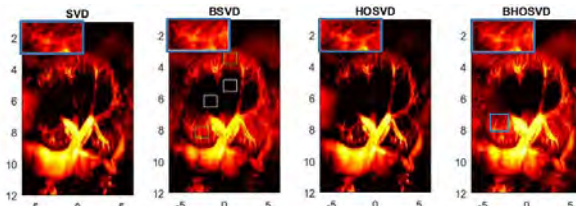


Fig 1: Normal mouse kidney imaged using global SVD, block-SVD (BSVD), global HOSVD and block-HOSVD. The images were generated by accumulating the relative echo power from all the moving scatterers and compressed to 30dB dynamic range.

1:45 PM

Adaptive grayscale mapping to improve molecular ultrasound difference imagesJasmine Shu¹, Dongwoon Hyun², Lotfi Abou-Elkacem³, Juergen Willmann², Jeremy Dahl⁴¹Bioengineering, Stanford University, Stanford, CA, United States, ²Department of Radiology, School of Medicine, Stanford University, Palo Alto, CA, United States, ³Stanford University, United States, ⁴Radiology, Stanford University, CA, United States**Background, Motivation, and Objective**

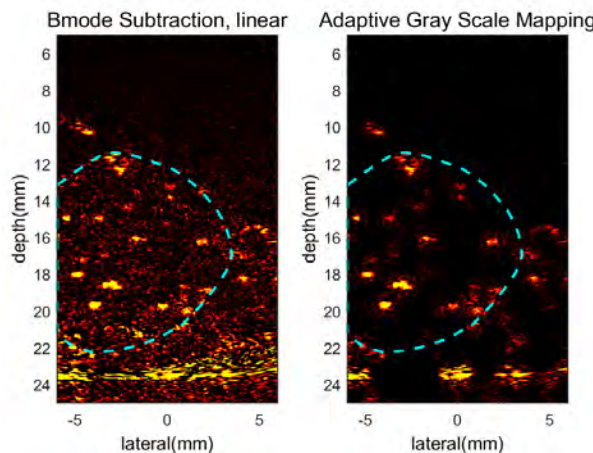
Molecular ultrasound is an imaging technique that uses targeted microbubbles (MBs) to detect molecular markers. Targeted MB imaging is a relatively new method without an established or optimized pipeline for image acquisition and display of information. Furthermore, targeted MBs can be difficult to visualize due to movement of unbound MBs, low MB dose and binding, or low SNR. A commonly used image processing method to identify targeted MBs is to subtract images before and after MBs are cleared with a destructive pulse, thus subtracting background and tissue noise from the stationary MB signals. However, misalignment, moving MBs, or distortion of the images can result in subtraction noise. We propose an adaptive grayscale mapping technique to improve visualization of stationary MBs.

Statement of Contribution/Methods

We modified the adaptive grayscale mapping technique, a geospatial mapping algorithm intended to reduce difference image artifacts, to improve detection and visualization of targeted MBs. Nontargeted microbubbles were injected into a tissue-mimicking microchannel flow phantom and held stationary. A layer of bovine tissue was placed between the transducer and the phantom to emulate *in vivo* conditions. Motion was caused by manually holding the probe during data acquisition. Ultrasound images before and after bursting the MBs were corrected for motion, averaged across 10 frames and subtracted before application of the proposed method. *In vivo* mice experiments ($n=10$) were performed with Thy1-targeted MBs injected in mice with subcutaneous tumors. Similar to the phantom experiment, a porcine tissue layer was placed between the transducer and the mouse. All results were quantified with signal-to-noise ratio (SNR).

Results/Discussion

Images from the phantom experiments demonstrated an SNR improvement of 5.23 dB with the proposed method. Most of the subtraction artifact in the tissue area was removed, while the microbubble signal was conserved. Similarly, the *in vivo* mouse images showed an SNR improvement of 4.15 dB. Qualitatively, the method reduces artifacts and background noise while improving visualization of MBs localized to the tumor (see Fig. 1 with tumor outlined).



2:00 PM

Understanding the origin of flashing artefacts due to Singular Value Decomposition clutter filter

Jiaqi Zhu¹, Jemma Brown², Kai Riemer¹, Sevan Harput¹, Kirsten Christensen-Jeffries², Chris Dunsby³, Robert Eckersley², Peter D. Weinberg¹, Mengxing Tang¹

¹Bioengineering, Imperial College London, London, United Kingdom, ²Biomedical Engineering Department, School of Biomedical Engineering and Imaging Sciences, King's College London, United Kingdom, ³Physics and Centre for Pathology, Imperial College London, London, United Kingdom

Background, Motivation, and Objective

Singular value decomposition (SVD) based clutter filters have extensively demonstrated efficient separation of clutter and blood or microbubbles in ultrafast plane wave imaging. However, a fluctuation in intensity (flashing) can often be observed experimentally and in simulation after SVD filtering. Understanding the sources of this flashing is necessary for clinical interpretation of the data, particularly in flow and perfusion quantification. The aim of this study is to understand the underlying causes and the factors influencing the flashing artefacts in SVD based filter techniques.

Statement of Contribution/Methods

A set of simulations, *in vitro* and *in vivo* experiments were conducted to investigate the fluctuation in intensity by using the contrast-to-tissue ratio (CTR) as a comparison metric. Simulations of single flowing microbubbles were performed using k-Wave to simulate wave propagation through tissue media and the Marmottan model to model the bubble response to high frame rate (HFR) plane wave ultrasound. Experimentally, HFR plane wave imaging was acquired using a Verasonics Vantage research platform. *In vitro* experiments were performed by imaging microbubble flow in a 300 μ m tube surrounded by a tissue mimicking phantom. *In vivo* experiments were conducted in the abdominal aorta of a New Zealand White rabbit.

Results/Discussion

The flashing occurs after SVD in all data sets, even in simulation when bubble signals are known to be constant over time. In *in silico* and *in vitro* experiments, fluctuation after SVD filtering was found to depend on image stack size (Fig. 1a), flow speed (Fig. 1b) and probe motion. A decrease in stack size or a decrease in flow speed resulted in fluctuations of higher frequency and amplitude. *In vivo*, fluctuation of image brightness are attributed to motion and pulsatility of the blood flow (Fig. 1c).

In this work we have demonstrated that image intensity fluctuation after SVD filtering is an artefact and not representative of physiological information. Understanding the different factors and how they affect the artefact will help to avoid misinterpretation on clinically and technically relevant level.

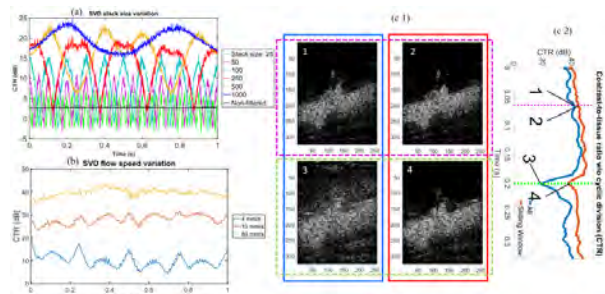


Fig. 1(a) Effects of stack size in silico, (b) Effects of flow speed *in vitro*, (c1&2) Flashing attributed to motion and pulsatility (blue) is reduced with a sliding window SVD filter (red). Adapting the stack size to cardiac cycle leads to better a CTR (pink,2) and a substantial decrease of flashing amplitude (green, 4) and frequency.

2:15 PM Identifying Directional Components in an Augmented Pulse Wave: A Spatial-Velocity Gradient Approach

Adrian J. Y. Chee¹, Jason Au¹, Alfred C. H. Yu¹¹Schlegel-UW Research Institute for Aging, University of Waterloo, Waterloo, ON, Canada**Background, Motivation, and Objective**

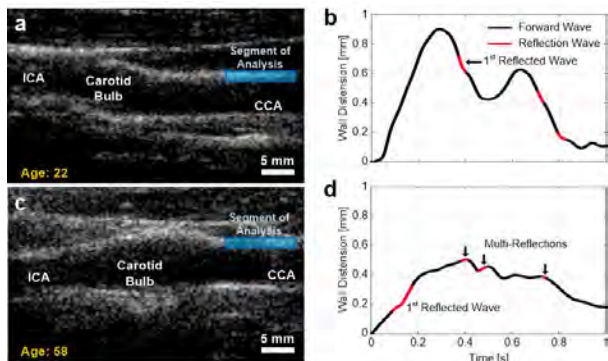
Blood pressure variation over a cardiac cycle is an augmentation of a forward cardiac pulse with multiple backward reflection waves. Analysis of such pressure variation (commonly known as pulse wave analysis) can critically reveal insight into arterial function and vascular health, especially if the characteristics of reflected waves are taken into account. However, reflected waves are often bundled and assumed as one composite backward wave in pulse wave analysis due to the lack of sensitivity in applanation tonometry to capture and discern individual waves. Here, we propose a new pulse wave analysis framework that is capable of identifying individual reflected waves. This framework is based on high frame rate ultrasound (HiFRUS) measurement principles.

Statement of Contribution/Methods

Premised upon the assertion that a transiting wave would induce a spatial gradient in the radial wall velocity, our framework involves three main stages: 1) HiFRUS acquisition to capture fast traveling waves; 2) tissue Doppler processing to increase wave detection sensitivity; 3) spatial gradient analysis of wall velocity to deduce wave propagation direction. HiFRUS images were acquired in-vivo (on two subjects: 22 and 58 yrs old) using a US4US platform with an SL1543 probe (plane wave Tx° -10°, 10°; 6 kHz PRF) at the right common carotid artery (CCA) bifurcation. Tissue Doppler analysis was performed on a 10 mm segment of the CCA's anterior wall (see Fig. A). Wall velocities at the CCA segment were estimated using a 10 ms Doppler processing window, slid along the slow-time axis. Spatial velocity gradient was estimated using robust regression, and wave direction was deduced from the sign of the gradient. Time-varying pressure waveform was finally constructed by integrating the wall velocities along its time axis.

Results/Discussion

For the 22 yrs old adult, Fig. b shows that augmentation of reflected waves occurs only in late systole. In contrast, for the 58 yrs old adult, presence of reflection waves were noted before the pressure contour peaks (Fig d). This is attributed to the close proximity of the studied segment to the bifurcation (Fig. c), as well as the stiffer arteries (note the arterial distensibility differences in Fig. b. More instances of wave reflection were observed in Fig. d, suggesting multi-site reflections in the artery's distal end.



2:30 PM

Fetal heart rate measurements of twins using a single flexible ultrasound transducer matrixPaul Hamelmann¹, Massimo Mischi¹, Rik Vullings¹, Alexander Kolen², Judith van Laar³, Jan Bergmans¹¹Eindhoven University of Technology, Netherlands, ²Philips Research, Netherlands, ³Máxima Medical Center, Veldhoven, Netherlands**Background, Motivation, and Objective**

The increased use of assisted reproductive technology and increasing maternal age have led to a significant increase of twin births in Western countries. Twin pregnancies are associated with higher risk and, therefore, monitoring fetal health is crucial. Fetal health is typically assessed by measuring the fetal heart rate (fHR) using a Doppler Ultrasound (US) transducer. In twin pregnancies, two independent US transducers need to be manually positioned on the maternal abdomen, which requires skill and experience. Common clinical problems are: 1) both hearts lie in the sample volume (SV) of one transducer, leading to erroneous fHR registration, 2) the heart locations change due to fetal movement, 3) registration of the maternal heart rate and 4) both US transducers measuring the same fHR. In this study, we propose twin-fHR measurements using a flexible US transducer matrix. The array aperture allows measuring the Doppler power from multiple SVs simultaneously to localize both fetal hearts in 3D. Furthermore, automated Doppler signal clustering enables unambiguous determination of the fHR of both fetuses.

Statement of Contribution/Methods

In total, 25 transducer elements are embedded into a flexible silicone layer and connected to an open US research system (Vantage 256, Verasonics). For each element, Doppler signals from SVs at different depths are computed and their respective power P is calculated. The matrix geometry, estimated from the average maternal abdominal curvature, allows estimating each SV location, providing a coarse 3D visualization of P to indicate the origin of the Doppler signals (Fig. 1). All SV locations with Doppler power P above threshold t_P are fitted to a two-component Gaussian mixture model and, subsequently, clustered. The median fHR is then computed from the Doppler signals of each cluster. The method is evaluated using a dedicated *in-vitro* twin-fHR setup.

Results/Discussion

Our results confirm that a single flexible sensor matrix can enable localization and visualization of twin fetal hearts. With the proposed clustering algorithm, the two fHRs can be detected without the aforementioned problems of manually positioning two US transducers. This may lead to improved clinical workflow and better fetal health monitoring in twins.

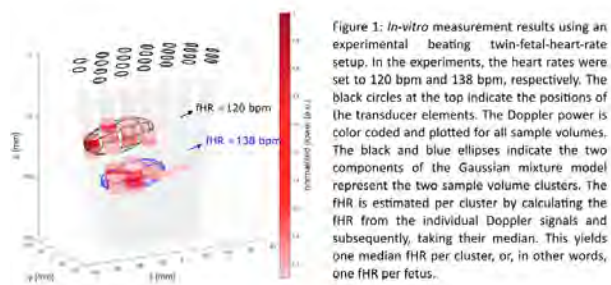


Figure 1: *In-vitro* measurement results using an experimental beating twin-fetal-heart-rate setup. In the experiments, the heart rates were set to 120 bpm and 138 bpm, respectively. The black circles at the top indicate the positions of the transducer elements. The Doppler power is color coded and plotted for all sample volumes. The black and blue ellipses indicate the two components of the Gaussian mixture model represent the two sample volume clusters. The fHR is estimated per cluster by calculating the fHR from the individual Doppler signals and subsequently, taking their median. This yields one median fHR per cluster, or, in other words, one fHR per fetus.

2:45 PM **Unambiguous detection and visualizing of a catheter with multiple active acoustic sources: in-vivo validation in a swine model**Viksit Kumar¹, Minako Katayama², Azra Alizad³, Marek Belohlavek², Mostafa Fatemi¹¹*Department of Physiology and Biomedical Engineering, Mayo Clinic College of Medicine and Science, Rochester, MN, United States, ²Department of Cardiovascular Diseases, Mayo Clinic College of Medicine and Science, Scottsdale, AZ, United States, ³Department of Radiology, Mayo Clinic College of Medicine and Science, Rochester, MN, United States***Background, Motivation, and Objective**

Ultrasound-guided minimally invasive procedures are becoming more common in clinical practice. However, ultrasound guidance has its own challenges due to the same echogenicity of catheter and anatomy. Furthermore, distinguishing needle from catheter enables the precise guidance of needle to its desired location for applications like drug delivery. Previously an acoustically active catheter (AAC) navigation system had been developed which can detect and display the AAC in a unique color along with B-mode and color Doppler using the Symmetric frequency detection (SFD) algorithm.

Statement of Contribution/Methods

The SFD algorithm is extended to track two different objects (catheter and needle tip) and display them with unique colors. The AAC has a 9-Fr steerable sheath and a needle tube with a 20-gauge needle. The piezoelectric crystal placed on the tip of the catheter sheath (needle) is excited with 30 (20) volts continuous wave signal at 2 (3) kHz. The AAC was inserted from the right carotid artery through the ascending aorta and into the left ventricle. The chest cavity was opened and the pig heart was imaged using a linear array (L4-7). Attenuation pads were used to emulate the closed chest cavity. 32 ensembles of In-phase/ quadrature (IQ) data using zero angle plane wave transmission were collected. The spatiotemporal IQ signals representing the crystals show symmetric Doppler shifts in Fourier domain. Points having symmetric Doppler shifts at ± 2 and ± 3 kHz and meeting a required signal to noise ratio (SNR) threshold with respect to the neighboring noise floor are identified to represent the catheter and needle tip.

Results/Discussion

The symmetric Doppler pattern generated due to the interaction of the two vibrating piezoelectric crystal with the imaging ultrasound beam does not interfere with each other thus enabling the unique identification of both the crystals. Figure 1 shows the catheter inside the left ventricle with the catheter and needle tip displayed in green and yellow respectively. The display frame rate varies between 8 to 10 Hz with the ability to detect the crystals in full field of view. The 12 dB/cm-MHz attenuation pad decreases the SNR of the spot marker by 3 dB only. The results demonstrate the validation of the extended SFD algorithm in a swine model.

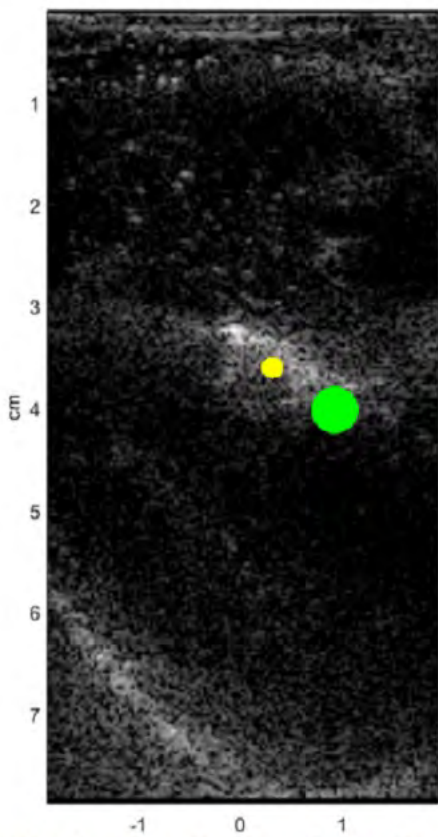


Fig. 1. Acoustically active catheter inside the beating left ventricle of a pig. The yellow and green markers show the location of the needle and catheter tip respectively.

3C - Nanodroplets Enhanced Imaging

Emerald (280)

Tuesday, October 23, 4:00 pm - 5:30 pm

Chair **Mingxi Wan**
Xi'an Jiaotong University

3C-1

4:00 PM Acoustic Wave Sparsely-Activated Localization Microscopy (AWSALM): A Fast and Flow Independent Ultrasound Super-Resolution Technique using Nanodroplets

Ge Zhang¹, Sevan Harput¹, Kirsten Christensen-Jeffries², Chee Hau Leow¹, Jemma Brown², Jiaqi Zhu¹, Robert Eckersley², Chris Dunsby³, Mengxing Tang¹

¹Department of Bioengineering, Imperial College London, London, United Kingdom, ²Biomedical Engineering Department, School of Biomedical Engineering and Imaging Sciences, King's College London, London, United Kingdom, ³Department of Physics and Centre for Pathology, Imperial College London, London, United Kingdom

Background, Motivation, and Objective

Currently flowing microbubbles with a low concentration are required for localization-based ultrasound super-resolution imaging to visualize microvasculature beyond the diffraction limit (Christensen-Jeffries et al., 2015). While the optical activation of high-boiling-point nanodroplets can also be used for ultrasound super-resolution imaging, the requirement of laser activation limits the imaging depth (Luke et al., 2016). In this study, ‘acoustic wave sparsely-activated localization microscopy (AWSALM)’, an acoustic counterpart of ‘photo-activated localisation microscopy (PALM)’ which does not require the presence of flow, is developed to super-resolve structures using activated nanodroplets in deep tissues.

Statement of Contribution/Methods

A high concentration of decafluorobutane nanodroplets with size distribution as illustrated in Figure (c) below were injected in a 200 μm crossed-tube phantom. The inlet and outlet of the tube phantom were stopped with a clip to ensure there was no flow in the tube. A Verasonics 128 research platform equipped with a L11-4v probe was used for experiments. A customised ‘Activation-Imaging’ acquisition sequence script was implemented to transmit 8 MHz, 2-cycle focused pulses ($\text{MI} = 1.3$) to activate the nanodroplets and perform plane wave ($\text{MI} = 0.25$, frame rate = 100 Hz) imaging at 4 MHz. Singular value decomposition processing was used to obtain the signals of activated nanodroplets without background signal. The ‘centroiding’ method was used to determine the signal locations. The full-width-half-maximum measurement of the localization distribution was used to estimate the diameter of the 200 μm tube.

Results/Discussion

The super-resolution image in figure (a) demonstrates the significant improvement in visualisation of the two micro-tube structures without flow by using AWSALM in 5 seconds. Figure (b) shows three representative image frames of activated nanodroplets signals acquired after successive activations. It should be noted that the conventional flow-based microbubble super-resolution techniques fail to produce an image under no flow condition. AWSALM has the potential for in vivo imaging of structures beyond the blood vessels, including the lymphatic system where flow is very slow.

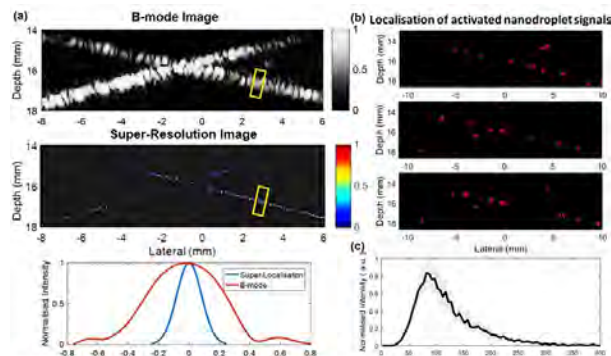


Figure (a) shows B-mode and super-resolution images of the 200-micron cellulose tube phantom and full-width-half-maximum measurement for the two images respectively. The panels in Figure (b) show the three representative images of activated nanodroplets signals after successive activations. Figure (c) shows nanodroplets are polydisperse with size ranging from 50 to 300 nm. Only a sparse subset of relatively large droplets randomly spatially distributed in the tube phantom are sensitive to the low activation pressure used ($\text{MI}=1.3$), which contributes to the sparse activation by the first activation pulse.

4:15 PM

Spontaneous Nucleation of Perfluorocarbon DropletsDavid Li^{1,2}, Sarah Schneewind¹, Matthew O'Donnell², Lilo Pozzo¹¹*Department of Chemical Engineering, University of Washington, Seattle, WA, United States*, ²*Department of Bioengineering, University of Washington, Seattle, WA, United States***Background, Motivation, and Objective**

Perfluorocarbon (PFC) nanodroplet-based phase-change agents have been proposed as an alternative to conventional microbubbles for contrast enhanced ultrasound imaging and therapy. Unlike microbubbles, phase-change agents are initially delivered as liquid nanodroplets. At the region of interest, a high amplitude acoustic pulse is used to vaporize the injected droplets to form larger gas bubbles. In the liquid phase, the droplets are typically five times diametrically smaller than the resulting bubble. The nanodroplets can be synthesized under 200 nm, allowing them to freely diffuse past the vessel wall for extravascular applications. Synthesis of perfluorocarbon droplets typically rely on methods of high-speed shaking, sonication, or homogenization of a liquid PFC in water. However, these methods do not translate well for low boiling point PFCs ($T_{boiling} < 20^{\circ}\text{C}$). For low boiling point PFCs a reverse condensation approach, where microbubbles are first synthesized followed by chilling and/or pressurizing the bubbles to condense the bubbles into its liquid phase, has been the only commonly used method.

Statement of Contribution/Methods

In this study, a new method of spontaneously nucleating PFC nanodroplets, referred to as the ouzo method, is presented. It can be used to synthesize nanodroplets using both liquid and gaseous PFCs. Conditions for droplet nucleation in ouzo phase space ranging from perfluorohexane (C_6F_{14} , $T_{boiling} < 56^{\circ}\text{C}$) to perfluoropropane (C_3F_8 , $T_{boiling} < 29^{\circ}\text{C}$) were explored. Droplet diameters were measured using dynamic light scattering and acoustic cavitation thresholds for the droplets were measured using passive acoustic cavitation detection.

Results/Discussion

Using the ouzo method, PFC droplets were easily synthesized with diameters as small as 38 nm (figure 1A). In general, the acoustic activation threshold reduced with increasing PFC volatility (i.e. lower boiling point). The use of ouzo synthesized nanodroplets as a phase-change agent was demonstrated in a simple tube phantom using a programmable ultrasound scanner (Verasonics 128, Verasonics Inc., Bothell, WA, USA) (Figure 1B and 1C).

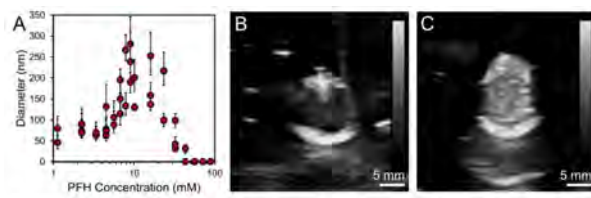


Figure 1: (A) The size distribution of droplets nucleated as a function of perfluorohexane (PFH) concentration. The droplets produced are typically less than 300 nm in diameter. An ultrasound tube phantom image (B) before the high amplitude activation pulse and (C) after activation. Before activation, only the boundaries of the tube are visible. After activation, image brightness within the tube increases due to successful vaporization of the nanodroplets.

4:30 PM

Manipulating the Dynamic Behavior of Laser-Activated Perfluorocarbon Nanodroplets Using Transmit Pulse Shape of Ultrafast Ultrasound Imaging

Yiying I. Zhu¹, Heechul Yoon¹, Andrew X. Zhao², Stanislav Emelianov^{1,2}

¹School of Electrical and Computer Engineering, Georgia Institute of Technology, Atlanta, GA, United States, ²Wallace H. Coulter Department of Biomedical Engineering, Georgia Institute of Technology and Emory University School of Medicine, Atlanta, GA, United States

Background, Motivation, and Objective

Under laser irradiation, perfluorocarbon nanodroplets (PFCnDs), a theranostic ultrasound (US) and photoacoustic (PA) agent, can repeatedly vaporize into gaseous bubbles and stochastically condense to liquid droplets, creating “blinking” ultrasound (US) signals. Their repeatable activation and random recondensation enable contrast-enhanced ultrasound (CEUS) and super-resolution imaging (SRI). However, the milliseconds long lifespan of the transient bubbles makes it difficult to capture the “blinking” signals even with ultrafast US imaging. Therefore, we explored the effect of the US imaging transmit pulse on the PFC bubble-to-droplet transition time to improve CEUS and SRI using laser-activated PFCnDs.

Statement of Contribution/Methods

The PFCnDs consisted of a perfluorohexane core (56°C boiling point), a stabilizing lipid shell (DSPE-PEG2k and DSPC), and a dye (1064 nm absorption peak) to enable optical triggering. The PFCnDs were distributed in a tissue-mimicking gel phantom. The phantom was irradiated with 5 ns laser pulses (10 Hz PRF, 1064 nm wavelength, 50 mJ/cm² fluence) and imaged using a 7 MHz US array transducer. A set of 50 images at 2 kHz (Vantage 256) per laser pulse was acquired. Two ultrafast US imaging transmit pulses were used, denoted as P-pulse (Fig. 1a: initial compressional phase) and N-pulse (Fig. 1b: initial rarefactional phase).

Results/Discussion

Under the same optical activation (Fig. 1c), the B-mode images of vaporized PFCnDs showed that US imaging with N-pulses led to a slower recondensation than with P-pulses (Fig. 1d). The quantitative results revealed that N-pulse imaging resulted in significantly higher signal-to-noise ratio (SNR) images of vaporized PFCnDs (Fig. 1e) and 4-6 times longer recondensation time of the PFC bubbles (Fig. 1f and Fig. 1g) compared to P-pulse imaging. This discovery that the phase of an imaging transmit pulse can affect PFCnD behavior has direct implications for SRI and molecular CEUS imaging where detection of individual or low-concentration PFCnDs is required. Indeed, extended detection time of vaporized PFCnDs in US imaging improves detection efficiency as well as contrast and spatial resolution by allowing for more averaging. Our results also suggest that encoded US imaging pulses can manipulate nanodroplet dynamics, which can be used for tumor microenvironment mapping.

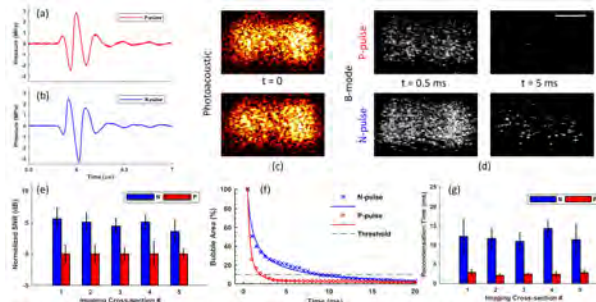


Figure 1. (a) P-pulse waveform: initial compressional phase. (b) N-pulse waveform: initial rarefactional phase. (d) PA images showing same PFCnD optical activation. (d) US B-mode images over time for P-pulse vs. N-pulse imaging showing vaporized PFCnD persistence [Bar = 50 mm]. (e) Normalized SNR of US images for 5 different imaging cross-sections for P-pulse vs. N-pulse, error bars represent standard deviation (N=10). (f) Normalized area of vaporized PFCnDs over time described using $s(t) = \alpha t^{-\beta} + r$ fit for P-pulse vs. N-pulse with recondensation threshold being 10% of the original detected bubble area. (g) Recondensation time based on recondensation threshold, error bars represent standard deviation (N=10).

4:45 PM

Individual perfluorocarbon nanodrop vaporization with 18-MHz plane wavesJeffrey Ketterling¹, Tiffany-Trang Nguyen², Mario L. Fabiilli^{2,3}¹*Lizzi Center for Biomedical Engineering, Riverside Research, New York, NY, United States*, ²*Department of Biomedical Engineering, University of Michigan, Ann Arbor, MI, United States*, ³*Department of Radiology, University of Michigan, Ann Arbor, MI, United States***Background, Motivation, and Objective**

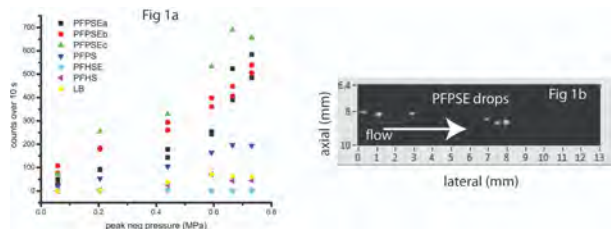
Perfluorocarbon (PF) nanodrops (NDs) undergo a phase change from liquid to vapor with an acoustic stimulation. The NDs then becomes echogenic which permits localization for imaging. Activation of NDs is accomplished with focused single-element transducers or with linear arrays with focused sub-apertures. Activation thresholds are established with relatively high-concentrations of NDs. Activating single NDs with high-frequency plane waves without the need to switch between transmit modes would allow uninterrupted high-speed imaging studies to be undertaken in microvasculature. We implement a flow phantom to detect the vaporization of NDs that pass through a plane-wave acoustic field.

Statement of Contribution/Methods

Lipid-coated perfluoropentane (PFP) or perfluorohexane (PFH) NDs were made via sonication (S) or sonication and extrusion (SE). A control sample consisted of lipid blend (LB) without PF. A Verasonics Vantage with an 18-MHz array was used to acquire backscatter data from activated NDs. A wall-less test tank with a 200 μm diameter input flow channel was used to pass a diluted (10^8 - 10^9 droplets/mL) concentration of NDs into the image plane of the array. The acoustic field was calibrated with a needle hydrophone. The injection flow rate was 55 mL/hr which resulted in peak flow velocity of approx 15 cm/s. Batches of 5 plane waves were transmitted at 22.2 kHz, over ± 5 degrees, every 5 ms for an effective PRF of 200 Hz. Data were collected over 10 s intervals. The plane-wave data were beamformed and then processed to count activation events. An event was defined as a backscatter signal that was 25 dB above the background noise.

Results/Discussion

The resulting z-average and polydispersity index for the ND formulations were as follows: PFPS (309 nm, 0.36), PFPSE (186 nm, 0.26), PFHS (309 nm, 0.49), and PFHSE (215 nm, 0.27). Fig 1a shows summary of counts over 10 s for each of the four ND formulations and LB. The PFPSE cases (3 runs) showed the highest counts at a given pressure. Agents appeared to be activated prior to entering the image plane (Fig 1b). The counts increased in linear fashion with pressure with a small jump above 0.6 MPa. The PFPS cases showed a reduced rate of activation but with a similar linear rise. The PFH and LB had minimal to no events. The data indicate some fraction of the injected agents were activated but do not indicate a distinct activation threshold was reached.



5:00 PM

HER2 Targeted Perfluorocarbon Nanodroplets for Super-Resolution Ultrasound Imaging**Austin Van Namen¹, Sidhartha Jandhyala¹, Christian NDong¹, Karl Griswold¹, Geoffrey Luke¹**¹Dartmouth College, Hanover, NH, United States**Background, Motivation, and Objective**

In the current standard of cancer imaging, there is a need for real-time, high-resolution molecular level information at subdermal depths to better identify tumor margin, metastases and intra-tumor heterogeneity. This study introduces a molecularly targeted contrast agent for ultrasound (US) and photoacoustic (PA) imaging that will provide cellular level spatial resolution imaging of cell surface markers. The developed perfluorocarbon (PFC) phase-change nanoparticle is part of an emerging class of US/PA contrast agents which, after exposure to an optical or acoustic trigger, can undergo a liquid-to-gas phase transition and generate strong US contrast. In addition, this phase transition generates a PA signature an order of magnitude stronger in amplitude than a conventional PA imaging agent.¹ In this work, we have used a high-boiling-point PFC which allows the nanodroplets to recondense back to their liquid nanodroplet state quickly post-vaporization. This repeatable vaporization is harnessed to achieve super-resolution and background-free ultrasound images.^{2,3}

Statement of Contribution/Methods

Despite the promise of these versatile agents there are not yet reliable methods to achieve molecular specific contrast with PFC nanodroplets.⁴ We have developed novel HER2-targeted PFC nanodroplets composed entirely of clinically approved materials. The nanodroplets are synthesized by encapsulating perfluorohexane and a hydrophobically modified indocyanine green (ICG) dye inside a lipid monolayer shell.⁶ We modified the surface of the particles with a layer of polyethylene glycol (PEG) to promote biocompatibility and stability. 4% of the PEG molecules contained a terminal maleimide functional group for molecular targeting conjugation. The particles were conjugated to Trastuzumab (the Fab region of the monoclonal antibody trastuzumab that targets HER2)⁵ via a maleimide-thiol bond. The molecular specificity was tested using two cell lines: 1) MCF-7 cells (HER2-negative), and 2) MCF-7 cells modified to overexpress HER2.

Results/Discussion

Optical microscopy shows strong labeling in the HER2 case and very little nonspecific labeling of the HER2-negative cells. UV-VIS results quantitatively confirm a statistically significant difference in targeted binding. Furthermore, preliminary *in vivo* studies show delivery of these particles to tumor sites. The nanodroplets preserve their ability to be optically triggered and generate strong PA/US contrast after molecular labeling. When combined with super-resolution US imaging³, these results demonstrate the ability to synthesize a nano-scale molecular-specific contrast agent that is the first bound particle mechanism for US/PA super-resolution imaging.

1. doi:10.1038/ncomms1627

2. doi:10.7150/thno.14961

3. doi:10.1021/acs.nanolett.6b00108

4. doi.org/10.1016/j.cbpa.2018.03.017

5. doi: 10.1021/nn403527r

6. doi:10.2147/ijn.s79367

5:15 PM

High-frequency molecular ultrasound imaging using targeted phase-change nanodropletsTrevor Mitcham¹, Dmitry Nevozhay¹, Stephen Lai², Konstantin Sokolov¹, Richard Bouchard¹¹*Imaging Physics, MD Anderson Cancer Center, Houston, TX, United States*, ²*Head and Neck Surgery, MD Anderson Cancer Center, Houston, TX, United States***Background, Motivation, and Objective**

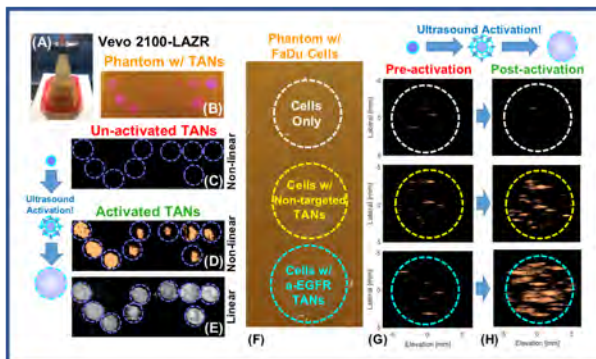
The goal of our research is to develop a targeted contrast agent to accurately identify micrometastases (mMets) in sentinel lymph nodes (SLNs) with high-resolution ultrasound (US) imaging. Our hypothesis is that targeted activatable nanodroplets (TANs) can specifically label cancer cells in SLN mMets and can be imaged in real-time with high contrast using high-frequency US, yielding immediate diagnostic information to facilitate timely and less-invasive treatment and/or to intraoperatively guide interventions. Our approach promises to deliver a uniquely versatile contrast agent with a size profile that is remotely changed from nano-scale (e.g., nanodroplet), which is required for molecularly targeted delivery, to micro-scale (i.e., microbubble) for high-frequency US imaging.

Statement of Contribution/Methods

To activate the TANs, Tx power, gate, and beamwidth were modulated in the Vevo 2100 (A) system's nonlinear mode (12.5-MHz Tx freq). Once a TAN-activation protocol was optimized, enhancement (i.e., comparing matched pre- to post-activation data) of nonlinear contrast from regions of interest containing TANs were assessed in tissue-mimicking phantoms (B,F) with inclusions of bare PFC-based TANs (C), untagged EGFR(+) FaDu cancer cells (white F), and FaDu cells incubated with either non-targeted (yellow F) or EGFR-targeted (cyan F) PFC-based TANs. 3D B-mode (E) and nonlinear (D) US scans were acquired before (G) and after (H) activation pulses.

Results/Discussion

US-transmit parameter settings were optimized to consistently activate PFC-based TANs on the Vevo system. Using these parameters, EGFR-targeted TANs experienced a 23 ± 3 dB contrast enhancement compared to just a 9 ± 3 dB enhancement for non-targeted samples, while untagged cells remained anechoic. In addition to improved spatial resolution, which could be critical for superficial clinical targets, high-frequency ultrasound affords nonlinear imaging with a transmit frequency closer to resonance for 1-micrometer bubbles (i.e., the nominal post-activation diameter). This work demonstrates this platform's potential to address all disadvantages of the current standard of care by providing a single, cancer-specific, non-radioactive contrast agent that can be noninvasively and clearly visualized using clinical US (i.e., the new Vevo MD clinical system) prior to or during surgery.



4A - Use of Microbubbles and Cavitation in Ultrasound Therapy

Sapphire (220)

Tuesday, October 23, 10:30 am - 12:00 pm

Chair **Elisa Konofagou**
Columbia University

4A-1

10:30 AM Correlation between passive cavitation imaging and positron emission tomography imaging of the radiolabeled-nanocluster delivery location and efficiency by FUS-mediated blood-brain barrier disruption

Yaoheng Yang¹, Dezhuang Ye², Xiaohui Zhang³, Shanshan Xu⁴, Yongjian Liu³, Hong Chen¹

¹*Biomedical Engineering, Washington University in St Louis, Saint Louis, MO, United States*, ²*Mechanical Engineering and Material Science, Washington University in St Louis, Saint Louis, MO, United States*, ³*Radiology, Washington University in St Louis, Saint Louis, MO, United States*, ⁴*Department of Biomedical Engineering, Xi'an Jiaotong University, China, People's Republic of*

Background, Motivation, and Objective

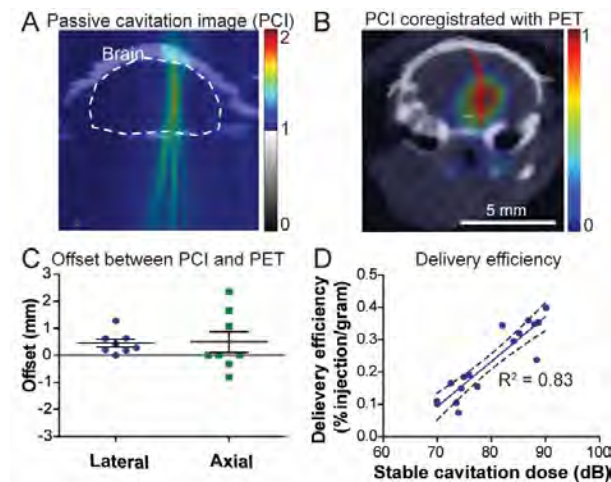
Cavitation monitoring is essential to the focused ultrasound in combination with microbubble-induced blood-brain barrier disruption (FUS-BBBD) because cavitation is the fundamental physical mechanism. Recently, passive cavitation imaging (PCI) has been introduced to monitor the spatial-temporal dynamics of FUS-activated microbubble (MB) cavitation activity. However, it is unknown whether PCI can predict the therapeutic agent delivery location and efficiency by FUS-BBBD. The objective of this study was to study the correlation between cavitation activity imaged by PCI and the radioactive nanocluster delivery localization and efficiency imaged by positron emission tomography (PET) post FUS-BBBD.

Statement of Contribution/Methods

This study used an ultrasound imaging-guided FUS system consisted of a single-element FUS transducer (1.5 MHz) and a co-axially aligned 128-element linear ultrasound imaging array (center frequency 12 MHz). Mice ($n=8$) were sonicated after MB injection, meanwhile acoustic emissions from MBs was acquired by the imaging probe and processed offline for PCI using the frequency-domain delay, sum, and integration algorithm. After the FUS treatment, ^{64}Cu -integrated gold nanocluster (^{64}Cu -AuNCs), used as the model drug, were injected intravenously, and their distribution in the brain was imaged using microPET/CT. The offset between the centroid of the PCI and the centroid of the radioactivity imaged by PET was calculated. The relationship between stable cavitation dose quantified using PCI and the ^{64}Cu -AuNCs delivery efficiency estimated using PET was also evaluated and verified by *ex vivo* quantification of radioactivity using gamma counting and gold concentration using inductively coupled plasma-mass spectrometry (ICP-MS).

Results/Discussion

PCI showed the spatiotemporal cavitation activity in the mouse brain *in vivo* (Fig. 1A, B). The offset between the centroids of stable cavitation (SC) maps and PET images were $0.45 \text{ mm} \pm 0.14 \text{ mm}$ and $0.49 \text{ mm} \pm 0.38 \text{ mm}$ in the lateral and axial directions, respectively (Fig. 1C). The SC dose was correlated with ^{64}Cu -AuNCs delivery efficiency quantified using *in vivo* PET imaging and verified by *ex vivo* measurements (Fig. 1D). These findings indicated that PCI may have the potential to predict ^{64}Cu -AuNCs delivery location and efficiency by FUS-mediated blood-brain barrier disruption.



10:45 AM

Artificial stone comminution and behavior of cavitation bubbles with annular focused ultrasoundShin Yoshizawa¹, Toshiya Yura¹, Kanta Sato², Daisaku Mashiko², Yoshifumi Saijo², Shin-ichiro Umemura²¹*Graduate School of Engineering, Tohoku University, Sendai, Japan*, ²*Graduate School of Biomedical Engineering, Tohoku University, Sendai, Japan***Background, Motivation, and Objective**

A renal stone can be eroded by the collapses of cavitation bubbles induced by a high-intensity focused ultrasound (HIFU) pulse, such as a histotripsy pulse. In our previous study, it was shown that peak-negative-enhanced waves by second harmonic superimposition improved a stone erosion rate at a high pulse repetition frequency (PRF). HIFU in the focal region has a peak-positive-enhanced pressure owing to the focusing after the nonlinear propagation. It causes the excessive cavitation cloud generation through the shock scattering mechanism. Therefore, the erosion rate improvement was probably because the shielding phenomenon of bubble clouds could be suppressed by reducing the peak positive pressure. The objective of this study is the further improvement of the stone erosion rate using a sector vortex annular focusing. In the focusing, the peak positive pressure at the focus should be smaller than a single spot-focusing because the lateral size of the focus is larger and the focal phase shift is smaller.

Statement of Contribution/Methods

A 128-channel array transducer at 1 MHz was placed in a water tank. The water was deionized and degassed (DO: 15–25%). The transducer had a focal length of 120 mm and a diameter of 147.8 mm. Model stones were prepared from commercially available cement powder. The stones were deaerated in a vacuum oven before the experiments. The three sequences were tested; a single spot-focusing (SF) at a peak negative pressure of -24 MPa and a pulse length of 3 μ s, a sector vortex annular focusing (SV) at -5 MPa and 3 μ s, and a switching sequence between SV and SF (SV+SF) with a switching delay of 45 μ s. The total acoustic power of the SF and SV sequences were the same. In the sector vortex focusing, a vortex mode number of 5 was applied. The radius of annular focus formed was approximately 3 mm.

Results/Discussion

Figure 1 shows cavitation bubbles induced by SV on a sapphire glass in the focal plane and stone erosion rates at a PRF of 0.1 – 1 kHz. For the result of the cavitation image, a different transducer with a diameter of 120 mm and a different peak negative pressure of -4 MPa were used. The SV sequence showed a higher erosion rate than the SF sequence at high PRFs. Furthermore, highly efficient fragmentation was achieved by the SV+SF sequence. It was hypothesized from a highspeed camera observation during HIFU exposure that the SF flushed out the residual fragments formed by the SV.

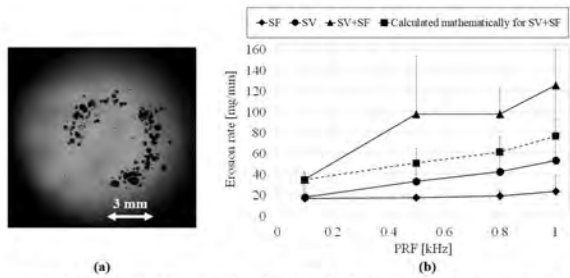


Figure 1 Cavitation by SV on a sapphire glass in the focal plane (a) and stone erosion rates (b).

11:00 AM Differentiation of tissue, cavitation bubbles and blood flow imaging in cavitation-enhanced high-intensity focused ultrasound treatment

Hayato Ikeda¹, Shin Yoshizawa², Maxime Lafond³, Ryosuke Iwasaki¹, Moe Maeda¹, Ryo Nagaoka⁴, Shin-ichiro Umemura¹, Yoshifumi Sajio¹

¹*Graduate School of Biomedical Engineering, Tohoku University, Sendai, Japan*, ²*Graduate School of Engineering, Tohoku University, Sendai, Japan*, ³*Department of Internal Medicine, Cincinnati University, Cincinnati, OH, United States*, ⁴*Graduate School of Science and Engineering, University of Toyama, Toyama, Japan*

Background, Motivation, and Objective

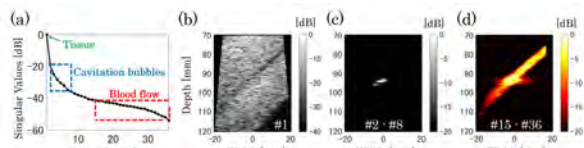
Occlusion of feeding artery is an efficient way to treat a large volume of tissue through coagulating a small volume by high-intensity focused ultrasound (HIFU). Cavitation bubbles can accelerate the thermal coagulation by HIFU, but conventional methods based on Doppler analysis are not suitable for monitoring blood flow in the presence of cavitation bubbles. In this study, we proposed a novel filtering method to separate tissue, cavitation bubbles, and blood flow, based on the differences in spatiotemporal characteristics and signal amplitudes, by employing singular value decomposition (SVD). The three components were automatically separated using the spatial and temporal covariance matrices of SVD. This study aims such automatic separation for real time imaging.

Statement of Contribution/Methods

A tissue and blood flow mimicking phantom containing cellulose as ultrasonic scatterers was chosen as the sample to test the proposed method. The flow was at 20 cm/s. HIFU exposure at 10 kW/cm² for 100 µs was carried out twice with an intermission of 20 ms for generating cavitation bubbles. Between the intermission and after the second exposure, ultrasonic images of 18 frames were acquired via ultrafast ultrasonic imaging at a frame rate of 1.0 kHz, respectively. The tissue, cavitation bubbles and blood flow components were separated automatically by applying an SVD filter to the 36 frames, and then used to reconstruct power integral images.

Results/Discussion

The singular values with respect to signal amplitudes: the tissue component (the singular value #1), cavitation bubbles component (the singular values #2-8), and blood flow component (the singular values #15-#36), are plotted in Fig. (a). The singular values corresponding to the blood flow were smaller than those of tissue and cavitation bubbles by up to 40 dB. Figs. (b)-(d) show a 2D image of the integrated power of each component separated automatically by the SVD filter. The proposed method using an SVD filter based on the differences in spatiotemporal characteristics and signal amplitude was able to separate tissue, cavitation bubbles and blood flow components.



Figures (a): Singular values corresponding to the signal amplitude.
 (b): Tissue power integral image (the singular value #1).
 (c): Cavitation bubbles power integral image (the singular value #2-8).
 (d): Blood flow power integral image (the singular value #15-#36).

11:15 AM

Enhancement of Radiation Response Using Ultrasound-Stimulated Microbubbles: ASMase Dependence**Gregory Czarnota^{1,2,3}, Ahmed El Kaffas⁴, Anoja Giles¹**

¹Radiation Oncology, Sunnybrook Health Sciences Centre, Toronto, ON, Canada, ²Physical Sciences, Sunnybrook Research Institute, Canada, ³Radiation Oncology, and Medical Biophysics, Faculty of Medicine, University of Toronto, Canada, ⁴Stanford University, United States

Background, Motivation, and Objective

It is now appreciated that radiation not only damages the DNA inside tumour cells *in vivo* but may act by damaging the endothelial cells of the vasculature. In this study we tested the hypothesis that microbubble agents *in vivo* may be used *a priori* to cause endothelial cell perturbations thus causing "radiosensitization" of tumours and the dependence of this on the ASMase pathway.

Statement of Contribution/Methods

Fibrosarcoma xenograft-bearing mice ($n=500+$) were exposed to combinations of ultrasound, activated-microbubbles, and radiation (8 animals per group). Animals were exposed to 500 kHz center frequency 570kPa peak negative pressure for treatment. For treatments, Definity bubbles (Bristol Myers-Squibb) were administered. For radiation 160 kVp X-rays were used at doses of 2 and 8 Gy. Representative tumour sections were examined using immunohistochemistry. Clonogenic assays and growth delay studies were also carried out. Experiments were carried out in *asmase* $+/+$ and $-/-$ mice to investigate endothelial cell apoptosis effects. As a control the *asmase* pathway was inhibited as well in *asmase* $+/+$ animals with sphingosine-1-phosphate (S1P) treatment.

Results/Discussion

Analyses in *asmase* $+/+$ mice indicated a synergistic increase in tumour cell kill due to vascular disruption that was *asmase* dependent caused by the combined therapies that increased when microbubbles were used in conjunction with radiation with increases of cell kill from 5% to over 50% with combined single treatments. Immunohistochemistry indicated endothelial cell apoptosis and activation of the ceramide cell-death pathway to be caused by microbubbles. Experiments conducted with *asmase* $-/-$ mice indicated no such effect. Specifically, results confirmed an interaction between treatments with ultrasound-stimulated microbubbles and ionizing radiation at 24 hours ($P < .001$), with a decrease in tumor perfusion of up to 46.5% by three hours following combined treatments. This peaked at 24 hours, persisting for up to 72 hours, and was accompanied by extensive tumor cell death. In contrast, statistically nonsignificant and minimal tumor responses were noted in S1P-treated and *asmase* knockout mice for all treatments.

Radiation effects were synergistically enhanced by using microbubbles to perturb tumour vasculature prior to the administration of radiotherapy. Analyses indicated activation of ceramide-mediated apoptotic cell death in endothelial cells leading to vascular disruption in tumours. Results indicate the acid-sphingomyelinase ceramide pathway as critical to the therapeutic effect of microbubbles.

11:30 AM Ultrasound-mediated microbubble destruction suppressed mouse glioblastoma growth as effectively as radiation therapy

Lifei Zhu¹, Michael Altman², Yimei Yue¹, Arash Nazeri³, Hong Chen^{1,2}

¹Department of Biomedical Engineering, Washington University in St Louis, Saint Louis, MO, United States,

²Department of Radiation Oncology, Washington University in Saint Louis, Saint Louis, MO, United States,

³Mallinckrodt Institute of Radiology, Washington University in St. Louis, Saint Louis, MO, United States

Background, Motivation, and Objective

Glioblastoma multiform (GBM) is the most common primary brain tumor with a median survival of about one year after diagnosis. Current standard-of-care therapy for GBM consists of initial surgical resection, followed by radiation therapy (RT) or chemotherapy. Previous studies have shown that ultrasound-mediated microbubble (MB) destruction (UMMD) by itself can induce vascular damage, shut down blood flow, and inhibit the growth of tumor outside the brain. The objectives of this study were: (1) evaluate the efficacy of UMMD in suppressing GBM growth; (2) compare the UMMD treatment efficacy with that of RT.

Statement of Contribution/Methods

An orthotopic mouse model of GBM was established by stereotactic implantation of mouse glioma cells (GL261) into mouse brains. Tumor volumes in all mice were measured using contrast-enhanced MRI. When the tumors reached 2 mm in diameter, mice were divided into 3 groups: (1) UMMD, (2) RT, and (3) control (no treatment). For group 1, sonication was performed using an MR-guided HIFU system (Sonalleve, Profound Medical) customized for small animal treatment. MBs were bolus injected into the mouse tail vein, followed by FUS sonication (1.44 MHz central frequency, 2 min duration, 5 Hz pulse repetition frequency, 1.5 MPa peak negative pressure, 3.33% duty cycle). UMMD was performed twice per week for 3 weeks. Mice in group 2 were irradiated with a dose of 2 Gy / day, 5 days per week for 3 weeks. Mice were sacrificed when they reached the endpoints of this study: tumor diameter > 8 mm or body weight drop > 20%. Mann-Whitney test was used for statistical analysis. H&E and TUNEL staining were used to access vascular disruption and tumor cell apoptosis, respectively.

Results/Discussion

Both UMMD and RT caused significant growth inhibition (Fig. A) compared to the control group ($p<0.05$ for both groups at 14 and 19 days after implanting tumor), without a significant difference between the UMMD and RT groups. Erythrocyte extravasation was detected in the tumors of mice in the UMMD group. TUNEL staining (Figs. B, C, D) found the number of apoptotic tumor cells in treated groups were substantially higher than the control group. This study demonstrated that UMMD suppressed tumor growth of the GBM-bearing mice, potentially by vascular disruption and/or tumor apoptosis, and the tumor growth inhibition effect was not significantly different from that achieved with RT.

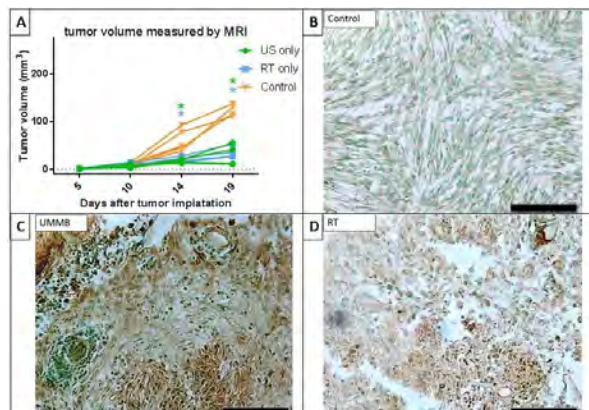


Figure (A) Tumor volume measured by contrast enhanced MR images. * indicates $p<0.05$ when comparing the treated group with the control group. (B, C, D) Representative TUNEL staining of brain tumor in UMMB, RT, and control group, respectively. The scale bar represents 100 μ m.

11:45 AM

Tumor Vascular Normalization by Oxygen-Microbubbles with UltrasoundShu-Wei Chu¹, Yi-Ju Ho¹, Chih-Kuang Yeh¹¹*Department of Biomedical Engineering and Environmental Sciences, National Tsing Hua University, Taiwan***Background, Motivation, and Objective**

Tumor vascular normalization (VN) improves blood perfusion and oxygenation by improving vessel maturity under the inhibition of angiogenesis. Anti-angiogenic agents (e.g. Avastin) reduce the secretion of vascular endothelial growth factor (VEGF) to improve the efficiency of drug delivery within a transient “time window” of VN (typically 3–7 days). Ultrasound-stimulated oxygen-microbubbles (O₂-MBs) can locally release O₂ to address tumor hypoxia. The degradation of hypoxia-inducible factor-1 α (HIF-1 α) under the normoxic condition by O₂ sensor prolyl-hydroxylase 2 (PHD2) would restrict VEGF secretion, which provides a potentiality to accomplish VN by regulating the upstream pathway of VEGF. Therefore, our study investigated the feasibility of VN induced by O₂-MBs with ultrasound.

Statement of Contribution/Methods

The mean diameter and O₂ concentration of O₂-MBs (C₃F₈: O₂=7:5 in volume ratio) was 1.02±0.03 μ m and 8.90±0.02 mg/L, respectively. After TRAMP cell implanting 7 days, mice (N=15) were separated to the control, C₃F₈-MBs, O₂-MBs 0.5 \times , O₂-MBs 1 \times and O₂-MBs 2 \times groups (concentration issue). Tumor-bearing mice were intravenously injected O₂-MBs (2x10⁷ MBs/mouse for 1 \times dosage) to locally release O₂ within tumors by ultrasound sonication (2-MHz, 2 MPa, 1000 cycles, PRF of 2 Hz, 20 min for whole tumor scanning). Because tumor perfusion is an important index to VN outcome, tumor perfusion was estimated over time (12 days). To unravel the probable pathway of VN process, the expressions of PHD2, HIF-1 α , and VEGF with tumors were evaluated by Western blot at day 4 after O₂-MBs delivery with US. Finally, the histological images were introduced to evaluate the vessel maturity of tumors by calculating the ratio of vessel density (CD31) and pericyte coverage (α -SMA).

Results/Discussion

Tumor perfusion was increased at 4–8 days (time window) in the O₂-MBs 1 \times (2.3±0.7-fold) and O₂-MBs 2 \times (2.1±0.3-fold) groups with respect to the control group. The perfusion ratio relative to day 0 was 0.77±0.25, 0.54±0.26, 0.95±0.30, 1.49±0.17, and 1.43±0.15 at day 4 in the control, C₃F₈-MBs, O₂-MBs 0.5 \times , O₂-MBs 1 \times , and O₂-MBs 2 \times groups, respectively. Comparison with the control group, the reduction of 60±16%, 55±21%, and 47±8% in PHD2, HIF-1 α , and VEGF expression certified the pathway of VN induced by O₂-MBs. Moreover, vessel maturity in the O₂-MBs group was 2.4±0.5-fold higher than the control group to show the increasing of pericyte coverage ($p<0.05$). Our study demonstrated that local releasing of O₂ in tumors can restrict VEGF expression to improve tumor perfusion, which provided a similar mechanism with anti-angiogenesis agents for inducing VN. Because the *in vivo* dosage of O₂-MBs was associated with the perfusion improvement, the possibility of regulating the time window of VN by O₂-MBs with ultrasound would be investigated in future.

4B - Contrast Imaging Applications

Sapphire (220)

Tuesday, October 23, 1:30 pm - 3:00 pm

Chair **Jeffrey Ketterling**
Riverside Research

4B-1

1:30 PM

Contrast enhanced ultrasound imaging of chronic rat spinal cord injury

Matthew Bruce¹, Ryan Hammond¹, Bryan Cunitz¹, Zin Z Khaing¹, Charles Tremblay-Darveau², Peter N. Burns³, Christoph Hofstetter¹

¹University of Washington, Seattle, WA, United States, ²Philips Medical Systems, United States, ³Medical Biophysics, University of Toronto, Toronto, ON, Canada

Background, Motivation, and Objective

Traumatic spinal cord injury (tSCI) often leads to debilitating neurological disabilities that in addition to loss of sensory and motor capabilities, also include frequent infections in the bladder and kidneys and other issues. A near complete loss of blood flow at the site of injury as well as ischemia surrounding the injury can result in progressive additional cell death. Counteracting secondary injury of spinal cord tissue surrounding tSCI, referred to as "rescueable" tissue, is an active area of research to improve patient prognosis. There are no existing techniques to assess simultaneously both temporal and spatial changes in blood flow of contused spinal cord tissue in experimental settings. The goal of this work was to visualize temporal and spatial changes of blood flow following tSCI in a chronic rat spinal cord injury model.

Statement of Contribution/Methods

We have developed a pre-clinical tool enabling visualization of blood flow in both the micro- and macro-circulations of a rat spinal cord injury model utilizing ultrasound contrast agents. Using an ultrasound research platform (Verasonics Vantage, USA) combined with a 15Mhz linear array transducer (Vermon, France), plane-wave nonlinear Doppler acquisition sequences were implemented enabling visualization of changes in blood flow in a rat's spinal cord. Nine rats were imaged at mid-line immediately before, 15 minutes, and 8 weeks after a contusion type injury at two different severities (Infinite Horizon at T7/T8; 150 or 200 kDyne). Acquisition sequences were also developed to assess bolus kinetics.

Results/Discussion

We report for the first time, the development and progression of blood flow changes immediately following injury out to 8 weeks after injury. The changes in perfusion and higher velocity flow signals at the site of injury (1b and 1e), corresponded to areas of spinal cord tissue and vascular remodeling at 8 weeks (1c and 1f). Acutely, moderate contusions(150 kDyne) resulted in smaller areas of perfusion deficits($1.79 \pm 0.14 \text{ mm}^2$) compared to animals with a severe contusions(200 kDyne) ($2.88 \pm 0.38 \text{ mm}^2$)($p < 0.03$). At 8 weeks post injury, larger and more numerous cystic like regions appeared for the severe contusions. Additionally, Figure 1 illustrates the development of tortuous vessels immediately following injury (1e) which grew extending over several vertebral segments after 8 weeks (1f).

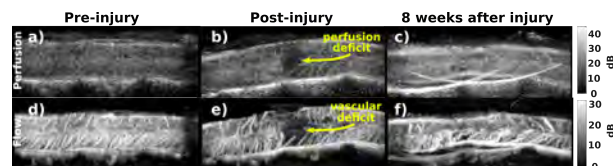


Figure 1. Perfusion(1a-1c) and vascular flow(1d-1f) changes from spinal cord injury in a rat following a bolus of Definity contrast agent before, after and 8 weeks after injury. The higher velocity flow(1d-1f) is segmented from perfusion signals by singular value decomposition wall filtering.

1:45 PM

Quantification of lipid microbubble shell pharmacokinetics enabled by copper-porphyrin-lipid labelingManeesha Rajora^{1,2}, Carly Pellow^{1,3}, Lili Ding¹, Juan Chen¹, David Goertz^{3,4}, Gang Zheng^{1,2,3}¹*Princess Margaret Cancer Centre, University Health Network, Toronto, ON, Canada*, ²*Institute of Biomaterials and Biomedical Engineering, University of Toronto, Toronto, ON, Canada*, ³*Department of Medical Biophysics, University of Toronto, Toronto, ON, Canada*, ⁴*Sunnybrook Research Institute, Toronto, ON, Canada***Background, Motivation, and Objective**

Despite the pervasive use of lipid microbubbles (MBs) as ultrasound contrast and drug delivery agents, quantitative pharmacokinetic (PK) characterization of their lipid shell components remains limited. Previous studies quantifying MB shell fate in vivo relied on radioisotope labeling strategies that could disrupt MB structure, required purification and/or used short half-life radioisotopes. Ultimately, this has prevented the reliable quantification of MB lipid PK beyond a 2 hr timeframe post injection. Here, we present a one-pot purification-free labeling strategy that allows us to formulate Definity®-mimicking porphyrin-lipid microbubbles (pMBs) that can be chelated to ⁶⁴Cu for sensitive and complimentary fluorescence imaging, PET and quantitative γ -counting of MB shell fate in vivo.

Statement of Contribution/Methods

PMBs were fabricated via a one-pot synthesis (Fig A). PMB size/concentration and porphyrin yield were obtained by Coulter counting and UV-Vis spectrometry respectively. Copper chelation efficiency was quantified by ICP-MS and γ -counting. Blood clearance of the porphyrin-lipid shell was monitored via fluorometry of healthy BALB/c mice plasma following pMB i.v. injection. PMB shell biodistribution was evaluated for 48 hr in healthy BALB/c mice and subcutaneous KB-bearing nude mice via Xenogen fluorescence imaging, PET and γ -counting +/- tumor sonication (SoniGene 1 MHz, 2 W/cm², 50% duty cycle).

Results/Discussion

PMBs were generated as $2.2 \pm 0.9 \mu\text{m}$ particles at a concentration of $1.8 \times 10^9 \text{ MB/mL}$ with uniform loading of porphyrin-lipid throughout the shell (Fig B). The one-pot chelation conserved pMB structure, size and stability (Fig C) while yielding a $96 \pm 1\%$ chelation efficiency that remained stable following SoniGene sonication. This robustness allows for the multimodal imaging properties of porphyrin-lipid to be applied viably for MB shell PK evaluation in vivo (Fig D): the porphyrin-lipid shell had a 4 hr circulation half-life and accumulated predominantly in the spleen and liver for at least 48 hr. This longitudinal quantification, and the versatility of these results (translating to C16/C18 lipid chain MBs with varying porphyrin compositions) demonstrate that lipid MBs have an in vivo residence time well beyond the 2 hr reported in literature, which could have off-target biological implications for drug-conjugated MBs.

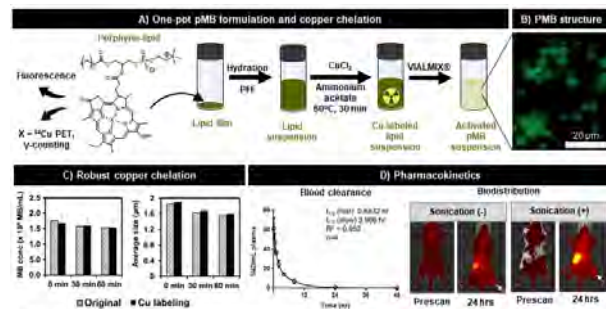


Figure: (A) Schematic of the self-assembly process, and copper chelation reaction leading to the generation of pMBs. (B) Fluorescence microscope image of a pMB suspension (100x magnification, 705 nm ex/725 nm em). (C) pMB concentration and size measured via Coulter counting after activation with and without copper chelation (values presented as mean \pm standard deviation of 3 samples). (D) Porphyrin-lipid blood clearance established in healthy BALB/c mice (administered 6 mL/kg pMBs through the tail vein) using a two-compartment model, and in vivo fluorescence imaging of porphyrin-lipid (Xenogen IVIS, 675 nm ex/720 nm em) shell fate in hind limb subcutaneous KB tumor-bearing nude mice administered pMBs (6 mL/kg) through the tail vein with or without the application of 1 MHz ultrasound sonication (2 W/cm², 50% duty cycle, 60 s) at the tumor site (arrow).

2:00 PM

Contrast-Enhanced Micro-Vasculature Imaging: A New Statistical ApproachBilly Y. S. Yiu¹, Raksha Urs², Harriet Lloyd², Jeffrey Ketterling³, Ronald Silverman², Alfred C. H. Yu¹¹Schlegel-UW Research Institute for Aging, University of Waterloo, Waterloo, ON, Canada, ²Columbia UniversityMedical Center, New York, NY, United States, ³Lizzi Center for Biomedical Engineering, Riverside Research, New York, NY, United States**Background, Motivation, and Objective**

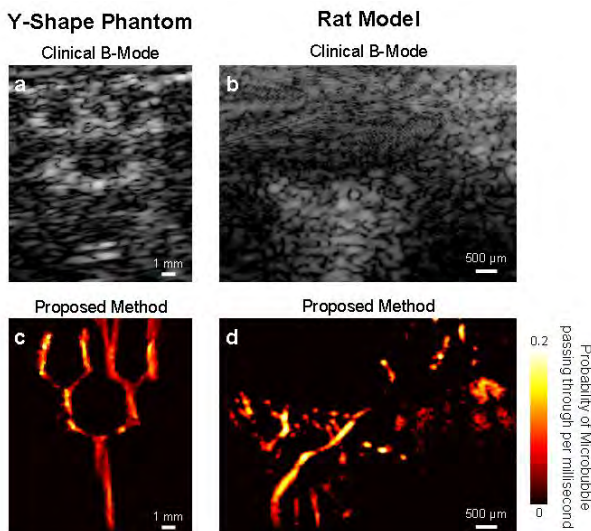
Pathological neovascularization that generates abnormal microvessels plays an important role in various diseases such as proliferative retinopathies and malignant tumors. However, it is difficult for current imaging modalities to detect and visualize these microvessels non-invasively due to limited spatial resolution. Here, we have developed a new plane-wave contrast imaging technique that leverages a statistical approach to identify microvessels.

Statement of Contribution/Methods

Microvessels were mapped by analyzing the probability of microbubbles (MB) passing through a pixel. The framework begins by acquiring full-view images using unsteered plane wave transmission. After that, clutter filtering was performed on each image frame to suppress stationary tissue echoes while retaining the echo signatures from moving MBs. The filtered image set was then matched against an MB template pattern using normalized cross correlation to generate correlation values. Next, we estimated the probability of an MB present in a pixel by analyzing the correlation values of that pixel over a fixed period using histogram (note: a pixel with high MB presence probability has a histogram shape skewed towards the right side, and vice versa for those with low MB presence rate). Finally, microvessels were visualized by displaying the MB presence probability across the entire image. To evaluate the image resolution of our framework, we conducted experiments on a Y-shaped flow phantom with one inlet (ID: 1 mm) and four outlets (ID: 500 μ m) using a SonixTouch scanner with unsteered plane wave firings (L14-5; 3-cycle 5 MHz burst; 2 kHz PRF). In-vivo data was also acquired from rat eye using slightly different settings (L26-13; 3-cycle 16 MHz burst; 6 kHz PRF).

Results/Discussion

For the Y-shaped flow phantom, Fig a & c respectively show the B-mode image and the MB presence probability map. It can be seen that the microvessels were not clearly visible on B-mode, but the MB presence probability map clearly highlighted the Y-shaped vessel topology. The lumen width at the outlets was measured to be $575 \pm 96 \mu\text{m}$ (FWHM). This observation was further confirmed in the in vivo rat eye experiment. Microvessels that were not visible in the B-mode (Fig. b) can be clearly highlighted using our proposed method (Fig. d).



2:15 PM Precise collection of microbubbles by acoustic vortex under flow conditions

Wei Chen Lo¹, Chih-Kuang Yeh¹¹*Department of Biomedical Engineering and Environmental Sciences, National Tsing Hua University, Taiwan***Background, Motivation, and Objective**

Microbubbles (MBs) can be pushed through blood circulation under radiation force guidance and facilitate the drug adhesion via cavitation. However, the retention and accumulation of MBs on the target site is typically unstable under flow conditions, particularly in the regions of endarterial region and thrombosis. In this study, we propose the acoustic vortex tweezers (AVT) precisely collecting MBs at specific locations under different flow conditions and ultrasound parameters. Owing to the features of long working distance (>10 mm) and single beam configuration, the AVT become feasible in vivo applications. Moreover, the AVT trapping drug-loaded MBs perform drugs accumulation at specific site within blood vessel and B-mode images can see the manipulating process of MBs.

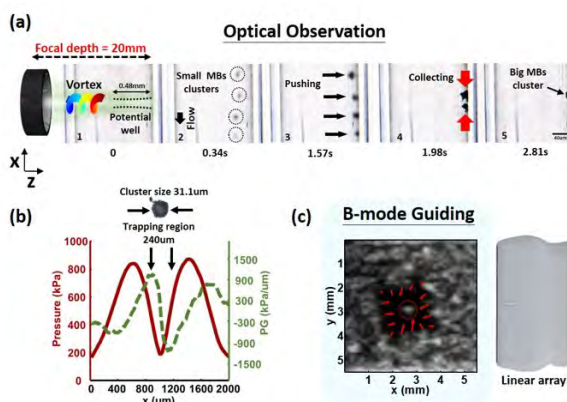
Statement of Contribution/Methods

The AVT trapping process was optically observed in a 200- μm capillaries mimic tube and acoustically monitored by a 7 MHz B-mode imaging in a tissue mimic phantom. Self-made MBs (sizes of 1.2 μm) were injected at a flow rate 2 ml/hr (i.e., 1.7 cm/s). The AVT was realized by a 4-element customized transducer (F# of 1) with 90-degree phase different in each adjacent element (frequency: 3.1 MHz, pressure: 800 kPa, duty cycle: 9.6%). The -6dB beam pattern of the transducer was 20 mm in depth and 1 mm in lateral direction and the depth of focus was 0.48 mm which can cover the whole tube (Fig. a(1)).

Results/Discussion

When the AVT was applied, primary radiation force (PRF) displaced MBs perpendicularly from the center streamline (Fig. a(2)) and then, the secondary radiation force pushed the MBs getting together to form a cluster of 12-14 μm . Afterwards, the AVT collected (Fig. a(4)) the MBs clusters toward the potential-well to generate a larger cluster of 31.1 μm (Fig. a(5)) and the MBs cluster stayed against the tube wall.

Figure (b) show the MBs trapping region (size of 240 μm) estimated by the maximum pressure gradient (PG). The retaining larger cluster can be detected by B-mode imaging (Fig. c). These results suggested that AVT are useful in precise retention of MBs under flow conditions and the surveillance ability can ensure process safety. Future work includes realizing the AVT system by using a 2-D array imaging system.



2:30 PM

Real-Time Closed-Loop Spatiotemporal Control of Cavitation Activity with Passive Acoustic MappingScott Schoen Jr.¹, Arpit Patel¹, Costas Arvanitis²¹*Mechanical Engineering, Georgia Institute of Technology, Atlanta, GA, United States*, ²*Mechanical Engineering and Biomedical Engineering, Georgia Institute of Technology and Emory University, Atlanta, GA, United States***Background, Motivation, and Objective**

Ultrasoundically actuated microbubble oscillations hold great promise for minimally invasive interventions in the brain. While several preclinical studies have demonstrated the therapeutic potential of this technology, real-time methods to control the amplitude and type of microbubble oscillations (stable vs inertial acoustic cavitation) and ensure that cavitation occurs within the targeted region are needed for their successful translation to the clinics. Here we developed, for the first time, a real-time controller based on passive acoustic mapping (PAM), which can localize and characterize cavitation activity and provide feedback to adjust the applied pressure to achieve a desired level thereof.

Statement of Contribution/Methods

The proposed controller is a real-time nonlinear state controller that uses specific frequency bands of the microbubble acoustic emissions (harmonic, ultra-harmonic, etc.) to control cavitation activity (observer states). To attain both spatial and temporal control of cavitation activity with high signal to noise ratio, we implement a controller using fast frequency-selective PAM based on the angular spectrum approach. The controller includes safety states based on the recorded broadband signal level and is able to reduce sensing inaccuracies with the inclusion of multiple frequency bands. In its simplest implementation the controller uses the peak intensity of the maps reconstructed with the 3rd harmonic (4.896 ± 0.019 MHz) of the excitation frequency. To assess the robustness of the controller we used a range of controller parameters, multiple observer states concurrently (harmonic, ultra-harmonic, and broadband), noise levels (-6 to 12 dB SNR), and bubble concentrations.

Results/Discussion

Our results show that the proposed real-time nonlinear state controller based on PAM is able to reach the targeted level of observer state (harmonic emissions) in less than 6 seconds and remain within 10 % of tolerance for the duration of the experiment (45 seconds). Similar response was observed using the acoustic emissions from single element passive cavitation detection as feedback, albeit with higher susceptibility to background noise and lack of spatial information. The performance of the controller using PAM was found to be robust to added noise up to SNRs of unity, and to bubble concentrations from 300 to 18 000 bubbles per microliter. Finally, the controller was not sensitive to the control law parameters providing additional evidence about its robustness.

In conclusion, the proposed real-time nonlinear controller based on PAM is able to perform, for the first time, spatial and temporal control of cavitation activity and provides the basis for safe and effective acoustic cavitation mediated interventions in the brain and elsewhere.

2:45 PM

Dual-Frequency-Chirp Passive Cavitation Imaging in Brain**Hsiang-Ching Lin¹, Chih-Kuang Yeh¹**¹*Department of Biomedical Engineering and Environmental Sciences, National Tsing Hua University, Taiwan***Background, Motivation, and Objective**

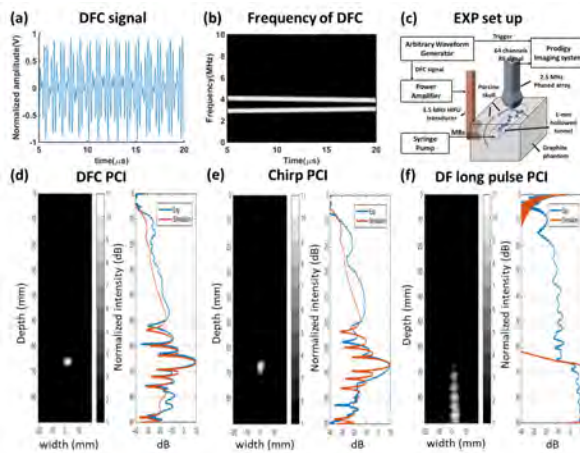
One of the major challenges that limits the cavitation-mediated application in brain such as blood-brain barrier (BBB) opening is difficult to locate the region of microbubbles (MBs) cavitation. Passive cavitation imaging (PCI) has gained attention due to its real-time monitoring by listening the acoustic cavitation activities. However, the long-length transmitting pulses degraded the axial resolution of PCI. In addition, the nonlinear components of cavitation resulted in the interference in chirp pulse compression technique. This study proposed a dual-frequency-chirp (DFC) technique for inducing MBs cavitation and the chirp signal had better penetration capability after trans-skull and better axial resolution by near perfect pulse compression.

Statement of Contribution/Methods

The DF insonation with MBs generated not only harmonics but also sum and difference of DF fundamental frequencies. The DFC consisted of a 3-MHz up-sweep and a 4-MHz down-sweep chirp (25 μ s) to make the difference of frequencies be 60% bandwidth 1-MHz down-sweep chirp (fig.1 (a)-(b)). Here, the difference of DFC was the key for PCI and designed away from MBs harmonics to avoid distortion after pulse compression. The experiments setup of DFC PCI is shown in Fig.1 (c) with transmitting *in situ* pressure 1.2 MPa. The 4-mm porcine skulls were placed in front of both transducers. Note that the chirp pulse of 1-MHz with 60% bandwidth and DF-long-pulse consisting of 3-MHz and 4-MHz tone burst generating 1-MHz difference pulse were included for comparisons.

Results/Discussion

Figs. 1(d)-(f) show PCI and its axial profile of DFC, chirp pulse and DF-long-pulse PCI, respectively. The axial resolutions (FWHM) of DFC and chirp pulse were 3.35 and 4.95 mm, respectively. The simulation result shows the ideal axial resolution being 3.15 mm. The case of DF-long-pulse is too long and out of image window. The DFC, chirp and DF-long-pulse provide the SNRs of 22.1, 21 and 15.2 dB, respectively. The proposed DFC method performed good pulse compression with chirp component because its difference component is away from harmonics of fundamental frequencies. Future work included concurrent BBB opening and PCI using DFC method with drug-carrying microbubbles for brain glioma theranostics.



4C - Microbubbles and Nanoparticles

Sapphire (220)

Tuesday, October 23, 4:00 pm - 5:30 pm

Chair **Nobuki Kudo**
Hokkaido University

4C-1

4:00 PM

Enhancing Checkpoint Inhibitor Therapy with Ultrasound Stimulated Microbubbles

Sharshi Bulner¹, Aaron Prodeus¹, Jean Gariépy¹, Kullervo Hyynen¹, David Goertz¹

¹*Sunnybrook Research Institute, Toronto, ON, Canada*

Background, Motivation, and Objective

Checkpoint inhibitor (CI) immunotherapy inhibits the ability of tumors to evade the immune system and boosts the activity of anti-tumor T-cells. However, CI immunotherapy has shown to be effective and durable only in a subset of patients with certain cancers (i.e. melanoma). There are widespread efforts at combining CIs with other therapies and in particular those that evoke an immune response that may be complementary to immunotherapy. Physical approaches such as ultrasound are appealing as they can be spatially targeted and do not suffer from dose limitation issues. While it is recognized that different forms of therapeutic ultrasound can elicit a spectrum of immune responses, it remains to be established if they can be employed to effectively potentiate the effects of CIs. In this study, we explore the combination of anti-PD-1 (aPD-1) therapy with ultrasound stimulated microbubbles (USMBs). More specifically, we use a level of ultrasound exposure that is non-thermal but elicits vascular injury within the tumor.

Statement of Contribution/Methods

Murine colon carcinoma (CT26.wt) was initiated subcutaneously in the hindlimb of female Balb/c mice. When tumors reached 50-100 mm³, animals were split into four groups: MBs, USMBs, aPD-1, USMBs + aPD-1. The drug aPD-1 was administered intraperitoneally at a dosage of 200 µg to respective groups prior to treatment and subsequently administered every 3 days for a total of 5 doses. The MBs used in this study were an experimental phospholipid encapsulated agent administered in bolus form prior to insonation. Ultrasound exposures were applied with a single element spherically focused 1 MHz transducer with the entire tumor within the -3dB beam width. The sonication scheme that was employed was as follows: 50 of 0.1 ms long pulses (1.65 MPa peak negative pressure) spaced 1 ms apart, which were repeated at 10 s intervals for a duration of 3 mins. This scheme was repeated twice, spaced 10 mins apart. Longitudinal studies were done to evaluate the efficacy of each treatment on tumor growth. Acute experiments were done, which included flow cytometry and ELISPOT to assess how T-cell populations/activity changed with each treatment.

Results/Discussion

Longitudinal experiments (n=5-6) showed that USMBs + aPD-1 treatment significantly inhibited tumor growth relative to MB-only, USMB-only group and aPD-1 group at Day 6 (p<0.0001, p<0.01, p<0.01, respectively) and at Day 9 (p<0.0001, p<0.01, p<0.05, respectively). This inhibition of tumor growth with combinatorial treatment translated to longer survival times (endpoint: tumor volume >1000mm³) compared to MBs (p<0.01), USMBs (p<0.01) and aPD-1 (p<0.005). Flow cytometry (n=5-7) and ELISPOT (n=6) data did not clearly illustrate a T-cell dependant mechanism for the inhibition of tumor growth. Therefore, the results provide a first demonstration of the ability of USMBs to enhance CI therapy, while the specific mechanisms of enhancement remain to be established.

4:15 PM

Targeted microbubble-cell interactions elucidated with combined confocal microscopy and Brandaris 128 ultra-high speed imaging

Ines Beekers¹, Merel Vegter¹, Kirby R. Lattwein¹, Frits Mastik¹, Robert Beurskens¹, Antonius F. W. van der Steen^{1,2}, Martin D. Verweij^{1,2}, Nico de Jong^{1,2}, Klazina Kooiman¹

¹Department of Biomedical Engineering, Erasmus MC, Rotterdam, Netherlands, ²Acoustical Wavefield Imaging, Delft University of Technology, Netherlands

Background, Motivation, and Objective

Vascular drug delivery can be locally enhanced with ultrasound (US) insonification of gas-filled microbubbles (MB) [Kooiman et al, Adv Drug Del Rev, 2014]. However, the underlying mechanism is still unknown. Elucidating the mechanism is challenging because of the nanometer and nanosecond resolution needed to visualize the cellular effects and MB oscillation. We now achieved these resolutions with our recently developed state-of-the-art optical imaging system: the Brandaris 128 ultra-high speed camera [Chin et al, Rev Sci Instru, 2003] coupled to a custom built Nikon A1R confocal microscope. With this system we aim to elucidate the MB-cell interaction for drug delivery.

Statement of Contribution/Methods

Human Umbilical Vein Endothelial Cells (HUVEC) were grown to confluence in a CLINIcell (50 µm, Mabio, France). Homemade MB were targeted to an angiogenic endothelial receptor ($\alpha_v\beta_3$). The cell membrane was stained with Cell Mask Green, the nuclei with Hoechst, and sonoporation was evaluated with Propidium Iodide (PI). The cellular response of a single MB upon insonification (n=140) was monitored with the confocal microscope (0.65 fps, 100x objective). The confocal recording started before US (2 MHz, 100 to 400 kPa, single 10-cycle burst) and continued for >3 min after US. Before US, cells were classified for either partial or full junctions with the neighboring cells. After US, the cellular response was evaluated for PI uptake and cellular retraction due to rupture of junctions. MB oscillation was recorded with the Brandaris 128 (~16 Mfps) and MB excursion was defined as the difference between maximum and resting radius.

Results/Discussion

When HUVEC showed PI uptake, the median excursion was 0.93 µm (Fig 1A, B) while this was 0.49 µm when no PI was observed. Fewer cells retracted upon insonification (20%) when they had full junctions than with partial junctions (65%, Fig 1C). Thus, junctions ruptured more often when a cell was not fully attached to the neighboring cells. Almost all cells with full junctions that retracted also showed PI uptake (92%). In conclusion, MB oscillation was related to both cellular retraction and PI uptake, while also assessing cellular junctions. Using the state-of-the-art optical imaging system, we are now able to elucidate the MB-cell interaction for ultrasound-mediated drug delivery.

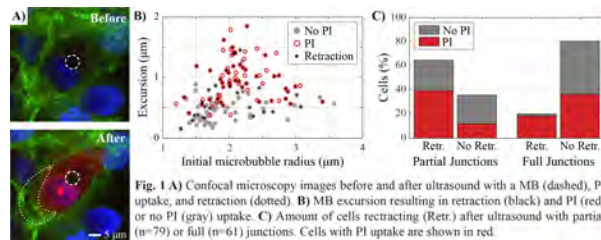


Fig. 1 A) Confocal microscopy images before and after ultrasound with a MB (dashed). PI uptake, and retraction (dotted). B) MB excursion resulting in retraction (black) and PI (red) or no PI (gray) uptake. C) Amount of cells retracting (Retr.) after ultrasound with partial (n=79) or full (n=61) junctions. Cells with PI uptake are shown in red.

4:30 PM The effect of sonication on extravasation and distribution of nanoparticles and dextrans in tumor tissue imaged by multiphoton microscopy

Petros Tesfamichael Yemane¹, Andreas Åslund¹, Kristin Grendstad¹, Astrid Bjørkøy¹, Sofie Snipstad¹, Annemike Van Wamel¹, Sigrid Berg^{2,3}, Yrr Mørch⁴, Rune Hansen^{2,3}, Bjørn Angelsen^{3,5}, Catharina de Lange Davies¹

¹*Department of Physics, Norwegian University of Science and Technology (NTNU), Trondheim, Norway*, ²*SINTEF Technology and Society, Trondheim, Norway*, ³*Circulation and Medical Imaging, Norwegian University of Science and Technology (NTNU), Trondheim, Norway*, ⁴*SINTEF Materials and Chemistry, Trondheim, Norway*, ⁵*Surf Technology, Trondheim, Norway*

Background, Motivation, and Objective

Ultrasound (US) and systemic administration of microbubbles (MBs) have been shown to improve the delivery of drugs and nanoparticles (NPs) to tumor tissue. The enhancement of the drug accumulation may be due to thermal and/or non-thermal effects. Non-thermal mechanical effects, mainly cavitation and acoustic radiation forces, cause bio-effects such as enhanced permeability across vessel walls or cellular membranes and acoustic streaming, thereby enhancing extravasation and penetration of drugs and NPs through the tumor interstitium.

A better understanding of these effects is crucial for effective delivery of NPs and drugs. The aim of this study was to elucidate the kinetics of extravasation events in the millisecond to minute range and to characterize the vessels and vessel flow where extravasation occurs. This was done by real-time intravital multiphoton microscopy during US sonication. We chose to study the effects of four different pressures levels while injecting SonoVue® or in-house made MBs. These MBs are formed by the self-assembly of polymeric, fluorescent NPs (NP-MBs).

Statement of Contribution/Methods

Human osteosarcoma cells were grown in a dorsal window chamber on the back of BALB/c nude mice. Two weeks after implantation, the tumor was sonicated for 5 min at 1 MHz, pulse length of 10 ms, pulse repetition frequency of 0.5 Hz, and mechanical index (MI) 0.2, 0.4, 0.6 and 0.8. FITC labeled dextran (2 MDa) was injected for visualization of the blood vessels. The in-house made NP-MBs or SonoVue® MBs co-administered with polymeric fluorescent NPs were injected in the tail vein and sonication started immediately after injection. The fluorescent NPs were imaged with a multiphoton microscope in resonance mode before, during, and after sonication to observe the effect of cavitation on vessel opening and/or vessel rupture, indicated by extravasation of NPs and the 2MDa dextrans. In addition, the intra- and extravascular distribution of the NPs and dextran were quantified.

Results/Discussion

We observed that high MI (0.8) induced a violent extravasation of both NPs and dextrans. The cavitation probably ruptured the capillary wall. Using lower MIs (0.2-0.6), the extravasation was less violent and occurred in capillaries with larger diameters compared to MI 0.8. The rate of extravasation of both NPs and dextrans, and the mean displacement of NPs and dextrans from the vessel into the tumor tissue, correlated with MI. In addition, at MI of 0.8, rupture of the blood vessels, which could be due to the violent collapse of the MBs, was observed for both MB types. The observed extravasation events seemed to appear randomly both in time and space, and happened within seconds to minutes during the US exposure. This real-time observation using intravital multiphoton microscope reveals new knowledge on the temporal and spatial extravasation of NPs and dextran during US exposure, which is highly useful for optimizing such treatments.

4:45 PM Development of a microvascular phantom for studies on microbubble dynamics and bubble-cell interaction inside a capillary

Shinji Imai¹, Nobuki Kudo¹

¹*Graduate School of Information Science and Technology, Hokkaido University, Sapporo, Japan*

Background, Motivation, and Objective

For better understanding of *in vivo* sonoporation, studies on bubble-cell interaction inside capillaries are essential because their total surface area is 700 times larger than that of the arteries. In this study, a microvascular phantom with cells cultured on the lumen surface was developed and used for high-speed observation of bubble dynamics inside a narrow lumen and confocal microscopic observation of resulting cell damage.

Statement of Contribution/Methods

To mimic the stiffness of biological cells, the vascular phantom was made using an acrylamide gel of 2.3 kPa in young's modulus. A tungsten wire of 60 μm in diameter was inserted across a mold case, and a gel solution was poured to fill the case. After gelation, the wire was removed to make the lumen, which was coated with collagen (Cellmatrix type I-C, Nitta Gelatin). A suspension of human prostate cancer cells (PC-3) was then introduced inside the lumen, and the phantom was incubated for 2 weeks while flipping every 2 to 3 days. Before sonication, a suspension of lipid shelled microbubbles of about 3 μm in diameter was introduced into the lumen to make the bubbles attached to the cells. Ten-cycle burst ultrasound of 1 MHz in center frequency and 1.0 MPa in peak-negative pressure was irradiated, and 256 frames were taken at a framing rate of 10 Mfps using a high-speed video camera (HPV-X2, Shimadzu). A confocal laser-scanning microscope (Ti C2 si, Nikon) with 40 \times Plan Fluor objective lens (N.A. 0.60) was used for confocal observation.

Results/Discussion

Figure 1(a) is a confocal image of the phantom taken before ultrasound exposure, confirming the introduced microbubbles adhering to the cells cultured on the lumen surface. Figure 2 shows high-speed images visualizing bubble contraction and expansion adjacent to the cells. The confocal image taken after ultrasound exposure (Fig. 1(b)) shows a decrease in a bubble number and the appearance of Sytox Blue fluorescence inside the cells around which bubble oscillation were observed, suggesting the bubble oscillation caused cell membrane damage. Observation of oscillating bubbles inside a lumen is ongoing, and improvement of the cell culture process that enables use of endothelial cells instead of PC-3 cells is our future task for elucidating the mechanisms of sonoporation and BBB opening. This work was supported by JSPS KAKENHI Grant Number 17H00864.

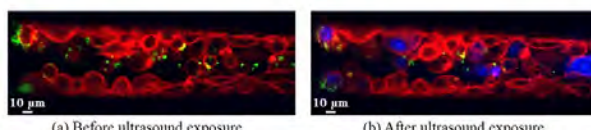


Fig. 1. Confocal observation of a microvascular phantom. Plasma membrane of the cells were stained with Cell Mask (red), and a shell material of the bubbles were stained with NBD (green). Membrane damage was detected using Sytox Blue (blue).

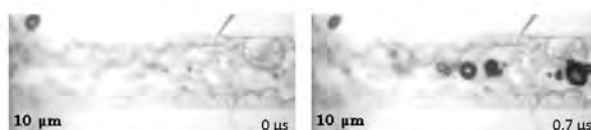


Fig. 2. High-speed observation of bubble dynamics inside the microvascular phantom

5:00 PM

Dynamics and Mechanisms of Ultrasound and Microbubble Facilitated Intracellular Plasmid DNA UptakeNing Rong¹, Hao Zhou², Ruming Liu², Yan Wang¹, Zhenzhen Fan^{1,3}¹*Biomedical Engineering, Tianjin University, Tianjin, China, People's Republic of,* ²*College of Life Sciences, Nankai University, Tianjin, China, People's Republic of,* ³*State Key Laboratory of Acoustics, Institute of Acoustics, Chinese Academy of Sciences, Beijing, China, People's Republic of***Background, Motivation, and Objective**

Ultrasound and microbubble has shown a great potential in gene therapy as this technology can achieve non-invasive and effective intracellular gene delivery and transfection both in vitro and in vivo. However, the mechanisms of how plasmid DNA intracellular uptake occurs are not fully understood. This study aims to reveal the dynamic process of ultrasound and microbubble mediated plasmid DNA intracellular uptake and unveil the mechanisms involved on single cell level.

Statement of Contribution/Methods

Targeted microbubble conjugated with RGD was attached to membrane of Hela cells. High pressure short pulse (0.44MPa, 10μs) and low pressure long pulse (0.13MPa, 1ms) were applied to stimulate different bubble dynamics with high viability and good transfection efficiency. Real time fluorescent microscopy of propidium iodide (PI) was employed to track the membrane perforation process. To correlate the plasmid DNA uptake with bubble-cell interactions, confocal microscope and high speed camera imaging were applied. Endocytosis inhibitors were used to confirm the role of endocytosis route played in the plasmid DNA uptake process.

Results/Discussion

Plasmid DNA radius was measured to be of 35.1 ± 10.6 nm using AFM. Numerical simulation shows that plasmid DNA with such dimension is possible to transport through the transient pore on cell membrane with radius of 86.5 ± 45 nm. Confocal fluorescent microscopic images show the spatial correlation between bubble and trans-membrane plasmid DNA, demonstrating that transient pore is an effective route for plasmid DNA uptake. The volumetric oscillation of the bubbles generated 1.1 to 15.4 kPa shear stress on cell membrane under high pressure short pulse, while 0.02 to 2.30 Pa under low pressure. The endocytosis inhibition indicates that endocytosis was initiated under both ultrasound conditions. Moreover, the plasmid DNAs in the entire 3D cytoplasm not correlated with bubble or membrane vesicles suggest that other global and fast mechanisms may be involved under both ultrasound conditions [1]. In sum, we conclude that the plasmid DNA intracellular uptake process involved multi-mechanisms determined by bubble-cell interactions.

References:

- [1] N Rong, H Zhou, R Liu, Y Wang, Z Fan. Ultrasound and microbubble mediated plasmid DNA uptake: A fast, global and multi-mechanisms involved process. *J. Control. Release* 273(2018):40-50.

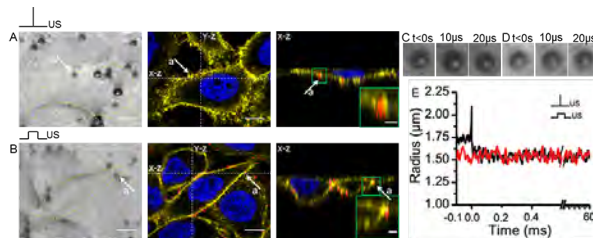


Figure 1. Plasmid DNA intracellular distribution in Hela cell and bubble dynamics under different ultrasound conditions.

5:15 PM

New Insights in the Actin Cytoskeleton Dynamics of the Sonoporated Human Umbilical Vein Endothelial CellsCaixia Jia¹, Jianmin Shi¹, Tao Han¹, Fan Li², Ping Cai¹, Alfred C. H. Yu³, Peng Qin¹¹*Instrument Science and Engineering, Shanghai Jiao Tong University, China, People's Republic of,* ²*Medical Ultrasound, Shanghai General Hospital, China, People's Republic of,* ³*ECE, University of Waterloo, Waterloo, ON, Canada***Background, Motivation, and Objective**

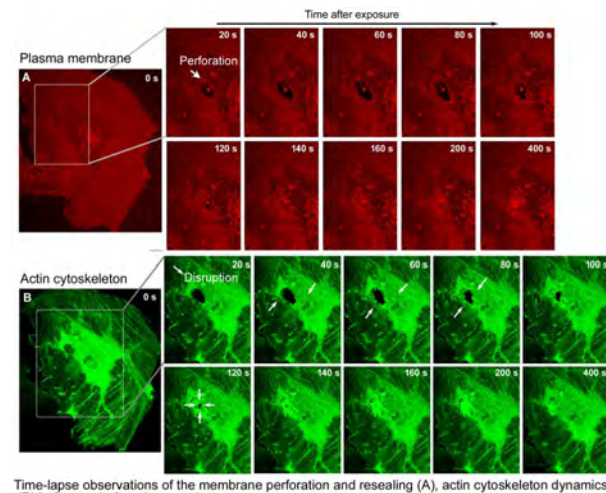
Sonoporation has shown great potential for drug delivery. However, some concomitant cellular and molecular responses, which dominate the resealing of the perforated membrane and the long-term cell fate, could be triggered by sonoporation, thereby influencing therapy efficiency and biosafety. Cytoskeleton, as a bridge for converting external mechanical stimulus to intracellular biochemical signals, directly interconnect with the membrane, and may be affected by acoustic cavitation. The objectives of this study are to understand how the cytoskeleton dynamics is affected by sonoporation, and how the disturbed cytoskeleton restores to initial status.

Statement of Contribution/Methods

A platform was established for performing acoustic cavitation and observing cellular responses at the single-cell level. 1.5 MHz ultrasound with 13.33 μ s duration and 0.7 MPa peak negative pressure was applied to trigger the collapse of microbubble, which contacted with the membrane of Human Umbilical Vein Endothelial Cell (HUVEC), inducing the membrane perforation at the bubble site. The membrane and actin cytoskeleton were labelled by CellMask deep red and Actin-GFP, respectively, to simultaneously record the dynamics of membrane perforation and cytoskeleton response by confocal microscope at 20-s interval over 30-min post-exposure. Calcein blue-AM was used to evaluate the viability of the sonoporated cells at 35-min post -exposure.

Results/Discussion

We obtained the following results by observing 28 reversibly sonoporated HUVECs: 1. The spatially disrupted fibrous actin (F-actin) was observed at the perforation site, and was synchronized with the time course of the perforated membrane by the collapsing bubble. 2. During the membrane resealing (within ~200 s), some actin components, such as cortex actin, rapidly depolymerized. Particularly noted that some actin filaments were partially disassembled, forming polymers of globular actin, which then directionally migrated to the disruption site along F-actin, and subsequently accumulated and aggregated(Figure B 20-140 s). 3. With the completion of membrane resealing, the accumulated polymers reassembled to form new F-actin. As such, the disrupted actin was repaired and returned to initial status(Figure B 400 s). These findings provide new insight into understanding the cytoskeleton dynamics in sonoporation.



Time-lapse observations of the membrane perforation and resealing (A), actin cytoskeleton dynamics (B) before and after ultrasound exposure.

5A - SAW Device & Application

Ikuta (200)

Tuesday, October 23, 10:30 am - 12:00 pm

Chair **Hiroyuki Nakamura**
Skyworks Solutions, Inc.

5A-1

10:30 AM Coexisting Surface and Bulk Gyroscopic Effects

Visarute Pinrod¹, Benyamin Davaji¹, Amit Lal¹

¹School of Electrical and Computer Engineering, Cornell University, Ithaca, NY, United States

Background, Motivation, and Objective

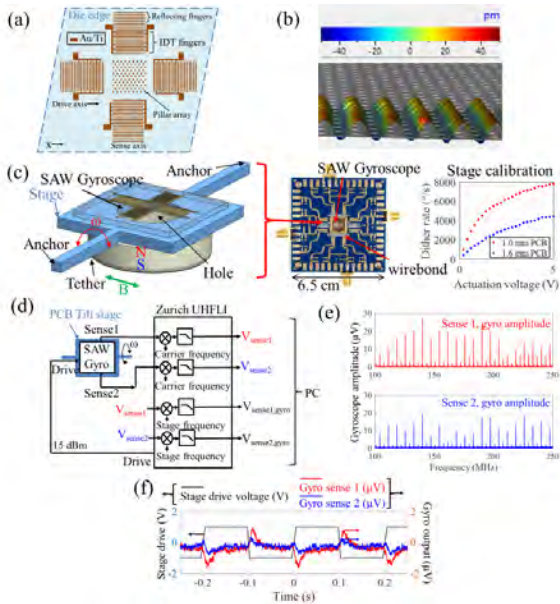
SAW gyroscopes have the potential of operation under high shock and vibration, such as driverless cars. They use Coriolis effect on oscillating mass excited by SAW to create secondary waves corresponding to rotation rates. Recent papers have demonstrated SAW gyroscope functions, but have not definitively elucidated the mechanism of operation with a theory that can be matched to measured response. In an attempt to identify the physics of gyroscopic operation, we establish that the bulk-modes excited with SAW IDTs can also lead to gyroscopic effect. We identify the continuum of thickness-mode bulk modes, and SAW modes, and measure the gyroscopic response of each of these modes. Gyroscopic response from multiple surface and bulk modes potentially enables temperature compensation since the temperature coefficients for these modes are different.

Statement of Contribution/Methods

SAW gyroscopes consist of 2 SAW resonators with distributed Coriolis mass array in the shared cavity (Fig. 1a). We present a lithium niobate based SAW/BAW gyroscope that is characterized using a novel test setup using a magnetically driven dither stage (Fig. 1c). The stage is formed by a PCB with an attached ring magnet with a hole for optical access. The magnet is actuated by an external electromagnet. The drive SAW resonator is driven with an RF generator, and the sense outputs are measured while applying a rotation dither rate. Devices are fabricated on the 128 Y-cut Lithium Niobate substrates by lift off process (200nm Au/10nm Ti).

Results/Discussion

The surface of the device is characterized by a laser Doppler vibrometer (UHF120) to identify the mode shapes. The dither stage was characterized by measuring reflected laser scanning length. The stage can apply rate as high as 8000 deg/s (Fig. 1c). The drive RF frequency is swept while dithering. The outputs from both sense ports are demodulate at RF frequency (Fig. 1d). Then, they are demodulated again at stage frequency. Peaks indicates that specific drive RF frequency results in gyroscopic outputs (Fig. 1e). These peaks occur at spacing of ~7.2 MHz, with Q ≈ 30,000. COMSOL predicts thickness mode frequency starts at 3.75 MHz, with spacing of 7.5 MHz. We identify that the modes of the bulk and SAW waves are established. The bulk waves in the thickness mode are established between the top and bottom of wafer, while the SAW waves are excited by the top and IDT electrodes.



10:45 AM

AlN based dual LCAT filters on a single chip for duplexing applicationYao Zhu¹, Nan Wang¹, Geng Li Chua¹, Bangtao Chen¹, Srinivas Merugu¹, Navab Singh¹, Yuandong Gu¹¹*Institutes of Microelectronics, A*STAR, Singapore***Background, Motivation, and Objective**

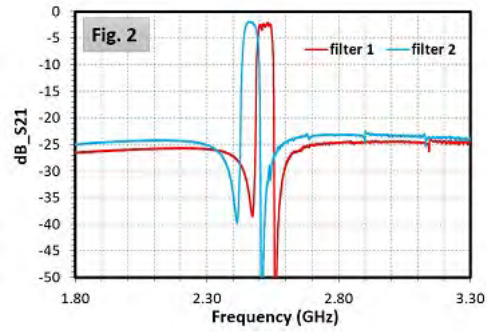
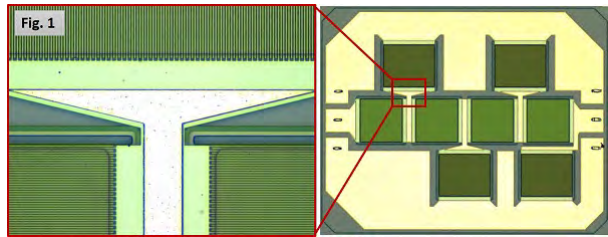
RF frontend filters in mobile phones nowadays are dominated by SAW technology for the low and mid band, and BAW technology for the mid and high band. One limitation for BAW technology is that one wafer can only deliver one frequency band, since the resonant frequency is determined by the stack thickness. This paper presents two filters fabricated on the same wafer operating at different frequencies for high band integrated duplexer application.

Statement of Contribution/Methods

Two filters delivering two adjacent frequency bands are designed and fabricated on the same wafer. Each filter is constructed by two sets of AlN based lateral coupled alternating thickness (LCAT) mode resonators in a ladder topology. The LCAT mode resonator is capable of delivering a BAW resonator comparable coupling coefficient, with its frequency adjustable by the design of the electrode pitch. In this work, a modified LCAT mode resonator with the bottom electrode being a floating plate is adopted to reduce the process complexity and fabrication cost, with minor compromise of the filter bandwidth.

Results/Discussion

The microphoto of one of the filters is shown in Fig. 1 and the measured S21 using 50Ω terminations of both filters are plotted in Fig. 2. Two inductors are connected at the input and output port to flatten the passband. The filters operate around 2.465GHz and 2.47GHz, respectively. Within 40MHz bandwidth, the average insertion loss of the lower frequency filter is 2.56dB, and of the higher frequency filter is 2.30dB. With such low passband insertion loss and an overall out of band rejection of 25dB, the LCAT filters demonstrate great potential for integrated duplexer and multiplexer applications.



11:00 AM

Leaky SAW devices with Beryllium electrodesVictor Plessky¹, Julius Koskela¹, Robert Hammond²¹GVR Trade SA, GORGIER, Switzerland, ²Resonant Inc., Goleta, CA, United States**Background, Motivation, and Objective**

The reduction of losses in SAW devices continues to be a relevant topic. Leaky SAW devices on rotated Y-cut LiNbO₃ and LiTaO₃ suffer from losses due to “leakage”, *i.e.* radiation of slow shear bulk-acoustic waves weakly coupled to the surface wave. It is well known that the leakage on LiTaO₃ can be reduced by optimizing the thickness of aluminum electrodes and the crystal cut angle [1]. It is also known that heavy metal electrodes (Pt, Mo, W) can slow down the leaky wave in LiNbO₃ so strongly that the leakage can be suppressed [2]. But what about other metals? Can a light metal, such as Beryllium (Be), be useful?

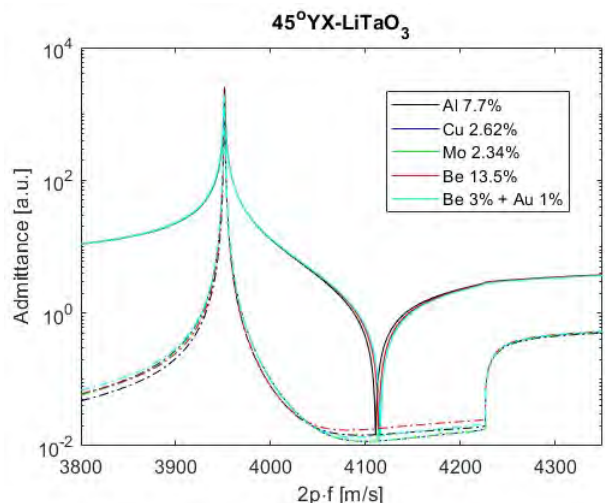
Statement of Contribution/Methods

In this work we show that the amount of leakage on rotated Y-cut LiTaO₃ depends on two parameters: the crystal cut angle and the mass of electrodes. With suitable chosen combination of the two, the leakage can be essentially suppressed at one frequency point. This cancellation can be achieved with many different metals. However, many heavy materials are not feasible in practice – the demanded thickness is so small that the resistivity of electrodes will be not acceptable. An excellent candidate seems to be Beryllium – being a very light material with low internal acoustic losses and relatively low resistivity.

Results/Discussion

For a synchronous resonator on LiTaO₃ we can minimize the leakage at a single frequency within the resonance–antiresonance region. As an example, Figure 1 illustrates simulated admittance (Re(Y) and Abs(Y)) for an infinite IDT structure on 45°-cut with Metallization ratio 0.5; resistivity and viscous losses in electrodes are not taken into account. For the leaky losses all studied metals seem fairly interchangeable. The structure was optimized to give about the same leaky loss at resonance and at the anti-resonance, with these losses being minimal about in the middle between these frequencies (around $2p^*f=4020\text{m/s}$). For thicker Be electrodes of $h/l=13.5\%$ we have resonance at $2p^*fr=3951.3\text{m/s}$ and anti-Resonance at 4114.0 m/s (Q-factors due to the leaky loss >4000).

- [1] O. Kawachi, et al, “Optimum cut of LiTaO₃ for high performance leaky surface acoustic wave filters”, Proc. IEEE Ultrasonics Symp., 1996, pp. 71-76.
- [2] V. P. Plessky, C. S. Hartmann and J. Koskela, “Suppression of the leakage effect in 64°YX-LiNbO₃ for thick aluminium electrodes,” 1996 Ultrason. Symp. 1996, p. 1603.



11:15 AM Advanced characterization of surface acoustic wave fields at high temperatureRobert Weser¹, Andrei Sotnikov^{1,2}, Hagen Schmidt¹¹*IFW Dresden, Germany*, ²*Ioffe Institute, St. Petersburg, Russian Federation***Background, Motivation, and Objective**

The application of wireless surface acoustic waves (SAW) sensors is state of the art for several years. These sensors are capable to measure physical quantities in harsh environments [1]. Beside electrical characterization, the SAW wave field, i.e. the lateral distribution of surface normal displacements, gives significant information on the behavior of SAW devices, so on loss evolution [2] and parasitic mode generation [3]. This also supports custom design of SAW devices with desired sensor functionality for extreme conditions.

Statement of Contribution/Methods

We present for the first time results of in-situ wave field measurements in a SAW resonator operated at high temperature. The absolute amplitude of the surface-normal wave field component is measured with a scanning Laser Doppler Vibrometer (Polytec UHF 120) at high resolution in a long-term stabilized setup. For this, the SAW device is mounted into a temperature stage (Linkam HFS 600E) in order to realize sample temperatures between 90K and 600°C.

Results/Discussion

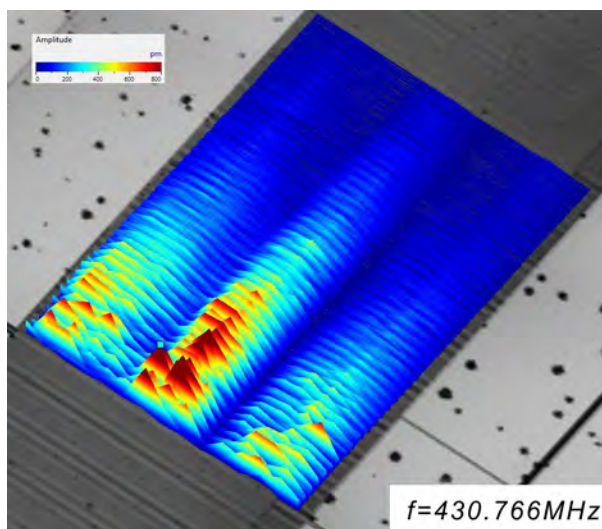
SAW sensors based on one-port resonator designs are well-suited for temperature dependent wave field investigations since different design parameters as well as the SAW device characteristics as a whole are very temperature sensitive. Figure 1 shows the measured wave field inside one half of a one-port resonator, measured at 300°C. The temperature-dependent evolution of the absolute amplitude maximum as well as the lateral distribution are important for the lifetime of the device. The stress loading of materials involved, which is already high due to the high temperature, is further increased within the region of maximum SAW amplitude (see Fig.) and can lead to premature failure of the sensor.

First results are captured at 300°C depending on maximum temperature capabilities of conventional substrate electrode material combinations. We present further results for different high temperature substrate-electrode systems and temperatures up to 600°C. The knowledge about temperature-dependent wave field characteristics can help to improve the design of SAW sensors in order to make them more robust and reliable, especially for applications in harsh environments.

[1] J.M. Friedt et al. *J. Appl. Phys.* **109**, 034905 (2011).

[2] M. Solal et al., *Proc. IEEE Int. Ultrasonics Symp.*, 324-332 (2011).

[3] M. Solal, *Proc. IEEE Int. Ultrasonics Symp.*, (2016).



11:30 AM

High Quality Factor SAW Resonators Based on Al / AlN / Sapphire for High Temperature Wireless ApplicationsJérémie Streloue¹, Julien Camus², Thierry Laroche³, Florian Bartoli^{1,4}, Sami Hage-Al¹, Thierry Aubert⁴, Mohamed-Abdou Djouadi², Sylvain Ballandras³, Omar Elmazria¹¹*Institut Jean Lamour, Université de Lorraine, CNRS, Nancy, France*, ²*Institut des Matériaux Jean Rouxel, Université de Nantes, CNRS, France*, ³*frec|n|sys, Besançon, France*, ⁴*LMOPS, CentraleSupélec - Université de Lorraine, Metz, France***Background, Motivation, and Objective**

AlN piezoelectric thin films grown on sapphire are strong candidates for high temperature SAW sensors, due to their thermal stability, high velocity and suitable electromechanical coupling (K^2). However, thin-film resonators need more design efforts than those based on bulk crystals. This work presents an optimization of AlN/Sapphire SAW resonators for high quality factors (Q), using aluminum electrodes for their low density and resistivity, as an alternative to heavier electrodes like Pt. It proves the interest of Al as a reliable electrode material up to 600°C, which can be sustained with further passivation. Standard, synchronous resonators are first presented and tested. A quasi-synchronous, optimized design is then proposed for higher quality factors and wireless sensing compliance.

Statement of Contribution/Methods

Two series of SAW devices were fabricated on AlN thin films deposited by reactive magnetron sputtering on sapphire substrates. The AlN thickness (3 μm) was chosen to offer high K^2 around the 433 MHz ISM band. The 200 nm thick electrodes were deposited by DC magnetron sputtering. The first series of devices, used to extract the material parameters for design optimization purposes, was based on synchronous resonators ($\lambda = 6.5$ and 13 μm , aperture = 40 λ , 100 pairs, 2 x 200 reflectors). A second series of devices was then based on an optimised design, and characterized with respect to the temperature in air atmosphere using a network analyzer and a RF prober designed for temperatures up to 600°C. Thus, resonance frequencies, Q and K^2 could be extracted over this temperature range.

Results/Discussion

The synthesized AlN films are highly textured despite their thickness, and show typical XRD FWHM rocking-curve values of 0.8° for the (002) reflex. Experimental characterizations of the first resonators series show typical values of $Q = 650$ and $K^2 = 0.4\%$. The frequency evolution for high temperatures remains quasilinear up to 593°C (Fig. 1.a), with a TCF of -50 ppm/°C, and shows a good reversibility. As expected, the optimised design shows a much better impedance matching (Fig. 1.b), with return losses over -15 dB and Q values up to 8200, despite a smaller K^2 : 0.038%. Measurements show that aluminium IDTs are stable up to at least 600°C, and that the Q factor of Al/AlN/Sapphire structure remains almost constant, making this design compatible with wireless sensing.

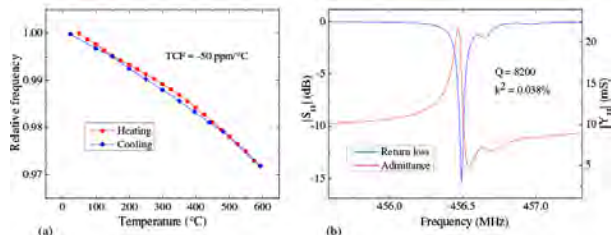


Fig. 1. Temperature evolution of phase velocity obtained from RF characterizations up to 593°C (a). Return loss and admittance plots of an optimized resonator (b).

11:45 AM Separation of Frequency and Amplitude Modulation Contributions due to External Vibration on a SAW Resonator

Anin Maskay^{1,2}, Donald Hummels¹, Mauricio Pereira da Cunha^{1,2}

¹*Electrical and Computer Engineering, University of Maine, Orono, ME, United States*, ²*Laboratory for Surface Science and Technology, University of Maine, Orono, ME, United States*

Background, Motivation, and Objective

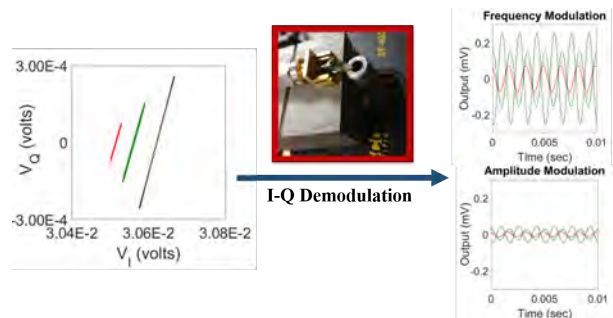
SAW resonators (SAWR) are widely used in radio-frequency (RF) communications, frequency-control, and sensing applications. External vibration-induced modulations of a SAWR's RF response can be detrimental in communications and frequency-control as it generates undesired spurious signals and unwanted phase noise. In sensing applications, vibration-induced response can either be a primary measurand or an undesired spurious signal that reduces sensor accuracy and precision. Therefore, characterization of vibration-induced modulations is important to improve device performance in all the applications listed above.

Statement of Contribution/Methods

This paper presents an in-phase and quadrature signal (I-Q) analysis technique to demodulate a SAWR RF signal exposed to external vibrations and separate the contributions of amplitude modulation (AM) and frequency modulation (FM). A SAWR was mounted in a cantilever configuration and exposed to external mechanical vibrating signals using a vibration generator (center inset figure). The SAWR was excited close to its resonant frequency using a RF synthesizer and its echo response was measured using a vector signal analyzer.

Results/Discussion

The figure (left) shows a plot of the measured in-phase voltage component (V_I) in the horizontal axis and quadrature voltage (V_Q) component in the vertical axis for three different values of vibration generator (single tone vibration at 600Hz) input voltage: 300mV_{p-p} (left curve); 600mV_{p-p} (center curve); and 900mV_{p-p} (right curve). The demodulated FM (top right inset) and AM (bottom right inset) time responses obtained for the three vibration cases illustrate: (i) the existence of both FM and AM contributions for the externally applied vibration signal; (ii) that both FM and AM signals are directly proportional to the vibration source amplitude; and (iii) that FM is the dominant mode of modulation, over five times greater than AM. The obtained experimental results confirm that the I-Q analysis developed in this work are effective not only to determine the frequency and spectral amplitude of a mechanical vibrating signal on a SAWR, but also to separate the AM and FM contributions. This analysis contributes to the quantification and understanding of induced external vibrations on SAWRs used in contemporary communications, frequency control, and sensing applications.



5B - SAW Modeling & Design 1

Ikuta (200)

Tuesday, October 23, 1:30 pm - 3:00 pm

Chair **Karl Wagner**
RF360 Europe GmbH

5B-1

1:30 PM

Thin Film Acoustoelectric GHZ SAW Amplifier Design

Donald Malocha¹, Chris Carmichael², Scott Smith³, Arthur Weeks³

¹Pegasense, Winter Springs, FL, United States, ²University of Central Florida, FL, United States, ³University of Central Florida, United States

Background, Motivation, and Objective

Surface acoustic wave (SAW) acoustoelectric (AE) theory and device embodiments have been demonstrated from the 1960s to the present. The ability to produce a practical integrated SAW AE amplifier in filters and resonators would provide new opportunities for SAW RF filters and oscillators. The Defense Advanced Research Project Agency (DARPA) has funded the Signal Processing at RF (SPAR) program, where one goal is to research and develop a SAW AE amplifier. In particular, the AE amplifier is one component of a SAW-based simultaneous transmit and receive (STAR) radios at approximately 1 GHz using spread spectrum RF filtering.

Practical passive AE devices have been developed for SAW sensors, which operate in the attenuation mode by modulating the SAW propagation loss with changes in the surface thin film resistivity. In these devices, the travelling SAW electric field couples to the film free-charge carriers resulting in an increase or decrease in the propagation loss with an applied gas or other material.

For amplification, an active AE device requires an external DC bias applied to an interaction layer that couples to the SAW. There are 3 principal surface interaction layer approaches that have been researched: an air-gap coupled semiconductor, a bonded semiconductor layer, and a thin film deposited layer. Each of the approaches has challenges, and to date a practical manufacturable AE amplifier has not been developed.

Statement of Contribution/Methods

This paper will present research efforts on development of a thin film AE amplifier on LiNbO₃. In the development of a practical SAW AE amplifier, the following design parameters need to be considered and investigated:

- Manufacturability for practical applications
- Device embodiments – single versus multi-segmented distributed amplifier
- Thin film parameters
 - Carrier concentrations and mobility
 - SAW propagation loss
 - Carrier drift velocity vs applied fields
- Amplifier applied DC voltage limits
- Substrate coupling coefficient
- DC maximum power
- AE Gain
- AE figure of merit (S_{21}/S_{12})
- Noise figure

Part I of the paper will discuss and provide plots that consider the boundaries and coupled-interactions of the design parameters for practical AE thin film amplifiers. Part II will provide the most recent results of the AE amplifier research efforts using graphene on lithium niobate. The graphene AE amplifier approaches many of the desired design requirements; including practical manufacturability.

Results/Discussion

Results of several different embodiments using single element and distributed AE elements, for GHz range SAW AE amplifier filters using graphene thin films are provided. To date, results on graphene AE devices, operating to 1500 MHz, show figure of merit of 2-6 dB. A video will show CW amplifier S_{21} and S_{12} results. Results to date are very encouraging, but net-positive gain has yet to be achieved. The many remaining challenges and opportunities for practical thin film AE amplifiers will be discussed.

1:45 PM

Simplified BEM Model for Fast and Accurate Simulation of Surface Acoustic Wave DevicesTakao Suzuki¹, Kazuhiro Takigawa¹, Ryo Nakagawa¹, Ken-ya Hashimoto²¹Murata Manufacturing Co., Ltd., Kyoto, Japan, ²Graduate School of Engineering, Chiba University, Chiba, Japan**Background, Motivation, and Objective**

Acoustic scattering at discontinuities is one of major loss mechanisms in SAW filters and duplexers, and its accurate modelling is highly demanded in numerical simulation used in the design stage. Although FEM and FEM/BEM seems to be solutions, their calculation speed is not acceptable for the iterative optimization.

In [1], one of the authors derived a closed-form 1D equation with respect to the surface charge from the full wave form by applying simplifications underlying the coupling-of-modes (COM) model for SH SAWs. The final result is similar to the delta function model but takes the SAW/BAW interaction into account.

Statement of Contribution/Methods

This paper proposes a high-speed and accurate simulation technique of SAW devices where the SAW/BAW scattering at structural discontinuities is taken into account. The method is based on the equation given in [1] but is expanded to a convolution form between the Green function and surface charge like BEM for the analysis of finite structures.

Another significant merit is compatibility of the parameters required for the analysis with those for the COM analysis which have already been established for device design.

Results/Discussion

Two DMS filters were designed using the conventional COM. Figure 1 shows variation of the normalized grating pitch with the position. Design A possesses smaller variation than Design B. Figure 2(a) shows the simulated pass-band characteristics obtained by the traditional COM. They are almost identical.

Figure 2(b) shows the measured pass-band responses of the fabricated filters. Although the pass-band shape is similar, insertion loss of Design B is about 0.1 dB larger than that of Design A. Figure 2(c) shows the simulated result obtained by the present method. Agreement is excellent with the experiments.

The excess insertion loss is not predictable by the traditional COM but by the present method. This means that it is caused by the BAW scattering at structural discontinuities.

In this simulation condition, the calculation time is about one-tenth compared with the FEM simulation under almost the same PC spec. It should be noted that further drastic speed up is possible because the computation time is mostly spent on the Green function calculation, and spatial sampling interval is uniform in the present analysis.

[1] K. Hashimoto, Proc. IEEE Ultrason. Symp. (2013) pp.1399-1402

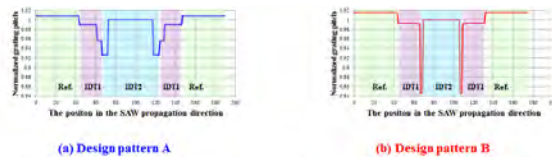


Fig.1 Variation of the normalized grating pitch with the position in the SAW propagation direction.

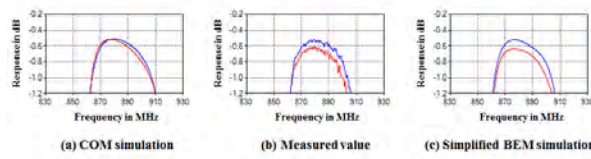


Fig.2 Pass-band characteristics after removal of miss-matching loss

Blue line: Design pattern A
Red line: Design pattern B

2:00 PM **Multi-mode P-matrix models for the description of interacting modes in TCSAW and LSAW devices****Markus Mayer¹, Thomas Ebner¹, Karl Wagner¹**¹*RF360 Europe GmbH, Munich, Germany***Background, Motivation, and Objective**

SAW devices in present day LTE bands frequently employ temperature compensated (TCSAW) material systems, where a SiO₂ compensation layer is deposited on a rotated Y-cut lithium niobate substrate. A major issue in the design of these devices is the suppression of the spurious SH mode. As described in [Huang et al. 2017] the excitation of the SH mode depends on the interaction of the main Rayleigh mode and the SH mode. It is therefore desirable to take into account these effects in the COM and P-matrix simulation models, employed at design stage.

A general, numerically stable P-matrix formalism for multi-mode P-matrix models has already been derived for surface diffraction description: the 2D P-matrix method [Wagner et al. 2006]. In the present work this formalism is applied to the 1D problem of interacting modes in the sagital plane.

The model of multiple interacting modes can also elucidate the occurrence of a second mode at the upper stopband edge in LSAW devices, e.g. 42YX-lithium tantalate, the so called surface bulk hybrid (SBH) mode [Naumenko et al. 2001], which cannot be predicted by single mode COM and P-matrix models.

Statement of Contribution/Methods

A multi-mode P-matrix formalism accounting for energy conservation, causality and reciprocity is presented. The P-matrix of a single cell, i.e. an electrode, is represented as product of P-matrices for propagation, excitation and reflection. Reflection considers the interaction of forward and backward propagating waves of the same mode as well as different modes. We do not assume a collinear coupling of modes, i.e. the coupling of waves of different modes with identical propagation direction as in [Huang et al. 2017]. Instead the modes are assumed to be dispersive, which is reasonable due to the presence of the surface layer. Model parameters are determined by fit to dispersion relation and harmonic admittance, both obtained from FEM computations.

A multi-mode model for LSAWs is set up by employing one main LSAW mode and a quasicontinuum of BAW modes. In this way the SBH mode and other characteristic features of LSAW devices automatically emerge.

Results/Discussion

The model was applied to TCSAW devices. A two-mode model accounting for the Rayleigh and the SH-mode was determined. For a filter, results of the new model, FEM computations and measurement are in excellent agreement.

Application of the model to 42YX-lithium tantalate allows for simulation close to FEM, in particular with an accurate description of the upper passband skirt, at a reasonable computational cost.

2:15 PM Nonclassical power law of third order intermodulation in TC-SAW devices**Thomas Finteis¹, Werner Ruile¹, Markus Mayer¹, Ingo Bleyl¹, Karl Wagner¹**¹*RF360 Europe GmbH, Munich, Germany***Background, Motivation, and Objective**

Many investigations of the SAW community in the last few years have been focused on nonlinearities due to their growing importance because of the combination of multiple bands and channels (carrier aggregation). However, up to now it has been implicitly assumed that these nonlinearities can be described by classical power laws. The aim of this paper is to show that for TC-SAW devices on LiNbO₃-rot128YX with SiO₂-layer there are deviations from this classical behavior that can be empirically described by a simple model.

Statement of Contribution/Methods

In the most simple case, nonlinear behavior is described by a Taylor expansion. For an experiment with two input carriers, this approach yields both all the newly generated frequencies and also their powers' dependence on the input parameters f_1 , f_2 , $P(f_1)$, and $P(f_2)$. Whereas the nonlinear frequencies are most often well described by this model, the predicted nonlinear powers' dependence on the input powers $P(f_1)$ and $P(f_2)$, in case of third order e.g. $P(2f_1-f_2) = k_3 \cdot P(f_1)^2 \cdot P(f_2)$ or rather $10 \lg P(2f_1-f_2) = P_0 + 2 \cdot 10 \lg P(f_1) + 10 \lg P(f_2)$ on a logarithmic scale, deviate in some cases from the experimental observations.

In contrary to filter devices based on LiTa3-42YX, whose nonlinear third order powers depend perfectly well on the input powers as described by the Taylor expansion, we observed for temperature compensated SAW filter devices with a SiO₂ layer a more sophisticated power law. Not only does the third order exponent for identical input powers $P(f_1) = P(f_2)$ deviate from the classical value of 3. Additionally, if we choose $P(f_1)$ and $P(f_2)$ in such a way that $P(f_1)^2 \cdot P(f_2)$ remains constant, a maximum appears in contrast to the classically expected constant behavior. In short, the surface $10 \lg P(2f_1-f_2)$ spanned above the plane constituted by $10 \lg P(f_1)$ and $10 \lg P(f_2)$ is not anymore planar as for the Taylor expansion but is bent along a certain line. We propose a simple extension of the classical power law to describe these experimental observations.

Results/Discussion

We present experimental data of TC-SAW devices of IMD3 for both third order frequencies $2f_1-f_2$ and $2f_2-f_1$. These data clearly demonstrate the power law's deviation from the Taylor expansion outcome.

The proposed new power law fits well to these experimental data and includes the classical power law as a special case.

2:30 PM

Transverse modes in temperature compensated surface acoustic wave devicesKen-ya Hashimoto^{1,2}, Xinyi Li^{1,3}, Jingfu Bao³, Yulin Huang^{1,3}, Benfeng Zhang^{1,2}, Tao Hao²¹*Dept. EEE, Graduate School of Eng., Chiba University, Chiba, Japan,* ²*Shanghai Jiao Tong University, China, People's Republic of,* ³*University of Electronic Science and Technology of China, China, People's Republic of***Background, Motivation, and Objective**

Currently, the SiO₂/LiNbO₃ (LN) structure combined with heavy metal electrodes is widely used to realize high performance surface acoustic wave (SAW) devices with temperature compensation. In comparison with conventional 42°YX-LiTaO₃ case, two additional issues must be addressed for their development. One is suppression of spurious resonances caused by a secondary SAW, and another is suppression of those caused by lateral SAW propagation called the transverse resonances.

The author's group pointed out that these two issues are closely related to each other, and coupling between two SAW modes gives significant influences to behavior of these spurious resonances.

Statement of Contribution/Methods

This talk discusses influence of the coupling between two SAW modes to the spurious resonances. It should be noted that the influence is apparent only when their velocities are close to each other.

Results/Discussion

It is shown that the effective K^2 of the secondary SAW becomes zero when the coupling and the velocity difference are appropriate. In the situation, K^2 for the primary SAW takes a maximum.

It is also shown that shape of SAW slowness curves changes with the coupling. This makes various impacts on the lateral SAW propagation, which are not explained by the traditional scalar potential theory. Its extension, the thin plate model, is used to reveal how variation of the slowness curves influence transverse mode characteristics.

Finally, a few device configuration are designed using the thin plate model. Their performances are calculated by the 3D FEM, and validity of all the analyses is confirmed.

5C - BAW Device

Ikuta (200)

Tuesday, October 23, 4:00 pm - 5:30 pm

Chair **Rich Ruby**
Broadcom Ltd

5C-1

- 4:00 PM A Fast Thermo-Piezoelectric Finite Element Model of 3D Transient FBAR Dynamics under Large RF Signal**
Christopher Kirkendall¹, Brice Ivira¹
¹*Broadcom Inc, United States*

Background, Motivation, and Objective

As high power RF filtering applications become increasingly relevant, there is a need to quickly predict the effect of nonlinear interactions between thermal and piezoelectric fields. Yet, traditional finite element methods (FEM) for 3D piezoelectric resonators impose unreasonable memory and time requirements. Here, we develop a fast finite element model of thermo-piezoelectric physics based on a generalized series expansion of the governing equations. Together with transient, thermal IR measurements of film bulk acoustic resonator (FBAR) under large signal, the model is used to explain a range of nonlinear phenomena reported here for the first time.

Statement of Contribution/Methods

Our custom FEM enables orders of magnitude speedup compared to methods based on standard piezoelectric equations (solve time of 10 to 20 seconds per frequency for 3D FBAR). The model accounts for self-heating by coupling power dissipation density from the acoustic field into the heat transfer PDE. A pulsed S-parameters technique combined with high speed thermal IR imaging is used to measure the transient thermal response under large signal to compare to FEM.

Results/Discussion

Figure 1 shows how temperature profiles in panels a) and b) are closely linked to the non-uniform heat source in the resonator (Fig. 1d). The temperature gradient can create distinct regions in the active area: one vibrating below its local f_s and the other above (Fig. 1c). Figure 2 shows the transient thermal response at various frequencies near f_s . The spatially non-uniform heat source depends on both time and driving frequency, which explains the multi-step thermal responses: the FBAR can start below its effective f_s and reach steady state above it. In summary, our results give deep insight into FBAR physics in the nonlinear regime.

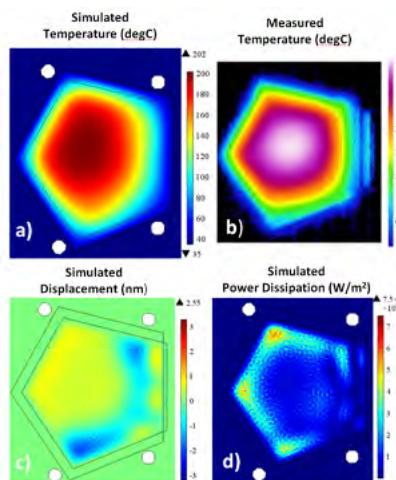


Figure 1

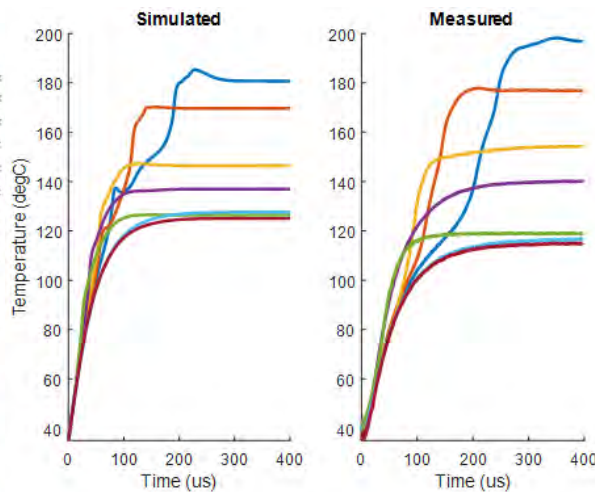


Figure 2

4:15 PM

Determining the Off-resonance 3rd Order Nonlinear Constants of a BAW resonatorJing Wu¹, Dave Feld¹¹Wireless Semiconductor Division, Broadcom, San Jose, CA, United States**Background, Motivation, and Objective**

Filters operated at high power levels and comprising BAW resonators produce 2nd & 3rd order harmonic emissions (H2 & H3) and intermodulation response (IMD3). To model the emissions of a BAW resonator, Feld and Shim constructed a nonlinear Mason model, which implements an “extended” pair of piezoelectric constitutive equations containing arbitrary 2nd & 3rd order terms:

$$T = [c^E S - eE] + [\frac{1}{2}\delta_3 c^E S^2 - \delta_1 eSE + \frac{1}{2}\delta_2 \varepsilon^S E^2] + [1/3\gamma_4 c^E S^3 - \gamma_1 eS^2 E + \gamma_2 \varepsilon^S SE^2 + 1/3\gamma_3 eeS^2 E^3/c^E]$$

$$D = [eS + \varepsilon^S E] + [\frac{1}{2}\delta_1 eS^2 - \delta_2 \varepsilon^S SE + \frac{1}{2}\delta_4 eeS^2 E^2] + [1/3\gamma_1 eS^3 - \gamma_2 \varepsilon^S S^2 E - \gamma_3 eeS^2 E^2/c^E + 1/3\gamma_5 (eS)^2 E^3/c^E]$$

c^E , e , ε^S , $\delta_1 - \delta_4$, $\gamma_1 - \gamma_5$ are the 1-D stiffness, piezoelectric, and dielectric, 2nd & 3rd order constants respectively. In our previous work we demonstrated a method by which the 2nd order constants $\delta_1 - \delta_4$ could be extracted from measurement of the small signal response of a resonator under a large dc bias voltage. This work is an extension of that work which allows us to extract the dominant 3rd order coefficients γ_5 , which gives rise to the H3 and IMD3 responses for a resonator when measured away from the resonance frequency.

Statement of Contribution/Methods

We use a network analyzer and a bias tee to measure the dependence of the small signal capacitance (at 400 MHz) as a function of the applied dc voltage. That capacitance is expressed as:

$$C = C^T * (1 + a_1 V + a_2 V^2)$$

Where C^T is the stress-free capacitance of the resonator, a_1 & a_2 are the linear & quadratic coefficient of C/C^T versus V_{dc} . A simple theory, expresses γ_5 in terms of a_2 :

$$\gamma_5 = a_2 t^2 c^E / \varepsilon^S (1 + e^2 / (e^S c^E))$$

Where t , is piezo thickness.

Results/Discussion

We select a piezoelectric AlN resonator, fabricated using a Mo-AlN-Mo piezoelectric layer stack, with metal and piezoelectric layer thickness chosen arbitrarily. We note that there is a small quadratic dependence superimposed on the linear response (Fig.1 (a)). We extracted the quadratic coefficient: $a_2 = 1.03e-7$. Using the equations stated above, we computed the 3rd nonlinear constant of the resonator: $\gamma_5 = 558$.

To verify this method, we plugged these constants, along with the linear materials properties and thicknesses of the piezo and metal films, into our non-linear Mason model. We simulated the response of our resonator by applying two 27 dBm fundamental tones, separated by 20 MHz incident on our resonator, measuring the emitted high side band IMD3 product. The measured and simulated IMD3 responses were in strong agreement (Fig.1 (b)).

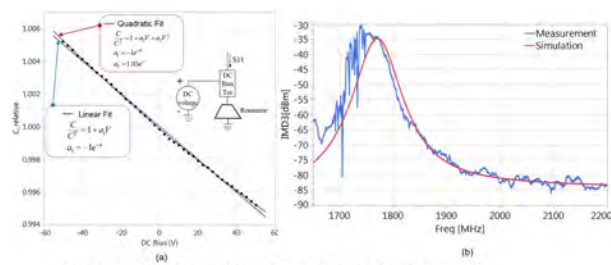


Fig.1 (a) Relative capacitance (C/C^T) of BAW resonator versus V_{dc} ; (b) Simulated and Measured IMD3

4:30 PM

Prediction of the H2 Response of an FBAR Resonator Using Finite Element Method**Zongliang Cao¹, Ruonan Liu¹, Jing Wu¹, Dave Feld¹**¹*Broadcom Inc, San Jose, CA, United States***Background, Motivation, and Objective**

Little effort has been given to modeling the 2nd and 3rd order harmonic emissions (H2 & H3) response of FBAR resonators exhibiting significant lateral mode behavior. Multi-Branched Butterworth-Van Dyke (MBBVD) circuit models have been used to incorporate lateral mode behavior of resonators. Global nonlinear parameters common to all branches can be incorporated into such a model to approximate a resonator's H2 & H3 response, but such an approach has limitations. In this work a Finite Element Analysis (FEA) tool incorporating both the linear and nonlinear physics is used to model the response of the aforementioned resonators.

Statement of Contribution/Methods

COMSOL FEA is used to simulate the H2 & H3 emissions of an FBAR resonator by incorporating weakly nonlinear terms into the stress and electric displacement tensors of the piezoelectric layer. We solve the weakly nonlinear problem using a perturbation approach to reduce simulation time. In this approach the field solution at the fundamental frequency is solved first using standard linear analysis driving the resonator plates with a power source. The 2nd order solution is found by re-solving the same set of physical equations as was used to solve the problem at the fundamental, but by replacing the external power source with a 50 Ω load and distributing a set of 2nd order sources throughout the piezoelectric medium which are derived from the field solution at the fundamental.

Results/Discussion

COMSOL FEA was used to simulate the S_{11} & H2 emissions responses of a circular resonator (including lateral physics) and was compared with measurements of the same. The S_{11} response for the measured and modeled devices was found to be in good agreement [Fig. 1a] in that the lateral Eigenmodes in the simulation were found to occur at the same frequency, and with approximately the same amplitude as in measurement. The discrepancy in the amplitude is primarily due to the difference in the measured and simulated Q (quality factor). The H2 response was also measured and modeled by recording the H2 emissions when a frequency swept +10 dBm tone was incident on the measured / modeled resonator and showed agreement too. The difference in the S_{11} lateral mode amplitudes between simulation and measurements is reflected in the H2 response [Fig. 1b]. We discuss the advantage of using this physical FEA approach over that of more simplistic MBBVD circuit models.

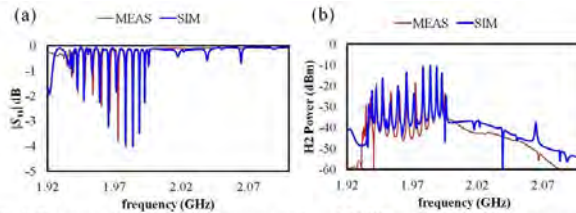


Fig. 1. The comparison of (a) the linear response S_{11} and (b) H2 response of a circular resonator between COMSOL and measurement

4:45 PM

A Hybrid 3D Thermal / 1D Piezoelectric Finite Element Model for Rapid Simulation of FBAR Filter Response under High Power**Christopher Kirkendall¹, Brice Ivira¹**¹*Broadcom Inc, United States***Background, Motivation, and Objective**

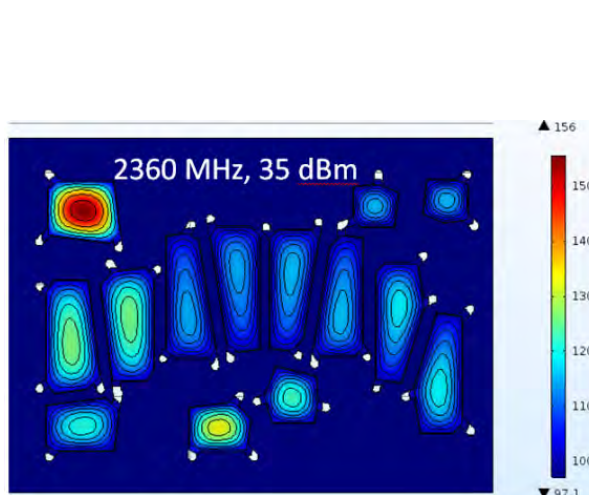
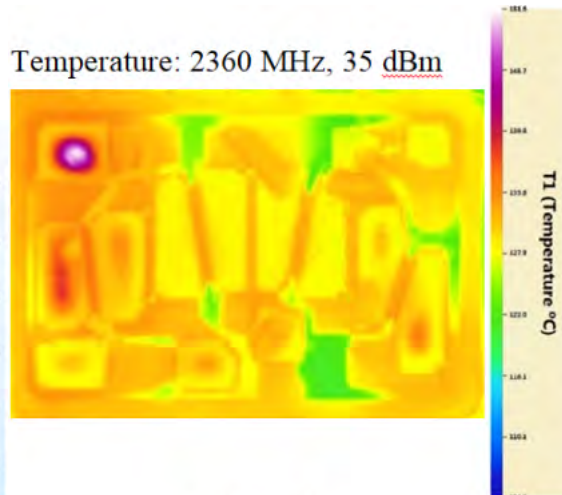
The increasingly stringent power requirements imposed on BAW filter technologies has made coupling between thermal and piezoelectric physics relevant to the design process. Existing lumped filter models do not account for the effect of a non-uniform temperature over each resonator. Here we report a new finite element based method for rapid simulation of filter response under high power that captures these effects.

Statement of Contribution/Methods

In order to preserve the speed of traditional lumped element filter models, a hybrid approach is taken in which the piezoelectric physics are modeled by 1D equations and the thermal physics by 3D equations. However, to capture the feedback of a non-uniform temperature distribution on the piezoelectric response, the active area of each resonator is divided into multiple segments. The boundaries between segments are defined by isothermal contours due to a heat source over the resonator. By choosing enough segments, each region is approximately isothermal and can be represented by a Mason model in parallel with those of other segments. The method accurately predicts frequency dependent drift of the filter response under high power.

Results/Discussion

Figure 1 shows the simulated temperature profile of each resonator in the filter for a CW driving frequency near the high band edge. It can be seen that each segment aligns with isothermal contours specific to the active area shape. Figure 2 is a thermal IR measurement of the filter under identical conditions as simulated in Fig. 1. Excellent agreement is achieved using the new isothermal segmentation approach. In summary, our method enables design and validation of BAW filters for high power applications.

**Figure 1****Figure 2**

5:00 PM

Hafnium nitride as high acoustic impedance material for fully insulating acoustic reflectors

Mario DeMiguel-Ramos¹, Marta Clement², Jimena Olivares², Teona Mirea², Valeriy Felmetser³, Andrew J. Flewitt¹, Enrique Iborra²

¹*Electrical Engineering Division, Department of Engineering, University of Cambridge, Cambridge, United Kingdom,*

²*GMME-CEMDATIC ETSI de Telecomunicacion, Universidad Politecnica de Madrid, Madrid, Spain, ³OEM Group, Gilbert, AZ, United States*

Background, Motivation, and Objective

Solidly mounted resonators (SMR) made of AlN piezoelectric thin films working at GHz frequencies are currently used in various fields (e.g. telecom, sensors) showing excellent performance. The confinement of the acoustic energy in the piezoelectric area is a major concern for designers and manufacturers, because it affects the quality factor of the device. To prevent acoustic leakage of the waves into the substrate, SMRs use an acoustic reflector that consists of alternated layers of low and high acoustic impedance (Z_A) materials. The mismatch between the high and low Z_A of the two materials used in the stack must be as high as possible, and it depends directly on the density (ρ) and the acoustic velocity (V_A) of the material ($Z_A = \rho V_A$). To this end, metals such as Mo or W are commonly used as high Z_A layer and SiO₂ is used as low Z_A layer. However, the use of metallic layers in the reflector is very damaging for certain applications, especially when there are several resonators on the chip (e.g. electrical filters) or when a long transmission line needs to be used. In those cases, the parasitic capacitance generated between the transmission line and the first metallic layer of the reflector has a huge detrimental effect on the response of the device and causes cross-talk between nearby resonators. To overcome this problem, patterning of each metallic layer is needed, complicating the fabrication process. Alternatively, insulating high acoustic impedance materials, such as AlN or Ta₂O₅, can be used. However, these materials offer a much lower acoustic impedance compared to metals, therefore manufacturers need to increase the number of layers of the reflector, making the fabrication process more difficult and costly. In this work we investigate HfN as a possible candidate for high acoustic impedance material in fully insulating acoustic reflectors because of its theoretical high Z_A .

Statement of Contribution/Methods

HfN films were deposited in a high target utilization (HiTUS) sputtering system using different N₂ concentrations in the Ar plasma. The density of films was assessed by X-Ray reflectance and the sound velocity by inducing an overtone resonance using a well-known Mo/SiO₂ reflector, a thick HfN layer and an AlN resonator. By fitting the electrical response of the resonators with the Mason model, the sound velocity is easily derived knowing the mass density and thickness of the HfN layer.

Results/Discussion

We have fabricated HfN thin films that display a density close to 11000 kg/m³, which is 80% of the nominal bulk value (13800 kg/m³), and a longitudinal velocity of 5400 m/s. These values result in a Z_A of 59.4 Mrayl, which is considerably higher than that obtained for the most used insulating high acoustic impedance materials (AlN and Ta₂O₅, 36.3 Mrayl and 38.9 Mrayl respectively) and very close to that of Mo sputtered films (64.7 Mrayl). A five layer acoustic reflector centered at 3.5 GHz made of HfN/SiO₂ is quantitatively compared with a standard Mo/SiO₂ reflector.

5:15 PM

Alloy Engineered Single Crystal BAW RF Filters for 5-6GHz Applications

Ramakrishna Vetur¹, Jeffrey Shealy¹, Michael Hodge¹, Shawn Gibb¹, Daeho Kim¹, Pinal Patel¹, Michael McLain¹, Ya Shen¹, Ken Fallon¹, Joonbum Kwon¹, Evan Grundman¹, Mary Winters¹, Rohan Houlden¹

¹Akoustis, Huntersville, NC, United States

Background, Motivation, and Objective

In 5-6GHz spectrum, emerging WiFi, 5G & infrastructure applications use multiple bands and complex architectures (CA, Diversity & MIMO), requiring higher filter counts and smaller filters, with improved insertion loss (IL), out of band rejection & linearity. Both wide and narrow band filters are required across the 1-6GHz and in the 5-6GHz spectrum. Infrastructure applications require high power handling capability at high frequency along with high linearity. Polycrystalline, highly oriented AlN materials face challenges at 5-6GHz spectrum as material stacks become thinner as frequency increases. This convergence of high frequency, high power, small size & *flexible* bandwidth motivates the requirement for innovation in piezoelectric materials.

Statement of Contribution/Methods

Single crystal MOCVD AlN, is promising for BAW filters at high frequencies [Akoustis:IMS 2017 & IEDM 2017]. X-ray diffraction scans of single crystal AlN show narrower peak widths i.e. better crystallinity vs sputtered AlN, for thick and thin (below 0.5μm) AlN layers. In addition, single crystal AlN enables piezoelectric coefficient e_{33} and resonator k_t^2 eff to be *flexibly* optimized for any specific application. (Fig 1).

Results/Discussion

5.2GHz resonators show a measured Q_p of 1644, Q_S of 1450 and a Q_{MAX} of 2136, and a k_t^2 eff of 6.259% leading to a FOM of 134. Filters at a center frequency of 5.2GHz measured -2.15dB insertion loss & 175MHz of 3dB bandwidth. Using alloy engineering, both wide (345MHz bandwidth and -2.1dB insertion loss at 5.7GHz) and narrow filters (75MHz bandwidth and -1.51dB insertion loss at 5.9GHz) were successfully simulated. Measured filter performance and simulated results demonstrate the excellent potential and great promise of single crystal BAW RF Filters for 5-6GHz applications.

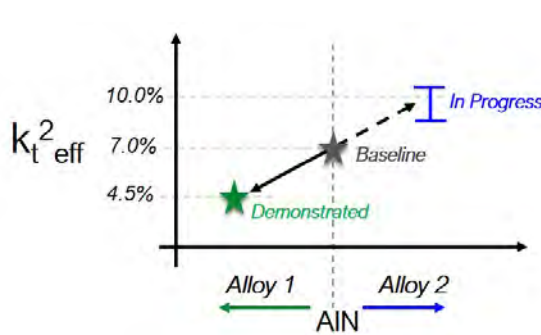


Fig 1: Flexible filter bandwidth and k_t^2 eff using alloy engineered single crystal AlN.

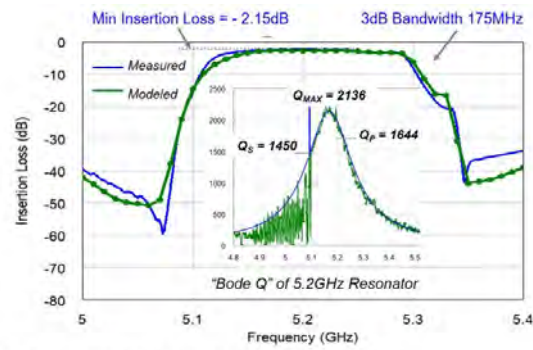


Fig 2: Measured and simulated response of 5.2GHz filter. Inset shows Bode Plot of 5.2GHz Resonator. Filter Measurement is taken on-wafer. Out of band rejection and wideband performance improves after packaging.

6A - Special Medical Systems

Nunobiki (150)

Tuesday, October 23, 10:30 am - 12:00 pm

Chair **John Hossack**
University of Virginia

6A-1

10:30 AM A lightweight, motorized 3D ultrasound probe for remote monitoring of astronauts health from ground

Cyril Mossuz¹, David Voisin¹, Erwan Filoux¹, Rémi Dufait¹, Philippe Auclair¹, Didier Chaput², Philippe Arbeille³
¹VERMON S.A., TOURS, France, ²Centre National d'Etudes Spatiales, TOULOUSE, France, ³Unité de Médecine et de Physiologie Spatiales, Université de Tours, France

Background, Motivation, and Objective

Various experiments are conducted aboard the International Space Station (ISS) to study the impact of prolonged exposure to microgravity on human health. The ECHO investigation aims at evaluating a tele-operable ultrasound scanner to perform health monitoring of crew members in space. Once the astronaut has placed the ultrasound probe at an acoustic window where the organ can be insonated from, the fine transducer orientation and image optimization are performed remotely by an expert on ground. Remote control of the imaging plane required the development of a compact motorized probe enabling fast and precise orientation of the transducer. On top of probe reliability, robustness and compactness, high image quality was essential to perform efficient medical diagnoses.

Statement of Contribution/Methods

VERMON developed a lightweight, high-performance, 3D acoustic probe made of a 128-element, curvilinear array mounted on 2 motorized axes allowing for $\pm 170^\circ$ rotation of the imaging plane around the probe central axis, and $\pm 40^\circ$ tilt from the same axis. Commercially-available, compact stepper motors coupled to a custom mechanical system were used to ensure responsive and accurate positioning of the array. All components of the acoustic stack (backing, piezoelectric elements, matching layers, silicone lens) were manufactured in-house and tuned to achieve optimal acoustic performances. Custom piezo-composite material was used to provide higher sensitivity and bandwidth.

Results/Discussion

The 3D probe performances were evaluated through standard pulse-echo measurements in water, using commercial pulser-receiver and custom data acquisition setup. A central frequency of 4.2 MHz was obtained with a fractional bandwidth of 75%. The probe was designed and all elements were carefully selected to achieve a total weight of about 400g, motors included. It was successfully used with French astronaut Thomas Pesquet during his 6-month mission aboard the ISS (Fig. 1). High-quality abdominal data were remotely acquired and used to characterize the effects of microgravity on human tissues. The system is now routinely used for several Canadian and European programs requiring remote echography, and is considered for a future human spaceflight towards planet Mars, but also for applications on Earth to provide ultrasound expertise to patients living in remote areas.

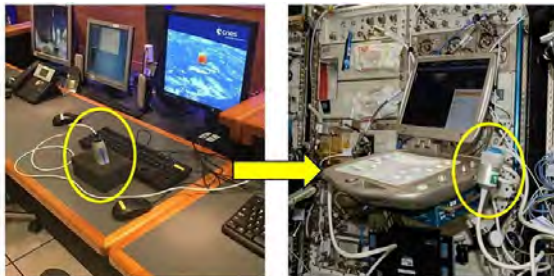


Fig. 1. 3D ultrasound probe in the ISS (right) remotely controlled from ground by a joystick (left).

10:45 AM

Development of a mechanically-scanning microultrasound capsule endoscopy device and demonstration in vivo

Yongqiang Qiu¹, Yaocai Huang², Jiehan Hong², Zhiqiang Zhang², Xingying Wang², Benjamin Cox³, Peitian Mu², Congzhi Wang², Holly Lay¹, Gerard Cummins⁴, Marc P.Y. Desmulliez⁴, Eddie Clutton⁵, Hairong Zheng², Sandy Cochran¹, Weibao Qiu²

¹School of Engineering, University of Glasgow, Glasgow, United Kingdom, ²Shenzhen Institutes of Advanced Technology, Chinese Academy of Sciences, China, People's Republic of, ³School of Medicine, University of Dundee, Dundee, United Kingdom, ⁴Heriot-Watt University, United Kingdom, ⁵Royal (Dick) School of Veterinary Studies, University of Edinburgh, United Kingdom

Background, Motivation, and Objective

Capsule endoscopy (CE) enables remote, minimally invasive observation of the gastrointestinal (GI) tract. Video capsule endoscopy (VCE) is limited to imaging of the GI mucosal surface. Information within the lumen wall cannot be acquired and microultrasound capsule endoscopy (μ USCE), with this capability, is thus a complementary solution. This paper describes the development and demonstration of a μ USCE device based on mechanical scanning with a high frequency (>20 MHz) ultrasound transducer.

Statement of Contribution/Methods

The prototype μ USCE device included a micromotor, a transducer holder and an ultrasound transducer based on piezocrystal LiNbO₃ (Fig. 1a). The micromotor rotated the transducer 360° in an oscillatory manner, alternately clockwise and counterclockwise. The motor rotation was controlled by varying the amplitude and direction of the input DC current. During rotation, the transducer emitted ultrasound vertically through an acoustic window in the capsule shell and received echoes from the wall of the surrounding lumen. The thickness of the parylene on the acoustic window was optimised to reduce the energy loss. The capsule shell was made of biocompatible poly(methyl methacrylate) (PMMA) coated with parylene and a tether was provided for power supply and data communications. To demonstrate the device's effectiveness, an *in vivo* study was performed in the oesophagus and small bowel of anaesthetised female Landrace. The study was conducted under UK Home Office License (PPL: 70/8812).

Results/Discussion

The 10 mm diameter and 30 mm length of the prototype devices conformed to commercial VCE dimensions found to be acceptable for clinical use. The centre frequency of the ultrasound transducer is $f_c \approx 28.5$ MHz, $\lambda \approx 52$ μ m. The focal distance of the transducer is ~8 mm. Imaging performance was initially evaluated with phantom consisting of multiple Ø 20 μ m tungsten wires, giving axial and lateral resolutions of 67.4 μ m and 130.6 μ m, respectively. Two prototypes were tested in the oesophagus and small bowel of two anaesthetised pigs and ultrasonic echoes were collected during experiments. Post mortem CT scans were performed to determine the location of the capsule in the small bowel. An example of a reconstructed and post-processed image of the small bowel is shown in Fig. 1b, giving clear differentiation of the lumen layer structure.

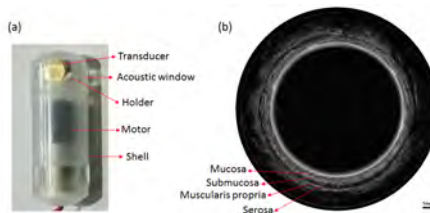


Figure 1 (a) Prototype μ USCE device, Ø 10 mm and (b) microultrasound image of porcine small bowel *in vivo*.

11:00 AM

Feasibility study of a coherent multi-transducer US imaging systemLaura Peralta¹, Alberto Gomez¹, Joseph Hajnal¹, Robert Eckersley¹¹*Biomedical Engineering Department, King's College London, London, United Kingdom***Background, Motivation, and Objective**

Ultrasound images can be difficult to assess, because of the limited resolution and view-dependent artefacts that are inherent to the small aperture transducers used clinically. An extended aperture has the potential to greatly improve imaging performance. This work introduces a fully coherent multi-transducer ultrasound imaging system, formed by several ultrasound transducers that are synchronized, freely located in space and transmit plane waves (PW). Through coherent combination of the different transducers, a larger effective aperture is obtained and then an improved final image. First phantom images produced using this technique are presented here.

Statement of Contribution/Methods

The method was experimentally validated in an ultrasound phantom. Wire targets at a depth of 77 mm in distilled water were imaged to measure resolution. Experiments were performed using two ULA-OP 256 imaging platforms (University of Florence, Italy) equipped with 2 linear array probes LA332 (Esaote, Italy). The systems were synchronized, i.e. with the same trigger and sampling times in both transmit and receive mode. The two probes were mounted on xyz translation and rotation stage (Thorlabs, USA). For each probe in an alternating sequence, i.e. only one probe transmits at each time while both probes receive, 121 PW were transmitted (-30° to 30°, 0.5° step) at 3 MHz and PRF of 4 kHz. Since every transmitted PW is received by all arrays, including the transmitting one, each PW shot yields 2 RF datasets.

The subwavelength localization accuracy required to merge information from multiple probes is achieved by optimizing the spatial coherence function of the backscattered echoes coming from the same point source insonated by all probes and received by the same one, without the use of an external tracking device. 2D PW beamforming of all received data was performed using the estimated positions of the probes to produce a high-resolution image.

Results/Discussion

Figure 1 shows a comparison between a conventional reconstruction with a single transducer and a coherent multi transducer image. The multi transducer image of the wire targets was clearly improved. The resolution was reduced from 0.65 mm to 0.19 mm. Effects of PW sector angle and k-space representation of the resulting images were also investigated and discussed. Further investigations with a tissue mimicking phantom are underway.

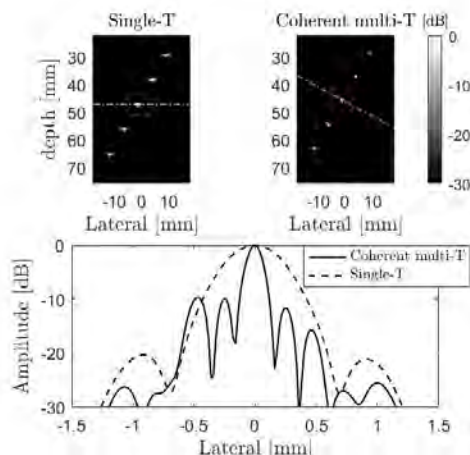


Figure 1. Experimental images of a wire phantom produced with a single transducer and coherently compounding the images acquired by both transducers; Transverse cut of the PSF at the scatterer depth indicated with dashed lines and that leads to the best resolution in each case.

11:15 AM

Reconfigurable 1.5D Source Arrays for Improved Elevational Focussing in All-Optical Ultrasound Imaging**Erwin Alles^{1,2}, Sacha Noimark^{1,2,3}, Edward Zhang¹, Paul Beard^{1,2}, Adrien Desjardins^{1,2}**¹*Department of Medical Physics & Biomedical Engineering, University College London, London, United Kingdom,*²*Wellcome / EPSRC Centre for Surgical and Interventional Sciences, University College London, London, United*³*Kingdom, ³Materials Chemistry Research Centre, Department of Chemistry, University College London, London, United Kingdom***Background, Motivation, and Objective**

All-optical ultrasound, where ultrasound is both generated and detected using light, is a viable alternative to electronic technology. Recently, we developed centimetre-scale photoacoustic optical ultrasound generator membranes that exhibit sufficiently low inter-element crosstalk to obviate the need for mechanical source separation. Instead, spatial confinement of excitation light can be used to define the geometry of the optical ultrasound source, and through scanning optics source arrays of arbitrary geometry can be synthesised (and dynamically reconfigured). Here, this flexibility in source aperture geometry is used to improve the elevational resolution in a 2D imaging setup.

Statement of Contribution/Methods

Pulsed laser light was focussed onto an optical ultrasound generator membrane comprising carbon nanotubes and polydimethylsiloxane, in which broadband ultrasound was generated photoacoustically. Back-scattered ultrasound was recorded using a fibre-optic detector comprising a Fabry-Pérot cavity. A single eccentric optical ultrasound source (dimensions: 1 mm elevational, 200 µm lateral) was sequentially moved to 200 lateral positions (16 mm aperture, irregularly spaced), which spatially partially overlapped. The source positions either coincided with the image plane (1D) or were distributed across 9 lines spaced 0.25 mm apart elevationally (1.5D, sparsely sampled). A point target (50 µm diameter) was placed at elevational offsets ranging between ±1.5 mm, and 2D images acquired for each position were stacked to determine the 3D point spread function (PSF) of the system.

Results/Discussion

The elevational extent (full width half maximum) of the PSF was improved from 1.1 mm with a 1D aperture to 0.9 mm with a 1.5D aperture, while the axial and lateral resolutions and the acquisition time were unaffected (Fig. 1). However, the image contrast was reduced by 3.4 dB due to a larger propagation distance and lower source density in each elevational line. Furthermore, the 1.5D source aperture enabled out-of-plane object localisation at a resolution of down to 0.7 mm across the elevational aperture. The demonstrated ability to arbitrarily reconfigure the geometry of the source array thus enables image optimisation paradigms that hitherto were impractical to implement, and allows for seamless switching between different imaging modes.

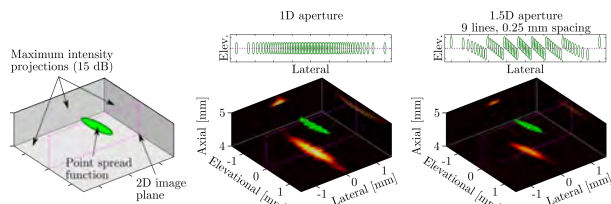


Fig. 1 - Schematic (left) and 3D point spread functions measured using a 1D (middle) and 1.5D array (right).

11:30 AM

Fibre-Optic Ultrasound Imaging Devices for Guidance of Minimally Invasive Procedures

Richard Colchester^{1,2}, Erwin Alles^{1,2}, Sacha Noimark^{1,2,3}, Charles Mosse^{1,2}, Sunish Mathews^{1,2}, Edward Zhang¹, Callum Little^{2,4}, Roby Rakshit^{2,4}, Ioannis Papakonstantinou⁵, Paul Beard^{1,2}, Malcolm Finlay^{1,2,6}, Adrien Desjardins^{1,2}

¹Department of Medical Physics & Biomedical Engineering, University College London, London, United Kingdom,

²Wellcome/EPSRC Centre for Surgical and Interventional Sciences, University College London, London, United Kingdom, ³Materials Chemistry Research Centre, Department of Chemistry, University College London, London, United Kingdom, ⁴Department of Cardiology, Royal Free Hospital, London, United Kingdom, ⁵Department of Electronic and Electrical Engineering, University College London, London, United Kingdom, ⁶William Harvey Cardiovascular Research Institute, Queen Mary University of London and Barts Health Centre, London, United Kingdom

Background, Motivation, and Objective

Recently, all-optical ultrasound has made rapid progress as a technique for medical imaging, moving from bench top to *in vivo* studies. With this technique, ultrasound is generated and received using light, enabling wide bandwidths, high sensitivity, and device miniaturisation. These properties make it well-suited for guidance of minimally invasive procedures. Using two optical fibres, one for ultrasound transmission and a second for reception, a series of devices can be fabricated. We discuss recent innovations, including real-time m-mode imaging, side-viewing intravascular imaging, and dual-modality ultrasound and photoacoustic imaging.

Statement of Contribution/Methods

In these devices, ultrasound generation occurs via the photoacoustic effect, with pulsed excitation light delivered to an optically absorbing coating on the end of an optical fibre. By applying this coating to the cleaved end surface of an optical fibre, ultrasound can be generated co-linear with the fibre axis. Using such a device we have demonstrated forward-viewing real-time m-mode imaging *in vivo* (Fig 1. a). Alternatively, by redirecting light from the optical fibre to a side surface, ultrasound can be transmitted perpendicular to the fibre axis. Rotating the ultrasound beam then facilitates the acquisition of a 2D image. Using this method, we acquired rotational images with a depth resolution $< 40 \mu\text{m}$ and an angular resolution *ca.* 14° (Fig 1. b). The carbon nanotube – polydimethylsiloxane composite coatings used for both these devices exhibit broadband optical absorption. In a recent advance, we have fabricated coatings with wavelength-selective absorption. Using these coatings, we demonstrated co-registered ultrasound and photoacoustic imaging of diseased vessels (Fig 1. c).

Results/Discussion

We present innovations in all-optical ultrasound imaging which have enabled real-time, rotational, and multi-modality imaging. The broad bandwidths generated by these devices has led to high resolutions (axial: *ca.* $40 \mu\text{m}$) and it is hoped these innovations will lead to the clinical translation of all-optical ultrasound soon.

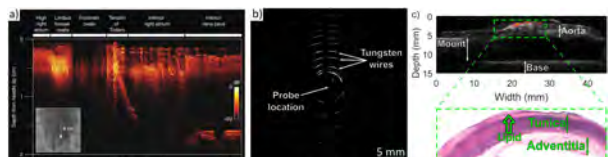


Fig 1. a) Real-time m-mode imaging during needle translation in the right atrium of a swine heart *in vivo*. b) Rotational imaging of a tungsten wire phantom. c) Dual-modality ultrasound (grayscale) and photoacoustic (red) imaging of diseased human aorta *ex vivo*.

11:45 AM Design of a fully populated phased array for transcranial HIFU therapies based on shock-wave exposures with aberration correction

Pavel Rosnitskiy¹, Oleg Sapozhnikov^{1,2}, Leonid Gavrilov³, Petr Yuldashev¹, Vera Khokhlova^{1,2}

¹Physics Faculty, Moscow State University, Russian Federation, ²Applied Physics Laboratory, University of Washington, United States, ³N.N. Andreyev Acoustics Institute, Russian Federation

Background, Motivation, and Objective

High-intensity focused ultrasound (HIFU) hemispherical arrays are used in clinics to induce thermal destruction of deep brain structures through an intact skull [Hynynen, Jolesz, UMB, 24(2), 1998]. However, this method may lead to overheating of surrounding tissues and skull bones. As an alternative, a boiling histotripsy (BH) approach that utilizes short bursts with shocks of 70-100 MPa amplitude can be used to mechanically ablate brain tissue [Khokhlova *et al.*, JASA, 130(5), 2011]. The objective of this study was to design an array that could enable reaching BH conditions in deep brain structures taking into account the effects of aberrations, reflections, absorption, nonlinearity, shear waves in the skull, and existing technical limitations on the intensity at the array elements (40 W/cm²).

Statement of Contribution/Methods

A model of 1 MHz 256-element array in the form of a spherical segment was proposed. A novel method based on the capacity-constrained tessellation was used to develop a fully populated random pattern of equal area polygonal elements at the array surface (Fig. (a)) [Rosnitskiy *et al.*, IEEE UFFC, 65(4), 2018]. A numerical algorithm that combines three different models was developed to simulate a 3D ultrasound beam when focusing through the skull. The Rayleigh integral method was used in water outside the head, a linear k-space Kelvin-Voigt model – inside the skull and adjacent tissues [Treeby, Cox, JASA, 136(4), 2014], and nonlinear Westervelt model was used inside the homogeneous absorptive brain tissue [Yuldashev *et al.*, Phys. Med. Biol., 58(8), 2013]. A 3D model of the head was created using segmentation of the MRI scan from open database (Fig. (b)). Aberration correction based on combining k-space and ordinary least squares (OLS) methods was proposed (Fig. (b), (c)).

Results/Discussion

A HIFU array for BH of deep brain structures was proposed. A combined modeling method for simulating ultrasound focusing through the skull and evaluating the degree of nonlinear waveform distortion at the focus was developed. The proposed OLS method for aberration correction provided tight focusing and formation of shocks of 70 MPa sufficient for BH (Fig. (c)) at intensity at the array elements of 25 W/cm². Work supported in parts by the RSF 14-12-00974, the Ph.D. student stipend from “Basis” Foundation, and the stipend of the President of Russia SP-2644.2018.4.

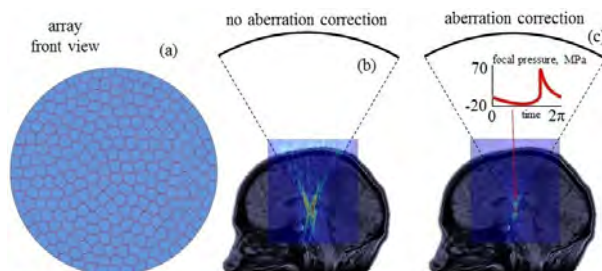


Figure. (a) A front view sketch of the 256-element fully populated random array. Simulated 2D distributions of the peak positive pressure from a fully populated array focused through an intact skull into the thalamus region obtained (b) without aberration correction, (c) with aberration correction. The arrow marks that shock front is present in simulated waveform at the focus.

6B - Transducers

Nunobiki (150)

Tuesday, October 23, 1:30 pm - 3:00 pm

Chair **Kentaro Nakamura**
Tokyo Institute of Technology

6B-1

1:30 PM

Printed polymer transducers for mid-air haptic feedback

Paul van Neer¹, arno volker¹, Arthur Berkhoff¹, Hylke Akkerman², Albert van Breemen², Gerwin Gelinck²

¹TNO, Netherlands, ²Holst Centre, Netherlands

Background, Motivation, and Objective

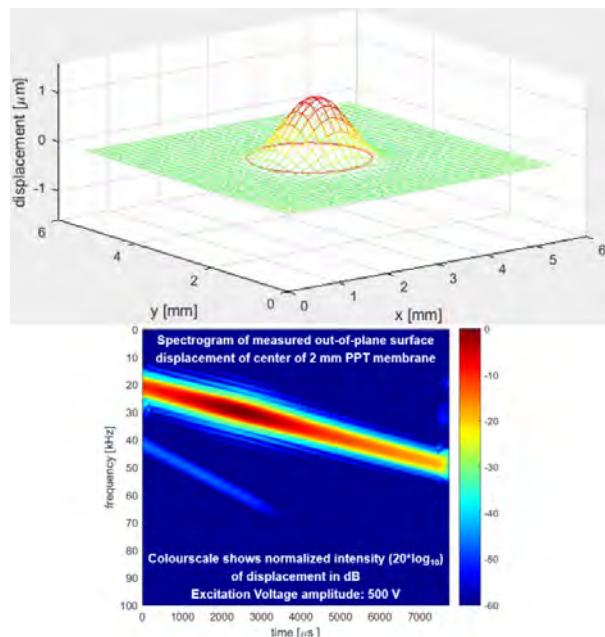
Recently, there has been considerable interest in the development of ultrasound based mid-air haptic feedback devices. These devices allow for tactile sensations to be induced at any position and time without constraints to human motion, which is useful for virtual user interfaces, augmented/virtual reality and feedback buttons. The haptic feedback mechanism is a combination of acoustic streaming and radiation force. Most work reported in literature induce said effects using matrices of 'standard' single element transducers, which are rigid, bulky and heavy. Our research focuses on the development of printed polymer transducers (PPTs): piezomembranes deposited using a printing process. The membrane is a sandwich of polyimide and PVDF. As PPTs are fully flexible, < 0.25 mm thick and light, they can be easily integrated onto curved surfaces. However, the piezoelectric charge coefficients of PVDF are low compared to regular PZT5A/H, making it challenging to achieve the required sound pressure. This work investigates the feasibility of using PPTs for haptic feedback.

Statement of Contribution/Methods

The surface displacement, transfer functions, crosstalk, electrical impedance, and acoustic far field response of PPTs with different geometries and materials were modeled in air using the COMSOL FEM package and custom built models. PPTs with diameters of 2, 4, 6, and 8 mm were built, separately and in arrays. Their out-of-plane surface displacement versus frequency and spatial locations was measured using a laser vibrometer mounted in an xyz-stage. Also, the membranes' acoustical responses were measured using a microphone setup.

Results/Discussion

The peak transmit transfer function of a 6 mm membrane in air was modeled to be 1.6 Pa/V at 7.4 kHz and measured to be 1.5 Pa/V at 7.7 kHz. Laser vibrometer measurements of a 2 mm membrane excited using a 500 V chirp showed a peak displacement of 1.6 μm @ 29.5 kHz in air with a 2nd harmonic of < -45 dB (see figure). The peak pressure produced by our chosen array design (annular array, aperture 30x30 cm^2 , membrane radius 0.6 mm) was modeled to be 156 dB re 20 μPa at 40 kHz in air using a 300V excitation. The calculated peak force on a finger due to acoustic streaming and radiation force was 0.26 and 2.0 mN respectively, which is much higher than the tactile threshold of 0.01 mN reported in literature. Thus, using PPTs for haptic feedback appears feasible.



1:45 PM

Linear Ultrasonic Array Development incorporating Cantor Set Fractal GeometryHaoyu Fang¹, Zhen Qiu¹, Anthony Mulholland², Richard O'leary³, Anthony Gachagan⁴¹*University of Strathclyde, Glasgow, United Kingdom*, ²*Mathematics and Statistics, University of Strathclyde, Glasgow, United Kingdom*, ³*Centre for Ultrasonic Engineering, University of Strathclyde, Glasgow, United Kingdom*, ⁴*Electronic and Electrical Engineering, University of Strathclyde, Glasgow, United Kingdom***Background, Motivation, and Objective**

Naturally occurring resonating system utilize structures containing a range of length scales to produce a broad operating bandwidth. In our previous work [1], a piezoelectric composite transducer, with components in varying length scales based on a fractal geometry, resulted in a wider operational bandwidth and a higher sensitivity. This work is now extended to an ultrasonic array device using a Cantor Set (CS) fractal geometry. The behavior of this CS fractal array is explored and compared with a conventional 2-2 linear array. A second advanced fractal geometry comprising orthogonal CS fractal geometries, known as the Cantor Tartan (CT), is also investigated to further enhance the bandwidth performance of the array.

Statement of Contribution/Methods

The design space of the CS microstructure was explored using finite element (FE) modeling (PZFlex, OnScale, USA); it was found that a CS structure of fractal generation Level II provided enhanced bandwidth, sensitivity and dilation quality when compared to a standard 2-2 connectivity piezocomposite. Prototypes of 24-element CS and regular 2-2 array were fabricated using the dice-and-fill technique. The experimental performance of both arrays was characterized and the imaging and defect sizing capability was assessed based on a full matrix capture (FMC) and total focusing method (TFM) imaging using a wire-water phantom.

Results/Discussion

The simulated pulse-echo response indicated that the CS fractal array elements possessed a wider - 6 dB bandwidth (57.3 % vs. 49.4 %), and a higher sensitivity, (113.9 vs. 89.0 mVp-p) compared with a conventional 2-2 design. The experimental pulse-echo response data of both array elements correlated well with the FE data. FMC/TFM images produced by the two arrays showed that the CS fractal array outperforms the conventional 2-2 array in terms of image resolution.

Finally, the possibility of further increasing the bandwidth of an ultrasonic array was investigated by considering the CT fractal geometry. It was found that array elements comprising a combination of Level II CS in azimuth and Level IV CS in elevation resulted in an enhanced -6 dB bandwidth of 68.1 %, when compared with other devices in this study.

[1] H. Fang, et al, "Improving the operational bandwidth of a 1-3 piezoelectric composite transducer using Sierpinski Gasket fractal geometry," Proc IEEE IUS, 2016.

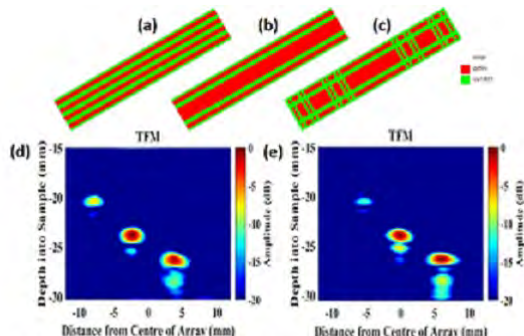


Fig. 1: Array element of (a) conventional 2-2 array; (b) CS fractal array in generation Level II; (c) CT fractal array; TFM imaging of (d) CS fractal array; (e) conventional linear array

2:00 PM

Broadband Piezocrystal Transducer Array for Non-Destructive Evaluation Imaging ApplicationsZhen Qiu¹, Haoyu Fang¹, Richard O'leary¹, Anthony Gachagan¹¹*Centre for Ultrasonic Engineering, University of Strathclyde, Glasgow, United Kingdom***Background, Motivation, and Objective**

Bandwidth plays an important role in ultrasound inspection in Non-Destructive Evaluation (NDE), and has direct impact on imaging resolution. With increasing demands of detecting smaller sized defects at earlier stage, particularly where the propagation medium presents a challenge to SNR, broadband transducers with high sensitivity are highly desirable. However in conventional piezoelectric ceramic transducers, bandwidth and sensitivity are mutually exclusive. The recent development of piezocrystals within $(1-x)\text{Pb}(\text{Mg}_{1/3}\text{Nb}_{2/3})\text{O}_3\text{-xPbTiO}_3$ (PMN-PT) family provide a means of advancing both the bandwidth and imaging sensitivity simultaneously. The large electromechanical coupling ($k_{33} \approx 90\%$) and large piezoelectric charge coefficient ($d_{33} > 2000 \text{ pc/N}$) of piezocrystals can result in improved resolution, higher SNR, and increased depth of view in NDT ultrasound imaging.

Statement of Contribution/Methods

A 32-element, 5MHz linear array, incorporating PMN-PT 1-3 piezo-polymer composite, has been designed using finite element modelling approach (PZFlex, OnScale Inc, Cupertino, CA). The Elasto-Electric material properties of the PMN-PT samples were characterized and evaluated with the FE model to fundamentally ensure accurate corroboration. The array configuration was then investigated, including array microstructure, matching and backing material selection – taking cognisance of the requirement for unimodal operation with minimal inter-element cross talk. Array sensitivity and bandwidth were assessed using pulse echo results from a steel block incorporating side-drilled hole defects. Imaging performance was then undertaken, employing full matrix capture (FMC) and total focusing method (TFM). A reference array comprising of conventional PZT5H ceramic was also implemented following the same designing criteria for comparison.

Results/Discussion

The piezocrystal array is predicted to produce a broad bandwidth of 87% at -6 dB and a gain-bandwidth product improvement of 160% when compared to the reference ceramic array. Both mechanical and electrical cross-talk were found to be minimal at better than -20 dB. The TFM imaging also demonstrates that the piezocrystal array has better defect detection and sizing ability. Implementation of the array is now in progress and experimental results will be presented.

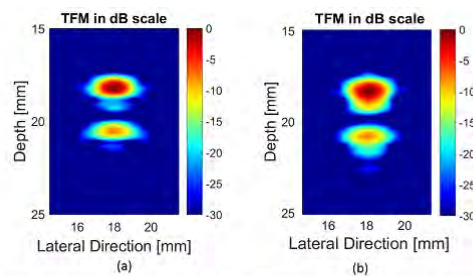


Figure 1. Predicted TFM images of two SDHs (0.6mm, $\sim\frac{1}{2}\lambda$, dia.) from: (a) piezocrystal array and (b) ceramic array. -6dB measurements are 1.32mm vs 1.34mm in lateral direction and 0.7mm vs 0.9mm in axial direction

2:15 PM

A novel design of piezoelectric ultrasonic transducer with high temperature resistanceXianwei Yuan¹, Shimin Yu², Xiyang Yu², Wenping Song²¹*Harbin Institute Of Technology, Harbin, China, People's Republic of*, ²*Harbin Institute of Technology, Harbin, China, People's Republic of***Background, Motivation, and Objective**

Ultrasonic cavitation has been proved to be an effective way to accelerate or change the chemical reaction processes, such as modification of asphalt and reduce of crude viscosity. However, when the temperature of liquid medium disposed by ultrasonic transducer is high, huge heat will be inevitably conducted to the piezoelectric ceramics of transducer and cause a high temperature rise. It causes the degradation of performances of the ultrasonic transducer. In this study, a novel sandwich piezoelectric ultrasonic transducer with a water cooling component is proposed and fabricated.

Statement of Contribution/Methods

The specific structure of the ultrasonic transducer is shown as Fig. 1. The horn is cooled down by the liquid coolant which is circulated in the cooling component. Firstly, dimensions of the sandwich vibrator, horn, cooling component and tool head are determined by the frequency equations, which are developed by the electromechanical equivalent and the transfer matrix. Then, the size and position of the cooling component are optimized by finite element method (i.e., FEM) using ANSYS. In addition, the heat conduction in the transducer while dealing with high-temperature liquid is analyzed by FEM analysis. Finally, an experiment is implemented using the set-up shown as Fig. 2, in which the transducer is immersed in an oil bath of 180°C.

Results/Discussion

The resonance frequencies calculated by the frequency equations and FEM analysis are in good agreement. The ultrasonic transducer designed in this study is proved to be able to work stably in the 180°C oil bath. The resonance frequency is 19.8 kHz and the input power can reach 2000W. Consequently, this ultrasonic transducer can be used to process the high temperature liquid, such as heated crude and asphalt.

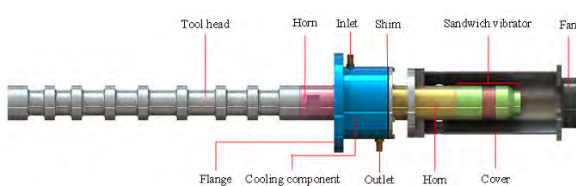


Fig. 1 Specific structure of the ultrasonic transducer

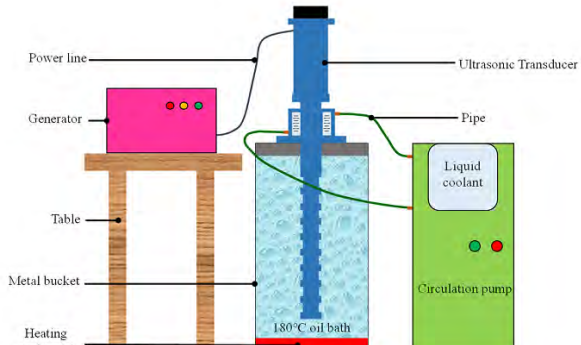


Fig. 2 Schematic of experiment set-up

2:30 PM

Densification behavior and Mechanical Properties of PBX Substitute Composites Fabricated by Ultrasonic Assisted Pressing of Powder

Kezhen Lyu¹, Chao Han¹

¹*Institute of Chemical Materials, China Academy of Engineering Physics, China, People's Republic of*

Background, Motivation, and Objective

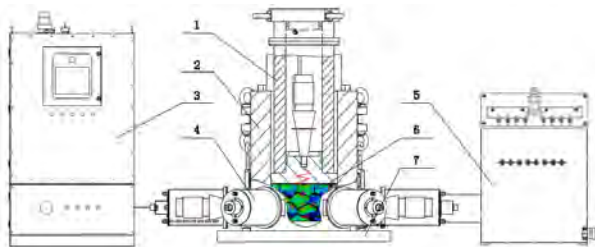
Pressing form is a well-established process to manufacture PBX parts of different shapes with desired mechanical properties. Residual porosity, structural non-homogeneities and poor mechanical properties are the most challenging issues in the area of the powder densification processes. In comparison with conventional, ultrasonic assisted powder compaction not only has the advantages to overcome these shortcomings but also has the ability of easy molding. To the best of our knowledge, published literature reports so far suggested that no attempt has been made to produce the PBX substitute by pressing of powder assisted ultrasonic vibration. The aim of this research was to study the feasibility of ultrasonic assisted PBX powder compaction and the optimal compaction condition of the powder, some effects such as compaction pressure, duration of ultrasonic vibrations, the amplitude of vibration and particle size distribution on mechanical properties was investigated.

Statement of Contribution/Methods

In order to fabricate PBX substitute parts with ultrasonic vibrations, an ultrasonic vibration assisted molding system was designed and manufactured based on axial and radial ultrasonic vibration loading technology. Each sample is composed of 2kg PBX substitute powder which is then converted into a cylinder of 200 mm in height and 45 mm in diameter after the pressing operations. Ultrasonic assisted PBX substitute powder compaction is carried out at a room temperature but three different pressure, i.e. 60, 90 and 150 MPa.

Results/Discussion

Fig. 1 shows the schematic view of ultrasonic vibration assisted pressing setup. The effects of particle size and vibration amplitude and pressure on the densification behavior and mechanical properties of PBX substitute powder are discussed. The results show that PBX substitute composite was successfully fabricated by pressing of powder with ultrasonic vibration, applying ultrasonic vibration leads to a higher relative density and an improved homogeneity, and the growth of the size of the pressed sample can be reduced with the ultrasonic vibration and the larger of static pressure, the smaller of the pressed sample size change. In addition, ultrasonic vibration has a great effect on the finer particles and the surface temperature of the sample is not obviously increased with ultrasonic vibration.



2:45 PM **High Temperature condition monitoring with a novel, flexible, thin film sensor**Daniel Irving¹, Ivan Shorokhov¹, Heather Trodden¹, David Allan Hughes¹¹*novosound, Motherwell, United Kingdom***Background, Motivation, and Objective**

Ultrasonic inspection is the go to tool for a range of industrial NDE applications. There are, however, severe limitations when applying the technology in high temperature environments. For sectors such as oil & gas and nuclear power this makes the monitoring of assets at elevated temperatures challenging; often requiring costly and inconvenient shutdown. Suitable sensors can be permanently fitted to high temperature infrastructure and this will significantly improve monitoring and reduce asset downtime.

The work presented here demonstrates fit and forget sensors which have consistent output at elevated temperatures and are durable enough to withstand the industrial environment. An additional benefit of these sensors is that they are truly flexible, which allows them to conform to curved surfaces (e.g. pipes) without the need for a couplant material.

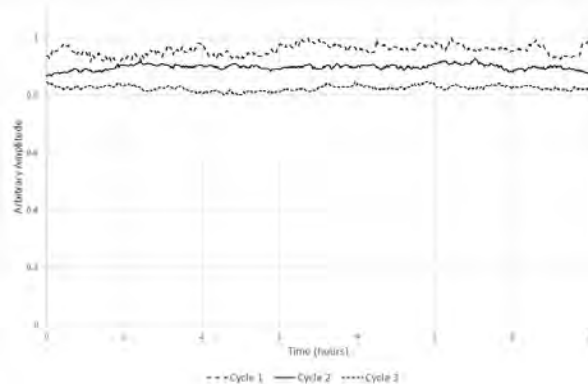
Statement of Contribution/Methods

A proprietary piezoelectric thin-film material is used to produce a large number of consistent 15MHz single element contact transducers. The material is a metal oxide-based alloy, deposited with a novel reactive sputtering process onto a flexible metallic substrate. The performance of the transducers is measured over long-term heating and cooling cycles at 250°C and 500°C. The transducer is fixed to a section of steel pipe on a hot plate. Backwall reflections of the steel pipe are recorded every minute throughout the cycling using standard ultrasonic NDT equipment.

Results/Discussion

Results obtained showed that the sensors operated effectively through repeated heating, demonstrating that they can withstand prolonged temperature and operation. Typical amplitude data from 3 sequential heating cycles (duration 7 hours) is shown in Figure 1. As shown, the output remains stable whilst held at elevated temperature, with no statistical significance in the output amplitude (Students T-Test, $p<0.08$).

By measuring the electrical characteristics of the transducer, the minor reduction of output after repeated cycles was found to be attributable to the clamping system loosening with repeat expansion and contraction. Further work will concentrate on the adhesion of the sensor to the pipe to reduce the variation in signal due to these effects. Other small fluctuations in output were observed and these were found to correlate to changes in the ambient temperature and easily compensated for.



6C - NDE

Nunobiki (150)

Tuesday, October 23, 4:00 pm - 5:30 pm

Chair **Jafar Sanie**
Illinois Institute of Technology

6C-1

4:00 PM GPU-based parallel processing for inverse computation of full-field material properties based on quantitative laser ultrasound visualization

Sheng-Po Tseng¹, Che-Hua Yang¹

¹*Graduate Institute of Manufacture Technology, National Taipei University of Technology, Taiwan*

Background, Motivation, and Objective

Ultrasonic guided waves become an important tool for nondestructive evaluation of structures and components. Guided waves are used for the purpose of identifying defects or evaluating material properties in a nondestructive way. While guided waves are applied for evaluating material properties, instead of knowing the properties directly, preliminary signals such as time domain signals or frequency domain spectra are first revealed. With the measured ultrasound data, inversion calculation can be further employed to obtain the desired mechanical properties.

Statement of Contribution/Methods

This research aims at the development of high speed inversion calculation technique for obtaining full-field mechanical properties from a quantitative laser ultrasound visualization system (QLUVS). The QLUVS employs a mirror-controlled scanning pulsed laser to generate guided acoustic waves traveling in a two-dimensional target. Guided waves are detected with a piezoelectric transducer located at a fixed location. With a gyro-scanning of the generation source, the QLUVS has the advantage of fast, full-field and quantitative inspection.

Results/Discussion

The QLUVS and inversion process have been investigated before, however, suffer the drawback of excessive computation time. This research introduces two important tools to improve computation efficiency. First graphic procession unit (GPU) with large amount of cores are introduced. Furthermore, combining the CPU and GPU cores, parallel procession scheme is developed for the inversion of full-field mechanical properties based on the QLUVS data. The newly developed inversion scheme is applied to investigate the computation efficiency for single-layered and double-layered plate-like samples. The computation efficiency is shown to be 80 times faster than unparalleled computation scheme. This research demonstrates a high speed inversion technique for the characterization of full-field material properties based on quantitative laser ultrasound visualization system. Significant computation efficiency is shown, however not reaching the limit yet. Further improvement can be reached by improving the parallel computation. Utilizing the development of the full-field mechanical property inspection technology, full-field mechanical property measured by non-destructive, high-speed and high-precision measurements can be obtained in qualitative and quantitative results. The developed high speed computation scheme is ready for applications where full-field mechanical properties are needed in a nondestructive and nearly real-time way.

4:15 PM

Optoacoustic Tissue Differentiation using a Mach-Zehnder Interferometer: Preliminary Results**Herve Ngendon Kenhagho¹, Georg Rauter², Raphael Guzman³, Philippe Cattin⁴, Azhar Zam⁵**¹*Department of Biomedical Engineering, Biomedical Laser and Optics Group (BLOG), University of Basel, Allschwil, Switzerland, ²Department of Biomedical Engineering, Bio-Inspired RObots for MEDicine-Lab, University of Basel, Switzerland, ³Department of Neurosurgery, University Hospital Basel, Swaziland, ⁴Department of Biomedical Engineering, Center for medical Image Analysis and Navigation, University of Basel, Swaziland, ⁵Department of Biomedical Engineering, Biomedical Laser and Optics Group (BLOG), Department of Biomedical Engineering, Allschwil, Switzerland***Background, Motivation, and Objective**

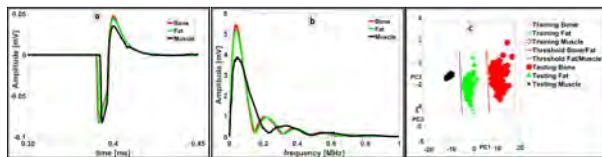
Laser osteotomes enable controlled contactless bone ablation leading to faster bone healing and less thermal damage compared to conventional mechanical osteotomes. To further extend the advantages of laserosteotomes over conventional osteotomes, also real-time feedback on the type and properties of the tissues being cut would be desirable. In this paper, we integrated an optoacoustic feedback in the laserosteotome to discriminate bone from surrounding soft tissue based on cutting sounds.

Statement of Contribution/Methods

In a study, 180 acoustic shock waves were recorded that were emitted during laser-tissue-ablation. For laser ablation, a frequency-doubled Nd:YAG laser at a pulse repetition rate of 1 hertz and pulse energy of 200 mJ was used. The goal was to differentiate various tissue types: bone, fat and muscle tissues of a fresh porcine upper tigh. For sound recording, the probing beam of the Mach-Zehnder interferometer was placed 5 cm away from the ablation spot. The shock waves caused spatiotemporal variations of the light refractive index that were measureable by light intensity changes of the built Mach-Zehnder probing beam. For offline tissue differentiation, we investigated the data by looking at the amplitude spectrum using the Fast Fourier Transform. Then, we used the Principle Component Analysis (PCA) to reduce dimensionally and the threshold method to discriminate the measured light intensities from each specimen. The first 40 measured data were used as ‘training data’ and the last 140 ones were considered as ‘testing data’.

Results/Discussion

Peak-to-peak amplitudes of light intensity changes measured by the photodiode of the Mach-Zehnder interferometer for bone, fat and muscle specimens were 0.85 mV, 0.84 mV, and 0.83 mV, respectively. The analysis of the frequency responses revealed that bone and fat produced three amplitude peaks from at near direct current -1 MHz compared to muscle tissue which produced only two. In addition, the features that were chosen for PCA were explained 98.26 % of the variance in the recorded data. Hereby, the first principle components PC1 explained 93.70 % of variance and was used to differentiate tissue types. From the confusing matrix, accuracy of the experimental based scores of each specimen is 100 %. Preliminary results of this study demonstrate a promising technique to differentiate bone, fat and muscle tissue.



4:30 PM

Monitoring Changes in Mechanical Properties of Rock Bolts Using a Low-Power Coded-Excitation SchemeJohan E. Carlson¹, Erik Andrén¹, Medhat Mohamad¹, Jaap van de Beek¹¹Luleå University of Technology, Luleå, Sweden**Background, Motivation, and Objective**

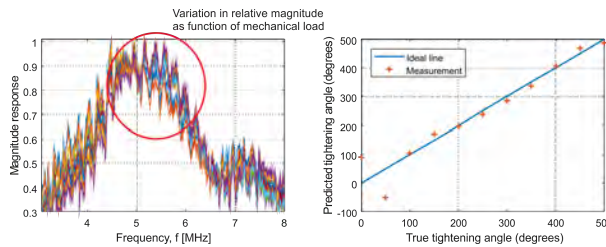
Rock-bolts are critical load-bearing structural elements ubiquitously used in mining industries and infrastructure projects for securing tunnel walls and ceilings. Today, there are no reliable techniques available for assessing the integrity of bolts already installed or to monitor changes in installed bolts over time. This is problematic when planning maintenance and service since safety is critical and the consequences of a failure are unacceptable. Hence, it is likely that more bolts than necessary are installed, as a precaution. A reliable technique for identifying faulty bolts or trending mechanical changes in bolts over time, would therefore enable more cost-efficient maintenance. To be practical, an instrument for this must, however, be portable and ideally also battery-powered.

Statement of Contribution/Methods

This paper presents initial results of using a low-power (low voltage) pulser for coded excitation of wide-band ultrasound signals. The pulser operates at a voltage of less than 1 V r.m.s. and we demonstrate that this can be used to drive a 5 MHz ultrasound transducer at its full available bandwidth (also around 5 MHz). By using a coding scheme borrowed from wireless communications, we are able to estimate the combined transfer function of the transducer and a one meter long rock bolt. This enables monitoring of changes over time in the transfer function, and consequently, of changes in mechanical properties of the rock bolt. The method is validated in a laboratory environment on a one meter segment of a rock bolt.

Results/Discussion

A rock bolt was mounted so that a force could be applied at one end to extend the bolt in the longitudinal direction. The ultrasound transducer was mounted at the opposite end of the bolt, operating in a pulse-echo mode to. Using a communication scheme called OFDM (Orthogonal Frequency Division Multiplexing), a 0.3 ms long burst of known data was transmitted into the bolt and the reflection from the back-end was recorded. The knowledge of the transmitted data sequence was then used to estimate the transfer function of the system, i.e. the channel. By studying how this channel changes (left figure), we show that the elongation or load applied to the bolt can be estimated based on the waveform alone, disregarding changes in absolute amplitude and time-of-flight (right figure).



4:45 PM

Experimental validation of non-collinear wave mixing modelHector Hernandez Delgadillo^{1,2}, Richard Loendersloot¹, Doekele Yntema², Remko Akkerman¹¹*University of Twente, Enschede, Netherlands*, ²*Wetsus, Leeuwarden, Netherlands***Background, Motivation, and Objective**

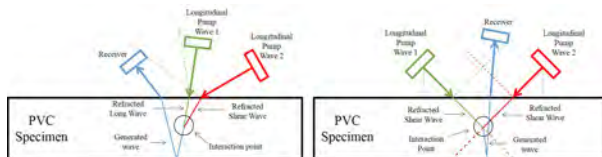
In this research a single sided non-collinear wave mixing technique is investigated in order to assess the condition of polyvinyl chloride (PVC) drinking water pipes. In an inline inspection system there is access to only one surface; thus constraining the possible wave mixing processes as well as the measurement parameters. In order to select the optimal wave interaction process, the response of the generated wave to the frequency ratio (ω_2/ω_1) of the two pump waves was experimentally investigated. The results, presented in this paper are used for validation of an analytical model.

Statement of Contribution/Methods

Two wave mixing processes were selected. These two processes consist of two waves mixing, either shear or longitudinal components and are: $SV(\omega_1)+SV(\omega_2) \rightarrow L(\omega_1+\omega_2)$ and $L(\omega_1)+SV(\omega_2) \rightarrow L(\omega_1+\omega_2)$. The experimental set-up for these is shown in Figure 1 a) and b) respectively. The frequency ratios were selected subsequently, as the ones with the highest amplitude from the analytical solutions found in literature. For the generation of the two pump waves, two broad-band transducers were used both with a 1 MHz central frequency. The receiving sensor (blue sensors in Figure 1) used was a 2.25 MHz central frequency transducer. The parameters extracted from the measurements were corrected by using the frequency response data of each sensor form the sensor supplier.

Results/Discussion

There is a difference in amplitude of one order of magnitude between the two interaction processes, where the long + shear interaction process is the highest. The experimentally determined optimal frequency ratio is 0.65 and 1.7 for shear + shear and long + shear respectively. These experimental results qualitatively correlate with both the analytical solutions found in literature as well as with the analytical model performed in this work. The solution of the analytical model is dependent, amongst other parameters, on the third order elastic constants, Lame parameters and speed of sound in the material.



5:00 PM

Full-field Laser-Ultrasound for Practical Nondestructive Inspection**Eric Flynn¹**, Nicholas Stull²¹*Intelligence and Space Research Division, Los Alamos National Laboratory, Los Alamos, NM, United States,*²*Engineering Institute, Los Alamos National Laboratory, Los Alamos, NM, United States***Background, Motivation, and Objective**

Full-field measurements of propagating ultrasonic waves in solid structures can be made remotely using scanning laser Doppler vibrometry (LDV). By repeatedly exciting the structure with the same transient ultrasonic signal, and measuring the response at a grid of points using the LDV, one can reconstruct the full-field propagation time history as if it was made simultaneously at all points. These full-field response measurements can provide valuable information for detecting structural defects such as cracking, corrosion, and delamination. However, the sensitivity of LDV systems is limited at typical ultrasonic frequencies and response levels, making it necessary to coat the inspection surface with a retroreflective layer, utilize dangerous laser power levels, or perform the scan very slowly with many averages at each point. These limitations have restricted full-field laser ultrasound to laboratory experiments and make it impractical for many deployed nondestructive inspection and structural health monitoring applications.

Statement of Contribution/Methods

Our research focuses on the use of steady, harmonic excitation in place of repeated transient excitation for full-field laser ultrasound inspection. With harmonic excitation, we realized several orders of magnitude improvement in signal level in ultrasonic LDV measurements, enabling scans with eye safe lasers on unmodified inspection surfaces at speeds of up to five square meters per minute. We've found that two classes of full-field analysis techniques to be especially effective when properly modified for harmonic response measurements: wavenumber spectroscopy and local gradient estimation. Wavenumber spectroscopy, which is effective at detecting in-plane defects, involves local analysis of the wavelengths of the ultrasonic waves in order to quantify changes in effective thickness using the Rayleigh-Lamb equations. Local gradient estimation, used for detecting out-of-plane-defects, attempts to identify discontinuities in the propagating waves that, in-turn, imply discontinuities in the material.

Results/Discussion

Through a mix of Cramer-Rao Lower Bound calculations, lab experiments, and field trials, we explored the theoretical and real-world performance limitations of these harmonic laser ultrasound techniques for imaging composite delamination in aerospace structures, hidden corrosion in civil infrastructure, and in-plane cracking in steel containment vessels.

7A - Abdominal and Pelvic Tissue Characterization

Kikusui (140)

Tuesday, October 23, 10:30 am - 12:00 pm

Chair **Timothy Hall**
University of Wisconsin-Madison

7A-1

10:30 AM Measured fractional calculus parameters for shear waves in swine liver

Tom Humphrey¹, Rebeca Pereira², Matthew Urban³, **Robert J. McGough¹**

¹Michigan State University, United States, ²Mayo Clinic, MN, United States, ³Department of Radiology, Mayo Clinic, Rochester, MN, United States

Background, Motivation, and Objective

Shear waves are highly attenuated in soft tissue, and the attenuation of shear waves in soft tissue follows a power law. To better understand the role of power law attenuation in noninvasive ultrasonic methods that characterize soft tissue mechanical properties with shear waves, complex shear modulus values are measured before and after swine liver samples are immersed in formalin for 1 hour. These measurements are performed with 10 samples obtained from 3 livers, and then the frequency-dependent shear wave attenuation is computed from these measurements to facilitate the calculation of shear wave parameters with a fractional calculus model.

Statement of Contribution/Methods

The attenuation constant and the power law exponent for shear waves in liver are not well-known, and to address this deficiency, shear wave measurements are performed in *ex vivo* swine liver samples using a RheoSpectris C500+ machine (Rheolution, Inc., Montreal, Quebec, Canada). The liver is cut into cylindrical samples with diameter of 10 mm. The storage modulus and loss modulus are then measured from 10 Hz to 2 kHz with an interval of 10 Hz. For each liver sample, the complex moduli are measured multiple times, and the result is obtained by averaging the measured values. The attenuation constant and power law exponent are then calculated from the storage and loss moduli with a power series model.

Results/Discussion

Measured shear wave attenuation values are plotted as a function of frequency in Fig. 1 for a representative liver sample. The attenuation constant is 2.81 Np/m/Hz^y and the power law exponent is 0.89 before the liver sample is immersed in formalin (Fig. 1a). The attenuation constant is 0.29 Np/m/Hz^y and the power law exponent is 1.01 after the liver sample is soaked in formalin (Fig. 1b). The range of power law exponents before the samples were immersed in formalin is 0.64-0.89, and the range of power law exponents after the samples were immersed is 0.92-1.50, where the shear wave attenuation constants are consistently much lower and the power law exponents are slightly higher after immersion. Simulations of shear waves based on these measured values will also be shown. These measurements provide new data for fractional calculus simulations of shear wave elasticity imaging, which are needed to evaluate the impact of power law attenuation on shear wave parameter estimates and images.

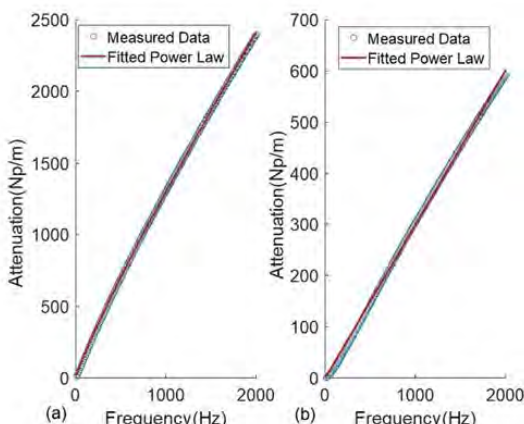


Figure 1: Measured power law attenuation and fitted values a) in swine liver and b) in swine liver Immersed in formalin.

10:45 AM

Quantitative ultrasound imaging and characterization of uterine peristaltic waves

Yizhou Huang¹, Federica Sammali¹, Celine Blank², Nienke Kuijsters², Chiara Rabotti¹, Benedictus Schoot², **Massimo Mischi¹**

¹Eindhoven University of Technology, Netherlands, ²Catharina Hospital Eindhoven, Netherlands

Background, Motivation, and Objective

Uterine peristalsis (UP) plays an important role in the generation of intrauterine streams; upstream towards the ovaries to support conception and downstream to favor menstrual emptying. Our understanding of the uterine mechanical behavior is however hampered by a lack of quantitative analysis, limiting identification and treatment of uterine dysfunctions. Building on our recent work on dedicated speckle tracking for uterine strain analysis, here we present the first algorithm for spatiotemporal assessment of UP. In particular, we aim at characterizing the propagation of contraction waves along the uterus.

Statement of Contribution/Methods

Nine women were scanned with B-mode transvaginal ultrasound during the late follicular phase, which coincides with the fertile period and is known to be the most active phase. The speckle was tracked on the gray-level videos by optical flow. The method accuracy was further improved by an adaptive spatial-warping approach. The method was first optimized and validated with a dedicated setup producing controlled motion of an ex-vivo uterus. In vivo, a grid of points with regularly-spaced coordinates (Fig. 1a) was positioned on the inner layers of the myometrium and tracked over time relative to the uterine longitudinal axis. The transversal displacement of the myometrium was then extracted to generate a time-space representation along the longitudinal axis (Fig. 1b). This was analyzed in the 2D Fourier domain (Fig. 1c) for the assessment of UP (contraction wave) speed and direction, determined by the two dominant spectral peaks.

Results/Discussion

The ex-vivo results confirmed the accuracy of the implemented adaptive optical flow method for uterine speckle tracking. In vivo, different propagation directions (upstream, downstream) were observed. In few cases, the presence of standing waves was detected. The estimated UP speed was 1.048 ± 0.488 mm/s, which is in line with the literature based on visual inspection. These promising results represent a first step towards a better characterization and understanding of UP. Extended studies with more patients will elucidate on the actual limits of the method, and the role it can play in clinical practice, with emphasis on fertilization procedures.

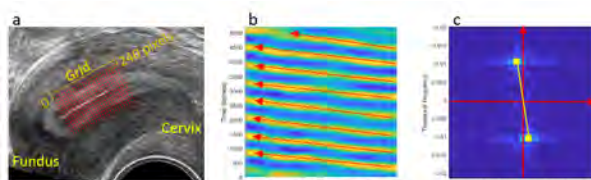


Figure 1: (a) Grid of points positioned on the inner layers of the myometrium; (b) Example of time-space plot representing the time evolution of the transversal displacement. The red arrows indicate the UP propagation downstream, from fundus (right) to cervix (left); (c) 2D Fourier transform of the transversal displacement time-space evolution. Both axis are normalized between $[-\pi, \pi]$. The two evident spectral peaks reflect both speed and direction of the peristaltic waves.

11:00 AM Temporal Correlations Between Cervical Smooth Muscle Force Generation and Acoustic Backscatter Coefficient Parameters

Andrew Santoso¹, Joy Vink², George Gallos³, Helen Feltovich^{1,4}, Timothy Hall¹

¹*Medical Physics, University of Wisconsin-Madison, Madison, WI, United States*, ²*Obstetrics & Gynecology, Columbia University Medical Center, New York, NY, United States*, ³*Anesthesia, Columbia University Medical Center, New York, NY, United States*, ⁴*Maternal Fetal Medicine, Intermountain Healthcare, Provo, UT, United States*

Background, Motivation, and Objective

Smooth muscle cells are present in the cervix, predominantly in a circumferential arrangement near the internal os (the area where the cervix meets the uterus), but their role, particularly in pregnancy, is unclear. A necessary step toward understanding the role of these cells in cervical function is to assess muscle activity, but noninvasive tools for this purpose are lacking. We explored parameters derived from the acoustic backscatter coefficient (BSC) as potential biomarkers of muscle force generation resulting from smooth muscle contractions in the *ex vivo* uterine cervix.

Statement of Contribution/Methods

After informed consent, whole cervix specimens were obtained from 5 nonpregnant women undergoing total hysterectomies for benign indications. Transverse slices of the cervix were obtained near the internal os, suspended in organ baths, and attached to a force transducer that measured muscle force generation. A frame of radiofrequency echo data was acquired every 2 seconds using a Siemens Acuson S3000 with a 14L5SP transducer operating at a nominal frequency of 10 MHz. The Reference Phantom Method was used to obtain BSC estimates before and after administration of 1 μ M of oxytocin. BSCs were parameterized in terms of frequency dependence and magnitude by calculating effective scatterer diameter (ESD) and average BSC (ABSC) within 4-9 MHz, respectively. To mitigate concerns of bias in parameter time series, bulk motion was assessed on B-mode images by computing center-of-mass deviations for all specimens. To assess the ability of parameters to detect smooth muscle activity, Pearson correlation coefficients (r) were computed between muscle force and BSC parameters. Calculation of r was performed for parameter estimates during the first 5 minutes (short) and then for 30 minutes (long) post-drug on data smoothed with a 30 second moving average filter. Results of the short and long temporal correlations are summarized in terms of the median and interquartile range [Q₁-Q₃] among specimens.

Results/Discussion

Center-of-mass deviations during acquisitions for all samples were less than 1.0 mm. For short temporal correlations, positive r values were observed for muscle force and ESDs ($r = 0.88$ [0.54-0.93]) while ABSCs were more varied ($r = -0.27$ [-0.90-0.26]). For long temporal correlations, positive correlations were maintained for ESDs ($r = 0.71$ [0.53-0.81]) while ABSCs changed direction of correlation ($r = 0.23$ [0.11-0.37]). These findings suggest that ESDs correlate with muscle force generation in the human cervix. This parameter is promising as a noninvasive tool for detecting muscle activity in the cervix. Future work will explore translation of these techniques to *in vivo* animal models.

Research supported by National Institutes of Health Grants T32CA009206 from the National Cancer Institute and R01HD072077, 1R01HD082251-01A1, and K08HD088758 from the Eunice Kennedy Shriver National Institute of Child Health and Human Development.

11:15 AM

Development of double Nakagami distribution model for quantitative evaluation of early-stage fatty-liver diseaseKazuki Tamura¹, Jonathan Mamou², Kenji Yoshida³, Hiroyuki Hachiya⁴, Tadashi Yamaguchi³¹*Graduate school of engineering, Chiba university, Japan*, ²*Lizzi Center for Biomedical Engineering, Riverside Research, New York, NY, United States*, ³*Center for Frontier Medical Engineering, Chiba University, Japan*, ⁴*School of Engineering, Tokyo Institute of Technology, Japan***Background, Motivation, and Objective**

Often fatty-liver disease evolves from a metabolic syndrome to become irreversible with the development of fibrosis as the disease progresses. In this study, we investigated early-stage fatty-liver disease (i.e., 20 % of hepatocytes contain lipid droplets) using novel envelope statistics methods applied to RF echo signals acquired from rat livers using a 15-MHz single-element transducer that yielded axial and lateral spatial resolutions of 100 and 150 μm , respectively.

Statement of Contribution/Methods

The fatty liver was hypothesized to have the structure of a healthy liver with the addition of lipid droplets. This model can be expressed using a probability density function (PDF), $p_{mix}(x)=(1-\alpha)p_L(x|\mu_L,\omega_L)+\alpha p_F(x|\mu_F,\omega_F)$ where p_L and p_F are two Nakagami distributions used to model the luminal structure in a healthy liver and the lipid droplets, respectively. μ_L was given the Nakagami parameter of a healthy liver obtained from healthy rat livers.

Parameter estimation was applied to a normalized echo by replacing ω_L with $\omega_L=1-\omega_F\alpha/(1-\alpha)$. Then, Nelder–Mead optimization was applied to estimate the remaining three parameters of the model: μ_F , α and ω_F . The proposed algorithm was applied in experimental and simulated data. Experiment data were acquired from nine excised healthy, early fatty, and serious fatty rat livers (three in each group). For simulations, a mixed low scatterer concentration numerical phantom was generated. To perform parameter estimation, RF data were separated into three dimensional regions (five times the spatial resolution in each dimension).

Results/Discussion

The relationships among the envelope amplitude and PDF models (single and double Nakagami PDF) are shown in Fig. 1(a). The double Nakagami PDF model fitted the echo signal PDF is better than the single Nakagami PDF model. Estimated parameters (μ_F and α) are illustrated in (b)–(d). Different parameter distributions are visible as the disease progresses. Results summarized in (e) show a clear upward trend of the fit parameters as a function of disease progression. This approach can detect early-stage fatty liver using values of μ_F and α which cannot be accomplished using a conventional Nakagami PDF model. In summary, our envelope-statistics approach using a double Nakagami PDF model can be used to easily quantify and monitor fatty-liver disease.

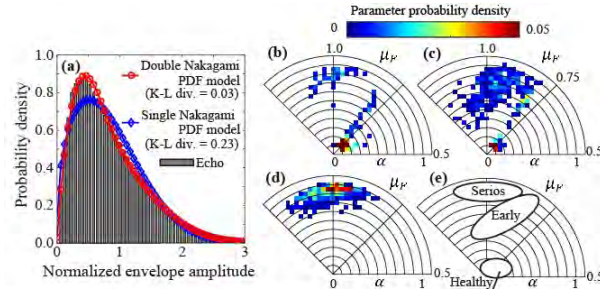


Figure 1 (a): the simulated low scatterer concentration PDF and fitted PDFs of the echo amplitude envelopes from a fatty-liver. (b)–(e): Different parameter distributions are shown in each disease progress. Radius and angular arc α and μ_F , respectively. (b)–(d) are healthy-liver, early and serious-fatty liver result, respectively. (e) is an image of parameter transition diagram.

11:30 AM

System-Independent Ultrasound Attenuation Coefficient Estimation Using Spectra NormalizationPing Gong¹, Pengfei Song¹, Chengwu Huang¹, Joshua Trzasko¹, Shigao Chen¹¹*Radiology, Mayo Clinic College of Medicine and Science, Rochester, MN, United States***Background, Motivation, and Objective**

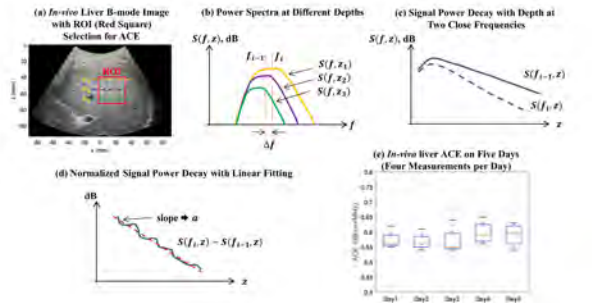
Ultrasound attenuation coefficient estimation (ACE) has great potential for use in many clinical applications such as quantifying liver fat content. The two commonly used ACE methods are spectral shift method and reference phantom method. The spectra shift method ignores beam diffraction effects, whereas the reference phantom method requires a well-calibrated phantom, which is not always available in practice. In this study, we propose a novel system-independent ACE technique, referred to as reference frequency method (RFM). RFM is based on spectra normalization between adjacent frequencies and does not require a reference phantom, which makes it applicable to different ultrasound systems with different transducer geometries and beam patterns.

Statement of Contribution/Methods

Fig. 1a shows an *in-vivo* liver ultrasound B-mode image acquired from a healthy volunteer. The signal power spectra $S(f, z)$ were calculated along axial direction at different depth (e.g., z_1, z_2, z_3) as shown in Fig. 1b. Fig. 1c shows the signal power decay curves as a function of depth z at two frequencies, f_i and f_{i-1} , which only differs by a few percent. Due to ultrasound attenuation, the logarithm of signal power should decay linearly with depth. However, such linear decay trend is often affected by system effects such as focusing or time gain compensation as illustrated in Fig. 1c. We assume that the differences in system effects between two close frequencies are negligible. Therefore, these effects can be normalized by calculating the difference between logged power at two close frequencies as $S(f_i, z) - S(f_{i-1}, z)$ as shown in Fig. 1d. A linear fitting can be applied to derive the ultrasound attenuation coefficient a . Attenuation coefficients calculated at different frequencies can be averaged over the entire spectrum for improved robustness.

Results/Discussion

The accuracy of RFM was validated by through transmission measurement on a tissue mimicking phantom. The difference between estimated ACE values from the two methods was below 5%. Fig. 1e show the liver ACE values measured from the healthy volunteer on five different days. The mean ACE values across different days range from 0.57 to 0.60 dB/cm/MHz, with a maximum standard deviation of ± 0.05 dB/cm/MHz. No significant differences ($p > 0.05$) were found using Analysis of Variance. These values also agree well with the findings in literatures.



11:45 AM

A deep learning method of transient elastography for assessment of liver fibrosisYongshuai Li¹, Qiong He¹, Jinhua Shao², Jianwen Luo¹¹School of Medicine, Tsinghua University, Beijing, China, People's Republic of, ²Wuxi Hisky Medical Technology Co., Ltd, Wuxi, China, People's Republic of**Background, Motivation, and Objective**

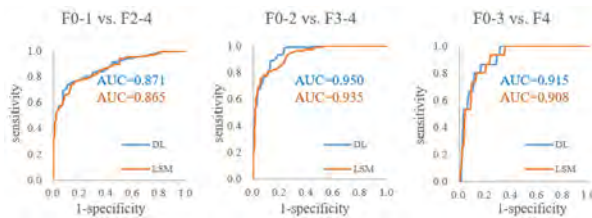
Transient elastography (TE) is a well-established modality, which performs liver stiffness measurement (LSM) and adopts certain thresholds to assess liver fibrosis. For LSM, an M-mode strain image is obtained from the M-mode RF data of the liver acquired after an external vibration. On the hypothesis that the M-mode strain image contains richer information than LSM, we propose a deep learning (DL) method of TE based on the M-mode strain image to improve the performance of fibrosis staging.

Statement of Contribution/Methods

A multicenter study was conducted where both TE and liver biopsy were performed on 421 patients. The M-mode RF data were acquired with a commercial TE system (FibroTouch, Wuxi Hisky, China. vibration freq. = 50 Hz, $f_0 = 2.5$ MHz, $f_s = 25$ MHz). Then, a normalized cross-correlation method (window length = 2 mm) was applied on the RF data for displacement estimation. The M-mode strain image was obtained from the derivative of the displacements. Finally, 245 patients with 3386 data were qualified and were randomly divided into training set (163 patients) and test set (82 patients). For the DL method, considering the trade-off between prediction losses and over-fitting, an optimal convolutional neural network (CNN) with 13 layers (5 convolutional layers, 3 pooling layers, 3 fully-connected layers and 2 dropout layers) was built. It took the M-mode strain images (160×160 pixels) as the input and the liver fibrosis stages according to Metavir standard (F0-F4) as the output. Trained on the training set for 100 epochs, the CNN was then evaluated on the test set. LSMs were also used to assess liver fibrosis on the test set for comparison, while liver biopsy acted as the gold standard. The receiver operating characteristic (ROC) curve was plotted to evaluate the performance for assessing significant fibrosis ($\geq F2$), advanced fibrosis ($\geq F3$) and cirrhosis (F4). 3-fold cross-validation was implemented, the ROC curves were averaged, and the area under ROC curve (AUC) was calculated from the average curve.

Results/Discussion

As shown in the figures, the AUCs of the DL method are 0.871 for $\geq F2$, 0.950 for $\geq F3$ and 0.915 for F4, respectively, slightly better than those of the LSM method (0.865 for $\geq F2$, 0.935 for $\geq F3$ and 0.908 for F4, respectively). To conclude, the DL method performs better than the LSM method and could be used in transient elastography for assessment of liver fibrosis.



7B - Carotid Elasticity

Kikusui (140)

Tuesday, October 23, 1:30 pm - 3:00 pm

Chair **Chris de Korte**
Radboud University Medical Center

7B-1

1:30 PM Evaluation of carotid biomechanical properties by simultaneous analysis of arterial stiffening and deformation

Guillaume Goudot¹, Tristan Mirault², Lina Khider², Maxime Gruet¹, Mickaël Tanter¹, Mathieu Pernot³, Emmanuel Messas²

¹*Institut Langevin, INSERM U979, Paris, France*, ²*PARCC INSERM U970, Paris, France*, ³*Institut Langevin, INSERM U979, Paris, France*

Background, Motivation, and Objective

Evaluation of arterial stiffness remains difficult *in vivo* due to the interdependence of stiffness with diameter and blood pressure variation. In this work, we aimed at developing ultrafast ultrasound acquisitions that allow us to evaluate both arterial deformation and stiffening during the cardiac cycle in a same acquisition. We then aimed at evaluating stiffening parameters in a series of healthy patients.

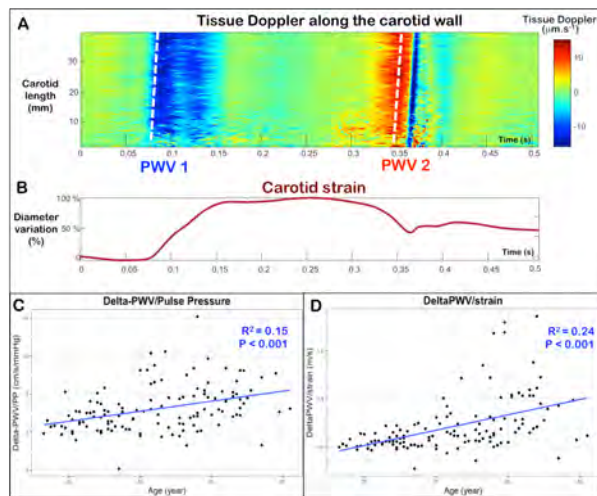
Statement of Contribution/Methods

Bilateral evaluation of common carotid arteries by UF was carried out by a linear probe (15-4 MHz, 256 elements, pitch 0.2 mm, SuperSonic Imagine[®]). Acquisitions had 3 angles (-5; 0; 5) and were triggered by the QRS. The high frame rate (2000/s) allowed us to measure the PWV at the foot of the waveform (PWV1), generated at the diastolic blood pressure (DBP) and at the dicrotic notch (PWV2), at the systolic blood pressure (SBP). The carotid diameter variation, obtained by tracking the wall by ultrafast Doppler imaging, allowed us to evaluate the circumferential arterial strain and distensibility. Arterial pressure was recorded with an oscillometric device.

Results/Discussion

140 patients were prospectively evaluated. As stiffness is depending on pressure, we therefore reported each PWV measured to their corresponding arterial pressure. PWV2/SBP better correlated with age than PWV1/DBP ($R^2=0.23$ vs. $R^2=0.03$ respectively) (Figure 1.A and 1.B). Arterial stiffening during the cardiac cycle, evaluated with Delta-PWV (PWV2-PWV1) divided by the pulse pressure (SBP-DBP) correlated with age ($R^2=0.15$) (Figure 1.C). In order to overcome blood pressure measurement, our acquisition allowed us to evaluate Delta-PWV ratio divided by arterial deformation. This index had a better correlation with age ($R^2=0.24$) (Figure 1.D).

Conclusion: The combination of PWV and distensibility measurements from a single acquisition allowed us to simply assess arterial stiffening during the cardiac cycle.



1:45 PM

Strain Discontinuities in Carotid Atherosclerotic Plaques – a Novel Marker for Plaque Vulnerability?Tim Vonk¹, Evelien Hermeling¹, Floris Schreuder², Werner Mess³, Eline Kooi¹¹*Radiology and Nuclear Medicine, Maastricht University Medical Center, Maastricht, Netherlands, ²Neurology, Radboud university medical center, Nijmegen, Netherlands, ³Neurophysiology, Maastricht University Medical Center, Maastricht, Netherlands***Background, Motivation, and Objective**

Rupture of atherosclerotic plaques is an important underlying cause of stroke and is ultimately a biomechanical event. Local ultrasound strain measurements may identify vulnerable plaques. We aim to develop and validate a novel method using ultrasound radiofrequency (RF) measurements to determine intraplaque inhomogeneities in the strain distribution with a high axial resolution.

Statement of Contribution/Methods

Ultrasound examinations were performed on common (CCA) and internal carotid arteries (ICA) of 22 patients, 17 with recent ischemic stroke / transient ischemic attack and 5 asymptomatic patients (39 CCAs and ICAs). The strain distribution was computed from RF data with a depth resolution <0.5mm using a custom MATLAB algorithm.

In the plaque-free CCA the radial wall strain was compared with the relative diameter change to validate the strain computation. Two observers analyzed the data for intra-observer variation analysis. In the ICAs, strain inhomogeneities in symptomatic and asymptomatic plaque were studied.

Results/Discussion**Results:**

Within the CCA wall, the strain (observer 1: $-7.4 \pm 2.7\%$, observer 2: $-6.4 \pm 2.6\%$) had reasonably good intra-subject precision (1.6%) and accuracy (correlation with relative distension, observer 1: $r=0.69$; $p<0.0001$, observer 2: $r=0.68$; $p<0.0001$). Intra-observer variability had an ICC of 0.681 (two-way mixed, single measure). In the ICA, strain inhomogeneities had an elongated shape (mean: $0.7 \times 11\text{mm}$) and demarcated in 58% of the cases the plaque-adventitia boundary. The percentage of ICAs with 1 or more strain inhomogeneities was increasing with the degree of stenosis ($p=0.03$, 95%-CI). Strain inhomogeneities were more frequent in ICAs at the symptomatic side of stroke/TIA patients as compared to the contralateral arteries and both carotid arteries of the asymptomatic subjects combined (odds's-ratio=4.7; $p=0.07$). In contrast to the average strain, strain in the deviating strain regions was higher at the symptomatic compared to the asymptomatic side ($p=0.02$).

Conclusion:

The proposed method to assess local radial strain distribution proved to be accurate and precise in the CCA. In the ICA, areas with high strain inhomogeneities were more frequent in symptomatic plaques as compared to asymptomatic plaques. These strain inhomogeneities could be a promising novel marker for plaque vulnerability.

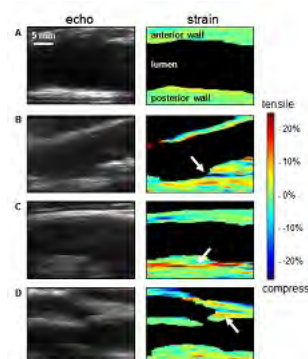


Figure 1. Examples of strain distribution in carotid plaques
Crude B-mode (echo, left panels) and corresponding strain distribution in the ICA (right panels); blood flow direction is from right to left. Note that in some cases the strain distribution is rather homogeneous (A), whereas in other cases a more heterogeneous distribution of strain is observed (B-D). Narrow but elongated regions with highly deviating strain (indicated by the white arrows) are often found near the boundary between the plaque and the supporting adventitia layer (B and D) and can appear either as diastolic-to-systolic wall compression (B) or as wall tension (C and D).

2:00 PM

In vivo 3D strain imaging of the carotid arteryStein Fekkes¹, Hendrik Hansen¹, Jan Menssen¹, Anne Saris¹, Chris de Korte¹¹*Medical Ultrasound Imaging Centre MUSIC, Radboud university medical center, Netherlands***Background, Motivation, and Objective**

The risk for getting a cerebral event is associated with carotid plaque composition. Strain imaging has demonstrated to be a technique capable of identifying plaque composition. Three-dimensional vascular strain estimation might improve the detection of rupture prone plaques in carotid arteries. This study shows the first results of in vivo 3D principal strain imaging of the carotid artery bifurcation.

Statement of Contribution/Methods

We developed a device that enables precise positioning and translation of a Philips L11-3 linear array transducer ($f_c = 9$ MHz, pitch = 135 μm , 288 elements) at the carotid bifurcation of a healthy subject (Figure 1 left). For 350 equally spaced (0.1 mm) elevational positions, ultrasound series were acquired of the systolic phase at 50 Hz synchronized using a trigger at the ECG R-top. Each series consisted of ultrasound plane waves transmitted at 3 sequentially alternating angles (0° , -19.5° , 19.5°) at a frequency of 10 kHz using a Verasonics Vantage 256 system. After delay-and-sum beamforming a rigid registration was applied to correct for breathing induced spatial miss-alignment before stacking into a 3D matrix of RF data. Inter-frame displacements were estimated using a normalized 3D cross-correlation-based algorithm. The 0° axial displacement was used as vertical displacement component. Horizontal displacements were obtained by projection of the $+19.5^\circ$ and 19.5° axial displacements. Elevational displacements were obtained by median selection of the 0° , -19.5° , and 19.5° elevational displacements. After 3D median based regularization and linear tracking, strains were derived for all three principal directions. Finally, the maximum and minimum principal strains were selected and presented as the tensile and compressive strains together with its direction.

Results/Discussion

3D displacement estimation of the CA during systole was feasible using the ECG triggered temporal synchronization of the US acquisitions. Figure 1, (middle & right) shows the derived 3D maximum and minimum principal strains for the complete volume yielding insight in the 3D deformation of the CA even in a complex geometry part as the bifurcation. This study shows for the first time 3D strain imaging in vivo. In patient acquisitions will have to prove the clinical benefit of this technique.

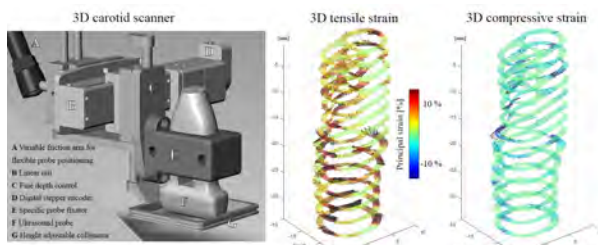


Figure 1: **Left:** device to acquire multi-slice ultrasound plane wave ultrasound of the carotid bifurcation. **Middle:** maximum principal strain values and directions indicating tensile strain. **Right:** Minimum principal strain values and directions indicating compressive strain of the vessel wall of the carotid bifurcation.

2:15 PM

Carotid elastography for detection of vulnerable atherosclerotic plaques: An inter-operator reproducibility study

Zhi Liu¹, Zhiyong Bai², Chengwu Huang¹, Manwei Huang³, Lingyun Huang⁴, Dongxiang Xu⁵, Huabin Zhang², Chun Yuan^{1,5}, Jianwen Luo¹

¹Department of Biomedical Engineering, Tsinghua University, Beijing, China, People's Republic of, ²Department of Sonography, Beijing Tsinghua Changgung Hospital, Beijing, China, People's Republic of, ³Department of Sonography, China Meitan General Hospital, Beijing, China, People's Republic of, ⁴Clinical Sites Research Program, Philips Research China, Shanghai, China, People's Republic of, ⁵Department of Radiology, University of Washington, Seattle, WA, United States

Background, Motivation, and Objective

Rupture of carotid atherosclerotic plaque is a major cause of ischemic stroke. Early detection of vulnerable plaques is essential to prevent the occurrence of ischemic events. Carotid elastography has been developed to detect vulnerable plaques. In this work, the inter-operator reproducibility of this technique was studied.

Statement of Contribution/Methods

Ultrasound RF data of 45 carotid arteries (including 53 plaques) were acquired separately by two clinicians (i.e., operators) in the long axis view, with a Philips iU22 system and an L9-3 probe. Then, the inter-frame axial strain rate (ASR) was estimated by an optical flow method. Next, the frame with the largest $|ASR|$ was chosen in each cardiac cycle. Finally, the 99th percentile of $|ASR|$ of the plaque was averaged over 2-4 cycles. The maximum 99th percentile of $|ASR|$ of all plaques in an artery was used as the elastographic index.

Each carotid artery was scanned with a Philips 3T MR scanner. MR images were used to identify the calcification, lipid-rich necrotic core (LRNC), and intraplaque hemorrhage (IPH). Vulnerable plaques were defined as those with IPH or a maximum LRNC area ratio $>20\%$ in the cross-section. The artery including the vulnerable plaque was considered as the vulnerable case.

The intraclass correlation coefficient (ICC) was used to assess the inter-operator reproducibility (poor: 0-0.2, fair to good: 0.4-0.75, and excellent: >0.75). The Bland-Altman plot was used to inspect the inter-operator agreement and systematic bias. The receiver operating characteristic (ROC) curve and area under the ROC curve (AUC) were used to evaluate the diagnostic performance. The difference between the ROCs of two operators was analyzed by a *U* test and a *p* value <0.05 indicated the statistical significance (SS).

Results/Discussion

Fig. 1 shows the inter-operator reproducibility. The ICC is 0.66, which indicates a good level. Fig. 2 depicts the Bland-Altman plot. No systematic bias is noticed, and all points except two are located within the 95% limits of agreement. Fig. 3 shows the ROC curves for detection of vulnerable plaques. No SS is found between the ROCs of two operators (*p*=0.53). From the ROC of the mean measurements, a sensitivity of 71.4%, a specificity of 87.1%, and an accuracy of 82.2% are obtained at a threshold of 1.37 s^{-1} . Carotid elastography is proved reproducible and reliable for detection of vulnerable plaques.

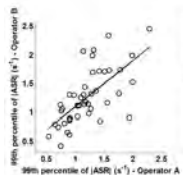


Fig. 1. The inter-operator reproducibility.

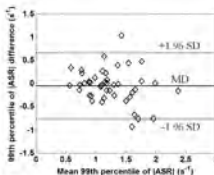


Fig. 2. The Bland-Altman plot for inter-operator variability analysis. MD = mean difference. SD = standard deviation.

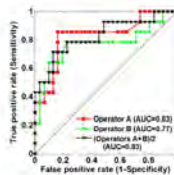


Fig. 3. The ROC curves for detection of vulnerable plaques.

2:30 PM

A Machine Learning Approach to Delineating Carotid Atherosclerotic Plaque Structure and Composition by ARFI Ultrasound, In Vivo

Gabriela Torres¹, Tomasz Czernuszewicz¹, Jonathon Homeister², Mark Farber³, Caterina Gallippi⁴

¹Joint Department of Biomedical Engineering, The University of North Carolina at Chapel Hill, United States,

²Department of Pathology and Laboratory Medicine, The University of North Carolina at Chapel Hill, United States,

³Department of Surgery, The University of North Carolina at Chapel Hill, United States, ⁴Joint Department of Biomedical Engineering, The University of North Carolina at Chapel Hill, Chapel Hill, NC, United States

Background, Motivation, and Objective

Vulnerable atherosclerotic plaques have high risk for rupture, with rupture potential related to plaque composition and structure. We have previously shown that soft (intraplaque hemorrhage (IPH), and lipid rich necrotic core (LRNC)) are differentiated from stiff (collagen (COL), and calcium (CAL)) plaque elements in human carotid plaques by Acoustic Radiation Force Impulse (ARFI)-derived peak displacement (PD). However, PD had lower performance for differentiating between features with similar stiffness. *We hypothesize that ARFI delineation of carotid plaque structure and composition is improved by machine learning algorithms.*

Statement of Contribution/Methods

This study analyzed 20 carotid plaques imaged *in vivo* in patients undergoing carotid endarterectomy (CEA). Prior to CEA, B-Mode and ARFI imaging were performed, and after CEA, specimens were harvested and processed for spatially-matched histological validation. From the B-Mode data, SNR was measured, and from the ARFI data, displacement profiles were calculated using 1D axial normalized cross-correlation. SNR, cross-correlation coefficient, and displacement were used as inputs (in all combinations of 2 or 3 parameters) to random forest (RaF) and support vector machine (SVM) algorithms. The algorithms were trained to identify IPH, LRNC, COL and CAL by 5-fold cross-validation with ground truth identified from histology. From the output likelihood matrices, CNR between IPH and LRNC and between COL and CAL were calculated and compared to the corresponding CNR achieved by ARFI PD.

Results/Discussion

See Figure 1 for representative B-Mode (a), ARFI PD (b), RaF (c), and SVM (d) images of a type VI plaque and CNR outcomes (e). Both RaF and SVM achieved statistically higher ($p<0.01$, Wilcoxon) CNRs when using all 3 versus any combination of 2 input parameters. CNR between IPH and LRNC was 24.92% higher for SVM (3.05 ± 0.20) versus RaF (2.29 ± 0.18), whereas CNR between COL and CAL was 7.80% higher for RaF (4.10 ± 0.21) versus SVM (3.78 ± 0.15). Differences between RaF and SVM were not statistically different ($p=0.21$). Importantly, both RaF and SVM achieved higher CNRs for distinguishing between features with similar stiffness than ARFI PD alone. These results suggest that, relative to PD, machine learning improves ARFI discrimination of carotid plaque components that are correlated to vulnerability for rupture.

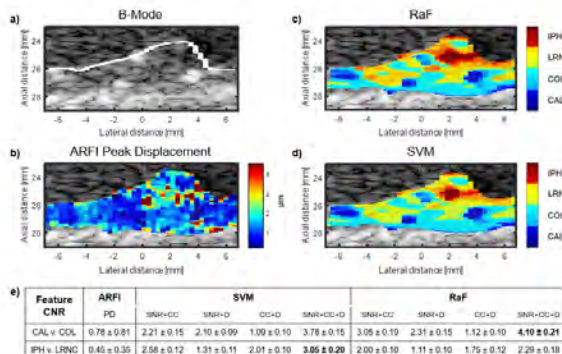


Figure 1. Matched B-Mode (a, white contour delineates plaque-lumen boundary), ARFI Peak Displacement (b), RaF (c), and SVM (d) parametric images, for a Type VI plaque in the carotid artery of a 63 year-symptomatic female. Colors indicate presence of calcium deposits (CAL – blue), collagen (COL – light blue), lipid-rich necrotic core (LRNC – yellow), and intraplaque hemorrhage (IPH – red), with colors combined as the weighted average of RaF or SVM predicted likelihoods. Panel (e) reports CNR for CAL vs. COL, and for IPH vs. LRNC, derived from ARFI PD, RaF, and SVM outcomes.

2:45 PM

Hadamard Encoded Multi-element Synthetic Aperture Imaging (H-MSA) for High Quality Tracking of Shear Waves

Rifat Ahmed¹, Marvin Doyley¹¹*University of Rochester, United States*

Background, Motivation, and Objective

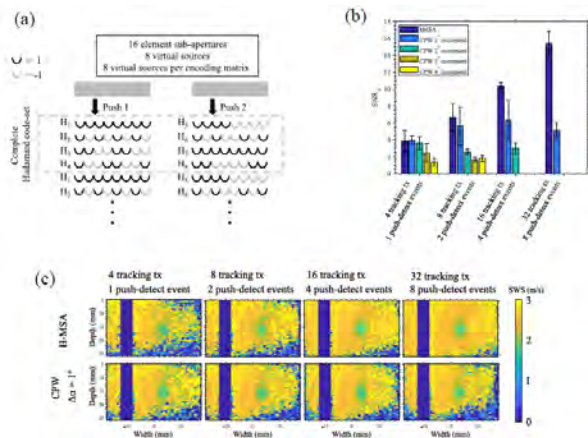
In shear wave elasticity imaging (SWEI), high frame rate tracking of transient shear waves is usually performed using plane or diverging beams. Imaging with these wide beams results in wider point spread functions (PSFs) that reduce image contrast which can be improved by coherently compounding multiple steered beams. However, such wide beam imaging and beam steering with conventional lambda-pitch transducers result in grating lobe artifacts. This condition is exacerbated at large steering angles. In this work, we propose the use of multi-element synthetic aperture imaging (MSA) which uses multiple laterally-shifted virtual sources to reduce PSF width without performing beam steering. To improve the transmit power of MSA, we used Hadamard encoded transmission (H-MSA). We present novel techniques to optimally distribute a large number of encoded virtual sources over multiple push-detect events to achieve high quality shear wave speed maps.

Statement of Contribution/Methods

Virtual sources (VSs) with 15-element sub-apertures are transmitted at multiple lateral sites following the transmission of push pulses. Four configurations were tested where 4, 8, 16, and 32 unique VSs were transmitted over 1, 2, 4, and 8 push-detect events, respectively. Each set of 8 consecutive transmissions spanning over 2 push-detect events were encoded with Hadamard codes to achieve high transmit power. Performance of H-MSA methods was evaluated on attenuating homogeneous and inclusion phantoms, and compared against plane wave imaging for equivalent numbers of push-detect events and transmissions. Feasibility of chirp coded transmission will be evaluated to further enhance the transmit power.

Results/Discussion

Fig. 1(a) shows the beam sequence for H-MSA with 16 encoded VSs distributed over 2 push-detect events. Fig. 1(b) shows that elastographic SNR of H-MSA was 200% higher than compounded plane wave (CPW) based SWEI. Fig. 1(c) shows that H-MSA achieves better lesion visualization than CPW-based SWEI.



7C - Vascular Elasticity

Kikusui (140)

Tuesday, October 23, 4:00 pm - 5:30 pm

Chair **Richard Lopata**
Eindhoven University of Technology

7C-1

4:00 PM Stiffness Evaluation of Aortic Aneurysm using an Ultrafast Regularized Tissue-Doppler Optical-Flow Principal Strain Estimator

Diya Wang¹, Boris Chayer¹, François Destrempe¹, François Tournoux¹, Guy Cloutier¹

¹*University of Montreal Hospital, Canada*

Background, Motivation, and Objective

Aortic stiffness is altered by cardiovascular diseases and exacerbated in innate or pathological conditions, which might be detected by noninvasive vascular elastography (NIVE). However, accuracy and robustness of conventional NIVE with low frame rate and lateral resolution limitations are expected to deteriorate due to the rapid motion and large 3D deformation of the aortic arch. Considering that tissue-Doppler imaging (TDI) is advantageous for large deformation conditions and optical flow (OF) is accurate for small motions, an ultrafast regularized TDI-OF principal strain estimator is proposed to objectively evaluate aortic stiffness *in vitro* and *in vivo*.

Statement of Contribution/Methods

Two aorta-mimicking phantom models were designed and driven by a hydraulic pump to simulate wall deformations under normal and pathological aortic aneurysm conditions. One normal volunteer and a patient with a documented ascending aortic aneurysm were also analyzed. Deformation data were recorded by ultrafast diverging echoes using a Verasonics platform equipped with a 2.5 MHz phased array scanner (frame rate: 4500 Hz). Contrast and resolution were enhanced by coherent compounding with TDI motion compensation (Porée et al., IEEE TMI, 2016, 36: 1647-57). Aortic principal strain maps and regional strain curves were then estimated by using the proposed model, which was modified by the regularization and time-ensemble strategies and treated as a least-squares problem to improve the estimation robustness.

Results/Discussion

The aortic stiffness was evaluated by the 2D principal strain maps in systole, early diastole, and during atrial contraction. Cumulated strain curves of superior and inferior aortic walls were documented. *In vitro* and *in vivo* principal strain ranges were smaller in the case of the aortic aneurysm compared with normal aorta. Heterogeneous strain patterns were also observed. These results suggest that the proposed model could detect and evaluate aortic aneurysm stiffness and may be useful clinically for the early and timely detection of degraded mechanical properties to impact patient outcomes.

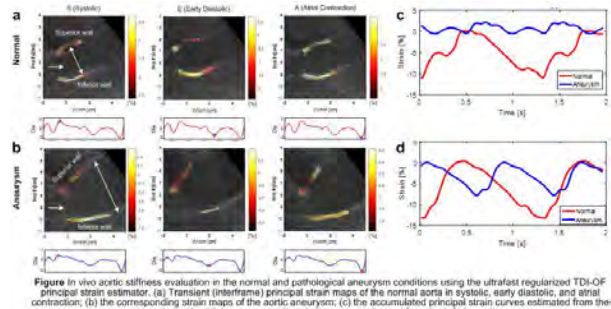


Figure In vivo aortic stiffness evaluation in the normal and pathological aneurysm conditions using the ultrafast regularized TDI-OF principal strain estimator. (a) Transient (interframe) principal strain maps of the normal aorta in systolic, early diastolic, and atrial contraction; (b) the corresponding strain maps of the aortic aneurysm; (c) the accumulated principal strain curves estimated from the superior walls; (d) the corresponding strain curves estimated from the inferior walls.

4:15 PM

A Longitudinal Study of the Mechanical Properties of Abdominal Aortic Aneurysms: the First ResultsEmiel van Disseldorp¹, Niels Petterson², Frans van de Vosse³, Marc van Sambeek⁴, Richard Lopata³¹Biomedical Engineering, Eindhoven University Of Technology, Eindhoven, Netherlands, ²Eindhoven University of Technology, Eindhoven, Netherlands, ³Eindhoven University of technology, Netherlands, ⁴Catharina Hospital Eindhoven, Netherlands**Background, Motivation, and Objective**

Rupture of an abdominal aortic aneurysm (AAA) will result in a life-threatening hemorrhage in 90% of all cases. Therefore, according to current clinical guidelines, surgery is recommended when the maximum aortic diameter reaches 5.5 cm or when it has grown more than 1 cm/year. This method has its shortcomings, and a more patient-specific method is required. In a previous study, we demonstrated a fully automated method to characterize the mechanical properties of AAAs using 4D ultrasound (US) based finite element analysis and elastometry. In this study, we monitored these patient-specific material properties over time to assess its relation with the diameter and its growth rate.

Statement of Contribution/Methods

In total 26 AAA patients (diameter 32 – 50 mm) were included in this study. 4D-US data were acquired using a Philips iU22 (X6-1 transducer) during breath hold while brachial pressure was measured simultaneously. Afterwards, these patients were followed for 3 – 32 months, which resulted in 2 – 10 consecutive moments where data were recorded. All patients were divided in a small (< 38 mm), moderate (38 – 45 mm), and large (> 45 mm) AAA group.

The aortic geometry was automatically segmented and tracked over time using 3D speckle tracking. The diastolic geometry was converted into a mesh (wall thickness of 2 mm) which was inflated to the patient-specific systolic pressure. Finally, the patient-specific shear modulus was estimated using an inverse method, by matching the measured 4D US displacements to the model displacements. The aortic stiffness (shear modulus x wall thickness) was calculated for all consecutive time moments.

Results/Discussion

Figure 1A shows the aortic stiffness at the first time measurement as a function of the diameter. A significant difference in aortic stiffness was measured between the small, and the moderate large AAAs. For each group the mean growth rate was assessed (small: 1.2, moderate: 1.6, and large: 3.8 mm/year), and afterwards each AAA was divided in a slow or rapid growing group. Figure 1B shows that the rapid growing AAAs in the large AAA group have a lower aortic stiffness compared to the slow growing AAAs. However, inclusion of more patients is needed to strengthen this finding.

In conclusion, using 4D US mechanical properties of the AAA wall can be assessed over time and the first results revealed differences between the slow and rapid growing AAAs.

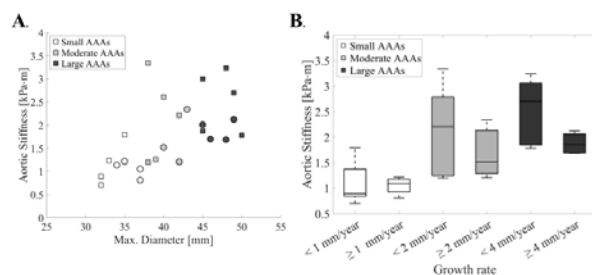


Figure 1A: Aortic stiffness as a function of the maximum diameter for the small, moderate, and large AAAs. The squares represent the AAAs with a relatively low growth rate while the circles have a relatively high growth rate.

B: Box-and-whisker plots of the aortic stiffness for each different group.

4:30 PM

Comparison of the shear wave velocities in anastomosis between excised pig aorta, Dacron, PTFE and custom made arterial models using shear wave elastography

Miguel Bernal^{1,2}, Indrani Sen³, Matthew Urban²

¹Grupo Dinámica Cardiovascular, Universidad Pontificia Bolivariana, Medellin, Colombia, ²Department of Radiology, Mayo Clinic, Rochester, MN, United States, ³Department of Vascular Surgery, Mayo Clinic, Rochester, MN, United States

Background, Motivation, and Objective

Cardiovascular disease is the leading cause of mortality in the USA with an overall death rate of 27.8%. Surgical revascularization with synthetic vascular grafts (Polytetrafluoroethylene, Dacron) is necessary in a subset of patients. These grafts are relatively non-compliant and susceptible to dilatation, neointimal hyperplasia and thrombosis over time. These have been associated with mismatch of the elasticity of the vascular implants, causing an increase in shear stress in the wall. The purpose of this study was to compare the mechanical properties of clinical grafts with excised arteries and custom made arterial models.

Statement of Contribution/Methods

Five descending aortas were collected from pigs at a local butcher shop. A 5 cm region-of-interest (ROI) was marked on each vessel and mounted on a frame at different longitudinal strains (0 to 40%). For each strain, the aortas were pressurized between 20 and 180 mmHg and tested using shear wave elastography (SWE). The arteries were then cut at the distal edge of the ROI and anastomosed with the surgical replacements (Dacron, PTFE) and custom made arterial models made of PVA (10% by weight) and a reinforcing mesh (PRAM). The same experimental procedure (SWE) was repeated for each of the anastomosis.

Results/Discussion

In this study we report the values for group velocity (C_g , m/s) as a surrogate for the Young's modulus. The arteries presented values between 4.8 m/s (20 mmHg and 0% strain) and 9.6 m/s (180 mmHg and 40% strain). The Dacron showed a higher increase going from 5.7 m/s to 19.1 m/s (same pressures and strains). The PTFE showed higher overall C_g values ranging from 14.2 to 22.5 m/s. The aortic models presented very similar behavior to those of the pig aortas with values from 4.4 m/s (at 20 mmHg and 0% strain) to 9.2 m/s (at 180 mmHg and 40% strain). Figure 1 shows all the mean values for C_g for the different combinations of pressure and strain.

The results from this study suggest that the synthetic vascular replacements (PTFE, Dacron) have much higher mechanical properties than healthy aortas. These differences in elasticity might explain the high failure rates of the synthetic replacement. The aortic models (PRAM) tested in this study showed almost identical behavior to the healthy aortas in a wide range of pressures and strain. The design of future vascular replacements should consider the matching of the mechanical properties.

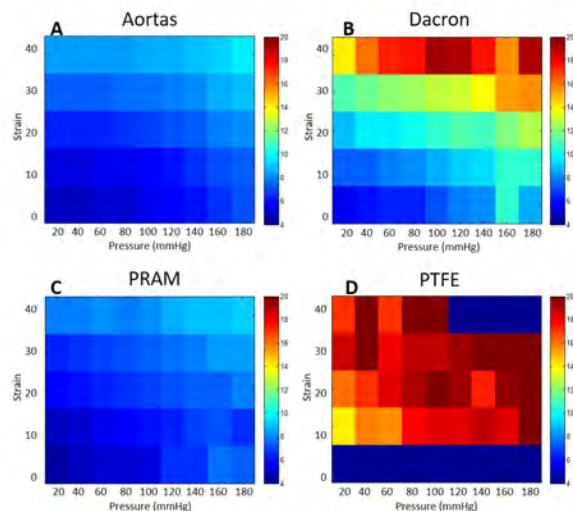


Figure 1. Comparison in the mean C_g (m/s) for healthy excised pig aortas (A), surgical Dacron (B), customized aortic models, PRAM (C) and surgical PTFE (D), at different strains (0 to 40%) and pressures (20 to 180 mmHg).

4:45 PM

Pulse Wave Imaging for monitoring non-linear material behavior in an Ang-II induced hypertensive mouse model

Paul Kemper¹, Matthew McGarry¹, Iason Zacharias Apostolakis¹, Elisa Konofagou^{1,2}

¹Biomedical Engineering, Columbia University, New York, NY, United States, ²Radiology, Columbia University, New York, NY, United States

Background, Motivation, and Objective

Hypertension is a major risk factor for various cardiovascular diseases, and current guidelines are mainly based on brachial blood pressure, which is not always representative of central arteries. A local assessment of central arteries such as the aorta is preferred. So far, Pulse Wave Imaging (PWI), developed by our group, relied on a single compliance value. However, the mechanical behavior of arterial tissue is non-linear. A change in elastin and collagen content is indicative of damage or remodeling caused by hypertension, which changes the non-linear elastic behavior of the arterial wall. In this study, the change in non-linear elastic behavior in Angiotensin-II (Ang-II) induced hypertensive mice was investigated using two different methods.

Statement of Contribution/Methods

The abdominal aorta of seven ($n=7$) Ang-II induced mice was imaged longitudinally for 5 weeks (4 weeks of Ang-II) using a 40 MHz linear array (MS550D, MicroScan). Coherent compounding sequences (Verasonics) with 3 plane waves were used (5376 Hz). Axial wall velocities were depicted over time to generate spatiotemporal maps of the pulse wave propagation (Fig. 1A and B). Propagation of two pulse waves are known to occur at diastolic and end-systolic pressure respectively. Regional PWV and corresponding compliance at these two different pressures were calculated **1)** using linear regression and the Bramwell-Hill equation (Fig. 1B), and **2)** by iteratively adapting bi-linear material properties of the arterial wall and the inlet pressure, until the simulated arterial wall displacements using the 1-D wave propagation model were in agreement (i.e. displacement error below 10%) with *in-vivo* measured displacements.

Results/Discussion

After 4 weeks of Ang-II infusion, the compliance at diastolic pressure was found to be 15% lower ($1.1 \cdot 10^{-10} \text{ m}^2/\text{Pa}$ versus $1.3 \cdot 10^{-10} \text{ m}^2/\text{Pa}$), while the compliance was 116% lower at end-systolic pressure ($3.1 \cdot 10^{-10} \pm 1.1 \cdot 10^{-11} \text{ m}^2/\text{Pa}$ versus $6.7 \cdot 10^{-10} \pm 3.0 \cdot 10^{-11} \text{ m}^2/\text{Pa}$) using the inverse problem approach ($p<0.05$) (Fig. 1C). The linear regression method yielded similar trend and values (i.e. within 20%), with higher variance at end-systolic compliance ($2.5 \cdot 10^{-10} \pm 2.1 \cdot 10^{-11} \text{ m}^2/\text{Pa}$) after 4 weeks. These findings indicate that PWI could potentially help clinicians detect early vascular remodelling or damage in hypertensive patients.

Supported in part by NIH-1R01HL135745

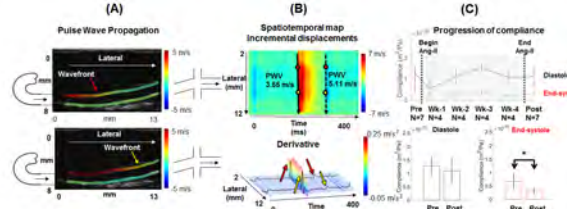


Figure 1 Axial wall velocities were depicted at the wall at two different moments during the propagation of the pulse wave (A), these axial wall velocities were depicted over time to generate spatiotemporal map of the pulse wave propagation. The derivative of this spatiotemporal map shows the foot of the two waves (B). The compliance progression over time shows a decrease in compliance within one week after the start of inducing AngII, after the diastolic compliance returns close to normal. The compliance at end-systolic remains lower after 5 weeks ($p<0.05$) (C).

5:00 PM Establishing Reliable Reference Values for Ultrasound Pulse Wave Velocity Measurement Methods: An Arterial Phantom Validation Study**Adrian J. Y. Chee¹, Hélène So^{1,2}, Alfred C. H. Yu¹**¹*Schlegel-UW Research Institute for Aging, University of Waterloo, Waterloo, ON, Canada*, ²*Sciences pour l'ingénieur, Sorbonne Université, Paris, France***Background, Motivation, and Objective**

Arterial phantoms play a key role in the development of ultrasound pulse wave velocity (PWV) analysis methods. In principle, theoretical PWV values may be derived in phantoms using the Moens-Korteweg (M-K) equation. Yet, one frequently overlooked caveat is that the theoretical PWV values themselves may be incorrect if the M-K equation is bluntly applied. Such estimation errors greatly jeopardize the arterial phantoms' reliability as PWV calibration tools for ultrasound PWV estimation techniques. Here, we have devised a new validation protocol based on direct pulse transit time measurements to investigate the accuracy of theoretical PWV values derived from the M-K equation. In turn, pertinent error sources in the M-K equation are identified and addressed to more dependably derive theoretical PWV values from arterial phantoms.

Statement of Contribution/Methods

Polyvinyl alcohol (PVA)-based arterial phantoms were fabricated using our injection molding framework (UMB, 2018; 44(4): 872-883). Phantom stiffness is varied by manipulating: i) material elasticity (1 to 5 freeze-thaw cycles) and ii) vessel wall thickness (1.5 to 3 mm in steps of 0.25 mm; 2 freeze-thaw cycles). Eight specimens were fabricated for each configuration using 10 % PVA solution. To measure PWV directly through pulse transit time principles, the phantoms were connected to a flow pump generating 0.1 s burst pulses of 10-mL/s peak flow rate at 20 bpm, minimizing measurement bias due to wave reflection. Two pressure transducers were attached at both ends of the phantom (220 mm apart) to measure pulse transit time using the foot-to-foot approach. PWV values were averaged over six pulse cycles. To quantify vessel elasticity in the circumferential direction, the vessels were progressively inflated by injecting 5 mL of water into its lumen and the corresponding intraluminal pressures were recorded. Hoop stress and strain was calculated to derive the elastic modulus. Theoretical PWV corresponding to the elastic moduli were derived using the M-K equation to compare with the measured PWV.

Results/Discussion

PWV of the tested phantoms ranged from 1.9 to 4.2 m/s. While measured and theoretical PWV were found to be correlated ($P = 0.91$) across arterial phantoms of different material elasticity, M-K derived PWV was severely underestimated (19%) when lumen diameter is same as the wall thickness. Such difference is attributed to the fact that the M-K model assumes the lumen diameter to wall thickness ratio to be at least 20. When this error is rectified using a modified M-K equation (Bergel's correction) to account for increased wall thickness, the underestimation was reduced to 7.3%. To conclude, errors from the M-K equation are significant and cannot be disregarded, especially when estimating local elastic modulus of individuals with subclinical vascular disease (and therefore thicker arterial walls). A modified M-K equation should be considered when translating PWV values to elastic modulus.

5:15 PM

An ultrasound phantom material with unique features: changing viscoelastic properties while keeping the speed of sound constant

Benjamin Meirza¹, Sandra Sjöstrand¹, Maria Evertsson¹, Ingrid Svensson¹, Lorenzo Grassi¹, Luciana C. Cabrelli², Theo Pavan², Tomas Jansson^{1,3}, Magnus Cinthio¹

¹Lund University, Sweden, ²University of São Paulo, Brazil, ³Skåne Medical Services, Lund, Sweden

Background, Motivation, and Objective

Realistic phantoms for ultrasound measurements are essential for developing new ultrasound methods and evaluating imaging techniques. To date, several tissue mimicking materials have been proposed. However, to the best of our knowledge, none of these existing materials give the possibility of changing the viscoelastic properties while keeping the speed of sound constant. Here we propose an oil-based phantom material for which the viscoelastic properties can be changed while keeping the speed of sound approximately constant. The aim of this study was to evaluate the novel material.

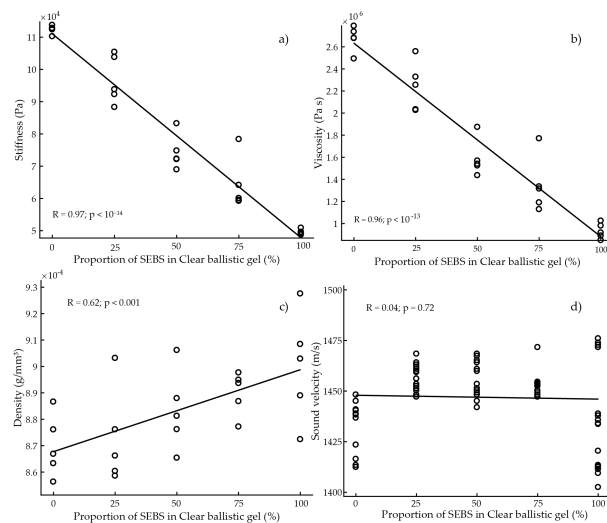
Statement of Contribution/Methods

The novel material was made by mixing two translucent oil-based gels: 1) styrene-ethylene/butylene-styrene (SEBS) copolymer in mineral oil and 2) Clear ballistic gel. In this study we evaluated the viscoelastic properties, the speed of sound and the density for five ratios (0%, 25%, 50%, 75% and 100%) of SEBS in Clear ballistic gel (five samples for each ratio). The mechanical response of the samples was evaluated through stress relaxation tests. The obtained force-displacement response was then fitted to a standard linear viscoelastic solid model to extrapolate the material parameters such as Young modulus and viscosity. The speed of sound was measured using a time of flight method and the density was calculated from mass and volume.

Results/Discussion

As shown in figure a) the instantaneous stiffness ($R = -0.97; p < 10^{-14}$) and b) the viscosity ($R = -0.96; p < 10^{-13}$) decreased whereas c) the density increased ($R = 0.62; p < 0.001$) linearly with the ratio between SEBS and Ballistic gel. As shown in figure d) the speed of sound showed no correlation with the ratio between SEBS and Ballistic gel ($R = -0.04; p = 0.72$).

In this study, a novel mix of ultrasound phantom materials was developed and characterized. It was shown that the material retained its speed of sound constant while the viscoelastic properties changed linearly with the ratio between SEBS and Clear ballistic gel. SEBS, Clear ballistic gel and its mixtures are stable, easy to use and manufacture, and are versatile. The results suggest that combining SEBS and Clear ballistic gel produces a promising phantom material for ultrasound imaging. The material is potentially useful for manufacturing ultrasound phantoms for development and evaluation of elastographic and photo-acoustic imaging methods.



8A - Therapeutic Transducers

Ruby (200)

Tuesday, October 23, 10:30 am - 12:00 pm

Chair **Yongrae Roh**
Kyungpook National University

8A-1

10:30 AM Treatment of breast tumors using a toroidal HIFU transducer. Preliminary experiments in human samples.

Marine Sanchez¹, Victor Barrere¹, Nicolas Chopin², David Melodelima¹

¹*LabTAU - INSERM unité 1032, LYON, France*, ²*Centre Léon Berard, LYON, France*

Background, Motivation, and Objective

Breast cancer is the most common among women. Breast-conserving surgery is the standard early-stage therapeutic approach. Lesser invasive treatments (radiofrequency, laser) have shown promising results with reduced morbidity and hospital stay. High Intensity Focused Ultrasound (HIFU) is an attractive technology due to its non-invasiveness though limited by the time required to achieve a complete ablation of the tumor volume. We recently developed toroidal HIFU transducers that enable fast and large volume treatments. We report here the first use of a completely non-invasive treatment of breast human tissues using a toroidal HIFU device.

Statement of Contribution/Methods

The HIFU transducer has a toroidal shape and was divided into 32 concentric rings of equal surface (78mm^2). The diameter of the transducer and its radius of curvature were 70 mm. The operating frequency was 3 MHz. The focal zone observed in the focal plane is a ring of 30 mm in diameter. Due to the geometrical characteristics of a torus, the ultrasound beams coming from each of the 32 emitters intersect between the principal focal ring and the transducer to form a secondary focal zone, which contributes to reinforce the size and homogeneity of the lesion. A 7 MHz ultrasound imaging probe was placed in the center of the HIFU device.

Experiments were conducted in 23 human samples of normal breast tissue recovered from mastectomies. Ablations in breast tissues were performed by placing the HIFU probe on the skin and using electronic beam steering to place the lesion at 15 mm under the skin. The free-field acoustic power varied from 100 to 140 watts and was applied for durations ranging from 45 to 180 seconds. Attenuation measurements were performed in the frequency range of 2 to 4 MHz, using the pulse-echo method, before and after HIFU treatment.

Results/Discussion

In total, 10 HIFU lesions were created. The dimensions of the lesion had an average diameter of 22.5 ± 4.4 mm while preserving skin integrity. The distance between the skin and the HIFU lesion was on average 15.1 mm. Necrosis of the treated zone in the breast was confirmed with histology. The attenuation coefficient was higher in HIFU-treated breast tissues ($0.27 \pm 0.08 \text{ Np.cm}^{-1}.\text{MHz}^{-1}$) than in the untreated tissues ($0.16 \pm 0.09 \text{ Np.cm}^{-1}.\text{MHz}^{-1}$).

These results suggest that it is possible to ablate a breast tumor of 10-15 mm in diameter with safety margins using a fully non-invasive HIFU exposure performed by a toroidal transducer. Particularly, this study highlights the creation of large ablation zones in a short period of time without the need of mechanically juxtaposing several lesions or the need to displace the HIFU device.

In conclusion, these preliminary results support the translation of the toroidal HIFU transducer to a Phase I – II clinical trials of breast cancer treatment. In parallel additional work is ongoing to continue increasing the ablation volume while keeping the same treatment time.

10:45 AM

Design, fabrication and testing of a dual-frequency transducer for Acoustic Cluster Therapy activationKenneth K. Andersen¹, Andrew Healey², Nigel L. Bush³, Martijn Frijlink¹, Lars Hoff¹¹*Department of Microsystems, University College of Southeast Norway, Horten, Norway*, ²*Phoenix Solutions AS, Oslo, Norway*, ³*Joint Department of Physics, Division of Radiotherapy and Imaging, The Institute of Cancer Research, London, United Kingdom***Background, Motivation, and Objective**

Acoustic Cluster Therapy (ACT) [1] is a two-component micro-particle formulation currently being developed for ultrasound-mediated drug delivery and opening of the blood-brain barrier. The ACT relies on using two distinct ultrasound frequencies: First exposure, above 2 MHz, causes the formulation to undergo a phase change to a gaseous state, forming approx. 20 μm diameter bubbles; further insonification at 0.5 MHz enhances the uptake of co-administered chemotherapeutic drugs, Fig.1 (a). Administering these two different ultrasound frequencies normally requires a two-transducer set-up, with careful and time-consuming alignment of the ultrasound beams.

Statement of Contribution/Methods

The aim of this study was to design, build, and validate a dual-frequency transducer for preclinical studies of ACT on murine tumor models (approx. 6 mm linear dimension). The transducer must deliver sufficient energy at both frequencies to activate the ACT formulation. To achieve this, a transducer was designed using a single circular piezoceramic disk operating at both its 1st and 5th harmonics, transmitting at 0.5 MHz and 2.7 MHz, respectively. The electrode pattern was arranged to achieve two different active apertures, giving overlapping sound fields from the two frequencies. Two acoustic matching layers were optimized using a numerical method [2] to reduce the ringing of the pulse at the 5th harmonic.

Results/Discussion

The transducer's ability to activate the ACT formulation was tested at the Institute of Cancer Research, London. The results show that microbubble activation was obtained both *in vitro* and *in vivo*. The activation levels were comparable to results obtained using the previous two-transducer setup. We conclude that the new dual-frequency transducer is suited for activation of the ACT formulation. Compared to a two-transducer setup, this removes the need for alignment, reducing the time per measurement and the probability of error.

References

- [1] A. van Wamel et al., Acoustic Cluster Therapy (ACT) enhances the therapeutic efficacy of paclitaxel and Abraxane for treatment of human prostate adenocarcinoma in mice, *Journal of Controlled Release*, Volume 236, 2016.
- [2] K. K. Andersen et al., Numerical optimization of ultrasound transducers by the linearity of the phase spectrum, 2017 IEEE International Ultrasonics Symposium, Washington, DC, 2017.

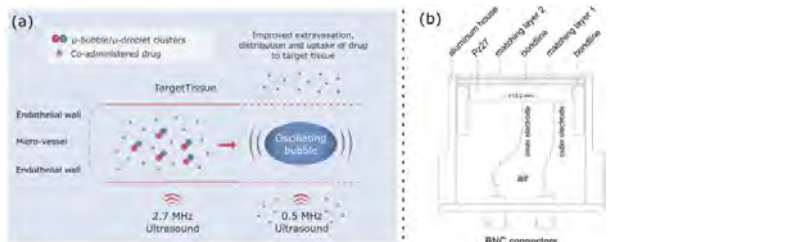


Figure 1. (a) 2.7 MHz ultrasound insonify the two-component micro-particle formulation with co-administered drug in the microvasculature. The gaseous state is achieved and a larger bubble is formed. Next, 0.5 MHz ultrasound enhances extravasation and distribution of the co-administered drug in the target tissue. (b) Cross-sectional view of the dual-frequency transducer.

11:00 AM

Development of Magnetic Resonance(MR) Compatible Transcranial 3072-elements Ultrasonic 2D Array for Deep Brain Stimulation and Neuromodulation

Teng Ma¹, Yongchuan Li¹, Ming Qian¹, Jiqing Huang¹, Ruibiao Guo¹, Xiaojing Long¹, Ye Li¹, Congzhi Wang¹, Weibao Qiu¹, Hairong Zheng¹

¹*Paul C. Lauterbur Research Center for Biomedical Imaging, Shenzhen Institutes of Advanced Technology, Chinese Academy of Sciences, China, People's Republic of*

Background, Motivation, and Objective

Ultrasonic neuromodulation is a fast-developing technology that has the great potentials to non-invasively obtain the information about neuronal circuits and treat neurological and psychiatric disorders. Functional magnetic resonance imaging(fMRI) is well-recognized and widely used for real-time monitoring the brain activities and evaluating the brain response of neuromodulation on nonhuman primates and humans. However, most of the commercial ultrasonic transducers are not MR compatible, which would lead to significant magnetic field inhomogeneity and cause unsuppressed artifacts in the MR image. In this study, we aim to develop four MR-compatible 3072-element ultrasonic 2D arrays for the precisely transcranial delivery of focused ultrasound to the targeted brain regions and achieve multidimensional, multisite, dynamic ultrasonic neuromodulation.

Statement of Contribution/Methods

As shown in Fig.1(A), the four 2D arrays are designed in coordination with the structure of the MR transmit coil and receive coil. Modified PZT 1-3 composite materials with a volume fraction of 51% are fabricated by using dice-and-fill technology. The sub-array with 256 elements are initially fabricated and the customized flexible printed circuits board is used to connect each individual element to the system. Each 2D array is designed to be a combination of 12 sub-arrays, which allows for the easy change and replacement of sub-array for the actual experiments (Fig1.(B)). All the electrodes and interconnectors used in the transducer fabrication are electromagnetic shielding and tested for MR compatibility. The thickness of piezoelectric material layer and matching layer is 1.5 mm and 0.75 mm, respectively.

Results/Discussion

The actual image of the two 3072-element 2D arrays is shown in Fig.1(C). The electrical impedance curve of one element of the array is shown in Fig.1(D). The 2D array has a center frequency about 1.03 MHz. The beam profile and transcranial capability of the sub-array is tested by using OptiSon Ultrasound Beam Analyzer. As shown in Fig.1(E-F), by applying 2 cycle of 200Vpp square wave excitation and proper time delay, the focused ultrasound generated by the MR-compatible 2D array could successfully penetrate the cadaver Rhesus macaque skull and form a steerable acoustic field for the deep brain stimulation and neuromodulation.

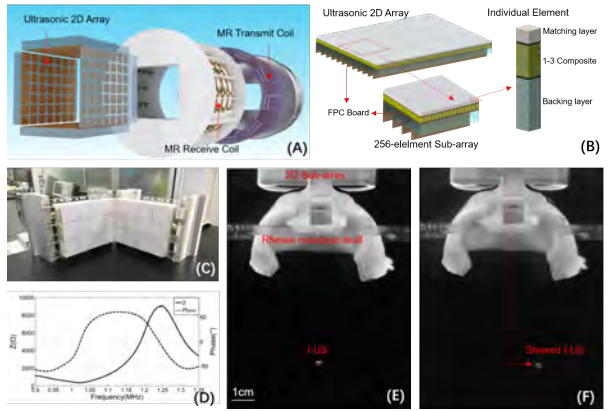


Fig.1 (A) Schematic of four ultrasonic 2D array with MR radiofrequency coil; (B) Design schematic of ultrasonic 2D array, sub-array and individual element; (C) Photography of two 2D ultrasonic array; (D) Electrical impedance curve of array element; (E) Instantaneous focused ultrasonic beam with skull; (F) Instantaneous steered focused ultrasound beam with skull;

11:15 AM

A 5 mm x 5 mm Square, Aluminum Lens Based Histotripsy Transducer: Reaching the Endoscopic Form FactorJeffrey Woodacre¹, Eric Simpson¹, Thomas Landry¹, Jeremy Brown¹¹Biomedical Engineering, Dalhousie University, Halifax, NS, Canada**Background, Motivation, and Objective**

Minimally invasive procedures (MIPs) have become commonplace in recent years as they result in less blood loss, fewer complications, and faster recovery times compared to open surgery. Conventional histotripsy is a cavitation-based ultrasonic ablation technique that could itself be considered an MIP as it can ablate transdermally using large highly focused transducers. Certain regions within the body do not lend themselves to this large range histotripsy either because the region of interest is blocked by bone (eg. the skull), or the precision requirements are too high. Our lab has been developing histotripsy tools to assist in burr hole surgeries with the end goal of creating an endoscopic form factor histotripsy device with co-registered imaging, enabling precision ablation. In this work, we will present a 5 mm by 5 mm square histotripsy transducer capable of tissue ablation. This 5 mm x 5 mm size is an important achievement as this makes it a clinically relevant endoscopic form factor for most MIPs.

Statement of Contribution/Methods

A square aperture histotripsy transducer was created using a 5.0 MHz piezoelectric composite coupled to a machined, 5 mm focus, 5 mm by 5 mm aluminum lens (f#1). The device uses a quarter-wavelength matching layer to improve bandwidth and increase coupling to tissue. A needle hydrophone was used to measure pressure amplitude versus drive voltage as well as the -3 dB beam width and length. Optimum drive frequency was found, and a combination of drive voltage, pulse-repetition frequency and number of pulse cycles were examined to find values of each which produce a cavitation bubble cloud in degassed water. A tuning inductor was used to reduce the drive voltage needed, allowing pressure to be further increased without additional stress to the pulser circuit.

Results/Discussion

It was found that, in the linear regime, peak negative pressure increases as $8 \text{ MPa}/100 \text{ V}_{\text{drive}}$ at the optimum transducer drive frequency of 6.2 MHz so, to reach cavitation pressure in water, at least 300 Volts are needed. In practice a 6.2 MHz, 10 cycle pulsed drive signal at a drive voltage of 450 and a PRF of 1 kHz was found to create a consistent bubble cloud in de-gassed water. The addition of a tuning inductor reduced the needed supply voltage to create this bubble cloud from 450 Volts to 250 Volts. The -3 dB beam width was found to be 0.229 mm while the -3 dB beam depth of field was found to be 1.2 mm.



11:30 AM 3D Ultrasound Image Guidance and Therapy through the Rib Cage with a Therapeutic Random Phased Array

Muhammad Zubair¹, Sevan Harput¹, Robert Dickinson¹

¹*Bioengineering, Imperial College London, London, United Kingdom*

Background, Motivation, and Objective

A major problem in clinical HIFU is the ablation of tissue underlying the ribs by maintaining adequate quality of field distribution beyond the ribs without overheating them. We propose that by operating the array in alternate image and therapy mode, ribs can be detected in real time without using any external imaging modality and HIFU beam can be adjusted accordingly avoiding any damage to the ribs.

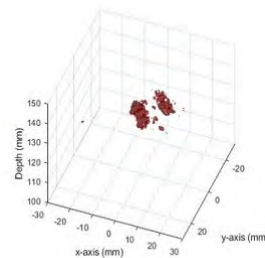
Statement of Contribution/Methods

Though Random Phased Arrays (RPA) are optimized for therapy only, the highly directional elements and the availability of almost 40% bandwidth encouraged us to assess its imaging capabilities. A 1 MHz 254-element random phased array, made by Acublate Ltd, London, UK is used both in therapeutic and imaging modes. Multiple simultaneous foci were generated and steered in simulations as well as experimentally. In imaging mode, the random phased array was integrated with Verasonics system via custom-built connectors to acquire raw RF data. Synthetic Aperture 3D beamforming technique was used to achieve 3D volumetric images of the region of interest. Plastic rib phantoms and ex-vivo ovine ribs were imaged both in simulation and experimentally in water bath.

Results/Discussion

Acoustic field distributions were calculated in the focal plane in an *xy* Cartesian coordinate grid with spatial step of 0.2mm. Patterns of multiple heating foci were generated and steered at ± 15 mm off the array axis and ± 20 mm along the axis. The measured -6dB full width of a single focused beam at geometric focus was 1.6mm. Point scatterers spaced laterally and axially were then imaged to measure the resolution of the system and the measurements were verified with MATLAB simulations. The FWHM of the lateral point spread function in simulated and experimentally acquired images was 1.6 mm. Ex-vivo study was performed to locate the ribs and geometric ray tracing method was used to focus the HIFU beam in the presence of ribs.

Integration of an imaging modality (MRI, CT or Ultrasound) with the HIFU system for imaging the ribs has been a hindrance in its clinical use. We have shown that with RPA, we can not only ablate the tissue but can also image the ribs and avoid damaging them. Moreover, RPA has very good spatial resolution at or near the geometric focus and we can locate the desired lesion target immediately prior to therapy.



11:45 AM

Planar CMUT annular-array and embedded imaging for ultrasound-guided HIFU therapy

Apoutou N'Djin¹, Christopher Bawiec¹, Guillaume Bouchoux¹, Nicolas Sénégond², Nicolas Guillen³, Jean-Yves Chapelon¹

¹*LabTAU, INSERM, Centre Léon Bérard, Université Lyon 1, Univ Lyon, Lyon, France*, ²*Vermon, France*, ³*EDAP TMS, France*

Background, Motivation, and Objective

Capacitive Micro-machined Ultrasound Transducers (CMUTs) used for biomedical applications have been mainly developed for imaging purposes and very few studies have proposed this technology for therapy. CMUTs have, however, already shown a potential for generating high intensity ultrasound. Although their operation in continuous wave (CW) mode remains challenging, their inherent characteristics could be of interest for improving some compromises made between the ultrasound imaging and therapy performances. In this study, CMUTs have been investigated for focusing ultrasound energy from a flat phased-array transducer, in the context of endocavitary ultrasound-guided High Intensity Focused Ultrasound (USgHIFU) for prostate therapy.

Statement of Contribution/Methods

The HIFU transducer consisted of a planar CMUT 64-element annular array divided into 4 quadrants ($f = 3$ MHz), with a central space containing a 256-element linear imaging array ($f = 7$ MHz). The CMUT rings were truncated in the width dimension making the total size of the array 57.5 mm long and 35 mm wide. CMUT prototypes were fabricated using a wafer bonding technique. An intermediary prototype was made of the HIFU part only, mounted on a 10-cm long, 4.5-cm wide flat rigid PCB. A final prototype of USgHIFU probe compatible with endocavitary prostate treatment approach was also developed. The probe final probes included the HIFU and imaging arrays, embedded electronics (pre-amplifying, mixing, matching circuits) and water circulation circuit for acoustic coupling with target tissues. The potential of this planar CMUT design for dynamic HIFU and guidance has been investigated in simulation and experimentally (hydrophone, radiation force, imaging phantoms).

Results/Discussion

The 64 planar CMUT rings could focus dynamically at 3MHz at distances ranging from 3-7 cm. The focal regions were comparable in size and shape to those modelled with the 16-ring spherical design of the Focal One® system used in clinic for prostate therapy. Focusing performances were confirmed experimentally at low power (hydrophone) and at high power by visualizing steady water fountains induced focally during several dozens of minutes. The array produced over 6W/cm^2 surface acoustic intensity, compatible with the generation of thermal lesions in prostate tissues. Increasing the DC bias voltage led to higher efficiencies ($\eta = 30\% @ V_{DC} = 120\text{V}$). The embedded CMUT linear-array allowed forming extended images (depth: 10 cm; widths: 3.5/10 cm) with resolutions ranging 0.3-0.7 mm. This work demonstrates the feasibility of utilizing planar CMUT arrays combined to perform high quality dynamic HIFU focusing and image guidance. Further improvements in the CMUT cell robustness should allow studying the repeatability of these performances at the preclinical level. This project was supported by the French Single Interministerial Fund (FUI, 2013), the Labex DEVweCAN and the Whitaker Foundation (2015).

8B - PTF & PTE: Thin Films and High Power Ultrasonics

Ruby (200)

Tuesday, October 23, 1:30 pm - 3:00 pm

Chair **Andreas Mayer**
HS Offenburg - Univ. of Applied Sciences, Gengenbach

8B-1

1:30 PM Evaluation method for high-power piezoelectric materials and devices

Takeshi Morita¹

¹*The Univ. of Tokyo, Kashiwa, Japan*

Background, Motivation, and Objective

It's well-known that the nonlinearity of the piezoelectric materials limits the performance of high-power ultrasonic devices. For developing these devices, understanding of the nonlinear piezoelectric vibration is essential challenge. However, the complicated phenomena, such as admittance curve deformation near the resonant peak, a jumping and a hysteresis between the different sweep directions, were obstacle to find the main sources of the nonlinearity. Therefore, it had been quite difficult to consider the maximum output power in designing the devices. In addition, for evaluating the piezoelectric materials, there had not been quantitative parameters suitable for hard-type piezoelectric materials; for example, quality factor measured with low vibration level has little meaning because under high-power vibration level, the quality factor changes dramatically because of the nonlinear effect.

Statement of Contribution/Methods

To clarify the nonlinear vibration mechanism of hard-type piezoelectric materials, two measurement methods, burst-mode method and admittance measurement under high power level were introduced. From the burst-mode method, the mechanical properties of the piezoelectric transducer can be obtained; on the other hand, the admittance curve is composed of both of the mechanical and electrical parameters. By comparing these results, it was found that the nonlinear terms exist only in mechanical compliance and mechanical damping in piezoelectric parameters. In other words, you can treat the force factor, the damped capacitor and the mechanical mass as constant parameters. Note that this model is valid only for the resonant drive with hard type piezoelectric materials. Anyway, the proposed model is effective in describing the nonlinear behavior.

Results/Discussion

Based on our nonlinear model, various simulations became possible. By evaluating the nonlinear parameters, it was clarified that the CuO-doped KNN ceramic has superior performance for high-power ultrasonic transducer compared to the conventional PZT ceramic. Putting the nonlinear parameters into the transfer-matrix model, the temperature effect under high-power operation could be taken into account. It means the high-power ultrasonic transducer can be designed including the temperature distribution. Recently, this nonlinear transfer-matrix model was adapted to the Langevin transducer and good agreement was confirmed between simulation and experimental results. Our nonlinear model would be useful for the future development of the high-power ultrasonic devices.

2:00 PM **An Ultrasonically Assisted Sagittal Saw****Daniel Richards¹**, Margaret Lucas¹¹*University of Glasgow, Glasgow, United Kingdom***Background, Motivation, and Objective**

Large bone cutting in modern surgery is predominately undertaken by power tools such as sagittal saws. For small bone surgeries, ultrasonic devices are also commonly used, principally in spinal, oral and maxillofacial procedures where their advantages over traditional saws and burs include high precision and low cutting force. To-date, research into ultrasonic devices for large bone surgery has been focused on longitudinal-mode cutting blades excited by a Langevin transducer. This new study investigates the potential for superimposing ultrasonic vibration on the reciprocating oscillatory motion of a sagittal saw blade, with the aim of demonstrating, in particular, a greater depth of cut for the same cut speed.

Statement of Contribution/Methods

The bone cutting device was based on a standard sagittal saw blade coupled with a Langevin-style transducer, where the front mass and sagittal blade formed a single part. The ultrasonic-sagittal saw (USS) device was designed using finite element analysis (Abaqus FEA, Dassault Systemes Simulia) with the aim of achieving a resonant device at 28.1 kHz, operating in the first longitudinal mode of the sagittal blade and with a nodal plane located at the piezoceramic stack of the transducer. The USS was subsequently fabricated and the modal parameters, impedance characteristics and nonlinear response were all characterised through experiments. The depth of cut and the current draw from the driving system defined cutting performance, and this was evaluated using a test rig designed to allow control of the cutting speed and applied load on the USS, for cut tests in a bone mimic material (White Renshape, Freeman). For these tests, the cutting speed was varied from 0.5 to 250 m/min, under applied loads of 8 and 16 N and the ultrasonic amplitude was varied from 4 to 12 μm . Tests were also carried out with no ultrasonic excitation of the USS device in order to compare with cut tests using a standard sagittal saw.

Results/Discussion

The predicted electrical impedance and modal frequencies of the USS were found to match their respective FEA predictions to within 1%. The tests showed that at low sagittal cut speeds and at the higher ultrasonic amplitude, a greater depth of cut could be achieved by the USS than the device operating with no ultrasonic excitation of the blade. However, at the higher sagittal cut speeds, more typical of sagittal saw operations, there was no discernible difference in cut depth with also little difference in current draw.

2:15 PM Improvement of crystalline orientation and electromechanical coupling in ScAlN film in view of negative ion bombardment during sputtering deposition

Shinji Takayanagi¹, Takahiko Yanagitani²

¹Nagoya Institute of Technology, Nagoya, Japan, ²Waseda University, Japan

Background, Motivation, and Objective

ScAlN films are widely studied for acoustic wave devices, because of their high piezoelectricity. A single sputtering source with a ScAl alloy metal target was used as one of the deposition technique. The large-size target of ScAl is, however, difficult to prepare and expensive. In previous study, we demonstrated Sc ingot sputtering deposition in which Sc ingots were set on an Al metal target. The c-axis orientation and electromechanical coupling in the Sc ingot sputtering were degraded compared with that in ScAl alloy sputtering, because of O⁻ and CN⁻ negative ion bombardment from Sc ingots to the substrate [1]. In this study, we investigated the method of decreasing the negative ion bombardment.

Statement of Contribution/Methods

In our study of ZnO sputtering, the negative ion bombardment decreased with the decrease of target temperature [2]. Based on the ion bombardment suppression, fifty Sc ingots whose mass were approximately 80 mg each were embedded in the surface of Al metal target (80 mm diameter) in order to cool them by water in the sputtering cathode. The amount of ion flux and ion energy which enter the substrate during the deposition by using an energy analyzer with a Q-mass spectrometer. ScAlN film was then grown on Ti/silica glass substrates by an RF magnetron sputtering. The crystalline orientation was determined by XRD analysis, and the conversion loss (CL) was measured by a network analyzer. These experimental results were compared with the results with the hot target where Sc ingots were just put on an Al metal disc.

Results/Discussion

The surface temperature of the Sc ingot during the sputtering deposition decreased from 890°C to 630°C by embedding Sc ingots in the Al target. Fig. 1(a) shows the energy distributions of CN⁻ negative ions which enter the substrate. Highly-energetic negative ions at 100-170 eV also decreased as expected. FWHM value of AlN(0002) ω -scan rocking curve in the ScAlN film sample with the cooled target was 2.5°, while that with the hot target was 4.6°. Furthermore, the minimal value of the CL in the sample with the cooled target was much lower than that with the hot target, as shown in Fig. 1(b). Therefore, the crystalline orientation and electromechanical coupling were improved by cooling Sc ingots.

[1] S. Takayanagi, et al., presented at *IEEE IUS 2017*, 7I-6.

[2] C. Takata, et al., presented at *IEEE IUS 2014*, P3C2-2.

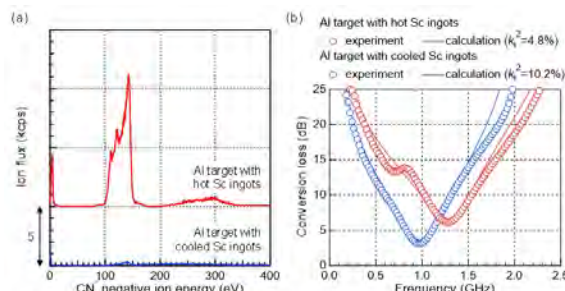


Fig. 1 (a) Energy distributions of CN⁻ negative ions entering the substrate during sputtering, and (b) frequency responses of the longitudinal-mode conversion losses of ScAlN films.

2:30 PM High-volume production and non-destructive piezo-property mapping of 30% Sc-doped aluminium nitride thin films

Stefan Mertin¹, Bernd Heinz², Andrea Mazzalai², Thorsten Schmitz-Kempen³, Stephan Tiedke³, Tuomas Pensala¹

¹*VTT Technical Research Centre of Finland, Espoo, Finland*, ²*Evatec AG, Trübbach, Switzerland*, ³*aixACCT Systems GmbH, Aachen, Germany*

Background, Motivation, and Objective

Scandium aluminium nitride (ScAlN) thin films exhibit a largely enhanced piezoelectric response in comparison to pure AlN (Akiyama et al., 2009). Both are compatible with well-established IC processing methods and can be sputter deposited at low temperatures such as 250–350°C. During the last International Ultrasonics Symposium a high-volume sputter process for ScAlN thin films was demonstrated (Mertin et al., 2017), providing the foundation for large-volume manufacturing of ScAlN based piezoMEMS.

Films with 30% or more Sc/(Sc+Al) content are of high interest for MEMS actuation, ultrasound generation, and energy harvesting applications (Akiyama et al., 2013 and Matloub et al., 2013). In comparison to conventional electrostatic designs, piezoelectric thin-film actuated MEMS devices offer a greater variety of in-plane and out-of-plane drive and sense modes. Based on its increased piezo-response and ease of process integration similar to AlN, ScAlN shows a high potential to improve device performances over AlN based. For the fabrication of devices, the designer needs accurate knowledge on material parameters, and for volume manufacturing, the knowledge on uniformity and repeatability of the parameters is crucial. In this work we measure the transversal and the longitudinal piezoelectric coefficients, $e_{31,f}$ and $d_{33,f}$, for ~30% ScAlN films fully mapped over 200-mm wafers.

Statement of Contribution/Methods

ScAlN is magnetron sputtered with pulsed DC on Pt coated 200-mm Si wafers with an Evatec CLUSTERLINE[©] 200 II tool. The film thickness and stress are mapped, and the crystalline orientation is monitored with X-ray diffraction (XRD). Top electrodes are sputter deposited and patterned to define test structures for measuring the piezoelectric parameters.

Using the aixACCT 4-point-bending setup (aix4PB) and a double-beam laser interferometry measurement tool (aixDBLI) with automated probe station, the transversal and the longitudinal coefficients ($e_{31,f}$ and $d_{33,f}$) of the ScAlN films are measured, respectively. The dielectric permittivity ϵ_r is determined from plate capacitor structures.

Results/Discussion

Material parameters ($e_{31,f}$, $d_{33,f}$, ϵ_r) of $\text{Sc}_{0.3}\text{Al}_{0.7}\text{N}$ thin films deposited in an Evatec CLUSTERLINE[©] 200 II are mapped over 200-mm wafer using aixACCT characterisation tools. A wafer map of each parameter is presented. Furthermore, scanning electron microscopy (SEM) cross-sectional views reveal typical columnar thin-film growth and XRD patterns confirm the c-axis thin-film texture in the desired AlN wurtzite phase. Expected typical values for the piezoelectric coefficients of the currently produced $\text{Sc}_{0.3}\text{Al}_{0.7}\text{N}$ coated wafers are in the order of $e_{31,f} = -2.3 \text{ C/m}^2$ and $d_{33,f} = 9.5 \text{ pm/V}$ or better.

2:45 PM

PZT epitaxial thick film for ultrasonic transducer at frequencies below 100 MHzYuka Mazda^{1,2}, Takahiro Shimidzu^{1,2}, Takahiko Yanagitani^{1,2,3}¹Waseda University, Japan, ²ZAIKEN, Japan, ³JST PRESTO, Japan**Background, Motivation, and Objective**

The frequency range of 20-100 MHz ultrasonics are promising for photoacoustic imaging, which is useful to image blood *in vivo* at high resolution. PVDF (Polyvinylidene Difluoride) is a well-known material for ultrasonic transducers for photoacoustic imaging. However, electromechanical coupling of PVDF ($k_t^2=4\%$) is not sufficient for practical application.

We previously reported high k_t^2 of $4.4 \mu\text{m}$ PZT epitaxial thin film ($k_t^2=25\%$) at 400 MHz [1]. In order to achieve lower frequency operation, thicker epitaxial film is required. However, it is difficult to obtain thick epitaxial PZT film due to their large internal stress. Many studies of PZT thick film transducers, therefore, were centered on the use of polycrystalline films. In this study we first reports high efficient PZT epitaxial thick film ($16.0 \mu\text{m}$) transducer operating in the 20-100 MHz.

[1] T. Yanagitani, K. Katada, M. Suzuki, and K. Wasa, IEEE IFCS2014, 121(2014).

Statement of Contribution/Methods

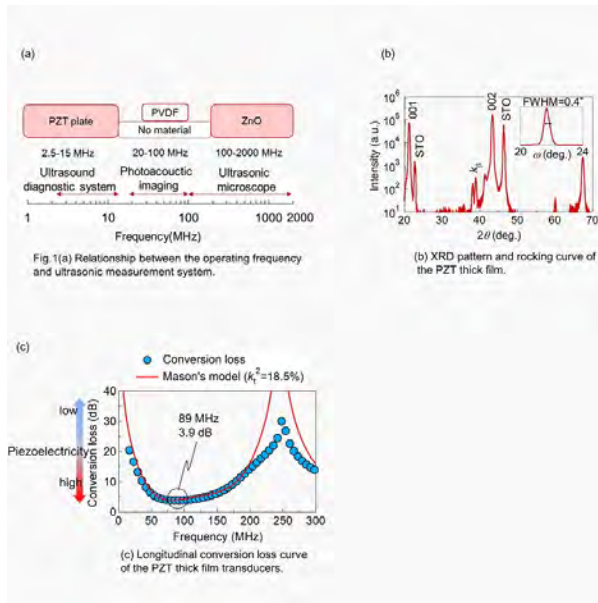
PZT thick films ($16.0 \mu\text{m}$) were grown epitaxially on conductive single crystal La-SrTiO₃ substrate by RF magnetron sputtering for 100 hours. The substrate is at the floating potential to reduce the effects of ion-irradiation-induced stress during the epitaxial growth. As shown in Fig.1(b), strong PZT (002) peak was observed at around $2\theta=43^\circ$. (002) peak rocking curve FWHM of the PZT were measured to be 0.4° which shows high crystalline quality.

[2] K. Wasa, S. Ito, K. Nakamura, T. Matsunaga, I. Kanno, T. Suzuki, H. Okino, T. Yamamoto, S. H. Seo, and D. Y. Noh, APL, **88**, 122903(2006).

[3] K. Iijima, Y. Tomita, R. Takayama, and I. Ueda, JAP, **60**, 361(1986).

Results/Discussion

We fabricated the high-overtone bulk acoustic resonator (HBAR) structure (Au/PZT/La-STO substrate). Longitudinal wave conversion loss is calculated from the impulse response, which is obtained by the inverse Fourier transform of the reflection coefficient S_{11} measured using a network analyzer. Fig.1(c) shows experimental conversion loss and theoretical one simulated by Mason's equivalent circuit model. The minimum conversion loss of 3.9 dB was found at 89 MHz. k_t^2 estimated by comparison of experimental and theoretical conversion losses was 18.5%, which is much higher than that of PVDF (4%). This transducer is well suited for photoacoustic imaging and medical ultrasonic applications.



8C - CMUT Design and Applications

Ruby (200)

Tuesday, October 23, 4:00 pm - 5:30 pm

Chair **Alessandro Stuart Savoia**
Roma Tre University

8C-1

4:00 PM Collapse-mode CMUT: design and characterization

Chris van Heesch¹

¹Philips Research

Background, Motivation, and Objective

Philips Research has been developing a CMUT platform during the last 10 years, aiming at a wide range of ultrasound transducers for various applications including conventional imaging probes and catheters, and potential new applications. The versatility of this platform results in a wide frequency range (1 to 50 MHz) and transducers dimensions in the range from ~1 mm² to ~25 cm², that can be designed with the CMUT technology.

This presentation shows the design of collapse-mode CMUTs using a single wafer CMOS compatible process. The measurements of both the electrical impedance, as a function of bias voltage, as well as the acoustical properties such as the output pressure and bandwidth, demonstrate their potential in terms of linearity and frequency tunability for ultrasound imaging.

Statement of Contribution/Methods

1

Results/Discussion

2

4:30 PM

A Robust and High Output Pressure CMUT Design for Ultrasound Imaging and HIFU Ablation

Ji Hoon Jang¹, Chienliu Chang¹, Morten Fischer Rasmussen¹, Kevin Brenner¹, Quintin Stedman¹, Arif Sanli Ergun², Butrus Khuri-Yakub¹

¹E.L. Ginzton Laboratory, Stanford University, Stanford, CA, United States, ²Electrical Engineering, TOBB University of Economics and Technology, Ankara, Turkey

Background, Motivation, and Objective

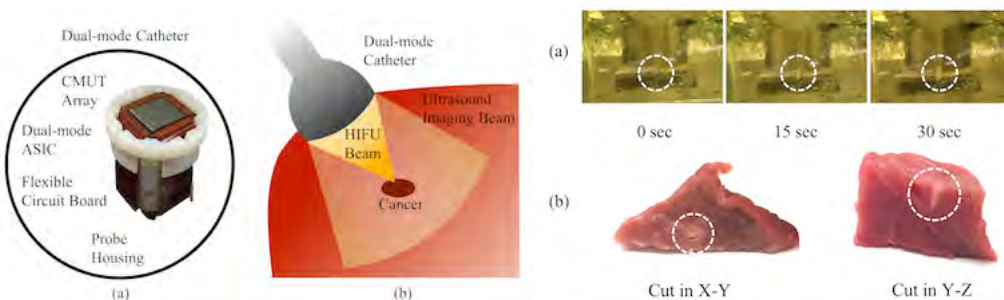
Capacitive Micromachined Ultrasonic Transducers (CMUTs) have a distinctive advantage over piezoelectric transducers in high intensity focused ultrasound (HIFU) applications in respect to a self-heating mechanism. However, obtaining high pressure levels that are needed for tissue ablation have been problematic with CMUTs due to device failure at high voltages which has been limiting the widespread use of CMUTs in HIFU applications. Therefore, we re-optimized a CMUT design for imaging and HIFU that can produce higher output pressure without breakdown or device failure.

Statement of Contribution/Methods

CMUT design requires many parameters to optimize, such as the thickness and location of top plate, gap height and material of the insulator and the plate. It is known that the output pressure generally increases with a larger gap height. However, when there is a limit on the AC and DC voltages, there is an optimum gap height that would generate the maximum output pressure. We designed and fabricated 2-D 32×32 elements CMUT array with a gap height of 0.13 μm and a top plate thickness of 1 μm.

Results/Discussion

After it is integrated with the dual-mode Application-Specific Integrated Circuit (ASIC), the dual-mode catheter was tested in an acoustic setup. Compared with previous published results, the device shows improved performance without device failure. The focused pressure at F-1 (8mm) was measured to 15.75 MPa peak-to-peak. An ablation test was successfully performed on HIFU phantom gel and ex-vivo tissue. We have shown that with proper design, CMUTs can produce high pressure levels reliably without device failure.



4:45 PM

Design of High-Frequency Ultra-Wideband 1-D CMUT Arrays for Acoustic Angiography ApplicationsOluwafemi Adelegan¹, Remzi Kemal², Feysel Yamaner¹, Paul Dayton³, Ömer Oralkan¹¹*Electrical and Computer Engineering, North Carolina State University, Raleigh, NC, United States*, ²*Electrical Engineering, Ozyegin University, Istanbul, Turkey*, ³*Joint Department of Biomedical Engineering, University of North Carolina at Chapel Hill and North Carolina State University, NC, United States***Background, Motivation, and Objective**

Broad range of medical imaging applications require high resolution in both lateral and axial directions. For superharmonic imaging applications involving the use of microbubble contrast agents, transducers that can transmit energy at low frequencies (less than 5 MHz) to excite the microbubbles, and at the same time detect scattered echoes at higher harmonics (greater than 20 MHz) are essential. Implementing such transducers using piezoelectric technology is extremely challenging. Capacitive micromachined ultrasonic transducers (CMUTs) have in recent years become an attractive alternative technology to the conventional piezoelectric transducers with ease of fabrication and possibility of achieving broader bandwidth as some of the inherent advantages. We have previously reported the design of 1-D broadband CMUT arrays with 29 MHz center frequency and 100% 3-dB fractional bandwidth (FBW). In this work, we designed ultra-wideband (2 MHz – 30 MHz) 1-D CMUT arrays by engineering the profile of the vibrating plate and optimizing the electrode shape.

Statement of Contribution/Methods

We used FEM to design 1-D ultra-wideband CMUT arrays for acoustic angiography applications. We investigated the effects of partially etched silicon plate and bottom electrode radius on the bandwidth of the devices. This design decouples the mass and stiffness components to give greater flexibility in the transducer design. The bottom electrode patterning enables greater control on higher order modes thereby increasing the bandwidth. A 0.7-mm thick, 100-mm glass wafer is used as the substrate. The 350-nm cavity depth is defined by dry etching, and the bottom electrode is defined by e-beam evaporation and liftoff. An SOI wafer with a 200-nm PECVD-silicon-nitride insulation layer is then bonded to the processed glass substrate using anodic bonding. After the bonding, the trapped gas inside the cavities is evacuated, and the cavities are sealed. The plate is patterned to complete the fabrication process.

Results/Discussion

The device fabrication requires seven masks. The bottom electrodes have been fabricated as shown in Fig. 1. FEM results for the devices show bandwidth from 1.7 MHz to 28 MHz pointing out the improvement enabled by reduced bottom electrode size and patterned plate.

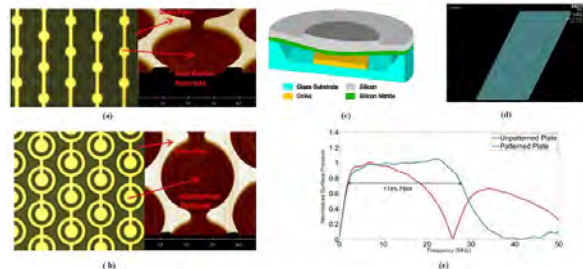


Fig. 1 (a) and (b) Optical (left) and AFM (right) images showing the glass post and patterned Cr/Au bottom electrode. (c) CMUT structure showing the optimized bottom electrode and patterned plate. (d) 3-D FEM structure used in simulation. (e) FEM analysis of the designed devices showing a Center Frequency of 15MHz and up to 174% FBW. The figure also shows the effect of patterned plate on the bandwidth.

5:00 PM Microbubble Contrast Agent Imaging Using Multi-Frequency CMUT Arrays
Mohammad Maadi¹, Chris Ceroici¹, Tarek Kaddoura¹, Roger Zemp¹
¹*Electrical and Computer Engineering, University of Alberta, Edmonton, AB, Canada*
Background, Motivation, and Objective

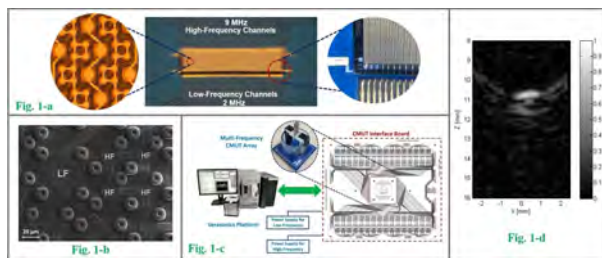
Ultrasonic transducers capable of operating over multiple frequency bands could have several interesting medical applications including imaging-therapy, super-harmonic contrast agent imaging, super-resolution imaging, image-guided drug delivery, and ultra-wideband ultrasound and photoacoustic imaging. Recently we introduced CMUT-based large-scale multi-frequency transducers for multi-scale imaging applications. These arrays can be used for microbubble contrast agent imaging applications in which low-frequencies are typically needed in transmission, while higher-frequencies are required in receive mode. Nonlinear micron-scale gas-scored agents strongly scatter ultrasound to enhance the contrast in the body. Pulse inversion or amplitude modulation techniques may be used to reject the signal coming back from linear scatterers.

Statement of Contribution/Methods

To ensure the minimization of grating lobes, large- and small CMUT membranes were fabricated in an interlaced fashion such that the pitch of high-frequency sub-arrays were 1λ or 2λ . Arrays of various sizes up to 128 elements were fabricated using a modified sacrificial release process with silicon nitride membranes and then wire-bonded to custom PCB boards mounted onto an interfacing board with voltage-protected pre-amplifiers, connected to a Verasonics programmable ultrasound platform. This system enables real-time imaging and programmable control over low- and/or high-frequency transmission and reception. To demonstrate contrast agent imaging, microbubbles with gas core and lipid shell were injected inside of a tube and then were imaged.

Results/Discussion

Fig. 1a shows the fabricated dual-frequency CMUT array with 128 low- and high-frequency elements. Fig. 1b demonstrates the SEM image of interlaced large- and small membranes. Fig 1c shows the setup used for the experiments. Different DC biases applied for low- (150 VDC) and high-frequency (200 VDC) elements. Fig 1d illustrates imaging of microbubbles (nonlinear scatterers) in which the linear scatterers were rejected. Results show promise for novel multi-scale multi-resolution imaging, imaging-therapy modes, superharmonic imaging and other applications.



5:15 PM

Broadband vs. sensitive CMUT linear array: a comparative study from bare chip up to the imageMaxime Hery¹, Tony Mateo², Dominique Gross², Nicolas Sénégond², Audren Boulme¹, Cyril Meynier², **Dominique Certon**¹¹*GREMAN - UMR CNRS 7347, Tours University, France*, ²*Vermon S.A., Tours, France***Background, Motivation, and Objective**

In a previous paper [1], we proposed a set of simple design rules in order to help the design of CMUT-based 1D arrays. The approach is based on properties of the radiation impedance of each element and the mechanical impedance of the CMUT membranes. It was shown that the mean mechanical stiffness of the membrane can be tuned to optimize either the bandwidth or the sensitivity of the transducer. This work follows this previous study and aims to verify experimentally these new design rules. Results and discussions presented here are focused on performances comparison between two 10MHz 1D arrays, one designed for large bandwidth (LB) and the other for sensitivity (SENS).

[1] Boulme et al., IEEE T-UFC, 2015

Statement of Contribution/Methods

The two arrays were initially designed by using the method proposed in [1], and fabricated thanks to a wafer bonding process. Only the size of the membranes was changed between these two configurations to reach the targeted specifications (LB: $40 \times 40 \mu\text{m}^2$, SENS: $30 \times 30 \mu\text{m}^2$). For each, a fully packaged probe prototype was fabricated. The devices were characterized at different steps of the workflow: mechanical displacements and pressure were measured on bare chips in oil, pressure measurements were performed with partially packaged devices, and finally pulse-echo measurements and image performances evaluation were performed with a Verasonics system on the final probes.

Results/Discussion

From the displacement measurements, one key parameter was particularly monitored: the mechanical cutoff frequency (f_{cut}) of the membrane, i.e. the frequency to which the average spatial displacement is zero. Simulated and experimental results showed the same f_{cut} values. As expected, the broadband prototype showed the lowest mean mechanical stiffness with a f_{cut} of 21 MHz, against 32 MHz for the sensitive device. The pressure measurements done with bare chips in oil and the packaged prototypes confirmed this result since the same f_{cut} were observed on the spectra. For the two arrays, the central frequency was lower than expected as the lenses were thicker than expected. Significant differences in sensitivity (9dB) and bandwidth (21%) were observed on the two probes, consistent from one experiment to another. The gain in sensitivity can clearly be ascribed to the gain of mechanical stiffness, since the sensitive device showed the lowest active surface ratio.

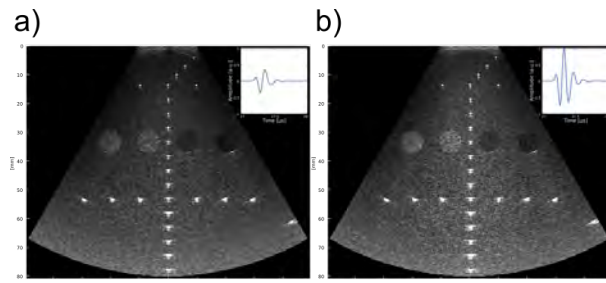


Figure 1: B-scans from plane wave imaging with 61 PW over $\pm 30^\circ$ and composite 2-ways impulse responses for
a) the broadband array and b) the sensitive array ($HV=20V$, $V_{\text{bias}}=80\% V_{\text{collapse}}$)

1D - Novel Contrast Agents

Topaz (400)

Wednesday, October 24, 8:00 am - 9:30 am

Chair **Ayache Bouakaz**
INSERM

1D-1

8:00 AM Bio-distribution of gas vesicles for cancer molecular ultrasound imaging

Guohao Wang¹, Lin SONG¹, Xuandi Hou¹, Lei Sun¹

¹Department of Biomedical Engineering, The Hong Kong Polytechnic University, Hong Kong

Background, Motivation, and Objective

Microbubbles based contrast-enhanced ultrasound plays a more and more important role in oncology. However, the utility of ultrasound for molecular imaging is significantly limited due to the lack of nanoscale contrast agents that can penetrate through tumor vasculature via the Enhanced Permeability and Retention (EPR) effect. Recently reported gas vesicles (GVs), isolated from buoyant photosynthetic microbes, demonstrated significant potentials as a novel nanoscale contrast agent for ultrasound molecular imaging. However, the actual capability of GVs to penetrate through EPR and reach tumor site has not been demonstrated.

Statement of Contribution/Methods

In this research, for the first time, we demonstrated that the surface modified GVs achieved high tumor uptake *in vivo*. With this result, we envision that GVs could serve as a unique and novel contrast agent for ultrasound molecular imaging.

Results/Discussion

In this research, we evaluated the bio-distribution of GVs in subcutaneous mouse tumor model with fluorescence imaging. First, *in vivo* fluorescence results showed little GVs retained in the tumor areas (Figure 1a). Then we utilized a biomaterial with good biocompatibility and targeting, Hyaluronic acid (HA), to improve the tumor uptake. Tumor accumulation and biodistribution of modified GVs was studied in MCF-7 tumor mouse model. Benefiting from good biocompatibility and targeting, strong fluorescent signals in tumor were observed in ICG-labeled HA-GV (HA-IGV) group steadily and peaked at 12 h (Figure 1). No significant fluorescent signals were observed at tumor sites in ICG-labeled GVs (IGV) group.

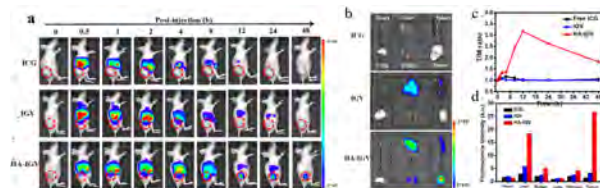


Figure 1. Biodistribution of GVs and HA-GV NPs *in vivo*. (a) In vivo NIR fluorescent imaging of MCF-7 tumor-bearing mice were taken at different times after intravenous injection of IGV, HA-IGV and free ICG respectively. Rounds indicate the tumors location. (b) Ex vivo fluorescence images of organs and tumors in tumor bearing mice after 12 h post-injection of free ICG, IGV and HA-IGV. (c) Tumor/muscle (T/M) ratio of MCF-7 tumor-bearing mouse model. (d) Fluorescence intensities of (b) ($\times 10^4$).

8:15 AM

Nonlinear X-wave ultrasound imaging of acoustic biomoleculesDaniel Sawyer¹, David Maresca², Guillaume Renaud³, Audrey Lee-Gosselin², Mikhail Shapiro⁴¹Bioengineering, Caltech, Pasadena, CA, United States, ²Chemical Engineering, Caltech, United States, ³Sorbonne Université, France, ⁴Caltech, United States**Background, Motivation, and Objective**

Recently, a new class of nanometric, stable, and genetically encodable contrast agents allowed biomedical ultrasound to image gene expression [Bourdeau 2018, *Nature*]. These air-filled proteins, known as gas vesicles, or GVs, can be engineered as harmonic variants (hGVs) that exhibit nonlinear scattering behavior due to buckling at acoustic pressures above 320 kPa [Lakshmanan 2016, *ACS Nano*], which allows amplitude-modulated (AM) ultrasound pulse sequences to distinguish hGVs from tissue. However, *in vivo* specificity is compromised by nonlinear propagation artifacts downstream of hGV inclusions. In highly nonlinear media like buckling GVs, the high amplitude waves of the AM code become distorted due to amplitude-dependent speed of sound and attenuation and carry that distortion downstream of the GV inclusion [Maresca 2016, *Appl Phys Lett*]. To address this issue, we present cross-amplitude modulation (xAM), an imaging paradigm that relies on axisymmetric cross-propagating plane-waves (Fig. 1a-c) to generate a transient AM code at their bisector. This preserves local nonlinearity but minimizes propagated nonlinearity due to the noncollinear geometry of the plane wave interaction.

Statement of Contribution/Methods

We implemented the xAM imaging sequence and beamforming on a programmable Verasonics Vantage ultrasound system with a 128-element linear array at 15.625 MHz using single-cycle pulses. To compare with a conventional AM imaging sequence, we implemented a parabolic AM (pAM) code. To evaluate artifact reduction *in vivo*, we injected into the colon of a mouse an agar-GV mixture containing a core of wild-type linearly scattering GVs (wtGVs) surrounded by a circular layer of hGVs (Fig. 2a). We imaged the *in vivo* gel at a depth range of $z = 2\text{ mm}$ to $z = 9.2\text{ mm}$ using both xAM and pAM and calculated the contrast-to-tissue ratio (CTR) and contrast-to-artifact ratio (CAR).

Results/Discussion

The superior specificity of xAM was demonstrated *in vivo*. The pAM image (Fig. 2c) contained a large artifact below the inclusion (CAR = -2 dB), parts of which blended with the hGV signal, displaying a potentially-misleading distribution of the contrast agent. In contrast, the annular hGV inclusion is almost entirely visible in the xAM image (CAR = 10 dB), with little-to-no artifact in the vicinity, and inner and outer contours more clearly delineated (Fig. 2e).

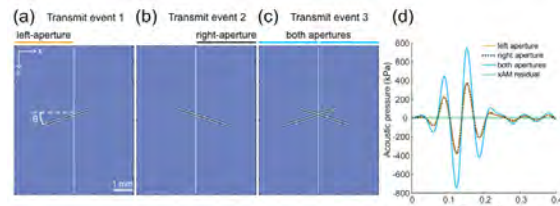


FIG. 1. Simulation of the xAM sequence for $\theta = 18^\circ$ with respect to the transducer array. (a-b) Half-aperture plane-wave transmissions. (c) Cross-propagating plane-waves transmission using both half-apertures. (d) Simulated waveform at the bisector intersection for $z = 3.6\text{ mm}$. The cross-propagating plane-waves peak positive pressure was 746.90 kPa (blue curve), while the residual peak positive pressure (green curve) was 0.13 kPa, or 0.018% of the cross-propagating plane-waves peak positive pressure.

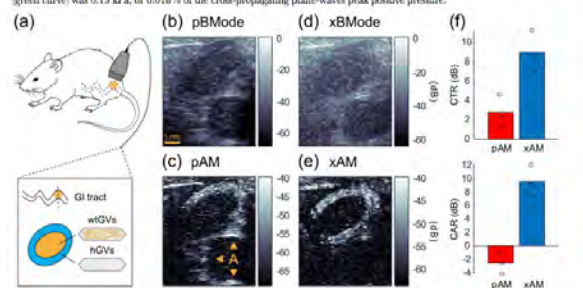


FIG. 2. *In vivo* pAM and xAM imaging of acoustic biomolecules. (a) Schematic of the experiment. A mixture of nonlinearly scattering hGVs and linearly scattering wtGVs was injected in a mouse gastrointestinal (GI) tract and imaged with pAM and xAM. (b) pBMode image, focus = 4 mm, f-number = 2.0. (c) pAM image, arrows point at the artifact (A). (d) xBMode, $\theta = 19.5^\circ$ (e) xAM image, pAM and xAM dynamic ranges are displayed relative to their respective BMode ranges. All images depths ranged from $z = 2\text{ mm}$ to $z_f = 9.2\text{ mm}$. (f) Comparison of xAM and pAM in terms of mean contrast-to-tissue ratios (CTR) and contrast-to-artifact ratios (CAR). N = 3.

8:30 AM

Acoustic Biomolecules as Genetically Encodable Nuclei for Inertial Cavitation

Avinoam Bar-Zion¹, Atousa Nourmahnad¹, David Mittelstein¹, Sangjin Yoo¹, Dina Malounda¹, Mohamad Abedi², Audrey Lee-Gosselin¹, David Maresca¹, Mikhail Shapiro¹

¹*Division of Chemistry and Chemical Engineering, California Institute of Technology, Pasadena, CA, United States,*

²*Division of Biology and Biological Engineering, California Institute of Technology, Pasadena, CA, United States*

Background, Motivation, and Objective

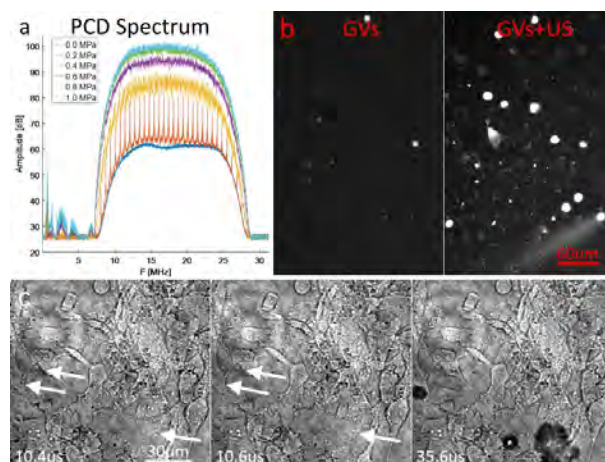
One of the main shortcomings of modern anticancer therapies is their limited ability to penetrate deep into cancerous tissue. Ultrasound-enhanced drug delivery is attractive due to ultrasound's availability and affordability; however, the use of this technology is currently limited by the properties of microbubbles as cavitation nuclei. Microbubbles' large sizes prevent extravasation, and their compositions lead to short circulation times. To overcome these challenges, we propose the use of gas vesicles (GVs), a unique class of physically stable, gas-filled protein nanostructures derived from buoyant photosynthetic microbes, as cavitation nuclei. Unlike microbubbles, GVs are genetically encoded, thus can be produced by e.g. tumor homing cells.

Statement of Contribution/Methods

The GVs were insonated using a 0.67 MHz Precision Acoustics HIFU transducer. A Verasonics scanner functioning as a passive cavitation detector (PCD) was used to detect cavitation and observe the effect of GV concentration and different pulse parameters on cavitation levels in purified GVs. Cavitation in GV-expressing E. coli was investigated via the same PCD setup. Sonoporation of U87 glioblastoma cells by membrane-attached GVs was imaged using fluorescence microscopy. Live imaging of GV cavitation was performed using a high frame rate (5MHz) camera. In order to examine GV cavitation *in vivo*, hind-limb MC26 tumors of 4 BALB/c mice were injected with purified GVs, and then co-aligned HIFU and imaging transducers were used to perform PCD at the injection site.

Results/Discussion

Using purified GVs, wideband spectral emissions were seen at pressure levels higher than 0.2MPa (Fig. 1a). Sonoporation of U87 cells by cavitation of attached GVs resulted in a statistically significant increase in propidium iodide-positive cells from 1% to 12.5% ($p<0.001$) following ultrasound exposure (Fig. 1b). High frame rate microscopy videos of GV cavitation supported a model in which GV collapse produces bubbles that nucleate cavitation (Fig. 1c). Inertial cavitation of GVs inside tumors resulted in a significant increase in wideband spectral emissions, compared to saline control ($P<0.01$). The use of GVs as cavitation nuclei could improve the efficacy and selectivity of cavitation-enhanced drug delivery, particularly in combination with emerging advancements in cell based therapeutics.



8:45 AM

Fluorine-modified Superhydrophobic Amorphous Calcium Carbonate-Doxorubicin Nanoparticles for Ultrasound Theranostics

Pei-Hua Chiang¹, Qiaofeng Jin², Chih-Kuang Yeh¹

¹Department of Biomedical Engineering and Environmental Sciences, National Tsing Hua University, Taiwan,

²Department of ultrasound, Union Hospital, Tongji Medical College, Huazhong University of Science and Technology, China, People's Republic of

Background, Motivation, and Objective

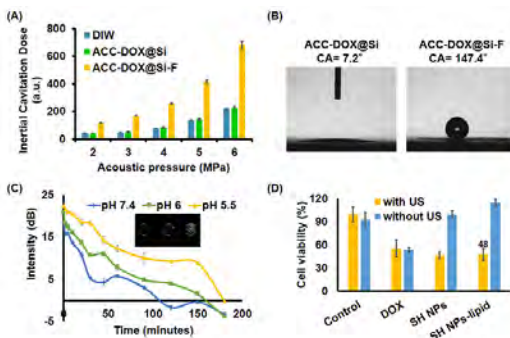
Ultrasound-induced microbubbles (MBs) cavitation effect has been widely applied in drug and gene delivery. However, the MBs properties of microsized, short lifespan and low drug payload limit their applications. The pH-sensitive Amorphous Calcium Carbonate-Doxorubicin Nanoparticles (ACC-DOX NP) could overcome these obstacles since their features of nanosized and high drug payload. In this study, we fluorinated NP into superhydrophobicity (SH) by trapping interfacial nanobubbles on the surface, which could induce cavitation effect with US to enhance blood vessel permeability and the fluorinated process improved the stability of ACC-DOX NP. Moreover, we coated lipid on the outer shell of SH NP to overcome the aggregation issue in aqueous solution. In other words, we designed a novel theranostic agent – ACC-DOX@ Silica- Perfluorodecyltriethoxysilane-lipid (Si-F-lipid). In addition, owing to the property of pH-sensitive of the NP, ACC-DOX could be dissolved and release CO₂ bubbles and DOX within tumor.

Statement of Contribution/Methods

ACC-DOX (86±0.2 nm) were synthesized by using a vapor-diffusion method. Then, ACC-DOX were coated with Si layers by Stöber method (123±2 nm) and fluorinated with F to obtain the SH NP (202±5 nm ACC-DOX@Si-F). The inertial cavitation doses (ICD) of NP were detected by a 10-MHz focused transducer under 2-MHz US insonations at 2-6 MPa. The static contact angles (CA) of NP films was measured using a CA analyzer (FTA-1000B). In vitro US imaging of ACC-DOX@Si-F-lipid was performed in phosphate buffer solutions at various pH (7.4, 6.5, and 5.5) using Terason 13000 through agarose gel (1.5%, w/v). Furthermore, the TRAMP cell experiments were conducted to assess the cytotoxicity under 2-MHz US excitation (50-cycle and 6 MPa at a PRF of 100).

Results/Discussion

The ICD of ACC-DOX@Si-F increased 3-fold with respect to that of ACC-DOX@Si and DI water (Figure A). The ξ-potentials were varied from +42mV (ACC-DOX) to -36 mV (ACC-DOX@Si-F). The CA from 7.2 and 147.4 degree showed that ACC-DOX@Si-F became SH after fluorination (Figure B). The US image intensity (from 5 to 12 dB) was augmented under pH 5 than pH 7 to indicate the pH-sensitive character (Figure C). The TRAMP cells incubated with ACC-DOX@Si-F-lipid presented a 48±4.1% cytotoxicity under US exposure (Figure D). Future work includes assessment of their capability as theranostic agents in vivo.



9:00 AM

Chemical and acoustic characterization of a novel ultrasound contrast agentSimone A. G. Langeveld¹, Ines Beeckers¹, Antonius F. W. van der Steen^{1,2}, Nico de Jong^{1,2}, Klazina Kooiman¹¹*Department of Biomedical Engineering, Erasmus MC, Rotterdam, Netherlands*, ²*Acoustical Wavefield Imaging, Delft University of Technology, Delft, Netherlands***Background, Motivation, and Objective**

Microbubbles (MBs) are ultrasound (US) contrast agents that are also attractive for molecular imaging and therapy [1]. A challenge is the variability in response to US of currently available MBs [2]. We hypothesize that this is caused by immiscible phospholipid components in the MB coating that are not in the same lipid phase. Cholesterol has been shown to affect phase distribution in lipid monolayers [3]. Therefore we developed and characterized novel phospholipid-coated ultrasound contrast agents containing cholesterol.

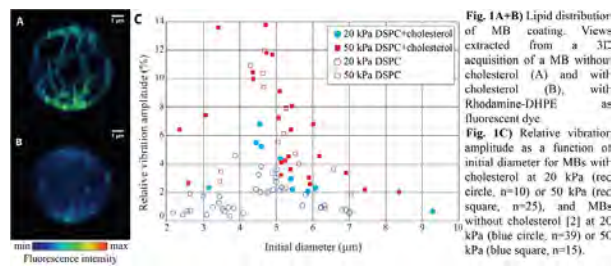
Statement of Contribution/Methods

Phospholipid-coated MBs (composition in mol%: DSPC 59.4; PEG-40 stearate 35.7; DSPE-PEG(2000) 4.1; DSPE-PEG(2000)-biotin 0.8) with or without 10 mol% cholesterol and a C₄F₁₀ gas core were made by sonication. MB size distribution was studied using a Coulter Counter. Fluorescent dye Rhodamine-DHPE was used (0.01 mol%) to study the lipid phase distribution of the MB coating. 4Pi microscopy was used to obtain high-axial-resolution images. MB response to US was studied in detail with the Brandaris 128 high-speed camera (20 to 50 kPa, 2 MHz, single 10-cycle burst) [4].

Results/Discussion

The size distribution of the newly synthesized MBs with cholesterol (mean diameter 3.7 μm) was comparable to the common in-house DSPC MBs (mean diameter 4.2 μm). 4Pi microscopy revealed a characteristic honeycomb pattern of lipid phase distribution in MBs without cholesterol (Fig. 1A). On the other hand, the MBs with cholesterol showed a more homogenous distribution of Rhodamine-DHPE (Fig. 1B). When insonified at 20 kPa, the MBs with cholesterol had a higher relative vibration amplitude than MBs without cholesterol (Fig. 1C). At 50 kPa, MBs with cholesterol showed a more similar behavior to MBs without cholesterol. Preliminary data shows characteristic resonance behavior of MBs with cholesterol in response to US. Our results indicate that cholesterol has a high impact on the miscibility of the phospholipid components in the MB coating while retaining a functional response to US.

[1] Kooiman et al, *Adv Drug Del Rev* 2014; [2] van Rooij et al, *Ultrasound Med Biol* 2015; [3] Yuan et al, *J Microsc* 2002; [4] Chin et al, *Rev Sci Instru* 2003. Acknowledgements – This project is funded by the Phospholipid Research Center in Heidelberg, Germany.



9:15 AM

Characterization of the in-vivo uptake of novel contrast agents using photoacoustic radiofrequency spectraYanjie Wang¹, Eno Hysi¹, Wenkun Bai^{2,3}, Elizabeth Berndl¹, Michael Kolios¹¹*Physics, Ryerson University, Toronto, ON, Canada*, ²*Ultrasound in Medicine, Shanghai Jiao Tong University, China, People's Republic of*, ³*6th People's Hospital, China, People's Republic of***Background, Motivation, and Objective**

Nobel metallic nanoparticles (NP) are effective contrast agents for photoacoustic (PA) imaging of tumor and as drug carriers for cancer treatment. However, the effectiveness of these carriers to be specifically delivered to target cells heavily depends on the targeting efficiency. We have developed a phase-change PA theranostic agent consisting of perfluorohexane (PFH) liquid and gold nanorods (GNRs) in the core and encapsulated by a biodegradable polymer, poly(lactic-co-glycolic acid) (PLGA). Here we demonstrate the potential of PA frequency-domain analysis for studying the in-vivo uptake of tumor targeted PLGA-GNRs.

Statement of Contribution/Methods

PLGA NPs loaded with PFH liquid, GNRs and DiD fluorescent dye were synthesized using a double emulsion method. The PLGA particle sizes (mean \approx 300 nm) were measured using the Archimedes system (Malvern Panalytical, UK). An antibody (Herceptin) was conjugated to the NP surface for specific binding to breast cancer cells that overexpress HER2 receptors. HER2-positive human breast cancer cells (BT474) were inoculated in the flanks in BALB/c B17 Scid mice ($N = 4$) four weeks prior to the imaging. The Herceptin conjugated PLGA-GNRs (PLGA-GNR-HER) were injected through tail veins. Tumors were imaged before injection and at 30min/3hr/6hr/12hr/18hr/24hr after injection using the VeoLAZR system (Fujifilm VisualSonics, Canada) at 21 MHz. The PA frequency spectra were studied as a function of time post-injection. Metrics such as integrated spectral power were used to compare the impact of tumor targeting.

Results/Discussion

Fig. 1a shows representative PA images of tumors acquired at 720 nm before (0 hr) and 6 hr after injection of PLGA-GNR-HER particles. There is a significant (15 dB) increase in contrast which is due to the NP targeting with HER2 receptors. The PA power spectra (Fig. 1b) show little enhancement ($\sim 1.1x$) of non-targeted PLGA particles at 6 hr. Additionally, the slope of the power spectrum for targeted particles decreases at 6 hr suggesting an increase in the effective absorber size due to increased PLGA-GNR tumor retention. The increased uptake is confirmed by the integrated spectral power (Fig. 1c) which is $\sim 30\%$ higher than non-targeted particles. This work shows the potential of analyzing frequency domain spectra for studying the in-vivo uptake and kinetics of novel NP contrast agents.

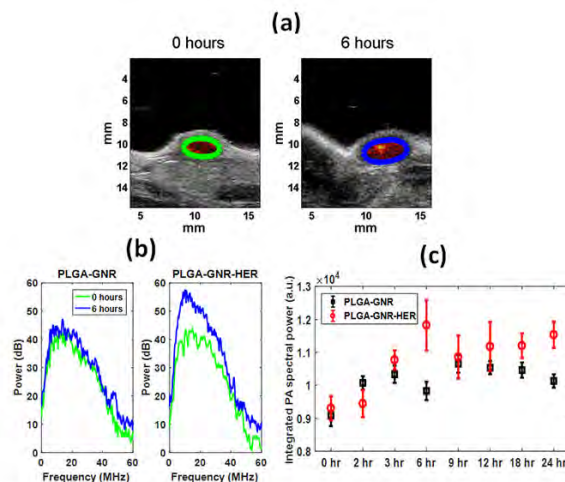


Fig. 1: (a) Representative PA images at 720 nm before (0 hour) and 6 hour post PLGA-GNR-HER injection. (b) Average power spectra for targeted and untargeted PLGA particles. (c) Integrated spectral power as a function of time post-injection. Error bars represent the standard deviation from 20 RF lines.

1E - Microbubbles and Nanobubbles

Topaz (400)

Wednesday, October 24, 10:30 am - 12:00 pm

Chair **Mike Averkiou**
University of Washington

1E-1

10:30 AM Molecular Modulation of Biological Membranes by Phospholipid Microbubbles

Eleanor Stride¹

¹*Oxford University, United Kingdom*

Background, Motivation, and Objective

Sonoporation - the temporary permeabilisation of cell membranes following exposure to microbubbles and ultrasound - has considerable potential for therapeutic delivery. However, understanding of the underlying mechanisms is far from complete. Recent studies have demonstrated that transfer of material takes place between phospholipid-coated microbubbles and cell membranes. The aim of our research was to investigate the impact of this transfer on membrane properties and cell permeability. Both artificial and biological cells were studied in an acoustofluidic device which enabled controlled exposure to both microbubbles and different ultrasound parameters. Quantitative fluorescence microscopy techniques were used to quantify changes in membrane molecular packing, viscosity and permeability to model drugs of different molecular weights. The results indicate that transfer of both phospholipids and other microbubble coating constituents can significantly alter the organization of molecules in both synthetic and biological membranes; and that this occurs even in the absence of ultrasound exposure. The relationship between molecular organization and permeability was found to be dependent upon multiple factors including the composition of the microbubble coating and the phase state of the cell membrane as well as the ultrasound exposure parameters. These results may help to explain why there is very wide variability in reported sonoporation efficiency. They also indicate the potential for optimising microbubble formulations for therapeutic applications.

Statement of Contribution/Methods

1

Results/Discussion

2

11:00 AM

Investigating nonlinear porphyrin nanobubble behaviour for vascular and extravascular applicationsCarly Pellow^{1,2,3}, Kullervo Hyynen¹, Gang Zheng², David Goertz¹¹*Physical Sciences, Sunnybrook Research Institute, Toronto, ON, Canada*, ²*University Health Network, Toronto, ON, Canada*, ³*Medical Biophysics, University of Toronto, Toronto, Canada***Background, Motivation, and Objective**

We recently reported the development of novel high payload porphyrin sono/photosensitizer-shelled MBs (pMBs), and their ultrasound (US)-triggered conversion to daughter nanobubbles (pNBs) with increased accumulation and retention (Fig 1B) in targeted tumor tissue (Huynh et al, *Nature* 2015). This has significant implications for optical and US imaging and photo/sonodynamic therapeutic applications. However, the acoustic response of NBs in general is poorly understood and harnessing their potential requires an understanding of their behavior in both intra- and extravascular compartments.

Statement of Contribution/Methods

We investigated the behavior of pMBs (0.8-6 μ m) and pNBs (0.2-0.4 μ m) at 10⁶ mL⁻¹ in vessel (0.5mm diameter) and tissue phantoms. A broadband 5 MHz transducer was employed to assess the response to 2.5 and 8 MHz center frequency pulses (8 μ s length, 1ms repetition frequency, 100 pulse sequences) from 100-1000kPa in 50kPa increments with n=5 acquisitions per pressure. Experimental results were compared to an encapsulated bubble model to gain mechanistic insights. We then acoustically induced conversion of pMBs in a two-photon window chamber setting and fluorescently monitored extravasation in a setup poised to investigate cavitation and phototherapeutic potential of daughter structures in tumor tissue.

Results/Discussion

The results provide a first direct observation that pNBs can initiate nonlinear scattering (Fig 1A) and do so at clinically relevant frequencies. pNBs notably exhibited a distinct pressure threshold at which scattered power rapidly increased, followed by a linear increase and plateau of similar power to their MB counterparts. Despite requiring higher driving pressures to achieve substantial oscillations, pNBs demonstrate sustained scattering in both tissue and vessel phantoms. Simulations indicated a substantial increase in scattered power upon sudden asymmetric radial oscillation sensitive to nonlinear shell rheology. These fundamental studies are supplemented by intravital imaging to demonstrate actively enhanced delivery and explore pMB and pNB cavitation *in vivo* (Fig 1C). The insights provided by this work suggest the potential of pNBs for imaging and therapeutic applications within the vascular and extravascular compartments.

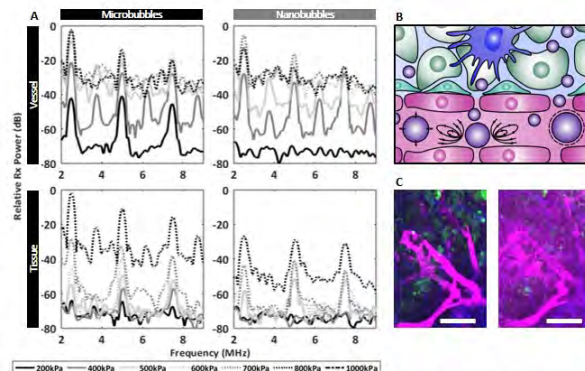


Figure 1. A) Received power spectra from MBs and NBs in vessel and tissue phantoms. Above threshold pressure levels, NBs exhibit distinct harmonics and ultraharmonics, and at higher pressures inertial cavitation. B) Concept sketch of MB conversion and subsequent permeabilization enhancement for daughter nanostructure extravasation. C) Two-photon dorsal window chamber microscopy images (blue: collagen, green: GFP-FaDu tumor cells, pink: fluorescent bubbles, scale=100 μ m) demonstrating pre- and post- US-triggered (1MHz, 2.5ms pulses for 2min at 4s PRP, 500kPa) vascular permeabilization.

11:15 AM

Stabilizing echogenic nanobubbles by nature-inspired elastic contrast shell design

Al de Leon¹, Reshani Perera¹, Christopher Hernandez¹, Michaela Cooley¹, Olive Jung¹, Grace Fishbein², Amin Sojahrood², Michael Kolios², Agata Exner¹

¹Case Western Reserve University, Cleveland, OH, United States, ²Ryerson University, Toronto, ON, Canada

Background, Motivation, and Objective

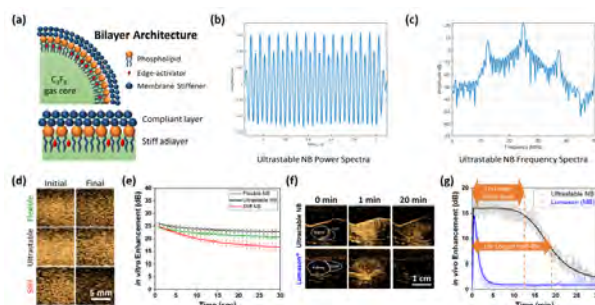
Of growing interest is the use of ultrasound contrast agents (UCAs) for cancer detection, image-guided biopsies, and theranostics. However, clinical UCAs or microbubbles (MB) typically range between 1-8 μm in diameter and are thus confined to the vasculature. Stability of MB is also poor, with typical half-life of <3 min. Our objective is the development of ultrastable nanobubbles (NB) with diameter less than 500 nm and which show persistent ultrasound signal for at least 20 minutes *in vivo*. Here we report the design and assess the stability of ultrastable NB as inspired by natural interfaces with elastic contrast (Fig 1a), which has been proven to provide synergistic improvement on toughness and resilience against defects as seen in blood vessels, red blood cells, and bacteria.

Statement of Contribution/Methods

Ultrastable NB with lipids plus either propylene glycol (flexible), glycerol (stiff) or both (ultrastable) in PBS followed by C₃F₈ gas exchange and activation via mechanical agitation. NB were purified by centrifugation, and size and concentration were measured by resonant mass measurement (Archimedes®, Malvern Panalytical). Power and frequency spectra of ultrastable NB was gathered with narrowband pulses at 25 MHz and 10% acoustic power (Veo-770, FUJIFILM VisualSonics). *In vitro* stability of NBs in phantom was determined through continuous exposure to US (Toshiba Aplio XG, 12 MHz, 0.1 MI, 15 fps). *In vivo* stability was determined using the same parameter but at 0.2 fps in normal mice (n=3) by injecting 200 μL of NB or MB via tail vein.

Results/Discussion

NB populations had a mean diameter of 282 ± 4 nm and concentration of $4.2\text{E}11 \pm 1.15\text{E}10$ NB/mL. Frequency and power spectra (Fig 1b, c) of ultrastable NB show a stable non-linear response. Ultrastable NB has a longer *in vitro* half-life compared to NB with different membrane properties (Fig 1d, e). *In vivo*, Lumason® showed a typical immediate and rapid decay ($t_{1/2} = 1.56$ min) following peak enhancement with signal dissipated within 5 min. Ultrastable NB signal remains for over 20 min (Fig 1f, g) with a 12X longer half-life ($t_{1/2} = 18.3$ min) and 19X longer decay onset compared to Lumason®. Ultrastable NB could provide a platform for augmented ultrasound applications in cancer molecular imaging and drug-delivery.



11:30 AM

Nanobubble Extravasation in Prostate Tumors Imaged with Ultrasound: Role of Active versus Passive Targeting**Reshani Perera¹, Al de Leon², Gopal Ramamurthy³, Xinning Wang⁴, James Basilion⁴, Agata Exner⁵**¹*Case Western Reserve University, United States*, ²*Biomedical Engineering, Case Western Reserve University, OH, United States*, ³*Case Western Reserve University, OH, United States*, ⁴*Case Western Reserve University, United States*, ⁵*Case Western Reserve University, OH, United States***Background, Motivation, and Objective**

Despite numerous clinical trials, contrast-enhanced ultrasound (US) with microbubbles (MB) has not shown consistent improvement in outcomes of prostate cancer (PCa) biopsies. Targeted nano-sized US contrast agents with improved capability to accumulate in tumors may result in prolonged signal enhancement and improved detection of PCa with US. Accordingly, we have developed long-circulating nanobubbles (NB) targeting prostate-specific membrane antigen (PSMA). In this study, using a unique US-pathology correlation scheme, we compared rapid tumor accumulation of PSMA-targeted NB (PSMA-NB) versus that of untargeted NB and commercially available MB.

Statement of Contribution/Methods

Shell-stabilized C₃F₈ NB were formulated by dissolving lipids and glycerol in propylene glycol. For active targeting, DSPE-PEG functionalized with PSMA-1 was incorporated into NB. After gas exchange and mechanical agitation, NBs were isolated by centrifugation and characterized (Archimedes, Malvern Panalytical). *In vivo*, mice with PSMA expressing tumors received tail vein injections of either PSMA-NB, NB or Lumason®. US images were acquired for 30 min (Fig.1a) using contrast harmonic imaging (Toshiba AplioXG, 12 MHz, 0.1 MI, 0.2 fps). To confirm extravasation, mice received fluorescent NBs and tumors were imaged before and after mouse perfusion. US data was validated by immunohistochemical (IHC) analysis of tumors extracted immediately after imaging.

Results/Discussion

PSMA-NB and NB had diameters of 277±11nm and 281±2.6nm, respectively and both had concentrations of 4E11 NB/ml. Both NB groups showed similar maximum peak enhancement which was > 2 fold higher than MB. 25 min after injection, PSMA-NB showed significantly higher accumulation (5-fold) in tumor (Fig.1b-c) compared to either NB or MB. After perfusion, PSMA-NB signal remained unchanged, confirming presence of intact extravasated bubble inside tumor parenchyma. IHC analysis (Fig.1d-e) confirmed 6-fold higher signal in PSMA-NB compared to NB. Our results demonstrate active targeting of NBs to PSMA enhances rapid tumor accumulation and is critical for tumor retention. The results also provide evidence that intact NBs extravasate and thus the process can be monitored with clinical ultrasound, providing future opportunities for facilitating real time US-guided PCa biopsies.

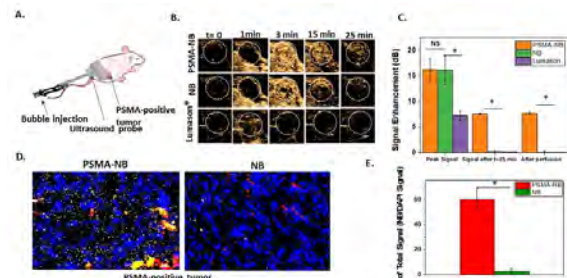


Figure 1: (a) Schematic of tumor model and US scan orientation. (b) Representative images of PSMA-NB, NB and MBs in murine flank tumors. (c) US signal in tumor: Peak signal, t=25 min after injection and after perfusion (d) Representative images of bubble distribution in tumor tissues (Blue=tumor cells, Red=vessels, Yellow=NB). (e) Signal intensity of bubbles as percentage of total tumor cells. NS = no significant difference, * P<0.01.

11:45 AM Virus-like and egg-yolk sandwich Fe₃O₄ mesoporous silica nanoparticles for photoacoustic imaging of prostate cancer

Wenkun Bai¹, Yan Wang², Krishnan Sathiyamoorthy³, Yuanyi Zheng¹, Michael Kolios³

¹Ultrasound in Medicine, Shanghai Jiao Tong University, Shanghai, China, People's Republic of, ²Ryerson University, Toronto, ON, Canada, ³Physics, Ryerson University, Toronto, ON, Canada

Background, Motivation, and Objective

Superparamagnetic iron-oxide nanoparticles (NP) have been designed for dual modal applications include photoacoustic (PA) and photothermal therapy. As the approach efficacy depends on the cellular uptake, virus-shaped nanoparticles that increase particle uptake were developed. Lasers could be used for both photoacoustic imaging and photo-thermally treatment of prostate cancer. In the present work, virus-like silica encapsulated superparamagnetic iron oxide NP were developed and their potential application in PA and photothermal therapy was investigated.

Statement of Contribution/Methods

The nanoparticle was synthesized via a novel single-micelle epitaxial growth approach in a low-concentration-surfactant oil/water biphasic system [1]. Different concentrations of nanoparticles (150 μ g/ml, 50 μ g/ml, 25 μ g/ml, 12.5 μ g/ml and 6.25 μ g/ml) were incubated with human prostate cancer cell PC-3 and cell proliferation was tested after 24hr, 48hr, and 72hr. A phantom containing different concentration of nanoparticles (12mg/ml, 6mg/ml, 3mg/ml, 1.5mg/ml, 0.5mg/ml and 0.25mg/ml) were prepared for PA measurement using the VovoLAZR system (Fujifilm VisualSonics) at 21 MHz. Continuous wave laser (810nm and 260 mW) was used for photothermal studies. The cell apoptosis was tested using AnnexinV/PI kit.

Results/Discussion

The average size of the particles was about 400 nm measured from TEM images using ImageJ software. PA images of NPs in phantom were acquired at 700 nm shown in Fig.1A. The high the NP concentration, the brighter the PA images at the location of the NPs. Fig. 1B shows that PA signal amplitude as a function of NP concentration. The photothermal studies show temperature rise non-linearly in NP concentration (Fig 1(D)). The concentration of 12 μ g/ml (biosafety concentration = 25 μ g/ml) exhibits the maximum temperature rise of about 11 °C for 12 min irradiation. For the photothermal study, cells treated with nanoparticles plus laser exhibit 5.8% apoptosis. Only 0.8% and 0.6% apoptosis was induced by NP alone, and laser alone, respectively. This degree of apoptosis is very similar to the control group. This study demonstrates that the new virus-like nanoparticles could be one of the potential candidates for photoacoustic image and photothermal therapy.

[1] W. Wang, et al., *ACS Central Science*, 2017, 3(8): 839-846.

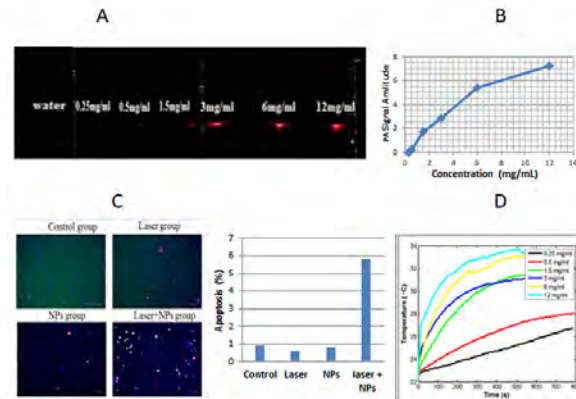


Fig. 1 (A) PA images of NPs at various concentration. (B) PA signal amplitude as a function to NP concentration. (C) Apoptosis test from different treatment group. (D) Photothermal studies of various concentrated nanoparticles.

1F - Advanced Systems and Devices for Real-Time Applications

Topaz (400)

Wednesday, October 24, 1:30 pm - 3:00 pm

Chair **Steven Freear**
University of Leeds

1F-1

1:30 PM **Real-Time, Multi-Angle Flow Vector Estimation with Dealising Using GPU**

Hassan Nahas¹, Takuro Ishii¹, Billy Y. S. Yiu¹, Alfred C. H. Yu¹

¹Schlegel-UW Research Institute for Aging, University of Waterloo, Waterloo, ON, Canada

Background, Motivation, and Objective

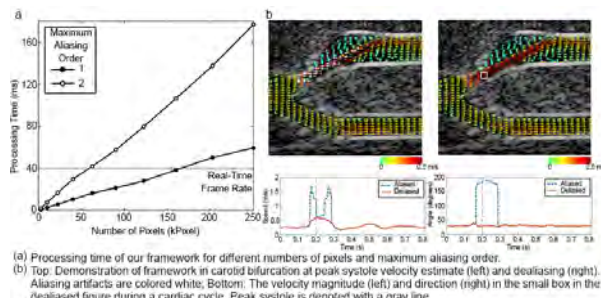
Plane-wave multi-angle vector Doppler imaging is inherently more prone to aliasing as the use of multiple transmit angles forces the maximum PRF (i.e. Doppler sampling rate) to be reduced. To address this issue, a dealiasing algorithm based on an extended least squares vector Doppler (ELS-VD) formulation has been proposed (UFFC, 2016; 63: 1745-57), where aliasing patterns are detected using least-squares fitting and block matching. While effective, ELS-VD's computational complexity is high, making it challenging to adopt for real-time use. Innovations in computing kernel design are thus critical to translate ELS-VD towards practical applications. Here, harnessing the vast parallel computing potential of GPU, we have successfully achieved the first real-time realization of robust multi-angle flow vector estimation through the ELS-VD approach.

Statement of Contribution/Methods

Our framework was built on three levels of parallelization: 1) Frame level (ELS-VD applied on every pixel); 2) Pixel level (multiple least square systems per pixel); 3) Operation level (parallelized matrix computations). ELS-VD was structured as six cascades of resource-optimized GPU kernels, and it was implemented using CUDA and a GTX 1080 device. Its computing throughput was tested for different parameters (max aliasing order, # of pixels). Also, the resulting flow vector estimation accuracy was analyzed in an aliasing-prone carotid bifurcation phantom imaging scenario (50% stenosis; 70 bpm pulsatile flow with 5ml/s peak flow rate). With this phantom setup, raw pre-beamform data was acquired using a SonixTouch scanner (with L14-5 array) that was configured to transmit plane waves over two angles (-10 and +10 deg; 6 kHz PRF; 5MHz freq; 3-cycle pulse). 7 Tx-Rx angle pairs were formed for the ELS-VD algorithm.

Results/Discussion

Real-time, aliasing-free flow vector estimation was achieved using our GPU-based ELS-VD framework. 160K and 62.5K flow vectors were computed in less than 40 ms (video range) for maximum aliasing order 1 and 2 respectively, with block matching size of 35x35 pixels (fig a). In the carotid phantom, our framework produced flow vector maps (with 39.6K pixels) that are free of artifacts in the flow jet zone with 0.6m/s peak systolic velocity (fig b). For this case, processing time was <10 ms per frame (max expected aliasing order of 1), which is well into the real-time range.



1:45 PM

High Frame Rate Vector Flow Imaging: Development as a New Diagnostic Mode on a Clinical ScannerYigang Du¹, Yingying Shen¹, Billy Y. S. Yiu², Alfred C. H. Yu², Lei Zhu¹¹Shenzhen Mindray Bio-Medical Electronics Co., Ltd., Shenzhen, China, People's Republic of, ²Schlegel Research Institute for Aging, University of Waterloo, Waterloo, ON, Canada**Background, Motivation, and Objective**

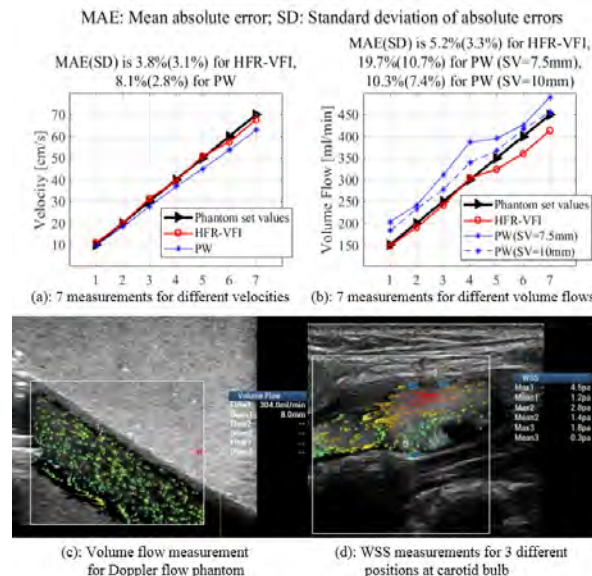
High Frame Rate Vector Flow Imaging (HFR-VFI) has been conceptualized previously in laboratories, their practical implementation on clinical scanners has not been a straightforward task because of the need to reconfigure transmit pulsing schemes and the need to redeploy on-board computing resources. This paper focuses on presenting the practical issues and solutions in the development of HFR-VFI on a clinical scanner.

Statement of Contribution/Methods

The HFR-VFI is done by multi-directional transmission (Tx) and reception (Rx), each Tx-Rx pair obtains corresponding velocity component based on Doppler technique and vector velocities are calculated by angle combination. Plane wave and focused wave are emitted alternatively and continuously, to get high temporal resolution flow image, and high spatial resolution B-mode image, respectively. The interrupted plane wave data are reconstructed by interpolation so continuous flow data can be obtained for dynamic vector velocities display. Velocity calculations including continuous FIR clutter filtering, lag-1 auto-correlation and angle combination, are with parallel processes using a GPU. The beamforming is made by FPGA, thus a streamline working process is achieved as the beamformed data are processed by GPU, meanwhile the FPGA starts to process new received RF signals for beamforming. The HFR-VFI is implemented in Mindray Resona 7 ultrasound platform with a linear array transducer. The volume flow and wall shear stress (WSS) can be measured based on vector velocities. For validation, measurements are made by a moving string phantom for velocity accuracy studies, and by a Doppler flow phantom (KS205D-1) for volume flow accuracy studies.

Results/Discussion

Results from the HFR-VFI and angle corrected commercial PW are compared to the values set by phantoms, as shown in Fig. a & b, where 7 measurements are made for different velocities and different volume flows. The MAE (mean absolute error) and SD (standard deviation of absolute errors) are shown in the figure, where SV means sample volume of PW. The HFR-VFI on clinical scanner gives better agreement in accuracy studies than PW. One example for volume flow measurement by the Doppler flow phantom is given in Fig. c. Clinical studies by this system can easily be made, as shown in Fig. d, where it can be seen that the WSS near the vortex is reduced compared to it near the laminar flow.



2:00 PM

Parallel implementation of randomized singular value decomposition and randomized spatial downsampling for real time ultrafast microvessel imaging on a multi-core CPUs architecture

U Wai Lok¹, Pengfei Song¹, Joshua Trzasko¹, Eric Borisch¹, Ron Daigle², Shigao Chen¹

¹Department of Radiology, Mayo Clinic, Rochester, MN, United States, ²Verasonics Inc., United States

Background, Motivation, and Objective

Singular value decomposition (SVD)-based clutter filter is widely used for functional ultrasound imaging such as super-resolution ultrasound localized microscopy and microvessel imaging. However, the demand of high computational complexity becomes the critical issue for the SVD-based clutter filter. Recently, randomized SVD-based clutter filter has been proposed for clutter suppression; the computational time can be dramatically reduced when combining with randomized spatial downsampling (Song et al. TUFFC 2017). In this study, we propose the use of multi-core CPU architecture to implement the randomized SVD-based clutter filter with randomized downsampling to demonstrate that it can perform in real time.

Statement of Contribution/Methods

The algorithm is shown in Fig. 1 (A). Baseband beamformed data are converted to spatially downsampled matrices, and then randomized SVD is applied to each output downsampled matrix. The illustration diagram of multi-core CPU architecture is shown in Fig. 1 (B). In the figure, two downsampled matrices are assigned to a specific thread. Randomized SVD-based clutter filter is performed to the downsampled matrices afterward. It should be noted that fully parallelization (each downsampled matrix is assigned to a specific thread) can be achieved as doubling the number of CPU cores. The algorithm was programmed using C language with P-thread architecture. In addition, MKL LAPACK and BLAS were used for QR decompositions and matrix multiplications of the randomized SVD process.

Results/Discussion

The proposed multi-core CPU architecture was embedded as an external function on a Verasonics Vantage system with 12 CPU cores (Verasonics Inc., Kirkland, WA, USA). The number of ensembles and pulse repetition frequency were set as 50 and 500 Hz, and 12x randomized downsampling factor was used in this experiment. This means that each downsampled matrix was assigned to a specific thread and fully parallelization was achieved. The B mode image and the micro-vessel image after passing through the randomized downsampling and SVD-based clutter filter are shown in Fig. 1 (C). The corresponding processing time required only around 25 ms. Noted that the computation time includes all the parallel processing of all downsampled matrices and associated overhead. The processing time was averaged from ten measurements.

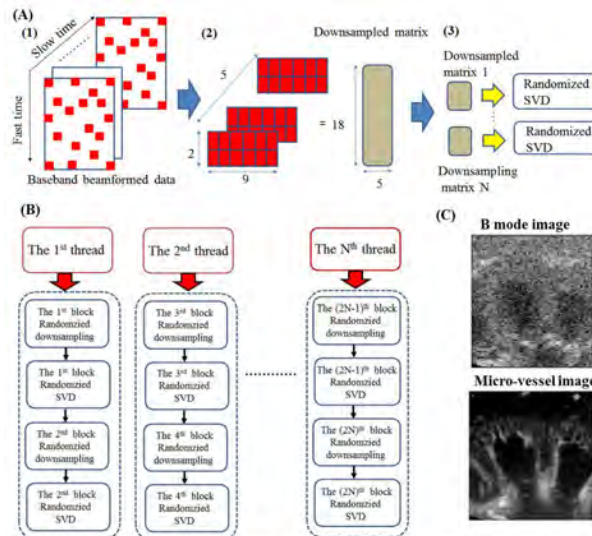


Figure 1. (A) Illustration diagram of the algorithm, (B) multi-thread architecture, and (C) B mode image and the microvessel image after randomized downsampling and randomized SVD.

2:15 PM

Acoustic Navigation of Intramyocardial Injection Needle Catheter Using Color Doppler Echocardiography

Minako Katayama¹, Viksit Kumar², David Zarbatany³, Veronica Vaitkus¹, David Fortuin¹, Mostafa Fatemi², Marek Belohlavek¹

¹Department of Cardiovascular Diseases, Mayo Clinic, Scottsdale, AZ, United States, ²Department of Physiology and Biomedical Engineering, Mayo Clinic, Rochester, MN, United States, ³Independent Engineering Consultant, Laguna Niguel, CA, United States

Background, Motivation, and Objective

Drug and stem cell intramyocardial therapeutic delivery in ischemic heart disease or cardiomyopathy has been tested using transendocardial approach guided by fluoroscopy and NOGA® navigation mapping systems. Precise localization of the injection needle tip with respect to the myocardial target would be ideal, but the exact location of the needle tip and, especially, the insertion depth within the myocardium are difficult to achieve.

We have been developing an acoustically active catheter (AAC) navigation system. The catheter tip is fitted with a piezoelectric crystal that vibrates and produces a color marker in Doppler echocardiography scans. The objective is to develop a prototype of an intramyocardial injection catheter that allows localization of the injection needle tip in the myocardium under the guidance of conventional 2D color Doppler echocardiography.

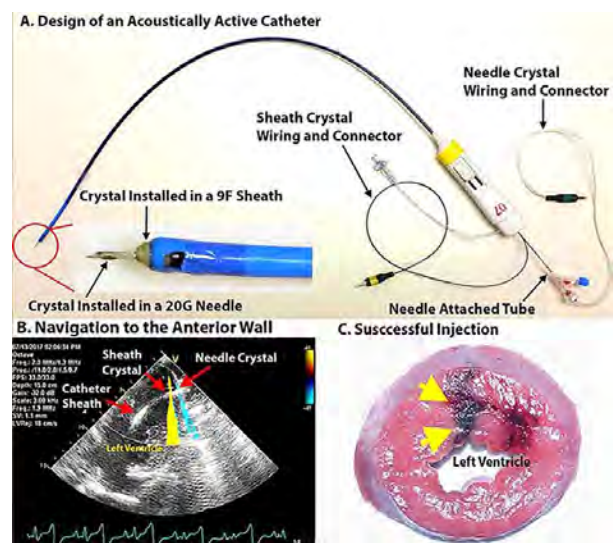
Statement of Contribution/Methods

A 9-Fr steerable catheter sheath tip is fitted with a piezoelectric ring crystal, which is assembled with a needle tube inside (Figure A). A 20-gauge needle has an embedded piezoelectric crystal in its wall close to the tip. The navigation and myocardial injection were tested in a beating heart in 14 adult domestic pigs. The AAC was inserted from the right carotid artery, and was retrogradely guided via the aorta into the left ventricle. Both crystals were driven by a waveform generator (square-wave driving signal) and produced acoustic interactions with Doppler beam resulting in instantaneous color markers in echocardiography scans.

Results/Discussion

Visualization of crystals was successful in all cases. A representative image is Figure B, which clearly shows the position of a sheath crystal (yellow marker; driven with 110 kHz and 2.0 V signal) at the endocardial border and a needle crystal (blue marker; driven with 97 kHz and 3.0 V signal) within the myocardium. Green color dye was injected through the needle tube lumen. Successful formation of a dye deposit is observed in the dissected heart (Figure C).

The concept of acoustically active navigation of the injection needle in a beating heart is presented. Guiding the injection needle within the left ventricle has potential to provide safer intramyocardial therapeutic delivery, utilizing a conventionally available echocardiography system.



2:30 PM **Matrix transducers for real-time 3D imaging: From intra-cardiac to trans-cranial applications**

Nico de Jong¹

¹*Erasmus Medical Centre*

Background, Motivation, and Objective

New developments in ultrasound imaging hardware, image reconstruction and molecular contrast agents are enabling completely new ranges of diagnostics and therapy in the cardiovascular and neurological field with ultrasound. This offers excellent opportunities to tackle the major existing and evolving healthcare threats, such as heart failure, arrhythmias, atherosclerosis, neurological disorders and cancer. So, new transducers for 4D cardiovascular function and flow, transducers to enable new 3D applications, and functional and anatomical ultrasound imaging of the brain are required.

We are developing matrix transducers ranging to be used inside very small vessels, intra-cardiac but also external devices to be used for carotid scanning and monitoring the brain of preterm babies. To realize matrix transducer we build the PZT transducer on top of a custom made ASIC (application specific intergrated circuit). The ASIC take care of selecting the elements in transmission and for amplifying the received signal and if appropriate perform pre-processing like micro-beam forming and/or digitisation. Examples of matrix transducers are 3D-forward looking IVUS having 80 elements (15 MHz, 80 µm) connected with only one coax cable. A second example is a miniature 3D TEE transducer for pediatric use or for prolonged monitoring in adults. Or a large-aperture 3D transducer for carotid imaging consisting of 20,000 acoustic PZT elements capable of acquiring 1000 volumes per second. Or a tiny 3D transducer for intracardiac use with digital output. Or a 3D transducer for monitoring the brain perfusion in preterm infants, through the fontanel anticipating to have a frequency of 15 MHz, a pitch of 50 µm and more than 50,000 elements. Finally, a spiral array will be presented with only 256 elements which is directly connected to a Ula-op and Verasonics system.

Statement of Contribution/Methods

1

Results/Discussion

2

1G - Functional Assessment by Remote Modulation

Topaz (400)

Wednesday, October 24, 4:00 pm - 5:30 pm

Chair **Jan D'hooge**
KU Leuven

1G-1

4:00 PM Towards Tomographic Reconstruction of Current Source Densities with Multichannel Acoustoelectric Brain Imaging (mABI) Using Ellipsoidal Human Head Model

Tushar Bera¹, Chet Preston², Alexander Alvarez², Pier Ingram¹, Cameron Wilhite³, Stephen Cowen⁴, Martin Weinand⁵, Russell Witte^{1,2}

¹Dept. of Medical Imaging, University of Arizona, United States, ²Dept. of Biomedical Engineering, University of Arizona, United States, ³Dept. of Physiology, University of Arizona, United States, ⁴Dept. of Psychology, University of Arizona, United States, ⁵Dept. of Surgery, University of Arizona, Tucson, AZ, United States

Background, Motivation, and Objective

Abnormal electrical activity in cortex and deep brain structures leads to a variety of disorders from Parkinson's to epilepsy. However, high resolution mapping of electrical sources deep in the brain remains challenging. Electroencephalography (EEG) provides real-time voltage maps from the surface of the brain or scalp, but suffers from poor resolution and reconstruction inaccuracy in resolving current sources. To address these limitations, we have developed multichannel acoustoelectric brain imaging (mABI) and tomographic reconstruction of current source densities based on conventional approaches to solving the inverse problem. In this study, we combine bench-top mABI experiments in a human head phantom with forward and inverse models based on boundary potentials for validation. Tomographic reconstruction with mABI potentially visualizes deep dipole sources in 4D (volume + time) at excellent spatial and temporal resolution.

Statement of Contribution/Methods

To demonstrate proof-of-concept of mABI, we used an agarose gel based human head phantom containing two platinum electrodes embedded 30 mm below the brain surface to produce EEG-like signals. A commercial ultrasound system (Vantage 64LE, Verasonics) with a linear array transducer (3 MHz, Verasonics P4-2) delivered a US pulse train at a repetition rate of 2 kHz. An electrocorticography (ECoG) grid array (Adtech Medical) was placed on the brain surface for multichannel recording of low frequency (EEG-like, <10 kHz) and high frequency (AE, >1 MHz) signals. Acquired signals were amplified, filtered and digitized and ABI image processing and tomographic reconstruction. An ellipsoid brain model was also developed in COMSOL yielding a forward solution. Using boundary potentials, likelihood localization of current sources is performed in the inverse solution with reciprocal techniques in MATLAB.

Results/Discussion

With a current injection of 40 mA (3 cycles at 200 Hz), the SNR for mABI was 41 dB, whereas the axial and lateral resolution of the system was 0.90 mm and 0.98 mm, respectively, at 30 mm depth. The average sensitivity obtained for the ABI images obtained for all channels was 5.05 μ V/mA. The inverse solution shows that the least squared error is minimum within 10 mm of the actual dipole position. mABI based tomographic imaging of brain can help the diagnosis and treatment for a variety of neural disorders.

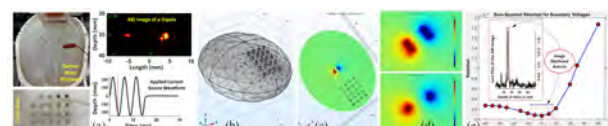


Figure 1: (a) mABI of human brain phantom (b) ellipsoidal head model with FEM mesh, (c) potential distribution obtained from forward solution (XZ plane), (d) potential distribution near dipole source (XY and ZX planes), (e) least squares error for dipole localization.

4:15 PM Real-time displacement and cavitation imaging of non-invasive neuromodulation of the peripheral nervous system via focused ultrasound

Stephen Lee¹, Mark Burgess¹, Antonios Pouliopoulos¹, Elisa Konofagou^{1,2}

¹*Biomedical Engineering, Columbia University, New York, NY, United States*, ²*Radiology, Columbia University, New York, NY, United States*

Background, Motivation, and Objective

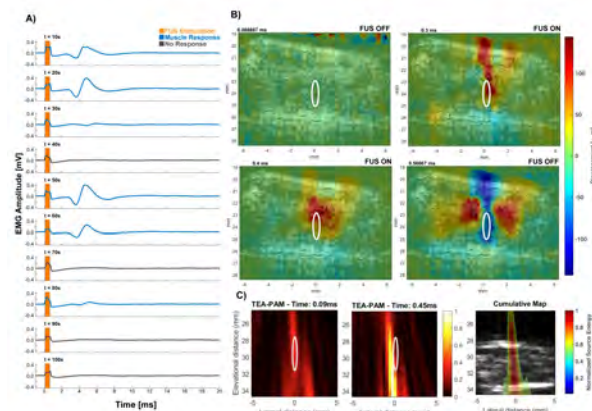
Focused ultrasound (FUS) neuromodulation could provide an important noninvasive surrogate with high specificity to current modulation techniques for treating peripheral neuropathies. The *in vivo* mechanism remains unknown with some theoretical models making assumptions that may not necessarily reflect the physical response of the nerve to FUS. Imaging and understanding neuromodulation during modulation is thus critical. Previously, we have demonstrated that FUS neuromodulation of the sciatic nerve can be imaged using displacement generated by FUS radiation force. In this study, the development of simultaneous real-time displacement and passive cavitation mapping (PAM) is discussed that can assist in targeting and monitoring FUS neuromodulation while also shedding light into the mechanism.

Statement of Contribution/Methods

A 4 MHz single-element HIFU transducer, with focal volume: 0.2 x 2 mm, (Sonic Concepts, WA) applied tone burst pulses of 0.5 ms, 0.01 Hz PRF, 30 MPa peak pressure, were used to generate action potentials recorded by electromyography (EMG). Real-time displacement images were acquired using an 18-MHz transducer (Vermon, France) and PAM were recorded at 7.8 MHz (Philips, MA). Displacement images were calculated by applying 1D cross-correlation (9λ window, 99% overlap) with compounded RF (frame rate of 10kHz). Cavitation was mapped through acoustic emissions from the HIFU transmit and calculation using a robust Capon beamformer (RCB-PAM). Both imaging methods were overlaid onto B-mode images of the mouse thigh.

Results/Discussion

Figure 1A depicts EMG recordings of 10 sequential sonifications (0.01 Hz PRF) on the nerve showing a time dependent relationship. Large amplitudes, up to 0.4 mV, were acquired during sonifications 1-3, 5-6, and 8. Figure 1B demonstrates using real-time displacement images for targeting increased the success rate of muscle activation by 33% and peak displacement for successful activation was 200 μm. In figure 1C, RCB-PAM indicated cavitation was located within 1.0 mm of the focus. Simultaneous cavitation and displacement imaging of FUS modulation may be capable of providing solid evidence for mechano-electric nerve conduction as well as monitoring the safety and efficacy of the methodology, rendering it thus a viable method for clinical application of ultrasound for peripheral neuropathy.



4:30 PM **Transcranial Acoustoelectric Brain Imaging: Progress and Challenges**

Russell Witte¹

¹*University of Arizona Health Sciences*

Background, Motivation, and Objective

Transcranial Acoustoelectric Brain Imaging (tABI) is a revolutionary concept capable of unprecedented resolution and accuracy for resolving current sources deep in the human brain. As a hybrid modality, tABI combines principles of ultrasound (US) imaging with radiofrequency recording of a signature acoustoelectric (AE) interaction signal to map physiologic current in 4D (volume + time). Unlike electroencephalography (EEG), which suffers from poor spatial resolution and inaccuracies due to blurring of electrical signals as they pass through the brain and skull, spatial resolution for tABI is primarily determined by properties of the US beam. This presentation will describe advantages and limitations of tABI technology, including recent progress and key challenges towards a new modality for noninvasive functional human brain imaging at the mm and ms scales. As a safe, mobile, and real-time platform designed for human brain mapping, tABI could revolutionize our understanding of a broad spectrum of brain disorders that are strongly associated with abnormal electrical conduction in the cortex and deep brain structures—from epilepsy and Parkinson’s to depression.

Statement of Contribution/Methods

1

Results/Discussion

2

5:00 PM

X-Ray Induced Acoustic Computed Tomography for Real-Time Monitoring of External Beam RadiotherapyWei Zhang^{1,2}, Hao Lei³, Ibrahim Oraiqat⁴, Zhipeng Liu², Jun Ni³, Issam El Naqa⁴, Xueding Wang¹¹*Department of Biomedical Engineering, University of Michigan, Ann Arbor, MI, United States*, ²*Institution of Biomedical Engineering, Chinese Academy of Medical Science & Peking Union Medical College, Tianjin, China, People's Republic of*³*Department of Mechanical Engineering, University of Michigan, Ann Arbor, MI, United States*,⁴*Department of Radiation Oncology, University of Michigan, Ann Arbor, MI, United States***Background, Motivation, and Objective**

As a newly invented technology, X-ray induced acoustic computed tomography (XACT) is a potentially solution for *in vivo* dosimetry and real-time online monitoring of X-ray beam position during external beam radiation therapy. In this work, via the experiments on soft tissue samples, we examine the feasibility of XACT in quantitatively mapping the X-ray dose deposition in the sample, and in real-time monitoring of the dose delivery position in relation to the target tissue.

Statement of Contribution/Methods

A prototype XACT system, which had an immersion ultrasound transducer scanning around target sample, was used to acquire X-ray induced acoustic (XA) signals produced by a medical linear accelerator to form an image of the X-ray energy deposition in the sample. Five lard cylinders imbedded into porcine gel were imaged to explore the dose sensitivity of XACT, and the results were verified by comparing to the measurements from radiochromic film. To locate the delivery position of the X-ray dose and track the motion of the treatment target in real-time, an integrated XACT and ultrasound (US) dual-modality imaging system was built on a Verasonics ultrasound platform. The performance of the system was evaluated using soft-tissue samples.

Results/Discussion

A difference in delivered X-ray doses as small as 2.9% can be measured by XACT ($p=0.02$). The intensities quantified in XACT images were highly correlated to the film measurements with correlation coefficients better than 0.986, demonstrating that XACT has a clinically acceptable sensitivity for mapping the dose deposition. The integrated XACT and US dual-modality imaging can track the movement of target tissue with spatial resolution better than 0.37 mm. The relative displacement of the X-ray beam and the target tissue can be visualized in the combined dual-modality image in a real-time fashion. In the future, a dual-modality imaging system may allow not only online monitoring of the X-ray beam position but also alignment of the X-ray beam to the treatment target.

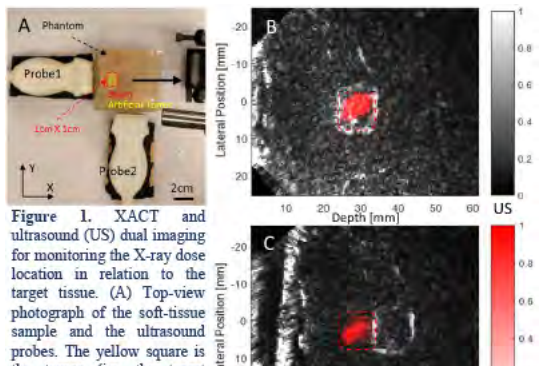


Figure 1. XACT and ultrasound (US) dual imaging for monitoring the X-ray dose location in relation to the target tissue. (A) Top-view photograph of the soft-tissue sample and the ultrasound probes. The yellow square is the tumor (i.e. the target tissue for treatment). The black arrow shows the sample moving steps. The red rectangle indicates the original location of the X-ray beam. (B)-(C) The pseudo-color XACT images (showing the location of X-ray dose deposition) superimposed on the gray-scale US images (showing the sample structure including the position of the tumor)

5:15 PM

On the Performance of Delay Estimators for Magnetomotive ImagingThomas Ersepke¹, Tim C. Kranemann¹, Georg Schmitz¹¹Ruhr-University Bochum, Germany**Background, Motivation, and Objective**

In Magnetomotive Ultrasound (MMUS), tissue embedded magnetic nanoparticles (NP) are mechanically excited by a magnetic field and the resulting motion of the tissue is tracked US-based to image the NP tracer distribution. To date, MMUS imaging procedures suffer from weak contrast-to-noise ratios (CNR) due to relatively small forces on the nanoparticles and hence small tissue displacements. Standard MMUS detection of the NPs is based on pixel-wise evaluation of the phase of the IQ-data under consideration of frequency and phase information of the magnetic excitation signal. Those methods do not make use of spatial information about the displacement of the surrounding tissue. We propose to incorporate spatial information by using a Bayesian displacement estimation, together with a generalized Gaussian-Markov random field (GGMRF) prior (Dumont et al., TUFFC, 2016) to reduce the estimation error and improve CNR. In this work, we evaluate the performance of the Bayesian displacement estimator as well as the normalized cross correlation (NCC) estimator for NP displacements in the sub-micrometer range. We demonstrate a considerable gain in CNR compared to pixel-wise MMUS imaging and prove that NP displacements below 1 μm can be tracked with sufficient contrast.

Statement of Contribution/Methods

The tracking parameters of the NCC and the Bayesian estimator were tuned by simulating sub-micrometer displacements of an NP bolus using the simulation toolbox FIELD II. For the phantom experiments a recently proposed magnetomotive excitation setup was used to apply a sinusoidally modulated force on the NP. A tube-shaped nanoparticle inclusion ($\varnothing = 5 \text{ mm}$, 23 mg Fe/ml, 7% gelatine w/w) embedded in a gelatin phantom (7% gelatine) was placed inside the excitation setup. US data were acquired using the Verasonics Vantage platform and an L12-3v transducer.

Results/Discussion

Compared to the pixel-wise method the NCC and the Bayesian estimator showed a mean gain (n=4) in CNR of 9.3 dB and 11.5 dB (see Figure 1). While for the pixel-wise method a high number of frames (400, 200 frames) was needed, the NCC and the Bayesian estimator returned satisfying results using only two frames. Besides the gain in CNR and the savings in required RF data, the two proposed estimation schemes also allow for additional phase and frequency sensitive filtering when tracking between successive frames is performed.

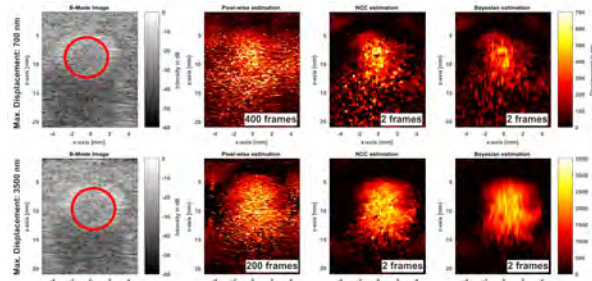


Fig. 1: Comparison of MMUS displacement estimation schemes. **Top row:** Phantom experiment with max. NP displacement of 700 nm. **Bottom row:** Phantom experiment with max. NP displacement of 3500 nm. **From left to right:** Column: B-Mode image (red circle: NP inclusion); pixel-wise frequency and phase sensitive estimation; normalized cross correlation estimation; Bayesian estimation.

2D - Tissue Ablation and Vascular Imaging using Photoacoustics

Diamond (300)

Wednesday, October 24, 8:00 am - 9:30 am

Chair **Michael Kolios**
Ryerson University

2D-1

8:00 AM Atrial RF ablation with dual wavelength photoacoustic imaging

Sophinese Iskander-Rizk¹, Pieter Kruizinga², Antonius F. W. van der Steen¹, Gijs van Soest¹

¹Thorax Center, Erasmus MC, Netherlands, ²Neuroscience, Erasmus MC, Rotterdam, Netherlands

Background, Motivation, and Objective

Atrial fibrillation is a cardiac arrhythmia stemming from abnormal electrical conduction/impulse formation in the atria. To restore cardiac rhythm an RF ablation (RFA) procedure, interrupting aberrant electrical patterns, is commonly performed. One way of improving the procedure (success rate~60%) is to enable visual feedback on lesion progression, thereby reducing complications linked to over ablation and mitigating recurrent conductivity due to under ablation. We have shown that the ratio of two photoacoustic (PA) images at 790/930 nm provides a robust and reliable lesion assessment (Iskander Rizk et al BOE 2018). In this study, we aim to monitor lesion progression using ultrasound (US), from an intracardiac echo (ICE) catheter, and PA, with illumination from a modified RFA catheter.

Statement of Contribution/Methods

We fitted the flushing channel of a commercially available RFA catheter with an optical fiber. We ablated porcine left atrium tissue with the modified catheter and a clinically approved ablation device (EPT 1000XP APM Boston Scientific, settings P ≤ 25W, T ≤ 93°C, t ≤ 20s). We received PA signals with a St Jude View Flex ICE catheter connected to a Verasonics vantage 256 system. The illumination/ablation was from the endocardial side, the transducer at the epicardium side and we toggled the laser source (Spitlight EVOI, Innolas) continuously between 790 and 930 nm at 100Hz. One acquisition frame consisted of 5 tilted diverging wave US acquisitions and 4 averaged PA acquisitions per wavelength (λ).

Results/Discussion

Using the ratio of PA images at 790/930 nm we can monitor RFA procedures *ex-vivo*. In Fig. 1, we compare images at 790 nm with ratio images overlaid on grayscale US. Prior to ablation and at the beginning of ablation, the dual wavelength images eliminate the PA signal from the catheter tip, emphasizing the absence of lesion. After ~10s of applying RF energy onto the tissue and up to the end of ablation, we can observe a signal change consistent with lesion formation. In conclusion, dual wavelength PA imaging can successfully monitor lesion progression and remove clutter such as the signal arising from the catheter tip. Using ICE and modified RFA catheters shows the potential to translate this work to the clinic. Future work targets eliminating interference from RFA signals and addresses motion artefacts for real time display of lesion progression.

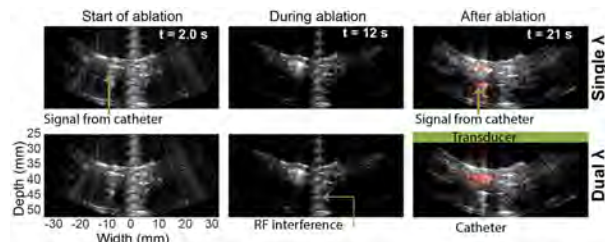


Figure 1- Ablation lesion progression monitoring snapshots. US in grayscale 40dB, in red scale PA signals (1st row: single wavelength 20dB thresholding; 2nd row: dual wavelength, thresholding ratio of 4). The green arrow illustrates the ablation catheter position pointing towards the endocardium and the green rectangle showcases the position of the ICE above the epicardium side. Initially the RFA catheter touches the tissue surface, at the end of ablation we move the catheter away from the tissue surface.

8:15 AM

Real-Time, Video-Rate and Depth-Resolved Imaging of Radio-Frequency Ablation using All-Optical Ultrasound

Erwin Alles^{1,2}, Richard Colchester^{1,2}, Yousuf Makki¹, Sacha Noimark^{1,2,3}, Edward Zhang¹, Paul Beard^{1,2}, Malcolm Finlay^{1,2}, Adrien Desjardins^{1,2}

¹*Department of Medical Physics & Biomedical Engineering, University College London, London, United Kingdom,*

²*Wellcome / EPSRC Centre for Surgical and Interventional Sciences, University College London, London, United Kingdom,*

³*Materials Chemistry Research Centre, Department of Chemistry, University College London, London, United Kingdom*

Background, Motivation, and Objective

Real-time ultrasound imaging of radiofrequency (RF) ablation lesion formation using conventional electronic imaging probes can be limited by RF noise, electronic interference, low bandwidths and poor tissue contrast. All-optical ultrasound imaging, where ultrasound is both generated and detected using light, is a promising alternative to RF ablation imaging due to its high resolution and inherent insensitivity to electromagnetic interference. Here, a benchtop all-optical imaging system was used to visualise RF ablation lesion formation in *ex vivo* tissue samples.

Statement of Contribution/Methods

Pulsed excitation light was focussed onto a nanocomposite membrane comprising multi-walled carbon nanotubes and polydimethylsiloxane, where it was converted into ultrasound *via* the photoacoustic effect. Using scanning optics, the resulting optical ultrasound source was translated to synthesise a 1D source aperture comprising irregularly spaced ultrasound sources. Back-scattered ultrasound was detected with a single fibre-optic acoustic receiver comprising a Fabry-Pérot cavity. 2D images were acquired, reconstructed and visualised at a sustained frame rate of 9 Hz, at an imaging depth >15 mm, and with an isotropic resolution of 100 µm. RF ablation lesion formation (max 30 W, 65°C, 60 s) was visualised *ex vivo* in both homogeneous (chicken breast) and inhomogeneous (pork belly) samples.

Results/Discussion

We present the first video-rate, depth-resolved 2D images acquired during RF ablation using an all-optical ultrasound imaging setup. In these images (Fig. 1), lesion formation was clearly visualised with contrast of up to 30 dB. For homogeneous tissue samples, lesions appeared to form isotropically, as is typically assumed in clinical practice. For inhomogeneous samples, however, heterogeneous lesion growth was observed, where rapid changes in ultrasonic appearance seemed to be localised to tendril-like regions, and lesion growth occurred along preferential directions. With its high miniaturisation potential, all-optical ultrasound imaging shows great promise for guiding interventional procedures, where real-time ablation lesion visualisation could optimise lesion delivery and improve patient outcomes.

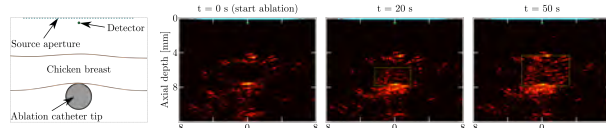


Fig. 1 - Schematic (left) and stills at different time points during real-time, video-rate all-optical ultrasound imaging of RF ablation.

8:30 AM Automatic detection of healthy arterial wall tissue *in vivo* using photoacoustic multi-spectral imagingTobias Erlöv¹, Rafi Sheik¹, Ulf Dahlstrand¹, Tomas Jansson^{1,2}, Malin Malm sjö¹, Magnus Cinthio¹¹Lund University, Sweden, ²Skåne Medical Services, Sweden**Background, Motivation, and Objective**

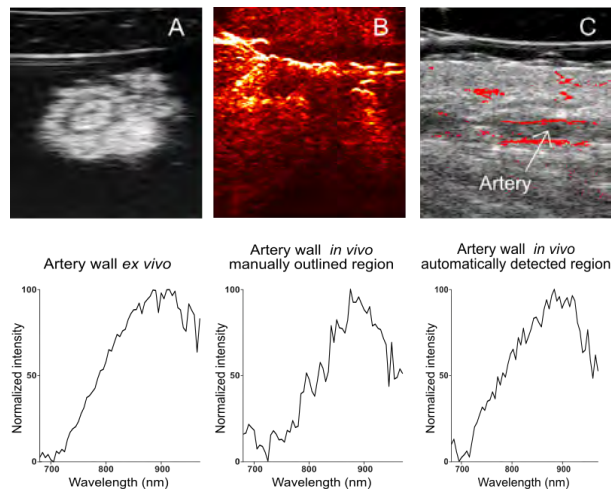
Photoacoustic multi-spectral imaging (PAI) can distinguish tissue based on molecular information. To be able to identify different type of tissue in a clinical setting the spectrum of the tissues-of-interest need to be known and the identification protocol as automatic as possible since manual delineation is very time-consuming. The overall objective in a larger study is to develop a method for non-invasive diagnosis of giant cell arteritis (GCA) using PAI. In this sub-study the aim was a) to automatically identify healthy artery walls in *in vivo* PAI using spectrums obtained from *ex vivo* PA images of healthy artery walls and b) to decrease spectral noise by implementing motion tracking in alternately acquired ultrasound images.

Statement of Contribution/Methods

Seven patients with suspected GCA (later found negative) were examined with PAI using the Vevo Lazzr-X (Visualsonics, Toronto, CA) before surgical removal of one of their temporal arteries. The arteries were then examined *ex vivo* with PAI and the artery wall spectrums covering 680-970 nm were obtained and averaged to produce a reference spectrum for the healthy artery wall. The reference spectrum was normalized and compared to all normalized spectrums in the *in vivo* PA images. The arterial wall was then automatically identified using a cost function and thresholding. To decrease noise in the resulting spectrums, the PA images were first corrected for motion artefacts using phase-based motion tracking on the ultrasound images.

Results/Discussion

The figure shows A) a B-Mode transverse cross-section of a human temporal artery in an *ex vivo* setup, B) an *in vivo* PA image (680 nm) of a human temporal artery (longitudinal cross-section) and surrounding tissue and C) a B-mode image of the same *in vivo* section. Figure C also shows, overlaid in red, the automatically detected samples with similar spectrum to that found from the artery wall *ex vivo*. The spectrums below demonstrate that tissue specific spectrums obtained *ex vivo* combined with this method can be very useful to automatically identify small sections of specific tissue *in vivo*. Manual delineation to identify tissue specific spectrums *in vivo* is both time consuming and suffers from motion artefacts and noise due to interference from other tissue. The novel method has potential to facilitate future non-invasive diagnosis of GCA as well as other clinical applications of PAI.



8:45 AM Multi-spectral photoacoustic morphology assessment of human carotid plaques using blind spectral unmixing and histologic validation

Mustafa Umit Arabul¹, Marcel Rutten¹, Marc van Sambeek², Frans van de Vosse¹, Richard Lopata¹

¹Biomedical Engineering, Eindhoven University of Technology, Eindhoven, Netherlands, ²Catharina Hospital Eindhoven, Netherlands

Background, Motivation, and Objective

Multi-spectral photoacoustic (PA) imaging is a promising imaging modality due to its inherent contrast mechanism based on biological chromophores such as blood and lipid. However, the composition of a carotid plaque is complex and mostly a mixture of chromophores present in the plaque. Therefore, having a priori spectrum of targeted tissue may not always be possible. In this study, we used multi-spectral PA and independent component analysis based blind spectral unmixing technique to reveal signatures of the composition.

Statement of Contribution/Methods

Human carotid samples ($n = 6$) were obtained in endarterectomy operations in the local hospital and measurements were performed ex vivo in a position-controlled immersion setup. The PA probe consisted of a diode laser ($E_p = 1 \text{ mJ}$, $t_p = 130 \text{ ns}$, $\lambda = 808, 915, 940, 980 \text{ nm}$, QUANTEL, FR) and a linear array transducer ($f_c = 7.5 \text{ MHz}$, ESAOTE, NL). Both ultrasound (US) and PA images were obtained by spatially compounding 36 images covering complete 360 degrees. Next, a modified version of independent component analysis (ICA) for non-negative sources was used to unmix different behavior of signal sources over the optical spectrum. The output of the ICA provided 4 different types of signal behavior without indicating any specific chromophore. Next, the high signal regions in unmixed ICs were qualitatively compared to histology images for ~50 cross-sections per plaque sample. Finally, same measurements were repeated using a vessel phantom with pure cholesterol, porcine blood, and thrombus embedded in its wall as an additional validation to the histology.

Results/Discussion

The preliminary investigation of histology images of 3 samples (~150 cross-sections) showed that ICA is promising for unmixing signal sources from recent hemorrhages, old hemorrhages, and cholesterol clefts. In Fig. 1, a typical slice shows that PA measurements alone do not provide unique information about the plaque content. However, the IC3 in Fig. 1-a shows high correlation with the intraplaque hemorrhage while IC1 corresponds to the area which is mostly populated by cholesterol clefts in histology images. Additionally, the results of phantom experiments were in agreement with the finding's in the histology.

In the future, additional staining methods will be used in histology new samples will be included to show clinical significance of the study.

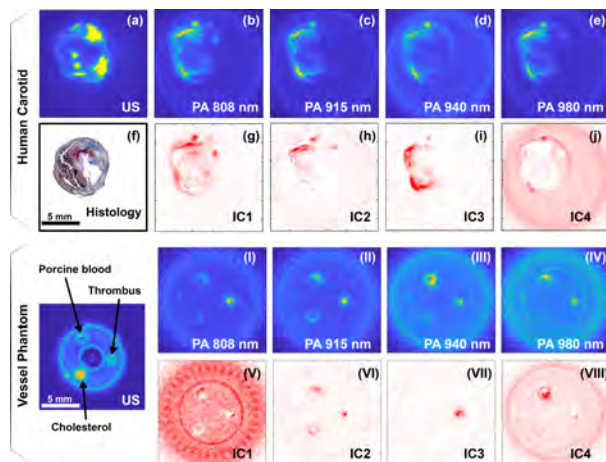


Figure 1: Results of blind spectral unmixing of 4 discrete wavelengths. (a) US image of a human plaque sample at the transverse plane. From (b) to (e) are the photoacoustic images (PA) obtained with respectively 808, 915, 940, 980 nm laser lights at the same transverse position with ultrasound (US). (f) The picture of Mason's Trichrome stained histologic section of the nearest cross-section. From (g) to (j) are the unmixed independent components (ICs). The results of the same measurements for the polyvinyl alcohol (PVA) phantom are denoted with roman numbers. From (I) to (IV) are the PA images and from (V) to (VIII) are the ICs. The order of the ICs does not carry any specific indication of the unmixed chromophore.

9:00 AM Simulation of photoacoustic imaging of red blood cell aggregation using a numerical model of pulsatile blood flow

Tae-Hoon Bok^{1,2,3}, Eno Hysi^{1,2,3}, Muhamad N. Fadhel^{1,2,3}, Michael Kolios^{1,2,3}

¹*Physics, Ryerson University, Toronto, ON, Canada*, ²*Institute for Biomedical Engineering, Science and Technology, Toronto, ON, Canada*, ³*Keenan Research Centre for Biomedical Science of St. Michael's Hospital, Toronto, ON, Canada*

Background, Motivation, and Objective

Photoacoustic (PA) imaging of blood flow can provide a label free and noninvasive assessment of the oxygen saturation (sO_2). Flow induced red blood cell (RBC) aggregation are typically not considered in sO_2 estimations even though RBC aggregates modify O₂ release. In this work, the pulsatile blood flow was simulated using particle motion based on the Doppler velocity of blood flow measured in the human radial artery (RA). In addition, the PA images were reconstructed for each temporal frame during the blood flow, and compared to *in vivo* PA images of the RA.

Statement of Contribution/Methods

A particle based model was constructed using the Doppler velocity of pulsatile blood flow (90 bpm) recorded from the RA. The positions of randomly distributed, identical spherical RBCs (radius - 2.7 μm) in the lateral axial plane ($20 \times 2 \text{ mm}^2$) were traced at each time step. The cells in the left hand side (LHS) from 0 mm moved toward the right hand side (RHS), based on the parabolic velocity profile in the axial position. When the cells flowing from the LHS overlapped the cells positioned to its right, the overlapped cells were considered a single spherical aggregate. At each step, the time dependent PA amplitude (PA_{amp}) from each cell (or aggregate) was computed by modeling and accounting for the directivity of a 21 MHz (9.2 ~ 32.8 MHz bandwidth) linear array. PA images of the RA were acquired using the VevoLAZR equipped with a 21 MHz linear array probe and compared to the developed model.

Results/Discussion

Fig. 1a shows the spatial distribution of the PA_{amp} at the initial, peak systolic, and end diastolic phases. The PA_{amp} on the parabolic front was larger due to RBC aggregates (larger absorber). The root mean square of the depth dependent PA_{amp} at each element was shown in the lateral direction, as a function of time up to 4 s (6 periods) (Fig. 1b). The spatiotemporal distribution of the measured PA_{amp} was reconstructed in the same way (Fig. 1c). The overall trend was similar in both cases. Specifically, the PA_{amp} at the LHS was ~10 dB smaller than the one at the RHS, suggesting that the simulated aggregation kinetics occur *in vivo*. These results can be used to study the *in silico*, label free, noninvasive assessment of the spatiotemporal distribution of sO_2 *in vivo*. Furthermore, the improved particle model can provide insights into the effect of RBC aggregation on PA wave generation during *in vivo* blood flow measurements.

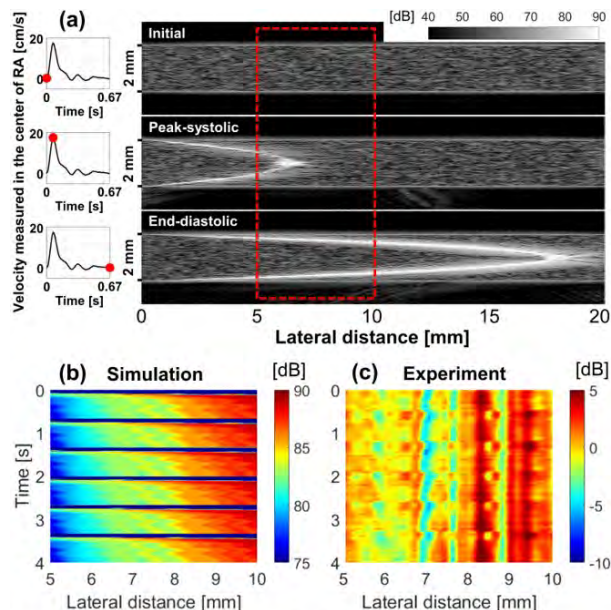


Fig. 1. (a) Simulated PA images in the axial-lateral plane at different time based on the measured blood flow velocity of the radial artery (RA). Spatiotemporal distribution of PA amplitude for simulation (b) and experiment (c). The time in (b) and (c) is a sequential time, repeating one period ($0.67 \text{ s} \times 6 \text{ periods} = 4 \text{ s}$)

9:15 AM

Improving tissue oxygenation estimation using photoacoustic spectral analysis**Muhammad N. Fadhel^{1,2,3}, Eno Hysi^{1,2,3}, Michael Kolios^{1,2,3}**¹*Keenan Research Centre for Biomedical Science of St. Michael's Hospital, ON, Canada*, ²*Institute for Biomedical Engineering, Science and Technology (iBEST), ON, Canada*, ³*Department of Physics, Ryerson University, ON, Canada***Background, Motivation, and Objective**

Photoacoustic (PA) signals convey information about tissue's chromophores and the light distribution. The wavelength dependence of the light distribution in tissue results in spectral coloring which affects chromophore quantification. Assessing oxygenation through linear spectral unmixing results a decrease in the estimated sO_2 with depth, rendering the technique inaccurate beyond a few millimeters depth. Fluence compensation is necessary to reduce the changes in the apparent sO_2 values. We propose to use the PA radiofrequency (RF) signal spectral slope ratio of different optical wavelengths to generate a frequency filter that corrects the optical fluence for the different illumination wavelengths to help improve sO_2 estimates with depth.

Statement of Contribution/Methods

The spectral slope is calculated by applying a line best fit to the ratio of the power spectra of windowed RF data at two optical wavelengths. Assuming that the same absorbers are imaged at both wavelengths, the ratio of power spectra yields information about the light distribution within the sample. An ultrasound frequency filter was designed based on the ratio of the power spectra.

The hind leg muscle of mice was imaged using the VevoLAZR PA system at 720 and 870nm. The mice were exposed to 100% O₂, 20% O₂ and 100% CO₂. A sliding rectangular window was applied to segment the RF signals. The fluence matching ultrasound frequency filter (FMFF) was applied to each segmented signal. The sO_2 maps (thresholded using Otsu's method) were computed using linear spectral unmixing and compared before and after applying the FMFF.

Results/Discussion

Estimated sO_2 maps of a representative mouse breathing 100% O₂ are show in Fig 1a before and after correction. sO_2 values of superficial vessels did not change after correction as the effects of spectral coloring were minimal. However, for deeper vessels, application of the FMFF increased the oxygenation estimates throughout the entire region (Fig 1b). Changes in the estimated sO_2 before and after correction for four ROIs (denoted in Fig 1a) of increasing depth are presented in Fig 1c. The results reveal an increase in the estimated sO_2 for mice exposed to 100% and 20% O₂ and an overall decrease for mice exposed to 100% CO₂. These results demonstrate that FMFF can provide more accurate sO_2 measurements which can be used to improve chromophore quantification using PA imaging.

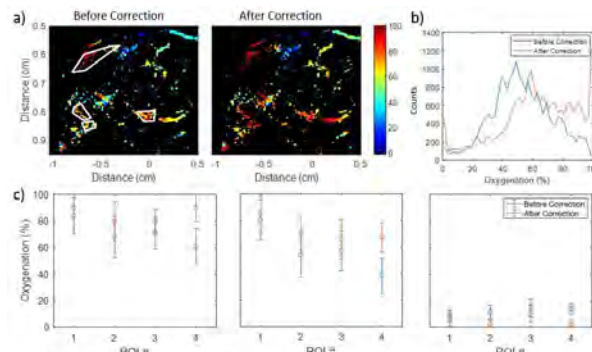


Fig1: (a) sO_2 maps of a mouse hind leg muscle exposed to 100% O₂ before and after correction using FM. The white outlines represent the 4 ROIs chosen for analysis in (c). (b) Histograms of the sO_2 map images presented in (a). (c) Left, middle, and right are the average oxygenation and standard deviation of the selected four windows with increasing depths before and after correction when the mouse was exposed to 100% O₂, 20% O₂, and 100% CO₂, respectively.

2E - Photoacoustics and Imaging

Diamond (300)

Wednesday, October 24, 10:30 am - 12:00 pm

Chair **William Wright**
University College Cork

2E-1

10:30 AM **Guided acoustic wave in a single Pt nanowire**

Hiroki Tamura¹, Akira Nagakubo¹, Teruo Ono², Hirotsugu Ogi¹

¹Osaka University, Japan, ²Kyoto University, Japan

Background, Motivation, and Objective

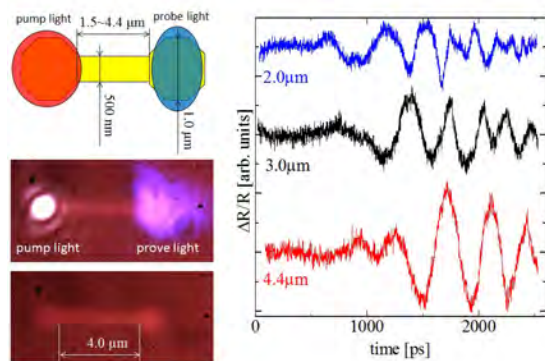
Recently, demand for sensitive and high-throughput biosensors grows in the fields of drug development and diagnosis. One promising candidate is an acoustic-wave biosensor, because it allows real-time and unlabeled measurements. Generally, the shorter the wavelength of the acoustic wave, the higher the biosensor sensitivity. However, conventional acoustic-wave biosensors, including QCM, use megahertz-order frequencies with micrometer-order wavelengths. We intend to drastically improve the sensitivity of the acoustic-wave biosensor with an ultrahigh-frequency picosecond laser ultrasonics (PSLU) measurement. The PSLU method excites coherent phonons with frequencies higher than 10 GHz. It is a pump-probe method. In the existing PSLU methods for biosensing, the laser-irradiation area and protein-detection area are the same, and the laser energy is transferred to immobilized proteins, inactivating the proteins. It is then important to separate the pump light from the probe light. Here, we aim to measure the coherent phonons transmitted in the in-plane direction along a nanowire.

Statement of Contribution/Methods

We developed a PSLU microscope system, which makes it possible to separately control the focusing positions of the pump and probe lights. We fabricated many 30-nm-thick Pt nanowires with various shapes and lengths on Si (111) substrate-using the electron beam lithography method. The wire lengths are 1.5, 2.0, 2.5, 3.0, 3.5, 4.0 and 4.4 μm , for example.

Results/Discussion

When we irradiate the same region about $1.5\text{--}4.4 \mu\text{m}$ on the wire specimen with the pump and probe light pulses, we were able to observe the through-thickness acoustic resonance of Pt thin film. We then separated the pump and probe light pulses, so that we were able to observe the guided acoustic waves. So we succeeded in measuring phonons in in-plane direction with this method; the main frequency of the acoustic guided wave exceeds 2 GHz.



10:45 AM

Imaging of wrinkles in CFRP composites with laser-ultrasound and tilt filter signal processing**Lukasz Ambrozinski¹, Jakub Mrowka¹, Geng-Shi Jeng², Matthew O'Donnell², Ivan Pelivanov²**¹*Department of Robotics and Mechatronics, AGH University of Science and Technology, Krakow, Poland,*²*Department of Bioengineering, University of Washington, Seattle, WA, United States***Background, Motivation, and Objective**

Carbon-fiber reinforced plastics (CFRP) are increasingly being used for structures manufacturing. They must meet the highest safety demands and require inspection both in production and in the field. Recent developments in laser-ultrasound (LU) have enabled high-resolution imaging of CFRPs in a fully non-contact manner [I. Pelivanov et al., *Photoacoustics* **2** (2014)]. Due to the broad bandwidth and high sensitivity of a recently developed fiber-optic Sagnac interferometer [I. Pelivanov et al., *J. Appl. Phys.* **115** (2014)], LU images providing sub-ply resolution can probe the details of CFRP structures. This capability can help identify different types of internal damage.

Waviness or wrinkles in a CFRP structure are extremely dangerous, dramatically changing the performance of a composite structure. However, wrinkles are one of the most difficult defects to characterize. Indeed, wrinkles do not produce large echoes like other flaws, which make them difficult to detect with routine ultrasonic inspection.

This work focuses on detecting wrinkles with a Sagnac-based LU scanner combined with two signal processing methods used in medical ultrasound: 'speckle-tracking' [M.A. Lubinski et al., *IEEE Trans UFFC* **46** (1999)] and 'tilt filtering' [L. Huang et al., *IEEE Trans UFFC* **56** (2009)].

Statement of Contribution/Methods

Figure 1(a) shows a B-scan of a wrinkled sample obtained with the LU scanner [I. Pelivanov et al., *IEEE Trans. UFFC* **62** (2015)]. Vertical streaks (i.e., A-scan streaks) in the image correspond to 'bad' surface points where signal reception is poor. A simple running average technique (Fig.1(b)) reduces the noise, but smooths the wrinkled structure. An alternate signal processing approach can be used paralleling US speckle tracking methods used in medical imaging. The idea is to interpolate signals and average along the instantaneous fiber direction rather than averaging adjacent A-scans. Additional information on changes in structural periodicity can be explored with local calculation of the structural signal carrier frequency (as we have previously demonstrated for heat damage analysis [I. Pelivanov et al., *Composites Part A* **84** (2015)]).

Results/Discussion

Results of this work clearly show the efficiency of LU method in combination with tilted interpolation and averaging (Fig.1(c)) for imaging of changes in composite periodicity (like wrinkles) in CFRPs.

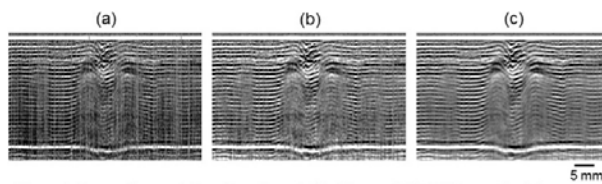


Figure 1. Laser-ultrasonic imaging of a wrinkled 5 mm thick CFRP sample: (a) – original B-scan consisting of 1000 single shot A-scans; (b) – B-scan after running averaging over 7 adjacent A-scans; (c) – B-Scan after 'tilt' filtering and interpolation.

11:00 AM New signal processing for fast and accurate QEPAS measurements
Raphael Levy¹, Maxime Duquesnoy¹, Guillaume Aoust², Jean-Michel Melkonian³
¹*ONERA- The French Aerospace Lab, Chatillon, France*, ²*MIRSENSE, palaiseau, France*, ³*ONERA- The French Aerospace Lab, palaiseau, France*
Background, Motivation, and Objective

Quartz Enhanced Photoacoustic Spectroscopy (QEPAS) gas sensors have been widely developed over the last decade. This technique takes advantage of a high quality factor micro tuning fork to enable high detectivity & high selectivity miniature gas sensors. Lock-in detection technique is classically used to measure the resonator amplitude proportional to gas concentration, but this technique is slow and does not follow the resonator frequency shift over temperature. This paper presents a new QEPAS signal processing technique that allows faster and more accurate measurements, that will enable accurate and fast multiple gas sensors.

Statement of Contribution/Methods

The principle of operation shown in figure 1 is as follows: the micro tuning fork is actuated at resonance by means of an oscillator circuit, the oscillator output signal is phase shifted and used to modulate the laser power. A phase quadrature is set between the actuation force from the oscillator circuit and the photoacoustic actuation force, this induces a frequency shift of the oscillator that is proportional to the photoacoustic force and thus to the gas concentration. This frequency shift is instantaneous allowing fast measurements and the frequency variations over temperature can be cancelled by adding a 180° periodic phase shift.

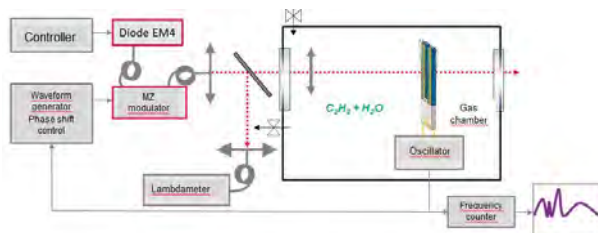
The additional phase shift to set takes into account the phase shift of the photoacoustic wave generation and the propagation delay of the acoustic wave to the tuning fork branches. Its calculation will be detailed in full paper.

This leads to a frequency variation over photoacoustic force that analytical expression has also been developed.

This new signal processing scheme and the analytical expression of the frequency variations over photoacoustic force have been validated first by numeric transient simulations, and then by photoacoustic experimental measurement over C₂H₂ with a laser diode at 6490 cm⁻¹.

Results/Discussion

This first measurement allowed to validate the fast measurement but with a poor signal to noise ratio. Work is currently in progress to optimize the oscillator circuit and the resonator electrodes configuration to improve signal to noise ratio.



11:15 AM Ultrasonic Phased Array TFM Detection in Highly Attenuating Materials based on Modified Golay-Coded Excitation
Teng Da¹, Zhu Wujun¹, Xiang Yanxun¹
¹*East China University of Science and Technology, Shanghai, China, People's Republic of*
Background, Motivation, and Objective

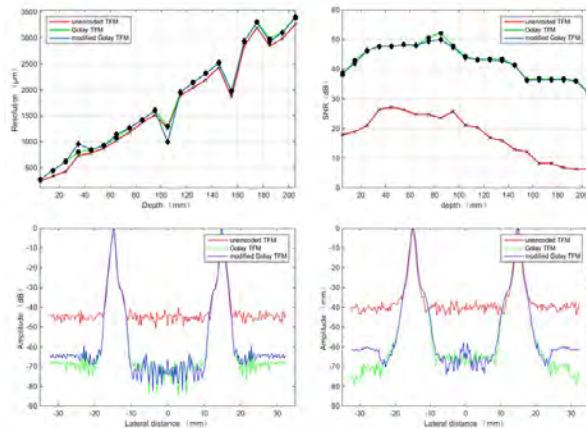
The total focusing method (TFM) attracts much interest because of high image resolution and large dynamic range. However, the signal-to-noise ratio (SNR) of TFM is relatively low due to single-element emission. Especially in highly attenuating materials, the signal amplitude may be reduced with depth to a level lower than the electronic noise introduced by the signal acquisition system. Golay-coded excitation was introduced to overcome this problem, however, the double-excitations reduce the time resolution and may lead to negative decoding performance due to the relative change of scanning positions. In this work, the AB code conversion factor was used to realize the TFM imaging based on Golay-coded single-excitation which has a good performance as traditional Golay-coded excitation.

Statement of Contribution/Methods

A multi-scatterers phantom, whose attenuation is 1.5×10^{-5} dB/(m×Hz), was simulated by commercial simulation soft Field II, in which a 5MHz 128-element linear transducer array with 0.1 mm inter-element spacing was applied. It was detected by TFM using un-coded excitation, Golay-coded excitation and modified Golay-coded excitation, respectively. Then, the image results were compared in terms of spatial resolution, SNR and point-spread function. Finally, experiments using above three methods to detect a PMMA test block with a series of 2mm holes were performed to verify the simulations.

Results/Discussion

The simulation results are shown in the figure below, lateral resolution at each depth of detection for above three methods yielded similar results. Modified Golay-coded TFM method shows approximately the same SNR as traditional Golay-coded TFM method at each depth of detection, average SNR gain is 25.2dB. The point-spread function at the depth of 55mm and 105mm clearly show the similar lateral resolution and clutter improvement (at least 20.3dB). Then according to the experimental result, modified Golay-coded excitation TFM based on single-excitation obtains the approximative result as traditional Golay-coded excitation based on double-excitations, and contribute to a 13dB SNR improvement when compared to un-coded TFM method while maintaining the resolution.



11:30 AM

Cortical bone microstructure assessed by acoustic microscopy in the tibia and proximal femur shaft is correlated with hip stiffness and strength

Gianluca Iori¹, Frans Heyer^{2,3}, Johannes Schneider¹, Andreas Reisinger⁴, Laura Peralta⁵, Caroline Wyers^{2,3}, Melanie Gräsel⁶, Reinhard Barkmann⁶, Dieter Pahr^{4,7}, Joop van den Bergh^{2,3}, Kay Raum¹

¹Berlin-Brandenburg Center for Regenerative Therapies, Charité - Universitätsmedizin Berlin, Berlin, Germany,

²Department of Internal Medicine, VieCuri Medical Center, Venlo, Netherlands, ³Department of Internal Medicine,

NUTRIM School for Nutrition and Translational Research in Metabolism, Maastricht, Netherlands, ⁴Division Biomechanics, Karl Landsteiner University of Health Sciences, Krems, Austria, ⁵Department of Biomedical Engineering, School of Biomedical Engineering & Imaging Sciences, King's College, London, United Kingdom, ⁶Klinik für Diagnostische Radiologie, Universitätsklinikum Schleswig-Holstein, Kiel, Germany, ⁷Institute for Lightweight Design and Structural Biomechanics, TU Wien, Vienna, Austria

Background, Motivation, and Objective

Most quantitative ultrasound (QUS) measurements are applied at distal sites of the skeleton (e.g., radius and tibia) to assess the fracture risk of patients. Ultrasound waves interacting with cortical bone contain structural information, such as its porosity and thickness. While the relation between microstructure and the mechanical resistance of bone tissue has been the subject of numerous studies, only a few works have investigated the effects of microstructural changes on whole organ mechanics. With a focus on the lower limb, we aimed at elucidating the relationship between the cortical bone microstructure in the tibia and proximal femur shaft and the mechanical properties of the hip.

Statement of Contribution/Methods

Tibia and proximal femur samples were collected from 20 pairs of human limbs (7 m, 13 f, age: 69-94 yrs, mean: 84±8 yrs). DXA and HR-pQCT scans were performed to image the entire hip. After this, a sub-set of 10 proximal femur pairs were tested mechanically until failure, assigning one side of the pair to side-fall (FALL) configuration testing, and counter legs to one-legged stance (STANCE) configuration, simulating the spontaneous fracture of the hip. Finite Element Models (FEM) were used to provide mechanical data in both configurations and for the entire data set. Mechanical tests and simulations were performed in quasi-static compression. Cross-sectional slices of the proximal shaft and of the tibia midshaft were extracted from all left samples for 100-MHz Scanning Acoustic Microscopy (SAM, pixel size: 12 µm, spatial resolution: 20 µm). Distributions of cortical bone tissue stiffness and microstructural properties were quantified.

Results/Discussion

Areal BMD (aBMD) from DXA as well as cortical thickness (Ct.Th), porosity (Ct.Po) and pore distribution heterogeneity (VORcv) were correlated with the mechanical competence of the hip. Correlations of microstructure with simulated hip strength/stiffness were stronger i) for STANCE than for FALL load conditions and ii) for tibia parameters than femur ones. Moreover, Ct.Po and Ct.Th obtained from the medial tibia shaft (a typical location for *in vivo* QUS application) showed correlation coefficients similar to those derived from the entire tibia cross-section.

In summary, our data shows that cortical bone structural parameters assessed at the tibia are correlated with hip stiffness and strength.

Table 1 DXA aBMD and cortical microstructure: correlation with simulated proximal femur strength and stiffness. N=16

| | | STANCE | | FALL | | Mean ± SD [mm ± mas] |
|-----------------|----------------------------|----------|-----------|----------|-----------|-------------------------|
| | | strength | stiffness | strength | stiffness | |
| Femur | aBMD [mg/cm ²] | 0.75 | 0.59 | 0.81 | 0.80 | 679 ± 121 [47.3 ± 96.4] |
| | Ct.Po [%] | ns | ns | ns | ns | 12.0 ± 3.4 [8.0 - 23.1] |
| | Ct.Th [mm] | 0.37 | 0.45 | ns | ns | 3.4 ± 1.1 [0.8 - 5.1] |
| | VORcv [%] | ns | ns | ns | ns | 95 ± 19 [66 - 150] |
| Tibia | Ct.Po [%] | 0.71 | 0.72 | ns | 0.54 | 112 ± 3.8 [6.8 - 24.2] |
| | Ct.Th [mm] | 0.85 | 0.85 | 0.60 | 0.63 | 3.0 ± 1.3 [0.5 - 5.5] |
| | VORcv [%] | -0.55 | 0.58 | ns | ns | 103 ± 54 [70 - 261] |
| | Ct.Po [%] | -0.58 | -0.58 | ns | ns | 10.2 ± 3.2 [6.2 - 18.8] |
| Tibia Medial | Ct.Th [mm] | 0.84 | 0.83 | 0.59 | 0.61 | 3.0 ± 1.4 [0.6 - 5.7] |
| | VORcv [%] | ns | ns | ns | ns | 80 ± 19 [61 - 128] |

Spearman's rho of the correlation with the hip mechanical properties, mean, standard deviation (SD), minimum (min) and maximum (max) values.

11:45 AM

Efficient and stable acoustical coupling for bottom Actuated GHz Subsurface Probe Microscopy

Benoit Quesson¹, Paul van Neer¹, Martijn van Riel¹, Maarten van Es¹, Daniele Piras¹, Kodai Hatakeyama¹, Abbas Mohtashami¹, Violeta Navarro¹, Tom Duivenvoorde¹, Hamed Sadeghianmarnani¹

¹TNO, Netherlands

Background, Motivation, and Objective

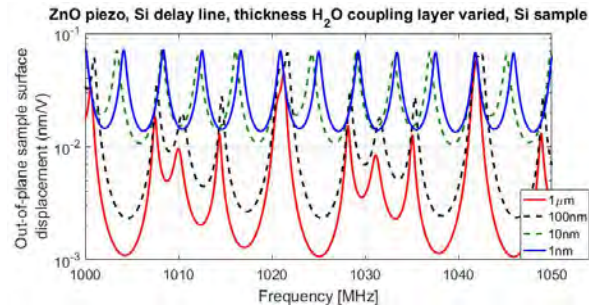
Many techniques are under development for the detection of subsurface defects or cracks. One such method is bottom actuated GHz subsurface probe microscopy (BA GHz SSPM). Here, modulated GHz elastic waves are transmitted through the bottom of a sample. The waves are scattered by buried features and detected using the cantilever of an atomic force microscope (AFM), which scans the top of the sample. To ensure that sufficient acoustical energy reaches the sample surface, an efficient and stable acoustical and mechanical coupling between the transducer and the sample is essential. As the GHz excitation is practically continuous, the attenuation and the standing wave patterns lead to a requirement on the coupling layer thickness and its stability in the micrometer and nanometer order, respectively. This study describes the design and modelling of a clamp and the associated acoustic measurement method to monitor and control the coupling thickness with nanometer accuracy.

Statement of Contribution/Methods

A 1 GHz transducer transmitted modulated elastic waves through the bottom of a sample. The out-of-plane sample surface displacement was read-out with an AFM. Samples typically measured 10x10x1 mm³. The coupling layer was water. Evaporation of the coupling layer was counteracted using a basin and the capillary effect. The combined acoustic behavior of the piezoelectric transducer, delay line, coupling layer and sample was modeled using the KLM model. The time dependent behavior of the coupling layer liquid was modeled analytically. The coupling layer thickness was controlled using the custom designed clamp and monitored in real-time using pulse-echo measurements and custom signal processing based on detecting the acoustic resonances of the transducer – coupling layer – sample stack.

Results/Discussion

The figure shows the out-of-plane sample surface displacement versus the carrier frequency. Its peak derivative was 3 dB/nm, hence a coupling layer thickness stability in the order of 2 nm was needed to ensure that the standing wave pattern remains sufficiently constant to allow for stable AFM measurements. The acoustic measurements showed that the clamp allowed for stable coupling layers (<1 μm in thickness with variations <2nm per 10mn) over a span of hours, allowing for successful BA GHz SSPM measurements.



2F - Novel Photoacoustic Imaging Techniques and Applications

Diamond (300)

Wednesday, October 24, 1:30 pm - 3:00 pm

Chair **Geoffrey Luke**
Dartmouth College

2F-1

1:30 PM Non-invasive mapping of rat visual cortex dynamics *in vivo* using transcranial photoacoustic voltage-sensitive dye imaging

Jeeun Kang¹, Maged M. Harraz², Adarsha Malla², Ping Yan³, Dean F. Wong⁴, Leslie M. Loew³, Peter L. Gehlbach⁵, Emad M. Boctor⁵

¹Johns Hopkins University, Baltimore, MD, United States, ²Johns Hopkins University, MD, United States, ³University of Connecticut Health, United States, ⁴Russell H. Morgan Department of Radiology and Radiological Science, Johns Hopkins University School of Medicine, United States, ⁵Johns Hopkins University School of Medicine, United States

Background, Motivation, and Objective

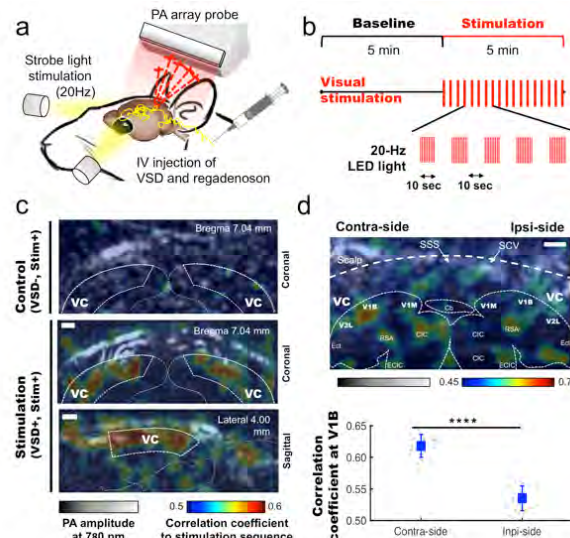
Non-invasive transcranial photoacoustic (PA) voltage-sensitive dye (VSD) imaging is promising modality to further improve current spatiotemporal resolution of functional neuroimaging. In this study, we present non-invasive mapping of rat visual cortex dynamics *in vivo* using PA imaging of near-infrared VSD.

Statement of Contribution/Methods

A preliminary study using visible light stimulation was conducted to directly prove the feasibility of the PA imaging of novel near-infrared cyanine VSD (PY6133, University of Connecticut) which has a peak absorbance at 800 nm with 81% higher absorbance than that of IR780 perchlorate, and yields $-16.80 \pm 1.17\%$ of fractional contrast in depolarization state of lipid vesicle model (Figure 1b). In this experiment, a 20-Hz strobe light was used for binocular/monocular stimulation onto rat eyes, with 10 sec of ON/OFF intervals, while the visual cortex (at bregma -7.04 mm) was monitored with the photoacoustic imaging (Figure 1a/c).

Results/Discussion

The correlation coefficient maps between neural activity index and stimulation sequence presented exclusively localized visual cortex dynamics in both the coronal and sagittal planes, while negative controls without VSD administration did not present any significant correlation (Figure c). The monocular stimulation was also conducted at the posterior visual cortex (bregma -9.16 mm, Figure 1d): The correlation coefficients measured from the contra- and ipsi-sided primary visual cortex were presented significantly different from each other, i.e., 0.62 ± 0.02 vs. 0.54 ± 0.02 , respectively. ($p < 0.0001$). Therefore, the proposed PA VSD imaging presented its feasibility of non-invasive mapping of real-time visual cortex dynamics, and suggests its efficacy in further advanced applications in neuroscience and clinics.



Transcranial photoacoustic imaging of rat visual cortex dynamics *in vivo*: (a) *in vivo* setup for photoacoustic imaging and (c) *in vivo* experimental protocol for stimulation. (d) Neural activity correlation coefficient maps for binocular stimulation in control group (VSD-, Stim+) and stimulation group (VSD+, Stim+). (f) Monocular stimulation and correlation coefficient at V1B region in rat visual cortex.

1:45 PM

Ultrasound/Photoacoustic Imaging Platform to Expedite Development of Novel Glaucoma Treatments**Kelsey Kubelick¹, Eric Snider¹, Andrei Karpouk², C. Ross Ethier¹, Stanislav Emelianov^{1,2}**¹*Wallace H. Coulter Department of Biomedical Engineering, Georgia Institute of Technology & Emory University, Atlanta, GA, United States, ²School of Electrical and Computer Engineering, Georgia Institute of Technology, Atlanta, GA, United States***Background, Motivation, and Objective**

Novel treatments for glaucoma, a disease associated with cell death at the trabecular meshwork (TM), seek to deliver stem cells to regenerate the TM. To understand and optimize the therapy and expedite clinical translation, longitudinal stem cell tracking *in vivo* is needed. Although optical coherence tomography (OCT) is widely used for retinal imaging, high scattering from the sclera and melanin absorbance make use of OCT very difficult in this application. Use of other imaging modalities is also challenging or limited. Thus, we developed an ultrasound (US) and photoacoustic (PA) imaging platform for *in vivo* tracking of mesenchymal stem cell (MSCs) in the anterior eye.

Statement of Contribution/Methods

Based on analysis of PA properties in the anterior segment, human MSCs were tagged with one of two custom-made optical absorbers: plasmonic citrate-stabilized gold nanospheres (AuNS) and photomagnetic dextran-coated Prussian blue nanocubes (PBNCs). Tagged MSCs were injected into the anterior chamber of *ex vivo* porcine eyes (250 μ L at 1,000-4,000 cells/ μ L) and eyes were perfused at a physiological rate of 2.5 μ L/min. US/PA datasets were acquired for up to 5 hours post-injection using the Vevo 2100 (20 MHz transducer) and LAZR (680-970 nm). A custom-built light delivery system was also integrated with the Vevo 2100 to direct light to the TM. Eye globes were dissected for histology and further spectroscopic PA imaging to verify results.

Results/Discussion

Single-wavelength imaging showed PA signals from melanin-rich tissues before injection (Fig. 1A) and from AuNS-MSCs immediately post-injection (Fig 1B). Spectroscopic analysis distinguished each signal (Figs. 1C & 1D), verifying the algorithm. AuNS-MSCs were detected up to 5 hours post-injection (Fig. 1E). Photomagnetic PBNC-MSCs were investigated to improve delivery efficiency. As an example, a disc magnet pulled PBNC-MSCs to the cornea and held the cells in place for 24 hours (Fig. 1F), indicating image-guided magnetic delivery to the TM is possible (Fig. 1G). To move towards clinical translation, we built a custom light delivery system (Fig. 1H) to concentrate light at the TM (Fig. 1I), thus improving detection capabilities and safety of our tool. Results show our US/PA imaging platform can successfully monitor stem cells in the anterior eye with potential for image-guided laser therapies and magnetic delivery.

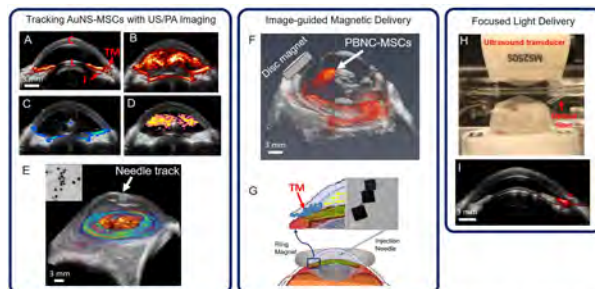


Figure 1. Single-wavelength PA images before (A) and after injection of AuNS-MSCs (B). C=cornea; L=lens; TM=trabecular meshwork; I=iris. Spectroscopic analysis separates signals from melanin (C) and AuNS-MSCs (D), which is important once cells localize to melanin-rich tissues, as seen at 5-hours post-injection (E). Blue=melanin; Orange=AuNS-MSCs. Instead of coating the lens, PBNC-MSCs were held at the cornea for 24 hours (F). PBNC-MSCs can be localized to the TM using a ring magnet (G). The custom light delivery system (H) only produces PA signals near the TM (I).

2:00 PM

Photoacoustic imaging of human inflammatory arthritis using light emitting diodeJanggun Jo¹, Guan Xu², Elena Schiopu³, Girish Gandikota², Xueding Wang^{1,2}¹*Biomedical Engineering, University of Michigan, Ann Arbor, MI, United States*, ²*Radiology, University of Michigan Medical School, Ann Arbor, MI, United States*, ³*Internal Medicine, University of Michigan Medical School, Ann Arbor, MI, United States***Background, Motivation, and Objective**

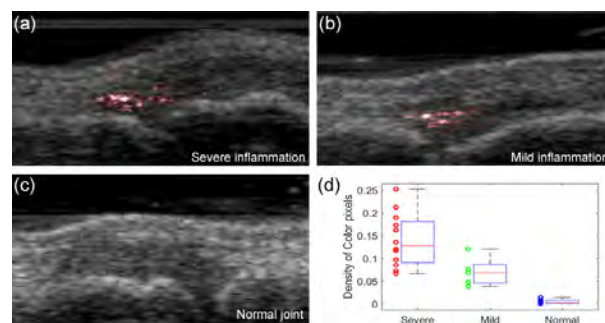
Our previous research demonstrated that photoacoustic imaging (PAI), by revealing vascular features suggestive of joint inflammation, could be a valuable supplement to musculoskeletal ultrasound (US). PAI systems involving class-IV lasers, however, are not ideal for rheumatology clinic due to their high cost, large footprint, immobility, and safety concerns.

Statement of Contribution/Methods

An LED-based PAI system integrated with a B-scan US enabling PA-US dual-modality imaging was employed in this study on human inflammatory arthritis. After validating the system performance through the experiments on normal volunteers, an initial study on arthritis patients was conducted. For each metacarpophalangeal (MCP) joint, 2D B-scan PA and US images were acquired along the sagittal sections. Along the same sections, US Doppler images were also acquired to be used as the gold standard. Images from 12 joints affected severe arthritis, 5 joints affected by mild arthritis, and 12 joints of normal volunteers were compared. The blood volume in each joint was quantified by counting the density of the color pixels in the pseudo-color PAI image. t-tests were conducted to evaluate whether PAI can differentiate the three groups.

Results/Discussion

The LED-based PAI is capable of mapping microvessels in subsurface tissue with an imaging depth up to 10 mm, at frame rate of up to 500 Hz. The increased blood volume in the joint space can be detected with excellent contrast-to-noise ratio. For the joint in the mild arthritis group where US Doppler failed to detect active flow in the joint space, mildly increased blood volume was successfully detected by PAI. For the t-tests conducted, $p < 0.001$ was achieved when comparing the mild arthritis group and the normal group; $p < 0.001$ was achieved when comparing the severe arthritis group and the normal group; while a p -value of 0.031 was achieved when comparing the severe arthritis group and the mild arthritis group. The results from this initial patient study suggest that LED-based PAI is capable of detecting increased blood volume as a biomarker of joint inflammation. Benefiting from the highly sensitive optical contrast, PAI could show better sensitivity than conventional Doppler US in detecting early and mild inflammation.



2:15 PM

Characterizing intestinal strictures with an endoscopic photoacoustic probe in rabbits *in vivo*Hao Lei¹, Laura Johnson², Jonathan Rubin³, Jun Ni¹, Xueding Wang⁴, Peter Higgins², Guan Xu³¹*Mechanical Engineering, University of Michigan, United States*, ²*Internal Medicine, University of Michigan, United States*, ³*University of Michigan, United States*, ⁴*Biomedical Engineering, University of Michigan, United States***Background, Motivation, and Objective**

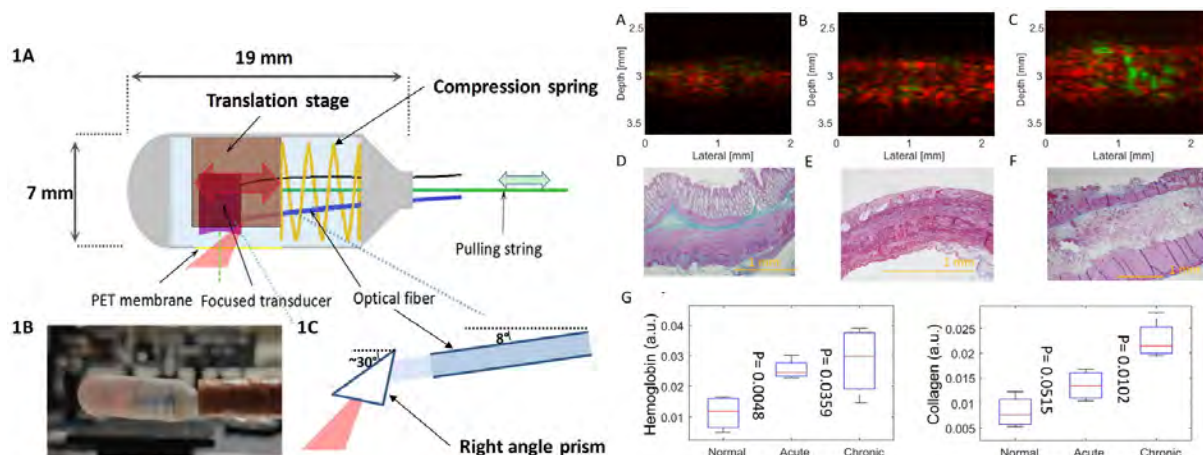
Crohn's disease (CD) is one type of inflammatory bowel disease, where inflammation and fibrosis cause the thickening of the bowel wall and intestinal strictures. The accurate assessment of the strictures is critical for the management of CD, since the fibrotic strictures must be removed surgically. The objective of this study is to validate our recently developed capsule-shaped acoustic resolution photoacoustic (PA) endoscopic probe in characterizing the intestinal strictures in a rabbit model *in vivo*.

Statement of Contribution/Methods

Fig. 1 shows the capsule PA endoscopic probe consisting of two fiber optics and a single element ultrasound transducer with a center frequency of 30MHz. Acute (with inflammatory stricture) and chronic (with mixed fibrotic and inflammatory strictures) diseases were generated in rabbits using trinitrobenzene sulfonic acid (TNBS). The endoscopic probe acquired the signals at 720 and 1310 nm targeting the hemoglobin and collagen contents, which are rich in the inflammatory and fibrotic intestinal strictures, respectively. The PA signal differences between the normal, acute and chronic groups, each including 4 animals, were observed. The longitudinal changes of the PA signals were observed in another 4 animals.

Results/Discussion

The representative PA images in Fig. 2, in agreement with the histology, show that 1) hemoglobin content increases by approximately twice in the acute and chronic subjects compared to the normal ones; and 2) collagen content increases by more than twice in the chronic subjects compared to the normal ones. Longitudinal study also agrees with the progressive disease conditions controlled by the doses of TNBS. These results support that the endoscopic PA probe can provide reliable characterization of the intestinal strictures.



2:30 PM

Development of an ultrasound and photoacoustic endoscopy system for imaging of gynecological disorders

Maryam Basij¹, Yan Yan¹, Suhail Alshahrani¹, Timothy Burton¹, Jacob Burmeister², Shelly Seward², Michael Dominello², **Mohammad Mehrmohammadi^{1,2}**

¹Biomedical Engineering, Wayne State University, Detroit, MI, United States, ²Barbara Ann Karmanos Cancer Institute, Detroit, MI, United States

Background, Motivation, and Objective

Gynecological cancer is known as the fourth most common cancer among women with nearly 18% of all women in the world. Early detection of gynecological cancers can significantly improve the patients' quality of life and reduce the mortality. Although there are some imaging modalities such as ultrasound (US), magnetic resonance imaging (MRI), computed tomography (CT), and optical imaging for gynecologic cancer imaging, due to lack of apparent symptoms and difficulty of accessing to the organs, early stage detection remains a challenge. In this study, we designed and developed of a miniaturized phased-array ultrasound (US) and a photoacoustic (PA) endoscope, capable of providing multi-modal diagnostic information of gynecological cancers such as cervical and ovarian cancer. The small size of the developed probe, enables potential passage through the cervical canal and access to internal organs.

Statement of Contribution/Methods

The proposed PA/US endoscope consists of three parts: a phased-array ultrasound endoscope, a compact light delivery system and a sheath. A 64-element phased array US probe was utilized for providing a high-resolution 90_degrees sector imaging within the range of 5-8 MHz. The diameter of US probe is about 9 mm. Six silica core optical fibers (600 μ m core diameter) was utilized for the light delivery system while they embedded surround US probe to divert the laser light toward the tissue in front of US aperture and yield an aligned and overlapped ultrasound and light beams. For providing desired light beam, the side-firing approach was used by polishing fibers at angle of 18 degrees which can cause the light exiting from the side within angular range of 18 to 50 degrees. A custom-built, 3D printed sheath was designed to enable integrating light delivery and US imaging as well as easy assemble and disassembling the probe for cross-patient imaging (**Figure 1a and 1b**).

Results/Discussion

Our primary results demonstrated the functionality of the developed endoscope to provide co-registered US and PA images of a calibration phantom (200 μ m wire phantom) with axial and lateral resolutions of 366 μ m and 466 μ m respectively (**Figure 1c and 1d**). The total diameter of proposed probe is about 7.5 mm which provides its potential ability for utilizing this technology for imaging various types of gynecological cancers in which the probe can become close to the target tissues.

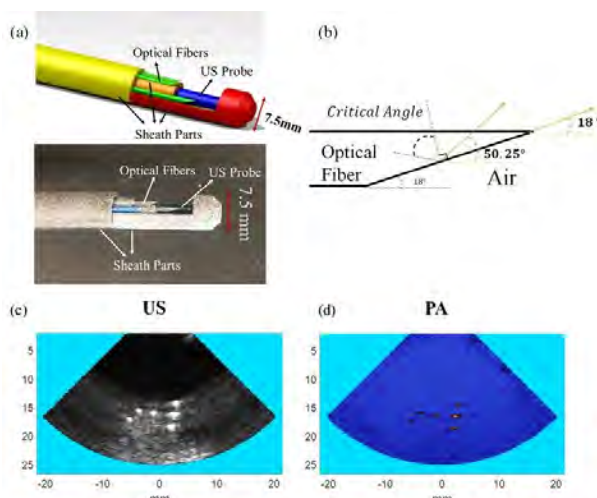


Figure 1: (a) 3-D visualization of combined US/PA endoscope including custom designed housing and a photograph of the developed endoscope; (b) A schematic of the side firing of fiber. Yellow lines indicate the light beam illumination from a polished fiber by 18 degrees; (c,d) US and PA imaging results obtained with the combined endoscope and from a characterization wire (200 μ m diameter) phantom.

2:45 PM

Fast label-free photoacoustic histology system using a MEMS scanner

Jin Woo Baik¹, Jin Young Kim², Hyojin Kim², Hyosang Ahn³, Kyung Hee Byun³, Hae Young Choi⁴, Seon Young Ryu², Chulhong Kim⁵

¹Pohang University of Science and Technology, Pohang, Korea, Republic of, ²Pohang University of Science and Technology, Korea, Republic of, ³Gachon University Graduate School of Medicine, Korea, Republic of, ⁴Medical Device Development Center, Korea, Republic of, ⁵Pohang University of Science and Technology (POSTECH), Korea, Republic of

Background, Motivation, and Objective

A frozen section examination is widely used in cancer surgery for assessment of surgical margin. However, this conventional method goes through a complicated process including sectioning and staining for about 15 minutes. Photoacoustic microscopy (PAM) is a novel imaging system, which combines the advantages of optical contrast and spatial resolution. Especially with UV laser, PAM can be a potential alternative of conventional intraoperative histology because DNA and RNA in cell nuclei can be imaged without sectioning and staining. However, current UV-PAM suffers from slow imaging speed because of motorized linear stages. In this study, we developed a photoacoustic imaging device for fast intraoperative histology using a 2-axis waterproof MEMS scanner.

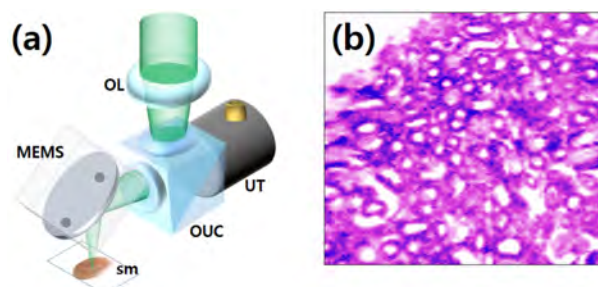
Statement of Contribution/Methods

A pulse laser with wave length of 266 nm was used to excite the sample because DNA/RNA in the cell nucleus has high absorption in this wave length. To enhance the lateral resolution, we construct a special optics for collimating and focusing after Z-max simulation. A UV-fused silica beam combiner was built to coaxially and confocally align UV laser with generated PA wave. A two-axis waterproof MEMS scanner, which was developed in our previous work, scan the aligned two beams along the X and Y axes. To enhance the reflectivity of UV laser, we conduct the UV enhanced aluminum coating on silicon mirror. Detected PA signal on the ultrasonic transducer was processed in PC via signal filtering, Hilbert transform and pseudo coloring.

Results/Discussion

We first quantified the spatial resolution to validate the developed system. Measured lateral and axial resolutions were 2.2 μm and 30 μm , respectively. The acquisition time for the image of 400 x 400 pixels took for 20 seconds. Finally, we acquired the PA image of frozen section sample in mouse kidney. As shown in the figure, characteristic tubular structures of kidney epithelial cells were clearly distinguished. In the future works, we will increase the lateral resolution to 1 μm . Then, we will apply this system to tissue directly.

Acknowledgement: Funded in part by the MOTIE (No.10067190), IITP (IITP-R0346-16-1007) and NRF (No. 2017R1D1A1B03034681, No. 2017R1D1 A1B03030087).



2G - POA: Opto-Acoustics

Diamond (300)

Wednesday, October 24, 4:00 pm - 5:30 pm

Chair **Vincent Laude**
CNRS

2G-1

4:00 PM Moving acoustic field for the control of electronic excitations in semiconductor nanostructures

Paulo Santos¹

¹*Paul-Drude-Institut für Festkörperelektronik, Berlin, Germany*

Background, Motivation, and Objective

A surface acoustic wave (SAW) propagating on a semiconductor structure produces a potential modulation of the underlying material, which can control and transport electronic excitations. Previous acoustic modulation studies on semiconductors focused on the transport of electrons and holes using the moving SAW piezoelectric field. Here, we review recent results on the transport and manipulation of excitonic species in semiconductor nanostructures by the moving SAW strain field. Excitons are neutral particles consisting of an electron-hole pair bound by the Coulomb interaction, which play a fundamental role in the absorption and emission of light in semiconductor structures. Excitons can be strongly coupled to photons in an optical microcavity to form Bose-Einstein-like polariton condensates (MP) at low temperatures (<10 K). We show that the combination of SAWs with specially designed nanostructures provide a powerful tool for controlling opto-electronic excitations as well as for interfacing them to photons.

Statement of Contribution/Methods

The studies were carried out on (001) (Al,Ga)As nanostructures grown by molecular beam epitaxy. SAWs along a non-piezoelectric <100> surface direction were generated by interdigital transducers (IDTs) placed on piezoelectric ZnO island. These purely mechanical SAWs are essential to avoid exciton dissociation by the SAW piezoelectric field. The experimental studies were carried out using time and spatially resolved photoluminescence at low temperatures to detect the transport of optically excited species along the sample surface.

Results/Discussion

We first show that electrically controlled excitons can be transported by the moving band-gap modulation induced by the SAW strain over several hundreds of micrometers. The acoustic exciton transport enables the realization of acoustic exciton transistors and acousto-optical multiplexers, which can be combined into complex and scalable excitonic circuits. We then address the manipulation of MP condensates by SAW fields. Due to the long (several tens of micrometer) spatial coherence lengths of the MP condensates, the strain modulation coherently fragments MP condensates leading to the formation of a lattice of mini-condensates trapped at the minima of the SAW potential. The lattice constant and inter-site interactions can be controlled by the wavelength and amplitude of the SAW potential, respectively. These acoustically tunable condensate lattices are solid-state analogs of optical lattices of cold atoms: they form, therefore, a prototype system for the investigation of many body interactions (such as Josephson coupling) in non-equilibrium solid quantum phases as well as for the realization of lattice-based quantum simulators.

4:30 PM

Structural and Functional Imaging with Concurrent Photoacoustic and Ultrasound MicroscopyYuqi Tang¹, Wei Liu¹, Yang Li², Qifa Zhou², Junjie Yao¹¹Duke University, Durham, NC, United States, ²University of Southern California, Los Angeles, CA, United States**Background, Motivation, and Objective**

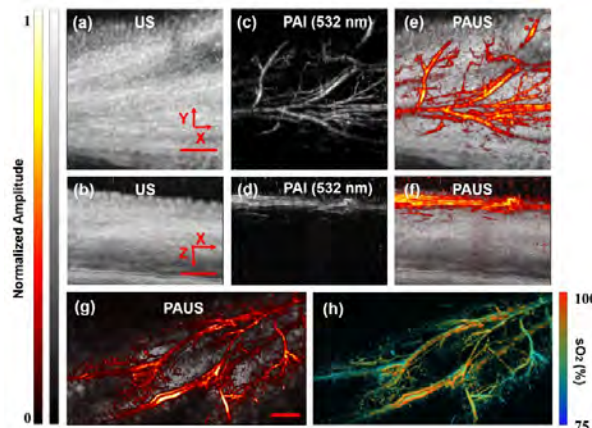
Photoacoustic imaging (PAI) relies on optical absorption from chromophores and reveals optical property of the tissue, but the contrast mechanism of PAI is limited to selective biomolecules (e.g. hemoglobin). Complementing PAI with ultrasound (US) imaging can provide general structural information at depths up to tens of centimeters that is typically absent from PAI. Most reported PAUS systems either rely on commercially available US transducers that have deep penetration detection at the expense of spatial resolution, or use high-frequency US transducers to detect PAI and US signals separately with long data acquisition time. In this work, we present a truly concurrent PAUS microscopy system that provides automatically co-registered PAUS images using a novel coaxial dual-element ultrasonic transducer (DE-UST).

Statement of Contribution/Methods

An Nd: YAG fiber laser (VPFL-G-20, V-Gen, Tel Aviv, Israel) delivered a 7 ns pulse with a pulse energy of 100 nJ at a wavelength of 532 nm for PAI excitation. The beam was focused and passed through the aperture of DE-UST. The 20 MHz element of DE-UST was connected to a US pulser-receiver (5800PR, Olympus, Waltham, MA, USA) for US transmission and the 40 MHz element was connected to an amplifier for receiving US and PA signals. A FPGA card (myRIO-1900, NI instrument, Austin, TX, USA) was used to implement a controlling time sequence. A 2-D raster scanning was performed and at each point, the laser firing and PA signal acquisition were followed by US transmission and receiving. In addition to the customized DE-UST, an alternative system was implemented by replacing the DE-UST with two identical commercially available single-elemental focused US transducers (V324, 25 MHz, Olympus, Inc.) that are confocally aligned. To validate the reliability and feasibility of the PAUS system, the hind paw of a mouse was imaged *in vivo*.

Results/Discussion

DE-UST acquired data are shown for US (a, b), PAI (c, d) and PAUS (e, f) with a FOV in the XY plane of $4.8 \times 4 \text{ mm}^2$. All scale bars represent 1 mm. Multiple-wavelength excitations were added, and fused PAUS and blood oxygenation level ($s\text{O}_2$) are shown for data acquired with Olympus transducer setup (g-h). In addition, our PAUS system can also be used to image microbubbles to provide blood flow velocity and nonlinear mechanical properties. We expect PAUS imaging to find a broad range of biomedical applications.



4:45 PM

Design of Acoustooptical Devices Based on KY(WO₄)₂ CrystalVladimir Molchanov¹, Konstantin Yushkov¹, Natalya Naumenko¹, Alexander Chizhikov¹¹*National University of Science and Technology MISIS, Russian Federation***Background, Motivation, and Objective**

Potassium rare-earth tungstates are used in photonics as active laser media but their acoustic and photoelastic properties had been studied only fragmentarily (M. Mazur et al. Ultrason. 54:1311, 2014). It has been reported that acousto-optic (AO) figure of merit M_2 of KY(WO₄)₂ and KGd(WO₄)₂ for isotropic light diffraction by a quasi-longitudinal bulk acoustic wave (BAW) is several times higher than in fused silica. High laser damage threshold of those crystals makes them promising for creating AO laser Q-switches and quasi-collinear dispersive delay lines for fs-pulse shaping (V. Molchanov et al. Appl.Opt. 48:C118, 2009). We aimed to design the quasi-collinear AO delay lines, filters and laser Q-switches based on KY(WO₄)₂ crystal.

Statement of Contribution/Methods

The quasi-collinear AO geometry uses a shear BAW propagating in the symmetry plane XY and polarized along the Z axis. The slowness curves, phase velocities, diffraction coefficients defining anisotropic acoustic divergences, and acoustical axes were investigated in details. Schaefer-Bergmann method (J. Pfeiffer et al. Appl.Opt. 57:C26, 2018) was used to determine effective photo-elastic constants for anisotropic quasi-collinear AO diffraction in KY(WO₄)₂.

Results/Discussion

We designed and fabricated an AO laser Q-switch using longitudinal BAW propagating along N_g dielectric axis. The Q-switch designed on the base of KY(WO₄)₂ crystal is shown in the figure. The Q-switch was commissioned in a Ho:YAG laser at the wavelength 2.1 μm demonstrating 70% at the driving power of 16 W. The laser damage tests were performed with the energy density up to 12 J/cm² (pulse duration 30 ns) without damaging the crystal. The quasi-collinear geometry of AO interaction in dispersion delay line using slow shear BAW in the region outside the acoustic axes (directions X-49.5° and X+5.1°) and corresponding to the maximum AO effect was also elaborated. It was demonstrated that KY(WO₄)₂ is more preferable for the creation of AO devices operating with high-power laser radiation than traditional quartz and TeO₂ crystals.



5:00 PM

High sensitivity sub-nanosecond pump probe measurement with surface plasmon resonance**Hayato Ichihashi¹, Hiromichi Hayashi¹, Shinji Takayanagi², Mami Matsukawa¹**¹*Doshisha university, Japan*, ²*Nagoya Institute of Technology, Japan***Background, Motivation, and Objective**

Non-destructive photo-thermal-acoustic measurement techniques of local properties are strongly necessary in the biomedical studies and the examination of small electronic components. The femtosecond pump probe technique and the nanosecond photoacoustic microscopy are often used for these demands in spite of the low detection ability. In recent years, the detection ability has been improved owing to the probe beam under the condition of surface plasmon resonance (SPR) [1,2]. However, there have been no studies in the range of sub-nanosecond. In this study, we tried to improve the detection ability of the pump probe technique in the sub-nanosecond range.

Statement of Contribution/Methods

Our pump probe measurement system is composed of a pulse laser (Pulse width: 790 ps, Coherent), 3 round trip automatic delay line and a differential detection system consisted of a balanced detector (Newport) and a lock in amplifier (NF). The wavelengths of the probe beam and the pump beam were 532 nm and 1064 nm, respectively. The energy of the pump beam was 0.1 mJ and the energy of the probe beam was hundredths times less than that of the pump beam. The Ag film (thickness: 53 nm, electron beam deposition) on a BK7 prism was used as a sample. The geometry arrangement of the sample is shown in Fig. 1(a).

Results/Discussion

Fig. 1 (b) shows the spot images of the reflected probe beam under the SPR condition and the non-SPR condition. As can be seen in Fig. 1 (b), the decrease of reflectivity due to SPR was confirmed as the disappearance of the center line. Fig. 1 (c) shows a detected signal due to the thermoelastic effect. Here, the signal was detected as the optical reflectivity change by the probe beam of P-polarization (SPR condition) whereas no signal was detected by the probe beam of S-polarization (non-SPR condition) in the same system. These data tell us that the SPR incredibly increase the thermoelastic signal and the applicability of the pump probe technique to the evaluation of local properties in the sub-nanosecond range.

[1] V. V. Temnov, et, al: Nature communications, **4** 1468 (2013)

[2] T. Wang, et, al: Appl. Phys. Let., **107** 153702 (2015)

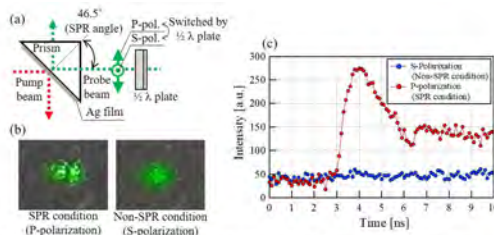


Fig. 1 The improvement results of the pump probe detection ability owing to SPR condition.

(a) The geometry arrangement of the sample.

(b) The spot images of the reflected probe beam under SPR condition and non-SPR condition.

(c) The thermoelastic signals of Ag film/ BK7 prism under SPR condition and non-SPR condition.

5:15 PM

Modelling the iono-acoustic wave field for proton beam range verificationKoen W.A. van Dongen¹, Anne de Blécourt¹, Eelco Lens², Dennis R. Schaart², Frans M. Vos¹¹*Department of Imaging Physics, Faculty of Applied Sciences, Delft University of Technology, Delft, Netherlands,*²*Department of Radiation Science & Technology, Faculty of Applied Sciences, Delft University of Technology, Delft, Netherlands***Background, Motivation, and Objective**

In proton therapy, cancer patients are irradiated with high energy protons. For a successful treatment it is important that the location with the highest energy deposition, the so-called Bragg-peak, is located inside the tumour and not in the healthy surrounding tissue. Here, we investigate if the iono-acoustic wave field generated by the protons can be used to monitor the Bragg-peak location during treatment.

Statement of Contribution/Methods

We present a new numerical method to model the expected pressure field generated by a clinical proton pencil beam. To compute the field, we convolved a 3-D Greens function, representing the impulse response of the medium, with a volume density of injection rate source. This source describes the expansion of the medium due to a local temperature increase caused by the energy deposited by the protons. An analytical model is used to compute the spatial and temporal shape of the proton dose distribution. Next, we used this method to compute the pressure field as would be measured by a linear array positioned behind the Bragg peak in the plane normal to the beam. By migrating the synthetic data back into the domain of interest, the location of the Bragg peak is revealed.

Results/Discussion

To validate our method we modelled the acoustic wave field generated by a 100 MeV clinical proton therapy beam in water. The selected beam parameters are representative for the Holland Proton Therapy Center. A cross section of the original proton dose distribution used to model the pressure field is shown in Fig. 1 (left). Next, we computed the resulting 3-D pressure field for this distribution. By positioning a transducer behind the Bragg-peak location, a set of A-scans is obtained, see Fig 1 (middle). The resulting A-scans had a centre frequency around 30 kHz and an amplitude of ~ 55 mPa. The A-scans show all the characteristics typical for the iono-acoustic wave field; the first pulse corresponds to the field generated by the protons at the Bragg-peak location, the second pulse to the protons entering the water. Migrating the measured data back into the volume of interest resulted in a reconstruction of the location of the Bragg peak, see Fig. 1 (right). To conclude, we have shown that the iono-acoustic wave field can be modelled and that the field can be used to reconstruct the Bragg-peak location.

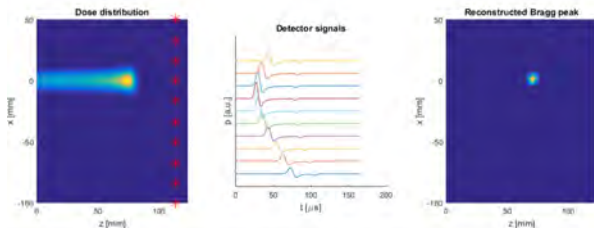


Figure 1. Bragg-peak localization using the iono-acoustic effect. (left) A cross-section of the original proton dose distribution for a 100 MeV clinical proton therapy beam in water. The red stars indicate the location of the 10 receivers. (middle) The pressure fields as would be measured by the linear array. (right) Migrating the pressure fields back into the volume of interest reveals the location of Bragg-peak.

3D - Advanced Beamforming I (Mustafa Karaman Memoriam)

Emerald (280)

Wednesday, October 24, 8:00 am - 9:30 am

Chair **Matthew O'Donnell**
University of Washington

3D-1

8:00 AM Multi-covariate Imaging of Sub-resolution Targets (MIST)

William Walker¹, Matthew Morgan², Gregg Trahey²

¹Biomedical Engineering / Electrical and Computer Engineering, Duke University, Durham, NC, United States,

²Biomedical Engineering, Duke University, Durham, NC, United States

Background, Motivation, and Objective

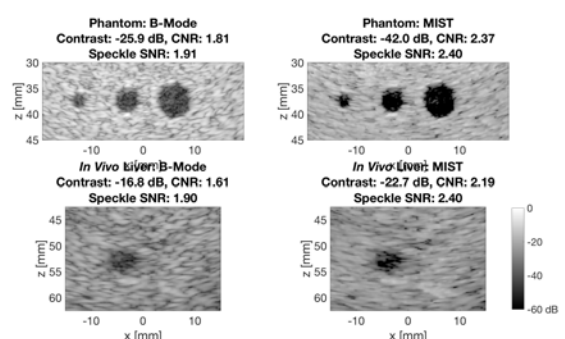
Delay-and-sum beamforming methods traditionally utilized in ultrasound imaging assume that targets consist of collections of point scatterers. Recently described coherence imaging methods take an *ad hoc* approach to image formation loosely based on the statistical properties of ultrasound backscatter. In this paper, we describe Multi-covariate Imaging of Sub-resolution Targets (MIST). MIST assumes that tissue consists of diffuse unresolvable targets, and takes a new approach to image formation derived from fundamental physical and mathematical principles. We hypothesize that this approach is better suited to the diffuse scattering environments that are nearly universal in medical ultrasound imaging.

Statement of Contribution/Methods

We evaluated MIST using simulated and experimental data sets. Simulated channel data was obtained using Field II with a 64-element, 5 MHz, phased array transducer on hypoechoic cyst and point targets distributed among a speckle generating background. Experimental phantom and *in vivo* channel data was acquired using a Verasonics Vantage research ultrasound scanner and a P4-2v 64-element phased array transducer imaging at 3 MHz. Channel data was acquired from hypoechoic cysts and point targets in a tissue-mimicking phantom, and from the livers of 5 human volunteers (under an approved IRB protocol). B-mode and MIST images were evaluated with regards to contrast, contrast-to-noise ratio (CNR), speckle signal-to-noise ratio (SNR), and resolution metrics. Multi-frame sequences of echo data were analyzed to assess the frame-to-frame stability of MIST.

Results/Discussion

MIST showed improved contrast (avg. +44%, + 42%, and +22%) and CNR (avg. +51%, +34%, and +29%) across simulation (N=3), phantom (N=3), and *in vivo* (N=9) datasets, respectively. Target conspicuity was increased significantly without an apparent loss in spatial resolution. Speckle was noticeably smoothed, with improved speckle SNR across datasets (avg. simulation: +47%, phantom: +29%, *in vivo*: +22%). MIST cine loops were stable under experimental noise and tissue motion. This initial work shows MIST to be a stable method capable of significantly improving image quality.



8:15 AM

Synthetic adaptive refocusing of ultrafast plane waves through aberrating media**Hanna Bendjador¹, Justine Robin^{1,2}, Thomas Deffieux¹, Mickaël Tanter¹**¹*Institut Langevin, ESPCI Paris, PSL Research University, CNRS UMR 7587, INSERM U979, PARIS, France*, ²*Dept. Neurology, Neurovascular and Neurosonology Unit, Hôpitaux Universitaires de Genève, Switzerland***Background, Motivation, and Objective**

A major challenging aspect in medical ultrasound imaging remains aberrations of the acoustic wave front which considerably affect image quality especially through complex layers such as skull or fat. Correcting these aberrations is key toward brain and quantitative imaging. Time-reversal of speckle noise is an iterative focusing technique retrieving the phase aberrations law. Backscattered signals are first virtually focused at different positions, echoes are steered back, corrected in phase and summed coherently to get a virtual point source. Last, signals are shifted from extracted time delays to correct the aberration.

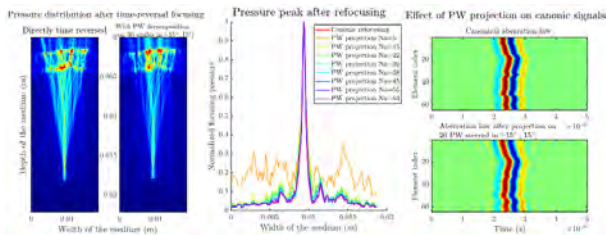
This approach has been used to improve imaging or sound speed estimation by considering homogenous sound speed correction and aberrating layers. Yet, such an algorithm relies on virtual focusing which in theory requires canonical emissions for both iterative process and image reconstruction. This limits its use for post-processing of ultrafast data or for fast moving media. In this work, we investigate matrix decomposition of aberrating laws on a limited set of plane wave transmits for synthetic adaptive refocusing of ultrafast data without compromising high frame rates.

Statement of Contribution/Methods

At each frequency, a theoretical matrix between the canonical and plane wave (PW) basis is defined from plane wave emission delays. A Moore Penrose pseudo-inversion is used to decompose phase aberration laws from canonical to plane waves. Ultrafast data can be corrected at each frequency in transmit and receive. Using different skull-like aberrating laws, synthetic refocusing was investigated both experimentally and in k-Wave 3D simulations.

Results/Discussion

Comparisons of canonical time-reversal refocusing and plane wave synthetic refocusing in simulation show good refocusing capability in skull-like medium. With a set of $Na = 15$ plane waves or more: peak displacement is negligible, FWHM increases by 3.6% ($Na = 64$) to 25% ($Na = 15$), side lobe-levels increase by 0.2dB ($Na = 64$) to 2dB ($Na = 15$). Similar results were obtained using tissue mimicking phantoms and a silicone aberrating layer: canonic and plane wave aberrations laws correlated at 91% for $Na = 33$. Those results demonstrate that efficient aberration corrections could be performed with a limited number of plane wave transmits allowing to adaptive focusing at ultrafast frame rates.



8:30 AM

Ultrasound Transcranial Imaging based on Fast Coherent-time-delay and Correlative Pixel-based BeamformingChen Bai^{1,2}, Xinyu Zhang¹, Xiaoyang Qiao¹, Yuchao Sang¹, Mingxi Wan¹¹*Department of Biomedical Engineering, School of Life Science and Technology, Xi'an Jiaotong University, China, People's Republic of, ²State Key Laboratory of Transient Optics and Photonics, Xi'an Institute of Optics and Precision Mechanics, Chinese Academy of Sciences, China, People's Republic of***Background, Motivation, and Objective**

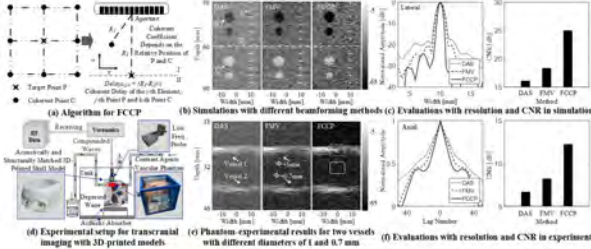
Fast minimum variance (FMV) algorithm has been developed to improve the contrast-to-noise ratio (CNR) in plane wave imaging with extremely reduced computation. However, in ultrasound transcranial imaging, FMV will be confronted with challenges raised by echoes with low intensities when calculating the beamformer contributions at points which are in a distance from the beam center line. In order to improve the CNR and resolution in low echo situation during transcranial imaging, this study combined FMV algorithm and unified pixel-based beamforming to propose the fast coherent-time-delay and correlative pixel-based (FCCP) beamforming by considering the influence of neighboring pixels, which can remove undesirable information whereas increasing diagnostic information.

Statement of Contribution/Methods

The influences of the neighboring points should be reflected by corresponding coherent time delays and the coherent coefficients. Therefore, after calculating the time delay from the active aperture to the target point and the neighbors, the covariance matrix was calculated. Then, the coherent coefficient, determining by the relative position of each pixel and its neighbors as well, was introduced to two plane waves with opposite phases. Through summing up the covariance matrices of each relevant point from the two opposite-phase pulses with multiplying by their corresponding coherent coefficients, the jointly covariance matrix of all points was acquired. Finally, combined with the compounded plane waves imaging and FMV algorithm, the FCCP weight vectors were calculated based on each transmit event.

Results/Discussion

The FCCP method was compared with delay-and-sum (DAS) and regular FMV beamforming both in simulations and phantom experiments with 9-angle compounded waves for all imaging. Among different beamforming methods in simulations, the lateral resolution in FCCP accounted for 46% and 72% in DAS and FMV beamforming, respectively. Whereas the CNR of each method was respectively 16.08, 18.32 and 24.97 dB. In terms of the transcranial phantom experiment and comparing to DAS and FMV beamforming, the axial resolution gain in FCCP was increased by 42% and 66%, while the CNR witnessed a similar increase with 1.57 and 5.62 dB. Therefore, it confirmed that FCCP beamforming can achieve an augmentation of resolution and CNR in transcranial imaging.



8:45 AM

Distributed Phase Aberration Correction Techniques Based on Local Sound Speed EstimatesRehman Ali¹, Carl Herickhoff², Jeremy Dahl²¹*Electrical Engineering, Stanford University, Palo Alto, CA, United States*, ²*Radiology, Stanford University, CA, United States***Background, Motivation, and Objective**

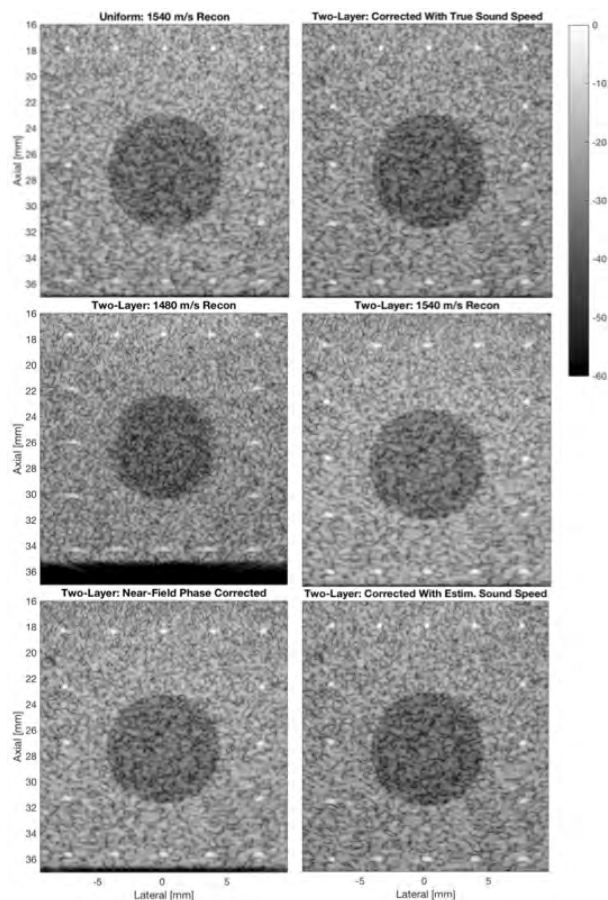
Phase aberration, reverberation clutter, and off-axis scattering have been identified as major sources of image degradation in medical ultrasound. Near-field and mid-field phase aberration correction techniques make assumptions about the sound speed distribution in the imaging medium that limit their efficacy in the presence of distributed aberrations; however, existing distributed aberration correction techniques perform poorly in media composed of diffuse scatterers. We propose a distributed phase aberration correction technique that aims to have greater flexibility and improve reconstruction accuracy in media with diffuse scatterers.

Statement of Contribution/Methods

Local sound speed in the medium was estimated by parabolic fitting of measured arrival times and model inversion. The eikonal equation was then used to calculate propagation times between each array element and each imaging point based on the local sound speed estimates. The resulting propagation delays were subsequently applied to full-synthetic aperture (FSA) datasets to obtain aberration-corrected images. This method, as well as conventional beamforming and near-field correction techniques, were applied to FSA data of two-layer media, from a fullwave simulation (top layer = 1480 m/s, bottom layer = 1600 m/s), and from experimental data acquired on a Verasonics Vantage 256 scanner from an L12-3v linear array in a graphite-formaldehyde slurry (~1540 m/s) on top of an ATS Model 549 phantom (~1460 m/s). Resolution (-6 dB width) and positional error of point targets relative to an ideal, uniform medium (1540 m/s) were measured to assess simulated image accuracy.

Results/Discussion

Compared to the ideal uniform medium, point target resolution (at 18 mm depth) in the simulated two-layer medium was degraded by 102% with conventional 1540 m/s beamforming and 45% with near-field phase-screen correction, while improving 4% with the proposed distributed aberration correction technique. Maximum position error of these point targets was 0.41, 0.38, and 0.07 mm laterally, and 0.57, 0.44, and 0.01 mm axially, for the three beamforming methods, respectively. In experimental data, the proposed distributed aberration correction technique produced 62% improvement in point target resolution relative to beamforming at the calibrated sound speed.



9:00 AM Matrix approach of ultrasound imaging and quantification

William Lambert^{1,2}, Laura Cobus¹, Mathias Fink¹, Alexandre Aubry¹¹Institut Langevin, Paris, France, ²SuperSonic Imagine, Aix-en-Provence, France**Background, Motivation, and Objective**

Conventional ultrasound imaging generally relies on two major assumptions. The back-scattered wave-field contains only singly-scattered echoes and the insonified medium is homogeneous, with a constant speed-of-sound. Nonetheless, when aberrations and/or multiple scattering events take place, those hypotheses are no longer valid. Liver imaging is an appropriate example in which ultrasonic waves propagate through multiple layers of fat and muscle tissues before reaching the organ. The image quality is then degraded and reverberation artefacts may appear. Moreover the speed of sound may vary with position, resulting in multiple isoplanatic patches (varying aberration laws in several areas of the image).

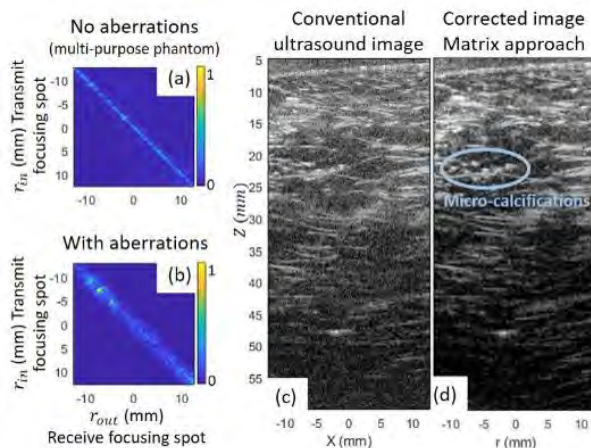
To maintain an optimal resolution, adaptive correction techniques have been developed. They consist in convolving the transmitted and received wave fronts by an adaptive filter that compensates for the wave-front distortions induced by the medium heterogeneities. Nevertheless, those methods require iterative focusing and are time-consuming. Above all, their range of action is limited to one single isoplanatic patch.

Statement of Contribution/Methods

In this work, a matrix approach of ultrasound imaging is developed and dedicated to the correction of aberrations and the removal of reverberations. This method is based on the study of the reflection matrix that contains all the back-scattered wave-fronts for a set of incident waves. This matrix formalism captures all the available information on the medium and simply projects the recorded data in any plane where aberration correction or artifacts removal is optimal (plane wave basis, transducer plane, etc.).

Results/Discussion

Fig.1 displays the result of our matrix approach applied to breast phantom imaging. By back-propagating the recorded data to the focal plane, a reflection matrix between the received and transmitted focusing spots is built (Fig. 1 a-b). Compared to the ultrasound image, this matrix contains additional information that can be used for correcting aberrations. Moreover, it enables a direct and local measurement of the focusing quality. Fig.1 (c-d) shows the result of the aberration correction on breast phantom. The contrast and resolution of the corrected image are clearly improved. The presence of micro-calcifications that are relevant biomarkers for tumors detection is revealed.



9:15 AM

Experimental Cross –Talk reduction for 3D multi-line transmissionEmilia Badescu¹, Lorena Petrusca¹, Denis Friboulet¹, Hervé Liebgott¹¹*Université de Lyon, CREATIS ; CNRS UMR5220 ; Inserm U1206 ; INSA-Lyon ; Université Lyon 1, France***Background, Motivation, and Objective**

The necessity of frame rate enhancement is particularly important in 3D echocardiography since full-volume acquisitions at a quality comparable to 2D imaging require increasing the number of transmissions. Despite the potential of Multi Line Transmission (MLT) in providing high frame rates while preserving the image quality, this method has a non-negligible limitation: the presence of cross-talks artefacts. Several studies proposed interesting solutions as using a proper apodization (Tong, TUFFC 2013) or making use of the 2D transducer geometry (Ortega, TUFFC 2016), but due to the difficulty in implementing this technique in practice, the analysis was limited mostly to simulations. The objective of this study is the experimental validation of cross-talk reduction by replacing the typical alignment of the transmissions parallel to the element lines or columns by an alignment along the transverse diagonal of the transducer.

Statement of Contribution/Methods

The data was acquired using a Verasonics 1024-channels imaging platform synchronized as explained in (Petrusca, *Applied Sciences* 2018). A Vermon probe was used to transmit 8 simultaneous focused beams 128 times in order to acquire a 32 by 32 volume. The transmissions were distributed in diagonal for reducing the side lobe interactions which are the main cause of cross-talk artefacts. The results obtained by using the classical transmission scheme (Fig1 A) were compared to a diagonal transmission (Fig1 B) in order to evaluate the cross-talk reduction.

Results/Discussion

As shown in Figure 1, the diagonal transmission scheme (ii) provides favorable results in comparison with the classical transmission (i). The transmission cross-talks are reduced for both XZ plane (iii compared to v) and XY plane (iv compared to vi). For providing a quantitative analysis, we measured the difference between the main lobe and the side lobe level in the focal point placed at 5cm. For the XZ plane, the measured difference was 7.97 dB for the diagonal transmission while a difference of only 2.82 dB was found for the classical transmission. Similarly, a difference of 7.98 dB compared to only 2.82 dB was measured in the YZ plane. Therefore, the cross-talk level was reduced more than 2 times relative to the classical MLT case, while the frame rate was increased 8 times compared to the conventional 3D focus imaging.

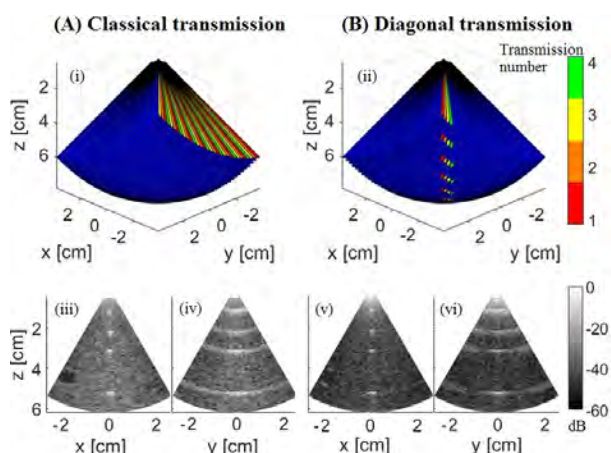


Figure 1. Transmission schemes and B-Mode images for a classical transmission (A) and a diagonal transmission (B)

3E - Advanced beamforming II

Emerald (280)

Wednesday, October 24, 10:30 am - 12:00 pm

Chair **Jeremy Dahl**
Stanford University

3E-1

10:30 AM Experimental Implementation of Resolution Enhancement Compression for Ultrasound Diverging Wave Compounding using a Tri-State Voltage Drive

Yanis Mehdi Benane¹, Denis Bujoreanu¹, Emilia Badescu¹, Roberto Lavarello², Hervé Liebgott¹, Christian Cachard¹, Olivier Basset¹

¹CREATIS, Univ.Lyon, INSA-Lyon, UCBL1, UJM-Saint Etienne, CNRS, Inserm, CREATIS UMR 5220, U1206, Villeurbanne, France, ²Laboratorio de Imagenes Medicas, Departamento de Ingenieria, Pontificia Universidad Católica del Perú, Lima, Peru

Background, Motivation, and Objective

Resolution Enhancement Compression (REC) improves the axial resolution of ultrasound images. It consists on emitting an amplitude modulated chirp signal that carries more energy at the frequencies where the ultrasound transducer is less efficient. Recent experimental implementations of REC on ultrasound scanners proved its advantages in comparison to conventional approaches, the only requirement being the capacity of the scanner to generate arbitrary waveforms. Here, we address the feasibility of REC excitation signals on an ultrasound scanner with a tri-state voltage drive in transmission, and show the first implementation of REC in Diverging Wave Compounding (DWC) ultrasound imaging on the platform Vantage 256.

Statement of Contribution/Methods

REC is based on the convolution equivalence showed in Eq.1. h_1 is the Impulse Response (IR) of the real probe, h_2 is the IR of the fictive probe having a larger bandwidth than h_1 and v_{lin} is a linear chirp that spans the full bandwidth of h_2 . The pre-enhanced chirp (v_{rec}) used as the excitation signal is calculated in the frequency domain. After emitting v_{rec} , the pulse compression on the received signals is performed with a modified Wiener filter (Eq.2), where γ (related to the power spectral density of the noise) can be tuned in order to adjust the trade-off between axial resolution and noise level. Nine diverging waves equally spaced between -30° and 30° (angular sector of 90°) are transmitted, received, compressed, beamformed and compounded. The results are compared to the Conventional DWC (C-DWC) imaging, where a short sinusoidal pulse is transmitted.

Results/Discussion

An overall better image quality is provided by REC-DWC (a) compared to C-DWC (b). These results are achieved by boosting the bandwidth of the probe by 46% using the proposed approach. An improvement of the axial resolution from 990.6 μm (C-DWC) to 679.2 μm (REC-DWC) is observed, in accordance with the bandwidth boost. As shown in (c), the penetration depth is higher for the proposed approach, a 15.4 dB brighter scatterer being measured at 11 mm depth for REC-DWC in comparison to C-DWC. The contrast to noise ratio measurements show gains of 2.11 dB (at 45 mm) and of 17.1 dB (at 115 mm) between REC-DWC and C-DWC. The enhanced image quality provided by the proposed approach proves the feasibility of REC excitation signals on ultrasound scanners with tri-state voltage drive.

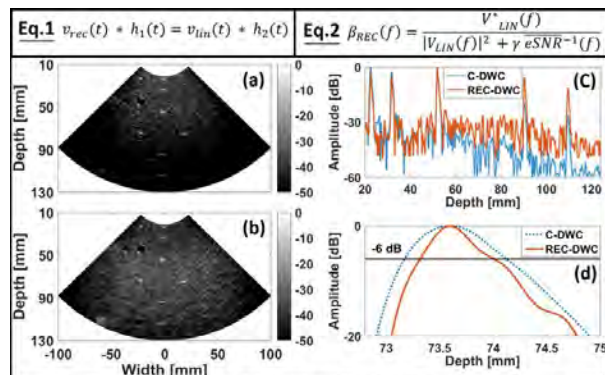


Figure: Obtained Bmode images with C-DWC (a) and with REC-DWC (b). (c) Vertical image line that passes through x=0mm. (d) Axial profile of the point spread function of the scatterer placed at (x = -22 mm, z = 74 mm).

10:45 AM

The Detection Probability of Adaptive Beamformers

Alfonso Rodriguez-Molares¹, Ole Marius Hoel Rindal², Jan D'hooge³, Svein-Erik Måsøy¹, Andreas Austeng⁴, Hans Torp⁵

¹Department of Circulation and Medical Imaging, and CIUS, Norway, ²Informatics, University of Oslo, Norway,

³Cardiovascular Sciences, KU Leuven, Leuven, Belgium, ⁴University of Oslo, Norway, ⁵Department of Circulation and Medical Imaging, and CIUS, Department of Circulation and Medical Imaging, and CIUS, Norway

Background, Motivation, and Objective

Many adaptive algorithms claim to provide higher contrast than delay-and-sum (DAS). These claims are often backed by estimations of the contrast-to-noise ratio (CNR). There are some discrepancies on how CNR is estimated, mostly due to the different nature of the algorithms and of their outputs.

Intuitively, we assume that higher CNR leads to higher probability of lesion detection, and this is indeed the case for DAS. However, non-linear processing can arbitrarily alter CNR values, and yet yield no improvement in the detection probability. The question, then, arises: do adaptive beamformers provide higher detection rate?

Statement of Contribution/Methods

We propose a new image quality index: the maximum success rate (MSR) given by the percentage of pixels that are successfully separated by a binary classifier, using an optimal threshold. Based on the statistics of speckle we derive an analytical expression for the MSR of DAS, as a function of the signal-to-noise-ratio (SNR). In practice, MSR can be estimated using hyper- or hypo- echoic regions on in vitro or in silico data. In that context the analytical solution for DAS can be used as reference.

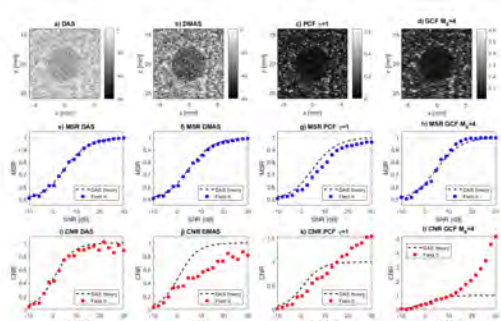
We estimate the detection probability of 4 beamforming algorithms: DAS, delay-multiply-and-sum (DMAS), phase coherence factor (PCF) with $\gamma=1$, and generalized coherence factor (GCF) with $M_0=4$. Using Field II simulations, we estimate the MSR for hypoechoic lesions embedded in uncorrelated Gaussian noise.

Results/Discussion

Figures a) to d) show the beamformed images for SNR=6.8 dB. Figures e) to h) show the estimated MSR. We observe a good agreement between DAS and its analytical solution. We observe that the three algorithms do not produce a significant improvement on MSR, being PCF slightly worse and GCF slightly better than DAS. Figures i) to l) show that two of the methods provide higher CNR than DAS, but only for SNR > 10 dB and without an impact on MSR.

This test can be applied to any algorithm, regardless of its nature or scale. The results below are only valid for speckle structures. The tested algorithms may perform better in the detection of coherent structures, such as single point scatterers.

These results put into question the relevance of contrast enhancement effects in some coherence-based beamforming algorithms. We believe the proposed index may be useful to review the significance of some of the metrics we take for granted.



11:00 AM Iterative ADMIRE for high dynamic range b-mode

Siegfried Schlunk¹, Kazuyuki Dei¹, Brett Byram²

¹Biomedical Engineering, Vanderbilt University, United States, ²Vanderbilt University, United States

Background, Motivation, and Objective

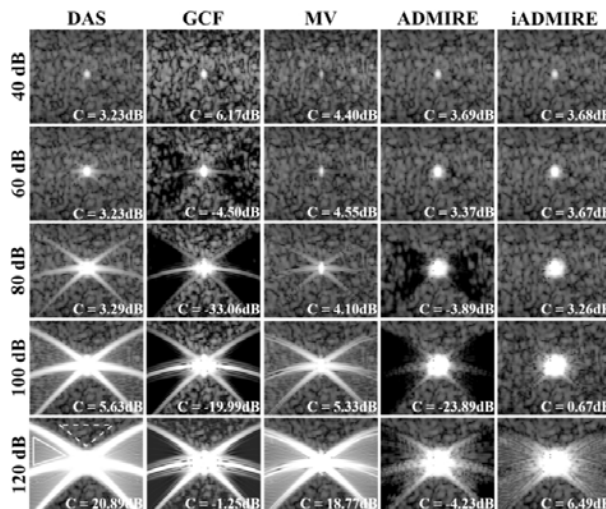
Some adaptive beamformers struggle with high dynamic range scenarios, as demonstrated by the occurrence of the dark region artifact (DRA), which can appear when these beamformers are applied in the proximity of strong acoustic sources such as kidney stones or near the lungs. Some have suggested that the DRA arises from a failure to differentiate mainlobe versus sidelobe signals. This is detrimental because the DRA may mask important features that are otherwise relatively weaker acoustically. In a previous paper, we used a version of our aperture domain model image reconstruction (ADMIRE) method that reduced the severity of the artifact but did not remove it completely. Here we introduce an iterative variant of ADMIRE (iADMIRE) that removes the artifact more effectively and across more cases, preserving the relatively weaker signals.

Statement of Contribution/Methods

iADMIRE estimates the clutter part of the signal in the elastic-net regularization step of ADMIRE and subtracts that clutter from the signal. This process is repeated until all detectable clutter is removed, which eliminates strong sidelobe clutter and allows for a better estimate of the region of interest. We applied delay-and-sum (DAS), generalized coherence factor (GCF, k=5), minimum variance (MV), ADMIRE, and iADMIRE to simulated channel data in cases with bright scatterers ranging from 0 dB up to 140 dB compared to the background speckle, with n=6 realizations for each case. All simulations were generated in Field II. The contrast of the DRA compared to the background speckle was calculated for each.

Results/Discussion

ADMIRE reduces the DRA in bright scatterer cases up 60 dB but did not fully mitigate the artifact in brighter cases. In comparison, iADMIRE was able to fully suppress the artifact in cases up to 100 dB. The included figure shows DAS plus the adaptive beamformers for bright scatterer cases from 40 dB to 120 dB on a 60 dB scale and the contrast of the DRA for each. For calculations, the DRA is indicated by the solid line and the background speckle is indicated by the dashed line. In cases up to 100 dB, iADMIRE was better than or equivalent to the other beamformers in maintaining a DRA contrast, and qualitatively it was able to completely preserve the speckle and suppress sidelobes in cases up to 100 dB. It was unable to fully preserve the speckle in the 120 dB cases, but these are unlikely to be encountered *in vivo*.



11:15 AM

Accelerating Nonlinear Speed of Sound Reconstructions Using a Randomized Block Kaczmarz AlgorithmAndreas Ihrig¹, Georg Schmitz¹¹Ruhr-University Bochum, Germany**Background, Motivation, and Objective**

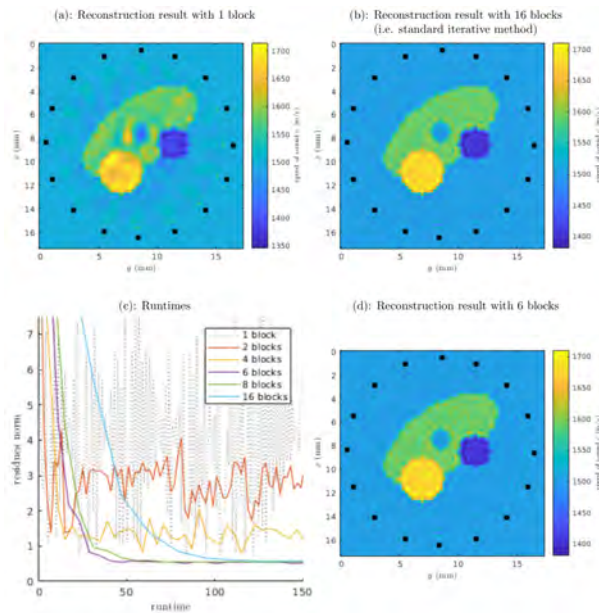
A main drawback of full waveform imaging methods is the high computational cost, associated with the non-linearity of those methods. Especially, the Kaczmarz method used for ultrasonic tomography (Hesse, Salehi, and Schmitz, 2013) suffers from long runtimes. Each reconstruction step of a sweep over all excitations solves the wave equation twice and is based on the preceding steps. Due to this iterative nature, those steps cannot be parallelized. Different approaches can be executed in parallel since the updates for all excitations are processed together. However, such methods converge slower. To achieve an acceleration, we propose using a block structured version of the Kaczmarz algorithm which can speed up the computation by finding a trade-off between both approaches. The different algorithms are compared, regarding imaging quality and execution times.

Statement of Contribution/Methods

The Kaczmarz algorithm (~, 1937) solves linear equation systems by iterative projections; in a randomized version (Strohmer and Vershynin, 2009), this method converges exponentially. Here, the randomized block Kaczmarz method (Needell and Tropp, 2014) is used. Instead of computing each projection separately, it combines subsets of the equation system and projects them onto sub-hyperspaces. The subsets, or blocks, are chosen randomly to maintain exponential convergence. We performed ultrasonic tomography reconstructions with a 16-elements ring transducer around a numeric object (Fig. (a), (b), (d)) and compared the reconstruction errors vs. estimated runtimes (Fig. (c)). For this comparison, the 16 transducer elements were split into different block sizes.

Results/Discussion

The reconstruction quality depends on the block size as shown by the achieved residues norm (Fig. (c)). As noted in Fig. (a), the reconstruction with 1 block (all 16 elements together) converges to a result only close to the standard Kaczmarz (16 blocks or 1 element per block; Fig. (b)). However, a comparable quality is reached by the 6 (and 8) blocks results (Fig. (d)). The computational effort in this case is about 2.4 times lower because the reconstruction converges much earlier. Here, we assume a full parallelization of the wave simulations. Thus the randomized block Kaczmarz algorithm enables partial parallelization and reduces the runtime by a factor of more than two.



11:30 AM High Frequency Ultrasonic Tomography Using Optimal Transport Distance

Andreas Ihrig¹, Georg Schmitz¹¹Ruhr-University Bochum, Germany**Background, Motivation, and Objective**

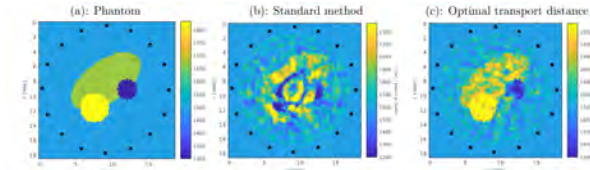
Ultrasonic tomography is known to suffer from the so called “cycle skipping” (Natterer, 2008). It describes the effect of a phase shift of more than 2π . This phase shift between measured and calculated signals depends on the center frequency and the speed of sound deviations of the measured object. For high phase shifts, the underlying least square based descent gradient approach tends to run into a local minimum. To circumvent this problem, frequency filtering methods have been proposed (Ihrig and Schmitz, 2017). Though, those approaches filter high frequency parts of the signal and are therefore restricted by the SNR and the systems bandwidth. In the field of seismic imaging, the optimal transport distance was used as an alternative to the least square approach (Métivier et al., 2016). We applied this technique to ultrasonic tomography. This contribution shows first reconstruction results.

Statement of Contribution/Methods

With the optimal transport distance, the error functional used as minimization criterion has no local minima anymore. Thereby the “cycle skipping” problem is avoided, i.e. the non-convex problem is replaced by a convex one. The calculation of the optimal transport distance is an optimization problem which is solved with a proximal splitting technique. We combined this approach with the Kaczmarz method where the solution of the optimization problem is used as the adjoint wavefield. The shown results are computed using a setup with a 16-elements transducer in circular arrangement around a numeric object (Fig. (a)). The signals center frequency was set to 1.5 MHz.

Results/Discussion

The chosen phantom induces a large phase shift of more than 6π ($\approx 2\pi$). Using the optimal transport distance, the Kaczmarz algorithm reconstructs this phantom, see Fig. (c). In comparison, the standard approach results in a local minimum only roughly showing the phantom borders and including wrong speed of sound values (Fig. (b)). We expect the convergence of this modified technique not to depend on the maximum signal center frequency anymore. Though, the computation is memory intensive which could be a limiting factor.



11:45 AM REFoCUS: Ultrasound focusing for the software beamforming age

Nick Bottenuus¹

¹*Biomedical Engineering, Duke University, Durham, NC, United States*

Background, Motivation, and Objective

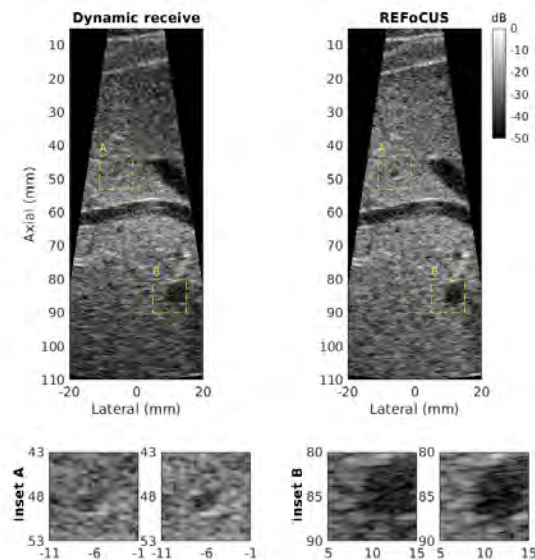
The evolution of ultrasound beamformers with increased parallel processing power has significantly improved diagnostic image quality. Traditional dynamic receive focused images suffered from a limited depth of field and low signal-to-noise ratio (SNR). The advent of synthetic transmit aperture beamforming has helped to overcome these issues by coherently combining the backscattered data from multiple transmissions in a sequence. However, synthetic aperture methods are fraught with details of the spatial beam distribution and assumed propagation geometry. In the case of focused beams, they also offer limited spatial overlap in which to perform adaptive transmit processing. Such focused transmissions are required to produce the harmonic signal that modern clinical imaging relies on to suppress acoustic clutter.

Statement of Contribution/Methods

Retrospective Encoding For Conventional Ultrasound Sequences (REFoCUS) overcomes these limitations using an element-based model to decompose a sequence of steered or translated transmissions into individual element contributions. These recovered signals can then be used to produce a synthetically focused image or for adaptive transmit aperture processing. I demonstrate the use of this technique for recovery of the effective transmit sources of the fundamental and harmonic backscattered signals. Experimental data were collected using the Verasonics Vantage 256 ultrasound system in phantom and in vivo targets. In addition to offline processing, online implementation is evaluated using an efficient approximate decoding method. The harmonic content of plane wave and focused transmissions are also compared using the REFoCUS decomposition.

Results/Discussion

REFoCUS successfully decomposes the harmonic backscattered signals from a transmit sequence into the effective source element contributions – the source aperture that would result at each depth from a linear backpropagation of the nonlinearly generated pressure field. In vivo harmonic images show improved depth of field and SNR across a variety of imaging environments, although some images show evidence of degradation from motion or acoustic clutter. The proposed efficient implementation of REFoCUS is computationally tractable with little compromise in image quality.



3F - Super Resolution Microbubble Imaging

Emerald (280)

Wednesday, October 24, 1:30 pm - 3:00 pm

Chair **Mickael Tanter**
INSERM

3F-1

1:30 PM

Deep-ULM: Super-resolution Ultrasound Localization Microscopy through Deep Learning

Ruud J. G. van Sloun¹, Oren Solomon², Matthew Bruce³, Zin Z Khaing³, Hessel Wijkstra⁴, Yonina Eldar², Massimo Mischi¹

¹Eindhoven University of Technology, Eindhoven, Netherlands, ²Technion, Haifa, Israel, ³University of Washington, Seattle, WA, United States, ⁴Academic Medical Center - University of Amsterdam, Netherlands

Background, Motivation, and Objective

Ultrasound localization microscopy has enabled super-resolution vascular imaging in laboratory environments through precise localization of individual ultrasound contrast agents across numerous imaging frames. However, analysis of high-density regions with significant overlaps among the agents' point spread functions (PSFs) yields high localization errors, constraining the technique to low-concentration conditions. As such, long acquisition times are required for sufficient coverage of the vascular bed. Algorithms based on sparse recovery have been developed specifically to cope with the overlapping PSFs of multiple microbubbles. While successful localization of densely-spaced emitters has been demonstrated, even highly optimized fast recovery techniques involve a time-consuming iterative procedure. In this work, we present a fast and precise method for obtaining super-resolution vascular images from high-density contrast-enhanced ultrasound imaging data based on deep learning.

Statement of Contribution/Methods

This method, which we term Deep Ultrasound Localization Microscopy (Deep-ULM), exploits modern deep learning strategies and employs a neural network to perform localization microscopy in dense scenarios. We adopt a fully convolutional architecture that consists of an encoder network which captures essential image information into a latent feature layer, and an expanding decoder network which maps this latent representation to precise localizations on a high-resolution grid. The network is trained using simulations of low-resolution ultrasound inputs and super-resolved targets. A sufficiently complete and representative dataset is formed by introducing many factors of variation (e.g. PSF model, concentration, backscatter, noise) during training.

Results/Discussion

We show that Deep-ULM attains super-resolution with challenging contrast-agent concentrations both in-silico and in-vivo, as we span from ultrasound scans of a rodent spinal cord in an experimental setting (see Figure 1) to standard clinically-acquired recordings in a human prostate. Deep-ULM achieves high quality sub-diffraction recovery, and is suitable for real-time applications, resolving about 2500 high-resolution 64x64-patches per second exploiting GPU acceleration.

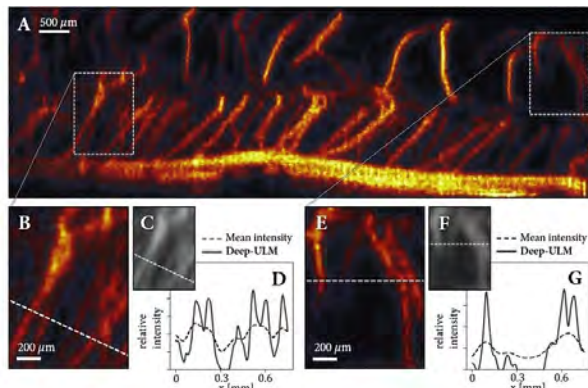


Figure 1. *In-vivo* Deep-ULM in a rat spinal cord. (A) Deep-ULM across 700 frames acquired at a frame rate of 400 Hz. (B, E) Close-ups of selected areas in the image and corresponding (C, F) mean intensity images. (D, G) Intensity profiles of the dashed-lines indicated in the close-ups. Deep-ULM achieves super-resolution beyond the diffraction limit.

1:45 PM

A Systematic Investigation of Microbubble Spatial Sampling Requirement and Microbubble Localization Methods for Super-resolution Imaging

Pengfei Song¹, Armando Manduca², Joshua Trzasko¹, Ron Daigle³, Shigao Chen¹

¹Department of Radiology, Mayo Clinic, Rochester, MN, United States, ²Department of Physiology and Biomedical Engineering, Mayo Clinic, Rochester, MN, United States, ³Verasonics Inc., United States

Background, Motivation, and Objective

Microbubble (MB) localization is a key step in super-resolution (SR) imaging, which involves using MB data sampled at a lower resolution grid to determine MB locations at a higher resolution grid. Accurate MB localization relies on a combination of robust localization processing methods and adequate spatial sampling resolution. The objective of this study is two-fold: 1) to systematically compare the performance of different MB localization methods at different SR imaging spatial resolutions; 2) to establish the minimum requirement for MB spatial sampling that yields minimal quantization error, so that SR data acquisition can be optimized with minimal computational load and overhead associated with beamforming and data storage.

Statement of Contribution/Methods

Seven MB localization methods (Table I) that are commonly used in SR imaging were studied, including methods that are based on the centroid and the peak intensity of the MB signal, and by parametric fitting (e.g., Gaussian) of the MB data. A Verasonics Vantage system was used to beamform the same sets of channel data at different spatial resolutions to study the effect of quantization error. The first part of the study was conducted on a 20 μm diameter wire target submerged in water, with wire movement finely controlled by a scanning stage. The second part of the experiment was conducted with a Gammex flow phantom and Lumason MB at a constant flow rate of 1.6 cm/s.

Results/Discussion

Table I summarizes the localization error of the wire target using different localization methods and spatial sampling resolutions. Fig. 1 shows selective SR images obtained from different methods at the lowest sampling resolution of 1 λ. These results indicate that parametric Gaussian fitting and centroid-based localization on upsampled (interpolation to 0.05 λ resolution) data have better overall MB localization performance and were less susceptible to quantization error than peak intensity-based localization methods. When spatial sampling is low, parametric Gaussian fitting has the best performance in suppressing quantization error, and could produce acceptable SR images with no significant gridding artifacts (Fig. 1). We also found that (results not shown) the Fourier analysis of an oversampled spatial profile of the MB signal could provide reliable guidance for selecting the proper spatial sampling resolution for SR imaging.

Table I. Summary of root-mean-square error (RMSE) of localization at different spatial sampling resolutions ($1\lambda \approx 0.17$ mm at 8.929 MHz center frequency)

| Axial quantization error (μm) | 0.25 λ | 0.5 λ | 1 λ |
|--|--------|-------|-------|
| Original data (no upsampling) and peak detection | 12.10 | 48.14 | 62.58 |
| 2D cubic interpolation and peak detection | 3.68 | 8.80 | 46.58 |
| 2D spline interpolation and peak detection | 3.27 | 5.37 | 42.64 |
| Original data (no upsampling) and centroid detection | 2.62 | 3.48 | 10.78 |
| 2D cubic interpolation and centroid detection | 2.66 | 2.53 | 11.00 |
| 2D spline interpolation and centroid detection | 2.66 | 2.51 | 12.49 |
| 2D Gaussian fitting | 3.54 | 4.20 | 6.27 |

| Lateral quantization error (μm) | 0.25 λ | 0.5 λ | 1 λ |
|--|--------|-------|-------|
| Original data (no upsampling) and peak detection | 20.62 | 35.96 | 74.40 |
| 2D cubic interpolation and peak detection | 8.80 | 12.67 | 22.48 |
| 2D spline interpolation and peak detection | 8.70 | 6.73 | 10.98 |
| Original data (no upsampling) and centroid detection | 3.69 | 8.06 | 12.78 |
| 2D cubic interpolation and centroid detection | 1.70 | 1.38 | 6.95 |
| 2D spline interpolation and centroid detection | 1.77 | 1.51 | 5.33 |
| 2D Gaussian fitting | 4.19 | 4.23 | 3.85 |

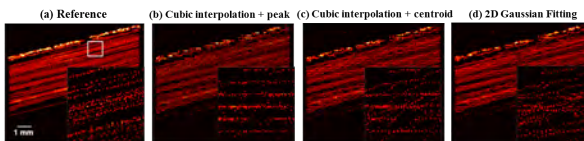


Figure 1. Super resolution (SR) vessel density images of the flow channel obtained from different microbubble localization methods (b-d, localization methods indicated in the subtitles). The axial and lateral beamforming resolution was both 1 λ (≈ 0.17 mm at 8.929 MHz center frequency). For each SR image, a magnified view of a small region inside the channel was displayed (as indicated by the white box in the top left image). For the reference data in (a), direct microbubble localization was performed on oversampled data at 0.1 λ spatial resolution.

2:00 PM

Assessment of Diabetic Kidney Disease Using Ultrasound Localization Microscopy on the Microvasculature in a Rat Kidney: An *in vivo* Feasibility Study

Yi Yang¹, Qiong He¹, Hong Zhang², Lanyan Qiu², Linxue Qian², Jianwen Luo¹

¹Department of Biomedical Engineering, Tsinghua University, Beijing, China, People's Republic of, ²Department of Sonography, Beijing Friendship Hospital, Beijing, China, People's Republic of

Background, Motivation, and Objective

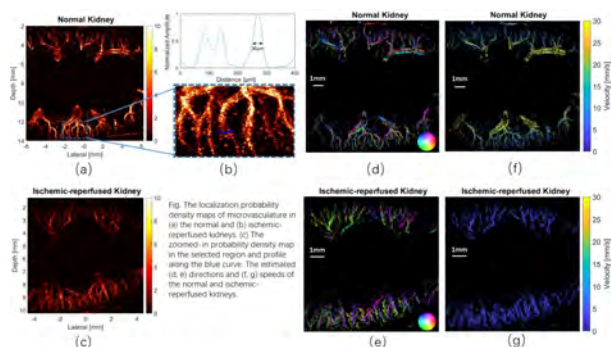
Diabetes mellitus is an incident and fateful disease. Kidney microvasculature changes with the deterioration of diabetic kidney disease (DKD). However, it cannot be observed by conventional ultrasound imaging because of diffraction limit. Recently, this limit was broken by ultrasound localization microscopy (ULM), which can obtain the microvasculature and estimate the blood flow velocity by localizing and tracking the flowing microbubbles. In this study, a comparison of microvascular morphology and velocity map between a normal rat kidney and an acute ischemic-reperfused rat kidney model was performed *in vivo* to validate the feasibility of ULM in evaluation of DKD.

Statement of Contribution/Methods

After anesthesia and open abdominal surgery, the renal artery of a normal rat was ligated by 45 minutes and then reperfused for 10 minutes, followed by data acquisition. Another normal rat served as the control. A bolus of 100 μ L microbubble (SonoVue) solution was diluted with saline by 1:9 and injected to the tail vein. 20 second after injection, a Verasonics Vantage system with an L20-10 probe was used to acquire the data transabdominally and *in vivo*. 6000 frames of 5-angle coherent compounding plane-wave images were acquired at PRF of 2 kHz for 15 seconds. After DAS beamforming, motion correction was applied to minimize the influence of breathing and heart beating. Thereafter, singular value decomposition (SVD) based spatiotemporal filtering was used to extract the microbubbles from the surrounding tissues. The individual microbubbles were localized by their weighted centroids. Finally, a localization density map with super-resolution was obtained by accumulating all the centroids. The blood flow direction and speed were estimated by tracking the microbubbles between adjacent frames.

Results/Discussion

More than 160k and 70k microbubble events were detected to form the localization probability density maps of the microvasculature in the normal and ischemic-reperfused kidneys, respectively (Figs. a and b). A resolution of 36 μ m was achieved (Fig. c). Blood flow directions (Figs. d and e) and speeds (Figs. f and g) were estimated. The blood flow speeds in the ischemic-reperfused kidney (typically < 10 mm/s) are much lower than those in the normal kidney (~ 30 mm/s). The *in vivo* feasibility of ULM in evaluation of DKD is thus validated.



2:15 PM Performance of Foreground-Background Separation Algorithms for the Detection of Microbubbles in Super-

Resolution Imaging

Marion Piepenbrock¹, Stefanie Dencks², Georg Schmitz²

¹Ruhr-University Bochum, Bochum, Germany, ²Ruhr-University Bochum, Germany

Background, Motivation, and Objective

For super-resolution imaging, the precise detection of microbubbles (MB) and the correction of their positions concerning tissue motion is fundamental. Preferably, the ultrasound sequence is separated into foreground for MB detection and background for tissue motion estimation. Recently, several techniques for the separation have been proposed, covering singular value decomposition (SVD) [1,2], rank filtering and spatiotemporal non-linear mean filtering (stNLM) [3]. In this contribution, we compare their performances in simulations of different motion types.

Statement of Contribution/Methods

A phantom with five vessels, flown through by individual rates, was simulated with the toolbox Field II. It is divided into three regions of different contrast-to-noise ratios of single MB ($CNR_1 = 30$ dB, $CNR_2 = 21$ dB, and $CNR_3 = 7$ dB) by varying the background. Further, three different scenarios of in-plane tissue motion were simulated: a periodic motion (**pm**), a periodic motion with simultaneous transducer displacement (**pdm**), and an aperiodic motion (**apm**). The maximal displacement from frame to frame was $6 \mu\text{m}$. For each scenario, the SNR was varied ($SNR_1 = 15$ dB, $SNR_2 = 20$ dB, $SNR_3 = 25$ dB).

For the extraction of foreground from the background, four approaches were applied: A rank filter, the stNLM [3], and two SVD based methods. The threshold for the singular values (SV) to separate tissue from MB was dependent on either the ratio of MB to tissue signal (SVD_1) [1], or on the covariance matrix of spatial singular vectors (SVD_2) [2]. Then, the MB were detected using the foreground, and the probability of false positive detections p_F and true positive detections p_T , were evaluated. The tissue motion was estimated by applying an optical flow algorithm to the background [4], and was compared to the ground truth by the absolute difference d .

Results/Discussion

The MB detection performance decreases with decreasing CNR and SNR. The SVD_2 is excluded for detection because it showed an insufficient $p_T = 0.4$ for the highest CNR. The other three methods led to similar $p_T = 0.98\text{-}1.0$ (CNR_1) for all motion types. However, the number of false detections varied. For **pm**, all three methods reached a p_F less than 0.02. For **pdm** and **apm**, p_F persists low after stNLM, but increases to $p_F = 0.25$ when applying SVD_1 . Rank filtering ranged between SVD_1 and stNLM. As a result, stNLM showed overall the best performance, and SVD_1 had weaknesses for aperiodic motion (**pdm & apm**).

For motion estimation, SVD_1 led to the largest maximum deviations, e.g. $d = 3.1 \mu\text{m}$ for **pdm**. The other three methods enable a more precise estimation, while rank filtering yields to the best result with $d = 0.8 \mu\text{m}$.

Summarizing, stNLM leads to the best performance, averaged over both applications. Nevertheless, we propose to combine stNLM for detection and rank filtering for motion estimation to increase the performance by exploiting the potential of each method.

[1] Demené et al., 2015.

[2] Arnal et al., 2016.

[3] Song et al., 2018.

[4] Dirks, 2016.

2:30 PM

Improved super-resolution by exploiting microbubble kinematics in ultrasound imagingOren Solomon¹, Ruud J. G. van Sloun², Hessel Wijkstra³, Massimo Mischi², Yonina Eldar¹¹*Technion, Haifa, Israel*, ²*Eindhoven University of Technology, Netherlands*, ³*Academic Medical Center - University of Amsterdam, Netherlands***Background, Motivation, and Objective**

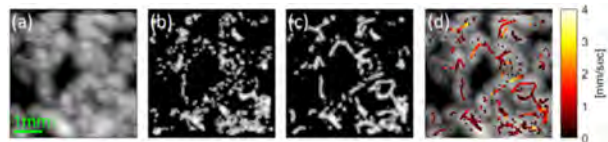
Ultrasound localization microscopy offers new radiation-free diagnostic tools for vascular imaging deep within the tissue. Despite its high spatial resolution, low microbubble (MB) concentrations dictate long acquisition periods, undesirable in many clinical scenarios. Recently proposed sparsity-based approaches reduce the total acquisition time, while maintaining good spatial resolution in settings with considerable overlap of the microbubble point spread functions. Here, we further improve sparsity-based super-resolution ultrasound imaging by exploiting *a-priori* knowledge on MB flow and kinematics. While doing so, we also provide quantitative measurements of MB velocities.

Statement of Contribution/Methods

CEUS data of a human prostate was acquired at the AMC university hospital, using a transrectal ultrasound probe and an iU22 scanner operating in a contrast-specific mode at a frame rate of 10 Hz. A 2.4-mL MB bolus of Sonovue was administered intravenously, and 150 frames (15 s) were collected for further analysis. Sparse recovery was performed on the first frame. Then, a Kalman filter was used to predict the MBs state to the next frame, including position and velocity. MBs velocities were initialized using optical flow (OF) estimation on the low-resolution frames. OF estimation over consequent frames served as the velocity measurements for state estimation. Using the estimated state error covariance matrix, a probability map of the predicted MB positions was then calculated and subsequently used for weighting the sparse recovery process of the next frame. Finally, automatic association of new measurements to existing MB tracks was performed using the multiple hypothesis tracking algorithm.

Results/Discussion

Panel (a) shows the maximum intensity projection (MIP) image. Panel (b) displays non-weighted sparsity-based reconstruction, after the accumulation of all localizations. Panel (c) displays the output of the proposed method of simultaneous localization and tracking of individual bubbles. Lastly, panel (d) corresponds to an overlay of the sub-diffraction MB trajectories over the MIP image, also displaying the estimated velocity magnitudes. Compared to a non-weighted sparse recovery, the proposed method achieves clearer and smoother depiction of the vascular bed, and it also provides quantitative information.



2:45 PM

What is the Resolving Power of Ultrasound Localization Microscopy? - Systematic Analysis Using a New Forked Microvessel Phantom Design

Hanyue Shangguan¹, Billy Y. S. Yiu¹, Adrian J. Y. Chee¹, Alfred C. H. Yu¹

¹Schlegel-UW Research Institute for Aging, University of Waterloo, Waterloo, ON, Canada

Background, Motivation, and Objective

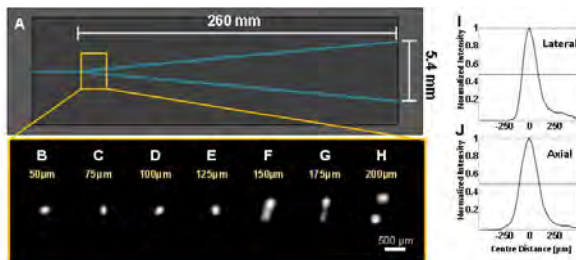
Ultrasound localization microscopy (ULM) has been demonstrated to resolve microvascular features on micron scale using contrast agents. However, the capability for ULM to resolve two flow channels at close proximity has yet to be systematically evaluated. Existing phantoms are usually straight microtubes and are incapable of calibrating vessel resolvability. Here, we propose the construction of a forking flow phantom that facilitates imaging at varying vessel separation distances that is adjusted by transducer placement. The system's vessel resolvability can hence be tested through the direct comparison of vessel separation resolved under ULM against the expected separation of the forked channels.

Statement of Contribution/Methods

Two flow channels with increasing separation were created by mounting 200 μm nylon wires in a 3D printed box drafted using Solidworks. The wires were positioned in a "Y" configuration (see Fig. A) kept in tension using attached weights on the forked outlet and secured to a common inlet. Agar was then casted as tissue mimic and microvessels were created upon wire retrieval. Microbubbles (USphere Prime, Trust Bio-Sonics) were diluted and gravity fed into the lumen. Imaging was done using a SonixTouch scanner with L14-5 array (plane wave Tx: -10° to 10° in 5° interval; 5 MHz; 3-Cycle; 5 kHz PRF; 4 sec acquisition). The probe was adjusted during acquisition using a micro-positioner stage to be perpendicular to the phantom and positioned where the lumens were 50 to 200 μm apart at 25 μm intervals. To localize the microbubbles, a normalized cross-correlation algorithm was applied to the compounded images.

Results/Discussion

Microvessels were inseparable when they were less than 150 μm apart (see Fig. B-E). Although the profile of two microvessels was noticeable at 150 μm separation (Fig. F), the individual vessels were indistinguishable. True separation was only observed for microvessels beyond 175 μm apart (Fig G & H). In Fig. I, we plotted the cross lumen profile for the top vessel of Fig H. The lumen size was measured at FWHM in both axial and lateral dimensions. Additionally, the average vessel diameter measured over each individualized lumens was $205 \pm 10 \mu\text{m}$. These results demonstrated the capacity of our phantom to evaluate new algorithms for microvessel imaging, especially for ULM.



3G - Super Resolution and Contrast Brain imaging

Emerald (280)

Wednesday, October 24, 4:00 pm - 5:30 pm

Chair **Nico de Jong**
Erasmus Medical Centre

3G-1

4:00 PM

Deep Transcranial Ultrasound Localization Microscopy of the adult human brain vascularization

Charlie Demene¹, Liene Puke², Justine Robin^{1,2}, Baptiste Heiles¹, Vincent Hingot¹, Olivier Couture¹, Mathieu Pernot¹, Fabienne Perren-Landis², Mickaël Tanter¹

¹Institut Langevin, ESPCI Paris, PSL Research University, CNRS UMR 7587, INSERM U979, PARIS, France, ²Clinical Neuroscience Department, LUNIC (Laboratory of Ultrafast-ultrasound Neuroimaging in Clinics), Université de Genève, Hôpitaux Universitaires de Genève, Switzerland

Background, Motivation, and Objective

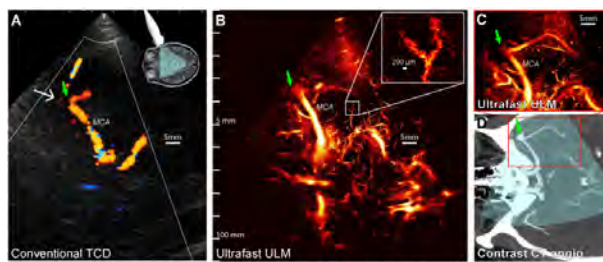
Human brain vascular imaging is very challenging across modalities as it usually requires contrast injection, ionizing (CT) or expensive (MRI) imaging devices. It is however widely practiced in clinics and key for management of cerebrovascular and neurological pathologies. It often eludes the blood flow time-dynamics and gives limited resolution (CT 0.6 mm, MRI 1 mm). Ultrasound (US), conversely, is poorly used for neuroimaging due to limited sensitivity and resolution at transcranial low frequencies. Recently US Localization Microscopy (ULM) [1] increased by almost two orders of magnitude the resolution for vascular US imaging in animals. Combined here with diverging wave transmissions, skull aberration corrections and tissue motion compensation, we show for the first time that ULM is readily achievable for clinical neuroimaging.

Statement of Contribution/Methods

Experiments complied with the Declaration of Helsinki and patients gave informed and written consent (protocol 2017-00353 Geneva CCER). Boluses of 0.3 mL of contrast agent (Sonovue) were administrated intravenously while imaging through the temporal window with a 3-MHz phased array (pitch 0.2 mm) and an Aixplorer ultrasound scanner. Ultrafast US sequences consisted in 4 diverging waves [2] fired at 4800 Hz, repeated at 800 Hz during 1s, looped every 4s, during 2 minutes. Tissue was filtered out by singular value decomposition, aberration corrections were calculated on isolated bubbles RF signatures and integrated in the beamforming, before motion compensation via speckle tracking. Geometric centers of bubbles were found using spline interpolation, tracked using Hungarian algorithm, and used to generate super-resolved images.

Results/Discussion

At typical f-numbers >4 in transtemporal imaging, theoretical US resolution is diffraction-limited to ~3 mm lateral and ~0.8 mm axial. Here we show that vascular beds with ~100-μm diameter can be delineated in the brain at depth >80 mm, largely beating the diffraction limit (x30) and resolution of other clinical modalities. Microbubbles motion speed can be computed based on efficient tracking. We show first clinical examples of small aneurysms invisible with regular US and fine vascular structures undetectable with any other neuroimaging modality. ULM could become a real game changer for neuroimaging and the management of cerebro-vascular diseases.



A Conventional transcranial color Doppler of a patient presenting a small (<3 mm) aneurysm on the right MCA (middle cerebral artery). The aneurysm is not visible and the overall image presents poor sensitivity. B Ultrasound localisation microscopy in the same field of view. Sensitivity and resolution are largely increased, depicting very small vessels (down to <200 μm). The aneurysm is slightly visible as an outgrowth of the visible section of the MCA (green arrow). C ULM in a slightly different plane, showing 2nd segment of the MCA and contrast take-in in the aneurysm. Very small vessels are also depicted. D Corresponding CT-angiogram: sensitivity to small vessels is much lower when using ULM and only the main branches are visible. Aneurysm location is confirmed.

[1] Ercole et al, Nature, 2015

[2] Papadacci et al, IEEE Transactions on Ultrasonics, Ferroelectrics, and Frequency Control, 2014

4:15 PM

Ultrafast Volumetric Ultrasound Localization Microscopy *in vivo*

Baptiste Heiles¹, Claire Rabut¹, Vincent Hingot¹, Line Rahal¹, Pauline Lopez^{1,2}, Mathieu Pernot¹, Mickaël Tanter¹, Olivier Couture¹

¹Institut Langevin, ESPCI Paris, PSL Research University, CNRS UMR 7587, INSERM U979, PARIS, France, ²Institut Cochin, INSERM U1016, France

Background, Motivation, and Objective

Inspired by FPALM in optics and exploiting ultrafast ultrasound imaging, ultrafast Ultrasound Localization Microscopy (ULM) allows the reconstruction of a full velocity map of the rat brain vasculature in 2D with a micrometric resolution ($8\text{ }\mu\text{m}$) [Errico et al. Nature, 2015]. Despite additional successes for tumour imaging [Lin et al. Theranostics, 2017], this plane-by-plane technique suffers from minute-long acquisitions, out-of-plane microbubble and tissue motion which cannot be corrected for [Hingot et al. Ultrasonics 2017] and the loss of information due to the projection of a 3D vascular structure into a 2D image. We previously proposed the use of an isotropic matrix array for 3D *in vitro* superresolution imaging at high frame rates. We present here the first applications of this process *in vivo*.

Statement of Contribution/Methods

The 2D matrix array with 1024 elements arranged in a 32x32 isotropic plane was controlled by the customised programmable 1024-channel system presented in [Provost et al. 2014]. Sprague Dawley rats underwent craniotomy surgery. Sonovue microbubbles were injected through a catheter in boli of 0.2mL while a Ketamine-Domitor solution was perfused. The brain was insonified with 9MHz plane waves inclined at 12 different angles with a compounded frame rate of up to 500 Hz. A 3D ULM process previously described [Heiles et al, submitted] was used to determine the position of the bubbles, track them and measure their velocities.

Results/Discussion

After implementation of this technique on 99900 volumes, a volumetric rendering of rat brain microvasculature was obtained (figure 1). At 9MHz, the conventional resolution with this 2D array is around $250\mu\text{m}$. The theoretical resolution obtainable with the technique proposed here is $5\text{ }\mu\text{m}$ in axial direction and $48\text{ }\mu\text{m}$ in lateral and elevational directions. Trajectories calculated allowed to yield velocity fields in microvessels of a few cm/s. Volumetric ULM allows to surpass the conventional resolution in 3 dimensions in a large volume with only 200s of acquisitions, however, the limited sensitivity of 2D matrix arrays, the data size, computation and transfer times remain major challenges.

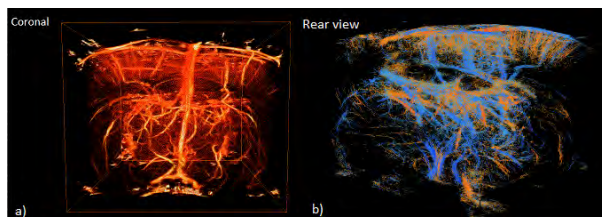


Figure 1. 3D rendering of rat brain after volumetric ULM on 99900 images acquired at 500Hz compounded volume rate
 a) Density of microbubbles
 b) Velocimetry (blue towards bottom, red towards top)

4:30 PM

In vivo 3D imaging of lymph nodes via high frame rate contrast enhanced ultrasound and super resolution

Jiaqi Zhu¹, Ethan Rowland¹, Chee Hau Leow¹, Sevan Harput¹, Kai Riemer¹, Karina Cox², Kirsten Christensen-Jeffries³, Ge Zhang¹, Jemma Brown³, Chris Dunsby⁴, Robert Eckersley³, Peter D. Weinberg¹, Mengxing Tang¹

¹Bioengineering, Imperial College London, London, United Kingdom, ²Surgery, Maidstone and Tunbridge Wells NHS Trust, London, United Kingdom, ³Biomedical Engineering Department, School of Biomedical Engineering and Imaging Sciences, King's College London, United Kingdom, ⁴Physics and Centre for Pathology, Imperial College London, London, United Kingdom

Background, Motivation, and Objective

The presence of metastases in tumour-draining lymph nodes (LN) remains an important marker of patient prognosis, but current imaging techniques in clinical use are generally poor at detecting them. Contrast enhanced ultrasound (CEUS) is a useful test to map lymphatic drainage in patients with breast cancer (Cox et al 2017). It has the potential to visualise malignant changes within individual LN. Morphological and functional disturbances occur in both lymphatic channels and blood vasculature before the onset of LN metastases, and ultrasound super resolution (SR) techniques have enabled non-invasive visualisation of sub-wavelength microvasculature and quantification of flow. The aim of this study is to demonstrate the in vivo feasibility of 3D reconstruction of complex LN vasculature via high frame rate (HFR) CEUS and ultrasound SR.

Statement of Contribution/Methods

An in vivo study was carried out to image popliteal LNs of New Zealand rabbits. To perform 3D HFR CEUS acquisition, a Verasonics system was synchronised with a mechanical scanning system to translate a 1D array transducer (L22-14v) along the elevation direction, covering 1.5 mm with a 100-μm step size. For each scanning position, 1200 plane wave B-mode images (18MHz, 15-angle compounding, 500 Hz) were acquired.

To increase image contrast, a spatio-temporal coherence technique, ASAP (Staniola et al. 2018), was used to suppress noise in the images after the SVD-based clutter filtering process. Individual microbubbles were subsequently identified (Christensen-Jeffries et al. 2015) to form a super-resolved 3D reconstruction of the LN vasculature.

Results/Discussion

Fig. 1A shows the original B-mode image acquired from single 2D slice with the red contour denoting the outline of the LN. In Fig. 1B, the intra-nodal vessels are clearly visualised and reconstructed in 3D after ASAP processing. Fig. 1C shows the maximum intensity projection of the SR images. The in vivo SR imaging method can resolve the microvasculature in the LN.

In conclusion, in vivo volumetric microvascular imaging of LN by a combination of HFR, CEUS and SR techniques has been demonstrated. The 3D reconstruction of LN vasculature offers the opportunity to detect early metastatic changes by revealing morphological and functional changes in the microvasculature prior to tumour cell invasion and architectural distortion.

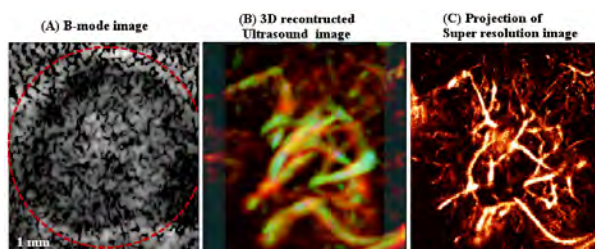


Fig. 1 HFR CEUS imaging of rabbit popliteal lymph node (A) original B-mode image at single slice, dynamic range: 40 dB (B) 3D vascular reconstruction from ASAP, (C) MIP of super resolution images. Scale bar: 1mm.

4:45 PM

Gas vesicles as hemodynamic enhancers for noninvasive functional ultrasound imaging of the mouse brain

David Maresca¹, Thomas Payen², Audrey Lee-Gosselin¹, Bill Ling¹, Dina Malounda¹, Charlie Demené², Thomas Deffieux², Mickaël Tanter², Mikhail Shapiro¹

¹California Institute of Technology, United States, ²Institut Langevin, ESPCI Paris, PSL Research University, CNRS UMR 7587, INSERM U979, France

Background, Motivation, and Objective

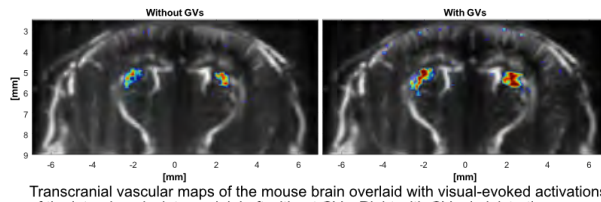
Recently, genetically encodable ultrasound contrast agents known as gas vesicles, or GVs, were introduced as ultrasound analogs to green fluorescent proteins [Bourdeau, *Nature* 2018]. These air-filled proteins can be purified to be used as nanoscale injectables in the blood stream. The analysis of their physical properties revealed that single GVs scatter ultrasound 3 times more strongly at 20 MHz than a red blood cells despite being 4000 times smaller. Unlike microbubbles, GVs are monodisperse, nanoscale, and inherently stable structures in equilibrium with their surroundings. Here, we assessed the performance of GVs as smooth hemodynamic enhancers for transcranial functional ultrasound imaging (fUS) of the brain in mice.

Statement of Contribution/Methods

fUS imaging was performed with a programmable ultrasound system connected to a 15 MHz probe. *In vitro* characterization was performed in a flow phantom with flow speeds ranging from 5 mm/s to 50 µm/s comparing GVs to microbubbles in a blood-mimicking fluid. fUS was performed in head fixed, anesthetized mice at a frame rate of 750 Hz after coherent compounding over 5 minutes long trials. We recorded visually-evoked activations of deep subcortical structures called the lateral geniculate nuclei using a light stimulation protocol (470 nm blue LED flashing at 3Hz for three periods of 15 seconds over the course of the trials). In each animal, we administered a single 50 µL bolus of GVs at a 6×10^9 GV/µL concentration via tail-vein injections. GV enhancement of fUS signals was compared to saline and microbubble injections at equal gas volume.

Results/Discussion

In vitro results showed that GVs can endure higher pressures than microbubbles (up to 646 kPa in a 2 mm/s flow), and stay stable in solution even in flows as slow as 50 µm/s when microbubbles sediment below 0.5 mm/s. In addition, our preliminary findings indicate a 40% peak enhancement of fUS activations in the presence of GVs compared to red blood cells alone. Peak correlation scores were increased by 16%. On the contrary, saline injections did not enhance neural activations, while microbubbles enhanced the signal the most but signal fluctuations hindered correlation. These preliminary results demonstrate that GVs are smoother hemodynamic enhancers than microbubbles and more accurate reporters of slow capillary flows, therefore emerging as the fUS contrast agent of choice.



Transcranial vascular maps of the mouse brain overlaid with visual-evoked activations of the lateral geniculate nuclei. Left without GVs, Right with GV administration.

5:00 PM

Kalman Filter-based Microvessel Inpainting for Super-Resolution ImagingPengfei Song¹, Joshua Trzasko¹, Armando Manduca², Shigao Chen¹¹*Department of Radiology, Mayo Clinic, Rochester, MN, United States*, ²*Department of Physiology and Biomedical Engineering, Mayo Clinic, Rochester, MN, United States***Background, Motivation, and Objective**

A common challenge in microbubble (MB)-based super-resolution (SR) imaging is the long accumulation time needed for adequate MB to populate the targeted microvasculature (MV). In practice, however, factors including tissue and probe motion, MB dose limit, imaging noise and various physiological conditions (e.g., slow MV perfusion) will limit the total available numbers of MB for SR processing. This can result in discontinuous MV depictions with missing MV structures and unreliable MV flow speed measurements (Fig. 1a). A linear fitting-based method (*IEEE TUFFC* 65 (2), 149-167) was recently proposed to address this issue using a constraint of constant local MB flow speed, facilitating a more robust MB accumulation and flow speed measurement (Fig. 1b). However, the assumption of locally constant speed may be suboptimal, and the linear fitting approach can be prone to noisy MB signals. Here we propose a Kalman filter-based MV inpainting method to facilitate robust SR imaging with limited or missing MB signals.

Statement of Contribution/Methods

The proposed inpainting method can be combined with both local and global MB tracking methods, from which the locations of a single MB that can be tracked in N consecutive frames can be used as inputs to the Kalman filter. The Kalman filter was configured with four states (lateral and axial MB displacements d_x and d_z , and flow speeds v_x and v_z) and a linear transition function ($d_t = d_{t-1} + v_{t-1}\Delta t$). After Kalman filtering, the estimated MB locations with flow speed higher than a preset speed limit were rejected, followed by an MB trajectory inpainting process based on spline interpolation, with the interpolation factor adaptively determined by the local MB flow speed.

Results/Discussion

Fig. 1c is the MV density map and MV flow speed map obtained from the proposed inpainting method, which shows marked improvement over the results from original data accumulation (Fig. 1a) and linear fitting-constrained accumulation (Fig. 1b). The proposed method could robustly reconstruct vessels with missing data points (indicated by the yellow and white arrows), better preserve the MV curvature and size (white arrow), and better resolve neighboring vessels (green arrow) than linear-fitting. The proposed method has the potential to accelerate and improve robustness of SR imaging by allowing robust MV characterization with limited or missing MB signals.

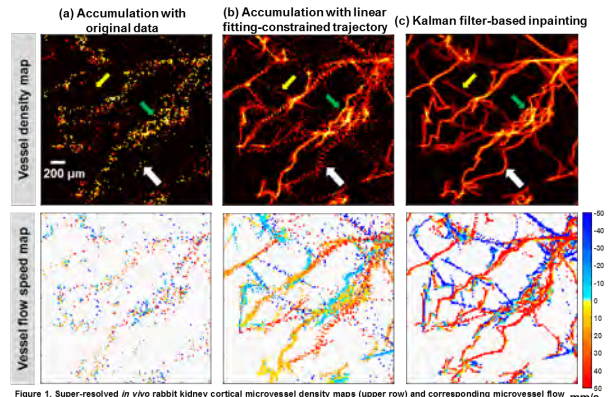


Figure 1. Super-resolved *in vivo* rabbit kidney cortical microvessel density maps (upper row) and corresponding microvessel flow speed maps (lower row) obtained from different methods (550 ms of data acquisition). (a) direct accumulation using original data. (b) accumulation using linear fitting-constrained microbubble movement trajectories. (c) Kalman filter-based microvessel inpainting. For the microvessel flow speed maps, microbubbles flowing away from the transducer (downward) were color-coded in red, and flowing towards the transducer (upward) were color-coded in blue.

5:15 PM

Human transcranial super-resolution imagingDanai Eleni Soulioti¹, David Espindola¹, Gianmarco Pinton¹¹*Joint Department of Biomedical Engineering, University of North Carolina at Chapel Hill and North Carolina State University, NC, United States***Background, Motivation, and Objective**

Transcranial ultrasound imaging in humans has been a persistent challenge for ultrasound, primarily due to degradation effects from aberration and reverberation. These mechanisms depend strongly on skull morphology and have high variability across individuals. Here we demonstrate that phase corrections in conjunction with a focused super-resolution approach successfully super-resolve a 208 μm microtube placed under a human skull phantom, at a clinically relevant depth (7 cm).

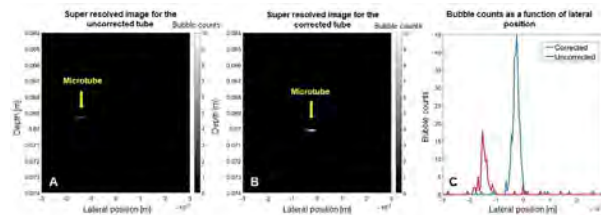
Statement of Contribution/Methods

Individual phase correction profiles for the parietal region of the human skull were calculated with a point target placed at the focal position, using a robust phase correlation technique. This correction was then applied to transmit-receive a custom focused super-resolution imaging sequence through a human skull phantom, targeting a 208 μm diameter microtube, at 7 cm in depth and at a frequency of 2.5MHz.

Microbubble contrast agents, with a characteristic mean diameter of less than 5 μm , were diluted to a concentration of 8×10^5 bubbles/mL and perfused at a flow rate of 25 $\mu\text{L}/\text{min}$. Acquisitions were performed using the phase corrected and uncorrected focal emissions at a frame rate of 1000Hz. Total acquisition time was 5 seconds in both cases.

Results/Discussion

We show that by correcting for the skull aberration, the raw signal amplitude from the tube improves by a factor of 2.44. The registration error of the tube's position in the uncorrected case was 1.12 mm and in the corrected case it was 0.37 mm, as measured in the point target B-mode images. Signal to Noise ratio values, calculated as the ratio of the RMS value within the tube region and the RMS value of the background region at the same depth, were 12.22 dB in the uncorrected super-resolved images and 24.54 dB in the corrected images. The super resolved images for the uncorrected and phase corrected cases are shown in images (A) and (B) respectively. The sensitivity in microbubble detection for the corrected case increases by a factor of 2.13, as shown by the sum of bubble counts laterally in plot (C). The tube size estimate, measured by the full width at half maximum, is 200 μm . In summary and conclusion, we demonstrate the feasibility of transcranial super-resolution in humans, by resolving a 208 μm sized target, and by improving its registration through a human skull.



4D - Prostate, Thyroid Elasticity, and Mechanical Anisotropy

Sapphire (220)

Wednesday, October 24, 8:00 am - 9:30 am

Chair **Caterina Gallippi**
University of North Carolina

4D-1

8:00 AM evaluation of transrectal ultrasound shear wave elastography (SWE) imaging in detection and characterization of clinically localized prostate cancer

Cheng Wei¹, Ghulam Nabi², Chunhui Li², Magdalena Szewczyk-Bieda³, Stephen Lang⁴, Zhihong Huang²

¹*School of Medicine, University of Dundee, DUNDEE, United Kingdom*, ²*University of Dundee, DUNDEE, United Kingdom*, ³*Department of Clinical Radiology, Ninewells Hospital, United Kingdom*, ⁴*Pathology department, Ninewells Hospital, DUNDEE, United Kingdom*

Background, Motivation, and Objective

Prostate cancer (PCa) accounts for the second most frequently diagnosed male cancer. Patients diagnosed with localized cancer are offered either active treatments or surveillance. Transrectal ultrasound (TRUS) is a non-invasive imaging method to detect cancer in early stage but traditional B-mode and Doppler imaging demonstrate limited accuracy. Ultrasound SWE is possible to assess tissue stiffness even for non-palpable small lesions. This study was designed to test the diagnostic accuracy of SWE for the detection and phenotypic characterization of PCa compared with whole-mount radical prostatectomy histopathology.

Statement of Contribution/Methods

228 consecutive men undergoing laparoscopic radical prostatectomy (LRP) for clinically localized PCa were recruited into the study. The primary outcome of the study was to determine the diagnostic accuracy of transrectal SWE for the detection and phenotyping of PCa. The secondary outcome was to determine the ability of the technology in detecting clinically significant PCa and to define risk threshold cut-off values for SWE. TRUS SWE was performed by an experienced urologist using an endocavity Aixplorer® ultrasound transducer (SuperSonic Imagine, Aix-en-Provence, France) through the rectal wall focussing on the prostate avoiding any pressure on the transducer. Quantitative stiffness data of the prostate gland was obtained in each patient and compared with detailed histopathological examination of radical prostatectomy specimen using 3-D printing mold based technology ensuring improved image-histology orientation. Receiver operator characteristic curves (ROC) were assessed between the groups.

Results/Discussion

Quantitative stiffness data estimated in kilopascals (kPa) was significantly higher in malignant compared with benign areas. With a cut-off value of 82.6 kPa, sensitivity and specificity of SWE were 96.8% and 67.8%, respectively ($p < 0.05$). Significant differences were observed for different grades of cancer with Young's moduli 91.6 kPa, 102.3 kPa and 131.8 kPa for low (Gleason score 6), intermediate (Gleason score 7) and high grade (Gleason score ≥ 8) PCa respectively ($p < 0.05$). SWE also detected capsular breaches with significant prediction of PCa pathologic staging. Potential limitations include selection bias and study being single center site.

Quantitative SWE via transrectal approach accurately detected cancer foci and showed significant differences between cancerous and benign tissue. Moreover, this technique can be used to reliably phenotype PCa aggressiveness.

8:15 AM

Prostate Shear Wave Elastography: Multiresolution Reconstruction Dependence on Push Beam Spacing

Derek Y. Chan¹, Samantha Lipman¹, Mark Palmeri¹, D. Cody Morris¹, Thomas J. Polascik², Ned C. Rouze¹, Kathryn Nightingale¹

¹Biomedical Engineering, Duke University, Durham, NC, United States, ²Surgery, Duke University, Durham, NC, United States

Background, Motivation, and Objective

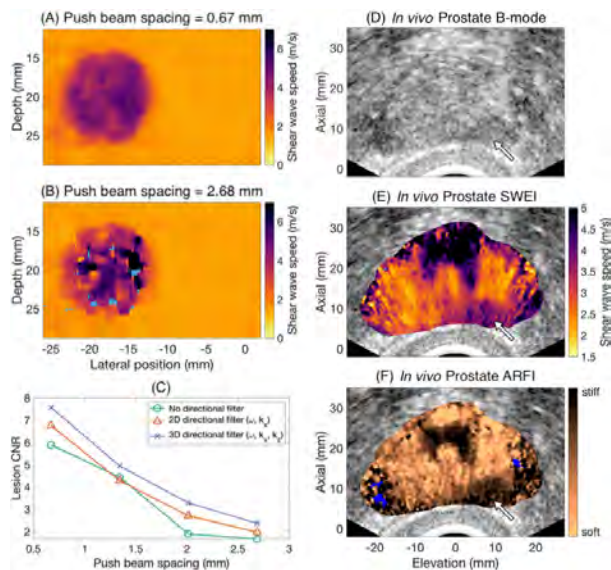
A transrectal ultrasound-guided biopsy is currently used for diagnostic confirmation of prostate cancer; however, lesion contrast in B-mode is often limited. We have developed a 3D ARFI/SWEI elasticity imaging system to provide targeted biopsy guidance, and hypothesize that using high-density pushes provides significant improvements to the resultant shear wave data. We demonstrate the implementation of a multiresolution shear wave tracking algorithm in phantoms and *in vivo* data to enable identification of prostate lesions and visualization of zonal anatomy.

Statement of Contribution/Methods

In an ongoing study, ARFI and SWEI data have been obtained with a combined sequence preoperatively in men expecting radical prostatectomy (29 subjects to date), on a Siemens SC2000 scanner with an Acuson ER7B side-fire transrectal probe. The shear wave arrival times were determined with cross-correlation of velocity signals in two dimensions after directional filtering [Song et al, UMB, 2014]. To combine data from serially interrogated lateral push locations, we extended the method to include alignment of arrival times for different pushes using the estimated propagation time between push locations. Estimates were resampled to a gridded shear wave speed (SWS) map with an algorithm weighted by distance and correlation coefficient. The impact of push beam density was examined by downsampling the high-density push beam data.

Results/Discussion

Figs. A and B show SWS maps for an 88 kPa phantom lesion in a 10 kPa background with push beam spacings of 0.67 mm and 2.68 mm, respectively, demonstrating a decrease in image quality with lower push density. Fig. C quantifies the impact of push spacing and directional filtering on phantom lesion contrast-to-noise ratio (CNR). The extended SWEI algorithm and 3D directional filtering tripled lesion CNR in phantoms compared to conventional SWEI beam spacing. Figs. D, E, and F show concurrently acquired *in vivo* axial prostate views of B-mode, SWEI, and ARFI. In addition to a visible lesion that appears stiff in both SWEI and ARFI (arrow; SWS = 3.83 ± 0.23 m/s; later confirmed Gleason 6 cancer), the soft peripheral zone of the prostate (SWS = 2.54 ± 0.24 m/s) can be distinguished from the stiffer central gland (SWS = 4.40 ± 0.38 m/s). This new SWEI algorithm facilitates visualization of prostate cancer and zonal anatomy that is concordant with ARFI imaging.



8:30 AM Correlation between 3D ARFI and quantitative imaging metrics from SWEI and multi-parametric MRI *in vivo* in normal and cancerous prostate tissue

D. Cody Morris¹, Derek Y. Chan¹, Mark Palmeri¹, Tyler J. Glass¹, Matthew M. McCormick², K. Jack Tay³, Thomas J. Polascik⁴, Rajan T. Gupta³, Kathryn Nightingale¹

¹Biomedical Engineering, Duke University, Durham, NC, United States, ²Medical Computing Group, Kitware Inc, Carborro, NC, United States, ³Radiology, Duke University, Durham, NC, United States, ⁴Surgery, Duke University, Durham, NC, United States

Background, Motivation, and Objective

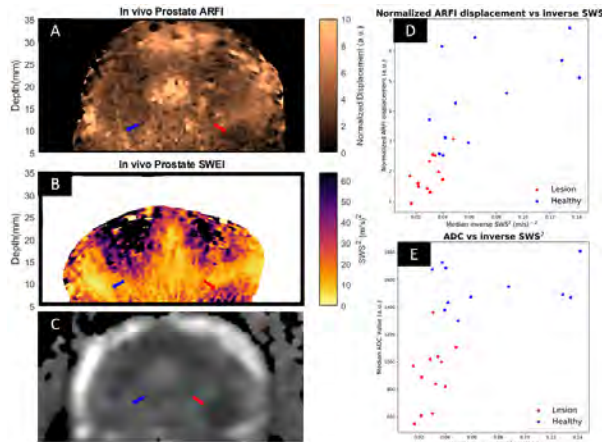
We have developed a Transrectal Ultrasound (TRUS) prostate elasticity imaging system which concurrently acquires 3D ARFI and SWEI data *in vivo*. In an ongoing study, we obtain *in vivo* ARFI/SWEI/B-mode and multi-parametric MRI image volumes, as well as post-prostatectomy whole mount histology from prostates in subjects receiving radical prostatectomy. We have obtained data in 24 subjects to date, and observe similar structures and regions of suspicion in the ultrasound and mp-MRI data. The goal of this study is to determine the correlation between higher resolution ARFI image data and corresponding quantitative metrics of shear wave speed (SWS) and MRI apparent diffusion coefficient (ADC).

Statement of Contribution/Methods

The ARFI/SWEI data were captured in a combined sequence on a Siemens SC2000 using an Acuson ER7B. The ARFI data was generated as described by Palmeri et al. [UMB 2016], and the SWSs were calculated using 2D vector tracking of directionally filtered velocity signals [Song et al., UMB 2014]. The index lesion was segmented in each ARFI volume. These segmentations were applied to the spatially matched SWEI volumes to determine the relationship between inverse SWS² and ARFI normalized displacement for identical voxels. The ADC volume was also segmented and a value for each index lesion was acquired. In patients where cancer was confined to a single hemisphere, the segmentations were left-right mirrored and the image metrics corresponding to the healthy tissue in the contralateral hemisphere were evaluated.

Results/Discussion

Figs. A, B, and C show matched axial prostate image slices from a single subject in ARFI, SWEI, and ADC, respectively, demonstrating concordant structural visualization across the three imaging modalities. A Gleason 7 tumor (red) and the healthy tissue (blue) are indicated with arrows. Fig. D shows the relationship between the median normalized ARFI displacement and the median SWEI derived shear modulus (inverse SWS²) in the segmented regions for 12 subjects. Fig. E demonstrates the relationship between the median MRI ADC value and the median SWEI derived shear modulus (inverse SWS²). In Figs D and E, the lesions are clearly separated from the healthy tissue. This separation and concordance between imaging metrics suggest that ADC, SWS², and normalized displacement can be combined and used to algorithmically detect prostate cancer.



8:45 AM

Elastography of the thyroid by tracking shear waves generated by vocal cords vibrationsSteve Beuve¹, Elise Khoury¹, Samuel Callé², Jean-Pierre Remenieras³¹UMR 1253 iBrain, Université de Tours, Inserm, Tours, France, ²Réseaux et télécommunications, GREMAN UMR 7347, Université de Tours, Tours cedex 2, France, ³UMR 1253, iBrain, Université de Tours, Inserm, France, Metropolitan**Background, Motivation, and Objective**

Some Thyroid diseases can be spotted by an uncommonly high hardness of tissue. Furthermore, this gland can't be accessible by a palpation test. The purpose of this study is to design a new shear wave elasticity method based on the propagation of diffuse field generated physiologically by a mono-frequency vibration of vocal cords. The high frame rate movies of the S wave propagation is obtained by Ultrafast Doppler and an inverse problem based on correlations already develop for passive elastography is apply to the dataset for Young modulus estimation.

Statement of Contribution/Methods

In vivo experiments were performed at 9MHz on a transverse cut of a volunteer's thyroid with a programmable ultrasound (US) scanner (Verasonics Vantage) equipped with a L11-4v probe. Ultrafast imaging was performed with tilted plane wave emission using 5 angles [-3°:1.5°:3°] in order to achieve a frame rate of 3kHz after coherent compounding. This set of angles was repeated 400 times to build cineloop during 132 msec. The probe is placed on the neck at the level of the carotid. Diffuse field are generated into the entire throat by singing to make the vocal cords vibrate. A 150Hz sound is played for reference on a speaker to emit a sound at the right frequency. A mask is applied on the region of interest in order to cancel values outside the thyroid (Fig A). An algorithm based on the ratio of the autocorrelation of the acceleration over the autocorrelation of the 2D space derivations of the axial particle velocity V_z was apply.

Results/Discussion

Movies of the wave field in function of the time clearly show a direction of propagation of the S waves, principally in the main direction of the thyroid. The wavelength can be observed (Fig B) for a fixed time. By setting a point in the mask and studying the signal as a function of time, a sine signal is observed with a fundamental at 148Hz with weak side lobes. The measurement of the space frequency at all location gives values of shear waves celerity between 0.8 m/s and 4 m/s. The cartography of the elasticity shows that the region of the thyroid in front of the trachea is harder (Fig C). The median values Young modulus are 26kPa in the hard spot and 2.5kPa for soft one.

This paper shows an elegant way to generate S waves physiologically with the voice without controlling the position of the sources associated with an efficient passive elastography inverse problem for elasticity estimation.

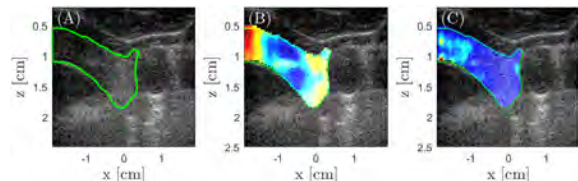


Figure (A): B mode and thyroid segmentation. (B): Particular velocity on the mask. (C): Elasticity on the mask

9:00 AM Assessing Mechanical Anisotropy in Transversely Isotropic (TI) Elastic Materials Using ARFI-Induced Peak Displacement (PD) at Electronically Steered Rotation Angles

Md Murad Hossain¹, Caterina Gallippi¹

¹*Joint Department of Biomedical Engineering, The University of North Carolina at Chapel Hill, Chapel Hill, NC, United States*

Background, Motivation, and Objective

The degree to which mechanical properties differ along versus across the axis of symmetry (AoS) in TI tissue, such as muscle or kidney, is diagnostically relevant. We have previously shown that degree of mechanical anisotropy is reflected by the ratio of ARFI-induced PD achieved when the long axis of a spatially asymmetric ARF excitation is aligned along versus across the material's AoS. Such anisotropy assessment was performed with physical transducer rotation and potential for misalignment. The objective of this work is to evaluate the feasibility of electronically rotating ARF excitations for mechanical anisotropy assessment using a multi-D array.

Statement of Contribution/Methods

ARF produced by a transducer with 3x192 (elevational x lateral) elements was simulated in Field II such that the long axis of the excitation was oriented, via electronic steering, at 0° or 59° (panels a-b) relative to the AoS of thirty-four modeled TI materials. The materials were linearly elastic and homogeneous, with material properties ranging as : $E_T = 12-15$; $E_L = 12-60$; $\mu_T = 4$; $\mu_L = 4 - 20$ KPa; $v_{LT} = 0.51-0.88$; $v_{TT} = 0.499$ where E = Young's modulus, μ = shear modulus, v = Poisson's ratio, L= along the AoS, and T= across the AoS. In these materials, ARF induced FEM modeled displacements were ultrasonically tracked using Field II, and the ratios of PDs were compared between all materials. As an experimental correlate to the simulation results, ARFI and SWEI imaging was performed in the excised biceps femoris muscles of two pigs. A Siemens VF7-3 linear array was mounted to a rotation stage and positioned such that the long axis of the ARF excitation was aligned at 0° and 60° relative to the AoS. PD and SWV ratios were compared between muscles.

Results/Discussion

See Fig.1. Both 0° and 59° simulated ARF excitations were asymmetric, with long over short axis lengths of 2.7 (a-b). PD ratio increased with increasing shear moduli ratio and did not statistically vary with Young's moduli ratio ($p>0.05$, (c)). PD ratio distinguished simulated materials with greater than 25% difference in shear moduli ratio (blue shade in (d)). Experimentally, PD and SWV ratios calculated from 0° and 60° orientations were statistically different between two *ex vivo* muscles (e). These data suggest the feasibility of using a multi-D transducer to electronically rotate ARF excitations for mechanical DoA assessment in anisotropic tissue.

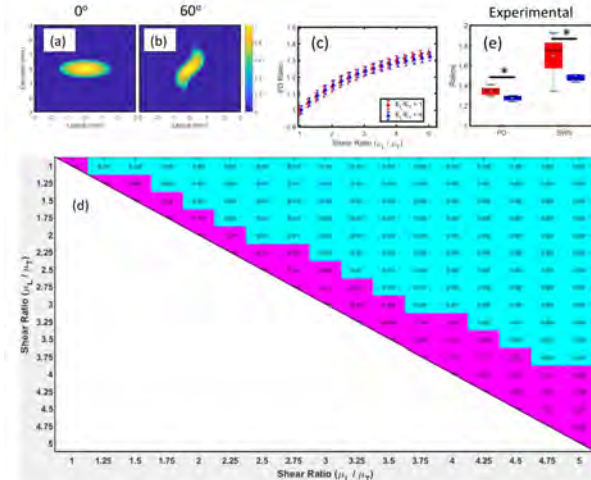


Figure 1. (a) Spatial distribution of ARF excitations in the lateral-elevation plane at the focal depth (30 mm) for a 0° (a) and 59°(b) orientations. The color bar indicates normalized nodal force, with normalization relative to the maximum nodal force. (c) The ratio of PDs (PD₀/PD₅₉) versus the ratio of shear moduli. For each shear moduli ratio, two materials are represented, one with a Young's moduli ratio of 1 (red) and one with a Young's moduli ratio of 4 (blue). PD ratio was not statistically different ($p>0.05$, Wilcoxon rank sum) between materials with the same shear but different Young's moduli ratio. (d) p-values for comparisons between PD ratios of materials with different shear moduli ratio. All materials had Young's ratio of 1. (e) PD ratios (PD₀/PD₅₉) and SWV ratios (SWV₅₉/SWV₀) measured in the excised *biceps femoris* muscles of two pigs (red versus blue).

9:15 AM

Anisotropic Constructive Shearwave Interference (ACSI) Measurements of Transverse Anisotropic Elasticity

Peter Hollender¹, Anna Knight¹, Niranjan Shashikumar¹, Inje Lee¹, Mark Palmeri^{1,2}, Kathryn Nightingale¹, Gregg Trahey^{1,3}

¹Biomedical Engineering, Duke University, Durham, NC, United States, ²Anesthesiology, Duke University Medical Center, Durham, NC, United States, ³Radiology, Duke University Medical Center, Durham, NC, United States

Background, Motivation, and Objective

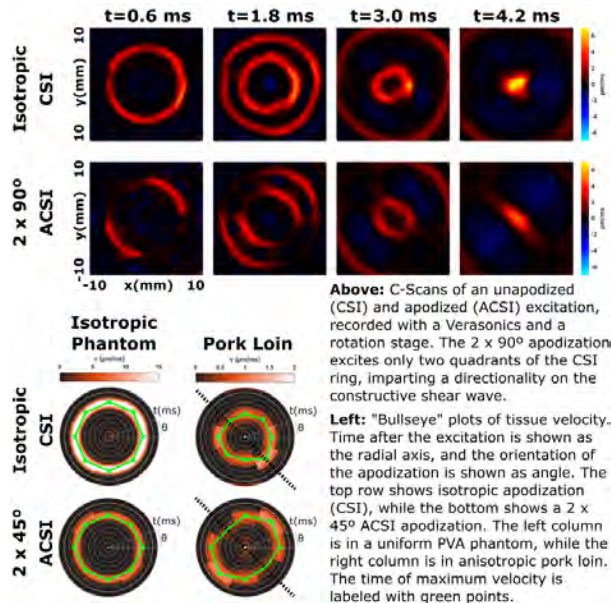
Shear Wave Elasticity Imaging (SWEI) is a powerful tool for noninvasively characterizing the elasticity of tissue. Traditionally, shear waves are tracked along the vector between a point source and the tracking beams. Tissues with anisotropic elasticity, such as skeletal muscle or myocardium, have orientation-dependent properties. It has been shown that shear wave propagation along different angles can be measured and used to assess anisotropic elasticity by either rotating the array (precluding real-time imaging) or imaging with a matrix array (expensive). Constructive Shearwave Interference (CSI) uses an annular array to generate a shear wave with a ring-shaped cross-section, and a single element to monitor the resulting constructive interference at the center. CSI has no directional sensitivity, so a method called Anisotropic CSI (ACSI) is proposed and demonstrated, which uses angular apodization to impose directionality on the constructively-interfering shear wave.

Statement of Contribution/Methods

A custom CSI system was adapted to mechanically apodize the aperture with 3D printed masks. The transmit beam patterns were validated with a hydrophone. To visualize anisotropic propagation, uniform elastic PVA phantoms were excited with the CSI system and imaged with a Verasonics system with a L12-3 linear array to visualize shear wave propagation, rotating the array to build up a 3D view. The CSI system was then used independently to measure isotropic phantoms and samples of pork loin, progressively rotating the pattern to interrogate different orientations.

Results/Discussion

When used in an isotropic phantom, no dependence on orientation was observed, although ACSI showed a 25% and 60% decrease in constructive shear wave amplitude when apodized to 2 x 90- and 2 x 45-degree opposing sectors, respectively. In pork loin, isotropic CSI showed no dependence on orientation, while apodized ACSI acquisitions recorded speeds along the visible orientation of the fibers faster than those across the fibers. Shear wave speed was more angle dependent with 45- than 90- degree sectors, indicating that the narrower apodization created a stronger directional sensitivity. ACSI could be implemented with electronic apodization of angular sectors to provide real-time measurement of tissue anisotropic elastic properties with limited hardware complexity.



4E - Abdominal Organ Elasticity

Sapphire (220)

Wednesday, October 24, 10:30 am - 12:00 pm

Chair **Shigao Chen**
Mayo Clinic

4E-1

10:30 AM Feasibility of Young's modulus mapping in Pancreatic Ductal Adenocarcinoma (PDA) tumors Using Harmonic Motion Elastography (HME) ex vivo and in vivo

Alireza Nabavizadeh¹, Thomas Payen¹, Niloufar Saharkhiz¹, Kenneth P. Olive^{2,3}, Elisa Konofagou^{1,3}

¹Biomedical engineering, Columbia University, United States, ²Department of Medicine and Pathology, Herbert Irving Comprehensive Cancer Center, Columbia University, United States, ³Department of Radiology, Columbia University Medical Center, United States

Background, Motivation, and Objective

Pancreatic ductal adenocarcinoma (PDA) is one of the most fatal cancers in developed countries. Also, the associated carcinoma is one of the stiffest among the human solid carcinomas. Mutation can gradually transform the ductal healthy cells to pancreatic intraepithelial neoplasia (PanIN) and eventually into PDA.

Statement of Contribution/Methods

HME A Focused Ultrasound (FUS) transducer generates harmonic motion at an excitation frequency of 50 Hz. At the same time, an imaging transducer aligned confocally with the FUS transducer acquires the RF signals at a sampling rate (frequency) of 1000 Hz. A 1-D cross correlation method is applied on RF signals to estimate the local displacement. To estimate the shear wave speed a 2D directional filter is used on 2D displacement. The 2D Young's modulus (E) map is reconstructed by measuring the time delay of shear wave propagation between two separated points at a known distance (6 or 8 ultrasound wavelength) in the lateral direction using cross-correlation. Then, the estimated shear wave speed is used for E estimation. In the noninvasive, *in vivo* study, we used 44 genetically engineered mice, categorized in four groups based on their different levels of fibrosis: 1) No fibrosis cases 2) less than 50% fibrosis cases 3) more than 50% fibrosis cases 4) PDA cases (full-fledged tumors), to investigate the efficiency of the HME method in differentiating between various level of fibrosis based on the generated 2D Young's modulus (E) maps. HME was also applied on 18 post-surgical human pancreatic specimens among which, 15 cases had no chemotherapeutic history while the others went through the chemotherapeutic treatment before surgery.

Results/Discussion

Results Figure 1 (g) summarizes the estimated E values of pancreatic tumors in mice at different fibrosis stages. Also figure 1 (j) demonstrates the estimated mean and standard deviation of E for tumors with no treatment (T^+ /chemo⁻) is $E = 36.7 \pm 15.3$ kPa; for their surrounding part (T^- /chemo⁻) is 6.5 ± 4.3 kPa; for tumor with chemotherapeutic history (T^+/chemo^+) is $E = 22.9 \pm 12.3$ kPa; and for their surrounding part (T^-/chemo^+) is 4.4 ± 3.3 kPa.

Conclusion Based on the presented results in figure 1, HME was found capable of differentiating the fibrosis stages in tumors in *in vivo* mice. This method was also capable of differentiating between softer and stiffer tumors in *ex vivo* human specimens.

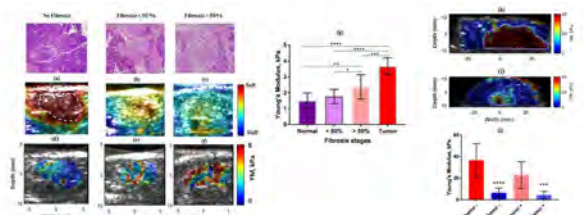


Figure 1: Different fibrosis stages with HME in mouse slices with 10x magnification, and the corresponding 1D displacement and Young's modulus (E) 2D maps overlaid on B-mode images. (a) 2D B-mode displacement map of pancreas with no fibrosis specified with white dashed regions. The estimated median displacement is $D = 16 \mu\text{m}$. (b) 2D B-mode displacement map of pancreas with less than 50% fibrosis. (c) 2D Young's modulus map of pancreas with no fibrosis. The estimated median Young's modulus is $E = 1.1$ kPa. (d) 2D Young's modulus map of pancreas with less than 50% fibrosis. The estimated median Young's modulus is $E = 2.3$ kPa. (e) 2D Young's modulus map of pancreas with more than 50% fibrosis and white dashed regions. The estimated median displacement is $D = 5.5 \mu\text{m}$. (f) 2D Young's modulus map of pancreas with no fibrosis. The estimated median Young's modulus is $E = 0.9$ kPa. (g) Bar chart showing Young's modulus (kPa) for Normal, <50%, >50% Fibrosis stages, and Tumor. (h) 2D Young's modulus map of pancreas with more than 50% fibrosis. (i) 2D Young's modulus map of tumor with no chemo history. (j) 2D Young's modulus map of tumor with chemo history. (k) Bar chart comparing E values for tumor and surrounding tissue. (l) Overlay of 2D Young's modulus map of pancreatic specimen on B-mode image with chemo history. The solid tissue is specified with blue line and the estimated E for this tissue is (5.9 ± 12.6) kPa and for tumor surrounding (5.1 ± 1.9) kPa. (m) Overlay of 2D Young's modulus map of pancreatic specimen on B-mode image with chemo history. The solid tissue is specified with blue line and the estimated E for this tissue is (1.1 ± 1.6) kPa and for tumor surrounding (1.1 ± 0.8) kPa. (n) Overlay of 2D Young's modulus map of pancreatic specimen on B-mode image with chemo history (Chemo+) and without chemo history (Chemo-). (o) Overlay of 2D Young's modulus map of tumor part (T^+) and its surrounding part (T^-) using bar chart. Comparison among 4 groups: $P < 0.0001$; T^+/Chemo^- vs. T^-/Chemo^- : $P < 0.0001$; T^+/Chemo^- vs. T^-/Chemo^+ : $P < 0.0001$; T^-/Chemo^- vs. T^-/Chemo^+ : $P = 0.19$; T^+/Chemo^+ vs. T^-/Chemo^+ : $P = 0.005$; T^+/Chemo^+ vs. T^-/Chemo^- : $P = 0.21$; T^+/Chemo^- vs. T^+/Chemo^+ : $P = 0.005$; T^-/Chemo^- vs. T^+/Chemo^+ : $P = 0.005$; T^-/Chemo^+ vs. T^+/Chemo^+ : $P = 0.005$; T^-/Chemo^- vs. T^+/Chemo^+ : $P = 0.005$.

10:45 AM

The influence of shear modulus on drug uptake in pancreatic ductal adenocarcinoma: an in vitro study

Hexuan Wang¹, Rifat Ahmed¹, Phuong Vincent², Reem Mislati¹, Solumtochukwu Nwabunwanne¹, Jason Gunn², Kayla Marra², Brian Pogue², Marvin Doyley¹

¹University of Rochester, United States, ²Dartmouth College, United States

Background, Motivation, and Objective

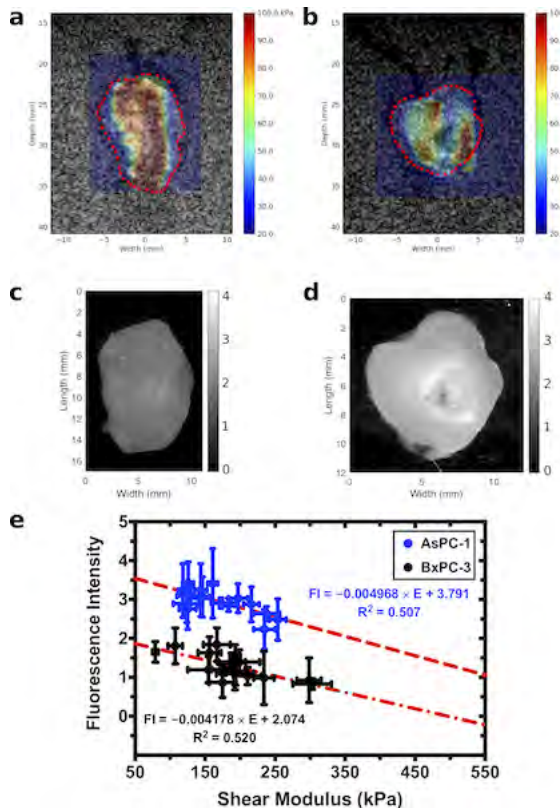
Pancreatic ductal adenocarcinoma (PDAC) is a prevalent form of pancreatic cancer with the 5-year survival rate less than 5% and a median survival of 4-6 months. The dense stroma is speculated to be a main factor in impairing delivery of both the existing chemotherapy agents and novel cancer-killing nanoparticle. We hypothesize that shear modulus measured with shear wave elasticity imaging influences drug delivery to pancreatic cancer tumors.

Statement of Contribution/Methods

We implanted AsPC-1 and BxPC-3 human pancreatic tumors in 50 immunodeficient Athymic Nude mice nu/nu by injecting 10^6 tumor cells in Matrigel (BD Biosciences, San Jose, California, USA) orthotopically into the pancreas. Drug verteporfin and perfused vessel marker lectin were injected 1 hour and 1 minute before animal sacrifice, respectively. Upon animal sacrifice, excised tumors were embedded in a gelatinous solution consisting of 10% gelatin, 1% corn starch, and water. A single tracking location shear wave elasticity imaging (STL-SWEI) method was implemented on a Verasonics Vantage 256 scanner with a 5 MHz L7-4 transducer. After STL-SWEI, each tissue sample was imaged for verteporfin uptake on a GE Typhoon 9410 flatbed scanner. Additional tissue samples were stained with Masson's Trichrome and lectin to investigate stromal density and vessel perfusion.

Results/Discussion

The SWEI elastography results reported an inverse relationship between tumor shear modulus distribution and verteporfin drug uptake, as indicated in figure 1(a - d). Linear regression test in figure 1(e) showed a strong inverse correlation for both the AsPC-1 tumors ($R^2 = 0.507$) and the BxPC-3 tumors ($R^2 = 0.520$). Between the two tumor lines, we measured the average fluorescence intensity (FI) of the drug uptake to be higher in the AsPC-1 tumors (FI = 2.95, n = 16) in comparison to that in the BxPC-3 tumors (FI = 1.314, n = 17). Those results demonstrated that shear modulus measured with SWEI affects verteporfin delivery to pancreatic cancer tumor, potentially establishing the usage of in vivo SWEI to evaluate the drug delivery efficiency in relevant studies.



11:00 AM Plane wave based single track location shear wave elasticity imaging (pSTL-SWEI) enables high resolution *in vivo* and *ex vivo* murine pancreatic tumor imaging

Rifat Ahmed¹, Hexuan Wang¹, Bradley Mills¹, Scott Gerber¹, Marvin Doyley¹

¹University of Rochester, United States

Background, Motivation, and Objective

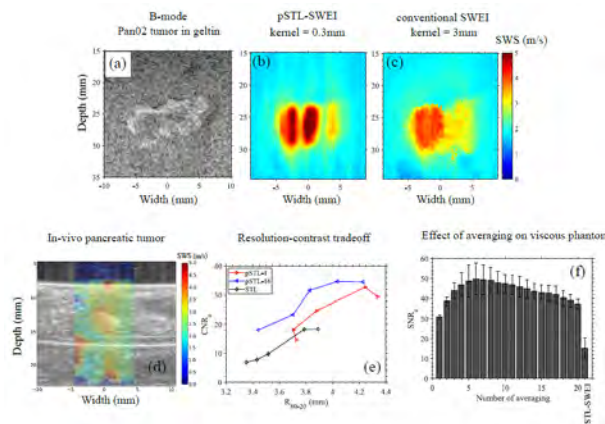
High resolution shear wave elasticity imaging of pancreatic ductal adenocarcinoma (PDA) is challenging due to the limitations imposed by the speckle bias and shear wave attenuation. The small processing kernels required for high resolution imaging of these heterogeneous tumors is prone to speckle noise. Also, the induced shear wave *in vivo* has low wave SNR. Recently proposed plane wave based single track location shear wave elasticity imaging (pSTL-SWEI) overcomes these limitations by utilizing the data redundancy of pixel-based parallel beamforming. In this work, we demonstrate the high resolution imaging capability of pSTL-SWEI for *in vivo* and *ex vivo* murine pancreatic tumors.

Statement of Contribution/Methods

A pSTL-SWEI beam sequence was designed with a push beam spacing of 0.3 mm (pitch of the L7-4 transducer used in the study). The synthetic transmit focusing of existing pSTL-SWEI was improved by using a larger number (9) of steering angles distributed over three separate sub-acquisitions. Averaging over 16 track lines was performed to remove noise. An animal study was performed by injecting Pan02 tumor cells in C57BL/6 mice ($n=8$). Spatial heterogeneity of elastograms will be evaluated quantitatively by comparing against regional distribution of collagen in histological images. The resolution and robustness to shear attenuation were evaluated on inclusion and viscous phantoms.

Results/Discussion

Fig. 1(a)-(c) shows B-mode, high resolution pSTL, and conventional STL shear wave speed maps, respectively, of an *ex vivo* tumor. The spatial heterogeneity of tumor is clearly visible in pSTL high-resolution mode. Fig. 1(d) shows the pSTL elastogram of an *in vivo* murine pancreatic tumor. Fig. 1(e) shows that pSTL can achieve similar contrast as STL at lower processing kernels. Fig. 1(f) shows that pSTL achieves higher elastographic signal-to-noise ratio than conventional STL in a viscous medium by performing track line averaging. Results demonstrate the effectiveness of pSTL-SWEI for pre-clinical evaluation of *in vivo* and *ex vivo* pancreatic tumors.



11:15 AM

3D Liver Shear Wave Absolute Vibro-Elastography with an xMATRIX Array – A Healthy Volunteer Study

Qi Zeng¹, Mohammad Honarvar¹, Julio Lobo¹, Caitlin Schneider¹, Robert Rohling¹, Anup Agarwal², Gerard Harrison², Changhong Hu², Scott Dianis³, James Jago², Septimiu E. Salecudean¹

¹Electrical and Computer Engineering, University of British Columbia, Vancouver, BC, Canada, ²Philips Healthcare, Bothell, WA, United States, ³Philips, Andover, MA, United States

Background, Motivation, and Objective

The progression of chronic liver disease, including hepatitis B, C and non-alcoholic steatohepatitis, is closely associated with advancing fibrosis. Magnetic resonance elastography (MRE), which quantitatively measures shear modulus over a volume, provides the most accurate imaging-based fibrosis staging when compared to biopsy [1]. While ultrasound-based elastography methods for liver fibrosis staging have been developed, they are confined to a 1D or a 2D region of interest and to a limited depth [2]. Our objective is to develop 3D ultrasound liver shear modulus imaging that performs similarly to MRE.

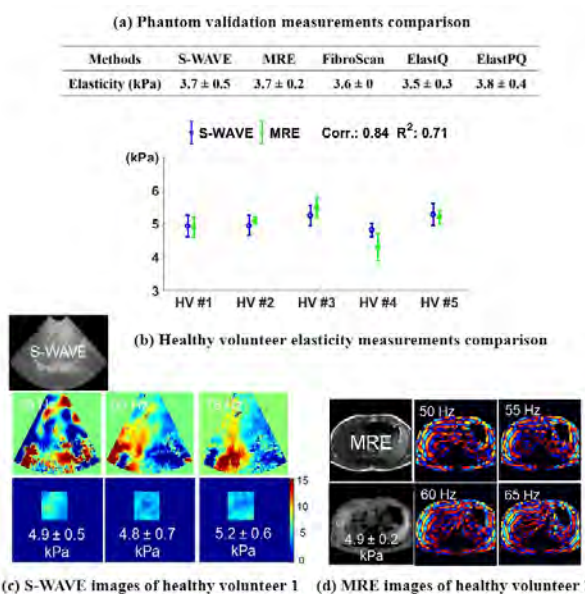
Statement of Contribution/Methods

We present a novel matrix array implementation of the live 3D shear wave absolute vibro-elastography (S-WAVE) [3] and validate its performance. We use an EPIQ 7 ultrasound machine with an X6-1 xMATRIX transducer (Philips Healthcare, Bothell, WA). Shear waves are generated by an activator coupled to the patient's back. A color Doppler scan sequence is used to sample tissue motion in 3D. The elasticity reconstruction is obtained using local frequency estimation. The system was validated in phantom studies with transient elastography (FibroScan, Echosens), ultrasound shear wave elastography point quantification (ElastPQ, Philips), 2D shear wave imaging (ElastQ, Philips) and MRE. Five healthy volunteers were imaged with MRE and S-WAVE with IRB-approval.

Results/Discussion

Validation results for a custom liver phantom (CIRS, Norfolk, VA) matched closely among different methods (Fig. a). MRE and S-WAVE results in healthy volunteers are also well matched (Fig. b). Typical image examples are presented in Fig. c-d. Our preliminary work indicates that S-WAVE with xMATRIX produces comparable results with MRE. Further evaluation in patients is warranted.

1. S. Singh et al, "Diagnostic Performance of Magnetic Resonance Elastography in Staging Liver Fibrosis: A Systematic Review and Meta-analysis of Individual Participant Data," *Clin. Gastroenterol. Hepatol.*, vol. 13, no. 3, 2015
2. R. G. Barr et al, "Elastography Assessment of Liver Fibrosis: Society of Radiologists in Ultrasound Consensus Conference Statement," *Radiology*, vol. 276, no. 3, pp. 845–861, 2015
3. J. Abeysekera et al, "Vibro-elastography: Absolute elasticity from motorized 3D ultrasound measurements of harmonic motion vectors," *2015 IEEE Int. Ultrason. Symp.*, 2015



11:30 AM Shear wave velocity and attenuation in 85 post-transplant liver patients with acute cellular rejection and comparison with biopsy findings

Ivan Nenadic¹, Luiz Vasconcelos², Rebeca Pereira³, Matthew Urban⁴, James Greenleaf², Shigao Chen⁴

¹Mayo Clinic, Rochester, United States, ²Mayo Clinic, United States, ³Mayo Clinic, MN, United States, ⁴Department of Radiology, Mayo Clinic, Rochester, MN, United States

Background, Motivation, and Objective

More than 6,000 liver transplants are performed each year in the United States. The 1-year, 5-year and 10-year survival rates of liver transplants are 84%, 68% and 54%, respectively. Acute cellular rejection (ACR) is the most common complication in the early post-transplant period occurring in 20-40% of patients. Blood labs characteristic of ACR are increases in serum aspartate transaminase (AST), alanine transaminase (ALT), alkaline phosphatase (ALP), gamma-glutamyl transpeptidase (GGT) and bilirubin levels, and is treated with corticosteroid therapy. Ischemia-reperfusion injury (IRI), a self-resolving tissue preservation injury that does not require therapy, is another common pathology that presents early in post-transplant period and is characterized by similar lab pattern. Clinical confirmation of ACR requires a liver biopsy, which is invasive and may cause hemorrhage and mortality. A noninvasive tool capable of differentiating between ACR and IRI with good negative predictive value for ACR would be highly beneficial in clinical settings.

Statement of Contribution/Methods

Attenuation Measuring Ultrasound Shearwave Elastography (AMUSE) is a shear wave based method that measures shear wave velocity and attenuation without the use of a rheological model that has been developed and validated in our lab. In this study, we compare shear wave velocity and attenuation to biopsy findings of acute cellular rejection in 85 transplanted livers. In addition, 15 patients were tracked longitudinally between day 7 when they were diagnosed with ACR and before they started therapy, and repeat biopsy on day 14. Focused radiation force was used to excite shear waves in the liver and pulse echo is used to track the wave motion. Two-dimensional (2D) Fourier Transform of the shear wave motion to obtain the k-space whose coordinates are the frequency (f) and the wave number (k). The velocity (c) at the given frequency is equal to f_0/k_0 , where f_0 and k_0 are the coordinates of the peak at the given frequency. The attenuation is calculated using $\alpha = (\pi/\sqrt{3}) \times FWHM$, where $FWHM$ is the full-width at half maximum of the peak along the wave number axis. Measurements of shear wave velocity and attenuation were made at 100, 200 and 300 Hz and the results were compared to clinical diagnoses made by liver biopsy in a blind study.

Results/Discussion

The results show that velocity and low attenuation correspond to biopsy findings of ACR, and that low velocity and high attenuation correspond to biopsy findings of no ACR. The results suggest that using both the shear wave velocity and attenuation improves the ability to differentiate between two groups of patients. The Hotelling trace criterion shows that using both velocity and attenuation increasing differentiation power. AMUSE was able to track changes in velocity and attenuation that show response to steroid therapy between days 7 and 14. Analysis shows that the AMUSE method has a good negative predictive value in ruling out presence of ACR.

11:45 AM

VisR, SWEI, and SDUV Ultrasound Detect Increased Degree of Mechanical Anisotropy Following Ischemia-Reperfusion Injury in Pig Kidney, In Vivo

Md Murad Hossain¹, Timothy Nichols², Elizabeth Merricks³, Dwight Bellinger⁴, Lauren Whimsey⁴, Melissa Caughey², Stephanie Montgomery³, Caterina Gallippi¹

¹Joint Department of Biomedical Engineering, University of North Carolina at Chapel Hill, Chapel Hill, NC, United States, ²Department of Medicine, University of North Carolina at Chapel Hill, United States, ³Department of Pathology and Laboratory Medicine, University of North Carolina at Chapel Hill, United States, ⁴Division of Comparative Medicine, University of North Carolina at Chapel Hill, NC, United States

Background, Motivation, and Objective

Renal cortex and medulla are mechanically anisotropic, and the degree of anisotropy (DoA) may change with renal pathology. In this work, the feasibility of using ARF-based methods for detecting DoA changes after ischemia-reperfusion injury (IRI) is tested *in vivo* in pig kidney. We hypothesize that: 1) IRI alters elastic and viscous DoA in the renal cortex and medulla; and 2) These DoA changes are detected by Viscoelastic Response (VisR), Shear Wave Elasticity Imaging (SWEI), and Shearwave Dispersion Ultrasound Vibrometry (SDUV).

Statement of Contribution/Methods

In 6 pigs, the renal artery was ligated for 1.5 hrs to induce ischemia. Then, the ligation was released to allow reperfusion for 2.5 hours, after which VisR, SWEI, and SDUV were performed in immediate succession. All data were acquired first with the transducer aligned along nephrons. The transducer was then rotated 90° for alignment across nephrons. In both alignment, FOV spanned the cortex and medulla. Data were acquired similarly in the left kidney, which did not undergo IRI and served as a control. VisR (relative elasticity (RE), relative viscosity (RV), peak displacement (PD)), SWEI (shear elastic modulus (μ)), and SDUV (shear elastic (μ) and viscous (η) moduli) outcomes were evaluated raw and as ratios to reflect DoA (longitudinal over transverse). Finally, IRI and control outcomes were compared (Wilcoxon). Kidneys were harvested for histological validation.

Results/Discussion

See Fig. 1. Histology confirms inflammation in both injured cortex and medulla, with predominantly tubule atrophy and casting in the medulla and cellular degeneration and edema in the cortex (a-d). Associated with tissue damage, VisR PD and RE indicate that the longitudinal shear elastic modulus increases in the medulla. In the cortex, VisR RE and PD, SWEI μ , and SDUV μ indicate that the transverse shear elastic modulus decreases (e). VisR PD and RE, SWEI μ , and SDUV μ demonstrate increased DoA after IRI in the medulla and cortex (except SWEI μ in cortex) (f-g). Notably, while elastic DoA increases in both medulla and cortex, the underlying causes differ (cortex: diminished transverse modulus v. medulla: elevated longitudinal modulus). VisR RV indicates decreased viscous DoA in the medulla after IRI. These results demonstrate that VisR, SWEI and SDUV detect changes in mechanical DoA, in association with tissue damage from IRI, *in vivo*.

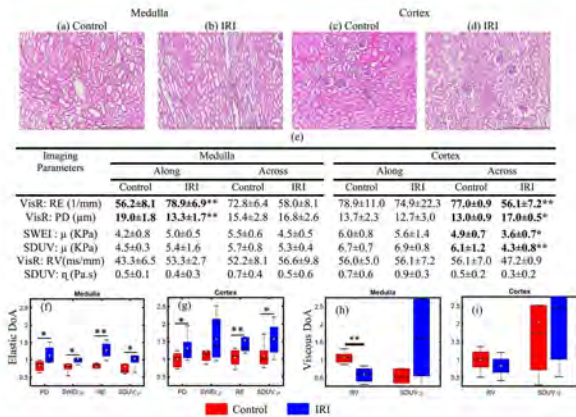


Figure 1. (a-d) Example H&E stains of IRI affected and control medulla and cortex. (e) VisR, SWEI, and SDUV outcomes measured along and across nephrons in the medulla and cortex. Significant difference between IRI and control cases are shown in bold by asterisk (* and ** represent p<0.1 and p<0.05, respectively). (f-g) Box-plots of elastic DoA from each outcome metric in IRI (blue) and control (red) medulla and cortex. (h-i) Box-plots of viscous DoA from each outcome metric in IRI (blue) and control (red) medulla and cortex.

4F - 3D Flow Imaging

Sapphire (220)

Wednesday, October 24, 1:30 pm - 3:00 pm

Chair **Jørgen Jensen**
Technical University of Denmark

4F-1

1:30 PM

Full 3D Power, Color & Vector Doppler imaging using large aperture Row Column Array transducers

Jonathan Porée¹, Jack Sauvage¹, Martin Flesch², Guillaume Ferin², Mickaël Tanter¹, Thomas Deffieux¹, Mathieu Pernot¹

¹Institut Langevin, ESPCI Paris, PSL Research University, CNRS UMR 7587, INSERM U979, France, ²Vermon SA, France

Background, Motivation, and Objective

Ultrafast 3D Doppler imaging can provide volumetric high frame rate and high resolution mapping of the vascular anatomy and function. Current approach relies on the use of relatively small aperture matrix arrays connected to high channel count electronics, which remain complex and costly. Row Column Addressed (RCA) approaches have been proposed as a low complexity alternative to matrix probe [1] for imaging of blood flows [2] including vector Doppler [3]. In this study, we investigate a dedicated sub-aperture beam forming method for full-3D Power, Color and Vector Doppler imaging in large field of view. This technique is validated *in vitro* on pipe flow phantoms and *in vivo* on human arteries.

Statement of Contribution/Methods

RCA prototypes of 8 and 15 MHz ultrasonic were designed and built (2×128 orthogonal arrays with 0.2 mm and 0.11 mm pitch respectively, Vermon ® France). They were driven by a VeraSonics® Vantage 256 research ultrasound systems. *In vitro* Doppler images were performed on a pipe flow phantom (1 mm cross section with velocity up to 20 mm/s). The pulse repetition frequency was set to 32 kHz for a maximum acquisition depth of 2 mm. Synthetic/Directional beam forming was performed using 32 tilted plane wave transmits (-8° to -8°) per arrays and 16 elements sub-apertures in receive for an effective frame-rate of 500 Hz and an equivalent F-number of 3. Five directional Color-Doppler images were reconstructed, after SVD-clutter filtering, using autocorrelation methods and combined in a least square system to recover the vector flow images.

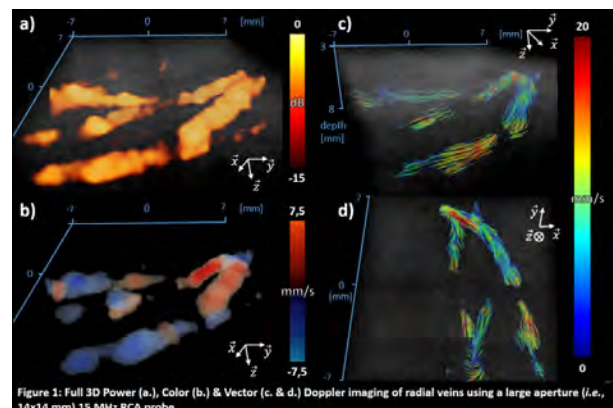
Results/Discussion

In vitro, estimated velocity were highly consistent with the expected values. *In vivo* (see Fig.1), despite the reduced sensitivity inherent to RCA probes, we could recover high-contrast and high-resolution 3D Power Doppler (Fig.1.a) and Color-Doppler (Fig.1.b) images in radial veins and carotid artery. Thanks to the synthetic/directional beamforming approach we could also resolved dense 3D velocity vector fields at ~50 frames per second. With this technology we can envision doing prospective 3D studies with already clinically available ultrasound scanners.

[1] Rasmussen, *et al.* (2015). *IEEE UFFC*, 62(5), 947-958.

[2] Sauvage *et al.* (2018). *PMB*

[3] Holbeck *et al.* (2016) *IEEE UFFC*, 63(11), 1799-1814.



1:45 PM

High-volume-rate 3D ultrasound imaging and stereoscopic PIV in a dynamic left ventricular phantom

Jason Voornedelv¹, Hicham Saaid², Christiaan Schinkel³, Franc van den Adel⁴, Nikola Radeljic⁴, Boris Lippe⁴, Antonius F. W. van der Steen^{5,6}, Frank Gijsen⁷, Nico de Jong^{6,8}, Tom Claessens⁹, Hendrik J. Vos^{1,6}, Sasa Kenjeres³, Johan G. Bosch¹⁰

¹Biomedical Engineering, Thorax Center, Erasmus MC, Rotterdam, Netherlands, ²Institute Biomedical Technology, Ghent University, Belgium, ³Transport Phenomena Section, Department of Chemical Engineering, Delft University of Technology, Netherlands, ⁴Oldehult Ultrasound, Netherlands, ⁵Thorax Center, Erasmus MC, Netherlands, ⁶Laboratory of Acoustical Wavefield Imaging, Delft University of Technology, Netherlands, ⁷Biomedical Engineering, Thorax Center, Erasmus MC, Netherlands, ⁸Erasmus MC, Netherlands, ⁹Department of Materials, Textiles and Chemical Engineering, Ghent University, Belgium, ¹⁰Biomedical Engineering, Erasmus MC, Netherlands

Background, Motivation, and Objective

Left ventricular (LV) blood flow is a 3D phenomenon and 2D quantification often ignores the effects of out of plane motion. In this study we describe a new experimental setup capable of producing realistic 3D LV flow patterns, suitable for stereoscopic optical particle image velocimetry (sPIV) concurrently with 3D ultrasound imaging. We use a prototype transesophageal (TEE) matrix probe for 3D high volume rate (4 kHz) imaging of the LV phantom, using ultrasound contrast agents to visualize the flow.

Statement of Contribution/Methods

A compliant, optically and acoustically transparent silicone LV chamber, encased in an acrylic box, was fitted with bio-prosthetic mitral and aortic valves (Edwards), connecting to atrial and compliance chambers (Fig.1A). The system uses a piston pump (ViVitro) to impose pressure and volume changes in the exterior chamber, causing realistic flow patterns to circulate inside the LV.

A compliant, optically and acoustically transparent silicone LV chamber, encased in an acrylic box, was fitted with bio-prosthetic mitral and aortic valves (Edwards), connecting to atrial and compliance chambers (Fig.1A). The system uses a piston pump (ViVitro) to impose pressure and volume changes in the exterior chamber, causing realistic flow patterns to circulate inside the LV.

Time resolved sPIV (double pulse acquisition with $\delta t = 250 \mu\text{s}$) was performed with fluorescent tracer particles. To construct a full 3D vector field, the imaging plane (1 mm thick, Fig.1B) was scanned at 2 mm intervals, for a total of 20 planes. Post-processing was done with DaVis 10 software (LaVision).

Results/Discussion

sPIV confirmed that the LV phantom could produce the high-energy diastolic 3D vortex ring (Fig.1C), with clinically relevant velocity magnitudes of approximately 1 m/s. It also confirmed the presence of large out of plane velocity components of 0.4 m/s. In the 4D ultrasound volumes (Fig.1D), we found coherent bubble motion with velocity components of at least 0.8 m/s axially and in the order of 0.4 m/s laterally, which was confirmed by sPIV (Fig.1C), suggesting that 3D flow tracking should be possible by using methods such as echoPIV.

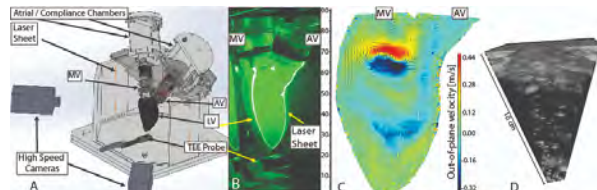


Fig 1 A) LV phantom with sPIV setup and TEE probe. B) Photograph of LV with laser sheet and bio-prosthetic mitral (MV) and aortic (AV) valves. C) sPIV result showing complex 3D nature of LV flow. D) 3D ultrasound volume obtained with matrix TEE probe with bubbles visible.

2:00 PM

The Helical Toroid Flow Phantom: A Twist for 3-D Flow Imaging InnovationsAdrian J. Y. Chee¹, Takuro Ishii¹, Billy Y. S. Yiu¹, Jason Au¹, Alfred C. H. Yu¹¹Schlegel-UW Research Institute for Aging, University of Waterloo, Waterloo, ON, Canada**Background, Motivation, and Objective**

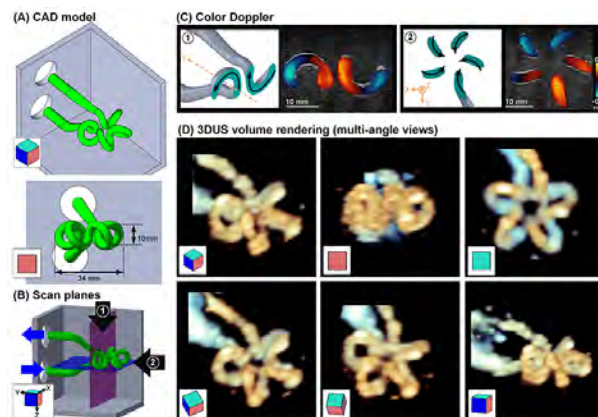
Recent breakthroughs in real-time 3D ultrasound imaging have sparked interest in visualizing blood flow in 3D and even quantifying its flow vectors at fine temporal resolution. To foster the development of new 3D flow estimation algorithms, a suitable flow phantom is needed to effectively assess the accuracy of the derived flow estimates. Yet, the conceptualization of such flow phantoms is not trivial as it should ideally incorporate multi-directional flow components to enable comprehensive evaluation of a 3-D flow estimator. Here, we present the design of a novel helical toroid flow phantom whose flow trajectory embraces all combinations of X, Y & Z directional components.

Statement of Contribution/Methods

Drawing inspiration from a toroid inductor, we drafted a 4 mm flow channel that was helically wounded for 5 revolutions over a toroid (see Fig A; drafted in SolidWorks). Radii of the toroid and helix were 10 and 5 mm respectively, resulting in a footprint diameter of 34 mm that corresponds to the left ventricular dimension (average of systole and diastole). One half of an outer helical loop was removed and was appended with two tubes for connection to a flow circuit. The phantom was physically fabricated using our established protocol (T-UFFC, 2017; 64: 25-38), and it was put into operation using a 5 ml/s constant flow pump. Using a SonixTouch scanner and an L14-5 array (5 MHz freq; 3-cycle duration; 6.7 kHz PRF), color flow imaging was performed at two cross-sectional planes (see Fig B). Then, 3D flow volumes were acquired using a Philips iE33 scanner and an X5-1 xMATRIX probe (3 MHz freq; 7 vps). Contrast agents (Definity-like; 3% bolus injections) were administered to highlight the flow region. For comparison, computational fluid dynamics (CFD) profiles were obtained using SolidWorks Flow Simulation.

Results/Discussion

Color flow scans in Fig. C indicated that helical loops directed flow about X & Y axes (C1), while the toroid loop steered flow about the Z axis (C2). These 3D flow patterns match well with those derived using CFD. 3D scans of the toroidal flow volume (Fig. D; rendered for different viewing angles) intuitively confirmed the multi-directional nature of flow generated within this phantom. These results demonstrate the merit of our helical toroid phantom in supporting the development of 3D flow imaging techniques, including vector estimation and visualization methods.



2:15 PM

Simultaneous 4D ultrafast blood flow and tissue Doppler imaging of the human heart

Clément Papadacci¹, Victor Fine¹, Olivier Villemain¹, Guillaume Goudot¹, Jean Provost¹, Mickaël Tanter¹, Mathieu Pernot¹

¹Institut Langevin, INSERM U979, ESPCI, CNRS UMR 7587, ART, France

Background, Motivation, and Objective

Echocardiography is routinely used in the clinic to evaluate heart function. Numerous cardiac indexes must be measured during each routine exam. The results highly depend on probe positioning and manual selections inducing operator variability and examination time. Standard 3D echocardiography cannot perform functional measurements such as Doppler flow or tissue Doppler due to its low volume rate [1]. In this study, we developed a novel ultrafast sequence and processing to simultaneously achieve 4D Doppler blood flow and tissue in the human heart to retrieve cardiac Doppler indexes.

Statement of Contribution/Methods

A 2.25MHz matrix array probe (1024 elements) connected to a 1024 channels electronics in emission/receive was positioned by a cardiologist on the apical four-chamber view centered on the left ventricle of a human volunteer. 5600 diverging waves were emitted at a volume rate of 4500 volumes/s to cover the entire cardiac cycle. N=3 acquisitions were performed and electrocardiogram (ECG) was co-registered. 4D Doppler flow and tissue were estimated using spatio-temporal filtering [2] and 1D cross-correlation on demodulated IQ volumes, respectively. Doppler flow and tissue index such as E, A, S, E/A, cardiac output (CO), e' , a' , s' , e'/a' , E/e' were assessed and compared to 2D clinical measurements.

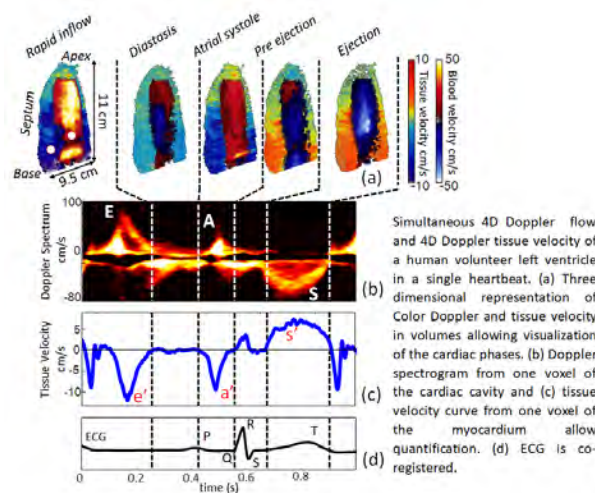
Results/Discussion

4D Doppler flow and tissue velocity were successfully assessed within a single cardiac cycle allowing the identification of each cardiac phase. The method enabled to assess a Doppler flow spectrogram and a tissue Doppler curve at each voxel of the cavity and the myocardium, respectively, allowing Doppler index quantifications: $E=83.6\pm2.4$ cm/s; $A=47.6\pm1.4$ cm/s; $E/A=1.7\pm0.06$; $S=100.1\pm2.4$ cm/s; $e'=12\pm0.4$ cm/s; $a'=10.2\pm0.1$ cm/s; $e'/a'=1.2\pm0.06$; $s'=5.8\pm0.3$ cm/s; $E/e'=7\pm0.5$; $CO=4.9\pm0.3$ L/min. These results were successfully compared to the measurement performed with the 2D clinical ultrasound machine.

Simultaneous 4D ultrasound ultrafast Doppler was developed to revisit the evaluation of the left ventricle indexes measured by ultrasound. The dedicated sequence includes a new acquisition and processing flow chart. It promises to improve patient care by accelerating examination time as well as results reproducibility by removing most of the operator dependency.

References

- [1] Nagueh SF et al. 2016
- [2] Demené et al. 2014



2:30 PM

Combining automatic angle correction and 3-D tracking Doppler for Aortic Stenosis severity assessmentStefano Fiorentini^{1,2}, Torvald Espeland^{1,2,3}, Erik Andreas Rye Berg^{1,2,3}, Svend Aakhus¹, Hans Torp^{1,2}, Jørgen Avdal^{1,2}¹*Department of Circulation and Medical Imaging, NTNU, Trondheim, Norway*, ²*Center for Innovative Ultrasound Solutions, Trondheim, Norway*, ³*Clinic of Cardiology, St. Olavs Hospital, Trondheim, Norway***Background, Motivation, and Objective**

Aortic Stenosis (AS) is a pathological narrowing of the aortic valve opening, which causes increased load on the left ventricle. This condition can lead to angina, myocardial hypertrophy and eventually heart failure.

Maximum velocity estimation using Continuous Wave (CW) Doppler is an important index in the assessment of AS, with velocities above 4 m/s indicating severe stenosis. In the attempt to align the aortic jet with the ultrasound beam, it is recommended to perform CW Doppler from multiple views [Baumgartner 2017]. The procedure is cumbersome, but failing to comply can lead to substantial underestimation of AS severity.

In this work, we perform 3-D high frame-rate imaging for retrospective maximum velocity estimation in AS jets. This is achieved using a combination of 3-D speckle tracking and 3-D tracking Doppler.

Statement of Contribution/Methods

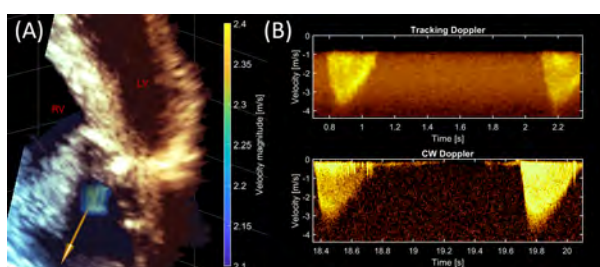
A non-compounded 3-D plane wave imaging scheme was enabled in a commercial US system (GE 4V probe and GE Vivid E95 scanner). High PRF mode was activated to avoid velocity aliasing while imaging at high depths. The AS jet direction was estimated automatically using a method that combines 1-D autocorrelation and 3-D blood speckle tracking [Wigen, 2016]. 3-D tracking Doppler [Fiorentini, 2018] was then used for spectral estimation, using the flow direction estimate from speckle tracking as tracking direction.

Results/Discussion

(A) Shows a 3-D duplex rendering from a patient with moderate AS, from a standard apical view. The arrow indicates the estimated jet direction from 3-D speckle tracking. The estimated beam-to-flow angle was 20°. (B) Shows a 3-D tracking Doppler sonogram estimated from the same flow dataset shown in (A). The results were generated using temporal window 75 samples, centre frequency 2 MHz, PRF 10 kHz and pulse length 3.5 cycles. A CW Doppler sonogram recorded from a non-standard lateral view is also shown for reference.

Results from 10 simulations of jet flow through an orifice show that the estimated trajectory from speckle tracking is $-0.04^\circ \pm 0.73^\circ$ and $32^\circ \pm 0.87^\circ$ at 0° and 45° respectively.

In-vivo results show that maximum velocity estimates from the combination of 3-D tracking Doppler and 3-D speckle tracking can match CW Doppler with less effort from the clinician, motivating further feasibility investigation.



2:45 PM

Using functional ultrasound imaging and 3D navigation for neonatal sleep phases discrimination

Jerome Baranger^{1,2}, Charlie Demené¹, Alice Frerot³, Miguel Bernal¹, Catherine Delanoe⁴, Stephane Auvin⁴, Valérie Biran³, Marianne Alison⁴, Jerome Mairesse⁵, Elisabeth Harribaud⁴, Mafalda Correia¹, Mathieu Pernot¹, Mickaël Tanter¹, Olivier Baud³

¹Institut Langevin, ESPCI Paris, PSL Research University, CNRS UMR 7587, INSERM U979, Paris, France, ²College Doctoral, Sorbonne Université, Paris, France, ³Neonatal Intensive Care Unit, Assistance Publique - Hôpitaux de Paris, France, ⁴Assistance Publique - Hôpitaux de Paris, France, ⁵Promoting Research Oriented Towards Early Central Nervous System Therapies (PROTECT), INSERM U1141, Paris, France

Background, Motivation, and Objective

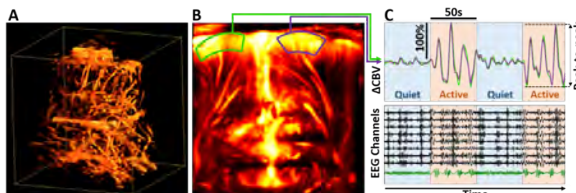
Functional Ultrasound (fUS) based on ultrafast imaging recently opened new perspectives for neonate neuroimaging. fUS can detect the neurovascular coupling by leveraging its sensitivity (down to 1mm/s blood flow speed), temporal resolution (1ms), and spatial accuracy (250 µm). Its portability makes it an unprecedented tool for research on neonate brain activity at bedside. In a first study, fUS was able to localize ictal events in pathological patients [1]. Here, we assessed the relevance of fUS coupled to electroencephalography (EEG) for studying neonates' sleep phases.

Statement of Contribution/Methods

A custom ultrasonic probe (128 elements, 0.2mm pitch, 6.4MHz) was mounted into a newborn-adapted headset along with 8 electrodes. An Aixplorer® research system was used to acquire custom fUS sequences (3 compounded plane waves, PRF 1950Hz, 370 frames) recording Ultrafast Doppler (UFD) every 1s, giving access to the Cerebral Blood Volume variations (ΔCBV) with acoustic intensities far below FDA requirements. The probe was placed on the fontanel and could be rotated with a servo-motor. 3D UFD plane-by-plane scans in both coronal and sagittal views were combined to reconstruct a volume of brain vasculature. Once in the section of interest, fUS and EEG were synchronously recorded on 6 near-term healthy neonates during 60min to observe phases of quiet and active sleep.

Results/Discussion

The 3D scan allowed probe positioning between patients in reproducible cerebral structures of interest. During sleep, fUS revealed oscillating patterns of ΔCBV (~0.05Hz), which amplitude increases more than threefold in active sleep as compared to quiet sleep. The high correlation ($r=0.8$, $p<0.0001$) between ΔCBV oscillations' peak-to-peak amplitude (> 50% of baseline) and the EEG-revealed sleep state showed the sensitivity of fUS to subtle neurovascular variations during the moderate brain electrical activity changes observed in healthy sleeping neonates. The huge metabolic demand recorded during active sleep is questioning the role of this sleep phase in brain development. By combining fUS, 3D navigation and synchronous EEG, this study paves the way for functional connectivity imaging [2] in neonates at bedside.



(A) 3D Ultrafast Doppler reconstruction of neonate vasculature (B) Ultrafast Doppler coronal slice at a given time (C) Time course of ΔCBV and EEG : ΔCBV peak-to-peak amplitude correlates with sleep phases visible in EEG

[1] Demené et al. "Functional ultrasound imaging of brain activity in human newborns." *STM*, 2017.

[2] Hassanpour et al. "Neonatal brain resting-state functional connectivity modalities." *Photoacoustics*, 2018.

4G - Vector Flow Imaging

Sapphire (220)

Wednesday, October 24, 4:00 pm - 5:30 pm

Chair **Enrico Boni**
University of Florence

4G-1

4:00 PM A fast 4D B-spline framework for model-based reconstruction and regularization in vector flow imaging

Thomas Groenli^{1,2}, Morten Wigen^{1,2}, Patrick Segers³, Lasse Lovstakken^{1,2}

¹Department of Circulation and Medical Imaging, Norwegian University of Science and Technology (NTNU), Trondheim, Norway, ²Centre for Innovative Ultrasound Solutions (CIUS), Norway, ³IBiTech-bioMMeda, Ghent University, Ghent, Belgium

Background, Motivation, and Objective

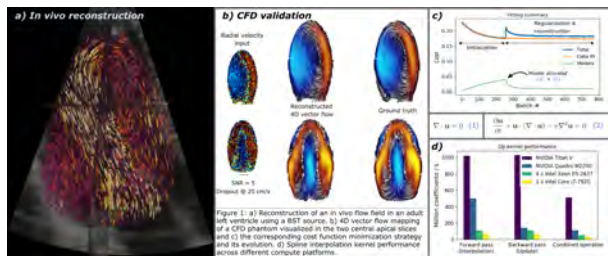
Ultrasound vector flow imaging (VFI) methods have shown promise for measuring intracardiac flow patterns, but are hampered by variance and clutter filter dropouts. Methods attempting to mediate often lead to feature blurring (smoothers) or scale poorly when moving to 4D imaging (model-regularizers). We propose a flexible reconstruction framework based on an efficient B-spline interpolation kernel and with model-based data regularization terms computed on the analytical spline gradients.

Statement of Contribution/Methods

A general purpose nD B-spline interpolator of arbitrary orders and differentials was developed in the open source TensorFlow framework. Sparse gradients supporting reverse mode automatic differentiation (AD) were implemented, enabling the use of stochastic gradient descent optimizers to minimize general differentiable cost functions even on memory constrained systems. This allows arbitrary models and data sources to be specified with a high level of implementation abstraction. Parallel forward pass and AD codes were written for CPU and GPU to increase performance across platforms. The framework was evaluated for vector flow reconstruction constrained by the incompressible Navier-Stokes (NS) equations.

Results/Discussion

Evaluation was done towards a computational fluid dynamics (CFD) phantom, subjected to semi-realistic artifacts and noise. Measurements were fitted to 4D spline grids, penalizing the deviation from the NS momentum and mass balance at each data point. This resulted in convincing reconstructions for moderately challenging scenarios, example seen in figure, where the (reconstructed) lateral and total RMSE were 3.5 mm/s and 3.0 cm/s respectively. The average 4D reconstruction time of the phantom on a NVIDIA Titan V was 3 minutes. An observed limitation with this model is the lack of inlet/outlet handling, leading to underestimation of the true velocities in these regions when momentum balance is strongly enforced. In vivo 4D data was acquired using a GE Vivid E95 system with a 4V probe, where VFI was done using 3D blood speckle tracking (BST), while the LV domain was extracted automatically using the open-source FAST library. We emphasize that the flexibility of the framework lies in the ease of specifying models and data sources, and its general purpose nature invites application to other regularization problems.



4:15 PM **Lagrangian coupling of SPH with ultrasound simulation for vector flow imaging investigation****Damien Garcia¹, Shahrokh Shahriari²**¹*Creatis, Lyon, France*, ²*ON, Canada***Background, Motivation, and Objective**

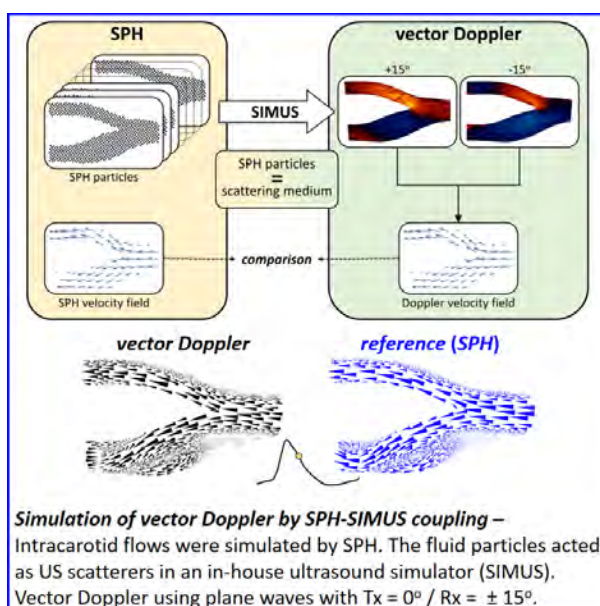
Before embarking on a series of *in vitro* or *in vivo* tests, design of flow-imaging modalities are generally more efficient through computational models as multiple configurations can be tested in a short time. To that end, simulations must generate realistic blood flow dynamics and realistic ultrasound signals. The current *in silico* ultrasound simulation techniques suffer mainly from uncertainty in providing accurate trajectories of moving ultrasound scatterers. When using mesh-based Eulerian methods for time-varying flow fields, pathline computation involves incremental interpolations. Truncation errors can accumulate significantly and make the pathlines unreliable. These errors distort beam-to-beam inter-correlation inherently present in ultrasound imaging. It is thus a technical issue to model a physically correct motion of the scatterers considering their interaction with boundaries and neighboring scatterers. Our hypothesis is that *in silico* analysis of emerging ultrasonic imaging modalities can be implemented accurately by using meshfree Lagrangian methods.

Statement of Contribution/Methods

We developed an original fluid-ultrasound simulation environment based on a meshfree Lagrangian CFD (computational fluid dynamics) formulation, which allows analysis of ultrasound flow imaging. This simulator combines smoothed particle hydrodynamics (SPH) and Fourier-domain linear acoustics (SIMUS = simulator for ultrasound imaging). In this meshfree method, the fluid particles also acts as individual ultrasound scatterers, resulting in a direct and physically sound fluid-ultrasonic coupling. We used the in-house algorithms for fluid and ultrasound simulations to simulate high-frame-rate vector flow imaging. The potential of the particle-based method was tested in two-dimensional simulations of vector Doppler for the intracarotid flow. The Doppler-based velocity fields were compared with those issued from SPH.

Results/Discussion

A movie of the SPH simulations is available in [www.biomedcardio.com/images/SPHmovie.gif]. In contrast to mesh-based methods, no numerical tricks were required to model a physically correct motion of the ultrasound scatterers. SPH-SIMUS coupling enables realistic simulations of ultrasound flow imaging. The proposed simulator has also the advantage to be 3-D compatible and easily parallelizable.



4:30 PM

Flow changes after biological and mechanical aortic valve implantation measured with VFI

Kristoffer Hansen¹, Hasse Møller-Sørensen², Jesper Kjaergaard³, Tin-Quoc Nguyen¹, Jørgen Arendt Jensen⁴, Michael Bachmann Nielsen¹

¹Dept. of Diagnostic Radiology, Copenhagen University Hospital, Copenhagen, Denmark, ²Dept. of Cardiothoracic Anesthesiology, Copenhagen University Hospital, Copenhagen, Denmark, ³Dept. of Cardiology, Copenhagen University Hospital, Copenhagen, Denmark, ⁴Technical University of Denmark, Lyngby, Denmark

Background, Motivation, and Objective

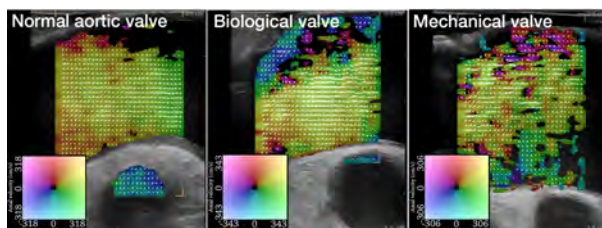
Aortic valve stenosis (AS) increases peak systolic velocity (PSV) and flow complexity in the ascending aorta (AA), and is treated with either biological or mechanical implants. Vector flow imaging (VFI) is an angle independent ultrasound method for flow assessment. In contrast to conventional ultrasound, VFI can quantify flow complexity i.e. vector concentration (VC) in long axis (LAX) and secondary rotation (SR) in short axis (SAX) view. Study aim was to evaluate flow changes only visible with VFI before and after valve implantation in patients (pts.) with AS.

Statement of Contribution/Methods

VFI on a commercial scanner (Pro Focus 2202 UltraView, BK Medical) with a linear transducer (Type: 8670, BK Medical) was applied intraoperatively on the AA. 4 pts. (mean: 69.5 y.o.) scheduled for biological valve implants and 4 pts. (mean: 62.8 y.o.) for mechanical valve implants were scanned before and after surgery. 4 pts. (mean: 57.3 y.o.) with normal aortic valve were scanned for comparison. VFI data of the AA were obtained in LAX and SAX view during systole. VC ranges from 0 to 1 (complex to laminar flow), and SR is measured in Hz. PSV was obtained with conventional spectral Doppler. The figure shows VFI of the AA in LAX view after valve implantation compared to the normal aortic valve.

Results/Discussion

All numbers are mean values (with standard deviation). Before surgery, pts. treated with mechanical (PSV: 356.3 (64.3) cm/s; SR: 15.3 (7.8) Hz; VC: 0.18 (0.03)) and biological valve (PSV: 350.0 (80.8) cm/s; SR: 17.9 (2.6) Hz; VC: 0.26 (0.07)) had more complex flow with higher velocities compared to pts. with normal aortic valve (PSV: 124.8 (16.7) cm/s; SR: 2.9 (1.1) Hz; VC: 0.83 (0.09)). After surgery, velocities were lower with mechanical (PSV: 214.5 (30.1) cm/s; SR: 5.6 (3.0) Hz) compared to biological valve (PSV: 241.5 (47.5) cm/s; SR: 13.2 (1.8) Hz). VC was higher with biological (0.68 (0.05)) compared to mechanical valve (0.56 (0.09)) indicating a more laminar flow despite higher velocities. The mechanical valve has a larger opening with cusps attached centrally in the lumen opposed to the biological valve, which may explain the differences found. Normal flow was neither found for biological nor mechanical implants. VFI can provide new parameters for flow evaluation and be useful for aortic flow assessment before and after valve implantation and in the development of mechanical valves.



4:45 PM

Vector Projectile Imaging to detect regional changes in extracranial blood velocity: A lower-body suction studyJason Au¹, Billy Y. S. Yiu¹, Hélène So^{1,2}, Danielle Greaves¹, Richard Hughson¹, Alfred C. H. Yu¹¹Schlegel-UW Research Institute for Aging, University of Waterloo, Waterloo, ON, Canada, ²Sciences pour l'ingénieur, Sorbonne Université, Paris, France**Background, Motivation, and Objective**

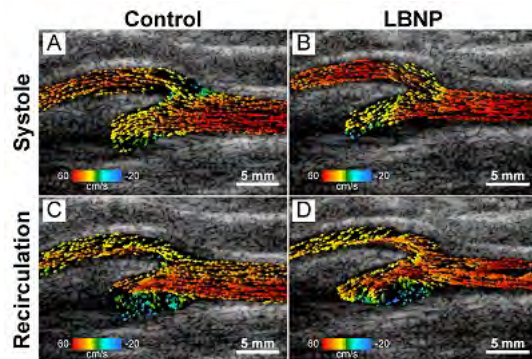
Recent innovations combining high frame rate ultrasound (HiFRUS) and multi-angle plane wave imaging have allowed full-field angle-independent blood velocity estimation, which may aid in the quantification of complex hemodynamic features. While there has been some success in applying vector projectile imaging (VPI) to qualitatively assess flow conditions, there have been few attempts to investigate the sensitivity of HiFRUS techniques to quantify experimental changes in complex hemodynamics *in vivo*. In this study, we examined the utility of HiFRUS to detect experimentally-induced reductions in conduit artery hemodynamics by reducing venous return using lower body negative pressure (LBNP).

Statement of Contribution/Methods

Seven healthy adults (27±4 years of age) participated in this study. Ultrasound images were acquired sequentially using both multi-angle HiFRUS (US4US; SL1543 probe; 6 kHz PRF; Tx° -10, 10; Rx° -10, 0, 10) and a conventional clinical ultrasound (Phillips iE33; L9-3 probe) at the right common carotid artery (CCA) bifurcation. VPI was used to visualize velocity vectors at the CCA before and after application of -45 mmHg LBNP, which was induced by controlled suction of air from an apparatus sealed at the participants' waists. Internal carotid artery (ICA) flow jet width and recirculation size were manually identified in two participants for whom all extracranial arteries could be visualized in one plane.

Results/Discussion

Application of LBNP elicited a reduction in cardiac output ($\Delta-1.2\pm0.5$ L/min; $P<0.01$). Peak CCA blood velocities were decreased using both conventional pulsed-wave Doppler ($\Delta-11.3\pm7.96$ cm/s; $P<0.01$) and angle-independent HiFRUS ($\Delta-9.98\pm11.23$ cm/s; $P=0.05$). In two participants, maximum ICA jet width was reduced following LBNP (1: 3.86 to 2.91 mm; 2: 4.09 to 3.17 mm; Fig1a, Fig1b) whereas the recirculation zone height appeared unchanged (1: 4.33 to 4.21 mm; 2: 3.14 to 4.07 mm; Fig1c, Fig 1d). Using a LBNP model, we demonstrated the sensitivity of HiFRUS to detect experimental changes in extracranial blood velocity, but also potential for VPI to reveal subtle changes in complex hemodynamic patterns during altered flow conditions in humans.



5:00 PM

Vector Flow Imaging Validated by Patient-Specific Fluid-Structure Interaction (FSI) Models

Marie Traberg¹, Sophie Nielsen², Carlos Villagomez-Hoyos³, Jacob Olesen³, Borislav Gueorguiev Tomov², Kristoffer Hansen⁴, Caroline Ewertsen⁴, Michael Bachmann Nielsen⁴, Jørgen Arendt Jensen⁵

¹*Electrical Engineering, Technical University of Denmark, Kongens Lyngby, Denmark*, ²*Technical University of Denmark, Denmark*, ³*BK Ultrasound, Denmark*, ⁴*Copenhagen University Hospital, Denmark*, ⁵*Technical University of Denmark, Lyngby, Denmark*

Background, Motivation, and Objective

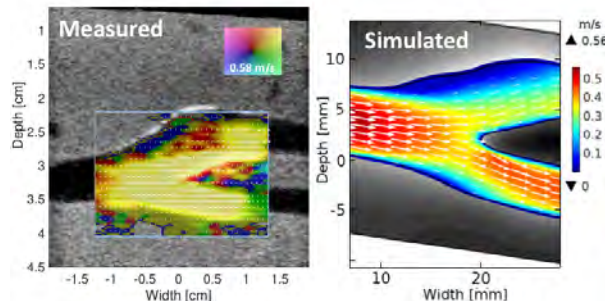
Synthetic aperture vector flow imaging (SA VFI) is a new ultrasound technique that visualises complex flow in the carotid bulb real time. But SA VFI requires validation prior to implementation in the clinical work-up of vascular diseases. Currently, it is impossible to validate SA VFI of complex flow as no other imaging modality is suitable. Fluid-Structure Interaction (FSI) models can potentially solve this. But an extensive number of test subjects is needed, and the models must be generic in the numerical solver setting and, at the same time, patient-specific. This paper presents a FSI model framework that applies to multiple cases and can be used for validation of SA VFI of complex flow. The models must be precise and accurate.

Statement of Contribution/Methods

Data were obtained from carotid arteries of 3 healthy volunteers. Wall-less tissue mimicking phantoms were constructed for each volunteer based on magnetic resonance imaging data. SA VFI data were acquired over 10 s for all phantoms using a linear array (BK9032, BK Medical) and the experimental ultrasound scanner SARUS. The imaging plane was aimed for the center of the carotid bulb. The FSI models were constructed using SolidWorks and Comsol Multiphysics. Model geometries include the vessel lumen surrounded by a block of tissue mimicking material. Inlet velocity profiles were obtained from the measured mean spatial velocity profile and pressure were applied on the outlets to match measured volume flow rates. Tissue displacement was obtained from B-mode imaging and compared to FSI simulation.

Results/Discussion

Fig. 1 shows the measured velocity field (from commercial scanner) and simulated with FSI model framework at peak systole. Visual comparison indicates comparable flow patterns. Peak velocity magnitude with SA VFI is 0.58 m/s, with FSI 0.56 m/s. For all cases deviation between SA VFI and FSI is 0.12 (+/-0.16) m/s. Maximum measured displacement is 0.26 mm, in FSI 0.35 mm. For all cases deviation between SA VFI and FSI is 0.21 (+/- 0.176) mm. The significant deviation is probably due to mismatch between tissue material properties in measurement and simulation. This requires more investigation. Regarding precision, the FSI model solution has a precision of 6.88%, SA VFI is precise within 10%. All this combined suggests that this generic FSI model is a step towards a validation tool for SA VFI in complex geometries.



5:15 PM

Combined contrast-enhanced echocardiography and 2D vector flow mapping at high frame rate using diverging waves

Luzhen Nie¹, Thomas Carpenter¹, David Cowell¹, James R. McLaughlan^{1,2}, Arzu Çubukçu³, Steven Freear¹

¹School of Electronic and Electrical Engineering, University of Leeds, United Kingdom, ²Leeds Institute of Cancer and Pathology, University of Leeds, United Kingdom, ³East Cheshire NHS Trust, United Kingdom

Background, Motivation, and Objective

The combination of diverging waves (DWs) and microbubbles (MBs) could revolutionize the paradigm in contrast enhanced echocardiography (CEE), by providing capabilities for high frame-rate (HFR) vector flow mapping (VFM) and improved image quality. However, the image formation by coherent summation of echoes from multiple steered DWs is subject to both tissue and MB motion, and thus a deterioration in the performance of spatial compounding. In this study, a method for 2D motion estimation (ME) and motion compensation (MC) was proposed for DW CEE. This enabled a HFR duplex cardiac imaging tool for simultaneous contrast mode imaging and 2D VFM *in vivo*.

Statement of Contribution/Methods

A Verasonics P4-2 transducer was connected to the Leeds Ultrasound Array Research Platform (UARP) performing DW amplitude modulation (4-cycle 2.78 MHz sinusoids, MI 0.12, 8 angles, PRF 4 KHz).

Multi-scale 2D ME was applied to *in-vivo* RF frames used for compounding in the polar grid. The first stage of ME involved the rigid block matching and correlation correction [Nie et al., IUS, 2016]. The coarse ME guided finer searching through deforming the kernels and iteratively decreasing the kernel size. MC was then applied to every RF frame prior to coherent summation. 2D VFM at 250 Hz was also calculated from ME without additional pulses.

Results/Discussion

Without MC, dark regions are found in (a) and (c) as highlighted by green arrows. After MC, the MB signal within the same region has been retrieved and the septum has been intact as shown in (b). The ability to differentiate the cardiac wall using the contrast imaging mode has also been strengthened after MC in (d). Fig. (e) shows the result of down-sampled 2D VFM and it demonstrates that the blood flow reaches its maximum velocity at around 0.6 m/s within the region that is dark in (a). In conclusion, MC is necessary for HFR CEE. Without extra pulses, the combined information of CEE and VFM in this study allows improved assessment of cardiac function.

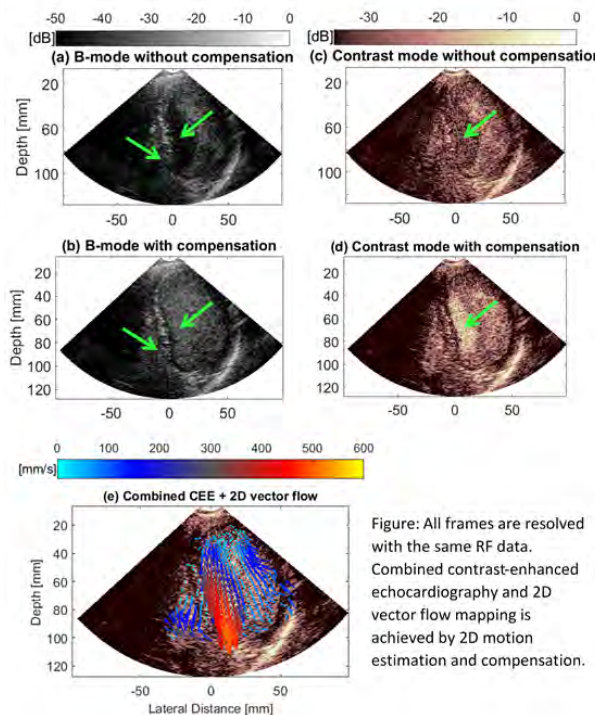


Figure: All frames are resolved with the same RF data. Combined contrast-enhanced echocardiography and 2D vector flow mapping is achieved by 2D motion estimation and compensation.

5D - PAT: Acoustic Tweezers and Particle Manipulation

Ikuta (200)

Wednesday, October 24, 8:00 am - 9:30 am

Chair **Eun Sok Kim**
University of Southern California

5D-1

8:00 AM **Magnetic-Free Radio Frequency Circulator Based on Spatiotemporal Modulation of MEMS Resonators**
Matteo Rinaldi¹
¹*Northeastern University*

Background, Motivation, and Objective

Circulators are well-known RF components that utilize nonreciprocal (i.e. unidirectional) electromagnetic (EM) wave propagation to isolate transmit and receive paths in a wireless system providing two-way communications on the same frequency channel. The conventional approach for realizing circulators is based on magnetic biasing and ferromagnetic materials. However, despite their maturity and broad availability, magnetic circulators are largely unattractive for integration, due to their relatively large size (larger than 25 mm), the incompatibility of magnetic materials with IC technology, and geopolitical issues related to the limited availability of such materials in nature. These problems drove attempts to design active magnet-free non-reciprocal devices based on transistors, exploiting the fact that transistors are inherently non-reciprocal components. These approaches never became popular, due to their poor linearity and noise performance. An alternative approach that has recently gained a lot of attention for magnet-less non-reciprocity is based on imparting an effective angular momentum to a resonant circuit, through spatiotemporal modulation of three strongly-coupled resonant cavities with signals of the same magnitude and phase difference of 120°. So far, this approach has been realized on a printed-circuit board by using LC tanks. However, the use of inductors with limited Q-factor inevitably increases the circulator insertion loss and the overall device size and it requires the use of a relatively large modulation frequency (~1/10 of the RF frequency). Furthermore, the use of solid state varactors to implement the frequency modulation fundamentally limits the linearity of the circulator and complicates the modulation network. This talk will introduce a revolutionary approach to the problem that merges for the first time angular-momentum biased devices with MEMS devices, thereby offering the possibility to build extremely high-Q resonators and filters while completely eliminating the need for inductors and solid-state varactors addressing the fundamental challenges that are currently hindering the full deployment of magnetic-free circulators. By means of fundamental innovations in MEMS design and fabrication, we demonstrated a magnetic-free radio-frequency (RF) Microelectromechanical Resonant Circulator (MIRC) architecture capable of achieving the linearity, bandwidth, insertion loss and isolation levels required for military and commercial systems at a chip-scale size, orders of magnitude smaller than any existing implementation of circulators commercially available to date. The magnetic-free non-reciprocity is achieved by imparting an effective angular momentum bias to a MEMS resonant circuit. The angular momentum is efficiently realized through spatiotemporal modulation of three strongly coupled high-Q (>1000) Aluminum Nitride (AlN) MEMS Resonators. Differently from previous demonstrations based on varactor-based frequency modulation of low-Q LC networks, we implemented the spatiotemporal modulation by means of switched capacitors which minimizes the complexity of the modulation network, increases the modulation efficiency and mitigates the fundamental linearity limitations associated with solid-state varactors. We experimentally demonstrated MIRC prototypes operating up to ~2.5 GHz with insertion loss < 4 dB; isolation>15 dB; P1dB>28 dBm and IIP3>40 dBm. Furthermore, due to the high Q of the MEMS resonators employed, strong non-reciprocity is achieved with an ultra-low modulation frequency (<0.5% of the RF frequency, orders of magnitude lower than previous demonstrations) which directly enables a total power consumption of only ~10s µW which is the lowest ever reported for magnetic-free RF circulators based on temporally modulated circuits.

test

Statement of Contribution/Methods

1

Results/Discussion

2

8:30 AM Trajectory Optimization of Levitated Particles in Mid-air Ultrasonic Standing Wave Levitators

Tatsuki Fushimi¹, Asier Marzo¹, Thomas L. Hill¹, Bruce W. Drinkwater¹

¹*Department of Mechanical Engineering, University of Bristol, Bristol, United Kingdom*

Background, Motivation, and Objective

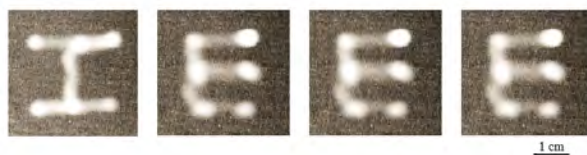
Ultrasonic standing wave levitators have a broad range of potential applications as a non-contact transportation method in pharmaceutical, chemical, or biological procedures. In these devices, the particle is held in mid-air and moved to the target position, either by mechanically translating the levitator or refocusing the standing wave with a phased-array. However, most acoustic levitators do not have feedback on the position of the particle and controlled manipulation has only been shown in near-field acoustic levitators. Without a control system, the path that the levitated particle follows differs from the desired path due to the presence of gravity, the system dynamics and the low damping of air. As tracking levitated millimeter-sized particles in mid-air at the required frame rates is technically challenging and costly, we explore offline optimization of the trajectory as a solution. Hence, the aim of this optimization is to increase the accuracy with which the desired path is followed and maximize the transport velocity, benefitting contactless transportation and manipulation applications. This method could also be applied to display technologies in which a fast travelling particle outlines different shapes to convey information.

Statement of Contribution/Methods

We use a mid-air single-axis acoustic levitator made of 60 transducers and operating at 40 kHz. The equilibrium point and trapping stiffness of the particle at each point is determined experimentally and compared against the simulated equilibrium point with good agreement. A dynamic trajectory generator is implemented to create complex trajectories, such as letters of the alphabet, to be followed by the particle. Various optimization schemes are explored, along with the relationship between the experimental configuration and the device performance.

Results/Discussion

Long exposure (3.2 seconds) trajectory of a 1mm diameter expanded polystyrene particle tracing the letters ‘IEEE’ is shown in Fig A. The optimization process has improved the path following accuracy and transport speed. There is a further scope of improvement of speed and accuracy by enhancing the optimization process, increasing the transducer power, and increasing the number of transducers.



8:45 AM

Acoustic Biomolecules Enable Acoustic Trapping and Manipulation of Genetically Engineered CellsDi Wu¹, Diego Baresch², Dina Malounda¹, Paulene Abundo¹, David Maresca¹, Mikhail Shapiro¹¹Caltech, United States, ²Imperial College London, United Kingdom**Background, Motivation, and Objective**

The ability to use ultrasound to position and apply force to specific biomolecules and engineered cells would have a large impact in multiple areas of biology and medicine. However, most biomolecules and cells lack the acoustic properties needed to experience differential acoustic radiation force (ARF) relative to other cells or biological media. Here, we describe a class of biomolecules and genetic elements that overcome these limitations, enabling acoustic manipulation. These biological constructs are based on gas vesicles (GVs), which are genetically encoded gas-filled protein nanostructures naturally found in buoyant cyanobacteria. Here we report that, in addition to their uses in molecular imaging [1,2], GVs enable molecular and cellular ARF.

Statement of Contribution/Methods

GV particles, harvested from their native cyanobacteria host, are fluorescently labeled for visualization. We isonified the particles while tracking their position, and quantified the ARF by applying a force balance with viscous drag force. Furthermore, we genetically engineered *E.coli* cells to express GVs, mixed these cells with wildtype bacteria, and isonified the mixed population. We visualized each population within their respective fluorescence filters.

Results/Discussion

Our results show that GVs experience significant ARF at MHz frequencies, allowing their trapping and positioning at pressure antinodes. To our knowledge, these are the first biomolecules and the first nano-sized particles to be directly trapped with ARF. Furthermore, we observed that *E.coli* cells genetically engineered to express GVs, can be similarly manipulated and trapped, and separated from wildtype *E.coli*. This work establishes GV encoding genes as the first genetic elements for ARF, and opens the door to potential applications in molecular and cellular navigation, patterning, and actuation in a broad range of *in vitro* and *in vivo* contexts.

[1]Shapiro, M. G. *et al.* Nat. Nanotechnol. 9, 311-316 (2014).

[2]Bourdeau, R. W. *et al.* Nature 553, 86-90 (2018).

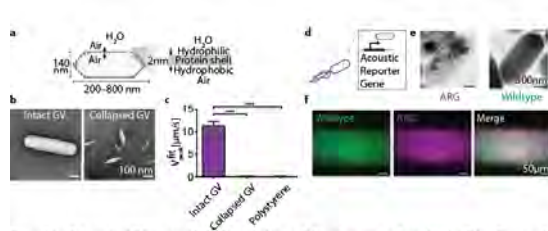


Figure 1 | a, Schematic of GV structure. b, TEM image of intact (left) and pressure collapsed (right) GVs. c, Fitted peak velocity of single particles in an acoustic field. d, Schematic of GV expression in bacteria via GV-encoding genes. e, TEM image of GV-expressing *E.coli* (left), and wildtype bacteria (right). f, fluorescence image of a mixed population of bacteria in an acoustic standing wave. Left: wildtype bacteria. Middle: GV-expressing bacteria. Right: image overlay. ARG, acoustic reporter gene.

9:00 AM Particle Manipulation and Separation Using Macro-Scale Bulk Angled Standing Waves
Kedar Chitale¹, Bart Lipkens¹, Walter Presz, Jr.¹, Benjamin Ross-Johnsrud¹
¹*Flodesign Sonics, Wilbraham, MA, United States*
Background, Motivation, and Objective

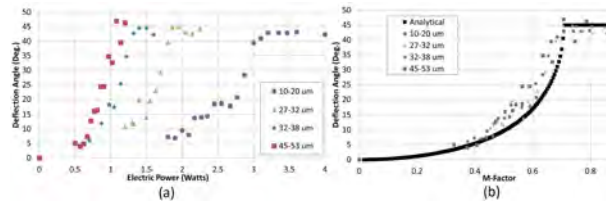
Tilted or angled standing waves have been used at MEMS scale to separate out particles of various sizes very effectively in previous studies. However, the mathematical understanding of such a problem is still limited. In this work, we propose a universal analytical solution for such a problem and study its physics. The motivation is to obtain a universal solution for deflection of a particle inside an angled standing wave for fast predictions. The mathematical formulation is validated with numerical simulations and experiments. Separation experiments are performed to determine the efficiency of macro scale angled wave system. The system shows 90+% efficiency in separating Jurkat T-cells from 30-micron beads. An advantage of such a macro-scale system is higher throughputs (several ml/min)

Statement of Contribution/Methods

A non-dimensional parameter (M) can be defined that represents the ratio of acoustic radiation force to the viscous drag force. This parameter plays a key role in determining particle deflection. An analytical solution is derived from the integral equations of time of flight using a Galilean transformation. The particle deflection is shown to depend on the wave angle and the M parameter. This analytical model can be used to obtain universal curves for all possible particle deflections based on their properties.

Results/Discussion

The analytical model has been validated using numerical trajectory calculations and experiments with known sized beads. The attached figure shows experimental results for particle deflection angle for beads of known size and acoustic contrast with variation in electrical power supplied to the transducer. The figure also shows the comparison of these results with the universal curve of M parameter. Experimental results of separation of Jurkat T-cells from 30-micron beads will be presented showing 90+% efficiency of separation. The application of this technology could be in affinity cell selection in cell therapy process.



9:15 AM Numerical simulation of particle motion in a phase modulated surface acoustic wave microfluidic device

Gergely Simon¹, Marco A.B. Andrade², Mathis O. Riehle³, Marc P.Y. Desmulliez¹, Anne L. Bernassau¹

¹School of Engineering and Physical Sciences, Heriot-Watt University, Edinburgh, United Kingdom, ²Institute of Physics, University of São Paulo, Brazil, ³Centre for Cell Engineering, Institute for Molecular, Cell and Systems Biology, CMVLS, University of Glasgow, United Kingdom

Background, Motivation, and Objective

Cell separation is an important enabling step in many research areas from biotechnology to food safety and diagnosis. Sorting techniques utilising acoustic methods are particularly favourable for their non-contact, label-free and scalable properties. A continuous phase modulated batch sorting technique using surface acoustic wave device was previously developed by our research group and validated against a theoretical framework. However, acoustic streaming was not included in this analysis. In this paper, we used the finite element package COMSOL Multiphysics to analyse particle motion in phase-modulated surface wave fields and identify critical particle diameter (CPD), below which streaming fields dominate motion and prevent efficient sorting.

Statement of Contribution/Methods

A two-dimensional cross section of the device has been modelled to reduce the computational complexity. Instead of using a coupled piezoelectric-structural mechanics-acoustics model, the simulation was further simplified and performed on a thermoviscous acoustic domain only, with appropriate impedance and velocity boundary conditions at the channel walls. The model was used to obtain the first order pressure field, which in turn was utilized to calculate the second order streaming velocity field. The pressure field was used to calculate the radiation force acting on particles using Gorkov's potential approach, and the streaming velocity field gave rise to the viscous drag force. The pressure and velocity fields were used in a particle tracing module to identify CPD, the radiation force, and streaming dominated regions within the channel. The investigation of particle motion was carried out for various relative phase of the two transducers to investigate different stages of particle sorting and to generate particle trajectories. Numerical simulations were validated with experiments for different particle sizes and materials.

Results/Discussion

The suitable mesh size was 1/10th of the viscous boundary layer thickness near the sidewalls and half of it in the bulk of the medium to be able to capture streaming fields due to thermoviscous effects. The effect of particle density on the critical diameter was analysed by varying materials: polystyrene (density 1.05 g/cm³, similar to cells), PMMA ($\rho = 1.25 \text{ g/cm}^3$), and iron-oxide filled PS ($\rho = 1.57 \text{ g/cm}^3$). Varying particle material in the model had no significant effect on the critical particle diameter, in all cases CPD was around 5 μm . Experimental validation was carried out to show that for particle diameter of 8 μm and above, more than 95% of particles were trapped and influenced by the primary radiation force. With particle diameters below 3 μm particle diameter this figure dropped to $\leq 20\%$. Simulation and experimental particle trajectories show excellent agreement for sizes larger than the CPD, 10 and 15 μm polystyrene particles and 10 μm polystyrene and iron-oxide particles were used for validation.

5E - SAW Modeling & Design 2

Ikuta (200)

Wednesday, October 24, 10:30 am - 12:00 pm

Chair **Marc Solal**
Qorvo, Inc

5E-1

10:30 AM **Study on High-Isolation SAW Duplexer with On-Chip SAW Compensation Circuit Optimized for Isolated Multiple Frequency Bands**

Masafumi Iwaki^{1,2}, Masanori Ueda¹, Yoshio Satoh³

¹TAIYO YUDEN CO., LTD., Japan, ²Graduate School of Engineering, Chiba University, Japan, ³TAIYO YUDEN Mobile Technology Co., Ltd., Japan

Background, Motivation, and Objective

There exist increasing demands for improving an isolation of acoustic duplexers that is used to cellular handsets to keep the communication quality. In the circumstances, we reported the method to improve the isolation by reducing the transmitter leakage to the receiver using the well-designed compensation circuit fabricated on the carrier substrate by a distributed constant line and L, C chip components [1-3]. However, the size of duplexer and variation of the electrical characteristics are large because it consists of the discrete off-chip components.

Statement of Contribution/Methods

In this paper, we present a method, which is providing the improvement of isolation in multiple frequency bands simultaneously using an on-chip small SAW compensation circuit. The basic working principle of the compensation circuit, which is the single series circuit consist of interdigital-capacitor as an attenuator and a double mode SAW (DMS) resonator as a phase shifter, is based on the idea to improve the isolation in a single frequency band [4].

In this work, we totally change the configuration of the interdigital transducer (IDT)s of the DMS resonator having more flexibility in the phase as like a DMS filter for a passband. By changing the design of the IDTs, the phase changes of lower and higher side slopes and poles in the DMS resonator fit separated frequency bands in the main filters. This method allows us to improve the isolation in two or more multiple separated frequency bands simultaneously.

Results/Discussion

We applied above method to the SAW duplexer utilizing Shear horizontal (SH)-SAW on a LiTaO₃ substrate for LTE Band-I. The compensation circuit was implemented between transmitter and receiver ports on the filter chip along with the main filter circuit. As a result, the isolation levels in a both transmitter and receiver bands were improved around 10 dB compared with the isolation in the no-compensation circuit duplexer.

In the proposed method, the compensation circuit is fabricated using a SAW process technology as same as that of the main filter circuit. Therefore, the variation in the isolation is better than that of the off-chip circuit case. Moreover, it is possible to adjust the phase of the compensation circuit finer than that of the off-chip circuit case too.

- [1] J. Tsutsumi, *et al.*, Proc. of 38th EuMC (2008) p.1066-1069
- [2] J. Tsutsumi, S. Inoue, M. Iwaki, *et al.*, Proc. of IUS2011 (2011) pp. 1833-1836
- [3] M. Iwaki, *et al.*, Proc. of EuMC2011 (2011) pp.751-754
- [4] M. Iwaki, *et al.*, Proc. of Symp. On Ultrasonic Electronics, Vol.38, 2017, 1P3-9.

10:45 AM

Low-loss, high-frequency and large-coupling SH SAW resonators based on SiN/LiNbO₃/Si

Jie Zou¹, Victor Plessky², Robert Hammond¹, Ventsislav Yantchev³, Patrick Turner¹, Sean McHugh¹, Sohrab Samadian¹, Neal Fenzi¹

¹Resonant Inc., Goleta, CA, United States, ²GVR Trade SA, GORGIER, Switzerland, ³Chalmers University of Technology, Goteborg, Sweden

Background, Motivation, and Objective

The loss mechanisms of SH mode on LT (LiTaO_3) and LN (LiNbO_3) have been intensively studied recently. By bonding the sub-wavelength-thick LT or LN layer to a high-velocity substrate, the SH mode no longer couples with the bulk mode in substrate and the leaky component is effectively eliminated. Given this, the acoustic propagation loss no longer dictates the choice of piezoelectric substrate cut angle and ultra large k^2 cuts can be taken advantage of, such as low cut angle YX-LN.

Emerging 5G communication standards require high frequency, low loss, and wide bandwidth filters. While the low-cut LN bonded to Si provides ultra large k^2 and low loss, the phase velocity is still low (3000-4000m/s), limiting its application in mobile phone filters. A high velocity layer beneath the piezoelectric LT or LN does not effectively increase the phase velocity of the SH mode; rather, by adding a high velocity layer overlay on top of the transducer and LN, the phase velocity of the SH mode can be significantly increased with a little trade-off on the k^2 . In this way, a resonator having low-loss, high-frequency, and large- k^2 SH-wave can be achieved and shows great potential for current and next-generation RF front ends.

Statement of Contribution/Methods

As depicted in Fig. 1, unlike LN substrates, the SH wave in LN/Si and SiN/LN/Si no longer couples with the bulk mode and leaks into the substrate, as the substrate bulk velocity is higher than the surface SH mode.

As shown in Fig. 2, there is a trade-off between the v_o and k^2 by varying SiN thickness for the SH wave propagating in SiN/LN/Si. The open phase velocity can be effectively boosted from 4400m/s to 5200m/s, showing a near 20% increase when h_{SiN} is up to around 0.3λ . Although the k^2 is decreased by increasing h_{SiN} , the absolute value for k^2 is still above 10% even with a large h_{SiN} due to the super large intrinsic k^2 of SH wave in low-cut YX-LN. This is very promising for mobile phone filter requirements.

Since the acoustic propagation loss is no longer the main concern for the cut angle selection, the optimal cut angle can be chosen to optimize v_o and k^2 for YX-LN. In Fig. 2, the phase velocity and coupling coefficient versus the rotation angle of Y-cut LN for the SH wave propagating in SiN/LN/Si show a similar trend compared with the LN substrate. For cut angles between -20° and 50°, the v_o can be around 5000m/s and k^2 7%-20% for h_{SiN} of 0.1λ - 0.3λ .

Results/Discussion

In this paper we present simulations of a sub-wavelength-thick LN layer on high-velocity Si substrate effectively eliminates the leaking component of the SH mode, and reduces the propagation loss. By overlaying a high-velocity layer such as SiN on top of LN/Si, the phase velocity of the SH wave can be largely enhanced at a small cost of k^2 . By carefully engineering the LN and SiN thicknesses, as well as LN rotation angle, the high-velocity and large- k^2 can be achieved simultaneously, and the high-performance SiN/LN/Si SH devices show great potential for current and next-generation RF front ends.

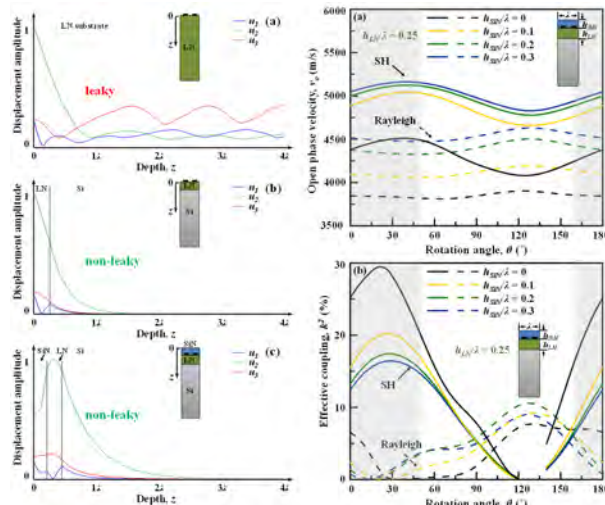


Fig. 1. Comparison of displacement profile of (a) LN substrate, (b) LN/St, and (c) SiN/LN/Si for the SH wave.

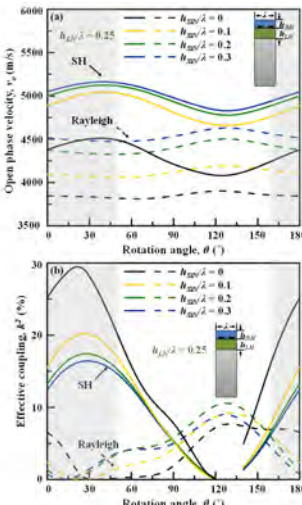


Fig. 2. Calculated (a) v_o and (b) k^2 for varied cut angle of YX-LN with $h_{\text{LN}}=0.25$.

11:00 AM

HIERARCHICAL CASCADING IN FEM SIMULATIONS OF SAW DEVICES**Julius Koskela¹**, Victor Plessky¹¹*GVR Trade SA, GORGIER, Switzerland***Background, Motivation, and Objective**

Fast development of SAW filters, which is becoming ever more complicated, demands precise and universal simulation tools. The finite element method (FEM) is very attractive due to its remarkable generality. FEM can handle arbitrary materials and crystal cuts, different electrode shapes, and structures including multiple metal and dielectric layers. Traditionally, the application of FEM to the SAW devices has been hampered by the difficulty of modeling the effectively semi-infinite substrate crystal, and by the very large memory consumption and long computation times required. These obstacles have been essentially removed by the recent introduction of the perfectly matched layers (PML) [1] and the hierarchical cascading method [2, 3]. The goal of this paper is to provide of an overview of the approach, focusing on aspects relevant to practical SAW modeling.

Statement of Contribution/Methods

The device geometry is analyzed and partitioned into small, repeatedly used building blocks. Identical building blocks need to be modeled with FEM only once. To avoid instabilities in the simulation, the PMLs need to be chosen according to the anisotropy of the substrate crystal. Moreover, to ensure efficient and accurate simulation, the computational mesh should be optimized to the substrate. The device is presented as a hierarchical cascading tree, where smaller blocks are combined into larger blocks until the multi-port electric admittance of the entire device has been simulated. Inverse cascading can be used to enable more options for analyzing the device, such as field and power flow visualization at every point of the device, and the evaluation of acoustic radiation losses and Q-factor.

Results/Discussion

The hierarchical cascading approach has proven an efficient and capable tool for simulating finite SAW devices. The electric response can be evaluated and loss mechanisms analyzed in complex layered SAW structures. 2D simulations typically require less than 16GB RAM and can be run in a few seconds per frequency point. The approach has been shown feasible for 3D simulation of finite SAW devices [4].

- [1] M. Mayer et al., 2007 IEEE International Ultrasonics Symp.
- [2] J. Koskela et al., 2016 IEEE International Ultrasonics Symp.
- [3] J. Koskela et al., TH02C_4, in Proc. of IMS, 2017, Honolulu, Hawaii.
- [4] M. Solal et al., 2017 IEEE International Ultrasonics Symp.

11:30 AM

Use of Hierarchical Cascading Technique for FEM Analysis of Transverse Mode Behaviors in SAW DevicesXinyi Li^{1,2}, Jingfu Bao¹, Yulin Huang^{1,2}, Benfeng Zhang^{2,3}, Tatsuya Omori², Ken-ya Hashimoto^{2,3}¹*University of Electronic Science and Technology of China, Chengdu, China, People's Republic of*, ²*Chiba University, Chiba, Japan*, ³*Shanghai Jiao Tong University, China, People's Republic of***Background, Motivation, and Objective**

Piston mode structures are widely used to suppress transverse resonances in SAW devices. In general, 3D FEM analysis is used to design the structural parameters. However, the traditional FEM is time consuming even when only one period is chosen as a model. In last IUS, the authors proposed use of the traveling wave source in the FEM analysis for selective excitation of a particular transverse mode. This technique allows us to evaluate reflection characteristics at electrode tips effectively. However, the calculation is slow because it is based on the 3D FEM.

Statement of Contribution/Methods

This paper describes use of the hierarchical cascading technique (HCT) to the 3D FEM analysis of transverse modes in SAW resonators. In addition to the admittance analysis, the scattering analysis at the finger tips are implemented by combining the HCT with the travelling wave source. Based on the simulated reflection coefficient Γ at the electrode tip, transverse mode suppression can be evaluated faster than obtaining admittance curves.

In 3D cases, HCT itself does not accelerate the calculation so much. However, the total execution time can be reduced significantly for parametric sweeping at the structural design because major portion of the FEM matrices is unchanged and their interim results can be reused.

Results/Discussion

In this calculation, the SiO_2 -overlay/Al-electrode/128°YX-LiNbO₃-substrate structure similar to the one in Ref.[1] is chosen. Thicknesses of SiO_2 and Al are 2 μm and 0.24 μm , respectively, and the electrode period and aperture are 2 μm and 100 μm , respectively. A Cu layer with thickness of 0.08 μm is placed on Al electrode tips to build a slow region for the piston mode operation.

Fig.1 shows variation of calculated admittance curves with the length L_s of the slow region from 1.2 μm to 2.8 μm with 0.4 μm step. It is seen how the spurious resonance levels change with L_s . Using HCT, the execution time is 3 min. for each case in parametric sweep for 1 frequency point. In contrast, it is about 30 min. for traditional FEM.

Fig.2 shows calculated $\angle\Gamma$ as a function of lateral wavenumber β_y with different L_s . Piston mode operation occurs when $\angle\Gamma=0$. It is seen that β_y giving $\angle\Gamma=0$ becomes small with L_s , and disappears when L_s is large. Note β_y increases with frequency, and the main resonance occurs at $\beta_y=0$.

[1] V. Yantchev, et al., Proc. IEEE IUS (2017) 10.1109/ULTSYM.2017.8091695

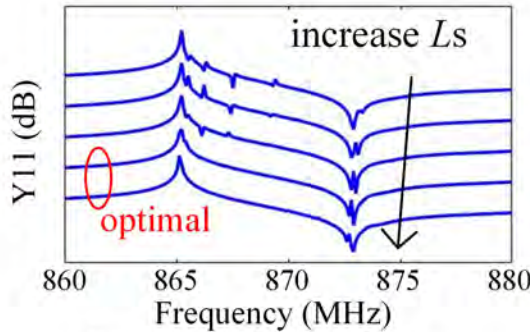


Fig.1 Simulated Y11 curves

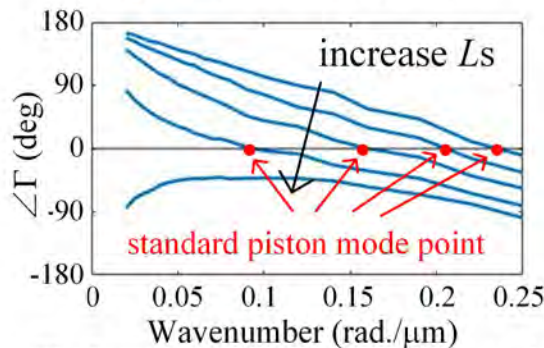


Fig.2 curves of $\angle\Gamma$ verses wavenumber

11:45 AM

FEM-calculation of nonlinear fields in SAW resonators with a finite number of electrodes**Andreas Mayer¹, Elena Mayer¹, Michael Smirnow², Werner Ruile², Markus Mayer², Ingo Bleyl², Karl Wagner²**¹*University of Applied Science, Offenburg, Germany*, ²*RF360 Europe GmbH, Munich, Germany***Background, Motivation, and Objective**

Nonlinearities will play an increasing role in specifying SAW devices because the combination of multiple bands and channels (carrier aggregation) generates nonlinearities that may corrupt signals, especially in Rx paths. Therefore, considerable effort has been spent to understand nonlinearities by finite element (FE-) simulations, since they allow to discriminate between the different contributions from materials, types (direct and cascaded nonlinearities) and mechanisms (elastic, dielectric etc.). However, up to now these FE calculations have been restricted to one single cell in an infinite array and therefore effects that only arise in structures with a finite number of electrodes could not be addressed.

Statement of Contribution/Methods

This approach is based on a perturbation theory, where the linear solutions are obtained from a commercial FE-program (ANSYS). From these linear solutions, i.e. the displacements and the potential, a nonlinear source term is calculated by taking into account all nonlinear material constants of all the materials that are involved. This source term acts as the inhomogeneity of the linear equations at the mixing frequency. Solving these equations with the same commercial FE program yields the nonlinear fields and currents. This approach enables us to use the full flexibility of the commercial FE-program without sacrificing the generality of the nonlinear calculation.

Results/Discussion

This paper shows all nonlinear fields in SAW-structures with a finite number of electrodes in comparison to the periodic cell and corresponding P-matrix calculations. Special focus will be on the transition between the IDT and reflectors and the field distribution at the frequencies of the stopband edges. The good agreement between simulation and measurement shows the validity of our approach.

5F - MEMS Resonator & Application

Ikuta (200)

Wednesday, October 24, 1:30 pm - 3:00 pm

Chair **Sunil Bhave**
Purdue University

5F-1

1:30 PM

S0-Mode Lithium Niobate Acoustic Delay Lines with 1 dB Insertion Loss

Ruochen Lu¹, Tomas Manzaneque¹, Yansong Yang¹, Songbin Gong¹

¹University of Illinois at Urbana-Champaign, Urbana, IL, United States

Background, Motivation, and Objective

The wireless connectivity and low power budget required by many Internet of Things (IoT) devices are demanding novel chip-scale radio frequency signal processing functions with little or no power consumption. Acoustic delay line structures (ADL) are a promising enabler as they can provide a variety of functions, including time delay, filtering, correlation, repeating, and sensing, while being passive and compact. These ADL functions have been previously explored on SAW platforms. However, their performance is limited in insertion loss (IL) and bandwidth (BW). Fundamentally, their high IL and small FBW arise from the insufficient electromechanical coupling (k^2) and narrowband uni-directionality in SAW devices.

Statement of Contribution/Methods

In this work, we resort to the S0 mode in suspended lithium niobate (LiNbO₃) thin films, which has recently been demonstrated with higher k^2 (30%) than SAW devices, to overcome the BW and loss limitations. The devices are built with a pair 250 nm Al IDTs that are separated with various distances on top of an 800 nm LiNbO₃ thin film. To minimize the IL due to bi-directionality in transduction, a single phase unidirectional transducer (SPUDT) design formed by unit cells of a periodicity of λ is employed (Fig. 1). Each cell consists of a pair of transduction electrodes ($\lambda/8$ wide) and a $3\lambda/8$ wide reflection electrode. In comparison to SAW devices, our design feature two major advantages. First, the higher k^2 of S0 permits a wider transducer bandwidth and lower loss. Second, a higher reflectivity per electrode can be achieved by mass loading a suspended film (as compared to a bulk substrate). Thus, a higher directionality can be obtained with less unit cells and wider bandwidth.

Results/Discussion

ADLs with 20 transducer cells and different gap widths (0.12 – 1.00 mm) were fabricated in-house. The measured S-parameters of the SPUDT-embedded delay line with 20 cells are shown in Fig. 2. The measured performance shows an IL as low as 0.9 dB and FBW of 4% for the shortest delay of 75 nS. The longest delay is measured around 200 ns with a slight larger IL of 1.3 dB. In conclusion, ADLs based on S0 mode on thin-film LiNbO₃ have been demonstrated with record-breaking low IL over a comparatively large bandwidth.

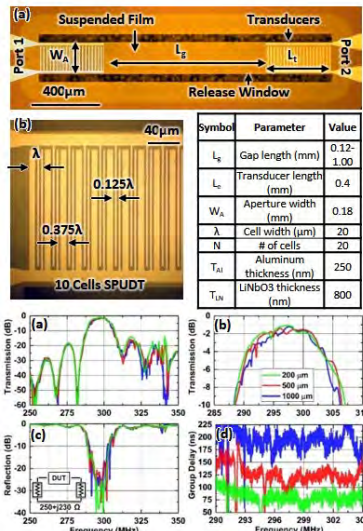


Fig. 1 Optical microscope images of the fabricated acoustic delay lines with single-phase unidirectional transducers (SPUDT), both (a) zoomed-out and (b) zoomed-in image. The parameters are listed in the inset Table.

Fig. 2 Measured S-parameters for delay lines with 20 transducer cells and different gap width (matched input and output port). (a) Zoomed-out and (b) zoomed-in transmission response show low IL (as low as 1 dB). (c) Reflection response and (d) group delay response for the measured devices. The ripples in the group delay are caused by the small multi-reflections between ports.

| Symbol | Parameter | Value |
|-----------|-----------------------------------|-----------|
| L_g | Gap length (mm) | 0.12-1.00 |
| L_t | Transducer length (mm) | 0.4 |
| W_a | Aperture width (mm) | 0.18 |
| λ | Cell width (μm) | 20 |
| N | # of cells | 20 |
| T_{Al} | Aluminum thickness (nm) | 250 |
| T_{LN} | LiNbO ₃ thickness (nm) | 800 |

1:45 PM

Investigations on the Quality Factor of Lithium Niobate Laterally Vibrating Resonators with Figure of Merit greater than 1,500

Luca Colombo¹, Abhay Kochhar¹, Gabriel Vidal-Álvarez¹, Gianluca Piazza¹

¹ECE, Carnegie Mellon University, Pittsburgh, PA, United States

Background, Motivation, and Objective

The growing interest for Internet of Things applications is fostering research on devices that can detect signals with almost no power consumption [1-3]. The use of micromechanical resonators for passive voltage amplification of the RF signature in ultra-low power Wake-Up Receivers (WuRx) is very appealing because of their small size and high performance [4]. In order to maximize the WuRx sensitivity, such resonators should simultaneously exhibit high quality factor at resonance (Q_s) and electromechanical coupling (k_t^2). We report on X-cut Lithium Niobate resonators with the highest Figure of Merit ($\text{FoM} = k_t^2 \cdot Q_s$) ever demonstrated. In this work, we investigate the impact of resonators' topology on the FoM of single elements and arrays of these resonators and identify the main sources of damping.

Statement of Contribution/Methods

We studied the influence of aperture (L_a), gap (g), anchor width (W_a), coverage (c), and electrical loading on the quality factor in 50 MHz (wavelength $\lambda = 116 \mu\text{m}$) devices (Fig. 1a-b). Vacuum and low temperature measurements were performed to characterize the main sources of damping. We also investigated the effect of frequency mismatch on the Q_s of an array of N_{el} parallel elements (Fig. 1c) with a Monte Carlo approach.

Results/Discussion

It was proven that aperture, gap, and coverage affect the quality factor of the resonators (Fig. 1d). Vacuum measurement highlighted a consistent increase (+20%) in Q_s (Fig. 1e). Low temperature measurements pointed out that electrical loading is one of the most important sources of damping for the devices in exam (Fig. 1f). For individual resonator, FoMs over 1500 were recorded in vacuum, with Q_s ranging from 3000 to 5000 and $k_t^2 > 30\%$ (Fig. 1g). A Monte Carlo simulation was used to simulate the Q_s of an array with different number of elements and estimate the changes in quality factor as a function of frequency mismatch and N_{el} (Fig. 1h).

[1] P.-H. P. Wang et al., Journal of Solid-State Circuits, 2018

[2] J. Moody et al., ISSCC 2018

[3] T. Wu et al., IEEE Sensors 2017

[4] R. Lu et al., MEMS 2018

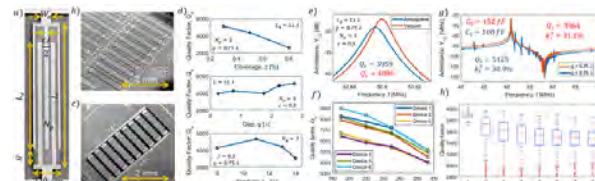


Fig. 1 – X-cut Lithium Niobate (LN) Laterally Vibrating Resonator SEM images of: (a) individual 50 MHz device, (b) 50 MHz devices with different geometry, (c) and array of $N_{el} = 9$ (d), Q_s as function of coverage, gap and aperture. (e) Effects of vacuum (5 mTorr) on Q_s . (f) Q_s as a function of temperature for different designs. (g) Effects of gap on Q_s and spurious modes for $g = 0.25 \mu\text{m}$ and $g = 2.75 \mu\text{m}$. (h) Box plot of simulated Q_s as a function of N_{el} (Monte Carlo simulation with 1000 samples, and a frequency mismatch characterized by $\mu = 50.75 \text{ MHz}$ and $\sigma_1 = 0.002 \text{ MHz}$).

2:00 PM PVDF-TrFE/SiO₂ Composite Film Bulk Acoustic Wave Resonator for Frequency-Modulated Sensor Application
Ryosuke Kaneko¹, Joerg Froemel¹, Shuji Tanaka¹
¹*Graduate school, Tohoku university, Sendai, Japan*

Background, Motivation, and Objective

Polyvinylidene fluoride trifluoroethylene (PVDF-TrFE) has been used in passive transducers such as hydrophones and tactile sensors, since it has moderate piezoelectric voltage constants, flexibility, small acoustic impedance and wide bandwidth. On the other hand, active transducers using PVDF-TrFE have been scarcely reported. It is interesting to use PVDF-TrFE-based acoustic wave resonators for new applications such as gas and humidity sensors. In this study, a high frequency film bulk acoustic resonator (FBAR) using 2 μm thick PVDF-TrFE was designed, fabricated and characterized for the first time.

Statement of Contribution/Methods

The fabrication process was newly developed, since the melting temperature of PVDF-TrFE is around 150°C, and PVDF-TrFE is damaged by most of organic solvents except alcohol. Photolithography was done below 105°C using ethanol as a photoresist stripper. XeF₂ etching was employed to release the device from a Si substrate. The poling was done by DC electric field of 100 V/ μm at 100 °C.

Results/Discussion

Fig. 1 shows the optical micrograph and cross-sectional structure of the device, which has a PVDF-TrFE/SiO₂ composite film. Fig. 2 shows the frequency characteristics of the thickness expansion mode at different temperatures (20-80°C). The temperature coefficient of frequency (TCF) is as large as -1105 ppm/°C. The quality factor is about 20 at 20°C, decreasing with temperature. A modified Butterworth-Van Dyke (MBVD) model for a lossy piezoelectric transducer was used to understand the measured characteristics. As shown in Fig. 3, the bulk capacitance (C_0) and dielectric loss ($\sim 1/C_0 R_0$) increase with temperature, which suggests the elastic relaxation and β phase relaxation of PVDF-TrFE^[1]. The frequency stability (Allan variance) is 777 Hz at an averaging time of 1.28 s, which will be improved by better design and fabrication for frequency-modulation sensing.

[1] K. Omote *et al*, J. Appl. Phys., Vol. 81, No. 6, 1997, pp. 2760-2769.

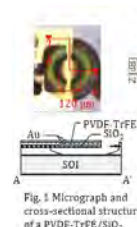


Fig. 1 Micrograph and cross-sectional structure of a PVDF-TrFE/SiO₂ composite FBAR.

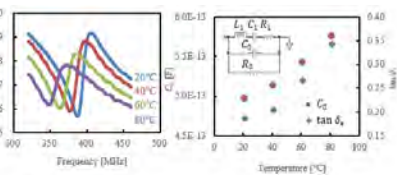


Fig. 2 Temperature dependency of thickness expansion mode.

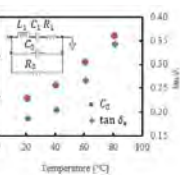


Fig. 3 MBVD model and temperature dependency of C_0 and $\tan \delta$.

2:15 PM

Spurious mode free 3.5GHz AlN plate mode resonator with high FoMNan Wang¹, Yao Zhu¹, Geng Li Chua¹, Bangtao Chen¹, Srinivas Merugu¹, Navab Singh¹, Yuandong Gu¹¹*Institutes of Microelectronics, A*STAR, Singapore***Background, Motivation, and Objective**

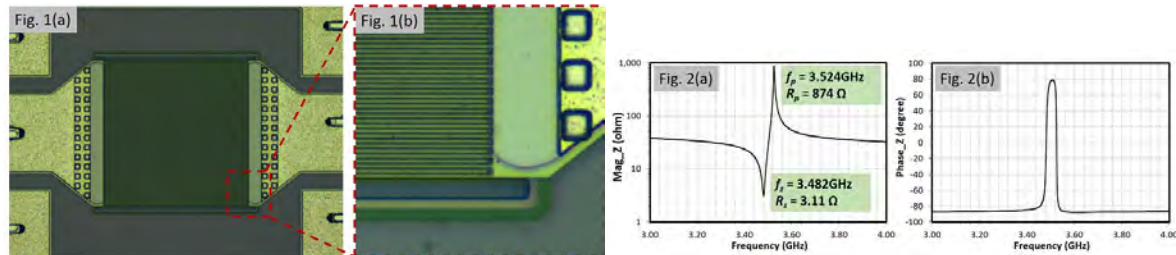
The ever-increasing volume of mobile communication data has driven the demand for high-frequency and high-quality filters. Since the operating frequency of Bulk Acoustic Wave (BAW) filters is determined by the film thickness, it is impossible to integrate multiple filters into a single chip. Moreover, as thinner piezoelectric film leads to poorer film quality, the performance of BAW filters will be degraded when frequency goes even higher. This work reports experimental data of a 3.5GHz AlN plate mode resonator with high FoM, which is a strong candidate for Band 42 applications.

Statement of Contribution/Methods

The resonator comprises of a 1μm-thick AlN layer, two sets of interdigitated top Mo electrodes and two sets of interdigitated bottom Mo electrodes, respectively. Both the width of the electrode finger and the space between adjacent fingers are 0.5μm. As shown in Fig.1, via contacts are defined to access the bottom electrodes. The distance between the electrode edge to the AlN plate edge is also carefully designed to suppress spurious modes.

Results/Discussion

Measurement results in Fig. 2 show that the resonant frequency (f_r) is around 3.5GHz, with a spurious mode free frequency response over a 1GHz range. The effective coupling coefficient (k_{eff}^2) is 3.15% and the Q factor (Q) is 1000, yielding an $f_r Q$ product of 3.5×10^{12} and $k_{eff}^2 Q$ of 31.5, respectively. Together with the series resistance of 3.11Ω and the parallel resistance of 874Ω , the proposed plate mode resonator is a potential candidate for mobile Band 42 applications.



2:30 PM

A Radio Frequency Comb Filter for Sparse Fourier Transform-based Spectrum SensingRuochen Lu¹, Tomas Manzaneque¹, Yansong Yang¹, Jin Zhou¹, Haitham Hassanieh¹, Songbin Gong¹¹*University of Illinois at Urbana-Champaign, Urbana, IL, United States***Background, Motivation, and Objective**

The increasing demand for wireless applications requires better spectrum access paradigm for efficient utilization of the RF spectrum. One promising approach is to adopt a multi-frequency dynamic spectrum access scheme, where the users sense the spectrum in real time and communicate within the idle channels. In such a scenario, a wide-band spectrum sensing system is the key for the technology. However, conventional spectrum sensing solutions using high-speed ADCs for sampling the full spectrum are power hungry and thus unsuitable for IoT applications. Recently, an alternative low-power approach using moderate-speed ADCs at sub-Nyquist rate by leveraging sparse Fourier transform (SFT), given a sparse spectrum, has been reported. Thus, the main challenge for more universal employment of SFT lies in sparsification of the spectrum in the RF front-end. In this work, we aim to demonstrate a passive low-IL RF comb filter based on high electromechanical coupling (k_t^2) acoustic devices, which can sparsify the spectrum by sampling the energy in various frequency bands (Fig. 1).

Statement of Contribution/Methods

Our approach employs lateral overtone bulk acoustic resonators (LOBARs), which have been recently demonstrated on the suspended LiNbO₃ thin film with high quality factor (Q) and k_t^2 simultaneously for multiple equally-spaced resonances. By networking LOBARs in a ladder topology (Fig. 2), a comb filter with periodic passbands is designed using 3 series resonators (200-μm-wide) and 2 pairs of shunt resonators (201-μm-wide). The center frequency is set to be around 400 MHz by setting the electrode pitch to 2.5 μm. Each resonator consists of 250 nm aluminum electrodes on an 800 nm suspended LiNbO₃ film, with a width around 200 μm that sets the spectral spacing (δf) between adjacent passbands to be around 20 MHz. These parameters lead to a designed sparsification ratio ($\gamma = \text{passband BW}/\delta f$) around 7% for the comb filter.

Results/Discussion

The measured transmission of the comb filter is shown in Fig. 3. As predicted in design, the multi-band filter is centered at 370 MHz and has a spectral spacing of 22 MHz. Low IL around 2 dB and FBWs around 0.6%, and $\gamma = 8\%$ have been obtained, while an out-of-band rejection around 25 dB has been achieved for more than 14 bands. The great performance demonstrated by the comb filter will serve to enable future sparse Fourier transform-based spectrum sensing.

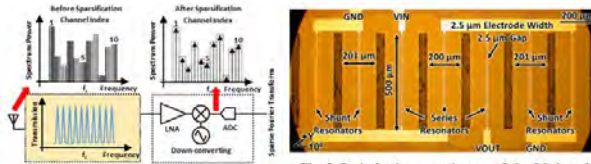


Fig. 1 Block diagram of an energy-efficient spectrum sensor front-end, consisting of a passive RF comb filter, reconfigurable RF circuits for sparsification. The output digital signals are used for sparse Fourier transform.

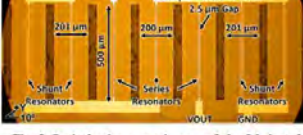


Fig. 2 Optical microscope image of the fabricated RF comb filter consisting of 7 LN LOBARs (3 series resonators and 4 shunt resonators) in a ladder filter topology. The resonances of series and shunt resonators are controlled by lithography. The dimensions are marked on the image.

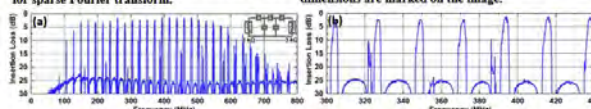


Fig. 3 Measured IL of the filter when both ports are matched to 3kΩ. (a) Wide-band and (b) zoomed-in performance show comb filter response with a frequency spacing of 22 MHz.

2:45 PM

Novel topology for a non-reciprocal MEMS filterMichele Pirro¹, Cristian Cassella², Piotr Kulik³, Giuseppe Michetti⁴, Yao Yu⁵, Guofeng Chen⁶, Matteo Rinaldi⁷¹ECE, northeastern univeristy, boston, MA, United States, ²Electrical and Computer Engineering, Northeastern University, Boston, MA, United States, ³northeastern univeristy, boston, MA, United States, ⁴ECE, Northeastern, Boston, MA, United States, ⁵Northeastern, Boston, MA, United States, ⁶Northeastern University, MA, United States, ⁷ECE, Northeastern University, Boston, MA, United States**Background, Motivation, and Objective**

Nowadays, RF-MEMS filters are at the base of wireless communication. We propose and demonstrate a new class of RF-filters based on Time Varying Networks (TVN) to improve the trade-off among area, performance and fabrication of the state of the art MEMS filters.

Statement of Contribution/Methods

Conventional ladder topologies employ MEMS resonators with different capacitances and resonance frequencies. In this work, we use 6 identical FBAR resonators arranged in 2 wyes. Each FBAR is connected to a switched capacitance system, modulated with a set time delay and frequency that creates a pass band only in one direction. The upper notch is the anti-resonance of the resonators, while the lower notch is induced by the TVN. There is an optimal value for the modulation parameters in order to get an opposite coupling among the resonators seen at each port that allows a non-reciprocal response. The path from the central node to the ground enables the matching conditions.

Results/Discussion

The filter exploited in-house FBAR resonators centered at 1 GHz, with 1 pF of static capacitance, k_t^2 of 6.5% and Q of 300. From port 2 to 1 there is -18 dB of isolation, while in the opposite direction there is a BW of 12 MHz at 3 dB around 1 GHz with -5.6 dB of insertion loss. The low insertion loss depends on the low Q resonators and on the parasitic of the switches, which should be taken into account in the simulation. The area reduction is almost by 40% when compared with a dual 50 ohm matched ladder filter. The approach is still valid for smaller resonators, making the area reduction even lower. In conclusion, this is the first prototype of a TVN filter made by identical resonators that guarantees 50 ohm matching (return loss >-20dB), a smaller area compared with traditional 3-resonators ladder filter and a non-reciprocal behavior in band.

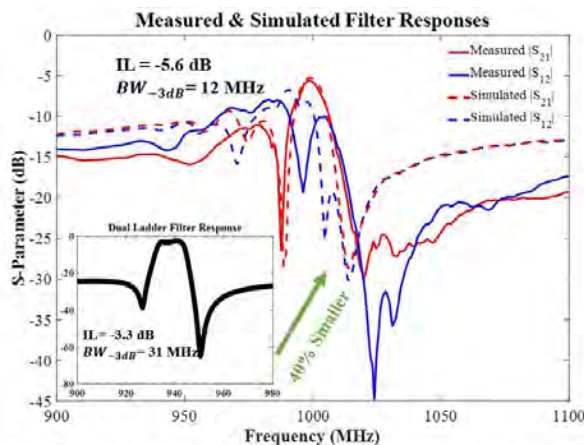


Fig. 1. Measured and simulated filter responses. Bottom left corner: response of a ladder filter composed of 3 FBARs, two of which are identical to the FBARs used in the experiment. The shunt resonator has same k_t^2 and Q but a different resonance frequency and a C_0 set for 50Ω matching.

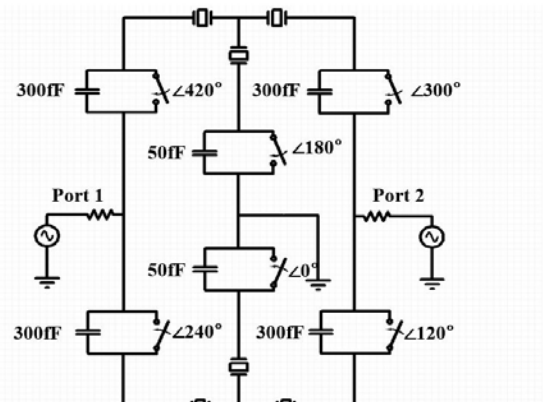


Fig. 2. Schematic of the proposed topology of the filter with identical FBAR MEMS resonators. Each resonator consists of $k_t^2 = 6.5\%$, $C_0 = 1 \text{ pF}$, $F_{res} = 1 \text{ GHz}$ and a $Q = 300$. The frequency of modulation is set at 10MHz.

5G - Novel Measurement Systems and Modeling Methods for Tissue Characterization

Ikuta (200)

Wednesday, October 24, 4:00 pm - 5:30 pm

Chair **Jonathan Mamou**
Riverside Research

5G-1

4:00 PM In vivo estimation of cortical thickness and porosity by axial transmission: Comparison with high resolution computed tomography

Donati Ramiandrisoa¹, Sylvie Fernandez², Christine Chappard³, Pascal Laugier⁴, Martine Cohen-Solal², Jean-Gabriel Minonzio⁴

¹Bleu Solid, Pomponne, France, ²Department of rheumatology, Hôpital Lariboisière, Inserm U1132, USPC Paris-Diderot, France, ³B2OA, UMR CNRS7052, University Denis Diderot, PRES Sorbonne Paris Cité, Paris, France,

⁴CNRS, INSERM, Laboratoire d'Imagerie Biomédicale (LIB), Sorbonne Université, France

Background, Motivation, and Objective

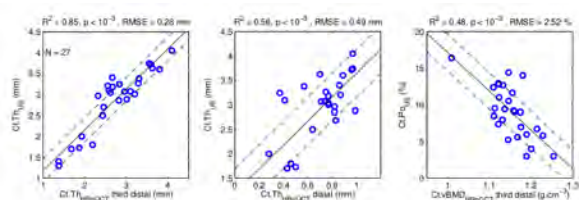
Estimation of key factors of fracture risk, such as cortical bone thickness and porosity, can be obtained using high resolution-peripheral quantitative computed tomography (HR-pQCT) [K. K. Nishiyama *et al* J Bone Miner Res 25:882–90, 2010]. The feasibility of *in vivo* cortical thickness estimation by analyzing the waveguide response of long bones using axial transmission (AT) has been previously evidenced [Q. Vallet *et al* IEEE UFFC 63:1361-71, 2016]. The aim of this study is to compare both AT parameters, cortical thickness and porosity, with HR-pQCT measurements done at the site matched and conventional locations.

Statement of Contribution/Methods

Twenty seven patients (21 females and 6 males, 30 to 89 years) underwent AT measurements using a 1-MHz prototype (Azalée, Paris, France) at the one-third distal radius. Singular value decomposition combined with 2-D spatio-temporal Fourier transform was applied to extract the dispersion curves. A model-based sparse inverse problem was used to estimate cortical thickness and porosity by fitting a 2-D transverse isotropic free plate model to the experimental dispersion curves. Site matched measurements at the one-third distal radius of cortical thickness and volumetric bone mineral density (vBMD g.cm⁻³) were obtained using HR-pQCT (Scanco, Brüttisellen, Switzerland). In addition, cortical thickness and vBMD (Dcomp), corresponding to conventional clinical index measured at the distal part of the radius, were automatically provided by the device software.

Results/Discussion

US-based estimates of Ct.Th and Ct.Po were successfully obtained on 27 patients. Highly significant Pearson correlations ($p < 10^{-3}$) were found between Ct.Th estimates and that measured with HRpQCT at the one-third distal radius ($R^2 = 0.85$, RMSE = 0.3 mm) and at the distal part ($R^2 = 0.56$, RMSE = 0.5 mm). A significant correlation between cortical porosity and vBMD was observed at the one-third distal radius ($R^2 = 0.48$, RMSE = 2.5 %), while no correlation existed with Dcomp at the distal site, partly due to thin cortical thickness (< 0.5 mm) limitation [A. Ostertag *et al* Bone 63:7-14, 2014]. This study shows the potential of AT measurements to provide *in vivo* cortical thickness and porosity estimates using a portable and non ionizing device.



4:15 PM

Assessment of cardiomyocyte contractility using high frequency ultrasoundEric Strohm^{1,2}, Neal Callaghan^{2,3}, Michael Koliou^{4,5}, Craig Simmons^{1,2,3}

¹Mechanical and Industrial Engineering, University of Toronto, Toronto, Canada, ²Translational Biology and Engineering Program, Ted Rogers Centre for Heart Research, Toronto, Canada, ³Institute of Biomaterials and Biomedical Engineering, University of Toronto, Toronto, Canada, ⁴Department of Physics, Ryerson University, Toronto, Canada, ⁵Institute for Biomedical Engineering, Science and Technology, Li Ka Shing Knowledge Institute, Keenan Research Centre, St. Michael's Hospital, Toronto, Canada

Background, Motivation, and Objective

Heart failure affects over 26 million people worldwide. It is not curable, and half die within five years of diagnosis. Induced pluripotent stem cell-derived cardiomyocytes (iPSC-CMs) are promising as a cell-based therapy for heart failure, and in drug testing platforms in vitro. Contractile function is the most important metric for evaluating iPSC-CMs, but current methods are inaccurate, low-throughput, or require complex set-ups. To address this need, we have developed a non-invasive label-free ultrasound technique to measure the CM beat rate, beat rhythm and force of contraction in vitro.

Statement of Contribution/Methods

Freshly isolated adult mouse primary CMs or iPSC-CMs were seeded onto standard 12-well plates, forming sparse monolayers. We developed a custom acoustic microscope to acquire 1000 signals per second from beating CMs using 200 MHz ultrasound at pulse burst repetition frequencies up to 1 MHz. Ultrasound signals were digitized at 10 GS/s with 14 bit resolution. The ultrasound echoes from the cell and substrate were separated in time and individually resolved (fig. 1A). Rapid variations in the amplitude and time of flight of the echoes from the cell were used to calculate the beat rate, beat rhythm and cell contraction, from which contractile forces were calculated using a linear elastic model.

Results/Discussion

The measured spontaneous beat rate of the CMs was 1-2 bps using ultrasound, and increased to 2-4 bps with epinephrine. Beat rates were validated with simultaneous optical imaging. The calculated peak force of contraction from different CMs ranged from 0.2-3.0 μ N (fig. 1B). These force measurements were validated with simultaneous traction force microscopy measurements, and agreed with published results. This preliminary study demonstrates that ultrasound can be used for the rapid non-invasive characterization of CM contractility using standard tissue culture platforms, with broad applicability towards CM phenotyping and drug screening applications in cardiac regenerative medicine.

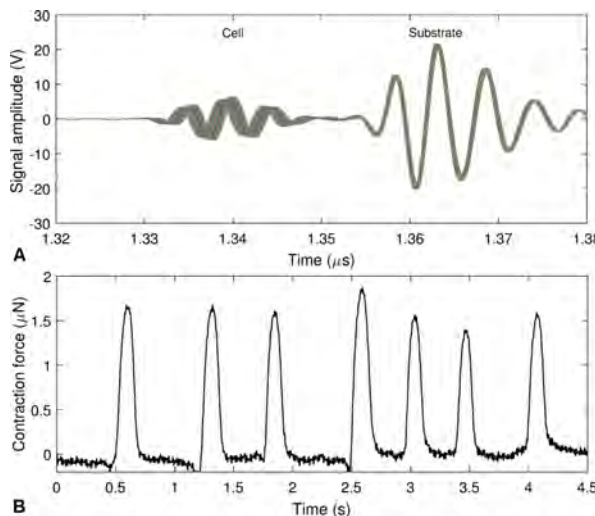


Figure 1: (A) Overlay of 2 seconds of acquisition time (2000 signals, 3 beats) showing the variation in the signals from a single adult beating cardiomyocyte. The echo from the substrate was static. (B) The calculated force of contraction of a single cell as a function of time.

4:30 PM

Estimation of viscoelastic properties of tissue with arbitrary power-law attenuation**Bharat Tripathi¹, David Espindola², Gianmarco Pinton³**

¹Joint Dept. of Biomedical Engineering, University of North Carolina-Chapel Hill and North Carolina State University, Chapel Hill, NC, United States, ²Biomedical engineering, University of North Carolina at Chapel Hill, NC, United States, ³Joint department of biomedical engineering, University of North Carolina at Chapel Hill and North Carolina State University, NC, United States

Background, Motivation, and Objective

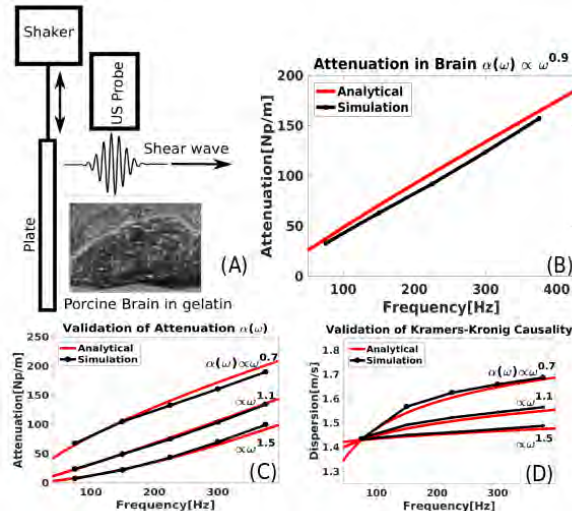
As in acoustics, the attenuation of shear waves in soft tissue is governed by empirical power laws. However, unlike acoustics, the attenuation for shear waves is two orders of magnitudes larger i.e. few wavelengths. Consequently, accurately modeling attenuation and dispersion is a critical component of the propagation physics. For example, even small variations in the attenuation model, can lead to large errors in estimates of Young's modulus. Current state-of-the-art models are based on linear power law attenuation. However, soft solids exhibit arbitrary fractional-power attenuation laws. We present a new model based on relaxation mechanisms for the propagation of shear waves in soft solids with ability to model attenuation and dispersion with a fractional power law. We also present a finite volume method (FVM) based numerical solver and a dedicated simulation tool for this model which, in conjunction with group shear wave speed method, can accurately characterize a wide range of viscoelastic materials.

Statement of Contribution/Methods

A collection of Maxwell bodies, i.e. relaxation mechanisms, is used to model arbitrary power laws. This, together with a nonlinear shear wave equation, is simulated using the piecewise parabolic method, a high-order FVM designed for transient wave propagation problems (unlike the FEMs which are intrinsically built for the elastostatic problems). The simulation method is experimentally validated with measurements of shear wave in fresh porcine brain and gelatin phantoms. Planar shear waves were generated by a plate embedded in the gelatin, which was then excited using a electromechanical shaker (fig-A). The shear waves were measured using our high-frame rate (6200 images/sec) ultrasound imaging technique and with custom adaptive displacement tracking algorithms designed for large amplitude shear waves.

Results/Discussion

Linear experiments were performed to calculate the attenuation law in brain (fig-B) which has a power law exponent equal to 0.9, and which can be modeled using the proposed method. A set of different attenuation laws were simulated, each with five different frequencies (fig-C & D). A close match between the numerical (black) and analytical (red) attenuation and dispersion is seen. This method is then used for the viscoelastic characterization of brain, and it can be extended to other tissues like liver.



(A) Experiments of planar shear waves in fresh porcine brain; (B) Power law in brain(red) with a non-Integral exponent shown vs the one from the numerical simulations(black); (C-D) Demonstrates the ability to model a range of power laws with fractional exponents: 0.7, 1.1, 1.5 calculated from the numerical simulations(black) compared with their corresponding analytical laws (red).

4:45 PM

Ultrasound Multiple Scattering in Cortical Bone: Effect of Pore Size and Pore ConcentrationYasamin Karbalaeisadegh¹, Omid Yousefian², Gianluca Iori³, Kay Raum⁴, Marie Muller⁵¹*North Carolina State University, NC, United States*, ²*Mechanical and Aerospace Engineering, North Carolina State University, United States*, ³*Charité – Universitätsmedizin Berlin, Germany*, ⁴*Berlin-Brandenburg Center for Regenerative Therapies, Charité - Universitätsmedizin Berlin, Berlin, Germany*, ⁵*Mechanical and Aerospace Engineering, North Carolina State University, NC, United States***Background, Motivation, and Objective**

Bone loss occurring with aging is manifested in cortical bone by the enlargement of the marrow-filled pores and emergence of new pores[1]. Quantitative Ultrasound (QUS) can provide a non-ionizing approach to the detection of structural changes related to bone loss[2]. Number of pores and their size affect ultrasound multiple scattering that takes place in bone. We calculate the diffusion constant (D) as a metric of the amount of scattering occurring during ultrasound propagation in cortical bone. We also study the effect of pore size and concentration on D to evaluate its potential to characterize cortical bone micro-structure.

Statement of Contribution/Methods

A cross-sectional image of femur cortical bone obtained by Scanning Acoustic Microscopy is modified to achieve desired constant pore sizes (30-100μm) and concentrations (5-30pore/mm²). The pores act as scatterers responsible for diffusing the propagation wave front within the medium. 2D FDTD simulations are developed from the modified bone geometries. A linear array transducer is modeled, in which each element successively emits an 8-MHz Gaussian pulse and the response is recorded on all elements. The inter-element response matrix of the transducer-medium system is obtained. Using an anti-symmetrization method, we extract the incoherent contribution of backscattered intensity. The temporal growth of the incoherent intensity allows the calculation of D [3]. This parameter is expected to be low when large amounts of scattering occur, and higher in cases where scattering by the pore distribution is not dominant.

Results/Discussion

In Fig.1-a, D is shown for geometries with constant pore concentration. It decreases as the average pore diameter increases. A similar trend is observed in Fig.1-c when pore concentration increases at constant average pore diameter. D is linearly correlated with pore diameter and concentration as shown in figures 1-b and 1-d respectively. These results suggest that the diffusion constant could be a relevant parameter in assessing cortical porosity as it is affected by both pore size and concentration independently.

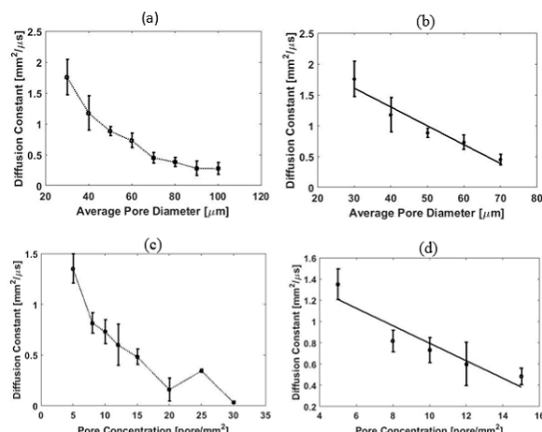


Figure 1. a: Diffusion constant vs. average pore diameter. b: Linear correlation between D and average pore diameter ($r=0.9709$, $p=0.0059$). In (a) and (b), the pore concentration is constant ($10^{\frac{pore}{mm^2}}$). c: Diffusion constant vs. pore concentration. d: Linear correlation between D and pore concentration ($r=0.9353$, $p=0.0195$). In (c) and (d), the average pore diameter is constant ($60\mu\text{m}$).

*Three different geometries were generated at each pore diameter/concentration to obtain the error bars.

References

- [1] R. L. Jilka, C. A. O'Brien, P. K. Roberson, L. F. Bonewald, R. S. Weinstein, and S. C. Manolagas, "Dysapoptosis of osteoblasts and osteocytes increases cancellous bone formation but exaggerates cortical porosity with age," *J. Bone Miner. Res.*, vol. 29, no. 1, pp. 103–117, 2014.
- [2] V. Egorov et al., "Osteoporosis detection in postmenopausal women using axial transmission multi-frequency bone ultrasonometer: Clinical findings," *Ultrasonics*, vol. 54, no. 5, pp. 1170–1177, 2014.
- [3] A. Aubry and A. Derode, "Ultrasonic imaging of highly scattering media from local measurements of the diffusion constant: Separation of coherent and incoherent intensities," *Phys. Rev. E - Stat. Nonlinear, Soft Matter Phys.*, vol. 75, no. 2, pp. 1–9, 2007.

5:00 PM

Sizing cells using acoustic flow cytometry

Eric Strohm^{1,2}, Vaskar Gnyawali^{3,4}, Joseph Sebastian^{4,5}, Robert Ngunjiri^{4,5}, Michael Moore^{4,5}, Scott Tsai^{3,4}, Michael Kolios^{4,5}

¹*Mechanical and Industrial Engineering, University of Toronto, Toronto, Canada*, ²*Translational Biology and Engineering Program, Ted Rogers Centre for Heart Research, Toronto, Canada*, ³*Mechanical and Industrial Engineering, Ryerson University, Toronto, Canada*, ⁴*Institute for Biomedical Engineering, Science and Technology, Li Ka Shing Knowledge Institute, Keenan Research Centre, St. Michael's Hospital, Toronto, Canada*, ⁵*Department of Physics, Ryerson University, Toronto, Canada*

Background, Motivation, and Objective

Flow cytometry is a high throughput technique commonly used to analyze cells using their physical, chemical and/or molecular properties. Current microfluidic cell sizing techniques use electrical impedance or optical imaging; however, these methods require complex fabrication techniques or may suffer from limited resolution. Here we present a device which combines ultrasound and a simple microfluidic design to rapidly size and count cells in a non-invasive, high-throughput, and label-free fashion.

Statement of Contribution/Methods

The microfluidic device was made of polydimethylsiloxane (PDMS) using a soft lithography technique. A 200 μm diameter inlet was bisected by two faster moving sheath flows, hydrodynamically focusing the cells axially and laterally within the 300 μm diameter channel (fig. 1A). The cells flowed single file past a 375 MHz ultrasound transducer at speeds of 1-5 cm/s, and were insonified using a pulse repetition frequency up to 1 MHz. From each cell, 10-30 ultrasound echoes were digitized at 4 GS/s and then averaged. To determine the cell size, periodic features within the power spectrum which are dependent on the cell size were compared to the Faran theoretical ultrasound scattering model. The system was validated using 3 μm polystyrene microbeads, and then human acute myeloid leukemia (AML) cells and HT29 colorectal cancer cells were measured.

Results/Discussion

The ultrasound spectra from the 3 μm microbeads were consistent with theoretical models, validating the technique. The mean diameter for the AML cells was $9.6 \pm 1.3 \mu\text{m}$ (2390 measurements), and for the larger HT29 cells, the mean diameter was $15.3 \pm 2.9 \mu\text{m}$ (1955 measurements) as shown in fig. 1B. These results agreed with measurements made using a Coulter Counter Multisizer 4, the current gold standard for cell sizing. This system demonstrates the ability of ultrasound to rapidly size single cells, which can be integrated into a variety of microfluidic platforms with the potential for multi-parameter cellular characterization using combined fluorescence, light scattering and/or quantitative photoacoustic techniques.

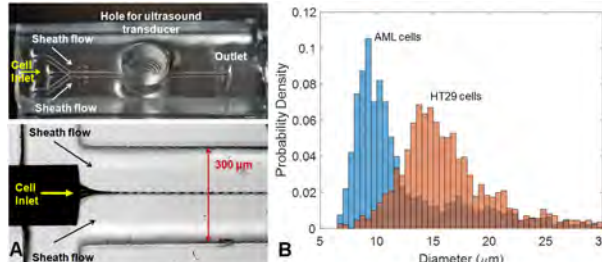


Figure 1: (A) The PDMS device used for flow focusing (top) and an optical view showing 3 μm beads focused into a narrow stream (bottom). (B) A histogram showing the diameter of the AML cells and HT29 cells measured using the acoustic flow cytometry technique.

5:15 PM

Skin Moisturizer Changes Morphology and Acoustic Impedance of SkinYoshifumi Saijo¹, Saaya Yokoshiki¹, Kazutoshi Kumagai¹, Kazuto Kobayashi², Naohiro Hozumi³¹*Graduate School of Biomedical Engineering, Tohoku University, Sendai, Japan*, ²*R & D Division, Honda Electronics Co., Ltd., Toyohashi, Japan*, ³*Toyohashi University of Technology, Toyohashi, Japan***Background, Motivation, and Objective**

Skin moisturizer is widely accepted cosmetic agent to increase skin hydration and to improve skin condition. The objective of the present study is to evaluate the effect of a skin moisturizer by high frequency ultrasound.

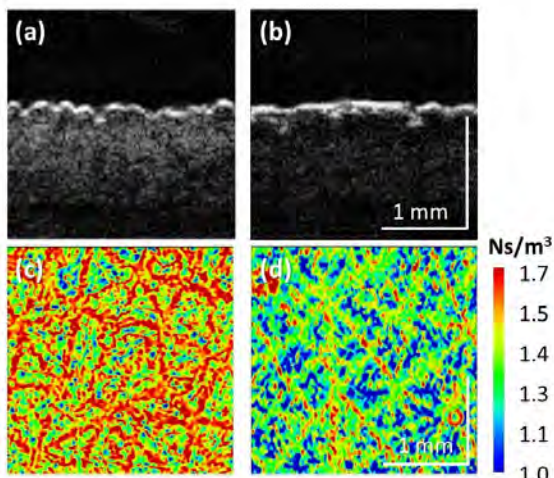
Statement of Contribution/Methods

Both B-mode and acoustic impedance mapping were obtained with a specially developed three-dimensional ultrasound microscope. P(VDF-TrFE) concave shaped transducer with the central frequency of 80 MHz, aperture diameter of 2.4 mm, and focal length of 3.2 mm was mechanically scanned over the object. For acoustic impedance mapping, ultrasound transmitted from the transducer, penetrated through the polystyrene plate with the thickness of 0.8 mm and reflected at the interface between the plate and the tissue. The acoustic impedance was calculated by the intensity of the reflection compared with that from the control object such as water or air. A conventional ultrasound diagnostic gel was used as the coupling medium for B-mode and water droplet was used as the coupling medium between the transducer and the plate.

Effect of a popular topical skin moisturizer (NIVEA Soft Moisturizing Creme) was investigated. Epidermal hydration was assessed by measuring the electrical capacitance before and 3 min after application of the moisturizer. B-mode imaging and acoustic impedance mapping were also obtained at the baseline and 3 min after application. The study was approved by the ethical committee of Tohoku University School of Engineering and the forearms of three healthy volunteers were investigated in the study.

Results/Discussion

The hydration was 33% at the baseline and 53% after application of the skin moisturizer. Figure (a) and (b) show B-mode images before and after application and (c) and (d) show acoustic impedance mapping before and after application. B-mode images show that the skin surface was smoothened because Vaseline, contained in the cream, formed a smooth layer. The acoustic impedance images clearly show the skin texture, and the average acoustic impedance decreased from 1.48 Ns/m³ at the baseline to 1.33 Ns/m³ after application of the moisturizer. The results indicate that the water content in stratum corneum is closely related to the acoustic impedance of the skin surface. High frequency ultrasound is useful to assess the effect of moisturizers on skin morphology and biomechanics.



6D - Flow Measurement and Industrial Applications

Nunobiki (150)

Wednesday, October 24, 8:00 am - 9:30 am

Chair **Nishal Ramadas**
Elster Instromet

6D-1

8:00 AM

3D flow mapping for Lorentz force driven liquid metal flows in crystallization experiments

Kevin Mäder¹, Norman Thieme¹, Dagmar Meier², Richard Nauber¹, Lars Büttner¹, Olf Pätzold², Jürgen Czarske¹

¹Laboratory of Measurement and Sensor System Techniques, Technische Universität Dresden, Dresden, Germany;

²Institute of Nonferrous Metallurgy and Purest Materials, Technische Universität Bergakademie Freiberg, Freiberg, Germany

Background, Motivation, and Objective

Conductive fluids, e.g. metallic melts, can be driven by magnetic fields, which is a branch of magnetohydrodynamics (MHD). MHD can be used for driving a melt flow during bulk crystal growth of semiconductors in order to improve the mass and heat transfer in the melt for better structural and electrical properties of the crystals. However, the optimal application of MHD requires a detailed understanding of the flow, which is generally complex and unsteady during crystal growth. Substantial knowledge about the flow is usually gained through numerical simulations and MHD model experiments at room temperature. For model experiments, a comprehensive flow mapping of complex and unsteady flow phenomena is required.

Statement of Contribution/Methods

We present an ultrasound array Doppler velocimeter (UADV) suited for 2D and 3D flow measurements in model experiments with low-melting metals, e.g. the alloy gallium-indium-tin (GaInSn, melting point 10.5 °C). The UADV employs arrays of large US elements (pitch > λ). Each element measures a flow velocity profile. Addressing the elements in a time- and space-division multiplexing scheme enables the parallelized measurement of flow profiles which are composed to 2D flow maps. Thereby frame rates of several 10 Hz are achieved which qualifies the UADV for the measurement of turbulent melt flows. The UADV supports up to 8 US arrays to measure multiple velocity components in multiple planes, e.g. four 2D vector flow fields with two orthogonally arranged arrays in each plane. Since the investigation of unsteady flow structures during the crystallization process may take several hours, the I-Q demodulation and the velocity estimation are executed on an FPGA, which can reduce the measurement data by a factor of 100. Approaches for the 3D flow reconstruction in cylindrical und square-based containers are presented.

Results/Discussion

The UADV was applied to a model experiment consisting of a cylindrical container filled with the molten alloy GaInSn that was driven by a travelling magnetic field. The figure shows a sketch of the experiment and a reconstructed 3D vector flow field.

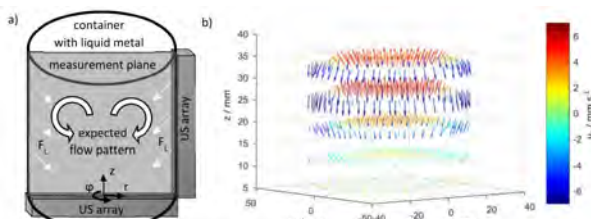


Fig.: a) Sketch of the container with the Lorentz force F_L and the expected poloidal flow pattern. b) 3D vector flow field measured at the sketched model experiment driven by a downward directed travelling magnetic field (400 Hz, 4 A)

8:15 AM

Feasibility of ultrasound flow measurements via non-linear wave propagationJack Massaad¹, Paul van Neer², Douwe van Willigen¹, Nicolaas de Jong¹, Michiel Pertjis¹, Martin D. Verweij¹¹TU Delft, Netherlands, ²TNO, Netherlands**Background, Motivation, and Objective**

Ultrasound flow meters are based on linear wave propagation. However, the nonlinear nature of wave propagation is well known. The harmonics build up progressively during wave propagation and the total bandwidth of the pressure pulse is thus effectively increased. In the context of ultrasonic flow measurements a larger available bandwidth leads to more precise measurements. However, it's not trivial if that works for the harmonics generated by nonlinear wave propagation, as the intensity of the 2nd harmonic is <-25dB of the fundamental. Alternatively, one could filter out the fundamental and harmonics separately and get an estimate for the flow speed from each component. Using nonlinear wave propagation could have a particular advantage for clamp-on flow meters because it would allow to lower the emitted frequency and thus to increase the wavelength in the pipe wall relative to its thickness and to increase the opening angle in the liquid. Here, we investigate the feasibility of using nonlinear wave propagation for ultrasonic flow measurements.

Statement of Contribution/Methods

Two Olympus transducers (V382, $f_c=3.5\text{MHz}$) were inserted into a pipe (40 mm ID) at a 45° angle with respect to the flow direction. A 150V pulse was used to excite a 5-cycle-Gaussian-apodized sine burst with a center frequency of 2.3MHz. The expected 2nd harmonic was centered around 4.6MHz. 1000 traces were recorded up and downstream of the flow. The flow speed was varied. The signal processing steps were: 1) window out noise, 2) separate the fundamental and the harmonic part of the received signals by filtering, 3) compute the arrival time difference between up and downstream measurements for each component.

Results/Discussion

The level of the 2nd harmonic was -30dB relative to the fundamental. For 8 different flow speeds, the standard deviations of the mean up/downstream time differences (σ_{mean}) were computed for the unfiltered, fundamental, and 2nd harmonic signals (Figure 1). The σ_{mean} was 0.013 - 0.029 ns and 0.017 - 0.031 ns for the fundamental and 2nd harmonic, respectively. If we correct for the systematic offset between fundamental and second harmonic data, the σ_{mean} of the combined fundamental and 2nd harmonic data was 0.011 - 0.021 ns: significantly lower than for the fundamental alone. These results show the feasibility of using nonlinear wave propagation for ultrasonic flow measurements.

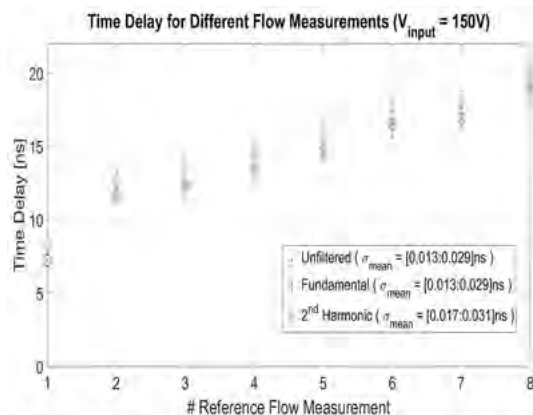


Figure 1: Time delay computed for eight different flow regimes using the fundamental and 2nd harmonic part of the recorded signals. Notice that the range of the mean standard deviations are very similar for the fundamental and 2nd harmonic, proving that later holds information about the flow and that non-linear wave propagation can be used to increase the amount of data (and therefore the precision) in the computation of flow.

8:30 AM

Development of a non-intrusive in-line tomographic ultrasonic velocity meter to measure liquid rheology

Paul van Neer¹, Uilke Stelwagen¹, Leon Geers¹, Daniele Piras¹, Francesc Corominas², Massimiliano Grosso³, Erwin Giling¹

¹TNO, Netherlands, ²Procter & Gamble, Belgium, ³University of Cagliari, Italy

Background, Motivation, and Objective

The number of chemical processes transferred from a batch-wise approach to continuous flow is increasing, due to several advantages of continuous over batch: processes can be operated at more extreme conditions, resulting in higher speed and efficiency. Thus it is critical to evaluate key performance indicators real-time and in-line. For fluid handling processes like mixing and filling, the viscosity of the process fluid is a critical parameter. Also, for non-Newtonian fluids the viscosity varies with the shear rate. Hence the measured rheology is affected by obstructing sensor designs. Moreover, in view of fouling prevention and safety, the pipe wall should not be punctured. We propose a concept to measure the viscosity as a function of the shear rate by measuring the liquid velocity profile and the pressure drop over the sensor. The concept is non-intrusive, in-line, and does not puncture the pipe wall. Here, we report on the development and performance of the tomographic ultrasonic velocity meter.

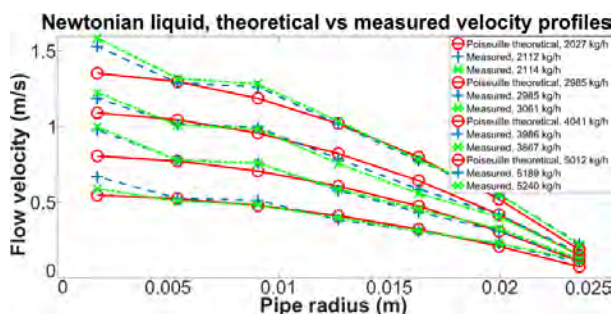
Statement of Contribution/Methods

The device consisted of 9 custom built transducers (0.85 MHz, width/length 0.6 mm) distributed along a cross-sectional plane which was tilted relative to the pipe axis (ID 5 cm). Signals produced by a waveform generator were amplified and routed to and from the transducers using a matrix switch. The received signals were pre-amplified and digitized. The full measurement chain including wave propagation, electronics and signal processing was modelled using custom models and the COMSOL FEM package. The acoustic wavefield emitted by the transducers was measured in water using a hydrophone mounted in an xyz-system. Tomographic time delay inversion was used to extract the velocity profiles. The device was tested using water and a 0.9 Pa.s Newtonian liquid.

Results/Discussion

The transducers had a peak transmit and receive transfer into water of 2.5 kPa/V and 45 μ V/Pa, respectively. The -6 dB opening angle of the transducers into the water was $>151^\circ$. Flow loop experiments (flow rate 0 – 5000 kg/h) showed standard deviations of the up/downstream time differences of 1.7 – 4 ns. The figure shows liquid velocity results (Newtonian, 0.9 Pa.s). The sensor successfully measured liquid velocity profiles.

This work was sponsored by H2020-SPIRE-2014 - Project CONSENS - Integrated Control and Sensing for Sustainable Operation of Flexible Intensified Processes.



8:45 AM Flow Imaging through a Multimode Waveguide using a Time Reversal Virtual Array

Richard Nauber¹, Arne Klass¹, Jürgen Czarske¹¹Laboratory for Measurement and Sensor System Technique, TU Dresden, Dresden, Germany**Background, Motivation, and Objective**

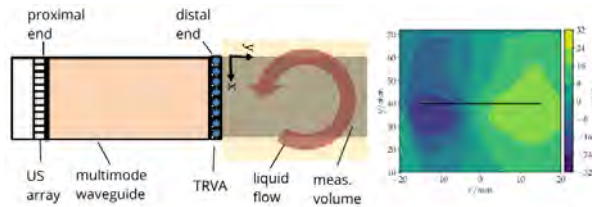
The resource-efficiency of many relevant industrial processes, such as continuous casting or plastics extrusion, strongly depends on the complex melt flow behavior. In order to control and optimize those processes, *in situ* flow imaging of hot, opaque liquids is required. Ultrasound Doppler velocimetry can be used in this context, if a waveguide separates the temperature-sensitive transducers from the measurement volume. Usually singlemode waveguides are employed due to their simple sound propagation properties, but they are mechanically complex, introduce strong sound attenuation and prevent fast planar imaging.

Statement of Contribution/Methods

We propose to use a multimode waveguide in combination with a novel signal processing method, the time reversal virtual array (TRVA), for ultrasound Doppler flow imaging. A multimode waveguide can carry the information of a complete, two-dimensional image, yet it is scrambled due to the complex sound propagation. TRVA exploits the time invariance of the wave equation in linear media to focus on a set of pre-calibrated points on the far (distal) end of the waveguide with a phased array transducer at the near (proximal) end. These points are combined to form a virtual array, which allows transmit and receive beamforming into the measurement volume.

Results/Discussion

In this contribution, we validate the TRVA principle numerically and experimentally using a generic ultrasound research platform, the phased array Doppler velocimeter (PAUDV). Furthermore, we demonstrate planar velocity imaging of a rotating flow in liquid gallium-indium-tin (GaInSn) through a borosilicate waveguide at room temperature. The measurement properties are characterized through a comparison with a velocity reference. This work provides a basis for *in situ* flow imaging of hot, opaque liquids in harsh environments.



Experimental set-up for flow imaging through a multimode waveguide and resulting flow field of a liquid metal (GaInSn alloy), which is driven by a counterclockwise rotating magnetic field.

- 9:00 AM 27 kHz Ultrasonic Complex Vibration Welding System Using Various Exchangeable Welding Tips for Different Welding Specimens**
Jiromaru Tsujino^{1,2}
¹Kanagawa University, Yokohama, Japan, ²LINK-US Co. Ltd, Japan

Background, Motivation, and Objective

Ultrasonic complex vibration welding systems with complex vibration converter using two-dimensional vibration stress were proved significantly superior welding method compared with conventional welding with linear vibration. 19.5 kHz complex vibration welding systems using various exchangeable welding tips have been shown significantly effective for welding of same and different metal parts and foils such as aluminum and copper electrode foils and terminals which are essential for electronic devices, Li-ion battery and other various industry fields.

To decrease required vibration amplitude and vibration damage of welding specimen, 27 kHz and 40 kHz complex vibration welding systems for various exchangeable welding tips were designed newly using equivalent electric transmission line method using measured acoustic impedance of slit part.

Statement of Contribution/Methods

Required vibration amplitudes for 27 kHz and 40 kHz welding systems are 62% and 34% compared with 19.5 kHz ultrasonic welding system by our research results on frequency characteristics of ultrasonic welding.

27 kHz complex vibration welding system using various welding tips was developed using complex vibration converter with diagonal slits. Schematic diagram and longitudinal and torsional vibration distributions between the free edge of the converter with welding tip installing spaces and a nodal part of driving longitudinal vibration horn are shown in Fig. 1. To secure sufficient working space, complex vibration converter was designed as one-wave longitudinal length mode. The complex vibration converter with slit part is 38 mm in diameter and vibrates in one longitudinal wavelength mode. Torsional vibration distribution is 7/4 wavelength along the vibration system between the free edge of the converter and the nodal part of longitudinal driving system.

Results/Discussion

The 27 kHz system is driven using 1 kW amplifiers and elliptical to circular vibration loci is obtained at the welding tip. Welding tip suited for special application could be installed at the free edge of converter using a connecting bolt. Using these various welding tips, welding specimens such as many lapped metal foils, terminals were welded successfully with material strength and small deformation and without vibration fatigue damages. 40 kHz complex vibration welding system is under testing.

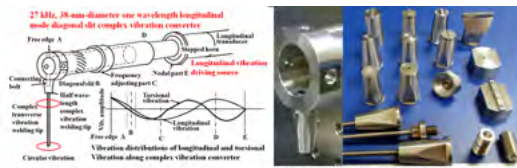


Fig. 1 Configuration of 27 kHz, 38-mm-diameter one-wavelength longitudinal mode diagonal slit complex vibration converter with four 12-mm-square installing parts for various exchangeable complex vibration welding tips driven by longitudinal vibration source, and various resonant and non-resonant type complex vibration welding tips.

9:15 AM Automatic estimation of borehole shape using ultrasonic data while drilling

Hadrien DOLLFUS¹, Henri-Pierre Valero¹, Jean-Christophe Auchere¹¹Schlumberger K.K, Sagamihara, Japan**Background, Motivation, and Objective**

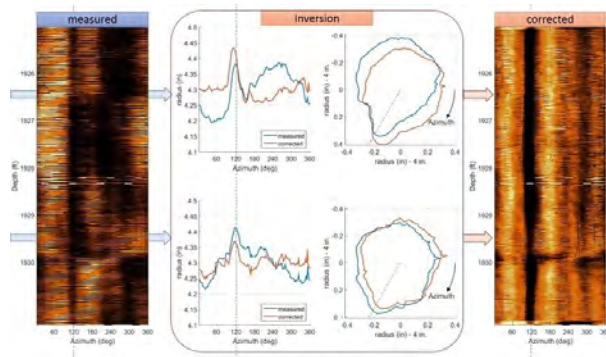
Drilling operations can be complex depending on the geomechanical properties of the drilled formation, and the ability to assess hole stability while drilling is critical. While-drilling measurement tools are widely used to get petrophysics and geomechanics properties of the formation. Drillers use the while-drilling data to assess drilling risks and optimize the drilling operation. A new method based on ultrasonic measurement acquired while drilling was used to estimate borehole shape and derive an image of the borehole wall. Data to assess the performances of this method were also obtained.

Statement of Contribution/Methods

The proposed method relies on a downhole acquisition system with four ultrasonic pulse-echo sensors mounted as two orthogonal pairs on the same plane. Echo signals reflected at wellbore surface are acquired and processed downhole in real time. Waveforms are first filtered then echo travel time and amplitude are automatically extracted for imaging. Travel time is converted to borehole radius using tool geometry and fluid parameters. The borehole cross section is assumed elliptic. The algorithm uses the four travel time inputs to estimate this shape represented by five degrees of freedom such as that surface area of the ellipse is minimized. The proposed solution returns the analytic expression of the ellipse, and hence the borehole shape.

Results/Discussion

The figure shows ultrasonic data recorded while drilling. Measured and corrected radius images are presented respectively in the left and right-most columns. In the center, the top and bottom row of graphs depict the inversion process of measured (blue curves) to corrected borehole radius (red curves) at two different depths. Center left and right graphs respectively present azimuthal profiles of radius and their polar plots with - 4 in. offset for detail cross-sectional analysis. Fine borehole features such as vertical drill marks, near 300°, and a 0.1 in. deep groove resembles to keyhole wear, near 120°, became clearly visible. Enhanced borehole features visible in the corrected image demonstrate the benefit of the inversion to ease image interpretation.



6E - Cancer

Nunobiki (150)

Wednesday, October 24, 10:30 am - 12:00 pm

Chair **Gregory Czarnota**
University of Toronto

6E-1

10:30 AM

Quantitative ultrasound-based detection of cancerous thyroid nodules

Daniel Rohrbach¹, Jason Smith¹, Poorani Goundan², Harshal Patel², Ernest Feleppa¹, Stephanie Lee²

¹Lazzi Center for Biomedical Engineering, Riverside Research, New York, NY, United States, ²Section of Endocrinology, Boston University School of Medicine, Boston Medical Center, Boston, MA, United States

Background, Motivation, and Objective

Thyroid cancer is the most-common endocrine malignancy worldwide. Most thyroid cancer occurs in nodules and the standard diagnostic method is a fine-needle aspiration biopsy (FNAB) of a thyroid nodule with cytological evaluation. Unfortunately, 20 to 30% of FNABs cannot differentiate benign from malignant thyroid nodules. Many of these patients require an additional surgical procedure for definitive histological diagnosis; however, only about 25% of those patients will have thyroid cancer. The objective of this study is to develop a non-invasive diagnostic approach using quantitative ultrasound (QUS) to detect thyroid cancer.

Statement of Contribution/Methods

RF data were acquired from 15 patients using a GE Logiq E9 research ultrasound system equipped with a 10-MHz, ML6-15 linear probe. QUS-estimate values, such as effective scatter diameter (ESD), effective scatter concentration (ESC), and spectral parameters (i.e., midband fit, slope, and intercept) were derived using a reference-phantom method. The phantom consisted of 60- μ m borosilicate beads. Additional QUS estimates were derived including envelope statistics employing a Nakagami distribution. Estimate values were used to train linear-discriminant (LD) and support-vector-machine (SVM) classifiers, and performance was assessed using area-under-the-curve (AUC) values obtained from receiver operating characteristic (ROC) analyses based on 10-fold cross validation.

Results/Discussion

Five patients had cytologically-confirmed thyroid cancer. A combination of ESD and EAC produced an AUC value of 0.85 and 0.81 when a LD or SVM was used, respectively. Classification performance of envelope statistics (i.e., $AUC_{LD} \sim 0.75$, $AUC_{SVM} \sim 0.78$) and spectral parameters (i.e., $AUC_{LD} \sim 0.86$, $AUC_{SVM} \sim 0.83$) were similar. The best classifier performance was obtained by combining envelope statistics, ESD and EAC, which produced an AUC of 0.87 when a SVM classifier was used. Our initial results with AUC values of 0.87 are very encouraging for developing a new tool for thyroid-cancer detection. These initial results suggest that QUS has promising potential to improve non-surgical evaluation of thyroid nodules.

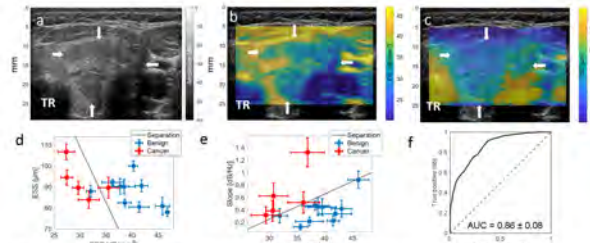


Figure 1 Transverse image of the left mid thyroid lobe containing a 4.3 x 2.3 x 2.6 cm (sagittal x anteroposterior x transverse) malignant nodule (white arrow). (a) B-mode greyscale image. (b) B-mode image with overlaid effective scatter concentration and (c) with effective scatter size. TR: trachea. (d-e) scatter plots of acoustic parameters (mean and standard deviation) and (f), ROC curve of linear discriminant classifier using spectral parameter features.

- 10:45 AM **Quantitative Ultrasound and Texture Predictors of Breast Tumor Response to Chemotherapy Prior to Treatment**
Gregory Czarnota¹, Lakshmanan Sannachi¹, Mehrdad Gangeh¹, William Tran¹, Ali Sadeghi-Naini¹
¹Sunnybrook Health Sciences Centre/University of Toronto, Toronto, ON, Canada

Background, Motivation, and Objective

Previous studies have demonstrated that quantitative ultrasound (QUS) is an effective tool for monitoring breast cancer patients undergoing neoadjuvant chemotherapy (NAC). Here, for the first time, we demonstrate the clinical utility of pre-treatment QUS texture features in predicting the response of breast cancer patients to NAC.

Statement of Contribution/Methods

Using a 6 MHz center frequency clinical ultrasound imaging system, radiofrequency (RF) breast ultrasound data were acquired from 100 locally advanced breast cancer (LABC) patients prior to their NAC treatment. QUS Spectral parameters including mid-band fit (MBF), spectral slope (SS), and spectral intercept (SI), and backscatter coefficient parameters including average acoustic concentration (AAC) and average scatterer diameter (ASD) were computed from regions of interest (ROI) in the tumor core and its margin. Subsequently, employing gray-level co-occurrence matrices (GLCM), textural features including contrast (CON), correlation (COR), energy (ENE), and homogeneity (HOM), and image quality features including core-to-margin ratio (CMR) and core-to-margin contrast ratio (CMCR) were extracted from the parametric images as potential predictive indicators. QUS results were compared with the clinical and pathological response of each patient determined at the end of their NAC.

Results/Discussion

Results from the 100 patients indicate that a combined QUS feature model demonstrated a favorable RECIST-based response (sensitivity=83%, specificity=79%, and AUC=82%), Miller-Payne based response (sensitivity=88%, specificity=71%, and AUC=83%), and were linked to patient survival (sensitivity=71%, specificity=92%, and AUC=82%) predictions. Best results were obtained using a radial-basis function support vector machine (RBF-SVM) machine learning algorithm. Only four features were selected in each binary response group classification.

The findings of this study suggest that QUS features of a breast tumor are strongly linked to tumor responsiveness. The ability to identify patients that would not benefit from NAC would facilitate salvage therapy and a clinical management that has minimum patient toxicity and maximum outcome (and a better quantity/quality of life). Future work will include investigations into the ability of a QUS model in predicting patient survival upon completion of chemotherapy and surgery, and the effect of including (i.e., estrogen/progesterone/human epidermal growth factor receptor 2 receptor status and histological grade) in the QUS-based predictive model.

11:00 AM

Predicting Radiotherapy Response in Head and Neck Patients Using Quantitative Ultrasound**William Tran¹, Irene Karam¹, Ian Poon¹, Harini Suraweera¹, Karina Quiaoit¹, Gregory Czarnota¹**¹*Sunnybrook Health Sciences Centre/University of Toronto, Toronto, ON, Canada***Background, Motivation, and Objective**

Treatment for patients with head and neck cancer typically require several weeks of radiotherapy leading to severe radiation-induced toxicity and variable response outcomes. This study examined using quantitative ultrasound to predict clinical response in patients receiving radiotherapy to the head and neck.

Statement of Contribution/Methods

This study was approved by the institution's ethics review board and 27 patients participated following written informed consent. All patients were diagnosed with carcinoma of the head of neck and underwent concurrent chemoradiation consisting of 70Gy/33 fractions.

Patients were scanned using a Clarity Ultrasound System at a centre frequency of ~7 MHz (Elekta Medical Corp, Montreal, Canada) prior to treatment (baseline), week 1, week 4 and after the completion of treatment at week 7. Quantitative ultrasound (QUS) data were collected and analysis included mean and texture-based features. The ground truth labels for patients were based on clinical response data from RECIST 1.1 criteria. Response classification was analyzed using a naïve Bayes, and k-nearest neighbour (k-NN) classifiers, and ROC analysis.

Results/Discussion

Preliminary QUS results demonstrated that for naïve-Bayes classification, the optimal sensitivity and specificity was 63%, and 100% respectively using a multiparametric model: SAS (scatterer spacing), and SI (spectral intercept)-contrast after 4 weeks of treatment. The AUC was 0.95 and the accuracy was 89%. For k-NN classification, the SAS (scatterer spacing) and SS (spectral slope)-energy demonstrated a sensitivity and specificity of 63%, and 95%, respectively at week 4. This corresponded with an AUC of 0.88 and an accuracy of 85%. Week 0 data was also predictive of response with an accuracy of up to 91% but using different QUS parameters.

Preliminary results demonstrate that quantitative ultrasound parameters combined with texture-based features can predict clinical response to radiotherapy in head and neck patients.

11:15 AM

In vivo diagnosis of metastasis in cervical lymph nodes using backscatter coefficients

Gloria Valenzuela¹, Rosa Laines², Joseph Pinto², Indira Tirado², Claudia Salazar², Imelda Chavez², Eduardo Gonzalez³, Jorge Guerrero², Roberto Lavarello¹

¹Pontificia Universidad Católica del Perú, Lima, Peru, ²Oncosalud-AUNA, Peru, ³Biomedical Engineering, Johns Hopkins University, United States

Background, Motivation, and Objective

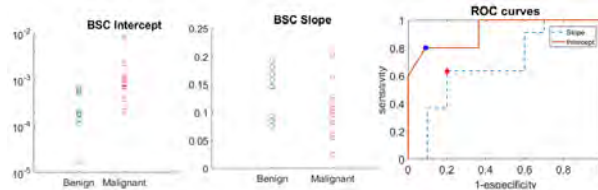
Sonographic evaluation is part of the workup of several solid tumors while lymph nodes characterization plays an important role in cancer staging and detecting local or distant recurrences. Previous studies have demonstrated the usefulness of ultrasonic backscatter coefficients (BSCs) at high frequencies (16.4 - 33.6 MHz) for detecting micro-metastasis of colorectal, gastric and breast cancers in lymph nodes. However, these studies were conducted ex vivo. In this work the feasibility of diagnosing metastatic cervical lymph nodes in vivo using BSCs within a clinical frequency range (3 - 10 MHz) was evaluated.

Statement of Contribution/Methods

The reference phantom method was used to estimate the BSC curves from 21 patients examined in a local oncology center for suspicious cervical nodes (metastatic spread at diagnosis or tumor recurrence). The average attenuation coefficient of muscle and lymph nodes were estimated using the regularized spectral log difference method. Values of attenuation coefficients for skin and subcutaneous fat were taken from the literature. The data was acquired using a SonixTOUCH (Ultrasonix, Richmond, Canada) scanner equipped with an L14-5 linear transducer. For all cases, the diagnosis was provided by a trained histopathologist through confirmatory biopsies. The patient median age was 51 years (19 – 91 years) and 17 cases (81%) were females. The operating points in the ROC curves were chosen to maximize Youden's index.

Results/Discussion

Overall, 10 out of 21 cases had malignant infiltration (48%). The median value of the BSC slope for the malignant cases was lower than the one for the benign cases (i.e., 0.1 vs. 0.15), resulting in a sensitivity of 63.6% and a specificity of 80%. On the other hand, the values of intercept for malignant cases were higher than the ones for the benign cases (i.e., 2×10^{-4} vs. 8.3×10^{-4}), resulting in a sensitivity of 80% and a specificity of 90.9%. These values are similar to the ones found in ex vivo studies. This works present the first report of *in vivo* assessment of lymph nodes for metastatic infiltration using BSCs. Our preliminary results suggest that it may possible to discriminate between benign and malignant nodes using BSCs *in vivo*.



11:30 AM

Machine-learning for the prediction of prostate cancer biopsy based on three-dimensional dynamic contrast-enhanced ultrasound quantification

Rogier R. Wildeboer¹, Ruud J. G. van Sloun¹, Pintong Huang², Hessel Wijkstra^{1,3}, Massimo Mischi¹

¹Department of Electrical Engineering, Eindhoven University of Technology, Netherlands, ²Second Affiliated Hospital of Zhejiang University, Hangzhou, Netherlands, ³Department of Urology, Academic Medical Center - University of Amsterdam, Netherlands

Background, Motivation, and Objective

Systematic biopsy (SBx) is still the guideline-recommended technique for the diagnosis of prostate cancer (PCa). Even though this procedure has a well-known risk of complications, underdiagnosis and overtreatment, imaging strategies that are currently in development have not yet reached sufficient accuracy to replace SBx. We propose a multiparametric ultrasound approach to distinguish malignancy from benign prostatic disease and to grade the aggressiveness of tumours. Our method exploits 3D dynamic contrast-enhanced ultrasound (DCE-US) quantification algorithms and combines them through machine learning to facilitate the prediction of individual-biopsy outcomes.

Statement of Contribution/Methods

Fourty-three patients at the 2nd Affiliated Zhejiang University Hospital underwent 2-minute 3D DCE-US and standard 12-core SBx. The 3D DCE-US recordings were analysed by voxel-based fitting of a local-density random walk model, voxel-to-voxel similarity analysis, voxel-to-voxel system identification, 3D convective-dispersion modelling and fractal dimension analysis. The median parameter values corresponding to each biopsy core were obtained by defining twelve regions in the estimated three-dimensional maps. Subsequently, a support vector machine (SVM) and a Gaussian mixture model (GMM) were trained to predict SBx outcomes. Single-parametric as well as multiparametric performance was validated in a leave-one-prostate-out fashion and measured by the area under the receiver-operating characteristics (ROC-AUC) curve.

Results/Discussion

Both the SVM and the GMM algorithms outperformed the single-parametric classification (see Figure 1), improving the ROC-AUC from 0.71 to 0.76 and 0.80 to 0.86 in distinguishing benign tissue from PCa and benign tissue from significant PCa, respectively. Our biopsy-validated dataset adequately represents the expected disease distributions in the SBx patient population and shows the diagnostic potential of multiparametric 3D DCE-US. An extended prostatectomy-based dataset might eventually confirm the ability of multiparametric 3D DCE-US to localize PCa.

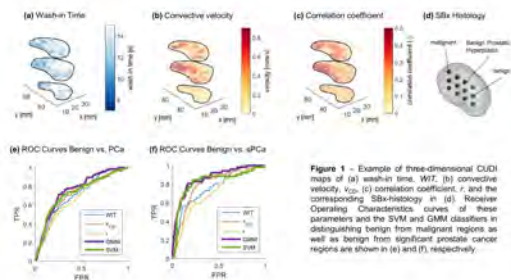


Figure 1 – Example of three-dimensional CUDI maps of (a) wash-in time, WIT, (b) convective velocity, V_{CO} , (c) correlation coefficient, r , and the corresponding SBx-histology in (d). Receiver Operating Characteristic (ROC) curves of these parameters and the SVM and GMM classifiers in distinguishing benign from malignant regions as well as benign from significant prostate cancer regions are shown in (e) and (f), respectively.

11:45 AM

Quantitative Ultrasound for in vivo monitoring of anti-angiogenic tumor therapyRégine Guillermin¹, Samantha Fernandez², Eric Debieu¹, Laure Balasse³, Benjamin Guillet³, **Emilie Franceschini¹**¹*Aix-Marseille université, CNRS, Centrale Marseille, France*, ²*Aix-Marseille Université, CERIMED, France*, ³*Aix-Marseille Université, INSERM, INRA, C2VN, France***Background, Motivation, and Objective**

Quantitative ultrasound (QUS) techniques providing insight into tissue microstructure are based on the frequency-based analysis of the signals backscattered from biological tissues. Previous studies (Czarnota & al. UMB 1997) have demonstrated the ability of QUS to monitor cell death during chemo- or radio-therapy. The aim of this study was to investigate the potential of QUS techniques to be sensitive to a change in tumor microvasculature and/or cell death during anti-angiogenic therapy using backscatter coefficient (BSC) measurements.

Statement of Contribution/Methods

In vivo experiments were conducted on human adenocarcinoma HT29 mouse models using the research echograph Visualsonics Vevo 2100 with a MS550D probe. Non-treated animals (N=3) and treated animals (N=3) with anti-angiogenic drug (Avastin) were imaged at 4 time points (day 10, 13, 17 and 20) after HT29 cells injection. For treated animals, the anti-angiogenic drug was injected at 4 time points (day 12, 14, 18 and 20) after HT29 injection. For each animal, RF data were collected from several scan planes within the tumor volume. BSC were measured using the reference phantom technique in the frequency bandwidth 15-40 MHz.

Results/Discussion

All the HT29 mouse tumors were heterogeneous containing two different areas as observed by histology: a cellular area with viable cells and a necrotic area with a majority of Natural Killer lymphocytes and no viable cells. The hyperechogenic zones observed in the B-mode ultrasound images were linked to the presence of small necrotic areas surrounded by viable HT29 cells. Results shows that mean BSC in the bandwidth 15-40 MHz increases with the growth of the tumor for non-treated animals, whereas the mean BSC decreases or remains stable for treated animals. On the examples shown in Figure 1, mean BSC increases of 6 dB for the non-treated animal and decreases of 5 dB for the treated animal. This study suggests that QUS techniques may be used to quantify the efficacy of anti-angiogenic therapy.

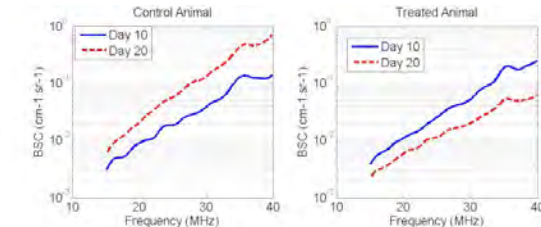


Figure 1 : Typical examples of measured BSC for one control and one treated animal

6F - Signal Processing

Nunobiki (150)

Wednesday, October 24, 1:30 pm - 3:00 pm

Chair **Erdal Oruklu**
Illinois Institute of Technology

6F-1

1:30 PM Information Transmission through Solids using Ultrasound

Jafar Saniie¹

¹*Illinois Institute of Technology, United States*

Background, Motivation, and Objective

Ultrasonic signals can be utilized as a viable communication method to transmit information through gas, liquid, and solid channels or a mixed media consisting of a solid interfaced with liquid and/or gas. For example, in underwater channels sound signals carrying data are efficient and consequently become a more practical and preferred communication method over electromagnetic message transmission which has limited signal penetration. But even with sound waves, underwater communication channels cause many challenges, often unforeseen, due to absorption, scattering, refractions, reverberations, multipaths, doppler shifts, temperature, salinity, and acoustic scintillation. Ultrasonic communication through the air is less prone to the environmental challenges that are often encountered in the underwater communications. Ultrasonic communication in solid channels is also adversely affected by absorption, scattering, refractions, reverberations, beam skewing, dispersion, mode conversion, multipaths, and above all these challenges are compounded by the geometrical structure of solids and type of ultrasonic waves.

Statement of Contribution/Methods

With solid structures many different ultrasonic wave types can be generated including Longitudinal (Compressional), Shear (Transverse), Surface-Rayleigh, Plate-Lamb (Symmetrical or Extensional Mode and Asymmetric or Flexural Mode), Plate-Love, and Stoneley (Leaky Rayleigh). The type of waves that can be used are governed by the position of the transmitters and receivers on a solid structure where the quality of the signal for communication is limited by the composition and geometrical shape of the solids.

Results/Discussion

For this study we have developed a testbed platform based on the ZYNQ SoC (System-on-Chip) FPGA by Xilinx which offers reconfigurability and high performance computational capability, high speed signal converters, transmitting power amplifiers, low noise receiving amplifiers and transducers to conduct ultrasonic communication experiments for transmitting data, audio, and video signals. Theoretically, ASK (amplitude shift keying) or any form of digital modulation can be tested with the system using the concept of the software-defined radio (SDR). The received signal is very complex, primarily caused by dispersion, reverberation, and multipath effects. We have examined this system using OOK (on and off keying), QPSK (quadrature phase shift keying), DQPSK (differential quadrature phase shift keying), and QAM (quadrature amplitude modulation). This system was tested using differently structured solid channels and the results in terms of transmission rate and bit-error rate were compared using 0.5 and 2.5 MHz ultrasonic transducers.

2:00 PM

Modelling of channels for intra-corporal communicationWentao Jiang¹, Thomas Bos², Win Dehaene², Marian Verhelst², Jan D'hooge¹¹*Cardiovascular Sciences, KU Leuven, Leuven, Belgium*, ²*Electrical Engineering, KU Leuven, Leuven, Belgium***Background, Motivation, and Objective**

Ultrasound has been proposed as a carrier for intra-corporal communication instead of radio waves given that it transmits more efficiently in water-like media and its good safety record in diagnostic imaging. Critically important to the design of communication protocols is to understand the characteristics of the channel. Although these properties can be obtained experimentally, it is labour-intensive, time-consuming and thus expensive as channel characteristics may vary significantly between applications. The aim of this work was therefore to lay the foundations of a model that enables to assess critical channel characteristics by computer simulation.

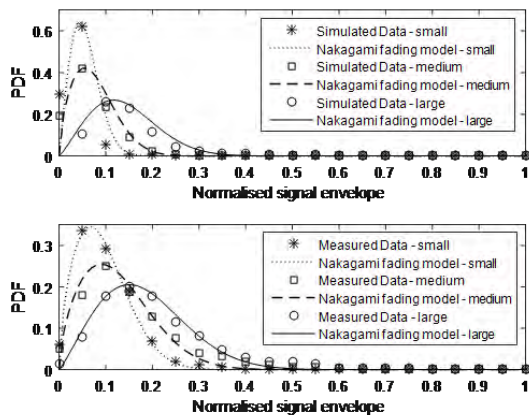
Statement of Contribution/Methods

Ultrasonic wave propagation was modeled considering three phenomena: diffraction (leading to transducer-dependent beam divergence loss); frequency-dependent attenuation; and reflection at media with different acoustic impedance. Importantly, the image-source method was used to incorporate multipath reflections based on geometrical considerations of the channel in combination with its reflection properties. Additionally, the frequency response of the ultrasound source and receiver were accounted for.

To test the validity of the simulation tool, simple geometric models of different dimensions (small – 40×40×20 mm³, medium – 40×40×40 mm³, large – 40×40×80 mm³) were generated and the channels' impulse response (IR) were determined by taking material constants from literature. The same IRs were then obtained experimentally using gelatine phantoms and a customized setup using 1 MHz transducers. To compare the experimental and synthetic findings, different IR metrics relevant for communication protocols were extracted, i.e. the signal delay spread, its coherence bandwidth and the Nakagami fading.

Results/Discussion

The simulated and measured signal delay spread and coherence bandwidth were equivalent (approx. 130 µs; 1.5 kHz) and both signal delay profiles could be fitted with a Nakagami fading model (Fig.). Although the absolute values of the channel metrics differed, relative changes were appropriately captured thereby indicating that the proposed model can describe trends in channel characteristics correctly. In future work, the model will be improved by implementing more realistic channel geometries corresponding to specific locations in the human body.



2:15 PM

Optical Imaging of Far-Field Diffraction of GHz AlN Transducers into Silicon: Towards Physical Fast Fourier Transform Computing

Yutong Liu¹, Justin Kuo², Mamdouh Abdelmejeed¹, Amit Lal³

¹*Electrical and Computer Engineering, Cornell University, Ithaca, NY, United States*, ²*Cornell University, Ithaca, NY, United States*, ³*School of Electrical and Computer Engineering, Cornell University, Ithaca, NY, United States*

Background, Motivation, and Objective

Image processors used in autonomous driving and robotic manipulation require Fast Fourier Transforms (FFT). The complexity of 2-D FFT is $O(N^2 \log N)$. We propose an analog-domain ultrasonic FFT (Sonic FFT) which approximates the transform with the Fraunhofer diffraction pattern generated by wavefront propagation from a transducer array. The complexity of the Sonic FFT is $1/\omega$ where the ω is the ultrasonic frequency. Given that the ω is comparable to the frequency of the state-of-the-art processors, the Sonic FFT reduces the complexity to $O(N)$. In this paper, we present the measurement of the diffraction pattern generated by a square Aluminum Nitride piezoelectric transducer, thereby demonstrating the feasibility of Sonic FFT.

Statement of Contribution/Methods

Under the condition that $z > 2.3(a/2)^2/\lambda$ where z is the silicon substrate thickness and a is the width of a square transducer, the ultrasonic waves propagate to the backside of the substrate in the Fraunhofer diffraction region. Driving the transducer at voltage V with frequency w , the pressure profile at the backside can be formulated as $p_0(x_0, y_0, z; \omega) \approx j\omega p_0 V / (2\pi R) * \exp(-jk[z + (x_0^2 + y_0^2)/(2z)] * F(x_1, y_1))$, where $j\omega p_0 V / (2\pi R)$ is a constant scaling factor, (x_0, y_0) is the source plane, and (x_1, y_1) is the focal plane as shown in Fig. 1a. The spatial frequencies in the x, y directions are $k_x = -kx_0/z$, $k_y = -ky_0/z$. We measure the displacement at the focal plane of an AlN transducer (Fig. 1b) driven by a 120ns pulsed 1GHz RF signal using a UHF Polytec interferometer. The amplitude and phase of the displacement are extracted from the output of the interferometer using IQ demodulation. The results of the 2-D Sonic FFT are shown in Fig. 1c&d. In Fig. 1e&f, we compare the amplitude and phase of a 1-D Sonic FFT between the experiment, the PZFlex simulation, and the Fraunhofer model.

Results/Discussion

Since our experiment is performed on the edge of the far-field, there exists a discrepancy between the obtained diffraction and the Fraunhofer diffraction. The Pearson correlation coefficients of 1-D magnitude and phase between experimental and analytical results are 0.929 and 0.883, respectively. This study indicates the Fraunhofer diffraction conforms with the calculated wavefronts. In order to derive the actual Fourier transform of the input field, additional ultrasonic components such as lenses are needed to cancel the wavefront phase.

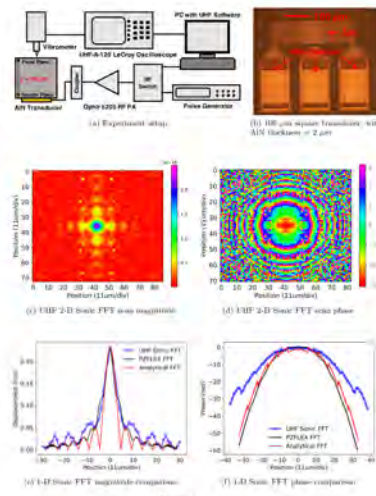


Figure 1

2:30 PM

GHz Ultrasonic Digital to Analog Converter for Wavefront Signal processing**Mamdouh Abdelmejeed¹, Justin Kuo¹, Amit Lal¹**¹*School of Electrical and Computer Engineering, Cornell University, Ithaca, NY, United States***Background, Motivation, and Objective**

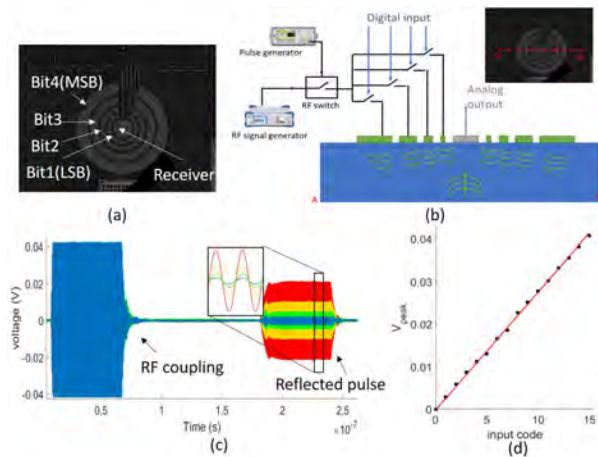
A 2D transducer array can produce an ultrasonic field that, when measured in the far-field, is the Fourier transform of the input field. This physics of field propagation approach has been used in optics for Fourier transform computation at the speed of light. However, optical systems occupy large area and are difficult to integrate with CMOS. In contrast, ultrasonic waves can be generated and received by systems that are more compact and easier to integrate. The transmitting aperture is formed from a 2D array of AlN piezoelectric pixels on top of a silicon substrate. The aperture is apodized to represent the input 2D function by assigning different actuation amplitudes to each pixel. A challenge in this architecture is the electronics overhead to drive each pixel with a different amplitude using circuit-based DAC. In this paper we present a digital to analog ultrasonic transducer pixel that allow for a simplified apodization for a 2D input plane aperture.

Statement of Contribution/Methods

A 4-bit version of the Sonic DAC is shown in Fig (a), each pixel is divided into concentric rings which are binary weighted in area. The far field pressure magnitude is proportional to the transducer area. As a result, the sensed pressure from the binary-weighted rings is also binary weighted. As shown in Fig (b), the piezoelectric transducers are actuated in the bulk mode by an RF pulse at the resonance frequency of the transducer. Digital input is used to determine which of the rings are actuated. The resulting acoustic pulses propagate through the silicon substrate and add up in the far field region. The pulse reflects from the back side of silicon then transduced back to electrical signal by the receiver circular transducer in the middle. The assumption that all the pressure waves add up in phase in the far field is only valid if the size of the whole pixel is in the order of the wavelength of the acoustic waves $\sim 9 \mu\text{m}$.

Results/Discussion

Fig. (c) shows the output signal for an input binary code of 0001, 0010, 0100, and 1000. Due to lithography limitation, the tested pixel size is $200 \mu\text{m}$ (~ 25 times the wavelength). As a result, the input phase of each ring is adjusted to compensate for the acoustic path length difference as well as the wirebonding mismatch to make sure waves from different rings add up in phase at the receiver. The input/output curve is shown in Fig (d). The DAC has a resolution of 2.7mV , DNL of 0.5 and INL of 0.4.



2:45 PM

An inverse approach for ultrasonic imaging by total focusing point for close reflectors separationNans Laroche^{1,2}, Ewen Carcreff¹, Sébastien Bourguignon², Jérôme Idier², Aroune Duclous³¹*The Phased Array Company, West Chester, OH, United States*, ²*LS2N, NANTES, France*, ³*LAUM, Le Mans, France***Background, Motivation, and Objective**

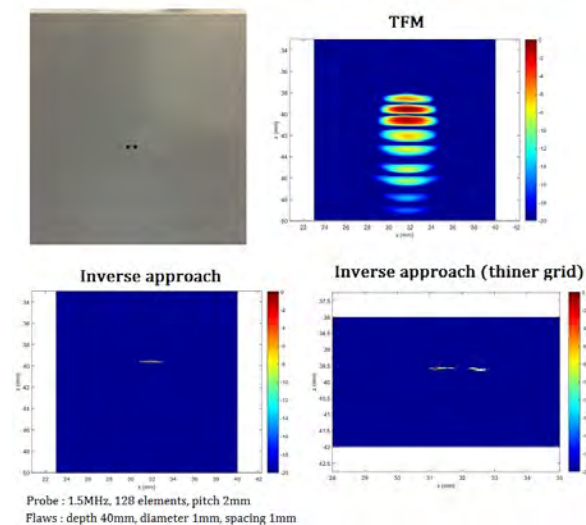
The total focusing method (TFM) becomes a common approach to process full matrix capture data in nondestructive testing. This method consists of transmitting an unfocused beam and performing focusing in reception at each point of a defined reconstruction grid. The quality of TFM images is generally better than conventional phased array focusing that can focus at only a few points. Nevertheless, flaw resolution in TFM images is not always sufficient, in particular when the defects are close.

Statement of Contribution/Methods

We propose to model the full matrix capture data as a linear operation between the concatenate reconstructed image and a matrix of waveforms. This matrix depends on the geometry of the inspection, the acoustical properties of the transducers and the media under inspection. This inverse problem is ill-posed, therefore, *a priori* information on the final image must be introduced to regularize the problem. Our proposal consists of inverting the system by minimizing a penalized least-squares criterion within an iterative procedure under a sparse assumption.

Results/Discussion

The first example shows the ability of the inverse approach to resolve flaws separated by a distance of $\lambda/4$ on synthetic data. The second example uses data acquired from two close side drilled holes (SDH) in an aluminum block. The proposed algorithm clearly resolved the two SDH that are also separated by a distance of $\lambda/4$. The proposed method is able to resolve close flaws despite their sub wavelength separation distance, it significantly outperforms the well known Rayleigh's criterion.



6G - Bio & Chemical Sensors

Nunobiki (150)

Wednesday, October 24, 4:00 pm - 5:30 pm

Chair **James Friend**
UCSD

6G-1

4:00 PM Design of Lab-on-a-Chip Surface Acoustic Resonance (SAR) Sensor with Enhanced Sensitivity and Integrated EIS

Kiryl Kustanovich¹, Aldo Jesorka¹, Ventsislav Yantchev¹

¹*Chalmers University of Technology, Goteborg, Sweden*

Background, Motivation, and Objective

Significant efforts are being directed into the development of biochemical sensor arrays. For this purpose the sensor must be small and reliable, while maintaining simple probing and robust integration with microfluidic systems. We have addressed these requirements through a novel sensing concept based on the surface acoustic resonance (SAR) implemented in a one-port Lab-Chip device [JMM Highlights]. Unlike SAW delay-lines, SAR sensors employ the *reflective gratings* as *sensing elements*. PDMS microfluidics is designed to supply the liquid over the reflectors, while isolating the IDT through an air-gap cavity. The SAR Lab-Chip platform has significantly smaller dimensions when compared to delay-line sensors, enabling easy read-out and fabrication.

Statement of Contribution/Methods

We demonstrate key-enabling enhancements in the SAR sensor design. A novel “acoustic trap” design is introduced, where the spatially varying reflectivity of the SAW reflectors enables SAW localization inside the sensing domain. We show an integration with a low frequency (<1MHz) electrochemical imp. spectroscopy (EIS). Here, the SAR port is independent from the EIS port (Fig. 1), thus enabling an *in-situ* calibration of the biochemical experiment.

Results/Discussion

More than **100%** improvement in mass-sensitivity is achieved. Our 187MHz SAR sensor demonstrates sensitivity comparable to a 900MHz SMR while significantly outperforming SAW delay lines in the 100MHz range. The enhanced sensitivity is accompanied with retained performance under highly viscous loads (Fig. 2). Detailed and time-resolved biochemical experiments reveal the ability of the SAR sensor to discriminate between mass loading and changes in layer elasticity, suggesting sensing capabilities beyond traditional microgravimetry.

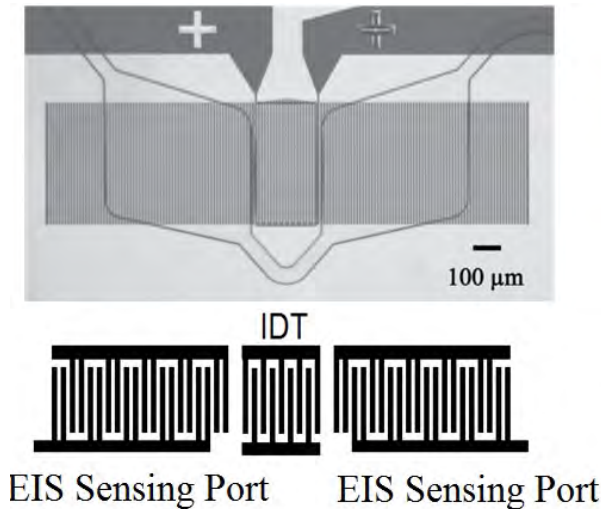


Figure 1

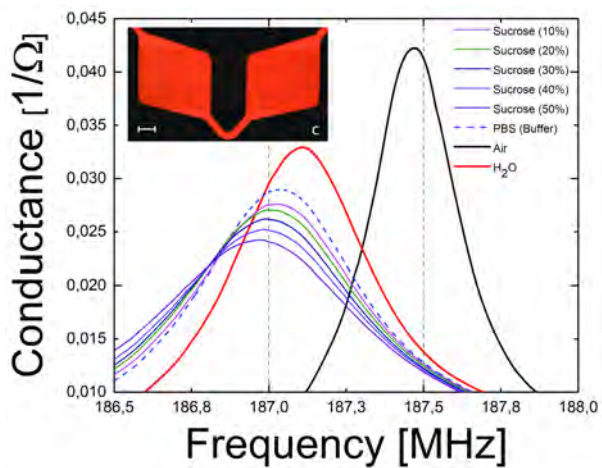


Figure 2

4:15 PM

c-axis tilted ScAlN film shear mode resonators for biosensingHana Yazaki^{1,2}, Rei Karasawa^{1,2}, Takahiko Yanagitani^{1,2,3}¹Waseda University, Japan, ²ZAIKEN, Japan, ³JST PRESTO, Japan**Background, Motivation, and Objective**

QCM (quartz crystal microbalance) and FBAR (thin film bulk acoustic resonator) are suitable for sensing the biomolecules [1,2]. The resonant frequency changes due to the mass loading caused by the biomolecules binding on the resonator surface. Thin resonators are required for accurate measurement because the sensitivity is inversely proportional to the mass of the entire resonator. QCM, however, has limitation in its thickness because of difficulty in the mechanical polishing. In contrast, the use of structure (FBAR) allows high sensitivity because of their small mass. In this study, we reported the detection of biochemical reaction using c-axis tilted ScAlN film shear mode resonators. Higher piezoelectricity of the ScAlN thin films makes it possible to improve signal-to-noise ratio.

[1] K. A. Marx, *Biomacromolecules*, **4**, 1099 (2003)

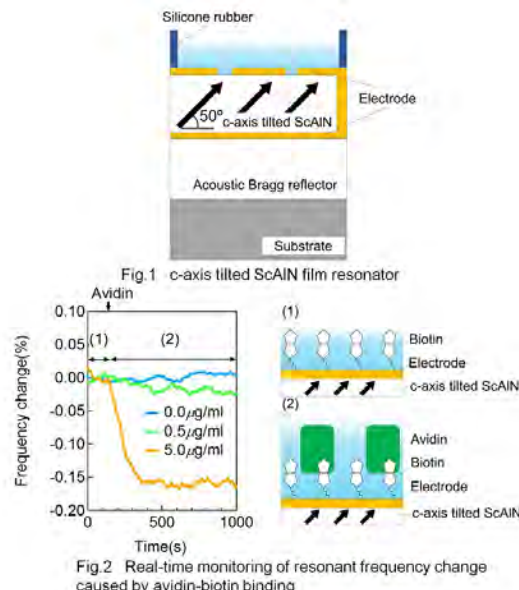
[2] J. Weber, W. M. Albers, J. Tuppurainen, M. Link, R. Gabl, W. Wersing, M. Schreiter, *Sensors and Actuators A*, **128**, 84 (2006)

Statement of Contribution/Methods

Figure 1 shows the sensor structure with c-axis tilted ScAlN films. First, c-axis tilted ScAlN films were grown by glancing angle sputtering deposition. c-axis tilt angle was measured to be 50° by using XRD pole figure analysis. k_{15} of the c-axis tilted ScAlN films was determined to be 9.7 % by using a resonance-antiresonance method. We measured the quasi-shear mode resonant frequency changes caused by avidin binding to biotin immobilized on the resonator surface. The resonant frequencies were measured every 2 seconds by using a network analyzer (Agilent Technologies, E5071C). The obtained data were smoothed by moving averages to reduce short-term variation.

Results/Discussion

Figure 2 shows the real-time monitoring of resonant frequency when avidin is introduced. First, the resonator coated with biotin was immersed in 30 μl of PBS (phosphate-buffered saline, pH 7.2) (Fig. 2 (1)). Next, 30 μl of avidin solution was introduced into the resonator at 200 seconds (Fig. 2 (2)). By comparing avidin concentration of 0.0 μg/ml with 5.0 μg/ml, we can see the apparent decrease of the resonant frequency due to the avidin-biotin binding. These results demonstrate that the c-axis tilted ScAlN film shear mode resonator is promising for biosensing applications.



4:30 PM

Wireless CO₂ SAW sensors with a nanoporous ZIF-8 sensing layerDavid Greve^{1,2}, Jagannath Devkota³, Paul Ohodnicki³¹*DWGreve Consulting, Sedona, AZ, United States*, ²*Department of Electrical and Computer Engineering, Carnegie Mellon University, Pittsburgh, PA, United States*, ³*National Energy Technology Laboratory, Pittsburgh, PA, United States***Background, Motivation, and Objective**

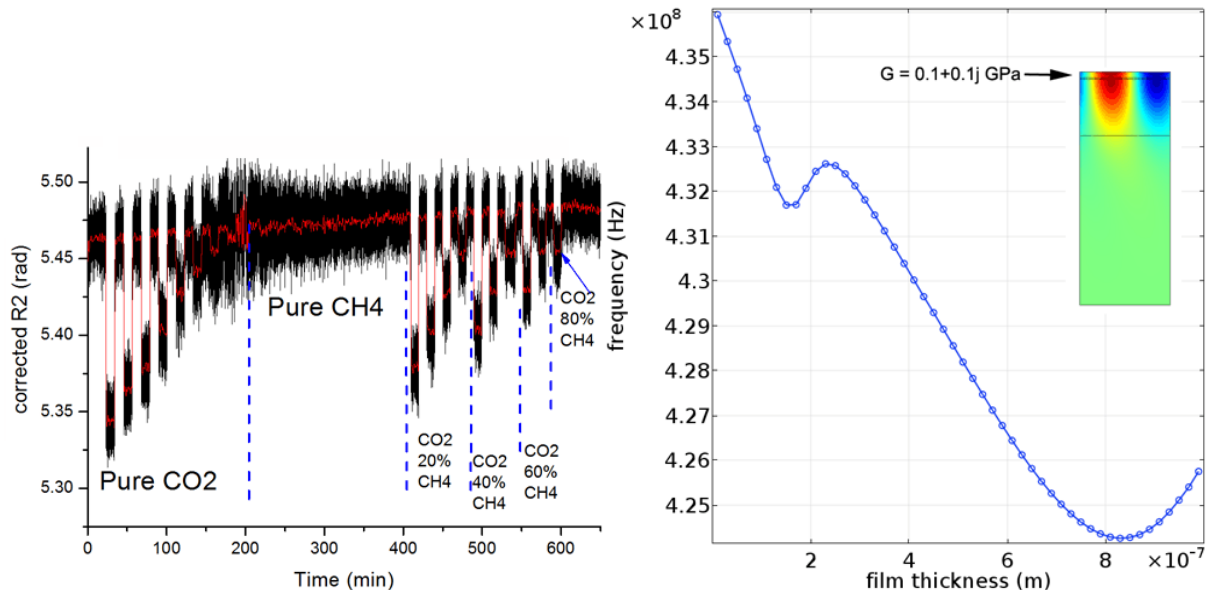
Wireless surface acoustic wave gas sensors are potentially valuable for detecting leakage from pipelines or carbon sequestration wells. Metal organic framework materials are potential sensing layers, having nanopores with engineered size for adsorption and desorption of particular gases. But in general overayers, especially mechanically soft overlayers, cause surface wave attenuation compromising signal levels.

Statement of Contribution/Methods

We have reported the fabrication and characterization of CO₂- sensitive wireless SAW sensors on LiNbO₃ substrates with ZIF-8 sensing layers. Designed to operate at ~436 MHz, the device consisted of an emitting/receiving interdigitated electrode and two reflectors on opposite sides at 2.38 mm and 3.08 mm. The longer delay path and associated reflector was coated with ZIF-8 while the shorter one was used to compensate for environmental effects. In this paper we focus on the attenuation and related unusual phenomena resulting from these overayers.

Results/Discussion

ZIF-8 overlays of 200 nm thickness exhibited additional attenuation of 1.06 dB/mm. Layers 500 nm thick showed higher sensitivity but also greater attenuation (1.65 dB/mm). Averaging was required in wireless mode so an increase in overlayer thickness and sensitivity would be desirable. However the mechanical characteristics of these layers impose limitations on the sensing layer thickness. The reported Poisson ratio is close to 0.5 leading to a low transverse velocity. Simulations and the literature show that standing waves can be formed in thick surface layers. This can cause an unusual dependence of velocity change on thickness. We will illustrate this effect in simulations and will report on attenuation, sensitivity, and response time of thick ZIF-8 sensing layers.



4:45 PM Post-Complementary-Metal-Oxide-Semiconductor Compatible Piezoelectric Micro-Machined Ultrasonic Transducers

Robert Reger¹, Adam Edstrand¹, Benjamin Griffin¹

¹*MEMS Technologies, Sandia National Laboratories, Albuquerque, NM, United States*

Background, Motivation, and Objective

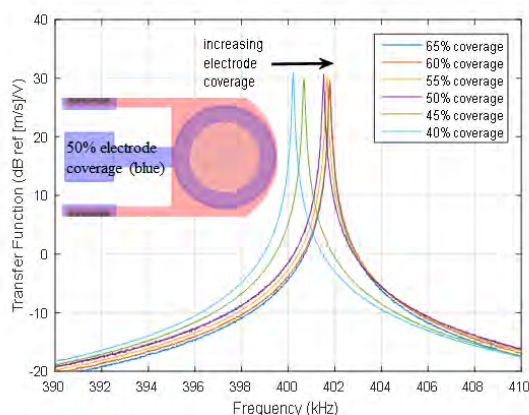
Fingerprint monitoring has become pervasive in the cellular telephone market. Current commercial state-of-the-art technology utilized in fingerprint monitoring is based on capacitive scanning. These scanners are fundamentally limited to two-dimensional surface measurements by their reliance on capacitance. This issue makes them unreliable when surface contamination is present. Recent research by Tsai et al. (2015) and Jiang et al. (2017) has investigated the use of arrays of piezoelectric micro-machined ultrasonic transducers (PMUTs) in fingerprint matching. Based on a pulse/receive architecture, the PMUT array creates a three-dimensional image of the epidermis and sub-surface layers making up the fingerprint, making them more secure and reliable in the presence of moisture and other surface contamination [Jiang, 2017]. In this work, we design, fabricate, and characterize a PMUT based pulse/receive ultrasonic imaging sensor utilizing piezoelectric aluminum nitride (AlN) for transduction.

Statement of Contribution/Methods

We are designing a PMUT based ultrasonic imaging sensor which relies on post-CMOS, monolithic integration rather than MEMS-to-CMOS wafer-to-wafer bonding. Initial electronics (amplifiers, multiplexers, etc.) and signal routing are designed in Sandia's 0.35 μm trench-isolated SOI CMOS7 process. Upon completion of the CMOS7 process, the PMUTs will be built directly on the CMOS wafers using Sandia's AlN micro-resonator process with via connections to the CMOS. This monolithic integration allows for intimate connection between PMUTs and electronics minimizing parasitic capacitances, frontside photolithographic definition of the back cavities of each of the devices in the PMUT array for frequency control, minimization of acoustic and mechanical cross-talk between devices, and limited mechanical stress due to bonding observed previously in work from Tsai et al. (2015) and Jiang et al. (2017).

Results/Discussion

Initial PMUT devices designed and fabricated in Sandia's AlN process are presented. Device characterization demonstrating a range of frequencies from 100 kHz to 800 kHz with varying electrode coverage are shown. Sample device design and representative results of the study are shown in the attached figure.



5:00 PM

A compact and sensitive liquid sensor based on a circumferential modeQin Lin^{1,2}, Feiyan Cai¹, Fei Li¹, Xiangxiang Xia¹, Zhanhua Mai², Wei Zhou¹, Hairong Zheng¹¹*Paul C. Lauterbur Research Center for Biomedical Imaging, Shenzhen Institutes of Advanced Technology, Chinese Academy of Sciences, China, People's Republic of*, ²*School of Information Engineering, Guangdong Medical University, China, People's Republic of***Background, Motivation, and Objective**

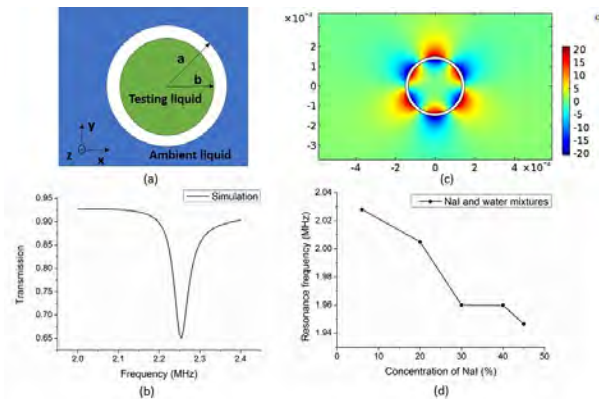
Acoustic wave devices are attractive for use in sensors because the wave characteristics are sensitive to outside parameters. The ability of confining an acoustic wave in an ultra-small region can strengthen the wave-matter interaction, which results in the improvement of sensing sensitivity and reducing the amount of the sample to be measured. Here, we report a liquid sensor based on a circumferential mode in a cylindrical shell. This sensor exhibits a high sensitivity and requires a minimal amount of liquid due to the field localized at the surface of the shell.

Statement of Contribution/Methods

As schematically shown in Fig. (a), the system consists of a glass cylindrical shell (white) whose inner and outer radius are 120 μm and 150 μm , respectively. The liquid to be sensed fills the cylindrical shell (green), while the ambient liquid surrounds the cylindrical shell (blue). The normal transmission spectrum and field distribution of this system are calculated by using the COMSOL Multiphysics software. As shown in Fig. (b), there is a transmission dip at frequency of 2.041MHz. The pressure field around the cylindrical shell at the resonance frequency is illustrated in Fig. (c), which is confined at the surface of the shell and can be demonstrated that is the 3-nd of circumferential mode.

Results/Discussion

To show the sensing capabilities of the cylindrical shell system, the resonance frequencies versus different concentrations of NaI-water mixtures filled in the cylindrical shell are shown in Fig. (d), which are showed to be dependent on the properties of NaI-water mixtures. Thus, the cylindrical shell based circumferential mode can be served as a compact and sensitive liquid sensor.



5:15 PM

Improvement of signal to noise ratio for Quartz Crystal Microbalance with viscous dampingSawit Na songkhla¹, Takamichi Nakamoto¹¹*Department of Information and Communications Engineering, Tokyo Institute of Technology, Yokohama, Japan***Background, Motivation, and Objective**

Quartz Crystal Microbalance (QCM) sensors are widely known using as sensor elements in odor sensing system. However, its signal to noise ratio decreases with viscous damping such as liquid loading or coating with viscous film. Here we aim to improve signal to noise ratio (SNR) using signal processing method.

Statement of Contribution/Methods

Our study introduces Vector Network Analyzer as a method to obtain resonance frequency. The feasibility was confirmed by the QCM in contact with glycerol-water solution with various concentration. Resonance frequency can be determined by reading the maximum conductance frequency. In principle using motional admittance method. Since viscous damping causes high noise level. We introduce curve fitting method by utilizing all data points within certain frequency range to obtain resonance frequency. Lastly, apply savitzky-golay filter, with polynomial approximation within moving window, to further smoothen the frequency data, keeping its sharp response.

Results/Discussion

We confirmed result by glycerol-water solution from at 40% (w/w). Figure 1 shows the temporal frequency shift at 40% (w/w) glycerol-water solution. The frequency deviation was more than 300 Hz for maximum conductance method compared to small noise using curve fitting method. From figure 2, by using curve fitting technique and savitzky-golay filter, the deviation was drastically reduced. we concluded that by apply both curve fitting technique and savitzky-golay filter should be applied to improve SNR of QCM sensor with viscous loading

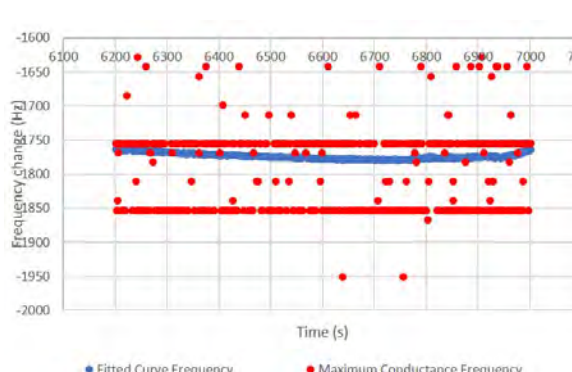


Fig 1. Sensor response by Maximum Conductance method compare to Curve fitting method (Sampling time 1.16 s)

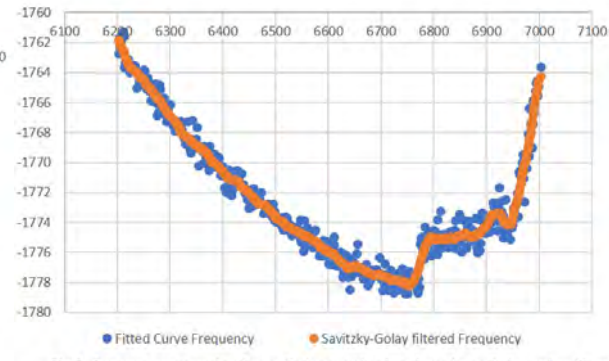


Fig 2. Sensor response by Curve fitting method and apply savitzky-golay filter (Polynomial order 3rd: Window width 33 points)

7D - New Developments in Medical Imaging

Kikusui (140)

Wednesday, October 24, 8:00 am - 9:30 am

Chair **Kang Kim**
University of Pittsburgh

7D-1

8:00 AM

Image-guided photo-mediated ultrasound therapy as a novel anti-vascular treatment for eye diseases

Xinyi Xie^{1,2}, Wei Zhang¹, Yu Qin^{1,3}, Qian Cheng³, Qinghuai Liu², Yannis Paulus^{1,4}, Xinmai Yang⁵, Xueding Wang^{1,3}

¹Department of biomedical engineering, University of michigan, Ann arbor, MI, United States, ²Department of Ophthalmology, the First Affiliated Hospital of Nanjing Medical University, Nanjing, China, People's Republic of,

³School of Physics Science and Engineering, Tongji University, China, People's Republic of, ⁴Department of

Ophthalmology, University of michigan, Ann arbor, MI, United States, ⁵Bioengineering Research Center and Department of Mechanical Engineering, university of kansas, lawrence, KS, United States

Background, Motivation, and Objective

Neovascularization occurs in eye diseases such as corneal neovascularization, diabetic retinopathy, and macular degeneration. Current treatment methods including anti-VEGF injection have drawbacks including frequent administration, high cost, and destructive nature. We have developed a novel photo-mediated ultrasound therapy (PUT) technique which concurrently applies nanosecond laser pulses and millisecond ultrasound bursts to precisely and safely remove microvessels in the eye. Here, we will present our recent development of image-guided PUT which can further improve the safety and efficacy in treating eye diseases.

Statement of Contribution/Methods

A multi-modality eye imaging system involving advanced photoacoustic microscopy (PAM) and optical coherence tomography (OCT) is integrated with PUT to provide real-time feedback and online evaluation of the treatment outcome. The laser in PAM system is the same one used for PUT. With this arrangement, the PAM can evaluate vascular response to treatment without interfering the treatment procedure. Sharing the same galvanometer, scan lens and ocular lens, the OCT system has its light beam coaxially aligned with the PAM laser beam to detect the cavitation in the vessels which is the fundamental mechanism of PUT. This image-guided PUT system was initially tested via the experiments on New Zealand white rabbits.

Results/Discussion

The image-guided PUT can precisely and efficiently remove choroidal vasculature with optimized parameters of 0.5-1.0 MPa ultrasound and 50-75 mJ/cm² laser fluence. The elimination of vessels in the treatment region was confirmed by fundus camera and fluorescence angiogram. Compared to these conventional methods, PAM, besides offering real-time treatment monitoring, presented more vascular details.(Figure 1) In addition, during the treatment, cavitation signals were observed by OCT, suggesting that OCT, with good sensitivity in detection microbubbles, can be another imaging modality for online monitoring and guidance of PUT. After a single treatment, the vascular occlusion was sustained beyond 4 weeks. The excellent safety was confirmed by histopathological analyses. In conclusion, image-guided PUT holds promise as a novel, non-invasive method for treating eye neovascularization.

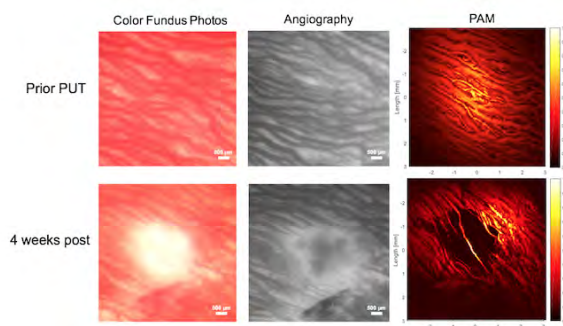


Figure 1. Color fundus photos, fluorescence angiography, and PAM images acquired before and 4 weeks after PUT treatment, showing the removal of rabbit choroidal vasculature in a long term.

8:15 AM High-resolution imaging of the breast using full-waveform inversion

Oscar Calderón Agudo¹, Lluís Guasch¹, Peter Huthwaite², Mike Warner¹¹*Earth Science and Engineering, Imperial College London, London, United Kingdom*, ²*Mechanical Engineering, Imperial College London, London, United Kingdom***Background, Motivation, and Objective**

Although ray-based tomographic algorithms are generally fast, the quality of recovered speed-of-sound models is limited by the size of the first Fresnel zone. Thus, small tumours, micro-calcifications or vessels in the breast can barely be imaged. In contrast, full-waveform inversion (FWI) methods honour the physics of wave propagation, and while they are more expensive to compute they result in models with much-higher spatial resolution, thus enabling imaging of small features. Nevertheless, the application of FWI to breast imaging with ultrasound is still in its infancy, especially in 3D.

Statement of Contribution/Methods

Utilising a highly realistic in-silico 3D model of the breast, we demonstrate the applicability of 3D FWI to ultrasound data, the importance of acquiring low-frequencies (below 1 MHz), and the impact of neglecting density, tissue absorption and 3D effects during model reconstruction. We then recover a speed-of-sound model of a breast from in-vivo clinical ultrasound data acquired with a 2D ring of transducers, and having little information about the exact acquisition geometry.

Results/Discussion

Simulations of the 3D in-silico breast model demonstrate the feasibility and potential of 3D FWI for breast imaging at high resolution, which is able to recover small features with limited prior information provided that low-frequency ultrasound data are acquired. The results also show that density and absorption can be safely neglected for average-density breasts, and that 3D effects as well as 3D data acquisition need to be considered to separate features in different planes. Application of FWI to an in-vivo dataset results in a highly resolved model despite the high level of noise in the data, the lack of low frequencies, and inaccurate positioning of the transducers. When compared to the low-resolution result obtained with ray-based time-of-flight tomography (Figure 1A), the speed-of-sound model obtained with FWI (Figure 1B) clearly shows sharper edges, continuous structures that may represent vessels, and a more heterogeneous high-velocity zone that may indicate the presence of a tumour.

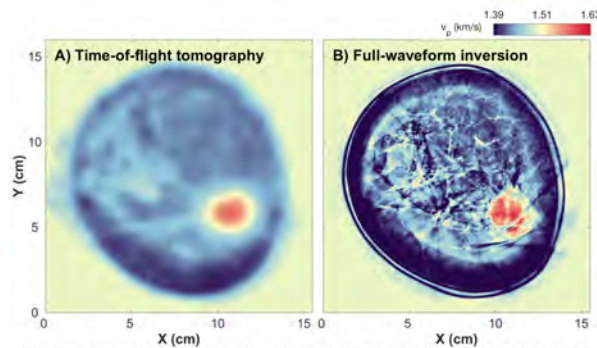


Figure 1. Recovered speed-of-sound models, for breast in-vivo ultrasound data, obtained with:
 (A) time-of-flight tomography, and (B) full-waveform inversion.

8:30 AM

Respiratory motion compensation for localization-based ultrasound super-resolution imagingJaesok Yu¹, Linda Lavery², Kang Kim^{1,2}¹*Bioengineering, University of Pittsburgh, Pittsburgh, PA, United States*, ²*Medicine, University of Pittsburgh, Pittsburgh, PA, United States***Background, Motivation, and Objective**

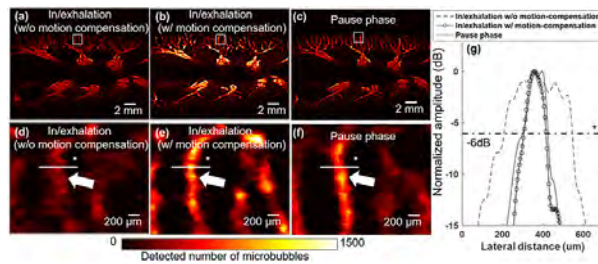
One of the biggest challenges of current microbubble (MB)-localization based super-resolution imaging (SRI) is the physiologic motion artifact. Despite recent efforts in significantly improving the temporal resolution of SRI such as deconvolution-based approach and super-resolution optical fluctuation imaging-based method, the scan time still remains longer than a typical breathing cycle of small animals due to the required large number of frames. This relatively long scan time critically hampers the performance of SRI. Here, we introduce a respiratory motion compensation (MC) method assuming a rigid body motion and present *in vivo* evaluation on a rabbit kidney.

Statement of Contribution/Methods

To evaluate our method, a deconvolution-based SRI was performed on a rabbit kidney during in/exhalation phase (motion) with and without MC and pause phase (no motion) right after exhalation phase as a baseline to compare with. MBs (150 μ L) was intravenously injected, and then a total of 1,000 three angle-compounded frames were acquired from the kidney at 500 Hz using a linear transducer (8.8 MHz) connected to Verasonics system. Selected 300 frames over in/exhalation and pause phase were reconstructed in B-mode. To compensate motion artifact, the motion vector of the following frames referenced to the initial frame during in/exhalation was estimated by using an efficient three-step search approach. The search block size was 2 mm \times 2 mm and the search range was 5 mm. The average motion vector was then applied to each frame to cancel the respiratory motion. The SR image over in/exhalation phase after MC was compared with the SR image over pause phase.

Results/Discussion

SR images reconstructed from 300 frames during in/exhalation phase were shown in (a) without and (b) with MC, and (c) during pause phase. Figs (d-f) are zoomed-in images of the areas indicated by the white rectangles in Figs (a-c). The diameter of the vessel indicated by a white arrow in the SRI over the in/exhalation phase (d, g) measures 336 μ m that is approximately 3 times larger than the size of the same vessel, 123 μ m, over the pause phase (f, g). The vessel size after MC (e, g), 109 μ m, is close to the size when no motion is involved (f, g). The overall increased signal intensity shown in (b) is mainly due to the increased number of MBs identified when breathing motion is canceled.



8:45 AM

3D Super-Resolution Ultrasound Imaging using a 2D Sparse Array with High Volumetric Imaging Rate

Sevan Harput¹, Kirsten Christensen-Jeffries², Jemma Brown², Jiaqi Zhu¹, Ge Zhang¹, Chee Hau Leow¹, Matthieu Toulemonde¹, Alessandro Ramalli^{3,4}, Enrico Boni³, Piero Tortoli³, Robert Eckersley², Chris Dunsby⁵, Mengxing Tang¹

¹Department of Bioengineering, Imperial College London, London, United Kingdom, ²Department of Biomedical Engineering, School of Biomedical Engineering and Imaging Sciences, King's College London, London, United Kingdom, ³Department of Information Engineering, University of Florence, Florence, Italy, ⁴Lab. on Cardiovascular Imaging & Dynamics, Dept. of Cardiovascular Sciences, KU Leuven, Leuven, Belgium, ⁵Department of Physics and Centre for Pathology, Imperial College London, London, United Kingdom

Background, Motivation, and Objective

Super resolution ultrasound (SR US) imaging has been achieved in 3D by mechanically scanning a volume with a linear probe, by co-aligning multiple linear probes, by using multiplexed 3D clinical US systems, or by using 3D US research systems. In this work, a 2D sparse array at a lower frequency closer to microbubble resonance was used to achieve SR in 3D. A high frame rate volumetric US imaging with plane waves was performed and experimental results of 3D SR US imaging are demonstrated.

Statement of Contribution/Methods

A sparse array was designed by selecting 512 elements from a 32×32 element array according to a density tapered 2D spiral layout. The 2D sparse array was specifically fabricated for 3D SR US with an element size of 300 × 300 μm, center frequency of 3.7 MHz and a bandwidth of 57%. Two ULA-OP256 systems were synchronized to transmit 9 plane waves steered within a range of ±10 degrees in the lateral and elevational directions from the 512 selected elements. Each compounded volume consisted of 9 volumetric datasets acquired in 3.6 ms at 2500 Hz PRF.

A 1:1000 diluted Sonovue solution was flowed through two 200 μm tubes arranged in a double helix shape as shown in Fig A. A total of 3000 volumetric US frames were acquired in 180 seconds and 3D localization of microbubbles were performed on every frame to generate the 3D super-resolved volumes. SVD was used to separate the microbubble signals from the echoes originating from the tube.

Results/Discussion

The FWHM of the 3D B-mode PSF was 793, 772, and 499 μm in X, Y, Z directions respectively and 3D SR images had a localization precision of 18 μm, which were measured before the experiments. Fig B shows the 3D visualization of microvessels overlaid on 2D B-mode slices, where it is not possible to visualize two 200 μm tubes. Fig C shows the 3D SR images of the sub-wavelength structures from different viewing angles, where the imaging wavelength is over 400 μm. The average FWHM of a single tube appeared as 112 μm due to higher number of localizations at the center of the tube and the 90% of the super-localizations were within a diameter of 266 μm.

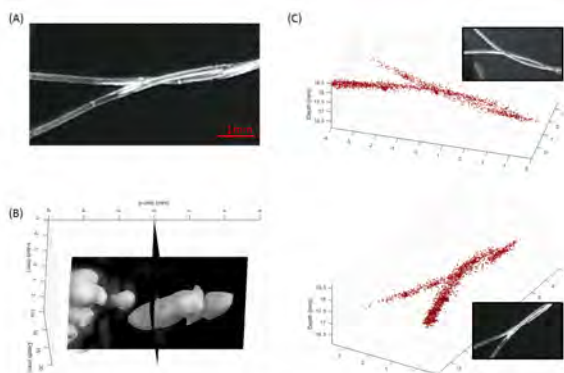


Figure (A) Optical Images of two 200 μm cellulose tubes arranged in a double helix pattern. **(B)** Isosurface of the 3D ultrasound image at 10 dB level overlaid on 2D B-mode slices. **(C)** Figures show 3D super-resolution images of two tubes from different viewing angles with corresponding optical images.

9:00 AM

Detection of distal forearm fractures using bone-enhanced 3D ultrasound imagingVon F. Botteicher¹, Adam J. Dixon¹, Christopher D. Thom², Mark R. Sochor², F. William Mauldin, Jr.¹¹Rivanna Medical, LLC, VA, United States, ²Emergency Medicine, University of Virginia, United States**Background, Motivation, and Objective**

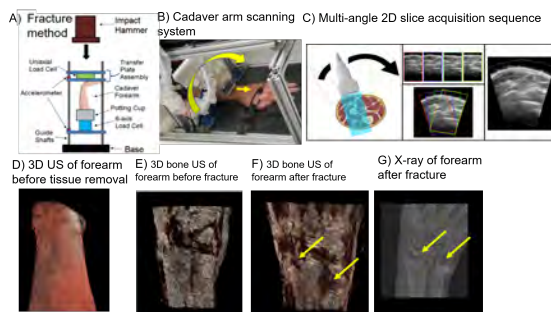
The use of x-ray imaging to detect distal forearm fractures has been the standard of care for over 100 years. However, with changes in emergency room workflows, there exists the need to rapidly differentiate between fractures and sprains at the bedside so as to best utilize emergency room resources and quickly triage patients between different treatment options (e.g. acquisition and interpretation of x-rays leading to casting versus splinting and rapid discharge). To this end, we present a 3D ultrasound imaging method intended to be performed at the bedside that produces 'CT-like' 3D reconstructions of boney wrist anatomy. Cadaver forearms were imaged before and after fracture and results are compared to conventional 2D x-ray images.

Statement of Contribution/Methods

Cadaver forearms were fractured using a drop tower to simulate common FOOSH (Fall On Out-Stretched Hand) fractures. Image acquisition was performed using an Alpinion E-Cube 12R research platform and a L3-12 linear array. The probe was affixed to a motion stage that translated the probe longitudinally along the forearm (0.5 mm increments), from the elbow to the hand, while also sweeping the probe around the circumference of the forearm to acquire data from 7 different angles (see fig). At each scanning location, multiple-angle beam steering was applied to collect specular reflections from the bone surfaces at several angles. Individual 2D frames were assembled into a 3D volume and bone-specific image processing was applied to automatically remove soft-tissue features and retain only reflections from bone surfaces.

Results/Discussion

Each 2D slice was comprised of 35 individual 2D acquisitions that were composited into a single image before being combined with other slices to form a volume. A total of 12 forearms were imaged, with high correspondence between anatomical features in the 3D bone US and x-ray images, as determined by clinician review. In particular, fractures were clearly evident in all 3D ultrasound images, representing early-stage validation of the technique. The 3D volumes shown below represent the first example of bone-segmented 3D ultrasound images of the distal forearm and demonstrate the promise of this approach for providing a large effective field of view rendering of boney anatomy to assist with fracture detection at the bedside.



9:15 AM

Implementation and Clinical Evaluation of a Fetal ALARA SystemKatelyn Flint¹, Nick Bottenus¹, Will Long¹, David Bradway¹, Patricia McNally², Sarah Ellestad², Gregg Trahey^{1,3}¹*Department of Biomedical Engineering, Duke University, Durham, NC, United States*, ²*Division of Maternal-Fetal Medicine, Duke University Medical Center, NC, United States*, ³*Department of Radiology, Duke University, Durham, NC, United States***Background, Motivation, and Objective**

Though diagnostic fetal ultrasound that adheres to FDA output guidelines has no known adverse bioeffects, it is desirable to minimize acoustic exposure. Studies have found that acoustic exposure metrics such as Mechanical Index (MI) are not usually used by sonographers to inform their choice of transmit power during a scan.

We developed an automated ALARA (As Low as Reasonably Achievable) tool using a Verasonics system that selects transmit power based on image quality feedback. Ultrasonic image quality is often assessed using contrast and contrast-to-noise ratio (CNR). However, their reliability suffers due to lack of a priori knowledge of the structures of interest. We based our tool on a novel image quality metric, Lag One Coherence (LOC). Previous work indicates that LOC is predictive of local signal-to-clutter level. It is degraded by the same sources as contrast and CNR, but only requires a soft tissue target, rather than both soft tissue and anechoic targets.

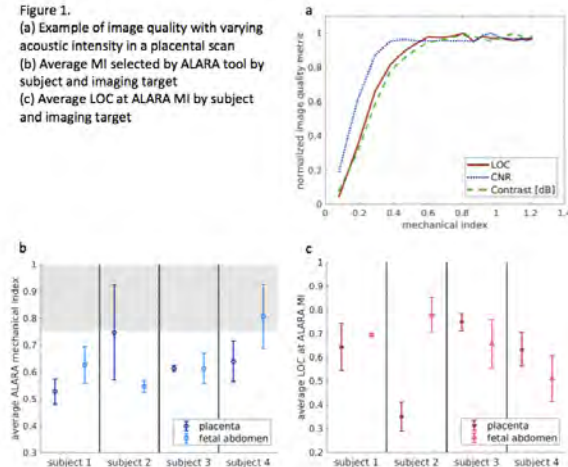
Statement of Contribution/Methods

We imaged four subjects using a C52v transducer. For each subject, LOC as a function of MI was assessed. A region of interest (ROI) centered at the transmit focus was placed on either the placenta or the fetal abdomen at distinct imaging windows to assess measurement variability within targets and across targets. Then, we swept through 18 transmit voltages that correspond to MIs ranging from 0.1 to 1.2 and the system automatically selected the optimum MI based on reaching 95% of the maximum LOC.

Results/Discussion

Figure 1a shows an example of matched measurements of LOC, CNR, and contrast with increasing MI for a representative placental scan. Figures 1b and 1c show the consistency of both LOC and the MI selected by the automated ALARA tool over multiple acoustic windows. Each data point represents the mean and standard deviation from three independent acquisitions. The shaded region on Figure 1b represents MI values commonly used in clinical practice. These results suggest that maximum image quality can be achieved with lower exposure levels than those that are currently used. The ALARA MI values vary between subjects and imaging windows, but this tool can be employed in real-time to optimize for specific conditions. Our results support the feasibility of automated, LOC-based implementation of the ALARA principle with regard to acoustic exposure for obstetric ultrasound.

Figure 1.
(a) Example of image quality with varying acoustic intensity in a placental scan
(b) Average MI selected by ALARA tool by subject and imaging target
(c) Average LOC at ALARA MI by subject and imaging target



7E - New Developments in Brain Imaging

Kikusui (140)

Wednesday, October 24, 10:30 am - 12:00 pm

Chair **Russell Witte**
University of Arizona

7E-1

10:30 AM

Ultrafast 4D Doppler Imaging of the rat brain with a large aperture Row Column addressed probe

Jack Sauvage¹, Jonathan Porée¹, Claire Rabut¹, Baptiste Heiles¹, Guillaume Ferin², Martin Flesch², An Nguyen-Dinh², Mickaël Tanter¹, Mathieu Pernot¹, Thomas Deffieux¹

¹*Institut Langevin, ESPCI Paris, PSL Research University, CNRS UMR 7587, INSERM U979, France, ²Vermon SA, 180 rue du General Renault, 37000 TOURS, France, France*

Background, Motivation, and Objective

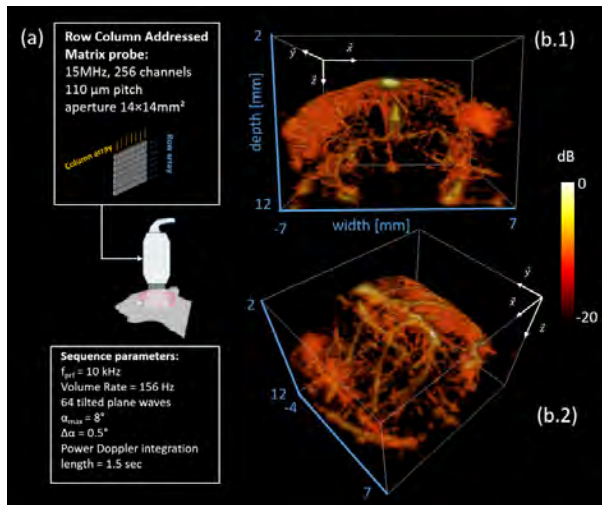
Ultrafast 4D Doppler imaging is a powerful modality to map the 3D vascular network [1] and neurovascular activation in brain. However, this approach requires expensive and complex high channel count electronics and has not yet been performed at high frequency (>10MHz) due to the challenges to manufacture high frequency 2D matrix. Different alternatives have been proposed, among them Row-Column arrays allow reducing the amount of channel from N*N to N+N [2] without compromise on the transducer aperture. By taking advantage of the orthogonal orientation of two arrays, we developed previously a dedicated Orthogonal Plane Wave (OPW) compounding strategy to obtain 3D images at high volume rate [3]. The objective of this work was to evaluate the capability of OPW to provide the full 3D mapping of the Rat Brain vascularization *in vivo* at high frequency using a new prototype of a large aperture 15 MHz RCA transducer.

Statement of Contribution/Methods

A prototype of 15MHz RCA transducer was designed and built by Vermon, Tours, France and consisted in 2 orthogonal arrays of 128 rows and columns elements with a pitch of 0.11 mm. The probe was driven by a research ultrasound system (Vantage 256, Verasonics) with a custom OPW sequence (PRF of 10kHz). The OPW sequence was optimized using field II simulations to compute the point spread function. Then, acquisition of 1.5 seconds were performed at a compounded volume rate of 156 Hz. The rat was anesthetized and trepanned and the probe positioned over the brain. Contrast agents (Sonovue, Bracco, Milan, Italy) were injected intravenously to enhance the SNR. Beamforming and clutter filter were implemented and Power Doppler Volumes were estimated by integrating over the slow time axis.

Results/Discussion

Simulations results showed that an angular pitch of 64 tilted plane waves allowed rejecting grating lobe artefacts out of the field of view. The optimized sequence consisted on the alternative transmission of 64 plane waves providing a total angular aperture of 16° on each direction (equivalent to F# = 3.6 in transmit). Reconstructed angiographic power Doppler volumes exhibits all major blood arteries and veins including inside the cortex and deep areas. Contrast agents allow to enhance the dynamic range by 10dB. Those results pave the way to 4D angiography and 3D functional ultrasound imaging with a 256 element conventional ultrasound research system.



10:45 AM 3D Transcranial Ultrasound Tomography of the Brain in Small Animals using Full-Waveform Inversion – an Initial Feasibility Study

Thomas Robins¹, Carlos Cueto¹, Oscar Calderon Agudo², Lluis Guasch², Mike Warner², Mengxing Tang¹

¹Bioengineering, Imperial College London, London, United Kingdom, ²Earth Science and Engineering, Imperial College London, London, United Kingdom

Background, Motivation, and Objective

Full-waveform inversion (FWI) is an iterative image-reconstruction technique capable of producing high-resolution tomographic images of different acoustic properties, such as speed of sound, absorption and density, by minimising the misfit between observed and modelled data. 2D FWI has already shown promise in breast imaging for soft tissue but has yet to be applied as a neuroimaging method in animal models where hard tissue is involved and 3D reconstruction is required. Here we demonstrate the feasibility of 3D small-animal transcranial ultrasound tomography using FWI *in silico*, based on a pair of 1D ultrasound arrays independently translated for 3D acquisition.

Statement of Contribution/Methods

A 3D transcranial dataset was obtained using forward simulation of a realistic mouse brain and skull model (with acoustic properties provided by the IT'IS Foundation) derived from an MRI and micro-CT dataset (129Sv strain, NeuroMouse Surgical Atlas). Fig.1a shows the 1152-element source and receiver plane arrays defined by simulating two 1D 96-element array probes, operating at 1.5 MHz, over 12 positions 2.5 mm apart along the z-axis. For the 3D acquisition, the full receiver plane was used to record each source element transmitting individually, resulting in a dataset of 1152×1152 unique source-receiver combinations. Reconstruction using this dataset was performed using a robust 3D FWI algorithm to find the misfit between observed data and an initial model, solved by a forward-modelling engine, while a local differential approach estimates the gradient and Hessian operators required to update the model such that this misfit is minimised. This process is repeated for each iteration of the model until a satisfactory minimum is reached. A starting model consisting of the skull and homogeneous water ($c = 1500$ m/s) was used to mitigate cycle skipping due to hard tissue being present.

Results/Discussion

Fig 1.b-c shows FWI results of the mouse brain and skull model. By comparing the reconstruction with the ground truth, a relative error of 0.110 % has been achieved (from a starting model relative error of 2.562 %). In future work we will investigate the impact of tissue elasticity and absorption-related effects on the inversion, and demonstrate the proposed method experimentally using dual phased-array probes (P4-1, ATL) for neuroimaging of *ex-vivo* brain and skull tissue.

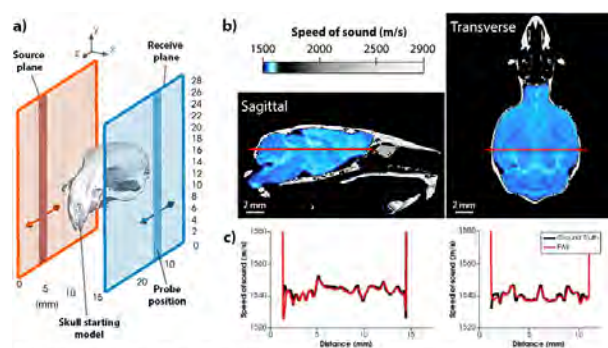


Fig 1. a) Experimental setup showing the dual P4-1 transducers being translated along the z-axis to form the source (orange) and receive (blue) planes either side of the imaging volume. b) Sagittal and transverse views of the 3D speed-of-sound mouse-brain model recovered using FWI. c) Speed-of-sound values sampled from the sagittal and transverse views (red) are plotted with corresponding ground truth values.

11:00 AM

Automatic segmentation of the cerebral ventricles in preterm neonates using deep learning with 3D reconstructed freehand ultrasound imaging.**Matthieu Martin¹, Bruno Sciolla¹, Philippe Delachartre¹, Philippe Quétin²**¹*Univ Lyon, INSA-Lyon, Université Claude Bernard Lyon 1, UJM-Saint Etienne, CNRS, Inserm, CREATIS UMR 5220, U1206, F-69100, LYON, France, France, ²CH Avignon, Avignon, France***Background, Motivation, and Objective**

Preterm neonates can be subject to ventriculomegaly, which is an enlargement of the cerebral ventricles (CV) that can lead to brain damages. In clinical practice, 2D coronal hand-held ultrasonographic scans are performed to assess CV dilation. Estimating CV volumes from 2D images is, however, imprecise and time consuming since 3D information is lacking. To address this issue, we proposed a 3D reconstruction technic and a segmentation algorithm based on an automatic deep learning method.

Statement of Contribution/Methods

2D image sequences (150 to 200 images/sequence) were acquired with a Siemens Acuson 9L4 transducer via the anterior fontanelle. Volumetric reconstruction of the CV was achieved in two steps. The US images were first stacked coherently through a rigid registration. A parametric model was then used to compensate for translation and rotation of the ultrasound probe during the clinical acquisition. These two steps allow a volumetric anatomical reconstruction in a 3D Cartesian grid. The model parameters were estimated (through L2-minimization) by matching major cerebral landmarks of the reconstructed image with those of a reference image. We trained a convolutional neural network with U-Net architecture including residual and skip connections to achieve the segmentation. The Dice coefficient was used as a cost function, and optimization of the network parameters was carried out using backpropagation and stochastic gradient descent. Gaussian filtering was finally applied to each segmented volume and we kept the three largest simply connected regions to determine the cerebral ventricular system.

Results/Discussion

The reconstruction accuracy was evaluated over 5 volumes by comparing the area of the corpus callosum on cross-sectional sagittal view to its area on a real sagittal image. The average area error was 30% before reconstruction and 7% after reconstruction. The accuracy of the segmentation algorithm was also assessed over 4 volumes after post-processing with Dice coefficient, Hausdorff distance and Mean Absolute Distance metrics. Respective average values of 0.77, 7.4 mm and 0.25 mm were obtained. The segmentation of one volume of size 256×256×256 was achieved in less than 10 s; qualitative results can be seen in Fig. 1. The proposed algorithm opens the way to quantitative volume measurements of preterm neonate cerebral structures.

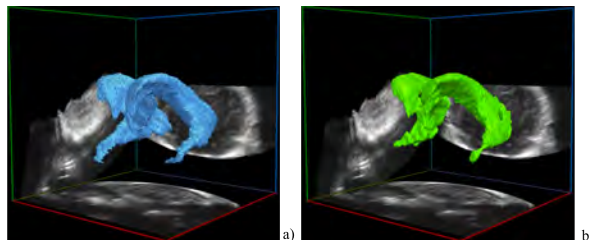


Figure 1. Manual a) and automatic b) segmentation of the cerebral ventricular system in a 3D reconstructed volume

11:15 AM

3D Multiplane Wave imaging for 4D Functional Ultrasound imaging of the whole-brain neuronal activityClaire Rabut¹, Mafalda Correia¹, Victor Finel¹, Mathieu Pernot¹, Thomas Deffieux¹, Mickaël Tanter¹¹*Institut Langevin, ESPCI Paris, CNRS UMR 7587, INSERM U 979, PSL Research University, 17 rue Moreau, Paris, PARIS, France***Background, Motivation, and Objective**

Ultrafast 3D Doppler imaging can provide volumetric high frame rate and high resolution mapping of the vascular anatomy and function [Provost 2015 IEEE]. Ultrafast 3D Doppler relies on coherent compounding of steered plane waves to produce high frame rate volumes with a trade-off between frame rate, resolution and sensitivity.

In this work, we have extended Multiplane Wave imaging [Tiran PhysMed 2015] to 3D Doppler (3D MWi) to allow for high sensitive 4D (3D space + time) Ultrafast imaging by virtually increasing the emission signal amplitude without compromising the frame rate. Applied to functional neuro imaging, we can image transient changes in blood volume in the whole brain at high spatiotemporal resolution.

Statement of Contribution/Methods

A 32x32 matrix phased array (0.3mm pitch, 9MHz) was used to insonify the brain of a trepanned and anesthetized rat. 3D MWi relies on the successive transmissions of N 2D multiple flat plane waves with different coded amplitudes and emission angles in a single transmit event. Data from each single plane wave of increased amplitude is then reconstructed by recombining the received data of successive events with coefficients given by Hadamard matrices H_N (N must be 1, 2 or multiple of 4)(fig a). We used $N=8$ angles and reached a PRF=390Hz during 350 ms (2 cardiac cycles) repeated every 2s.

To highlight the sensitivity of 3D MWi in neuro functional imaging, we followed the dynamics of blood volume during visual stimulation, induced epileptiform seizures as well as reconstructed Functional Connectivity (FC) matrix at rest between 3D registered brain structures.

Results/Discussion

We were able to obtain high sensitive 3D vascular volumes with an increase of the SNR by a factor $N=8$ compared to classic coherent compounding without reducing the volume rate. During induced epileptiform seizures, we could follow different spreading patterns of blood volume variations (fig b) such as slow propagation of cortical activity, called “spreading depression” crossing hemispheres (~ 2.2 mm/min), or waves traveling through the whole thalamus. At rest, we identified strong intrinsic functional connectivity patterns ($0.5 < r < 0.95$) similar to known major functional networks described in fMRI. The ability of 3D MWi to image volumic cerebral activity patterns with high sensitivity is of tremendous interest toward new neuro-imaging applications.

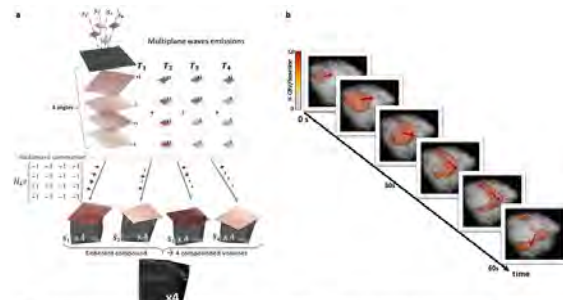


Figure. a) Schematic representation of multiplane wave compounding method, here explained with $N = 4$ plane waves. At transmit time T_1 , four wavefronts tilted with four different polarizations +1 or -1 given by the Hadamard matrix H_4 . Those coefficients are then used as combination for subtraction or addition operation to retrieve one plane wave individually with an amplitude 4 and cancel all the others. The virtual inverse of the emitted amplitude obtained by coherent summation results in an overall increase of the signal-to-noise ratio of the image. b) Propagation of a cortical depression wave from the back to the front of the brain during epileptic seizure induced by a cortical injection of a potassium channel blocker (4-AP). Power-Doppler blood volume increased between ISN and SON during ictal activity. Wave moving speed $\sim 2.2 \pm 0.3$ mm/min.

11:30 AM

Quantitative ultrasound brain imaging in 3D**Lluis Guasch¹, Oscar Calderon Agudo¹, Mengxing Tang², Parashkev Nachev³, Mike Warner¹**¹*Earth Science and Engineering, Imperial College London, United Kingdom*, ²*Bioengineering, Imperial College London, United Kingdom*, ³*University College London, United Kingdom***Background, Motivation, and Objective**

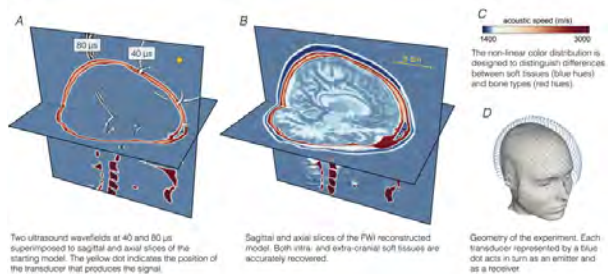
Existing ultrasound techniques are not able to produce brain images because the highly reflective nature of the skull obscures the signal in reflection-based imaging, and time-of-flight tomography that uses transcranial ultrasound provides diagnostically unusable low-resolution images. We propose the use of an imaging algorithm developed in the field of exploration seismology, full-waveform inversion (FWI), to overcome these limitations.

Statement of Contribution/Methods

We present the first successful in-silico three-dimensional brain images using transmitted ultrasound, and demonstrate that this approach can produce high-fidelity, high-resolution quantitative images of the brain. FWI takes into account the full physics of wave propagation to extract all the information present in the ultrasound waveforms, by numerically solving the wave equation (Figure-A), comparing the synthetised data to observations, and updating the model iteratively to minimise the mismatch between the two datasets. To demonstrate the potential of the proposed method we inverted a 3D in silico dataset generated with the experimental acquisition geometry detailed in Figure-D. The transmitted waveform signal is a 3-cycle tone burst centered on 400 kHz. Ex vivo ultrasound data acquired in the laboratory using real human skulls support our assumptions that the in-silico experiment mimics the signal penetration and signal-to-noise obtainable in real clinical applications.

Results/Discussion

FWI is a local optimisation technique that requires an initial guess model that is not too far removed from the target in order to converge. Our starting model is a 1500 m/s homogeneous model with the correct skull acoustic wave speed for the skull (Figure 1-A). The results demonstrate that FWI is able to reconstruct all relevant structures in the intracranial tissues, being able to distinguish not only small tissue contrasts, but also to resolve structures at sub-millimetre scales (Figure-B). Grey and white matter match well the target, both in absolute value and position, with enough resolution to allow direct identification of cortical folds. The potential for this novel neuroimaging modality covers a wide range of applications, from early stroke diagnosis to rapid assessment of head trauma, and its low cost and portability makes it particularly attractive for developing countries.



11:45 AM

Low Frequency Ultrasound Transcranial Imaging with Coherent Compounding of Diverging Chirp WavesChen Bai^{1,2}, Meiling Ji¹, Xiaoyang Qiao¹, Yuchao Sang¹, Mingxi Wan¹

¹Department of Biomedical Engineering, School of Life Science and Technology, Xi'an Jiaotong University, China, People's Republic of, ²State Key Laboratory of Transient Optics and Photonics, Xi'an Institute of Optics and Precision Mechanics, Chinese Academy of Sciences, China, People's Republic of

Background, Motivation, and Objective

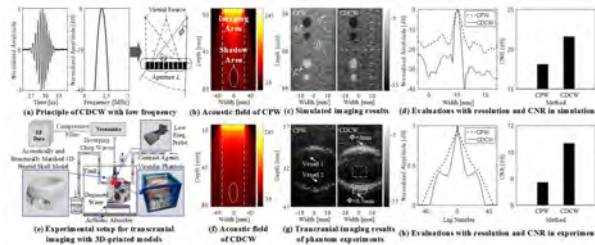
For transcranial imaging based on contrast microbubbles, the acoustic window is limited to the temporal bone with strong attenuation. Consequently, the images obtained with conventional compounded plane waves (CPW) transmission is often not good in contrast-to-noise ratio (CNR). This is partly attribute to that short pulse commonly has low ability to penetrate the temporal bone. And moreover, CPW will raise a shadow area in the relatively deep field where beams are not overlapped. Although this can be improved by increasing the numbers of transmitting angles, it will reduce the frame rate. Therefore, to realize improvement both in detective sensitivity of microbubbles and CNR in transcranial imaging, the compounding of diverging chirp waves (CDCW) was investigated in this study.

Statement of Contribution/Methods

The 5-angle diverging chirp waves, defined by their virtual sources spaced by virtual pitches and angular apertures, were sent independently with a custom-build array probe at a low center frequency of 2 MHz. Each diverging wave was backscattered and the received corresponding echos were firstly compressed by match filters. Then, by applying delays corresponding to a constructive wavefront of each diverging wave, beamforming was performed. Finally, the feasibility of this method was validated through simulations, and experiments with the acoustically and structurally matched 3D-printed skull model and cerebral vessel phantom, which has been investigated in our previous study for competently replacing the real skull.

Results/Discussion

For all simulations and experiments, 5-angle compounded waves in both CPW and CDCW imaging were transmitted with same frame rate of 300 Hz. Consequently, compared with CPW imaging in simulations, the CNR in CDCW increased 3.49 dB. In addition, according to lateral responses of point targets, the resolution in CDCW was 1.67 times more than that in CPW. In terms of transcranial phantom imaging, with the assistance of spatial-temporal filter, the two vessels with different diameters became more clear in CDCW imaging, indicating it has a strongly detective sensitivity of microbubbles. Specifically, both CNR and axial resolution gain witnessed an increase by 2.95 dB and 1.90 times in CDCW versus to CPW imaging. In summary, it confirmed that CDCW method can achieve transcranial imaging with relatively high qualities.



7F - Applications of Therapeutic Ultrasound

Kikusui (140)

Wednesday, October 24, 1:30 pm - 3:00 pm

Chair **Zhen Xu**
University of Michigan

7F-1

1:30 PM

Ultrasound and Microbubbles Promote the Retention of Fluorescent Compounds in the Small Intestine

Mihnea Vlad Turcanu¹, Fraser Stewart², Benjamin Cox³, Helen Mulvana¹, Inke Nähke², Sandy Cochran¹

¹Systems Power and Energy, Medical and Industrial Ultrasonics, University of Glasgow, Glasgow, United Kingdom,

²Cell and Developmental Biology, University of Dundee, Dundee, United Kingdom, ³School of Medicine, University of Dundee, Dundee, United Kingdom

Background, Motivation, and Objective

Focused ultrasound (US) is a novel means to increase the passage of medication through the wall of the small intestine. The motivation of this study was to determine the potential of US and microbubbles (MBs) to facilitate delivery of macromolecular therapeutic agents across the epithelial layer. The objectives were to determine (1) if delivery of model drugs through a cell monolayer *in vitro* is promoted by US and MB; (2) whether US and MB facilitate delivery of fluorescent compounds to the porcine small intestine *in vivo*.

Statement of Contribution/Methods

To investigate delivery across cell monolayers, Caco-2 cells (ATCC) seeded on ThinCert filters (Greiner Bio-One) were cultured for a minimum 3 weeks. A suspension of 20 µg/ml of 3 kDa dextran fluorescein-labelled with Alexa Fluor® 488 (ThermoFisher Scientific) +/- 5% MB (2–5 x 10⁸ MB/ml, SonoVue, Bracco) prepared in growth medium was introduced into a multiwell plate divided by the seeded ThinCert into apical and basal chambers. This was done with a syringe pump through a channel in the centre of a miniature focused US transducer (4 MHz, 1 MPa PNP, 15 mm focal length, 1.79 mm² focal area). The suspension was delivered for 1 min at 1 ml/min, concomitantly with application of US. Following treatment, fluorescent dextran in the basal chamber was quantified with a plate reader.

To investigate delivery *in vivo*, a tethered endoscopic capsule with an US transducer and a delivery channel, as previously reported [1], was inserted through a stoma into the small intestine of terminally anaesthetised Landrace X pigs (PPL 70/8812). 5% CdSeS/ZnS quantum dots (QDs) (Sigma UK) were delivered under the protocol described above. QDs retention in excised tissue was verified with UV imaging (365 nm).

Results/Discussion

US with MBs led to higher delivery of fluorescent dextran across Caco-2 cell monolayers than US alone, Fig. 1. US and MBs also led to delivery of QDs to the wall of porcine small intestine in four out of five cases. These results suggest that focused US and MBs decrease epithelial barrier function enhancing the passage of macromolecules. Our work indicates potential applications in targeted treatment of gastrointestinal disease and oral drug delivery.

[1] F. Stewart et al. ‘Development of a Therapeutic Capsule Endoscope for Treatment in the Gastrointestinal Tract: Bench Testing to Translational Trial’, IEEE Int. Ultrasonics Symp., 2017

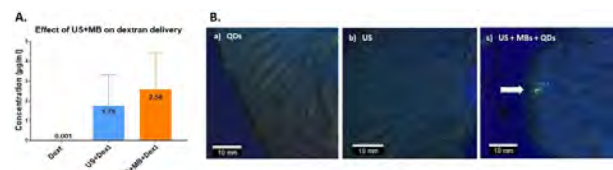


Fig. 1. A. US + MB + Dex facilitates drug delivery through a Caco-2 monolayer. Error bars represent SD of averages for n = 4.
Dex = Dextran; B. (a) Fluorescent QDs did not lodge into tissue when treated with QDs (a) or US (b), but they were observed after a combination of insertion, MB and QD delivery.

1:45 PM

Luminescence estimation of the region of reactive oxygen generation by focused ultrasound with multiple foci for sonodynamic treatment

Daisaku Mashiko¹, Shin-ichiro Umemura¹, Shin Yoshizawa²

¹Graduate School of Biomedical Engineering, Tohoku University, Sendai, Japan, ²Graduate School of Engineering, Tohoku University, Sendai, Japan

Background, Motivation, and Objective

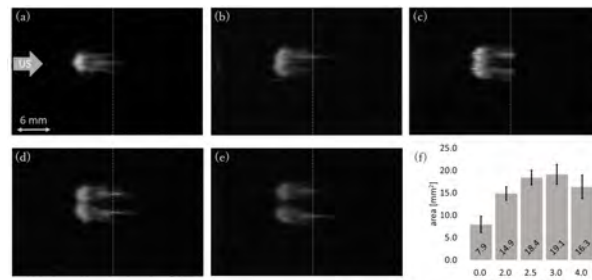
Sonodynamic treatment (SDT) using high-intensity focused ultrasound (HIFU) is a non-invasive cancer treatment. Cavitation bubbles induced by HIFU produce reactive oxygen species (ROS), whose cytotoxicity can be used for cancer treatment. For such a purpose, ROS has to be localized to avoid potential side effects on a normal tissue. Scanning the HIFU focal zone, chosen smaller than the cancerous region, so as to paint the whole cancerous region can be reasonable tactics. In this study, the region of ROS generation by scanned HIFU was visualized and the effect of the inter-focal distance between the HIFU foci was estimated.

Statement of Contribution/Methods

HIFU at 1 MHz, generated by a 128 channel array transducer, was focused onto a polyacrylamide gel, after soaked in 0.7 mM luminol. A trigger HIFU sequence, consisting of a high intensity pulse at 50 kW/cm^2 for 0.1 ms, and an immediately following long burst at 250 W/cm^2 for 10 ms, was used. This sequence was sequentially applied to two focal points with a separation distance 0, 2.0, 2.5, 3.0, and 4.0 mm, and repeated for 30 s. The region of ROS generation can be evaluated by photographing the light emitting region because luminol emits blue light when it reacts with OH radical. Although it may not be exactly the same ROS mediating SDT, luminol emission is useful for spatial investigation of the ROS generation.

Results/Discussion

Figures (a) to (e) show the blue component images, taken by DSLR camera with an exposure time of 30 s, for each inter-focal distance. Figure (f) shows the average ROS generation area obtained by binarizing the blue component images. When the focal distance was 2.5 mm or longer, the ROS generation area was twice or more than that with no distance. Furthermore, when the focal distance was set 2.5 and 3.0 mm, the area was blighter and significantly larger than that with a distance of 4.0 mm. This effect is thought based on high-speed camera observation to be because the remaining bubbles around the first focal point oscillated when HIFU was irradiated at the second focal point. To perform quantitative evaluation for optimizing the sequence, a method such as KI dosimetry should be combined.



Figures (a): Blue component images of the ROS generated region with the inter-focal distance of 0 mm, (b): 2 mm, (c): 2.5 mm, (d): 3 mm, (e): 4 mm.
(f): The average area of the ROS generation region.

2:00 PM

Antivascular photo-mediated ultrasound therapy for neovascularization in the eye**Xinmai Yang¹, Xinyi Xie², Yu Qin², Shuying Li², Wei Zhang², Yannis Paulus², Xueding Wang²**¹*University of Kansas, Lawrence, KS, United States*, ²*University of Michigan, Ann Arbor, MI, United States***Background, Motivation, and Objective**

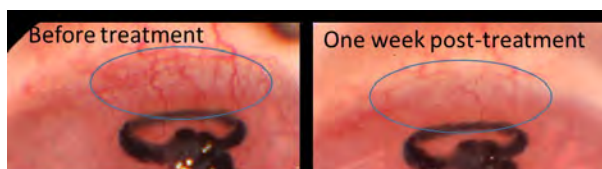
Neovascularization and pathologic microvasculature are common in several eye diseases, including corneal neovascularization, diabetic retinopathy, and macular degeneration. Current treatments, such as laser photocoagulation, photodynamic therapy (PDT), and anti-vascular endothelial growth factor (VEGF) therapy, impose significant burdens on patients, their families, and our health care system because of frequent administration, high cost, and their destructive nature. We developed a novel treatment, termed photo-mediated ultrasound therapy (PUT), that uses a combination of a low intensity nanosecond laser concurrently with ultrasound. PUT can remove microvessels noninvasively without damaging surrounding tissue in the eye. We present the first evaluation of PUT on a disease model of corneal neovascularization on rabbits.

Statement of Contribution/Methods

An integrated therapeutic ultrasound and laser treatment system was devised. Laser pulses, produced by a pulsed (Nd:YAG) laser at 532 nm with 5-ns pulse duration and 10-Hz repetition rate, synchronized with millisecond ultrasound bursts. New Zealand white rabbits were used. Corneal neovascularization was induced using an established animal model placing pro-inflammatory silk sutures in the cornea. The outcome of PUT treatment was evaluated by using imaging techniques such as photography, optical coherence tomography (OCT), fluorescein angiography, and photoacoustic microscopy (PAM). Imaging was performed before, after, and weekly following PUT treatment for 1 month.

Results/Discussion

Treatment with laser- or ultrasound-only resulted in no changes to the corneal neovascularization. PUT treatment with concurrent laser and ultrasound was able to remove the corneal neovascularization. The optimal parameters were 0.5 MPa ultrasound + 32 mJ/cm² laser. By 1 week, neovascularization in the region of treatment was greatly retreated (Figure 1). Quantified results from OCT indicated significant decrease in neovascularization. In conclusion, PUT holds significant promise as a novel non-invasive method to precisely remove microvessels in neovascular eye diseases by more selectively treating vasculature with minimized side-effects and no systemic photosensitizing dye.



2:15 PM

Ultrasound Convolutional Neural Networks Imaging for Monitoring of Microwave AblationSiyuan Zhang¹, Shaoqiang Shang¹, Shan Wu¹, Lei Zhang¹, Supin Wang¹, Mingxi Wan¹¹*Department of Biomedical Engineering, Xi'an Jiaotong University, China, People's Republic of***Background, Motivation, and Objective**

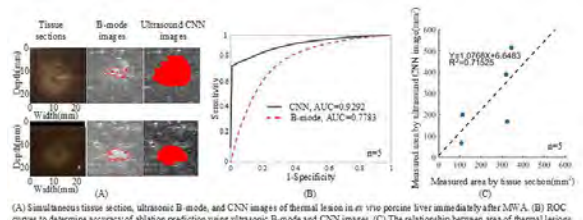
Ultrasound imaging can be easily integrated into thermal ablation treatments and has a number of other advantages, such as real-time imaging capabilities and portability, to monitor microwave ablation (MWA) treatments. Thermal lesions in tissue are sometimes not easily visualized with ultrasound image because of the low intrinsic contrast between ablated and normal tissues. In addition, acoustic posterior shadowing effects of bubbles resulting from boiling may influence the accuracy of defining the location and size range of an ablated thermal lesion. This study explored the feasibility of using ultrasound convolutional neural networks (CNN) imaging to evaluate thermal lesions induced by MWA in ex vivo porcine models.

Statement of Contribution/Methods

Thermal lesions were induced in the livers of domestic pigs using a clinical MWA system. 2-D RF data backscattered from the ablated region were captured by a modified diagnostic ultrasound scanner as training sample. Every point in the RF data matrix was detected by CNN to predict the thermal lesion. The classification results of RF data matrix were overlapped on the corresponding ultrasound B-mode image to generate ultrasound CNN image. Receiver operating characteristic (ROC) curves were employed to assess and compare the discrimination ability of ultrasonic imaging to predict the thermal lesions. Area under ROC (AUC) was calculated to measure the predictability statistically. The relationship between area of thermal lesions assessed using ultrasound CNN images and gross-pathology images was explored through plotting fitting line.

Results/Discussion

After thermal ablation, a bright hyper-echoic region appeared in the ultrasonic B-mode and CNN images, identifying the thermal lesion. AUC values calculated from ROC curves were 0.77 and 0.92 for ultrasonic B-mode and CNN images. Thermal lesion area, assessed using ultrasonic CNN images, shows a linear correlation to those obtained from the gross-pathology images ($R^2 = 0.71$). This preliminary study suggests that ultrasonic imaging based on deep learning methods may have a potential use in evaluating the formation of thermal lesions, and may be utilized as an alternative modality in developing monitoring systems for image-guided thermal ablation treatments.



(A) Histological tissue section, ultrasound B-mode, and CNN images of thermal lesion in ex vivo porcine liver immediately after 3.5W. (B) ROC curves to determine accuracy of ablation prediction using ultrasound B-mode and CNN images. (C) The relationship between area of thermal lesions assessed using ultrasound CNN images and gross-pathology images.

2:30 PM

A catheter based ultrasound device for treating chronic total occlusionsAlex Wright¹, Lindsey Di Bartolomeo¹, Bradley Strauss¹, Kullervo Hynynen¹, David Goertz¹¹Sunnybrook Research Institute, Toronto, ON, Canada**Background, Motivation, and Objective**

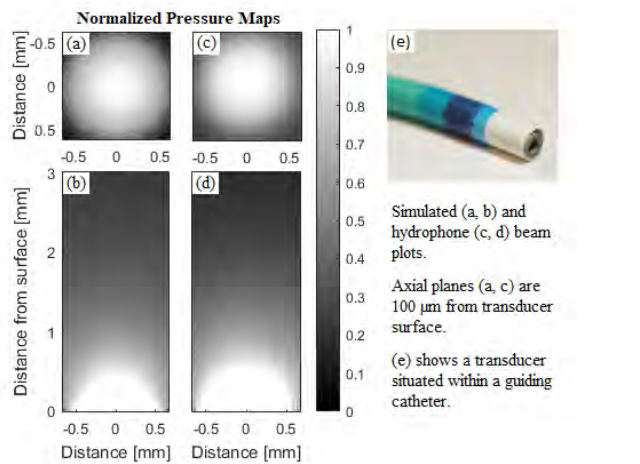
Chronic total occlusions (CTO) of the coronary arteries are thrombotic obstructions that can develop collagen rich proximal fibrous caps (PFC). Minimally invasive percutaneous (PCI) CTO revascularization is frequently unsuccessful due to the presence of stiff PFCs. A promising new method to soften CTOPFC is the injection of collagenase, which has recently shown favorable clinical trial results. We have also conducted animal experiments that demonstrated the ability of US stimulated microbubbles (MBs) to reduce the force required to cross CTOs. Here we present proof of principle for the design and development of a catheter that permits the delivery of collagenase, MBs and forward looking therapeutic ultrasound to the PFC region of CTOs. This can improve patient outcomes and enable procedures to be carried out within a single PCI session.

Statement of Contribution/Methods

The design uses a PZT-4 cylindrical transducer (1.2/0.8 mm outer/inner diameter, 3 mm length) that is radially polarized and situated at the catheter tip. Electrodes on the inner and outer cylindrical surfaces are stimulated at a frequency that excites length-mode oscillations. This reduces the electrical impedance and can direct MHz to sub-MHz in a forward looking direction. The inner hole can accommodate a guide wire to situate the tip adjacent to the PFC, and extraction provides a conduit through which enzymes and MBs can be introduced. Simulations performed in PZFlex™ assessed the effects of transducer geometry, electrode configurations, and mounting and sheath materials on the resulting acoustic fields within and away from the transducer. Prototype transducers were constructed with matching circuits and characterized with hydrophone scans. The prototypes underwent initial evaluation within anthropomorphic CTO phantoms where MBs were injected and cavitation was assessed with high speed microscopy and passive cavitation detection.

Results/Discussion

Hydrophone measured pressures closely matched simulation results. Pressures of over 1 MPa were achievable at the transducer surface, and over 500 kPa was attainable 1 mm from the surface. Transducers with thin wall steel tubes contacting the inner electrode performed similarly to those with a single wire contact. Phantom experiments demonstrated significant MB displacement and cavitation activity from MBs introduced through the catheter.



2:45 PM

Ultrasound Oncotripsy: Targeting Cancer Cells Selectively Via Resonant Harmonic Excitation**David Mittelstein¹, Erika Figueroa², M. Houman Fekrazad³, Michael Ortiz², Mikhail Shapiro⁴, Morteza Gharib¹**¹*Department of Medical Engineering, California Institute of Technology, United States*, ²*Division of Engineering and Applied Sciences, California Institute of Technology, Pasadena, CA, United States*, ³*Department of Medical Oncology & Therapeutics Research, City of Hope, United States*, ⁴*Division of Chemistry and Chemical Engineering, California Institute of Technology, Pasadena, CA, United States***Background, Motivation, and Objective**

Therapeutic ultrasound (US) is a promising non-invasive tumor ablation method as it is able to disrupt cells, enhance drug uptake, and stimulate anti-neoplastic immune response. However, high intensity focused US uses non-specific heating or cavitation and safe use requires precise tumor targeting to prevent off-target ablation. Low intensity focused US (LIFU) may allow for more selective US therapy. Pulsed US at <5 W/cm² has been shown to cause bioeffects, although its mechanisms are not well understood. We propose a new paradigm in which LIFU induces resonant cell membrane oscillation. “Oncotripsy” involves applying waveforms that exploit this resonance vulnerability to selectively lyse cancer cells (Fig 1a).

Statement of Contribution/Methods

We developed an *in vitro* testbed with mylar-bottom sample plates suspended over a water bath containing a focused US transducer. Pulsed US at 10% duty cycle 0.7 MPa PNP is applied for 1 min. We apply US at various frequencies and pulse durations (PD), while maintaining constant acoustic energy (Fig 1b). We assess cell death of myeloid cancer (K562), lymphoid cancer (U937) and healthy T cells using LIVE/DEAD fluorescence. We perturb cell’s mechanical properties using viscous isotonic sucrose instead of saline, 1 hr pretreatment with actin depolymerizing cytochalasin D, or 16 hr pretreatment with microtubule depolymerizing paclitaxel.

Results/Discussion

We confirmed that long PD LIFU (>10 ms) lead to irreversible cell death in cancer models. We observed that this cyo-disruption was frequency and cell-type dependent (Fig 1c). All trials used the same US intensity, but cancer selective targeting was achieved with 500 kHz 20 ms PD US ($p<.001$). Finally, perturbing mechanical properties altered the LIFU response. *In vivo*, we observed PD dependent necrosis in xenografted tumors after 670 kHz 1 MPa LIFU.

LIFU’s PD-dependent response that is sensitive to frequency, cell type, and mechanical properties supports the theory that growing resonant oscillations passing a lethal threshold may cause cell death. We are currently investigating alternate cavitation mechanisms. Our data suggest that adjusting US parameters can achieve cell-selective targeting without contrast agents. Furthering the reach of therapeutic US could provide clinicians access to the benefits of US ablation in regimes where it was previously unsafe.

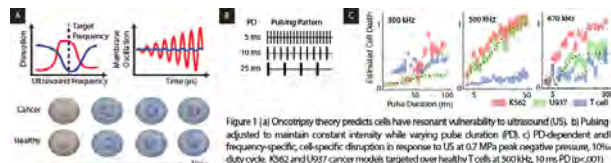


Figure 1 | i) Oncotripsy theory predicts cells have resonant vulnerability to ultrasound (US). ii) Pulsing adjusted to maintain constant intensity while varying pulse duration (PD). iii) PD-dependent and frequency-specific cell-specific disruption in response to US at 0.7 MPa peak negative pressure, 10% duty cycle. K562 and U937 cancer models targeted over healthy T cells at 300 kHz, 10 ms PD ($p<.001$).

7G - Monitoring and Mapping Methods in Ultrasound Therapy

Kikusui (140)

Wednesday, October 24, 4:00 pm - 5:30 pm

Chair

7G-1

4:00 PM

Self-adaptive 3D time reversal cavity for safe ultrasound therapy through the ribcage

Justine Robin^{1,2}, Alverède Simon¹, Mickaël Tanter¹, Mathieu Pernot¹

¹*Institut Langevin, ESPCI Paris, PSL Research University, CNRS UMR 7587, INSERM U979, paris, France*, ²*Dept. of Neurology, Neurovascular and Neurosonology Unit, Hôpitaux Universitaires de Genève, Genève, Switzerland*

Background, Motivation, and Objective

Ultrasound therapy is increasingly used for non invasive surgery and requires reaching very high pressures in small foci. In transcostal cardiac therapy the impedance mismatch between bone and soft tissue induces aberrations and attenuation of the wavefront, causing a pressure drop on target and potential injuries. With conventional devices, the energy reflected by the ribs is lost or at best cancelled by adaptive focusing techniques, resulting in a strong pressure drop at the focus. We recently proposed a non invasive adaptive focusing method for transcostal US therapy with a time reversal cavity (TRC) acting as a beam amplifier. Using the signals backscattered by the ribs through the TRC, we shape the therapy beam to pass in the intercostal space only (DORT method¹) which increases the focal power. We here demonstrate that this technique can enhance greatly the shock wave therapy generated by a 3D TRC.

Statement of Contribution/Methods

We built a 3D TRC by placing 2 rod forests (10 rod/cm^2 , 1 cm wide) in a $20 \times 15 \times 15 \text{ cm}^3$ reverberating cavity². A high power matrix array probe (4 x 64-elements, 1 MHz, Imasonics) was placed in the cavity, driven by a 256 vantage HIFU system (Verasonics).

Free field calibration

The TRC was calibrated in free field for time reversal focusing (TRF): $3 \mu\text{s}$ US pulses emitted through the cavity were spread to up to $300 \mu\text{s}$, and recorded by a HNC 400 hydrophone (Onda). This calibration step was repeated on a $6 \times 6 \text{ cm}^2$ grid 10 cm from the cavity aperture: the therapy targets. Once time reversed, these signals are a TRF library in all grid points. This process was repeated on a $9 \times 7 \text{ cm}^2$ control grid (5 mm step) placed between the cavity and the therapy targets. The control grid acts as a virtual array probe in front of the cavity. Finally, the signals focusing on each control grid points were emitted in free field. The backscattered signals were recorded, to constitute a reference library.

Adaptive focusing

The device was placed in front of a ribcage phantom, and the last step was repeated. For each point, the reference was subtracted from the backscattered signals and a 3D image of the ribs was built. The image was used to implement the DORT method in the control grid plane, to cancel the therapy beam in front of the ribs.

Lesion formation

An Ultracal phantom was targeted for 10s at 10Hz PRF in various points to form lesions in free field, or through the ribs with or without adaptive focusing.

Results/Discussion

In free field, the therapy focal spots are 2 mm thin. The maximum pressure is 21 MPa. Through the ribs with no adaptive focusing the pressure drops of 60%, making therapy difficult.

With adaptive focusing, the energy in front of the ribs decreases by 75%. Contrary to common therapy probes results, pressure on target increases by up to 30 %, matching TRF calculated through the ribs, and lesions were formed in the Ultracal phantom through the ribs. This paves the way to safer and more efficient transcostal cardiac therapy.

1. Cochard et al, Med. Phys. 36, 3495, 2009
2. Robin et al, PMB, 2017

4:15 PM

High-resolution Transcranial Passive Acoustic Mapping using Delay Multiple and Sum Beamformer**Shukuan Lu¹, Renyan Li¹, Xianbo Yu¹, Ayache Bouakaz², Mingxi Wan¹**¹*Department of Biomedical Engineering, School of Life Science and Technology, Xi'an Jiaotong University, Xi'an, China, People's Republic of,* ²*Université François Rabelais, Tours, France***Background, Motivation, and Objective**

Passive acoustic mapping (PAM) has been proposed as a means for real-time monitoring of US therapy in the brain by enabling spatiotemporal monitoring of inertial cavitation activity. However, conventionally used transcranial PAM, based on time exposure acoustics (TEA) algorithm, has poor resolution and spatial accuracy due to the limited aperture size, the propagation through inhomogeneous media (skull) and multiple bubble interaction, therefore possibly causing inaccurate estimation of cavitation localization. We propose here a high-resolution transcranial PAM using delay multiple and sum beamformer (DMAS-TEA), which may be useful for accurate monitoring and control of transcranial US therapy, particularly non-thermal cavitation-mediated applications such as BBB opening and drug delivery.

Statement of Contribution/Methods

The performance of the proposed transcranial PAM was validated by simulations and *in vitro* experiments. The simulations were based on a multi-bubble model to generate the prebeamformed data of cavitation sources. The experimental setup consisted of a linear array to receive cavitation signals induced by HIFU, and a piece of a temporal bone printed in 3D placed beneath the linear array (Fig. 1). As in TEA, the first step of the proposed algorithm was the time-shifting of the received signals, and then these signals were coupled and multiplied before adding them up. The variation of sound speed in different media was considered by using an average value in the proposed algorithm. The ratio of the full width at half maximum (FWHM) to the normalized source energy along the lateral and axial directions was used to evaluate the resolution improvement.

Results/Discussion

Simulations show clear tail artifacts in front of and behind the cavitation activity in the axial direction which makes cavitation not easily distinguishable when conventional PAM is used. However, the proposed method provides cavitation image with improved spatial resolution (Fig. 2a). Both lateral and axial resolutions are improved (Fig. 2b). Experimental measurements confirm that our method is able to reduce artifacts as appreciated by the 30% improvements in resolution (Fig. 3). In conclusion, the proposed PAM based on DMAS-TEA seems to be suitable to more accurately localize cavitation activity and hence improve the spatial resolution for transcranial cavitation mapping.

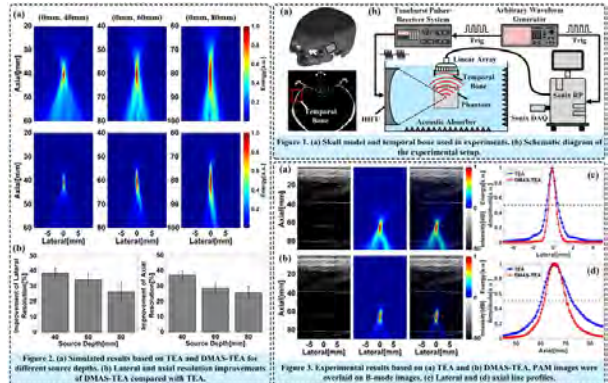


Figure 1. (a) Skull model and temporal bone used in experiments. (b) Schematic diagram of the experimental setup.

Figure 2. (a) Simulation results based on TEA and DMAS-TEA for different source depths. (b) Lateral and axial resolution improvement of DMAS-TEA compared with TEA.

Figure 3. Experimental results based on (a) TEA and (b) DMAS-TEA. PAM images were overlaid on B-mode images. (c) Lateral and (d) axial line profiles.

Figure 2. (a) Simulation results based on TEA and DMAS-TEA for different source depths. (b) Lateral and axial resolution improvement of DMAS-TEA compared with TEA.

Figure 3. Experimental results based on (a) TEA and (b) DMAS-TEA. PAM images were overlaid on B-mode images. (c) Lateral and (d) axial line profiles.

4:30 PM

Detection of the focused-ultrasound-induced blood-brain barrier opening by diffusion tensor imaging in non-human primates**Maria Eleni Karakatsani¹, Antonios Pouliopoulos¹, Michael Liu², Sachin Jambawalikar², Elisa Konofagou³**¹*Biomedical Engineering, Columbia University, New York, NY, United States*, ²*Radiology, Columbia University, New York, NY, United States*, ³*Biomedical Engineering, Columbia University, United States***Background, Motivation, and Objective**

Contrast-enhanced magnetic resonance imaging has been extensively used for the detection and confirmation of the blood-brain barrier opening (BBBo) induced by focused-ultrasound (FUS) coupled with the administration of microbubbles. The translation of the technique to the clinic is hindered by the toxicity of the currently available contrast agents (gadolinium (Gd)) as well as the lack of diffusion information. In this study we investigate the feasibility of diffusion-tensor imaging (DTI) in the detection of the BBBo and the directionality of the flow that does not require contrast.

Statement of Contribution/Methods

For this study, FUS coupled with systemic administration of microbubbles was employed to induce a BBBo at the caudate nucleus of non-human primates. The scanning routine involved a diffusion sequence followed by the injection of Gd and the acquisition of a contrast-enhanced T1-weighted image, enabling comparison with the emerging protocol. This routine was implemented once before the onset of the experiments (DTIPRE, Gd-T1WPRE) and was repeated after every sonication (DTIPOST, Gd-T1WPOST). The DTIPOST was registered to the DTIPRE by a deformable deformation matrix and corrected for eddy current distortions before the calculation of the tensor with the associated eigenvalues, eigenvectors and the fractional anisotropy (FA) map.

Results/Discussion

Figure 1 shows the successful detection of the BBBo with both scanning sequences. Gd-T1WPRE was subtracted from Gd-T1WPOST eliminating the signal from the vessels and the intact structures and enabling the visualization of the opening with the corresponding targeting overlayed on an anatomical scan in the axial plane. The difference between the fractional anisotropy maps before and after sonication ($FA_{POST} - FA_{PRE}$) is in agreement with the gold standard in detecting the opening at the targeted location. An outstanding observation is that the anisotropy of the diffusion increased after the BBBo suggesting that proton-dense molecules are diffusing towards a preferred direction and not uniformly. This finding was confirmed by the FA_{POST} as well as the vector field showing the preferred direction of flow at the sonicated site. These findings show, for the first time, the feasibility of DTI in detecting a BBB opening paving the way for contrast-free monitoring.

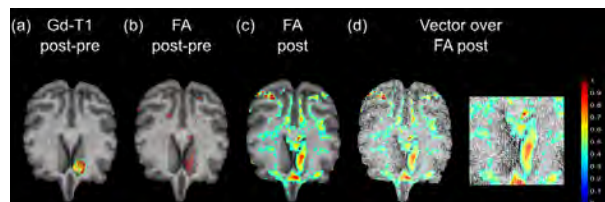


Figure 1: Blood-brain barrier opening detection with contrast enhanced T1-weighted (Gd-T1w) and diffusion tensor imaging (DTI). (a) The difference of the $Gd-T1w_{POST}$ to the $Gd-T1w_{PRE}$ enables visualization of the BBB opening (jet colormap) at the targeted location (yellow). The difference image is overlaid onto an anatomical scan. (b) The difference of the FA_{POST} to the FA_{PRE} shows the BBB opening at the same location as detected by the contrast imaging. (c) The FA_{POST} map acquired after the sonication shows an increase in the anisotropy suggesting a preferred direction of flow. (d) The preferred direction is confirmed by the vector field that shows the direction of flow in lower and higher magnification.

4:45 PM **Wideband Image-based Transskull Refocusing of Ultrasound Beams Using Dual-Mode Ultrasound Arrays: Ex****Vivo Results****Hasan Aldiabat¹, Parker O'Brien¹, Dalong Liu¹, Emad Ebbini¹**¹*Electrical and Computer Engineering, University of Minnesota--Twin Cities, Minneapolis, MN, United States***Background, Motivation, and Objective**

Transcranial focused ultrasound (tFUS) is capable of providing subtherapeutic and therapeutic ablative treatments for a variety of brain disorders. A major challenge towards widespread use of tFUS-based therapies stems from the complexity of the skull, which could result in severe loss of focusing gain as well as focus distortion. We present first results demonstrating the feasibility of image-based refocusing utilizing the full transducer bandwidth to maximize the localization and reclaim the focusing gain.

Statement of Contribution/Methods

Dual-mode ultrasound array (DMUA) was utilized to image and generate tFUS beams through rodent skull samples. Experiments were performed at a set of 32 discrete frequencies in the range 1.9 MHz - 5.0 MHz. Transskull measurements using a wideband hydrophones were performed (Fig. 1 (a)). In other experiments, skull samples were embedded in a tissue-mimicking phantom (Fig. 1 (b)) and positioned at a distance from the apex of the DMUA corresponding to the skull position during *in vivo* experiments. A thermocouple was inserted so that its junction was closest to the geometric focus. It served as a target as well as a sensor to measure the heating rate (focusing gain) of standard and refocused beams.

Synthetic-aperture and Single-transmit focus imaging along with a 3D skull volume scan imaging were used. Raw imaging echo data received by each array element were used to form focusing data matrices (FDMs) corresponding to the selected control points.

Results/Discussion

The transmission efficiencies of tFUS beams at any given location varied as a function of frequency in a nonmonotonic manner. Moreover, different locations of the same skull have different transmission characteristics. To demonstrate the increased therapeutic gain due to refocusing, both geometrically focused and optimally refocused ultrasound beams were used to transcranially heat the vicinity of a thermocouple used as a target. Temperature rise produced by each beam was recorded for each frequency. The results show that the focusing gain was increased for all frequencies, albeit to varying degrees. In addition, heating rates were estimated from the measured temperature profiles (Fig. 1 (c)). This result was typical, but variations in the refocusing gain were observed depending on the operating frequency and the part of the skull traversed by the tFUS beam.



Fig.1 (a)

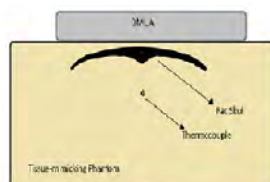


Fig.1 (b)

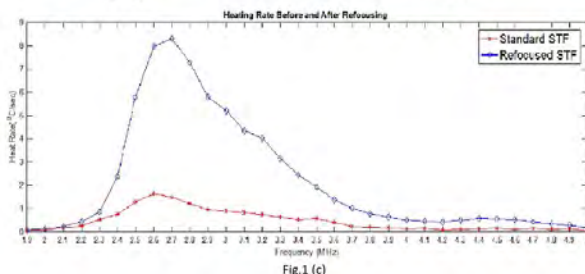


Fig.1 (c)

5:00 PM

Fast MR thermometry for FUS monitoring using an echo-shifted sequence with simultaneous multi-slice imagingChao Zou¹, Yuhong Peng², Yangzi Qiao¹, Changjun Tie¹, Faqi Li², Xin Liu¹, Hairong Zheng¹¹*Paul C. Lauterbur Research Center for Biomedical Imaging, Shenzhen Institutes of Advanced Technology, Chinese Academy of Sciences, China, People's Republic of*, ²*College of Biomedical Engineering, Chongqing Medical University, China, People's Republic of***Background, Motivation, and Objective**

MR temperature imaging is fundamental for HIFU therapy. The temporal resolution for temperature imaging is quite critical to prevent overheating. For accurate thermal dose calculations for safety concerns, the temporal resolution is preferably as high as possible. The spatial coverage of temperature monitoring during HIFU therapy is also very important as due to the unwanted heating in the tissue interface. Multiple-slice or volumetric temperature imaging is preferred for HIFU monitoring. However, the increase in spatial coverage would result in a longer acquisition time. To further improve the temporal resolution of the temperature imaging, taking greater coverage into account, a sequence based on echo-shifted RF-spoiled GRE with simultaneous multi-slice (SMS) imaging was designed for multi-slice temperature imaging in this study.

Statement of Contribution/Methods

The echo-shifted RF-spoiled GRE sequence with multi-band RF excitation pulse was designed. Controlled aliasing in parallel imaging results in higher acceleration (CAIPIRINHA) was implemented to decrease the overall noise amplification in the image unfolding procedure based on sensitivity encoding (SENSE) algorithm. Phantom experiment was conducted to calibrate the thermometric accuracy of the sequence using a fiber optical thermometer. Ex-vivo porcine liver experiment was performed to demonstrate its ability of monitoring the temperature change in both the focal and interface planes simultaneously.

Results/Discussion

The temporal resolution for the sequence was ~1 second per 2 slice when imaging resolution = 128. It was shown that the mean and standard deviation of temperature errors in the ROIs over the 300 measurements in the two slices were both $0.01 \pm 0.06^\circ\text{C}$, compared to the fiber optical thermometers.

The echo-shifted sequence had a better temperature noise performance compared to the traditional GRE sequence with the same temporal resolution due to the longer effective echo time.

The *ex vivo* heating experiment confirmed that by combining the SMS technique and echo-shifted sequence, the spatial coverage was increased without decreasing temporal resolution, while maintaining high temperature measurement precision. Both the focal plane and the interface were monitored during the ultrasonic sonication.

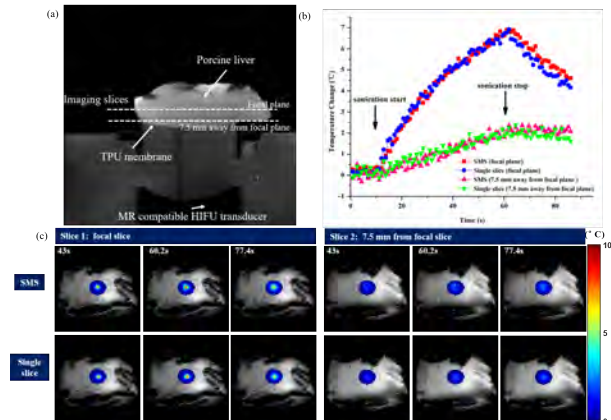


FIG. 1. The results of the HIFU heating experiment in ex vivo porcine liver. (a) Illustration of the setup of the HIFU heating experiment. An MR-compatible HIFU transducer was fixed at the bottom of water tank. The degassed porcine liver was placed on the water tank. A piece of TPU membrane separates the porcine liver from the water. Imaging planes were set perpendicular to the direction of the acoustic wave propagation. Two planes were mounted simultaneously using the proposed sequence. (b) Temperature change curves using SMS and single slice scan from HIFU heating in ex vivo porcine liver tissue of the heated focus area and 7.5 mm from the focus area measured by PRFS thermometry. (c) Three selected temperature change images of the SMS and single slice scans during HIFU heating, including two slices: a slice at the focal plane and a slice at 7.5 mm from the focal plane. The color bar represents the value of the temperature change.

5:15 PM Passive cavitation mapping during blood-brain barrier opening is facilitated through treatment with ultrasonic pulses of inverse polarity

Antonios Pouliopoulos¹, Mark Burgess¹, Elisa Konofagou¹

¹Biomedical Engineering, Columbia University, New York City, NY, United States

Background, Motivation, and Objective

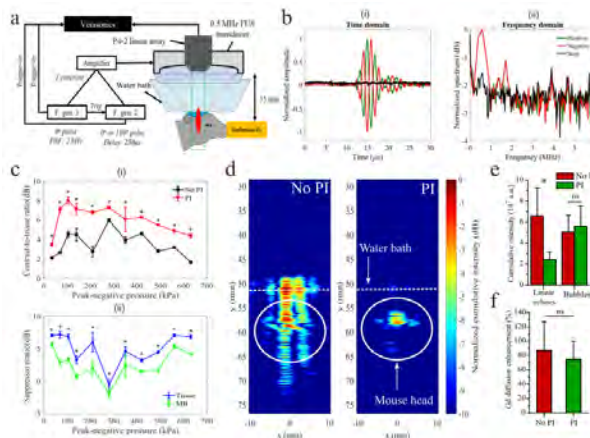
Focused ultrasound (FUS) in conjunction with pre-formed circulating microbubbles (MB) is being tested for a wide range of therapeutic applications such as non-invasive and reversible opening of the blood-brain barrier (BBB). An advantage of MB-based therapies is the ability to monitor their evolution by mapping the cavitation activity within the targeted area. However, skull and tissues limit our ability to detect low-amplitude MB activity, especially in clinical BBB opening applications. Linear echoes dominate the received signal when the therapeutic and passive imaging frequencies overlap. Here, we employ pulse inversion (PI) to improve the passive cavitation mapping during BBB opening by suppressing linear echoes within the FUS path.

Statement of Contribution/Methods

FUS with PI was achieved by synchronizing the emission of inverse short pulses (pulse length: 2-3 cycles, PRF: 4 kHz, peak-negative pressure: 35-630 kPa) through a focused 0.5-MHz FUS transducer driven by two function generators (fig. 1a). An ATL P4-2 linear array passively captured acoustic signals in synchrony with FUS emission, using absolute time-of-flight information. We tested the PI sequence in a 10% w/v gelatin phantom filled with 0.5% w/v Si particles. Polydisperse lipid-based MB (concentration: 2×10^6 MB/ml = 1x clinical dose) flowed through a 5-mm channel (flow speed: 1 mm/s) and exposed to FUS pulses of inverse polarity. FUS with PI was also tested *in vivo* to monitor BBB opening in a mouse model.

Results/Discussion

Summation of the inverse FUS pulses in free field led to a 15 dB cancellation of the time-domain signal (fig. 1b-i), mainly due to the suppression of the fundamental frequency and 3rd harmonic (fig. 1b-ii). PI increased the contrast-to-tissue ratio in the phantom by up to 5.5 dB compared to no PI (fig. 1c-i), due to the enhanced tissue signal suppression compared to the MB signal (fig. 1c-ii). Linear echoes were cancelled *in vivo* (figs. 1d and 1e), facilitating detection of MB activity during BBB opening. Both therapeutic schemes resulted in efficient BBB opening *in vivo*, with no significant difference in the delivery of gadolinium into the brain parenchyma (figure 1f). In conclusion, FUS with PI facilitates the passive mapping of weak MB signals both in a phantom and *in vivo* and can be applied in clinical BBB opening to suppress reflections from the thick human skull and brain tissue.



8D - High Frequency and IVUS

Ruby (200)

Wednesday, October 24, 8:00 am - 9:30 am

Chair **Jian Yuan**
ALS Shanghai

8D-1

8:00 AM In vivo imaging of a porcine coronary artery with a 30/80 MHz dual frequency intravascular ultrasound catheter

Chelsea Munding¹, Emmanuel Cherin², Natasha Alves², David Goertz^{1,2}, Brian Courtney^{2,3,4}, F. Stuart Foster^{1,2}

¹*University of Toronto, Toronto, ON, Canada*, ²*Sunnybrook Research Institute, Toronto, ON, Canada*, ³*Sunnybrook Health Sciences Centre, Toronto, ON, Canada*, ⁴*Conavi Medical Inc., Toronto, ON, Canada*

Background, Motivation, and Objective

Intravascular imaging can provide valuable information about vessel dimensions, plaque morphology and distribution, and stent placement. Two important modalities are intravascular ultrasound (IVUS) and optical coherence tomography (OCT). While conventional IVUS can usually penetrate the full thickness of the vessel wall and fatty plaques, its resolution is relatively poor (~70 - 200 μm). Some clinical and preclinical IVUS devices have achieved better resolution using higher frequencies (≥ 60 MHz), though with a corresponding loss of penetration depth. OCT achieves higher resolution (~10 - 20 μm), but is limited to 1-2 mm of tissue penetration and requires flushing of the blood. We have recently shown that a 3 French dual frequency IVUS (DF IVUS) catheter, operating at 30 and 80 MHz, was able to achieve complementary, co-planar images of ex vivo atherosclerotic arteries. However, questions relating to the clinical feasibility of this device remain. Importantly, it is unknown whether the 80 MHz transducer would be able to obtain useful images in the presence of blood or iodinated contrast agent (used for flushing in OCT).

Statement of Contribution/Methods

The DF IVUS catheter was designed and fabricated in-house. It incorporated two side-viewing transducer elements (30 and 80 MHz), facing opposite directions and sharing a common backing. The transducers were excited alternately using 20 cycle Tukey windowed chirps with 100% -6 dB bandwidth around their centre frequencies. The catheter was introduced into the left circumflex coronary artery (LCX) of a healthy 55 kg female pig via the left femoral artery. Pullbacks were acquired at 2.5 mm/s at 20 Hz frame rate in the presence of blood and while flushing with iodinated contrast.

Results/Discussion

Figure 1 shows an example of DF IVUS imaging in the mid-LCX. As expected, the 30 MHz image showed the full thickness of the vessel wall, despite the presence of blood. Surprisingly, the 80 MHz transducer was also able to image the superficial vessel wall despite high backscatter from blood and reduced penetration. The media is clearly delineated at 80 MHz. Axial and lateral resolutions were 50 and 220 μm (30 MHz) and 20 and 120 μm (80 MHz). Imaging through iodinated contrast was also successful. These results suggest that DF IVUS might be a promising approach for simultaneous imaging of both deeper vessel morphology and superficial detail.

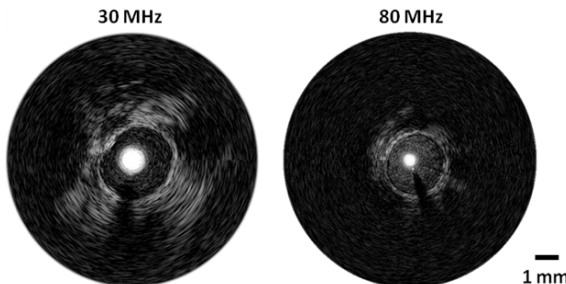


Figure 1: Example of *in vivo* DF IVUS imaging in the mid-left circumflex coronary artery of a healthy pig, in the presence of blood. The dynamic range of both images is 45 dB.

8:15 AM

Development of Dual-Element Intravascular Ultrasound Transducers for Third Harmonic Tissue ImagingJUNSU Lee¹, Ju-Young Moon², Jin Ho Chang^{1,3}¹*Department of Electronic Engineering, Sogang University, Korea, Republic of*, ²*Institute of Integrated Biotechnology, Sogang University, Korea, Republic of*, ³*Department of Biomedical Engineering, Sogang University, Korea, Republic of***Background, Motivation, and Objective**

Tissue harmonic imaging (THI) can provide images with high spatial and contrast resolutions. However, the conventional intravascular ultrasound (IVUS) transducers are difficult to use for THI, especially the third harmonic tissue imaging. This is so because IVUS transducers have a narrow fractional bandwidth (about 50%). Due to their small aperture (about 0.5 mm in diameter), additionally, the third harmonic signal both generated and received if possible is too weak to produce high-quality third harmonic tissue images. To solve this problem, we designed and fabricated a dual-element IVUS transducer for third harmonic tissue imaging without using contrast agents.

Statement of Contribution/Methods

The developed dual-element IVUS transducer consists of 35-MHz and 105-MHz elements as shown in Fig. 1(a). The 35-MHz element is responsible for ultrasound transmission and the 105-MHz element for reception of the third harmonic signal produced by the 35-MHz ultrasound. Each element has a square shape of which size is 0.5 mm x 0.5 mm. The aperture was spherically shaped in both lateral and elevation directions for geometric focusing at 2.5 mm. The 35-MHz element was constructed using PZT-5H as an active layer, two matching layers (2-3 silver epoxy and Parylene), and a backing layer (E-solder 3022). For the 105-MHz element, lithium niobate in conjunction with one matching layer (Parylene) was used. The ability to construct the third harmonic image of the developed IVUS transducer was evaluated in ex vivo experiments using pig blood vessels.

Results/Discussion

In the pulse-echo test, it was found that the 35-MHz and 105-MHz elements had center frequencies of 36.4 MHz and 111.7 MHz, respectively. As shown in Fig. 1(c) and (d), the image depth of the third harmonic imaging was deeper than that of the 105-MHz fundamental imaging due to the frequency-dependent attenuation of 105-MHz ultrasound. The third harmonic imaging provided a higher contrast resolution than the 105-MHz fundamental imaging due to lower side lobe levels. Additionally, the white ring images in Fig. 1(c) generated due to the pulser/receiver system (UT340) used in the experiments did not appear in the third harmonic image. We believe that the developed dual-element IVUS transducer is useful for examining vulnerable plaques and measuring the thickness of thin fibrous cap due to its high spatial and contrast resolution.

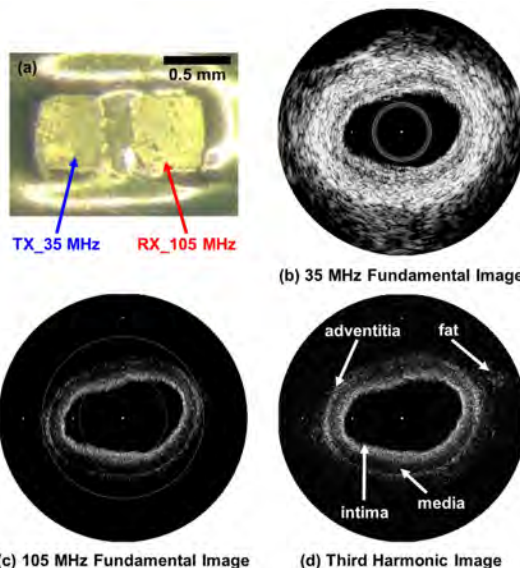


Fig. 1. (a) Photograph of the developed dual-element IVUS transducer, the fundamental images of the excised pig blood vessel obtained using (b) the 35-MHz and (c) 105-MHz elements, and (d) the third harmonic image obtained using the 35-MHz element for transmission and the 105-MHz element for reception. The white ring images in (c) are the artifacts generated due to the pulser/receiver system (UT340) used in the experiments. The space between the white bars on the images indicates 1 mm.

8:30 AM Axially-Segmented Cylindrical Transducer Array for Intravascular ARFI and SWEI Imaging

Arsenii Telichko¹, Carl Herickhoff¹, Jeremy Dahl¹¹Radiology, Stanford University, CA, United States**Background, Motivation, and Objective**

Cardiovascular disease affects millions of people worldwide. There is a clinical need to accurately assess vascular plaque vulnerability and base treatment decisions on quantitative analysis of plaque composition.

Here we describe a custom intravascular ultrasound (IVUS) transducer array prototype capable of generating acoustic radiation force impulse (ARFI). We demonstrate the application of ARFI and SWEI (shear wave elasticity imaging) with this transducer in experiments in a custom vessel phantom, to investigate the potential for IVUS-ARFI to distinguish soft lipid cores from stiffer surrounding tissues and quantifiably assess vascular plaques.

Statement of Contribution/Methods

A polyvinyl alcohol cryogel vessel phantom with an inclusion softer than the surrounding vessel wall ($G = 1 \text{ kPa}$ and $G = 6.2 \text{ kPa}$, respectively) was created. A 4.6-Fr cylindrical single-element transducer prototype was placed in the lumen of the vessel phantom and driven at 6 MHz to generate a radial ARFI push in the phantom. The resulting displacements in the phantom were tracked using a 15-MHz linear array probe connected to a Verasonics scanner.

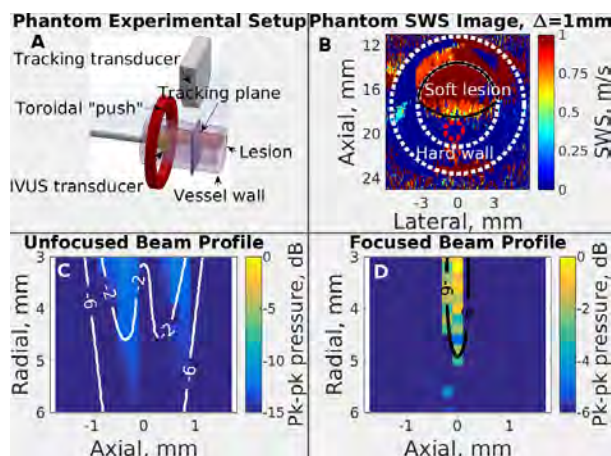
To enable electronic focusing of an ARFI push at a specified radius and axial position with respect to the catheter, an axially-segmented prototype array (12 elements, 205 μm pitch) was fabricated using a radially-poled, 4.6-Fr tube of PZT-4. The prototype array was connected to a Verasonics scanner, and a hydrophone was used to measure the intensity and distribution of the acoustic beam with the array either focused or unfocused at 7.1 MHz.

Results/Discussion

Tracked-displacement images of the vessel phantom were obtained at axial locations from 0 to 5 mm away from the plane of the ARFI push. No significant displacement was detected in the vessel wall, but the soft inclusion showed a maximum peak displacement of 2.4 μm , with shear-wave propagation detectable at 5 mm away ($c_s = 0.8 \pm 0.2 \text{ m/s}$ using the time-to-peak method).

Array measurements at a range of 5 mm showed a focal gain of up to 6.4x in intensity with respect to an unfocused excitation. The measured beam pattern shows good agreement with Field II simulations.

These results show that it is possible to construct an axially-segmented cylindrical transducer array capable of generating a stronger, electronically-controlled intravascular ARFI push to distinguish a soft inclusion from the vessel wall.



8:45 AM

A novel dual-frequency transducer for intravascular ultrasoundMin Su¹, Jiehan Hong¹, Zhiqiang Zhang¹, Suzi Liang¹, Congzhi Wang¹, Hairong Zheng¹, Weibao Qiu¹¹*Paul C. Lauterbur Research Center for Biomedical Imaging, Shenzhen Institutes of Advanced Technology, Chinese Academy of Sciences, China, People's Republic of***Background, Motivation, and Objective**

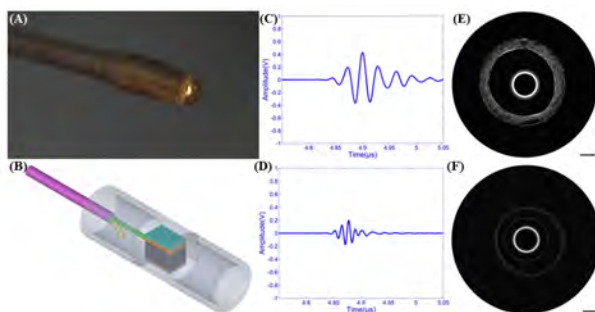
Currently, intravascular ultrasound (IVUS) is an important imaging modality for the evaluation of atherosclerotic plaques. It can provide real-time, high-resolution, and three dimensional images which offers valuable information including the dimension of lumen, plaque burden, and characteristics. The frequency of traditional IVUS ranges from 20 MHz to 45 MHz, providing 60-120 μm axial resolution. Ultra-high frequency (80 to 150 MHz) transducers were fabricated for IVUS, providing a very high axial resolution ($\sim 19 \mu\text{m}$), which is possible to achieve a comparable imaging resolution to optical imaging method. In this paper, a new method for dual-frequency IVUS has been proposed. Two different frequency (35MHz and 80 MHz) ultrasonic transducer elements were assembled with one common backing. Therefore only one coaxial cable is required for the catheter, which enables an easy implementation of dual frequency IVUS. Imaging results have been demonstrated of the proposed new IVUS scheme.

Statement of Contribution/Methods

In this work, a backing shared dual frequency ultrasound transducer was designed and fabricated for IVUS applications. PZT-5H was used for the piezoelectric material due to its stability and high Curie temperature. High frequency element and low frequency element were fabricated separately. A coaxial cable was arranged between in conductive backings of elements. Dual frequency elements were back to back arranged in a copper housing (as shown in Fig A). The schematic of the transducer is shown in Fig B.

Results/Discussion

A vector network analyzer was used to acquire the impedance of the transducer. The resonant frequencies of the transducer were 42 MHz and 124MHz respectively. Two polished steel reflectors were placed in a tank of deionized water positioned in front of two elements to acquire pulse echoes. A pulser/receiver was used to excite two ultrasonic elements simultaneously, and the receiver on the same unit was used to amplify the echoes before displaying them on a digital oscilloscope (Tektronix DPO 4104). Band pass filters were designed to filter out the pulse echoes. Dual-frequency echo after filter were shown in Fig. C (low frequency echo) and Fig. D (high frequency echo). Fig. C and D show the dual frequency images acquired from the same phantom. It therefore can provide a dual frequency intravascular ultrasound imaging with one catheter.



9:00 AM High frequency ultrasound needle transducer based on modified PMN-PT ceramic with ultrahigh clamped dielectric permittivity

Zhiqiang Zhang¹, Fei Li², Ruimin Chen³, Tianfu Zhang³, Xiaodong Cao⁴, Shujun Zhang², Thomas Shrout², Hairong Zheng¹, K. Kirk Shung³, Qifa Zhou³, Weibao Qiu¹

¹Shenzhen Institutes of Advanced Technology, Chinese Academy of Sciences, China, People's Republic of,

²Pennsylvania State University, United States, ³University of Southern California, United States, ⁴South China University of Technology, China, People's Republic of

Background, Motivation, and Objective

Needle transducers, housing a small piezoelectric element (usually less than 1 mm) into a commercially standard needle or catheter, have shown significant application in many minimally invasive procedures due to their safety, low cost, portability, and real-time visualization capability. However, the electrical impedance mismatch between the needled transducer and electrical terminations (usually $50\ \Omega$) usually deteriorate the transducer performance. Piezoelectric materials with large clamped permittivity and high piezoelectric properties are advantageous for fabricating needle transducers with high performance. In this work, a modified PMN-PT ceramic with ultrahigh clamped permittivity and high piezoelectric properties was proposed to design and fabricate a high performance needle transducer.

Statement of Contribution/Methods

A 40MHz needle transducer with a miniature aperture of $0.4\text{ mm} \times 0.4\text{ mm}$ was designed using Krimboltz, Leedom, and Mattaei (KLM) model-based simulation software PiezoCAD. A modified PMN-PT polycrystalline ceramics were used as the active element and prepared by the solid-state reaction method. Two matching layers were designed to compensate for the acoustic mismatch between the modified PMN-PT ceramic and the human body . The first matching layer was made of Insulcast 501, Insulcure 9, and $2\text{-}3\ \mu\text{m}$ silver. The second layer was made using parylene. E-solder 3022 with an acoustic impedance of 5.9 MRayl was selected as the backing layer.

Results/Discussion

The modified PMN-PT ceramic exhibited ultrahigh relative clamped permittivity ($\epsilon^S/\epsilon^0 = 3500$), high piezoelectric properties ($d_{33} = 1200\text{ pC/N}$, $k_t = 0.55$). The ultrahigh clamped permittivity of this modified PMN-PT ceramic can improve electrical matching of fabricated transducers with miniature aperture to the electrical system, thus improving the need transducer performance. The -6 dB fractional bandwidth and the two-way insertion loss of the fabricated needle transducer were 80% and -13 dB, respectively, indicating its good imaging resolution and high sensitivity. Wire phantom imaging and porcine eyeball imaging of the needle transducer were obtained, showing a good imaging capability. These results demonstrate the excellent performance of the modified PMN-PT ceramic needle transducer, making it a good candidate for minimally invasive procedures in medical applications.

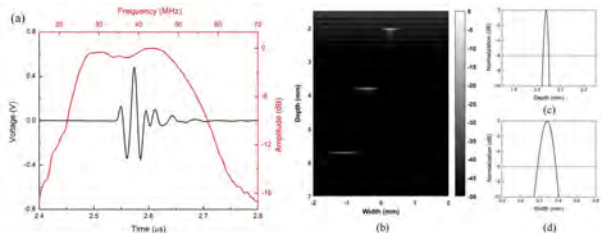


Fig. 1 (a) measured pulse-echo waveform and frequency spectrum of the modified PMN-PT ceramic needle transducer. (b) Wire phantom image of the modified PMN-PT ceramic needle transducer with dynamic range of 50 dB, (c) axial resolution (25.4 μm), and (d) lateral resolution (200 μm) of the modified PMN-PT ceramic needle transducer at about 2 mm depth.

9:15 AM

Development of a KNN ceramic based lead-free array transducer for high-frequency ultrasound

Zhiqiang Zhang¹, Ruimin Chen², Bo Wang³, Tianfu Zhang², Min Su¹, Rong Liu¹, Jiaxing Yang¹, Xiaodong Cao⁴, Yongxiang Li³, Hairong Zheng¹, K. Kirk Shung², Qifa Zhou², Weibao Qiu¹

¹Shenzhen Institutes of Advanced Technology, Chinese Academy of Sciences, China, People's Republic of, ²University of Southern California, United States, ³Shanghai Institute of Ceramics, Chinese Academy of Sciences, China, People's Republic of, ⁴South China University of Technology, China, People's Republic of

Background, Motivation, and Objective

High-frequency (higher than 15 MHz) ultrasound imaging has attracted increasing attention for many specified clinical applications such as ophthalmology, dermatology, cardiology, and endoscopy due to its improved imaging resolution. However, commercial available high frequency ultrasonic transducers are mostly made of lead-based piezoelectric materials, which are harmful to the environment and public health. Moreover, the array transducers have significant advantages over the single-element transducers, such as high frame rate imaging, capability of dynamic focusing, and clinical convenience. But complex process in fabrication restricts the development of high-frequency array. In this work, an 18.3 MHz lead-free linear array ultrasonic transducer was developed based on KNN piezoceramic.

Statement of Contribution/Methods

Krimboltz, Leedom, and Mattaei (KLM) model-based simulation software PiezoCAD (Sonic Concepts, Woodinville, WA) was used to simulate and optimize the design of the linear array single-element. Array elements were spaced at a 75- μm pitch, interconnected via a custom flexible circuit. The lead-free KNN based piezoceramic was used as the active element and prepared by the solid-state reaction method. The array element was fabricated by dicing and filling process. Two matching layers and a light backing materials were used to improve performance of the lead-free linear array.

Results/Discussion

A 64-elements high-frequency (18.3 MHz) lead-free linear array ultrasonic transducer based on KNN piezoceramic was developed successfully. The aperture size of active area of the linear array was 3 mm \times 4.785 mm. The measured results showed that the linear array exhibited a center frequency of 18.3 MHz, an average bandwidth of 42% at -6 dB, an average insertion loss of 41.8 dB at the center frequency, and a crosstalk between adjacent elements of less than -53 dB near the center frequency. The imaging capability of the fabricated lead-free linear array has been demonstrated by imaging a wire phantom. The axial and lateral resolutions were measured to be 105 μm and 166 μm , respectively. Based upon the results presented, the lead-free linear array appears to be a viable alternative for medical ultrasound imaging applications considering the protection of environment and public health.

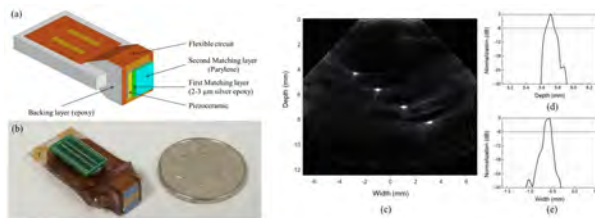


Fig. 1(a) a schematic diagram of the designed lead-free linear array and major designed components, (b) the photograph of the developed lead-free linear array transducer, (c) wire phantom image of the lead-free linear array, (d) axial resolution (105 μm), and (e) lateral resolution (166 μm) of the lead-free linear array at the second wire near the focus.

8E - Special Session: Technologies and Challenges for 3D Imaging

Ruby (200)

Wednesday, October 24, 10:30 am - 12:00 pm

Chair **Alfred Yu**
University of Waterloo

8E-1

10:30 AM Modular fabrication and assembly of large 2D Arrays with interface ASICs, PIN-PMN-PT composite, and 3D printed backing

Robert Wodnicki¹, Haochen Kang¹, Jayesh Adhikari¹, Rui Zhang², Ruimin Chen¹, Laiming Jiang¹, Nestor Cabrera-Munoz¹, Yu Liu², Victoria Chiu², Hayong Jung¹, Josquin Foiret², Qifa Zhou^{1,3}, Douglas N. Stephens², Katherine Ferrara²

¹*Department of Biomedical Engineering, University of Southern California, Los Angeles, CA, United States,*

²*Department of Biomedical Engineering, University of California, Davis, Davis, CA, United States, ³Department of Ophthalmology, University of Southern California, Los Angeles, CA, United States*

Background, Motivation, and Objective

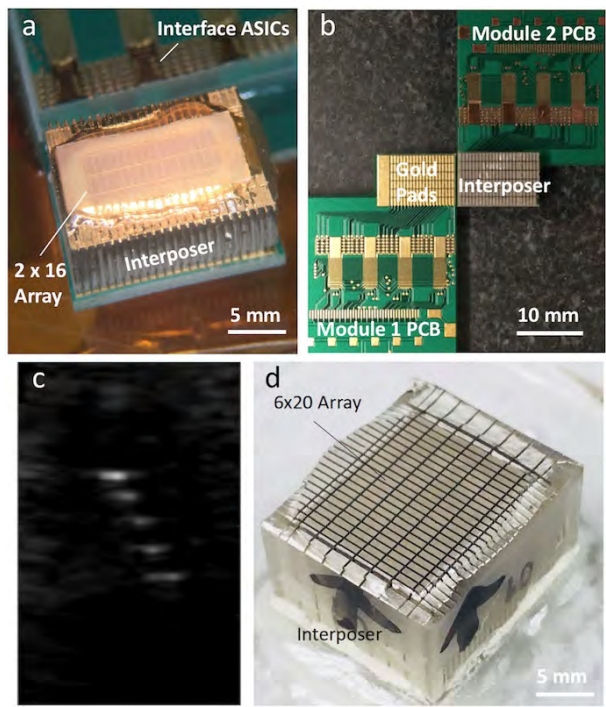
Large area ultrasound arrays with thousands of 2D array elements require dense interconnections to interface with front-end ASICs. For high yield, these arrays can be formed using multiple smaller modules that have been tested and sorted prior to assembly. We have been developing such densely interfaced acoustic/electrical array modules utilizing PIN-PMN-PT transducer material, 3D printed interposer backing structures, and multiple interface ASICs. The goal of this work is the realization of a large area 2D array for improved liver cancer screening.

Statement of Contribution/Methods

The proposed module implements a 2D array with 120 elements spaced at 600 μm in azimuth and 1600 μm in elevation. Each module has four interface ASICs designed for this application, implemented in a 0.35 μm 50V process and wire-bonded directly to the PCB. The ASICs multiplex 40 elements to 5 system channels using high voltage switches, and each element is buffered by a respective on-chip preamplifier and high voltage transmit/receive switch. The transducer array ($F_c = 3.8 \text{ MHz}$) is composed of a 1-3 composite of PIN-PMN-PT material and two matching layers and is mounted to a conductive backing interposer created by filling a 3D printed acrylic grid frame with E-Solder 3022 material. The individual acoustic modules are fabricated separately and then assembled to a tested four ASIC module using gold stud bumps and conductive adhesive.

Results/Discussion

Figure (a) illustrates a prototype acoustic module with 32 elements fabricated during process development and mounted to the 120-channel ASIC board. Fig. (b) illustrates array modularity: the left side PCB is bare, showing gold pads for acoustic stack assembly, the right side PCB has a full 120 element interposer assembled to it. The fabricated module in (a) was controlled by a Xilinx FPGA reading codes for synchronization and configuration from a Verasonics system. Data was transferred from local RAM in the FPGA to the ASICs to implement real-time synthetic aperture scanning. To illustrate the functioning device, 50 μm tungsten wires spaced at 1 mm in the axial direction were imaged using the 2 x 16 array prototype (c). A full acoustic stack with interposer and dual matching layers (d) has been fabricated showing 100% functional elements (no shorts/opens) and will next be assembled to a four ASIC PCB to implement the 6 x 20 element tileable 2D array module.



10:45 AM

Prototype 3D real-time imaging system based on a sparse PZT spiral arrayEnrico Boni¹, Alessandro Ramalli^{1,2}, Verya Daeichin³, Nico de Jong^{3,4}, Hendrik J. Vos^{3,4}, Piero Tortoli¹

¹Department of Information Engineering, University of Florence, Italy, ²Lab. on Cardiovascular Imaging & Dynamics, Dept. of Cardiovascular Sciences, KU Leuven, Belgium, ³Imaging Physics, Delft University of Technology, Delft, Netherlands, ⁴Biomedical Engineering, Thorax Center, Erasmus MC, Rotterdam, Netherlands

Background, Motivation, and Objective

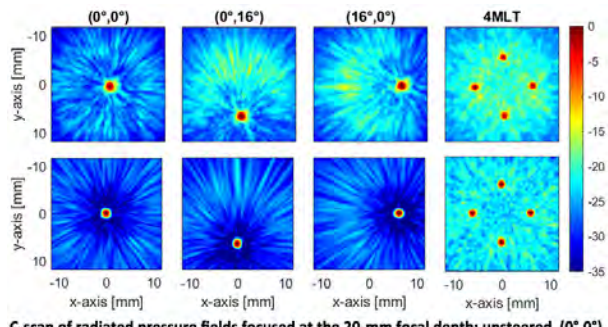
3D ultrasound imaging is costly and complicated mostly due to the need of controlling 2D probes with high numbers of elements (≥ 1024). A 256-element density tapered spiral array has been recently designed and realized in a piezoelectric probe prototype. The probe has now been connected to the ULA-OP 256 open scanner, suitably programmed to permit volumetric scanning in real-time. This paper reports on the first experimental transmit fields of such prototype system, including multi-line transmit fields that, in combination with parallel receive beamforming, may produce high volume rates in real-time.

Statement of Contribution/Methods

ULA-OP 256 was first configured to drive the 256 probe elements with 5MHz, 3-cycle sinusoidal bursts at 40 Vpp. Ultrasound beams were focused at 20 mm with 9 steering angles uniformly spaced between 0° and 32° in both elevation and azimuth planes. The linear high-power amplifiers of ULA-OP 256 were further exploited to test the simultaneous transmission of 4 beams (4MLT). The radiated fields were measured through a lipstick hydrophone (Onda Corp.), moved by an automatic positioning system, in steps of $0.2 \times 0.2 \times 1$ mm, within a $45 \times 45 \times 40$ mm³ volume. For all transmit modes, acquisitions were compared with Field II simulations in terms of lateral resolution and side-lobe level (SLL). ULA-OP 256 was then programmed to scan a $60^\circ \times 60^\circ$ region of interest with 3600 scanlines while continuously displaying two arbitrary cross-planes and beamforming the full volume in real-time.

Results/Discussion

Multiple beamplots confirming the probe capability of properly steering the beam within a volume have been obtained and some samples are shown in the figure. On average, the measured SLL was 15.9dB, while the -6dB lateral resolution was 1.25mm. With respect to simulations, measurements showed an average 7.5dB of SLL degradation and 33% wider lateral resolution; this could be due to 28 defective elements on the first prototype probe, but further investigation on this behaviour is in progress. The prototype system's capability of simultaneously transmitting multiple beams into arbitrary directions is shown in the figure (4MLT column). By exploiting the open system parallel beamforming capability, MLT can be combined with the multi-line acquisition (MLA) scheme (using, e.g., a 4MLT-4MLA setting) to produce B-Mode data over up to 30 volumes per second in real-time.



C-scan of radiated pressure fields focused at the 20-mm focal depth: unsteered ($0^\circ, 0^\circ$), steered ($0^\circ, 16^\circ$) and ($16^\circ, 0^\circ$) single beams and 4MLT beams. The top row shows the acquired fields while the bottom row the simulated ones; the dynamic range is 35dB.

11:00 AM

Single-Chip Reduced-Wire CMUT-on-CMOS System for Intracardiac Echocardiography

Gwangrok Jung¹, Amirabbas Pirouz¹, Coskun Tekes², Thomas M. Carpenter³, M. Wasequr Rashid¹, Ahmad Rezvanitabar¹, David Cowell³, Steven Freear³, Maysam Ghovalloo¹, F. Levent Degertekin^{1,2}

¹School of Electrical & Computer Engineering, Georgia Institute of Technology, Atlanta, GA, United States, ²G.W. Woodruff School of Mechanical Engineering, Georgia Institute of Technology, Atlanta, GA, United States, ³School of Electronic and Electrical Engineering, University of Leeds, Leeds, United Kingdom

Background, Motivation, and Objective

Intracardiac echocardiography (ICE) catheters are frequently used during interventional procedures for the diagnosis and treatment of structural heart diseases, but they are used under X-ray guidance. In order to use ICE catheters under MRI to avoid X-rays, the number of interconnect cables needs to be minimized to reduce RF-induced heating. This requires electronic integration with significant complexity at the tip of the catheter to handle large number of channels. For this purpose, we developed a CMUT-on-CMOS based single chip system with programmable transmit beamformer and front-end receiver using time division multiplexing (TDM).

Statement of Contribution/Methods

The system is designed to drive 64-channel CMUT array with 8:1 TDM analog receiver (Rx) with direct digital demultiplexing (DDD), and includes transmit (Tx)-beamformer logic, which is programmed with a single low-voltage differential signaling data line for wire reduction (Fig. 1-a). The ASIC is fabricated in 60-V, 0.18- μ m, HV CMOS/DMOS technology. Tx-beamformer logic generates a maximum delay of 10.235 μ s with resolution of 5 ns, using 200 MHz of clock frequency. The pulser circuitry drives each 1-D CMUT array element (~15 pF) with a 60-V unipolar pulse. The Rx block consists of Tx/Rx switch, low-noise amplifier, 4-level digital time gain compensation (TGC), buffer, and TDM circuitry operating at 1.8 V. The TDM signals are sent to high speed ADCs in the backend system, where DDD is performed in an FPGA for real-time image processing in the digital domain. The 64-element 1-D CMUT is fabricated using CMUT-on-CMOS approach with low temperature sacrificial release process.

Results/Discussion

The proposed CMUT-on-CMOS system occupies 2.6×11 mm² and reduces the number of wires from over 64 down to 22 with potential for larger reduction in 2-D arrays [1]. We successfully demonstrated the functionality of all system blocks including 8-pulse Doppler mode and TGC control. Results from a pulse echo experiment in oil are shown in Fig. 1-b. The signals show 5 MHz center frequency with 80% bandwidth, which is suitable for ICE catheters (Fig. 1-c). Imaging experiments using the single chip system is currently underway.

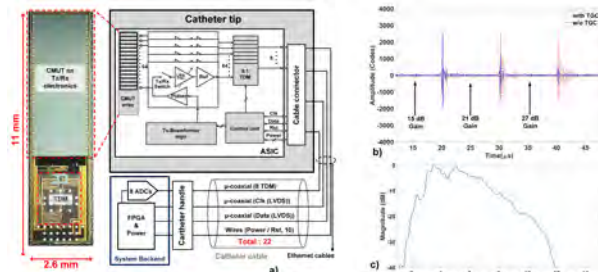


Figure 1. a) Simplified block diagram of ICE system, including the backend system, b) received pulse-echo signals with or without TGC control, c) frequency spectrum of the echo signals from plane reflector.
[1] G. Jung et al., "Single-Chip Reduced-Wire Active Catheter System with Programmable Transmit Beamforming and Receive Time-Division Multiplexing for Intracardiac Echocardiography," ISCC Dig. Tech. Papers, Feb. 2018.

11:15 AM Fast Orthogonal Row-Column Electronic Scanning with Bias-Switchable Crossed-Electrode Relaxor Arrays and GPU Accelerated Volumetric Reconstruction

Chris Ceroici¹, Katherine Latham², Benjamin Greenlay¹, Jeremy Brown³, Roger Zemp⁴

¹*Electrical and Computer Engineering, University of Alberta, Edmonton, AB, Canada*, ²*Electrical and Computer Engineering, Dalhousie University, Canada*, ³*Biomedical Engineering, Dalhousie University, Halifax, NS, Canada*,

⁴*University of Alberta, Canada*

Background, Motivation, and Objective

The Top-Orthogonal-to-Bottom Electrode (TOBE) architectures provide reduced channel count for large 2-D ultrasound imaging arrays using a cross-electrode wiring technique where top electrodes are connected along rows and bottom electrodes are connected along columns [A. Sampaleanu, et al. *IEEE UFFC*, 2014]. By using bias sensitive transducer elements, full control of a NxN array using only 2N connections can be achieved. Fast Orthogonal Row-Column Electronic Scanning (FORCES) is an imaging scheme which leverages the TOBE architecture and bias-switching for 3-D imaging. Hadamard bias-encoded transmit signals are used to achieve two-way focusing in the azimuthal direction, providing similar imaging quality to a linear array along with 3D imaging capabilities using electronic focusing in elevation. Decoding and volumetric reconstruction is accelerating using a GPU-based program.

Statement of Contribution/Methods

We use a 10 MHz 64x64 element bias-sensitive piezoelectric array fabricated from a 1-3 composite using PMN-38 electrostrictive relaxor material. Using a Verasonics programmable ultrasound platform along with custom interface and bias switching electronics, the FORCES imaging scheme is compared with other crossed-electrode imaging schemes as well as a linear array with the same number of channels. Imaging experiments are conducted on crossed-wire phantoms and a rat heart.

Results/Discussion

Figure 1 shows elevational B-scan slices of a rat heart using the FORCES imaging scheme and rectilinear crossed-electrode imaging, a commonly used crossed electrode imaging scheme described in [Seo, C. H., et al. *IEEE UFFC*, 2009]. The contrast between the heart wall and right ventricle was 3.08 for the FORCES imaging scheme and 0.27 for rectilinear imaging. Wire phantom experiments showed an azimuthal resolution of 0.31 mm using FORCES and 0.41 mm with a 64-channel linear array using 64 flash angle compounding. A GPU decoding and reconstruction program was created allowing for a 300 ms B-scan reconstruction time compared with a 78 s reconstruction time using a CPU based program resulting in a 20 elevational slice volumetric reconstruction speed of 0.17 volumes/s.

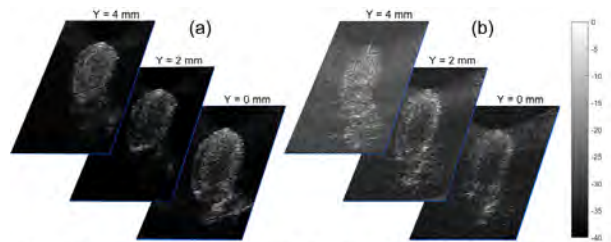


Figure 1: B-scan images of a sacrificed Sprague Dawley rat heart using (a) FORCES imaging scheme and (b) rectilinear crossed-electrode imaging.

8F - CMUT/PMUT

Ruby (200)

Wednesday, October 24, 1:30 pm - 3:00 pm

Chair **Qifa Zhou**
University of Southern California

8F-1

1:30 PM Design, Fabrication and Characterization of a Hybrid Piezoelectric-CMUT Dual-Frequency Ultrasonic Transducer

Alessandro Stuart Savoia¹, Tung Manh², Barbara Mauti¹, Lars Hoff², Trym Eggen³, Frederic Lanteri⁴, Jean-Francois Gelly⁴

¹*Department of Engineering, Roma Tre University, Rome, Italy*, ²*Department of Micro and Nano Systems Technology, University College of Southeast Norway, Borre, Norway*, ³*GE Vingmed, Horten, Norway*, ⁴*GE Parallel Design SAS, Sophia Antipolis, France*

Background, Motivation, and Objective

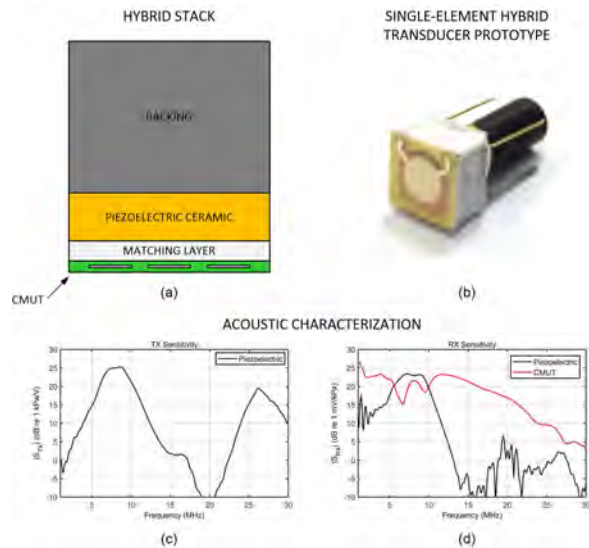
Dual-frequency ultrasonic transducers, capable of operating over distinct frequency bands, may be conveniently used in different applications such as harmonic imaging. Several dual-frequency transducer configurations, implemented using bulk piezoelectric or micromachined transducers, were investigated. Recently, a hybrid transducer configuration, consisting of a Capacitive Micromachined Ultrasound Transducer (CMUT) placed on top of a piezoelectric transducer stack, was proposed and investigated using Finite Element Modeling (FEM) [doi: 10.1109/ULTSYM.2016.7728599]. This paper presents the design and fabrication of a dual-frequency hybrid single-element transducer prototype. The prototype is characterized with the aim of evaluating the potentiality of the dual-frequency hybrid approach in nonlinear imaging applications.

Statement of Contribution/Methods

The hybrid transducer stack, shown in Fig.(a), was designed using FEM. The low-frequency (LF) transducer, i.e. a 4mm-diameter PZT ceramic disk supported by a backing and matched using a $\lambda/4$ layer, was designed to operate around 7 MHz. The high-frequency (HF) transducer, i.e. a 3.5mm single-element Reverse-Fabricated CMUT [10.1109/TUFFC.2012.2303], was designed to operate at a -3dB center frequency of 14 MHz. The hybrid transducer prototype shown in Fig.(b) was achieved by individually fabricating and successively assembling the LF and HF transducers. Electrical impedance measurements were performed before and after the transducer assembly. The hybrid transducer was then acoustically characterized by performing hydrophone and pulse-echo experiments in immersion in order to estimate transmit (TX) and receive (RX) frequency responses. Characterization results were compared with simulations.

Results/Discussion

Simulation and characterization results showed that the TX and RX responses of the LF transducer are not altered by the presence of the CMUT, whilst the RX response of the HF transducer is affected by the presence of the piezoelectric stack only at low frequency, as shown in Fig.(c)-(d). Moreover, the peak RX sensitivities of the LF and HF transducers are equivalent (16 mV/kPa) demonstrating that the proposed hybrid transducer approach can be leveraged to obtain an increased RX bandwidth towards high frequency leading to potential benefits in nonlinear imaging applications.



1:45 PM

36% Scandium ScAlN Air-coupled Piezoelectric Micromachined Ultrasonic TransducersYuri Kusano¹, Akihiko Teshigahara², Itaru Ishii², Guo-Lun Luo³, David Horsley^{1,3}¹*Electrical and Computer Engineering, University of California, Davis, CA, United States*, ²*Research Laboratories, DENSO Corporation, Aichi, Japan*, ³*Mechanical and Aerospace Engineering, University of California, Davis, CA, United States***Background, Motivation, and Objective**

Scandium aluminum nitride ($\text{Sc}_x\text{Al}_{1-x}\text{N}$) retains many features of AlN (e.g. CMOS compatibility, ease of deposition/etching) but possesses significantly increased piezoelectric properties compared to pure AlN [1,2]. However, most of the devices published to date have used Sc concentrations below 20%, where the piezoelectric coefficient is only modestly improved, because alloy targets are difficult to manufacture at higher concentrations. Here, we demonstrate PMUTs fabricated with 36% Sc films, a concentration close to the phase boundary where the piezoelectric coefficient is maximum. Through this increase in piezoelectric coefficient and improved mechanical design, we seek to realize air-coupled PMUTs that are capable of 10x greater transmit pressures than earlier AlN air-coupled PMUTs and comparable to pressures achieved in conventional bulk transducers.

Statement of Contribution/Methods

PMUTs consisting of an Al/ScAlN film stack were fabricated on a custom SOI wafer. The 5 μm thick Si device layer of the SOI was B-doped to achieve low resistivity and used as the bottom electrode. High Sc concentration ScAlN film (1 μm) was sputtered using ScAl alloy target. Aluminum top electrode was then formed by a lift off process. The PMUT membrane was defined by a backside Si DRIE followed by the BOX removal. The Sc concentration in the film was analyzed by electron probe microanalysis (EPMA). The device performance in air was characterized using laser Doppler vibrometer (LDV).

Results/Discussion

The concentration of Sc in the actual sputtered film was 36% from EPMA. The $\text{Sc}_{0.36}\text{Al}_{0.64}\text{N}$ with good crystal quality exhibited high d_{33} of 17 pC/N (Fig 1a), indicating 2x higher $e_{31,f}$ than AlN. The displacement sensitivity of a 1 mm diameter PMUT was 876 nm/V at the 84 kHz resonance frequency (Fig 1b/c). Because the maximum transmit pressure of a PMUT is usually limited by mechanical “spring-hardening” nonlinearity at large vibration amplitudes, the maximum displacements at voltages up to 20V_{pp} were measured (Fig 1d) using both a fixed 84 kHz input frequency and by adjusting the input frequency by a few kHz to follow PMUT resonance frequency. A large displacement of 4.8 μm was achieved at the fixed frequency. This represents a factor of 9 increase in transmit amplitude compared to prior art air-coupled PMUTs [3].

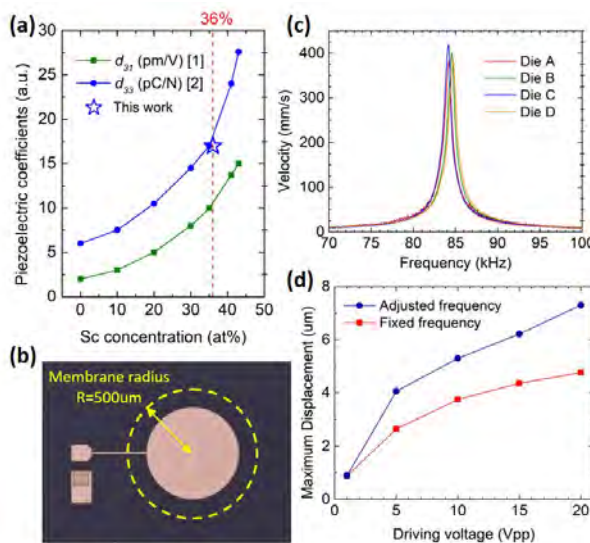
1. Akiyama *et al*, *APL* 20092. Akiyama *et al*, *APL* 20133. Przybyla *et al*, *IEEE JSSC* 2015

Fig. 1. (a) Piezoelectric coefficients of ScAlN film (b) optical top view image of PMUT (c) frequency response measured via LDV (d) maximum displacement.

2:00 PM

Thin Film PZT-based PMUT arrays

Susan Trolier-McKinstry¹, Christopher Cheng¹, Jeong Nyeon Kim¹, Richard L. Tutwiler¹, Kyusun Choi¹, Thomas N. Jackson¹, Yongqiang Qiu², Holly Lay², Sandy Cochran²

¹Penn State University, United States, ²Medical and Industrial Ultrasonics, University of Glasgow, Glasgow, United Kingdom

Background, Motivation, and Objective

Miniaturized high frequency ultrasound systems offer the opportunity to create small form factor systems for applications in medical imaging (including ultrasound pill cameras), acoustic control of motion of suspended particles, and detection of the veins in the fingers for improved identification systems. The goal in this work was to develop piezoelectric micromachined ultrasound transducers (PMUT) using PbZr_{0.52}Ti_{0.48}O₃ (PZT) films for these purposes. PMUTs were fabricated both on rigid silicon (Si) substrates and on flexible polyimide platforms.

Statement of Contribution/Methods

PMUTs were fabricated using two different approaches. In the first method, Si on insulator (SOI) wafers were used as substrates. Pt/PZT/Pt/Ti stacks were deposited by sputtering (or a combination of sputtering and chemical solution deposition) as blanket layers, and were subsequently patterned top-down using conventional nanofabrication processes. The final structures were then released by deep-reactive ion etching of the handle Si wafers. As an alternative, polyimide/Pt/Ti/PZT/Pt/Ti/Al₂O₃/ZnO stacks were grown on SiO₂/Si.

Following top-down patterning, the structures could be released from the underlying Si substrate by undercutting the ZnO layer in a dilute acetic acid bath. The latter method ultimately allows the preparation of flexible transducer arrays using high piezoelectric coefficient materials. Finite element modelling was used in both cases to design devices with resonant frequencies between 8 and 80 MHz.

Results/Discussion

Air-backed PMUT transducer arrays on deep reactive ion etched Si (See Fig. 1) were poled at 150°C for 15 minutes at high fields to provide a stable polarization direction for the piezoelectric film. After wire-bonding to a package and water-proofing with parylene, ~67% bandwidth was achieved in 35 MHz annular PMUT arrays. Data will also be presented for linear and 2D arrays.

Fig. 1 also shows a released PZT film on a polyimide substrate. While PMUTs could benefit immensely from flexible, reconfigurable polymeric substrates, a critical challenge lies in the discordance between the high crystallization temperatures of many perovskite materials and the low decomposition temperature of the plastic, thus leaving limited options for direct deposition of high strain piezoelectric films on polymers. The released PZT on polyimide exhibited enhanced dielectric response due to a reduction in clamping from the low stiffness, low thickness polymer layer. After release from the Si, polarization – electric field hysteresis measurements showed an increase in remanent polarization from 17.5 µC/cm² to 26 µC/cm² compared to the same films clamped on Si. In addition, poling to 3 times the coercive field at 125 °C led to more ferroelastic realignment in the released films. These films are now being explored for transducer arrays.

2:30 PM

1D Lumped Parameter Modeling of CPUT: A Capacitive Transducer Without DC Bias or Pre-ChargeSushruta Surappa¹, Molei Tao², F. Levent Degertekin³¹*Mechanical Engineering, Georgia Institute of Technology, United States*, ²*Mathematics, Georgia Institute of Technology, United States*, ³*ECE, Georgia Institute of Technology, Atlanta, GA, United States***Background, Motivation, and Objective**

Ultrasound power transfer has many advantages over RF-based wireless power transfer for powering implantable medical devices (IMDs) such as higher penetration depth and power levels allowed in the body. One drawback with using capacitive transducers as receivers in ultrasound power transfer is that a DC bias or an electret is required to operate the receiver. Capacitive parametric ultrasonic transducers (CPUTs), which can operate without a DC bias or pre-charge, overcome the limitations faced by traditional capacitive devices making them ideal for applications such as energy harvesting and powering of IMDs [1]. The objective in this study is to model and analyse the CPUTs for power transfer applications.

Statement of Contribution/Methods

The CPUT is modeled as an ultrasound driven piston (at 2ω) coupled to an RLC resonator (resonating at ω_0) resulting in a system of two coupled nonlinear ordinary differential equations (Fig. 1-a). SIMULINK is used along with an analytical approximation of the system to obtain the voltage across the capacitor and displacement of the piston. Parametric resonance threshold and ultrasound to electrical conversion efficiency are evaluated and the dependence of these performance metrics on the load resistance, input ultrasound intensity, forcing frequency, electrode coverage area, gap height and the mechanical Q-factor are studied. Guided by these results, practical device designs are obtained through COMSOL simulations and the feasibility of using CPUT in air is predicted.

Results/Discussion

Results for 1mm^2 CPUT at 2 MHz in water show that the mechanical input impedance of the CPUT can be matched to water by adjusting parameters such as the electrode coverage and load resistance to achieve acousto-electrical conversion efficiencies over 90% with power levels below FDA limit (fig. 1-b). This particular design uses $200\text{ }\mu\text{m}$ thick circular silicon plate over 120 nm gap. For air applications, similar efficiencies are predicted with 115 dB-SPL input sound level at an operation frequency of 50 kHz. These results demonstrate that the CPUT overcomes a significant challenge faced by capacitive transducers by offering a completely passive and highly efficient solution to wireless ultrasound power transfer at power levels relevant to biomedical implants and remote charging.

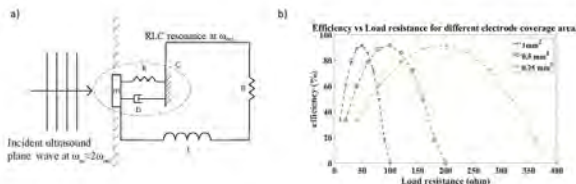


Fig. 1. a) 1D lumped parameter model of the CPUT b) Efficiency vs load resistance for different electrode coverage in water

[1] S. Surappa, S. Satit, and F. Levent Degertekin, "A capacitive ultrasonic transducer based on parametric resonance," *Appl. Phys. Lett.*, vol. 111, no. 4, p. 043503, Jul. 2017.

2:45 PM

Design and Implementation of Wideband CMUTs for Airborne ApplicationsOluwafemi Adelegan¹, Feysel Yamaner¹, Ömer Oralkan¹¹*Electrical and Computer Engineering, North Carolina State University, Raleigh, NC, United States***Background, Motivation, and Objective**

Wideband airborne ultrasound transducers are desired for the development of parametric arrays for directional sound, haptics, and gesture sensing. Piezoelectric transducers developed for these applications have large mechanical impedance mismatch with air, resulting in a narrowband frequency response. Capacitive transducers offer the advantages of better transmit and receive sensitivity without requiring a matching layer. We have previously reported a three-mask process for fabricating capacitive micromachined ultrasonic transducers (CMUTs) on a glass substrate using anodic bonding. We also reported an optically transparent air-coupled CMUT fabricated using adhesive bonding. In this work, we designed and fabricated annular and spiral shaped air-coupled CMUTs with improved bandwidth.

Statement of Contribution/Methods

We used FEM to design vacuum-sealed annular and spiral shaped CMUTs to operate at a center frequency of 80 kHz with up to 20% fractional bandwidth (FBW). The varying width of the spiral and annular cell designs contribute largely to the bandwidth improvement of these devices. The CMUTs presented in this work were fabricated with three masks using anodic bonding. We investigated two designs for implementing wideband air transducers. The 15- μm deep cavities in the glass substrate were defined by wet etching using HF (49%)/H₂O solution in a volumetric ratio 2:1. Cr/Au and AZ 4620 photoresist were used as the etch mask. The lateral etch was measured as 30 μm and it was incorporated in the masks design. After the deep etch, 300-nm Cr/Au was deposited in the cavities as the bottom electrode and defined by e-beam evaporation and liftoff. An SOI wafer with 25- μm thick device layer with a 300-nm PECVD-silicon-nitride insulation layer was bonded to the processed glass substrate using anodic bonding. The gas trapped inside the cavities during anodic bonding was evacuated after handle and BOX layer removal. The cavities were sealed with Benzocyclobutene (BCB) to achieve vacuum-sealed devices.

Results/Discussion

The devices were fully fabricated and are now being characterized. Based on FEM simulations, the fabricated devices are expected to have 20% FBW. The atmospheric deflection observed in the devices agrees with the FEM simulations. Comparing the simulation results with earlier demonstrations, spiral and annular shaped designs show improved bandwidth

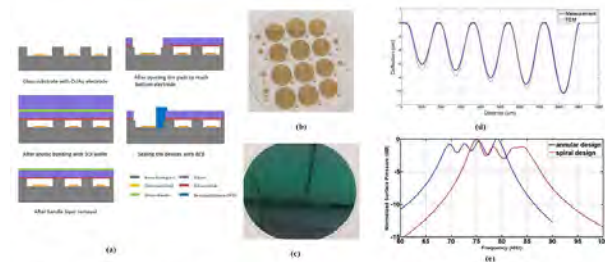


Fig. 1 (a) Simplified process flow for fabricating the devices. (b) Processed glass substrate showing the bottom electrode. (c) Bonded wafer after handle and BOX layers removal. (d) Atmospheric deflection profile of the annular device showing an agreement with the FEM simulations. (e) FEM simulations showing 20% FBW for the annular and spiral designs.

8G - Ultrasound Electronics

Ruby (200)

Wednesday, October 24, 4:00 pm - 5:30 pm

Chair **David Cowell**
University of Leeds

8G-1

4:00 PM ASIC design for a single-cable 64-element ultrasound probe

Douwe van Willigen¹, Jovana Janjic², Eunchul Kang¹, Zu Yao Chang¹, Emile Noothout³, Martin D. Verweij^{2,3}, Nicolaas de Jong^{2,3}, Michiel Pertuis¹

¹*Electronic Instrumentation Laboratory, Delft University of Technology, Delft, Netherlands*, ²*Thorax Centre, Erasmus MC, Rotterdam, Netherlands*, ³*Laboratory of Acoustical Wavefield Imaging, Delft University of Technology, Delft, Netherlands*

Background, Motivation, and Objective

The increasing number of elements used in medical ultrasound probes causes an increasing need for a reduction in the number of cables interfacing the probe with the imaging system. Especially in catheter-based ultrasound this is valuable to facilitate a more flexible probe shaft and leave room for a guide-wire.

A probe that uses a single cable connection, but can still produce 3D-ultrasound images is interesting as it can replace current single-element probes by a matrix array with 3D-imaging capabilities without changing the electrical infrastructure.

This work shows a prototype ASIC (Application Specific Integrated Circuit) that connects 64 piezo elements to an imaging system using a single coaxial cable.

Statement of Contribution/Methods

In this work an ASIC with a diameter of 1.5 mm has been designed that interfaces 64 PZT-elements with a center frequency of 12 MHz and a pitch of 100 μm to an imaging system by using a single cable. In transmit, a high-voltage pulse of up to 30 V applied to the cable can be passed to one or multiple elements. In reception, the signal received by a selected element is amplified by a low-noise amplifier. Thereafter, the signal is passed over the cable using current mode signaling, which is more power efficient than driving the cable with a voltage. The power supply to the amplifier is provided by a constant voltage on the cable. Configuration data is modulated on the power supply to select the TX and RX channels and set the programmable gain of the amplifier. A block diagram of the circuit is shown in the figure on the left.

Results/Discussion

The ASIC has been fabricated in a 0.18 μm high-voltage CMOS technology, and has been characterized in combination with a 42-AWG coaxial cable with a length of 1.5 m. Measurements show that transmit signals of up to 30 V can be successfully passed to the elements. The LNA has a 3 dB bandwidth of 21 MHz and dynamic range of 61 dB, plus 12 dB programmable gain, while consuming a power of 6 mW at 3 V. Using synthetic aperture imaging and delay-and-sum beamforming, an image of a needle phantom located in a water bag placed on top of the ASIC has been obtained, as shown in the figure on the right. The image shows a dynamic range similar to prior work using an interface of four or more cables. It is the first ASIC to interface a transducer array via a single micro-coaxial cable, thus greatly simplifying the realization of catheter-based 3D imaging devices.

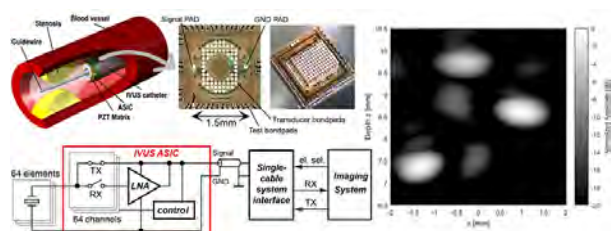


Figure 1: Top: Artist impression of the prototype ASIC inside an artery and micrographs with and without piezo elements.
Bottom: Block diagram of the prototype front end ASIC.
Right: Maximum projection of delay-and-sum beamformed image of a needle phantom containing three needles.

4:15 PM

Integrated Front End Circuitry for Microultrasound Capsule Endoscopy

Holly Lay¹, Christina Lemke¹, Benjamin Cox², Gerard Cummins³, Elena Ferrazzano¹, Calum West¹, Marc P.Y. Desmulliez³, Eddie Clutton⁴, Sandy Cochran¹

¹Medical and Industrial Ultrasonics, University of Glasgow, Glasgow, United Kingdom, ²University of Dundee, United Kingdom, ³School of Engineering and Physical Sciences, Heriot-Watt University, Edinburgh, United Kingdom, ⁴Royal (Dick) School of Veterinary Studies, University of Edinburgh, United Kingdom

Background, Motivation, and Objective

Capsule endoscopy (CE) was originally developed to address the limitation of conventional endoscopy and colonoscopy in accessing the small bowel as a remote part of the gastrointestinal tract. To further enhance the diagnostic ability of CE, microultrasound capsule endoscopy is under development for visualisation of sub-surface tissue layers and identification of diseased tissue at an earlier stage. To address key concerns about tissue coupling, image quality and multimodal system integration, a set of translational trial prototypes were developed for rapid validation and design iteration. Low-cost approaches with minimal manufacturing time were adopted to allow multiple rapid prototype design cycles and integrated front-end electronics were included to improve signal integrity and address issues with electrical interference.

Statement of Contribution/Methods

Prototype capsules were designed with four, 30 MHz PVDF transducers connected to a custom printed circuit board (PCB) housing a four channel front end analogue circuit comprising transmit/receive protection circuits (T/R, MD0101, Microchip Technology, Chandler, USA) and 12 dB pre-amplification implemented with 4-channel low-noise amplifiers (LNA, ADA4807, Analog Devices, Norwood, USA) in an inverting feedback configuration. These were housed in additively manufactured capsule shells and interconnection to benchtop electronics was achieved via single-core power wires and micro-coaxial cables (9442, Alpha Wire, Elizabeth, USA).

Following initial testing results, the front-end circuitry was modified to incorporate T/R protection with higher voltage tolerances (BAV99 diodes, Diodes Inc, Plano, USA) and an improved electrical ground topology. Grounding and channel isolation were also improved by reducing the channel count to two transducers in response to *in vivo* testing in a large animal model that showed this was sufficient for device validation. Coded excitation was investigated to counteract the signal to noise ratio (SNR) loss from the use of PVDF transducers in transmission mode and the electronic interference from multimodal circuitry.

Results/Discussion

The first prototype capsules were tested *in vivo* in a porcine model in collaboration with the Wellcome Trust Critical Care Laboratory for Large Animals (Roslin Institute) under license from the UK Home Office (PPL 70/8812). M-mode imaging was performed in the oesophagus and small bowel (via stoma) with saline coupling and an avalanche-mode transmitter/amplifier unit (DPR300, JSR Ultrasonics, Pittsford, USA). A second-generation prototype was tested in the small bowel and colon using both the avalanche-mode transmitter and coded excitation generated with an arbitrary waveform generator (DG4162, Rigol Technologies, Beijing, China) and amplified to 60 V_{pp} with a bespoke amplifier. Images obtained from the trials were assessed clinically to be of high quality and with good repeatability.

4:30 PM

A 256-Element Spiral CMUT Array with Integrated Analog Front End and Transmit Beamforming Circuits

Alessandro Stuart Savoia¹, Barbara Mauti¹, Luca Fanni¹, Alvise Bagolini², Enrico Boni³, Federico Guanziroli⁴, Stefano Passi⁴, Giulia Matrone⁵, Alessandro Ramalli³, Pierluigi Bellutti², Giosuè Caliano¹, Fabio Quaglia⁴, Andrea Mazzanti⁵, Piero Tortoli³

¹Department of Engineering, Roma Tre University, Rome, Italy, ²Fondazione Bruno Kessler, Trento, Italy, ³Department of Information Engineering, University of Florence, Florence, Italy, ⁴ST Microelectronics, Agrate, Italy, ⁵Department of Electrical, Computer and Biomedical Engineering, University of Pavia, Pavia, Italy

Background, Motivation, and Objective

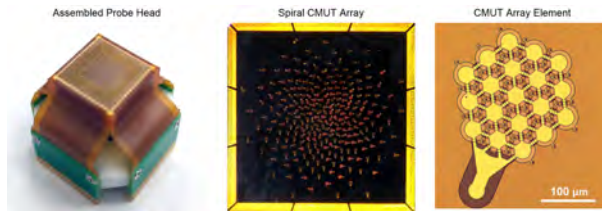
MEMS-based CMUT technology enables the development of advanced transducer-electronics multi-chip modules (MCM) for medical imaging applications, thanks to the high compatibility with 3D packaging methods. In this paper, we present the design, fabrication and characterization of an MCM comprising a 256-element CMUT spiral array interconnected to a 256-channel analog front end (AFE) ASIC in BCD-SOI technology, featuring high-voltage unipolar pulsers, capacitive-feedback low-noise amplifiers and a programmable transmit (TX) beamformer. The spiral array, designed to perform volumetric beam steering at 7 MHz, is characterized by a density-tapered layout of 220 μm-wide hexagonal elements distributed over a quasi-circular area of 10 mm diameter.

Statement of Contribution/Methods

A co-design of the CMUT and the AFE was carried out. CMUT and ASIC wafers were fabricated and further processed according to the recently proposed 3D packaging method [10.1109/ULTSYM.2017.8092991], which uses Cu pillars and solder reflow for electrical interconnection, and patterned benzocyclobutene for mechanical bonding. Two MCMs were assembled, i.e. a test module comprising the CMUT array and a dummy ASIC used to make the array elements directly accessible for basic transducer characterization, and a fully-functional module comprising both the CMUT and the programmable ASIC for complete testing. Each fabricated module was integrated in a probe head (see figure) and characterized. Air-coupled displacement and water-coupled TX pressure responses were measured on different array elements of the test module, using a laser Doppler vibrometer and a hydrophone, respectively, to verify the CMUT array functionality. ASIC programming sequences were then implemented on a digital pattern generator and used to configure the fully-functional modules for pulse-echo testing of the single array elements, and for one-way beampattern measurements in different array focusing and steering configurations.

Results/Discussion

Displacement and TX pressure measurement results confirmed the design specifications. Pulse-echo testing using 7MHz, 4-cycle TX pulses showed a variation of the echo signal amplitude of 3 dB across the CMUT array. Examples of unsteered and steered one-way beampatterns measurement results will be shown along with a quantitative estimation of the sidelobe levels.



4:45 PM

Real-Time FIR Filter Normalisation of Ultrasound Analog Front Ends for Broadband ImagingThomas Carpenter¹, David Cowell¹, Steven Freear¹¹School of Electronic & Electrical Engineering, University of Leeds, United Kingdom**Background, Motivation, and Objective**

A typical ultrasound imaging system Analog Front End (AFE) receiver consists of a transmit/receive switch, amplifiers and an analog to digital converter (ADC). Each component has a frequency dependent gain response resulting in distortion of the ultrasound echo signal. This paper proposes a method of calibration and real-time equalization of the AFE using per-channel Finite Impulse Response (FIR) filters.

Statement of Contribution/Methods

To perform calibration, the frequency response of the AFE must be determined as shown in Fig (a). An arbitrary waveform generator (AWG) produces a broadband chirp signal which is fed into the AFE. The signal is simultaneously measured at the AFE input via oscilloscope and by the AFE ADC. The frequency response is calculated by comparing the Fast Fourier Transform (FFT) of the voltage input with the ADC output.

Each AFE channel of the University of Leeds Ultrasound Array Research Platform (UARP) includes a real-time 94-Tap FIR filter. These filters are fully reprogrammable and can be repurposed for performing real-time filtering or gain correction/normalization by uploading the coefficients for the filter.

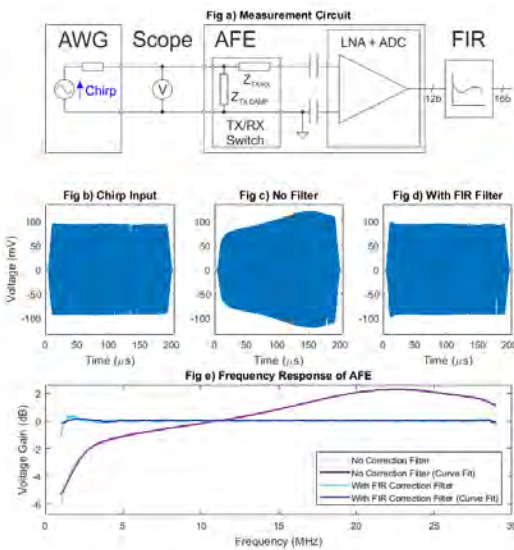
Correction of the AFE frequency response is performed by designing a matching filter with inverse response. FIR filter coefficients are calculated using MathWorks MATLAB. The resulting digital filter can then be uploaded to perform normalization in real time.

Results/Discussion

Calibration measurements were performed on the UARP to determine the gain response of the system. A Keysight 33612A AWG and Keysight MSO-S 104A scope were used to perform the measurements. The AWG was used to produce a broadband chirp signal, Fig (b), with 15MHz centre frequency and 30MHz bandwidth, allowing practical calibration over the range 1MHz to 29MHz.

Fig (c) shows the uncorrected time domain measurement performed by the UARP AFE. Due to the TX/RX switch and amplifiers in the front end, the response is distorted. Fig (e) shows the unfiltered frequency response of the AFE, from which an inverse correction filter was designed. Fig (d) and (e) show the measurement of the AFE in the time and frequency domain after the correction filter has been applied.

The presented results demonstrate how digital FIR filters can be used to correct the frequency response of the AFE in real-time using existing hardware FIR filters within the UARP ultrasound imaging system.



5:00 PM

A Power-Efficient Transmit Beamformer ASIC for 3-D Catheter-Based/ Endoscopic Probes

Zhao Chen¹, Eunchul Kang¹, Zu Yao Chang¹, Emile Noothout², Johan G. Bosch³, Martin D. Verweij^{2,3}, Nico de Jong^{2,3}, Michiel Pertijs¹

¹*Electronic Instrumentation Laboratory, Delft University of Technology, Delft, Netherlands*, ²*Laboratory of Acoustical Wavefield Imaging, Delft University of Technology, Delft, Netherlands*, ³*Biomedical Engineering, Thorax Center, Erasmus MC, Rotterdam, Netherlands*

Background, Motivation, and Objective

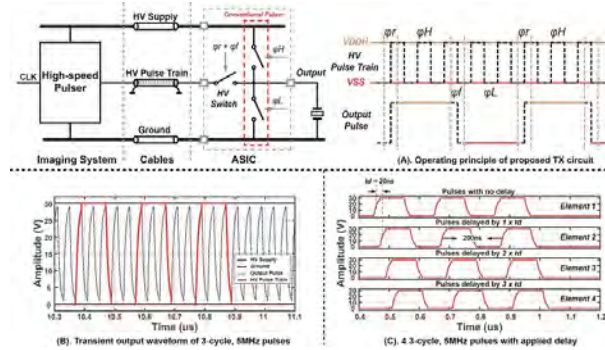
To reduce cable count in 3D catheter-based or endoscopic probes, generation of the (HV) transmit (TX) signals using an in-probe ASIC is a promising solution. However, such ASICs are subject to stringent power-consumption constraints to limit self-heating. The power consumed by conventional HV pulsers is at least fCV^2 , due to the periodic charging/discharging of the transducer element capacitance C. HV switches can be used to connect elements to a pulser in the imaging system, thus only dissipating a fraction of fCV^2 in the probe, but full TX beamforming (BF) cannot be realized using switches. In this work, we propose a power-efficient HV TX circuit capable of providing full TX BF using only 3 HV connections to the system. Implemented in a 0.18um BCD process, the ASIC was fully evaluated by means of post-layout simulations.

Statement of Contribution/Methods

Fig. (A) illustrates the concept of the proposed TX circuit: it combines a conventional pulser and a HV switch. The switch is connected to a high-speed pulse train from the system, which is pulsed at an integer multiple of the output pulse frequency. The output pulse is composed by connecting the output to the pulse train to realize the rising and falling edges, and clamping it to the HV supply and ground in between. Thus, the majority of the fCV^2 is dissipated in the system, strongly reducing the in-probe dissipation. The delay resolution is determined by the frequency of the pulse train. To realize 2× better delay resolution, two complementary pulse trains are used by adding a duplicate switch path. The realized ASIC thus generates 30V, 5MHz pulses with 20ns delay resolution, from a 30V supply and two complementary 30V pulse trains at 25MHz.

Results/Discussion

Fig. (B) shows the simulated output waveform of 30V, 3-cycle 5MHz pulses generated by the ASIC. The impact of the bandwidth limitation associated with the capacitance of the cables connecting the probe to the system is included in this simulation. When loaded by a 10pF transducer capacitance, and continuously pulsing at 5MHz, the proposed TX circuit consumes only 21.47mW, compared to 67.2mW for a conventional pulser. The BF function is verified by having 4 TX circuits generating 3-cycle pulses with 20ns delay step (Fig. (C)). Compared to conventional pulsers, the proposed TX circuit realizes a 3× power-reduction while still achieving a 20ns delay resolution when pulsing at 5MHz.



5:15 PM

Modified Harmonic Reduction Pulse Width Modulation (mHRPWM) for Switched Excitation of Resonant HIFU Transducers

David Cowell¹, Christopher Adams¹, Thomas Carpenter¹, Steven Freear¹

¹School of Electronic & Electrical Engineering, University of Leeds, Leeds, United Kingdom

Background, Motivation, and Objective

Compact and efficient excitation systems are desirable for high intensity focused ultrasound (HIFU) therapy arrays. Control of amplitude, frequency and phase are required for apodization and beamforming. HIFU transducers are typically highly resonant at their fundamental and low order harmonics. As such waveform distortion must be minimised to reduce disruption of the focal region.

Harmonic reduction pulse width modulation (HRPWM) has facilitated the design of waveforms with amplitude control and suppression of the third harmonic. However the high voltage and low channel resistance transistors required for HIFU excitation have slow switching times that impose limitations on waveform designs. This work defines a systematic modification to HRPWM to create waveforms that are compatible with the speed restrictions.

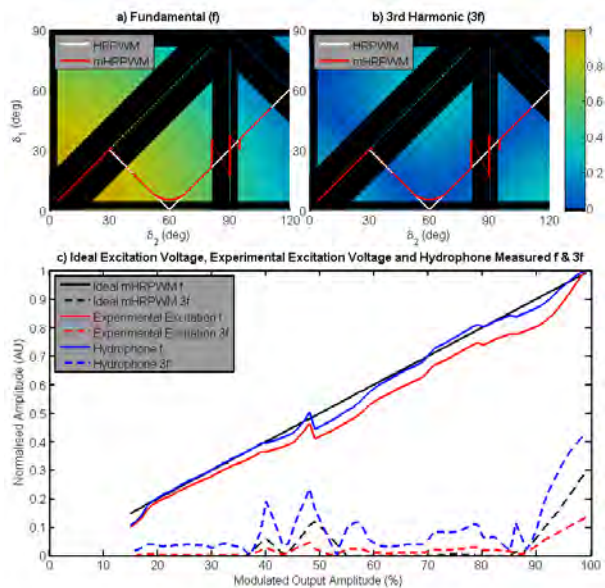
Statement of Contribution/Methods

Figures a) and b) illustrate the fundamental and third harmonic amplitudes using symmetric three or five level excitation. The switched waveforms are defined by δ_1 and δ_2 where δ_1 describes the phase of switching between ground and mid rails, and δ_2 between mid and full voltage rails. The white line indicates the modulation path of HRPWM with full amplitude control where 3rd harmonics are minimised.

The black regions are system dependent solutions that violate the dead time or minimum pulse width requirements of the transistors used. The full range of amplitudes on the standard HRPWM path cannot always be generated. By modifying the path to avoid these inaccessible regions, the modified HRPWM (mHRPWM) scheme, shown on fig (a) and (b) in red, regains full amplitude control using a combination of three-level and five-level-HRPWM waveforms, whilst still reducing the third harmonic at each amplitude compared with standard PWM techniques.

Results/Discussion

The proposed mHRPWM scheme was experimentally tested using the University of Leeds HIFU Array Research Platform (HIFUARP) as a switched excitation source for a H-102 transducer (Sonic Concepts, USA) with a 44 um membrane hydrophone (Precision Acoustics, UK) aligned at its natural focus. Fig (c) shows the oscilloscope (MSOS104A, Keysight, USA) measured excitation voltage plus hydrophone output voltage. The amplitude is shown to be controllable from 15-100% whilst minimising harmonics in the excitation waveform to at worst -17dB below the fundamental.



1H - Shear Wave Methods I

Topaz (400)

Thursday, October 25, 8:00 am - 9:30 am

Chair **Matthew Urban**
Mayo Clinic

1H-1

8:00 AM Ultrasound Shear Wave Elastography of Viscoelastic Media Using Local Phase Velocity Based Imaging (LPVI) Approach

Piotr Kijanka^{1,2}, Matthew Urban^{1,3}

¹Department of Radiology, Mayo Clinic, Rochester, MN, United States, ²Department of Robotics and Mechatronics, AGH University of Science and Technology, Krakow, Poland, ³Department of Physiology and Biomedical Engineering, Mayo Clinic, Rochester, MN, United States

Background, Motivation, and Objective

Assessment of soft tissue elasticity and viscosity is of interest in several clinical applications. Therefore, we present a new technique called local phase velocity based imaging (LPVI) to create images of phase velocity in viscoelastic soft tissues. The motivation is to provide an estimate of tissue elasticity and viscosity based on shear wave elastography.

Statement of Contribution/Methods

A focused acoustic radiation force push beam was used to produce a broadband propagating shear wave. A local phase velocity is then recovered from the acquisition. First, a wave mode isolation using narrow bandpass filter and directional filtering, is performed. Then, the spatio-temporal particle motion is transformed to the temporal frequency-domain via a one-dimensional (1D) Fourier transform (FT). Next, for a specified frequency, a short space two-dimensional (2D) FT is executed by multiplying the wavefield with a window function which is non-zero for only a small area in space. Then a 2D FT is applied on the windowed wavefield, resulting in a set of 2D wavenumbers. The peak in the wavenumber distribution is then identified in this plane and the phase velocity is calculated. Finally, a 2D shear wave velocity map is reconstructed by sliding the window over the whole domain. Based on the frequency-dependent shear wave speed maps, the elasticity and viscosity maps are deduced using a nonlinear least-squares curve fitting. The proposed method was tested on simulated data sets of numerical viscoelastic phantoms for which mechanical properties are known, a commercial viscoelastic elastography phantom and an *ex vivo* porcine liver.

Results/Discussion

Using the LPVI approach 2D shear wave phase velocity maps were reconstructed for the *ex vivo* porcine liver [Fig. 1]. By testing the LPVI method on simulated data sets and performing *ex vivo* experiments, we show that the ability of the proposed technique to generate phase velocity maps of the viscoelastic material properties are robust [Fig. 1c]. An increase in phase velocity with increasing frequency is observed [Fig. 1a] in the same manner as for a classical 2D-FT based method [Fig. 1c]. The LPVI technique opens new possibilities for noninvasive imaging and characterization of pathologies of viscoelastic tissues.

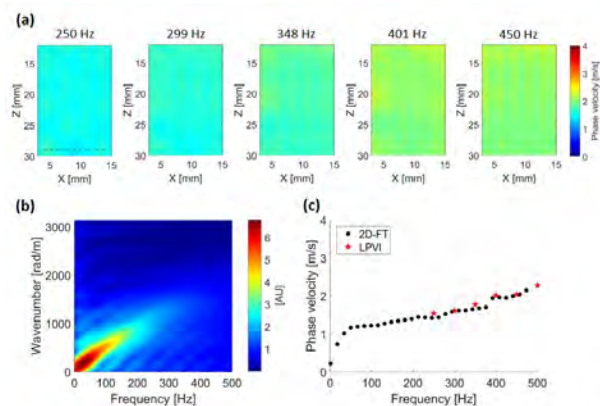


Figure 1. Two-dimensional shear wave phase velocity maps for a selected frequencies, for an *ex vivo* porcine liver (a). A 2D-FT based wavenumbers (b) and a phase velocity (c) reconstructed from (a) for a focused beam position. In (c) black dots represent data for 2D-FT and red markers represent a mean phase velocity evaluated from the LPVI results from a region-of-interest marked in first image of (a).

8:15 AM

Ultrasound Shear Wave Elastography of Small Inclusions Using Local Phase Velocity Based Imaging (LPVI) Approach

Piotr Kijanka^{1,2}, Matthew Urban^{1,3}

¹Department of Radiology, Mayo Clinic, Rochester, MN, United States, ²Department of Robotics and Mechatronics, AGH University of Science and Technology, Krakow, Poland, ³Department of Physiology and Biomedical Engineering, Mayo Clinic, Rochester, MN, United States

Background, Motivation, and Objective

Among the various methods used for shear wave elastography there are numerous techniques for reconstructing the mechanical properties. Most methods are based on measuring the time-of-flight of the shear wave in a local sense. Another way to estimate the shear wave velocity uses frequency-domain approaches. Here we present a method called local phase velocity based imaging (LPVI) to create images of phase velocity in soft tissues. The motivation is to create an optimal method to reconstruct the shear wave velocity of small inclusions in the frequency-domain without overestimating lesion dimension.

Statement of Contribution/Methods

Two separate acquisitions with acoustic radiation force push beams focused once on the left side and once on the right side of the inclusion were generated to produce a transient displacement. A local shear wave velocity is then recovered in the frequency-domain for both acquisitions. First, the spatio-temporal particle motion is transformed to the temporal frequency-domain using the 1D Fourier transform (FT). Then, for a particular frequency, a short space 2D FT is performed. The wavefield is multiplied by a window function which is non-zero for only a small area in space. Then a 2D FT is applied on the windowed wavefield, resulting in a set of 2D wavenumbers. The peak in the wavenumber distribution is then identified in this plane and the phase velocity is calculated. Ultimately, a 2D shear wave velocity map is reconstructed by sliding the window over the whole domain and combining maps from two separate acquisitions. Images at different frequencies can be reconstructed using a similar approach. A calibrated elastography phantom with stepped cylinder inclusions and a homemade gelatin phantom with an *ex vivo* porcine liver inclusion were used to test the LPVI method.

Results/Discussion

Using the LPVI approach 2D shear wave phase velocity maps were reconstructed at 1050 Hz [Fig. 1]. The proposed technique provides less shape distortions of reconstructed inclusions in comparison to the group velocity based method (comb-push ultrasound shear elastography, CUSE). The contrast-to-noise ratio for the LPVI method was 43, 36 and 26 dB whereas, for the CUSE method it is 35, 39 and 15 dB, for the inclusions size of 6.49, 4.05 and 2.53 mm, respectively. The LPVI method provides images of phase velocity that have strong contrast for small inclusions.

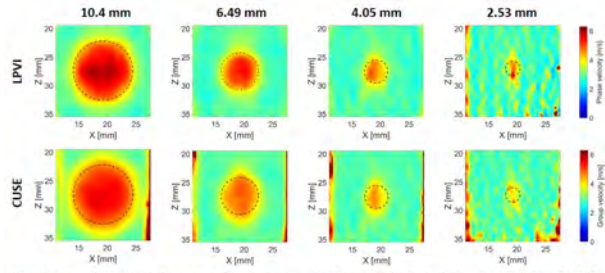


Figure 1. Two-dimensional shear wave phase and group velocity images for the inclusion size of 10.40, 6.49, 4.05 and 2.53 mm diameter, respectively. Phase velocity images were calculated with the LPVI approach whereas, group velocity maps are obtained from the CUSE method. The selected frequency used for the calculations was equal to 1050 Hz. Dashed lines present the true inclusion location as determined from the B-mode image.

8:30 AM

Enhanced Shear Wave Elastography for HIFU Monitoring of Stiff Uterine FibroidsSua Bae¹, Pilsu Kim¹, Kidong Kim², Jiyeoun Jeong², Tai-kyong Song¹¹*Department of Electronic Engineering, Sogang University, Korea, Republic of*, ²*Department of Obstetrics & Gynecology, Seoul National University Bundang Hospital, Korea, Republic of***Background, Motivation, and Objective**

High-intensity focused ultrasound (HIFU) therapy of uterine fibroids is now widely used in clinics and shear wave elastography (SWE) is one of the promising techniques for evaluation of thermal lesions. However, SWE for uterine fibroid requires high signal-to-noise ratio (SNR) and high frame rate (FR) since most of the uterine fibroids have complex structures and are stiffer than other tissues (i.e., higher shear wave speed). In coherent plane wave (PW) compounding, increasing the number of PW angles, N , enhances the SNR but also causes a decrease in effective FR. In this paper, we proposed a simple SWE method to increase the SNR without compromising the FR.

Statement of Contribution/Methods

Fig. 1(a) illustrates the proposed method in which N push-track sequences are repeated and one of the N angles is used for tracking in each sequence. Plane wave images which are captured with the same delay from the time of push are compounded and used for detection of shear wave motion. Therefore, the FR is not reduced after compounding and thus the N can be increased for SNR enhancement without decreasing the FR.

To evaluate its performance, SWE images of phantoms were acquired with an ultrasound system (Vantage 128, Verasonics) and an L7-4 array (Philips) using three methods; conventional one with 3 angles, proposed one with 3 angles, and proposed one with 21 angles (angle interval = 1.8°). In addition, to demonstrate its feasibility, three human uterine fibroid samples were thermally ablated by HIFU and their SWE images before and after HIFU were obtained using the proposed method ($N = 21$) in the setup of Fig. 1(b).

Results/Discussion

Fig. 1(c) shows that, compared to the conventional method, the proposed one provides higher SNR and better SWE images even when $N = 3$. This is because, in the proposed method, the plane wave images with exactly the same delay from the push were compounded, and the FR of compounded images was maintained.

In Fig. 2(d), thermal lesions inside the fibroid samples are well reconstructed in spite of such high stiffness, which demonstrates the feasibility of the proposed method for monitoring of uterine fibroid HIFU. In clinics, motion artifacts may be introduced but it will not be serious because the uterus is relatively less affected by breathing motion and the total data acquisition time for $N = 21$ was only 0.14 msec due to the fast shear wave speed.

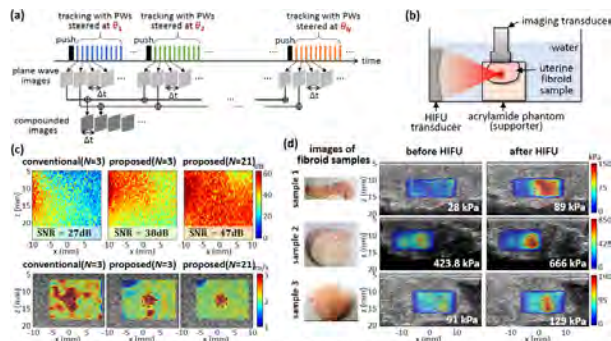


Fig. 1 (a) TX configuration and plane wave compounding of the proposed method (b) ex-vivo experimental setup (c) shear wave SNR maps of a homogeneous phantom (top row) and shear wave speed maps of a inclusion-contained phantom (bottom row) reconstructed using conventional and proposed methods (d) images of uterine fibroid samples and elasticity maps of the samples before and after HIFU using the proposed method ($N = 21$)

8:45 AM Near-field effect on elastic wave propagation in shear wave elastography

Salavat Aglyamov^{1,2}, Susobhan Das³, Chen Wu³, Kirill Larin^{3,4}¹*Mechanical Engineering, University of Houston, Houston, TX, United States*, ²*Biomedical Engineering, University of Texas at Austin, Austin, TX, United States*, ³*Biomedical Engineering, University of Houston, Houston, TX, United States*, ⁴*Molecular Physiology and Biophysics, Baylor College of Medicine, Houston, TX, United States***Background, Motivation, and Objective**

Measurement of shear wave velocity for the determination of tissue mechanical properties has been used in soft tissue assessment and clinical diagnosis. The use of dispersion analysis permits the quantitative measurement of not only elastic, but also viscous properties of tissues in order to improve the quality of diagnosis. The usual assumption behind these quantitative methods is that the measurements are performed in a far field zone, where the effect of the source of the acoustic radiation force is negligible. In such cases the mechanical parameters can be evaluated using the model of shear wave propagation in infinite medium, or models of Rayleigh and Lamb waves on the surface. In practice, however, shear wave measurements are characterized by wavelengths that are often comparable to the source-receiver distance due to the fact that elastic waves in soft tissues attenuate very quickly. Because most measurements are performed near the focus of the acoustic beam, in this study, we investigate the effect of such a near-field configuration on wave propagation.

Statement of Contribution/Methods

We performed both theoretical and experimental studies to evaluate effect of a source on elastic wave propagation, and to estimate limitations of the far field assumption. Theoretical calculations were based on analytical and numerical models of shear and surface waves in a viscoelastic medium. In experimental studies, a combined ultrasound and OCT system was utilized to measure elastic wave propagation on the surface of agar-based phantoms of different concentrations. A 3.5 MHz single element transducer was used to generate surface waves in phantoms, and the phase-sensitive OCT system with an A-line acquisition rate of 30 kHz was utilized to measure displacement profiles.

Results/Discussion

Results demonstrated the dependence of the phase velocity on the distance between the source and the points of measurement, when measurements were performed in vicinity of the source. In addition, the effect of the source for surface wave propagation was more pronounced than for shear waves. As shown in Fig. 1, the dispersion of the surface waves in near-and far-fields can have significant difference in the low-frequency range, such that analysis of the wave dispersion should take into account the source influence.

This study was supported by National Institute of Health grants EY022362.

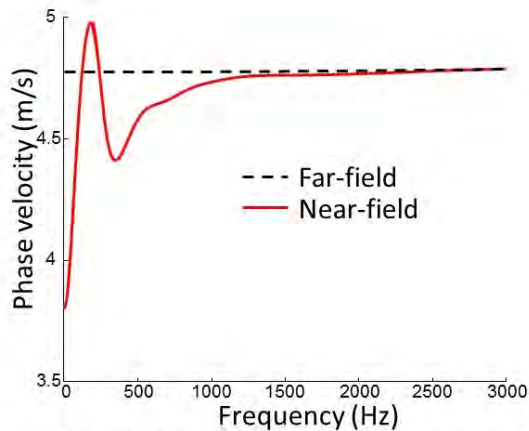


Fig.1 : Elastic surface wave dispersion in near-and far-field

9:00 AM

Cellquake elastography: applying shear wave elastography on cells

Pol Grasland-Mongrain^{1,2}, Ali Zorgani³, Shoma Nakagawa⁴, Simon Bernard^{2,5}, Lia Gomes Paim⁴, Greg FitzHarris⁴, Stefan Catheline³, Guy Cloutier²

¹*ENS de Lyon, Lyon, France*, ²*LBUM, CRCHUM, Université de Montréal, Montreal, QC, Canada*, ³*LabTAU, INSERM, Lyon, France*, ⁴*OBGYN, CRCHUM, Université de Montréal, Montreal, QC, Canada*, ⁵*LMA, Université Aix-Marseille, Marseille, France*

Background, Motivation, and Objective

Elasticity is a fundamental cellular property that is related to the anatomy, functionality and pathological state of cells and tissues. However, current techniques based on cell deformation, atomic force microscopy or Brillouin scattering are rather slow and do not always accurately represent cell elasticity. Shear wave elastography method, developed at the organ scale, could be adapted at the cellular level to get quick and robust measurements.

We aimed then to demonstrate the feasibility of the shear wave elastography technique on cells.

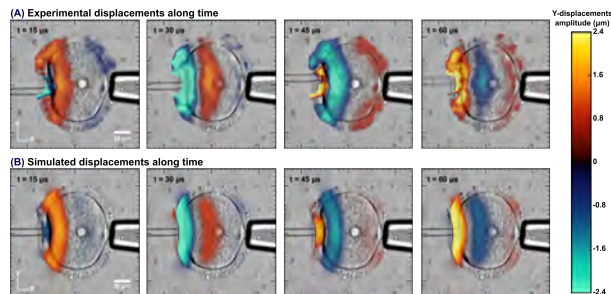
Statement of Contribution/Methods

In our study, a 80 μm diameter mouse oocyte was held by a pipette. Elastic waves were mechanically induced in live mammalian oocytes using a vibrating micropipette fixed to a 15 kHz piezoelectric actuator. The cell was observed with a 200,000 frames/second optical camera attached to a $\times 100$ microscope. Displacements were tracked with a Lucas-Kanade optical flow method. Whole cell elasticity was finally mapped using a passive elastography method.

Results/Discussion

Using this approach, we show that (1) shear waves have been successfully induced in the oocyte, with a good agreement between experimental and simulated results, (2) whole cell elasticity can be computed from the induced shear waves using passive elastography, and (3) as expected, elasticity of mouse oocyte is significantly ($p < 0.02$) decreased when the oocyte cytoskeleton is disrupted with cytochalasin B, a softening toxin.

The technique is fast (less than 1 ms for data acquisition), precise (spatial resolution of a few micrometers), able to map internal cell structures, robust, and thus represents a tractable novel option for interrogating biomechanical properties at the cellular scale.



9:15 AM

Dispersion analysis of guided waves in bounded media induced by acoustic micro-tapping

Liang Gao¹, Mitchell Kirby¹, Łukasz Ambroziński², Shaozhen Song¹, David Li³, Ivan Pelivanov¹, Ruikang Wang^{1,4}, Matthew O'Donnell¹

¹Bioengineering, University of Washington, Seattle, WA, United States, ²AGH University of Science and Technology, Krakow, Poland, ³Chemical Engineering, University of Washington, Seattle, WA, United States, ⁴Ophthalmology, University of Washington, Seattle, WA, United States

Background, Motivation, and Objective

Broadband mechanical waves in soft tissue can be generated in different ways [M. Kirby et al., J. Biomed. Opt. 22 (2017)]. Ultrafast phase sensitive OCT can track their propagation along the tissue surface and at shallow depths with great sensitivity, potentially enabling elastic modulus reconstruction in soft tissues such as cornea and skin.

However, the relationship between wave speed and elastic modulus is often complicated by sample geometry, boundary conditions, and excitation parameters. For example, wave propagation in cornea is guided and, in general, consists of multiple highly dispersive modes [M. Kirby et al., J. Biomed. Opt. 22 (2017)] (Fig. 1a). Thus, reconstruction of Young's modulus is not as simple as for the bulk case.

Statement of Contribution/Methods

Here we demonstrate the analytical solution for mechanical wave propagation in bounded materials, and perform numerical simulations and direct experiments to explore how elastic moduli of bounded tissues can be obtained from experimentally measured wave velocity data.

The influence of tissue viscosity as well as a curved medium geometry (in case of cornea) is also explored.

Numerical simulations were performed on the COMSOL platform.

A fully non-contact OCE system including AμT (launching broadband mechanical waves in tissues with ~ 1 MHz focused ultrasound through air [L. Ambrozinski et al., Scientific Reports 6 (2016)]) and ultrafast phase sensitive OCT is employed for all experiments. Both gelatin phantoms and ex-vivo porcine cornea samples were used.

Results/Discussion

Figures 1(b, c, d, e) show an example of time-space propagation of the mechanical wave in a 1.5 mm layer bounded on one side by a liquid and on the other side by air. Two modes are clearly visible. Note that simple Young's modulus reconstruction based on the group velocity, as in the majority of studies, produces serious errors. In contrast, broadband generation and detection of mechanical waves with accurate measurement of dispersion curves can be used to determine the high-frequency velocity asymptote that is simply related to the modulus. The proposed method has high potential for in-vivo studies utilizing OCE.

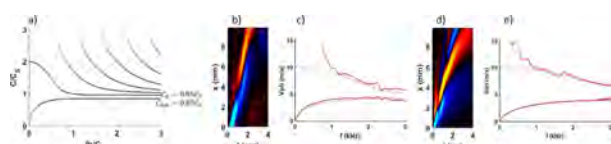


Figure 1. a) - Phase velocity dispersion for guided waves in a layer of incompressible medium bounded on one side by a liquid and on the other side by air; b) - XT plot of wave propagation along the surface of a 1.5mm gelatin phantom (experimental data); c) - dispersion curves calculated from the XT plot (red) and theoretical value (black); d) - XT plot obtained with simulation for a 1 mm gelatin layer; e) - dispersion curves calculated from the simulated XT plot(red) and theoretical value (black)

II - Shear Wave Methods II

Topaz (400)

Thursday, October 25, 10:30 am - 12:00 pm

Chair **Kathy Nightingale**
Duke University

II-1

10:30 AM Feasibility of monitoring HIFU treatments by passive elastography

Bruno Giammarinaro¹, Paul Greillier¹, Stefan Catheline¹, Cyril Lafon¹

¹*LabTAU, INSERM, Centre Léon Bérard, Université Lyon 1, Lyon, France*

Background, Motivation, and Objective

High Intensity Focused Ultrasound (HIFU) methods are known to allow ablation in deep tissues. However, monitoring the treatment is required to control limitations due to ultrasound propagation. Previous studies have demonstrated that the formation of lesion creates a change in tissue elasticity properties which can be observed by elastography. In soft tissues, the elasticity can be estimated in measuring the shear wave velocity. Most of these studies have been performed with shear waves created by acoustic radiation force, leading to some difficulties to measure deep tissue elasticity. However, in the human body, there is a natural noise due to, for examples, cardiac activities or arterial pulsatility. Passive elastography can estimate the shear elasticity from this wave field and it only depends on imaging techniques, allowing to measure elasticity of deep tissues. The objective of the present study is therefore to study the feasibility of the HIFU monitoring by passive elastography in soft tissues.

Statement of Contribution/Methods

For that purpose, a probe composed of 5 MHz 64-elements commercial imaging transducer and a 3-MHz HIFU transducer was used. The HIFU part was a spherical transducer with a 40 mm radius of curvature, divided into 8 elements permitting a 17-55 mm dynamic range. Lesions were produced *in vitro* in swine liver and heart samples with a 5 min sonication at 7 to 10.5 W.cm⁻² acoustic intensity on the transducer surface (35 % of duty cycle and 0.6 Hz of pulse repetition frequency). Imaging probe was used with a ultrasound scanner Vantage 256 (Verasonics Inc., Kirkland, USA) which allowed high frame rate ultrasound acquisitions between 700 and 1000 Hz. These acquisitions were obtained before and after lesion production using diverging wave emissions with 5 angles compounding. Sum-and-delay method was performed to beamform raw ultrasound data and shear-wave displacements were estimated by a speckle tracking algorithm. Passive elastography map was computed according to Catheline et al. (APL, 2013). Artificial shear-waves were produced by an external vibrator fixed on the sample holder with frequency sweep between 50-500 Hz.

Results/Discussion

Seven lesions were created and were visible on elastography maps, showing a tissue stiffening in the targeted area. In liver samples, shear waves velocity increased from $1.89 \pm 0.44 \text{ m.s}^{-1}$ to $6.04 \pm 1.36 \text{ m.s}^{-1}$ after sonication. In heart samples, it changed from $3.8 \pm 1.8 \text{ m.s}^{-1}$ to $7.35 \pm 3.34 \text{ m.s}^{-1}$. The comparison of the lesions dimensions measured macroscopically and by elastography showed average differences of -1.2 mm in length and 0.6 mm in width in the imaging plane. Observation of thermal lesions on macroscopic view and on shear wave velocity maps demonstrates the feasibility of monitoring HIFU treatments by passive elastography in *in vitro* tissues.

Work supported by the ANR, the FUS Foundation and Banque Publique d'Investissement (PIA, PSPC 2015)

10:45 AM

Real-time X-Plane Shear Wave Elastography Feasibility on Philips 2D xMatrix Transducer

Man Nguyen¹, Sheng-Wen Huang¹, Shiwei Zhou², Changhong Hu³, Nik Ledoux², Bernard Savord², Vijay Shamdasani³, Hua Xie¹

¹Philips Research North America, Cambridge, MA, United States, ²Philips Healthcare, Andover, MA, United States,

³Philips Healthcare, Bothell, WA, United States

Background, Motivation, and Objective

Though ultrasound shear wave elastography (SWE) has become a clinically accepted diagnostic tool for non-invasive tissue quantification, multi-planar stiffness measurement can only be carried out mechanically, suboptimal for characterizing anisotropic tissues such as musculoskeletal (MSK) tissue, myocardium, and arterial wall. In those applications, a 2D matrix array with large acoustic aperture, that provides both electronic 3D capability and high B-mode image quality, is preferred from workflow and standardization points of view. This study takes ultrasound SWE one step further onto a 2D matrix transducer, opening opportunities for characterizing anisotropic tissues. We demonstrated the feasibility of real-time X-plane elasticity quantification on a Philips commercial 2D vascular transducer (XL14-3).

Statement of Contribution/Methods

An XL14-3 was modified to support effective acoustic push-pulses (Fig. 1a). 2D push apertures for different depths were optimized by acoustic radiation force simulation and hydrophone measurement. SWE pulse sequence and post-processing were designed based on geometry, frequency, and imaging planes. Real-time elasticity point measurement was enabled on XL14-3 in X-plane consisting of a rectangular FOV (A-plane) and a virtual-convex FOV (B-plane) perpendicular to each other. We evaluated quantification performance on CIRS elasticity phantoms and ex-vivo porcine tenderloin tissue, as well as benchmarked the prototype against released elastography products on Philips C5-1 and eL18-4.

Results/Discussion

Our experimental results showed comparable elasticity measurements between the A- and the B-planes on CIRS isotropic elastic phantoms with stiffness ranging from 4 - 46 kPa (Fig. 1b). As anticipated, the measurements on ex-vivo sample indicated anisotropy of skeletal muscle, where shear modulus measured along the fiber is greater than that across the fiber (Fig. 1c). The results by XL14-3 also qualitatively agreed with those achieved by 2D shear wave imaging on an eL18-4 which was mechanically rotated between measurements (Fig. 1d). In summary, we demonstrated a SWE prototype capable of real-time X-plane point quantification on a Philips 2D xMatrix transducer suitable for characterizing anisotropic tissues. Future work includes performance optimization, circuit miniaturization, and clinical studies.

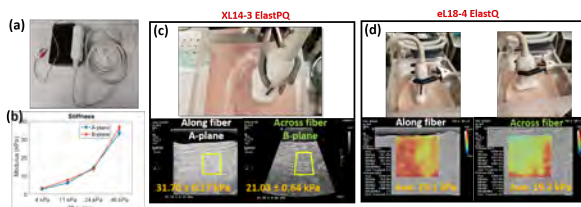


Figure 1. (a) Modified xMatrix vascular transducer XL14-3; (b) A-plane and B-plane measurements on CIRS phantoms; Experiment results on porcine tenderloin tissue with (c) XL14-3 ElastPQ, and (d) eL18-4 ElastQ

11:00 AM 3D Shear Wave Elasticity Tomography based on Laser Speckle Contrast Imaging

Pei-Yu Chao¹, Pai-Chi Li¹¹National Taiwan University, Taipei, Taiwan**Background, Motivation, and Objective**

3D elasticity imaging can be a valuable tool for disease characterization and mechanobiology. In our previous study, a 3D laser speckle contrast shear wave (LSC-SW) imaging system was developed, where a 3D elasticity image was reconstructed from multiple 2D elasticity images of different planes. In this report, a 3D SW tomographic imaging system is proposed, constructed and verified. In this system, projections of the SW wavefronts at different view angles are acquired. We hypothesize that visualization of the SW propagation in 3D can be realized by applying tomographic reconstruction algorithms on the projection data. Thus, the SW speed can be estimated along multiple directions. This approach can be applied to improve imaging of the mechanical properties of complex structures, and to provide a new tool for mechanobiology studies with 3D cell culture models.

Statement of Contribution/Methods

Propagation of the SW wavefront in a semi-turbid sample results in local blurring in the time-integrated speckle image of the sample. The speckle contrast is defined as $K = \sigma_s / \langle I \rangle$, where σ_s and $\langle I \rangle$ are the standard deviation and mean intensity of pixels within an image region. A 2-D speckle contrast map, which is obtained by computing speckle contrast of the speckle image using a kernel size of $160 \times 160 \mu\text{m}$, is thus a projection of the SW wavefront. By obtaining projections of the SW wavefront at different view angles, the 3D SW wavefront can be reconstructed using a tomographic approach.

Results/Discussion

A setup of the LSC-SW tomographic imaging system is illustrated in Fig. 1(a). Fig. 1(b) shows the flowchart of data acquisition and post-processing. Fig. 1(c) shows the projections of the SW wavefront, after a propagation time of 0.1, 0.7 and 1.3 ms, induced by an ultrasound transducer that was located at 0° to 355° around a homogeneous 0.6% agarose phantom. As shown in Fig. 1(d), the reconstruction of the 3D SW wavefront can be achieved by applying back-projection algorithm on the respective projection data. The SW speed estimated from the spatiotemporal map computed along Y-direction is 2.14 m/s, with an error of 3.6%. The volumetric reconstruction of the SW speed of the sample can be obtained by adopting a TOF algorithm along different SW propagation directions. More results will be presented in the full report.

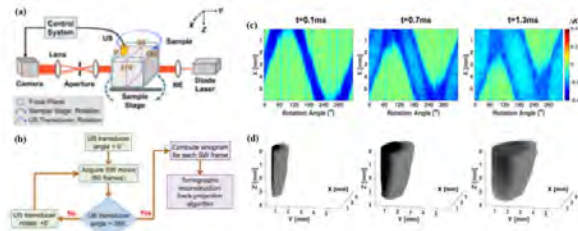


Fig. 1(a) Schematic of the imaging system and 1(b) data acquisition and post-processing flowchart. 1(c) Projections of SW wavefront acquired with the ultrasound transducer rotated from 0° to 355° , and 1(d) reconstructed SW wavefront, with a propagation time of 0.1ms, 0.7ms, and 1.3ms, using the back-projection algorithm.

11:15 AM

3-D Speckle Tracking with Two-Pass Searching and Phase-Rotated Correlation Filtering

Geng-Shi Jeng¹, Maria Zonak², Ivan Pelivanov¹, Nripesh Parajuli³, Allen Lu³, Kevinminh Ta³, Albert J. Sinusas³, James S. Duncan³, Matthew O'Donnell¹

¹Bioengineering, University of Washington, Seattle, WA, United States, ²Northeastern University, United States, ³Yale University, United States

Background, Motivation, and Objective

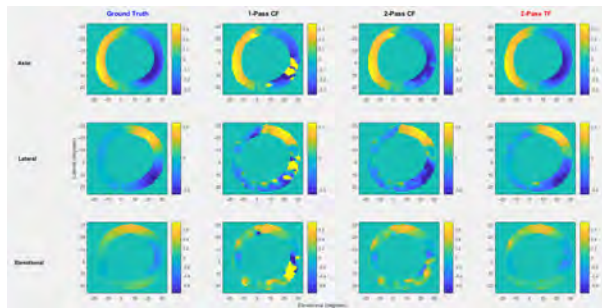
In 3-D cardiac elasticity imaging, speckle decorrelation due to low volume rates (i.e., large interframe motion) increases the possibility of detecting false secondary peaks of the normalized cross-correlation coefficient (NCC). We previously proposed a two-pass tracking approach where a randomized searching (i.e., PatchMatch) is employed in the first pass. The second pass uses conventional block matching with a tiny search region, followed by correlation filtering (CF). The peak hopping artifact is improved by a factor of 3 while reducing the computational load by 10. However, under high strain and rotational motion, the performance is limited because the true NCC peaks along the axial direction are misaligned at constant lag. When a CF is applied to NCCs at adjacent voxels, phase cancellation increases peak hopping artifacts. The purpose of this paper is to address such phase misalignment by employing a 3-D phase rotation technique (called tilt filtering, TF) associated with three spatial gradients in the axial displacement.

Statement of Contribution/Methods

Phases of successive NCCs along the axial direction under strain-induced deformation are approximately a linear function of lag, with frequency shifts equal to the three spatial derivatives of the axial displacement component. Thus, phase rotation can be applied to ensure phase alignment prior to CF provided that the strains are known in advance. Without an initial strain guess, we propose an autocorrelation method where three related strain components are estimated analogous to conventional Doppler mean frequency estimation.

Results/Discussion

Simulated and *in vivo* canine cardiac datasets were evaluated to estimate interframe displacements. Figure 1 shows the simulated result at end-systole where one-pass tracking with CF (2nd column), two-pass tracking with CF (3rd), and the proposed two-pass tracking with TF (4th) are compared with ground-truth displacements (1st). The axial displacement is in mm whereas lateral and elevational ones are in degrees. By evaluating from end-diastole to end-systole periods, improvements using TF over CF based on two-pass tracking are a factor of 1.3, 1.3, and 2.2 for lateral, elevational, and axial displacement components, respectively.



11:30 AM **Passive elastography: a seismic imaging of soft tissues**

Stefan Catheline¹

¹*LabTAU*

Background, Motivation, and Objective

Elastography, sometimes referred as seismology of the human body, is an imaging modality recently implemented on medical ultrasound systems. It allows to measure shear waves within soft tissues and gives a tomography reconstruction of the shear elasticity. This elasticity map is useful for early cancer detection. A general overview of this field is given in the first part of the presentation as well as latest developments. The second part, is devoted to the application of time reversal or noise correlation technique in the field of elastography. The idea, as in seismology, is to take advantage of shear waves naturally present in the human body due to muscles activities to construct shear elasticity map of soft tissues. It is thus a passive elastography approach since no shear wave sources are used. In the third part some examples are provided using ultrasounds, MRI or optic to detect shear waves and reconstruct a speed tomography in a human liver, thyroid, brain, in a mouse eye and a single cell.

Statement of Contribution/Methods

1

Results/Discussion

2

1J - Deep Neural Networks for Ultrasound Image Formation

Topaz (400)

Thursday, October 25, 1:30 pm - 3:00 pm

Chair **Adrian Basarab**
University of Toulouse

1J-1

1:30 PM **Evaluating the Robustness of Ultrasound Beamforming with Deep Neural Networks**

Adam Luchies¹, Brett Byram¹

¹Biomedical Engineering, Vanderbilt University, Nashville, TN, United States

Background, Motivation, and Objective

In the past, our group developed a model based beamforming method, called ADMIRE, with the goal of reducing the effects of clutter (e.g., off-axis scattering, etc.) on B-mode image quality. ADMIRE also demonstrated that beamforming can be posed as a nonlinear regression problem. Deep neural networks (DNN) can be used to solve nonlinear regression problems, most of the computation is completed during the training phase, and the inference (application) phase can be fast. Recently, we investigated using DNNs for ultrasound beamforming and were able to improve experimental ultrasound scans using DNNs trained with simulated training data.

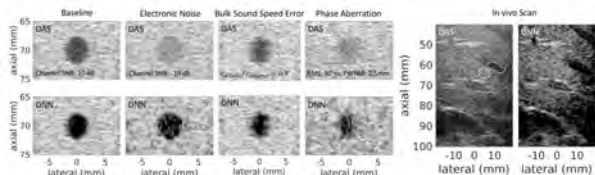
Statement of Contribution/Methods

For this work, we investigated the robustness of DNN beamforming to several common sources of image degradation, including electronic noise, bulk sound speed errors, and phase aberration. The DNNs were only trained to suppress off-axis scattering using simulated training data that consisted of the combined responses from one, two, or three point targets. Image contrast was measured when varying channel SNR, including error in the assumed sound speed, or introducing phase aberration using a near field phase screen in five simulated anechoic cysts. The DNNs were not trained to correct these sources of image degradation. The liver of a healthy individual was also scanned to demonstrate *in vivo* image quality improvements.

Results/Discussion

We studied image quality for various levels of image degradation, but we report the most extreme realizations in the included Table and Figure. For the included *in vivo* scan, the contrast-to-noise ratio (CNR) for delay-and-sum (DAS) and DNN beamforming were 4.3 dB and 5.0 dB, respectively. Overall, these results show that DNN beamforming is robust to the examined sources of image degradation.

| Degradation | Description | CNR (dB) | |
|------------------------|---|----------|---------|
| | | DAS | DNN |
| Baseline | 10 dB Channel SNR | 5.0±0.1 | 5.4±0.1 |
| Electronic Noise | -10 dB Channel SNR | 1.9±0.1 | 4.1±0.3 |
| Bulk Sound Speed Error | Assumed sound speed was 10% larger than the actual sound speed. | 4.7±0.3 | 4.9±0.2 |
| Phase Aberration | 2.5 mm FWHM and 30 ns RMS | 0.8±1.1 | 2.9±0.5 |



1:45 PM Beamforming and speckle reduction using deep neural networks

Dongwoon Hyun¹, Leandra Brickson², Kevin Looby¹, Jeremy Dahl¹

¹*Department of Radiology, School of Medicine, Stanford University, Palo Alto, CA, United States*, ²*Stanford University, United States*

Background, Motivation, and Objective

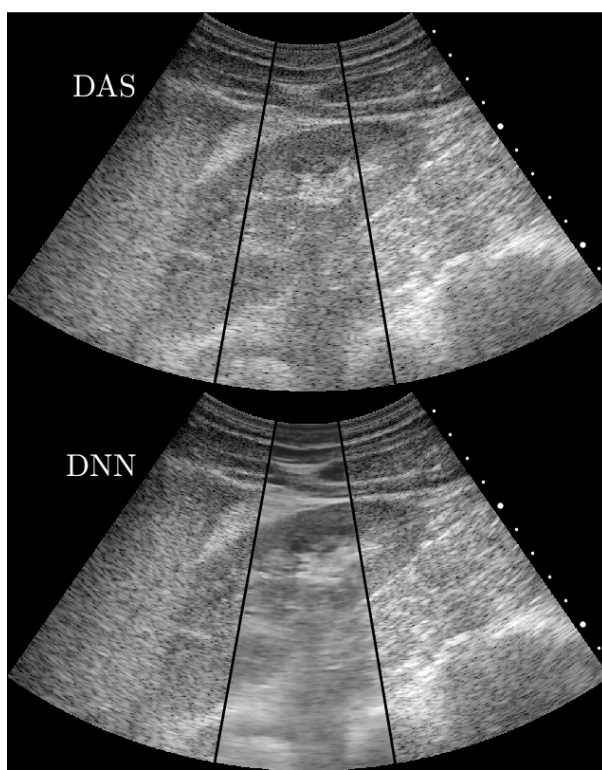
B-mode images contain speckle noise caused by the random interference of diffuse subresolution scatterers. Although speckle-reducing beamforming methods exist (e.g., spatial and frequency compounding), speckle reduction is often performed after beamforming using filtering techniques, such as anisotropic diffusion or non-local means. Recently, deep neural networks (DNNs) have demonstrated excellent performance across a wide variety of tasks, such as image classification and segmentation. In this work, we introduce a framework to utilize DNNs to beamform channel signals into speckle-reduced B-mode images.

Statement of Contribution/Methods

A fully convolutional DNN was trained to learn the beamforming mapping from focused channel signals to speckle-free B-mode images. The DNN was trained using 5000 Field II Pro simulations of channel signals from an L12-3v transducer and the corresponding maps of true echogenicity. The DNN was trained to minimize a novel ultrasound-specific loss function capable of handling images with high dynamic range and arbitrary units. Training performance was assessed versus loss function, network depth, and network width. The trained DNN was tested on simulations, in a phantom with a Verasonics Vantage 256 scanner, and *in vivo* with a Siemens S2000 scanner. Image quality was quantified using the pixel-wise error in echogenicity where ground truth was available and using speckle SNR in a homogeneous region otherwise. Performance was compared against delay-and-sum (DAS), receive spatial compounding (SC), and a nonlocal means (NLM) method.

Results/Discussion

The DNN trained most effectively using a combination of modified L1 and multi-scale structural similarity losses. The widest and deepest tested DNN had the best reconstruction errors (94% reduction in L2 error versus DAS in simulations). The DNN outperformed DAS and SC in speckle reduction and exhibited improved detail preservation over NLM in simulations, phantoms, and *in vivo*, achieving speckle SNRs of 11.0, 7.7, and 3.1, respectively. This work demonstrates that DNNs can be used for ultrasound beamforming and establishes that DNNs trained *in silico* can generalize to *in vivo* settings. Furthermore, we present live speckle-reduced imaging at 30 frames per second using a real-time implementation of the DNN beamformer on a Verasonics system.



2:00 PM Reverberation Noise Suppression in the Aperture Domain Using 3D Fully Convolutional Neural Networks

Leandra Brickson¹, Dongwoon Hyun², Jeremy Dahl³

¹*Electrical Engineering, Stanford University, Menlo Park, CA, United States*, ²*Department of Radiology, School of Medicine, Stanford University, Palo Alto, CA, United States*, ³*Radiology, Stanford University, CA, United States*

Background, Motivation, and Objective

Reverberation clutter is image noise resulting from multiple reflections between tissue layers and leads to image degradation. In addition, reverberation clutter diminishes the quality of the channel signals, thereby degrading the performance of techniques that require these aperture domain signals, such as phase aberration correction and adaptive beamforming. We propose a 3D fully convolutional neural network (FCNN) to selectively remove reverberation noise from ultrasound channel data.

Statement of Contribution/Methods

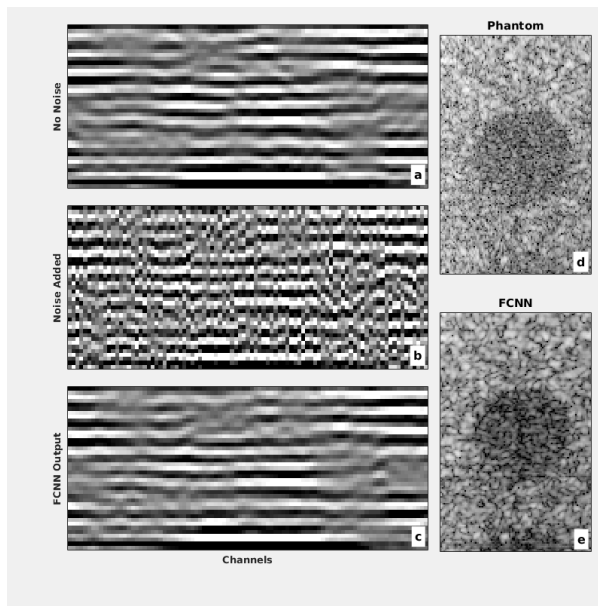
A 9,000 sample training set was generated using Field II Pro to simulate full synthetic aperture channel data. Reverberation noise was approximated by adding bandpass filtered noise to the noise-free simulated channel data. Thermal noise (range: -20 to 10 dB) was also added. Paired channel data, with and without noise, were used to train a 3D FCNN with a custom architecture to remove the reverberation and thermal noise. The input and output of this network are in the form of demodulated and time-delayed channel data.

After training, the network was evaluated with a 1,000 sample simulated test set with added reverberation noise varying between 10 and 20 dB. In addition, the network was tested on an ATS 549 phantom using a L12-3v transducer connected to a Verasonics Vantage 256 system. Steel wool was placed between the transducer and phantom to generate reverberation clutter.

Results/Discussion

Example channel data from one scanline of a simulated test set without and with reverberation noise are shown in figures a and b respectively. The noisy channel signals are input into the 3D FCNN to give the output shown in Figure c. The resulting image shows significant smoothing along the channels, and closely resembles the noiseless data, indicating that the network successfully removed the reverberation noise. Across the entire test set, the noisy dataset showed an increase in normalized correlation with the noise-free data from 0.69 to 0.92 after being decluttered using 3D FCNN.

Images generated from the phantom data channel signals before and after being passed through the network are shown in Figure d and e. The reverberation noise in the anechoic lesion has been suppressed, showing the network's ability to generalize to real data. In the images shown, the lesion CNR was increased from 1.12 to 1.23 and the lesion contrast was increased from -9.9 to -12.2 dB.



2:15 PM A fully convolutional neural network for beamforming ultrasound images

Arun Nair¹, Trac Tran¹, Muyinatu Bell¹

¹*Johns Hopkins, Baltimore, MD, United States*

Background, Motivation, and Objective

Plane wave ultrasound imaging is one of the fastest methods available to reduce latency for robotic tracking tasks, requiring multiple insonification angles to generate good image quality. However, the presence of acoustic clutter and speckle can confuse robot tracking algorithms. This work explores deep learning to extract information directly from the radiofrequency (RF) channel data [1] to locate targets, speed up existing acquisition rates, and provide suitable image quality with a single plane wave insonification angle.

Statement of Contribution/Methods

A fully convolutional neural network (FCN) was trained using 25,989 raw radiofrequency plane wave data created with Field II simulations of anechoic cysts. One plane wave was transmitted with a 0° insonification angle to image anechoic and -6dB contrast cysts. The cyst radius (2 - 8mm), axial position (40-70mm), lateral position (-10-10mm), and sound speed (1440 – 1640 m/s) was varied. We evaluated the network with held-out test sets of 6,498 anechoic cysts and 17, 199 -6dB hypoechoic cysts. We also tested with two 3 mm-radius, anechoic targets in a CIRS 054GS phantom at depths of 40mm and 70mm with 20 independent, single-angle plane wave acquisitions. An additional post-processing step was applied to suppress false positives by detecting and removing all connected components smaller than 120 pixels, which corresponds to cysts with radii ≤ 1 mm (a radius not included during training). Dice coefficients were measured to quantify overlap between true and FCN-determined cyst locations.

Results/Discussion

The mean Dice coefficient was 0.98 and 0.77 for the simulated anechoic and hypoechoic test sets, respectively. The 40 mm- and 70 mm-deep anechoic cysts in the phantom had B-mode image contrasts of -17dB and -9dB, respectively, and were segmented with mean Dice coefficients of 0.90 and 0.59, respectively, which agrees with the simulated data having better performance when cysts are closer to anechoic in the B-mode image. Images are presented in a new format that extracts information directly from the raw RF channel data, enabling us to ignore common degradations like acoustic clutter and speckle with a factor of 173 increase in speed and fewer transmits than traditionally required with plane wave imaging. Results are highly promising for autonomous robot tracking tasks.

[1] AA Nair, et al. IEEE ICASSP 2018

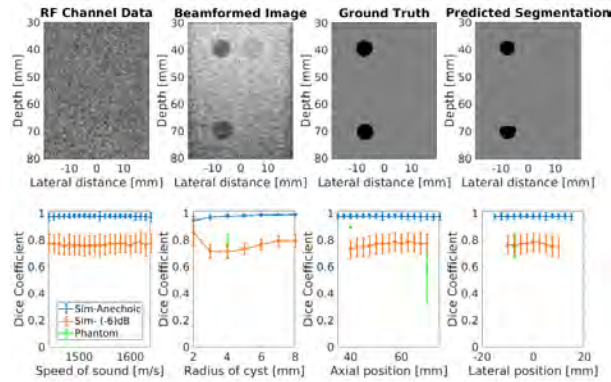


Fig. 1 Example segmentation predicted by the neural network and mean \pm one standard deviation of dice coefficients measured as a function of speed of sound, cyst radius, axial position and lateral position.

2:30 PM **Ultrasound image reconstruction using deep learning: a new paradigm**

Maxime Gasse¹

¹*Creatis Medical Imaging Research Centre*

Background, Motivation, and Objective

In the past few years, deep learning imposed itself as a disruptive technique that has been adopted in many scientific and industrial fields, along with a new problem-solving paradigm: machine learning. While the historical success of deep learning is grounded in natural image classification, remarkable results are regularly obtained on a wide range of tasks, e.g. image segmentation, object localization, speech synthesis, text-to-text translation, or game-playing. The medical imaging community naturally benefits from these recent advances, and deep learning is now a prominent tool for solving a wide range of problems, e.g. lesion detection, tumor grading, or tissue segmentation. It is only very recently that deep learning has been applied to image reconstruction in the context of ultrasound imaging, with promising results that outperform traditional approaches. In this context, the purpose of this talk is: i) to expose to the ultrasound imaging community the core ideas of deep learning (supervised learning, model architectures, back-propagation); ii) to highlight the difference between the analytical and the machine learning paradigms in the context of ultrasound imaging; iii) to show the great potential of this technique for ultrasound image reconstruction, with recent successes in learning PW compounding and beamforming models. We will conclude the talk by exposing some promising directions for deep learning in ultrasound imaging, as well as some typical problems and questions that arise with this new paradigm.

Statement of Contribution/Methods

1

Results/Discussion

2

1K - Fourier Beamforming and Passive Imaging

Topaz (400)

Thursday, October 25, 4:00 pm - 5:30 pm

Chair **Marvin Doyley**
University of Rochester

1K-1

4:00 PM

Implications of lag one coherence on real-time adaptive frequency selection

James Long¹, Will Long¹, Nick Bottenuis¹, Gianmarco Pinton², Gregg Trahey¹

¹Biomedical Engineering, Duke University, Durham, NC, United States, ²Joint department of biomedical engineering, University of North Carolina at Chapel Hill and North Carolina State University, NC, United States

Background, Motivation, and Objective

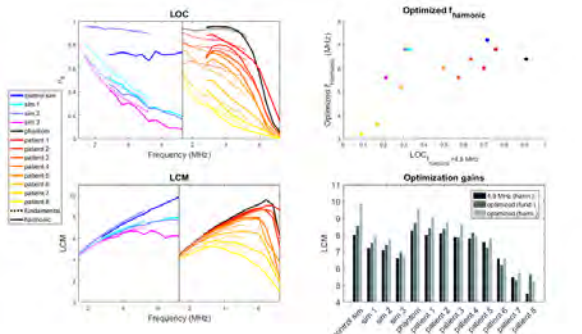
Abdominal image quality and measured spatial coherence have been shown to be degraded by the effects of phase aberration and reverberation. Optimal system configurations exist to minimize such sources of clutter, but there is currently no automated method by which parameters such as imaging frequency are selected. Adaptive imaging seeks to optimize these parameters using lag one coherence (LOC), a direct estimate of clutter levels *in vivo*, as a real-time feedback metric. The aim of this study is to determine the viability of using LOC to adaptively select imaging frequencies in the presence of clutter.

Statement of Contribution/Methods

Channel data were acquired using Fullwave simulations and Mast abdominal wall models, over a range of frequencies. LOC was calculated over a depth of field around the focus, for fundamental and harmonic receive cases. The lesion conspicuity metric (LCM), an image quality metric adapted from the work of Smith et al. 1983, was calculated using the LOC-estimated bounded contrast. The trends were compared to a control simulation with no abdominal wall, and phantom and *in vivo* liver data acquired using the C5-2v curvilinear transducer and Verasonics Vantage 256 ultrasound scanner. The expected contribution of thermal noise was subtracted from experimental data to minimize the effect of transducer bandwidth.

Results/Discussion

Initial results show that the imaging frequency that optimized image quality is correlated with LOC measured at a single frequency (4.8 MHz harmonic). The control simulation and phantom, having no near-field source of clutter and thus being the most favorable imaging environments, allow some of the highest optimized frequencies. These findings match the clinical experience, in which lower frequencies are used for difficult-to-image patients. In nearly all cases, the LCM is appreciably improved when moving from the transducer recommended frequency to an optimized frequency in fundamental or harmonic.



4:15 PM

Regularized Inversion Method for Frequency-Domain Reconstruction of Full Synthetic Aperture Dataset From Focused Transmissions**Rehman Ali¹, Carl Herickhoff², Jeremy Dahl², Nick Bottenu³**¹*Electrical Engineering, Stanford University, Palo Alto, CA, United States*, ²*Radiology, Stanford University, CA, United States*, ³*Duke University, Durham, NC, United States***Background, Motivation, and Objective**

Accurate recovery of the full-synthetic aperture (FSA) dataset from focused transmits can enable synthetic transmit focusing without the drawbacks of single-element and virtual-element transmissions and enable a wide array of imaging techniques that require the FSA dataset. Recovery of the FSA dataset has previously been performed using an adjoint-based pseudoinverse method [1]. We present a regularized inversion method of FSA dataset recovery that allows additional aperture specification to improve dataset accuracy and achievable image quality.

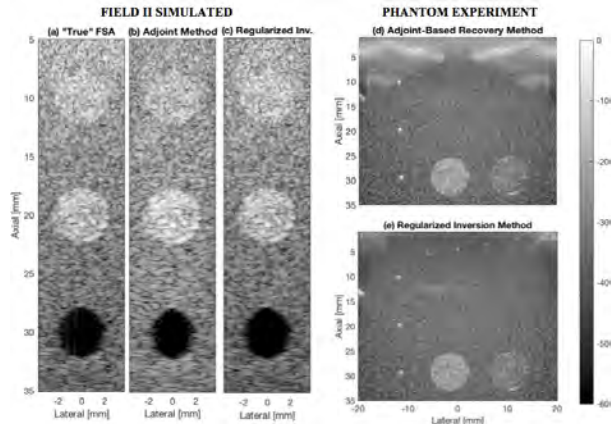
Statement of Contribution/Methods

The method formulates a frequency-domain transmit encoding matrix that incorporates both delay and apodization profiles. When applied to received, frequency-domain channel data from focused transmits, regularized inversion of this matrix can recover the FSA dataset at each frequency. Field II was used to simulate received channel signals from a single-element transmit FSA sequence as a gold standard, and a walking-aperture, focused-transmit pulse sequence. Similar data were captured using an L12-3v linear array with a Verasonics Vantage 256 scanner on a CIRS 040GSE phantom. Both regularized inversion and adjoint-based methods were applied to the focused-transmit data, and FSA image reconstruction was performed on the recovered and ‘true’ FSA datasets. Resolution, speckle structure, and artifacts in the resulting images were compared.

Results/Discussion

Simulations show that both the speckle structure and resolution of the ‘true’ FSA image (a) are better retained in the proposed method (c) compared to the adjoint-based method (b). At 33 mm depth, error in resolution (-6 dB width) was 28.7% and <0.1% for adjoint-based (b) and proposed (c) methods, respectively. The normalized RMS error in image reconstruction was 50% for adjoint-based method (b) and 7% for the proposed method (c). Experiments in phantoms show strong artifacts close to the transducer in adjoint-based method (d), which are improved in the proposed method (e).

[1] Bottenu³, N. *IEEE Trans on UFFC* 65.1 (2018)



4:30 PM

Frequency domain Two-Stage Beamforming for Phased Array Imaging using the Fast Hankel Transform**Fabian Fool¹, Jos de Wit¹, Deep Bera², Hendrik J. Vos^{1,2}, Martin D. Verweij^{1,2}, Nico de Jong^{1,2}**¹*Acoustical Wavefield Imaging, Imaging Physics, Delft University of Technology, Delft, Netherlands*, ²*Biomedical Engineering, Thorax Center, Erasmus MC, Rotterdam, Netherlands***Background, Motivation, and Objective**

The huge amount of data that needs to be transferred between probe and imaging system becomes a major issue when the data transfer capacity is limited, e.g. in handheld systems, wireless probes and miniaturized probes. The amount of data can be significantly reduced by using two-stage beamforming. The first stage consists of a fixed focus algorithm that compresses channel data to scanline data. This can be done by integrated electronics in the handle. In the second stage the scanline data is further beamformed in the imaging system to obtain images that are synthetically focused at all depths.

Currently, there are two approaches for the second stage: Synthetic Aperture Sequential Beamforming (SASB) and a full wave field approach. The latter has only been developed for linear arrays and is very fast compared to SASB. A full wave field method for phased arrays has not yet been developed, although a similar but slow method for a cylindrical geometry already exists. Here we present a full wave field method for phased arrays that is computationally efficient.

Statement of Contribution/Methods

To obtain a computationally efficient algorithm we have employed a change of variables from the original cylindrical wave solution after which a Fast Hankel Transform (FHT) could be used. Our Phased Array Migration (PAM) method is compared to Dynamic Receive Focusing (DRF) and Phased SASB (PSASB) using measurements on a commercial tissue phantom. The measurements were obtained using a P4-1 phased array probe connected to a Verasonics Vantage. The image quality is evaluated using the lateral resolution and the contrast to noise ratio (CNR). The computational efficiency is evaluated using the number of operations to construct the image.

Results/Discussion

The results presented in Fig. 1a and 1b show that PAM has a 17% better resolution compared to PSASB, which is subsequently better than DRF. The improved resolution does not come at the cost of artefacts in the image. The CNR, presented in Fig. 1c, is also improved as compared to both methods. For the presented examples, PAM has an almost equal amount of operations as PSASB and requires about 4 orders of magnitude fewer operations compared to the implementation without the FHT.

Our method can thus achieve a better lateral resolution compared to PSASB, without introducing additional artefacts and with a similar amount of operations.

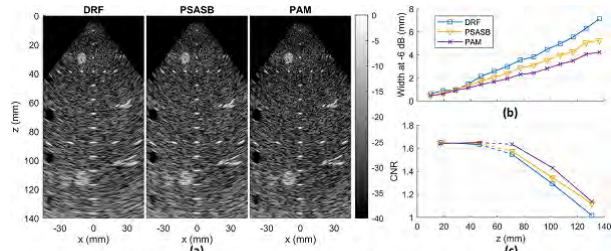


Fig. 1: (a) Images of the CIRS 040GSE. The main differences can be observed at the resolution wires (clear white dots) and the lower left anechoic cyst. (b) The FWHM obtained at the vertical resolution wires. (c) The CNR obtained at two anechoic cysts of 6.7 mm diameter at depths of about 15 and 40 mm, and three cysts of 10 mm diameter at depths between 70 and 130 mm.

4:45 PM

Full-wave ultrasound reconstruction with linear arrays based on a Fourier split step approachHans-Martin Schwab¹, Georg Schmitz¹¹*Medical Engineering, Ruhr-University Bochum, Germany***Background, Motivation, and Objective**

In ultrasound (US) imaging, the transmitted wave is usually modeled as a simple geometric shape, such as a line for plane wave imaging or an arc for diverging wave imaging. This allows for straight-forward algorithms but neglects wave front distortions due to diffractive effects or scattering, which leads to a loss of coherence during compounding and introduces reconstruction artifacts. An exact simulation of the transmitted wave is difficult, since the wave field depends on the unknown scatterer distribution. In this contribution, we propose a reconstruction algorithm that is based on a Fourier split step approach and alternates between a wave field extrapolation and a reflection parameter reconstruction for each depth, generating both a full wave field and a scatterer distribution. In addition, information about speed of sound (SOS) variations can be included at no extra computational cost to correct for aberration artifacts.

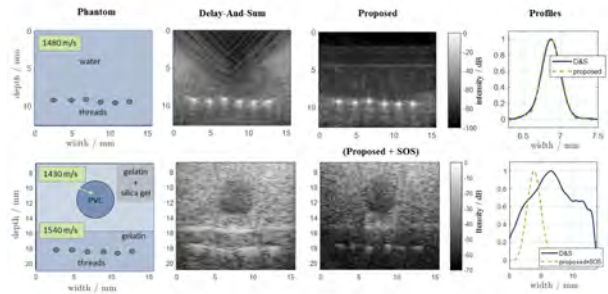
Statement of Contribution/Methods

The proposed reconstruction method decomposes the wave field into a forward and a backward propagating part with transmitted and received waves as respective boundary conditions at zero depth. Both fields are extrapolated in axial direction by a Fourier split step approach, which treats scattering and diffraction as two consecutive events. For each pixel at one depth, a reflection factor is derived as least squares solution to a scatter relation between the forward and backward propagating fields. Based on that reflection factor, the wave fields are extrapolated to the next depth and the process is repeated recursively to all depths. Local SOS deviations can be considered by phase adjustments during the extrapolation.

The method was tested on plane wave US acquisitions of two thread phantoms using a commercial ultrasound system (MyLabOne, Esaote) in combination with a research acquisition software. All algorithms were implemented in an in-house reconstruction toolbox to assure comparability.

Results/Discussion

The peak-to-background contrast was increased by 26.3 dB at equal lateral resolution compared to a delay-and-sum reconstruction. By additionally considering local variations in the SOS, the lateral resolution beneath a PVC inclusion was increased by 454%. Here, SOS values were manually assigned to segmented regions. In the future, the method will be combined with SOS imaging techniques.



5:00 PM

Advanced beamforming techniques for passive imaging of stable and inertial cavitation**Maxime Polichetti^{1,2}, François Varray¹, Jean-Christophe Béra², Christian Cachard¹, Barbara Nicolas¹**¹*University Lyon, INSA-Lyon, UCBL, UJM-Saint-Etienne, CNRS, Inserm, CREATIS UMR 5220, U1206, F-69100 Villeurbanne, France, France, ²LabTAU, INSERM, Centre Léon Bérard, UCBL, University Lyon, F-69003 Lyon, France, France***Background, Motivation, and Objective**

Passive Acoustic Mapping (PAM) could allow real-time imaging of the cavitation activity for ultrasound extracorporeal sonothrombolysis. A reproducible treatment requires accurate monitoring of the two types of cavitation: stable cavitation (oscillating bubbles producing mainly tissue heating) and inertial cavitation (collapsing bubbles producing mechanical damages). To improve their localization, we adapt the pDAS beamformer to PAM, since pDAS enhances resolution and contrast of B-mode images [Polichetti, 2018]. The proposed method is compared in simulation to PAM, and PAM with Phase Coherence Factor (PCF) [Boulos, 2016].

Statement of Contribution/Methods

PAM algorithm processes passively acquired acoustic bubbles signals. Pixels represent the energy of delayed and coherently summed signals integrated over time. We adapt pDAS beamforming to PAM: a p-th root compression of rephased bubbles signals emphasizes their coherent summation, and so, improve their localization. This amplitude-based beamformer is compared to our previously proposed phase-based one: the PCF.

We simulate a linear probe and a medium composed of two disjoint bubble clouds (Figure 1a): a cloud of high intensity stable cavitation scattering harmonic peaks from 1 to 5 MHz, and a little inertial cavitation cloud scattering broadband signals of random pulse trains [Vokurka, 2002].

Results/Discussion

First, both stable and inertial cavitation clouds are mapped simultaneously: no pre-filtering is applied on raw data (blue spectrum, Figure 1b). In this case, only the high energy of stable cavitation is visible (Figure 1c, d, e) and the thinnest resolution is obtained for PCF (lateral main lobe width at -3 dB for PAM: 3.0 mm, PCF: 1.9 mm, pDAS: 2.3 mm). Then, only the broadband inertial cavitation is mapped by using a comb notch filter to filter-out the narrowband components (red spectrum, Figure 1b). Both PCF and pDAS improve the localization of inertial cavitation (Figure 1f, g, h) compared to PAM. The contrast ratio (CR) is evaluated as the mean intensity within the expected cavitation region over the one measured within the artifact region (black squares on Figure 1 f, g, h). The CR values (PAM: 1.7 dB, PCF: 2.9 dB, pDAS: 4.6 dB) clearly illustrate the superiority of the amplitude-based beamformer pDAS compared to PCF to finely localize inertial cavitation from broadband received signals.

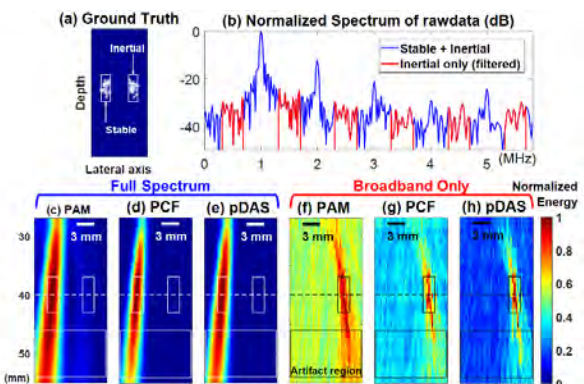


Figure 1: Results for cavitation mapping. Ground truth for bubble positions is given on (a): stable cavitation is on the left and inertial cavitation on the right. The spectrum of a received signal is plotted on (b). The full frequency content (in blue, b) is used to build the cavitation normalized energy maps with PAM (c), PCF (d), and pDAS (e). The filtered broadband frequency content (in red, b) is used to build the cavitation normalized energy maps with PAM (f), PCF (g), and pDAS (h).

5:15 PM

Decimated Analytic Signal based Beamformer for Efficient Reconstruction of Passive Acoustic MappingPilsu Kim¹, Tai-kyong Song¹, Jae Hee Song²¹*Department of Electronic Engineering, Sogang University, Seoul, Korea, Republic of,* ²*Cavitation Laboratory, Medical and Industrial Ultrasonics, School of Engineering, University of Glasgow, Glasgow, United Kingdom***Background, Motivation, and Objective**

Passive acoustic mapping (PAM) is current state-of-the-art imaging tool for monitoring cavitation activity during focused ultrasound therapy. However, it suffers from massive computational complexity for PAM reconstruction. Fortunately, frequency-domain PAM (PAM-FD) had been proposed to alleviate this computational burden. Nevertheless, it still requires a large number of fast Fourier transforms (FFT) including unutilized frequency components in PAM reconstruction. In this paper, we propose frequency domain passive acoustic mapping with decimated analytic signal (PAM-DeAS) for efficient implementation of passive beamforming.

Statement of Contribution/Methods

To alleviate the computational burden caused by redundant FFT, the PAM-DeAS perform decimation before FFT execution using band-limited analytic signal to prevent the aliasing during decimation. The decimation rate (M) is determined by sampling rate (f_s) and the bandwidth (BW) for PAM reconstruction ($f_s/BW \geq M$). To verify PAM-DeAS, periodic shock waves (PSWs) from single bubble was recorded by ultrasound research system (E-cube 12R, Alpinion medical systems) with 7.5-MHz centered linear array transducer. High-speed shadowgraphic imaging taken at 2Mfps ensures nucleation of a single acoustic bubble. The number of samples used for PAM reconstruction was set to 2048, 51.2 μ s when f_s is 40MHz. The peak signal-to-noise ratio and the spatial resolution were utilized as the evaluation metrics. Moreover, computational complexity was investigated with the number of multipliers for the entire processing. To demonstrate feasibility, we implemented PAM-DeAS using CUDA on GPU (GTX 970, NVIDIA) embedded in E-cube 12R to perform reconstruction in real-time.

Results/Discussion

Fig. 1(b) shows the PAM images reconstructed using the RF data with frequency components of 375-kHz bandwidth, which is the extremely decimated by a factor of $M=106$ for PAM-DeAS. Even though PAM-DeAS reduces the computational complexity by 96.53% as shown in Fig. 1(d), there is no significant degradation in image quality. Therefore, we demonstrate that PAM-DeAS efficiently reduces the computational complexity. Moreover, Fig. 1(c) demonstrates that PAM-DeAS correlates better with PAM-FD as BW increases (i.e. decreasing M). In addition, the PAM-DeAS applies not only for frequency domain PAM, but also angular spectrum based PAM.

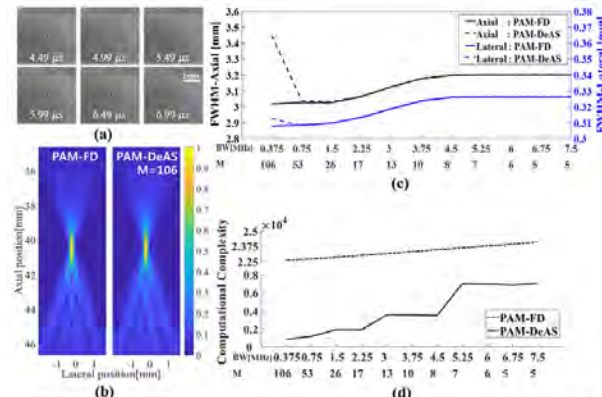


Fig.1. (a) Representative images extracted from a high speed sequence recorded at 2×10^6 fps, of cavitation activity. (b) Reconstructed PAM images using RF data with frequency components of 375kHz bandwidth. (c) The comparison of spatial resolution among the reconstructed images with full width at half maximum (FWHM) as a function of bandwidth (BW) and maximum decimation rate (M) (d) Evaluation of computational complexity

2H - Neuromodulation and Brain Applications

Diamond (300)

Thursday, October 25, 8:00 am - 9:30 am

Chair **William Apoutou N'Djin**
INSERM

2H-1

8:00 AM Inhibitory effects of motor neuron activity in mouse peripheral nerve system using ultrasound-guided focused ultrasound *in vivo*

Min Gon Kim¹, Stephen Lee¹, Hermes Kamimura¹, Elisa Konofagou^{1,2}

¹Biomedical Engineering, Columbia University, United States, ²Radiology, Columbia University, United States

Background, Motivation, and Objective

Noninvasively controlling neuronal activity remains a primordial challenge in neurology. Recently, we developed the use of focused ultrasound stimulation of peripheral nerve with safe and specific nerve targeting (Downs et al. 2018). In this study, we propose an approach to inhibit motor neuron activity of the mouse sciatic nerve *in vivo* by controlling the heating rate through the pulse repetition frequency (PRF). To verify the proposed approach, we selected five different PRF values (1-500Hz) and examined temperature effects on the motor neuronal activity in the gastrocnemius muscle *in vivo*.

Statement of Contribution/Methods

The experimental setup consists of electrical/ultrasound stimulations and EMG recording/analysis. After locating the sciatic nerve with an 18.5MHz, 128-element linear array, the proximal/distal sciatic nerve was exposed to electrical/ultrasound-guided focused ultrasound stimulations, respectively. The effects of induced neuromodulation (3.1MHz single element HIFU transducer with 1ms pulse duration/2s total time at different PRF's (1/10/40/250/500Hz) on the sciatic nerve were recorded and analyzed in terms of EMG amplitude/latency ($n=11$). To evaluate the safety, hematoxylin and eosin (H&E) staining was conducted in a blinded study between the negative control and experimental groups.

Results/Discussion

Fig. 1(a-b) illustrates quantification of the average normalized EMG amplitude/latency as a function of temperature elevation during ultrasound stimulation compared to the values before ultrasound exposure. For temperature elevation under 1°C (PRF: 1/10/40Hz), the average normalized EMG amplitude and latency were similar to the values without FUS modulation. On the other hand, the average normalized amplitude/latency were decreased to $93 \pm 3\%$ / $97 \pm 2\%$ by a 6.3°C temperature increase during FUS modulation (PRF: 250Hz) and $81 \pm 3\%$ / $89 \pm 5\%$ by 8.2°C temperature increase (PRF: 500Hz), respectively. Fig. 1(c-d) presents H&E staining and compared with the negative control group (Fig. 1(c)), the experimental group (Fig. 1(d)) did not detect any morphological changes of the treated sciatic nerve and its surrounding tissue. The experimental results show that ultrasound neuromodulation could be applied for a more selective control of motor neuron with the ability to noninvasively and selectively excite/inhibit neuronal activity.

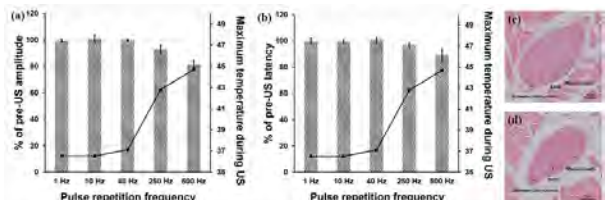


Fig. 1: The quantification of average normalized EMG amplitude/latency with temperature change controlled by different PRF. (Number of treated mice was 11) (a-b) Compared with pre-ultrasound stimulation amplitude/latency, at the maximum temperature of 36.5°C (1 Hz), 36.5°C (10 Hz), 37.1°C (40 Hz), 42.8°C (250 Hz), 44.7°C (500 Hz), (a) the average EMG amplitudes were $99.5 \pm 0.8\%$, $100.6 \pm 2.0\%$, $99.9 \pm 0.3\%$, $92.9 \pm 2.9\%$, and $81.2 \pm 2.8\%$ and (b) the average latency were $99.8 \pm 2.2\%$, $99.3 \pm 1.2\%$, $100.6 \pm 2.2\%$, $96.7 \pm 2.1\%$, and $89 \pm 4.7\%$. (c-d) H&E staining on the sciatic nerve and surrounding tissue between (c) negative control group and (d) experimental group. There were no obvious morphological changes of the sciatic nerve and its surrounding tissue by the experimental group compared with negative control group.

8:15 AM Low intensity pulsed ultrasound stimulation improves sensorimotor function in a mouse model of Parkinson's disease

Hui Zhou¹, Long Meng¹, Xiangxiang Xia¹, Lili Niu¹, Hairong Zheng¹

¹Paul C. Lauterbur Research Center for Biomedical Imaging, Shenzhen Institutes of Advanced Technology, Chinese Academy of Sciences, China, People's Republic of

Background, Motivation, and Objective

Although deep brain stimulation (DBS) is effective for the treatment of Parkinson disease, it is invasive as it implants one or more electrodes to the specific brain regions [Nature Reviews Neuroscience, 8(8): 623-35, 2007]. As ultrasound can noninvasively transmit through the skull bone in a focused manner, it is also a potentially powerful neurostimulation tool. We hypothesized that low-intensity pulsed ultrasound stimulation of primary motor cortex (M1) could improve behavior performance in an acute mouse model of Parkinson's disease induced by 1-Methyl-4-phenyl-1,2,3,6-tetrahydropyridine (MPTP) injection.

Statement of Contribution/Methods

The experimental setup of our study was shown in Fig. 1 (a). C57BL/6J mice (9 weeks old, male) were randomized into control, MPTP, shame-US+MPTP and US+MPTP treatment group (n=8 per group). Mice received MPTP injection (20 mg/kg body weigh; Sigma-Aldrich) at 2-h intervals or an equivalent volume of saline [Nature Protocols, 2(1): 141-51, 2007]. For US+MPTP treatment group, 7 days of LIPUS ($f = 800\text{ KHz}$, Ispfa = 240 mW/cm^2 , PRF = 100Hz, DC = 10%, 600 pulses, 10s intervals, 40min/day) was given. Behavior test was evaluated by adhesive removal test. In addition, c-FOS and hematoxylin and eosin (H&E) immunohistochemistry were performed to confirm the position and safety of ultrasound stimulation.

Results/Discussion

The expression of c-FOS in motor cortex was shown in Fig. 1(b). A one-way ANOVA found behavior differences for four groups ($p < 0.05$). The results suggested that US+MPTP treatment could improve sensorimotor function versus shame-US+MPTP group ($23.6 \pm 1.69\text{ s}$ vs. $59.67 \pm 2.08\text{ s}$ in day 1; $11.7 \pm 0.59\text{ s}$ vs. $14.6 \pm 0.6\text{ s}$ in day 3; $8.9 \pm 0.6\text{ s}$ vs. $10.93 \pm 0.5\text{ s}$; $p < 0.05$, $n = 8$). In addition, US+MPTP group mice didn't show statistically significant versus control group on day 5 ($8.9 \pm 0.6\text{ s}$ vs. $8.1 \pm 0.98\text{ s}$; $P > 0.05$, $n = 8$), as shown in Fig. 1(c). HE staining did not present any tissue damage with ultrasound stimulation, as shown in Fig. 1(d). Our findings reveal that ultrasound treatment significantly inhibits MPTP-induced Parkinsonism-like symptoms and could be potential application in neurotherapeutics for PD treatment.

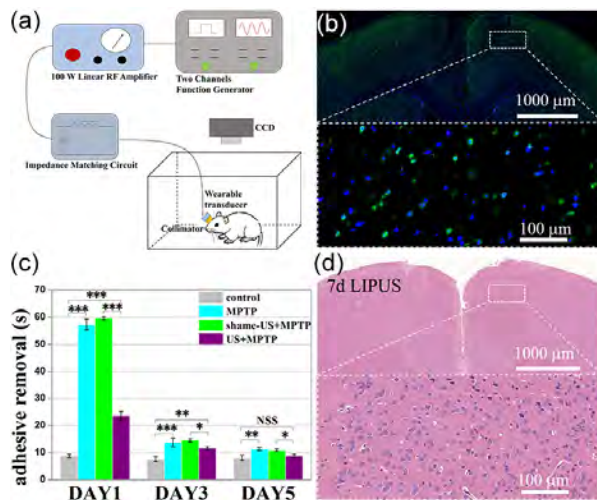


Fig. 1 (a) Schematic of experimental design. (b) c-FOS expression in motor cortex. (c) LIPUS protects from MPTP-induced impairment in sensorimotor of mice. (d) Hematoxylin and eosin (H&E) staining.

8:30 AM

Focused Ultrasound-enabled Brain Tumor Liquid Biopsy

Lifei Zhu¹, Galen Cheng¹, Dezhuang Ye², Arash Nazeri³, Yimei Yue⁴, Weijun Liu⁵, Xiaowei Wang⁵, Gavin P. Dunn^{6,7}, Allegra A. Petti^{8,9}, Eric C. Leuthardt^{1,6,10}, **Hong Chen^{1,5}**

¹*Department of Biomedical Engineering, Washington University in St. Louis, Saint Louis, MO, United States,*

²*Mechanical Engineering and Material Science, Washington University in St. Louis, Saint Louis, MO, United States,*

³*Mallinckrodt Institute of Radiology, Washington University School of Medicine, Saint Louis, MO, United States,*

⁴*Biomedical Engineering, Washington University in St. Louis, Saint Louis, MO, United States,* ⁵*Department of Radiation Oncology, Washington University in St. Louis, Saint Louis, MO, United States,* ⁶*Department of Neurosurgery,*

Washington University School of Medicine, Saint Louis, MO, United States, ⁷*Center for Human Immunology and*

Immunotherapy Programs, Washington University School of Medicine, Saint Louis, MO, United States, ⁸*McDonnell*

Genome Institute, Washington University School of Medicine, Saint Louis, MO, United States, ⁹*Department of*

Medicine, Washington University School of Medicine, Saint Louis, MO, United States, ¹⁰*Center for Innovation in*

Neuroscience and Technology, Washington University School of Medicine, Saint Louis, MO, United States

Background, Motivation, and Objective

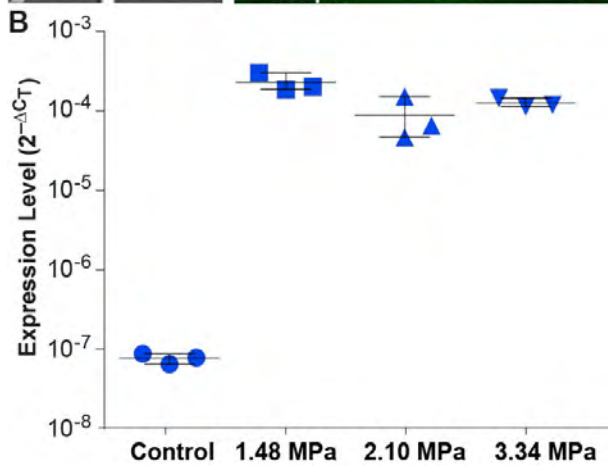
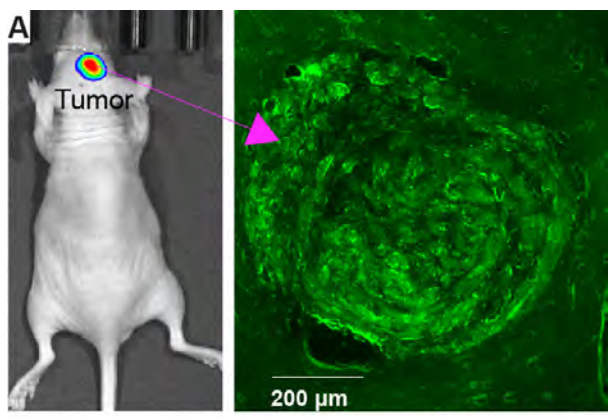
Glioblastoma multiform (GBM) is the most common primary brain tumor and one of the deadliest of all cancers. Direct surgical tissue biopsy to determine tumor molecular profiles is associated with potential complications such as hemorrhage and infection. Meanwhile, repeated tissue biopsies using surgical interventions to assess treatment response and recurrence may not be feasible given the increased risk for complications and morbidity. Although blood-based liquid biopsies have emerged as a promising non-invasive method to detect biomarkers in various cancers, limited progress has been made for brain tumors. One major obstacle is the blood-brain barrier (BBB), which hinders efficient passage of tumor biomarkers into the peripheral circulation. The objective of this application is to develop a novel technique - focused ultrasound-enabled liquid biopsy (FELB) - to noninvasively increase the concentration of biomarkers in the blood and enable the detection of GBM by blood testing.

Statement of Contribution/Methods

Two glioblastoma tumor models (U87 and GL261) were developed by intracranial injection of respective enhanced green fluorescent protein (eGFP)-transduced glioblastoma cells (Figure A). Microbubbles were injected systemically to the mice through the tail vein, followed by FUS sonication with acoustic pressures of 1.48 MPa, 2.10 MPa, and 3.34 MPa. FUS was targeted at the center of the tumor under the guidance of MRI. Blood samples of 500–800 µL were collected from the heart about 20 min after the FUS treatment and prepared for quantitative polymerase chain reaction (qPCR) analysis of eGFP mRNA.

Results/Discussion

eGFP mRNA was only detectable in the FUS-treated mice and undetectable in the untreated mice (maximum cycle number set to 40). The circulating levels of eGFP mRNA were 1,500–4,800 fold higher in the FUS-treated mice than that of the untreated mice for the three acoustic pressures (Fig. b). This study demonstrated the feasibility of FUS-enabled brain tumor liquid biopsies in two different murine glioma models across different acoustic pressures. Our findings established that FUS-mediated BBB disruption could enhance brain-to-blood trafficking. FUS may offer an enabling technique for noninvasive and regionally-specific brain tumor liquid biopsy that can be utilized in personalized brain cancer patient care.



8:45 AM

Improved performance and safety of drug delivery to the brain in vivo with Rapid Short-Pulse (RaSP) sequencesSophie V. Morse¹, Tiffany G. Chan², Matthew J. Coping¹, Antonios Pouliopoulos¹, Nicholas J. Long², James J. Choi¹¹*Bioengineering, Imperial College London, London, United Kingdom*, ²*Chemistry, Imperial College London, United Kingdom***Background, Motivation, and Objective**

Focused ultrasound and microbubbles can locally and noninvasively enhance the blood-brain barrier permeability for drugs. Although clinical results have been encouraging for glioblastoma treatment in adults, there are concerns for more sensitive patients - the elderly with dementia and children with brain cancer. With current ultrasound methods, drugs are delivered inefficiently to diseased regions and safety relies on a long healing process. Side effects include unpredictable drug distributions, high drug concentrations along vessels and red blood cell extravasation. Our group has developed a Rapid Short-Pulse (RaSP) sequence designed to improve cavitation distribution. Here, we evaluated the ability of RaSP to improve drug delivery performance and safety, by comparing the drug dose and distribution and the extent of morphological changes and red blood cell extravasation compared to conventional long-pulses.

Statement of Contribution/Methods

We tested a RaSP sequence in vivo that had a low-energy pulse (PL: 5 cycles, P: 350 kPa_{pk-neg}) and compared it to a long-pulse sequence that had a high-energy pulse (PL: 10,000 cycles, P: 350 kPa_{pk-neg}) in mice at 1 MHz. RaSP pulses were emitted at a rapid pulse and slow burst rate (PRF: 1.25 kHz, BRF: 0.5 Hz) while long-pulses were emitted at a slow pulse rate (PRF: 0.5 Hz). Fluorescent 3 kDa dextran and SonoVue® microbubbles were injected with emissions captured by a 7.5 MHz passive cavitation detector. Brains were imaged by fluorescence microscopy and stained with H&E to check for any damage and red blood cell extravasation.

Results/Discussion

Despite depositing 150 times less acoustic energy into the brain, RaSP sequences delivered a more uniform drug distribution with a similar dose to conventional long-pulses. Such improvement is thought to be due to a better spatiotemporal distribution of cavitation. Neuronal uptake was higher with RaSP and less dextran was observed within glial cells which are linked to a tissue response to damage. No red blood cell extravasation or morphological damage was observed with RaSP, while with long-pulses, one brain had haemorrhage and microvacuolations. These results indicate that low-pressure RaSP sequences could be used to deliver drugs with improved performance and safety to treat sensitive neurological diseases, such as neurodegenerative diseases and paediatric brain cancers.

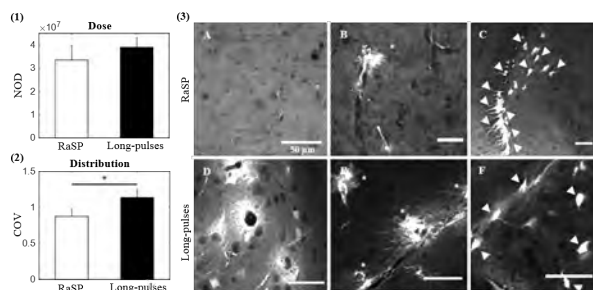


Figure. Drug dose and distribution in the brain with RaSP vs long-pulse sequences at 350 kPa_{pk-neg}. Quantification of (1) drug dose and (2) drug distribution was done by calculating the normalised optical density (NOD) – increased fluorescence in the targeted region (left hippocampus) compared to the control region (right hippocampus) – and coefficient of variation (COV) – standard deviation over the mean – respectively for RaSP and long-pulse treated brains. (3) In vivo drug distribution with (A) RaSP and (B) long-pulses observed from fluorescence images. (C) High uptake in neurons (arrows) and (D) in a few glial cells (asterisks) was observed with RaSP, while (E) lower neuronal uptake and (F) higher glial cell uptake was found with long-pulses.

9:00 AM

Bi-modal modulation of neuronal excitability by ultrasound stimulation in human temporal lobe epilepsy**Zhengrong Lin¹, Lili Niu¹, Long Meng¹, Wei Zhou¹, Xiaowei Huang², Hairong Zheng¹**¹*Paul C. Lauterbur Research Center for Biomedical Imaging, Shenzhen Institutes of Advanced Technology, Chinese Academy of Sciences, Shenzhen, China, CA, China, People's Republic of, ²Shenzhen Institutes of Advanced Technology, Chinese Academy of Sciences, Shenzhen, China, China, People's Republic of***Background, Motivation, and Objective**

Temporal lobe epilepsy (TLE) is a prevalent neurological disorder resulting in disruptive seizures and often associated with pharmacoresistance. Ultrasound stimulation as an emerging non-invasive neuro-stimulation technique has shown its effectiveness in suppressing the epileptic seizures in rodent animal models (Neuroimage 56, 1267-1275, 2011; BMC Neuroscience 12, 23, 2011; Epilepsy Behavior 49, 26-32, 2015). The effect of ultrasound stimulation on the seizures of human temporal lobe epilepsy (TLE) have been little addressed. In this study, we aimed to determine whether ultrasound stimulation was capable of inhibiting single neuronal excitability in brain slices of the temporal lobe from TLE patients.

Statement of Contribution/Methods

Fig. 1a shows a biopsy specimen removed from a TLE patient and the spontaneous activity of the neurons in the TLE slice was recorded using electrophysiological technique. Fig. 1b shows low-intensity pulsed ultrasound (frequency: 28 MHz, pressure: 0.25 MPa) was delivered into human TLE slices generated by the ultrasound stimulation system. The following pulsed ultrasound parameters were chosen and used in the present study: (1) single 5ms ultrasound pulse containing 140000 acoustic cycles of 28MHz at pulse repetition frequency (PRF) of 100Hz and (2) single 0.5ms ultrasound pulses containing 14000 acoustic cycles were repeated at PRF of 1000Hz.

Results/Discussion

Fig. 1c shows ultrasound stimulation could be bi-modal modulation of the burst discharge of 'epileptic neurons'. Single 5ms ultrasound pulse containing 140000 acoustic cycles of 28MHz at pulse repetition frequency (PRF) of 100Hz could effectively inhibit the burst discharge. A population of 13 neurons showed that the relative frequency rapidly decreased several-fold. Interestingly, another parameter with single 0.5ms ultrasound pulses containing 14000 acoustic cycles were repeated at PRF of 1000Hz showed a completely different effect on the burst discharge. A total of 7 neurons showed that the relative frequency rapidly increased several-fold. This suggests that ultrasound stimulation may be a valuable treatment modality for patients with epilepsy.

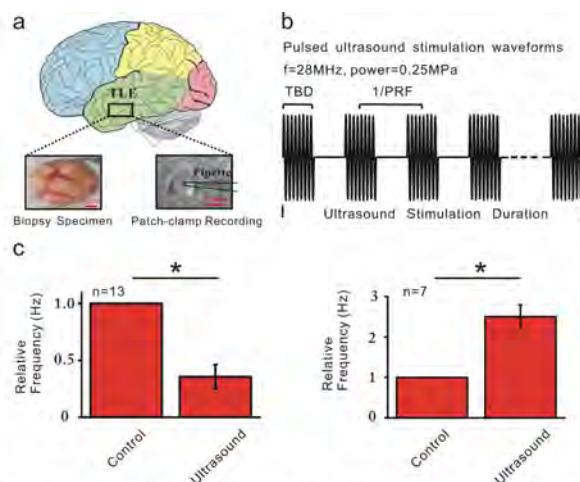


Fig 1. a. An example of biopsy specimen removed from a TLE patient and 40X photomicrograph of an neuron for electrophysiological recording in the TLE slice. b. Schematics of pulsed ultrasound stimulation protocols. c. Bi-modal modulation of burst discharge frequency of 'epileptic neurons' using ultrasound stimulation with different sonic parameters.

9:15 AM High-resolution, focused ultrasound-mediated neuromodulation and detailed analysis of electromyography characteristics reveals a high degree of spatial specificity in elicited responses in mice *in vivo*

Christian Aurup¹, Elisa Konofagou²

¹Columbia University, New York, NY, United States, ²Biomedical Engineering, Columbia University, United States

Background, Motivation, and Objective

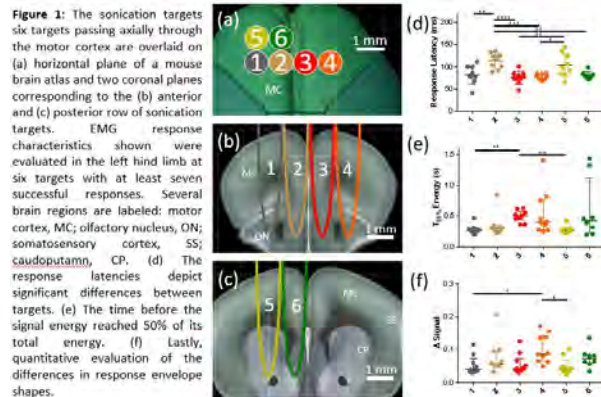
Focused ultrasound (FUS) is a promising technique for modulating neural activity. It provides a means for the non-invasive and non-pharmacological modulation of activity in deep and superficial brain structures with high spatial resolution. In this study, we determine the potential of FUS for motor circuit mapping by tailoring the EMG analysis to include metrics for signal energy distribution, response similarity, duration, success rates, and latency measured in all four limbs simultaneously and thus determining the degree to which these characteristics can differ throughout the brain.

Statement of Contribution/Methods

An FUS transducer operating at 2 MHz (1 kHz PRF, 50% duty cycle, 1.76 MPa peak negative pressure, 97 W/cm² ISPPA, 1mm x 8.5mm focal size) was used to sonicate 2x4 grid of targets, each target spaced 1mm apart, in three brain regions; one spanning the motor cortex bilaterally and the other two spanning areas posterior of the lambda skull suture in the left and right hemispheres, respectively. Each target was sonicated 10 times for 300ms every 5 seconds. EMG responses were measured in all four limbs using fine-wire bipolar electrodes in five mice. EMG characteristics evaluated were response latencies, response durations, the time the signal reaches 50% of total energy (T50%), success rates, and normalized signal change, which quantifies the signal envelope shape similarities.

Results/Discussion

It was shown that EMG characteristics differ significantly between brain regions and even neighboring targets for all four limbs. Figure 1 shows an example of how latency, T_{50%} time, and the normalized signal change may vary within a region. A total of 978 successful sonications were performed across 24 unique locations in the brain with an overall success rate of 94%. The combined mean latency and median T50% time for all trials was 106.5ms and 504ms, respectively. The median response durations for the front and hind limbs were 370ms and 1005ms, respectively. The responses were virtually all bilateral with no laterality of response characteristics. It is likely that the responses result from the modulation of a volume of neural tissue extending into deeper structures contained within the acoustic focus and not limited to cortical excitation. We determine that high resolution FUS can be used with a large complement of EMG analyses for potential circuit mapping in rodents.



2I - Neuromodulation and Cellular Bioeffects

Diamond (300)

Thursday, October 25, 10:30 am - 12:00 pm

Chair **Eleanor Stride**
University of Oxford

2I-1

10:30 AM Controllable Single Neuron GHz Ultrasonic Stimulation of Ion Channels in Vitro

Priya S. Balasubramanian¹, Amit Lal¹

¹Electrical and Computer Engineering, Cornell University, Ithaca, NY, United States

Background, Motivation, and Objective

Single neuron level signal manipulation is essential in neuroscience discovery, treatment, and neural network tissue engineering. Ultrasonic stimulation is a known method to influence neural signals, however current methods focus on the ~100kHz-MHz frequency range with deep tissue penetration but limited beam focusing where individual neurons cannot be accessed.² Here we demonstrate the use of ~1.5 GHz ultrasonics towards modulation of neural signals in *in vitro* neural systems. By operating at GHz frequencies, we can form sonic beams with 2-5 μm focal points with approximately 1-2 degree beam widths, that can be used to interrogate and scan a neuron of approximately 20-60 μm in diameter. While there is limited penetration depth (100s μm), GHz ultrasonic specificity allows for well-defined actuation.

Statement of Contribution/Methods

We use 75x75 μm Aluminum Nitride transducers microfabricated identically on *both* sides of a wafer (1a). The actuators on the bottom achieve far-field waves at the other surface of the chip.¹ This RF drive (0.5-2 V_{peak} 1.47 GHz continuous wave RF) leads to peak displacements of ~10 picometers on the opposite side of the wafer, measured using a Polytec UHF interferometer. The displacement corresponds to surface particle velocity of 10-20cm/s and surface intensity of 10-20 Watts/cm². We quantify changes in calcium flux using calcium imaging of 48-hour RA differentiated SH-SY5Y semi-confluent neuroblastoma cells (1b). We quantify dependency of ultrasonic dosage on cell culture medium.

Results/Discussion

We observe the potential for the use of GHz ultrasonics in an *in vitro* neural system given that we see changes in membrane potential due to calcium flux for cells with ultrasonic stimulus for a total of 14 cells (1b). This indicates that the ion channels on a differentiating cell membrane are responding to ultrasonics, causing a net change in transmembrane potential. Plausible mechanisms for this include acoustic radiation and streaming forces. We envision transducers integrated with CMOS that are wirelessly powered for neural actuation.

1. Kuo, Justin C., et al. "64-Pixel solid state CMOS compatible ultrasonic fingerprint reader." *MEMS, 2017 IEEE 30th International Conference on IEEE*, 2017.

2. Schuster, Anne, et al. "Neural stem cells influenced by ultrasound: Frequency and energy density dependencies." *Physics in Medicine* 4 (2017): 8-16.

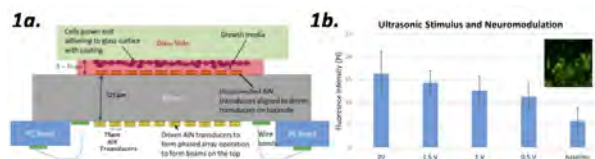


Figure 1a. Experimental details of setup used to expose cells to GHz Ultrasound. A silicon wafer, 700um thick has 2- μm thick AlN transducers fabricated on both sides of the wafer. Glass slide with cell adhesion layer is coated with cells in media with 5-10 μm gap. The transducers on backside are driven and aligned with cells using top transducers fabricated as mirror images of the bottom using dual sided alignment. **Figure 1b.** Inset shows typical optical calcium image from neuron clusters with changes in fluorescence observed with calcium flux. Graph indicates normalized emitted fluorescence intensity as a function of applied ultrasonic peak drive voltage, at 1.47GHz.

10:45 AM

Low-Frequency, Low-Intensity Ultrasound Induces Autophagy in SH-SY5Y Neuronal CellsXiaowei Huang¹, Zhengrong Lin¹, Lili Niu¹, Long Meng¹, Wei Zhou¹, Hairong Zheng¹¹*Paul C. Lauterbur Research Center for Biomedical Imaging, Shenzhen Institutes of Advanced Technology, Chinese Academy of Sciences, China, People's Republic of***Background, Motivation, and Objective**

Autophagy, cellular self-digestion, is an essential process to recycle obsolete cellular constituents and eliminate abnormal protein aggregates and organelles. Accumulating evidence has indicated that increased neuronal autophagy shows protective effect for neurodegenerative disorders (Nature Medicine, 19 (8): 983-997, 2013; Nature Reviews Neuroscience, 16 (6): 345-357, 2015). Low-intensity pulsed ultrasound (LIPUS) stimulation has reported as a promising technology for treating neurodegenerative disease. However, the effect of LIPUS stimulation on neuronal autophagy has been little addressed. The aim of this study was to investigate whether LIPUS stimulation could induce autophagy in SH-SY5Y neuronal cells.

Statement of Contribution/Methods

LIPUS was generated by a 0.68 MHz plane transducer (diameter = 8 mm) fabricated in our lab. The parameters of LIPUS stimulation for SH-SY5Y neuronal cells were as follows: pulse repetition frequency of 500 Hz, duty cycle of 5%, spatial peak temporal-average intensities (I_{spota}) of 75 or 250 mW/cm², sonication duration of 4 or 6 hours. LIPUS was transmitted from the plane transducer to the bottom of the culture chambers in a cell 37°C incubator with 95% air and 5% CO₂ (Figure 1a). Immunofluorescence analysis of LC3B (a marker of autophagic activity) was performed for detecting the autophagy of SH-SY5Y neuronal cells after LIPUS stimulation. Images were obtained by a confocal microscope (Leica TCS SP5) and the fluorescence intensity was measured using ImageJ software.

Results/Discussion

Figure 1 shows that a 4-hour LIPUS stimulation with I_{spota} of 250 mW/cm² significantly increased the autophagy of SH-SY5Y neuronal cells ($p < 0.01$). Similarly, increasing sonication duration and intensity of LIPUS stimulation improved the autophagy. Previous studies have reported that increasing autophagy can alleviate memory deficits and amyloid- β pathology in a mouse model of Alzheimer's disease and Parkinson's disease (Journal of Neuroscience, 29 (43): 13578-13588, 2009). Our results have demonstrated that ultrasonic stimulation is an effective tool to induce autophagy in SH-SY5Y neuronal cells, which may suggest that transcranial LIPUS stimulation is a potential therapeutic strategy for neurodegenerative disorders by enhancing the neuronal autophagy.

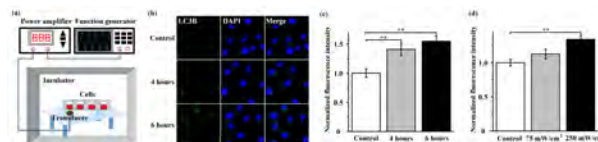


Figure 1. Low-intensity pulsed ultrasound (LIPUS) stimulation increased autophagy of SH-SY5Y neuronal cells. (a) Experimental apparatus. (b) Representative immunofluorescence images of LC3B (green) and DAPI (blue), scale bar = 25 μ m. (c) Autophagy induced by LIPUS stimulation with spatial peak temporal-average intensity (I_{spota}) of 250 mW/cm² for 4 and 6 hours. (d) Autophagy induced by LIPUS stimulation with I_{spota} of 75 and 250 mW/cm² for 4 hours ($^{**}p < 0.01$).

11:00 AM

Bioelectric identification of aggressive prostate cancer using ultrasound cell stimulation

Haichong K. Zhang¹, Jeeun Kang¹, Adarsha Malla¹, Ala Lisok¹, Zaver M. Bhujwalla¹, Martin G. Pomper¹, Maged M. Harraz¹, Emad M. Boctor¹

¹*Johns Hopkins University, MD, United States*

Background, Motivation, and Objective

It is well established that transmembrane voltage potential is linked to the proliferative ability of cells. Hence, cell types with high resting potential such as neurons do not proliferate. On the other hand, malignant cancer cells have low membrane potential and consequently high proliferative ability compared to the surrounding normal or less aggressive cells. High frequency ultrasound that can deliver sound waves at a specific energy is an emerging approach to evoke cell potential non-invasively. In this work, we propose a non-invasive approach to detect aggressive prostate cancer (PCa) using ultrasound cell stimulation.

Statement of Contribution/Methods

As in the proof-of-concept *in vitro* study, we conducted the comparative evaluation between normal prostate epithelial cells and two types of PCa cells; DU145 and PC3. After loading the cells with the DiBAC4 (3), a slow response voltage sensitive dye, ultrasound stimulation was performed while monitoring the membrane potential change for 6 min using fluorescence microscopy. Each cell type was exposed to 1-MHz continuous ultrasound stimulation at 0.53W/cm² power density for 10-seconds following a 1-min baseline. A positive control group was established with potassium chloride (KCl) administration at 1 min time point that induced depolarization by creating strong potassium gradient. The fluorescence intensity during the pre-stimulation baseline was regarded as the negative control.

Results/Discussion

The aggressive malignant prostate cell line PC-3 showed a significant change in membrane potential following ultrasound stimulation compared to sham treatment at 5-min time point (1.78 ± 0.68 vs. 0.83 ± 0.25 , $P < 0.02$), whereas normal prostate cells and less aggressive malignant cells, DU145, showed comparable membrane potentials between pre- and post-ultrasound stimulation phases (0.89 ± 0.25 vs. 0.89 ± 0.16 , $P = 0.52$, and 1.19 ± 0.35 vs. 1.10 ± 0.20 , $P = 0.19$, respectively). These results indicate that bioelectric sensing combined with the non-invasive ultrasound cell stimulation can be a tool for distinguishing aggressive from normal and less aggressive malignant cells.

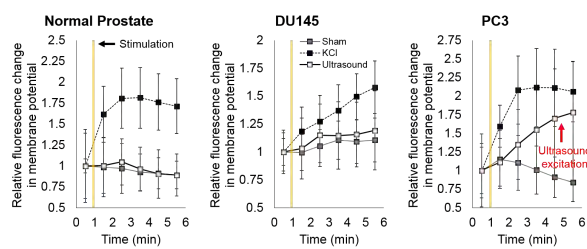


Figure: *In vitro* experiment results of membrane potential response upon ultrasound stimulation (white dot). KCl-induced depolarization (black dot) was regarded as the positive control to validate the function of voltage sensitive dye.

11:15 AM Ex-vivo recording of LEUS-generated neural responses from mouse brain slices using a MicroElectrode Array (MEA) system

Ivan Suarez Castellanos¹, Jérémie Vion-Bailly¹, Apoutou N'Djin¹, Magali Perier¹, Alain Birer¹, Alexandre Carpentier², Gilles Huberfeld², Jean-Yves Chapelon¹

¹INSERM, Lyon, France, ²Assistance Publique Hôpitaux de Paris, France

Background, Motivation, and Objective

Low Energy Ultrasound (LEUS) neurostimulation/modulation is a field that has drawn much attention in past years because of its therapeutic value in treating ailments of neurological and psychiatric nature by non-electrically stimulating nervous tissue. The objective of this work was to develop a MicroElectrode Arrays (MEA)-based set-up to record and explore the mechanisms involved in LEUS stimulation/modulation of neural responses using an ex vivo mouse brain model.

Statement of Contribution/Methods

An experimental platform integrating LEUS generation to a MEA recording system was developed. The LEUS stimulation system consisted of a focused piezoceramic transducer with working frequency of 1.78 MHz and focal distance of 1.5 cm coupled with a cone filled with a 0.2% agarose gel for transmission of the ultrasound wave to the MEA chip. In this set of experiments, hippocampal slices from adult mice were prepared and placed in the MEA chip. The MEA chip consisted of a grid of 120 extracellular electrodes (diameter: 30 μ m) spread every 200 micrometers, thus allowing the recording of single action potentials (APs), APs from multiple neurons (Multi Unit Activity) as well as synchronized synaptic potentials (Local Field Potentials). The ultrasound transducer was precisely placed using a micromanipulator to have the brain slice positioned in the focal region. LEUS exposures were then administrated as pulse trains of 1.1 MPa, 800 to 6200 cycles with PRF of 4 Hz.

Results/Discussion

The signals detected in response to LEUS stimulation corresponded to biphasic responses that appear to be similar in shape and magnitude to those reported by previous work performed *in vivo* on intact mouse brains. The magnitude of the positive peak exhibited a 6-fold increase when increasing the number of pulses/cycle from 800 to 6200. Similarly, the duration of the response increased 3-fold when increasing the number of cycles/pulse from 800 to 3200, but stayed constant when further increasing this number from 3200 to 6400. As a negative control, the same slice was perfused with TTX, a sodium channel blocker aimed at inhibiting the generation of electrical activity in the brain slice. We found that after adding TTX, the magnitude of the positive peak progressively decreased with time (by almost 86%, 12 min after the start of TTX perfusion).

Our results tend to suggest that focused LEUS exposures are capable of generating an electrical response from ex-vivo sliced mouse brains in what appears to be a sodium-dependent mechanism. However, further experiments are still necessary to isolate the neural response generated by LEUS stimulation from potential artifacts, while identifying membrane structures (i.e. ionic channels) involved in this process. This project was supported by the French National Research Agency (ANR 2016, N° ANR-16-TERC-0017) and the Laboratory of Excellence (LabEx) DevWeCan.

11:30 AM Experimental identification of the locus of interaction between Low-Energy UltraSound and the nervous system of *lumbricus terrestris* during the phenomenon of neurostimulation

Jérémie Vion-Bailly¹, Apoutou N'Djin², Alexandre Carpentier³, Jean-Yves Chapelon⁴

¹LabTAU, INSERM, Lyon, France, ²INSERM, France, ³Assistance Publique Hôpitaux de Paris, France, ⁴INSERM, LYON, France

Background, Motivation, and Objective

The interest for ultrasound neurostimulation and potential medical applications keep increasing, but few models are currently available to study the biophysical mechanisms at the preclinical level. In the present work, we aim to demonstrate the interest of an earthworm model of giant neurons to study the phenomenon of Low Energy UltraSound (LEUS) neurostimulation.

Statement of Contribution/Methods

The ventral nerve cord of the earthworm presents 3 giant axons: one Medial Giant Fiber (MGF), and 2 Lateral Giant Fibers (LGF). They receive their inputs from afferent nerves, themselves receiving inputs from mechanosensory ends. Mechanical (MStim) and electrical (EStim) stimulations interact with this nervous architecture at two different levels. MStim activates the mechanosensors and can generate series of Action Potentials (APs), while EStim acts downstream, instantaneously depolarizing the membrane of giant axons and triggering the generation of a single AP in both. Due to variations of the synaptic connections strength, the sensitivity to MStim is, unlike EStim, concentrated in two anteroposterior poles. In our study, experimental investigations have been conducted *in vivo* with this model to compare neural responses associated with LEUS stimulation (LEUStim), MStim and EStim: i) by mapping the anatomical distribution of sensitivity associated with LEUStim; ii) by analyzing the APs time delays. LEUStim was performed with a confocal transducer ($f=1.1$ MHz, Ncycles = 175, Pac-pp = 15 MPa, PRP = 10 Hz). EStim was performed with stimulating electrodes delivering an electrical pulse (8V, 50 μ s). Time of propagation (TOP) of the APs along the axons were estimated by using two sets of recording electrodes.

Results/Discussion

LEUStim triggered the generation of a single or series of APs, and the same excitability polarity as MStim was observed. This indicated that the interactions between LEUS and the nervous system occurred upstream the giant axons, in the neural structures responsible for the polarity. The response delays associated with MStim and LEUStim were longer than the estimated TOPs. Studying the time difference between the actual AP delay and the theoretical TOP highlighted a time interval between the stimulus onset and the generation of the AP in the giant axon, referred to as the time of generation (TOG). The TOGs associated with LEUStim were much shorter and more stable (med. 6.4 ms) than those associated with MStim (med. 32.5 ms). This suggested that the interactions between LEUS and the nervous system occurred downstream the mechanosensors. Thus, this causal study allowed precisely identifying the nervous structures interacting with LEUS during the phenomenon of neurostimulation. Several differences were highlighted between LEUStim, MStim and EStim which can be used to improve the understanding of LEUS neurostimulation. This project was supported by the French National Research Agency (ANR-16-TERC-0017) and the LabEx DEVweCAN.

11:45 AM

Potential of Low Energy UltraSound for inducing cardioprotection mechanisms: in-vitro investigations on a hypoxia-reoxygenation model of cardiac cells

Lorena Petrusca¹, Claire da Silva², W. Apoutou N'Djin³, Jean-Yves Chapelon³, Pierre Croisille¹, Michel Ovize², Magalie Viallon¹

¹Univ Lyon, UJM-Saint-Etienne, INSA, CNRS UMR 5520, INSERM U1206, CREATIS, F-42023, SAINT-ETIENNE, France, ²INSERM UMR-1060, Laboratoire CarMeN, Université Lyon 1, Faculté de Médecine, Rockefeller, Lyon, France, ³LabTAU, INSERM, Centre Léon Bérard, Université Lyon 1, Univ Lyon, F-69003, LYON, France

Background, Motivation, and Objective

After acute myocardial infarction, patients' prognosis is mainly determined by the final infarct size (IS) resulted from ischemia and reperfusion injury (IRI). Innovative "Cardio-protective" strategies may target edema and inflammation to alleviate IRI. Mechanotransduction (MT) (d'Agostino MC *et al*, Int J Surg. 2015; 24:147-53) represents a biologic pathway encompassing the molecular mechanisms by which cells can adapt to Low Energy Ultrasound (LEUS) stimulation. We propose that LEUS exposures might attenuate the detrimental effects of IRI. Specifically, our goal is to quantify and monitor the effects of MT using a cardiac cell model of ischemia-reperfusion.

Statement of Contribution/Methods

The study was conducted using a mono-layer cell model (H9C2 cardiomyoblasts) exposed to a prolonged hypoxia-reoxygenation (HR) challenge. Cells underwent 4.5 hours of nutrients and O₂ deprivation (PO₂ reduced to near 0.5%) followed by reoxygenation. Three groups were formed: i). **Normoxia**: cells incubated under normal conditions (5% CO₂, 37°C), ii). **HR**: cells submitted to hypoxia followed by reoxygenation period, and iii). **HR+PostCond-LEUS**: LEUS (pulsed sequence, $f = 2.7$ MHz, $MI < 0.4$) applied repeatedly for 20 min starting at the onset of reoxygenation. Cell death was evaluated by flow cytometry for each group at the end of US exposure. A research-dedicated US scanner and standard cardiac probes were used for LEUS delivery.

Results/Discussion

Cell viability was clearly improved in the HR+PostCond-LEUS group, at all time points during reoxygenation. Maximum protection was observed at t3 = 50 min after the onset of reperfusion, where the IP (% dead cells) was decreased by 19% in the HR+PostCond-LEUS group when compared to the HR group with no LEUS. Accordingly, the DilC1 (% live cells) was increased by 23% for HR+PostCond-LEUS group.

This study suggests a potential protective effect of LEUS on cardiomyoblasts exposed to a prolonged hypoxia-reoxygenation insult. Pulsed LEUS might be a promising approach to attenuate cellular damage following a prolonged ischemia-reperfusion. More complex *in vitro* models exploring potential protective mechanisms (SAFE and RISK signaling pathways (Abrial M *et al*, J Mol Cell Cardiol. 2014;68:56–65)) and *in vivo* models will follow for a better comprehension of the underlying mechanisms.

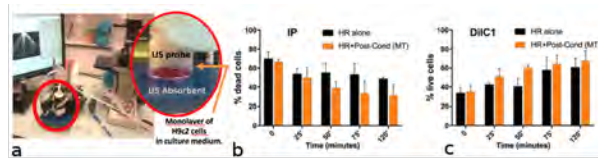


Fig. 1. a) Experimental setup including the LEUS probe and the monolayer of H9C2 cells in culture medium. b-c) Results obtained (in %) at different time-points after cell hypoxia for HR and HR+PostCond-LEUS groups for IP (b) and DilC1 (c).

2J - Ultrasound Mediated Agent Delivery

Diamond (300)

Thursday, October 25, 1:30 pm - 3:00 pm

Chair **Mark Borden**
University of Colorado Boulder

2J-1

1:30 PM Focused Ultrasound Enhanced Intranasal Delivery of Neurotrophic Factors Exhibit Neurorestorative Effects in Parkinson's Disease Mouse Model

Robin Ji¹, Morgan Smith¹, Vernice Jackson-Lewis², Serge Przedborski^{2,3}, Elisa Konofagou^{1,4}

¹*Biomedical Engineering, Columbia University, New York, NY, United States*, ²*Pathology & Cell Biology, Columbia University, United States*, ³*Neurology, Columbia University, United States*, ⁴*Radiology, Columbia University, United States*

Background, Motivation, and Objective

Focused ultrasound enhanced intranasal (IN+FUS) delivery is a unique, noninvasive approach that utilizes the olfactory pathway to administer drugs directly to the brain. Drugs that typically do not cross the BBB, or have short circulating half-life, can now gain direct access to targeted brain regions. Our group has shown that IN+FUS delivery of model drugs provide a more homogenous distribution of delivery when compared to IN delivery alone, and similar delivery efficiency to intravenous delivery after FUS induced BBB opening. The aim of this study was to investigate the delivery efficacy and therapeutic effects of IN+FUS administered brain-derived neurotrophic factor (BDNF) has on an early stage Parkinsonian mouse model.

Statement of Contribution/Methods

Wild-type mice were given a sub-acute dose of the 1-methyl-4-phenyl-1,2,3,6-tetrahydropyridine (MPTP) toxin daily for 5 days, causing bilateral degeneration of the nigrostriatal dopaminergic pathway. After a stabilizing period, the mice were split into a treated group and a control group (N=7/group). The treated group was dosed with IN+FUS of BDNF weekly for 3 weeks. Each week, 0.4 mg of BDNF was intranasally delivered followed by BBB opening in the left substantia nigra (SN) and caudate putamen (CP) using FUS and sized isolated microbubbles. After the 3rd week, the mice were survived for 2 months to allow for any neurorestorative effects to occur. Then behavioral testing through amphetamine-induced rotations was conducted. Brains were harvested via transcardial perfusions and sectioned coronally. Staining of tyrosine hydroxylase positive (TH+) neurons in the SN and terminals in the CP were used to assess the nigrostriatal dopaminergic pathway integrity.

Results/Discussion

Initial TH+ staining in the CP suggests a trend of greater staining in the ipsilateral side in treated mice (Fig. 1A) and similar staining bilaterally in control mice (Fig. 1B). Significant ipsilateral rotation in treated mice corroborate the initial TH+ staining (Fig. 1C), suggesting improved ipsilateral nigrostriatal dopaminergic pathway. These initial findings indicate a modest neurorestorative effect of IN+FUS BDNF on MPTP mice, demonstrating the potential of an alternative and efficient drug delivery route for brain treatment with FUS. Further TH+ staining and quantification in the SN and CP are ongoing to confirm these findings.

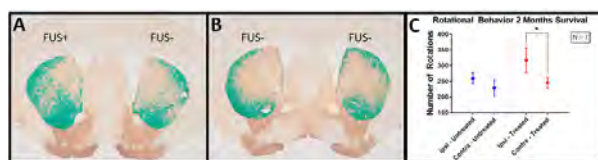


Fig. 1: (A) TH+ neurons in the CP of IN+FUS BDNF treated MPTP mouse with only the left side sonicated. (B) TH+ neurons in the CP of an untreated MPTP mouse with no sonication on either side. (C) Amphetamine-induced behavioral tests show a significant rotational bias toward ipsilateral side in IN+FUS BDNF treated MPTP mice but not in untreated MPTP mice. The mean and standard error is plotted.

1:45 PM

Comparison of focused ultrasound-mediated intranasal brain drug delivery and focused ultrasound-induced blood-brain barrier disruption in the delivery of gold nanoclusters to the brainstem

Dezhuang Ye¹, Xiaohui Zhang², Yimei Yue³, Sara Taylor⁴, Yuan-Chuan Tai², Joshua B. Rubin⁴, Yongjian Liu², Hong Chen^{3,5}

¹*Mechanical Engineering and Material Science, Washington University in St Louis, Saint Louis, MO, United States,*

²*Radiology, Washington University in St Louis, Saint Louis, MO, United States,* ³*Biomedical Engineering, Washington University in St Louis, Saint Louis, MO, United States,* ⁴*Pediatrics Hematology/Oncology, Washington University in St Louis, Saint Louis, MO, United States,* ⁵*Radiation oncology, Washington University in St Louis, Saint Louis, MO, United States*

Background, Motivation, and Objective

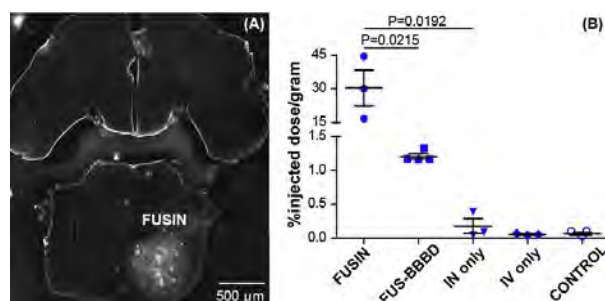
Focused ultrasound-mediated intranasal brain drug delivery (FUSIN) is a new brain drug delivery technique. Different from the established FUS-induced blood-brain barrier disruption (FUS-BBBD), FUSIN utilizes the nose-to-brain pathway for drug administration, which bypasses the BBB and minimizes systemic exposure; it uses FUS combined with microbubbles to enhance the accumulation of IN-administered agents at the FUS-targeted brain location. The objective of this study was to compare FUSIN with FUS-BBBD in terms of the drug delivery efficiency, systemic exposure, and drug delivery pathways.

Statement of Contribution/Methods

Texas red-labeled gold nanoclusters (TR-AuNCs) were used as the model drug and the brainstem was selected as the FUS targeted brain location. Mice were divided into five groups: FUSIN, FUS-BBBD, intranasal (IN) only, intravenous (IV) only, and control with no treatment. The distribution of TR-AuNCs in the mouse brain was visualized by fluorescence microscopic imaging of *ex vivo* brain slices from both FUSIN and FUS-BBBD groups ($n=3$ for each group). The delivery efficiency of TR-AuNCs to the mouse brain was quantified using inductively coupled plasma-mass spectrometry (ICP-MS), which measured the Au concentration in the brainstem of mice in all groups ($n=3$ for each group). The concentrations of TR-AuNCs in other major organs, as well as in nasal tissue, trigeminal nerves, and blood, were also quantified using ICP-MS.

Results/Discussion

The acquired fluorescence images showed that both FUSIN and FUS-BBBD enhanced the delivery of TR-AuNCs at the FUS-targeted brainstem (Fig. A). ICP-MS found the delivery efficiency of TR-AuNCs by FUSIN was 25-fold ($P=0.0192$) higher than that by FUS-BBBD, and 172-fold higher than that by IN only ($P=0.0215$) (Fig. B). The systemic exposure of TR-AuNCs by IN delivery was one-magnitude lower than that by IV in major organs except stomach and intestines. The Au concentrations in the nasal tissue and trigeminal nerves were respectively 290-fold and 72-fold higher in mice by IN delivery than by IV injection, while in the blood were 109-fold lower in mice by IN delivery than by IV injection. These findings suggest that FUSIN is a promising technique for spatially targeted and efficient brain drug delivery with minimized systemic exposure and the drug delivery pathway of FUSIN is different from that of FUS-BBBD.



2:00 PM

Ultrasound and microbubble-mediated targeted delivery of drug-loaded nanoparticles to porcine liver

Tommaso Di Ianni¹, Sunita Bachawal¹, Huaijun Wang¹, Rajendran J. C. Bose¹, Arsenii Telichko¹, Uday K. Sukumar¹, Carl Herickhoff¹, Sam Baker², Stephen A. Felt², Ramasamy Palmarugan¹, Jeremy Dahl¹

¹Radiology, Stanford University, United States, ²Comparative Medicine, Stanford University, United States

Background, Motivation, and Objective

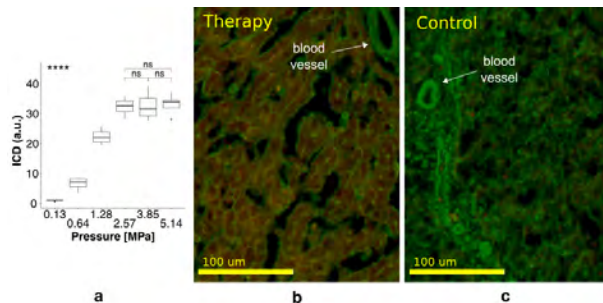
Hepatocellular carcinoma is a leading cause of cancer death, with poor prognosis and limited possibilities for surgical resection. Identification of new treatment approaches is highly needed to improve patient survival outcome. Use of focused ultrasound (US) and microbubbles (MB) has proven effective in facilitating delivery of drug-loaded nanoparticles to cancer in a targeted way in small animal models. The aim of this study was to adapt and validate the US/MB-mediated drug delivery platform for large animal models using clinically approved MB (SonoVue, Bracco Research) and a diagnostic US setup, as a further step toward clinical translation.

Statement of Contribution/Methods

Phantom and *in vivo* experiments were performed with a C5-2v curved array and a Verasonics Vantage 256 scanner for image guidance and therapy. A 2-MHz focused beam was used to induce MB cavitation at the treatment site. Acoustic parameters (peak negative pressure (P), pulse length, PRF, n. pulses) were optimized in a flow phantom by measuring the inertial cavitation dose (ICD). The optimized setup (3.21 MPa P; 10-cycle pulse length; 4 Hz PRF; 800 pulses) was tested *in vivo* on female swine ($n = 2$) injected with a solution of MB and semiconducting polymer nanoparticles (SPN) of ~150-nm diameter used as a model drug. Therapy was delivered in a liver lobe at a depth of 70 mm. The animals were euthanized after 24 h, and liver tissue was collected, fixed, and stained for F-actin. Immunofluorescence analysis was performed to assess the presence of nanoparticles in the liver parenchyma.

Results/Discussion

The ICD measured in phantom experiments increased significantly with increasing pressure (Fig. a; $p < 0.0001$). A plateau was reached at $P = 2.57$ MPa, and no differences were found between $P = 2.57$, 3.85, and 5.14 MPa ($p > 0.7$). Fig. b and c show the immunofluorescence of porcine liver tissue in the therapy region (b) and in a distal lobe as control (c). The cytoskeleton was stained in green, and SPN was stained in red. The amount of extravasated SPN was considerably increased in the therapy region compared to the control. In addition, nanoparticles were located inside the cells indicating enhanced cellular uptake of the model drug. In conclusion, US/MB-mediated targeted delivery of drug-loaded nanoparticles is feasible in deep liver tissue in large animals using clinically approved MB and a diagnostic US system.



2:15 PM

Focused-ultrasound mediated anti-alpha-synuclein antibody delivery for the treatment of Parkinson's disease

Hairong Zhang¹, Carlos Sierra¹, Nancy Kwon¹, Maria Eleni Karakatsani¹, Vernice Jackson-Lewis², Serge Przedborski^{2,3}, Elisa Konofagou^{1,4}

¹Department of Biomedical Engineering, Columbia University, New York, NY, United States, ²Department of Neurology, Columbia University, New York, NY, United States, ³Department of Pathology & Cell Biology, Columbia University, New York, NY, United States, ⁴Department of Radiology, Columbia University, New York, NY, United States

Background, Motivation, and Objective

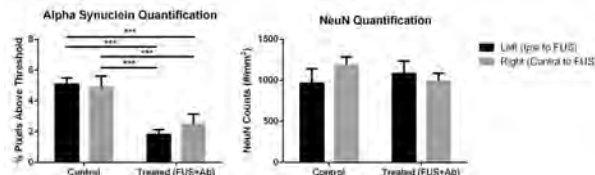
Parkinson's disease (PD) is associated with the selective death of dopaminergic (DA) neurons in the substantia nigra pars compacta (SNpc). While the specific cause of the neuronal loss remains elusive, the abnormal accumulation of alpha synuclein (α -syn), a major constituent of Lewy bodies, is considered to play a central role in the pathology of PD. Previous passive immunotherapy studies remain ineffective due to the presence of the blood-brain barrier (BBB), which hinders most therapeutic agents to diffuse to the brain parenchyma. Focused ultrasound in conjunction with microbubbles is a technique to achieve noninvasive, transient, and localized BBB opening to enhance drug delivery to the brain. Therefore, the objective of this study is to explore the potential of FUS-mediated delivery of anti α -syn antibodies for the treatment of Parkinson's disease.

Statement of Contribution/Methods

The study group consisted of ten A53T mice expressing the human α -syn which were divided into three groups: control, FUS-only, and FUS combined with anti- α -syn monoclonal antibodies. Mice were sonicated with FUS at the left hippocampus, left caudate putamen, and left substantia nigra at an acoustic pressure of 450 kPa, and the microbubbles were injected intravenously (with or without antibodies) through the tail vein immediately prior to sonication. To investigate the neuroprotective effects of FUS/Ab, mice received three weekly treatments at 6-7 months of age before significant alpha synuclein aggregation and were euthanized one month after the last treatment for perfusion and immunohistochemical analysis.

Results/Discussion

Quantification using a minimum error thresholding technique demonstrated reduced α -syn load in mice treated with both FUS and antibody compared to the control mice ($p<0.01$ by one-way ANOVA and multiple comparison test, Figure 1), without a significant change in neuronal cell counts ($p>0.5$ by one-way ANOVA, Figure 1). Reduction of α -syn aggregation was detected bilaterally in the treated brain, indicating a possible bilateral effect of unilateral FUS treatment. The FUS treatment was found to be safe as assessed by both MRI and TUNEL staining. These findings indicate that weekly treatments with FUS and anti- α -syn antibodies can successfully reduce α -syn load in transgenic mouse models of PD.



2:30 PM

Ultrasound-Enhanced Distribution and Treatment Efficacy of Dox-loaded Intratumoral In Situ Forming Implants in Murine HCT-15 Tumors

Selva Jeganathan¹, Emily Budziszewski¹, Peter Bielecki¹, Christopher Hernandez¹, Agata Exner^{1,2}

¹Biomedical Engineering, Case Western Reserve University, Cleveland, OH, United States, ²Radiology, Case Western Reserve University, Cleveland, OH, United States

Background, Motivation, and Objective

Systemic chemotherapy suffers from adverse toxicity in healthy tissues and a heterogeneous distribution within the tumor parenchyma. To overcome these challenges, injectable *in situ* forming implants (ISFI) can be used for continuous release of a high dosage of drugs directly at the tumor site. However, drug penetration away from the implant-tumor interface is limited to 2-3 mm due to the highly heterogeneous tumor microenvironment and irregular vasculature. Ultrasound has been used in numerous studies to improve distribution of drugs delivered via micro- and nanoparticles. Here we examined the effects of combining ultrasound with locally delivered chemotherapeutic drugs in a murine model of human colorectal cancer.

Statement of Contribution/Methods

ISFIs consisting of Doxorubicin (Dox) and poly(lactic-co-glycolic acid) co-dissolved in an organic solvent, N-methyl-2-pyrrolidone, were intratumorally injected into subcutaneous HCT-15 tumors. All animals received ISFI injection ($n=6$) and a sub-group of 3 mice received TUS treatment (4 cm² surface probe, 3 MHz, 2.2 W/cm²) for 5 min at 33% duty factor. Exposure to TUS in this model has been shown to increase the local temperature by $\sim 13^{\circ}\text{C}$. To determine effects of hyperthermia on drug release and distribution, ISFIs were injected into PBS pre-heated to 50°C and into an acrylamide phantom submerged in a 50°C water bath. *In vitro* and *in vivo* Dox distribution was monitored with a fluorescence imaging system (CRI Maestro) and analyzed using ImageJ (NIH). Tumors were measured with calipers every other day following treatment.

Results/Discussion

Representative fluorescent images intratumoral ISFI are seen in Fig 1A. ISFI + TUS showed a 3-fold increase in area of Dox distribution (1.93 cm² vs 0.64 cm²) and 2-fold increase in total Dox fluorescence (1647.38 a.u. vs 786.30 a.u.) immediately after treatment, compared to ISFI alone (Fig 1B, C). ISFI + TUS also resulted in significantly slower tumor growth (481.20 \pm 319.72 mm³ vs 1832.74 \pm 467.84 mm³) (Fig 1D). H&E staining showed increased necrosis (not shown). ISFIs exposed to 50°C showed no significant increase in drug release or distribution, *in vitro* (not shown). Overall ISFI + TUS showed increased *in vivo* Dox penetration into tumors and significantly inhibited tumor growth. Future studies will examine the effects of TUS-induced hyperthermia alone on tumor growth inhibition *in vivo*.

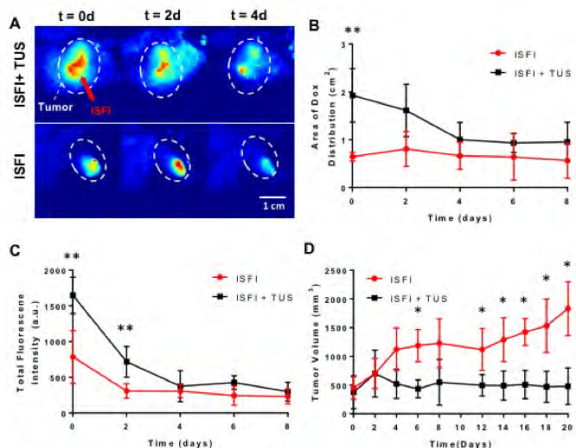


Figure 1: (A) Representative images of intratumoral ISFI. Effects of low frequency ultrasound applied to ISFIs on (B) area of drug distribution, (C) total fluorescence intensity, and (D) tumor growth. Exposure to TUS shows an increase in drug distribution and reduction in tumor growth. Significant difference: * $p < 0.05$, ** $p < 0.01$.

2:45 PM

Abraxane delivery with microbubble-assisted ultrasound in human pancreatic cancer mouse modelJean-Michel Escoffre¹, Diane Bressand^{1,2}, Anthony Novell¹, Thierry Lecomte², Ayache Bouakaz¹¹*University of Tours, Inserm UMR1253 iBrain, Tours, France*, ²*Gastro-enterology and Digestive Cancerology, University Hospital CHU, Tours, France***Background, Motivation, and Objective**

Microbubble-assisted ultrasound (US) is a potential method for non-invasive targeted delivery of anticancer drugs. This method increases the local drug concentration in the tumor tissue while reducing the systemic adverse sides. The present study aims to evaluate the therapeutic effectiveness of this technique both in-vitro and in-vivo for Abraxane delivery.

Statement of Contribution/Methods

In-vitro, a suspension of human pancreatic cancer BxPC3 cells was exposed to US (1 MHz, 100 µs PRP, 40% DC, 400 kPa, 30s) in presence of microbubbles (QA3216 MBs/cell ratio 5:1) and Abraxane (2.5 ng/mL). 72 hours later, MTT assay was performed to assess cell viability.

In-vivo, BxPC3 tumors were induced by a subcutaneous injection of 5×10^6 cells in both flanks of nude mouse. When the tumor volume reached 50 mm^3 , the treatment was initiated as follows: An i.v. administration of Abraxane (5 or 20 mg/kg) followed by an i.v. administration of MBs (70 µL). US insonation was applied using a single-element transducer at 1 MHz (100 µs PRP, 40% DC, 400 kPa, 3 min). The therapeutic efficacy was determined by monitoring the tumor volume growth using US imaging.

Results/Discussion

In-vitro, results indicated that the acoustically-mediated Abraxane delivery led to a 10% additional decrease in cell viability in comparison with Abraxane treatment alone ($p < 0.05$).

As shown in Fig.1, MBs and US did not affect tumor growth compared to the control group. After 37 days, chemotherapy with 5 or 20 mg/kg Abraxane dose alone led to a 1.5- and 5-fold decrease in the tumor volume compared to control group ($p < 0.05$). Combination of US, MBs and chemotherapy with 5 or 20 mg/kg Abraxane dose resulted in a 1.5- and 3-fold additional decrease in the tumor volume compared to chemotherapy alone ($p < 0.05$). More interestingly, Abraxane at 20 mg/kg in combination with US and MBs induced a total shut down of tumor volume growth.

In conclusion, this study demonstrates the potential of this method to improve the therapeutic effectiveness of Abraxane in pancreatic cancer.

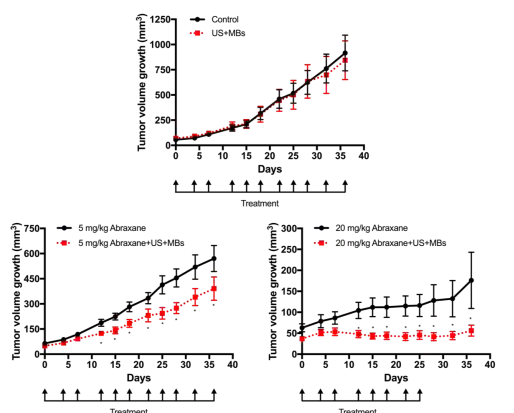


Figure 1 - Abraxane delivery using microbubble-assisted ultrasound in human pancreatic cancer mouse model

2K - Coding, Beamforming and Parametric Contrast Imaging

Diamond (300)

Thursday, October 25, 4:00 pm - 5:30 pm

Chair **Chih-Kuang Yeh**
National Tsing Hua University

2K-1

4:00 PM Nondestructive targeted microbubble detection using a dual-frequency beamforming deep neural network

Dongwoon Hyun¹, Leandra Brickson², Lotfi Abou-Elkacem¹, Jeremy Dahl¹

¹*Department of Radiology, School of Medicine, Stanford University, Palo Alto, CA, United States*, ²*Department of Electrical Engineering, Stanford University, Stanford, CA, United States*

Background, Motivation, and Objective

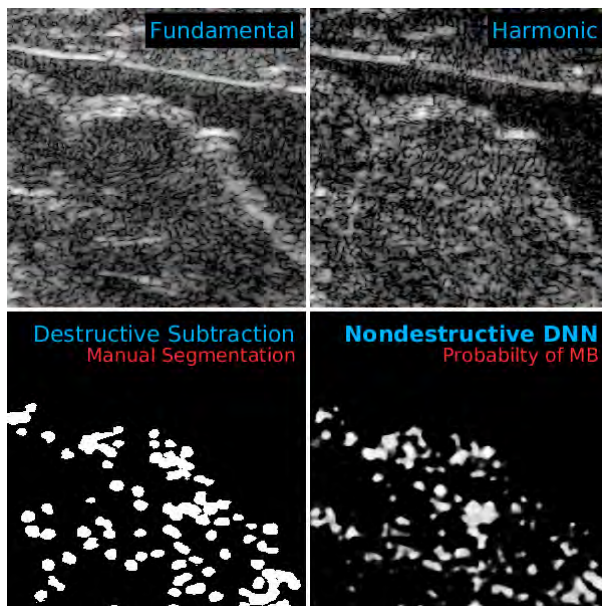
Ultrasound molecular imaging (USMI) is accomplished by detecting targeted microbubbles (MBs) that bind to desired molecular targets. Targeted MBs are imaged using low pressure pulses to avoid bursting, leading to echoes with low signal-to-noise ratio. Currently, the gold standard for targeted MB detection *in vivo* preclinically is to use a strong destructive pulse to burst the MBs and to subtract a post-burst image from a pre-burst image, enhancing the targeted MB signal and suppressing background tissue noise and non-stationary MBs. However, this approach can lead to tissue damage, is not real-time, and is highly sensitive to motion artifacts. We propose to detect targeted MBs nondestructively using a novel deep neural network (DNN) beamformer that processes channel data from dual-frequency transmissions.

Statement of Contribution/Methods

A DNN was designed to accept focused channel data from one 10 MHz and two pulse-inverted 5 MHz plane waves for interleaved fundamental and harmonic imaging at 10 MHz. The output of the DNN was a pixel-wise probability of MB presence. The DNN was trained to identify MBs according to 20 manually segmented destructive subtraction images that were used as ground truth. A Verasonics Vantage 256 scanner and L12-3v transducer were used to obtain channel data from VEGFR2-targeted MBs in a microvessel flow phantom and a subcutaneous tumor in a mouse model of hepatocellular carcinoma. Porcine tissue was placed between the transducer and the target to emulate *in vivo* conditions and to serve as a region known to contain no MBs. The trained DNN was tested on 5 previously unseen USMI datasets, including one control dataset acquired without MBs. Segmentation quality was quantified using the AUC metric and Dice coefficient (DC) of the image thresholded at $p > .5$.

Results/Discussion

In 5 test datasets, the DNN achieved a mean AUC of .91 and DC of .56 compared to the destructive subtraction images. The DNN accurately detected MBs within the tumors and the flow phantom and not in the porcine tissue, surrounding gel, or control dataset. These results show that the DNN can nondestructively distinguish MBs from tissue and noise by exploiting characteristic differences in their fundamental and harmonic responses. The nondestructive dual-frequency DNN beamformer enables safe and real-time USMI and can aid in the translation to clinical applications.



4:15 PM

Improved Contrast-Enhanced Ultrasound Imaging by combining Hadamard-encoded Multi-pulses with Multiplane Wave Transmission

Ping Gong¹, Pengfei Song¹, Chengwu Huang¹, Shigao Chen¹

¹Radiology, Mayo Clinic College of Medicine and Science, Rochester, MN, United States

Background, Motivation, and Objective

Contrast-enhanced ultrasound (CEUS) imaging has great potential for use in many new ultrasound clinical applications by improving the contrast between blood and tissue. However, the low mechanical index (MI) used in CEUS may result in low signal-to-noise ratio (SNR) in deeper imaging regions. To address this challenge, we recently proposed a new microbubble sequence, Hadamard-encoded multi-pulses (HEM), to improve the SNR and contrast-to-tissue ratio (CTR) in CEUS imaging. Multiplane wave (MW) imaging is another new technique that was recently proposed to improve SNR in plane wave imaging. In this study, we propose to combine the HEM pulse with MW imaging to further improve SNR and CNR without elevating MI in plane-wave-based CEUS imaging.

Statement of Contribution/Methods

Fig. 1a shows an example of MW-HEM pulse design with two compounding angles. This MW-HEM sequence consists of four transmission events (i.e., TX #1-TX #4), each with four tilted plane wave emissions. These four emissions can be further separated into two HEM pulse pairs, with each pair containing two consecutive pulses steering at the same angle (i.e., +1° or -1°). The polarity of each emitted pulse follows the 4th-order Hadamard matrix (labeled in red). The received radiofrequency (RF) signals can be decoded with the same Hadamard matrix to recover the signals as if they were obtained from individually exciting each pulse at each steering angle in separate transmission events. The signal amplitude, however, is significantly enhanced. Tissue signal can be suppressed by recombining the decoded HEM pulse pairs. Final image is then constructed following the standard plane wave beamforming and compounding process.

Results/Discussion

Fig. 1b shows the flow phantom images acquired with the proposed MW-HEM sequence as well as the AM, MW-AM and HEM sequences. MW-HEM provides the highest CTR among the four sequences. This enhancement is because the multiple fast pulse polarity changes induced by the MW-HEM pulses lead to significantly improved microbubble nonlinear responses, and thus further enhanced SNR and CTR as compared to HEM alone or other CEUS sequences. These results showed great potential for MW-HEM to improve CEUS imaging quality in deep abdominal organs and the heart.

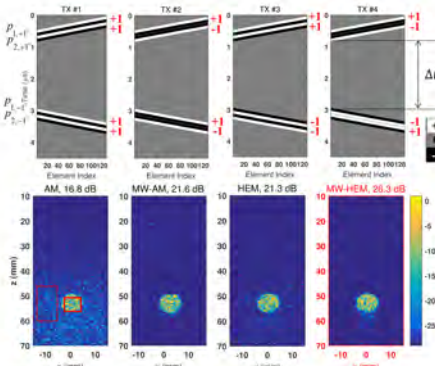


Fig. 1a: MW-HEM design example using a tristate pulser. Fig. 1b: CEUS images acquired from a tissue mimicking phantom with a microbubble flow-cell in the center, using plane-wave-based amplitude modulation (AM), multiplane wave AM, HEM, and MW-HEM. The dotted (tissue) and solid (contrast) boxes indicate the region-of-interest (ROI) selections for CTR quantification with values shown in the subtitles.

4:30 PM

Acoustic sub-aperture processing (ASAP) for super-contrast microvascular imaging: in vivo demonstration for preclinical contrast and non-contrast imaging

Chee Hau Leow¹, Marta Braga², Nigel L. Bush³, Antonio Stanziola¹, Anant Shah³, Javier Hernández-Gil^{2,4}, Nicholas J. Long^{2,4}, Eric O. Aboagye², Jeffrey Bamber³, Mengxing Tang¹

¹Department of Bioengineering, Imperial College London, United Kingdom, ²Department of Surgery & Cancer, Imperial College London, United Kingdom, ³Joint Department of Physics and Cancer Research UK Cancer Imaging Centre, Institute of Cancer Research, United Kingdom, ⁴Department of Chemistry, Imperial College London, United Kingdom

Background, Motivation, and Objective

We recently developed ASAP processing for super-contrast vasculature imaging and demonstrated its feasibility for high-frame rate contrast-enhanced ultrasound (CEUS). This technique relies on the spatial coherence of the backscattered echoes over different acquisitions to substantially reduce the noise floor compared to the power Doppler (PD) technique. In this study, our objectives are to demonstrate the feasibility of applying ASAP processing for non-contrast enhanced microvascular imaging, and compare it with contrast enhanced ASAP as well as standard PD.

Statement of Contribution/Methods

A Balb-c mouse was anaesthetised and high frame-rate imaging was performed of the kidney using a high frequency probe (L22-14v, 7 angle compounding, frame rate=500Hz). Non-contrast B-mode images were first acquired followed by the contrast B-mode images after a 50 μ l bolus injection of a relatively dilute solution of home-made microbubbles (1×10^6 microbubbles/ml). Singular value decomposition (SVD) was used for clutter filtering and microvascular images were generated using PD and ASAP processing for comparison.

Results/Discussion

Figure 1 shows the images obtained from PD and ASAP processing using autocorrelation lag-0. The signal-to-noise ratio (SNR), quantified from the green and white boxes, were found to be -1.1, 6.2, 1.3 and 9.8dB for the non-contrast PD, non-contrast ASAP, contrast PD, and contrast ASAP, respectively. Vascular images with higher contrast can be seen when using ASAP compared to PD. Higher SNRs were expected for contrast images than for non-contrast, and more microvasculature can indeed be seen after contrast injection. In conclusion, we demonstrated the feasibility using ASAP *in vivo* for non-contrast microvascular imaging, and the advantages of using contrast agents in microvascular imaging.

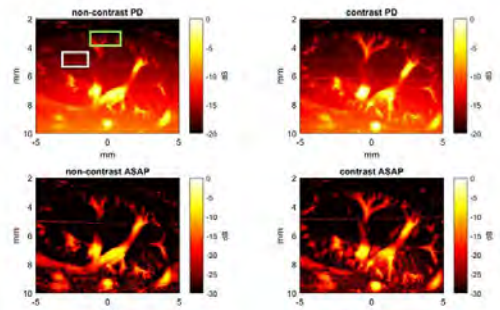


Fig 1: In-vivo demonstration of mouse kidney processed using Power Doppler (PD) and Acoustic Sub-Aperture Processing (ASAP), with and without contrast. The vascular images were generated by accumulating the relative echo power from moving scatterers over 3 seconds acquisition and displayed in log-scale.

4:45 PM

Multi-Parametric Assessment of Treatment Response from 3D Dynamic Contrast-Enhanced Ultrasound

Ahmed El Kaffas¹, Assaf Hoogi², Albert Tseng², Isabelle Durot³, Jarrett Rosenberg², Dimitre Hristov², Daniel Rubin², Juergen Willmann³

¹Radiology, Stanford University, Stanford, CA, United States, ²Stanford, United States, ³Department of Radiology, School of Medicine, Stanford University, Palo Alto, CA, United States

Background, Motivation, and Objective

Volumetric dynamic contrast-enhanced ultrasound (DCE-US) can yield 3D parametric maps to assess spatial changes in tumor perfusion heterogeneity during cancer treatment. Here, quantitative multi-parametric biomarkers based on texture and histogram-based features from 3D parametric maps were evaluated as surrogates of treatment response.

Statement of Contribution/Methods

We used a total of 78 mice bearing colon cancer tumors on the hind leg to identify multi-parametric biomarkers and develop a model that can predict treatment response. Data included LS174T and CT26 tumors randomized into control or treated conditions. Treatments consisted of the anti-angiogenic therapy (Bevacizumab; 3x10 mg weekly) at 0, 1, 3, 7, and 10 days. Imaging was performed using Philips EPIQ7/iU22 with an X6-1 transducer. Animals were imaged following a bolus of 5×10^7 Definity microbubbles at days 0, 1, 3, 7 and 10. Parametric map generation based on voxel-by-voxel bolus perfusion parameters was carried out on high-performance computing cluster as previously described. Greater than 1000 texture or histogram features were extracted for each animal on each imaging day, and a selection pipeline that assessed sensitivity to treatment and repeatability, followed by a principal component analysis, was used to select the best feature sets. Linear discriminant and GLMNET models were used on features to form multi-parametric approaches to differentiate between responders and non-responders. Models were tested in a separate set of pre-clinical data with histological assessment, and on preliminary clinical data consisting of n=7 patients (HIPPA compliant study) imaged longitudinally, and confirmed against RECIST criteria as responders or non-responders through.

Results/Discussion

Features selected yielded multi-parametric biomarkers that are better than the conventional perfusion parameters at discriminating between pre-clinical responders and non-responders ($\text{ROC-AUC} > 0.97$), and that can be directly translated to the clinic to differentiate between responders and non-responders within 14 days of treatment ($\text{ROC-AUC} = 1.00$) (Figure). Multi-parametric biomarkers were significantly correlated to histology ($p < 0.02-0.01$; Spearman R > 0.77). In contrast, conventional parameters had a $\text{ROC-AUC} < 0.33$, and did not correlate with histology.

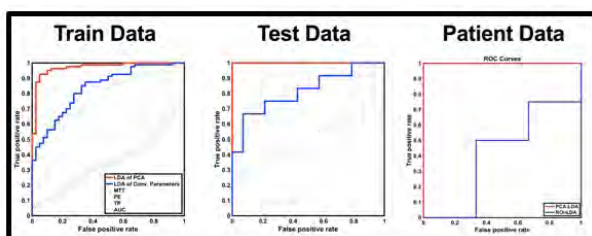


Figure 1 - Left: ROC of all data used to train simple LDA statistical model. Mid: ROC results for separate data set used to test this LDA model. Right: ROC results for patient data set used to test LDA model. Red line is ROC for LDA model from all selected features and blue line is ROC for LDA model from combined conventional perfusion parameters. Fine lines are ROC for each conventional parameter alone.

5:00 PM High-contrast 3D *in vivo* microvascular imaging using scanning 2D ultrasound and acoustic sub-aperture processing (ASAP)

Chee Hau Leow¹, Marta Braga², Nigel L. Bush³, Antonio Stanziola¹, Anant Shah³, Javier Hernández-Gil^{2,4}, Nicholas J. Long^{2,4}, Eric O. Aboagye², Jeffrey Bamber³, Mengxing Tang¹

¹Department of Bioengineering, Imperial College London, United Kingdom, ²Department of Surgery & Cancer, Imperial College London, United Kingdom, ³Joint Department of Physics and Cancer Research UK Cancer Imaging Centre, Institute of Cancer Research, United Kingdom, ⁴Department of Chemistry, Imperial College London, United Kingdom

Background, Motivation, and Objective

Imaging of microvascular structure and flow is of clinical interest to study the progression and response of various diseases. Our recent development of 2D-ASAP imaging has shown unprecedented contrast for vascular imaging. However, 2D imaging is insufficient to represent the volumetric structure of the vascular environment. In this work, we aim to generate 3D vascular images using multiple slices of 2D non-contrast enhanced images processed using ASAP.

Statement of Contribution/Methods

2D high frame-rate Bmode images of an athymic nude (NCR-Fox1^{nu}) mouse liver were acquired using a Verasonics Vantage™ and an L22-14v probe (18MHz, 500Hz). A stepper motor was synchronised with this system to move the transducer along the elevation direction with a step size of 500um and total travel range of 3 mm. For each step, 1500 frames of 15-angle plane-wave images were acquired and processed using the ASAP technique to generate a vascular 2D image. To avoid artefacts from respiratory motion, principle component analysis was applied to reject any frames affected by the motion. Multiple 2D vascular images were finally stacked into a 3D volume and rendered using local maximum intensity projection technique.

Results/Discussion

Figure 1 shows example of *in vivo* 2D and 3D vascular images of a normal mouse liver. The signal-to-noise ratio quantified from the mid-plane vascular image (green and yellow boxes) were 6.6 and 14.7dB for PD and ASAP, respectively. High contrast mages processed using ASAP facilitate the visualisation of the vascular information in both 2D and 3D. In the future, we expect to extract and quantify the vascular structural information generated using ASAP to study various diseases such as cancer.

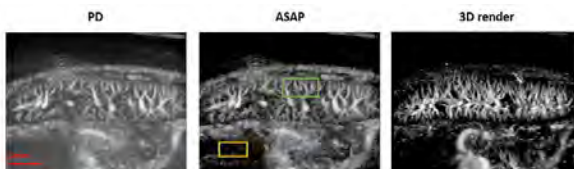


Fig 1: 2D vascular image of the mouse liver generated using (left) Power Doppler and (middle) ASAP. (Right) 3D vascular volume visualised using local maximum intensity projection after ASAP processing. The vascular images were generated by accumulating the relative echo power from the moving scatterers over all acquisition frames in each imaging plane and compressed to 30dB dynamic range for visualisation.

5:15 PM

Novel Motion Correction Algorithm for 3D Dynamic Contrast Ultrasound Without Anatomical Bmode ImagesAhme El Kaffas¹, Jia-Chu Chen², Maged Goubran³, Dimitre Hristov³, Juergen Willmann⁴¹*Radiology, Stanford, Stanford, CA, United States*, ²*Brown University, United States*, ³*Stanford, United States*,⁴*Department of Radiology, School of Medicine, Stanford University, Palo Alto, CA, United States***Background, Motivation, and Objective**

Dynamics contrast-enhanced ultrasound (DCE-US) is highly susceptible to motion artifacts arising from patient movement, respiration, and operator experience. Motion artifacts can be especially problematic in the context of perfusion quantification. In conventional 2D DCE-US, motion correction algorithms take advantage of accompanying side-by-side anatomical Bmode images that contain time-stable features. However, current commercial implementations of 3D DCE-US do not provide side-by-side Bmode images, which makes motion correction challenging. Here, we detail and validate a novel motion correction algorithm for 3D DCE-US.

Statement of Contribution/Methods

In brief, the motion correction algorithm first splits the 4D sequence into short temporal windows consisting of 3-6 frames (based on similarity assessment). These are then registered locally to a representative window reference. Window-based references are then registered to a master reference derived from a weighted average of all frames. A brief overview of the algorithm is presented in Figure. The motion correction algorithm was evaluated using 9 patients imaged with 3D-DCE US. The imaging studies were acquired from patients with metastatic lesions in the liver, and who provided written consent under IRB and met all inclusion criteria. The 3D-DCE US scanning was performed by an experienced sonographer using the current-commercial implementation of the Philips X6-1 matrix transducer at a frame rate of 1-3 Hz. For each patient, we evaluated improvements in original vs. motion corrected 3D DCE-US cine using: i) the frame-to-frame volumetric overlap of segmented lesion, ii) the R-value correlation coefficient (RCC) between frames (similarity analysis), and iii) the r-square quality-of-fit from a fitted time intensity curves (TIC) extracted from a segmented lesion.

Results/Discussion

Results demonstrate significant decreases in 3D DCE-US motion after applying the proposed algorithm. We noted overall significant ($p < 0.05$) improvements in frame-to-frame lesion overlap. Across all patients, the average overlap was $67\% \pm 15\%$ without motion correction, and $84\% \pm 3\%$ with motion correction. Frame-to-frame similarity also improved, with average RCCs of $69\% \pm 8\%$ and $87\% \pm 3\%$ for originals and motion corrected cine, respectively.

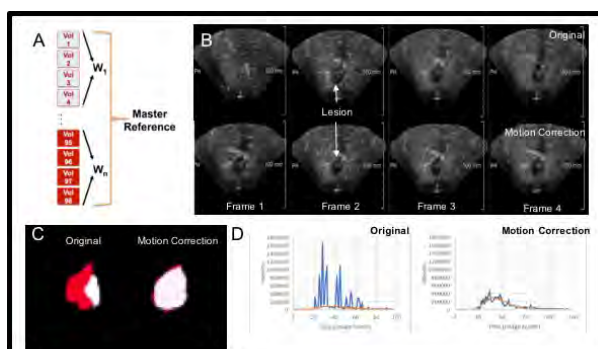


Figure - A) Overview of motion correction algorithm that functions only on contrast-mode images obtained in 4D. B) Example of 4 subsequent frames with and without motion correction applied. Lesion in center can be noted to remain in place only in motion corrected data. C) Lesion segmentation masks obtained from two subsequent frames (white, then red). Note improved overlap between both masks after motion correction. D) TIC curves (blue) with lognormal fit (red), with and without motion correction.

3H - Automated Image Quantification

Emerald (280)

Thursday, October 25, 8:00 am - 9:30 am

Chair **PIERO TORTOLI**
University of Florence

3H-1

8:00 AM Experimental Validation of an Improved Local Speed-of-Sound Estimator Using Pulse-Echo Ultrasound

Marko Jakovljevic¹, Rehman Ali², Dongwoon Hyun¹, Scott Hsieh³, Jeremy Dahl¹

¹Radiology, Stanford University, United States, ²Electrical Engineering, Stanford University, United States, ³Radiology, University of California, Los Angeles, United States

Background, Motivation, and Objective

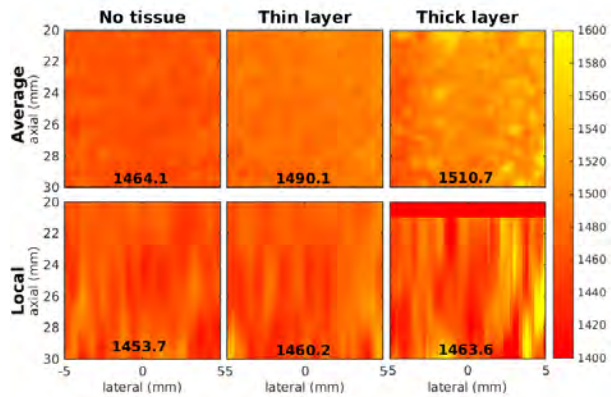
Speed of sound is a key acoustic parameter for both beamforming and tissue characterization. For example, knowledge of the speed of sound in localized areas of tissue can be utilized to improve image reconstruction (e.g. distributed aberration correction) as well as quantify tissue properties (e.g. fat concentration). We have recently introduced a model-based approach to estimating sound speed using pulse-echo ultrasound. Here, we improve upon our method and validate the approach in simulations and phantom experiments.

Statement of Contribution/Methods

The proposed model relates the average sound speed (measured quantity) to the local sound speed (estimated quantity) of a medium. The model assumes uniform sampling in time of the reflected waves, and then infers the local sound speed from the average sound speed by solving the model directly by the method of gradient descent. Regularization is utilized to mitigate high-frequency noise as a result of the inherent differentiation process. Validation of the method was performed in simulations of two-layered media with different sound speeds (1480 m/s for the top layer; 1520, 1540, and 1570 m/s for the bottom layer). Validation in phantoms was performed with an ATS 549 phantom (calibrated speed of sound: 1460 m/s) with and without porcine tissue placed between the phantom and transducer.

Results/Discussion

In the two-layer simulations, the model-based estimator yielded high accuracy in the sound speed estimates in the bottom layer, with biases of 4.7, -1.3, and 1.5 m/s in the 1520, 1540, and 1570 m/s media, respectively. Comparatively, the average sound speed measurements showed biases of -33.2, -46.9, and -66.7 for the same media, respectively. The figure compares the average and local sound speed estimates in the ATS phantom for none, thin (4 mm), and thick (10 mm) porcine tissue layers. The bias of the local sound speed estimates was -6.3, 0.2, and 3.6 m/s for the three layers, respectively, while the average sound speed measurements had a bias of 4.1, 30.1, and 50.7 m/s, respectively. We were able to reduce the standard deviation of the local estimates from 12 m/s to 7.8 m/s by incorporating multiple directions of wave propagation (5 angles) in the model. For comparison, the standard deviation of the average measurements was 6.8 m/s.



8:15 AM Fully automatic real-time ejection fraction and MAPSE measurements in 2D echocardiography using deep neural networks

Erik Smistad^{1,2}, Andreas Østvik^{1,2}, Ivar Mjåland Salte³, Sarah Leclerc⁴, Olivier Bernard⁴, Lasse Lovstakken^{1,2}

¹Department of Circulation and Medical Imaging, Norwegian University of Science and Technology (NTNU), Trondheim, Norway, ²Centre for Innovative Ultrasound Solutions (CIUS), Trondheim, Norway, ³Sørlandet Hospital, Kristiansand, Norway, ⁴CREATIS, Lyon, France

Background, Motivation, and Objective

Automated measurements in echocardiography has the potential to improve workflow by reducing time spent on manual annotation and contouring. It can also reduce interobserver variability known to be significant in echocardiography. In order to fully automate ejection fraction (EF) and mitral annular plane systolic excursion (MAPSE) measurements, several automated components are needed: view classification, left ventricle (LV) segmentation, extraction of apex and base points, identification of end-diastolic (ED) and end-systolic (ES) frames, and volume calculation. This study presents deep neural network methods for the automation of all these steps in an integrated software which receives ultrasound images directly from a GE Vivid E95 scanner in real-time.

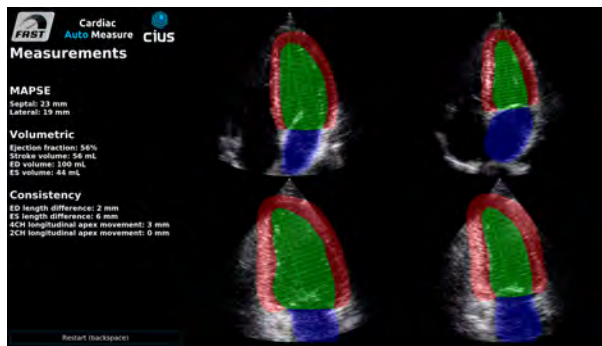
Statement of Contribution/Methods

View classification and LV segmentation were performed using deep convolutional neural networks. A network with inception blocks and a dense connectivity pattern, trained with images from 200 patients, was used for view classification. For segmentation, a U-net architecture was used, trained on 4CH and 2CH images from both ED and ES of 500 patients. View classification and segmentation was executed for each incoming image frame. LV area was extracted from the segmentation, and the ED and ES frames were determined using the min- and maximum area. Segmentation contours were extracted at ED and ES, and used to extract the apex and base landmarks. The volume was estimated using Simpson's biplane method with 20 disks. MAPSE was calculated in 4CH view using the base septal and lateral landmarks.

Results/Discussion

The ED and ES images for 4CH and 2CH views were visualized together with the measurements as shown in the figure. In the software, all measurements were calculated without any user interaction and updated in real-time while scanning, this was achieved using GPU processing through the FAST framework.

A Bland-Altman analysis of EF and MAPSE was performed using a separate test dataset with recordings from 72 patients. The results showed a mean difference of -13.7 and standard deviation of 8.6 for EF and -1.0 and 4.5 mm for MAPSE. The large bias was due to a consistent difference in the two expert's annotations of the training and test datasets. Most of the test dataset was marked as having low image quality, thus the preliminary results show promise for automating these measurements.



8:30 AM

Zonal segmentation in transrectal ultrasound images of the prostate through deep learning

Ruud J. G. van Sloun¹, Rogier R Wildeboer¹, Arnoud W. Postema², Christophe K Mannaerts², Maudy Gayet³, Hessel Wijkstra², Massimo Mischi¹

¹Eindhoven University of Technology, Netherlands, ²Academic Medical Center - University of Amsterdam, Netherlands,

³Jeroen Bosch Hospital, Den Bosch, Netherlands

Background, Motivation, and Objective

Automatic segmentation of the prostate in transrectal ultrasound (TRUS) images has been a challenge in medical image analysis. The prostate may appear in many forms, shapes, and orientations depending on the imaging plane, prostatic boundaries may be poorly visible or obscured by speckle noise or shadow artefacts, and image quality and formation may differ among manufacturers. Even more challenging is the segmentation of the prostate into its main zones: the transitional zone and the peripheral zone. Although adequate and automatic extraction of zonal and organ contours is of high relevance for e.g. biopsy fusion systems, state-of-the-art algorithms for prostate segmentation in TRUS (based on edge detection, modelling, or local textures) lack robustness and do not enable reliable zonal segmentation. In this work, we exploit modern deep learning strategies to perform accurate organ as well as zonal segmentation of the prostate.

Statement of Contribution/Methods

We performed TRUS imaging in 84 patients using an iU22 ultrasound scanner (Philips Healthcare, Bothell, USA) equipped with either a C10-3v or a C8-4v probe. In total, 210 imaging planes were included. All patients signed an informed consent. The outer and zonal contours of each two-dimensional image were delineated in consensus by a panel of five experts, consisting of 2 engineers and 3 urologists. Zonal segmentation was performed using a fully convolutional neural network, consisting of an encoder, mapping the input TRUS images to a latent feature space, and a symmetric decoder, mapping this latent space to a semantic output segmentation. We trained the network on 150 images from 54 patients, by minimizing the categorical cross-entropy between the target expert-annotated labels, and the neural network predictions. High network generalization and robustness was attained through the use of aggressive on-line data augmentation techniques (e.g. non-rigid image deformation).

Results/Discussion

Validation was performed on a test set of 60 TRUS images from 30 patients which were excluded from training. On this set, the pixel-wise accuracy for zonal segmentation was 0.93, the mean intersection over union was 0.80, and the mean Dice coefficient was 0.88. Figure 1 displays several example segmentations along with the expert annotated ground truths, illustrating the high potential of the proposed technique.

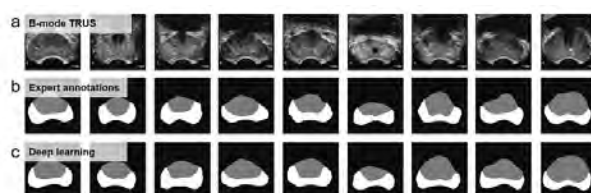


Figure 1. Input B-mode TRUS images (a), expert-annotated zonal segmentation (b) and corresponding zonal segmentation by the proposed deep learning strategy (c).

8:45 AM Automated Detection of Fetal Presentation and Gestational Age using Low-cost Ultrasound and Deep Learning in a Resource-Limited Setting

Thomas van den Heuvel¹, Bram van Ginneken^{1,2}, Chris de Korte^{1,3}

¹Department of Radiology and Nuclear Medicine, Radboud university medical center, Nijmegen, Netherlands,

²Fraunhofer MEVIS, Bremen, Germany, ³MIRA, University of Twente, Enschede, Netherlands

Background, Motivation, and Objective

Worldwide, 99% of all maternal deaths occur in low-resource settings. Ultrasound can be used to determine gestational age (GA) and detect breech presentation. Estimation of GA is essential for obstetric management and detection of breech presentation is important, because it increases risk during delivery. Although low-cost portable ultrasound devices have been introduced, wide spread of prenatal ultrasound is limited by the lack of trained sonographers that can acquire and interpret the images. In 2011, DeStigter introduced the obstetric sweep protocol (OSP), which can be taught to any health care worker within one day. In this work we combined low-cost ultrasound and the OSP with a deep learning algorithm to automatically detect the fetal presentation and estimate GA.

Statement of Contribution/Methods

The OSP was acquired from 247 pregnant women using the low-cost Telemed MicrUs in St. Luke's Hospital, Woliso, Ethiopia. The OSP consists of six pre-defined free-hand sweeps with the ultrasound transducer over the abdomen of the pregnant women (Figure 1.A.). A deep learning system was trained to detect if a frame contains the fetal head, body or side, or if the transducer was detached from the abdomen of the pregnant women (Figure 1.B.). This automated frame classification was used to automatically separate the six sweeps and determine the presentation of the fetus. A second deep learning system was used to estimate the head circumference (HC) from the frames that were classified as fetal head. The curve of Hadlock (Radiology. 1984;152(2):497-501) was used to determine the GA from the HC and this estimated GA was compared to the reference GA determined from the HC which was measured in the standard plane. The system was evaluated using a five-fold cross-validation.

Results/Discussion

The proposed system was able to estimate GA with a mean difference of -1.3 ± 14.2 days (Figure 1.C.) compared to the reference GA. The system was also able correctly detected all 31 breech presentations and only misclassified one of the 216 cephalic presentations as breech. This system therefore shows feasibility to estimate GA and detect breech presentation using low-cost ultrasound without the need of a trained sonographer to both acquire and interpret ultrasound images.

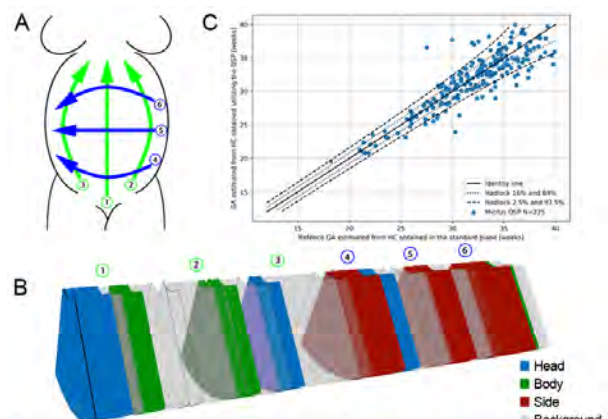


Figure 1. A: Schematic overview of the obstetric sweep protocol. B: Frame classification of the deep learning system. C: Scatterplot with the reference GA on the x-axis and the automatically estimated GA from the OSP on the y-axis.

9:00 AM

Fully Automatic Assessment of Mitral Valve Morphology from 3D Transthoracic EchocardiographyJoão Pedrosa¹, Sandro Queirós², João L. Vilaça^{2,3}, Luigi Badano⁴, Jan D'hooge¹¹*Cardiovascular Sciences, KU Leuven, Leuven, Belgium*, ²*Universidade do Minho, Portugal*, ³*Instituto Politécnico do Cávado e do Ave, Portugal*, ⁴*Università degli Studi di Padova, Italy***Background, Motivation, and Objective**

Quantitative assessment of the mitral valve (MV) morphology is important for diagnosing MV pathology and for planning of reparative procedures. Although this is typically done using 3D transesophageal echocardiography (TEE), recent advances in the spatiotemporal resolution of 3D transthoracic echocardiography (TTE) have enabled the use of this more patient friendly modality. However, data analysis remains manual and is therefore time consuming and operator dependent. In this study, we propose and validate a fully automatic method for MV segmentation and tracking in 3D TTE.

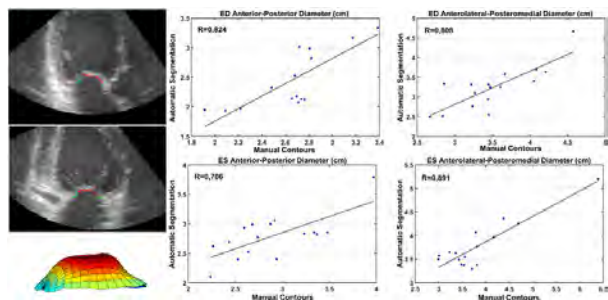
Statement of Contribution/Methods

Given the field of view of TTE, the proposed framework takes advantage of a validated left ventricle (LV) segmentation framework [Pedrosa, J. et al. IEEE TMI 2017] to localize the MV in the image and initialize the segmentation. MV segmentation is then performed in two steps, the first using a threshold based energy function and the second using a localized region-based energy. The orientation of the MV is obtained according to the automatically detected right ventricular insertion point and the LV outflow tract. Following the segmentation, the MV surface is cropped to the MV annulus and divided into posterior and anterior leaflets using a dynamic programming technique refined by consulting an atlas of manually contoured MVs. The segmented MV at ED is then propagated to end systole (ES) using localized anatomical affine optical flow. Because the orientation and leaflet division is known, relevant clinical parameters can then be extracted from the mesh at any time point.

The framework was tested on 16 cases of the CETUS challenge data, a multi-center multi-vendor database. Manual contouring was performed by an expert at ED and ES and the quality of the automatic segmentation expressed as the mean absolute distance (MAD) and the Hausdorff distance (HD).

Results/Discussion

The proposed framework showed excellent segmentation results with a MAD and HD of 1.19 ± 0.25 mm and 5.79 ± 1.25 mm at ED and 1.39 ± 0.32 mm and 6.70 ± 1.97 mm at ES. Correlations of different clinical parameters were good as shown in Fig. 1 (R ranging from 0.70 to 0.93). In conclusion, an automatic method for MV segmentation was proposed which could provide valuable clinical information currently difficult to assess.



9:15 AM

Semi-automatic 3D geometry assessment of bifurcated carotid arteryJoerik de Ruijter¹, Frans van de Vosse², Marc van Sambeek³, Richard Lopata²¹Eindhoven University of Technology, Netherlands, ²Eindhoven University of technology, Netherlands, ³Catharina Hospital Eindhoven, Netherlands**Background, Motivation, and Objective**

Plaques in the carotid artery are a common cause of stroke. High peak stresses in the shoulders or cap of the plaque are related to rupture risk. Patient-specific, 3D biomechanical models are required for a reliable calculation of the magnitude of the peak stresses, which requires an accurate 3D geometry. This is currently not feasible with available 3D transducer technology. In this study, a high-resolution 2D linear array is used in combination with a magnetic probe tracking device, maintaining the high spatial and temporal resolution of 2D ultrasound. An automated segmentation and meshing method was developed to create a patient-specific mechanical model with minimal user input.

Statement of Contribution/Methods

The method was tested in vivo on 20 healthy volunteers. By making a slow sweep (6 cm) over the patient's neck, the full geometry of the bifurcated geometry of the carotid artery is captured. In the first frame, seeds were placed in the centers of the internal and external carotid. The extended Star-Kalman method was used to approximate the center and the size of the vessel(s) for every frame. Images were filtered with a Gaussian low-pass filter before conversion into the 2D monogenic signals, multiscale asymmetry features were extracted from these data, enhancing low lateral wall-lumen contrast (**Fig 1A**). These images, in combination with the initial ellipse contours, were used for an active deformable contour model to segment the vessel lumen.

Distension of the wall due to the change in blood pressure is present in the resulting contours. Hence, all contours were translated to the $r\theta$ -domain, the heart rate is detected, and with a low-pass filter in the r -time-domain the influence of the heartbeat and high frequency noise were removed (**Fig 1B**). Finally, the contours were converted into a 3D hexahedral mesh for finite element analysis in ANSYS (**Fig 1C**). Results were compared to manual segmentation performed by an experienced observer.

Results/Discussion

The segmentation algorithm performed well with an average Similarity Index of 0.90 and an average Hausdorff distance of 0.8 ± 0.4 mm. For the CCA an average diameter of 6.8 ± 1.1 mm was found and for ICA/ECA 5.4 ± 0.7 mm. With minimal user input, finite element or fluid structure interaction models are created directly from an in vivo measurement (**Fig 1C**). In future work, these models will be extended to diseased carotid arteries.

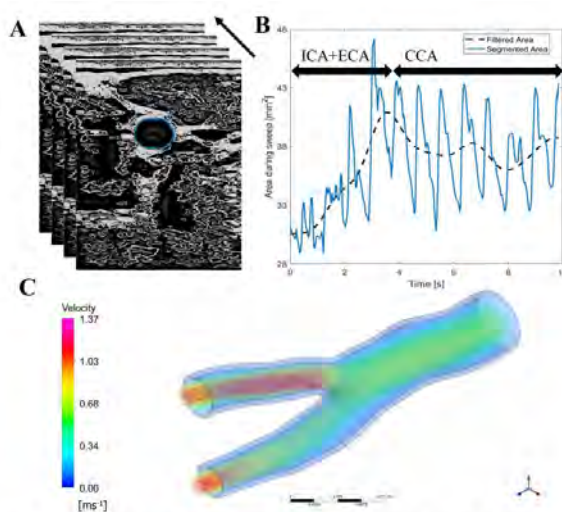


Figure 1: A: US images after adjustments and the segmented contour of CCA. B: Segmented area over time of multiple heart cycles (blue line), area after low-pass filtering (dotted line). C: Fluid-structure interaction simulation of bifurcated carotid artery.

3I - Machine Learning for Image Reconstruction and Interpretation

Emerald (280)

Thursday, October 25, 10:30 am - 12:00 pm

Chair **Olivier Bernard**
INSA Lyon

3I-1

10:30 AM Machine learning to improve breast cancer diagnosis by multimodal ultrasound

Laith Sultan¹, Susan Schultz², **Chandra Sehgal²**

¹*University of Pennsylvania, Exton, PA, United States*, ²*Radiology, University of Pennsylvania, Greater Philadelphia Area, PA, United States*

Background, Motivation, and Objective

Despite major advances in breast cancer imaging, the yield for biopsying a breast lesion continues to be low and up to 85% of biopsies are found to be benign. There is compelling need to improve confidence and reliability of characterizing breast lesions by imaging to reduce unnecessary biopsies. In this study we demonstrate the use of machine learning with multimodal ultrasound to enhance breast cancer diagnosis

Statement of Contribution/Methods

160 surgically proven solid breast lesions were studied using grayscale and Doppler ultrasound imaging. Lesions were segmented on the grayscale images and partitioned into five-degree sectors. Eight morphological features describing lesion margin and shape were extracted by analyzing grayscale characteristics of each sector. Similarly, three vascular features representing mean flow velocity, vascular area and mean flow in the lesion were extracted from Doppler images. The features that showed statistical difference $P < 0.05$ were used with logistic regression to train and test lesion differentiation. Leave-one-out cross validation was used for determining probability of malignancy. Using small perturbation theory the reliability of each machine learning cycle was measured by cumulative dispersion in the weighting of the individual features. Cases with highest dispersion representing weak learning (low confidence diagnosis) were identified and pruned. Diagnostic performance was measured by the area under ROC (AUC) and sensitivity (Sen) and specificity (Spe) was measured at the Youdons index

Results/Discussion

Results: Of the eleven features, three grayscale morphologic sonographic and three Doppler vascularity features were found to be significantly discriminating ($P < .02$). Diagnostic performance of grayscale morphologic features including all training cycles had AUC of 0.85 (Sen 87, Spe = 69), which improved to 0.89 (Sen 79, Spe = 89) when Doppler features were added to the analysis. The improvement was significant, $P = 0.04$. This level of performance is comparable to that of human observers. The high level of performance by machine learning further improved when weak learner cases were identified. Using dispersion measurement as a metric for the quality of training, 18 training cycles out of 160 (11.3%) were found to be weak. Pruning these cases improved diagnostic performance to AUC of 0.96 (Sen 92, Spe = 95) at the cost of no decision on 11% cases.

Conclusion: Machine-learning methodology with multimodal ultrasound including grayscale and Doppler can achieve high sensitivity and specificity for breast cancer diagnosis that is comparable to that human observers. Identifying weak-learners in machine learning methodology can markedly enhance the diagnosis. Implementation and further validation of this approach using a larger dataset has a potential to reduce unnecessary breast biopsies

10:45 AM

Machine learning for quality assurance of myocardial strain curves**Mahdi Tabassian¹, Olivia Zulaica Iglesias¹, Serkan Ünlü², Jens-Uwe Voigt^{1,2}, Jan D'hooge¹**¹*Department of Cardiovascular Sciences, KU Leuven, Leuven, Belgium*, ²*Department of Cardiology, University Hospitals Leuven, Leuven, Belgium***Background, Motivation, and Objective**

Speckle tracking echocardiography (STE) is a well-established technique to quantify regional cardiac function. However, STE-derived strain curves depend strongly on the quality of the acquired B-mode image and can significantly be influenced by image artefacts. Unfortunately, these tracking errors can lead to deformation patterns that are similar to those obtained in pathology. It would thus be clinically very relevant to get feedback on the reliability (i.e. quality) of the extracted strain curves. As such, the aim of this study was to examine the use of machine learning in the identification of artefactual strain curves.

Statement of Contribution/Methods

Longitudinal strain curves were measured using GE EchoPac from the apical 2- and 4-chamber views (frame rate 60Hz) in a set of 52 patients with previous myocardial infarction and 5 healthy volunteers using a GE Vivid E9. Based on visual assessment of an expert cardiologist trained in STE, the curves were categorized as artefactual or not. Each measured curve was also imputed using the non-artefactual concatenated curves of the two views through weighted k -nearest neighbor (WKNN). The measured and imputed curves were then compared assuming that a non-artefactual curve would look similar to its imputed version. Hereto, the measured curve and its imputed version were concatenated and modeled using principal component analysis (PCA) to then be classified as artefactual or not using WKNN (Figure 1). Training and testing sets were created by randomly selecting 70% and 30% of the subjects, respectively. This process was repeated 200 times and the average classification performance was computed using ROC analysis.

Results/Discussion

The machine learning framework yielded an average and standard deviation area under the curve of $70\pm6\%$ and accuracy, sensitivity and specificity of $64\pm10\%$, $64\pm15\%$ and $64\pm12\%$, respectively. Given the relatively small database used for the imputation, these results are promising and show the potential of machine learning for quality assurance of the STE-derived strain curves. The clinical implication of these results is significant since having feedback on the quality of the measured strain curves will facilitate their interpretation and thus their diagnostic power.

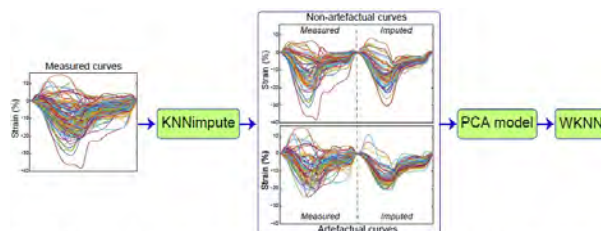


Figure 1. The proposed machine learning framework for automatic identification of the artefactual strain curves. All the individual measured curves were imputed using weighted k -nearest neighbor (WKNN) and the concatenated non-artefactual curves of the apical 2- and 4-chamber views. The measured and imputed curves were then concatenated to be statistically modeled using PCA. The modeled patterns were finally classified as artefactual or not using WKNN.

11:00 AM

High-quality Reconstruction of Plane-wave Imaging Using Generative Adversarial NetworkXi Zhang¹, Jing Liu¹, Qiong He¹, Heye Zhang², Jianwen Luo¹¹*Department of Biomedical Engineering, Tsinghua University, Beijing, China, People's Republic of*, ²*Shenzhen Institutes of Advanced Technology, Chinese Academy of Sciences, Shenzhen, China, People's Republic of***Background, Motivation, and Objective**

Coherent plane wave (PW) compounding (PWC) using tens of steered PWs can obtain high quality images, but it reduces the gain in frame rate. Recently a new strategy using convolutional neural network (CNN) was proposed to recover high quality images from only 3 PWs (Gasse et al, TUFFC, 2017). Considering the excellent performance of generative adversarial network (GAN) in image reconstruction, we propose to use GAN to reconstruct high-quality ultrasound images from 3 PWs.

Statement of Contribution/Methods

A Verasonics Vantage system with an L10-5 linear array ($f_0 = 7.5$ MHz) was used to acquired 6530 frames of channel data, i.e., 2030 from a CIRS 040GSE phantom, 500 from swine muscles *ex vivo*, and 4000 from carotid artery and brachioradialis of three healthy human subjects *in vivo*. Each frame contained 31 steered PWs (-15° to 15° with 1° steps). 6000 frames were used as the training data, including the input and label. The input was three images of DAS beamformed RF data from steering angles of 0° and ±15° respectively. The label was the RF image obtained by PWC with 31 PWs (PWC-31). The remaining 530 frames were used as the test data, with the RF images corresponding to the above 3 PWs as the input.

A GAN model with residual networks (including generative network and discriminative network) was built in TensorFlow (Google). The GAN was trained by minimizing the loss function via stochastic gradient descent with Adam optimizer (Tesla P100, NVIDIA). The images obtained by GAN with 3 PWs were compared with those by CNN with 3 PWs, and PWC with 3 PWs (PWC-3) and PWC-31, respectively. The full width at half maximum (FWHM) of a wire at 40 mm depth (yellow arrow in Fig. 1a), the contrast ratio (CR) and contrast-to-noise ratio (CNR) between a cystic region and the background (red circles in Fig. 1a, r = 1 mm) in the phantom were quantified.

Results/Discussion

The B-mode images of the phantom and carotid artery show that GAN obtains better performance than PWC-3 and CNN (Figs. 1a - 1c), and obtains similar images to PWC-31. Quantitatively, the FWHMs of GAN, PWC-3 and PWC-31 are close, which are smaller than that of CNN. The CR of GAN is higher than those of PWC-3 and CNN, and is slightly lower than that of PWC-31. The CNR of GAN is close to that of CNN, lower than that of PWC-31, and higher than that of PWC-3. To conclude, GAN can reconstruct high-quality ultrasound images from 3 steered PWs and performs better than CNN.

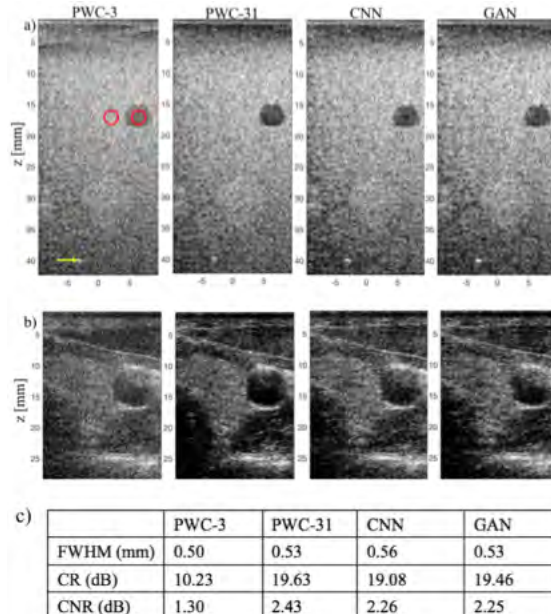


Fig. 1. B-mode images of (a) the phantom and (b) carotid artery using PWC-3, PWC-31, CNN (3 PWs) and GAN (3 PWs), respectively. c) Quantitative results.

11:15 AM

Automatic functional imaging in echocardiography using deep learning based segmentation and flow estimationAndreas Østvik^{1,2}, Erik Smistad^{1,2}, Torvald Espeland^{1,2,3}, Lasse Lovstakken^{1,2}¹*Department of Circulation and Medical Imaging, Norwegian University of Science and Technology, Norway*, ²*Centre for Innovative Ultrasound Solutions (CIUS), Norway*, ³*Clinic of cardiology, St. Olavs hospital, Trondheim, Norway***Background, Motivation, and Objective**

Evaluation of the contractile abilities of the heart involves geometric measures such as ejection fraction and visual interpretation of myocardial morphophysiology. Tissue doppler imaging and speckle tracking has further enabled sensitive methods for assessing the myocardial deformation pattern. Recent work in the field of deep learning (DL) suggest that motion estimation can be treated as a learnable problem[1]. Herein, we investigate this approach in combination with segmentation to achieve fully automatic functional imaging.

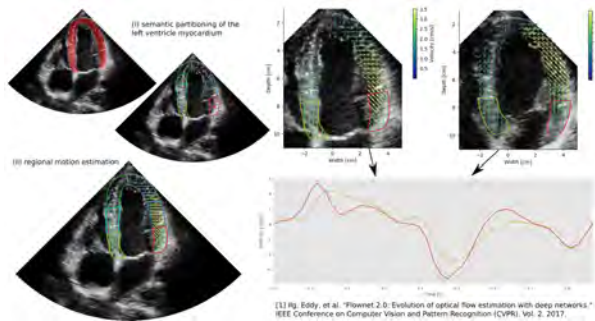
Statement of Contribution/Methods

The proposed pipeline consists of two central components, (i) semantic partitioning of the left ventricle (LV) myocardium, and (ii) regional motion estimates. A U-Net type of convolutional neural network (CNN) was developed to classify muscle tissue, partitioned into six segments based on LV length and orientation. Dense tissue motion was predicted using stacked U-Net architectures with image warping of intermediate flow, designed to tackle variable displacements. Training was performed on synthetic data. The resulting tracking was used as basis for functional measures such as velocity and strain.

For reference, 2D B-mode images from four healthy volunteers was acquired using a GE Vivid E95. Data was analyzed by an expert using a semi-automatic tool for longitudinal function estimates in GE EchoPAC, and further compared to output of the proposed method.

Results/Discussion

Qualitative assessment showed comparable velocity and deformation trends as the clinical analysis software. As seen in the figure, the fundamental events in the heart cycle was apparent and synchronous. The average deviation for the basal velocity in peak systole, early- and late-diastole was (-0.2 ± 1.2) cm/s, while the relative average absolute error of global strain estimates was $(10.5 \pm 4.3)\%$. The system was implemented with Tensorflow, and working in an end-to-end fashion without any ad-hoc tuning. Using a modern graphics processing unit, the average inference time is estimated to (87.5 ± 0.9) ms per frame, where flow prediction accounts for approximately 80% of compute time. Future work includes further method development and training, optimization for real-time use, and evaluation on a larger reference material.



11:30 AM

Deep Convolutional Neural Network for Ultrasound Image EnhancementDimitris Perdios¹, Manuel Vonlanthen¹, Adrien Besson¹, Florian Martinez¹, Marcel Ardit¹, Jean-Philippe Thiran^{1,2}¹*Signal Processing Laboratory (LTS5), Ecole Polytechnique Fédérale de Lausanne (EPFL), Switzerland*, ²*Department of Radiology, University Hospital Center (CHUV) and University of Lausanne (UNIL), Switzerland***Background, Motivation, and Objective**

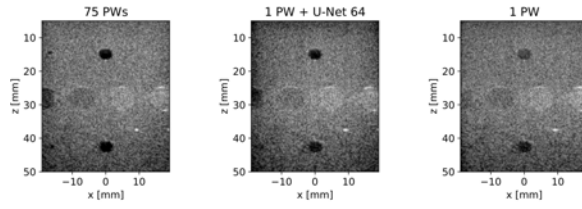
The problem of improving image quality in ultrafast ultrasound (US) imaging has raised an important interest in the US community, mostly in the field of regularized iterative algorithms. In the last years, deep-learning methods have shown impressive results but comprehensive studies of such architectures are still lacking. U-Net has recently been introduced for image reconstruction in computerized tomography [Jin *et al.*, TIP2017]. Thanks to its multiscale characteristic combined with multichannel filtering, it remarkably captures representative structures of images in its hidden layers allowing it to learn a non-linear mapping between subspaces of low-quality and high-quality images. This mapping is later used to produce high-quality images.

Statement of Contribution/Methods

We propose to use the U-Net architecture to improve images from a single plane wave (PW) with normal incidence. The idea is to learn a mapping from the subspace of beamformed radio-frequency (RF) images obtained with 1 PW to the subspace of synthetic aperture images reconstructed from 128 insonifications. The network first performs a dyadic scale decomposition through multiple convolutional layers of 3x3 kernels followed by reconstruction layers with skip connections for residual learning. Three number of channels are tested namely 16, 32 and 64. The network is trained on 4k images simulated on an in-house simulator with a L11-4v probe. The phantoms and medium properties are randomly generated from typical tissue zones. The evaluation is performed on the PICMUS dataset.

Results/Discussion

The images below (60dB range) demonstrate that the proposed method with the higher number of channels (U-Net 64) achieves an impressive enhancement, with a resulting quality comparable in both resolution and contrast to an image obtained with 75 PWs. It has to be noted that the network is exclusively trained on simulated images and remains extremely robust on *in-vitro* images. Few artefacts which are mostly located on the boarders still remain, but they can be efficiently reduced with a larger architecture. Such a visual assessment is confirmed by the quantitative metrics reported on the table below. Furthermore, image improvement with the proposed U-Net architecture can be compatible with real-time imaging and paves the way to high-quality imaging with a single PW insonification.



PICMUS numerical phantom metrics table

| Metrics | 75 PWs | 1 PW + U-Net 64 | 1 PW |
|----------------|--------------|-----------------|--------------|
| CNR [dB] | 16.4 | 15.7 | 7.2 |
| Lat. res. [mm] | 0.46 | 0.39 | 0.53 |
| Ax. res. [mm] | 0.4 | 0.41 | 0.41 |
| Linearity | Success | Success | Success |
| Speckle | Passed – 6/6 | Passed – 5/6 | Passed – 6/6 |

11:45 AM **Ultrasound image processing based on deep learning**Fabian Dietrichson¹, Erik Smistad¹, Andreas Østvik¹, Lasse Lovstakken¹¹Department of Circulation and Medical Imaging, Norwegian University of Science and Technology (NTNU), Trondheim, Norway**Background, Motivation, and Objective**

The raw ultrasound B-mode images go through a significant amount of post-processing before displayed. One example is speckle reduction for improving image contrast. State-of-the-art image processing algorithms are not necessarily compatible with real-time requirements. Deep neural networks (DNN) may be able to learn the characteristics of advanced algorithms while simplifying the implementation. The aim of this work is 1) to investigate if DNNs can learn an advanced ultrasound image processing algorithm, and 2) to see if this approach can provide a practical path to real-time performance by utilizing the optimized DNN GPU backends.

Statement of Contribution/Methods

Two DNN approaches were investigated for speckle reduction: autoencoders and generative adversarial networks (GAN).

The networks were developed using Keras and Tensorflow.

The scanconverted images were resized to 512x512. A dataset of 600 samples from 200 patients was used to train the networks. This dataset consists of heart images from the apical four chamber view only. Images from 10% of the patients were used for parameter optimization during training. A second dataset of 170 samples from 55 patients was created to test the network.

All images were processed using an optimized non-local means (NLM) speckle reduction algorithm [1]. These NLM processed images were the target for the training and used for evaluation on the test set.

Results/Discussion

The DNNs were able to learn principal features of NLM, thus reducing speckle in a similar manner.

However, only the GAN was able to reduce speckle while maintaining important edges. Therefore, only results for the GAN method is presented.

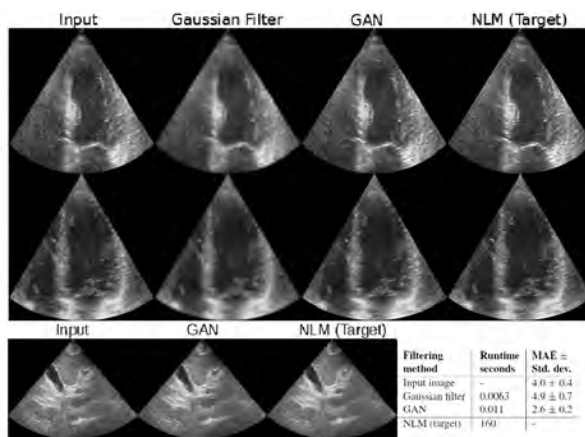
For comparison, the results of a simple Gaussian filtering method is included.

The figure below show a comparison of the Gaussian filter, GAN and NLM methods on two images.

Images from the liver were also acquired to check if the trained network is applicable to other organs as well.

For quantitative evaluation, the mean absolute error (MAE) and standard deviation was calculated for each pixel and sample in the test set. The accuracy was calculated using image intensities in the scale of 0 to 255.

The results indicate that GANs can learn advanced ultrasound image processing algorithms by only having input and target images, and perform these image processings at sufficiently low run time for real time performance.



[1] L. Zhu, P.A. Heng et al, A Non-local Low-Rank Framework for Ultrasound Speckle Reduction, IEEE Conference on CVPR, 2017

3J - High Frame Rate Cardiac Imaging

Emerald (280)

Thursday, October 25, 1:30 pm - 3:00 pm

Chair **Massimo Mischi**
Eindhoven University of Technology

3J-1

1:30 PM

High frame rate imaging of natural shear waves in the human heart

Pedro Santos¹, Aniela Monica Petrescu¹, João Pedrosa¹, Marta Orlowska¹, Vangjush Komini¹, Jens-Uwe Voigt¹, Jan D'hooge¹

¹Department of Cardiovascular Sciences, KU Leuven, Leuven, Belgium

Background, Motivation, and Objective

Cardiac shear wave (SW) elastography has been proposed to non-invasively assess myocardial stiffness and may provide a new diagnostic tool to evaluate cardiac (systolic/diastolic) function, as suggested from initial *in-vivo* studies using SWs induced by acoustic push beams. The use of SWs occurring naturally due to heart valve closures has also been proposed, but available data is sparse. The aims of this study were therefore to: i) demonstrate the feasibility of detecting these natural SWs in healthy volunteers and report on the normal propagation speeds; ii) show that natural SW speed changes with disease or intervention.

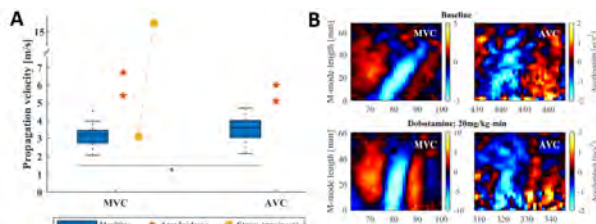
Statement of Contribution/Methods

Parasternal long axis views were acquired in 22 healthy volunteers and 3 patients (2 cardiac amyloidosis and 1 dobutamine stress test) to ensure alignment between the main component of the SW motion (i.e. perpendicularly to the myocardium) and the US beam. Channel data was acquired with an experimental scanner (HD-PULSE) and a commercial 3.5 MHz phased array (P2-5AC, Samsung Medison). High frame rate (HFR) was achieved with a 6 DW sequence (21 transmitting elements sliding over the aperture) followed by coherent compounding.

Tissue velocity and acceleration were obtained with frame-to-frame Doppler and used to create septal color M-modes on which the SWs associated with mitral valve closure (MVC) and aortic valve closure (AVC) were tracked using an automatic correlation-based algorithm. The SW propagation speed at AVC and MVC was compared using a paired t-test.

Results/Discussion

HFR imaging detected the transient vibrations in response to MVC and AVC in 22 and 23 recordings, respectively. For normal volunteers SWs were faster at AVC than at MVC (3.5 ± 0.7 vs 3.1 ± 0.6 m/s, $p=0.013$ – Fig A) consistent with what has been reported using push beams. The cardiac amyloidosis patients (“stiff heart syndrome”) showed higher SW speeds (~5.5 m/s and ~6.1 m/s, respectively), whereas the scanning during the stress echo had normal values at baseline but strongly elevated (>15 m/s) after dobutamine infusion (Fig B). Both groups showed changes consistent with the alterations in stiffness/contractility expected clinically. In conclusion, naturally occurring SWs in the heart can systematically be detected and vary with the cardiac condition of the subject. Understanding the exact cause of the observed changes is the topic of ongoing work.



(A) Natural shear wave velocities at mitral valve closure (MVC) and aortic valve closure (AVC) obtained for the 3 groups (tracking failed at AVC for the stress test). (B) MVC and AVC shear waves during the dobutamine stress echo (baseline and after infusion).

1:45 PM

Longitudinal and Transversal Particle Motion Induced by Aortic Valve Closure in the Interventricular Septum

L.B.H. Keijzer¹, Mihai Strachinaru^{1,2}, Johan G. Bosch¹, B.M. van Dalen^{2,3}, I. Heinonen^{4,5,6}, Martin D. Verweij^{1,7}, Antonius F. W. van der Steen^{1,7}, Nicolaas de Jong^{1,7}, Hendrik J. Vos^{1,7}

¹Biomedical Engineering, Thorax Center, Erasmus MC, Rotterdam, Netherlands, ²Cardiology, Thorax Center, Erasmus MC, Rotterdam, Netherlands, ³Franciscus Gasthuis & Vlietland, Rotterdam, Netherlands, ⁴Experimental Cardiology, Erasmus MC, Rotterdam, Netherlands, ⁵University of Turku and Turku University Hospital, Turku, Finland,

⁶Department of Clinical Physiology and Nuclear Medicine, University of Turku and Turku University Hospital, Turku, Finland, ⁷Acoustical Wavefield Imaging, ImPhys, Delft University of Technology, Delft, Netherlands

Background, Motivation, and Objective

Lamb waves (LWs) induced by aortic valve closure (AVC) in the interventricular septum (IVS) might be used to non-invasively measure the stiffness of the heart muscle. Earlier studies used either a parasternal [Kanai, IEEE TUFFC 2005; Vos et al, UMB 2017] or an apical view [Brekke et al, UMB 2014] to track the LWs. Since Tissue Doppler is sensitive to axial particle motion only, a parasternal view would mainly track transversal particle motion on the IVS, which is dominant in antisymmetric LWs, while an apical view would mainly track longitudinal particle motion, dominant in the symmetric mode. Symmetric LWs have higher propagation speeds than antisymmetric LWs, and thus knowing the LW mode enables correct translation of propagation speeds into tissue stiffness; yet, multiple modes may be present simultaneously, and even other waves might exist. As a single mode can only have one propagation speed, we track the particle motion with high resolution in all directions and investigate the presence of multiple LW modes by analysing propagation speeds.

Statement of Contribution/Methods

Three pigs with open chest were scanned in long-axis parasternal and 4-chamber apical view. High-resolution high-frame rate B-mode images were recorded (Aixplorer, SSI, France; L15-4 probe in plane wave mode). Speckle-tracking was used to compute axial and lateral particle motion. These were then converted to longitudinal and transversal particle motion along the IVS. A Radon transform was used to obtain propagation speeds from either type of particle motion.

Results/Discussion

Fig 1 shows the results. Overall, we found three ranges of propagation speeds: larger than 8 m/s, with associated high variation; 4 - 7 m/s; and 2 - 4 m/s. As the two data points per measurement are obtained simultaneously, the different propagation speeds indicate the presence of two simultaneous waves. No significant difference was found in propagation speed of the transversal particle motion in parasternal view compared to the longitudinal particle motion in apical view, which supports the finding in an earlier study [Kanai, IEEE TUFFC 2005], suggesting that the same mode can be measured in both views. These preliminary results suggest that multiple modes of LWs are simultaneously induced by AVC, which would require caution when translating propagation speeds into tissue stiffness.

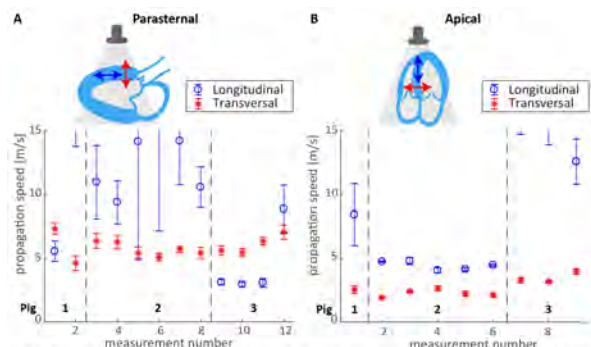


Fig 1: Overview of the mean and standard deviations of propagation speeds obtained for the M-panels with longitudinal and transversal particle motion in parasternal view (A) and in apical view (B). For every measurement, 10 anatomical M-lines were drawn.

2:00 PM

Monitoring canine myocardial infarction formation and recovery with transthoracic cardiac strain imagingVincent Sayseng¹, Rebecca Ober², Christopher Grubb³, Rachel Weber¹, Elisa Konofagou⁴¹*Biomedical Engineering, Columbia University, New York, NY, United States*, ²*Institute of Comparative Medicine, Columbia University Medical Center, New York, NY, United States*, ³*Medicine - Division of Cardiology, Columbia University, New York, NY, United States*, ⁴*Biomedical Engineering, Columbia University, United States***Background, Motivation, and Objective**

Myocardial Elastography (ME), a strain imaging technique, could be proven useful in assessing myocardial infarction. Previous studies have shown that canine myocardial infarcts produced via coronary ligation gradually recover through collateral perfusion after 4 weeks. A canine model was employed to demonstrate the ability of ME to localize and assess infarct severity during formation and subsequent recovery using radial strain (ϵ) and validating with histology.

Statement of Contribution/Methods

Myocardial infarcts were produced in 9 mongrel canines (24 ± 2.4 kg, male) through surgical ligation of their left anterior descending coronary artery. Using a Verasonics system, transthoracic imaging at the short-axis base, mid, and apical level was performed with a coherently compounded diverging wave sequence (3000 Hz PRF, 10 virtual sources, 2.5 MHz) prior to ligation and up to 28 days post-ligation. Cumulative ϵ was estimated using axial and lateral displacements calculated by cross-correlation of RF data and accumulated throughout systole. Sacrifice was performed on days 3-4 ($n = 5$) or 28 ($n = 4$) to allow for validation during both infarction formation and recovery, respectively. The excised myocardium was divided into 5 mm slices and stained with 1% tetrazolium chloride. The median ϵ within the image ROI (ϵ_{median}) was correlated with the percent infarcted area, defined as the infarcted area over the total area ($n=8$).

Results/Discussion

ME was able to localize infarcts as areas of near-zero magnitude ϵ (Fig. 1a, outlined in green) as confirmed in histology (Fig. 1b). High correlation between ϵ_{median} and percent infarcted area was found ($R^2=0.77$, $p<0.001$) (Fig. 1c). Tracking the temporal change in mean ϵ_{median} across subjects illustrated infarct formation and recovery (Fig. 1d). Significant differences in mean ϵ_{median} at baseline (day 0) and during infarct formation (days 1-3) was achieved at the mid ($p<0.05$) and apex ($p<.001$) levels using Tukey's multiple comparison test. Perfusion at the base level, located superior to the ligation site, was expected to be unaffected. Confirming physiological expectations, base ϵ_{median} was statistically equivalent throughout the 4-week imaging period. ME ϵ was shown to be a good predictor of infarct severity and was capable of localizing infarct formation and monitoring recovery at the short-axis base, mid and apex levels.

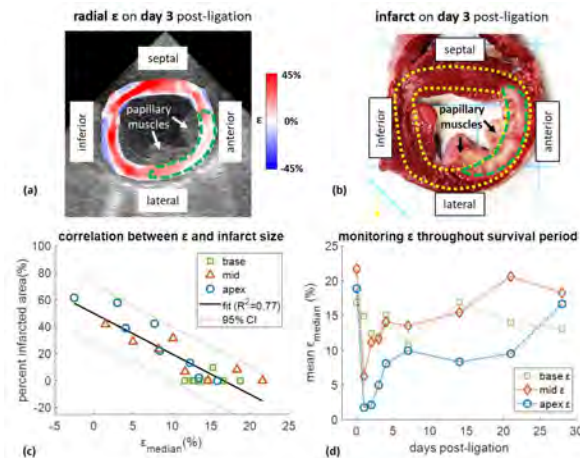


Figure 1. ME radial strain (ϵ) measurement in a canine 3 days post-ligation at the mid short-axis level shows healthy tissue as regions of high positive strain, and the infarct as an area of near-zero magnitude strain (outlined in green) (a). Infarct location was confirmed by histology (b). Median strain within the image ROI, ϵ_{median} , was well correlated with percent infarcted area (c), defined as the infarct area (outlined in green, in b) over the total area (outlined in yellow, in b). Infarct formation was evidenced by a drop in mean ϵ_{median} across subjects, while the subsequent increase in mean ϵ_{median} illustrated infarct recovery(d).

2:15 PM

An angle independent motion estimator for high frame rate cardiac data sets

Bidisha Chakraborty¹, Pedro Santos¹, Vangjush Komini¹, Aniela Monica Petrescu¹, Marta Orlowska¹, João Pedrosa¹, Brecht Heyde¹, Jens-Uwe Voigt¹, Jan D'hooge¹

¹*Cardiovascular Sciences, KU Leuven, Leuven, Belgium*

Background, Motivation, and Objective

Myocardial strain imaging has been introduced to assess local myocardial contractile function. However, strain is highly sensitive to loading conditions (e.g. blood pressure). On the other hand, peak systolic strain rate (SR) is primarily linked to local contractility. To date, a time-resolved estimate of SR is only possible by narrow sector-angle (to get a frame rate (FR) of ~180Hz) tissue Doppler imaging (TDI) which makes clinical implementation challenging. The goal of this study was therefore to show: i) that high frame rate (HFR) imaging enables measuring SR accurately in wide sector-angle images; ii) that these data sets benefit from Doppler angle correction.

Statement of Contribution/Methods

Apical views of 12 healthy volunteers (30.9 ± 4.2 years) were acquired using a 3.5MHz phased array in a 90° sector by transmitting 6 diverging waves at a PRF of ~5600Hz resulting in a FR of ~900Hz. Channel data was collected at 25MHz and reconstructed offline using compounding.

Inter-frame displacements were computed by RF-based non-rigid image registration (NRIR; i.e. displacement model: tensor product cubic B-splines; similarity measure: sum of squared differences; regularizer: bending energy) where in a multi-resolution setting envelope followed by RF data were aligned. SR was computed as the spatial gradient of velocities estimated i) in the anatomical direction of the myocardium (i.e. angle independent) and ii) by projecting the local motion on the axial direction (i.e. Doppler velocity). Segmental peak systolic (S') and diastolic (E' and A') SR were extracted. Finally, strain was obtained by time integrating the SR curves and the peak systolic strain (PS) was obtained.

Results/Discussion

SR and strain traces followed a physiologic pattern (Fig. 1A) and the measured S', E', A' and PS peaks were similar to TDI estimates reported in [1] (Fig. 1B) thereby validating the extracted SR / strain curves. Moreover, angle corrected SR was – as expected – slightly higher (Fig. 1B; $p < 0.01$) resulting in higher PS (i.e. $-21.8 \pm 8.25\%$; $p < 0.01$). In conclusion, 2D RF-based NRIR enabled accurate estimation of segmental SR in wide-angle HFR cardiac data sets. Importantly, the estimator enables to correct for angle, which is particularly relevant in wide-angle HFR recordings where the image line and myocardial wall are intrinsically misaligned.

[1] J Am Soc Echocardiogr, 13, 6, 588 – 598, 2000

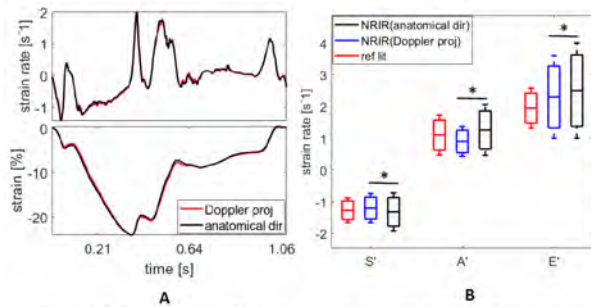


Figure 1. **A.** Example segmental strain rate and corresponding strain trace for both the components extracted from NRIR . **B.** S', A' and E' extracted from the strain rate traces for the reference and the components extracted both the ways from the NRIR. * $p < 0.01$.

2:30 PM

4D ultrafast imaging of myocardial contraction activation in normal and pathological isolated rat heartsVictor Finel¹, Philippe Mateo¹, Clément Papadacci¹, Jean Provost¹, Mickaël Tanter², Mathieu Pernot²¹Institut Langevin, INSERM U979, ESPCI, CNRS UMR 7587, ART, France, ²Institut Langevin, ESPCI Paris, PSL Research University, CNRS UMR 7587, INSERM U979, paris, France**Background, Motivation, and Objective**

The sequence of myocardium contraction activation is crucial for blood ejection, but the evaluation of cardiac activation remains challenging in the clinical setting. Electromechanical Wave Imaging [1] was developed to map the transient deformations of the myocardium following electrical activation in 2D imaging planes. In this study, we present 4D ultrafast imaging of Myocardial Contraction Activation (4DMCA) for the analysis of cardiac activation within a single heartbeat. The objective was to investigate the potential of 4DMCA on isolated rat hearts and validate the activation time against physiological gold standards measurements.

Statement of Contribution/Methods

A 2D matrix array (8MHz, 32x32 elements, 0.3mm pitch) driven by a customized, programmable, 1024-channel ultrasound scanner was used to perform 600-ms-long 2D plane-wave acquisitions during pacing at 3000 volumes/s in five isolated rat hearts in the apical view. Inter-volume axial displacements and accelerations were mapped in the myocardium using the Kasai algorithm and a smooth derivative filter, respectively. A correlation algorithm was then applied to compute 3D mechanical activation maps automatically. Two-lead epicardial potentials were recorded simultaneously during ultrasound acquisitions. The temperature of the heart was varied from 27°C to 37°C to study the effect of hypothermia on the activation sequence. Ischemia was achieved by the ligation of the LAD coronary artery.

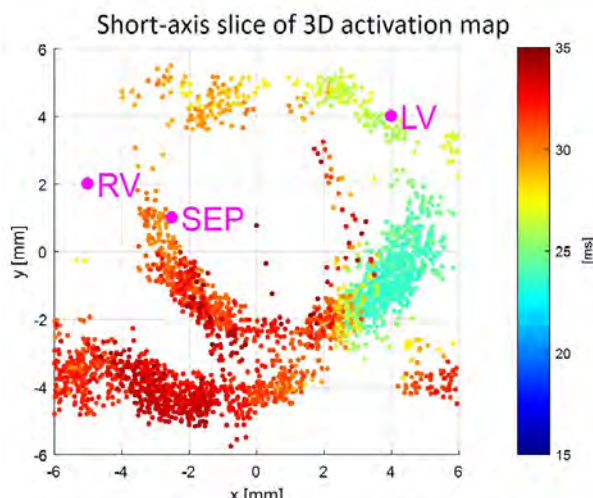
Results/Discussion

The 3D myocardial contraction activation was imaged in five rat hearts. The effect of hypothermia from 37 to 27°C augmented the hearts' electrical and mechanical activations times of $72.7 \pm 9.8\%$ and $73.7 \pm 14.1\%$, respectively. The corresponding relative change in propagation speeds was found to be $-41.3 \pm 3.9\%$ and $-40.9 \pm 4.0\%$, which is in good agreement with the value of $5.6\%/\text{°C}$ reported in the literature [2]. The modification of the activation time was quantified in the ischemic heart.

In this work, we showed that 4DMCA can provide a full 3d mechanical activation map of the heart within a single heartbeat. We demonstrated that 4DMCA can accurately quantify mechanical delays induced by hypothermia or ischemia. Further work will focus on *in-vivo* imaging.

[1] Provost et al., Proc. Nat. Acad. Sci., 108(21):8565-70, 2011

[2] Nygren et al., Am J Physiol Heart Circ Physiol 284: H892–H902, 2003



Short axis view of 3D activation map. RV stands for right ventricle, LV for left ventricle and SEP for septum.

2:45 PM

Enhancing Cardiac Positron Emission Tomography using Ultrafast Ultrasound Imaging

Jonathan Porée¹, Mailyn Pérez-Liva^{2,3}, Beatrice Berthon¹, Joevin Sourdon^{2,3}, Thomas Viel^{2,3}, Anikitos Garofolakis^{2,3}, Mickaël Tanter¹, Bertrand Tavitian^{2,3}, Jean Provost¹

¹Institut Langevin, ESPCI Paris, PSL Research University, CNRS UMR 7587, INSERM U979, Paris, France, ²Paris Descartes University, Sorbonne Paris Cité University, Inserm U970, Paris, France, ³Cardiovascular Research Center at Hôpital européen Georges Pompidou, Paris, France

Background, Motivation, and Objective

Although a promising approach for the characterization of cardiac viability, Positron Emission Tomography (PET) has seldom been used for that purpose. One reason is the uncertain localization of the PET signal induced by heart motion during the minutes-long, ECG-gated acquisitions, which imply high costs and exposure. We have recently shown that it is possible to perform co-registered Ultrafast Ultrasound Imaging (UUI) and PET simultaneously [1], without fundamental modifications to existing hardware. Herein, we propose a novel UUI non-rigid-registration algorithm that enables the reconstruction of metabolism images in Lagrangian coordinates.

Statement of Contribution/Methods

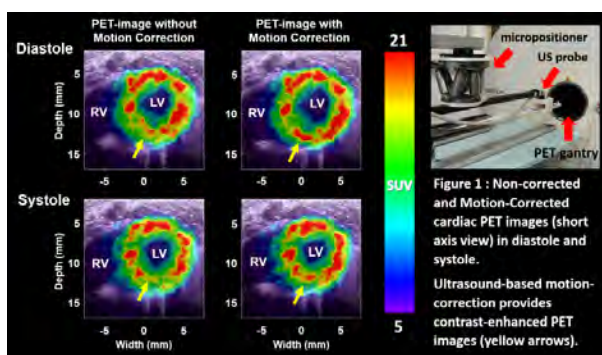
A 30-min-long, 8-frame ECG-gated, simultaneous PET-UUI was performed in rats ($n = 5$) using a small-animal PET-CT (Nano-PET-CT, Mediso, Hungary) and a 12-MHz UUI system (Aixplorer, Supersonic Imagine, France), 30 min after FDG injection. The UUI probe was positioned using a 6-degree-of-freedom micropositioner (H811, Physik Instrumente, Germany) and co-registered to the PET-CT device. UUI was performed at 750 frames/s using 20 plane waves. Multidirectional Tissue Doppler images were first computed after Gabor filtering using autocorrelation methods. Lagrangian coordinates of the myocardium were then computed as the minimizer of a quadratic cost function that is the weighted sum of : 1) the l^2 -norm of Tissue-Doppler residual and 2) a quadratic regularizer enforcing spatiotemporal continuity of the coordinates. Motion-corrected PET images were found by projecting ECG-gated frames onto Lagrangian and averaging.

Results/Discussion

Figure 1 shows the contrast enhancement due to the motion-correction. Spatial resolution was similar with and without motion correction, while the contrast increased from 11.2 to 15.1 dB.

Simultaneous CT-PET-UUI acquisitions can drastically enhance contrast of cardiac metabolic imaging without any change in the PET acquisition process. Contrast enhancement could be leveraged to better characterize cardiac viability in pathological situations such as myocardial infarcts. Alternatively, images of similar quality could be acquired over shorter acquisition times or using lower quantities of radiotracer. This could potentially lead to a reduction in cost and radiation exposure.

[1] Provost, J., et al. (2018) *Nature Biomedical Engineering*



3K - Cardiovascular Imaging

Emerald (280)

Thursday, October 25, 4:00 pm - 5:30 pm

Chair **Jean Provost**
Polytechnique Montreal

3K-1

4:00 PM Differentiation of carotid artery plaque composition in asymptomatic individuals using compound ultrasound strain imaging validated by magnetic resonance imaging

Hendrik Hansen¹, Inge van den Munckhof², Eveline van der Kolk¹, Anton Meijer¹, Marinette van der Graaf¹, Joost Rutten², Chris de Korte^{1,3}

¹*Department of Radiology and Nuclear Medicine, Radboud university medical center, Nijmegen, Netherlands*, ²*Internal Medicine, Radboud university medical center, Nijmegen, Netherlands*, ³*Physics of Fluids Group, University of Twente, Enschede, Netherlands*

Background, Motivation, and Objective

The rupture of vulnerable plaques is a main initiator of transient ischemic attacks and stroke. To detect atherosclerotic plaques with a rupture prone composition dedicated ultrasound strain imaging techniques have been developed to accurately and noninvasively measure deformations/strains of the carotid artery wall induced by the pulsating blood flow. Multiple studies have confirmed the relation between strain and plaque composition. However, studies in transverse imaging planes were only performed in patients with severe symptomatic stenosis. This study investigates if strains obtained with a strain imaging technique designed for transverse planes also correlate with MRI-based plaque composition in an asymptomatic population.

Statement of Contribution/Methods

Ultrasound radiofrequency (RF) data of 51 carotid plaques from 31 asymptomatic participants with an increased cardiovascular risk profile were recorded by an experienced sonographer in a dedicated three-angle (0° , $+20^\circ$ and -20°) focused acquisition mode using a Samsung Medison Accuvix V10 ultrasound system equipped with an L5-13IS transducer. Additionally, MR angiography and high resolution MR vessel wall data were obtained using a Siemens 3.0 T MAGNETOM Skyra MRI scanner (Erlangen, Germany) with a dedicated 4-channel Machnet Phased Array Carotid Coil (Eelde, the Netherlands). Principal radially-oriented strains were derived from the RF data using our previously published compound strain imaging approach and cumulated over the diastolic phase. The resulting strain map was normalized with respect to pulse pressure as measured with a sphygmomanometer. Two strain parameters were calculated from the strain map values in those parts of the circumference where the wall was at least 2 mm thick: 1) the median value, and 2) the percentage of strain values exceeding 0.5% strain. We studied the performance of both strain parameters for differentiating plaques classified as fatty, haemorrhagic, calcified, or aspecific/fibrous by an experienced neuroradiologist based on the MRI data and blinded to the ultrasound data.

Results/Discussion

Overall, both strain parameter values were highest for fatty plaques compared to the other plaques, although no significant differences were detected using a Kruskall-Wallis test. After grouping the plaques with a composition associated with vulnerability, i.e. fatty (n=9) and haemorrhagic plaques (n=5), and those with a stable composition, i.e. calcified (n=14) and aspecific/fibrous plaques (n=23), it was observed that both strain parameters were significantly higher for the first group (Mann-Whitney test, P<0.05). Median strain and percentage strain >0.5% for the vulnerable plaques were 0.95% and 53.4% versus -0.02% and 47.1% for the stable plaques, respectively. Thus, even in this small asymptomatic population, compound strain imaging discriminated between plaques with vulnerable and stable features.

4:15 PM New Denoising Unsharp Masking Methods for Improved Intima Media Thickness Measurements with Active Contour Segmentation

Asraf Moubark¹, David Cowell¹, Sevan Harput², Steven Freear¹

¹*University of Leeds, Leeds, United Kingdom, ²Bioengineering, Imperial College London, London, United Kingdom*

Background, Motivation, and Objective

The automated snake active contour (SAC) based segmentations play a vital role in determining the intima-media wall thickness (IMT) for assessing the risk related to cardio vascular diseases (CVD). However, the speckle and clutter noise in the ultrasound B-mode images are known to interfere with the contour formation during segmentation. Both noise sources act as false external energy in SAC and thus influence the resulting boundary definition. A high number of iterations are needed for the SAC to settle on the intended boundary and in worse case totally miss the boundary when the noise presents. Thus in this work we have applied the new denoising unsharp masking (UM) method in order to reduce the speckle and clutter noise in the B-mode image before the segmentation process takes place for faster and accurate measurement.

Statement of Contribution/Methods

The proposed UM method can be represented by the following equation:

$$B(x,t)_{\text{improved}} = |B(x,t)_{\text{coherent}} + \sigma[B(x,t)_{\text{coherent}} - B(x,t)_{\text{non-coherent}}]|$$

where $B(x,t)_{\text{improved}}$ represents a new improved B-Mode image, $B(x,t)_{\text{coherent}}$ represents coherent compound plane wave imaging (CPWI), $B(x,t)_{\text{non-coherent}}$ represents non-coherent CPWI and σ represents the weighting factor. The performance of the proposed methods was evaluated with experimental data obtained from ultrasound array research platform (UARP II) excited with 2-cycles sinusoidal signal using a 7.5 MHz linear ultrasound probe. The RF data was acquired from the right side carotid artery wall with 13 CPWI and beamformed with delay and sum (DAS). The IMT thickness is computed between the two boundaries, intima-media along the arterial far wall segmented by the SAC.

Results/Discussion

The UM denoising methods are able to attenuate the clutter and speckle noise intensity on the Media regions as shown in Fig. 1(d). This facilitates faster snake active contour formation on the adventitia borders compared to with noise as shown in Fig. 1(c) and (d). Total of 200 iterations are required with UM-DAS (Fig. 1(f)) and 400 iterations with DAS (Fig. 1(g)) for the SAC to settle on the adventitia borders. With the new proposed UM methods, the number of iterations for the SAC can be reduced by half thus speeding up the IMT measurements processing time and improving accuracy. The measured IMT on the DAS and UM-DAS are [mean = 0.70 mm, 0.75 mm], [maximum = 0.81 mm, 0.85 mm] and [minimum = 0.67 mm, 0.69 mm].

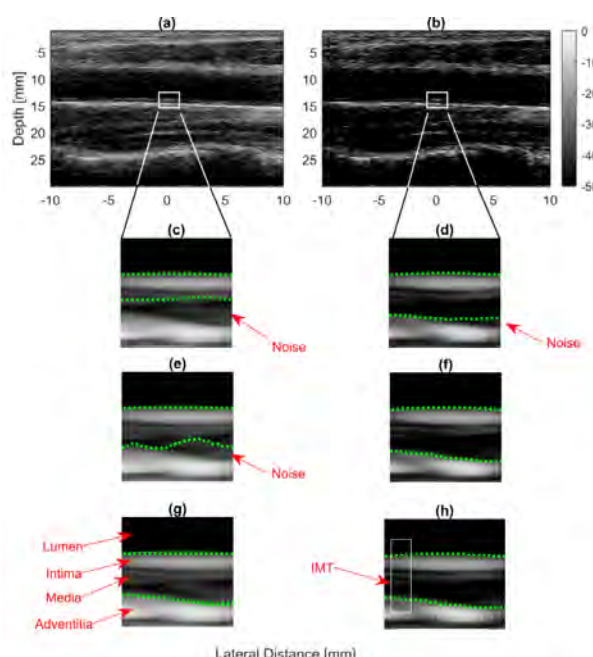


Fig. 1: The carotid artery beamformed with a) DAS and denoised with b) UM-DAS. The SAC (green dashed lines) implemented within the selected kernel regions after 100 iterations (c and d), 200 iterations (e and f), 400 iterations (g and h). The IMT measured between the two green dashed lines as shown in (h).

4:30 PM Non-invasive myocardial performance mapping using 3D echocardiographic stress-strain loops: validation against PET

João Pedrosa¹, Jürgen Duchenne¹, Sandro Queirós², Ganna Degtiarova³, Piet Claus¹, Jens-Uwe Voigt¹, Jan D'hooge¹

¹*Cardiovascular Sciences, KU Leuven, Leuven, Belgium*, ²*Universidade do Minho, Portugal*, ³*Nuclear Medicine & Molecular Imaging, KU Leuven, Leuven, Belgium*

Background, Motivation, and Objective

In clinical practice, the regional contribution to left ventricular (LV) ejection is most often assessed through visual wall motion readings. Such readings are however subject to high intra- and inter-observer variability. Although regional deformation imaging has been introduced to tackle this problem, it is highly dependent on loading conditions. As such, true myocardial (MYO) performance can only be assessed by relating deformation and loading conditions.

In this work, we propose a method for 3D automatic MYO performance mapping by 3D MYO segmentation and tracking, thus giving access to local geometry and strain. This is then used to assess local LV stress-strain relationships which can be seen as a measure of local MYO work. The proposed method was validated against 18F-fluorodeoxyglucose F 18 positron emission tomography (FDG-PET), the reference method to assess local metabolism clinically.

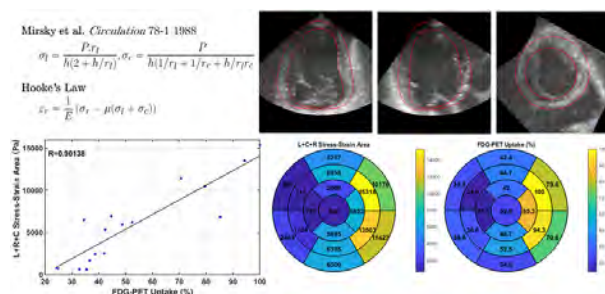
Statement of Contribution/Methods

12 non-ischemic patients that underwent FDG-PET and 3D echocardiography 1 week prior to cardiac resynchronization therapy implantation were selected from the WORK-CRT study.

Fully automatic 3D MYO segmentation using shape-based B-spline Explicit Active Surfaces was performed at end diastole. This myocardial mesh was tracked throughout the cardiac cycle using an optical flow algorithm, providing local strain estimates. The obtained local geometric characteristics were then used together with an approximated intraventricular pressure curve to estimate local longitudinal (L) and circumferential (C) stress using the equations by Mirsky et al. This pressure curve was obtained with the method by Russel et al. that scales a typical LV pressure trace based on valve opening/closing and measured blood pressure. Next, the generalized 3D Hooke's law was applied to estimate radial (R) stress. Finally, for each component (i.e. R, L and C) the corresponding stress-strain loop was calculated and the sum of these 3 loop areas was taken as an estimate of local MYO work.

Results/Discussion

Fig. 1 shows the performance maps obtained for one patient as well as the FDG-PET map and the correlation between the two. Averaged over all patients, the mean correlation between FDG-PET and the L+C+R loop area was 0.67 ± 0.18 . In conclusion, the proposed method shows promising results for fully automatic non-invasive estimation of regional MYO performance.



4:45 PM

3D direct visualization and non-invasive localization of atrial and ventricular arrhythmias using Electromechanical Wave Imaging in patients

Lea Melki¹, Christopher Grubb², Pierre Nauleau¹, Rachel Weber¹, Hasan Garan², Eric S. Silver³, Leonardo Liberman³, Elaine Wan², Elisa Konofagou^{1,4}

¹Biomedical Engineering, Columbia University, New York, NY, United States, ²Medicine - Division of Cardiology, Columbia University, New York, NY, United States, ³Pediatrics - Division of Pediatric Cardiology, Columbia University, New York, NY, United States, ⁴Radiology, Columbia University, New York, NY, United States

Background, Motivation, and Objective

Arrhythmia localization prior to catheter ablation is critical for clinical decision making and treatment planning. The current standard lies in 12-lead ECG interpretation, but this method is non-specific and anatomically limited. Accurate localization requires intracardiac catheter mapping prior to ablation. Electromechanical Wave Imaging (EWI) is a high frame-rate ultrasound modality capable of non-invasively mapping the electromechanical activation in all cardiac chambers *in vivo*. In this study, we evaluate 3D-rendered EWI as a technique for consistently localizing the origin in different atrial (flutter, tachycardia) and ventricular (Wolff Parkinson White, premature contraction) arrhythmias in patients.

Statement of Contribution/Methods

A 2 kHz diverging sequence (Verasonics) was used to image 40 patients (age: 7-89, median 34, 53% male) with evidence of ECG abnormalities (10/40 atrial arrhythmias), immediately prior to catheter ablation in four transthoracic apical views. Electromechanical strains were computed with 1D RF cross-correlation followed by a 5 mm kernel least-squares estimator. Activation times were defined as the timing of the first sign change in incremental axial strain after the QRS and the p-wave onset, for the ventricles and atria respectively. 3D rendering of the activation maps was then generated by registering the multi-2D views around the left ventricle longitudinal symmetry axis and performing a linear interpolation around the circumference. Two electrophysiologists predicted the arrhythmic location on 12-lead ECG. Double-blinded EWI isochrones and clinician assessments were compared to the ground truth (successful ablation site) using a segmented template of the heart with 21 ventricular and 3 atrial regions.

Results/Discussion

3D-rendered EWI was shown capable of consistently localizing abnormal regions in (37/40) 92.5% of arrhythmic cases (Fig. 1) and 100% of the cases when excluding the three poor quality B-modes. Clinical ECG interpretation correctly predicted the origin with an accuracy of 69%. Our method also differentiated irregular beats from sinus rhythm on the same patients (Fig. 1 b-c). These findings indicate that EWI could inform current diagnosis and expedite treatment planning of various arrhythmias in tandem with an ultrasound scan within the standard clinical routine.

NIH support R01 HL140646 01

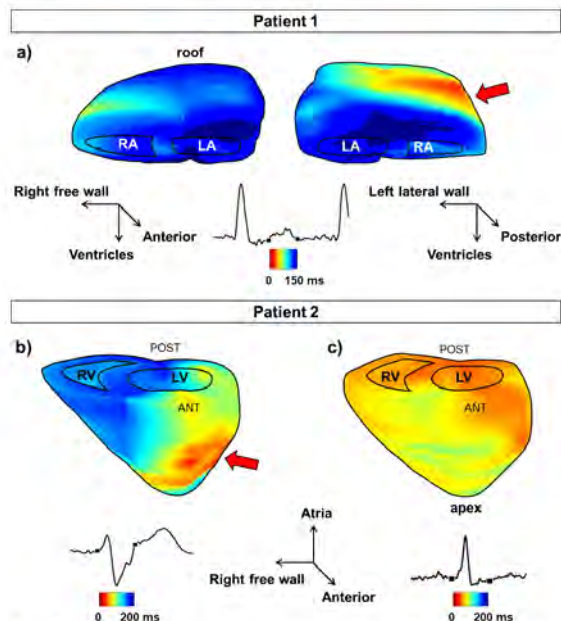


Fig.1: EWI activation maps in two different arrhythmic subjects prior to their catheter ablation. a) Patient 1; 3D rendered atrial isochrones of a focal tachycardia coming from the mid posterior right atrium in both anterior (left) and posterior (right) views. b) Patient 2; 3D rendered ventricular map of a premature ventricular contraction originating from the left anterior papillary muscle in anterior view. c) Patient 2: same patient imaged in a consecutive non ectopic beat (sinus rhythm) in anterior view.

5:00 PM Ultrafast imaging of the heart dynamics with cascaded-wave ultrasound
Yang Zhang¹, He Li¹, Wei-Ning Lee^{1,2}
¹*Electrical and Electronic Engineering, The University of Hong Kong, Hong Kong*, ²*Medical Engineering Programme, The University of Hong Kong, Hong Kong*
Background, Motivation, and Objective

Ultrafast cardiac imaging techniques based on pulsed-wave ultrasound have emerged to permit quantification of rapid heart dynamics, such as myocardial deformation and blood flow, but they suffer from limited sonographic signal-to-noise ratio (SNR) due to insufficient energy delivery. We hereby propose ultrafast cascaded-wave ultrasound imaging to map heart dynamics with higher SNR than pulsed-wave ultrafast ultrasound.

Statement of Contribution/Methods

Our ultrafast ultrasound cascaded-wave imaging sequence design takes full advantage of both the spatial and temporal domains of the array. On transmission, the array is divided into M ($M = 2^m$, $m = 0, 1, 2, \dots$) sub-apertures, and this is similar to the virtual-source-based synthetic aperture imaging (SA) and the Hadamard encoded SA (H-SA). Ours, however, is distinct in that the M sub-apertures transmit simultaneously and that each sub-aperture transmission is a train of divergent waves which contains N ($N = 2^n$, $n = 0, 1, 2, \dots$) cascaded waves with short time intervals and +1 or -1 polarity coefficients. Our method is hereby coined as “cascaded synthetic aperture imaging (CaSA)”. In order to tackle the tradeoff between spatial resolution and penetration (i.e., the length of transmitted signals), we design a spatiotemporal coding matrix for the polarity coefficients of each cascaded wave transmission. On reception, we design a spatiotemporal decoding scheme for subsequent image formation to increase the SNR ($10 \log_{10}(NM)$ Vs. SA) without compromising spatiotemporal resolutions.

In vivo human heart (male, 26 y.o.) and a calibration phantom (CIRS) were scanned using a Vantage system (Verasonics, Kirkland, WA) with an ATL P4-2 probe (center frequency 2.5 MHz, acquisition rate 4000 fps, $M = 4$ and $N = 32$). Myocardial motion was estimated by cross-correlation and blood flow was mapped using power Doppler with spatiotemporal filtering.

Results/Discussion

The proposed CaSA imaging not only improved SNR (+20.46 dB Vs. SA, + 14.83 dB Vs. H-SA) with comparable spatiotemporal resolutions in the calibration phantom but also enhanced the delineation of myocardium wall with about 10 dB noise suppression in the heart ventricle as evidenced in Fig. 1A. CaSA generated higher quality images, thus yielding more accurate mapping of myocardial motion (Fig. 1B) and higher contrast (about 7 dB) Doppler flow imaging (Fig. 1C) than benchmark methods.

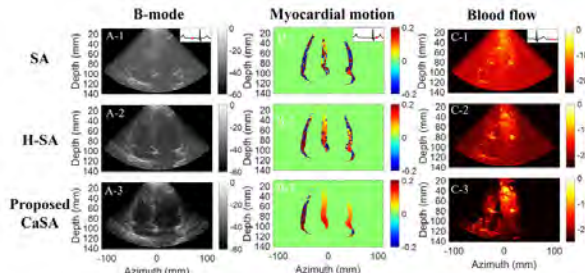


Fig. 1. *In vivo* human heart: The B-mode images (A) displayed in 60 dB dynamic range, axial tissue velocity maps of the myocardium (B) displayed from -0.2 m/s to 0.2 m/s, and power Doppler flow images (C) by spatiotemporal filtering. A-1, B-1 and C-1 are obtained from the virtual-source-based synthetic aperture imaging (SA); A-2, B-2, and C-2 from the Hadamard encoded SA imaging (H-SA); and A-3, B-3, C-3 from our proposed cascaded SA imaging (CaSA). The SA, H-SA and CaSA sequences were sequentially scanned frame by frame to ensure the quasi-simultaneous acquisition of the same region of interest of the beating heart. Electrocardiogram (ECG) is shown on the upper right corner of each image in the first row; the red dot represents the phase within the cardiac cycle that corresponds to the displayed images.

5:15 PM

Ventricular tachycardia re-entry mapping with 3D electromechanical wave imagingJulien Grondin¹, Christopher Grubb², Elisa Konofagou³¹Columbia University, United States, ²Medicine - Division of Cardiology, Columbia University, New York, NY, United States, ³Biomedical Engineering, Columbia University, United States**Background, Motivation, and Objective**

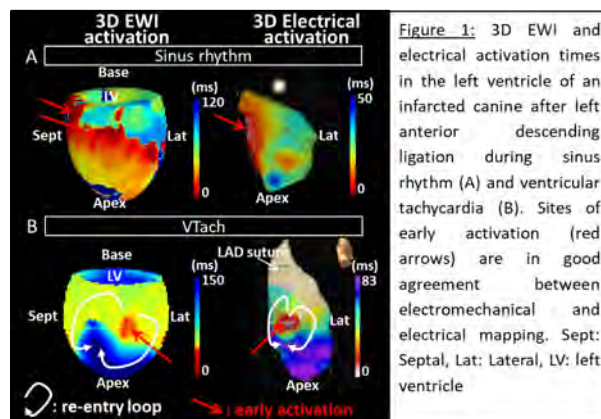
Myocardial infarction resulting from coronary artery occlusions can alter electrical conduction in the infarct region, where re-entry loops can form and lead to ventricular tachycardia (VTach) and fibrillation. Localization of the re-entrant pathway is critical to treat the arrhythmia and is performed invasively with an electrical mapping catheter under fluoroscopy in the clinic. 3D electromechanical wave imaging (EWI) is an ultrasound-based methodology that can map the electromechanical activation of the full heart at high volume-rate in a single heartbeat. The objective of this study is to show the feasibility of mapping the origin of VTach with 3D EWI *in vivo*.

Statement of Contribution/Methods

A myocardial infarct was induced in a canine model by ligating the left anterior descending (LAD) artery. Three days after the infarct formation, VTach was induced after 10-20 s of ventricular pacing with a cycle length of 160-280 ms in the infarct border zone and sustained for 5-30 min. A 32x32-element array, with 3-MHz center frequency and connected to two Verasonics Vantage systems with a 2:1 multiplexer was used for 3D EWI. Ultrasound radiofrequency channel data were acquired at 1000 Hz using diverging wave imaging and inter-volume axial displacements were estimated using 1-D normalized cross-correlation. Inter-volume axial strains were estimated with a least-squares estimator and the electromechanical activation times were calculated as the time of first zero-crossing. Electrical mapping of the epicardial surface was performed with 3D electroanatomical mapping (EnSite, St. Jude Medical). 3D EWI and electrical mapping were both performed during sinus rhythm and VTach.

Results/Discussion

Good agreement was found between 3D EWI and electrical activation times in an infarcted canine after LAD ligation during both sinus rhythm and VTach (Figure 1). The site of origin of VTach was found to be in the anterior region at the mid-level in the territory perfused by the LAD. During VTach, the earliest (0-40 ms) and latest (150-200 ms for EWI and 80-90 ms for electrical) activation sites were adjacent, which indicates that the underlying mechanism for this VTach is a re-entry loop in that area. This study shows that 3-D EWI can map the site of origin of VTach, which could potentially open new avenues for noninvasive VTach diagnosis and treatment monitoring in a clinical setting.



4H - Beamforming for Other Applications

Sapphire (220)

Thursday, October 25, 8:00 am - 9:30 am

Chair **Georg Schmitz**
Ruhr-Universität Bochum

4H-1

8:00 AM Segmenting bone structures in ultrasound images with Locally Weighted SLSC (LW-SLSC) beamforming

Eduardo Gonzalez¹, Muyinatu Bell¹

¹*Johns Hopkins University, Baltimore, MD, United States*

Background, Motivation, and Objective

Registering preoperative computed tomography (CT) images with intraoperative ultrasound (US) is a challenging task, due to the poor similarity of reconstructed images. Existing CT-US registration approaches rely on accurate segmentation of bone structures in US images, which are often subject to ultrasound speckle noise, clutter, and acoustic shadowing. The objective of this work is to explore Short-Lag Spatial Coherence (SLSC) beamforming as an alternative to delay-and-sum (DAS) beamforming to reduce speckle noise and enhance bone boundaries. In addition, we propose Locally Weighted SLSC (LW-SLSC) beamforming to further improve bone segmentation.

Statement of Contribution/Methods

Instead of averaging the cumulative sum up to a lag value M (out of a preselected total of N lags, where $M \leq N$), LW-SLSC beamforming computes the weighted coefficients for N lags by minimizing the total variation of the weighted sum within a moving kernel. In order to preserve the high resolution located at higher lags, this adaptive solution is regularized using the L2-norm with a gradient operator. US channel data was acquired for 10 different views of a human vertebra submerged in deionized water using an Alpinion ECUBE-12R system and SP1-5 phased array probe (3.8 MHz center frequency, 65 mm depth, 50 mm focus). SLSC images were computed with M varying from 1 to 25, and DAS images were created with the dynamic range (DR) varying from -60 to -40 dB. LW-SLSC images were computed with a 1.20 mm (lateral) x 1.92 mm (axial) kernel, $N=50$, 50% overlap and 0.1 regularized coefficient obtained from L-curve tests. The Gradient Correlation (GC) was measured to evaluate the bone structure similarity of each ultrasound imaging method when compared to CT images.

Results/Discussion

Example CT, DAS, SLSC and LW-SLSC images are shown in Fig. 1 alongside the mean \pm standard deviation of GC measurements. Overall, SLSC outperforms DAS for a range of parameters commonly used in the literature (e.g., $M=5-25$, DR=-50 to -60 dB) when considering the similarity of bone structures in the CT and US-based images. An additional improvement is observed with LW-SLSC over SLSC (e.g., 8.2 dB mean contrast-to-noise ratio increase, 0.10 mean GC increase). These results indicate that SLSC and LW-SLSC provide improved bone segmentation over traditional DAS, with possible applications to improving US-CT registration for spine surgery.

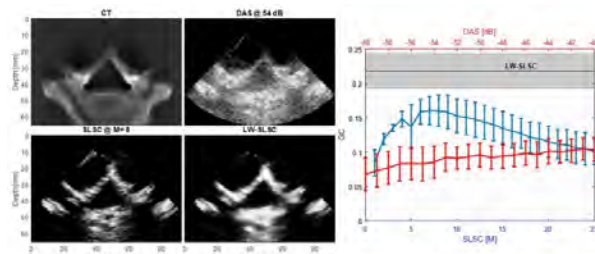


Figure 1. Left: examples of reconstructed CT, DAS, SLSC and LW-SLSC images. Observe that both SLSC and LW-SLSC have similar lateral resolution. Right: Mean \pm standard deviation of GC measurements when comparing DAS, SLSC and LW-SLSC images to CT images. Note that the neither x-axis applies to the LW-SLSC result as the multiple possible parameters were fixed for all 10 images.

8:15 AM

Influence of beamforming methods on velocity estimation: in vitro experiments**Maxime Polichetti^{1,2}, Vincent Perrot¹, Hervé Liebgott¹, Barbara Nicolas¹, François Varray¹**¹*University Lyon, INSA-Lyon, UCBL, UJM-Saint-Etienne, CNRS, Inserm, CREATIS UMR 5220, U1206, F-69100 Villeurbanne, France, France, ²LabTau, INSERM, Centre Léon Bérard, UCBL, University Lyon, F-69003 Lyon, France***Background, Motivation, and Objective**

Ultrasound is becoming more and more a functional and tissue characterization modality providing additional information thanks to improved motion estimation (flow velocity, tissue deformation) along sequences of images. Many beamforming methods have been developed as an alternative to conventional Delay-And-Sum (DAS) algorithm. Fourier-based methods decrease the computational load, while adaptive ones enhance B-mode image quality. These beamformers were mainly evaluated using image quality metrics on static media, such as resolution and contrast, but never on motion estimation. Herein, the influence of six beamformers on velocity estimation is quantitatively evaluated experimentally with a rotating disk.

Statement of Contribution/Methods

An agar and silica based rotating disk was imaged at different constant velocities (50, 100, 150 and 200 deg/s) using a Verasonics system and a L7-4 linear probe. Axial velocity maps were computed with a phase-based estimator using the complex autocorrelation of beamformed signals (Loupas 1995). The conventional DAS was compared with several beamformers introduced in the literature: two Fourier-based techniques (Lu's and FK), and three adaptive ones (Minimum Variance (MV), Phase Coherence Factor (PCF) and DAS with p-th root compression of signals (p-DAS)). Adaptive effects were tuned with the spatial smoothing rate for MV (p_{L}), the rejecting weight of PCF (γ), and the p-th root order for p-DAS (p). For each beamformer, the bias and the standard deviation (STD) of velocity estimations were compared.

Results/Discussion

The experimental results demonstrate that advanced beamformers are compatible with velocity estimation. Fourier-based methods slightly outperformed DAS (Figure 1e: averaged bias for DAS: 5%, Lu: 4%, FK: 4%). Adaptive beamformers can offer comparable velocity maps as DAS (Figure 1b, c) with similar statistics in terms of bias (Figure 1e: DAS: 5%, MV- $p_{L}30$: 5%, 1.2-DAS: 5%, PCF- $\gamma1$: 6%) and STD (Figure 1e: DAS: 5%, MV- $p_{L}30$: 6%, 1.2-DAS: 6%, PCF- $\gamma1$: 6%). However, their performances decreased when increasing the adaptive effect. For example, using p-DAS, when the value of p increased, the lateral resolution and contrast of B-mode images were improved, but the quality of the velocity estimates was decreasing (Figure 1e: bias for DAS: 5%, 1.5-DAS: 6%, 2-DAS: 9%, and STD for DAS: 6%, 1.5-DAS: 7%, 2-DAS: 11%).

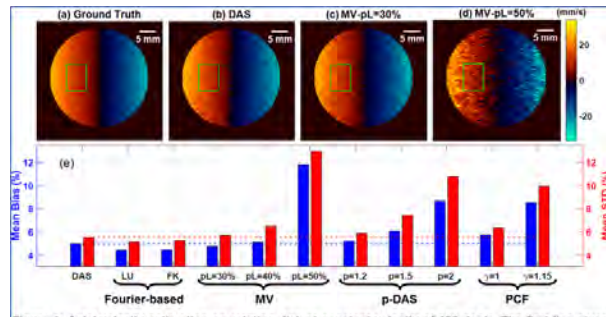


Figure 1: Axial velocity estimation on rotating disk at constant velocity of 100 deg/s. The first line gives instantaneous velocity maps between two successive frames (PRF = 1000 Hz, f = 5.2 MHz): (a) ground truth, (b) estimation after conventional DAS beamforming, and estimations after adaptive MV beamforming for two different values for spatial smoothing parameter (c) $p_{L} = 30\%$ and (d) $p_{L} = 50\%$. For each pixel bias and standard deviation are computed considering 253 frames. The graph (e) represents the averaged bias and averaged standard deviation in the region of interest in the green box. Metrics are normalized with respect to the theoretical maximum velocity of 26 mm/s.

8:30 AM

Evaluation of coherence-based beamforming for B-mode and speckle tracking echocardiography

Pedro Santos¹, Nadezhda Koriakina¹, Bidisha Chakraborty¹, João Pedrosa¹, Aniela Monica Petrescu¹, Jens-Uwe Voigt¹, Jan D'hooge¹

¹Department of Cardiovascular Sciences, KU Leuven, Leuven, Belgium

Background, Motivation, and Objective

Speckle tracking (ST) is the main clinical tool for quantifying cardiac function, whereas B-mode is used for anatomical assessment. The success of both depends on B-mode quality, often degraded eg. by clutter and off-axis scattering. Lately, several beamformers showed improved resolution/contrast, mostly validated on B-mode images. Interestingly, ST may indirectly benefit from the same algorithms.

At IUS 2017 we presented a preliminary *in-silico* study on ST performance with phase coherence beamforming. In the present work, we performed a more thorough *in-vivo* analysis with the aims of: i) comparing image quality of different beamformers in a clinical setting; ii) assessing the performance of ST on these datasets.

Statement of Contribution/Methods

Channel data was acquired with an experimental scanner (HD-PULSE) in 10 healthy volunteers with average acoustic window (good quality datasets were discarded). Six beamformers were used: delay-and-sum (DAS), phase coherence factor (PCF), sign coherence factor (SCF), generalized coherence factor (GCF), short-lag spatial coherence (SLSC) and filtered-delay multiply and sum (FDMAS).

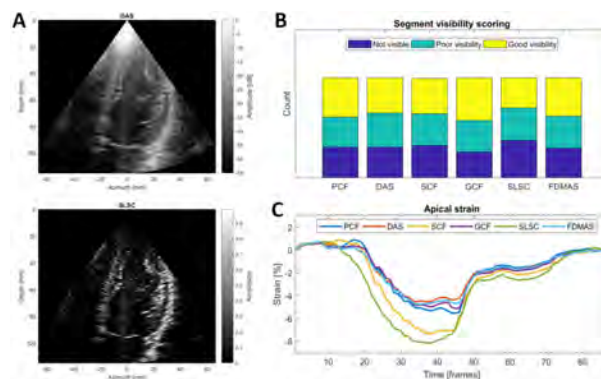
Images were shown in random order to 4 sonographers who scored them based on myocardial segment visibility and overall image quality. They were then tracked using a validated non-rigid registration algorithm to estimate segmental strain from which peak systolic values were extracted and compared using a Friedman test.

Results/Discussion

Advanced beamforming reduced artifacts particularly in the near field where visibility was on average worst (Fig A), as confirmed by a slight change in score across methods (Fig B). Although no method was systematically favorable ($p=NS$), GCF and FDMAS showed a trend for better visibility.

Significant differences in peak strain were found in mid-septal ($p=.013$) and apical segments ($p<.001$). Consistent with the above, apical strain curves benefited from alternative beamforming as they partially recovered from the severe underestimation seen for DAS (Fig. C). No method outperformed in all segments/volunteers suggesting the presence of different artifacts.

In conclusion, although advanced beamformers can benefit cardiac imaging, their impact on image quality and ST is variable between subjects. Further research is thus required to understand under which conditions each method shows most benefit.



[A] DAS and SLSC B-mode for one volunteer, depicting better contrast for the latter. [B] Summary of segment visibility scoring for all 4 reviewers. [C] Apical strain curves for the subject in A, showing higher underestimation for DAS.

8:45 AM

Assessment of tissue boundary delineation using fundamental and harmonic ADMIRE and SLSC for percutaneous biopsy guidance

Kazuyuki Dei¹, Siegfried Schlunk¹, Adam Luchies¹, Daniel Brown², Brett Byram¹

¹Department of Biomedical Engineering, Vanderbilt University, Nashville, TN, United States, ²Department of Radiology, Vanderbilt University Medical Center, Nashville, TN, United States

Background, Motivation, and Objective

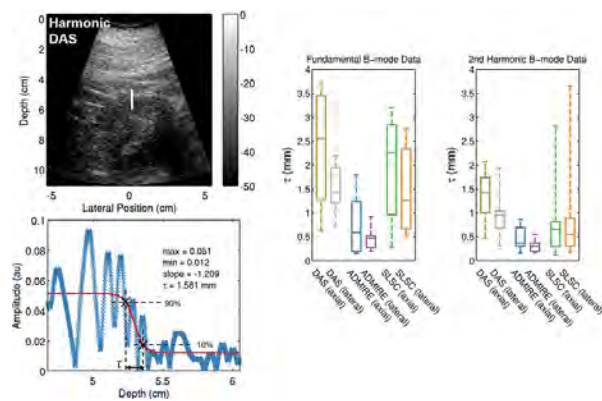
Ultrasound is used extensively for percutaneous biopsy guidance. In ultrasound guidance, it is important to delineate boundaries, but conventional ultrasound images may be of poor quality. This may be worse in the presence of an acoustically bright needle, and in general, high levels of clutter will blur boundaries. To tackle this shortcoming, numerous beamformers have been developed, including aperture domain model image reconstruction (ADMIRE) and short-lag spatial coherence (SLSC). To determine whether ADMIRE and SLSC provide better delineation of boundaries, we quantify the sharpness of axial and lateral edges at the boundary of the kidney. We consider both fundamental and harmonic implementations.

Statement of Contribution/Methods

We acquired *in vivo* kidney data from six patients undergoing biopsy and cryoablation using a Siemens SC2000. The data set consists of channel data acquired using fundamental frequency and 2nd harmonic pulse inversion sequencing. We then applied ADMIRE and SLSC to the data. Using uncompressed enveloped signals at axial and lateral kidney boundaries, we fit sigmoid functions in order to estimate the transition length between 10% and 90% of amplitude difference at the boundary of the kidney. Shorter transitions indicate sharper boundaries. We applied this method to delay-and-sum (DAS), ADMIRE and SLSC data for fundamental and harmonic cases.

Results/Discussion

An example of estimates of the transition length (i.e., τ) using a sigmoid function is demonstrated in the figure. Results of measured τ are also shown in box plots for fundamental and harmonic data. The axial/lateral values of τ using DAS, ADMIRE and SLSC are $2.38 \pm 1.21/1.51 \pm 0.51$ mm, $0.75 \pm 0.64/0.46 \pm 0.24$ mm and $1.86 \pm 1.12/1.51 \pm 0.90$ mm, respectively, for the fundamental data, while the harmonic cases have $1.36 \pm 0.54/0.97 \pm 0.50$ mm, $0.47 \pm 0.26/0.31 \pm 0.13$ mm and $0.84 \pm 0.90/0.96 \pm 1.21$ mm, respectively. Based on the findings, ADMIRE has the shortest transition length laterally and axially for both fundamental and harmonic cases, suggesting that ADMIRE provides better axial and lateral boundary delineation than DAS and SLSC. It is also interesting to note that the transition length of SLSC shows large variance in the harmonic data.



9:00 AM

Clinical Feasibility of Coherence-Based Beamforming to Distinguish Solid from Fluid Hypoechoic Breast Masses

Alycen Wiacek¹, Kelly Myers², Eniola Falomo², Ole Marius Hoel Rindal³, Kelly Fabrega-Foster², Susan Harvey², Muyinatu A. Lediju Bell^{1,4,5}

¹Department of Electrical and Computer Engineering, Johns Hopkins University, United States, ²Department of Radiology and Radiological Science, Johns Hopkins Medicine, United States, ³Department of Informatics, University of Oslo, Norway, ⁴Department of Biomedical Engineering, Johns Hopkins University, United States, ⁵Department of Computer Science, Johns Hopkins University, United States

Background, Motivation, and Objective

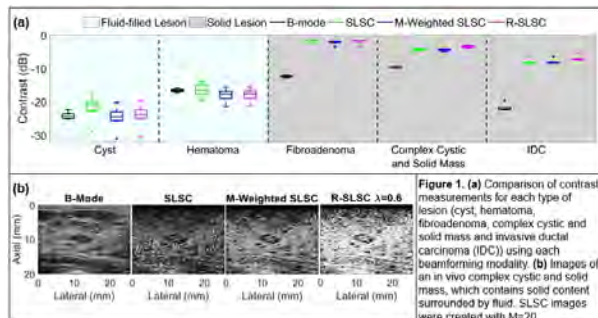
Ultrasound imaging is a key diagnostic and screening tool for early breast cancer detection. However, the dense breast tissue that makes ultrasound favorable over mammography introduces acoustic clutter that contributes to high false positive rates, diagnostic uncertainty, and excessive follow-up exams and biopsies. Coherence-based beamformers, such as short-lag spatial coherence (SLSC), directly display spatial coherence, while M-Weighted SLSC and Robust SLSC (R-SLSC) imaging additionally leverage the sparse information at higher spatial lag values, which is promising for hypoechoic breast masses with uncertain fluid or solid content due to acoustic clutter (Nair *et. al.* IEEE T-UFC 2018). The objective of this work is to explore the ability of these methods to distinguish between solid and fluid-filled hypoechoic breast masses.

Statement of Contribution/Methods

Four patients were enrolled in our ongoing study after informed consent and approval from the Johns Hopkins Medical Institutions. Each patient had at least one hypoechoic lesion of interest (i.e., simple cyst, complex cystic and solid mass, hematoma, fibroadenoma, and invasive ductal carcinoma) that was scanned using an Alpinion ECUBE12R research ultrasound scanner connected to either an Alpinion L3-8 or L8-17 linear array transducer with center frequencies of 8MHz and 12.5MHz, respectively. Each lesion was insonified using 256 focused transmissions. Lesion contrast was compared across matched B-mode and coherence-based images created from the same channel data.

Results/Discussion

Fig. 1a shows the measured contrast of the 5 lesions when visualized using the 4 beamforming techniques. Fluid-filled lesions demonstrate comparable contrast between B-mode and the three coherence-based images. Conversely, solid lesions demonstrate significantly lower contrast in the coherence-based images ($p < 0.001$). Fig. 1b shows example images from one of the solid lesions (i.e., complex cystic and solid mass), which exhibits improved border delineation in addition to accentuated solid content with R-SLSC imaging. These initial results are promising for the introduction of coherence-based ultrasound imaging techniques to provide additional classification of suspicious breast lesions prior to biopsy, potentially reducing the current rate of false positives with ultrasound imaging.



9:15 AM Cardiac deformation imaging based on coherent compounding of diverging waves with coded excitation

Feifei Zhao¹, Jianwen Luo¹¹*Department of Biomedical Engineering, Tsinghua University, Beijing, China, People's Republic of***Background, Motivation, and Objective**

Diverging wave transmit based on phased array offers a potential solution for cardiac deformation imaging at high frame rate. Diverging wave compounding (DWC) imaging has been developed to improve the imaging SNR and contrast as well as the performance of cardiac strain estimation. We previously proposed to use coded excitation in DWC imaging to improve the B-mode image quality without sacrificing the frame rate. This study proposes to apply coded excitation in DWC imaging for cardiac deformation imaging, and investigates its performance both *in silico* and *in vivo*.

Statement of Contribution/Methods

Three imaging schemes were considered and contrasted, i.e., non-coded, chirp-coded and orthogonal Golay pairs-coded (OGPs-coded) DWC imaging with 8 steering angles, at 4 kHz PRF (effective frame rate: 500 Hz). Full aperture (20 mm) of a 2-MHz, 64-element phased array was used both *in silico* and *in vivo*, and the virtual sources moved along an arc centered at the center of the probe. In the *in silico* study, short-axis view of the left ventricle in the systolic phase was simulated. The cardiac motion model was derived from a realistic 3D synthetic echocardiographic database. Axial, lateral and radial inter-frame strains were estimated and compared to the true values for calculation of the mean relative errors. The correlation coefficients in motion estimation were also compared. In the *in vivo* study, the heart of a healthy volunteer was scanned in an apical four-chamber view with a ULA-OP system. For each imaging scheme, the spatiotemporal variation of tissue velocities along the septum and temporal profile of velocities at one point (white arrow in Fig. 1(a)) were derived during the systolic phase.

Results/Discussion

For the *in silico* study, compared to non-coded scheme, chirp- or OGPs-coded schemes achieve lower mean relative errors in strain estimation and higher correlation coefficients (Table I). For the *in vivo* study, spatiotemporal tissue velocities extracted from atrial septum show an improved penetration depth both in chirp- and OGPs-coded schemes (see arrows in Figs. 1(b-d)). The noise level of the velocity profile is lower in coded excitation schemes than in non-coded one (Fig. 1(e)). The *in silico* and *in vivo* results indicate that DWC with coded excitation can achieve more reliable cardiac deformation estimation, which is important for characterization of cardiac function.

Table I. Mean relative errors of estimated strains and correlation coefficients

| Imaging scheme | Axial strain error (%) | Lateral strain error (%) | Radial strain error (%) | Correlation coefficient |
|----------------|------------------------|--------------------------|-------------------------|-------------------------|
| Non-coded | 127 | 776 | 134 | 0.993 |
| Chirp-coded | 103 | 391 | 54 | 0.999 |
| OGPs-coded | 110 | 473 | 62 | 0.999 |

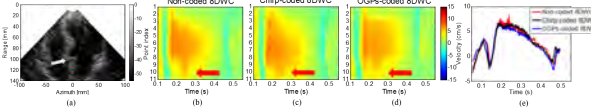


Figure 1. (a) 11 different locations along the septum superimposed on B mode image and (b-d) the extracted spatiotemporal tissue velocity maps. (e) Velocity vs. time at one point (indicated by the white arrow in (a)).

4I - Compressed Imaging

Sapphire (220)

Thursday, October 25, 10:30 am - 12:00 pm

Chair **Yonina Eldar**
Technion

4I-1

10:30 AM Structured Ultrasound Microscopy

Jovana Janjic¹, Pieter Kruizinga², Pim van der Meulen³, Geert Springeling⁴, Frits Mastik¹, Geert Leus³, Johan G. Bosch¹, Antonius F. W. van der Steen^{1,5}, **Gijs van Soest¹**

¹Thorax Centre, Erasmus MC, Rotterdam, Netherlands, ²Dept. of Neuroscience, Erasmus MC, Rotterdam, Netherlands,

³EWI, TU Delft, Netherlands, ⁴Experimental Medical Instrumentation, Erasmus MC, Rotterdam, Netherlands, ⁵Faculty of Applied Science - ImPhys, TU Delft, Netherlands

Background, Motivation, and Objective

High-resolution wide-field ultrasound microscopy creates high resolution images in different applications such as non-destructive testing, tissue microscopy and intravascular imaging. Traditional scanning acoustic microscopy (SAM) works by translation of a focused beam across an object. The depth-varying, anisotropic resolution, the large number of sampling points needed for full 3D coverage and the complexity of manufacturing high-frequency focused transducers limit the utility of SAM in many practical applications. In this work, we propose Structured Ultrasound Microscopy (SUM), a wide-field imaging technique with isotropic high resolution.

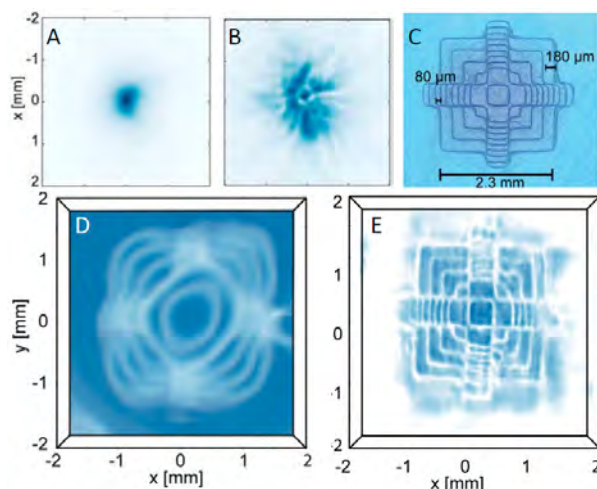
Statement of Contribution/Methods

SUM creates a volumetric image by recording reflected echoes of ultrasound waves with a structured phase front using a moving single-element transducer and computational reconstruction. A priori knowledge of the acoustic field produced by the single element relates the received echoes to a 3D scatter map within the acoustic beam itself. A 3D-printed aberration mask in front of the acoustic element imposes the phase structure, broadening the beam and breaking the spatial coherence between different voxels at equal acoustic propagation delay, increasing the uniqueness of the reconstruction (Kruizinga *et al.* Sci Adv 2017;3:e1701423). By translating the transducer, we synthetically enlarge the imaging aperture. The image is reconstructed by solving the linear equation $\mathbf{u} = \mathbf{Hv} + \mathbf{n}$ for the object \mathbf{v} , using the multiple overlapping and spatially sparsely sampled measurements \mathbf{u} and the system matrix \mathbf{H} , containing the knowledge of the acoustic field.

Results/Discussion

We demonstrate microscopic imaging at 20 MHz of a 2.3x2.3x1.2 mm object in water, with a smallest feature size of 80 μm . All features were successfully resolved, demonstrating an isotropic resolution of < 80 μm . The proposed approach allows for wide-field 3D imaging at isotropic microscopic resolution using a small unfocused ultrasound sensor and multiple spatially sparsely sampled measurements. This technique may find applications in many other fields where space is constrained, device simplicity is required, and wide-field isotropic high-resolution imaging is desired.

Figure: **A** acoustic beam for SAM; **B** phase-encoded SUM beam; **C** 3D pyramid object; reconstructed image using **D** conventional SAM-like imaging, and **E** SUM.



10:45 AM

Joint optimization of coding mask and scan positions for compressive single sensor imaging**Pim van der Meulen¹, Pieter Kruizinga², Johan G. Bosch³, Geert Leus¹**¹*Department of Microelectronics, Delft University of Technology, Netherlands*, ²*Department of Neuroscience, Erasmus Medical Center, Netherlands*, ³*Biomedical Engineering, Erasmus Medical Center, Netherlands***Background, Motivation, and Objective**

Recently, we introduced a 3D ultrasound imaging device consisting of a single ultrasound transducer covered by an irregularly shaped coding mask [1]. Needing only one sensor, the device is useful for space limited applications, but can also be used for structured ultrasound scanning microscopy by raster scanning the object of interest. In this work, given a fixed number of spatial measurements, we want to find the best scanning positions, as well as the best coding mask.

Statement of Contribution/Methods

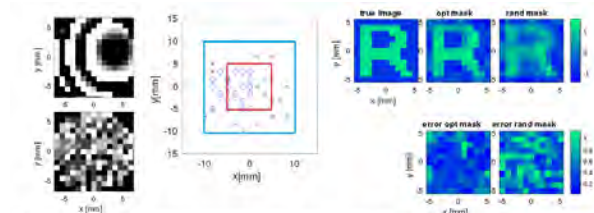
The sampled pulse-echo measurements \mathbf{y} are represented by a linear system of equations $\mathbf{y} = \mathbf{Ax}$, where \mathbf{x} contains the image pixel intensities, and \mathbf{A} contains the spatiotemporal transfer functions relating the image to the measurements. Using a Wiener filter to estimate \mathbf{x} with image and noise covariance matrices \mathbf{C}_x and \mathbf{C}_n , we consider minimizing various functions of the image estimation error covariance matrix

$\mathbf{C}_e = (\mathbf{C}_x^{-1} + \mathbf{A}^H \mathbf{C}_n^{-1} \mathbf{A})^{-1}$, such as the average MSE, $f(\mathbf{A}) = \text{tr}(\mathbf{C}_e)$, or the log volume of the confidence ellipsoid, given by the function $f(\mathbf{A}) = -\log \det \mathbf{C}_e^{-1}$. By discretizing the mask surface into channels, we express \mathbf{A} in terms of the mask thickness per channel as well as the sensing positions. Our problem is then cast as a selection problem where we want to select from a finite set of thickness levels per mask channel, and simultaneously select from a finite set of sensing positions by gridding the sensor space, such that $f(\mathbf{A})$ is minimized. We solve this problem using a successive greedy selection algorithm.

Results/Discussion

We optimized for a circular 4-6 MHz transducer with a 12 mm diameter and define an ROI of 10x10 mm at a depth of 12 mm. We further choose a uniform rectangular grid of potential sensing positions covering an area of 20x20 mm at a depth of 0 mm, and let the algorithm select 20 sensing positions. With a fixed noise energy, and $\text{var}(\mathbf{x}) = 1$, the optimized setup has an MSE of 0.46 (averaged over all \mathbf{x}), and an SNR of 18.7 dB (averaged over all \mathbf{x}). To estimate the average performance of a random design strategy, we test 1,000 configurations with a random mask and random scanning positions, giving an average MSE of 0.61 and an average SNR of 10.6 dB. The figure below shows a simulation-based experiment for a particular \mathbf{x} using the optimized configuration, and one particular random setup. Future work focuses on translating these results to real experiments.

[1] P. Kruizinga et. al., *Science Adv.* 2017



Left: optimized mask (top) and one particular random mask (bottom). Center: positions selected by the optimization algorithm (diamonds) and by a random selection procedure (crosses). The ROI of 11x11 pixels is shown in red, a grid of 13x13 sensor positions is indicated in blue. Right: image reconstructions of a letter P with $\|x\|_1=1$, using the mask profiles and sensing positions shown in the left. The optimized and random configurations reconstruction MSEs are 0.29 and 0.46, respectively.

11:00 AM

Sparse Beamforming based on Cantor ArraysRegev Cohen¹, Yonina Eldar¹, Adi Apotheker², Raphael Azeroual¹¹Technion, Haifa, Israel, ²Technion, Israel**Background, Motivation, and Objective**

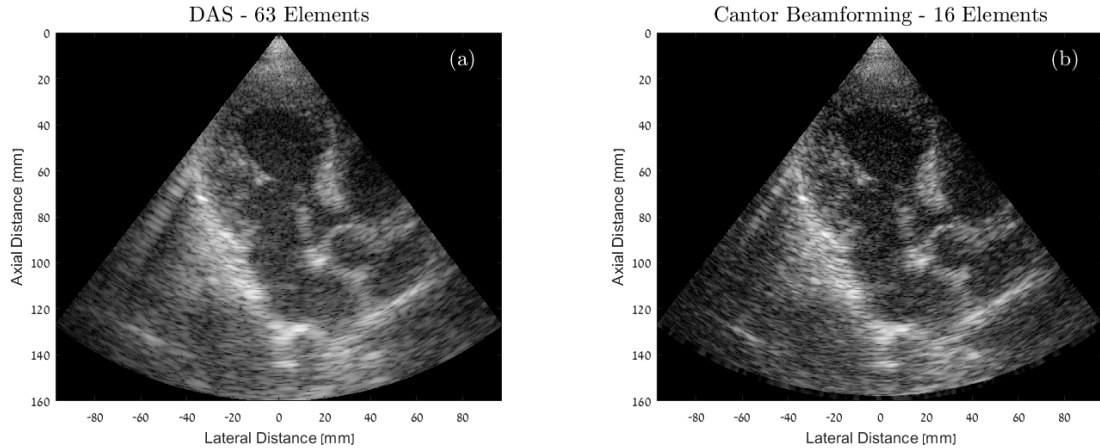
Conventional medical ultrasound systems generate B-mode images using the standard delay and sum (DAS) beamforming. However, DAS exhibits limited image resolution and contrast, which are mainly determined by the center frequency and the aperture size of the ultrasound transducer. Manufacturing a probe with a large aperture by increasing the number of elements improves resolution but at the same time increases the data size and the system cost due to the receive electronics required for each element. Hence, we aim to reduce the number of receiving channels while producing high quality images.

Statement of Contribution/Methods

We present a non-linear beamforming method called Cantor beamforming which enables a significant element reduction while providing B-mode images with improved resolution and contrast with respect to DAS. The proposed beamformer, based on Cantor arrays that are sparse symmetric arrays with a fractal geometry, has $N=2^k$ non-uniformly spaced physical sensors and generates a beam pattern which is equivalent to that generated by DAS operating on 3^k uniformly spaced elements. Thus, Cantor beamforming leads to increased image resolution and contrast while using exponentially fewer elements.

Results/Discussion

We validated the proposed Cantor beamforming by applying it on *in vivo* cardiac data, acquired by GE breadboard ultrasonic scanner where 63 channels were used. The radiated depth was 16 cm, the probe carrier frequency was 3.4 MHz and the system sampling frequency was 16 MHz. The results below show the resultant images obtained by (a) DAS and (b) Cantor beamforming. Both images are presented with a dynamic range of 70 dB. Cantor beamforming requires only 16 elements out of 63 (~25%) and leads to improved resolution and contrast in comparison with DAS, as seen from the images.



11:15 AM

3D anatomical scanning using a conical transmit wave: preliminary simulation findings**Pedro Santos¹, Fu-Feng Lee², Alejandra Ortega¹, Jianwen Luo³, Jan D'hooge¹**¹*Department of Cardiovascular Sciences, KU Leuven, Leuven, Belgium*, ²*Department of Biomedical Engineering, Tsinghua University, Beijing, China*, ³*School of Medicine, Tsinghua University, Beijing, China*, *People's Republic of***Background, Motivation, and Objective**

Clinical assessment of all left ventricle segments currently requires multiple 2D acquisitions, as the frame rate (FR) of 3D SLT/MLA remains limited. We have previously suggested to scan only an anatomically relevant region (ie. a conical ring enclosing the myocardium – Fig A) and further improved FR by using multi-line transmit (MLT)/MLA. However, high MLT count can lead to long/complex excitation waveforms (hence prone to transducer heating) and crosstalk artifacts (as the beams get closer). Both problems may thus impact the achievable FR. Moreover, MLA requires slightly-defocused beams, effectively spreading the combined energy profile around the entire anatomical region. Therefore, we have investigated an hybrid scheme that allows 3D anatomical imaging at higher FR and with less transmitter complexity – the conical wave imaging (CWI).

Statement of Contribution/Methods

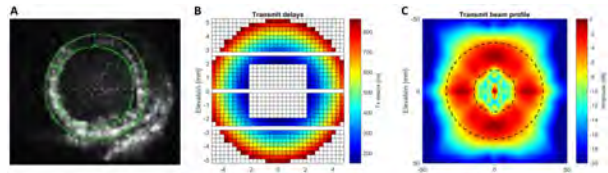
A statistical region of interest (ROI) was defined by retrospectively measuring opening angles for both endo- and epicardial myocardial borders from 3D echo recordings. Mean angles of $\pm 14^\circ$ and $\pm 30^\circ$, respectively, were found.

Anatomical volumetric insonification was then investigated by using diverging wave delays onto a masked matrix array (Fig B). Transmit beam profiles were simulated in Field II for a 32x32-elements array to optimize the aperture layout and maximize pressure within the ROI while reducing it outside.

A dual-transmission sequence was implemented: one emission from the aperture ring was followed by a second emission from the aperture edges with opposite polarity. Both shots were combined to suppress edge waves.

Results/Discussion

The combination of the aperture opening with the edge wave transmission effectively suppressed the energy transmitted in the central region when compared to the anatomical ROI (~8dB lower). The insonified region thus becomes similar to the one of anatomical MLT. Notably, CWI has a significant benefit in FR (~2500Hz vs ~200Hz) and excitation simplicity, although at the expense of side lobe levels. Compared to a full diverging wave, CWI not only has a more suited transmit beam pattern (circular) but also has the potential to improve contrast (especially when strong reflectors exist in the cavity, eg. calcifications or prosthetic valves) and reduce transmit element count. Experimental validation of CWI as well as an extension to compounding is ongoing.



(A) C-section of a 3D apical recording showing the circular myocardial geometry. (B) Transmit delay and aperture for generating a conical wave. (C) Resulting transmit profile (dashed lines show the statistical anatomical ROI).

11:30 AM Performance of F-DMAS beamforming with adjustable maximum spatial lag in Multi-Line Transmission ultrasound imaging

Giulia Matrone¹, Alessandro Ramalli^{2,3}, Jan D'hooge², Piero Tortoli³, Giovanni Magenes¹

¹*Department of Electrical, Computer and Biomedical Engineering, University of Pavia, Pavia, Italy*, ²*Lab. on Cardiovascular Imaging & Dynamics, Dept. of Cardiovascular Sciences, KU Leuven, Leuven, Belgium*, ³*Department of Information Engineering, University of Florence, Florence, Italy*

Background, Motivation, and Objective

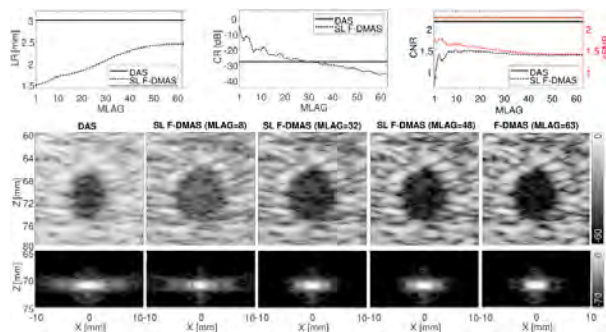
In Multi-Line Transmission (MLT) ultrasound imaging, high frame-rate is achieved by the simultaneous transmission (TX) of multiple focused beams along different directions. Image contrast is potentially degraded by cross-talk artifacts that, however, can be successfully attenuated e.g. by Filtered-Delay Multiply And Sum (F-DMAS) beamforming. F-DMAS is based on the computation of the autocorrelation of the aperture in reception (RX), which is related to the spatial-coherence (SC) of backscattered signals. SC in turn is affected by the two-way beam shape. Since MLT has a major effect on SC, a new F-DMAS formulation, called Short-Lag (SL) F-DMAS, is here proposed that allows to set the maximum lag (MLAG) between the echo signals used for image reconstruction; the performance of the new approach in MLT imaging is assessed through simulations.

Statement of Contribution/Methods

Images of a point-scatterer and of a 10-mm-diameter cyst phantom were simulated in Field II, considering a 2 MHz 64-element phased-array. The TX focus was set at 70 mm and 192 lines were acquired over a 90° sector, implementing standard single-line transmission (SLT) and MLT with different numbers of simultaneous TX beams (4, 6, 8, 12). Tukey apodization was applied in TX to reduce TX cross-talk; images were then reconstructed using either DAS with RX Tukey apodization or SL F-DMAS with different MLAGs (standard F-DMAS corresponds to MLAG=63). Lateral resolution (LR) at -6 dB, contrast ratio (CR), contrast-to-noise ratio (CNR) and speckle signal-to-noise ratio (sSNR) were evaluated at the focal depth.

Results/Discussion

Lateral resolution in MLT images is always better with SL F-DMAS than with DAS: the smaller the MLAG value, the better the resolution. CNR and sSNR with SL F-DMAS instead are worse than with DAS; shorter MLAGs worsen the CNR but enhance sSNR, since cross-talk rejection is weakened but speckle uniformity is improved. CR instead improves with increasing MLAGs and outperforms DAS for higher values (e.g. MLAG=32 for MLT with 4 TX beams (4-MLT)). These trends are confirmed by the PSF and cyst-phantom images obtained with SL F-DMAS at different MLAGs. The figure shows sample results for the 4-MLT case. In conclusion, SL F-DMAS provides valuable indications to select the MLAG (thus, a certain trade-off between contrast, resolution and sSNR) based on the specific application requirements.



11:45 AM

Compressed Sensing Reconstruction of Synthetic Transmit Aperture Dataset for Volumetric Diverging Wave Imaging: A Simulation Study

Yinran Chen¹, Jing Liu¹, Jianwen Luo¹

¹Department of Biomedical Engineering, Department of Biomedical Engineering, Tsinghua University, Beijing, China, People's Republic of

Background, Motivation, and Objective

Matrix array based 3D ultrasound imaging suffers from several limitations: 1) low volume rate due to a large number of firings, 2) poor lateral resolutions (LR) due to a small aperture size, and 3) massive transmit/receive channels required (e.g., 1024). The problems could be mitigated by using 1) 3D diverging wave compounding (DWC), 2) 3D synthetic transmit aperture (STA), and 3) sparse array, respectively. In this study, a compressed sensing (CS) based technique [Liu et al, TUFFC, 2018] was extended to 3D (i.e., 3D CS-STA) to reconstruct the complete dataset of STA from a series of apodized 3D DWs, in order to increase volume rate while improving LRs. Moreover, a sparse matrix array was used to release the data storage burden.

Statement of Contribution/Methods

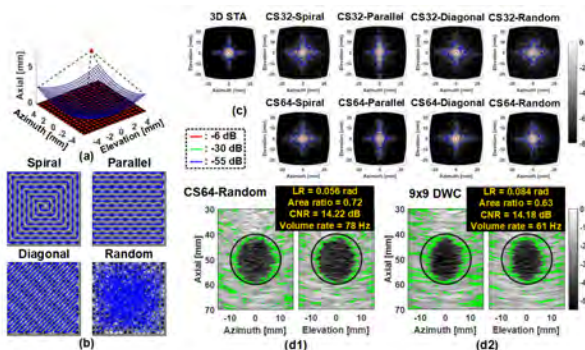
A periodic sparse array with 16×16 elements and $0.6 \text{ mm} \times 0.6 \text{ mm}$ pitch was setup by down-sampling a typical 32×32 -element matrix array with 3 MHz center frequency. A series of 3D DWs were transmitted from a fixed virtual source, with the i^{th} DW apodized by the i^{th} row of a 256-order Hadamard matrix [Fig. (a)]. Four layouts of element numbering for apodizations, i.e., Spiral, Parallel, Diagonal, and Random [Fig. (b)] and transmit events of 32 and 64 were investigated. CS reconstruction and transmit delay compensation were applied to the acquired channel data in the slow-time direction to recover the complete dataset of 3D STA. Finally, standard STA beamforming was used to obtain the volumetric images.

Point spread functions (PSFs) of 3D CS-STA setups were compared with that of 3D STA. And CS-STA with the optimal setup was compared with 9×9 DWC by imaging a cystic phantom. LR, contrast-to-noise ratio (CNR), and area ratio between estimated and true cystic regions were quantified.

Results/Discussion

PSFs of 3D CS-STA and STA from a C-plane view at 50 mm depth are given in Fig. (c), showing similar LRs and improved side lobes as the number of firings increases while unbalanced side lobes found in Parallel layout. B-mode images and quantitative results of the cystic phantom, acquired from 3D CS-STA with 64 firings and Random layout and 9×9 DWC are given in Fig. (d). 3D CS-STA obtains a ~32% improvement of LRs, higher area ratio and volume rate, and a competitive CNR when compared with 9×9 DWC.

To conclude, 3D CS-STA was proposed to increase volume rate while keeping LRs of 3D STA. Moreover, it outperformed 9×9 DWC in terms of image quality and volume rate.



4J - Flow Processing: Methods and Applications

Sapphire (220)

Thursday, October 25, 1:30 pm - 3:00 pm

Chair **Lasse Lovstakken**
NTNU

4J-1

1:30 PM

Dual-Frequency Alias-Free Color Doppler using Chirping and Pulse Compression

Vincent Perrot¹, Yanis Mehdi Benane¹, Emilia Badescu¹, Hervé Liebgott¹, Damien Garcia¹

¹CREATIS, Univ.Lyon, INSA-Lyon, UCB Lyon 1, UJM-Saint Etienne, CNRS, Inserm, Villeurbanne, France

Background, Motivation, and Objective

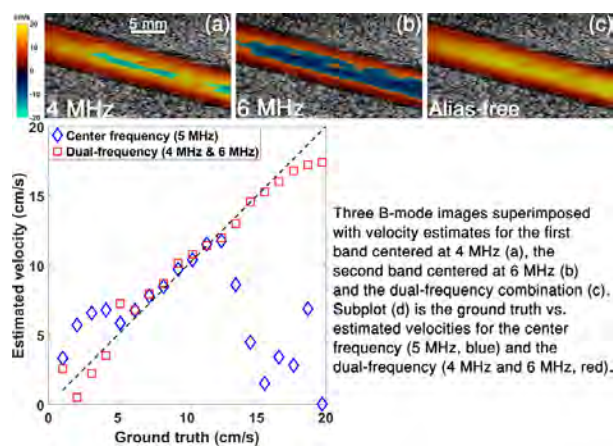
Color Doppler is one of the most popular non-invasive technique for blood flow analysis and visualization. Plane-wave ultrasound can be used to yield high frame rates and broaden the clinical perspectives of color flow imaging. As with conventional ultrasound, however, aliasing may occur if the flow information is time-sampled insufficiently. The Nyquist velocity limit depends upon PRF (pulse repetition frequency) and center frequency. One approach for extending this Nyquist limit is to transmit signals using a dual-PRF scheme (Posada *et al.*, IEEE TMI, 2016) and combine the two aliased estimates to recover alias-free velocities. Instead of transmitting at dual PRFs, it is similarly possible to use a dual-frequency approach to increase Nyquist velocity. Our objective was to increase the Nyquist limit while increasing range resolution. To this end, we used chirp signals and matched filtering to obtain a spread spectrum for dual-frequency dealiasing.

Statement of Contribution/Methods

A 20° slanting vessel (Gammex Doppler 403) was scanned with a Verasonics Vantage system and a linear array probe. Poiseuille flows with velocities ranging between 2-20 cm/s were analyzed. Linear up-chirps were transmitted with plane wavefronts in the 3-7 MHz band. The received signals were matched-filtered through pulse compression to recover a wide frequency band. The delayed-and-summed signals were then bandpass filtered at 4 and 6 MHz, respectively, to provide two signals at different center frequencies. Two series of Doppler velocities were finally obtained by using a slow-time autocorrelator. These Doppler fields were combined to extend the Nyquist velocity and return alias-free color Doppler images.

Results/Discussion

Our results show (Fig. 1a-b) that aliasing was present in the two Doppler estimates (20 cm/s), at 4 and 6 MHz. After dual-frequency combination, an alias-free velocity map was extracted (Fig. 1c). Fig. 1d also shows that there was a good concordance between the dealiased estimated velocities and the ground-truth velocities, up to 20 cm/s. These findings demonstrate that the dual-frequency method with pulse compression allows extending the Nyquist velocity limit with a good range resolution. Further improvements are expected with the use of CMUT probes and wider frequency bands.



1:45 PM

In-vivo Abdominal Microvasculature Evaluation based on Ultrafast Curved Array Imaging**Jinbum Kang¹, Dooyoung Go¹, Yangmo Yoo^{1,2}**¹*Electronic Engineering, Sogang University, Seoul, Korea, Republic of,* ²*Biomedical Engineering, Sogang University, Seoul, Korea, Republic of***Background, Motivation, and Objective**

Ultrafast small vessel or microvessel imaging, which utilizes the large amount of spatial and temporal samples within a short acquisition time, has been growing interest in recent years since it effectively enables the visualization of microvascular without contrast agent. Along with the ultrafast imaging using a linear (or phased) array transducer, ultrafast imaging with curved array transducers (e.g., curvilinear, endocavitory and micro-convex) may be useful for abdominal and pelvic applications. However, ultrafast curved array imaging must consider element directivity and field-of-view (FOV) in a wide beam transmission strategy. In this study, we evaluate the performance of the microvascular imaging based on ultrafast curved array imaging method in abdominal applications.

Statement of Contribution/Methods

In the ultrafast curved array imaging, plane wave and diverging wave are transmitted using a linear source and a point virtual source, respectively, and the received signals with any number of steering angles are constructively summed to improve spatial resolution and SNR. For data acquisition, the plane wave and diverging wave (both 10 angles ($\pm 18^\circ$)) were alternately transmitted to obtain the same image frames in an irregular *in vivo* environment. Also, an abdomen region from a healthy volunteer was scanned using an ultrasound research platform (Vantage, Verasonics Inc., Kirkland, WA, USA) with a C5-2 curved array transducer. For power Doppler imaging, each post-compounding set of 250 frames with a PRF of 250 Hz (data acquisition time = 800 ms) was obtained, and a spatio-temporal clutter filter was applied to acquire flow signals.

Results/Discussion

Figs. 1(a)-(c) and 1(d)-(f) represent the results of the B-mode and microvascular imaging using plane wave and diverging wave transmission for the liver and kidney scan, respectively. As illustrated in Figs. 1(c) and 1(f), the diverging wave shows more vascularity (white arrow region) in the liver and kidney than the plane wave in the ultrafast curved array imaging method. Furthermore, the diverging wave imaging shows higher flow signal-to-clutter ratio (SCR) value than the plane wave imaging, i.e., 6.35 vs. 4.26 dB, respectively, in the microvessel region of the kidney. These results demonstrate that ultrafast curved array imaging is of great advantage to high-sensitive microvascular imaging with a wide FOV.

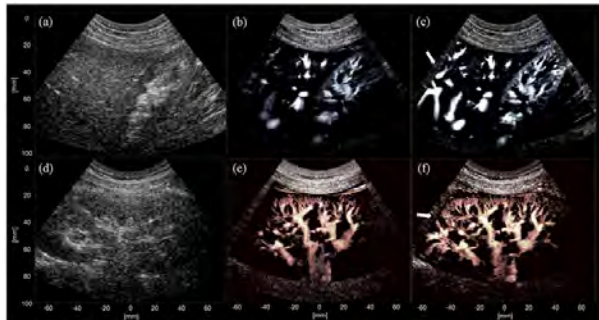


Fig. 1. The results of the B-mode ((a) and (d)) and microvascular imaging using plane wave ((b) and (e)) and diverging wave ((c) and (f)) transmission for a human liver (in the first row) and kidney (in the second row), respectively.

2:00 PM

High Sensitivity Liver Vasculature Visualization Using a Real-time Coherent Flow Power Doppler (CFPD)**Imaging System: A Pilot Clinical Study**You Li¹, Dongwoon Hyun¹, Isabelle Durot¹, Juergen Willmann¹, Jeremy Dahl¹¹*Department of Radiology, School of Medicine, Stanford University, Palo Alto, CA, United States***Background, Motivation, and Objective**

Power Doppler (PD) imaging is a commonly used technique for flow detection. Thermal noise and reverberation clutter can reduce sensitivity to small vessels and slow flow. To improve flow detection and visualization without sacrificing acquisition rate, we have proposed coherent flow power Doppler (CFPD), which detects blood flow based on the spatial coherence of backscattered echoes, and improves the SNR by 7-12 dB over PD using the same ensemble lengths (8-16). However, the computational time of CFPD using CPUs is prohibitively long for real time imaging and hinders the clinical application of CFPD.

Statement of Contribution/Methods

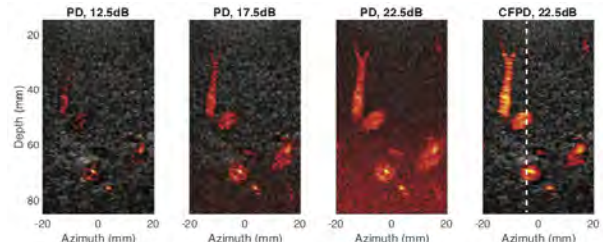
We have built a real-time CFPD imaging system using a Verasonics Vantage 256 scanner and an abdominal curvilinear transducer. The real-time CFPD processing was implemented in CUDA C++ on a commercial GPU card. An ensemble length of 8 was used throughout the study. Using the system, we have conducted a pilot clinical study on 15 healthy human subjects. In each subject, the liver vasculature was identified by a radiologist using real-time display of CFPD images, and Doppler channel data was recorded over a 256 ms clip. With the recorded data, 132 sets of PD and CFPD video streams were produced and analyzed off-line.

Results/Discussion

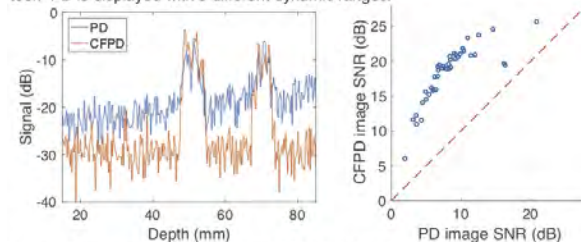
Using GPU processing, we have reduced the total acquisition and processing time for each CFPD image from several minutes to under 0.1 second, enabling real time imaging. The acquisition and data transfer use 52% of the total time, and the CFPD computation requires only 29%, implying that CFPD processing is no longer a bottleneck for real time imaging.

The clinical study results are shown in the figure panels. Fig. (a) shows an example of PD and CFPD images, with PD displayed using 3 dynamic ranges. The vessels appear fragmented in the 12.5 dB dynamic range case, and overwhelmed by noise in the 22.5 dB case. The CFPD image shows complete vessels free from noise. Fig. (b) shows the axial cross-sections of the vessels, which indicate that the depth-dependent noise increase in the PD image is removed in the CFPD image. Fig. (c) shows the SNR measurement of the PD and CFPD images produced from the 132 data sets. In all cases, CFPD produces higher SNR than PD, with an average improvement of 8.6 dB.

Therefore, the clinical feasibility of real-time CFPD imaging, and its improvement in clinical visualization of liver vasculature were demonstrated.



(a) Examples of PD and CFPD images acquired from the left liver lobe of one volunteer. PD is displayed with 3 different dynamic ranges.



(b) Axial cross-section of the PD and CFPD images (location indicated by dashed line in (a)).

(c) SNR measurements of PD and CFPD from the 132 data sets.

2:15 PM In vivo Adaptive focusing for clinical Transcranial Ultrafast Ultrasound Imaging by Time Reversal of Moving Speckle Noise

Justine Robin^{1,2}, Charlie Demené¹, Hanna Bendjador¹, Fabienne Perren-Landis², Mathieu Pernot³, Mickaël Tanter³

¹*Institut Langevin, ESPCI Paris, PSL Research University, CNRS UMR 7587, INSERM U979, Paris, France*, ²*Dept. of Neurology, Neurovascular and Neurosonology Unit, Hôpitaux Universitaires de Genève, Genève, Switzerland*, ³*Institut Langevin, ESPCI Paris, PSL Research University, CNRS UMR 7587, INSERM U979, Paris, France*

Background, Motivation, and Objective

Spatial heterogeneities and high discrepancy between the acoustic sound speed in the skull bone and soft tissues lead to aberrations that strongly affect image quality during Transcranial Color Doppler (TCCD) Ultrasound. Along with the strong reflections and attenuation in the skull, it makes transcranial imaging very challenging. To overcome this beam degradation, adaptive focusing methods for TCCD have been thoroughly developed with limited success. A potential solution was proposed by creating a virtual point-like reflector using independent realizations of speckle summed coherently¹. Here we implement for the first time this technique based on Time Reversal of Moving Speckle Noise (TRMSN) to improve *in vivo* transcranial Doppler images in human adults.

Statement of Contribution/Methods

Acquisitions

Trans-temporal ultrasound RF data were acquired with a phased ultrasonic probe (96 elements, 0.2mm pitch, 2MHz) using ultrafast diverging wave sequences (100 frames, frame rate 100Hz, 29 virtual sources) on a SuperSonic Imagine Aixplorer™, to enable decorrelation of the red blood cells signals in large vessels between each frame. Blood signal was isolated from brain tissue by a SVD based clutter filter, and then beamformed using classical delay and sum. 5 points of interest in blood vessels were identified in the PW Doppler Image.

TRSN algorithm

In post processing, the 29 virtual sources RF data are combined with delays focusing on a point of interest. The 100 compound frames are as many speckle realizations that are rephased at a given depth (or time of arrival) and summed to create a virtual bright spot. The aberration law of the skull is extracted from the distorted wavefront. This law is then used to correct the initial delay law and the process is repeated (5 iterations). At each iteration, the integral of the coherence function is used to assess focus quality².

Image correction

RF data were beamformed using spherical laws corrected by the calculated aberration law.

Results/Discussion

On average after 5 iterations the area under the spatial coherence function of backscattered echoes was improved by 17 % using the corrected focal law, and the contrast on PW Doppler image was improved by 3 dB. These preliminary *in vivo* results pave the way for future transcranial Ultrafast Doppler imaging with high sensitivity by maximizing antenna gain through the temporal bone window.

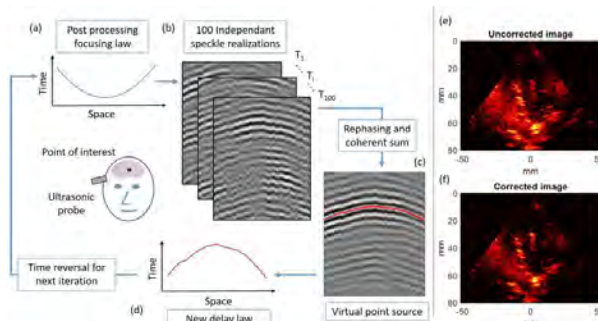


Figure: Left: Iterative aberration correction method. (a) Focused law to recombine the 29 virtual sources RF Data, (b) 100 compound frames are used as 100 independent speckle realisations; (c) A virtual source is created by coherent summation, (d) A corrected delay law is extracted and used in the next iteration. **Right: Trans-temporal Power Doppler image.** RF data were beamformed using (e) spherical delay laws and (f) corrected delay laws using TRMSN

¹ B.F. Osmanski, et al, IEEE Trans. Ultrason. Ferroelectr. Freq. Control 59, 1575 (2012).

² Montaldo et al, Physical Review Letters 2009

2:30 PM

High frequency functional ultrasound in mice

Bas Koekkoek¹, Sadaf Soloukey Tbalvandany^{1,2}, Bas Generowicz³, Bas van Hoogstraten¹, Nina de Oude¹, Henk-Jan Boele¹, Christos Strydis¹, Geert Leus³, Johan G. Bosch⁴, Antonius F. W. van der Steen⁴, Chris de Zeeuw^{1,5}, **Pieter Kruizinga**^{1,4}

¹Department of Neuroscience, Erasmus MC, Netherlands, ²Department of Neurosurgery, Erasmus MC, Netherlands,

³EWI, TU Delft, Netherlands, ⁴Thorax Center, Erasmus MC, Netherlands, ⁵Netherlands Institute of Neuroscience, Royal Dutch Academy for Arts and Sciences, Netherlands

Background, Motivation, and Objective

Functional ultrasound (fUS) is a new imaging modality to study the brain with a high spatiotemporal resolution and a wide field-of-view [1]. In fUS detailed images of cerebral blood volume (CBV) are used to derive functional information, as changes in local CBV may reflect neuronal activation through neurovascular coupling. Most fUS studies so far have been performed in rats. Translating fUS to mice, which is a favorable animal model for neuroscience, pleads for a higher spatial resolution than what has been reported so far [2]. As a consequence the temporal sampling of the blood flow should also be increased, as the Doppler shifts are inversely proportional to the spatial resolution. Here we present our first detailed images of the mouse brain vasculature at very high spatiotemporal resolution.

Statement of Contribution/Methods

We have performed whole brain fUS imaging in anesthetized head-fixed C57BL/6 mice. For the ultrasound data acquisition, we used an ultrasound research system (Vantage 64-LE, Verasonics Redmond, WA, USA) interfaced with a 128 element, high frequency linear array (L35-16v, 69 µm pitch) driven at 30 MHz. Because of the 64 channel acquisition, two transmit-receive events were needed to address the complete aperture. We developed our own CPU/GPU data processing software, to achieve continuous, real-time imaging for a long period of time, including the storage of raw beamformed images. The major processing steps include Fourier domain beamforming, SVD clutter filtering, and Power Doppler image (PDI) formation, real-time display and data storage.

Results/Discussion

We successfully imaged several mice with high spatial (<60 µm) and high temporal resolution. The maximum achievable temporal resolution depends on the specific imaging settings. In our implementation this can be as high as 0.5 ms, while maintaining real-time display (20 Hz) and continuously raw frame storage (2 KHz), when using for example 6 angled plane waves and an 8.8 x 8 mm field-of-view. In figure 1 we show two examples of the high resolution PDI's containing the microvasculature of the mouse brain we obtained with our high frequency implementation of fUS. Having established high resolution imaging of the CBV in mice brain we will now further focus on unraveling brain dynamics during learning tasks in the cerebellum.

[1] Macé et al., Nature 2011

[2] Deffieux et al., Cur. Opin. in Neurobiol. 2018

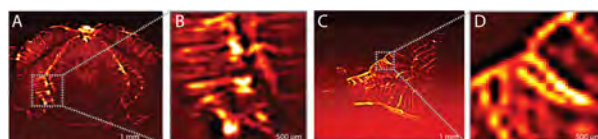


Figure 1. High frequency functional ultrasound in mice. (A) Power Doppler image of a coronal view (Bregma -3.80) of the vasculature inside the mouse brain. (B) Zoom-in of a subsection of A, showing the hippocampus. (C) Power Doppler image of a sagittal view of the vasculature of the mouse cerebellum and brainstem. (D) Zoom-in on a cerebellar lobule displayed in C, emphasizing the high spatial resolution.

2:45 PM

Simultaneous Noise Suppression and Incoherent Artifact Reduction In Ultrafast Ultrasound Microvessel Imaging

Chengwu Huang¹, Pengfei Song¹, Ping Gong¹, Joshua Trzasko¹, Armando Manduca², Shigao Chen¹

¹Department of Radiology, Mayo Clinic, Rochester, MN, United States, ²Department of Physiology and Biomedical Engineering, Mayo Clinic, Rochester, MN, United States

Background, Motivation, and Objective

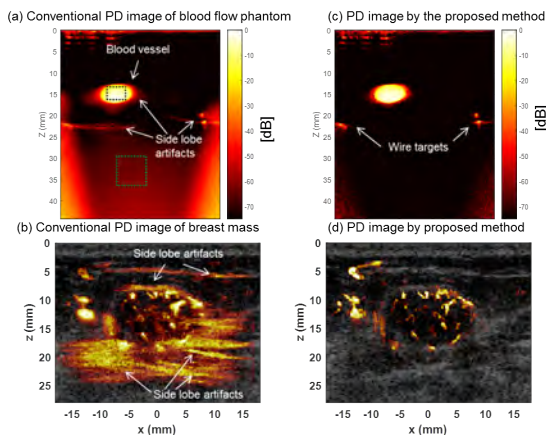
Ultrasound microvessel imaging (UMI) based on plane wave imaging and singular value decomposition (SVD) clutter filtering has recently demonstrated superior performance in small vessel detection. However, UMI is susceptible to electronic noise, leading to a classic ramp-shaped background noise profile (Figs 1a). In addition, incoherent lateral side-lobe artifacts originating from strong scatterers that resemble the blood signal in the spatiotemporal domain cannot be completely removed by the SVD filter, creating a strong mask on top of the blood signal that severely undermines the small microvessel visibility (Figs. 1a, 1b). To address these issues, we propose a novel method that can simultaneously suppress the background noise and the incoherent artifacts in UMI.

Statement of Contribution/Methods

The method is based on the framework of plane wave compounding, from which we propose to divide the tilted plane wave transmissions into two groups (e.g., angle 1-8 as group 1, and 9-16 as group 2). Instead of a coherent sum on all the angles for compounding, we propose to compound the tilted angles for each group, generating two compounded data sets (e.g., each data set is with 8-angle compounding). A SVD-based clutter filter will then be applied to each data set, followed by a zero-lag cross-correlation between the two clutter filtered data sets to produce a power Doppler (PD) image. The cross-correlation process can effectively suppress incoherent electronic noise and the side-lobe artifacts, but preserve and enhance blood signal which can be assumed to be coherent thanks to the ultrafast imaging frame rate. The method was validated on a tissue-mimicking blood flow phantom and an *in vivo* breast mass based on a Verasonics Vantage system (Verasonics Inc., Kirkland, WA) and a linear array transducer 9LD (GE Healthcare, Wauwatosa, WI).

Results/Discussion

Fig. 1a and 1c demonstrate the effectiveness of the method in simultaneous suppression of the background noise and the side lobe artifacts generated by the wire targets of the phantom. The b-SNR (power ratio of blood and background regions indicated by dashed boxes in Fig. 1a) increases by 21 dB. The side lobes of the blood vessel can also be reduced using the proposed method, leading to an improved lateral resolution. Similar findings are shown in the breast mass data (Figs. 1b and 1d), demonstrating the *in vivo* feasibility of the method.



4K - Flow Processing: Segmentation

Sapphire (220)

Thursday, October 25, 4:00 pm - 5:30 pm

Chair **Matthew Bruce**
University of Washington

4K-1

4:00 PM Non-Contrast Perfusion Ultrasound Imaging for Assessment of Trans-arterial Chemoembolization of Hepatic Malignancy

Jaime Tierney¹, Kathryn Ozgun¹, Anthony Borgmann², Daniel Brown², Brett Byram¹

¹Vanderbilt University, Nashville, TN, United States, ²Vanderbilt University Medical Center, Nashville, TN, United States

Background, Motivation, and Objective

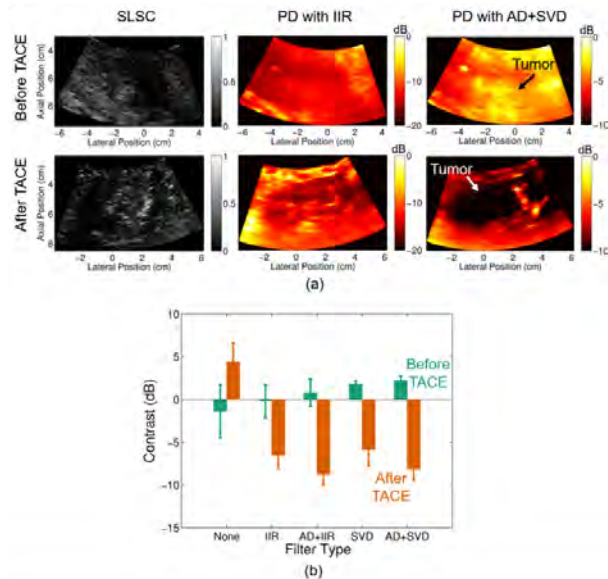
We previously developed an adaptive demodulation (AD) method to address challenges associated with non-contrast perfusion ultrasound imaging, namely tissue clutter spectral broadening. Here, we propose AD in combination with other slow flow methods as a tool to monitor trans-arterial chemoembolization (TACE) treatment of liver tumors. TACE is a minimally invasive procedure to treat liver tumors by simultaneously delivering high doses of chemotherapy and occluding the arterial supply. Because TACE acutely changes tumor perfusion, it provides a unique clinical scenario to evaluate AD and other slow flow algorithms. Furthermore, this study tests these methods at deeper depths (down to 10cm) and with a lower transmit frequency than typically used for proof-of-concept studies.

Statement of Contribution/Methods

This study was approved by Vanderbilt's institutional review board and 5 patients undergoing TACE consented. A Verasonics C5-2 probe with a 4.2MHz frequency was used to acquire a 6cm focused scan followed by 0.5s of plane wave data immediately before and after TACE for each patient. Focused short-lag spatial coherence (SLSC) imaging was used for anatomical reference. The plane wave sequence used 9 angles between -8° and 8° at a PRF of 5.4kHz (600Hz frame rate). We compared a conventional 30Hz (5mm/s) infinite impulse response (IIR) filter to an adaptive singular value decomposition (SVD) filter with and without AD. We computed tumor-to-background contrast in power Doppler (PD) images before and after TACE for each filter type and averaged across patients. Because TACE intends to substantially reduce blood supply to the tumor, our hypothesis is that after treatment there will be decreased power in the tumor and decreased contrast.

Results/Discussion

Fig. 1(a) shows example SLSC and PD images for a single patient. Qualitatively, AD+SVD produces PD images that have increased power (i.e., perfusion) in the tumor before TACE and decreased power after, which is consistent with the hypothesis and less apparent with conventional filtering. Fig. 1(b) shows average contrast before and after TACE for each filter. Contrast is highest before TACE (2.2dB) and lowest after TACE (-8.7dB) when AD+SVD and AD are used, respectively. These results suggest that combining slow flow techniques could potentially make non-contrast perfusion imaging a viable tool for monitoring TACE.



4:15 PM

Adaptive SVD clutter filter for Ultrafast Doppler imaging using Spatial Similarity Matrix**Jerome Baranger^{1,2}, Bastien Arnal¹, Fabienne Perren-Landis³, Olivier Baud^{4,5}, Mickaël Tanter¹, Charlie Demené¹**¹*Institut Langevin, ESPCI Paris, PSL Research University, CNRS UMR 7587, INSERM U979, Paris, France*, ²*College Doctoral, Sorbonne Université, France*, ³*Dept. of Neurology, Neurovascular and Neurosonology Unit, Hôpitaux Universitaires de Genève, Genève, Switzerland*, ⁴*Neonatal Intensive Care Unit, Assistance Publique - Hôpitaux de Paris, France*, ⁵*Inserm U1141, Fondation PremUp, Robert Debré University Hospital, France***Background, Motivation, and Objective**

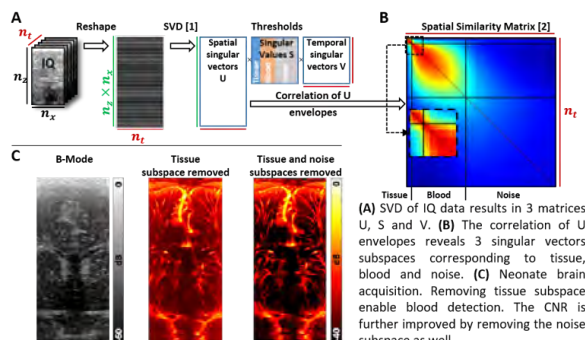
The ability of plane-wave Ultrafast ultrasound imaging to detect small blood flows strongly relies on the clutter filtering process. Singular value decomposition (SVD)-based filters applied to ultrafast raw data have shown great performances to separate tissue, blood and noise signals into relatively distinct singular vectors subspaces [1]. The accuracy of these subspaces boundaries estimation determines the filter ability to maximize blood detection and vascular contrast. Here, we introduce an automated and efficient estimator for the tissue/blood threshold based on the correlation matrix of spatial singular vectors envelopes, called the Spatial Similarity Matrix (SSM), and compare it to existing estimators relying on energetic and temporal SVD features, for both *in vitro* and *in vivo* conditions. A 2nd SSM-based blood/noise threshold was also studied to lower the noise-floor.

Statement of Contribution/Methods

An ATS flow phantom with flowing blood-mimicking fluid was imaged with an ultrasonic probe (128 elements, 0.2mm pitch, 6.4MHz) mounted on a 4-axis motor stage (3 translations, 1 rotation) and ultrafast compound plane wave sequences (PRF 1000Hz, 5 angles) were implemented on a SuperSonic Imagine Aixplorer™. 576 sets of flow speeds, probe speeds, movement axis and ensemble length, were considered, with 100 trials for each set. By segmenting the canal in B-Mode, the Contrast to Noise Ratio (CNR) was computed for all possible SVD thresholds, its maximum unveiling the optimal cut-off. The thresholds were then estimated using the SSM, or with estimators based on either the singular values magnitudes or the temporal singular vectors' spectra. The CNR obtained with each estimated threshold was compared to its optimum value, allowing a quantitative assessment of each estimator's performances. The adaptive filter was then tested *in vivo* on neonate brain, adult kidney, carotid and thyroid.

Results/Discussion

The estimator based on the SSM turned out to be the most robust of all for tissue/blood discrimination [2]. In more than 74% of the 576 sets, it resulted in a CNR that was less than 10% below the optimal value. Moreover, both tissue and noise subspaces can be identified on the SSM. In neonate brain, suppressing this two subspaces lowered the background by at least 5dB as compared to tissue suppression only.



[1] Demené et al. "Spatiotemporal Clutter Filtering of Ultrafast Ultrasound Data Highly Increases Doppler and Ultrasound Sensitivity," IEEE Trans Med Imaging, vol. 34, no. 11, pp. 2271–2285, 2015.

[2] Baranger et al. "Adaptive spatiotemporal SVD clutter filtering for Ultrafast Doppler Imaging using similarity of spatial singular vectors," IEEE Trans Med Imaging, 2018.

4:30 PM **3D HOSVD clutter filtering with automatic cutoff selection applied to circular wave cardiac Doppler imaging**Julia Faurie¹, Guy Cloutier², Damien Garcia³¹Université de Montréal, Montreal, QC, Canada, ²LBUM, Université de Montréal, Montreal, QC, Canada, ³Université de Lyon, CREATIS ; CNRS UMR5220 ; Inserm U1206 ; INSA-Lyon ; Université Lyon 1, France**Background, Motivation, and Objective**

Separation of blood and tissue is a matter of utmost importance in Doppler imaging to get accurate estimation of blood velocity. Cardiac flow imaging is also inherently challenging owing to the ventricle and mitral valve motions and to the small slow-time samples due to duplex modalities. High-frame-rate (ultrafast) imaging based on wide wavefronts also highlighted the need of an improved clutter filter because of reduced sensitivity around the mitral valve. SVD-based clutter filtering recently regained interest in ultrafast flow imaging as it was shown to improve Doppler flow images. However, 1) the choice of the singular-value threshold remains a difficult issue, especially with small Doppler samples, and 2) SVD filtering is confined to the slow-time direction.

Statement of Contribution/Methods

To improve clutter filtering, we propose a filter based on higher-order singular value decomposition (HOSVD) dealing with the three dimensions of I/Q ultrasound signals. To make the clutter filter unsupervised, the HOSVD was associated with an automatic threshold selection by minimizing the Akaike information criterion (AIC, Fig 1). Since it is multilinear, HOSVD takes advantage of the slow-time, fast-time and lateral information concomitantly by doing a 3-D decomposition (based on a SVD in each direction). The AIC criterion tends to minimize the number of singular vectors that are necessary to reconstruct the tissue Doppler signal, which also determines the filtered modes. We used the corrected AIC as it is adapted for small sample sizes. The HOSVD clutter filter was tested in volunteers on circular-waves duplex ultrasound sequences for cardiac imaging. We compared the output color Doppler images with those obtained with an automatic 1D SVD.

Results/Discussion

HOSVD 3D filtering helped in reducing clutter and noise through the contribution of the spatial information. Figure 1 shows the comparison between SVD- and HOSVD-based automatic filters in a human left ventricle. The automatic HOSVD reveals a stronger Doppler signal and the lateral diastolic vortex ring becomes apparent, in contrast to the 1-D SVD in which the signal is disturbed along the walls. HOSVD clutter filtering enabled qualitative improvement during diastole and systole.

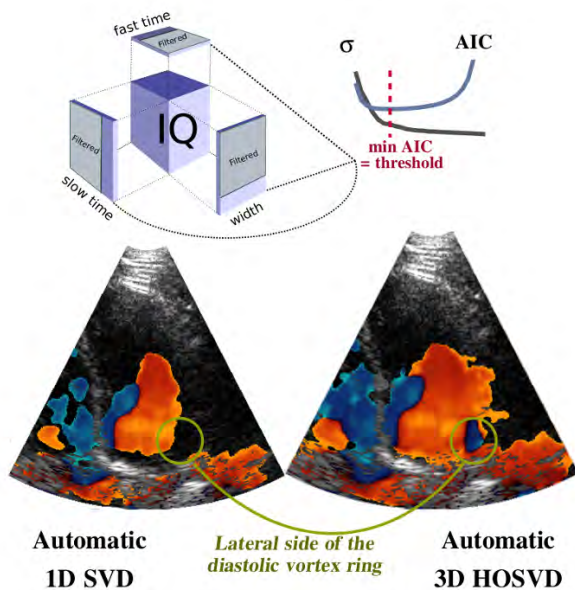


Fig 1. Top : 3D HOSVD decomposition combined with Akaike (AIC) threshold (σ for singular values). Bottom : Comparison between SVD and HOSVD filter in a 4-chamber view

4:45 PM

Noise Debiasing for Real-Time SVD Clutter Filter-Based Ultrafast Microvessel Imaging**Chengwu Huang¹, Pengfei Song¹, Ping Gong¹, Joshua Trzasko¹, Armando Manduca², Shigao Chen¹**¹*Department of Radiology, Mayo Clinic, Rochester, MN, United States*, ²*Department of Physiology and Biomedical Engineering, Mayo Clinic, Rochester, MN, United States***Background, Motivation, and Objective**

Ultrasound microvessel imaging (UMI) based on singular value decomposition (SVD) clutter filtering and plane wave imaging has shown highly improved Doppler sensitivity. However, real-time implementation of UMI is hindered by the high computational cost and low blood signal-to-noise-ratio (b-SNR) due to the lack of transmit focusing of plane waves. A fast SVD clutter filter based on randomized SVD (rSVD) and randomized spatial downsampling (rSD) was recently proposed (Song et al. TUFFC 2017), which demonstrated real-time UMI capability. Here we propose a noise debiasing method to be combined with the fast SVD clutter filter to realize real-time UMI with high b-SNR throughout the field-of-view (FOV).

Statement of Contribution/Methods

A 10-angle coherent compounding plane wave imaging sequence (frame rate = 500 Hz) based on a Verasonics Vantage system (Verasonics Inc., Kirkland, WA) and a curved array transducer C1-6-D (GE Healthcare, Wauwatosa, WI) was used to acquire data from an *in vivo* human kidney in this study for UMI. Clutter filtering was conducted with rSVD alone and rSVD combined with rSD (Fig. 1a). Noise debiasing was achieved by collecting noise signals using the identical imaging sequence as UMI, but with the ultrasound transmission turned off. The estimated noise power (Fig. 1b) can be subtracted from the original power Doppler (PD) image (Fig. 1a) to obtain noise debiasing (Fig. 1c). Quantitative b-SNR was measured using the regions indicated in Fig. 1e.

Results/Discussion

Fig. 1a and Fig. 1c show that the proposed noise debiasing method could effectively remove the background ramp-shaped noise. The b-SNR was improved significantly by 23 dB (from 7.7 dB to 30.7 dB). The cortical kidney vessels can be much better visualized after noise debiasing (Fig. 1c). Fig. 1d shows that the proposed noise debiasing method can be effectively combined with rSVD and rSD for real-time clutter filtering. Albeit the slight drop of b-SNR to 27.1 dB (Fig. 1d), the computational speed was significantly improved by 10X when combining rSVD and rSD, demonstrating real-time imaging capability. These results suggest that the proposed noise debiasing method provides a viable solution to the noise issue of real-time SVD clutter filtering technique, facilitating high quality, real-time UMI imaging based on SVD clutter filters.

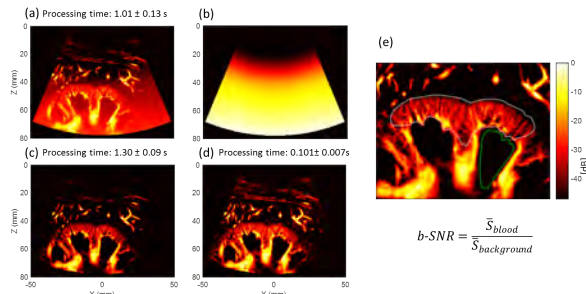


Fig. 1. (a) PD image processed by rSVD filtering. (b) Experimentally measured noise power image. (c) PD image by rSVD filtering with noise debiasing. (d) PD image by rSVD and rSD filtering with noise debiasing. (e) Magnified display for b-SNR definition; \bar{S}_{blood} and $\bar{S}_{background}$ are mean power of blood signal and background noise indicated by regions within the white dashed line and green dashed line, respectively.

5:00 PM

**Non-invasive small vessel imaging of human thyroid using motion-corrected Power Doppler Imaging:
Preliminary *in vivo* study**

Rohit Nayak¹, Viksit Kumar², Jeremy Webb¹, Mostafa Fatemi², Azra Alizad¹

¹Department of Radiology, Mayo Clinic, Rochester, MN, United States, ²Department of Physiology and Biomedical Engineering, Mayo Clinic, Rochester, MN, United States

Background, Motivation, and Objective

Singular value decomposition (SVD) based spatiotemporal clutter filtering (STF) can significantly improve the sensitivity of non-contrast power Doppler (PD) imaging. Although SVD based STF suppress tissue clutter, coherent integration of clutter filtered Doppler signal can be challenging and unreliable in the presence of large motion -- especially for imaging small vessels. We hypothesize that motion correction of the Doppler ensemble can enable coherent integration of Doppler signal, and thus improve the visualization and detection of small vessel perfusion.

Statement of Contribution/Methods

The efficacy of the proposed technique was evaluated on 5 *in vivo* thyroid lesions -- typically incur large motion due to its proximity to the pulsating carotid artery. Compounded plane wave imaging was used for scanning. Depth dependent imaging frame rate varied from 600-700 Hz across patients. Thyroid motion was estimated using 2D normalized cross-correlation, prior to clutter suppression. SVD based STF was used for tissue clutter rejection. Subsequently, motion correction was performed to re-register each clutter-filtered ultrasound frame to the first frame.

Results/Discussion

The results demonstrated that in the absence of motion correction, the PD images were visibly corrupted with motion artifacts due to signal distortion, blurring and occurrence of shadow vessels (Fig. 1 a-d). The vessel intensity profile revealed incoherent lateral shift of the PD signal, in the direction of motion. Consequently, the estimated PD signal displayed two separate peaks instead of one stronger peak -- creating visuals of artificial blood vessels (Fig. 1e). In contrast, the results obtained using motion correction demonstrated coherent integration of the PD signal, which considerably improved the quality of the PD images. For patient #1 (Fig. 1), motion correction improved contrast ratio (CR) and contrast-to-noise (CNR) by a remarkable 12 dB and 5.5 dB, respectively. In the overall patient population, CR and CNR improved by up to 19.6 dB and 11.6 dB, respectively, with the highest improvement observed for lesion with largest motion. This technique is particularly valuable in non-contrast agent based PD imaging, in which low intensity flow signals can be easily corrupted by motion. The preliminary results obtained from this study were encouraging to warrant more *in vivo* validation.

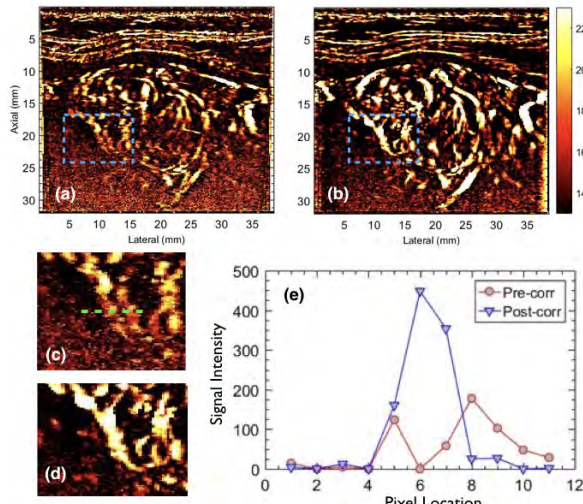


Fig. 1 displays the power Doppler images estimated without (a) and with (b) motion correction. Representative zoomed inset of (a, b) are displayed in (c, d), respectively, which clearly displays the improvement in visualization of small vessels upon motion correction. The corresponding spatial intensity profile of the PD images, along the indicated green segment in (c), is displayed in (e).

5:15 PM

Wall Signal Removal in Doppler Ultrasound using Principal Component Pursuit**Gustavo Chau^{1,2}, You Li¹, Marko Jakovljevic³, Jeremy Dahl³, Paul Rodriguez²**¹*Bioengineering Department, Stanford University, Stanford, CA, United States*, ²*Electrical Engineering Department, Pontificia Universidad Católica del Perú, Lima, Peru*, ³*Department of Radiology, Stanford University, Palo Alto, CA, United States***Background, Motivation, and Objective**

Discriminating between tissue and blood signals is a crucial pre-processing step in doppler ultrasound. Recently, spatio-temporal approaches based on singular value decomposition (SVD) have arisen as a better alternative to separate tissue and blood echoes. However, SVD still presents sensitivity to clutter and low noise rejection capabilities when tissue motion is present. In this work, we propose to use a video background modelling approach using principal component pursuit (PCP) which reduces both the noise and clutter artifacts.

Statement of Contribution/Methods

Our proposed method adapts a relaxation of the PCP problem which finds an additive decomposition of the ultrasound ensemble sequence into low-rank (modeling the static or slow-moving tissue) and sparse components (which captures the blood motion). The optimization problem is solved by alternating low-rank approximations and projections onto the L1-norm ball. We compare our method on fullwave simulations and flow phantom data with SVD and conventional high-pass filtering (HPF) approaches in terms of signal-to-noise (SNR) and signal-to-clutter (SCR) ratios. The simulations consisted of three realizations of 10 cm/s blood flow in a vessel located below a model of an abdominal wall. Physiologically relevant tissue motion of 1, 2 and 3 mm/s and various clutter impedance mismatches were included. All low-rank approximations are of rank 4 and the cut-off frequency of the HPF is taken at 0.1π normalized frequency.

Results/Discussion

Figure 1 shows representative power Doppler images obtained in the simulations with a 60% impedance mismatch and a tissue motion of 2 mm/s for HPF (a), SVD (b) and the proposed PCP method (c). The regions used in the calculations for signal (white), noise (blue) and clutter (green) are shown in (a). PCP presents visual improvements both in the tissue zone (reduction of clutter and noise) and under the vessel (reduction of noise). Figures 1d and 1e show the SNR and SCR for different impedance mismatches at 2 mm/s motion. The proposed method obtained average SNR enhancements of 7 dB in all simulated speeds and the flow phantom experiments. Average SCR improvements of 7, 9 and 4 dB were obtained at tissue speeds of 1, 2 and 3 mm/s, respectively. These results show that the proposed method presents a better performance in the presence of noise and clutter than previous wall-signal rejection methods.

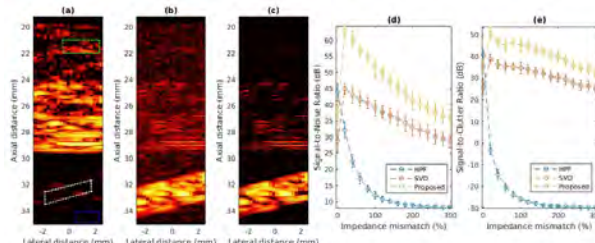


Figure 1. Power Doppler Images (shown with a 60 dB dynamic range) of the fullwave simulations with a 60% impedance mismatch and a tissue motion of 2 mm/s for HPF (a), SVD (b) and the proposed PCP method (c). Regions used in the calculations for signal (white), noise (blue) and clutter (green) are shown in (a). The SNR and SCR for the tissue motion of 2 mm/s for different impedance mismatch values are shown in (d) and (e), respectively.

5H - Acoustic Microfluidics

Ikuta (200)

Thursday, October 25, 8:00 am - 9:30 am

Chair **David Greve**
DWGreve Consulting

5H-1

8:00 AM Omnidirectional spiral surface acoustic waves for particles manipulation and multi-size particles separation in a microliter sessile drop

Naiqing Zhang¹, Gopesh Tilwawala¹, James Friend¹

¹Center for Medical Devices and Instrumentation, University of California, San Diego, La Jolla, CA, United States

Background, Motivation, and Objective

Surface acoustic wave (SAW) induced mixing and separation in sessile drops has shown superiority and importance due to rapid fluid actuation and biocompatibility. Straight interdigital transducers (IDTs) with a sessile drop located at an offset position from the center of the SAW propagation direction has been developed for fluid spinning, particle concentration and separation due to asymmetric SAW actuation. However, asymmetric material properties, difficulty in accurately locating sessile drops, and large SAW energy losses because of the offset position impede its efficiency, accuracy, and repeatability. Our objective is to develop an axisymmetric SAW design for efficient transfer of energy from all directions into an accurately located sessile drop.

Statement of Contribution/Methods

We presented a novel omnidirectional spiral surface acoustic wave (OSSAW) design to conduct more efficient fluid spinning and mixing. We further demonstrated accurate particle manipulation and multi-size separation in a microliter (μl) drop. Specifically, a novel spiral design was developed for OSSAWs such that the wave propagation directions, which are perpendicular to the spiral structure's fingers, are rotationally symmetric with a constant offset angle α relative to the inner circular region (Fig. a & b).

Results/Discussion

A phase scan of inner annular region demonstrated rotational waves propagating into the inner region (Fig. c). A 60MHz OSSAWs device performed ultrafast fluid spinning (~3000rpm) and rapid uniform mixing (~1s) in μl -scale sessile drops. An integrated frequency-based OSSAW design was further developed, with 40MHz and 100MHz resonance frequencies for inner and outer spiral IDT patterns (Fig. d1). Due to frequency-based acoustic radiation force (Fig. d2 & d3), centrifugation and concentration of polystyrene (PS) particles can be rapidly achieved (~1s) with input frequencies of 40MHz and 100MHz respectively. Moreover, when the input signal was alternated between 40MHz and 100MHz at a much smaller time scale (0.01s) compared to particles' dynamic motion in the fluid (~1s), multi-size particle separation was performed in one μl -scale sessile drop (Fig. e) for the first time. These advancements potentially provide an effective platform for whole blood separation and point-of-care diagnostics without need for micro or nanoscale fluidic enclosure.

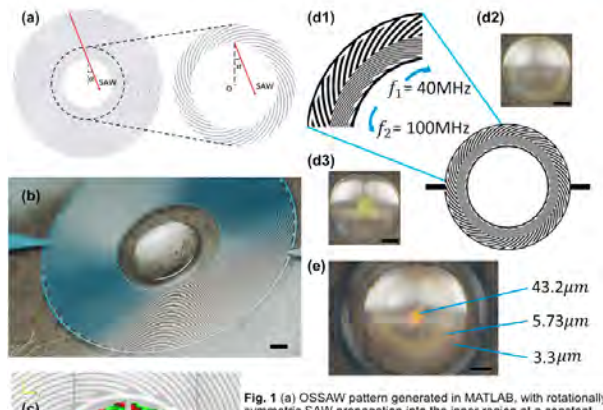


Fig. 1 (a) OSSAW pattern generated in MATLAB, with rotationally symmetric SAW propagation into the inner region at a constant angle α . (b) Image of 60MHz OSSAW device with microliter sessile drop on a glass substrate. (c) Laser Doppler vibrometry phase scan of OSSAW inner annular region, showing rotational waves propagating into inner region. (d1) Design of frequency-based OSSAW with resonance frequencies for the inner and outer spiral IDT patterns of 100MHz and 40MHz, respectively. (d2) Image of outer ring formation of $5.73 \mu\text{m}$ PS particles when activating frequency $f_1=40\text{MHz}$. (d3) Image of concentrated middle pattern of $5.73\mu\text{m}$ PS particles when activating frequency $f_2=100\text{MHz}$. (e) Image of simultaneous separation of $3.3\mu\text{m}$, $5.73\mu\text{m}$, and $43.2\mu\text{m}$ PS particles in one drop, with 0.01s actuation time for each of the two 40MHz and 100MHz signals, alternating back and forth. Scale bar: 0.5mm .

8:15 AM Safe and rapid recharging in lithium metal batteries possessing significantly greater charge capacities via integrated surface acoustic wave turbulent electrolyte mixing

An Huang¹, James Friend²

¹Medically Advanced Devices, Materials Engineering, University of California, San Diego, La Jolla, CA, United States,

²Medically Advanced Devices, Mechanical and Aerospace Engineering, UC San Diego, La Jolla, CA, United States

Background, Motivation, and Objective

A rapidly growing and sustainable means of transport, electric vehicles demand energy capacity and recharging speed that even the best batteries today do not achieve. There is an extraordinary need for better battery technologies, and we have achieved a breakthrough via rechargeable liquid electrolyte lithium metal batteries (LMB) through inclusion of robust, fingernail-sized, and solid-state \sim 100-MHz surface acoustic wave (SAW) microdevices that produce turbulent acoustic streaming. Lithium (Li) is the best anode material for rechargeable batteries, however, rechargeable lithium metal batteries (LMB) have languished due to *dendrite formation*, resulting in thermal runaway and fire or explosion. During charging, Li⁺ ions non-uniformly deposit onto the Li metal anode from the cathode via electrolyte, forming dendrites, due to the existence of a thick (>400 μ m) Li⁺ ion depletion layer. Our objective is to reduce this diffusion layer from 400 μ m to 1 μ m by using SAW-driven mixing flow.

Statement of Contribution/Methods

We employ custom, low-power 100-MHz SAW microdevices to induce acoustic streaming of the electrolyte. Needed only during charging, the induced turbulent flow reduces both the Li⁺ ion depletion layer adjacent the anode to <1 μ m during charging and the characteristic diffusion time of Li⁺ ions by over three orders of magnitude. In our crude LMBs, we have achieved rapid recharging of up to 3C (20 min to full charge at 15 mA/cm²) for greater than 250 cycles without dendrite formation with Li as an anode, Cu as a cathode, and 1M LiPF₆ in 1:1 (w/w) EC/DEC as an electrolyte, maintaining charge capacities fully 90% of the theoretical 170 mAh/g. These same devices also provide detection of the intrinsic morphology, a significant improvement in safety.

Results/Discussion

In our prototype swagelok LMB with a SAW device (see Figure) we show are able to suppress the effects of remarkably fast (3C) charging in LMB batteries using SAW where even slow charging (<0.1C) leads to dendrites easily long enough to destroy the battery. We will provide concrete evidence of the technique with prototype battery results alongside an explanation of the physics and what this could mean in terms of reducing battery charging times for electric vehicles by one order of magnitude, more than doubling battery life, reducing the amount of lithium required, and dramatically improving battery safety.

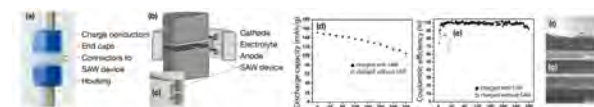


Figure 1(a,b) A prototype LMB with (b) SAW. For trials, the charge conductors are 10 mm in diameter and the anode-cathode gap is 100 μ m. Applying 100 mW at 100 MHz produces acoustic streaming. (c) In an LMB without SAW, cycling at 1C rapidly degrades the battery's capacity to 40% in 40 cycles. With SAW to reconstitute the electrolyte, however, 70% of the battery's capacity is preserved after 280 cycles at 3C. Moreover, (d) the Coulombic efficiency is \sim 98% in the SAW-LMB, far superior to \sim 70% without SAW, and (e) dendrite reach a dangerous >100 μ m in length. With SAW, there are (f) no dendrites after 280 cycles.

8:30 AM

Localized Microfluidic Mixer Using Planar Fresnel Type GHz Ultrasonic Transducer**Adarsh Ravi¹, Amit Lal²**¹*School of Electrical and Computer Engineering, Cornell University, Ithaca, United States*, ²*School of Electrical and Computer Engineering, Cornell University, Ithaca, NY, United States***Background, Motivation, and Objective**

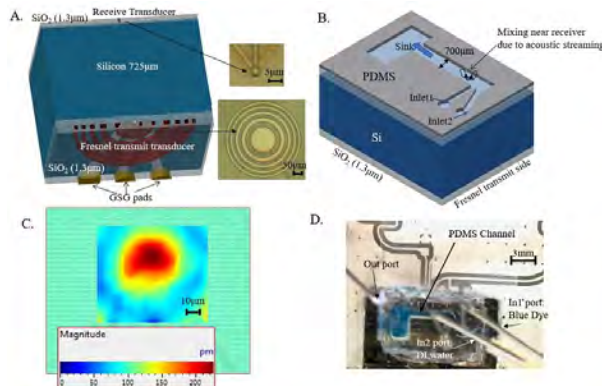
Rapid mixing of small quantities of liquids find applications in drug screening, medical diagnosis, chemical synthesis, and protein folding studies. Several active microfluidic mixers employing external electrical, magnetic or acoustic energy sources are reported. However, acoustic based mixers are advantageous as they perform contactless fluidic mixing without any restriction on the physical properties of the fluids. Traditional acoustic mixers based on BAW, SAW or membranes use acoustic bubbles to efficiently generate vortices to rapidly mix fluids. Further, as the fluid is placed on the same side of the transducers, considerable chip area is required to isolate the electrical interconnects of the transducers from the fluidic sample. SAW waves require electrodes on the same side as the fluidics. In the GHz ultrasonic transducers presented here, the transducers are on the opposite side of the fluidics, enabling easier integration of transducers and fluidics in a distributed manner. We present a localized acoustic wave mixer that focuses GHz ultrasonic waves, which decay within 20-50 microns into the fluid. The shorter penetration depth thereby produces strong localized streaming forces and radiation forces.

Statement of Contribution/Methods

The GHz transducer uses focusing transducers placed in a Fresnel lens configuration, which generates bulk acoustic waves through the silicon substrate adding in phase at the focus (Fig. 1a). A 5 element Fresnel lens transmit transducer of outermost radius 165 μ m was designed and fabricated on a 725 μ m thick silicon wafer. A receive transducer of 2 μ m radius is placed on the opposite side of the wafer. A PDMS channel with two inlets is attached on top of the receive transducer (Fig. 1 b, d). The transducer is driven at its resonant frequency of 1.06GHz, determined by the maximum displacement on the receive transducer.

Results/Discussion

The transducer is planar and is fabricated with a CMOS compatible process, with no thin-film release steps. Peak displacement of 250pm was measured at the focus using Polytec UHF vibrometer with 5V amplitude input (Fig. 1c). The high frequency and narrow beam width results in high acoustic forces in the fluid thereby creating streaming vortices near the receive transducer. Microfluidic mixing of blue dye and water was observed with 80% efficiency.



8:45 AM

Real-Time Monitoring of Size and Concentration of Nanoparticles inside a reactor using ultrasound

Gert-Jan van Groenestijn¹, Nicole Meulendijks², Arno Volker², Paul van Neel^{2,3}, Pascal Buskens^{2,4,5}, Guillaume Pierre⁶

¹TNO, The Hague, Netherlands, ²TNO, Netherlands, ³Delft University of Technology, Netherlands, ⁴Hasselt University, Belgium, ⁵Zuyd University, Netherlands, ⁶Sonaxis, France

Background, Motivation, and Objective

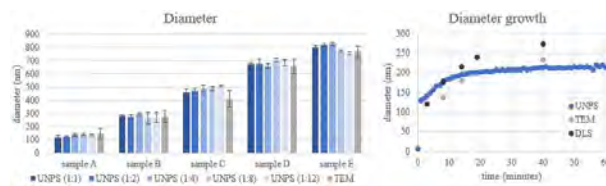
Nanoparticles are applied in an increasing number of products (e.g. medicine). There is a need to real-time monitor the growth of nanoparticles during production inside the chemical reactor. However, standard particle sizing methods such as dynamic light scattering (DLS) and a transmission electron microscopy (TEM) cannot do this. A suitable candidate may be ultrasonic transmission spectroscopy (UTS). Here, the sound speed and attenuation are measured of a dispersion and a physics based model is inverted and fitted to the measurements. The model describes the wave propagation effects at the particle-liquid boundary. Hence, performing UTS in a reactor is very challenging: at the start of a growth reaction the particle size and concentration are both very low. Moreover, the properties of the liquid medium may vary considerably during particle formation and other structures may be formed during the reaction. Also, high temperature, basic or very acidic conditions may exist in the reactor. Here, we investigate the feasibility of monitoring the growth of nanoparticles inside a reactor in real-time using a new ultrasound nanoparticle sizer (UNPS).

Statement of Contribution/Methods

The UNPS method is based on ultrasound transmission spectroscopy (50-250 MHz). The changes in the speed of sound and attenuation of sound waves in the dispersion caused by the nanoparticles are measured, and via an inversion translated into a particle diameter and concentration. We validate the UNPS with the use of TEM by measuring silica particles in water in several dilutions. A Stöber reaction, where silica particles are formed in an ethanol-water-ammonia mixture starting from a tetraethyl orthosilicate precursor, is real-time monitored inside the chemical reactor by the UNPS. Its measurements were verified with DLS and TEM by removing samples from the reactor.

Results/Discussion

There is a good agreement between the UNPS and TEM measurements of the mean diameter in the figure left. The figure right shows the growth of the mean particle diameter of the particles during a Stöber reaction. The UNPS' measurements every minute are fast enough to follow the reaction. These results qualified the UNPS as an instrument that can measure particle size during a chemical reaction inside the reactor.



9:00 AM

Evaluation of viscoelastic properties of liquids based on the oblique incidence technology using shear horizontal waves at frequencies above 100 megahertz from c-axis tilted ScAlN thin films

Yui Yamakawa^{1,2}, Takahiko Yanagitani^{1,2,3}

¹Waseda University, Japan, ²ZAIKEN, Japan, ³JST-PRESTO, Japan

Background, Motivation, and Objective

The ultrasonic reflection method [1] has been reported which is one of the ways to evaluate viscoelastic properties of liquids such as the complex acoustic impedance, the shear modulus, and the shear viscosity. These properties can be determined from the complex reflection coefficient of the viscoelastic liquid. The low angle incidence of shear horizontal (SH) wave on the surface is required for accurate evaluation. Although there have been many studies of this technique, shear waves at frequencies above 100 MHz have not been used in these studies because shear mode piezoelectric films have not been achieved. In this study, the sensitive evaluation of viscoelastic properties of liquids was conducted in the VHF range by using quasi-shear mode c-axis tilted ScAlN thin films.

[1] W. P. Mason, W. O. Baker, H. J. Mcskimin, and J. H. Heiss, Phys. Rev., **75**, 936 (1949).

Statement of Contribution/Methods

For the purpose of oblique incidence of SH wave, the trapezoidal silica glass prism was used as shown schematically in Fig. 1. The SH wave transducer consisting of c-axis tilted ScAlN piezoelectric thin film was fabricated on the prism by RF magnetron sputtering. The complex reflection coefficient of six glycerin solutions at various concentrations was measured by a network analyzer (Agilent Technologies, E5071C).

Results/Discussion

Figure 2 shows the time response characteristics of the prism. The SH wave from the piezoelectric film propagating through the route ABCBA (88 mm) in Fig. 1 is observed. The peaks every 23.4 μ s in Fig. 2 are found to be those of the SH wave because the shear wave velocity of silica glass is 3768.9 m/s [2]. Fig. 3(a)(b) shows the complex reflection coefficient Γ^* which is obtained by Fourier transforming the time response SH1 in Fig. 2.

While the amplitude decreases monotonically with increasing glycerin concentration, there is considerable variation in the phase of Γ^* . This irregularity affects the calculation of the shear modulus and the shear viscosity as shown in Fig. 3(c)(d). The trapezoidal prism is so large that the propagation distance increases, and the temperature control of the entire prism is difficult, which causes errors in the result. We intend to improve temperature control and conduct the experiment at higher frequencies by using thinner piezoelectric films in the future.

[2] J. Kushibiki, T. Wei, Y. Ohashi, and A. Tada, J. Appl. Phys., **87**, 3113 (2000).

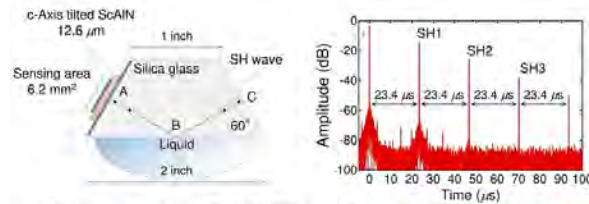


Fig. 1 Trapezoidal transducer for oblique incidence of SH wave

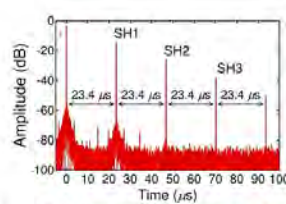


Fig. 2 Time response characteristics of the trapezoidal transducer

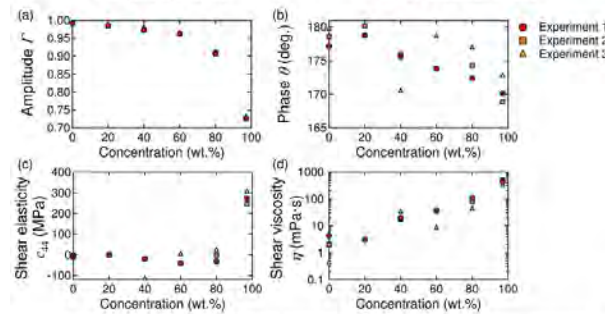


Fig. 3 Experimental results of (a)(b)complex reflection coefficient and (c)(d)viscoelastic properties of glycerin solutions

9:15 AM

Forces and torques on rods in an ultrasonic standing waveDavid Greve^{1,2}, Erin Dauson³, Irving Oppenheim³¹DWGreve Consulting, Sedona, AZ, United States, ²Department of Electrical and Computer Engineering, Carnegie Mellon University, Pittsburgh, PA, United States, ³Civil and Environmental Engineering, Carnegie Mellon University, Pittsburgh, PA, United States**Background, Motivation, and Objective**

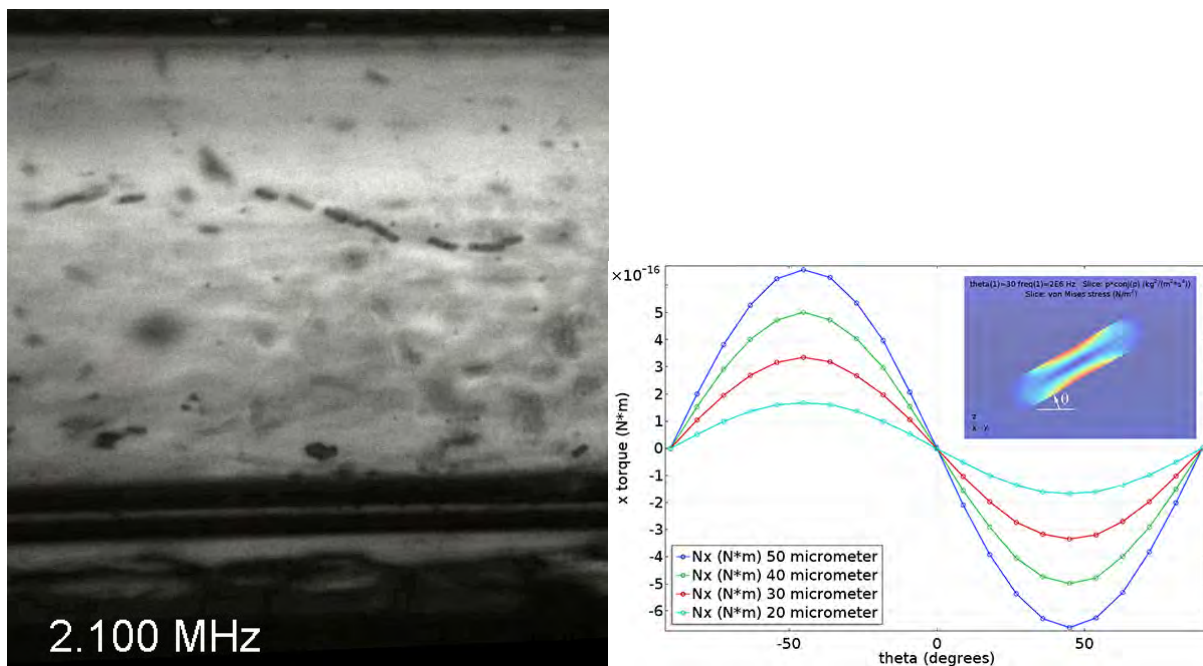
Ultrasonic standing waves have recently been used to align non-spherical objects for the deposition of ordered two-phase materials [Deposition of ordered two-phase materials using microfluidic print nozzles with acoustic focusing, R.R. Collino *et al.*, Extreme Mechanics Letters **8** (2016) 96–106]. In order to understand the alignment process, it is useful to calculate the forces and torques on objects in acoustic standing waves. There are many works addressing spherical objects but non-spherical objects have received less attention and are much less amenable to analytic approaches.

Statement of Contribution/Methods

In this paper we observe and simulate the effect of ultrasonic standing waves on cylindrical objects, including interactions between multiple objects. Alignment of 25–40 micrometer long and 10 micrometer diameter glass rods has been observed in water when standing waves were excited by a PZT actuator at 2.1 MHz. COMSOL has been used to simulate the acoustic fields for one or more rods in water. The stress tensor was determined from the acoustic field, and then the force and torque on the rods was calculated using well-established expressions.

Results/Discussion

Forces and torques have been calculated for single rods at various positions in an acoustic standing wave. Based on the calculated torques, the order of magnitude of the alignment time is predicted to be much less than a second, in agreement with observations of immediate alignment upon turning on the field. Forces between rods have also been calculated. Attractive forces are predicted for short separations between rods, consistent with the observed behavior.



5I - Material and Defect Characterization

Ikuta (200)

Thursday, October 25, 10:30 am - 12:00 pm

Chair **Walter Arnold**
Saarland University

5I-1

10:30 AM Ultrasonic evaluation of segmental variability in additively manufactured metal components

Manish Roy¹, Kenneth Walton¹, **Joel B. Harley²**, Mikhail Skliar¹

¹University of Utah, United States, ²University of Florida, United States

Background, Motivation, and Objective

Selective laser melting (SLM) additive manufacturing sequentially melts metal powder to produce intricate metal parts. The set-up cost for this method is low, but parts experience spatial variability in their thermal cycling history. This causes microstructure heterogeneity, residual stresses, and spatial variation in mechanical properties [1]. X-ray Computed Tomography (CT) can characterize microstructure heterogeneity, but there is no technology to characterize the internal varying mechanical properties. This paper adapts an ultrasound method for segmental temperature distribution (US-MSTD) to estimate this spatial variability.

Statement of Contribution/Methods

Traditional nondestructive ultrasound evaluation only provides an aggregate characterization of spatially distributed elastic properties. US-MSTD was developed to resolve this difficulty for temperature distributions [2,3] by (a) using a structured propagation path with multiple echogenic features to create ultrasound echoes (i.e., multiple TOFs) and (b) parametrizing “admissible” temperature distributions by prescribing a functional form. In this study, the same ideas are implemented for isothermal samples with spatial material property variability in different regions of 3D-printed metal parts.

Results/Discussion

Selective laser melting was used to fabricate three metallic waveguides (Fig. 1a) from different metal powders (aluminum and titanium alloys and stainless steel). Three small internal echogenic features were introduced along the centerline of each waveguide to produce reflections in response to an excitation at the waveguide base. The echoes timing illustrated in Fig. 1b was used to estimate the spatial distribution of elastic modulus along the waveguide. The results showed correlation with the heterogeneity from X-ray CT and indicate the feasibility of characterizing mechanical spatial heterogeneity with the proposed method.

[1] Y. Liu et al., Appl. Phys. A, Nov. 2017.

[2] Y. Jia et al., Ultrasonics, 2016.

[3] Y. Jia and M. Skliar, Energy Fuels, 2016.

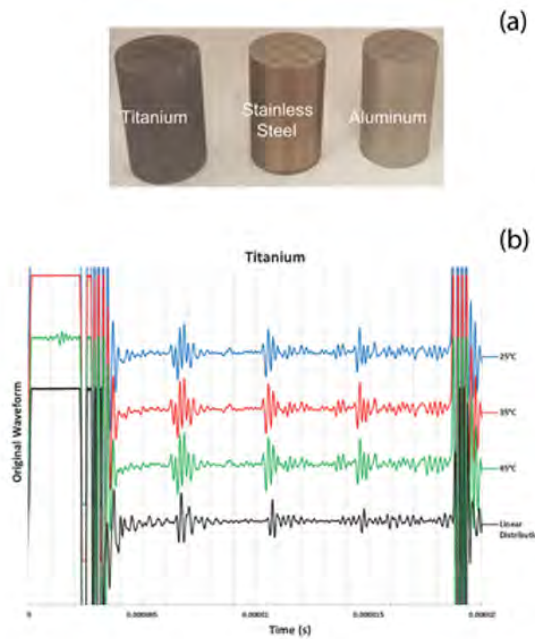


Fig. 1: (a) Waveguides with echogenic features obtained by selective laser melting. (b) Echoes from internal echogenic features shown for the titanium waveguide maintained at different temperatures.

10:45 AM

Full waveform inversion for material property mapping using ultrasonic phased arraysKatherine Tant¹, Russell Niven¹, Anthony Mulholland², Anthony Gachagan³¹*University of Strathclyde, United Kingdom*, ²*Mathematics and Statistics, University of Strathclyde, Glasgow, United Kingdom*, ³*Electronic and Electrical Engineering, University of Strathclyde, Glasgow, United Kingdom***Background, Motivation, and Objective**

Typically, imaging algorithms within the ultrasonic non-destructive testing community assume that waves travel at a constant wave speed within the material under inspection. This is a poor assumption when the medium under inspection is of a heterogeneous nature and it can contribute to the misplacement of defects. Prior knowledge of the material's internal structure would allow corrective measures to be taken, but this is seldom available. The work presented here endeavours to reconstruct the spatially varying wave speed maps of heterogeneous media from ultrasonic phased array measurements. This is achieved via a semi-analytical approach to full waveform inversion and the reversible-jump Markov Chain Monte Carlo (rj-MCMC) method.

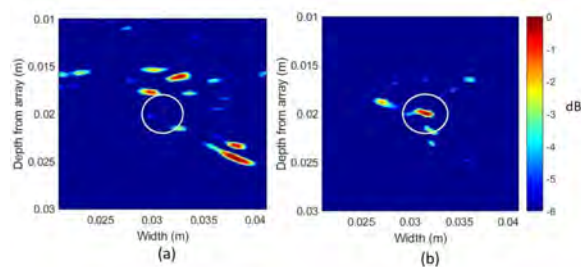
Statement of Contribution/Methods

The material's structure is parameterised using Voronoi diagrams, where each region is assigned a local wave speed. A semi-analytical 1D model of the wave's interaction with the regional boundaries has been derived to approximate the A-scans that would arise from the ultrasonic phased array inspection of this material. For each transmit-receive pair of ultrasonic array elements, the Pearson correlation coefficient between the modelled and observed A-scans is calculated. Using this as the basis for the objective function, the material parameterisation is perturbed iteratively, and the model space is searched for wave speed maps which minimise this. Due to the Bayesian framework of the rj-MCMC, a distribution of maps is obtained from which we can approximate the internal structure of our component and quantify the uncertainty attached to it. The resulting map is used in conjunction with an imaging algorithm to produce a more reliable reconstruction of defects.

Results/Discussion

The data examined arises from a simulated through-transmission inspection of a random medium. Figure 1 shows the image generated when the standard Total Focussing Method is used and exhibits an error in flaw placement of 8.15mm (measured from the highest amplitude point). Correcting for the heterogeneity using the map reconstructed by the rj-MCMC, we obtain image (b) which exhibits a misplacement of only 0.7mm.

Figure 1. Reconstruction of a 4mm diameter void embedded in a heterogeneous medium where (a) a constant velocity has been assumed and (b) the rj-MCMC map has been utilised to correct for the the spatially varying velocity.



11:00 AM **Automated Robotically Enabled Ultrasonic Sensing for Additive Manufacturing**

Anthony Gachagan¹

¹Electronic and Electrical Engineering, University of Strathclyde, Glasgow, United Kingdom

Background, Motivation, and Objective

Statement of Contribution/Methods

Results/Discussion

11:15 AM

Characterizing Micro- and Nano- Materials based on their Ultrasonic Dispersion Properties: A Feasibility StudyDaniel Alabi¹, Mehrdad Ramezani¹, **Joel B. Harley¹**, Roozbeh Tabrizian¹¹*Department of Electrical and Computer Engineering, University of Florida, Gainesville, FL, United States***Background, Motivation, and Objective**

Current methods typically characterize morphological and/or elastic properties of materials with laser spectrometers or x-ray diffraction. These methods are expensive, slow, bulky, and cannot be applied *in situ*, and are not effective for micro- and nano-scale thin films. In this paper, we present an ultrasound technique for characterizing micro- / nano-scale materials based on ultrasonic dispersion (i.e., frequency-dependent wavenumbers). In contrast with current approaches, ultrasonic transduction can utilize inexpensive hardware in real-time and is applicable for material characterization at the micro- / nano-scale.

Statement of Contribution/Methods

To analyze materials at the micro- and nano-scale, we target extraction of their dispersive behaviour through measuring particle displacements across a semiconductor waveguide, shown in Figure 1, and over a wide frequency range. We then compute the spatial Fourier transform to produce a dispersion diagrams, which will later serve to identify morphological and elastic properties of the film. In this work, we compare this representation for silicon (Si) and molybdenum (Mo), to demonstrate our capability to distinguish materials with different elastic properties.

Results/Discussion

COMSOL Multiphysics was used to extract different resonance mode shapes for <100> Si and Mo waveguides, over 67-80 MHz. The wavenumbers of the waves were extracted for each resonance mode to reconstruct the dispersion diagram. Figure 2 shows the dispersion diagram for Si and Mo, highlighting their significant distinction, which can be used to distinguish materials and their elastic properties. While simulations are used in this example, in practice, dispersion diagrams will be extracted using a test-vehicle actuated by a thin piezo transducer.

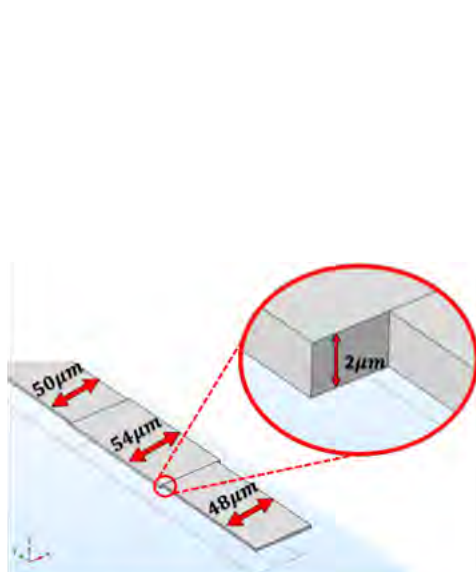


Figure 1. Three waveguides with different widths cascaded to help energy trapping and achieve high-Q resonance modes in the test vehicle.

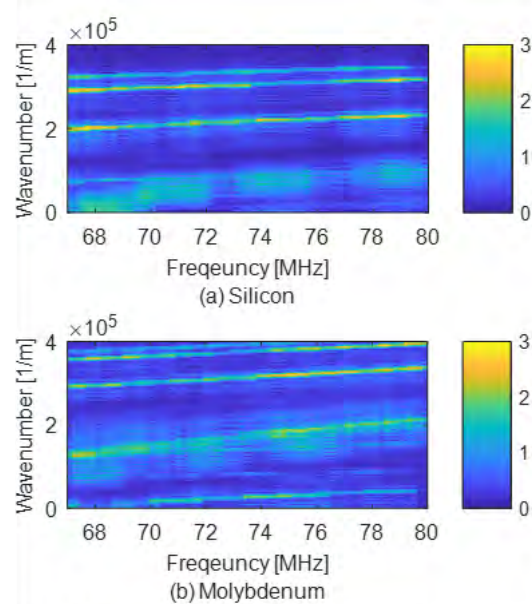


Figure 2. The extracted dispersion diagrams for <100> Si and Mo.

11:30 AM Mechanical Properties of Comet 67P/Churyumov-Gerasimenko Measured by CASSE and DIM on Board Rosetta's Lander Philae

Walter Arnold¹, Hans-Herbert Fischer², Martin Knapmeyer³, Harald Krüger⁴

¹*Department of Material Science and Engineering, Saarland University, Saarbruecken, Germany*, ²*MUSC, DLR MUSC, Köln, Germany*, ³*Asteroids and Comets, DLR Institute of Planetary Research, Berlin, Germany*, ⁴*Max-Planck-Institut for Solar System Research, Göttingen, Germany*

Background, Motivation, and Objective

In August 2014, the ESA spacecraft Rosetta encountered comet 67P. Rosetta carried the lander Philae that landed on the comet's nucleus on November 12th 2014. Philae housed ten different instruments including the Surface Electric Sounding and Acoustic Monitoring Experiment (SESAME), comprising CASSE. The objective of the Rosetta mission was to determine the properties of comet 67P. The mission ended on September 30th 2016 with the deorbiting of Rosetta onto comet 67P.

Statement of Contribution/Methods

The Comet Acoustic Surface Sounding Experiment (CASSE) is housed in the six soles of Philae's landing feet. It consists of three piezoelectric tri-axial accelerometers, and three transducers. This allowed for both passive listening to the comet's seismic activity and active sounding of the comet surface. Deceleration signals occurring in the first ms of the touchdown at the first landing site at an impact velocity of approx. 1 m/s were recorded. They contained information on Young's modulus E and on the crushing strength σ of the comet soil. A first analysis based on an inversion scheme exploiting Hertzian contact mechanics together with laboratory calibration tests was presented at the IEEE-IUS in 2015 (abstract 5 D-2), followed by a recent detailed account of the CASSE results /1/.

The MUPUS listening experiment was a joint operation of two instruments on Philae: The Multi- purpose Sensors for Surface and Sub-Surface Science (MUPUS), and CASSE. While the main goal of MUPUS was to measure the thermal conductivity and the heat flow of the surface comet material by driving an instrumented rod into the ground /2/, a joint operation was carried out at the final landing site Abydos, since MUPUS used a hammering mechanism with stroke energies up to 4 Joules, constituting a strong source for surface waves in the 100 Hz to 2 kHz range /3/.

Results/Discussion

We will first give a summary of the data recorded by CASSE and MUPUS-CASSE, followed by an interpretation in terms of relations known in material science. The data support the concept that the elastic (E) and strength properties (σ) of the comet material correspond to very porous solids constituted by the regolith particles with porosities up to 80%. The σ/E ratio $\approx 1/1000$ agrees well with relations known in material science /4/. There is a gradient in the elasticity as derived from the dispersion of surface waves generated in the MUPUS-CASSE experiment indicating a structural layering of the comet surface. The data also allow an estimate of the fracture toughness K_{Ic} which is compared with data for crack growth observed in the neck of the comet /5/.

/1/ D. Möhlmann et al., Icarus, 303, 251 (2018).

/2/ T. Spohn et al., Science 349 (6247), aab0464-1 (2015).

/3/ M. Knapmeyer et al., Icarus, (2018), DOI: 10.1016/j.icarus.2017.12.002, in print.

/4/ L. J. Gibson, M. F. Ashby, *Cellular solids* (1997), Cambridge University Press, Cambridge, UK.

/5/ M. R. El-Maarry et al., Geophys. Res. Letters, 42, 5170, (2015).

5J - Sensors and Actuators

Ikuta (200)

Thursday, October 25, 1:30 pm - 3:00 pm

Chair **Robert Addison**
Rockwell Science Center

5J-1

1:30 PM

High-temperature Microwave Acoustic Vibration Sensor

Anin Maskay^{1,2}, Donald Hummels¹, Mauricio Pereira da Cunha^{1,2}

¹Electrical and Computer Engineering, University of Maine, Orono, ME, United States, ²Laboratory for Surface Science and Technology, University of Maine, Orono, ME, United States

Background, Motivation, and Objective

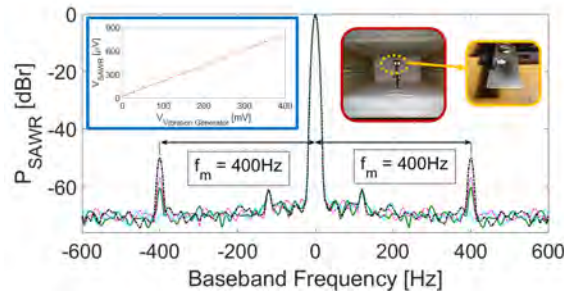
High-temperature vibration sensors are desired in a number of contemporary harsh-environment applications, namely: power plants, metallurgy, aerospace, and defense. The detection of vibrations in these applications is important for providing structural and system based condition-based maintenance, thus reducing operating and maintenance costs, improving industry efficiency, and increasing safety. Microwave surface acoustic wave resonator (MSAWR) sensors have the potential of being used as high-temperature vibration sensors due to their proven harsh-environment operation, small size, battery-free, and wireless capability.

Statement of Contribution/Methods

This paper explores the MSAWR as a vibration sensor mounted and tested up to 500°C. A 193MHz langasite-based MSAWR sensor was attached to a custom-designed constant-stress Inconel cantilever test beam (figure right inset) using a high-temperature capable Al₂O₃-based epoxy. The beam was mounted in a box furnace and exposed to vibrations using a stainless steel rod attached to a vibration generator outside the furnace. The measured MSAWR's RF power spectral response was used to sense and quantify vibration magnitude and frequency at high-temperatures.

Results/Discussion

The main plot in the figure shows the measured MSAWR sensor power spectra at 400°C for four vibration generator input signal levels: (i) 25mV_{p-p} (dotted); (ii) 99mV_{p-p} (solid); (iii) 150mV_{p-p} (dashed); and (iv) 300mV_{p-p} (dashed-dotted). The 0Hz peak is the baseband representation of the MSAWR excitation frequency at 193MHz and the 400Hz peaks are due to the vibration-induced modulations of the MSAWR RF signal (note: the 120Hz peaks are spurious from the testing system unrelated to measured vibration). The measured data in this power spectra plot allow the determination of both vibration frequency and magnitude. The left inset shows the measured MSAWR voltage levels (vertical axis) potted against the vibration generator input voltage (horizontal axis) for seven different vibration levels. The curve reveals a linear dependence with a correlation coefficient of 0.994 and sensor sensitivity of 1.97μV/mV. These measured results at high-temperatures confirm the viability of the MSAWR sensor to detect both vibration frequency and magnitude for high temperature industrial, defense, aerospace, and power sector applications.



1:45 PM

Ultra-Wide-Band SAW Sensor with HFM Etched Reflectors**Victor Plessky¹, Aleksey Shimko², Rimantas Miskinis³, Dmitrij Smirnov³, Soumya Yandrapalli^{1,4}**¹*GVR Trade SA, GORGIER, Switzerland*, ²*Tai-Saw Co. Ltd, Taiwan*, ³*FTMC, Lithuania*, ⁴*EPFL, Switzerland***Background, Motivation, and Objective**

Remotely controlled SAW sensors are used in different harsh environments. It is especially attractive to include UWB coding directly onto the sensor [1], and to apply “matched to signal” filtering of sensor feedback to the “reader” device. However, the sensor temperature can vary in a wide range and the thermal variation of SAW delays changes the coding. This complicates the reader algorithm. Also, for UWB SAW devices, a strong piezo-substrate is necessary and any long electrode structure will have many internal reflections perturbing the desired response. We propose solution based on Hyperbolically Frequency Modulated (HFM) signals and reflectors.

Statement of Contribution/Methods

The HFM signals have a unique property – that their extension in time is equivalent to their shift [2]. We present the sensors operating in 2.0-2.5 GHz frequency range, including etched reflectors with dispersive delay of 1000ns. The sensor includes two acoustic channels with reflectors off-set of 500ns. The “reader” can compress sensor responses into short (about 2.5 ns) pulses independent of the sensor temperature, however the delays between pulses is temperature dependent and allows temperature measurements.

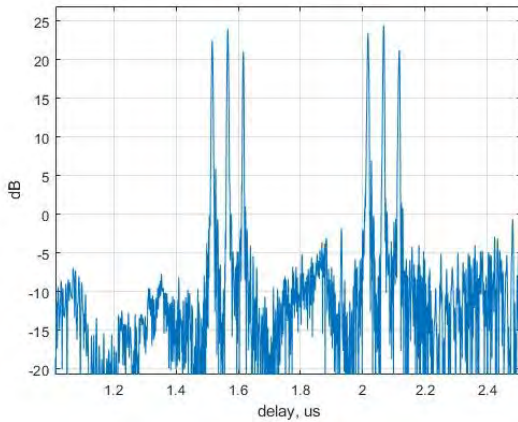
Results/Discussion

The remotely simultaneously measured frequency responses of 3 sensors, which were compressed using the same numeric matched to signal filter are shown in Fig.1. The time slot allocated for each sensor was sufficient for unique identification of two reflection peaks each from all 3 sensors. The nominal offset of reflectors was the same 500ns for all sensors, but, in practice, it depends on the sensor temperature and the measurement of delays between pairs of peaks gives temperature from all 3 sensors. The precision of the measurement is about 0.1°C and depends on Signal-to-Noise (S/N) ratio, etc. Power levels of the reader are being measured in different regimes.

This work is done in the frame of the Swiss-Lithuanian Eurostars Project No. E!10640 UWB_SENS and was co-funded by the State Secretariat for Education, Research and Innovation. The authors express their gratitude.

[1] S. Harma, V. P. Plessky and Xianyi Li, "Feasibility of ultra-wideband SAW tags," 2008 IEEE Ultrasonics Symposium, Beijing, 2008, pp. 1944-1947.

[2] V. Plessky and M. Lamothe, *Electron. Lett.*, Vol. 49, No24, 21 Nov. 2013, p. 1503



2:00 PM

Microwave Resonator Ultrasound ReceiversTom S. Robbins¹, James Seddon¹, Erwin Alles², Adrien Desjardins³, Ioannis Papakonstantinou², Cyril C. Renaud¹¹*Department of Electronic and Electrical Engineering, University College London, United Kingdom, ²University College London, London, United Kingdom, ³Department of Medical Physics & Biomedical Engineering, University College London, London, United Kingdom***Background, Motivation, and Objective**

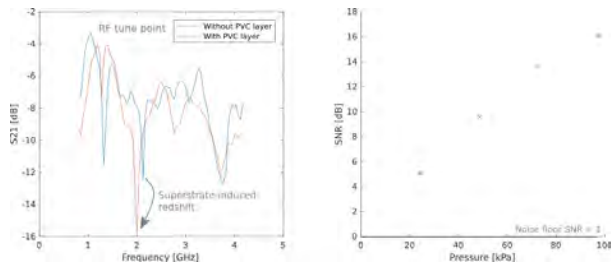
To detect ultrasound waves, most devices either transduce directly into current by the piezoelectric effect, or use laser interferometry to detect small strains in a suitable material. We propose an ultrasound receiver which works by modulating a GHz-range electromagnetic carrier signal with an ultrasound amplitude (or phase) envelope. In our present work, this is achieved by covering a waveguide coupled metamaterial resonator with a thin superstrate of high electrical permittivity and low Young's modulus. As the superstrate layer is deformed, the effective electric permittivity of the waveguide changes, causing the resonance to shift and the amplitude of the carrier signal (tuned near the resonance, see left figure) to be modulated. This device is essentially a microwave-frequency version of a Bragg fibre optical hydrophone, but one which allows spatial multiplexing of ultrasound signals over a potential 1D or 2D array (since each resonator element can have its own microwave channel), while retaining the broadband sensitivity of each element.

Statement of Contribution/Methods

Our theoretical analysis considers the effect of static strains on dielectric-covered microstrip lines, and we derive an equation which extends this to microwave resonators. This is combined with an expression for the change in thickness of the superstrate layer under ultrasound illumination, treating the layer as an ultrasound cavity, giving an expression for the device sensitivity. Simulations using FDTD (CST Microwave Studio) and FEM (COMSOL Multiphysics) are used to design high Q-factor resonators. A proof-of-concept device was fabricated using a circuit board for the substrate and shrink-wrapped PVC for the superstrate, and its response measured for harmonic ultrasound signals using a spectrum analyser.

Results/Discussion

Our proof-of-concept device was found to be able to detect a 5 MHz harmonic ultrasound signal delivered from a ultrasound-gel-coupled piezo source (see right figure), demonstrating the viability of the principle. Further experiments are planned which use pulsed ultrasound and an envelope detector to analyse the device response in the time domain. We propose schemes for miniaturisation and suggest ways to increase the sensitivity by using a higher frequency carrier signal, and optimising the material of the superstrate layer.



2:15 PM Wireless inertial sensing platform self-powered by piezoelectric energy harvester for industrial predictive maintenance

Maxime Benchemou¹, Guillaume Ferin¹, Bogdan Rosinski¹, Philippe Vince¹, An Nguyendinh¹

¹*Advanced Research, Vermon SA, Tours, France*

Background, Motivation, and Objective

Piezoelectric materials have long been recognized for their efficacy in a wide range of applications such as sensors, actuators and electromechanical energy harvesters. Their robustness and budget-friendly implementation make them well suited for reliable, cost effective sensing systems in medical or industry.

The growing IoT market increasingly requires more miniaturization, low power electronics and quasi-inexhaustible source for extended autonomy and sustainable performance.

Our work presents the development of a wireless sensing platform self-powered by a piezoelectric vibrational energy harvester for predictive maintenance applications on industrial machines.

Statement of Contribution/Methods

An autonomous wireless sensor module have been developed and manufactured with a modular 3-D packaging approach: it is made of several stacks, keeping the form factor well under the volume of two AA batteries (only $3.3 \times 3 \times 0.66$ cm³). The device embeds all the electronics required to deploy a predictive maintenance application: communication (BLE), sensing (accelerometer), piezoelectric energy harvester, thin-film backup battery and a microcontroller which manages the whole system.

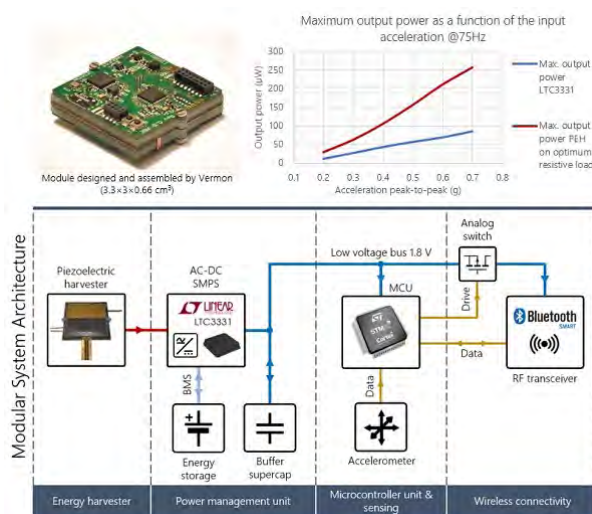
Thanks to the modular design, each main function can be interchanged and tuned in accordance with the installation and its environment (ambient vibration characteristics, sensing, wireless protocol, etc.).

Results/Discussion

The Piezoelectric Energy Harvester, manufactured by Vermon, relies on a proprietary thinned-bulk process. After the power conversion, a useful power of 85 μ W has been recorded at a frequency of 75 Hz and at 0.7 g of acceleration, which fits with industrial machine vibrations.

This level of energy is sufficient to power up the system, thanks to off-the-shelf ultra-low power electronics. The power production-to-consumption budget is balanced taking into account the amount of data to be transferred, the signal processing and the measurement duty cycle. This offers several degrees of freedom to optimize the monitoring method.

In conclusion, this solution, which can easily be networked, is a breakthrough to offer a self-powered low-power sensing platform over a long lifetime for predictive maintenance while performing cost savings.



2:30 PM

Modeling and experimental parametric study of a dual-cantilever piezo-magneto-elastic energy harvester**Xiaobo Rui¹, Yibo Li¹, Hui Zhang¹, Hao Feng¹, Zhuochen Wang¹, Zhoumo Zeng¹**¹*State Key Laboratory of Precision Measurement Technology and Instrument, Tianjin University, Tianjin, China, People's Republic of***Background, Motivation, and Objective**

Piezoelectric energy harvesting technology has attracted wide attention due to its potential to power the wireless sensors. Motivated by the need to increase the harvesting efficiency and the bandwidth of the cantilever type energy harvester, a novel dual-cantilever piezo-magneto-elastic energy harvester (DPEH) is presented in this paper. The DPEH combines the characteristics of linear arrays and nonlinear transverse magnetics configurations. The structure has two same-size parallel symmetric cantilever beams, and two opposite cylindrical magnets are attached at the end of the beams.

Statement of Contribution/Methods

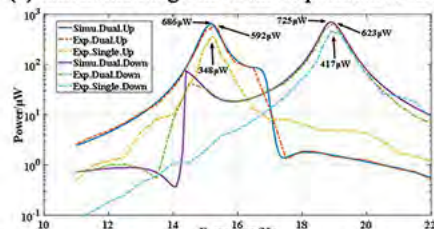
For the DPEH structure, we develop an approximated distributed-parameter model based on the Galerkin discretization method. The model is based on magnetic dipole aligned and none vertical magnet misalignment assumptions, and includes the initial magnet static position effect analysis. To validate the model and study its parametric performance, an experimental energy harvester with MFC-M8514-P2 piezoelectric patches and 6061-T6 aluminum alloy cantilever beams with magnet tip-masses was excited by an electromagnetic shaker.

Results/Discussion

The results confirmed that the distributed-parameter model can generally reflect the characteristics of DPEH, but there is a certain error in the prediction of the amplitude with the experiment. A possible explanation for the deviation might be that damping ratio variety with frequency change. The most obvious finding to emerge from this study is that the harvester can broaden the resonance bandwidth and have an increase power output of about 59% in this setting. Because of the different tip masses settings of the two beams, their first-order resonance frequencies are separated. Due to the nonlinear characteristics, some side lobes are overlapped to widen the band. It is demonstrated that the DPEH has the potential to be a wideband efficient energy harvesting structure in this paper. Finally, the influence of the magnetic surface flux and distance parameters are studied based on the model.



(a) Schematic diagram of the experimental setup



(b) Power evaluations of simulation and experiment

2:45 PM **Accelerated aging procedures of bending piezoelectric structures using electrical stress induced approaches**

Thien Hoang^{1,2}, Guillaume Ferin¹, Claire Bantignies¹, Bogdan Rosinski¹, Philippe Vince¹, An Nguyen-Dinh¹

¹*Vermon SA, Tours, France, ²GREMAN, UMR 7347 CNRS, Université de Tours, INSA-CVL, Blois, France*

Background, Motivation, and Objective

Piezoelectric material has long been recognized for its efficacy in a wide range of applications as sensors and actuators. Their robustness and budget-friendly implementation make them well suited for reliable, cost effective systems and their aging capabilities were usually tested with regards to the targeted application field and expected lifetime.

Recently, piezoelectric materials have been designed and processed to address energy harvesting applications. Such miniaturized piezoelectric structures allow to power up industrial, domestic or automotive wireless sensors for a quasi-infinite operating lifetime (>30 years). However, if the reliability has been extensively studied for piezoelectric sensors and actuators, aging capabilities of such semi-perpetual system are difficult to assess using direct mechanical solicitation approaches since a representative test would require several billion cycles and would mostly be an aging test for the test equipment itself.

We herein propose an alternative relying on the resonating property analysis of a well-known clamped-free cantilever beam when electrically stressed on its first eigen flexural mode. Such a strategy consist in simplifying the mechanical fixtures at its maximum to reduce its own aging impact and dramatically accelerate the aging process.

Statement of Contribution/Methods

The tested clamped-free cantilever beam structure is constituted of two piezoelectric layers separated by an inner shim material. The stress level, the beam deformation shape and its resonating behavior are related to the beam dimensions (length, width, thickness) and its tip mass weight, shape and position.

Using FEM analysis, we have confirmed the equivalency of the stress distribution of a clamped-free cantilever when mechanically operated using external actuator and electrically operated at its first eigen frequency with a simple waveform generator [Gwinstek GFG-3015].

Based on the electrical solicitation technique, it is indeed possible to get the same stress distribution profile but for a higher resonating frequency (X20), thus considerably accelerating the aging process.

We develop a dedicated and fully automated test bench where the beam shape and the stress is continuously monitored using high frequency LASER telemeter (Keyence LK-G5000).

Results/Discussion

We demonstrated that mechanical stress exhibited in the bimorph cantilever beam with electrical solicitation is found equivalent to mechanical solicitation by FEM. An automated test bench with electrical solicitation was developed to perform and survey accelerated aging test. Using this approach, 10 samples tested during 4 months under a maximum stress of 69MPa operated at 470Hz have reached up to 5 billion cycles representing 8 years of equivalent lifetime and demonstrating the capability of the electrical solicitation approach for accelerated aging of long lifetime vibrating piezoelectric energy harvesting device.

5K - Structural Health Monitoring

Ikuta (200)

Thursday, October 25, 4:00 pm - 5:30 pm

Chair **Patrick Johnston**
NASA Langley Research Center

5K-1

4:00 PM Exploiting complex boundaries through full waveform ultrasonic imaging

Fan Shi¹, Peter Huthwaite²

¹*Mechanical Engineering, Imperial College London, London, United Kingdom*, ²*Mechanical Engineering, Imperial College London, United Kingdom*

Background, Motivation, and Objective

Characterisation of defects located near complex boundaries of engineering components is challenging. Scattered waves from defects are often masked by unwanted reflections from complex boundaries, causing artefacts to appear in images. However, in fact multiple scattered waves between defects and backwalls contain vital information which can be decoded to reveal important features of defects. The objective of this paper is to utilise full waveform imaging methods including wave interactions between defects and complex boundaries, to achieve significant improvements in defect characterisation.

Statement of Contribution/Methods

The main contribution of this study is the development and application of an ultrasonic full waveform imaging algorithm to enhance the reconstruction of defects. An initial estimate model of the defect is given and updated by minimising the difference between the simulated waveforms and the actual physical measurements. In this way, the complex interactions between backwalls and defects are considered in the imaging algorithm, which enable the improvement of the reconstruction of the defect. In particular the algorithm reveals the shadowing region of the defect which is not ‘seen’ directly by probing ultrasonic waves.

Results/Discussion

We simulate the ultrasonic array full waveform imaging of a side drilled hole (SDH) located close to a backwall. The initial estimate model is assumed to have the same model setup without the SDH. By running the full waveform imaging algorithm, we successfully reconstruct the shape of the SDH as shown in Fig. 2(b). Note that the back face of the SDH which is shadowed from the incident waves is reconstructed, by considering wave interactions between the SDH and the backwall. For comparison, Fig. 2(a) shows the image obtained by neglecting the SDH-backwall scattering, which only reconstructs the front face ‘seen’ by the probing waves. The talk will discuss this, as well as potentially looking at areas including more complex backwalls and where the backwall is unknown.

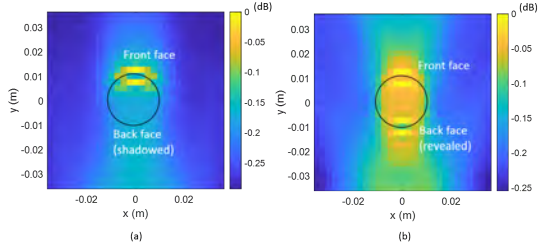


Fig. 1. (a) Reconstructed SDH without considering multiple scattering between the SDH and the backwall.
(b) Reconstructed SDH considering multiple scattering between the SDH and the backwall. The back face of the SDH is recovered.

4:15 PM

Ultrafast Phased Array Imaging: an Application to Closed Crack CharacterizationYoshikazu Ohara¹, Sylvain Haupert², Sinan Li³¹*Department of Materials Processing, Tohoku University, Sendai, Japan*, ²*Laboratoire d'Imagerie Biomedicale, Sorbonne University, PARIS, France*, ³*Verasonics Inc, Kirkland, WA, United States***Background, Motivation, and Objective**

Ultrafast imaging in ultrasound refers to imaging with a frame rate higher than thousands of frames per second (fps). The high frame rate is typically achieved by transmitting plane waves or some other forms of unfocused beams into the region of interest, eliminating or minimizing the needs for beam scans. Recent biomedical ultrasound research has been largely progressed by ultrafast imaging [1,2]. In this paper, we present ultrafast imaging in NDT to observe the nonlinear dynamics of the closed cracks.

Statement of Contribution/Methods

The combination of a pump wave at low frequencies and a probe wave at high frequencies has been widely studied to examine the elastic nonlinearity, e.g. in closed cracks, for simultaneous high vibration amplitude and good probing spatial resolution. Constrained by the frame rate of typical phase array imaging, dynamics of closed cracks was previously studied only at very low frequencies using a servohydraulic tensile stress pump [3] and a thermal stress pump [4], with limited insights into complex elastic nonlinearity signatures such as hysteretic behaviors and material conditioning [5]. In this study, the sample is pumped at its resonant frequency ~7 kHz with a PZT disk glued on it, and at the same time, the closed crack responses are imaged in a stroboscopic way using ultrafast plane wave imaging technique with an effective frame rate > 50kfps (interleave multiple frames acquired at thousands fps).

Results/Discussion

The slow motion replay resolves the closed crack dynamics with good sensitivity, contrast and temporal resolution. The pixel intensities in the region change as the crack opens and closes. The intensity curve suggests the most energy resides in the fundamental resonant frequency with small spreading over to the higher order harmonics. The method could be useful applied to detect closed or micro-cracks and fundamental to study nonlinear dynamics in solids.

References:

1. C. Errico, J. Pierre, S. Pezet, Y. Desailly, Z. Lenkei, O. Couture and M. Tanter, *Nature*, 527, 499-502, 2015
2. A. Urban, C. Dussaux, G. Martel, C. Brunner, E. Mace and G. Montaldo, *Nature Methods*, 12, 873-878, 2015.
3. Y. Ohara, S. Horinouchi, M. Hashimoto, Y. Shintaku, K. Yamanaka, *Ultrasonics*, 51, 661-666, 2011.
4. Y. Ohara, K. Takahashi, S. Murai, K. Yamanaka, *Applied Physics Letters*, 103, 031917-1-5, 2013.
5. J. Riviere, M. C. Remillieux, Y. Ohara, B. E. Anderson, S. Haupert, T. J. Ulrich, P. A. Johnson, *Journal of Nondestructive Evaluation*, 33, 216-225, 2014.

4:30 PM

High frequency ultrasonic and photoacoustic studies of polymer composites with nanoinclusions**Vytautas Samulionis¹, Jan Macutkevic¹, Juras Banys¹, Olga Shenderova², Ala Zak³**¹*Physics Faculty of Vilnius University, Vilnius, Lithuania*, ²*International Technology Center, Raleigh, NC, United States*, ³*2HIT - Holon Institute of Technology, Holon, Israel***Background, Motivation, and Objective**

Polymer materials are well known for their flexibility in practical applications due to easy formability, lightweight, color and transparency. In order to improve their properties or modify their range of applications, the fabrication of composites with various types of nanoinclusions is a common practice. Nowadays it is well known that nanotube structures is not specific to carbon, but is a generic property of two dimensional layered inorganic materials, such as MoS₂, or WS₂. Multifunctional materials produced from composites of polymers containing inorganic nanotubes, which can be designed at the nanoscale, are expected to have the great impact on industrial applications in the future. Among the broad range of available polymer matrices PDMS and polyurethane are widely used. Polyurea elastomers are a new kind of elastomeric materials with the enhancement of mechanical, chemical and thermal properties. Ultrasonic spectroscopy allows to observe and evaluate relaxation processes that govern nanocomposites elastic behaviour and to reveal variation of these processes because of the change of the filler concentration.

Statement of Contribution/Methods

In this contribution we present extensive temperature investigations of longitudinal ultrasonic velocity and attenuation in various types of polymer composites with nanoinclusions: polyurea elastomers with MoS₂ nanotubes, polyurethane with WS₂ nanotubes, and polydimethylsiloxane (PDMS) composites with onion-like carbons (OLC). The computer controlled pulse-echo system was used for measurements of ultrasonic velocity and attenuation. The system have large dynamic range and large input ultrasonic power, therefore the large ultrasonic attenuation values could be measured.

Results/Discussion

In all composites above the glass transition region the ultrasonic velocity dispersion and large ultrasonic attenuation maxima were observed in pure and doped composites. The positions of ultrasonic velocity dispersion and attenuation peaks were slightly shifted to higher temperatures after doping with MoS₂, WS₂ and OLC nanoparticles. This upshift of the glass transition temperature with addition of nanoparticles can be attributed to attractive interaction between polymer and nanoparticles. The increase of ultrasonic attenuation in PDMS composites with increasing of MoS₂ and OLC particle concentration was observed at room temperature and such behaviour was attributed to the ultrasound interactions with nanoparticles dispersed in the polymer matrix. In all investigated composites with carbons and inorganic nanoinclusions the increase of ultrasonic attenuation was observed after illuminating samples by white light using optical waveguide. Such photoacoustic phenomenon could be related to the ultrasonic interaction with nanoparticles of sufficiently higher temperature than polymer matrix.

4:45 PM

GPU-accelerated matrix-free 3D reconstruction for ultrasonic nondestructive testing**Jan Kirchhof^{1,2}, Sebastian Semper², Florian Römer¹**¹*Fraunhofer IZFP, Germany*, ²*Technische Universität Ilmenau, Germany***Background, Motivation, and Objective**

In nondestructive testing, the reconstruction of 3D images often involves computations of a high complexity, especially if high resolutions are desired, which renders algorithms that scale moderately in time and memory consumption indispensable.

We show that the forward and backward operator appearing in ultrasonic imaging admits an efficient parallelized frequency domain based matrix-free implementation.

This facilitates its direct application to recent sophisticated reconstruction techniques such as sparsity based algorithms.

Statement of Contribution/Methods

We provide a matrix-free implementation of the operator on a GPU to perform the reconstruction of 3D ultrasound images. This approach leverages the rich structure in the operator while maintaining flexibility in the choice of the physical model. Note that for a suitable model a single backward projection step is equivalent to the Synthetic Aperture Focusing Technique (SAFT).

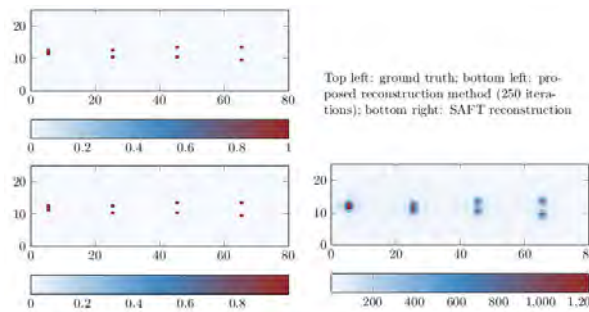
Our operator allows to localize defects in a specimen from ultrasonic measurement data using a variety of reconstruction methods such as FISTA or OMP.

Most of these methods require certain parameters that depend on the scenario, where a fast convergence of the algorithm requires a proper choice. This is crucial in large-scale problems to minimize the number of projections of the operator.

We discuss the efficient choice of these parameters in the matrix-free setup without brute-force exhaustive search.

Results/Discussion

We compare the reconstruction performance of a particular sparsity based iterative method to a conventional SAFT image based on a 3D synthetic dataset. The parameters of the former are not manually optimized, but chosen based on the aforementioned estimation strategy and both images are computed based on the same underlying forward model. Note that in contrast to SAFT, the sparse reconstruction image has the same focusing quality also in the depth dimension, which is not shown in the C-scan. In the full paper, we apply our proposed method to measured data.



5:00 PM Outer wall inspection using acoustic irradiation induced vibration from UAV for noncontact acoustic inspection method

Tsuneyoshi Sugimoto¹, Kazuko Sugimoto¹, Itsuki Uechi¹, Noriyuki Utagawa², Chitose Kuroda²

¹Graduate School of Engineering, Toin University of Yokohama, Japan, ²Technical Research Institute, SatoKogyo Co., Ltd., Japan

Background, Motivation, and Objective

In Japan, it is necessary to inspect the whole surface of all buildings constructed over 10 years before by the hammering test, but it is not realistic because of the large cost burden of temporary scaffolding etc. Therefore, development of a noncontact inspection method is required. In our noncontact acoustic inspection method using LDV and acoustic irradiation induced vibration, problems of angle dependence and environmental noise existed. However, it is expected that these problems will be solved when a sound source is mounted on an unmanned aerial vehicle (UAV). Therefore, we conducted a basic verification experiment to confirm the feasibility of our proposed method this time.

Statement of Contribution/Methods

A flat speaker, an aiming laser pointer and a laser rangefinder are mounted on the prototype UAV. A simulated defect sheet (thickness 1mm) with a different planar scale is buried in the outer wall tile specimen ($2 \times 1.6 \times 0.2 \text{ m}^3$) in the depth of 9 mm from the tile surface. Acoustic wave irradiation experiments from UAV were performed on eight simulated defects (defect size 50 to 200 mm²) in two rows on the upper side of the outer wall specimen. The UAV faced almost to the simulated defect position as shown in Fig.1. The tone burst wave including the flexural resonance frequency of the target defect was used.

Results/Discussion

An example of the result based on the vibration energy ratio in the frequency band used is shown in Fig.2. As can be seen from this figure, all defects are detected. We confirmed that it is possible to detect delamination defects of outer wall tiles by our proposed method utilizing flexural resonance even using a compact sound source that can be mounted on UAV. Therefore, it is expected that it will be possible to carry out long-distance measurement up to the measurable limit of LDV.

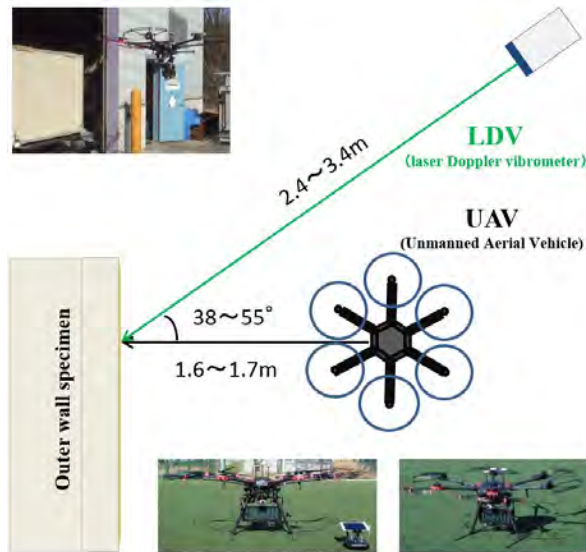


Fig.1. Experimental setup.

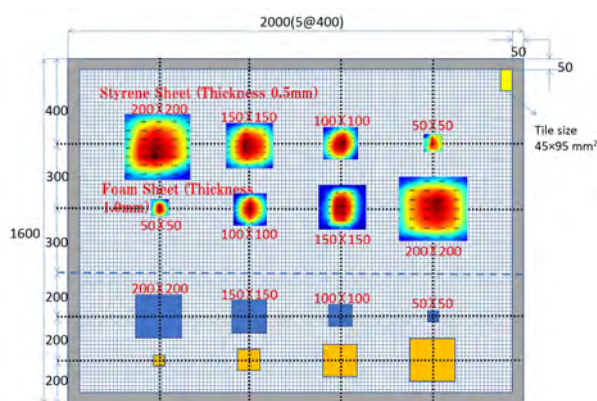


Fig.2. Experimental result.

5:15 PM

Progressive online 3-D SAFT processing by matrix structure exploitation

Fabian Krieg^{1,2}, Rick Pandey², Jan Kirchhof^{1,2}, Alexander Ihlow², Florian Römer¹, Giovanni del Galdo^{2,3}, Ahmad Osman^{1,4}

¹*Fraunhofer Institute for Nondestructive Testing IZFP, Germany*, ²*Technische Universität Ilmenau, Germany*,

³*Fraunhofer Institute for Integrated Circuits IIS, Germany*, ⁴*Hochschule für Technik und Wirtschaft des Saarlandes htw Saar, Germany*

Background, Motivation, and Objective

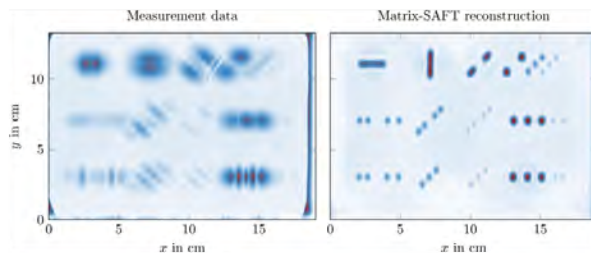
The Synthetic Aperture Focusing Technique (SAFT) is a reconstruction strategy for ultrasonic inspection, which allows the focusing of multiple measurements by superposition. It is usually applied in post-processing due to its high computational demands. Time-critical applications are mostly approached by incorporating elaborate computing infrastructure and massive parallelization. In contrast, the goal of this contribution is to apply SAFT in a progressive manner simultaneous to the measurement process, where the reconstruction is updated with each newly acquired A-scan. Compared to common post-processing schemes this allows to adapt the measurement strategy based on intermediate results and to identify critical regions which require more in-depth investigation at measurement time. The system is meant to be deployed at Fraunhofer-IZFP to aid engineers at complicated measurement tasks.

Statement of Contribution/Methods

It is known that time-domain SAFT can be formulated as matrix-vector product, where all geometric information is encapsulated in a huge structured matrix. Based on this, we show how these multilevel Block-Toeplitz matrices can be implemented and evaluated efficiently, rendering the reconstruction feasible both memory- and computation-time-wise. Furthermore, we extend the scheme by a consecutive decomposition and masking of the matrix. By appropriate selection of a subset of the defining tensors of the matrix, the reconstruction can be updated memory-efficiently and time-efficiently with each newly recorded A-scan.

Results/Discussion

We derive an efficient time-domain SAFT scheme that exploits redundancy imposed by geometrical constraints for a planar cartesian setup. This new approach provides the same results as the naive one. However, computational and memory requirements can be reduced significantly. A comparison of the implementations schemes is given based on measurement data.



6H - Ultrasonic Transducer & Sensor

Nunobiki (150)

Thursday, October 25, 8:00 am - 9:30 am

Chair **Mauricio Pereira da Cunha**
University of Maine

6H-1

8:00 AM Fabrication of transparent capacitive micromachined ultrasonic transducers (CMUTs)

Zhenhao Li¹, Afshin Kashani Ilkhechi¹, Roger Zemp¹

¹University of Alberta, Canada

Background, Motivation, and Objective

Growing demands of integrating methods of acoustics with optical techniques have prompted the need for transparent ultrasonic transducers. For example, the photoacoustic imaging could benefit from trans-illumination through the transducer for high SNR imaging. Capacitive micromachined ultrasonic transducer (CMUT) technology offers advantages of wide bandwidth, precise array-fabrication and feasibility for CMOS integration. However, CMUTs are typically fabricated with non-transparent materials. Recently, CMUTs transparent in the visible wavelength range were reported, but the operational frequency is less than 100 kHz with poor sensitivity to high-frequency photoacoustic signals. Therefore, our work is focusing on producing transparent CMUTs for future photoacoustic imaging applications.

Statement of Contribution/Methods

We fabricated CMUTs using glass substrate and indium-tin-oxide (ITO) electrodes, which have more than 80% transparency in the visible range. Adhesive wafer bonding was applied using photosensitive benzocyclobutene (BCB) as both the adhesive layer and the structural layer. Vacuum cavities with diameters of less than 50 μm and a sub-micron-level cavity depth were patterned in the BCB layer and sealed by a layer of low pressure chemical vapor deposited silicon nitride film. The transparency of the CMUTs is measured with a spectrophotometer in the visible range. The C-V response and the impedance of the CMUTs are measured in-air with a semiconductor characterization system to demonstrate the functionality.

Results/Discussion

As can be found from Figure 1, we demonstrated the feasibility of fabricating CMUTs with the feature size of sub-hundred-micron level targeting an operational frequency in the MHz range. Based on the results from spectrophotometer tests, a CMUT structure that contains layers of glass, ITO, BCB and silicon nitride showed a transparency of about 70% to 90% in the wavelength range from 515 nm to 1055 nm. This attractive feature suggested the possibility of applying CMUTs in photoacoustic imaging and other applications.

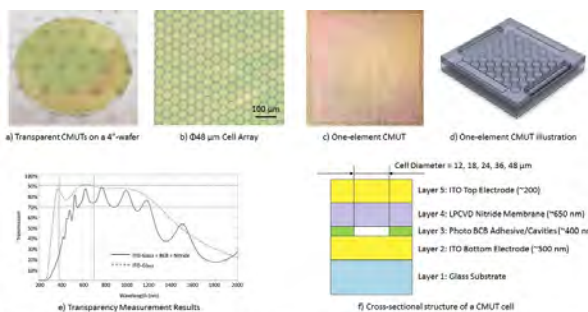


Figure 1 (a) Photo of the transparent CMUTs (b-c) The fabricated CMUTs were placed on a metal plate before taking microscopy images. The scratches on the metal plate surface can be observed through the transparent CMUT. An illustration of a designed one-element CMUT is given in (d). The transparency measurement result is given in (e). The materials used for each layer are explained in the cross-sectional drawing (f).

8:15 AM

Research on Ultrasound-sensitive Ion Channels by using Ultrasound Neuro-modulation ChipXinhui Wang^{1,2}, Wei Zhou¹, Lisheng Xu², Yudong Yao², Lili Niu¹, Long Meng¹, Hairong Zheng¹¹*Paul C. Lauterbur Research Center for Biomedical Imaging, Shenzhen Institutes of Advanced Technology, Chinese Academy of Sciences, China, People's Republic of*, ²*Northeastern University, shenyang, People's Republic of China, China, People's Republic of***Background, Motivation, and Objective**

As a non-invasive method, ultrasound can pass through the intact skull and activate deep brain neurons, gaining increasing attention. Nevertheless, the fundamental mechanisms of ultrasound neuro-modulation have not been elucidated. The nematode *Caenorhabditis elegans* (*C. elegans*) is an excellent model organism and has been widely used in the neurobiology research. Our previous work has shown that mechanical effects of the ultrasound enable to initiate reversal behaviour and activate ASH neurons of *C. elegans*. The aim of the study is to investigate which ion channel responds to ultrasound mechanical stimulation.

Statement of Contribution/Methods

The ultrasound neuro-modulation chip consists of interdigital transducers and an agar plate. The device was fabricated using a standard microelectromechanical system technology, ensuring the stability and repeatability. Worms were transferred from standard culture plates to the surface of agar mounted on the substrate, and recorded the behaviour with a frame rate of 30 fps(Frequency: 22.85MHz; input electronic power 5W; cycle: 180k). Calcium imaging was carried out to investigate which kind of the ion channel could be activated by the ultrasound. Besides, the *mec-4* mutants were stimulated by ultrasound and the behavior was recorded.

Results/Discussion

Fig. 1a and fig. 1b show the neurons of ALM and PLM, having the *mec-4* ion channel, could be activated by ultrasound, with fluorescence increased by 12% and 9% respectively. The results indicate that ultrasound stimulation is similar to general body touch which is referred to *mec-4* ion channel. Furthermore, fig. 1c shows that the *mec-4* mutant has almost no response to ultrasound. There was a statistically significant difference compared to the wild type. The results indicated that the *mec-4* is the main ion channel responded to the ultrasound stimulation and *mec-4* could be transferred to other ultrasound-insensitive neurons, achieving sonogenetics.

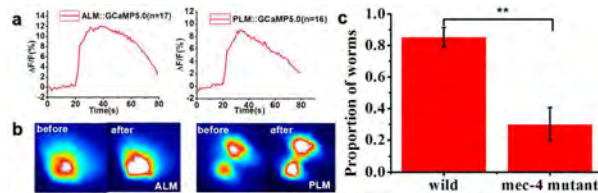


Fig 1. a. ALM and PLM neurons are sensitive to ultrasound stimulation. Average ratio change of fluorescence intensity in ALM and PLM under ultrasound stimulation at $t = 20$ s. b. Fluorescence in the ALM and PLM cell body. False-color images showing the changes in GCaMP5.0 fluorescence in ALM and PLM neurons responding to the ultrasound stimulation. Warmer colours indicate Ca^{2+} elevations in ALM and PLM neurons. c: The proportion of worms displaying reversal is 83.33% for the wild type group while that of the *mec-4* mutant group is 30%. All behavioural data were analysed using the Fisher's exact test, with error bars showing the standard error of the proportion. The difference between the two groups is statistically significant ($p < 0.01$).

8:30 AM

Novel pMUT-Based Acoustic Duplexer for Underwater and Intra-Body Communication

Flavios Pop¹, Bernard Herrera¹, Guofeng Chen¹, Emrecan Demirors¹, Raffaele Guida¹, Cristian Cassella¹, Tommaso Melodia¹, Matteo Rinaldi¹

¹*Northeastern University, Boston, MA, United States*

Background, Motivation, and Objective

pMUTs have been explored for medical imaging, power transfer and fingerprint sensors. For underwater and intrabody communication, these devices have been less explored since their quality factor, compared to conventional PZTs, translates into less transferred energy and less efficient communication. In this work, a novel pMUT-based acoustic duplexer that enables large data-rates and full-duplex operation in intra-body and underwater data-links is proposed.

Statement of Contribution/Methods

This work demonstrates for the first time an acoustic duplexer based on Aluminum Nitride pMUTs as radiating elements. The duplexer has the function of efficiently separating independent data-streams coming from the transmit and receive modules while minimizing the noise injected in the channel through the achievement of large out-of-band rejections (Fig. 1). As a result, this permits to reach levels of bit-error-rates (BER) that are comparable to those achieved through the use of commercial PZT transducers (Fig. 2). Furthermore, the simultaneous use of two communication bands allows much higher data-rates than traditional resonant approaches, thus enabling much larger data throughputs.

Results/Discussion

The transmission power of the full system has been characterized (Fig. 1). Once the duplexers are added to the pMUT arrays, both the power transfer and frequency selectivity improves by rejecting the out-of-band signal. An Orthogonal Frequency-Division Multiplexing with Binary Phase-Shift Keying is implemented using two Universal Software Radio Peripherals (Fig. 2 inset). This demonstrates the capability of the duplexer to simultaneously transmit and receive on different bands using a single pMUT array. Furthermore, for levels of $\text{BER} > 10^{-4}$, standard videos can be transmitted.

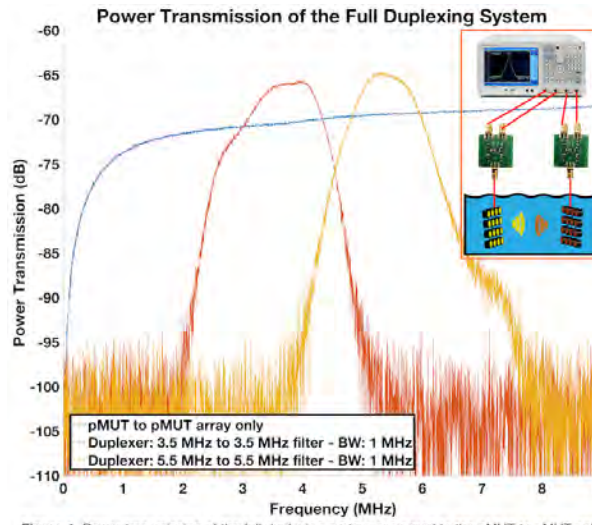


Figure 1. Power transmission of the full duplexing system compared to the pMUT to pMUT-only link. Two communication bands can be distinguished (3.5 MHz and 5.5 MHz). The power transmission and the out of band rejection, compared to the pMUT only, improves. In the inset is shown the measurement setup. A network analyzer is connected to the duplexer PCB boards, connected to the pMUT arrays and submerged in a water tank.

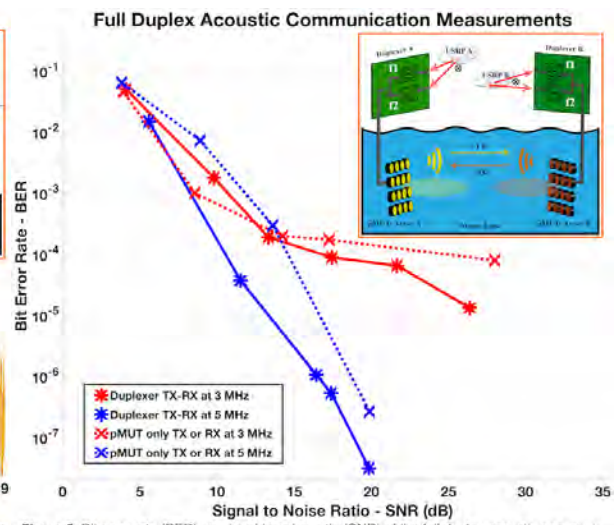


Figure 2. Bit error rate (BER) vs. signal to noise ratio (SNR) of the full duplex acoustic communication system. The measurements are done for the pMUT-only link for each transmission band and compared to the simultaneous transmission with the duplexers on the same bands. In the inset, the communication set-up is shown. Two Universal User Software Radio Peripherals (USRP) are used to implement simultaneous transmit and receive on two different bands.

8:45 AM

Immersion PMUTs Fabricated with a Low Thermal-Budget Surface Micromachining ProcessGuo-Lun Luo¹, Yuri Kusano¹, David Horsley¹¹*University of California, DAVIS, CA, United States***Background, Motivation, and Objective**

High fill-factor PMUT arrays yield higher pressure output. Earlier PMUT arrays required through-wafer DRIE to form released membranes, causing large space between PMUTs and resulting in low fill-factor (34%) [1]. In [2], we demonstrated a surface micromachining process to fabricate PMUT arrays with small inter-PMUT spacing. However, unbalanced stresses in the multi-layer structure resulted in low manufacturing yield, and non-optimal layer thicknesses resulted in small transmit amplitude. Here, we propose a new fabrication process with in-situ vacuum sealing resulting in high fill-factor PMUTs with good acoustic matching for immersion.

Statement of Contribution/Methods

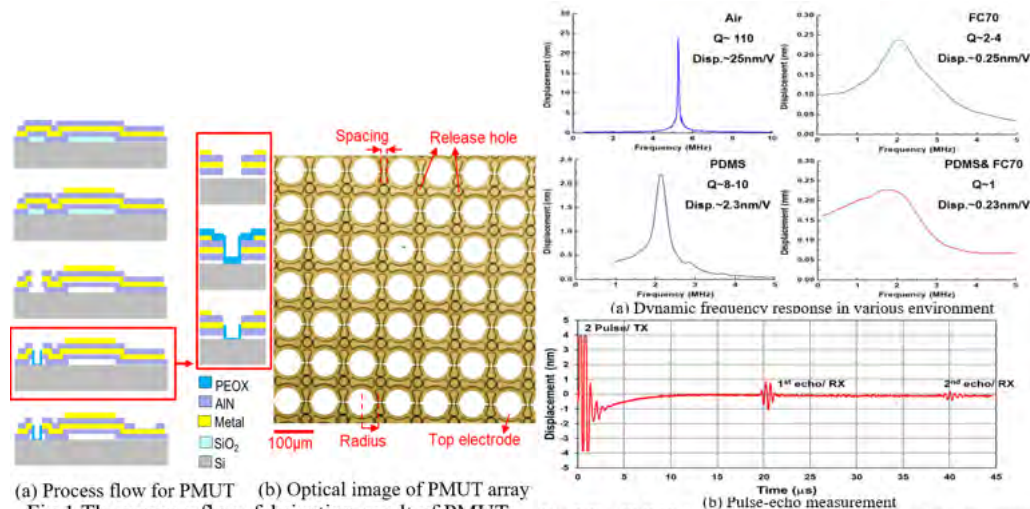
The new process, Fig. 1a, enables PMUTs with a minimum spacing of 10 μm , resulting in 64% fill-factor, Fig. 1b, 2X larger than in [1]. The AlN-AlN unimorph structure was designed to achieve 10X larger displacement and, compared to earlier AlN-SiO₂ structures, the symmetric AlN-AlN laminate results in lower residual stress and higher manufacturing yield. The structure is in-situ vacuum sealed in a SiO₂ PECVD reactor, enabling fluid-immersion of arrays. After sealing, the array is coated with a 100 μm thick PDMS, and pulse-echo experiments were conducted using LDV to monitor PMUT transmit and receive vibrations.

Results/Discussion

Fig.2a shows the PMUT frequency response in air and immersed in fluid, where a 65% bandwidth is achieved. Fig.2b shows pulse-echo measurements with the echo around 1.3 kPa for a 7x7 array. Relative to [2], this work has improved the pressure output 3X and doubled the bandwidth.

[1] J. Jung et al., *J. Micromech. Microeng.*, 23, 125037, 2013.

[2] G. Luo et al., *TRANSDUCERS 2017*, pp. 1053-1056.



9:00 AM

Neuronal stimulation and calcium imaging of retinal neurons using surface acoustic waves**Melanie Stamp^{1,2,3}, Wei Tong¹, David Garrett¹, Christoph Westerhausen^{3,4}, Steven Prawer¹, Achim Wixforth^{3,4}**¹*School of Physics, University of Melbourne, Melbourne, Australia*, ²*University of Augsburg, Germany*, ³*Nanosystems Initiative Munich, Munich, Germany*, ⁴*Physics, University of Augsburg, Augsburg, Germany***Background, Motivation, and Objective**

Given the lack of treatment for many neurological disorders, devices that interact with neural systems such as hearing or vision are in high demand. These devices communicate with the nervous system and have the potential to bypass damaged or diseased tissue and return function to the user. For example, retinal stimulation devices are of benefit to people with retinal diseases, which result in a loss of photoreceptors with retinal ganglion cells and other neuronal elements still remain viable and can respond to electrical stimulation.

Electrical stimulation of retinal neurons leads to neuron signal translation through the optic nerve to the visual cortex. A bionic prosthesis can restore a sense of vision to blind users. To investigate if cells can be triggered by an electrical signal, calcium imaging techniques are applied. Fluorophores that respond to changes in calcium concentration are introduced into neurons. When neurons fire, the calcium concentration inside the neuron changes dramatically. Thus, neuronal depolarization can be optically detected using these fluorophores. Introducing these large fluorophores into neurons, in particular into whole tissue, can result in a high incidence of cell death. A facile method to introduce fluorophore dyes into whole neuronal tissue without killing cells will be a highly valuable technique in electrophysiology. A common method in nano drug delivery is the use of acoustic wave driven systems for particle uptake or ultrasonic, cavitation bubbles to interact and penetrate cell membranes.

Statement of Contribution/Methods

We here present a new approach based on acoustic driven pumping systems for dynamic stimulation of calcium stain uptake in neurons and mammalian cells. Using acoustic streaming, we induce a modulated and well-defined pressure field on cells to open pores in the membrane and transport calcium ion based fluorescent dye into the cells. In addition, we create a microfluidic mixing via acoustically driven chaotic advection.

In a miniaturized lab-on-a-chip system, surface acoustic waves are excited on optical transparent chips to induce acoustic streaming. Retina cells inside the device are locally exposed to a shear spectrum ranging from 0 to 8000 s⁻¹. As we employ optical transparent piezo-electric materials like LiNbO₃, the experiments allow for live video observation. A successful dye-uptake is then measured and quantified via fluorescence microscopy.

Results/Discussion

Our results indicate that cells exposed to acoustic streaming show an up to 20% higher dye uptake compared to control samples. Simulations show the particles are well distributed due to the chaotic advection whereas in the control sample, particles are only distributed via diffusion. Further research will provide insight of the SAW induced shear flow and the advanced dye uptake in cells.

9:15 AM

Evaluation of SH-SAW Biosensor in Whole BloodKoji Kano¹, Takashi Kogai¹, Hiromi Yatsuda¹, Szu-Heng Liu², Yi-Qi Huang², Yu-Tung Huang², Pei-Jer Chen³¹*Japan Radio Co., Ltd., Fujimino-shi, Japan*, ²*TAI-SAW TECHNOLOGY CO., LTD., Taiwan*, ³*Graduate Institute of Clinical Medicine, National Taiwan University College of Medicine, Taiwan***Background, Motivation, and Objective**

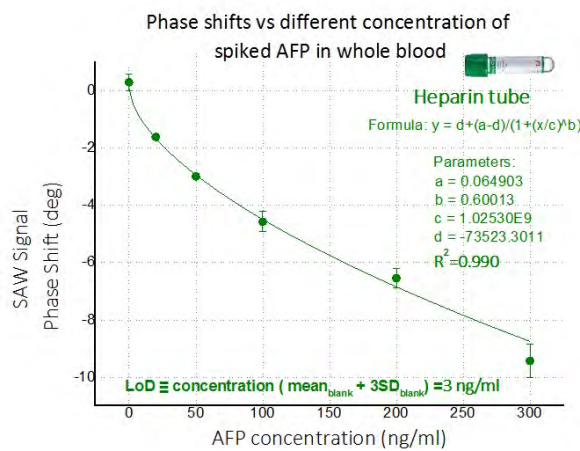
Infectious diseases, including HIV, Hepatitis, Influenza and Zika virus, are transmitted to patients subconsciously and become epidemic unpredictably. Once epidemics happened, it brings not only health sufferings, but also economic losses, infectious diseases are serious threats to human being. In fighting to infectious diseases, early case detection is considered important to prevent epidemics. To increase early diagnostics efficiency, patient side analysis, which is conducted outside of hospital, become considerably important. In this kind use, diagnostic devices are required different features from conventional hospital use analyzers, such as mobility and operability in the field. Shear-Horizontal SAW(SH-SAW) based immunoreaction biosensor is one of the promising devices in this kind application. Distinctive feature of SH-SAW biosensor is to be able to detect immunoreaction without bond/free(B/F) separation. This feature makes SH-SAW sensor a dominant candidate in the mobile diagnostics.

Statement of Contribution/Methods

To confirm SH-SAW biosensor potential in mobile diagnostic applications, measurement capability with and without B/F separation in a typical antigen-antibody reaction is compared. The comparison is conducted by applying an antigen diluted specimen onto a quartz-based 250MHz SH-SAW sensor surface which is coated with specific antibody to the antigen. The diluent for the antigen contains different concentration of Bovine Serum Albumin(BSA) to rehearse an impurities interaction which is assumed in the actual usage. After confirmation of fundamental properties, a practicality in pre-clinical tests is evaluated by measuring Alpha-fetoprotein(AFP) which is widely used as a diagnostic marker for hepatocellular carcinoma. The AFP evaluation measures antigen spiked whole blood(AFP-WB). Before AFP-WB applying onto SH-SAW sensor, 20nm gold particle conjugated antibody is mixed with AFP-WB to amplify signal. AFP measurement is accomplished by one step process.

Results/Discussion

Measured result is shown in the graph. Clear correlation between spiked AFP concentration and SH-SAW biosensor 5 min. phase-shift is observed. Also, Limit of Detection(LoD) which shows the lowest distinguishable target analyte concentration of SH-SAW system is 3ng/mL. These results suggest SH-SAW sensor has promising potential in POCT field.



6I - Multi-Parametric and Multi-Wave Tissue Characterization

Nunobiki (150)

Thursday, October 25, 10:30 am - 12:00 pm

Chair **Roberto Lavarello**
Pontificia Universidad Católica del Perú

6I-1

10:30 AM In vivo assessment of interstitial fibrosis in renal allografts using quantitative ultrasound – comparison with estimated glomerular filtration rates

Roberto Lavarello¹, Gabriela Torres², Carolina Amador³, Sara Aristizabal⁴, Maria Luisa Montero⁵, Andrew Rule⁶, Naim Issa⁷, Thomas Atwell⁸, Matthew Urban⁹

¹Departamento de Ingeniería, Pontificia Universidad Católica del Perú, Lima, Peru, ²Joint Department of Biomedical Engineering, The University of North Carolina at Chapel Hill, NC, United States, ³Ultrasound Imaging and Interventions, Philips Research North America, United States, ⁴Well Living Lab, United States, ⁵Departamento de Ciencias, Pontificia Universidad Católica del Perú, San Miguel, Peru, ⁶Division of Nephrology and Hypertension, Department of Internal Medicine, Mayo Clinic, MN, United States, ⁷Division of Nephrology and Hypertension, Department of Internal Medicine, Mayo Clinic, MN, United States, ⁸Department of Radiology, Mayo Clinic, MN, United States, ⁹Department of Radiology, Mayo Clinic, Rochester, MN, United States

Background, Motivation, and Objective

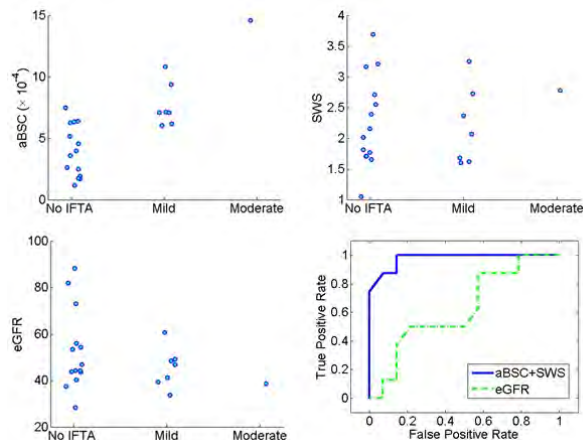
Renal transplant is the preferred long-term treatment for end-stage renal disease. Graft survival and renal function are monitored over the course of the graft's life using blood tests, medical imaging and renal biopsy. The estimated glomerular filtration rate (eGFR) is often used as a surrogate marker of kidney function, and is calculated using equations that include the serum creatinine (SCr) or serum cystatin C levels, age, race, sex, and body size. However, previous studies suggest that eGFR is a poor predictor of early histopathologic changes in renal allografts. In this study, the performance of quantitative ultrasound using the average backscatter coefficient (aBSC) and shear wave speed (SWS) estimates was compared against eGFR for the detection of interstitial fibrosis in renal allografts.

Statement of Contribution/Methods

Data were obtained from 22 renal transplant patients scheduled for protocol biopsies. Experiments were performed using a General Electric Logiq E9 with a C1-6-D curvilinear array transducer operating in Comb-push Ultrasound Shear Elastography mode. Both SWS and aBSC from each recipient's kidney was estimated from the same datasets. Kidney biopsies were obtained, and the degree of interstitial fibrosis (ci) was scored as absent (ci=0, N=14), mild (ci=1, N=7), and moderate (ci=2, N=1). The SCr level at the time of the biopsy was measured and the IDMS-traceable Modification of Diet in Renal Disease (MDRD) study equation was used to calculate the eGFR. Classification between the ci=0 and ci>0 groups was performed using linear logistic regression.

Results/Discussion

The aBSC ($\text{in } \text{sr}^{-1} \cdot \text{cm}^{-1}$), SWS (in m/s), and eGFR (in mL/min/1.73m²) values from all allografts are shown in the figure, together with the ROC curves when using aBSC and SWS values and eGFR values. The model that uses both aBSC and SWS obtained an accuracy of 0.91 and an area under the curve (AUC) of 0.98 when differentiating between allografts with and without interstitial fibrosis. In contrast, the use of the eGFR resulted in an accuracy of 0.59 and an AUC of 0.63. These results suggest that multi-wave QUS may be a useful tool for the non-invasive diagnosis of renal interstitial fibrosis and may provide a superior performance when compared to currently available blood tests. This research was supported by grant 012-2014- FONDECYT-C1 from the Peruvian government and R01DK092255 from the NIDDK.



10:45 AM

Evaluation of the microstructural changes occurring in the myopic sclera using high-frequency quantitative ultrasound

Jonathan Mamou¹, Sally A. McFadden², Quan V. Hoang^{3,4}

¹*F. L. Lizz Center for Biomedical Engineering, Riverside Research, New York, NY, United States*, ²*Hunter Medical Research Institute and School of Psychology, Faculty of Science, University of Newcastle, Newcastle, Australia*,

³*Department of Ophthalmology, Columbia University Medical Center, New York, NY, United States*, ⁴*Singapore Eye Research Institute, Singapore National Eye Centre, DUKE-NUS, Singapore, Singapore*

Background, Motivation, and Objective

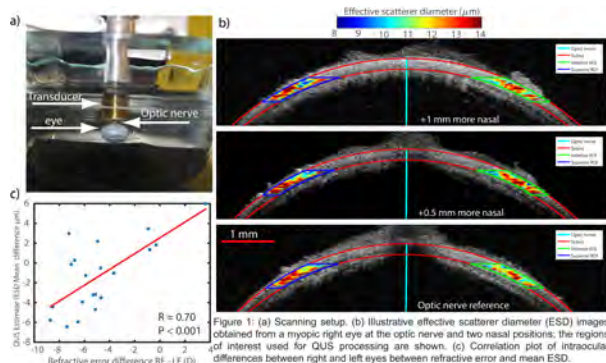
Myopia is a condition that affects up to 2.3 billion people. In myopia, images are focused anterior to the retina. More than 95% of myopia cases result from excessive axial eye length. Although minimal levels of myopia are considered a minor inconvenience, high myopia is associated with sight-threatening pathology in 70% of patients. Anatomic changes underlying eye elongation and vision-threatening staphyloma formation may occur in the posterior sclera. Therefore, high-frequency quantitative ultrasound (QUS) was applied to eyes of a guinea pig model of myopia to investigate whether QUS estimates can sense the microstructural changes in the sclera during myopia development.

Statement of Contribution/Methods

21 guinea pigs were form-deprived in the right eye (RE) from 5 to 20 days of age to induce myopia. At 20 days, refractive error and axial length were measured *in vivo*. Following euthanasia, both eyes were enucleated, immersed in PBS, and anchored in a normal anatomical position with corneal sutures (Fig. 1a). 3D RF data were collected from 41 eyes by raster scanning an 80-MHz transducer focused in the posterior sclera of the eye. The transducer had a focal length of 2.2 mm, an f-number of 2, and a -6-dB bandwidth extending from 41 to 109 MHz. The mean and standard deviation of 4 QUS estimates were computed from the RF data in 6 regions of the posterior sclera (Fig. 1b). Effective scatterer diameter (ESD) and acoustic concentration (EAC) were derived by fitting a Gaussian scattering model to the backscatter coefficient, and Nakagami shape and scale were derived using a maximum-likelihood estimator. Regression and correlation analyses were used to determine whether QUS estimates showed contrast between control and myopic eyes or were correlated with axial length or refractive error.

Results/Discussion

Statistically significant contrast existed between control left eyes (LEs) and myopic REs for several QUS estimates. The standard deviation of ESD was larger in LEs (i.e., $1.88 \pm 0.41 \mu\text{m}$) than REs (i.e., $1.63 \pm 0.34 \mu\text{m}$, $p < 0.05$). Significant correlation occurred between intraocular differences (i.e., LE minus RE) in values of the refractive error and mean ESD ($R = 0.70$, $p < 0.001$, Fig. 1c). These results indicate that QUS can provide novel information about the microstructure of the myopic sclera and can provide new biomarkers for monitoring and managing high-myopia patients.



11:00 AM

Multi-parametric Acoustic Imaging of Cervical Insufficiency

Yan Yan¹, Maryam Basij¹, Zhijie Wang¹, Adeel Siddiqui¹, Edgar Hernandez-Andrade^{2,3}, Sonia Hassan^{2,3}, Ali Alhousseini², Nardhy Gomez-Lopez², **Mohammad Mehrmohammadi¹**

¹Biomedical Engineering, Wayne State University, Detroit, MI, United States, ²Obstetrics and Gynecology, Wayne State University, Detroit, MI, United States, ³Perinatology Research Branch, Wayne State University, Detroit, MI, United States

Background, Motivation, and Objective

Spontaneous preterm birth (sPTD) is a dangerous health problem for newborns, and this occurs in about 10% of the births in the United States [1]. In standard health care, the approach for determining the risk of sPTD is measuring the cervix length. We propose that by using ultrasound (US) and photoacoustic (PA) imaging to detect features of the cervical tissue, more accurate detection of cervix ripening can be provided, and this can potentially lower the risk of sPTD.

Statement of Contribution/Methods

An integrated endocavity US and PA imaging system (ECUSPA), which consists of a transvaginal US transducer and an optimized integrated light delivery system (using fiber optics), has been designed and characterized. We determined that the US microstructural features, such as effective scatterers diameter (ESD) and effective scatterers acoustic concentration (EAC), could be used to obtain the orientation and integrity of the collagen fibers network in the cervix. For PA features, we collected broad-spectroscopy PA (sPA) information ($\lambda=1150$ to 1650 nm) from a set of pregnant mice cervices at gestational age (GA) of 13.5 to 19.5 days. We determined that the sPA was sensitive to collagen-water ratio changes, and we also observed sPA amplitude changes while the collagen fiber disorganized. Furthermore, in a set of ex-vivo experiments, controls of the scatter of the collagen fibers were applied to confirm that the scattering properties of the collagen network affected the sPA amplitude. These results were cross-checked with histology studies. The collagen concentration was detected by chemical staining, and the fiber polymerization of the collagen was shown with a 20X polarized light microscope.

Results/Discussion

From the experimental results, we determined that ESD and EAC could be used to indicate when the acoustic waves were transmitted parallel and perpendicular to the orientation of the fibers. The sPA showed that the collagen-water ratio decreased when the mice got close to delivery. The observed degradation of the collagen signal is likely to be the result of the change in scattering properties of the tissue. In addition, the water content of the ripened tissue is increased and could be well visualized in sPA imaging. Therefore, with combined sPA and histologic analysis, we can conclude that collagen fiber degradation can be detected and visualized by sPA imaging (**Figure 1**).

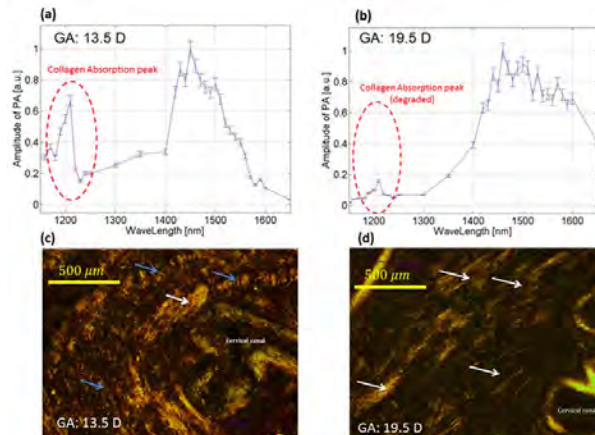


Figure 1: (a) and (b) Photoacoustic signal amplitudes and wavelengths from cervical tissues of pregnant mice 13.5 and 19.5 days. The collagen absorption peak around 1200 nm degraded along the cervix ripening. (c) and (d) Transversal slide of mouse uterus, at 13.5 and 19.5 days of gestation, stained with Sirius Red and observed under polarized light with 20x magnification. The position of the cervical canal or lumen is indicated as the reference. Organized concentric fibers of collagen that can be observed as rods of variable diameter (blue arrows); some of them have the appearance of disaggregated or ripened fibers (white arrow).

11:15 AM

Acoustically stimulated electromagnetic imaging in biomedical tissuesKenji Ikushima¹, Hisato Yamada¹, Nobuo Niimi², Yoshitsugu Kojima², Yutaka Yabe³, Yoshihiro Hagiwara³¹*Department of Applied Physics, Tokyo University of A & T, Japan*, ²*Nippon Sigmax, Japan*, ³*Department of Orthopaedic Surgery, Tohoku University School of Medicine, Japan***Background, Motivation, and Objective**

Ultrasonic techniques are widely used in medical and industrial fields. Because reflected or transmitted ultrasonic waves are usually measured, the majority of existing applications are restricted to diagnosing structural or elastic properties of matters. In recent years, however, electric or magnetic properties have been successfully visualized by ultrasonic focusing and scanning. The principle of this technique is based on the generation and detection of acoustically stimulated electromagnetic (ASEM) waves through electro- or magneto-mechanical coupling [1]. In the ASEM method, electric or magnetic polarization is temporally modulated with the radio frequency (rf) of irradiated ultrasonic waves. The EM response emitted from a focal spot of ultrasonic beams are sensitively detected using a narrow-band tuned antenna. In ferromagnetic materials typified by steel, magnetic imaging and local hysteresis measurements have been performed[2-4].

In this paper, we focus on the ASEM response in biomedical tissues. Owing to the ubiquity of electromechanical coupling attributed to collagen fibrils, the ASEM method may find broad application in biological and clinical researches. We here present the experimental results of ASEM imaging in artificial skin (collagen sheet), bone and fibrotic heart due to myocardial infarction (MI).

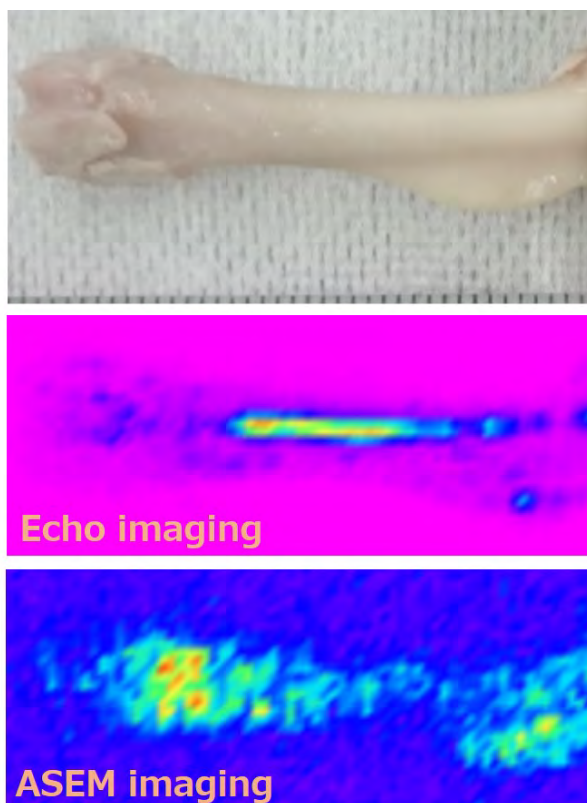
Statement of Contribution/Methods

A rectangular 50 ns wide pulses are applied at a repetition rate of 1 kHz by a pulser/receiver. The signals are measured by using a capacitive resonant antenna, in which the electric polarization parallel to the irradiated longitudinal-wave direction is detected.

Results/Discussion

The ASEM response is successfully observed in 0.3mm-thick collagen sheets, normal and decalcified bones (rat femur). The signal amplitude in the decalcified bone is comparable to that in a normal bone, indicating that the origin of ASEM response in bone is attributed to the collagen fibrils. Furthermore, it is turned out that the signal amplitude has a tendency to be reduced in osteoporosis models. We will also discuss the potential applications for non-invasive MI detection of heart.

[1] K. Ikushima *et al.* Appl. Phys. Lett. 89, 194103 (2006). [2] H. Yamada *et al.*, Rev. Sci. Instrum. 84, 044903 (2013). [3] H. Yamada *et al.*, Jpn. J. Appl. Phys. 54, 086601 (2015). [4] H. Yamada *et al.*, Jpn. J. Appl. Phys. 57, 07LB09 (2018).



11:30 AM Carotid artery plaque components classification using homodyned-K parametric maps, elastograms and echogenicity analysis

Marie-Hélène Roy Cardinal¹, François Destrempe¹, Gilles Soulez¹, Guy Cloutier¹

¹*University of Montreal Hospital, Canada*

Background, Motivation, and Objective

Multiple quantitative ultrasound (QUS) features are available from a single ultrasound radiofrequency (RF) acquisition. The objective was to test if the combination of homodyned-K (HK), elastogram, and echogenicity features could improve carotid artery plaque components characterization compared to these same features taken separately.

Statement of Contribution/Methods

Thirty-one patients with carotid atherosclerotic plaques underwent magnetic resonance imaging to quantify plaque components (lipid and calcium content). Ultrasound RF data acquisitions were performed on patients and were used to compute HK parametric maps, strain elastograms, and B-mode gray level (GL) images. QUS features were extracted from these maps. Classification tasks were then performed to detect: a large area of lipid; a small area of lipid; and a large area of calcification. Feature selection and classification were based on a random forest machine learning algorithm. A maximum of 3 features per classification task was used to avoid overfitting of the data. The 0.632+ bootstrap and Jackknife methods were used, respectively, to compute area under ROC curves (AUC) and 95% confidence intervals (CI).

Results/Discussion

Fig. 1 shows examples of parametric maps. For detection of a large area of lipid, the highest AUC (0.90, CI 0.80 - 0.92, p<0.001) was obtained with combined HK, elastography and B-mode GL features; for a small area of lipid, the highest AUC (0.79, CI 0.77-0.83, p=0.022) was based on elastography and B-mode GL features. To detect a large area of calcification, the highest AUC (0.95, CI 0.94 - 0.96, p<0.001) was obtained with HK, elastography and B-mode GL features. When using elastography features only in the classification tasks, AUCs decreased by 2% to 17% (p<0.001). AUCs also decreased by 1% to 7% (p<0.05) when HK and B-mode GL features were used without elastography. Combining different QUS features extracted from the same RF sequence significantly increased the accuracy of classification.

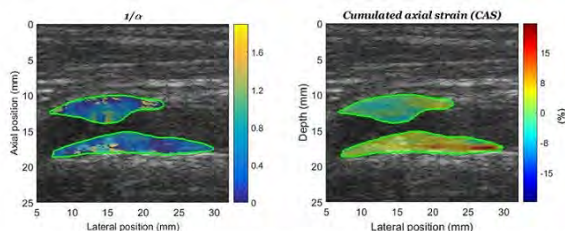


Fig. 1 Example of a HK parametric map ($1/\alpha$ in logarithmic scale) and of an elastogram (CAS: cumulated axial strain) of a plaque on the near and far walls of the carotid artery superimposed on a longitudinal B-mode image. A lower value of $1/\alpha$ indicates a greater acoustical homogeneity. CAS was cumulated during the diastolic phase of the cardiac cycle.

11:45 AM Fatty liver assessment using ultrasound multifeatures based on machine learning

YingHsiu Lin¹, CheWei Chu², PoHsiang Tsui¹¹*ChangGung University, Taiwan*, ²*National Taiwan University, Taiwan***Background, Motivation, and Objective**

Nonalcoholic fatty liver disease (NAFLD) is a type of hepatic steatosis that results in advanced liver diseases. Ultrasound imaging provides fast screening and qualitative descriptions of NAFLD. To assist in the diagnosis by physicians, quantitative evaluation of NAFLD is highly required clinically. Note that liver steatosis results in changes in several sonofeatures, including echo intensity, attenuation, and speckle pattern. Therefore, compared to using the individual feature, combination of the above three sonofeatures may provide more clues and physical meanings to improve the accuracy for NAFLD examinations. In this study, we proposed a machine learning-based diagnostic approach based on ultrasound multifeatures for the assessment of NAFLD.

Statement of Contribution/Methods

The patients with different degree of steatosis were recruited and divided into two groups: Groups A (n=111) and B (n=74) were used for training and testing in the analysis of machine learning, respectively. For each patient, the percentage of liver steatosis was estimated using pathological section images ($>10\%$ was used to identify diseased cases). A commercial ultrasound scanner equipped with a 3-MHz convex transducer was used to acquire envelope data for calculating the parameters, including the integrated backscatter (IB, a measure of echo intensity), Q factor (proposed as a new estimate of frequency downshift due to attenuation), and homogeneity factor (HF, a new parameter proposed to describe the speckle pattern). Support vector machine (SVM) based on different kernel functions (linear, radial basis function (RBF), and polynomial) was used to combine the above three parameters for comparisons of accuracies between single- and multifeatures in NAFLD assessment.

Results/Discussion

Each parameter is able to discriminate between normal and fatty patients. Importantly, SVM-based multifeatures approach allows characterization of NAFLD with the highest accuracy (86.49%) and area under the receiver operating characteristic curve (AUROC; 0.8899). Ultrasound multifeatures based on machine learning improve the accuracy for NAFLD diagnosis.

Table. 1 The accuracies of ultrasound multifeatures using different kernels. f (•): function of SVM.

| | Feature Select | linear | RBF | poly |
|---------------------|---------------------|--------|--------|--------|
| Accuracy (%) | f(IB) | 77.03 | 77.03 | 81.08 |
| | f(Q factor) | 68.92 | 64.86 | 68.92 |
| | f(HF) | 79.73 | 79.73 | 79.73 |
| | f(IB, Q factor) | 79.73 | 81.08 | 82.43 |
| | f(IB, HF) | 83.78 | 81.08 | 81.08 |
| | f(Q factor, HF) | 78.38 | 77.03 | 78.38 |
| f(IB, Q factor, HF) | f(IB, Q factor, HF) | 86.49 | 86.49 | 86.49 |
| | Cut-off value | 0.6363 | 0.6448 | 0.6363 |
| | Sensitivity (%) | 92.86 | 92.86 | 92.86 |
| | Specificity (%) | 66.67 | 66.67 | 66.67 |
| | LR ⁺ | 2.79 | 2.79 | 2.79 |
| | LR ⁻ | 0.11 | 0.11 | 0.11 |
| | PPV (%) | 89.66 | 89.66 | 89.66 |
| | NPV (%) | 75 | 75 | 75 |
| | Accuracy (%) | 86.49 | 86.49 | 86.49 |
| AUROC | | | | |
| 0.8899 | | | | |

6J - New Class of SAW Device

Nunobiki (150)

Thursday, October 25, 1:30 pm - 3:00 pm

Chair **Clemens Ruppel**

6J-1

1:30 PM Prof. Eric Adler's Legacy to Microwave Acoustics

Mauricio Pereira da Cunha^{1,2}

¹*Dept. of Electrical and Computer Engineering, University of Maine, Orono, ME, United States*, ²*Laboratory for Surface Science and Technology, University of Maine, Orono, ME, United States*

Background, Motivation, and Objective

Eric passed away on November 06, 2017, after a long and bright career in microwave acoustics that helped, inspired and motivated students and colleagues. Advisor, mentor, righteous guide, friend, clear, sharp, focused and objective in addressing any situation or problem, always ready to listen and ponder. What else could one ask from an outstanding engineer, educator, colleague, and friend? As his last doctoral student before his retirement, I had the opportunity to enjoy all those qualities in a mix of blessed opportunities. Eric retired in 1995, one year after I finished my PhD, and I certainly did not want to let him step down in peace. I was fortunate to continue to discuss technical issues with him for more than a decade after his retirement.

Statement of Contribution/Methods

Eric's contributions to our society were significant. His 2001 Achievement Award of the IEEE Ultrasonics, Ferroelectrics, and Frequency Control Society rightfully reads "*For his extensive contributions to the understanding and analysis of bulk, surface and pseudo-surface acoustic waves in single crystals and layered structures, and his years of service to the Society.*" Advised on his PhD by Gerry Farnell, Eric co-authored with him fundamental papers and chapters on bulk, surface, and pseudo-surface acoustic wave propagation on anisotropic crystal, and crystal orientations and properties. Throughout several decades, his work broadened to encompass surface, bulk, and multilayer thin film propagation and transduction modeling, which led to several of the current microwave acoustic device applications in frequency control, sensors, and mobile systems that we enjoy today.

Results/Discussion

Eric's impressive credentials include being an electrical engineer educator since the late 1950's; Professor Emeritus; Associate Dean (Academic) at McGill Faculty of Engineering; IEEE Fellow; IEEE UFFC Distinguished Lecturer; UFFC-Society Adcom member; and reviewer for this conference, IEEE UFFC transactions, and other acoustic wave journals. Even though Eric's physical presence and mentorship will be missed in our day-to-day activities, we will continue to benefit from his past service, research, publications, and acoustic wave propagation and modeling programs. His legacy to our society and our field will remain strong, and continue to guide researchers and students throughout the world.



2:00 PM Suprious-Free, Near-Zero-TCF Hetero Acoustic Layer (HAL) SAW Resonators Using LiTaO₃ Thin Plate on QuartzMichio Kadota¹, Yoshimi Yunoki¹, Takehito Simatsu², Miyuki Uomoto², Shuji Tanaka¹¹*Graduate school, Tohoku university, Sendai, Japan*, ²*FRIS, Tohoku University, Sendai, Japan***Background, Motivation, and Objective**

A better performance (higher $Q k^2$ product and smaller TCF) of acoustic wave devices is continuously required for mobile communication. Recently, new types of acoustic wave devices, Hetero Acoustic Layer (HAL) SAW devices, have been intensively studied by different groups. In our previous study [1, 2], HAL SAW devices with a LiTaO₃ thin plate on a quartz substrate were fabricated, and a very large impedance ratio of 82 dB and a Bode Q as high as 3000 were demonstrated. In this paper, the LT/ quartz HAL SAW resonators are compared with a LiTaO₃/ SiO₂/ Si one to figure out the features.

Statement of Contribution/Methods

42°YX or 20°YX LiTaO₃ is used as a piezoelectric thin plate, and 42°45°Y90°X quartz, 50°Y90°X quartz or thermally-oxidized Si is used as a support substrate. The LiTaO₃ thin plate is 0.44–0.53 μm thick, and the thermal oxide is 1 μm thick. The IDT and grating reflectors are made of Cu. The frequency characteristics were measured from 300 MHz to 14 GHz to investigate far-off-resonance spurious responses. The TCF of the LiTaO₃/ quartz HAL SAW resonators were measured to compared with that of the LiTaO₃/ SiO₂/ Si one.

Results/Discussion

Fig. 1 compares the measured wide-range frequency characteristics of the LiTaO₃/ quartz and LiTaO₃/ SiO₂/ Si HAL SAW resonators. For the LiTaO₃/quartz device, the resonance with an impedance ratio of 73 dB is found around 1 GHz, and there is no significant spurious response up to 14 GHz. For the LiTaO₃/ SiO₂/ Si device, on the other hand, large spurious responses appear at 1.7 and 1.9 GHz. In simulation, the spurious responses approach the main resonance, if the SiO₂ layer becomes thicker to improve TCF. The super-clean frequency characteristic of the LiTaO₃/quartz device is preferable for the synthesis of multiband filters.

Fig. 2 shows the measured temperature characteristics of series resonance frequency for different designs of HAL SAW resonators. The best TCF of +2 ppm/°C was obtained by the device using 0.126λ-thick 42°YX LiTaO₃ on quartz. Comparison in TCF with the LiTaO₃/ SiO₂/ Si device will be discussed in a full paper.

References

- [1] Proc. IEEE Int. Freq. Contr. Symp., 206, 017.
- [2] Proc. IEEE Int. Ultrason. Symp., 5F-5, 2017.

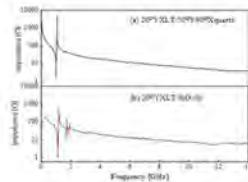


Fig. 1 Wide-range frequency characteristics of HAL SAW resonators with (a) 20°YX LiTaO₃/ 50°Y90°X quartz; and (b) 20°YX LiTaO₃/ SiO₂/ Si structures.

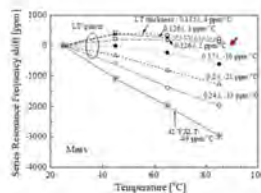


Fig. 2 Temperature characteristics of series resonance frequency of 42°YX LiTaO₃/ 42°45°Y90°X quartz HAL SAW resonators.

2:15 PM

Transverse Modes in I.H.P. SAW Resonator and Their Suppression MethodHideki Iwamoto¹, Tsutomu Takai¹, Yuichi Takamine¹, Takeshi Nakao¹, Toshiyuki Fuyutsume¹, Masayoshi Koshino¹¹Murata Manufacturing Co., Ltd., Nagaokakyo-shi, Kyoto 617-8555, Japan**Background, Motivation, and Objective**

Recently, a multi-layered substrate including a thin piezoelectric crystal plate with SAW energy confinement effect have been studied. Some of the authors reported that a SAW resonator on 50YX LiTaO₃/SiO₂/Si substrate realizes very high-Q and good temperature stability, which is called I.H.P. SAW (Incredible High-performance SAW) [1]. It is known that a simple 42YX LiTaO₃ does not show transverse modes in a resonator structure, such as aluminum electrodes one-port resonator; however I.H.P. SAW resonators reveal transverse mode spurious response. This paper describes causes of generation and a suppression method for the transverse spurious.

Statement of Contribution/Methods

Using finite element method (FEM), slowness curves on the surface were calculated, and it was found that the curve on I.H.P. SAW have been changed by an effects of under-layers. Although the slowness curve profile for 42YX LiTaO₃ is a concave shape in the vicinity of the propagation direction, that profile for I.H.P. SAW is a convex shape. A numerical propagation analysis shows that a wave guide effect occurs in the I.H.P. SAW resonator and transverse resonances are generated. A tilted electrodes resonator is proposed to suppress the transverse modes, and a numerical analysis for it leads an optimum tilt angle with respect to the propagation direction.

Results/Discussion

Figure 1 shows a concept of the tilted resonator and measured frequency characteristics of I.H.P. SAW resonator. It is shown that the transverse modes can be suppressed at 5° of the tilt angle, and a maximum Bode-Q more than 4000 has been achieved. In the case of this structure, since the convex slowness curve is close to a flat shape, the transverse modes can be suppressed at the small tilt angle; as the result, it is also possible to maintain the high Q-factor.

[1] T. Takai, et al., Proc. IEEE Intl. Ultrason. Symp. (2017), p.p. 1-8.

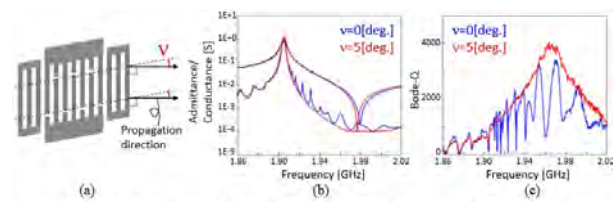


Fig. 1 (a) Conceptual diagram of tilted resonator. v means a tilt angle with respect to the propagation direction, (b) measured admittance characteristics of 1.9GHz one-port resonator, (c) measured Bode-Q characteristics.

2:30 PM

Oriented single-crystal LiTaO₃ thin film on Silicon for high performances SAW components

Marie Gorisse¹, Alexis Drouin¹, Yann Sinquin¹, Isabelle Huyet¹, Émilie Courjon², Florent Bernard², Thierry Laroche², Marie Bousquet³, Alexandre Reinhardt³, Éric Butaud¹, Sylvain Ballandras², Ionut Radu¹

¹Soitec, Bernin, France, ²frec|n|sys, Besançon, France, ³CEA Tech, Grenoble, France

Background, Motivation, and Objective

The RF filter market for mobile devices is exploding and requirements are more and more stringent in particular for frequencies above 2 GHz. Surface acoustic wave (SAW) filters provide high selectivity, low losses and small form factor at reasonable cost. However, conventional SAW filters or multiplexers based on bulk piezoelectric materials are pushed toward their actual limits and do not allow for temperature compensation. Therefore new concepts are evaluated for high performances SAW filters.

The thin film piezoelectric on insulator (POI) structure provides two main advantages [1]: guided modes having higher acoustic velocities with higher quality factor, and minimal temperature coefficient of frequency (TCF) at desired frequencies.

[1] T. Pastureaud *et al.*, TUFFC 54 (4), p. 870-876, 2007

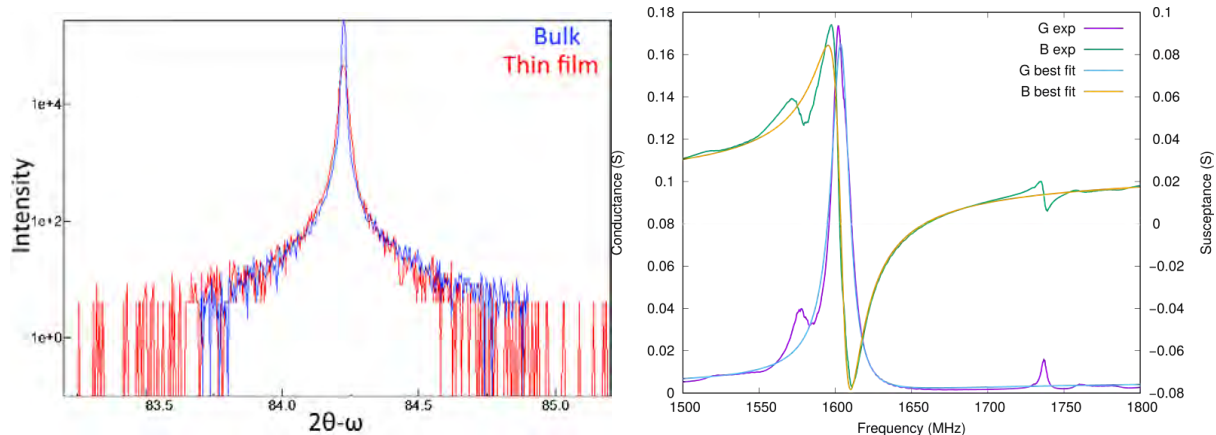
Statement of Contribution/Methods

High quality transfer of single-crystal (XYI)42° LiTaO₃ thin films is demonstrated on 150-mm diameter oxidized Si wafers using the Smart Cut™ process, overcoming process challenges previously faced [2]. An extensive characterization of the transferred film based on direct measurement of crystal properties (fig. 1: $2\theta-\omega$ XRD pattern of bulk and thin film LTO showing no FWHM broadening) and film polarity is reported. SAW devices fabricated on POI substrates are then experimentally and theoretically investigated.

[2] A. Tauzin *et al.*, Elec. Let. 44 (13), 2008

Results/Discussion

Single port SAW resonators operating from 1.4 to 2.3 GHz are demonstrated as shown in fig. 2 (resonator impedance measurement and BVD-based fit), exhibiting coupling coefficient near 8%, reflection coefficients in excess of 12%, loss factor of some tens dB per wavelength and TCF down to -2 ppm.K⁻¹, consistent with theoretical estimations, paving the way to new SAW filters at high frequencies.



2:45 PM Spurious Free SAW Resonators on Layered Substrate with Ultra-High Q, High Coupling and Small TCF

Shogo Inoue¹, Marc Solal¹¹Acoustic Technology R&D, Qorvo, Inc., Apopka, FL, United States**Background, Motivation, and Objective**

Filters using leaky surface acoustic wave (LSAW) on rotated Y-cut LiTaO₃ (LT) are commonly used in smart phone applications. A large portion of the acoustic energy in LSAW resonators is lost by bulk radiation into the substrate. In recent years, the SAW devices on thin LT layer bonded on a high acoustic velocity substrate to avoid the bulk radiation have been actively studied by many groups including us [1, 2]. These resonators potentially have higher electromechanical coupling coefficient (k^2) and smaller temperature coefficient of frequency (TCF) as well as higher Q than regular LSAW resonators. This paper focuses on the design of layered substrate not only to optimize its narrow band characteristics (Q, k^2 , TCF) but also for eliminating the spurious responses due to higher order modes in the film.

Statement of Contribution/Methods

By using a finite element method / boundary element method (FEM/BEM) approach, requirements for the substrate are derived to maximize the Q and k^2 while keeping a small TCF and avoiding the presence of spurious modes. The theoretical results are experimentally confirmed for two different support substrates.

Results/Discussion

Based on the analysis, sapphire is selected as the first demonstration substrate. Experimental results are an ultra-high Q of over 7,000, a high k^2 of 9.0%, and small TCF of -2 ppm/K at 1 GHz. However, strong spurious modes above main response due to higher order modes are obtained. The second used support substrate is quartz. The fabricated LT/quartz SAW resonators exhibit a spurious free response above the main mode and an ultra-high Q of over 6,000, a high k^2 of 9.9%, and a small TCF of -23 ppm/K at 1 GHz as shown in Fig. 1, while LSAW resonators fabricated on regular LT show 1,000 of Q, 8.0% of k^2 , and -38 ppm/K of TCF. These results indicate that SAW devices on layered substrate have the potential to improve filter performance drastically. For smart phone multiplexers which call for very clean response out of the band, LT/quartz is more suitable than LT/sapphire.

[1] T. Takai et al., "Incredible High Performance SAW Resonator on Novel Multi-Layered Substrate," IEEE Ultrason. Symp., 2016.

[2] S. Inoue et al., "SAW Resonators with Ultra-High Q, High Coupling and Small TCF," 7th Int. Symp. on Acoustic Wave Devices for Future Mobile Communications Systems, 2B-2, 2018.

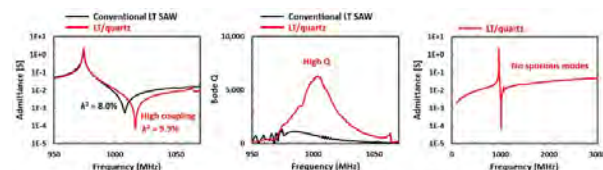


Fig. 1. Measurement results of fabricated LT/quartz SAW resonator

6K - Material for Acoustic Wave Device

Nunobiki (150)

Thursday, October 25, 4:00 pm - 5:30 pm

Chair **Omar Elmazria**
Université de Lorraine

6K-1

4:00 PM

SAW based wireless flexible temperature sensors for on-body applications

Cécile Floer¹, Sami Hage-Ali¹, Jérémie Streque¹, Florian Bartoli^{1,2}, Sergei Zhgoon³, Stefan Mc Murtry¹, Thierry Aubert², Omar Elmazria¹

¹Institut Jean Lamour UMR 7198, Université de Lorraine - CNRS, Nancy, France, ²CentraleSupélec, Metz, France,

³National Research University "MPEI", Moscow, Russian Federation

Background, Motivation, and Objective

The continuous monitoring of the human body parameters is a growing trend in the biomedical, sport or cosmeceutical sectors. To address this challenge, a new class of electronics has emerged: the epidermal electronics, where devices can be stretched, bent or twisted to follow the body deformations. With these new connected objects, continuous and long-term measurements of physiological parameters (such as the temperature) become possible. In this context SAW devices, which are totally passive and can be remotely interrogated, are highly attractive. In our previous work [1], it was shown that low-profile packageless Waveguiding Layer Acoustic Wave (WLAW) devices could be used as temperature sensors, even in contact with soft matter. Here, we report the development of wireless, flexible WLAW sensors towards on-skin sensing applications.

Statement of Contribution/Methods

A WLAW device based on a LiNbO₃ substrate Y-128°-X cut with aluminum interdigital transducers (IDTs) was designed to operate around the 868 MHz ISM band. It was fabricated by electron beam lithography and ion beam etching, followed by the sputtering of ZnO (2 μm) and AlN (8 μm) (see [1] for more details). To ensure its remote interrogation, it was connected to a specifically optimized electrically-small, flexible antenna. The antenna was designed with FEM numerical simulations, that are in good agreement with experimental off-body and on-body S₁₁ measurements (Fig.1a). For the prototyping tests, we used a 25 μm thick Kapton sheet as base for the flexible antenna, coupled to the WLAW device (Fig.1b).

Results/Discussion

We successfully performed a remote interrogation using a second antenna, which is itself connected to a network analyzer. The prototype was measured under a very gentle heat source (lamp), generating a frequency shift of 0.68 MHz for the WLAW mode around 845 MHz, and 0.96 MHz for the other mode. According to [1] the WLAW mode has a temperature coefficient of frequency (TCF) of -106 ppm/°C, so a temperature change of around 7°C was detected remotely. Finally, we present first results on the manufacturing of stretchable antennas made on the Solaris elastomer (Smooth-on, USA) using the transfer printing technique, and connected to SAW sensors (Fig.1c). More results on these elastomeric devices will be presented at the conference.

[1] C. Floer *et al.*, Proc. IEEE IUS 2017.

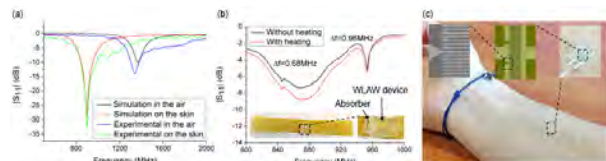


Fig. 1. (a) Reflection coefficients of the antennas with respect to their environment (b) Wireless temperature measurement of the flexible WLAW prototyping sensor. An elastomeric absorber, mimicking the mechanical properties of the skin is placed onto the sensor. (c) SAW device connected to an elastomeric antenna and placed on the skin

4:15 PM

Piezoresistive Graphene SAW TransducerBenyamin Davaji¹, Shrinidhi Kulkarni¹, Visarute Pinrod¹, Alexander Ruyack¹, Amit Lal¹¹*School of Electrical and Computer Engineering, Cornell University, Ithaca, NY, United States***Background, Motivation, and Objective**

SAW gyroscopes, owing to lack of moving elements, have the potential of operation under high shock and vibration environments. In SAW gyroscopes, the drive resonator couples waves into the sense resonator through the Coriolis force. Challenges in SAW gyroscope instrumentation include the matching of drive and sense resonance frequencies, matching to 50Ω impedances for electronics, and maximizing sensitivity while minimizing noise. Piezoresistive graphene resistive transducers, with high sensitivity, and ultralow mass loading of SAW waves, and matching to 50Ω by proper sizing, can provide a pathway to improving SAW gyroscope performance. We presented the superior sensitivity of graphene piezoresistive pickup for SAW [1]. Here we applied design hypothesis on the placement of the graphene transducer in a two port SAW resonator to maximize the sensitivity.

Statement of Contribution/Methods

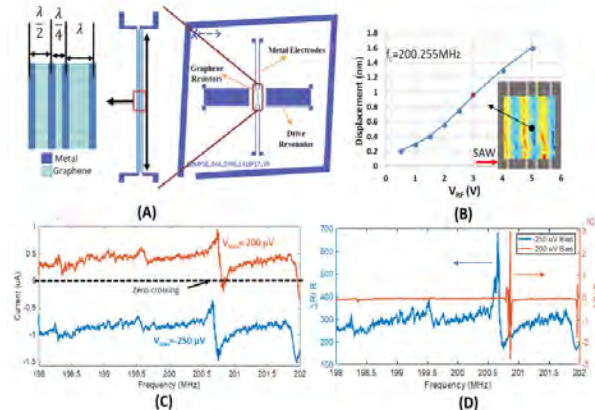
A two port SAW resonance cavity with symmetric configuration is selected to excite standing wave SAW along the cavity at 200.3 MHz ($\lambda_{IDT}=19.71\mu m$) in 128° Y-cut lithium niobate substrate. Graphene resistors are fabricated in the SAW cavity with gold electrodes as external connections. To characterize the enhancement of the sensitivity, the width of pick up graphene resistor is varied by $\lambda/4$, $\lambda/2$ and λ (Figure 1A). The length of the resistors is kept same as the acoustic aperture of the IDTs (50λ). The metal structures are patterned by lithography, metal deposition (Au/Ti) and lift-off. A commercially available monolayer CVD graphene is transferred with wet PMMA transfer technique, patterned by lithography and O₂ plasma.

Results/Discussion

The drive SAW standing wave profile is measured using Doppler microscopy as shown in Figure 1B. A low-noise SMU is used to bias the voltage across the graphene resistor and measure the current as a function of SAW amplitude. By adjusting the current at fixed RF amplitude, the SAW induced current inside the graphene is cancelled. To characterize the sensitivity of graphene electrodes, the effective gauge factor, $EGF = \frac{\Delta R/R}{\epsilon}$, is calculated using the measured displacement at 3V_p RF excitation (954 pm). We discovered that the $\lambda/4$ electrodes aligned between the node and antinode will be the most sensitive configurations equivalent to $EGF=1 \times 10^8$. This high gauge factor, enabled by fast digital processing, can be a key for higher sensitivity of SAW gyroscopes.

References:

- [1] A Ruyack, B Davaji, S Kulkarni and A Lal, Characterization of graphene electrodes as piezoresistive SAW transducers, 2017 IEEE International Ultrasonics Symposium (IUS), 2017.



4:30 PM

Investigation of Temperature Characteristics and Substrate Influence on AlScN-based SAW Resonators

Anli Ding¹, Markus Reusch¹, Yuan Lu¹, Nicolas Kurz², Tim Christoph¹, Roger Lozar¹, Rachid Driad¹, Agne Zukauskaite¹, Oliver Ambacher^{1,3}

¹Fraunhofer IAF, Freiburg, Germany, ²Laboratory for Compound Semiconductor Microsystems, IMTEK, University of Freiburg, Freiburg, Germany, ³Sustainable Systems Engineering, INATECH, University of Freiburg, Germany

Background, Motivation, and Objective

It has been found that introducing up to ~40% Sc into AlN to form $\text{Al}_{1-x}\text{Sc}_x\text{N}$ [1] can lead to a significant increase in piezoelectric response, making AlScN a promising material for electro-acoustic devices, such as frequency filters for mobile communications. For AlScN thin film surface acoustic wave (SAW) resonators, device performance strongly depends on material quality, Sc concentration, substrate, and operating temperature, however, their influence was not investigated in detail until now.

Statement of Contribution/Methods

1 μm thick highly c-axis oriented $\text{Al}_{1-x}\text{Sc}_x\text{N}$ ($x=0; 0.14; 0.23; 0.32$) thin films were deposited on 100 mm Si(001) and Al_2O_3 (0001) substrates by an optimized process [2] using reactive pulsed-DC magnetron sputtering, and SAW resonators with wavelengths $\lambda = 2\text{-}24 \mu\text{m}$ were fabricated. X-ray diffraction (XRD), scanning electron microscopy (SEM) and atomic force microscopy (AFM) measurements confirmed the high quality of the material. Device performance was evaluated by vector network analyzer (VNA) between room temperature and 125 °C as well as by laser Doppler vibrometry (LDV). The measurements were fitted by modified Butterworth-Van Dyke (mBVD) model to extract the electromechanical coupling (k_{eff}^2), phase velocity (v_{ph}), and quality factor (Q).

Results/Discussion

k_{eff}^2 of the resonators improved with increasing Sc concentration, for instance, the $\lambda = 2 \mu\text{m}$ AlN ($f_{\text{res}} = 2.1 \text{ GHz}$) and $\text{Al}_{0.68}\text{Sc}_{0.32}\text{N}$ ($f_{\text{res}} = 1.83 \text{ GHz}$) resonators exhibited k_{eff}^2 of 0.75 % and 2.6 %, respectively. As shown in Fig. 1(a), for all the resonators v_{ph} decreased with increasing Sc concentration, thus confirming the theoretically predicted material softening with higher amount of incorporated Sc [3]. Using Al_2O_3 substrates instead of Si resulted in increased v_{ph} as long as the surface acoustic wave penetrated into the substrate (i.e. for small normalized thickness h_{AlScN}/λ). Moreover, as it can be seen from Fig. 1(b), temperature coefficient of frequency (TCF) only slightly changed with increasing Sc concentration, the temperature dependence of the overall device performance will be discussed in detail.

- [1] M. Akiyama et al., Appl. Phys. Lett. 95, 2009, 162107
- [2] Y. Lu et al., Phys. Status Solidi A 2017, 1700559
- [3] M. A. Caro et al., J. Phys.: Condens. Matter 27, 2015, 245901

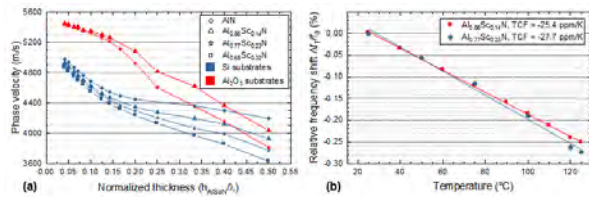


Figure 1. (a) Phase velocity dispersion curves of the fabricated SAW resonators.
(b) Relative frequency shift of SAW resonators ($\lambda = 2 \mu\text{m}$) at different operating temperatures.

4:45 PM

Polarity inverted ScAlN multilayer for application to transformer in rectifying antennaRei Karasawa^{1,2}, Takahiko Yanagitani^{1,2,3}¹Waseda University, Japan, ²ZAIKEN, Japan, ³JST PRESTO, Japan**Background, Motivation, and Objective**

Harvesting energy from the surrounding environment is a key technology for wireless sensor networks. RF energy harvesting is generally achieved by a rectifying antenna consisting of a diode and an antenna. One of the problems is a low RF to DC conversion efficiency due to a weak RF input signal[1]. Therefore, a voltage multiplier, such as a Dickson charge pump[2], is installed in the rectenna to amplify the signal. However, its low efficiency, large size, and poor impedance matching are the problem. In this study, we present polarity inverted FBAR transformer to overcome this problem. As shown in Fig. 1(a), an RF input signal can be enhanced with increasing number of output layers. We previously reported the 12-layer c-axis zig-zag polarization inverted ScAlN film operating around 600 MHz[3]. We here report a 12-layer ScAlN film stack operating in the 2.45 GHz Industrial, Scientific, and Medical (ISM) band, which is commonly used for wireless communication.

[1] T.-W. Woo and K. Chang, IEEE Trans. Micro. Theory and Tech., Vol. 40, pp.1259-1266, (1992).

[2] A. N. Parks, A. P. Sample, Y. Zhao, and J. R. Smith, Proc. IEEE WiSNET, pp-154-156, (2013).

[3] R. Karasawa and T. Yanagitani, Proc. IEEE Ultrason. Symp., (2017).

Statement of Contribution/Methods

c-Axis tilted ScAlN films were RF magnetron sputtered on Ti bottom electrode/ silica glass substrate by a glancing angle deposition. After the deposition of the first layer, the substrate was rotated by 180° and the following layers were grown. Repeating this process 11 times, the 12-layer c-axis zig-zag structure was obtained without breaking the vacuum.

Results/Discussion

Fig. 1(b) shows the cross sectional SEM image of the 12-layer c-axis zig-zag ScAlN stack. The c-axis zig-zag structure was clearly observed. The thickness of each layer was determined to be 730 nm. c-Axis tilt angle of the layers was determined to be 51-53 degrees by an XRD pole figure analysis. As shown in Fig. 1(c), 12th shear mode operation of the 12-layer c-axis zig-zag polarization inverted ScAlN film resonator was observed at 2.45 GHz. The experimental curve is almost in line with the theoretical one, derived from Mason's equivalent circuit model, around 2.45 GHz. This new type of device is promising for a voltage transformer in the rectenna.

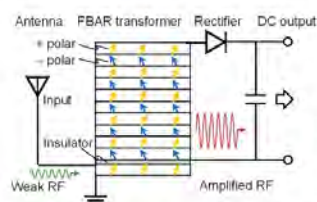


Fig. 1 (a) FBAR transformer rectifying antenna. The arrows indicate piezoelectric polarizations of the layers.

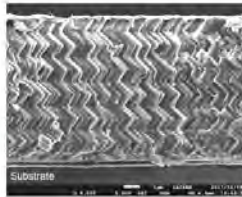


Fig. 1(b) Cross sectional SEM image of the 12-layer c-axis zig-zag ScAlN film stack.

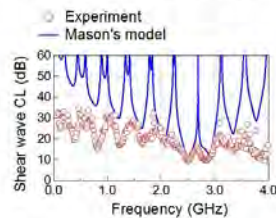


Fig. 1(c) Quasi-shear wave conversion loss of the 12-layer c-axis zig-zag ScAlN film resonator.

5:00 PM

Extraction of electromechanical coupling coefficient of film/substrate structure by using the ratio of a third mode resonant frequency to a fundamental mode resonant frequency

Makoto Totsuka^{1,2}, Takahiko Yanagitani^{1,2,3}¹Waseda University, Japan, ²ZAIKEN, Japan, ³JST PRESTO, Japan

Background, Motivation, and Objective

A resonance-antiresonance method is recommended for the determination of electromechanical coupling coefficient k_t^2 for the piezoelectric film, according to the IEEE standard [1]. However, a self-standing film structure (FBAR) is required to use this method. To apply the resonance-antiresonance method to film/substrate structure (HBAR), we tried to determine resonant frequencies and antiresonant frequencies in HBAR by using Mason's model. As shown in Fig.1, we tried to determine the resonant frequency (f_r) and the antiresonant frequency (f_a) of the piezoelectric film in HBAR from the maximum point of the envelope obtained from multiple resonant frequencies and antiresonant frequencies in HBAR, respectively. The simulation using Mason's model shows large discrepancy between f_a of piezoelectric film obtained from HBAR and f_a from FBAR (Fig.1 (a)), while f_r from HBAR corresponds to f_r from FBAR (Fig.1 (b)). This simulation demonstrated that k_t^2 in HBAR cannot be determined by the resonance-antiresonance method. On the other hand, Onoe showed the ratio of a third mode f_r to a fundamental mode f_r in FBAR depends on k_t^2 of the piezoelectric film and reported k_t^2 determination method comparing the experimental ratio with the theoretical one in FBAR without using f_a [2]. In this study, we considered that k_t^2 can be determined by using this ratio method for HBAR because the f_r of piezoelectric film from HBAR corresponds to the f_r from FBAR.

[1] IEEE Std., 176-1987

[2] M. Onoe, et al., JASA., 36 (1963)

Statement of Contribution/Methods

AlN and ScAlN were grown on a Ti bottom electrode on a silica glass substrate by using RF magnetron sputtering to prepare HBAR samples. We compared k_t^2 determined by the resonant frequency ratio method in this study with ones determined by three different k_t^2 extraction methods to demonstrate the validity of k_t^2 determination in this method.

Results/Discussion

In the resonant frequency ratio method, k_t^2 is determined by comparing the experimental ratio of the third mode f_r to the fundamental mode f_r measured by a network analyzer with theoretical one, as shown in Fig.2. The validity of k_t^2 determination by the resonant frequency ratio method was demonstrated because the difference between k_t^2 determined by this method and one by the resonance-antiresonance method is within 7%. This new method is promising for k_t^2 determination before the FBAR fabrication.

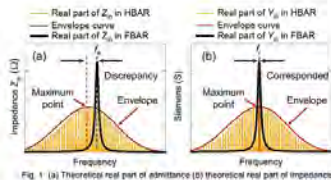


Fig. 1 (a) Theoretical real part of admittance in HBAR and FBAR simulated by Mason's equivalent circuit model

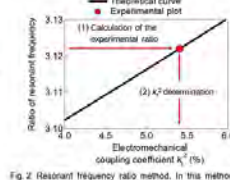


Fig. 1 (b) Theoretical real part of admittance in HBAR and FBAR simulated by Mason's equivalent circuit model

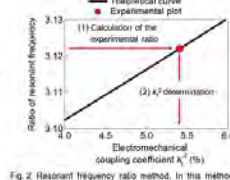


Fig. 2 Resonant Frequency ratio method. In this method, the experimental ratio of a third resonant frequency to first resonant frequency is calculated by a network analyzer (a red dot). The ratio is compared with the theoretical ratio of a third resonant frequency to first resonant frequency including electrode layers to determine k_t^2 of the piezoelectric film in HBAR.

| Table 1 Comparison of k_t^2 determination method | | | | | | | |
|--|----------------|---------------------|--|--|--|---|---|
| Piezoelectric film | Thickness (μm) | Resonant curve FWHM | Conversion loss method k_t^2 (%) [3] | Resonant spectrum method k_t^2 (%) [4] | Resonance-antiresonance method k_t^2 (%) | Resonant frequency ratio method k_t^2 (%) (in this study) | Difference between resonant frequency ratio method and resonance-antiresonance method (%) |
| AlN | 8.8 | 1.6 | 5.1 | 0.3 | 5.8 | 5.4 | -6.8 |
| Sc _{0.9} Ti _{0.1} N | 5.2 | 3.2 | 9.6 | 9.6 | 10.6 | 10.2 | -3.8 |
| Sc _{0.9} Ti _{0.1} N | 5.5 | 4.3 | 13.9 | 14.5 | 15.1 | 14.1 | -6.6 |
| Sc _{0.9} Ti _{0.1} N | 10.5 | 1.9 | 21.4 | 20.3 | 23.0 | 22.1 | -3.8 |

[3] T. Yanagitani et al., JAP, 2410 (2007) [4] Y. Zhang, et al., IEEE Trans. Ultrason. Ferroelectr. Freq. Control, 52, 121 (2005)

5:15 PM

A new method for extracting Q factor of the piezoelectric film without removing substrate**Sarina Kinoshita^{1,2}, Makoto Totsuka^{1,2}, Rei Karasawa^{1,2}, Takahiko Yanagitani^{1,2,3}**¹*Waseda University, Japan*, ²*ZAIKEN, Japan*, ³*JST PRESTO, Japan***Background, Motivation, and Objective**

Q factors of piezoelectric thin films determine the sharpness of resonance of FBAR filters. Self-standing film structures (FBAR, Fig. 1(a)) without substrate is required to determine Q factors of the films. In this study, we introduce a new method for estimating Q factors of films using piezoelectric film/substrate structures (HBAR, Fig. 1(b)) without removing substrates. In contrast to FBAR, multiple peaks caused by the resonance of thick substrate are observed in HBAR as shown in Fig. 2. Q factor of multiple peaks in the vicinity of the thick external mode resonant frequency of the film is most affected by the mechanical loss of films. When Q factor of the substrate (Q_{sub}) is higher than that of the film (Q_{piezo}), Q factor of the entire HBAR (Q_{HBAR}) decrease due to the damping of the film which have larger mechanical loss, only in the vicinity of the resonant frequency of the film.

Therefore, Q_{piezo} can be estimated from the amount of reduction in the Q_{HBAR} when Q_{sub} is known. In this study, we test a new method to extract Q_{piezo} without removing substrate.

Statement of Contribution/Methods

It is well known that Q factor of ScAlN is lower than that of pure AlN [1]. To confirm the principle of the method, we investigated whether the difference of the Q factor between pure AlN and ScAlN is able to be detected. The real part of impedance (Z_{real}) of pure AlN film (8.8 μm) and $\text{Sc}_{0.35}\text{Al}_{0.65}\text{N}$ film (7.2 μm) / silica glass substrate (0.5 mm) HBAR samples (Table 1) were measured by network analyzer. Experimental Q_{HBAR} obtained from FWHM of the Z_{real} peaks were compared with the simulated ones using Mason's equivalent circuit model.

[1] M. Moreira, J. Bjurström, I. Katardjev, and V. Yantchev, "Aluminum scandium nitride thin-film bulk acoustic resonators for wide band applications," *Vacuum*, vol. 86, no. 1, pp. 23-26, 2011.

Results/Discussion

As shown in Fig. 3, Q_{HBAR} decrease depending on Q_{piezo} in the vicinity of the resonant frequency of the film, when Q_{sub} is constant. As shown in Fig. 4, obvious decrease of experimental Q_{HBAR} in the vicinity of the resonant frequency of pure AlN film (570 MHz) and ScAlN film (470 MHz) was observed as expected in the simulation (Fig. 3). The amount of reduction of ScAlN is larger than that of pure AlN, indicating that mechanical Q_{piezo} of ScAlN is lower than that of pure AlN as expected. This method is attractive to extract Q_{piezo} from the wafer before the FBAR fabrication.

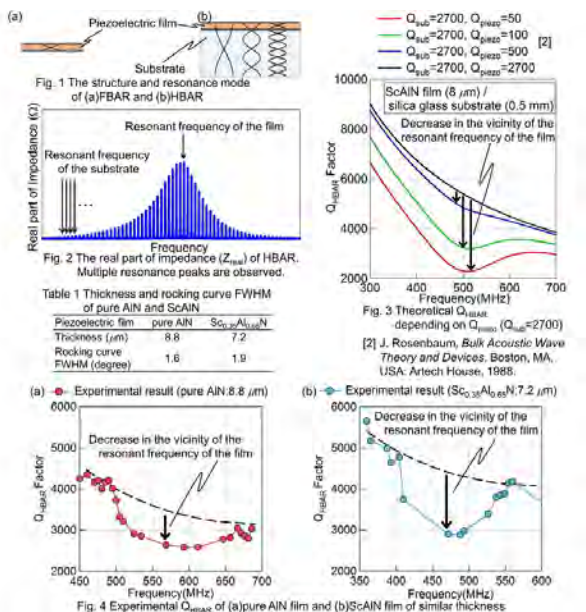


Table 1 Thickness and rocking curve FWHM of pure AlN and ScAlN

| Piezoelectric film | pure AlN | $\text{Sc}_{0.35}\text{Al}_{0.65}\text{N}$ |
|-----------------------------|----------|--|
| Thickness (μm) | 8.8 | 7.2 |
| Rocking curve (degree) | 1.6 | 1.9 |

(a) ● Experimental result (pure AlN 8.8 μm)

(b) ● Experimental result ($\text{Sc}_{0.35}\text{Al}_{0.65}\text{N}$ 7.2 μm)

Decrease in the vicinity of the resonant frequency of the film

Decrease in the vicinity of the resonant frequency of the film

Decrease in the vicinity of the resonant frequency of the film

Decrease in the vicinity of the resonant frequency of the film

Decrease in the vicinity of the resonant frequency of the film

Decrease in the vicinity of the resonant frequency of the film

Decrease in the vicinity of the resonant frequency of the film

Decrease in the vicinity of the resonant frequency of the film

Decrease in the vicinity of the resonant frequency of the film

Decrease in the vicinity of the resonant frequency of the film

Decrease in the vicinity of the resonant frequency of the film

Decrease in the vicinity of the resonant frequency of the film

Decrease in the vicinity of the resonant frequency of the film

Decrease in the vicinity of the resonant frequency of the film

Decrease in the vicinity of the resonant frequency of the film

Decrease in the vicinity of the resonant frequency of the film

Decrease in the vicinity of the resonant frequency of the film

Decrease in the vicinity of the resonant frequency of the film

Decrease in the vicinity of the resonant frequency of the film

Decrease in the vicinity of the resonant frequency of the film

Decrease in the vicinity of the resonant frequency of the film

Decrease in the vicinity of the resonant frequency of the film

Decrease in the vicinity of the resonant frequency of the film

Decrease in the vicinity of the resonant frequency of the film

Decrease in the vicinity of the resonant frequency of the film

Decrease in the vicinity of the resonant frequency of the film

Decrease in the vicinity of the resonant frequency of the film

Decrease in the vicinity of the resonant frequency of the film

Decrease in the vicinity of the resonant frequency of the film

Decrease in the vicinity of the resonant frequency of the film

Decrease in the vicinity of the resonant frequency of the film

Decrease in the vicinity of the resonant frequency of the film

Decrease in the vicinity of the resonant frequency of the film

Decrease in the vicinity of the resonant frequency of the film

Decrease in the vicinity of the resonant frequency of the film

Decrease in the vicinity of the resonant frequency of the film

Decrease in the vicinity of the resonant frequency of the film

Decrease in the vicinity of the resonant frequency of the film

Decrease in the vicinity of the resonant frequency of the film

Decrease in the vicinity of the resonant frequency of the film

Decrease in the vicinity of the resonant frequency of the film

Decrease in the vicinity of the resonant frequency of the film

Decrease in the vicinity of the resonant frequency of the film

Decrease in the vicinity of the resonant frequency of the film

Decrease in the vicinity of the resonant frequency of the film

Decrease in the vicinity of the resonant frequency of the film

Decrease in the vicinity of the resonant frequency of the film

Decrease in the vicinity of the resonant frequency of the film

Decrease in the vicinity of the resonant frequency of the film

Decrease in the vicinity of the resonant frequency of the film

Decrease in the vicinity of the resonant frequency of the film

Decrease in the vicinity of the resonant frequency of the film

Decrease in the vicinity of the resonant frequency of the film

Decrease in the vicinity of the resonant frequency of the film

Decrease in the vicinity of the resonant frequency of the film

Decrease in the vicinity of the resonant frequency of the film

Decrease in the vicinity of the resonant frequency of the film

Decrease in the vicinity of the resonant frequency of the film

Decrease in the vicinity of the resonant frequency of the film

Decrease in the vicinity of the resonant frequency of the film

Decrease in the vicinity of the resonant frequency of the film

Decrease in the vicinity of the resonant frequency of the film

Decrease in the vicinity of the resonant frequency of the film

Decrease in the vicinity of the resonant frequency of the film

Decrease in the vicinity of the resonant frequency of the film

Decrease in the vicinity of the resonant frequency of the film

Decrease in the vicinity of the resonant frequency of the film

Decrease in the vicinity of the resonant frequency of the film

Decrease in the vicinity of the resonant frequency of the film

Decrease in the vicinity of the resonant frequency of the film

Decrease in the vicinity of the resonant frequency of the film

Decrease in the vicinity of the resonant frequency of the film

Decrease in the vicinity of the resonant frequency of the film

Decrease in the vicinity of the resonant frequency of the film

Decrease in the vicinity of the resonant frequency of the film

Decrease in the vicinity of the resonant frequency of the film

Decrease in the vicinity of the resonant frequency of the film

Decrease in the vicinity of the resonant frequency of the film

Decrease in the vicinity of the resonant frequency of the film

Decrease in the vicinity of the resonant frequency of the film

Decrease in the vicinity of the resonant frequency of the film

Decrease in the vicinity of the resonant frequency of the film

Decrease in the vicinity of the resonant frequency of the film

Decrease in the vicinity of the resonant frequency of the film

Decrease in the vicinity of the resonant frequency of the film

Decrease in the vicinity of the resonant frequency of the film

Decrease in the vicinity of the resonant frequency of the film

Decrease in the vicinity of the resonant frequency of the film

Decrease in the vicinity of the resonant frequency of the film

Decrease in the vicinity of the resonant frequency of the film

Decrease in the vicinity of the resonant frequency of the film

Decrease in the vicinity of the resonant frequency of the film

Decrease in the vicinity of the resonant frequency of the film

Decrease in the vicinity of the resonant frequency of the film

Decrease in the vicinity of the resonant frequency of the film

Decrease in the vicinity of the resonant frequency of the film

Decrease in the vicinity of the resonant frequency of the film

Decrease in the vicinity of the resonant frequency of the film

Decrease in the vicinity of the resonant frequency of the film

Decrease in the vicinity of the resonant frequency of the film

Decrease in the vicinity of the resonant frequency of the film

Decrease in the vicinity of the resonant frequency of the film

Decrease in the vicinity of the resonant frequency of the film

Decrease in the vicinity of the resonant frequency of the film

Decrease in the vicinity of the resonant frequency of the film

Decrease in the vicinity of the resonant frequency of the film

Decrease in the vicinity of the resonant frequency of the film

Decrease in the vicinity of the resonant frequency of the film

Decrease in the vicinity of the resonant frequency of the film

Decrease in the vicinity of the resonant frequency of the film

Decrease in the vicinity of the resonant frequency of the film

Decrease in the vicinity of the resonant frequency of the film

Decrease in the vicinity of the resonant frequency of the film

Decrease in the vicinity of the resonant frequency of the film

Decrease in the vicinity of the resonant frequency of the film

Decrease in the vicinity of the resonant frequency of the film

Decrease in the vicinity of the resonant frequency of the film

Decrease in the vicinity of the resonant frequency of the film

Decrease in the vicinity of the resonant frequency of the film

Decrease in the vicinity of the resonant frequency of the film

Decrease in the vicinity of the resonant frequency of the film

Decrease in the vicinity of the resonant frequency of the film

Decrease in the vicinity of the resonant frequency of the film

Decrease in the vicinity of the resonant frequency of the film

Decrease in the vicinity of the resonant frequency of the film

Decrease in the vicinity of the resonant frequency of the film

Decrease in the vicinity of the resonant frequency of the film

Decrease in the vicinity of the resonant frequency of the film

Decrease in the vicinity of the resonant frequency of the film

Decrease in the vicinity of the resonant frequency of the film

Decrease in the vicinity of the resonant frequency of the film

Decrease in the vicinity of the resonant frequency of the film

Decrease in the vicinity of the resonant frequency of the film

Decrease in the vicinity of the resonant frequency of the film

Decrease in the vicinity of the resonant frequency of the film

Decrease in the vicinity of the resonant frequency of the film

Decrease in the vicinity of the resonant frequency of the film

Decrease in the vicinity of the resonant frequency of the film

Decrease in the vicinity of the resonant frequency of the film

Decrease in the vicinity of the resonant frequency of the film

Decrease in the vicinity of the resonant frequency of the film

Decrease in the vicinity of the resonant frequency of the film

Decrease in the vicinity of the resonant frequency of the film

Decrease in the vicinity of the resonant frequency of the film

Decrease in the vicinity of the resonant frequency of the film

Decrease in the vicinity of the resonant frequency of the film

Decrease in the vicinity of the resonant frequency of the film

Decrease in the vicinity of the resonant frequency of the film

Decrease in the vicinity of the resonant frequency of the film

Decrease in the vicinity of the resonant frequency of the film

Decrease in the vicinity of the resonant frequency of the film

Decrease in the vicinity of the resonant frequency of the film

Decrease in the vicinity of the resonant frequency of the film

Decrease in the vicinity of the resonant frequency of the film

Decrease in the vicinity of the resonant frequency of the film

Decrease in the vicinity of the resonant frequency of the film

Decrease in the vicinity of the resonant frequency of the film

Decrease in the vicinity of the resonant frequency of the film

Decrease in the vicinity of the resonant frequency of the film

Decrease in the vicinity of the resonant frequency of the film

Decrease in the vicinity of the resonant frequency of the film

Decrease in the vicinity of the resonant frequency of the film

Decrease in the vicinity of the resonant frequency of the film

Decrease in the vicinity of the resonant frequency of the film

Decrease in the vicinity of the resonant frequency of the film

Decrease in the vicinity of the resonant frequency of the film

Decrease in the vicinity of the resonant frequency of the film

Decrease in the vicinity of the resonant frequency of the film

Decrease in the vicinity of the resonant frequency of the film

Decrease in the vicinity of the resonant frequency of the film

Decrease in the vicinity of the resonant frequency of the film

Decrease in the vicinity of the resonant frequency of the film

Decrease in the vicinity of the resonant frequency of the film

Decrease in the vicinity of the resonant frequency of the film

Decrease in the vicinity of the resonant frequency of the film

Decrease in the vicinity of the resonant frequency of the film

Decrease in the vicinity of the resonant frequency of the film

Decrease in the vicinity of the resonant frequency of the film

Decrease in the vicinity of the resonant frequency of the film

Decrease in the vicinity of the resonant frequency of the film

Decrease in the vicinity of the resonant frequency of the film

Decrease in the vicinity of the resonant frequency of the film

Decrease in the vicinity of the resonant frequency of the film

7H - PPN: Phononics

Kikusui (140)

Thursday, October 25, 8:00 am - 9:30 am

Chair **John Larson**
Broadcom Ltd

7H-1

8:00 AM Radiative damping of vibrational modes of a microsphere on an elastic substrate

Alexei Maznev¹

¹*Department of Chemistry, MIT, Cambridge, MA, United States*

Background, Motivation, and Objective

Acoustic vibrations of micro- and nano-objects such as spheres and rods is a subject of active research. In many experimental studies, the vibrating particles are in contact with a supporting substrate. The elastic contact with the substrate shifts the frequencies of vibrational modes and in some cases causes mode splitting via degeneracy lifting; it also gives rise to low-frequency contact-based modes in which the particle moves as a rigid body. Another important effect caused by the contact with the substrate is damping of acoustic vibrations via radiation of acoustic waves into the substrate. In this report, I will provide an analytical treatment of radiative damping of contact-based and spheroidal vibrations of a spherical particle on an elastically isotropic substrate.

Statement of Contribution/Methods

I assume a Hertzian contact between the particle and the substrate. The radius of the contact area, controlled by the adhesion force, will typically be much smaller than both the particle size and the wavelength of acoustic waves radiated into the substrate by the vibrating particle. In this case, the contact can be treated as a point spring, and the radiation loss is given by the power dissipated by a harmonic point force acting on the surface of the substrate. In addition, I take advantage of the fact that for spheroidal modes the contact can be treated as a small perturbation. Within these assumptions, analytical results for radiative damping of contact-based and spheroidal modes, accounting for the radiation of both bulk and surface acoustic waves, are obtained. The key parameter needed to calculate the radiation loss is the spring constant of the contact, which can be determined experimentally from the frequency of the contact-based axial vibrational mode or estimated using adhesion models.

Results/Discussion

I will present results for the axial and horizontal-rotational contact-based modes as well as for the spheroidal breathing mode, which is most often seen in experiment. We will also consider vibrations of particle assemblies: it will be shown that radiative damping is greatly enhanced for a monolayer of particles. On the other hand, radiative damping can be eliminated altogether for collective modes of the monolayer with a high enough in-plane wavevector. The available experimental results for both individual particles and close-packed monolayers will be reviewed. Finally, we will touch upon radiative damping of vibrations of nanorods/nanowires which can be treated using the same methodology.

8:15 AM

Coupled phonons, photons and RF read-out for phononic circuits

Daniel Navarro Urrios¹, David Garcia Fernandez², Jeremie Maire², Martin F. Colombano^{2,3}, Guillermo Arregui^{2,4}, Alejandro Martinez⁵, Nestor E. Capuj⁶, Nikolaos Kehagias², Marianna Sledzinska², Clivia M. Sotomayor Torres²

¹Departament d'Electrònica, Universidad de Barcelona, Barcelona, Spain, ²ICN2, Bellaterra (Barcelona), Spain,

³Dept. of Physics, Universidad Autónoma de Barcelona, Spain, ⁴Dept. of Physics, Universidad Autonoma de Barcelona, Spain,

⁵Nanophotonics Technology Center, Universitat Politècnica de València, Spain, ⁶Universidad de La Laguna, Spain

Background, Motivation, and Objective

The coupling of phonon and photons brings forward a series of physical interactions one of them being optomechanics (OM). OM has shown to be a rich research area where the control of this interaction, in the GHz-THz range, and its link to radio frequencies provide a wide range of possibilities for both, fundamental and applied research. At room temperature, mechanical Q factors in the 1000s can be reached, sufficient for classical studies of photon-phonon coupling, especially in the beam configuration of OM crystals consisting of a cavity to confine photons and phonons simultaneously into small modal volumes [1]. In fact, there is a myriad of engineered optomechanical structures operating mostly at cryogenic temperatures and mainly directed to quantum technologies. Our work is oriented to scalable phonon circuit concepts using OM in a silicon-compatible nanobeam configuration for room temperature operation.

Statement of Contribution/Methods

We use silicon technologies, opto-mechanical coupling methods and fibre optics. Our studies are all in ambient conditions.

Results/Discussion

We have shown the quantitative impact of thermo-optic effects and free carrier absorption [2], have generated coherent phonons up to 5 GHz [3] and established three modulations schemes for it. We have demonstrated the transition from the lasing regime to chaotic behavior (fig.1) [4] and show that fabrication imperfections can be exploited to enhance light-matter interaction [5].

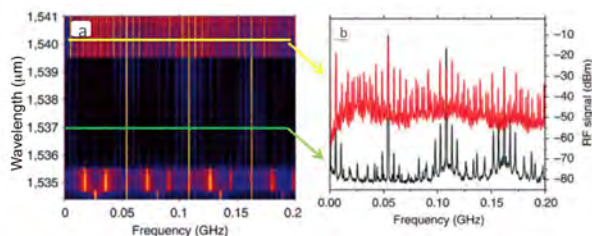
We will discuss factors affecting the integration of phonon sources, phonon detectors, waveguides and other phononic components.

References.

1. see, e.g., J. Gomis-Bresco et al., Nature Comm. 5, 4452 (2014)
2. D. Navarro Urrios et al., J. Applied Physics 116, 093506 (2014)
3. D. Navarro-Urrios et al., Scientific Reports 5, 15733 (2015)
4. D. Navarro-Urrios et al., Nature Comm. 8 14965 (2017)
5. P. D. Garcia et al., Physical Review B 95, 115129 (2017)

Figure caption:

Non-linear dynamics of an OM cavity. (a) Colour contour plot of the radio-frequency spectrum as a function of the laser wavelength obtained at a laser power of $P_l=44\text{mW}$. (b) Shows radio-frequency spectra below 1,537.05 nm (green curve) and above the bifurcation marking the onset of chaos (1,540.70 nm, yellow curve).



8:30 AM Surface-mediated mechanical coupling of pillar pairs

Laetitia Raguin¹, Olivier Gaiffe¹, Roland Salut¹, Valérie Soumann¹, Jean-Marc Cote¹, Vincent Laude¹, Abdelkrim Khelif¹, Sarah Benchabane¹

¹*Femto-st, CNRS, Université de Bourgogne Franche-Comté, Besançon, France*

Background, Motivation, and Objective

Interaction between guided waves and mechanical resonators has been widely studied in the field of phononic crystals or elastic metamaterials, where many works have been devoted to periodical arrangement of local resonators. Most of the literature however deals with the collective behavior of such physical objects. In this work, we focus on the intrinsic properties of isolated resonators coupled to surface acoustic waves (SAW), with the aim of controlling propagation at a subwavelength scale. We investigate the interaction and coupling between a substrate excited by SAW and a pair of phononic resonators. The influence of the orientation of the source as well as of the distance between the two neighboring resonators is experimentally studied.

Statement of Contribution/Methods

Pairs of platinum pillars were grown using focused ion beam induced deposition on a Y-cut lithium niobate substrate. Their diameter and height were set at 4.4 μm and 4 μm respectively, leading to a resonance frequency of the order of 70 MHz for the first flexural mode. SAWs were launched on the substrate surface using interdigital transducers. The elastic energy distribution at the surface of the pillars and of the substrate was measured using optical interferometry, giving access to the frequency responses for each pillar and to the orientations of the modes as a function of the incident SAW wave vector.

Results/Discussion

The experimental observation of frequency splitting of the pillar pair response, which is not present for an isolated pillar, is an evidence of coupling. The characteristics of this splitting depend on the orientation of the source and on the distance between the resonators. Two coupling regimes can be identified: a weaker coupling, where the two pillars resonate at different frequencies, respectively blue and red shifted compared to the individual pillar natural response, and a stronger coupling regime, where the two pillars present the same behavior and two separated modes, as shown by the obtained split frequency response. Preliminary investigations in addition show that nonlinearities can be observed at higher drive power for particular configurations. These results prove that, by choosing appropriate configurations, the combination of SAW and mechanical resonators can be used either to control the elastic energy distribution at the microscale, or, reciprocally, to manipulate pillar ensembles by changing the excitation conditions.

8:45 AM

Double Negativity in Double-sided Pillared MetamaterialBernard Bonello¹, Wei Wang¹, Bahram Djafari-Rouhani², Yan Pennec², Jinfeng Zhao³¹CNRS/Sorbonne Université, Paris, France, ²Lille University - IEMN, France, ³Tongji University - Shanghai, China, People's Republic of**Background, Motivation, and Objective**

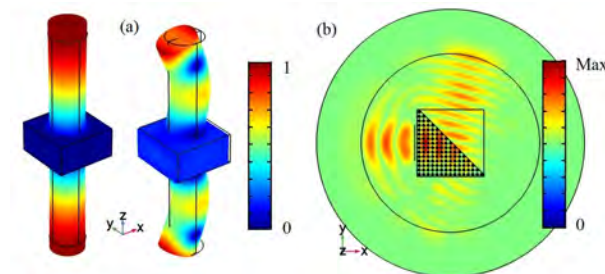
Owing to their locally resonant substructures, the effective parameters of elastic metamaterials can be dynamically set to a positive, zero or negative value, enabling the control of the propagation of elastic waves at the subwavelength scale. The doubly-negative properties can be realized by combining two different substructures, each supporting a different resonant mode. This leads to an overall structure that may be difficult to achieve. In this work we followed another route that consists of investigating a single phase, double-sided pillared metamaterial where two resonances occur in the same frequency range. We show that this structure exhibits double negativity and that it allows for the propagation of the zero order symmetric Lamb wave in a frequency interval where the propagation of the antisymmetric Lamb wave is forbidden.

Statement of Contribution/Methods

The unit cell consists of two identical steel pillars arranged symmetrically on each free surface of a steel plate (Fig. 1a). A finite element method is employed to solve the eigenvalue equation and to obtain the band structure of the metamaterial. We used a displacement perturbation method to calculate the effective mass density. We propose a simplified mass-spring model to explain the occurrence of the doubly negative property.

Results/Discussion

We show that the negative mass density is achieved within a frequency range where both the symmetric bending resonance and the antisymmetric compression resonance of the pillars occur, whereas the negative elastic modulus only involves the symmetric compression resonances (Fig. 1a). Comparisons with the case of the single-sided pillared metamaterial allow highlighting the mechanisms leading to this double negativity. Actually, it is analytically shown that the effective elastic modulus of the single-sided pillared structure is always positive, whereas its effective mass density gets negative close to the resonance frequency of both the bending and compressional modes of the pillars. We further demonstrate the negative refraction of an incident symmetric Lamb wave which wavelength is larger than the lattice constant by one order of magnitude, at the interface between the double-sided pillared metamaterial and the substrate (Fig. 1b).



9:00 AM

Topologically Valley-protected Lamb Waves in Pillared MetamaterialWei Wang¹, Bernard Bonello¹, Bahram Djafari-Rouhani², Yan Pennec²¹Sorbonne Université, UPMC Université Paris 06 (INSP–UMR CNRS 7588), Paris, France, ²Lille University - IEMN, France**Background, Motivation, and Objective**

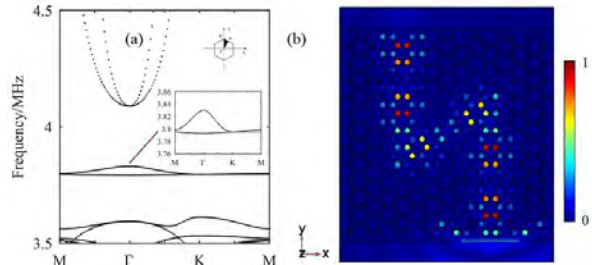
Elastic analogues of quantum valley Hall effect (QVHE) in phononic crystals and metamaterials featuring topologically protected edge waves immune from backscattering in the presence of imperfections have attracted more and more interest. QVHE exploits valley states instead of spin states with the advantage that the lattice site needs to have only one degree of freedom, reducing geometrical complexity. Moreover, the corresponding topological phase transition can be easily realized by breaking the inversion symmetry in the unit cell. In this work we investigate the topological valley-protected transport of the zero-order symmetric Lamb wave in a pillared metamaterial. We show that the proposed configuration provides a new design diagram to manipulate the symmetric Lamb wave at the subwavelength scale.

Statement of Contribution/Methods

We use a finite element method to solve the eigenvalue equation and to draw the band structure of the metamaterial. The valley edge modes of the configurations we considered are predicted by finite strip dispersion analyses. Wave propagation in frequency domain is carried out to investigate the valley-protected edge modes.

Results/Discussion

Two pairs of identical double-sided pillars are involved and arranged symmetrically over a thin plate in a regular honeycomb lattice. In this configuration, multiple Dirac points at corner K (K') in the Brillouin zone are formed due to the band folding effect (FIG. 1(a)). Furthermore, Dirac points at K (K') can be split by slightly adjusting the relative height of the adjacent pillars to break inversion symmetry. The opposite vortex chirality are put into evidence according to the phase distribution of in-plane displacement of matrix plate which represent pseudospin up and down respectively. We further numerically demonstrate the topological valley-protected backscattering suppression of the symmetric Lamb wave in a curved waveguide along the interface constructed by two kinds of pillared metamaterials with opposite valley Chern numbers (FIG. 1(b))).



9:15 AM

Lamb wave propagation in coupled-resonator elastic waveguidesYan-Feng Wang¹, Ting-Ting Wang¹, Yue-Sheng Wang¹, Vincent Laude²¹*Beijing Jiaotong University, Beijing, China, People's Republic of*, ²*Institut FEMTO-ST, Besançon, France***Background, Motivation, and Objective**

Waveguides based on linear chains of coupled cavities have been shown theoretically to allow very strong wave confinement and low group velocity transmission. In this work, we observe experimentally for the first time highly confined propagation of Lamb waves along coupled-resonator elastic waveguides (CREWs). We also observe that sharp 90° bends can be included to form phononic circuits.

Statement of Contribution/Methods

Numerical simulations are conducted using the FE method in order to understand better the experimental results. A supercell technique is used to investigate the dispersion relation and eigenmodes of CREWs. Traction-free boundary conditions are set on the top and bottom surfaces and inside the holes, and periodic Bloch boundary conditions are applied on the other boundaries. Displacements are also measured using a Polytec PSV-500 scanning vibrometer.

Results/Discussion

We investigate experimentally Lamb wave propagation in coupled-resonator elastic waveguides (CREWs) formed by a chain of cavities in a two-dimensional phononic crystal slab with cross holes. A waveguide and a wave splitting circuit with exact 90° bends are designed, fabricated and measured. Elastic Lamb waves are excited by a piezoelectric patch attached to one side of the phononic slab and detected using a scanning vibrometer. Strongly confined guidance along waveguides and splitting at waveguide junctions are clearly observed. Numerical simulations are conducted to obtain the band structure of the waveguides and the transmission of the circuits. They are found to be in excellent agreement with experimental results and allow the identification of the involved resonant cavity modes. The work in this paper has implications for the design of innovative phononic devices.

7I - PMI: Modelling and Inversion

Kikusui (140)

Thursday, October 25, 10:30 am - 12:00 pm

Chair **Robert Thalhammer**
Broadcom Ltd

7I-1

10:30 AM Redatuming for Breast Ultrasound

Ulas Taskin¹, Joost van der Neut¹, Koen w.a. van Dongen¹

¹Department of Imaging Physics, Faculty of Applied Sciences, TU Delft, Delft, Netherlands

Background, Motivation, and Objective

One of the leading causes of death for women is breast cancer. To increase the survival rate, there is an increasing interest in using ultrasound together with full-wave inversion to detect and characterize small breast lesions. A limiting factor to apply inversion is the long computation time involved. This computation time is generally proportional to the size of the imaging domain. To reduce the size we propose a technique referred to as redatuming. This technique is often used in seismics to back-propagate the field from the planar surface where the measurements have been done to a second surface near the volume of interest. Unfortunately, these seismic methods are not applicable to the curved scanning geometries used for breast ultrasound. Consequently, we investigate a new approach that does allow us to redatum the field measured on a closed cylindrical surface.

Statement of Contribution/Methods

To employ redatuming we describe the measured wave fields using Hankel functions. Once Hankel decomposition of the field is done, redatuming of the field towards any location in the homogeneous background becomes possible.

The method is tested on data measured with the Delft Breast Ultrasound Scanner (DBUS); a circular scanning system that operates at 0.5 MHz central frequency. First, a full scan is made for a receiver radius of 0.1 m. Then, we redatum the data to a receiver radius of 0.05 m. Finally, imaging by Born inversion is done for both the original and redatumed data.

Reconstruction results of both data sets are shown in Figure 1. The first two images are based on four frequency components obtained before (left) and after (middle) applying redatuming. The resulting images are highly similar, with the second image being computed four times faster than the first image. Next, we increase the number of frequency components from four to sixteen. Compared to the first image, the computation time remained the same, while the reconstruction improved significantly.

Results/Discussion

A new technique to redatum breast ultrasound measurements is presented. The method has been validated successfully using experimental data in combination with Born inversion. In addition, we showed that reducing the size of the spatial domain lead to a significant reduction in computation time. This is important when solving computationally demanding 3-D inverse problems.

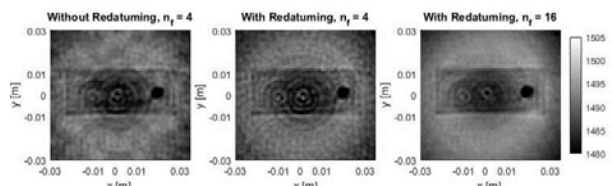


Figure 1: Born inversion applied on a circular scan of a rectangular agar phantom containing two copper threads and one plastic straw. Results obtained using four frequency components before (left) and after (middle) redatuming the wave field. By redatuming the wave field it becomes feasible to increase the number of frequency components for Born inversion to 16 (right).

10:45 AM

Sparse recovery of strong reflectors with an application to non-destructive evaluation**Eric Bezzam¹, Adrien Besson¹, Hanjie Pan², Dimitris Perdios¹, Jean-Philippe Thiran^{1,3}**¹*Signal Processing Laboratory 5, Ecole Polytechnique Fédérale de Lausanne, Lausanne, Switzerland*, ²*Audiovisual Communications Laboratory, Ecole Polytechnique Fédérale de Lausanne, Switzerland*, ³*Department of Radiology, University Hospital Center and University of Lausanne, Lausanne, Switzerland***Background, Motivation, and Objective**

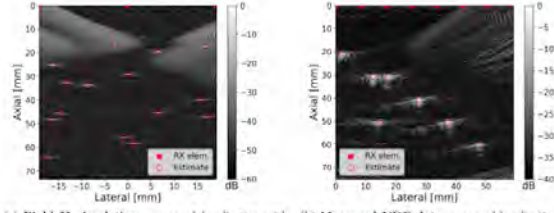
In several applications, the localization of strong reflectors in an insonified medium is of significant interest: cracks in non-destructive evaluation (NDE) and microbubbles in medical imaging. We propose a high frame rate method to accomplish this with plane wave transmission, sub-Nyquist sampling and three receive (RX) channels. Sub-Nyquist recovery is typically performed by modelling each channel's measurement as a stream of pulses located at the appropriate time-of-flights (TOFs). With a suitable sampling kernel, reconstruction can be done in the discrete or continuous domain, e.g. L1-minimization or finite rate of innovation (FRI) methods. FRI places practical constraints on the sampling kernel, namely bandpass filters.

Statement of Contribution/Methods

The proposed method achieves strong reflector localization in two steps: TOF estimation with FRI and localization with Euclidean Distance Matrices (EDMs). Standard FRI is highly sensitive to pulse estimate errors. We therefore use the generalized framework (GenFRI) [Pan et al, Towards Generalized FRI Sampling] which is more robust to such errors while requiring the same minimum number of samples for recovery: $2K+1$ for K TOFs. In GenFRI, reconstruction is recast as a constrained optimization in order to recover a stream of pulses that is consistent with the measurements. With the TOFs across multiple channels, beamforming is not needed to recover the reflector locations. Given two TOFs of the same reflector, its position can be determined by solving a system of quadratic equations. The challenge is identifying the TOFs correspondence across channels. A minimum of three sensors is sufficient to uniquely match TOFs by exploiting the rank property of EDMs. Our method thus requires $3(2K+1)$ samples for localization. More samples and channels can be used for noisy measurements and model inaccuracies.

Results/Discussion

In Fig. 1a we apply the proposed method with standard FRI to simulated pulse-echo RF data. We recover the 15 strong reflectors in white noise (10.4 dB SNR) with three RX channels and an 8x sampling rate reduction. In Fig. 1b we tackle NDE data but apply GenFRI as the exact pulse shape is unknown. Seven holes in an aluminium block are correctly localized with 8 RX channels and a 7x sampling rate reduction. With the proposed method, a reduction in the number of ADCs, the sampling rate and data is thus possible.



(a) **Field II simulation:** proposed localization with 3 RX channels at 2.61 MHz sampling rate (8x reduction) overlaid on DAS beamforming with 128 RX channels at 20.8 MHz. Reconstruction accuracy of 44 dB.
(b) **Measured NDE data:** proposed localization with 8 RX channels at 7.18 MHz sampling rate (7x reduction) overlaid on DAS beamforming with 64 RX channels at 50 MHz.

Figure 1: (a) Proposed algorithm with standard FRI applied to Field II generated data (128 transmit elements, 0.3 mm pitch, 5.2 MHz center freq., 1 plane wave normal incidence); (b) Proposed algorithm with GenFRI applied to measured NDE data provided by Advanced OEM Solutions (64 transmit elements, 0.93 mm pitch, 5 MHz center freq., 1 plane wave normal incidence).

11:00 AM Resolution analysis and uncertainty quantification for ultrasound computed tomography

Christian Boehm¹, Naiara Korta Martiartu¹, Vaclav Hapla¹, Andreas Fichtner¹

¹ETH Zurich, Switzerland

Background, Motivation, and Objective

Ultrasound Computed Tomography (USCT) is a widely used imaging technology for breast cancer screening, and there is a variety of image reconstruction algorithms working either with ray-based approximations, or by simulating the (visco)-acoustic wave equation. The final image is typically assembled from several pieces, considering both transmission and reflection data, as well as different tissue properties like speed of sound, density or attenuation. Despite the computational complexity of solving this non-linear inverse problem, another major challenge is the assessment of the quality of the reconstructed image in terms of spatial resolution and parameter tradeoffs. The goal of this work is to enhance tomographic images with this information by applying Bayesian inference.

Statement of Contribution/Methods

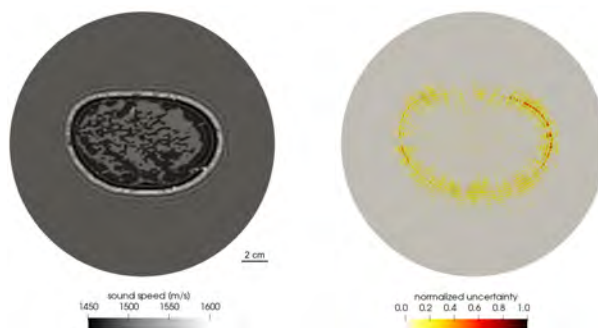
We present a framework for analyzing the resolution and the uncertainties in USCT images. The method is based on a Bayesian formulation of the inverse problem that enables us to extract statistical quantities, such as means and pointwise variance fields from the posterior distribution.

The main ingredients are (1) the computation of a joint posterior distribution resulting from imaging with transmission and reflection data, (2) an approximation of the data misfit covariance based on a low rank approximation of the Hessian and adjoint techniques, (3) an efficient strategy to sample the posterior that relies on concurrently solving a deterministic inverse problem approximately, and (4) an extension to non-Gaussian priors, in particular those resulting from a total variation regularization.

The method is applicable to both ray-based and full waveform imaging techniques.

Results/Discussion

We present several numerical examples for USCT breast imaging using both simulated data generated with the OA-Breast database (Lou et al., 2017) and real data provided by the USCT Data Challenge 2017 (Ruiter et al., 2017). Fig. 1 shows the reconstructed speed of sound of a synthetic breast phantom using waveform inversion (left) and the estimated normalized uncertainty (right). The skin is poorly resolved, because reflection data is not taken into account. This is reflected by high spatial uncertainties in this region. Furthermore, we discuss how this approach can help to objectively assess the quality of the reconstruction, and to tune acquisition and imaging systems.



11:15 AM Modeling of Wave Propagation in Heterogeneous Media Using a Modified Mixed Domain Method
Juanjuan Gu¹, Yun Jing¹
¹*Mechanical and Aerospace Engineering, North Carolina State University, Raleigh, NC, United States*
Background, Motivation, and Objective

High intensity focused ultrasound (HIFU) has been applied to treat a variety of diseases. Numerical models can be utilized as an alternative or adjunctive approach to study the safety and effectiveness of HIFU device. A mixed domain method (MDM) for modeling linear/nonlinear wave propagation in dissipative, weakly heterogeneous media has been studied. To extend the MDM for modeling wave propagation in more strongly heterogeneous media, phase and amplitude corrections to the MDM are proposed and evaluated in this paper.

Statement of Contribution/Methods

The original MDM solves the Westervelt-like equation with appropriate assumptions and it is accurate for cases with small variations of speed of sound. A phase correction term is theoretically derived. As the transmission coefficient due to the variation of sound speed is not considered in the original MDM, an amplitude correction is also proposed and applied in the wave-vector domain. The resulting method is denoted as the modified mixed domain method (MMDM).

Results/Discussion

We first validated the MMDM using a layered medium (Fig. 1(a)). Sound speed and density are 1500 m/s and 1000 kg/m³ in the blue layer and are 3000 m/s and 2000 kg/m³ in the red layer. Results from the angular spectrum approach (ASA) are used as the benchmark. The center frequency is 1 MHz. The geometrical focus is 12 mm and the aperture size is 15 mm. Spatial step size in the ASA is 1/32λ (λ is the wavelength and it is 1.5 mm). The temporal resolution dt is 0.05 μs for both methods. The L2 norm errors evaluated at the geometrical focus at step size 1/4λ, 1/8λ and 1/16λ are 2.4131, 2.3868 and 2.2010 for MDM and are 0.1854, 0.1423 and 0.1242 for the MMDM. The results with step size 1/8λ are shown in Fig. 2 (b).

A clinically relevant case (Fig. 3) is studied and tissue properties are shown in table I. Results from k-Wave are used as benchmark. Transducer diameter in this case is 62.7 mm and focal length is 62.9 mm. Center frequency is 0.7 MHz. Time step in MMDM is 0.0714 μs and in k-Wave is 0.0022 μs. Spatial step size in both methods are 0.1650 mm. The L2 norm error in time domain is 0.1099 for MMDM. Fig. 3 shows the pressure at the geometrical focus. Fundamental and second-harmonic wave fields are in Fig. 4.

Overall, the MMDM does significantly improve upon the MDM for moderately heterogeneous media. In the future, we would like to add reflections to further increase the accuracy of the model.

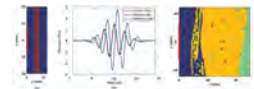


Figure 1. (a) A layered medium with a slice showing contour of 2.0 for both the density and speed of sound. Components are shown in (b).

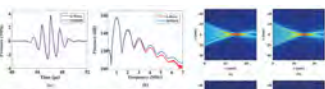


Figure 2. Tissue map. The superficial layer is skin tissue, then in fat with connective tissue and muscle.

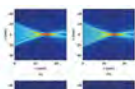


Figure 3. Comparison for the wave pressure at the geometrical focus of the transducer between the simulation results in (a) time domain and (b) frequency domain.

| Table I | | | |
|------------|--------------------------|---------------------------|--------------------|
| | Nonlinearity coefficient | Density Kg/m ³ | Speed of sound m/s |
| connective | 5 | 1120 | 1613 |
| fat | 5.8 | 937 | 1479 |
| muscle | 5.5 | 1070 | 1566 |
| tissue | 5.5 | 1000 | 1540 |

Table I. Properties for the fundamental frequency field simulated by (a) MMDM and (b) k-Wave.

Properties for the second-harmonic field simulated by (c) MMDM and (d) k-Wave.

Figure 4. Pressure for the fundamental frequency field simulated by (a) MMDM and (b) k-Wave.

Pressure for the second-harmonic field simulated by (c) MMDM and (d) k-Wave.

11:30 AM

Strongly Nonlinear Ultrasound Simulations in an Axisymmetric Coordinate System using k-Wave**Bradley Treeby¹, Elliott Wise¹, Filip Kuklis², Jiri Jaros², Ben Cox¹**¹*University College London, United Kingdom, ²Brno University of Technology, Czech Republic***Background, Motivation, and Objective**

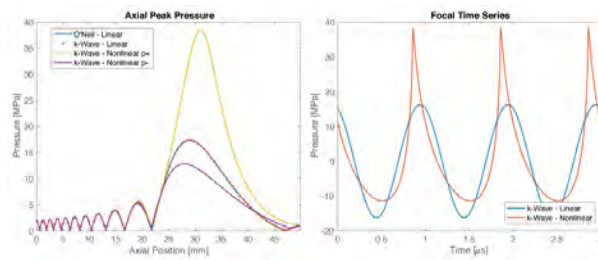
Full-wave nonlinear ultrasound models in 3D have many applications. Simulations have now been demonstrated by many groups, and the open-source k-Wave toolbox provides a freely available tool for this purpose. The largest k-Wave simulations to date use 4096^3 grid points. While well beyond the limits imagined a decade ago, this still requires many days on a large supercomputer. Moreover, for a 20 cm domain and a 1 MHz source frequency, even simulations this size are only accurate up to 15 harmonics, which is not sufficient for modelling high-intensity sources used in emerging ultrasound therapies. In this work, an axisymmetric k-Wave model is developed capable of modelling highly-nonlinear fields with modest computational resources.

Statement of Contribution/Methods

A pseudospectral time domain (PSTD) solution of the first-order conservation equations (equivalent to a generalised Westervelt equation) in an axisymmetric coordinate system is derived. Spatial gradients are computed using a spectral collocation method with a Fourier basis. The FFT and discrete trigonometric transforms (DTTs) are used to compute gradients in the axial and radial dimensions, respectively. Time integration is performed using a first-order forward difference with a k-space correction (derived using the framework of non-standard PSTD schemes) to minimise numerical dispersion. The model is implemented in C++ for a single shared-memory computer. The FFTs and DTTs are computed using the FFTW library. Element-wise operations are parallelized using OpenMP and streaming SIMD extensions.

Results/Discussion

The code is validated against other numerical models and analytical solutions for grid sizes up to 16384×8192 grid points. For linear simulations of plane piston and focused bowl transducers, the error in the axisymmetric model at 3 points per wavelength is <1% compared to analytical solutions (see figure). For a nonlinear plane wave, the error is <0.2% compared to the Mendousse solution. A more general example of the nonlinear field from a focused bowl transducer is shown in the figure. This uses a grid size of 5120×2048 , modelling up to 75 harmonics, and was computed in 37 minutes on a typical server using <1 GB of memory. Compared to simulations in 3D, the axisymmetric model allows the efficient computation of highly-nonlinear fields. The model will form part of the next k-Wave release.



11:45 AM Distinguishing between noncausal and nonlocal behavior in a time-fractional wave equation

James F. Kelly¹, Robert J. McGough¹
¹Michigan State University, United States

Background, Motivation, and Objective

There is some confusion in the ultrasound literature with regards to the distinction between noncausal and nonlocal behavior in fractional wave equations that describe power law attenuation. In a causal system, the effect follows the cause, and in a noncausal system, a nonzero response occurs before the input is applied. In contrast, local operators only relate values at a single point, and nonlocal operators include information from distant sources. Causality strictly describes the time response, whereas temporal and spatial operators determine the locality. Causality and locality are thus two separate concepts, which will be reinforced through the presentation of several different examples.

Statement of Contribution/Methods

The distinction between causality and locality is demonstrated through analysis of the power law wave equation, which exhibits four different combinations of causality and locality for different values of the power law exponent y . The power law wave equation is causal for power law exponents $0 \leq y < 1$, and the power law wave equation is noncausal for $1 < y \leq 2$. Also, the power law wave equation is local for integer values of y , and the power law wave equation is nonlocal for noninteger values of y . Causal and noncausal responses are described through calculation of time-domain Green's functions for the power law wave equation, which are shifted and scaled stable densities that are readily computed with the Stable Toolbox. Local and nonlocal behavior is demonstrated through integer and fractional derivatives of inputs with finite temporal duration.

Results/Discussion

Fig. 1a shows an example of a causal response for a nonlocal system with power law exponent $y=1/2$, Fig. 1b demonstrates a noncausal response for a nonlocal system with power law exponent $y=3/2$, and Fig. 1c describes a noncausal response for a local system with power law exponent $y=2$. All three of these examples evaluate time-domain Green's functions multiplied by $4\pi r$ for a sound speed constant $c_0 = 1450$ m/s and an attenuation constant $\alpha_0 = 0.086$ Np/cm/MHz^y. From these three plots, the causal and noncausal responses are easily identified, whereas separate mathematical analysis is required to distinguish between local and nonlocal behavior.

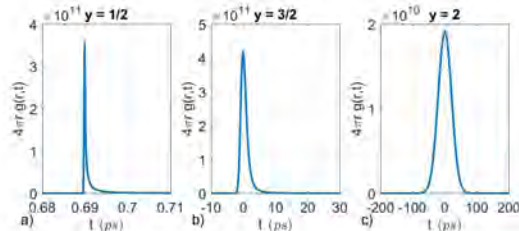


Figure 1: Time-domain Green's functions for the power law wave equation multiplied by $4\pi r$ evaluated at $r = 1$ nm for power law exponents a) $y = 1/2$, b) $y = 3/2$, and c) $y = 2$. Panel a) shows an example of a causal time-domain Green's function, and panels b) and c) contain noncausal time-domain Green's functions. Panels a) and b) are computed with nonlocal operators, and panel c) is computed with a local operator.

7J - PGP & PNL: General Physical and Non-Linear Acoustics

Kikusui (140)

Thursday, October 25, 1:30 pm - 3:00 pm

Chair **Dave Feld**
Broadcom Ltd

7J-1

1:30 PM **Multiple steerable acoustic fields using a single element bowl transducer and 3D-printed kinoform**

Michael Brown¹, Ben Cox¹, Bradley Treeby¹

¹*Medical Physics and Biomedical Engineering, University College London, London, United Kingdom*

Background, Motivation, and Objective

Acoustic kinoforms are objects that can be used to generate complex focused acoustic fields from planar single element transducers. They are 3D printed lenses that map the transducer field onto a pre-calculated phase hologram via variations in thickness. While promising for applications in particle manipulation and neurostimulation, a present limitation is that the pattern generated by each kinoform is fixed.

Two methods that exploit the chromatic properties of these kinoforms can be used to overcome this drawback. First, using a focused rather than a planar transducer allows for scaling of the pattern at the focal depth by varying the driving frequency. Second, the dependence of the generated phase offsets on frequency allows for distinct patterns to be encoded onto different driving frequencies. The aim of this work was to investigate combining both methods to create multiple scalable patterns from a single element transducer.

Statement of Contribution/Methods

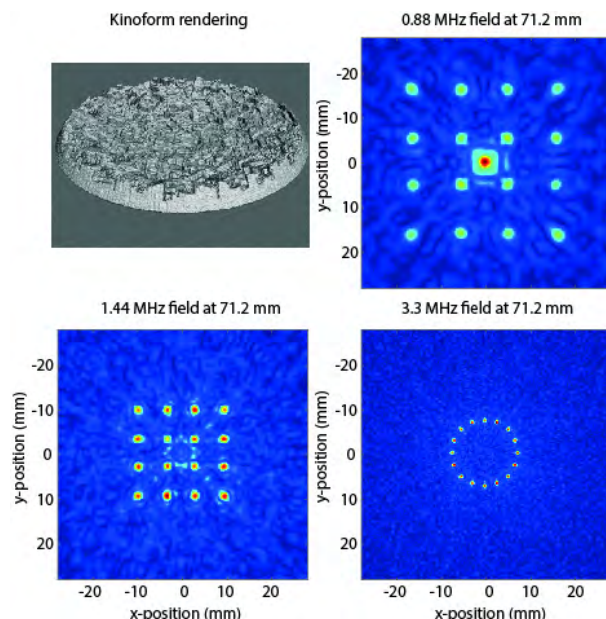
An optimisation approach using direct search was implemented to design the kinoforms. This searched for the thickness at each position on the transducer that minimised a cost function penalising variation between the target and output field at each design frequency. The k-Wave toolbox was used to simulate the output field of each kinoform and to quantify the effect of changing different design and experimental parameters.

The approach was then validated experimentally. A kinoform was designed for a 1.1 MHz bowl transducer with a 64 mm diameter and 63.2 mm radius of curvature. Different patterns were encoded onto the fundamental and the third harmonic. The kinoform was fabricated via 3D printing and the acoustic field was characterised driving the transducer at a range of frequencies.

Results/Discussion

Both the simulated and experimental results demonstrated that multiple scalable patterns can be generated at a fixed depth with this approach. This is illustrated by the figure which shows a rendering of a kinoform and its simulated field at three frequencies. Both the change in size of the pattern at the fundamental and the distinct pattern at the third harmonic can clearly be seen and there is no visible cross-talk.

This result could find applications in many areas of physical acoustics. For example, for particle manipulation the spacing between a set of objects could be flexibly changed by varying the driving signal.



1:45 PM Source Correction for k-space Pseudospectral Time Domain Models

Ben Cox¹, Bradley Treeby¹¹*University College London, United Kingdom***Background, Motivation, and Objective**

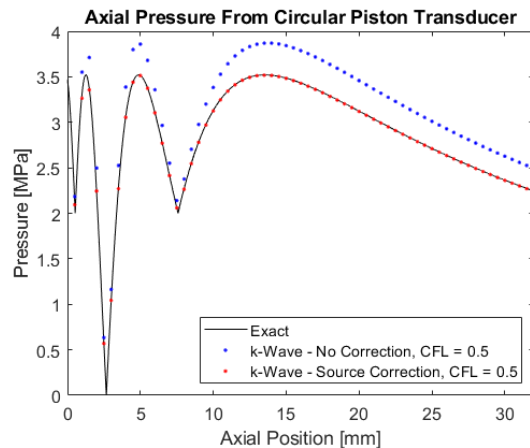
Non-standard pseudospectral time domain methods, often called k-space methods, are widely used in acoustics for modelling wave propagation through large domains, and form the basis of the open-source k-Wave toolbox. These methods combine the calculation of spatial gradients using a Fourier collocation spectral method, with a k-space corrected finite-difference time step. For initial value problems in homogeneous and lossless media, the k-space correction factor makes the method exact and unconditionally stable, and for more general media, significantly reduces dispersion errors. However, the k-space correction is derived from the source-free wave equation. This means when time-varying sources are introduced, noticeable amplitude errors can arise (see figure). While this error converges away when increasing the number of points per period (reducing the CFL), this can significantly decrease performance.

Statement of Contribution/Methods

In this work, an exact time-stepping scheme is derived for the wave equation including a time-varying source term. This is based on an exact solution for the inhomogeneous wave equation with a single-frequency continuous wave source [<http://dx.doi.org/10.1121/1.5021245>]. Using the underlying dispersion relation, this results in a simple form for the source correction that can be expressed as a function of either the source frequency, or the spatial frequency. The former gives a simple scalar amplitude scaling factor, but relies on knowledge of the source frequency. The latter can be applied to broadband sources without needing to specify the frequency, but requires two additional FFTs per time step.

Results/Discussion

The source correction terms were implemented in k-Wave. Simulations were compared against the acoustic field propagator (AFP) and analytical solutions for simple source geometries. When the source correction was applied, k-Wave simulations for single frequency sources agreed with the AFP to machine precision. For multi-frequency or broadband sources, the error was less than 1% when compared to analytical solutions. The figure shows an example for the axial pressure from a circular piston transducer driven at two frequencies along with the analytical solution. The source correction will be included as part of k-Wave, and significantly improves the accuracy and efficiency of modelling time-varying sources.



2:00 PM

Changing the Speed of Ultrasonic Pulses Through Spatial Structuring of the Acoustic WavefrontGrace Richard¹, Holly Lay², Sandy Cochran², Gabriel Spalding³, Martin Lavery¹¹School of Engineering, University of Glasgow, Glasgow, United Kingdom, ²Medical and Industrial Ultrasonics, University of Glasgow, Glasgow, United Kingdom, ³Department of Physics, Illinois Wesleyan University, Bloomington, IL, United States**Background, Motivation, and Objective**

Phase controlled arrays of ultrasonic transducers are used for imaging in medical ultrasound [1], the manipulation of particles with acoustic tractor beams [2] and many other applications. A particular form of spatial shaping creates helical wavefronts that carry a property known as orbital angular momentum (OAM). This interesting property was first noted by Allen et al. in 1992 [3] where a wavefront with an azimuthal phase dependence of $\exp(i\ell\phi)$, where ℓ is an unbounded integer and ϕ is the angular coordinate, carry an OAM of $\ell\hbar$ per photon. Subsequently in 1998, Hefner and Marston demonstrated the presence of OAM in acoustic waves [4].

Recent studies in optics have indicated the spatial shaping of optical wavefronts have induced changes in the group velocity of photons [5]. In this paper, we investigate the slowing of an ultrasonic pulse that arises from the spatial shaping of sound. Our results indicate that we observe a change in propagation speed of an ultrasonic pulse by 2% when the pulse is carrying a OAM of $1\hbar$.

Statement of Contribution/Methods

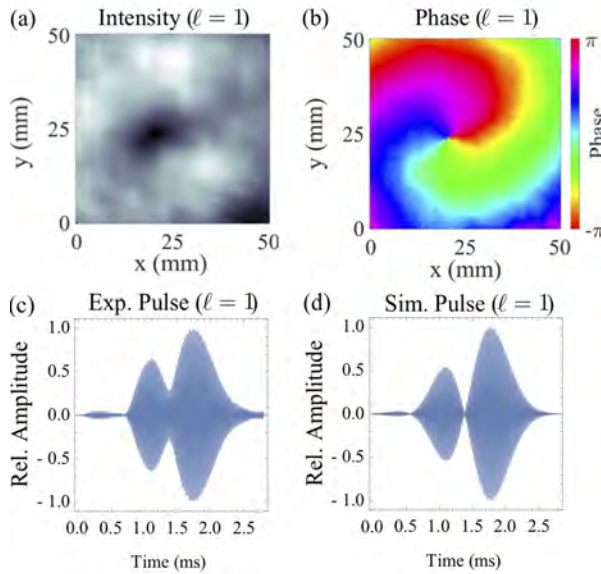
We generate our structured sound using 28, 40 kHz transducers to create a bespoke phased array antenna. Each transducer is coupled into a 3D printed tapered waveguide that guides the sound to form a square array of apertures half a wavelength apart and are individually addressable to allow for the generation of Ultrasonic OAM modes. Using a scanning ultrasonic microphone we can measure both the intensity, Fig 1(a), and the phase, Fig 2(b), of the wavefront generated by our bespoke phased array antenna.

Results/Discussion

Our array generates 2 π acoustic pulses that is subsequently measured by a microphone with a collection area of 14mm, which is placed at the centre of the wavefront. Our results show an amplitude variation in pulse indicative of variation in the speed of sound across the area of the microphone, Fig.1(c). This amplitude arises from beating from the spatial variation in the speed of sound across the microphone's aperture, Fig.1(d). We will discuss our results in full and further present experimental data for a range of structured ultrasonic modes.

References

- [1] J. A. Jensen, Prog Biophys Mol Biol., 93, 1, 2007.
- [2] C. E. M. Démoré et al., Phys. Rev. Lett., 112, 17, p. 174302, 2014.
- [3] L. Allen, et al., Phys. Rev. A, 45, 11, pp. 1992.
- [4] B. T. Hefner et al., J. Acoust. Soc. Am., 103, 5, 1998.
- [5] D. Giovannini et al., Science, 347, 6224, 2015.



2:15 PM

Focused Ultrasonic Transducer with Electrically Controllable Focal-Point LocationLurui Zhao¹, Eun Sok Kim¹¹UNIVERSITY OF SOUTHERN CALIFORNIA, United States**Background, Motivation, and Objective**

Focused ultrasonic transducers are used in imaging, medical therapeutics, microfluidic mixing, etc. However, the electrical controllability of the focal point has not been reported without a phased array that requires many power amplifiers or high-voltage phase shifters for high intensity application, while a time-shared phase array with one power amplifier and one phase shifter reduces the focused intensity. We recently reported a design with electrical controllability over the focal length, but not the focal position over a plane. We now describe electrically tuning of the focal position over a focal plane.

Statement of Contribution/Methods

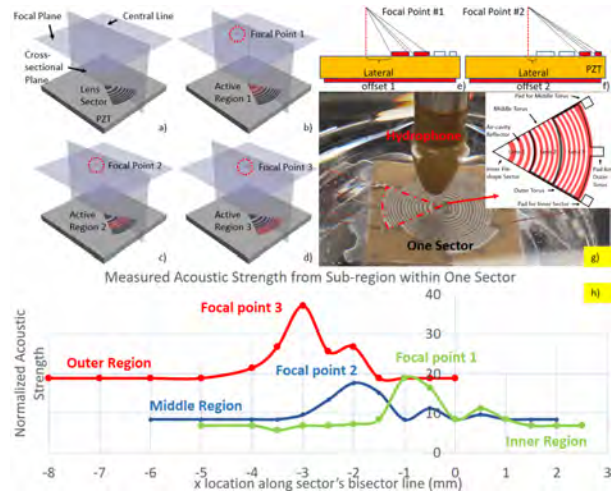
Fresnel zone-plate focuses ultrasound through near-field effect. Since the focal point of a Fresnel zone-plate is along the line perpendicular to the center of the annular ring, we make the focal points off-centered by offsetting the centers of the ring patterns in different regions of the transducer, so that the focal points of different regions may be at different locations. By electrically selecting and actuating the electrodes in each of the regions, the focal position can be electrically changed.

The transducer is fabricated on a 1.02mm thick PZT deposited with nickel electrodes. The front nickel layer is patterned into 6 sectors, with each sector divided into 3 sub-regions along its radius (i.e., inner pie-shape sector, middle torus, and outer torus) with 0.05 mm spacing between the regions. Each electrode is made to be individually accessible. On top of the patterned electrode, off-centered Fresnel zone-plate pattern is defined with 20μm-thick-Parylene-sealed air-cavities. Focal positions of the three lenses are offset from the device center by 3, 2, 1, -1, -2, and -3mm.

Results/Discussion

By electrically actuating the different sub-regions within a sector, we have observed the focal point position varying a total of 6mm on the focal plane. Figure h shows the measured pressures for three cases (i.e., 3, 2 and 1).

With a transducer designed for 5mm focal length, we demonstrated its electrical tunability of the focal point through measuring the acoustic field with a point hydrophone (Figure g). With the transducer immersed in water and driven under pulsed 2.25 MHz sinusoidal signal at $V_{pp}=30V$, the measured results confirm the electrical controllability of the focal point over a 2-dimensional plane.



2:30 PM

Bayesian spectrum analysis of non-linear ultrasound contrast microbubble signalsKonstantinos Diamantis¹, James Hopgood², Vassilis Sboros¹¹*Heriot-Watt University, United Kingdom*, ²*University of Edinburgh, United Kingdom***Background, Motivation, and Objective**

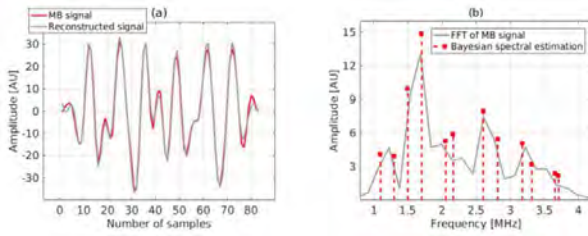
The localization of individual contrast microbubbles (MBs) is key to the emerging field of super-resolution ultrasound. The Fourier Transform (FT) is typically used for the frequency domain analysis of MB signals in ultrasound contrast imaging. Bayesian spectrum analysis offers a viable solution to overcome the limited frequency resolution achieved by the FT for linear scatter. This work investigates the uniqueness, robustness, and parsimoniousness of the solution derived by the Bayesian spectrum analysis. It also provides an assessment of such a method for the reconstruction of non-linear MB signals.

Statement of Contribution/Methods

The Bayesian method attempts to represent any given input signal as a sum of sinusoids in noise. The number of frequencies, their values, their associated amplitude and phase are all unknown parameters that are being estimated. The algorithm is based on the exploitation of prior knowledge and on repetitive realizations for the estimation. A modified transducer is used to acquire echo signals from individual MBs with 20 MHz sampling rate. The Bayesian method is employed to calculate all signal parameters which lead to signal reconstruction. The similarity between original MB echo and reconstructed signal is measured using the correlation coefficient, r . The method is then applied to the reconstructed signal. This second round of reconstruction allows the one to one comparison of all estimated parameters.

Results/Discussion

A set of 2 signals is shown in Fig.(a) as an example, and the r is calculated to 0.99 showing close resemblance between MB and reconstructed signal. The signal duration is limited to \approx 80 samples which is equivalent to a frequency resolution of 250 kHz using the FT as the temporal and spectral resolution are inversely proportional. Fig. (b) shows that the Bayesian spectral estimation results in 12 distinct frequency components many of which are separated by less than 250 kHz. The smallest separation is 52 kHz. Overall, the result matches relatively well with the FT, is reproducible for the second stage of reconstruction (all 12 frequencies are always resolved), and promises high spectral resolution without sacrificing the temporal one. Further, the MB non-linear signal can be well differentiated from that of linear scatter. A 80% correct signal classification can be achieved based on the spectral content of the 2 signal types.



2:45 PM

HIFU beam: a software package for modeling axially-symmetric nonlinear ultrasound beams radiated by focused therapeutic transducersPetr Yuldashev¹, Ilia Mezdrokhin¹, Pavel Rosnitskiy¹, Oleg Sapozhnikov^{1,2}, Vera Khokhlova^{1,2}¹*Physics Faculty, Moscow State University, Russian Federation*, ²*Applied Physics Laboratory, University of Washington, United States***Background, Motivation, and Objective**

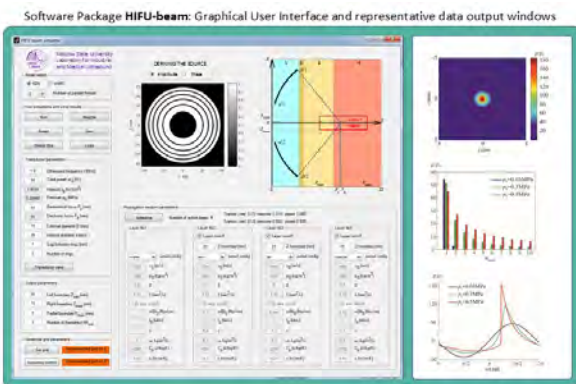
High Intensity Focused Ultrasound (HIFU) transducers operate over a wide range of power outputs including the conditions when beam focusing is strongly affected by nonlinear propagation effects. User-friendly wave simulators can serve as an effective tool for predicting the pressure levels in nonlinear HIFU fields and designing transducers capable to reach the desired parameters of such fields.

Statement of Contribution/Methods

A software package "HIFU beam" with a graphical user interface (GUI) implemented as a MATLAB application was developed and includes simulation of two wave equations in axially-symmetric formulation. The Khokhlov-Zabolotskaya-Kuznetsov (KZK) nonlinear parabolic equation is generalized to include an equivalent source boundary condition for modeling strongly focused beams. The Westervelt equation is represented through the split-step Pade approximation of the diffraction operator for one-way propagation and is termed as a wide angle parabolic equation (WAPE) [Yuldashev et al., *Acoust. Phys.*, 64(3), 2018]. HIFU transducer is defined as an annular focusing array. Both equations are solved in the frequency domain. A method of fractional steps with an operator splitting procedure is implemented and individual algorithms are used for modeling diffraction, nonlinearity, and absorption effects. A user can configure the geometrical parameters and power of the array, and acoustic properties of up to 10 layers of the propagation medium (See Fig.). Electronic focus steering along the beam axis is also included. The solver is parallelized using OpenMP and can be executed on a PC with multiple cores. Visualization and output of various acoustic field parameters such as waveforms, peak pressures, intensity, and heat deposition rate are provided.

Results/Discussion

The software package "HIFU beam" is developed for modeling nonlinear HIFU beams in layered medium such as water and different types of tissue. Axially symmetric formulation greatly reduces the computation time when shock fronts are developed as compared to fully 3D simulations. Even if transducer geometry is not quite symmetric, it often can be represented by an equivalent radially-symmetric source [Rosnitskiy et al., *IEEE UFFC*, 64(2), 2017]. The package can be downloaded and used for free from the website <http://limu.msu.ru> from 1 October 2018. Work was supported by RSF №14-12-00974.



7K - Ultrasonic Devices

Kikusui (140)

Thursday, October 25, 4:00 pm - 5:30 pm

Chair **Margaret Lucas**
University of Glasgow

7K-1

4:00 PM A novel swimmer actuator via leaky surface acoustic wave

Deqing Kong¹, Minoru Kurosawa¹

¹Tokyo Institute of Technology, Japan

Background, Motivation, and Objective

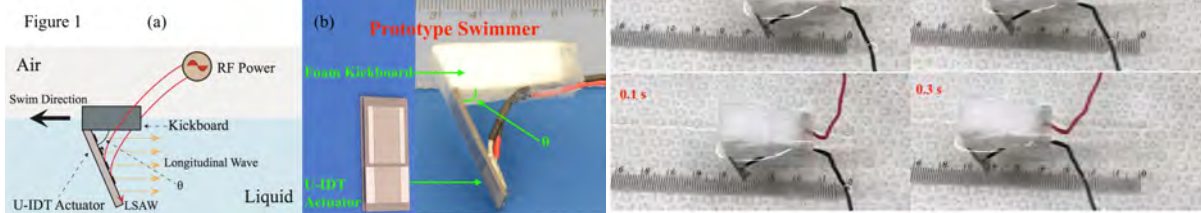
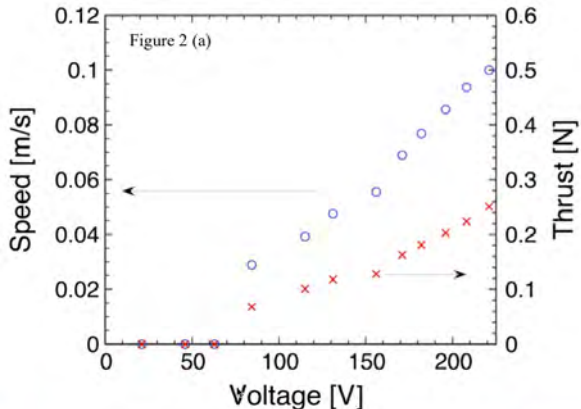
Robotic swimmer represents a rapidly emerging and fascinating research area. Particularly, small size swimmer is attempt to be a drug carrier or fixer inside the human body. In this study, a novel approach to the swimmer actuator via leaky surface acoustic wave (LSAW) is first proposed in the world. The swimmer converts acoustic streaming propulsion of the longitudinal wave via LSAW into movement in water.

Statement of Contribution/Methods

A schematic view of the swimmer with LSAW is displayed in Fig. 1 (a). A unidirectional interdigital transducer (U-IDT) actuator is utilized to generate the acoustic streaming in water, based on the 128°y-rotated x-propagation lithium niobate substrate. A kickboard is set to make the swimmer float in water. 22° angle θ is kept between the U-IDT actuator and the kickboard to make the horizontal acoustic streaming propulsion in the rear of swimmer. A prototype swimmer is displayed in Fig. 1 (b).

Results/Discussion

At 9.61 MHz driving frequency, the velocities and thrusts of the swimmer versus the driving voltage are shown in Fig. 2 (a). The velocity was measured out, when the driving voltage was up to 85 V_{pp}. At 225 V_{pp} driving voltage, 0.1 m/s velocity was confirmed. Furthermore, even the swimmer did not move less than 85 V_{pp} driving voltage, 0.25 N thrust was measured at 225 V_{pp}. The movement of the swimmer in water is recorded per 0.1 second, when the driving voltage is 225 V_{pp}, as observed in Fig. 2 (b). The prototype swimmer moves by one centimeter per 0.1 second, according to the set scale in the bottom of the tank. The LSAW swimmer actuator is first presented and demonstrated in the world. Because the surface acoustic wave device is easy to be miniaturized, the LSAW swimmer actuator can be expected for the small robot inside the human body.



4:15 PM

Ultrasonic Propeller with Electrically Controllable Propulsion DirectionLurui Zhao¹, Eun Sok Kim¹¹UNIVERSITY OF SOUTHERN CALIFORNIA, United States**Background, Motivation, and Objective**

Immersive micropropeller has potential applications in drug delivery, microfluidics, robotics, etc. However, there has been no report on micropropeller with electrical controllability over propulsion direction. The new device described here offers highly efficient, immersive, propeller with electrical controllability of the propulsion direction.

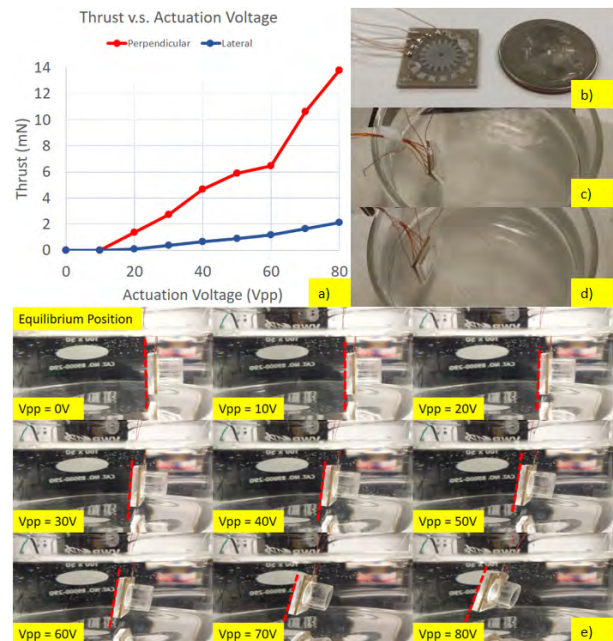
Statement of Contribution/Methods

A focused ultrasound transducer immersed in liquid produces an intensified acoustic beam at the focal point, which delivers momentum to the liquid, resulting in propulsion force on the transducer, as the propelled liquid mass is replenished from the surrounding region. With Fresnel lens based on annular rings, the in-plane or lateral acoustic forces cancel each other out, leading to a thrust force perpendicular to the lens surface. However, if the annular rings are sectored into pie shape and the actuation on one sector is weaker than other sector(s), there exists unbalanced acoustic force, which will result in a lateral thrust. By controlling the actuation amplitudes on all the sectors, the propelling direction can be finely tuned.

The propeller is made on a 1.02mm thick nickel-coated PZT substrate, with the front nickel layer patterned into 18 sectors. Fresnel lens with air-cavity-reflectors are added over the sectored electrodes for the acoustic focusing, so that the electrodes do not need to be finely patterned in order to ensure minimum heat generation from the electrode joule effect. Propellers with and without the air-cavity-reflectors have been fabricated and packaged (Figure b).

Results/Discussion

The fabricated propeller is tested in water with a flexible wire suspending the device. Upon actuation, the propeller is propelled to leave its equilibrium position. The thrusts under different driving conditions are characterized by measuring the angle of the suspension wire. A maximum perpendicular thrust of 13.8mN is measured under 80V_{pp} driving voltage with all sectors on, while a maximum lateral thrust of 2.1mN is measured under 80V_{pp} voltage with a single sector on. With all the sectors actuated, the net thrust will be perpendicular (Figure e). By actuating only a selected sector, directional thrust is exerted to make the transducer turn left or right (Figures c and d).



4:30 PM

Special Nonlinear Effects of the Harmonic 3rd Overtone Thickness-shear Mode on its Fundamental Mode in f-3f Modal Interactions and Drive Level Dependency

Yook-Kong Yong¹, Xiangnan Pang¹, Ji Wang²

¹Civil and Environmental Engineering, Rutgers University, Piscataway, NJ, United States, ²Ningbo University, China, People's Republic of

Background, Motivation, and Objective

Previous papers and experiments have documented well the drive level dependency in a single mode. Recent experiments[1] were reported on AT-cut and SC-cut quartz resonators where the fundamental thickness shear (f_1) mode was observed to interact nonlinearly with its 3rd harmonic ($3f_1$) and its 3rd harmonic overtone mode (f_3). The parameters governing drive level dependency in quartz resonators are still not well understood and are still problematic for the industry. We show in this paper the role of 3rd harmonic overtone of thickness shear (f_3) mode and 3rd harmonic of the fundamental thickness shear mode ($3f_1$) on the drive level dependency of a fundamental thickness shear (f_1) mode resonator.

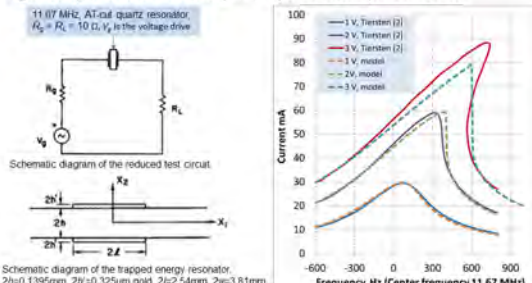
Statement of Contribution/Methods

We present for the first time in quartz thickness shear resonators the nonlinear finite element frequency responses of multi-modal interactions. We have developed a finite element program/model for nonlinear frequency responses of f - $3f$ modal interactions and drive level dependency in quartz resonators. We show that the drive level dependency was not due solely to a single mode Duffing resonator, but also dependent on its 3rd harmonic ($3f_1$) and 3rd harmonic overtone (f_3) modes.

Results/Discussion

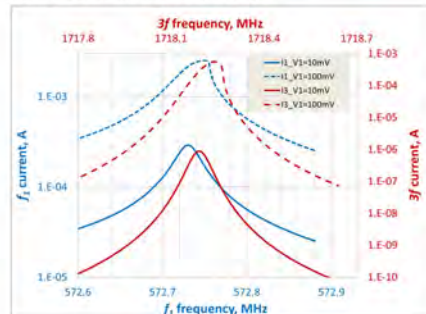
Our results were first validated by comparison with Tiersten's paper[2] for the nonlinear vibrations of an AT-cut quartz resonator as shown in Fig.1. Fig. 2 showed the f - $3f$ frequency response curves for a 573 MHz fundamental thickness shear mode resonator. The drive level dependency in the resonator was due to the nonlinear elastic constants and the proximity of 3rd harmonic overtone (blue curves) modal frequency to 3 times the fundamental mode frequency (red curves). Strong f - $3f$ modal interactions were generated by high drive levels at the fundamental mode.

Fig. 1: Comparison of drive level dependency of an AT-cut quartz resonator



[1] "Special Amplitude-Frequency Effects in VDF Quartz Resonators", Randall Kubena, Richard Joyce, Brian Rose and Yook-Kong Yong, *Proceedings of the 2013 IEEE International Frequency Control Symposium*, Taipei, Taiwan, 2013, pp. 1-6, DOI: 10.1109/IFCS.2013.6689982
 [2] "Analysis of nonlinear resonators in thickness shear and trapped energy resonators", H.F. Tiersten, *Journal of Acoustical Society of America*, Vol. 59, No. 4, April 1976, pp. 888-892.

Fig. 2: Voltage drive level dependency of the fundamental mode (blue) and its 3rd harmonic overtone mode (red).



4:45 PM

A Quasi-LTI Frequency-Selective SAW CirculatorGiuseppe Michetti¹, Cristian Cassella¹, Flavius Pop¹, Ahmed Kord², Dimitrios Sounas², Andrea Alù², Matteo Rinaldi¹¹Northeastern University, Boston, MA, United States, ²University of Texas at Austin, United States**Background, Motivation, and Objective**

Recent studies have shown how MEMS based Linear Time Varying (LTV) networks can realize efficient nonreciprocal components. We demonstrate here the first symmetric 3 port MEMS circulator with high frequency selectivity, based on time modulated SAW filters arranged in an Angular Momentum Bias(AMB) network. The unique features of MEMS resonators in this context enable the achievement of an unprecedented figure of distortion and full bandwidth operation.

Statement of Contribution/Methods

Three High-Q MEMS multi-pole SAW filters were time modulated with a single AMB core for the first time, so to ensure an almost flat nonreciprocal transfer function: interestingly, no loss overhead due the modulation can be observed, (Fig.1), as well as negligible spectral distortion (Fig.2) compared to static filters. IC switches were adopted to achieve the capacitance variation required, and an inductor was envisioned to resonate the average value of capacitance within the pass band. The switching frequency (F_m) was carefully selected at the edge of the pass band: this feature, together with the strong passive off-band rejection of the filter (Fig.2) was engineered to parametrically suppress Intermodulation (IM) tones. Moreover, thanks to its High-Q dynamics, the presented architecture enables lower F_m than attained with other AMB networks, thus confirming the impact of using MEMS resonators in nonreciprocal time-modulated RF components.

Results/Discussion

As expected, relative isolation was observed in excess of 7dB (Fig.1), with excellent threefold symmetry; both the bandwidth of the device and the F_m were found to be close to the same value (respectively 1.1% and 1.7% of RF frequencies) and the first IM product was found at -40dBc(Fig.2), the highest ever reported to our knowledge.

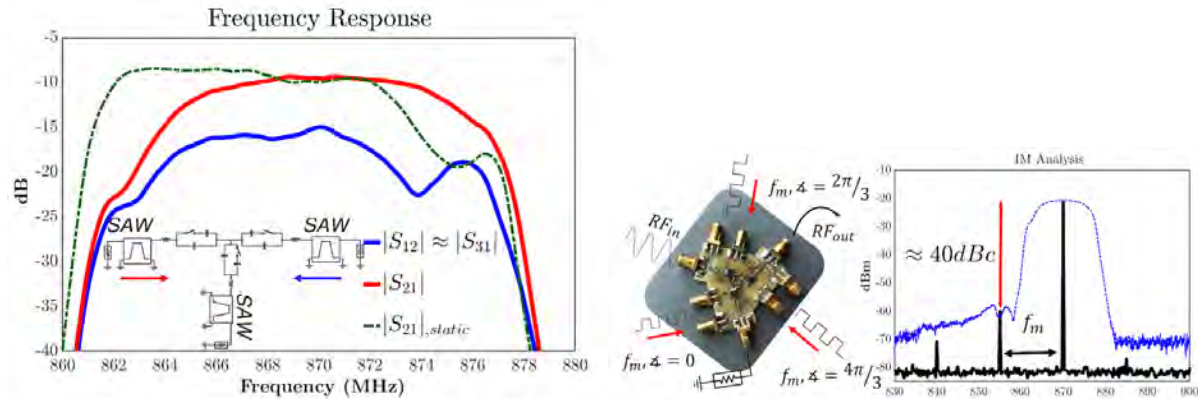


Fig.(1) Nonreciprocal architecture, displaying low dynamic losses induced by the modulation.

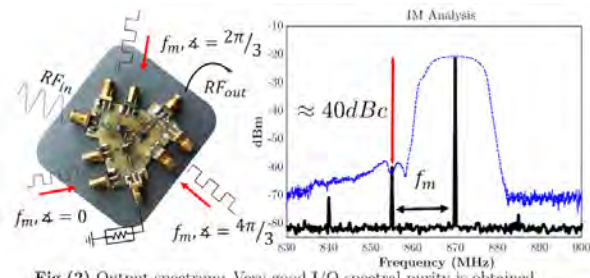


Fig.(2) Output spectrum: Very good I/O spectral purity is obtained, thanks edge-of-band modulation and strong off-band rejection of the SAW filter (in dashed blue, out of scale filter S21)

5:00 PM

A Radio Frequency Non-reciprocal Network Based on Switched Low-Loss Acoustic Delay LinesRuochen Lu¹, Tomas Manzaneque¹, Yansong Yang¹, Anming Gao¹, Liuqing Gao¹, Songbin Gong¹¹*University of Illinois at Urbana-Champaign, Urbana, IL, United States***Background, Motivation, and Objective**

RF non-reciprocal networks, e.g. circulators, are critical for implementing full-duplex radios. Conventionally, non-reciprocity is achieved by Faraday effect in ferrite materials. Recently, non-reciprocal components based on time-varying systems have been demonstrated. Despite their promising performance, these demonstrations require either a large structure for long delays or a high-frequency modulation due to the fast phase velocity of EM waves. Moreover, the bandwidth of non-reciprocity is limited by either the modulation frequency or the phase matching condition. To overcome their limitations, we harness SH0 waves in a LiNbO₃ thin film to produce long delays (280 ns) with sub-4 dB IL over 1-mm size. Combining with a nonreciprocal framework based on switched delays, this work has achieved wideband non-reciprocity employing unprecedentedly low temporal effort (e.g. modulation frequency and depth).

Statement of Contribution/Methods

The 4-port non-reciprocal system consists of 2 delay lines and 4 single pole single throw switches [Fig. 1 (a)]. The switches are controlled by four signals [Fig. 1(b)], with a period 4 times the delay line's group delay (δ). Control signals on opposite sides of the delay lines are offset by δ . In operation, the signals flowing into Port 1 are time-multiplexed onto the two delay lines and subsequently de-multiplexed to Port 2 by turning on the switches connected to Port 2 δ time after the signals are launched from Port 1. The time-reversal symmetry is broken through sequentially timing the switching from one side of the delay lines to the other side. Consequently, signals fed to Port 2 are rejected by Port 1's closed switches and received by Port 3.

Results/Discussion

We implemented 2 standalone switch boards and a delay line board, which are assembled as the circulator seen in Fig. 2 (b). On the delay line board, a pair of in-house fabricated LiNbO₃ acoustic delay lines, were wirebonded to LC matching networks with a measured 4 dB IL and 280 ns delay. As shown in Fig. 3, the measured S-parameters of the circulator exhibit great performance symmetry between ports, a minimum insertion loss around 6.7 dB, and an isolation larger than 27 dB over a bandwidth of 13.6 MHz (8.7% FBW). The loss is limited by the SPUDT delay line and matching networks, which will be significantly reduced by further optimization.

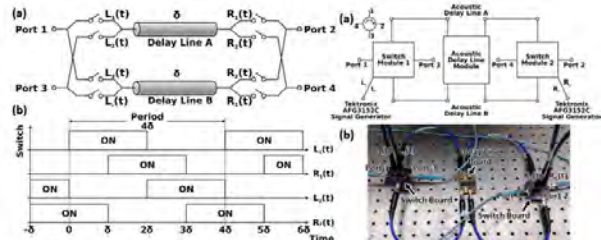


Fig. 1 (a) Schematic of 4 port circulator based on switched delay lines. (b) Switch control waveforms for nonreciprocal response

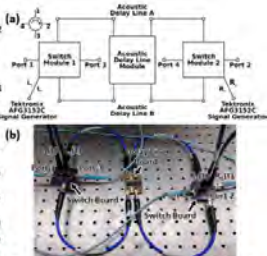


Fig. 2 (a) Block diagram of the constructed 4-port circulator. (b) Experiment setup of 4-port circulator.

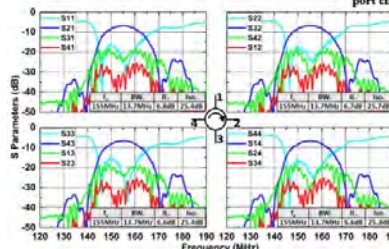


Fig. 3 Measured S-parameter performance. Great performance symmetry is shown in the measurement. Minimum insertion loss (IL) around 6.7 dB is measured at different ports. A bandwidth of 13.6 MHz (8.7% FBW) is obtained. Directivity larger than 21 dB is obtained between the forward and backward propagation path (e.g. between S12 and S21). Return loss is better than 15 dB at each port. Control signals are set to be 877.2 kHz (1.14 μ s period).

5:15 PM

Measurement of elastic constants of monoclinic Ga_2O_3 using resonant ultrasound spectroscopy**Takeuchi Naoto¹, Kanta Adachi², Hirotsugu Ogi³, Hideyuki Watanabe⁴, Toshimitsu Ito⁴, Yasuko Ozaki⁴**¹*Osaka university, Japan*, ²*Iwate university, Japan*, ³*Osaka University, Japan*, ⁴*National Institute of Advanced Industrial Science and Technology, Japan***Background, Motivation, and Objective**

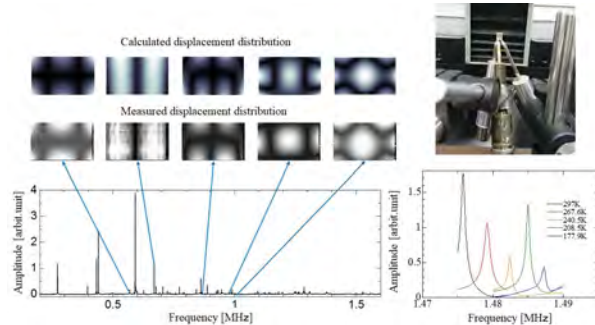
$\beta\text{-Ga}_2\text{O}_3$ has been recognized as a promising semiconductor material because it shows large band gap and dielectric breakdown voltage. However, the elastic constants, which are fundamental physical properties and needed for designing the devices, have not been reported yet because of its low crystallographic symmetry. We here study the elastic constants C_{ij} of $\beta\text{-Ga}_2\text{O}_3$, exhibiting thirteen independent C_{ij} of monoclinic symmetry ($C2/m$), by resonant ultrasound spectroscopy (RUS).

Statement of Contribution/Methods

We measured many free-vibration resonance frequencies of $\beta\text{-Ga}_2\text{O}_3$ at room temperature using originally developed piezoelectric tripod. We then identified their modes by comparing measured and calculated displacement distributions on the vibrating specimen with laser-Doppler interferometry. Using more than 110 resonance frequencies, we inversely determined all thirteen C_{ij} for the first time. Moreover, we studied temperature dependence of C_{ij} at low temperatures, revealing strong anisotropy in the temperature coefficient of C_{ij} .

Results/Discussion

At room temperature, C_{ij} of $\beta\text{-Ga}_2\text{O}_3$ was determined as follows: $C_{11}=243$, $C_{22}=344$, $C_{33}=347$, $C_{44}=47.8$, $C_{55}=88.6$, $C_{66}=104$, $C_{12}=128$, $C_{13}=160$, $C_{23}=70.9$, $C_{15}=-1.62$, $C_{25}=0.36$, $C_{35}=0.97$, and $C_{46}=5.59$ GPa. The strong stiffness anisotropy is found in the diagonal elastic constants: C_{11} is smaller than C_{22} and C_{33} by about 30 %, and the difference between C_{44} and C_{66} exceeds 50 %. In the low temperature experiment, C_{44} showed the highest temperature dependence among the diagonal elastic constants. It is expected that Gr neisen parameter of C_{44} has significantly larger since there is a positive correlation between the temperature dependence of elastic constants and Gr neisen parameter.



8H - Piezoelectric Transducers

Ruby (200)

Thursday, October 25, 8:00 am - 9:30 am

Chair **Sandy Cochran**
University of Glasgow

8H-1

8:00 AM The impact of local structural heterogeneity on piezoelectric properties of perovskite ferroelectrics

Shujun Zhang¹, Fei Li², Long-Qing Chen², Thomas Shroud²

¹*University of Wollongong, Australia*, ²*Pennsylvania State University, United States*

Background, Motivation, and Objective

Perovskite ferroelectric materials are at the heart of numerous electronic devices, such as imaging transducer, piezoelectric sensors and energy harvesting, to name a few. Relaxor-PT ferroelectrics show superior dielectric/piezoelectric properties, outperforming conventional ferroelectric PZTs, which greatly benefit medical ultrasound imaging. The good properties of relaxor-PT based materials are inherently associated with their unique local structural heterogeneity: the existence of nanoscale heterogeneous regions that coexists with normal ferroelectric domains. Despite two decades of extensive studies, the contribution of polar nanoregions to the underlying piezoelectric properties of relaxor ferroelectrics has yet to be established, which is the purpose of this research.

Statement of Contribution/Methods

In this research, we combined the cryogenic dielectric/piezoelectric measurements and the mesoscale phase field simulation to confirm the polar nanoregions contributions quantitatively to the dielectric properties. Guided by phenomenological theories and phase-field simulations, we propose an alternative design strategy to commonly used morphotropic phase boundaries to further flatten the energy landscape, by judiciously introducing local structural heterogeneity to manipulate interfacial energies (that is, extra interaction energies, such as electrostatic and elastic energies associated with the interfaces). To validate this, we synthesize rare-earth-doped $\text{Pb}(\text{Mg}_{1/3}\text{Nb}_{2/3})\text{O}_3-\text{PbTiO}_3$ (PMN-PT), as rare-earth dopants tend to change the local structure of Pb-based perovskite ferroelectrics.

Results/Discussion

Based on the paradigm, recent developments have experimentally confirmed that modest changes in the polarizability of local structure, can be regarded as “seeds” to further enhance the dielectric properties of ABO_3 perovskite solid solutions. The contribution of these local structures has been theoretically modelled to be the origin of the ultrahigh dielectric and piezoelectric activities of relaxor based perovskite ferroelectric crystals, accounting for 50-80% of their respective room temperature values [1-2]. The modified polycrystalline ceramics exhibit ultrahigh dielectric and piezoelectric properties compared to their non-modified counterparts, being on the order of 13,000 and 1500 pC/N respectively [3]. The relationship between local structure and macroscopic properties has been established, try to understand the impact of local structure on dielectric properties, to explore high performance ferroelectric materials for transducer applications.

References:

[1] F. Li, et al., *Nature Communications*, 7, 13807 (2016). [2] F. Li, et al., *Adv. Funct. Mater.*, 27, 1700310 (2017). [3] F. Li, et al., *Nature Materials*, 17, 349-354 (2018).

Acknowledgement: This work was supported by ONR and ONR Global.

8:15 AM **Piezoelectric Single Crystal Standard Development**Lynn Ewart¹, Zuo-Guang Ye²¹*Naval Undersea Warfare Center, RI, United States*, ²*Simon Fraser University, Burnaby, BC, Canada***Background, Motivation, and Objective**

Piezoelectric single crystals (piezocrystals) of lead magnesium niobate-lead titanate (PMN-PT) and lead zinc niobate-lead titanate (PZN-PT) have extremely large electromechanical coupling coefficients and exhibit strains of over one percent. The technical significance of these properties to devices is enormous and includes a doubling of bandwidth, decreased package size, and increased resolution. The exploitation of electroactive single crystals is currently being pursued for naval sonar and medical ultrasound transducers. To accelerate the maturation and implementation of piezocrystals from the research arena into commercial devices, an international working group completed an IEEE material standard that was published in 2017: IEEE-SA Std 1859TM-2017, "Standard for Relaxor-Based Piezoelectric Single Crystal Materials for Transducer and Actuator Applications". The working group is now working on extensions to this standard including into ternary piezocrystal materials.

Statement of Contribution/Methods

The group has had three major accomplishments to date. First, device designers and materials specialists wrote a standard that serves the two communities. Second, the materials and device communities that use piezocrystals developed mutually agreed upon terminology for discussing piezocrystals and a common understanding of each other's materials needs and concerns. Third, the group has identified near term piezocrystal development areas opportune for future addition to the standard.

Results/Discussion

The standard covers the physical and electromechanical requirements for [001]-poled relaxor-based piezoelectric single crystal materials for use in medical, industrial, and military transducers, actuators, and sensors. The focus is on three compositions from each of the PMNT and PZNT systems. The central content is the eight properties provided for each composition: free relative dielectric permittivity (K_3^T), dielectric loss tangent ($\tan\delta$), temperature of the first anomalous event in free relative dielectric permittivity (T_{RF}), rod extensional coupling factor (k_{33}), transversely poled length extensional coupling factor (k_{31}), longitudinal mode piezoelectric coefficient (d_{33}), transversely poled length extensional mode (d_{31}), elastic compliance at constant electric displacement (s_{33}^D). This presentation will discuss the standard, the underlying contributions of the working group, and the extensions of the standard, including to ternary piezocrystals, that are underway.

8:30 AM Piezoelectric PMN-PZT Single Crystal-Polymer Composites with Wide Usage Range of Temperature and Driving Electric Field

Dong-Ho Kim¹, Ho-Yong Lee¹

¹Ceracomp Co., Ltd., Korea, Republic of

Background, Motivation, and Objective

Relaxor-PT single crystals, specifically PMN-PT and PZN-PT, offer much higher piezoelectric and electromechanical coupling coefficients ($d_{33} > 1,500$ pC/N, $k_{33} > 0.9$), when compared to PZT ceramics [1]. Made into piezocomposites, they also have significant performance advantages such as higher thickness mode coupling coefficient ($k_t > 0.8$), higher piezoelectric figure of merit ($FOM = d_{33}xg_{33}$), and higher sensitivity in both transmission and reception. Therefore, the piezoelectric single crystal-polymer composites have been expected to be widely used in three main markets for piezoelectric ultrasonic transducers of non-destructive testing (NDT), biomedical imaging (and therapy), and underwater sonar. However, there are several remaining issues for their application: (1) a cost difference between single crystals and PZT ceramics, (2) machinability problem, and (3) significant temperature dependence at relatively low temperatures. Their temperature-dependent behavior at relatively low temperatures is due to their low rhombohedral-tetragonal phase transition temperatures ($T_{RT} \sim 90^\circ\text{C}$) and may limit their application in many environments.

Statement of Contribution/Methods

In this investigation we have developed new PMN-PZT single crystals of high T_{RT} ($> 165^\circ\text{C}$) and coercive electric field E_C ($> 5\text{kV/cm}$) by using a solid-state single crystal growth (SSCG) technique. Compared to conventional single crystal growth methods, the SSCG process is very cost-effective and suitable to mass production. After crystal growth, their machinability was tested by using a standard dicing saw. The various kinds of PMN-PZT single crystal-polymer composites with different internal structures as well as resonant frequencies were fabricated by using a standard dice-and-fill method. The “1-3” PMN-PZT single crystal-polymer composites were characterized and also compared with those of PMN-PT single crystals and PZH-5H ceramics.

Results/Discussion

The “1-3” PMN-PZT single crystal-polymer composites show high thickness mode coupling coefficient ($k_t > 0.85$), high piezoelectric constants ($d_{33} > 1,000$ pC/N), high piezoelectric figure of merit ($FOM = d_{33}xg_{33}$), and very low temperature-dependent behavior because of their high T_{RT} ($> 165^\circ\text{C}$) as well as E_C ($> 5\text{kV/cm}$). Compared to the 1-3 composites of PMN-PT single crystals and PZH-5H ceramics as shown in Fig. 1, the 1-3 composites of high T_C/T_{RT} PMN-PZT single crystals showed the higher k_t at room temperature and the lower temperature-dependent behavior of k_t . These results demonstrate that the high T_C/T_{RT} PMN-PZT single crystal-polymer composites have great advantages in the applications of ultrasonic transducers.

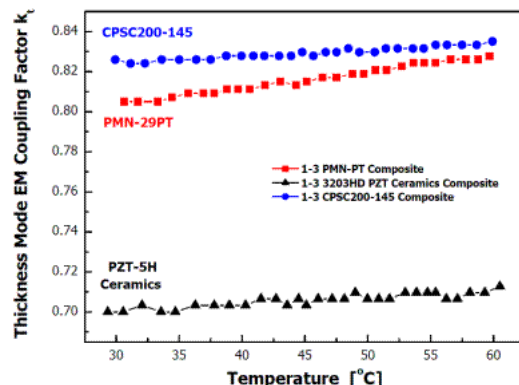


Fig. 1. Temperature dependence of thickness mode electromechanical coupling factor [k_t] of 1-3 composites: (a) (001) PMN-PZT single crystal [CPSC200-145; $T_{RT}=145^\circ\text{C}$; $T_C=200^\circ\text{C}$], (b) (001) PMN-29PT single crystal [$T_{RT}=90^\circ\text{C}$; $T_C=150^\circ\text{C}$], and (c) PZT-5H ceramics [$T_C=230^\circ\text{C}$]

8:45 AM Progress towards Piezocrystal and Pb-Free Piezoceramic Performance Prediction for High Power Ultrasound Devices

Nicola Fenu¹, Nathan Giles-Donovan¹, Muhammad Sadiq², Sandy Cochran¹

¹*Medical and Industrial Ultrasonics, University of Glasgow, Glasgow, United Kingdom*, ²*Active Needle Technology Ltd, United Kingdom*

Background, Motivation, and Objective

For medical and industrial applications requiring high power ultrasound, high piezoelectric coefficient, d , electromechanical coupling, k_{33} , and mechanical quality factor, Q_m , are generally required. Third generation Mn-doped piezocrystals outperform PZT in these respects, with simultaneously high $d_{33} > 1100 \text{ pC/N}$, $k_{33} > 0.85$, and Q_m in the range 700 - 1000 reported. However, Mn segregation may impact this performance. Additionally, environmental considerations motivate a search for Pb-free piezoceramics, which currently exhibit low Q_m .

In both cases, accurate material characterisation is essential for virtual prototyping with finite element analysis (FEA). Additionally, piezomaterials frequently experience varying mechanical, thermal and electrical stresses, either deliberate or as artefacts, in high power applications. Such conditions affect material properties, potentially altering operational modes and reducing device performance. Hence, an effective process for high power material characterisation is needed.

Statement of Contribution/Methods

The full piezoelastoelectric matrices for 4mm Mn:PIN-PMN-PT piezocrystal (TRS Technologies, PA, USA) and 6mm piezoceramic PIC700 (PI Ceramics, Lederhose, Germany) have been obtained through resonant ultrasound spectroscopy combined with an optimisation algorithm based on the Levenberg–Marquardt and Nelder–Mead approaches using exactly cubic samples. The conventional multi-sample IEEE method was also applied to characterise PIC700 and further validation was performed with FEA and laser Doppler vibrometry (LDV). This allows mode shapes to be reconstructed, visualised and animated for comparison and identification.

Results/Discussion

All the d_{ij} coefficients have been measured with LDV and the use of the Berlincourt method and the changes that result from environmental temperatures below T_c and uniaxial pressure have been determined. The resulting experimental data (example shown in Fig. 1) have been successfully matched with simulated mode shapes thus validating the method. Characterisation under varying conditions has an impact on material performance suggesting the use of complex constants in FEA and a frequency tracking system for practical adoption of these materials in high power applications.

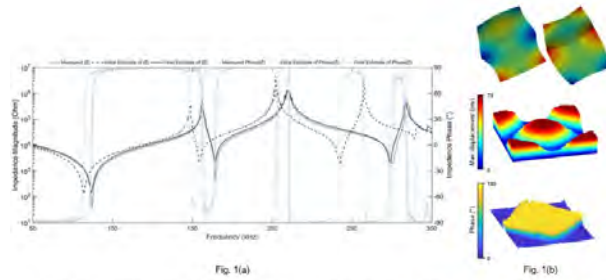


Fig. 1(a) Electrical impedance magnitude and phase spectra for measured, initial estimate and final estimate for exactly cubic Mn:PIN-PMN-PT sample and (b) Sample shapes for mode at c. 165 kHz: top, P2Flex FEA; middle, measured peak displacement; bottom, measured phase.

9:00 AM

Determination of elastic and piezoelectric properties of Al_{0.84}Sc_{0.16}N thin filmsNicolas Kurz¹, Fazel Parsapour², Vladimir Pashchenko², Vadim Lebedev³, Pascal Nicolay⁴, Paul Muralt², Oliver Ambacher⁵¹ *Microsystems Engineering, University Freiburg, 79110, Germany, ²EPFL, Switzerland, ³Fraunhofer IAF, Germany,*⁴*CTR AG, Austria, ⁵Sustainable Systems Engineering, University Freiburg, Germany***Background, Motivation, and Objective**

AlScN has an up to 400 % increased piezoelectric coefficient d_{33} as compared to AlN (Akiyama et al., 2009). It therefore attracted a lot of interest for applications in ultrasonic RF devices such as SAW and BAW filters. The knowledge of all elastic, piezoelectric, and dielectric tensor components of AlScN are crucial for designing and simulating such devices. However, the investigation of AlScN material parameters is still at an early stage. In this work, we fabricated bar- and disk-shaped resonators to determine the tensor components s_{11}^E , s_{12}^E , and d_{31} of Al_{0.84}Sc_{0.16}N.

Statement of Contribution/Methods

Bar- and disk-shaped membrane-resonators based on 1.2 μm thick sputtered Al_{0.84}Sc_{0.16}N films were fabricated and are shown in fig.1a-b. Resonance and antiresonance frequencies of length-extensional modes (LEM) of the bar resonators and radial-extensional modes (REM) of the disk resonators were characterized by a vector network analyser. 15 resonators of each type were characterized on the wafer-level. Finite element modelling (FEM) was employed for extracting material parameters. The simulated mode displacement of the LEM and REM is shown in fig. 1c and d, respectively. FEM sensitivity analysis of the resonators was carried out to identify the dominating elastic and piezoelectric tensor components, as well as to assess the anchor influence.

Results/Discussion

The sensitivity analysis of the resonators with respect to s_{ij}^E and d_{ij} revealed that both LEM and REM are sensitive to s_{11}^E , s_{12}^E , and d_{31} . Interestingly, the sensitivity of the LEM to s_{12}^E is majorly caused by the anchor. As a result, LEM and REM cannot be treated independently. Therefore, finite element analysis in conjunction with an iterative algorithm was implemented to minimize mean squared error of simulated and experimental resonance frequencies by adjusting s_{11}^E , s_{12}^E , and d_{31} . Using our approach, we determined $s_{11}^E = 4.083 \times 10^{-12} \text{ Pa}^{-1}$, $s_{12}^E = -1.684 \times 10^{-12} \text{ Pa}^{-1}$, and $d_{31} = -3.627 \text{ pC/N}$. Comparing with theoretical values (Caro et al., 2015), the d_{31} is in good agreement with theory, whereas the absolute values of the elastic parameters are larger compared to theoretical predictions meaning that the thin films are softer. These findings will help to obtain complete elastic and piezoelectric tensors of Al_{0.84}Sc_{0.16}N.

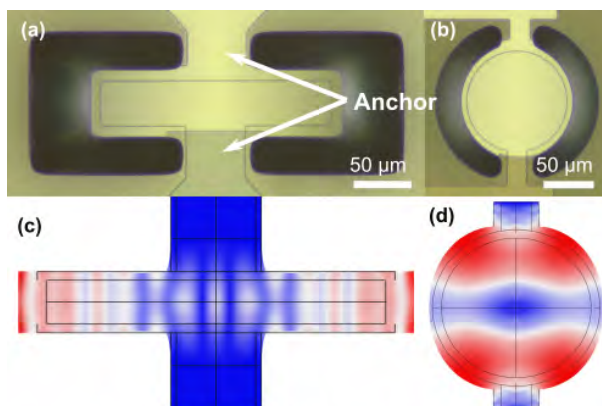


Fig 1. (a) top view of bar resonator. (b) Top view of disc resonator.
(c) Simulated mode-shape of LEM. (d) Simulated mode-shape of REM.

9:15 AM High Piezoelectric Properties and Complex Phase Transformations in New Ternary Perovskite Single Crystals**Zuo-Guang Ye^{1,2}, Zenghui Liu², Hua Wu³, Wei Ren²**¹*Department of Chemistry, Simon Fraser University, Burnaby, BC, Canada*, ²*Xi'an Jiaotong University, China, People's Republic of*, ³*Donghua University, China, People's Republic of***Background, Motivation, and Objective**

Piezo-/ferroelectrics are essential materials for electromechanical sensors and actuators in a wide range of technological applications. Relaxor-based single crystals of complex perovskite solid solutions, $\text{Pb}(\text{Mg}_{1/3}\text{Nb}_{2/3})\text{O}_3-\text{PbTiO}_3$ and $\text{Pb}(\text{Zn}_{1/3}\text{Nb}_{2/3})\text{O}_3-\text{PbTiO}_3$, exhibit high piezoelectric coefficients, large electromechanical coupling factors and high strain levels, making them the materials of choice for the next generation of high-end electromechanical transducers, including (i) high-power underwater projectors and medical therapy, (ii) medical diagnostic imaging and nondestructive evaluation, (iii) sensors and receivers, such as hearing aid devices and pyroelectric applications. However, to further improve the binary materials' properties, new generations of piezocrystals need to be developed, including ternary relaxor-PT solid solutions (GE II) and doped relaxor-PT solid solutions (GE III), with higher Curie temperature (T_C) and high-performance. Understanding the relationship between the complex domain structures and macroscopic properties is a key to this development.

Statement of Contribution/Methods

In order to understand the complex phase symmetry and phase transitions, and to illustrate the microscopic mechanisms of high piezoelectricity, single crystals of a new ternary complex perovskite system, $\text{Pb}(\text{Mg}_{1/3}\text{Nb}_{2/3})\text{O}_3-\text{Bi}(\text{Zn}_{2/3}\text{Nb}_{1/3})\text{O}_3-\text{PbTiO}_3$ (PMN-BZN-PT), are grown by the high temperature solution growth method and their domain structure, dielectric and ferro-/piezoelectric properties, and phase transformation behavior are investigated by various techniques. These studies provide new insights into the intricate morphotropic phase symmetry and phase components in complex perovskite solid solutions, and a better understanding of the microscopic mechanisms of high piezoelectric response in relaxor-based piezocrystals, which in turn will be helpful for designing better piezoelectric single crystals.

Results/Discussion

Different phase symmetries including the rhombohedral, tetragonal and monoclinic are found in these crystals, indicating that the composition of the crystals is close to the morphotropic phase boundary (MPB) region. Most interestingly, unusual phase transformation sequences of rhombohedral \rightarrow monoclinic \rightarrow cubic, and monoclinic \rightarrow cubic are directly observed by polarized light microscopy and confirmed by the dielectric and birefringence results. Moreover, an ultrahigh piezoelectric coefficient $d_{33} \approx 2000 \text{ pC/N}$ is obtained in these crystals, making these crystals useful for applications as electromechanical transducers. The unusual phase transformation sequences and the high piezoelectric response are explained from the polarization rotation mechanism, which has been evidenced in this work. Based on these results, a temperature-composition phase diagram is established, which illustrates the complex phases present and their transformation behavior.

8I - Multimodal Imaging Transducers

Ruby (200)

Thursday, October 25, 10:30 am - 12:00 pm

Chair **Christine Démoré**
Sunnybrook Research Institute

8I-1

- 10:30 AM Technology development of Photoacousitic imaging system in CANON**
Ken-ichi Nagae¹
¹*Canon Inc.*

Background, Motivation, and Objective

Photoacoustic imaging is an attractive technology to visualize blood vessels in human body without invasiveness or ionizing radiation.

Canon had researched and developed photoacoustic imaging technologies in collaboration with Kyoto University, which was named the "Innovative Techno-Hub for Integrated Medical Bio-imaging" (CK Project), from 2006 to 2015. In that time, we demonstrated the diagnostic performance for breast cancer patients by exploratory clinical research with using photoacoustic imaging system prototype.

In the project, we developed a hemisphere array scanning system for high-resolution 3D imaging.

Statement of Contribution/Methods

In CK project, we developed a photoacoustic imaging system, called "PAI-04", for breast imaging. To image various sizes of the blood vessels, 500CH CMUT sensors with large-bandwidth were installed to the hemisphere array. The PAI-04 works for clinical research in Kyoto University hospital.

In order to expand clinical application area, we promote research and development of the photoacoustic technologies under a program which was taken over by ImPACT (Impulsing Paradigm Change through Disruptive Technologies Program) established in the Council for Science, Technology and Innovation (CSTI) of the Cabinet Office, Japan. The ImPACT program aims to develop real-time 3D visualization technologies by using photoacoustic imaging that can image blood vessels in which abnormalities appear with illnesses.

We developed another photoacoustic imaging system, called "PAI-05" under the ImPACT program in collaboration with Hitachi, Ltd. and JAPAN PROBE CO., LTD. The hemisphere array in PAI-05 has over 1000CH Piezo-composite sensors to realize real-time 3D imaging. The PAI-05 works for clinical research study in ImPACT program.

In our talk, we introduce these photoacoustic imaging systems.

Results/Discussion

2



Fig.1 photoacoustic imaging system PAI-04



Fig.2 photoacoustic imaging system PAI-05

11:00 AM

Development of a Transrectal Probe for Combined Ultrasound and Photoacoustic ImagingJihun Jang¹, Jin Ho Chang^{1,2}¹*Electronic Engineering, Sogang University, Seoul, Korea, Republic of,* ²*Biomedical Engineering, Sogang University, Seoul, Korea, Republic of***Background, Motivation, and Objective**

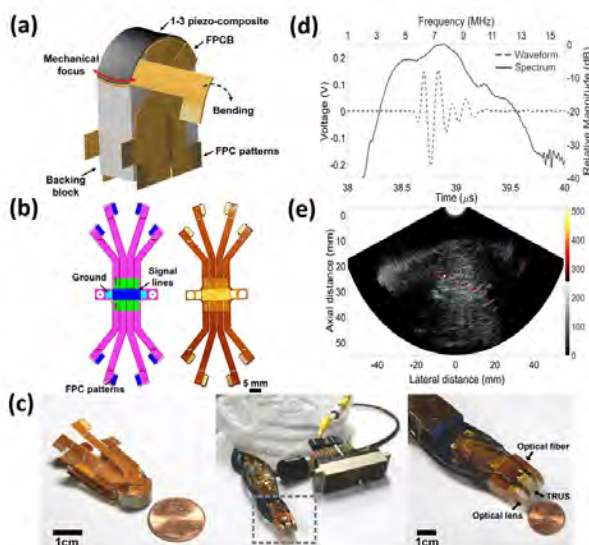
Transrectal ultrasound (TRUS) image-guided biopsy is mandatory to confirm the malignancy of the suspicious tumor. However, the diagnostic accuracy of initial biopsy is only 20 to 30% due to low contrast of TRUS images, thus requiring repeated biopsies despite patient's pain. Transrectal ultrasound-photoacoustic (TRUS-PA) imaging can be one solution to this problem if the overall size of a TRUS-PA probe, in which an ultrasound array transducer and optical fibers are integrated, is as small as possible for the convenience of the patients, while providing the desired performances. Here, we report a recently developed TRUS-PA probe of which size is less than 15 mm in diameter and the results of performance evaluation.

Statement of Contribution/Methods

The TRUS-PA probe consists of a 128-element, 7-MHz convex array and two convex optical lenses with 3-mm thickness connected to bifurcated outlets of an optical fiber bundle. The size of the array were 11.4 and 5 mm in the lateral and elevation directions, respectively. The field-of-view was determined to be 134° and the elevational focal length was selected as 30 mm, considering the typical prostate gland volume of 30 (anteroposterior) x 40 (width) x 50 (longitudinal) mm³. Also, we developed a new type of FPCB as a key element to downsize the overall size of the probe (See Fig. 1(a), (b), and (c)). The final diameter of the TRUS-PA probe is expected to be less than 15 mm, considering the housing.

Results/Discussion

The peak-to-peak voltage, center frequency and -6 dB bandwidth of the fabricated array transducer were measured 359 mV, 6.75 MHz and 4.5 MHz (66%) (See Fig. (d)). The ability of the TRUS-PA probe to produce combined US and PA images was verified in *ex vivo* experiments using the chicken breast tissue containing five graphite rods with a diameter of 0.3 mm. In the US image, the speckle pattern of the chicken breast tissue was clearly observed, but the graphite rods were hard to differentiate from the tissue. On the other hand, the PA image demonstrated the ability of the developed TRUS-PA probe to distinguish the graphite rods from the surrounding tissue with a stark contrast (See Fig. 1(e)). This result showed the advantage of the combined US and PA imaging and implied that the developed TRUS-PA probe is capable of acquiring the PA image of deeply-lying optical targets such as blood vessels in and around the prostate gland.



11:15 AM

Dual Frequency array for contrast superharmonic imaging

Emmanuel Cherin¹, Jing Yang², Jianhua Yin¹, Chris Chaggares³, Pang Guofeng³, Oleg Ivanytskyy³, Isabel Newsome⁴, Paul Dayton⁴, F. Stuart Foster^{1,2}, Christine Demore^{1,2}

¹*Physical Sciences, Sunnybrook Research Institute, Toronto, ON, Canada*, ²*Medical Biophysics, University of Toronto, Toronto, ON, Canada*, ³*Fujifilm Visualsonics, Toronto, ON, Canada*, ⁴*Joint Department of Biomedical Engineering, University of North Carolina at Chapel Hill and North Carolina State University, NC, United States*

Background, Motivation, and Objective

Superharmonic imaging (SI) exploits microbubble nonlinear behavior to visualize the microvasculature with resolution typical of μ CT. SI has been performed in animal models using a previously reported dual frequency transducer consisting of a 2-4 MHz ring coaligned with a 25-30 MHz single element focused transducer [1], however, mechanical scanning, single focus and limited focal depth hinder its clinical translation. These limitations can be alleviated using dual-frequency arrays (DFA).

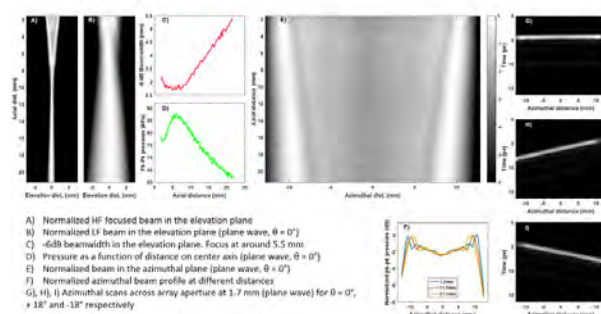
Statement of Contribution/Methods

We built a prototype DFA in a vertical topology, with a 32-element low frequency (LF, 2 MHz) transmitter array positioned behind a 256-element high frequency (HF, 20 MHz) receiver array. Both arrays were built from piezoelectric composites. The HF backing material between the two piezoelectric layers is weakly and strongly attenuating at 2 MHz and 20 MHz, respectively. Matching layers were used to improve transmission throughout the whole array structure. An elevation lens was added to focus the receive component at around 9 mm. Electrical matching was used to improve the electro-mechanical characteristics of the LF elements. Hydrophone measurements were performed to evaluate the variations between individual LF elements, characterize the LF beam in plane wave mode and evaluate steering capability.

Results/Discussion

The HF array imaging performances are typical of Visualsonics 20 MHz arrays (A). Matched LF element electrical impedance is $47.2\Omega \pm 2.6\Omega$ with a phase of $-60.1^\circ \pm 5.5^\circ$. Single element pk-pk pressures measured at 1.7 mm from the lens are 1.51 kPa/V in the 6-130V range, with a variation of 5% across the elements. In plane wave transmission ($\theta=0^\circ$), the pressure is 3 times higher than for a single element. Focusing is observed in the elevation plane at 5.5 mm, with a -6dB beamwidth of 2.7 mm (B, C). Past the focus, the pressure drops as the wavefront diverges (D). In the azimuth, the beam is relatively uniform (without apodization) with a variation of 2dB relative to the maximum on the edges (E, F). Beam steering is achieved for $\pm 18^\circ$ angles (G-I) allowing for plane wave compounding. These promising results demonstrate the capabilities of our vertical topology. Future work will focus on decreasing the elevation beamwidth, to improve pressure and CTR and focusing deeper for clinical applications.

[1] Lukacs et al. doi.org/10.1109/ULTSYM.2009.5441806



11:30 AM

High performance ultrasonic transducers from nanostructured and multilayered piezoelectric materialsKui Yao¹, Weng Heng Liew¹, Qingqing Ke¹, Shuting Chen¹, Lei Zhang¹, Chin Yaw Tan¹¹IMRE, A*STAR, Singapore, Singapore**Background, Motivation, and Objective**

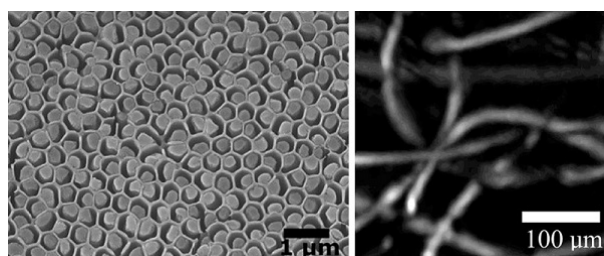
As a key electromechanical active component in an ultrasonic imaging system including photoacoustic imaging, the specifications of the ultrasonic transducer, typically made of piezoelectric material, often determine the overall performance of the imaging system. Thus the design and selection of the piezoelectric material and the resulting electrical and mechanical characteristics are vital to the advancement of the ultrasonic imaging technology.

Statement of Contribution/Methods

Two types of the advanced piezoelectric materials produced in our lab for ultrasonic transducer applications, including multilayer piezoelectric materials and one-dimensional (1D) nanostructured piezoelectric materials, will be introduced in this presentation. Theoretical analyses show that the multilayer piezoelectric configuration has the great potential in maximizing the transmission of electrical signal attributed to the tunable electrical impedance customized to match with various external circuitries, which becomes particularly important with highly miniaturized transducer array elements. Through our study on 1D piezoelectric materials and bottom-up nano-fabrication approach, we obtain large area nanostructures consisting of millions of vertically aligned piezoelectric nanotubes with the desired polarization orientation and outstanding electromechanical performance in comparison with the thin film benchmark.

Results/Discussion

Multilayer ultrasonic transducers made of our piezoelectric multilayer materials have been tested with significantly enhanced sensitivity in both pulse-echo and transmission modes as compared to single layer of the same materials. Multi-element multilayer ultrasonic transducers with enhanced performance has been demonstrated for photoacoustic imaging. High frequency ultrasonic transducers (above 100 MHz) with broad bandwidth (> 125 % (-6 dB)) have been obtained from the piezoelectric nanotube array. High-resolution scanning ultrasonic imaging and photoacoustic imaging using the obtained nanotube array transducers have been demonstrated. Figure 1 shows an image of piezoelectric P(VDF-TrFE) nanotube array fabricated in ordered anodized alumina membrane (AAM) (Left), and a high resolution scanning ultrasonic imaging obtained with a high frequency nanotube array ultrasonic transducer (Right).



11:45 AM

A novel Row-Column Addressed stack architecture for enhanced cardiac imaging

Guillaume Ferin¹, Marie-Coline Dumoux¹, Martin Flesch¹, Emmanuel Montauban¹, Agnes Lejeune¹, Bogdan Rosinski¹, Tony Mateo¹, Jonathan Porée², Jack Sauvage², Thomas Deffieux², Mathieu Pernot², Mickaël Tanter², An Nguyen-Dinh¹

¹Vermon SA, Tours, France, ²Institut Langevin, ESPCI Paris, PSL Research University, CNRS UMR 7587, INSERM U979, Paris, France

Background, Motivation, and Objective

Matrix transducers have for long been the gold standard in volumetric imaging, and in particular for echocardiography. However, their inner constitution (N^2 elements) accounts for highly dense and individual interconnection of thousands of elements.

There are several ways of reducing cable count such as using a micro beamformer or reducing the number of active elements over a wide aperture with a sparse array and also Row Column Addressed (RCA) matrices, which are made of two independent electrode arrays patterned perpendicularly one to each other ($2N$ elements). The latest have recently drawn probes manufacturers attention as there is no need to embed a specific electronic system as for driving a micro beamformer.

However, RCA matrices in their raw constitution are not suitable for volumetric echocardiography as a diverging field of view is required and that they only allow for a front axial projection of volume reconstruction.

Furthermore, RCA architecture suffers from a lack of true electrical ground and would require dedicated electronic.

Statement of Contribution/Methods

As to answer this dual issue, a “stack” ($\lambda/4$) architecture is proposed (patent pending), where the two independent piezoelectric arrays are stacked together with internal common ground allowing for an increased SNR compared to embedded electronic solutions and allowing for precise amplitude and phase control of elements over the total aperture.

Moreover, instead of using a diverging lens [1] that would account for decreased sensitivity, we suggest a smooth mechanical deformation process achieved through relevant tools and single crystal-based 1-3 piezocomposite materials.

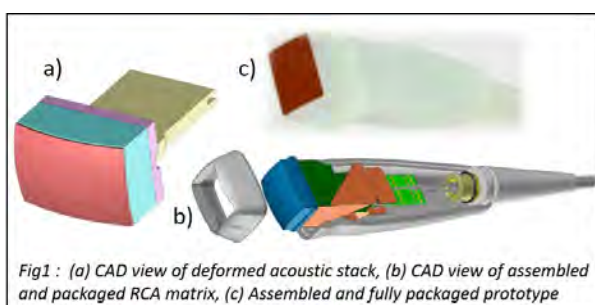
Results/Discussion

A standard RCA matrix and a fully packaged single crystal stack RCA matrix (3MHz center frequency, 96x64 elements, 240µm square pitch, 24x16.32mm active footprint) have been manufactured and implemented on the Verasonics Research platform to assess for their performances. Measurements show enhanced directivity pattern allowing for beam deflection flexibility and +10dB SNR gain measured on pulse-echo in favor of the “stack” RCA matrix.

Thanks to mechanical deformation of the acoustic stack, a field of view of 30° is obtained.

Furthermore, being electronic-less makes the conceived transducer a cost efficient and plug & play solution for basic cardiac imaging exam.

[1] M.Engholm et al, Ultrasonics, 2018



8J - Compressed Sensing and Quantification

Ruby (200)

Thursday, October 25, 1:30 pm - 3:00 pm

Chair **Miaomiao Zhang**
KU Leuven

8J-1

1:30 PM

Ultrasound signal reconstruction from sparse samples using a low-rank and joint-sparse model

Miaomiao ZHANG¹, Ivan Markovsky², Colas Schretter³, Jan D'hooge¹

¹*Cardiovascular Sciences, KU Leuven, Leuven, Belgium*, ²*Department ELEC, Vrije Universiteit Brussel (VUB), Belgium*, ³*Department of Mathematics, Vrije Universiteit Brussel (VUB), Belgium*

Background, Motivation, and Objective

With the introduction of very dense sensor arrays in ultrasound (US) imaging, data transfer rate and data storage can become a bottleneck in ultrasound system design. To reduce the amount of sampled channel data, several strategies based on compressive sensing (CS) have been proposed. However, the reconstruction accuracy of CS-based methods is highly dependent on the sparse basis and the number of measurements for each channel cannot be lower than the sparsity thereby limiting the data reduction rate. The aim of the current study was therefore to further reduce data rates by exploiting more properties of US signals.

Statement of Contribution/Methods

The pre-beamformed US signals from different transducer elements are joint-sparse in the Fourier domain and strongly correlated between channels and transmissions. Both properties imply that they show a low-rank structure when represented as a matrix. Therefore, a new method based on a low-rank and joint-sparse model is proposed to exploit these correlations. In order to solve the proposed model, a novel optimization algorithm based on the simultaneous direction method of multipliers is proposed. To validate the proposed methodology, *in vivo* cardiac channel data (center frequency $f_c = 3.5$ MHz; sampling frequency $f_s = 25$ MHz) was captured using an experimental ultrasound system and reconstructed from a subset of samples obtained at different sampling rates (SR). Next to a visual appreciation, CNR was quantified to evaluate the quality of the reconstructed images.

Results/Discussion

Figure 1 shows the B-mode images reconstructed for different sampling rates together with the corresponding CNR. Image quality remained good even when using only 10% of the samples. In comparison, given the sparsity of the problem (i.e. $2f_c/f_s$), CS-based strategies would maximally achieve a SR of 28%. In conclusion, the proposed methodology enables to further reduce data rates over CS-based approaches while maintaining image quality.

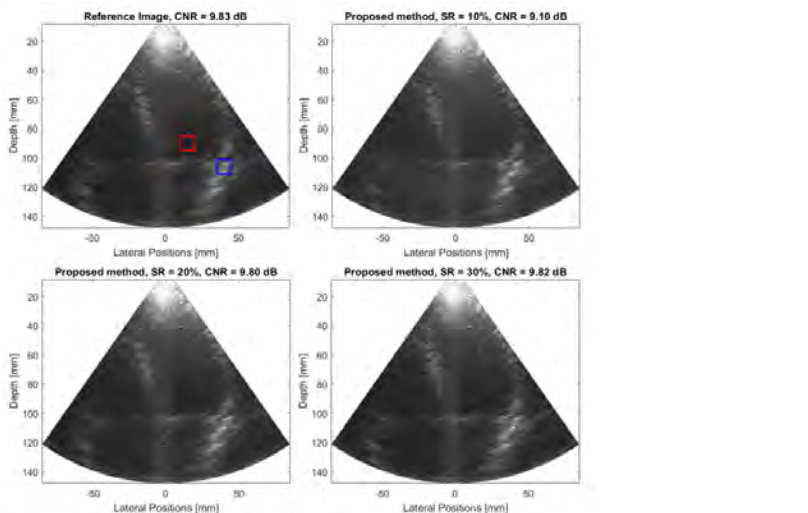


Figure 1. Original *in vivo* cardiac image and the images reconstructed by the proposed method with different sampling rates. The red and blue block in the reference image represent the regions used to compute CNR.

1:45 PM

Compressive Multiplexing of Ultrasound SignalsAdrien Besson¹, Dimitris Perdios¹, Marcel Ardit¹, Yves Wiaux², Jean-Philippe Thiran^{1,3}¹*Signal Processing Laboratory 5, Ecole Polytechnique Fédérale de Lausanne, Lausanne, Switzerland*, ²*Institute of Sensors, Signals, and Systems, Heriot-Watt University, Edinburgh, United Kingdom*, ³*Department of Radiology, University Hospital Center and University of Lausanne, Lausanne, Switzerland***Background, Motivation, and Objective**

High-quality 3D ultrasound (US) imaging requires a US probe with a high channel-count, which necessitates an unrealistic number of coaxial cables and analog-to-digital converters (ADC). To address this problem, micro-beamforming methods have been developed, where sub-array analog beamforming is performed in the probe-head, allowing to achieve 3D imaging using systems with a complexity similar to 2D imaging systems but resulting in a significant reduction of the image quality. Sparse 2D arrays have also been designed, where a subset of transducer-elements are used in receive, also resulting in a significant decrease of the image quality due to higher side lobe levels.

Statement of Contribution/Methods

We propose a novel multiplexing method which relies on compressed-sensing (CS) principles to significantly reduce the number of coaxial cables and ADCs. We exploit the compressive multiplexer (CMUX) introduced in the radar community to multiplex signals in the probe-head. Such a CMUX considers sets of N channels as inputs, modulates them with chipping sequences working at a rate Ω , and sums them together to form y . Each output y is transferred to the back-end system, resulting in a reduction by a factor N of the number of cables and ADCs. In the reconstruction, we propose two methods: one solving a CS-based problem exploiting the sparsity in a pulse-stream model (CS-PS) and one solving a least square problem in the Fourier domain (LS-F).

We evaluate the two methods on a sequence of *in-vivo* carotid data acquired with a Verasonics system (ATL L7-4v, 128 el., 5.2MHz central freq., 62.5MHz sampling freq.) using a single plane wave with normal incidence on transmit. In the CMUX architecture, N is set to 8 and the chipping sequences are chosen as random sequences of +1 and -1. For CS-PS, the reconstruction is performed using the fast iterative soft thresholding algorithm. Delay-and-sum beamforming is employed followed by envelope detection and log-compression.

Results/Discussion

Both visual assessment and the quantitative metrics in Fig. 1 demonstrate high quality reconstructions, with better results for LS-F, probably due to pulse-mismatch in CS-PS. These methods may be combined with spatial compression methods, such as micro-beamforming, to achieve data reduction and provide 3D imaging with less image degradation than conventional approaches.

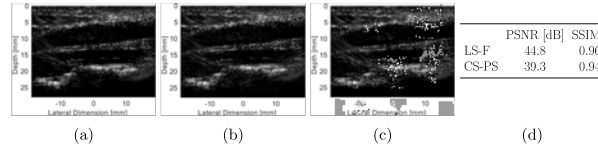


Figure 1: (a) Reference log-compressed B-mode image for 1 PW insonification; (b) Reconstructed log-compressed B-mode image from CMUX measurements using LS-F; (c) Reconstructed log-compressed B-mode image from CMUX measurements using CS-PS; (d) Average PSNR and SSIM over the sequence for LS-F and CS-PS.

2:00 PM Strategic lateral undersampling and Compressed Sensing recovery in ultrasound imaging

Anand R¹, Arun K. Thittai¹

¹Applied Mechanics, Indian Institute of Technology Madras(IITM), Chennai, India

Background, Motivation, and Objective

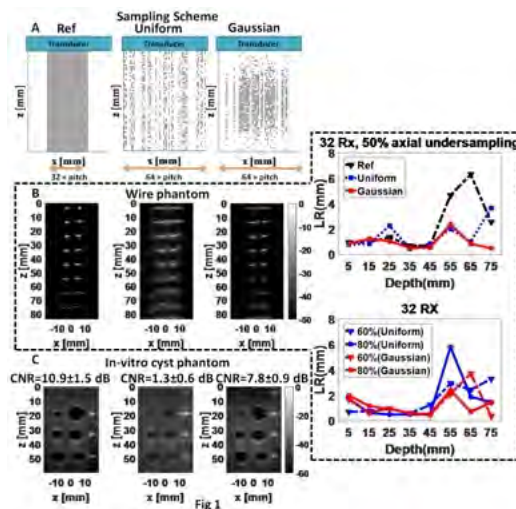
Affordable point-of-care ultrasound systems have demanding requirement for data transfer and storage due to limited hardware resources and wireless data transfer speed. To overcome this limitation, data reduction using Compressed Sensing (CS) has been proposed earlier to recover fully-sampled RF data from axially undersampled data. However, there is no detailed investigation on lateral-undersampling of the RF data, which may offer additional data reduction and it may probably be easier to implement as well. This work investigates two such schemes to under-sample the received RF data in lateral as well as axial directions and compares the CS recovery performance for the proposed schemes.

Statement of Contribution/Methods

Wire phantom and in-vitro cyst phantom were imaged with L14-5/38 (Sonix Touch Q+, Analogic^(R)) operating at 5MHz and 40 MHz sampling rate. The transmit focus and number of active elements were fixed to 35mm and 64, respectively. Two sampling schemes based on uniform and Gaussian distribution have been implemented to randomly under-sample the RF data in both lateral and axial directions, which is illustrated in Fig. 1A. Subsequently, CS was used to recover the fully sampled RF data using the standard Fourier basis as sparsifying function and then, beamformed using delay-and-sum (DAS) to obtain the image. Reference image was obtained by applying DAS to the RF data from 32 consecutive elements (50% lateral data). Lateral Resolution (LR) at various depths and Contrast to Noise Ratio (CNR) computed at 35mm depth were estimated to compare the performance.

Results/Discussion

From the images and the two LR plots for the wire phantom shown in Fig. 1B, it could be inferred that the LR shows improvement for CS recovered data when compared to that of reference especially, beyond the focus point. Also, no significance difference in LR values were found among the CS schemes for various axial undersampling rate, in spite of discarding 90% of the samples (50% lateral and 80% axial) from the fully sampled data. Furthermore, despite discarding 75% of the samples from the cyst phantom data, Gaussian undersampling shown in Fig 1C is comparable to the reference image. CS with Gaussian undersampling outperforms the uniform undersampling due to the fact that the former sampling strategy is similar to the apodization function (eg. Hanning) used during the beamforming process.



2:15 PM

In-silico validation of microstructure estimation from cortical bone backscatterJuan Du¹, Kay Raum¹¹Berlin-Brandenburg Center for Regenerative Therapies, Charité - Universitätsmedizin Berlin, Berlin, Germany**Background, Motivation, and Objective**

Cortical bone pore density (Ct.Po.Dn) and pore diameter (Ct.Po.Dm) are important factors in determining bone toughness and strength [1-3]. However, they cannot be directly assessed with established diagnostic tools. In principle, the backscatter amplitude of a cortical pore exhibits a linear relationship with Ct.Po.Dm within a certain frequency range (3-11 MHz), while Ct.Po.Dn is frequency independent. In [4], Ct.Po.Dm and porosity (Ct.Po) have been accessed by means of spectral analysis. However, multiple factors, e.g. multiple scattering, mode conversions, and attenuation caused by absorption and scattering may influence the backscatter spectrum. In this paper, we have conducted a numerical study to establish the dependencies of cortical backscatter on Ct.Po.Dn and Ct.Po.Dm.

Statement of Contribution/Methods

A 2D parametric FDTD study was performed using a 4-mm thick plate with randomly distributed spherical pores yielding Ct.Po (2-18%) and Ct.Po.Dm (10-200 μm). Material properties of bone matrix and pores were taken from [5]. The absorption in bone and pores was set to 2.1 and 0.002 dB/mm, respectively. The plate was placed 4 mm below the surface of an unfocused linear array transducer. Single element, transmit and receive aperture sizes were 0.3, 4.8, and 9.6 mm, respectively. A broadband 5-MHz pulse was used for excitation. All simulations were performed using Simsonic.

A sliding-window (0.6- μs Hanning) spectral analysis was performed for each receive channel. Spectra originating from the plate surface were averaged to produce a reference spectrum. For all spectra, the reference spectrum was subtracted to produce a depth (z) and frequency (f) dependent normalized backscatter spectrum $Y_{\text{norm}}(f,z)$. The following model was fitted to $Y_{\text{norm}}(f,z)$ in the frequency and depth ranges of $3 \leq f \leq 7$ MHz and $1 \leq z \leq 3$ mm, respectively:

$$Y_{\text{norm}}(f,z) = a_0 + a_z \cdot z + a_{fz} \cdot f \cdot z.$$

Each model was generated ten times and the derived coefficients were averaged.

Results/Discussion

The coefficients a_z and a_{fz} were highly correlated with Ct.Po.Dn (Pearson, $0.57 < |\rho| < 0.78$) and Ct.Po.Dm (Pearson, $0.78 < |\rho| < 0.84$), and can be predicted by a multivariate model ($0.81 < R^2 < 0.83$, Figure 1c).

In conclusion, this study has confirmed that the coefficients of the established model are sensitive to cortical bone structural properties. The properties can be retrieved from cortical backscatter spectrum.

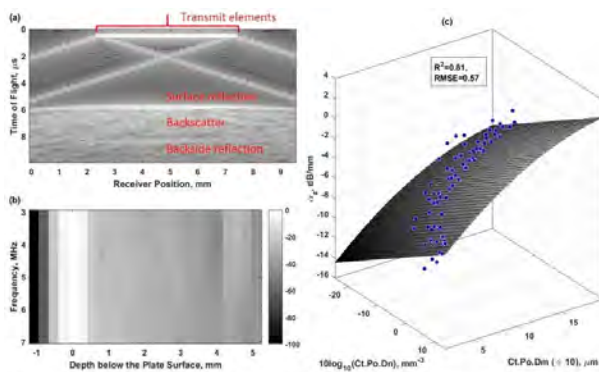


Figure 1. Representative simulation model with Ct.Po.Dm 55 μm and Ct.Po 6% (a); Depth and frequency dependent normalized spectrum $Y_{\text{norm}}(f,z)$ (b); Correction of a_z with Ct.Po.Dn and Ct.Po.Dm (c).

Reference:

- [1] Granke et al., Journal of Biomechanics, vol. 49, no. 13, pp. 2748-2755, 2016.
- [2] Yeni et al., Bone, vol. 21, no. 5, pp. 453-459, 1997.
- [3] Bell et al., Bone, vol. 24, no. 1, pp. 57-64, 1999.
- [4] Kilappa et al., IEEE International Ultrasonics Symposium (IUS), 2017.
- [5] Rohrbach et al., Journal of Biomechanics, vol. 45, no. 13, pp. 2264-2270, 2012.

2:30 PM

Quantification of multispectral photoacoustic images: unsupervised unmixing methods comparison**Aneline Dolet^{1,2}, Rita Ammanouil³, Thomas Grenier¹, Cédric Richard³, Piero Tortoli², Didier Vray¹, François Varay¹**¹*Univ.Lyon, INSA-Lyon, Université Claude Bernard Lyon 1, UJM-Saint Etienne, CNRS, Inserm, CREATIS UMR 5220, U1206, F-69621, CREATIS, Lyon, France, Metropolitan*²*Department of Information Engineering, University of Florence, Florence, Italy, ³Laboratoire Lagrange, Université de Nice Sophia-Antipolis, France, Metropolitan***Background, Motivation, and Objective**

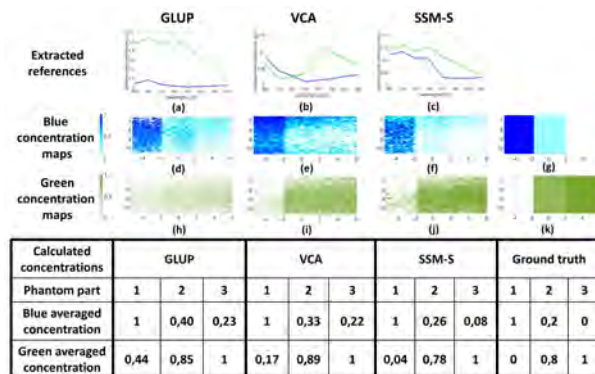
Photoacoustic imaging is a promising modality to image and discriminate biological tissues. Each medium is characterized by a specific multispectral photoacoustic signal which allows its quantification. This is of interest to follow-up diseases like carcinoma quantifying oxygenated and deoxygenated blood in tissue. Classically, quantification methods are supervised and required reference spectra. The optimization of their estimation is still a tricky task marginally discussed in the literature. This study aims at comparing unsupervised methods able to extract these reference spectra from the data. Group Lasso with Unit sum and Positivity constraints (GLUP) and Virtual Component Analysis (VCA), typically used in hyperspectral fields, are compared to the Spatio-Spectral Mean-Shift (SSM-S) already applied to cluster photoacoustic data.

Statement of Contribution/Methods

The signal of each pixel in the data is considered as a weighted sum of the references, corresponding to pure media, where the weights represent these media concentrations. GLUP, VCA and SSM-S are used to extract these references and the parameters of these methods were tuned optimally by experts. To compare these method performances, an inverse problem is solved to estimate the concentrations (weights) of the extracted references in each pixel of the data. The experimental multispectral photoacoustic images used in this study were acquired with a Vevo LAZR system and a coloured 4% agar phantom with three different colours: fully blue, mix of 20% blue and 80% green and fully green.

Results/Discussion

The Figure shows the extracted references using GLUP, VCA and SSM-S (a-b-c), and the corresponding concentration maps estimated (d-e-f-h-i-j). Table (l) gives the average concentration for each phantom part. The extracted references are different due to the different extraction criteria of each method. Nevertheless, GLUP and VCA results are relatively close to the ground truth (g-k). Whereas the SSM-S gives the best results with 0.26 for 0.2 of blue ink and 0.78 for 0.8 of green ink. The SSM-S quantification performance makes it the most preferable method for accurately estimating the media concentrations with multispectral photoacoustic imaging. It could then be used to quantify the oxygenation in tumors blood and hence could allow the discrimination of benign/malignant tumors.



Extracted references obtained with: (a) GLUP, (b) VCA, (c) SSM-S. Blue and green concentration maps obtained with: GLUP (d) and (h), VCA (e) and (i), SSM-S (f) and (j), ground truth (g) and (k) respectively. Table (l): averaged concentrations of the three phantom parts, blue concentrations, respectively green, are normalized according to phantom part 1, respectively 3.

- 2:45 PM** **Improved arbitrary waveform synthesis for tri-state transmitters by an impulse response factorization enabling use of the Viterbi algorithm**
John Flynn¹
¹*Verasonics, Inc, Kirkland, WA, United States*

Background, Motivation, and Objective

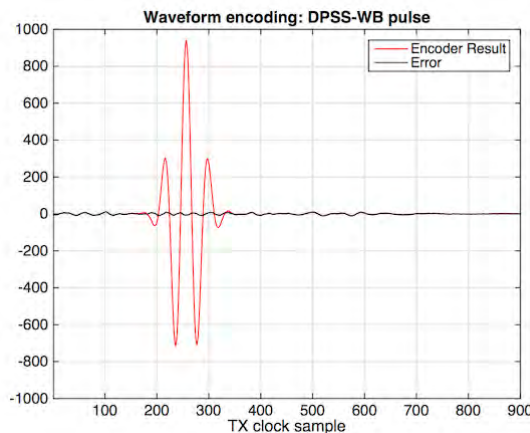
While tri-state transmitters enable cost-effective hardware implementation with large channel counts and high power capacity, performance of encoders for useful waveform synthesis is critical in achieving acoustic fidelity. Examples of waveforms with complex specifications include LFM chirps, and those with minimal time-bandwidth products such as discrete prolate spheroidal (DPSS) pulses. One extant encoder with good performance is structurally similar to linear equalizers for communications, and uses knowledge of transducer impulse response (IR) to enable a linear deconvolution process for whitening the design signal, which is then quantized by a memoryless slicer. Though low in complexity, these methods are suboptimal to those based on constrained optimization, such as Dynamic Programming (DP). This motivates the investigation of nonlinear methods to design pulse sequences for emission of specified waveforms.

Statement of Contribution/Methods

A good candidate for a DP approach to encoding is the Viterbi Algorithm (VA). The utility of VA is in reducing the computation cost of optimal inference from being exponential in signal length, to being exponential in the length L of the IR. Unfortunately, the long IR of typical ultrasound transducers means that direct use of the VA becomes intractable. However, we show that the VA can be employed by defining an abstracted two-stage IR model. Here we factorize the IR into a shorter prototype IR (say, H) of length suitable for the VA, and a longer abstracted convolutional factor G to be processed linearly. In this way, an abstracted signal is presented to the VA for tractable inference of transmit symbols through H and subsequently G .

Results/Discussion

Using the empirical IR for a 5MHz commercial transducer, we demonstrate encodings of LFM and DPSS waveforms for a tri-state transmitter with a 250 MHz pulse clock. Compared to a previously disclosed linear encoder, the proposed factorized encoding process shows improvements in fidelity of approximately 10 and 14 dB RMSE for these two waveforms respectively.



8K - Novel Designs and Applications

Ruby (200)

Thursday, October 25, 4:00 pm - 5:30 pm

Chair **Valsala Kurusingal**
Thales Australia

8K-1

4:00 PM Fibonacci Spiral Arranged Ultrasound Phased Array for Mid-Air Haptics

Adam Price¹, Benjamin Long¹
¹*Ultrahaptics, Bristol, United Kingdom*

Background, Motivation, and Objective

Ultrasound phased arrays are most commonly used in nondestructive testing and medical diagnostic applications. More recently mid-air haptic technology has utilized the acoustic radiation force to produce skin deformations and thus recreate the sensation of touch. The acoustic radiation force is the time-averaged force exerted by an acoustic wave on a medium and can be spatially and temporally controlled using electronically steered phased ultrasonic arrays. An important problem with most phased arrays has been the presence of grating lobes arising from the periodicity of array element spacing and arrangement that are detrimental to haptic sensations. We show that by arranging the elements of an array in a Fibonacci spiral, one can suppress grating lobes. We discuss the benefits of fabricating Fibonacci spiral arrays as opposed to sparse arrays. We also discuss the benefits of removing grating lobes for mid-air haptic applications such as control panels for automotive dashboards and immersive experiences in VR.

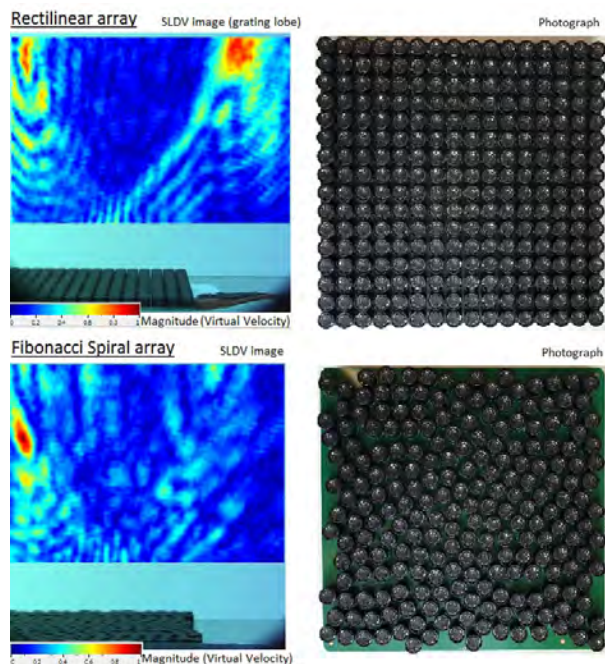
Statement of Contribution/Methods

In the present work we show that by arranging transducer elements of an array in a Fibonacci spiral one can suppress grating lobes. The acoustic fields of both periodic and Fibonacci spiral arrangement arrays have been simulated and then experimentally verified. A number of experimental methods have been used including acoustic field images acquired using a scanning laser Doppler vibrometer (SLDV), microphone scans with the array placed on a turntable and microphone scans with the array fixed and the microphone moved.

Previous work has either focused on showing that array elements within half a wavelength can suppress grating lobes [Konetzke, 2015, IUS] or considered the problem purely from simulation without optimizing the design or testing it experimentally [Legg, 2017, ICSV24].

Results/Discussion

Simulations agreed well with experiment, grating lobes do not appear in microphone scans or SLDV images of the acoustic field (Fig 1). The Fibonacci spiral pattern is a better solution for mid-air haptic technology than a sparse array as it allows for greater focusing range and therefore a larger 'Interaction zone' for mid-air haptic applications such as control panels for automotive dashboards and immersive experiences in VR. The absence of grating lobes would also be useful for other applications such as acoustic imaging.



4:15 PM

Lead-free sodium potassium niobate based piezoelectric thick film bimorph structure for energy harvesting

Claire Bantignies¹, Thien Hoang¹, Hugo Mercier², Danjela Kuscer³, Barbara Malic³, Franck Levassort², An NguyenDinh¹

¹VERMON, TOURS, France, ²GREMAN UMR 7347, Université de Tours, Tours, France, ³Jožef Stefan Institute, Ljubljana, Slovenia

Background, Motivation, and Objective

Piezoelectric materials have long been recognized for their efficiency in a wide range of applications as sensors, actuators and energy harvesters. Their robustness and budget-friendly implementation make them well suited for reliable, cost effective sensing systems in medical or industry.

Recently, IoT, wireless sensing networks... increasingly require low power consumption electronics and quasi-inexhaustible source for extended autonomy and sustainable performance. They represent opportunities for piezoelectric designs to take up new challenges and therefore to come up with integrated solutions for powering the devices autonomously.

On the other hand most widespread piezoelectric materials are based on lead zirconate titanate (PZT) and thus are containing lead which is now restricted in many countries due to its toxicity to human health and environment. Among alternative piezoelectric solution, sodium potassium niobate based ((K,Na)NbO₃, KNN) ceramics are considered as one of the most promising candidates. They exhibit a very high Curie temperature, and a good d₃₁ value.

What we propose here is to realize, to characterize and to show the potential of a piezoelectric energy harvesting bimorph demonstrator based on lead-free material.

Statement of Contribution/Methods

Ceramics with the nominal composition (K_{0.5}Na_{0.5})_{0.99}Sr_{0.005}NbO₃ (KNNSr) were prepared from a stoichiometric mixture of K₂CO₃, Na₂CO₃, SrCO₃ and Nb₂O₅. The homogenized powder mixture was calcined at 800°C for 4 H, milled and re-calcined at 750°C for 4 H. The powder compacts with dimensions 40 mm x 40 mm x 10 mm were sintered at 1120 °C for 2 hours in oxygen. These plates with sputtered gold electrodes were poled with a DC-electric field of 2 kV/mm at 120°C for 40 min and then field-cooled to 25°C.

A bimorph structure was manufactured with the thinned-bulk approach: 2 plates of the KNNSr ceramic were laminated including a brass shim layer between them. Each layer was then thinned down to a thickness of 60 µm and gold plated. A 1 g tip mass was added to decrease the resonance frequency in order to scavenge vibrations from the environment (human body, industrial equipment ...). This bimorph was then clamped on one side in a cantilever beam structure for characterization on a vibrational test bench.

Results/Discussion

A first electromechanical performance evaluation of plates showed a k_t value around 40% and a dielectric constant at 370 (ϵ_{33}^S) for the thickness mode. A lead-free bimorph demonstrator for energy harvesting was realized using the thinned-bulk approach. It exhibits the power density of 13 µW/G²/cm³ and the resonance frequency of 24 Hz which is highly compatible with vibrations at low external frequencies. It is also competitive with MEMS based energy harvesters that have difficulties to lower their resonance frequencies below one hundred Hz.

This concept is very promising to address the growing demand of IoT and the forthcoming prohibition of lead in piezoelectric materials.

4:30 PM

Sparse volumetric PZT array with density tapering

Hendrik J. Vos^{1,2}, Filippo Piccardi^{2,3}, Andrea Traversi^{2,3}, Davide Galeotti^{2,3}, Emile Noothout², Enrico Boni³, Alessandro Ramalli^{3,4}, Verya Daeichin², Martin D. Verweij^{1,2}, Piero Tortoli³, Nico de Jong^{1,2}

¹Biomedical Engineering, Thorax Center, Erasmus MC, Rotterdam, Netherlands, ²Acoustical Wavefield Imaging, ImPhys, TU Delft, Netherlands, ³Microelectronics Systems Design Lab, University of Florence, Italy, ⁴Lab. on Cardiovascular Imaging & Dynamics, Dept. of Cardiovascular Sciences, KU Leuven, Leuven, Belgium

Background, Motivation, and Objective

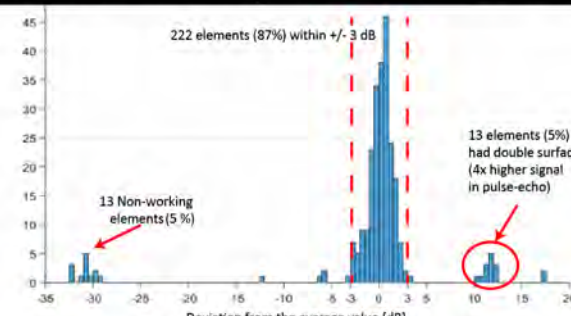
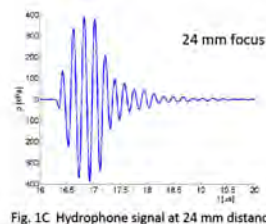
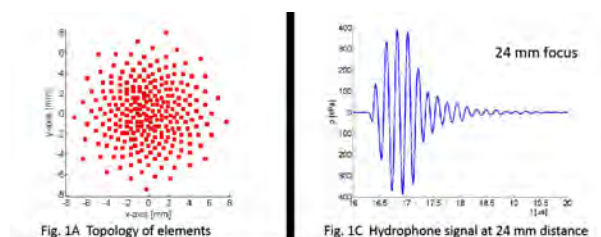
Volumetric medical ultrasound imaging currently provides either high resolution or high frame rates. Efforts to obtain both at the same time involve either expensive and complex multi-channel (1000+) ultrasound systems or in-probe electronics to reduce cable count. We propose a sparse array probe with only 256 elements that are density tapered. All elements are directly wired to an ultrasound engine, thus being flexible in transmission and reception. Here we present the design, realization, and characterization of a probe prototype for carotid 3D high frame rate scanning.

Statement of Contribution/Methods

The distribution of the 256 elements was based on a density tapered spiral [Ramalli et al. TUFFC 2015] (Fig. 1A). The aperture was 16 mm, the center frequency 5 MHz and the element size 200×200 µm. The array was made of PZT material (3202HD, CTS Corp.) built on a rigid high-precision PCB (RushPCB). The PCB has functions of acoustic backing, mechanical stabilization, and electric conductance between the individual element pads and the outer connectors. The front matching layer had an acoustic impedance of 4.7 MRayl, was electrically conductive and after cutting with a diamond saw it was connected to ground via a thin conductive foil. Receive signal amplification and line driving was done with MAX4805 high-voltage-protected OpAmps (MAXIM Integrated). The probe was connected to a Vantage-256 scanner (Verasonics) for acoustic characterization of single elements and of the full probe.

Results/Discussion

Fig. 1B shows that 95% of the elements was acoustically active, and 87% was within ±3 dB sensitivity range compared to the average, in pulse-echo. Center frequency was 5.3 MHz, and fractional one-way -6dB bandwidth (FBW) was 32 %, narrower than the designed one (50% FBW), due to an unexplained ringing effect. One-way -6 dB opening angle of a single element was 70° which is in close agreement with the opening angle of a piston. The transmit efficiency of a single element was 4 kPa/V at 1.5 mm distance. When the full probe was focused at 24 mm with a 20 V peak, 3-cycle tone burst, the peak pressure in focus was 400 kPa (Fig. 1C). The OpAmps improved SNR by 13 dB with 1m cable attached. In preliminary tests, we could detect invisibly small air bubbles in tap water in pulse-echo mode with a single diverging transmit wave. These results show that the probe is viable for volumetric imaging tests.



4:45 PM

A Broadband Technique for Couplant-Corrected Pulse-Echo Measurements in a Large Volume Pressure CellBlake Sturtevant¹, Eric Moss², Yoshio Kono³, Nenad Velisavljevic²¹*Materials Physics & Applications, Los Alamos National Laboratory, Los Alamos, NM, United States*, ²*Explosive Science & Shock Physics, Los Alamos National Laboratory, Los Alamos, NM, United States*, ³*HPCAT, Advanced Photon Source, Argonne National Laboratory, Argonne, IL, United States***Background, Motivation, and Objective**

Knowledge of a material's third order elastic constants (TOEC) is needed for applications such as the design of acoustic devices subjected to high accelerations. One way to determine TOEC is to measure a material's sound speeds as a function of pressure using pulse-echo in a pressure cell. In all pulse-echo measurements consisting of a buffer rod—couplant—sample, the acoustic wave acquires phase shifts upon transmission through, and reflection from, the buffer rod/sample interface. The net phase shift, Φ_{net} , leads to a difference between the measured time of flight τ_m , and the desired time of flight in the sample τ_s :

$$\tau_m = \tau_s + \Phi_{\text{net}}/2\pi. \quad (1)$$

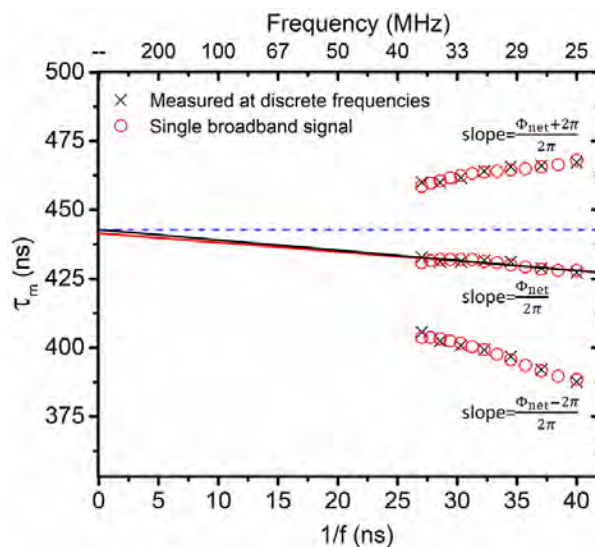
This phase shift can be accounted for by measuring τ_m at multiple frequencies and extrapolating to $f \rightarrow \infty$ where $\tau_m = \tau_s$. The collection of τ_m at multiple frequencies can take ~10 minutes. The pressure in a pressure cell may decrease by 5-10% over this time period due to relaxation of the sample and cell components, leading to uncertainty in the actual pressure at which the data were collected.

Statement of Contribution/Methods

To reduce the time needed for data acquisition, a method was developed to perform pulse-echo measurements using a single broadband (20 MHz) signal that is later digitally frequency filtered. The result is that a single waveform contains all of the information that is traditionally obtained by measurements at many discrete frequencies. Broadband pulse echo measurements have recently been performed in a large volume pressure cell *in-situ* at the HPCAT sector of the Advanced Photon Source. Simultaneous X-ray diffraction and radiography enable precise determination of the sample pressure and physical dimensions, respectively. The determined τ_s and sample dimension are used to determine sound speeds, elastic moduli, and their pressure dependence.

Results/Discussion

The figure shows an example of data collected at 7 frequencies over a period of ~10 minutes as well as the data collected in < 1 minute using a single broadband signal and filtered offline. Linear fits of each set extrapolated to $f \rightarrow \infty$ yield τ_s that agree within 2 ns. The dashed line helps to visualize the magnitude of the correction, $\tau_m - \tau_s$, when compared to τ_m measured at a single frequency. At 25 MHz, this difference is 39 ns, nearly 10% of τ_s given the very short travel time in the sample shown here. Further examples of sound speeds and their pressure dependence will be presented.



5:00 PM A 30 MHz, 3D Imaging, Forward Looking Miniature Endoscope based on a 128-element Relaxor Array**Katherine Latham¹, Christopher Samson¹, Eric Simpson¹, Roger Zemp², Jeremy Brown¹**¹*Biomedical Engineering, Dalhousie University, Halifax, NS, Canada*, ²*University of Alberta, Canada***Background, Motivation, and Objective**

3D Ultrasound systems present several technical challenges, particularly the large number of elements inherent to a 2D array, high electrical impedance of small elements, and long image acquisition time. Crossed electrode arrays address some of these issues, especially the huge reduction in number of elements where only $2N$ elements are required instead of N^2 . However, even with $2N$ elements, there remain practical challenges in packaging a high-frequency crossed electrode array into an endoscopic form factor. This work describes the design, fabrication and characterization of a 128-element crossed electrode array in a miniature endoscopic form factor.

We have previously demonstrated a fast and simple 3D imaging approach for crossed electrode arrays referred to as Simultaneous Azimuth and Fresnel Elevation (SAFE) compounding. The principle behind this technique is to perform conventional compound imaging with an azimuth set of electrodes, while implementing a bias controllable Fresnel elevation lens with an elevation set of electrodes. While a Fresnel lens would usually result in unacceptable secondary lobe levels, these lobes can be suppressed by compounding different Fresnel patterns in parallel with the conventional plane wave compounding in the azimuth dimension. The Fresnel lens is implemented by using an electrostrictive ceramic (eg. Pulse polarity depends on a DC bias) as the array substrate.

Statement of Contribution/Methods

A 30MHz, 64x64 element crossed electrode relaxor array was fabricated on a electrostrictive 1-3 composite substrate. The array was designed with λ pitch and a single quarter wavelength matching layer. A process has been developed that uses a thinly diced strip of flex circuit to bring the back-side connections to common bond surface, which allows the final size of the endoscope to measure only 5.4 x 6.4 mm.

Imaging performance was tested using a custom 64 channel beamforming system with a 3D imaging module that provides the 64 reconfigurable biasing channels. 3D images were generated by imaging two perpendicular wire phantoms in a water bath using a reconfigurable acoustic Fresnel lens to focus to a series of elevation slices to build the volume image. A diverging wave compounding scheme was implemented in the azimuth direction. In both the elevation and azimuth directions, 64 insonifications were used to compound and reconstruct each 2D slice.

Results/Discussion

The electrostrictive composite array elements had a measured electromechanical coupling coefficient (k_t) of 0.62 with a bias voltage of 40V and a measured one-way pulse bandwidth of 55%. The electrical impedance magnitude on resonance was measured to be 70 ohms with a peak phase angle of -60 degrees. Hydrophone measurements were completed to confirm the pulse polarity and fast switching speed (< 3μs). Preliminary 3D images were generated of a wire phantom using the SAFE compounding technique. Full beam radiation beam profile measurements are ongoing.

5:15 PM

Backside clamped phased array transducer : From FEM to characterizationCyril Meynier¹, Marie-Coline Dumoux¹, Guillaume Ferin¹, Claire Bantignies¹, An Nguyen-Dinh¹¹*Vermon SA, Tours, France***Background, Motivation, and Objective**

Recent transducer array designs incorporate high-impedance material, also known as dematching layer, to clamp the backside of the active material. Such a design strategy represents an interesting alternative to dramatically increase the elementary capacitance and thus improve its electrical compatibility with Front-End electronics. It also paves the way of interesting interconnection features allowing to increase contact amounts and density.

Phased Array (PA) transducers centered near 3MHz are one of the major segments within the medical imaging probe industry. They are mainly used for external (intercostal) cardiac imaging on high-end echocardiography systems. In this work, a 3 MHz phased array probe including a tungsten clamping layer was designed with the help of FEM modeling, manufactured and characterized. Modeled and measured responses are compared.

Statement of Contribution/Methods

A commercial, generic FEM tool (COMSOL Multiphysics, COMSOL Group, Sweden) was used for the design and optimization of the transducer. Computing limitations impose the use of a 2D model, which assumes variables are constant along elevation axis. Thus, in order to be able to calculate the far-field response, a mixed 2D-3D model has been developed: the pressure field calculated in 2D is exported to a 3D model and thus geometric focusing (performed by a conventional lens) can be taken into account.

Experimentally, a corresponding prototype was extensively characterized. In particular, the pressure field was recorded using a calibrated hydrophone (ONDA corp, USA), both in front of the transducer and along a circle. Electrical impedance was also measured, in various loading conditions.

Results/Discussion

A mixed 2D-3D FEM model has been developed for addressing computing limitations and successfully validated through experimental measurements. Figure 1 c) compares the time-frequency FEM response (convoluted by recorded excitation) with the experimental one (compensated by hydrophone calibration data). Similarly, electrical impedance and angular response of the transducer were also measured, attesting for the electrical and acoustical benefits of the proposed design, and compared to the model. A good match is obtained, exhibiting the high reliability of the model. Furthermore, the merits of using a passive electrical impedance matching are also studied.

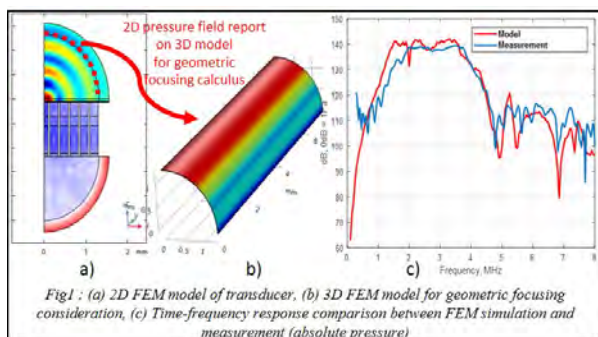


Fig1 : (a) 2D FEM model of transducer, (b) 3D FEM model for geometric focusing consideration, (c) Time-frequency response comparison between FEM simulation and measurement (absolute pressure)

P1-A10 - Cardiovascular System

Kairaku (posters 1)

Tuesday, October 23, 9:30 AM - 4:00 PM

Chair: **Chih-Chung Huang** National Cheng Kung University

P1-A10-1

Characterizing the erythrocyte aggregation using the anisotropy of ultrasonic backscatter

Julien Rouyer¹, Lenin Chinchilla¹, Olivier Lombard¹, Emilie Franceschini¹

¹Aix-Marseille université, CNRS, Centrale Marseille, France

Background, Motivation, and Objective

Quantitative ultrasound techniques for characterizing red blood cell (RBC) aggregation rely on a theoretical scattering model to fit the measured BackScatter Coefficient (BSC). The scattering theories commonly used assume spherical shape of RBC aggregates and an isotropic structure factor. The aim of this work was to study the anisotropy of ultrasonic backscatter from blood to determine if measuring the angular dependent BSCs could improve the differentiation between healthy and pathological RBC aggregation (i.e. anisotropic rouleaux versus isotropic clumps).

Statement of Contribution/Methods

Experiments were conducted at a physiological hematocrit of 40% on porcine blood sheared in a Couette flow device combined with a 15-MHz focused transducer. The transducer was placed in order to obtain different insonification angles ranging from 60° to 120° with respect to the flow streamlines. The flow contains disaggregated RBCs or RBCs treated with dextran 500 kDa to promote aggregation. In parallel, simulations were conducted by considering a collection of spherical and rouleaux-shaped scatterers. Scatterers are uniformly randomly distributed using a Monte Carlo algorithm.

Results/Discussion

Results exhibit angular dependent BSC behavior for aggregating blood in both simulations and experiments. The peak of BSC amplitude at 90° observed in experiments could be explained by rouleaux structures aligned with the streamlines. For individual RBCs re-suspended in saline solution, the experimental BSC amplitude versus insonification angle is also strongly anisotropic with a minimum value at 90°, which was not expected. This anisotropic behavior cannot be simulated by considering the Monte Carlo algorithm but are due to hydrodynamic and contact effects on microstructure, as reported previously in (Blanc, Journal of Rheology, 2013) for hard spheres. To conclude, the anisotropy observed in sheared blood originates from both aggregate structure (aligned or not with the flow) and the anisotropic structure factor of effective scatterer.

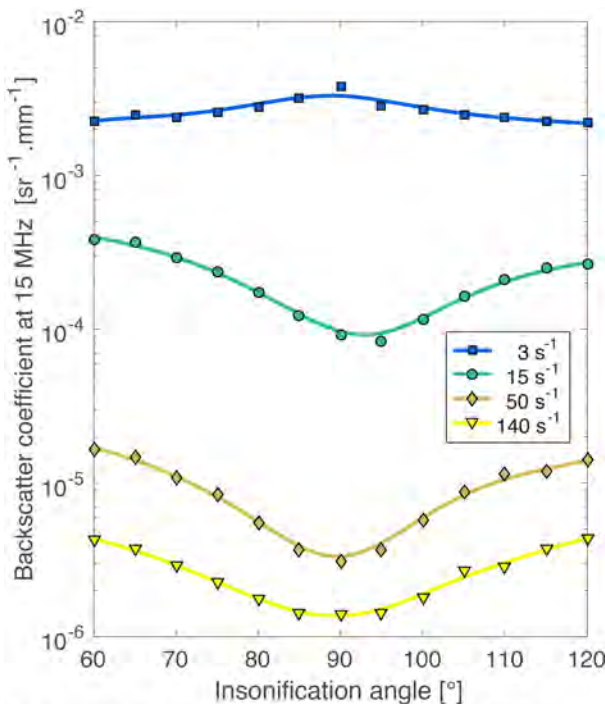


Figure. Values of the BSCs at 15 MHz as function of the insonification angles ranging from 60° to 120° in the case of an aggregating RBC sample at 40% hematocrit. The sample was studied under different shear rates from 3 s⁻¹ up to 140 s⁻¹.

Coronary Plaque Characterization from IVUS Image by using Artificial Intelligence Technique

Yi-Chen Li¹, Wei-Ting Chang², Chih-Chung Huang¹

¹Department of Biomedical Engineering, National Cheng Kung University, Taiwan, ²Division of Cardiovascular Medicine, Chi-Mei Medical Center, Taiwan

Background, Motivation, and Objective

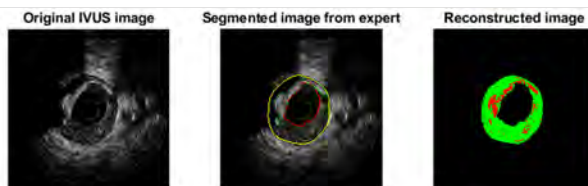
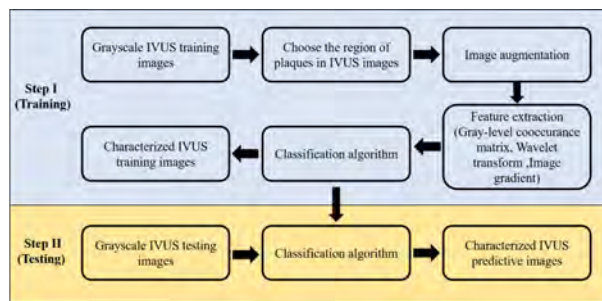
Hypertension, hyperlipidemia, smoking, and diabetes are the major risk factors for atherosclerosis, which is the main cause of cardiovascular diseases (CVD). Physicians believe that analyzes the distribution and morphology of the plaque can improve the treatment strategy of CVD. Currently, gray-scale IVUS is a common technique for visualization of intravascular structure and plaque distribution. Commercial IVUS systems provide the software for analyzing the types of plaque and the size of lumen by using the backscattering signals from tissues. However, there are still some limitations, for example, the RF attenuation and shifting problems. In addition, the automatic results from commercial systems sometime conflict with the determination from physicians. Therefore, physicians still have to spend times for labeling IVUS image manually. It prompts us to develop a new approach based on machine learning to automatically characterize plaque components from IVUS image.

Statement of Contribution/Methods

The gray-scale IVUS images from patients with CVD were obtained from Division of Cardiovascular Medicine, Chi-Mei Medical Center, Tainan, Taiwan. Each image was labeled by the experts for classification of plaque manually: the calcified plaques, other plaque regions defined as soft plaques between the borders of media-adventitia, and lumen size. The block diagram of the proposed algorithm for plaque characterization using IVUS images is shown in Fig. 1(a). Texture analysis algorithms including gray-level co-occurrence matrix, wavelet transform, and image gradient were used for feature extraction. In classification step, the supervised machine learning algorithms: AdaBoost Classifier and Error-Correcting Output Codes (ECOC) were selected for training.

Results/Discussion

The characterized results are shown in Fig 1(b), including a typical original grayscale IVUS image, the segmented image characterized by the expert, and the reconstructed image from machine learning algorithm. In the segmented image, the yellow contour refers to the border of media-adventitia. The red one is the lumen border, and the green represents the calcified plaques. In reconstructed image, the green label is the soft plaque, and the red means calcified plaque. Average accuracy for the images that participated in validation is higher than 72% compared to the experts in this study.



Quantitative ultrasound spectroscopy measurements of erythrocyte aggregation within superficial veins

Guy Cloutier¹, Boris Chayer¹, Louise Allard¹, Julian Garcia-Duitama¹

¹University of Montreal Hospital, Canada

Background, Motivation, and Objective

An enhanced inflammatory response is a trigger to the production of blood macromolecules involved in abnormally high levels of red blood cell (RBC) aggregation. This study aimed to demonstrate the clinical feasibility of a non-invasive ultrasound-based erythrocyte aggregation measurement method for potential application in critical care medicine.

Statement of Contribution/Methods

RBC aggregation was evaluated using modeling of the ultrasound backscatter coefficient with the structure factor size and attenuation estimator (SFSAE). SFSAE spectral parameters W (packing factor describing spatial organization of RBCs) and D (fractal dimension of RBC aggregates) were measured within the antebrachial vein of the forearm and tibial vein of the leg in 50 healthy participants at two flow shear rates. Recordings were performed with a Vevo770 Visualsonics scanner equipped with a 35 MHz probe. Experimental conditions considered natural flow or reduced flow controlled by a specially designed pressurized bracelet applied on the skin. Blood samples were also collected to measure RBC aggregation ex-vivo with a laser erythroaggregometer (parameter S10).

Results/Discussion

W and D measured in-vivo were positively correlated with ex-vivo S10 index for both measurement sites and shear rates (correlations between 0.35 - 0.81, $p < 0.05$). SFSAE W and D measurements on the forearm were correlated with values over the leg for similar shear rates ($p < 0.05$). For both venous sites and shear rates (natural flow at 37 s-1 on average, and reduced flow at 0.8 s-1 on average), intra-observer variability for 5 repeated measures of D varied between 26.3 - 28.2%, whereas it was higher (34.1 – 48.9%) for W. In conclusion, the designed bracelet coupled to the high-frequency SFSAE ultrasound measures may found applications for continuous patient monitoring in critical care units to predict sepsis events. However, repeatability might have to be improved by readjusting the bracelet applied pressure and position between each measure.



Figure 1: Recording device made of a pressurized bracelet applied over the brachial vein and of a 35 MHz single-element oscillating transducer acquiring radiofrequency data (Visualsonics, Vevo770).

Experimental verification of relationship between red blood cell aggregation degree and peak frequency of ultrasonic reflection spectrum with real blood**Takayuki Sato¹**¹*Graduate School of Science and Engineering, Tokyo Metropolitan University, Tokyo, Japan***Background, Motivation, and Objective**

We propose that the red blood cell (RBC) aggregation degree can be estimated from the peak frequency (PF) of the reflection spectrum using a 20-MHz ultrasonic transducer and the RBC-mimicking particles of several materials. By using the relationship between the wavelength of medical ultrasound and the RBC diameter, the attenuation of the ultrasound, which is due to Rayleigh scattering, can be determined. In our previous work, the PF proportionally declined with the logarithm of the aggregation degree. This study aims to experimentally verify the relationship between the aggregation degree and the PF with actual blood and develop a monitoring technique for RBC aggregation degree for extracorporeal treatment.

Statement of Contribution/Methods

For controlling the RBC aggregation degree, dextran 70, which is regarded as an effective flocculant for RBC, was used in porcine blood. The interface sedimentation velocity (ISV) was measured as an aggregation index. The ISV had the advantage that it was capable of evaluating the blood sample aggregation degree with a hematocrit of over 40 % against the aggregation diameters obtained by microscopic observation. The quantitative relationship between the aggregation degree observed with a microscope and the ISV was confirmed in our previous work. The porcine blood was adjusted to hematocrit 40 % in advance. An aqueous solution of dextran 70 with 0.9 % saline was added to set the concentrations from 0 to 3.0 % in the blood samples. Subsequently, under a constant temperature of 36 degrees centigrade, the samples were left in test tubes, and the height of the interface was obtained for 180 minutes. The PFs were obtained using the samples prepared by the same method as that for the ISV. Stainless steel containers were filled with each sample, and reflection boards were placed on the bottoms of the containers. A broadband transducer with a center frequency of 20 MHz and an element diameter of 6.2 mm was immersed in the suspensions to vertically face the reflection boards placed in the container at a distance of 10 mm. Scattering attenuation, which depends on the aggregation diameter, is reflected in the echo signals at the reflection board. After fast Fourier transform processes, the PFs were specified.

Results/Discussion

In the cases of dextran 70 concentrations from 0 to 2.0 %, the ISVs increased from 0 to 0.63 mm/min, and the PFs declined from 13.7 to 12.3 MHz. In the cases of dextran 70 concentrations over 2.0 %, the ISVs declined, and the PFs ascended. The correlation coefficient between the ISVs and the PFs was -0.98. By confirming the quantitative relationship between the aggregation degree and the blood viscosity, a simple technique that uses the PF for real-time monitoring of blood viscosity could be realized.

Red blood cell aggregation measurement with 40-MHz ultrasound has a possibility for noninvasive evaluation of blood glucose level in patients with diabetes

Kanta Nagasawa¹, Hiroki Sakaki¹, Shohei Mori², Mototaka Arakawa¹, Satoshi Yashiro³, Yasushi Ishigaki³, Hiroshi Kanai²

¹Graduate School of Biomedical Engineering, Tohoku University, Sendai, Japan, ²Graduate School of Engineering, Tohoku University, Sendai, Japan, ³Department of Internal Medicine Division of Diabetes and Metabolism, Iwate Medical University, Morioka, Japan

Background, Motivation, and Objective

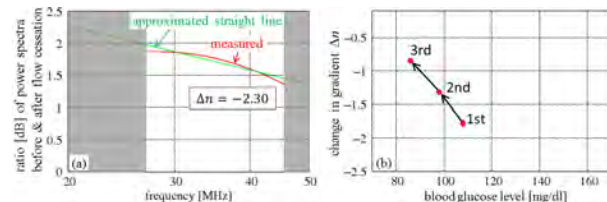
Diabetic patients must measure their blood glucose level (BGL) by multiple-times skin-puncture for achieving optimal BGL control, resulting a burden due to invasiveness and high cost. Though several methods for non-invasively measuring BGL have been developed, they have not yet become clinically available. Red blood cells (RBCs) aggregation, which is a reversible adhesion phenomenon, is an essential determinant of hematological properties (viscoelasticity), and the blood viscosity is increased when BGL is high. Therefore, the BGL can be assumed to be correlated with RBC aggregation. The present study experimentally shows that ultrasonic measurement of RBC aggregation at low shear rates has a possibility for noninvasive evaluation of the BGL.

Statement of Contribution/Methods

The theoretical scattering property of each size of scatterer strongly depends on frequency f , and each slope of the scattering power spectrum $|S(f)|^2$ can be approximated by $C \times f^n$ in a certain frequency bandwidth, where C is a coefficient and n is the power index. Actually, the power spectrum of the measured echo includes four properties other than $|S(f)|^2$, which are the transducer input, the transducer transmission property, the spatial sound pressure distribution, and the attenuation property in the medium. For eliminating these four properties to clarify the scattering property, the present study evaluates the degree of RBC aggregation at a low shear rate by introducing a novel parameter Δn which shows change in gradients (power indexes) of the power spectra of the echoes scattered from the venous lumen before and after cessation of blood flow. The ultrasound of 40 MHz was transmitted and Δn was evaluated in the frequency range of 27 to 45 MHz as in Fig. (a) and compared with the BGL level, which was invasively obtained just after the ultrasonic measurements.

Results/Discussion

After confirming the accuracy of the proposed parameters by basic experiments using microspheres, Δn was compared with the BGL for one healthy subject. Both measurements were applied just after glucose of 18 g was ingested after fasting for 12 hours. Both measurements were applied 3 times at intervals of about 30 minutes. As shown in Fig. (b), Δn became higher as the BGL decreased. The parameter Δn determined by the proposed method has a potential in clinical noninvasive evaluation of BGL for patients with diabetes.



Nonlinearly Generated Second Harmonic Ultrasonic Backscatter for Determining Composition of Human Carotid Plaque

Russell Fedewa¹, Sheronica James¹, Heather Gornik², Sean Lyden³, D. Geoffrey Vince¹

¹Biomedical Engineering, Cleveland Clinic, Cleveland, OH, United States, ²Cardiovascular Medicine, Cleveland Clinic, Cleveland, OH, United States, ³Vascular Medicine, Cleveland Clinic, Cleveland, OH, United States

Background, Motivation, and Objective

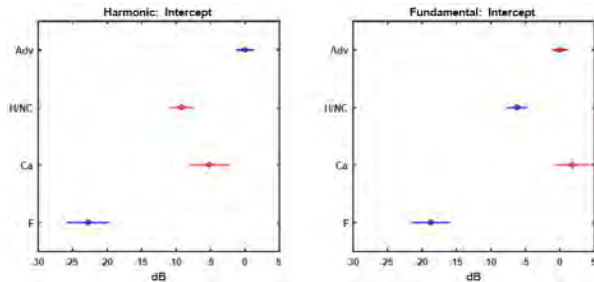
Carotid atherosclerotic plaque is an important cause of stroke. Current imaging approaches measure the extent of stenosis, while plaque composition is unavailable at the point of care outside of calcium burden provided by CT. The goal of this effort is to provide a robust non-invasive measure of plaque composition. The specific focus of this abstract is to determine if the nonlinearly generated second harmonic portion of the signal can aid the fundamental portion in determining plaque composition.

Statement of Contribution/Methods

A pilot clinical study, enrolled 14 subjects and obtained pulse inversion RF backscatter prior to carotid endarterectomy using a Siemens S3000 with Axius Direct software and a 9L4 probe. Transverse serial histology slices of the surgically removed plaque were prepared and matched to ultrasound frames. Homogenous regions of interest (ROI) were located within each stack of slides and placed into one of three categories (# of ROIs): Ca – calcium (20), F – fibrous (18), and H/NC – hemorrhagic and/or necrotic core (53). Ultrasound data was collected from adventitial (Adv) regions of six normal subjects to obtain 202 ROI's. Each ROI contained 15 pulse inversion pairs by 64 points (40 MHz) and corresponded to a 1.2mm square. The pulse inversion pairs were processed to obtain the harmonic and fundamental traces with 20dB bandwidths of 2.5 - 6.9 MHz and 4.9 - 10.1 MHz. Power spectrum for each ROI was obtained using a Yule-Walker approach of order 20. The power spectra were normalized by data obtained from a uniform 0.5 dB/cm-MHz phantom. The estimate of the backscatter transfer function was adjusted by a depth and frequency dependent attenuation estimate derived from adventitial backscatter of normal subjects.

Results/Discussion

The figure displays Bonferroni adjusted 95% confidence intervals of the means of each tissue type for the fundamental (right) and harmonic (left) intercept linear fit parameter. Non-overlapping confidence intervals indicates that the parameters are significantly different. A significant difference for both bandwidths for the mean of F was found. The fundamental has the mean of H/NC being significantly different from other types, in contrast the harmonic has the mean of Adv being significantly different from other types. In conclusion, the harmonic parameters provide additional discriminatory information for plaque composition.



Laser-generated focused ultrasound back-scattered signal analysis for differentiating blood and clot: A quantitative study
Deblina Biswas¹, Jeongmin Heo¹, Hyoung Won Baac¹
¹*Sungkyunkwan University, Korea, Republic of*
Background, Motivation, and Objective

Recently, laser-generated focused ultrasound (LGFU) has emerged as a cavitation based therapeutic technique since it can generate large amount of micro-bubbles which can be used for drug delivery.

Statement of Contribution/Methods

Citrated mouse blood was coagulated with 0.2M CaCl₂ solution which was poured into thin plastic container and placed at the focal point of the LGFU system.

Results/Discussion

Figure 1 illustrates the frequency spectra obtained from blood and blood clot. This clearly illustrates two-fold increase in the dominant frequency in case of clot compared to that of the blood. Differentiation is also observed in the mean frequency as shown in Fig.2.

Consistent results were confirmed for six different samples from three different mice. Temporal change of blood clot elasticity could be also characterized quantitatively with frequency spectral information of LGFU-BS signal. This demonstrates the potential of our LGFU-BS analysis technique to spectrally differentiate blood and blood clot which can be further applied for in-vivo micro-clot identification.

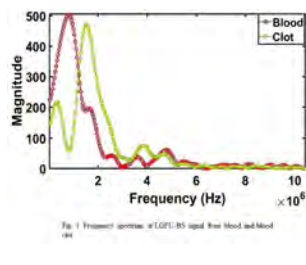


Fig. 1. Frequency spectrum of LGFU-BS signal from Blood and Clot

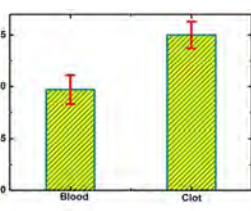


Fig. 2. Bar graph indicates mean frequency obtained from Blood and Blood clot LGFU-BS signal frequency spectrum

P1-A11 - Histotripsy, SonoThrombolysis and HIFU

Kairaku (posters 1)

Tuesday, October 23, 9:30 AM - 4:00 PM

Chair: **Shin Yoshizawa** Tohoku University

P1-A11-1

Non-invasive Histotripsy Aberration Correction for Soft-Tissue using Cavitation-induced Shockwaves

Jonathan Macoskey¹, Tim Hall¹, Jonathan Sukovich², Sang Won Choi¹, Kimberly Ives¹, Eric Johnsen³, Charles Cain¹, Zhen Xu¹

¹*Biomedical Engineering, University of Michigan, Ann Arbor, MI, United States*, ²*Biomedical Engineering, University of Michigan, MI, United States*, ³*Mechanical Engineering, University of Michigan, United States*

Background, Motivation, and Objective

Spatial variations of physical parameters in heterogeneous soft tissue, e.g., sound speed, can severely defocus ultrasound propagation resulting in phase aberrations. Histotripsy is a therapeutic ultrasound method that fractionates tissue via cavitation. Cavitation microbubbles can function as point-source signals and have been used for aberration correction (AC) in ultrasound imaging and therapy. This paper is the first study to investigate the feasibility of using shockwaves emitted from histotripsy-induced cavitation for AC using a histotripsy array with both transmit and receive capability.

Statement of Contribution/Methods

A 500-kHz, 112-element phased array was used to generate cavitation clouds in water through four 5-cm thick porcine abdominal tissue samples. Each element of this array was also used to receive shockwaves emitted from the cavitation. The arrival time of shockwaves on each element was calculated and compared to a reference signal to determine the time delay required to correct for phase aberrations. This shockwave AC (SAC) method was compared to a gold standard hydrophone AC (HAC) method, in which a hydrophone placed at the transducer focus measures arrival times directly.

Results/Discussion

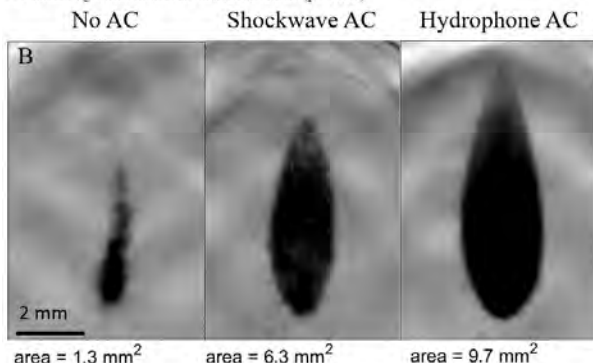
Focal pressures were measured with no AC, HAC, and SAC (Figure 1A). HAC and SAC methods respectively resulted in an average increase in focal pressure of 55.5% and 20.9% with the same transducer power input compared to no AC. As a result, the cavitation cloud generated was significantly larger with HAC and SAC compared to no AC at the same power level (Figure 1B). HAC and SAC methods also resulted in a 50% and 31.5% decrease in transducer power threshold required to generate cavitation, respectively. This study demonstrates the proof-of-concept for using histotripsy cavitation for AC.

A: Sub-Cavitation Threshold Focal Pressures Through Tissue

| | Focal Pressure (MPa) | % Recovered |
|-----------------------------------|----------------------|------------------|
| Baseline pressure without tissue* | 2.19 | 100.0% |
| No AC | 1.09 ± 0.05 | $0.0 \pm 4.5\%$ |
| Hydrophone AC** | 1.70 ± 0.10 | $55.5 \pm 9.1\%$ |
| Shockwave AC** | 1.32 ± 0.03 | $20.9 \pm 2.7\%$ |

* Pressure at the focus of the histotripsy array aligned with the hydrophone method in the free-field without any pre-focal aberration medium

** Indicates significant difference from No AC values ($p < 0.005$)



Histotripsy Volume Ablation Enabled by Electronic Focal Steering and Bubble Coalescence**Jonathan Lundt¹, Akshay Rao², Tim Hall¹, Charles Cain¹, Zhen Xu¹**¹*Biomedical Engineering, University of Michigan, Ann Arbor, MI, United States, ²Computer Engineering, University of Michigan, MI, United States***Background, Motivation, and Objective**

The persistence of residual microbubbles following histotripsy cavitation collapse hinders treatment speed and homogeneity. Previous studies in our lab have demonstrated the use of low-amplitude (~ 1 MPa) pulses interleaved with histotripsy pulses to drive bubble coalescence (BC) via the secondary Bjerknes force. In a recent proof-of-principle study, low-gain regions (~ 20 dB) of the histotripsy beam approximately 2λ outside the electronic focal steering (EFS) focus were shown to drive BC. In this manner, each pulse served the dual-purpose of generating cavitation at the current EFS position while simultaneously driving BC at recently treated foci which harbored populations of residual microbubbles. Based on this result, the present study investigates the use of a specialized EFS sequence to increase the speed and homogeneity of histotripsy volume ablation.

Statement of Contribution/Methods

Histotripsy was applied using a 250 kHz, 256-element hemispherical phased array transducer with a 15-cm focal distance, generating 1.5-cycle pulses at 400 Hz PRF with estimated $P_0 = 52$ MPa. An algorithm was developed to construct an EFS sequence which strategically arranged the spatiotemporal position of each EFS position such that residual microbubbles were exposed only to low-gain regions of the therapy beam for at least 20 pulses immediately following the histotripsy pulse. Our previous study showed exposure to low-gain acoustic regions for 6.7 ± 0.8 pulses was sufficient to achieve BC at 400 Hz PRF. Performance of the algorithmic EFS sequence was compared to an EFS sequence arranged in a raster pattern. The two EFS sequences were applied to tissue-mimicking phantoms containing a thin layer of red blood cells (RBCs). The phantom, initially opaque, became translucent as RBCs were fractionated by histotripsy, allowing treatment progression and homogeneity to be monitored by optical imaging.

Results/Discussion

The algorithmic sequence required significantly ($p < 0.01$) fewer pulses (89.3 ± 16.8) to achieve 97% ablation of a 22-cm^3 target than the raster sequence (168 ± 24.3 pulses). These results provide strong evidence that a specially designed EFS sequence which utilizes low-gain acoustic regions to drive BC has the potential to increase speed and homogeneity of histotripsy ablation without the deposition of any additional acoustic energy.

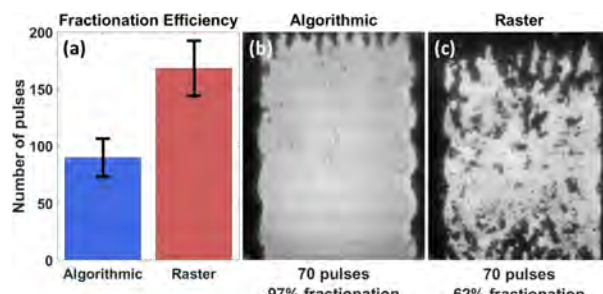


Fig. 1. (a) Number of pulses required to achieve 97% fractionation for algorithmic (blue) and raster (red) sequences ($p < 0.01$, $N=3$). Characteristic images of RBC phantom treated with 70 pulses using (b) algorithmic EFS sequence and (c) raster EFS sequence. After delivering 70 pulses, the algorithmic sequence achieved 97% fractionation, whereas the raster sequence achieved 62% fractionation.

Rapid Histotripsy Treatment Using Protocol of Fundamental and Second Harmonic Superposition Combined with Hundred-Microsecond Ultrasound Pulses with Sector Array Approach: Initial Experiments

Mingzhu Lu¹, Dan Han¹, Rui Wang¹, Yujiao Li¹, Yanshan Liu¹, Yizhe Geng¹, Xuan Wang¹, Mingxi Wan¹

¹*The key Laboratory of Biomedical Information Engineering of Ministry of Education, Xian Jiaotong Univ., Xian, China, People's Republic of*

Background, Motivation, and Objective

Histotripsy is a non-invasive therapy modality and can mechanically disintegration of target tissue for tumor treatment. In this study, in order to speed up histotripsy treatment we propose a strategy of using 4-element sector array, fundamental and second harmonic pressure superposition, and waveform of hundred-microsecond pulses and two stages. Hopefully, the rapid histotripsy process can be achieved through increasing one-spot lesion volume, enhancing pressure from cavitation reflection and multi boiling bubbles

Statement of Contribution/Methods

A custom-designed 4-element sector array (Fig.1 (a)) operated at 1.2 MHz (1,4 elements) and 2.4 MHz (2,3 elements) with 146 mm aperture, 100 mm geometric focal length. By controlling the phase shift between neighbor elements, one, two and four foci in focus plane can be generated. In our initial experiments, in order to obtain high pressure at focus we used the one focus pattern with acoustic focus dimension of 0.7 mm by 3 mm (lateral by axial length) and the peak negative pressure of each frequency exceeding -10 MPa. The histotripsy waveform scheme of hundred-microsecond pulses and two stages was used: stage 1, pulses with a pulse duration (PD) of 400 μ s, much higher 4% duty factor and pulse repetition frequency (PRF) of 100 Hz; stage 2, same PD and PRF as those in stage 1 and 1% duty factor. The experiments were implemented in gel-phantom with bovine serum albumin (BSA), ex vivo porcine kidneys, monitored via high speed camera or passive cavitation detection (PCD).

Results/Discussion

As expected, the experiments achieved successfully the disintegrated lesions with typical dimension of 5 mm by 7 mm (lateral by axial length) in porcine kidneys (Fig.1 (b) and (c)). The slide of H&E stained shows the lesion region (Fig.1 (g)) where tissue fractionates into acellular debris with sharp boundary. The filtered-PCD mean square waveform indicates the enhanced inertial cavitation energy. The selected images (Fig.1 (e) and (f)) from high speed imaging show the cavitation cloud structure and cavitation-bubble-layer reflection effects toward to transducer in prefocal region. The large sized lesion with wider 5-mm lateral dimension generated in prefocal region can attribute to dual-frequency parallel beams with shock waves, strong cavitation-bubble-layer reflection effects, and the parallel boiling bubbles of two frequencies.

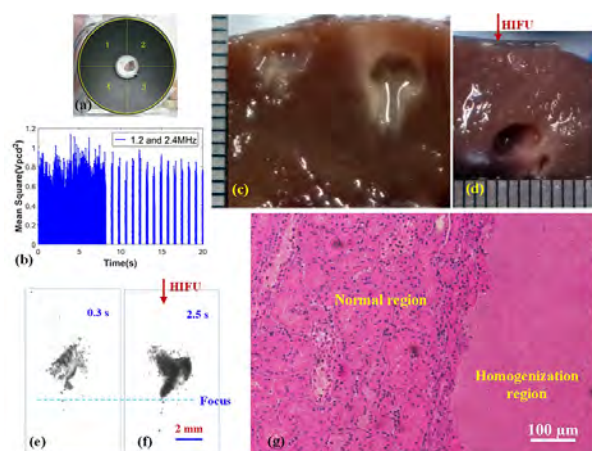


Fig.1 Histotripsy of hundred-microsecond pulses and two stages using (a) 4- element sector array operating at 1.2 and 2.4 MHz. (b) Filtered-PCD mean square waveform. (c) and (d) Lesions generated in ex vivo porcine kidneys under different depths, exhibited complete disintegration of target tissues. (e) and (f) Images from high speed imaging. (g) H&E stain slide of pig kidney.

Thrombotripsy for venous recanalization using a high frequency transducer of 2.25MHz in a porcine model of femoral venous thrombosis

Guillaume Goudot¹, Lina Khider², Costantino Del Giudice², Tristan Mirault², Patrick Bruneval², Alexandre Galloula³, Michaël Vion⁴, Mickaël Tanter¹, Emmanuel Messas², Mathieu Pernot¹

¹Institut Langevin, INSERM U979, Paris, France, ²PARCC INSERM U970, Paris, France, ³Vascular medicine, APHP, Paris, France, ⁴Cardiawave SAS, Paris, France

Background, Motivation, and Objective

Histotripsy has been shown promising for non-invasive treatment of deep venous thrombosis [Ref]. Important challenges remain, however, to perform a safe and accurate treatment in human patients. We have shown previously *in vitro* that a high-frequency approach enables accurate and targeted recanalization by reducing the size of the focal spot. The objective of this work was to evaluate 1) the feasibility of this approach assisted by a robot to recanalize effectively a venous thrombosis *in vivo* and 2) the safety of our device on venous wall injury and risk of pulmonary embolism.

Statement of Contribution/Methods

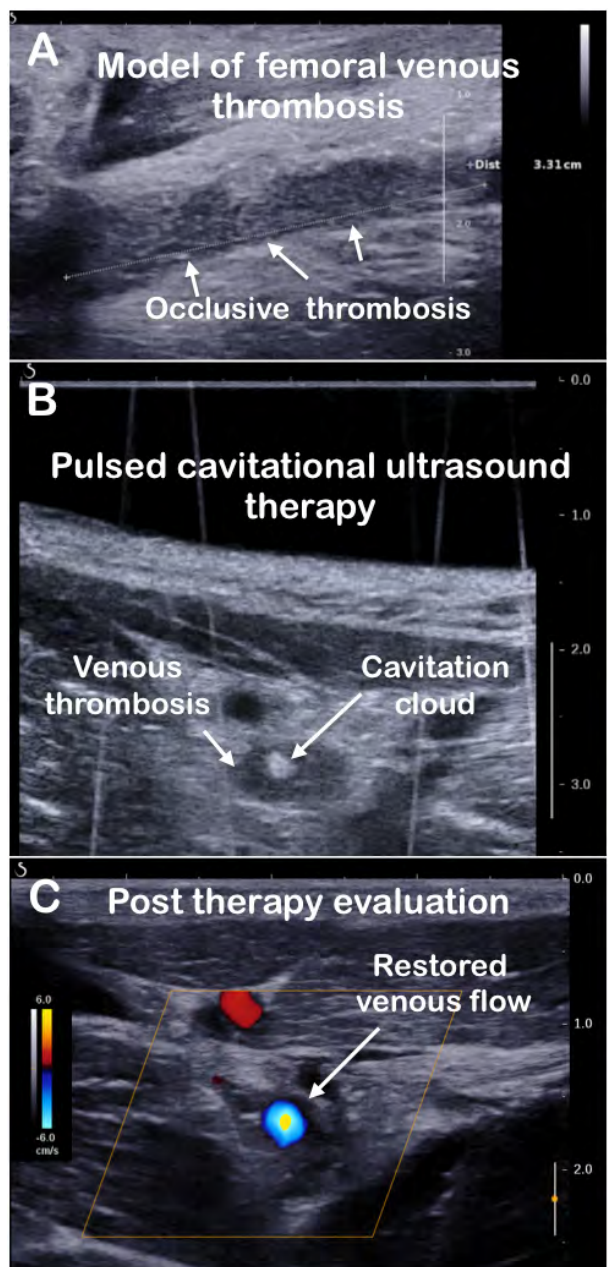
A femoral venous thrombosis of 9 pigs weighing 49.6 kg was systematically created. To obtain occlusive thrombosis, we used a double jugular and femoral approach to position the balloons. A thrombosis was obtained after 2h of stasis associated with 50 IU of human thrombin. A 2.25 MHz transducer (Imasonic[®]) centered by a linear probe (SL10-2, SuperSonic Imagine[®]) was used and cavitation was obtained in the center of the vein. After manual determination of the thrombus, a 6-axis robotic arm was used to automatically move the transducer along the thrombus trajectory. Success of recanalization was evaluated by the flow restoration evaluated with color-Doppler imaging and by the passage of contrast agent with phlebography (Figure). The safety was assessed by local hematoma research with ultrasound imaging and histological analysis of the lungs for embolism.

Results/Discussion

7 occlusive and 2 subocclusive venous thromboses were obtained with a mean length of 2.8±0.4 cm. Among them, only 7 were accessible for recanalization because 2 thromboses were too deep (>3cm). Recanalization was systematically obtained among the 6 occlusive cases, with improvement of flow in the case of partial thrombosis. No extravasation of contrast product or hematoma was observed with radioscopie and ultrasound imaging. The pulmonary arterial tree was macroscopically free from embolism.

Conclusion: Thrombotripsy performed at high frequency (2.25MHz) is an effective and safe tool to enable non-invasive and thrombolytic venous recanalization.

Ref: Maxwell AD *et al. J Vasc Interv Radiol* 2011;22:369–77.



Generation of medium-high intensity focused acoustic vortex and its application in sonothrombolysis

Shifang Guo¹, Xuan Du¹, Xin Wang¹, Xuyan Guo¹, Mingxi Wan¹

¹Department of Biomedical Engineering, School of Life Science and Technology, Xi'an Jiaotong University, China, People's Republic of

Background, Motivation, and Objective

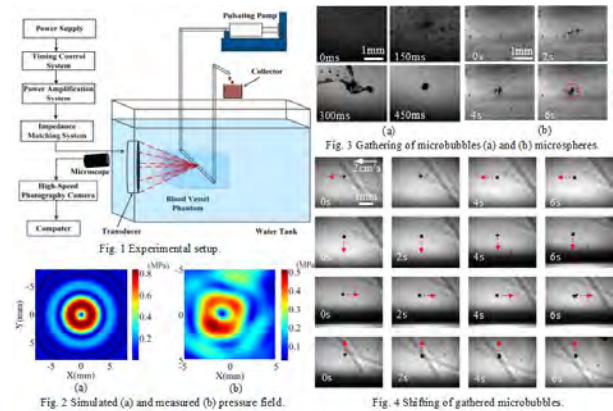
Clot debris produced in sonothrombolysis has the risk of blocking the downstream vessels due to their size, potentially causing hazardous emboli. Multiple fragmentation of debris via confining them in the focal region proved effective in reducing their size. Though the feasibility of using acoustic vortex to capture particles has been demonstrated, the low intensity in current studies makes it unlikely to induce cavitation, especially inertial cavitation, which was the underlying mechanism for ultrasound therapy. In this work, we developed a generation system of medium-high intensity focused acoustic vortex to induce inertial cavitation and explored its application in thrombolysis in an effort to reduce debris size.

Statement of Contribution/Methods

A generation system of medium-high intensity focused acoustic vortex, including a power supply, a timing control system, a power amplification system, an impedance matching system and a focused spherical transducer composed of sixteen split arrays (active diameter = 120 mm, geometrical length = 120 mm), was developed. The amplitude of each array kept the same but the phase between adjacent arrays increased by $2\pi/16$. Besides, a transparent phantom with a vessel of 6 mm diameter was used to mimic a blood vessel in soft tissue. Disperse microbubbles (mean diameter: 2.5 μm) and polystyrene microspheres (mean diameter: 50 μm) were pumped into the vessel separately, and the latter were used to simulate clot debris. The distribution of microbubbles and microspheres was observed through a microscope (cf. Fig. 1).

Results/Discussion

Primary results showed this system could generate the desired acoustic vortex with a focal region less than 1 mm (cf. Fig. 2), showing an excellent ability to capture microbubbles and microspheres (cf. Fig. 3). Disperse microbubbles could be aggregated into the focal region within 1 s, and no microbubbles could be observed in the vicinity, which may be beneficial to ensure effective thrombolysis in focal areas while avoiding damages to surrounding tissues. Microspheres could also be effectively aggregated though it took longer. Furthermore, the morphology of gathered microbubbles was demonstrated to be maintained when they were shifted, even when against the direction of blood flow (cf. Fig. 4). The application of medium-high intensity focused acoustic vortex in sonothrombolysis is in process.



Dual-frequency ultrasound thrombolysis using a high intensity focused ultrasound transducer arrayWu Sun¹, Suzi Liang¹, Yun Jing², Erik Dumont³, Hairong Zheng¹, Weibao Qiu¹¹*Paul C. Lauterbur Research Center for Biomedical Imaging, Shenzhen Institutes of Advanced Technology, Chinese Academy of Sciences, China, People's Republic of*, ²*Mechanical and Aerospace Engineering, North Carolina State University, Raleigh, NC, United States*, ³*Image Guided Therapy, France***Background, Motivation, and Objective**

Ultrasound thrombolysis has emerged as a promising non-invasive treatment approach for ischemic diseases. Cavitation has been attributed to one of the main mechanisms for sonothrombolysis. Dual-frequency sonication has been demonstrated for the reduction of the inertial cavitation threshold [1]. However, there are no reports on the efficacy of dual-frequency sonothrombolysis using high intensity focused ultrasound (HIFU) transducer arrays. This study attempts to investigate dual-frequency ultrasound for thrombolysis using a 128-element HIFU transducer array.

Statement of Contribution/Methods

Porcine blood clots were prepared in a similar fashion as in [1]. All experiments were conducted in a water tank with a 3D translational stage. A sketch of the experimental setup is shown in Fig.(a). A 128-element transducer array with four passive cavitation detection elements (IMASONIC,France) was driven by the Image Guide Therapy system. Each clot was cut into about 20mm long pieces and initially weighted (m_1). Then the clot was pushed into the PVC tube for sonication. During the treatment, the 3D translational stage moved the tube to achieve thorough thrombolysis. At each treatment position, the tube stayed for $t/5$, where t is the total treatment time. After treatment, the debris was injected into a 100 μm filter and weighted (m_2). The thrombolysis efficiency was calculated by,

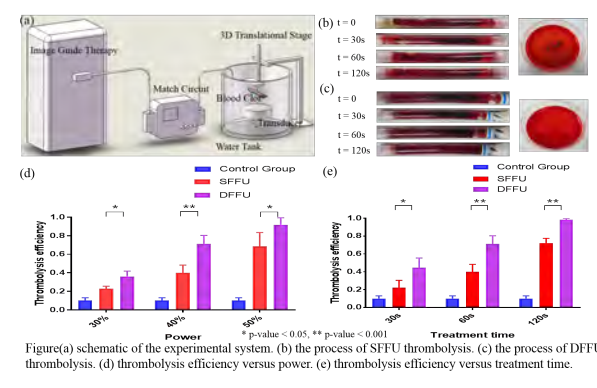
$$\eta = (m_1 - m_2) / m_1$$

Several groups of experiments with different parameters were performed at single frequency focused ultrasound (SFFU, 650 kHz) and dual-frequency focused ultrasound (DFFU, 64 elements driven at 650 kHz and others driven at 700 kHz).

Results/Discussion

The experiments of thrombolysis based on SFFU and DFFU were shown in Fig. (b) and Fig. (c), respectively. It was shown that DFFU has less blood clot debris left compared with SFFU. Fig.(d) and (e) show the relationship between thrombolysis efficiency and power (at 60s treatment time and 3% duty cycle) as well as between thrombolysis efficiency and treatment time (at 80W power and 3% duty cycle) respectively . There was no ultrasound treatment for the control group. As a conclusion, DFFU was able to accelerate thrombolysis and promote treatment performance compared with SFFU.

[1] Dingjie Suo et al., *Physics in Medicine & Biology*, 2015



High intensity focused ultrasound (HIFU) combines shear wave optical coherence elastography (SW-OCE) for diseases treatment and evaluation

Kanheng Zhou¹, Guan Wang¹, Yan Wang², Kairui Feng¹, Faqi Li², Chunhui Li¹, Zhihong Huang¹

¹School of Science and Engineering, University of Dundee, Dundee, United Kingdom, ²State Key Laboratory of Ultrasound Engineering in Medicine Co-Founded by Chongqing and the Ministry of Science and Technology, Chongqing Key Laboratory of Biomedical Engineering, College of Biomedical Engineering, Chongqing Medical University, Chongqing, China, People's Republic of

Background, Motivation, and Objective

HIFU is a non-invasively acoustic therapeutic technique that utilizes high intensity acoustic field in the focus to kill the targeted tissue for disease treatment purpose. The mechanical properties of targeted tissue, e.g. Young's modulus, usually change before and after HIFU treatment. This change can be accurately detected by shear wave elastography. Thus, it is usually used for evaluating HIFU treatment effect. Not only to improve the low spatial resolution in ultrasound shear wave elastography, but also to perform diseases treatment and evaluation using the same transducer in the same system, a new setup that combines HIFU and phase-sensitive optical coherence tomography (PhS-OCT) system was proposed in this study to do the both: 1) HIFU treatment with the transducer working at high energy level, 2) treatment effect evaluation using SW-OCE with the transducer working at low energy level.

Statement of Contribution/Methods

In this study, a customized 10.3 MHz single element HIFU transducer was employed for treatment and shear wave inducing, and a M-B mode PhS-OCT with micrometre level resolution was used as the wave tracker. Ex-vivo bovine liver tissue was treated at the same energy level for different time (1s, 5s, 9s) in this research. SW-OCE was performed on the lesion area of the sample after HIFU treatment, and the elastogram was reconstructed by the time of flight time method.

Results/Discussion

The elastogram results clearly show the boundary of HIFU lesion area and surrounding normal tissue, even for 1s treatment time. Elasticity of the lesion grows as the treatment time increases. Combined with OCT needle probe, the proposed method has a large potential not only to be used for superficial diseases treatment, but also to be used for high-precision-demanded diseases treatment, e.g. nervous disease treatment.

Low-cost ultrasound thermometry for HIFU therapy using CNN

Younsu Kim¹, Chloe Audigier¹, Nicholas Ellens¹, Emad M. Boctor²

¹Johns Hopkins University, Baltimore, MD, United States, ²Johns Hopkins University School of Medicine, United States

Background, Motivation, and Objective

High intensity focused ultrasound (HIFU) therapy can be used to non-invasively heat a target region for hyperthermia or thermal ablation. Temperature monitoring is required to deliver an appropriate amount of thermal dose. In a previous work, we developed a HIFU thermometry using an ultrasound element. Due to sparse time of flight (ToF) information, the thermal image reconstruction accuracy highly depends on the ultrasound element location. In this work, we propose a thermal image reconstruction method using a convolutional neural network (CNN), which could be less sensitive to ultrasound element location.

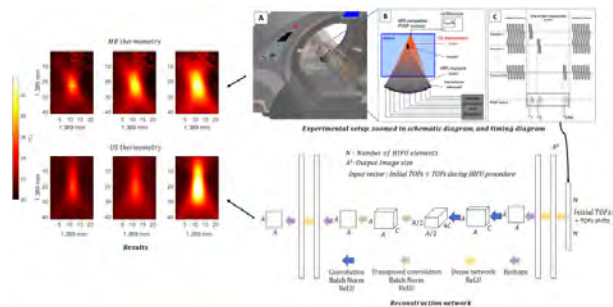
Statement of Contribution/Methods

We propose a thermal image reconstruction method using CNN. The input for the network is a concatenated vector of ToF acquired at the beginning and ToF shifts during the HIFU procedure. This approach utilizes an ultrasound modality that sound velocity varies with temperatures, therefore ToF changes as HIFU delivers thermal energy to a target tissue.

One of the challenges of machine learning approach is to collect large amount of training sets to increase the accuracy. To overcome this, we used a physics-based HIFU simulation able to generate an unlimited number of training sets using various tissue types, HIFU powers and heating durations. Since the ultrasound thermometry system is MR-compatible, we trained the model with simulated data and tested it with phantom data acquired under MR thermometry as well.

Results/Discussion

We simulated 21,384 datasets at 162 different element locations with 132 temperature images. The dataset was randomly split into 16,038 training and 5,346 validation sets. The result on the validation sets show 0.13 ± 0.07 C° of mean and 1.16 ± 0.75 C° of maximum errors. To test the trained model, we performed phantom experiments. We built a soft tissue mimicking phantom using agar and silicon dioxide. We evaluated our method with the phantom experiment and compared with MR thermometry. The result shows a mean and maximum temperature difference of 0.81 ± 0.23 C° and 3.78 ± 0.66 C° respectively. Those promising results show the feasibility of thermal monitoring using an external ultrasound element and CNN reconstruction.



Feasibility Study on Noise Reduction Using Continuous Wave Response of Therapeutic Ultrasound for High Intensity Focused Ultrasound Treatment

Ryo Takagi¹, Shin Yoshizawa²

¹National Institute of Advanced Industrial Science and Technology (AIST), Tsukuba, Japan, ²Graduate School of Engineering, Tohoku University, Sendai, Japan

Background, Motivation, and Objective

In ultrasonic monitoring of high intensity focused ultrasound (HIFU) treatment, it is difficult to ultrasonically monitor tissue changes while irradiating therapeutic ultrasound because it overlaps with diagnostic ultrasound signals. In our previous study, noise reduction method utilizing continuous wave response of HIFU signals has been developed and it was applied to the static cases, where the tissue samples were not moved. However, the target body and organs are moving randomly at relatively slow speed because of breathing and also rapid tissue changes such as cavitation bubble generation occur in the actual HIFU treatment. In this study, the developed noise reduction method was applied to the cases, where the excised block of gel phantom was moved assuming the respiration-induced motion and the feasibility of this method for the actual HIFU treatment was investigated.

Statement of Contribution/Methods

The polyurethane gel phantom was placed on the stage which is controlled by a PC and the speed of the stage was increased in increments of 5 mm/s up to 45 mm/s. RF images with and without HIFU noise was obtained using a phased array probe alternately at a rate of 10 Hz during HIFU exposure and the proposed method was applied to the noisy RF images. In this method, the reference RF signals to estimate entire HIFU noise was chosen in the water bolus during HIFU exposure and estimated HIFU noise was subtracted from the original noisy RF images. The driving frequency of diagnostic and therapeutic ultrasound was 2.50 and 1.67 MHz, respectively. In these experiments, plane wave was used to produce RF images for the detection of rapid tissue changes.

Results/Discussion

Figure.1 (a) (b) show one of the average power spectra of received RF signals in all channels and actual RF images with and without HIFU noise and after signal processing in a case that gel phantom was moved at a speed of 45 mm/s. As shown in Fig. 1(a) (b), the fundamental component of HIFU noise was reduced by about 20 dB and decreased to the original signal level even when the target phantom was moved during HIFU exposure. These results imply that our proposed method could be practically applicable for the case of respiratory motion during HIFU treatment. We are planning to investigate the feasibility of this method for the case, where cavitation bubbles are generated while target phantom is moved during HIFU exposure in near future.

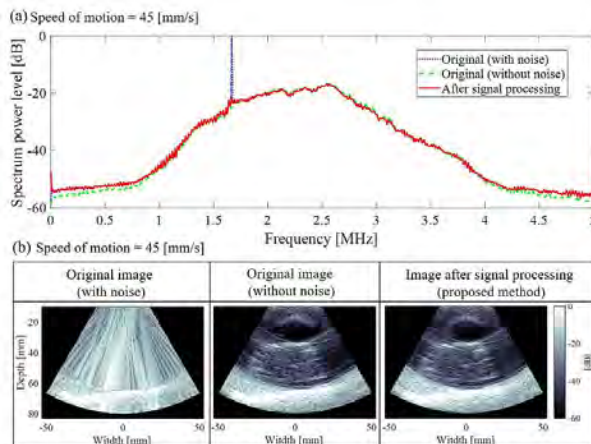


Fig.1 (a) One of the average power spectra of received RF signals in all channels and (b) actual RF images with and without HIFU noise and after signal processing in the cases that gel phantom was moved at a speed of 45 [mm/s]

Patched Optimal Scanning Pathway with Brute-force Approach for Time Reduction in High Intensity Focused Ultrasound Treatment

Euisuk Chung¹, Pilsu Kim¹, Tai-kyong Song¹

¹*Department of Electronic Engineering, Sogang University, Seoul, Korea, Republic of*

Background, Motivation, and Objective

In high intensity focused ultrasound (HIFU) treatment, there are arising interest to enhance the treatment efficiency by reduction of treatment time. The previous researches had revealed the spiral pattern from the outside to the center is efficient scanning pathway. However, these researches were conducted by evaluating among the previously known pattern, which is not guaranteed the optimal treatment time. In this paper, we propose the patched optimal scanning pathway with brute force approach (P-Optimal) which can effectively lower the treatment time.

Statement of Contribution/Methods

In the P-Optimal, the optimal scanning pathway is heuristically determined by the brute force investigation on every possible patterns. In the small area, optimal pathway to minimize the treatment time can be easily found using brute force approach. For the large area, using brute force approach is impossible due to enormous cases. Thus, as illustrated in Fig.1 (b), P-Optimal can be determined by dividing the target area into multiple sub-regions, which allow to obtain the optimal path way through brute force investigation. The brute-force investigation was conducted with finite element method simulation with MATLAB. To verify the P-Optimal, we perform *in-vitro* and *ex-vivo* studies on transparent commercial BSA phantom (ONDA Co) and bovine liver for 3x3 and 9x9. The thermal lesion size on the phantom is recorded by digital camera during HIFU experiments. The size of thermal lesion from the results were calculated by pixel counting. The ratio of intersection over union(IoU) and lesion area was utilized as the evaluation metrics.

Results/Discussion

Fig.1(a) shows results of *ex-vivo* study for 3x3. Thermal lesion size generated by three methods have acceptable IoU compared to simulation results as illustrated by dashed black line. Using optimal method determined by brute force, the treatment time was reduced by 8% compared with raster scanning. P-Optimal have significant time reduction as increasing of target size as shown in Fig.1(b). The experimental results for 9x9 were expressed by Fig.1(c) and Fig.1(d), which demonstrate that P-Optimal is able to ablate accurately and effectively diminish the treatment time. Moreover, the feasibility of P-Optimal was confirmed by R^2 value of 0.987 between the results of experiment and simulation in the Fig.1(d).

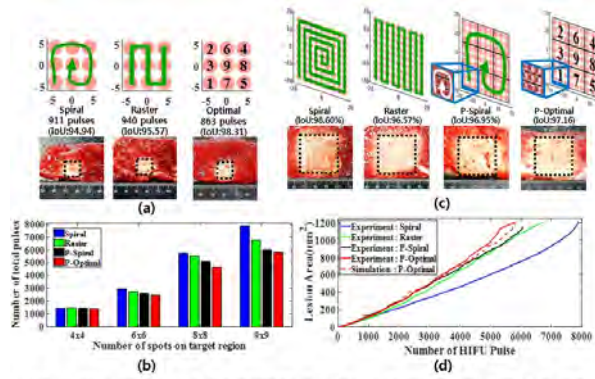


Fig. 1 (a) Illustration for 3x3 Scanning pathway of Spiral(left), Raster(middle) and Optimal(right) and experimental results for HIFU lesions using the methods (black dashed line express the simulation region) (b) the comparison of number of total pulse between methods depends on the target size. (c) Illustration for 9x9 Scanning pathway of Spiral, Raster, P-Spiral and P-Optimal and experimental results for HIFU lesions using the methods (black dashed lines express the simulation region) (d) thermal region size as function of HIFU pulses at 9x9 size of BSA phantom

P1-A12 - Micromachined Transducers - I

Kairaku (posters 1)

Tuesday, October 23, 9:30 AM - 4:00 PM

Chair: **Omer Oralkan** North Carolina State University

P1-A12-1

Efficiency and bandwidth of experimental capacitive and commercial piezo transducers

Borislav Gueorguiev Tomov¹, Jørgen Arendt Jensen², Mathias Engholm³, Andreas Havreland⁴, Søren Elmin Diederichsen⁵, Erik Vilain Thomsen⁴, Christopher Beers⁶, Lars Moesner⁷

¹DTU Electrical Engineering, Technical University of Denmark, Kongens Lyngby, Denmark, ²Technical University of Denmark, Lyngby, Denmark, ³The Technical University of Denmark, Kongens Lyngby, Denmark, ⁴Technical University of Denmark, Denmark, ⁵DTU Nanotech, Technical University of Denmark, Kgs. Lyngby, Denmark, ⁶Sound Technology Inc., United States, ⁷BK Ultrasound, Denmark

Background, Motivation, and Objective

The image quality and price of medical ultrasound scanners depend greatly on the transducers that they employ. The development of transducers based on new principles, f.ex. capacitive micromachined ultrasound transducers (CMUT), promises increased flexibility of the design of the active transducer area, lowered cost in mass production, and natural integration with electronics in the transducer handle, hence paving the way for compact and affordable scanners. The goal of this study was to compare several generations of CMUT in terms of transmit and receive performance between them and to existing commercial piezo transducers.

Statement of Contribution/Methods

The measurements have been made in water bath, using transducers that have been prepared for use on patients, with appropriate insulation properties and with acoustic lenses where applicable. A hydrophone was positioned below (in front of) each of their elements, which was excited by a series of stochastic signals. The pressure signal for each individual excitation was recorded and later correlated with it, leaving theoretically only the impulse response of the element plus noise. Averaging across the series improves both the signal-to-noise ratio and the decoding performance. The recorded signals were compensated for the spatial impulse response effect using the Field II simulation program, yielding the impulse response of the transducer material from voltage to emitted pressure. The pulse-echo (PE) recording was done by sending and receiving with each transducer element in turn, reflecting off a Plexiglas plate. The PE response can only be used for comparisons between transducers with identical geometry (the linear arrays; the 62+62 element row-column arrays).

Results/Discussion

The measurement-derived performance figures of the transducers are presented in the table. It can be observed that in the CMUT designs the transmit efficiency and receive sensitivity can be traded off for bandwidth. With several iterations, a CMUT transducer can be made to exceed its equivalent piezo reference in one or more parameters. This approach for testing can be (and was) used for determining the direction for future designs, with the goal of optimizing their performance for their specific area of application.

| Transducer type | Tx sensitivity, Pa/Vs | Tx bandwidth, % | Pulse-echo response, mV/V | Pulse-echo bandwidth, % |
|------------------|--------------------------|-----------------------|---------------------------------|-------------------------------|
| Linear, PZT | 3.08×10^{16} | 88 | 14.1 | 62 |
| Linear, CMUT, 2g | 6.38×10^{15} | 96 | 12.1 | 75 |
| Linear, CMUT, 3g | 1.36×10^{16} | 81 | 26.3 | 61 |
| RC, PZT, 62+62 | 5.31×10^{15} | 75 | 9.1 | 67 |
| RC,CMUT,62+62,1g | 3.09×10^{15} | 135 | 3.5 | 90 |
| RC,CMUT,92+92,3g | 8.73×10^{15} | 106 | 4.6 | 73 |

A PMUT array with dynamic directivity: A study of its underwater acoustic power intensity

Sina Sadeghpour¹, Michael Kraft¹, Robert Puers¹

¹Department of Electrical Engineering (ESAT), KU Leuven, Leuven, Belgium

Background, Motivation, and Objective

Because of their ease of fabrication, small size, and high efficiency, piezoelectric micromachined ultrasound transducers (PMUTs) tend to replace conventional transducers in many fields, such as biomedical imaging. However, there has been little analysis and application of PMUTs for underwater communication and localization. Two important properties in the design are the desired directivity and the maximum acoustic power intensity, which define the maximum transmission distance range. Therefore, a PMUT array is proposed and its properties are investigated.

Statement of Contribution/Methods

A detailed analysis as well as FEM simulations were conducted to characterize the dependency of the output acoustic power of a PMUT array on its directivity. Based on specifically derived analytical equations, design and fabrication procedures were introduced to tune the directivity and maximize the output acoustic power. Accordingly, a 12x12 PZT PMUT array was fabricated using a DRIE process on SOI (Fig. 1a) with an element diameter of 410 μm . They can selectively be actuated as a 6x6, 8x8, or 12x12 array. The array was designed to have an underwater center frequency of 300 kHz. It was measured by a Laser Doppler Vibrometer (LDV) in air (Fig. 1a) and will be further characterized by a needle hydrophone in a 600 liter water tank.

Results/Discussion

The equations of the output pressure and power intensity ratio of a directional to an omnidirectional array were derived. It was shown analytically that by keeping the number of elements in an array constant the total output acoustic power decreases by increasing the directivity and the power intensity ratio remains constant and equal to 1. Fig. 1b shows the FEM simulation and calculation of the directivity of three 1D arrays and the ratio of the power intensity to the one of an omnidirectional array with respect to the spacing. The same analysis was performed on a 2D array (Fig. 1c). This illustrates that making an array directional has no benefit for the transmission distance. It will be explained that in practice a directional array can even have a lower power intensity than an omnidirectional one. Fig. 1d shows the simulated and analytical results of the beam pattern of a 6-element 1D array with three different spacings. The underwater measurement of the array and its comparison to analytical and simulated results will be presented in the full paper.

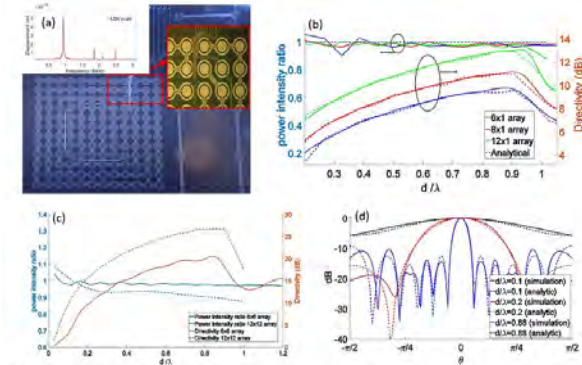


Fig. 1. (a) The fabricated PMUT array; left inset shows the LDV measurement; (b) The FEM simulation and calculation of the power intensity ratio and the directivity of three 1D array respect to the spacing; (c) the FEM simulation of the directivity and the power intensity of a 6x6 and 12x12 array respect to the spacing; (d) beam pattern of three 6-element 1D arrays with three different spacings. In all figures d and λ are the distance between elements (spacing) and the wavelength, respectively.

Study on Wide-band Piezoelectric Micro-machined Ultrasound Transducers (pMUT) by Combined Resonance Frequencies and Controlling Poling Directions.

Kenji Suzuki¹, Yuta Nakayama¹, Naoki Shimizu¹, Takashi Mizuno¹

¹KONICAMINOLTA, INC., Tokyo, Japan

Background, Motivation, and Objective

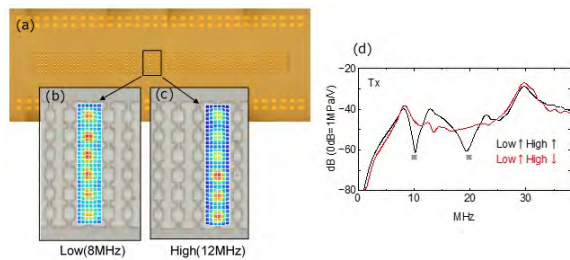
We are developing high sensitivity ultrasonic transducers by combining high performance piezoelectric thin film and MEMS fine processing technology. By utilizing PMUT structure, that is, diaphragm structure and flexural vibration, acoustic impedance matching from the transducer to human tissue is effectively improved against conventional structure based on bulk piezoelectric material, and it could improve sensitivity. On the other hand, there is a problem that the frequency bandwidth that can be imaged is narrowed in this vibration mode. In order to solve the problem, attempts to broaden the bandwidth by combining PMUTs that simultaneously excite a plurality of resonance frequencies have been reported. However, in our study, it is known that deep valley of frequency response (dead zone) occurs in the coupled band because the propagation phase of the oscillator is inverted around the resonance frequency. Therefore, the purpose of this study is to elucidate the cause of the dead zone and to broaden the bandwidth as much as conventional transducers, in particular by controlling the poling directions of the piezoelectric thin film.

Statement of Contribution/Methods

A 64 channel 1-dimensional array by alternately arranging two types of PMUT structures with the resonant frequencies of 9MHz (Low) and 12MHz (High) is designed by FEM and is fabricated with MEMS processing. The layer structure of the substrate with piezoelectric film is Si/SiO₂/Ti/Pt/PZT/Ti/Pt. Evaluate vibration displacement and radiation field characteristics in water using the poling direction (upward or downward) for Low and High-PMUT as parameter respectively. Then analyze the relationship between the difference in poling direction and the in-band shape.

Results/Discussion

The figure to the left shows a fabricated 1-dimensional PMUT array, (a) the optical view from radiation side, (b) the displacement response of Low-PMUTs at 8MHz, (c) the displacement response of High-PMUTs at 12MHz. The figure to the right shows transmission frequency response in water due to difference in combination of polling direction to Low and High PMUTs. When the polarization is opposite to each other, the frequency dead zones seen in parallel case are disappeared and the bandwidth is increased.



High Voltage Excitation and Nonlinear Transmission of a 16 MHz AlN-Based Piezoelectric Micro-Machined Ultrasonic Transducer

Wen-Juan Liu^{1,2,3}, Wei-Jiang Xu¹, Jia Zhou², Nikolay Smagin¹, Malika Toubal¹, Le-Ming He², Xu-Bo Wang², Hao Yu³, Yuandong Gu⁴, Lynda chehami¹, Denis Remiens¹, Jun-Yan Ren²

¹IEMN-DOAE, France, ²School of Microelectronics, Fudan University, Shanghai, China, People's Republic of, ³School of Electrical and Electronic Engineering, Nanyang Technological University, Singapore, ⁴Institutes of Microelectronics, A*STAR, Singapore

Background, Motivation, and Objective

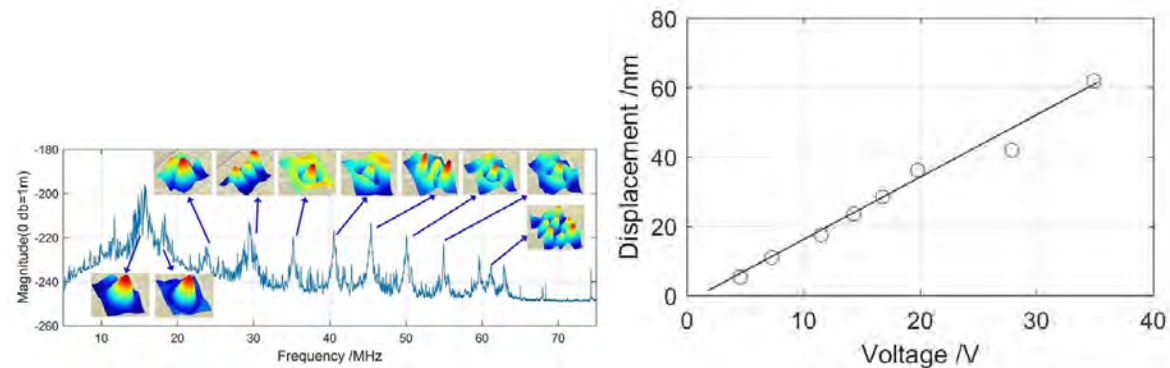
Piezoelectric micro-machined ultrasonic transducers (PMUT) are being applied to portable and miniaturized system for high frequency acoustic imaging. Aluminum nitride (AlN) is an ideal material for MEMS fabrication of high frequency transducers due to its compatibility with CMOS, while it has a low electromechanical coefficient. To increase the transmission sensitivity, this work reports the performance of a 16MHz AlN-based PMUT under high voltage excitation and determining the limit of power transmission capability.

Statement of Contribution/Methods

The proposed PMUT array consists of 44x39 elements fabricated on a silicon-on-insulator with 1 μm AlN thin film on 5 μm silicon membrane. The diameter of the pitch, cavity, and transducer are 70, 60, 50 μm , respectively. The electrical impedance was measured using Network Analyzer and the vibration modes were characterized by Laser Doppler Vibrometer (LDV) when the elements are electrically connected together. The nonlinear response and high order resonances of the device were tested in both frequency burst and wideband short pulse.

Results/Discussion

The total electrical impedance of the PMUT array was 11.6-j30 Ω at 15.8 MHz resonant frequency in air and 4.72-j25 Ω at 13.9 MHz when water charged. The LDV measurements showed that the transmission sensitivity and the bandwidth for free vibration were 1.7 nm/V and 2.1%, respectively. The resonance modes were specifically associated with the substrate and the cavity structure but they are 10~15 dB less in amplitude than the fundamental resonance of the array. Nonlinear behavior was observed when increasing the burst amplitude and the PMUT array broke down when the input mean power applied on the single element exceeded 5.2 mW.



A Row–Column-Addressed 2D Probe with an Integrated Compound Diverging Lens

Mathias Engholm¹, Christopher Beers², Andreas Havreland¹, Borislav Gueorguiev Tomov³, Jørgen Arendt Jensen³, Erik Vilain Thomsen¹

¹*Department of Micro- and Nanotechnology, Technical University of Denmark, Kgs. Lyngby, Denmark*, ²*Sound Technology Inc., United States*, ³*Center for Fast Ultrasound Imaging, Department of Electrical Engineering, Technical University of Denmark, Kgs. Lyngby, Denmark*

Background, Motivation, and Objective

The number of transmit and receive channels needed to perform real-time 3D ultrasonic imaging can be greatly reduced if row–column-addressed (RCA) 2D transducer arrays are used. However, the field-of-view (FOV) is limited to the forward looking rectilinear volume region in front of the transducer. For applications such as abdominal and cardiac imaging, a curvilinear volume region is necessary. A diverging lens can be used to increase the FOV. However, common lens materials result in a convex lens shape. A flat sole is a requirement to obtain good patient contact. By using a compound acoustic diverging lens, the FOV can be extended to a curvilinear volume region, while retaining a flat sole. The objective is to develop an RCA probe with an integrated diverging compound lens to obtain a curvilinear FOV.

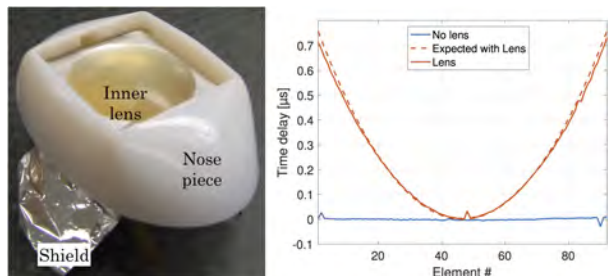
Statement of Contribution/Methods

Two 4.5 MHz, $\lambda/2$ -pitch 92 + 92 channels RCA 2D CMUT arrays were fabricated using a LOCOS process. They were mounted and wire-bonded on flexible printed circuit boards (PCBs), which were connected to two rigid PCBs with pre-amplifiers. The arrays mounted on the PCBs were encapsulated in 3D printed handles, and an electromagnetic shielding layer and the acoustic lens were applied to the front-side of the array. One array was assembled into a probe with a flat lens without any focusing, and the other with a compound diverging lens. The compound lens was composed of two materials: the inner lens material was a urethane, Hapflex 541, and the outer lens material was a silicone, RTV615, loaded with a Bi_2O_3 nano-powder. The diverging compound lens was designed to obtain an FOV of $30.1^\circ \times 30.1^\circ$.

The transmit impulse responses of the rows of both probes were measured using an AIMS III intensity measurement system with an Onda HGL-0400 hydrophone connected to the SARUS experimental ultrasound scanner.

Results/Discussion

The left image shows the transducer after the inner lens was cured. The transducer was then glued to the 3D printed nose piece before the outer lens was added. The right plot shows the measured time delay of the impulse responses across the row elements compared to expected time delay. The diverging effect of the lens is visible as signals are delayed more at the edges than at the center. The FOV can be determined as 28.5° from the delay profile. The 1.6° discrepancy could be due to the probe having been slightly deformed during curing of the outer lens material.



Flexible piezoelectric micromachined ultrasonic transducers towards new applicationsSheng Sun¹, Yuan Jiang¹, Chuanhai Gao¹, Chongling Sun¹, Wei Pang¹, Menglun Zhang¹¹*State Key Laboratory of Precision Measuring Technology and Instruments, Tianjin University, China, People's Republic of***Background, Motivation, and Objective**

Currently, piezoelectric micromachined ultrasonic transducers (PMUTs) are based on silicon substrate. The mechanical rigid nature and limited area prevent their full implementation as ultrasonic transducers and limit their potential applications, since ultrasonic waves by nature have plenty of unique properties that we can leverage. Flexible electronics have been considered as disruptive technologies and seen a promising future. In terms of ultrasonic transducers, after miniaturization (i.e. PMUT and CMUT), transforming them into flexible realm is believed to be another revolution to free ultrasonic transducers from their physical shackles. Flexible PMUT will find new applications in medical imaging, therapeutics, surgery, industry and consumer electronics, thanks to the mechanical compliance, light weight, small element size, large array area and high integration level.

Statement of Contribution/Methods

This work demonstrate a flexible PMUT array, which is fabricated by a ground-breaking technology[1], FlexMEMS, to endow rigid PMUT array with flexibility while its high performance is preserved. The details on fabrication will be fully disclosed. Furthermore, several interesting applications (e.g. wearable smart patch for medical imaging and physical therapeutics, variable HIFU, implantable ultrasonic wireless power transmission) will also be demonstrated or envisioned.

Results/Discussion

Figure 1 (a) and (b) shows the schematic drawing and the as-prepared PMUT array on PET substrate. The mechanical and electrical properties of the PMUT devices were characterized in air and in water respectively. Meanwhile, we have studied the long term stability in water and the influence of substrate bending to the PMUT performance. The results indicate that the performance of the flexible PMUT is as good as the conventional PMUT on silicon substrate. The optimization is still ongoing and we will present the best possible results at the conference. The flexible PMUT with high performance opens up brand new applications.

[1] Jiang Y, Zhang M, Duan X, et al. A flexible, gigahertz, and free-standing thin film piezoelectric MEMS resonator with high figure of merit[J]. Applied Physics Letters, 2017, 111(2): 023505.

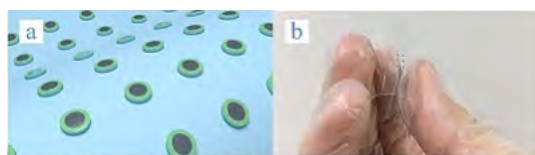


FIG.1 (a) The schematic drawing and (b) the as-prepared PMUT array on flexible substrate

A Study on Structural Parameters for Optimizing Wide-band Property of Diaphragm-Type Transducer Using Piezoelectric Thick Film

Yuya Ishiguro¹, Masatoshi Suzuki¹, Norio Tagawa¹, Masasumi Yoshizawa², Takasuke Irie^{1,3}

¹Electrical Engineering and Computer Science, Tokyo Metropolitan University, Tokyo, Japan, ²Tokyo Metropolitan College of Industrial Technology, Japan, ³Microsonic Co., Ltd, Japan

Background, Motivation, and Objective

A diaphragm-type transducer is suitable for the MEMS manufacturing method as a PMUT, but generally has a narrow band characteristic. This is the result of using a thin film as the piezoelectric material to improve the film vibration efficiency. From the result in [1], we infer that it is possible to increase the bandwidth by thickening the piezoelectric film and by superimposing the thickness vibration on the film vibration. Conversely, when the thickness vibration becomes dominant, it is expected that the narrow band characteristic appears again. Therefore, in this study, we hypothesize that the degree of coexistence of both vibrations depends on the aspect ratio defined as the ratio between the size and the film thickness and that there is optimal aspect ratio.

Statement of Contribution/Methods

Firstly, we confirm a wide band characteristic realized by thickening the PZT film by FEM simulation. After that, we aim to determine the optimal aspect ratio of a PZT thick film to maximize the bandwidth. At that time, we also compute the realized frequency band. As a result, by specifying the desired frequency band, it is possible to determine the optimal size and thickness of the PZT film.

Results/Discussion

We modeled the PZT film as a square diaphragm, and let L be the length of one side of it and h be the thickness. The left figure of Fig. 1 is a simulation result of the specific bandwidth (orange line) and the maximum reception sensitivity (blue line) with respect to h , and L is used as a parameter. As L increases from 50 μm to 100 μm , both lines move to the right. Of course, the larger the size, the higher the overall sensitivity. The relationship between h and L to realize bandwidth maximization is extracted from the left figure and is shown as orange circles in the right figure of Fig. 1. In the figure, the corresponding frequency band is indicated by a blue bar and the center frequency is also indicated by a green circle. Furthermore, the straight line fitted to the data set $\{(h, L)\}$ by least squares criterion is indicated by the solid orange line. This line is expressed as $L = 6.89h + 9.87$. By renormalizing bias 9.87 to L and redefining L' , the optimal aspect ratio defined by L'/h is found to be constant value 6.89. Based on this result, the optimal diaphragm structure for a desired frequency band can be determined.

[1] Y. Ishiguro et al., IEEE Int. Ultrasonics Symp., 10.1109/ULTSYM.2016.7728534 (2016).

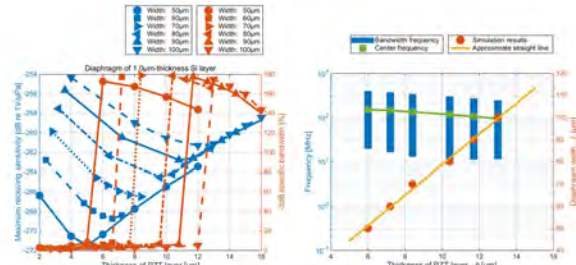


Fig.1 Characteristic evaluation on difference in size and thickness of PZT film: (a) Relationship between specific bandwidth/maximum reception sensitivity and thickness with size as a parameter; (b) Relationship between thickness and size to realize bandwidth maximization for desired design frequency (left blue vertical axis).

A 6-Degree-of-Freedom Piezoelectric Vibration Microstage with Reduced Cross-Axis Coupling

Yi Zhang¹, Jingfu Bao¹, Feng Qin¹, Xinyi Li^{1,2}, Muhammad Ammar Khan¹, Xiaosheng Zhang¹, Ken-ya Hashimoto²

¹School of Electronic Science and Engineering (National Exemplary School of Microelectronics), University of Electronic Science and Technology of China, ChengDu, China, People's Republic of, ²Graduate School of Engineering, Chiba University, Chiba, Japan

Background, Motivation, and Objective

Vibration microstage plays an important role in the practical applications of inertia MEMS (micro-electro-mechanical systems) devices, especially accelerometers and gyroscopes. It provides on-chip stimuli to help the sensors realize self-calibration and improve long-term stability. The key limitation of the current progress of microstage is reducing the cross-axis coupling while increasing the degree of freedom (DOF) simultaneously.

Statement of Contribution/Methods

Herein, we proposed a microstage with six DOF, and moreover, a new structural geometry was developed to decline the cross-axis coupling. Figure 1 shows the as-presented piezoelectric microstage, which is connected to eight crab-leg supporting structures through serpentine flexures. The top electrode of PZT of crab legs was designed with two separated strips to offer in-plane and out-of-plane bending. The novel design of symmetric geometry of crab legs and the combination of serpentine flexures significantly suppress the cross-axis coupling. Furthermore, the serpentine flexures can be utilized to strengthen the displacement of microstage.

Results/Discussion

The systematical study revealed that the displacement of the developed microstage increases linearly with the driven voltage. The driven modes of translation along X-axis and Y-axis exhibit the same displacement value due to the structural symmetry, and the tilting modes around X/Y-axis show the similar situation. FEA simulation results of cross-axis actuation indicate the desired movement along X axis was enhanced to 25 μm while the unwanted cross-coupling movements were significantly suppressed by three-order times. In summary, the axis coupling was effectively reduced down to about 0.02%.

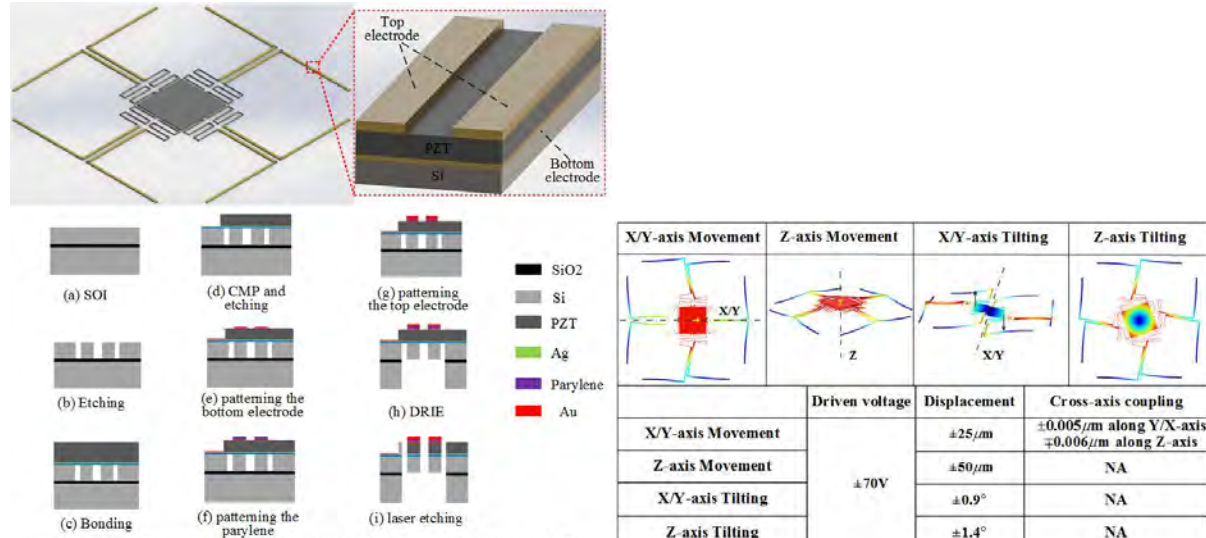


Fig. 1: The schematic view of the proposed 6-DOF micro stage and its fabrication process flow.

Fig. 2: Displacements and cross-axis coupling during static actuation of the stage.

Electrical Tuning of Focal Size with Single Focused Ultrasonic Transducer
Yongkui Tang¹, Eun Sok Kim¹
¹*Electrical Engineering, University of Southern California, Los Angeles, CA, United States*
Background, Motivation, and Objective

Electrical tuning of the focal diameter of focused ultrasound is highly desirable, as the focal diameter is usually varied by physically replacing convex/concave lens on top of a piezoelectric transducer which is labor-intensive. Electrical tuning of a focal diameter can be obtained with phased array, which requires many bulky power amplifiers if high intensity is required. Our aim is to develop an inexpensive high-intensity focused ultrasonic transducer with easy electrical tunability of the focal size.

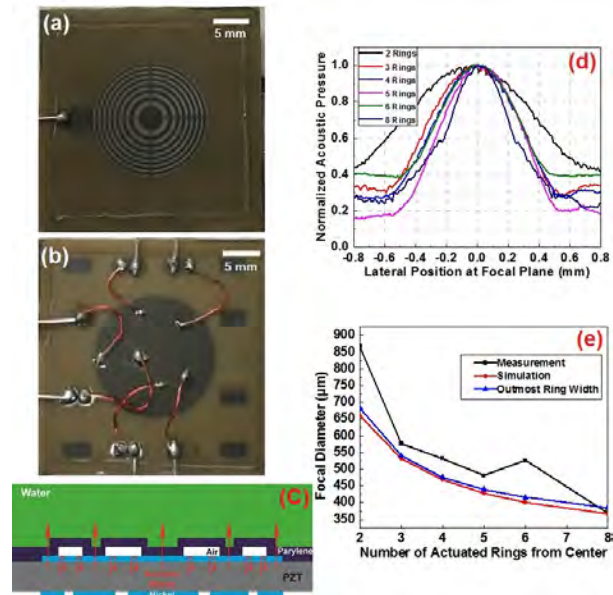
Statement of Contribution/Methods

We designed and microfabricated a focused ultrasound transducer on a 1 mm thick PZT substrate with (1) Fresnel lens with annular rings of air cavities on the top for effective focusing and (2) individually-accessible annular-ring electrodes on the bottom, so that the number of Fresnel rings being activated could be electrically controlled for varying focal size.

On circular top electrode on the PZT substrate, we formed 8 annular-ring air cavities with Parylene (Fig. 1a). The radii of the annular rings are designed into half-wavelength band sources for 6 mm focal length. Due to acoustic impedance mismatch between air and solid, acoustic waves contributing to destructive interference are reflected back, while the waves in the non-air-cavity areas propagate through the lens, and interfere constructively at the focal point, producing high acoustic intensity. On the PZT's bottom side (Fig. 1b), the electrode is patterned into 6 individually-accessible annular rings that overlap with the first two, the 3rd, 4th, 5th, 6th, and the last two Fresnel rings on the top. This design (Fig. 1c) allows us to electrically select any combination of the 6 electrode rings to produce acoustic waves that will pass through the air-cavity lens for focusing. According to Fresnel lens theory, the focal size of a Fresnel lens is close to the width of its outmost ring, which decreases as the ring order gets higher.

Results/Discussion

Acoustic pressure was measured at the focal plane (Fig. 1d) through laterally scanning a hydrophone. During measurement, the voltage level was adjusted in each case to keep the maximal intensity level the same, as we varied the number of the actuated electrode rings. By controlling the number of Fresnel rings being driven from the center, we were able to tune the focal size between 371 and 866 μm (Fig. 1e), while keeping 6 mm focal length at 2.32 MHz.



P1-A13 - Micromachined Transducers - II

Kairaku (posters 1)

Tuesday, October 23, 9:30 AM - 4:00 PM

Chair: **Omer Oralkan** North Carolina State University

P1-A13-1

A 120+120-Element Crisscross CMUT Probe with Real-Time Switchable Electronic and Fresnel Focusing Capabilities

Alessandro Stuart Savoia¹, Enrico Boni², Barbara Mauti¹, Monica Scaringella², Luca Fanni¹, Piero Tortoli², Giosuè Caliano¹

¹*Department of Engineering, Roma Tre University, Rome, Italy;* ²*Department of Information Engineering, University of Florence, Florence, Italy*

Background, Motivation, and Objective

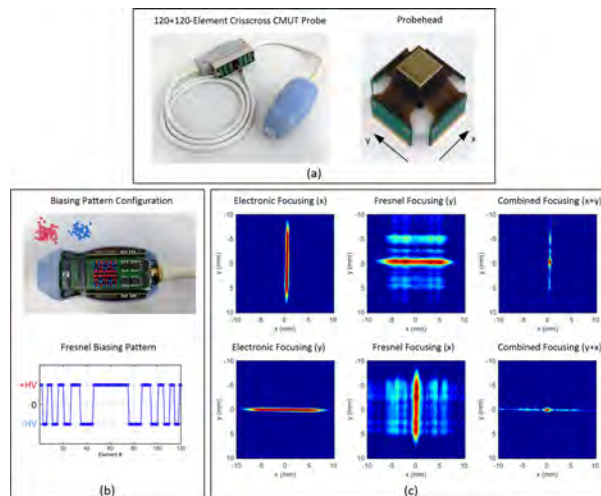
Biplane modality, consisting in the real-time formation of perpendicular B-Mode images, is frequently used in medical ultrasound applications. In some cases (e.g., cardiac imaging), biplane imaging is achieved using fully-sampled 2-D transducer arrays, which typically have high number of elements. Significant element count reduction can be achieved by using crossed array configurations (e.g., Row-Column-Addressed and Crisscross Arrays), in which two orthogonal 1-D arrays co-exist on the same area. However, the imaging performance is limited by the absence of focusing capability in the arrays respective elevation directions. In this paper, we present a novel 120+120-element 7MHz Crisscross CMUT probe, designed for biplane vascular imaging, in which the orthogonal arrays are both provided with Fresnel elevation focusing capability.

Statement of Contribution/Methods

The CMUT array has been designed with a 110 μ m element pitch and 13.2mm length. The packed probehead [Fig.(a)] was connected to in-probe low-noise receivers and high-voltage switches, which allow fast switching (<200 μ s) of the CMUT bias voltage of each array element between 0 V and high voltages up to ± 300 V. The configuration of the bias polarity of each element is provided statically by using a set of micro jumpers [Fig.(b)]. The bias polarity selection enables the elevation aperture Fresnel focusing, while the switching capability allows to alternately apply the elevation bias pattern to the two orthogonal arrays in real-time during biplane scan. The focusing capabilities were tested by interfacing the probe to the ULA-OP 256 scanner, which was configured to transmit 7MHz beams focused at 25 mm with each array using “Electronic focusing only”, “Fresnel focusing only” and both focusing together, with Electronic and Fresnel focusing on X and Y directions and vice-versa. C-scans of radiated pressure fields were acquired at the focal depth with a resolution of 0.2x0.2 mm. Side lobe level (SLL) and peak pressure levels were evaluated.

Results/Discussion

Fig.(c) shows measured pressure fields with a 20dB dynamic range. The SLL were -21 dB and -13 dB for the Electronic and Fresnel focused beams, respectively. The beams obtained by combining the two focusing approaches were found to be mostly equivalent, confirming that this Crisscross probe implementation shows the same performance along the two directions.



CMUT based air coupled transducers for gas-mixture analysis

Priyadarshini SHANMUGAM¹, Luis Iglesias², Jean-Francois Michaud¹, Isabelle Dufour², Daniel ALQUIER¹, Laurent Colin¹, Dominique Certon¹

¹GREMAN UMR-CNRS 7347, Université de TOURS, Tours, France, ²IMS CNRS UMR 5218, Univ. Bordeaux, Bordeaux, France

Background, Motivation, and Objective

Air-ultrasound is an efficient way to monitor binary gas mixture concentrations. Method consists of sensing simultaneously the variations of ultrasonic velocity and attenuation, then by inverse problem, to find the concentration of each gas mixture components. Air-coupled transducers used are particularly significant for the quality of measures. Frequency bandwidth is essential because it defines the frequency range on which the ultrasonic attenuation of gas is measured and the duration of the emitted pressure pulse. The present study aims to develop a specific measuring cell to monitor the real-time hydrogen concentration. It is made of two capacitive micro-machined ultrasound transducers (CMUTs) facing each other in order to perform ultrasonic time of flight (TOF) and attenuation measurements.

Statement of Contribution/Methods

CMUT were fabricated by using a SiN-based surface micromachining process. The total size of emitter and receiver were fixed by the final application. The volume of the measuring cell had to be lower than 3 mL with a distance between emitter and receiver lower than 10 mm. This led to choose square-shape single element transducers with a surface of 12 mm². The CMUT-cells were designed by using non-linear time domain model in order to optimize the frequency bandwidth of the transducer, for a central frequency comprised between 500 kHz and 1 MHz. Several parameters were previously fixed, the membrane and electrode thicknesses (500 nm and 450 nm resp.). The following solution was retained: membrane size of 40x40 μm^2 and gap height of 400 nm. The fabricated transducers were glued on a specifically designed PCB, and then placed face to face in the measuring cell.

Results/Discussion

For the first electroacoustic tests, emitter was excited with one period of sine-shaped pulse centred at 1 MHz ($V_{pp} = 40$ V) and biased with $V_{bias} = 40$ V. A charge amplifier was used to drive the receiver. The measured impulse response was centred at 1 MHz, with amplitude of 150 mV and a -6 dB fractional bandwidth of 105% (fig.1). To validate the general principle of the proposed detection method, a first test on varying the concentration of helium in the cell was performed. A shift in the time of flight (TOF) of the stationary wave was observed (fig.1). As quoted in objective, this method can be applied to other binary gas mixture, and tests with hydrogen will also be performed.

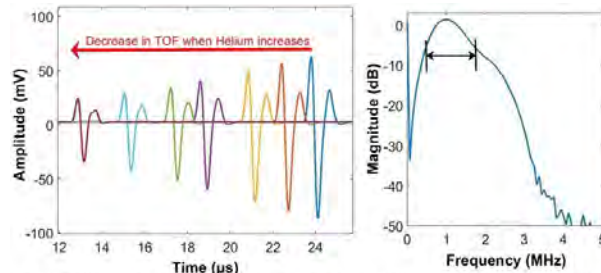


Fig 1: Decrease in TOF when the concentration of helium increases in the measuring cell (left) and spectrum corresponding to the signal at 0% of He (-6dB fractional bandwidth of 105%) (right)

CMUT-based single element transducer applied to 1D transient ultrasound elastography

Dominique Certon¹, Stephane Audiere², Laurent Colin¹, Nicolas Sénégond³, Daniel Alquier¹, Jean Marc Gregoire⁴, Laurent Sandrin², Veronique Miette²

¹*GREMAN UMR-CNRS 7347, Tours University, TOURS, France*, ²*Echosens, PARIS, France*, ³*Vermon, TOURS, France*,

⁴*iBRAIN-UMR INSERM U1253, Tours University, TOURS, France*

Background, Motivation, and Objective

Vibration-Controlled Transient Elastography (VCTE) based FibroScan® device (Echosens, France) is widely used in routine clinical practice for the assessment of liver fibrosis and liver steatosis in patients with chronic liver diseases. Based on single element ultrasound transducer, working typically at 2.5 or 3.5 MHz depending on the probe type, the signal degradation arising from tissue attenuation (often caused by subcutaneous fat or by large exploration depth) is one of the limitations of this technique. The use of only one transducer able to operate in wider frequency band would enable to tune in real-time the frequency working according to the patient. Capacitive Micromachined Ultrasonic Transducers (CMUT) with typical frequency bandwidth of 110 % could be an interesting alternative to overcome this limitation. The present study aims to fabricate and test CMUT-based transducer for VCTE. The fabricated prototype was connected to the Fibroscan® device and compared with its counterpart PZT-based technology.

Statement of Contribution/Methods

The CMUT specifications were based on the PZT transducer used in the Fibroscan® device: a surface of 50 mm² and a center frequency of 3 MHz. CMUTs size and membrane thickness were fixed to meet both acoustic and process specifications (surface micromachining process): square cells of 37x37 μm², with 500 nm SiN membrane covered with 500 nm Al electrode and gap height of 400 nm. Individual transducers were bonded on specifically designed PCB and packaged by covering with a polymer silicone. For the first tests, to avoid that the sensitivity results are biased, no integrated preamplifiers circuits were used to drive the CMUT as receivers.

Results/Discussion

As a first result, CMUT showed very promising performances. Pressure values were measured at different frequencies, with one sinus-shape pulse as excitation (40 Vpp for a collapse voltage of 60 V), from 1.5 MHz up to 7.5 MHz. In all the frequency range, the pressure amplitude was almost constant, 300 kPa-pp, with similar temporal response (1.5 period at the excitation frequency). For the first VCTE tests, the same result than the PZT probe (@ 2.5 MHz) was obtained (fig. 1). As expected, a sensitivity difference was measured (10 dB). But this value should be improved easily by the use of preamplifiers since many electronic circuits, with reasonable costs, are now commercially available.

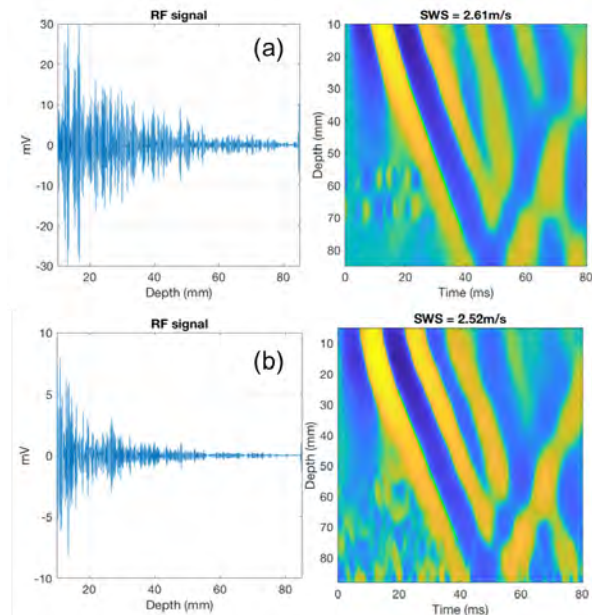


Figure 1 : Comparison between PZT (a) and CMUT (b) probe. Left : RF signal Right : 2D Elastogram

Capacitance-Voltage Characterization of CMUT Arrays: Analytical modeling, simulations, and experiments

Erik Thomsen¹, Søren Elmin Diederichsen¹, Andreas Havreland¹, Jørgen Arendt Jensen², Ole Hansen¹

¹DTU Nanotech, Technical University of Denmark, Kgs. Lyngby, Denmark, ²Technical University of Denmark, Lyngby, Denmark

Background, Motivation, and Objective

Typical ultrasound arrays based on Capacitive Micromachined Ultrasonic Transducers (CMUTs) have hundreds of elements and automated wafer scale measurements are needed for quality control.

Capacitance-Voltage (CV) measurements are widely used to characterize CMUTs. From the CV curve parameters such as the minimum capacitance and the corresponding voltage can be determined. CV measurements can also reveal charging effects and assist in optimizing device design and process development.

The objective of this work is to present a non-destructive measurement method for the uniformity of the pull-in voltage for CMUT arrays. The method is based on CV characterization performed at voltages much smaller than the pull-in voltage and it is a characterization methodology suitable for on-wafer automated measurements.

Statement of Contribution/Methods

We present an analytical electrostatic theory, Eqns. 1-4, predicting the shape of the CV curve and show, that for voltages smaller than approximately 40% of the pull-in voltage the CV curve can be described by the Eq. 1, shown in the figure. V is the applied voltage, C_{\min} is the minimum capacitance, and V_0 is the voltage offset. The pull-in voltage, V_p , can be calculated from the curvature parameter B using Eqns. 2-4. Thus, the pull-in voltage can be determined by a CV measurement, and the proposed method can be used to non-destructively characterize CMUT arrays.

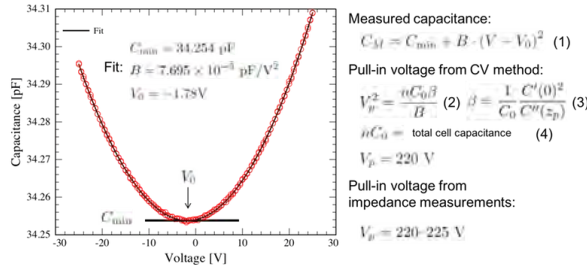
CV measurements were performed on CMUT devices using a Cascade 12K Summit semi-automatic wafer prober and a KEYSIGHT B1500A Semiconductor Device Parameter Analyzer equipped with a B1520A multi frequency capacitance measurement unit.

The CV measurements were performed first from negative to positive bias ("up") and then from positive to negative bias ("down"). Finally, the pull-in voltage was measured using impedance spectroscopy.

Results/Discussion

The obtained CV curves were analyzed by fitting Eq. 1 to the data. One example is shown on the figure where both the up and down CV curves are identical and the CV curve has a minimum close to zero volts showing the absence of charging effects. The pull-in voltage was determined using Eq. 2 to be 220 V, which is close to the value of 220-225 V obtained from impedance spectroscopy.

In conclusion, CV characterization of CMUTs can be used to non-destructively determine the pull-in voltage in CMUT array transducers.



Electrode resistance considerations for large CMUT arrays

Andreas Havreland¹, Mathias Engholm¹, Borislav Gueorguiev Tomov², Jørgen Arendt Jensen³, Erik Thomsen¹

¹DTU Nanotech, Technical University of Denmark, Kongens Lyngby, Denmark, ²Center for Fast Ultrasound Imaging, Technical University of Denmark, Denmark, ³Center for Fast Ultrasound Imaging, Technical University of Denmark, Lyngby, Denmark

Background, Motivation, and Objective

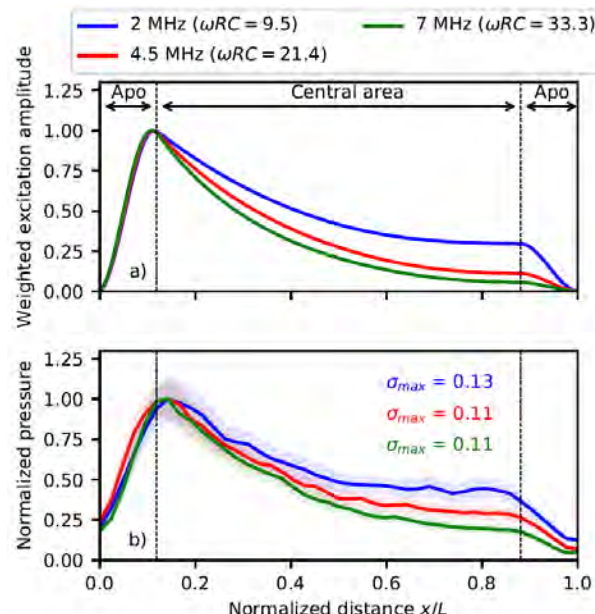
The number of transmit and receive channels needed to perform real-time 3D ultrasound imaging can be reduced, from N^2 to $2N$, if Row-Column Addressed (RCA) 2D transducer arrays are used instead of fully populated matrix arrays. Common for all 2D transducers is that the footprint scales with N^2 . It introduces challenges that are not relevant for 1D transducers, such as increased resistance along the element. High resistance in an element causes attenuation of applied high frequency AC signals, leading to a decreased emitted pressure field along the element. The objective of this work is to develop a model to calculate the required electrical properties of the electrodes needed to operate a CMUT array.

Statement of Contribution/Methods

This work presents a 4.5 MHz 92+92 RCA transducer with integrated apodization, abbreviated Apo. The footprint of this transducer is $2.3 \times 2.3 \text{ cm}^2$ with $\lambda/2$ pitch equal to $180 \mu\text{m}$. The CMUT is fusion bonded, which requires a high annealing temperature ($\approx 1000^\circ\text{C}$), so doped silicon is used as bottom electrode, as metal electrodes melt at such elevated temperatures. The resistivity of the silicon electrode is 0.1 cm , sufficient for a 1D CMUT array, it is however too high for the presented 2D CMUT array. A delay line model has been developed to calculate the required electrical parameters in a CMUT process. By modelling the CMUT element as a delay line, one can show that the determining factor in this system is the non-dimensional product ωRC , where ω is the angular frequency, R is the resistance and C is the capacitance of the CMUT element.

Results/Discussion

The model prediction of AC attenuation along an element is shown in Figure a). The weighted excitation amplitude is plotted as function of position along an element (normalized) for three different values of ωRC , corresponding to excitation frequencies of 2 MHz, 4.5 MHz and 7 MHz. The pressure field was measured 1 cm from the transducer surface by moving an Onda HGL-0400 hydrophone in a grid consisting of 45×45 points. Figure b) shows the average measured peak to peak pressure of all 92 elements as function of position along the element (normalized), with 1 standard deviation (shaded region). Qualitatively, this model captures all the effects in the pressure field along an element, and can be used to calculate the required electrical properties of CMUT arrays used for ultrasound imaging.



Tunable Manipulation of Microparticles by CMUT

Changde He^{1,2,3}, Feiyan Cai², Fei Li², Wendong Zhang¹, Yiheng Du¹, Licheng Jia¹, Chenyang Xue¹, Shengdong Zhang³, Hairong Zheng²

¹*Key Laboratory of Instrumentation Science & Dynamic Measurement, Ministry of Education, North University of China, Taiyuan, China, People's Republic of;* ²*Paul C. Lauterbur Research Center for Biomedical Imaging, Shenzhen Institutes of Advanced Technology, Chinese Academy of Sciences, Shenzhen, China, People's Republic of;* ³*School of Electronic and Computer Engineering, Peking University, Shenzhen, China, People's Republic of*

Background, Motivation, and Objective

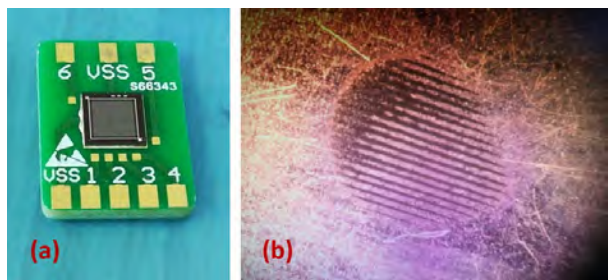
The ability to manipulate microparticles based on ultrasonic wave is highly desirable as its various applications ranging from targeting drug delivery to additive manufacturing. A tunable and miniature sound source is essential for precision particles manipulation. The traditional Piezoelectric (PZT) source array can be used to generated tunable acoustic field, however, are hardly miniaturized. Here, we achieve microparticles manipulation by using a miniature capacitive micromachined ultrasonic transducer (CMUT), which can generate tunable acoustic radiation force resulting from the localized acoustic field at its structured surface interaction with the microparticles.

Statement of Contribution/Methods

As shown in Fig. 1(a), the CMUT device is fabricated by wafer direct bonding technology consist of 40×40 micro-capacitors, the radius and thickness of each micro-capacitor are $46 \mu\text{m}$ and $2 \mu\text{m}$, respectively. The manipulated polystyrene particles with radius of $15 \mu\text{m}$ are placed on the flat upper surface of a phononic crystal plate, which consists of a thin steel plate patterned with a periodical array of the rectangular steel gratings on the bottom surface. The phononic crystal plate is placed on the surface of the packaged CMUT. The whole system is immersed in a water vessel. The phenomenon of particle manipulation is observed through a microscope at the top of the system.

Results/Discussion

When the CMUT device generates a continuous wave with frequency of 3.5 MHz, which is the resonant frequency of the phononic crystal plate, the disorder particles are arranged regularly, as shown in Fig. 1(b). The experimental results show that the sound field generated by the CMUT device is feasible for particles manipulation. Further work about replacing the packaged surface with phononic crystal plate is carried out.



A 50MHz CMUT Probe for Medical Ultrasound ImagingSteve Zhuang¹, Danhua Zhao², Lei Chen²¹Kolo Medical Inc., San Jose, CA, United States, ²Kolo Medical Inc., United States**Background, Motivation, and Objective**

Kolo Medical has developed a number of CMUT probes suitable for ultra-high-frequency ultrasound imaging for applications such as neonatal, dermatology, rheumatology, MSK etc. This paper presents a 50MHz CMUT linear probe prototype.

Statement of Contribution/Methods

We have successfully developed a 50MHz linear CMUT transducer fully packaged into the probe form. The CMUT wafers are fabricated in a commercial foundry. The CMUT chips are packaged into acoustic modules in a commercial packaging house. The probe assembly and testing are performed in house.

The finished 50MHz probe has 256 elements. A 2:1 multiplexer is utilized to connect the 256 elements to the 128 channels of an imaging system. A DC-DC convertor is placed inside the ZIF connector to convert a low DC voltage ranging between 3.3V and 12V to any desired high bias voltage ranging from 120V to 250V. Table 1 shows the physical parameters of the array.

Results/Discussion

The probe was tested in a water tank with a Panametrics 5073PR. All 256 elements are active. A measured pulse-echo waveform is plotted in Fig. 1(a). The corresponding spectrum is plotted in Fig. 1(b). The acoustic data demonstrates that this prototype probe is suitable for ultra-high frequency imaging. Our next step is to refine the peripheral component design and assembly techniques to improve the array performance.

Table 1. Physical parameters

| | |
|----------------------|-----|
| Number of elements | 256 |
| Element pitch (um) | 40 |
| Elevation (mm) | 1.5 |
| Elevation focus (mm) | 5.0 |

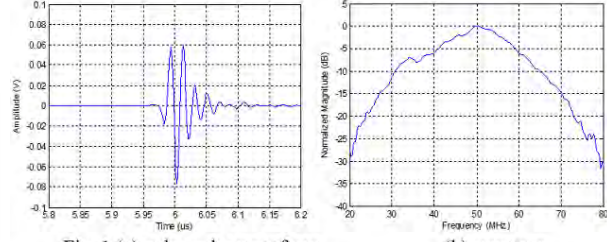


Fig. 1 (a) pulse-echo waveform

(b) spectrum

CMUT surface functionalization with imine-based polymer for SO₂ gas detection applications**Dovydas Barauskas^{1,2}, Donatas Pelenis^{1,2}, Darius Virzonis^{1,2}**¹*Panėvėžys Faculty of Technologies and Business, Kaunas University of Technology, Panėvėžys, Lithuania*, ²*Panėvėžys Mechatronics Center, Panėvėžys, Lithuania***Background, Motivation, and Objective**

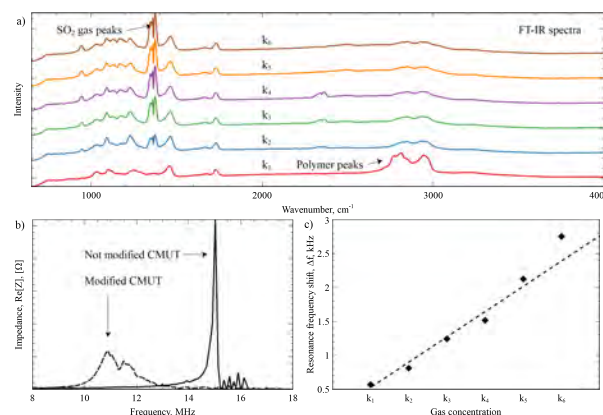
Due to increase of air pollution and greenhouse gas emissions, demand for robust, reliable, sensitive and highly selective gas sensing systems which are cost effective at the same time and could be used in various applications of environmental control is constantly growing. Capacitive micromachined ultrasound transducers (CMUTs) have been already demonstrated as suitable platform for gas detection sensors. Since CMUT structure is composed of an array of many small vibrating membranes, it is extremely sensitive to any mechanical mass loading. However, the need for development of functional coatings required for cross-selective detection of multiple gases is still holding back this type of the gas sensors from entering the market. Objective of our research was to explore the functionalization of the CMUT working surface with imine-based polymers making it sensitive to greenhouse effect gases.

Statement of Contribution/Methods

Thin layer of imine-based polymer was spin coated over the CMUT devices. The thickness of the layer was controlled by diluting the polymer in a solvent with different ratios. Resonant CMUT characteristics before and after modification are shown in fig. 1b. To analyze the formed thin layers, we have used Raman spectroscope from WITec, GmbH, Germany and FT-IR with in situ chamber for real time monitoring. CMUT devices with functional coatings were placed into the chamber and flushed with dry nitrogen. While doing real-time FT-IR signal acquisition, greenhouse gases with various concentrations, ranging from k_1 to k_6 were introduced into the chamber and were absorbed by the functional imine-based film on the CMUT surface. Synchronously, resonance frequency shift of CMUT was recorded.

Results/Discussion

Changes in the polymer FT-IR spectrum peaks were observed after interaction with the SO₂ gas as shown fig. 1a. This change was reflected by the corresponding changes in CMUT resonant frequency. Increased concentration of the gas increased the downshift of the CMUT resonance frequency (fig. 1c). We explain this by the increase of the mass of the functional imine-based film due the gas absorption. We here conclude that imine-based polymers are suitable candidates for CMUT gas sensing applications.



Analysis and Design of High Frequency CMUT Arrays in Non-Collapsed Mode

Evrin Arkan¹, F. Levent Degertekin²

¹George W. Woodruff School of Mechanical Engineering, Georgia Institute of Technology, Atlanta, GA, United States, ²ECE, Georgia Institute of Technology, Atlanta, GA, United States

Background, Motivation, and Objective

High frequency ultrasound imaging is utilized in a wide range of applications with the desired resolution and operation frequency steadily increasing. Among the available devices, CMUT arrays possess several preferable characteristics, such as ease of fabrication, ease of electronics integration, and flexibility of geometries. To determine the performance limitations of high frequency CMUT arrays for both pulse-echo and photoacoustic imaging, a comprehensive model is utilized to analyze the array behavior and the limiting factors.

Statement of Contribution/Methods

The CMUT array model for non-collapsed operation developed by Satir *et al* is used for calculations in this analysis [1]. Receiver performance is analyzed through receiver parameters extracted from simulations, namely, thermal mechanical current noise, plane wave pressure sensitivity, and pressure noise spectrum. Transmit/receive performance is analyzed through the simulated pulse-echo response from a perfect planar reflector and thermal mechanical current noise limited SNR. 1D CMUT arrays of 40 MHz center frequency and 300 μ m width and 500 μ m height, suitable for guidewire IVUS, is considered as the case study. Square Si₃N₄ membranes of 4 different width (Fig. 1a) are used to populate the analyzed arrays with 12 or 16 elements. In these arrays, fill factor is kept at 64% and the distance between membranes (d_m) in both vertical and horizontal directions are the same. The DC bias is set at 60 V and the gap is adjusted for 90% collapse. Pulse-echo analysis is conducted for unipolar pulsing with a perfect reflector at 5 mm distance.

Results/Discussion

The pressure noise spectrum of arrays demonstrate that the receiver performance of CMUT array elements can be close to an ideal piston with integrated low noise electronics (Fig. 1b). The frequency band of the arrays are delimited by the crosstalk actuated modes around the single membrane resonance (f_{single}) and the Bragg resonance ($f_{\text{Bragg}} = c_0/d_m$), where c_0 is the speed of sound in water. Utilization of smaller membranes consistently improves the bandwidth (BW), whereas SNR decreases after a certain value (Fig. 1c). It is observed that the lower -6 dB limit of the reflection current can be estimated as f_{single} and the -6 dB frequency span can be estimated as $f_{\text{Bragg}}/4$ for an ideal transimpedance receiver.

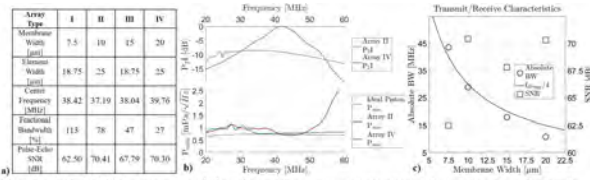


Figure 1: a) Evaluated CMUT array parameters, b) Normalized receiver pressure sensitivity and noise, c) pulse-echo response characteristics.

[1] S. Satir and F. L. Degertekin, "A nonlinear lumped model for ultrasound systems using CMUT arrays," *IEEE Transactions on Ultrasonics, Ferroelectrics, and Frequency Control*, vol. 62, no. 10, pp. 1865-1879, 2015.

P1-A2 - Cell Stimulation, HIFU, and Pressure Measurement

Kairaku (posters 1)

Tuesday, October 23, 9:30 AM - 4:00 PM

Chair: **Kenichi Kawabata** Hitachi

P1-A2-1

Behavioral responses of ultrasonic neuromodulation in freely moving mice

Guofeng Li¹, Qiuju Jiang¹, Min Su¹, Zhiqiang Zhang¹, Weibao Qiu¹, Hairong Zheng¹

¹Shenzhen Institutes of Advanced Technology, Chinese Academy of Sciences, China, People's Republic of

Background, Motivation, and Objective

Ultrasound (US) brain stimulation has been demonstrated to be a promising approach for noninvasive neurostimulation *in vivo*. However, conventional methods always require animals to be under anesthesia and body constraint to achieve stable operation with bulky US transducer and equipment. The neural activity related to perception, cognition, and behavior would be interfered. Minimized the setup for US stimulation in freely moving mouse will significantly benefit for obtaining credible neural response from brain stimulation. This study investigates the behavioral responses of ultrasonic neuromodulation in freely moving mouse with a head-mounted US device.

Statement of Contribution/Methods

A miniature US transducer, which consists of an electrical socket, a transducer housing, a backing gasket, a piezoelectric ceramic (PZT-4, 2MHz, 5 mm in diameter), and a focus lens, was designed and fabricated to perform neuromodulation in mouse. Two pieces of such transducers were installed on the bilateral regions (S1BFs) of each skull of 13 mice (C57BL/6). Figure (a) and (b) illustrate the schematic and the experimental procedures of ultrasonic neuromodulation using the two stimulators. Those stimulators can generate alternate stimuli in the left and right S1BFs every 6 seconds. The US propagates through the mouse skull into the S1BF to achieve non-invasive neuromodulation. Head-turning test of the freely moving mouse was carried out in a quiet dark case to assess the effect of ultrasonic neuromodulation. The experimental processes were videoed by an infrared camera to allow offline analysis.

Results/Discussion

Figure (c) shows the snapshots of an infrared video to demonstrate the head-turning responses of a mouse in a trial of US stimuli. The mouse head turned right following the onset of the US stimulus performed in the right S1BF. Figure (d) compares the statistic result of the head-turning responses. The quantity of head-turning response to normal stimuli in S1BF is significantly larger than the value of no response and control stimuli, which indicates that US modulation in S1BFs can evoke behavioral responses of the mice. In a word, the proposed head-mounted ultrasonic neuromodulation device can be used in awake and freely moving rodents, which could potentially promote the development of ultrasonic neuromodulation to more extensive neuroscience studies.

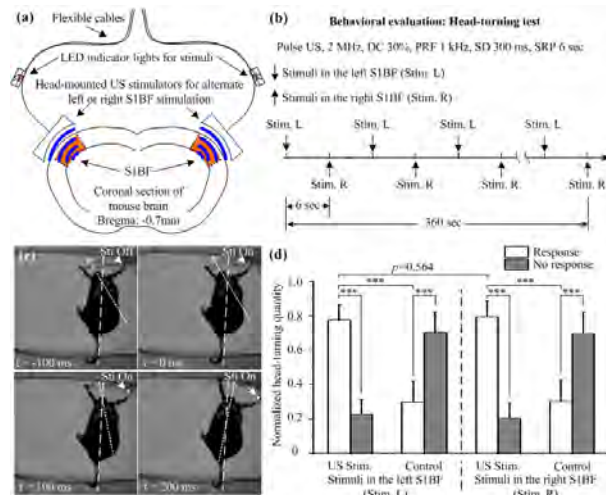


Figure (a) Schematic of the two ultrasound stimulators and the stimulation positions. (b) Experimental procedures for ultrasonic stimulation. LED, light-emitting diode; US, ultrasound; S1BF, primary somatosensory cortex barrel field; DC, duty cycle; PRF, pulse repetition frequency; SD, stimulus duration; SRP, stimulus repetition period, sec, second; Stim., stimulus. (c) Snapshots of the behavioral responses to ultrasound stimuli at different time points. (d) Statistic result of the head-turning responses of 13 mice to different stimulation conditions. Two-sample t-tests were used to analyze the differences ($n=13$, *** $p<0.001$).

Ultrasound stimulation of dopamine neurons in the ventral tegmental area induces reanimation from general anesthesiaTianyuan Bian¹, Zhengrong Lin¹, Long Meng¹, Lili Niu¹, Yingzhe Liu¹, Hairong Zheng¹¹*Paul C. Lauterbur Research Center for Biomedical Imaging, Shenzhen Institutes of Advanced Technology, Chinese Academy of Sciences, China, People's Republic of***Background, Motivation, and Objective**

Delayed awakening from general anesthesia remains one of the biggest challenges. It has been demonstrated that optogenetic or electrical stimulation enables to activate ventral tegmental area (VTA) dopamine neurons in rodent and induces emergence from general anesthesia (Anesthesiology 121, 311-9, 2014; PNAS 113, 12826-31, 2016). As ultrasound can noninvasively transmit through the skull bone in a focused manner, it is also a potentially powerful neurostimulation tool (Biomed. Eng. Lett. 7, 135-42, 2017). However, whether ultrasound stimulation of dopamine neurons in the VTA can induce reanimation from general anesthesia is still unknown.

Statement of Contribution/Methods

Fig. 1a shows the experimental setup. The mice were placed in an acrylic chamber and anesthetized with isoflurane. The mice were randomized into control and US group ($n = 8$ per group). Single 1ms ultrasound pulse containing 3300 acoustic cycles of 3.3MHz at PRF of 500Hz was delivered into VTA (Fig. 1b). The arousal scores were calculated according to spontaneous exercise intensity of the head, limbs, beard, and tail of the mice recorded by a video camera during the course of the experiment. At the same time, we embedded DSI implants in mice to monitor EEG in real time during ultrasound stimulation.

Results/Discussion

The behavioral scores of mice in different groups under different acoustic pressures were shown in Fig. 1d. The total score of US group was significantly higher than control (US: 7.75 ± 0.14 , control: 0.875 ± 0.20 , $p < 0.001$). Fig. 1e shows the normalized and averaged power spectra computed from EEG. The ultrasound stimulation during general anesthesia induced a rapid increase in θ (4-8 Hz) and β (12-30 Hz) power. While there was no statistically significant change after ultrasound stimulation. The results suggested that Ultrasound stimulation of VTA is sufficient to induce the transition from an anesthetized, unconscious state to an awake state, suggesting critical involvement in behavioral arousal.

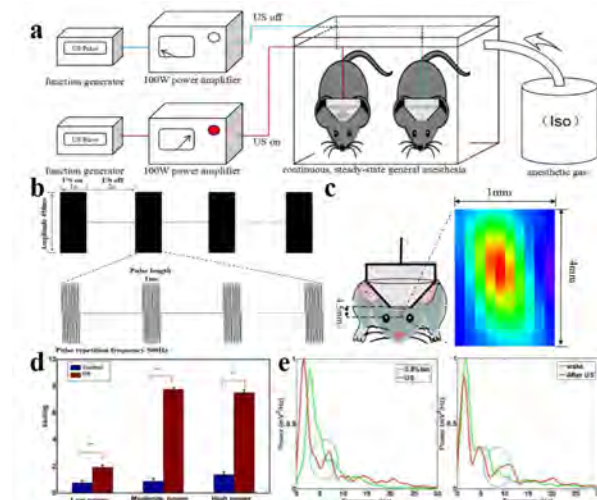


Fig 1. a. Schematic diagram of the experimental device; b Ultrasonic parameters in the experiment (amplitude 0.60Mpa, pulse repetition frequency 500 Hz, pulse length 1 ms); c. Sound field distribution after ultrasound probe penetrates the skull; d. There was a significant difference between the ultrasound stimulation group and the control group under different gradient excitation voltages, as determined using a Independent T test (For different excitation voltages, $n=16$ mice per group were divided into 8 experiments, ** $P < 0.01$); e. During anesthesia, the ultrasound stimulation induced a rapid increase in θ (4-8 Hz) power; The Power spectra between wake and after Ultrasound stimulation has no statistically significant changes.

Ultrasound brain stimulation via activation of Piezo1

Zihai Qiu¹, Lei Sun¹, Jinghui Guo¹, Shashwati Kala¹, Jiejun Zhu¹, Quanxiang Xian¹, Guofeng Li², Hairong Zheng³, Lei SUN¹

¹*Department of Biomedical Engineering, The Hong Kong Polytechnic University, Hong Kong*, ²*Shenzhen Institutes of Advanced Technology, Chinese Academy of Sciences, China, People's Republic of*, ³*Paul C. Lauterbur Research Center for Biomedical Imaging, Shenzhen Institutes of Advanced Technology, Chinese Academy of Sciences, China, People's Republic of*

Background, Motivation, and Objective

Ultrasonic (US) brain stimulation, capable of non-invasive transmission through skull with fine focal size (~mm), has been demonstrated to noninvasively alter neuron activity in animals and humans. It is limited however, the bio-effects of US are unclear and lacks of selectivity to specific neurons in the targeted brain region. Here we focus on the mechanisms of gating mechanosensitive ion channels (MCs) by US

Statement of Contribution/Methods

On gating MCs by US was verified on HEK293t cells, neuron cell lines and primary cultured neurons expressing Piezo1. GsMTx-4 and siRNA were used to test the role of Piezo1 in US neural activation. In addition, neurons with Piezo1 targeted nanobubbles were utilized to verify the tether model for MCs activation. Calcium imaging and whole cell patch clamp techniques were utilized to characterize the responses. AAV virus containing Piezo1 gene were used to deliver Piezo1 into neuron cell line and primary neurons to gain ultrasonic sensitivity for subsequent ultrasound activation. Based on these proof of concept results, sono- and acoustic mechano-genetic toolkits for neuron activity controlling and visualization simultaneously were developed.

Results/Discussion

It is shown that US can mediate membrane tension which can be tuned up to one order magnitude higher than which required for gating MCs, here Piezo 1. Different frequency stimulation (0.5-2 MHz) on the cells expressing Piezo1 showed that it is more sensitive to lower frequency US. Experimental results clearly demonstrated that US can activate Piezo1-HEK293t cells while no response can be detected for the control cells. The induced inward current and calcium influx are US pressure dependent for Piezo1 overexpressed HEK293T and neurons which can be blocked by GsMTx-4. These results show that ultrasound can modulate neuronal activity by gating mechanosensitive ion channels by membrane tension or localized tether force. It demonstrates reliable precise control of neuron activity by ultrasound. The toolkit for sonogenetics and acoustic mechanogenetics are being developed.

Transcranial focus ultrasound stimulation modulates saccadic behaviors in monkey
Xiaojing Long¹, Guofeng Li¹, Teng Ma¹, Weibao Qiu¹, Yongchuan Li¹, Lin Wang¹, Hairong Zheng¹
¹*Paul C. Lauterbur Research Center for Biomedical Imaging, Shenzhen Institutes of Advanced Technology, Chinese Academy of Sciences, China, People's Republic of*
Background, Motivation, and Objective

Transcranial focus ultrasound stimulation (tFUS) is increasingly used to assess the causal effect on performance of cognitive tasks by perturbing brain regions of interest non-invasively. In this study, we targeted the frontal eye field (FEF) of a macaque to investigate the impact of ultrasound on visually guided saccades.

Statement of Contribution/Methods

An adult male Rhesus macaque was trained to perform the memory guided saccade task while its eye movement was recorded. At the beginning of the trial the monkey fixated a small red dot at the center of the screen for 150ms, then another red peripheral cue was flashed for 200ms. The monkey was required to maintain fixation throughout the cue period and the subsequent delay period with 500 to 800ms randomly interleaved interval. At the end of the delay interval the fixation disappeared and the monkey was expected to make a saccade to the remembered location of the cue. The monkey was rewarded if his eye position fell within a 5 deg circle window around the cue location within 300ms of fixation offset. Four possible cue locations were equally spaced at the diagonals of the clock face. In each experiment session, the monkey performed six blocks where non-stimulation and stimulation blocks were alternated. The tFUS pulses induced by a 500 kHz single element transducer were delivered to the left FEF. The stimulation was triggered by the onset of peripheral cue and lasted to the end of saccade. The pulse repetition frequency was set to 1kHz, duty cycle was 50%, and the pressure amplitude at focus was 1MHz. The location of sham stimulation was sidewardly moved 20mm with the same stimulation design. The average deviation of eye movement and task error rate were calculated.

Results/Discussion

Ultrasound stimulation on FEF significantly increased eye movement dispersion and task error rate in monkey, which suggested that ultrasound modulation may cause interruption of visual information processing across FEF. This study demonstrated a behavioral effect induced by tFUS in alert monkey performing a cognitive task, which may open new opportunities for measuring behavioral consequences of tFUS in the primate brain, and ultimately for human-monkey comparisons.

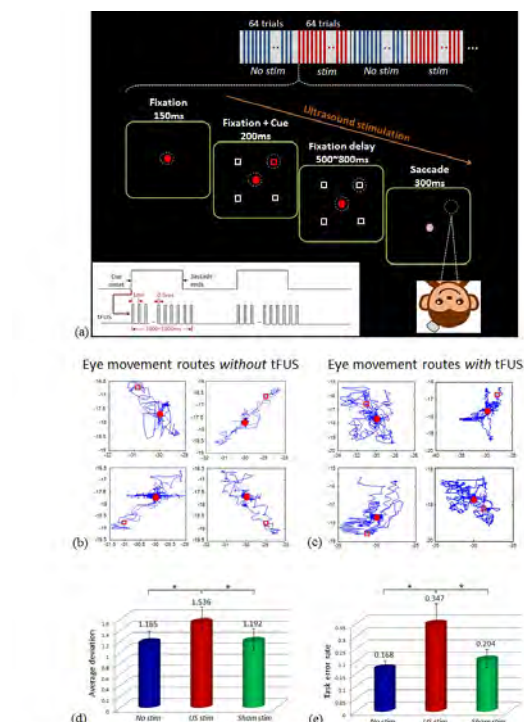


Figure 1. (a) Experimental design and task paradigm. (b)(c) Representative eye movement routes without stimulation and with stimulation. Eye movement was notably dispersed during saccadic tasks with ultrasound stimulation on FEF. (d) Quantitative comparison of average deviation values also demonstrated significant difference on eye movement with and without stimulation. (e) Task error rate increased while stimulation was applied to FEF.

High Intensity Focused Ultrasound Induced Assembly of Suprametallomolecular Hydrogel

Umesh Jonnalagadda¹, Feifei Li², Atsushi Goto³, Jim Lee⁴, Minh Nguyen⁴, James Kwan¹

¹School of Chemical and Biomedical Engineering, Nanyang Technological University, Singapore, Singapore, ²Nanyang Technological University, Singapore, Singapore, ³School of Physical and Mathematical Sciences, Nanyang Technological University, Singapore, Singapore, ⁴Institute of Chemical and Engineering Sciences, A*STAR, Singapore

Background, Motivation, and Objective

Chronic venous diseases (CVD) are vasculature with malformations and abnormalities, which are no longer capable of unidirectional blood flow. Treatments rely on blocking methods that may result in post-operative complications (e.g., ischemia) and surgery. Physiologically safe blocking materials are required to improve CVD treatment. Yet current methods for acoustic gel synthesis require organic/aqueous solvent mixtures, which cannot address the challenges of CVD treatment. We propose the use high intensity focused ultrasound (HIFU) to induce hydrogel synthesis for biomedical applications.

We synthesized a metal binding ligand (M1) and copolymerized it to poly(ethylene glycol) methacrylate (PEGMA), resulting in a water soluble polymer that responds to HIFU. Our findings demonstrate the potential for HIFU induced *in situ* synthesis of hydrogels, thereby enhancing the flexibility of sonochemistry for clinical application.

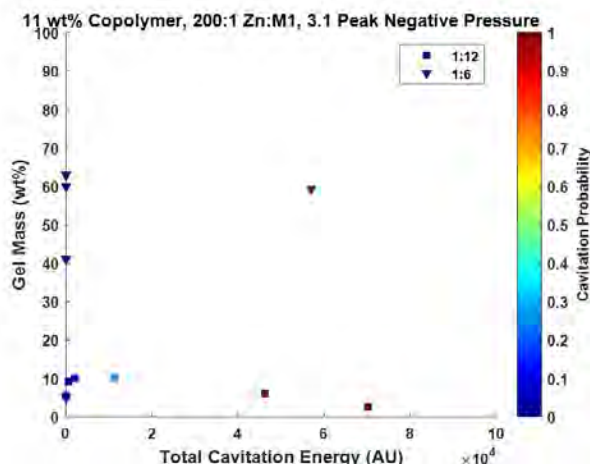
Statement of Contribution/Methods

An aqueous solution (11 wt% copolymer and 200:1 molar mix of Zn ions to M1 in H₂O) was introduced into an eppendorf tube and immersed in a degassed water tank to trigger hydrogel synthesis. The gelation reaction was explored with two different concentrations of M1:PEGMA (1:6 and 1:12). For the HIFU treatment, the copolymer solution was exposed to acoustic bursts (50000 cycles at 0.5 MHz and 10% duty cycle) for 4 minutes to induce gelation. For a given sample, the peak negative pressure ranged from 1.86 to 3.1 MPa.

Results/Discussion

For both the 1:12 and 1:6 copolymers, the highest gel mass yield was observed when the copolymer solution was exposed to a peak negative pressure of 3.1 MPa (Figure 1). HIFU stimulation of the 1:6 copolymer synthesized gel upwards of 50 wt% of the initial solution volume, while the 1:12 copolymer samples synthesized gel averaging 10 wt% following acoustic stimulation. This discrepancy is likely a result of the 1:6 copolymer containing more crosslinking groups, thereby increasing the network's affinity for trapping water.

Mechanically activated material synthesis offers novel prospects for creating materials *in vitro* and *in vivo*. In this abstract, we presented the potential of HIFU to trigger hydrogel formation within an Eppendorf tube. Future work will involve translating the system to a physiological relevant model to investigate the practicality of this system as an embolic therapy.



On the use of spatial coherence for in situ peak rarefaction pressure estimation

Bofeng Zhang¹, Will Long¹, Gianmarco Pinton², Kathryn Nightingale¹

¹Biomedical Engineering, Duke University, Durham, NC, United States, ²Joint department of biomedical engineering, University of North Carolina at Chapel Hill and North Carolina State University, NC, United States

Background, Motivation, and Objective

The Mechanical Index (MI) uses linearly derated water peak rarefaction pressure (PRP) to predict *in situ* PRP. *In vivo*, however, tissue heterogeneity leads to considerable variability in PRPs. The Effective Mechanical Index (MIE) has been proposed as a metric that uses the MI equation with the estimated *in situ* PRP instead of derated water PRP. Previously, using 3D nonlinear simulations, we have shown that the MIE for a tightly focused transmit (i.e. F/1-3) in the presence of a bodywall is consistently lower than the MI, primarily because of phase aberration [Zhang, IEEE IUS 2017]. Phase aberration causes beam defocusing which leads to lower spatial correlation [Pinton, IEEE TUFFC 2014]. Our overall goal is to develop a robust method for estimating MIE on a patient specific basis. In this work, we investigated the hypothesis that MIE is correlated with spatial coherence.

Statement of Contribution/Methods

We simulated nonlinear full-wave ultrasound through heterogeneous, attenuating bodywalls to quantify the MIE and collect backscattered speckle coherence data. 6 different histologically stained bodywall sections were mapped by tissue acoustic properties (density, sound speed, attenuation, and nonlinearity). An F/1.5 linear transmit aperture focused at 5 cm was modeled with a 2 cycle, 2.2 MHz transmit pulse. MIE was derived from simulated field PRP. Spatial coherence was computed at the focal depth on the receive channels and summed across lags 1-20, thus quantifying the short lag spatial coherence (SLSC). B-mode was modeled across 40 focused transmit beams spaced 0.13 mm apart. Fundamental and pulse-inverted harmonic signals were analyzed.

Results/Discussion

Figure 1 shows MIE through bodywalls are considerably lower than in the no bodywall control. It also shows linear regression between MIE and harmonic SLSC (Fig 1a, $R^2=0.93$) to have a better goodness-of-fit than with fundamental SLSC (Fig 1b, $R^2=0.43$). We hypothesize that this is because fundamental signal traverses the aberrating bodywall twice (transmit and receive), whereas harmonic signal is generated near the focus and the MIE is quantified near the focus, so these parameters reflect only one-way bodywall propagation. The excellent correlation between harmonic SLSC and MIE support the potential for this relationship to be exploited for more accurate patient specific estimation of *in situ* pressures.

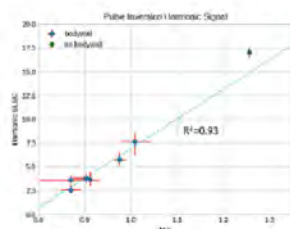


Figure 1(a)

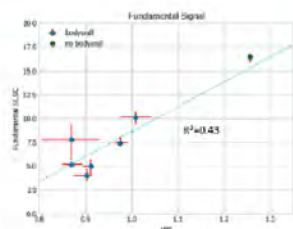


Figure 1(b)

Ultrasound stimulates insulin secretion via activating mechanical sensitive ion channels in pancreatic islet β cellsJinghui Guo^{1,2,3}, Zhihai Qiu¹, Rui Zhang¹, Jingyao Wang¹, Long Meng⁴, Hairong Zheng⁴, Hsiao Chan¹, Lei SUN¹¹*Department of Biomedical Engineering, The Hong Kong Polytechnic University, Hong Kong, ²Department of Physiology, School of Medicine, Jinan University, China, People's Republic of, ³School of Biomedical Sciences, The Chinese University of Hong Kong, Hong Kong, ⁴Paul C. Lauterbur Research Center for Biomedical Imaging, Shenzhen Institutes of Advanced Technology, Chinese Academy of Sciences, China, People's Republic of***Background, Motivation, and Objective**

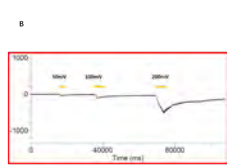
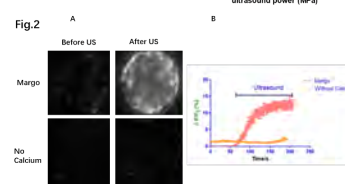
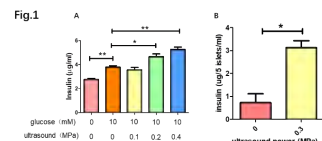
Abnormal insulin secretion is the key cause for diabetes. Current treatment for diabetes mainly focuses on the regulation of insulin secretion through drugs or electrical stimulus. Ultrasound has been demonstrated capable of inducing mechanical stress and activating mechanosensitive ion channels, which play important roles in insulin secretion. In this research, we investigated the mechanism of ultrasound-induced insulin secretion via activating mechanosensitive ion channels.

Statement of Contribution/Methods

RINm5F cells, a well-known pancreatic islet beta cell line, were seeded in the 35mm culture dish or coverslips. Calcium imaging and patch clamp techniques were utilized to investigate the effect of ultrasound on the electrophysiology of pancreatic islet β cells. Culture medium from cells treated with ultrasound was collected for Elisa analysis. Low frequency (1 MHz) and low intensity (200 cycles per pulse, pulse repetition frequency of 1kHz, a duration of 0.2 second with acoustic pressure range of 0.1-0.6MPa) was generated by a customized ultrasound stimulation system. For patch clamp experiments, a surface acoustic wave chip with central frequency of 28.04MHz was utilized to induce the inward current.

Results/Discussion

It is shown that ultrasound can increase insulin secretion significantly in both pancreatic beta cell line RINm5F cells and primary isolated pancreatic islets (Fig. 1). As insulin secretion depends on the elevation of intracellular calcium, calcium imaging is applied to investigate the effect of ultrasound in intracellular calcium. Our data demonstrated that ultrasound can induce calcium influx but not calcium release in pancreatic islets. (Fig.2) Moreover, with whole-cell patch clamp recording, ultrasound has been found to induce an inward current with an ultrasound intensity-dependent pattern (Fig.3). These results together draw our conclusion that ultrasound can activate mechanosensitive ion channel that help to elevate intracellular calcium and facilitate insulin secretion in pancreatic islet, which has shed a new light for diabetes treatment in the future.



Study on dependence of mechanotransduction sensitivity on cytoskeletal development using cultured cardiomyocytes.
Shota Negishi¹, Nobuki Kudo¹
¹*Graduate School of Information Science and Technology, Hokkaido University, Sapporo, Japan*
Background, Motivation, and Objective

We have been studying the effect of ultrasound exposure on cardiac pulsation using cultured cardiomyocytes isolated from neonatal rats. Our previous study showed that cardiomyocytes cultured on a scaffold with lower stiffness have a higher threshold of ultrasound intensity for induction of pulsation disruption, and the fact that cells cultured on a scaffold with lower stiffness have a less developed cytoskeleton suggests dependence of cell mechanotransduction sensitivity on cytoskeletal development. In this study, the development of the myocyte cytoskeleton was controlled by using an actin polymerization inhibitor, and its effect on the sensitivity for pulsation disruption was investigated to confirm the role of the cytoskeleton in cell mechanotransduction.

Statement of Contribution/Methods

Cardiomyocytes were isolated from 2-3-d-old neonatal rats and cultured on a coverslip. After 3-d incubation, a cell sample with autonomous pulsation was incubated with 100 nM or 1000 nM of an actin polymerization inhibitor (Latrunculin A, Wako) for 24 h. A control sample that was cultured for the same period without an inhibitor was also prepared. Cell samples were irradiated by a series of ultrasound burst pulses of 1 MHz in center frequency and 13.5 MPa in peak negative pressure. The threshold condition of a burst length required for induction of pulsation disruption was then determined. The effect of the inhibitor on cytoskeleton development was observed using confocal microscopy.

Results/Discussion

Figure 1 shows typical cells without and with loading of 50 nM of the inhibitor. Cardiomyocytes are outlined by red lines, and green fibrous structures inside the cells represent actin fibers, indicating that extension of the cytoskeleton in (a) was suppressed in (b). Figure 2 shows the minimum burst lengths required to induce pulsation disruption. The thresholds of burst length were 6 ± 1 cycles in control cells ($n = 6$, mean \pm S.D.), 71 ± 104 cycles in cells treated with 100 nM of the inhibitor ($n=6$), and 210 ± 207 cycles in cells treated with 1000 nM of the inhibitor ($n=3$). Preparation of cell samples with similar vulnerable sensitivities of autonomous pulsation was difficult and, therefore, there was no significant difference between the groups ($p = 0.22, 0.30$); however, the results indicate the importance to consider *in vivo* cell morphology in studies on mechanotransduction.

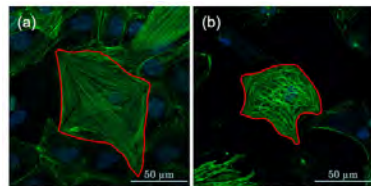


Fig. 1 Fluorescence image of cytoskeleton. Confocal images of cardiomyocytes stained using Acti-stain 488 phalloidin (green) and Hoechst 33342 (blue) (a) without and (b) with an actin polymerization inhibitor.

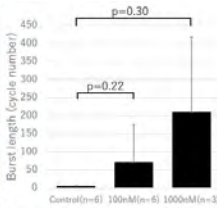


Fig. 2 Threshold of burst length for pulsation disruption

Real-time field mapping using an ultrasound scanner

Kazuhiro Matsui^{1,2}, Apoutou N'Djin¹, Takashi Azuma³, Ichiro Sakuma⁴, Françoise Chavrier¹, Rémi Souchon¹

¹LabTAU, INSERM, France, ²University of Tokyo, Japan, ³Center for Disease Biology and Integrative Medicine, The University of Tokyo, Tokyo, Japan, ⁴The University of Tokyo, Japan

Background, Motivation, and Objective

The objective of this work was to develop a method for imaging ultrasonic fields in real-time. Device testing, treatment planning and marketing clearance are based on measurement of pressure fields. Pressure measurements are usually performed using a hydrophone and a motorized scanning system. This task requires precise alignment of the hydrophone with the device under test, and motorized scanning. The process can be time consuming.

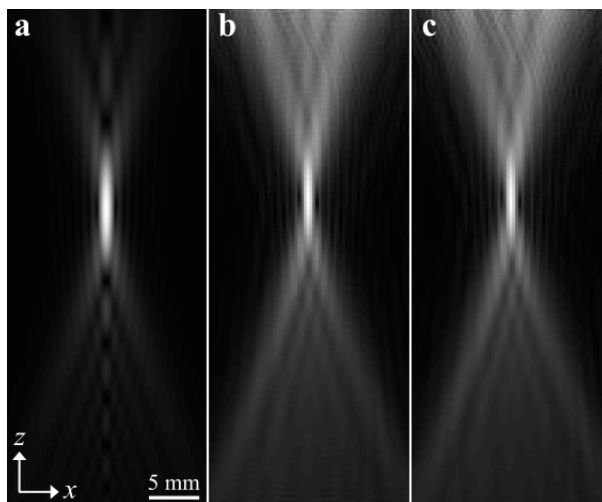
Statement of Contribution/Methods

A real-time field mapping technique was developed based on an ultrasound scanner. Each element of the imaging array was acting as an independent hydrophone. The ultrasound field was captured simultaneously on all elements. Then the image of the ultrasound field was calculated using time reversal. A prototype system was developed and implemented on a Verasonics Vantage scanner with a 128-elements linear array (Philips L7-4). The performance of the acquisition system was tested experimentally in water. The device under test was a 2.4 MHz HIFU transducer. Accuracy was assessed by comparison with measurements obtained from a standard hydrophone (Onda HGL). Scanning time and acquisition frame rate were also recorded.

Results/Discussion

The prototype system was capable of imaging the position and dimensions of the focal area accurately and in real-time. The acquisition time for 40x100 mm imaging plane was less than 100 µs with the scanner, and several hours with a conventional hydrophone. The ultrasound field was acquired and displayed in real-time, with frame rate on the order of 10-20 frames per second.

Current limitations are (1) the bandwidth of imaging probes is limited compared to that of hydrophones, (2) accurate quantitative field mapping is possible ,but requires an imaging probe with a large footprint and small elements.



Retrospective analysis and theoretical simulation of the first HIFU treatment point of isointense uterine fibroids on T2WI: a retrospective comparative study

Faqi Li¹, Chengbin Guo¹, Huan Liu¹, Haoran Huang¹, Yurong Zhang¹

¹*State Key Laboratory of Ultrasound Engineering in Medicine Co-founded by Chongqing and the Ministry of Science and Technology, College of Biomedical Engineering, Chongqing Medical University, China, People's Republic of*

Background, Motivation, and Objective

High intensity focused ultrasound (HIFU) is a novel non-invasive surgical technique, which has been used in various tumor treatment. However, how to select irradiation dose (irradiation power, pulse parameters, irradiation time) to achieve the first treatment point necrotic is a major problem in HIFU treatment. For this reason, we conducted a retrospective analysis on the necrotic range of the first HIFU treatment point of isointense uterine fibroids on T2WI. Besides, we adopted the irradiation parameters of the first treatment point of uterine fibroids to simulate the necrosis range, and then compared the results of retrospective analysis and theoretical simulation.

Statement of Contribution/Methods

We selected 54 patients with isointense uterine fibroids on T2WI as research objects, whose uterus were anterior uterus and uterine fibroids were located in the anterior uterine wall by preoperative MR scanning. The ultrasound monitoring image at the time of grayscale variation occurred at the first treatment point through retrospectively analysis of ultrasound monitoring videos during HIFU intraoperative. The variation range of B-mode ultrasound grayscale was obtained through image processing, which served as the coagulative necrosis range of the first treatment point. The layered media model (degassed water, skin, fat, rectus abdominis, bladder, uterine fibroid) was used in simulation, and the thickness of each layer was measured through the B-mode ultrasound image during the first treatment point irradiating. The HIFU transducer parameters and irradiation doses used in simulation were consistent with those in clinical. For simulation, KZK equation and Pennes biological heat conduction equation were combined to calculate the temperature distribution within the tissue. Thermal dose in tissue was calculated with the equivalent thermal dose model, and threshold of thermal lesion was set at 240EM.

Results/Discussion

The simulated lesions area range of the first HIFU treatment point in 54 patients with isointense uterine fibroids on T2WI was 7.087 ~ 102.946 mm². The area range of B-mode ultrasound grayscale change obtained from retrospective analysis was 12.994 ~ 92.208 mm². The Spearman correlation coefficient was 0.788 ($p = 0.000$). The results indicated that the layered medium model based on B-mode ultrasound image and radiation parameters in HIFU ablation of uterine fibroids can provide a reference for predicting HIFU treatment effect.

Investigation on interaction between ultrasound and living tissue

Satoshi Sobue¹, Shogo Shido¹, Keiichi Nakagawa², Tatsuya Murakami³, Etsuo Susaki³, Hiroki Ueda³, Shu Takagi⁴, Takashi Azuma⁵

¹Department of Mechanical Engineering, The University of Tokyo, Japan, ²Department of Bioengineering, School of engineering, The University of Tokyo, Tokyo, Japan, ³Department of Medical Science, The University of Tokyo, Japan, ⁴The University of Tokyo, Japan, ⁵Center for Disease Biology and Integrative Medicine, The University of Tokyo, Tokyo, Japan

Background, Motivation, and Objective

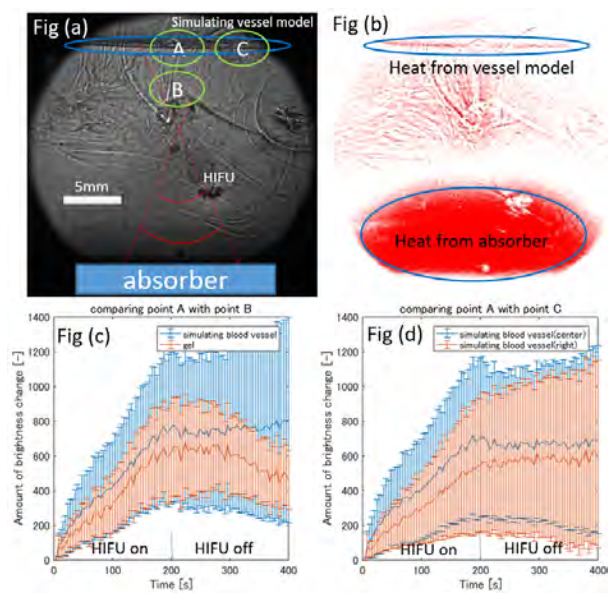
Regarding ultrasonic propagation in the body, it has been treated as attenuating in proportion to the propagation distance at a constant attenuation factor determined by empirical studies. Based on this idea, focal heating in ultrasonic therapy and acoustic radiation force in shear-elastography are estimated. The actual living body is composed of various size scale structures, and discontinuous interface called “acoustic boundary layer (ABL)” exists between the elastic body and fluid. The empirical attenuation coefficient can be explained by a stack of local attenuation due to the ABL. Recently, it became possible to optically capture the interaction between transparent mouse’s brain and sound waves. In this research, we propose a method to improve the sensitivity of observation by accumulating the interaction between ultrasonic and biological structure, that is, by observing local density changes in objects after irradiation, we are aiming to observe the heating and generation of strain.

Statement of Contribution/Methods

We used an acrylamide gel with an artificial hole with a diameter of 0.2 mm simulating blood vessel and observed the change of density distribution, namely heating by schlieren method. We used a HIFU transducer whose both aperture width and focal length are 40 mm and frequency is 3.35 MHz. Every 4s we took an image and repeated this for 100 cycles. In the first half 50 cycles, we irradiated HIFU for 3.95s, and during the rest 0.05s, took an image. In the latter half of 50 cycles, we stopped the irradiation and just took an image every 4s. The irradiation focus position and the arrangement of the simulated blood vessel are as shown in Fig1.(a). To prevent reflection from the bottom, we put absorber at the bottom.

Results/Discussion

Micro heating was successfully detected and be imaged in our system. Fig1 (b) is the subtracted image of first condition and the image taken after HIFU irradiation for 200s. This shows that mainly heat was generated at the vessel model and absorber. Fig1 (c), (d) are local view of temperature change and temporal profile of heating at vessel model is clearly detected. We will investigate the relationship between the local heating by ABL and the macro average attenuation in the continuum by comparing this with experiment data with transparent living tissue.



P1-A3 - Multifunctional Bubbles and Applications

Kairaku (posters 1)

Tuesday, October 23, 9:30 AM - 4:00 PM

Chair: Agata Exner Case Western Reserve University

P1-A3-1

Biomimetic synthesis of neutrophil-microbubble for robust in vivo targeting of atherosclerotic vulnerable plaques

yang mao¹, Fei Yan², Pengfei Zhang³, Fei Li²

¹The Key Laboratory of Cardiovascular Remodeling and Function Research, Chinese Ministry of Education, China, People's Republic of, ²shenzhen institutes of advanced technology, Chinese academy of sciences, China, People's Republic of, ³Qilu Hospital, Shandong University, China, People's Republic of

Background, Motivation, and Objective

Amongst all kinds of cardiovascular diseases (CVDs), atherosclerotic (AS) vulnerable plaque rupture is of the highest morbidity and mortality. By now, improvements on the differentiation of vulnerable atherosclerotic plaques are still needed for early diagnosis and intervention of AS. As a key step in the advanced stage of AS plaque formation, inflammatory fibrous cap appears to be a valuable target. Evidences showed that circulating neutrophils possess inflammatory endothelial targeting property by the intrinsic cell adhesion molecules on neutrophils. Inspired by this mechanism and in order to realize accurate localization and evaluation of vulnerability of atherosclerotic plaques, we designed a novel bionic microbubble by assembling neutrophils-microbubble complexes, named "BionicBells".

Statement of Contribution/Methods

BionicBells assembled through binding of targeted microbubbles ($\sim 2\mu\text{m}$) to neutrophil via a CD11b antibody. Adherence of BionicBells and negative control microbubble (MB-CON) to TNF- α (1ng/ml) stimulated endothelial cells (*B.end3*) was determined in vitro by using a parallel plate flow chamber at variable shear stress (4-16 dynes/cm 2). After confirming their specificity in flow chamber cell attachment studies, BionicBells were used in vivo adhesion molecules targeted contrast-enhanced ultrasound imaging. Aortic arch plaques were established by fed Apolipoprotein E-deficient (apoE-/-) mice with a high-fat diet for 8, 16, 24 weeks. H&E, Oil Red O staining, α -actin, CD68 and Sirius Red staining was used to evaluate the vulnerability of the plaque. Immunohistochemistry and western-blots demonstrated the expression level of adhesion molecules (ICAM-1) and E-selectin in aortic segments of AS plaque. A-20804 (ICMA-1 and E-selectin inhibitor) was used in vitro study to confirm the role of ICMA-1 and E-selectin in the process of BionicBells cell attachment and plaque attachment.

Results/Discussion

BionicBells were successfully synthesized and had excellent affinity to inflammatory endothelial (*B.end3*) under physiological shear stress conditions. Ultrasoundograms of aortic plaques were enhanced significantly by the BionicBells in apoE-/- mice than in control C57 mice ($P<0.05$). Compared with MB-CON the enhancement of BionicBells was more significant ($P<0.05$), and the enhancement could be blocked with ICMA-1 and E-selectin neutralizing antibodies. Abundant expression of ICAM-1 and E-selectin in the plaque endothelial was demonstrated by immunohistochemical staining which is corresponded to the adherence and localization of BionicBells. Moreover, the extent of BionicBells enhancement positively correlated with the vulnerable index of the aortic plaques.

BionicBells were successfully synthesized, and this targeted contrast agent helped to better differentiation of AS vulnerable plaques.

In vivo acoustic trapping of microbubbles by a resonant stentFei Li¹, Pengfei Zhang², Feiyan Cai¹, Yang Mao², Wei Zhou¹, Min Su¹, Jiqing Huang¹, Long Meng¹, Hairong Zheng¹¹shenzhen institutes of advanced technology, Chinese academy of sciences, China, People's Republic of, ²Qilu Hospital, Shandong University, China, People's Republic of**Background, Motivation, and Objective**

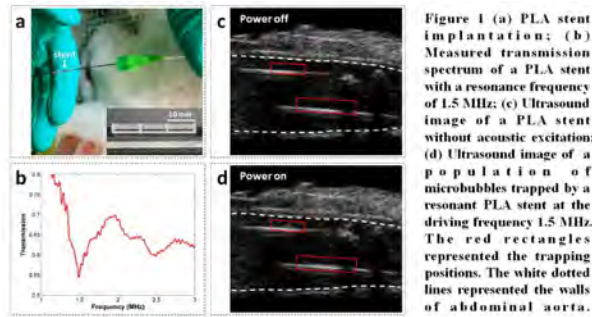
Although the percutaneous coronary intervention plays an indispensable role in management of acute cardiovascular events, the treatment of patients with in-stent restenosis (ISR) and in-stent thrombus (IST) remains a challenge and represents a major clinical problem. Here, using poly lactic acid (PLA) with good biocompatibility and biodegradability, we designed a kind of PLA stent with an interesting acoustic manipulation function and validated its trapping effect *in vivo*, which may be a potential tool for inhibition of ISR and IST by combining with the drug-loaded microbubbles.

Statement of Contribution/Methods

The PLA stent was fabricated by the additive manufacturing, which had a primary resonance frequency of 1.5 MHz by the acoustic transmission measurement. The stent was inserted into the abdominal aorta of a rabbit by a standard stent implantation. The embedded stent was observed by a commercial ultrasound scanner Vovo™ 2100, and it was excited by continuous waves from a transducer for acoustic manipulation. Commercial SonoVue™ microbubbles were injected into the ear vein, and flowed into the abdominal aorta via the blood circulation.

Results/Discussion

The measured transmission spectrums showed the existence of the resonance frequency, which originated from the excitation of the quasi-Scholte wave mode on the surface of the PLA stent. The velocity of blood flow in the center of the aorta reached a maximum value of ~5 m/s by using Doppler ultrasound. We experimentally observed that the microbubbles were trapped and accumulated onto the surface of the stent at the driving frequency of 1.5 MHz. When the transducer for acoustic manipulation was powered off, those trapped microbubbles were flushed away by the blood flow due to the loss of trapping force. In conclusion, this *in vivo* study confirmed the acoustic trapping effect of the resonant PLA stent, and may be used to inhibit ISR and IST.



Ultrasound Driven Penetration of Gold Nanocones in a Tissue Model

Xiaoqian Su¹, Umesh Jonnalagadda¹, James Kwan¹

¹Nanyang Technological University, Singapore

Background, Motivation, and Objective

Diffusion limited drug delivery remains a challenge for treatment of some diseases. Ultrasound-assisted strategies (e.g., acoustic cavitation) provide an attractive means to promote drug distribution into tissue. Acoustic cavitation is the dynamic oscillations of gas/vapor bubbles in a liquid exposed to pressure waves. Cavitation promotes a multitude of mechanical effects to enhance the penetration and distribution of therapeutics. Presently, microbubbles and solid cavitation nuclei are widely used to reduce the acoustic pressure required to induce cavitation. However, these cavitation nuclei have disease specific limitations owing to their large size, rapid acoustic destruction, or relatively high cavitation threshold pressure amplitudes. Here, we investigate conical-shaped gold nanoparticles as a candidate for gas-stabilising on its surface and subsequent acoustic response. Furthermore, we observe the cavitation driven penetration depth of the gold nanocone in an agarose tissue model after exposure to high intensity focused ultrasound (HIFU).

Statement of Contribution/Methods

Gold nanocones (GNCs) were manufactured using an ultrasound-assisted interfacial growth method. PEG was used to functionalize the surface of GNCs to prevent GNC agglomeration. GNC product was lyophilized and resuspended in deionized water, allowing bubbles to be trapped. Acoustic cavitation thresholds were determined using a methodology outlined in Kwan et al. 0.5 mg/ml of GNCs was sealed in the channel of a 2% agarose phantom and exposed to 0.5 MHz HIFU.

Results/Discussion

The cone-shaped structure of GNCs with a base diameter of 108.3 ± 23.0 nm was confirmed by TEM (Fig. 2a). The GNCs show well-defined hollow cavities and rough surfaces. This suggests that GNCs will trap gas bubbles. The probability of cavitation was measured at pressure amplitudes between 0.1 and 2.5 MPa (Fig. 2b). GNCs without gas stabilization displayed negligible cavitation activity over the tested pressure range. In contrast, gs-GNCs required 1.75 MPa to reliably nucleate cavitation. Once we confirmed the inertial cavitation threshold, we measured the penetration of gs-GNCs into tissue mimicking agarose phantom. Cross-sectional images of the agarose phantoms indicated that gs-GNCs generated sufficient cavitation to propel neighboring gs-GNCs deep into agarose.

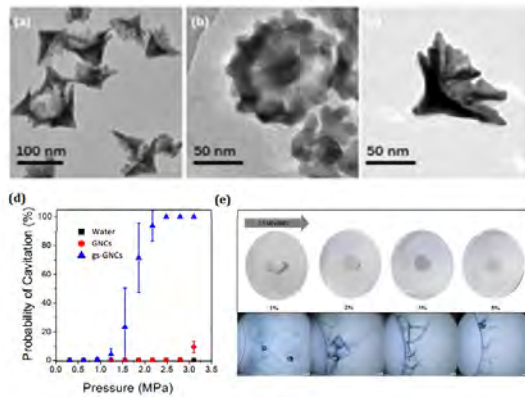


Fig. 1 (a-c) TEM images of GNCs. (d) Probability of Cavitation of DI water, GNCs, and gs-GNCs with increasing peak negative pressure amplitude. (e) Photograph and corresponding microscopy images of GNCs imbedded in 1%, 2%, 3%, and 5% agarose phantoms.

Indirect assessment of nanobubble size through agarose trapping and ultrasound M-Mode imaging

Michael Moore^{1,2,3}, Christopher Hernandez⁴, Nico Arezza^{1,2,3}, Agata Exner^{4,5}, Michael Kolios^{1,2,3}

¹Ryerson University, Toronto, ON, Canada, ²Institute for Biomedical Engineering, Science and Technology, St. Michael's Hospital, Toronto, ON, Canada, ³Keenan Research Centre, Li Ka Shing Knowledge Institute, St. Michael's Hospital, Toronto, ON, Canada, ⁴Department of Biomedical Engineering, Case Western Reserve University, OH, United States, ⁵Department of Radiology, Case Western Reserve University, OH, United States

Background, Motivation, and Objective

Nanobubbles (NB) have been proposed as agents for enhancing drug delivery and ultrasound (US) contrast. While their small size allows NBs to extravasate outside of hyper-permeable vasculature of various pathologies into regions inaccessible to conventional microbubbles, it also presents a challenge when trying to assess NB morphology. NB sizing using optical techniques is limited by inadequate spatial resolution, and techniques such as electron microscopy or resonant mass (RM) measurements are costly and dependent on sample preparation. In this work, we investigate a US based gel trapping technique for indirectly assessing NB size and echogenicity.

Statement of Contribution/Methods

Sub-micron C₃F₈ core, lipid shell NBs were prepared by self assembly driven by mechanical agitation. Larger bubbles were removed by differential centrifugation. Solutions of 600 μ L of either 0.5% or 1.5% (w/v) molten low melting point agarose (LMPA) and 50 μ L of activated NB stock were prepared. The molten NB/LMPA solutions were poured into separate petri dishes and allowed to solidify at room temperature for 30 minutes. The expected pore sizes for the 0.5% and 1.5% LMPA are 1 μ m and 200 nm, respectively. The phantoms were imaged using a 400 MHz US transducer at 37°C. RF lines ($n = 10000$) averaged 30x at a 121 kHz pulse repetition frequency were acquired at 5 scan locations, and corresponding M-Mode images were generated. Regions of interest (ROI) within each M-Mode image were selected, and the average autocorrelation (AC) as a function of slow time was computed.

Results/Discussion

Representative M-Mode images are shown in Fig 1b. Significant amplitude fluctuation was observed in the 0.5% phantom, indicative of NB motion. In contrast, features in the 1.5% phantom were predominantly stationary, indicating NB entrapment. ACs (Fig 1c) from the 0.5% phantom decayed more rapidly than those from the 1.5% phantom, further demonstrating NB motion in the 0.5% phantom and minimal change for the 1.5% phantom ROIs. These results suggest that the NBs used in the study were on the order of 200 nm, which agreed with the size distribution measured by a RM particle sizer (Archimedes, Malvern Panalytical). Going forward we plan to use intermediate concentrations of LMPA to further refine the range of NB sizes. This technique could be used as a low cost alternative for determining NB size and echogenicity.

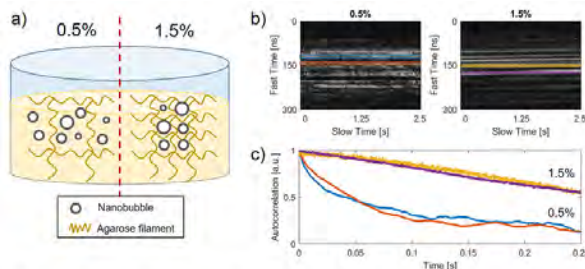


Fig 1: a) Schematic representation of nanobubbles (NB) embedded in 0.5% and 1.5% agarose gels. b) M-Mode images of 0.5% and 1.5% agarose phantoms. Intensity fluctuations indicate significant NB motion in the 0.5% agarose phantom, and very little motion in the 1.5% phantom. Negligible backscatter was observed from LMPA phantoms devoid of NBs. c) Average autocorrelation of pixels from the colour matched ROI's indicated in b).

Acoustic characterization of microbubbles with indocyanine green derivatives for dual contrast imaging using ultrasound and near infrared fluorescence

Kenji Yoshida¹, Katsuya Saito², Taro Toyota³, Tadashi Yamaguchi¹, Hideki Hayashi²

¹Center for Frontier Medical Engineering, Chiba University, Japan, ²Chiba University, Japan, ³The University of Tokyo, Japan

Background, Motivation, and Objective

Near infrared (NIR) fluorescence imaging have been powerful tool for visualizing small vessels in surface of tissue although it has limitation in penetration depth. In contrast, contrast enhanced ultrasound enables to visualize the vessels in deeper tissue. Development of novel contrast agent, which can work in both methods, will be effective technique in clinical situation, e.g. leading to surgery navigation for sentinel lymph-node biopsy. Thus the vesicle including gas as ultrasound contrast agent and indocyanine green (ICG) derivative as NIR fluorescence contrast agent were developed. We demonstrated the acoustic resonant characteristic of the agent by measuring the attenuation coefficient to investigate how the anchoring of ICG affects the resonance.

Statement of Contribution/Methods

The agent, microbubble with ICG derivatives (ICGB) as shown in Fig. 1(a), was fabricated. The ICG derivatives (ICG-C18) with more hydrophobic characteristic was fixed to the phospholipid shell. The anchoring of ICG was confirmed by using a NIR fluorescence microscope. The agents without ICG-C18, control bubble (CB), were also made for comparison. A brief flow system was employed for the attenuation measurement, where the bubble suspension with concentration of 610^3 1/mm³ circulated in a silicone tube with inner diameter of 2 mm with flow volume of 450 mm³/s. A coaxial annular transducer with two elements was used for emitting and receiving ultrasound with pressure of 0.19 MPa and pulse repetition frequency of 100 Hz. The echo signals were recorded with interval of 10 sec during 60 sec after keeping stable flow in the channel. The attenuation was analyzed in -20 dB band width of 2-5 MHz by dividing the power spectrum of echo signal in the presence of bubbles by that in the absence of bubbles.

Results/Discussion

Figure 1(b) shows the bright field and NIR fluorescence image of the ICGBs. The fluorescence from the outer shell with ICG was clearly confirmed. The radius of ICGBs was typically ranged in 0.5-4 μ m. Figure 1(c) shows the frequency characteristic of attenuation coefficient of ICGBs and CBs. The peak frequency of attenuation shifted from 2.8 to 2.5 MHz in case of ICGBs and shifted from 2.6 to 2.3 MHz in case of CBs. Although the peak frequency of ICGBs was slightly higher than that of CBs, it was supposed that the anchoring of ICG did not drastically change the resonance of bubble oscillation.

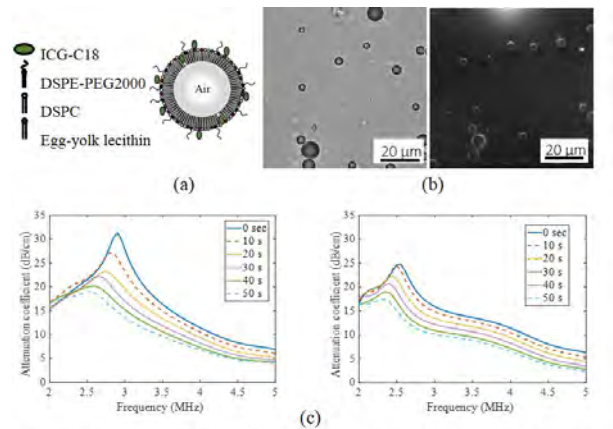


Fig. 1(a) Structure of ICG bubbles, (b) microscopic bright field (left) and near infrared fluorescence image of ICG bubbles, (c) frequency characteristic of attenuation coefficient of ICG bubbles (left) and control bubbles (right).

Porphyrin/Camptothecin-Fluorouridine Triad Microbubbles Along with Ultrasound and Photodynamic Therapy for Overcoming Multidrug Resistance in Colorectal Cancer

Min Chen¹, Xiaolong Liang², Mengxuan Wang¹, Zhifei Dai¹

¹*Department of Biomedical Engineering, Peking University, China, People's Republic of*, ²*Department of Ultrasound, Peking University Third Hospital, Beijing, China, People's Republic of*

Background, Motivation, and Objective

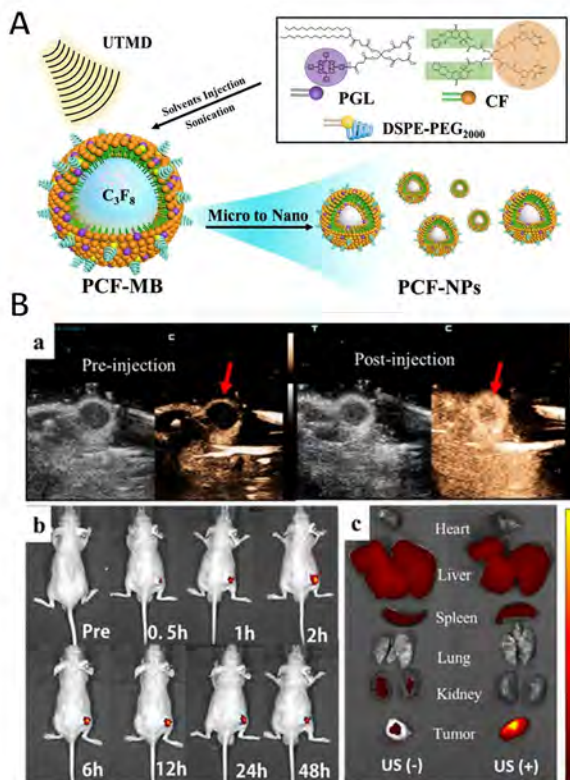
Multidrug resistance remains one of the main obstacles to efficient chemotherapy of colorectal cancer. Traditional drugs are still limited due to their low bioavailability and poor permeability through cancer even with current delivery system such as liposomal nanocarriers. In addition, other blocking mechanisms apart from chemical agents should be combined with chemotherapy for more efficiently overcome MDR. Therefore, we urgently need a kind of site-specific cancer penetrating delivery strategy which is able to increase the therapeutic effect of chemotherapy and simultaneously reduce activation of unwanted recurrence pathways. Herein, an efficient drug delivery and combination therapeutic strategy is proposed based on porphyrin/camptothecin-fluorouridine triad microbubbles (PCF-MBs), showing highly stable co-delivery drug combinations with fairly high drug loading content, and no premature release (**Scheme 1**).

Statement of Contribution/Methods

The triad MBs (PCF-MBs) were constructed by mixing porphyrin grafted lipid (PGL) and amphiphilic CF drug-drug conjugate to encapsulate perfluoropropane (C_3F_8). The ultrasound signal was seen diminished immediately upon ultrasound irradiation (1.0 MHz, 1 W/cm², 50% duty, 1 min) due to ultrasound triggered conversion of PCF-MBs into nanoparticles.

Results/Discussion

The triad PCF-MBs can act not only as a contrast agent for ultrasound/fluorescence bi-modal imaging but also a multi-modal therapeutic agent for synergistic combined chemo-photodynamic therapy. Upon local ultrasound exposure under the guidance of ultrasound imaging, *in situ* conversion of PCF-MBs into PCF NPs leads to high accumulation of chemo-drugs and photosensitizer in tumor, greatly reducing the risk of systemic exposure. *In vivo* anticancer activity showed that the PCF-MBs in combination of ultrasound and laser irradiation could achieve a 90% tumor inhibition rate of HT-29 cancer with no recurrence. Therefore, such triad PCF-MBs based combination therapeutic strategy shows great promise for overcoming drug resistance of colorectal cancer and other cancers.



Ultrasound contrast agent of camptothecin-floxuridine microbubbles for achieving in situ tumor drug accumulation and enhancing combined chemotherapeutic efficacy

Xiaolong Liang¹, Mengxuan Wang², Yunxue Xu², Chuang Gao², Yiming Zhou², Nisi Zhang², Zhifei Dai²

¹Department of Ultrasound, Peking University Third Hospital, Beijing, China, People's Republic of, ²Department of Biomedical engineering, Peking University, Beijing, China, People's Republic of

Background, Motivation, and Objective

Ultrasound-targeted microbubble destruction has been demonstrated to be an emerging technique for noninvasive drug delivery to the tumor sites. Yet, very limited drug-loading capacity of conventional microbubbles (MBs) remains a great obstacle to efficacious cancer therapy. Herein, a highly symmetric Janus camptothecin-floxuridine (CF) conjugate with two hydrophobic camptothecin (CPT) molecules and two hydrophilic floxuridine (FUDR) molecules was synthesized through hydrolyzable ester bonds linking to multivalent pentaerythritol. Its amphiphilic structure facilitates the self-assembly of CF MBs, resulting in highly stable co-delivery drug combinations with ultrahigh drug loading content, a fixed CPT/FUDR molar ratio of 1:1 and no premature release.

Statement of Contribution/Methods

CF MBs were fabricated by mechanical oscillation method with perfluoropropane (C_3F_8) gas encapsulation. 4T1 tumor-bearing mouse injecting with CF MBs was applied to the contrast enhanced ultrasound imaging (USI) using the Mindray resona 7 ultrasound (US) system with the L12-3U probe (MI=0.04). *In vivo* fluorescence imaging was performed on the IVIS Spectrum fluorescent imaging system when the 4T1 tumor-bearing mice were treated by CF MBs with or without US sonication (1.03 MHz, 50% duty, 1 W/cm², 3 min). Finally, 5 groups of mice of the same 4T1 tumor volume (100mm³) were applied to various treatments and their tumor sizes were recorded every day for 14 days to investigate the therapeutic efficacy.

Results/Discussion

The contrast enhanced USI (Fig.1a) showed no contrast signal in the tumor before MBs injection (0s) and 5s-post injection with the strongest signal. Low frequency US exposure (24s) led to the in situ conversion of CF MBs to nanoparticles (NPs) and an instantaneous decrease of the contrast signal, with the CF MBs re-perfusion and contrast signal partly recovering afterwards (50s). The *in vivo* fluorescence signal (Fig.1b) indicated the significant enhancement of CF MBs accumulation in tumor with US and remarkable lower drug concentration in other organs. And the tumor volume (Fig.1c) treated with both CF MBs and US was considerably reduced compared to other groups, suggesting the enhanced therapeutic efficacy by combining CF MBs with US. Therefore, CF MBs have the potential to be used in US guided drug delivery for cancer theranostics.

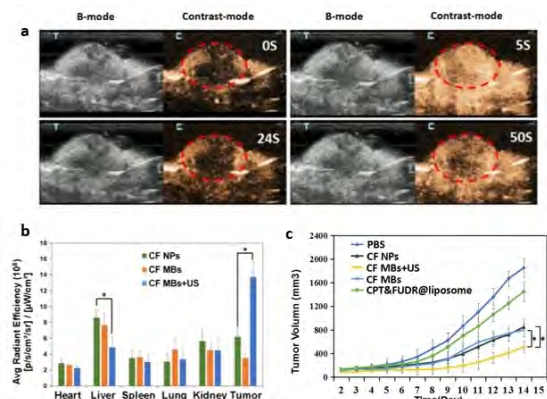


Figure 1. (a) CF MBs were intravenously administrated into the 4T1 tumor-bearing mice and the tumor was imaged with a clinical ultrasound probe, and the dashed circles indicate subcutaneous tumor regions. (b) Quantitation of the fluorescence intensity of tumors and main organs after 24 h injection. (c) Tumor volume change with increasing time after different treatments.

The Effect of Lipid Solubilization on the Performance of Doxorubicin-loaded Nanobubbles

Pinunta Nittayacharn¹, Al de Leon², Eric C. Abenojar², Agata Exner^{1,2}

¹Biomedical Engineering, Case Western Reserve University, OH, United States, ²Radiology, Case Western Reserve University, OH, United States

Background, Motivation, and Objective

Microbubbles (MB) have been widely used for ultrasound-guided drug delivery, but their effectiveness *in vivo* is limited by their large size (1-8 μm). Drug-loaded nanobubbles (NB) with a footprint of 100-500 nm can facilitate extravasation, resulting in higher drug accumulation in tumors and improved efficacy. Here we report on the formulation of doxorubicin-loaded lipid-shelled NB (Dox-NB) via two different preparation methods. For each NB, the size, concentration, drug encapsulation efficiency and *in vitro* acoustic properties were measured and compared to unloaded controls.

Statement of Contribution/Methods

Dox-NB were prepared with lipids (DBPC, DPPA, DPPE, DSPE-PEG2k) via either pre-dissolution in chloroform and hydration with PBS+Dox (formulation A) or direct lipid dissolution in PBS+Dox (formulation B). NBs w/o Dox were formulated as controls. Following air exchange with C_3F_8 , NBs were formed by mechanical agitation and isolated by centrifugation. Size and concentration of buoyant/non-buoyant particles were measured using resonant mass measurement (RMM) (Archimedes, Malvern). Encapsulation efficiency (%EE) of Dox was determined using fluorescent measurement after centrifuge filtration technique. Initial enhancement (IS) and signal decay rate were measured by imaging NBs in PBS in an agarose phantom using contrast harmonic imaging (ApplioXG SSA-790A, Toshiba) at 12MHz, 1 fps, and 0.1 MI (Fig1A).

Results/Discussion

Formulation A produced Dox-NB with a higher IS (21.0 ± 1.1 dB vs 14.7 ± 0.9 dB) (Fig 1B,C) but showed a faster signal decay compared to formulation B ($t_{1/2} = 10.1 \pm 0.2$ min vs $t_{1/2} = 12.7 \pm 3.2$ min). This is likely a result of a higher amount of smaller buoyant particles (Fig 1D) present in the population. RMM also showed consistent size of buoyant/non-buoyant particles in the range of 200-300 nm and no particles larger than 1 μm were observed. %EE of Dox was higher in formulation A, but the differences were not significant (Fig 1E). Importantly, following Dox loading, acoustic properties were comparable to NBs without Dox, indicating that Dox does not affect NB performance. Overall, these results provide evidence that Dox-loaded NBs, with loading efficiencies comparable to reported Dox-loaded micelles, can easily be formulated with minor modification. These findings could pave the way for advancing therapeutic applications of NBs.

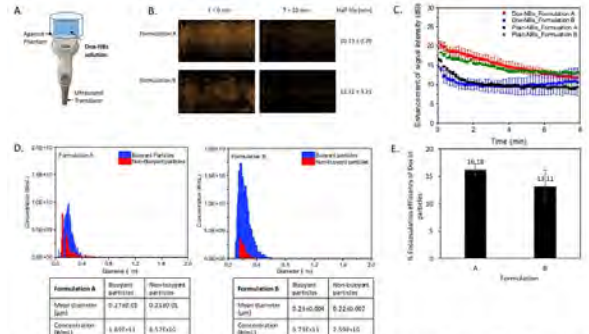


Figure 5. (A) Schematic of the ultrasound transducer (bottom) and agarose phantom sample location; (B) US contrast images and half-life of signal intensity measured by clinical US. (C) Enhancement of US signal intensity over time. (D) Size distribution of buoyant and non-buoyant particles measured by RMM. (E) Encapsulation efficiency of Dox (%) in particles (both buoyant and non-buoyant particles) from nanobubbles.

P1-A4 - Contrast-Enhanced Ultrasound

Kairaku (posters 1)

Tuesday, October 23, 9:30 AM - 4:00 PM

Chair: Hairong Zheng Shenzhen Institutes of Advanced Technology

P1-A4-1

3D local convective-dispersion characterisation in dynamic contrast-enhanced ultrasound recordings based on a finite-element scheme

Rogier R. Wildeboer¹, Ruud J. G. van Sloun¹, Christophe K. Mannaerts², Johannes C. van der Linden³, Pintong Huang⁴, Hessel Wijkstra^{1,2}, Massimo Mischi¹

¹Department of Electrical Engineering, Eindhoven University of Technology, Netherlands, ²Department of Urology, Academic Medical Center - University of Amsterdam, Netherlands, ³Department of Pathology / DNA laboratories, Jeroen Bosch Hospital, 's-Hertogenbosch, Netherlands, ⁴Second Affiliated Hospital of Zhejiang University, Hangzhou, Netherlands

Background, Motivation, and Objective

The introduction of three-dimensional (3D) dynamic contrast-enhanced ultrasound (DCE-US) imaging enables the macroscopic visualisation of perfusion and vasculature to the full extent. Characterisation of the vascularity can for instance be used for localisation of prostate cancer (PCa), as the angiogenic nature of the malignancy alters the local vascular architecture. Modelling of contrast-agent behaviour as a convective-dispersion process has shown promise for this purpose; however, the relatively low spatial and temporal resolution of 3D recordings complicates the reliable estimation of local concentration gradients. In this work, we exploit a stable finite-element scheme to locally assess the convective-dispersion contrast-agent behaviour in the prostate.

Statement of Contribution/Methods

Based on the 3D convective-dispersion equation, a finite-element Crank-Nicolson scheme was formulated to describe the contrast-agent concentration behaviour. Subsequently, local convective-dispersion parameters were consecutively estimated through least-squares minimization in a small 3D kernel at different locations covering the full measurement space. Convective-dispersion vector fields were visualised through probabilistic tractography. To this end, streamlines were computed using the anisotropically-filtered velocity vector field with random perturbations that scale with the estimated spatial dispersion. The method was evaluated *in silico* in 2D (10 Hz) and 3D (1 Hz), assuming the images to be a combination of all bubbles represented by a 3.5-MHz modulated 0.5-mm Gaussian-shaped point spread function in all dimensions. A ~0.25 Hz 3D DCE-US video acquired at the 2nd Affiliated Hospital of Zhejiang University in a patient referred for radical prostatectomy was used to test the method *in vivo*.

Results/Discussion

In silico, the method demonstrated the ability to resolve simulated vascular structures (see Figure 1A and 1B). An example of the method's ability to visualise macroscopic vascular behaviour with *in-vivo* data is depicted in Figure 1C. These preliminary results suggest that the method has potential for the visualisation of contrast convective-dispersion behaviour in 3D, however, further development of the method *in vivo* is still to be performed as well as an assessment of its clinical value.

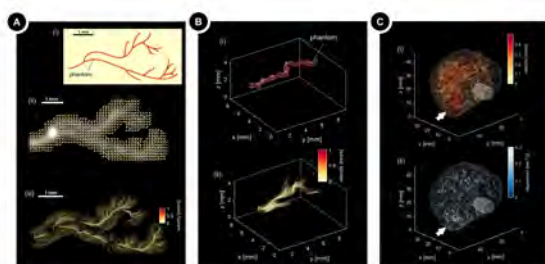


Figure 1 – Streamline representations of the convective dispersion field: (A) simulation of (i) a 2D vasculature depicting (ii) the velocity vector field overlaid on the maximum-intensity projection and (iii) streamline representation; (B) simulation of a 3D vessel depicting (i) the phantom and (ii) the streamline representation; and (C) streamline representations of an *in-vivo* DCE-US acquisition showing (i) velocity and (ii) transparency-scaled dispersion. A Gleason 4+5 prostate cancer lesion is indicated by an arrow.

Contrast-agent detection using orthogonal decoding with pulse-inversion harmonic suppression in Hadamard-encoded multi-pulses (HEM) transmission

Che-Chou Shen¹, Jyun-Hong Yan¹, Guan-Heng Lai¹

¹Department of Electrical Engineering, National Taiwan University of Science and Technology, Taipei, Taiwan

Background, Motivation, and Objective

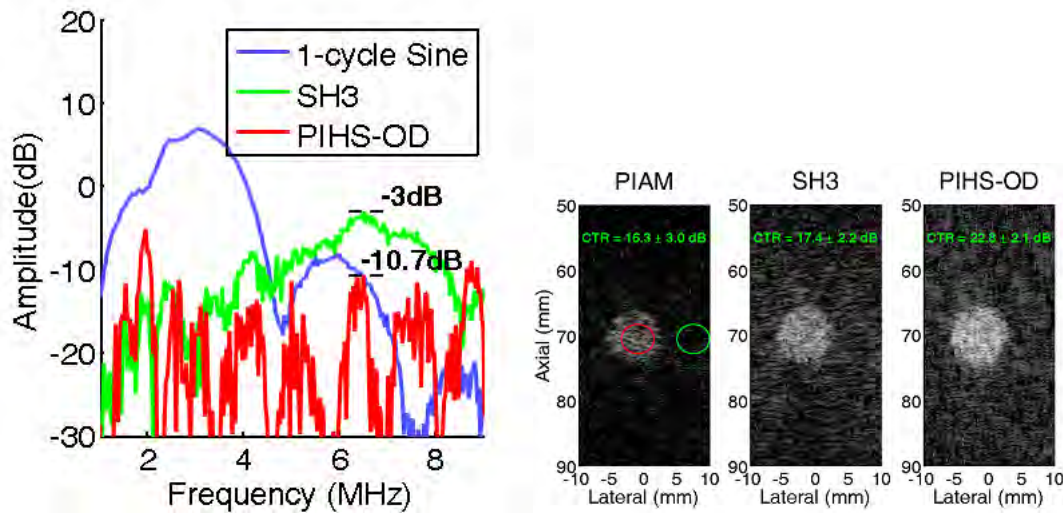
Recently, Hadamard encoded multi-pulses (HEM) transmit has been utilized for background suppression in ultrasound contrast agent (UCA) imaging to enhance contrast-to-tissue ratio (CTR). Nonetheless, second harmonic component does not comply with HEM encoding and thus lead to residual tissue background after decoding, especially in the presence of memory effect which considers the nonlinear contribution of previous bit waveform into next one in the progress of harmonic generation.

Statement of Contribution/Methods

In this study, orthogonal decoding of HEM transmit is proposed with pulse-inversion harmonic suppression (PIHS) to remedy memory effect on tissue background. Pairs of received HEM echoes are respectively correlated with its orthogonal decoding filter and then combined to eliminate linear component. PIHS further removes second harmonic by subtracting the positive echo from the negative echo. In PIHS orthogonal decoding, echoes from inverted transmission contain the same harmonic interferences from memory effect and thus can be effectively suppressed using pulse subtraction.

Results/Discussion

Hydrophone measurement and B-mode imaging are performed to compare the efficacy of Hadamard decoding (SH3) and PIHS orthogonal decoding. Compared to Hadamard decoding, hydrophone-measured spectra in Fig. (a) shows that PIHS orthogonal decoding improves tissue harmonic suppression by 7.7 dB at focal depth. The corresponding UCA imaging in Fig. (b) also shows that PIHS orthogonal decoding increases CTR by 5.4 dB. It is shown that PIHS orthogonal decoding of HEM transmit can alleviate residual tissue background in the presence of memory effect. It demands for the same firings as Hadamard decoding and is comparable in temporal resolution and possible motion artifacts.



Contrast-Enhanced Time-Resolved Vector Flow Imaging of Urinary Flow DynamicsTakuro Ishii¹, Chung Kit Ho¹, Hassan Nahas¹, Billy Y. S. Yiu¹, Alfred C. H. Yu¹¹Schlegel-UW Research Institute for Aging, University of Waterloo, Waterloo, ON, Canada**Background, Motivation, and Objective**

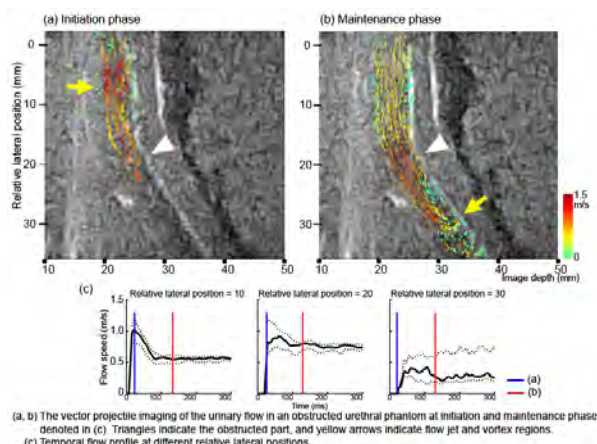
Visualization of urine flow passing through the urethra can critically help reveal hydrodynamic symptoms that are attributed to voiding dysfunction. On this topic, high frame rate vector flow imaging is a potential solution, as it can temporally resolve the complex urine passage process. However, urine typically has an acoustic scattering strength lower than that of blood. This makes it difficult to acquire high-quality vector flow image frames from the urinary tract and, in turn, pose major signal processing challenges in identifying recirculatory flow and resolving aliasing artifacts in fast flow jet zones. To overcome such problem, we have investigated the feasibility of performing high-frame-rate contrast-enhanced vector flow imaging to visualize urinary flow dynamics.

Statement of Contribution/Methods

An ultrasound research scanner (SonixTouch+SonixDAQ) with a L14-5 transducer (2 Tx angles, 10 kHz PRF, 5 MHz freq) was utilized to acquire high-frame rate plane wave image frames. Before micturition, a 0.5 ml bolus of contrast (20 % USphere Prime) was injected into the bladder through catheterization, and then image data was acquired over the first 1 s of micturition. Flow vectors were derived in two steps. First, for each Tx angle's contrast-enhanced raw data frame, it was analyzed with slow-time lag-one autocorrelation to estimate frequency shift on 7 Rx angles (ensemble size 128; slide 4; effective frame rate 1250 fps). Second, the extended-least square vector estimation method (UFFC, 2016; 63: 1745-57) was applied to calculate dealiased flow vectors. Finally, the derived flow vectors were rendered dynamically using the Vector Projectile Imaging (VPI) algorithm (UMB, 2014; 40: 2295-2309). This framework was tested on a walled urethral phantom that resembled the deformation of the urinary flow tract during micturition. The phantom was connected to a pump that generated 1 s constant flow pulses (7ml/s flow rate).

Results/Discussion

We observed various urinary flow patterns caused by the obstruction (Figure), including low speed vortex (median 0.20 m/s; IQR 0.17-0.67 m/s) and flow jet formation (median 1.2 m/s; IQR 0.91-1.26 m/s). The spatiotemporal dynamics of urinary flow during the initiation of voiding and the maintenance phase were also lucidly visualized. These results assert the potential of the proposed contrast imaging technique in urinary diagnostics.



Characterization of Heterogeneous Perfusion in Contrast-enhanced Ultrasound
Michelle Kleckler¹, Soheil Mohajer², Emad Ebbini²
¹*University of Minnesota Twin Cities, MINNEAPOLIS, MN, United States*, ²*Electrical and Computer Engineering, University of Minnesota Twin Cities, Minneapolis, MN, United States*
Background, Motivation, and Objective

Perfusion imaging using CEUS is a promising functional imaging modality with applications in the evaluation of tumors, vascular disease, stroke and other abnormalities. In many applications, heterogeneous perfusion presents a challenge to quantitative CEUS imaging. While regions with high perfusion can be easily seen on B-mode ultrasound, regions with medium and low perfusion require nonlinear imaging modes with higher sensitivity and specificity to UCA. Tissue motion and deformation together with noise can also mask subtle UCA activity in low perfusion regions.

Statement of Contribution/Methods

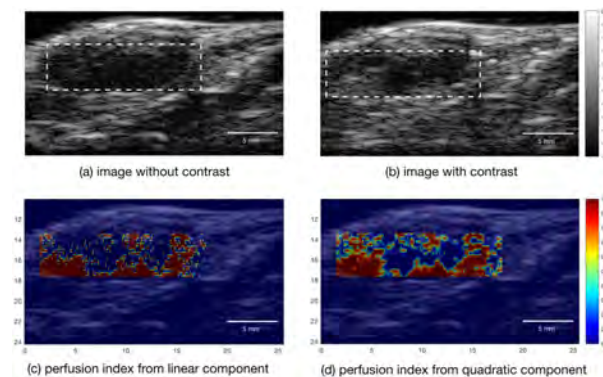
RF data was collected while imaging a subcutaneous LNCaP tumor at 26 fps (approximately 4 s) *in vivo* under approved protocol. A nonlinear third-order Volterra filter (TVF) applied to the RF data generated linear, quadratic, and cubic data from with and without UCA. Grayscale data from the VF components were preprocessed to compensate for motion and remove the spatial mean. An ROI within the tumor containing regions of high and low perfusion was identified. The differential data within the ROI was partitioned into axial segments 15 samples at 40 MHz and formed into M-mode matrices.

The singular values (SVs) of the M-mode segments were obtained and the largest SV was removed, being largely insensitive to UCA. Mid-range SVs were retained while low-order ones were dropped, being largely sensitive to noise.

Fig. 1 shows the ROI within the tumor. The UCA image (b) shows a high perfusion region in the lower left quadrant and a low perfusion region to the right. Approximately 19% of the tumor samples were labeled as either high or low perfusion based on manual inspection. Eighty percent of the selected samples were used to train a 2-layer, 10 neuron feed-forward back-propagation neural network using SVs from corresponding M-mode segments with and without UCA. The network output was calibrated to produce a *perfusion index* with 1 for highly perfused and 0 for no perfusion.

Results/Discussion

The figure shows the CNN output when applied to the ROI mapped on a B-mode image frame. The index values obtained using the LVF component resulted in 86% accuracy while the QVF and CVF components produced 96% accuracy. Compared to the LVF, the QVF and CVF produce index profiles largely free of false positives. Combining machine learning with nonlinear imaging provides characterization of heterogeneous perfusion.



Validation of NSSA-based filtering using differential targeted enhancement

Elizabeth B. Herbst¹, Sunil Unnikrishnan¹, Alexander L. Klibanov¹, F. William Mauldin¹, John A. Hossack¹

¹University of Virginia, United States

Background, Motivation, and Objective

Microbubbles (MBs) are highly echogenic ultrasound contrast agents capable of identifying vascular disease markers through targeted adhesion. A previous study showed that it is possible to use normalized singular spectrum area (NSSA), a statistical property of data, to differentiate between adherent MBs, non-adherent MBs, and static tissue in the environment of a mouse hindlimb tumor model, without the use of destructive ultrasound pulses typically used in “gold standard” differential targeted enhancement (dTE) imaging. This study validates past results by comparing the NSSA of MB signal to dTE using the pre-burst minus post-burst method.

Statement of Contribution/Methods

C57BL/6 mice were implanted with subcutaneous hindlimb MC38 cells. They were administered retro-orbital injections of 2×10^7 MBs conjugated with either VEGFR2 (a molecular marker of tumor angiogenesis) or isotype-control antibody. Mouse tumors were imaged using a Verasonics Vantage 256 programmable ultrasound scanner and a linear array transducer. (Transmit frequency = 5.5 MHz; receive frequency = 11 MHz.) For each type of MB, destruction pulses were administered at either 1 min or 6 min post-injection.

To analyze the data, regions of interest (ROIs) were manually selected within the tumor interior. NSSA values within these ROIs were calculated from ensembles of frames collected just before the destruction pulse. dTE was calculated by averaging the MB signal intensity in ensembles of frames collected before and after the destruction pulse.

Results/Discussion

NSSA measurements had a strong linear correlation with dTE measurements (R^2 value: 0.72; MSE: 0.21) (Fig. 1A). These data suggest that freely circulating MBs exhibit lower dTE and higher signal decorrelation, resulting in higher NSSA values. Conversely, adherent MBs exhibit higher dTE and lower signal decorrelation, resulting in lower NSSA values. The results suggest that NSSA is capable of predicting MB adherence throughout the entire time course of MB administration, without the use of destructive acoustic energy (Fig. 1B).

Both dTE and NSSA measurements revealed that our isotype control MBs demonstrated non-specific adhesion to the tumor vasculature. It is believed that this is most likely due to the size of the microbubbles (mean diameter approx. 2.5 μm).

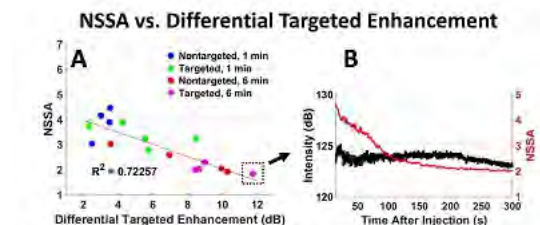


Figure 1. A. NSSA is linearly correlated with the differential targeted enhancement (dTE) of adherent MBs. The linear correlation between dTE and NSSA validates NSSA as a reliable measurement of MB adhesion. B. NSSA provides a sensitive real-time measurement of MB adherence through time. After injection of targeted MBs, the mean signal intensity inside the tumor is almost constant, and no information about adherence can be obtained without the use of a destruction pulse. Conversely, NSSA measurements of the MB signal show that the MBs adhere rapidly during the first 100 seconds after injection, as indicated by the sharp downward slope in NSSA values.

Dynamic contrast enhanced ultrasound imaging; the effect of imaging modes and parameter settings for a microvascular phantom

Elahe Moghimirad¹, Jeffrey Bamber¹, Emma Harris¹

¹Joint Department of Physics and CRUK Cancer Imaging Centre, The Institute of Cancer Research and Royal Marsden NHS Foundation Trust, Sutton, London, United Kingdom

Background, Motivation, and Objective

Dynamic contrast enhanced ultrasound (DCE-US) imaging provides perfusion information, an indicator for tumor response to radiotherapy. To increase the reproducibility of time-intensity curve (TIC) characteristics, we are developing a 3D DCE-US imaging system. There are, however, many choices to be made in system design, such as whether to use plane wave (PW) or focused imaging (FI), and the values to use for parameters such as focal depth (FD), F-number (F#), mechanical index (MI) and number of angles (NA) for focusing (for PW imaging). Here we evaluate the effect of such choices on TICs for a microvascular flow phantom *in vitro*.

Statement of Contribution/Methods

DCE-US images were obtained using a Vantage™ (Verasonics Inc.) and a pulse-inversion algorithm. Default parameters which gave similar contrast and microbubble disruption rate for both FI and PW imaging were: FD=20mm (for FI), F#=4, MI=0.15, transmit frequency = 4 MHz, NA=7 (for PW imaging). To evaluate TICs, 800 frames were recorded at 10 Hz for PW and FI, using a phantom containing ~100,000 parallel microtubes, each 200 μm diameter. All measurements were repeated 3 times, injecting 0.4 ml of contrast agent (SonoZoid™) into the system running at 1ml/sec and changing one parameter at a time, using the values: FD = 20, 40 mm; F# = 2, 4; MI = 0.11, 0.15, 0.25; NA = 3, 7, 11.

Results/Discussion

Fig. 1(a) shows a B-scan of the phantom, which provided reproducible TICs that were tumor-like in being dependent on distance from the center. Reducing the MI reduced TIC intensities for PW imaging and FI. For the example (large) region of interest (ROI) shown, TICs were sharp and single-peaked for F2 but broader and double-peaked for F4 (Fig. 1b), consistent with F4 averaging over a greater focal volume than F2. Choosing a smaller ROI reduced the effect but did not eliminate it completely. Placing the focus deeper than the center reduced the TIC intensity (Fig. 1b) due to attenuation but also resulted in less region dependence and a flatter TIC. PW intensity was highest for 3 angles (Fig. 1c) with evidence (not shown) that this may be due to side lobe artefacts added to the contrast signal. TIC characteristics are thus expected to be highly sensitive to imaging parameters. This should be considered in longitudinal studies.

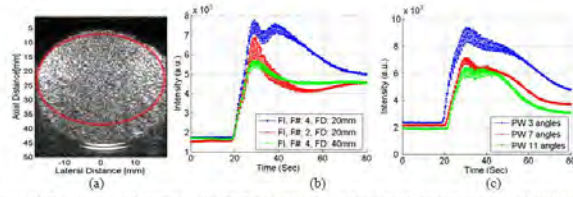


Figure 1. (a) B-mode image of the phantom and the TIC ROI (in red). TICs are shown for: (b) different FI's and focal depths (FI only, MI=0.15), and (c) various numbers of angles (PW only, MI=0.15).

A fluid dynamic model for quantitative contrast-enhanced ultrasound imaging: validation for the assessment of uteroplacental perfusion

Baudouin Denis de Senneville¹, Anthony Novell², Chloé Arthuis³, Vanda Mendes³, Paul-Armand Dujardin⁴, Frédéric Patat⁴, Ayache Bouakaz⁵, Jean-Michel Escoffre⁶, Franck Perrotin³

¹UMR 5251 CNRS/University of Bordeaux/INRIA, Institut de Mathématiques de Bordeaux, Talence, France, ²University of Tours, Inserm UMR1253 iBrain, Tours, France, ³Obstetrics, Gynecology and Fetal Medicine, University Hospital of Tours, Tours, France, ⁴Inserm CIC 1415, University Hospital of Tours, Tours, France, ⁵Université François Rabelais, Tours, France, ⁶Inserm UMR1253 iBrain, Tours, France

Background, Motivation, and Objective

Contrast-enhanced ultrasound (CEUS) is a non-invasive imaging technique extensively used for blood perfusion imaging of various organs. In this study, we introduce the use of a fluid dynamic model for the analysis of dynamic CEUS (DCEUS). The efficiency of proposed methodology is evaluated in-vivo, for the classification of placental insufficiency (control versus ligature) of pregnant rats from DCEUS.

Statement of Contribution/Methods

Implemented fluid dynamic model –Physiological activity and motion of the ultrasound probe were first compensated on the DCEUS images. Subsequently, the microbubble transport (\dot{I}) was estimated using the following transport equation: (I denotes the grey level intensity on DCEUS images and I_t the partial temporal derivative of I). The left part of this equation is composed by a transient term (I_t) and a transport term (\dot{I}), which stand for any temporal and spatial grey intensity variations, respectively.

CEUS examination –20 pregnant rats (11 rats with a ligature of the uterine horn pedicle, 9 control rats) were individually placed on a thermostatically controlled pad. Ultrasound B-scans were used to image fetal-placental unit in cross-section. A bolus of 200 µL of contrast agent (0.5 mL/kg) was intravenously injected. Subsequently, a video clip of 150 s was recorded to investigate the utero-placental perfusion.

CEUS analysis –Utero-placental perfusion was quantitatively analyzed both using our methodology and using the existing TIC-based approach. The four following parameters were extracted from the TIC: peak enhancement (PE), wash-in rate (WiR), time to peak (TTP), area under the curve during wash-in (WiAUC), using the CEUS analysis software Vevo-CQTM.

Results/Discussion

The spatio-temporally averaged microbubble transport amplitude was significantly higher ($p\text{-value}=1.1\times10^{-3}$) in the control group than in the ligature group. The proposed classification criterion was thus demonstrated to be a good binary classification criterion for ligature/non-ligature rat placentas. On the other hand, none of tested TIC-based parameters led to a significant difference between control and ligature populations (p -values obtained using PE, WIR, TTP and WiAUC were equal to 0.098, 0.348, 0.972 and 0.285, respectively). Our methodology opens great perspectives for the evaluation of the proposed technique for the clinical diagnostic of obstetrical disorders.

P1-A5 - New Elasticity Imaging Methods

Kairaku (posters 1)

Tuesday, October 23, 9:30 AM - 4:00 PM

Chair: Arun Kumar Thittai IIT Madras

P1-A5-1

Hybrid elastography: a new technique for the assessment of tissue stiffness.

Hugo Lorée^{1,2}, Cécile Bastard¹, Didier Cassereau^{2,3}, Veronique Miette¹, Laurent Sandrin¹

¹Echosens, Paris, France, ²Laboratoire d'Imagerie Biomédicale, UMR S 1146/UMR 7371, Paris, France, ³ESPCI, Paris, France

Background, Motivation, and Objective

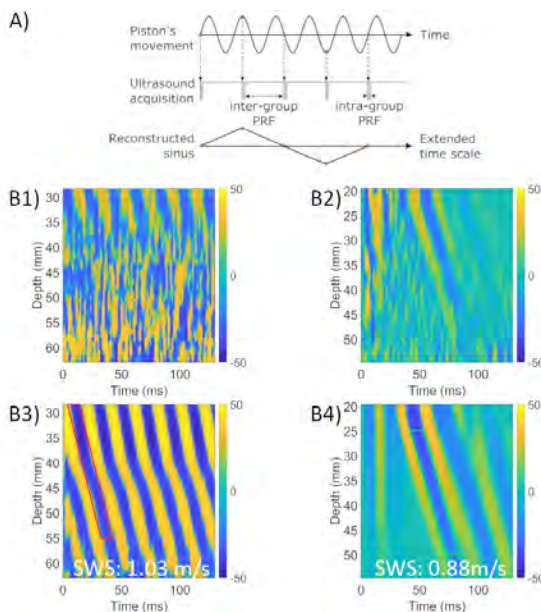
Vibration-Controlled Transient Elastography (VCTE) is a clinically well validated method to assess liver stiffness (LS) using FibroScan (Echosens, Paris, France). The operator relies on ultrasound (US) A- and M-mode images to locate the liver. Finding a good measurement window is key to get a good penetration of the SW and therefore a valid LS measurement. However, relying only on US may be suboptimal to identify the right measurement position. We developed a novel technique called Hybrid Elastography (HE) that combines continuous and transient elastography, respectively to assist the operator in finding an optimal measurement position and to perform the measurement.

Statement of Contribution/Methods

During continuous elastography, the US transducer vibrates at 50 Hz with an amplitude of 300 μm peak-to-peak. US acquisitions are performed as groups of two emission-reception sequences executed with an inter-group Pulse Repetition Frequency (PRF) of 47 Hz and an intra-group PRF of 6 kHz (Fig A). This stroboscopic method allows to reconstruct the displacements induced in the tissues by the continuous vibration within a limited number of low frequency periods. Displacements induced in the tissues are measured using a standard correlation technique applied to RF lines groups to construct the Elastic Wave Propagation Map (EWPM).

Results/Discussion

We used an elastography phantom (CIRS, Norfolk, USA) with a reference Shear Wave Speed (SWS) of 0.91 m/s. Fig B shows the EWPM obtained with continuous (left) and transient (right) modes on a phantom containing a plastic rib. The presence of the rib clearly reduces the propagation depth of elastic waves to about 45 mm in continuous and transient modes (Fig B1 and B2) compared to the propagation in a homogeneous part of the phantom (Fig B3 and B4). As expected SWS assessed during continuous elastography is overestimated due to the superimposition of compression and shear waves ($\text{SWS}_{\text{continuous}} = 1.03 \text{ m/s}$, $\text{SWS}_{\text{transient}} = 0.88 \text{ m/s}$). However continuous elastography is useful to guide in real time the operator in positioning the probe in front of a large portion of homogeneous tissues which is a good indication that the transient measurement will be successful. HE is a promising technique that adequately combines both continuous and transient elastography techniques for real-time guidance and measurement respectively.



Design and Experimental Validation of Miniature External Mechanical Vibrators towards Clinical Ultrasound Shear Wave Elastography

Heng Yang¹, Carolina Carrascal², Hua Xie², Vijay Shamdasani³, Brian Anthony¹

¹Department of Mechanical Engineering, MIT, Cambridge, MA, United States, ²Philips Research, Cambridge, MA, United States,

³Philips Healthcare, Bothell, WA, United States

Background, Motivation, and Objective

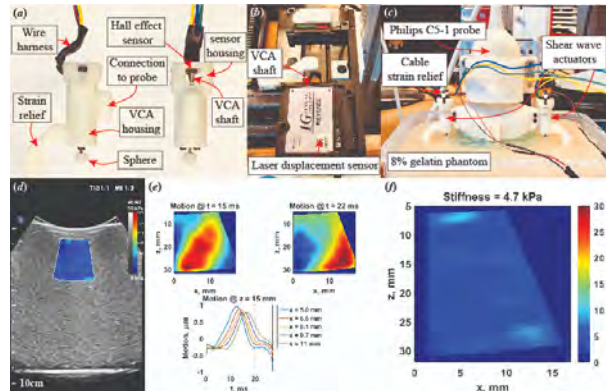
Ultrasound shear wave elastography (SWE) is mostly available on premium systems with effective acoustic radiation force (ARF) to induce detectable shear waves in soft tissues. External mechanical vibration (EMV) is a cost-effective alternative of ARF that has potential to enable SWE on low-end systems. Previously at IUS2017 we presented an EMV prototype integrated with a commercial imaging scanner that could vibrate multiple point sources to induce shear wave propagation. In this study, we design and construct miniature shear wave vibrators to achieve the ergonomic form factor suitable for routine clinical practice. The newly designed miniature actuators have significantly reduced form factor from their predecessor: 5% of the original volume size. We also use the commercial SWE feature on Philips EPIQ 7G as a benchmark to validate the EMV based SWE function on elasticity phantoms.

Statement of Contribution/Methods

Fig. 1(a) shows a shear wave actuator, including a miniature voice coil actuator (VCA) (BEI Kimco, Vista, CA), a hall effect sensor (Allegro MicroSystems, Worcester, MA), a VCA housing with strain relief protrusion, a sensor housing fastened to the VCA housing, and a sphere threaded to the VCA as the vibrating point source. The hall effect position sensor is calibrated using a laser displacement sensor (Keyence, Osaka, Japan), as shown in Fig. 1(b). Shear wave actuators can be easily attached to an ultrasound probe either in the imaging plane (in-plane), or transverse to the imaging plane (cross-plane). Transient mechanical vibration is synchronized with shear wave tracking pulses from the imaging scanner. Fig. 1(c) depicts an experimental setup with two actuators attached in-plane to a Philips curvilinear C5-1 probe imaging an elasticity phantom fabricated with 8% gelatin.

Results/Discussion

The reconstructed stiffness map from 50 Hz EMV excitation shown in Fig. 1(f) is visually in agreement with the ARF based stiffness map shown in Fig. 1(d). Quantitatively, the averaged stiffness from ARF and EMV were 5.5 kPa and 4.7 kPa, respectively. The intermediate displacement results shown in Fig. 1(e) illustrate successfully generated shear wave propagation by EMV. Such miniature EMV is a promising step towards clinical ultrasound SWE for low-end and portable ultrasound systems where ARF push may be limited. Future work includes *ex vivo* and *in vivo* feasibility study.



Quantitative quasi-static ultrasound elastography using reference layer: A preliminary Assessment

Sathyamoorthy Selladurai¹, Arun K. Thittai¹

¹Applied Mechanics(Biomedical Group), Indian Institute of Technology Madras(IITM), Chennai, India

Background, Motivation, and Objective

Changes in tissue elasticity are generally correlated with pathological phenomena. Quasi-static elastography is used to visualize regions with different relative stiffness. However, its major limitation is its qualitative nature. This can be overcome by using a reference layer with known stiffness, sandwiched between the transducer and the tissue surface. This enables us to normalize and quantitatively image the unknown modulus of the examined tissue. The performance of the method was studied through simulations and experiments on phantoms, having the range of Young's modulus appropriate to liver. We characterized and used a commercially available gel pad as reference layer and used the modulus contrast transfer efficiency to determine modulus value from the estimated strain ratio.

Statement of Contribution/Methods

Developed a method for measuring the elastic modulus of an underlying homogeneous tissue using the calibrated reference layer, for quasi-static ultrasound elastography (see Fig. 1).

Young's modulus was obtained from the strain ratio estimate: where, $1/C_s = 2/(1+C_m)$, C_s is the strain contrast ($C_s = S_1/S_2$), S_1 -strain in the reference layer, S_2 - strain in the phantom, C_m is the corresponding modulus contrast. We can obtain the unknown target modulus using $M_1 = C_m * M_2$.

Where, M_1 (unknown) - Modulus of phantom target, M_2 (known) - Modulus of reference layer.

Results/Discussion

Fig. 2 shows simulation results of the axial , Lateral Displacement(LD), and axial strain elastogram from two different configurations. Notice the conspicuous changes in the LD, which depict the reference layer undergoing less displacement compared to the phantom, when the reference layer is stiffer than the phantom. Further, axial strain image shows that the phantom undergoes more strain compared to the reference layer. As expected, the exact opposite, i.e., phantom undergoing less strain than the reference layer and the LD being more in the reference layer than in the phantom is observed in configuration 2. Fig.3 showing the experimental results of the LDand axial strain distribution, exhibits similar behavior as noted in simulations. The unknown modulus value of the phantom was estimated and it was compared with the modulus values of phantom samples measured using Universal Testing Machine (UTM) . The results obtained in simulations and experiments (Table 1 and 2, respectively).

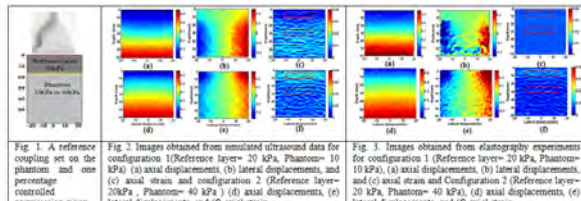


Fig. 2. Images obtained from simulated ultrasound data for configuration 1 (Reference layers= 20 kPa, Phantom= 10 kPa) (a) lateral displacement, (b) lateral strain measurements, (c) axial strain and configuration 2 (Reference layers= 20 kPa, Phantom= 40 kPa) (d) axial displacements, (e) lateral displacements, and (f) axial strain

Fig. 3. Images obtained from elastography experiments for configuration 1 (Reference layer= 20 kPa, Phantom= 10 kPa) (a) lateral displacement, (b) lateral strain measurements, and (c) axial strain and Configuration 2 (Reference layer= 20 kPa, Phantom= 40 kPa). (d) axial displacements, (e) lateral displacements, and (f) axial strain

| Table 1. The mean and standard deviation values of elastic properties obtained in simulations | | | |
|---|---------------------------------|------------------|-------------------|
| Configuration | Measured Strain ratio (C_s) | Estimated (kPa) | Ground Truth(kPa) |
| 1 | 0.76 ± 0.05 | 10.43 ± 1.95 | 10 |
| 2 | 1.52 ± 0.08 | 40.8 ± 4.2 | 40 |

| Table 2. The mean and standard deviation values of elastic properties obtained in experiments | | | |
|---|---------------------------------|-----------------|-------------------|
| Configuration | Measured Strain ratio (C_s) | Estimated (kPa) | Ground Truth(kPa) |
| 1 | 0.73 ± 0.07 | 9.2 ± 2.23 | 10.257 ± 1.84 |
| 2 | 1.48 ± 0.12 | 39.2 ± 4.10 | 40.826 ± 3.75 |

A Convolution Neural Network-based Speckle Tracking Method for Ultrasound Elastography**Bo Peng¹, Yuhong Xian¹, Jingfeng Jiang²**¹*School of Computer Science, Southwest Petroleum University, Chengdu, China, People's Republic of,* ²*Biomedical Engineering, Michigan Technological University, MI, United States***Background, Motivation, and Objective**

Accurate tracking of tissue motion is critically important for several ultrasound elastography methods including strain elastography and shear wave elastography. Many speckle tracking methods used in conjunction with ultrasound elastography are correlation-based and, in this study, we investigate a novel alternate approach. More specifically, a convolution neural network (CNN) was applied to accurately estimate tissue motion as a deep-learning problem.

Statement of Contribution/Methods

We adopted an end-to-end learning approach (FlowNet, Dosovitskiy et al., ICCV, 2015) to predict tissue motion between a pair of pre- and post-deformed RF signals. First, given a dataset consisting of ultrasound echo signal pairs and known tissue displacements, we train a CNN to predict the two-dimensional displacement fields. Of Note, during the training process, finite element (FE) simulated data from a realistic breast phantom (Wang et al., Medical Physics, 2015) were used for training. Then, the trained CNN was used to estimate tissue motion in tissue-mimicking (TM) phantoms and *in vivo* breast imaging data (Hall et al., UMB, 2003). Results obtained by this novel CNN-based method were compared to a published 2D high-quality speckle tracking method by our group (Jiang and Hall, PMB, 2015).

Results/Discussion

Our preliminary results showed that the trained CNN worked very well on other FE-simulated data, TM phantoms and *in vivo* breast data. Under a 1% frame-to-frame compression, the CNN-based method yielded comparable signal-to-noise ratios (SNRs) in all data tested. For instance, in the FE-simulated data, similar SNRs were obtained (6.4 vs 6.5). In the TM phantom results, the proposed CNN-based method achieved similar contrast-to-noise ratios (3.23 vs 3.43), as compared to the correlation-based high-quality speckle tracking method. Furthermore, the novel approach maintained the similar performance in terms of CNR (0.81 vs 0.83) and motion-compensated normalized cross-correlation values (0.75 vs 0.76) for *in-vivo* breast data.

Currently, the inference process after the training of the proposed CNN can achieve approximately 60 frames/second for 2D speckle tracking under the NVIDIA TensorRT™ framework.

Overall, we conclude that applying the proposed CNN-based speckle tracking method is feasible and high-quality strain elastography data can be obtained in TM phantoms and *in vivo* breast data. Our future work includes applying this technique to *in vivo* 3D whole breast ultrasound data (Wang et al., Ultrasonic Imaging, 2017). We expect that accelerated 3D speckle tracking can be obtained using the proposed CNN.

Mechanical waves in time-dependent media may offer a new view on tissue elasticity imaging
Alberico Sabbadini¹, L.B.H. Keijzer², Henry den Bok¹, Hendrik J. Vos^{1,2}, Nicolaas de Jong^{1,2}, Martin D. Verweij^{1,2}
¹*Acoustical Wavefield Imaging, ImPhys, Faculty of Applied Sciences, Delft University of Technology, Delft, Netherlands,*
²*Biomedical Engineering, Thorax Center, Erasmus MC, Rotterdam, Netherlands*
Background, Motivation, and Objective

Obtaining the mechanical properties of a tissue medium using medical ultrasound imaging requires a model of wave propagation in that medium. Models currently assume that the properties of the medium are constant over time, but this is not always the case. For instance, at the beginning of diastole, the heart undergoes a rapid relaxation whose rate is connected to cardiac health and which may affect shear wave (SW) elastography measurements. While the effects of time-dependent medium properties on wave phenomena have been described extensively for electromagnetic waves [Fante, IEEE Trans Ant & Prop, 1971], they have not been thoroughly investigated for mechanical systems, nor have they been related to imaging applications. We experimentally and numerically studied these effects on 1D mechanical waves and show their potential for medical acoustic imaging.

Statement of Contribution/Methods

To obtain an experimental ‘medium’ in which all properties are fully known, we have built a 4 m long Wave Machine [Fig. 1A] in which angular displacement of a series of rods propagates as a torsional wave. The tension applied to the eccentric wires can be varied to change the wave speed during propagation. Wave motion was captured by a camera, and the space-time coordinates of the tips of the rods were extracted. Moreover, we described the setup with a Finite Difference Time Domain model to explore the effects of the amount and the rate of change in wave speed.

Results/Discussion

In our experiments, we observed that reducing the tension during propagation causes the initial wave to split into two components, a transmitted (TW) and a reflected (RW) wave, travelling in opposite directions [Fig. 1B]. Moreover, the wavelength remains constant and the frequency varies proportionally to the change in wave speed, as does the amplitude of TW. The amplitude of RW depends instead on the rate of such change. Simulations matched well with these results [Fig. 1B]. Using our model, we predict that the frequency of a SW travelling through the myocardium would decrease by 15% during diastolic relaxation with time constant of $\tau = 50$ ms (healthy), whereas for $\tau = 100$ ms (infarcted) the frequency would decrease by 5% only. This study shows that time-varying mechanical properties of tissue can affect wave phenomena significantly, and may thus be exploited in e.g. SW imaging to assess the diastolic relaxation of the heart muscle.

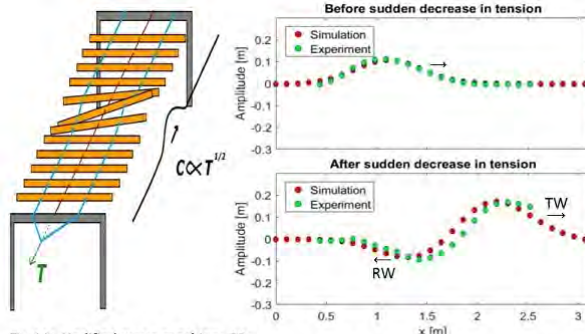


Fig 1A: Modified wave machine. 32 aluminium rods (yellow) are traversed by a metal wire (red) which provides the pivot, and by two nylon wires (blue). The tension T applied to the nylon wires determines the speed of torsional waves and can be varied manually during propagation.

Fig 1B: Propagating wave before and after a rapid (~ 30 ms) drop in tension, from 32 N to 8 N. The initial amplitude of the wave is 0.11 m, the amplitude of TW is 0.19 m and that of RW is 0.09 m. The wavelength remains 1.32 m throughout the whole experiment.

Non-contact sub-surface elastography using airborne ultrasound surface motion cameraAntoine Aminot¹, Pavel Shirkovskiy¹, Mathias Fink¹, Ros Kiri Ing¹¹*Institut Langevin, CNRS, ESPCI Paris, PSL Research University, 75238 Paris Cedex 05, France***Background, Motivation, and Objective**

Elastography plays a key role in characterizing soft media such as biological tissue. With few exceptions this method require direct physical contact with the object of interest. For medical examination on the eye cornea, physical contact is not desired and may even be prohibited. Here we propose a new approach to non-contact ultrasound elastography using airborne ultrasound surface motion camera (AUSMC) operating at 40 kHz. This device was developed for non-contact 2D surface-vibrometry by combining multi-element airborne ultrasound arrays, a synthetic aperture implementation and pulsed-waves. This approach is demonstrated and validated in specular reflection regime on x12 scaled eye phantoms.

Statement of Contribution/Methods

AUSMC uses two separate emission and reception aperture and operates in pulse echo mode. Inter-element acoustic impulse responses are acquired. Acoustic images are computed in post-processing. Afterwards, acoustics images are successively cross-correlated to determine for each pixel of the surface the normal displacement velocity in function of time. Finally the surface motion camera allows us to track surface wave propagations on any surface - planar or non planar - and assuming the medium as semi-infinite, sub-surface elasticity map may therefore be calculated.

Results/Discussion

The study presents preliminary results that support the capability of the AUSMC system to estimate without contact the elastic modulus of semi-infinite media or even thin layer over semi-infinite media. We will show movies of surface wave propagations on planar and non planar surfaces including x12 scaled eye phantom. First results using a prototype of an air-coupled 500 kHz transducer system will also be presented. All those preliminary results will define the next generation of surface motion camera working at 500 kHz to measure elasticity of eye cornea.

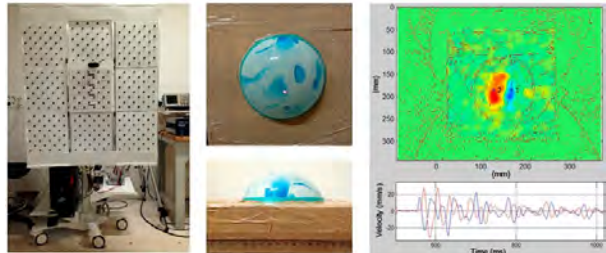


Figure 1. Left: Picture of AUSMC system (40kHz version). Middle: Picture of x12 scale eye phantom. Upper-right: Experimental velocity map. Bottom-right: velocity versus time for two measurement points (n°1 and 2 in upper map).

Toward a Shear Wave Based Mode to Sonographically Monitor the Enrichment of Iron Oxide Nanoparticles in Drug Targeting Applications

Michael Fink¹, Stefan Lyer², Christoph Alexiou², Helmut Ermert¹

¹Chair of Sensor Technology, University of Erlangen-Nuremberg, Germany; ²Section for Experimental Oncology and Nanomedicine, University Hospital Erlangen, Germany

Background, Motivation, and Objective

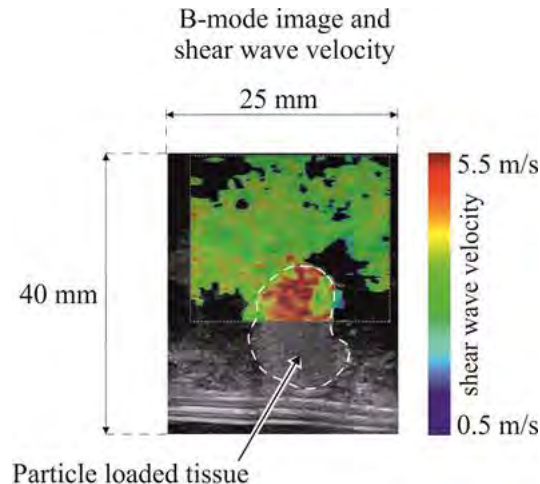
Magnetic Drug Targeting (MDT) is a cancer treatment technique that enables a local chemotherapy. In MDT chemotherapeutic drugs are bound to magnetic nanoparticles and are accumulated in the tumor area by means of an external magnetic field. Hereby, a well-defined particle concentration in the cancerous tissue requires monitoring of the particle accumulation. Unfortunately, classical ultrasonic pulse-echo imaging modes are not capable to display nanoparticles due to their weak backscattering. Therefore, as an alternative to magnetomotive concepts, we for the first time present as a new approach an ultrasound based imaging technique capable to detect quantitatively the concentration of iron oxide nanoparticles in biological tissue based on shear wave elastography.

Statement of Contribution/Methods

The measurement is based on differences between the bulk acoustic material properties of the utilized nanoparticles and of the biological tissue. The speed of sound values as well as the acoustic impedances of particle loaded tissue differ from those of tissue that is free from particles. For example, the velocity of low frequency shear waves in tissue is higher in tissue enriched by iron oxide particles than in particle free tissue. Similar to shear wave elastography, a shear wave can be induced into the target tissue and the shear wave speed of sound can be tracked. The variation of the spatial distribution of the speed of sound with respect to time permits conclusions regarding the local and temporal enrichment of nanoparticles. Moreover, this modality is capable to determine the enrichment quantitatively as the the shear wave velocity is proportional to the content of nanoparticle material in the biological tissue.

Results/Discussion

We have produced tissue mimicking phantoms that include areas perfused by different nanoparticle concentrations. In the particle loaded tissue, the nanoparticles are randomly distributed. The dependence of speed of sound with respect to the particle concentration has been experimentally demonstrated. The particle loaded areas could be identified employing a push pulse shear wave elastography mode. The figure shows the B-mode image partly combined with the color coded shear wave velocity values of the tissue mimicking phantom. The particle loaded tissue is marked by a dashed line.



Shear Wave Computed Tomography with Directional FilteringChia-Lin Lee¹, Yung-Shao Yang¹, Pai Chi Li¹¹National Taiwan University, Taiwan**Background, Motivation, and Objective**

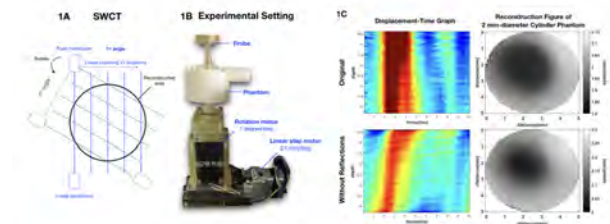
In our previous study, we presented a system for shear modulus computed tomography (SWCT). In clinical applications, the shear wave image format is the same as the corresponding B-mode so that the shear modulus distribution can be overlaid with the anatomy. Our proposed SWCT approach, on the other hand, performs image reconstruction at the plane perpendicular to the ultrasound beam. The system thus inherently can achieve higher spatial resolution from tomographic reconstruction and the imaging setup is more suitable for cell studies using 3D culture systems. The main purpose of the current study is to refine the SWCT approach by adding directional filtering to remove reflected shear waves.

Statement of Contribution/Methods

The data acquisition is similar to that of X-ray computed tomography. A 20MHz transducer is used to generate shear waves and a 40MHz transducer is used to detect the shear wave arrival time. The distance between focal points of the two transducers is 5mm and the shear wave speed is calculated based on the time-of-flight, which is related to the integration of the inverse of shear wave speed along the propagation path. A step motor stage is used to move and rotate the sample. At each angle, linear projection of the shear wave propagation time is done by linearly translating the two transducers at 51 steps with a step size of 0.1mm. The rotation is from 0 to 180 degrees with a 1 degree step size. The filtered back projection method is used for reconstruction of shear wave speed. To improve estimation accuracy, reflection waves were removed using a directional filter.

Results/Discussion

Agar based phantoms were constructed and tested. The diameter of the reconstruction area is 5mm and shear wave speed ranges from 1.8m/s to 2.3m/s. Effects of the directional filter are clearly demonstrated in the left panels of Figure 1C, and the final images shown in the right panels of Figure 1C also demonstrate improvement in spatial resolution.



1A SWCT data acquisition, 1B System Setup, 1C Displacement Maps (left) and Reconstructed Images (right)

P1-A6 - Cardiovascular Elasticity Imaging

Kairaku (posters 1)

Tuesday, October 23, 9:30 AM - 4:00 PM

Chair: **Hendrik Hansen** Radboud University Medical Center

P1-A6-1

Estimation of the spatial resolution of a 2D strain estimator using synthetic cardiac images

Bidisha Chakraborty¹, Sophie Giffard-Roisin², Martino Alessandrini¹, Brecht Heyde¹, Maxime Sermesant³, Jan D'hooge¹

¹Cardiovascular Sciences, KU Leuven, Leuven, Belgium, ²Laboratoire d'Accélérateur Linéaire, CNRS, Université Paris-Sud, France, ³Epione Project, Inria, Université Côte d'Azur, France

Background, Motivation, and Objective

Although strain analysis is often used clinically to quantify regional myocardial function, to date, the spatial resolution of speckle tracking algorithms has not been tested. As such, the minimum size of resolvable dysfunction area with these techniques remains unknown while this is relevant for clinical use. The aim of this study was therefore to determine the spatial resolution of our previously validated non-rigid image registration (NRIR) based strain estimates in an *in-silico* setting.

Statement of Contribution/Methods

Ultra-realistic 2D synthetic apical images were generated by combining a complex electromechanical model of the heart with a novel ultrasound simulation approach. Next to a model mimicking a normal heart, 9 data sets with dysfunctional areas ranging from 1.6 cm to 5.2 cm were generated by locally modifying the active contractile force and stiffness. The ground truth dysfunctional areas were defined as the regions with reduced regional strain with respect to the normal heart model.

Inter-frame displacements were obtained by NRIR (i.e. tensor product cubic B-splines as displacement model; sum of squared differences as similarity metric; bending energy as regularizer) and longitudinal segmental strains at end-systole (ES) were obtained. Similar to the ground truth model, pixels were defined as dysfunctional if the measured strain was lower than that in the same location of the normal heart model. The size of the dysfunctional area was determined as the largest spatially continuous dysfunctional region across the ventricle.

To quantify tracking performance, the Pearson's correlation coefficient (CC) was computed between NRIR-based and ground truth ES. Tracking resolution was estimated by computing the CC between the NRIR-based and ground truth size of the dysfunctional area. In addition, to assess dysfunction, sensitivity, specificity and accuracy was computed on a pixel-by-pixel basis and the dysfunctional size was defined to be resolved when accuracy was > 60 %. Finally, the area under curve (AUC) was also computed.

Results/Discussion

The CCs of ES strain and the size of the dysfunctional area against the ground truth were 0.97 and 0.92 respectively (Fig.1). The accuracy from 1.6cm to 5.2cm of dysfunction increased from 52% to 82%; while the AUC increased from 0.49 to 0.95. Overall, we found that NRIR can resolve dysfunctional areas down to 1.9 cm.

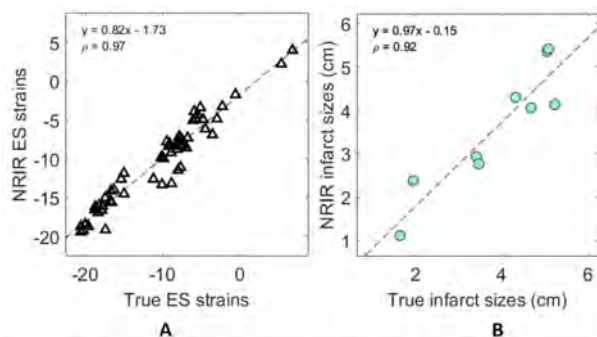


Figure 1. Correlation plots of the **A.** NRIR-based vs. true ES strains. **B.** NRIR-based vs. true infarct sizes

Investigating the degree of shear wave speed anisotropy in function of studied ventricular zone
Annette Caenen¹, Peter Hollender², Nick Botteman², Patrick Segers¹, Gregg Trahey², Mark Palmeri²
¹*IBiTech-bioMMeda, Ghent University, Ghent, Belgium*, ²*Biomedical Engineering, Duke University, Durham, NC, United States*
Background, Motivation, and Objective

From literature it is known that shear wave propagation in cardiac shear wave elastography (SWE) is affected by the changing myocardial fiber orientation across tissue thickness, leading to spatially varying group speeds. Additionally, the intrinsic cardiac fiber organization can alter depending on the studied ventricular region. Therefore, our objective was to quantify the degree of shear wave speed anisotropy in function of the analyzed ventricular position to determine its susceptibility to fiber orientation. To that end, we studied the shear wave anisotropy in the basal, mid-ventricular and apical zones of the left ventricular (LV) lateral free wall and interventricular septum (IVS).

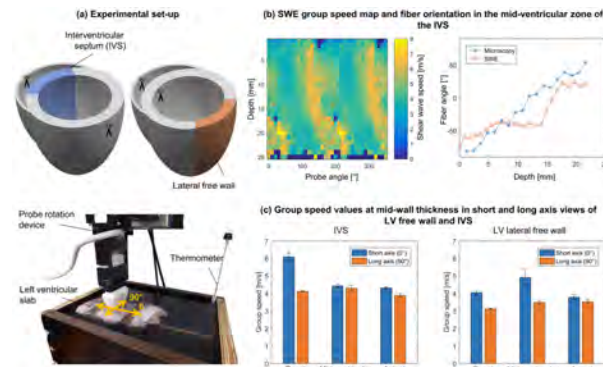
Statement of Contribution/Methods

Two porcine hearts were cut open to obtain rectangular slabs of the LV lateral free wall and the IVS (fig. a). A L7-4 transducer coupled to a Verasonics system was used to apply a pushing beam in the middle of the cardiac wall (f_0 of 6.9 MHz and Δt of 400 μ s) and to image shear wave propagation (ultrafast frame rate of 4.8 kHz). SWE acquisitions were performed while rotating the probe from -90° to 90° in steps of 10° (fig. a). Axial velocity data were processed with a time-of-flight method to estimate the depth-varying group speed. Assuming ellipsoidal group speed surfaces parallel to the cardiac wall allowed fiber orientation extraction at every depth.

The cardiac samples were cut with a Leica CM3050 S cryostat into slices of 300 μ m, and the anisotropic tissue structure of each 4th slice was analyzed under a Zeiss microscope. A quantitative description of the fiber anisotropy and orientation was obtained from the microscope image using an ImageJ plug-in, FibrilTool.

Results/Discussion

The shear wave anisotropy in the group speed map of the mid-IVS zone (left panel of fig. b) reflected well the myocardial fiber orientation (right panel of fig. b). Investigating typical transthoracic cardiac SWE views in fig. c, i.e. short and long axis views at mid-wall thickness, we clearly observe a higher shear wave speed in the long axis view than in the short axis view for all zones in both IVS (4.3-6.1 vs. 3.9-4.3 m/s) and LV lateral free wall (3.8-4.9 vs. 3.1-3.5 m/s). Furthermore, the mid-IVS and the apical lateral zone seem to be less susceptible to fiber orientation in the studied short (4.4 and 3.8 m/s, respectively) and long axis view (4.3 m/s and 3.5 m/s, respectively) of fig. c.



High frame rate imaging to assess myocardial contractility

Marta Orlowska¹, Aniela Monica Petrescu¹, Pedro Santos¹, Bidisha Chakraborty¹, João Pedrosa¹, Jens-Uwe Voigt¹, Jan D'hooge¹

¹Cardiovascular Sciences, KU Leuven, Leuven, Belgium

Background, Motivation, and Objective

Myocardial deformation imaging allows to assess regional myocardial function non-invasively. Although strain has been used extensively to quantify function, peak systolic strain rate (SR) is known to be less load dependent and more closely linked to intrinsic contractile function. Unfortunately, current deformation imaging approaches based on speckle tracking typically operate at ~60Hz and cannot estimate SR in a time resolved manner. This problem might be overcome by high frame rate (HFR) imaging approaches. The aim of this study was then to show: i) that HFR imaging allows to accurately assess myocardial SR; ii) that peak systolic SR allows to detect subtle changes in myocardial contractility.

Statement of Contribution/Methods

7 healthy volunteers were imaged at rest and during isometric exercise (i.e. handgrip) in an apical 4-chamber view using HD-PULSE, an experimental ultrasound system with 256 independent channels, equipped with a 3.5 MHz phased array using a sequence of 6 Diverging Waves transmitted from 21 elements sliding over the aperture. The channel data was captured and reconstructed offline using a compounding scheme. From the reconstructed RF images, velocity was computed using cross correlation (10 wavelengths x 11 lines kernel, 80% overlap, spline interpolation for subsample motion estimation and obtaining an estimate at every pixel). The obtained velocities were filtered with a 11x5 median filter and given as input to a 1D least-squares strain estimator with a 12mm estimation length. Next, a point placed in the apical, medial and basal part of the interventricular septum was manually tracked throughout the cardiac cycle to extract SR curves from which systolic (S') and diastolic (E' and A') SR peaks were extracted. Finally, a paired t-test was performed to test the significance of our findings.

Results/Discussion

The extracted SR curves at rest and during exercise showed a physiological pattern (Fig 1A). As expected, heart rate increased during exercise as did the atrial component to filling A' by 46% (Fig 1B). Importantly, peak systolic SR significantly increased during exercise by 14% (Fig 1B) pointing at an increased contractile status of the heart. These results show that HFR allows to assess segmental myocardial SR adequately and thus enables to detect subtle changes in regional myocardial contractility independently of loading conditions.

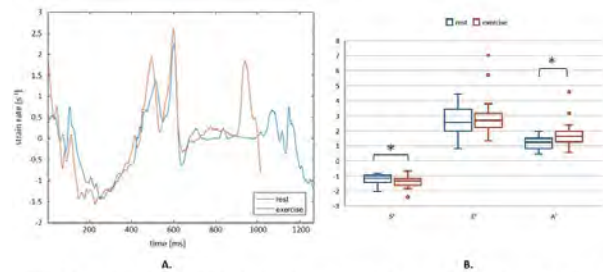


Figure 1. A. Example of obtained SR curve at rest and during isometric exercise. B. S', E' and A' measured in strain rates: * P<0,05

Imaging the contraction of mechanically supported ex vivo beating hearts

Louis Fixsen¹, Niels Petterson¹, Frans van de Vosse¹, Marcel Rutten², Richard Lopata³

¹Eindhoven University of Technology, Eindhoven, Netherlands, ²Biomedical Engineering, Eindhoven University of Technology, Eindhoven, Netherlands, ³Eindhoven University of technology, Netherlands

Background, Motivation, and Objective

In patients with a mechanical circulatory support (MCS) device, clinicians lack the tools (MRI) to monitor the condition of the heart due to metals in the body. Factors such as the maximum rate of pressure change in the left ventricle (dP/dt_{max}) and changes in contraction pattern are valuable in assessing cardiac function. These parameters have yet to be quantified in MCS patients. Ultrasound (US) strain imaging could enable the study of these effects. However, due to a high level of illness it is difficult to validate new methods in MCS patients. Therefore, in this study, 2-D US strain imaging was used to investigate the change in heart mechanics in left ventricular assist device (LVAD) supported hearts, with an isolated beating porcine heart platform.

Statement of Contribution/Methods

The *ex vivo* porcine hearts were implanted with Thoratec HeartMate II (n=2) and MicroMed DeBakey (n=2) LVADs, with pump inflow at the apex and outflow at the aorta. Healthy hearts (n=4, no LVAD) were included for comparison. The hearts were attached to a mock loop, re-perfused with oxygenated blood, resuscitated and paced at 120 bpm (PhysioHeart, LifeTec). Measurements at four time points were performed whilst the LVAD-supported hearts deteriorated from baseline condition (based on cardiac output). Radio-frequency US data were acquired (Esaote MyLab 70 US system, curved array transducer) at pump speeds from 0 (no outflow) to 10.5 krpm. Data were manually segmented and local radial (e_{rad}) and circumferential strain (e_{cir}) were estimated over each heart cycle. The unloaded 0 krpm initial geometry was used as an initial condition for all further pump speeds at each time point.

Results/Discussion

Figure 1a shows pump speed and circumferential strain against measured dP/dt_{max} in one heart. As the pump speed is increased, dP/dt_{max} reduces. A similar increase can be seen in the e_{cir} magnitude. This shows that circumferential strain estimated using US strain imaging can be related to dP/dt_{max} . Figure 1b shows spatial plots of time to peak strain around the left ventricle. As the pump speed is increased and heart condition degrades, regions of early and late contraction grow in size and magnitude. This is a first step in unravelling the interplay between pump-action and remaining cardiac function. Further work includes investigating these results using 3-D imaging, and in patients.

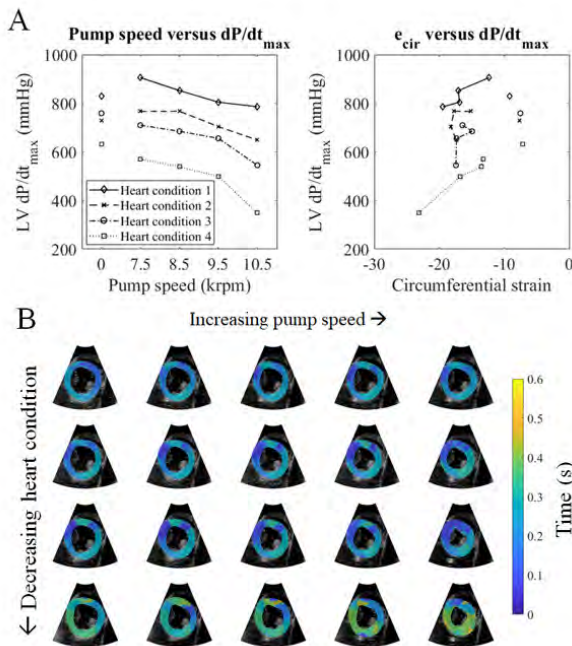


Figure 1: A: Left: Plots of pump speed versus left ventricular (LV) dP/dt_{max} in an *ex vivo*, left ventricular assist device supported heart. Right: Plots of circumferential strain versus LV dP/dt_{max} in the same heart. B: Ultrasound images of *ex-vivo* heart overlaid with spatial plots of time to peak strain.

Bi-directional Ultrasound Assessment of Nonlinear Mechanical Behavior of Physiologically Pressurized Artery in Both Normal and Hardening Conditions

Yahua Wang¹, Dan Ran¹, He Li¹, Wei-Ning Lee^{1,2}

¹*Electrical and Electronic Engineering, The University of Hong Kong, Hong Kong, Hong Kong*, ²*Medical Engineering Programme, The University of Hong Kong, Hong Kong*

Background, Motivation, and Objective

Ultrasound investigation of nonlinear arterial mechanical behavior on multiple directions in response to dynamic intraluminal pressure is scarce in literature. In this study, we present a bi-directional ultrasound elastographic imaging framework, which encompasses our in-house vascular guided wave imaging (VGWI) and ultrasound strain imaging (USI), to quantify arterial wall deformation and stiffness simultaneously. Strain-stiffness loops of the physiologically pressurized artery over multiple cycles are further proposed to assess nonlinear behavior of the artery in two principal directions of a porcine aorta *in vitro* before and after hardening.

Statement of Contribution/Methods

One excised porcine aorta prior to and after 2-minute immersion in a 36.5% formaldehyde solution (Sigma-Aldrich®) was examined. The formaldehyde-treated aorta mimicked arterial hardening. The aorta (with a 17% longitudinal pre-stretch) was pressurized under sinusoidal fluid flow at 1 Hz by an AccuFlow-Q® flow pump with cyclic intraluminal pressure ranging from 60 to 125 mmHg. A Verasonics® Vantage 256 system with an L7-4 linear array probe (5.2MHz) mounted on a Newport® rotation stage was used for bi-directional VGWI and USI data acquisitions at a frame rate of 8000 Hz for 3 consecutive flow cycles, each of which had 12 imaging events at equally spaced time intervals. Coherent plane wave compounding with three steering angles (-4°, 0, 4°) was performed. Longitudinal (μ_L) and circumferential (μ_T) shear moduli were estimated by VGWI, and radial strain (ε_r) was estimated by USI.

Results/Discussion

The magnitudes of ε_r estimated for the fresh aorta were slightly larger than those for the hardened aorta (Fig. 1). Both the μ_L and μ_T increased nonlinearly with ε_r magnitude, but more drastic changes in $\mu_T - \varepsilon_r$ loops indicated that $\mu_T - \varepsilon_r$ loops were more sensitive to the arterial condition than $\mu_L - \varepsilon_r$ ones. Both $\mu_L - \varepsilon_r$ and $\mu_T - \varepsilon_r$ loops for hardened aorta exhibited an upward shift, an increased slope, and a greater loop area. Good repeatability was also achieved as evidenced by the three consecutive cycles, especially for the $\mu_L - \varepsilon_r$ loops. Our results show that the proposed framework and the strain-stiffness relationships could 1) evaluate nonlinear arterial mechanical behavior under dynamic loading in two principal directions and 2) differentiate hardening from normal conditions of the aorta.

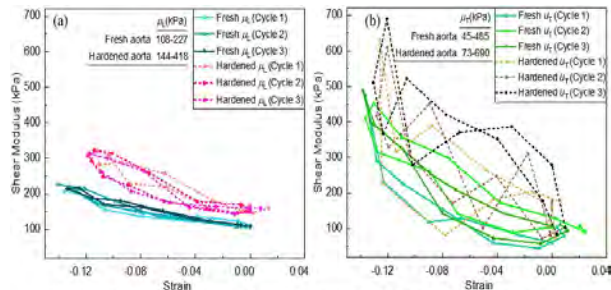


Fig. 1. ε_r - μ loops over three consecutive flow cycles in the (a) longitudinal and (b) circumferential directions of the aorta before (solid lines) and after (dash lines) hardening.

In Vivo Pulse Wave Imaging for Mice Carotid Artery Based on 40 MHz Array Ultrafast Ultrasound Vector Velocity Estimation
Yi-Jie Wang¹, Hsin Huang¹, Chih-Chung Huang¹
¹*National Cheng Kung University, Taiwan*
Background, Motivation, and Objective

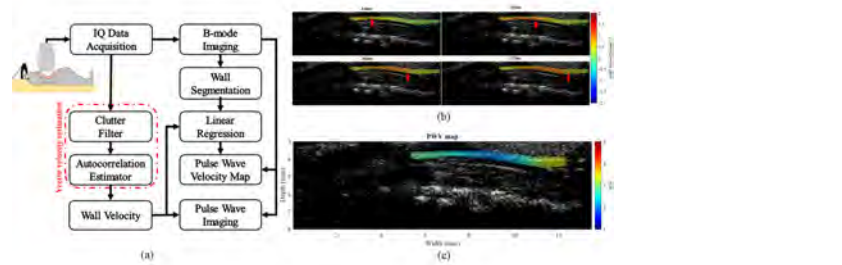
Pulse wave velocity (PWV) has been considered as a indicator for evaluating arterial stiffness. Pulse wave imaging (PWI) was also proposed for visualization of the PWV along the vessel wall for stiffness measurement by normalized cross-correlation (NCC). For example, the 40MHz single-element transducer system was used to measure the atherosclerotic artery of mice. Since the PWV is fast, the high frame rate retrospective imaging is needed, which was obtained by ECG gating. However, the retrospective imaging is affected by heart arrhythmia which may lead to the disorder of the time sequence for ultrasound imaging. In addition, use of NCC to track wall motion may neglect the longitudinal motion as well as that NCC is limited by small arterial displacement estimation. Therefore, the vector velocity estimation method based on a 40 MHz ultrafast ultrasound imaging was developed for PWI of mice in this study.

Statement of Contribution/Methods

Fig. 1(a) shows the block diagram of PWI procedure in this study. IQ data from the mice carotid artery was acquired by Vantage 256 (Verasonics) with a 40 MHz array transducer (MS550D). Three title plane waves with angles were transmitted to mice for acquiring the compounding image of carotid artery at a high frame rate of 5 kHz for 0.5 s. The motion velocity from the wall of carotid artery was estimated by vector flow velocity algorithm. After a segmentation process for anterior wall, the vector velocity data were plotted as a function of time on the B-mode image. A piecewise linear regression method was used to calculate the PWV which defines as the slope between travel time and motion speed.

Results/Discussion

Fig. 1(b) shows PWI from mice carotid artery at different times. The PW propagation was observed obviously along the vessel wall. The red arrows indicate the propagation of the PW. The PWV value overall of the carotid artery was 2.18 m/s and the correlation coefficient for linear regression was 0.98. Fig. 1(c) shows the piecewise PWV of the mice carotid artery. An increase of the PWV values around the bifurcation, which may be due to the narrowing of the carotid artery into external carotid artery. All experimental results show that high frequency ultrasound vector velocity estimation exhibits a good sensitivity for PWI in small animal applications.



High Spatio-Temporal Resolution Arterial Pulse Wave Assessment Using Multiplane Wave Sliding Decoding Sequence

Jinbum Kang¹, Yangmo Yoo^{1,2}

¹Electronic Engineering, Sogang University, Seoul, Korea, Republic of, ²Biomedical Engineering, Sogang University, Seoul, Korea, Republic of

Background, Motivation, and Objective

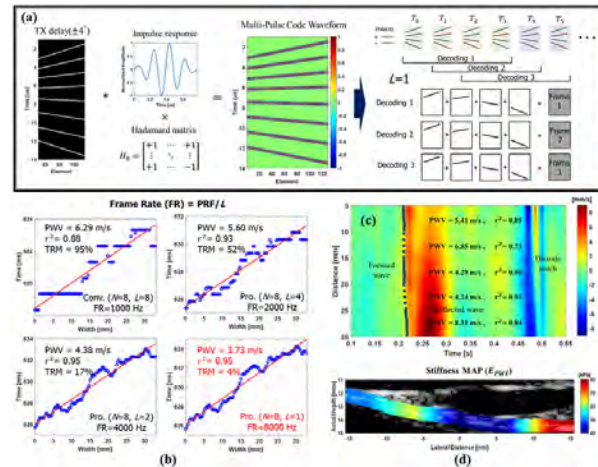
Higher arterial stiffness is associated with the increased risk of cardiovascular events, such as myocardial infarction and stroke. The recently-introduced pulse wave velocity (PWV) measurement using ultrafast ultrasound imaging has been introduced as a useful noninvasive technique for a surrogate marker of arterial stiffness. However, ultrafast ultrasound imaging still presents challenges due to an inherent tradeoff between temporal resolution and image quality. To overcome this constraint, we newly propose an improved arterial pulse wave evaluation method based on multiplane wave sliding decoding sequence.

Statement of Contribution/Methods

As illustrated in Fig. 1(a), in the proposed method, multiple delay-encoded multiplane waves are emitted and a decoding is sequentially conducted using a sliding window with a step size (L) to create high SNR scanline data without sacrificing frame rates. Therefore, it can achieve significant improvements in temporal resolution compared to the conventional plane wave and multiplane wave imaging (e.g., frame rate = PRF at $L=1$). Based on the proposed method, arterial wall motion to measure PWV can be more accurately estimated and it can more adequately sampled the propagation of the pulse wave (> 4 m/s). To evaluate the performance of the proposed method, a fabricated soft vessel phantom and *in vivo* carotid artery were evaluated, and channel data were obtained with an ultrasound research platform (Vantage, Verasonics Inc.) with multiplane wave transmission ($N=8, \pm 8^\circ, \text{PRF}=8 \text{ kHz}$) using a L7-4 linear array transducer. To compute Young's modulus (E), the pressure change was also measured in the phantom study (PWV = 3.88 m/s and $E = 0.18 \text{ MPa}$).

Results/Discussion

In the phantom study, both the PWV and the coefficient of determination values (r^2) were more accurately measured with the proposed method ($L=1$), compared to the conventional multiplane wave imaging, i.e., 3.73 m/s (0.16 MPa) vs. 6.29 m/s (0.46 MPa), respectively, as shown in Fig. 1(b). In the *in vivo* study, a regional PWV can be measured with very high spatio-temporal resolution as shown in the Fig. 1(c) and a stiffness mapping (E_{PWV}) was successively derived by the measured regional PWV as depicted in the Fig. 1(d). From the studies, the proposed method showed improved PWV measurement, thus, it can be used as a more accurate and reliable assessment tool for focal arterial stiffness.



P1-A7 - New Methods and Techniques for Imaging

Kairaku (posters 1)

Tuesday, October 23, 9:30 AM - 4:00 PM

Chair: **Hiroshi Kanai** Tohoku University

P1-A7-1

Characterization of B-mode image quality using lag-one coherence (LOC)

Will Long¹, Nick Bottenuis¹, Rendon Nelson², Gregg Trahey^{1,2}

¹Biomedical Engineering, Duke University, Durham, NC, United States, ²Radiology, Duke University, Durham, NC, United States

Background, Motivation, and Objective

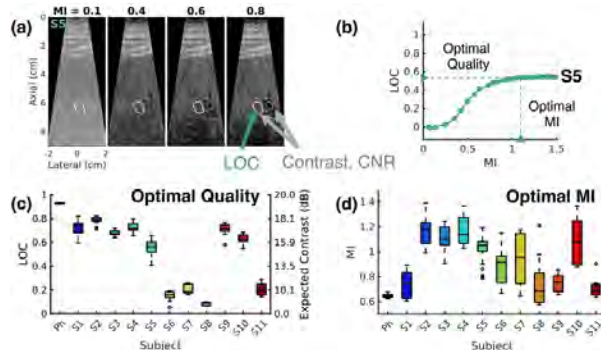
Adaptive ultrasound systems designed to automatically adjust system controls present a promising solution to mitigate the user-dependence of ultrasound imaging. However, the development of such systems has been stymied by the lack of suitable metrics for providing reliable image quality feedback. To address this challenge, we are investigating the use of spatial coherence, specifically the lag-one coherence (LOC), as a single region-of-interest (ROI) measure of thermal noise and acoustic clutter. The objectives of this work are to introduce LOC as an ultrasonic image quality metric and demonstrate its clinical feasibility in the adaptive selection of acoustic output.

Statement of Contribution/Methods

Theory was derived to relate LOC to the conventional metrics of contrast and contrast-to-noise ratio (CNR) for the case of spatially incoherent noise. Simulation and phantom experiments were performed to validate this theory and compare the sensitivity and variance of LOC and conventional metrics for targets with known contrast under varying levels of channel noise. To examine the feasibility of acoustic output selection using LOC, custom sequences were implemented on a Verasonics system to acquire channel data for a series of harmonic images formed with mechanical index (MI) values from 0.05 to 1.51 (34 images in 1.7 s). Variable MI data were collected from liver in 11 subjects and used to compute matched measurements of contrast, CNR, temporal correlation, and LOC.

Results/Discussion

Simulation and phantom results agree with theory and reveal lower variability in measurements of LOC compared to contrast and CNR for a range of clinically relevant noise levels. For acquisitions in the liver, this translates to higher monotonicity in LOC with changes in MI compared to matched measurements of contrast and CNR in 88.6% and 85.7% of acquisitions, respectively. Under conditions with minimal thermal noise, LOC is well-correlated with contrast ($r=0.74$) and CNR ($r=0.66$) when measuring acoustic clutter. As shown in the figure, high repeatability in measurements of LOC across different acoustic windows and ROIs provide reliable characterization of the maximum image quality (c) and the MI needed to achieve maximum image quality (d) in each subject. Results demonstrate feasibility in acoustic output selection using LOC and its application for in vivo image quality assessment.



Receive angle steering and clutter reduction for imaging the speed-of-sound inside large blood vessels
Maju Kuriakose¹, Jan-Willem Muller², Patrick Stahli¹, Martin Frenz¹, Michael Jaeger¹
¹*Institute of Applied Physics, University of Bern, Bern, Switzerland*, ²*Eindhoven University of Technology, Netherlands*
Background, Motivation, and Objective

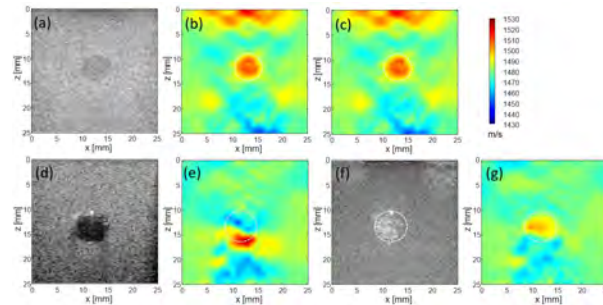
Computed ultrasound tomography in echo-mode (CUTE) images the speed-of-sound (SoS) of tissue using echo ultrasound (US): The phase shift of echoes when varying the ultrasound transmit (Tx) angle is measured in a spatially resolved way and related to the distribution of the SoS. A promising application is in angiology, to assess atherosclerotic plaque rupture risk via the dependence of the SoS on plaque composition. The challenges are: (1) Arterial flow leads to decorrelation of blood echoes in-between successive Tx angles. (2) Surrounding tissue clutter obscures blood echoes. Conventionally, both result in phase noise and SoS artifacts, which inhibits a proper identification of the plaque's SoS. Our objective was to adapt CUTE for solving this problem.

Statement of Contribution/Methods

Following modifications have been made: (1) Echo phase shift is measured as function of receive (Rx) as opposed to Tx angle. This allows to reduce the number of plane wave acquisitions, minimizing flow-related echo decorrelation. (2) The acquisition sequence is repeated at time intervals that can be chosen such that subtraction of the resulting signals removes stationary clutter but highlights moving blood echoes.

Results/Discussion

The equivalence of Tx and Rx CUTE was investigated in a phantom containing a cylindrical inclusion with uniform echogenicity (Fig. a, B-mode US). Conventional Tx CUTE reveals the elevated SoS inside the cylinder (Fig. b). The Tx steering range was -25° to 25° for phase tracking, and the Rx aperture was -5° to 5° . Correspondingly, Rx CUTE was based on 21 plane-wave acquisitions spanning a $[-5^\circ:0.5^\circ:5^\circ]$ Tx range, and tracking was performed in Rx. The resulting SoS image (Fig. c) is identical to Fig. b, demonstrating the equivalence. In a flow phantom mimicking the carotid (Fig. d, B-mode US), this high-quality (HQ) Rx CUTE still leads to flow and clutter artefacts in the SoS image (Fig. e). The Tx angle range was thus further reduced to $[-5^\circ:2.5^\circ:5^\circ]$ (5 acquisitions), and clutter was removed by the subtraction technique, resulting in well-correlated vessel echoes (Fig. f, B-mode US). These echoes were combined with the HQ Rx-CUTE data from outside the vessel, to obtain a final image with an improved delineation of vessel SoS (Fig. g). In conclusion, our results suggest that SoS imaging is feasible inside large blood vessels, which is a prerequisite to image plaque.



Computationally Efficient Spatially Variant Deconvolution in Ultrasound Imaging

Mihai Florea¹, Adrian Basarab², Denis Kouamé², Sergiy Vorobyov¹

¹Signal Processing and Acoustics, Aalto University, Finland, ²IRIT, University of Toulouse, Toulouse Cedex, France

Background, Motivation, and Objective

Ultrasound (US) images have limited spatial resolution that can be improved in post-processing by deconvolution, based on the hypothesis that RF images can be modeled by 2D deconvolution of the tissue reflectivity function (TRF) and the system PSF. For computational reasons, most of existing methods, except a few very recent attempts, consider the PSF spatially invariant. However, this assumption is violated in practice for any emission-reception scheme. We propose a computational efficient method of deconvolving US images able to account for point-wise spatial variability of the PSF.

Statement of Contribution/Methods

The contributions of this paper are: i) to establish an efficient matrix-free spatially variant US image formation model, ii) to express the adjoint operator (used by proximal splitting optimization algorithms) in a form of equal complexity as the forward model operator, iii) to address the resulting inverse problem using a recent computationally efficient optimization technique (with a convergence rate superior to algorithms such as FISTA). Interestingly, while standard deconvolution methods consider circular boundary conditions (without any physical justification but to exploit the diagonal matrix forward model in the Fourier domain), the proposed spatially variant convolution model can incorporate any padding operator to handle the boundary conditions (e.g., circular, replicate, symmetric, and zero-padding), without increasing computational complexity.

Results/Discussion

Our method was validated on simulated data with TRF ground truth knowledge. A particular case for our model consists in the axially variant laterally invariant PSF case which accurately simulates the pulse-echo sequence. We generated a collection of PSFs, one for each depth, and a TRF based on data from the Visible Human Project. Fig. 1 shows the TRF, PSF variation and the US image. The results show the importance of taking into account the variability of the PSF in the inversion process. The capacity of the proposed method to restore high frequencies suppressed by the PSF can be appreciated in the zooms in Fig. 1. Aside from this example, our framework is capable of modeling virtually any US acquisition, and is particularly suitable for ultrafast imaging. Preliminary results on diverging waves support our theoretical findings.

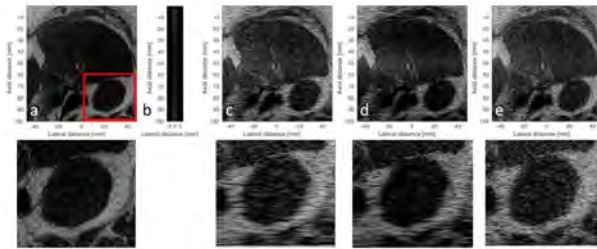


Fig. 1 Illustrative result showing the resolution improvement obtained with spatially variant image deconvolution compared to standard deconvolution. 1st row: (a) simulated TRF, (b) PSF examples for 20 depths, (c) RF image, (d) spatially-invariant deconvolution results, (e) deconvolution result with proposed method. 2nd row: zooms corresponding to the red rectangular in (a).

Development of extended field of view, extended aperture and 3D spatial compounding of 3D images to improve ultrasound-based localization of the uterus for radiotherapy treatment

Sarah Mason¹, Ingrid White², Tuathan O'Shea², Helen McNair², Matthew Blackledge¹, Susan Lalondrelle², Jeffrey Bamber¹, Emma Harris¹

¹Institute of Cancer Research, United Kingdom, ²Royal Marsden Hospital, United Kingdom

Background, Motivation, and Objective

Variable image quality and small field of view make it challenging to use US to localize the uterus during radiotherapy. As a potential solution, a novel method using optical technology to track a 3D probe was developed to spatially-compound in 3D and with an extended 2D aperture and extended 3D field of view (FOV). Image quality was evaluated as a function of the number of US volumes used to create a compounded image in a phantom and *in vivo*.

Statement of Contribution/Methods

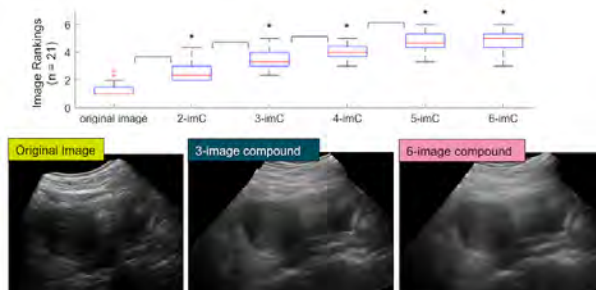
3D US images were acquired from different positions in an US quality assurance phantom (7 images), and transabdominally of the uterus from four volunteers (6 images/imaging session/volunteer, 21 total sessions), and from four cervical cancer patients (4 images/fraction/patient; 15 total fractions). Images were resampled onto a common frame of reference. Compounded images (imCs) were created by averaging 2, 3, 4, 5, 6 or 7 individual images. Phantom: Differences in (1) contrast-to-noise-ratio (CNR) in four grayscale targets and (2) spatial resolution were determined between the non-compounded image and each imC using ANOVA. *In vivo*: Three observers independently ranked randomized sets of images (noncompounded and imCs) for image quality of the uterus (1 representing poorest image quality). A Wilcoxon-signed-rank test was used to measure differences in mean rank (MR) of 3 observers between the compounded and non-compounded images.

Results/Discussion

Phantom: Compounding increased the CNR significantly, by 35% to 104%, depending on the number of individual images in the IMC and grayscale target assessed. Spatial resolution was not significantly altered, compared with non-compounded images.

In vivo: The non-compounded image had significantly poorer MR than any imC, with mean [range] MRs of 1.3 [1 – 2.7] (volunteers, see figure) and 1.6 [1 – 2.3] (patients). MR increased significantly with increasing number of 3D US images used in each ImC, up to 4.7 [3.3- 6] for imCs comprised of 5 US volumes and 3.1 [2 – 3.7] for imCs comprised of 3 US volumes for volunteers and patients, respectively.

3D extended aperture spatial compounding improves US image quality compared with non-compounded images in both the phantom and *in vivo*.



A new adaptive frequency compounding method based on a saliency map
Sunyoung Oh¹
¹*SOGANG UNIVERSITY, SEOUL, Korea, Republic of*
Background, Motivation, and Objective

Ultrasound imaging has an advantage of spatial resolution over other medical imaging modalities. However, its clinical usefulness is sometimes limited due to speckle noise, which leads to degradation in contrast resolution. Frequency compounding (FC) is the one of speckle reduction methods has been widely used, but it is challenging to determine the blending ratio between different frequency components to achieve improved speckle reduction while preserving contrast resolution.

Statement of Contribution/Methods

In this paper, a new FC method, in which weighting factors between frequency components are dynamically updated depending on a saliency map, is proposed. In the proposed adaptive frequency compounding method (i.e., AFC), a saliency map is first generated based on intensity information of each frequency component image by considering that intensity changes are smaller in speckle regions compared to feature regions. Then, the regions are divided depending on the depth, and the weighting factor minimizing the variance of speckle region is determined by minimizing root mean square (RMS) error as follows:

$$\theta = -\sum_k S_{fb} h_k (S_{fb}^* h_k - S_{fg} h_k) / \sum_k (S_{fb}^* h_k - S_{fg} h_k)^2$$

Moreover, the image quality of the feature region can be further improved by using frequency-dependent characteristics, such as spatial resolutions and penetration. For examples, taking advantage of the fact that low frequency images are good in penetration, find the region where the depth is deep and the saliency is low in high frequency image whereas high in low frequency image, and give the weighting factor of low frequency image heavier. In this way, it is possible to maintain the feature signal from the deep area even there exists a signal loss due to attenuation in high frequency image.

Results/Discussion

To evaluate the performance of the proposed ADA method, the phantom study was conducted. In the phantom study, beamformed RF data were captured by using a flexible research ultrasound system (Vantage 128, Verasonics Inc.) and processed in off line. For quantitative analysis, contrast-to-noise ratio (CNR) and speckle signal-to-noise-ratio (SSNR) were measured. As shown in Figs. 1(a) and 1(b), the low and high frequency component images shows higher SNR and spatial resolution with low contrast due to speckles. On the other hand, the proposed ADA method showed improved CNR and comparable SSNR, compared to the conventional FC method (CON), i.e., 2.52 and 5.05 vs. 0.58 and 5.05, respectively. These results indicate that the proposed adaptive frequency compounding method can improve image quality by effectively reducing speckles.

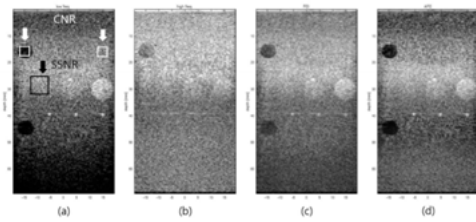


Figure. (a) low freq. image (b) high freq. image (c) Conventional FC (d) Proposed method (new Adaptive-FC)

| | (a) | (b) | (c) | (d) |
|------|------|------|------|------|
| CNR | 0.11 | 0.66 | 0.58 | 2.52 |
| SSNR | 3.55 | 4.21 | 5.05 | 5.05 |

Figure 1. Ultrasound B-mode images with (a) low frequency component, (b) high frequency component, (c) conventional frequency compounding, and (d) adaptive frequency compounding.

Table 1. Measured contrast-to-noise ratio (CNR) and speckle signal-to-noise ratio (SSNR).

Transcranial Imaging Using Coded Multiple Transmit Focus Wavefront Synthesis
Parker O'Brien¹, Hasan Diabat¹, Dalong Liu¹, Emad Ebbini¹
¹*Electrical and Computer Engineering, University of Minnesota Twin Cities, Minneapolis, MN, United States*
Background, Motivation, and Objective

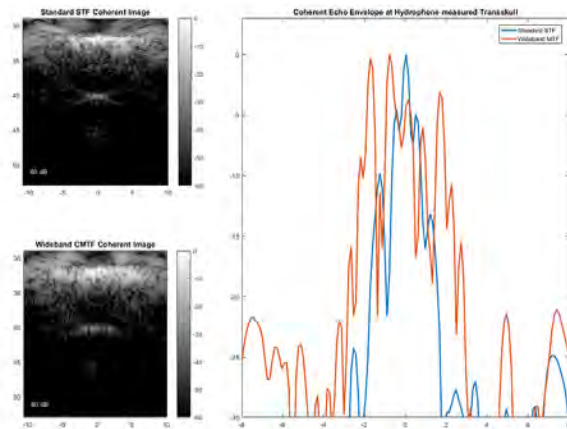
Single transmit focus (STF) imaging is a useful mode for guidance and monitoring of therapeutic procedures using FUS, including transcranial applications. However, STF's small FOV can limit its utility in applications where the target region undergoes significant lateral motion and deformation. We have recently introduced a wavefront synthesis method for generating coded multiple transmit focus (cMTF) wavefronts that extend the FOV to allow 2D/3D tracking of tissue targets of FUS therapy. MTF wavefronts still provide high focusing gain at selected points in the target region while limiting the transmit energy outside the region of interest. The goal of this paper is to assess the robustness of cMTF synthesis in the presence of strongly scattering obstacles such as the skull in tFUS applications.

Statement of Contribution/Methods

A 3.2 MHz, concave (40 mm roc) DMUA transducer 32 elements was used for generating STF and cMTF patterns in three settings: degassed water with and without skull obstacle, and transcranially *in vivo* under approved protocol. In the first two settings, a needle hydrophone (Onda, HNP-200) served as a target and for measuring the transmitted STF and cMTF wavefronts in the target region. MTF wavefronts were synthesized to focus at 5 points at $(0, \pm 0.7, \pm 1.4)$ mm from the DMUA geometric center at 40 mm axially. Pulse-echo DMUA channel data were collected synchronously with the hydrophone at each focus location. For the water and trans skull experiments, received echoes were compared directly with the hydrophone measurements pre- and post-beamforming. For the *in vivo* experiments, STF and cMTF images were formed and compared for a variety of coded wavefronts.

Results/Discussion

Comparison between hydrophone and echo data in water and trans skull have confirmed the desired waveforms were transmitted to the focus locations for each of the cMTF patterns. More importantly, STF and cMTF images confirmed the feasibility forming coded wavefronts trans skull that experienced the same level of aberration as STF wavefronts. Fig. 1 gives an example of coherently summed images from the 5 hydrophone positions for the STF and broadband cMTF wavefronts. The line plots show the lateral echo profile from STF (blue) and wideband cMTF (red), which were consistent with synthesized wavefronts. Skull aberrations affected both STF and cMTF to the same degree *in vitro* and *in vivo*.



Shear shock wave focusing in human skull phantom: observations with high-frame rate ultrasound imaging and matched simulations

Bharat Tripathi¹, Sandhya Chandrasekaran², David Espindola³, Gianmarco Pinton⁴

¹Joint Dept. of Biomedical Engineering, University of North Carolina-Chapel Hill, Chapel Hill, NC, United States, ²North Carolina State University, United States, ³Biomedical engineering, University of North Carolina at Chapel Hill, NC, United States, ⁴Joint department of biomedical engineering, University of North Carolina at Chapel Hill and North Carolina State University, NC, United States

Background, Motivation, and Objective

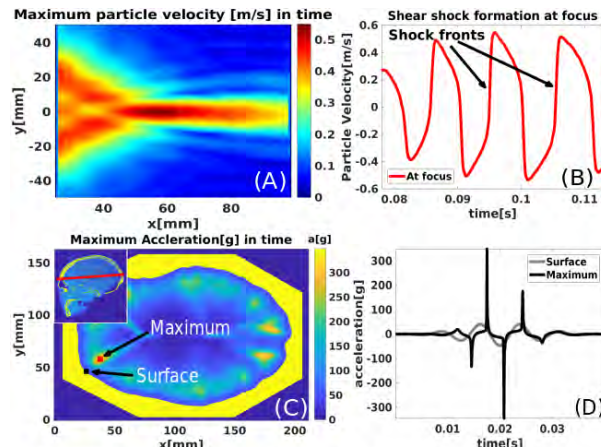
We have recently observed that smooth low acceleration shear waves develop into destructive high acceleration shocks as they propagate in fresh ex vivo porcine brain. We hypothesize that the local amplification of acceleration at the shear shock front can damage neurons and may be responsible for a wide range of traumatic brain injuries. Unlike compressional waves, shear shock waves are relatively unstudied and there are currently no measurements or simulation tools for it, in the human head. Therefore, new quantitative imaging tools along with new theoretical models for nonlinear shear waves propagation in soft tissue with a high degree of anatomical fidelity are necessary to understand the injury biomechanics in humans.

Statement of Contribution/Methods

We present 1) a system of conservation laws modeling polarized nonlinear shear full-wave propagation 2) a generalized Maxwell body describing the arbitrary power law attenuation in soft tissue, 3) a high-order piecewise parabolic method (PPM) that solves 1) and 2). It is shown that the nonlinear solver satisfies the Rankine-Hugoniot theoretical conditions, and that the relaxation mechanisms accurately model a wide range of arbitrary fractional-power laws. This 2D solver is then validated experimentally using our high frame-rate (6200 fps) ultrasound imaging method designed for shock wave tracking. A 3D printed human skull, i.e. a complex geometry, with brain-mimicking gelatin is used to study shear shock waves focusing with high anatomical fidelity.

Results/Discussion

Particle velocity maps from the shear shock focusing experiment (fig-A), and its waveform at the focus (fig-B), demonstrates that steep shock fronts (30g to 180g) are formed near the focus. This experiment is then used to validate the numerical solver. The simulations, based on human CT skull morphology (fig-C) show a sub-wavelength focusing of shear shocks in the brain, as predicted by experiments. The local acceleration at the focus increases (30g to 300g) by a factor of 10 compared to the surface acceleration (fig-D) due to focusing and nonlinear effects. In conclusion, the validated nonlinear shear wave PPM solver is capable of describing polarized shock wave physics in the brain. It can be used to understand the contribution of this recently discovered phenomenon to TBI by capturing complex scenarios that are not realizable *in vivo* in humans.



(A) Experimental results of focusing of shear shock waves in gelatin; (B) Waveforms at the point close to the plate and that at the focal position, a steep shock profile can be observed; (C-D) Simulations of shear shock formation in domain obtained from a cross section of a human skull, with physical parameters of brain showing the amplification of local acceleration more than 300g (D).

3D Motion Correction for Volumetric Super-Resolution Ultrasound Imaging

Sevan Harput¹, Kirsten Christensen-Jeffries², Jemma Brown², Jiaqi Zhu¹, Ge Zhang¹, Robert Eckersley², Chris Dunsby³, Mengxing Tang¹

¹Department of Bioengineering, Imperial College London, London, United Kingdom, ²Department of Biomedical Engineering, School of Biomedical Engineering and Imaging Sciences, King's College London, London, United Kingdom, ³Department of Physics and Centre for Pathology, Imperial College London, London, United Kingdom

Background, Motivation, and Objective

Localization based super resolution ultrasound (SR US) imaging has two key limits on the maximum achievable resolution. Firstly, the SNR of the imaging system and processing method and secondly error introduced by motion. For 2D imaging, motion correction (MC) is impossible in the elevational direction in presence of out-of-plane motion. For 3D imaging with plane waves, the motion can be compensated in every direction thanks to the availability of full volumetric information at each acquisition. In this study, an extension of two stage MC method was proposed in 3D and its accuracy was evaluated [1]. The capability of the proposed method was demonstrated with a 3D SR US simulation to compensate for handheld probe motion.

Statement of Contribution/Methods

A 3.7 MHz 512-element 2D matrix probe was used to acquire 3000 volumes/second driven by 2 ULA-OP256 systems. 9 angle plane wave compounding was performed within a range of ± 10 degrees. To demonstrate the MC, two 100 μm wires arranged in a cross shape were imaged with a handheld probe.

A SR simulation environment was created by combining tissue echoes generated in Field II and microbubble signals generated with the Marmottan model. Microbubble flow in a Y and S shaped microvessel was simulated with motion extracted from the handheld measurements. Tissue signal was removed by using background subtraction for the MC case. SVD was used to remove tissue signal for the case with motion.

Results/Discussion

Fig A shows the motion of the handheld probe while imaging the wire phantom over 300 ms. The absolute motion was over 50 μm , which is larger than typical localization precisions achieved for SR imaging. Fig B shows the elevational PSF measured from a single volume without motion as 840 μm , from 100 volumes with motion as 893 μm , and from 100 volumes with MC as 856 μm .

After verifying the feasibility of the 3D MC experimentally, the method was demonstrated on 3D SR US imaging simulations. Fig C shows the simulated microvascular structure, the SR image with motion and with MC, respectively. The average localization error was reduced from 49 to 32 μm , and the maximum error was decreased from 250 to 160 μm after MC. The S shaped microvessel with sub-wavelength spacing was recovered with 3D MC.

[1] Harput et al., Two-Stage Motion Correction for Super-Resolution Ultrasound Imaging in Human Lower Limb, IEEE Trans Ultrason Ferroelectr Freq Control 65(6), 2018.

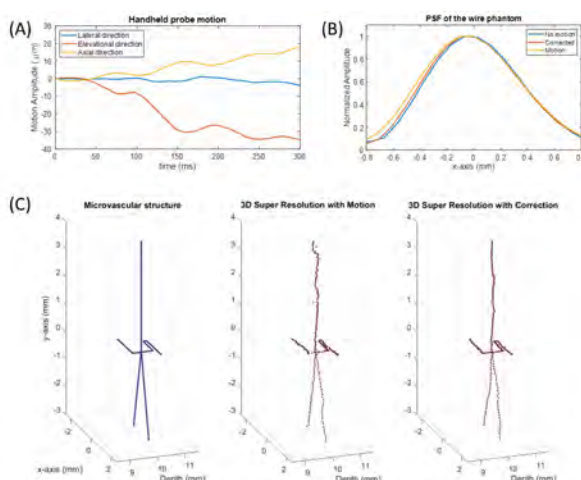


Figure (A) Motion of the handheld probe in the axial, lateral and elevational directions over a duration of 300 ms. (B) Elevational PSF of a wire phantom measured with high frame rate 3D US is plotted without motion (from a single volume), with motion, and with motion correction. (C) Three subplots show the shape of the simulated microvascular structure, the SR image with motion, and the SR image with motion correction, respectively.

A Harmonic Motion Imaging (HMI) clinical system for detection and characterization of in-vivo human breast tumors – Initial feasibility

Niloufar Saharkhiz¹, Yang Han¹, Alireza Nabavizadeh¹, Richard Ha², Elisa Konofagou^{1,2}

¹Department of Biomedical Engineering, Columbia University, New York, NY, United States, ²Department of Radiology, Columbia University, New York, NY, United States

Background, Motivation, and Objective

Breast cancer is associated with alterations in the mechanical properties of breast tissues. Although several methods have been proposed for breast cancer imaging, a need for low cost, non-ionizing, non-invasive imaging technique with high sensitivity still remains. Harmonic Motion Imaging (HMI) is an ultrasound-based elasticity imaging technique that generates localized harmonic motions at the focal region and therefore, measures the mechanical properties of the underlying tissue. Previous studies from our group have demonstrated the capability of HMI to characterize and differentiate relative stiffness in post-surgical lumpectomy and mastectomy breast specimens. The objective of this study is to assess the potential of HMI as a complementary method for in-vivo human breast tumor detection and differentiation.

Statement of Contribution/Methods

The HMI clinical setup consists of a 7.8 MHz phased array imaging probe co-aligned through the central opening of a 4 MHz FUS transducer. A robotic arm was controlled by a PC workstation to move the HMI setup in a point-by point 1-D raster scan with a step size of 3 mm and a total scan duration of 2 minutes. The scan was performed on a 53-year-old female patient diagnosed with fat necrosis. The FUS exposure lasted 0.08 seconds at each point, resulting in 4 cycles of 50 Hz amplitude-modulated oscillations at the focal region during which 80 RF frames were acquired using a Verasonics system at 1 kHz pulse repetition frequency. The axial displacements were estimated using 1-D cross correlation with a 0.98 mm window and 95% overlap. The induced peak-to-peak displacements were used to reconstruct the 15×50 mm² HMI displacement map.

Results/Discussion

HMI displacements were averaged within a 5 mm diameter circular region of interest resulting in 1) $2.38 \pm 0.46 \mu\text{m}$ with a maximum of $3.16 \mu\text{m}$ within the tumor area, and 2) $3.70 \pm 1.09 \mu\text{m}$ with a maximum of $6.63 \mu\text{m}$ within the normal tissue. These findings indicate that the mass was twice stiffer than the peripheral tissue (Figure 1) and the measured size was correlated with B-mode. In this study, HMI was shown to be capable of mapping relative stiffness in breast cancer patients for the first time. A clinical study is currently ongoing to assess whether HMI can differentiate and characterize tumor types based on the displacements and further optimize the clinical HMI system for real-time acquisition.

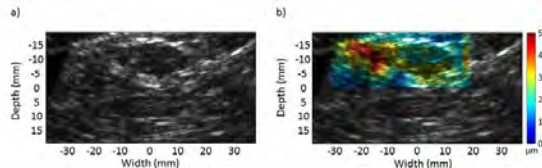


Figure 1. a) B-mode image and b) overlaid image (B-mode+HMI displacement map) of a patient with breast mass. The displacement values are displayed with a color map where red shows high displacement (soft) and blue shows low displacement (stiff).

Quantitative analysis of uterine motion outside pregnancy by dedicated ultrasound speckle tracking

Federica Sammali¹, Celine Blank², Yizhou Huang¹, Nienke Kuijsters², Chiara Rabotti¹, Benedictus Schoot², Massimo Mischi¹

¹Eindhoven University of Technology, Netherlands, ²Catharina Hospital Eindhoven, Netherlands

Background, Motivation, and Objective

Infertility is a large-scale problem concerning an increasing number of women. For this reason, assisted reproductive technologies are rapidly developing. However, their success rate remains below 30%. There is evidence that fertilization outcome is affected by uterine motion, but solutions for quantitative analysis of uterine motion are lacking. Here we present a dedicated method for quantification of uterine motion and strain by B-mode transvaginal ultrasound (TVUS).

Statement of Contribution/Methods

Motion analysis was implemented by speckle tracking based on block matching using sum of absolute differences as a matching criterion. Prior to the analysis, the speckle-size was regularized by Wiener deconvolution and Singular Value Decomposition (SVD) filtering used to enhance the uterine motion. The SVD filter and speckle tracking parameters were first optimized *ex vivo* by a dedicated setup and then translated *in vivo*. *In vivo*, the speckle tracking was accelerated by a diamond search (DS) strategy. Robustness to speckle decorrelation was improved by taking the median shift of surrounding blocks. The method feasibility was tested on 9 healthy women. An ultrasound scanner WS80A (Samsung) with transvaginal probe V5-9 was employed for the acquisition. 3-min TVUS scans were performed on every woman at four selected phases of the menstrual cycle, namely, menses, late follicular (LF), early luteal (EL), and late luteal (LL) phase. For each image sequence, four sites where selected around the internal lining of the uterus (Fig. 1a) and tracked over time to derive distance and strain signals along the longitudinal and transversal direction of the uterus (Fig. 1b). Frequency and amplitude features were extracted from these signals and evaluated for their ability to discriminate between the different selected phases, which are known to show different motion characteristics.

Results/Discussion

Among the considered features, median frequency and contraction frequency showed significant difference between menses and LF phase as well as between LF and LL phase. These promising results suggest our proposed method to produce effective enhancement and tracking of uterine motion and motivate towards an extensive validation in the context of fertilization procedures.

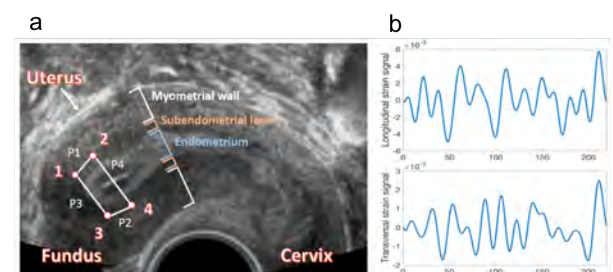


Figure 1. (a) Longitudinal view of uterine B-mode TVUS. The rounded extremity on the left side represents the fundus while the extremity on the right side represents the cervical end (cervix). The white segments indicate the myometrial wall, the orange segments indicate the subendometrial layer (inner lining of the myometrium); the blue segment indicates the endometrium. Four sites (1, 2, 3, and 4) are manually defined on the inner lining of the myometrium and tracked over time to derive distance and strain signals. (b) Example of strain signal derived from P1# along the longitudinal direction (upper graph) and from P4# along the transversal direction (bottom graph) during 3-min recording.

Characterization of the performances of 4D DCE-US

Virginie Grand-Perret¹, Ning Yao¹, Maxandre Jacqueline¹, Julie Lachaux², Gilgueng Hwang², Anne-Marie Haghiri², Ingrid Leguerney³, Nathalie Lassau^{1,4}, Stéphanie Pitre-Champagnat¹

¹IR4M UMR8081 (CNRS, Univ. Paris-Sud, Université Paris-Saclay), Villejuif, France, ²C2N (CNRS, Univ. Paris-Sud, Université Paris-Saclay), Marcoussis, France, ³Research Department, Gustave Roussy, Villejuif, France, ⁴Research department, Gustave Roussy, Villejuif, France

Background, Motivation, and Objective

Tumor microvascularization is a promising biomarker of response to anti-angiogenic drugs in cancer treatment [1]. Microvascular flows can be imaged by dynamic contrast-enhanced Ultrasound (DCE-US) using microbubbles as a contrast agent (CA). However, 2D DCE-US imaging is limited by user-variability. Therefore, 4D imaging is a promising technique that makes it possible to depend less on the operator and thus improves the clinical reproducibility [2].

In order to assess the instrumental performances of 4D DCE-US, specific flow phantoms have been developed. In particular, the aim of our study was to measure the spatial resolution and the partial volume effect using a new generation of flow phantom based on a microfluidic setup.

Statement of Contribution/Methods

1. Phantom design

Ecoflex 00-30 (Smooth-On, USA) was chosen between several silicones including PDMS, being the best compromise in terms of acoustical properties measured at 10 MHz. A micro-machined mold was used to create phantoms of various geometries using microfluidic technology. In particular, series of 14 channels of $100 \times 200 \mu\text{m}^2$ separated by $450 \mu\text{m}$, 1.2 mm, and 3.2 mm were designed to study partial volume effects. Ecoflex 00-30 was cast on the mold, and then stucked to a 2 mm layer of the same material using a stamp-and stick technique.

Setup

The CA, Sonovue® (Bracco, Italy), was mixed to Phosphate Buffered Saline at a 1:1 ratio to stabilize the bubbles and was driven continuously in the channels by a MFCS-EZ microfluidic flow control system (Fluigent, France) at 250 mbar.

Ultrasound data acquisition

An Aplio500 ultrasound scanner (Toshiba Medical Systems, Japan) with a 12 MHz 3D mechanical probe PLT1204BT was used. Raw data were acquired during 25 minutes. The primary acquisition plane was the one including the cross-section of the channels, and the volume angle was 5° . Ultrasound parameters were: focus depth 1.3 mm, mechanical index 0.23, frame rate at 1 volume per second. Raw data were processed using a homemade software for spatial characterization.

Results/Discussion

Spatial resolution in the primary plane was found to be 1.5 mm. The design of the phantoms made it possible to have the same flow in all the channels: difference of mean intensities in a $0.12 \times 0.24 \text{ mm}^2$ cross-sectional ROI was <9% between two channels. Total intensity in 14 channels of $100 \times 200 \mu\text{m}^2$ section was 110 A.U. when separated by 1.2 mm vs 7.9 A.U. when separated by $450 \mu\text{m}$, suggesting a partial volume effect in 4D DCE-US. These results will be further investigated and compared to a preclinical study on 2D vs 3D.

[1] N. Lassau *et al.*, “Validation of Dynamic Contrast-Enhanced Ultrasound in Predicting Outcomes of Antiangiogenic Therapy for Solid Tumors The French Multicenter Support for Innovative and Expensive Techniques Study,” *Invest. Radiol.*, vol. 49, no. 12, pp. 794–800, Dec. 2014.

[2] J. R. Eisenbrey, J. K. Dave, and F. Forsberg, “Recent technological advancements in breast ultrasound,” *Ultrasonics*, vol. 70, pp. 183–190, Aug. 2016.

P1-A8 - Image Guidance and Acoustic Microscopy

Kairaku (posters 1)

Tuesday, October 23, 9:30 AM - 4:00 PM

Chair: **Shinichiro Umemura** Tohoku University

P1-A8-1

3-D observation of punctual needle by 2-D shear wave imaging under forced vibration of needle

Yoshiki Yamakoshi¹, Masato Ota¹, Ziheng Liu¹, Kana Taniuchi¹

¹*Grad. School, Science & Technology, Gunma University, Kiryu, Japan*

Background, Motivation, and Objective

Central venous catheterization (CVC) is performed under ultrasound guidance. However, it is difficult to insert a puncture needle (PN) at a correct position, because the contrast of PN in B mode image is low and the position of PN cannot be known until the PN reaches the image plane. We propose a novel shear wave imaging method, which realizes high contrast 3-D imaging of PN using real-time 2-D shear wave imaging.

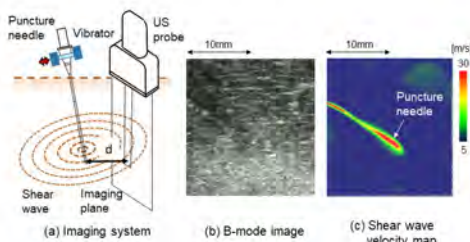
Statement of Contribution/Methods

PN vibrates at small amplitude (less than 100 μm) with an exciter attached to the base of the PN. Frequency of vibration satisfies a frequency condition of shear wave imaging: CD SWI (Color Doppler Shear Wave Imaging)¹⁾ (Fig. (a)). The shear wave radiated from PN produces a cylindrical shear wave's field around the PN. When shear wave phase is reconstructed by CD SWI using 2-D ultrasound probe, an orthogonally projected image of the PN appears on the shear wave velocity map, even if the PN does not reach the ultrasound imaging plane. In this method, the distance between the ultrasound imaging plane and the PN is observed from the width of the projection image, because the width, which is measured at K times the shear wave velocity of the surrounding medium, is proportional to the distance. The position of the tip of PN is calculated from the shear wave velocity on the extended line of the projected image of the PN. The contrast of the PN image by the proposed method is larger than that of the B mode, because the maximum shear wave velocity of the projected image is much higher than that of the surrounding medium.

Results/Discussion

In experiment, PNs of 22G and 24G were inserted into chicken breast meat. The needle was excited with frequency of 276.5 Hz. Figs.(b) and(c) are the B-mode image and the shear wave velocity map, which are observed when the distance d between the PN and the ultrasound imaging plane is set to 2 mm. Since the PN does not reach the image plane, it is difficult to observe on B mode image, but PN is clearly visualized on the shear wave velocity map which is reconstructed by CD SWI. The imaging method of PN using shear wave radiated from PN provides high contrast 3-D observation of PN effective for accurate needle puncture in CVC.

1) Y. Yamakoshi et al. IEEE Tran. UFFC, 64, 340 (2017).



In vivo microultrasound visualisation of nerve trauma due to regional anaesthesia needle insertion and injection

Anu Chandra¹, Yohannes Soenjaya², Judy Yan², Brandon Morningstar², Malachy Columb³, Graeme McLeod⁴, Christine Demore²

¹University of Dundee, United Kingdom, ²Sunnybrook Research Institute, Canada, ³Manchester University Hospitals Foundation Trust, United Kingdom, ⁴Ninewells Hospital, United Kingdom

Background, Motivation, and Objective

Regional Anesthesia (RA), used for many surgical procedures to numb peripheral nerves, uses a needle to deliver anesthetic fluid around a nerve. Intraneuronal injection is unintended but frequent and 10% of patients have acute or chronic peripheral nerve pain post surgery. Factors that can contribute to nerve damage include mechanical trauma, high injectate pressure (recommended maximum: 15 psi) and high flow rate, but the mechanisms are poorly understood and disputed. This study used microultrasound (microUS) to visualise the changes in nerve geometry, the fascicles (bundles of neurons) and epineurium (protective connective tissue) concurrently with measurement of injectate pressure during replicated RA nerve blocks to better understand physical mechanisms of nerve damage.

Statement of Contribution/Methods

Median, ulnar, and radial axillary nerves of anesthetized pigs were surgically exposed. MicroUS (40 MHz array; Vevo 2100, VisualSonics Inc.) videos were recorded of 21g needle insertions into nerves followed by 0.5 mL saline injection at 1, 6 or 12 mL/min using an infusion pump, and an inline sensor to measured injectate pressure. Needle tip position, nerve structure changes and fluid distribution were recorded for 235 individual injections across 56 block procedures on 4 pigs. Injection with the needle tip extraneural, in forceful contact with nerve epineurium, and intraneuronal were attempted to replicate clinical practices that may lead to nerve damage.

Results/Discussion

MicroUS enabled *in vivo*, real-time visualisation of the fascicle structure in 100% attempted blocks. The effects of needle position and injectate distribution on fascicles and epineurium were correlated with injectate pressure (Fig. 1). Intraneuronal injection was characterised by swelling of the whole nerve, swelling immediately around the nerve, rupture of the epineurium, and/or failure to return to pre-injection morphology on needle withdrawal. Mixed model statistical analysis showed significant ($P<0.0001$) increase in injectate pressure with intraneuronal injection and forceful needle-epineurium contact, even at low flow rates. Injectate was pressure <15 psi in 47% of intraneuronal injection and needle-epineurium contact, indicating the limit should be reduced. The onset of nerve structure changes could be observed at 1 mL/min flow, with time to stop or reposition the injection.

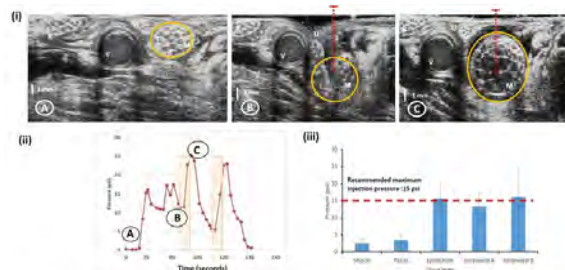


Fig. 1: (i) MicroUS image frames showing B- radial nerve, U- ulnar nerve, M- Median nerve, F- fascicles and V- vessel. (ii) pressure measurement during needle insertion into median nerve (marked in yellow circle) and 0.5 ml bolus injection (at 6 mL/min). A – before needle insertion; B – entry of the nerve, during attempt to penetrate the epineurium; fluid distribution starts above nerve when the needle is in the epineurium and continues to intraneuronal injection. C – intraneuronal injection showing expansion of the nerve and distribution of fluid inside and around the nerve (needle trajectory marked in dashed red line). (iii) Peak pressure measured at the needle tip during injection for different needle tip positions within tissue

Thermal Strain Imaging for Sonodynamic Therapy Monitoring: ex vivo and in vivo Feasibility Studies

Fu-Feng Lee¹, Qiong He¹, Min Chen², Yi Yang¹, Mengxuan Wang², Zhifei Dai², Jianwen Luo¹

¹Department of Biomedical Engineering, Tsinghua University, Beijing, China, People's Republic of, ²Department of Biomedical Engineering, Peking University, Beijing, China, People's Republic of

Background, Motivation, and Objective

Sonodynamic therapy (SDT) is an emerging therapeutic method against cancers based on the synergistic effect of combined ultrasound and sonosensitizer with tumor affinity. A low-intensity continuous wave ultrasound is focused on the tumor to enhance the drug cytotoxicity of the sonosensitizer, resulting in a small temperature elevation within the tumor ($< 2^{\circ}\text{C}$). The aim of this study is to assess the feasibility of thermal strain imaging (TSI) in monitoring the ultrasound irradiation during SDT.

Statement of Contribution/Methods

The system diagram is shown in Fig. 1. HT-29 colon cancer xenografts were transplanted into the male BALB/c nude mice (4-6 week old, 20 g). When the tumor grew to a size of 10 mm in the longest dimension, a single-element transducer (1L0112HP, CTS, USA) was used to transmit low-intensity focused ultrasound (LIFU) at 1 MHz and $< 1 \text{ W/cm}^2$ into the tumor for 50 seconds. A SonixMDP system equipped with SonixDAQ (Analogic, USA) and L40-8 probe (transmit frequency = 10 MHz) were utilized to acquire RF frames using 5-angle plane wave imaging at a sample frequency of 40 MHz. The control sequence of the irradiation and imaging was implemented in PC (Liang et al, IUS 2017).

The relationship between the temperature elevation and the strain in the tumor was investigated in the *ex vivo* experiments. A thermocouple was inserted into the extracted tumor near the focal spot of LIFU to monitor the temperature. A correlation-based method was used to compensate for the respiratory motion of mice in the *in vivo* experiments. The reference frame was acquired before the irradiation, and the frames highly correlated to the reference frame were collected. The thermal strain images were obtained by using 2D cross-correlation algorithm (lateral \times axial: 0.1 mm \times 1 mm, 80% overlap) and 2D Savitzky-Golay differentiation filter (lateral \times axial: 0.7 mm \times 4 mm).

Results/Discussion

Fig. 2 shows the temperature elevation and strain varied with the irradiation time in the *ex vivo* experiments. A temperature rise of 0.3°C produces a strain decrease of $\sim 0.02\%$ in the tumor at an ambient temperature of 22°C . Fig. 3 shows the thermal strain images within the tumor at different irradiation time in the *in vivo* experiments. The region with lower strains indicates the focal spot of LIFU, and the strain magnitude decreases with time. In conclusion, the *in vivo* feasibility of SDT monitoring using TSI is validated.

Fig. 1

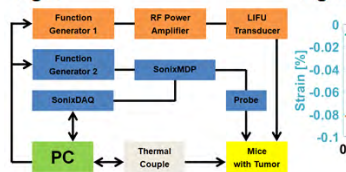


Fig. 2

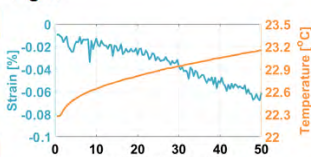
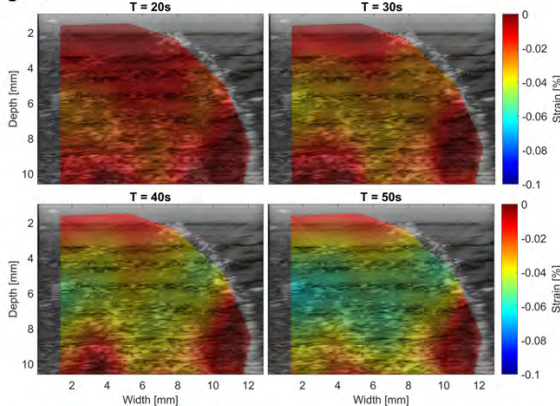


Fig. 3



Reconstruction of Quantitative Acoustic Microscopy Images from RF Signals Sampled at Innovation Rate

Jong-Hoon Kim¹, Jonathan Mamou², Denis Kouamé¹, Alin Achim³, Adrian Basarab¹

¹*IRIT, University of Toulouse, Toulouse Cedex, France*, ²*Lizzi Center for Biomedical Engineering, Riverside Research, NYC, NY, United States*, ³*Visual Information Lab, Merchant Venturers School of Engineering, University of Bristol, Bristol, United Kingdom*

Background, Motivation, and Objective

In quantitative acoustic microscopy (QAM), 2D acoustic maps are estimated from an RF data cube acquired by transmitting short ultrasound pulses into a thin section of soft tissue affixed to a microscopy slide. For each x-y position, the received RF echo signal consists of two main reflections due to the water-tissue and tissue-glass interfaces. These reflections are time shifted, linear frequency-dependent attenuated, and scaled versions of a reference reflection signal obtained from a water-glass interface. Despite their limited degrees of freedom (i.e., 5), QAM RF signals are currently sampled beyond the Nyquist rate, e.g., at 2.5 GHz for 250-MHz scanners. In this work, we show that RF signals in QAM can be sampled at the innovation rate, without affecting the estimation of the acoustic parameters.

Statement of Contribution/Methods

The class of signals with limited degrees of freedom is usually called finite rate of innovation (FRI). For such signals, existing theoretical results show the possibility of reconstructing them from samples acquired at innovation rate, much below the Nyquist rate. The originality of our work is twofold: i) incorporate the frequency-dependent attenuation in the FRI model, ii) combine the few samples acquired at innovation rate with a model-based acoustic parameter estimator. Fig. 1(a) illustrates the main steps of the proposed method. After classical demodulation and low-pass filtering in the analog domain, the RF signals are sampled at a very low rate (162.5 MHz). The resulting samples are used to retrieve the Fourier coefficients further used by the model-based process to estimate the acoustic parameters.

Results/Discussion

Fig. 1 (b,c) show the speed-of-sound maps obtained for an *ex vivo* lymph node samples obtained from a breast-cancer patients scanned at 250 MHz, for both classical sampling at 2.5 GHz and with the proposed method at 162.5 MHz. We show the ability of estimating very similar (PSNR>53dB) acoustic parameter maps from RF signals sampled at a much lower rate than with current scanners. The proposed framework could significantly reduce costs and experimental challenges in current QAM system because of the current need for ultra-precise and fast sampling cards.

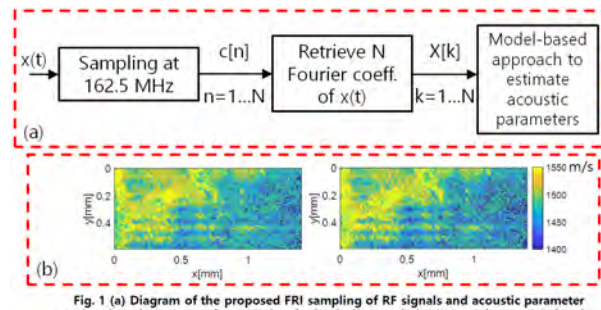


Fig. 1 (a) Diagram of the proposed FRI sampling of RF signals and acoustic parameter estimation, (b) SoS map from RF signals classically sampled (200 samples per RF signal), (c) SoS map from RF signals sampled at innovation rate ($N = 13$ samples per RF signal).

A Study for B-Mode Imaging using 100-MHz-Range Ultrasound through a Fused Quartz Fiber
Takasuke Irie¹, Masakazu Sato², Norio Tagawa³, Masasumi Yoshizawa⁴
¹*Microsonic Co., Ltd, Japan*, ²*Microsonic. co., ltd, Japan*, ³*Tokyo metropolitan university, Japan*, ⁴*Metropolitan college of industrial technology, Japan*
Background, Motivation, and Objective

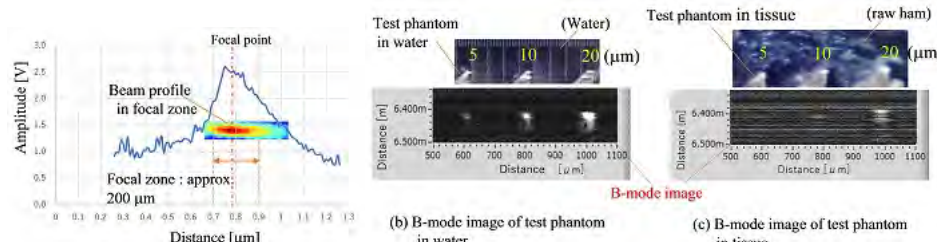
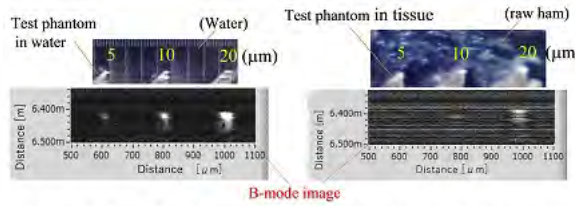
The tissue diagnosis in the current pathological examination has two drawbacks. (1) It takes time, and (2) it gives burden on the patient. The main objective of the study is to enable an operator to observe directly microscopic image of the tissue in real time without taking out the tissue sample from the patient. To achieve the objective, we are developing a needle-type ultrasonic microscope that uses a thin fiber as an ultrasonic probe.

Statement of Contribution/Methods

We have reported that the microscopic C-mode and B-mode images of the tissue samples were obtained using the focused ultrasonic-beam radiated from the quartz fiber. In this paper, a method to improve the detectability of the echo from tissue using the ultrasonic-beam with a long focal-zone and the experimental result are described. The ultrasonic-beam is focused by lens. In the experiment, we measured the focal zone of the beam using the reflected echo from a stainless steel plate in water. The results are shown in Fig. 1. We performed the B-mode imaging of a test phantom with extremely small size (1, 3, 5, 10, 20 μm , and so on) targets (Fig. 2) in order to estimate the detectable-size of the target not only in water but also in tissue (a piece of ham with 400-600 μm thickness).

Results/Discussion

The ultrasonic-beam with a focal zone of approximately 200 μm -length (frequency band: approximately 80-130MHz) was obtained (Fig. 1). The minimum detectable-size of the target on the B-mode image was 5 μm in water. On the other hand, it was 10 μm in tissue. It seems that the reduction of detectability due to the attenuation (approximately 10-15dB) of the ultrasound in tissue. As the result of the experiment, we could obtain a B-mode image of the target with 10 μm size in tissue. Next, we will improve the sensitivity and signal to noise ratio of the system.


Fig. 1 Focal zone of ultrasonic-beam
Fig. 2 Detectable size of target of test phantom


In vitro volume imaging of articular cartilage using chirped coded high frequency ultrasound**Anowarul Habib¹, Juha Vierinen¹, Ashraful Islam², Inigo Zubiaurre Martinez², Frank Melandsø¹**¹*Department of Physics and Technology, UiT The Arctic University of Norway, Norway*, ²*Institute of Clinical Medicine, UiT The Arctic University of Norway, Tromsø, Norway***Background, Motivation, and Objective**

Articular cartilage is a hyaline and highly specialized connective tissue in the diarthrodial joints. Cartilage degeneration is the central hallmark of osteoarthritis, a complex musculoskeletal disorder with numerous contributory genetic, constitutional and biomechanical factors. Changes in biomechanical properties for articular cartilage can indicate tissue degeneration e.g. in rheumatoid arthritis or osteoarthritis. In vitro cartilage samples prepared as thin (typical 5-50 µm) slices have previously been investigated by scanning acoustic microscopy (SAM). This approach has been successful in terms of producing high-resolution 2D images. However, ultrasonic imaging of 3D dimensional global cartilage structures will typically require thicker samples, involving increased complexity in terms of for example, wave attenuation and scattering variation. Our objective has therefore been to facilitate high resolution imaging of larger cartilage volumes combining SAM and chirp-coded waveforms.

Statement of Contribution/Methods

Human articular cartilage samples were obtained from The University Hospital Tromsø, Norway and sliced into 1.0 to 1.5 mm thick sections and imaged using a SAM platform with an Olympus 50MHz focused PVDF transducer. This custom-made platform which was build up around a Leica DMI8 inverted microscope and an ASI MSI-2000 stage system, was designed to handle long arbitrary coded waveforms using FPGA FlexRIO hardware from National Instruments. Chirp-coded waveforms were investigated with results visualized as C- and B-scans after compression with both match- and Wiener filters.

Results/Discussion

The experimental results show that chirp-coded waves in combination with appropriate compression filters can enhance the image quality significantly without inducing significant artifacts from sidelobes. This is illustrated in the figure under were a C-scan obtained from a single broad-banded Ricker pulse [Fig (a)] was re-imaged using a chirped pulse [Fig. (b)] under the same conditions. Figure (b) obtained from compression with a Wiener filter, provides more details in weak scattering domains (dark areas) due to its increased dynamical range and SNR.

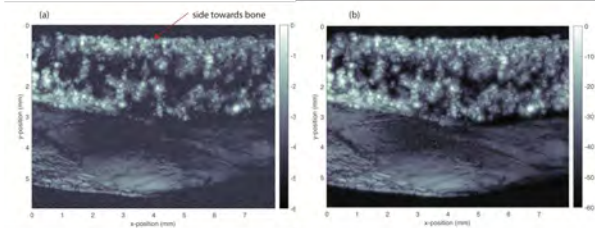


Figure: (a) Acoustic image of articular cartilage sample using a Ricker pulse
 (b) using coded signal and Wiener filter was used

P1-A9 - Leveraging Deep Learning and Pulse Compression

Kairaku (posters 1)

Tuesday, October 23, 9:30 AM - 4:00 PM

Chair: **Mathieu Pernot** INSERM

P1-A9-1

Learning Doppler with convolutional neural networks (DopplerNet) and its application to intra-cardiac echography

Ruud J. G. van Sloun¹, Harm Belt², Massimo Mischi¹

¹Eindhoven University of Technology, Netherlands, ²Philips Research, Eindhoven, Netherlands

Background, Motivation, and Objective

Cardiac ablation therapy is an effective treatment for atrial fibrillation and ventricular tachycardia that relies on the creation of electrically isolating scars through heat. The ability to reliably visualize and assess the formation of these lesions during the procedure would greatly enhance the therapy's success rate. Tissue Doppler echography enables measurement of tissue strain, and could therefore be used to monitor and quantify the stiffening of developing lesions. In tissue Doppler, the tradeoff between spatiotemporal resolution and estimation accuracy/precision is balanced by manually tweaking the fast- and slow-time range gates, with the optimal settings varying across measurements and desired clinical objectives. Convolutional neural networks have shown remarkable performance at learning to execute a large variety of signal and image processing tasks. In this work, we show how a deep neural network can be trained to robustly fulfill Doppler imaging functionality: DopplerNet.

Statement of Contribution/Methods

We take an end-to-end learning approach to predicting Doppler estimates from quadrature demodulated IQ data, by learning a set of nonlinear operations that can approximate the behavior of the well-known Kasai auto-correlator. We exploit convolutional networks based on an encoder-decoder architecture to learn Doppler features at a hierarchy of scales and abstractions, while the use of small latent ‘bottleneck’ space inherently de-noises the estimates and compactly compresses the relevant information. The neural network’s ability to mimic Doppler functionality was validated using *in-vivo* M-mode intra-cardiac echography of the left-ventricular apex of canines (Haines *et al.*, 2017).

Results/Discussion

Figure 1 shows the envelope-detected M-mode image (top), standard Kasai axial velocity estimates (middle), and DopplerNet predictions (bottom). DopplerNet qualitatively displays good agreement with Kasai’s method, with reduced noise levels and artifacts. Moreover, the ability to perform Doppler using a neural network opens up new possibilities for learning dedicated data compression schemes to reduce the bandwidth for probe-scanner communication (edge computing) and optimal Doppler-related feature extraction for the purpose of tissue classification.

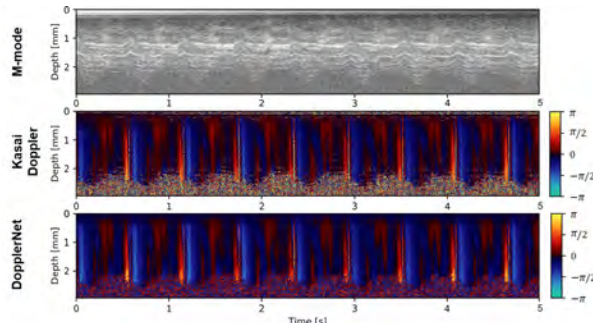


Figure 1. Intra-cardiac M-mode ultrasound of the left atrial wall (top), Doppler estimation from the IQ data based on the Kasai autocorrelator (middle), and the deep learning based DopplerNet (bottom). Note that training for the latter is based on separate acquisitions.

WaveFlow – Towards Integration of Ultrasound Processing with Deep Learning**Piotr Jarosik¹, Michał Byra^{2,3}, Marcin Lewandowski⁴**

¹*Department of Information and Computational Science, Institute of Fundamental Technological Research, Polish Academy of Sciences, Warsaw, Poland*, ²*Department of Ultrasound, Institute of Fundamental Technological Research, Polish Academy of Sciences, Warsaw, Poland*, ³*Department of Radiology, University of California, United States*, ⁴*Laboratory of Professional Electronics, Institute of Fundamental Technological Research, Polish Academy of Sciences, Warsaw, Poland*

Background, Motivation, and Objective

In recent years, we have observed a growing interest in the use of deep learning methods and GPU processing for ultrasound imaging. The idea of applying machine learning to signal processing is highly promising. The ultimate goal of this work is a real-time processing framework for ultrasound image reconstruction augmented with machine learning. To attain this, we have implemented WaveFlow – a set of ultrasound data acquisition and processing tools for TensorFlow.

Statement of Contribution/Methods

We have chosen the TensorFlow framework as a base for our implementation, because of its widespread usage in the machine learning community, active development, and data flow abstracted from a processing device (CPUs or GPUs) enabling easy extensibility.

WaveFlow includes an ultrasound Environments and signal processing Operators (ops) library. The Environment is a connection point between the input raw RF data source (i.e. dataset, simulation or hardware scanner) and TensorFlow. It provides current state and metadata as a collection of tensors understandable to the framework. Tensors can be processed in real-time by algorithms available in both TensorFlow and WaveFlow. Currently, WaveFlow provides ops for image reconstruction (beamforming), pre- and post-processing and quantitative ultrasound. The ops have implementations for both the CPU and GPU, as well as built-in automated tests and benchmarks.

Results/Discussion

To demonstrate WaveFlow's performance, ultrasound RF data for wire and cyst phantoms was acquired and elaborated using selected sequences of the ops. We implemented and evaluated: a Delay-and Sum beamformer, synthetic transmit aperture (STA), plane-wave imaging (PWI), an FIR filter, an envelope detector and dynamic range clipping. The benchmarks were executed on the NVidia® Titan X GPU integrated in the USPlatform research scanner (us4us Ltd., Poland).

We achieved B-mode image reconstruction throughput: STA for tensors with shape (acquisitions=128, channels=64, samples=2048): 73fps, PWI for tensors with shape (11, 192, 2048): 20 fps. The results prove the feasibility of real-time ultrasound image reconstruction using WaveFlow operators in a TensorFlow framework.

WaveFlow provides well-defined and mutually exchangeable steps of the signal processing flow. A tight integration with TensorFlow provides the possibility to directly apply machine learning algorithms to data from ultrasound systems. Additionally, the standard ultrasound algorithms can be augmented with deep learning tools available in the framework. This opens a new area of possibilities for ultrasound and artificial intelligence researchers.

Waveflow is open-source (github.com/waveflow-team/waveflow) and open to contributors.

Localization of partially visible needles in 3D ultrasound using dilated convolutional neural networks

Arash Pourtaherian¹, Nenad Mihajlovic², Farhad Ghazvinian Zanjani¹, Svitlana Zinger¹, Gary Ng³, Hendrikus Korsten⁴, Peter de With⁵

¹Eindhoven University of Technology, Eindhoven, Netherlands, ²Philips Research Eindhoven, Netherlands, ³Philips Ultrasound, Bothell, WA, United States, ⁴Catharina Hospital Eindhoven, Eindhoven, Netherlands, ⁵Faculty of Electrical Engineering, Eindhoven University of Technology, Netherlands

Background, Motivation, and Objective

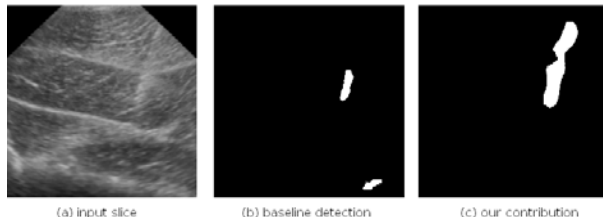
Guidance of needles for interventions that involve percutaneous advancing of a needle to a target inside the body is one of the key applications of ultrasound, i.e. for biopsies, ablations, and nerve blocks. During these procedures, image-based detection of the needle can circumvent complex needle-transducer alignment by ensuring an adequate visualization of the needle during the entire procedure. However, successful localization in sector and curvilinear transducers is challenging as the needle can be invisible or partially visible, due to the lack of received beam reflections from parts of the needle. Therefore, it is necessary to explicitly model the global information present in the data for correct localization of the needle to compensate for the lost signal.

Statement of Contribution/Methods

We present a novel image-based localization technique to detect partially visible needles in phased-array 3D ultrasound volumes using convolutional neural networks. In order to recover the missing information from the needle, we propose to model both local and global information at multi scales using dilated convolutions. Our method efficiently models both low and high-order structures by exploiting pyramid pooling features, while preserving the spatial accuracy. Needle segments are detected in thick cross-sections perpendicular to the coronal planes and analyzed to localize the position and orientation of the needle in 3D. The main contributions of this study are: (1) effective modeling of local and global information in the data to localize partially visible needles and (2) robust localization and visualization of virtually invisible needles in sector and curvilinear 3D ultrasound data.

Results/Discussion

The proposed algorithm is evaluated on 3D US data of a porcine leg, acquired with a X6-1 phased-array transducer. The dataset consists of 40 trials of standard 17G and 22G needles, inserted at various steepness angles (55° – 80°), in which the shaft is partially visible. The proposed algorithm successfully detects the needle plane with accuracy in the sub-millimeter domain, as shown in Figure 1. In this work, we present a novel image processing system to robustly detect a needle in 3D US volumes when a major part of the needle is invisible, thereby strongly supporting challenging clinical interventions and eliminating the need for external tracking devices.



(a) input slice

(b) baseline detection

(c) our contribution

Grading severity of rheumatoid arthritis on ultrasound images with deep convolutional neural networks

Jian Tang¹, Zhibin Jin², Xue Zhou¹, Hongzuo Chu¹, **Jie Yuan¹**, Min Wu², Qian Cheng³, Xueding Wang^{3,4}

¹Nanjing University, Nanjing, China, People's Republic of, ²Nanjing Drum Tower Hospital, Nanjing, Jiangsu, China, China, People's Republic of, ³Tongji University, China, People's Republic of, ⁴University of Michigan, United States

Background, Motivation, and Objective

Rheumatoid arthritis (RA) is one of the most common autoimmune diseases which is characterized by pain, swelling, and stiffness of the joints, affecting almost 1% of the population around the world. Detecting the diseased finger joint region of RA patients and quantifying its severity are important for diagnosis, making treatment decision and predicting disease progression. Clinically, RA severity is assessed using the composite OMERACT-EULAR power Doppler and grey-scale ultrasound (PDUS) score, which is a 4-grade semi-quantitative scoring system. However, quantifying RA severity has always been a difficult diagnostic problem due to the semi-quantitative score criterion, even experienced doctors cannot always guarantee the accuracy, reliability and consistency of diagnosis results.

Statement of Contribution/Methods

In this contribution, we present a RA grading system based on GoogLeNet. Gray-scale ultrasound images of finger joints are taken as inputs while the output is the accuracy of corresponding RA grading results. The samples were split into 80% training and 20% test set. In order to make up for the lack of large annotated training dataset, we performed data augmentation to increase the number of samples from 600 RA images to 7200 images. Then we employed the Caffe framework to implement and train the chosen 22-layer GoogLeNet Inception V1 network. Motivated by the approach of transfer learning, we pre-trained the GoogLeNet on ImageNet as a feature extractor and then fine-tuned it on our own dataset. Meanwhile we rename the fully connected layers to train these layers with random initial weights so that it can fit our own classification task.

Results/Discussion

Our experiment results demonstrate that the proposed method achieves performance comparable to RA experts on multi-class classification. The final 4-grade classification accuracy on the testing samples reaches 95%. Especially, we obtain high accuracy on binary classification problems such as Grade 0 (normal) vs Grade 1-3(abnormal) and Grade 1 (minimal) vs Grade 3(severe), which are the main concern of doctors. We effectively boost the classification accuracy via data augmentation and transfer learning techniques, thus solves the problem that is widely existed in the deep learning studies on medical images classification and rating. And the loading of pre-trained Convolutional Neural Network (CNN) model effectively avoids the cost of training the whole CNN from scratch. To summarize, the proposed CNN-based RA grading method has the potential to provide an objective and accurate reference for clinicians in clinical management of RA treatment.

Improved Decorrelation Based Elevational Motion Estimation with Singular Value Decomposition and Machine Learning
Ching-Yen Lee¹, Pai Chi Li¹¹*National Taiwan University, Taiwan*
Background, Motivation, and Objective

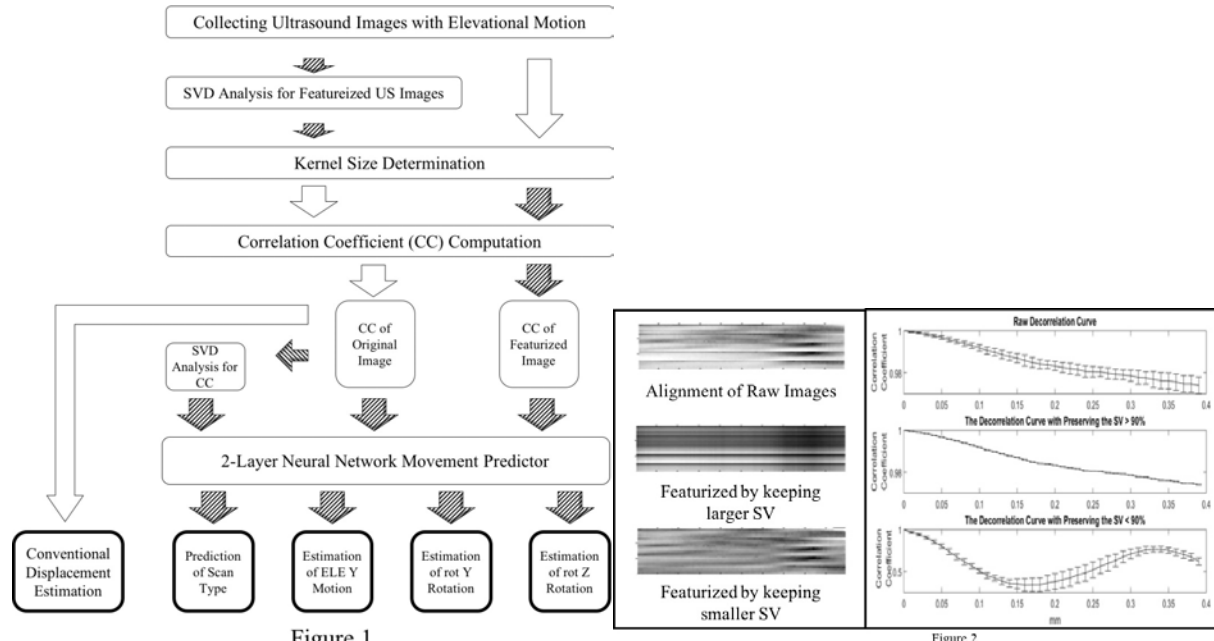
Speckle decorrelation based elevational motion estimation has been widely investigated. Generally, the correlation coefficient (CC) of two images with and without motion is mapped to the beam pattern to estimate the displacement. However, its performance has been limited due to several factors, including the signal-to-noise ratio, focusing quality and inherent speckle variance. In this study, we propose a modified approach that utilizes singular value decomposition (SVD) and machine learning for significantly lower estimation variations. In other words, calculations of the CCs are improved with the introduction of singular value decomposition. In addition, mapping of the CCs to the beam pattern is replaced with a neural-network based estimator.

Statement of Contribution/Methods

Figure 1 shows the flow chart of the proposed algorithm. A series of ultrasound images are captured and the CC curve (CC as a function of elevation displacement) is calculated with a step size of 0.01 mm along the elevational direction. The SVD is used to extract features from a group of ultrasound images. By properly selecting the kernel size and the preserved singular values, a set of features can be generated for training a two-layer neural network estimator for the displacement estimation.

Results/Discussion

Figure 2 shows the CC curves. Based on experimental phantom data with a 7-MHz, 128-element linear array, the accuracy of the elevational motion estimation by the proposed method is 96% and the estimation error is less than 0.001 mm. On the other hand, the estimation error using the conventional decorrelation method is larger than 0.03 mm under the same scan conditions. The proposed method can be applied to other types of motion estimation. Its performance on human imaging will also be tested.



Ultrasound Probe Bandwidth Enhancement Combined with Non-Stationary Compression Filters to Improve Image Quality

Yanis Mehdi Benane¹, Denis Bujoreanu¹, Hervé Liebgott¹, Christian Cachard¹, Olivier Basset¹

¹CREATIS, Univ.Lyon, INSA-Lyon, UCBL1, UJM-Saint Etienne, CNRS, Inserm, CREATIS UMR 5220, U1206, Lyon, France

Background, Motivation, and Objective

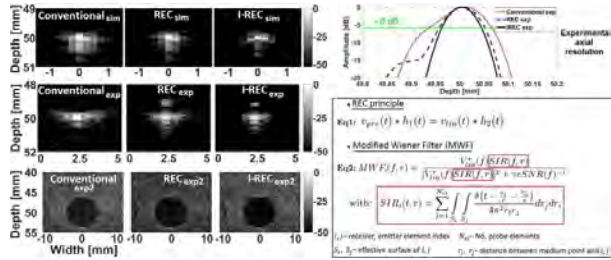
Resolution Enhancement Compression (REC) is a pulse compression technique which provides significant image quality improvements, compared to conventional ultrasonic imaging approaches. In order to do so, REC employs amplitude modulated chirp signals in transmission (to increase the energy at the frequencies where the probe is less efficient) and Wiener filters in reception (to adjust the tradeoff between bandwidth / noise level). However the performance of REC is not optimal since the Spatial Impulse Response (SIR) of the probe varies across the medium while the compression filters are spatially invariant. In this work, an adaptation of REC compression filters as a function of the SIR of the probe is proposed (I-REC). I-REC was compared to a conventional imaging technique and to classical REC (without SIR compensation).

Statement of Contribution/Methods

In the figure below, Eq1 shows the pre-enhanced chirp (v_{pre}), used as the excitation of the probe in REC. v_{lin} is a frequency modulated chirp tapered with a 20% Tukey window. Since the desired Impulse Response (IR) h_2 is designed to be larger than the real IR of the probe (h_1), v_{pre} is able to boost the effective bandwidth of the probe. The expression of the Modified Wiener Filter (MWF) is shown in Eq2. The dependency on SIR makes the MWF optimal for each backscattered echo. I-REC was implemented in simulation (Field II) and in experiments (using the research platform UlaOP-256), by considering the experimental IR of the probe (h_1), measured using a hydrophone. The performance of the MWF was evaluated on both single target and anechoic cyst phantoms, using a focalised acquisition scheme.

Results/Discussion

The obtained results show that I-REC provides the better image quality. Indeed, simulations and experiments reveal bandwidth improvements (53% and 51%, respectively) for I-REC in comparison to the conventional technique, consistent with the intended bandwidth boost of 54%. When the REC approach is used (SIR not compensated), only 36% bandwidth enhancement is observed in comparison with the conventional technique. Axial resolution follows the same trend (i.e. I-REC: 87.4 μm , REC: 99.1 μm , conventional: 132.8 μm). The obtained cyst images demonstrate that I-REC improves also CNR by 3.43 dB when compared to the conventional technique while REC increase it by only 2.21 dB, (i.e. I-REC: 7.34 dB, REC: 6.12 dB, conventional: 3.91 dB).



Enhanced Second Harmonic Imaging using a Pulse Compression Technique Combined with Ultrasound Pulse Inversion

Yanis Mehdi Benane¹, Denis Bujoreanu¹, Roberto Lavarello², Adeline Bernard¹, Christian Cachard¹, Olivier Basset¹

¹CREATIS, Univ.Lyon, INSA-Lyon, UCBL1, UJM-Saint Etienne, CNRS, Inserm, CREATIS UMR 5220, U1206, Villeurbanne, France,

²Laboratorio de Imagenes Medicas, Departamento de Ingenieria, Pontificia Universidad Católica del Perú, Lima, Peru

Background, Motivation, and Objective

Pulse Inversion (PI) is an emission technique used for harmonic imaging. By transmitting two phase inverted signals, which allow cancelling out the fundamental component, PI is able to achieve better image quality thanks to the reduced clutter / reverberation and to the improved bandwidth of the second harmonic. Here, a technique based on Resolution Enhancement Convolution (REC) that improves the performance of PI is proposed. It consists in boosting the energy of the excitation signal at the frequencies where the probe is less efficient, which further improves the bandwidth of the second harmonic signal. The proposed approach (REC-PI) is combined with a focused transmission scheme and implemented on the UIAOP 256 ultrasound scanner.

Statement of Contribution/Methods

A linear chirp v_{lin} of $T=10 \mu s$ duration, that spans between $f_0=2.9 \text{ MHz}$ and $f_1=5.5 \text{ MHz}$ was designed in order to boost the bandwidth h_1 of the probe (a). Then, using the REC convolution equivalence (Eq1), the pre-enhanced excitation v_{rec} is obtained (a). From (Eq1), one can deduce that the signal that propagates inside the medium is v_{lin} , which implies that the nonlinearity will generate a harmonic signal v_{harm} that can be deduced using (Eq2). Since the recorded echo of the second harmonic is a temporal convolution between v_{harm} and h_1 , the optimal compression filter can be deduced using (Eq3). As shown in (a), the bandwidths of v_{lin} and v_{harm} slightly overlap (under -12dB), however this clutter is removed thanks to successive emission / coherent addition of echoes of v_{lin} and its phase inverted counterpart. REC-PI was tested experimentally using a phantom characterized by a low nonlinearity ($B/A=6.7$).

Results/Discussion

An improvement of image quality is observed when using REC-PI (c) in comparison to classical PI (b). An enhancement of 25.4% of the axial resolution was noticed for the scatterer placed at $(x = -0.9 \text{ cm}, z = 2 \text{ cm})$. A better speckle size was also obtained, confirmed by the calculation of the radiofrequency auto correlation length in the axial direction. Indeed, REC-PI provides 20.1% improvement in comparison to classical PI consistent with the previous resolution enhancement. A better penetration depth of REC-PI is demonstrated by its ability to reconstruct the deeper scatterer which is not visible in the conventional PI. The cyst reveals a gain of 18.2 dB in contrast to noise ratio for the proposed approach.

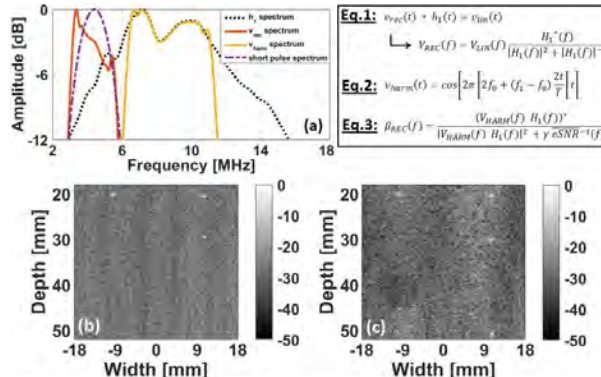


Figure: (a) Spectra of the transmitted signals (in both approaches) and of the chirp signal used to compress the received echoes for REC-PI. (b) Bmode image obtained for conventional PI. (c) Bmode image obtained for REC-PI

P2-A1 - PTF & PTE: Thin Films and High Power Ultrasonics

Waraku (posters 2)

Tuesday, October 23, 9:30 AM - 4:00 PM

Chair: **Koen W.A. van Dongen** TU Delft

P2-A1-1

DC-induced piezoelectric cubic PMN-PT/ piezoelectric tetragonal PZT epitaxial stack polarity inverted resonators for frequency switchable filters

Takahiro Shimidzu^{1,2}, Takahiko Yanagitani^{1,2,3}

¹Waseda University, Tokyo, Japan, ²ZAIKEN, Tokyo, Japan, ³JST PRESTO, Tokyo, Japan

Background, Motivation, and Objective

Currently, mobile communication devices have become more complex because of increasing the number of bandpass filters due to global roaming. Frequency switchable filters are a promising solution to the problem. We previously reported frequency switchable two-layered PZT/PbTiO₃ epitaxial film resonators, which make it possible to switch between fundamental and second mode resonance by applying the intermediate coercive field of PZT and PbTiO₃ [1]. However, PbTiO₃/PZT/PbTiO₃/PZT... multilayer is difficult to obtain since Curie temperature and growth temperature of PbTiO₃ are higher than those of PZT. On the other hands, 0.95Pb(Mg_{1/3}Nb_{2/3})O₃-0.05PbTiO₃ (PMN-PT) is a cubic perovskite, whose polarization and piezoelectricity can be induced only during the application of DC field. Their polar directions are inverted by changing direction of DC field. In this study, we considered that polarity inverted PZT/PMN-PT/PZT... multilayer can be obtained during the application of DC field less than coercive field of PZT (Fig.1(a)).

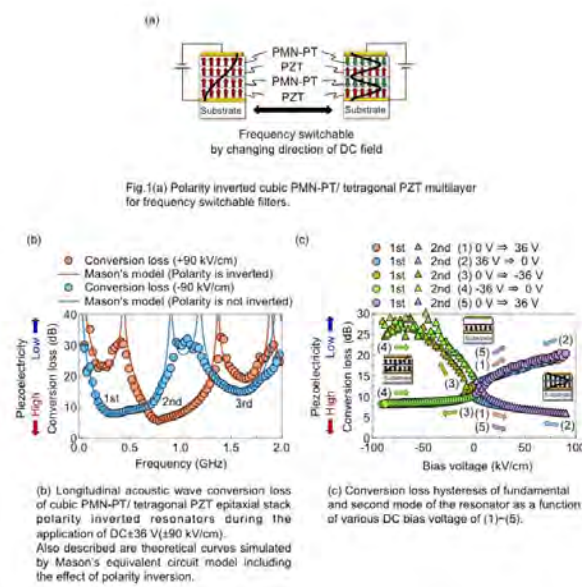
[1] T. Mori, M. Suzuki, and T. Yanagitani, IEEE Ultrason. Symp., 6H-1 (2016)

Statement of Contribution/Methods

First, PZT epitaxial films were grown on conductive La-SrTiO₃ substrate by RF magnetron sputtering. Next, PMN-PT epitaxial films were grown on the PZT films. Longitudinal wave conversion loss was measured by a network analyzer with various bias voltage.

Results/Discussion

Fig.1(b) shows conversion loss curves at DC \pm 36 V. Also described are theoretical curves simulated by Mason's model including polarity inversion. Fundamental mode resonance at 0.33 GHz was observed, whereas second mode resonance was suppressed with +36 V (+90 kV/cm) applied. In contrast, second mode resonance at 0.78 GHz was observed, whereas fundamental mode resonance was suppressed with -36 V (-90 kV/cm) applied. These results demonstrate frequency switching by changing direction of DC field. Fig.1(c) shows conversion loss hysteresis as a function of various bias voltage of (1)-(5). When the voltage is decreased 36 V to -36 V, the resonance mode is switched from second to fundamental at around 0 V. Next, the voltage is decreased -36 V to 36 V, the resonance mode is switched again from fundamental to second at around 0 V, as expected. These results show polarity inversion of cubic PMN-PT layer.



Evaluation of frequency shifts in thickness-shear mode resonator consisting of c-axis parallel oriented ZnO film for viscosity measurement
Masaya Miyata¹, Shinji Takayanagi², Mami Matsukawa¹, Takahiko Yanagitani³
¹Doshisha university, Japan, ²Nagoya Institute of Technology, Japan, ³Waseda University, Japan

Background, Motivation, and Objective

Thickness-shear mode resonators are used for viscosity measurements, because of small energy leakage of the shear wave into the liquid. A quartz crystal microbalance (QCM) is widely studied as the conventional thickness-shear mode resonator. Shifts of series resonant frequency f_s due to the liquid viscosity are generally measured in these studies. On the other hand, Itoh and Ichihashi reported that the frequency at maximal susceptance f_{im} is sifted twice [1]. In previous study, we have fabricated a thickness-shear mode resonator with c-axis parallel oriented ZnO film. We then demonstrated that a large amount of frequency shift was obtained in frequency of minimum impedance f_m [2]. In this study, detailed frequency characteristics of the resonator were evaluated with the shifts of f_s , f_m , and f_{im} .

Statement of Contribution/Methods

Our resonator consists of top electrode ($0.35\ \mu\text{m}$) / c-axis parallel oriented ZnO film ($2.6\ \mu\text{m}$) / bottom electrode ($0.35\ \mu\text{m}$) / SOI layer ($9.7\ \mu\text{m}$). Glycerol solutions were loaded on the resonator in order to measure the liquid loading properties. Concentrations of the glycerol solutions were 0-40 wt. %. Frequency characteristics were then measured by a network analyzer. The frequency shifts of f_s , f_m or f_{im} at each sample loading were calculated by subtracting f_s , f_m or f_{im} at 0 wt. % sample loading. Theoretical frequency shifts of f_s , f_m or f_{im} also calculated based on a one-dimensional transmission line model with Mason's equivalent circuit.

Results/Discussion

f_s , f_m and f_{im} at 1st mode in the condition of 0 wt. % sample loading were 131.519, 131.314, and 131.185 MHz, respectively. Fig. 1 shows the experimental and theoretical frequency shifts of f_s , f_m and f_{im} . These frequencies decreased as increasing the glycerin concentration. Experimental results showed the same tendency with theoretical results. The frequency shifts of f_s , f_m and f_{im} in the condition of 40 wt. % sample loading were -485, -837, and -963 ppm, respectively. The frequency shifts of f_{im} were twice as large as that of f_s which is generally used and, in addition, larger than that of f_m which was measured in our previous study [2]. f_{im} is expected as a high-sensitive parameter for viscosity measurement, because f_{im} is strongly affected by viscous load.

[1] A Itoh and M Ichihashi: *Meas. Sci. Technol.* **22** (2011) 015402

[2] R. Iwanaga, et al., presented at *IEEE IUS 2016*, 6H-2.

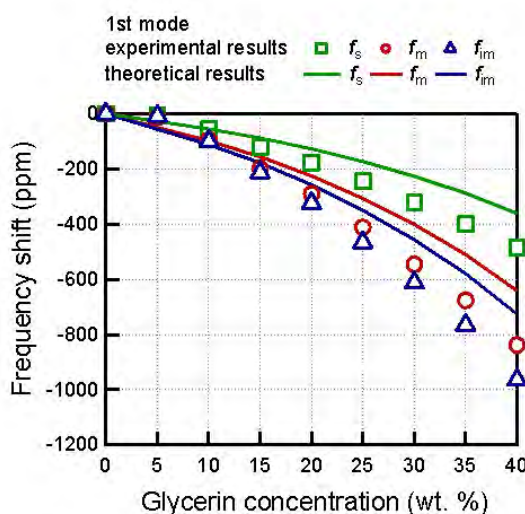


Fig. 1 frequency shifts of f_s , f_m and f_{im} in the multilayered resonator with liquid loading.

ScAlN free-standing 0.1 mm plates with 30-50 MHz resonance frequencyChiaki Masamune^{1,2}, Rei Karasawa^{1,2}, Takahiko Yanagitani^{1,2,3}¹Waseda University, Japan, ²ZAIKEN, Japan, ³JST PRESTO, Japan**Background, Motivation, and Objective**

Ultrasonic microscopy for biological imaging uses the frequency range of 100-300 MHz. High frequency ultrasound has high spatial resolution. Higher frequency, however, induces lower deep resolution because of the large sound attenuation. In recent years, tissues *in vivo* observation by ultrasonic microscopy with 80 MHz PVDF (Polyvinylidene Difluoride) transducer was reported. However, their electromechanical coupling coefficient k_t^2 of 4% is too small for practical use [1, 2]. We previously reported the transducer with ScAlN thick film on silica glass rod, operating at 44 MHz ($k_t^2=11.9\%$) [3]. Lead-free ScAlN with large piezoelectricity is suitable for medical applications. In this study, we report for the first time the fabrication of ScAlN free-standing plates with 0.105 mm and 0.117 mm thickness by using high rate sputtering growth.

[1] K. Inoue, et al., IEICE 113 (13), (2013).

[2] H.Ohigashi, J. Appl. Phys., vol.47, No.3, (1976)

[3] K-H. Sano, et al., Proc., IEEE Ultrason. Symp.(2017).

Statement of Contribution/Methods

Two ScAlN thick films (plates) were grown on Ti bottom electrodes/ silica glass substrates by hot target RF magnetron sputtering technique. We used self-made ScAl alloy metal target fabricated by e-beam melting in vacuum. Au top electrodes were deposited on the films. The free-standing plates were obtained by peeling off the thick films from the substrates. Next, the real part of admittance (Y_{real}) and impedance (Z_{real}) were measured by a network analyzer. The k_t^2 was measured by a resonance anti-resonance method using the peak of Y_{real} and Z_{real} .

Results/Discussion

Fig.1 (a) shows the X-ray diffraction (XRD) pattern of the 0.105 mm thick ScAlN free-standing plate. The rocking curve FWHM (0002) peak of the ScAlN free-standing film was measured to be 2.6°. Fig.1 (b) shows the experimental frequency response of the admittance, the real part of the admittance, and the real part of the impedance of the 0.105 mm thick plate. In Table. I , resonance frequency, film thickness, rocking curve FWHM, and k_t^2 of the plates are summarized. The k_t^2 of each plate was determined to be 12.4% at 43 MHz and 13.6 % at 38 MHz by using a resonance anti-resonance method. These k_t^2 were much larger than that of PVDF membrane. Therefore, the lead-free ScAlN transducer has a bright promise for ultrasound biological imaging.

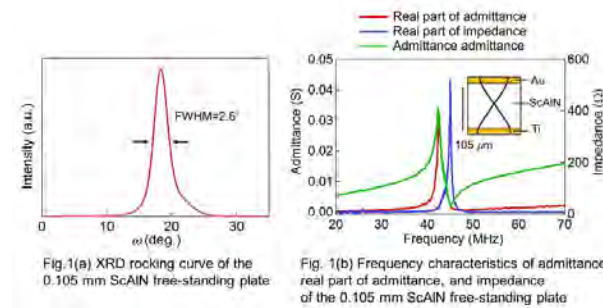


Fig.1(a) XRD rocking curve of the 0.105 mm ScAlN free-standing plate

Fig.1(b) Frequency characteristics of admittance, real part of admittance, and impedance of the 0.105 mm ScAlN free-standing plate

Table. I Resonance frequency, film thickness, rocking curve FWHM, and k_t^2 of the ScAlN plates

| | ScAlN plate (a) | ScAlN plate (b) |
|---------------------|-----------------|-----------------|
| Resonance frequency | 43 MHz | 38 MHz |
| Film thickness | 0.105 mm | 0.117 mm |
| Rocking curve FWHM | 2.6° | 5.7° |
| k_t | 0.352 | 0.369 |
| k_t^2 | 12.4% | 13.6% |

Picosecond-ultrasound study on interlayer interaction of monocrystal graphiteAtsuki Wake¹, Hirotugu Ogi¹, Akira Nagakubo¹, Koichi Kusakabe¹, Kensuke Murashima², Mutsuaki Murakami²¹*Osaka University, Japan*, ²*Kaneka Corporation, Japan***Background, Motivation, and Objective**

Graphite shows high thermal conductivity in the in-plane direction, where carbon atoms are bonded covalently. Concerning the out-of-plane bonding or interlayer bonding, the van der Waals force has been recognized as the dominant interaction cause, but the detail has not been clarified. The out-of-plane elastic constant C_{33} directly reflects the interlayer interaction and will contribute to clarifying the bonding mechanism. C_{33} is obtained from the longitudinal-wave sound velocity propagating along the c-axis of graphite.

Previously, highly oriented pyrolytic graphite (HOPG) was widely used for studying the interlayer interaction. However, HOPG usually contains many interlayer grain boundaries and interlayer defects and is not suitable for accurately evaluating C_{33} . Recently, it has become possible to synthesize monocrystal graphite films without defects by using polyimide films. The thickness is, however, $\sim 1 \mu\text{m}$ at most, for which conventional ultrasonic methods with longer wavelength ($>\sim 0.1 \text{ mm}$) cannot be adopted. We determine C_{33} of well-oriented and high quality graphite monocrystal films using picosecond ultrasonics, which allows ultra-high frequency ($\sim 10 \text{ GHz}$) measurements.

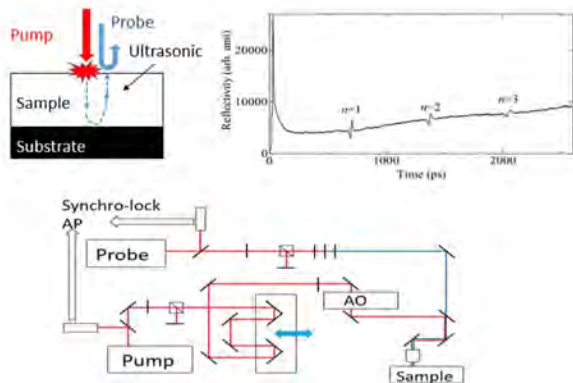
Statement of Contribution/Methods

Picosecond ultrasonics is a kind of pump-probe spectroscopy; the femtosecond pump light pulse induces ultra-high-frequency coherent acoustic wave through the thermal-phonon interaction. The ultrasonic strain pulse changes material's reflective index for the probe light. We used two Ti-S pulse lasers which synchronized in $\sim 100 \text{ fs}$ jittering. By changing the delay time for the pump light pulse to the probe light pulse and measuring the reflectivity change, it is possible to evaluate the sound-wave propagation time, and then determine the c-axis velocity of sound.

It is well accepted that incohesive bonds at grain boundaries significantly decrease the elastic constants. We developed a microscopic picosecond ultrasonics system and measured the propagation time inside the graphite grain to evaluate the true C_{33} .

Results/Discussion

Figure shows a typical reflectivity change for a graphite crystal with thickness about 1200 nm, where three pulse echoes are clearly observed. We thus precisely determined the sound velocity and then the elastic constant. The film thickness was evaluated by the cross-section observation with a field-emission.



Morphology Change of Ultrathin Films Studied by Noncontact Piezoelectric Resonance Method**Tomoya Ueno¹, Nobutomo Nakamura¹, Ryuichi Tarumi¹, Hirotugu Ogi²**¹*Graduate School of Engineering Science, Osaka University, Japan*, ²*Graduate School of Engineering, Osaka University, Japan***Background, Motivation, and Objective**

In the early stage of metallic film deposition, it frequently appears the morphology change from island to continuous structure on a substrate material. In a previous study, we developed the *in situ* and noncontact piezoelectric resonance method which detects the morphology change from internal friction of the resonator placed beneath of the substrate. Application of the method for various materials revealed that the behavior of the internal friction differs depending on the rate and type of the material deposited on the substrate. In this study, we develop a theoretical model which relates the morphology change and the internal friction variations. In addition, we simulate the dynamical behavior of film growth processes based on the internal friction experiment.

Statement of Contribution/Methods

When the piezoelectric resonator is vibrating at a resonant frequency, an electric field is generated around it. The field causes the electric current in deposited material. Then, the current yields the energy loss by Joule heating process, where total amount of the heat depends on the *apparent* electric resistance. That is an electric resistance determined from the morphology of the material deposited on the substrate. It is for this reason that the morphology of the thin film can be detected through the internal friction measurement. In this study, we develop a theoretical model which explain the entire film growth process. At first, we calculate the morphology of the deposited material, *e.g.* changes in the number and diameter of the material islands, from rate equation. Here, the surface diffusion coefficient, deposition rate, and contact angle between the island and substrate are used as material parameters. The apparent electrical resistivity as well as the internal friction are then calculated as a function of deposition time.

Results/Discussion

We experimentally observed the morphology change for some metallic films. The internal friction was generally stable just after starting deposition and increased sharply at the moment where morphology change from the island structure to the continuous film occurs. When the deposition rate increased, the morphology change appeared at smaller thickness. Present theoretical model successfully explains the experimental behavior and which confirm the validity. When Cu was deposited, the internal friction started to increase immediately after deposition started. From the calculation using different parameters, it was expected that larger islands are formed faster and their contact angle on substrate is smaller in Cu films. The morphology change occurs when the film thickness is about 2 nm. *In situ* observation of the morphology is not straightforward. However, our model enables us to expect morphology of such thin films. In the presentation, detailed experiment and analysis results are shown.

Deposition of Pd semicontinuous films using resistive spectroscopy for hydrogen sensor**Nobutomo Nakamura¹, Sosuke Iwaki², Keitaro Horikawa¹, Hirotugu Ogi³**¹*Graduate School of Engineering Science, Osaka University, Japan*, ²*School of Engineering Science, Osaka University, Japan*,³*Graduate School of Engineering, Osaka University, Japan***Background, Motivation, and Objective**

During deposition of metallic material on substrate, morphology of the deposited material changes from isolated islands to continuous film, and just before the continuous film is formed, the semicontinuous structure appears, in which inter-island distance is significantly small. Because the electrical conductivity between the islands increases drastically when they contact with each other, the electrical conductivity of the semicontinuous film is sensitive to variation of island shape. Pd is a hydrogen-absorbing metal, and it expands in hydrogen atmosphere. Therefore, change in the conductivity of a Pd semicontinuous film is expected to become a highly sensitive hydrogen sensor. However, the semicontinuous film appears when film thickness is around a few nanometers, and it is very difficult to fabricate the Pd semicontinuous films; there was no guide for letting us know the formation of the semicontinuous film. In our previous study, we developed a method that detects the morphology change using resonant vibrations of a piezoelectric material and we named this method the resistive spectroscopy. Using the resistive spectroscopy, we prepared Pd films with different morphologies and evaluated conductivity variations in hydrogen atmosphere.

Statement of Contribution/Methods

In the resistive spectroscopy, a piezoelectric material vibrating at a resonant frequency is placed beneath a substrate. Around the piezoelectric material, an oscillating electric field is generated, and when metallic material is deposited on the top surface of the substrate, the electric field causes current flow in the deposited material. Then, attenuation of the piezoelectric material increases, and the attenuation coefficient takes a maximum when the continuous film is formed. Using this phenomenon, the morphology change is detected. In this study, Pt was deposited on Si substrates using the RF-magnetron sputtering method. Pd films with different morphologies were prepared, and conductivity change under hydrogen atmosphere (180 ppm in N₂) was measured.

Results/Discussion

Discontinuous, semicontinuous, and continuous films were prepared, and their conductivity variations were measured. Change ratios of electric resistances in semicontinuous films were larger than those in other films. In addition, the response speed with the semicontinuous films was higher. By considering different conductivity-variation mechanisms, these results were explained. From these results, it was demonstrated that thin films with different morphologies were easily obtained by using the resistive spectroscopy and it was applicable to development of Pd films for hydrogen sensing.

Investigation of morphotropic phase boundary in sputter-grown Pb(Zrx,Ti1-x)O3 epitaxial films
Ryuta Noda^{1,2}, Takahiro Shimidzu^{1,2}, Kiyotaka Wasa³, Takahiko Yanagitani^{1,2,4}
¹*Waseda University, Japan*, ²*ZAIKEN, Japan*, ³*Yokohama City University, Japan*, ⁴*JST PRESTO, Japan*
Background, Motivation, and Objective

$\text{Pb}(\text{Zr}_x\text{Ti}_{1-x})\text{O}_3$ (PZT) ceramics display tetragonal-rhombohedral morphotropic phase boundary (MPB) around $x = 0.53$. In general, PZT ceramics show the anomalously high piezoelectricity and dielectric constant near the MPB [1]. However, PbTiO_3 sputter-epitaxial films at $x = 0$, where is far from the MPB, showed higher k_t^2 than PZT near the MPB in our previous studies with good reproducibility [2]. Such phenomena may occur because of the damage of the film caused by the negative ion bombardment from the target. In this study, in order to show that PZT sputter-epitaxial films do not display MPB, we measured k_t^2 , dielectric constant and coercive field as a function of x (Zr concentration).

[1] D.A. Berlincourt, C. Cmolik, and H. Jaffe, Proc. IRE, 48 (1960)

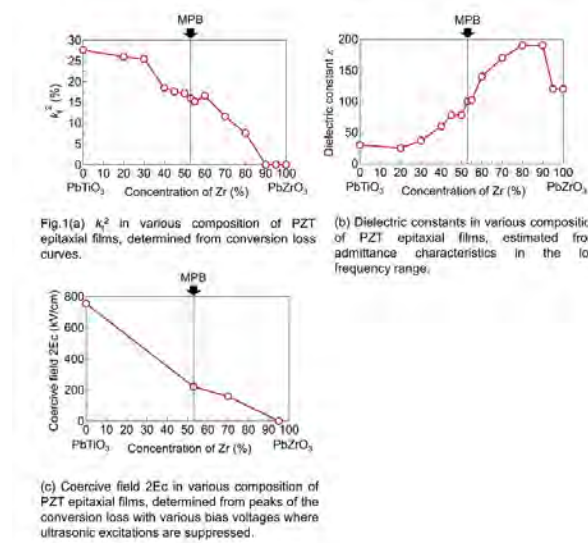
[2] T. Mori, M. Suzuki and T. Yanagitani, IEEE Ultrason. Symp., 6H-1 (2016)

Statement of Contribution/Methods

Fourteen different compositions of PZT epitaxial films were grown on conductive La-SrTiO_3 substrate by RF magnetron sputtering with powder target. First, longitudinal wave conversion loss (CL) with the various bias voltages were measured by a network analyzer (E5071C, Agilent Technologies). Next, k_t^2 were determined by comparison of theoretical CL curves simulated by Mason's equivalent circuit model with experimental CL curves. Dielectric constants were estimated from admittance characteristics in the low frequency range. Finally, coercive fields were determined from peaks of the CL with various bias voltages where ultrasonic excitations are suppressed.

Results/Discussion

FWHM of ω -scan (002) rocking curves of all samples were less than 0.5° . Figure 1 (a) and (b) show the k_t^2 and the dielectric constant in various compositions of PZT films, respectively. The anomalously high piezoelectricity and dielectric constant were not observed near the MPB. Figure 1 (c) shows the coercive field $2Ec$ in various compositions of PZT films. The coercive field may be influenced by the crystal structure change near the MPB. However, a specific change of the experimental coercive field near the MPB was not observed. From these results, PZT sputter-epitaxial films did not display the MPB, as expected. We considered that such phenomena observed in sputter-epitaxial films were attributed to the degradations by the negative oxygen ion bombardment on the films.



Polymer films joining with High-Intensity Focused Ultrasound: investigation of the physical principles

Coralie Koo Sin Lin¹, Klaus-Vitold Jenderka², Marko Liebler³

¹Chair of Processing Machines and Processing Technology, Technische Universität Dresden, Germany, ²Departement of Engineering and Natural Sciences, University of Applied Sciences Merseburg, Germany, ³Robert Bosch GmbH, Germany

Background, Motivation, and Objective

Previous studies showed that using a 1 MHz solid waveguide transducer based on High-Intensity Focused Ultrasound (HIFU) enables 320 μm thick low density polyethylene (LDPE) films heating over the melting temperature within 200 ms. However, the physical mechanisms causing the heating of polymer films thinner than half a wavelength are still unknown. It is not clear if the waves can be transmitted and concentrated.

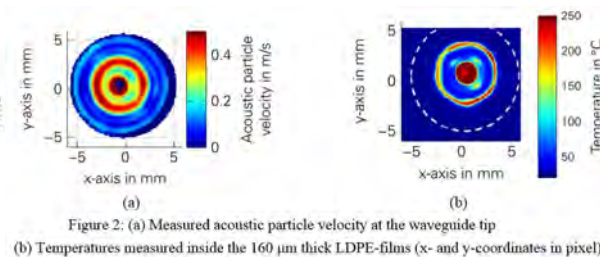
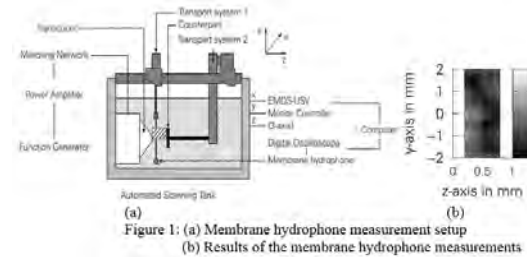
An innovative polymer film joining technology is presented and the physical principles responsible for polymer films heating are investigated using sound field, vibrometry (sLDV) and infrared measurements.

Statement of Contribution/Methods

A focused ultrasound transducer ($R=48.5 \text{ mm}$, $f=1.088 \text{ MHz}$) coupled to a solid waveguide is used to heat 160 μm thick LDPE films with an electrical power of 175 W applied for 3 s. The heating of the films was measured by infrared camera (Infratec, ImageIR 8300). The particle velocities at the waveguide tip were measured with sLDV (Polytec, PSV-500), applying an electrical power of 6 Watt (cw-signal) and the sound field in water between waveguide and counterpart was measured using a PVDF membrane hydrophone (Gampt, SF100).

Results/Discussion

The sound field distribution measured does not look like the typical focused sound field (Figure 1). In the gap, being smaller than half a wavelength, the waves cannot propagate to generate an energy concentration. Depending on the gap size an irregular superposed wave field occurs. A correlation between the acoustic particle velocity at the waveguide tip and the heating inside the polymer is found (Figure 2). From these findings it can be concluded that the heating in LDPE films is caused by waveguide tip hammering on the films leading to intermolecular frictions and not by the absorption of the sound wave inside the film.



P2-A10 - SAW Modeling & Design I

Waraku (posters 2)

Tuesday, October 23, 9:30 AM - 4:00 PM

Chair: **Ryo Nakagawa** Murata Manufacturing Co., Ltd.

P2-A10-1

Acoustic Wave Filter Topologies for enhanced performance

Jordi Mateu¹, Carlos Collado¹, Alberto Huertes¹, Rafael Perea-Robles¹, Robert Aigner², Nadim Khlat³

¹*Universitat Politècnica de Catalunya, Spain*, ²*Qorvo, United States*, ³*Qorvo, France*

Background, Motivation, and Objective

Acoustic wave (AW) filters have been for more than a decade one of the driving technologies on the development of handset wireless due to the outstanding achievable filter responses in an extremely compact size, in comparison with any other technology at those frequencies.

However, due to the nature of acoustic resonators and the usual filter topologies, as ladder, there still exist intrinsic limitations on the achievable filter responses, such as the position of transmission zeros and the achievable bandwidth. The question is, will AW filters continue driving the future development of handset components? The answer is: as long as they provide the electrical filter requirements they will continue playing a fundamental role on the telecom industry.

The motivation and objective of this work is to help onwards that direction by proposing a novel filter topology that can offer responses unachievable with the current ladder or lattice topologies.

Statement of Contribution/Methods

This work presents a novel filter topology based on a transversal configuration of the resonators forming the filter, in such a way that the frequency response is created by the contribution of each signal path. This allows to obtain any type of response such as wider band, multiband and self-equalized responses, and with arbitrary position of transmission zeros.

This can be achieved without dependence on the electro-acoustic coupling coefficient, which can be set with full flexibility by the designer from the very beginning. Additional flexibility exists on the selection of the resonator impedances and resonant frequencies, with the possibility of selecting all the resonators with uniform impedance and/or a selected families of resonant frequencies

Results/Discussion

The paper will present synthesized responses that meet the current requirements of existing bands and will illustrate filter responses with multiband and self equalized performances.

Implementation of this topology might be very significant on the development of a new generation of filters for the full deployment of 5G, where complex multiplexing filtering stages, carrier aggregation access and the need of coexistence of several systems in a single device is a must.

Even a more important benefit is the ability to give response to the spectrum development which pushes the communication bands to higher frequency. The fact that filter responses do not depend on the coupling coefficient opens the possibility to move the technology to higher frequency without the constrain of maintaining a high coupling coefficient and focus on other important parameters as the Q factor of the resonators.

Fast SAW Device Simulation in COMSOL Using the Hierarchical Cascading MethodAleksey Shimko¹, Victor Plessky²¹Tai-Saw Technology Co. Ltd, Taiwan, ²GVR Trade SA, GORGIER, Switzerland**Background, Motivation, and Objective**

Using the finite element method (FEM) for modeling SAW resonators, it is possible to achieve high accuracy, by considering influence of shape of the electrodes, the parameters of multilayer structures, etc. However, commercial software products (e.g. COMSOL) require considerable time and a large amount of RAM to simulate a full-sized SAW device. Therefore, COMSOL is often used to model an infinite periodic 2D SAW transducer structure, and Y-parameters of such a structure are used to extract Coupling of Mode (COM) parameters. The device simulation and optimization is then carried out with the help of a fast COM-model. This approach lowers the accuracy of the simulation.

The method of hierarchical cascading proposed in [1] demands significantly less memory and radically reduces the computation time of the quasi-periodic SAW. In this paper, we show how this approach can be used together with COMSOL Multiphysics 5.2a.

Statement of Contribution/Methods

To correctly take into account the component of displacement perpendicular to the sagittal plane in COMSOL 5.2, a 3D model of unit block was used (see Fig.1). Continuity of variables on the front and back surface was imposed. To successfully apply the method, the grid/mesh on the left and right edges must be identical, as well as the grid on the front and back surface. Then, using the COMSOL module Live Link for MATLAB, the system matrix is transferred to MATLAB as:

$$K \cdot U + N^T \cdot A = L$$

$$N \cdot U = 0,$$

where U is the vector containing the nodal DOFs; K is stiffness matrix; L is Load vector; N is Constraint Jacobian; N^T is Constraint force Jacobian; A is Lagrange multiplier vector.

The structure of matrix N allows us to find a matrix C such that $C^T K C = A$, where A is the *Eliminated stiffness matrix*, corresponding to the A -matrix in Koskela's *et al* paper [1].

Results/Discussion

Exclusion of internal variables and use of hierarchical cascading, as in [1], was done in Matlab. Increase of the computational speed of more than 30 times was seen in case of the synchronous resonator, consisting of 200 Al electrodes in the IDTs and 20 in the reflectors, compared to simulation of such a structure entirely in COMSOL. COMSOL is used for the mesh generation, etc.

References

- [1] J. Koskela, et al. "Hierarchical cascading... " *Ultrason. Symp.*, 2016, p.

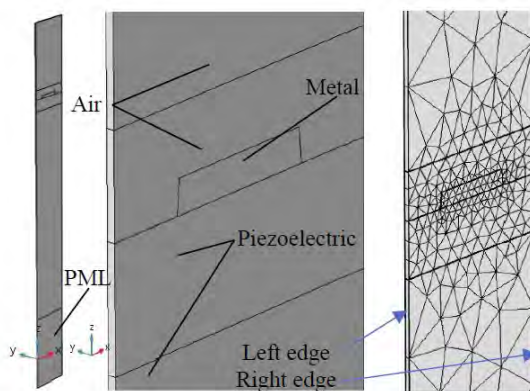


Fig. 1. 3D model of a unit block with a single electrode and mesh. From top to bottom: vacuum, metal, piezoelectric, PML

A nonlinear FEM model to calculate third harmonics and intermodulation in TC-SAW devices

Vikrant Chauhan¹, Markus Mayer², Elena Mayer³, Werner Ruile², Thomas Ebner², Ingo Bleyl², Karl Wagner², Robert Weigel¹, Andreas Mayer³, Amelie Hagelauer¹

¹*Institute for Electronics Engineering, Friedrich-Alexander-University Erlangen-Nuremberg, Erlangen, Germany*, ²*Advanced Development Department, RF360 Europe GmbH, Munich, Germany*, ³*Offenburg University of Applied Science, Offenburg, Germany*

Background, Motivation, and Objective

The generation of third harmonics (H3) and third order intermodulation products (IMD3) are typical problems caused by the nonlinearity in acoustic devices. Previously, we employed a nonlinear FEM simulation model [1] to better understand the origin of nonlinearities in such acoustic devices. By applying a single scaling factor for the Silicon dioxide (SiO_2) nonlinear material constants and another single scaling factor for the electrode material Copper (Cu) nonlinear material constant, we identified metal as the main cause of IMD3 [2]. In this model, we apply a similar scheme to both IMD3 and H3.

Statement of Contribution/Methods

In this work, we extended our nonlinear FEM model to include H3. In the employed perturbation approach, different contributions to the total H3, the direct and indirect contribution, are considered. Since this time, H3 and IMD3 measurements were fitted simultaneously using two scaling factors for SiO_2 (3rd and 4th order elasticity) and two scaling factors for those of Cu (3rd and 4th order elasticity) nonlinear material constants. Also in this work we employ P-matrix simulations as intermediate step: Firstly, measurement and nonlinear P-matrix calculations for finite devices are compared and coefficients of the P-matrix simulation are determined. Secondly, nonlinear P-matrix and FEM calculations for an infinite periodic system are compared and the scaling factors are determined.

Results/Discussion

We investigated test TC-SAW filters with varying metallization ratios and period lengths. Different IMD3 and H3 measurements are considered to determine the scaling factors of nonlinear material constants. Based on the FEM simulations, the contributions of the different materials to the nonlinear behavior of SAW devices are compared, in particular the direct and cascaded contributions to H3 are considered in some detail. Finally, the role of electric and acoustic contributions to the nonlinear responses of TC-SAW devices is discussed.

[1] A. Mayer, E. Mayer, M. Mayer, P. Jäger, W. Ruile, I. Bleyl, and K. Wagner, "Full 2D-FEM calculations of third-order intermodulation in SAW devices", IEEE International Ultrasonics Symposium 2016.

[2] V. Chauhan, M. Mayer, E. Mayer, W. Ruile, T. Ebner, I. Bleyl, K. Wagner, R. Weigel, A. Mayer, and A. Hagelauer, "Investigation on third-order intermodulation distortions due to material nonlinearities in TC-SAW devices", IEEE Transactions on Ultrasonics, Ferroelectrics and Frequency Control (UFFC), April 2018.

P-matrix model for third order electric and acoustic nonlinearities in TC-SAW devices

Vikrant Chauhan¹, Markus Mayer², Thomas Fintets², Werner Ruile², Thomas Ebner², Ingo Bleyl², Karl Wagner², Robert Weigel¹, Amelie Hagelauer¹

¹Institute for Electronics Engineering, Friedrich-Alexander-University Erlangen-Nueremberg, Erlangen, Germany, ²Advanced Development Department, RF360 Europe Gmbh, Munich, Germany

Background, Motivation, and Objective

Suppression of nonlinearities is crucial, especially in the design of LTE devices. Thereto, it is essential to understand the interaction of nonlinearities in different bands. Since these bands may be separated by hundreds of MHz, not only acoustic but also electric and mixed electro-acoustic nonlinearities contribute to intermodulation products.

Previously Nakagawa et al. [1] proposed a model to describe third order nonlinearities on 42° YX-LiTaO₃ (Lithium Tantalate) substrate depending on acoustic and electric fields. In former work, P-matrix models were based on the acoustic field only [2] and therefore provided the description of intermodulation products with small tone differences only. In this work, we introduce a P-matrix approach considering acoustic and electric source terms, requiring 8 nonlinear parameters. It is applied to describe the generation of third harmonics (H3) and third order intermodulation (IMD3) products in temperature compensating (TC)-SAW devices on 128° YX-LiNbO₃ (Lithium Niobate) substrate.

Statement of Contribution/Methods

The nonlinear P-matrix approach of [2] is extended by considering source terms of mixed acoustic and electric origin. As in [1] the nonlinear sources are written as sum of mixed third order terms in strain and electric field. Two kinds of nonlinear sources are considered: directly induced nonlinear currents at the electrodes (vertical dielectric displacement D_z) and acoustic sources distributed in the device, which indirectly lead to nonlinear currents at electrodes. For TC-SAW devices, the wave considered in the P-matrix model is the vertical displacement u_z. From symmetry considerations, horizontal electric field E_x and the strain S_{xz} give rise to nonlinear stress T_{xz}, the acoustic source, while vertical electric field E_z and strain S_{zz} give rise to D_z. In total 8 source terms and therefore 8 coefficients are needed.

Results/Discussion

The extended P-matrix approach is applied to single filters and duplexers operating in different LTE frequency bands such as band-2, band-8 and band-1. The third order nonlinear simulation model for TC-SAW devices shows a good fit to H3 and IMD3 measurements. Finally, the role of electric and acoustic contribution to the nonlinear responses of TC-SAW devices are discussed.

[1] R. Nakagawa, T. Suzuki, H. Shimizu, H. Kyoya, and K. Hashimoto, "Study on generation mechanism of third-order nonlinearity in SAW devices", IEEE International Ultrasonics Symposium (IUS), Sept 2015.

[2] M. Mayer, E. Mayer, W. Ruile, J. Johnson, I. Bleyl, K. Wagner, and A. Mayer, "Rigorous COM and P-matrix approaches to the simulation of third-order intermodulation distortion and triple beat in SAW filters", IEEE International Ultrasonics Symposium (IUS), Sept 2013.

Electrothermal modeling of TC SAW filter

Wolfgang Akstaller¹, Jan H. Kuypers², Kimmo Kokkonen³, Robert Weigel¹, Amelie Hagelauer¹

¹Institute for Electronics Engineering, Friedrich-Alexander-University Erlangen-Nueremberg, Erlangen, Germany, ²Qorvo, Inc., Apopka, FL, United States, ³Qorvo Munich GmbH, Munich, Germany

Background, Motivation, and Objective

Ongoing miniaturization of RF frontend modules for mobile hand-sets results in greater power densities and increasing temperatures within acoustic filters. The increase in device temperature in combination with the resonators' temperature coefficient of frequency leads to a frequency shift of the filter transfer function that is problematic due to the stringent specifications. With the high power levels typical for a TX filter, the frequency shift remains a challenge even with the current temperature compensation (TC) techniques. Furthermore, increased device temperature is detrimental to the filter performance and lifetime, and therefore, it is desirable to include the thermal aspect in the SAW filter modeling.

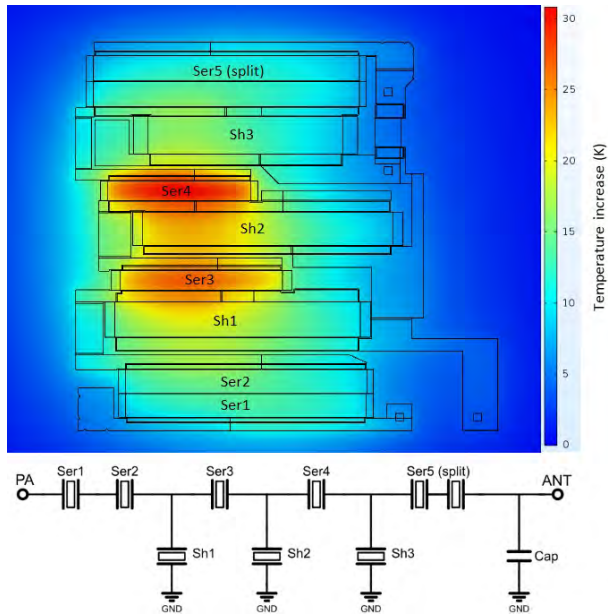
Statement of Contribution/Methods

We present an electro-thermal model for a filter test structure on wafer level. The filter layout is imported to FEM-simulation software to calculate a thermal impedance matrix. It is used in AWR circuit simulator together with temperature dependent acoustic resonator models and models which represent the losses occurring in the routing to simulate the electro-thermal response of the filter test structure. To validate the temperature predictions, the filter test structure includes resistive temperature sensors, which enable the measurement of the effective temperature of two series resonators within the filter. In our measurements, the filter is excited with a high-power CW load tone and the temperatures of the target resonators are monitored.

Results/Discussion

The simulated temperature increases at two resonators of the test structure are compared to measurement. The model enables to separate the contributions to the resonator temperatures into self-heating of the resonator and mutual-heating from surrounding structures which can be used to determine the crucial heat sources. Consequently, this implementation of the electro-thermal model can be applied to the design optimization of arbitrary filter geometries.

Fig. Example of simulated temperature distribution on the wafer level SAW filter test structure. A +29 dBm load tone is applied at a frequency close to the upper band edge of the filter. At this frequency the resonators SER3 and SER4 show highest temperatures and are spreading heat into the surrounding area. The test filter circuit topology is shown at the bottom.



P2-A11 - SAW Device & Application I

Waraku (posters 2)

Tuesday, October 23, 9:30 AM - 4:00 PM

Chair: **Jidong Dai** Murata Electronics North America, Inc.

P2-A11-1

Experimental observation of high-velocity surface acoustic wave (HVSaw) on highly-textured ScAlN/Sapphire bilayer structure. Application to high frequency devices.

Florian Bartoli¹, Jérémie Streque², Mohammed Moutaouekkil², Thierry Aubert¹, Philippe Pigeat², Jaafar Ghanbaja², Sylvie Robert², Sami Hage-Al², Omar Elmazria²

¹LMOPS, CentraleSupélec, France, ²Institut Jean Lamour, Université de Lorraine, Nancy, France

Background, Motivation, and Objective

One of the important tasks for further development of SAW filters is to increase their operating frequency and bandwidth. This requires substrates or structures exhibiting simultaneously a high elastic velocity (v) and a large electromechanical coupling coefficient (K^2). To date, the highest velocities were obtained from structures using diamond as substrate. However, the unavailability of industrial diamond wafer production lines combining large size, high quality and low cost prohibits its use. In the present work, we experimentally investigate the ScAlN/Sapphire structure as a potential solution allowing the combination of high acoustic velocity (> 10 km/s) and high K^2 (3%).

Statement of Contribution/Methods

(002) $\text{Sc}_{0.09}\text{Al}_{0.91}\text{N}$ and $\text{Sc}_{0.18}\text{Al}_{0.82}\text{N}$ films have been grown on (0001) sapphire substrates by reactive magnetron sputtering. The growth process was optimized in order to maximize the texture of the films. X-ray diffraction (XRD) and energy-dispersive X-ray spectroscopy coupled to transmission electron microscopy (TEM-EDXS) measurements were performed to get access to the microstructure and the local composition of the samples respectively. Several surface acoustic waves (SAW) resonators were fabricated using different wavelengths (λ) and ScAlN film thicknesses (h). K^2 and v were determined from S_{11} measurements for each observed mode.

Results/Discussion

XRD FWHM rocking-curve values of 0.8° and 1.2° for the (002) reflex were obtained for the optimized $\text{Sc}_{0.09}\text{Al}_{0.91}\text{N}$ and $\text{Sc}_{0.18}\text{Al}_{0.82}\text{N}$ films, respectively. TEM observations confirm this result, and show that the films are textured in the plane as well, demonstrating an epitaxial nature. SAW characterizations reveal that, depending on the ratio h/λ , different modes are excited. In particular, one mode, identified as high-velocity surface acoustic waves (HVSaw) [1], is observed for several devices with different parameters (λ and h), and shows a velocity greater than 10 km/s. The figure 1-a shows an example of a SAW response which exhibits this mode. In that case, the K^2 value is equal to 1.7% (Fig. 1-b). We experimentally obtained a maximum K^2 of 3.3% for this mode. By reducing λ to $1.2\ \mu\text{m}$ and h to $0.5\ \mu\text{m}$, in order to keep the ratio h/λ constant, a frequency of 8.5 GHz is expected. The fabrication of such a device is in progress.

[1] N. Naumenko and I.S. Didenko, Appl. Phys. Lett., vol. 75, pp. 3029 (1999).

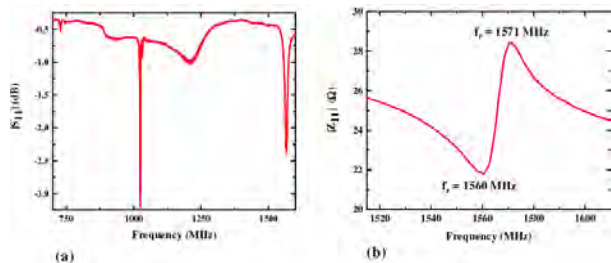


Fig. 1 : S_{11} response of a $\lambda = 6.5\ \mu\text{m}$ and $h = 2.76\ \mu\text{m}$ device (a),
Impedance of the HVSaw mode located at 1.56 GHz (b).

Study for Temperature Coefficient of Frequency of Surface Acoustic Wave Devices with SiO_xN_y Film Using LiTaO₃ Substrate**Atsushi Nishimura¹, Satoru Matsuda¹, Yoshiro Kabe¹, Hiroyuki Nakamura¹**¹*Skyworks Solutions, Inc., Japan***Background, Motivation, and Objective**

Surface acoustic wave (SAW) devices are increasing in demand in recent years. These devices often suffer from the passivation film formation process that affects the frequency and TCF (Temperature Coefficient of Frequency). It is reported that the sound velocity and TCV (Temperature Coefficient of Velocity) of the SiO_xN_y film correlate with its refractive index [1, 2]. When SiO_xN_y film is used as a passivation film, it is expected that the frequency and TCF can be controlled by manipulating the refractive index. In previous research reports, the authors uncovered the correlation between the frequency of the one-port resonators and the refractive index of the SiO_xN_y films [3, 4]. In this study, the correlation between the TCF of the one-port resonators and the refractive index of the SiO_xN_y films is investigated.

Statement of Contribution/Methods

One-port resonators were fabricated by forming interdigital transducer (IDT) electrode with Al on 42°Y-X LiTaO₃ substrate. Then, a dielectric film of SiO₂, Si₃N₄ or SiO_xN_y was deposited on IDT electrode and we investigated whether TCF of one-port resonators correlates with refractive index of dielectric films. Here, refractive index of SiO_xN_y film was varied by changing O₂/N₂ gas flow ratio in RF sputtering.

Results/Discussion

We have uncovered that the TCF of the one-port resonator correlates with the refractive index of the dielectric film deposited on the IDT electrode. Our data shows that when SiO_xN_y film is deposited, TCF of the one-port resonators is likely to shift from SiO₂ film side to Si₃N₄ film side as the refractive index increases.

[1] S. Tsuboi et al., presented at (72nd Spring Meet., 2017); The Physical Society of Japan, 17pC43-4 [in Japanese].

[2] S. Tsuboi et al., presented at IEEE Ultrason. Symp., 2017, P4-A2-1.

[3] A. Nishimura et al., Proc. Symp. on Ultrasonic Electronics, 1J3-1, 2017.

[4] A. Nishimura et al., to be published in Jpn. J. Appl. Phys.

Longitudinal Leaky SAW with Low Attenuation on LiTaO₃ Thin Plate Bonded to Quartz Substrate

Junki Hayashi¹, Kosuke Yamaya¹, Shiori Asakawa¹, Masashi Suzuki¹, Shoji Kakio¹, Hiroyuki Kuwae², Toshifumi Yonai³, Kazuhito Kishida³, Jun Mizuno²

¹University of Yamanashi, Kofu, Japan, ²Waseda University, Tokyo, Japan, ³The Japan Steel Works, Ltd., Tokyo, Japan

Background, Motivation, and Objective

To develop next-generation mobile communication systems, surface acoustic wave (SAW) devices with a high frequency and a large electromechanical coupling factor (K^2) are required. The longitudinal leaky SAW (LLSAW) has attracted interest owing to its high phase velocity close to that of a longitudinal bulk wave. The authors previously reported that, when LiNbO₃ (LN) or LiTaO₃ (LT) thin plate with a thickness smaller than the wavelength λ was bonded to an AT-cut 45°X-propagating quartz (AT45°X-Q) substrate, the particle displacement of the LLSAW was concentrated in the thin plate and a larger K^2 than that on the single LN or LT was obtained. However, it was difficult to achieve a high Q factor because the attenuation of the bonded structure remained large. In this study, to obtain a bonded structure with low attenuation for an LLSAW, the propagation and resonance properties of an LLSAW on an LT thin plate bonded to an X-cut quartz substrate were investigated.

Statement of Contribution/Methods

First, for the structure of an X-cut 31°Y-propagating LT (X31°Y-LT) thin plate with a large K^2 for an LLSAW bonded to a quartz substrate, the dependence of LLSAW attenuation on the cut angle of the quartz substrate was calculated. An X32°Y-Q substrate was found to have the optimum cut angle to obtain low attenuation. Then, simple delay line samples with the propagation path length L ($L=25$ and $50\ \lambda$) and interdigital transducer (IDT)-type resonator samples were fabricated on the bonded structure of X31°Y-LT/X32°Y-Q with an LT thickness h of $6.0\ \mu\text{m}$. A single-electrode IDT with a period λ of $96\ \mu\text{m}$ ($h/\lambda=0.063$) and 30 finger pairs was fabricated on the LT surface using a $5500\text{-}\text{\AA}$ -thick Al thin film. For comparison, similar samples of X31°Y-LT/AT45°X-Q with an LT thickness of $9.0\ \mu\text{m}$ ($0.094\ \lambda$) were also fabricated. The propagation loss PL was experimentally determined from the slope of the minimum insertion loss as a function of L . In addition, using a finite element method (FEM) system, the ideal resonance properties of the LLSAW on models consisting of an infinite periodic IDT with the same parameters as above were simulated.

Results/Discussion

An LLSAW attenuation of $0.0005\ \text{dB}/\lambda$ was obtained theoretically for X31°Y-LT/X32°Y-Q with $h/\lambda=0.062$ for a metallized surface. The measured values of PL were 0.016 and $0.024\ \text{dB}/\lambda$ for X31°Y-LT/X32°Y-Q and X31°Y-LT/AT45°X-Q, respectively. From the simulated resonance properties, the Q factors of 33800 , 990 , and 42.6 were obtained for X31°Y-LT/X32°Y-Q, X31°Y-LT/AT45°X-Q, and single LT, respectively. On the other hand, the measured Q factors were 71 and 73 for X31°Y-LT/X32°Y-Q and X31°Y-LT/AT45°X-Q, respectively. The electrode parameters will be optimized to obtain a high Q factor in a future experiment.

Optimized Y-rotated cut of LiNbO₃ with least anisotropic and higher electromechanical in-plane properties for omnidirectional surface acoustic waves propagation

Naiqing Zhang¹, Jiyang Mei¹, Gopesh Tilwala¹, James Friend¹

¹*Center for Medical Devices and Instrumentation, University of California, San Diego, La Jolla, CA, United States*

Background, Motivation, and Objective

Surface acoustic wave (SAW) has been widely generated and propagated on 128° Y-rotated X-propagating (YX) cut lithium niobate (LN) for fluid actuation, particle manipulation, and various biological and chemical applications. But 128° YX cut LN can generate SAW of the same frequency and amplitude only in one direction. Any veering from the primary propagation direction is affected by beam steering and changes in frequency and electromechanical coupling coefficients (K^2). So high frequency SAW devices made using LN substrates are limited to a single direction for SAW propagation if optimal performance is desired. Our objective is to proposed an optimized YX cut of LN for omnidirectional SAW propagation with least anisotropic and comparable electromechanical properties for acoustofluidics applications.

Statement of Contribution/Methods

Tensor analysis and L^2 -norm comparison under rotational transformation of LN were used, for the first time, to obtain the exact cut of LN, 121° YX cut, with least anisotropic in-plane properties. A physical model with closed governing equations for SAW propagation on the surface of a piezoelectric material was then presented to analytically obtain SAW velocity and K^2 of 121° YX cut LN with respect to propagation direction. Finally, experimental device was designed (Fig. 1c), fabricated and tested on 121° YX cut LN substrate to verify the analytical calculation and further demonstrated its practical effectiveness for SAW generation and propagation.

Results/Discussion

Stiffness tensor of 0 degree YX cut LN on propagation surface was compared with isotropic in-plane material via L^2 -norm $\min\{\|c_{3qr3}^E - c_{iso}\|_2\}$ (Fig. 1a). Because of the poor quality of SAW generation and propagation on Z-cut LN ($\theta=0$ or 180°), $\theta=121^\circ$ YX cut of LN turned to be the optimum cut with least anisotropic properties. Analytical calculation of K^2 with respect to propagation direction (Fig. 1b) showed that K^2 of 121° YX cut LN is larger than that of 128° YX cut LN in most of propagation directions. The standard deviation and accumulation of K^2 in all directions quantified that 121° YX cut LN is 29.2% less anisotropic and 5.87% more electromechanically efficient than the widely used 128° YX cut LN. Experimental results (Fig. 1d) also verified the effectiveness of the analytical calculation, and further emphasized its superior electromechanical effects for SAW propagation.

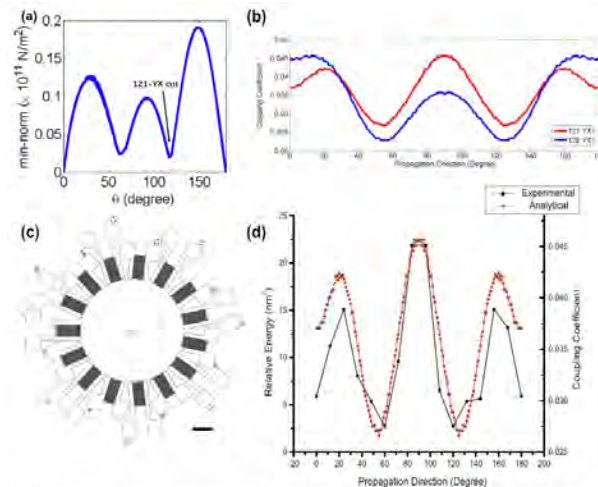


Fig. 1 (a) Analytical $\min\{\|c - c(iso)\|_2\}$ with respect to 0 degree YX-cut LN, showing the 121° YX-cut LN has the least anisotropic properties. (b) Analytical coupling coefficient of 121° and 128° YX-cut LN with respect to propagation direction, showing that 121° YX-cut also has high electromechanical effects for SAW propagation. (c) Experimental device design for testing the coupling coefficient of 121° YX-cut LN. (d) Experimental results from laser Doppler vibrometry (UHF-120 Polytec, Germany) compared to analytical results for 121° YX-cut LN. Scale bar: 2mm.

Novel Cuts of Quartz Crystals for SAW Resonators with Cubic Frequency-temperature RelationsShaoyun Wang¹, Ji Wang¹, Longtao Xie¹, Aibing Zhang¹, Jianke Du², Yook-Kong Yong³¹*Ningbo University, Ningbo, China, People's Republic of*, ²*Faculty of Mechanical Engineering and Mechanics, Ningbo University, China, People's Republic of*, ³*Rutgers University, United States***Background, Motivation, and Objective**

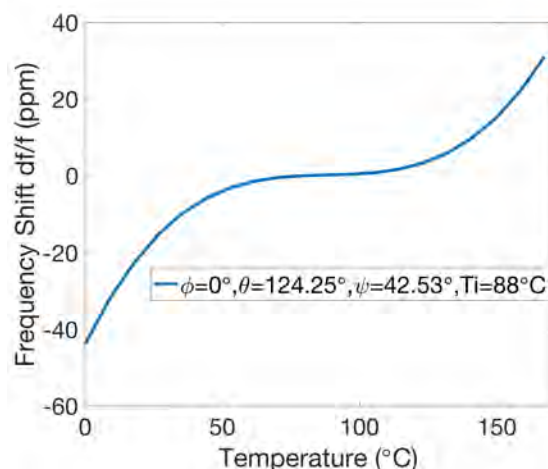
Frequency-temperature relations of acoustic wave resonators of bulk and surface types are vital in applications from consumer to communication electronics. Recently, it is found that with the theory of incremental thermal field, high frequency vibrations of piezoelectric solids can be formulated in a systematic manner for the vibration frequency and mode shapes, and the optimal frequency-temperature relation can be obtained by changing essential variables such as orientations and configuration to obtain the cubic frequency-temperature relations.

Statement of Contribution/Methods

Applying the incremental thermal field theory, the propagation of surface acoustic waves in a piezoelectric solid is formulated with the consideration of Euler angles as orientation and thermal properties as shown in earlier studies. For surface acoustic waves in a thermal field, the frequency is obtained as a function of orientations and temperature. To achieve ideal frequency-temperature relations of cubic curves, we let the first- and second derivatives of the frequency-temperature function to vanish, and all orientation angles of the triply-rotated quartz crystals are obtained. In doubly-rotated quartz crystals, orientations with cubic frequency-temperature curves and inflection temperature slightly above 85°C are found and they may have potential applications in high precision SAW resonators with much improved thermal properties. The existing cuts of quartz crystals with superior thermal behavior for surface acoustic wave substrates are validated, and more novel and promising cuts are found to drive further studies for new cuts with such excellent frequency-temperature properties.

Results/Discussion

With the theory of incremental thermal field for the high frequency vibrations of quartz crystal substrates, the frequency-temperature relation of surface acoustic waves is obtained for optimization of orientations to realize the much needed cubic frequency-temperature relations. With a powerful numerical procedure, optimal orientations with cubic frequency-temperature relations are obtained after checking over three Euler angles in a systematic manner. In addition, more novel cuts are found for further studies for the accurate properties of thermal effect and vibration modes.



P2-A12 - BAW Device & Application I

Waraku (posters 2)

Tuesday, October 23, 9:30 AM - 4:00 PM

Chair: **Amelie Hagelauer** University of Erlangen-Nuremberg

P2-A12-1

A Hybrid Acoustic-Wave Resonator and Lumped-Element Ladder Filter

Michael Wagner^{1,2}, Stephan Leuschner², Robert Weigel³, Amelie Hagelauer³

¹Friedrich-Alexander-University Erlangen-Nuremberg, Germany, ²Intel Deutschland GmbH, Germany, ³Institute for Electronics Engineering, Friedrich-Alexander-University Erlangen-Nuremberg, Erlangen, Germany

Background, Motivation, and Objective

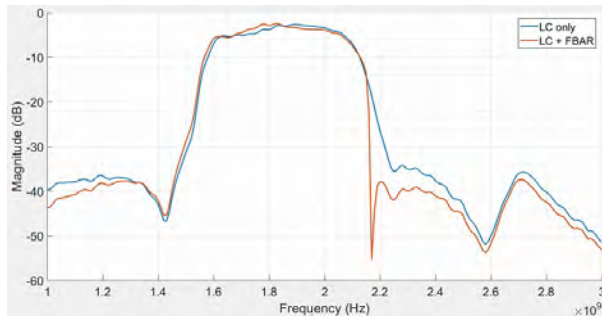
RF frequency filters employing acoustic-wave resonators are used in modern handsets for mobile communication. Their characteristics depend on employed materials and technology. They offer high quality and stability but achievable fractional bandwidth is limited by the electro-mechanical coupling factor $k_2 t$. Instead, classic filter design theory is dealing with lumped reactive elements (L, C) for the realization of any-order filter designs. Achievable bandwidth is theoretically unlimited while exhibiting rather low quality in practice. A new approach for the combination of these two filter types, preserving their respective benefits, is presented. Theoretical aspects, design process and measurement results will be outlined. Other recent hybrid filter designs are discussed.

Statement of Contribution/Methods

The presented design is a combination of an LC filter core with added FBARs at the input and output in a ladder-type filter topology. The difference to other recent proposals is that no series or parallel elements are added to the resonator dipole, i.e. its respective resonance frequencies are not manipulated. The advantage is that there is no inherent restriction in achievable bandwidth. Due to their high quality, the FBARs account for steep filter skirts at the passband edges without degrading passband performance significantly. The overall filter behavior (esp. stopband suppression) is defined by the LC filter core. A hybrid filter of this type was built with discrete components on a PCB. [Schematic, photograph of the PCB will be shown.]

Results/Discussion

Fractional 3 dB-bandwidth is greater than 22 % at a center frequency of approx. 1.8 GHz. Simulated IL is 2.5 dB, measured approx. 3 dB. Stopband suppression is greater than 38 dB. A much steeper filter skirt on the upper side of the passband is achieved compared to the pure LC filter — this is due to the employed FBARs. The initial objective of the proposed design is met. The combination of different filter concepts is a major advancement in general filter design methodology. The presented filter design is a practical approach of combining lumped elements and acoustic-wave resonators while preserving its respective benefits.



Resonant and antiresonant frequencies behavior with temperature changes in gravimetric sensors**Teona Mirea¹, Marta Clement², Jimena Olivares², Jesus Sangrador¹, Enrique Iborra³**¹*Universidad Politecnica de Madrid, Madrid, Spain*, ²*Universidad Politecnica de Madrid, Spain*, ³*Universidad Politécnica de Madrid, Madrid, Spain***Background, Motivation, and Objective**

The gravimetric response of thin film solidly mounted resonators (SMRs) consists in shifts in their resonant frequency upon mass attachment to their surface. To accurately apply them as gravimetric sensors, either in liquid or gaseous media, other factors that can influence their sensitivity need to be considered. Probably, the most important one is the temperature. The temperature coefficient of frequency (TCF) takes into account the influence of the actual temperature of the sensor on the shift of a characteristic frequency (resonant or antiresonant, overmodes, etc.). If the TCF value is well-known, it can be used to correct measurements, eliminating the temperature influence. On the other hand, it is common to use the resonant frequencies of two identical devices (same TCFs): one to monitor the mass deposition and the other as reference to monitor temperature variations. In this work we study the possibility of using the resonant and antiresonant frequencies of the same vibrational mode of AlN-based SMRs to assess the mass and temperature sensitivities with the aim of employing the same device for both mass sensing and temperature monitoring.

Statement of Contribution/Methods

Our devices are shear mode AlN-based SMRs resonating at around 1.5 GHz intended to be used as in-liquid biosensors. They are composed of insulating acoustic reflectors made of seven alternating layers of SiO₂/AlN and Ir and Mo bottom and top electrodes. We are able to design different reflector stacks with different TCF values of the shear resonance by using partial TCF compensation. We test the resonators mass sensitivity by sequentially depositing very thin films of SiO₂ on their active surface and assessing their resonant and antiresonant frequencies shifts after each cycle. To measure their TCFs we subject the devices to temperatures ranging from 20°C to 100°C using a controlled heating system with a Peltier cell and track the admittance and impedance real part maximums through a specifically designed LabView® application with an accuracy below 1 kHz.

Results/Discussion

The assessment of the mass sensitivities showed identical values of around $-2.5 \cdot 10^{12} \text{ Hz} \cdot \text{cm}^2/\text{g}$ for both resonant and antiresonant frequencies, while TCF values appeared to be different in around 3-4 ppm/°C in the range of -20 ppm/°C. Since the resonant and antiresonant mass sensitivities are identical, the difference in TCFs can be exploited to numerically compensate shifts in frequency due to temperature variations and extract correct values of frequency shifts due solely to mass deposition.

FBAR oscillator stabilized by Rb atomic resonator for SHF/EHF band wireless devices

Motoaki Hara¹, Yuichiro Yano¹, Masatoshi Kajita¹, Shinsuke Hara¹, Akifumi Kasamatsu¹, Masaya Toda², Hiroyuki Ito³, Takahito Ono², Tetsuya Ido¹

¹National Institute of Information and Communications Technology, Tokyo, Japan, ²Tohoku University, Sendai, Japan, ³Tokyo Institute of Technology, Yokohama, Japan

Background, Motivation, and Objective

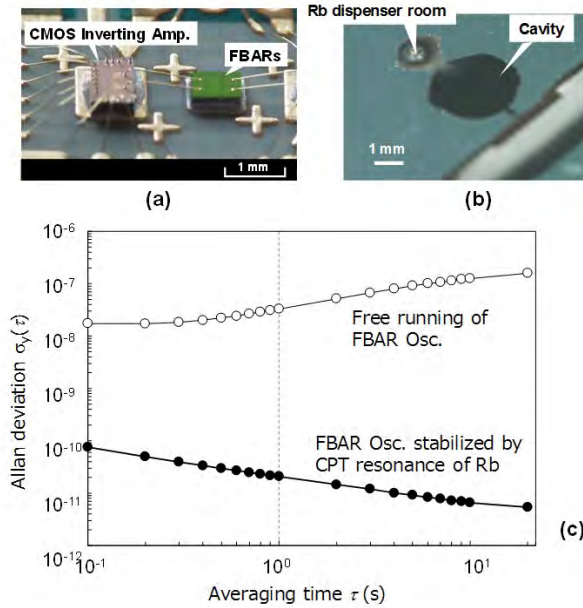
To efficiently utilize high frequency up to millimeter wave band for wireless communication, high efficient time domain duplexing (TDD) and mixer first configuration are much anticipated. A key to such a configuration is a highly accurate clock device. Quartz has been used as a local oscillator in the past, however, it has problems in the integration with the silicon device and power consumption. Also, in generation of a reference signal above GHz frequencies, heavy frequency multiplication must be crucial problem. In this report, we attempt to employ the thin film bulk acoustic resonator (FBAR) to generate the reference signal and to stabilize it using atomic resonance.

Statement of Contribution/Methods

In the FBAR based oscillator, oscillation in the GHz band is easily attained with simple configuration. So, unlike the quartz having the resonance frequency in the MHz band, amount of frequency multiplication can be mitigated. However, it is tough scheme to apply the FBAR oscillator instead of the crystal one due to the frequency instability of the FBAR. In this study we propose to stabilize the frequency of the FBAR oscillator by using coherent population trapping (CPT) resonance of Rb. This configuration has been proposed to miniaturize a Cs atomic clocks. Encapsulating the Rb gas into the silicon cavity fabricated by MEMS technology, the CPT resonance of the Rb atom (clock transition) is optically acquired with simple configuration including VCSEL and PD chips. Obtained resonance peak can be used to stabilize the FBAR oscillator. The resonance frequency of the FBAR is designed to the 3.4 GHz band to match the clock transition frequency of Rb. Also, regarding the manufacturing variance of the FBAR, a locking system using phase modulation was newly adopted in our feedback system.

Results/Discussion

Figure 1 (a) is a prototype of FBAR oscillator. Inverting amplifier was implemented in a 65-nm CMOS technology. Figure 1 (b) is a silicon gas cell with 3 mm in diameter, in which Rb gas and nitrogen as buffer gas were encapsulated. Figure 1(c) shows the results of evaluating the frequency stability of the oscillator. The frequency stability of the FBAR-VCO plotted by a white circle was gradually deteriorate due to the drift. Contrarily, when stabilizing with the CPT resonance (see filled circle plot), the frequency stability improved with time and reached to 2.1×10^{-11} at 1 s.



Laterally acoustically coupled BAW filters at 3.6 GHzTuomas Pensala¹, Tapani Makkonen¹, James Dekker¹, Markku Ylilammi¹¹MEMS, VTT Technical Research Centre of Finland, Espoo, Finland**Background, Motivation, and Objective**

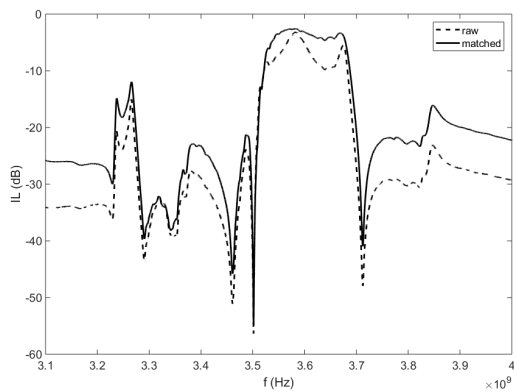
GHz-range Laterally Acoustically coupled thin film BAW (LBAW) filters utilize horizontal evanescent wave acoustical signal coupling from input to output in a similar manner as in the quartz-based monolithic crystal filters (MCFs). They combine the manufacturing technology and thin film layer structure of thin film BAW filters and the interdigitated electrode structures similar to those in SAW filters. The advantages sought with LBAW technology include small size, simple manufacturing, and large bandwidth. In order to explore the applicability of LBAW to higher frequencies, AlN based solidly mounted LBAW filters were designed and manufactured for 3.6 GHz center frequency.

Statement of Contribution/Methods

An AlN-based solidly mounted LBAW filter based on SiO₂-W reflector was designed for 3.6 GHz center frequency using a FEM-based design flow. The filters were manufactured using the VTT 150 mm process platform, and characterized with a vector network analyzer on wafer level. The filter responses were computationally matched with inductances. Comparison to simulation and to scaled performance of 1.9 GHz devices was done.

Results/Discussion

An exemplary filter shows a matched minimum insertion loss of -2.6 dB (-3.2 dB raw) and a relative bandwidth of 4.1 % at 3.58 GHz. Suppression level is below -30 dB for the raw filter and below 20 dB for the matched data, respectively, apart from spurious peaks.



Investigation of thermal and non-linear effects on the performance of the power amplifier - BAW filter - chain in a LTE transmitter

Uwe Stehr¹, Matthias Hein¹, Vikrant Chauhan², Victor Silva², Robert Weigel², Amelie Hagelauer², Astrid Frank³, Steffen Michael³

¹TU Ilmenau, Ilmenau, Germany, ²Institute for Electronics Engineering, Friedrich-Alexander-University Erlangen-Nueremberg, Erlangen, Germany, ³Institut für Mikroelektronik- und Mechatronik-Systeme gemeinnützige GmbH, Ilmenau, Germany

Background, Motivation, and Objective

In radio frequency (RF) integrated circuits for LTE transmitters (Tx), the consideration of temperature- and RF power-induced coupling between the power amplifier (PA) and adjacent RF filters, realized by bulk acoustic wave (BAW) resonators, is crucial in view of thermal and non-linear variations of the material parameters and geometric tolerances. In order to achieve a successful system design and reliable system performance, we have investigated the influence of the PA on the BAW filter transmission by comparing the results with those of individual BAW filters.

Statement of Contribution/Methods

In this work, a LTE transmitter chain (band 2, 1880 MHz), utilizing a Gallium Arsenide (GaAs) power amplifier and a matched BAW Tx filter, has been co-designed and implemented in the silicon-ceramic (SiCer) substrate technology. This substrate combines a stack of low-temperature co-fired ceramic (LTCC) layers with a thin silicon wafer in a monolithic composite substrate. The composite substrate displays superior RF properties in the LTCC part, while the silicon part provides excellent mechanical properties for the integration of micro-electromechanical devices. The influence of non-linear and thermal effects caused by the RF input power level and DC power dissipation has been analyzed for the individual constituents and the complete TX chain by means of an electrothermal numerical simulation using Keysight ADS and Ansys software. The generation of second harmonics (H2) and third-order intermodulation distortion (IMD3) are typical problems caused by the non-linearity in the BAW components and it has been modeled using the non-linear Mason model.

Results/Discussion

We present the linear parameters like input and output matching and small-signal gain, as well as non-linear parameters like gain compression, second-order harmonic generation (H2) and third-order intermodulation distortion (IMD3), both for the individual constituents and of the complete TX chain. The degradation of the performance of the TX chain due to the non-linear response of the BAW filter and its frequency shift due to substrate heating caused by the PA power dissipation are analyzed and experimentally verified. Based on these results, strategies for circuit/ layout improvements are presented.

P2-A13 - MEMS & Application I

Waraku (posters 2)

Tuesday, October 23, 9:30 AM - 4:00 PM

Chair: **Shuji Tanaka** Tohoku University

P2-A13-1

On the implementation of mode localization between physical and digital resonators

Claude Humbert¹, Thérèse Leblois¹, Thomas Bertin¹, Gwenhaël Goavec-Merou¹

¹FEMTO-ST, France

Background, Motivation, and Objective

In the field of sensing MEMS, mode localization has risen great interest for the past years due to its high sensitivity to mass or stiffness change when the resonators are balanced and the coupling is weak [1], [2]. However, the perfect balance condition is hard to reach due to microfabrication uncertainties and the coupling value is seldom tunable. Furthermore, it may happen the excited mode shape makes a physical coupling difficult to create (such as SAW or bulk shear waves). The purpose of this work is to generate mode localization between a physical resonator and a numerical one, enabling to tune enough parameters in the digital part to go over these limitations and reach a maximal sensitivity.

Statement of Contribution/Methods

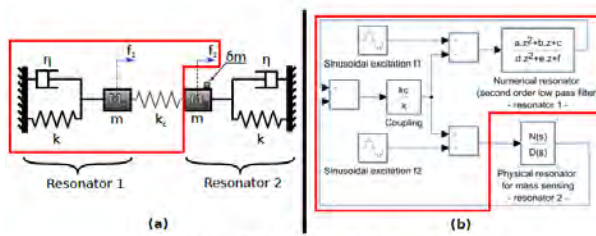
Figure 1a represents a two degrees of freedom mechanical discrete model and the idea is to replace the elements surrounded in red with a numerical circuit and keep only the resonator 2 as a physical interface catching the mass to be sensed. Indeed, for the first time in the literature, we integrate a physical resonator in a closed loop simulating in real time the presence of an additional resonator using the calculation of the coupling contribution in mode localization conditions. The digital part, also surrounded in red on figure 1b, is implemented in a Field Programmable Gate Array (FPGA) doing parallel calculations and so making possible the programming of a resonator network until a few MHz, compatible with MEMS natural frequencies. FPGA blocks are written using Z transform and communicate with resonator 2 through analog-digital converters.

Results/Discussion

Our FPGA design was tested separately on a piezo and an electrical resonator. Concerning the latter for instance, we got a normalized sensitivity of 7 after tuning each parameter in the FPGA, which is the maximum reachable value for this resonator Q factor (25), according to the analytical model. These satisfying results are very encouraging for further tests on real MEMS mass sensors having greater Q factors.

[1] Zhao C, Montaseri MH, Wood GS, Pu SH, Seshia AA and Kraft M (2016) A review on coupled MEMS resonators for sensing applications utilizing mode localization. Sensors and Actuators A, 249. pp. 93-111

[2] Manav M, Reynen G, Sharma M, Cretu E and Phani S (2014) Ultrasensitive resonant MEMS transducers with tuneable coupling. Journal of Micromechanics and Microengineering, Volume 24, Issue 5



Microbubble Non-linear Oscillation Induced Acoustic Micromixing within Microfluidic DevicesWenjun Zhang^{1,2}, Lili Niu¹, Long Meng¹, Wei Zhou¹, Yuchen Wang¹, Xiufang Liu¹, Hairong Zheng¹¹*Paul C. Lauterbur Research Center for Biomedical Imaging, Shenzhen Institutes of Advanced Technology, Chinese Academy of Sciences, Shenzhen, China, People's Republic of;* ²*Key Laboratory of E&M, Ministry of Education & Zhejiang Province, Zhejiang University of Technology, Hangzhou, China, People's Republic of***Background, Motivation, and Objective**

Microfluidics is of great significance in terms of biomedical research and chemical engineering. Liquid mixing is an essential and necessary procedure for the sample preparation. For the microfluidic device, laminar flow is dominant due to the low Reynolds number. Thus, liquid mixing by diffusion is time consuming and it is difficult to achieve uniform mixing within a microfluidic channel. The aim of this study was to design oscillating microbubble-based acoustic micromixer.

Statement of Contribution/Methods

By designing the circular structure on the bottom surface, microbubble (MB) can be generated when the fluid flowed through the circular structure due to surface tension. A piezoelectric transducer (PZT) was placed adjacent to the polydimethylsiloxane (PDMS) microfluidic device on the same glass substrate with ultrasound coupling gel; the width and depth of PDMS microchannel were 240 μm and 40 μm , respectively. To verify whether ultrasound could induce MB cavitation, the passive cavitation detection (PCD) system was established. A solution of polystyrene particles with the diameter of 2 μm was injected into the microchannel to characterize the microstreaming induced by the MB oscillation. The mixing performance was evaluated by measuring the grayscale value.

Results/Discussion

When the MB was excited by the PZT at the resonant frequency, MB oscillated immediately and a symmetrical flow pattern throughout the liquid around the MB was observed. Fig. 1(a) shows power spectrum of the MB exited by PZT at 165 kHz. It can be seen that high-order harmonics was generated by the MB oscillation, as depicted in Fig. 1(b), illustrating stable cavitation occurs. The mixing process was ultrafast, within 37.5 ms, and high mixing uniformity of 92.7% could be achieved when input power applied to PZT was 8.08W (Fig. 1(c-d)). The strong vortical microstreaming facilitated the rapid interchanging of liquid between the two fluids, providing a highly efficient and ultrafast mixing.

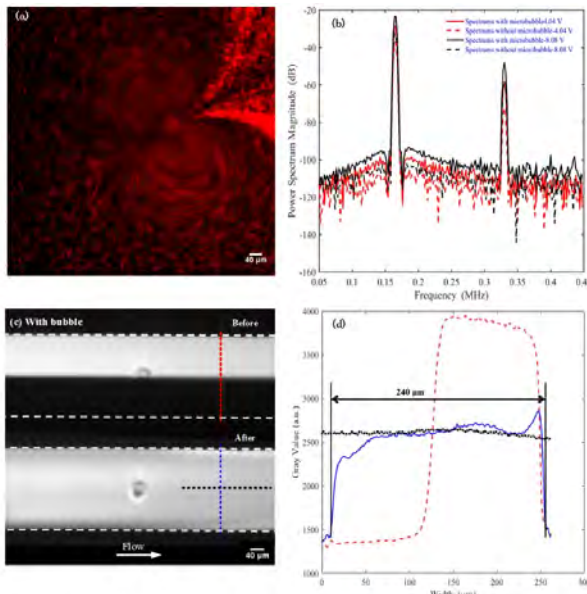


Fig. 1. (a) Trajectory of the PS fluorescent particles in the microstreaming; (b) The frequency spectrum of the PCD signal generated by microbubble oscillation; (c) Mixing process of liquid in the microchannel; (d) Gray value of liquid in microchannel before and after microbubble oscillation.

Nanocrystalline Optomechanical Cavity Excited by SAW Launchers**Jouni Ahopelto¹**¹*VTT Technical Research Centre of Finland, Espoo, Finland***Background, Motivation, and Objective**

Cavity optomechanics has become a very active research field [1]. The potential applications range from quantum technologies to telecommunication to sensors. Typically, the devices are made of silicon-on-insulator (SOI) substrates, i.e., the structures are single crystalline.

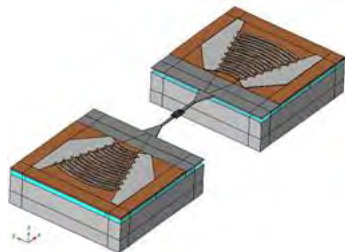
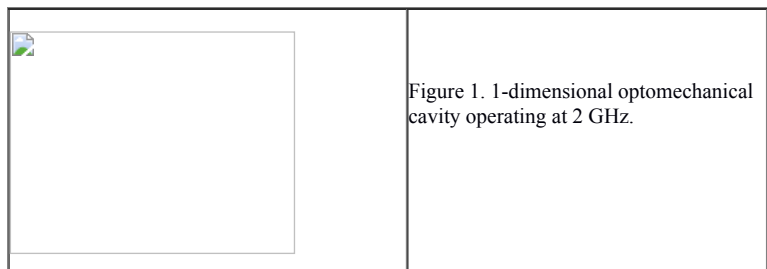
Statement of Contribution/Methods

Recently it was shown that nanocrystalline silicon has very interesting properties arising from the strong nonlinearity of the material. Phonon lasing based on self-pulsing and chaotic behaviour was demonstrated at room temperature in optomechanical nanobeams [2]. An advantage of the nanocrystalline silicon is that the strain, doping and dimensions can easily be controlled by process parameters, in contrast to the commercial SOI wafers, giving degrees of freedom in designing the devices. Usually the optomechanical cavities are pumped by photons.

1. M. Aspelmeyer, T. J. Kippenberg, and F. Marquardt, Cavity optomechanics, Rev. Mod. Phys. 86, (2014) 1391.
2. D. Navarro-Urrios, N. E. Capuj, J. Maire, M. Colombano, J. Jaramillo-Fernandez, E. Chavez-Angel, L. L. Martin, L. Mercade, A. Griol, A. Martinez, C. M. Sotomayor-Torres, and J. Ahopelto, Nanocrystalline silicon optomechanical cavities, Optics Express 26 (2018) 9829.

Results/Discussion

Here we will describe an OM cavity excited by interdigitated transducers focussing surface acoustic waves into a 1-dimensional beam forming the cavity. The operation frequency is 2 GHz and, in addition to the mechanical excitation, the cavities can be characterised by optical means. The designed structure is shown in the Figure 1 below. The optical cavity is formed by the holes in the beam and the mechanical cavity by the stubs on the sides of the beam. In this talk, we will discuss the interesting properties nanocrystalline silicon can bring to optomechanical structures, the self-pulsing mechanism and the coupling of the SAW to the optomechanical cavity.



Improving PMUT Transmit Performance via Sub-Micron Thickness Scaling

Xiaoyue Jiang¹, Guo-Lun Luo², David Horsley³

¹UC Berkeley, United States, ²UC Davis, United States, ³MAE, UC Davis, CA, United States

Background, Motivation, and Objective

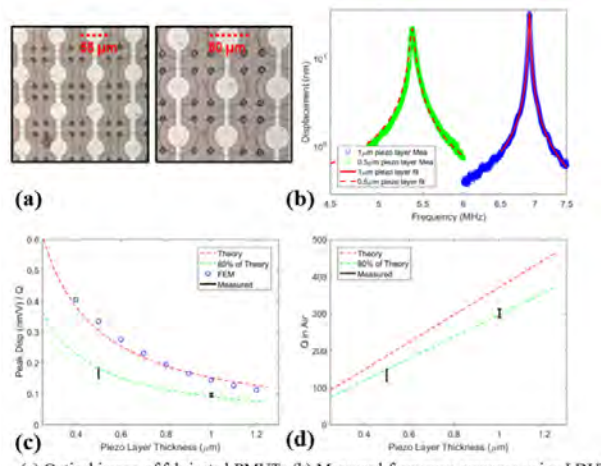
Analytical models for micromachined ultrasonic transducers (MUTs) show that the transmit voltage sensitivity (Pa/V) has an inverse dependence on thickness. However, the ability to scale capacitive MUTs (CMUTs) to submicron thickness is limited by electrostatic pull-in instability. PMUTs are not subject to pull-in instability, making them an ideal vehicle to explore the benefits of thickness scaling. Using analytical model, FEM, and experiment measurements, we demonstrated individual PMUT's transmit voltage sensitivity at the same frequency is inversely proportional to the device thickness, while the quality factor dominated by the acoustic radiation loss linearly scales with the device thickness. AlN PMUTs with 500 nm and 1 μm piezo layer thickness were fabricated to demonstrate an improved transmit voltage sensitivity via sub-micro thickness scaling.

Statement of Contribution/Methods

The analytical and FEM models for circular AlN PMUTs at 6 MHz showed that the transmit performance (η/k) is inversely proportional to the device thickness (Fig c.), while the quality factor linearly scales with thickness (Fig d.). 29 μm and 40 μm radius PMUTs with 500 nm and 1 μm piezo layer were fabricated to compare the transmit performance at 6 MHz (Fig a.). Experiments were performed using a laser Doppler vibrometer (LDV) to measure the PMUT's displacement as shown in Fig b. The peak displacement ($Q\eta/k$) is normalized by the quality factor as the figure-of-merit to compare the transmit performance.

Results/Discussion

As shown in Fig c. and Fig d., the measured figure-of-merit and Q follows the trend of the model. The difference between the model and experiment can be attributed to variations in piezo material properties and stack thickness. The experiment results have demonstrated that 6 MHz PMUTs with 500 nm thick piezo layer has 1.7 times better transmit performance and 45% of the Q when compared to that with 1 μm piezo layer.



Specificity and sensitivity characterization of a resonant bio-sensor made of gallium arsenidePierre Boiteux¹, Céline Elie-Caille¹, Thérèse Leblois¹¹FEMTO-ST, Besançon, France**Background, Motivation, and Objective**

Gallium Arsenide (GaAs) Sensors have been being developed for a few years [1]. One of its applications is the detection and quantification of bio-entities such as proteins or microorganisms since GaAs has interesting crystal characteristics for biosensors : its piezoelectricity, biofunctionalization abilities and common micromanufacturing cleanroom processes. However, one of the current challenges is the integration of both microfluidic and biosensing aspects in one resonator. Our project consists in designing and fabricating a microsensor able to go over this limitation by capturing specific biological entities in a complex liquid environment such as blood. After a study characterizing the environment influence (T, pH, [NaCl]) on the resonant frequency shift, the present work consists in the determination of our GaAs biosensor specificity and sensitivity.

Statement of Contribution/Methods

Our sensor is made of a resonant membrane with bio-interface on one side and electrodes on the other. These electrodes generate shear acoustic waves using Lateral Field Excitation and enable at the same time impedance measurement. The bio-interface consists in specific antibodies (Ab) (chosen in accordance with the targeted antigen (Ag)) which are temporally grafted to a mixed Self-Assembled Monolayer of thiols themselves strongly fixed to the GaAs membrane. Then the grafting of the Ag on the Ab triggers a resonant frequency shift and so a measurable impedance shift. We have carried out measurements at each step of the biointerface generation : 1/ thiolation on the GaAs membrane (90% MUDO chains (thiolates of 11 carbons with a terminal group of hydroxyle) + 10% MHDA chains (thiolates of 16 carbons with an activable carboxylic acid terminal group), 2/ activation with EDC-NHS, 3/ Ab grafting, 4/ inactivation with ethanolamine [2]. We finally measured the resonant frequency shift after incubation with an Ag solution at 10 nM for the sensor with and without the Ab monolayer. At last the bio-interface can be regenerated by glycine solution at pH 2, that breaks up the Ab/Ag interaction.

Results/Discussion

We successfully proved that, after incubation with the Ag solution, only the biofunctionalized sensor with Ab shows a significant resonant frequency shift ($\Delta f = -43,75 \cdot 10^{-6}$ Hz with Ab, $-3,563 \cdot 10^{-6}$ Hz without Ab for a 1mm^2 membrane area), confirming that the captured Ag are the source of this frequency deviation. The next step consists in determining the link between frequency shift and the analyte concentration in the biological liquid.

[1] H. Yamaguchi, GaAs-based micro/nanomechanical resonators, Semicond. Sci. Technol. 2017, 32 103003

[2] A. Bienaime et al, Influence of the thiolates chemical layer on the GaAs (100) biofunctionalization: an original approach coupling AFM and mass spectrometry methods, Materials 2013, 6(11), 4946-66

High-throughput sonoporation of single cells within a microfluidic chip

Xiufang Liu^{1,2}, Long Meng¹, Yuchen Wang¹, Lisheng Xu², Lili Niu¹, Wei Zhou¹, Wenjun Zhang¹, Hairong Zheng¹

¹*Paul C. Lauterbur Research Center for Biomedical Imaging, Shenzhen Institutes of Advanced Technology, Chinese Academy of Sciences, Shenzhen, China, People's Republic of*, ²*Northeastern University, shenyang, China, China, People's Republic of*

Background, Motivation, and Objective

The modulation of membrane permeability employing ultrasound has a great significance in gene therapy. Stable cavitation induced reversible pores in membrane is capable of improving the membrane permeability and receives increasing attention. Due to the wide size distribution of the microbubbles, however, the sonoporation events seem to be random process, and it is difficult to realize the homogenization sonoporation at single cell level. To address the above issue, this paper demonstrates a microfluidic device that enables to achieve high-throughput, parallel and high-efficient sonoporation at the single cells level.

Statement of Contribution/Methods

A polydimethylsiloxane (PDMS) microfluidic chip was designed by the standard replica moulding technique and a multi-rectangular cavity structure with the size of 40.8 μm in width was established in the main channel. A piezoelectric ceramics (PZT) whose resonance frequency equals to the resonant frequency of air bubble was adhered to the glass slide to excite the bubble stable cavitation. Passive cavitation detection (PCD) system was established to verify whether the ultrasonic wave could induce stable cavitation. Single suspension cells, human breast cancer cell of MDA-MB-231, were combined with Calcein AM and Propidium Iodide(PI) to detect the cell viability and membrane permeability.

Results/Discussion

When the cell solution flowed through the microchannel, semicircular air bubbles at the opening hole was generated due to the discontinuity at the fluid/PDMS interface. With the presence of ultrasound, piezoelectric ceramics (PZT) drove the trapped air microbubble to start oscillating and microstreaming was generated. Fig. a shows higher harmonics could be detected by PCD, indicating stable cavitation occurred. When input power was 7.4 W, the single cells could be trapped at the individual microbubble surface within 0.6 s due to the second acoustic radiation force induced by microbubble oscillation. (Fig. b). A merged fluorescence image of Calcein-AM/PI, depicted in Fig. c, shows the reversible sonoporation efficiency was $88.89 \pm 2.35\%$. This device provides an excellent tool for massively parallel single cells sonoporation through air microbubble array oscillations within sidewall cavities, which has potential applications in gene therapy.



First steps towards simultaneous isolation and detection of exosomes with carbon nanotube-based SMRs

Teona Mirea¹, Jimena Olivares², María Yáñez-Mó³, Mar Valés-Gómez⁴, Enrique Iborra⁵

¹*Universidad Politécnica de Madrid, Madrid, Spain*, ²*Universidad Politécnica de Madrid, Spain*, ³*Centro de Biología Molecular Severo Ochoa, Madrid, Spain*, ⁴*Departamento de Inmunología y Oncología, CNB-CSIC, Madrid, Spain*, ⁵*Universidad Politécnica de Madrid, Madrid, Spain*

Background, Motivation, and Objective

Exosomes are extracellular vesicles (20-150 nm) carrying valuable information within cells. They have become important in disease diagnosis or disease evolution tracking. The biggest bottleneck in exosome research are the inefficient and time-consuming standard purification methods from body fluids (e.g. ultracentrifugation). The newest technologies for exosomes isolation include nanofiltration, size discrimination with surface acoustic waves or affinity capture methods. Although efficient, these technologies still present disadvantages, like the use of expensive nanolithography, isolation without size discrimination below 150 nm, or the need of optical read-out means in all cases. Microfluidic devices including carbon nanotube (CNT) forests have proven to be an alternative filtering method overcoming the nanolithography need by controlling the tubes distance for specific size isolation. Nevertheless, optical read-out methods are still needed. We propose using solidly mounted resonators (SMRs) with integrated CNT forest for simultaneous isolation and gravimetric detection of exosomes. We present our initial progresses by functionalizing the CNTs with specific antibodies against exosomes and monitoring the response of the devices.

Statement of Contribution/Methods

CNT forests are directly grown by chemical vapor deposition on the active top electrode area of 1.5 GHz AlN-based shear mode SMRs. The distance between the forest tubes ranges between 10 nm to 80 nm. We perform a covalent functionalization of the CNTs sidewalls using MES + EDC + NHS as activation buffer combined with streptavidin and the immobilization of a CD63 antibody, to which exosomes specifically bind. The process is performed in a fluidic system with a peristaltic pump and a PDMS structure.

Results/Discussion

The frequency shifts of the device are monitored during the functionalization process, including the attachment of streptavidin to the CNT sidewalls and the immobilization of CD63 on them, and finally the exosomes detection. As an example, during a standard functionalization process, frequency shifts around 100 kHz for streptavidin (with a concentration of 248 nM or 13 ng/μl) and 280 kHz for the CD63 antibody (8 nM or 1.3 ng/μl). These responses prove the ability of our devices to gravimetrically detect the species attached to the CNT sidewalls. Moreover, the 280 kHz shift produced with a very low concentration of antibody improves previous results with devices without CNTs (bare top electrodes) by enlarging the active surface sites where the species can bind. Finally, the shifts in resonant frequency upon exosome attachment are variable depending on the amount of exosomes quantity and their sizes. Experiments to fully characterize them are ongoing.

P2-A2 - POA: Opto-Acoustics

Waraku (posters 2)

Tuesday, October 23, 9:30 AM - 4:00 PM

Chair: **Koen W.A. van Dongen** TU Delft

P2-A2-1

Sparsity-promoting opto-acoustic imaging with source estimation

Rajiv Kumar¹, Diego Dumani², Shashin Sharan¹, Mathias Louboutin³, Rongrong Wang⁴, Stanislav Emelianov⁵, Felix J. Herrmann^{1,3}

¹School of Earth and Atmospheric sciences, Georgia Institute of Technology, atlanta, GA, United States, ²Wallace H. Coulter Department of Biomedical Engineering, Georgia Institute of Technology & Emory University, Atlanta, GA, United States, ³School of Computer Science and Engineering, Georgia Institute of Technology, atlanta, GA, United States, ⁴Department of Computational Mathematics, Science and Engineering, Michigan State University, MI, United States, ⁵School of Electrical and Computer Engineering, Georgia Institute of Technology, Atlanta, GA, United States

Background, Motivation, and Objective

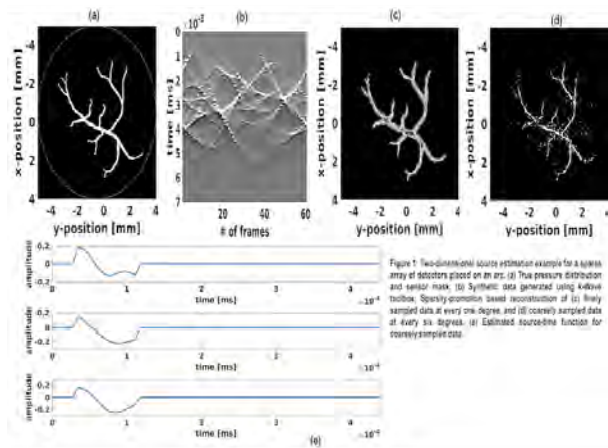
The field of opto-acoustic imaging has made tremendous progress in creating high-fidelity images using wave-equations valid in media where wavespeeds vary. While these images are of great diagnostic value, they are based on three key limiting assumptions, namely (i) the opto-triggered sources fire all at the same time and with the same source-time function; (ii) data is densely sampled; and (iii) the wavespeed in the medium is known accurately. We propose a new method where we relax at least two of these assumptions and obtain estimates of both the source locations and their source-time functions. We argue that the latter may offer additional diagnostic value.

Statement of Contribution/Methods

By solving a wave-equation based source localization problem with sparsity promotion in space and minimal energy and short-pulse duration constraints along time, we recover the full source wavefield everywhere without making assumptions on the source-time mechanism for each source position. We obtain these results by combining sophisticated techniques from convex optimization (duality) and scientific computing to implement a code that works with highly optimized numerical 2- and 3-D wave-equation solvers.

Results/Discussion

Estimating the full source wavefield as a function of space and time is challenging and requires sophisticated constraints to overcome the problem of non-radiating sources. Our mixed L1/L2-norm minimization deals with this problem and leads to an implementation that makes fewer assumptions on the source function and sampling while producing somewhat noisy but interpretable images that include estimates for the source-time function for each point. We obtained the result in the figure below from synthetic data generated by k-Wave toolbox, where the estimated locations and source-time functions using the proposed sparsity-promotion based formulation are displayed for finely sampled data at every one degree and coarsely sampled at every six degrees. The result indicates that we can indeed handle situations where data is incomplete. We also argue that the point-wise estimates for the source-time function could potentially lead to a new diagnostic tool.



Regularized Capon Beamformer using L1-Norm Applied to Photoacoustic Imaging

Roya Paridar¹, Moein Mozaffarzadeh^{1,2}, Maryam Basij³, Mohammad Mehrmohammadi³, Mahdi Orooji¹

¹Biomedical Engineering, Tarbiat Modares University, Tehran, Iran, ²Research Center for Biomedical Technologies and

Robotics, Institute for Advanced Medical Technologies, Tehran, Iran, ³Biomedical Engineering, Wayne State University, Detroit, MI, United States

Background, Motivation, and Objective

Recently, sparse-based algorithms have been used for image formation, especially in tomographic image reconstruction where the difference between the measured signals and the predicted sparse beamformed data is considered to be minimized through a least square model. In addition, some regularization terms are combined with the mentioned minimization problem in order to suppress the artifacts caused by the limited-view and improve the Photoacoustic (PA) image quality.

Statement of Contribution/Methods

In this paper, it is proposed to add a new L_1 -norm sparse constraint to the existing Minimum Variance (MV) beamformer after some modifications in order to enhance the image quality and further suppress the sidelobes. The newly added constraint can be interpreted as the sparsity of the output which is forced to the entire beampattern. The optimum weight would be obtained from a simple iterative algorithm. We have converted the L_p -norm form into the L_2 -norm form to make the optimization problem solvable. From this new form of the minimization problem, the optimum weight would be obtained using the Lagrange multiplier method. To evaluate the introduced algorithm and its effect on PA image improvement, phantom experiments were performed in which a phantom consists 2 light absorbing wires with a diameter of 150 μm placed 1 mm apart from each other in a water tank. We utilized a Nd:YAG pulsed laser, with the pulse repetition rate of 30 Hz at wavelengths of 532 nm. A programmable digital ultrasound scanner (Verasonics Vantage 128), equipped with a linear array transducer (L11-4v) operating at a frequency range between 4 to 9 MHz was utilized to acquire the PA RF data. A high speed FPGA was used to synchronize the light excitation and PA signal acquisition.

Results/Discussion

As demonstrated in Figure 1, Delay-and-Sum (DAS) results in a low resolution image along with high sidelobes. MV improves the resolution, but the sidelobes and background noise still affect the reconstructed image. On the other hand, Modified Sparse-MV (MS-MV) leads to a high resolution while the sidelobes are degraded, and the presence of noise is suppressed in the image, as can be seen in Figure 1.

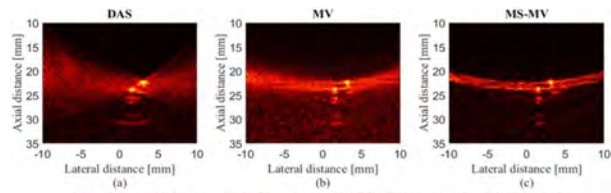


Figure 1. Reconstructed experimental PA images using (a) DAS, (b) MV and (c) MS-MV ($\beta=1$). All the images are shown with a dynamic range of 50 dB. Two wires were used as the imaging target.

Effect of Backing on Carbon-Polymer Nanocomposite Sources for Laser Generation of Broadband and High Amplitude Ultrasound

Srinath Rajagopal^{1,2}, Bradley Treeby¹, Ben Cox¹

¹*Medical Physics and Biomedical Engineering, University College London, London, United Kingdom*, ²*Ultrasound and Underwater Acoustics, National Physical Laboratory, Teddington, United Kingdom*

Background, Motivation, and Objective

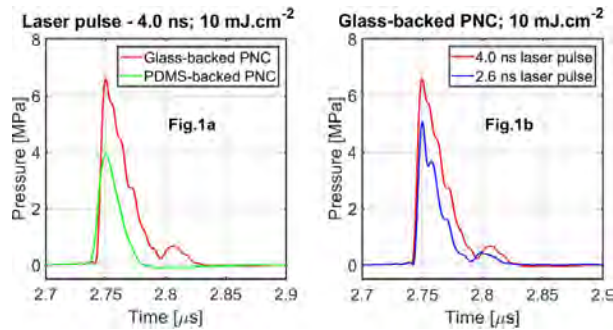
Nanocomposites made of light absorbing nanoparticles supported in a bulk polymer matrix has been widely investigated as a photoacoustic source of broadband and high amplitude ultrasound in biomedical imaging. Increased performance requires the nanocomposite to be highly optically absorbing. Fabrication of such sources has always involved intense and elaborate chemistry, which is difficult to replicate by other researchers for validation purposes. Here, a relatively simple method is exploited in which the amplitude performance of the nanocomposite is improved by up to 60% without affecting the bandwidth by experimenting with the backing substrate supporting the nanocomposite.

Statement of Contribution/Methods

PNC sources were fabricated by dispersing multi-walled carbon nanotubes (3.5% by-weight) in PDMS using a speed-mixer. A thin film of this mixture of ~20 µm was backed on glass and PDMS substrates of 1 mm thickness, and subsequently oven cured to complete the source fabrication process. Each source was tested with a 4 ns and 2.6 ns duration pulsed lasers operating at 1064 nm with a laser fluence of 10 mJ.cm⁻². A broadband hydrophone was used to measure the laser generated ultrasound (LGUS) pressure pulse.

Results/Discussion

The LGUS pressure pulses from glass- and PDMS-backed PNC sources are shown in Fig.(1a) for a 4 ns laser and fluence of 10 mJ.cm⁻². The peak pressures from both sources should be nominally identical except for pulse durations. However, the peak-pressure from glass-backed PNC source is 60% higher compared to PDMS-backed PNC. When isochoric thermalization is not satisfied, the built-up pressure within the PNC will start to leave the PNC volume whilst that volume is still undergoing thermalization. For a homogenous media the two pressure waves leaving the PNC travels in opposite direction without interaction. If one-side of the PNC is backed with an acoustically reflecting surface such as glass, then the backward travelling wave for e.g. is reflected into the PNC. Since thermalization is still under way, the reflected pressure and the pressure increase from thermalization add up increasing the overall pressure within the PNC. If the heating duration is reduced, then the pressure increase in the case of glass-backed PNC source should be lower as shown in Fig.(1b).



Magnetically mediated thermoacoustic signal enhanced by coupled magnetic resonanceYunqi Luo¹, Xiaohua Feng², Ruochong Zhang², Wensong Wang², Yuanjin Zheng²¹*Electrical & Electronic Engineering, Nanyang Technological University, Singapore, Singapore*, ²*Nanyang Technological University, Singapore, Singapore***Background, Motivation, and Objective**

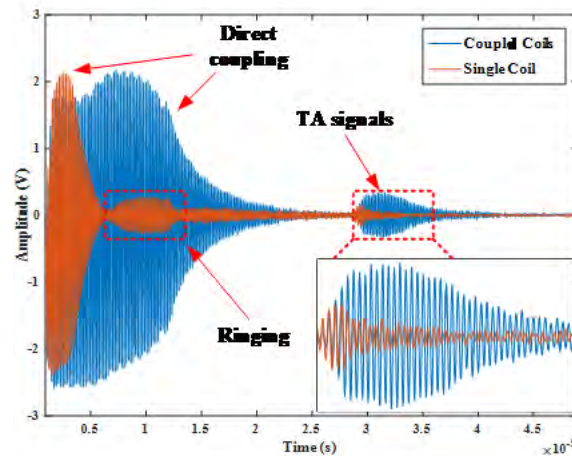
Thermoacoustic sensing probes electrical contrast of matter at ultrasonic resolution and by using low frequency magnetic field, it generally offers deeper penetration up to several centimeters. However, due to lower absorption of matter at low frequency, it suffers from degraded signal to noise ratio (SNR) at depths. To enhance the SNR without resorting to higher power amplifiers, we propose here a coupled magnetic resonance method to improve the SNR of thermoacoustic signals that uses low frequency magnetic field for radiation, which is termed as magnetic resonance mediated thermoacoustic sensing (MRMTA).

Statement of Contribution/Methods

Contrasted with previous magnetically mediated thermoacoustic sensing systems that use a single coil for near field radiation, our method adds in a secondary coil to form with the primary coil a coupled resonance system. Such coupled resonance systems can confine the electromagnetic field to be between the two coils and enhance the magnitude of the field therein, leading to larger absorption of matter and hence an improved SNR. Since it physically enhances the field in a localized manner, it is equally applicable for incoherent pulsed thermoacoustic imaging and coherent frequency domain method.

Results/Discussion

Both simulation and experiment results demonstrated SNR improvement using the coupled magnetic resonance method without the increase in coil current. Circuit simulation results indicate that current in the secondary coil is larger than that in the primary coil, and primary and secondary current are in phase, indicating that the electric field between these two coils is the superposition of the electric field of the primary and secondary coil, and is definitely enhanced. Electromagnetic field simulation results show that the maximal amplitude of electric field of the two coupled coils system is approximately twice of that in one single coil, and electric field is confined well between these two coupled coils, which contributes to the enhancement of thermoacoustic signals. Experiment results show that thermoacoustic signal amplitude increase approximately 4 times compared with TA signal generated by one single coil (Fig. 1), and SNR has also been improved.



Improved lateral resolution using sub pitch sampling of ultrasound data for pulsed laser diode-based photoacoustic imaging
Sowmiya Chandramoorthi¹, Arun K. Thittai¹
¹*Applied Mechanics, Indian Institute of Technology Madras(IITM), Chennai, India*
Background, Motivation, and Objective

In Photoacoustic Tomography (PAT), image quality and resolution is mainly dependent on the receive ultrasound (US) probe parameters such as pitch, wavelength, aperture length among others . It is more practical to use linear array for PAT due to ease of availability. However, its lateral resolution (LR) is limited by pitch and wavelength (λ). Further, commonly used PAT reconstruction techniques assumes point detector, and continuous sampling among other assumptions, violating which causes degradation in spatial resolution and appearance of streak artifacts in PAT reconstructed image. Manufacturing transducer with "sub- λ " pitch, especially at higher frequencies (>10 MHz) is very difficult to achieve. Hence, there is a need for alternate ways of increasing discrete array sampling in PAT. It has been recently shown for pulse echo US imaging that translation of the linear array and acquisition of sub-pitch location data can result in improved LR [1]. In this work, we have adapted this sub-pitch translation method for PAT and report the improvements observed in LR.

Statement of Contribution/Methods

Improvement in LR of a reconstructed PAT image has been analyzed by acquiring new RF A-lines at sub-pitch location by translating the US linear array probe. A pulsed laser diode (PLD) module of 905 nm, upto 220W power/pulse, 120 ns pulse width and 5kHz PRF was used as optical source. A gelatin phantom containing a 0.7 mm lead was used as target medium. The PLD was integrated with a Sonix Touch US scanner by external triggering with function generator. A 5MHz, 128 element linear array probe with 0.3mm pitch was used. The setup is shown in Fig.1a.

Results/Discussion

Preliminary results were obtained by reconstructing using a) 64 elements with 0.6mm pitch and b) full 128 elements data with 0.3mm pitch. The results showed significant improvement in LR and reduction in streak artifacts when using (b) as can be observed in Fig 1. Although only the concept is demonstrated in this 1-page abstract, comparison between 0.3mm pitch and 0.15mm pitch is currently under progress using a custom-built transducer that has integrated actuator to translate the array by sub-pitch amount.

- [1] S. Selladurai and A. K. Thittai, "Strategies to Obtain Subpitch Precision in Lateral Motion Estimation in Ultrasound Elastography," *IEEE Trans. Ultrason. Ferroelectr. Freq. Control*, vol. 65, no. 3, pp. 448–456, Mar. 2018.

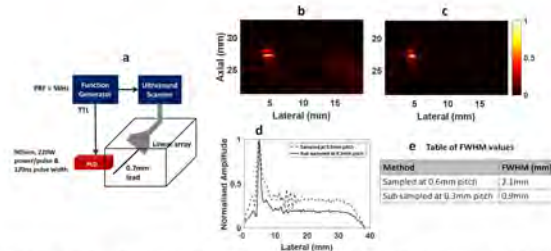


Figure 1: Image showing preliminary results obtained from sub-sample evaluation of point scatterer using linear array- PAT system a) The experimental setup of pulsed laser diode based photoacoustic imaging system, b) B-mode image of PSF using 0.6 mm pitch, c) B-mode image of PSF using 0.3 mm pitch, d) Lateral profile plots comparing the two methods and e) shows the table of the FWHM values obtained.

Analysis of Elastic Vortex Waves for Optical Orbital-Angular-Momentum Mode Conversion by Acoustooptic Interaction
Takuya Shoro¹, Hiroki Kishikawa², Nobuo Goto²
¹*Department of Optical Science, Tokushima University, Tokushima city, Japan*, ²*Tokushima University, Japan*
Background, Motivation, and Objective

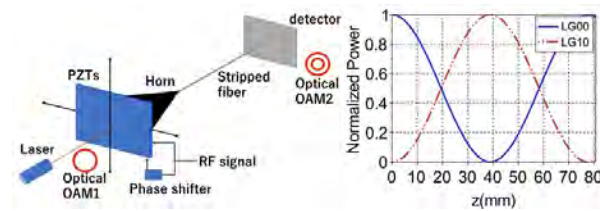
In recent years, novel methods of increasing optical transmission capacity are keenly required. Optical orbital angular momentum (OAM) mode multiplexing is powerful technology for increasing transmission capacity. Flexible handling of plural OAM modes is indispensable to execute OAM mode multiplexing. In this paper, we theoretically analyze elastic vortex wave (EVW) for OAM mode conversion in an optical graded index fiber.

Statement of Contribution/Methods

We clarify acoustooptic (AO) mode conversion between Laguerre-Gaussian modes (LG modes) having OAM using EVW, which is acoustic wave having OAM, in a graded-index fiber. EVW is generated by two orthogonal flexural waves. This EVW causes perturbation of dielectric constant. Mode coupling is induced via this perturbation. Dielectric constant is explained by 6 components. Firstly, we analyze OAM mode conversion by EVW. Moreover, we evaluate the contribution from each of the 6 components.

Results/Discussion

We consider mode conversion from LG00 to LG10. Here, we must consider phase matching condition between LG modes and EVW. We use EVW at about 0.3918MHz which satisfies the phase matching condition. Fig.1 shows a AO mode conversion configuration and mode conversion between LG00 to LG10. These graphs indicate that OAM mode conversion can be successfully executed by EVW in graded index fiber. Moreover, we confirmed that all components of dielectric constant contribute the mode coupling.



Acousto-Optic Modulator Driven by Longitudinal Leaky Surface Acoustic Waves on Bonded Structures**Kentaro Hakiri¹, Masashi Suzuki¹, Shoji Kakio¹**¹*Integrated Graduate School of Medicine, Engineering, and Agricultural Sciences, University of Yamanashi, Kofu, Japan***Background, Motivation, and Objective**

A light wave that is guided to the propagation region of a surface acoustic wave (SAW) is Bragg-diffracted by an acousto-optic (AO) effect and shows an optical frequency shift caused by the SAW. To increase the amount of frequency shift, the authors previously fabricated an AO modulator (AOM) using a longitudinal leaky SAW (LLSAW) that is 1.5–2-fold higher phase velocity than Rayleigh-type SAWs (R-SAWs) on an X-cut 36° Y-propagating LiNbO₃ (X36°Y-LN) substrate with a high electromechanical coupling factor for an LLSAW and evaluated its diffraction properties. However, the driving voltage required for optical diffraction by the LLSAW was higher than those when using R-SAWs cases because the LLSAW lost energy through the radiation of bulk waves into the substrate. On the other hand, it was reported that the propagation properties of LLSAWs could be improved by use of a structure consisting of an LN thin plate bonded with a high-velocity substrate such as quartz or sapphire (Al₂O₃). In this study, to lower the driving voltage of the AOM using an LLSAW, the AOM was fabricated on an LN thin plate bonded with a quartz or Al₂O₃ substrate, and its diffraction properties were evaluated.

Statement of Contribution/Methods

The process of fabricating the AOM is as follows. First, as an optical waveguide mask with a width of 5 mm, a 2500-Å-thick SiO₂ film was deposited on 2.0- or 3.4-μm-thick X36°Y-LN thin plate bonded with an AT-cut 45°X-propagating quartz (AT45°X-quartz) or c-plane Al₂O₃ (c-Al₂O₃) substrate. Then, the samples were immersed in benzoic acid at 240 °C to fabricate a proton-exchanged (PE) optical waveguide with a depth of 0.65 or 1.2 μm. Then, interdigital transducers (IDTs) with a period of 20 μm and an overlap length of 3 mm were fabricated on a SiO₂ mask using a 2500-Å-thick Al thin film.

Results/Discussion

A He-Ne laser light with a wavelength of 0.633 μm was guided to a PE optical waveguide using a rutile prism coupler. An RF burst signal was applied to the input IDT and LLSAWs on X36°Y-LN/AT45°X-quartz or X36°Y-LN/c-Al₂O₃ were excited by adjusting the frequency of the input RF signal to 347 or 403 MHz. The intensity of the undiffracted light was measured using a photomultiplier and the diffraction efficiency was determined from the decrease in the intensity. The maximum diffraction efficiency in the TE₀ mode and the required driving voltage by the LLSAWs were 91% and 5.1 V for X36°Y-LN/AT45°X-quartz, and 60% and 11 V for X36°Y-LN/c-Al₂O₃, respectively. The diffraction properties of the LLSAWs on the bonded structures were improved compared with those of the single LN.

Minimization of group delay dispersion for platelet piezoelectric transducers of acousto-optic devicesVladimir Molchanov¹, Oleg Makarov¹, Konstantin Yushkov¹¹National University of Science and Technology MISIS, Russian Federation**Background, Motivation, and Objective**

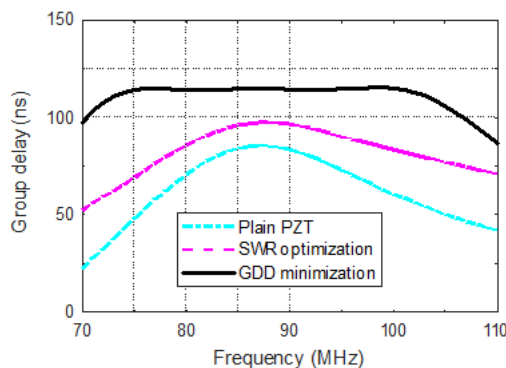
Lithium niobate PZTs are used to excite BAWs in acousto-optic (AO) devices in the typical frequency domain from few MHz to few hundred MHz. AO deflectors, tunable filters, and dispersive delay lines for ultrashort laser pulse shaping require broadband electrical impedance matching to provide effective BAW excitation in an octave-spanning range (V. Molchanov, O. Makarov. Opt. Eng. 38:1127, 1999). Coherent light processing, e.g. heterodyning and ultrashort laser pulse shaping, require the group delay dispersion (GDD) of the PZT to be minimized in the broad frequency range.

Statement of Contribution/Methods

We developed a new method for broadband electrical impedance matching of a PZT providing minimized GDD and linear phase response. Phase transfer function of a LiNbO₃ shear PZT on a TeO₂ crystal is derived from a Mason equivalent circuit. T-shaped electrical circuit of LC components is used for adjusting the phase response and efficiency of the PZT. Nominal values of LC elements are calculated using numerical global optimization (differential evolution genetic algorithm) with BAW group delay to be flattened in the predefined frequency range. Initial data for the optimization algorithm were obtained from measurement electrical impedance of the PZT.

Results/Discussion

Optimization of the phase response has been applied to a platelet PZT bonded to TeO₂ by vacuum cold welding nanotechnology. A quasi-collinear AO dispersive delay line with indirect BAW excitation was studied (V.Ya. Molchanov et al. Appl. Opt. 48:C118, 2009). The fundamental antiresonance frequency of the PZT was 85 MHz. The result of the optimization is <0.6 ns group delay in 75–95 MHz range with SWR<5.3. The plots show the resulting group delay of the unmatched PZT, the optimized circuit for minimum SWR, and the optimized circuit for minimum GDD. The results demonstrate almost 50-fold reducing of BAW group delay deviation compared to conventional broadband electrical matching over the typical instantaneous frequency band of the AO dispersive delay line.



P2-A3 - Adaptive Beamforming

Waraku (posters 2)

Tuesday, October 23, 9:30 AM - 4:00 PM

Chair: **Francois Varray** INSA Lyon

P2-A3-1

A New Compensated Coherence Factor Beamforming Method for Ultrasound B-mode Imaging: Preliminary Evaluation in Simulation and in-vivo Breast Studies

Younjo Oh¹, Jinbum Kang¹, Ilseob Song¹, Yangmo Yoo^{1,2}

¹*Electronic Engineering, Sogang University, Seoul, Korea, Republic of*, ²*Biomedical Engineering, Sogang University, Seoul, Korea, Republic of*

Background, Motivation, and Objective

- Coherence factor (CF) is one of the representative adaptive beamforming methods measuring coherence of array signals. In CF, incoherent and coherent sums are estimated before and after receive beamforming, respectively. Thus, while the incoherent sum means the energy of signals from on and off-axis targets, the coherent sum represents the energy of signals from on-axis targets. This difference of data domains lowers the CF values corresponding to transmit beam width rather than beamforming quality, leading to undesired artifacts, including decreased overall image brightness, increased speckle variance, and black region artifacts around hyperechoic target, and reduction of speckle pattern. Therefore, to reduce the artifacts of CF, it is necessary to compensate for this domain difference.

Statement of Contribution/Methods

In this paper, a new beamforming method based on compensated coherence factor (CCF) is proposed. Unlike the CF method, in CCF, the incoherent sum is first calculated and modified with transmit beam width estimates so that it only account for the energy from on-axis targets. Thus, the CCF can represents beamforming quality more accurately compared to the CF, resulting in the reduction of the artifacts. To evaluate the proposed CCF method quantitatively and qualitatively, the Field II simulation and *in-vivo* breast studies with the ultrasound research system (SonixTouch, Ultrasonix Corp., Canada) using a 10-MHz linear array probe were conducted.

Results/Discussion

In the Field II simulation study, contrast-to-noise ratio (CNR) for cystic targets and contrast ratio (CR) for massive targets were measured with conventional delay-and-sum (DAS), CF, and CCF. As shown in Figs. 1(a)-(c), the CCF method outperformed over the DAS and CF methods in terms of CNR values, 9.44 vs. 6.57 and 7.88, respectively. In addition, for CR, the CCF method showed comparable results with the DAS while the CF suffers from black region artifacts, i.e., 9.52, 9.01, and 12.90, respectively. These results were further verified with *in-vivo* breast studies as shown in Figs. 1(d)-(f). The enhanced delineation of lesion boundaries and less clutter inside hypoechoic regions were observed with the CCF method. This results indicate that the proposed CCF method can improve image contrast by reducing the artifacts and clutter noise, and provide better image quality than DAS and CF methods.

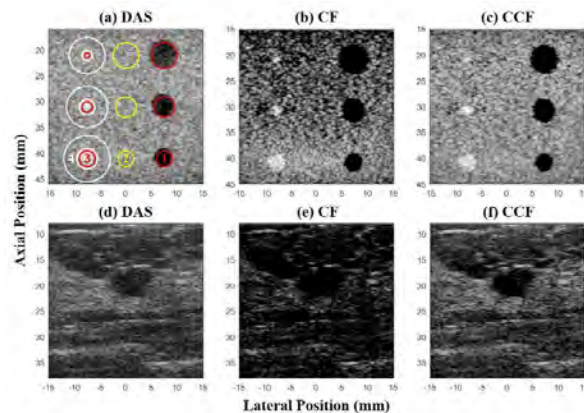


Figure 1. (a)-(c) Field-II simulation. (d)-(f) *in-vivo* breast with lesion. The focal depth of both simulation and *in-vivo* data sets is 40mm. In (a), region 2 and 4 are background regions, and region 1 and 3 are cystic and massive regions respectively.

Short-lag Spatial Coherence Imaging in 1.5-D and 1.75-D Arrays: Beamforming and Array Design Considerations

Matthew Morgan¹, Dongwoon Hyun², Gregg Trahey^{1,3}

¹Biomedical Engineering, Duke University, Durham, NC, United States, ²Radiology, Stanford University School of Medicine, Palo Alto, CA, United States, ³Radiology, Duke University Medical Center, Durham, NC, United States

Background, Motivation, and Objective

Conventional one-dimensional (1-D) ultrasound transducers employ an acoustic lens to limit slice thickness and provide a fixed elevation focus. To improve elevation focusing, transducers have also been developed to include multiple rows of elements in elevation, which can be mirrored (1.5-D) or individually connected (1.75-D). These arrays often employ a Fresnel-style geometry to minimize the time delay error across the elevation aperture.

Short-lag spatial coherence (SLSC) imaging forms images based on the spatial similarity of received echoes across the aperture, and has demonstrated improved image quality over delay-and-sum beamforming. While SLSC imaging has been studied using 1-D and 2-D arrays, the effects of elevation aperture geometry on SLSC image quality are not well understood. The objective of this work is to evaluate SLSC imaging performance using a variety of 1.5-D and 1.75-D elevation geometries.

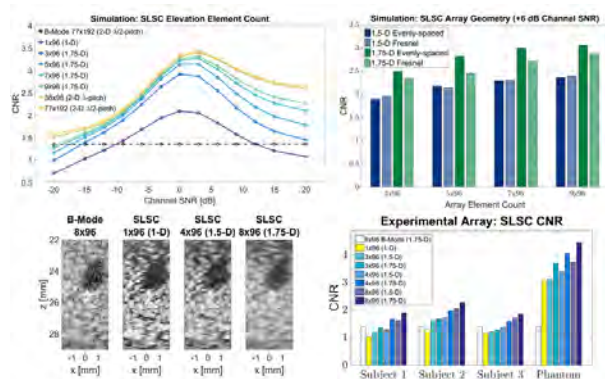
Statement of Contribution/Methods

Field II simulations of cyst targets of anechoic, -12, and -6 dB contrasts were performed using a 3 MHz array with 96 lateral elements. Arrays with 3, 5, 7 and 9-element elevation elements (evenly-spaced and Fresnel geometries) were compared to a 1-D array, and matrix arrays with wavelength and half-wavelength element spacing. SLSC images were formed for each array; the short-lag region for each element was defined based on the predicted inter-element correlation for a diffuse target. Contrast, contrast-to-noise ratio (CNR), and speckle statistics were measured as a function of channel signal-to-noise ratios between -20 and 20 dB.

Channel data was acquired from phantom and *in vivo* targets using a custom 8.9 MHz, 8x96 array transducer and a Siemens SONOLINE Antares scanner. Elevation channels were summed to form subapertures and create SLSC images using effective 8, 4, 3, and 1-element elevation arrays, with and without mirroring. Image quality was evaluated as a function of elevation aperture geometry.

Results/Discussion

Increasing elevation element count improved SLSC image quality in simulation and experimental datasets. Elevation symmetry in 1.5-D arrays forced the inclusion of additional long-lag pairs into the short-lag region, which resulted in a slight loss in CNR. Even element spacing out-performed Fresnel-style geometries, and 1.75-D geometries demonstrated improved SLSC image quality over 1.5-D arrays.



Benefits of adaptive beamforming methods for contrast enhanced high frame-rate ultrasound

Antonio Stanziola¹, Matthieu Toulemonde², Richard Corbett³, Virginie Papadopoulou¹, Robert Eckersley⁴, Neill Duncan³, Mengxing Tang⁵

¹*Bioengineering, Imperial College London, South Kensington, United Kingdom*, ²*Department of Bioengineering, Imperial College London, London, United Kingdom*, ³*Imperial College Renal and Transplant Centre, Hammersmith Hospital, United Kingdom*, ⁴*Department of Biomedical Engineering, King's College London, London, United Kingdom*, ⁵*Imperial College London, London, United Kingdom*

Background, Motivation, and Objective

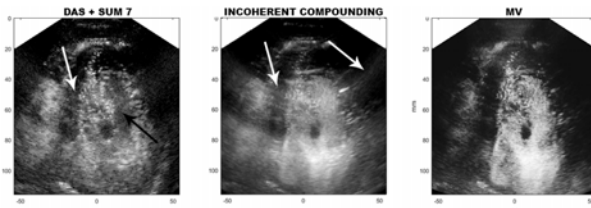
High frame-rate (HFR) ultrasound allows a frame-rate up to thousands of images per second, at the expenses of resolution and contrast. To improve image quality, successive transmissions at different steering angles are coherently compounded together. Such approach assumes static targets between different transmissions, a requirement often violated for fast flowing contrast agents, especially in fast moving organs. An alternative is to incoherently average multiple transmissions (incoherent compounding, IC): this reduces both motion artefacts and the suppression of interferences. The aim of this study is to evaluate adaptive beamforming methods, such as minimum variance beamforming (MV), to generate contrast enhanced ultrasound (CEUS) images, which to the best of our knowledge has not been studied yet.

Statement of Contribution/Methods

The proposed technique uses a modified mid-way MV approach [P. Stoica, IEEE Trans. on Signal Processing, 2008], restricted to the lower dimensional signal subspace [A. B. Mohammadzadeh, IEEE Trans. UFFC, 2010]. HFR CEUS heart images of a healthy human volunteer have been acquired by transmitting 11 (x2 for pulse inversion) diverging waves at 1.5 MHz (angle range of 30°, PRF ~ 5500Hz) and a second harmonic filter is used to enhance contrast to tissue ratio. The same 7 frames have been processed using standard delay and sum with incoherent averaging of 7 frames (DAS + SUM 7) [M. Toulemonde, IEEE IUS, 2016], IC and MV beamforming.

Results/Discussion

Figure 1 shows the results using DAS + SUM 7, IC and MV. Images are displayed in their own optimal dynamic ranges, that is (from left to right): 30dB, 25dB and 120dB. The images highlight how DAS + SUM7 and Incoherent Compounding generates artefacts, both as intensity reductions in the left ventricular (LV) chamber (black arrow) as well as interference signals (white arrow). MV improves the image quality by attenuating such artifacts, as well as improving the visualization of cardiac structures, like the papillary muscle in the center of the LV chamber or the vortex close to the apex. In conclusion, we demonstrated how adaptive beamforming methods can be used to improve the quality of contrast images compared to classical DAS methods, especially with fast flow or fast-moving organs.



A dynamic generalized coherence factor based on Van Cittert-Zernike theorem

Ali Fatemi^{1,2}, Hans Torp^{1,2}, Alfonso Rodriguez-Molares^{1,2}

¹Department of Circulation and Medical Imaging, NTNU, Trondheim, Norway, ²Center for Innovative Ultrasound Solutions (CIUS), NTNU, Norway

Background, Motivation, and Objective

Reverberation in medical ultrasound reduces the diagnostic value of images and is still a big issue in many cases. Coherent-based beamformers have been used to reduce reverberation noise. However most of them have the side effect of increasing the variance of the speckle signal, which has an impact on the detection of weak lesions. The exception is the generalized coherence factor (GCF) that can produce a uniform speckle distribution by including M0 components of the aperture spatial spectrum. The choice of M0 is user-based, and can vary in different parts of the image if dynamic expanding aperture or different transmit and receive apertures are used.

Statement of Contribution/Methods

As per Van Cittert-Zernike's (VCZ) theorem, the lateral correlation of speckle signal corresponds to the autocorrelation of the aperture function. The spectrum of speckle signal across the aperture is therefore a function of the spectrum of the aperture function. For any given aperture function and F-number, VCZ can be applied to obtain an optimal M0 value.

We compare a GCF with a dynamic M0, to other adaptive methods such as the coherence factor (CF), the phase coherence factor (PCF), the short-lag spatial coherence (SLSC) for Q=0.3, and the GCF for a fixed M0. We estimate the receiver operating characteristic (ROC) curve to evaluate the ability of each method to separate speckle and reverberation.

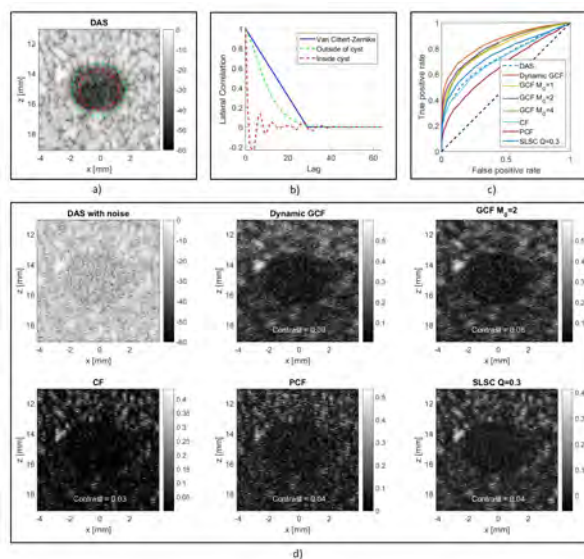
Experimental data was recorded by a Verasonics Vantage 256 research scanner with a L11 probe. As the target, we imaged a 3 mm anechoic cyst in a CIRS phantom (Model 040GSE) and added band-pass Gaussian noise with a channel SNR=-10 dB.

Results/Discussion

Figure 1 a) shows a delay and sum (DAS) B-mode image of the anechoic cyst. We define two regions: speckle (outside the green circle) and reverberation (inside the red circle). Figure 1 b) shows the lateral correlation as a function of lag for the two regions, together with the VCZ theory.

Figure 1 c) shows the ROC curves for all tested methods with added noise. GCF curve is calculated for three different M0. The dynamic GCF shows a better detection compared to GCF with a fixed M0.

Figure 1 d) shows the images obtained from all tested methods for SNR = -10dB. The contrast between the two regions is included on each image. The dynamic GCF shows the highest contrast.



Adaptive loading in minimum variance beamforming for passive imaging of acoustic cavitation

Tao Sun^{1,2}, Calum Crake¹, Brian Tracey², Costas Arvanitis³, Eric Miller², Nathan McDannold¹

¹Radiology, Brigham and Women's Hospital, Harvard Medical School, United States, ²Electrical and Computer Engineering, Tufts University, United States, ³Mechanical Engineering and Biomedical Engineering, Georgia Institute of Technology, Atlanta, GA, United States

Background, Motivation, and Objective

Passive cavitation imaging (PCI) has been shown promise in monitoring cavitation-mediated ultrasound therapy. Traditional PCI relies on non-adaptive delay-and-sum (DAS) beamforming, leading to poor axial resolution and low contrast. Adaptive techniques such as the minimum variance distortionless response (MVDR) beamformer, although generally providing superior interference rejection ability over DAS, are often oversensitive, suppressing sources of interest due to errors in array calibration, knowledge of the medium, etc. Diagonal loading can control the adaptation of MVDR but has not been extensively used and discussed for PCI. Here we applied the white noise gain constraint (WNCG) to adaptively control the loading level, so that the sensitivity of MVDR can be adjusted in a spatially selective manner. Proportional diagonal loading (PDL), used successfully in active ultrasound imaging, was also compared.

Statement of Contribution/Methods

Data were acquired in a clinical MR-guided FUS system (ExAblate 4000, InSightec) with a milk-based phantom filled in an *ex vivo* macaque skull. A 1024-element phased array was driven to transmit 10-ms pulsed FUS at 220 kHz. The 64 elements of a 128-element linear array (L382, Acuson; center frequency: 3.21 MHz; bandwidth: ~75%) were used for the passive recordings. Transmitting and receiving systems were synchronized and the first 180 μ s of RF data were recorded for each burst. The cavitation-enhanced heating was monitored using MR temperature imaging, where the heated spots served as the ground truth of source locations. The image resolution and contrast were compared in DAS, unloaded MVDR, PDL- and WNCG-guided MVDR beamformers.

Results/Discussion

WNCG-controlled MVDR was demonstrated to significantly improve the source localization over DAS, unloaded MVDR and PDL-controlled MVDR methods. Reduced “tail” artifact was accomplished. The main lobe areas of WNCG were significantly smaller than those of the other approaches (Fig. 1, ****; $P < 0.0001$, *t*-tests, $n = 36$). Axial full widths (FWs) at 75% maximum were tightened from 31.0 ± 2.8 mm in DAS down to 8.2 ± 3.4 mm in WNCG. Transverse FWs at 75% maximum were decreased from 3.6 ± 0.2 mm in DAS to 1.22 ± 0.4 mm in WNCG. Contrary to previous findings shown in active imaging, PDL added the loading term ϵ less adaptively (Fig. 1c) and failed to offer better cavitation localization compared to DAS.

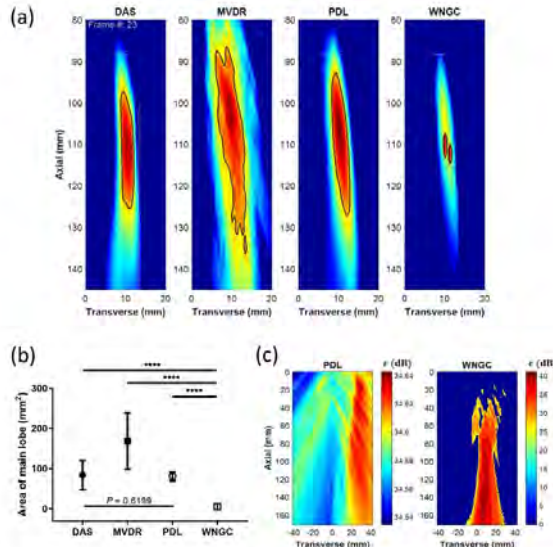


Fig. 1. (a) Image reconstructions via DAS, unloaded MVDR, PDL- and WNCG-controlled MVDR methods. The black contour represents the 80% level of the peak output power. All images were scaled to 0 to ~ 3 dB. (b) shows quantitative evaluation of the main lobe area across all frames ($n = 36$). (c) shows representative loading level maps using PDL and WNCG methods.

Plane-Wave Phase Coherence Imaging with Singular Value DecompositionHideyuki Hasegawa¹, Ryo Nagaoka²¹*University of Toyama, Japan*, ²*Graduate School of Science and Engineering, University of Toyama, Toyama, Japan***Background, Motivation, and Objective**

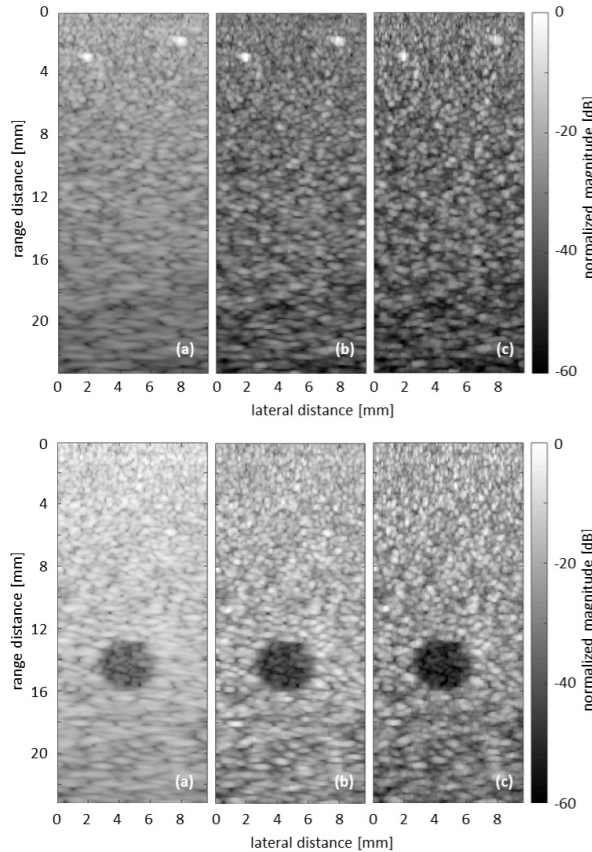
Phase coherence factor (PCF) was introduced to ultrasound imaging for improvement of image quality. It evaluates focusing quality using phases of echo signals received by individual transducer elements. We previously showed that the performance of PCF was improved by reducing out-of-focus echoes by sub-aperture beamforming prior to estimation of phases of echo signals. In the present study, the performance of PCF was shown to be improved further by singular value decomposition (SVD).

Statement of Contribution/Methods

PCF evaluates the variance of phases of echo signals. Echo signals received by individual elements contain not only an echo from a focal point but also out-of-focus echoes. They interfere with each other and such interferences increase the phase variance. Sub-aperture beamforming suppresses out-of-focus echoes and the phase variance of an echo from a focal point can be evaluated more accurately. In the present study, SVD was applied to outputs from sub-apertures to further suppress out-of-focus echoes (in other words, extract an echo from a focal point). Outputs from sub-apertures were stacked into a matrix and SVD was applied. The components in the matrix, which corresponds to the first (largest) singular value, were used as the final outputs from the sub-apertures. In this process, the components correspond to the first singular value were regarded as the echo from the focal point.

Results/Discussion

In the present study, each plane wave was transmitted with 96 elements and echoes received by the same 96 elements were acquired. In each transmission, 24 receiving beams were obtained, each of which was created with 72 elements. A B-mode image consisting of 96 receiving beams was obtained with 4 transmissions. In the figure, upper and lower figures show B-mode images of string and anechoic cyst phantoms, respectively. Figures (a) were obtained by conventional delay-and-sum (DAS) beamforming. The lateral full width at half maximum (FWHM) and contrast were 0.50 mm and 4.0 dB, respectively. Figures (b) are obtained with conventional PCF evaluated using echo signals received by individual elements, and FWHM and contrast were improved to 0.38 mm and 5.2 dB, respectively. Figures (c) are obtained with PCF evaluated using outputs from 8 sub-apertures (9 elements/sub-aperture) subjected to SVD. FWHM and contrast were further improved to 0.20 mm and 5.3 dB, respectively.



Low-complexity Delay-Multiply-and-Sum (DMAS) beamforming using baseband spatial coherenceChe-Chou Shen¹, Pei-Ying Hsieh¹¹*Department of Electrical Engineering, National Taiwan University of Science and Technology, Taipei, Taiwan***Background, Motivation, and Objective**

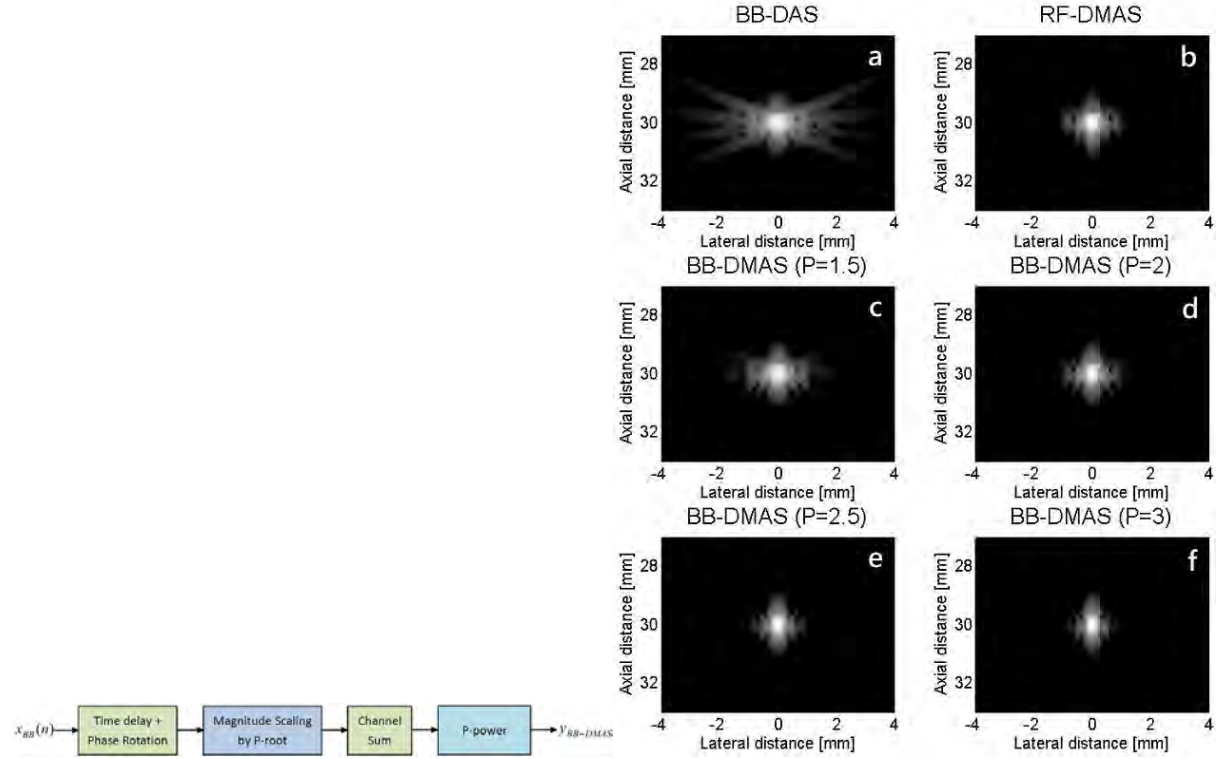
Compared conventional Delay-and-Sum (DAS) beamforming, Delay-Multiply-and-Sum (DMAS) imaging utilizes multiplicative coupling of channel pairs for spatial coherence of receiving aperture to improve image resolution and contrast. However, present DMAS imaging is based on the radio-frequency (RF) channel signals and thus requires large oversampling to avoid aliasing and additional band-pass (BP) filtering to isolate the corresponding spectral components for imaging.

Statement of Contribution/Methods

Baseband (BB) DMAS in this study is based on the demodulated channel signals to provide similar results but with simplified signal processing. The BB-DMAS scales the magnitude of time-delayed channel signal by P-th root while maintaining the phase as in Fig. 1. After channel sum, the output dimensionality is restored by P-th power. The multiplicative coupling in BB-DMAS still renders baseband signal and thus the need for oversampling and additional BP filtering is eliminated. Besides, the BB-DMAS can use any rational P values to provide flexible image quality.

Results/Discussion

Simulations are performed using Field II with a 128-element array at 5 MHz. Fig. 2(a, b) show the simulated point-spread-function (PSF) of DAS and RF-DMAS, respectively and (c, d, e, f) are the results of BB-DMAS with $P = 1.5, 2.0, 2.5$ and 3.0 . Results show that the PSFs in (b) and (d) are similar, which indicates comparable characteristics between BB-DMAS and RF-DMAS. It is also noticeable that the decrease of lateral side lobe level can be smoothly manipulated by the rational P value in BB-DMAS beamforming. Results indicate that the proposed BB-DMAS requires lower computational load but still performs comparably to RF-DMAS and provides higher flexibility due to rational P value.



Phase aberration correction of focused ultrasound by optimized refraction-compensation methodJun Yasuda¹, Hideki Yoshikawa¹¹Hitachi, Ltd., Tokyo, Japan**Background, Motivation, and Objective**

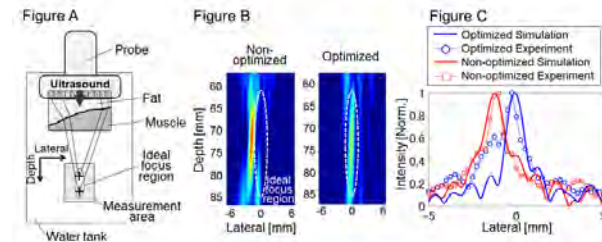
Phase aberration of focused ultrasound by tissue structure causes focus region shift and deformation and they drops quality of ultrasound images. To improve image quality, it's important to correct such phase aberration adaptively for each patients. Refraction at a boundary between subcutaneous fat and muscle is one of a key reasons for the phase aberration. An objective of this study is to propose a method for correcting phase aberration caused by refraction and demonstrate correction effect.

Statement of Contribution/Methods

To achieve the objective, we proposed optimized refraction-compensation method. In this method, firstly, boundary shape was detected by a B-mode image. Next, ultrasound paths from probe elements to multiple points in ideal focal region is calculated based on Snell's law. Then, delay time of each probe elements is optimized for maximizing total acoustic energy in focus region with considering the phases and amplitudes on each paths calculated by length of paths, sound of speed and attenuation. Correction effect of the proposed method was evaluated by both experiments and simulations. In experiments, biological tissue (pork) which consists of fat and muscle layers was set in front of a 64-ch linear ultrasound probe as shown in Figure A. Then, focused ultrasound using non-optimized and optimized delay time was transmitted from the probe at a frequency of 6 MHz with Verasonics and ultrasound intensity around focus region was measured by a hydrophone. To evaluate correction effect, focus shape and position in the case of non-optimized and optimized was compared. Numerical simulations under the same condition as the experiments were also performed to evaluate theological correction effect.

Results/Discussion

Figure B shows distribution of acoustic intensity in the simulations. In non-optimized case, focus region deformed and shifted. In optimized case, both focus deformation and shift were corrected. Figure C shows lateral profile of acoustic intensity at depth = 75 mm in both simulation and experiment. Ideal focus position is lateral = 0 mm. Results of the simulations and the experiments were agreed well. In non-optimized case, focus was shifted 1.1 mm. On the other hand, in optimized case, focus shift was corrected to ideal focus position. From these results, both theoretical and experimental correction effect of proposed method were demonstrated.



A New Compounding Method for High Contrast Ultrafast Ultrasound Imaging Based on Delay Multiply and Sum
Dooyoung Go¹, Jinbum Kang¹, Yangmo Yoo^{1,2}
¹*Electronic Engineering, Sogang University, Seoul, Korea, Republic of*, ²*Biomedical Engineering, Sogang University, Seoul, Korea, Republic of*
Background, Motivation, and Objective

Ultrafast ultrasound imaging based on coherent plane-wave compounding has enabled new high-frame-rate applications, such as shear wave elastography and ultrafast Doppler imaging. However, it generally suffers from low contrast resolution resulting from side, grating, and axial lobe artifacts since a limited number of frames can be used for compounding in order to attain high frame rates. In this paper, we present a new compounding method for increasing contrast of ultrafast imaging without sacrificing frame rates by adopting a nonlinear beamforming technique, called as the delay multiply and sum (DMAS).

Statement of Contribution/Methods

In the proposed method, unlike the conventional coherent compounding where frames acquired by using multiple plane-waves tilted at different angles are summed, the frames are coupled in pairs and multiplied, generating signals with squared dimensionality, i.e., $[V^2]$. In addition, a signed square root operation and band-pass filtering are applied in order to bring the signals back to their original dimension [V] and filter out unwanted signal components, such as DC. Finally, the filtered signals are summed together to form a single compounded frame. This approach is similar to the previously-proposed DMAS-based receive beamforming technique since the compounding is interpreted as a synthetic transmit focusing. To evaluate the performance of the proposed method, a Field-II simulation study and an *in-vivo* study based on an ultrasound research platform (Vantage, Verasonics Inc., Kirkland, WA, USA) were performed with 20 different plane-wave insonifications ($-9^\circ \sim +9^\circ$) using a L7-4 linear array transducer.

Results/Discussion

Figs. 1(a)-(b) are simulated B-mode phantom images based on the conventional coherent compounding method and the proposed DMAS-based compounding method, respectively. As shown in the images, the proposed method showed an increased contrast ratio compared to the conventional method (i.e., -37.5 dB vs. -27.8 dB, respectively). In addition, Figs. 1(c)-(d) show that our method provides enhanced image quality for B-mode imaging of *in-vivo* carotid artery by reducing artifacts inside the vessel. These results indicate that the proposed DMAS compounding method can enhance image contrast of the ultrafast imaging method.

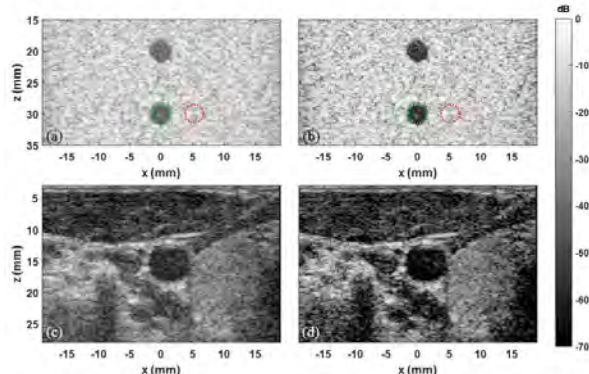


Fig. 1. Simulated B-mode images based on (a) coherent compounding and (b) proposed DMAS compounding, and *in-vivo* carotid B-mode images based on (c) coherent compounding and (b) DMAS compounding. The dotted lines in (a) and (b) indicate cyst (green) and background (red) regions used for measurements of the contrast ratios.

A real-time lag one coherence tool for adaptive imagingNick Bottenus¹, Will Long¹, James Long¹, Gregg Trahey^{1,2}¹*Biomedical Engineering, Duke University, Durham, NC, United States*, ²*Radiology, Duke University, Durham, NC, United States***Background, Motivation, and Objective**

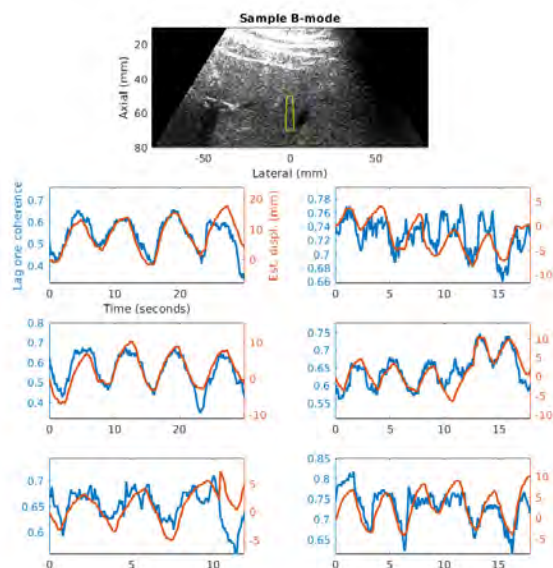
Ultrasound imaging has historically relied on pre-programmed sequences to make images in real-time. Although optimizations of focal configuration, transmit waveform, or other system properties may exist, sonographers do not often take advantage of them. We have demonstrated that lag one coherence (LOC), an aperture-domain signal quality metric, reflects image quality in the presence of *in vivo* clutter effects. Increased system bandwidth and computing power now make it possible to estimate LOC in real-time and adaptively make decisions about transmit sequencing or post-processing. We demonstrate a Verasonics-based platform for real-time temporal correlation and spatial coherence estimation during B-mode imaging. A study of abdominal image quality under varying common scanning conditions is presented using the tool. Implementations of several applications are also exhibited, including automated transmit intensity optimization and quality-triggered elasticity measurements.

Statement of Contribution/Methods

Pulse inversion (PI) harmonic B-mode imaging (128 rays/frame) was implemented with the C5-2v curvilinear transducer and Verasonics Vantage 256 ultrasound scanner. This sequence was augmented with 10 PI transmissions (2 repeated at 5 spatial locations) for temporal and spatial correlation. The receive data were delayed and Hilbert transformed to produce I/Q data. Pointwise estimation of temporal correlation (between repeated firings) and LOC (between neighboring receive channels) was efficiently performed using the complex dot product and averaged over a 2 cm x 4 degree for live display to the user. In this experiment, axial force was applied cyclically to the transducer to compress the abdominal tissues. We hypothesize that the image quality improvements associated with applied compression will be reflected in the LOC.

Results/Discussion

Temporal and spatial coherence estimates were provided to the user alongside the B-mode frames at 12 fps. In post-processing, the temporal noise component was removed from the spatial coherence estimates and the residual LOC is displayed in the attached figure for six sample acquisitions from one volunteer. The estimated axial displacement of the transducer correlates well with the LOC, indicating that the spatial clutter level decreases with increasing applied compression.



P2-A4 - Vector Flow Measurements

Waraku (posters 2)

Tuesday, October 23, 9:30 AM - 4:00 PM

Chair: **Adrian Chee** University of Waterloo

P2-A4-1

Quantitative vascular blood flow imaging: A comparison of vector velocity estimation schemes

Ingvild Kinn Ekroll^{1,2}, Morten Wiggen¹, Solveig Fadnes¹, Jørgen Avdal¹

¹CIUS, Norwegian University of Science and Technology, NTNU, Norway, ²St Olavs Hospital HF, Kirurgisk Klinikk, Norway

Background, Motivation, and Objective

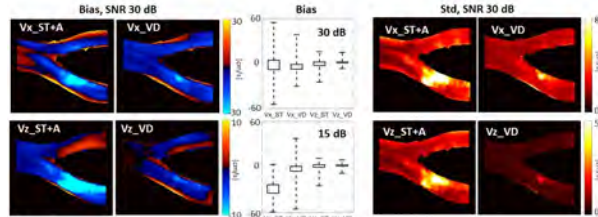
Vector velocity imaging of blood flow can provide detailed information on flow patterns present in a vessel or cavity. For derived measurements, such as estimation of wall shear stress, quantification of high velocity flow through a stenosis or calibration of spectral Doppler curves, an estimator with high accuracy and precision is desirable. Over the years, several estimators have been suggested, with speckle tracking and vector Doppler as the most widespread techniques. Similar to most ultrasound velocity estimators, they have relatively high variance. Multiple flow field realizations tend to require unreasonably long simulation times, whereas performance analyses based on single realizations of flow fields are hampered by the need to use spatial averaging.

Statement of Contribution/Methods

In this work, we utilize the in-house developed, flow line based simulation tool FLUST to obtain the statistically expected 2D vector velocity field for two different estimators: 1) A least squares vector Doppler estimator with four transmit/receive angle combinations (VD), and 2) an estimator based on a combination of speckle tracking in the lateral direction and autocorrelation in the axial direction (ST+A). The results are based on 100 realizations of a 3D flow field with realistic spatial and temporal gradients, where the true velocity field is taken from a patient specific carotid bifurcation model developed by Swillens et al. (2012). Transmit angles +/-15 and 4.5 cycles pulse were used in the VD acquisition, whereas no steering and 2.5 cycles pulse were used for ST, at twice the Doppler PRF, yielding equal temporal observation window. White noise was added to the beamformed data.

Results/Discussion

The left panels show the statistically expected bias in the horizontal (V_x) and vertical (V_z) velocity components for the two setups at 30 dB SNR. These results are summarized in the topmost boxplot, whereas the lower boxplot shows the expected bias at 15 dB SNR. The velocity component based on speckle tracking (V_x _ST+A) shows the largest increase in bias at decreased SNR. Standard deviation in the velocity components at various spatial positions is shown in the right panels. Further work includes using FLUST to find the best acquisition and beamforming parameters for each estimator, and determine which estimator yields the best performance for vascular blood flow measurements.



Intraventricular blood velocity measurements – a comparison between iVFM and blood speckle tracking

Magnus Sælemsminde¹, Thomas Groenli¹, Patrick Segers², Siri Ann Nyrnes^{1,3}, Lasse Lovstakken¹

¹CIUS, Dept. Circulation and Medical Imaging, Norwegian University of Science and Technology (NTNU), Norway, ²IBiTech-bioMMeda, Ghent University, Ghent, Belgium, ³St. Olavs Hospital, Norway

Background, Motivation, and Objective

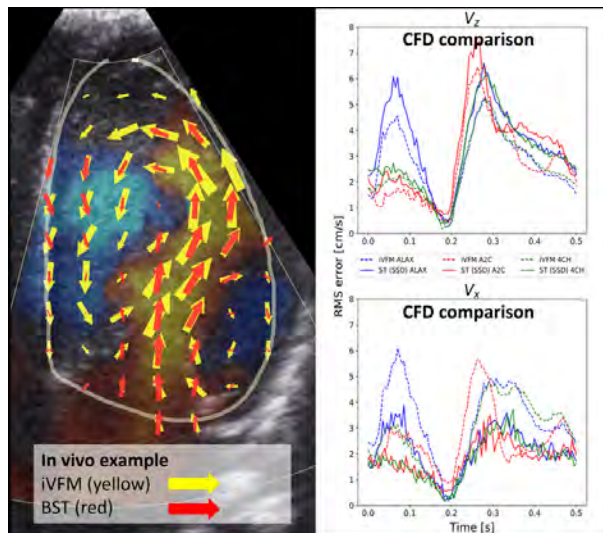
Several methods have been proposed to measure complex intraventricular blood velocities using ultrasound. *Intraventricular vector flow mapping* iVFM is based on reconstructing the velocity field using the radial blood velocities from color-Doppler imaging (CDI), the endocardial border definition, and by enforcing mass conservation. Blood speckle tracking (BST) is a direct measurement of the blood velocity vectors, based on high frame rate imaging and image pattern matching. Our aim is here to compare the two methods *in silico* and *in vivo* for cardiac flow patterns.

Statement of Contribution/Methods

iVFM was calculated using conjugate gradient with preconditioning. An additional regularization term was added to restrict high radial velocities outside the CDI mask. Blood speckle tracking was implemented using sum-of-squared differences (SSD), and using a hybrid approach combining radial color-Doppler with lateral tracking. Computational fluid dynamics (CFD) was used to simulate time-varying 3D intraventricular flows in a model of the left ventricle, and used to compare the methods quantitatively. Ultrasound IQ-data was generated using the fast ultrasound simulation tool in k-space (FUSK), which provided a basis for color-Doppler and envelope data. The methods were compared for three planes mimicking the standard cardiac views. Further, *in vivo* 2D image data from healthy and diseased pediatric patients was investigated qualitatively.

Results/Discussion

The figure shows an *in vivo* example from a healthy pediatric subject, as well as results from the quantitative comparison based on CFD for the different cardiac views. While iVFM and BST often agrees on the direction of flow, we observed that iVFM tended to overestimate while BST underestimated the true velocity. Overall, BST was able to capture more correctly details in the lateral velocities and thus reduce global error. A major source of error in iVFM for the CFD analysis was out-of-plane motion. When including an additional elevation source in the divergence regularization term, we could significantly improve results. Since iVFM is sensitive to parameter choices and boundary conditions, the current results may be improved by further tuning.



High Frequency Ultrafast Ultrasound Vector Flow Imaging for Mice Brain Without Contrast AgentsChin-Fang Hsieh¹, Hsin-Che Li¹, Hsin Huang¹, Chih-Chung Huang¹¹National Cheng Kung University, Taiwan**Background, Motivation, and Objective**

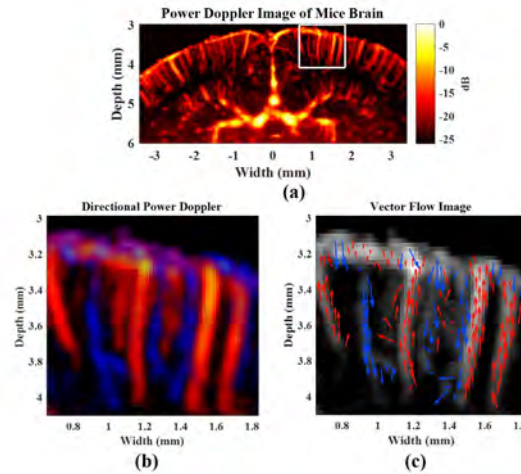
It is well known that functional magnetic resonance imaging (fMRI) and positron emission tomography (PET) have been used widely for brain imaging, particularly for hemodynamic response diagnosis, but they lack good temporal and spatial resolution for small animal brain imaging. Recently, high-resolution blood flow image based on ultrafast plane wave imaging has been proposed for rats and mice brain by applying contrast agents (CA) for enhancing the blood signals, but the amount of CA and its injection duration must be controlled carefully. Increase of ultrasound frequency is another solution for high spatial resolution blood flow mapping without CA. Therefore, the 40 MHz ultrafast Doppler imaging was proposed for mice brain in this study. Since the microvascular distribution of brain is complicated, the vector flow imaging (VFI) was also proposed to determine the blood flow directions in the mice brain.

Statement of Contribution/Methods

An ultrafast ultrasound imaging system (Vantage 256, Verasonics) with a 40 MHz high frequency array transducer (Vevo MS550D) was used for data acquisition. The plane wave compounding image at a frame rate of 1k fps was obtained at three angles (+3°, 0°, -3°). After using a high-pass filter (cutoff frequency of 70 Hz) to extract the blood signals, components of flow vectors at all pixels were individually calculated by lag-one autocorrelation from each angle. Subsequently, the VFI was generated by compositing the power Doppler image (PDI) and its corresponding flow vectors. For animal experiments, the head of an anesthetized mouse was placed in a stereotaxic frame, and a cranial window was surgically opened to expose the upper surface of the mouse brain.

Results/Discussion

Fig.1(a) shows the high-resolution PDI of mice brain without using CA. The microcirculation in cerebral cortex and hippocampus was observed obviously. Fig.1(b) shows the directional PDI corresponding to the region of interest (ROI) in Fig.1(a). The image size is about 1.2x1.2 mm, however, the blood flow directions and microvascular structure were observed clearly. Fig. 1(c) shows the high-resolution VFI from the same ROI in Fig.1(a), and the flow direction and velocity were represented by the arrow and its length. All the experimental results show the ability of high frequency ultrafast VFI for providing the flow information of each vessel for micebrain hemodynamics.



VORTEX RING PHANTOM FOR INVESTIGATION OF ULTRASOUND VECTOR FLOW IMAGINGEmilia Badescu¹, Simone Ambrogio^{2,3,4}, John Fenner^{3,4}, Hervé Liebgott¹, Denis Friboulet¹, Damien Garcia¹¹*Université de Lyon, CREATIS ; CNRS UMR5220 ; Inserm U1206 ; INSA-Lyon ; Université Lyon 1, France, France, ²Leeds Test Objects Ltd., Boroughbridge, UK, United Kingdom, ³Mathematical Modelling in Medicine Group, Department of Infection, Immunity and Cardiovascular Disease, University of Sheffield, UK, United Kingdom, ⁴Insigneo Institute for In Silico Medicine, University of Sheffield, Sheffield, UK, United Kingdom***Background, Motivation, and Objective**

The emergence of high-frame-rate ultrasound imaging has enabled important progress in blood flow quantification, as it makes it possible to acquire wide-field data at fine temporal steps. Before considering bench-to-bedside translation, there is a need in evaluating the multi-component time-resolved velocity fields provided by the new imaging methods. Our objective was to test an in-house vortex ring generator for investigation and validation of vector flow imaging. Such donut-shaped vortex forms in the left heart during cardiac relaxation, as blood flows through the mitral valve.

Statement of Contribution/Methods

The proposed phantom can generate non-turbulent vortex rings of different diameters and propagation speeds. It is controllable and compatible with optical particle image velocimetry (PIV) to obtain experimental ground-truths. The vortex rings are theoretically well characterized. Vector flow imaging by echo-PIV and vector Doppler was evaluated with vortex rings of various diameters and velocities (2 and 2.5 cm, 1-7 cm/s). Plane waves were transmitted at a frequency of 4 kHz using a Verasonics research scanner with a 5-MHz linear transducer. Multi-scale cross-correlation was used for echo-PIV. The signals were beamformed at two receive angles ($\pm 15^\circ$) for vector Doppler.

Results/Discussion

As shown in Fig. 1A, high-frame-rate ultrasound vector flow imaging can be successfully applied in complex flows, such as those generated by the proposed vortex ring phantom. Since we did not have a ground truth, we investigated the link between the rotational and translational speeds. The two velocity components were highly correlated ($r^2 = 0.95$, Fig. 1B), in accordance with theory (Tinaikar A *et al.*, *J. Fluid Mech.*, 2018). Therefore, the vortex ring phantom represents a good candidate for optimizing and validating ultrasound flow imaging methods in controllable, non-stationary, three-dimensional complex flows.

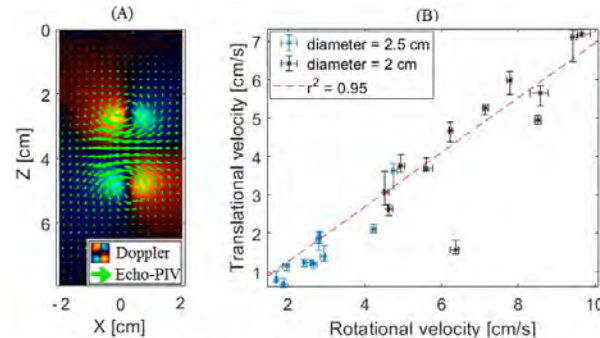


Figure 1. (A) Velocity field estimation by Doppler and echo-PIV for a translational velocity of 4 cm/s, and (B) Linear relationship between the rotational and translational velocities ($n = 12$ velocities $\times 2$ orifice diameters = 24)

Inter-leaved Synthetic Aperture Sequences for Measuring High Vector Flow Velocities**Jørgen Jensen¹**¹*Center for Fast Ultrasound Imaging, Technical University of Denmark, Lyngby, Denmark***Background, Motivation, and Objective**

Synthetic Aperture (SA) flow imaging uses the combination of Low Resolution Images (LRIs) acquired from N emissions to form a High Resolution Image (HRI). It increases resolution and contrast in the HRI resulting in increased velocity estimate precision and improved tissue components removal for excellent detection of both high and low velocities. The effective pulse repetition frequency, $f_{prf,eff}$, and thereby the maximum detectable velocity V_{peak} are, however, reduced by N . This makes it very difficult to estimate high velocities in e.g. the heart, where a good contrast is desired, which necessitates long sequences. A new method using inter-leaved emissions is suggested to obtain the highest possible $f_{prf,eff}$, equal to the emission pulse repetition frequency, f_{prf} resulting in the highest possible V_{peak} .

Statement of Contribution/Methods

SA emissions are ordered from 1 to N and repeated to give continuous data. The new scheme inter-leaves emissions as: $1^{(1)} 1^{(2)} 2^{(1)} 2^{(2)} \dots N^{(1)} N^{(2)}$. The first HRI⁽¹⁾ is made from $1^{(1)} 2^{(1)} \dots N^{(1)}$ and HRI⁽²⁾ from $1^{(2)} 2^{(2)} \dots N^{(2)}$. The time distance between HRIs is only $1/f_{prf}$ resulting in the highest possible V_{peak} . The approach was implemented on the SARUS scanner using a 3 MHz 128 elements phased array and simulated using Field II. Five virtual sources were used for the flow sequence and each emission was repeated 3 times with a positive, negative, and positive emission making pulse inversion possible. Directional data were beamformed for all depths using Transverse Oscillation and a new cross-correlation based estimator (DTO) was used. Measurements were made on a circulating flow rig with a parabolic profile with a peak velocity of 0.52 m/s at beam-to-flow angles of 60, 75, and 90° and at $f_{prf}=[4500, 1000, 450, 225]$ Hz with similar simulations. The velocities were estimated using 8 HRIs, and the relative Standard Deviation (SD) to the peak velocity was calculated as the averaged across the estimated profiles.

Results/Discussion

For simulated data SDs from 2.0% to 9.9% were obtained for all angles and f_{prf} values from 4500 to 450 Hz for the lateral velocity component, when using the DTO estimator. For measured data SD was ranging from 2.5% to 10.5%. Scaling f_{prf} to 5 kHz thereby gives a V_{peak} of at least 5.8 m/s or 11.6 m/s at 10 kHz. Beamformation along the flow direction can increase precision. At $f_{prf}=225$ Hz and 90°, SD was lowered from 30.8% to 8.7% using this with a cross-correlation estimator demonstrating a possible peak velocity of 23.1 m/s at $f_{prf}=10$ kHz, when the flow angle is known. The new SA scheme can, thus, give continuously available data everywhere in the imaging, which has an infinite observation time and at the same time estimate the highest peak velocities encountered in clinical ultrasound. This makes it possible to replace continuous wave Doppler measurement, and thereby correctly reveal both velocity magnitude and direction as a function of depth.

Simultaneous Tissue and Flow Estimation using Plane Waves and Transverse Oscillation on In Vivo CarotidVincent Perrot¹, Hervé Liebgott¹, Anne Long¹, Didier Vray¹¹*CREATIS, Univ.Lyon, INSA-Lyon, UCB Lyon 1, UJM-Saint Etienne, CNRS, Inserm, Villeurbanne, France***Background, Motivation, and Objective**

Tissue motion, pulse wave velocity (PWV) and blood flow are significant vascular features which are inherently related. They reflect the cardiovascular physiology like artery stiffness, blood pressure and heart dynamics. Consequently, simultaneous assessment of these parameters is essential for studying, understanding and monitoring the cardiovascular system. Unfortunately, due to the differences in terms of signal intensity between blood and tissue (up to a ratio of 100 dB) and in terms of velocities (can exceed 1 m/s for flow, while tissue velocity is in the order of 1 cm/s), two different ultrasound sequences and processing techniques are usually used. A sequence and processing technique have previously been validated on a phantom vessel to respond to the expressed need. This work aims at studying it with *in vivo* carotid data.

Statement of Contribution/Methods

Carotid arteries from healthy volunteers were imaged with a Verasonics Vantage 256 system coupled to a linear array probe. An ultrafast ultrasound sequence was used based on horizontal plane wave transmissions without compounding with a 3-cycles excitation signal. After beamforming, transverse oscillation was introduced in the Fourier domain and wall motion was extracted with a 2D phase-based estimator. A temporal adaptive FIR was designed based on the estimate wall velocities to remove clutter from the lumen. Afterwards, flow was extracted with the same methods than the wall motion.

Results/Discussion

Results (Fig. 1) show that the flow and wall motion can be assessed simultaneously with the proposed technique. PWV (Fig. 1 a) was extracted by tracking the wall velocity front at diastolic notch. For this volunteer, measured PWV was 3.15 m/s. Moreover, the technique is able to extract peak flow (Fig 1 b) and slow-moving flow (Fig 1 c). Finally, this method provides a simultaneous extraction of tissue motion and flow, which permits to compare synchronization between the difference phenomena during the cardiac cycle, in particular the delay between systolic flow wave and pulse wave. Applied to atherosclerosis of the carotid bifurcation, these techniques may be valuable to study plaque vulnerability.

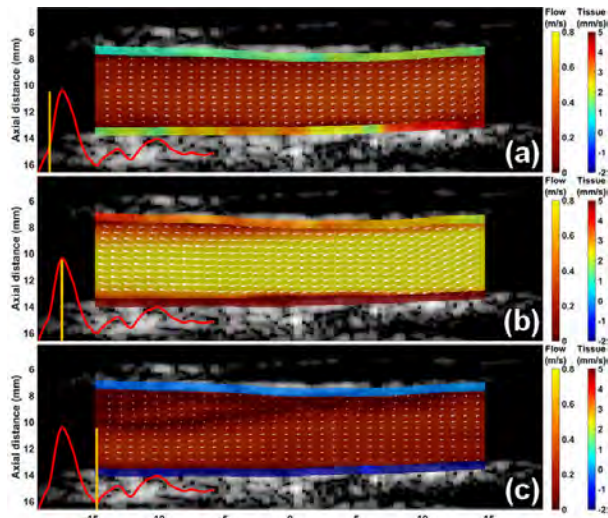


Figure 1 - B-mode images superimposed with flow (m/s) and tissue velocity (mm/s, sign is related with expansion/contraction) estimation at three different times: (a) pulse wave arriving from the right edge of the carotid (velocity front at 10 mm along the lateral axis), (b) peak flow and (c) minimum flow.

In Vivo 40 MHz Ultrafast Ultrasound Vector Doppler Imaging (VDI) for Mice Carotid Artery**Hsin Huang¹, Chih-Chung Huang¹**¹*National Cheng Kung University, Taiwan***Background, Motivation, and Objective**

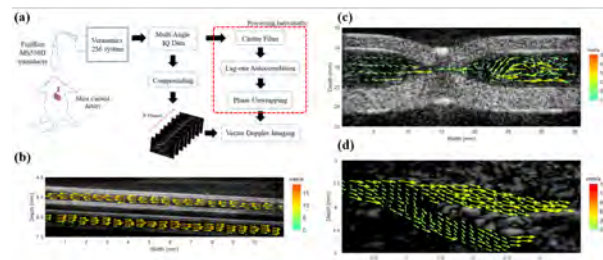
Ultrafast ultrasound Doppler imaging has been used for many applications with an operational frequency range from 3-20 MHz. Since Ultrafast ultrasound image is usually based on multi-angles plane wave imaging, vector Doppler imaging (VDI) was proposed for depicting the blood flow in all directions without Doppler angle correction. Recently, VDI has also been used for small animal applications. However, the image resolution is not good enough for visualizing the micro-structure tissues. This problem can be solved by applying high frequency (HF) ultrasound. However, the maximum flow velocity estimation was limited by operational frequency according to Doppler aliasing equation. This phenomenon is obvious for small animal applications, such as at carotid artery and aorta. The purpose of this study is to develop a 40 MHz VDI, and overcomes the aliasing problem by the phase unwrapping algorithm. Performance verification was carried out by phantoms and in vivo mice study.

Statement of Contribution/Methods

Data acquisition was performed by Verasonics Vantage 256 system with a 40 MHz linear array (Visualsonics MS550D), as shown in Fig 1(a). The plane wave compounding image at a frame rate of 4 k fps was obtained from three angles ($+5^\circ$, 0° , -5°). VDI was performed on slow-time analysis with an individual angle collection. Clutter filters including high pass filters and SVD-based filters were utilized to suppress the unwanted signals. Spatial and temporal phase unwrapping methods were carried out to overcome the aliasing problem. Experiments were performed by flow phantoms and in vivo mice carotid artery for verification.

Results/Discussion

Fig 1(b) shows the HF VDI from two-way steady flow phantom. The arrow in the image represents the flow direction, and length of arrow represents the velocity value. The measured velocity was around 5.5 mm/s, which is consistent with the experimental setup. Fig 1(c) shows the VDI from a narrowed PVA tube. A turbulent of flow was observed obviously at the outflow area. Fig 1(d) shows the in vivo HF VDI of the mice carotid artery (dia. 0.5-1 mm). The flow direction and velocity from carotid artery branch was also observed obviously. The average flow velocities were 82, 61, and 104 mm/s for CCA, ECA, and ICA. All the experimental results show that HF VDI exhibits a good performance for measuring the complex flow dynamics for preclinical small animal researches.



P2-A5 - Novel Instrumentation and Approaches in Photoacoustic Imaging

Waraku (posters 2)

Tuesday, October 23, 9:30 AM - 4:00 PM

Chair: **Sophinese Iskander-Rizk** Erasmus Medical Center

P2-A5-1

An automated breast ultrasound scanner with integrated Doppler flow imaging and shear wave elastography

Corey Kelly¹, Julio Lobo², Yanan Shao³, Mohammad Honarvar¹, Tim Salcudean¹

¹*University of British Columbia, Vancouver, BC, Canada*, ²*Electrical and Computer Engineering, University of British Columbia, Vancouver, BC, Canada*, ³*University of British Columbia, Canada*

Background, Motivation, and Objective

Whole-breast automated ultrasound scanning has been shown to improve tumour detection in radiographically dense breasts, where mammography (the current screening standard) lacks sensitivity[1]. More sophisticated ultrasound modalities, in particular Doppler flow and elasticity imaging [2, 3], can further improve detection accuracy to avoid unnecessary biopsies.

The aim of this study is to integrate 3D shear wave absolute elastography and Doppler flow imaging into an existing automated breast ultrasound scanner (ABUS), with the goal of acquiring multimodal volumetric data in one fast, operator-independent scan.

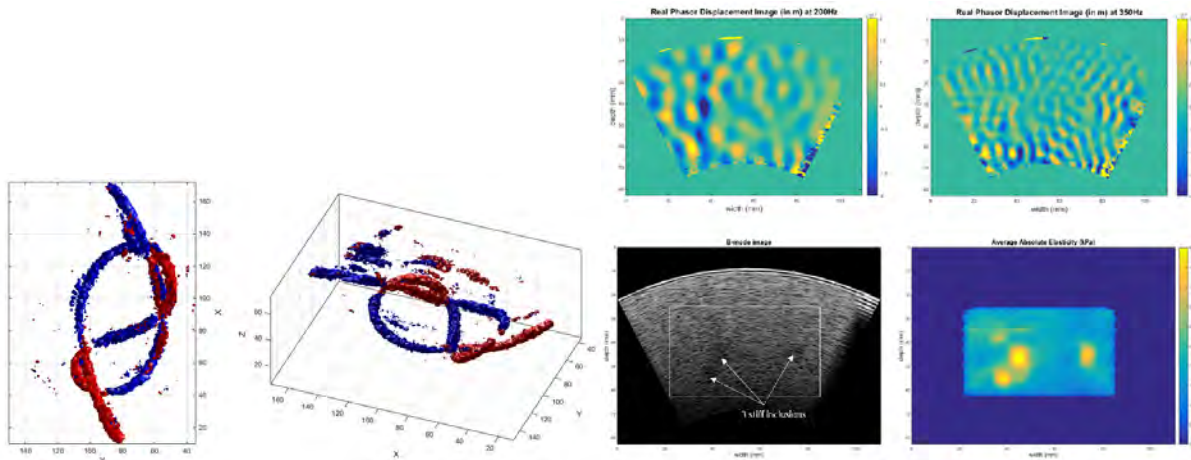
Statement of Contribution/Methods

This work consists of three primary contributions. First, we designed and built a shear wave tissue exciter compatible with the SonixEmbrace ABUS. Second, we developed the sequencing for the 384-element ABUS transducer while maintaining the high acquisition speed necessary for accurate elasticity measurement. Third, we completed the 3D scan conversion and display of these multimodal data.

Results/Discussion

We have developed a system which can acquire 3D B-mode, Doppler flow, and elasticity images of an entire breast volume in under ten minutes. This system can display real-time 2D data for all three modalities during acquisition. The volumetric data are reconstructed for display offline.

Figure 1 shows 3D Doppler flow in a phantom containing a knotted tube. Figure 2 shows 2D phasor and absolute elasticity images acquired in a breast phantom.



3D Photoacoustic and Ultrafast Ultrasound Volumetric Flow Imaging with a Bias-Switchable Row-Column 2D ArrayChris Ceroici¹, Quinn M. Barber², Katherine Latham³, Jeremy Brown⁴, Roger Zemp²¹*Electrical and Computer Engineering, University of Alberta, Edmonton, AB, Canada*, ²*University of Alberta, Canada*,³*Electrical and Computer Engineering, Dalhousie University, Canada*, ⁴*Biomedical Engineering, Dalhousie University, Halifax, NS, Canada***Background, Motivation, and Objective**

The combination of ultrasound flow imaging and photoacoustic imaging holds promise for visualizing biomarkers in context of surrounding vasculature, as well as functional estimation of oxygen metabolism, among other things. 3D visualization of flow and biomarkers may have significant implications for future biological and medical imaging applications. Ultrafast volumetric imaging methods have been proposed using large row-column arrays, however, ultrasound B-scans have degraded image quality, owing to only one-way focussing. Additionally, these arrays are not suitable for photoacoustic imaging, which requires read-out from each subelement of a 2D array. Recently, we introduced bias-switchable row-column arrays, enabling desired read-out capabilities at a greatly reduced channel count when compared with a fully-wired array. These arrays are investigated here for ultrafast volumetric flow imaging, photoacoustic (PA) imaging, and high-quality ultrasound B-scan imaging.

Statement of Contribution/Methods

We implemented 3D PA/US imaging using a 64x64 element, top-orthogonal-to-bottom-electrode (TOBE) relaxor array. The TOBE architecture enables our row/column channels to be bias-switchable allowing for 3D photoacoustic imaging using bias-encoded receive apodizations, increasing our signal-to-noise ratio compared to conventional approaches while maintaining high-resolution. We imaged two crossed wires in an optically scattering medium to validate this.

Orthogonal Plane-wave Compounding [M Flesch *et al* 2017 *Phys. Med. Biol.*] was used to generate 3D Power Doppler (PD) images, using 36 total transmits with $\pm 10^\circ$ angular span. A 1 mm diameter tube was submerged in water, and a blood-mimicking fluid was flowed through the tube at 10 cm/s. PD images were reconstructed in MATLAB using an SVD filter.

Results/Discussion

We were able to demonstrate both PA and PD imaging using our 2D TOBE relaxor array. Figure 1a shows a volumetric PA reconstruction of a crossed-wire phantom at 1 cm depth in a tissue-mimicking phantom. Axial, azimuthal and elevational resolution was measured to be 220 μm , 311 μm , and 369 μm . Using bias-encoding the SNR was improved by 16.5 dB over single-column biasing. Figure 1b and c shows ultrafast volumetric PD flow images of the aforementioned flow phantom. Ongoing work aims to estimate oxygen consumption in phantoms and *in vivo*.

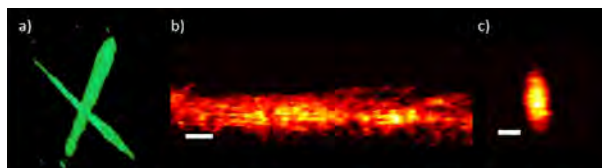


Fig 1. 3D PA image of two wires 1 cm apart (a), and lateral (b) and cross-sectional (c) PD images of a 1 mm tube. Scale bar is 0.5 mm.

Laser-generated focused ultrasound system using CNT-PDMS optoacoustic lenses for micro-precision tissue treatment**Jeongmin Heo¹, Pilgyu Sang¹, Mingyu Joo¹, Aavish Abbasi¹, TaiAnh La¹, Hyoung Won Baac¹**¹*Sungkyunkwan university, Korea, Republic of***Background, Motivation, and Objective**

Laser-generated focused ultrasound (LGFU) is an emerging modality that is highly suitable for micro-precision histotripsy. For such cavitation-based treatment on a microscale spot, optoacoustic lenses coated with a CNT-PDMS composite film have been used, converting an incident high-energy laser pulse (5–10 ns) into a powerful focused ultrasonic pulse (15-MHz center frequency and 70-MPa pressure peak). LGFU could be applied to mechanical disruption of stones and cells. We have developed robust and highly energy-efficient optoacoustic lenses with a variety of designs in terms of focal length (up to 40 mm), aperture (3–50 mm), focal gain, and focal spot width (down to 20 μm). Moreover, an LGFU system has been significantly improved with a waveguide mold and an additional sensor to monitor the location of focus. We present our recent progress for LGFU system development and characterization together with applications to micro-histotripsy.

Statement of Contribution/Methods

Solution-based CNT-PDMS lenses were used to generate LGFU under pulsed laser irradiation with a few to tens of mJ/pulse. First, focal waveforms and focal spot dimensions were characterized. As cavitation is a key for histotripsy, we have characterized cavitation threshold for a single LGFU pulse using a non-thermal excitation condition, i.e., with a pulse repetition rate of 10~20 Hz. Then, we performed LGFU-induced mechanical fragmentation first on aluminum foils with respect to pressure amplitude and the number of pulse accumulation. Next, tissue mimicking gel (agarose gel; 1%), mouse brain and pig heart muscle were used for micro-histotripsy ex vivo and in vivo demonstration. Moreover, for facile optoacoustic systems, an ultrasound propagation guide mold was integrated with a CNT-PDMS lens with a 2-mm hole at the center for monitoring the focus.

Results/Discussion

LGFU strength was first characterized on an alumina foil. LGFU-induced cavitation could form dents with different scales (100~500 nm in width) that were generated depending on incident laser energy (23~103 mJ/pulse) and geometrical focus. Then, cavitation-based micro-histotripsy was performed using agarose gels and tissue, resulting in the width of approximately 100 μm for the laser energy fluence of >20 mJ/cm² at the optoacoustic lens. The agarose gel experiment shows that LGFU amplitudes are sufficiently high to produce free-field micro-cavitation. Targeted tissue fragmentation and cavitation behaviors under LGFU were monitored by a passive cavitation detection (PCD) system, integrated onto the LGFU system, which allows us to find the axial position of the focus (resolution: 100 μm). For lateral targeting of the focus, we used a visible laser guidance through the central hole of optoacoustic lens (resolution: 300 μm) Finally, we utilized a waveguide frame (fabricated by a 3-D printer) mounted on the CNT-PDMS lens, confirming the enhancement of focused ultrasound amplitude.

The effectiveness of the omnidirectional illumination in full-ring photoacoustic tomography

Suhail Alshahrani¹, Yan Yan¹, Alexander Pattyn¹, Mohammad Mehrmohammadi^{1,2,3}

¹Department of Biomedical Engineering, Wayne State University, Detroit, MI, United States, ²Department of Electrical and Computer Engineering, Wayne State University, Detroit, MI, United States, ³Barbara Ann Karmanos Cancer Institute, Detroit, United States

Background, Motivation, and Objective

We have previously introduced a novel photoacoustic tomography (PAT) system for breast cancer imaging. In our proposed method, the object (i.e., breast tissue) is illuminated omnidirectionally using a set of the cone and conical ring mirrors. A ring ultrasound (US) transducer is utilized to acquire PA signals and form PAT images. Using omnidirectional illumination can provide a more uniform illumination pattern within the tissue and enable PAT imaging at larger depths. In this study, we report for the first time the integration of large size optical components into a clinical ultrasound tomography system for performing US/PA tomography in breast size objects. In addition, we report a quantitative comparison between omnidirectional illumination and a reported common strategy for light illumination in PAT using a single laser beam. This examination and comparison were conducted by using a small optical prototype with the linear-array transducer.

Statement of Contribution/Methods

The large size optical prototype consists of the cone-shaped reflector and 25 cm diameter parabolic reflector which able to create full-ring beam from a collimated beam. The diameter of the ring-shaped beam could be changed by adjusting the distance between the optical system and the subject (**Fig. 1a**). The ability of the full-ring illumination mode in precisely targeting specified cross-sectional slice from the tissue-mimicking phantom including light absorbing materials was tested using a linear-array US transducer. In addition, the effectiveness of the full-ring illumination mode was investigated by comparing it with single-point illumination (side and center illumination) (**Fig. 1b**).

Results/Discussion

The results indicated: (a) at almost the same energy level (44 mJ/pulse), the full-ring illumination mode visualized all objects in the targeted cross-sectional slice of the tissue-mimicking phantom while side and center point illumination generated a large PA signal on the object close to the entrance point; (b) the full-ring illumination provides relatively uniform PA signal within the selected cross-section, indicating uniform fluence distribution. The mean PA amplitude of all objects in the targeted cross-sectional area is illustrated in **Figure 1c**.

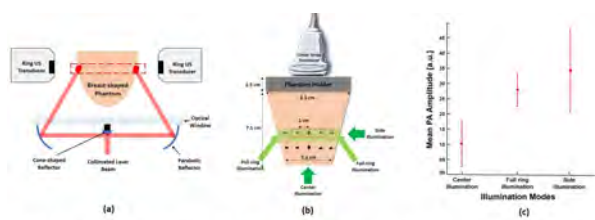


Figure 1: (a) The schematic of the large-scale optical prototype integrated with ring ultrasound transducer (b) experimental setup on the tissue-mimicking phantom to study full-ring, side, and center illumination modes at 44mJ/pulse. (c) The graph shows the mean value of measured PA amplitudes in each illumination mode.

Internal-illumination Photoacoustic Computed Tomography with 15-cm Penetration DepthMucong Li¹, Wei Liu¹, Junjie Yao¹¹Duke University, United States**Background, Motivation, and Objective**

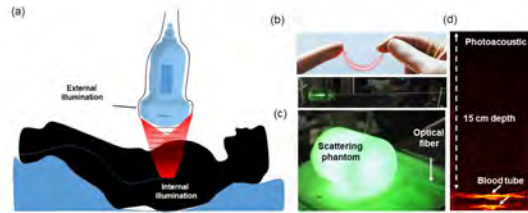
Photoacoustic imaging (PAI) is a hybrid imaging modality that combines optical excitation with ultrasound detection. Compared to pure optical imaging, PAI is less limited by optical diffusion for deep tissue imaging, taking advantage of both ballistic and diffused photons. However, the traditional external light illumination in PACT usually limits the penetration depth to a few centimeters from the tissue surface, mainly due to strong optical attenuation along the light propagation path from the outside in.

Statement of Contribution/Methods

Unlike the traditional PAI systems using external illumination, internal light illumination combined with external ultrasound detection can potentially detect much deeper targets (**Fig. 1a**). Here, we report a photoacoustic computed tomography (PACT) system using a customized optical fiber with a cylindrical diffuser to internally illuminate deep targets. Different from previous internal illumination PACT implementations using forward-looking optical fibers, our internal-illumination PACT system uses a customized optical fiber with a three-centimeter-long conoid needle diffuser attached to the fiber tip (**Fig. 1b**), which can homogeneously illuminate the surrounding space and substantially enlarge the field of view.

Results/Discussion

We characterized the internal illumination distribution (**Fig. 1c**) and we performed tissue phantom and *in vivo* animal studies to further demonstrate the superior imaging depth using internal illumination over external illumination. We imaged a 15-cm-deep leaf target embedded in optically scattering medium (**Fig. 1d**) and the beating heart of a mouse overlaid with 3.7 cm thick chicken tissue. Our results have collectively demonstrated that the internal light illumination combined with external ultrasound detection might be a useful strategy for imaging internal organs that are deeply seated in the human body but close to the body cavity nearby, including the prostate close to the rectal cavity, the bladder and kidney close to the urethra and ureter, and the lung close to the trachea.



Axial-Resolution Improved Optical Resolution Photoacoustic Microscopy Using Minimum-Variance Spectral Apodization and Coherence Weighting

Hong-Sheng Chen¹, Meng-Lin Li¹

¹National Tsing Hua University, Taiwan

Background, Motivation, and Objective

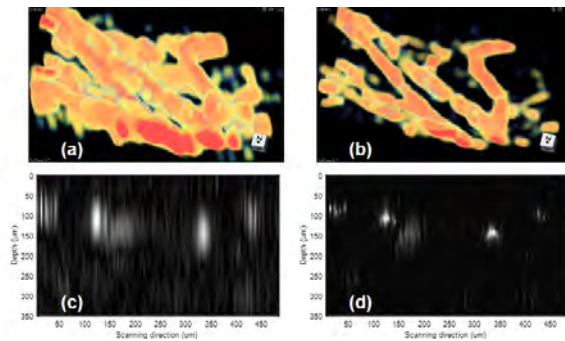
Optical resolution photoacoustic microscopy (OR-PAM), though possessing high lateral resolution via optical focusing, has been limited by its poor axial resolution. Its axial resolution mainly depends on the bandwidth of the ultrasound detector. To form images with isometric spatial resolution, high frequency ultrasound detectors larger than 100 MHz along with a Wiener deconvolution method have been proposed, yet suffering severe high-frequency acoustic attenuation and thus limited imaging depth and working distance.

Statement of Contribution/Methods

In this study, we propose a novel minimum-variance (MV) spectral apodization technique along with coherence weighting to improve axial resolution of OR-PAM without physically increasing the detection bandwidth. The MV technique and coherence weighting are originally proposed to apply over array data in both ultrasound and photoacoustic array imaging to improve lateral resolution. Via the help of spectral whitening, the MV method can be adapted to the frequency components which synthesize the OR-PAM signal at a desired depth, minimizing the interference from other depths thus improving the axial resolution. Here the ratio of the energy of the MV spectral apodized signal to the total energy of the frequency components at the desired depth is calculated and used as coherence weighting to the MV spectral apodized signal to further reduce the axial mainlobe width and suppress the axial sidelobes.

Results/Discussion

In vivo 25-MHz OR-PAM of mouse-ear microvasculature was performed to verify our idea. Figure (a) and (c) showed the original 3D and B-mode images of the mouse-ear microvasculature, respectively, while their corresponding axial-resolution improved 3D and B-mode images were presented in figure (b) and (d). A micro-vessel with its measured diameter of 88.7 μm in figure (c) was chosen to estimate the performance of the proposed method. With the proposed method, the diameter of the imaged microvessel became 21.1 μm , providing 4.2 times improvement in axial resolution. The performance of the proposed technique with a higher frequency transducer, e.g., a 50-MHz transducer will also be presented.



Simultaneous photoacoustic and ultrasound imaging using a hemispherical sensor array

Shunto Takaoka¹, Kengo Kondo¹, Takeshi Namita¹, Makoto Yamakawa¹, Tsuyoshi Shiina²

¹Graduate School of Medicine, Kyoto University, Kyoto, Japan, ²Faculty Consort of Human Health Sciences, Kyoto University, Kyoto, Japan

Background, Motivation, and Objective

A hemispherical sensor array[1] enables photoacoustic (PA) imaging with spatially isotropic and finer vasculature compared to planar sensor array. Combining ultrasound (US) image with PA image helps us to determine structural relations of tissues and vessels. Although a piezoelectric element of the hemispherical sensor array has the ability to perform pulse-echo, the array is very sparse due to limited number of channels on data acquisition systems, therefore beamforming cannot be applied properly and enough quality US image has not been obtained. In this study, we used mechanical scanning and synthetic aperture imaging to improve quality of US images, and it enables PA and US simultaneous measurements by hemispherical sensor array.

Statement of Contribution/Methods

PA imaging by hemispherical sensor array acquires PA signals with mechanical scanning in order not only to broaden the field of view but also to improve contrast by virtually increasing the number of sensors. During PA scanning, we also acquire US signals transmitted from each sensor element between laser pulse intervals, then synthetic aperture imaging[2] is applied to emulate a large number of sensors. Experiments were performed on a tissue-mimicking agar phantom (Figs. 1 (a), (b)). The phantom consisted of agar gel mixed with acoustic scatterers, agar gel inclusion without scatterers, agar gel mixed with ink, and acrylic rod, which mimic background tissue, tumor, vessels, and bone, respectively. A hemispherical sensor array (100 mm diameter, 256 elements, 2 MHz center frequency) located on mechanical stage was connected to a Verasonics Vantage 256 research ultrasound system. Laser pulses (800 nm, 30 Hz PRF) were used to generate PA signals.

Results/Discussion

Figs. 2 (a)-(c) show the results. In Fig. 2 (a), PA image clearly visualized optical absorbers but other structures did not appear. Fig. 2 (b) indicates that the obtained contrast was too low to distinguish inclusion from surrounding tissue due to high grating lobes when sensor is not scanned. In contrast, in Fig. 2 (c), scanning sensors improved the contrast and the field of view. Low echoic inclusion and acrylic rod can be identified. In addition, combining PA and US images helps us to easily determine where optical absorbers were located.

References

[1] R. A. Kruger et al., Med. Phys. 40, 113301, 2013.

[2] J. A. Jensen et al., Ultrasonics, 44, e5-e15, 2006.

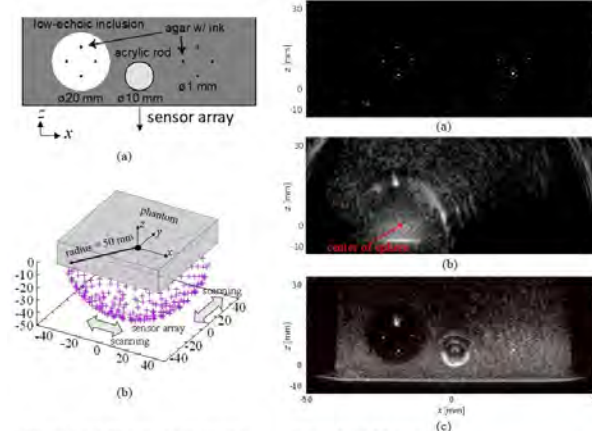
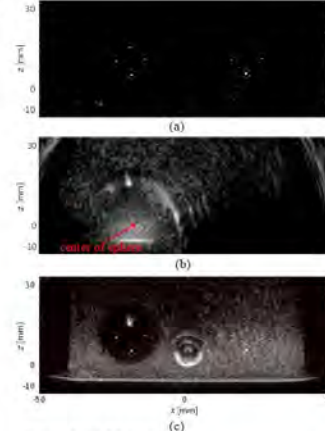


Figure 1 (a) Phantom schematic.
(b) Experimental system setup.

Figure 2 (a) PA image.
(b) US image without mechanical scanning.
(c) Overlaid PA (red) and US (gray) images obtained by mechanical scanning.



P2-A6 - All-Optical Photoacoustic Imaging and Computational Approaches

Waraku (posters 2)

Tuesday, October 23, 9:30 AM - 4:00 PM

Chair: Meng-Lin Li National Tsing Hua University

P2-A6-1

Dual-modality All-Optical Ultrasound and Photoacoustic Imaging Using Permanent Marker Ink

Richard Colchester^{1,2}, Sacha Noimark^{1,2,3}, Edward Zhang¹, Paul Beard^{1,2}, Adrien Desjardins^{1,2}

¹Department of Medical Physics & Biomedical Engineering, University College London, London, United Kingdom,

²Wellcome/EPSRC Centre for Surgical and Interventional Sciences, University College London, London, United Kingdom,

³Materials Chemistry Research Centre, Department of Chemistry, University College London, London, United Kingdom

Background, Motivation, and Objective

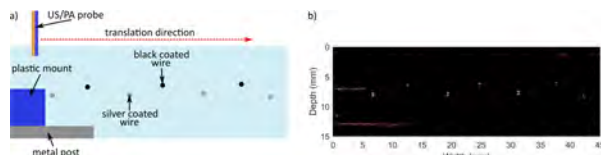
High frequency miniaturised ultrasound (US) probes are desirable for guiding minimally invasive procedures. Optical generation and reception of US is emerging as an alternative method for US imaging. Here, US is generated using pulsed or modulated excitation light and received with optically sensitive elements. These devices have several advantages, including the potential to generate and receive wideband US required for high resolution imaging. In addition, use of download optics, i.e. optical fibres instead of electric wiring, allows for the integration of secondary optical capabilities. We present a fibre-optic US and photoacoustic (PA) transmitter fabricated using a wavelength-selective polydimethylsiloxane (PDMS) and permanent marker ink composite.

Statement of Contribution/Methods

An optical US transmitter comprising PDMS and permanent marker was fabricated on the end of an optical fibre. The composite was created by re-dispersing dried permanent marker ink (2 ml) in 1 ml of xylene, adding 1 g PDMS and sonicating the resultant polymer solution. The distal tips of optical fibres were manually dipped into the polymer solution and the coating left cure. The optical absorption and US generation properties of the coating were characterised. Subsequently, the transmitter was paired with a Fabry-Pérot fibre optic sensor to create an imaging device. Two phantoms were imaged; a 25 µm diameter tungsten wire phantom and a coated copper wire phantom.

Results/Discussion

The optical absorption was > 95% from 400 nm to 700 nm and < 5% for wavelengths > 1000 nm. This gave two wavelength regions, an optically absorbing region for US generation and an optically transmitting region for PA light delivery. Ultrasound generated within the coating had a peak-to-peak pressure > 200 kPa with a -6 dB bandwidth > 15 MHz. The US resolution in the axial dimensions was < 200 µm. Co-registered US and PA imaging demonstrates the capability of the device (Figure 1). In this work, we have shown it is possible to make dual-modality US transmitters using a low-cost, commercially available ink.



Adaptive All-Optical Ultrasound Imaging through Temporal Modulation of Excitation Light**Erwin Alles^{1,2}, Richard Colchester^{1,2}, Adrien Desjardins^{1,2}**¹*Department of Medical Physics & Biomedical Engineering, University College London, London, United Kingdom*, ²*Wellcome / EPSRC Centre for Surgical and Interventional Sciences, University College London, London, United Kingdom***Background, Motivation, and Objective**

Conventional electronic ultrasound transducers typically derive their sensitivity from mechanical resonance. As such, their frequency and bandwidth, and hence the corresponding spatial resolution and tissue penetration depth, are fixed during fabrication. Recently, all-optical ultrasound imaging, where ultrasound is both generated and detected using light, has been demonstrated as a viable alternative modality that exhibits great miniaturisation potential. Not relying on resonance effects, high bandwidths have been reported for optical ultrasound sources that were excited with nanosecond duration light pulses. In contrast, here a temporally modulated light source is used to vary and constrain the optical and corresponding acoustic bandwidth, thus allowing dynamic control over the imaging depth and resolution.

Statement of Contribution/Methods

A broadband fibre-optic ultrasound detector (comprising a Fabry-Pérot etalon) and a fibre-optic ultrasound generator (comprising a nanocomposite based on multi-walled carbon nanotubes and polydimethylsiloxane) were paired to create an all-optical ultrasound imaging probe. B-mode ultrasound images were obtained by translating the imaging probe along a linear aperture during continuous pulse-echo data acquisition, followed by time reversal reconstruction. Either broadband (Q-switched laser generating 2 ns duration pulses) or spectrally-constrained excitation light (laser diode modulated by a linear chirp of 4 μ s duration of adjustable spectral content) was used to generate broadband (1-35 MHz; limited by the sound generating coating) or spectrally constrained ultrasound, respectively. In the latter case, the axial resolution was recovered through pulse compression.

Results/Discussion

Images of *ex vivo* tissue samples confirmed that adjusting the spectral content of the excitation light enabled dynamic control over the image resolution and penetration depth. Using a single all-optical imaging probe, images were acquired at low resolution but deep penetration (Fig. 1c), as well as at high resolution but short penetration (Fig. 1d), without the need for band-pass filtering and associated power losses. The demonstrated dynamic control over imaging parameters will allow for seamless multiscale imaging without the need for changing transducers, and can strongly benefit interventional imaging.

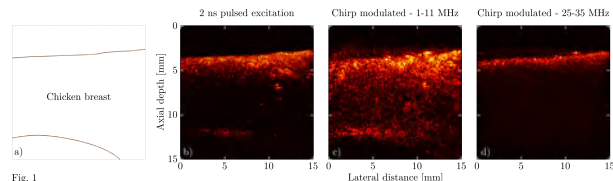


Fig. 1

Deep learning for limited-view photoacoustic tomography reconstructionYuan Zhou¹, Jianwen Luo¹, Junjie Yao²¹Tsinghua University, China, People's Republic of, ²Duke University, Durham, NC, United States**Background, Motivation, and Objective**

High quality and accurate reconstructed photoacoustic (PA) image can give a quantification of the tissue properties. Usually the PA image are reconstructed from the partial-scan acoustic data, for the ease of use of the linear PA transducer. However, the PA image reconstructed by the traditional PA reconstruction algorithms suffers from the artefacts because of the limited-view data.

The objective is to use a deep learning based approach to the image reconstruction from the limited-view linear PA transducer measurements, to overcome the artefacts and low-quality induced by the traditional PA reconstructed algorithm.

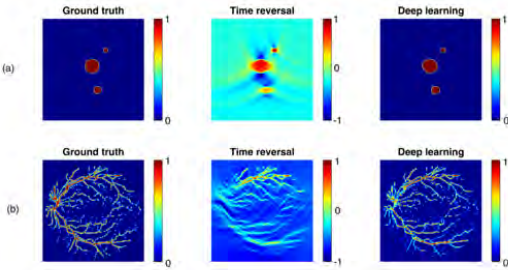
Statement of Contribution/Methods

A deep learning model, U-Net, was used to estimate the initial pressure from the reconstructions of the limited-view PA data by the traditional algorithm. The images of initial pressure were first reconstructed by the time reversal (TR) algorithm from the raw limited-view data. Then the TR reconstructions were input into the U-Net and the final reconstructions of initial pressure were output from the U-Net. The U-Net was a fully convolutional network which can realize the image-to-image mapping. Two models of U-Net were trained for reconstructing different types of structures, using random disc and blood vessel simulated data.

Results/Discussion

Figure 1 shows the ground truth, TR reconstruction and deep learning reconstruction results, of both random disc and blood vessel simulated data. The deep learning model removed the artefacts and recovered more details with better image quality, comparing with the TR reconstructions.

We proposed a deep learning based approach to the image reconstruction from the limited-view PA measurements. In this approach we first performed the traditional TR algorithm to obtain the reconstructions with much artefacts and then applied a U-Net to generate the final reconstructions of the initial pressure. According to the results of both the simulated random discs and blood vessel data, the proposed deep learning based image reconstruction method can remove the artefacts and provide high quality images with more details from the reconstructions of the traditional PA reconstruction algorithm. The simulation results also prove the feasibility of the deep learning on PA image reconstruction and processing and can provide an option for further phantom and *in vivo* PA applications.



Using deep neural networks to remove photoacoustic reflection artifacts in ex vivo tissue

Derek Allman¹, Muyinatu Bell²

¹Electrical and Computer Engineering, Johns Hopkins University, United States, ²Johns Hopkins, Baltimore, MD, United States

Background, Motivation, and Objective

Photoacoustic (PA) imaging has promising potential to guide surgeries by providing the information needed to avoid accidental injury to major blood vessels. However, PA imaging is often hampered by reflection artifacts, which may result from hyperechoic structures such as bone or subcutaneous fat. We previously demonstrated a deep convolutional neural network (CNN) to distinguish between PA sources and reflection artifacts using the raw channel data as an input, in both simulated and phantom data [1]. This work evaluates our novel approach in *ex vivo* tissue.

Statement of Contribution/Methods

A deep neural network was first trained with simulated channel data, then transferred to experimental PA data of a needle tip inserted in *ex vivo* tissue. A total of 19,992 frames of PA channel data were simulated in k-Wave (80% for training and 20% for testing). Each image contained two acoustic wavefronts, one originating from a true source and the other representing a reflection artifact. White Gaussian noise was randomly added, resulting in channel SNR ranging from -5dB to 2dB. A CNN was trained using the Faster region-based CNN (Faster-RCNN) algorithm VGG16 network architecture to identify sources and reflection artifacts in raw PA channel data [1]. The outputs of the network (class, confidence score, and bounding box location) were used to generate usable images we refer to as CNN-based images. Once trained this, network's source detection capability was evaluated on simulated data as well as 17-31 frames of *ex vivo* channel data from chicken breast, bovine liver, steak, and a chicken thigh containing bone.

Results/Discussion

The chicken and liver datasets achieved 100% source classification accuracy and 0% misclassification rate. The steak dataset achieved 100% source classification accuracy and a 23.5% misclassification rate. The chicken thigh dataset achieved 83.9% source classification accuracy and 8.89% misclassification rate. True signal locations were displayed with a diameter corresponding to two standard deviations of the location errors measured with testing of simulated data (i.e. 0.28 mm), as shown in the CNN-based image of Fig. 1. Results establish the feasibility of testing CNNs with simulated data and transferring them to experimental tissue data to remove reflection artifacts and detect low-amplitude PA sources.

[1] D Allman, A Reiter, MAL Bell, IEEE TMI 2018

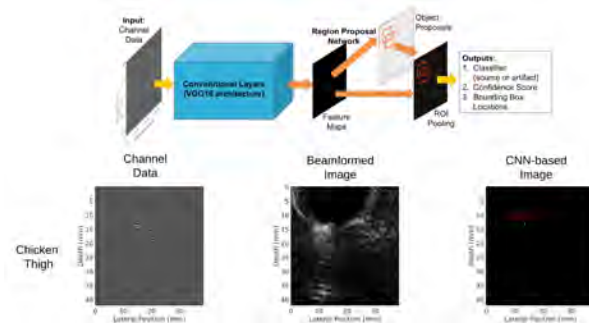


Fig. 1: Schematic diagram of our convolutional neural network approach and sample images obtained in an *ex vivo* chicken thigh.

P2-A7 - Industrial Applications

Waraku (posters 2)

Tuesday, October 23, 9:30 AM - 4:00 PM

Chair: **Kentaro Nakamura** Tokyo Institute of Technology

P2-A7-1

Evaluation of engine oil deterioration using shear horizontal surface acoustic wave sensor based on acoustoelectric interaction

Saya Kobayashi¹, Jun Kondoh¹

¹Shizuoka University, Hamamatsu-shi, Japan

Background, Motivation, and Objective

Oils have been widely used in transportation systems, machines, etc. On-line measurement of oils is required. In this paper, a shear horizontal surface acoustic wave (SH-SAW) based on the acoustoelectric interaction is applied to measure oil. Viscosity measurements of oil are normally carried out using the acoustic wave sensors. However, in this paper, we focused the electrical property change. First, we compared new and used engine oils, which was extracted from a motorbike. The conductivity and relative permittivity of the used engine oil was increased. If the mechanism of the changes is explained using the SH-SAW sensor, oil monitoring systems using the SH-SAW is realized. In this paper, influences of particles in the oil, heating effect of the oil, and water contained in the oil were experimentally discussed.

Statement of Contribution/Methods

The used SH-SAW sensor was fabricated on 36YX-LiTaO₃. Center frequency was 50 MHz. The sensor has two delay lines for detecting the acoustoelectric interaction. A liquid cell was placed on the sensor surface and sample liquids were injected into the cell. The reference liquid was an olive oil. Iron and carbon powders were mixed in the oil to discuss the influence of the particle. Concentrations of the water in the oil were 1 and 10 wt%. The water was ultrasonically mixed with the new engine oil.

Results/Discussion

Figure 1 shows the measured results of new and used engine oils. As particles were observed in the used olive oil, iron and carbon powders were mixed in the new engine oil. Whereas the relative permittivity increases with the amount of the particles, the conductivity was the constant. The influence of the particles are not the main causes. Secondly, the effect of oxidization by heating was measured. The new engine oil was kept at 100 °C. Heating times were varied from 400 to 3000 h. The color of the oil after 3000 h heated was similar with the used engine oil. However, the electrical properties of the heated oils do not agree with the used one. Thirdly, the influence of the water contained in the oil was measured. The results are plotted in Fig. 1. The result of used engine oil almost agrees with the result of 1 wt% water. Therefore, the mechanism of the deterioration of the engine oil used is the influence of the contained water. The results indicates that the SH-SAW sensor based on the acoustoelectric interaction can be applied for oil monitoring system.

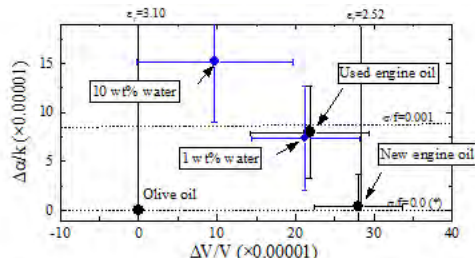


Fig. 1. Experimental results of the new and used engine oils, and the water contained oils.
 ϵ : relative permittivity, α/f : conductivity normalized by frequency, (*: $\times 10^{-8}$ S/m/Hz)

Application of Ultrasonic Assisted End Milling for Glass Material

Akira Yoneyama¹, Tsuyoshi Shimizu², Yoshihito Hagihara¹, Teruo Ishiguro¹, Masaaki Sano¹, Takaaki Ishii²

¹Yamanashi Industrial Technology Center, Kofu, Japan, ²University of Yamanashi, Kofu, Japan

Background, Motivation, and Objective

In recent years, the use of glass materials for Micro-TAS devices and electronic substrates has expanded, and micromachining technology is required for making micro-channels. Generally, in the case of end milling of glass materials, chippings occur on the machined surface, and the surface roughness becomes not so well, and the tool life becomes short. For these reasons, there are very few end milling cases for glass material. Therefore, the purpose of this research is to improve the quality of machined surface by adopting ultrasonic assisted end milling method. In this research, ultrasonic vibration in the axial direction is excited to the rotating tool, and improvement of machinability can be expected from conventional machining.

Statement of Contribution/Methods

Figure 1 shows the experimental setup. A three-axis machining center and an ultrasonic vibration unit with a built-in Langevin transducer are used. The specifications of this unit are oscillation frequency of 54 kHz, amplitude of about 3 μm , maximum rotational speed of 20000 rpm. Workpiece material used in this study is a soda-lime glass plate whose geometrical size is 50×50×3mm. Cemented carbide square end milling cutters 0.3mm in diameter with diamond coating were used for grooving with a width of 0.3mm and a depth of 0.05mm.

Results/Discussion

Figure 2 shows the comparison of the grooving surface morphology which are ultrasonic assisted pocket milling and conventional pocket milling. The result shows that ultrasonic assisted end milling can indeed reduce edge chipping when machining glass material.

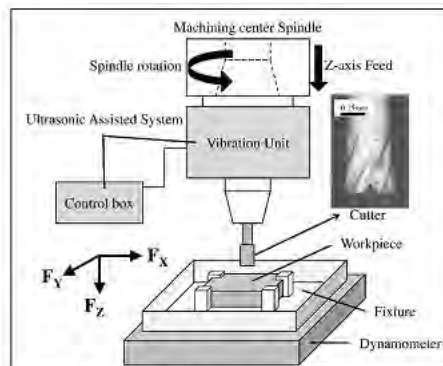


Figure 1. Experimental setup.

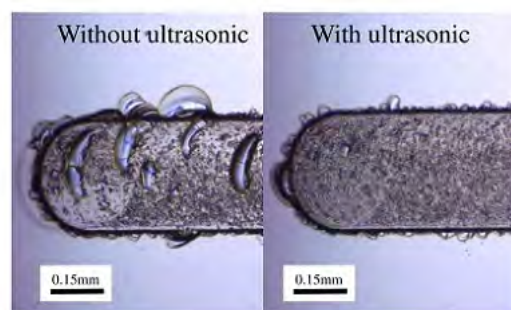


Figure 2. Machined surface comparison.

An ultrasonic flextensional array for acoustic emission techniques on concrete structuresMonica La Mura¹, Nicola Lamberti¹, Giosuè Caliano², Alessandro Stuart Savoia²¹*Department of Industrial Engineering, University of Salerno, Fisciano, Italy,* ²*Department of Engineering, Roma Tre University, Rome, Italy***Background, Motivation, and Objective**

The monitoring of concrete buildings is important to assess their solidity and promptly intervene in case of damage. Concrete structures suffer the formation of micro-cracks and the propagation of macro-cracks, due to ageing or to mechanical stresses. These cracks are sources of acoustic emission, and can be distinguished according to the frequency and intensity of the acoustic wave they generate. The acoustic emission of concrete structures occurs at frequencies ranging from 20 kHz to 180 kHz, and a good transducer for acoustic emission should have a flat bandwidth and a high gain of the pressure-to-voltage transfer function in this frequency range. Flextensional piezoelectric transducers are known for their wider bandwidth with respect to thickness-mode transducers, commonly used for this application; therefore, we designed a flextensional transducer optimized for acoustic emission applications.

Statement of Contribution/Methods

In this work, we use a FEM model to design a flextensional array for the detection of ultrasonic waves for acoustic emission techniques applied to concrete structures. The array (based on DOI: 10.1109/TUFFC.2015.2496300) is designed to have a broadband sensitivity in receive mode. The flexural movement of an elastic front plate causes the bending of an array of underlying PZT5-H piezoelectric disks. Coupled to the plate, a layer of FR-4, patterned with circular holes slightly bigger than the piezoceramics, defines the geometry of the vibrating membranes by clamping the front plate to a rigid backing made of brass. We modeled in ANSYS the device coupled to concrete, and varied its dimensions in order to obtain a broadband pressure-to-voltage transfer function. Due to technological constraints, the cell diameter was fixed at 6 mm.

Results/Discussion

The frequency of the first flexural axisymmetric mode of the 6 mm membrane was increased by increasing the membrane and the piezoelectric disk thickness, in order to make it fall within the frequency range of interest. Increasing the thickness, though, also results in a narrowing of the bandwidth due to the sharper resonance peak of the mechanical impedance. A trade-off between the bandwidth and the gain of the receive sensitivity was found in a thickness of 400 μm for the front plate and 600 μm for the piezoceramics. The presence of a laminate layer under the front plate caused a resonant peak of the sensitivity that contributed to widen the bandwidth; its thickness was varied until the two peaks of the reception transfer function were almost equal in amplitude. The back plate was designed to maintain its thickness mode resonance outside the bandwidth and to keep the sensitivity gain ripple inside a 6 dB range; the resulting thickness of the brass backing was 6 mm. The obtained transducer has a -6 dB bandwidth of 200 kHz, ranging from 12 kHz to 212 kHz.

Modelling and electrical characterization of a cantilever mechanical energy harvester

Thien Hoang^{1,2}, Maxime Bavencoffe², Guylaine Poulin-Vittrant², Guillaume Ferin¹, Franck Levassort², Claire Bantignies¹, An Nguyen-Dinh¹, Marc Lethiecq²

¹*Vermon SA, Tours, France*, ²*GREMAN, UMR 7347 CNRS, Université de Tours, INSA-CVL, Blois, France*

Background, Motivation, and Objective

Ambient vibration energy harvesting by piezoelectric materials enables to convert wasted mechanical energy available in our environment into useful electrical energy. The two main structures of piezoelectric cantilever beams used in vibration energy harvesting are the unimorph, constituted of one piezoelectric layer bonded on an elastic layer, and the bimorph, made of two piezoelectric layers separated with an inner elastic shim material.

To understand and predict the behavior of such clamped-free cantilever-based mechanical energy harvesters, numerical models have to be developed and compared to experimental measurements.

This objective first requires an accurate set of material properties. We herein propose an original approach based on the characterization of the piezoelectric material before its integration into a piezoelectric bimorph cantilever. We indeed started characterizing a 39mm x 4mm x 150 μ m PZT layer in free mechanical boundary conditions to get an accurate set of parameters of the thinned piezoelectric material. To this end, a 1D analytical admittance model has been used to identify effective parameters. To move towards experimental results, the set of material parameters used for the numerical modelling has been adjusted using mechanical and dielectric losses. Then, we evaluated the full tensor of material constant matrix by using 3D finite element (FE) model. Now, the pursued goal is to build a 3D FE model for the design of a cantilever-based mechanical energy harvester.

Statement of Contribution/Methods

Based on the characterized PZT layer, a 14 μ m thick layer of brass has been added to form a 164 μ m thick unimorph structure. In the same way, another PZT layer has been added to the unimorph structure to constitute a 314 μ m thick bimorph structure.

For each structure, a numerical study based on the FE method has been carried out. In particular, a frequency domain study has been performed on a 3D FE model in free mechanical boundary conditions to calculate the electrical response of the considered sample in the frequency range of 40kHz-100kHz.

The electrical impedance of the sample has been measured in the frequency domain thanks to an impedance analyzer and compared to the numerical results.

Results/Discussion

The set of effective parameters of the considered PZT material has been previously characterized, taking into account mechanical and dielectric losses.

Then, 3D FE modelling of different energy harvesters were performed successfully and compared to experimental measurements: the discrepancy between modelling and experiment is less than 2% in frequency. This therefore demonstrates the good accuracy of our modelling tool to predict the electrical behavior of energy harvesters in free mechanical boundary conditions.

The next step of this work is to model the clamping fixture as the pursued goal will be to build a 3D FE model to predict the vibrational behavior of the piezoelectric cantilever-type energy harvester.

P2-A8 - NDE

Waraku (posters 2)

Tuesday, October 23, 9:30 AM - 4:00 PM

Chair: **Robert Addison** Rockwell Science Center

P2-A8-1

A GPU-based Portable Phased-Array System with Full-Matrix Capture

Marcin Lewandowski^{1,2}, Mateusz Walczak^{1,2}, Beata Witek^{1,2}

¹Laboratory of Professional Electronics, Institute of Fundamental Technological Research, Polish Academy of Sciences, Warsaw, Poland, ²us4us Ltd., Warsaw, Poland

Background, Motivation, and Objective

The widely adopted ultrasound Phased-Array (PA) systems for nondestructive testing (NDT) use standard beamforming for line-by-line image creation. The introduction of new full-matrix capture (FMC) technique enables the implementation of advance processing algorithms (e.g. the total focusing method, multi-pass adaptive techniques). However, the limited availability of portable PA systems with FMC capabilities prevents widespread introduction. Our goal was to demonstrate the feasibility of a portable PA solution with FMC and advanced processing with the help of a mobile GPU.

Statement of Contribution/Methods

Using an OEM ultrasound front-end module (us4us Ltd., Poland), we integrated a complete PA system with an embedded Nvidia® Tegra X2 module (pictured below). An external probe adapter enables a direct connection to commercial Olympus-NDT PA probes with up to 128-elements (32 active RX aperture). The system is fully programmable, both in the front-end (TX/RX schemes, acquisition parameters), as well as in the digital signal processing chain. Raw RF data is acquired and transferred to mobile GPU memory for processing. The algorithm can be conveniently implemented using a standard Nvidia CUDA toolkit. We implemented real-time B-mode imaging with the total focusing method for demonstration purposes.

Results/Discussion

The presented all-in-one system is a fully flexible tool for the research and evaluation of novel Phased-Array FMC methods and complex signal processing algorithms. An extended programmability and real-time access to raw channel data allows to create custom solutions specifically dedicated for any one NDT application. Mobile GPU parallel processing provides a strong enough performance for real-time imaging. Its small size and low power consumption makes the system an ideal candidate for a portable industrial flaw detector. We believe that FMC will be the method of choice for the ultrasound-'difficult' materials (e.g. composites).



Stress dependence of magnetic hysteresis properties through acoustically stimulated electromagnetic response in steel

Yuhei Suzuki^{1,2}, Hisato Yamada¹, Tomohiro Ozaki³, Kenji Ikushima¹

¹Tokyo Univ. of A & T, Japan, ²IHI Inspection & Instrumentation, Japan, ³Denshikiki Industry, Japan

Background, Motivation, and Objective

Steel is a major component used in machines, automobiles, buildings and infrastructures. Undesirable residual stress introduced on the manufacturing process is often a cause of premature failure of critical components. There are many techniques used to measure residual stress, but the nondestructive technique for visualizing residual stress is under development. We here focus on the acoustically stimulated electromagnetic (ASEM) method that is a magnetic probe technique by ultrasonic excitation [1-4]. In this method, the local magnetic hysteresis curves within a focal spot of ultrasonic waves is obtained through magnetomechanical coupling. The purpose of this paper is to clarify the stress dependence of the ASEM hysteresis curve in steel and to find the proper index for quantitative evaluation of residual stress.

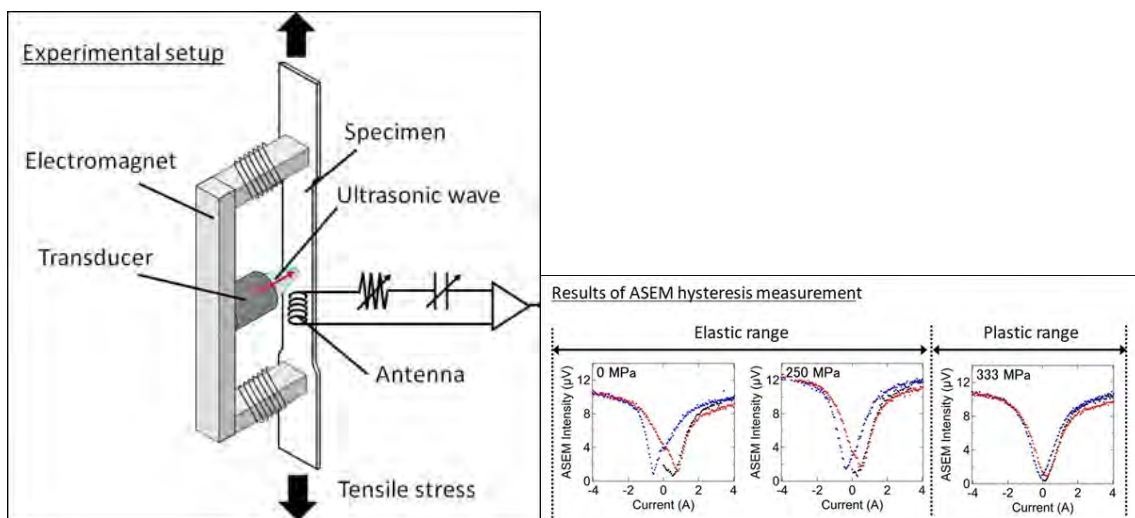
Statement of Contribution/Methods

We prepared a 6-mm-thick carbon steel plate (S25C, JIS G4051:2009) for tensile testing. The direction of the applied tensile stresses and magnetic fields is parallel to the rolling direction of the steel plate. ASEM measurements in the tensile testing were carried out up to the plastic deformation range (above 300 MPa).

Results/Discussion

We clearly observed the stress dependence of ASEM hysteresis curves. Particularly, the coercive force can be a good index for evaluating stress between 100 and 300 MPa. We also found that the ASEM response is very sensitive to the surface condition of steel. We will discuss the surface treatment required in practical applications.

[1] K. Ikushima *et al.* Appl. Phys. Lett. **89**, 194103 (2006). [2] H. Yamada *et al.*, Rev. Sci. Instrum. **84**, 044903 (2013). [3] H. Yamada *et al.*, Jpn. J. Appl. Phys. **54**, 086601 (2015). [4] H. Yamada *et al.*, Jpn. J. Appl. Phys. **57**, 07LB09 (2018).



Defect detection in billet using plane-wave and time-of-flight deviation with transmission method
Ryusuke Miyamoto¹, Koichi Mizutani², Naoto Wakatsuki², Tadashi Ebihara²
¹*Graduate school of systems and information engineering, University of Tsukuba, Tsukuba, Japan,* ²*Faculty of Engineering, information and systems, University of Tsukuba, Tsukuba, Japan*
Background, Motivation, and Objective

To inspect a steel billet, which is a semi-finished product of steel products, pulse echo method is commonly used in billet manufacturing line. However, the pulse echo method has difficulty with inspecting near the surfaces of billet because the echo from the defects may overlap a sending pulse or bottom echo. Therefore, we have proposed inspection methods for billet using time-of-flight (TOF) of transmitted wave[Miyamoto *et al.*, JJAP, 2016]. Although these methods can detect defects regardless of the positions of defects, they take long measurement time in spite of reducing measurement paths using linear scanning compared to tomographic methods.

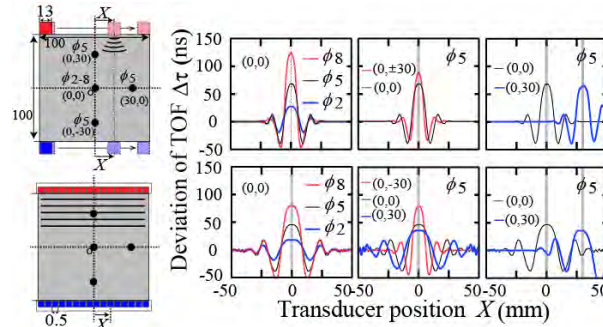
In this study, we introduced a one-shot measurement using plane-wave with TOF based transmission method instead of stepwise measurements to accelerate the inspection. Although plane-wave is used in the medical field, few studies in NDT field have been used plane-wave. In addition, TOF of transmitted plane-wave has not been focused on, while the echoes from defects are commonly used. In this paper, the proposed method using plane-wave is validated by comparing with linear scanning method using wave propagation simulations.

Statement of Contribution/Methods

The measurements are validated by numerical wave propagation simulations using finite-difference time-domain (FDTD) method. In the simulation, a cross section of a billet is measured by transmitting a plane-wave from transmitter array and receiving the wave at each receivers on the opposite side. TOF deviation caused by defects, $\Delta\tau$, is obtained by calculating cross-correlation function between $m(t)$ and $r(t)$, which are a received signal at a measurement plane and a received signal at a reference plane without defects, respectively. TOF profile, which is the relationship between receiver position X and $\Delta\tau$, is used to detect defects.

Results/Discussion

Figures below show the simulation conditions and TOF profiles at each conditions calculated by simulations. Upper graphs show TOF profiles of linear scanning method, and lower graphs show those of plane-wave method. The effects of a defect appear in TOF profiles of plane-wave method, although the $\Delta\tau$ is smaller than that of linear scan method. The defects which are not on the center position also can be detected from TOF profiles. As seen above, defects in billet can be detected using plane-wave and TOF by one-shot measurement.



Study about non-contact measurement of the acoustic property in an incline-sided tissue using pass-through airborne ultrasound**Shinnosuke Hirata¹, Daisuke Hanawa¹, Hiroyuki Hachiya¹**¹*Department of Systems and Control Engineering, Tokyo Institute of Technology, Japan***Background, Motivation, and Objective**

Quantitative ultrasound (QUS), ultrasonic bone assessment using the speed of sound (SOS) or broadband ultrasound attenuation (BUA), is one of the diagnosis methods of osteoporosis and widely applied in clinical screening. In typical devices for QUS, ultrasonic transducers are brought into contact with tissue surfaces through an ultrasonic gel to effectively propagate ultrasound. We have proposed non-contact QUS using airborne ultrasound passed through a tissue. The pass-through ultrasound is extremely attenuated due to large reflections at boundaries between the air and the tissue. Furthermore, the propagation direction also changes due to refractions at boundaries. In the proposed method, first, inclinations of tissue sides are measured from multiple reflections between surfaces of the transducer and the tissue. Then, directions of transducers are adjusted to the receivable angle of the pass-through ultrasound. The M-sequence-modulated signal is transmitted from one transducer, and the received signal of the other transducer is correlated with the transmitted M-sequence. The signal-to-noise ratio (SNR) of the pass-through ultrasound could be greatly improved by employment of a very long M-sequence. In this report, accuracy of the proposed method is evaluated through experiments using a tissue mimicking phantom.

Statement of Contribution/Methods

In experiments, a pair of the ultrasonic transducer and the condenser microphone was arranged at each side of the tissue. In the case of the inclination measurement of tissue sides, ultrasound modulated by the 8th-order M-sequence was transmitted from both transducers. The frequency of ultrasound was 166.7 kHz, which is approximately the central frequency of transducers. Multiple reflections between each transducer and each tissue side were received by each microphone. When both surfaces become parallel, multiple reflections are the most long-lasting. Therefore, the inclination of each tissue side could be estimated from the length of multiple reflections. In the case of the measurement of acoustic property, the 17th-order M-sequence was employed to improve the SNR of the path-through ultrasound. The SOS in the tissue was estimated from the TOF and propagated lengths of the path-through ultrasound and the SOS in the air.

Results/Discussion

The agar phantom, whose mass ratio was 2.5%, was used for experiments. Inclinations of both sides and the SOS were measured by the non-contact method at 30 times of different positions. The average and standard deviation of SOSs were 1.52×10^3 m/s and 18.8 m/s. For comparison, the SOS was also measured by the contact method using parallel sides. The average and standard deviation of SOSs were 1.53×10^3 m/s and 10 m/s. The SOS of the agar phantom could be measured with the similar accuracy although the variation increased.

Ultrasonic Pattern Recognition Algorithm based on Multilayer Perceptron Neural NetworkBoyang Wang¹, Jafar Saniie¹¹*Illinois Institute of Technology, United States***Background, Motivation, and Objective**

Ultrasonic Non-Destructive Evaluation (NDE) of materials for detecting flaw echoes in presence of high microstructure scattering noise is a challenging problem that demands statistical signal processing and pattern recognition. Conventional signal processing methods such as Split Spectrum Processing (SSP), Discrete Wavelet Transform (DWT) and Match Filtering (MF) have been applied to ultrasonic signal for target detection with limited success. In this study, a machine learning algorithm called multilayer perceptron neural network (MLPNN) is used for ultrasonic target detection in presence of clutter. Furthermore, the neural network is combined with conventional signal processing methods such as SSP and DWT to enhance and optimize the performance and the accuracy of the target detection algorithms.

Statement of Contribution/Methods

For this study, the data is collected through an embedded NDE platform. The system is built based on ZYNQ System-on-Chip (SoC). Ultrasonic pulser, Transmit/Receive switch, voltage-controlled amplifier and high frequency analog to digital converter are integrated as a programmable and reconfigurable system to generate and receive ultrasonic signals. The specimen under test is a steel block with an embedded flaw (i.e., a flat button hole) at a known position. By computing the speed of the sound in the steel block, we know exactly the position of the flaw echo. The training and recognition algorithms for flaw detection are implemented using the TensorFlow with GPU acceleration. To explore the performance of training, the acquired signals are pre-processed with feature extraction methods such as DWT, SSP, and spatial segmentation. After training of pre-processed datasets, TensorBoard is used to display and compare the performance and accuracy of training with different pre-processing methods.

Results/Discussion

This paper presents the theory and application of ultrasonic pattern recognition for flaw detection using MLPNN combined with SSP and DWT algorithms. The testing data were acquired with 5 MHz PZT transducers at the sampling rate of 100M samples/second. Using SSP, DWT and spatial segmentation combined with neural network, we are able to clearly detect flaw echoes with 0 dB signal-to-noise ratio.

Study of amount of gas in soft container using the noncontact acoustic inspection methodShigeya Kawai¹, Tsuneyoshi Sugimoto², Yutaka Nakagawa²¹Graduate School of Engineering, Toin University of Yokohama, kanagawa-ken, Japan, ²Toin University of Yokohama, Japan**Background, Motivation, and Objective**

In metal can containers, it is possible to measure the amount of internal gas in a noncontact manner from the frequency change of vibration sound due to electromagnetic force. Electromagnetic force cannot vibrate the soft drink container made of a paper or a plastic without magnetism. However, by using acoustic irradiation excitation, it is possible to vibrate easily even with a soft container without magnetism. Therefore, we investigated whether or not the gas change inside the soft container inside the soft container can be inspected by noncontact acoustic inspection method combining sound wave irradiation excitation and laser Doppler vibrometer (LDV).

Statement of Contribution/Methods

Figure 1 shows the experimental setup when a paper container is used as a specimen as an example of a soft container. In order to prevent the dispersion of the internal gas, A flat speaker was used as a sound source, and a scanning vibrometer was used as LDV. A tone burst wave including frequencies from 500 Hz to 10 kHz is used as the excitation waveform and the maximum sound pressure is set to 96 dB. From the vibration velocity spectrum, the amount of vibration energy in frequency band was calculated and used for evaluation.

Results/Discussion

Fig. 2 shows the measurement results of the vibration energy amount of 0 cc, 0.5 cc, and 2.0 cc of the internal gas. It can be seen from this figure that the vibration energy increases according to the amount of internal gas. From this result, it can be seen that the difference in the gas amount in the soft container can be inspected by the noncontact acoustic inspection method. This means that it is possible to measure the amount of gas generated due to gas leakage sucking and corruption of a soft container in a short time, and in the future it is expected to shorten warehouse storage time.

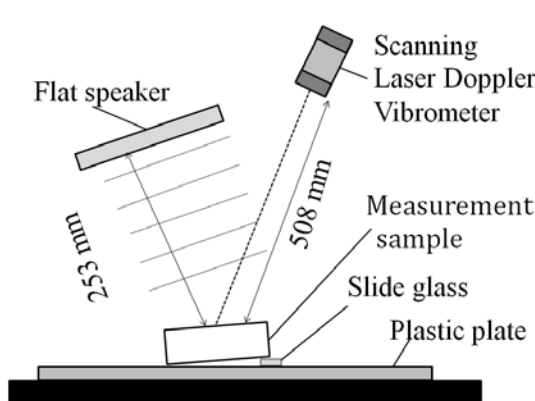


Fig.1 Experimental setup of noncontact acoustic inspection method when a paper container is tilted.

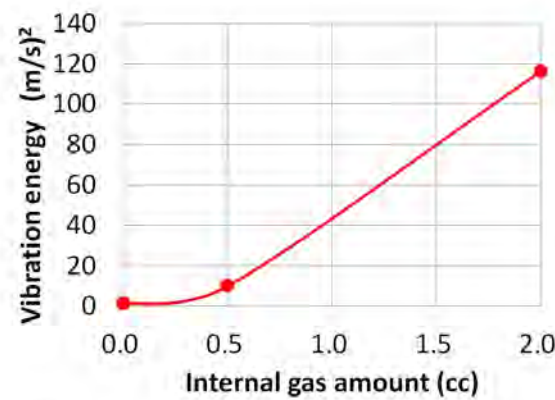


Fig.2 Vibration energy characteristics of paper part of a tilted paper container.

Ultrasonic Communication System Design using Electromagnetic Acoustic Transducer

Xin Huang¹, Jafar Saniie¹, Sasan Bakhtiari², Alexander Heifetz²

¹*Illinois Institute of Technology, United States*, ²*Argonne National Laboratory, United States*

Background, Motivation, and Objective

Electromagnetic acoustic transducer (EMAT) is a non-contact sensor for ultrasonic wave generation and reception, and it is widely used in many industrial applications as energy transformers for nondestructive testing. For this study, EMAT is designed and implemented for an acoustic communication system using steel plates and pipes as communication channels. Excitation frequency and plate or tube thickness governs the acoustic wave propagation modes. Therefore, EMAT architecture can be tuned for improved communications and mode selection. In this study, a mode-based analytical model is used for simulating the shear wave propagation and attenuation in the channel. In EMAT design, periodic permanent magnet is used to generate and receive shear horizontal waves for communication through stainless-steel plates and pipes.

Statement of Contribution/Methods

Shear wave has a more predictable dispersion characteristic and it is less vulnerable when propagates in the steel plate compared with Lamb wave. Channel characterization is important for the development of communication and signal processing. In experimental ultrasonic communication platform, an NI arbitrary function generator (AFG) and a 50dB gain power amplifier are used to excite SH2 or SH3 modes. On the receiver side, the signal is picked up by the SH-wave EMAT receiver and amplified before sampling by a PXI digital oscilloscope.

To improve the shear wave signal quality, both transmitter and receiver are connected to an impedance matching network. The AFG and the PXI digital oscilloscope can be programmed by the computer allowing to test the performance of different communication channels. A random binary message is modulated with different modulation techniques and the received message is processed to recover the binary code to examine Bit Error Rate (BER).

Results/Discussion

PZT transducers may suffer from the ambiguity in signal quality due to uncertainty in a coupling condition. In contrast, EMAT is a non-contact transmitter and receiver of ultrasonic waves and becomes a promising choice for communication through solids. In this paper, the simulation and experimental results prove that using EMAT as transmitter and receiver in a communication system is achievable and efficient. In particular, experiments of transmitting SH waves for digital communication through 154cm steel plate channel are conducted with SH-EMAT. We will present the simulation models and experimental results for channel characterization, and the accuracy of transmitted information within the frequency band from 400kHz to 600kHz. The objective is to transfer digital data at 10kb per second without any error in presence of undesirable multipath and wave dispersion effects.

P2-A9 - Sensors

Waraku (posters 2)

Tuesday, October 23, 9:30 AM - 4:00 PM

Chair: **David Greve** DWGreve Consulting

P2-A9-1

ULTRA SONIC CAVITY RESONANCE METHOD FOR FLUID QUALITY MONITORING APPLICATION

Daijiro Miyazaki¹, Kazuo Hasegawa¹, Heewon Jeong¹

¹TE connectivity, Japan

Background, Motivation, and Objective

As a conventional ultrasonic technology of measuring fluid quality, the sensors which adopted the time of flight (TOF) method is famous and widely used. However, due to the wait time between the wave emission and receiving, some dead time should be inevitable. This article introduces the ultrasonic cavity resonance (USCR) method as a new candidate to solve above issue. We established an analytical model to calculate the sensor scale factor and proved the effectiveness of USCR in experimental ways also.

Statement of Contribution/Methods

Figure.1(a) shows sensor system configuration of the USCR fluid quality sensor. We used a PZT (lead zirconate titanate, Pb[ZrxTi1-x]O3) plate as a ultrasonic transducer. The emitted acoustic wave from the transducer is transferred to the cavity which is fulfilled with a sample fluid and come back to the transducer by reflection at a reflector.

The USCR sensor forms one or several standing waves in a specifically designed cavity. Where, the acoustic pressure and vibration energy is accumulated in the cavity and build a resonator with some mechanical quality factor. Under this condition, some changes in fluid quality disturb the resonance conditions of the resonator and make the resonant frequency shift. So, the USCR sensor doesn't make dead time to monitor the fluid quality and do realize real-time response. We adopted model based design (MBD) approach, which consists of Mason and acoustic wave propagation transfer function models, to investigate and design the behaviors of the sensor, such as the sensor scale factor against the change of sample fluid quality and spurious frequencies. In the experiment, NaCl solution was used as a sample fluid to prove the USCR concept. We changed NaCl density from 0 wt% to 25 wt% and compared the resonant frequency shift with the simulation result.

Results/Discussion

Figure.1 (b) shows the scale factor of USCR sensor from both of simulation and experiment. The scale factor was roughly consistent as 7.32 kHz per wt% from both the simulation and experiment. This is enough scale factor even for detection the sea water which has around 3.5 wt% NaCl, even more for a saline solution having around 0.9 wt% NaCl. However, since we didn't consider damping effects in the analytic model, the amplitudes of each resonance peak are not consistent with the experiment. Future study should move forward to improving the discrepancy.

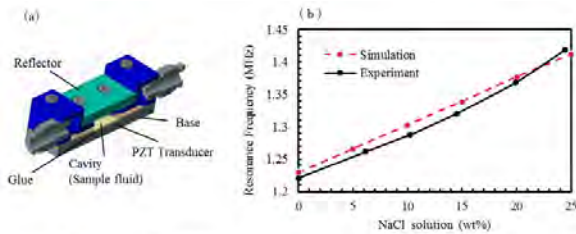


Fig 1. (a) Schematic of USCR (b) Scale factor of USCR sensor against wt% NaCl solution

Acoustic sensor for non-contact analysis of bacterial cells in conducting suspensions

Irina Borodina¹, Boris Zaitsev¹, Olga Guliy², Andrey Teplykh¹

¹Laboratory of Physical Acoustics, Kotel'nikov Institute of Radio Engineering and Electronics of RAS, Saratov Branch, Saratov, Russian Federation, ²Institute of Biochemistry and Physiology of Plants and Microorganisms of RAS, Saratov, Russian Federation

Background, Motivation, and Objective

The development of novel sensors for detecting the microorganisms in real conducting liquids is now an urgent problem. There exist the biological sensors for detecting the cells directly in suspension but they have the significant drawback, which is associated with the need for thorough cleaning and controlling the surface of waveguide after the contact with the suspension under study. This requires the use of the special procedures to remove the remains of the previous biological samples and to control the quality of cleaning. This problem may be solved by using the contactless analysis methods, in which the container with the suspension under study is isolated from the sensor surface. This paper describes the sensor based on the slot mode in the acoustic delay line with a propagating shear horizontal acoustic wave of zero order. The container with the biological suspension under study is isolated from the delay line and this suspension does not contact the surface of the wave guide. The sensor capabilities for recording the biological interaction “bacterial cells – specific antibodies” in the electrically conducting suspensions were studied.

Statement of Contribution/Methods

As the main element of the sensor for study bacterial cells is delay line based on the plate of Y-X lithium niobate. Two interdigital transducers (IDTs) for excitation and reception of acoustic wave with shear – horizontal polarization of zero order were deposited on the plate surface. The liquid container was placed above the waveguide of delay line between IDTs with given gap. The bottom of the container was made of plate of Z-X lithium niobate. The measurement of the frequency dependence of the insertion loss of output signal was carried out by using meter of S – parameters. The frequency dependence of the insertion loss of such delay line contained the clearly expressed resonant peaks caused by excitation of slot wave. These dependencies were measured for liquid container with the buffer solution with given conductivity and bacterial cells of the certain concentration. Then the antibodies were added in the container and the measurement was repeated. The measured dependencies allowed to determine the values of frequency and depth of the resonant peaks.

Results/Discussion

It has been found that the specific interaction of bacterial cells with antibodies in suspensions leads to a change in the depth and frequency of the resonant peaks in the frequency dependence of the insertion loss of the sensor output signal. Dependences of the depth and frequency of the resonant peaks on the conductivity of the buffer solution for different cell concentrations were obtained for the pointed specific interaction. The possibility of using the slot mode for the contactless analysis of bacterial cells in suspensions with an initial conductivity of 5-20 $\mu\text{S}/\text{cm}$ was shown.

The work is supported by grant of RFBR 16-07-00818.

A Delay-line Sensor Based on Wedge Waves**Che-Hua Yang¹, Sheng-Po Tseng¹**¹*Graduate Institute of Manufacture Technology, National Taipei University of Technology, Taiwan***Background, Motivation, and Objective**

The study aims at developing an ultrasound transducer system by introducing a new type of acoustic delay-line based on wedge waves. Delay lines based on wedge wave have unique features of one-dimensional propagation, relatively large amplitude at wedge tips, non-dispersive behavior without truncation and low energy attenuation. As a consequence, the wedge delay-line transducer (WXDR) have advantages including point contact nature, high spatial resolution, coupler-free, and multiple polarizing direction measurements by using a single transducer.

Statement of Contribution/Methods

Experimental configuration consists of a 5MHz shear wave transducer and a wedge delay-line transducer for ultrasonic excitation and detection. In this research, the wedge delay-line transducer is composed of a 2.25MHz shear piezoelectric transducer and an aluminum wedge with an apex angle of 70°. The end point of wedge delay line is contacted at the specimen surface in a point-wise contact way to measure the vibration signal without coupling agent. The signal is measured by different contact angle contact angle start from 35° to 90° with an interval angle is 5°.

Results/Discussion

Good SNR is demonstrated using the wedge-wave delay line sensor. In the meanwhile, the amplitude of anti-symmetric flexural mode is found to increase as the contact angle increases. The result shows when contact angle is approaching to 90°, the in-plane shear wave can be observed with better detection efficiency, but opposite for the out-plane detection. More importantly, the delay line is shown to be used as polarization-sensitive detection of elastic waves. The wedge delay-line transducer are characterized experimentally. While the wedge delay line is in a configuration of contact angle near 90°, the detection for the in-plane shear wave is found to be very efficient. Advantages of wedge delay-line transducer include point-wise contact area, no coupling agent needed and directivity by specific contact angle. This research aims at the development of a new signal-detection method based on wedge delay-line.

Quantifying the performance of state of the art fiber optic sensors to measure guided elastic waves
Gert-Jan van Groenestijn¹, Paul van Neer^{2,3}, Lun Cheng², Rob Jansen², Mark Jacobs⁴
¹*TNO, The Hague, Netherlands*, ²*TNO, Netherlands*, ³*Delft University of Technology, Netherlands*, ⁴*Optics11, Netherlands*
Background, Motivation, and Objective

Nowadays, the reception of guided waves has been reported using different sensors, such as piezos, FBGs, ring resonators etc. As the physics behind these sensors is very different, it is not trivial to compare the performance of these sensors for a particular application (e.g. inspection of wind turbines). To be able to make the right choices in the design of measurement applications we need quantitative SNR information of the sensors. Measuring this SNR is hard, as for some sensors it is below 50 dB. It is also important to know which signal a sensor has to measure, as e.g. an S0 wave has significantly less vertical movement than an A0 wave.

In this work we quantitatively compare five sensor types presented in literature: piezo, in-fiber interferometer, FBG, free-space interferometer, and ring resonator sensors in their ability to receive S0 and A0 guided waves. The experimental results are backed up by simulations.

Statement of Contribution/Methods

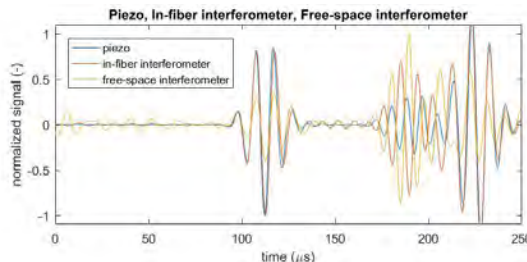
Our setup consists of a steel 8 mm plate where a source piezo emits a Gaussian pulse with a center frequency around 90 kHz. Only A0 and S0 guided waves are generated below 200 kHz in said plate. The five sensors are located 60 cm further. In the measured data we isolate regions of interest: only noise, an S0 pulse train, and an A0 pulse train. We calculate the SNR based on the only noise region and the S0 pulse train.

Results/Discussion

Figure 1 shows three of the five measured sensors, the piezo (blue) the in-fiber interferometer (red), and the free-space interferometer measuring contactless vertical displacement only (yellow), after averaging over a number of measurements. As can be seen, the noise (0-80 μ s), S0 (80-135 μ s) and, A0 (160-200 μ s) regions can be isolated in time. Note the amplitude ratio differences between the S0 and A0 waves for each sensor.

Using our well-defined setup we quantified the performance, expressed in SNR relative to the piezo, of each sensor: piezo (0 dB), in-fiber interferometer (-38 dB), free-space interferometer at 45° (-42 dB), ring resonator (-47 dB), FBG (-51 dB), free-space interferometer at 0° (-56 dB).

Given that piezos are cheap and outperforming the others it seems that other sensors need to find niche applications (e.g. EMI presence or long distance). However, as the others are researched intensively this may change quickly.



Integrated Transmitting and Receiving Mode Graphene Microphone Array
Kaihua Cao¹, Xinhua Guo²
¹*School of Mechanical and Electronic Engineering, Wuhan University of Technology, Wuhan, China, People's Republic of,*
²*Wuhan University of Technology, China, People's Republic of*
Background, Motivation, and Objective

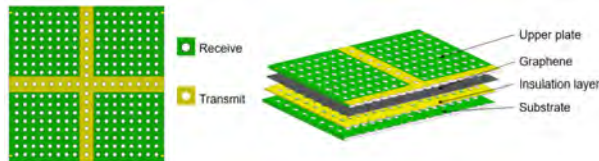
Microphone array is used widely for speech recognition, acoustic imaging and sound source location. Information, such as the image of outer contour of the measured object can be acquired through multiple synchronous acoustic sensors. We have previously demonstrated a graphene-based microphone array, which proves that graphene, with unique combination of electronic and mechanical properties, helps improve the sensitivity of microphone. Here we propose a graphene-based microphone array with transmit & receive mode integrated.

Statement of Contribution/Methods

The proposed microphone array (measuring 120×120mm) consists of three parts: upper plate with graphene film attached on, lower plate constituted by a metal array placed on the substrate and an insulation layer to avoid a direct contact between graphene film and metal array, which may cause a short circuit. As is shown in Fig.1, the upper plate is constituted by a 17×17 perforated array and graphene film. The horizontal and vertical lines in the medium divide the array into four parts, four 8×8 sub-arrays. The horizontal and vertical lines in the medium are designed for transmitting while the remaining sub-arrays are used for receiving the ultrasound wave. The transmitting area is separated from receiving area by the surrounding insulation material to avoid a mutual interference. A constant DC voltage is loaded between the graphene film and substrate during both transmitting and receiving. In transmitting mode, the graphene film generates ultrasound wave by vibrating around a static deflection point when a superimposed AC voltage is biased. The receiving sub-arrays operate in a voltage constant condition, deflection of graphene film caused by sound pressure is transformed into the change of current. To achieve the synchronization of transmitting and receiving, the voltage of transmit and receive area is loaded independently.

Results/Discussion

We propose a two-dimensional acoustic sensor array based on graphene film with function of synchronous transmitting and receiving ultrasound wave. Related simulation based on finite element method is proposed to verify the performance of the microphone array. Results show that the array, operating in receiving mode, has a central frequency of 90kHz and a sound pressure level of 26dB when the graphene film radiates ultrasound wave.



Gas sensor based on the piezoelectric resonator with lateral electric field and film of chitosan gluconate

Boris Zaitsev¹, Fedor Fedorov², Alexander Semyonov¹, Andrey Teplykh¹, Irina Borodina¹, Artem Grebenko², Albert Nasibulin², Gleb Filkov³, Alexander Trofimenco³, Georgy Sviridov³

¹Laboratory of Physical Acoustics, Kotelnikov's Institute of Radio Engineering and Electronics of RAS, Saratov Branch, Saratov, Russian Federation; ²Laboratory of Nanomaterials, Skolkovo Institute of Science and Technology, Moscow, Russian Federation;

³Laboratory of special medical equipment, technologies and pharmaceuticals, Moscow Institute of Physics and Technology, Dolgoprudny, Moscow Region, Russian Federation

Background, Motivation, and Objective

At present, the piezoelectric resonators with a lateral electric exciting field cause the great interest of researchers and such resonators are widely used for the development of liquid and biological sensors. It is also well known that a change in the conductivity of a thin layer located near the free side of the resonator lead to the change in the parallel resonant frequency and the maximum of the real part of the electrical impedance. Obviously, that this fact allows to develop a gas sensor if the conductivity of the layer located near the resonator changes with the change in the composition of the surrounding gaseous medium. In this paper, the possibility of realizing a gas sensor based on a piezoelectric resonator with a lateral electric field and a gas sensitive film of the chitosan glycolate was shown.

Statement of Contribution/Methods

The piezoelectric resonators with a lateral electric field based on a plate of PZT ceramics 3.5 mm thick with shear dimensions of 20x18 mm were experimentally and theoretically investigated. The polar axis was oriented along the size of 18 mm. One side of the plate was covered with an aluminum film with a gap in the center 4 mm wide, which was oriented perpendicular to the polar axis. At a distance of 0.18 mm from the free side of the resonator a film of chitosan glycolate with thickness of 0.02 mm, deposited on a glass plate, was set. This structure was placed in a sealed chamber, which was filled by the saturated vapors of the investigated liquids. By using the LCR meter, the frequency dependences of the real and imaginary parts of the electrical impedance of the resonator at different points of the time in the presence of gas under study and in air were measured.

Results/Discussion

The sensor was examined in the presence of ammonia and also saturated ethanol and water vapor. It was established that the parallel resonant frequency and the maximum value of the real part of the electrical impedance after placing in the investigated gaseous medium decreased monotonically and reached the saturation after reaching the time T1. Exposure to air for a time T2 led to a complete restoration of the initial parameters of the structure. Below the values of the relative change in the maximum value of the real part of the electrical impedance dR/R and the frequency of the parallel resonance df/f for resonator with the chitosan glycolate film in various gaseous media are presented. Ethanol: T1 = 260 min, T2 = 14 min, $dR/R = 9.6\%$, $df/f = 0.1\%$; for water vapor T1 = 110 min, T2 = 130 min, $dR/R = 25\%$, $df/f = 0.6\%$; for ammonia T1 = 90 min, T2 = 160 min, $dR/R = 19\%$, $df/f = 0.7\%$. These results correlate with the data on the conductivity measurement of the chitosan glycolate film in these media. The results open up the prospect of developing the gas sensors based on the described structure.

The work is supported by grant of RFBR 16-07-00821

Influence of Viscoelastic Stress Relaxation of Glass-frit Sealing layer on the Frequency Stability of a Dual-mode Quartz Pressure Sensor under extreme Pressure Conditions
Mihir Patel¹, Bikash Sinha²
¹*Schlumberger Tech Corp, MA, United States*, ²*Schlumberger Tech Corp, United States*
Background, Motivation, and Objective

A new crystalline orientation of quartz was discovered (Sinha, 1981), where the slow thickness-shear mode (C-mode) is temperature compensated and the fast thickness-shear mode (B-mode) is stress compensated. This new crystalline orientation of quartz called the SBTC-cut (Stress compensated B-mode Temperature compensated C-mode) was experimentally verified and showed good pressure sensitivity of the C-mode for pressure sensor applications. The axisymmetric loading of the probe enabled a smaller size and simple design of the pressure sensor with reduced manufacturing cost. The simple design consists of a SBTC-cut bi-convex quartz resonator disk sealed between two SBTC-cut quartz end-caps using a glass-frit bonding layer. Thus, the discovery of SBTC-cut angle of quartz enabled the development of the next generation dual-mode axisymmetric quartz pressure sensor (AXQG) and was recently commercialized for use in a reservoir characterization tool operating up to a pressure (P) of 210 MPa and temperature (T) of 210 degC. In addition to the high accuracy, resolution, and fast response time, the long-term stability of the AXQG pressure sensor was one of the key meteorological requirements for pressure measurements during drilling operations.

One of the factors affecting the long-term stability of quartz pressure sensors is the viscoelastic stress relaxation in the glass-frit layer introduced during the sealing process of the end-caps with the resonator. This becomes a major source of frequency drifts due to the inelastic stress relaxation caused by the viscoelastic deformation of the glass-frit film. The main objective was to determine the temporal change in the normal stresses at the center of the AXQG resonator due to the viscoelastic stress relaxation in the current glass-frit and then calculate its influence on the frequency change of the thickness-shear C- and the B-mode of the AXQG sensor.

Statement of Contribution/Methods

In this paper, we have developed a 3D-FEA based model for the AXQG pressure sensor to understand the influence of stress relaxation caused by the viscoelastic deformation of the glass-frit layer on the frequency stability of the AXQG pressure sensor. Analytical method based on Sinha-Tiersten technique helps to estimate the frequency shift of the slow and fast thickness-shear modes based on the changes in viscoelastic stress-relaxation values.

Results/Discussion

Results show that with an increase in temperature the stress relaxation due to the viscoelastic deformation of the glass-frit becomes significant that affects the frequency stability of the thickness-shear modes of the AXQG sensor. The magnitude of the frequency drift increases substantially under the influence of high P & T . However, at low temperature and high pressure the frequency drift is negligible and is confirmed with the experimental data.

Pressure and Temperature Sensitivity of a Dual-mode Quartz Pressure Sensor for High Pressure Applications**Mihir Patel¹, Bikash Sinha²**¹*Schlumberger Tech Corp, MA, United States*, ²*Schlumberger Tech Corp, United States***Background, Motivation, and Objective**

High precision quartz pressure sensors have been used in the oil-field services for the past several decades as they provide a reliable estimate of the formation permeability and oil/water interfaces in reservoirs that help in an optimal completion of wells for oil and gas production. Since 1991, Crystal Quartz Gauge (CQG) owing to its dual-mode operation achieved by modifying the SC-cut orientation to a new cut angle angle called Without-Activity-Dip (WAD) enabled fast response time under rapidly varying thermal gradients and was the industry standard pressure sensor. The low tensile strength of quartz under uniaxial loading conditions limited its operating pressure range to 103 MPa. To overcome this limitation and given a high mechanical strength of quartz under compression, led to the discovery of the Stress-compensated B-mode, Temperature compensated C-mode (SBTC) orientation of quartz that possessed piezoelectric coupling for both the modes.

This discovery of SBTC-cut angle was one of the key enabler for the recently developed next generation dual-mode axisymmetric quartz (AXQG) pressure sensor for extreme pressure (P) and temperature (T) operating range up to 210 MPa and 210 degC, respectively. To ensure an activity dip free operation of AXQG for this entire operating range it is necessary to determine the modal characteristics of not only the main modes of interest but also its overtones and anharmonics as a function of P & T. The objective of this paper was to develop a method for accurately determining the frequency changes of the B-mode, C-mode and the anharmonic modes for the SBTC-cut based AXQG pressure sensor when subjected to extreme static pressure and temperature changes.

Statement of Contribution/Methods

In this paper, we developed a 3-D FEA model by implementing the incremental stress equations in Lagrangian formulation [Lee, Yong & Patel] to calculate the effect of P & T on the sensitivities of different modes of interest for a doubly rotated contoured thickness-shear SBTC-cut resonator. These set of equations includes the third-order elastic constants and the temperature derivates of the second-order elastic constants of quartz. We have also developed reliable 3D stress analysis models for fast and efficient computation of normal stresses at the center of the resonator which can be used with existing Sinha-Tiersten perturbation technique.

Results/Discussion

3D-FEA results for the AXQG sensor probe showed an excellent agreement with the measured data for all the modes for (P,T) varying to (210 MPa, 210 degC). Based on this investigation, we identify the interaction of the C-mode anharmonic with the fundamental B-mode leading to an activity dip at high P & T. This helped to provide accurate and reliable guidelines for the effect of different design parameters on the P & T sensitivities of the different modes, prevent activity dips, and their subsequent improvement on the metrological performance of the AXQG pressure sensor for extreme P & T.

Equivalent Circuit Analysis of a Piezoelectric Multilayered Structure for In-Air Ultrasound Sensors
Muhammad Shakeel¹, Hayeong Shim¹, Yongrae Roh¹
¹*Kyungpook National University, Daegu, Korea, Republic of*
Background, Motivation, and Objective

Ultrasonic sensors in air are used in various applications like automobiles, robots, and consumer electronics. The ultrasonic sensor using piezoceramics has typically a multilayered structure and its performance is highly dependent on dimensions, boundary conditions, and material properties of each layer. For development of good sensors, the characteristics of the multilayered structure need to be analyzed accurately and thoroughly. The characteristics have been commonly analyzed by simplified theoretical equations or time-consuming numerical methods. In this work, we have developed an electroacoustic equivalent circuit for more efficient and reliable estimation of the characteristics of the piezoelectric multilayered structure as an in-air ultrasonic sensor.

Statement of Contribution/Methods

The multilayered structure is composed of a vibrational plate, a piezoceramic disk, a bonding layer, and a backing load. The electromechanical characteristics of the structure were first rigorously analyzed to derive the vertical deflection of the whole system as a function of the applied voltage, geometry, and anisotropic material properties of the constituent layers. Then the electroacoustic equivalent circuit was constructed using the derived functional forms of the deflection. The circuit systematically considers both the vibration characteristics of the structure and the consequent ultrasound field so that the results can be realistic. Once the circuit became ready, we could investigate the performance of the multilayered structure with much higher efficiency and rapidity than with other techniques like finite element analysis (FEA).

Results/Discussion

Using the equivalent circuit, we analyzed the effects of various structural parameters on the acoustic properties of the structure such as resonant frequency, electromechanical impedance, pulse-echo response, and radiation pattern. The validity of the results was verified by comparing them with those from the FEA of the same structure. Based on the analysis, the geometry of the multilayered structure was optimized to achieve the highest pulse-echo response. The validity the optimal design was verified by fabricating a prototype sensor and comparing its measured performance with the design. The comparison in Fig.1 showed a good agreement, which confirmed the efficacy of the equivalent circuit.

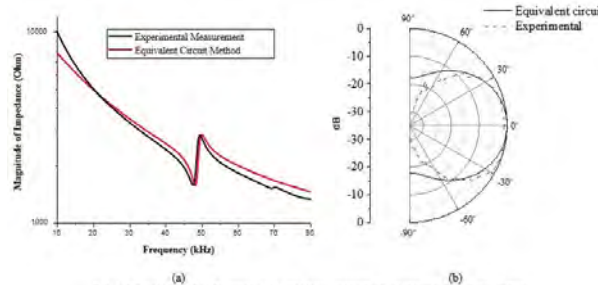


Fig. 1 Comparison of performance (a) impedance magnitude spectrum and (b) beam pattern

Blood Coagulation Time Measurement Using a 1 μ L of Whole Blood on a TE Mode BAW ResonatorNegar Majidi¹, Mohammad Rahim Sobhani², Stephane Evoy², Goksenin Yaralioglu¹¹*Electrical and Electronics Engineering, Ozyegin University, Istanbul, Turkey*, ²*Electrical and Computer Engineering, University of Alberta, Canada***Background, Motivation, and Objective**

Blood clotting, which occurs to stop bleeding, is a result of a consecutive biological interactions. Coagulation time is a vital indicator of specific factors in blood and their adequacies. In this regard, various tests are performed at hospitals, where requires patients to travel to these medical centers. Although, portable healthcare kits have been developed to identify amount of these factors. But the amount of the blood required for existing devices (5to10 μ L) usually cannot be provided by a simple finger prick. Nevertheless, by considering the BAW resonator as a sensor which its performance depends on the acoustic impedance of the adjacent layers (mediums) with a high operation frequency, the required blood amount may be decreased. Therefore, the TE mode BAW devices which are more sensitive to immersed environments, are good candidates to be used for blood coagulation time determination by investigating the input impedance and quality factor over the time.

Statement of Contribution/Methods

A BAW device composed of Au/ZnO/Au/Fused Quartz was used with layers thickness of 150nm, 8um, 150nm, and 1.2mm, respectively with an active area of 500x500 μ m. A 1 μ L of blood droplet was put on the fused quartz substrate, where the thin-film located on the opposite side of the substrate as shown in Fig. 1. Previously, the same device had been used to perform a time measurements of blood coagulation by utilizing a pulse-echo method at 400MHz. In this work, the input impedance of the transducer was investigated versus the frequency for a same volume of the liquid (blood) samples. In operation, the reflection coefficient of the substrate and blood (liquid) interface changes due to impedance mismatches by different stages of blood coagulation processes. This affects the overall trapped acoustic energy inside the bulk film and consequently changes the resonator parameters. The method requires only 1 μ L of whole blood without centrifuging which makes the proposed methodology much more patient friendly.

Results/Discussion

An analytical KLM modeling was implemented along the COMSOL simulations and practical measurements. The sensitivity of the device to liquid shows itself in input impedance as illustrated in Fig. 2. The parameters of the resonator for different samples and bloods were compared and reported from both practical and analytical results.

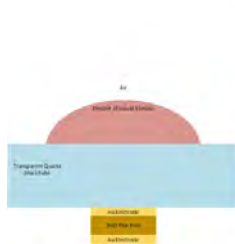


Fig 1. Schematic of the device.

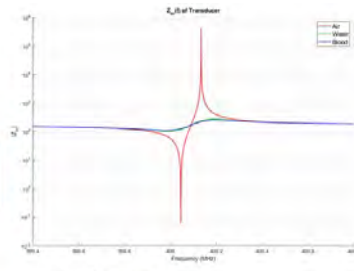


Fig 2. Input impedance.

Non-contact measurement of surface wave speeds and estimation of Young's moduli of tissue-mimicking phantoms by using focused airborne ultrasound

Marie Tabaru¹, Takahiro Aoyagi¹
¹Tokyo Institute of Technology, Japan

Background, Motivation, and Objective

There are increasing demands of non-contact measurements in medical and agricultural fields. Non-contact methods have advantage when measuring objects are soft or delicate. Although quantitative elastic properties are one of important factors to diagnose, there are few studies about the properties. In this report, we investigate a possibility of non-contact measurement of surface wave speed and Young's modulus with tissue-mimicking phantoms as a feasibility study.

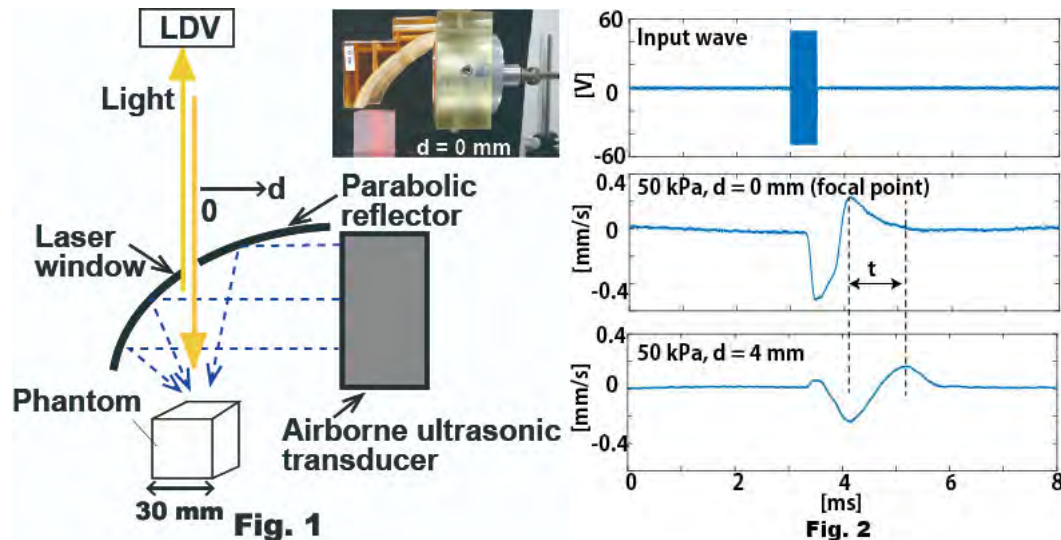
Statement of Contribution/Methods

Fig. 1 shows the developed system. First, a plane-wave was exposed by an airborne ultrasound transducer (NCG100-D50, Ultran) ($\Phi: 50$ mm). The wave was focused on a specimen with a parabolic-reflector. Acoustic radiation force, which was produced by the focused wave, caused mechanical low-frequency vibration on the surface. The radiation pressure was 1440 Pa (@14 V_{0p}). The vibration velocity was measured by a laser Doppler velocimeter (LDV). A laser window ($\Phi: 3$ mm) was made to the reflector at the focal position ($d = 0$ mm) so that the LDV could detect the vibration. Another parabolic reflector was made with different laser window position ($d = 4$ mm) to measure surface wave speed.

Four phantoms (Young's moduli $E: 15, 30, 50, 75$ kPa, 30 mm^3 , OST) were used. Burst waves (50 V_{0p}, 100 kHz, 50 cycles) were inputted to the transducer, and velocities were measured. Surface wave speeds, c , were calculated with the arrival time difference, t , between two positions. Young's moduli were calculated by $3pc^2$ (ρ : density).

Results/Discussion

Fig. 2 shows the input wave and the velocities. The resulted c were 2.2, 3.1, 3.9, and 5.1 m/s and E were 14, 30, 46, and 78 kPa. The estimated values were within the allowable error, 15%. We confirmed that the non-contact system enable to estimate quantitative elastic properties.



A Novel Phase Evaluation Method for Range Detection by Hybrid SAW sensors

Zixiao Lu¹, Honglang Li¹, Yabing Ke¹, Lina Cheng¹, Yahui Tian¹

¹*institute of acoustics, chinese academy of sciences, China, People's Republic of*

Background, Motivation, and Objective

Wireless and passive SAW sensors have prospect to apply for range detection by round-trip time-of-flight (RTOF) estimation, received signal strength (RSS), or phase evaluation method. Thomas F. Bechteler uses RTOF to achieve the range accuracy of 20cm. Darmindra D. Arumugam use both RTOF and RSS to improve the range accuracy up to 3.17cm. Phase evaluation method has higher accuracy theoretically in range detection, which is proposed to improve the range accuracy for SAW sensors. Corresponding experiments are also performed to verify the method.

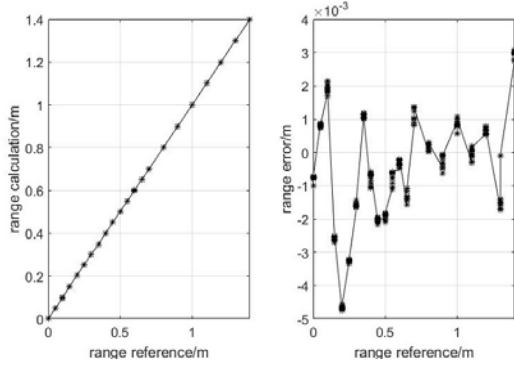
Statement of Contribution/Methods

Firstly, the phase information of SAW tag or SAW resonator is calculated. Secondly, phases at suitable multiple frequencies are combined to achieve the unambiguous phase. Finally the unambiguous phases evaluate the range accurately.

In experiment, a 2.40~2.48GHz SAW tag, a 433MHz resonator, and a FSCW reader are used. The sensor is located at several distances (0m~1.4m) from reader antenna. From the frequency response of sensor, the phases at 2.42GHz, 2.46GHz, 433MHz are calculated respectively firstly, and a synthetic phase at 40MHz is calculated by the subtraction of two phases at 2.42GHz and 2.46GHz. Then the three phases at 40MHz, 433MHz and 2.46GHz are combined to calculate the unambiguous phase at 2.46GHz, which is used to calculate the range.

Results/Discussion

The unambiguity phase at 2.46GHz is almost linear with respect to the range, which demonstrate that the proposed method accurately solve the problem of the phase ambiguity. The experimental calculated range is shown in Fig.1, which shows that the range accuracy is less than 1cm at 0m~1.4m. Therefore, the experiment demonstrates that the proposed phase evaluation method by Hybrid SAW sensors (SAW tag and SAW resonator) can achieve high accuracy of range detection.



P1-B10 - Spectral-Based and Elastographic Tissue Characterization

Kairaku (posters 1)

Wednesday, October 24, 9:30 AM - 4:00 PM

Chair: **Emilie Franceschini** CNRS

P1-B10-1

In situ calibration to account for transmission losses in backscatter coefficient estimation.

Trong Nguyen¹, Minh Do², Michael Oelze²

¹University of Illinois at Urbana Champaign, Champaign, IL, United States, ²University of Illinois at Urbana-Champaign, United States

Background, Motivation, and Objective

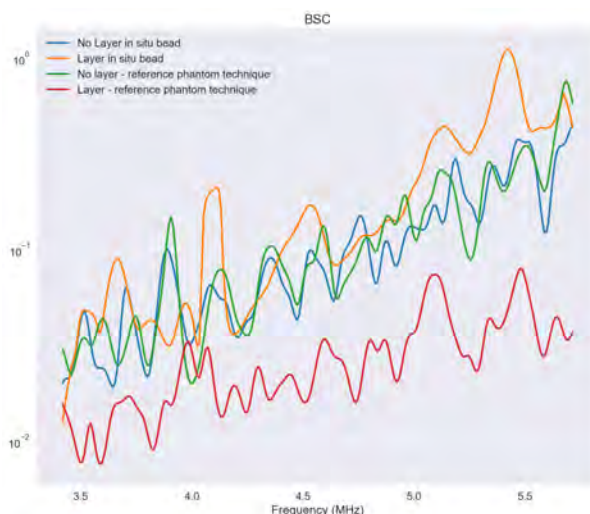
The backscatter coefficient (BSC) has demonstrated the ability to classify disease state and to monitor changes in tissue due to therapy. However, traditional methods of estimating the BSC *in vivo* using a reference phantom technique do not account for transmission losses due to intervening layers between the ultrasonic source and interrogated tissues. The intervening layers result in increases in bias and variance of BSC-based estimates. To accurately account for the transmission losses, an *in situ* calibration approach is proposed to obtain a more robust estimate of the BSC. The technique employs the use of a biocompatible sphere that is well-characterized ultrasonically and embedded inside a sample or tissue. Ultrasound scattered from the sphere encounters the same transmission loss and attenuation as the investigated sample and can be used as a reference spectrum to provide a more accurate estimate of the BSC.

Statement of Contribution/Methods

A 2-mm diameter titanium sphere was embedded inside a homogeneous phantom containing glass bead scatterers with diameters $\leq 90 \mu\text{m}$ placed spatially at random. A layer of fatty meat was placed on top of the phantom to produce transmission losses from a layer. The BSC was estimated from the phantom with and without the layer on top and compared using a traditional reference phantom technique and using the *in situ* sphere as a calibration target. Estimates of the effective scatterer diameter (ESD) were obtained for each condition and compared.

Results/Discussion

Figure shows the BSC estimated with and without the layer using the reference phantom technique and the *in situ* calibration approach. The BSCs estimated using the *in situ* calibration approach with and without the layer present overlapped with the BSC estimated using the reference phantom approach without the layer present. The BSC estimated using the traditional reference phantom approach with the layer present did not overlap with the other curves. Estimates of the ESD were 83 μm , 72 μm , 76 μm and 89 μm using the *in situ* calibration approach without the layer, with the layer and using the reference phantom approach without layer and with the layer present, respectively. The results indicate that an *in situ* calibration target can account for overlying tissue losses thereby improving the robustness of BSC-based estimates. This work was supported by a grant from the NIH (R21 EB020766).



Quantitative ultrasound and immunohistochemistry characterization at different stages of murine tumor developmentJerome Griffon¹, Delphine Le Guillou-Buffello¹, Michele Lamuraglia^{1,2}, Lori Bridal¹¹Laboratoire d'Imagerie Biomédicale (Sorbonne University, CNRS, INSERM), Paris, France, ²Beaujon Hospital (Medical Oncology, AP-HP), France**Background, Motivation, and Objective**

Relating quantitative US parameters to tumor microstructure should help interpret data for cancer therapy follow-up. We compared *in vivo* US evaluation of tumor size, elasticity and microvascular flow with whole-slice, fluorescent immunohistochemical marker maps at different stages of murine tumor development.

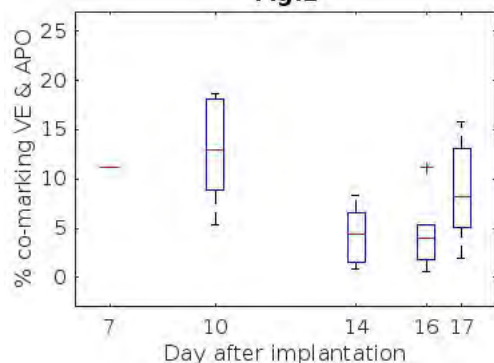
Statement of Contribution/Methods

Murine colorectal carcinoma (CT26) was subcutaneously implanted in 49 mice on Day 0 (D0). Mice were randomized for data acquisition on D7, D10, D14, D16 and D17 ($n = 10$ each day except for D16 $n = 9$). Tumors were measured in B-mode along major transverse and longitudinal axes to estimate ellipsoidal volume. Contrast-Enhanced Ultrasound (CEUS; Sequoia 512, 7-14 MHz probe) data and Shear-Wave Elastography (SWE; SSI, Aixplorer, SL 15-4 probe) maps were acquired along the longitudinal axis. Tumors were then excised and frozen at -80°C. Whole-slice histological sections (10 μm thick) were prepared with fluorescent immunohistochemical staining and parametric maps were made with in-house software to estimate the % area of nuclei, apoptosis (APO) and vascular endothelium (VE) marker (pixel resolution ~0.2 mm). Regions with no contrast-enhancement were identified to estimate % perfused area (%P) and to construct perfused (P) and nonperfused (NP) masks that were then rigidly co-registered to SWE maps so that mean and standard deviation (SD) of the SWE could be calculated in whole tumor, P and NP zones. Average contrast intensity vs. time curves in the P zone were fit to a lognormal model to estimate Area Under the Curve (AUC) and Time to Peak (TTP). The non-parametric Wilcoxon rank test was used to test parameter evolution as a function of tumor growth and differences between P and NP zones.

Results/Discussion

SWE and CEUS parameters did not correlate. SWE did not differ significantly for P and NP zones. Both SD-SWE ($RS = 0.65, p < 0.001$, non-parametric Spearman correlation coefficient) and TTP ($RS = 0.62, p < 0.001$) correlated positively with tumor volume. Overall, %P was high ($\geq 75\%$) and did not correlate with tumor volume. Individual histological parameters did not change significantly with time or tumor volume, but % area of strong co-marking of VE and APO decreased significantly between D10 and D14/16 (Fig.1). Lack of correlation between SWE and CEUS suggests they may provide complementary information.

Work funded by FRM (grant DBS20131128436)

Fig.1

Coherent ultrasound scattering in the young Rhesus macaque brain: effects of exposure to anestheticsIvan Rosado-Mendez^{1,2}, Laura Castañeda¹, Chrysanthy Ikonomidou³, James Zagzebski², **Timothy Hall²**¹*Instituto de Fisica, Universidad Nacional Autonoma de Mexico, Mexico City, Mexico*, ²*Medical Physics, University of Wisconsin-Madison, Madison, WI, United States*, ³*Neurology, University of Wisconsin-Madison, Madison, WI, United States***Background, Motivation, and Objective**

We are developing Quantitative Ultrasound (QUS) biomarkers to non-invasively detect neuroapoptosis caused by exposure of the newborn brain to anesthetics. Preliminary work in a nonhuman primate model (NHP) of the thalamus suggested that QUS parameters based on diffuse scattering, including the effective scatterer size, changed in proportion to the amount of apoptosis. However, significant inter-subject variability was also observed which can be attributed, in part, to coherent scattering caused by the complex structure of the thalamus (neuron nuclei surrounded by bundles of axon fibers). This work aims at (1) assessing the prevalence of coherent ultrasound scattering in the neonatal NHP thalamus using advanced spectral and speckle statistics analysis on ultrasound echo signals and (2) evaluating the effects of exposure to the anesthetic sevoflurane (SEVO).

Statement of Contribution/Methods

Fourteen 2-7 day-old Rhesus macaques were exposed to SEVO for 5hrs. A Siemens ACUSON S3000 system was used to scan the thalamus coronally with a 10V4 transducer through the sagittal suture at 0.5hrs (no apoptosis expected) and 6hrs (significant apoptosis expected) after initiation of SEVO exposure. Radiofrequency (RF) echo signals (10-15 frames) were obtained from each scan using the Axius Direct Ultrasound Research Interface [1]. Signals were processed to detect the presence of different scattering conditions: diffuse scattering, low scatterer number density, specular reflectors, and periodic scatterers [2]. This was achieved by analyzing parameters of the echo-signal generalized spectrum and of the signal's speckle statistics within 25mm² regions of interest. Classification decisions were made by comparing the values of test parameters to those computed for a reference material with diffuse scattering conditions. The analysis was applied to echo signals with spectral SNR larger than 15dB within ROIs at the left and right portions of the thalamus in each RF data frame.

Results/Discussion

Among 721 ROIs, 23% were classified as having only diffuse scatterers, 38% as exhibiting a low scatterer number density, 36% as containing specular reflectors, and 3% as containing periodic scatterers. The distribution of scattering scenarios was consistent in estimates made 0.5hrs and 6hrs after SEVO exposure. Based on the strong evidence of coherent scattering, we are refining the analysis of QUS biomarkers based on diffuse scattering and supplementing them with other coherent-scattering biomarkers that might be sensitive to SEVO exposure.

Lung Mass Density Analysis using Deep Neural Network and Lung Ultrasound Surface Wave Elastography: a sponge phantom study

Boran Zhou¹, Xiaoming Zhang¹

¹Mayo Clinic, Rochester, MN, United States

Background, Motivation, and Objective

Lung mass density is directly associated with lung pathology. Currently, there is no technique available to directly measure the lung mass density. We have developed a lung ultrasound surface wave elastography (LUSWE) technique to measure the surface wave speed (SWS) of superficial lung tissue. The objective of this study is to develop a method to estimate lung mass density using a deep neural network (DNN) and experimental data from LUSWE.

Statement of Contribution/Methods

A lung sponge phantom model is used in this study. The volume and weight of a dry sponge were measured to calculate its density. It was then injected with water at an interval of 3 ml from 0 to 30 ml and the corresponding mass density of sponge was calculated. After each injection, the surface wave speeds were measured at five frequencies 100, 150, 200, 250 and 300 Hz. A mechanical shaker was used to generate the harmonic vibration on the sponge phantom surface. A Verasonics Vantage system with a L11-5v probe (6.4 MHZ) was used to measure the surface wave speed.

The viscoelasticity of the sponge was calculated using the Voigt model. The synthetic training dataset of lung mass density (50 – 1000 kg/m³), shear elasticity μ_1 (2 – 14 kPa), shear viscosity μ_2 (2 – 17 Pa·s), vibration frequency and corresponding SWS from LUSWE (800000 in total) was used to train the DNN model. The DNN was composed of 3 hidden layers of 1024 neurons for each layer and trained for 10 epochs with a batch size of 4096 and a learning rate of 0.001 with Adam optimizer and L2 regularizer. The validation dataset (cross-validation ratio is 0.2) was used for fine tuning of hyper-parameters. The test dataset obtained from LUSWE of sponge phantom was used to predict the sponge density and evaluate its accuracy compared with experimentally measured sponge density. The DNN was implemented using the Python API of Tensorflow and TFLearn framework.

Results/Discussion

The obtained results showed that predictions matched well with experimental measured densities (Fig 1, validation accuracy was 0.92). This method may be useful to analyze lung mass density by using the DNN model together with the LUSWE and lung stiffness measurements for patients with interstitial lung disease or pulmonary edema.



Determination of Thermal Dose for Ablation Therapies: An Ex Vivo Tissue Experiment
Ami Kling¹, Jingfeng Jiang²
¹*Biomedical Engineering, Michigan Technological University, Houghton, MI, United States*, ²*Biomedical Engineering, Michigan Technological University, MI, United States*
Background, Motivation, and Objective

Thermal ablation therapy is a minimally invasive technique with the potential to allow eradication of tumors using highly localized heating. Protein coagulation induced by the heating is thought to induce a change at the microscopic level, thereby manifesting itself as measurable changes of tissue's viscoelastic properties. The objective of this study was to determine the relationship between clinically relevant thermal doses and a novel biomechanical parameter that is measurable using ultrasound.

Statement of Contribution/Methods

Ex vivo pig liver tissue was cut into ~2.6cm cubic pieces. Samples were administered clinically relevant thermal doses using a temperature-controlled water bath. Thermal doses were calculated as cumulative equivalent minutes at 43°C (CEM₄₃). Heated tissue samples were then cut into approximately half-inch cubes prior to mechanical testing. Unconfined uniaxial compression and stress-relaxation tests were performed using an ElectroForce® 3200 mechanical testing machine (TA Instrument Inc., MN).

Stress and strain data were fit to a Kelvin-Voigt fractional derivative (KVFD) model of tissue viscoelasticity. In the KVFD model, the alpha parameter is the order of the fractional derivative ($0 < \alpha < 1$) and represents the amount of collagen microstructure change due to protein coagulation.

Results/Discussion

Analysis of experimental results suggests a predictable nonlinear relationship between thermal dose received during simulated thermal ablation therapy and an increase of the alpha parameter.

In short, the relationship between thermal dose and mechanical properties of heated tissue may be used to develop new imaging techniques to reliably determine the amount of ablated tissues. In the future, we are going to develop techniques allowing us to measure the proposed alpha parameter *in vivo* using elastography techniques since the correlation between the thermal dosage and the alpha parameter has now been demonstrated.

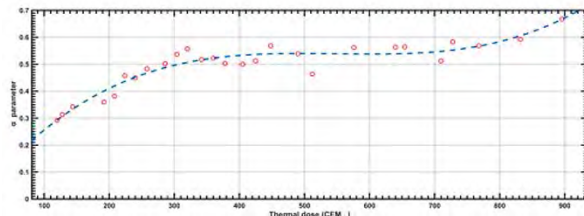


Figure 1. Calculated alpha parameter values (unitless) as a function of applied thermal doses (CEM₄₃). Experimental data are plotted as red circular points and a third-degree polynomial fit line is plotted as a dotted blue line ($R^2=0.9005$).

Analysis of the accuracy and precision of the least square fitting method for simultaneous estimation of backscatter and attenuation coefficients

Johan Polack¹, Andres Coila², Michael Oelze², Roberto Lavarello³

¹Pontifica Universidad Católica del Perú, Peru, ²University of Illinois at Urbana-Champaign, United States, ³Pontificia Universidad Católica del Perú, Lima, Peru

Background, Motivation, and Objective

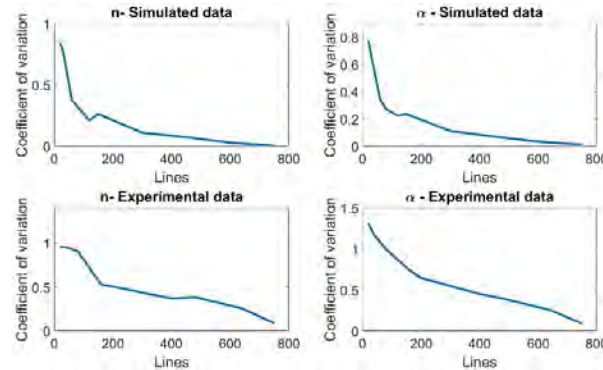
The backscatter coefficient (BSC) has proven to be a valuable tool for tissue characterization. Unfortunately, the estimation of BSCs requires knowledge of the total attenuation between the transducer and the region of analysis. Methods that simultaneously estimate the BSCs and the total attenuation have been proposed in the past, such as the least square fitting (LSF) method, but have not been extensively evaluated. In this study, the trade-off between estimation variance and spatial resolution for the LSF method was analyzed using both simulated and experimental data.

Statement of Contribution/Methods

Simulated data were obtained with Field II using a 7-MHz linear array. The synthetic media contained 10 scatterers per resolution cell and an attenuation coefficient slope (ACS) of 0.5 dB/cm/MHz. The BSCs of the sample and reference media were modeled using an exponential form factor with correlation lengths of 40 and 80 μm , respectively. The experimental data were obtained from calibrated agar-based physical phantoms embedded with glass beads located spatially at random throughout. The reference phantom had an approximated ACS of 0.4 dB/cm/MHz with glass beads of diameters between 75-90 μm , while the sample phantom had an ACS of 0.7 dB/cm/MHz with glass beads of diameters between 9-43 μm . The data were acquired using a SonixOne scanner with an L9-4/38 transducer having a center frequency of 5 MHz. For both simulated and experimental data, the LSF method was applied with analysis regions centered at the focus with an axial size of 12λ and a lateral size ranging from 20 to 750 scan lines. The LSF was applied assuming that the BSC could be modeled as $b f^n$, where f is the frequency and b and n are constants, while the attenuation coefficient was modeled as αf , where α is the ACS.

Results/Discussion

In simulations, the coefficient of variation (CoV) ranged from 0.01 to 0.78 for the ACS, and from 0.003 to 0.84 for n , as the number of scan lines decreased from 750 to 20. A similar trend was observed with the experimental data, with CoVs ranging from 0.09 to 1.31 for the ACS, and 0.09 to 0.96 for n for the same number of lines. The estimation bias was not significantly affected as a function of the number of scan lines (i.e., variations of bias of less than 20% for all parameters). These results suggest that the precision of the LSF method may be more compromised than its accuracy when imaging small tissue regions .



Relative quality of tumor growth equations describing volume and vascular evolution assessed with ultrasoundJerome Griffon¹, Zixin Yang¹, Delphine Le Guillou-Buffello¹, Alexandre Dizeux¹, Lori Bridal¹¹Laboratoire d'Imagerie Biomédicale (Sorbonne University, CNRS, INSERM), Paris, France**Background, Motivation, and Objective**

Mathematical models have been developed to simulate tumor growth and help predict therapy effect. We implemented three of these models and investigated their agreement with ultrasound image-based data on tumor size and microvascular flow evolution in a murine tumor model.

Statement of Contribution/Methods

Three ordinary differential equation tumor growth models were implemented in Matlab. The exponential-linear model (EL) assumes growth rate tends to linear after initial exponential growth as nutrient support becomes limited. The Gompertz model (G) describes demographic growth with a fixed carrying capacity because growth cannot exceed the capacity of the environment. The dynamic carrying capacity model (DCC) assumes this carrying capacity can change with time, for example, due to angiogenesis or necrosis formation. Experimental data were acquired in 11 control and 10 antiangiogenic (AA)-treated mice with ectopic murine colorectal carcinoma (CT26) on days 7, 9, 13, 18 and 21 after implantation (therapy started at day 7). Ellipsoidal volume V was estimated from B-mode measurements of the major transverse and longitudinal axes and used to estimate Relative Growth Rate, $RGR(t_n) = [V(t_n) - V(t_{n-1})] / [(t_n - t_{n-1}) \cdot V(t_{n-1})]$. Contrast-Enhanced Ultrasound (CEUS; Sequoia 512, 7-14 MHz probe) data were acquired along the longitudinal axis. Regions with no contrast-enhancement were identified to estimate % perfused area (%P). Average contrast intensity vs. time curves in the P zone were fit to a lognormal model to estimate Area Under the Curve (AUC) and Time To Peak (TTP). The Akaike Information Criterion (AIC) was used to evaluate the relative quality of the models to describe the tumor size evolution. AIC penalizes models with more parameters to deal with the trade-off between goodness of fit and the model's simplicity.

Results/Discussion

Initial implementation of the models using a fixed (1 mm^3) and free initial tumor size were compared. In this data set where earliest measured tumor size (day 4) varied from 15 to 39 mm^3 , the additional free parameter resulted in improved mean AIC (EL: 37 vs. 40 ; G: 37 vs. 41 ; DCC: 43 vs. 45 - free and fixed initial volume respectively). AIC was lowest on average for the G model in control mice. For each day, there was no significant difference using the non-parametric Wilcoxon rank test between the control group and the AA group for the volume, AUC, %P and TTP. Data were then pooled. The AUC at t_n was linked with prior RGR between t_{n-1} and t_n ($RS = 0.36$, $p < 0.001$, non-parametric Spearman correlation coefficient). This implies that the microvascular function includes additional information related to tumor growth. Work is on-going to integrate %P and AUC into the mathematical models so that size and vascularization evolution can be taken into account together. Such a model will provide a better framework for integration of complementary data from quantitative ultrasound images.

Work funded by FRM (grant DBS20131128436)

P1-B11 - Neuromodulation and Brain Applications

Kairaku (posters 1)

Wednesday, October 24, 9:30 AM - 4:00 PM

Chair: **James Kwan** Nanyang Technological University of Singapore

P1-B11-1

Measurement of Focused Ultrasound Neural Stimulation; Somatosensory Evoked Potential at Two Separate Skin Temperatures

Lu Xu^{1,2}, Yan Gong^{1,2}, Donald Kimball^{2,3}, Rahul Singh⁴, Ramesh Rao^{1,2}, Imanuel Lerman^{2,5}

¹*Jacob School of Engineering, UC San Diego, LAJOLLA, CA, United States*, ²*Calit2, UC San Diego, LAJOLLA, CA, United States*, ³*Maxentric LLC, La Jolla, CA, United States*, ⁴*Farus LLC., San Diego, CA, United States*, ⁵*UC San Diego School of Medicine, UC San Diego, LAJOLLA, CA, United States*

Background, Motivation, and Objective

Focused ultrasound stimulation (FUS) can induce thermal or tactile somatic sensations(Tyler et al. 2008) that can be measured with evoked potentials from somatosensory cortex (Legon et al. 2012). Here we compare focused ultrasound neural stimulation to electrical neural stimulation at two different skin temperatures (baseline temperature at 30°C and cooled skin at 20°C).

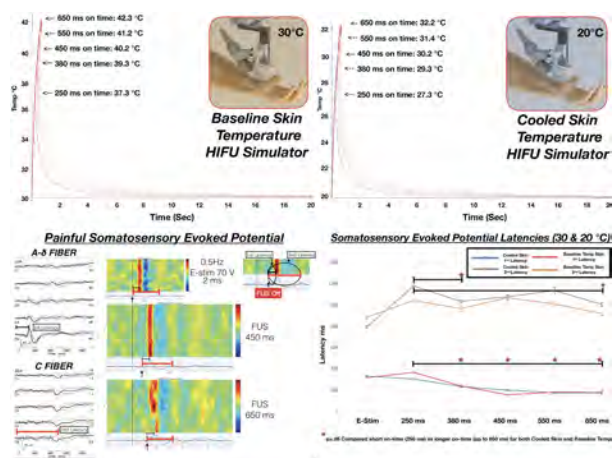
Statement of Contribution/Methods

An Olympus transducer A382S-Su-F-0.83-IN-PTF was used to deliver FUS with an input electric power of 5 to 10 W average pulse power. Using a function generator, 3.57 MHz(f_c) sine wave with on-times of 250, 380, 450, 550 and 650 ms(50 trial each) with a constant 20 sec off-time, and 2 MPa peak acoustic power was applied to left hand radial longitudinal crease. The transducer was mounted on a 3-axial system with 0.1mm accuracy for fine-tuning of focal point position(0.5 mm below dermis). Somatosensory evoked potential(SSEP) was collected with Micro 1401 and Spike2 (10,000Hz, 4 seconds epochs) and post-processed with EEGLab filtered with 1-2Hz bandpass filter. SSEP latency was analyzed with MATLAB. HIFU Simulator was used to model FUS effects on subdermal tissue. Protocol was approved by UCSD IRB (#171154).

Results/Discussion

Results: Subdermal FUS of skin (at 20°C and 30°C) with above on-times show identical temperature rises and linear slopes. SSEP data acquired from subdermal FUS was compared to electrical stimulation(E-stim) at supra-motor stimulation(~70V). Characteristic peak (A-δ and C-Fiber) for pain stimuli are identified in both SSEPs from painful E-stim and painful FUS (time locked to FUS offset). For both skin temperatures, FUS showed decreases in latencies(1st peak and 2nd peak) with increasing on time(250 ms short vs longer on-times) suggesting typical heat effects on SSEP. Similar SSEP latencies of(1st peak and 2nd peak) compared between 30°C and 20°C are demonstrated at on-times(380, 550 and 650 ms for 1st peak), and(450 ms for 2nd peak).

Conclusion: FUS result in consistent characteristic pain mediated SSEP(A-δ and C-Fiber) peak that show time synced latency to offset of FUS. Baseline skin temperature(30°C and 20°C) does not significantly impact SSEP latency, while on-time does. Therefore radiation forces and velocity streaming are likely critical in FUS of subdermal neuronal structures.



Temperature and cavitation monitoring for FUS peripheral neuromodulation

Hermes Kamimura¹, Min Gon Kim¹, Antonios Pouliopoulos², Stephen Lee³, Elisa Konofagou³

¹Columbia University, New York, NY, United States, ²Biomedical Engineering, Columbia University, New York, NY, United States, ³Biomedical Engineering, Columbia University, United States

Background, Motivation, and Objective

Noninvasive focused ultrasound (FUS) is capable of modulating the central and the peripheral nervous system (PNS) [1, 2]. FUS modulation of the PNS is a promising approach to treat neuropathic diseases as an alternative to drug therapy, electrical stimulation and surgical intervention. Although, a range of acoustic parameters (< 5.7 MPa) was found safe in mice [2], the clinical translation of this technique requires a reliable control of parameters. Monitoring thermal and cavitation effects in real time allow conducting safe sonication in humans. In this study, thermal evaluation and cavitation mapping were performed in chicken breast samples and in murine tibialis anterior muscle in vivo as a preliminary evaluation of our human setup.

Statement of Contribution/Methods

Sonications were performed at 3.1 MHz (Sonic Concepts) in male C57BL/6 mice in vivo and ex vivo chicken breast samples with average pressure attenuation of 3.5 dB/cm@1 MHz (similar to human muscle) were sonicated with pulse durations (PD) varying within 32-1000 µs and peak negative pressure (PNP) levels from 3 to 11 MPa. Thermal assessments were performed using a T-type thermocouple. A P12-5 (Philips) array passively recorded cavitation signals, which were processed with a passive cavitation imaging (PCI) algorithm [3] to map acoustic emissions.

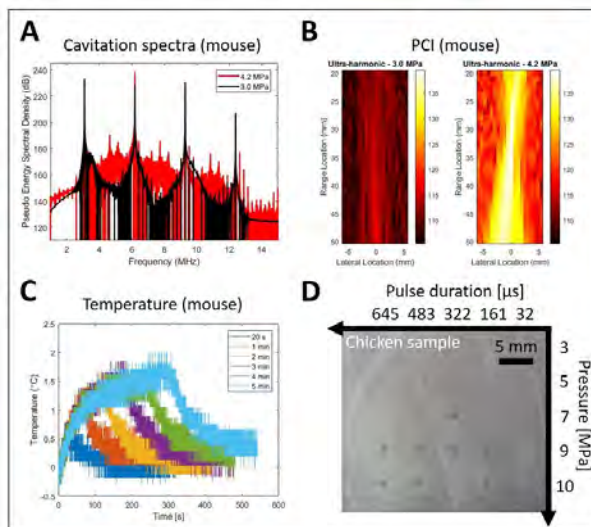
Results/Discussion

PCI revealed a threshold of 4.2 MPa for broadband and ultra-harmonic emissions in the muscle in mice (Fig A, B). Modest temperature increase (<2°C, 5 min, Fig C) was detected 5 mm from the focus at 11 MPa, 1 ms PD and 1 Hz PRF. Tissue fragmentation was observed in chicken sample (Fig D) for PNP ≥ 7 MPa, 161 µs PD, 0.3 Hz PRF and sonication duration of 2 min. Safe sonication was thus found to be limited to PNP < 7 MPa despite the fact that the thermal dose remained under 0.001 CEM at lower PRF (≤ 1 Hz). These results indicate a PNP range (4.2 - 7 MPa) where cavitation is present without measurable thermal effects or any gross damage. In ongoing studies, EMG measurements will be conducted in human subjects at the identified safe PNP levels where cavitation can be minimized (≤ 4.2 MPa) and explore whether these safe cavitation levels (at $4.2 \leq \text{PNP} < 7$ MPa) and thermal effects (at $\text{PRF} > 1$ Hz) can enhance neuromodulatory responses in humans.

[1] Kamimura et al 2016 Med Phys 43 5730-5

[2] Downs et al 2018 Phys Med Biol 63 035011

[3] Haworth et al 2017 IEEE T Ultr Ferroelec Freq Contr 64 177-191



Transcranial Focused Ultrasound Stimulation Decreases Blood Pressure in Spontaneously Hypertensive Rats

Dapeng Li¹, Siyuan Zhang¹, Zhiwei Cui¹, Yabo Yang¹, Ayache Bouakaz², Mingxi Wan¹

¹The Key Laboratory of Biomedical Information Engineering of Ministry of Education, Department of Biomedical Engineering, School of Life Science and Technology, Xi'an Jiaotong University, xi'an, China, People's Republic of, ²UMR 1253, iBrain, Université de Tours, Inserm, France

Background, Motivation, and Objective

The ventrolateral periaqueductal gray (VLPAG) resides within the midbrain and its role in lowering blood pressure has been studied extensively in animals. Reports have shown that deep brain electric stimulation of the VLPAG can reduce blood pressure both in hypertensive patients and spontaneously hypertensive (SH) rats. Electrical stimulation using implanted electrodes is precise and effective, but requires invasive procedures for placement. Ultrasound (US) transcranial neurostimulation has been successfully evaluated as a non-invasive and spatially specific technique in various animal species. In this study, we aimed at exploring the feasibility of using US neuromodulation to the VLPAG as a noninvasive treatment for hypertension in a rat hypertensive model.

Statement of Contribution/Methods

The rats were fixed on the brain stereotaxic instrument and anesthetized using 2% isoflurane during the experiment. US (620 KHz, Pulse Duration=2ms, Pulse Period=4ms, Pulse Number=50) field was focused through the rats' skull and aimed to the VLPAG. Seven SH rats (blood pressure range: 140-190mmHg) were selected as experimental group and treated with US for 20 minutes each time respectively. The other 4 SH rats were used as control group without US stimulation. Blood pressure was measured at half an hour before the experiment and 1, 2 and 3 hours after the experiment in three consecutive days.

Results/Discussion

The mean blood pressure of the experimental group was reduced by 14.8% after 1 hour. After 2 hours, the decrease dropped to 7.1% and 3 hours later to 1.7%. There was no significant change of the control group within 3 hours. However, after two days of US treatment, the mean blood pressure of experimental group dropped from 168 to 145 mmHg. The results demonstrate the potential of US neuromodulation aimed to ventrolateral periaqueductal gray as a noninvasive treatment for hypertension. However, further work is needed to optimize this technique and evaluate its safety.

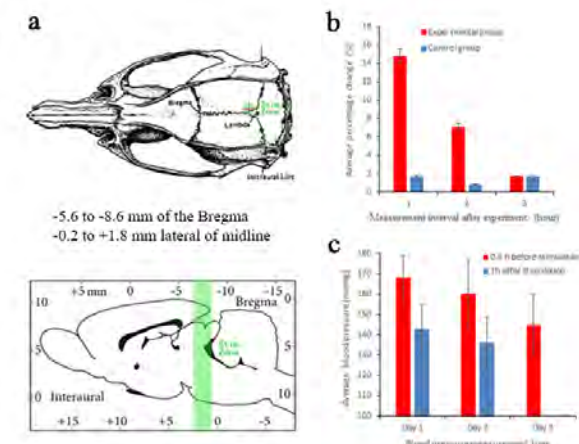


Fig.1.a) Diagrams showing the anatomical locations where transcranial pulsed US was delivered.
b) Comparison of the average percentage change of blood pressure of experimental group (red) and control group (blue). Error bars indicate standard errors of the mean. Experimental group indicates statistically significant differences ($p < 0.05$) with control group. **c)** Diagram showing changes of blood pressure of experimental group during three days. Error bars indicate standard errors of the mean.

Noninvasive delivery of adenoviral-mediated suicide gene to treat glioma through focused ultrasound-induced BBB opening

Min Pan¹, Yi Zhang², Guobin Hong², Hairong Zheng³, Fei Yan³

¹Shenzhen Hospital (Futian) of Guangzhou University of Chinese Medicine, China, People's Republic of, ²The Fifth Affiliated Hospital of Sun Yat-sen University, China, People's Republic of, ³Paul C. Lauterbur Research Center for Biomedical Imaging, Shenzhen Institutes of Advanced Technology, Chinese Academy of Sciences, China, People's Republic of

Background, Motivation, and Objective

Glioma is the most common primary malignant brain tumor and considered one of the most difficult curable tumors because of its typical characteristics such as rapid proliferation, strong invasiveness and unsatisfactory prognosis. Although radiotherapy, chemotherapy or their combination treatments are also widely used for consolidating the surgical effect, they indeed cause a range of side effects and seriously lower the quality of the patient's life. Therefore, it is desirable to develop alternative treatment modalities for safer and more efficiently killing tumor cells and extending patient survival. Adenoviral-mediated suicide gene therapy has been shown great prospects for tumor treatment. However, it is still a great challenge for its application in the glioma. A main cause is the blood-brain barrier (BBB) limits the delivery of adenoviral vectors, greatly compromising their efficacy. The purpose of the present study is to use focused ultrasound (FUS) induced microbubble cavitation to locally and reversibly open BBB for enhancing gene delivery and its efficacy.

Statement of Contribution/Methods

Recombinant adenoviral Ad-CMV-TK-IRES-EGFP (Ad-TK-EGFP) carrying the herpes simplex virus thymidine kinase (HSV-TK) and EGFP transgenes was chose as gencidine and Ad-CMV-IRES-EGFP (Ad-EGFP) as the control. The C6 tumor cell killing effects were firstly examined by CCK-8 assay and flow cytometry. Rat brain tumors were developed and the in vivo anti-tumor efficacy of Ad-HSV-TK-EGFP/GCV also investigated through FUS-induced BBB opening.

Results/Discussion

The in vitro experiments showed that Ad-TK-EGFP had a high infection efficiency for C6 glioma cells, producing good tumor cell killing effects when these cells were exposed to more than 10 µg/ml ganciclovir (GCV). Taking advantage of FUS-induced BBB opening (Fig.1a), Ad-TK-EGFP could be effectively delivered into the brain tumors, getting the overexpression of HSV-TK gene in the tumor cells. After exposure to GCV, the significantly stronger anti-tumor efficacy and longer survival time were observed in tumor-bearing mice treated with Ad-TK-EGFP + FUS than those treated with Ad-EGFP + FUS or only Ad-TK-EGFP (Fig.1b and 1c). Our study provided a new strategy to efficiently and locally deliver recombinant adenoviral vector-mediated HSV-TK gene into the brain to treat glioma.

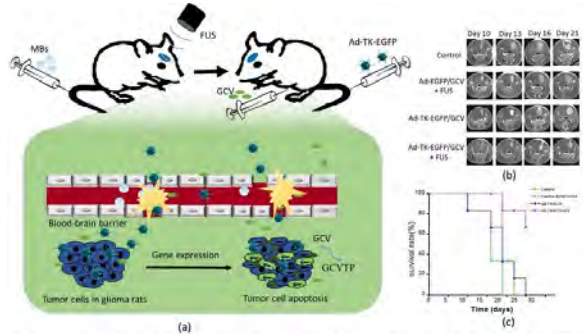


Figure 1. (a) Schematic diagram of adenoviral-mediated HSV-TK to treat glioma through FUS-induced BBB opening. (b) Representative contrast-enhanced T1 weighted MR images taken on day 10, day 13, day 16 and day 21. (c) Survival rates of C6 orthotopic tumor-bearing mice after gene treatments.

Ultrasonic-magnetic Hybrid Gene-delivery System for Parkinson's Disease Treatment**Chun-Yao Wu¹, Ching-Hsiang Fan¹, Jih-Yang Huang¹, Chien-Wen Chang¹, Chih-Kuang Yeh¹**¹*Department of Biomedical Engineering and Environmental Sciences, National Tsing Hua University, Taiwan***Background, Motivation, and Objective**

Genetic treatment for Parkinson's disease (PD) by plasmid glial cell-line derived neurotrophic factor (pGDNF) has the potent trophic effect on damaged dopaminergic neurons. Ultrasound (US)-based plasmid DNA (pDNA) delivery is a promising mean for central nervous system treatment. However, three barriers including, (1) cell membrane reducing intracellular pDNA uptake, (2) lysosome degrading the delivered pDNA and (3) nucleus envelope lowering pDNA entry into nucleus, hamper pDNA transfection and expression (typically 4-10 %). This study proposed the polyethylenimine (PEI)-superparamagnetic iron oxide-pDNA loaded microbubbles (PSp-MBs) in conjunction with US and two-step magnetic force to increase the efficiency of gene delivery. In other words, the intracellular accumulation of PSp complexes was enhanced by concurrently performing US (cavitation) and step I magnetic force (magnetic effect). Secondly, the PEI allowed PSp complexes escaping from lysosome degradation (proton sponge effect). In final, the amount of pDNA entering nucleus could be increased by step II magnetic-mediated cytoskeletons re-organization (magnetic effect).

Statement of Contribution/Methods

The PSp-MBs (3.61 pg PSp/MB) were prepared by loading PSp (150±5.4 nm) onto the lipid-shell of MBs (1±0.21 μm) by electrostatic force. The plasmid green fluorescence protein (pGFP) and pGDNF were used to quantify the efficiency of gene delivery and repair dopaminergic neurons in SH-sy5y neuron-like cell and genetic PD mice (MitoPark), respectively. The PSp delivery was carried out by FUS (frequency = 1 MHz, pressure = 0.3 MPa, duty cycles = 0.5 %, sonication duration = 1 min) and step I magnetic force (0.37 T, 20 mins) with PSp-MBs. After lysosome escape, the step II magnetic force (0.37 T, 60 mins) was applied to the right side of cells for pDNA transporting into nuclear. To verify the *in vivo* treatment outcome, the time for crossing an 80 cm-beam and the walking distance in open field by PD's mice ($N=30$) were recorded weekly to trace the motor balance and willingness, respectively.

Results/Discussion

The gene transfection rate in the proposed system was 2 fold higher than that of the commercial agent (TransIT®-LT1). The transfection rates could be boosted up ~11%, ~7%, and 2% by cavitation-magnetic hybrid enhanced cell membrane permeabilization, proton sponge effect and magnetic-assisted cytoskeleton-reorganization, respectively. *In vivo* data suggested that the system improved 1.8 and 1.6 folds of motor balance and willingness compared to untreated PD mice, individually. This study proposed a novel US-magnetic hybrid gene delivery platform and potentially could be integrated with other therapeutic genes for treating neurodegenerative diseases in future.

Study on the antitumor effect of sonodynamic therapy on nude mice bearing intracranial glioblastoma xenografts

Yongpeng Huang¹, Zhaoke Pi¹, Xin Chen^{1,2}, Siping Chen^{1,2}, Yuanyuan Shen^{1,2}

¹School of Biomedical Engineering, Shenzhen University, Shenzhen, China, People's Republic of; ²National-Regional Key Technology Engineering Laboratory for Medical Ultrasound, Shenzhen, China, People's Republic of

Background, Motivation, and Objective

Sonodynamic therapy (SDT) utilizes a certain frequency of ultrasonic irradiation to activate the sonosensitizer, which has become a promising non-invasive method for cancer treatment. For brain tumors, blood-brain barrier presents a formidable obstacle to the delivery of sonosensitizers to tumor sites. In this study, the antitumor effect of SDT on glioblastoma (GBM) was investigated using sinoporphyrin sodium (DVDMS) as the sonosensitizer, which was delivered by low-intensity ultrasound with microbubbles (Fig. 1a).

Statement of Contribution/Methods

U87 MG Red FLuc cells (1.0×10^5 cells) were implanted into the right striatum of male nude mice (20 ± 2 g). They were randomly divided into four groups: the control group without SDT (Control), injection of DVDMS (2 mg/kg) alone (DVDMS), FUS sonication alone (FUS), and SDT (acoustic power: 2 W/cm^2 ; center frequency: 0.996 MHz; duration: 1 min) after enhanced delivery of DVDMS (SDT). The delivery of DVDMS was performed 3 hrs before SDT by ultrasound with microbubbles. Treatments were applied every three days starting on the seventh day after tumor implantation. 3D bioluminescence imaging (BLI) method was used to monitor tumor growth (IVIS SPECTRUM; PerkinElmer Inc., Waltham, MA, USA). The survival data of each group were recorded and analyzed.

Results/Discussion

Figure 1b showed representative 3D bioluminescence images of the intracranial GBM in each group two weeks after the treatments. It can be seen that the GBM growth of the SDT group was significantly suppressed. Compared with the control group ($133 \pm 5 \times 10^7$ photons/sec), the bioluminescence photon emission value of SDT group was significantly lower ($0.768 \pm 0.149 \times 10^7$ photons/sec) two weeks after tumor implantation (Fig. 1c). Moreover, the median survival period of the SDT group increased to 30 days, while the control group was 24 days (Fig. 1d). The results suggested that SDT with DVDMS may provide a promising therapeutic strategy against glioblastoma.

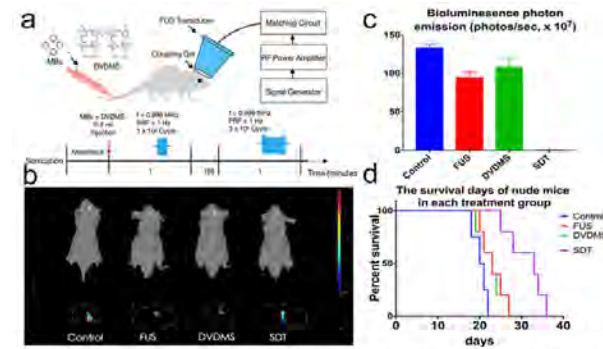


Figure 1 (a) The SDT experimental setup and the experimental timeline of the single treatment procedure. (b) Representative 3D bioluminescence images and (c) the corresponding photon emission counts of the intracranial GBM in the four groups two weeks after the treatments ($n \geq 3$, mean \pm SD). (d) The survival curves of nude mice in each treatment group ($n=5$).

P1-B12 - Catheters and High-Frequency Transducers

Kairaku (posters 1)

Wednesday, October 24, 9:30 AM - 4:00 PM

Chair: Nicolas Felix Vermon SA

P1-B12-1

Development of High-Frequency Miniature PNN-PZT-based Ceramic Ultrasonic Transducer

Qi Zhang¹, Xuming Pang², Zhiqiang Zhang³, Min Su³, Hairong Zheng³, Weibao Qiu³, Kwok Ho Lam¹

¹Department of Electrical Engineering, The Hong Kong Polytechnic University, Hong Kong, ²School of Mechanical and Power Engineering, Nanjing University of Technology, China, People's Republic of, ³Paul C. Lauterbur Research Center for Biomedical Imaging, Shenzhen Institutes of Advanced Technology, Chinese Academy of Sciences, China, People's Republic of

Background, Motivation, and Objective

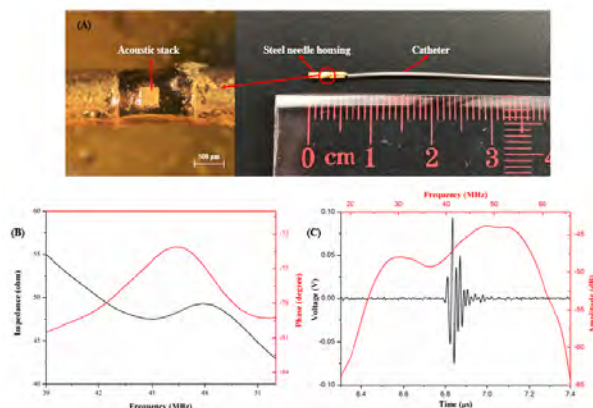
Intravascular ultrasound (IVUS) imaging, stretching a catheter combined with a miniature ultrasonic transducer into the blood vessel, has been an effective diagnosis method to determine the amount of atheromatous plaques in the coronary arteries. It is known that the transducer performance usually deteriorates when the aperture size is reduced at high frequencies. To develop miniature ultrasonic transducers, a high-frequency material with outstanding dielectric permittivity and piezoelectric performance is highly desired. In this work, a high-frequency (>40 MHz) side-looking miniature transducer based on novel high-performance piezoelectric ceramic was developed.

Statement of Contribution/Methods

In this research, a novel $\text{Pb}(\text{Ni}_{1/3}\text{Nb}_{2/3})\text{O}_3\text{-Pb}(\text{Zr}_{0.3}\text{Ti}_{0.7})\text{O}_3$ (PNN-PZT)-based ceramic with ultrahigh dielectric permittivity and high electromechanical coupling capability was developed using the conventional solid-state reaction method. A high-frequency side-looking ultrasonic transducer based on the PNN-PZT-based ceramic with a very small aperture of $0.33 \text{ mm} \times 0.33 \text{ mm}$ was designed and fabricated using conventional transducer technology.

Results/Discussion

The modified PNN-PZT ceramic exhibited an ultrahigh clamped dielectric constant ($\epsilon^S/\epsilon_0 = 3409$) and a high electromechanical coupling coefficient ($k_t = 0.60$). The fabricated miniature side-looking transducer prototype is shown in Figure A. The frequency dependences of electrical impedance and phase, as shown in Figure B, present that the transducer exhibited the resonance frequency of 45 MHz with the electrical impedance of 47.5Ω . The measured pulse-echo response and its frequency spectrum present that the center frequency was 41 MHz while the -6 dB bandwidth was 79.8% as shown in Figure C. The insertion loss of the transducer was measured as 24.9 dB. The results demonstrate that the transducer performance was still excellent even the aperture size was so small, which shows great potential of using the novel PNN-PZT-based ceramic for miniature transducer applications such as IVUS imaging.



High Performance 60MHz Single Crystal PMN-PT Composite for Medical Ultrasound Applications**Ramanarao Bommema¹, Patrick McGowan², Brian Harrison², Brandon Stone², Jian Tian²**¹*CTS ADVANCED MATERIALS, BOLINGBROOK, IL, United States*, ²*CTS Advanced Materials, United States***Background, Motivation, and Objective**

Piezoelectric single crystals such as lead magnesium niobate - lead titanate (PMN-PT) have superior dielectric and piezoelectric properties suitable for medical ultrasound with notable advantages of broad bandwidth and high sensitivity. The advantage of single crystal is limited when used as monolithic crystal at high frequency (e.g., > 30 MHz) however, crystal composite offers an effective means to extensively exploit the excellent properties of single crystals at high frequency. A higher electromechanical coupling factor for composite compared to monolithic single crystal PMN-PT makes it a viable choice for a transducer used in medical imaging. These single crystal PMN-PT based transducers have demonstrated improved performance characteristics in both low and high frequency medical ultrasound applications. In our previous work we have reported the development of 50MHz single crystal PMN-PT composite transducers that are currently gaining extensive interest in the medical imaging market. A high performance single crystal PMN-PT transducer at 60MHz can provide better resolution than the current technologies (50MHz) being used for multimodality imaging.

Statement of Contribution/Methods

In this paper we present the development of a high performance 60MHz single crystal PMN-PT composite transducer that can be used for intravascular medical ultrasound imaging and emerging technologies. The high frequency transducers have been developed using a combination of micro-electromechanical (MEMS) fabrication techniques and state of the art mechanical finishing processes. The composite development has been focused on maximizing the coupling factor by optimizing the geometry of the single crystal pillars to obtain a high aspect ratio without compromising the manufacturing feasibility of the transducer during subsequent process steps. Electrical characterization of the transducers has been performed using an Agilent 4294 impedance analyzer for evaluating the dielectric and piezoelectric properties of the crystal composite. Acoustic pulse echo measurements have been performed using an Olympus pulser/receiver and a Tektronix oscilloscope to evaluate the bandwidth (BW), sensitivity (Vpp) and the center frequency (Fc) of the transducers.

Results/Discussion

The results for a 60MHz single crystal PMN-PT composite transducer with coupling factor around 0.77, fractional bandwidth 65%, and sensitivity around 0.6V are presented.

Highly Sensitive Array Transducer based on a KNN-NTK Composite Lead-free Piezoelectric Ceramic for High-frequency Ultrasonic Imaging Application

Ruimin Chen¹, Laiming Jiang^{2,3}, Robert Wodnicki¹, Haochen Kang¹, Takayuki Matsuoka⁴, Ahmad Safari⁵, K. Kirk Shung¹, Qifa Zhou^{1,2}

¹Department of Biomedical Engineering, University of Southern California, Los Angeles, CA, United States, ²Roski Eye Institute, Keck School of Medicine, University of Southern California, Los Angeles, CA, United States, ³College of Materials Science and Engineering, Sichuan University, Chengdu, China, People's Republic of, ⁴NGK Spark Plug Co., LTD., Aichi, Japan, ⁵Department of Materials Science and Engineering, Rutgers University, Piscataway, NJ, United States

Background, Motivation, and Objective

High-frequency (HF) ultrasonic imaging ($> 10\text{-MHz}$) with improved spatial resolution has been widely applied to many specified clinical applications. Over the last decade, lead-based piezoelectric materials represented by $\text{Pb}(\text{Zr},\text{Ti})\text{O}_3$ (PZT) ceramics and $\text{Pb}(\text{Mg}_{1/3}\text{Nb}_{2/3})\text{O}_3\text{-PbTiO}_3$ (PMN-PT) single crystals have been extensively used to manufacture HF ultrasonic transducers due to their excellent piezoelectric and electromechanical properties. Recently, a lot of efforts has been made to develop environmental friendly lead-free piezoelectric materials with comparable properties to the lead-based ones for the application in highly sensitive HF ultrasonic transducers. $(\text{K},\text{Na})\text{NbO}_3$ (KNN) is one of the most promising lead-free piezoelectric materials due to its particularly high piezoelectric characteristics. In this work, we present the development of a 20-MHz 64-element HF linear array ultrasonic transducer based on a new $(\text{K},\text{Na})\text{NbO}_3\text{-KTiNbO}_5$ (KNN-NTK) composite lead-free piezoelectric ceramic [1].

Statement of Contribution/Methods

Simulation software packages including PiezoCAD and Field II were employed in order to optimize the performance of the lead-free linear array. The composites used in the array was fabricated by dice-and-fill technique. Array elements were spaced at a 1λ pitch, interconnected via a custom flexible circuit. Two matching layers and light backing materials were used to improve sensitivity and bandwidth. A number of performance benchmarks, including electrical impedance, pulse-echo response, insertion loss, and crosstalk, were measured to evaluate the performance of the array.

Results/Discussion

The electrical impedance was measured to be $180\text{-}\Omega$ on resonance in a representative array element (Fig. 1a). Two-way pulse-echo response measured from the element exhibits a center frequency of 18.9-MHz, a high received peak-to-peak voltage of 370-mV without gain, a -6dB bandwidth of 43% (Fig. 1b), and an insertion loss of 29.1dB. A Verasonics Vantage research ultrasound imaging system will be employed with the array to perform B-mode imaging on a 20- μm tungsten wire phantom to measure lateral and axial spatial resolutions. As our intended application for this array, we will further perform *ex-vivo* imaging on the anterior segment of a porcine eyeball to demonstrate imaging capability of the array.

[1] T. Matsuoka et al., J. Appl. Phys., 2014.

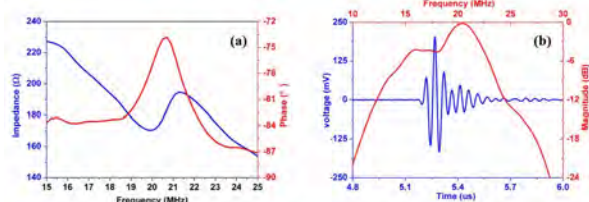


Figure 1. Measured (a) electrical impedance and (b) pulse-echo response and its FFT spectrum of a representative array element.

High speed high frequency miniature forward-looking ultrasound system for clinical applications

Xueqiao Wang¹, Guijun Huang¹, Zhiyu Zhou¹, Di Li², Xuejun Qian^{2,3}, Runze Li^{2,3}, **Qifa Zhou^{2,3}**

¹*Newway Technology (US), Inc, United States*, ²*Department of Biomedical Engineering, University of Southern California, United States*, ³*USC Roski Eye Institute, University of Southern California, United States*

Background, Motivation, and Objective

To dynamic monitor tissue morphological structure with high resolution and high frame rate has been proved great important in many clinical applications such as intracranial surgery and intravascular diagnosis. Unfortunately, an imaging device with a high resolution capability to provide 2D cross-sectional imaging fields deep inside the body is still lacking. Herein, we newly developed a 60 MHz PVDF based miniature ultrasonic device, which would be an important step forward in clinical surgery and help physicians to have a better visualization of target tissues during the surgery.

Statement of Contribution/Methods

The design and fabrication process of the ultrasonic device is described as below: First, the PVDF was diced into small cylinder with diameter of 1 mm and housed in the polyimide tube for electrical isolation. Then, a wire was connected to the backing layer and then the other side of acoustic stack was connected to the housing by conductive epoxy to form the ground plane connection. Next, all the connections were sealed by epoxy for electrical isolation and water proof. Finally, the transducer was put on the motor-based device to achieve fast rotation scanning by using customized micro motor and rotator as shown in Fig. 1a.

Results/Discussion

The photography of the miniature ultrasonic device was shown in Fig. 1b. The spatial resolution was tested using a 20 μm diameter wire phantom. The -6 dB bandwidth was used to define the imaging resolution, which is 80 μm axially and 450 μm laterally as shown in Fig. 1c. The maximum operating angle of the device is +/- 15 degree, which covers a 2 mm lateral view and up to 4 mm in depth direction. Up to 30 frame/seconds rate satisfies the clinical requirements. All these results demonstrate that the high speed high resolution imaging capability of the miniature ultrasonic device could benefit for clinical surgery, especially when integrated with a needle biopsy.

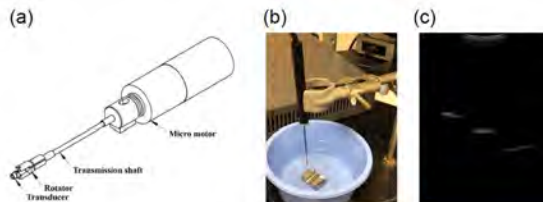


Figure. 1

Novel thin film transducers for durable high-resolution imaging in industry and medicineIvan Shorokhov¹, Daniel Irving¹, Heather Trodden¹, David Allan Hughes¹¹*Novosound Ltd, Biocity, Bo'ness Road, Newhouse, Scotland, United Kingdom***Background, Motivation, and Objective**

The mass-manufacture of high-resolution ultrasound transducers remains a challenge. This work presents a scalable, additive manufacturing method for producing ultrasound transducers. The thin-film based sensors are easy to assemble, highly customizable, provides large bandwidth at high frequency as well as consistent performance in harsh environments.

Statement of Contribution/Methods

A novel sensor material is deposited on to a flexible substrate using a reactive sputtering method and assembled into a tightly focused ultrasound transducer. A, B and C-mode data (as shown in Figure 1) was recorded with a DPR 500 (JSR Electronics), 140V excitation, 0dB pre-amplifier gain, 5-300MHz bandwidth by mechanically scanning the transducer. The high-frequency thin-film transducer was used to produce images several test objects. In particular, a UK coin image demonstrates spatial and axial resolution, and a porcine tooth to demonstrate imaging of both hard and soft-tissues.

Results/Discussion

The results show that high-frequency probes based on thin-film technology could be used in acoustic microscopy and medical imaging. The probes were characterized with an aluminium reflector and found to have an average centre frequency of 45MHz, and -20dB bandwidth of 86%. The axial resolution of the probe was measured to be 50.9µm and the spatial resolution was 295µm corresponding to an f-number of 1.88. Representative images are displayed in Figures 1b-c, demonstrating high image quality and resolution.

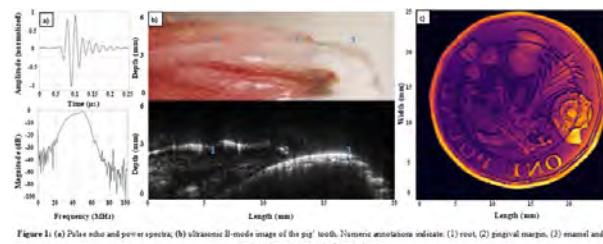


Figure 1: (a) Pulse echo and power spectra; (b) ultrasonic B-mode image of the pig's teeth. Numeric annotations indicate: (1) root, (2) gingival margin, (3) enamel and dentin; (c) one pound coin C-mode image

A Distal Micro-Motor Ultrasonic Imaging Catheter

Yunfei Li^{1,2}, Lucai Ma^{1,2}, Hu Tang^{1,2}, Siping Chen^{1,2}, Jue Peng^{1,2}

¹National-Regional Key Technology Engineering Laboratory for Medical Ultrasound, China, People's Republic of, ²Guangdong Provincial Key Laboratory for Biomedical Measurements and Ultrasound Imaging, School of Biomedical Engineering, Shenzhen University Health Sciences Center, Shenzhen, China, People's Republic of

Background, Motivation, and Objective

Intravascular ultrasound (IVUS) is the gold standard in clinic for diagnosing cardiovascular diseases. The images of vessels are acquired in this way with a rotation transducer which is controlled by the long flexible driving shaft. However, non-uniform rotation often occurs when a catheter passes through a long bending vessel owing to the frictional force between the flexible drive shaft and catheter wall, causes image distortion. One approach to solve this problem is to develop a catheter driven by a distal motor. In this study, a catheter integrated distal micro-motor and high-frequency transducer was developed. The schematic of the IVUS catheter is shown in Fig. 1(a).

Statement of Contribution/Methods

A micro distal motor with 3.7 mm length and 1.2 mm outer diameter was proposed as an actuator for the IVUS catheter, as shown in Fig. 1(b). A three-phased micro motor using the electromagnetic method with a new structural design was proposed. A 0.5 mm × 0.5 mm Pb(Mg_{1/3}Nb_{2/3})O₃-PbTiO₃ (PMN-PT) single crystal 1-3 composite single-element transducer was designed and manufactured. The setup of the imaging system combined with multiple devices and in vitro imaging experiments is implemented to test the imaging performance of the catheter that is integrated with the micro motor and ultrasound transducer.

Results/Discussion

An IVUS catheter combining a micro-motor with a high-frequency transducer was designed. Fig. 1(c) shows the photograph of the wire phantom image captured by the IVUS catheter. The wire phantom in one direction can be fully displayed, but the other direction is not displayed completely. The reason is that transducer signal line which integrates in catheter has an effect on the rotating mirror. We will optimize the structure of the IVUS catheter to improve the imaging quality, and perform in vitro vascular experiments. With the improvement of the IVUS catheter, it will provide more accurate images for evaluating lumen dimensions and guiding intervention for clinical application.

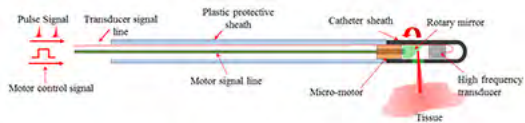


Fig. 1(a) A diagram of the IVUS catheter.



Fig. 1(b) Photograph of the fabricated intravascular ultrasound catheter.



Fig. 1(c) Images of the tungsten wires.

Modeling and Characterization of an Acousto-optical Transducer for Catheter Tracking in Interventional Magnetic Resonance Imaging

Yusuf Yaras¹, Robert Lederman², Ozgur Kocaturk³, F. Levent Degertekin¹

¹School of Electrical and Computer Engineering, Georgia Institute of Technology, Atlanta, GA, United States, ²Division of Intramural Research, National Heart Lung and Blood Institute, United States, ³Institute of Biomedical Engineering, Bogazici University, Turkey

Background, Motivation, and Objective

RF induced heating is a significant safety concern for Magnetic Resonance Imaging (MRI) especially when long metallic structures are inserted in the body during interventional MRI procedures due to the concentrated eddy currents. Current position tracking sensors used during interventional MRI rely on long conductor cables to carry local MR signal from coils to MR system. Resonances on these conductors can exacerbate RF heating. An acousto-optical transducer in which the RF signal is converted optical modulation and sent to the MR system over optical fiber can make the system immune to RF induced heating [1]. Here, we discuss detailed modeling and experimental characterization of this device.

Statement of Contribution/Methods

The proposed transducer is composed of a coil, a piezoelectric transducer and a fiber Bragg grating (FBG). The piezoelectric transducer converts electrical signal collected by the coil into mechanical waves, which in turn modulates the reflected light from the FBG. Two different π -phase shifted FBG sensors were used with a notch bandwidth of 50 MHz and 250 MHz at 1550nm. Combination of different numerical methods and analytical approaches were used to model the acousto-optical transducer. Coupled mode theory (CMT) was used to model the FBG and implemented in MATLAB [2]. The piezoelectric transducer was modelled with an FEA tool, COMSOL. Photodetector response is calculated analytically. The pressure sensitivity of the FBG was obtained through hydrophone measurements in water. A proof of concept sensor prototype [1] was fabricated using a 250 MHz FBG and a 21 MHz PZT5A piezoelectric transducer operated around its third harmonic frequency. The prototype was tested in 1.5T MRI and results are compared with simulations.

Results/Discussion

The pressure sensitivity of the bare FBG sensor is calculated using the model and confirmed experimentally as 81mV/kPa for the 50MHz FBG and 12mV/kPa for the 250MHz FBG. Minimum detectable pressure for the FBG sensor is calculated as 20Pa for a bandwidth of 100kHz at 64 MHz whereas the shot noise limited minimum detectable pressure is calculated as 7.5 Pa. An output signal of 1.72V with 57 dB SNR at 64 MHz is measured from the prototype in MRI during RF transmission, which is on the same order of the modelling results.

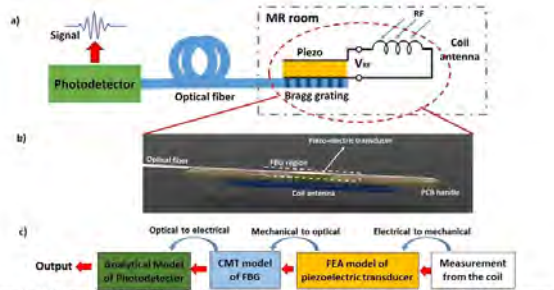


Figure 1. a) Schematic of the FBG based ultrasonic sensor b) Illustration of the prototype c) Model of the sensor
 [1] Y.S. Yaras et al., "Acousto-optic Based Active MRI Marker for Interventional MRI Devices," in ISMRM, 2017.
 [2] S.M. Norton, T. Erdogan, and G.M. Morris, "Coupled-mode theory of resonant-grating filters," *J Opt Soc Am A*, vol. 14, no. 3, p. 629, 1997.

High frequency Transducer Based on Ultrathin Li doped ($K_{0.45}Na_{0.55}NbO_3$) Single Crystal for 80MHz Intravascular Ultrasound and Photoacoustic Imaging

Tao Zhang¹, Ziyu Wang², Rui Xiong², Xiaofei Yang¹, Wei Wei³, Benpeng Zhu¹

¹Huazhong University of Science and Technology, China, People's Republic of, ²Wuhan University, China, People's Republic of,

³Hubei Cancer Hospital, China, People's Republic of

Background, Motivation, and Objective

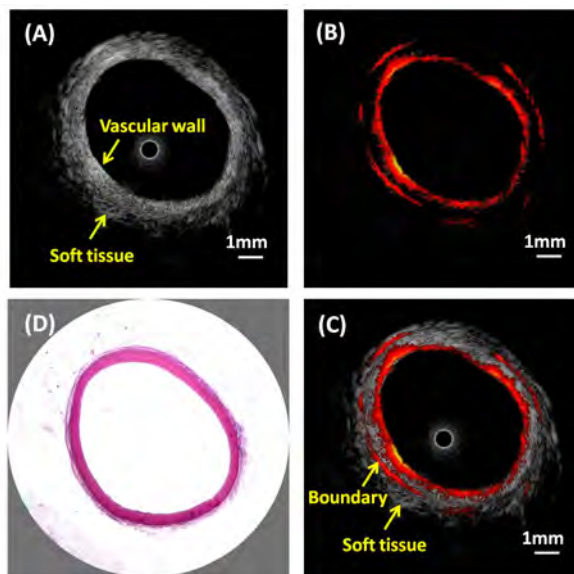
The development of miniaturized transducers at frequency range 20~50MHz for IVUS imaging has attracted much attention, whereas the axial/lateral resolutions are still inferior to intravascular Optical Coherence Tomography (OCT) imaging. Actually, the drawback of OCT imaging is the pretty low penetration depth (~1mm). With this in mind, to enhance the imaging performance and provide more details about coronary artery, further increasing the tiny ultrasound transducer's operational frequency and combining with other imaging modalities are considered as effective alternatives. To date, only limited researches about high frequency ($\geq 80\text{MHz}$) IUVS and intravascular photoacoustic (IVPA) imaging have been carried out; because it is a great challenge to fabricate highly sensitive miniaturized transducers at such high frequency. The aim of the present study is to demonstrate the feasibility of ultrathin KNN-based single crystals to be implemented in IVUS and IVPA applications at higher frequency (~80MHz).

Statement of Contribution/Methods

In this study, we present the preparation of ultrathin KNN-based single crystal with high piezoelectric performance, the fabrication process of a highly sensitive miniaturized high frequency transducer and the 80MHz IVUS and IVPA imaging of a healthy rabbit.

Results/Discussion

The $28\mu\text{m}$ KNN-based single crystal exhibits a stable k_t value, as high as 0.55, comparable to the k_t values of PMN-PT and PIN-PMN-PT single crystals. Most importantly, its $d_{33,f}$ is determined to be $\sim 490 \text{ pm/V}$, which is much larger than those values of KNN-based films. The ultrasound transducer, with a 82 MHz central-frequency and a fractional bandwidth of 57.3% at -6 dB, which was determined with a pulse echo test, was slightly tilted toward the fiber to achieve a maximized overlap of the optical/acoustic beam. In Fig. 1(A) and (B), the 80-MHz IVUS and IVPA images are displayed with a dynamic range of 50 dB and a dynamic range of 35 dB, respectively. By fusing the IVUS and IVPA images together, as shown in Fig. 1(C), the boundary between surrounding soft tissue and vessel wall can be easily seen. These promising results indicate that the ultrathin KNN-based lead free piezoelectric single crystal is competent for high frequency (~80MHz) IVUS and IVPA imaging. This research opens a path for the application of lead-free piezoelectric single crystal.



P1-B13 - Acoustic Imaging

Kairaku (posters 1)

Wednesday, October 24, 9:30 AM - 4:00 PM

Chair: **Joel Harley** University of Utah

P1-B13-1

Preliminary experiments of 3-dimensional Fourier beamforming with no approximate interpolation for wavenumber matching

Chikayoshi Sumi¹, Taku Asakawa²

¹*Info & Commun Sci, Sophia University, Tokyo, Japan*, ²*R & D, Japan Probe Co., Ltd, Japan*

Background, Motivation, and Objective

In fields of a medical ultrasound and a nondestructive evaluation, an ultrasonic Fourier beamforming is performed to achieve a higher speed processing than a precise delay-and-summation (DAS) beamforming. Such a beamforming will be more effective on 3-dimensional (3D) imaging with more data than on 2-dimensional (2D) one. However, except for nonsteered synthetic aperture (SA), all methods developed by other groups require approximate interpolations of angular spectra for a wavenumber matching. This causes sever artifacts indeed [see Sumi in ITEC 2015].

Statement of Contribution/Methods

The author has developed Fourier methods such as of a steered synthetic aperture (SA) and a steered reception dynamic focusing with respect to a steered, focused transmission and a steered, nonfocused transmission such as of a plane or spherical wave etc. The advantage of the author's developed methods includes no performing of any approximations for a wave number matching by performing the multiplication of complex exponentials [ITEC 2015]. In this report, 3D Fourier beamforming was performed on steered SA and steered reception beamforming with respect to a steered plane wave transmission, respectively. The imaging targets were three stainless wires (0.23 mm-dia.) positioned at about 30 mm depths (z) in a water with 6 mm pitch in y-direction and running in x-direction (Fig. 1). A 2D linear-array type probe having 16×16 elements with 1.5 MHz nominal frequency, 0.35 × 0.35 mm widths, and 0.05 mm kerfs (Ueda Japan Radio Co., Ltd) was set at the surface of a water. An rf-echo data acquisition system (20 MHz) with a motorized positioner (Japan Probe Co., Ltd) was used to acquire $64 \times 64 \times 1500$ monostatic SA data.

Results/Discussion

Fig. 2 shows Images of y-z or x-z planes obtained by (a) SA and (b) reception beamforming with respect to a plane wave transmission. The results were obtained by steering beams only in y-z planes with 0 and 20, and -20 deg, respectively. In both beamformings, images of targets were successfully formed. Since the transmission/reception sensitivities of peripheral elements of a 2D array were small, the images of targets became discontinuous in a running direction (x-direction).

The Fourier beamformings were successfully performed. The medical and nondestructive applications will be reported in the near future. Other probes, a virtual source and a sector scan will also be used.

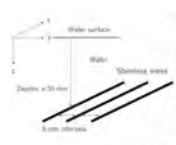


Fig. 1. Targets.

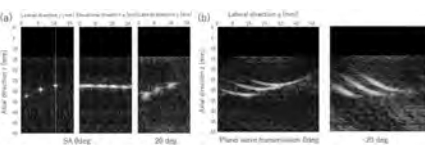


Fig. 2. Obtained images: (a) SA and (b) plane wave transmission.

Ultrasonic Array Imaging through Reverberating Layers for Industrial Process Analysis

Marcus Ingram¹, Anthony Gachagan¹, Jerzy Dziewierz¹, Anthony Mulholland², Alison Nordon³, Martin Hegarty⁴

¹*Electronic and Electrical Engineering, University of Strathclyde, Glasgow, United Kingdom*, ²*Mathematics and Statistics, University of Strathclyde, Glasgow, United Kingdom*, ³*Centre for Process Analytics and Control Technology, University of Strathclyde, Glasgow, United Kingdom*, ⁴*BP Chemicals Ltd, United Kingdom*

Background, Motivation, and Objective

In this paper, we investigate the application of ultrasonic phased arrays as an imaging tool for industrial process analysis. Non-invasive process measurement, via transmission of information through a vessel wall, typically requires a window to create an optical path between the sensor and the process. Ultrasonic array imaging provides a means to overcome this barrier as it is specifically used to image into optically opaque structures. However, in typical process analysis environments, there is a large acoustic impedance mismatch between the steel vessel and the fluid process. At this acoustic boundary most energy is reflected back towards the transducer, reducing the energy that is transmitted into the process, leading to reverberation clutter in the time domain signals. The motivation of this work is to demonstrate how this reverberation clutter can be minimised, thus enabling visualisation of an industrial process.

Statement of Contribution/Methods

A 32 element linear array with a 5 MHz centre frequency was designed in PZFlex (PZFlex, OnScale Inc., USA) to represent a typical process analysis environment. The array was positioned on the outside wall of a 10 mm steel layer and four void reflectors were suspended in a water load on the adjacent side of the steel layer. The array was deployed using Full Matrix Capture (FMC) followed by the Total Focussing Method (TFM). Existing methods of clutter removal include background subtraction or deconvolution, however the background response of an industrial process is not always available. Therefore, to identify the location of reflections deriving from reverberations, a method has been developed called the Reverberation Pattern Gain Correction Method (RP-GCM). Using ray-tracing to predict the path length of reverberations within the steel layer, the pattern of echoes for a given transmit-receive combination can be reconstructed. This pattern is then translated into a gain filter to reduce the local signal amplitude in the FMC data set, prior to application of the standard TFM process.

Results/Discussion

Upon application of the RP-GCM to the simulated FMC data set, there is a 15 dB increase in the signal-to-noise ratio corresponding to the void reflectors in the TFM image. This results in effective imaging of the void reflectors and minimisation of the reverberation signals. However, this method assumes there is a good repeatability of the reverberation pattern and that material heterogeneity has a negligible impact on the time-of-flight estimation. Therefore, to increase the robustness of the algorithm for experimental application, methodologies including subspace analysis will be discussed to enhance the clutter minimisation. The conclusion of this work demonstrates the applicability of ultrasonic phased array imaging to dynamic, non-invasive industrial process analysis.

Large-Panel Multitouch Ultrasonic Touchscreen using Lamb waveKi Chang Kang¹, Young Hun Kim¹, Kwan Kyu Park¹¹*Mechanical Convergence Engineering, Hanyang University, Seoul, Korea, Republic of***Background, Motivation, and Objective**

Touchscreen sensors are used in a variety of devices, including smartphones, tablets, and large panels. Capacitive touch technologies are the most commonly used, but they have disadvantages in the implementation on large panels such as manufacturing cost, hardware complexity. Ultrasonic touchscreen is can be potential candidate to solve this issue. However, existing ultrasonic methods have been implemented only on small panels less than 23 inches and have never been implemented on panels of several tens of inches. In this study, we developed ultrasonic touch screen technology capable of multi-touch on 55 inches glass using A_0 mode of lamb wave. If multi-touch can be realized in a large panel, the technology can be used for large touch screen display, smart window glass, car exterior, etc.

Statement of Contribution/Methods

Considering the center frequency and signal strength, $3 \text{ mm} \times 3 \text{ mm} \times 1 \text{ mm}$ PMN-PT was used for transmitting (TX) and receiving (RX) sensor. Four pairs of sensors (4 TX, 4 RX) are located on 3-mm thick glass and the measured center frequency is 220 kHz. Classical synthetic aperture imaging method were used to detect the location of the fingertip. A single frame is made of four transmitting sequence. At each sequence, one TX-RX sensor pair is performing pulse-echo and received signal was compensated by reference signal. The received signals were processed by delay and sum method to enable finger detection in real time. We also developed a multi-point detection algorithm optimized for multiple point targets, which enable to detect multiple fingertips with different reflection strength.

Results/Discussion

Detection of multiple fingers on 55 inches glass panel was successfully implemented by using PMN-PT sensor pairs. The system currently implements images at a rate of 0.9 frames per second due to the limitation of current synthetic imaging hardware. Based on the wave propagation time the frame rate can be improved up to 166 fps. From our preliminary result, four device pair can cover more than 50% of the total glass panel. The current 3-dB spot size of a finger image is 5.5 cm. The center location of the fingertip was calculated by weighted average. The resolution of the fingertip location is 1.7 mm based on $\pm 3\sigma$. This study has realized a multi-touch technology using a small number of sensors in a large touch screen.

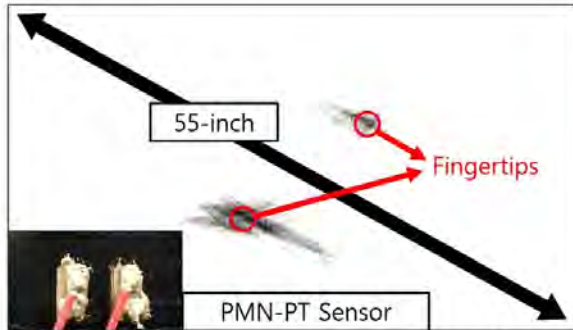


Figure 1. PMN-PT sensor pair and 5dB delay and sum image of 2 fingertips

Ultrasonic focusing through a steel layer for acoustic imaging

Andreas S. Talberg^{1,2}, Hefeng Dong^{1,2}, Tonni Franke Johansen^{2,3,4}, Svein-Erik Måsøy^{2,4}, Tarjei Rommetveit⁵, Svein Brekke⁵
¹Department of Electronic Systems, NTNU, Norway, ²Centre for Innovative Ultrasound Solutions (CIUS), Norway, ³Digital,
SINTEF, Norway, ⁴Department of Circulation and Medical Imaging, NTNU, Norway, ⁵Archer BTC, Norway

Background, Motivation, and Objective

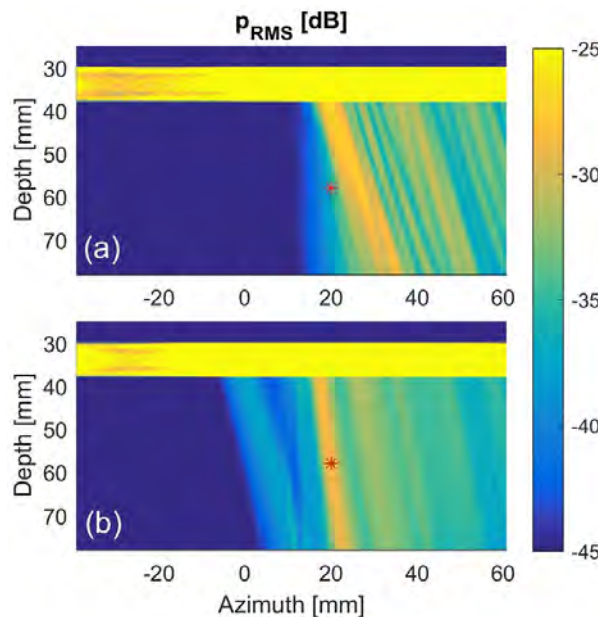
Ultrasonic tools are being used for imaging in a large variety of fields, spanning from medical applications in a hospital to applications deep down in oil and gas wells. When applying ultrasonic imaging techniques to image through elastic materials, such as steel, one of the main challenges these tools have to overcome is the high impedance differences between the steel and the surrounding media, making it a barrier for the acoustic wave. Putting effort into studying acoustic focusing through steel, maximizing the energy propagating to a point on the outside of the elastic layer, we aim to use back scattered pulses from this point to conduct imaging of the volume outside a steel layer.

Statement of Contribution/Methods

An ultrasonic array consisting of 64 elements (0.6 mm pitch, 0.51 mm width) has been replicated in a 2D FDTD simulation setup. The geometry of the model consists of two water layers, separated by a flat, 8 mm thick, steel layer. Using time reversal (TR) techniques by inserting a point source in the lower water layer and receiving at the positions corresponding to the ultrasonic array placed in the upper water layer, the aim is to improve the focusing of the acoustic wave through the steel plate.

Results/Discussion

The 64 element array was placed 30 mm above the steel layer, set to receive an ultrasonic pulse emitted from a point source placed 20 mm below the plate and 20 mm to the right of the center of the array. By logging the time of arrival at each array element and using these to calculate the delays for transmitting, improved focusing of the ultrasonic pulse was achieved. The figure displays the RMS pressure in the domain below the steel plate summed over 70 μ s, normalized, and plotted in decibel. The horizontal yellow area marks the position of the steel layer while the red point indicates the desired focus point. Figure (a) shows the focusing acquired by calculating the time delays as the transmitter where to focus its beam as it was only propagating in water. At the desired focus depth, the -3 dB beamwidth is 7.5 mm and the maximum can be found at 27 mm in x-direction. Implementing the focusing acquired using TR through steel (fig (b)), the beamwidth is reduced to 4.15 mm and the maximum is found at 19.9 mm in x-direction, close to the desired focus point at 20 mm. Hence, the TR technique makes it possible to improve the focusing by precisely targeting the desired area with a narrower beam.



A Study on Marked Muscle Fiber for Ultrasonic Skeletal Muscle

Pan Li¹, Jianzhong Guo¹, Guanjun Yin², Shuyu Lin², Hui Cao²

¹Shaanxi Normal University, Xi'an, China, People's Republic of, ²School of Physics and Information Technology, Shaanxi Normal University, Xi'an, China, People's Republic of

Background, Motivation, and Objective

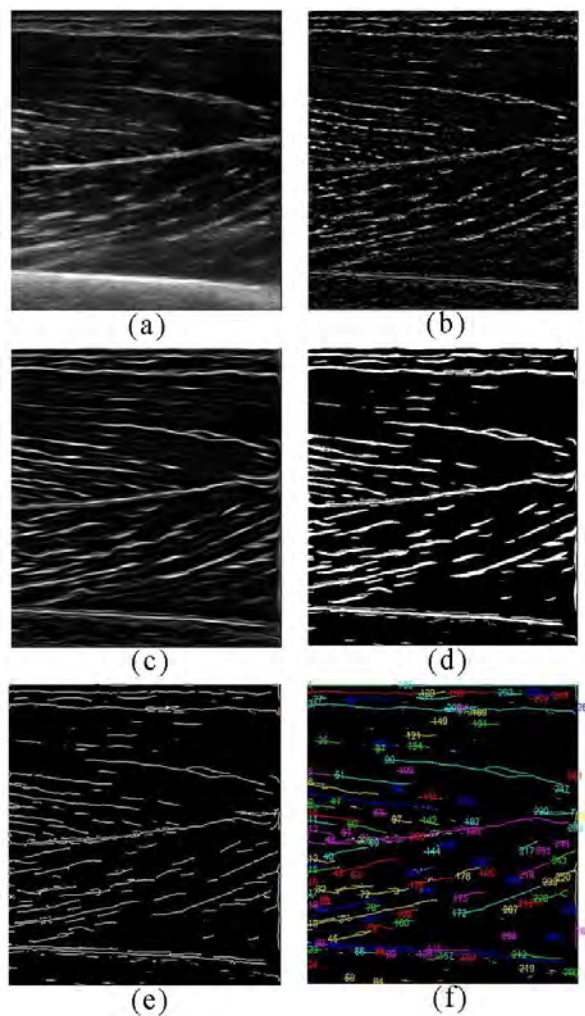
Skeletal muscles play an important role to keep human body movement. Over recent years, B-mode ultrasound imaging has been used widely to assess skeletal muscles function and state. The distribution properties of the length and direction and thickness of the muscle fibers are very important for muscle function. Traditionally those properties were marked by drawing lines on ultrasound images manually for research and clinical applications. It's obvious that there are very poor efficiency.

Statement of Contribution/Methods

In this paper, we propose an automatic method to extract muscle fiber on ultrasonic imaging. First we use nonlinear anisotropic diffusion filter to decrease the speckle noise. Then, the coherence enhancing diffusion filter is applied to enhance muscle fiber structures. At last, extract muscle fiber by the mathematical morphology method. The original ultrasound image of the biceps of left arm, de-noised image, enhancement structures and final muscle fiber extraction result are shown in Fig. 1(a-f). Actually, the extracted muscle fiber in Fig. 1(e) are clearly clearer than the original.

Results/Discussion

The final results shows that our method could automatically extract muscle fiber. And the processing results are effective to mark the muscle fiber. In ultrasonic muscle image it is convenient to be used for automatic estimation muscle fiber properties such as thickness, pennation angle, fascicle length, and so on.



The Coupling Effects in Three Parallel Waveguides

Guanjun Yin¹, Pan Li¹, Jianzhong Guo¹, Shuyu Lin¹, Hui Cao¹

¹School of Physics and Information Technology, Shaanxi Normal University, Xi'an, China, People's Republic of

Background, Motivation, and Objective

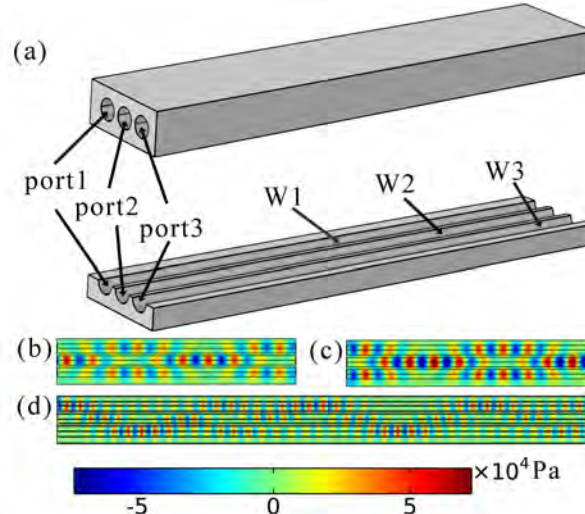
Coupled mode theory (CMT) has always been a hot topic in electromagnetism and optics. The coupling effect owns important value in controlling and steering waves. Over past decades, the coupling phenomena in optical waveguides have attracted much attention of researchers in optics. While, there are little reports about the effects in the acoustic cladding waveguides (ACW). Recently, the coupling effects in two parallel ACWs were investigated and demonstrated; furthermore, the focusing phenomena in the nested waveguide structures are also illustrated based on the coupling effect.

Statement of Contribution/Methods

In this paper, using the finite-difference time domain method, we studied and showed the coupling effects in three parallel ACWs under different input modes. The fabricated structure is shown in Fig. 1(a). Three evenly spaced hollows are arranged parallel along an aluminum block. The core zones—hollows are filled with water. The input waves are plane sinusoidal signals of 180 kHz.

Results/Discussion

With three input modes, the instantaneous acoustic pressure distributions in the structure are demonstrated. In Fig. 1(b), the input waves cover port 2. Along the propagation direction, the waves in the W2 transfer into the W1 and W3 and then back into the original waveguide periodically with a fixed coupling length (CL). In Fig. 1(c), the input waves cover ports 1 and 3. The waves in the W1 and W3 transfer into the W2 and then back into the two original waveguides periodically with the same CL in Fig. 1(b). In Fig. 1(d), the input waves cover port 1. The phenomenon is more complicated than the two situations above, and the CL is different from the above two cases. The waves transfer from the W1 into the W3 and then back to the W1 periodically through the W2. In the coupling process between the W1 and W3, the W2 acts as an intermediary.



Nonlinear Behavior of Contact-Resonance Atomic Force Microscopy due to Stick-Slip phenomena**M Kalyan Phani¹, V Pfahl², C. Ma³, Anish Kumar⁴, Walter Arnold⁵, K. Samwer²**¹*Metallurgical and Materials Engineering, OP Jindal University, Raigarh, India*, ²*1. Physikalisches Institut, Georg-August-Universität, Germany*, ³*Department of Precision Machinery and Precision Instrumentation, University of Science and Technology, China, People's Republic of*, ⁴*Indira Gandhi Centre for Atomic Research, India*, ⁵*Department of Materials Science and Engineering, Saarland University, Germany***Background, Motivation, and Objective**

In the last two decades, contact-resonance atomic force microscopy (CR-AFM) has emerged as an advanced scanning probe microscopy technique for materials characterization with very high lateral resolution down to 5 nm. In CR-AFM, contact resonances (CR) of the AFM cantilever may be excited either by an ultrasonic transducer beneath the sample (Atomic Force Acoustic Microscopy, AFAM mode) or by the piezo-element on the cantilever chip (Ultrasonic Atomic Force Microscopy, UAFM mode). The contact-resonance frequency can be used to derive the tip-sample contact stiffness and in-turn the elastic modulus of the material under examination after proper calibration. The width of the resonance curve can be used to measure the viscoelastic loss or damping of the contact. In addition to the internal friction in the material and the air damping, partial slip or sliding of the tip at the surface also contributes significantly to the measured contact damping and the CR spectra becomes nonlinear at high excitation amplitudes while under relatively low contact stiffnesses. The transition from linear to nonlinear behaviour indicates the onset of mechanical yielding of the contact from sticking to sliding and hence also from elastic to plastic deformation. The sliding depends on the friction coefficient of the tip material, usually Si, against the material examined. The present study aims at understanding the influence of excitation amplitude (causing the tangential force) and applied load (normal force) on the non-linearity in the CR spectra and the loss Q^{-1} in different materials.

Statement of Contribution/Methods

CR-AFM was used to acquire CR spectra at different applied loads and excitation amplitudes on fused silica, silicon (100), a metallic glass and a La_{0.6}Sr_{0.4}MnO₃ (LSMO) thin film. The nonlinearity was studied in terms of the increased Q^{-1} , the sudden drop in the amplitude in the CR spectrum, and by the use of Duffing oscillator model where a nonlinear coefficient, β , was calculated.

Results/Discussion

The study demonstrates that Q^{-1} increases with decreasing load at all the excitation amplitudes. Further, at a given load, Q^{-1} increases with increasing excitation amplitude. The β coefficient of the Duffing oscillator obtained for all the samples was found to be decreasing with increase in the applied load. The increase in Q^{-1} and appearance of nonlinearity in the CR spectra at higher excitation amplitudes and/or lower contact stiffness were analysed in view of Mindlin's theory of micro-slip under tangential loading between contacting bodies. At larger loads and lower excitation amplitudes, Q^{-1} provides the internal friction in the specimen. The results of this study widen the applicability of ultrasonic AFM techniques.

A study on feasibility of method using high-intensity aerial ultrasonic waves for detection of foreign substance inside soft material

Li Jin¹, Ayumu Osumi¹, Youichi Ito¹

¹Electrical Engineering, Graduate School of Science and Technology, Nihon University, Tokyo, Japan

Background, Motivation, and Objective

As one method for detection of foreign substance, a measurement method using high-intensity aerial ultrasonic waves and laser Doppler vibrometer (LDV) was proposed. In the previous research, we succeeded in detecting the hard foreign substance which is in the form of a cylinder with a diameter of 20 mm inside soft material.

In order to make the method practicable, it's necessary to understand the impacts which are given by intensity of acoustic waves, irradiation angles and surface properties of soft materials on measurement results.

In this paper, we made a study of the imaging accuracy of the proposed method when the irradiation angle of acoustic waves changed.

Statement of Contribution/Methods

The experimental devices are made up of a source of high-intensity aerial ultrasonic waves (frequency: 28 kHz), an LDV, a data logger, and a PC that controls other equipment.

The experimental procedure is shown as followings. First, high-intensity focused acoustic waves (sound pressure: 4 kPa) which are irradiated at an angle θ with respect to the normal axis of the sample surface are generated and stopped at 1 second interval. Linked with this, the vibration velocity of the sample surface is measured by the LDV. In this case, the vibration velocity waveform measured by the LDV includes the changes in velocity of the static surface displacement due to the acoustic radiation force. Therefore, the velocity information of the surface displacement is extracted from the signals and the static displacement can be calculated by this.

Results/Discussion

Fig. 1(a), (b) show the measurement results. The sample which is used in the experiment is made of silicone rubber and foreign substance inserted is made of harder silicone rubber (a cylinder with a diameter of 20 mm). The center (the position of the black line) of measurement area is the insertion portion of foreign substance and the measurement range is 61 mm \times 61 mm with steps of 2 mm.

In the results, when acoustic waves are irradiated at an angle θ of 0° and 30°, both of them can image the foreign substance. In the case of $\theta=30^\circ$, though the displacement of a part of area free from defect descend, the SN ratio is enough to image the foreign substance. In other words, by the proposed method, even if the irradiation angle to the object surface is 30°, it can be confirmed that it's possible to image the foreign substance.

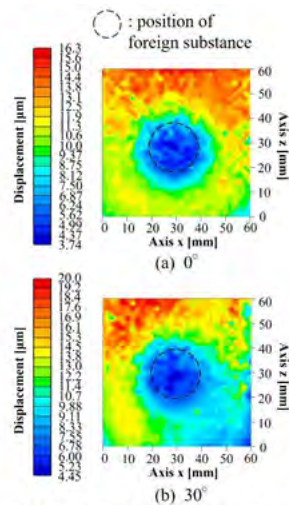


Fig.1. Static displacement distribution

A Compressed Sensing Based Miniaturized Photoacoustic Imaging System

Haoran Jin¹, Eryong Wu², Yunqi Luo¹, Liqiang Li², Ruochong Zhang¹, Yuanjin Zheng¹

¹*Nanyang Technological University, Singapore, Singapore*, ²*College of mechanical engineering, Zhejiang University, China, People's Republic of*

Background, Motivation, and Objective

The miniaturized PA systems have a great potential in measuring and monitoring physiological parameters in a continuous and noninvasive manner. To reduce the burden of power consumption and system volume, the data are always transmitted to user end (PC, mobile phone) for processing. One major challenge of the design is the conflict among huge amount of data transmission, limited battery life of portable devices and limited communication bandwidth. Because of this challenge, data usually needs to be compressed before transmission. In fact, most of the physiological signals are redundant, which means that they can be compressed using some transform encoders like discrete wavelet transform (DWT) based methods. However, this method consists of many matrix-vector multiplication, sorting and arithmetic encoding which consequently increase the hardware requirement and consume the power significantly. Compressed sensing (CS), is a technique for reconstructing signal with less measurement whose signal is sparse or can be sparsely represented based on some transformed domains. Herein, we introduce CS into PA systems as a lossy compression method to reduce the data transmission burden.

Statement of Contribution/Methods

We proposed a CS-model based compression and reconstruction method for portable and wearable photoacoustic system. The compression method is optimized for digital signal processing so that could be effectively implemented in a FPGA in parallel manner without any multipliers. To better recover the original signal, CS algorithm should incorporate physical information into the optimization procedure. In the case of PA measurement, the spatial pulse response of PA signal is utilized to build the sparse basis. Then the CS reconstruction is implemented by orthogonal matching pursuit (OMP) based on this sparse basis.

Results/Discussion

Experiment on B-scan imaging showed that CS-model based compression and reconstruction causes little degradation to photoacoustic signals while significantly suppresses the signal noise. The compressive sensing method could accurately recover photoacoustic signal and significantly suppress the undesired noise. The Signal Noise Ratio (SNR) has been improved by 16.9dB, 7.1dB and 5.3dB for 50%, 20% and 10% compression ratio respectively. It has been implemented and demonstrated on our portable and wearable photoacoustic system.

Imaging of disbond and delamination using flexural vibrations generated by laser modulationTakahiro Hayashi¹, Shogo Nakao²¹Kyoto University, Kyoto, Japan, ²Kyoto University, Japan**Background, Motivation, and Objective**

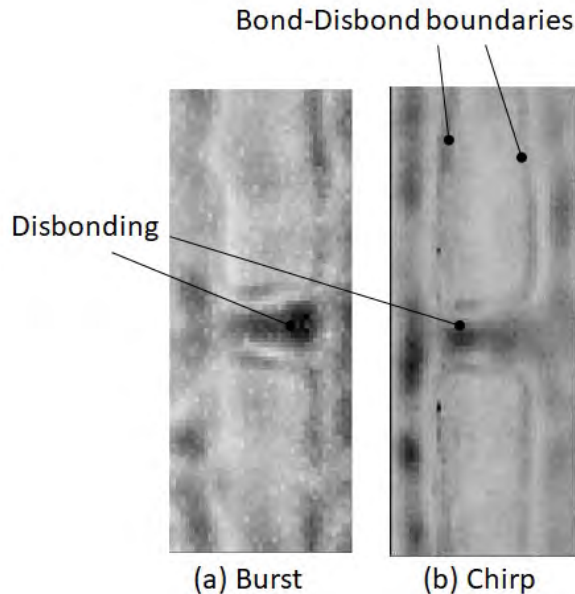
For the purpose of weight saving of automobiles and air-crafts, carbon composite laminates and aluminum alloy plates are increasingly used and their adhesive bonding has become popular. Therefore, nondestructive evaluation techniques are indispensable to evaluate the quality of bonding. Moreover, because the carbon composite laminates used in the body of air-crafts are occasionally damaged during the formation and processing, nondestructive inspection before shipping is required to find a delamination in the laminated plates. This paper describes imaging technique of the disbond and delamination in a non-contact and nondestructive manner.

Statement of Contribution/Methods

Authors have been developing defect imaging technique for plate-like structures using energy variation of flexural vibration generated by laser irradiation. This study applies this imaging technique to evaluations of adhesive bonding and delamination.

Results/Discussion

Numerical analysis using a semi-analytical finite element method revealed that large energy variations are observed at the boundaries of bonded and disbanded regions, and in the other areas, larger energy is roughly observed at disbanded regions than one at bonded regions. Next, adhesive bonding of a hat-top section and a flat plate that are often seen in actual bonded structures of automobiles were experimentally visualized. The visualization results showed the similar tendencies with numerical results, and spurious images were strongly obtained due to resonance in the structure when using narrowband burst wave (Figure a). To reduce the resonance and the spurious images, we used broadband chirp wave generated by appropriate laser modulation, which worked well for improving the image of the disbond (Figure b).



Suppression of surface wave signal artifacts in laser-ultrasound imaging of CFRP composites

Lukasz Ambrozinski¹, Jakub Mrowka¹, Matthew O'Donnell², Ivan Pelivanov²

¹Department of Robotics and Mechatronics, AGH University of Science and Technology, Kraków, Poland, ²Department of Bioengineering, University of Washington, United States

Background, Motivation, and Objective

Carbon-fiber reinforced plastics (CFRP) are widely used for structure manufacturing due to their efficient stiffness to mass ratio. A number of failures can occur in these materials; therefore, inspections are required both in production and in the field. Recent developments in laser-ultrasound (LU) enable high resolution imaging of CFRPs in a fully non-contact manner [I. Pelivanov et al., *Photoacoustics*, **4** (2016)].

In general, laser excitation operating in the thermo-elastic regime can produce different elastic modes simultaneously. Shear and surface waves signals superimposed with longitudinal waves create image artifacts hindering data interpretation and damage detection in B-scans. The objective of this work is to develop a signal processing technique to suppress these unwanted components.

Statement of Contribution/Methods

Figure 1(a) shows a B-scan obtained with the LU scanner [I. Pelivanov et al., *IEEE Tran. UFFC* **62** (2015)] in an impact damaged sample. An impulse corresponding to the front surface as well as the back-wall echo can be clearly seen from the image. Additionally, reflections from delaminations created at a number of layers can be seen in the middle part of the image. Surface waves can be observed in Fig. 1(b) as a low frequency component, which can be also seen as a dark area reaching a depth of 1.5 mm in the B-scan of Fig. 1(a). To suppress this artifact, a signal deconvolution procedure was developed. It is based on designing a reference signal reassembling temporal and frequency characteristics of the surface wave signal (Fig.1(b)). In the next step, the reference signal was used for inverse filtration of the original A-scans.

Results/Discussion

The performance of this approach can be observed at the A-scan level (Fig.1(b)), as well as by comparing the B-scan presented in Figure 1(a) to the processed image in Figure 1(c). A near surface area containing reflections from subsequent layers can be clearly seen in the processed image that is absent in the original one. Moreover, it is evident that the processing technique preserves damage-reflections and high frequency structure components. The back-wall reflection is enhanced due to time-gain correction applied to the image. Overall, the image quality is greatly improved by suppressing artifacts resulting from shear/surface waves

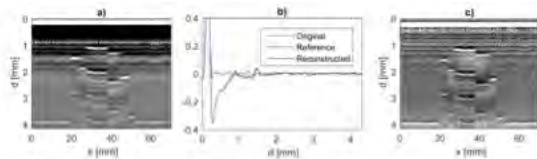


Figure 1. (a) - Laser ultrasound B-scan of an impacted composite sample. (b) - Comparison of original, reference and reconstructed A-scan waveforms. The original and reconstructed signals were taken from the damaged area in the middle of the B scan. (c) - Resulting image obtained with the proposed signal deconvolution procedure.

P1-B14 - Signal Processing

Kairaku (posters 1)

Wednesday, October 24, 9:30 AM - 4:00 PM

Chair: **Erdal Oruklu** Illinois Institute of Technology

P1-B14-1

A Subspace Based Method for Near Transducer Interference Suppression

Johan E. Carlson¹, Simon Ranefjärd¹, Felix Trulsson¹

¹DIv. of Signals and Systems, Luleå University of Technology, Luleå, Sweden

Background, Motivation, and Objective

For pulse-echo ultrasound, both when using transducer arrays and when using single-element transducers, the excitation from the pulser causes a strong transient interference. This prevents detection of echoes originating from scatterers near the transducer surface, resulting in a so called *blind zone*. One remedy is to introduce a delay-line or a wedge between the specimen and the transducer. This solution causes, however, an energy loss due to reflections between the delay-line and the specimen. In some applications, this loss causes problems, and direct-contact measurement is preferred.

The transducer itself is fully capable of transmitting and receiving at the same time, so if the transient from the excitation can be suppressed sufficiently well, it should be possible to detect echoes from scatterers, even close to the transducer surface.

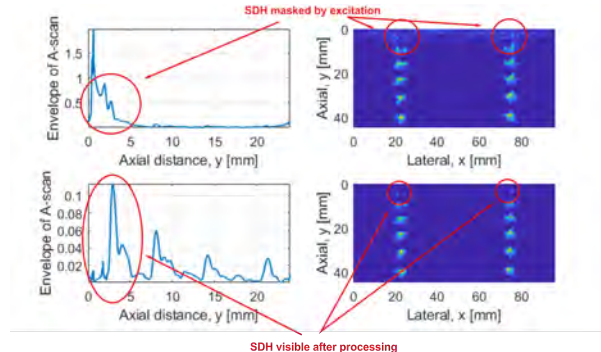
This paper presents and evaluates a technique for suppressing this interference, and shows with experiments using both a single-element transducer and a linear transducer array, that sufficient suppression is possible for detection defects close to the transducer, which were previously masked by the excitation.

Statement of Contribution/Methods

The interference from the excitation of the transducer is not deterministic, but exhibits some random properties, stemming from variations in excitation pulses, coupling effects between the probe and the medium, sampling jitter, etc. Based on calibration measurements, a basis is formed spanning the subspace containing the variation of the interference. Suppression in subsequent measurements is then achieved by projecting the recorded A-scans onto the orthogonal complement of this basis.

Results/Discussion

The figure shows the result of measurement on an aluminum block with near surface side-drilled holes (SDH) with a diameter of 1 mm. To the left we see the result of using a single-element probe and to the right is the result of imaging with FMC/TFM. The top figures show the envelopes A-scan and the image (generated using TFM), respectively, with no pre-processing applied. The bottom figures show the corresponding result after the proposed interference suppression algorithm has been applied to the raw data. It is clear that the interfering transient from the excitation has been suppressed sufficiently well to reveal the presence of the SDHs.



Sparse Representation with Partially Known Support and Subspace Expansion for Echo Estimation in Ultrasonic NDE Applications

Yufeng Lu¹, Jafar Saniie²

¹*Bradley University, United States*, ²*Illinois Institute of Technology, United States*

Background, Motivation, and Objective

In ultrasonic NDE applications, the change of echoes in the returned signal is governed by the physical properties along the propagation path. To unravel these information, various signal decomposition algorithms have been applied to separate these echoes and perform parameter estimation if echo model or dictionary is established. Out of these algorithms, the matching pursuit (MP) has become a framework of iterative dictionary decomposition. Various improvements to MP such as orthogonal matching pursuit (OMP), regularized OMP, stagewise OMP, generalized OMP and subspace pursuit have been developed. Nevertheless, it remains a challenge to decompose ultrasonic signal for NDE applications. Depending on the criteria used in the process, different decomposition results are obtained. These results not necessarily coincide with the physical reality of the application. To have meaningful decomposition results, a priori system information can play a major role in the decomposition strategy. This study aims to explore sparse representation of ultrasonic NDE signal via matching pursuit with partially known support for echo estimation.

Statement of Contribution/Methods

Since ultrasound reflectors are randomly distributed in the medium, echo estimation with local optimization is highly sought out. In this paper, we introduce the maximum a posteriori (MAP) estimation to the MP framework. The transducer specifications and the front surface echo are used to provide partially known support of atoms in a dictionary. The dictionary is built upon six-parameters chirplet, model. These parameters are adaptively estimated to best match the signal via correlation operation. The decomposition by default starts from the echo with the most energy concentration per iteration. During the iterative process, a subspace expansion and estimation back-tracing strategy is employed to achieve a better outcome of sparse representation. Those dominant echoes with parameters satisfying the a priori condition are registered to form subspaces. For those echoes with near-same parameters such as time-of-arrival are regrouped and retracted back to the signal residue for decomposition. The iteration process is completed until the energy of signal residue stop decreasing.

Results/Discussion

Ultrasonic signals including echoes with different level of overlapping conditions are evaluated. The simulation study shows that the proposed algorithm successfully tracks these echoes and estimates the parameters accurately, especially for the scenario of severe overlapping condition. For the experimental study, an ultrasonic signal is acquired from a steel block sample with a flat bottom hole. The flaw echo is embedded in strong backscattered grain noise. The proposed algorithm can not only obtain a sparse representation of the ultrasonic signal, but successfully detects the flaw echo.

Mode Separation and Reconstruction of Ultrasonic Guided Waves Based on Synchrosqueezed Wavelet Transform

Zhenli Liu¹, Kailiang Xu², Dan Li¹, Dean Ta¹, Lawrence H Le³, Jianqiu Zhang¹

¹Department of Electronic Engineering, Fudan University, Shanghai, 200433, China, People's Republic of, ²Institut Langevin, CNRS, INSERM, ESPCI Paris, PSL Research University, 17 rue Moreau, 75012, Paris, France, ³Department of Radiology and Diagnostic Imaging, University of Alberta, Edmonton, AB, T6G 2B7, Canada

Background, Motivation, and Objective

Human long bone can support the propagation of ultrasonic guided waves. The properties of guided waves are very sensitive to the cortical bone geometry and elasticity. It holds the potentials for developing a new technique for long bone evaluation. Guided wave signals are typically measured as a combination of multiple dispersive wave-packets, which brings challenges for signal interpretation and bone parameter inversion. In this study, we propose an automatic method based on synchrosqueezed wavelet transform (SWT) for individual mode extraction.

Statement of Contribution/Methods

SWT is employed to obtain the time-frequency representation of the guided wave signal. Watershed transform is applied to divide the spectrogram into several segments, each of which corresponds to an individual component. In order to extract the time-frequency energy of each component, a region growing algorithm is introduced to remove the noise time-frequency energy. Based on the segmentation result, the maximum energy time-frequency ridges of different modes can be extracted by a greedy algorithm. From the extracted ridges, we can finally reconstruct each guided wave mode in time domain by using inverse SWT.

Results/Discussion

Both simulated and experimental signals in a 4 mm-thickness bovine tibia were employed to investigate the performance of the algorithm. In the simulation, the spectrogram of the multimodal signal was in good agreement with the theoretical curves, and the region of each mode could be correctly distinguished (see Fig.1a). A high correlation coefficient can be obtained between the reconstructed and original signals at various signal-to-noise ratios (SNRs) (see Fig.1b). The correlation coefficients increase with the SNR increasing. When SNR = 0 dB, they are 0.980, 0.976 and 0.953 for A1, S1 and S2 mode respectively. In the experiment, the energy trajectory of each reconstructed mode was extracted (see Fig.2). It could be observed that the group-velocity frequency representation of each mode matched the corresponding theoretical curve. The method based on SWT could be used to extract the individual modes from a multimodal guided signal. The proposed method can be realized automatically without any pre-knowledge and only a single-channel signal is required.

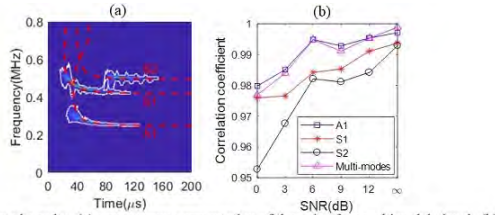


Fig1 Simulated results: (a) spectrogram segmentation of the noise-free multimodal signal; (b) correlation coefficients between the reconstructed and the original signals at different SNRs

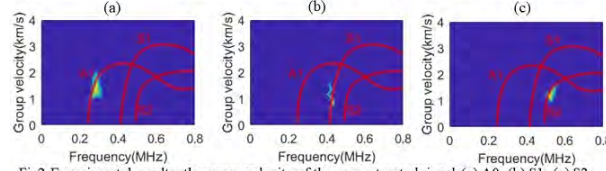


Fig2 Experimental results: the group velocity of the reconstructed signal (a) A0; (b) S1; (c) S2

A High Performance Communication Platform for Ultrasonic ApplicationsBoyang Wang¹, Jafar Saniie¹, Sasan Bakhtiari², Alexander Heifetz²¹*Illinois Institute of Technology, United States*, ²*Argonne National Laboratory, United States***Background, Motivation, and Objective**

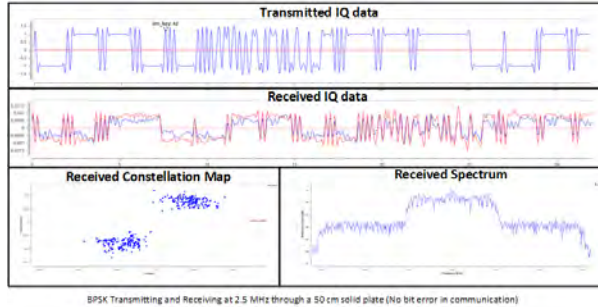
This paper presents a software defined communication system for transmitting and receiving information using ultrasonic signals. Experiments are conducted to evaluate the ultrasonic communication in different type of solid channels such as pipes, metal bars, plates, acrylic columns, etc.

Statement of Contribution/Methods

For this study, we developed a software defined ultrasonic communication system based on a ZYNQ System-on-Chip (SoC). ZYNQ SoC consists of ARM processor and FPGA on the same chip, which makes it an ideal platform to build a digital communication system. The ARM processor will be the main controller of the system while Digital Up Converter and Digital Down Converter implemented on the FPGA will handle the high frequency signal from and to the high frequency ADC and DAC in the system. Power amplifier on the transmitting side and low noise amplifiers on the receiving side are used to condition the signal to improve the signal-to-noise ratio.

Results/Discussion

Using ultrasonic signals for communication is a desirable solution when RF communication is not preferable in the channel. In this study, a software defined ultrasonic communication platform based on ZYNQ SoC is designed to conduct experiments. With IQ modulation and demodulation implemented on FPGA, high frequency ADC and DAC on the board, the system becomes programmable and adaptable for a series of experiments using different channel configurations. The following figure shows an experimental result with the software defined ultrasonic communication system.



Fluid layer thickness measurement using a shift-invariant sparse approachQuanchang Li¹, Wenbin Huang¹¹*Chongqing University, China, People's Republic of***Background, Motivation, and Objective**

Lubricant film thickness is one of the most important parameters to indicate the operating condition of machine elements, such as mechanical seals and hydrostatic slideway, etc. Ultrasonic pulse-echo methods, including the time of flight model, spring model and resonance model, have been used extensively in measuring the thickness of layered structures as well as those of thin adhesive interface layers with thickness values from high to low. However, a fluid layer within microns to tens of microns belongs to the unreachable region of these conventional methods by using an usual ultrasound transducer. Hence, novel pulse-echo signal processing method is desired to interpret the fluid layer thickness within such range.

Statement of Contribution/Methods

In this paper, a shift-invariant sparse based method is explored to extract the film thickness from its reflection ultrasonic signals. Firstly, an ultrasonic transducer sends pulses and receives all reflected echoes in the sample. Secondly, the reference signal, which can be called the main reflected signal, is also collected by the transducer. Thirdly, the reference signal is used as the atom to accomplish shift-invariant sparse learning of reflection signal in the time-frequency domain. Finally, by transforming time-frequency sparse approximation into time-scale waveform, the time interval of each echo can be found, which is used to obtain the thickness value of liquid layer. Among them, the reference signal is denoised in advance to have better characteristics. As an extension of traditional sparse representation, the shift-invariant sparse allows each dictionary to be replicated at each time offset within the signal, which is in accordance with the characteristics of pulse echoes. Compared to dictionary-based deconvolution, the proposed algorithm used the main reflection signal as the only dictionary to achieve sparse analysis, which avoids the complex construction of dictionary sets and has a better features matching with different echoes from the acquired data.

Results/Discussion

The algorithm was validated via experiments using fluid layer with various thicknesses between flat metal surfaces. Film thickness values in the range 10-200 um were recorded, which agreed well with theoretical predictions. Experimental results show that the thickness can be obtained accurately while compared with the results of other methods, and the error is within the allowable range.

A Multi-Resolution Convolutional Neural Network Architecture for Ultrasonic Flaw DetectionKushal Virupakshappa¹, Michael Marino¹, Erdal Oruklu¹¹*ECE Department, Illinois Institute of Technology, Chicago, IL, United States***Background, Motivation, and Objective**

In this work, a Convolutional Neural Network (CNN) architecture with a novel feature selector based on Wavelet Packets (WP) is introduced for ultrasonic flaw detection applications. CNN is among the key Deep Learning algorithms that have gained increased attention in recent years due to their success in machine vision, pattern recognition and classification tasks. CNN consists of multiple layers and it can extract features in a hierarchical manner to construct a high-level abstraction of the original data. We design a CNN for 1-D Ultrasonic data (A-scan) using wavelet coefficients as feature inputs and investigate optimal topologies such as number of parallel convolution networks, number of filters and output classifiers.

Statement of Contribution/Methods

A CNN is composed of convolution layers and pooling/dropout layers cascaded consecutively to form a deep neural network. The convolution layer contains a linear transformation filter and an activation layer. A classification layer is added at the end of the CNN. The algorithm pipeline for this work consists of a WP block, a feature selector block, and the CNN. The WP decomposition (wherein both low-pass and high-pass signals can be filtered) of A-scan data results in increased flexibility for selection of subbands which can be searched for optimal separation of clutter and flaw echo signals. Therefore, the feature selector is designed to perform a permutation of the subbands to yield best validation results during training. Assuming a selection of N subbands by the feature selector, N parallel CNNs are trained. Each CNN has four convolution layers and three pooling layers sandwiched between the convolution layers. The final convolution layer is appended with a max pooling layer and the output of these max pooling layer for all N CNNs are fed to a fully connected neural network classifier. The depth of convolution layers in each CNN is 8, 16, 16 and 32 respectively and the filter size of convolution operation is 1x5 while the filter size of pooling filter is 1x2.

Two different implementations of fully connected neural network have been used. One is used for binary classification to indicate presence of flaw and the other is used for regression analysis to indicate position of flaw. A Transfer Learning technique is used so that only the final layer of fully connected neural network needs to be trained.

Results/Discussion

All the training and testing is performed with the TensorFlow library running on AWS cloud computing infrastructure with NVIDIA GPU instances. During training phase, epochs of [2,3,5], learning rate of [0.1,0.05,0.01] and batch size of 70 have been used. An experimental data set of approximately 300 A-scans was used for the initial investigation. Preliminary tests yielded a detection accuracy of 86.5% for epoch of 3 and learning rate of 0.05. A confusion matrix has been generated to analyze results while validation losses and accuracy have been tracked to understand performance during training phase.

Human Activity Recognition Based on Two-Dimensional Acoustic Arrays

Xinhu Guo^{1,2}, Xiaonan Hu¹, Xiaodong Ye¹, Chaoyue Hu¹

¹School of Mechanical and Electronic Engineering, Wuhan University of Technology, China, People's Republic of, ²Hubei Provincial Engineering Technology Research Center for Magnetic Suspension, China, People's Republic of

Background, Motivation, and Objective

Human activity recognition (HAR) is widely used in many fields, monitoring of smart home, fire searching and rescuing, hospital patient management, etc. Acoustic is one of effective methods in HAR. In the traditional way, one or few ultrasonic sensors are used to receive signals, which requires a few feature quantities of extraction from the received data to improve recognition accuracy. In this study, time- and frequency-domain features of the data from acoustic arrays are used to obtain high recognition accuracy.

Statement of Contribution/Methods

The experiments of human activity recognition are carried out by two-dimensional acoustic arrays, which are composed of 4 transmitters and 256 receivers (16×16). The experimental setup is shown in Fig. 1(a). Four kinds of human activities (standing, sitting, falling, and walking) of each person are collected, as shown in Fig. 1(b). Each activity is repeated 10 times. The data is processed and classified by the algorithm of convolutional neural network (CNN).

Results/Discussion

The results showed that four kinds of human activities were effectively recognized by the algorithm of CNN. The accuracy of the activities is shown in Fig. 2. The total accurate rate of recognition is 100% for frequency-domain data, and 97.5% for time-domain data. In future work, we need further to build a large amount of data of human activity, and a model of human activity for application.

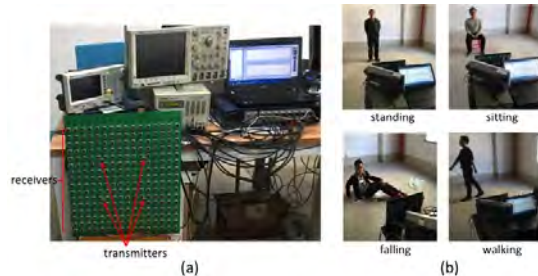


Fig. 1. (a) Photograph of the experimental setup, (b) four kinds of human activities.

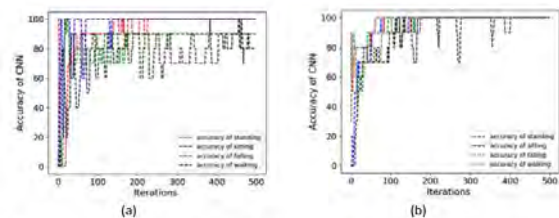


Fig. 2. (a) Accuracy of time-domain data by CNN method, and (b) accuracy of frequency-domain data.

A Recurrent Neural Network Classifier for Ultrasonic NDE ApplicationsMichael Marino¹, Kushal Virupakshappa¹, Erdal Oruklu¹¹*ECE Department, Illinois Institute of Technology, Chicago, IL, United States***Background, Motivation, and Objective**

This work presents a new classifier architecture for Ultrasonic Non-Destructive Evaluation (NDE) applications which can robustly detect the presence and location of flaws using Recurrent Neural Networks (RNN). RNN is a popular choice for deep learning networks used in language modeling, speech recognition (such as Apple SIRI), image recognition and characterization, financial data processing, and memory optimization techniques. As opposed to the traditional Neural Networks which are feedforward only, RNN adds memory to the analysis and enables modeling of sequential and spatiotemporal information. There are various implementations of RNN in the literature. We propose a bi-directional, partially recurrent RNN with reduced complexity for ultrasonic flaw detection.

Statement of Contribution/Methods

In the proposed method, Wavelet Transform (WT) is used as the feature extractor for raw ultrasonic signals since WT can analyze both time and frequency information simultaneously. WT filters out higher frequency clutter data via the selection of the appropriate wavelet kernel and number of decomposition levels. After WT, feature selections (wavelet coefficients) are subjected to the RNN classifier. The goal of the RNN is to further reduce the clutter information by predicting the output to be either a flaw echo signal with a high numerical rating, or clutter echo with a low numerical rating.

A bi-directional RNN algorithm is used in processing the data. This evaluates the input using both backward and forward time samples. The gradient descent method with least squares cost function was chosen for training the network. The specific RNN architecture was the partially recurrent Elman network which contains carefully selected feedback connections. This is a three layer fully connected network consisting of input, hidden, and output layers. There can be an arbitrary number of hidden layers, each with an arbitrary number of nodes. Each hidden layer has a memory context layer. The proposed Elman RNN is investigated with up to 2 hidden layers and a maximum of 80 nodes each. A threshold detector is used on the output of the RNN to detect for the presence and location of a flaw. We also investigate the use of LSTM cells with RNN. LSTM is designed to overcome long term dependencies and vanishing or exploding gradient effects. One drawback of LSTM is that additional A-scan data are needed for training due to increased number of parameters.

Results/Discussion

Experimental ultrasonic data acquired from steel blocks with defects were used for training and testing. For implementation of the RNN classifier, we utilize the TensorFlow platform by Google and Tesla GPUs by Nvidia. Experimental results indicate that the proposed architecture offers highly reliable flaw detection and localization with significant Flaw to Clutter Ratio (FCR) enhancements (an average of 30dB FCR improvement is observed). This architecture also performs well when multiple neighboring flaws exist.

Analog computing for acoustic spatial signals based on metasurfaces

Qi Wei^{1,2}, Xing-Feng Zhu¹, Jie Yao¹, Da-Jian Wu¹, Zheng Xu³, Xiao-Jun Liu²

¹School of Physics and Technology, Nanjing Normal University, Nanjing, China, People's Republic of, ²Department of Physics, Nanjing University, Nanjing, China, People's Republic of, ³Department of Physics, Tongji University, Shanghai, China, People's Republic of

Background, Motivation, and Objective

Metasurfaces have attracted extensive attention in both academic research and engineering as the planarization of metamaterials with subwavelength thickness. A metasurface can effectively manipulate electromagnetic (EM) and acoustic waves over a subwavelength scale, resulting in numerous extraordinary phenomena and functionalities, such as anomalous reflection/refraction, wave bending, focusing, cloaking, holography and asymmetric propagation. In particular, EM analog computing has been realized recently using a metasurface suitably designed to perform complex mathematical operations, such as spatial differentiation, integration and convolution. Metasurface-based analog computing (MBAC) platforms offer miniaturized and integrable wave-based computing systems, which may lead to fascinating applications in future supercomputing. The emerging advances in such designs inspire the development of acoustic MBAC. However, mapping the success of EM MBAC to acoustics is challenging, mostly owing to the distinct inherent wave–matter interactions between EM and acoustic waves. The EM metasurface performing complex mathematical operations exhibits both inhomogenous phase and amplitude responses, while the primary emphasis of research on the acoustic metasurface has been tailoring the phase delay only. Meanwhile, although some acoustic computing devices, such as acoustic diodes, switches and logic gates, have been demonstrated based on phononic crystals or bulk metamaterials, they suffer from the limitations of simple functionality, high losses and geometrical complexity.

Statement of Contribution/Methods

Numerical simulations are performed in Pressure Acoustic module of COMSOL Multiphysics v4.3, a finite-element analysis and solver software.

Results/Discussion

We present a two-dimensional acoustic MBAC system that performs complex mathematical operations on input acoustic signals. The system consists of three cascaded metasurfaces; i.e., two focusing metasurfaces (FMs) and one space filtering metasurface (SFM). The FMs function as spatial Fourier transformers while the SFM exhibits independent phase and amplitude responses to mimic mathematical operations in the Fourier domain. The FMs and SFM are constructed from layered labyrinthine metamaterials, which can provide broad modulation ranges on the phase and amplitude of the input acoustic signals. Three complex mathematical operations, namely spatial differentiation, integration and convolution, are designed and demonstrated using full-wave simulations based on the finite element method. The proposed MBAC system has great flexibility for efficient acoustic amplitude and phase manipulations with compact geometry, and offers a feasible solution of constructing compact devices for acoustic computing applications, signal processing and acoustic wave manipulations.

P1-B2 - Emerging Methods and Initiatives

Kairaku (posters 1)

Wednesday, October 24, 9:30 AM - 4:00 PM

Chair: **Giulia Matrone** University of Pavia

P1-B2-1

Density- and Compressibility-Weighted Ultrasound Scattering Tomography

Quinn Barber¹, Roger Zemp²

¹University of Alberta, Edmonton, AB, Canada, ²University of Alberta, Canada

Background, Motivation, and Objective

Microcalcifications (MC) in breast tissue are an early indicator of breast cancer, however, for conventional ultrasound, they are difficult to discern from background speckle. High resolution and high depth of imaging are also important for MC imaging. We develop a novel reconstruction technique for ultrasound tomography (UST) that can amplify signal from highly-dense scatterers while suppressing background speckle. Our technique exploits the fact that a scatterer's compressibility produces monopole scattering profiles, while its density produces dipole scattering profiles. Because UST grants us ultrasound scatter data from a wide range of angles, we utilize this anisotropy to produce compressibility- and density-weighted images (C-WI and D-WI). MCs are highly dense, thus we propose that this technique will allow better differentiation of MCs, compared to conventional ultrasound imaging. UST is also capable of isotropic resolution reaching the half-wavelength diffraction limit at depths of 5 cm.

Statement of Contribution/Methods

We developed a novel reconstruction method to form C-WI and D-WI using conventional UST data. By weighting each signal trace by the cosine of the appropriate scattering angle, we can amplify the angle-dependent signal due to the target's density and suppress the angle-independent signal due to its compressibility. Delay-and-sum is then applied to form the final images. First, simulations were conducted to show the efficacy of these techniques. A phantom study (with compressible and dense scatterers placed in a scattering medium) was then performed. We used a 256-element, 256°, 5 MHz ring array transducer coupled to a Verasonics ultrasound platform. Resolution measurements were conducted for C-WI and D-WI.

Results/Discussion

Resolution was measured to be ~150 µm for the new reconstruction technique. We found that we could better differentiate between dense and compressible targets and suppress background signal in our D-WI (compared to C-WI, see Fig 1). We also compared our method to a 5 MHz linear array, and found a 6.5x enhancement in our minimum-detectable density-contrast sensitivity. We believe these results demonstrate the benefit of our method for MC imaging.

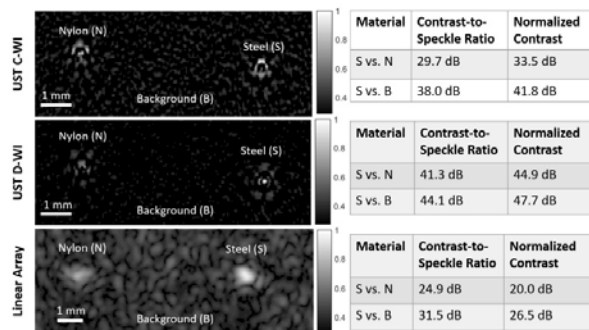


Fig 1. UST C-WI, UST D-WI and Linear Array images of nylon and wire phantoms in a scattering medium. Contrast-to-Speckle (difference in signal between A vs B divided by the variance of speckle) and Normalized Contrast (difference in signal between A vs B normalized by the mean of the background signal) for each image is found on the right.

The Ultrasound File Format

Olivier Bernard¹, David Bradway², Hendrik Hansen³, Pieter Kruijzinga⁴, Arun Nair⁵, Dimitris Perdios⁶, Stefano Ricci⁷, Ole Marius Hoel Rindal⁸, Alfonso Rodriguez-Molares⁹, Matthias B. Stuart¹⁰, Carlos Villagomez-Hoyos¹¹, Pedro Santos¹²

¹CREATIS, Lyon, France, ²Duke University, United States, ³Medical UltraSound Imaging Centre, Radboud university medical center, NIJMEGEN, Netherlands, ⁴Erasmus MC, Rotterdam, Netherlands, ⁵Johns Hopkins University, United States, ⁶Signal Processing Laboratory 5, Ecole Polytechnique Fédérale de Lausanne, Lausanne, Switzerland, ⁷University of Florence, Italy, ⁸Informatics, University of Oslo, Norway, ⁹Department of Circulation and Medical Imaging, and CIUS, Norway, ¹⁰Technical University of Denmark, Lyngby, Denmark, ¹¹Technical University of Denmark, Denmark, ¹²Cardiovascular Sciences, KU Leuven, Leuven, Belgium

Background, Motivation, and Objective

Systems able to save channel data have become widely available in research laboratories, making possible the development of advanced sequences and processing techniques. Despite of its popularity, channel data is often stored in custom formats, defined by the laboratories according to their research interests and preferred processing tools.

Custom formats hinder data dissemination as they rarely include proper documentation. Custom formats are frequently fitted to specific sequences, systems, or array geometries, and often omit information that would be required by a third party to use the data. Custom formats are difficult to maintain or expand, and rely heavily on “patches” to be adapted to new scenarios.

During the IEEE IUS 2017 conference, 11 research groups met to start the Ultrasound File Format (UFF) initiative. The 11 groups agreed upon the need for a common format for channel and beamformed data that would facilitate dissemination of data, replication of results, and comparison of processing techniques.

Statement of Contribution/Methods

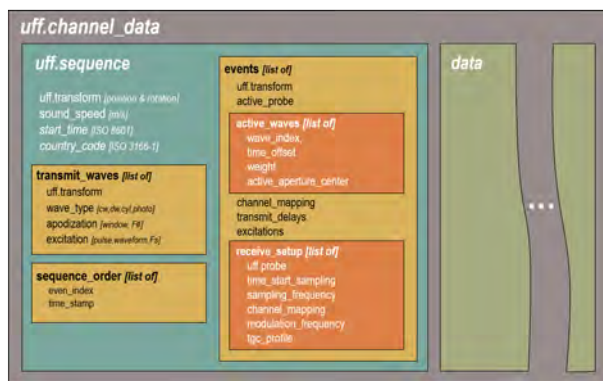
After the initial meeting at IUS, the UFF taskforce was created, formed by one member from each laboratory, with the objective of developing the format. The taskforce started by examining the formats in use in each of the laboratories. Differences, advantages, and disadvantages were discussed.

It was agreed that the Hierarchical Data Format (HDF5) will be used due to its ability to store and organize large amounts of data. HDF5 is platform independent, and many scientific and programming environments already include APIs to interact with it.

Results/Discussion

Currently, the taskforce works on the first UFF draft. Solutions are being tested to cover any probe geometry, and all the sequences in the state-of-the-art. Effort is being put into making the format as general as possible, without sacrificing efficient data access. The Figure below shows the structure at present. More information can be accessed at https://bitbucket.org/ultrasound_file_format/uff/src/master/.

The UFF taskforce believes this initiative will support a more transparent dissemination of research. Enabling data sharing and comparison of results will render into a higher impact on society. A common format will also bring a boost in productivity by reducing the amount of time that each laboratory must invest in maintaining and expanding their own format.



Improving quality of high-frame-rate imaging with coherent and incoherent processing

Jian-yu Lu¹

¹Bioengineering, The University of Toledo, Toledo, OH, United States

Background, Motivation, and Objective

High-frame rate (HFR) imaging based on Fourier reconstruction was first developed in late 1990s and has found many applications in recent years. Steered plane wave (SPW) and limited-diffraction beam (LDB) are two HFR imaging methods, where images are reconstructed with either coherent (high contrast but high speckle noise) or incoherent (low speckle noise but low contrast) superposition of sub-images obtained from different transmissions.

Statement of Contribution/Methods

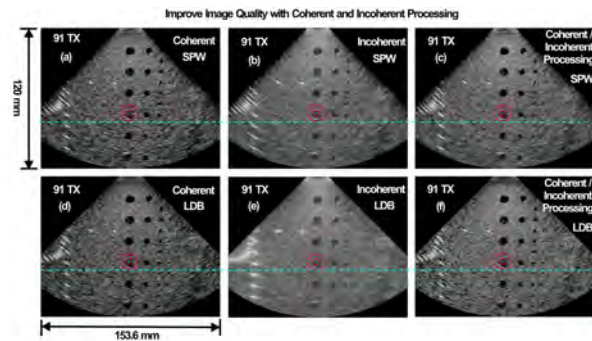
In this paper, a coherent and incoherent processing method was developed to obtain images of both high contrast and low speckle noise. In this method, the incoherent image is divided by the coherent image to obtain a ratio image. The ratio image is used to determine the portions of the coherent image to be used to modify the corresponding portions of the incoherent image.

Experiment was performed with a home-made HFR imaging system to demonstrate the efficacy of the method. In the experiment, a wide-band transducer of 128 elements and 2.5-MHz center frequency was used. The dimensions of the transducer aperture were 19.2-mm (width) and 14-mm (height). An ATS539 tissue-mimicking phantom was used. The dimensions of the reconstructed images of the phantom were 153.6 mm in width and 120 mm in depth. Images were log-compressed at 50 dB dynamic range.

Results/Discussion

Images reconstructed with SPW and LDB methods are shown in the first (Figs. (a), (b), and (c)) and second (Figs. (d), (e), and (f)) rows, respectively. Images obtained with coherent superposition (Figs. (a) (signal-to-noise ration or SNR=41.33dB and contrast C=-26.10) and (d) (SNR=39.23dB and C=-24.67)), incoherent superposition (Figs. (b) (SNR=54.26dB and C=-11.97) and (e) (SNR=76.72dB and C=-10.35)), and the coherent and incoherent processing method (Figs. (c) (SNR=50.35dB and C=-27.00) and (f) (SNR=48.27dB and C=-27.42)) are shown in the first, second, and third columns, respectively. The SNR was calculated (average of pixel values divided by the standard deviation) along the horizontal dashed lines (cyan color) and the contrast was calculated with the average value of pixels in the green circle divided by that of pixels in the background area between the two red circles.

The results show that images obtained with the newly developed coherent and incoherent processing method can have both high image contrast and low speckle noise (high SNR).



Synthetic transmit aperture beamforming for sound velocity estimation using channel-domain differential phase gradientChe-Chou Shen¹, Sheng-Hsuan Hsiao¹, Kuan-Lin Tu¹¹*Department of Electrical Engineering, National Taiwan University of Science and Technology, Taipei, Taiwan***Background, Motivation, and Objective**

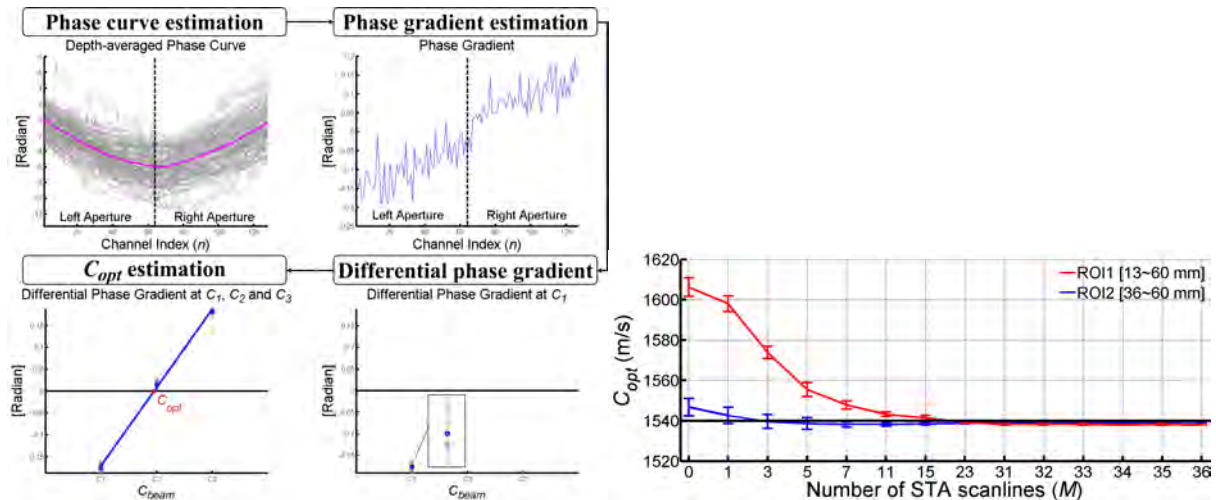
Loss of ultrasound image quality occurs due to mismatch between beamforming sound velocity (C_{beam}) and tissue sound velocity (C_t). Channel-domain phase gradient (ϕ_x) has been proposed to optimize C_{beam} but its efficacy is limited to transmit focal depth which is difficult to locate with unknown C_t . At non-focal depth, however, low spatial coherence of channel signal often leads to over-estimation of sound velocity.

Statement of Contribution/Methods

To reduce the estimation bias from transmit focal localization, synthetic transmit aperture (STA) beamforming is utilized to restore the spatial coherence of the entire image depth. After combining channel signals in adjacent scanlines, the optimal sound velocity is determined by taking linear regression to find the zero of differential phase gradient ($\Delta\phi_x$) between the left and right sub-apertures after depth and scanline averaging as shown in Figure 1.

Results/Discussion

Ultrasonic image of speckle phantom is simulated with $C_t = 1540$ m/s and transmit focus at 55 mm. The proposed sound velocity estimation is performed with two ROIs of different depth ranges (ROI1: 13~60 mm and ROI2: 36~60 mm) in Figure 2. As the number of combined scanlines (M) in STA beamforming increases, the estimated sound velocity in both ROIs converges to 1540 m/s. When $M = 31$, the estimated sound velocity in ROI1 is 1538.2 ± 0.4 m/s. In experiments using ATS commercial phantom, the estimated sound velocity is 1441.3 ± 1.2 m/s, which is close to its nominal value of 1440.5 m/s at 23°C. Results indicate that channel-domain phase gradient estimation in combination with STA beamforming can provide robust C_{beam} optimization even when the ROI contains non-focal depth. This method could be recursively applied to minimize the bias between optimized C_{beam} and C_t .



Efficient Pseudo-dynamic Delay Calculation using Optimal Zone Segmentation for Ultra-portable Ultrasound Imaging System

Pilsu Kim¹, Jeeun Kang², Tai-kyong Song¹

¹Department of Electronic Engineering, Sogang University, Korea, Republic of, ²Russell H. Morgan Department of Radiology, Johns Hopkins University, Baltimore, MD, United States

Background, Motivation, and Objective

A dynamic delay calculation is a burden within the limited resources of an ultra-portable ultrasound imaging. A pseudo-dynamic delay calculation (PDC-Conv) method dividing imaging depth into zone segments with uniform length. However, there have been no clear design guidelines to regulate beamforming accuracy and hardware complexity. In this paper, we propose an efficient PDC method using optimal zone segmentation with non-uniform intervals (PDC-Optimal) for an ultra-portable ultrasound imaging system.

Statement of Contribution/Methods

The PDC-Optimal method is implemented using a delay accumulator and LUT allocated in a channel (Fig. a). The LUT stores a preset for each zone segment: the zone segment length and a delay increment. Each preset parameter is determined based on a heuristic optimization to restrict the delay error between pseudo and ideal delays with an user-definable error allowance, τ . In Field-II simulation evaluation, the imaging specifications were assumed based on a 15-MHz linear array transducer with 100 μm of element pitch. Target imaging depth was set to 20 mm. Note that the identical LUT size was used for PDC-Conv and PDC-Optimal methods. We also implemented/synthesized a 32-channels portable system of a conventional dynamic delay calculation (DDC) and PDC-Optimal methods on Artix-7 FPGA (xc7A200T, Xilinx Inc., US).

Results/Discussion

Fig. b presents the mean number of zone segments and LUT size as a function of bit quantification (i.e., Q). The lower or higher Q than optimal point presented suboptimal LUT size due to a lack of resolution for error regulation or wider bit width, respectively. The LUT size could be alleviated with the higher τ with the reduced number of zone segments. A Field-II simulation presents that the PDC-Optimal method yielded the better image quality than that by PDC-Conv method (Fig. c). The correlation coefficient to that of DDC was shown as follows: 1.00 ± 0.00 , 0.99 ± 0.00 , 0.97 ± 0.01 , 0.84 ± 0.05 for PDC-Optimal method and 0.99 ± 0.01 , 0.98 ± 0.01 , 0.82 ± 0.27 , 0.60 ± 0.28 for PDC-Conv method were for 0.125 , 0.25 , 0.5 , and 1 of τ , respectively. In addition, the PDC-Optimal method significantly alleviates the hardware complexity compared to DDC: 84.30% and 87.53% of the reduction in the use of flip-flops (FF) and LUT, which lead to up to 94.53 % less dynamic power consumption.

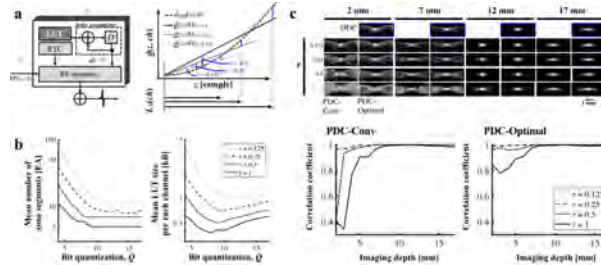


Fig. (a) The schematic diagram of the proposed PDC-Optimal method. (b) the mean zone size and LUT size averaged over entire channels as a function of bit quantification and τ . (c) Representative point-spread functions at 2-, 7-, 12-, and 17-mm depth. Correlation coefficients of PSF in (b) PDC-Conv and (c) PDC-Optimal methods for varying τ .

P1-B3 - Microbubbles, Droplets, and Nanoparticles

Kairaku (posters 1)

Wednesday, October 24, 9:30 AM - 4:00 PM

Chair: **Katsuro Tachibana** Fukuoka University

P1-B3-1

Reduction of ultrasound energy to induce cellular damage by selective intracellular aggregation of phase-change nano-droplets

Ayumu Ishijima¹, Takashi Azuma², Satoshi Yamaguchi³, Etsuko Kobayashi⁴, Yoshikazu Shibasaki³, Teruyuki Nagamune^{5,6}, Ichiro Sakuma^{1,4,6}

¹Medical Device Development and Regulation Research Center, The University of Tokyo, Japan, ²Center for Disease Biology and Integrative Medicine, The University of Tokyo, Japan, ³Research Center for Advanced Science and Technology, The University of Tokyo, Japan, ⁴Department of Precision Engineering, The University of Tokyo, Japan, ⁵Department of Chemistry & Biotechnology, The University of Tokyo, Japan, ⁶Department of Bioengineering, The University of Tokyo, Japan

Background, Motivation, and Objective

Phase-change nano-droplets (PCNDs) are ultrasound responsive liquid state perfluorocarbon (PFC) nanoparticles that vaporize into microbubble upon ultrasound exposure with sufficient peak negative pressure. Recent studies utilized the mechanical effects of the vaporization phenomena for treating tumour. In terms of avoiding the damage to the non-targeted tissue sites, ultrasound energy to induce vaporization must be low enough to avoid non-specific cavitation.

Statement of Contribution/Methods

Here we showed that pressure threshold to induce cellular damage through vaporization can be significantly reduced by selectively introducing PCNDs inside the targeted tumour cells. In order to introduce PCNDs selectively to the targeted tumour cells, a monoclonal antibody 9E5 was conjugated to the PCND. Previously we have shown that 9E5-conjugated PCNDs can be selectively introduced inside the tumour cells and exposure of ultrasound induced intracellular vaporization that leads to rapid disruption of cellular structure [1]. In this study, we compared the cytotoxicity of vaporization inside and outside the cells and showed that intracellular delivery of PCNDs can reduce the required ultrasound energy to damage cells by vaporization.

Results/Discussion

Confocal laser scanning microscopy (CLSM) observation clearly showed the selective targeting and intracellular aggregation of 9E5-conjugated PCNDs toward DLD-1 cells (Fig 1). Comparison on the cytotoxic effects of outside and intracellular vaporization indicated that the significant cell viability decreases were observed for the cells which incorporated PCNDs after ultrasound exposure of 5 MHz, 5 cycles, 2.0 MPa ($59 \pm 10\%, N = 5, p < 0.01$), whereas the viability did not decrease for the cells without PCNDs-incorporation but with PCNDs-attachment to the cellular membrane ($87 \pm 3\%, N = 5$). These results indicated that selective intracellular delivery of PCNDs can reduce the required ultrasound pressure to damage cells through vaporization. Although the strategy to reduce the vaporization threshold by using non-selective cellular function (phagocytosis) have reported previously [2], this is the first report to show in a selective manner.

References

- [1] A. Ishijima *et al.*, *Scientific Reports*, vol. 7, 44077, 2017.
[2] A. L. Martin *et al.*, *Ultrasound in Medicine & Biology*, vol. 38, no. 10, pp. 1799–1810, 2012.

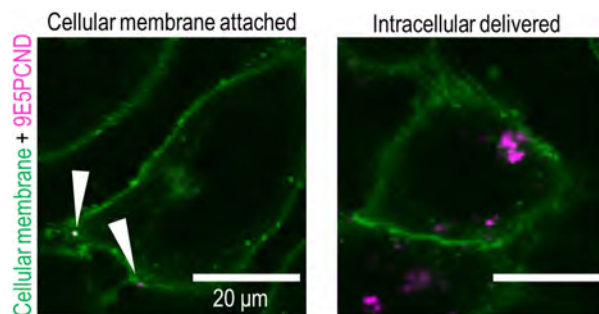


Fig. 1 | CLSM images of cellular membrane attached PCNDs and intracellular aggregated PCNDs.

Acoustic droplet vaporization induced physicochemical effects at the single-cell level**Ching-Hsiang Fan¹, Yi-Ting Lin¹, Yu-Chun Lin², Chih-Kuang Yeh¹**¹*Department of Biomedical Engineering and Environmental Sciences, National Tsing Hua University, Taiwan*, ²*Institute of Molecular Medicine, National Tsing Hua University, Taiwan***Background, Motivation, and Objective**

The medical application of acoustic droplet vaporization (ADV) conducted by perfluoropentane droplets with ultrasound have been widely explored. However, one of the major challenges for successfully developing of ADV-associated therapy as an effective and safe strategy is hard to precisely estimate the spatially cellular bioeffects after ADV. This study combined high-speed camera imaging and live-cell microscopic imaging to observe droplets transient dynamics during ADV and to evaluate the mechanical force to cells. In other words, the dynamic behaviors of droplets near cells, droplets-cell interactions, and associated cell responses at the single-cell level were investigated in this study.

Statement of Contribution/Methods

C6 glioma cells were co-incubated with Dil-labeled droplets (diameter: 1.5 μm). An acousto-optical system that allowed high-speed bright field (500 kfps) and fluorescence (40 kfps) microscopic imaging for visualizing the dynamics of the droplets under ultrasound excitations (frequency = 5 MHz, pressure = 5-8 MPa, cycle number = 3, pulse number = 1). A live-cell microscopic imaging was used to monitor the cell morphology, cell membrane permeabilization, and cell viability by membrane-anchored Lyn-yellow fluorescence protein, Propidium Iodide staining, and Calcein Blue AM staining, respectively.

Results/Discussion

The spatial distribution of ADV-induced bioeffects could be well mapped with the physical dynamics of droplets vaporization. For droplets with 1.5 μm diameter, the distance threshold for ADV-induced cell death ($5.5 \pm 1.9 \mu\text{m}$) and reversible membrane permeabilization ($11.3 \pm 3.5 \mu\text{m}$) exhibited well correlation with the distance of ADV-bubble pressing downward to the floor ($5.7 \pm 1.3 \mu\text{m}$) and maximum distance of droplet expansion ($11.5 \pm 2.6 \mu\text{m}$), respectively. These distances were enlarged by increasing the droplet sizes and insonation acoustic pressures. The live-cell imaging results showed that ADV-bubbles would directly disrupt cell membrane layer and induce intensive intracellular substance leakage. Further, the droplets shed off the payload beyond maximum distance of droplet expansion during ADV. These suggested that the ADV could directly induce the adjacent cells death by physical force and perform enhanced-chemotherapy to distal cells, providing new insights into ADV-medicated physicochemical synergic effect for medical applications.

Effects of Pulse Length and Pulse Repetition Frequency on the Cavitation Dynamics of the flowing Microbubbles Population

Mouwen Cheng¹, Fan Li², Tao Han¹, Alfred C. H. Yu³, Peng Qin¹

¹Instrument Science and Engineering, Shanghai Jiao Tong University, China, People's Republic of, ²Medical Ultrasound, Shanghai General Hospital, China, People's Republic of, ³ECE, University of Waterloo, Waterloo, ON, Canada

Background, Motivation, and Objective

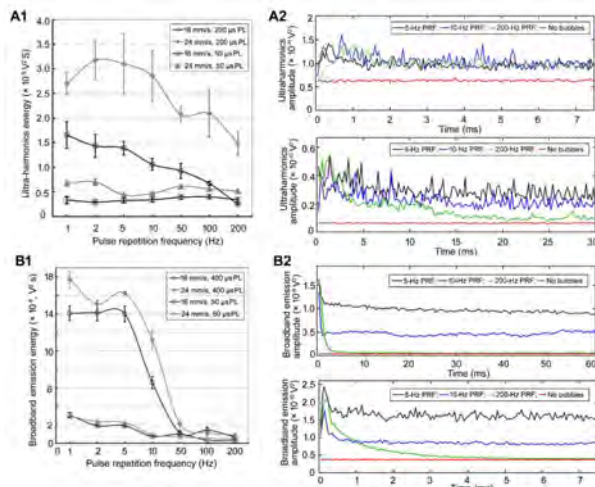
Acoustic cavitation could induce diverse bioeffects for therapeutic applications. To avoid under- or over-treated regions in targeted tissue and improve therapy efficacy and biosafety, it is crucial to design efficient acoustic pulses for producing adjustable cavitation activity with uniform distribution. This study aims to comprehensively understand how the pulse length (PL) and pulse repetition frequency (PRF) affect the magnitudes and temporal distributions of stable cavitation (SC) and inertial cavitation (IC) of the flowing bubbles.

Statement of Contribution/Methods

An in vitro phantom was fabricated to allow the bubbles to flow with a constant velocity. A spherical focused transducer (1 MHz, FWHM≈3 mm) was used to sonicate the flowing bubbles at a wide variation of peak negative pressures (PNPs) (0.1~1.2 MPa), PRFs (1~800 Hz) and PLs (10~600 µs). The signals from bubbles were passively detected by another 7.5 MHz plane transducer, and then recorded at 50-M samples s⁻¹. The ultra-harmonics and broadband emissions were respectively quantified to evaluate the energies of SC and IC in the focal region. The amplitudes change of the ultra-harmonics and broadband emissions with the acoustic pulses were used to respectively analyze the temporal distributions of SC and IC.

Results/Discussion

There is a PRF_{threshold} to ensure that the focal region could be filled with the flowing bubbles in the off-time between two pulses. The PRF_{threshold} could be approximately calculated by v / FWHM (v : fluid velocity, PRF_{threshold} is ~5.3 Hz at a 16 mm/s fluid velocity). We obtained the following results. 1. PRFs below threshold had no influence on the SC dynamics at shorter or longer PLs. However, the effect of PRFs above threshold on the SC dynamics was dependent on PL due to acoustically driven diffusion. Specifically, at shorter PLs, PRFs above threshold produced almost same SC energy with uniformly temporal distribution, but at longer PLs, SC energy, gradually reducing with the acoustic pulses, was negatively correlated with PRFs. 2. At either shorter or longer PLs, PRFs below threshold had no influence on the energy and dynamics of IC. Increasing PRF above threshold caused the decrease in the IC magnitude, which mainly dominated in the first pulses, and then followed by lower magnitude of IC. Such results could guide the design of acoustic pulses with respect to flow conditions for therapy.



The relationship between PRF and ultra-harmonics energy (A1) and broadband emission energy (B1) which were obtained in different PL and fluid velocity through 150 acoustic pulses.

The temporal-distribution of ultra-harmonics amplitude (A2) and broadband emission amplitude (B2) through 150 acoustic pulses at 5- (black line), 10- (blue line), and 200-Hz (green line) PRF

Tumor hypoxic microenvironment alteration and cancer therapy with biogenic nanoparticle-based oxygen delivery

Lin Song¹, Guohao Wang², Xuandi Hou³, Zhihai Qiu³, Lei Sun³

¹The Hong Kong Polytechnic University, Hong Kong, ²Department of Biomedical Engineering, The Hong Kong Polytechnic University, HONG KONG, Hong Kong, ³Department of Biomedical Engineering, The Hong Kong Polytechnic University, Hong Kong

Background, Motivation, and Objective

Tumor hypoxia is believed to be closely associated with increased tumor progression and aggressiveness, which hamper patients' survival. Direct or indirect methods of reducing hypoxic micro-environment would have considerable therapeutic value. Given the role of hypoxia in tumor progression and resistance to therapy, it has been considered to be a validated target of anticancer therapy. Besides developing drugs that could target hypoxia-related genes or change metabolism in hypoxic tumors, one main strategy to overcome tumor hypoxia is to increase the delivery of oxygen. Currently, there are no medications that can be administered to improve oxygen level at the tumor site. The recent development of novel oxygen-carrying particles may provide a possible means for local oxygen delivery and hypoxia alteration.

Statement of Contribution/Methods

In the present study, we explored the potential of nanometer size biogenic gas vesicles (GVs) as an oxygen carrier to alleviate tumor hypoxia. GVs are hollow bubbles formed by cyanobacteria with an average size of 100-300 nm. To achieve the goal of oxygen delivery, GVs were modified by a layer of polydopamine (PDA). The size and zeta potential of PDA-GVs were determined respectively.

Results/Discussion

We found that the size of the PDA-GVs (0.01mg/ml DA) was approximately 310nm. Moreover, PDA surface modification decreased the zeta potential of GVs and the negative charge of PDA-GVs was sufficiently high to prevent nanobubble aggregation (Fig.1.). Next, we tested the stability of PDA-GVs, the results showed that there were no significant size and concentration change for the prepared PDA-GVs formulation for 7 days (Fig.2.). What's more, to determine whether surface modification by PDA could increase the oxygen-carrying capability of GVs, we detected the oxygen content of the formulation with an oxygen purge (Fig.3.). We found that PDA-GVs showed superior oxygen carrying capacity than PBS. Next, we will evaluate and optimize the oxygen carrying capability of GVs in hypoxic solutions, cells, and *in vivo* tumor models. Also, the potential of GVs to revert the expression of hypoxia-related protein markers will be examined. In summary, PDA-GVs have a good potential to be as an effective oxygen carrier which may be applied to alleviate tumor hypoxia, as well as other hypoxia-related diseases in the future clinical treatment.

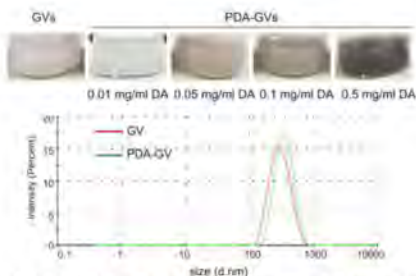


Figure 1. Photographic images and size distribution curves of GVs and PDA-GVs.

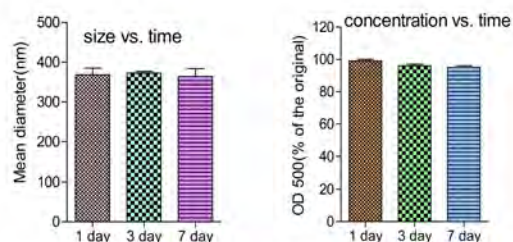


Figure 2. Stability of PDA-GVs over 7 days. Single PDA-GV particle size and concentration of PDA-GVs solution were determined respectively.

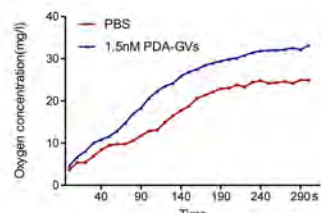


Figure 3. Oxygen concentration of PDA-GVs with an O₂ purge. PBS and PDA-GVs were purged with oxygen for 5 minutes. Oxygen content of these formulations were determined respectively. We can find that PDA-GVs showed superior oxygen carrying capacity than PBS.

Acoustic phase-shift nanodroplets mediated miRNA therapy for hepatocellular carcinomaWei Dong¹, Jixiu Huang¹, Jiangying Long¹, Di Zhou¹, Xinxing Yang², Shanshan Xu¹, Yi Feng¹, Mingxi Wan¹, Yujin Zong¹¹*Department of Biomedical Engineering, Xi'an Jiaotong University, China, People's Republic of*, ²*Xijing Hospital, Fourth Military Medical University, China, People's Republic of***Background, Motivation, and Objective**

PIK3CA encoded the p110 α subunit that was frequently mutated or amplified in solid and hematological tumors, including hepatocellular carcinoma (HCC). Post-transcriptional regulation on the suicide gene could be an effective way to treat cancers. For successful therapy, it is necessary to efficiently deliver gene into cancer cells. This study aimed to find a most effective miRNA inhibiting PIK3CA, and then attempted to utilize submicron acoustic phase-shift nanodroplet (PSND) as a vector to deliver pre-miRNA plasmid to enable efficient transfection after ultrasound (US) activation.

Statement of Contribution/Methods

We summarized all the proven miRNAs targeting PIK3CA that were down-regulated in HCC reported in previous literature by prediction online. Then qRT-PCR and western-blots were performed to verify the inhibitory effect after SMMC-7721 cancer cells were transfected with pre-miRNA plasmids. Additionally, lipid-shelled NDs were prepared by sonicating the mixture of hydrated lipid and C₅F₁₂. The pre-miRNA plasmid was electrostatically bound to the ND surface and delivered to the SMMC-7721 cells under 1.2 MHz focused US exposure. During US exposure, passive cavitation detect was used to monitor and quantify the phase-shift. After treatment, expression of GFP fluorescent protein in the cells was detected by fluorescence microscopy and flow cytometer. And then qRT-PCR and western-blots were performed to validate the gene therapeutic effect. The *in vivo* effect of PSNDs mediated miRNA delivery was evaluated by measuring the tumor size of mouse xenograft HCC model.

Results/Discussion

The qRT-PCR and western-blots results revealed that has-pre-miR-378a, one of the five down-regulated miRNAs, could most effectively inhibit the expression of PIK3CA in HCC (Fig. 1). The mean diameter of NDs was about 300 nm as determined by dynamic light scattering, and the zeta potential was about +20 mV. The fluorescent results showed that PSNDs combined with 1.2 MHz US exposure (5.5MPa peak negative pressure) could effectively transfect pre-miRNA plasmid into the cells (Fig. 2A,C). Although with the increase of pulse duration (60 to 100 cycles), the numbers of cells detached from petri dish increased, many detached cells were still transfected (Fig. 2B,D). The treatment effect of pre-miRNA plasmid transfected under PSNDs acoustic vaporization was validated on the mouse model.

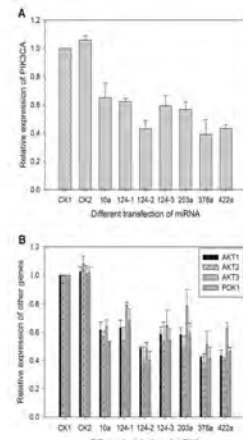


Fig. 1 Expressions of PIK3CA and downstream genes

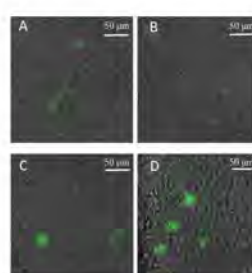


Fig. 2 GFP fluorescence microscopic image in cells after ultrasonic treatment (5.5MPa negative peak pressure, 40Hz pulse repetition frequency, A: 60cycles, attached cell; B: 60cycles, detached cell; C: 100cycles, attached cell; D: 100cycles, detached cell)

Real-time investigation of cell membrane damage induced by acoustic droplet vaporization in tissue mimicking hydrogelLei Zhang¹, Yi Feng¹, Dui Qin¹, Han Liu¹, Guoyou Huang¹, Ayache Bouakaz², Mingxi Wan¹¹School of Life Science and Technology, Xi'an Jiaotong University, China, People's Republic of, ²Université François Rabelais, Tours, France**Background, Motivation, and Objective**

Acoustic droplet vaporization (ADV) has shown a great potential in extravascular tumor-targeted theranostics. It might also cause cell dysfunction with significant irreversible cell damage *in vivo* or *in vitro*. However, the interaction of cells with droplets in the tissue remains not very clear. Thus, a tissue mimicking hydrogel was introduced to the study. The interaction of cells with droplets in hydrogel was studied with high-speed microscopic imaging and fluorescence imaging.

Statement of Contribution/Methods

Tissue mimicking hydrogel with different stiffnesses was prepared with the mixture of collagen and HeLa cervical cancer cell line ($10^7/\text{ml}$). Perfluoropentane (PFP) nanodroplets (1-3 %, v/v) was mixed into the cell culture and filled around the tissue hydrogel. ADV was triggered with a single pulse (5 MHz, 10 μs , 4.2 MPa) focused on the cell in hydrogel. A confocal acousto-optical microscopic system was used to investigate the process of ADV on nearby cells in hydrogel in real time with high-speed microscopic imaging and fluorescence imaging. Calcein-AM and Propidium iodide (PI) was used to indicate cell membrane integrity and evaluate cell viability after ADV in real-time.

Results/Discussion

Upon ultrasound exposure, rapid ADV and subsequent ADV bubble-cell interaction caused irreversible cell damage in a distance-dependent manner (Fig. 1). PI uptake vs. time shows an increase of the intracellular fluorescence intensity in the cell indicating cell damage which might be attributed to the formation of irreversible pores on the cell membrane (Fig. 2). Compared to the effects of ADV on cells *in vitro*, the distance to induce irreversible cell damage in mimic tissue hydrogel reduced significantly. SEM images reveal the formation of voids or holes in hydrogel (Fig. 3) which give the droplets enough space to move freely in the hydrogel. The elasticity of hydrogel makes the cells avoid from the direct mechanical forces of ADV, might be the main reason. It revealed that increasing the local concentration of droplets would be important to achieve effective cell damage *in vivo*.

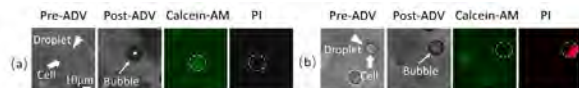


Figure 1. (a) Bright-field, Calcein-AM and PI fluorescence images of survived HeLa cell Post-ADV. (b) Bright-field, Calcein-AM and PI fluorescence images of damaged HeLa cell Post-ADV.

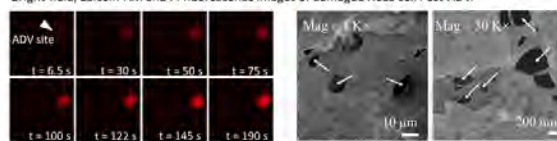


Figure 2. Time-lapse fluorescence images of damaged HeLa cell Post-ADV.

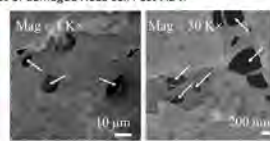


Figure 3. The hole in hydrogel [Collagen Concentration 3mg/ml] by SEM.

Lysosome Exocytosis Involved in the Resealing of the Perforated Membrane by Acoustic Cavitation
Caixia Jia¹, Jianmin Shi¹, Tao Han¹, Ping Cai¹, Alfred C. H. Yu², Peng Qin¹
¹*Instrument Science and Engineering, Shanghai Jiao Tong University, China, People's Republic of*, ²*ECE, University of Waterloo, Waterloo, ON, Canada*
Background, Motivation, and Objective

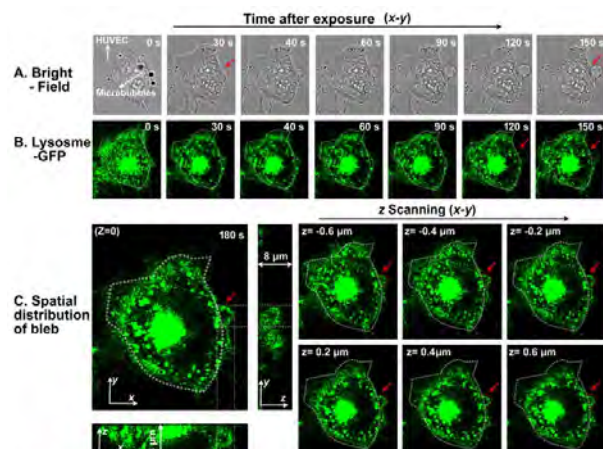
Sonoporation entails two sequential biophysical processes, membrane perforation by acoustic cavitation, and pore resealing through biological mechanism. The resealing ability of perforated membrane dominates the short- and long-term fate of the sonoporated cells, thereby affecting therapy efficiency and biosafety. Although early studies showed some blebs protruded around the sonoporated cell's membrane, it remains unclear which cellular mechanisms mediate the formation of blebs for membrane resealing. To clarify this question, based on the membrane resealing theory, we hypothesize that lysosome exocytosis may be involved in the blebs formation to reseal the perforated membrane by cavitation.

Statement of Contribution/Methods

A customized platform was used for 1.5 MHz ultrasound exposure (13.33 μ s duration and 0.70 MPa peak negative pressure) and recording cellular responses at the single cell level. The collapse of microbubble was triggered to induce the localized membrane perforation of the Hela cervical cancer cell. Propidium iodide and Calcein Blue-AM were used to evaluate the degree of sonoporation. The spatiotemporal dynamics of the lysosomes was analyzed by 3D imaging the transfected luminal domain Lamp-1 with green fluorescence protein at 20-s interval over 15-min post-exposure.

Results/Discussion

The following results were obtained. 1. During the perforated membrane resealing, a single bleb, which spatially located at the perforation site, began to emerge, and then gradually expanded to spherical shape, subsequently gently contracted to disappear. This dynamic process maintained about hundreds of seconds, and the temporal-duration and spatial size of the bleb were positively correlated with the degree of the reversible sonoporation. 2. During the expansion of bleb, some lysosome-GFP was observed in the contour of the bleb at different time-points post-exposure (Fig. B), suggesting lysosomes were delivered to the membrane surface by exocytosis, and then fused with membrane to facilitate resealing. Fig. C by scanning multi-z axis positions showed lysosome-GFP nonuniformly distributed in the periphery of the bleb in xz and yz planes. These results suggest lysosome exocytosis is involved in the resealing process of perforated membrane, and provide new evidence to reveal the resealing mechanism of the perforated membrane by cavitation.



Time-lapse observations of the morphology of the cell (A) and intracellular lysosomes distribution (B) in x - y plane before and after ultrasound exposure. (C) The spatial distribution of lysosomes around bleb in multi- z axis positions.

Experimental study for active control of bubble-surrounded cells by acoustic radiation force with considering optimal production and cell viability
Kohji Masuda¹, Takuya Otsuka¹, Masakazu Seki¹, Riki Oitate¹, Johan Unga², Ryo Suzuki², Kazuo Maruyama²
¹Tokyo Univ. of A&T, Japan, ²Teikyo Univ., Japan

Background, Motivation, and Objective

To contribute various cellular immune therapies, we proposed a method to carry therapeutic cells under ultrasound exposure, which is based on the production of bubble-surrounded cells (BSCs). Although the controllability of BSCs under ultrasound exposure has been confirmed in advance, we were unable to optimize the condition to produce BSCs. Furthermore, the viability of the cells in BSCs after ultrasound exposure has not investigated. In this study, we report our attempts of induction performance of BSCs under observation of fluorescent imaging considering the cell viability.

Statement of Contribution/Methods

We introduced CD8-positive T lymphocytes as the cells, which were dyed with tetramethyl rhodamine. We have also prepared anti-CD8 antibody-modified bubbles, where the antibody was covalently linked onto the surface. The suspension of the cells and the bubbles was diluted in phosphate-buffered saline, where the adhesion of bubbles onto the cells was enhanced. Then the viability of the cells was investigated using Cell Counting Kit-8 after various conditions of burst wave exposure. Next, an artificial blood vessel with a bifurcation was used for induction of BSCs to a lower path by acoustic radiation force, where a pair of identical ultrasound transducers emit plane waves to produce and sweep the nodes in the standing wave.

Results/Discussion

We have optimized the bubble concentration upon production of BSCs as shown in Fig.1, where the cell concentration at $1.0 \times 10^5/\text{mL}$ and the bubble concentration at 0.3 mg/mL . According to the cell viability investigation, when the sound pressure was limited to 400 kPa-pp for the duration of exposure of 60 s , we confirmed there was no significant effect in the cell viability except the specific condition of BSCs with the frequency of 3 MHz , where the viability decreased to 70% .

Fig.2 shows the fluorescent images of the bifurcation under continuous ultrasound exposure at a maximum sound pressure of 200 kPa-pp for each transducer with a node velocity of 5 mm/s . There was a significant induction of BSCs to a lower path with the frequency of 3 and 5 MHz . However, when the frequency was 7 MHz , we found no effect of induction despite the node intervals in a standing wave become narrower. Therefore, we have to consider not only the cell viability but also ultrasound attenuation at higher frequencies rather than the node intervals.

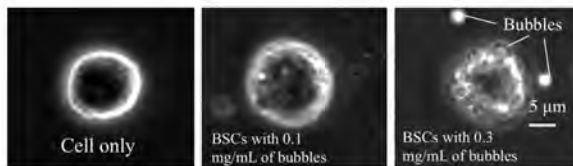


Fig.1 Microscopy images of a cell and BSCs

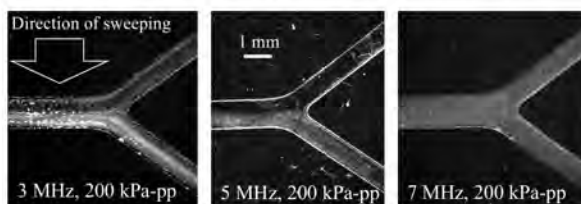


Fig.2 Fluorescence images in artificial blood vessel under ultrasound exposure when the suspension of BSCs was injected

Ultrasound-Induced Acid-Base Neutralization-Generated CO₂ microbubbles on Epidermal PenetrationHui-Ching Hsu¹, Yi-Ju Ho¹, Chih-Kuang Yeh¹¹*Department of Biomedical Engineering and Environmental Sciences, National Tsing Hua University, Taiwan***Background, Motivation, and Objective**

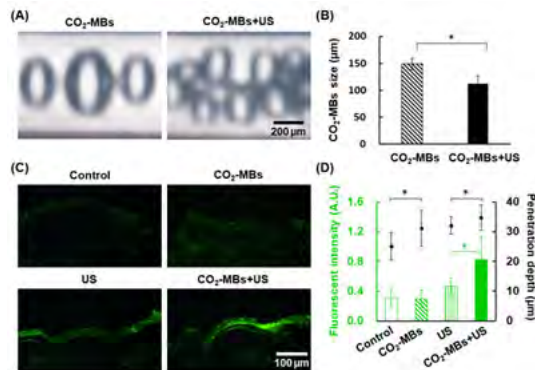
The stratum spinosum of epidermis (30–50 μm in depth) distributes Langerhans cells, which can activate adaptive immunity after epidermal vaccination. However, the epidermal diffusion of vaccine (50–100 kDa) might restrict penetration depth and induce skin allergies to influence immune activation. Ultrasound (US)-induced microbubble cavitation increases cellular permeability for drug penetration to provide a potential way for improving the efficiency of vaccine penetration. Therefore, our study investigated the epidermal penetration to evaluate the feasibility of non-invasive vaccination by using US-induced acid-base neutralization-generated CO₂-microbubbles (CO₂-MBs) cavitation.

Statement of Contribution/Methods

In this study, we applied the acid-base neutralization-generated CO₂ to simply produce MBs for US theranostic applications. CO₂-MBs were generated by mixing the 7% citric acid solution and 3% NaHCO₃ in propylene glycol (volume ratio of 1:1). The size and number of CO₂-MBs generated by US stimulation (3.1 MHz, 2 W/cm², 50% duty cycle) were quantified in the PE100 tube with the flow rate of 20 mL/h under microscope. The *in vivo* epidermal penetration was investigated on the abdominal skin of Sprague-Dawley rats ($N=12$). After CO₂-MBs generation and cavitation by US stimulation, FITC-conjugated hyaluronic acid (100–300 kDa) was applied evenly on the skin and then rested 15 min for penetration. Finally, the skin tissue was sectioned to evaluate the improvement of penetration depth by US-induced CO₂-MBs cavitation.

Results/Discussion

The mean size and number of CO₂-MBs generation was 112±14 μm and 318±83 MBs/10 s under US stimulation. In the CO₂-MBs+US group, fluorescent intensity and penetration depth was improved 2.8±1.0-fold and 1.4±0.1-fold relative to the control group ($p<0.01$). Epidermal penetration depth of 34.6±4.3 μm induced by CO₂-MBs with only 1 min US sonication revealed the possibility of promoting vaccine penetration into stratum spinosum. Moreover, CO₂-MBs might regulate vascular permeability to further assist the efficiency of drug or vaccine delivery. Our study proposed to establish a product combining acid-base neutralization-generated CO₂-MBs, vaccine/drug, and commercial US instrument for personal medicine in future.



Microscopic examination of sonothrombolysis process inside the transparent to ultrasound parallel plate flow chamber

Wojciech Secomski¹, Ziemowit Klimonda¹, Katarzyna Majka^{2,3}, Robert Olszewski¹, Andrzej Nowicki⁴

¹Institute of Fundamental Technological Research, Poland, ²Military Institute of Medicine in Warsaw, Poland, ³Medical University of Warsaw, Poland, ⁴Department of Ultrasound, Institute of Fundamental Technological Research, Polish Academy of Sciences, Warsaw, Poland

Background, Motivation, and Objective

Parallel plate flow chambers are widely used for the cell research in conditions of constant or pulsatile liquid flow. They are also used to analyze the formation of thrombi. Authors designed a flow chamber that is transparent to ultrasound, thus enabling the microscopic observation of the thrombus dissolution process by interaction of drug, microbubbles and ultrasound in real time, in-vitro.

Statement of Contribution/Methods

Sonothrombolysis was performed for nine ultrasound frequencies from 40 kHz to 6 MHz at space averaged time averaged intensities of 0.4 – 1.6 W/cm². 1 mm thick slices of the human blood clots were exposed to ultrasound in presence of the Actilyse tissue plasminogen activator at concentration of 10 µg/ml flowing around the sample. Next the Sonovue microbubbles at concentration of 3x10⁵/ml effect on the dissolution of the thrombus was investigated. Thrombus size changes were observed under a 4x magnification microscope and were recorded as a function of time.

Results/Discussion

The efficacy of thrombus dissolution was observed by means of a designed parallel plate flow chamber (fig.1) and the time of thrombus complete dissolution was measured. The best result was recorded for the 1 MHz frequency and 1.6 W/cm² intensity, where the thrombus was dissolved within 5.3 min (fig.2). The noticeable effect of microbubbles on the thrombolysis process appeared at 3.3 MHz; at an intensity of 1.6 W/cm², the thrombus dissolved in 12 minutes.

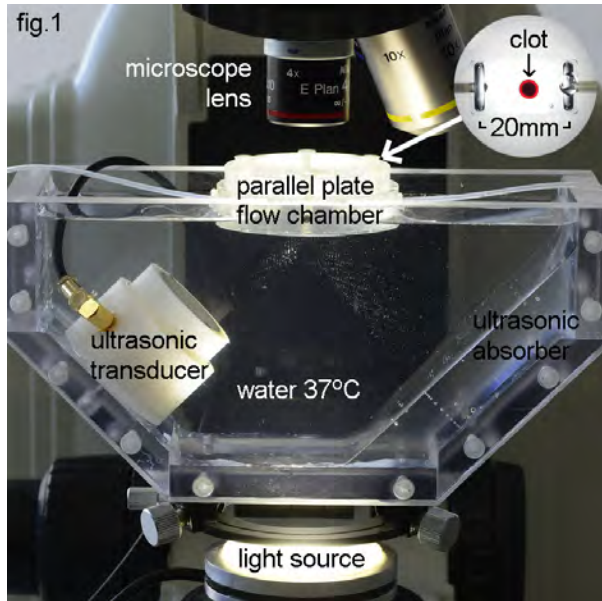
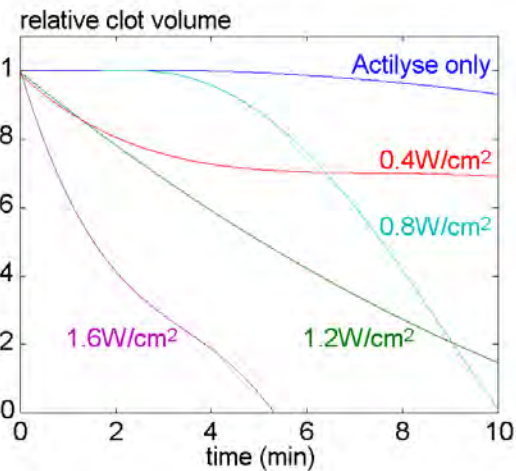


fig.2 relative loss of the clot volume under the influence of 1MHz ultrasound



P1-B4 - Acoustic Droplets and Bubbles Applications

Kairaku (posters 1)

Wednesday, October 24, 9:30 AM - 4:00 PM

Chair: **Klazina Kooiman** Erasmus Medical Center

P1-B4-1

Evidence of Laser-Activated Perfluorocarbon Nanodroplet Extravasation In Vivo

Steven K. Yarmoska¹, Heechul Yoon², Vadakkancheril S. Jisha², Yiyiing I. Zhu², Eleanor Donnelly², Stanislav Emelianov^{1,2}

¹Wallace H. Coulter Department of Biomedical Engineering, Georgia Institute of Technology and Emory University, Atlanta, GA, United States, ²School of Electrical and Computer Engineering, Georgia Institute of Technology, Atlanta, GA, United States

Background, Motivation, and Objective

Laser-activated perfluorocarbon nanodroplets (PFCnDs) are a promising ultrasound photoacoustic (USPA) contrast agent for extravascular imaging. Yet extravasation of PFCnDs has not been demonstrated in a realistic, orthotopic model of cancer. The objective of this work was to provide evidence of extravasation via a PFCnD capable of both USPA imaging and FRET fluorescent emission via histology.

Statement of Contribution/Methods

PFCnDs were made with a perfluorohexane (FluoroMed) core, lipid shell, and near-infrared (NIR) dye (Epolight 3072; Epolin) for optical droplet vaporization. The shell also included a 1:10 ratio of encapsulated Cy3 carboxylic acid (Lumiprobe) and Cy5 PE (Avanti), enabling intact PFCnDs to exhibit FRET. The ratio of PEG2000 PE (Avanti) to Cy5 PE to DSPC (NanoCS) was 8:1:1. PFCnD size distribution was assessed by a NanoSight NS300 (Malvern). Fluorescence emission was recorded by a spectrofluorometer (Fluorolog 3-21; Horiba). USPA images were captured by a Vantage 256 (Verasonics) driving an integrated USPA transducer (LZ400; VisualSonics) coupled to a 10 Hz pulsed Nd:YAG laser (Phocus Mobile; Optotek) outputting 1064 nm light. Six week old athymic female mice (nu/nu; JAX) were inoculated in the right-lower mammary fat pad with 1×10^6 4T1 rat breast carcinoma cells in a 1:1 mixture of media and Matrigel Matrix (Corning). Tumors were allowed to grow until they were 5-10 mm in diameter (1 week). After preliminary imaging, mice were injected with 70 μ L of 2×10^{10} PFCnD/mL solution via jugular vein. Mice were reimaged after 24 hours both *in vivo* and after perfusion prior to tumor resection.

Results/Discussion

PFCnDs had a median size of 240 nm (**Fig. 1A**). These PFCnDs exhibited on-particle FRET *in vitro* (**Fig. 1B**, bottom), with decreased observed fluorescent emission compared to Cy3-Cy5 nanomicelles (**Fig. 1B**, middle) likely due to particle scattering and NIR dye absorption. Imaging shows contrast enhancement at 24 hours compared to pre-injection imaging (**Fig. 1C**) in both PA and differential ultrafast US images (**Fig. 1D**). Contrast persists even after perfusion (**Fig. 1E**). These preliminary results suggest PFCnDs extravasated in an orthotopic primary breast tumor. Ongoing studies will examine histology for FRET signal from intact PFCnDs in the tumor stroma and attempt to localize these in the extravascular space by staining for vascular markers (e.g., VCAM-1).

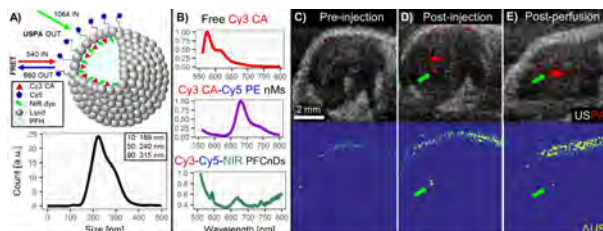


Fig. 1. (A) Cartoon schematic of near-infrared laser activated / FRET-trackable PFCnDs (top) with corresponding droplet size distribution from nanoparticle tracking analysis (bottom). (B) Normalized fluorescence emission [a.u.] after 540 nm excitation for Cy3 CA (top), Cy3 CA-Cy5 PE nanomicelles (middle), and multifunctional PFCnDs (bottom); USPA (top) and differential ultrafast US (bottom) images of the murine breast tumor during pre-injection imaging (C) as well as 24-hour post-injection imaging (D) and post-perfusion imaging (E) showing PFCnDs (arrow).

Ultrasound and Optical Imaging of Perfluorocarbon Nanodroplet Adhesion to Endothelial Cells under Atheroprone Flow Conditions

Ge Zhang¹, Kuin Pang^{1,2}, Mean Ghim¹, Peter D. Weinberg¹, Mengxing Tang¹

¹Department of Bioengineering, Imperial College London, London, United Kingdom, ²Institute of Molecular and Cell Biology, Agency for Science, Technology and Research (A*STAR), Singapore

Background, Motivation, and Objective

Ultrasound molecular imaging with microbubbles targeted to inflammatory activation of endothelium, which is involved in the initiation and progression of atherosclerosis, could improve risk stratification for atherosclerotic complications. Nanodroplets, may have advantages over microbubbles as they have smaller dimensions, a longer *in vivo* circulation time, and activation that can be controlled in both space and time. Such nanodroplets offer opportunities for ultrasound molecular imaging of atherosclerosis. In this study we investigated *in vitro* the targeting of native perfluorocarbon nanodroplets to endothelial cells under atheroprotective versus pro-atherogenic flow conditions.

Statement of Contribution/Methods

(Porcine Aortic Endothelial Cells) PAEC were seeded in 6 well-plates and cultured until confluent. The plates were placed on an orbital shaker in the incubator to allow cells to experience low magnitude multidirectional (pro-atherogenic) flow and high magnitude uniaxial (atheroprotective) flow in the centre or at the edge of the swirling well, respectively. Nanodroplets were added into the wells for 30 mins, followed by three washes before the ultrasonic exposure. A Verasonics 128 research platform equipped with a L11-4v probe was used to activate and subsequently image the nanodroplets. A customised ‘Imaging-Activation-Imaging’ Matlab script was used to transmit 8MHz, 2-cycle focus pulses ($MI=1.5$) to activate the nanodroplets and to perform a plane wave ($MI=0.1$) imaging at 4MHz.

Results/Discussion

Figure (a) shows, after ultrasonic activation, the signals from activated nanodroplets were predominantly located at the centre of the swirled well while the signals were uniformly distributed in the static well. Figure (b) shows microscopic images of activated nanodroplets on cells at the centre and edge of the well. A large number of activated nanodroplets adhered to PAEC sheared with pro-atherogenic flow at the centre of the swirled well.

This study showed that nanodroplets adhered to the cells sheared with pro-atherogenic flow, but not to the cells sheared with atheroprotective flow, even without a receptor targeting mechanism. This finding could be developed further to develop a novel technique to detect the early development and progression of atherosclerosis, without the need of receptor conjugation to the agents.

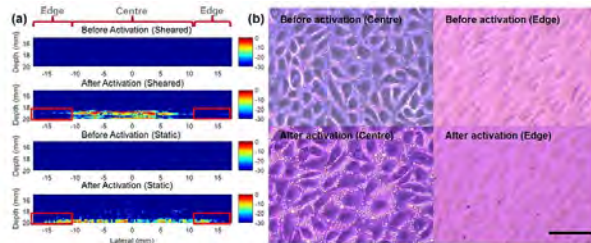


Figure (a) shows the ultrasound signals before and after activation of nanodroplets, after subtraction of signals before activation. Figure (b) shows the microscopic images of PAEC at the center and periphery of the well pre- and post-activation. A large number of activated nanodroplets adhered to PAEC sheared with atheroprone flow at the centre of a swirled well were observed.

Enhanced Extravasation of Magnetic Perfluorocarbon Nanodroplets with Bimodal Size Distribution by Two-step Magnetic/Ultrasound Synergistic Manipulation
Jixiu Huang¹, Wei Dong¹, Jiangying Long¹, Huiying Jiang¹, Yiyi Zhang², Di Zhou¹, Shanshan Xu¹, Mingxi Wan¹, Yujin Zong¹
¹*Department of Biomedical Engineering, Xi'an Jiaotong University, Xi'an, China, People's Republic of, ²Xi'an AbborBio Co. LTD, China, People's Republic of*
Background, Motivation, and Objective

Phase-shift nanodroplets (NDs) are reported as potential theranostic agents for tumor diagnosis and therapy because of its submicron size and acoustic triggerability. An increased interstitial fluid pressure in tumor tissue hinders convectional transport of nanodroplets across blood vessel walls, thus extravasation of sufficient amounts of nanodroplets remains a major challenge. In this paper, SPIO nanoparticles (NPs) were dispersed into the liquid perfluoropentane (PFP) phase of lipid-shelled ND to prepare magnetic phase-shift ND (MPND) that had bimodal size distribution. And a two-step magnetic/ultrasound synergistic manipulation was used as enhanced extravasation strategy for these MPNDs. The MPNDs were accumulated near the vessel wall by the external magnet, then focused US acoustically vaporized the larger NDs, thereby the smaller MPNDs can penetrate and retain within the phantom guided by magnetic force.

Statement of Contribution/Methods

SPIO NPs synthesized by co-precipitation were perfluorinated with 1H,1H,2H,2H-perfluoroctyl trimethoxysilane to well disperse in liquid PFP. Then MPNDs were prepared by extruding the mixture of hydrated lipid and SPIO-dispersed PFP using an extruder until the mean diameter was reduced to about 200nm. Monodisperse MPNDs with a mean diameter of 800 nm were prepared via solvent dissolution from microfluidic-generated precursor microdroplets. 1% agarose gel vessel phantom that has a pore size range of 200-800 nm was prepared to mimic the leaky tumor vascular. MRI images of the vessel phantom were acquired to compare the MPND extravasation when the phantoms through which the MPNDs flowed were processed by magnet alone, US alone and external magnet combined with US.

Results/Discussion

The prepared SPIO NPs have an average diameter of 10nm (Fig.1). The MPNDs can be effectively accumulated by an external magnet (Fig.2) and negatively enhanced the T2-weighted MR images (Fig.3). While the phase shift threshold of the MPNDs decreased with the incorporation of SPIO and the increase of droplet size. The MPNDs with a bimodal size distribution could be obtained by mixed the NDS with different size. Enhanced extravasation could be observed after magnetic/ultrasound synergistic manipulation. The reason might be that the cavitation effect accomplished with the phase shift of larger MPNDs could further increase the permeability.



Fig. 1 TEM image of SPIO nanoparticles synthesized by co-precipitation

Fig. 2 Prepared MPNDs (left: no external magnet, right: MPND were effectively accumulated by external magnet)

Fig. 3 T2-weighted MR images
(A. Control, no SPIO; B. 5mg/mL SPIO;
C. 10mg/mL SPIO)

Effects of Flowing Lipid-shelled Microbubbles and Phase-shift Nanodroplets on the Characteristics of Cavitation during Focused Ultrasound Exposure

Tianqi Xu¹, Siyuan Zhang¹, Zhiwei Cui¹, Dapeng Li¹, Fu Mo¹, Shan Wu¹, Supin Wang¹, Mingxi Wan¹

¹The Key Laboratory of Biomedical Information Engineering of Ministry of Education, Department of Biomedical Engineering, School of Life Science and Technology, Xi'an Jiaotong University, China, People's Republic of

Background, Motivation, and Objective

As artificial cavitation nuclei, encapsulated gas-filled microbubbles (MBs) are commonly used to enhance local cavitation during focused ultrasound (FUS) exposures. For phase-shift nanodroplets (NDs), the properties of nano-level size, long-lasting and high stability show the advantages of safety and high efficiency in therapeutic ultrasound. This study investigated and compared the characteristics of cavitation activity between lipid-shelled MBs and phase-shift NDs with various velocities at different acoustic pressures during FUS exposures.

Statement of Contribution/Methods

Passive cavitation detection (PCD) method was used to monitor cavitation activity, and broadband noise was collected when solutions of either lipid-shelled MBs (SonoVue™) or phase-shift NDs (Perfluoropentane) flowed at various velocities through a wall-less vessel in a transparent tissue-mimicking phantom during FUS exposures with a 1.06 MHz working frequency and the mode of continuous waves at different acoustic pressures. Root-mean-square (RMS) amplitudes of broadband noise were calculated as a trace over time. The inertial cavitation dose (ICD) was qualified as the integration of RMS over the recording duration.

Results/Discussion

The RMS amplitude increased from 35 to 80 for NDs and decreased from 52 to 38 for MBs when they were static. Meanwhile, the increase of cavitation for the phase-shift NDs and decrease of cavitation for the lipid-shelled MBs had slowed down when they flowed through the vessel at 10 cm/s. At the acoustic power of 2 W, the normalized ICD values for lipid-shelled MBs increased with the increasing velocities from 5 to 30 cm/s. However, the normalized ICD for phase-shift NDs increased from 5 to 15 cm/s, and decreased from 15 to 30 cm/s. At the acoustic power of 15 W, both NDs and MBs had increasing trends of normalized ICD values with the increasing flow velocities. The effects of the flowing phase-shift NDs on the characteristics of cavitation were inverse to those of flowing lipid-shelled MBs during FUS exposure.

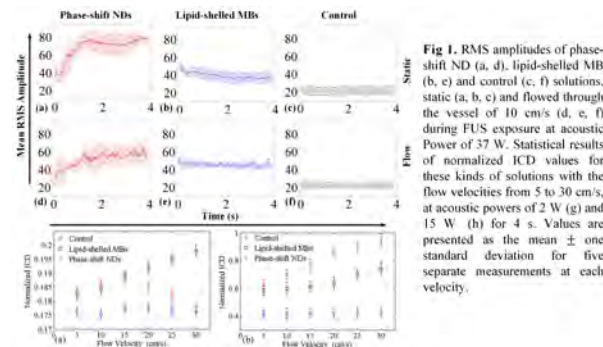


Fig 1. RMS amplitudes of phase-shift ND (a, d), lipid-shelled MB (b, e) and control (c, f) solutions, static (a, b, c) and flowed through the vessel of 10 cm/s (d, e, f) during FUS exposure at acoustic Power of 37 W. Statistical results of normalized ICD values for these kinds of solutions with the flow velocities from 5 to 30 cm/s, at acoustic powers of 2 W (g) and 15 W (h) for 4 s. Values are presented as the mean \pm one standard deviation for five separate measurements at each velocity.

Synchronized ADV and ODV for enhanced cavitationSy-Han Huang¹, Wei-Wen Liu¹, Pai Chi Li¹¹National Taiwan University, Taiwan**Background, Motivation, and Objective**

Sonoporation can enhance the delivery efficiency of therapeutic agents into cells. Our previous study used nanodroplets to significantly enhance the effectiveness of sonoporation relative to using conventional microbubbles. It was demonstrated that combined continuous wave (CW) laser and ultrasound strongly enhanced the tumor therapeutic efficacy through inducing gold nanodroplets (AuNDs)-based sonoporation. In this study, we propose a new droplet vaporization strategy to more reliably induce such cavitation under lower acoustic and laser energy levels. The new strategy synchronizes ultrasound with pulsed wave (PW) laser such that laser triggering is applied during rarefaction. With the new triggering strategy, not only the laser power for inducing optical droplet vaporization (ODV) can be reduced significantly to avoid safety concerns, photoacoustic (PA) imaging can also be performed at the same time for monitoring the ODV since the same PW laser is used for both ODV and PA imaging.

Statement of Contribution/Methods

The AuNDs consisted of dodecaperfluorocarbone cores and human serum albumin shells. The encapsulated gold nanorods were synthesized with absorbance wavelength at 808 nm. To trigger the ODV, we used a wavelength-tunable OPO laser to generate 808-nm PW laser pulses with 20 Hz pulse repetition rate. To induce the acoustic droplet vaporization (ADV) and measure the cavitation signals, we used a 1-MHz focused transducer for transmission and a 10-MHz ultrasound transducer for receiving differential inertial cavitation dose (dICD) signals. To detect vaporization, we calculated the square root of the total energy and the root mean square value of 2nd to 4th harmonic of the received signals.

Results/Discussion

We successfully induced vaporization of AuNDs by delivering a 6-mm-wide laser beam with the laser fluence of 12.02 mJ/cm² at the ultrasound rarefaction phase. We also found that when the peak negative pressure was -526.1 Kpa, the dICD values varied in a 1-μs period consistent with the driven acoustic pressure (at 1MHz). In comparison to the power of the CW laser we applied in our previous study for inducing the ODV, the laser power here was reduced from 2 W/cm² to 0.24 W/cm². In conclusion, we successfully reduce the vaporization threshold through the proposed approach by synchronizing the pulsed ODV with ADV. Concurrent PA imaging can also be performed.

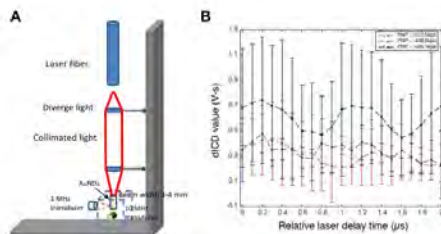


Figure 1. (A) Schematic system setup. (B) The dICD value as a function of the time delay between the pulsed ODV and the ADV peak negative pressure time point.

Ultrasound-based Cell Sorting with Microbubbles

Thomas Matula¹, Oleg Sapozhnikov^{1,2}, Lev Ostrovsky^{3,4}, Andrew Brayman¹, John Kucewicz¹, Brian MacConaghay¹, Dino De Raad¹

¹Univ. of Washington, Seattle, WA, United States, ²Moscow State University, Russian Federation, ³University of Colorado, Boulder, United States, ⁴Institute of Applied Physics, Nizhni Novgorod, Russian Federation

Background, Motivation, and Objective

Cell-based immunotherapies exploit the use of cell surface antigens to identify and purify cell lines. Fluorescence-based sorters require relatively large sample volumes and are too costly for small labs. Magnetic sorters are less expensive but require enzymatic digestion to remove magnetic particles. We propose to label cells with antibody-conjugated microbubbles (MBs) and selectively sort them using ultrasound. After sorting, the MBs can be removed with a small overpressure. The objective here was to determine the feasibility of separating cells from erythrocytes as a first step in cell purification.

Statement of Contribution/Methods

TargeStar-SA microbubbles (MBs) were conjugated to leukemia cells expressing CD7 antigens. Conjugated cell suspensions were placed in a flow with erythrocytes (which lack CD7) and imaged under magnification. Cell motion was quantified with or without ultrasound insonation (1 MHz, 20-80 kPa, variable pulse lengths). The acoustic radiation force (ARF) acting on a cell-MB conjugated pair was modeled by assuming the driving force is associated with the MB, and the viscous drag is due to the much larger cell. A separate observation of cell-MB rotation caused by the ARF was explained by considering the torque on the cell, where adherent MBs act as point forces. The ARF can be extracted from either observation.

Results/Discussion

Under insonation, tagged cells were observed to rotate to align with the ARF, and to move in the direction of the ARF. If a tagged cell was adherent to the observation coverslip, it only rotated. The theoretical model for rotation-only behavior fit well with this data ($R^2=0.996$). The ARF extracted from the fit was 1.7×10^{-12} N. This agreed with the ARF calculated from the cell displacement observations. Under flow, tagged leukemia cells were deflected by ultrasound, while erythrocytes were unaffected (figure 1). These initial studies showed that tagged cells can easily be manipulated relative to untagged cells, providing a new way for isolating and sorting cells. (Funded in part by LSDF #3292512, RBBR 17-02-00261, NIH P01 DK43881, and NSBRI via NASA NCC 9-58).

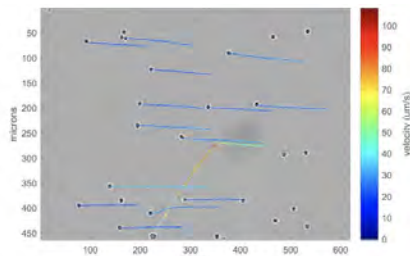


Figure 1. Path of a tagged leukemia cell relative to erythrocytes. Ultrasound propagates from above..

Separation of contrast agents from tissue via an unfolded deep learning schemeOren Solomon¹, Regev Cohen¹, Liran Taieb¹, Daniel Toberman¹, Yonina Eldar¹¹*Electrical Engineering, Technion, Israel***Background, Motivation, and Objective**

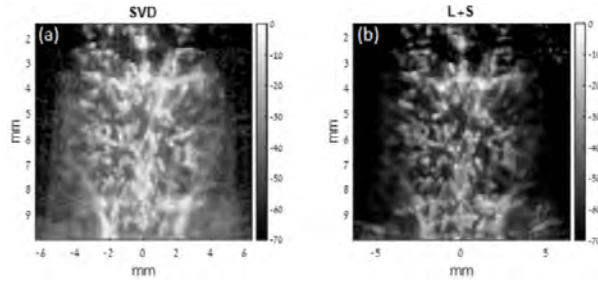
Contrast enhanced ultrasound (CEUS) imaging enables vascular visualization with high contrast using inert microbubbles (MBs), injected into the bloodstream. CEUS processing requires separating tissue signal from the MB signal, prior to subsequent processing. Several separation techniques exist, such as the well-known SVD filtering. However, selection of the cutoff threshold in SVD is data-dependent and wrong choice often results in noisy or cluttered CEUS signals. Here, we propose a low-rank and sparse (L+S) decomposition to solve the separation problem, which alleviates the need to a-priori estimate the rank of the tissue signal matrix and is considered to be robust in the presence of sparse outliers (MBs). We then unfold the corresponding iterative algorithm via recently developed deep-learning techniques to improve its convergence speed, reconstruction quality and reduce its computational complexity.

Statement of Contribution/Methods

CEUS scan of two rat brains were acquired using a Verasonics scanner, courtesy of the center for biomedical imaging research, Tsinghua University. After demodulation and beamforming of 100 CEUS frames, the complex analytical clip is modeled as a sum of a low-rank (tissue) and sparse matrix (MBs). Next, we solve an optimization problem, based on the L+S decomposition, using the fast iterative shrinkage/thresholding algorithm (FISTA/ISTA). We later unfold the iterative scheme of ISTA over a few iterations, where each iteration is a layer in a deep network. We train the network on the FISTA recovery obtained from the experimental data from the first mouse. We test the performance of the network on the second mouse and compare it with the naïve SVD decomposition and FISTA.

Results/Discussion

The following are preliminary results, showing the benefits of using an L+S decomposition over SVD. Panel (a) shows the CEUS signal after performing a naïve SVD decomposition (attained from keeping the 50 smallest eigenvalues out of 100). Panel (b) shows the CEUS signal obtained from the FISTA minimization of the L+S decomposition over 20000 iterations. Both images have a dynamic range of 70dB, and are obtained by estimating the pixelwise variance from the separated CEUS movie. The L+S decomposition shows a cleaner and sharper image of the vasculature, as compared with the naïve SVD approach, due to its robustness to sparse outliers and noise handling.



P1-B5 - Abdominal Elasticity Imaging

Kairaku (posters 1)

Wednesday, October 24, 9:30 AM - 4:00 PM

Chair: **Jianwen Luo** Tsinghua University

P1-B5-1

Kidney biopsy score prediction based on shear wave elastography measurements and machine learning

Luiz Vasconcelos¹, Carolina Amador², Sara Aristizabal³, Ivan Nenadic¹, Matthew Urban⁴

¹*Department of Physiology and Biomedical Engineering, Mayo Clinic, Rochester, MN, United States*, ²*Ultrasound Imaging and Interventions, Philips Research North America, Cambridge, MA, United States*, ³*Well Living Lab, Rochester, MN, United States*,

⁴*Department of Radiology, Mayo Clinic, Rochester, MN, United States*

Background, Motivation, and Objective

The kidneys are responsible to maintain metabolic and fluid balance of the body. End-stage renal disease (ESRD) can rapidly deteriorate the capacity of the body to sustain homeostasis. Kidney transplant is the preferred treatment for ESRD because it provides a better survival rate and quality of life than dialysis. Protocol biopsies using Banff diagnostic criteria, for features like interstitial fibrosis and tubular atrophy (IFTA), are the gold standard procedure for rejection assessment with the limitation of being an invasive procedure that can cause complications and cannot be performed frequently. An alternative to biopsy could be noninvasive imaging such as elasticity imaging that can potentially assess changes in renal allografts directly related to pathological processes. Shear wave elastography (SWE) techniques have been very useful for the analysis of tissue rheological properties and pathologies. The objective of this research is to develop supervised machine learning algorithms that can predict biopsy scores based on SWE measurements and other physiological biomarkers.

Statement of Contribution/Methods

The dataset used for this study was composed by 97 kidney transplanted patient that had SWE scans performed right before their routine biopsy procedure at Mayo Clinic. Multiple machine learning techniques were compared to assess its capabilities to predict IFTA classifications with the rheological and physiological features obtained during their routine check-up. The parameters obtained from the SWE measurements included group velocity, shear modulus, phase velocity and attenuation at frequencies 100-300 Hz, and parameters from fitting a Kelvin-Voigt fractional derivative rheological model. The biopsy scores were used as labels to train the models. All techniques shared the same pre-processing steps to assure a common starting point for performance evaluation. Neural networks (NN), support vector classifier (SVC) and K-nearest neighbors (KNN) were used to predict the biopsy results and were evaluated with respect to their sensitivity and specificity for each biopsy score class and binary IFTA classification.

Results/Discussion

NN had the best overall performance and generalization capacity. With sensitivity and specificity of 76.3% and 73.7%, respectively, for binary rejection classification, it showed a good potential for kidney IFTA diagnosis given the small number of patients analyzed. SVC showed lower sensitivity and specificity, at 65.7% and 54.3%. KNN showed similar performance, with 51.4% and 69.7%. Along with the size of the dataset, the proper balancing of the classes proved to be the main challenge for all machine learning techniques. The vast majority of healthy biopsy outcomes can mislead the algorithm, but fine class weighting techniques helped the models to overcome this issues. These results showed potential to be used clinically for noninvasive evaluation of renal allografts.

Obtaining Equivalent Liver Shear Wave Speed Measurements with Multiple Transducers

Mallory Selzo¹, Stephen Rosenzweig¹, Andy Milkowski¹

¹Siemens Healthineers, Issaquah, WA, United States

Background, Motivation, and Objective

The diagnostic utility of Siemens Virtual Touch Quantification (VTQ) for measuring liver stiffness has been reported by numerous studies, establishing cut-off velocities for grading liver fibrosis¹. It is important when introducing transducers, signal processing algorithms, and acquisition formats that shear wave speeds remain consistent with previously published values; however, due to the viscoelastic nature of tissues, these all can affect shear speed measurements.

This work demonstrates how data driven optimization of processing parameters can minimize differences in shear wave speeds clinically.

Statement of Contribution/Methods

Shear speeds were measured in the livers of 26 healthy volunteers. VTQ measurements were acquired with a 4C1 transducer on a Siemens S2000 (Mountain View, CA) scanner using the method described in [2]. Measurements and raw data were collected with 3 additional transducers in multiple acquisition formats. In total, 10 repeated measurements were taken for each transducer/format resulting in 60 measurements for each patient. Measurements were also acquired in four custom CIRS, Inc. (Norfolk, VA) elasticity phantoms at depths spanning the ranges appropriate for each transducer. Calibrated phantom shear speeds, measured independently at Duke University using QIBA guidance³, ranged from 1.04 – 3.82 m/s.

Phantom and clinical data for each transducer and acquisition format were reprocessed offline using approximately 5,000 different permutations of propagation distances, harmonic/fundamental blending ratios, directional filter settings, low-pass filter cutoff values, and quality thresholds. Clinical data sets generated from each permutation, or ‘parameter set’, were compared to VTQ on the 4C1 using two methods: the 2-sample Student’s t-test to compare the distributions of the 260 measurements, and the paired t-test to compare patient medians. Phantom data sets were compared to the calibrated values. Parameter sets which resulted in data that was either statistically significantly different than VTQ ($p<0.05$) or not consistent with calibrated phantom values were eliminated from consideration. Of the remaining parameter sets, the parameters which minimized patient variability, expressed as IQR/median ratio, were selected for each transducer and acquisition format.

Results/Discussion

Prior to optimization, measurements obtained with two of the three transducers were statistically significantly different from those obtained with 4C1 transducer on the S2000 ($p<0.05$). Furthermore, significant differences in shear velocity were observed across the different transducers and acquisition formats. Following optimization, there were no significant differences between measurements from any of the transducers or acquisition formats ($p>0.3$).

[1] Bota S, et al. Liver Int 2013; 33(8): 1138-47

[2] Barr RG, et al. Radiology 2015; 276(3): 845-61

[3] Deng Y, et al. IEEE Trans UFFC 2017; 64(1): 164-76

Could ultrasound elastography reflect liver function reserve?

Tingting Qiu¹, Hong Wang¹, Jinzhen Song¹, Gang Guo², Yan Luo¹

¹Department of ultrasound, West China Hospital, Sichuan University, China, People's Republic of, ²Research Institute of Pathology, West China Hospital, China, People's Republic of

Background, Motivation, and Objective

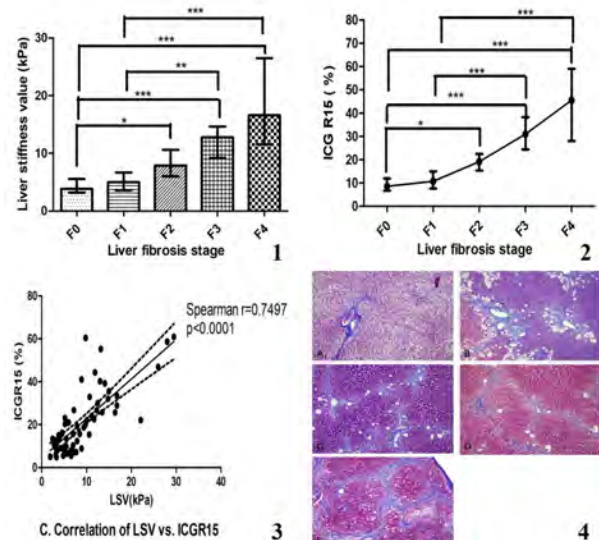
Evaluation of liver function reserve is crucial for treatment and prognosis. Liver stiffness measurement has been proved useful for assessing liver fibrosis stage and is easy to perform clinically. The purpose of this study was to investigate whether liver stiffness measured by ultrasound elastography could reflect liver function reserve with relation to liver fibrosis histology.

Statement of Contribution/Methods

Sixty-five New Zealand rabbits were divided into experimental ($n=45$) and control group ($n=20$). In the experimental group, liver fibrosis (F1-F4) was induced by subcutaneous injection of carbon tetrachloride. Point shear-wave elastography (pSWE) and indocyanine green (ICG) elimination test were performed for the two groups at a 4-week interval for 56 weeks. The liver stiffness value (LSV) and ICG retention rate at 15 minutes (ICGR15) were obtained and the correlation between them were investigated.

Results/Discussion

The median LSVs of F0-F4 stages were 3.92 kPa (1.91-8.53 kPa), 5.02 kPa (2.39-8.91 kPa), 7.87 kPa (5.21-12.26 kPa), 12.83 kPa (5.92-16.79 kPa), and 16.64 kPa (9.76-29.50 kPa) respectively. The median ICGR15 of F0-F4 stages were 8.7% (4.8-15.6%), 10.8% (5.6-20.3%), 19.2% (12.3-26.7%), 31.0% (20.9-41.0%) and 45.6% (22.1-60.9%). A positive correlation was found between LSV and ICGR15 ($r=0.7497$, $p<0.0001$). A strong correlation was observed between liver stiffness and liver function reserve, indicating ultrasound elastography may be able to primarily reflect liver function reserve in different degrees of liver fibrosis.



Large Field-of-View Shear Wave Imaging for Hepatocellular Carcinoma Screening
Samantha Lipman¹, Mark Palmeri¹, Kathryn Nightingale¹
¹*Biomedical Engineering, Duke University, Durham, NC, United States*
Background, Motivation, and Objective

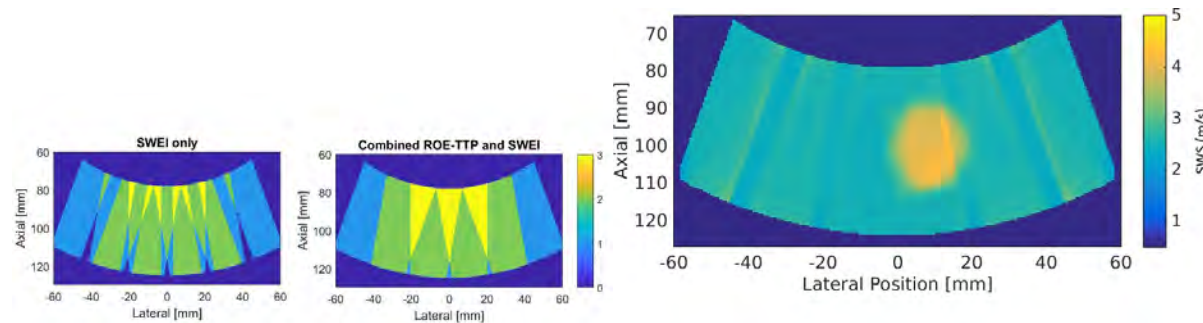
Patients with liver cirrhosis or Hepatitis C have an increased likelihood of developing hepatocellular carcinoma (HCC) and are screened every six months with ultrasound; however, B-mode has demonstrated a low sensitivity for detecting small, early stage HCC. Studies using ultrasonic elasticity methods have shown increased HCC lesion contrast compared to B-mode, but current elasticity systems are limited to a depth penetration of 8 cm.

Statement of Contribution/Methods

A proposed, large-aperture, matrix array is presented for increasing depth penetration of acoustic radiation force excitations. Sparsity in the reconstructed shear wave elasticity imaging (SWEI) occurs in the region of excitation (ROE). Our previously proposed on-axis method uses a lookup table (LUT) and relates the ROE time-to-peak (TTP) displacement to underlying material stiffness. The ROE-TTP methods were extended to include the near-field region (± 3 mm) of the shear wave source and can be combined with traditional off-axis time of flight methods (Figure 1). The same field-of-view (FOV) using only SWEI would require 60% more excitations. Finite element simulations in homogeneous, elastic phantoms were used to create a LUT. Imaging of a 20 mm diameter spherical lesion in three liver disease states was simulated, including an HCC in a fibrotic liver.

Results/Discussion

Figure 2 shows a reconstruction combining on-axis and off-axis methods with an HCC lesion CNR of 4.31. The ROE-TTP methods have increased bias in high stiffness materials increasing from 4% bias in SWEI estimates up to 19 % bias in ROE-TTP estimates in a 60 kPa phantom. Even with increased bias, on-axis methods can reduce the sparsity that would otherwise occur inside the ROE, which allows a larger FOV to be interrogated with a reduced number of excitations.



A Two-dimensional (2D) Systems Biology-based Discrete Liver Tissue Model for Simulations of Ultrasound Shear Wave Elastography (SWE)

Jingfeng Jiang¹, Yu Wang²

¹Biomedical Engineering, Michigan Technological University, MI, United States, ²Biomedical Engineering, Michigan Technological University, Houghton, MI, United States

Background, Motivation, and Objective

Computer simulations have played important roles in understanding complicated interactions between biological tissues and external mechanical stimuli, thereby gaining insight related to the image formation in elastography. However, to date, most numerical phantoms used in these computer simulations are too simple to reflect the complexity of biological tissues. Our primary objective is to incorporate a biologically-relevant tissue model for advanced elastography simulations [1] using the framework of systems biology.

Statement of Contribution/Methods

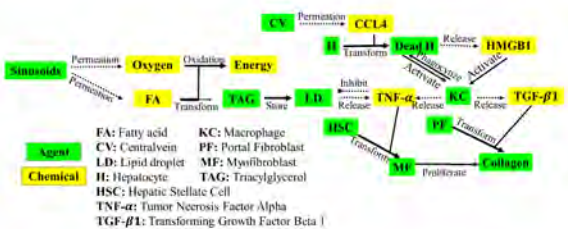
As shown in Figure, the proposed fibrotic liver tissue model leverages established knowledge of histopathology. Specifically, in the framework of systems biology, rules derived from molecular and histopathological knowledge [2-3] related to hepatic wound/healing including inflammation, fibrosis, and lipid accumulation were implemented into an agent-based software platform (SPARK [4]). Through dynamic simulations in SPARK, histological progressions of liver fibrosis with or without steatosis can be realistically produced. These systems biology results were converted to microscopic compositions of liver tissues (at a 50 – 100-micrometer scale). To demonstrate the validity of the proposed systems biology-based discrete liver tissue model, SWE and speed of sound (SOS) simulations were performed by an open-source wave simulator K-Wave. To verify the physical soundness of the proposed model, virtual shear wave speed measurements were performed to results in the clinical literature [5-7].

Results/Discussion

Our initial results demonstrated that the simulated virtual liver tissues with and without steatosis qualitatively can reproduce results reported in the clinical literature. Specifically, the simulated SWS values increased with the progression of liver fibrosis (from 1.5 m/s [Fibrosis stage 1] to 4 m/s [Fibrosis stage 4]). Similarly, the simulated SOS values were within the range of clinical data (from 1575 m/s [Fibrosis stage 0-3] to 1594 m/s [Fibrosis stage 4]).

References:

1. Wang, Y. et al., PMB, 2017.
2. Schleicher, J., Biochim Biophys Acta 2014.
3. Hubscher, S. G., Histopathology 2006.
4. Dutta-Moscato, J., Front Bioeng Biotechnol 2014.
5. Yeh Wen-Chun, IEEE Int Ultrason Symp 2001.
6. Kemper A, ESV 2009.
7. Jeong J. Y. World J Gastroenterol 2014, 20.



P1-B6 - Elasticity in Pre-Clinical and Clinical Applications

Kairaku (posters 1)

Wednesday, October 24, 9:30 AM - 4:00 PM

Chair: **Gianmarco Pinton** University of North Carolina

P1-B6-1

Subresolution displacements and shear shock wave tracking in the human brain

Sandhya Chandrasekaran¹, Bharat Tripathi², David Espindola², Gianmarco Pinton²

¹North Carolina State University, United States, ²University of North Carolina at Chapel Hill and North Carolina State University, United States

Background, Motivation, and Objective

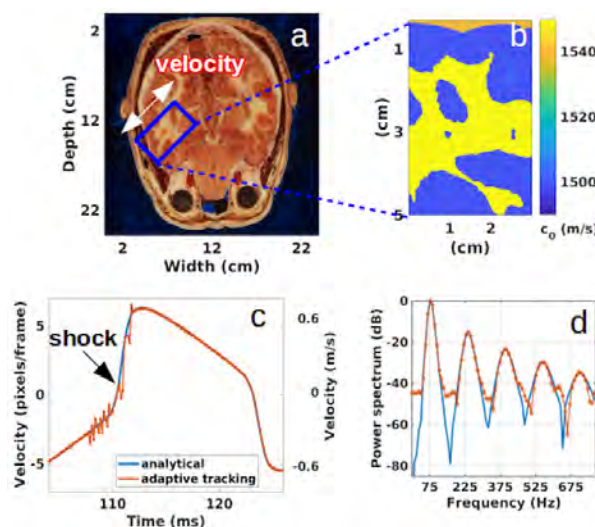
Highly realistic finite difference simulations of acoustic wave propagation can be used to describe ultrasound imaging in soft tissue. They have recently been shown to also model the backscattering physics from the subresolution motion of distributed scatterer fields. Here, we present a general method that models displacements in complex tissue maps, specifically the human brain. The proposed method is used to i) model tissue motion due to shear shock wave propagation in the brain, which we hypothesize is a primary mechanism for traumatic brain injuries ii) obtain the backscattered signal from an imaging pulse, and iii) estimate the imposed displacements from the simulated RF data. The high anatomical fidelity of the tissue maps combined with the high accuracy of the displacement model are used to validate the performance of the tracking algorithms and to design imaging sequences that detect the unique odd harmonic spectral signature generated by the cubic nonlinearity of shear shocks.

Statement of Contribution/Methods

Brain maps from the Visible Human Project dataset (Fig. (a)) were converted to acoustical maps (Fig. (b)) for the Fullwave ultrasound simulations of an ultrasonic probe (ATL-Philips L7-4) operating at 5.2 MHz. Sub-pixel interframe displacements ($1.9 \mu\text{m}$), generated by shear shock waves were calculated using an experimentally validated custom piecewise parabolic method that models the shear shock wave physics in the brain. These displacements were then imposed by varying the impedance of scatterers and tissue interfaces. The resulting phase shift was measured from the beamformed RF data using a custom adaptive correlation-based tracking algorithm.

Results/Discussion

It is shown that the average error in the shear shock wave displacement tracking (Fig. (c)) is small compared to the wavelength ($\lambda/674$) with a standard deviation of ($\lambda/4235$). Jitter and bias errors were measured to be 0.39 ns and 0.57 ns, respectively. Consistently with theoretical predictions, the characteristic odd harmonics signature of shear shock waves was detected up to the 9th harmonic (Fig. (d)). This method, validated here for a challenging discontinuous displacement model, can be applied to less complex motion, such as linear shear waves generated for shear wave elasticity imaging.



Measurement of the nonlinear elastic properties of ex vivo porcine brain: applications to traumatic brain injury
David Espindola¹, Bharat Tripathi¹, Gianmarco Pinton¹
¹*Joint Department of Biomedical Engineering, University of North Carolina at Chapel Hill and North Carolina State University, NC, United States*
Background, Motivation, and Objective

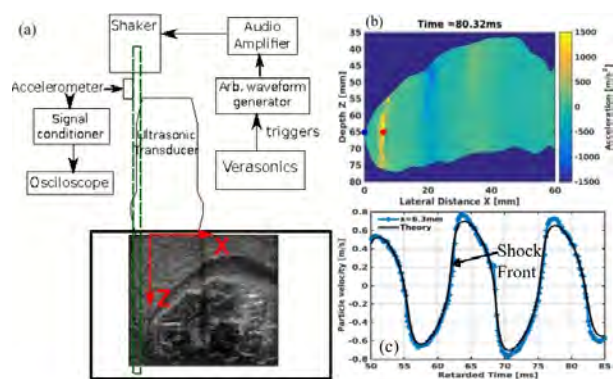
The rapid transient motion associated with traumatic brain injury results in a complex deformation of the brain. We have recently demonstrated that shear shock waves are easily generated in the brain under conditions that are mild (as low as concussive accelerations). These shock waves are driven by a cubic nonlinearity which can be characterized by a nonlinear parameter of the brain, β . Measuring shear shock wave physics is challenging due to the combination of frame-rate, penetration, and motion detection accuracy that is required to characterize the nonlinear viscoelastic behavior. Measurements of the elastic beta, which are currently absent from mechanical models of the brain, may be fundamental for the biomechanics of traumatic brain injury. Here we compare experimental measurements of shear shock waves with numerical simulations to directly estimate the nonlinear elastic wave parameter of the brain.

Statement of Contribution/Methods

High frame-rate ultrasound imaging (6200 images/second), of an ex-vivo porcine brain measure the displacements imposed by an external plate driven at 75 Hz (a). An adaptive tracking algorithm and a customized parallel receive high frame-rate beamforming method is used to detect the development and propagation of shear shock waves.

Results/Discussion

Much like an acoustic wave the smooth shear wave generated by the plate develops into a shock front that has a sharp and almost discontinuous transition from positive to negative velocities. Fig. (b) shows a snapshot of the acceleration into the brain. At the surface of the brain the acceleration is nearly monochromatic with an amplitude of 48g. However at 6.5 mm from the surface, the acceleration reaches 400 g. Thus, the shear shock wave locally amplifies the acceleration up to a factor of 8.5 suggesting that shear shocks are a primary mechanism for traumatic injuries. A custom piecewise parabolic method (PPM) was developed to model nonlinear shear wave propagation on a retarded time frame of reference in an attenuating elastic medium. By matching experiment with the PPM numerical simulation, we have found that the brain has a $\beta = 13 \pm 6$. Thus, it is shown that these shock waves closely match theoretical predictions (c) as measured temporally and by the a specific odd harmonic signature predicted by theory describing a cubically nonlinear elastic soft solid.



A novel non-invasive ultrasound vibro-elastography technique for assessing patients with unilateral papilledema and choroidal folds

Boran Zhou¹, Arash Kazemi², John Chen³, Arthur J. Sit², Xiaoming Zhang¹

¹Department of Radiology, Mayo Clinic, Rochester, MN, United States, ²Department of Ophthalmology, Mayo Clinic, Rochester, MN, United States, ³Department of Ophthalmology and Neurology, Mayo Clinic, Rochester, MN, United States

Background, Motivation, and Objective

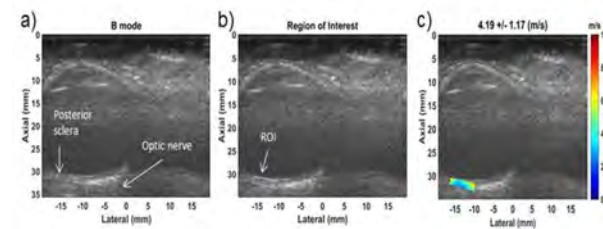
Idiopathic intracranial hypertension (IIH) is a condition of increased intracranial pressure of unknown cause producing papilledema (optic nerve swelling), choroidal folds, and visual loss. We hypothesize that the variability of the papilledema in relation to a given intracranial pressure is due to differences in the biomechanical properties of the posterior sclera. The purpose of this study is to evaluate our novel ultrasound vibro-elastography (UVE) technique for assessing patients with unilateral papilledema and choroidal folds by noninvasively measuring viscoelastic properties of posterior sclera.

Statement of Contribution/Methods

Under an IRB approved protocol, both eyes of a patient with unilateral papilledema and choroidal folds in the left eye were evaluated. A 0.1 second vibration was noninvasively generated on the eyelid using an indenter of the handheld shaker. The resulting wave propagation in the eye was measured using a Verasonics Vantage system with a L11-5v probe (6.42 MHz) and a plane wave imaging sequence with a 0.1 s data accumulation (PRF = 2 kHz) (Fig. 1a). Vibration excitation was performed at 100, 150 and 200 Hz. A directional filter was then applied upon the shear wave field to extract the axial and lateral propagating shear waves. Local shear wave speed was recovered using a time-of-flight method based on both axial and lateral speed maps. A region-of-interest (ROI) was selected to measure the wave speed in the area of the posterior sclera (Fig. 1b) and the corresponding shear wave speed (SWS) of ROI was calculated (Fig. 1c). Viscoelasticity of posterior sclera was calculated based on the SWS at three frequencies using Voigt model.

Results/Discussion

The SWS within the posterior sclera of the patient was significantly lower in the left eye (2.26 ± 0.55 , 2.87 ± 0.87 , 3.57 ± 0.98 m/s) compared to the right eye (3.51 ± 1.14 , 4.69 ± 1.29 , 5.08 ± 0.38 m/s; $p < 0.05$) at three frequencies. There was no significant difference in the elasticity between left (3.05 ± 3.17 kPa) and right (5.74 ± 6.68 kPa, $p > 0.05$) eyes. However, there was a significant difference in viscosity between the left (5.85 ± 1.09 Pas) and right (12.89 ± 4.03 Pas, $p < 0.05$) eyes, which suggests that the viscoelasticity of the posterior sclera does play a role in the susceptibility to papilledema from raised intracranial pressure and can be accurately measured with UVE.



Texture Features in Viscoelastic Response (VisR) Ultrasound Images Differentiate Dystrophic from Control Skeletal Muscles in a Dog Model of Duchenne Muscular Dystrophy, In Vivo

Christopher Moore^{1,2}, Mallory Selzo³, Juan Prieto⁴, Kathy Spaulding⁵, Melissa Caughey⁶, Amanda Bettis⁷, Heather Heath-Barnett⁷, Martin Styner⁴, Joe Kornegay⁸, Caterina Gallippi⁹

¹University of North Carolina at Chapel Hill, Chapel Hill, NC, United States, ²Electrical and Computer Engineering, North Carolina State University, Chapel Hill, NC, United States, ³Biomedical Engineering, University of North Carolina at Chapel Hill, Chapel Hill, NC, United States, ⁴Computer Science, University of North Carolina at Chapel Hill, Chapel Hill, NC, United States,

⁵Large Animal Clinical Sciences, Texas A&M University, United States, ⁶Cardiology, University of North Carolina at Chapel Hill, Chapel Hill, NC, United States, ⁷Veterinary Integrative Biosciences, Texas A&M University, United States, ⁸Veterinary Medicine, Texas A&M University, United States, ⁹Joint Department of Biomedical Engineering, The University of North Carolina at Chapel Hill, Chapel Hill, NC, United States

Background, Motivation, and Objective

In Duchenne muscular dystrophy (DMD), repeating cycles of muscle fiber inflammation and necrosis followed by fibrous and fatty deposition cause progressive muscle wasting. These degenerative changes are associated with altered elastic and viscous muscle properties that can be assessed noninvasively by Viscoelastic Response (VisR) ultrasound. *We hypothesize that the spatial distributions of VisR-derived elastic and viscous features, assessed by computational texture feature analysis, differ between dystrophic and control skeletal muscles, in vivo.*

Statement of Contribution/Methods

VisR imaging was performed in the rectus femoris (RF), vastus lateralis (VL), cranial sartorius (CS), and semitendinosus (ST) muscles of 10 Golden Retriever Muscular Dystrophy (GRMD) dogs and in 10 age-matched littermate pairs with no known neuromuscular disorders. In each dog, serial VisR imaging occurred at 3, 4.5, 6, 9 and 12 months of age. Tissue samples were harvested for histological processing at 6 and 12 months. The acquired VisR data were processed to render parametric images of relative elasticity (RE) and relative viscosity (RV), to which computational texture analysis was applied using a custom C++ implementation of gray level run length analysis. Resulting texture features included: small lesion index (SLI), heterogeneity index (HI), entropy, and long run index (LRI).

Results/Discussion

See Fig. 1. Cross-sectionally, GRMD and control exhibited statistical differences ($p<0.1$, Wilcoxon) as follows: RF (RE entropy and HI at 6, 9, and 12 mos; RV entropy and HI at 6 mos, LRI and SLI at 9 mos); VL (RE entropy and HI at 12 mos, LRI at 9 mos; RV LRI at 3 mos, SRI at 3 and 9 mos); CS (RE entropy at 12 mos, SRI at 6 mos); ST (RE entropy at 12 mos, HI at 6 and 12 mos); Longitudinally, GRMD and control exhibited statistically different linear slope of texture feature v. time as follows: RF (RE HI and SLI); ST (RV LRI). These results are consistent with expectation and with histological validation showing that the RF undergoes earlier and more severe dystrophic degeneration than the other examined muscles. Overall, this study suggests that the spatial distributions of elastic and viscous properties in dystrophic muscles, as detected by VisR ultrasound, may be diagnostically relevant to clinically monitoring dystrophic muscle degeneration in boys with DMD.

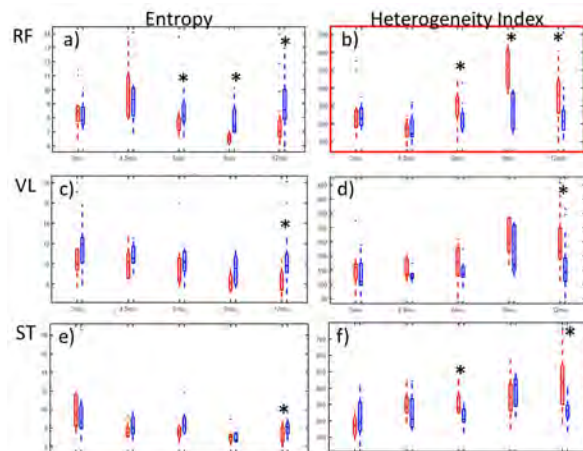


Figure 1: Entropy and Heterogeneity Index (HI) versus imaging time point in the RF (a, b), VL (c, d), and ST (e,f) muscles of GRMD (blue) and litter-mate control (red) dogs. Cross-sectionally, statistical difference ($p<0.1$, Wilcoxon) between GRMD and control in terms of texture value at single time points is indicated by an asterisk. Longitudinally, statistical difference between GRMD and control in terms of slope of texture feature versus time is indicated by the red panel outline (b). For brevity, RV results, LRI and SRI outcomes, and results in the CS are not shown.

Measurement of Passive Elastic Property of Human Gastrocnemius Muscle in Vivo using Dynamic Ultrasound B-mode and Shear-wave Elastography Image Sequences

Yang Xiao¹, Congzhi Wang¹, Hairong Zheng¹, Jinhua Yu²

¹Shenzhen Institutes of Advanced Technology, Chinese Academy of Sciences, China, People's Republic of, ²Fudan University, China, People's Republic of

Background, Motivation, and Objective

Musculoskeletal application of shear-wave elastography (SWE) is just beginning to be realized and studied. Since skeletal muscle is a dynamic tissue and its mechanical properties will change throughout the functional process, a certain elastic modulus value can not fully characterize the changed properties. The purpose of this preliminary study is to propose a physiologically meaningful parameter α , termed stiffness index, from the elastic modulus-length curve obtained by tracking dynamic B-mode and SWE image sequences during human gastrocnemius muscle (GM) passive stretching, and apply the new parameter for clinical evaluation of muscle atrophy.

Statement of Contribution/Methods

In this study, B-mode and SWE examinations of resting right GM were implemented in 9 subjects (7 healthy, 2 atrophy) during passive ankle angle from 40°plantarflexion to 20°dorsiflexion performed on an isokinetic dynamometer (Fig.a). The distal muscle-tendon junction of GM was visualized by B-mode image sequences and its positional change, defined as muscle length l change, was tracked by using an open-end gradient vector flow snake based on a modified energy function (Fig.b). Mean elasticity value in region of interest (ROI) of GM belly was measured as muscle elastic modulus E (Fig.c). A piecewise exponential model was proposed to describe the passive elastic modulus-length ($E-l$) relationship of GM. The Gauss-Newton algorithm was used to estimate stiffness index α from the $E-l$ curve.

Results/Discussion

The $E-l$ data were well fitted to the piecewise exponential model ($0.933 < R^2 < 1$, Fig.d, e) to calculate the parameter α . The α values differed significantly between healthy and atrophy subjects (mean standard deviation: 148.2 ± 18.4 versus 681.2 ± 343.2 , $p < 0.05$, Fig.d, e, f). The constant α existing in the passive stretching process reflects the ‘invariability within variability’ (slope of normalized $E-l$ curve), and better quantifies the essential elastic property of skeletal muscle. Furthermore, the new elastic parameter has the potential to provide valuable information for diagnosis of muscle disorders and in monitoring disease progression and treatment response.

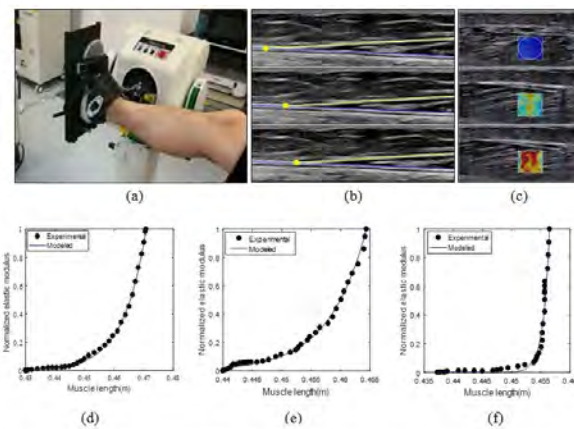


Fig. 1. (a) An isokinetic dynamometer for GM passive stretching. (b) Distal muscle-tendon junction of GM tracking using dynamic B-mode image sequences for muscle length measurement. (c) Muscle elastic modulus measurement using dynamic SWE image sequences. (d) Healthy subject 1 ($\alpha=128.6$). (e) Healthy subject 2 ($\alpha=156.6$). (f) Atrophy subject 1 ($\alpha=923.8$).

Pulmonary edema model study using lung ultrasound surface wave elastographyJinling Zhou¹, Boran Zhou¹, Xiaoming Zhang¹¹*Mayo Clinic, Rochester, MN, United States***Background, Motivation, and Objective**

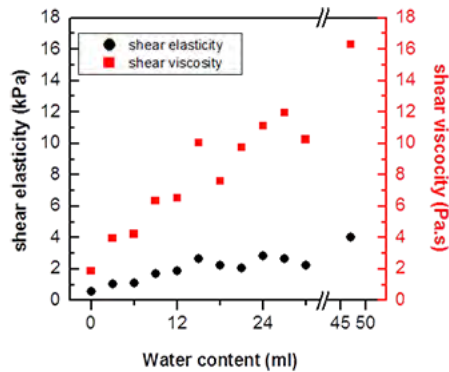
Lung ultrasound surface wave elastography (LUSWE) was developed as a novel noninvasive technique to measure superficial lung stiffness for assessing interstitial lung disease. The purpose of this study is to develop LUSWE for assessing pulmonary edema which is common for patients suffering from a heart failure.

Statement of Contribution/Methods

Pulmonary edema was modeled in a lung phantom model using cellulose sponges injected with different amount of tap water. The cellulose sponge was cut into a rectangular shape with a dimension of 3.0 cm x 1.9 cm x 8.0 cm. Tap water was injected onto three locations 1.0 cm apart on the 1.9 cm x 8.0 cm side. The total injected water was from zero to 30 ml in steps of 3 ml. An additional measurement was taken when the sponge was on the edge of dripping. This pulmonary edema phantom model was measured by LUSWE, where a shaker generated a harmonic vibration on the sponge surface and an ultrasound probe was used to detect the sponge surface wave propagation. The wave propagation was measured for waves at 100, 150, 200, 250 and 300 Hz. The surface wave speeds at these five frequencies were combined with the corresponding sponge density to estimate the sponge viscoelasticity. The measurement was repeated for all water levels and the results were compared.

Results/Discussion

Calculated by dividing the angular frequency by the rate of phase change with distance, the sponge surface wave speeds were larger for waves with higher frequencies; the sponge surface wave speeds at different water levels remained similar. The sponge viscosity and elasticity nevertheless increased with the water level. This study suggests that LUSWE is useful to evaluate the water content in the lung sponge phantom. Further study will be performed on *ex vivo* swine lung tissues.



Comparison of placental elastography and contrast-enhanced ultrasound imaging in a murine intrauterine growth restriction model

Emmanuel Simon¹, Jean-Pierre Remenieras¹, Chloé Arthuis², Ayache Bouakaz¹, Samuel Calle³

¹UMR 1253, iBrain, University of Tours, Inserm, Tours, France, ²Obstetrics, Gynecology and Fetal Medicine, University Hospital of Tours, Tours, France, ³Réseaux et télécommunications, GREMAN UMR 7347, Tours cedex 2, France

Background, Motivation, and Objective

Shear Wave Elastography (SWE) is a promising tool for the detection of placental pathologies. However, the relations between the elasticity of this organ and the uteroplacental perfusion are not known. We used a murine model of intrauterine growth restriction (IUGR) to study the shear wave speed (SWS) according to the parameters of Microbubble-based contrast-enhanced ultrasound (CEUS).

Statement of Contribution/Methods

IUGR was created by ligation of the left uterine artery of six Sprague–Dawley rats on day 17. The model validity was checked after cesarean section with the weighing of the fetuses in each uterine horn. CEUS scans were performed on day 19 using the Vevo2100 (Visualsonics Inc., Toronto, Canada) and a 21MHz (MS250) probe at a mechanical index of 0.43.

Ultrasound contrast agents were injected in a 200 µL bolus at a concentration of 1 mL/kg of Definity® microbubbles (Lantheus Medical Imaging, Billerica, MA), diluted in 1 mL of 0.9% saline in a 24-gauge catheter located in the caudal vein of the rat.

The following parameters were quantified: Peak Enhancement (PE), Time To Peak (TTP), Wash in Rate (WiR) and Wash in Area Under the Curve (WiAUC).

At the same time (day 19), a SWE examination was conducted using an Aixplorer system (Supersonic Imagine, France) and a US linear probe (128 elements centered at 2.8 MHz). SWS measurements were performed in two placental regions (deep and superficial) and repeated 3 times by 2 operators. In addition, SWS values have been measured before injection of microbubbles, 2, 3 and 4 minutes after injection.

Results/Discussion

In the superficial region of placenta, the mean SWS value was 1.68m/s +/-0.35 for the control horn, and 1.44m/s +/-0.29 for the ligated horn ($P=0.011$). In the deep region, the SWS values for the control and ligated horns were 2.08m/s +/-0.42 and 1.77m/s+/-0.50 respectively ($P=0.019$). No significant evolution of SWS has been observed before and after injection of microbubbles. Intra and inter reproducibility of SWS measurement was good.

No correlation has been found between perfusion parameters (PE, TTP, WiR, WiAUC) and SWS values (in ligated and non-ligated horns).

Our study found a decrease in SWS in case of vascular ligation. However, there is no significant relation between the elastographic and perfusion parameters. These two evaluations seem independent.

SHEAR WAVE SPEED DISPERSION COMPARISON IN NORMAL AND ABNORMAL PLACENTAS

Emmanuel Simon¹, Jean-Pierre Remenieras², Marie-Coline Dumoux³, Frédéric Pataf⁴, Franck Perrotin⁵, Samuel Callé⁶

¹UMR 1253, iBrain, University of Tours, Inserm, Tours, France, ²UMR 1253, iBrain, Université de Tours, Inserm, France,

Metropolitan, ³Vermon SA, France, ⁴Inserm CIC 1415, University Hospital of Tours, Tours, France, ⁵Obstetrics, Gynecology and Fetal Medicine, University Hospital of Tours, Tours, France, ⁶Réseaux et télécommunications, GREMAN UMR 7347, Tours cedex 2, France

Background, Motivation, and Objective

In case of intra-uterine growth restriction (IUGR) or preeclampsia (PE), changes in placental tissue architecture could cause variations in elasticity. Among the ultrasound (US) elastography methods, transient elastography (TE) seems suitable for such an application. We evaluated the interest of a frequency analysis for shear wave speed (SWS) in order to distinguish the elasticity of normal and abnormal placentas.

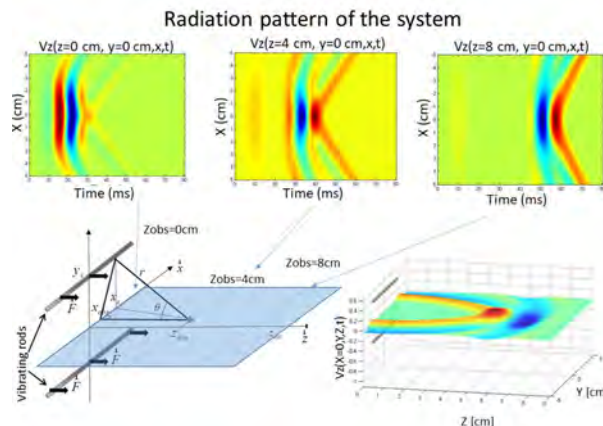
Statement of Contribution/Methods

We developed a 2D TE system, based on the coupling of a shear wave generated by 2 vibrating rods and US images acquired at an ultrafast rate. Two electrodynamic excitors, decoupled from the US linear probe (128 elements centered at 2.8 MHz), generated the vibration of the rods. Beamformed demodulated IQ data were acquired with an ultrafast US scanner (Aixplorer, Supersonic Imagine, France): acquisition at 2.8 MHz during 128ms with a PRF of 4 kHz. The particle velocity was computed using extended autocorrelation method. Calculating the spatial FFTs of $Vz(z,\omega)$, the SWS dispersion curve was obtained between 20 Hz and 80 Hz. The experimental data obtained from TE were fitted with a fractional rheological model $G^*(\omega) = Ge + K[\omega]^n$. The method has been applied *ex vivo* on 22 uncomplicated pregnancies, 9 IUGR, and 4 PE. Measurements (3 times with repositioning, 2 operators) have been performed on 2 regions, central and peripheral. Then, the experiment has been conducted *in vivo* on 2 pregnant women (normal pregnancies).

Results/Discussion

The mean SWS (at 50 Hz) was lower in case of IUGR (1.05 m/s +/- 0.05) than in control group (1.77 m/s +/- 0.48, $P < 0.001$) or in PE cases (1.20 m/s +/- 0.22). In addition, the mean exponent n value of the model was lower in case of IUGR (1.01 +/- 0.24) compared to control group (1.27 +/- 0.11, $P = 0.006$) or PE cases (1.18 +/- 0.36). We found no difference between central and peripheral regions. The optimal cutoff values of SWS and n for distinguishing normal and pathological situations were 1.37 m/s and 1.13 respectively, with AUC of 0.98 (IC 95% 0.94-1) and 0.75 (IC 95% 0.51-0.99) respectively. Intra and interobserver reproducibility was good for both Cs and n values. The *in vivo* experiments demonstrated feasibility of this method during pregnancy.

The frequency analysis of SWS could improve the ability of TE to distinguish normal and abnormal placentas.



P1-B7 - Cardiovascular Imaging

Kairaku (posters 1)

Wednesday, October 24, 9:30 AM - 4:00 PM

Chair: **Marie Traberg** Technical University of Denmark

P1-B7-1

Ultrasonically measured propagation speed of myocardial contraction rapidly decreased in swine heart just after avascularisation of coronary artery

Akane Hayashi¹, Mototaka Arakawa¹, Shohei Mori², Hiroaki Yamamoto³, Susume Morosawa³, Hiroaki Shimokawa³, Hiroshi Kanai²

¹Graduate School of Biomedical Engineering, Tohoku University, Sendai, Japan, ²Graduate School of Engineering, Tohoku University, Sendai, Japan, ³Graduate School of Medicine, Tohoku University, Sendai, Japan

Background, Motivation, and Objective

Fatal necrosis of the myocardium can be avoided by prompt re-perfusion at the onset of myocardial ischemia. Therefore, rapid identification of ischemic regions is essential for diagnosis and treatment of the early stage of ischemic heart disease. In the present study, in order to establish an ultrasonic-based method of identification of ischemic regions, the change of the myocardial contraction response from normal to ischemic conditions was elucidated by ultrasonic measurement.

Statement of Contribution/Methods

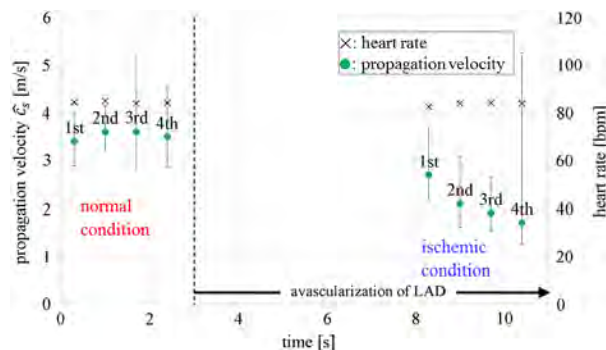
Ultrasonic measurement was applied to the interventricular septum (IVS) of an open-chest heart of 5 swine under normal conditions. For each swine, just after that ischemia in the IVS was induced by avascularizing the left anterior descending coronary artery, ultrasonic measurement of the ischemic septum was applied within a few seconds. The number of the scanning ultrasonic beams in the heart was restricted to 13 in order to keep the high pulse repetition interval.

By applying the phased-tracking method [IEEE Trans on UFFC Vol. 43, pp. 791-810, 1996.] to the acquisition signals in each condition, velocity waveforms with minute vibration were simultaneously obtained at about 3,000 points in the IVS. By applying a cross-correlation between the resultant vibration velocity waveforms at each measurement point and that at the reference point, the propagation of the myocardial contraction was evaluated as transition of the delay time. The propagation speed was quantitatively determined by applying the straight line to the delay for the onset time of the contraction response.

Results/Discussion

In the IVS, the myocardial contraction response propagated from the basal side to the apical side. For the swine, its propagation velocity was 3.4 m/s under normal conditions and 2.7 m/s under ischemic conditions, and a decrease of the propagation velocity was observed during the avascularization as shown in Figure. Similar results were observed for other 4 swine. In addition, for the short period of 10 seconds, the propagation velocity rapidly decreased as avascularization time elapsed.

Using the proposed measurement and analysis, change of the myocardial contraction response from normal to ischemic conditions was confirmed. It was suggested that myocardial ischemic regions are identified noninvasively by ultrasonic measurement.



Ultrasound imaging of cardiac fiber orientation: What are we looking at?

Alessandro Ramalli¹, Pedro Santos¹, Jan D'hooge¹

¹Lab. on Cardiovascular Imaging & Dynamics, Dept. of Cardiovascular Sciences, KU Leuven, Leuven, Belgium

Background, Motivation, and Objective

Myocardial tissue is very complex: sarcomeres are linked to form myofibrils that combine into myocytes that, in turn, group into muscle fibers; the latter are organized in a complex 3D network governing cardiac mechanics and function. As such, cardiac fiber imaging might be an important diagnostic tool. Hereto, Papadacci et al. (Sci. Rep. 2017) enabled the assessment of the transmural fiber orientation during the cardiac cycle by 3D Backscatter Tensor Imaging; however, which histologic structure it detects remains unclear. The aim of our work was therefore to propose and validate, by computer simulation, a theoretical framework that addresses this issue.

Statement of Contribution/Methods

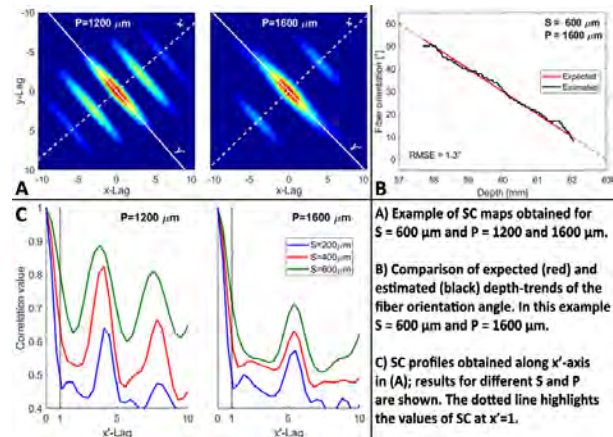
The theory shows that, for an unfocused transducer, the spatial coherence (SC) of the echo field equals the autocorrelation of the spatial scattering amplitude distribution of the area illuminated by the transmitted beam. Hence, the SC maps do not only carry information on fiber direction (i.e. the direction of highest correlation) but also have a one-to-one relationship with the fiber properties such as size (S) and pitch (P): the main-to-secondary lobe distance of SC relates to P while the width of the main lobe relates to S.

Field II simulations were carried out by modeling a 32×32 array. Numeric phantoms were also developed: the background consisted of random scatterers with a Gaussian scattering amplitude distribution; the fibers were scatterers whose amplitudes were modulated by a periodic function. Different models were constructed: the fibers were defined by S (200–800 μm) and P (400–2000 μm); their orientation was varied along depth from 60° to 0° . Synthetic RF signals were processed to compute SC and estimate the fiber characteristics.

Results/Discussion

Example SC maps are presented in A clearly showing main and secondary lobes. The RMSE of the estimated fiber orientations was $1^\circ \pm 1^\circ$ (B). Importantly, the SC characteristics depended on P and S (C): averaged over all models, the main-to-secondary lobe distance linearly correlated with P ($R^2=98\%$) while the value of the SC at lag 1 (i.e. an estimate of the main lobe width) linearly correlated with S ($R^2=92\%$).

In conclusion, as predicted by the proposed theory, the SC maps not only allow assessing the local fiber direction but also allow estimating fiber pitch and size thus providing information on the microstructures being investigated.



Detection of mechanical activation of the left ventricle using high frame rate ultrasound imaging

Kaja Kvåle^{1,2,3}, Jørn Bersvendsen^{1,2}, Pål Brekke², John Aalen^{2,4}, Espen Remme^{2,4}, Thor Edvardsen^{2,3}, Egil Samset^{1,2,3}

¹GE Vingmed Ultrasound, Horten, Norway, ²Center for Cardiological Innovation, Oslo University Hospital, Oslo, Norway,

³University of Oslo, Oslo, Norway, ⁴Institute for Surgical Research, Oslo University Hospital, Oslo, Norway

Background, Motivation, and Objective

Information on regional timing of myocardial mechanical activation (MA) is of potential clinical interest when diagnosing pathologies such as conduction system abnormalities or ischemia. With the advent of high frame rate (HFR) echocardiography, there is potential to map the MA of the myocardium and uncover rapid events not seen by conventional imaging. In this work we present a pilot study investigating the feasibility of using HFR echocardiography to determine spatio-temporal information about onset of MA in the left ventricle (LV).

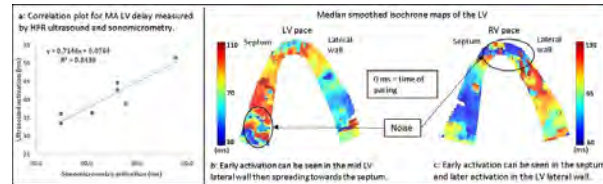
Statement of Contribution/Methods

HFR ultrasound imaging (1000 fps) was performed using a GE Vivid E95 scanner on 3 anesthetized open chest dogs during epicardial right ventricular (RV) and LV free wall pacing. Sonomicrometric crystals were implanted to measure strain rate in the basal / equatorial LV regions.

The start of MA was defined as the zero crossing of the strain rate curve in a 0.15 s time interval after pacing. Strain rate was obtained by first estimating the tissue velocity from radio-frequency data using autocorrelation on two consecutive frames. Then, strain rate was estimated from smoothed velocity data using a least squares algorithm and a segment length of 12 mm. The delay in activation between walls measured by HFR ultrasound was compared to simultaneous sonomicrometry measurements. Zero crossings in strain rate curves were manually selected from areas in the image corresponding to sonomicrometry sensor locations. After manual segmentation of the LV, isochrone maps were created by an automatic zero cross detection method.

Results/Discussion

Fig. a shows the correlation between LV wall MA delay as measured by ultrasound and sonomicrometry. An R^2 -value of 0.84 indicates a strong correlation. Fig. b shows an automatically generated isochrone map of LV pacing, with early activation in the mid lateral wall which spreads towards the septum. Fig. c shows RV pacing with early activation in the septum then spreading to the lateral wall. Some noise and discontinuities can be observed in the isochrone maps in fig. b and c. This can be explained by limited robustness of the automatic detection of zero-crossing in strain rate. However, when manually defining strain rate zero crossing, MA measured by ultrasound had good agreement with invasive measurements. Thus, HFR ultrasound shows potential as a non-invasive tool for LV MA mapping.



Spiral complex movements of the heart wall at the beginning of myocardial contraction detected by high frame speckle tracking

Hiroshi Kanai¹, Itsuki Kobayashi¹, Shohei Mori¹, Mototaka Arakawa²

¹Graduate School of Engineering, Tohoku University, Sendai, Japan, ²Graduate School of Biomedical Engineering, Tohoku University, Sendai, Japan

Background, Motivation, and Objective

Ischemia causes abnormality in excitation propagation of the local myocardium. Therefore, measuring myocardial contractile movement caused by electrical excitation leads to early detection of abnormalities of cardiomyocytes due to disease. However, the detail mechanism of the transition process in the myocardium from dilation to contraction is still unclear.

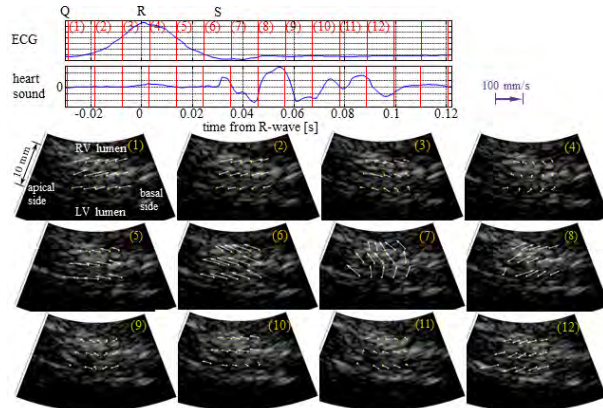
Statement of Contribution/Methods

In the present study, we acquired ultrasonic RF signals with a high frame rate of 1.2 ms using the parallel beam forming [IEEE Trans. UFFC, 2008;55:2626] by transmitting a plane wave from a sector probe. Furthermore, velocity and displacement in the 2D direction, the ultrasonic beam direction, and the direction orthogonal to the ultrasonic beam (lateral direction), were simultaneously estimated by applying the speckle tracking method, where the cross-correlation coefficient was interpolated so that the spatial resolutions in displacement estimation along the axial and lateral directions were increased to 1.0 and 2.2 μm , respectively. We then detected the propagation of contraction response due to electrical excitation along the ultrasound beam and lateral directions around the R-wave of ECG.

Results/Discussion

Figure shows the instantaneous velocity vector mapping of the ventricular septal wall for a healthy male obtained every 8.2 ms from the Q-wave. The yellow dots and arrows show the analysis points and the instantaneous 2D velocity vectors, respectively. As in Figs. (1) and (2) just after the Q-wave, the myocardium moved toward the base of the heart and the right ventricle (RV), which corresponds to the expansion. After this, the myocardium began to move to the side of the left ventricle (LV), it began to move towards the apical side a few ms later, and contraction of the LV started (Figs. (3)-(6)). From the S-wave, the myocardium moved so that the LV expanded in the direction of the RV and the base of the heart (Figs. (7)-(8)). The motion then became smaller and contraction of the LV temporarily stopped (Figs. (9)-(11)). Finally, from the end of the first sound, the myocardium moved again to the LV sides and the apex, and substantial contraction of the LV started (Fig. (12)). The contraction response propagates spirally with 1-4 m/s from Q-wave to the first sound.

These results suggest that the proposed method would be useful for evaluating the cardiac contractile function.



Adaptive Normalized Convolution for 4D reconstruction of freehand- rotated 2D TEE sequences

Raja Sekhar Bandaru¹, Mihai Strachinaru^{2,3}, Sophie van Malderen³, Gerard van Burken², Marcel Geleijnse³, Sing-Chien Yap³, Tamas Szili Torok³, Johan G. Bosch²

¹Biomedical Engineering, Erasmus MC, Rotterdam, Netherlands, ²Biomedical Engineering, Erasmus MC, Netherlands,

³Cardiology, Thoraxcenter, Erasmus MC, Netherlands

Background, Motivation, and Objective

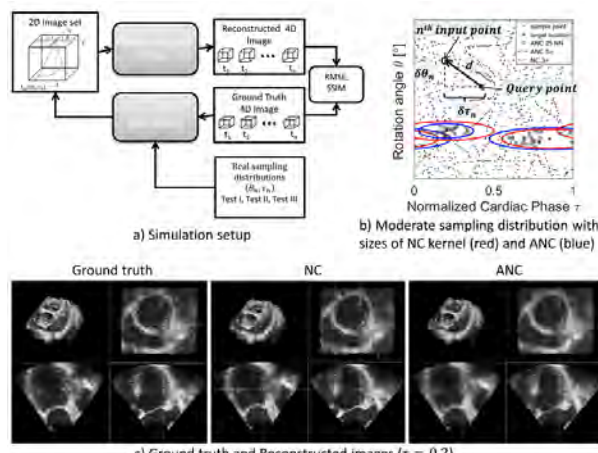
4D reconstruction of moving anatomy from 2D micro-TEE images with manual plane rotation requires sparse/irregular data interpolation. We earlier reported Normalized Convolution (NC) [1,2] methods with kernel sizes optimized for the expected density of the distribution [2]. However, performance depends on the actual irregularity of the spatio-temporal sampling distribution: the variable cardiac rhythm and manual probe plane rotation can lead to large holes in the angle/phase (θ, τ) sampling distribution. The fixed 2D smoothing kernel of NC may lead to sharp angle artifacts in undersampled areas and excessive smoothing in oversampled areas.

Statement of Contribution/Methods

We propose an Adaptive Normalized Convolution (ANC) approach using a 2D Gaussian kernel with a local size adjusted to the nearest samples. The sampling distribution was first rescaled in τ direction by 1/6 based on the optimum kernel aspect ratio found from overall ANC kernel optimization. For each query point, the 25 nearest samples in rescaled (θ, τ) space were selected by their Euclidean distance and average absolute distance in θ and τ determined the local kernel size. We compare results of ANC and NC in a simulation setup (fig 1a). A 4D dataset of high spatial and temporal resolution acquired with a commercial matrix TEE probe was used as ground truth. Test 2D TEE images were generated from the 4D TEE using three distinct angle/phase sampling distributions chosen from many actual micro-TEE rotating acquisitions: a)good, b)moderate (fig 1b) and c)poor. Root Mean Square Error (RMSE) and Structure Similarity (SSIM) metrics were calculated over the complete 4D data for NC and ANC. For NC, kernel sizes (0.03, 0.015) as previously optimized [2] were used.

Results/Discussion

ANC resulted in lower RMSE (a)13.9, b)14.25, c)16.9) and higher SSIM (0.9213, 0.92, 0.90) than NC (14.7, 14.8, 18.2 & 0.9125, 0.9125, 0.89). ANC reduced RMSE by 6, 4 and 7% for the three cases. ANC improved the image quality by adapting to the local distribution. Moreover, ANC is less sensitive to the variabilities in the actual sampling distributions.



[1] J.G. Bosch et.al. Medical Imaging 2006, p. 61470Q.

[2] A. Haak et.al. Ultrasonics Symposium 2012, pp. 703-706

Ultrasound Sub-pixel Speckle Tracking with Off-plane Motion Detector for Precise Vascular Imaging

Hideki Yoshikawa¹, Taku Yamamoto¹, Shin Yoshizawa², Shin-ichiro Umemura³

¹Research & Development Group, HITACHI Ltd., Tokyo, Japan, ²Graduate School of Engineering, Tohoku University, Sendai, Japan, ³Graduate School of Biomedical Engineering, Tohoku University, Sendai, Japan

Background, Motivation, and Objective

Frame accumulation with motion compensation is a feasible technique to provide clear vascular images. Recently, with the use of high-frame-rate systems, the sizes of vessels potentially have become much smaller, so the motion tracking needs to be more precise. In addition, how to reduce artifacts due to off-plane motion that is perpendicular to the imaging plane remains a critical issue to be solved. In this article, sub-pixel motion tracking with an off-plane motion detector is proposed.

Statement of Contribution/Methods

The tracking algorithm consists of SAD (sum of absolute differences), interpolation, and the KLT (Kanade-Lucas-Tomasi) feature tracker. SAD is a pixel-based tracking method that uses the residual brightness value. And KLT is a sub-pixel tracking method that uses the gradient of brightness between neighboring pixels. By combining both methods, accurate and robust tracking for various motions is achieved. The off-plane motion detector (OPMD) was defined by using statistical analysis of the distribution of the residual values obtained by SAD. The sensitivity of the detector was evaluated by phantom experiment. Lastly, the feasibility of the proposed algorithm was evaluated by applying the algorithm to frame accumulation of power Doppler images and contrast-enhanced images with rabbit vascular images.

Results/Discussion

Fig. 1 shows the simulation result of the sub-pixel speckle tracking against in-plane motion, and an accuracy of about 0.2 pixels ($20 \mu\text{m}$) was achieved. Figs. 2 (a) and (b) show the relation between the tracking results and the OPMD against the off-plane motion. Note that off-plane motion (d) is normalized by the axial beam width (W) of the transmission pulses. Focusing on the OPMD, the value rapidly increases at $W = 0.3$, and most importantly this occurs before the tracking failures at $W = 0.4$. That means the detector can practically work as an indicator to predict tracking failures. The threshold value of OPMD is also evaluated to be independent of frequencies and probe types. Figs. 3 show the results of the *in vivo* experiment. Rabbit vessels are clearly imaged in Fig. 3 (a) with motion compensation and Fig. 3 (b) with removing frames detected by OPMD. However, these vessels are obviously blurred in Fig. 3 (c) without motion compensation and Fig. 3 (d) without removing frames detected by OPMD.

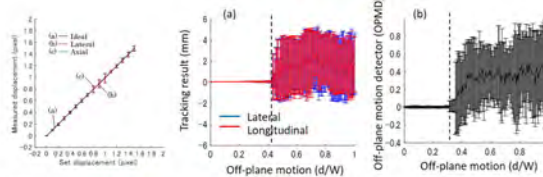
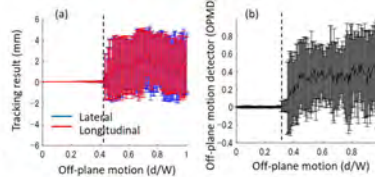
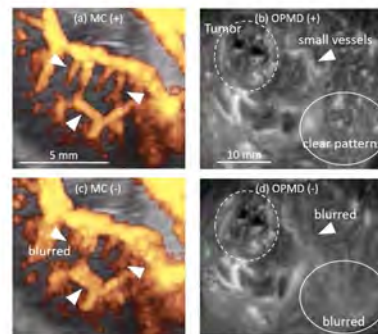


Fig. 1 Simulation results of motion tracking



Figs. 2 Relation between tracking result (a) and OPMD (b).



Figs. 3 Vascular images of rabbit kidney with frame accumulation. Left: Power Doppler images (a) with and (c) without motion compensation (MC). Right: Contrast-enhanced Images (b) with and (d) without OPMD.

Automatic quantification of Extra-Medial Thickness in carotid ultrasound
Guillaume Zahnd¹, Michael Skilton², Nassir Navab¹
¹*Chair for Computer Aided Medical Procedures & Augmented Reality, Technische Universität München, Germany*, ²*Boden Institute of Obesity, Nutrition, Exercise and Eating Disorders, University of Sydney, Australia*
Background, Motivation, and Objective

Ultrasound imaging of the intima-media thickness (IMT) is one of the most widely adopted methodologies to assess cardiovascular risk. However, this surrogate marker does not reflect the structural modifications to the adventitia that accompany atherosclerotic disease progression. A novel marker, dubbed EMT (Extra-Medial Thickness), has recently been described. EMT is defined as the combined thickness of the adventitia, jugular wall, interstitial tissue, and perivascular tissue. This index was demonstrated to be more strongly associated with modifiable risk factors than the established carotid IMT technique. Nevertheless, EMT measurements are still performed manually with calipers or operator-intensive adaptation of existing semi-automated methods; there is as yet no EMT-specific semi or fully automated method.

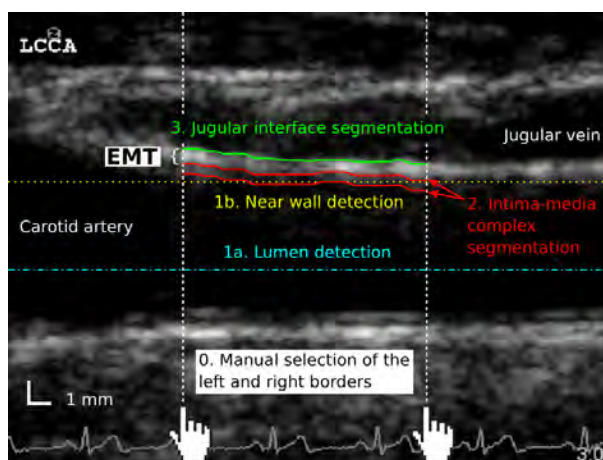
Statement of Contribution/Methods

The main contribution of this work is a framework to segment the arterial tissues and quantify the EMT. Two main issues make this task challenging: The presence of two lumens (jugular and carotid) with a similar layered structure, and a less favorable echogenicity on the near wall compared to the far wall.

The only user interaction is to indicate the left and right borders of the region to be processed. The remaining of the method is based on three fully automatic steps. 1. A pre-processing phase is conducted to extract the approximate carotid lumen centerline and the depth of the near wall. This is conducted by detecting peaks and valleys intensity points. 2. The contours of the lumen-intima and media-adventitia interfaces are simultaneously extracted via a front propagation in a 3D search space, where the minimum-cost path describes both the centerline and the spacing of the target contours. 3. The extracted intima-media complex is used as an unambiguous anchor point to further locate the contour of the jugular interface via a second front propagation in a circumsized region.

Results/Discussion

A total of 35 participants (21 healthy volunteers and 14 at-risk patients) were involved in this study. The method was successfully applied to all participants. The lumen and the near wall were automatically detected in all cases. The average absolute error (\pm STD) of EMT quantification was $115 \pm 196 \mu\text{m}$ (pixel size: $52 \mu\text{m}$). This automatic method has potential to be a novel tool for cardiovascular risk analysis in routine clinical practice.



Automatic spatial mechanical inhomogeneity detection in atherosclerotic carotid arteries in-vivo
Grigoris Marios Karageorgos¹, Iason Zacharias Apostolakis², Pierre Nauleau¹, Paul Kemper³, Elisa Konofagou³
¹*Biomedical Engineering, Columbia University, New York, NY, United States*, ²*Columbia University, NY, United States*,

³*Biomedical Engineering, Columbia University, United States*
Background, Motivation, and Objective

Pulse wave imaging (PWI) is an ultrasound-based method, which can regionally map the pulse wave velocity (PWV). The aims of this study were to present a novel method that utilizes the PWI information to automatically detect spatial inhomogeneities along the imaged blood vessel, and employ this method to analyze the wall dynamics in human atherosclerotic common carotid arteries (CCAs) in-vivo.

Statement of Contribution/Methods

The CCAs of N=6 normal (6 M, 25.3 ± 3.1 y.o.) and N=10 (7 F, 3 M 68.3 ± 6.8 y.o.) atherosclerotic human subjects with moderate ($> 50\%$) to high-grade ($> 80\%$) stenosis were imaged at 5 MHz in vivo, using a 5-plane wave coherent compounding sequence at a frame rate of 1667 Hz. By applying a cross correlation technique, the arterial distension at each lateral position versus time ($v_i(t)$, $i=1,2,\dots,128$) was obtained.

Two markers of homogeneity were calculated at each position: i) the 50% upstroke ($T_{50\%,i}$) of $v_i(t)$, which denotes the linearity of the PW propagation; ii) the area under the curve (AUC_i) of the cross-correlation between $v_1(t)$ and $v_i(t)$. Using solely those markers as inputs, a dynamic programming algorithm over a graph modeling framework was developed to optimally divide the imaged artery into the most homogeneous segments. The borders of those segments indicate inhomogeneous regions. In atherosclerotic CCAs, the algorithm also detected the borders of the stenotic segment.

By fitting a line to $T_{50\%,i}$, the PWV, as well as the average peak distension (v_{peak}) were calculated across multiple lateral positions in healthy CCAs, the stenotic and pre-stenotic segment in atherosclerotic CCAs.

Results/Discussion

The number of inhomogeneous CCA regions identified was significantly higher in diseased compared to healthy CCAs ($p<0.001$), indicating that atherosclerosis leads to the vessel inhomogeneity increase. The absolute value of PWV and v_{peak} were lower in the stenotic segment compared to the pre-stenotic one ($p<0.01$ and $p<0.001$, respectively) and healthy CCAs ($p<0.01$ and $p<0.0001$, respectively). The decrease of PWV and v_{peak} in the stenotic segment can be related to the stiffness, and thus, the plaque composition.

In conclusion, a novel, automated approach for detecting inhomogeneities in arteries was presented, demonstrating the potential to enhance the PWI's mapping information and aiding in quantitative atherosclerosis diagnosis and monitoring.

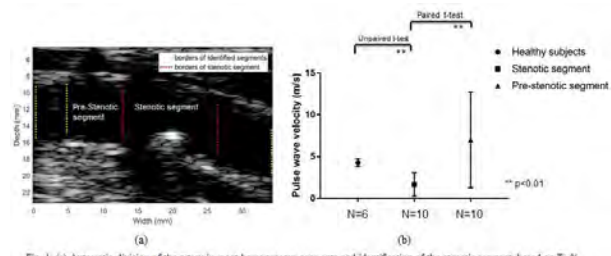


Fig. 1: (a) Automatic division of the artery in most homogeneous segments and identification of the stenotic segment, based on $T_{50\%}$ and AUC. The yellow dashed lines indicate the interfaces of those segments, while the red dashed lines show the borders of the automatically detected stenotic segment. (b) Mean and standard deviation of PWVs in healthy CCAs, stenotic and pre-stenotic segments in atherosclerotic arteries.

P1-B8 - Functional Assessment by Remote Modulation

Kairaku (posters 1)

Wednesday, October 24, 9:30 AM - 4:00 PM

Chair: Alessandro Ramalli University of Florence

P1-B8-1

Mobile Platform for Acoustoelectric Brain Imaging in Rats

Alex Burton¹, Cameron Wilhite², Tushar Bera³, Pier Ingram³, Stephen Cowen^{2,4}, Russell Witte^{1,3}

¹Department of Biomedical Engineering, University of Arizona, United States, ²Department of Physiology, University of Arizona, United States, ³Department of Medical Imaging, University of Arizona, United States, ⁴Department of Psychology, University of Arizona, United States

Background, Motivation, and Objective

Electrical brain mapping is important to help diagnose or treat diseases, such as Parkinson's, epilepsy, and depression. However, existing techniques for mapping surface potentials (e.g. electroencephalography) have severe limitations, including poor spatial resolution and accuracy. To overcome these limitations, we developed an acoustoelectric (AE) imaging device, which uses an ultrasound pressure wave to locally modulate tissue resistivity; in the presence of evoked potentials, the AE effect produces a high frequency modulation electrical signals. The purpose of this study is to test the feasibility of using acoustoelectric brain imaging (ABI) to map physiological activity in the rat hippocampus using depth and surface recording electrodes.

Statement of Contribution/Methods

We developed a mobile ABI platform containing a custom per-amplifier, fast DAQ board, function generator, and open ultrasound (US) system (Vantage 64LE Verasonics) coupled with a 2.5 MHz transducer (P4-1, Philips). A rat brain phantom (RBP) composed of saline and Agarose™ was molded with needle wires to generate an electric dipole field (3 cycles at 200 Hz and 5V). The US system produced modulated (1-4 MHz) chirp pulses (8KHz). Recorded signals on tungsten electrodes were conditioned a pre-amplifier, digitized, and processed for imaging. After following baseline AE characterization in the RBP, the imaging system was transferred to a surgical suite for ABI in anesthetized rats. Rats were fitted with either an array of 4 depth electrodes or a 16 channel surface electrode (NeuroNexus). Biphasic pulses (750µA, 100µs) were used to stimulate the perforant pathway in the hippocampus. Signals were collected at multiple points using electrical US beam steering at the recording sites and processed similarly to the RBP experiments to form ABI maps.

Results/Discussion

Spatial resolution of ABI is defined by the US focus with FWHM at 0.83 mm. RBP experiments show ability to conduct ABI with low injected currents (>0.1mA). Sensitivity is 2.8mV/mA with imbedded electrodes and 2.1mV/mA at US pressure of 2.75MPa. Preliminary results also show similar slow time response between AE image and evoked potentials in the rat hippocampus (>10mV). Preliminary data suggest that ABI could provide non-invasive, high-resolution 4D maps of human brain activity.

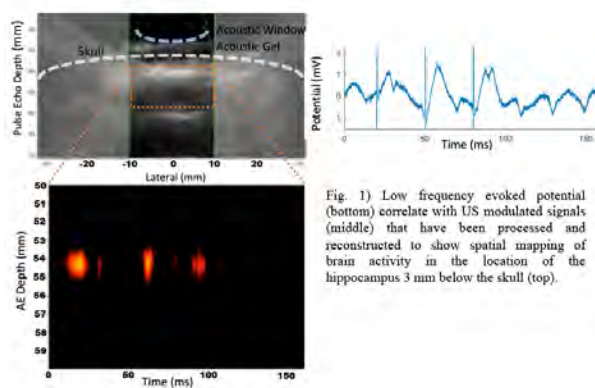


Fig. 1) Low frequency evoked potential (bottom) correlate with US modulated signals (middle) that have been processed and reconstructed to show spatial mapping of brain activity in the location of the hippocampus 3 mm below the skull (top).

Effects of Ultrasound Frequency and Beam Pattern on Acoustoelectric Cardiac Imaging

Alexander Alvarez¹, Jonathan Ferng², Chet Preston¹, Charles Ingram³, Russell Witte^{1,3}

¹Biomedical Engineering, University of Arizona, United States, ²Medicine, University of Arizona, United States, ³Medical Imaging, University of Arizona, United States

Background, Motivation, and Objective

Real-time, accurate, high-resolution maps of cardiac electrical propagation could lead to better tools for arrhythmia diagnosis and therapy. However, conventional electroanatomic mapping (EAM) is limited in resolution and accuracy. Acoustoelectric Cardiac Imaging (ACI) based on the interaction between an ultrasound (US) wave and tissue resistivity has been proposed to overcome these limitations. Though ACI of the cardiac activation wave has been exhibited in *ex vivo* rabbit hearts, these studies employed low frequency, single element transducers, impeding translation of ACI to humans. As such, we investigated the impact of US arrays with different center frequencies and beam patterns on the quality of ACI spatial resolution and sensitivity in tissues of varying myocardial thickness and fiber orientation.

Statement of Contribution/Methods

We used two setups to study the ACI resolution-sensitivity tradeoff in numerical simulations and tissue phantom experiments: 1) a monopole in saline with well-controlled current densities, and 2) cylindrical current sources with different radii (0.2-5mm) and orientations embedded in tissue (Fig. 1a). In each case, arrays with center frequencies from 0.6 to 5.5 MHz were used to generate plane waves or focused beams. For simulations, we used COMSOL to generate electric fields from current sources (Fig. 1b), FOCUS to generate pressure fields from the arrays, and custom MATLAB software to determine ACI resolution upon interaction of these fields. For phantom studies, a function generator injected ECG-like signal (Fig. 1c) through platinum electrodes into saline or tissue and a Verasonics Vantage 64 electronically steered the US array at a pulse rate of 4 kHz to generate ACI signal. This signal was recorded on an EAM lasso catheter and passed to a custom amplifier before digitization for analysis of resolution and sensitivity.

Results/Discussion

Higher US frequency with both focused and plane wave beam patterns improved lateral resolution of ACI with an ECG-like signal - from 3.81 mm FWHM in a 0.6 MHz array to 0.70 mm in a 5.5 MHz array (Fig. 1d) - but decreased sensitivity with increased tissue thickness and fiber complexity. Our results demonstrate that a broadband array with tunable frequency might allow for the best balance of the ACI resolution-sensitivity tradeoff for mapping of arrhythmias in heterogeneous cardiac tissue.

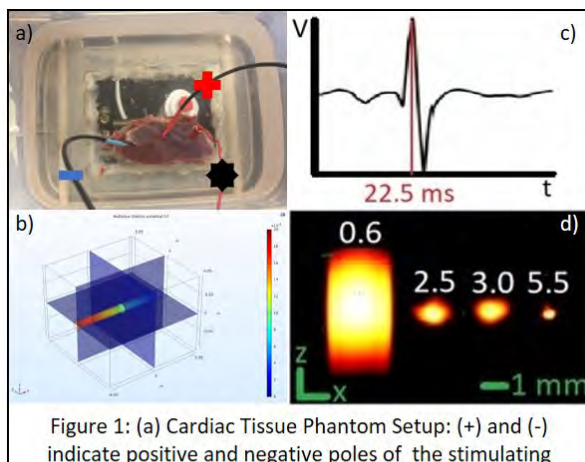


Figure 1: (a) Cardiac Tissue Phantom Setup: (+) and (-) indicate positive and negative poles of the stimulating dipole, respectively; (*) indicates recording electrode; (b) Electric Potential Field of simulated current source in COMSOL; (c) Low-frequency, ECG-like signal recorded from tissue; (d) ACI B-mode magnitude image for monopole in saline at peak of ECG-like signal (red line in c) using ultrasound arrays of different center frequencies (white numbers)(in MHz).

2D mapping of the electrical activation in the live heart using the acoustoelectric effect: a parametric study**Beatrice Berthon¹, Philippe Mateo¹, Nathalie Italy-Radio¹, Mickaël Tanter¹, Mathieu Pernot¹, Jean Provost¹**¹*Institut Langevin, ESPCI Paris, PSL Research University, CNRS UMR 7587, INSERM U979, Paris, France***Background, Motivation, and Objective**

Ultrafast Acoustoelectric Imaging (UAI) is a novel method for the mapping of biological currents, which may lead in the future to better diagnosis and treatment monitoring of cardiac activation diseases such as arrhythmias. We have previously shown the feasibility of mapping electrical activation in live hearts using UAI. In this study we assessed the impact of three key parameters in the optimization of image quality in UAI: mechanical contraction of the myocardium, frequency of the ultrasound wave and position of the measuring electrodes.

Statement of Contribution/Methods

UAI was performed in isolated rat hearts ($n = 10$) perfused with a nutritive Krebbs-Henseleit solution. For $n=5$ rats, 2,3-butane dione monoxime (BDM) was mixed in the perfusion solution to suppress the mechanical contraction of tissues. A fully integrated UAI system described previously was used to image the hearts via a pair of Ag/Cl electrodes placed on the myocardium wall, after differential amplification and high pass filtering. The electrocardiogram (ECG) was measured simultaneously via the same electrode pair. Data were acquired using up to 33 tilted plane waves emitted with a maximum peak negative pressure of 3 MPa (MI=1.4) for three ultrasound probes centered at 3-MHz, 5-MHz and 12 MHz. The experiment was repeated for 6 different positions of the measuring electrodes for $n=3$ hearts.

Results/Discussion

2D current density maps were obtained from the received UAI signals with a frame rate of up to 10000Hz during several heart cycles, and overlaid onto B-mode images obtained simultaneously. No signals were visible for the 12MHz probe. For the 3MHz and 5MHz probes, high intensity UAI signals visible on the averaged maps at the atrio-ventricular node (AV) node, ventricular walls and apex were temporally periodic, with a frequency matching the simultaneously measured ECG signals. This was observed even when BDM was used, confirming that the measured signals were independent from tissue contraction. High intensity peaks for these different regions were obtained at different time points of the ECG, which corresponded to the QRS complex for the AV node. These data allowed estimating the electrical activation propagation from the AV node to the apex at 0.30 mm/ms. As expected, different electrode positions led to UAI signals visible in different parts of the myocardium, allowing for the generation of 2D maps of the electrical activation in the whole myocardium by combining the corresponding images. Our results suggests that Ultrafast Acoustoelectric Imaging at frequencies of 5 MHz and below allows for real-time imaging of the current density in the whole myocardium and of the electrical activation propagation in the live heart. Work is in progress to demonstrate its use as a non-invasive technique for the diagnosis and study of cardiac activation diseases in-vivo.

Real-time Thermoacoustic Imaging and Thermometry Using a Linear Ultrasound ArrayChandra Karunakaran¹, Srishti Sarawat¹, Jin-pil Tak¹, Hao Xin¹, Russell Witte¹¹*University of Arizona, United States***Background, Motivation, and Objective**

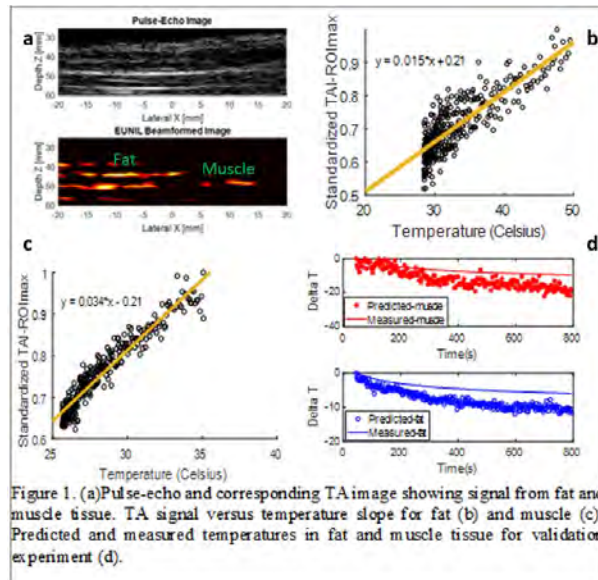
In recent years, there has been a progressive trend towards minimally invasive treatments for breast cancer, such as thermal ablation with focused ultrasound or microwaves. However, thermal therapies usually require real-time temperature monitoring for feedback. Whereas thermocouples are invasive and provide only point measurements, MR thermometry requires expensive equipment. As a result, there remains an unmet need for an accurate, real-time, low cost modality for monitoring temperature during ablation therapy. Hence, we propose real-time thermoacoustic (TA) imaging and thermometry for mapping tissue dielectric properties and monitoring temperature. The primary goal of this study was to quantify the temperature dependence of the TA signal from different types of tissue (muscle and fat) and then predict and validate tissue temperature during a separate heating experiment.

Statement of Contribution/Methods

A microwave source was used to produce short microwave pulses (2.8 GHz, 4 kW, 340 ns) for TA imaging. TA images were collected with a 96-element 2.5 MHz linear ultrasound array (P4-1, Philips, Vantage 64LE, Verasonics). A slab of fresh bovine muscle and porcine fat (0.5 cm thick) were placed side-by-side, wrapped in a thin film, heated to approximately 60 °C before placing in the imaging tank filled with mineral oil. Thermocouples were placed in the fat and muscle samples independently to record temperatures every second during the cooling period. The peak TA signal within defined regions corresponding to the muscle and fat tissue were then correlated with the thermocouple measurements, and the best-fit slopes were calculated. A second validation experiment was used to predict the change in temperature for muscle and fat based on the previous calibration, and compared it with actual temperature measurements.

Results/Discussion

Strong correlation between temperature and peak TAI signal was observed for both muscle ($R^2=0.716$) and fat ($R^2=0.92$) with slopes of 1.5%/°C and 3.4%/°C, respectively. In predicting tissue temperatures, root-mean-square errors (RMSE) were 0.24 °C and 0.14 °C per °C increase in temperature of muscle and fat, respectively. In the future, real-time 3D TA thermometry may improve accuracy and monitoring of temperature in heterogeneous tissue during delivery of thermal therapies for treatment of breast cancer.



Detectability of Model Thrombus as a Function of Size and Stiffness using Magnetomotive UltrasoundBenjamin Levy¹, Md Murad Hossain², Justin Sierchio¹, Diwash Thapa¹, Caterina Gallippi², Amy Oldenburg^{1,3}¹*Department of Physics and Astronomy, The University of North Carolina at Chapel Hill, Chapel Hill, NC, United States*, ²*Joint Department of Biomedical Engineering, The University of North Carolina at Chapel Hill, Chapel Hill, NC, United States*,³*Biomedical Research Imaging Center, The University of North Carolina at Chapel Hill, Chapel Hill, NC, United States***Background, Motivation, and Objective**

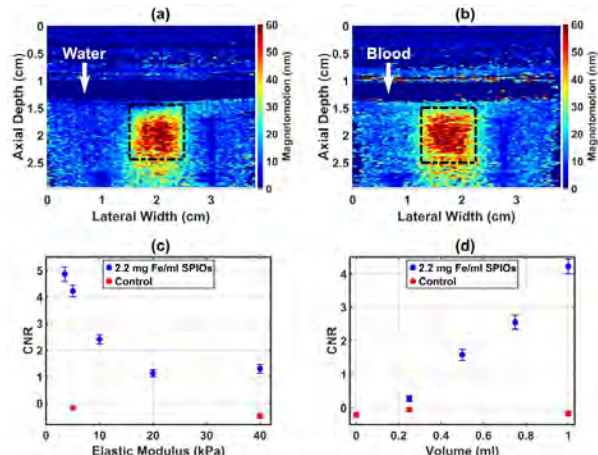
Thrombosis, a leading cause of heart attacks, pulmonary embolisms, and strokes, requires rapid diagnosis and treatment monitoring. Magnetomotive Ultrasound (MMUS) using thrombosis-targeting super-paramagnetic iron oxide (SPIO) particles as a contrast agent is a promising new imaging solution which, unlike Doppler and Compression, can contrast thrombi against a dark-field. Such a modality shows promise for *in situ* detection of thrombus volume and elastic modulus, which are clinically relevant in several thromboembolic diseases. By using porcine blood, pumped in a pulsatile manner we show that MMUS is sensitive to simulated thrombus volume and elastic modulus in gelatin tissue-mimicking phantoms, even in the presence of artificial cardiac motion.

Statement of Contribution/Methods

Blood vessel phantoms were constructed from tissue-mimicking gelatin with an SPIO-labeled model thrombus hidden beneath a tube with a 6 mm lumen and a physiologically-relevant elastic modulus. Water or blood was pumped through the tube with a peristaltic pump which mimicked the pulsations of cardiac motion. The open-air MMUS system created a 2 Hz sinusoidal magnetic force, and ultrasound RF data was collected. For thrombus detection, a frequency and phase-locking algorithm was used to determine the portions of the image containing 2 Hz motion. Contrast-to-noise ratio (CNR) was measured for model thrombus volumes and elastic moduli ranging from 0.25 to 1.0 ml, and 3.5 to 40 kPa respectively. The water was then replaced with porcine whole blood, and experimentation was repeated.

Results/Discussion

As expected, thrombus volume correlated positively with CNR ($r = 0.99$), while elastic modulus correlated negatively ($r = -0.81$). Results were independent of flow rate and pump-induced vibration amplitude, indicating that MMUS is robust to cardiac-like motion. Model thrombi as small as 0.5 ml, and as stiff as 40 kPa were detectable (CNR >1). A transition to a more physiologically-realistic model has begun. When water was replaced with porcine whole blood, no qualitative change in detectability was observed. Volume and elastic modulus trends also held, indicating that MMUS has promise for quantitative thrombosis imaging *in-vivo*. Current work involves using SPIO-labelled platelets for targeted MMUS imaging of damaged regions in *ex-vivo* porcine blood vessels integrated into the flow system.



(a) MMUS image of gelatin blood vessel phantom under pulsatile water flow, and (b) porcine whole blood flow. The true location of the SPIO-laden model thrombus below the vessel-mimicking tube is shown dashed. (c) Average CNR as a function of thrombus elastic modulus in the presence of pulsatile water flow, and (d) Average CNR as a function of volume in the presence of pulsatile water flow.

Real-Time Magnetomotive Ultrasound Imaging Using a Recursive EstimatorTim C. Kranemann¹, Thomas Ersepke¹, Georg Schmitz¹¹*Chair for Medical Engineering, Ruhr-University Bochum, Bochum, Germany***Background, Motivation, and Objective**

Real-time capability is a valuable feature of ultrasound (US) imaging methods. It is also considered necessary for the clinical application of magnetomotive (MM) US. However, frame rates >1 Hz have not been reported to date. Here, we implemented an algorithm that is real-time capable and improves the motion estimation.

MMUS imaging is the identification of nanoparticle labeled tissue by detecting a magnetically induced, often sinusoidal motion. Hence, the phase of IQ-data per pixel over time, which corresponds to the in-pixel motion, is evaluated with a discrete-time Fourier transform (DFT) at the MMUS frequency. Magnitude and phase of the DFT are used for motion display. In practice, it needs to be accounted for an instationarity in the MMUS signal due to interfering tissue motion, which requires trading of time and frequency resolution of the estimate. Therefore, a recursive spectral estimator with a sliding window is used here.

Statement of Contribution/Methods

A modified sliding windowed infinite Fourier transform (SWIFT) was implemented. Thereby, incoming data updates a previous motion estimate. An exponential decaying window gives more weight to recent data, allowing for adjusting efficiency against tracking ability in instationary motion. Due to the infinite nature, motion can be tracked at any frequency. The algorithm has similar computational complexity, but significantly less memory requirement compared to the DFT approach. Due to the recursive update, the computer can call the corresponding function at any time, which solves several interdependencies between software processing and hardware constraints.

The algorithm was compared offline to the DFT approach with a simulation of radio frequency (RF) lines in Field II containing a 0.1-1 μm scatter motion. White Gaussian noise was added to the RF-data resulting in a signal-to-noise ratio of 30 dB. A pulse repetition frequency (PRF) of 5.25 kHz was set to track a 105 Hz motion in groups of 350 frames, corresponding to a 15 Hz B-mode display rate. The SWIFT estimate was updated for one second; the same data was used by the DFT-approach.

To evaluate real-time feasibility, an US platform (Vantage 256 with P4-2v transducer, Verasonics) was programmed to acquire data with the PRF and B-mode rate. The SWIFT-based implementation in MATLAB was executed on a GPU (Tesla K40, Nvidia) with the aim to display the MMUS estimate together with the B-mode image.

Results/Discussion

An MMUS algorithm optimized for real-time execution was proposed which also improves the estimator performance. In the simulation, a 3 dB improvement in mean absolute error of motion was achieved with SWIFT over the DFT using the same data. An improvement of 12 dB is achieved when 350 frames are used for the DFT, corresponding to a 15 Hz display rate. The US hardware processed the SWIFT-based algorithm in 58 ms for 350 frames of 4902 px, which allowed to display a latest SWIFT estimate in real-time together with a B-mode image.

P1-B9 - High-Frequency Tissue Characterization

Kairaku (posters 1)

Wednesday, October 24, 9:30 AM - 4:00 PM

Chair: **Eric Strohm** University of Toronto

P1-B9-1

Estimating the change in cellular size variance during cell death using the polydisperse structure factor model

Emilie Franceschini¹, Laure Balasse², Sandrine Roffino³, Benjamin Guillet²

¹Aix-Marseille université, CNRS, Centrale Marseille, France, ²Aix-Marseille Université, INSERM, INRA, C2VN, France, ³Aix-Marseille Université, CNRS, ISM, France

Background, Motivation, and Objective

Quantitative UltraSound (QUS) techniques for determining the tissue microstructure are promising tools to detect and quantify cell death, and thus monitor the tumor response to therapy. Previous *in vitro* experimental studies suggested that the changes in the backscatter coefficient (BSC) during cell death were linked to the increase of the cellular size variance. The aim of this work was to estimate the change in cellular size variance from the polydisperse structure factor model (SFM) by using experimental ultrasonic measurement before and after therapy.

Statement of Contribution/Methods

The polydisperse SFM was recently demonstrated to be efficient for explaining the measured BSCs on cell pellet biophantoms. Cell pellet biophantoms consist in centrifuged densely packed cells and serve as simplified *in vitro* versions of real tumors. Ultrasonic backscatter measurements were performed at frequencies ranging from 10 to 42 MHz on colon adenocarcinoma cell pellet biophantoms treated with staurosporine, a drug which induces mainly cell apoptosis. Blind estimates of QUS parameters were performed by fitting one measured BSC with a standard ultrasonic scattering model, namely the fluid sphere model (FSM). A novel approach was also proposed to estimate QUS parameters from the polydisperse SFM by using two measured BSCs before and after therapy. Finally, the relationship between the percentage of dead cells and QUS parameters was investigated.

Results/Discussion

When using the FSM, the averaged scatterer diameter (ASD) was found to increase with the percentage of HT29 dying cells, which is consistent with an increase in the cellular size variance. Plotting the percentage of dead cells against the standard deviation of scatterer diameter estimated by the polydisperse SFM show a good correlation coefficient $r^2=0.79$ (against $r^2=0.71$ for the ASD estimated by the FSM). The blind estimation of the change in cellular size variance may be thus a complementary parameter to assess the cell death index. This procedure could be easily translated in clinical practice by using the measured BSC before and after treatment in the same region-of-interest within the tumor under treatment.

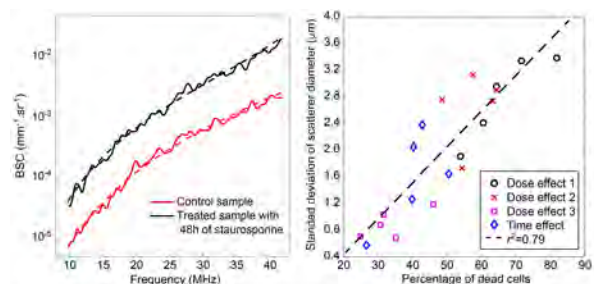


Figure. (On the left) Examples of measured backscatter coefficients (solid lines) and corresponding fitting curves using the polydisperse structure factor model. (On the right) Standard deviation of the scatterer diameter estimated by the polydisperse structure factor model as a function of percentage of dead cells for the four experimental series.

Verification of error factors and accuracy improvement in speed of sound analysis at ultra-high frequency

Toshiki Matsuzaki¹, Atsuko Yamada¹, Kazuki Tamura¹, Kazuyo Ito², Kenji Yoshida³, Tadashi Yamaguchi³

¹Chiba University, Japan, ²Graduate School of Engineering, Chiba university, Chiba, Japan, ³Center for Frontier Medical Engineering, Chiba University, Japan

Background, Motivation, and Objective

Applying the autoregressive (AR) model in exponential to deconvolute pulses is known as one of the method to analyze speed of sound (SoS) by scanning acoustic microscopy (SAM) and being put into practical use. However, the accuracy of analysis is unknown in over the center frequency of 100 MHz. In addition, the influence of the surface shape of the target sample on the accuracy of SoS analysis has not been examined. This study aims to understand optimal measuring and analysis conditions to analyze SoS through the echo simulations.

Statement of Contribution/Methods

The wave propagation in two dimensions was simulated by finite-difference time-domain (FDTD) method. The target tissues were set on each glass plate and ultrasound pulse of 250 MHz was irradiated to it via the water. The acoustic impedance of the tissue sample imitated the actual liver and the basic thickness was 6 μm . The signal to noise ratio was 50 dB, and the lateral resolution in focus depth was 7 μm . To consider the influence by analysis and tissue conditions, the experiments were conducted with thickness and surface shape of tissue, and AR order (number of echo components deconvoluted in) as various.

Results/Discussion

Figures 1(a)-(c) are showing the propagation images of echo from tissue surface. In a flat surface sample shown in Fig. 1(a), echoes are obtained almost as equivalent to the shape of the transmit beam. In Figs. 1(b) and (c), that have complex surface obtained by laser scanning of actual thin samples, interference of echoes was confirmed. The calculated SoS from separated echo components (eg. from sample surface, from glass surface, multiple reflections, etc.) by AR model is shown in Fig. 1(d). In Sample 1 as well as Sample 3, SoS was not accurately calculated unless the AR order was 4 or more. Therefore, it can be confirmed that multiple reflections inside the sample are included in the echo even in a flat shape. Also, in cases with excessive thickness difference, the calculation error of SoS is large regardless of AR order. This is because most of reflected waves having a large time difference interfere each other, and the independent components were increased. If the echo conditions were similar to this experiment, 7th or 8th order is appropriate.

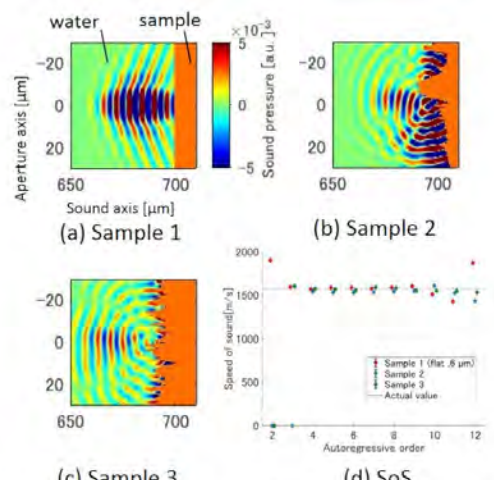


Fig. 1 Wave propagation images simulated by FDTD and evaluated speed of sound. (a) plane surface (sample 1), (b) with different thickness (sample 2), (c) with extreme unevenness (sample 3), (d) relationship between AR order and speed of sound.

Speed of sound analysis from micro to macro size by wide area ultrasound microscopic measurementTakuya Ogawa¹, Kazuki Tamura², Kazuyo Ito², Masaaki Omura¹, Toshiki Matsuzaki¹, Kenji Yoshida³, Tadashi Yamaguchi³¹*Graduate School of Science and Engineering, Chiba University, Chiba, Japan*, ²*Graduate School of Engineering, Chiba university, Chiba, Japan*, ³*Center for Frontier Medical Engineering, Chiba University, Japan***Background, Motivation, and Objective**

Many studies for evaluating acoustic characteristics of biological tissue with several microns resolution have been reported, and it is possible to discriminate difference of cell organelles (Irie, 2016). Because the measurement and analysis area were limiting on usual scanning acoustic microscopy (SAM), there is no study to analyze acoustic characteristics from macro size as like whole organs with micro scale resolution with ultra-high frequency ultrasound. We developed new SAM system to acquire radiofrequency (RF) echo signals from 100 mm square areas of sliced specimens, and evaluated the speed of sound (SoS) of rat organs with ultrasound of 80 and 250 MHz center frequency.

Statement of Contribution/Methods

The new SAM system consists of three precision moving tables with a minimum moving distance of 0.1 μm , and the maximum sampling frequency is 2 GHz. A PVDF-TrFE transducer of 80 MHz center frequency and a ZnO single-element transducer of 250 MHz center frequency were used to this study. The SoS of target tissue was calculated from the RF echo signals of front and back of the thin sliced specimen. The optimized autoregressive (AR) model of 5 order was applied to each normalized power spectrum to separate to echoes from tissue surface, glass plane, and others (Tanaka, 2005).

Results/Discussion

Figure 1(a) and 1(b) show the intensity image of excised rat kidney observed by 80 and 250 MHz, i.e. the normalized positive maximum of received RF echo signal for each scan line, and Fig. 1(c), 1(d), 1(e) and 1(f) show the SoS maps. In Fig. 1 (c) and (d), which are macro scale maps, it clearly show that there is a difference in SoS and tissue density between renal cortex and renal medulla. From the microscale maps, Fig. 1 (e) and (f), it can be confirmed that there are multiple glomeruli in 1 mm square renal medulla and that the SoS of inside of glomerulus is lower than medulla.

The average \pm the standard deviation of SoS in glomerulus calculated from each map of 80 and 250 MHz are $1604.9 \pm 36.0 \text{ m/s}$ and $1636.5 \pm 47.1 \text{ m/s}$, respectively. This difference is due to the difference in the lateral resolution ($20 \mu\text{m}$ in 80 MHz, $7 \mu\text{m}$ in 250 MHz). We are examining how much the macro acoustic characteristics evaluated by the spatial resolution in the clinical ultrasonic scanner reflects the micro-characteristics of the living tissue.

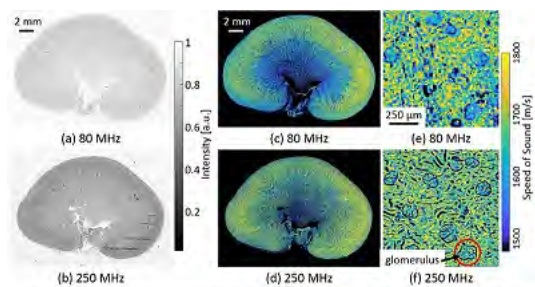


Fig.1 Observation and analysis results of rat kidney Intensity map (a), (b), 2D SoS map (c), (d) and enlarged view of 2D SoS map (e), (f) with a center frequency of 80 and 250 MHz.

Three-dimensional Acoustic Impedance Imaging for Cultured Biological Cells

Naohiro Hozumi¹, Nur Dalila Binti Jalaluddin¹, Thomas Tiong², Tomohiro Kawashima¹, Yoshinobu Murakami¹, Sachiko Yoshida², Kazuto Kobayashi³

¹Dpt. Electrical & Electronic Information Engineering, Toyohashi University of Technology, Toyohashi, Japan, ²Dpt.

Environmental & Life Sciences, Toyohashi University of Technology, Toyohashi, Japan, ³R & D Division, Honda Electronics Co., Ltd., Japan

Background, Motivation, and Objective

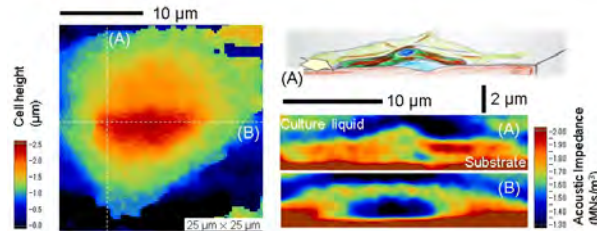
Acoustic microscope is a powerful tool for observation of biological matters. Non-invasive *In-situ* observation can be performed without any staining process. Unlike optical microscopy of which contrast is based on optical refractive index, the acoustic microscopy is contrasted by elastic parameters like sound speed and acoustic impedance. We have proposed the acoustic microscope that can acquire three-dimensional acoustic impedance profile, and applied to cell-size observation. The presentation will deal with its hardware and signal processing, as well as the observation result of a cultured glial cell.

Statement of Contribution/Methods

Glial cells are cultured on a 70 μm -thick polypropylene film substrate. A highly focused ultrasound beam is transmitted from the rear side of the film substrate, and the reflection is received by the same transducer. A pulse acoustic wave of which spectrum is briefly spreading from 100 to 450 MHz is employed. The transducer is scanned along x and y direction by using piezoelectric stage, of which field of view is 65 μm square. The data set for one observation is composed of 200×200 scanning points; each point corresponds to time resolved 200 points of waveform. The waveform is acquired by 125 ps in time interval.

Results/Discussion

The reflection signal corresponding to each scanning point was converted into characteristic acoustic impedance, making use of an algorithm that is similar to time-domain reflectometry. As the result, a data set composed of $200 \times 200 \times 200$ points in acoustic impedance was created. The figure displayed in color scale shows an example of the observation. Cell height (left) was estimated by thresholding the acoustic impedance. Cross-sectional acoustic impedance profiles corresponding to lines (A) and (B) are displayed on the right side. Spatial resolution along the beam direction looks as fine as 0.2 μm . Nucleus is found at the top of the cell, and pseudopodia are found its underneath with a high acoustic impedance. It is remarkable that internal structure of living cell has been visualized in terms of acoustic property that is corresponding to elasticity. The method is believed to be powerful in monitoring internal cell condition.



Enhancement of bandwidth and SNR with ultra-high-frequency ultrasound using chirps for acoustic microscopy
Kazuyo Ito¹, Kazuki Tamura¹, Daniel Rohrbach², Kenji Yoshida³, Tadashi Yamaguchi³, Jonathan Mamou²
¹*Graduate School of Engineering, Chiba University, Chiba, Japan*, ²*Lazzi Center for Biomedical Engineering, Riverside Research, New York, NY, United States*, ³*Center for Frontier Medical Engineering, Chiba University, Chiba, Japan*
Background, Motivation, and Objective

Chirp-encoded excitation and pulse compression have been used in ultrasonic imaging at lower frequencies (e.g., $f_c < 40$ MHz) to increase signal to noise ratio (SNR) and penetration depth, and to expand the -6 dB bandwidth. Although, in theory, chirp-encoded excitation at ultra-high frequencies (i.e., $f_c > 100$ MHz) also is expected to increase SNR and bandwidth, no studies of chirp encoding at ultra-high frequencies have been performed to date. This study investigates chirp-encoded excitation at ultra-high frequencies and illustrates it on a 250-MHz scanning acoustic microscopy (SAM) system.

Statement of Contribution/Methods

An optimally weighted, 0.8- μ s long, linear chirp sweeping from 1 to 500 MHz was used. The weighting envelope was designed to enhance the bandwidth following compression, and was based on a filtered version of the inverse of the combined impulse response of the transducer and the system. The received RF echo signals were compressed with the time-reversed chirp weighted by a Chebyshev window to restore axial resolution and increase SNR. In the SAM experiments, the weighted linear-chirp waveform and a conventional monocyte excitation were used to excite the 250-MHz single-element transducer. The received echo signals were digitized using an oscilloscope. Experimental SAM data were collected from a 6- μ m thick healthy rat-liver tissue specimen that was put on the glass plate and raster scanned in two dimensions using conventional monocyte and chirp excitation.

Results/Discussion

The -6 dB bandwidths of chirp and monocyte signals were 176 MHz and 156 MHz, respectively (i.e., the bandwidth was 13 % wider in chirp-coded signal). In terms of SNR (which is defined as the peak of the signal divided by the noise floor), SNR of the chirp was 37.0 dB whereas the SNR of the pulse was 32.2 dB. In the two-dimensional speed-of-sound (c) map obtained by processing the RF data at each scan location, 96.8 % and 93.6% of the pixels were considered to be well estimated (i.e., $1485 < c < 1900$) with the chirp and monocyte excitation, respectively. Overall, results demonstrate that the proposed method improves the accuracy of the estimation due to better SNR and -6 dB bandwidth. This novel technique could be particularly relevant to SAM investigations of fresh tissue because its lower acoustic impedance contrast typically yields challenging SNR conditions.

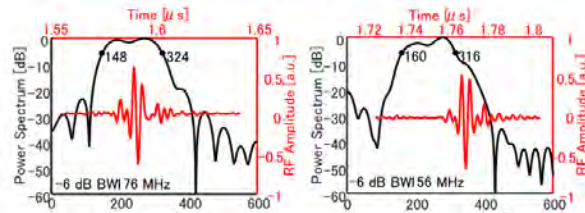


Fig. 1 Received RF signal from tissue (red), and corresponding power spectrum (black) of chirp(a) and monocyte(b) excitation.

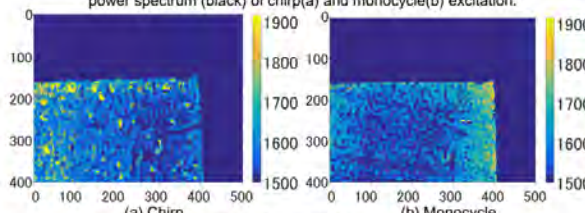


Fig. 2 Two-dimensional of computed speed of sound with of chirp(a) and monocyte(b) excitation. The navy parts represent the glassplate area, and the other parts are tissue.

Non-invasive intracellular observation of cancer cells associated with proliferation

Thomas Tiong Kwong Soon¹, Rahma Rahayu Hutami¹, Kyouichi Takanashi², Naohiro Hozumi², Sachiko Yoshida¹, Kazuto Kobayashi³

¹*Environmental & Life Sciences, Toyohashi University of Technology, Toyohashi, Japan*, ²*Electrical and Electronic Information Engineering, Toyohashi University of Technology, Toyohashi, Japan*, ³*R & D Division, Honda Electronics Co., Ltd., Japan*

Background, Motivation, and Objective

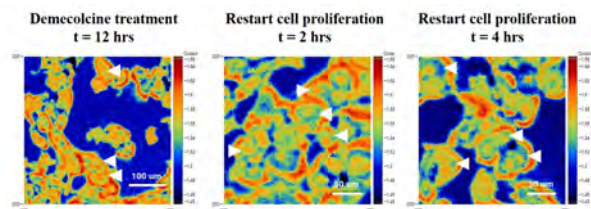
Ultrasonic microscope (UM) is a useful tool for living organ and tissues observation as it works quickly and non-destructively without chemical staining. Previously, the cytoskeleton was successfully mapped by utilizing the cell elasticity, which corresponds to changes in acoustic impedance. In this research, we switched the focus to the intracellular dynamics which govern by the cellular organelles to illustrate the biological phenomenon under cellular level. This study is designed to observe and evaluate the morphological changes, which define the effects of anticancer drugs in cultured cancer cells to improve the current cancer screening technique and treatment strategies.

Statement of Contribution/Methods

C127I, murine breast cancer cells were proliferated on a 50 micrometer-thick polystyrene substrate (PS film dish). Acoustic pulse wave spreading 200 - 400 MHz was focused on the interface between the cell and the substrate and sent through the substrate. The reflection was received by the same transducer and interpreted into acoustic impedance profile by mechanical scanning. Anticancer drugs were applied to the cultured cells to observe the changes of organelles; demecolcine (DEM, 0.05 µg/ml) targeting cell nucleus and betulinic acid (BA, 50 µg/ml) targeting mitochondria in C127I murine breast cancer cells.

Results/Discussion

DEM was used to arrest cancer cells in M phase in order to reveal the cell nucleus for observation and evaluation (Fig. 1). The crescent shapes ($1.63 \times 10^6 \text{ Nsm}^{-3}$) and round shapes ($1.58 \times 10^6 \text{ Nsm}^{-3}$) observed and recorded indicates the changes during M phase which are nuclear division and cytokinesis. This shows that phenomena in the mitosis. Similar morphology was seen by both optical and acoustic observation but acoustic was much easier to clarify intracellular structure because it was contrasted by difference in elasticity. Such a structure is not visible by optical without staining. The application of BA decreased the overall acoustic impedance in C127I, which did not reveal the mitochondrial changes.



Acoustic impedance analysis for internal structure of cultured cells by 250 MHz ultrasound
Tamaki Honda¹, Kenji Yoshida², Kazuyo Ito³, Hitoshi Maruyama⁴, Tadashi Yamaguchi²
¹*Graduate School of Science and Engineering, Chiba University, Japan*, ²*Center for Frontier Medical Engineering, Chiba University, Japan*, ³*Graduate School of Engineering, Chiba University, Chiba, Japan*, ⁴*Graduate School of Medicine, Chiba University, Chiba, Japan*
Background, Motivation, and Objective

The acoustic impedance of free fatty acids (FFA), which is an important role in NASH progression, could be evaluated as each FFA by scanning acoustic microscopy (SAM), even if they were in solution or absorbed by cells (Ito, 2017). However, it has been still unknown how the acoustic impedance relates to the microscopic structure and composition in the cells. To precisely understand this relationship, the cultured cells were measured by SAM, and the minute echo signal from the internal structures were extracted in each scan line and the three-dimensional acoustic impedance was evaluated.

Statement of Contribution/Methods

Swiss 3T3 fibroblasts were cultured in 5% CO₂ at 37°C with a DMEM+10% FBS medium and penicillin/streptomycin, and were seeded on a dish made of polystyrene thin film with thickness of 50 μm. A SAM (modified AMS-50SI, Honda Electronics Co., Ltd, Japan) equipped a 250-MHz center-frequency transducer which has the spatial resolution of 7 μm was employed for measurement of cells. The signal from internal structure of the cell was analyzed by subtracting the echo signals of film interface from each measurement point. Acoustic impedance was calculated by comparing the amplitude of subtracted signals with the amplitude of the signal from a coupling medium.

Results/Discussion

Figure 1(a)-(c) show a microscopic optical image of a cell, a C-mode image at 3.1 μm deeper section from the boundary face between film and cell surfaces, and B-mode images at lines A and B on Fig. 1(c) which were constructed from the normalized envelope amplitude of the subtracted signal, respectively. It was confirmed strong echoes reflected from internal structure at 2-3 μm deeper area from the film surface.

Figure 1(d) is an acoustic impedance map of the internal structure of the cell at the same depth from Fig. 1(b) evaluated from the subtracted signal, assuming that the acoustic impedance of water as coupler medium was 1.55 and polystyrene was 2.37 Mrayl. The acoustic impedance of point C and D are 1.46 Mrayl, and 1.91 Mrayl, respectively. As a result of examining the evaluation results at other depths and the morphological features of the cells, it is assumed that there is a cell nucleus at point C with low acoustic impedance. Currently, we are investigating the relationship between uptake of each FFA into cells and distribution change of acoustic impedance value.

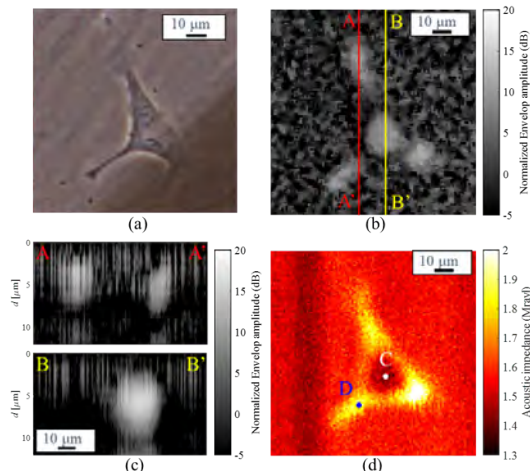


Fig. 1. (a) An optical image of a cell, (b) a C-mode image at $d = 3.1 \mu\text{m}$, (c) B-mode images, and (d) an acoustic impedance map of the internal object of the cell.

In vivo attenuation coefficient estimation of the healthy forearm and thigh human dermisAna Saavedra¹, Andres Coila², Junior Arroyo¹, Benjamin Castaneda¹, Roberto Lavarello¹¹Pontificia Universidad Católica del Perú, Lima, Peru, ²University of Illinois at Urbana-Champaign, IL, United States**Background, Motivation, and Objective**

Few studies of *in vivo* normal dermis characterization have been reported. In the forearm, Raju *et al.* (UMB, 27(11): 1543) reported an attenuation coefficient slope (ACS) of $2.1 \text{ dB}\cdot\text{cm}^{-1}\cdot\text{MHz}^{-1}$ for the age range of 19-36 years whereas Guittet *et al.* (UMB, 25(3): 421) reported an ACS of $2.63 \text{ dB}\cdot\text{cm}^{-1}\cdot\text{MHz}^{-1}$ for the age range of 15-30 years. This study uses the regularized spectral log-difference (RSLD) method for the estimation of the ACS in the forearm and thigh dermis with the objective of complementing previous studies on characterization of the forearm dermis and exploring the variations of ACS at different anatomic sites.

Statement of Contribution/Methods

Ten volunteers without skin injuries (age range of 19-27 years) were scanned in the middle of the ventral side of the forearm and of the anterior side of the thigh. The acquisition was performed using a VEVO 2100 (Fujifilm Visualsonics Inc., Toronto, ON, Canada) scanner equipped with an MS250 transducer operating at 21 MHz. A positioning system was used to hold the transducer and a water-based couplant (Aquaflux®, Parker Laboratories, Fairfield, USA) was placed between the skin and the transducer active surface. When using the RSLD method, diffraction effects were compensated using data from a calibrated agarose-milk matrix phantom with embedded glass beads of $18.3 \mu\text{m}$ diameter. The ACS was estimated within an analysis band spanning from 8 to 27 MHz. Statistical differences between the ACSs in the forearm and thigh were assessed using a Wilcoxon test.

Results/Discussion

The average ACS in the forearm dermis was $2.07 \text{ dB}\cdot\text{cm}^{-1}\cdot\text{MHz}^{-1}$, which is in closer agreement with the slope determined by Raju *et al.* In addition, a significant difference ($p < 0.05$) was found between the ACS in the forearm dermis and the thigh dermis (average ACS of $2.54 \text{ dB}\cdot\text{cm}^{-1}\cdot\text{MHz}^{-1}$), which is consistent with the expected reduced collagen content in the forearm dermis due to an increased sun exposure. Therefore, these results suggest the ACS has the potential to be used as a tool for *in vivo* skin characterization. This research was supported by grant 012-2014- FONDECYT-C1.

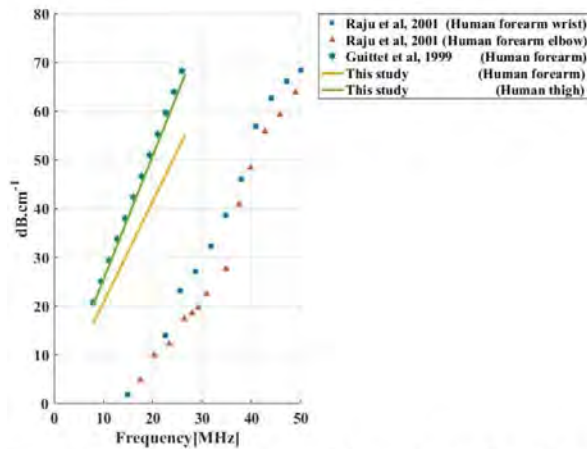


Figure 1. Comparison of *in vivo* attenuation coefficient average curve of the dermis from this study with literature.

P2-B1 - PAT: Acoustic Tweezers and Particle Manipulation

Waraku (posters 2)

Wednesday, October 24, 9:30 AM - 4:00 PM

Chair: **Minoru Kurabayashi Kurokawa** Tokyo Institute of Technology

P2-B1-1

Ultrasound-driven self-assembly of gold nanocages with different patterns

Mian Chen¹, Long Meng², Xin Chen¹, Haoming Lin¹, Minhua Lu¹, Xinyu Zhang¹, Chien Ting Chin¹, Hairong Zheng², Siping Chen¹

¹School of Biomedical Engineering, Shenzhen University, Shenzhen, China, People's Republic of, ²Paul C. Lauterbur Research Center for Biomedical Imaging, Shenzhen Institutes of Advanced Technology, Chinese Academy of Sciences, China, People's Republic of

Background, Motivation, and Objective

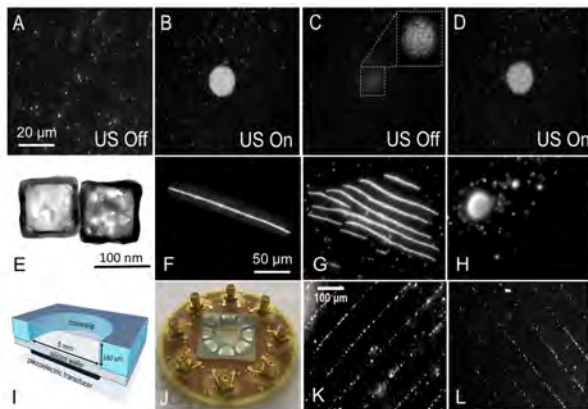
As the rapid progress of nanoscience, the ability to control and regulate the collective behavior of nanoparticles will lead to new and exciting developments from manufacturing engineering to nanomedicine. Ultrasonic manipulation have been demonstrated as an effective method for the control of micro-particles or bigger ones. However, as the particle size is reduced to nanoscale, the acoustic force decreases rapidly, and Brownian motion of the nanoparticles by the collisions with water molecules increases significantly. Thus, the precise manipulation of nanoparticles based on ultrasonic is extremely challenging.

Statement of Contribution/Methods

In the previous research, for the first time, we proposed that the hollow nanostructures could significantly enhance the interaction of metal nanoparticles with acoustic field, leading to acoustic levitation and swarm aggregations, as shown in Figure 1A-D (Adv. Sci. 2017, 1600447). In this paper, we tried to acoustically manipulate the gold nanocages (AuNCs, as shown in Figure 1E) self-assembly with different patterns. A standing wave field formed by using a piezoelectric ceramic transducer (as shown in Figure 1I) and a surface acoustic wave field formed by using interdigital transducers (IDTs, as shown in Figure 1J) were conducted, respectively.

Results/Discussion

Figure 1F-H showed that a standing wave field could further drive AuNCs to self-assemble into other patterns, including chain assembly, multi-chain assembly, and rotating patterns. These patterns corresponded to different applied acoustic frequencies. Figure 1K, L showed that a surface acoustic wave field could also lead to well-defined patterns of AuNCs assemblies. The pattern direction and displacement were flexibly regulated by the optimized combination of IDTs and the phase-shift method. Based on the unique properties of AuNCs, we anticipate that these results will be highly desirable for further applications.



Experimental feasibility study of non-contact acoustic picker considering effect of stage**Yutaka Yamamoto¹, Kan Okubo¹**¹*Electrical Engineering and Computer Science, Tokyo Metropolitan University, Japan***Background, Motivation, and Objective**

In recent years, there are some studies that report the method to levitate and manipulate a particle using ultrasonic waves and/or ultrasonic transducer array. However, in the conventional acoustic levitation method using compact acoustic delay-lines device, it was so difficult to pick up a particle located on the stage or table. In this research, we examine a new approach to make it possible to pick up a particle left on the stage.

Statement of Contribution/Methods

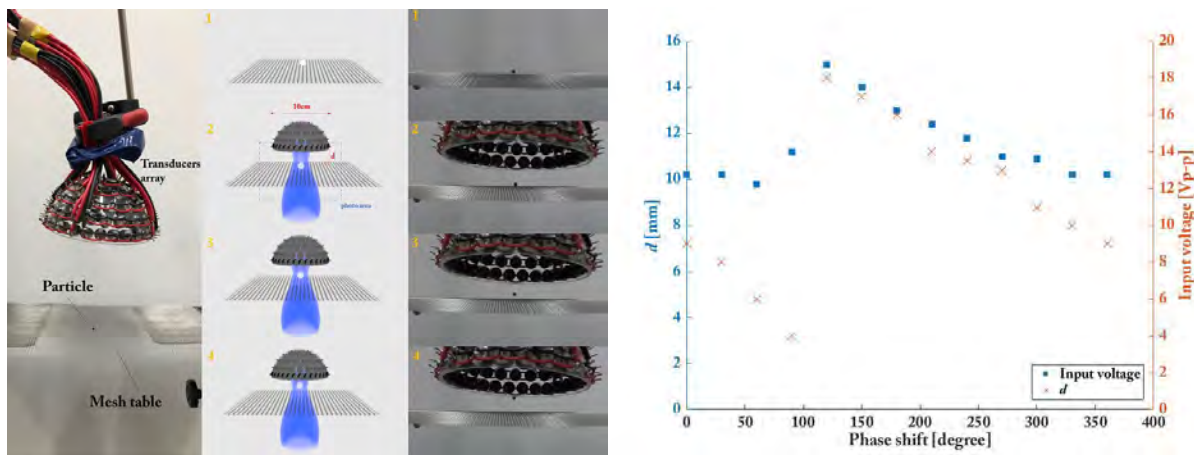
The hemispherical-like ultrasonic transducers array (see Fig. 1) enables to levitate a particle near the center of the hemisphere by phase inversion control. However, when trying to apply this method to a particle on a normal table top of a stage, the reflection of a sound wave from the stage affected the sound field near a particle, and which makes it impossible to pick up the particle. Therefore, we examined an effective method which enable to pick up a particle located on the stage by the use of special materials and phase shift control. Here, mesh structure stage and sound absorbing material are employed as a stage material.

Results/Discussion

Figure 1 shows a photograph of hemispherical-like transducers array (left), image diagrams of the acoustic picker (middle), and time-sequence photos of experiment (right). We used polystyrene spheres with a diameter of 3 mm as a particle to pick up in our experiment. Moreover, it was possible to control the picking up distance d from the stage by phase control.

The method of the phase control is shifting the phase of upper transducers from lower transducers. As shown in Fig. 2, d can be controlled by phase shift. This figure also plots a relationship to minimum input voltage to pick up a particle.

Through this study, we have demonstrated the non-contact acoustic picker employing effective stage and phase control.



Immobilization of single cells by an array transducer based single-beam acoustic tweezersChanghan Yoon¹, Hae Gyun Lim², Haekyu Park¹, Myeongjin Song¹, Hyung Ham Kim²¹Inje University, Korea, Republic of, ²Pohang University of Science and Technology, Korea, Republic of**Background, Motivation, and Objective**

Many biological studies often involve immobilizing (or trapping) particles and cells under investigations. In the single-beam acoustic tweezers, similar to the mechanism of the optical tweezers, a tightly focused acoustic beam produces high acoustic gradient force, thus targets (e.g., microparticles and cells) can be attracted toward the beam center and trapped within its area. Here, we present ultrasound-array-based single-beam acoustic tweezers that can trap and manipulate a single cell or multiple cells. Since acoustic beam steering and scanning can be conducted electronically with an array transducer, manipulating of microparticles and cells by using the array transducer is simpler and faster than single-element based acoustic tweezers which requires mechanical translation of the transducer.

Statement of Contribution/Methods

In the experiments, a customized 30-MHz array transducer with an interdigitally bonded (IB) 2-2 piezo-composite was employed to immobilize MCF-12F cells. The MCF-12F cells were suspended in a petri-dish filled with HBSS. It was mounted on a microscopy and the images were recorded using a high-sensitive CMOS camera. A custom-built field programmable gate array (FPGA) based 64-channel ultrasound imaging system was utilized to transmit ultrasound waves. A 300-cycles of 30 MHz sinusoidal burst with 40 Vpp was transmitted and pulse repetition period was 1 ms; thus duty factor was 1 %.

Results/Discussion

Figure 1 illustrates a cell motion during the immobilization experiment. A single cell rests 40 μm away from a white dotted line that is the initial focusing region in the lateral direction (Fig. 1a). As shown in Fig. 1b, when the transducer was turned on, the cell was attracted to the white dotted line and immobilized. After the cell settled at the initial focus, the focal spot was shifted the opposite direction to the attracted direction. As can be seen in Figs. 1c and d, the cell was moved to the focus as if the cell was tethered to the acoustic beam focus. Overall, our studies demonstrate that the array based single-beam acoustic tweezers can be utilized as a manipulator of particles and cells, and would pave the way for exploring new biological applications.

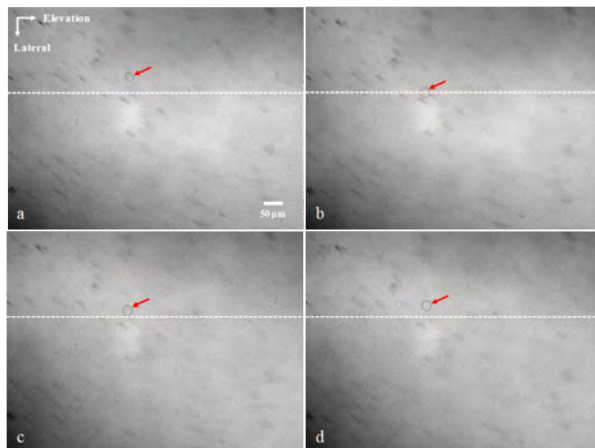


Figure 1. Example of a single cell immobilization where the initial focus is assumed to be located on a white dotted line. (a) The cell (a red arrow) was positioned at 40 μm away from the focus and (b) gradually attracted to it when the high-frequency ultrasound was on. (c) and (d) After immobilized, the transducer was moved to the upper direction and the cell was pulled by the trapping force.

Ultrasonic manipulation of particles on fluid surface using 2-D CMUT array

Chang Hoon Lee¹, Bum Hoon Park¹, Kwan Kyu Park¹

¹Mechanical Convergence Engineering, Hanyang University, Seoul, Korea, Republic of

Background, Motivation, and Objective

Recently, there have been several studies on transporting and classifying particles using ultrasound. The ultrasonic method has the advantage of not damaging the particles being examined as it enables us to control without making direct contact. Current works use standing wave or focused transducers. It is difficult to change the position of the particle because the standing wave method is trapping the particles at the node position. Focused transducer has the disadvantage of requiring mechanical movement. These methods only work in fluids. In this study, we aim to move particles (or group of particles) freely on a fluid using a transducer array.

Statement of Contribution/Methods

To manipulate the particles arbitrarily, an array device which controls each channel independently is required. Furthermore, manipulation is performed by pulse-based impulse excitation method instead of CW-based standing wave method for manipulation on fluid. The device used for the experiment is a 5 x 5 2-D capacitive micromachined ultrasonic transducer (CMUT) array fabricated through a direct wafer bonding process. The cell radius of the used CMUT is 105 μm and the element size is 800 μm . Each channel consists of nine cells. The designed center frequency is 2 MHz and the operating bias voltage is 80 V. The experiment is conducted with an input AC voltage of 70 Vpp and a burst cycle of 100,000 cycles. Pulse repetition frequency (PRF) is performed at 2 Hz and 10 Hz. The 2.6 mm thickness oil is used as the medium. Cork particles are used as oil floating objects. The size of the cork is 1 mm and the density is 0.22 to 0.26 g / cm³. The particles are moved by the pressure generated by the CMUT.

Results/Discussion

Due to the large-number of burst numbers, the surface of the oil springs up by standing waves and radiation forces. As a result, the particles are pushed out. With the effect of this repulsion and the array, particles can be driven to target locations in 2-D space. The surface pressure of the device was measured at 500 kPa at a center frequency of 2 MHz. The movement of the particles were confirmed when put into the same condition of the excitation. Particle velocities were proportional to PRF according to the results, and measured particle velocities were 50 $\mu\text{m/s}$ and 100 $\mu\text{m/s}$ with the PRF of 2 Hz and 10 Hz respectively.

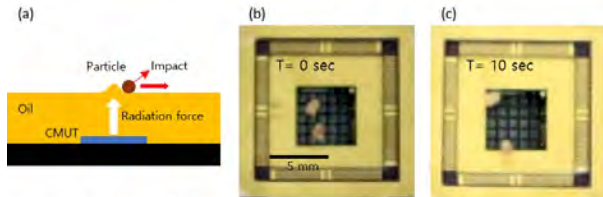


Figure 1. (a) System schematic diagram (b) t = 0 (c) t = 10 sec

Finite element analysis of acoustic streaming in a Kundt tube with artificial ridge boundaryYuji Wada¹, Kohei Yuge¹¹*Faculty of Science and Technology, Seikei University, Tokyo, Japan***Background, Motivation, and Objective**

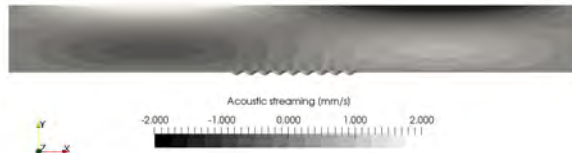
The Kundt tube problem, that is, the mysteriously aligned powder ridges formed in an acoustic tube, has been one of the unsolved problems in acoustics since the nineteenth century. Since acoustic radiation force and acoustic streaming currently play important roles in industrial or medical applications, the elucidation of this powder-ridge generation mechanism is important for future applications of nonlinear acoustic.

Statement of Contribution/Methods

The acoustic streaming near an artificially prescribed rigid bended boundary is calculated, and the analyses are performed at different intervals and heights of the artificial ridge pattern. A viscoacoustic harmonic finite element analysis (FEA) and a static-fluid FEA are coupled using an acoustic streaming driving force to derive acoustic streaming. The pattern, where the acoustic streaming vortices are strongest, is compared with literature values. Although these artificial boundaries is equivalent to the actual powder ridges, determining the most possible boundary among them would be informative for mechanism elucidation.

Results/Discussion

Figure 1 shows the x-component acoustic streaming distribution in a Kundt tube with partially bended boundary when the half-wavelength mode is excited in an acoustic tube with 1 kHz driving frequency. Many series of small vortex flows of Schlichting streaming near every ridge are superposed in ambient Rayleigh streaming. The maximum velocity of these circular flows is 2.6 mm/s, which is three times higher than that of ambient Rayleigh streaming. When the ridge interval is changed, the Schlichting streaming velocity has a single peak. The higher ridge induces faster Schlichting streaming. When the ridge height is 4 mm, the streaming has a peak at 2-mm interval, which agree with the ridge pattern size in the literature. The mechanism underlying the regular ridge interval is related to the streaming bifurcation just above the ridge valley, which is determined by ridge height, interval, and boundary thickness.



Simulation of interparticle radiation force between solid elastic spheres in a standing wave field

Gergely Simon¹, Marco A.B. Andrade², Mathis O. Riehle³, Marc P.Y. Desmulliez¹, Anne L. Bernassau¹

¹*School of Engineering and Physical Sciences, Heriot-Watt University, Edinburgh, United Kingdom*, ²*Institute of Physics, University of São Paulo, Brazil*, ³*Centre for Cell Engineering, Institute for Molecular, Cell and Systems Biology, CMVLS, University of Glasgow, United Kingdom*

Background, Motivation, and Objective

Cell separation is a crucial step in various research areas including sample preparation, diagnosis, or therapy. To achieve separation, acoustic sorting methods are advantageous for their non-invasive, biocompatible, and flexible properties. However, with increasing particle or cell concentration, a secondary acoustic radiation force arises and can lead to particle aggregation, which is unfavourable for sorting. This interaction force has been investigated by many in the past using theoretical, experimental and simulation, all utilising a fluid particle approximation, and neglecting shear waves within the object. This approach can lead to a variance of up to 50% in compressibility and consequently the real interaction force can be significantly altered. In this paper we investigate and quantify this difference for various particle types, such as polystyrene, PMMA, or iron-oxide filled PS using two different numerical models implemented in COMSOL.

Statement of Contribution/Methods

Two simulation methods are widely used for acoustic radiation force calculation: Gorkov's potential approach can be applied directly at the centre of the scatterer, assuming a spherical object and using the primary pressure and velocity fields. Alternatively, a tensor field, dependent on the pressure and velocity fields, can be integrated over a surface which encloses the particle, which in this case can be of arbitrary shape. The first method neglects re-scattering events between the two particles, while the second method provides a more complete picture, but requires a 3D simulation domain. In both cases, the total radiation force is obtained directly, therefore the primary radiation force has to be subtracted. To account for shear effects within the solid particles, our simulations utilize a coupled solid-acoustic model, instead of relying on an acoustic domain only for both the Gorkov approach and the tensor field method.

Results/Discussion

Particles both in water and air were investigated. First, we analysed the effect of changes in compressibility on the primary radiation force. The models were used without the second scatterer particle to provide this force. We observed excellent agreement with theory when the compressibility corresponding to a solid sphere was used instead of the isentropic fluid compressibility. For the secondary radiation force, the difference between theory utilizing fluid particle model and either of the simulations was more pronounced, >20%. This difference increased with particle density up to 90% for the iron-oxide particles, due to their fluid-solid compressibility difference. The two simulation models showed better agreement, less than 10% error for all spatial positions. From these results we conclude that for particles with similar physical properties as of the medium, the theoretical fluid model might be adequate, but for more rigid particles a numerical 3D solid-acoustic simulation is required.

Acoustic manipulation of microbubbles based on implantable and biodegradable artificial structuresFei Li¹, Pengfei Zhang², Feiyan Cai¹, Yang Mao², Wei Zhou¹, Min Su¹, Jiqing Huang¹, Long Meng¹, Hairong Zheng¹¹Shenzhen Institutes of Advanced Technology, Chinese Academy of Sciences, China, People's Republic of, ²Qilu Hospital, Shandong University, China, People's Republic of**Background, Motivation, and Objective**

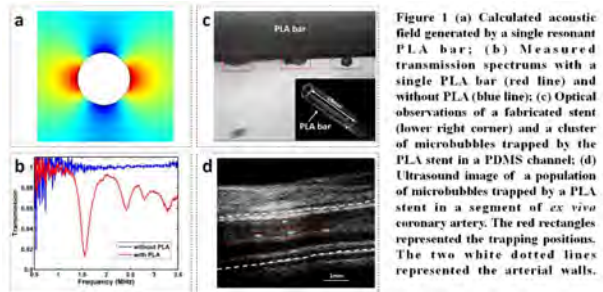
Poly lactic acid (PLA) with good biocompatibility and biodegradability has become one of the most important biomedical materials in fields such as drug delivery, tissue engineering, bone fixing, man-made skin and three-dimensional scaffold etc. Here we explored an interesting acoustic trapping of microbubbles based on a resonant PLA stent. The trapping mechanism was originated from the gradient force induced by the quasi-Scholte wave-excited localized field on the surface of a single PLA bar.

Statement of Contribution/Methods

The stent composed of PLA bars with a mean diameter of 300 μm was fabricated by the additive manufacturing. The stent had a primary resonance frequency of 1.5 MHz by the acoustic transmission measurement, which was nearly the same as the resonance frequency of a single PLA bar. The stents were located in a PDMS channel and a segment of *ex vivo* coronary artery, which were then observed by an optical microscope and a commercial ultrasound scanner VovoTM 2100, respectively. Commercial ultrasound contrast agent SonoVueTM microbubbles were pumped into the channel and vessel with a flow rate of 70 ml/h. Continuous waves were generated to excite the stents at the resonance frequency. A linear acoustic model was used to calculate the first order resonant acoustic pressure and velocity fields of a single PLA bar.

Results/Discussion

The simulated acoustic field from the resonant PLA with a shear wave speed lower than the acoustic speed in water showed the characteristic of evanescent wave, and an integral number of wavelengths fitted into the circumference of the bar. It indicated the excitation of the quasi-Scholte wave mode on the surface of the PLA bar. The measured transmission spectrums showed the existence of the resonance frequency. We experimentally observed that the microbubbles were trapped onto the surface of the stent at the driving frequency of 1.5 MHz. And the microbubbles were gathered as the trapping force dragged them onto the bar. This study might provide *in vivo* acoustic manipulation of particles with a potential tool for drug delivery.



Acoustic trapping of microparticles at the inner and outer wall of a glass capillaryQin Lin^{1,2}, Feiyan Cai¹, Fei Li¹, Xiangxiang Xia¹, Zhanhua Mai², Wei Zhou¹, Hairong Zheng¹¹*Paul C. Lauterbur Research Center for Biomedical Imaging, Shenzhen Institutes of Advanced Technology, Chinese Academy of Sciences, China, People's Republic of*, ²*School of Information Engineering, Guangdong Medical University, China, People's Republic of***Background, Motivation, and Objective**

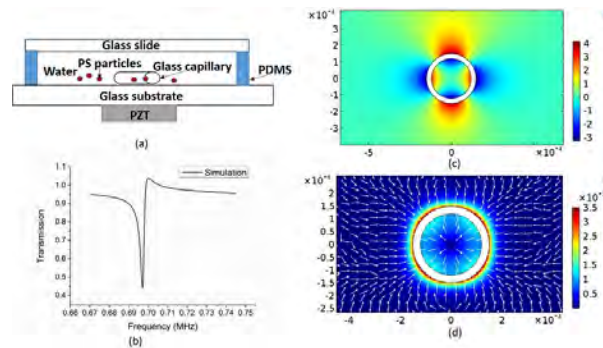
The ability to manipulate microparticle flexibly is critical for the development of active microsystems. Acoustic tweezers based on standing field are excellent tools for manipulation kinds of microparticles, and these microparticles are usually trapped at pressure node or antinode depending on the elastic properties of the object and the surrounding medium. However, the standing wave patterns which are usually generated directly by acoustic transducers, cannot be redesigned easily, nor can their corresponding acoustic trapping positions be modulated efficiently. Here, we report acoustic trapping of microparticles at the inner and outer wall of a glass capillary, which supports circumferential mode with gradient field at the surface of capillary.

Statement of Contribution/Methods

As schematically shown in Fig. 1(a), the system consists of a glass capillary with 120 μm inner radius, 150 μm outer radius and 10mm in length. Polystyrene (PS) microparticles with diameters of 15 μm are scattered in the inner and outer wall of the glass capillary. Both the capillary and PS microparticles are immersed in water confined by a PDMS channel. A PZT is an actuator for generating ultrasonic wave. The normal transmission spectrum, pressure field and acoustic radiation force distribution of this system are calculated by using the COMSOL Multiphysics software. As shown in Fig. (b), there is a transmission dip at frequency of 0.6988MHz. The pressure field around the capillary at the resonance frequency is illustrated in Fig. (c), which is confined at the surface of the capillary and can be demonstrated that is the 2-nd of circumferential mode. Furthermore, the numerical map of acoustic radiation forces exerted on a PS particle near the surface of capillary are shown in Fig. (d).

Results/Discussion

It is clearly illustrated that PS particles may suffer the acoustic trapping forces, moving towards the inner and outer surface of the capillary. Most interestingly, the trapping force reported here is mainly contributed by the intensity gradient force originating from the resonance of circumferential mode of the capillary. Also, this trapping force is insensitive to the source position and can trapped objects at the inner and outer wall of a glass capillary located at arbitrary position.



High Frequency Ultrasonic Levitation of Red Blood Cells Aggregation

Hae Gyun Lim¹, Jeongwoo Park¹, Dasom Heo¹, Kyungmin Kim¹, Hyunhee Kim¹, Jinhee Yoo¹, Yeonggeon Kim¹, Hyung Ham Kim¹

¹Department of Creative IT Engineering, Pohang University of Science and Technology, Korea, Republic of

Background, Motivation, and Objective

Ultrasonic levitation techniques have been developed as a promising tool for drug delivery in the human body since ultrasound can levitate and manipulate a single object or objects through air and water. The single-beam acoustic trapping has a definitive advantage over other acoustic tweezer methods since it only employs a one-sided ultrasound. In this study, we elucidated that single-beam acoustic tweezers (SBAT) could levitate red blood cells (RBCs) aggregation and successfully performed the manipulation of levitated cell aggregation. This work is a significant step forward in three dimensional manipulation of cell aggregates using high frequency acoustic tweezers.

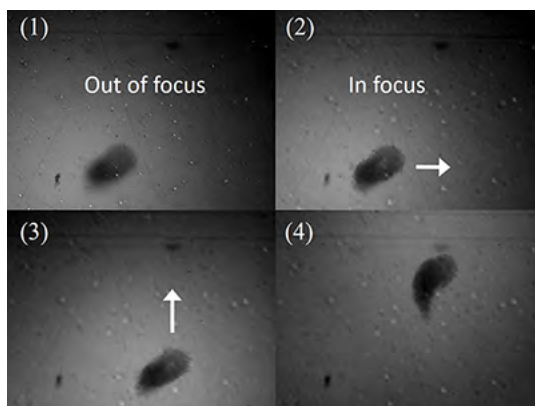
Statement of Contribution/Methods

Lithium niobate transducer (center frequency of 45 MHz and *f-number* of 1.5) was fabricated for the experiment of ultrasonic levitation. This transducer was mounted on a three-axis motorized linear stage and set in the chamber of deionized water. The movement of cell aggregates using acoustic tweezers was observed by the inverted microscope and recorded by CMOS camera. As the transducer was driven by a function generator and a power amplifier, RBCs was levitated from the bottom of cell culture dish and formed cell aggregation.

Results/Discussion

As shown in Fig. 1 (1), the focal plane of the microscope was placed at the bottom of the petri dish to demonstrate that trapped RBCs aggregates were levitated. As a result, RBCs aggregates have been seen as a blurry image. The RBCs was in-focused in Fig. 1 (2~4) which proved that the transducer could effectively levitate cells and formed 2-D cell aggregates in the space. As the transducer was moved in the transverse direction, cell aggregates were manipulated along the movement of the transducer. The white arrows represented the steps of cell locomotion, and same background images were given as a reference to show the cell manipulation.

In this study, we ascertained that SBAT was a potential tool for manipulation of levitated RBCs aggregates with non-contact and label-free. Using focused ultrasound field generated by a high frequency single-element transducer, we first report the levitation and transportation of cell aggregates in the space.



P2-B10 - Imaging Transducers

Kairaku (posters 1)

Wednesday, October 24, 9:30 AM - 4:00 PM

Chair: **Richard O'Leary** University of Strathclyde

P2-B10-1

A 360° Electronic Radial Ultrasound Endoscope Based on Designed PMN-PT Single Crystal/Epoxy 2-2 Composite

Ting Zhang^{1,2}, Xiaozhen Li^{1,2}, Hu Tang^{1,2}, Siping Chen^{1,2}, Jue Peng^{1,2}

¹National-Regional Key Technology Engineering Laboratory for Medical Ultrasound, China, People's Republic of, ²Guangdong Provincial Key Laboratory for Biomedical Measurements and Ultrasound Imaging, School of Biomedical Engineering, Shenzhen University Health Sciences Center, Shenzhen, China, People's Republic of

Background, Motivation, and Objective

Endoscopic ultrasound (EUS) is an imaging technique to obtain accurate and detailed information regarding the digestive tract and surrounding organs or tissues. The 360-degree fully functional EUS can simultaneously display optical and 360-degree sideward view ultrasound images through the combination of endoscopy and an radial array transducer. To improve the imaging resolution and operational convenience, the higher optical and ultrasonic resolution, the smaller external diameter (less than 10 mm), are required. In this paper, a EUS probe integrating an 8.25 MHz, 128 elements radial array transducer based on PMN-PT single crystal/epoxy 2-2 composite and a wide-angle 5-million-pixel CMOS camera module is presented.

Statement of Contribution/Methods

We designed a PMN-PT single crystal/epoxy 2-2 composite to fabricate the 8.25 MHz, 128 elements radial ultrasound transducer, which has high uniformity among elements and excellent performance. To improve optical imaging resolution, a 128.3-degree 5-million-pixel CMOS camera module was integrated with the ultrasound transducer. Finally, the integrated 360-degree electronic radial EUS has small packaged size equal to 9.5 mm outer diameter, which can simultaneously display the real-time optical and ultrasound image.

Results/Discussion

Figure 1(a) showed the schematic of the 360-degree electronic radial EUS probe. Photograph of the radial array based on 2-2 composite was shown in Fig.1 (b). Figure 1(c) showed that the array has a center frequency of 8.25 MHz, a -6 dB fractional bandwidth of 81.21%. And a two-way insertion loss of 28.29 dB was obtained at the average center frequency. In Fig. 1(d), the annulus phantom can be distinctly imaged with the radial array, which demonstrates the high uniformity among elements. As shown in Fig. 1(e), the porcine esophagus inner surface can be distinctly imaged in vitro with the wide-angle CMOS camera module. Therefore, the 360-degree electronic radial EUS based on PMN-PT single crystal/epoxy 2-2 composite can ensure a desirable imaging resolution for digestive tract imaging.

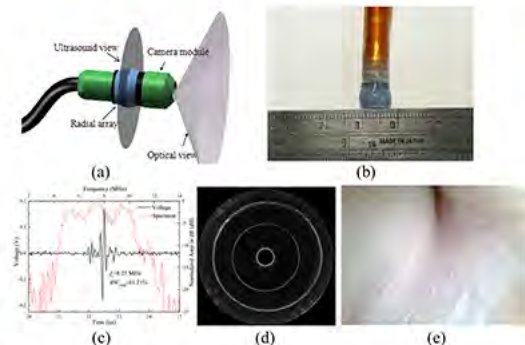


Fig.1 (a) schematic of the 360° electronic radial EUS probe (b) photograph of the radial array based on 2-2 composite (c) pulse-echo response and spectra (d) the image of an annulus phantom with the radial array(e) the porcine esophagus inner surface image with the camera module

A kerfless PVDF array for photoacoustic imaging

Reza Pakdaman Zangabad¹, Geert Splingering¹, Emile Noothout², Robert Beurskens¹, Nico de Jong^{1,2}, Antonius F. W. van der Steen^{1,2,3}, Gijs van Soest¹, Verya Daeichin²

¹Biomedical Engineering, Erasmus Medical Center, Rotterdam, Netherlands, ²Imaging Science & Technology, Delft University of Technology, Delft, Netherlands, ³Chinese Academy of Sciences, Shenzhen Institutes of Advanced Technology, Shenzhen, China, People's Republic of

Background, Motivation, and Objective

Photoacoustic (PA) in human plaque generates very broadband signals (2 - 15 MHz) which can be detected by using an off resonance PVDF transducer [1]. Minimizing pitch and kerf in ultrasound transducer to improve lateral resolution is of great importance. Making a kerfless array where the electrodes are patterned onto the piezoelectric surface to define the elements is a simpler manufacturing approach. We have characterized such a kerfless PVDF array both numerically and experimentally and realized a kerfless, off resonance, PVDF array for PA imaging.

Statement of Contribution/Methods

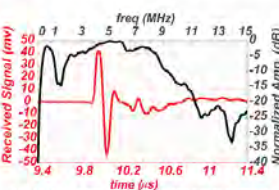
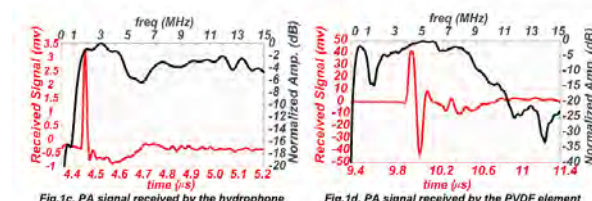
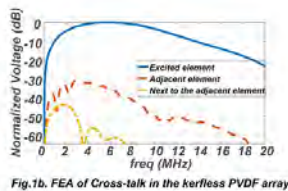
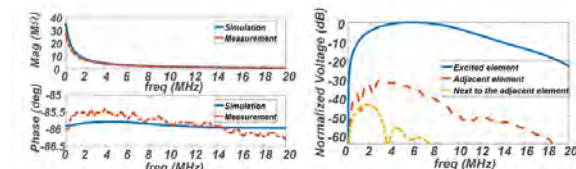
3-D Finite Element Analysis (FEA) was carried out using COMSOL Multiphysics® for characterizing the kerfless PVDF array of 10 elements with dimensions of $1\text{mm} \times 1.5\text{mm} \times 28\mu\text{m}$. We matched the high impedance of the PVDF elements with low impedance of acquisition system through an appropriate LNA (25dB amplification over 10MHz BW). The array was glued to a quartz layer of 1mm as a backing layer. A short wire (~3 mm) was glued to each element and connected to a PCB where the LNA was placed. A laser source of 800nm wavelength, 4mJ, and 200Hz PRF was shined on a tungsten wire with diameter of 35 μm and the generated PA signal was detected with a 0.2 mm needle hydrophone in water and with our device immersed in Galden to prevent from electrical short circuit.

Results/Discussion

Based on FEA and measurement results depicted in Fig.1a, the phase change in the off-resonance PVDF is negligible. The simulated crosstalk between the elements (Fig.1b) is -30dB for the adjacent element indicating that it won't have detrimental effect on the beam profile of the array. Figure 1.c and 1.d depict the received PA signal in time and frequency domain detected by the hydrophone and one element of our array respectively. Notice that the dip at 1.5 MHz in the frequency response of the PVDF is due to the suboptimal backing. When calibrated with the hydrophone, our device provides an output voltage with a sensitivity of about 1.38 $\mu\text{V}/\text{Pa}$ at 3 MHz. The RMS output noise level is 240 μV over the entire bandwidth (10Hz - 10 MHz).

We have designed and manufactured a broadband, kerfless, off resonance PVDF array for PA imaging with low mechanical crosstalk (-30 dB) between the elements and high sensitivity in receive which can significantly improve the detection of PA signals of human plaques.

[1] Daeichin V, et al., Ultrasound in Med. & Biol., (2016) 42: 2017-2025



An ultrasonic probe to measure both radial arterial pressure and diameter at identical position for early diagnosis of arteriosclerosis**Mototaka Arakawa^{1,2}, Takumi Saito¹, Shohei Mori², Shigeo Ohba², Kazuto Kobayashi³, Hiroshi Kanai^{1,2}**¹*Graduate School of Biomedical Engineering, Tohoku University, Sendai, Japan*, ²*Graduate School of Engineering, Tohoku University, Sendai, Japan*, ³*R & D Division, Honda Electronics Co., Ltd., Japan***Background, Motivation, and Objective**

Arteriosclerosis is a serious factor of cardiovascular diseases. Some indices, such as pulse wave velocity (PWV) and ankle-brachial index (ABI), were proposed. However, these are used for diagnosis of irreversibly advanced lesions and not suitable for diagnosis at an extremely early stage.

Our group has proposed an estimation method of the viscoelastic parameters using the stress-strain characteristics by measuring a relationship between radial arterial pressure and diameter, in order to evaluate the vascular endothelial functions. In the previous study, those were measured by pressure sensors and ultrasonic diagnosis equipment [Jpn. J. Appl. Phys. (2016)]. However, measurements at the different position caused timing errors because the PWV varies according to change in the arterial pressure around the arrival time of the pulse wave. In the present study, therefore, we developed an ultrasonic probe in order to measure both the blood pressure and diameter at the same position.

Statement of Contribution/Methods

In order to realize the measurement, a linear array probe with a center frequency of 7.5 MHz and 128 channels was customized. One cord connecting the piezoelectric element at the center of the probe and the ultrasonic diagnosis equipment was cut off to measure the arterial pressure. The output from the element was amplified 100 times, filtered with a low pass filter, and acquired with an oscilloscope. The arterial diameter was measured using the other 127 elements with the ultrasonic diagnosis equipment by the phased-tracking method [IEEE Trans.UFFC (1996)]. To synchronize the oscilloscope and the ultrasonic diagnosis equipment, a trigger pulse from a function generator was used. The measured arterial pressure waveform was calibrated with the measurement result using a sphygmomanometer.

Results/Discussion

The left radial artery of 22-years-old healthy subject was measured. From the theoretical analysis, it was found that the blood pressure waveform measured by the piezoelectric element became a differential form of the actual blood pressure. Then, the waveform was integrated. The measured relationship between the diameter and pressure during a heartbeat is shown in figure. The hysteresis loop was successfully confirmed. Therefore, this probe is useful for the evaluation of the vascular endothelial functions.



Design of a novel zig-zag 192+192 Row Column Addressed Array Transducer for Rodent Super Resolution Imaging: A Simulation study.

Mikkel Schou¹, Andreas Havreland², Mathias Engholm³, Erik Vilain Thomsen², Matthias B. Stuart⁴, Jørgen Arendt Jensen⁴

¹Center for Fast Ultrasound, Department of Electrical Engineering, Technical University of Denmark, Kgs. Lyngby, Denmark,

²Technical University of Denmark, Denmark, ³The Technical University of Denmark, Kongens Lyngby, Denmark, ⁴Technical University of Denmark, Lyngby, Denmark

Background, Motivation, and Objective

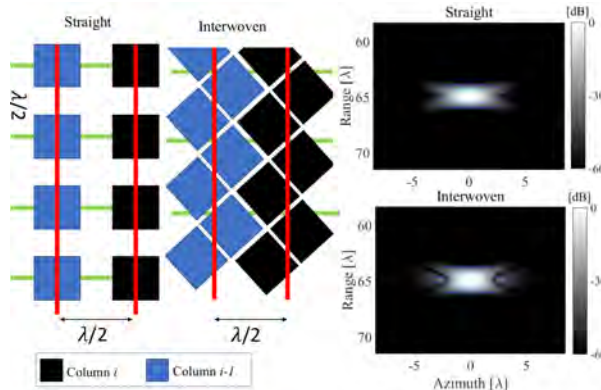
Super resolution imaging (SRI) can benefit greatly from full 3D imaging to compensate for vessel structures moving out of the image plane. Row Column Addressed (RCA) arrays can provide such 3D imaging with low-complexity. A RCA probe is being designed for a rat kidney with 192 + 192 elements to ensure low sidelobes and an imaging volume of 15x15x15 mm³. The design space of such a transducer is investigated with this in mind. Capacitive micromachined ultrasonic transducer (CMUT) technology allows for new geometric shapes, including a kerf-less zig-zag interwoven structure, which provides flexibility in the design process of new RCA. This work compares the image quality of a straight element RCA array with a kerf-less RCA array with an interwoven zig-zag structure by simulations, to test the image quality of a zig-zag structured RCA.

Statement of Contribution/Methods

Two design layouts for 192+192 RCA rodent transducers are tested with Field II simulations. The first being a straight element RCA transducer and the second a novel RCA design with an interwoven zig-zag structure. They are designed to have $\lambda/2$ -pitch, with a center frequency of 10 MHz, which resolves to a footprint of the desired size of a rat kidney. The point spread function (PSF) is simulated using a point scatter at a depth of 1 cm, and a volume is beamformed using Synthetic Aperture Imaging (SAI). 192 single row element emissions are summed to reveal a single high-resolution volume for each of the RCA designs. The cystic resolution at 20 dB (CR) and Full-Width-Half-Maximum (FWHM) are used to quantify the performance, normalized to wavelengths (λ), of the two designs.

Results/Discussion

Fig. 1 shows a cutout of the interwoven zig-zag and the straight structured RCAs to the left. The right panel shows the corresponding Azimuth-Range planes, beamformed with RCA SAI. The PSF proved symmetric in azimuth and in elevation. The straight design had a lateral FWHM of 1.96λ compared to 1.87λ for the interwoven. The interwoven design showed a slight contrast loss over the straight design which was quantified by the CR. The CR at 20 dB for the straight design was 1.89λ , compared to 1.79λ of the interwoven design. The two designs had comparable PSF metrics. The interwoven zig-zag structure is therefore a viable solution to meet the requirements of the rodent experiment and provides a new level of design flexibility for RCA transducer arrays.



A row-column array for ultrasound-based tissue anisotropy measurement**Huaiyu Wu¹**¹*Mechanical and Aerospace Engineering, NC state university, Raleigh, NC, United States***Background, Motivation, and Objective**

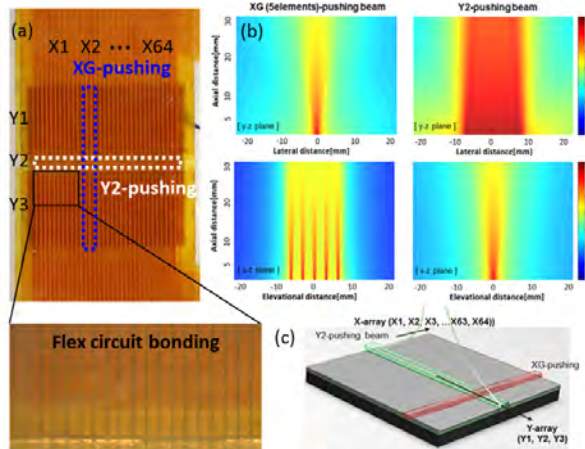
Degree of anisotropy is a rapidly emerging biomarker for tissue pathology that is correlated to fatty infiltration in dystrophic skeletal muscle. Studies suggest that ultrasound is a promising method for anisotropy measurement due to its low cost relative to MRI diffusion-tensor imaging (DTI). However, conventional shear wave velocity-based methods are limited by tissue inhomogeneities and misalignment errors caused by physical rotation of conventional linear arrays. Though 2D arrays could enable electronic aperture rotation, the high cost and complicated fabrication procedures are challenges. To solve these problems, a custom row-column array is proposed in this paper, which can be used to rotate the imaging plane electronically and measure mechanical anisotropy by Viscoelastic Response (VisR) ultrasound.

Statement of Contribution/Methods

A custom 3×64 array transducer was designed and fabricated. The $15 \times 15\text{mm}^2$ array has 64 elements ($X_1 \dots X_{64}$) in the x-direction, with a pitch size of $230\mu\text{m}$. In the y-direction, the array has 3 columns (Y_1, Y_2, Y_3) with widths of 7mm, 1.2mm and 7mm. To fabricate the array, a bulk material of PZT-5H ceramic was lapped to $280\mu\text{m}$ (5 MHz). Then, a 1 mm thick backing layer of Esolder was bonded to it. After curing, the elements were diced and aligned and bonded with a custom designed flex-circuit by epoxy. The ground wire was connected to the backing layer, and the flex circuit was bonded to PCB board. To characterize performances of the array, the impedance of each element were measured with an impedance analyzer. Then, the loop sensitivity of each element was tested with a pulser/receiver. Also, the pressure output was measured with a hydrophone.

Results/Discussion

Initial characterization results show that the capacitance and dielectric loss of the Y_1/Y_3 elements are 56 pF and 68 mU. Those of Y_2 elements are 18 pF and 21 mU. The measured loop sensitivity was 115.6 mV and 21.6 mV for the Y_1/Y_3 and Y_2 elements with the central frequency of 4.63 MHz and -6 dB bandwidth of 39%. The performance of the array was predicted with Field II for beam patterns in different directions. The simulation results are shown for Y_2 elements pushing and the X-group pushing with 5 elements fired. In the future, beamforming tests will be performed in a tissue mimicking phantom, and the array will be used to implement VisR imaging for assessing mechanical anisotropy in tissue.



(a) Fabricated prototype (b) Simulated beam patterns
(c) Design of the prototype

A quantitative study on the impact of bit errors on image quality in ultrasound probes with in-probe digitization

Zhao Chen¹, Mehdi Soozande², Hendrik J. Vos^{2,3}, Johan G. Bosch², Martin D. Verweij^{2,3}, Nico de Jong^{2,3}, Michiel Pertijs¹

¹Electronic Instrumentation Laboratory, Delft University of Technology, Delft, Netherlands, ²Biomedical Engineering, Thorax Center, Erasmus MC, Rotterdam, Netherlands, ³Laboratory of Acoustical Wavefield Imaging, Delft University of Technology, Delft, Netherlands

Background, Motivation, and Objective

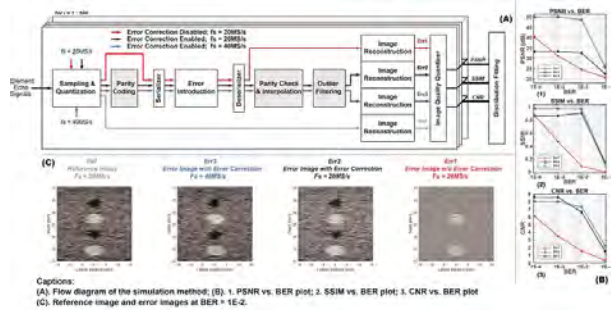
Integrating ultrasound transducers with ASICs which digitize and multiplex the received echo signals (Chen, ISSCC, 2018) effectively mitigates the burden of signal transmission for 3-D catheter-based or endoscopic probes. Multiplexing the echo signals from multiple elements onto a cable reduces the cable count, but requires a higher data rate per cable, which typically involves a trade-off between power consumption and bit-error rate (BER). Understanding the impact of finite BER on the resulting image quality is a necessity to optimize the cable count and power consumption. In this work, this impact is quantitatively assessed using Matlab simulations. The effectiveness of error correction (EC) is also investigated.

Statement of Contribution/Methods

A 5MHz, 128-element linear array transducer is simulated in Field-II to produce the raw echo signals, scanning a phantom consisting of background scatterers, anechoic and hyperechoic regions. 29 elements are active in each pulse-echo acquisition. Fig. (A) illustrates the flow diagram of the simulation: If EC is off, the raw element echo signals are sampled and digitized with 10-bit resolution; then bit errors are randomly introduced to the serialized data with a prescribed BER; a reference image and an error image are reconstructed from the digitized signals and the deserialized error data respectively, and saved in log-scale; lastly, peak signal-to-noise ratio (PSNR), structural similarity (SSIM) (Razaak, JBHI, 2014) and contrast-to-noise ratio (CNR) are calculated from a Monte-Carlo simulation. If EC is on, parity bits are added to the digitized samples before serialization; after deserialization, data with disparities are corrected by a spline interpolation; a following outlier filter provides further error rejection.

Results/Discussion

Fig. (B) shows the PSNR, SSIM and CNR vs. BER plots. Without EC, all the metrics decrease dramatically when BER is worse than 1E-4; while with EC, the corner moves to 1E-2. Doubling the sampling frequency (fs) also improves the image quality at BER = 1E-2. Fig. (C) shows the reference image and the 3 error images reconstructed at BER = 1E-2. When EC is on and fs = 40MS/s, the error image can be barely distinguished from the reference image. This implies that much higher BER can be tolerated than in typical digital data links, allowing substantially higher data rates per cable to be achieved.



Magnetostrictive-Vibration Isolated Probe Design for Backward-Mode Magnetomotive UltrasoundMing-Chen Lu¹, Meng-Lin Li¹¹*National Tsing Hua University, Taiwan***Background, Motivation, and Objective**

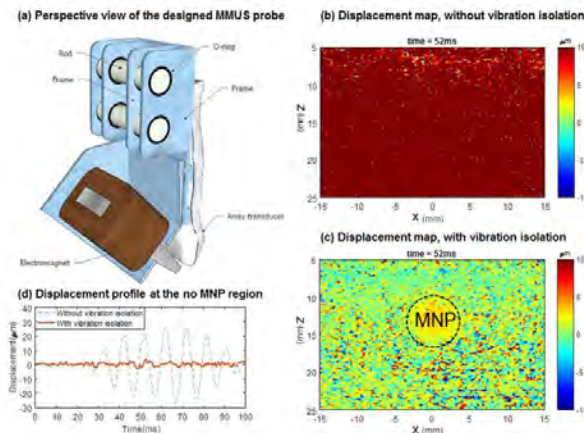
Magnetomotive ultrasound (MMUS), capable of imaging *in vivo* magnetic nanoparticle (MNP) distribution, has shown its potential in extravascular ultrasound molecular imaging, magnetic nano-drug delivery monitoring, and sentinel lymph node identification. To date, MMUS is mainly implemented in forward mode where the imaging object has to lie in between an ultrasound probe and an electromagnet, which is not clinically translatable. To facilitate clinical translation of MMUS, previously we proposed backward-mode MMUS featuring an MMUS probe integrating an array transducer and an electromagnet. However, the MMUS displacement map was overwhelmed by magnetostrictive vibration of the electromagnet because of such an integration, and thus sophisticated signal processing was required to locate MNPs.

Statement of Contribution/Methods

Here we propose a novel MMUS probe design for backward-mode MMUS. The aim of the new design is to isolate the ultrasound array transducer from the magnetostrictive vibration of the working electromagnet. Such vibration is presented in the field of view with the same frequency and appearing timing as those of the magneto-motion of the excited MNPs, causing difficulties in distinguishing MNPs from the background. The design (see Fig. (a)) is based on two separated frames which carry the transducer and electromagnet, respectively. Utilizing high stiffness rods to link the two frames and applying O-rings around joints stabilize the whole structure and isolate the vibration effectively. This probe along with our magnetic pulser can perform cyclic pulsed magnetic excitation with 0.25-Tesla maximum magnetic field intensity.

Results/Discussion

Phantom experiments were used to validate the proposed probe design. Fig. (b) showed the MMUS displacement map obtained by the MMUS probe without vibration isolation. It was overwhelmed by the artifact resulting from the magnetostrictive vibration of the electromagnet and it was difficult to localize the embedded MNPs. Fig. (c) showed the displacement map obtained with the new probe. The vibration artifact was suppressed (see also Fig. (d)), and the distribution of the embedded MNPs was clearly imaged without any sophisticated signal processing. Overall, the present MMUS probe is a promising design enabling backward-mode MMUS, which is more clinically translatable.



Development of Flexible and Kerfless Phased Array Using Sol-Gel Composite Spraying TechniqueMasayuki Tanabe¹, Makiko Kobayashi¹, Kei Nakatsuma¹¹*Faculty of Advanced Science and Technology, Kumamoto University, Kumamoto, Japan***Background, Motivation, and Objective**

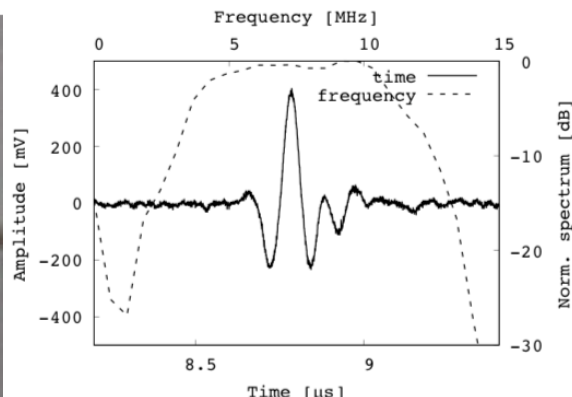
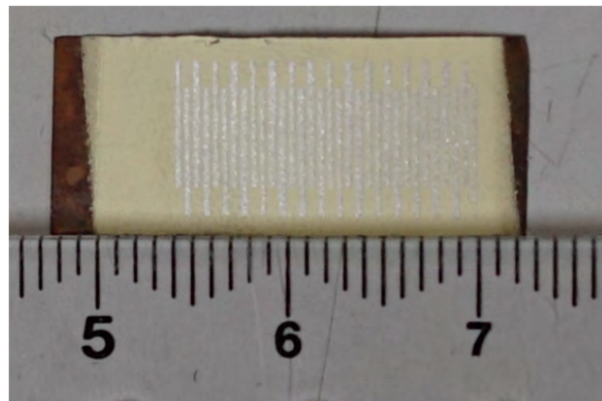
A flexible and kerfless phased array transducer has been fabricated using sol-gel composite spraying technique for curved surface regions of human body. This transducer fabrication technique has been used for non-destructive testing because of mainly its high-temperature durability. The sol-gel composite transducer has many holes generated in the fabrication process and this porosity leads to high flexibility and low mechanical and acoustic crosstalks. These features are also suitable for medical imaging. This research reports a design and fabrication of a sol-gel based PZT/PZT phased array transducer, and the flexibility and crosstalks are investigated.

Statement of Contribution/Methods

Figure 1 shows the fabricated transducer. A PZT/PZT layers with approximately 100 μm is fabricated by a sol-gel spray method on a 100 μm thick stainless substrate. The mixture of PZT powder and PZT sol-gel solution is sprayed onto the substrate sequentially until the desired thickness. Linear electrode arrays with 500 μm pitch and 200 μm kerf are put on the PZT/PZT layer. The transducer can be bent many times and it has not been broken after bend testing.

Results/Discussion

Pulse-echo experiment is conducted for each element with a pulser receiver (DPR300, JSR Inc.) and a stainless steel block. The example of obtained echo is illustrated in Fig. 2. The center frequency is 7 MHz and the frequency bandwidth is approximately 100 %. Crosstalk between elements is below -60 dB.



Design, Fabrication and Testing Highly Sensitive Single Element Doppler TransducersPer Kristian Bolstad¹, Lars Hoff², Hans Torp³, Tonni Franke Johansen⁴¹*University of Southeast Norway, Jar, Norway*, ²*Department of Microsystems, University College of Southeast Norway, Borre, Norway*, ³*Department of Circulation and Medical Imaging, NTNU, Norway*, ⁴*Digital, SINTEF, Norway***Background, Motivation, and Objective**

Doppler measurements are a common diagnostic technique used in ultrasound to detect blood flow or muscle movement, to assess the state of blood vessels and functions of organs. The weak ultrasound echoes from blood require high sensitivity transducers, while bandwidth and pulse length are often less important. The aim of this study was to design, build, test, and compare a variety of single element ultrasound transducer designs, optimized for high sensitivity.

Statement of Contribution/Methods

All transducers were designed for 8 MHz center frequency, with one acoustic matching layer in front and air backing. Three different piezoelectric materials were tested, Pz29, Pz27 and Pz24. Soft piezoelectrics, e.g. Pz29 and Pz27, having large dielectric constant ϵ_r , are commonly preferred in medical ultrasound applications. However, for single-element Doppler transducers having a large aperture area, the resulting high capacitance and low impedance may be hard to drive electrically, especially through a long, thin cable. Hence, for this particular application, a hard piezoelectric with lower ϵ_r , e.g. Pz24, might be preferred. Two different geometries were tested, circular and rectangular, with equal surface areas. The housed transducers were electrically shielded to reduce noise pick-up, and the transducers were electrically matched to the scanner by adding a transformer and a parallel inductor at the transducer end.

Results/Discussion

Transducers were simulated in one-dimensional circuit models and finite element models for comparison and evaluation of results. Fabricated transducers were characterized by electrical impedance measurements, pulse-echo measurements, beam profile measurements. A system for measuring and comparing the signal to noise ratio of the transducers was set up where the reflector is a sphere with diameter 18 mm positioned 157 mm away from the transducer. When comparing the transducers with circular aperture using the signal to noise measurement setup, the hard PZ24 yielded a 3 dB improved sensitivity over the soft PZ27. A comparison between the two soft PZT materials in transducers with rectangular aperture indicated that the PZ29 material gave a 3 dB improved sensitivity over PZ27, likely due to the higher coupling coefficient, K_t , of the material. Overall, the transducers performed well with a signal strength of 75-85 dB over the recorded noise level. -3dB bandwidth for the transducers was found to range from 25% to 50% depending primarily on the thickness of the matching layers.

Feasibility of genetic algorithms in 2D ultrasound array optimization
Bakary Diarra¹, Ravi Samikannu¹, Hervé Liebgott², Joseph Chuma¹, Christian Cachard²
¹*Electrical, Electronics, Computer & Telecommunication Engineering Department, Botswana International University of Science & Technology (BIUST), Palapye, Botswana*, ²*CREATIS, Univ Lyon, INSA-Lyon, Université Claude Bernard Lyon 1, UJM-Saint Etienne, CNRS, Inserm, CREATIS UMR 5220, U1206, Lyon, France*
Background, Motivation, and Objective

The optimization of medium and large 2D ultrasound arrays for 3D ultrasound applications remains a challenge. The most efficient algorithm in this optimization is the simulated annealing (SA) which requires a lot of time and resources due to its functioning principle. In SA, each elements of the array is visited at each iteration slowing down the process as thousands of iterations are required to satisfy the different constraints on the beam profile. This paper proposes to use the genetic algorithms (GA) and compare their performance to those of the SA in terms of time and output beam profiles. The optimization is carried out on a 128 2D array varying the parameters of the genetic algorithms to get the best from them for a reliable comparison to simulated annealing.

Statement of Contribution/Methods

To apply GA to the arrays, a number N=20 of 2D arrays of the 128 active elements are generated randomly. The N arrays are then randomly crossed over to minimize the cost function accounting for the beam side and grating lobes and the main lobe width. To get the best from GA for comparison purpose to the SA, four different selection methods are employed for the offspring generation. After the crossover and mutation, instead of going elements by elements as in SA, GA permit to evaluate the energy of the entire arrays in a relative short time giving a clear advantage. The footprint of the 3.9 MHz 24x8 array is constant and only the position of the 128 active elements varies. The element size is fixed to 0.94λ . with no apodization.

Results/Discussion

The results of Fig. 1a) and b) show that with GA, the final result is obtained between 500 and 920 iterations whereas SA needs more than 1000 iterations to get the same cost function value. Beam profile from Field II simulation of a scatterer placed at 50 mm on the arrays axis shows that the tournament selection in GA leads to a lateral resolution of 0.66° against 0.76° for the reward based selection when SA gives 0.72° (Fig. 1c). In terms of grating lobes, SA performs better with maximum grating lobes of -42 dB against -24 dB for all the GA methods. For scanning angle between 0° and 90° , the GA gives comparable results to the SA whereas for large angles, SA clearly surpasses the GA with grating lobes twice lower. These results confirm, in addition to its speed, the potential of GA to compete with SA in terms of beam profile too using reward based selection and carrying out further investigation.

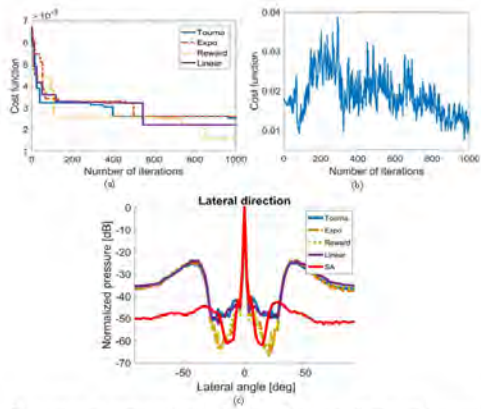


FIG. 1: Cost function evolution as a function of iteration using (a) genetic algorithms with tournament, exponential, reward based and linear selection methods, (b) simulated annealing and (c) comparison between the beam profiles of the optimized arrays of the (a) algorithm over the whole space with the scatterer placed at 50 mm on the array ($0^\circ, 0^\circ$). The average gain and the lobes are about -48 dB for simulated annealing and -24 dB for all the genetic algorithm configurations. The main lobe width is less than 0.66° and 0.76° depending on the GA selection methods against 0.72° for the SA. Element size is 0.94λ .

Basic study on ultrasonic imaging using piezoelectric elements with polarization-inverted layer

Ryo Nagaoka¹, Shin-ichiro Umemura², Yoshifumi Saijo³, Hideyuki Hasegawa¹

¹Graduate School of Science and Engineering, University of Toyama, Toyama, Japan, ²Ultrasound Enhanced Nanomedicine Laboratory, Graduate School of Biomedical Engineering, Tohoku University, Sendai, Japan, ³Biomedical Imaging Laboratory, Graduate School of Biomedical Engineering, Tohoku University, Sendai, Japan

Background, Motivation, and Objective

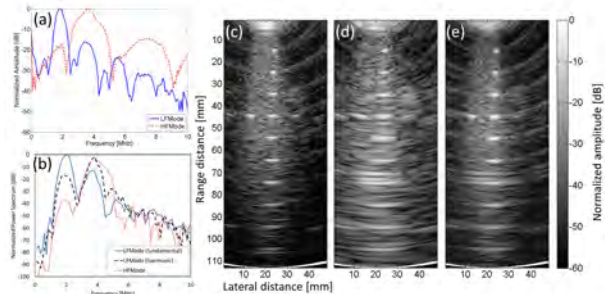
A portable ultrasound system has been developed for emergency medical cares. However, separate arrays are required for imaging at different ultrasonic frequencies. Alternatively, one probe with low frequency is used for the portability at the expense of spatial resolution. In this study, an ultrasonic probe with two different resonant frequencies was developed to solve this issue. Such a probe can also be used for harmonic imaging.

Statement of Contribution/Methods

We developed a two-layered piezoelectric element. The resonance frequency of each layer was 1.8 MHz, and that for an entire thickness of each element was 1.8 MHz. The two layers were bonded and an electrode (2nd) was placed in between them. Two more electrodes (1st and 3rd) were placed on the other surfaces of the two layers, where the 3rd electrode was next to a backing layer. The directions of polarizations of the two layers were opposite. The 1.8-MHz component was generated by applying a pulse voltage both to the 1st and 3rd electrodes. The 3.6-MHz component was generated by applying a pulse voltage to the 1st electrodes. The 2nd electrode was always connected to ground. Those excitation modes were named as LFMode and HFMode, respectively. LFMode can also be used for harmonic imaging. In LFMode, the fundamental components in the signals received by the 1st and 3rd electrodes were in phase, and the second harmonic components were reverse phase. Hence, addition and difference of the signals received by the 1st and 3rd electrodes could enhance the fundamental and second harmonic components, respectively, without the pulse inversion method.

Results/Discussion

Figure (a) shows power spectra of ultrasonic pulses generated by LFMode and HFMode measured with a hydrophone. As can be seen in the figure, LFMode and HFMode successfully generated ultrasonic pulses at central frequencies of 1.8 MHz and 3.6 MHz, respectively. Figure (b) shows power spectra of echoes from a phantom obtained by the respective modes. HFMode could obtain echoes at 3.6 MHz, and LFMode could obtain both the fundamental (1.8 MHz) and second harmonic (3.6 MHz) components. Figures (c)-(e) show B-mode images of a phantom obtained by HFMode, LFMode (fundamental), and LFMode (harmonic), respectively. Those results show that the developed array can obtain ultrasonic images at different frequencies and, also, it can also be used for harmonic imaging.



P2-B11 - SAW Modeling & Design II

Waraku (posters 2)

Wednesday, October 24, 9:30 AM - 4:00 PM

Chair: **Maximilian Pitschi** RF360 Europe GmbH

P2-B11-1

FEM-Based Estimation of SAW Power Flow Angle in Periodic Gratings

Benfeng Zhang^{1,2}, Tao Han¹, Xinyi Li^{2,3}, Yulin Huang^{2,3}, Luyan Qiu², Tatsuya Omori², Ken-ya Hashimoto²

¹*Shanghai Jiao Tong University, China, People's Republic of*, ²*Chiba University, Japan*, ³*University of Electronic Science and Technology of China, China, People's Republic of*

Background, Motivation, and Objective

Non-zero power flow angle (PFA) is not desirable in common SAW device design because grating electrodes are needed to be inclined with an angle equal to PFA. Its miss setting will result in lateral energy leakage from the grating structure. Nevertheless, piezoelectric substrates with this property are often chosen to utilize other features such as temperature stability.

Traditionally, PFA has been evaluated from the SAW slowness curve for free or metallized surface. However, it was unclear whether the grating structure influences PFA or not especially near the resonance.

Statement of Contribution/Methods

This paper proposes a FEM-based technique to estimate SAW PFA in periodic grating structures. It is an extension of the technique proposed by the authors' group[1] to characterize lateral SAW propagation in grating structures with zero PFA. First, the frequency f dependence of lateral wavenumber β_y is calculated by FEM where the longitudinal wavenumber β_x is fixed at π/p (p is the grating period). Next, the calculated f dependence is fitted with that given by a mathematical model which is similar to the thin plate model proposed by the authors' group[2] but non-zero PFA is newly taken into account. After fitting, PFA is estimated from parameters in the mathematical model.

Results/Discussion

Figure 1 shows the f dependence of β_y of the Rayleigh SAW on the Al grating/(0°, 132.75°, -60°) quartz substrate structure at $\beta_x=\pi/p$. The Al thickness h is $0.02p$. In the figure, both the FEM and fitted results are shown. Their agreement is excellent. Frequencies giving $\beta_y=0$ correspond to those at the stopband edges of the main resonance. In general, f increases with β_y when PFA=0. In contrast, two curves exhibit opposite β_y dependency in this case. This is due to nonzero PFA. Note that f increases with β_y when β_y is large.

Figure 2 shows variation of estimated PFA with h . It is seen that the PFA increases gradually with h . In the figure, PFA estimated for the fully metallized case is also shown for comparison. In the case, PFA scarcely changes with h .

[1] G. Tang et al., Jpn. J. Appl. Phys., **55**, 07KD09, 2016.

[2] G. Tang et al., Jpn. J. Appl. Phys., **55**, 07KD08, 2016.

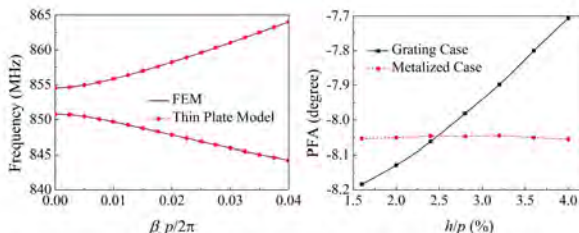
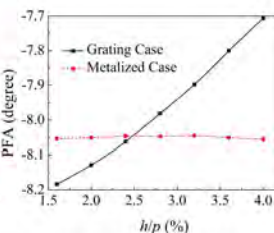


Fig.1 Frequency dispersion of β_y for Al/quartz structure (Al thickness: $0.02p$, $p=2\mu\text{m}$)

Fig.2 Change of PFA with Al thickness for grating and metallized surface cases



Theoretical analysis and design of longitudinal leaky SAW device consisting of ScAlN film / piezoelectric single crystal substrate

Masashi Suzuki¹, Shoji Kakio¹

¹University of Yamanashi, Japan

Background, Motivation, and Objective

Longitudinal leaky SAW (LLSAW) devices are more suitable for applications to high frequency filters than Rayleigh-type SAW devices, because of their high electromechanical coupling factor (K^2) and high phase velocity. However, the LLSAWs on monolayer piezoelectric substrates possess high attenuation which cause a low Q factor. Our group reported that the attenuation of the LLSAW was reduced by loading a high velocity AlN film on LiNbO₃ (LN) or LiTaO₃ (LT) substrate. We expected that the high K^2 , high phase velocity, and low attenuation in LLSAW would be obtained by loading the giant piezoelectric ScAlN film on the piezoelectric single crystal substrate. In this study, the LLSAW propagation characteristics on ScAlN films/piezoelectric single crystal substrates (Quartz and LN) were theoretically analyzed to determine the optimized layered structure for LLSAW devices.

Statement of Contribution/Methods

The phase velocity, attenuation, and K^2 of LLSAWs on (0° 90° 90°) ScAlN/Quartz or LN were calculated by Farnell and Adler SAW propagation analysis method (Fig. 1 (a)). In addition, the frequency characteristics of the admittance of LLSAWs on these layered structures were simulated by the FEM (Fig. 1 (b)). The IDT period λ and the thickness of the infinite periodic Aluminum IDTs in the FEM simulations were set to be 8 μm and 100 nm, respectively.

Results/Discussion

As shown in Fig. 1 (a), the K^2 maximum of 20 % at ScAlN film thickness $h/\lambda=0.09$ on (0° 90° 90°) ScAlN/X36°Y-LN was approximately 1.4 times higher than that of X36°Y-LN. However, the attenuation was not reduced in the ScAlN/LN structure. On the other hand, the attenuation minimum of 0.003 dB/ λ were observed at $h/\lambda=0.1$ on (0° 90° 90°) ScAlN/AT35°Y-Quartz. The K^2 of 7 % at $h/\lambda=0.1$ in the ScAlN/Quartz structure was higher than that of approximately 5 % in a standard LSAW device with a 36°-42°YX LT substrate for frequency filters. Moreover, as shown in Fig. 1 (b), the Q factor and admittance ratio of LLSAW in (0° 90° 90°) ScAlN ($h/\lambda=0.1$) /AT35°Y-Quartz were much higher than that in X36°Y-LN. These theoretical results suggest that the layered structure with ScAlN/Quartz may have a high Q and a high K^2 in LLSAW devices. In the presentation, we will discuss the effect of the Euler angle (c-axis direction) of the ScAlN films, cut angle of the substrates, and SAW propagation direction on the LLSAW characteristics in the layered structures.

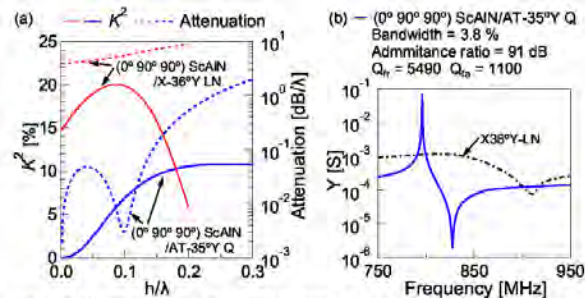


Fig. 1 (a) K^2 and attenuation of LLSAW on ScAlN/LNbO₃ (LN) and on ScAlN/Quartz(Q) as a function of ScAlN film thickness h/λ . (b) Frequency characteristics of admittance of LLSAW on ScAlN($h/\lambda=0.1$)/Q, simulated by the FEM.

Analysis of SAW Scattering at Discontinuity Between Periodic Gratings Using Travelling Wave Excitation and Hierarchical Cascading Technique

Yulin Huang^{1,2}, Jingfu Bao¹, Xinyi Li^{1,2}, Benfeng Zhang^{2,3}, Tatsuya Omori², Ken-ya Hashimoto^{2,3}

¹*University of Electronic Science and Technology of China, China, People's Republic of*, ²*Chiba University, Japan*, ³*Shanghai Jiao Tong University, China, People's Republic of*

Background, Motivation, and Objective

SAW resonators are composed of multiple periodic gratings, and discontinuities are often introduced between the gratings for the synthesis of frequency characteristics. For example, inclusion of structural discontinuities is essential for operation of double mode SAW filters. Although it is known that SAW scattering at the discontinuities gives significant impact on device performances, there was no practical way to analyze it theoretically. It is empirically known phase shift in the discontinuities is not simply given by their physical lengths, in particular for leaky SAWs on 42-LT. Thus as a pessimistic solution, tricks are often introduced in COM-based simulation tools for good coincidence with experimental data.

Statement of Contribution/Methods

This paper proposes use of hierarchical cascading[1] and the travelling wave source[2] for the FEM analysis of SAW scattering at discontinuities. The hierarchical cascading allows us to analyze SAW scattering at a discontinuity sandwiched in between two extremely long periodic grating. The traveling wave source allows us to excite one particular SAW mode selectively from one periodic grating, and scattered SAW amplitudes can be estimated from the FFT spectra of the calculated SAW fields on the surface.

Results/Discussion

Scattering properties of Leaky SAWs on 42-LT are analyzed. The IDT period p_1 and thickness of the gratings are set at 4 mm and 0.32 mm, respectively, and a gap is inserted between two gratings as a discontinuity. Damping mechanisms are given at the outer ends of the gratings.

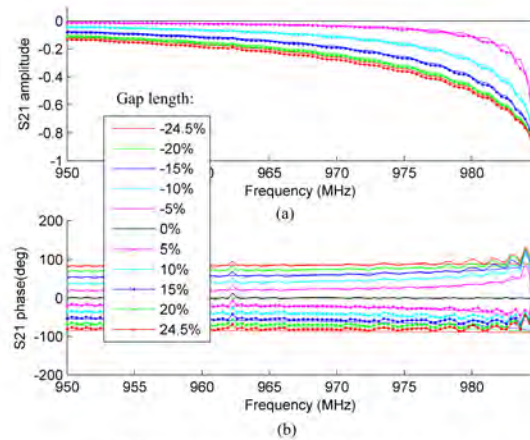
Figure 1(a) shows variation of the transmission coefficient (amplitude) $|S_{21}|$ of gap region with the driving frequency f , and the gap length d relative to p_1 is chosen as a parameter. The amplitude becomes small with $|d|$ as well as f . This is mainly due to increase of the reflection coefficient but scattering into bulk waves is not negligible. It is interesting that the sign of d scarcely influences to the magnitude. Note 985 MHz corresponds to the lower stopband edge of the gratings.

Figure 1(b) shows DS_{21} . It is almost proportional to d when f is much lower than 985 MHz. On the other hand, when f is close to 985 MHz, the phase changes rapidly.

Further analyses including modeling will be given at the presentation.

[1] J.Koskela, et al., *Proc. IEEE Ultrason. Symp.* (2016) p.122.

[2] X.Y.Li, et al., 10.1109/ULTSYM.2017.8092845



Transmission coefficient of gap region in
(a) amplitude and (b) phase (deg)

Love Wave Mode Resonator with a Wide Stable Temperature Range

Yang Yang¹, Qiaozhen Zhang¹, Yirou Shi¹, Tao Han¹, Ping Li¹, Yumei Wen¹

¹Department of Electronic Information and Electrical Engineering, Shanghai Jiao Tong university, Shanghai, China, People's Republic of

Background, Motivation, and Objective

One-port love wave mode resonator has the potential of a wireless sensing platform for measuring physical or chemical parameters, such as magnetic field, gas and liquid, because of its sensitivity to mass loading and enhanced sensing areas. However, the reported frequency shift of the sensor due to the working temperature is close to or even greater than that caused by the measured parameters. Therefore, some temperature-compensated love wave devices, for example the relative frequency shift <50ppm in 20°C~50°C for ZnO/ST90°quartz structure^[1], have been explored. To design a love-wave sensor using one-port resonator with better temperature compensation characteristics, a layered structure of ZnO/SiO₂/quartz with embedded electrodes is proposed.

Statement of Contribution/Methods

The amorphous SiO₂ is filled in the groove between electrodes for temperature compensation. The propagation characteristics of love wave in the proposed ZnO/SiO₂/quartz structure(as shown in Fig.1) are modeled and analyzed by COMSOL. The temperature behavior of love wave mode is calculated by pre-stress analysis using the thermal mechanical coupling model. The thermal strain matrix including shear strain is added into model. The third-order elastic parameters are imported into the non-liner thermal biasing field by using weak form equations in finite element analysis. The cut orientation of quartz with zero temperature coefficient of frequency(TCF) at room temperature is determined. The variation trend of TCF is calculated by changing the metallization ratio and thicknesses of ZnO thin film, SiO₂ and electrodes.

Results/Discussion

The quartz with Euler angle of (0,35°,90°) is used as substrate. The characteristics of love wave phase velocity, electromechanical coupling coefficient and TCF with different thicknesses of ZnO and SiO₂ layers are analyzed. The wide stable temperature range of proposed structure is achieved by adding SiO₂. The relative frequency shift temperature dependence of proposed structure is investigated (Fig.2 compared with[1]), which is $\Delta f/f < 10\text{ppm}$ in -10°C~80°C with cubic function. The optimal thicknesses of ZnO, SiO₂ and electrodes are obtained for the wide range of temperature compensation. The results contribute to designing love wave resonant wireless sensors with a wide and stable operation temperature range for working under various environmental conditions.

[1] F. Moreira, M.E. Hakiki, et al. Numerical Development of ZnO/Quartz Love Wave Structure for Gas Contamination Detection[J]. IEEE Sensors Journal, 2007, 7(3):336-341.

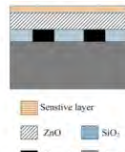


Fig.1 Love wave resonator structure

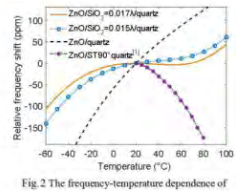


Fig.2 The frequency-temperature dependence of ZnO/SiO₂/quartz structure

P2-B12 - SAW Sensor & Actuator I

Waraku (posters 2)

Wednesday, October 24, 9:30 AM - 4:00 PM

Chair: **Tao Han** Shanghai Jiao Tong University

P2-B12-1

Wireless, Direct Pressure Sensing with SAW Devices at Elevated Temperatures

Gudrun Bruckner¹, Jochen Bardong¹, Paul Szász²

¹HIT, CTR AG, Villach, Austria, ²Sensor Solutions, ABB AG, Ladenburg, Germany

Background, Motivation, and Objective

For process control in industrial applications pressure is the most important parameter after temperature. As the applied sensing elements are often vulnerable against temperature these sensors cannot be placed in direct contact with the medium to measure if the operation temperature is above 150°C. Instead a transmitter medium like oil must be used to transfer the pressure to the sensing element that is placed in low temperature environment. In addition to measurement inaccuracies inherent in the method, these installations require an amount of additional membranes and pipelines which can be avoided by the application of SAW based pressure sensors. As SAW devices can withstand medium (300°C) or high temperatures (800°C) depending on device substrate, they can be operated wirelessly as direct pressure and temperature sensors.

Statement of Contribution/Methods

While the suitability of SAW devices as temperature, pressure or torque sensors is well known, this work focusses on design considerations indispensable for the practical usage. Our design applies SAW delay lines, working at 2.45 GHz on Lithiumniobate as sensing elements. A membrane made of stainless steel transfers the pressure to the sensing element that is bent like a cantilever. The design of the membrane and the delay-lines was adjusted to optimize signal to noise ratio and to cover a wide pressure range. Attention was set to the choice of temperature stable materials, avoiding of thermal stresses and a fixation method free of organic adhesives. Additional delay lines are used for temperature compensation and temperature measurement on the same device. The demonstrators have been extensively tested versus pressure and temperature in a climate cabinet. In addition cyclic lifetime tests were performed for about one year as well as studies on the performance in wireless reading.

Results/Discussion

The experimental investigations demonstrated the suitability of the SAW based devices as pressure and temperature sensors for temperatures up to 300°C provided that no organic material is used in the setup and careful choice of all materials especially for the electrodes. The devices showed a sensitivity of ~ 0.4% FS for pressure measurements and ~ 0.1°C for temperature readings. The lifetime was deduced to be 1.5 years at 300°C. Wireless reading could be achieved up to 1.5 m with 9dBi antennas.



Novel acoustic gratings with high reflection constant for surface acoustic wave gyroscopes

Ashraf Mahmoud¹, Tamal Mukherjee¹, Gianluca Piazza¹

¹ECE, Carnegie Mellon University, Pittsburgh, PA, United States

Background, Motivation, and Objective

SAW Gyroscope (SAWG) [1] has been pursued as an alternative to MEMS and optical gyroscopes for operation in high shock environments. Despite promising demonstrations, there is a need to enhance SAWG noise performance specifically lower Angle Random Walk (ARW) and bias instability by increasing the quality factor (Q) of the SAWG drive and sense resonators while keeping a small form factor. To frequency match the drive and sense resonators, the SAWG is designed on a Y-cut Lithium Niobate (LN) with wave propagation along +/- 45° with respect to the Z-axis [2]. This reduces the K_t^2 of the LN resonators, further motivating high performance mechanical reflectors [3]. By exploiting MEMS processing techniques, we significantly increase the reflectivity of the reflector gratings. We simultaneously etch the LN film and process thick films of materials with very high acoustic impedance. The enhancement in reflectivity translates to an increase in Q (by >6x), gyro sensitivity and ARW (by 12x).

Statement of Contribution/Methods

Grating structures formed by combining metal array (MA) and groove array (GA) with various electrical boundary conditions were designed via finite element analysis, fabricated and measured (Fig.1a-b). We investigated the combination of thick etches of LN with the patterning of thick electrodes with high acoustic impedance (W). Other metals such as Au, Pt and Al were also explored for comparison purposes and different electrical boundary conditions were applied to the reflectors. Resonators were built using these reflectors and their performance characterized.

Results/Discussion

The reflection constant of W was found to be much higher than Al. Using W MAs with GAs yields the highest reflection constant, which compares well with theoretical expectations (Fig.1c). The Q of the rotated resonators is significantly enhanced with respect to prior demonstrations (Q of 6240 vs. 1,000 at 115 MHz) (Fig.1d). The resulting SAWG is expected to exhibit a decrease in ARW by more than 12x, while simultaneously reducing the device footprint by ~2x (Fig.1e).

[1] H. Oh,et.al, Sensors and Actuators A: Physical, 2011 – Elsevier

[2] A. Mahmoud, et.al, Inertial Sensors 2018

[3] C. Dunnrowicz, et.al, Ultrasonics Symposium 1976

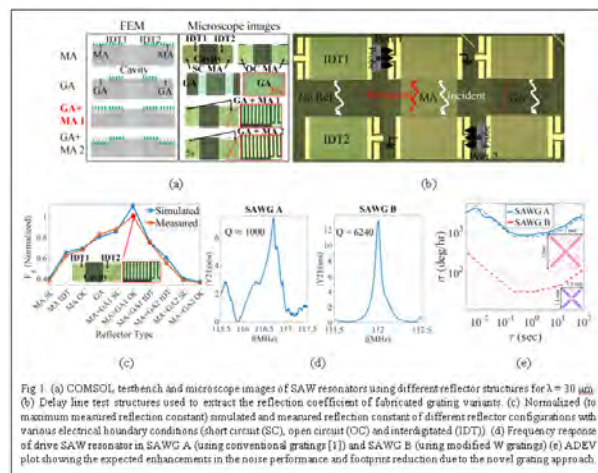


Fig 1. (a) COMSOL, terphenyl and microscope images of SAW resonators using different reflector structures for $\lambda = 30 \mu\text{m}$ (b) Delay line test structures used to extract the reflection coefficient of fabricated grating variants. (c) Normalized (to maximum measured reflection constant) simulated and measured reflection constant of different reflector configurations with various electrical boundary conditions (short circuit (SC), open circuit (OC) and interdigitated (IDT)). (d) Frequency response of drive SAW resonator in SAWG A (using conventional gratings (1)) and SAWG B (using modified W gratings) (e) ADEV plot showing the expected enhancements in the noise performance and footprints reduction due to the novel grating approach.

Cell detachment using guided surface acoustic waves

Jiyang Mei¹, Takumi Inui², Yuta Kurashina², James Friend¹, Kenjiro Takemura²

¹Center for Medical Devices and Instrumentation, University of California, San Diego, La Jolla, CA, United States,

²Mechanical Engineering, Keio University, Yokohama, Japan

Background, Motivation, and Objective

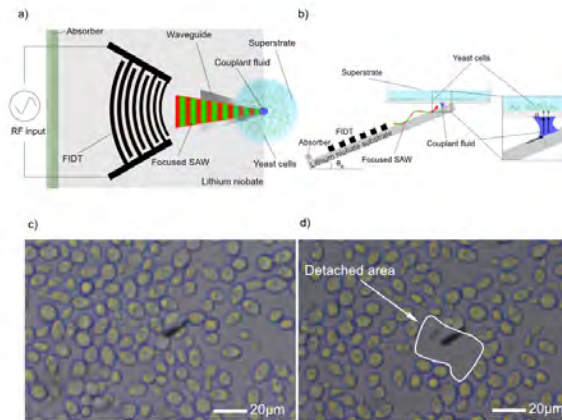
Tissue engineering has been widely studied for decades to regenerate a variety of tissues, where processes of seeding, culturing, detaching and collecting cells are involved. In the recent years, bio-engineers sometimes are interested in a specific limited amount of targeted cells. There consequently grows a necessity of a "friendly" method of cell detachment and manipulation of a small area, or even single cell, as most of the techniques induce damage. This study shows one potential bio-related, contact-free application applying surface acoustic waves (SAW), with which a controllable small amount of cells can be detached by acoustic radiation.

Statement of Contribution/Methods

SAW-based acoustofluidic device is composed of a piezoelectric substrate (128 YX lithium niobate) and focused interdigital transducers (FIDT) with resonant frequency at 100 MHz, deposited on top. A thin aluminum strip of tip width comparable to the wavelength, as a wave-guiding structure, was deposited as well at where the FIDT geometrically focus, trapping the wave from dissipating. The SAW generated from the FIDT travels into a thin layer of liquid and diffracts at the Rayleigh angle, so that the acoustic radiation is coupled and propagates into the superstrate through the couplant fluid, exerting force on the cells which are cultured on the superstrate. The acoustic radiation force overcomes the adhesion force between the cells and the surface and realizes cell removal at the designated area.

Results/Discussion

The FIDT and waveguide are proven to possess the ability of focusing waves to a small spot, 40 μm in radius, according to the amplitude measurement from a laser Doppler vibrometer (LDV, UHF-120, Polytec). As shown in the figure, when a radio frequency (RF) power (the threshold is approximately 80 mW) is applied to the SAW device, acoustic radiation transmitted through the couplant fluid layer is able to detach a targeted region of yeast cells, size $\sim 5 \mu\text{m}$, in less than 1 second. The detached area has a radius about 40 μm , accord with the SAW focused size. Our results have proved the potential of using SAW in cell engineering, such as rapid and accurate manipulation of small amount of cells in fluid environment.



a) Top view of the experiment setup. Focused SAW are generated and propagate to the tip of waveguide. b) The SAW device is mounted at the Rayleigh angle, so that acoustic radiation goes up straight when coupling through the liquid layer. c) The yeast cells, size $\sim 5 \mu\text{m}$, attached to the surface. d) A small area of yeast cells are detached after applying RF power.

Shape effects and response to an applied magnetic field in (TbCo₂/FeCo) multilayer-based SAW resonators. Shape effects and response to an applied magnetic field in (TbCo₂/FeCo) multilayer-based SAW resonators.

Harshad Mishra¹, Mohammed Moutaouekkil¹, Sami Hage-Ali¹, Vincent Polewczuk¹, Karine Dumesnil¹, Daniel Lacour¹, Michel Hehn¹, Omar Elmazria¹, Nicolas Tiercelin², Abdelkrim Talbi², Olivier Bou Matar²

¹Institut Jean Lamour, Université de Lorraine, Nancy, France, ²Univ. Lille, CNRS, Centrale Lille, ISEN, Univ. Valenciennes, UMR 8520 – IEMN, LIA LICS/LEMAC, Lille, France

Background, Motivation, and Objective

Previous studies on Surface Acoustic Wave (SAW) devices have revealed their high potential as magnetic field sensors (MSAW) [1-3]. Both delay line and resonator configurations were considered and sensitive magnetostrictive film was used as IDT or additional layer. Recently, we have shown the influence of the shape of the magnetic sensing layer on the MSAW response [4,5]. In this work we investigate, both experimentally and numerically the IDT shape effects in (LiNbO₃/TbCo₂/FeCo) SAW resonators and their impact on the MSAW response.

Statement of Contribution/Methods

25 bi-layers of [TbCo₂ (3.7nm)/ FeCo (4nm)] capped by a 5nm Ru layer were deposited by RF sputtering to form an approximately 190nm thick metallized layer over a 128° Y-cut LiNbO₃ substrate. Using photolithography and ion beam etching, SAW resonators were fabricated in two configurations: one with the intrinsic magnetic anisotropy parallel to the length of the IDT and the second perpendicular to it. 4mm × 4mm square samples were fabricated for in-plane vibrating sample magnetometer (VSM) tests, in which the metallized full film layer was subjected to lithography and etching to develop IDT finger structures corresponding to the device ($\lambda = 6.5\mu\text{m}$ & $\eta = 60\%$) as well as other different geometries by considering an array of different IDT widths (4μm, 5μm, 6μm, 8μm).

Results/Discussion

Fig 1(a) shows that the anisotropy of the system decreased when the magnetic anisotropy was perpendicular to the IDT and increased when it was parallel to the IDT. The physics behind this is directly correlated to the shape anisotropy, induced during fabrication. This effect is observed in a more pronounced way in thinner IDT fingers, thereby fortifying the shape anisotropy. The data from the VSM tests were used as input of the magnetic properties in the simulations. Fig. 1(b) shows a comparison of the simulated MSAW response when the experimental magnetization of a full film is used vs that of IDT fingers. These results validate the effect of shape induced anisotropy and thus enable us to engineer sensors with specific desirable properties including sensitivity and detection range.

[1] H. Zhou *et al. Appl. Phys. Lett.* 104 114101 (2014)

[2] Kadota *et al. Jpn. J. Appl. Phys.* 50 07HD07 (2011)

[3] M. Elhosni *et al. Sensors and Actuators A* 240 41–49 (2016)

[4] H. Mishra, *et al. Proc. of IEEE Sensors* 2017

[5] V. Polewczuk *et al. Phys. Rev. Applied* 8 024001 (2017)

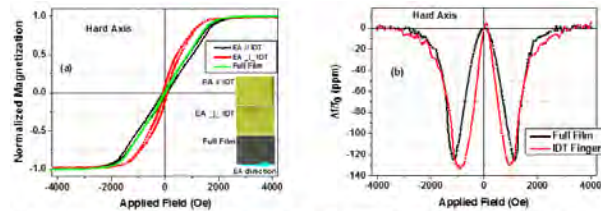


Figure 1. (a) Comparison of the magnetization along the hard axis of the full film with that of IDT fingers

corresponding to devices ($\lambda=6.5\mu\text{m}$, $\eta=60\%$)

(b) Simulated MSAW response using VSM data from IDT fingers vs full film, for a device with magnetic

anisotropy perpendicular to IDT (EA ⊥ IDT)

Acoustofluidics with high selectivity using spatio-temporal modulated SAWsLiqiang Li¹, Eryong Wu¹, Kun Jia², Jiang Zhu³, Keji Yang¹¹*College of mechanical engineering, Zhejiang University, Hangzhou, China, People's Republic of*, ²*School of Aerospace Engineering, Xi'an Jiaotong University, Xi'an, China, People's Republic of*, ³*Zhejiang University, Hangzhou, China, People's Republic of***Background, Motivation, and Objective**

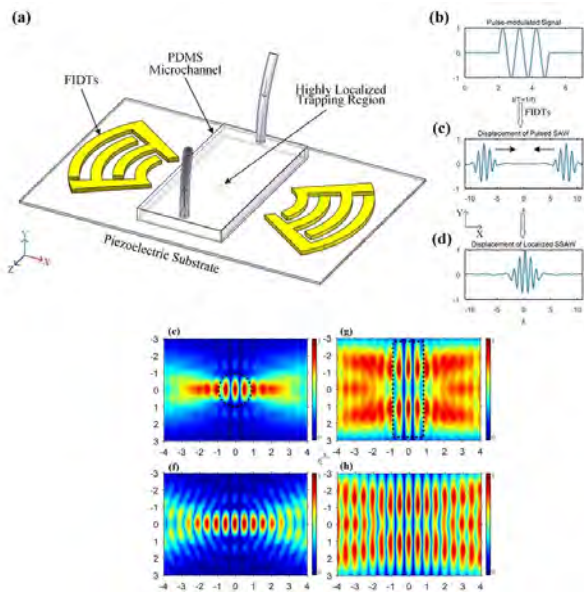
Surface acoustic waves (SAWs) based microfluidics show promising applications in bio-particle processing. With the attributes of simple fabrication and high efficiency, the further development of this technology lies on the improvement of spacial selectivity. In ultrasonic manipulations, the focused transducer and sound field synthesis technique are successfully implemented to achieve localized trapping. Recently, an alternative method, modulating the incident wave in time domain, has been proposed. In this work, we propose a hybrid method, combining the spacial and temporal modulation of incident waves to build acoustofluidics with two-dimensional high selectivity.

Statement of Contribution/Methods

Fig. 1 (a) shows the proposed device, including a pair of focused interdigital transducers (FIDTs), a piezoelectric substrate and a liquid-filled PDMS channel. The FIDTs are actuated by modulated sine signals with a pulse width less than the spread time between opposing transducers (Fig. 1 (b)). As the generated waves only encounter in the center region of the device, horizontally localized trapping region is established, which improves selectively in x-axis. Due to the focused wavefront resulting from FIDTs, the selectivity in y-axis is further improved.

Results/Discussion

A simplified 2D finite-element model is adopted to predict the device performance. Two opposing SAW pulses are actuated on the piezoelectric substrate by the FIDTs (Fig. 1(c)). These two pulses overlap in the substrate and the instantaneous displacement of the standing wave is showed in Fig. 1(d). Accordingly, the time-averaged acoustic field in the fluid is illustrated in Fig. 1(e). For direct comparison, the pressure field only using FIDTs with continuous actuation, non-focused IDTs with pulsed actuation, and non-focused IDTs with continuous actuation are calculated and illustrated in Fig. 1(f), (g) and (h) respectively. It is clear to see the smallest range of pressure node and anti-node (marked by the dashed circle) is established in Fig. 1(e), ensuring the two-dimensional high selectivity of trapping targets. Experiments with 7um polystyrene particles are performed, in which the targets are trapped in a small region as expected. By adjusting the pulse width, the localized target region can be tuned and the proposed device even has the potential to achieve single particle manipulation.



SAW Delay-Line Sensors Only Using Two Reflectors

Jingping Ruan¹, Ruchuan Shi¹, Yang Yang¹, Jiashi Lv¹, Xupeng Zhao¹, Tao Han¹

¹Department of Electronic Information and Electrical Engineering, Shanghai Jiao Tong University, Shanghai, China, People's Republic of

Background, Motivation, and Objective

Surface acoustic wave (SAW) delay-line sensors have their application advantages especially in harsh environments. Phase difference between reflectors is commonly measured to derive the measured parameters. Due to the 2π ambiguity of phase measurement, currently, in SAW delay-line sensors at least three reflectors, whose locations are elaborately designed, have to be adopted in order to guarantee wide measurement range and high accuracy. However, this limits the multi-accessed sensor number by time division. Therefore, a sensing method to guarantee wide measurement range and high accuracy only using two reflectors is proposed. Multi-frequency interrogation signals (MFIS) are used to prevent 2π ambiguity of phase difference between reflectors.

Statement of Contribution/Methods

A method to guarantee wide measurement range and high accuracy only using two reflectors in SAW delay-line sensors is proposed. Three pulses with different carrier frequencies are used to interrogate SAW delay-line sensors. Using the extracted ambiguous phase of echo signals, undetermined equations for estimating the integer period number of unambiguous phase difference between reflectors are constructed. The unambiguous phase difference between reflectors is obtained by seeking the roots of equations based on the group delay interval in a certain range. The measured parameters can then be obtained by unambiguous phase difference between reflectors. The theoretical measurement accuracy and range with the relationship of the sensor sensitivity, the maximum phase measurement error, and the distance between two reflectors are discussed.

Results/Discussion

A SAW reflective delay-line with two reflectors is designed on 128°YX-LiNbO₃ substrate, where the distance between two reflectors is 4.386 mm. A reading system working in 922.5MHz with 10MHz bandwidth is used as the experimental platform. Three interrogation signals of 917.5MHz, 925MHz and 927.4MHz are used to implement MFIS. There is serious 2π ambiguity when measuring temperature. The temperature sensing experiment has been carried out in the range of 0~250°C. The temperature measurement accuracy reaches $\pm 1^\circ\text{C}$. It can be concluded that the proposed evaluation scheme guarantees wide measurement range and high accuracy simultaneously. Furthermore, the number of wireless SAW sensor accessed through time division can be increased.

SAW based tube rotation with wireless power transferSergey Biryukov¹, Andrei Sotnikov^{1,2}, **Hagen Schmidt¹**¹*IFW Dresden, Germany*, ²*Ioffe Institute, Russian Federation***Background, Motivation, and Objective**

During last two years it was found both experimentally [1], [2] and theoretically [3] that a cylindrical piezoelectric tube with a symmetric polarization perpendicular to its surface can be rotated due to the excitation of counter-propagating surface acoustic waves (SAWs) with different amplitudes. The excitation of the waves has been realized by a ring unidirectional transducer (RUDT) placed along the tube surface. This leads to the appearance of a permanent torque that rotates the tube as a whole. Such a structure can be considered as a motor without any stator. But in practice the presence of a thread of suspension for the tube and as well as electrical wires contacting the RUDT strongly hinder and limit the rotation effect. The objective of this work is to consider a wireless power transfer (WPT) system in order to enhance the rotation effect of the piezoelectric tube.

Statement of Contribution/Methods

Unlike the first experimental sample described in [1] and [2] as a piezoelectric tube with RUDT hanging on a thread and directly connected by wires to power amplifier and generator, the WPT system has been developed now. The WRT coil excites without any mechanical contact a second coil electrically connected to the RUDT on the piezoelectric tube surface. This second coil is mounted on the metallic spindle of the tube suspended by a thread. In order to keep the spindle along the system axis a lightweight plastic sphere with 20 mm radius equal to the internal radius of the tube is used. The external radius of the tube, its height and total mass of the sample are equal to 22 mm, 25 mm, and 64 g, respectively. The inertia moment of the sample has been calculated to be $23.1 \cdot 10^{-6} \text{ kg}\cdot\text{m}^2$. The transducer pattern consists of a periodic structure with two electrode fingers of different width per RUDT period and comprises 10 periods covering the whole external surface of the tube.

Results/Discussion

The free operation of the sample suspended from the thread only as a torsional pendulum is characterized by a long period of oscillation $T=140$ s in contrast to the case of previous experiments with $T=9$ s [1], [2]. This means that the suspension elasticity coefficient is much smaller now. As a result, in the present system (generator-amplifier-WRT) the sample rotation angle due to the permanent torque is one order of magnitude larger than in the case without WRT. After switching on the generator at any frequency within the SAW excitation range of 273–278 kHz, the oscillating rotation of the tube is to be seen. Due to the permanent torque the equilibrium center of the sample oscillations is shifted in one direction. This shift reaches 5° and it is visible to the naked eye. The permanent torque responsible for this shift has been calculated as 4 nN·m.

- [1] S. V. Biryukov, A. Sotnikov, H. Schmidt, *APL*, **108**, 134103, 2016.
- [2] S. V. Biryukov, A. Sotnikov, H. Schmidt, In *Proc. 2016 IEEE IUS*, ID 318.
- [3] S. V. Biryukov, M. Weihnacht, A. Sotnikov, H. Schmidt, In *Proc. 2017 IEEE IUS*, ID 207.

Glue-less and robust assembly method for SAW strain sensors**Pascal Nicolay¹, Jochen Bardong², Hugo Chambon³, Pierre Dufilié⁴**¹*CTR AG, Villach, Austria*, ²*HIT, CTR AG, Villach, Austria*, ³*CTR AG, Austria*, ⁴*Microsemi, United States***Background, Motivation, and Objective**

The appropriate mounting of SAW strain sensors is a complicated task. The sensors are usually thoroughly glued in a well-controlled environment. However, glue generates many issues, throughout the sensor's life. Among others, glue doesn't age well, damps the applied strain and undergoes changes over time (hysteresis, creep etc.). A better solution is therefore required, to mount SAW strain (and torque) sensors on mechanical components that operate under heavy load and extreme conditions (high temperature, corrosive environment, high cycle rate etc.).

Statement of Contribution/Methods

We developed a glue-less assembly method, based on reactive NanoFoils®. Once ignited, the foils generate a huge amount of heat in a fraction of a second. The heat can be used to fuse together two thin layers of noble metal and therefore, to bond components whose surfaces are previously coated with Au or Ag. The method was applied to bond SAW strain sensors (Quartz Delay Lines) on steel blades. A specific 433MHz Design was developed, to minimize the temperature sensitivity to almost zero, at room temperature. The applied pressure (a critical parameter to ensure high-quality bonding) was controlled during the bonding operation. A pneumatic test-bench was designed to accurately strain the blades. Reference DMS gages were used, on the back side of the blades. The relative frequency shift of the strain sensors was recorded, using a NWA in phase-tracking mode.

Results/Discussion

Results are presented in Fig. 1. The frequency was observed to change linearly, versus applied strain. This demonstrates the feasibility of the method. However, the center frequency was systematically shifted by more than +20MHz. In addition, the temperature coefficient of frequency (TCF) of the bonded sensors was strongly modified. It was linear over a wide temperature range, close to -16ppm/°C. There is no definitive explanation yet, for the observed changes of properties. It is believed that the dies reached a temperature much higher than 573°C (a-b transition), before quickly cooling down (quenching). This might have changed the crystal orientation of the dies, and therefore, their acoustic properties. Residual thermal stress and strain fields might also (partly) explain some of the observed changes. These hypotheses are supported by FEM computations, presented in more details in the paper.

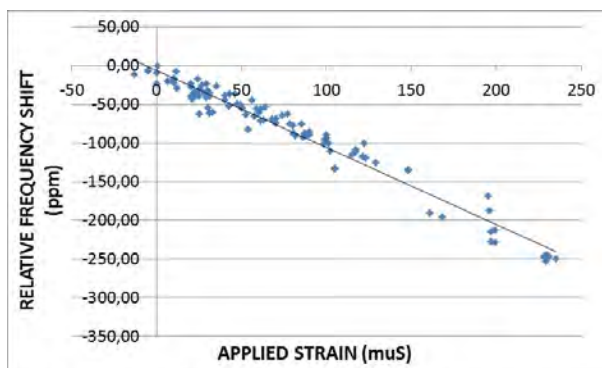


Fig. 1. Characteristic curve of a SAW Strain Sensor mounted on a Steel Blade, using NanoFoils®

P2-B13 - BAW Device & Application II

Waraku (posters 2)

Wednesday, October 24, 9:30 AM - 4:00 PM

Chair: **Masanori Ueda** TAIYO YUDEN CO., LTD.

P2-B13-1

High frequency optical probe for BAW/SAW devices

Hugo Chambon¹, Pascal Nicolay¹, Thomas Moldaschl¹, Claude Humbert¹, Aoun-Amin Awan¹, Maximilian Schiek², Thomas Metzger², Ayech Benjeddou³

¹*CTR AG, Villach, Austria*, ²*RF360 Europe GmbH, Munich, Germany*, ³*Roberval (UTC/CNRS), Université de Technologie de Compiègne - UTC, Compiègne, France*

Background, Motivation, and Objective

Optical probes make it possible to better understand the acoustic behavior of the devices through direct visualization of losses and other design effects and issues. The next generation of 5G filters will operate at high frequency (up to at least 5GHz). It is therefore necessary to develop visualization tools that will be able to characterize these high-frequency SAW/BAW devices, in a highly efficient way.

Statement of Contribution/Methods

An optical probe based on a heterodyne interferometer was implemented. The setup is based on a stabilized 633nm Laser. The beam is divided into a measurement beam and a reference beam by means of an acousto-optic modulator (AOM) operating at 80MHz. After passing through a microscope objective, the measurement beam probes the device under test (DUT), which is connected to a first high-frequency and tunable frequency synthesizer. The two beams are then recombined. The resulting interference pattern is observed using a fast photodiode. After amplification, a custom-built electronic system processes the obtained, high-frequency interferometric signal. This system down converts the input signal to low intermediate frequency, using a large bandwidth I/Q demodulator. The latter is driven by a second, tunable frequency synthesizer. The low frequency signal is then converted into a numerical signal, using an ADC which amplitude is computed. For the sake of frequency and phase stability, the two synthesizers share the same reference clock, which is that from the AOM driver itself. The setup was designed to characterize DUTs operating in a wide frequency range, up to 6GHz. 2D scans are possible, thanks to an XY accurate translation stage.

Results/Discussion

The setup has been used already to characterize high-frequency test BAW devices. In one selected case, the filter was supplied with a 15dBm signal at 1993 MHz. The figure 1 shows the amplitude (in dBm) of the signal detected at the photodiode output. The noise floor was around -145dBm. The acquisition time was 100ms per spatial point. Surface displacements were then computed. The minimal detectable displacement was 2pm. The size of the Laser spot on the DUT was characterized. For 60×, 0.85NA objectives, it was found to be close to 1.4μm in diameter. Future works include the reduction of the spot size to its theoretical limit (<600nm), as well as the development of a fast frequency scanning method.

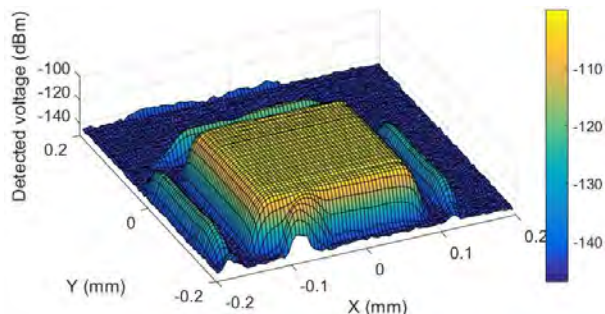


Fig. 1. Surface characterization of a BAW device at 1993MHz, detected voltage at photodiode output.

New Technique to Cancel IMD3 in Electroacoustic Filters
Marta González-Rodríguez¹, Carlos Collado¹, J.M. González-Arbesú¹, Jordi Mateu¹
¹*Universitat Politècnica de Catalunya (UPC), Barcelona, Catalunya, Spain*
Background, Motivation, and Objective

Recent growing demands in wireless applications such as LTE-A puts further stress on the utilization of multiple bands in a limited bandwidth. This scenario presents a variety of challenges. One of them is to face the desensitization or RF receivers due to the generation of spurious signals by the nonlinearity of components inside the handset.

The generation of IMD3 in frequency selective devices is becoming a major concern in the design of RF transceivers where the transmitter and receiver share the antenna because it can cause interfering signals at a given receiver band affecting its sensitivity. Acoustic wave devices are among them. IMD3 in electroacoustic devices is coming either from direct generation due to second order nonlinearities or from remixing effects due to first order nonlinearities. The concept of a new technique to cancel this undesired signal will be presented.

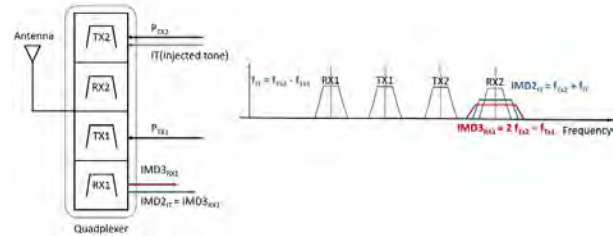
Statement of Contribution/Methods

Knowing that in BAW devices third order effects, such as IMD3, are lower than second order effects, such as IMD2, is possible to cancel second order nonlinearities without the need of high-power (HP) levels by using an injected jamming signal and generating the IMD2 that falls exactly at the same frequency of the undesired IMD3, with the same magnitude and opposite phase.

Fig.1 depicts how the proposed method makes use of a signal at $f_{IT} = f_{Tx2} - f_{Tx1}$ injected at the selective device to cancel the generated IMD3 at $f_{Rx1} = 2f_{Tx2} - f_{Tx1}$ that arise when the device is driven by two HP signals f_{Tx1} and f_{Tx2} . By adjusting the amplitude and phase of the low frequency signal f_{IT} , the IMD2 due to first order nonlinearities that falls exactly at the same frequency of the undesired IMD3 may cancel this last signal.

Results/Discussion

The concept of this technique will be demonstrated by doing measurements of an on-wafer resonator as a proof of concept. The measurement system, including cancellation algorithm will be described. The cancellation achieved with this technique is in good agreement with nonlinear circuit simulations. A proper modeling and a good resonator characterization is needed to demonstrate the concept. The application of this technique to a real environment will be also outlined.



Monolithic FBAR resonators using AlScN piezoelectric layers.

Mohanraj Soundara pandian¹, Elio Marigo Ferrer¹, Jazril Bin Jamil Din¹, Chan Buan Fei¹, Arjun Kumar Kantimahanti¹, Andrea Mazzalai²

¹SilTerra Malaysia Sdn Bhd, Malaysia, ²Evatec AG, Switzerland

Background, Motivation, and Objective

Passive high frequency resonators manufactured using Micro-Electro-Mechanical-Systems (MEMS) technology are an attractive solution for active radio frequency (RF) components like oscillators and filters. These high performance, small form factor devices are fabricated using the MEMS silicon batch processing techniques. After MEMS fabrication, these devices are externally connected with the active application specific integrated circuits devices (ASIC devices).

The motivation is to develop a truly monolithic fabrication technique to integrate thin film piezoelectric resonators directly on top of the ASIC devices. This technique will enable small form factor active filters and programmable oscillators.

The developed monolithic technique has limitations in terms of acoustic energy confinement. Aluminum Scandium Nitride (AlScN) piezoelectric layer is evaluated to improve the electromechanical coupling coefficient and minimize the insertion loss.

Statement of Contribution/Methods

The fabricated device is shown in Figure 1a. The top metal layer of a conventional Complementary-Metal-Oxide Semiconductor (CMOS) device is used to electrically interconnect the top and bottom electrodes. Aluminum layers of 400nm and 350nm are used as top and bottom electrodes respectively. Two types of piezoelectric layers are evaluated, Aluminum Nitride and Aluminum Scandium Nitride.

Results/Discussion

The bulk acoustic resonator is designed to operate at the ISM band. The piezoelectric thickness is 1300nm . The coupling is determined by the electrodes area, as shown in the Figure 1a. The resonator magnitude transmission response is extracted employing RF probes previously calibrated-connected to a vector network analyzer with output power of 0dBm, In the Figure 1b the response for the AlN and Al_{0.91}Sc_{0.09}N test studies is shown. The center frequency is 2.27GHz employing AlN and it shift to 2.19GHz when Al_{0.91}Sc_{0.09}N is used. This shift is expected due to the fact that the acoustic velocity will be different for both piezoelectric materials. The electromechanical coupling coefficient is improved by 60% which translates in higher acoustic energy propagation and thus higher quality factor. The improvement of the resonator performance translates into an improvement of 3.9dB of insertion loss.

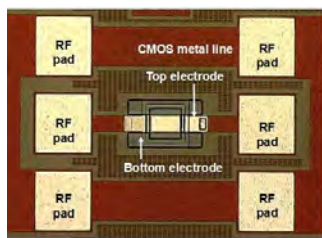


Figure 1a:

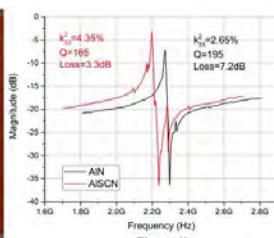


Figure 1b:

Fast Nonlinear Procedure for the Nonlinear Analysis of BAW Resonators and FiltersRafael Perea-Robles¹, David Garcia-Pastor¹, Jordi Mateu¹, Carlos Collado¹, Robert Aigner²¹*Universitat Politècnica de Catalunya (UPC), Barcelona, Catalunya, Spain*, ²*Qorvo, United States***Background, Motivation, and Objective**

Electroacoustic technology is the preferred one to implement the filters at the RF stage of a portable device. However, this technology suffers of some nonlinear problems, which must be considered in the early stages of the design. The interaction of thermic, acoustic and electric domains implies that different mechanism can be the sources of different undesired effects, such as harmonics and IMD.

Proper nonlinear models, usually solved with Harmonic Balance (HB) simulations, have been well stablished. However, if nonlinear distributed models of resonators are required, the circuit size increases considerably and the HB simulations are very time consuming. We will present an alternative method with the aim of reducing the computation time.

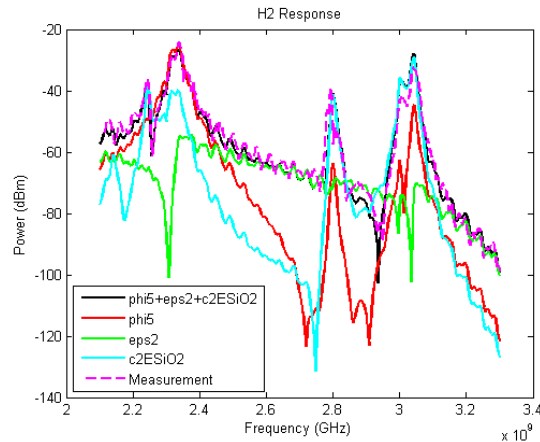
Statement of Contribution/Methods

The presented procedure is able to simulate the generation of IMD and harmonics of any circuit comprising several interconnected resonators and lumped components. The analysis is based on the Y matrix of the whole circuit, including the discretized resonators providing current and voltage values at any point of the circuit. The circuit is defined by means of a Netlist that lists the components, their parameters and their electrical nodes, and its linearly solved at the fundamental frequencies of the sources. The distributed nonlinear voltage sources of the new frequencies of interest are calculated using the nonlinear constitutive equations and its solved again considering those sources. If thermal effects are required, the dissipated power is calculated at any lossy component and heat generation and propagation is included.

Results/Discussion

Measurements and examples of the usefulness of the proposed modelling will be presented, including comparison with standard HB simulations. This analysis is able to analyze the contribution of each nonlinear coefficient in one single simulation. Fig 1 shows an example of measurements and the contribution of different sources of H2 generation.

This method is accurate if the nonlinearities are low. There is no restriction to interconnect resonators and lumped components. Furthermore, the part of the circuit that describes the heat propagation may be calculated independently reducing considerably the computation time in comparison with standard HB simulations.



AlN-based solidly mounted resonators on glass substrates for high temperature applicationsTeona Mirea¹, Jimena Olivares¹, Marta Clement¹, Jesus Sangrador¹, Enrique Iborra¹¹GMME-CEMDATIC-ETSIT-Universidad Politecnica de Madrid. Spain., Spain**Background, Motivation, and Objective**

Acoustic wave resonators have been widely investigated as sensors for operating at high temperature (up to 1000°C) due to their low cost and good performance. One of the most explored devices is surface acoustic wave (SAW) resonators made on langasite or AlN. Although efficient, these devices still have drawbacks, like using long and narrow metallic strips for the IDT, which are subjected to destructive agglomeration when working at high temperature, or the need of high resolution nanolithography if high frequencies are pursued. In previous works we proposed AlN-based solidly mounted resonators (SMR) as a promising alternative. We showed that these devices can sustain up to 1000°C (by showing non degraded before and after annealing measurements). However, during measurements at high temperature, their response was degraded. We found the main responsible to be the fact that the high resistivity silicon substrates on which we deposited fully-insulating reflectors become conductive when temperature increases due to the exponential increase of the intrinsic carrier density, which makes the material to have a quasi-metallic conductivity above 400°C. Conductive substrates in BAW technology make the design of layouts very complex because the appearance of parasitic capacitive coupling between the top electrode and the substrate which short-circuits the device. To solve this problem, now we present the characterization at high temperatures of SMRs deposited on glass plates, which does not vary its high resistivity at high temperatures.

Statement of Contribution/Methods

The SMRs are composed of seven alternating layers of SiO₂/AlN deposited on a mechanically polished 7059 corning glass, which can sustain up to 639°C before softening. Piezoelectric stack was composed by an evaporated Ir bottom electrode, on which we sputter a *c*-axis oriented AlN, and a Mo top electrode. The top electrodes are extended 1.7 mm to bigger pads where the GSG probes of a home-made RF high temperature cable are bond. To avoid capacitive coupling of the electrical extensions to the bottom electrode, the Ir bottom electrode is etched below them. For high temperature in-situ electrical characterization, we calibrate the system, including our home-made RF cable, with specifically designed calibration kits using ITO as the conductive layer for load standard resistance, on which we define Au pads with similar geometries to our devices.

Results/Discussion

As an initial test, we have annealed 3 GHz devices at 550-600°C during several hours. Assessment of their electrical response before and after the treatment shows identical responses, proving their performance is not degraded. Devices with a coupling factor of more than 5.7% and quality factors of around 300 were used for these experiments. The structural integrity of the devices is also preserved. Their in-situ characterization at the same temperatures and higher is on-going.

P2-B14 - Material for Acoustic Wave Device I

Waraku (posters 2)

Wednesday, October 24, 9:30 AM - 4:00 PM

Chair: **Sergei Zhgoon** National Research University "MPEI" (Moscow Power Engineering Institute)

P2-B14-1

Temperature characteristics of ScAlN/SiO₂ BAW resonators

Honoka Igeta^{1,2}, Makoto Totsuka^{1,2}, Masashi Suzuki³, Takahiko Yanagitani^{1,2,4}

¹Waseda University, Japan, ²ZAIKEN, Japan, ³University of yamanashi, Japan, ⁴JST PRESTO, Japan

Background, Motivation, and Objective

AlN films have been used in high Q RF filter for mobile communications. However, the effective electromechanical coupling k_{eff}^2 which determines the bandwidth of the filters is low. Piezoelectricity of Sc doped AlN film increases five times compared to that of AlN film [1,2]. TCF degradation may occur in the ScAlN films compared to AlN. In this study, we experimentally investigated TCF of $\text{Sc}_x\text{Al}_{(1-x)}\text{N}$ films with various Sc concentration. Furthermore, using the TCF values, we simulated TCF of the layered of ScAlN/SiO₂ FBAR which having positive TCF. We investigated to find optimal SiO₂ thickness which has both high k_{eff}^2 and good TCF, using Mason's equivalent circuit models.

[1] M. Akiyama, T. Kamohara, K. Kano, A. Teshigawara, Y. Takeuchi, and N. Kawahara, *Adv. Mater.*, **21**, 593-596 (2009).

[2] T. Yanagitani, and M. Suzuki, *Appl. Phys. Lett.* **105**, 12907(2014).

Statement of Contribution/Methods

Three ScAlN samples for each Sc concentration were prepared total 36 samples. TCF were determined by averaging the measured TCF at three samples. In the simulation, TCF and k_{eff}^2 for fundamental mode and second mode of ScAlN/SiO₂ FBAR were compared to those of AlN. TCF of SiO₂ used in the simulation was assumed to be 116.8 ppm/°C[3].

[3] J. Kushibiki, and A. Tada, *Phys.*, **87**, 3113(2000)

Results/Discussion

As shown in Fig. 1, TCF is nearly constant in the region of $x < 0.2$. TCF is deteriorated in the region of $x > 0.2$. Fig. 2 (a) and (b) show k_{eff}^2 and TCF for fundamental mode and second mode at high Sc concentration (Sc=41%) as a function of SiO₂/ScAlN thickness ratio. In the second mode, k_{eff}^2 of ScAlN/SiO₂ FBAR is much lower than that of AlN. On the other hand, high k_{eff}^2 and stable TCF in fundamental mode are found compared with AlN at the thickness ratio near 0.25. The simulated results of fundamental mode at high Sc concentration (Sc=41%) and low Sc concentration (Sc=9.5%) of ScAlN/SiO₂ FBAR are summarized in Table.I. At low Sc concentration, k_{eff}^2 and Q factor are both lower than those of AlN when zero TCF is achieved. At high Sc concentration, k_{eff}^2 of ScAlN/SiO₂ FBAR exceeds that of AlN when both have the same TCF. k_{eff}^2 of ScAlN/SiO₂ FBAR is comparable to that of AlN even if TCF is zero. In conclusion, high k_{eff}^2 of ScAlN/SiO₂ FBAR at high Sc concentration is promising for FBAR where k_{eff}^2 and TCF exceed those of AlN. This structure, however, does not have high Q factor compared with AlN.

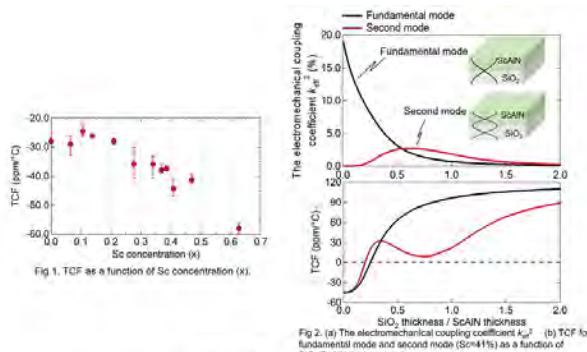


Table I. k_{eff}^2 , TCF and Q factor of AlN, ScAlN, and ScAlN/SiO₂ FBAR

| Piezoelectric material | SiO ₂ / ScAlN | Electromechanical coupling coefficient k_{eff}^2 (%) | TCF(ppm/°C) | Q factor (@ 20Hz) |
|---------------------------------------|--------------------------|---|-------------|-------------------|
| AlN | 0.0 | 6.4 [2,4] | -27.2 | 3200 [4] |
| SiO ₂ | 2.0 | 0.0 | 116.8 [3] | 2700 [5] |
| ScAlN (Sc=9.5%) | 0.0 | 9.2 [4] | -25.2 | 1900 [4] |
| ScAlN (Sc=41.0%) | 0.0 | 19.0 [6] | -45.0 | — |
| SiO ₂ +ScAlN (Sc=9.5%) | 0.31 | 3.2 | ±0.0 | 2005 |
| SiO ₂ +ScAlN (Sc=41.0%) | 0.37 | 5.2 | ±0.0 | — |
| SiO ₂ +ScAlN (Sc=41.0%) | 0.26 | 7.9 | -27.2 | — |

[1] R. Aigner, Int. Symp. Acoust. Wave device Future Mobile Comm. Syst. (2011)

[2] B.A. Auld, *ACOUSTIC FIELDS AND WAVES IN SOLIDS*, p 98

[3] K. Sano, R. Karasawa, and T. Yanagitani, *Proc. 2017 IEEE Ultrason. Symp.*, 1-4 (2017)

Effects of post-deposition vacuum annealing on piezoelectric performance of AlScN thin films sputtered on 200 mm production wafers

Marta Clement¹, Valeriy Felmetser², Teona Mirea¹, Jimena Olivares¹, **Enrique Iborra¹**

¹GMME-CEMDATIC-ETSIT-Universidad Politécnica de Madrid, Spain, ²OEM Group, AZ, United States

Background, Motivation, and Objective

Sc-doped AlN polycrystalline films are attractive active layers for electro-acoustic devices working at 5G frequencies, owing to the significant enlargement of the AlN piezoelectric activity with the increasing Sc content. Besides, MEMS industries are claiming for better piezoelectric material than pure AlN, where low Sc doping levels can offer the advantage of considerably increasing the electromechanical coupling factors while keeping the elastic constants relatively high. A configurable cathode based on a variable, non-homogeneous Sc content could be a better solution than alloyed targets when fine-tuning of the Sc content for each particular application is needed. This method, complemented with post-heat treatments, gives layers with 7 at% of Sc and 8.6% material electromechanical coupling factor (k^2). The method was implemented in an Endeavor-AT cluster tool from OEM Group, adapted for sputtering on 200 mm wafers.

Statement of Contribution/Methods

The sputtering module is equipped with a dual-cathode S-gun magnetron. AC (40 kHz) power is applied between two pure Al targets containing embedded 12 mm in-diameter Sc pellets, the number of which can be varied to achieve the desired composition in the deposited film. The 180 mm inner target can contain up to 20 Sc pellets, whereas the 280 mm outer target can accommodate up to 14 pellets. In this work we use a Sc pellets combination to obtain around 7 at% of Sc in the films, which has been measured with RBS. After deposition, thermal treatments at different temperatures and times were studied for optimizing the Sc rearrangement in the network lattice. Two types of acoustic mirrors were used for fabricating test resonators. First a non-optimized Al/Mo mirror was deposited on 200 mm wafers for as-deposited AlScN characterization. Second, well performing SiO₂/Mo mirrors deposited on 100 mm wafers were used for thermal treatment studies.

Results/Discussion

AlScN films were sputtered on 200 mm Si wafers covered with non-optimized Al/Mo-based acoustic mirrors intended for fabricating test resonators and studying radial homogeneity. The composition of the films assessed by RBS measurements, gave Sc contents around 7 at% with reasonably good homogeneity across the wafers. The electrical characterization of the resonators yielded k^2 of the as-deposited material of around 7%. XRD measurements revealed that AlScN films are highly *c*-axis oriented, with plane spacing of 5.00 Å ± 0.005 Å and FWHM of the rocking curve around the (00·2) reflection ranging from 1.6° to 2° across the wafers. We also present a study of thermal treatment to increase the stability of the samples and to increase the piezoelectric activity to obtain values of k^2 of more than 8.6%. Additionally, we present a method for assessing the compositional changes by using a non-destructive technique based on IR reflectance measurements.

Evaluation of bonded wafer for SAW devices using The Line-Focus-Beam Acoustic MicroscopeOsamu Kawachi¹, Rei Oikawa¹, Jun-ichi Kushibiki²¹TAIYO YUDEN Mobile Technology Co., LTd., Shinmachi Ome, Japan, ²Department of Electrical Engineering, Tohoku University, Sendai, Japan**Background, Motivation, and Objective**

Recently, bonded wafers for SAW devices have been actively developed. In this development, it is of great importance to evaluate such characteristics of the bonded wafer itself as to realize stable performance. So far, we have employed a conventional method using comb patterns fabricated on the wafer that measure SAW velocities and evaluate coupling coefficient and propagation loss for SAW devices. However, it is difficult to evaluate bonding situation. In this report, we try to apply a line-focus-beam (LFB) acoustic microscope technology developed by Kushibiki and Chubachi to evaluate the bonded wafer as well as piezoelectric substrates of LiTaO₃ and supporting substrates of sapphire.

Statement of Contribution/Methods

LFB acoustic microscopy can measure the propagation characteristics, viz., phase velocity and attenuation of leaky SAW (LSAW) on the water-loaded specimen surface by V(z) curve measurements. This system enables to do quantitatively characterizing elastic and structural changes of the specimens with very high accuracy. So, this evaluation method is extremely useful for sensing the bonding interface located within a wavelength of LSAWs. We first characterized a piezoelectric substrate and a supporting substrate as reference data and then measure the LSAW propagation characteristics of the bonded wafer as a function of frequency in a range from 100 to 275 MHz.

Results/Discussion

We prepared several specimens of thick 42YX-LiTaO₃ bonded on R-plane of sapphire with orientation flat set to 45deg. Average velocity of the sapphire substrate was 5927 m/s, while that of 42YX-LiTaO₃ substrate was about 3130 m/s. For the bonded wafer of 3 μm thickness we observed typical velocity changes of 940 m/s decreasing between 100 and 275 MHz. The measured result of line-scanned along X-axis is exhibiting a maximum change of 110 m/s depending upon the position (Fig. 1). The velocity changes must contain the information of film thickness distribution and bonded condition. We also obtained velocity change due to the bonding condition.

***Conclusion**

We started characterizing bonding interface used for the new SAW devices by LFB acoustic microscope technology. We are collecting technical data concerned with the bonding as well as data of piezoelectric LiTaO₃ substrate and supporting sapphire substrate. We will develop the SAW devices by optimizing the bonding conditions.

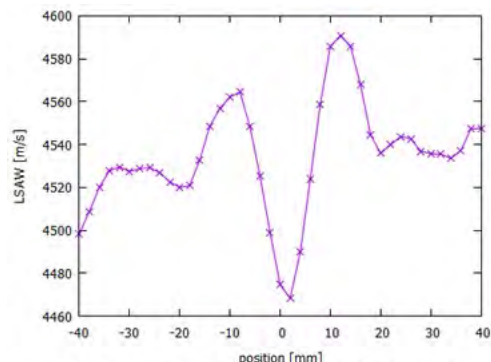


**Fig.1 X-line scan of bonded wafer
(LiTaO₃/Sapphire)**

Stress control for highly doped Aluminum Scandium Nitride films

Sergey Mishin¹

¹AMS, Inc., Goleta, CA, United States

Background, Motivation, and Objective

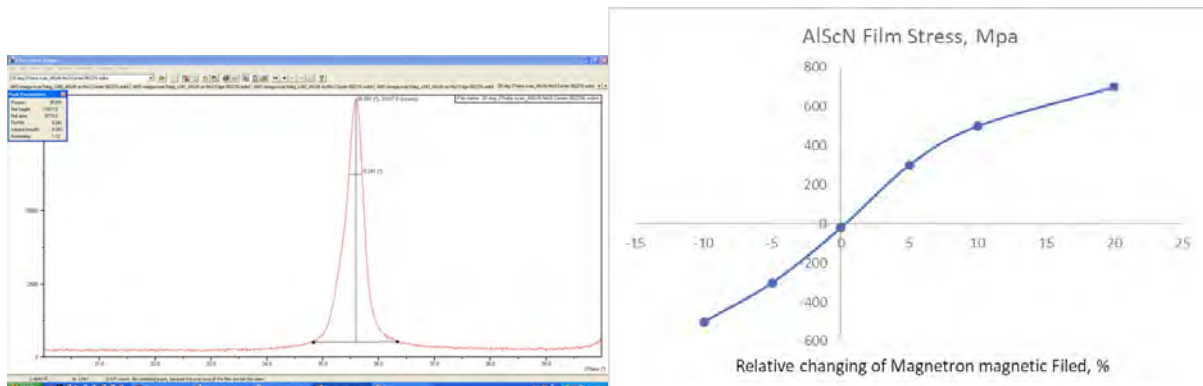
Recently highly Sc doped aluminum nitride films have been used for variety of applications ranging from microphones to PMUT sensors. Deposition on different substrate surfaces such as Pt, Mo, SiO₂ and GaN (both patterned and un-patterned) lead to requirement to be able to control stress over 1GPa range. In order to obtain zero stress on different surfaces, equivalent process condition on Si wafers requires large stress offset. Stress is typically controlled by adjusting deposition pressure and substrate bias. For concentrations above 20%atomic Sc, stress control using substrate bias results in non-uniform stress across wafer. Stress control using adjustment in deposition pressure can produce good stress control across wafer, but can only produce stress adjustment with good thickness uniformity control over a limited stress range. Furthermore, at Sc concentrations above 30%, sporadic crystal growth is observed on more tensile depositions.

Statement of Contribution/Methods

In this investigation, we demonstrated stress control over 1 GPa range, by using a secondary magnetic field that is easily adjusted from outside of the magnetron.

Results/Discussion

We were able to obtain stress variation across 200mm wafer below 100MPa. No sporadic crystal growth was observed between 20% Sc and 32% Sc range.



P2-B2 - PPN: Phononics

Waraku (posters 2)

Wednesday, October 24, 9:30 AM - 4:00 PM

Chair: **Minoru Kurabayashi Kurosawa** Tokyo Institute of Technology

P2-B2-1

Experimental evidence of compact waveguide based on whispering gallery in phononic crystals plate

Jinfeng Zhao¹, Weitao Yuan¹, Bernard Bonello², Yongydong Pan¹, Zheng Zhong¹

¹School of Aerospace Engineering and Applied Mechanics, Tongji University, Shanghai, China, People's Republic of, ²Sorbonne Université, UPMC Université Paris 06 (INSP–UMR CNRS 7588), Paris, France

Background, Motivation, and Objective

Phononic crystals (PCs) based waveguides are made, in general, by introducing an accurately designed linear defect into a perfect PC. This kind of guide features a relatively broad frequency range as the width of defect increases. However, there is another kind of guide allowing for filtering Lamb modes within a very narrow frequency range, based on the whispering gallery modes (WGM) of hollow pillars embedded in the defect.

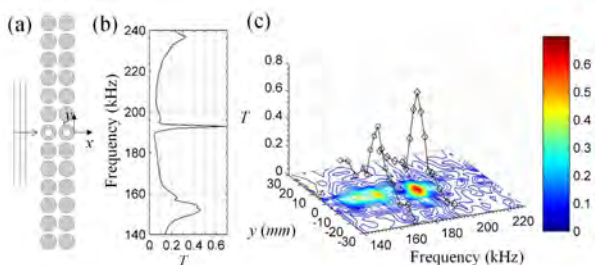
Statement of Contribution/Methods

Following this point, we proposed a compact waveguide for the lowest order antisymmetric Lamb modes (A0). In particular, two hollow pillars are introduced on the central axis of aligned lines of full pillars, as shown in Fig. 1(a). These steel pillars are bonded to the aluminum plate in square lattice by the epoxy adhesive.

Results/Discussion

The WGMs are computed to appear around 193 kHz when the hollow pillar features the inner diameter $d_2 = 2.8\text{mm}$, the outer diameter $d_1 = 5\text{mm}$, the height pillar $h_p = 2.4\text{mm}$, on a 1.5mm thickness aluminum plate. The calculated transmissivity, as shown in Fig. 1(b), leads to a narrow spot centered at $f = 193\text{ kHz}$ ($T_{max} = 0.69$) within an otherwise stop bands. We then used the air-coupled method and the laser ultrasonic technique to characterize the wave propagation. We show in Fig. 1(c) the T recorded at a distance $x = 6\text{ mm}$ behind the sample. One bypassing spot that features the maximum $T_{max} = 0.70$ when $f = 191\text{ kHz}$, corresponds well to the frequency interval of WGMs based guidance in Fig. 1(b).

In summary, the experimental evidence of compact waveguide based on the WGMs is shown for A0 mode.



Transferable Analytical Model of Phononic Bandgap in Cross-hole Phononic Crystals
Takahiro Nishino¹, Kenji Tsuruta¹, Atsushi Ishikawa¹
¹*Electrical and Electronic Engineering, Okayama University, Okayama, Japan*
Background, Motivation, and Objective

Phononic Crystal(PnC) is a periodic composite material capable of selectively transmitting and controlling propagation of acoustic waves, and is suitable for the development of advanced technological devices such as acoustic filters, resonators, acoustic diodes, topological acoustics. Precise control of the phonon band is a key to realization of these applications. A recent report demonstrated numerically and experimentally that the position and the width of phononic bandgap (PBG) of PnC can be controlled by varying the shape of unit cell structure. However, the design method has relied on empirical selection of the shape parameter depending strongly on the materials chosen. The purpose of the present study is to develop an analytical model for PBG control that can be applied to wide range of operation frequency. We show numerically and theoretically that band structure of the PnC in plates can be tuned precisely by adjusting shape, size, and materials of periodic cells for MHz and kHz ranges.

Statement of Contribution/Methods

We adopted a PnC with cross hole in the periodic cell, as illustrated in Fig. 1(a). First, the band structure of the PnC with AlN plates with parameters $\{a, b, h\} = \{500\mu\text{m}, 450\mu\text{m}, 250\mu\text{m}\}$ is calculated using the Finite Element Method (FEM). The shape of the cross holes is varied by changing another parameter c ($0 < c/a < 1$) to control position and width of PBG in MHz region. The FEM data at lower and upper edge of the bandgap frequency are then modeled by three types of vibrational modes. Finally, it is demonstrated that the analytical model developed for the AlN plate can be applied to PnC with acrylic plate with PBG in kHz region.

Results/Discussion

Figure 1(b) shows the relationship between the geometrical parameter (c/a) and the bandgap. Three different vibrational modes were confirmed at the upper and lower edge of the PBG (Fig. 1(c)-(e)): An out-of-plane mode at point B (Fig. 1(c)); an in-plane mode of beams with fixed ends at point C (Fig. 1(d)); a local resonance mode of the beams and lumps at point D (Fig. 1(e)). To model these identified modes, we apply three types of analytical expression; the flexural wave dispersion relation (point B) and *Bernoulli-Euler beam theory* (point C) for upper edges, and the *spring-mass model* for lower edge (point D). We further show that this modeling method is applicable to a kHz region by the same phononic structure in an acrylic plate.

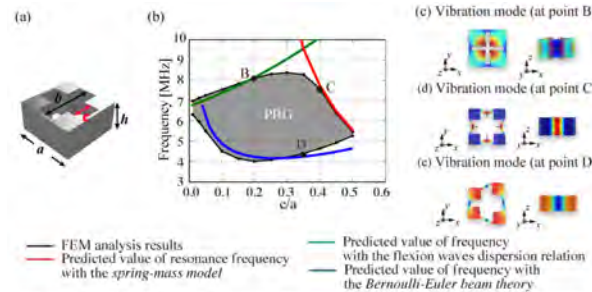


Fig. 1(a) Schematic of the unit cell of a cross-hole structure. (b) Comparison between the numerically simulated PBG and the corresponding theoretical result. (c)-(e) Vibration modes

Design and Assessment of Phononic Crystals for Controlling Ultrasonic Wave via Optical Measurement Method**Kensuke Manabe¹, Atsushi Ishikawa¹, Ken Yamamoto², Takefumi Kanda¹, Kenji Tsuruta¹**¹*Graduate School of Natural Science and Technology, Okayama University, Okayama, Japan*, ²*Department of Pure and Applied Physics, Kansai University, Osaka Prefecture, Japan***Background, Motivation, and Objective**

Recent advances in acoustic-wave control based on artificial structures, such as acoustic lenses¹⁾, waveguides, and acoustic diodes²⁾, require complex design strategies which hamper performance assessment via direct measurement of wavefront inside the structures. Non-invasive techniques as well as numerical simulations are thus indispensable for an efficiency improvement and miniaturization of those acoustic devices. In the present work, we develop an optical measurement technique to visualize ultrasonic wavefront in phononic crystals without interfering the propagation. Our approach achieves non-invasive time-resolved imaging of an ultrasonic wavefront in artificial acoustic structures, paving the way toward an important step of acoustic device design for an advanced ultrasonic wave control.

Statement of Contribution/Methods

Using the finite element method (FEM), we have first designed the phonon dispersion of a two-dimensional phononic crystal consisting of a square array of copper wires in water in order to realize phonon band gap, defect mode, negative refraction at a desired ultrasonic frequency. We then fabricated the designed structures and conducted an optical measurement based on the Fresnel diffraction method³⁾ [Fig. 1(a)] to characterize the acoustic responses of the phononic crystals. The light illumination from xenon lamp is diffracted by density variation in the ultrasonic wave induced by a transducer, and then captured synchronously by a camera to visualize the wavefront.

Results/Discussion

Figure 1 (b) shows the experimentally visualized ultrasonic propagations in the phononic structure with a bended waveguide for 200 kHz. Note that a single wire placed at the corner of the waveguide plays effectively as a scatterer to bend the guided wave upward, and the position of the wire can be adjusted to optimize the transmittance by the time-resolved imaging. Also, this experimental observation of the wavefront is well re-produced by the corresponding numerical simulation in Fig.1 (c). Our approach is also shown to be applicable to direct measurement of wavefront in phononic structures in solid media such as Poly Dimethyl Siloxane (PDMS).

- 1) Y. Kanno, K. Tsuruta, K. Fujimori, H. Fukano, S. Nogi, Electron. Commun. Jpn. **97**, 22 (2014).
- 2) A. Ishikawa and K. Tsuruta, Jpn. J. Appl. Phys. **56**, 07JB01 (2017).
- 3) K. Yamamoto, Acoust. Sci. Tech. **26**, 378 (2005).

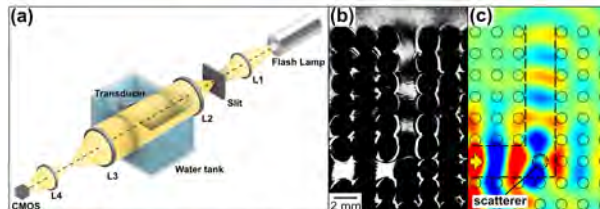


Fig.1 (a) The schematic of our experimental setup.
(b) Experimental visualization and (c) numerical simulation.

Effective slowness surfaces for anisotropic elastic composites**Vincent Laude¹, Muamer Kadic²**¹CNRS, Besançon, France, ²Université de Franche-Comté, Besançon, France**Background, Motivation, and Objective**

The problem of the homogenization of periodic elastic composites at low frequencies or long wavelengths is a rather old one. With the recent interest in phononic crystals and acoustic metamaterials, however, it has become important to predict accurately the effective wave properties for arbitrary materials, lattice types, and structures. Our motivation is to devise formulas for the estimation of the effective phase and group velocities in periodic composites containing sharp discontinuities of material distribution within a unit cell. Once this objective is achieved, we can obtain effective slowness surfaces and in particular estimate the anisotropy of wave propagation that results from a periodic structuration.

Statement of Contribution/Methods

Basing on previous studies that used the plane wave expansion method to obtain formulas for the effective phase velocity [1,2], we constructed estimation formulas that are based on a variational formulation that is easily implemented with finite element analysis. Our derivation is based on second-order perturbation theory, with the propagation direction dependent zero-order solution being a simple uniform displacement and the first-order correction resulting from material discontinuities. In practice, in order to obtain an effective slowness surface it is only necessary to solve one periodic boundary value problem per propagation direction. The method is hence numerically very efficient.

Results/Discussion

The method is applied to sonic crystals (for pressure waves in fluids) and to phononic crystals (for elastic waves in solids). Formulas valid for all cases are obtained, including the case of anisotropic constituents. Effective slowness surfaces are obtained and plotted. If a connected propagation matrix extends throughout the unit cell, it is usually found that the effective anisotropy is very small and is furthermore rather independent of the lattice type. If a solid skeleton is considered instead, such as in the case of pentamode materials, the effective anisotropy can in contrast be quite large. By including resonant structures within the unit cell, it is furthermore possible to combine anisotropy with resonant and negative effective mass densities.

[1] Krokhin, Arkadii A., Jesús Arriaga, and L. N. Gumen. "Speed of sound in periodic elastic composites." *Physical review letters* 91.26 (2003): 264302.

[2] Torrent, Daniel, Yan Pennec, and Bahram Djafari-Rouhani. "Resonant and nonlocal properties of phononic metasolids." *Physical Review B* 92.17 (2015): 174110.

Surface wave attenuation mechanisms in pillar-based phononic crystals**Sebastien Aubert¹, Luc Chommeloux¹, Sarah Benchabane², Mahmoud Addouche², Abdelkrim Khelif²**¹*SENSeOR SAS, VALBONNE, France*, ²*Femto-st, Besançon, France***Background, Motivation, and Objective**

The aim of this work is to perform an investigation of the attenuation mechanism responsible for the occurrence of band gaps for surface acoustic waves (SAWs) in pillar-based phononic crystals (PnCs) and to investigate its evolution. We pay particular attention to the interplay of Bragg scattering and local resonances (LR) that can lead to complete band gaps with very high attenuation under certain geometrical parameters, avoiding coupling other modes. The proposed structures may represent a reliable alternative to classical Bragg mirrors in microelectromechanical systems (MEMS) as acoustic reflectors.

Statement of Contribution/Methods

The PnCs consist of a periodical arrangement of aluminium pillars on a quartz substrate. Advanced dispersion diagrams taking into account the modes in the radiative zone were obtained using the finite element method by integrating the total displacement in the pillars and in the deep surface of the computation domain. Transmission calculations through a series of pillars were then performed to evaluate the attenuation resulting from the PnC. The transmission is obtained with a finite length model where wave reflections from the borders are prohibited by perfectly matched layers. Coupling these two simulation tools allows distinguishing the contribution of the acoustic energy contained in the pillars from the energy propagating in the deep surface. This method makes it possible to evaluate the attenuation of SAWs resulting from Bragg mechanism and local resonances in the radiative and non-radiative regions.

Results/Discussion

As expected, the Bragg band gaps are affected by the filling fraction and the number of periods. In this case, the pillars scatter the SAWs that can interfere destructively and open a band gap. In the LR band gap, due to the hybridization of resonating pillars and surface mode, the elastic energy is first stored by the pillars then reflected to the entrance of the crystal. A strong attenuation is observed in the case of tall pillars: increasing the height of the pillar does not only shift the LR band gaps to lower frequencies, it also reduces the coupling in the radiative zone and enhances the reflection of SAW in the band gap frequencies. Finally, when the pillar resonance occurs in the Bragg region, the two mechanisms can be combined and the choice of geometrical parameters can enhance one of them. These results can play an important role in an efficient design of phononic devices that require strong attenuation or reflection of surface waves.

P2-B3 - PMI: Modelling and Inversion

Waraku (posters 2)

Wednesday, October 24, 9:30 AM - 4:00 PM

Chair: **Minoru Kurabayashi Kurosawa** Tokyo Institute of Technology

P2-B3-1

Theoretical analysis of the slot acoustic waves in two piezoelectric plates of finite length separated by vacuum gap

Andrey Teplykh¹, Boris Zaitsev¹, Irina Borodina¹, Alexandr Semyonov¹

¹*Laboratory of Physical Acoustics, Kotelnikov's Institute of Radio Engineering and Electronics of RAS, Saratov Branch, Saratov, Russian Federation*

Background, Motivation, and Objective

It is well known that acoustic waves propagating in thin piezoelectric plates have a high electromechanical coupling coefficient, and are accompanied by the strong electric field penetrating in the vacuum around the plate. Therefore, there are exists slot modes of acoustic waves propagating in a system of two thin piezoelectric plates separated by a narrow vacuum or air gap. The situation, when both plates have infinite length, has been well studied before. However, we recently have discovered experimentally, that when the upper plate in the structure has a finite length of about 10-20 wavelengths, the well formed equidistant resonant peaks on the frequency dependence of the insertion loss are observed. This means that on certain frequencies the losses in system increase sharply, which may be explained by the appearance of a standing wave in the upper plate and by the transfer of energy from the lower plate to the upper plate. In this paper, the causes of this phenomenon and the influence of the position and parameters of the upper plate on the characteristics of the slot mode are theoretically studied in detail.

Statement of Contribution/Methods

The slot acoustic wave propagating in a system of two lithium niobate piezoplates was investigated. The lower plate is a delay line based on the 0.2 mm thick plate of Y-X lithium niobate. In this delay line, the zero order shear-horizontal (SH_0) acoustic wave is excited and received by the interdigital transducers (IDT) located on the lower side of the piezoplate. The period of the IDT is 1.25 mm, the aperture is 8 mm, and the distance between the IDTs is 27 mm. At a distance of 30 μ m from the upper side of the delay line, there is a second plate made of Z-X lithium niobate. The thickness of the upper plate is 0.5 mm, the length along the propagation direction is 20 mm, and upper plate completely covers the wave aperture. The whole structure was modeled using the finite element method. The insertion loss (parameter S21) in the 2.4 - 4.0 MHz band was calculated. Thus, a series of resonance peaks with a width less than 50 kHz and a depth of about 15 dB were observed.

Results/Discussion

As a result, theoretical dependences of the insertion losses were obtained, which are in good agreement with the experimental results. This allowed us to verify the correctness of the model. It is shown that at resonant frequencies a standing SH_0 wave exists in the upper plate, which holds more than 80% of the acoustic energy of the system. The influence of the position, width and thickness of the upper plate and the gap between plates on the frequencies and depths of the resonant peaks were investigated. It is shown that the electric boundary conditions on the upper side of the upper plate strongly influence the resonant peaks, which makes this structure suitable for analyzing liquids in contact with the upper plate.

The work is supported by grant of RFBR 16-07-00818

Acoustic waves guided at the intersection of interfaces and surfaces**Pavel Pupyrev¹, Ilya Nedospasov², Andreas Mayer³**¹*Prokhorov General Physics Institute of the Russian Academy of Sciences, Russian Federation*, ²*Kotelnikov Institute of Radioelectronics and Electronics of the Russian Academy of Sciences, Russian Federation*, ³*Hochschule Offenburg, Germany***Background, Motivation, and Objective**

The intersection line between the interface of two different elastic quarter-spaces and their common surface (Fig. 1a) is known to guide non-dispersive acoustic waves [1] with strain fields decaying exponentially away from this line (x-axis). In the case of welded contact between the two media, the range of existence in parameter space is much smaller than that of Stoneley waves. If the contact between the two media allows for slip, the existence range becomes larger and the guided waves become dispersive [2]. In view of their relevance for non-destructive evaluation by ultrasonics methods and in various geophysical contexts, a numerical search has been carried out for the existence of analogous guided waves in geometries shown in Fig. 1b,c with welded contacts between the solid media. The system of Fig. 1c may be regarded as a wedge cut in two pieces that are linked via a second elastic medium. It may represent two pieces of rock with a gap filled by another material or two components of a technical device connected by an elastic bond.

Statement of Contribution/Methods

A semi-analytic finite element model was set up with perfectly matched layers to simulate infinite systems. In order to ensure sufficient accuracy, the results obtained with this method for some of the systems investigated were partly validated with calculations based on an expansion of the displacement field in a double series of Laguerre functions or Laguerre and Legendre functions.

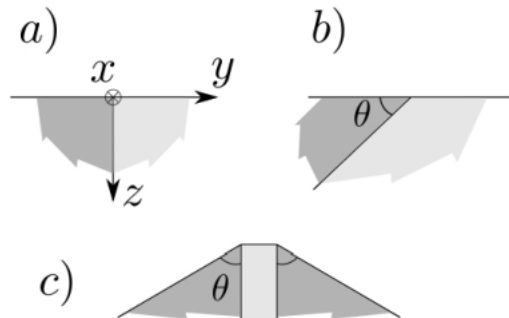
Results/Discussion

For two Poisson media, the existence range of the guided modes in the systems of Fig. 1b has been determined. It was found to strongly depend on the angle θ and even extends beyond the existence area of Stoneley waves for angles smaller than 50° . Phase velocities and displacement patterns are analyzed and discussed in connection with those of wedge waves.

Depending on the material constants, a variety of guided modes was found to exist with strain fields decaying exponentially away from the x-axis. Their dispersion curves are determined and discussed in detail. In addition, leaky waves with a high degree of surface and interface localization were identified in simulations with a time-harmonic external stress. The dependence of their damping on the geometry parameters is analyzed.

[1] E.S. Sokolova, A.S. Kovalev, A.A. Maznev, A.P. Mayer, *Wave Motion* 49, 388 (2012).

[2] B.C. Abell, L.J. Pyrak-Nolte, *JASA* 134, 3551 (2013).



P2-B4 - Multi-Line and Multi-Plane Imaging

Waraku (posters 2)

Wednesday, October 24, 9:30 AM - 4:00 PM

Chair: **Dongwoon Hyun** Stanford University

P2-B4-1

Spatial coherence based beamforming in multi-line transmit echocardiography

Giulia Matrone¹, Alessandro Ramalli^{2,3}, Jan D'hooge², Piero Tortoli³, Giovanni Magenes¹

¹Department of Electrical, Computer and Biomedical Engineering, University of Pavia, Pavia, Italy, ²Lab. on Cardiovascular Imaging & Dynamics, Dept. of Cardiovascular Sciences, KU Leuven, Leuven, Belgium, ³Department of Information Engineering, University of Florence, Florence, Italy

Background, Motivation, and Objective

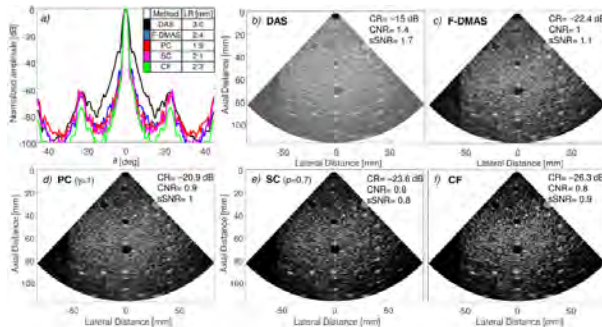
High frame rate ultrasound imaging can be achieved by implementing different techniques, in transmission (TX) and/or reception (RX). Multi-line transmission (MLT) has recently gained interest for cardiac applications and several approaches have been proposed to address its main limitation, i.e. the limited contrast due to cross-talk artifacts. In particular, we have presented Filtered-Delay Multiply and Sum (F-DMAS) beamforming as a method able to improve cross-talk rejection compared to the reference Delay and Sum (DAS) with Tukey TX/RX apodization. In this work, we analyze the MLT imaging performance of Phase Coherence (PC), Sign Coherence (SC) and Coherence Factor (CF) weighting that, similarly to F-DMAS, are based on the spatial coherence of backscattered echoes.

Statement of Contribution/Methods

Simulations and experiments were carried out using a 2MHz, 64-element phased array to scan 192 lines over a 90° sector; the TX focus was set at 70 mm depth and Tukey apodization was applied in TX to reduce TX cross-talk. Single Line Transmission (SLT) and MLT with 4 TX beams (4-MLT) were implemented. In simulations, Field II was used to generate images of a point scatterer at the focal depth. In experiments, the ULA-OP system was used to scan a tissue mimicking phantom and to acquire pre-beamforming signals that were post-processed in Matlab. The images produced by PC, SC and CF were compared to the reference images obtained with DAS plus Tukey RX apodization and F-DMAS, in terms of lateral resolution (LR), contrast ratio (CR), contrast-to-noise ratio (CNR) and speckle signal-to-noise ratio (sSNR).

Results/Discussion

Results are shown in the figure for 4-MLT. The lateral profile of the simulated PSF (panel *a*) and experimental phantom images (panels *b-f*) demonstrate that: CF (panel *f*) outperforms the other methods in terms of cross-talk rejection and CR; CF, PC and SC achieve better LR (<2.2 mm) than F-DMAS (panel *a*). All spatial-coherence-based beamformers (panels *c-f*) show a reduced CNR and sSNR compared to DAS (panel *b*), as speckle quality is degraded; however, LR significantly improves and CR is up to ~11 dB higher. In conclusion, all the analyzed methods can represent a promising solution for cardiac imaging, achieving a similar or even better image quality than standard methods used in clinical practice but with higher frame-rate.



Tri-plane cardiac imaging using multi-line transmission on a spiral array: a feasibility study
Alessandro Ramalli^{1,2}, Pedro Santos¹, Piero Tortoli², Jan D'hooge¹
¹*Lab. on Cardiovascular Imaging & Dynamics, Dept. of Cardiovascular Sciences, KU Leuven, Leuven, Belgium*, ²*Department of Information Engineering, University of Florence, Florence, Italy*
Background, Motivation, and Objective

The assessment of regional cardiac function requires imaging all segments of the left ventricle. As full 3D echocardiography is limited in space-time resolution, tri-plane imaging has been proposed as an intermediate solution. Although its time resolution was further improved by a multi-line transmission (MLT) scheme [Santos et al., IUS 2017], its implementation is still impractical since it requires a fully wired 32x32 array. The aim of this study was therefore to test the feasibility of MLT-based tri-plane imaging using a 2D array with low element count.

Statement of Contribution/Methods

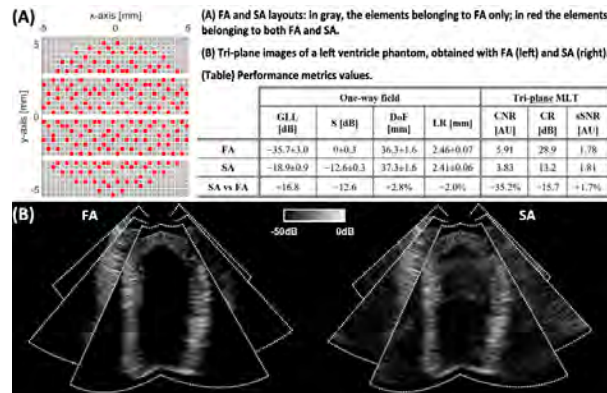
A spiral array (SA) was designed based on a 32x32 full array (FA) (3 MHz; 70% bandwidth; 300µm pitch) using a uniform, 10mm-wide spiral with 200 seeds. For both the SA and FA, 3D one-way pressure fields were simulated using Field II, setting the focal distance at 40 mm and using 81 steering angles, i.e. the combinations of 9 uniformly spaced angles between -40° and 40° in both elevation and azimuth planes. The performance of both arrays was then assessed by estimating the grating-lobe-level (GLL), sensitivity (S), lateral resolution (LR), and depth of field (DoF).

Next, tri-plane images from a cardiac software phantom were simulated in MLT using both arrays. The 3 reconstructed B-mode images were positioned at rotational angles of 0°, 90° and 45°, respectively, while their opening angle was 80°. Imaging performance was quantified using CR, CNR and sSNR.

Results/Discussion

The layouts of both arrays are shown in Fig. A. As shown in the table, LR (2.46 vs 2.41 mm) and DoF (36.3 vs 37.3 mm) were equivalent for both arrays while sensitivity was reduced by -12.6dB for the SA given it only has 19.5% of the elements of the FA. Furthermore, due to the larger average distance between elements, GLL of the SA increased by 16.8dB up to -18.9dB. In terms of imaging performance, the latter corresponded to 35% reduction of CNR and -15.7dB CR while a marginal 1.1% improvement of sSNR was shown.

In conclusion, despite an unavoidable loss in image quality, tri-plane imaging using MLT on a SA seems feasible, as qualitatively confirmed in Fig. B. This would enable volumetric functional analysis of the heart using a 256-channel system.



Orthogonal Frequency Division Multiplexing Combined with Multi Line Transmission for Ultrafast Ultrasound Imaging: Experimental Findings

Libertario Demi¹, Alessandro Ramalli^{2,3}, Enrico Boni³, Jan D'hooge²

¹Dept of Information Engineering and Computer Science, University of Trento, Trento, Italy, ²Lab. on Cardiovascular Imaging & Dynamics, Dept. of Cardiovascular Sciences, KU Leuven, Leuven, Belgium, ³Microelectronics Systems Design Lab, University of Florence, Italy

Background, Motivation, and Objective

Recently, orthogonal frequency division multiplexing (OFDM) and multi line transmission (MLT) beamforming have been shown capable of increasing the data acquisition rate of ultrasound imaging by transmitting multiple focused beams in parallel. For both, increasing the number of parallel beams, and thus the data acquisition rate, results in image artifacts (due to inter-beam cross-talk) and deterioration of the image quality compared to standard beamforming. To minimize the cross-talk, OFDM allocates each transmitted beam to a sub-band of the available bandwidth; differently, MLT optimizes the spatial distribution of the transmitted beams.

In this study, we investigated experimentally whether and how the combination of MLT and OFDM could be used to achieve a high number of parallel beams with reduced cross talk.

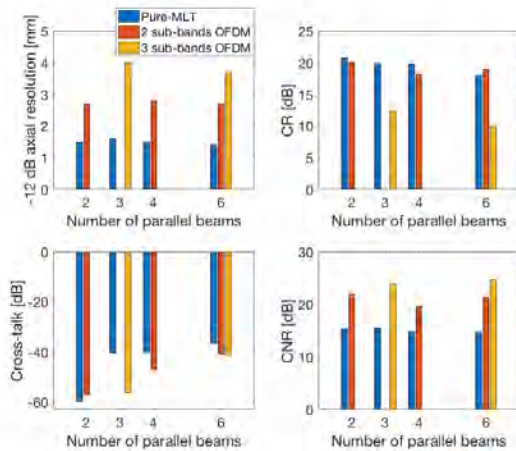
Statement of Contribution/Methods

90°-sector images, consisting of 144 lines, of wire targets and of the 040GSE phantom (Cirs Inc, Norfolk, VI, USA) were generated using the ULA-OP 256 system equipped with a 2.4 MHz phased array (SP2430, Esaote, Firenze, Italy). Different configurations were tested, with 2, 3, 4, 6 simultaneously transmitted beams. Both standard wide-band bursts and OFDM pulses with 2 or 3 different sub-bands were used. The latter were centered at 1.8 and 3 MHz, and at 1.6, 2.4 and 3.2 MHz, respectively; while the wideband burst was centered at 2.4 MHz and covered the entire 80% transducer bandwidth. In these experiments, the improved data acquisition rate was spent to increase the frame rate. The frame rates for the described setups were respectively 70, 105, 140 and 210 Hz, for an imaging depth of 15 cm. Beamformed RF signals were acquired, and the wire targets data were used to evaluate axial resolution and the inter beam cross talk; the images obtained from the tissue-mimicking phantom were used to assess contrast ratio (CR) and contrast to noise ratio (CNR).

Results/Discussion

The plots below summarise the results. As an example, combining MLT with 2 sub-bands OFDM to achieve 6 parallel beams, improved CNR (21.3 vs 14.7), cross-talk rejection (-41.0 vs -36.7) and CR (18.9 vs 18.0) compared to pure 6-MLT, but worsened the axial resolution (2.7 vs 1.4 mm).

In conclusion, combining MLT and OFDM is effective to achieve a high data acquisition rate with limited cross talk and higher CNR, with the drawback of reduced axial resolution and slightly diminished CR.



Multi-Line Transmission and Multi-Line Acquisition with Synthetic Transmit and Filtered Delay Multiply and Sum Receive Beamforming in Cardiac Ultrasound Imaging

Grigoriy Zurakhov¹, Ling Tong^{2,3}, Alessandro Ramalli⁴, Piero Tortoli⁵, Jan D'hooge⁶, Zvi Friedman¹, Dan Adam¹

¹Biomedical Engineering, Technion - IIT, Israel, ²Department of Cardiovascular Sciences, KU Leuven, Belgium, ³Supersonic Imagine, France, ⁴Lab. on Cardiovascular Imaging & Dynamics, Dept. of Cardiovascular Sciences, KU Leuven, Leuven, Belgium, ⁵Department of Information Engineering, University of Florence, Italy, ⁶Cardiovascular Sciences, KU Leuven, Leuven, Belgium

Background, Motivation, and Objective

Multi-line transmission (MLT) and multi-line acquisition (MLA) are two methods to achieve high frame rate in cardiac ultrasound imaging at the expense of potential image artifacts. However, filtered delay multiply and sum (F-DMAS) beamforming was shown to be effective in alleviating MLT caused artifacts, whereas synthetic transmit beams (STB) alleviate artifacts from MLA in delay-and-sum (DAS). The objective of this work was, therefore, to experimentally verify whether MLA with STB can be used alongside MLT with F-DMAS to achieve high frame-rate with minimal compromises on image quality.

Statement of Contribution/Methods

A 128-element phased array probe was connected to an ultrasound advanced open platform (ULA-OP) to scan 89°-wide sector using a 6MLT sequence with 15 transmit events. In-vivo radiofrequency data were acquired and beamformed off-line in MLA/STB modes, using DAS and F-DMAS beamforming. The STB was performed prior to F-DMAS processing. DAS with transmit/receive Tukey apodization was compared to F-DMAS with transmit-only Tukey apodization, by measuring contrast ratio (CR) and contrast-to-noise ratio (CNR). The intensity of MLA artifacts was measured for DAS using correlation analysis.

Results/Discussion

The proposed 6MLT-2STB F-DMAS provides 10.7 dB higher CR than 6MLT-2STB DAS, with attenuation of both MLT and MLA artifacts as compared to 6MLT-2MLA DAS, leading to a gain in frame rate by a factor of 12 over a single-line transmission and single-line acquisition (SLT-SLA) setup. As expected, the achieved CNR was lower than that of 6MLT-2STB DAS (0.71 vs 1.08). The intensity of MLA artifacts for DAS data was reduced from 17.3 to 1. Qualitatively, the MLA artifacts for F-DMAS were found to be lower than for DAS. The proposed setup may be an alternative to 12MLT, bearing less potential MLT artifacts and reducing the energy transferred to the body, thus improving safety issues.

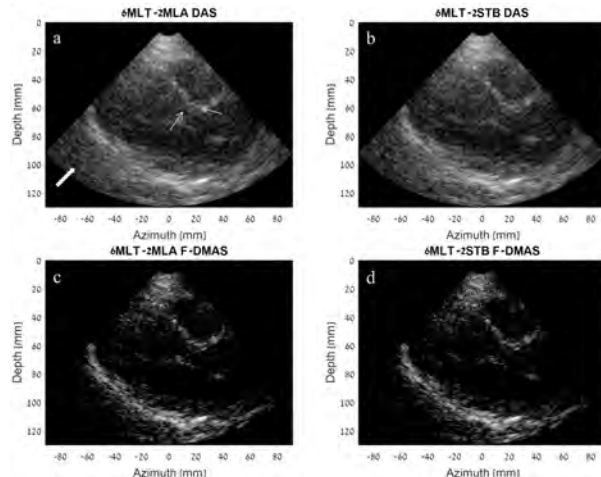


Fig. 1: Images of the parasternal long axis acquired using different imaging strategies with Tukey apodization on transmit: (a) 6MLT-2MLA DAS with Tukey apodization on receive; (b) 6MLT-2STB DAS with Tukey apodization on receive; (c) 6MLT-2MLA F-DMAS and (d) 6MLT-2STB F-DMAS. All images are presented in a dynamic range of 6dB dB. Thin white arrows depict regions used for calculation of the CR and CNR. Thick white arrow depicts region with MLT artifact.

S-sequence Encoded Multiplane Wave Imaging: Phantom and In-vivo ValidationsYinran Chen¹, Jianwen Luo¹¹*Department of Biomedical Engineering, Tsinghua University, Beijing, China, People's Republic of***Background, Motivation, and Objective**

Plane wave with coherent compounding (PWC) has shown promise in ultrafast ultrasound imaging, but at the expense of limited signal-to-noise ratio (SNR). Hadamard (HD)-encoded multiplane wave imaging was recently proposed to increase SNR without sacrificing frame rate. However, HD encoding requires an inverted copy of transmit pulse, which may introduce extra harmonic artifacts in conventional B-mode imaging. Furthermore, transmission of zero-degree plane wave is always missing due to the constraint in the size of the HD matrix (i.e., the powers of 2). To mitigate this problem, S-sequence (SS) encoding, firstly proposed in synthetic transmit aperture beamforming, was implemented in multiplane wave imaging in this study, as an alternative imaging strategy which omits the inversion of transmit pulse, and includes transmission of zero-degree plane wave.

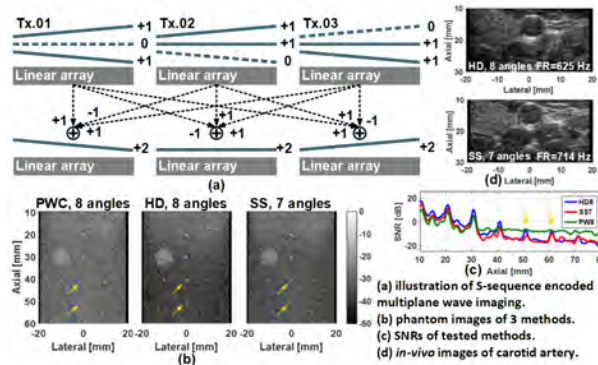
Statement of Contribution/Methods

The SS matrix for encoding is formed by deleting the first row and column of a HD matrix, and replacing 1 by 0, and -1 by 1 in the rest of the matrix. In analogy with HD encoding method, each row of the SS matrix is used to encode the multiple steered plane waves in each transmit event, with a 3-order SS encoding case shown in Fig. (a). Then decoding was performed by using the inverse of SS matrix. SS-encoded multiplane wave imaging was implemented on a Verasonics Vantage system, with 7 steering angles of [-7°, -5°, -3°, 0°, +3°, +5°, +7°]. For comparison, PWC and HD encoding setup with 8 steering angles of [-7°, -5°, -3°, -1°, +1°, +3°, +5°, +7°] were applied.

A standard wire phantom and the carotid artery of a healthy volunteer were imaged. Transmit voltage was set to 2 V and SNR was quantified for comparison.

Results/Discussion

Images of the wire phantom and the SNRs of the wires at different depths are given in Fig. (b) and (c), respectively. SS encoding provides a moderate SNR performance when compared with HD encoding and PWC. This is reasonable due to a smaller number of transmit events and zero-encoding [see Fig. (a)] in the SS setup, resulting in much less effective pulses compared with HD encoding (28 vs. 64). *In-vivo* images are presented in Fig. (d), showing that SS encoding provides higher frame rate, at the expense of slightly lower SNR. To conclude, SS-encoded multiplane wave imaging achieves ultrafast imaging with higher frame rate and a moderate SNR performance in between conventional PWC and HD encoding.



Reducing Cross-Talk Artifacts for Ultrafast Ultrasound Imaging with Arbitrary Level Codes: Beam Clustering and Optimization Dimensionality Reduction
David Egolf¹, Roger Zemp²
¹*University of Alberta, Edmonton, AB, Canada*, ²*University of Alberta, Canada*
Background, Motivation, and Objective

One strategy for ultrafast ultrasound imaging is to simultaneously transmit a large number of beams. Unfortunately, the resulting cross-talk between these beams seriously degrades image quality. To address this problem, we are exploring the use of complementary encoded transmissions to reduce cross-talk while still allowing for image formation in as few as two transmit events. Previously, we introduced an optimization framework for code design in this setting [Egolf et al. IUS 2017]. The practicality of the derived framework was limited by the high dimensionality of the nonlinear optimization problem it used to design codes and also by its assumption of an even spacing between simultaneously transmitted beams. We aim to address these limitations by reducing the dimensionality of the optimization problem, and by introducing beam clustering for further reduction of cross-talk artifacts.

Statement of Contribution/Methods

We first show that not all cross-talk is equally undesirable and use this to motivate the idea that clustering transmitted beams will tend to reduce cross-talk artifacts. Next, recognizing that complementarity is important for preserving axial resolution, we show how requiring complementarity from the start reduces the dimensionality of the optimization problem used to generate codes by a factor of two. Finally, we illustrate the resulting image quality improvements in a Field II simulation setting.

Results/Discussion

The reduced dimensionality optimization framework allowed for faster and more precise design of arbitrary level codes for ultrafast ultrasound imaging. In particular, it allowed for design of code sets with different interference levels between different focal zones. The resulting optimized codes, together with the proposed beam clustering approach, resulted in improved image quality. As an example, the Field II cyst simulations in Figure 1 show an increase in the background-signal-to-cyst-signal ratio (BCR). Fig.1(b) and (c) improve the BCR by factors of 1.4 and 2.4 respectively relative to the unoptimized baseline of Fig.1(a). Ongoing work is exploring implementation on a programmable ultrasound system and is comparing performance to plane wave imaging. The introduced optimizations represent a step towards providing improved image quality and SNR for ultrafast imaging applications, such as ultrafast flow imaging.

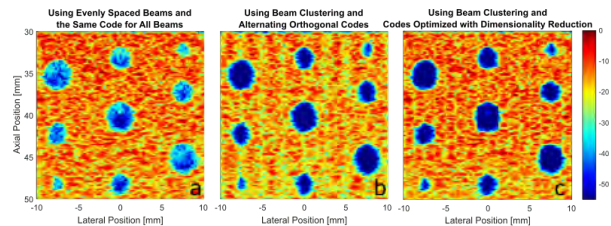


Fig.1. Using the codes generated by the new optimization system, together with beam clustering, resulted in increased cyst contrast. All images were formed from eight transmission events and were generated using the Field II simulation software.

P2-B5 - Flow Estimation Methods and Applications

Waraku (posters 2)

Wednesday, October 24, 9:30 AM - 4:00 PM

Chair: Pengfei Song Mayo Clinic

P2-B5-1

Spatiotemporal filtering for synthetic aperture slow flow imaging

Guillermo Galán Olleros¹, Carlos Villagomez-Hoyos², Kristoffer Hansen³, Matthias B. Stuart¹, Jørgen Arendt Jensen¹

¹Technical University of Denmark, Lyngby, Denmark, ²BK Ultrasound, Herlev, Denmark, ³Copenhagen University Hospital, Denmark

Background, Motivation, and Objective

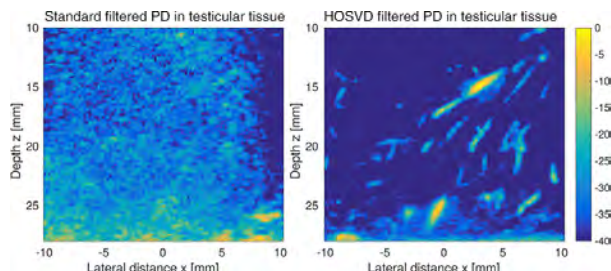
Recent developments in microvascular flow imaging have produced unprecedented results in murine brain imaging and other slow flow targets. Long ensemble lengths are needed for stationary clutter separation from the slow flow signal, and are typically obtained from plane wave compounding using a static probe. In this study, slow flow power Doppler (PD) is obtained using duplex synthetic aperture (SA) focused spherical waves on human in-vivo tissue with a handheld probe. To overcome the effects of motion blur, microvascular flow detection is enhanced by using a spatiotemporal higher order singular value decomposition (HOSVD) filter.

Statement of Contribution/Methods

An 8 MHz BK8670 linear array was used on the SARUS research scanner to acquire images of testicular parenchyma from a healthy volunteer. SA *high resolution* images were combined from 5 *low resolution* emissions with a fPRF of 12.5 kHz (thus an effective flow fPRF of 2.08 kHz including a B-mode emission). The beamformed data were temporally grouped in *Doppler frames* of 32 consecutive acquisitions. The time between Doppler frames is 15 ms (65 Hz), giving a sampling interval that represents the slow flow variation. Doppler frames were processed using a 3D spatiotemporal filter, taking into account the 2 temporal dimensions and the spatial dimension. The dimensions of the core 3D tensor of the filter were adjusted to filter out static clutter and random noise while maintaining slow moving flow.

Results/Discussion

An ultrasound scan of 4.3 seconds of data was recorded using the previously described duplex SA sequence, corresponding to 53760 emissions. After beamforming and filtering, color flow mapping (CFM) videos were produced. An image frame extracted from the video (40 dB dynamic range) from testicular tissue is provided below before and after the filtering process was applied, where the vessels of the testis are clearly visible. The imaged vessels are under 1 mm in diameter and the velocity of the flow within them is below 0.5 cm/s. The data shown therefore supports the use of sparse synthetic aperture sequences combined with eigen-filtering for slow flow imaging in human tissue. The proposed technique delivers improved visualization of the testicular vasculature and is of clinical importance in diagnosing of e.g. testicular torsion and cancer.



An Adapted Coherent Flow Power Doppler Beamforming Scheme for Improved Sensitivity Towards Blood Signal EnergyKathryn Ozgun¹, Jaime Tierney¹, Brett Byram¹¹*Biomedical Engineering, Vanderbilt University, Nashville, TN, United States***Background, Motivation, and Objective**

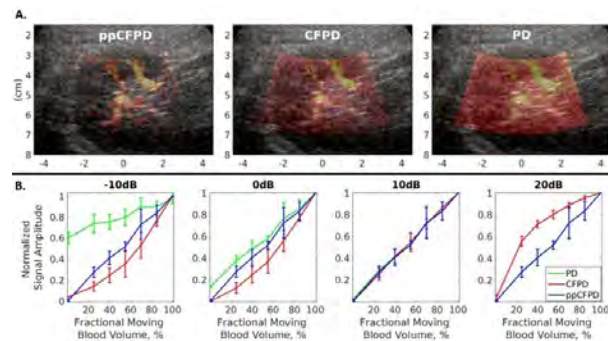
Prior studies have demonstrated that Coherent Flow Power Doppler (CFPD) may offer improved sensitivity towards blood flow compared to power Doppler (PD), especially in cluttered environments. However, CFPD images depict the normalized spatial coherence of the backscattered echo, which uncouples the image intensity from the underlying signal energy. As such, CFPD images are not a robust measure of the blood signal energy and have lower sensitivity towards flow gradation. Comparatively, PD images are proportional to the number of moving blood scatterers within a region. Assessment of the fractional moving blood volume is clinically valuable, as it is indicative of relative vascularity, an important biomarker in the study of malignancy.

Statement of Contribution/Methods

We propose a modified Doppler scheme which we call Power Preserving Coherent Flow Power Doppler (ppCFPD). Motivated by the van Cittert-Zernike theorem, we demonstrate how the implementation of a modified coherence metric preserves the underlying blood signal energy, while maintaining greater rejection of clutter in comparison to conventional PD imaging. Single-vessel simulations developed in Field II were employed to assess the efficacy of ppCFPD in the presence of flow velocities ranging from 0.1 to 5cm/sec and varied clutter environments. Blood signal energy preservation was studied by controlling the fraction of moving blood scatterers. Additionally, a preliminary assessment was performed in a human kidney to demonstrate *in vivo* efficacy.

Results/Discussion

Assessment of ppCFPD simulation results yielded up to a 13dB improvement in root-mean-square SNR, 14dB gain in contrast, and an increase of 1.1 in CNR in comparison to PD. Fig. 1(a) shows ppCFPD, CFPD, and PD images of kidney perfusion on a 30dB scale, overlaid on B-mode. Qualitatively, ppCFPD provides greater noise suppression, while preserving the relative amplitude of blood flow. Fig. 1(b) depicts how the ppCFPD signal amplitude remains a linear approximation of the number of moving blood scatterers. Further, ppCFPD was robust to varied clutter conditions, where the blood signal to noise ratio was varied from -10 to 20dB.



High-frame-rate Ultrasound Motion Estimation Based on Pre-beamformed Multi-angle Plane Wave Images
He Li¹, Yang Zhang¹, Wei-Ning Lee¹
¹*Electrical and Electronic Engineering, The University of Hong Kong, Hong Kong*
Background, Motivation, and Objective

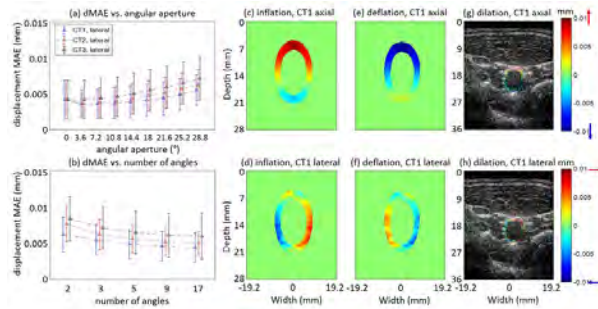
High-frame-rate ultrasound imaging (HFRI) enables assessment of rapid tissue dynamics for additional clinical insights. Previous studies have proposed micron-level displacement estimation using pre-beamformed channel data acquired by non-steered plane waves. In this study, we propose and investigate motion estimation using pre-beamformed channel data acquired by multi-angle plane wave imaging (MAPWI).

Statement of Contribution/Methods

Field II was used to simulate ultrasound channel data of a homogeneous phantom ($40 \times 40 \text{ mm}^2$, interframe lateral displacement = 0.01 mm) in MAPWI configurations using an L7-4 probe (5.2 MHz), with N tilted angles ($1 \leq N \leq 17$) ranging from -6° to 0° . Channel data of a vessel-mimicking PVA phantom (5 freeze-thaw cycles) pressurized by an AccuFlow-Q flow pump and an *in vivo* human carotid artery were acquired using a Verasonics® Vantage 256 system with an L11-4v (6.6 MHz) and the L7-4 probe, respectively. HFRI was achieved using 3 tilted angles (-5° , 0° , 5°) and a pulse repetition frequency of 6 kHz. Time shift in each channel was estimated using autocorrelation, and the shift profile along the aperture was used to construct an overdetermined system of element-shift relations. Three compounding strategies were considered: 1) including all the element-shift relations from N angles in the overdetermined system (CT1), 2) compounding the shift profiles from N angles and taking the compounded profile as that yielded by a non-steered plane wave (CT2), and 3) compounding channel data from N angles before time shift estimation and taking the shift profile as that yielded by a non-steered plane wave (CT3). The overdetermined system then derived a least-squares solution of in-plane displacements.

Results/Discussion

The displacement mean absolute errors (dMAEs) suggested that compounding improved motion estimation accuracy, and that CT1 outperformed the other two methods. With a fixed number of tilted angles ($N = 3$), the mean value of dMAEs first decreased and then increased with θ (Fig. a), indicating an optimal steered angle. With the fixed largest angular aperture (28.8°), dMAEs decreased with more tilted angles used (Fig. b). Figs. c-h show that CT1 could estimate in-plane displacements (~tens of microns) both *in vitro* and *in vivo*. The proposed method with CT1 shall provide more detailed characterization of rapid tissue dynamics for clinical diagnosis.



De-aliasing color flow mapping with staggered pulse sequence at improved frame rate**Rei Asami¹, Tomohiko Tanaka²**¹*Hitachi, Ltd, Japan*, ²*Hitachi, Ltd, Japan***Background, Motivation, and Objective**

Aliasing is a classic problem present in ultrasound color flow mapping (CFM). To estimate de-aliased velocities, several methods using staggered pulse repetition frequencies (PRF) are reported. For example, the multi-PRF method [1] recovers unwrapped velocities based on different Doppler velocities obtained at different PRFs of specific ratio. The obvious drawback of these methods is that they require multiple times the number of pulse transmission depending on the number of PRFs used, which results in much slower framerate. While this might not be an issue in emerging ultrafast ultrasound trend, it could be a critical issue in conventional platform, as well as volumetric ultrasound. The aim of this study is to propose an algorithm that reduces the number of pulse transmission of Multi-PRF method while maintaining performance of de-aliased velocity estimation.

Statement of Contribution/Methods

As illustrated in fig.1a, proposed method acquires Doppler shifts from every other pulse at the interval of PRT3 where $PRT3 = PRT1 + PRT2$. Unlike Doppler shifts at PRT1 and 2, Doppler shifts at PRT3 can be acquired from successive pulses requiring less numbers of pulse transmission to attain same number of Doppler shifts for averaging. Using PRT3 in place of PRT2, de-aliased velocity is recovered. The Field II program [2] was used to assess the de-aliased velocity estimation performance using a digital flow phantom with a parabolic flow profile. The multi-PRF method and proposed method was used to estimate de-aliased velocities. In this study, the second PRT was assigned such that $PRT2 = 4/3PRT1$. Other parameters were set similar to those of clinical ultrasound scanners. In addition, *in vitro* flow phantom experiment is performed using Verasonics® scanner.

Results/Discussion

In simulation study, proposed method estimated de-aliased velocity of MRS error of 2.6 % within the extended velocity range, which was comparable to that of multi-PRF (1.9 %). The proposed method also performed as well as multi-PRF method in the phantom study (fig.1b). The results indicate that our proposed method is a valid method to reduce the number of pulse transmission while maintaining the de-aliasing performance.

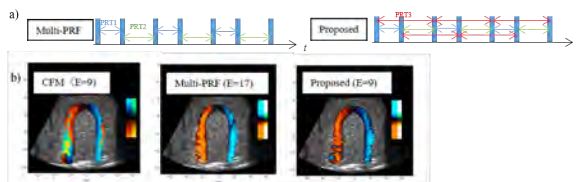


Figure 1 a) Schematics of proposed method. b) *in vitro* experiment result

Super-resolution measurement of fluid velocity profiles within sub-wavelength microtubesDavid Espindola¹, Ryan DeRuiter¹, Francisco Santibanez¹, Paul Dayton¹, Gianmarco Pinton¹¹*Joint Department of Biomedical Engineering, University of North Carolina at Chapel Hill and North Carolina State University, NC, United States***Background, Motivation, and Objective**

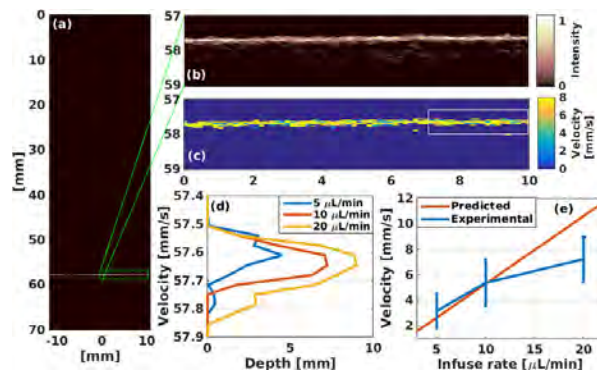
Contrast-enhanced super-resolution ultrasound imaging localizes microbubble contrast agents circulating in the vasculature. By accumulating bubble detection events, maps of the in-vivo microvasculature have been produced with a 20 μm resolution. This technique can be extended to measure microvascular flow by tracking the positions of the microbubbles over time. Here we present a super-resolution technique that can measure the local flow dynamics within a 200 μm diameter tube at a 4 cm depth under ex-vivo pork belly tissue using a custom correlation-based tracking algorithm.

Statement of Contribution/Methods

A 200 μm microtube was placed under a 4 cm thick pork belly under water and it was connected to a motorized pump that generated a constant flow of microbubbles (1e6 bubbles/mL concentration). Once the flow was completely established, B-mode images were acquired using an ultrafast plane-wave sequence (700 fps) with a probe ATL L7-4 operating at central frequency of 5.2 MHz. The bubble signal was extracted from these images using a singular value decomposition (SVD) filter. To detect the bubbles with sufficient accuracy we developed a custom high accuracy correlation-based tracking algorithm that measures bubble displacements across the microtube diameter. Then, by combining the displacement and position of the bubbles, velocity profiles were obtained.

Results/Discussion

As validation, experiments were repeated under water, without tissue. The super-resolution velocity technique was able to obtain super-resolved images of the microtube (a, b). The cross-section of the tube (not shown) was measured to be 197 μm . Using our tracking approach, velocity maps of flow within the tube were created (c, d). The mean value of the profile is consistent with theoretical predictions based on conservation of mass (e). For a calibrated flow of 10 $\mu\text{L}/\text{min}$, which is typical of small blood vessels, a parabolic profile with a peak velocity of 7.21 mm/s and an average of 5.4 mm/s was measured. Theory predicts an average velocity profile of 5.3 mm/s. The ex-vivo application of the same technique through attenuating pork belly showed similar results. These results demonstrate that highly accurate velocity flow maps can be created with super-resolution imaging, providing additional information regarding microvascular flow dynamics in-vivo.



An ultrafast ultrasound microvessel imaging technique for assessing patients with unilateral papilledema and choroidal folds

Boran Zhou¹, Arash Kazemi², John Chen³, Arthur J. Sit⁴, Xiaoming Zhang¹

¹Mayo Clinic, Rochester, MN, United States, ²Department of Ophthalmology, Mayo Clinic, Rochester, MN, United States,

³Ophthalmology and Neurology, Mayo Clinic, United States, ⁴Ophthalmology, Mayo Clinic, United States

Background, Motivation, and Objective

Idiopathic intracranial hypertension (IIH) is a condition of increased intracranial pressure of unknown cause producing bilateral papilledema (optic nerve swelling), choroidal folds, and visual loss. Pseudo-papilledema is most commonly caused by optic disc drusen and measurement of optic nerve sheath is regarded as an indirect indicator of raised intracranial pressure. So far, there is no direct way to differentiate pseudo-papilledema from papilledema. Rarely, IIH can cause unilateral papilledema. We hypothesize that IIH may result in increased blood volume in the optic disc in cases of unilateral papilledema. This work proposes to use ultrafast ultrasound microvessel imaging for measuring the blood volume and axial velocity of the optic disc in patients with unilateral papilledema and choroidal folds from IIH.

Statement of Contribution/Methods

Under an IRB approved protocol, both eyes of one patient who had unilateral papilledema in the left eye from IIH were evaluated with a Verasonics Vantage system (Verasonics Inc.). L11-5v probe with a central frequency of 6.42 MHz was used for a plane wave imaging sequence with a 0.1 s data accumulation (Fig. 1a). A 3-angle spatial compounding (-4° to 4°) was used to improve imaging SNR. The post-compounding ensemble size with an effective pulse-repetition-frequency (PRF) of 2000Hz. A numerical Butterworth high-pass filter of the fifth order with a cutoff frequency of 30 Hz was used to remove tissue signal. The Power Doppler Intensity (PDI) of each pixel was obtained by the incoherent temporal mean of the blood signal and converted to decibel scale (dB). Color flow images were generated by using the 2-D autocorrelation method. A region-of-interest (ROI) was selected to measure the PDI in the optic disc (Fig. 1a) and the corresponding axial velocity of ROI was calculated (Fig. 1b).

Results/Discussion

The PDI within the optic disc of the patient was significantly higher in the left eye (-39.55 ± 2.74 dB) compared to the right eye (-45.34 ± 3.3 dB; $p < 0.05$), which corresponds to higher blood volume. There was no significant difference in the axial velocity between left (0.45 ± 1.67 mm/s) and right (-0.63 ± 1.54 mm/s, $p > 0.05$) eyes. This suggests that the blood volume of the optic disc does correlate with the unilateral papilledema from raised intracranial pressure and can be accurately measured with ultrafast ultrasound microvessel imaging.

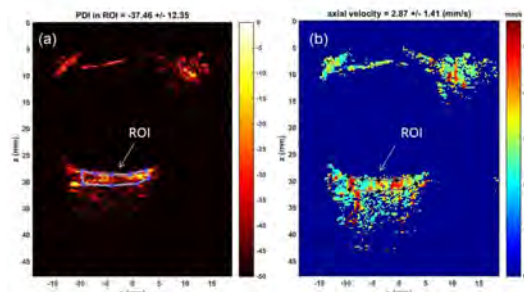


Figure 1. Power Doppler (a) and color flow images(b) of the patient with unilateral papilledema. Region of interest (ROI) was selected for calculating PDI and axial velocity of optic disk.

RADIAL ARTERY REACTIVE RESPONSE AND SHEAR RATE MEASUREMENTS USING 20 MHZ SYSTEM

Andrzej Nowicki¹, Barbara Gamin¹, Zbigniew Trawiński¹, Wojciech Secomski¹, Michał Szubielski², Marzena Parol³, Robert Olszewski^{4,5}

¹Institute of Fundamental Technological Research - PAS, Warsaw, Poland, ²Mazovia Regional Hospital in Siedlce, Siedlce, Poland, ³The John Paul's II Western Hospital in Grodzisk Mazowiecki, Grodzisk Mazowiecki, Poland, ⁴Robert Olszewski,

Institute of Fundamental Technological Research - PAS, Warsaw, Poland, ⁵National Institute of Geriatrics, Rheumatology and Rehabilitation, Warsaw, Poland

Background, Motivation, and Objective

There is growing interest in the application of non-invasive clinical tools allowing to assess the endothelial function, preceding atherosclerosis. A comparison of 7-12 MHz and 20 MHz scanners for flow mediated dilation (FMD) and shear rate (SR) measurements in radial artery is reported. The experiments in vitro using closely spaced food plastic foils proved over three times better resolution of the high frequency 20 MHz scanner (<0.1 mm) over the 7-12 MHz one. Also the sensitivity of the external single transducer 20 MHz pulse Doppler proved to be over 20 dB better (in terms of SNR) than the pulse Doppler incorporated into linear 7-12 MHz linear array. These results justified designing of a high-frequency scanning system consisting of a 20 MHz linear array transducer combined with 20 MHz pulsed Doppler probe to validate its usefulness in estimation of the degree of radial artery FMD and SR after 5 minutes of reactive hyperaemia.

Statement of Contribution/Methods

In our pilot studies, 12 healthy volunteers (38–71 yr old) and 14 patients (36–77 yr old) with chronic coronary artery disease (CAD) were included. The diagnosis of chronic CAD was based on the presence of symptoms of stable angina or a positive myocardial ischemia stress test. The Imaging/Doppler system was modified by adding the single element 20 MHz pulse Doppler with a sample volume size being equal 0.3 mm axially and 0.8 mm laterally, to the linear array transducer, providing to high precision FMD and SR measurements. The normalization of FMD to shear rate is done by dividing the peak FMD by the accumulated value of shear rate area under the curve (AUC). Hereafter in this work, we will use the abbreviation “SR” for the time integral of shear rate, thus SR is a dimensionless quantity. The time variable shear rate is calculated from the blood velocity recordings by the external Doppler device or by Duplex scanning, and next, SR is calculated for the time span between releasing the cuff and peak dilation.

Results/Discussion

The in vivo usefulness of the system was evaluated in two groups of patients. In group I, comprising 12 healthy volunteers, FMD was $15 \pm 4.8\%$, and in group II, comprising 14 patients with chronic coronary artery disease, FMD was significantly less at $4.6 \pm 4\%$. A similar difference in tests groups was observed after normalizing to account for the effect of time integral of shear rate (SR). Specifically, the ratio FMD/SR, was equal to $5.36 \pm 4.83 \cdot 10^{-4}$ in group I and $1.3 \pm 0.89 \cdot 10^{-4}$ in group II. Statistically significant differences between the two groups were confirmed by a Wilcoxon-Mann-Whitney test for both FMD and FMD/SR (p -values < 0.01). AUCs of ROC curves for FMD and FMD/SR were greater than 0.9. The results confirm the usefulness of the proposed measurements of radial artery FMD and SR in differentiation of normal subjects from those with chronic coronary artery disease.

Coded Multiple Parallel Focal Zone Scanning for Ultrafast Power Doppler Blood Flow ImagingTarek Kaddoura¹, Roger Zemp²¹*University of Alberta, AB, Canada*, ²*University of Alberta, Canada***Background, Motivation, and Objective**

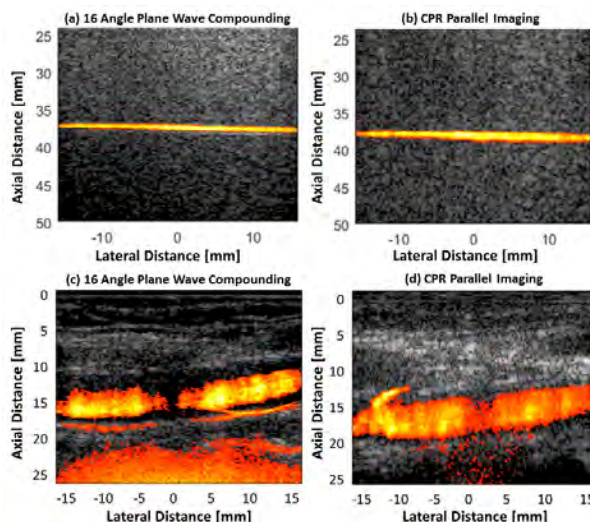
Cutting-edge applications such as ultrafast blood flow imaging, functional brain imaging, and supersonic shear-wave elastography methods are all enabled by ultrafast imaging methods, which offer much larger Doppler ensemble-sizes than conventional color- and power-Doppler methods for each pixel in an image, thus providing high sensitivity to subtle motions. However, fast plane-wave imaging methods may suffer from low image quality, especially for aberrating tissues and larger depths. We propose a multiple parallel focal zone imaging strategy that uses complimentary-pseudorandom codes (CPR) transmitted in parallel to different focal zones to increase signal-to-noise and sensitivity to flow, especially at larger depths, while retaining the same imaging speed.

Statement of Contribution/Methods

A Verasonics ultrasound system was used to obtain images of (1) a flow phantom, and (2) an *in-vivo* image of a carotid from a human volunteer obtained in the longitudinal view. The flow phantom consisted of a single tube surrounded by 10% w/w of cornstarch and gelatin mixed with water. A mixture of 5% w/w of cornstarch and water was flowed through the tube at a constant velocity to simulate blood flow. Singular Value Decomposition (SVD) was applied on the obtained image frames to separate the blood flow from the background tissue and obtain a blood power image, which was then thresholded and overlaid on the B-Mode image. 500 images were obtained at 600 fps with the proposed method using 16 parallel focal zones, and then compared with 16-angle plane-wave compounding to match the imaging speed.

Results/Discussion

Here we present our results for the blood flow comparison. Fig. 1 shows the overlaid blood power images for (a) the flow phantom imaged with 16-angle plane wave compounding, (b) the flow phantom imaged with CPR parallel imaging with 16 parallel focal zones, (c) a human carotid imaged with 16-angle plane wave compounding, and (d) a human carotid imaged with CPR parallel imaging. In the flow phantom (Fig. 1a-b), we see very similar results for the flow visually between both methods, but quantitatively, the CPR imaging method resulted in a decrease of 0.05 for standard deviation of the blood flow. In the *in-vivo* image (Fig. 1c-d), we see an increase in sensitivity for blood flow within the tube in the case of CPR imaging, while compounded-flash imaging suffers from more noise at larger depths.



Towards Oxygen Metabolism Estimation with Ultrafast Speckle-Decorrelation Imaging and Functional Photoacoustic Imaging

Mayara Nascimento de Oliveira¹, Bingjie Ma¹, Quinn M. Barber¹, Min Choi¹, Tarek Kaddoura¹, Roger Zemp¹

¹Electrical and Computer Engineering, University of Alberta, Edmonton, AB, Canada

Background, Motivation, and Objective

Oxygen metabolism is an important physiological measure that indicates tissue metabolic activity. Therefore, non-invasive methods to imaging and estimating the rate of oxygen consumption are important for understanding diseases such as cancer and diabetes, which shows abnormal oxygen metabolism. Other studies have addressed this issue using optical resolution photoacoustic microscopy (OR-PAM), which has a limited penetration depth. Furthermore, our research group previously used deep PAM to estimate oxygen metabolism by estimating oxygen saturation (sO_2) in conjunction with a single-element transducer to estimate flow using ultrasound bandwidth-based Doppler [Jiang et al, JBO 2018]. However, the single-element transducer required mechanical scanning, which leads to limited frame rates. This project proposes the use of deep PAM combined with linear array methods for real-time flow estimation using a high-frequency 21-MHz array.

Statement of Contribution/Methods

We propose two ultrafast methods to estimate blood flow: ultrafast angled-beam Doppler and ultrafast speckle-decorrelation imaging. The first one is best for imaging transverse sections of vessels but cannot estimate flow in multiple out of plane vessels, while the latter can estimate flow through cross-sections including estimating flow in multiple feeding and draining vessels. To improve perfusion sensitivity, we designed a clutter filter based on high-order singular value decomposition (HOSVD). The sO_2 can be estimated using the peak amplitude of photoacoustic signals at optimal wavelengths, and the cross-section area of vessels can be estimated using power Doppler ultrasound. A phantom study (with tissue mimicking base) was performed to show the feasibility of our method using a high-frequency programmable system and array. In addition, *in vivo* studies are being implemented.

Results/Discussion

The estimated sO_2 can be seen in Fig. 1a, while a velocity image from our flow phantom can be seen in Fig. 1b. Using the ultrafast speckle-decorrelation technique blood flow was estimated in vessel cross-sections, which can be seen in Fig. 1c. Fig. 1d shows Power Doppler imaging of a mouse kidney *in vivo*. With further work, we anticipate our approach being able to estimate oxygen flux and oxygen metabolism in deep tissues with many possible clinical applications.

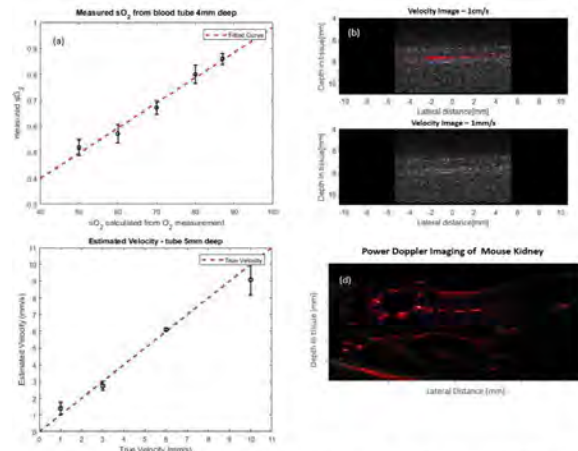


Figure 1 – (a) Estimated sO_2 (from peak amplitude PA signal) vs. Preset sO_2 (b) Velocity Image of blood tube using angled-beam Doppler technique (c) Estimated velocity (from ultrafast speckle-decorrelation method) vs. True velocity (d) Power Doppler image of a mouse kidney.

P2-B6 - Photoacoustic Contrast and Theranostic Agents

Waraku (posters 2)

Wednesday, October 24, 9:30 AM - 4:00 PM

Chair: Kelsey Kubelick Georgia Institute of Technology

P2-B6-1

Monitoring liposome payload release by photoacoustic spectroscopy of indocyanine green

Adam J. Dixon¹, John A. Hossack¹, Alexander L. Klibanov¹

¹Biomedical Engineering, University of Virginia, Charlottesville, VA, United States

Background, Motivation, and Objective

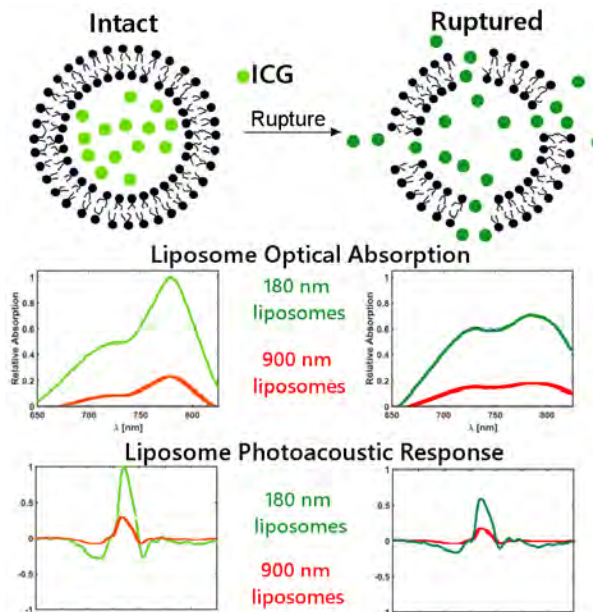
Remote monitoring of liposome payload release is of relevance to drug delivery and molecular imaging. However, conventional methods of monitoring release (e.g. fluorescence dequenching, luciferase) are difficult to apply at depths > 5 mm *in vivo*. In this study, we evaluate the photoacoustic (PA) imaging potential of a novel formulation of indocyanine-green (ICG) loaded liposomes. Specifically, we prepared two liposomes formulations of different mean diameter (180 nm vs 900 nm) and characterized the PA response before and after liposome destruction to determine if dye release resulted in a change in the PA response of the dye.

Statement of Contribution/Methods

Two separate liposome preparations were evaluated in this study, one of 180 nm diameter and the other of 900 nm mean diameter (DLS). Liposomes (1M calcium acetate) were prepared by reverse phase evaporation from a 2:1:1 mass ratio of DSPC, cholesterol, and PEG2000-DSPE, followed by repeated filtration with either 200 nm or 1000 nm Nuclepore filters. External salt was removed by Zeba spin column, followed by overnight incubation with aqueous ICG that entered the liposome core via remote loading (DSPC:ICG mass ratio was 2:0.035). Repeated centrifugation (100000 x g, 1 hr) was performed to remove free dye. Dye loading efficiency was assessed via UV-Vis spectroscopy (Nanodrop). Liposomes were diluted in 10 mM HEPES buffer (pH 7.4) and were evaluated by a custom PA spectroscopy system. Dye release was achieved via light sonication with a microtip sonicator and PA spectroscopy was repeated.

Results/Discussion

Dye loading efficiency was 90% in the 180 nm liposome formulation and 25% in the 900 nm formulation. When intact, both liposomes of both sizes exhibited a narrow optical absorption peak near 780 nm, although absorption and PA responses of the smaller formulation was approximately 5-fold greater due to more entrapped dye. Following rupture, the optical absorption spectra broadened significantly, with a broad peak near 750 nm that was 35% lower than the intact liposomes. PA amplitudes broadly mirrored the optical absorption spectra. This study is the first to demonstrate monitoring of dye contents release from liposomes using PA spectroscopy. The liposome preparation may be used as blood pool contrast agents, molecular imaging agents, or markers of drug delivery processes in PA or optical imaging applications.



IR808-Anchored MnO Nanoparticles Imaging Tumor and Inducing Enhanced Phototherapy Effect via Mitochondria-mediated Pathway

Lihua Zhou¹, Guanjun Deng¹, Sanpeng Li¹, Xiaoqing Meng¹, Zhen Xu¹, Wenjun Li¹, Ping Gong^{1,2}

¹Shenzhen Institutes of Advanced Technology, Chinese Academy of Sciences, China, People's Republic of, ²Dongguan Key Laboratory of Drug Design and Formulation Technology, Key Laboratory for Nanomedicine, Guangdong Medical University, Dongguan 523808, PR China, China, People's Republic of

Background, Motivation, and Objective

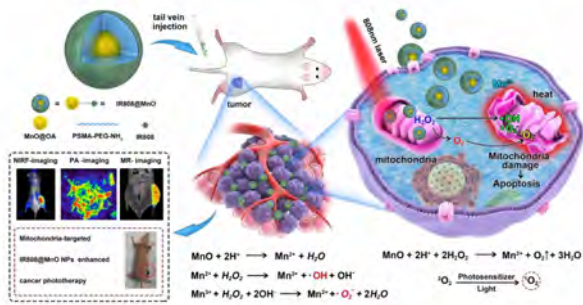
As cancer is proliferating fast, the innovated diagnostic and therapeutic strategies are imperative for early detection and precision treatment. Theranostics provides good strategies to monitor response to treatment real-timely, as well as to optimize the efficacy and safety of therapy for potentially transformative advances in biomedicine. Theranostics seems to can streamline the entire drug development process and results in significant cost savings for the overall healthcare system. Therefore, theranostic probes containing both diagnostic imaging and therapeutic functions in one integrated system are emerging as an alternative to independently administered diagnostic contrast agents and traditional cancer therapy strategies.

Statement of Contribution/Methods

In our approach, a multifunctional dye-anchored manganese oxide nanoparticle as a kind of theranostic probe was constructed by assembling the prefabricated MnO nanoparticles and IR808 dye. Then, physicochemical properties of IR808@MnO NPs were characterized. And then IR808@MnO NPs were used to image tumor by photoacoustic, fluorescent and magnetic resonance tri-modal imaging. Finally, we evaluated *In vitro* and *In vivo* phototherapy effect of IR808@MnO NPs on tumor.

Results/Discussion

IR808@MnO NPs could target and image tumor. Furthermore, IR808@MnO NPs could preferentially accumulate in the tumor tissue, attenuate tumor hypoxia, and completely inhibit tumor growth. Moreover, metabolic kinetics experiments showed that IR808@MnO NPs were biocompatible and could be removed by uropoietic and excretory system. These results suggested that IR808@MnO NPs are expected to be an effective nanophotosensitizer for cancer imaging and treatment.



Transcranial photoacoustic imaging of NMDA-evoked focal circuit dynamics in rat forebrain

Jeeun Kang¹, Shilpa Kadam², Joshua Elmore³, Brennan Sullivan², Heather Valentine³, Adarsha Malla², Maged M. Harraz², Arman Rahmim³, Jin U. Kang⁴, Leslie M. Loew⁵, Michael Baumann⁶, Anthony Grace⁷, Albert Gjedde⁸, Emad M. Boctor², Dean F. Wong³

¹Russell H. Morgan Department of Radiology and Radiological Science, Johns Hopkins University School of Medicine, Baltimore, MD, United States, ²Johns Hopkins University School of Medicine, United States, ³Russell H. Morgan Department of Radiology and Radiological Science, Johns Hopkins University School of Medicine, United States, ⁴Johns Hopkins University, United States, ⁵University of Connecticut Health, United States, ⁶National Institute on Drug Abuse, NIH, United States, ⁷University of Pittsburgh, United States, ⁸University of Copenhagen, Denmark

Background, Motivation, and Objective

Non-invasive transcranial photoacoustic (PA) voltage-sensitive dye (VSD) imaging is promising modality to further improve current spatiotemporal resolution of functional neuroimaging. In this study, we present *in vivo* differentiation between N-methyl-D-aspartate (NMDA)-evoked circuit dynamics at two distinct compartments in rat forebrain, i.e., sensorimotor cortex and hippocampus.

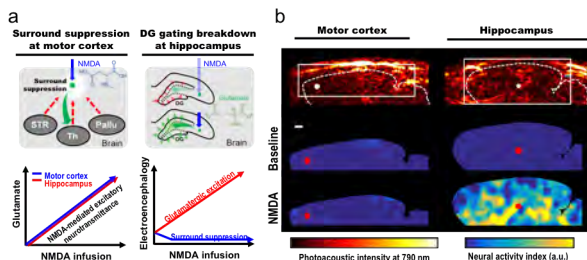
Statement of Contribution/Methods

We hypothesized that NMDA-evoked focal glutamate release in both circuits would correlate with PA and EEG signals with spatiotemporal domain. In both circuits, 0.3, 1 and 3 mM NMDA was infused with 2 μ l/min rate over 60 min via an inlet of microdialysis probe, while collecting dialysate samples in every 20 min through its outlet. The focal changes in extracellular glutamate release was quantified by high-performance liquid chromatography (HPLC). Concurrent quantitative EEG (qEEG) recorded real time circuit dynamics. Transcranial PA imaging was conducted in sagittal plane at the contralateral position of an implanted microdialysis probe.

Results/Discussion

Microdialysis at 0.3, 1 and 3 mM showed dose-dependent increases of glutamate (39%, 200% and 670 %, respectively) in hippocampus. Recorded qEEG at 3 mM NMDA infusion confirmed induction of focal seizure activity. Transcranial PA VSD imaging provided up to 301.45 ± 42.48 % of fractional neural activity index change measured with 3 mM NMDA infusion, while presenting -24.48 ± 34.16 % of fractional decrease with 0.3 mM NMDA infusion. This clearly suggests the dentate gyrus (DG) gatekeeping function in hippocampus.

On the other hand, Intracerebral NMDA infusion at 0.3 mM concentration produced the anticipated increase of glutamate release, but with a decrease of qEEG spectral power for 20 min of post-NMDA infusion phase, which suggests surround inhibition mechanism triggered by preferential activation of inhibitory interneurons. Transcranial PA VSD imaging consistently provided -13.22 ± 37.08 % of fractional neural activity index change in the same time duration. The results show this emerging technology to be an innovative and significant advance of functional neuroimaging.



Transcranial photoacoustic imaging of distinct electrophysiology in rat forebrain. (a) Surround suppression at motor cortex and dentate gyrus (DG) gating breakdown at hippocampus to a glutamate release evoked by focal NMDA infusion. (b) Near-infrared photoacoustic sagittal plane imaging at 790 nm and neural activity imaging during baseline and NMDA infusion phases. NMDA, N-methyl-D-aspartate; STR, subthalamic nucleus; Th, Thalamus; Pala, Palidus.

P2-B7 - Disease and Therapy Monitoring using Photoacoustics

Waraku (posters 2)

Wednesday, October 24, 9:30 AM - 4:00 PM

Chair: **Pai Chi Li** National Taiwan University

P2-B7-1

Photoacoustic imaging for assessing flow-mediated oxygenation for peripheral arterial disease.

Kathryn Khaw¹, Susan Schultz¹, Mustafa Mohammad¹, Zhen Chen¹, Khalid Ashi¹, **Chandra Sehgal¹**

¹*Radiology, University of Pennsylvania, Greater Philadelphia Area, PA, United States*

Background, Motivation, and Objective

Peripheral arterial disease (PAD) is a common cardiovascular disease that afflicts a large population worldwide. Reduced blood flow to the limbs by the narrowing of the arteries makes it difficult to meet the demands of physical activities like walking and results in mild to severe claudication. PAD is a risk factor for coronary heart disease and stroke and if left untreated could lead to gangrene and amputation. The goal of this study is to develop a photoacoustic imaging (PAI) technique for diagnosis and monitoring of PAD

Statement of Contribution/Methods

The studies were performed in nine mice where each animal was scanned bilaterally with a pulsed laser at optical wavelengths of 750 nm and 850 nm using a VovoLazr 2100 scanner. The photoacoustic signals generated by the two-wavelength irradiation was unmixed to generate parametric map of estimated oxygen saturation. The parametric map was superimposed in color on grayscale ultrasound images at a frame rate of 0.5 Hz. PAI was performed before and after tie-off of femoral muscles between the external iliac and femoral arteries. Following 5 minutes of occlusion, the tie-off was released and re-oxygenation of the muscles was imaged again with PAI. Femoral muscles distal to external iliac artery were outlined on pre-, during and post occlusion images and oxygen saturation (sO₂) was measured within the region of interest. The time-oxygenation (TO) waveform for each imaging session was used to determine pre-occlusion, during-occlusion and post-occlusion sO₂s.

Results/Discussion

Results: Photoacoustics successfully imaged limb oxygenation with a well-defined TO waveform in all the animals. Marked reduction in oxygenation during occlusion was observed followed by hyper-oxygenation that exceeded baseline value during post-occlusion. Occlusion caused the sO₂ to decrease on average to $36.8\% \pm 10.5\%$ (range 26.3% - 47.3%) from the baseline (pre-occlusion) value of $51.9\% \pm 0.5\%$ (range 51.4% - 52.4%). Following the tie-off release, post-occlusion showed a rapid increase in sO₂ to $74.7\% \pm 15.5\%$ (range 59.2% - 90.2%). The overshoot above the baseline pre-occlusion value was observed in all cases. The average excess oxygenation for all the animals studied was $23.2\% \pm 12.4\%$. The overshoot in oxygenation from the baseline was significant ($P < 0.0001$). After peaking, the post-occlusion sO₂ decreased gradually but it did not return to the baseline value over 5 minutes of image recording.

Conclusion: This study reports a novel approach using photoacoustic imaging to observe changes in oxygen saturation in response to stress induced by ischemia. The results show hyper-oxygenation occurs following stress release where sO₂ exceeds the baseline due to endothelium-mediated dilation of the microvasculature. Measurement of flow-mediated hyper-oxygenation and its kinetics by photoacoustic imaging could provide a novel approach for assessing endothelial function noninvasively in PAD subjects

Integration of Endovenous Laser Ablation and Photoacoustic Imaging Systems for Enhanced Treatment of Venous Insufficiency

Samuel John¹, Yan Yan¹, Loay Kabbani², Nicole A. Kennedy², **Mohammad Mehrmohammadi^{1,3}**

¹Biomedical Engineering, Wayne State University, Detroit, MI, United States, ²Henry Ford Hospital, MI, United States,

³Electrical and Computer Engineering, Wayne State University, MI, United States

Background, Motivation, and Objective

The treatment methods for venous insufficiency such as varicose veins disease include minimally invasive techniques such as endovenous laser ablation (EVLA) procedures. Currently, ultrasound (US) imaging modality helps vascular surgeons to guide the ablation fiber through the diseased veins. However, in perforating veins, US imaging is unable to track and visualize the fiber because it suffers from angular dependency, low contrast to noise (CNR) ratio. Besides, US imaging lacks the ability to distinguish between the fiber tip and the cross section of the fiber body. In addition, existing clinical EVLA procedures lack real-time temperature monitoring inside the diseased vein, which may lead to an insufficient thermal dose or endovenous heat induced thrombosis. In this study, we propose to integrate photoacoustic (PA) imaging and EVLA using a simple, cost-effective and practical solution for accurate fiber tip tracking and real-time temperature monitoring.

Statement of Contribution/Methods

The ability of PA imaging for fiber tip tracking and real-time monitoring the temperature are evaluated through a set of tissue-mimicking experiments using a clinical ablation catheter. A short pass dichroic mirror with cut-off wavelength of 650 nm was used to couple both pulsed laser beam at $\lambda=532$ nm and continuous wave (CW) laser at $\lambda=800$ nm into a single fiber for simultaneous ablation and PA imaging. Vascular mimicking phantom with both straight and angled vessels were used to perform US and PA fiber tracking and compare their performance in terms of ability to detect angled fibers, differentiating between fiber tip and fiber body, and image CNR. In addition, PA imaging was performed in a range of ambient temperatures ranging from 20 to 85 degrees to evaluate the performance of PA for thermometry.

Results/Discussion

Compared to US imaging which visualizes the fiber body and the background tissue, PA imaging provided angle-independent, artifact-free, high CNR images of the fiber tip in the straight and angled orientations (**Figure 1 a-c**). Also, PA imaging was able to differentiate between the fiber tip and the cross section of the fiber body since the PA signal is only generated at the tip where the light interacts with tissue. From the thermometry studies, a clear increment in the amplitude of the PA signal was observed with an increase in the surrounding temperature (**Figure 1 d-e**).

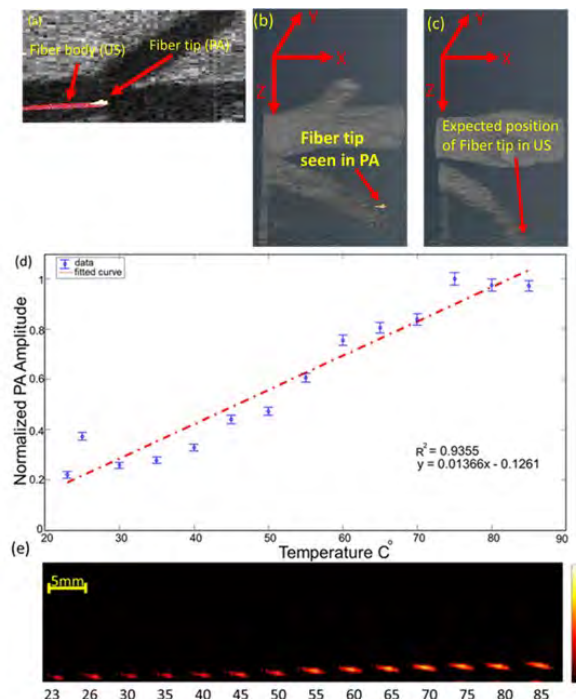


Figure 1: Straight fiber tip tracking – (a) Volumetric image of the fiber in both US and PA indicating that PA is only visualizing the fiber tip while US imaging shows the whole fiber body. Angled fiber tip tracking - (b) Volumetric image showing the fiber tip is seen using PA imaging. (c) Volumetric image showing the fiber tip is lost using US imaging. (d) Plot indicating normalized amplitude of the PA signal obtained versus surrounding temperature, blue dots indicate measurements and the red dotted line represents the linear fit. (e) PA images of the fiber tip at different surrounding temperatures.

Photoacoustics for non-invasive monitoring of kidney damage due to diabetes and hypertension
Elizabeth Berndl^{1,2,3}, Xiaolin He^{2,4}, Darren Yuen^{2,4}, Michael Kolios^{1,2,3}
¹*Department of Physics, Ryerson University, Toronto, ON, Canada*, ²*Institute for Biomedical Engineering, Science and Technology (iBEST), Toronto, ON, Canada*, ³*Keenan Research Centre for Biomedical Science of St. Michael's Hospital, Toronto, ON, Canada*, ⁴*Division of Nephrology, Department of Medicine, University of Toronto, Toronto, ON, Canada*
Background, Motivation, and Objective

One in 10 Americans has kidney disease in their lifetime. Kidney transplantation has revolutionized kidney failure outcomes, yet a shortage of donors has led to expanding kidney waiting lists. With approximately 93 000 people on the kidney transplant wait list in the United States, wait times are from 3 – 8 years. Each year, almost 5 000 people die on the kidney waiting list. Loosening eligibility for donors to include older “expanded criteria donors” with poorer kidney function or hypertension has reduced wait times, but long term outcomes of these kidneys is highly variable.

Assessing donor kidney quality relies on non-specific, insensitive measures that do not directly assess injury burden. Biopsies can evaluate donor kidney damage due to fibrosis or microvascular injury histologically, but risks injuring the kidney, and has a small sampling volume. A non-invasive technique capable of directly evaluating a larger portion of donor kidneys may provide more complete information about its quality prior to transplant, permitting the selection of the most appropriate kidneys.

Statement of Contribution/Methods

TTRhRen^{+/−} mice (n=4) were injected with STZ (Ren-STZ) to induce a diabetic, hypertensive phenotype, and RF data of photoacoustic (PA) spectral sweeps (680 - 970 nm) of three planes of the left kidney were collected at 0, 4 and 8 weeks post-injection by a VevoLAZR system at 21MHz, and compared to wild-type littermates (n=6) injected with citrate (WT-citrate). For each plane, the average PA amplitude within the kidney was calculated. 20 weeks post-injection, animals were sacrificed and kidneys were assessed by picrosirius red (PSR) staining.

Results/Discussion

PSR staining (Fig A) shows that Ren-STZ mice have increased collagen at 20 weeks compared to the WT mice, indicating that the diabetic-hypertensive phenotype scars the kidney, which is associated with their decreased function. Changes in PA signal amplitude in the kidneys (Fig B) were dependent on both time and phenotype ($p < 0.001$), with Ren-STZ amplitude at W8 (1.223 ± 0.009) statistically different from the next nearest group (WT-citrate at W8; 0.719 ± 0.008).

Increased PA amplitude appears to be a simple indicator of increased damage in kidneys. Further research in both animals and humans will determine if this is associated with all types of damage or if it is specific to damage due to hypertension and diabetes.

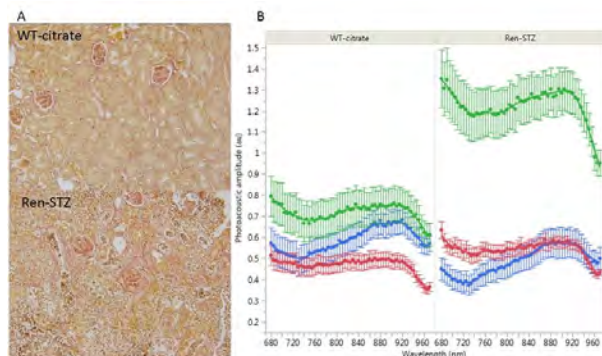


Figure 1: (A) Representative PSR staining of WT-citrate and Ren-STZ kidneys at week 20. Increased red staining is associated with increased collagen content, and scarring. (B) Average photoacoustic amplitude in WT-citrate (left) and Ren-STZ (right) kidneys at 0 (blue), 4 (red) and 8 (green) weeks. Increased signal in the W8 Ren-STZ is statistically significant ($p < 0.0001$). Values are mean \pm SE.

Pathology Study for Blood Vessel of Ocular Fundus Images by photoacoustic tomography

Jiayao Zhang¹, Kai Deng², Bin Chen¹, Meng Zhou¹, Hengrong Lan¹, Fei Gao¹

¹ShanghaiTech University, Shanghai, China, People's Republic of, ²Beijing University of Posts and Telecommunications, China, People's Republic of

Background, Motivation, and Objective

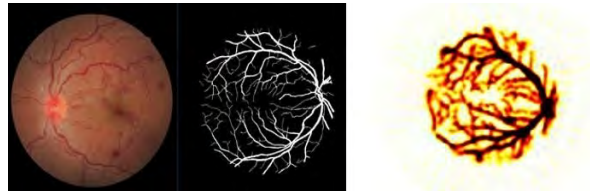
Blood vessel of ocular fundus is the only blood vessel that can be directly observed and has great application value in the medical field. Photoacoustic Tomography (PAT) is an emerging technique that can obtain high-resolution 3D in-vivo images of absorbed optical energy by sensing laser-generated ultrasound signals. Therefore, in this article, based on a deep learning algorithm, we will analyze the differences between the diabetics and normal people by the ocular fundus segmentation photoacoustic images of blood vessel, which may open up new methods for ocular fundus medical image processing.

Statement of Contribution/Methods

This model includes a convolutional neural network (CNN) to fundus segmentation of blood vessel images. The network introduces the convolution layer as the main feature extraction layer. The weight-sharing network structure of the convolution layer is more like a biological neural network. The entire network can be directly trained without pre-training, making the training process more simplified. Next, we use 2D Time Reversal photoacoustic simulation based on k-WAVE MATLAB toolbox to convert the fundus segmentation of blood vessel images into photoacoustic images. Finally, we use the Resnet Network for the diagnosis of diabetes, in which the input data are the diabetics and the normal people' images of the fundus segmentation of blood vessel.

Results/Discussion

The Resnet Network structure is a 27-layer convolutional layer. Each three convolution layers are connected across layers. After each convolution layer we use Relu in the activation function, followed by BatchNorm. The final output layer function uses sigmoid function, whose output value represents the probability that the input sample has diabetes; we set the threshold to 0.5. when the output probability is greater than 0.5, then it is judged to be the diabetic patients, and vice versa; the final loss function uses cross entropy. We have achieved 85% accuracy with 40 training samples. These results demonstrate the power of using deep learning for the analysis of diabetes through the ocular fundus segmentation photoacoustic images of blood vessel.



Photoacoustic spectral analysis at ultraviolet wavelength for assessing the aggressiveness of prostate cancer
Guan Xu¹, Yunhao Zhu², Mandy Davis³, Javed Siddiqui³, Scott Tomlins³, John Wei⁴, Evan Keller⁴, Xueding Wang²
¹*Radiology, University of Michigan, United States*, ²*Biomedical Engineering, University of Michigan, United States*, ³*Pathology, University of Michigan, United States*, ⁴*Urology, University of Michigan, United States*
Background, Motivation, and Objective

During the past two decades, prostate cancer (PCa) has become the most commonly diagnosed cancer in American men. Currently, the diagnostic challenge for PCa is to differentiate aggressive PCa cases from indolent ones to prevent metastasis. The aggressiveness of prostate cancer is quantified under a Gleason grading system, which describes the cellular level architectural heterogeneity of the prostate tissue. Taking advantage of the strong optical absorbing properties of cell nuclei at ultraviolet wavelengths, this study examines the feasibility of quantifying the PCa aggressiveness using photoacoustic (PA) spectral analysis (PASA).

Statement of Contribution/Methods

In this study, PA signals were generated at 266 nm with optical density of 2 mJ/cm^2 and acquired by a needle hydrophone with a bandwidth of 0.1-10 MHz. The prostates of an animal model, TRAMP mice, were scanned *ex vivo* and *in vivo*. The *in vivo* measurements were achieved using our recently developed needle PA probe. Human prostate cancer tissues were also examined *ex vivo*. The fluctuations of the PA signals were quantified by PASA slopes as a reflection of the tissue heterogeneity.

Results/Discussion

Fig. 1 shows the *ex vivo* images of normal and cancerous mouse prostates. Higher heterogeneities were observed in the cancerous prostate. Fig. 2 shows significant difference between the cancerous and normal prostates in mice *in vivo* and between nonaggressive and aggressive cancers in human prostate tissues *ex vivo*. Both sets of results support that the proposed method is capable of quantifying the PCa aggressiveness.

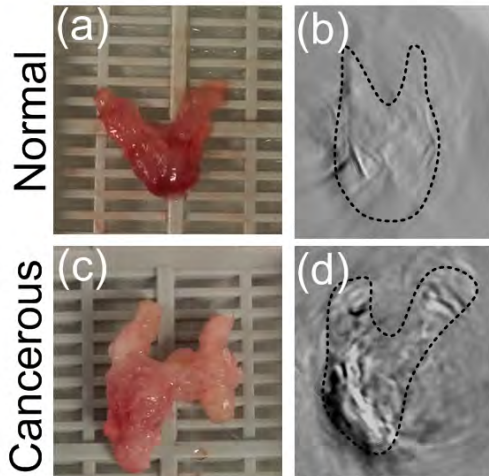


Fig.1 Gross pathology and PA images of the normal and cancerous mouse prostates

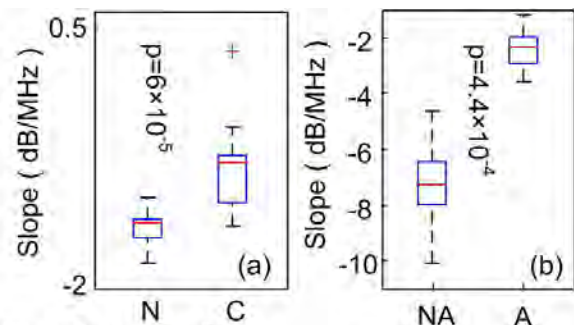


Fig.2 Statistics of the quantitative PA parameters derived from (a) mouse prostates *in vivo* and (b) human prostate tissue *ex vivo*. N: normal. C: Cancer. NA: nonaggressive. A: aggressive.

Photoacoustic cepstrum analysis for studying vascular networks

Eno Hysi^{1,2}, Muhamnad N. Fadhel^{1,2}, Michael Moore^{1,2}, Jason Zalev^{1,2}, Eric Strohm^{3,4}, Michael Kolios^{1,2}

¹*Physics, Ryerson University, Toronto, ON, Canada*, ²*Institute for Biomedical Engineering, Science and Technology, Toronto, ON, Canada*, ³*Mechanical and Industrial Engineering, University of Toronto, ON, Canada*, ⁴*Translational Biology and Engineering Program, Ted Rogers Centre for Heart Research, University of Toronto, ON, Canada*

Background, Motivation, and Objective

Photoacoustic (PA) images contain speckle due to the random superposition of absorbers within the imaging transducer's resolution volume. When imaging vasculature using ultrasound resolution PA imaging with linear arrays, an abundance of sub-resolution vessels generates speckle, making it difficult to resolve individual blood vessels. We introduce PA cepstral analysis as a means of probing the spatial arrangement of sub-resolution vessels using fractal-based models of normal and tumor vasculature.

Statement of Contribution/Methods

Spherical absorbers: The cepstral algorithm based on the logarithmic Fourier Transform of PA signals was tested in simulated 3D phantoms imaged with a 21 MHz linear array. The phantoms consisted of random and periodic absorbers. The location of the dominant cepstral peak for phantoms with varying spacing was compared to the true absorber spacing.

Cylindrical absorbers: A fractal model was used to construct normal and tumor vasculature networks. The model uses cylindrical bases which bifurcate to give rise to daughter branches. Normal and tumor vasculature was modeled across 9 branching orders (average diameter 26 μm ; average length 352 μm) by randomly changing the bifurcation angle in the 27-30° (normal) and 25-140° (tumor) range, respectively. PA signals were detected using a 40 MHz linear array. Cepstral peaks were used to differentiate the two models of vasculature.

Results/Discussion

Fig. 1a shows the PA image of the spherical absorber phantom. The PA power cepstrum (Fig. 1b) identifies the periodicity within the phantom (~ 1 mm) without the need to resolve individual absorbers. This extends to a wide range of absorber concentrations (Fig. 1c) and estimates are nearly identical to the true spacing. The PA images from normal and tumor vascular networks are shown in Fig. 1d. One cannot resolve individual vessels from the PA images but the cepstra (Fig. 1e) reveal differences. The first prominent peak of the tumor vasculature is $\sim 200 \mu\text{m}$ lower than normal vessels. It is postulated that due to the chaotic organization of tumor vasculature (i.e. larger branching angle) vessels are closer to one another than in normal tissue. These results suggest that PA cepstral analysis can be used to probe the spacing of non-resolvable vascular networks. It may be possible to differentiate and/or colorize regions of tissue with different vascular structure.

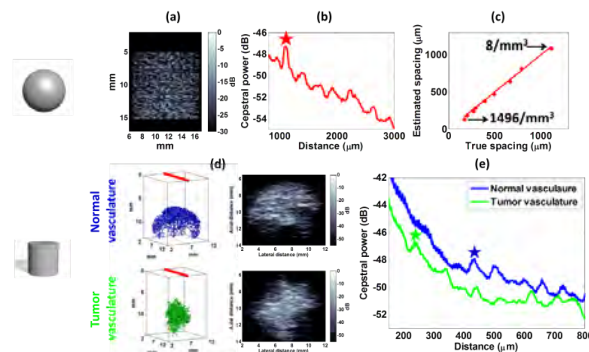


Fig. 1: (a) Representative PA B-mode image from 20 μm spherical beads arranged in a grid (15%) and random (85%) pattern. (b) Average power cepstrum (star denotes most prominent peak). (c) Comparison of the estimated absorber spacing with the true spacing for various number densities. (d) Fractal-based vascular tree model and PA B-mode images at 40 MHz for normal and tumor vasculature. (e) Average PA power cepstrum for normal and tumor vasculature.

P2-B8 - Application-Specific Systems and Real-Time Acceleration

Waraku (posters 2)

Wednesday, October 24, 9:30 AM - 4:00 PM

Chair: **Billy Yiu** University of Waterloo

P2-B8-1

A portable ultrasound device for measuring the stiffness of carotid artery: comparison with SphygmoCor carotid-femoral pulse wave velocity

Chieh-Ju Tang¹, Yi-Hsiang Chuang¹, Po-Yang Lee¹, Chih-Chung Huang¹

¹Department of Biomedical Engineering, National Cheng Kung University, Taiwan

Background, Motivation, and Objective

Arterial stiffness is an important clinical index for preventing cardiovascular diseases, such as stroke and atherosclerosis. Carotid-femoral pulse wave velocity (cfPWV) is an acceptable index for evaluating the regional arterial stiffness (Fig 1(a)). However, it is difficult to evaluate the accurate distance between carotid and femoral sites which makes errors for cfPWV measurements. Recently, many studies have indicated that local PWV measurement exhibits more clinical significance, which can be used as an early diagnosis tool for identifying the local atherosclerosis. However, only a few commercial ultrasound systems provide the local PWV measurement function. Therefore, there are two purposes of this study: (1) developing a portable ultrasound device for automatically measuring the local PWV from carotid artery and (2) demonstrating that local PWV can predict cfPWV.

Statement of Contribution/Methods

A portable ultrasound device with an eight 5 MHz elements transducer was designed in this study (Fig. 1(b)). The system hardware including eight channels pulser/receiver, Pre-Amp, VGA, 12 bit ADC, Altera FPGA chip, and Bluetooth module. Fig 1(c) shows the signal processing procedure in the system. An automatic positioning approach based on Doppler measurement was designed for the operators, and the vessel wall motion tracking algorithm was developed for measuring the local PWV. A total of 13 healthy volunteers was included in this study. The cfPWV from volunteer was also measured by commercial device SphygmoCor, which uses a tonometric sensor to determine the cfPWV between femoral and carotid arteries.

Results/Discussion

Fig 1.(d) shows the relationship between cfPWV and local PWV obtained from ultrasound device. A good linear correlation was found between cfPWV and local PWV ($r= 0.85$) in normal subjects. The measured PWVs are 6.8 ± 0.6 and 4.8 ± 0.5 m/s for cfPWV and local PWV, respectively, which in a good agreement with previous study that the cfPWV is higher than local PWV from carotid artery. Further studies are needed to recruit more subjects and to evaluate the clinical significance for using local PWV from ultrasound device in routine clinical practice for the assessment cardiovascular diseases risk.

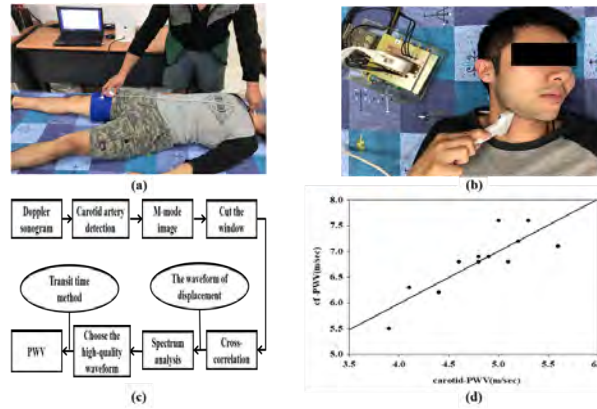


Figure1

A Low-Cost Software-Defined Ultrasound System Capable of High-Speed Ultrasound Bubble TrackingPascal Alexander Hager¹, Pascal Jud¹, Luca Benini¹¹*Integrated Systems Lab, ETH Zürich, Switzerland***Background, Motivation, and Objective**

Localizing and tracking of individual bubbles is an operation required for several new imaging modalities: In ultrafast Ultrasound Localization Microscopy (uULM) individual bubbles injected into the blood flow are localized to map the vascular network below the diffraction limit. Furthermore, by tracking the bubble movement over time the streaming velocity of the fluid is measured.

For reliable localization and tracking of bubbles, an ultrafast imaging system providing a frame rate above 100 Hz over multiple seconds is required. Due to the huge amount of data (>1GB), data-rates (>10Gbit/s) and the required processing performance, ultrafast imaging is currently supported only in large research systems or expensive high-end commercial systems.

In this work, we want to show that high-speed bubble tracking can be implemented on a low-cost ultrasound system based on a digital ultrasound probe equipped with a high-speed digital link to connect to a standard PC.

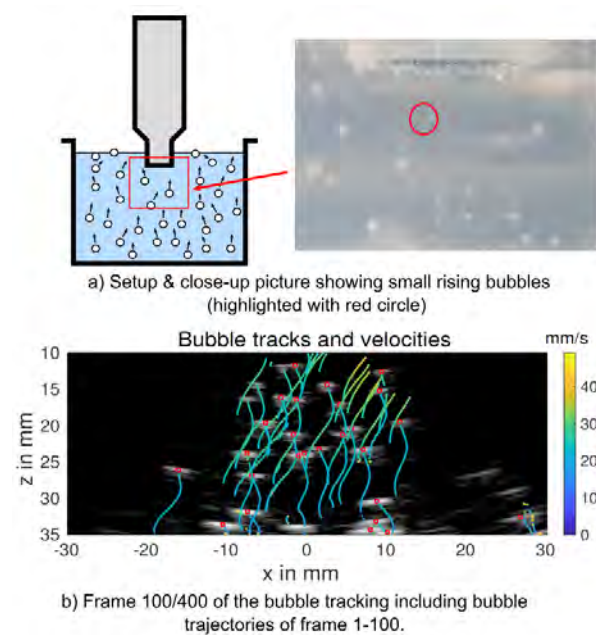
Statement of Contribution/Methods

We demonstrate 200fps high-speed ultrasound bubble tracking of air bubbles in water using the UltraLight ultrafast imaging platform (IUS2017). The platform features a 4 MHz 64-channel digital ultrasound probe, which integrates the analog frontend and connects to a GPU-equipped PC over a 25Gbit/s fiber optical link. The link allows to transfer the raw RF samples from all channels continuously to the PC.

For the experimental setup, a salt-activated sparkling water bath is used with intensive bubbling. We recorded 400 frames in 2s (200 fps) using a TX sequence of 13 defocused virtual source emissions (3 kHz PRF). The acquired raw data is moved to the PCs main memory. The data is beamformed on the GPU to create a B-mode sequence, which is feed to our offline bubble detection/tracking pipeline.

Results/Discussion

Prior to implementation, we simulated the imaging system and computed a bubble tracking accuracy of 1.2um lateral and 14.5um axial direction with a correct bubble detection and step tracking rate of 95.8% and 99.1%. In the experimental setup we are able to track 321 bubbles over 3-242 Frames (median 9) over a length of 0.04-28.0mm (median 1.1mm). The observed velocities were in a range of 0-149.7 mm/s. Current work focuses on moving from air to microbubbles and speeding up the processing pipeline for real-time imaging.

**Figure 1: Setup & Result**

Automatic B-mode Ultrasound Image Optimization for a Wireless Mobile Ultrasound Imaging System

Hojung Lee¹, Jinbum Kang¹, Ilseob Song¹, Min Kim¹, Tai-kyong Song¹, Yangmo Yoo^{1,2}

¹Electronic Engineering, Sogang University, Seoul, Korea, Republic of, ²Biomedical Engineering, Sogang University, Seoul, Korea, Republic of

Background, Motivation, and Objective

A mobile ultrasound imaging system now plays an important role in point-of-care (POC) diagnosis with a smart-device compatible wireless ultrasound probe. The ultrasound imaging, however, is highly user-dependent, so it must be adjusted appropriately by the user for clinical use. Thus, for the mobile ultrasound system applied in POC diagnosis, it is necessary to automatically optimize the ultrasound image by adjusting some of key imaging parameters, including time gain compensation (TGC), overall gain and dynamic range (DR).

Statement of Contribution/Methods

In the developed wireless mobile ultrasound imaging system, the smartphone handles back-end processing to reconstruct an ultrasound B-mode image by using a GPU with OpenGL ES3.0 in Android 7.0 as shown in Fig. 1(a). An input data's scanline average intensity along the depth is first computed to estimate signal attenuation and linearly approximated to get a proper TGC gain curve for attenuation compensation. The overall gain value is adjusted by comparing reference's average intensity. Finally, DR is calculated by comparing reference image's distance between average intensity to maximum and minimum intensities. The proposed method was implemented in the commercial smartphone (Galaxy S7, Samsung electronics Inc., South Korea) as shown in Figs. 1(a)-(b). To further evaluate the proposed method, *in-vivo* thyroid data were captured using a 7.5-MHz linear array transducer on the commercial ultrasound system (Accuvix V10, Samsung Medison Inc., Seoul, South Korea) and analyzed with Matlab (Mathworks Inc., Natick, MA, USA).

Results/Discussion

The reference, input and output B-mode images with the proposed automatic image optimization method are shown in the left, center and right sides of Fig. 1(c). The corresponding axial intensity profiles are shown in Fig. 1(d). As shown in Fig. 1(d), the proposed method optimally adjusted a TGC curve of the input image. The adjusted overall gain and DR values were 1.17 and 74.35 dB, respectively. To evaluate the gain and DR values, correlation coefficient of intensity histogram between output and reference images were measured. It scored 0.93 and represents that the output image's overall brightness and contrast are comparable to those of the reference image. To validate the impact of the automatic optimization on POC diagnosis, further clinical evaluation is under investigation.

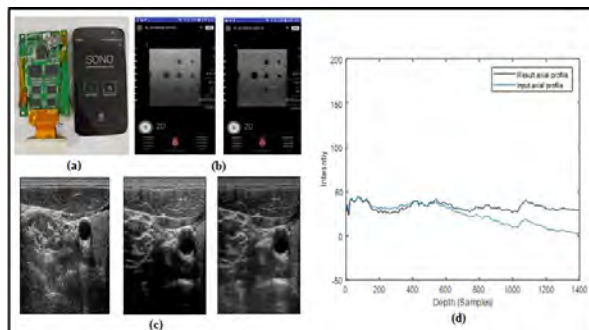


Fig. 1. (a) Wireless ultrasound probe and smartphone application (b) Mobile ultrasound image before optimization (left) and Optimized result (right) (c) Reference image (left), input image before optimization (center) and result image of simulation (right) (d) vertical profile values of result image

A Point-of-Care Ultrasound Scanner with Software Beamforming on Nvidia Tegra mobile GPU**Marcin Lewandowski^{1,2}, Mateusz Walczak^{1,2}, Beata Witek^{1,2}**¹*Laboratory of Professional Electronics, Institute of Fundamental Technological Research, Polish Academy of Sciences, Warsaw, Poland, ²us4us Ltd., Warsaw, Poland***Background, Motivation, and Objective**

Point-of-Care Ultrasonography (POCUS) is a novel approach to the application of ultrasound diagnostics that greatly extend the users' base and offer diagnostic at the site of patient care. POCUS requires a new class of portable, low-cost, and low-power devices. Many new devices targeting this application have been introduced in recent years. Unfortunately, all these developments are based on hardware line-by-line beamforming, which prevents the introduction of a more advanced synthetic aperture approach.

We have proposed an architecture with software-based image reconstruction that fulfills the paradigm of Software Defined Ultrasound (SDU). A newly developed, compact ultrasound front-end module featuring 128 TX/32 RX channels supplemented by the Nvidia® Tegra mobile GPU module can support all standard ultrasound modalities, as well as new advanced algorithms (eg. Plane-wave, vector Doppler).

Statement of Contribution/Methods

We integrated a compact high-performance ultrasound front-end module (us4us Ltd., Poland) supporting 128 TX and 32 RX channels and featuring raw channel data acquisition and real-time streaming with PCIe gen.3 interface. The module interfaces to an Nvidia® Tegra X1 evaluation board, where the entire signal processing and user interface is implemented.

The system can work with standard medical piezo probes; in our case, we fitted an adapter for commercial probes by Esaote (Italy). The system supports all types of probes with up to 128-elements. A plain CUDA implementation of time-based Plane-Wave Imaging (PWI) algorithm was tested and benchmarked on the embedded Nvidia Tegra processor.

Results/Discussion

We therefore present a functional demonstrator of a portable, low-cost/low-power programmable ultrasound scanner featuring real-time software-based PWI (framerate 50 fps) on a mobile GPU. The scanner can be easily extended and adapted to custom applications through software-only modification. The total system power is under 30W, making it a good candidate for a portable device (laptop form factor).

We are convinced that the presented system can become the ultimate platform for the introduction of ultrafast imaging and other advanced ultrasound modalities in POCUS.



A Spline-based Spatial Impulse Response Ultrasound Simulator with GPU Implementation

Dimitris Perdios¹, Florian Martinez¹, Adrien Besson¹, Marcel Ardit¹, Jean-Philippe Thiran^{1,2}

¹Signal Processing Laboratory (LTS5), Ecole Polytechnique Fédérale de Lausanne (EPFL), Switzerland, ²Department of Radiology, University Hospital Center (CHUV) and University of Lausanne (UNIL), Switzerland

Background, Motivation, and Objective

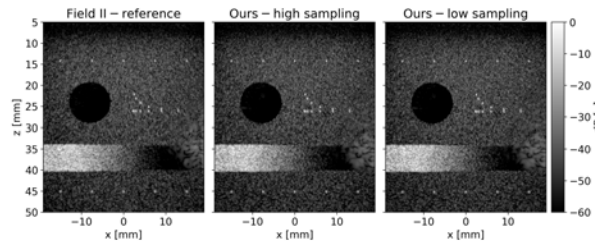
The need for fast and accurate ultrasound (US) simulation tools is as great as ever. Such tools are used on a daily basis in a myriad of applications such as array optimization, image reconstruction, and dataset generation for machine learning. Many US simulators targeting various applications are already available. Among them, Field II is certainly the most widely used. It is based on the spatial impulse response (SIR) model. Tx and Rx apertures are discretized by planar elements and the surface integrations are performed using a far-field approximation. Last year, FAMUS II was introduced. It is also based on the SIR model but uses a point-source approximation for accelerating the computations at the cost of less accurate surface integrations. Both rely on CPU implementations, which prevents a full benefit from the high parallelizability offered by SIR.

Statement of Contribution/Methods

We propose to take advantage of spline representations for both time and aperture domains. Using non-uniform rational B-spline to compute the SIR allows exact representations of common transducer-element geometries. The surface integrations are performed with the Gauss-Legendre quadrature rule providing high-order approximations with few integration points. Cubic B-splines are used in the time domain, which proved to be the best trade-off. To demonstrate the high parallelizability of this method, we achieved a first GPU implementation with minimal memory requirements, allowing the computation of 2D and 3D scenarios in a reasonable time.

Results/Discussion

We compared our approach to Field II on images reconstructed by synthetic aperture (SA) imaging on the PICMUS phantom. The probe is a 128-element linear array (L11-4v) and the transmitted pulse is centered at 5.2 MHz with 67% bandwidth. The phantom is composed of ~140'000 scatterers. The Field II reference (left) is obtained using 7x35 sub-elements at 100 MHz. Our approach is evaluated on a high-sampling setting at 100 MHz with 8x128 integration points (center), and a low-sampling setting at 20 MHz with 2x32 integration points (right). The images are remarkably similar, while our initial GPU implementation already provided a decrease in computation time exceeding 200x compared to Field II. Furthermore, the new simulator successfully generated a SA dataset composed of 4k images for machine learning tasks in less than a day.



Feasibility of hands-free acquisitions of the skeletal muscles and the heart during exercise
Marloes Sjoerdsma¹, Maarten Heres¹, Frans van de Vosse¹, Richard Lopata¹
¹*Eindhoven University of Technology, Eindhoven, Netherlands*
Background, Motivation, and Objective

Continuous, dynamic ultrasonic evaluation of architectural and mechanical parameters of skeletal muscles is challenging. In addition, for many applications, intra-exercise measurements are more relevant compared to post-exercise parameters. A constant FOV is often essential for measurement accuracy, however, the orientation and position of the probe are difficult to reproduce and preserve. Probe fixation might improve the FOV stability and enable continuous acquisitions during exercise. In this study, the feasibility of hands-free acquisitions was investigated in two distinctively challenging fields, i.e. myosonography and echocardiography.

Statement of Contribution/Methods

The FOV stability obtained by trained sonographers was compared to a fixated probe. In myosonography, longitudinal images of the vastus lateralis muscle were acquired in ten healthy volunteers whilst cycling. In echocardiography, eight exercise stress tests were performed. For both, a MyLab 70 US system (Esaote, NL) was used.

To overcome inter-observer variability and bias, feature-based algorithms were implemented to detect and measure muscle diameter and pennation automatically. The FOV stability was assessed based on the temporal deviation in these functional parameters and the structural similarity (CW-SSIM) of the images.

For feasibility demonstration in an uncontrolled environment, the muscular functional parameters of three marathon runners were measured hands-free with a Lumify L12-4 probe (Philips, USA).

Results/Discussion

In myosonography, the FOV stability was significantly superior compared to two trained sonographers (Fig. 1A-B). In the marathon runners, the CW-SSIM index, pennation angles and diameter were overall stable (< 1%, < 5% and < 1% variability, respectively) for the measurement distance (+/- 10 km).

Figures 1C-D show the FOV stability of apical and parasternal views. Overall, the hands-free FOV was at least equal to those obtained by the trained sonographers. However, the parasternal FOV variation of the observer was lower, due to manual corrections made for respiration induced cardiac dislocation.

The demonstrated feasibility of hands-free, continuous, dynamic acquisitions promises to be beneficial in many clinical fields and sports. Moreover, it has the potential to decrease work-related musculoskeletal afflictions in sonographers.

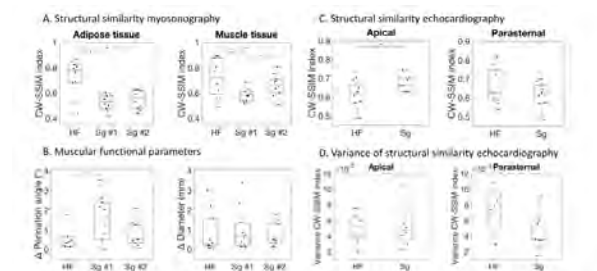


Figure 1: FOV stability results of the skeletal muscles (A-D) and the heart (C-D) obtained during exercise. For all, the final 10 seconds were compared to first 10. **A:** Image structural similarity indexes of the adipose and muscle tissue. **B:** Absolute changes in pennation angles and diameters. **C:** Image structural similarity indexes of the apical and parasternal views and **D:** their variances.

Experimental study to bend thin catheter independent to ultrasound propagation direction by tempo-spatial division emission using multiple transducers

Hidetaka Ushimizu¹, Toshiya Suzuki¹, Takashi Mochizuki¹, Kohji Masuda¹

¹Tokyo Univ. of A&T, Japan

Background, Motivation, and Objective

We have already confirmed the displacement of the tip of a thin catheter in proportion to the applied sound pressure. We succeeded in bending the catheter in the direction perpendicular to ultrasound propagation using a single matrix array transducer, which produced a focal point and steered it by changing the delay time of sound elements. Considering various clinical situations, developing the method of bending the catheter in any direction is necessary due to a limitation of the installation position of ultrasound transducers on the body surface. In this study, we introduced two matrix array transducers to bend the catheter in the direction independent to ultrasound propagation by establishing tempo-spatial division emission of focal point.

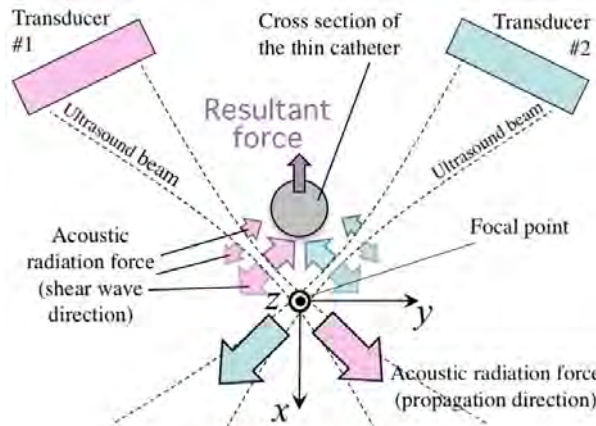
Statement of Contribution/Methods

Figure shows the experimental setup with two matrix array transducers, where the ultrasound propagation direction is in the x - y plane, and the catheter is placed along the z -axis. The direction of gravity corresponds to the x -axis. We consider that the interaction of the acoustic radiation forces in shear wave direction produces a resultant force to bend the catheter in the negative x -axis direction.

We prepared a thin catheter, which is made of a perfluoroalkoxy (PFA) copolymer with outer diameter of 0.20 mm, length of 50 mm, and a bulk elasticity of $E_f = 600$ MPa in water. Also we prepared two identical transducers, which have 128 elements with central frequency of 3 MHz. The maximum sound pressure of the focal point was 500 kPa-pp with a duty ratio of 60%. The driving equipment was set to generate a burst wave to electrically shift the focal point with the transition rate of 0.4 mm/s.

Results/Discussion

We set the transducers with facing each other along x -direction with the distance of 120 mm to produce the initial focal point in the middle, and observed the behavior of the tip of the catheter by changing initial position of the catheter. When the catheter was set to the initial focal point, the tip was oscillated in the x - y plane. On the other hand, when the catheter was set 0.5 mm above (in the negative x -direction) from the initial focal point, the tip was lifted according to the transition of the focal point with the maximum displacement of 0.25 mm. We are now searching the effective conditions with not only the acoustic condition but also three-dimensional position relationship between the catheter and the focal point.



Comparison of longitudinal-mode and longitudinal-torsional mode ultrasonic bone biopsy devices

Rebecca Cleary¹, Margaret Lucas¹

¹*University of Glasgow, Glasgow, United Kingdom*

Background, Motivation, and Objective

Previous research by the authors has demonstrated the efficacy of a novel ultrasonic bone biopsy device that operates in a longitudinal (L) mode at 25 kHz. Ultrasonic longitudinal-torsional (L-T) coupled vibration has proven successful in several applications including ultrasonic surgical devices. In this work, an L-mode ultrasonic bone biopsy device was geometrically modified by introducing helical slits to degenerate the longitudinal vibration into a composite L-T motion. The performance of the L-T biopsy needle device was then compared with the L-mode needle device based on their ability to penetrate animal bone samples.

Statement of Contribution/Methods

Finite element analysis (Abaqus FEA, Dassault Systemes Simulia) was used to design the L-T needle. The depth and pitch of the helical slits were systematically modified in the FEA model with the aim of maximising the achievable torsional displacement while ensuring sufficient frequency spacing between the L-T mode and the neighbouring flexural modes. Experimental modal analysis (EMA) of the fabricated ultrasonic device was used to identify the modal parameters and validate the FEA model. Bone penetration tests were carried out using the L-mode and L-T mode needle devices. The needles were driven under the same conditions, penetrating the metaphysis of swine femur, noting the ease of operation while observing the quality of the sample and hole.

Results/Discussion

The ultrasonic bone biopsy needle designed using FEA was demonstrated to operate in an L-T mode at 25 kHz using EMA. Comparative bone penetration tests showed that to achieve penetration with the L-mode device, the operator was required to apply a slow alternating twisting action as well as the small forward force, to attain a forward motion and avoid imprinting of the needle tip in the bone. The resulting hole was conical in shape and the twisting action caused micro-damage on the hole surface. The L-T mode device, however, could penetrate the same animal bone sample only applying a small forward force, hence simplifying the procedure, increasing precision and resulting in a cylindrical, less damaged hole surface.

Future work will focus on increasing the penetration speed and precision, and reducing temperature.

Volumetric Ultrasound Image Reconstruction from a Single-Element Forward-Looking Intracardiac Steerable Catheter using 3D Adaptive Normalized Convolution

Jovana Janjic¹, Awaz Ali², Frits Mastik³, Merel Leistikow⁴, Johan G. Bosch⁵, Paul Breedveld², Antonius F. W. van der Steen^{6,7}, Gijs van Soest¹

¹*Thorax Centre, Erasmus MC, Rotterdam, Netherlands*, ²*Faculty pf 3mE - Biomechanical Engineering, TU Delft, Netherlands*,

³*Erasmus MC, Netherlands*, ⁴*In-body Systems, Philips Research, Netherlands*, ⁵*Biomedical Engineering, Erasmus MC, Netherlands*,

⁶*Thorax Center, Erasmus MC, Netherlands*, ⁷*Faculty of Applied Science - ImPhys, TU Delft, Netherlands*

Background, Motivation, and Objective

Image-guided minimally-invasive treatment has become a viable and safe option for many cardiac diseases, including structural and electrophysiological conditions. Intracardiac echography (ICE) is a robust and versatile technique to visualize cardiac anatomy and interventional devices. Commercially available ICE catheters provide a 2D image acquired with a side-looking linear array transducer: these are complex, expensive disposables. In this work, we set out to demonstrate 3D imaging from a simple, forward-looking (FL) single element catheter.

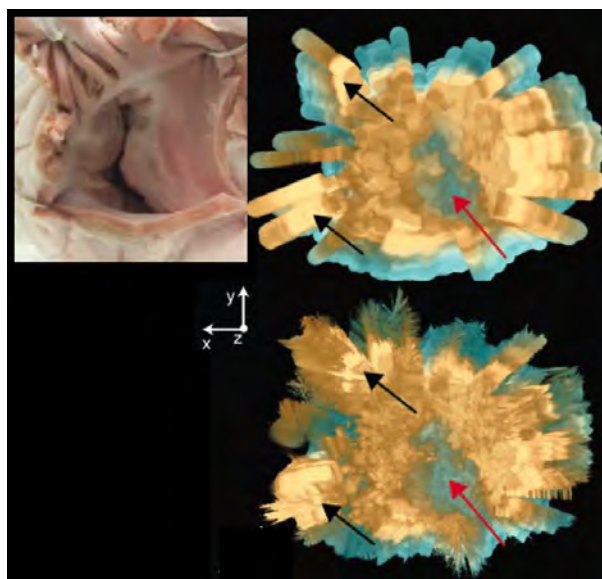
Statement of Contribution/Methods

We investigated FL 3D imaging by integrating a 7 MHz single-element ultrasound transducer at the tip of a custom-built multi-steerable intracardiac catheter with an integrated optical shape sensing fiber (OSS), which allows us to position and orient the ultrasound A-scans. We tested the imaging capability of the integrated device on an ex-vivo pig heart. By continuously acquiring ultrasound data at different locations while steering the catheter tip, a sparse 3D image is obtained. To reconstruct a volumetric image from the sparse data we implemented an adaptive Normalized Convolution (NC) algorithm where the dimension, orientation and angle of the 3D anisotropic kernel change dynamically according to the scanning path.

Results/Discussion

We acquired A-scans of the tricuspid valve and computed the 3D image using NC with both an isotropic kernel and an anisotropic kernel, interpolating the sparse data to obtain volumetric images. With an anisotropic kernel, a 3D reconstruction is achieved with more detail compared to the reconstruction obtained using an isotropic kernel. It successfully visualized key anatomic details of the valve and annulus. This experiment demonstrates the potential of FL image guidance during intracardiac procedures using a single-element transducer integrated in a steerable catheter with an OSS fiber.

Figure: 3D depth-colored rendering of the porcine tricuspid valve (inset) obtained with serial A-line scanning, steering the probe tip, and processing with isotropic normalized convolution (top) compared to adaptive normalized convolution with an anisotropic kernel (bottom). Red arrow: valve; black arrows: needles. Dynamic range is 50 dB.



Sonopill: Progress Towards Microultrasound Capsule Endoscopy

Holly Lay¹, Gerard Cummins², Joseph Norton³, Yongqiang Qiu¹, James Martin³, Christina Lemke¹, Rachael McPhillips¹, Mohammed Al-Rawhani¹, James Beeley¹, Piotr Slawinski⁴, Fraser Stewart⁵, Mihnea Vlad Turcanu¹, David Cumming¹, Pietro Valdastrì³, Eddie Clutton⁶, Inke Nähke⁵, Marc P.Y. Desmulliez², **Sandy Cochran¹**

¹School of Engineering, University of Glasgow, Glasgow, United Kingdom, ²School of Engineering and Physical Sciences, Heriot-Watt University, Edinburgh, United Kingdom, ³University of Leeds, United Kingdom, ⁴Vanderbilt University, United States, ⁵Cell and Developmental Biology, University of Dundee, Dundee, United Kingdom, ⁶5. Royal (Dick) School of Veterinary Studies, University of Edinburgh, United Kingdom

Background, Motivation, and Objective

Video capsule endoscopy (VCE) is now well-established as a diagnostic tool for gastrointestinal (GI) diseases, with more than 4 million devices used to date and new applications emerging, e.g. in diagnosis of stomach and colon cancer. Microultrasound (μ US) capsule endoscopy (μ USCE) is a potentially valuable complementary technique, allowing imaging of features within the thickness of the gut wall.

The work reported here was motivated by the need to establish the feasibility of μ USCE and the devices required to realise it. The objectives were (1) to demonstrate detection of tissue features corresponding to GI diseases including inflammation and cancer, (2) to develop initial prototypes for use *in vivo* in large animal models and to test technical compatibility with other diagnostic modalities, and (3) to gain results from experiments *in vivo* to validate the performance of these prototypes.

Statement of Contribution/Methods

Detection of relevant tissue features was explored using genetically-adapted mouse models for cancer and mice with diets modified to create a model of inflammation. Tissue from these models was resected and imaged with high-sensitivity, broadband piezocomposite transducers operating at centre frequencies in the range $20 < f_c < 55$ MHz ($75 > \lambda > 28$ mm). Resected human tissue was also scanned.

Initial prototypes included custom-made integrated electronics operating μ US devices principally at 30 MHz and the same capabilities were also incorporated in a multimodal device for hybrid VCE / μ USCE. A porcine model was developed for *in vivo* testing in the oesophagus, small bowel and colon and data were collected, processed and assessed clinically.

Results/Discussion

Indications of inflammation and of early tissue dysplasia characteristic of cancer were obtained from the murine models. Bespoke experimental prototypes designed for use *in vivo* were characterised successfully on the bench and were then applied in more than 10 terminally-anaesthetized healthy female Landrace X pigs under UK Home Office License PPL PF5151DAF. μ US images were obtained and hybrid VCE / μ USCE was demonstrated. This work has established the potential value of μ USCE as a complementary technique to VCE and its viability for use *in vivo* for examination of the GI tract.

P2-B9 - Spectral Doppler and Clutter Filters

Waraku (posters 2)

Wednesday, October 24, 9:30 AM - 4:00 PM

Chair: **Jorgen Avdal** Norwegian University of Science and Technology

P2-B9-1

Spectral Doppler Measurements with 2-D Sparse Arrays

Paolo Mattesini^{1,2}, Alessandro Ramalli^{1,3}, Emmanuel Roux⁴, Lorena Petrusca², Hervé Liebgott², Olivier Basset², Piero Tortoli¹

¹*Microelectronics Systems Design Lab, University of Florence, Italy*, ²*CREATIS, Univ Lyon, INSA-Lyon, Université Claude*

Bernard Lyon 1, UJM-Saint Etienne, CNRS, Inserm, Lyon, France, ³*Lab. on Cardiovascular Imaging & Dynamics, Dept. of Cardiovascular Sciences, KU Leuven, Leuven, Belgium*, ⁴*Laboratoire Hubert Curien, Univ Lyon, INSA-Lyon, Université Claude Bernard Lyon 1, UJM-Saint Etienne, CNRS, Inserm, France*

Background, Motivation, and Objective

2-D arrays allow extending Doppler velocity measurements to an entire volume. The use of 2-D sparse arrays may be particularly attractive since such arrays reduce the channel count and may be coupled to a scanner by means of cables of reasonable dimensions. The aim of this work was to experimentally assess how the use of sparse rather than full gridded arrays impacts on spectral Doppler measurements.

Statement of Contribution/Methods

The 1024 elements of a 3 MHz 2-D array probe (Vermon, Tours, F) were individually connected to four synchronized Verasonics Vantage 256 systems. These were programmed to activate 3 sets of elements: all active (ref1024); 256 randomly selected (rand256) and 256 optimally (10.1109/TUFFC.2016.2614776) selected (opti256). 3-5-7 cycles of 3 MHz square waves were used to focus the beam at 40 mm depth into a disc-shaped homogeneous agar phantom, rotating at two speeds ($\omega=100$ or $200^\circ/\text{s}$). For each experiment, two steering angles were tested: $\theta=0^\circ$ and $\theta=12^\circ$. Raw echo-data were acquired; the related 128-point Doppler spectra were computed off-line and compared in terms of mean Doppler frequency (Fm), -6dB bandwidth (BW) and SNR.

Results/Discussion

The measurement results obtained by transmitting 3-cycle bursts and $\omega = 100^\circ/\text{s}$ are summarized in the Table. The estimation of Fm for $\theta=0^\circ$ is not affected by sparsity, while it is marginally affected for $\theta=12^\circ$ (max difference between ref and sparse arrays: 1.3 % of the Nyquist velocity). Similarly, BW is marginally affected by sparsity (max difference: 6.7%). However, as expected, SNR is attenuated by 6-9 dB ($\theta=0^\circ$) or 8.5-10 dB ($\theta=12^\circ$); on average, opti256 performs 1.4dB better than rand256. Equivalent results were obtained for all other settings.

In conclusion, the results of spectral Doppler measurements are not significantly affected by the use of sparse arrays rather than a full gridded array. Even the spectrum shape didn't appreciably change. Nevertheless, SNR is significantly affected, but experimental tests have confirmed that the SNR may be improved by 6dB exciting the sparse array probe elements with higher voltage, to produce the same focal pressure as the full array. This SNR recovery might be important in applications with critical SNR conditions.

| | 0° steering | | | 12° steering | | |
|--|-------------|-------|----------|--------------|-------|----------|
| | Fm | BW | SNR (dB) | Fm | BW | SNR (dB) |
| Ref1024 | 0,066 | 0,052 | 46 | 0,032 | 0,031 | 45 |
| Rand256 | 0,065 | 0,047 | 36,7 | 0,037 | 0,034 | 34,7 |
| Opti256 | 0,066 | 0,05 | 40,3 | 0,034 | 0,034 | 36,4 |
| <i>Fm and BW are normalized to PRF/2</i> | | | | | | |

A New Flow Disturbance Mapping Technique Based on Doppler Bandwidth Measurements

Billy Y. S. Yiu¹, Guo Tang², Alfred C. H. Yu¹

¹Schlegel-UW Research Institute for Aging, University of Waterloo, Waterloo, ON, Canada, ²Bioprober Corporation, Seattle, WA, United States

Background, Motivation, and Objective

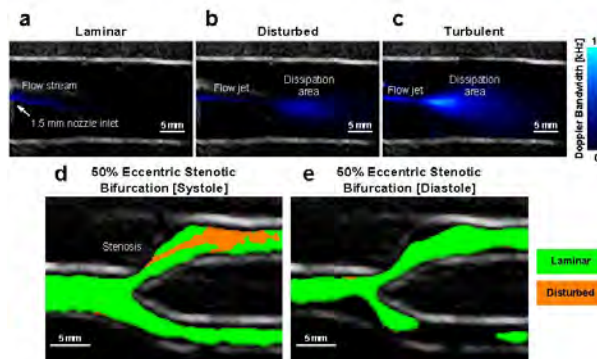
Flow disturbance has been shown to contribute to the initiation and development of atherosclerosis that may eventually lead to the onset of a cardiovascular event. Yet, previously it has been challenging to classify flow disturbance non-invasively using ultrasound due to inadequate time resolution on an image level. To overcome these issues, we have devised a new high frame rate Doppler ultrasound technique that can quantitatively identify flow disturbance zones by measuring the instantaneous Doppler bandwidth (BW). This new technique leverages the fact that disturbed flow and turbulence are marked by a presence of a wide velocity range within a range gate over a short period.

Statement of Contribution/Methods

Our framework is based on: 1) full-view insonation by plane wave transmission; 2) coherent full-view image formation by parallel beamforming; 3) simultaneous slow-time sampling for all pixels; 4) spectral estimation by autoregressive (AR) modeling of Doppler signal. Altogether, they enable consistent derivation of Doppler power spectral estimate (PSE) and measurement of Doppler BW, and in turn the velocity range within different range gates. The proposed method was evaluated on a straight tube flow model with flow conditions from laminar to turbulent flow. Using a SonixTouch scanner and an L14-5 array, pre-beamform RF data were collected with steered plane wave (-10°, 5-cycle 5MHz pulse; 10 kHz PRF). Parallel beamformed from RF data, coherent images were clutter filtered and then AR modelled along slow time. For each pixel, the AR modeling took 256 samples and estimated the corresponding PSE using Burg's method. From the PSE, Doppler BW is measured at FWHM. This process is repeated to generate Doppler BW maps at multiple time instances.

Results/Discussion

Fig. a-c respectively show the averaged Doppler BW map acquired under different flow conditions. The turbulent flow showed the highest BW at the flow jet and the dissipation area, while disturbed and laminar flow showed mid and lowest BW. From this, the proposed method can classify flow regions into laminar, disturbed or turbulent flow based on the Doppler BW, as demonstrated by Fig. d and e when applied to a stenotic bifurcation model with 20 ml/s systolic flow rate. The disturbed flow region at ICA was highlighted by the orange color during systole; the flow region turned green as the flow returned to laminar at diastole.



Sparse Transmission Strategy for Transverse Doppler Spectrum Estimation**Regev Cohen¹, Ruud J. G. van Sloun², Yonina Eldar¹**¹*Technion, Haifa, Israel*, ²*Eindhoven University of Technology, Netherlands***Background, Motivation, and Objective**

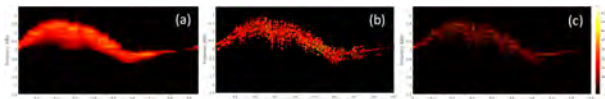
plex ultrasonography is a non-invasive imaging modality which allows visualizing anatomical structures of the body (B-mode) and the blood velocity distribution at a chosen point a spectrogram (Doppler mode). While high-resolution B-mode imaging is attained using wide-band pulses, high spectral resolution Doppler is achieved with narrow-band pulses. atry for alternating B-mode and Doppler emissions is required, leading to deterioration of the B-mode frame rate. Moreover, conventional approaches do not assess flow trans am direction, thus providing only partial information about blood flow.

Statement of Contribution/Methods

present a sparse transmission strategy and signal recovery approach which allows reconstruction of the transverse blood spectrum from a significantly decreased amount of tr cently, a sparse Doppler emission scheme, referred to as nested sampling, was introduced to recover axial blood spectrum using reduced number of transmissions. In this paper, we sted emission pattern with a transverse oscillation technique (TO) to enable measurement of the transversal flow velocities. Two real-time techniques for recovering the trans ectrum are presented. The first assumes that the Doppler frequencies lie on the Nyquist grid and reconstructs the transverse spectrum with enhanced resolution. The seco ntinuous recovery with no grid assumptions, thereby avoiding spectral leakage.

Results/Discussion

The proposed combined scheme is evaluated using realistic Field II simulations for pulsating flow from the femoral artery. For an observation window consisting of 256 pulses, Fig. 1(a) shows the transverse spectrogram reconstructed by Welch's method with no apodization. Fig. 1(b) and Fig. 1(c) show the transverse spectrograms of the continuous and discrete recovery methods respectively. Both latter spectrograms are reconstructed from the nested sparse emission pattern, sending only 31 Doppler pulses out of 256 (12%). Both proposed methods result in precise recovery of the transverse spectrum with fewer emissions, thereby enabling a duplex mode in which B-mode images are updated frequently while the axial and transverse blood velocities are displayed.



Motion Tracking using Neural Networks for a 2D Sample Volume based Spectral Doppler Imaging

Jihye Baek¹, Jinbum Kang¹, Ilseob Song², Yangmo Yoo¹

¹Electronic Engineering, Sogang University, Seoul, Korea, Republic of, ²Sogang University, Seoul, Korea, Republic of

Background, Motivation, and Objective

The objective of this study is to enhance the sensitivity in spectral Doppler imaging with tissue movement. Due to nonstationary tissue motions, it is impossible to continuously monitor hemodynamics with a conventional spectral Doppler imaging where 1D sample volume (SV) is used. However, the motion may be traced with 2D SV, which is generated by using wide-beam transmission and multi-beam receive beamforming.

Statement of Contribution/Methods

In this paper, a new motion tracking method based on Neural Network (NN) is proposed for 2D SV spectral Doppler imaging. As shown in Fig. 1(a), wide-beam transmission was performed by 13-mm line focusing with hamming apodization and 32 multi-beam scanlines were reconstructed without lowering pulse-repetition frequency (PRF). For motion tracking, the previous single scanline of blood flows, tissue signals and their derivatives in 1D SV is assigned to an input prototype vector in a modified Hamming Network of NN. Similarly, the current 32 scanlines from 2D SV are used as a weight vector. In the modified Hamming Network of NN, the correlation between the previous single scanline and current 32 scanlines is computed and the most competitive scanline is selected as an output scanline for updating a spectrogram in the 2D SV based spectral Doppler imaging.

Results/Discussion

The performance of the proposed method was evaluated with Field II simulation and *in-vivo* studies. In the Field II simulation, respiratory motion ($f=0.4259$) was applied as global motion. With the proposed motion tracking method based on NN, as shown in Fig. 1(b), output scanlines were correctly classified 70.2% (± 0.5 scanline) and 87.6% (± 1 scanline). In addition, the proposed method successfully represents pulsatile flows in the presence of respiratory motion while the spectrum disappears in the conventional spectral Doppler imaging with 1D SV as shown in Fig. 1(c).

In vivo-study was also performed in carotid artery using an ultrasound research platform (Vantage 128, Verasonics Inc., Kirkland, WA, USA) with a 5.2-MHz linear array transducer. In this case, the lateral movement was tracked and the signal-to-noise ratio of blood flow signal is increased by 2.5 dB in Fig. 1(d). This study represents that the proposed 2D SV based motion tracking method with NN can enhance image quality of spectral Doppler imaging by compensating of tissue movements.

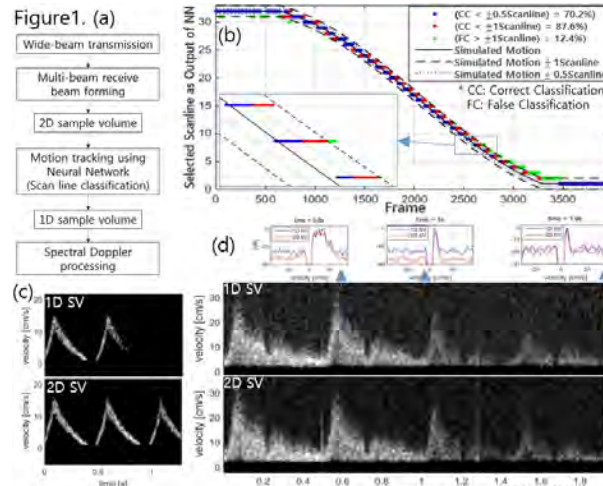


Figure 1. (a) the block diagram of the proposed motion tracking method based in Neural Networks, (b) correct and false classification results with the simulated motion, (c) spectral Doppler image with 1D and 2D SV approaches from the Field II simulation, and (d) spectral Doppler image with 1D and 2D SV approaches from the carotid *in vivo* study.

Low-Complexity Rank-revealing Spatiotemporal Microvascular Clutter Filter**John Flynn¹**¹*Verasonics, Inc, Kirkland, WA, United States***Background, Motivation, and Objective**

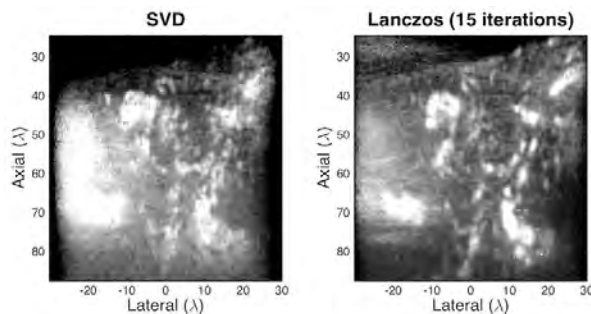
Effective clutter rejection filters are critical to detection performance in microvascular Doppler flow planewave (PW) imaging, for example in mouse brain studies. The use of the singular value decomposition (SVD) as a tool for approximating the clutter image sequence has provided successful spatiotemporal (ST) decluttering for some of these applications. However, the need to adapt to local pixel neighborhood motion dynamics has guided the use of the SVD toward approximating many overlapping small neighborhoods. Unfortunately, the SVD is computationally intensive, and has been resistant to efficient implementation in the small-neighborhood regime typical for microvascular data. This motivates alternate approaches to the SVD for ST clutter filtering.

Statement of Contribution/Methods

As an alternative to the SVD for computationally-efficient ST clutter filtering, we evaluate a technique employing matrix bidiagonalization (BD). This rank-revealing decomposition is based on Lanczos iterations, and constructs a bidiagonal orthogonal factorization while incurring a computation cost dominated by matrix-vector multiplications. In one formulation we evaluate, this matrix is the Casorati matrix of the pixel neighborhood scattering estimates resulting from PW imaging reconstruction of a Doppler acquisition ensemble. Because the BD weights are ordered, termination after R iterations sets the model rank to be R. Thus, the low-rank nature of the tissue clutter data ensures good approximation without requiring complete decomposition, so that the flow signal is readily computed by the orthogonal complement. The resulting clutter filtering is effective in microvascular Doppler PW imaging applications, and uses operations efficient in contemporary numeric libraries.

Results/Discussion

Using PW reconstructions of a thyroid measured at 5MHz, we demonstrate the effectiveness of the Lanczos-based BD, and compare to that of the SVD. Clutter rank R is dictated by the algorithm iteration count, which we set to values ranging from 15 to 45 for a 10-wavelength pixel neighborhood to give effective clutter rejection. Computation time is improved several times over, and resulting Doppler imagery is effectively reproduced as shown in the figure.



Efficient and flexible spatiotemporal clutter filtering of high frame rate images using subspace tracking

Bas Generowicz¹, Geert Leus¹, Sadaf Soloukey Tbalvandany^{2,3}, Bas van Hoogstraten², Christos Strydis², Johan G. Bosch⁴, Antonius F. W. van der Steen⁴, Chris de Zeeuw^{2,5}, Bas Koekkoek², Pieter Kruizinga^{2,4}

¹*EWI, TU Delft, Netherlands*, ²*Department of Neuroscience, Erasmus MC, Netherlands*, ³*Department of Neurosurgery, Erasmus MC, Netherlands*, ⁴*Thorax Center, Erasmus MC, Netherlands*, ⁵*Netherlands Institute of Neuroscience, Royal Dutch Academy for Arts and Sciences, Netherlands*

Background, Motivation, and Objective

Ultrafast Doppler imaging has gained popularity due to its high temporal resolution which is required to distinguish blood motion from slow moving tissue. To remove the clutter signals associated with the slow moving tissue, a Singular Value Decomposition (SVD) has been shown to be effective [1]. Conventionally the SVD is calculated from an ensemble of frames after which the first dominant eigenvectors, are removed. The Power Doppler Image (PDI) is then computed by averaging over the remaining components. This technique has two drawbacks: it is 1) computationally intensive, and 2) not flexible, as it requires a fixed ensemble length. Here we present a computationally efficient method allowing us to sequentially estimate and remove the principle components, while also offering flexibility for calculating the PDI, e.g. by using any averaging filter.

Statement of Contribution/Methods

Our method uses the PASTd algorithm [2], which is an iterative method that processes images sequentially. At every iteration, the algorithm has as input a data vector $\mathbf{x}(t)$, corresponding to a new ultrasound image. The projections of the data vector onto the r most dominant eigen components are sequentially removed, leaving a new data vector containing only the components of the blood motion signal. Furthermore, these r most dominant eigenvectors are updated using the new image. The PASTd algorithm has a computational complexity of $O(n \times r)$ while the SVD method maintains a complexity of $O(n \times n_e^2)$ where n is the length of the data vector and where n_e is the ensemble length.

Results/Discussion

Figure 1(a) shows a PDI of a mouse brain, obtained using a 28 MHz linear array transducer coupled to an ultrasound system (Vantage 64-LE). Figure 1(b)-(c) shows for the two different methods, the intensity variations over time for one PDI pixel during a functional measurement. For functional ultrasound these signals are correlated with a known stimulus pattern. The SVD method provides a Pearson correlation coefficient of 0.24 for the unfiltered, and 0.49 for the smoothed PDI pixel. We used moving average filters of lengths 100 and 800 to calculate the PDI for the PASTd method, which resulted in a correlation coefficient of 0.33 and 0.55 respectively, highlighting the potential of the PASTd method for use in ultrafast Doppler imaging.

[1] Demené et al., IEEE Trans. Med. Imag., 2015

[2] Bin, IEEE Trans. Sig. Proc., 1995

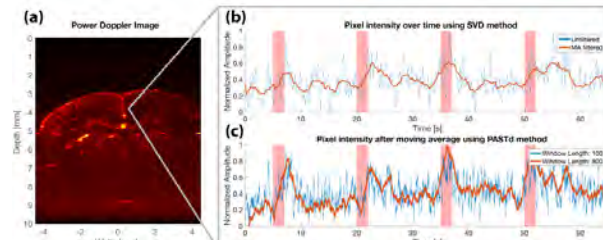


Figure 1: Efficient and flexible spatiotemporal clutter filtering of high frame rate images using subspace tracking
 (a) A Power Doppler Image of the vasculature of a mouse brain obtained with the PASTd method. (b) The PDI pixel intensity over time using the conventional SVD spatiotemporal clutter filter. Red box - Applied stimulation duration. Blue line - Unfiltered intensity of a pixel over time. Orange line - Pixel intensity after moving average. (c) The pixel intensity using the PASTd method for the same pixel as with the SVD method. Blue line - Pixel intensity after moving average filter of window length 100. Orange line - Pixel intensity after moving average filter of window length 800.

Low-Rank Adaptive Clutter Filtering for Robust Ultrasound Vector Flow Imaging

Yigang Du¹, Mengyi Zhang², Alfred C. H. Yu³, Weichuan Yu⁴

¹Shenzhen Mindray Bio-Medical Electronics Co., Ltd., Shenzhen, China, People's Republic of, ²Department of Computer Science and Engineering, The Chinese University of Hong Kong, Hong Kong SAR, China, People's Republic of, ³Schlegel Research Institute for Aging, University of Waterloo, Waterloo, ON, Canada, ⁴Department of Electronic and Computer Engineering, The Hong Kong University of Science and Technology, Hong Kong SAR, China, People's Republic of

Background, Motivation, and Objective

Multi-angle plane wave vector flow imaging (VFI) can measure vector velocities of blood flow at a high frame rate. But the blood signal is weak due to unfocused plane wave. The clutter noise is very strong due to the scattering of ultrasound waves from surrounding tissue, vessel wall and its motion at systole. Reducing clutter noise and influence of wall motion is therefore much desired to improve plane wave based VFI.

Statement of Contribution/Methods

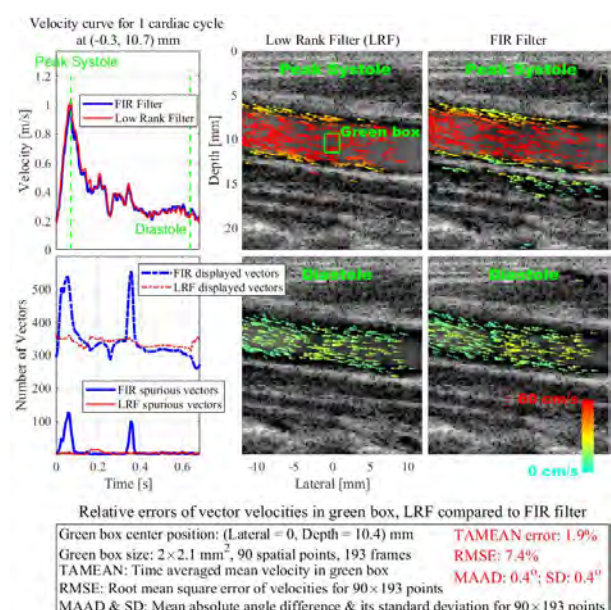
We assume that the beamformed M×N image is composed of clutter and flow signal. A series of slow-time beamformed images can be represented as a 2D matrix with each column of the matrix denoting one beamformed MN×1 image. Thus, the 2D matrix is the sum of one clutter matrix and one flow signal matrix. The rank of the clutter matrix should be small as the strength from tissue reverberation echoes is much stronger than the backscattered red blood cell echoes, and the flow signal matrix should be spatially sparse as the image contains both tissue and blood flow. In this way, we formulate a signal decomposition problem with penalty on rank and sparsity. This is non-convex optimization, but can be relaxed as a convex problem by using a nuclear norm to replace the rank penalty and using the ℓ_1 norm to enforce the sparsity. The convex problem is solved by Inexact ALM [1]. The number of columns of the low rank filter (LRF) is adaptively determined based on the mean velocities in the current and previous frames. The weighting coefficient between the nuclear norm and ℓ_1 norm is selected based on the number of displayed vectors in the current and previous frames. Data from a common carotid artery are beamformed, and then decomposed by LRF, and also processed by a conventional FIR high-pass filter as benchmark for comparison. The vector velocities are generated using VPI [2].

[1] Lin et al. UILU-ENG-09-2214, 2010

[2] Yiu et al. UMB, 40(9):2295-2309, 2014

Results/Discussion

One cardiac cycle in-vivo data containing 193 frames are used for comparison studies. The number of spurious vectors outside the vessel due to the tissue motion, and total displayed vectors are counted for each frame. By LRF, the average displayed/spurious vectors per frame are 337.7/3.5, and by FIR filter is 345.4/12.2. The figure clearly shows that the spurious vectors are largely reduced by LRF, particularly at the peak systole. Relative errors of vector velocities in green box are shown in the figure.



Spatial and Temporal Adaptive FIR Clutter Filtering

Vincent Perrot¹, Jørgen Avdal², Lasse Lovstakken², Sébastien Salles², Didier Vray¹, Hervé Liebgott¹, Ingvild Kinn Ekroll^{2,3}

¹CREATIS, Univ.Lyon, INSA-Lyon, UCB Lyon 1, UJM-Saint Etienne, CNRS, Inserm, Villeurbanne, France, ²Department of Circulation and Medical Imaging, Centre for Innovative Ultrasound Solutions (CIUS), NTNU, Norway, ³St Olavs Hospital, Norway

Background, Motivation, and Objective

Clutter filtering is an important step in flow estimation. Ideally the cutoff frequency of the filter should be chosen in accordance with the tissue velocity. A too high frequency will remove signal from blood scatterers while a low value will not sufficiently suppress the clutter signal. Because the tissue velocity changes during the cardiac cycle, temporal adaptive filters can perform better than the non-adaptive ones (Ekroll *et al.*, 2017). In order to take into account the spatial tissue velocity variation, a spatial and temporal adaptive FIR filter was developed.

Statement of Contribution/Methods

Carotid arteries were imaged with a Verasonics Vantage 256 system and a linear array probe. An ultrafast ultrasound sequence was used based on horizontal plane waves. Axial tissue velocities were extracted with a phase-based estimator. Afterwards, three FIR clutter filters were compared: *i*) Standard with one cutoff for the whole sequence based on the maximum tissue velocity; *ii*) Adaptive, with a temporal adaptive cutoff depending on the maximum tissue velocity at each frame; *iii*) Spatial and temporal adaptive, where the filter cutoff is computed locally based on the estimated tissue velocities and a measured point spread function. After clutter filtering, transverse oscillations were introduced in the Fourier domain and 2D vector velocities were estimated using a phase-based estimator.

Results/Discussion

Fig 1 shows that the standard filter approach yields the least robust velocity estimates close to the wall. The two adaptive filters are more robust in time than the non-adaptive and yield similar velocity estimates. In fact, the temporal evolution of the flow is close to identical when estimated by the two adaptive filters (Fig. 1 b and d). The spatial and temporal adaptive filter enables estimation of the flow profile a little closer to the wall than the others (Fig. 1 c). However, prior to estimation of e.g. wall shear stress, both adaptive filters would outperform the standard filters in periods of low flow velocity (e.g. diastole). In conclusion, this *in vivo* study shows that in terms of velocity estimation (both spatial and temporal) the two adaptive filters have very similar performance. Due to the higher computational cost of the spatiotemporal filter, however, the temporal adaptive FIR seems sufficient.

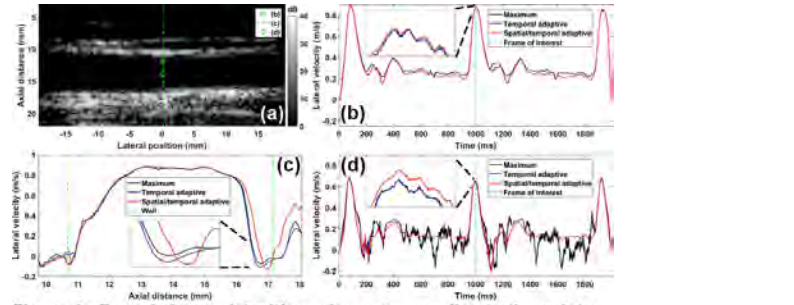


Figure 1 - B-mode image (a) with marks corresponding to the points for extracting the temporal evolution of the flow in the center of the lumen (b) and close to the wall (d) and the flow profile at a specific time along the central element (c). The dashed green lines in (b) and (d) correspond to the time when the flow profile (c) is showed. In (c) the dashed green lines show the position of the artery wall. Three close-up views allow better distinguishing the differences of flow estimation between the three FIR methods. The standard approach, using one cutoff based on the maximum velocity is displayed in black. The temporal adaptive technique is showed in blue. Finally, the spatial and temporal method is in red.

Adaptive Independent Component Analysis-Based Clutter Filtering for Improved Non-Contrast Perfusion Ultrasound Imaging

Jaime Tierney¹, Don Wilkes¹, Brett Byram¹

¹Vanderbilt University, Nashville, TN, United States

Background, Motivation, and Objective

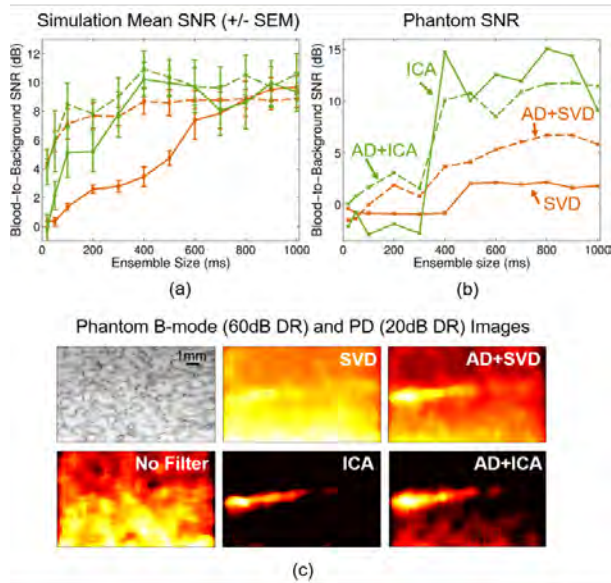
Tissue motion makes perfusion ultrasound imaging without contrast difficult. We previously developed an adaptive demodulation (AD) method to correct for this motion prior to tissue filtering. Additionally, 2D space and time eigen-based clutter filtering has been shown to be superior to conventional frequency domain filtering performed only in the slow-time dimension, especially when long ensembles are used. We have shown that combining AD with singular value decomposition (SVD) filtering can improve slow blood flow detection. Here, we aim to develop and evaluate an adaptive independent component analysis (ICA) approach to clutter filtering and compare it to adaptive SVD filtering with and without AD using simulations and a single vessel phantom.

Statement of Contribution/Methods

For the simulations we used a 0.5mm diameter vessel of blood scatterers within a 0.6 by 1cm area of tissue scatterers. Blood moved laminarly at a peak velocity of 1mm/s. Displacements estimated from hand motion phantom data were used to displace the tissue and blood to generate 6 tissue motion realizations. For the phantoms we used a polyvinyl alcohol and graphite mixture to make a phantom with a 0.6mm diameter vessel within a 2 by 3cm mold. A syringe pump was used to flow blood mimicking fluid through the vessel at an average velocity of 1mm/s. For both the simulations and phantom, a 9-angle plane wave sequence was used to acquire 1s of data at a PRF of 9kHz (1kHz frame rate) and a 7.8MHz frequency. SVD and a maximum likelihood approach to ICA were used for tissue filtering (both with adaptive cutoff selection). Blood-to-background signal-to-noise ratios (SNR) were computed on power Doppler (PD) images made using ensembles between 20ms and 1s. B-mode and PD images were scaled to individual maximums and fixed dynamic ranges (DR).

Results/Discussion

Figs. 1(a) and (b) show SNR for each filtering method and ensemble for the simulations and phantom, respectively. AD+ICA produces the highest simulated SNR for most ensembles and the highest phantom SNR for small ensembles. Fig. 1(c) shows phantom B-mode and PD images for the 400ms ensemble. The vessel is seen in the AD+SVD (3.7dB SNR) image, but the background is suppressed the best in the ICA (14.7dB SNR) and AD+ICA (10.1dB SNR) images. These results suggest that ICA filtering in combination with AD could further improve non-contrast perfusion ultrasound imaging.



P1-C10 - Liver

Kairaku (posters 1)

Thursday, October 25, 9:30 AM - 4:00 PM

Chair: **Michael Oelze** University of Illinois

P1-C10-1

Sensitivity analysis of reference-free quantitative ultrasound tissue classification.

Trong Nguyen¹, Minh Do², Michael Oelze²

¹Electrical and Computer Engineering, University of Illinois at Urbana Champaign, United States, ²University of Illinois at Urbana-Champaign, United States

Background, Motivation, and Objective

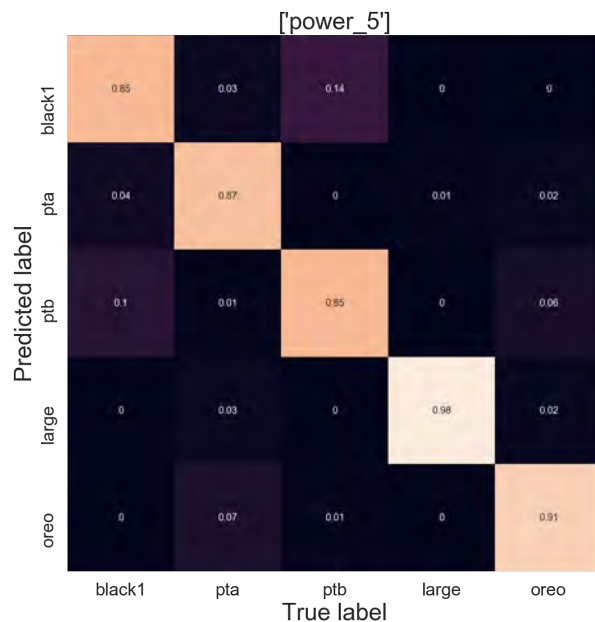
To implement spectral-based quantitative ultrasound (QUS), currently it is necessary to take a reference scan from a well-characterized tissue-mimicking material for each scanner setting that is used. The purpose of this study was to evaluate if a reference-free approach could be adopted, which would eliminate the need for multiple reference scans while still maintaining the ability to objectively classify different tissue states. Specifically, we utilized a convolutional neural network (CNN) to classify tissues and tissue-mimicking phantoms without taking a reference for each setting used and compared the performance to conventional QUS approaches using a reference phantom.

Statement of Contribution/Methods

Rabbits that were maintained on a high fat diet for 0, 1, 2, 3 or 6 weeks with three rabbits per diet group (total N = 60) were scanned ultrasonically and classified into two groups based on their liver lipid levels: low fat (< 8%) and high fat (> 8%). An array transducer L9-4 with center frequency of 4 MHz was used to gather RF backscattered data *in vivo* from the rabbits. In the conventional QUS approach, the RF signals were calibrated from a reference phantom and used to estimate an average BSC for each rabbit. In the reference-free approach, a CNN was trained on the time domain RF signals to classify the rabbit livers. To assess the reliability of the CNN to classify when the settings of the scanner were adjusted, five tissue-mimicking phantoms with different but known properties were scanned under different system settings: power, time gain compensation and number of transmit foci. The CNN was first trained on one system setting and then tested on data acquired from each phantom with the other settings. This was repeated for each individual setting. Finally, the CNN was trained with data from the phantoms using all settings combined and then tested for each individual system setting.

Results/Discussion

The testing accuracy of *in vivo* rabbit liver classification using the CNN without a reference was 73% compared to 68% when using the conventional QUS. The figure shows a confusion matrix when using the CNN to classify the phantoms by training on one setting and testing using a different setting. The results demonstrated that the CNN can accurate and robust classification without having to use a reference for each setting. This work was supported by a grant from the NIH (R21 EB020766).



Investigation of A Method for Quantifying Diffuse Liver Disease Based on Histogram of Ultrasound Signal-to-Noise Ratio

Takuma Oguri¹, Naohisa Kamiyama¹, Sachio Noguchi¹, Yuko Kanayama¹, Yudai Fujiwara², Tamami Abe², Yuriko Mikami², Hidekatsu Kuroda²

¹Ultrasound General Imaging, GE Healthcare, Hino, Japan, ²Division of Hepatology, Department of Internal Medicine, Iwate Medical University, Morioka, Japan

Background, Motivation, and Objective

Analysis of signal-to-noise ratio (SNR) of the ultrasound RF signals has potential to characterize a grade of the diffuse liver disease [e.g., H. Kuroda, World J. Gastroenterol, 2012]. However, since SNR decreases with fibrosis generation and increases with generation of fat droplets (steatosis), the analysis will have more difficulty in the combined situation (i.e., fibrosis generation in the fatty liver). In this report we proposed a method which enables to quantify steatosis and fibrosis separately from the mixed cases, and evaluated it with clinical data.

Statement of Contribution/Methods

RF signals for 194 consecutive chronic liver disease patients who underwent liver biopsy on the same day were acquired at transmission and reception frequency of 4.0 MHz. Ultrasound scanner LOGIQ E9 prototype (GE Healthcare) with a 3.5 MHz convex probe (C1-6-D) were used. Percentage of steatosis (PS) and fibrosis (PF) were calculated from bioptic specimens by ImageJ (NIH), and categorized as L0: [PS and PF < 5%], L1: [PS > 5% and PF < 5%], L2: [PS < 5% and PF > 5%], and [L3: PS and PF > 5%]. SNR average (SA), SNR standard deviation (SSD) and SNR histogram area ratio (SHAR) [%], which is a ratio of the areas which are smaller and larger than threshold in the normalized histogram of SNR, of a region of interest (ROI) was calculated from the RF signals of the corresponding B-mode image. As the calculation method, first local SNR was calculated by 4-kernels method, which four kernels surround a target pixel and maximum value of SNR of each kernel is calculated [T. Oguri, RCGI, 2017]. Second, SA, SSD and the normalized histogram of SNR were calculated. Finally, SHAR was calculated. A position of ROI was selected manually to avoid the diaphragm or large vessels. The threshold was defined by SA and SSD.

Results/Discussion

Fig. 1 shows the local SNR images of L0 (PS = 1.8% and PF = 3.5%) and L3 (PS = 20.7% and PF = 13.5%), and Fig. 2 shows the combination of SA and SHAR in all data. The value of SA varied according to the biopsy category, but there is no significant difference between L0 and L3 though the overall difference was shown in local SNR images (Fig.1). For the SHAR on the other hand, L0 and L3 showed significant difference, i.e., this 2D plot describes sufficient difference for all four categories. In conclusion, it is suggested that our proposed method can quantify fibrosis generation in the fatty liver.

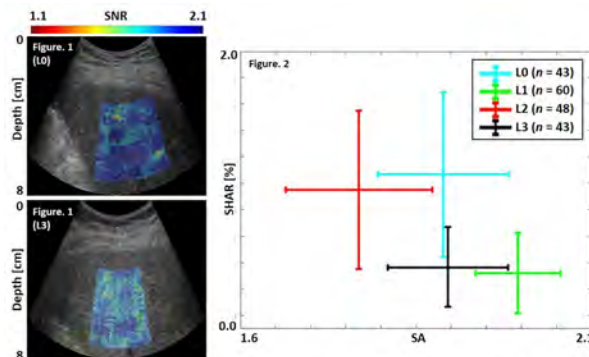


Figure 1 is the SNR image reconstructed local SNR values to the corresponding B-mode image, and Figure 2 is the relationship between SNR average (SA) and SNR histogram area ratio (SHAR). Percentage of steatosis of (L0) and (L3) are 1.5 % and 27.7%, respectively. Percentage of fibrosis of (L0) and (L3) are 3.8% and 20.7%, respectively.

Quantitative Ultrasound Spectroscopy to Differentiate Between Cirrhotic and Non-Cirrhotic Patients

Ahmed El Kaffas¹, Isabelle Durot², Jarrett Rosenberg³, Juergen Willmann²

¹Radiology, Stanford University, Stanford, CA, United States, ²Department of Radiology, School of Medicine, Stanford University, Palo Alto, CA, United States, ³Stanford, United States

Background, Motivation, and Objective

Liver fibrosis is a wound-healing response to chronic liver injuries that can result in serious hepatic conditions, including the development of cirrhosis and hepatocellular carcinoma. Histology following liver biopsy remains the standard of care for evaluating and grading liver fibrosis, but several non-invasive imaging modalities are being introduced to evaluate liver tissue and fibrosis. Quantitative ultrasound spectroscopy (QUS) is a promising tool that may enable quantitative assessment of tissue morphological and structural changes such as those that manifest through the development of fibrosis and cirrhosis. This study aimed to perform a clinical assessment of QUS parameters for differentiating cirrhotic from non-cirrhotic liver parenchyma.

Statement of Contribution/Methods

Data was obtained through a HIPAA-complied study approved by the institutional IRB. A total of 18 patients (12 male, 6 female) with confirmed cirrhosis were evaluated with QUS parameter measurements. Cirrhosis was confirmed with ultrasound or MR elastography. QUS measurements were obtained in 37 patients with no signs of cirrhosis (either confirmed by ultrasound/MR elastography or in healthy volunteers). For all patients, Ultrasound RF data was acquired using an Ultrasonix Tablet (Analogic) coupled to an C7-3/50 transducer. Data was acquired for each of the eight liver segments to survey the whole organ. Each liver location was imaged with 2 center frequencies (3.3 and 5 MHz) and 4 focal depths (3, 6, 9 and 12 cm), for a total of 8 sets of images per liver segment, per patient. ROIs were drawn by one observer on the liver parenchyma within the focus region, for each image acquired in each patient. The average normalized (using glass-bead phantom) power spectrum for each ROI was extracted and a linear regression was fit within the -6 dB bandwidth window of the power spectrum, from which the mid-band fit (MBF) was extracted. Differences in QUS parameters between the ROIs in cirrhotic vs healthy livers were tested by a student Mann-Whitney test.

Results/Discussion

Results suggest that for the 3.3 MHz frequency, QUS parameter can significantly ($p < 0.0001$) differentiate between cirrhotic and non-cirrhotic livers. The average MBF parameters in cirrhotic livers was 4.4 dBr (CI: 4.2 – 4.6 dBr), and 3.1 (CI: 2.9 – 3.2 dBr) in non-cirrhotic livers.

Envelope statistics and backscattered power-spectrum analysis of rat livers with high-frequency annular arrayTakeru Mizoguchi¹, Kazuki Tamura², Kenji Yoshida³, Jonathan Mamou⁴, Jeffrey Ketterling⁴, Tadashi Yamaguchi³¹*Graduate School of Science and Engineering, Chiba University, Japan*, ²*Graduate School of Engineering, Chiba University, Japan*,³*Center for Frontier Medical Engineering, Chiba University, Japan*, ⁴*Lazzi Center for Biomedical Engineering, Riverside Research, New York, NY, United States***Background, Motivation, and Objective**

High-frequency ultrasound (HFU, >20 MHz) and quantitative ultrasound (QUS) methods provide a means to understand the relationship between anatomical and acoustical characteristics. However, the depth of field (DOF) of HFU transducers is limited which also constrains the range where QUS parameters can be estimated. In this study, we aim to improve the accuracy of HFU QUS based-parameters on the envelope statistics and backscattered power-spectrum analysis by using an annular array that allows for an extended DOF.

Statement of Contribution/Methods

A 20-MHz annular-array transducer with 5 elements (total aperture: 10 mm, focal length: 26 mm) was employed for the measurements and data were obtained for each transmit-to-receive pair. Fresh excised control and fatty model rat livers were scanned with a 30- μm step size. The data were synthetically focused in post-processing. Histological images were also obtained from each liver. For the envelope statistics, we estimated the QUS parameters with a Nakagami distribution. For the backscattered power-spectrum analysis, we estimated the scatterer diameter and acoustic concentration. The size of ROI was decided as six times the resolution of each direction. The analyses were performed with data obtained from the whole of liver region.

Results/Discussion

Figure 1 shows the B-mode images, QUS parameters (μ of Nakagami distribution and estimated scatterer diameter) overlaid on B-mode and corresponding histology. The μ and scatterer size are homogeneous values versus depth for the annular array analysis. In fatty liver, the μ and scatterer size are larger than the control liver and the characteristics of living tissue confirmed by histology can be evaluated markedly. However, some compensations are necessary because backscattered power-spectrum analysis is not successful deeper into tissue because of acoustic attenuation. These results show improved accuracy-versus-depth compared to single-element transducers that display inhomogeneous values in the axial direction due to the influence of sound field characteristics.

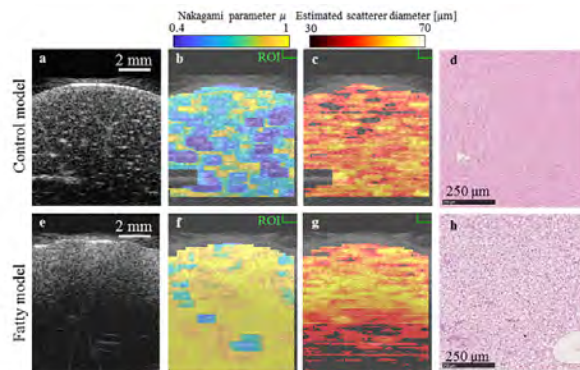


Fig. 1 Images of control (a-e) and fatty (e-h) model rat liver. (a, e) B-mode images. (b, f) and (c, g) QUS parameters (μ of Nakagami distribution and estimated scatterer diameter) overlaid on B-mode images. (d, h) Histological images.

Characterization of concentrated scattering media using ultrasound parametric imaging based on Homodyned-K Distribution

Jui Fang¹, Zhuhuang Zhou², Po-Hsiang Tsui³

¹*Ph.D. Program in Biomedical Engineering, Chang Gung University, Taiwan*, ²*College of Life Science and Bioengineering, Beijing University of Technology, China, People's Republic of*, ³*Medical Imaging and Radiological Sciences, Chang Gung University, Taiwan*

Background, Motivation, and Objective

Homodyned-K (HK) distribution and its approximation, Nakagami distribution, have been demonstrated as general models for ultrasound backscattering. Their parameters (μ parameter of HK distribution and m parameter of Nakagami distribution) have been extensively explored for scatterer concentration detection. Compared to the m parameter, the μ parameter works in differentiating concentrated media under fully developed speckle. However, the estimation of the μ parameter is more sensitive to the sample size, which further affects the performance of parametric imaging in scatterer characterization. This study explored the appropriate window side length (WSL) for reliably μ parametric imaging, which was further compared with the m image in characterizing concentrated media.

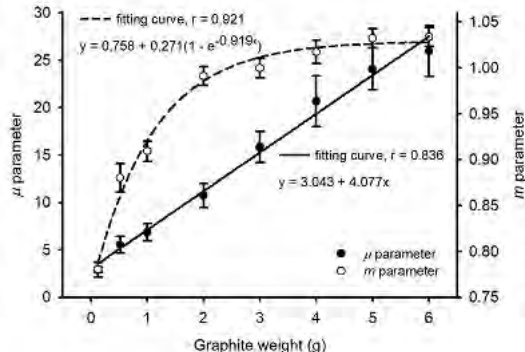
Statement of Contribution/Methods

We made agar phantoms by adding 0.13, 0.52, 1, 2, 3, 4, 5, and 6 g graphite powder with diameters $< 20 \mu\text{m}$ (Model 282863, Sigma-Aldrich, St. Louis, MO, USA) as acoustic scatterers. A commercial ultrasound scanner (Model 3000, Terason, Burlington, MA, USA) equipped with a 7-MHz linear array transducer (Model 10L5, Terason) was used to obtain the envelope data for parametric imaging. The pulse length of the transducer is 0.7 mm. To visualize changes in scatterer concentration, parametric images of μ and m were constructed through the standard sliding window technique using different WSLs. Parameters μ and m were obtained from XU (i.e., X- and U- statistics method) and moment-based estimators, respectively.

Results/Discussion

The m parameter increased and gradually reached a plateau ($m = 1$) with increasing graphite weight when WSL = 3 times the pulse length, which is well-known criterion as an appropriate WSL. We tested μ imaging using WSL ranging from 1 to 10 times the pulse length. The linearity between μ parameter and graphite weight was observed when WSL ≥ 5 times the pulse length. This study identified the minimum requirement of WSL for reliable μ parameter imaging, allowing scatterer characterization of concentrated media. This finding was also validated by rat models of liver steatosis (data were not shown due to word limits).

Fig. 1 Parameters μ (WSL = 5 times the pulse length) and m (WSL = 3 times the pulse length) as function of graphite weight.



Quantitative evaluation method for liver fibrosis in clinical ultrasound B-mode image based on optimized multi-Rayleigh model

Shohei Mori¹, Shinnosuke Hirata², Tadashi Yamaguchi³, Hiroyuki Hachiya²

¹Department of Electronic Engineering, Tohoku University, Japan, ²Department of Systems and Control Engineering, Tokyo Institute of Technology, Japan, ³Center for Frontier Medical Engineering, Chiba University, Japan

Background, Motivation, and Objective

To quantitatively evaluate liver fibrosis, we have focused on a property of probability density function (PDF) of ultrasound echo envelope. A multi-Rayleigh (MRA) model which is a mixture of Rayleigh (RA) distributions is a suitable model for expressing the PDF of echo envelope from the fibrotic liver [IEEE IUS 2016]. In previous studies, we addressed several challenges to quantitatively evaluate liver fibrosis using the MRA model in the clinical condition. In this paper, we integrated past achievements as the optimized MRA model and evaluated the clinical ultrasound B-mode image of fibrotic liver.

Statement of Contribution/Methods

Each RA component in the MRA model expresses each tissue in the fibrotic liver such as nodule, normal or fibrotic tissues; therefore, the fibrotic tissue characteristics can be evaluated using the fibrotic component parameters in the MRA model [IEEE IUS 2015]. However, in the clinical condition, a number of tissue components in the clinical B-mode image (i.e., a number of RA components in the MRA model) is unknown. In addition, there are non-speckled signals from such as small vessel walls which cannot be expressed by the MRA model. In the present study, we proposed an optimized MRA model to deal with these difficulties in the clinical condition. In the optimized MRA model, the effect of non-speckled signals was removed based on the amplitude distribution property and the number of RA components in the MRA model was adaptively changed based on the statistical property of echo envelope.

Results/Discussion

Figure (a) shows clinical B-mode images of normal (F0) and fibrotic (F1 – F3) livers with automatically determined ROI [IEEE IUS 2015]. Figure (b) shows a distribution of liver fibrosis parameters estimated by the optimized MRA model. The origin point is a condition of normal liver and shifts of the distribution to radial and angular directions indicate the increase of fibrotic tissues and progression of liver fibrosis, respectively. Figure (c) shows fibrotic probability images estimated using the optimized MRA model. Using the optimized MRA model, the fibrotic tissue characteristics could be quantitatively and correctly evaluated in the clinical condition; therefore, the change of estimated fibrotic tissue characteristics according to the liver fibrosis stage well corresponded to the actual tissue structural change caused by liver fibrosis.

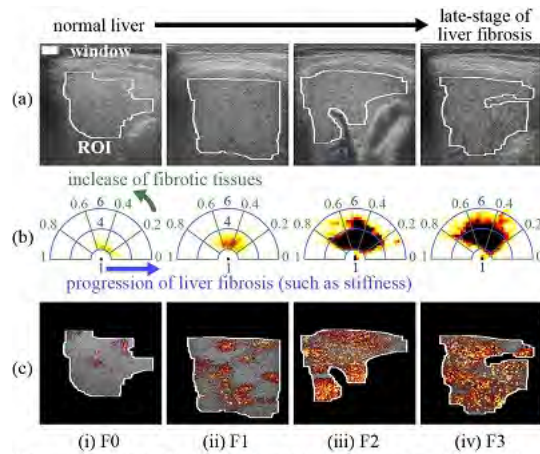


Figure (a) Clinical ultrasound B-mode image of (i) normal liver and (ii) early-stage, (iii) moderate-stage, and (iv) late-stage of liver fibrosis. (b), (c) Estimated results of (b) liver fibrosis parameters and (c) fibrotic probability image based on optimized multi-Rayleigh model.

Verification of frequency dependence and accuracy in backscatter coefficient analysis of fatty liver

Atsuko Yamada¹, Kazuki Tamura¹, Emilie Franceschini², Kenji Yoshida³, Tadashi Yamaguchi³

¹Chiba University, Japan, ²Aix-Marseille université, CNRS, Centrale Marseille, France, ³Center for Frontier Medical Engineering, Chiba University, Japan

Background, Motivation, and Objective

In order to establish quantitative ultrasound, research focusing on backscatter coefficient (BSC) using various frequencies is actively carried out. However, satisfactory discussion about appropriate measurement conditions and the theoretical model is not conducted. In this study, to understand scattering sources in fatty liver, the measurement and analysis conditions for accurately obtaining the BSC of the biological tissue are clarified by actual measurements using tissue mimicking phantoms as a basic study.

Statement of Contribution/Methods

10 phantoms were prepared containing scatterer with an average diameter of 5, 10 μm and with 1, 5, 10, 15 and 20 v/v%. The RF signal was measured with single element transducers with center frequency of 15, 25 MHz. The BSC was estimated using the reference phantom method with a 0.5 v/v% phantom for both scatterer diameter. Scatterer diameters were estimated using fluid spherical model (FSM), structural factor model (SFM), and particle model (PM).

Results/Discussion

Figure 1 shows the relationship between the actual volume fractions and the estimated scatterer diameter. In case of estimation results in 15 MHz, there is no difference depending on the volume fractions in scatterer diameter of 5 μm , but the accuracy decreases with high density in 10 μm . On the other hand, in case of estimation results in 25 MHz, the results of FSM and PM are approximated in both scatterer diameters. With a scatterer diameter of 5 μm , a large difference was confirmed between FSM and other models. The reason that the estimation accuracy decreases when the density is high (> 10%) is because the frequency is too low and the structure factor does not work effectively. In the case of Fig. 1(d), the estimation results have large error even if $0.5 < ka < 1.2$, which is a condition for obtaining theoretically high estimation accuracy. This is because the models used in this study are based on the assumption of the monodisperse scatterer diameter, but the actual scatterer has polydisperse diameters. This problem is expected even in case of the actual biological tissue. In current, we are pursuing further verification using some computed liver models with actual acoustic impedances of normal liver and fat droplets estimated by acoustic microscopy.

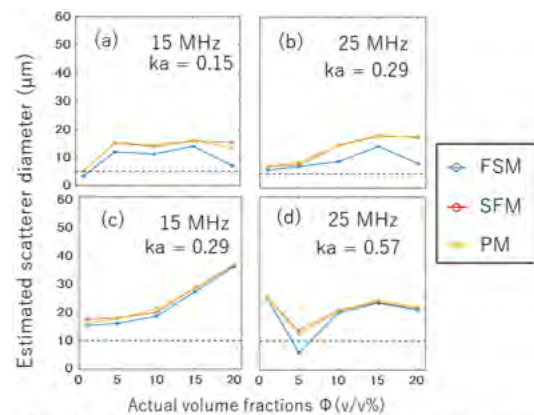


Figure 1 Estimated scatterer diameter from BSC. (a)(b)and(c)(d) are result of estimation with 5 and 10 μm diameter phantoms, respectively. (a)(c)and(b)(d) are result of estimation by 15 and 25 MHz, respectively. Actual diameters are illustrated as dashed lines.

P1-C11 - Applications of Therapeutic Ultrasound

Kairaku (posters 1)

Thursday, October 25, 9:30 AM - 4:00 PM

Chair: **Hong Chen** Washington University at St. Louis

P1-C11-1

Tumor Recruitment by Fusogenic Nanodroplets in Stem Cell-Mediated Drug-Delivery System

Yi-Ju Ho¹, Yu-Jung Chiang¹, Chih-Kuang Yeh¹

¹*Department of Biomedical Engineering and Environmental Sciences, National Tsing Hua University, Taiwan*

Background, Motivation, and Objective

Stem cell can be a biocarrier to passive delivery drugs into tumors because of the property of tumor recruitment. Since the real-time theranostic information of stem cell migration and drug release into tumors is lacking, the therapeutic efficiency of cellular drug delivery system during treatment is difficult to regulate. Acoustic phase-changed nanodroplets can be triggered to locally release drugs and generate bubbles under ultrasound stimulation. The process of acoustic droplet vaporization (ADV) provides an ability to be the theranostic agent for cellular drug delivery system. Moreover, the fusogenic ability of nanodroplets growing to microdroplets within a close-packed condition might be accomplished in the cytoplasm to improve the ADV efficiency. Therefore, present study investigated the feasibility of using camptothecin-loaded fusogenic nanodroplets (CPT-FNDs) as ultrasound theranostic agents in cellular drug delivery system.

Statement of Contribution/Methods

To fabricate the CPT-FNDs, 1.25 mg CPT and 75 μ L perfluoropentane were added in the lipid solution (molar ratio of POPC:POPE:cholesterol:DSPE-PEG-2000= 1:1:0.263:0.027) to sonicate 15 min. The *in vitro* fusion condition of 37 °C for 24 h was designed to simulate the environment of cytoplasm and evaluate the feasibility of CPT-FNDs fusion result in improving ADV efficiency and CPT release. Melanoma-bearing mice were intravenously injected 1×10^6 CPT-FNDs-loaded adipose-derived stem cells (ADSCs) for 24 h tumor recruitment. An image-guided focused ultrasound system (2-MHz, 12 MPa, 1000-cycle, PRF 18 Hz) was used to induce ADV for releasing CPT, generating bubbles, and causing physical damage within tumors. Finally, the intratumoral distribution of ADSCs was demonstrated by histological assessment.

Results/Discussion

The fusion ability of CPT-FNDs was demonstrated by the size growing (82 ± 4 to 1044 ± 28 nm) and ultrasound-triggered CPT release improving (22 ± 2 to $38 \pm 2\%$) in the fusion condition. After 24 h CPT-FNDs-loaded ADSCs migration, the intratumoral ADV-generated bubbles (increasing 3.24 ± 0.47 dB) and ADSCs distribution were showed on ultrasound and histological images to demonstrate the feasibility of theranostic information provided by CPT-FNDs. Therefore, the CPT-FNDs can be used as theranostic agents in cellular drug delivery system to provide the ultrasound contrast imaging, local drug release, and physical damage after ADV.

Catalase-Loaded Mesoporous Zeolite as Implantable Nanocapsules for Ultrasound-Guided Oxygen Self-Sufficient Photodynamic Therapy against Pancreatic Cancer**Zonghai Sheng¹, Zhuwen Chen², Dehong Hu¹, Teng Ma¹, Fei Yan¹, Mei Hong², Hairong Zheng¹**¹*Shenzhen Institute of Advance Technology Chinese Academy of Sciences, China, People's Republic of*, ²*School of Chemical Biology & Biotechnology, Peking University Shenzhen Graduate School, China, People's Republic of***Background, Motivation, and Objective**

Pancreatic cancer (PC) is one of the deadliest malignancies worldwide, and its five-year survival rate is less than 5% after diagnosis. Photodynamic therapy (PDT) as an alternative strategy has been employed for the minimally invasive therapy of the unresectable PC. It employs a photosensitizer, light, and oxygen (O_2) molecules to generate singlet oxygen (1O_2) for inducing PC cell apoptosis. However, tumor hypoxia microenvironment, a characteristic feature of solid tumors, severely reduces the 1O_2 generation efficacy, resulting low PDT efficiency and high recurrence rates. Previous works have demonstrated that catalase could efficiently decompose endogenous H_2O_2 (~50–100 μM) and in-situ produce O_2 gas bubbles inside the tumor tissue for regulating tumor hypoxia. Importantly, O_2 gas-releasing inside the nanocarriers enabled the enhanced ultrasound (US) contrast for specific guidance of PDT. However, the natural enzyme tends to be degraded rapidly during blood circulation by protease, resulting in inefficient accumulation in tumor tissue and low US contrast.

Statement of Contribution/Methods

Mesoporous zeolite (MZ) was prepared via a one-pot wet chemical method for highly efficient loading of catalase and photosensitizer for US imaging-guided PDT of PC. Upon implantation into the tumor region of mice under the US imaging guidance, MZ nanocapsule realized a highly efficient O_2 gas bubble release for overcoming tumor hypoxia and simultaneously enhanced US contrast, enabling sensitive US imaging-guided oxygen self-sufficient PDT of PC.

Results/Discussion

The average hydrodynamic diameter of MZ was measured to be 531 nm with a high Brunaure-Emmett-Teller (BET) surface area (101.59 m^2/g) and large pore volume (0.18 cm^3/g). The catalase immobilization efficacy was measured to be 145 mg/g. Under the US imaging guidance, the nanocapsule was accurately implanted into the tumor tissue. The MC nanocapsule-treated group showed slow formation of O_2 bubbles for US contrast enhancement. The generation of O_2 gas bubbles in tumor tissue facilitated to increase the oxyhemoglobin levels for enhancing PDT. The tumor growth was completely inhibited for 18 days after a single therapy with MC nanocapsule and light in mice model. The survival of tumor-bearing mice was significantly prolonged. Beyond the specific PDT using zeolite for delivery of photosensitizer, the nanomaterials may inspire other therapeutic methods that utilizes the zeolite for localized delivery and sustained release of chemotherapeutics and immune adjuvant for cancer combination therapy.

Investigation of Combined Sonodynamic and Radiotherapy for Pancreatic Cancer

Richard Browning¹, Sarah Able¹, Estelle Beguin², Heather Nesbitt³, Sukanta Kamila³, Eleanor Stride², Anthony McHale³, John Callan³, Katherine Vallis¹

¹University of Oxford, Oxford, United Kingdom, ²Engineering Sciences, University of Oxford, Oxford, United Kingdom,

³University of Ulster, Coleraine, United Kingdom

Background, Motivation, and Objective

Pancreatic cancer is a disease with poor prognosis. With a symptomless early progression, the cancer typically presents as a hypoxic, chemo- and radio-resistant tumour with desmoplasia. The current gold standard drug is gemcitabine, which modestly increases survival.

It has been shown that release of oxygen (O_2) from lipid microbubbles (MBs) can temporarily relieve tumour hypoxia. When combined with gemcitabine (Gem) and the sonosensitiser Rose Bengal (RB), this led to improved survival and tumour growth delay in a murine model¹. As radiotherapy (IR) is also enhanced by O_2 and Gem, a further combination is proposed (as shown in the Figure) to determine additional additive and synergistic effects.

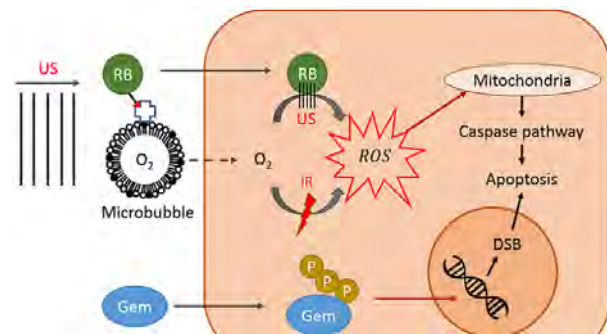
(1 - Nesbitt H et al. (2018) *J Control Release* 279:8-16)

Statement of Contribution/Methods

Biotinylated RB was prepared and bio-conjugated to a sulphur hexafluoride lipid MB. These were sparged with O_2 to form RB-loaded oxygen MB (O_2 MB-RB). O_2 MB-RB with ultrasound was tested *in vitro* with different combinations and timings of Gem and IR under normoxic and hypoxic conditions using pancreatic cell lines, with relative cytotoxic contributions determined by cell survival assays. Subcutaneous xenograft tumours were established in athymic nude mice and treated with combinations of O_2 MB, Gem and IR.

Results/Discussion

The IC₅₀ values for 24 hr Gem exposure for PANC-1 and PSN-1 cell lines were found to be 356 nM and 26.0 nM respectively under normoxia, and 704 nM and 31.2 nM under hypoxia. The combination of O_2 MB and RB was shown to generate singlet oxygen with an expected cytotoxic effect. Data from the *in vivo* experiments on tumour inhibition will also be presented. The sensitisation of cancer to radiotherapy by gemcitabine and oxygen loaded microbubbles, combined with cytotoxic sonodynamic therapy, would provide an inexpensive and effective method for management of pancreatic cancer.



Schematic concept of the proposed combination therapy. Ultrasound (US) causes microbubble release of Rose Bengal (RB) and O_2 in the tumour area. US activation of RB and radiation (IR) convert O_2 to reactive oxygen species (ROS) leading to mitochondrial damage and pro-apoptotic signals. Also, gemcitabine (Gem) enters cells and is phosphorylated (P). This form incorporates into DNA to cause double strand breaks (DSB) leading to apoptosis.

Accumulation of Magnetic Nanoparticles Employing High Intensity Focused Ultrasound for Drug Targeting ApplicationsMichael Fink¹, Benedikt George¹, Stefan J. Rupitsch¹, Helmut Ermert¹¹*Chair of Sensor Technology, University of Erlangen Nuremberg, Germany***Background, Motivation, and Objective**

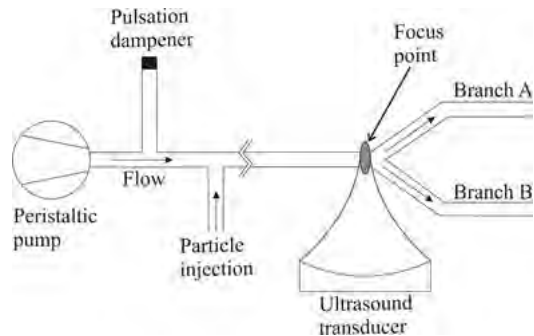
Magnetic Drug Targeting (MDT) is a cancer treatment technique that enables a local chemotherapy. In MDT, chemotherapeutic drugs are bound to magnetic nanoparticles and are accumulated in the tumor area by means of an external magnetic field. Unfortunately, a single magnet can only generate a pulling magnetic force. However, in some applications a pushing force on the nanoparticles could be advantageous. One possibility to do so is to exploit the acoustic radiation force caused by a high intensity focused ultrasonic transducer. In this contribution, we investigate the ability of ultrasonic waves for nanoparticle accumulation in drug targeting applications.

Statement of Contribution/Methods

In order to investigate whether the acoustic radiation force can be utilized to guide drug carrying nanoparticles through the vascular system, a test bench was built that emulates the anatomy of the vascular system. It contains a peristaltic pump, acting as the human heart, a damping element acting as the aorta and a pipeline that branches into sub-pipes acting as the actual network of bloodstreams (see figure). The focus of the ultrasonic transducer is adjusted to the branching point of the pipeline system. The transducer is positioned in such a manner that the pushing force on the nanoparticles should increase the particle concentration in branch A. To verify the change of particle concentration, the content of iron in both branches is determined using microwave plasma atomic emission spectrometry (Agilent MP-AES 4200).

Results/Discussion

The ultrasonic transducer emitted an ultrasonic wave at 835 kHz and the pressure value in the focus point was 0.63 MPa. This leads to a mechanical index of 0.69, which is below the maximum value that the FDA mandates for diagnostic ultrasound scanners. After the measurements, the particle concentration in each of the branches was determined. Without acoustic irradiation the branching point, the iron content was approximately 2918.7 µg/l in both branches. However, with acoustic irradiation the content of iron increased in branch A to 4379.5 µg/l (standard deviation 23.9 µg/l) and decreased in branch B to 2473.0 µg/l (standard deviation 70.2 µg/l). Therefore, the acoustic radiation force could be employed for particle accumulation in drug targeting applications.



Controlled Transdermal Hepatitis B Immunization using Focused Ultrasound

Mei Yang¹, Haoqiang Huang¹, Yixin Hu^{1,2}

¹Biomedical Engineering, Health Science Center, Shenzhen University, Shenzhen, China, People's Republic of, ²National-Regional Key Technology Engineering Laboratory for Medical Ultrasound, China, People's Republic of

Background, Motivation, and Objective

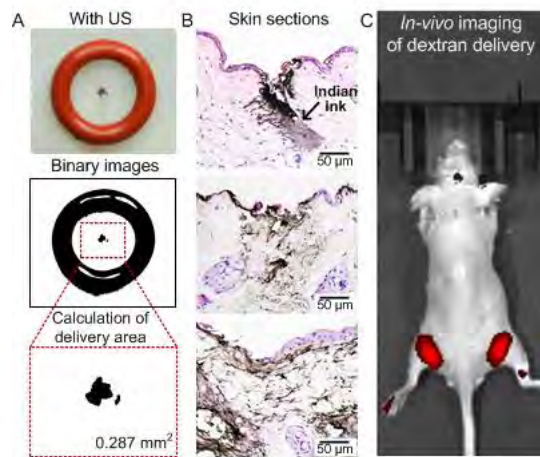
Although ultrasound-mediated transdermal delivery has been proven to be effective in the delivery of low-molecular-weight therapeutics, the clinical application of this method is still challenged by its inconsistent performance in creating localized transport regions (LTRs) on the target skin. In previous reports, the locations of the LTRs were unpredictable and the areas of the LTRs varied greatly. To improve the controllability of ultrasound-mediated transdermal delivery, this study employed a highly-focused ultrasound transducer to create well-defined LTRs with sub-millimeter diameters at pre-defined locations. This study also examined the question whether this proposed new method is able to deliver large molecules of Hepatitis B antigen to the skin immune system.

Statement of Contribution/Methods

The ultrasound wave was produced by a highly-focused transducer (60-mm-diameter, 1.1MHz). To guide the ultrasound energy to the skin, a delivery patch was designed. BALB/c mice of 6-8 weeks were used in this study. As for the in-vitro experiments, a tissue staining dye of Indian ink was first used to label the LTRs, and then the areas of the LTRs were quantified by ImageJ software. As for the in-vivo experiments, fluorescently-labeled dextran (10 kDa) was used as the model drug to quantify the total delivery dosage of the proposed method. To examine the immunization efficiency, Hepatitis B antigen was added to the delivery patch (201 µg/ml), and the antibodies produced against the antigen were measured by ELISA assay.

Results/Discussion

First of all, by concentrating the ultrasound energy at the center of the delivery patch, single-site creation of skin LTR was consistently observed. Secondly, the measured area of the LTRs ranged from 0.42 to 4.75 mm², and the depth of the LTRs measured in skin sections ranged from 150 to 960 µm. Specifically, ultrasound exposure with shorter duration, higher peak negative pressure and longer exposure time resulted in a larger and deeper LTR. Furthermore, in-vivo fluorescent imaging demonstrated that the total amount of the delivered dextran was around 10 µl. ELISA results showed that the new delivery method was effective in transdermal delivery of Hepatitis B antigen, and more antibodies were produced in animals treated with vaccine solutions containing DMSO.



Ultrasound targeted microbubble destruction promotes the homing of MSCs in rat model of acute injury liver**Fan Li¹, Ting Sun¹**¹*Medical Ultrasound, Shanghai General Hospital, China, People's Republic of***Background, Motivation, and Objective**

Bone marrow mesenchymal stem cells (BMSCs) has been considered as a therapeutic strategy for acute liver injury (ALI). However, the insufficient homing of BMSCs in vivo limited their applications. Ultrasound targeted microbubble destruction (UTMD) has shown the potential in promoting the homing of stem cells into ischemic myocardium. We therefore explored whether UTMD could promote BMSCs' homing in ALL rat models and its corresponding therapeutic effect.

Statement of Contribution/Methods

Bone marrow mesenchymal stem cells (BMSCs) were obtained from the femurs of Sprague-Dawley (SD) rats. The characteristics of BMSCs including the proliferative viability, diversified differentiation ability and specific cell surface markers' expression were verified by flow cytometry. In order to find the appropriate ultrasound parameters, the normal rat liver was exposed to different intensity of ultrasound (1.2W/cm^2 , 1.5W/cm^2 , 2.0W/cm^2) with $300\mu\text{l}$ microbubbles, and the expression of tumor necrosis factor α (TNF- α) and stromal cell-derived factor 1 (SDF-1) were detected at 24h post-treatment. The ALI models were established via a single intraperitoneal injection of d-galactose on 32 SD rats, which then were randomly assigned into four groups: blank, BMSCs, UTMD, and UTMD+BMSCs. After the BMSCs were stably transfected with a lentivirus for expressing green fluorescent protein (GFP), these cells were then injected through tail vein in a concentration of $2\times10^6/\text{mL}$. Forty-eight and 72 hours after the treatment, the protein expression levels of SDF-1, intercellular cell adhesion molecule1(ICAM-1), vascular cell adhesion molecule 1(VCAM-1) and monocyte chemotactic protein 1 (MCP-1) of exposed liver were analyzed, and the number of GFP-transfected BMSCs were observed as well. Serum alanine transaminase (ALT), aspartate transaminase (AST), alkaline phosphatase (ALP) activities were tested after 2 weeks of treatment.

Results/Discussion

The isolated rat BMSCs demonstrated good proliferation, osteogenic and adipogenic differentiation and the expression of CD29+, CD90+, CD45-, CD11b/c-. After the application of UTMD, the expression level of SDF-1 and TNF- α on exposed liver was markedly higher in 2.0W/cm^2 group than in the 1.5 W/cm^2 and 1.2W/cm^2 group ($p<0.05$). The ALI models were successfully established on 32 SD rats. The ultrasound parameters were 1.2W/cm^2 for 10min. After the treatments, the number of GFP-labeled BMSCs in UTMD+BMSCs group were significantly increased comparing with BMSCs groups ($p<0.05$), as well as the protein expression of SDF-1, ICAM-1, VCAM-1 and MCP-1 ($p<0.01$). The ALT, AST and ALP activities were much lower in UTMD+BMSCs, and the apoptotic rate of hepatocytes in UTMD+BMSCs group was significantly decreased by 58% relative to the control group (all $p<0.05$). Through up-regulation of adhesion molecular and cytokines, UTMD could enhance the homing of BMSCs in rat models of ALI and improve the function of acute injured liver.

Photoacoustic Imaging in the Spinal Cord: Monitoring Stem Cell Therapies for Image-Guided Regenerative Medicine

Kelsey Kubelick¹, Diego Dumani¹, Stanislav Emelianov^{1,2}, Eleanor Donnelly²

¹Wallace H. Coulter Department of Biomedical Engineering, Georgia Institute of Technology & Emory University, Atlanta, GA, United States, ²School of Electrical and Computer Engineering, Georgia Institute of Technology, Atlanta, GA, United States

Background, Motivation, and Objective

Regenerative stem cell therapies have great potential to treat diseases and injuries in the spinal cord. MRI has been used to track stem cells in the spinal cord to aid development of therapies, but drawbacks include high cost, low portability, and slow image acquisition. Thus there is a need for a real-time, longitudinal tracking technique to monitor transplanted cells in the spinal cord over 3-dimensional (3D) volumes to better assess treatment outcomes. We developed an ultrasound/photoacoustic (US/PA) imaging tool to intraoperatively guide stem cell injections into the spinal cord, confirm and quantify delivery, and track stem cells longitudinally.

Statement of Contribution/Methods

Mesenchymal stem cells (MSCs) were incubated with citrate-stabilized gold nanospheres (AuNS) for 24 h to tag cells. Per the clinical procedure, rat spinal columns were isolated and a laminectomy was performed. AuNS-MSCs were injected (5 μ L at 1,000-5,000 cells/ μ L) *ex vivo* at 16 nL/s. During injection, US/PA images were acquired using the Vovo LAZR (40 MHz and 20 MHz transducers, 680-970 nm). After injection, samples were 3D imaged using PA tomography (PhotoSound) at 700 nm for quantitative analysis. A similar experimental protocol was followed using photomagnetic Prussian blue nanocubes (PBNCs) to label MSCs.

Results/Discussion

Real-time single-wavelength US/PA imaging guided needle placement and tracked AuNS-MSC delivery (Fig. 1A). Less than 1,000 AuNS-MSCs were detectable, indicating high sensitivity of our imaging platform. Spectroscopic PA analysis and image segmentation identified each optical absorber (Fig. 1A). Tomographic PA imaging was used for quantitative analysis (Fig. 1B&C). Total PA signal increased according to number of MSCs delivered (Fig. 1D&E). We also investigated photomagnetic PBNCs to enable tri-modal US/PA/MRI. PBNC-MSCs were injected as above, and the previously-excised layer of muscle was replaced over the cord. PA imaging again detected less than 1,000 PBNC-MSCs (Fig. 1F), providing further proof-of-concept as we move to *in vivo* studies. Beyond imaging, magnetic properties of PBNCs can be used to retain stem cells at an injection site to improve therapeutic outcomes. Overall, our 3D US/PA imaging platform provides critical clinical benefits, including real-time imaging, injection guidance, quantitative assessment, and longitudinal feedback.

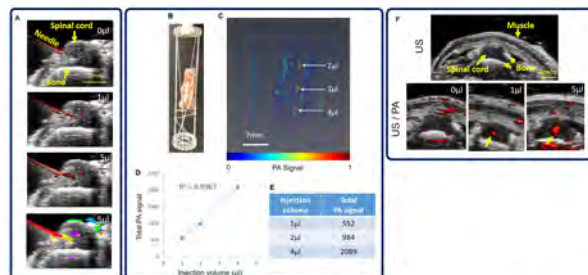


Figure 1. AuNS-MSCs were detected in real-time throughout the injection (A). PA signals from the needle (red), AuNS-MSCs (teal), degenerated plasma, impregnated tissue, and both species of hemoglobin (blue) were segmented and quantified. The total PA signal increased with increasing injection volume and thereby varied according to cell density, allowing for quantitative imaging (D & E). PBNC-MSCs were imaged after replacing muscle on the spinal cord, per the clinical procedure. PBNC-MSCs were detected in spite of the additional tissue layer (F).

Ultrasound stimulation of synthetic platelets in vitro. Influence of cross-linkage, applications to healing and effect on drug release kinetics.

Seema Nandi¹, Daniel Chester¹, Ashley Brown¹, **Marie Muller²**

¹*Biomedical Engineering, North Carolina State University, NC, United States*, ²*Mechanical and Aerospace Engineering, North Carolina State University, NC, United States*

Background, Motivation, and Objective

Synthetic platelets are highly deformable, ultra-low cross-linked (ULC), fibrin-binding microgels. They can emulate the behavior of natural platelets by spreading within a fibrin network and inducing a fibrin clot collapse, which promotes healing. However, the time required for the clot collapse to occur with synthetic platelets is of the order of days, as opposed to hours with natural platelets. We propose to use ultrasound to stimulate the deformation of these microgels to accelerate the clot collapse. Because these microgels can be loaded with drugs for targeted delivery, the ability to tune their deformability using ultrasound would also provide control over the kinetics of drug release.

Statement of Contribution/Methods

Microgels with various concentrations (0 to 4 mg/ml) and various degrees of cross linking (by incorporating 0% to 7% of N,N-dimethylenebis(acrylamide)) were added to agar gelatin gels containing aluminum oxide particles. Ultrasound stimulation was applied by transmitting plane continuous waves (from 0.5 to 4 MHz), using a plane single element transducer. Plane wave ultrafast imaging of the phantom was performed during ultrasound stimulation using a Verasonics L11-4v linear array connected to a Verasonics Vantage 128 scanner. The aluminum oxide particles were tracked using a Loupas 2D correlation, which provided indirect information on the microgel deformations. Because the frame rate allowed by ultrasonic imaging was not sufficient to capture a full cycle of deformations in the MHz range, a stroboscopic approach was used and the deformation cycle was reconstructed from multiple consecutive stimulation cycles.

Furthermore, ultrasound stimulation was applied to fibrin clots containing fibrin-binding microgels with various degrees of cross linking. The clots were imaged using cryogenic scanning electron microscopy (CryoSEM) 24 and 72 hrs after polymerization.

Finally, the microgels were loaded with 20 kDa Dextran and drug release kinetics were monitored over 24 hours using fluorescence analysis in the presence and absence of ultrasound stimulation.

Results/Discussion

Combining ultra low crosslinked microgels and ultrasound lead to displacements in the gelatin phantoms that were four times higher than phantoms containing no microgels. Phantoms containing microgels with higher degrees of cross-linking showed a more moderate response to ultrasound stimulation, with displacements 30% smaller than those observed with the ultra low cross linked microgels. We also show that the combination of ultrasound and fibrin binding microgels resulted in a higher density and connectivity of the fibrin clots. This suggests that ultrasound stimulation of synthetic platelets enhances fibrin clot collapse, and is likely to promote wound healing. Finally, the drug release kinetics were 30% slower with the ultrasound stimulated microgels, suggesting that ultrasound could be used to tune drug release kinetics.

P1-C12 - Transducer Modeling and Characterization

Kairaku (posters 1)

Thursday, October 25, 9:30 AM - 4:00 PM

Chair: Stefan Rupitsch Friedrich-Alexander University

P1-C12-1

Assessment of Electromechanical Coupling Coefficient for a Completed PIN-PMN-PT Array

Douglas N. Stephens¹, Robert Wodnicki², Ruimin Chen³, Laiming Jiang⁴, Kyle Morrison⁵, Katherine Ferrara⁶

¹Biomedical Engineering, University of Calif, Davis, Davis, CA, United States, ²Department of Biomedical Engineering, University of Southern California, CA, United States, ³University of Southern California, United States, ⁴Roski Eye Institute, Keck School of Medicine, University of Southern California, United States, ⁵Sonic Concepts, Inc., United States, ⁶University of California, Davis, United States

Background, Motivation, and Objective

After the matching layers are added to a piezoceramic array, there are only poorly qualified formulas available to guide the assessment of the electromechanical coupling coefficient (EMCC). However, the EMCC can drop in processing at (e.g.) ASIC soldering, or at oven cure steps. We are developing a very large 2D aperture array (3.75 MHz, PIN-PMN-PT, 1-3 composite) for use in deep liver imaging; the array prototype modules will be multiplexed with custom ASICs. We have derived a practical expression for the EMCC for an array with matching layers. Prototypes of our composite array design have been experimentally tested to demonstrate the effects of heating on EMCC.

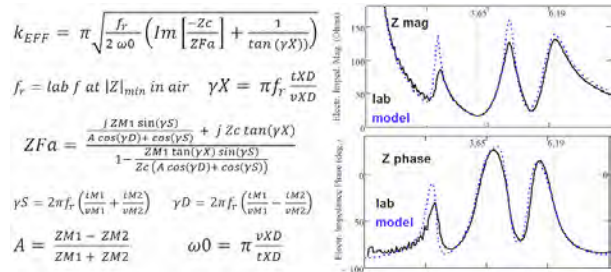
Statement of Contribution/Methods

The principal contribution of this work is the development of a new closed form EMCC expression which predicts coupling of a completed array with matching layers. A custom KLM model is used in comparison against the predictive ability of this new EMCC expression ("kEFF," see figure). The KLM model establishes the accurate 1-3 composite acoustic velocity. Laboratory tests on a prototype composite array were completed to explore the use of this new expression. After the fully assembled array velocity is established, and the other dimensional and material properties of the layers are obtained by conventional means, the kEFF value can be computed with the resonance frequency at the $|Z|$ minimum measured in the lab. Echo and impedance lab measurements were made with 256 array elements in parallel creating a 6.4 mm by 6.4 mm aperture. We measured the electrical impedance spectra in air before and after heating the packaged array in an oven at 160 C for 15 min. The kEFF derivation results were compared against the full KLM model prediction for EMCC.

Results/Discussion

Two EMCC expressions (using either lossy or lossless array parameters) were established and tested; both provide equal accuracy (kEFF shown in figure is for lossless parameters). The calculated kEFF values pre and post heating were within 1% of the full KLM model predictions. Heating in a 160C oven for 15 min reduces the composite velocity (2.7%), dielectric constant (7.9%), mechanical Q (38%), and the EMCC (5.0%). The EMCC decrease due to heating is most sensitive to the decrease in velocity. The expression for kEFF reduces to the classical EMCC "tangent" formula if matching layers are omitted.

Supported by NIH/NCI R01 CA211602.



Comparison of two models for power dissipation and temperature in piezoelectric transducers
Marcus Wild¹, Martin Bring², Lars Hoff¹, Karina Hjelmervik¹
¹*Faculty of Technology, Natural Sciences and Maritime Sciences, University of South-Eastern Norway, Borre, Norway*, ²*Subsea Division, Kongsberg Maritime, Horten, Norway*
Background, Motivation, and Objective

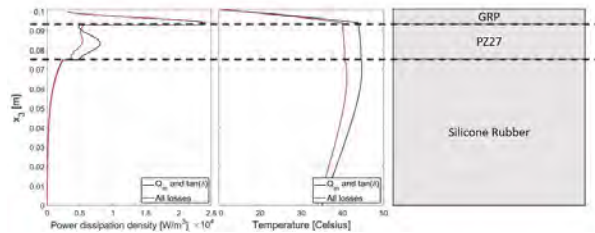
Piezoelectric materials are commonly characterized using the ANSI/IEEE 176-1987 Standard on Piezoelectricity. Losses, in this model, are described by two parameters, the mechanical quality factor Q_m and the dielectric loss tangent $\tan(\delta)$. Other models, such as the one developed by Holland, represent loss in piezoelectric materials by making the material tensors complex, including the piezoelectric constant. A good model for the power dissipation is important to predict the temperature rise in a transducer. This study compares the power dissipation and temperature profile in a transducer as a result of the losses described by either the IEEE standard, or the more complete model with complex tensor components.

Statement of Contribution/Methods

The study uses published material parameter values for PZ27. These values are input into a 1D Mason model for a piezoelectric plate to generate an impedance curve, and the material parameters Q_m and $\tan(\delta)$ are determined from this curve, as described in the IEEE standard. The piezoelectric plate is part of an acoustic stack, with a soft backing material consisting of silicone rubber and a quarter wavelength matching layer of glass reinforced plastic. The spatially dependent power dissipation density throughout the transducer is then calculated firstly from the parameters Q_m and $\tan(\delta)$, then from the complex material tensor components. These results are inserted into a 1D heat model in COMSOL. The resulting temperature profiles from the two datasets are then compared, in order to quantify the importance of the piezoelectric loss.

Results/Discussion

The two different formulations of the piezoelectric material parameters result in a clear discrepancy between the power dissipation density curves (see figure). Most of the discrepancy is concentrated around the piezoelectric layer, but differences are also seen in the matching layer. In the temperature profile, this translates into 4 to 5°C temperature difference inside the piezoelectric layer. This highlights the importance of a good model for the loss mechanisms when considering power dissipation and temperature profiles in acoustic transducers. The complex tensor formulation is assumed to give the more correct values, but this needs to be verified experimentally.



A FEM-based Method for Complete Parameter Identification of Thin Piezoceramic Bars
Amirfereydoon Mansoori¹, Marcus Wild², Lars Hoff³
¹*Faculty of Technology, Natural Sciences and Maritime Sciences, University College of Southeast Norway, Norway*, ²*University College of Southeast Norway, Norway*, ³*Department of Microsystems, University College of Southeast Norway, Borre, Norway*
Background, Motivation, and Objective

Reliable acoustic modeling of ultrasonic transducer arrays requires accurate estimates for the piezoelectric material parameters. Supplier data are often not sufficient for accurate modeling a specific sample shape, particularly after material processing. The objective of this study is to develop a tool to find the complete set of piezoelectric parameters, by minimizing the error between the simulated and measured impedance curves over a wide frequency range. The sample under study is a typical 1D array element in which the length dimension (l) is much larger than the other dimensions (w, t).

Statement of Contribution/Methods

In the case of PZT, there are thirteen parameters to be identified; ten real material parameters and three loss tangents corresponding to elastic, piezoelectric and dielectric isotropic losses. The sample is a PZT bar with dimensions $l=13$ mm $w=0.5$ mm $t=0.5$ mm. A sensitivity analysis is carried out to ensure the impedance curve characteristics of the sample are sufficiently influenced by the full set of parameters in the determined frequency range. The FEM model is implemented in COMSOL. The geometric symmetry and the fact that $w,t \ll l$ allows the FEM model to be reduced to a 2D model of the quarter of the bar. The optimization was performed in MATLAB, using the interior-point algorithm implemented in the *fmincon* function, and supplier data was chosen as initial values. The method was first tested on a synthetic impedance curve generated from a random set of material parameters. Subsequently, the method was applied to estimate material parameters of a sample made of the piezoceramic L303, based on a measured impedance curve.

Results/Discussion

The study on the synthetic data showed that the method was able to reproduce the accurate material parameters where the maximum difference was found for d_{15} and ϵ^T_{11} which is less than 2%. This difference is explained by these parameters having less influence on the impedance curve for the sample. In the case of L303 piezoceramic bar, figure 1 shows that we found a much better fit between the measured and simulated impedance curves when using our optimized parameter values, than when using supplier values. We conclude that the described method can be used to obtain improved material parameter values using only one sample, but only for the parameters having sufficient influence on the impedance curve in the given frequency range.

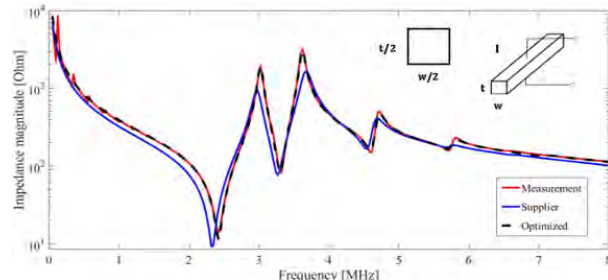


Fig 1. Electrical impedance for a thin bar of PZT type L303. Measured (red), simulated from supplier data (blue) and from optimized tensor values (black)

Temporal evolutional acoustic pattern generated by a 3D printed Fresnel lens-focused transducer
Chunlong Fei¹, Zhihai Qiu², Pengfei Lin¹, Qiang Chen¹, Xinyu Yang¹, Lei Sun², Qifa Zhou³
¹*Xidian University, Xi'an, People's Republic of*, ²*Department of Biomedical Engineering, The Hong Kong Polytechnic University, Hong Kong*, ³*University of Southern California, United States*
Background, Motivation, and Objective

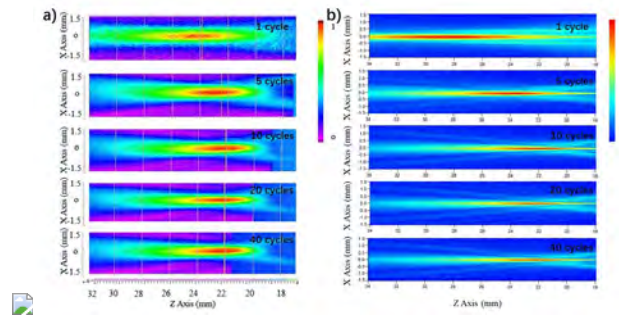
The controlled coupling of acoustic field has the potential to address grand scientific challenges for biological imaging, particle manipulation, therapy and intervention. However, current technologies have limited flexibility and poor control over acoustic pattern generated by a given transducer design. We report a Fresnel lens-focused ultrasonic transducer for generating excited signal dependent acoustic pressure patterns, which may support a simple way for acoustic pattern control.

Statement of Contribution/Methods

A 3D-printed Fresnel lens is bonded to a 5 MHz ultrasonic transducer built using conventional technology. The schematic of the Fresnel lens and the photo of the lens-focused transducer are shown in Fig.1. The normalized intensity maps of the acoustic pressure fields from the Fresnel lens-focused transducer under various cycle numbers of excited signal were characterized and compared with finite-element analysis.

Results/Discussion

The experimental results demonstrated that the focal depth changed from 23.8 mm to 21.9 mm when the cycle numbers of excited signal increased from 1 to 40, and remained unchanged after 10 cycles, which is agree with the simulation results (as shown in Fig.2). These results demonstrated that under different cycle excitation, a temporal evolution acoustic intensity at various longitudinal locations along the focus can be generated and controlled by a 3D printed Fresnel lens focused ultrasound transducer. It suggests a simple way for acoustic pattern control which can have broad application in the future.



Multilayered Carbon Nanotube Yarn Based Optoacoustic Transducer

Zeyu Chen¹, Yue Wu², Yang Yang¹, Qifa Zhou¹, Benpeng Zhu²

¹University of Southern California, Los Angeles, CA, United States, ²Huazhong University of Science and Technology, Wuhan, China, People's Republic of

Background, Motivation, and Objective

Carbons assemblies such as nanotube buckpaper, arrays sheets and yarns are capable of converting absorbed laser or modulated light into high intensity ultrasound. Besides, This study presents a novel optoacoustic transducer consisted of multilayered carbon nanotube yarn and gold particles. It also unveils the gold particles' enhancement mechanisms for optoacoustic effect.

Statement of Contribution/Methods

Two types of transducer were fabricated with freestanding layered Carbon Nanotube (CNT) yarn, which were CNT yarn-gold nanoparticle-PDMS structure (type I) and CNT yarn-PDMS structure (type II), respectively. A 6 ns pulsed laser with 532 nm wavelength (Lapa-80) was shined on the transducer. A piezoelectric hydrophone with 0.2mm diameter (Precision Acoustic, UK) was used to detect the acoustic wave. The signals were then recorded by an oscilloscope (TDS, 2024B, Tektronix, USA). The temperature variation on the interface was simulated by COMSOL Multiphysics.

Results/Discussion

Through a specifically designed PDMS/Au-CNT yarn-PDMS structure, the acoustic pressure and energy conversion efficiency of Type I transducer achieve 33.6MPa and 2.74×10^{-2} , respectively. The temperature variation on the interface illustrated that light absorption can be further enhanced by exciting localized surface plasmon resonance (LSPR). This transducer can also manipulate micro particle along certain direction. These results indicate that high intensity ultrasound enabled by the novel optoacoustic transducers and device can bring us tremendous possibilities in applications such as microfluidic flow control system and drug delivery.

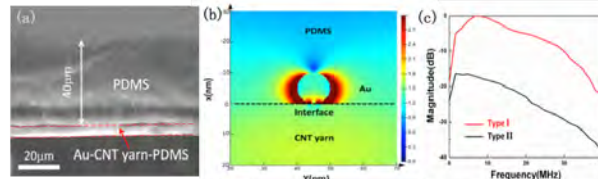


Figure 1: (a) The SEM cross-sectional view of PDMS/Au-CNT Yarn-PDMS structure (type I). (b) Temperature variation on the interface of type I transducers. (c) Spectrum of two types of transducers.

Micro-Stereolithography of KNN Piezoceramics for Ultrasonic Transducers

Weicen Chen¹, Kang Yan¹, Yuanhao Zhang¹, Dawei Wu¹

¹*State Key Lab of Mechanics and Control of Mechanical Structures, Nanjing University of Aeronautics and Astronautics, Nanjing, China, People's Republic of*

Background, Motivation, and Objective

Alkaline niobate (KNN) based piezoelectric ceramics are promising materials for ultrasonic transducers due to their non-toxicity, good piezoelectric properties ($d_{33}=416\text{pC/N}$), and high curie temperature ($T_c>250^\circ\text{C}$). Considering that piezoceramics are hard and brittle to be machined using traditional manufacturing methods, micro-stereolithography (μSL), an additive manufacturing approach, is supposed to be a promising way for piezoelectric components, especially for the design of complex constructions. However, the uneven uniformity and poor crystallinity of KNN powders pose a great challenge to μSL . The objective of this research is to fabricate KNN piezoceramics for ultrasonic transducers by a μSL based additive manufacturing method.

Statement of Contribution/Methods

The high solid loading, high reactive, and low viscosity KNN ceramic suspensions were prepared to meet requirements of thin layer recoating and low light intensity of μSL . With thermogravimetric analysis, a two-step debinding and sintering process was designed to achieve highly-dense crack-free piezoceramic components. The phases of the sintered components were identified by XRD analysis. The microstructures were characterized by SEM. The piezoelectrical properties of printed ceramics were measured after poling. The dielectric properties were evaluated in a thermal cycling chamber using HIOKI3532 LCR meter. Ferroelectric hysteresis loops were measured by a precision ferroelectric work station.

Results/Discussion

The KNN ceramic suspensions with solid loading of 65wt% were prepared and printed successfully. The density of sintered KNN was 4.05g/cm^3 , corresponding to 92% of the density of the bulk material. The XRD measurement showed that sintered KNN parts possessed a pure perovskite structure (Fig1.(a)). The piezoelectric constant and relative permittivity were 160pC/N and 1500 respectively. The curie temperature was about 220°C . The piezoceramic transducer arrays with high geometric accuracy and good electrical properties were initially printed (Fig1.(b)) and characterized. This work demonstrated that high performance KNN-based lead-free piezoceramics can be fabricated via 3D printing technique for ultrasonic transducers.

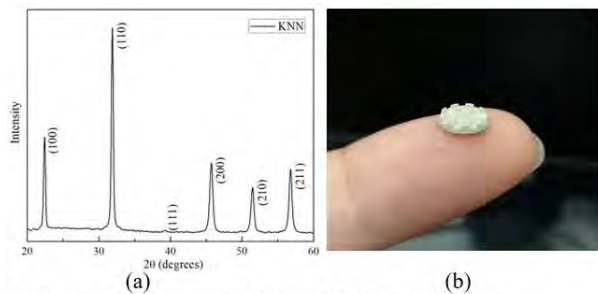


Fig1. (a) XRD pattern; (b) Printed KNN transducer array.

Theoretical Electroelastic Moduli of Porous Textured Piezoceramics

Antoine Balé^{1,2}, Rémi Rouffaud¹, Anne-Christine Hladky-Hennion², Pascal Marchet³, **Franck Levassort¹**

¹*Université de Tours - GREMAN UMR 7347 CNRS, TOURS, France*, ²*IEMN UMR 8520 CNRS, ISEN Department, LILLE, France*, ³*Université de Limoges - IRCER UMR 7315 CNRS, LIMOGES, France*

Background, Motivation, and Objective

Textured polycrystalline piezoelectric materials are expected to provide improved electromechanical performance compared to untextured ceramics, and can approach those of single crystals (SC). These materials which can be produced in large areas represent an important issue for ultrasonic transducer applications. Tempered grain growth (TGG) enables the fabrication of such materials by aligning few % vol. of SC templates (plate-shaped) in a tape casted slurry containing polycrystalline powder. Modeling of textured ceramics to deduce effective properties when the material is considered homogeneous at long-wavelength approximation has already been studied when taking into account the crystal orientation distribution for very high degree of texture. Meanwhile, during the process, additional porosity often appears and can be considered as isolated pores in the surrounding material. We propose in this theoretical work to take into account this porosity content and to highlight the corresponding effect on electromechanical performance of the whole material.

Statement of Contribution/Methods

To describe the spatial arrangement of the several phases, the concept of connectivity is used and extended to textured ceramic considering two piezoelectric phases. After sintering, the SC oriented phase is self-connected in three dimensions in the residual matrix (same consideration for this second phase). 3-3 connectivity defines this biphasic material. Moreover, in taking into account the closed porosity, the 3-(0-3) connectivity is retained for the whole material. A simple model called the matrix method is used to obtain the effective electroelastic moduli of a porous textured ceramic. The method is based on the generalization of series and parallel connections (2-2 connectivity) and was adapted to our considered materials.

Results/Discussion

For the matrix method calculation, two close-phase composition (templates and matrix) systems were studied (PMN-PT and lead-free system KNN-based compositions). Abacus of several parameters such as the thickness coupling factor as a function of SC and porosity volume fractions were represented. Results clearly show that porosity has a beneficial effect and increases the electromechanical properties. This was confirmed on one configuration using FEM. Typically, for the studied PMN-PT system, k_t value is improved from 48% to 58% for a relatively high degree of texture (and consequently SC volume fraction) and 15% porosity. Moreover, results show that a trade-off between the SC and the porosity content can be adjusted according to the studied compositions. In particular for the used KNN composition, porosity content is directly linked to improved performances. This work highlights that porosity content is not a critical parameter but inversely improves material performance (coupling factor and lower acoustical impedance) which is advantageous for transducer applications.

Eccentric design of Fabry-Perot interferometer for high sensitivity and broadband ultrasound sensing
Binxue Liu¹, Lijun Xu^{1,2}, Jianguo Ma^{1,2}
¹*School of Instrumentation Science and Opto-electronics Engineering, Beihang University, China, People's Republic of,* ²*Beijing Advanced Innovation Center for Big Data-based Precision Medicine, Beihang University, China, People's Republic of*
Background, Motivation, and Objective

Ultrasound sensing with broadband and high sensitivity enables high resolution and large penetration in ultrasound imaging as photoacoustic imaging and non-destructive testing. Traditional piezoelectric ultrasound transducers suffer from limited bandwidth and sensitivity. On the contrary, fiber-based Fabry-Perot (FP) interferometer exhibited very high sensitivity on vibrations, which potentially acted as a high sensitivity ultrasound sensor. However, due to the high quality factor of silica in fibers, its reverberation lasts long time, leading to a narrow bandwidth and a high noise level. In order to overcome this weakness, we designed a large-size multi-core fiber (MCF) FP sensor, and applied finite-element method (FEM) to optimize the performance.

Statement of Contribution/Methods

In this research, we focus on the acoustic vibration of the optical fiber and try to eliminate the reverberation. In optical fibers, both fiber core and cladding layers are made of silica, which are almost identical for acoustic vibrations. Consequently, we considered the fiber as a uniform bar, and used 2D-axisymmetric models at fiber tip in COMSOL (COMSOL Inc., Stockholm, Sweden) to reduce the computation consumption. In this research, we designed multi-core single-mode fibers by varying the cladding diameters and remaining 10 μm Parylene C coverage as the interference cavity. We investigate both the acoustic pressure field and the strain of fiber tip under the excitation of a cycle of sinusoidal wave at 100MHz in time domain. Positions of the fiber cores are optimized with FEM to avoid significant resonance and minimize the reverberations.

Results/Discussion

Deformation and strain distribution of the 500 diameter, multi-core fiber illustrate that the reverberation is much stronger in the center because symmetric boundaries generate constructive interference (Fig. 1 A). At the eccentric fiber cores (Fig. 1 B), the reverberation diminishes to -20 dB within 8 ns after excitation (Fig. 1 C), equivalent to a broadband response. Meanwhile, there is no sacrifice on the sensitivity. The design of off-axis fiber cores is applicable for either single-fiber sensor or multiple-fiber arrays. In conclusion, we designed FP interferometer with off-axis fiber cores, which eliminated reverberation and remained high sensitivity, pioneering a promising future of ultrasound sensing.

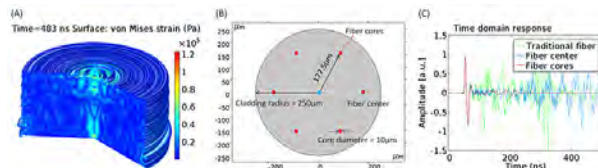


Fig.1 (A) Deformation and strain of the fiber tip at 483 ns in the modeling. (B) MCF design. (C) Normalized signal response in time domain.

P1-C13 - Therapeutic Transducers

Kairaku (posters 1)

Thursday, October 25, 9:30 AM - 4:00 PM

Chair: **Ho-yong Lee** Ceracomp Co., Ltd

P1-C13-1

Minaturized Sub-megahertz Focused Ultrasound Transducers Composed of Multilayer Hard PZT ceramics

Ho-Wuk Kim¹, Jinwook Kim², Xiaoning Jiang¹

¹*North Carolina State University, United States*, ²*Biomedical Engineering, University of North Carolina - Chapel hill, United States*

Background, Motivation, and Objective

Therapeutic ultrasound is a versatile tool for diverse medical therapies. In this application, relatively high power, low frequency ultrasound has been utilized to enhance the targeted bioeffects. In our previous research, a soft piezoelectric ceramic (PZT-5A) was employed for the miniaturized multilayer design, but the feasibility using other piezo materials has not been fully studied. We hypothesize that the maximum usable pressure can be enhanced by using a hard-type PZT, such as PZT-4, because it exhibits a relatively sharp frequency response owing to its terrific mechanical quality factor. Furthermore, its stiff material characteristic allows higher electric field than PZT-5A material, thus leading to greater acoustic power.

Statement of Contribution/Methods

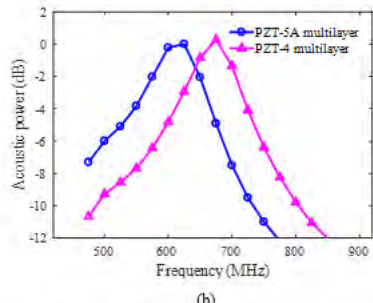
Multilayer PZT-4 transducer is designed based on numerical simulation, and its performance was validated by an experiment. First, multilayer transducers are designed for each material in the same geometric condition, where a metallic concave lens is embedded on them in order to focus the acoustic energy effectively. Second, electric impedances are analyzed to characterize their resonance frequencies, using a commercial software, ANSYS. Third, acoustic powers transmitted from each transducer are simulated in order to figure out the frequency characteristics in acoustic pressure transmission of each transducer. Based on the simulation results, multilayer transducers (Fig. 1(a)) are fabricated with two different PZTs. Finally, three samples for each type are tested to examine their maximum acoustic pressure.

Results/Discussion

Two types of miniaturized multilayer transducers were designed through simulations and fabricated, respectively. Fig. 1(b) exhibits the acoustic powers measured at 0.75 mm distance from the aperture. While the maximum power of PZT-4 transducer retains the similar level compared to that of PZT-5A transducer, frequency bandwidth becomes narrower (about 15.6 %) than that of PZT-5A. Then, PZT-4 multilayer shows not only a long ringing-down in the pulse-echo response owing to its sharp frequency characteristic, but also exhibits higher acoustic pressure than PZT-5A with greater input voltage; it can make up the limitation in PZT-4 transducer. To conclude, the multilayer transducer employing the hard PZT, may be more appropriate for high acoustic power generation.



(a)



(b)

Figure 1. Photo image of forward-looking multilayer transducer (a) and acoustic power with respect to frequency (b).

High intensity focused ultrasound (HIFU) combines Optical Coherence tomography (OCT) for skin superficial diseases treatment and evaluation

Guan Wang¹, Kanheng Zhou¹, Yan Wang², Faqi Li², Kairui Feng¹, Chunhui Li¹, Zhihong Huang¹

¹School of Science and Engineering, University of Dundee, Dundee, United Kingdom, ²State Key Laboratory of Ultrasound Engineering in Medicine Co-Founded by Chongqing and the Ministry of Science and Technology, Chongqing Key Laboratory of Biomedical Engineering, College of Biomedical Engineering, Chongqing Medical University, Chongqing, China, People's Republic of

Background, Motivation, and Objective

High intensity focused ultrasound (HIFU) is a medical technology that is in various stages of development to treat a range of disorders including skin superficial diseases. Optical coherence tomography (OCT) is a rapid development imaging technique in recent 10 years. OCT is a good monitoring tool of skin because of the millimetre-level detection depth with high resolution. This paper aims to develop a new high frequency transducer for the superficial treatments. The focal length of the transducer is 3mm which is suitable for the skin superficial diseases. OCT system is used to monitor the tissue during HIFU treatment. The transducer together with OCT monitoring system bring huge potential for future dermatology applications and superficial treatment and monitoring of superficial area of cancer.

Statement of Contribution/Methods

A customized single element transducer has been used in this study for the treatment at 10.3MHz. Acoustic power mapping test and radiation force balance test had been finished before the experiment which are essential factors to characterize the transducer. In this research, ex-vivo bovine liver tissue and ex-vivo chicken breast were treated at the same energy level for different time: 2 s, 4 s, 6 s, 8 s, 10 s, 15 s, 20 s, respectively. During the treatment, OCT images were collected on the lesion area of the sample to monitor the effect of treatment. After HIFU treatment, OCT images were reconstructed to generate a 3D model by Amira.

Results/Discussion

After HIFU treatment, different volume of the lesion area corresponding to different treatment time can be seen very clearly. Shape of the lesion area is like a 'cigar' which is perfectly matching the acoustic power mapping results. Also, the boundary between lesion area and surrounding healthy tissue was easy to tell, which means the HIFU treatment can positioned to the lesion location accurately. The precisely control of the focal length (3mm) by the customized transducer is perfectly for the treatment of skin superficial diseases. Combined HIFU and OCT system, the data will correlate with the histology results.

Development of low frequency (20 kHz) clinically viable ultrasound applicator for chronic wound treatment

Olivia Ngo¹, Evan Niemann¹, Vivinya Gunasekaran¹, Prabagar Sankar¹, Alec Lafontant¹, Sumati Nadkarni¹, Rose Ann DiMaria-Ghalili², Michael Neidrauer¹, Leonid Zubkov¹, Michael Weingarten³, David Margolis⁴, Peter Lewin¹

¹Drexel University School of Biomed, Philadelphia, PA, United States, ²Drexel College of Nursing, Philadelphia, PA, United States, ³Drexel College of Medicine, Philadelphia, PA, United States, ⁴University of Pennsylvania, Philadelphia, PA, United States

Background, Motivation, and Objective

Chronic wounds, such as venous and diabetic ulcers, cost the U.S healthcare system \$25 billion annually. In a 2017 study by the University of Toronto, the median health-care cost of a hospital treatment for a chronic ulcer was found to be \$16,400. A reduction of healing time directly translates into a reduction of healthcare costs; thus a positive clinical outcome would create a substantial societal impact. The primary goal of this work was to systematically delineate the process of the design and hardware implementation of the clinically viable ultrasound applicator. The applicator was specifically devised to treat chronic wounds and is the first truly wearable device with a proven record of successful treatment of human patients.

Statement of Contribution/Methods

The applicator *actively* promotes healing – a fundamentally different treatment from commercial ultrasound systems that offer *passive* wound management in the form of debridement. Debridement removes necrotic tissue through the use of cavitation (inertial cavitation) ultrasound, and is intended to maintain a wound environment that is conducive to the natural healing process but does not actively promote healing. In contrast, the proposed applicator uses non-cavitation and non-thermal levels of ultrasound energy. The prototype operates in the kHz (20-100) range of frequencies; hence, in the absence of inertial cavitation and temperature elevation, the tissue-ultrasound interaction is considered to be dependent on stable cavitation (if any) and radiation force. The peak acoustic output pressure amplitude is limited to 55 kPa, corresponding to a spatial peak temporal peak intensity of 100 mW/cm². This level of intensity is considered to be safe to apply for extended (up to four hours) periods of time.

Results/Discussion

The patch-like applicator design is suitable to be embedded in wound dressing and with its light weight (<20g), and circular (40 mm dia) disk shape architecture, is well suited for chronic wound treatment. The quantitative absolute calibration (to within +/-10%) of the device acoustic output is conveniently implemented in the frequency range considered (here 20-100 kHz) making use of reciprocity calibration. The calibration permits linkage of exposure parameters with the rate of wound closure, allowing personalization of patient treatment. Finally, a small (n=8) pilot study on the effects of the applicator on diabetic ulcers healing time is presented. The average time to wound closure was 4.7 weeks for subjects treated with the active ultrasound applicator, compared to 12 weeks for subjects treated with a sham applicator, suggesting that patients with diabetic ulcers may benefit from the proposed treatment.

Virtual Prototyping of a Catheter Transducer Array for Internal Hepatic Sonoporation

Alexandru Moldovan¹, Jerzy Dziewierz¹, Holly Lay², Sandy Cochran³, Anthony Gachagan¹

¹Electronic and Electrical Engineering, University of Strathclyde, Glasgow, United Kingdom, ²School of Engineering, University of Glasgow, Glasgow, United Kingdom, ³Medical and Industrial Ultrasonics, University of Glasgow, Glasgow, United Kingdom

Background, Motivation, and Objective

Sonoporation is a minimally-invasive targeted drug delivery technique based on cavitation which aims to increase therapeutic efficacy in the treatment of various pathologies. It uses high power ultrasound to oscillate and collapse microbubbles (MBs) in proximity of the endothelial cells that are constitutive elements of blood vessels. The mechanical interaction between the MBs and the cells increases the cells' permeability to exogenous agents and has proven successful in studies *in vitro* [1] and *in vivo* [2]. The liver is particularly difficult to sonoporate because of its movement during patient respiration, the surrounding fat layer and the presence of the ribs which shadow the ultrasound beam. The objective of the current work is to design a catheter transducer that circumvents these issues by providing sonoporation from within a larger hepatic blood vessel.

Statement of Contribution/Methods

A 1-3 piezocomposite transducer design is optimised through a multiparametric sweep of volume fraction (VF), thickness and pillar number using finite element analysis (PZFlex, Glasgow, UK). The cost function of the optimisation targets a transducer to achieve a sufficiently high pressure variation in blood to sustain MB cavitation. Other considerations include control of transducer self-heating and beam steering quality.

The simulation framework for the parameter sweep has been developed as a MATLAB graphical user interface (The MathWorks, Cambs, UK) with PZFlex as the computational engine. Once set up, the procedure is automatic, with minimum user input. A typical execution time for a 10-step VF sweep is approximately 2 hours on a high-end workstation. The simulation process has been validated against a PZT-5A piezocomposite device manufactured for the purpose.

Results/Discussion

The procedure has been used to design a linear array transducer to fit a catheter of size 8 Fr (2.7 mm). The array thickness is approximately 0.40 mm and it is comprised of 8 square elements with a maximum element width of 1.50 mm. Several active materials have been modelled, including PZT-5H, PMN-29%PT and 26%PIN-PMN-32%PT coupled with a polymer filler (EpoFix, Struers, UK). The simulation indicates the optimal solution is obtained for PMN-29%PT composite with a thickness of 0.42mm, a VF of 0.60 and 15x15 pillars per element which produces a peak negative pressure of 2.60MPa per single element, driven at 100V, with natural focus at 1.27mm.

Future work will involve modelling the entire array, followed by fabrication and characterisation of the optimised design for all three candidate active materials. The transducers' efficiency in cavitating MBs will be tested in immersion with high speed video imaging and passive acoustic mapping.

[1] K. Kooiman, M. F.Harteveld, A. F. Steen, N. Jong, *Journal of Controlled Release*, vol. 154, no. 1 (2011), pp. 35–41

[2] G. Shapiro et al., *Journal of Controlled Release*, vol. 223 (2016), pp. 157–164

LEAD-FREE PIEZOCERAMIC BASED ULTRASONIC DEVICE FOR MEDICAL APPLICATION**Muhammad Sadiq¹, Mike Irvine¹, Nicola Fenu², Sandy Cochran², Ian Quirk¹**¹*Active Needle Technology Ltd., Abingdon, United Kingdom, ²Medical and Industrial Ultrasonics, University of Glasgow, Glasgow, United Kingdom***Background, Motivation, and Objective**

A novel ultrasonic needle biopsy device has been developed (ANT Ltd, Oxford, UK), based on a traditional lead (Pb)-based piezoceramic material (PZT), to address the clinical need of improved accuracy of needle placement in image-guided biopsy procedures.

Worldwide, including in the EU, regulatory agencies have begun to restrict the use of Pb, a cumulative toxicant. Due to its 60% by weight Pb-content, PZT has been identified formally as a substance of very high concern (SVHC). However, it enjoys exemption from restrictions till 2021 due to the lack of suitable Pb-free alternatives. Hence Pb-free alternatives need to be identified and qualified with urgency.

Building on the recent advances in the field of Pb-free materials and to assess the feasibility of these materials in medical applications, this paper reports a version of the ANT biopsy device developed using commercial Pb-free piezoceramic material (PIC700, PI Ceramics, Lederhose, Germany). In doing so, the paper also draws a performance-based comparison between PIC700 and current PZT8 piezoceramic devices.

Statement of Contribution/Methods

Prior to fabrication, in-depth virtual prototyping of the PIC700 device was carried out using time-domain finite element analysis to achieve the desired operational characteristics. While PZT8 is an established piezoceramic material with a complete property set readily available, comprehensive data for PIC700 was obtained experimentally, based on IEEE characterization techniques.

Post fabrication, complete characterization was carried out to measure and compare the performance of the PIC700 device with its PZT8 counterpart. Key performance parameters, including k_{eff} , Q_M , and displacement amplitude at the tip of the needle, were considered.

Furthermore, to assess the device's feasibility in clinical practice, image-guided biopsy studies were carried out on tissue-mimicking phantoms.

Results/Discussion

Comparing key application specific parameters, performance gaps between PIC700 and PZT8 were observed. Due to the low density (ρ) and dielectric constant (ϵ_{33}^s rel), the PIC700 device was designed with a piezoelectric stack approximately twice the length of the PZT8 stack to achieve the desired operational frequency and impedance characteristics.

| Material | Density ρ (kg/m ³) | Dielectric Constant ϵ_{33}^s rel (-) | Strain coefficient d_{33} (pC/N) | Coupling Coefficient k_{33} (-) |
|----------|--|--|---------------------------------------|---|
| PZT8 | 7800 | 1200 | 265 | 0.66 |
| PIC700 | 5750 | 685 | 88.5 | 0.38 |

While PIC700 has piezoelectric properties with relatively low piezoelectric activity, devices based on it showed satisfactory performance during the biopsy studies. It is expected that design optimization and on-going advances will permit Pb-free piezoceramic to replace Pb-based piezoceramics, especially in less demanding medical applications.

P1-C14 - Transducer Design and Applications

Kairaku (posters 1)

Thursday, October 25, 9:30 AM - 4:00 PM

Chair: **Xiaoning Jiang** North Carolina State University

P1-C14-1

Development of anti-cavitation hydrophone -Study on the novel hydrophone with new cap structure titanium front plate

Michihisa Shiiba¹, Mayu Yahagi², Takeshi Morishita², Nagaya Okada³, Minoru Kurosawa⁴, Shinichi Takeuchi²

¹Nihon Institute of Medical Science, Saitama, Japan, ²Toin University of Yokohama, Japan, ³Honda Electronics Co., Ltd., Japan,

⁴Tokyo Institute of Technology, Japan

Background, Motivation, and Objective

Recently, ultrasound treatment methods such as sonoporation for gene transfer, high-intensity focused ultrasound (HIFU) for cancer therapy and sono dynamic therapy (SDT) are developed and used actively. Furthermore, ultrasound cleaners and ultrasonic particle dispersion systems are used in the industrial field. There is a tendency that ultrasound is irradiated frequently in these applications. These acoustic field distributions should be measured with a hydrophone. However, electrodes or piezoelectric elements of the hydrophones were broken by effect of high sound pressure and acoustic cavitation when acoustic fields formed by ultrasound apparatus with high intensity ultrasound like ultrasound cleaner or HIFU device were measured by using normal commercial hydrophones. Therefore, it was difficult to measure such high intensity acoustic field by using normal commercial hydrophone. We presented the durability test of our conventional anti-cavitation hydrophone at IEEE IUS 2015 in Taipei TAIWAN.

We will presents the novel anti-cavitation hydrophones were fabricated by deposition of hydrothermally synthesized lead zirconate titanate (PZT) polycrystalline film on the reverse side of titanium front plate. These hydrophones were not damaged by measurement of high intensity ultrasound field.

Statement of Contribution/Methods

We proposed and fabricated novel anti-cavitation hydrophone with new cap structure type titanium front plate (acoustic receiving surface) and titanium backing material with specific acoustic impedance of 27 MRayl for measurement of high intensity ultrasound in this study.

A durability test on our fabricated anti-cavitation hydrophone was performed by exposure to the ultrasound acoustic field with the generation of acoustic cavitation in the water tank of an ultrasound cleaner (Honda Electronics HCL-280A) at 22.5 kHz. The maximum input electric power of the ultrasound cleaner is 48 W. Output voltages from the hydrophone under test were measured at 5.0 MHz for the durability test.

Results/Discussion

The receiving sensitivity of our fabricated hydrophone did no decrease even after ultrasound cleaner exposure for 14 hours. The frequency characteristics of the receiving sensitivity was not changed. The electrode (titanium front plate) of our fabricated anti-cavitation hydrophone was not damaged at all even after sonication. However, exposure was done sonication with an ultrasound cleaner, a pinhole was formed near the center of the titanium front plate after 15 hours. In the future we will review the structure and fabrication method again to improve the frequency response of the receiving sensitivity.

High efficiency ultrasonic transducer using polarity inverted ZnO thin film

Tsuyoshi Majima^{1,2}, Takahiro Shimidzu^{1,2}, Takahiko Yanagitani^{1,2,3}

¹Waseda University, Japan, ²ZAIKEN, Japan, ³JST-PRESTO, Japan

Background, Motivation, and Objective

Ultrasonic microscope is generally operated in the frequency range of 100 MHz to 2 GHz. To achieve 50 ohm impedance matching, emission area S reduces with increasing frequency. Emission area S reduction decreases S/N because sound pressure lowers when ultrasonic wave is focused. As shown in Fig.1(a), polarity inverted n -layered transducer resonates in n -th mode. Piezoelectric film thickness and emission area increase by n -times compared to single-layered transducer when operating frequency is same. We previously reported the control of ZnO polarity [1], and reported the fabrication of polarity inverted ZnO films. In this study, we first report polarity inverted two-layered ZnO transducer on silica glass buffer rod. Characteristics of new two-layer transducer are compared with single-layered transducer.

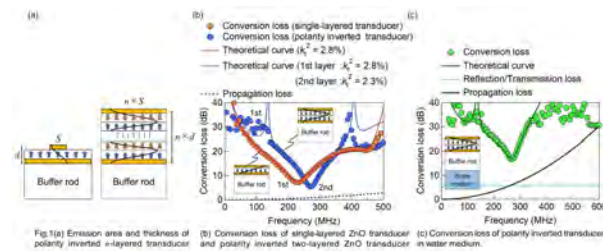
[1] R. Ikoma, et al., IEICE Technical Report, US2012-61, Sep. 2012 (in Japanese).

Statement of Contribution/Methods

O-polar ZnO film grows in the case of a usual sputtering, where a substrate is heated and is set outside of the discharge. In contrast, Zn-polar ZnO film grows in the case of an unusual sputtering, where a substrate is set inside of the discharge without heating. Single-layered transducer (Au electrode layer / O-polar ZnO (11.5 μ m) / bottom electrode / SiO₂ buffer rod (12 mm)) and two-layered transducer (Au electrode layer / Zn-polar ZnO(11.5 μ m) / SiO₂ layer(0.5 μ m) / O-polar ZnO(11.5 μ m) / bottom electrode / SiO₂ buffer rod(12 mm)) were fabricated. SiO₂ layer is inserted between first and second layer to decrease the effect of the polarity of first ZnO layer.

Results/Discussion

The theoretical conversion loss was simulated by multilayered Mason's equivalent circuit model taking polarity inversion into consideration. Fig.1(b) shows conversion loss of single-layered transducer and two-layered transducer. Two-layered transducer resonates in second mode. The minimum conversion loss was improved from 7.1 dB to 5.3 dB. Thickness and emission area were also increased from 13.9 μ m to 23.4 μ m and from 2.2 mm² to 3.0 mm², respectively. Fig.1(c) shows comparison of experimental and theoretical conversion loss of two-layered transducer in water medium. The experimental curve agrees with theoretical curve. The minimum conversion loss was 16.7 dB. Polarity inverted transducer is promising for ultrasonic microscope applications.



New Lead-Free Bi₄Ti₃O₁₂ Based Sol-Gel Composites for Ultrasonic TransducersShohei Nozawa¹, Tomoya Yamamoto¹, Makiko Kobayashi¹¹Kumamoto University, Kumamoto, Japan**Background, Motivation, and Objective**

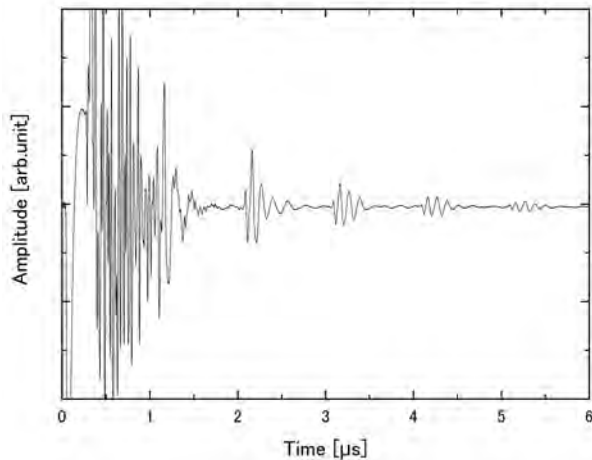
In recent years, ultrasound non-destructive testing (NDT) in operation has been demanded for industrial fields because of safety assurance and economical reason. Sol-gel composite materials could be suitable because of no couplant/backing material requirement. Ultrasonic transducers made by Bi₄Ti₃O₁₂(BiT)/Pb(Zr,Ti)O₃ (PZT) sol-gel composite has been developed and it showed stable ultrasonic performance up to 400°C. However, BiT/PZT is lead-containing material, so lead-free sol-gel composite material is preferred for high temperature applications. In previous study, BiT/BiT sol-gel composite demonstrated stable ultrasonic performance up to 500°C. However, poling process of BiT/BiT required high temperature because BiT sol-gel has lower dielectric constant than that of BiT bulk material. It has been desired to develop new lead-free sol-gel composite with high temperature durability and poling facility. In this study, new sol-gel composite, BiT/TiO₂ was developed. TiO₂ was chosen as sol-gel material because it has relatively high dielectric constant and high resistivity.

Statement of Contribution/Methods

BiT/TiO₂ samples were fabricated by sol-gel spray technique. The mixture of BiT powder and TiO₂ sol-gel solution mixed and sprayed on 3mm thick titanium substrates. Drying at 150°C and firing at 650 °C for 5 min each were performed. 100μm thick films on substrates were fabricated by repeating these processes. After film fabrication process, polarization process was carried out at room temperature. Top electrodes were made by silver paste.

Results/Discussion

The sample was set onto a hot plate and the temperature was changed every 50°C up to 500°C. After 5 min holding time at each temperature, ultrasonic waveform in pulse-echo mode was recorded by a digital oscilloscope. Fig.1 shows the ultrasonic response of the BiT/TiO₂ film poled at room temperature at 500°C. The signal amplitude was stable at 500°C and signal to noise ratio was high enough to confirm multiple reflected echoes from the bottom surface of the titanium substrate. Further research is required for repeatability and material characterization.



Near-field multiple traps of acoustic vortices generated by a sector transducer array and its application in object manipulation

Qingyu Ma¹, Caojin Yuan¹, Shaotong Feng¹, Qingdong Wang¹, Juan Tu², Dong Zhang²

¹*School of Physics and Technology, Nanjing Normal University, China, People's Republic of, ²Nanjing University, China, People's Republic of*

Background, Motivation, and Objective

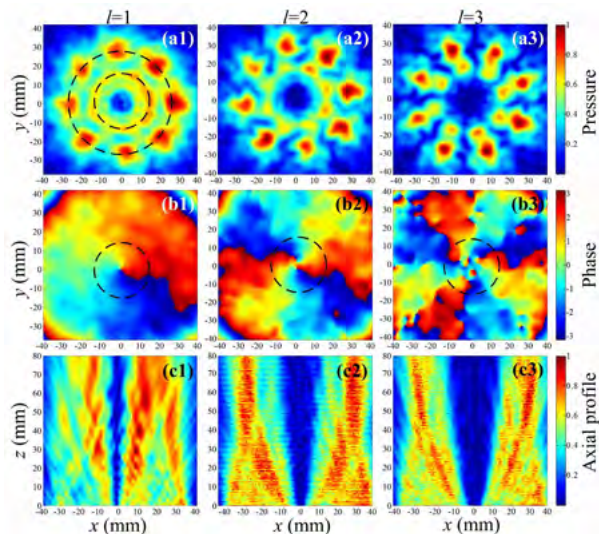
As a kind of special acoustic field, the helical wavefront of an acoustic vortex (AV) beam has a pressure zero with phase singularity at the center. The orbital angular momentum (OAM) of AVs can be applied in particle manipulation, which attracts more and more attention in acoustic researches. However, the trapping capability of side-AVs generated by side lobes is still unsatisfactory for the lower-level potential gradient in the near field, and the trapping efficiency of the main-AV is also limited by the reduced pressure at a longer axial distance in the far field.

Statement of Contribution/Methods

In order to improve the capability of particle trapping close to the source plane, theoretical and experimental studies on near-field multiple traps of paraxial AVs generated by a phase-coded sector transducer array are conducted. The acoustic pressure of the AV beam is derived in cylindrical coordinates with explicit formulae and the corresponding pressure distributions are simulated for an 8-source transducer array. The acoustic gradient forces (AGFs) of the AV beam in the near and far fields are calculated to analyze the capability of object trapping. The numerical results are also verified by the measurements of axial and radial pressure distributions using the experimental transducer array.

Results/Discussion

It is proved that strengthened AGFs of near-field multiple AVs with higher peak pressures and smaller vortex radii can be produced at a small topological charge. Axial distributions of the equivalent potential gradient indicate that the AGFs of the near-field AVs are much higher than that in the far field, and the corresponding vortex antinodes are the ideal trapping positions with relatively higher AGFs. With the established 8-channel experimental system, the formation of near-field multiple AVs is verified by the cross-sectional circular pressure distributions with perfect phase spirals around the center axis at a pressure zero, and the trapping capabilities of the vortex nodes and antinodes along the center axis are demonstrated by the AGFs at different distances. The favorable results demonstrate the feasibility of near-field multiple traps with strengthened AGF using the sector transducer array, and suggested the potential applications of close-range and multi-position particle trapping in biomedical engineering.



Ultrasonic auger for narrow-gauge bore-hole drillingDavid Firstbrook¹, Kevin Worrall¹, Patrick Harkness¹, Thaleia Flessa¹, Euan McGookin¹, Douglas Thomson¹¹*School of Engineering, University of Glasgow, Glasgow, United Kingdom***Background, Motivation, and Objective**

Normal pipe installation requires disruptive cut-and-cover mechanisms, and the ongoing BADGER project is looking at developing a wireline mole-like driller to counteract this. Utilisation of this robotic system should reduce the infrastructure footprint, minimise damage, and shorten delays. One issue of the wireline approach is that the overhead weight and torque cannot be supplied by a ground-station, and must be reacted by the device down hole, requiring significant power and complex mechanisms. The research reported in this paper looks at miniaturising the BADGER technology by utilising an ultrasonically-assisted drilling head in order reduce the force and torque requirements to levels that can be reacted by a small device.

Statement of Contribution/Methods

Several stainless steel conical augers have been modelled using the Finite Element Analysis (FEA) program Abaqus. Various configurations of design have been explored in order to achieve adequate acoustical properties, whilst also providing a shape that could drill soil and clay efficiently. To compare drilling characteristics, two augers have been chosen to be brought forward to manufacture, shown in the figure. One has been designed with a longer length and sharper tip angle to resonate in the L2 mode, whilst the other has a shorter, blunt drill head, designed for the L1 mode. Both consisted of a double-helix auger, and resonated within the region 19.5 kHz – 20.5 kHz. The predicted vibration characteristics have been verified using Experimental Modal Analysis (EMA) and impedance analysis. A bore-hole stabilising casing, slightly narrower than the widest part of the conical auger, was fitted behind the drill-head, allowing drill depths of up to 50 cm.

Results/Discussion

The vibrational properties of the augers have been measured and identified, and found to closely match with the predicted values. A selection of substrates have been chosen to represent a broad range of conditions, ranging from initial lab tests using granular material, to full field trials in clay and soil. It has been found that utilising ultrasonic vibration improved performance of drilling by reducing the levels of overhead force and torque, potentially paving the way for development of a narrow-gauge boring device.



Lead free Ceramic Transducers for Sonar Applications

Valsala Kurusingal¹, Christopher Dean², George Gatsios²

¹*Thales Australia, Rydalmere, Australia*, ²*Thales Australia, Australia*

Background, Motivation, and Objective

With the adoption of the Restriction of Hazardous Substances (RoHS) Directive on the use of certain hazardous substances in electrical and electronic equipment, lead free piezoelectric ceramic materials are gaining interest from researchers and underwater acoustic transducer designers around the world. In order to obtain performance levels similar to those achieved using PZT materials, development activities of lead free materials has been expanding over the last two decades. Thales Australia is currently focusing its development efforts on hard and soft lead free materials for underwater applications.

Statement of Contribution/Methods

Thales Australia has developed hard and soft Barium Titanate compositions for underwater transmitters and receivers. Ceramics were manufactured using conventional ball milling and sintering processes. The performance of a barrel-stave flexensional transducer, manufactured with hard BaTiO₃, was evaluated in terms of transmit voltage response (TVR), sound pressure level (SPL), and directivity pattern. Linear array hydrophones made using BCZT (Ba_{1-x}Cax(ZryTi_{1-y})O₃) were used for studying receive voltage sensitivity and directivity pattern. Transmitters were tested in a lake with sufficient depth and lateral dimensions to measure the far field characteristics. Receiver arrays were characterised in an Acoustic Test Tank. Performance of the developed transmitter and receiver arrays were compared with the standard PZT based devices.

Results/Discussion

BaTiO₃ transmitters exhibited a typical TVR greater than 130 dB re 1 Pa/V @ 1 m and a SPL of 186 dB re 1 Pa @ 1 m which is comparable to what is reported in the open literature for PZT barrel-stave flexensional transducers.

Receiver arrays made using BCZT exhibited a sensitivity 3 dB less than a standard TLZ-1 hydrophone array.

These results demonstrate that there is still a performance difference between lead free and PZT based underwater sensors, although the gap is narrowing.

P1-C2 - Improving Image Quality with Limited Data

Kairaku (posters 1)

Thursday, October 25, 9:30 AM - 4:00 PM

Chair: **Pieter Kruizinga** Erasmus Medical Center

P1-C2-1

Sparse Orthogonal Diverging Wave Imaging on a High-Frequency Phased Array Endoscope

Christopher Samson¹, Eric Simpson¹, Rob Adamson¹, Jeremy Brown²

¹Biomedical Engineering, Dalhousie University, Canada, ²Biomedical Engineering, Dalhousie University, Halifax, NS, Canada

Background, Motivation, and Objective

Ultrafast imaging systems with frame rates in the kilohertz range have enabled several exciting new imaging modes such as shear wave imaging, super-resolution imaging, and functional brain imaging. The measurement and analysis of these images offer clinically significant insight that cannot be as easily obtained from conventional line-by-line focusing systems. For phased arrays, diverging wave imaging is the most common ultrafast imaging method. This approach, however, suffers from reduced SNR since only a sub-aperture of the array is used for each insonification. This work presents a new ultrafast phased array imaging technique whereby orthogonal Hadamard codes are ‘surfed’ on top of a diverging wave emitted from the full aperture. The number of Hadamard codes can be sparsely selected from the Hadamard matrix allowing for a trade-off between frame rate and image quality, yet still providing a significant SNR improvement over the gold standard sub-aperture method. The beamforming scheme was implemented and evaluated using a custom beamforming system with a 64-element 40MHz phased array endoscope.

Statement of Contribution/Methods

Hadamard coding allows for synthetic aperture (SA) beamforming to be performed and is equivalent to transmit pulsing N elements individually, but with an SNR improvement of N, where N is the number of elements in the array. As a result, a complete set of orthogonal basis codes is defined by N orthogonal Hadamard codes. The number of codes can be reduced by sparsely selecting rows from the Hadamard transmit matrix so that only the codes containing the lowest spatial frequency components are used. When an incomplete set of Hadamard codes are used, however, the directivity of the insonifications deteriorates. This study shows that this effect can be mitigated by surfing the codes on a virtual point source diverging wave. In this study, the directivity and radiation patterns were theoretically and experimentally compared for 64, 32, 16, 8, and 4 Hadamard codes using a 64 element, 40 MHz phased array. Images were collected for each configuration and the SNR was compared between each transmit scheme as well as with conventional transmit-receive beamforming.

Results/Discussion

The secondary lobe levels were found to be at -65, -60, -58, -53, and -48 dB for 64, 32, 16, 8, and 4 Hadamard encoded insonification events. Using the same number of Hadamard codes, the FWHM directivity was found to be 136°, 160°, 140°, 128°, and 112°, compared to 136°, 56°, 30°, 19°, and 18° when the Hadamard codes were not surfed on a diverging wave. The SNR when using N Hadamard codes was approximately 2dB better than the conventional transmit-receive focusing case measured with our variable sampling imaging system. Thereafter, SNR decreases by approximately 2dB each time the number of Hadamard codes is halved.

Deepforming: a deep learning strategy for ultrasound beamforming applied to sub-sampled dataWalter Simson¹, Nassir Navab¹, Guillaume Zahnd¹¹*Chair for Computer Aided Medical Procedures & Augmented Reality, Technische Universität München, Germany***Background, Motivation, and Objective**

Receive beamforming plays a critical role in ultrasound image generation. This operation can be summarized as follow. A back-scattered wave is received by an aperture window, corresponding to a range of piezoelectric elements. The ensemble of signals captured this way, called a raw scan line (of dimension 2), are combined together to create a single radio frequency signal (RF, of dimension 1) which represents an image column. This operation is repeated by shifting the central element of the aperture window along the length of the transducer to beamform the entire image.

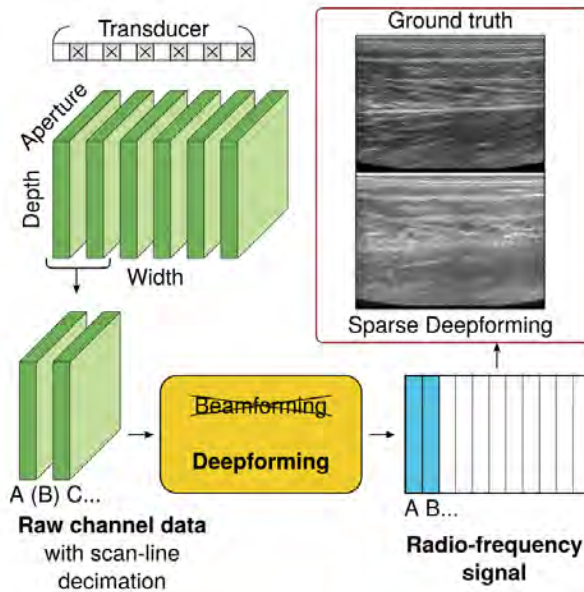
A major trade-off generally exists between beamforming strategies that enable a relatively high frame rate (eg, Delay and Sum, 20-100 fps) at the cost of a lower image quality, and strategies that provide a greater resolution and contrast (eg, Minimum Variance) but are prohibiting for real-time applications. An approach that brings the best of both worlds is yet to be put forward.

Statement of Contribution/Methods

This study is based on a recent so-called "Deepformer" pipeline, that completely replaces the traditional "explicit" beamforming operation by an "implicit" deep learning approach. The aim of this work is to combine Deepforming with image sub-sampling (50% sparsity) to further speed up acquisition time by skipping every other scan line, allowing for twice the acquisition frame-rate. A deep residual neural network is trained to act as a delay and sum pipeline by mapping raw channel data to RF signals. A Cephasonics cQuest Cicada scanner with a 128 elements linear transducer (CPLA12875, 7 MHz) is used to acquire the data in combination with the open-source SUPRA software on GPUs.

Results/Discussion

The method is trained on 8625 *in vivo* images (19 healthy volunteers, 4 separate anatomies) and validated on another 1828 images (3 further volunteers and 3 previously unseen anatomies). The produced deepformed images are closely comparable to ground truth frames created with an explicit delay and sum strategy. No quality drop-off is observed between trained and unseen anatomies, showing the robustness of the approach. In summary, the method of Deepforming is able to perform a beamforming operation on sparse raw data. A constant inference speed combined with the potential ability to map virtually any beamforming algorithm paves the way for a new paradigm in ultrasound imaging.



The partial Hadamard matrix for performance optimization of compressed sensing based synthetic transmit apertureJing Liu¹, Jianwen Luo¹¹School of Medicine, Tsinghua University, Beijing, China, People's Republic of**Background, Motivation, and Objective**

We previously proposed compressed sensing (CS) based synthetic transmit aperture (CS-STA) to reconstruct the synthetic transmit aperture (STA) dataset from a smaller number of randomly apodized plane wave (PW) firings with CS algorithm. In CS-STA, the apodization of the i^{th} PW firing is the i^{th} row of the measurement matrix. Sparsely representing STA data with *sym8* wavelets, we validated that CS-STA can increase the frame rate (FR) and contrast-to-noise ratio (CNR) of STA while maintaining its high resolution by choosing a random matrix as the measurement matrix (Liu et al, IEEE TMI 2017). However, for this choice, the reconstruction is time-consuming, and the FR and image quality improvements are limited. To solve these issues, we propose to use the partial Hadamard matrix as the measurement matrix in this study.

Statement of Contribution/Methods

For an n -element array, the partial Hadamard matrix of CS-STA with m firings (CSm-STA) is the first m rows of the n^{th} order Hadamard matrix and the entries of the corresponding random matrix obey a continuous uniform distribution $U(0, 1)$. We investigated the CS-STA performance with these two measurement matrices on a 128-element linear array (pitch = 0.3 mm, f_0 = 6.25 MHz, bandwidth = 60%) by comparing CS8-STA and CS16-STA with STA. We carried out the experiments on a CIRS 040 phantom with a Verasonics Vantage 256 system. The pulse repetition frequency was 12.8 kHz.

Results/Discussion

As Fig. 1 shows, with 16 \times higher FR, CS8-STA with random matrix deteriorates the image quality of STA while CS8-STA with Hadamard matrix improves the image quality of STA. As Table I shows, CS8-STA with Hadamard matrix and STA obtain similar lateral FWHMs (~ 0.42 mm) while CS8-STA with random matrix has 0.16 mm larger FWHM. The CNR of STA is 1.47 dB, which is higher than that of CS8-STA with random matrix (-5.11 dB) and lower than that of CS8-STA with Hadamard matrix (5.26 dB). In addition, the reconstruction speed of CS-STA with Hadamard matrix is $\sim 100\times$ faster than that with random matrix. Although CS16-STA performs better than CS8-STA, Hadamard matrix still outperforms random matrix. The higher performance of Hadamard matrix is because it is less coherent with sparse basis (i.e., *sym8* wavelets in this study) than random matrix. To conclude, the partial Hadamard matrix can optimize the performance of CS-STA and further increase the FR and image quality of STA.

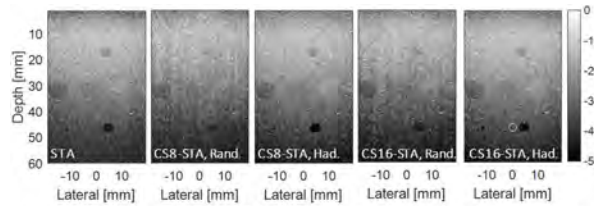


Fig. 1. The B-mode images of different methods. The red and white circles indicate the region-of-interest and the corresponding background for the CNR calculation.

Table I. The frame rate (FR), reconstruction time (recon time), lateral FWHM and CNR for different methods.

| Method | Measurement matrix | FR [Hz] | Recon time [min] | Lateral FWHM [mm] | CNR [dB] |
|----------|--------------------|---------|------------------|-------------------|----------|
| STA | ~ | 100 | ~ | 0.42 | 1.47 |
| CS8-STA | Random | 1600 | 280.41 | 0.66 | -5.11 |
| CS8-STA | Hadamard | 1600 | 2.99 | 0.43 | 5.26 |
| CS16-STA | Random | 800 | 376.20 | 0.58 | -1.83 |
| CS16-STA | Hadamard | 800 | 3.63 | 0.42 | 6.36 |

Virtually Extended Array imaging improves lateral resolution in high frame rate volumetric imaging

Mehdi Soozande¹, Fabian Foo², Maysam Shabanimotagh², Michiel Pertijs³, Martin D. Verweij^{1,2}, Hendrik J. Vos^{1,2}, Johan G. Bosch¹, Nico de Jong^{1,2}

¹Biomedical Engineering, Thorax Center, Erasmus MC, Rotterdam, Netherlands, ²Laboratory of Acoustical Wavefield Imaging, Department of Imaging Physics, Delft University of Technology, Delft, Netherlands, ³Electronic Instrumentation Laboratory, Delft University of Technology, Delft, Netherlands

Background, Motivation, and Objective

Matrix arrays for endoscopic and catheter-based applications are restricted to small physical apertures, which limits their lateral resolution. In addition, when aiming for high volume rate imaging and utilizing the recent methods of transmitting a single or few diverging waves, lateral resolution further deteriorates. In this work, we suggest a high frame rate transmission scheme which outperforms the recent methods in lateral resolution.

Statement of Contribution/Methods

In general, the lateral resolution in an ultrasound image is determined by the imaging aperture, which is a convolution of the effective transmit and receive aperture. A synthetic transmit aperture (STA) has the largest imaging aperture size and triangular natural apodization in co-array analysis (Hoctor, Kassam. Proc IEEE 1990), hence it can provide a high lateral resolution and low side lobe level, but at the cost of a high number of transmissions. To cut this number while keeping the same imaging aperture as STA, we propose to transmit only on either side of the array (Daft et al. IUS 2007). Furthermore, to achieve similar lateral resolution and contrast as STA, we weigh the channel data as to obtain a same triangular apodization. We tested this Virtually Extended Array (VEA) concept in watertank experiments on a 24×20 elements matrix array (7.5MHz), by consecutively transmitting a diverging wave from the first and last columns. The final volume was reconstructed by voxel-based delay and sum. Apart from using two single-columns for transmit, which provide relatively low transmit power and low SNR, we also used larger sub-apertures of 24×10 elements (both halves of the array) to generate diverging waves with higher transmission power. PSF, CR and SNR were used to compare the image quality of single diverging wave, STA, single-column VEA (CVEA) and sub-aperture VEA (SVEA) methods.

Results/Discussion

The proposed method (SVEA) reduces the PSF width by 16±3% (average ±standard deviation), compared to a single diverging wave. The SNR for diverging wave, STA, CVEA and SVEA was 52, 51, 46, and 55 dB and the CR was 32, 41, 38, and 36 dB, respectively. In conclusion, we have shown that SVEA can improve the lateral resolution using only two transmissions while providing acceptable SNR, at the cost of halving the framerate, compared to a single diverging wave.

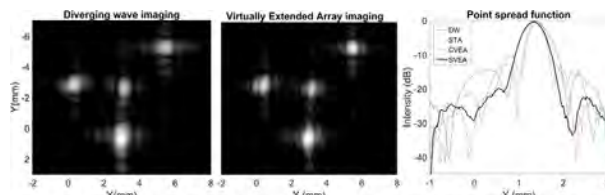


Figure 1. C-plane images of a four-needle phantom at 10 mm depth reconstructed with A) DW and B) CVEA. C) PSF of a single needle phantom image acquired by DW, STA, CVEA and SVEA imaging.

Gap-filling method for suppressing the grating lobes in ultrasound imaging

Bae-Hyung Kim¹, Viksit Kumar¹, Azra Alizad², Mostafa Fatemi¹

¹Department of Physiology and Biomedical Engineering, Mayo Clinic College of Medicine & Science, Rochester, MN, United States, ²Department of Radiology, Mayo Clinic College of Medicine & Science, Rochester, MN, United States

Background, Motivation, and Objective

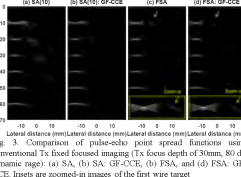
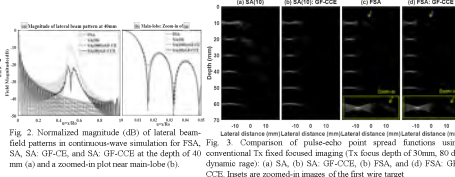
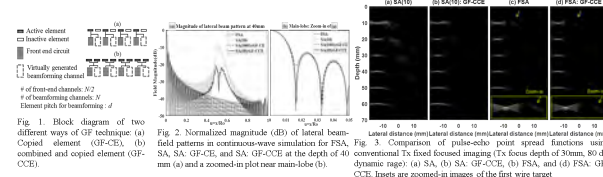
The grating lobe (GL) artifact due to the sparsity of sampled array aperture results in degradation of the ultrasound imaging quality. Sparse array (SA) techniques which leave inactive elements in array aperture were introduced to reduce the active channel count in ultrasound imaging systems. However, the GL level of SA is higher than the fully sampled array (FSA) due to more increased inter-element spacing of array aperture. In this paper, a novel method for suppressing the GL in the SA or FSA is presented.

Statement of Contribution/Methods

Based on a given or known data sets of radio frequency (RF) echo acquired from active elements of an array, RF echo data in inactive and/or non-existing elements of array can be created virtually and used to suppress the GL artifact of the SA or FSA. This paper presents the gap-filling (GF) or gap-interpolation (GI) approaches to generate virtual channel data, which are not actually acquired. Fig. 1 shows the diagrams of two different GF techniques as the simplest approach: 1) GF-CE technique that uses the copied element (CE) where the active channel data is copied to the data of inactive element, and 2) GF-CCE technique where two elements are combined and original channel data is acquired by the left channel and is copied to the right channel. The GF technique can reduce the original GL by incoherently summing with other GLs generated by virtually created source aperture. For demonstrating the proof of concept, continuous-wave simulation using Rayleigh Sommerfeld scalar wave diffraction formula and pulsed-wave simulation using Field II tool were performed with a centre frequency of 7.5 MHz, element pitch of 0.2 mm, element width of 0.19 mm, 64 elements of the array aperture, 64 Tx/Rx channels in FSA and 32 Rx channels in SA.

Results/Discussion

As seen in the simulation results of Figs. 2 and 3, it has been shown that the GF technique can be realized in conventional beamforming system, reducing the GLs by about 16 dB without sacrificing the lateral resolution as indicated by the main-lobe width or any appreciable changes in the side-lobe levels. The GF technique can also be used for FSA to improve the near-field image by virtually generating RF data in inter-channels and having an effective pitch size less than the original pitch size. This paper shows the feasibility of providing improved image quality with reduced number of active channel using the GF technique.



Optimal virtual sources distribution in 3-D Diverging Wave Ultrasound Imaging: an experimental study
Paolo Mattesini^{1,2}, Emmanuel Roux³, Emilia Badescu², Lorena Petrusca², Olivier Basset², Piero Tortoli¹, Hervé Liebgott²
¹*Microelectronics Systems Design Lab, University of Florence, Italy*, ²*CREATIS, Univ Lyon, INSA-Lyon, Université Claude*
Bernard Lyon 1, UJM-Saint Etienne, CNRS, Inserm, Lyon, France, ³*Laboratoire Hubert Curien, Univ Lyon, INSA-Lyon, Université Claude Bernard Lyon 1, UJM-Saint Etienne, CNRS, Inserm, Lyon, France*
Background, Motivation, and Objective

In a previous study we have experimentally demonstrated that sparse 2D arrays can be used to implement fast volumetric ultrasound imaging based on the transmission (TX) of Diverging Waves (DW). However, the optimal location of the virtual sources (VS) used for the 3D DW transmission is still undefined (for both sparse and full configurations).

The aim of this work is to experimentally analyse how the VS distribution affects the images produced by: a reference 2-D array, a random sparse array and a sparse array optimised for focused TX.

Statement of Contribution/Methods

Two VS positioning strategies have been considered: regular VS (on a grid) and spiral VS (on a spiral). In both cases, two maximum angular widths were tried (60° and 120°). In all tested settings, 25 VS were used and located at 40 mm behind the 2-D array centre.

The experiments were performed by three different 2-D array configurations: a 32x32 element array (considered as reference: Ref1024) and two 256-elements sparse arrays (Opti256 and Rand256 [10.1109/TUFFC.2016.2614776]) obtained by properly selecting the elements from Ref1024.

The 1024 elements of a 3 MHz 2-D array probe (Vermon) were individually connected to four synchronized Verasonics Vantage 256 systems as described in [Petrusca, Applied Sciences 2018]. The image quality was evaluated on a Gammex (Sono410 SCG) and a CIRS (054GS) phantom. The performance metrics include the lateral and axial full width at half maximum (FWHM), contrast ratio (CR) and contrast to noise ratio (CNR).

Results/Discussion

In Ref1024, average improvements of CR (3.4 dB) and CNR (2.9 dB) are obtained by using the spiral VS distribution rather than a grid. The axial resolution remains the same, while the lateral resolution is worse (up to 0.4 mm coarser). For Opti256 and Rand256 the trend is similar: with the spiral VS distribution the CR and CNR are, on average, improved by 2.2 dB and 4.8 dB, respectively, but the resolutions are worse (up to 0.4 mm coarser for the lateral and up to 0.2 mm for the axial). On average, the CR and CNR are improved by 4.2 dB and 8.2 dB respectively when using the 60° angle range instead of 120°. The complete results are reported in the Table.

The results show that, compared to a regular one, a spiral VS distribution increases the contrast while reducing the lateral resolution, confirming that VS position optimization is crucial to improve the imaging quality.

| Ref1024 VSs d. 40mm | | | | |
|----------------------------|----------------------|---------------------|--------------|--------------|
| | Mean Lat. Reso. [mm] | Mean Ax. Reso. [mm] | CR [dB] | CNR [dB] |
| Grid 60° | 1,98 | 0,47 | -8,8 | -10,2 |
| Grid 120° | 2,13 | 0,44 | -2,3 | -15,4 |
| Spiral 60° | 2,39 | 0,47 | -11,5 | -8,8 |
| Spiral 120° | 2,29 | 0,45 | -6,4 | -11,0 |
| | | | | |
| Rand256 VSs d. 40mm | | | | |
| | Mean Lat. Reso. [mm] | Mean Ax. Reso. [mm] | CR [dB] | CNR [dB] |
| Grid 60° | 2,06 | 0,45 | -3,0 | -16,2 |
| Grid 120° | 2,06 | 0,58 | 0,4 | -31,0 |
| Spiral 60° | 2,46 | 0,67 | -5,5 | -12,7 |
| Spiral 120° | 2,49 | 0,75 | -1,1 | -24,7 |
| | | | | |
| Opti256 VSs d. 40mm | | | | |
| | Mean Lat. Reso. [mm] | Mean Ax. Reso. [mm] | CR [dB] | CNR [dB] |
| Grid 60° | 3,11 | 0,44 | -2,5 | -17,5 |
| Grid 120° | 2,78 | 0,49 | 0,6 | -27,9 |
| Spiral 60° | 3,35 | 0,55 | -4,6 | -16,6 |
| Spiral 120° | 3,14 | 0,47 | -2,2 | -19,6 |

Best (green) and worst (red) performances for each column are highlighted

Improving contrast and grating lobe suppression in sparse array imaging using convolutional neural network
Viksit Kumar¹, Bae-Hyung Kim¹, Po-Yang Lee², Mostafa Fatemi³, Azra Alizad⁴
¹*Department of Physiology and Biomedical Engineering, Mayo clinic, Rochester, MN, United States,*
²*National Cheng Kung University, Taiwan,*
³*Department of Physiology and Biomedical Engineering, Mayo Clinic, Rochester, MN, United States,*
⁴*Department of Radiology, Mayo Clinic, Rochester, MN, United States*
Background, Motivation, and Objective

Sparse array (SA) techniques are used to reduce the number of active channels in an ultrasound system. However, SA suffers from grating lobe (GL) artifacts resulting in poor image quality and low contrast to noise ratio (CNR). The high correlation between the neighboring channel data can be leveraged to interpolate the signal for inactive channels in SA, which is termed as gap-filling (GF).

Statement of Contribution/Methods

1800 pre-beamformed radio frequency (RF) echo data is acquired at a center frequency of 6.25 MHz from a calibrated phantom using zero angle plane-wave transmission with a 128 element linear array (L11-4v). Custom convolutional neural network (CNN) algorithm is developed to create pseudo-RF data which can fill the inactive channels of SA. A supervised training is performed with 64-channel data (odd channels of 128-channel data) as the input and 128-channels as the output of CNN. Mean absolute error is used as the loss function.

Results/Discussion

Figure 1(a), (b) and (c) show an example image of original 128-channel fully sampled array, 64-channel SA and 128-channel pseudo SA with even channels as the output of CNN algorithm respectively. The corresponding beamformed (BF) images are shown in fig. 1(d), 1(e) and 1(f) respectively. The GL present in 1(e) is obscuring the hypoechoic region due to the clutter caused by increased inter-element spacing. The hypoechoic region is recovered using CNN in fig. 1 (f). Table 1 summarizes the improvement in CNR and contrast ratio (CR). The hyperechoic region of BF data using 128 pseudo channels has CR and CNR higher than the BF data using original 128-channel data. In conclusion, GF technique based on CNN algorithm can provide improved CNR, CR and GL suppression with a reduced number of active channels.

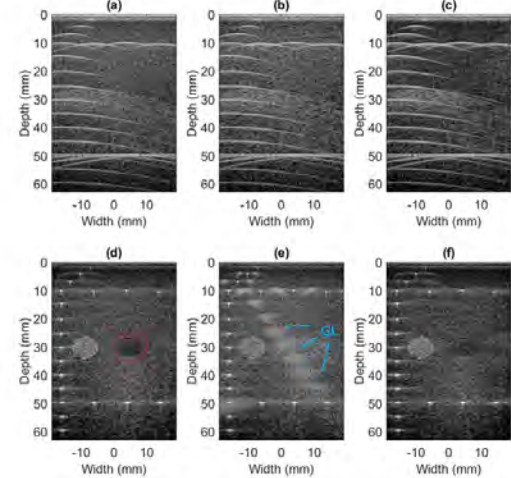


Table 1: Comparison of contrast and contrast to noise ratio for hypoechoic and hyperechoic regions from 64-channel sparse array, 128-channel pseudo array and 128-channel fully sampled array.

| | Contrast ratio (dB) | Contrast to noise ratio (dB) |
|---------------------------------|---------------------|------------------------------|
| Hypoechoic | | |
| 64-channel sparse array | 0.57 | -23.26 |
| 128-channel pseudo array | 3.48 | -7.50 |
| 128-channel fully sampled array | 6.07 | -2.67 |
| Hyperechoic | | |
| 64-channel sparse array | 6.75 | -1.55 |
| 128-channel pseudo array | 9.38 | 1.52 |
| 128-channel fully sampled array | 9.31 | 1.29 |

Fig. 1: Montage showing pre beamformed RF echo data for (a) 128-channel fully sampled array, (b) 64-channel sparse array and (c) 128-channel pseudo fully sampled array. The second row shows the beamformed RF data for (d) 128-channel fully sampled array, (e) 64-channel sparse array and (f) 128-channel pseudo fully sampled array. The grating lobe (GL) obscuring hypoechoic region (red circle) in 1(e) is completely removed in 1(f).

Portable Ultrasound through Compressive Beamforming with Improved ContrastJovan Mitrovic¹, Lynn La Pietra², Zeljko Ignjatovic¹¹*University of Rochester, United States*, ²*Carestream Inc, United States***Background, Motivation, and Objective**

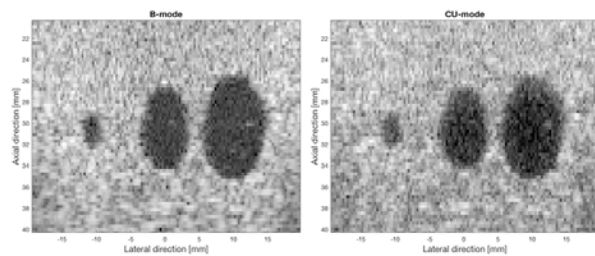
Medical ultrasound is a go-to modality for medical imaging as it provides good quality pictures of soft tissue without any ionizing radiation and damage. To further support point-of-care testing and diagnostic tools, there have been numerous efforts aimed towards the development of portable ultrasound. However, with portability usually comes lower contrast-to-noise ratio (CNR) which may diminish its advantages as compared to traditional full-aperture delay-and-sum (DAS). Our objective is to develop and characterize a portable ultrasound system with the same or better CNR and contrast than traditional systems.

Statement of Contribution/Methods

Our method (compressive ultrasound – CU) employs the principles of compressive sensing to spread the information across the spectrum and compress it into a fewer number of channels by changing the polarity of transducer elements' signals in a pseudo-random manner before summation into a single channel. The compressed data is then fed to an elastic nets estimation algorithm to reconstruct the full-aperture RF data, which is then beamformed and displayed as a grayscale image. The proposed method enables reduced front-end complexity of an ultrasound system while providing comparable image quality.

Results/Discussion

Verasonics V1 scanner, 5 MHz linear array, and ATS ultrasound phantom were used to validate the CU method and compare against full-aperture DAS. The CU consistently performs on par or better than DAS (Fig 1). Measured contrast ratio for DAS and CU (with 16:1 compression ratio) is 0.82 and 0.9, respectively. Also, the measured CNR for DAS and CU is 1.92 and 2.01, respectively. This improvement is enabled by the non-linear nature of elastic nets, where a balance between sparsity and energy smoothness can be introduced when needed.



Artifact Suppressed Sparse Coherent Plane Wave Compounding Using Modified Vernier-Interpolation Angle SequenceYa-Ling Hsieh¹, Meng-Lin Li¹¹*National Tsing Hua University, Taiwan***Background, Motivation, and Objective**

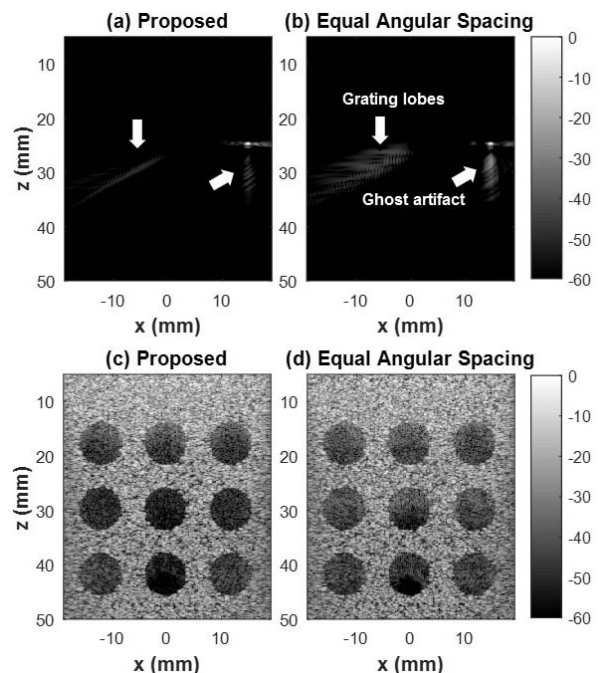
Coherent plane-wave compounding (CPWC) is a retrospective transmit focusing technique capable of providing equivalent beam quality to optimal multifocus imaging techniques. The more tilted plane wave data, the higher image quality. However, in most applications such as cardiovascular imaging, equal-angular-spacing decimation in the angle sequence is commonly used to significantly lower down the number of titled plane wave emissions; thus reducing motion artifacts and saving power since the computational load and the transmit number are reduced. Unfortunately, such sparse CPWC inevitably causes grating lobe artifacts.

Statement of Contribution/Methods

Here we propose a modified vernier-interpolation angle sequence for sparse CPWC to avoid grating lobe artifacts associated with sparse CPWC using equal-angular-spacing decimation. We explore the relation between transmit elements in conventional focusing and plane wave steering angles in CPWC. Based on this relation, sparse plane wave steering angles can be selected to optimize the two-way effective aperture function. Angle sequence with our proposed modified vernier interpolation being applied is designed to synthesize an effective vernier sparse periodic transmit array aperture, which was similar to that proposed by Lockwood for sparse periodic linear array design avoiding grating lobes. Given the number of the total titled plane wave emissions, the synthesized effective aperture by the sparse CPWC with our proposed angle sequence approximates to the desired two-way effective aperture with appropriate width, shape, and effective element pitch smaller than half wavelength; thus enabling grating-lobe suppression.

Results/Discussion

Field II simulation was used to verify our idea. 10-angle sparse CPWC was performed. Figs. (a) and (c) were with the sparse CPWC using our proposed angle sequence and Figs. (b) and (d) were with the sparse CPWC using equal-angular-spacing-decimation angle sequence. With our proposed angle sequence, the grating lobe was suppressed by at least 10 dB, and 34 % contrast-to-noise ratio improvement was achieved. Overall, we demonstrated the efficacy of our proposed angle sequence for grating-lobe artifact suppression. Moreover, it is found that our proposed angle sequence can highly suppress ghost artifacts (see Figs. (a) and (b)), for which further study is required.



High-frame rate 3D-synthetic transmit aperture imaging with a reduced number of receiving channelsYing Li¹, Michael Kolios¹, Yuan Xu¹¹*Physics, Ryerson University, Toronto, ON, Canada***Background, Motivation, and Objective**

The cost of a system using a fully addressed 2D matrix array for 3D ultrasound imaging is prohibitively high. Moreover, the amount of RF data in 3D-STA (synthetic transmit aperture) imaging is usually large and can prohibit real-time imaging. Therefore, we propose a high frame rate 3D-STA ultrasound approach with a reduced number of receiving channels to image a small field of view (FOV) with the image quality of a full array. The FOV can be steered to cover a larger imaging area.

Statement of Contribution/Methods

Assume that a 2D array has $N \times N$ elements. Along both the lateral and the elevational direction, we combined L (K) adjacent transmit (receive) elements to form a transmit (receive) group, each of which contains $L \times L$ ($K \times K$) elements. K and L were prime to each other (no common factor) to suppress the grating lobe artifacts. Thus, the total number of measurement channels M (the product of the number of transmission events (n_T) and receiving channels (n_R)) was reduced from N^4 to $N^4/(L \times K)^2$. The transmission and receiving beams were focused at the specific region of interest (ROI) by introducing the element delays within each group. After M channels of RF data were acquired, a spatial matched filter (SMF) approach was used to reconstruct the images. The two-way SMF, which depends on the size and location of the group element, was generated dynamically for each imaging pixel.

A $\lambda/2$ -pitch 2D array with 64×64 elements using a center frequency of 5-MHz was simulated in Field II. The simulated point target was placed at $(x, y, z) = (0, 0, 30)$ mm. The imaging performance was assessed by calculating the full width at half maximum (FWHM) and the clutter-energy-to-total energy ratio (CTR) of a simulated 3-D point target.

Results/Discussion

By using $(n_T, n_R) = (N^2/9, N^2/49)$ ($L = 3$ and $K = 7$) to acquire data for one frame, the lateral and elevational FWHM in the proposed method were 1.06 mm, comparable with that of the full-array STA (1.00 mm). Also, the CTR value in the proposed method and full STA were -23.65 and -24.01, respectively. The cross-section image in x-z and y-z planes and the line plots are shown in the Fig. 1. We have demonstrated using this approach images of comparable quality with a 9-fold reduction in transmission events and 49-fold reduction in receiving channels. The approach may help in realizing clinical applications of real-time 3D ultrasound imaging technology using large arrays.

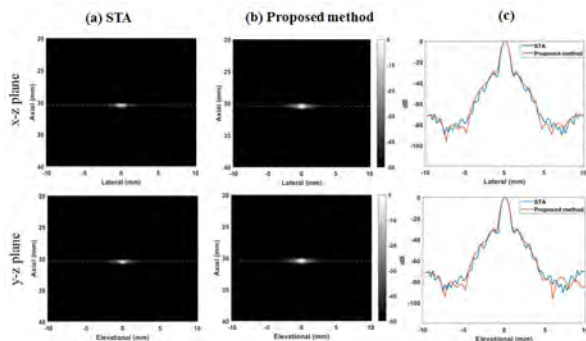


Fig.1 The log-enveloped beamformed images obtained from (a) STA with full array, (b) The proposed method , and (c) Comparison line plot through the center of the point target (indicated with a dashed green line). Top row of the figure represents the x-z plane, bottom row is y-z plane.

Ultrafast Ultrasound Imaging with Stretchable Probe on Nonplanar Surface: A Simulation Study
Congzhi Wang¹, Yang Xiao¹, Weibao Qiu¹, Teng Ma¹, Hairong Zheng¹
¹*Paul C. Lauterbur Research Center for Biomedical Imaging, Shenzhen Institutes of Advanced Technology, the Chinese Academy of Sciences, China, People's Republic of*
Background, Motivation, and Objective

Ultrasound imaging is generally obtained by rigid probes with regular shape (planar or convex). However, when the surface to be examined is too complex, it is difficult to obtain high quality images even though the ultrasonic couplant is used. Recently, the stretchable ultrasound probe that can be conformed to nonplanar surfaces has been reported [1]. To reconstruct the image with it, the synthetic aperture method was used, in which only one element was activated in each insonification and thus the flying-time of the forward propagating wave can be accurately estimated. However, it is still a big challenge to obtain the image with single insonification of all elements, like in the plane-wave imaging, to increase the frame rate, as the irregular positions and different directivities of the elements make it difficult to determine the exact time-delay between the pulse emission and echo reflection.

Statement of Contribution/Methods

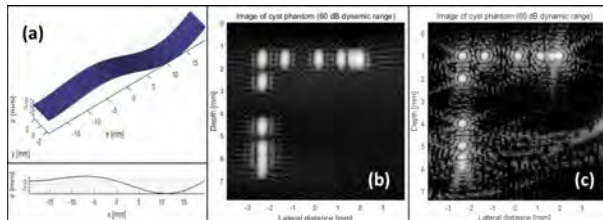
In this paper, a novel framework for ultrasound image reconstruction is proposed, which can avoid the estimation of any flying-time of wave-front and thus can be used to achieve ultrafast imaging with the stretchable probe. A linear relationship, $R=GI$, is established between the acquired RF signals R and the image I with a matrix G , which is the assembling of all the Point Spread Functions (PSF) at each image pixel. The PSFs are obtained by the simulation in the Field II, and the RF signals are then obtained on a simulated phantom with several point scatterers. At last, the inverse problem is solved using a sparsity regularization method, $\min\|\Phi I\|_1 \text{ s.t. } \|R-GI\|_2^2 \leq \beta^2$, which is similar to that used in [2], and the image can be correctly reconstructed.

Results/Discussion

The shape of the curved probe is arbitrarily defined and shown in Figure 1 (a), the upper one is the 3D contour of its surface and the lower one is the side view. Figure 1 (b) shows the image obtained by a regular linear array probe with 127 steering plane-wave insonifications and reconstructed by the coherent compounding method on the same phantom. Figure 1 (c) is the image obtained by the curved probe with one insonification and reconstructed by the proposed method. We hope this image reconstruction method can help the stretchable ultrasonic probe to be used in the special applications of NDE and medicine.

[1] Hu et al., Sci. Adv. 2018;4:eaar3979

[2] David et al., J. Acoust. Soc. Am. 137(5), 2015, 2773-84



P1-C3 - Modelling in Beamforming

Kairaku (posters 1)

Thursday, October 25, 9:30 AM - 4:00 PM

Chair: Sebastian Salles NTNU

P1-C3-1

Determination of Delay Resolution in Baseband I/Q Beamformer Using Error Model of Array Gain

Jintae Jang¹, Sua Bae¹, Hyunwoo Song¹, Kangsik Kim², Tai-kyong Song¹

¹Department of Electronic Engineering, Sogang University, Korea, Republic of, ²Samsung Electronics Co., Ltd, Seoul, Korea, Republic of

Background, Motivation, and Objective

Baseband I/Q beamformer (IQBF) has been widely used because it requires a lower sampling rate and smaller memory compared to RF beamformer (RFBF); the low complexity of beamformer allows parallel beamforming for various advanced imaging methods. However, despite its popularity, there exist only a few studies on IQBF in terms of performance depending on the delay resolution which determines the complexity of beamformer. In this paper, a criterion for determining delay resolution of IQBF is proposed by comparing the gain loss of IQBF and RFBF as a function of delay resolution.

Statement of Contribution/Methods

We formulated an error model of array gain by assuming that 1) the ultrasound signal has an envelope of a Gaussian function with a -6dB bandwidth of B and 2) the timing error is uniformly distributed in the interval $[-T/2, T/2]$ where T is a delay resolution. To verify proposed error model, simulation, phantom and in vivo studies were conducted using plane wave compounding (6 angles from -10° to 10°). In Field II simulation, B-mode images were reconstructed with a 128-element linear array (center frequency : $f_0 = 5.2$ MHz, B = 70%) varying $1/T$ from $2f_0$ to $16f_0$, and contrasts of the images were measured. In phantom and in vivo experiments, images of a phantom (ATS 549, ATS Lab.) and a human carotid were obtained with an ultrasound system (Vantage 128, Verasonics) and a linear probe (L7-4, Philips) and reconstructed using IQBF and RFBF ($1/T = 4f_0$ or $16f_0$).

Results/Discussion

Fig. 1(a) shows the theoretical gain loss of IQBF and RFBF expected by the error model as a function of $1/T$ assuming B = 70%. Fig. 1(b) presents the measured contrasts of simulated images, which agrees well with the expected gain loss in Fig. 1(a) since the gain loss leads to contrast degradation. The theoretical gain loss as a function of B when $1/T$ is $4f_0$ or $16f_0$ is shown in Fig. 1(c) and the phantom and in vivo results are presented in Fig. 1(d) and Fig. 1(e), respectively. From the phantom and carotid images, it can be observed that the image quality of IQBF with $4f_0$ is similar to that of RFBF with $16f_0$ and much better than that of RFBF with $4f_0$. It can also be recognized through contrast ratio in Fig. 1(d). These results are consistent with the theoretical prediction in Fig. 1(c) as bandwidth of the L7-4 is around 50%. Thus, we concluded that delay resolution of IQBF can be determined by the proposed error model to achieve the desired image quality.

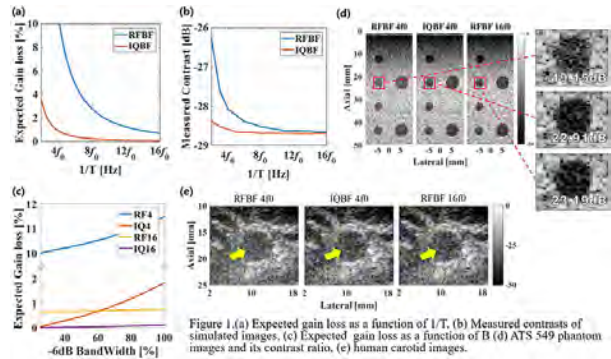


Figure 1.(a) Expected gain loss as a function of $1/T$, (b) Measured contrasts of simulated images, (c) Expected gain loss as a function of B (d) ATS 549 phantom images and its contrast ratio, (e) human carotid images.

A simple, artifact-free virtual source modelOle Marius Hoel Rindal¹, Alfonso Rodriguez-Molares², Andreas Austeng¹¹*University of Oslo, Norway*, ²*Norwegian University of Science and Technology, Norway***Background, Motivation, and Objective**

Virtual sources (VS) allow intuitive implementations of synthetic aperture imaging. However, when the VS lie within the image scan, an artifact occurs due to a discontinuity of the VS model. VS are placed within the imaging plane in techniques such as retrospective beamforming (RTB), synthetic aperture sequential beamforming (SASB), and can be used for multiple line acquisition (MLA). We present a simple modification of the VS model to correct this artifact.

Statement of Contribution/Methods

Nguyen and Prager [1] introduced a complete VS model of the wave propagation that resolves the discontinuity in the wave path and corrects the artifact. However, their solution is cumbersome to implement and computationally expensive.

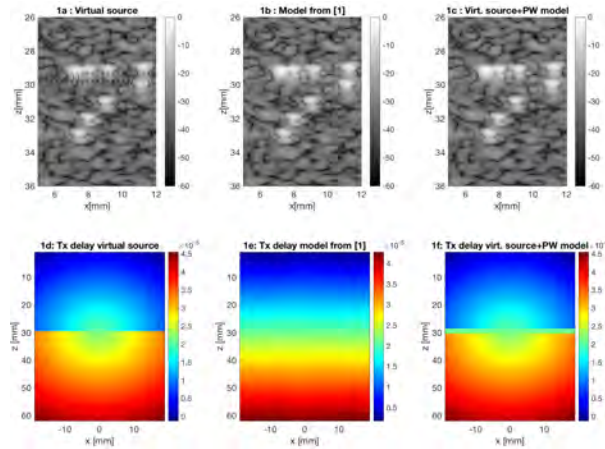
We introduce an alternative solution that is both easy to implement and less computationally expensive. We modify the VS model by assuming plane-wave (PW) propagation in a small region before and after the focus.

These two approaches are implemented for linear and sector scans in the UltraSound Toolbox (USTB) for both RTB and MLA reconstruction. For demonstration, a RTB sequence was recorded on the Verasonics Vantage 256 system using a Philips L7-4 probe. 128 VS were placed at 29.6 mm depth, ranging from -19 to 19 mm in the lateral direction. A commercial CIRS phantom (Model 054GS) was used as target. The channel data was beamformed with USTB using 4 MLAs and full RTB reconstruction. The data and code are available through www.ustb.no/examples/hybrid_virtual_source_model.

Results/Discussion

Fig. 1 shows the resulting RTB images around the focus, and the transmit delays for the center wave. The discontinuity in the transmit delays of the VS model can be observed in Fig. 1d, producing the artifact shown in Fig. 1a at 29.6 mm depth. The model proposed in [1] eliminates the discontinuity in the transmit delays (Fig. 1e) and corrects the artifact (Fig. 1b). The transmit delays of the proposed model are shown in Fig. 1f. Even though the discontinuity is not removed, it is moved out of the insonified area, effectively correcting the artifact (Fig. 1c). This modification does not affect lateral resolution noticeably since focused beams are almost plane at the focal depth.

[1] Nguyen & Prager (2016). High-Resolution Ultrasound Imaging With Unified Pixel-Based Beamforming. IEEE Trans. Med. Imaging.



Modeling the acoustic field produced by diagnostic ultrasound arrays in plane wave modeTing-Yu Lai¹, Michalakis Averkiou¹¹*University of Washington, United States***Background, Motivation, and Objective**

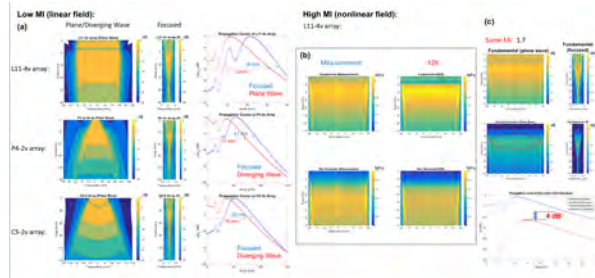
Recent advances in ultrafast contrast imaging that combine plane wave imaging (PWI) and contrast imaging have further facilitated innovations such as super-resolution imaging and ultrafast contrast-enhanced Doppler imaging. Combining PWI and THI may offer improvements in image quality in applications that use PWI such as 3D THI and harmonic color flow. However, no studies have yet investigated the acoustic field produced by diagnostic arrays in plane wave mode for these clinical applications. The aim of the present study is to model 3 diagnostic arrays, the Verasonics L11-4v linear array, C5-2v convex array, and P4-2v phased array with the KZK nonlinear parabolic wave equation. We have 2 specific objectives: first, to investigate increased nearfield bubble destruction due to the nature of the plane and diverging fields in low MI contrast imaging; and second, to investigate the feasibility of combining PWI and THI by quantifying the 2nd harmonic component generated by these fields.

Statement of Contribution/Methods

A KZK code that numerically solves the KZK equation in time domain and accounts for elevation focus and either plane or diverging geometries in the azimuthal plane was developed. For modeling the L11-4v array, the field of view was set to 4 cm, consistent with the typical field of view in carotid imaging. For the C5-2v and the P4-2v arrays, the depth was set to 15 cm, which is the typical depth in abdominal and cardiac imaging. Simulation results from KZK were compared with the results from Field II and hydrophone measurements in a water tank.

Results/Discussion

The linear and nonlinear field of 3 diagnostic ultrasound arrays operating in plane/diverging wave mode was investigated. In Fig. 1(a), use of such arrays in low MI contrast imaging produces slightly greater bubble destruction than conventional partial aperture focused beams. Reducing the sector width (degree of divergence) will increase penetration at the expense of a narrower field of view. In Fig. 1(b), simulation results (KZK) of the nonlinear field produced by the L11-4v array in plane wave mode agree with the acoustic measurement in the water tank. In Fig. 1(c), the 2nd harmonic of PWI beams was found to be lower than that of focused beams by 4 dB when operated at the same MI (1.7). Yet this suggests that combining PWI and THI would still be possible despite some signal loss when compared with conventional imaging.



P1-C4 - Bubbles Imaging

Kairaku (posters 1)

Thursday, October 25, 9:30 AM - 4:00 PM

Chair: **Wei-Ning Lee** University of Hong Kong

P1-C4-1

Comparing Microbubble Detection Algorithms for Super-Resolution Imaging

Jemma Brown¹, Kirsten Christensen-Jeffries¹, Sevan Harput², Ge Zhang², Jiaqi Zhu², Mengxing Tang², Chris Dunsby³, Robert Eckersley¹

¹Biomedical Engineering Department, School of Biomedical Engineering and Imaging Sciences, King's College London, London, United Kingdom, ²Bioengineering, Imperial College London, London, United Kingdom, ³Department of Physics and Centre for Pathology, Imperial College London, London, United Kingdom

Background, Motivation, and Objective

Visualisation of vasculature beyond the diffraction limit can be achieved by localising signals from isolated microbubbles. Various techniques to extract these signals from the surrounding tissue have been presented in the literature, relying on either the bubble non-linearity or movement. There is a need to comprehensively investigate the factors influencing the efficacy of these techniques. This work has developed a simulation environment where the techniques of pulse inversion (PI), differential imaging (DI) and singular value decomposition (SVD) filtering can be quantitatively compared.

Statement of Contribution/Methods

Building on previous work (Brown et al., 2017) the simulation has been expanded to investigate the wide parameter space over which super-resolution imaging is possible. Modelling of wave propagation through tissue was modelled using k-Wave and the bubble response over a size distribution of microbubbles incorporated using the Marmottant model. Signal onset was used to determine microbubble localisations (Christensen-Jeffries et al., 2017b). Each method was assessed over different transmit centre frequencies, transducer bandwidths and geometries, and flow velocities relevant to tumour microvasculature in terms of CTR and localisation precision and accuracy.

Results/Discussion

Figure 1A shows CTR and localisation dependence on centre transmit frequency for a bubble moving laterally at 0.5mm/s. PI generated a CTR improvement of 3.4 dB at a transmit frequency of 2 MHz over SVD and 36.2 dB over DI. However, at higher frequencies, Figure 1B shows that SVD and DI imaging had improved precision. When transducer bandwidths were included, the results showed that PI was more affected by transducer sensitivity and varying bubble sizes than the linear techniques.

The influence of flow velocity was investigated at suitable frequencies and bandwidths for each method. The results showed that PI was independent of bubble velocities for speeds between 0-2mm/s. SVD and DI were dependent on flow velocity. For example, SVD dependence on speed meant that the axial localisations for the weighted bubble distribution varied by 221 μ m over the speeds investigated.

This work has shown the importance of careful choosing the bubble detection algorithm to match the application and explored some of the factors that will introduce localisation error.

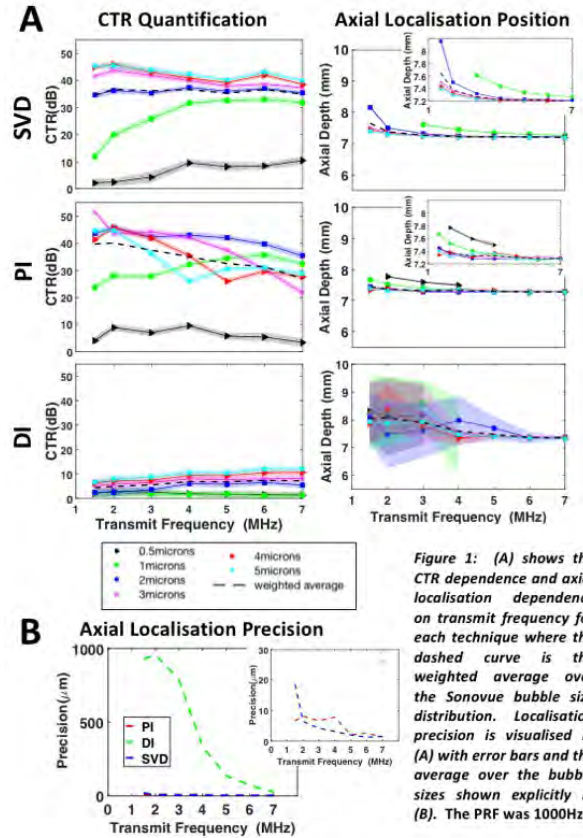


Figure 1: (A) shows the CTR dependence and axial localisation dependence on transmit frequency for each technique where the dashed curve is the weighted average over the Sonovue bubble size distribution. Localisation precision is visualised in (A) with error bars and the average over the bubble sizes shown explicitly in (B). The PRF was 1000Hz.

Development of Simultaneous Optical Imaging and Super-Resolution Ultrasound to Improve Microbubble Localisation Accuracy

Jemma Brown¹, Kirsten Christensen-Jeffries¹, Samradnyee Kolas¹, Cahil De Menezes¹, Ge Zhang², Jiaqi Zhu², Sevan Harput², Chris Dunsby³, Mengxing Tang², Robert Eckersley¹

¹*Biomedical Engineering Department, School of Biomedical Engineering and Imaging Sciences, King's College London, United Kingdom*, ²*Bioengineering, Imperial College London, London, United Kingdom*, ³*Department of Physics and Centre for Pathology, Imperial College London, London, United Kingdom*

Background, Motivation, and Objective

Super-resolution techniques which localise isolated microbubbles require a comprehensive understanding of the relationship between microbubble response and position. Boundaries, neighbouring bubbles and flow velocities can influence the bubble response and introduce localisation errors. Previous authors have acquired simultaneous optical and acoustic images of individual bubbles, either by entrapment or using very low concentrations. For flowing microbubble distributions appropriate to super-resolution, the relative depths of field of wide-field optical microscopy and ultrasound imaging make it challenging to match corresponding optical and acoustic data. This work introduces the novel approach of using an adjustable optical aperture to extend the depth of field. This system has the flexibility of reducing the numerical aperture without changing the magnification.

Statement of Contribution/Methods

An adjustable aperture (Thorlabs) was inserted as close to the back aperture of a water immersion x40 microscope (LUMPLANFLN, Olympus) as permitted by the optomechanics used, and the image focused on a CMOS sensor (Ximea). The resolution over the depth of field was characterised using a sector star resolution target.

A 200 μm cellulose tube was chosen as a vessel phantom. Modelling of the parabolic microbubble flow within the tube enabled the required aperture width to be calculated. A dilute microbubble solution was introduced, and real-time processing of the optical images enabled automatic triggering of plane wave ultrasound acquisition using an ULA-OP system (MSD Lab, University of Florence) when a bubble was detected.

Results/Discussion

Figure 1A shows how the introduction of the aperture enabled the smallest structure in the resolution target, 4.4 μm , to be resolved at a distance of 100 μm from the optical focus. This corresponds to the depth of field required to detect microbubbles of radius 2.2 μm over the whole extent of the tube phantom. Simple modelling showed that the required depth of field was reduced due to buoyancy. For example, bubbles of 1 μm radius will only be found in the top 50 μm of the tube after travelling 50 mm. Figure 1B shows an example microbubble detected over 50 μm . Extending the depth of field will enable frames containing a number of microbubbles to be optically validated and matched to the corresponding acoustic acquisition.

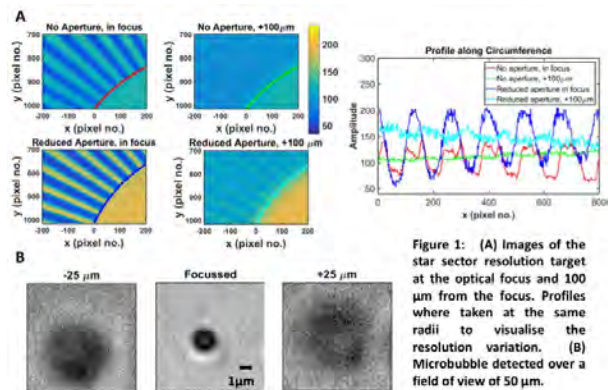


Figure 1: (A) Images of the star sector resolution target at the optical focus and 100 μm from the focus. Profiles were taken at the same radii to visualise the resolution variation. (B) Microbubble detected over a field of view of 50 μm .

Subharmonic Plane Wave Imaging of Liposome-loaded Microbubbles

Luzhen Nie¹, James R. McLaughlan^{1,2}, David Cowell¹, Thomas Carpenter¹, Steven Freear¹

¹School of Electronic and Electrical Engineering, University of Leeds, United Kingdom, ²Leeds Institute of Cancer and Pathology, University of Leeds, United Kingdom

Background, Motivation, and Objective

A key component of targeted drug delivery using liposome-loaded microbubbles (LLMBs) and ultrasound is the ability to track these drug vehicles in real time, which guides payload release at the desired location. As the uniquely identifiable emission from microbubbles (MBs), subharmonic (SH) signal is of great interest for this purpose. Acoustic characterization of LLMB populations confirmed the decreased pressure threshold for SH emissions (50 kPa vs. 200 kPa for normal MBs). This finding has been related to the 'expansion-only' behaviour whereby MBs are enforced to a buckled state by the packed liposome layer. Plane wave imaging (PWI) spreads the spatial peak acoustic intensity over multi-pulses to preserve the survival rate of MBs, but the imaging depth is limited because of the lack of Tx focus. This study aimed to investigate whether the lowered threshold for the production of SH with LLMBs could improve their ability to perform SH PWI.

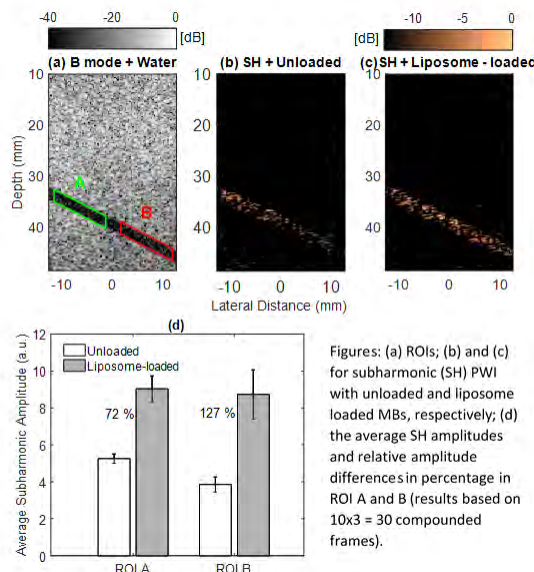
Statement of Contribution/Methods

Both unloaded MBs and LLMBs were diluted to a concentration of 1.9×10^6 MBs/mL and pumped through a wall-less flow phantom with a mean velocity of 20 mm/s.

For SH PWI, the Leeds UARP system was programmed to transmit 6-cycle 9 MHz pulses (MI 0.09, Rx 4.5 MHz) using a L11-4 probe with a pulse sequence of 15 plane waves (PWs), steered from -5° to 5° , at a PRF of 6 kHz. Each pulse sequence was separated by a 2s period to allow replenishment of MBs between two acquisitions. Each measurement comprised of ten transmissions of this sequence and the measurement was repeated three times with fresh MB solution preparations.

Results/Discussion

Two ROIs are delimitated in Fig.a and average SH amplitudes within these two ROIs (relative to the noise floor) are given in Fig.d. Fig.b shows that the SH signals from unloaded MBs diminish with increased depth, but this phenomenon is not obvious with LLMBs in Fig.c. Fig.d shows that the average SH amplitude in ROI A is higher with LLMBs. The amplitude difference between unloaded MBs and LLMBs has been more significant in ROI B (percentages in Fig.d). These occurred as a result of the lack of Tx focus with PWs. Pressures were gradually attenuated with increased depth and thus lower than the threshold to elicit SHs at deep locations for unloaded MBs. However, for LLMBs, SH nonlinearity sets in with a reduced acoustic pressure threshold. This enables SH PWI providing a tool for specific tracking of LLMBs.



Figures: (a) ROIs; (b) and (c) for subharmonic (SH) PWI with unloaded and liposome loaded MBs, respectively; (d) the average SH amplitudes and relative amplitude differences in percentage in ROI A and B (results based on $10 \times 3 = 30$ compounded frames).

3D In Vitro Ultrasound Super-Resolution Imaging using a Clinical System

Kirsten Christensen-Jeffries¹, Sevan Harput², Jemma Brown³, Jiaqi Zhu⁴, Ge Zhang², Mengxing Tang⁵, Chris Dunsby⁶, Robert Eckersley⁷

¹Department of Biomedical Engineering, Kings College London, London, United Kingdom, ²Bioengineering, Imperial College London, London, United Kingdom, ³Biomedical Engineering Department, School of Biomedical Engineering and Imaging Sciences, King's College London, United Kingdom, ⁴Department of Bioengineering, Imperial College London, London, United Kingdom, ⁵Imperial College London, London, United Kingdom, ⁶Department of Physics and Centre for Pathology, Imperial College London, London, United Kingdom, ⁷Department of Biomedical Engineering, King's College London, London, United Kingdom

Background, Motivation, and Objective

Visualisation of complex and disordered 3D vasculature, such as that of a tumour, using ultrasound super-resolution techniques requires an acquisition strategy which can additionally localise bubbles in the elevational plane with high precision. Existing demonstrations of super-resolution have been predominantly two-dimensional, where the elevational resolution remains restricted to around the millimetre range, while 3D demonstrations have required customised or state-of-the-art research systems to achieve true super-resolution in the third dimension. In this study, 3D super-resolution and velocity tracking *in vitro* is demonstrated using a currently available clinical ultrasound system.

Statement of Contribution/Methods

In vitro experiments were performed using a clinical Philips EPIQ7 system with a X5-1 2D matrix array probe at 1.25 MHz transmit frequency in contrast enhanced imaging mode. A microvessel phantom was constructed by setting a twisted 200 μm cellulose tube into medium density paraffin gel wax. An infusion pump circulated a low concentration of SonoVue (Bracco, Milan) microbubbles through the phantom. Imaging was performed at 54 volumes/second at a depth of 3.5 cm. Video segments were acquired for 11 seconds each. A rolling background subtraction was applied to remove background signals. Bubbles were then localised by calculating the onset of the extracted signal. Twenty-three segments were processed in the final images. Bubble signals were tracked to generate 3D velocity information. The distance of the localisation positions to the tube centreline was assessed.

Results/Discussion

Three-dimensional super-resolved volumetric imaging of a twisted microvessel phantom far smaller than the transmit wavelength ($\lambda \approx 1200 \mu\text{m}$) is possible with a clinical ultrasound system at depth (Figure A). Velocity tracking detected changes in direction, θ , of 3D velocity vectors as bubbles travel along the twisted structure (Figure B). Absolute distances of onset localisations from the centreline are shown in Figure C. Corresponding histograms demonstrate 66% of the onset bubble localisations were inside the estimated internal diameter of the tube (Figure D). In the future, 3D localisation using microbubble signal onset could allow considerably improved visualisation of the human microvasculature using clinical ultrasound imaging systems.

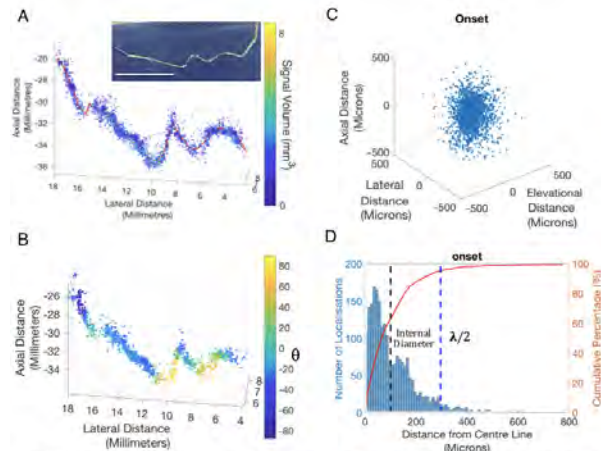


Figure A: Three-dimensional localisation map of twisted tube using onset method with centreline in red. Optical image of phantom inset, scale bar 5 mm. Three dimensional onset localisations with colour bar representing elevational angle, θ are shown in Figure B. Figure C and D show the absolute distance of each localisation from the nearest point on centreline and the corresponding histogram respectively.

A study of radiation force effects in plane-wave transmission mode

Francesco Guidi¹, Outi Supponen², Connor Slagle², Hendrik J. Vos^{3,4}, Mark Borden², Piero Tortoli¹

¹*Information Engineering, University of Florence, Italy*, ²*Mechanical Engineering, University of Colorado, CO, United States*,

³*Biomedical Engineering, Thorax Center; Erasmus MC, Rotterdam, Netherlands*, ⁴*Acoustical Wavefield Imaging, ImPhys, Delft University of Technology, Netherlands*

Background, Motivation, and Objective

Significant microbubble displacements due to the primary radiation force have been observed in the focal region of single-element and array probes. This effect has been harnessed to increase contact between ligand-bearing microbubbles and targeted endothelium for targeted drug delivery and ultrasound molecular imaging applications. In this study, microbubble displacements associated with plane-wave (PW) transmission (TX) are investigated and compared to displacements obtained in focussed-wave (FW) TX at equivalent peak negative pressures (PNP).

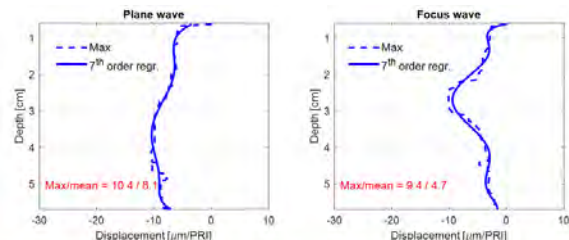
Statement of Contribution/Methods

Size-isolated microbubbles of 1-2, 3-4, 4-5 and 5-8 μm diameter, as well as polydisperse microbubbles (AMB Labs, Boulder, CO) were diluted with purified water to 10^4 to 10^5 mL^{-1} in a 1 L tank. The microbubbles were insonified at 4 kHz PRF by the LA332 linear array probe (100% bandwidth around 4.6 MHz) connected to the 64-channel ULA-OP open scanner. For each microbubble size, multiple experimental conditions were established by varying the TX frequency (range: 3-7 MHz) and the burst duration (1-10 μs), to transmit PW or FW beams with 100-330 kPa PNP. For each TX event, the raw echo-data received over at least 250 ms were acquired and processed using a multi-gate spectral Doppler approach. This analysis allowed estimation of the peak microbubble displacements (PMDs) along the axis of the insonified region.

Results/Discussion

In all PW experiments, the TX of 1- μs pulses yielded PMDs lower than 2 μm per TX event. Displacement significantly increased for longer TX pulses, especially at a TX frequency close to the microbubble resonance. For example, with pulses of 10 μs and 260 kPa PNP, PMDs were measured up to 20 μm . In FW mode, the PMDs were similar to, although typically slightly lower than, the values measured for PW.

These results suggest that: 1) when short (wideband) pulses are transmitted (as in B-mode), the radiation force effects are negligible; 2) by using, e.g., 10- μs duration and 260 kPa PNP pulses, 50 pulses near the resonance frequency are sufficient to move bubbles by 1 mm; and 3) for a same PNP, PW TX moves the bubbles slightly more than FW TX. The uniform radiation force experienced by microbubbles in PW mode may be advantageous to promote more uniform microbubble-endothelium contact throughout a tissue mass for applications in targeted drug delivery and ultrasound molecular imaging.



Displacement profiles in PW (left) and FW @ 25 mm (right) modes, obtained with 7 MHz TX frequency, 260 kPa PNP, 10 μs pulses, 1-2 μm bubble diameter, and 8×10^4 bubbles/ml concentration. Values reported on horizontal axis are peak displacements measured per TX event.

Poisson Statistical Model of Ultrasound Super-Resolution Image Acquisition Time

Kirsten Christensen-Jeffries¹, Jemma Brown², Sevan Harput³, Ge Zhang³, Jiaqi Zhu⁴, Chris Dunsby⁵, Mengxing Tang⁶, Robert Eckersley¹

¹Department of Biomedical Engineering, King's College London, London, United Kingdom, ²Biomedical Engineering Department, School of Biomedical Engineering and Imaging Sciences, King's College London, United Kingdom, ³Bioengineering, Imperial College London, London, United Kingdom, ⁴Department of Bioengineering, Imperial College London, London, United Kingdom, ⁵Department of Physics and Centre for Pathology, Imperial College London, London, United Kingdom, ⁶Imperial College London, London, United Kingdom

Background, Motivation, and Objective

A crucial aspect of all ultrasound super-resolution (SR) methods using single bubble localisation is the efficient detection of individual bubble signals in each frame. Due to the need for bubbles to circulate through the entire vasculature during acquisition, slow flows associated with the microcirculation limit the minimum acquisition time needed to obtain adequate spatial resolution. In this study, a model is developed to investigate the combined effects of imaging parameters, bubble concentration, and vascular flow on SR image acquisition time.

Statement of Contribution/Methods

Firstly, Poisson statistics were used to generate a distribution of signal densities with expectation value based on bubble concentration and vascular volume fraction. The localisation number per frame was determined by the probability of imaging single bubbles within the diffraction limit and resolution limit. The number of localisations needed for SR images depends on the system localisation precision and the desired contrast in the SR rendering. Finally, the acquisition time was limited for slow blood flows by effectively restricting the frame rate to allow new spatial information to be obtained by moving bubbles in each frame. This was explored over different vascular densities and flow rates, as well as varying depths, transmit wavelengths, λ , and improvements in resolution using SR.

Results/Discussion

The acquisition procedure, transmit frequency, localisation precision, and desired SR image contrast together determine the minimum acquisition time for a given flow velocity and local signal density. Frame rate limits for blood velocities ranging from the microvasculature ($< 1 \text{ mm/s}$) to the aorta ($\sim 45 \text{ cm/s}$) at 5 cm depth are restricted by the bubble velocity at low blood flows ($< 150 \text{ mm/s}$), but are only restricted by the time-of-flight at higher flows (Figure A). The estimated minimum time needed for SR increases both for slower blood velocities, and resolution improvement (Figure B). To obtain a SR of $\lambda/10$ while imaging the microvasculature, the estimated minimum time is 56 seconds, while for $\lambda/20$ improvement this increases to 13 minutes. Exploring the effects of both system parameters and details of the target vasculature can allow better choice of acquisition settings, and provide improved understanding of the completeness of SR information.

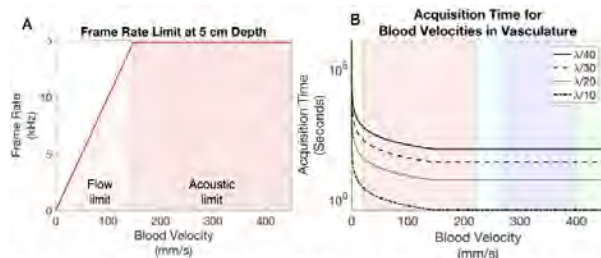


Figure A) Frame rate limits are defined by the bubble velocity at low blood flows, while imaging at high blood flows becomes restricted only by the time-of-flight. Figure B) Acquisition time required to create super-resolution images for a target region at 5 cm depth with blood velocities ranging between the microvasculature (yellow), veins and arterioles (red), vena cava (blue), arteries (purple) and aorta (green). The graph demonstrates an increase in acquisition time with improvements in resolution compared to the transmit wavelength, λ .

Chirp-Coded Excitation for Enhancing the Transcranial Penetration in Ultrasound Localization Microscopy: An ex vivo Validation Study

Fu-Feng Lee¹, Yi Yang¹, Qiong He¹, Nisi Zhang², Zhifei Dai², Jianwen Luo¹

¹Department of Biomedical Engineering, Tsinghua University, Beijing, China, People's Republic of, ²Department of Biomedical Engineering, Peking University, Beijing, China, People's Republic of

Background, Motivation, and Objective

Ultrasound localization microscopy (ULM) is a novel approach for super-resolution vascular imaging based on localizing and tracking contrast agent microbubbles. The morphology and blood flow features of microvessels in the rat brain have been obtained *in vivo* in a transcranial manner (Errico et al, Nature, 2015). A thinned-skull window is required to reduce the acoustic attenuation caused by the skull. The aim of this study is to assess the feasibility of achieving non-invasive ULM without skull thinning using chirp-coded excitation.

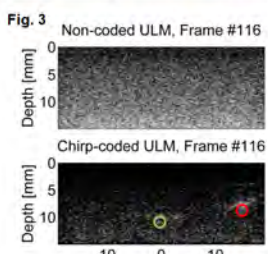
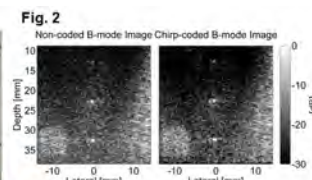
Statement of Contribution/Methods

Ex vivo experiments were conducted on a CIRS 040GSE phantom and home-made agar (1.5% by mass concentration) phantom, respectively, as shown in Fig. 1. The extracted rat skull was placed on the top of both phantoms. A PTFE tube (inner diameter = 200 μm) was embedded in the home-made phantom at a depth of 10 mm. One end of the tube was connected to a syringe filled with contrast agents (SonoVue, Bracco, Italy) with a concentration of 3×10^7 microbubbles per mL. A Vantage system (Verasonics, USA) equipped with an L8-3 linear probe (transmit frequency = 5.5 MHz) were utilized to acquire RF frames using 5-angle plane wave imaging at a frame rate of 400 Hz and sample frequency = 23 MHz. A linear frequency-modulated chirp signal with a bandwidth of 9 MHz (1 - 10 MHz) over a time of 3.74 μs was adopted for coded excitation.

The performance of coded excitation was firstly validated in terms of signal-to-noise ratio (SNR) using the CIRS phantom. Validation was then performed on the home-made phantom where the agent injection was controlled using a syringe pump at a flow rate of 0.02 mL/s. The time-reversed chirp signal was used to decode the acquired images. ULM was achieved using singular-value decomposition (SVD) applied to the decoded images to localize the microbubbles.

Results/Discussion

Fig. 2 shows the B-mode images of the CIRS phantom. The SNR has a significant improvement from 5.06 to 12.47 dB after applying chirp-coded excitation. Fig. 3 shows the ULM results of the home-made phantom. The microbubbles can be localized only in chirp-coded ULM. The estimated velocity of microbubbles (~ 188 mm/s) is close to the reference one (159 mm/s) with errors within 20%. In conclusion, chirp-coded ULM is preliminary validated through *ex vivo* experiments. More systematic assessment and *in vivo* study of this approach is the topic of ongoing work.



P1-C5 - Elasticity Imaging of the Skin

Kairaku (posters 1)

Thursday, October 25, 9:30 AM - 4:00 PM

Chair: **Brett Byram** Vanderbilt University

P1-C5-1

Young's Modulus of Dermis and Hypodermis of Healthy Volunteers Measured with High Frequency Transient Elastography

Caroline Chartier¹, Yassine Mofid², Annabel Maruani³, Katell Vie⁴, Laurent Machet³, **Frederic Ossant**¹

¹UMR Inserm U1253, Tours, France, ²UMR Insert U1253, Tours, France, ³CHRU Tours, Department of Dermatology, Tours, France, ⁴Clarins Company, France

Background, Motivation, and Objective

Skin ageing and effectiveness of cosmetics are today evaluated by a bundle of techniques: colorimetry, micro-relief and several methods. The objective of this study was to evaluate, on healthy subjects, the interest of a high-frequency transient elastography (HF-TE) for

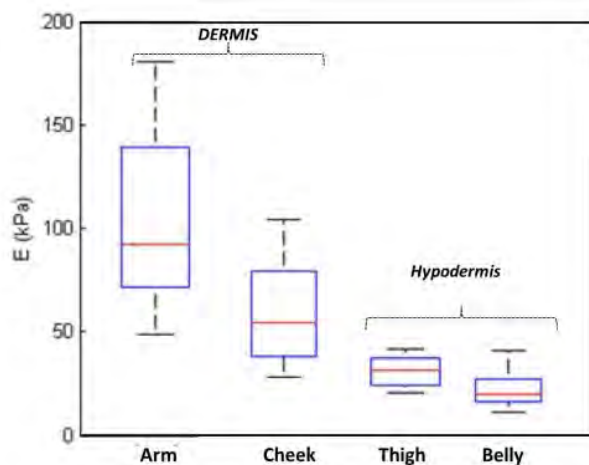
Statement of Contribution/Methods

A HF electronic system (Echosens™, Paris, France) has been developed with HF ultrasound (US) emission/reception (sinusoidal waveform, 15MHz US frequency, 2 US cycles, 48 kHz as the pulse repetition frequency allowing an exploration depth of 15mm with acquisition time of 20ms. The mechanical pulse had one cycle sinusoidal waveform, a pic-pic amplitude of 0.5 mm and a frequency of 400Hz). A freehand probe including HF transducer and mechanical vibrator, was coupled with 2-foot stand system used to place the US transducer perpendicularly to the skin surface and to control the pre-compression of the skin.

15 healthy volunteers (women between 20 and 60 years old) were enrolled at the Clarins Company (Paris, France) in an institutional review board-approved study. Measures of E (10 measures per cm² of skin zone) were realized in the dermis (arm and cheek) and superficial hypodermis (belly and thigh) of each subject.

Results/Discussion

Dermis of arm and cheek had E median values between 50 and 100 kPa while hypodermis of thigh and belly had E median values of a few 10 kPa. As expected, Young's modulus values measured in the hypodermis were clearly lower than those measured in the dermis. Otherwise, the dispersion of the values in the hypodermis were relatively low despite the age differences of the subjects and the measurement in a few mm.



Clinical Interest of High Frequency Transient Elastography to Assess Dermis Fibrosis in Patients with Venous Insufficiency

Yassine Mofid¹, Annabel Maruani², Caroline Chartier¹, Geoffroy Falaewc³, Laurent Machet², **Frederic Ossant¹**

¹UMR Inserm U1253, Tours, France, ²CHRU Tours, Department of Dermatology, Tours, France, ³CHRU Tours, CIC1415, Tours, France, France

Background, Motivation, and Objective

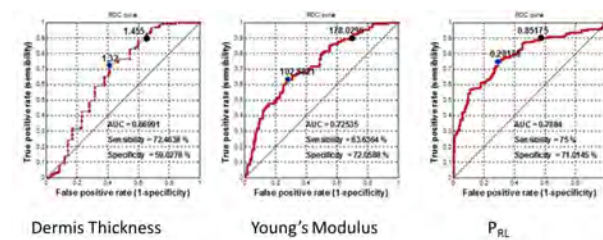
Chronic Venous Disorder (CVD) is a public health issue because of its high prevalence and because of the important socioeconomic impact. Transient elastography (TE) has demonstrated excellent diagnostic performance in the detection and monitoring of liver fibrosis (Echosens Compagnie). This clinical study aimed to evaluate the performance of a high frequency transient elastography (HF-TE) in the case of CVD diagnosis.

Statement of Contribution/Methods

48 patients with CVD and 48 paired healthy volunteers were enrolled at the CHRU of Tours in an institutional review board-approved study. For each patient, clinical examination has been conducted to classify CVD patients in 3 stages (stage 1-2 for low, stage 3-4 for medium and stage 5-6 for high stage disease) and 3 parameters of the dermis were estimated on 3 skin zones of the leg for each subject: the dermis thickness (DT), the Young's modulus (E) with a specific HF-TE prototype device and an acousto-elastographic parameter, PRL, based on a logistic regression model using both E and DT values.

Results/Discussion

The median value of E parameter for skin zone 3 was 103 kPa in patients at stage 1-2 of CVD, 125 kPa at stage 3-4, 155 kPa at stage 5-6 and 80 kPa in the control group. However, PRL parameter is the most efficient to discriminate CVD patients to volunteers for any grade and any zone, and this discriminant capacity is well described with ROC analysis (figure below: area under ROC curve (AUC) values was highest for PRL with good sensitivity and specificity). Moreover, if we consider this parameter only for skin zone 3, AUC values varying from 0.72 for stages 1-2, 0.75 for stages 3-4 and 0.89 for stages 5-6. These results showed HF-TE potential for diagnosis of skin fibrosis.



On-Axis Acoustic Radiation Force-based Elasticity Measurement in Homogeneous and Layered, Skin-Mimicking Phantoms
Kristy Walsh¹, Mark Palmeri², Brett Byram¹
¹*Biomedical Engineering, Vanderbilt University, Nashville, TN, United States*, ²*Biomedical Engineering, Duke University, Durham, NC, United States*
Background, Motivation, and Objective

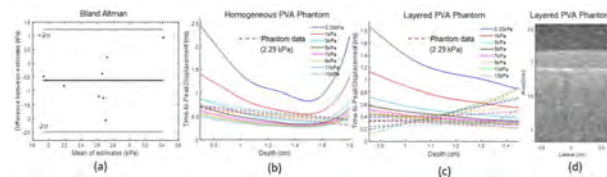
Shear wave elasticity imaging has been difficult in inhomogeneous tissue, such as skin, where thin layers cause bias in shear wave estimates. Instead, we propose an FEM-based look-up table to estimate shear modulus at the on-axis location rather than at lateral locations. We estimate the time-to-peak on-axis displacement at each depth and use a look-up table to estimate shear modulus. Here we test the on-axis stiffness estimates in polyvinyl-alcohol (PVA) phantoms.

Statement of Contribution/Methods

We generated a stiffness look-up table using a 3D FEM model coupled to Field-II simulations. We simulated shear moduli of 1-13kPa using a CL15-7 transducer, 1.125cm axial push focus, 8.9MHz push frequency, 10.4MHz tracking frequency, and plane wave tracking. The experimental cases use the same imaging parameters as the simulations. The displacements were estimated using an advanced Bayesian displacement estimator. The PVA phantoms were prepared by dissolving 15g of PVA into 200mL of water heated to 85°C, and then adding 6% by weight concentration of graphite for scattering. The elasticity of PVA phantoms can be increased with additional freeze-thaw cycles. Before the phantoms were sliced into thin layers, we computed three independent shear wave speeds at the same depth that would be sliced and took the average. The PVA skin phantoms had a top layer between 1.5-2.5mm thick (1 freeze/thaw cycles) and a thicker, stiffer bottom layer (3 freeze/thaw cycles). After slicing and layering the phantoms, we tested the on-axis method and compared it to shear wave speed-derived shear modulus estimates.

Results/Discussion

The presliced homogeneous PVA phantoms had a mean shear wave speed-derived shear modulus of 2.29kPa and standard deviation of 0.76kPa. The Bland-Altman plot (Fig. (a)) compares the shear wave speed-derived shear modulus to the on-axis method's estimates. The time-to-peak displacement results are shown in Fig. (b) for the homogeneous PVA phantom where the results are most accurate and match the simulations at the focal depth of 1.125cm. Fig. (c) show the time-to-peak displacements for the layered phantoms. The plot suggests the look-up table will need to be updated to estimate the shear modulus in the layer more accurately. The mean shear modulus for the on-axis method and shear wave speed-derived estimates in the layer was 11.2+-5.2kPa and 101+-309kPa, respectively.



Noninvasive measurement of lung and skin stiffness for assessing interstitial lung disease and skin involvement in systemic sclerosis**Xiaoming Zhang¹, Boran Zhou², Jinling Zhou¹, Thomas Osborn¹, Brian Bartholmai¹, Sanjay Kalra¹**¹*Mayo Clinic, United States, ²Mayo Clinic, Rochester, MN, United States***Background, Motivation, and Objective**

Ultrasoundography is not widely used for lung assessment because ultrasound cannot usefully image deep lung tissue. We have developed a lung ultrasound surface wave elastography (LUSWE) technique for measuring superficial lung tissue stiffness which has potential for assessing patients with interstitial lung disease (ILD). ILDs include multiple chronic lung disorders with lung parenchymal damage and fibrosis. Many of these have predominantly peripheral involvement, making them especially accessible to our measurement technique.

Statement of Contribution/Methods

In LUSWE, a 0.1 second harmonic vibration is generated on the chest wall of a subject using a handheld vibrator. An ultrasound probe is positioned in the same intercostal space as the indenter of the vibrator to measure the generated surface wave propagation on the lung. The Verasonics ultrasound system with an ultrasound probe of L11-4 with a central frequency of 6.4 MHz is used. A human subject is examined in a sitting position. The lung testing is performed with full inspiration breath hold and through three intercostal spaces on each side. Skin testing is performed at forearm and upper arm on each side. The surface wave speeds are measured at 100 Hz, 150 Hz, and 200 Hz.

Results/Discussion

In this study, LUSWE was used to measure both lung and skin characteristics in 91 patients with ILD and 30 healthy control subjects. The surface wave speeds of patients' lungs were significantly higher than those of control subjects. Patient skin elasticity and viscosity were significantly higher in patients than those of control subjects. We also analyzed ILD patients as two groups, ILD patients with ($n=41$) and without ($n=50$) systemic sclerosis (SSc) - no significant differences were found between the two patient groups. LUSWE is a safe and noninvasive technique for generating and measuring surface wave propagation on the lung. LUSWE may complement the clinical standard high-resolution computed tomography for assessing ILD. LUSWE may be useful for screening early stage ILD patients and monitoring disease progression.



High resolution SAW elastography for ex-vivo porcine skin specimen**Kairui Feng¹, Kanheng Zhou², Chunhui Li³, Zhihong Huang³**¹*University of Dundee, Dundee, United Kingdom*, ²*School of Science and Engineering, University of Dundee, dundee, United Kingdom*, ³*University of Dundee, DUNDEE, United Kingdom***Background, Motivation, and Objective**

The mechanical properties of soft tissue, i.e. Young's modulus, usually changes with tissue pathological changes. Thus, quantitative evaluation of true elasticity of skin tissue is demanded for diagnosis and treatment monitoring for many skin diseases. Surface acoustic wave (SAW) elastography has been proven to be a non-invasive, non-destructive method for accurately characterizing tissue elastic properties. However, current SAW elastography technique using laser vibrometer only detects and records the generated SAW impulse point by point which are a few millimeters away. Therefore, the reconstructed elastography has low lateral resolution. This study aims to improve the existing SAW elastography technique by employing phase-sensitive Optical Coherence Tomography (PhS-OCT) system as a wave detector to track the focused ultrasound induced SAW impulse. A 2D fast Fourier transform based phase velocity analysis algorithm was employed to retrieve the surface acoustic wave dispersion curve, from which the high resolution elastogram were reconstructed.

Statement of Contribution/Methods

Ex-vivo porcine belly skin was chosen as the sample to mimic vertically heterogeneous material. The whole experimental setup can be divided into two parts: the focused ultrasound transducer works as a SAW impulse inducer, and PhS-OCT system works as a SAW impulse detector. The ultrasound transducer is triggered by the signal generator and synchronised with OCT system to induce the surface acoustic wave propagating on samples. PhS-OCT system is simultaneously performing to detect the wave travelling.

Results/Discussion

To improve the lateral resolution of current SAW elastography, a new method, that combines a focused ultrasound transducer for SAW impulse inducing and a PhS-OCT system for wave tracking, was proposed in this paper. Ex-vivo porcine skin specimen was tested under this proposed method. The datasets were processed by a 2D FFT based phase velocity analysis algorithm and the elastogram was approximated by relating the phase velocity and its corresponding penetration depth. The estimated Young's modulus of different layers in ex-vivo porcine skin were 1.13 ± 0.08 MPa, 1.37 ± 0.13 MPa and 0.29 ± 0.02 MPa for all layers, dermis layer and hypodermis layer, respectively. The average Young's modulus (1.13 ± 0.08 MPa) agrees well with the reference value. The reconstructed elasticity map shows higher lateral resolution than that from current SAW elastography technique, and different layers in ex-vivo porcine skin sample could also be distinguished. This proposed SAW elastography technique may have a large potential to be widely applied in clinical use for skin disease diagnosis and treatment monitoring.

P1-C6 - Methods for Elasticity Imaging

Kairaku (posters 1)

Thursday, October 25, 9:30 AM - 4:00 PM

Chair: **Hideyuki Hasegawa** University of Toyama

P1-C6-1

Optimization of angular displacement compounding in plane-wave ultrasound imaging to improve accuracy of lateral displacements and strain estimates.

Gijs Hendriks¹, Chuan Chen¹, Anne ten Dam¹, Hendrik Hansen¹, Chris de Korte^{1,2}

¹Medical UltraSound Imaging Centre, Radboud university medical center, NIJMEGEN, Netherlands, ²Physics of Fluids group, University of Twente, Enschede, Netherlands

Background, Motivation, and Objective

Ultrasound breast elastography is a method to detect lesion stiffness (strain) and bonding (rotation and shear strain). Lateral strain estimation is typically less accurate than axial strain estimation due to the lack of phase information. To improve accuracy, angular displacement compounding (ADC) can be applied in which displacements along beam-steering angles are estimated and combined. The aim of this study was to investigate the performance of ADC in estimating lateral displacements, shear and lateral strain for breast elastography using plane wave transmissions. Furthermore, the effect of transmit apodization and plane-wave reconstruction parameters were evaluated.

Statement of Contribution/Methods

Element data were collected by 3 transducers using steered plane-wave acquisitions ($\pm 30^\circ$) with(out) Tukey (0.7) transmit apodization before and after a lateral transducer shift of 1 pitch, a phantom rotation of 1.9° , or a lateral phantom deformation of 1%. RF data were beam-formed with Hamming apodization and dynamic focusing in receive (F-number between 0 - 2). Axial displacements per angle were estimated using coarse-to-fine block-matching, lateral displacements calculated by ADC of two opposite angles and (shear) strains estimated by least-squared-strain estimation. As performance metric the Root-Mean-Squared Error (RMSE) was calculated.

Results/Discussion

Figure 1 shows that for pure lateral translation maximum steering provided the lowest RMSE, whereas for rotation and lateral strain an optimum was found for steering angles of 15° for all transducers. This difference might be due to the fact that in rigid-block matching, blocks cannot rotate or stretch resulting in reduced performance when applying strain or rotation. The already reduced performance in those cases might be amplified by grating lobes. This might also explain the higher RMSE for small wavelength-pitch ratio (0.8 for 12L4VF and 1 for the other transducers). An F-number of ~ 0.8 seemed optimal for rotation and strain in all transducers. For pure lateral translation the F-number did not seem to affect results. Finally, apodization in transmit seemed to improve the accuracy of the estimates for all F-numbers, angles and transducers which might be related to reduced side-lobes. To conclude, ADC combined with transmit apodization provided the most accurate displacements and strains.

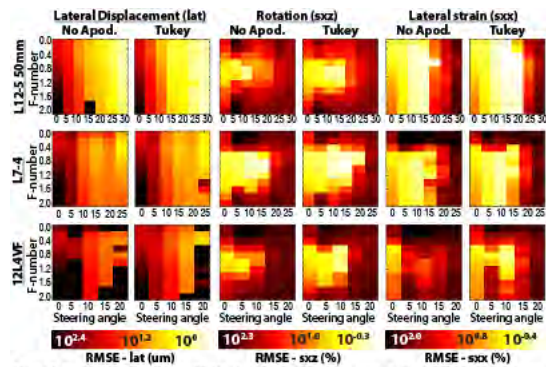


Figure 1. Root-mean-squared error (RMSE) of estimated lateral displacements (1 pitch shift); rotation (sxz, 3.4%); and lateral strain (sxx, 1.0%) using spatial displacement compounding (\pm steering angle); no or Tukey (0.7) apodization in transmit; F-numbers varying between 0.0 and 2.0 in dynamic focusing in receive; and three transducers (L12.5 50mm, ATL; L7.4, ATL; 12L4VF, Siemens) connected to a Verasonics V1 Research system to enable beam-steered plane-wave acquisitions. The colormaps are logarithmic.

Multi-frequency 3D phase tracking method with phased-array beamforming in Cartesian coordinate systemSoichiro Nunome¹, Ryo Nagaoka¹, Hideyuki Hasegawa¹¹*Graduate School of Science and Engineering, University of Toyama, Toyama, Japan***Background, Motivation, and Objective**

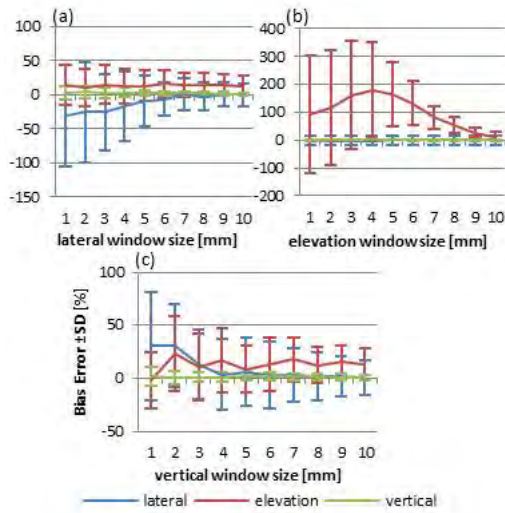
For accurate motion estimation, it is necessary to estimate tissue motion in 3D space while keeping high frame rate. In this study, a multi-frequency 3D phase tracking method with phased-array beamforming in the Cartesian coordinate system was developed for a relatively small-scale ultrasonic probe, e.g., 256 elements.

Statement of Contribution/Methods

Volume datasets were obtained by Field II simulation. A 3-MHz matrix array probe with 32 x 8 elements (pitch: 0.5 mm in every direction) was simulated. A volume data was obtained by a single diverging wave emitted with 256 elements to achieve a high frame rate of 1000 Hz. The transmit beam was a plane wave in the elevation direction and diverging in the lateral direction. The aperture for receive beamforming was also composed of 256 elements, and beamformed ultrasonic data was created in the Cartesian coordinate system with the horizontal (lateral and elevation) and vertical sampling intervals of 0.2 mm and 0.02464 mm (31.25 MHz), respectively, in other words, 201 x 51 (lateral x elevation) vertical scan lines. The target was a homogeneous phantom including 100,000 scatterers moving at 5 mm/s in every direction. The multi-frequency tracking method developed by our group (Hasegawa, Appl. Sci., 2016) was expanded for 3D motion estimation and applied to the beamformed data. The fast Fourier transform (FFT) was used to obtain frequency spectra of beamformed RF signals.

Results/Discussion

Figures (a), (b), and (c) show bias errors and standard deviations of velocity estimates when the FFT window sizes in lateral, elevation, and vertical directions were varied from 1 mm to 10 mm, respectively. These results show that a FFT window size of about 10 mm in every direction is required to obtain good velocity estimates. A window size of 10 mm is similar to a typical kernel size in the speckle tracking method (STM). However, in STM, a similarity function, such as cross correlation function, needs to be obtained at multiple lags between volume sets to estimate a sub-sample displacement using an interpolation method. Therefore, STM requires a larger volume data, which requires a larger aperture size or large steering angle in receive beamforming. A larger aperture size increases the scale of a probe, and a large steering angle degrades the accuracy in velocity estimation. In conclusion, the proposed method is very effective for 3D motion estimation.



Intra-Scan Variability of Natural Shear Wave Measurements

L.B.H. Keijzer¹, Johan G. Bosch¹, Martin D. Verweij^{1,2}, Nicolaas de Jong^{1,2}, Hendrik J. Vos^{1,2}

¹Biomedical Engineering, Thorax Center, Erasmus MC, Rotterdam, Netherlands, ²Acoustical Wavefield Imaging, ImPhys, Delft University of Technology, Delft, Netherlands

Background, Motivation, and Objective

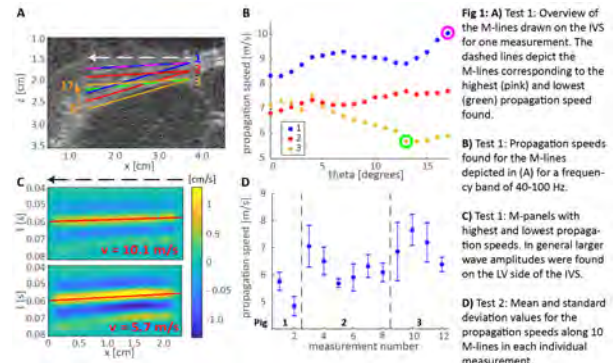
Shear wave (SW) elastography can potentially diagnose increased stiffness of the myocardium for patients with diastolic dysfunction [Villemain et al, JACC 2018]. We focus on the natural SWs induced in the interventricular septum (IVS) by the aortic valve closure. SWs are measured along a manually-drawn line on the IVS (anatomical M-line). We studied the influence of M-line location and orientation on the measured SW propagation speed, and tested the intra-scan variability in anticipation of clinical diagnostic application.

Statement of Contribution/Methods

We performed in-vivo measurements on 3 Göttingen minipigs with open chest, and in-vitro measurements using a custom PVA slab phantom. For in-vitro testing, the effect of angle error between the M-line and the wave propagation direction was systematically tested. For in-vivo testing, high frame rate images with a PRF of 1000 Hz were recorded in long-axis parasternal view (Aixplorer, SSI France, L15-4 probe). A one-lag autocorrelation method was used to obtain Tissue Doppler values. Propagation velocities were computed with a Radon transform. Two tests were performed on the in-vivo data. Test 1 investigated the effect of global M-line location and angle over the thickness of the IVS (Fig 1A). Test 2 investigated local changes on the propagation speed by test-retest over 10 M-lines at the left ventricle (LV) side of the IVS (based on test 1) to test intra-scan reproducibility.

Results/Discussion

The in-vitro measurements show a maximum increase of 10% in propagation speed when rotating the M-line up to $\theta = 20$ degrees, explained by a $1/\cos(\theta)$ bias. In test 1, differences up to a 100% were found for the in-vivo measurement in Fig 1B. Therefore, they are expected to have physiological causes, such as inhomogeneities of the IVS and differences in fiber orientation. In general, higher wave amplitudes and lower propagation velocities on the LV side of the IVS are found (Fig 1B-C), suggesting higher SNRs and lower angle bias. In test 2, the mean of the standard deviations of all recordings was 0.5 m/s (Fig 1D). These variations are now expected to be caused by measurement inaccuracy, in which precision can be improved by averaging over multiple M-lines. This study shows that averaging over multiple M-lines is required for precise measurements of propagation speed.



Fast randomized singular value decomposition based clutter filtering for shear wave imagingYuanyuan Wang¹, Qiong He¹, Jianwen Luo¹¹*Department of Biomedical Engineering, Tsinghua University, Beijing, China, People's Republic of***Background, Motivation, and Objective**

Clutter filter wave imaging (CFWI) has previously been proposed to detect shear wave propagation without motion estimation. We have also found that singular value decomposition (SVD) based CFWI (SVD-CFWI) outperforms Butterworth filter based CFWI (BW-CFWI) with higher SNR and smaller bias. However, the computational load of SVD is a major challenge for practical implementation. In this study, we propose randomized SVD (rSVD) based CFWI (rSVD-CFWI) to accelerate shear wave velocity (SWV) estimation and compare it with BW-CFWI, SVD-CFWI and 1D cross-correlation based speckle tracking (ST).

Statement of Contribution/Methods

RSVD accelerated SWV estimation by approximating SVD with the first k ranks of singular values corresponding to tissue motion induced by shear wave. Assuming that the beamformed RF data was A (with the size of $xy \times t$), a reduced matrix B ($xy \times k$, $k < t$) was obtained by multiplying A with a random matrix C ($t \times k$). An orthonormal matrix Q containing k columns was then computed through QR factorization of B. After that, the first k ranks approximation of A was obtained as $Q \times Q^T \times A$. The shear-wave motion was removed from A and the filtered sequence D was obtained as $D = A - Q \times Q^T \times A$. Conventional post-processing methods in CFWI were applied on D to obtain a tissue “acceleration” map and SWV map.

The proposed method was tested on the type-II inclusion of CIRS 049 phantom. A Verasonics V1 system with an L10-5 probe was used to induce shear wave. Plane wave compounding images with 3 steering angles were acquired at an effective frame rate of 4.9 kHz. A region of interest (ROI, $7 \times 7 \text{ mm}^2$) was selected from the inclusion to calculate the mean, standard deviation (SD) and signal-to-noise ratio (SNR). The computational time was evaluated on Dell XPS 8500 (Intel Core i7-3770 CPU @ 3.4GHz, 8GB RAM) running MATLAB.

Results/Discussion

As shown in Fig. 1, the spatial resolution of the shear wave acceleration maps obtained with rSVD-CFWI is comparable to that obtained with SVD-CFWI and ST and is better than that obtained with BW-CFWI. RSVD-CFWI achieves smaller SD and higher SNR than BW-CFWI, and obtains comparable SD and SNR to SVD-CFWI and ST. The computational time of rSVD-CFWI is similar to that of BW-CFWI and is an order of magnitude smaller than that of SVD-CFWI and ST (Table 1). In conclusion, rSVD-CFWI can remarkably accelerate SWV estimation while obtaining comparable SD and SNR to SVD-CFWI and ST.

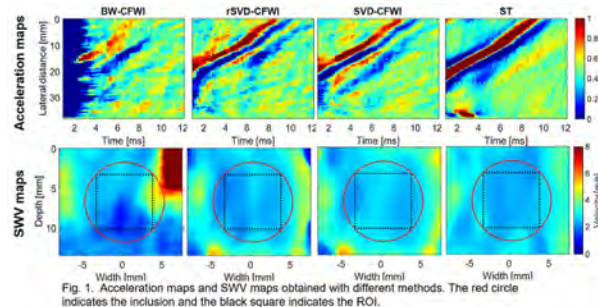


Fig. 1. Acceleration maps and SWV maps obtained with different methods. The red circle indicates the inclusion and the black square indicates the ROI.

Table 1. SWV results of ROIs ($7 \times 7 \text{ mm}^2$) in the inclusion

| | SWV (m/s) | SNR (dB) | Computational time (ms) |
|-----------|-----------|----------|-------------------------|
| BW-CFWI | 2.31±0.69 | 3.35 | 331 |
| rSVD-CFWI | 2.32±0.16 | 12.64 | 338 |
| SVD-CFWI | 2.50±0.16 | 15.74 | 3886 |
| ST | 2.36±0.15 | 16.83 | 4704 |

A Comparative Study of Displacement De-noising Strategies: An In Vivo Feasibility Study Using 3D Whole Breast Ultrasound Data

Jingfeng Jiang¹, Bo Peng²

¹Biomedical Engineering, Michigan Technological University, MI, United States, ²Southwest Petroleum University, China, People's Republic of

Background, Motivation, and Objective

FDA-approved 3D automated breast ultrasound (ABUS) systems (e.g. GE InveniaTM; Siemens Acuson S2000 ABVS) are available. The recent “Somo-Insight” trial (a prospective multicenter study involving 15,318 patients) has concluded that the combination of ABUS and mammography yielded “an additional 1.9 detected cancers per 1000 women screened”. Other clinical relevant information such as full shear deformation and strain anisotropy will further enhance diagnosis and characterization of breast lesions. However, in order to achieve that, high-quality non-axial displacements are required. Thus, our primary objective is to compare 3D displacement de-noising strategies.

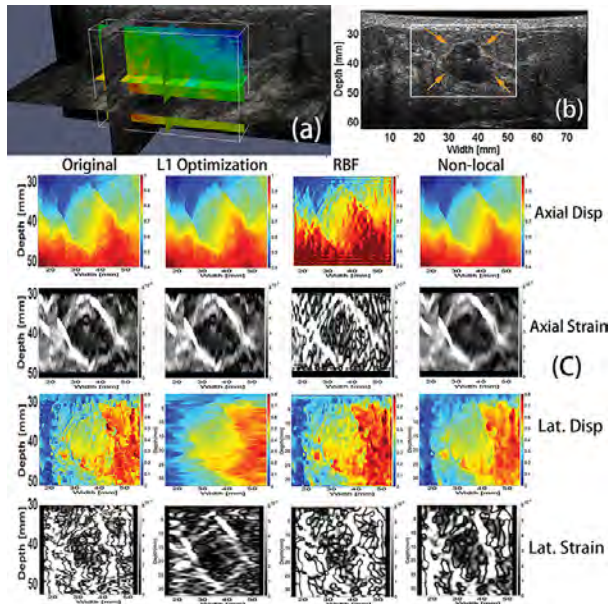
Statement of Contribution/Methods

Three different de-noising strategies were compared. 3D ultrasound data were obtained using a slightly modified Siemens Acuson S2000 ABVS scanner (Wang et al., Ultrasonic Imaging, 2017). A correlation-based speckle tracking algorithm (Jiang and Hall, PMB, 2015) was first used to obtain relatively accurately 3D displacement fields. Then, three different denoising algorithms were applied and evaluated. The first denoising algorithm is a partial differential equation (PDE)-based algorithm and the incompressibility was enforced through iterative optimization (Jiang et al., Ultrasonic Imaging, 2015). The second method (Busch et al., MRM, 2013) utilizes radial basis function (RBF) to enforce the incompressibility, while the third algorithm (Buades et al, CVPR, 2015) is a non-local median filter method.

Results/Discussion

Using FE-simulated data, the PDE-based algorithm achieved the lowest incompressibility among three different algorithms. As compared to the raw displacement estimates, reduction rates of incompressibility were approximately 95%, 50% and 63% after three denoising algorithms had been applied, respectively. The analysis of 3D ultrasound data containing an *in vivo* fibroadenoma showed that the PDE based algorithm can provide most consistent lateral strain images as shown in the Figure below.

In conclusion, our preliminary results demonstrated that denoising can significantly improve non-axial displacement estimates. Our future work is to further develop the denoising technique so that full shear deformation and strain anisotropy can be reliably estimated for 3D whole breast ultrasound data.



2D motion estimation based on diverging wave coherent compounding and transverse oscillations**Feifei Zhao¹, Jianwen Luo¹**¹*Department of Biomedical Engineering, Tsinghua University, Beijing, China, People's Republic of***Background, Motivation, and Objective**

Diverging wave (DW) based ultrafast imaging with transverse oscillations (TOs) has been developed to benefit 2D motion tracking in phased array, while coherent compounding can improve the quality of DW imaging. The combination of DW compounding and TOs has not been investigated. The objective of this study was to develop TOs for DW compounding to improve the performance of 2D motion estimation in phased array.

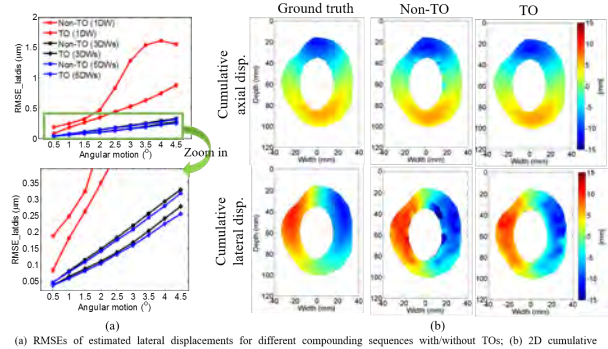
Statement of Contribution/Methods

1, 3 and 5 steered DWs were transmitted by setting virtual focuses behind a 2-MHz, 64-element phased array probe at 4 kHz PRF. Non-TO images were obtained with compounding of 1, 3 and 5 DWs. TO images were obtained by a filtering method from the non-TO images (Salles et al, IEEE TUFFC 2015) with angular wavelengths and extents equal to 0.1 and 0.04 rad, respectively. A homogeneous phantom ($80 \times 80 \text{ mm}^2$) in rigid angular motions (0.5°–4.5°, 0.5° steps) was simulated in Field II to test the performances of different imaging modes. 2D cross-correlation was used for motion estimation (window size: 4.6 mm \times 7 beams, overlap: 90%). Root-mean-square errors (RMSEs) of lateral motion estimation were calculated by comparing the estimated values to theoretical values.

A realistic cardiac model (Alessandrini et al, IEEE TMI 2015) was also involved (interpolated from 33 to 4000 datasets in one cardiac cycle) by compounding of 5 DWs with/without TOs. RF signals of the myocardium in the short axis view were simulated. 2D cross-correlation was used for motion estimation (window size: 3.85 mm \times 5 beams, overlap: 90%). The performances of motion estimation from non-TO and TO images were compared by quantifying RMSEs of the cumulative axial and lateral displacements during the systolic phase.

Results/Discussion

In the phantom simulations, for lateral motion estimation, TO images obtain smaller RMSEs than non-TO images with different compounding angles. Compounding of 5 DWs with TOs perform the best in all imaging modes (Fig. a). In the cardiac model, the estimated 2D cumulative motions from TO images are closer to the ground truth compared to those from non-TO images (Fig. b). The RMSEs are 0.99 and 0.84 mm in axial direction, and are 2.25 and 1.56 mm in lateral direction for non-TO and TO images respectively. Overall, the results demonstrate that it is feasible to introduce TOs by the filtering method in DW compounding for assisting the 2D motion estimation in phased array.



(a) RMSEs of estimated lateral displacements for different compounding sequences with/without TOs; (b) 2D cumulative displacements estimated from non-TO and TO images by compounding of 5 DWs and the ground truth.

Influence of Factors on Motion Artifacts in Strain Estimation with Spatial Angular Compounding
Zonghui Pan¹, Qiong He¹, Zhi Liu¹, Jianwen Luo¹
¹*Department of Biomedical Engineering, Tsinghua University, Beijing, China, People's Republic of*
Background, Motivation, and Objective

Carotid elastography has been developed to image strain distributions of plaques. Spatial angular compounding (SAC) improves the performance of lateral estimation in elastography. However, arterial motion and deformation during multi-angle acquisition causes motion artifacts in strain estimation with SAC. In this study, the influence of key factors such as the pulse repetition frequency (PRF) and number of steering angles (NSA) on motion artifacts in strain estimation with plane wave imaging (PWI) and SAC was investigated through both simulations and *in vivo* experiments.

Statement of Contribution/Methods

A 3D heterogeneous model with a cylindrical inclusion (Young's modulus = 25 kPa) embedded in the center of the background (80 kPa) was simulated. The model was imaged with a linear array ($f_0 = 6.25$ MHz, $f_s = 100$ MHz). Axial strain rate of 2 s^{-1} was applied, as a typical value in vulnerable plaques. PWI with PRFs of 200 Hz-10 kHz was performed with 1 (0°), 3 (0° and $\pm 15^\circ$) and 7 (0° , $\pm 5^\circ$, $\pm 10^\circ$, $\pm 15^\circ$) steering angles, respectively.

In the *in vivo* study, the right common carotid artery (CCA) of a 26-year-old, healthy male volunteer was imaged by a Vantage 256 system equipped with an L12-5 transducer ($f_0 = 6.25$ MHz, $f_s = 50$ MHz). PWI data (3 angles) was acquired with PRFs of 3 kHz and 429 Hz, respectively.

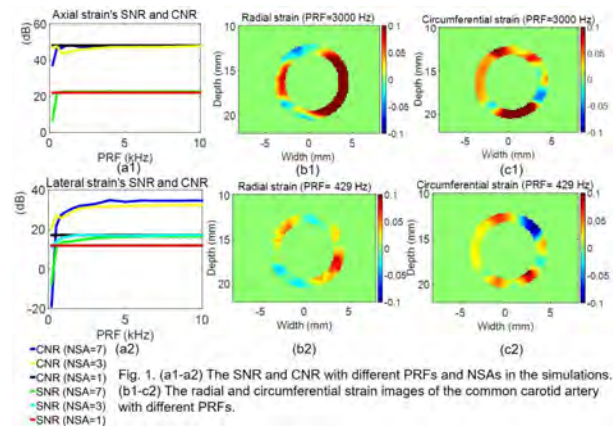
In both the simulations and *in vivo* study, after DAS beamforming, an optical flow method was used for motion estimation and the final 2D displacements were compounded from multiple axial estimates with SAC. At last, the 2D strains were calculated from the derivative of the displacements. The signal-to-noise ratio (SNR) and contrast-to-noise ratio (CNR) of the strains were used to assess the estimation performance in simulations.

Results/Discussion

In the simulations, the SNR and CNR of both axial and lateral strains increase with the PRF when $\text{PRF} < 4000$ Hz, and then remain constant when $\text{PRF} > 4000$ Hz; the SNR and CNR with an NSA of 3 are higher than those with an NSA of 7 when $\text{PRF} < 1000$ Hz, but they are similar when $\text{PRF} > 1000$ Hz (Fig. 1 a1-a2).

In the *in vivo* study, the radial and circumferential strain images with a PRF of 3 kHz are smoother and more homogeneous than those with a PRF of 429 Hz (Fig. 1 b1-c2).

In conclusion, both the PRF and NSA have influence on motion artifacts in strain estimation with PWI and SAC. For CCA, a PRF of 3-4 kHz and an NSA of 3 are suggested to obtain strain images with smaller motion artifacts.



Shear-wave based monitoring of radiofrequency ablations at clinically relevant depthsJochen Kruecker¹, Shriram Sethuraman¹, Can Meral¹, William Shi¹, William Pritchard², John Karanian², Bradford J. Wood²¹Philips Research North America, United States, ²National Institutes of Health, Bethesda, MD, United States**Background, Motivation, and Objective**

Thermal ablation is a widely used interventional cancer therapy. Current imaging methods are sub-optimal for ablation monitoring and none depict ablations accurately. While quantitative ultrasound-based methods like shear wave imaging holds great promise, visualizing the distal margins of ablations at clinically relevant depths remains a challenge with phase-based Young's Modulus reconstructions. We present a method using both phase and amplitude of ultrasonic shear waves for improved ablation detection at depths of up to 7 cm.

Statement of Contribution/Methods

A custom framework for ablation detection was developed on a modified commercial shear wave imaging platform (Philips Epiq 7 with C5-1 probe). To improve detection sensitivity at greater depth, both shear wave phase and amplitude were used for reconstructing elastography maps. The custom mode was tested on *ex vivo* bovine (N=6) and *in vivo* porcine (N=11) RF liver ablation studies. In *ex vivo* studies, optimal thresholds for segmenting ablations in the elastography maps were found by comparison with gross pathology using dice similarity and ellipsoidal fit methods. In the *in vivo* studies, the elastography maps were compared with contrast CT

Results/Discussion

All 6 *ex vivo* ablations were visualized using the imaging framework. The mean and range of thresholds for optimal segmentation of ablations in the elastography maps determined using the dice and elliptical fit methods were 12.2 kPa (8.6 – 15.9 kPa) and 10.2 kPa (6.4 – 16.1 kPa), respectively. The radii measurements agreed satisfactorily, with 10% relative difference. In *in vivo* studies, 10 of the 11 ablations could be visualized. Figures 1 and 2 are example *in vivo* results. We demonstrated feasibility of shear-wave based ablation monitoring at clinically relevant imaging depths.

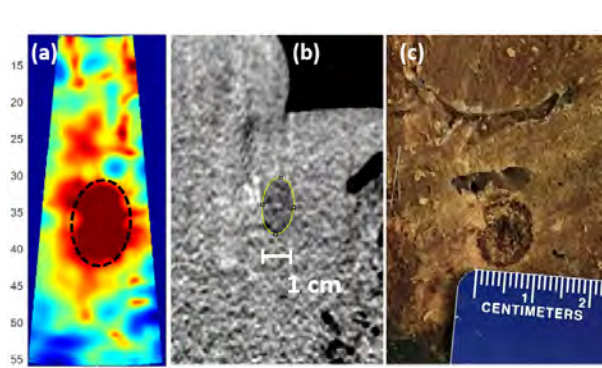


Figure 1. (a) Elastographic map after an *in vivo* ablation at 35mm depth, (b) contrast CT image, and (c) gross pathology photograph.

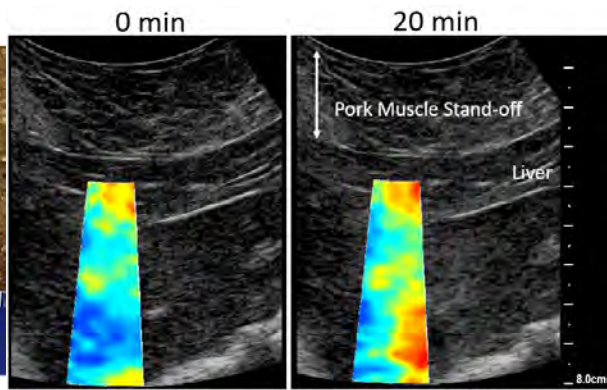


Figure 2. *In vivo* elastographic monitoring of RFA lesion centered at 7 cm imaging depth in a porcine liver

P1-C7 - Machine Learning for Image Processing

Kairaku (posters 1)

Thursday, October 25, 9:30 AM - 4:00 PM

Chair:

P1-C7-1

Automatic classification of cardiac events from ultrasound images using deep learning

Adrian Meidell Fiorito^{1,2}, Andreas Østvik^{1,2}, Erik Smistad^{1,2}, Sarah Leclerc³, Olivier Bernard³, Lasse Lovstakken^{1,2}

¹Department of Circulation and Medical Imaging, Norwegian University of Science and Technology, Trondheim, Norway, ²Centre for Innovative Ultrasound Solutions (CIUS), Norway, ³CREATIS, Lyon, France

Background, Motivation, and Objective

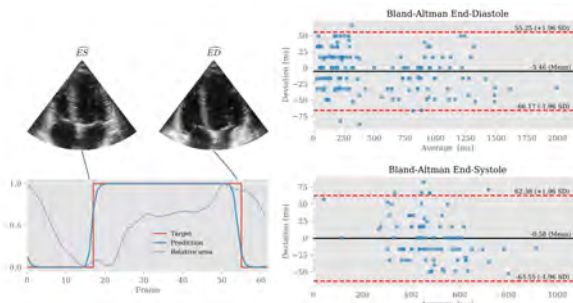
A proper definition of cardiac events such as end-diastole and end-systole is important for quantitative measurements in echocardiography (e.g. ejection fraction (EF) or stroke volume). The manual approach is based on M-mode measurements and/or by looking for valve closure events in B-mode images. While end-diastole can be found using ECG, end-systole is difficult to extract from ECG alone. Further, on handheld devices ECG is not available or cumbersome. Several other methods for automatic timing estimation have been proposed in the recent years. Following the success of convolutional neural networks (CNN) in image classification, state-of-the-art methods propose using 2D CNN followed by recurrent layers. These methods however ignore temporal correlations at the pixel level.

Statement of Contribution/Methods

We propose a 3D CNN to extract spatiotemporal features, which are further input into a dual-layer recurrent network (LSTM) for classifying whether frames belong to either diastole or systole. End-systole and end-diastole is then automatically detected as the switch between the two states. The model works on arbitrary length sequences, whereas previous models have only used fixed length input videos. The dataset consists of standard B-mode images of four- and two-chamber views from 500 patients acquired at the University Hospital of St-Etienne (France) using a GE Vivid E95 system. A total of 100 videos was randomly selected for testing.

Results/Discussion

The method performs favourably compared to other machine learning approaches, with an average deviation from reference of (-5.5 ± 28.2) ms and (-0.6 ± 31.8) ms on ED and ES respectively. The mean absolute error was 1.53 and 1.55 frames from ED/ES reference. The figure illustrates an example of phase transition frames, and the Bland-Altman plots for ED and ES. Model inference is fast, using (5.5 ± 1.4) ms per frame on a modern graphics processing unit. 3D CNN lend themselves well for spatiotemporal tasks, while LSTM is good for filtering the output of the CNN. Saliency studies show that the model output can be attributed mostly to movement of the mitral and tricuspid valves, as well as the septum wall. Future work includes testing in practice, and detection of additional cardiac events.



Ultrasound image synthesis and anatomical encoding using generative adversary neural networks

Oudom Somphone¹, Bo Zhang¹

¹Philips Research France, France

Background, Motivation, and Objective

Ultrasound image synthesis usually involves specific speckles and wave-propagation computation. However, in situations where we look for generating a large number of images, physical modeling can be practically computationally prohibitive. In this work, we propose an alternative data-driven approach within the generative adversary neural network (GAN) framework, to synthesize images visually similar to a given training base. Furthermore, our first results show that the proposed design seems to exhibit capability of anatomical encoding.

Statement of Contribution/Methods

We designed a specific adversary neural network that combines several generative components and a single discriminating component. Each generative network is driven by a random code, and all the components are combined into a synthetic image. Sparsity and decorrelation constraints are applied on these generated components. The rationale lies on the intent of letting the learning algorithm find the optimal anatomical decomposition within a given database of a single image class. The user controls individually the code element on each generative part to form a visually realistic image.

Results/Discussion

This method has the advantage of implicitly learning anatomical information during the training phase (Figure 1). Our first result shows a very interesting anatomy encoding capability, and therefore facilitates the user control. Indeed, different noise code element seems to generate complementary anatomical information (Figure 2). The combined image produces realistic ultrasound look. The entire synthesis based on network inference is also computationally friendly.

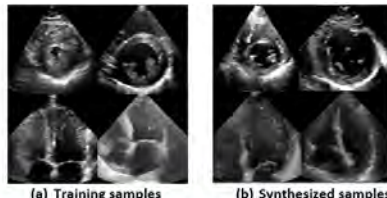


Figure 1 Image synthesis with the proposed method. (a) short-axis (SA) and 4-chamber long-axis (LA) training samples; (b) synthesized SA and LA samples.

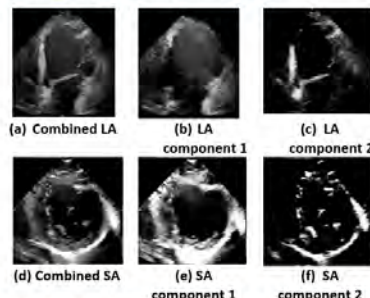


Figure 2 Our network seems to exhibit anatomical encoding capability. (a) shows a synthesized sample of LA image. (a) is combined from the two components separately generated from the network, i.e., (b) and (c). Notice that (b) encodes the major geometry information; (b) encodes the information at a more detailed level such as cardiac septum and valves. Similar observation applies on the SA synthesis sample (d), reconstructed from the components (e) and (f).

Ultrasound – computerized tomography registration using generative adversarial networks

Naama Cohen¹, Yuval Ron¹, Oren Solomon¹, Regev Cohen², Eyak Berkovich³, Yonina Eldar⁴

¹EE, Technion, Israel, ²Technion, Israel, ³Medical imaging, Rambam healthcare center, Israel, ⁴Technion, Haifa, Israel

Background, Motivation, and Objective

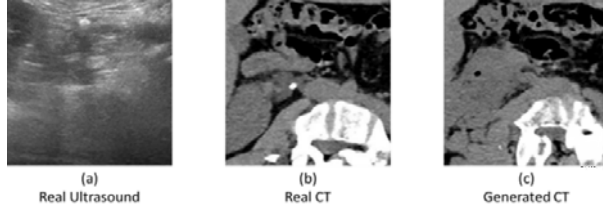
The orientation and position of ultrasound (US) images are strongly affected by the expertise and probe positioning of the US operator. In contrast, computerized tomography (CT) scans are produced according to a pre-defined and fixed coordinate system. In some clinical applications, such as real-time diagnosis in operation or trauma rooms, real-time CT scans can help guide surgeons during medical procedures. To reduce the patient and surrounding staff to radiation, it is more beneficial to perform radiation-free US scans for such procedures. Today, alignment of a pre-acquired CT scan to real-time US scan is custom-made using specifically calibrated US systems as the US images are scanned. However, if the two modalities are taken in different times, the alignment procedure is more challenging. Here we propose to use a generative adversarial network (GAN) to produce a CT scan from a given US scan to perform alignment.

Statement of Contribution/Methods

GANs constitute a class of deep-learning training policies which comprise of two competing networks (generative and adversarial) in a zero-sum game. At the end of the training process, the generative network can mimic a wide range of data distributions. We use a conditional GAN to translate a given US image into an aligned CT image. The goal of the trained GAN is to find a mapping between the spaces of US images to that of the CT images. Thus, given a US scan, the GAN produces an artificial CT-like image of the corresponding organ, aligned with the US scan in a fully automated manner. Then, we aim at correlating the produced CT-like image to a pre-acquired set of CT scans to find the best CT segment match to present to the operating medical staff.

Results/Discussion

We train a GAN using aligned pairs of CT and US scans acquired with a Logiq E9 US machine (GE healthcare). For the training process, we use a total of 2500 pairs taken from 20 patients as the training data and train the network to output a CT-like image, given a US image. Panel (a) presents a US scan, while panel (b) shows the corresponding aligned CT scan. Panel (c) displays the CT-like generated image, as the output of the generative network. Clearly, the CT-like image has close resemblance to the originally acquired CT scan, and with good alignment



Deep learning applied to multi-structures segmentation in 2D echocardiography : a preliminary investigation of the required database size

Sarah Leclerc¹, Erik Smistad², Thomas Grenier¹, Andreas Østvik², Florian Espinosa³, Lasse Lovstakken², Olivier Bernard¹

¹*CREATIS, Lyon, France*, ²*CIUS, NTNU, Trondheim, Norway*, ³*Cardiovascular department, CHU St-Etienne, Saint-Etienne, France*

Background, Motivation, and Objective

With the recent advances in machine learning, and their successful application to medical imaging, the building of medical databases big enough to learn the intrinsic heterogeneity of corresponding applications has become a priority. In this study, we set up a specific database to investigate the number of patients needed by learning methods to obtain accurate segmentation results in 2D echocardiography.

Statement of Contribution/Methods

The database contains daily exams from 500 patients of the University Hospital of St-Etienne (France). The left ventricle endocardium (LV-endo) and epicardium contours (LV-epi) were manually delineated by an expert at end diastole (ED) and end systole (ES) on two chambers (2CH) and 4CH views. The dataset was divided into 10 subfolds of 50 patients each, such that each subfold has the same distributions in terms of image quality and ejection fraction class.

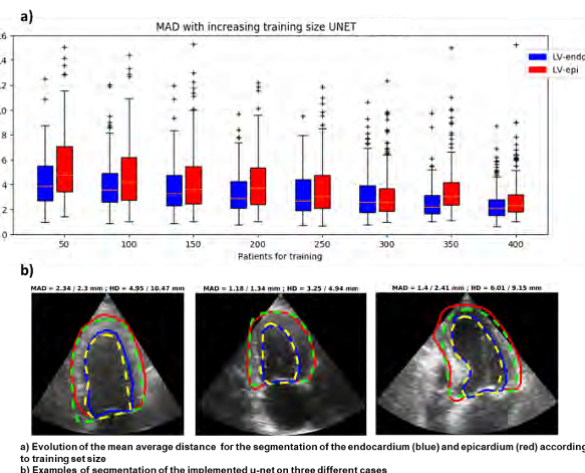
A deep convolutional network (U-Net) and a structured random forest (SRF) were trained with an incremental increase of the number of sub-folds involved in the training set, from 1 to 8 sub-folds for a total of 400 patients. The same validation and test sub-folds were kept aside from the training data and used to respectively optimize the parameters of each learning method and assess performance based on mean absolute (MAD) and Hausdorff (HD) distances.

Results/Discussion

Using the full training set, the average results showed for the U-net a MAD of LV-endo : 2.3 mm / LV-epi : 2.6 mm, and 3.3 mm / 3.7 mm using the SRF. The same tendency can be observed for the HD with 7.3 mm / 8.1 mm for the U-Net compared to 12.7 mm / 14.2 mm for the SRF. This clearly hints at the superiority of U-Net when compared to SRF.

It is worth noting from the boxplot underneath that from 300 patients onward, the U-Net implemented - while still improving in mean performances - appears to slowly reach a plateau, and that it was already able to produce accurate segmentation results learning on 50 cases. More evaluation metrics and discussion on the results will be provided in the full length paper.

These preliminary observations suggest that U-Net is a good candidate to solve 2D echocardiography automatic segmentation and doesn't necessarily require a huge amount of patients to capture the variability of the two cardiac structures present in these standard views.



The Feasibility of Classification of thyroid nodules integrated experiences based inference of radiologist and extracted feature vectors in ultrasound images

Shijie Zhang¹, Huarui Du², Yaqiong Zhu³, Zhuang Jin³, Fang Xie³, Mingbo Zhang³, Ying Zhang³, Ziyu Jiao³, Xiaoqi Tian³, Yukun Luo³, Jue Zhang⁴

¹Academy for Advanced Interdisciplinary Studies, Peking University, China, People's Republic of, ²State Information Center, China, People's Republic of, ³Ultrasonography Department, General Hospital of Chinese PLA, China, People's Republic of,

⁴Academy for Advanced Interdisciplinary Studies, College of Engineering, Peking University, China, People's Republic of

Background, Motivation, and Objective

Although Computer-aided diagnosis (CAD) systems have been reported in the assessment of lung and breast cancer, there are a limited number of studies that use CAD systems in diagnosing thyroid nodules with ultrasound scans. Current research focuses on the classifications of benign and malignant tumors in the diagnosis of thyroid nodules, but there are few studies that are based on the combination of CAD and the experiences based inference of radiologists. Following the necessity of manual intervention in diagnoses that use a CAD system, we prospectively developed a new method for classifying thyroid nodules that integrate human inference and classifiers for ultrasound images.

Statement of Contribution/Methods

The training data set was extracted from thyroid ultrasound images captured with ten distinct Ultrasound device models and consisted of 2,000 thyroid ultrasound images. Experts independently evaluated patients individually and described specific features, filling the TI-RADS requirements. We present a method for a TI-RADS automatic scoring system based on a binary classification neural network (binary network) and a multitask neural classification network (multitask network). We use a binary network to distinguish between benign and malignant nodules as well as a multitask network to detect clinical features (composition, echogenicity, shape, margin and echogenic foci). Radiologists adjusted the results of clinical features. Finally, the trade-off between each couple clinical features was made according to benign and malignant classifications from the binary network. Ultimately, we fused binary network output and clinical features and calculated the risk of thyroid nodules based on TI-RADS.

Results/Discussion

In this experiment, 501 thyroid nodules from 300 patients were included. Of those, 208 (41.5%) were benign and 293 (58.4%) were malignant. As Table 1 shows, cooperation between the classifier and the experiences based inference of radiologist offered significantly improved performance, compare to using either the classifier or radiologist separately. These results show our classifier-human based approach is a more effective way to increase the diagnostic accuracy of detecting thyroid cancer.

Table .1. Classification performances on experiment.

| | Sensitivity(%) | Specificity(%) | Accuracy(%) | Youden index |
|------------------------|----------------|----------------|-------------|--------------|
| ResNet 50 | 82.9 | 70.2 | 77.6 | 0.53 |
| VGG-16 | 80.5 | 67.3 | 75.0 | 0.48 |
| Radiologist | 52.6 | 95.7 | 70.5 | 0.48 |
| ResNet 50+ Radiologist | 98.6 | 83.7 | 92.4 | 0.82 |

Deep CNN-based ultrasound super-resolution for high-speed high-resolution B-mode imaging

Woosuk Choi¹, Mina Kim¹, Jae Hak Lee², Jungho Kim², **Jong Beom Ra¹**

¹School of Electrical Engineering, KAIST, Daejeon, Korea, Republic of, ²Samsung Electronics Co., Ltd., Gyeonggi-do, Korea, Republic of

Background, Motivation, and Objective

In real-time high-resolution B-mode ultrasound (US) imaging, the lateral resolution, or the number of scan lines, may be limited due to the speed of sound, if a longer penetration depth is needed as in obese patient imaging. To deal with this limitation, in this study, we propose to apply a super resolution (SR) technique to US B-mode scan images of low lateral and high depth resolutions. Recently, several convolutional neural networks (CNNs), such as VDSR and SRResNet, have shown good performance in SR of natural images. However, they usually provide rare improvement on image textures. To alleviate this problem, SRGAN is proposed for natural color images. In the US image, speckle noise can be considered texture. It is also observed that its degree of fineness is important to determine the image resolution, in addition to structural sharpness. We hence adopt and modify SRGAN to make B-mode US images of low lateral resolution similar to their original high-resolution (HR) images.

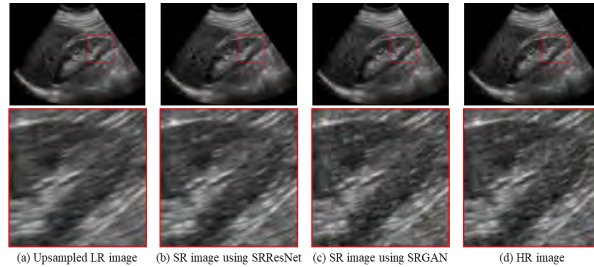
Statement of Contribution/Methods

We first define US SR as the recovery of HR images from 4-to-1 laterally subsampled low-resolution (LR) images. Those LR images are acquired by using a quarter of the number of scan lines required for HR images so that the scanning speed can be four times faster. LR images thereby have asymmetric resolution, or a low lateral and high depth resolution. It should be noted that the beam width is widened four times with respect to the acquisition of HR images, to reduce unwanted aliasing artifacts along the lateral direction. In order to improve the resolution, we adopt SRGAN and slightly modify its network architecture and the corresponding VGG loss so that they can be applicable for US asymmetric SR.

Results/Discussion

We train the modified SRGAN network using LR and HR image pairs selected from nineteen B-mode US scan sequences, which are captured from the abdomens of different patients. Figures below show (a) bicubic upsampled LR image obtained via four times faster scanning than HR image, (b) SR image obtained from LR images by using SRResNet, (c) SR image by using the modified SRGAN, and (d) the corresponding HR image. As shown in the figures, the proposed SR image in (c) is perceptually more similar to the HR image, by improving the fineness of speckle noise texture as well as the resolution of organ structures.

Work supported by Samsung Medicine, Co., Ltd.



(a) Upsampled LR image

(b) SR image using SRResNet

(c) SR image using SRGAN

(d) HR image

Cardiac Motion Estimation with Dictionary Learning and Robust Sparse Coding in Ultrasound Imaging

Nora Ouzir¹, Patricia Chiril², Adrian Basarab², Jean-Yves Tourneret¹

¹IRIT/INP-ENSEEIHT, University of Toulouse, Toulouse, France, ²IRIT, University of Toulouse, Toulouse Cedex, France

Background, Motivation, and Objective

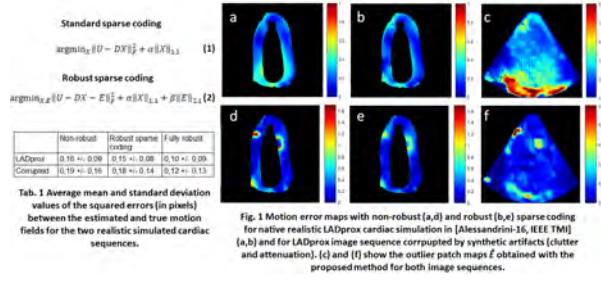
Cardiac motion estimation (CME) from ultrasound (US) images is an ill-posed problem that needs regularization to stabilize the solution. A large variety of regularizations exist, ranging from local parametric models (affine) to global functions (B-splines, total variation). In this context, we recently showed the interest of constraining the cardiac motion fields to be patch-wise sparse in a learned overcomplete dictionary that contains patterns of training motions [Ouzir-18, IEEE TIP]. More precisely, combining total variation and patch-wise sparsity regularizations with an optical flow-based data fidelity term provides a cost function, which can be minimized to provide estimated motion fields. In this work, we further improve this method by integrating automatic detection of (abnormal) motion patches that do not have a sparse representation in the dictionary. The existence of these patches is justified by the presence of anatomical motion boundaries or image artifacts (shadowing, clutter).

Statement of Contribution/Methods

Our CME method alternates between two optimization problems: i) motion field estimation, ii) determination of patch-wise sparse codes in the dictionary. The main contribution is to robustify the second problem in order to handle patches that are not sparse in the dictionary. Eqs. (1) and (2) show the difference between the non-robust and robust sparse coding optimization problems, where U is the motion field, D the dictionary, X contains the sparse codes and α, β are two hyperparameters. Note that the $\ell_{2,1}$ -norm of E in (2) captures the information associated with non-sparse patches (large values of E correspond to patches that cannot be decomposed sparsely in the dictionary) and limits the number of such patches. Problem (2) can be solved efficiently by an ADMM-based optimization algorithm.

Results/Discussion

Two realistic simulations (native, and corrupted by synthetic attenuation and clutter) with ground truth cardiac motion are used to evaluate the contribution of the robust sparse coding in CME. The results are shown quantitatively and qualitatively in Tab. 1 and Fig. 1. Fig. 1 also shows the estimated outlier map E , which fits the myocardium boundaries and the regions with artifacts. Note that the method can be further improved by robustifying the total variation term yielding a fully robust algorithm, whose performance is shown in Tab. 1.



Quality assessment of transperineal ultrasound images of the male pelvic region using deep learning

Saskia Camps^{1,2}, Tim Houben¹, Christopher Edwards³, Maria Antico^{4,5}, Matteo Dunnhofer⁶, Esther Martens⁷, Jose Baeza⁷, Ben Vanneste⁷, Evert van Limbergen⁷, Peter de With¹, Frank Verhaegen⁷, Gustavo Carneiro⁸, Davide Fontanarosa^{3,4}

¹Faculty of Electrical Engineering, Eindhoven University of Technology, Netherlands, ²Oncology solutions, Philips Research, Netherlands, ³School of Clinical Sciences, Queensland University of Technology, Australia, ⁴Institute of Health & Biomedical Innovation, Queensland University of Technology, Australia, ⁵School of Chemistry, Physics and Mechanical Engineering, Queensland University of Technology, Australia, ⁶Department of Mathematics, Computer Science and Physics, University of Udine, Italy, ⁷Department of Radiation Oncology (MAASTRO), GROW – School for Oncology and Developmental Biology, Netherlands, ⁸Australian Centre of Visual Technologies, the University of Adelaide, Australia

Ultrasound Imaging Improved by the Context Encoder Reconstruction Generative Adversarial Network

Chao-Yi Huang¹, Oscal Tzyh-Chiang Chen¹, Guo-Zua Wu², Chih-Chi Chang², Chang-Lin Hu²

¹National Chung Cheng University, Taiwan, ²Industrial Technology Research Institute, Taiwan

Background, Motivation, and Objective

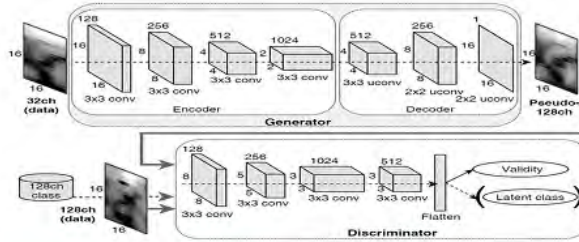
Portable ultrasound devices with less numbers of transducers become popularly spread soon or later. Accordingly, this work explores how to make quality of ultrasound images from 32 channels approaching to that from 128 channels by using Deep Neural Networks (DNN) of Convolutional Neural Network (CNN), Residual Nets (ResNet), Auxiliary Classifier Generative Adversarial Network (AC-GAN), and Context Encoder Reconstruction GAN (CERGAN).

Statement of Contribution/Methods

Based on the concepts of auto-encoder, context encoder, semi-supervised latent-class learning, and context-conditional GAN, we develop the CERGAN, as shown in Fig. 1(a), which adopts the contour learning mechanism to construct the relationship between 32-channel and 128-channel Point Spread Functions (PSF) via the mini-batch training. The encoder and decoder of the generator have the corresponding dimensional layers of convolution and de-convolution. Both generator and discriminator are designed by leaky ReLU of ResNet with local response normalization. The stacking order of a cell is convolution, batch normalization, and leaky ReLU layer plus dropout for removing dead neurons.

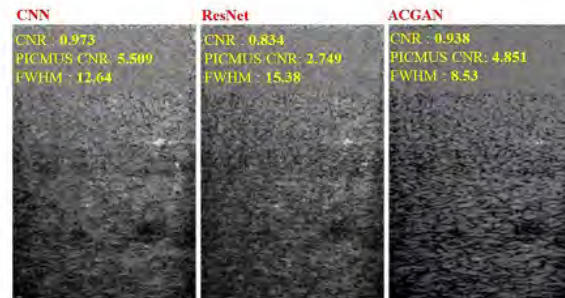
Results/Discussion

In our experiments, 20 pairs of 32/128-channel ultrasound images were used where the way of “leave one person out” was employed for cross-validation. Our CERGAN automatically encodes 32-channel PSF blocks, and generates pseudo 128-channel PSF ones which are matched with real 128-channel ones to obtain discrimination and amendment from the adversarial mechanism. Finally, these pseudo blocks are used to yield an improved image. The evaluation criteria adopt Contrast Noise Ratio (CNR), PICMUS CNR, and Full Width at Half Maximum (FWHM). The experimental results reveal that the proposed CERGAN outperforms the other three DNNs, as depicted in Fig. 1(b). In FWHM, the minimum distinguishable pixel lengths from the 32-channel, CERGAN, and 128-channel images are 13.34, 11.15, and 8.62, respectively. In CNR/PICMUS CNR, the scores of the 32-channel, CERGAN, and 128-channel images are 0.939/4.762, 1.508/13.004, and 1.422/12.005, respectively. The favorable score from CERGAN is because the background speckle noise is lowered to some extent. Hence, our CERGAN is a reliable architecture that effectively ameliorates the quality of 32-channel ultrasound imaging, close to that of 128-channel one.



(a)

| 32 channels | 128 channels | CERGAN |
|--|--|---|
| CNR : 0.939 PICMUS CNR: 4.762 FWHM : 13.34 | CNR : 1.422 PICMUS CNR: 12.005 FWHM : 8.62 | CNR : 1.508 PICMUS CNR: 13.004 FWHM : 11.15 |



(b)

Fig. 1 Proposed CERGAN associated with (a) architecture, and (b) result comparison.

RF Data Restoration using Deep Neural Network in Subjects Including Bone for Ultrasound Computed TomographyYoshiki Watanabe¹, Hongxiang Lin², Naoki Tomii³, Shu Takagi², Takashi Azuma⁴¹*Department of Bioengineering, The University of Tokyo, Japan*, ²*Department of Mechanical Engineering, The University of Tokyo, Japan*, ³*Center for Disease Biology and Integrative Medicine, The University of Tokyo, Japan*, ⁴*Center for Disease Biology and Integrative Medicine, The University of Tokyo, Tokyo, Japan***Background, Motivation, and Objective**

Ultrasound Computed Tomography (USCT) can obtain various valuable information such as sound speed, attenuation, and B-mode image. From the view point of the achieved spatial resolution, B mode imaging using a ring array have been studied. One of advantages of the ring array is shadow-less, isotropic imaging possibility. This feature has huge advantage in the case of imaging object including bone. In this study, we try to remove bone effects from RF data to enhance the advantage of shadow-less imaging, and improve imaging quality by using Deep Neural Network (DNN). For training of the DNN, numerical simulations as an efficient development method was used.

Statement of Contribution/Methods

One way to reduce artifact is to apply DNN to reconstructed images, but we apply it to RF signal because it has much more information to distinguish a scattering wave of bone from the others. Simulation and training condition is detailed on Fig. 1 (a), (b). By learning for each pixel, it was possible to generate a large amount of data from a single propagation simulation using K-wave. We adopted RF data on an including bone condition as input data, and a no bone condition as a correct answer data for training DNN. Training data was created from the whole RF data by extracting region corresponding to 10 pulses around the time of interest. After training, the learning results were applied to RF data acquired in different bone and point scatterer distribution. After that, image reconstruction was performed on recovered RF data.

Results/Discussion

From the view point of RF signal restoration, it was confirmed samples that trained network selectively removed the reflection waves from the bone while scatter waves from point scatters were preserved. Figure 1 (d), (e) shows the reconstructed images. Reconstruction from raw RF data contained strong artifacts. On the other hand, the one from the restored RF had no artifact from the bone, while almost of all point scatters were clearly imaged. Now a transmitter is only one element, then shadow area of the bone is hide the point scatters. When multi transmitter RF data is used for training of DNN, it is thought that the system can realize not only RF signal restoration but also perfect shadow-less imaging.

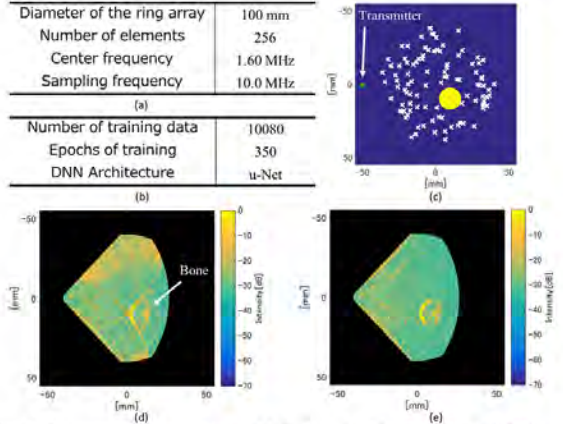


Figure 1. The reconstructed images on region including bone. (a) Simulation condition; (b) DNN training condition, (c) Schematic view of a medium of the validation data. White cross marks indicate position of scatterers, a yellow circle indicates bone; (d) Reconstruction result from raw RF data; (e) Reconstruction result from restored RF data

Machine learning of regional myocardial strain curves to predict myocardial viability
Mahdi Tabassian¹, Serkan Ünlü², Jens-Uwe Voigt^{1,2}, Jan D'hooge¹
¹*Department of Cardiovascular Sciences, KU Leuven, Leuven, Belgium*, ²*Department of Cardiology, University Hospitals Leuven, Leuven, Belgium*
Background, Motivation, and Objective

Speckle tracking echocardiography (STE) is a well-established method to assess regional cardiac function. Despite considerable research focused on accurate implementation of STE, little attention has been given to the objective assessment of the measured curves to aid clinical decision-making. The goal of this study was therefore to investigate the utility of machine learning to identify myocardial scar tissue from the STE-derived strain curves.

Statement of Contribution/Methods

Longitudinal strain curves were measured using GE EchoPac from the apical 2- and 4-chamber views in a set of 53 patients with previous myocardial infarction and 5 healthy volunteers using a GE Vivid E9 at 60 Hz. Based on correlative MRI late enhancement data, a transmural extent of scar was attributed to each myocardial segment in the range of 0 to 100%. Partial least square regression (PLSR) was used to model the whole temporal profile of the strain trace in order to predict scar transmurality. Two independent PLSR models were trained using individual segmental curves and locally concatenated curves. In the latter case, not only the curve obtained in a given segment but also those of its adjacent segments were modeled to help identifying scar tissue. The regression results were used to categorize the segments into non-transmural or transmural scar for ROC analysis where a segment with transmurality > 50% was considered transmurally scarred. Training and testing sets were created by randomly selecting 60% and 40% of the subjects, respectively. This process was repeated 200 times and the average classification performance was computed.

Results/Discussion

The classification results obtained with the PLSR models are shown in Figure 1. For all computed metrics, PLSR trained with the adjacent segments outperformed its counterpart trained with the individual segments and showed an average and standard deviation area under the curve of $88 \pm 3\%$ and accuracy, sensitivity and specificity of $79 \pm 3\%$, $78 \pm 6\%$ and $79 \pm 4\%$, respectively. In conclusion, this study shows that myocardial viability can be predicted with good accuracy by careful analysis of the regional strain curve and the curves of its neighboring segments. The clinical implication of these results is significant since ultrasound currently lacks a reliable methodology to assess segmental viability.

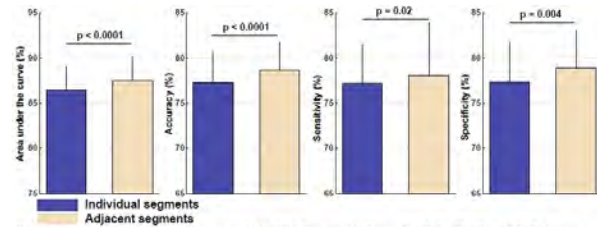


Figure 1. Classification results (averages and standard deviations) obtained with the PLSR models that were trained with the individual and adjacent segments. Accuracy, sensitivity and specificity rates were computed using the optimal cut-off points applied to the ROC curves and statistically compared for the two PLSR models.

Use of Deep Learning to Reconstruct Limited-Angle Ultrasound Tomography Images in Prostate Cancer: A Simulation Feasibility Study

Alexis Cheng¹, Younsu Kim², Emran Anas², Arman Rahmim², Emad M. Boctor², Reza Seifabadi¹, Bradford J. Wood¹

¹National Institutes of Health, United States, ²Johns Hopkins University, United States

Background, Motivation, and Objective

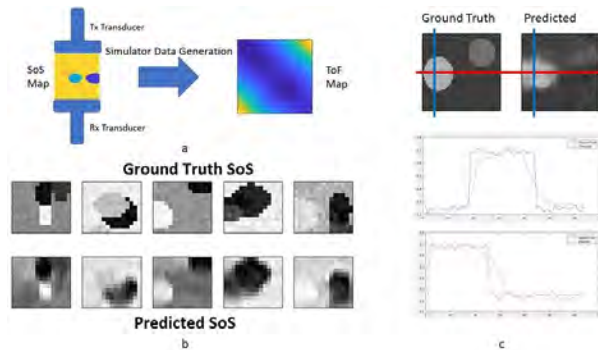
The gold standard for prostate cancer diagnosis is B-mode transrectal ultrasound-guided prostate biopsy. The inability to distinguish tumors within ultrasound (US) images result in blind prostate biopsies and it has led to the use of MRI or US/MRI fusion systems to perform targeted prostate biopsies. Given the assortment of high costs associated with using MRI and the success of ultrasound tomography (UST) for breast cancer detection, UST for prostate cancer detection may be feasible. However, the prostate anatomy precludes one from using a full-angle UST system. We previously proposed a limited-angle UST approach in which the prostate is imaged between two linear probes, inside the rectum and on the abdomen. Image reconstruction methods for such a system have focused on an $Ax=b$ approach where A is the system matrix, x is the slowness (reciprocal of speed-of-sound (SoS)), and b is the time-of-flight (ToF). There has been some early work using deep learning-based frameworks in MRI and CT sparse data reconstruction problems. Inspired by their promising results, we explore a deep learning-based framework to solve the limited-angle UST image reconstruction problem.

Statement of Contribution/Methods

The contribution of this work is to obtain the SoS in a limited-angle UST setup from ToF measurements with a deep learning-based framework. The network architecture consists of a fully connected layer followed by a series of encoder and decoder convolutional neural network layers. This network was trained with data simulating the SoS observed in healthy and cancerous prostate tissue and the ToF detected by our limited-angle UST setup. A total of 40000 images were used for training and 10000 images were used for validation.

Results/Discussion

Models based on deep learning can reconstruct regions with different SoS. Quantitatively, this method and an expectation-maximization method resulted in 0.0066 and 0.0074 normalized mean squared error between the predicted and ground truth SoS images respectively. Areas for improvement include using more realistic acoustic simulation packages to generate training data, as well as extending to experimental physical data. Limited angle UST simulation models are feasible using deep learning-based image reconstruction methods and they merit experimental assessment of ability to improve image reconstruction algorithms on raw data.



P1-C8 - Signal Processing for Hard and Soft Tissue Imaging

Kairaku (posters 1)

Thursday, October 25, 9:30 AM - 4:00 PM

Chair: **Veronica He** Infraredx Inc.

P1-C8-1

Enhancing Microcalcifications in Breast Images by Shrinkage of Wavelet Coefficients

Stine M. Hverven¹, Alan J. Hunter^{1,2}, Bastien Dénarié³, Andreas Austeng¹

¹*Department of Informatics, University of Oslo, Oslo, Norway*, ²*University of Bath, Bath, United Kingdom*, ³*GE Vingmed Ultrasound, Horten, Norway*

Background, Motivation, and Objective

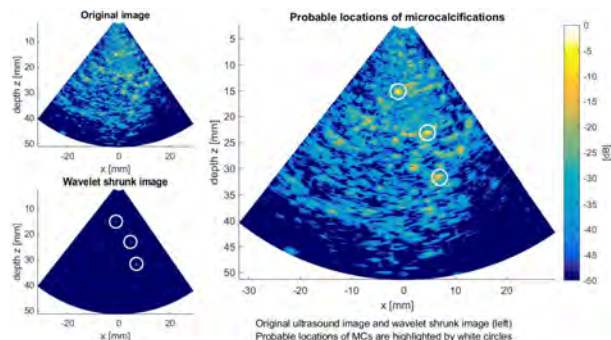
Detection of microcalcifications (MCs) in ultrasound images is important in early breast cancer diagnosis. MCs are small, hard calcium deposits that appear as point scatterers in an ultrasound image. They can be very difficult to identify and differentiate from surrounding breast tissue. Several detection algorithms have been proposed, but they generally suffer from many false positives. A promising technique uses shrinkage of wavelet coefficients and exploits frequency characteristics of speckle background (Hverven et al., IUS 2017). The proposed method is an extension of this technique by further exploiting three dimensional (3D) volumetric data. By exploiting that speckle is independent in each 2D plane, the technique can be run over several directions and the resulting estimates can be combined into a more certain 3D estimate. The proposed method can thus greatly reduce the probability of false positives.

Statement of Contribution/Methods

The method performs the wavelet shrinkage technique for three orthogonal directions separately. For each direction, it forms a 3D estimate of possible MCs by calculating a series of 2D wavelet shrunk images. These 3D estimates are then combined using coherence. To reduce false positives, points that are present in all three direction estimates are retained. Speckle points and MC candidates that are not present in all direction estimates will consequently be suppressed by the method.

Results/Discussion

The method was tested on a tissue-mimicking breast phantom with several hyperechoic areas and point scatterers. A 3D ultrasound image was recorded on a state of the art GE Vivid E95 scanner using a 4D volume transducer (GE 6VT-D) with center frequency at 5 MHz. Analysis in three orthogonal directions and further coherence-based shrinkage greatly reduces the number of MC candidates. For the presented ultrasound image, the method reduces the number of candidates from an average of 18 when using only one of the direction estimates, to the final three candidates shown in the figure. The results using the tissue-mimicking breast phantom are promising for further testing using transducers with higher frequency and larger aperture size on real breasts with MCs.



Parameter-sweep inversion for thickness and elastic velocities of long bone using axially-transmitted ultrasonic guided waves

Tho N.H.T. Tran¹, Lawrence H. Le^{1,2,3}, Mauricio D. Sacchi², Dean Ta³

¹*Department of Radiology and Diagnostic Imaging, University of Alberta, Canada*, ²*Department of Physics, University of Alberta, Canada*, ³*Department of Electronic Engineering, Fudan University, China, People's Republic of*

Background, Motivation, and Objective

Ultrasonic guided waves (UGW) are powerful non-destructive testing tools, which are used intensively in structural health monitoring and material characterization because of their long range propagation and low energy dissipation. In the last decade, long cortical bone assessment by UGW using pitch-catch or axial transmission (AT) setup has gained considerable attention. Inversion of AT ultrasound data to extract bone properties is challenging due to the complexity and co-existence of the multimodal UGW signals. In this work, a model-based parameter sweep inversion scheme has been developed to recover the thickness and elastic velocities of the cortex.

Statement of Contribution/Methods

The multimodal inversion scheme is formulated in the frequency-phase velocity ($f\text{-}c$) domain. To solve the model-based inverse problem, i.e. to extract bone properties from ultrasound data, a forward modeling has been developed to simulate the $f\text{-}c$ dispersion curves given a bone model. A semi-analytical finite element (SAFE) method is used to compute the dispersion curves for complex structures such as cortical bone plate coupled with surrounding soft tissues. A parameter sweep is used to seek within a range of values an optimized solution with the least cost. The proposed method optimizes the mismatch between the measured and simulated dispersion curves with a least-square constraint. Numerical and experimental data examples are presented to illustrate the technique's performance.

Results/Discussion

The feasibility of the proposed approach is demonstrated via both a numerically simulated data for a 2 mm soft tissue-6 mm bone bilayer and an *ex-vivo* dataset from a bovine femur plate with an overlying 2 mm-thick soft-tissue mimic. The *ex-vivo* AT scan was performed using a TomoScan Focus LT™ ultrasound system (Olympus NDT Inc., Canada) with two 1 MHz-exciting array transducers. Using the proposed inversion technique, the simulation input parameters (cortical thickness h , compressional-wave velocity V_p , and shear-wave velocity V_s) were exactly retrieved. For the *ex-vivo* case, the recovered values were 6 mm (h), 4000 m/s (V_p), and 1980 m/s (V_s) respectively. The cortical thickness and compressional-wave velocity were reasonably determined with less than 5% error compared to the average CT-measured thickness (5.89 mm) and the ray-traced velocity (4012 m/s). Refining the grid spacing may improve the accuracy but will result in excessive computational cost. Axial transmission ultrasonography shows the potential clinical application for cortical bone quality assessment.

Application of Dynamic Time Warping Technique to Evaluate Microstructures of Cancellous Bones

Boyi Li¹, Ying Li¹, Chengcheng Liu², Feng Xu¹, Lawrence H. Le³, Dean Ta¹

¹Department of Electronic Engineering, Fudan University, Shanghai, China, People's Republic of, ²Institute of Acoustics, Tongji University, Shanghai, China, People's Republic of, ³Department of Radiology and Diagnostic Imaging, University of Alberta, Edmonton, AB, Canada

Background, Motivation, and Objective

Osteoporosis is a systemic skeletal disease, which is characterized by the deterioration of microstructures and decrease of bone mineral density (BMD). Being non-ionizing and non-invasive, ultrasonic backscatter technique has a promising potential to evaluate microstructures and BMD of cancellous bone for the clinical diagnosis of osteoporosis. The dynamic time warping (DTW) algorithm, measuring the similarity and extracting features between two signals, has been widely used in speech recognition. The purpose of this feasibility study is to investigate the application of DTW to estimate the microstructure of cancellous bones. The dynamic time warped distance (DTWD) was calculated from the cost matrix between the ultrasonic backscatter signals and the reference signal.

Statement of Contribution/Methods

Ultrasonic backscatter measurements were performed on twenty-six bovine cancellous bone specimens using an ultrasonic backscatter bone diagnostic system with a focused broadband transducer, which has a center frequency of 1.04 MHz, and a -6dB frequency band from 0.67 MHz to 1.40 MHz. Each specimen was measured at 100 locations within the evenly-spaced grid points of the place of acquisition and data was acquired at each location 128 times and averaged for each record. Both the Pearson-correlations and Partial-correlations were analyzed and compared between DTWD, the apparent integrated backscatter (AIB), the backscatter spectral centroid shift (SCS), the zero frequency intercept of apparent backscatter (FIAB), the frequency slope of apparent backscatter (FSAB) and the micro-CT parameters of the average trabecular number (Tb.N), the average trabecular spacing (Tb.Sp), and BMD.

Results/Discussion

The results showed that DTWD correlates strongly with the bone microstructure characteristics ($|R|=0.57\text{--}0.86$, $p<0.05$) and BMD ($|R|=0.86\text{--}0.89$, $p<0.05$). The DTWD yields a negative correlation with Tb.N ($R=-0.86\pm0.09$, $p<0.0001$) and BMD ($R=-0.86\pm0.08$, $p<0.0001$), and a positive correlation with the Tb.Sp ($R=0.71\pm0.12$, $p<0.0001$). The positive correlation between BMD and Tb.N ($R=0.84\pm0.07$, $p<0.001$) and the negative correlation between BMD and Tb.Sp ($R=-0.63\pm0.13$, $p<0.001$) were observed. With the effect of BMD removed, the DTWD still displays a statistically significant Partial negative correlation with Tb.N ($R=-0.51\pm0.15$, $p<0.05$), and a Partial positive correlation with Tb.Sp ($R=0.42\pm0.15$, $p<0.05$).

In conclusion, ultrasonic backscatter provides a potential measurement for the microstructures of the cancellous bone. The DTWD has demonstrated the feasibility to evaluate the bone microstructure. Our future work will involve more samples to investigate the efficacy of DTW both in vitro and in vivo.

Ringdown suppression for a sonothrombolysis catheter using principal component analysis filteringAdam J. Dixon¹, John A. Hossack²¹Biomedical Engineering, University of Virginia, Charlottesville, VA, United States, ²University of Virginia, United States**Background, Motivation, and Objective**

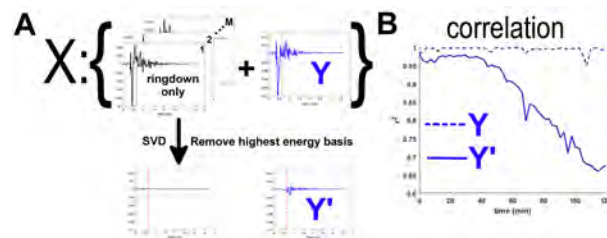
Therapeutic ultrasound catheters accelerate thrombus dissolution via sonothrombolysis. These catheters emit high pressure, low frequency, long cycle waveforms and are poorly suited for imaging. However, it would be advantageous to offer a catheter-based treatment monitoring mode to report the extent of clot dissolution to the user. An impediment to this goal is the ringdown artifact that extends for several millimeters into the pulse-echo RF data and obscures the signal derived from clot and tissue. In this study, we present a principal-component analysis (PCA) based filter that separates ringdown from tissue-derived signals and permits the analysis of a decorrelation-based metric of clot erosion. The method is demonstrated via results computed on simulation data and is verified using an EkoSonic therapeutic ultrasound catheter in an *in vitro* blood clot dissolution model.

Statement of Contribution/Methods

A PCA filter for removing ringdown artifact from a single element of an EkoSonic catheter was developed using experimental data. 1000 realizations of pure ringdown signal were collected in a data matrix, X, of size MxN (M observations, N samples). The waveform to be filtered, Y, comprising the ringdown plus tissue signal, was added as the 1001st row of X. Singular value decomposition was performed to derive data-specific basis functions. The highest energy singular value was assumed to correspond to ringdown and was removed. Y', the filtered version of Y, was reconstructed from the remaining basis functions. This method was experimentally validated using an EkoSonic catheter in an *in vitro* blood clot dissolution model.

Results/Discussion

The PCA filter is shown in Figure A. As shown, > 99% of the energy in the pure ringdown signal(s) was removed by exclusion of the highest energy basis, but signal remained in the filtered waveform, Y', corresponding to information not in the 1000 ringdown realizations. The filter was applied to 120 min of continuous pulse/echo A-line data acquired by an EkoSonic catheter during a thrombolysis experiment using bovine blood clots. Filtered versions of the waveforms were analyzed for decorrelation over time, which demonstrated a reduction in correlation from $r^2 > 0.95$ to $r^2 \sim 0.70$ after 120 min. Overall, the results demonstrate this technique's potential to permit a decorrelation-based assessment of clot erosion during sonothrombolysis.



Reconstruction acceleration for compressed sensing based synthetic transmit aperture using quadrature sampling**Jing Liu¹, Jianwen Luo¹**¹*School of Medicine, Tsinghua University, Beijing, China, People's Republic of***Background, Motivation, and Objective**

Previously, we proposed compressed sensing (CS) based synthetic transmit aperture (CS-STA) to reconstruct the radio-frequency (RF) dataset of synthetic transmit aperture (STA) from that of a smaller number of randomly apodized plane waves (PWs). We validated that CS-STA can increase the frame rate (FR) and contrast-to-noise ratio (CNR) of STA while maintaining its high resolution (Liu et al, IEEE TMI 2017). In CS-STA, CS reconstruction should be repeated on all samples and receive channels. Because the sampling frequency (f_s) of RF data is usually tens of MHz, the CS reconstruction is time-consuming. To reduce the reconstruction time, we reconstruct the in-phase/quadrature (IQ) dataset of STA from that of PWs in this study. This method is also of practical significance because many clinical and research systems only provide IQ data.

Statement of Contribution/Methods

We adopted the partial Hadamard matrix as the apodizations in CS-STA firings. We investigated the CS-STA performance with RF and IQ data on a 128-element linear array (pitch = 0.3 mm, f_0 = 6.25 MHz, bandwidth = 60%) by comparing CS-STA with 8 and 16 PW firings (i.e., CS8-STA and CS16-STA, respectively) with STA. We carried out the experiments on a CIRS 040 phantom with a Verasonics Vantage 256 system. In this system, the f_s of RF data ($f_{s, RF}$) is $4f_0$, i.e., 25 MHz. We obtained the IQ data from RF data by quadrature sampling, i.e., $I(n)=(-1)^n RF(3nT/2)$ and $Q(n)=(-1)^n RF(3nT/2+T/4)$ while $T=1/f_0$. Therefore, the f_s of IQ data ($f_{s, IQ}$) is $2f_0/3=4.17$ MHz.

Results/Discussion

As Fig. 1 shows, compared with STA, CS8-STA and CS16-STA present clearer image with 16× and 8× higher FR, respectively. CS-STA images with RF and IQ data appear to have no differences. Quantitative results in Table I are in agreement with these observations. The lateral full-widths at half maximum (FWHMs) are all about 0.42 mm. CS-STA achieves at least 3.44 and 3.48 dB higher CNR and contrast ratio (CR) than STA, respectively. CS-STA with RF and IQ data has similar CNR or CR. CS-STA with IQ data slightly increases the axial FWHM due to IQ data based beamforming. In addition, the reconstruction speed with IQ data is 3× faster than that with RF data, because RF data has $f_{s, RF}/2f_{s, IQ}$ times more samples than the I and Q data. To conclude, reconstructing IQ data can accelerate the CS-STA reconstruction by $f_{s, RF}/2f_{s, IQ}$ times without reducing the image quality significantly.

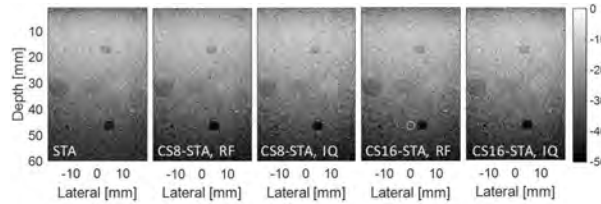


Fig. 1. The B-mode images of different methods. The red and white circles indicate the region-of-interest and the corresponding background for the CNR and CR calculations.

Table I. The frame rate (FR), reconstruction time, lateral and axial FWHMs, CNR and CR for different methods.

| Method | FR [Hz] | Recon time [min] | FWHM [mm] | | CNR [dB] | CR [dB] |
|--------------|---------|------------------|-----------|-------|----------|---------|
| | | | Lateral | Axial | | |
| STA | 100 | ~ | 0.42 | 0.26 | 1.47 | 19.72 |
| CS8-STA, RF | 1600 | 2.99 | 0.43 | 0.26 | 5.26 | 23.28 |
| CS8-STA, IQ | 1600 | 0.99 | 0.41 | 0.34 | 4.83 | 23.21 |
| CS16-STA, RF | 800 | 3.63 | 0.42 | 0.26 | 6.36 | 24.81 |
| CS16-STA, IQ | 800 | 1.11 | 0.41 | 0.34 | 6.65 | 24.49 |

Wavelet-based Cepstral Analysis for the Estimation of the Mean Scatterer Spacing

Remie Nasr¹, Omar Falou^{1,2}, Eno Hysi^{3,4}, Ahmad Shahin¹, Lauren Wirtfeld³, Elizabeth Berndl^{3,4}, Michael Kolios^{3,4}

¹Lebanese University, Lebanon, ²American University of Culture and Education, Lebanon, ³Ryerson University, Toronto, ON, Canada, ⁴Institute for Biomedical Engineering, Science and Technology (iBEST), Toronto, ON, Canada

Background, Motivation, and Objective

The potential of ultrasound (US) cepstral analysis for the characterization of scatterer spacing in normal and diseased tissue is hindered by the difficulty in identifying recurrent periodic peaks from the noisy backscatter signal. Wavelet transforms have the potential to extract features in noisy signals and to detect periodicities. In this work, the continuous wavelet transform (CWT) is applied to cepstra to estimate the mean scatterer spacing from simulated and experimental US backscatter from cancer cell aggregates.

Statement of Contribution/Methods

Two colon cancer (HT-29) cell pellets were imaged using a 55 MHz single element transducer (Vevo770, VisualSonics, Toronto, ON). H&E histological images were obtained and the location of each cell was extracted from the image using the circle Hough transform. The spatial coordinates and diameter of each cell were measured, and then used in simulations to generate backscattered signals by convolving the histologically based scattering medium with a 55 MHz Gaussian RF pulse.

For each of the 30 RF signals in 12 frames, the power cepstrum was computed and averaged. The CWT was applied to the average cepstrum and a basic global threshold was used to extract peaks. The spacing between each two consecutive peaks was computed and averaged across all frames. The simulated and measured spacings were compared to the diameter of HT-29 cells.

Results/Discussion

Fig. 1A shows a representative H&E histology image of an HT-29 pellet sample, which was used to extract the location of each cell for the simulation (Fig. 1B). Figs. 1C and 1D show the results of the CWT cepstral algorithm applied to the simulated and experimental RF lines from the pellet backscatter, respectively. The mean scatterer spacing values were estimated to be $13.00 \pm 2.40 \mu\text{m}$ for the simulation and $13.56 \pm 0.14 \mu\text{m}$ for the pellets, resulting in a difference between these two values of 4.31%. The estimated spacing was close to the $13 \mu\text{m}$ average diameter of the HT-29 cells. This is consistent with the fact that cells in the tightly packed pellet are spaced approximately one cell away from each other. This study suggests that estimating the mean scatterer spacing from US signals can be accomplished with this new algorithm. The cepstral analysis algorithm can be used to aid in the estimation of average scatterer size in a tightly packed medium, with applications in tissue characterization.

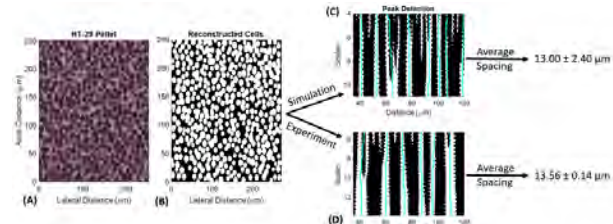


Fig. 1: (A) H&E histology image of a representative HT-29 cell pellet. (B) Location of each cell reconstructed from the histology image. (C) Simulated and (D) experimental binary CWT for the average cepstrum. The mean scatterer spacing is computed from the horizontal distance between detected peaks (blue lines), and the standard deviation between two consecutive spacings is estimated.

Jointly Optimized Modulation / Filtering Technique for Pseudo-Orthogonal Binary Sequences

Denis Bujoreanu¹, Yanis Mehdi Benane¹, Barbara Nicolas¹, Hervé Liebgott¹, Jean-Marie Gorce², Leonardo S. Cardoso², Denis Friboulet¹

¹*CREATIS, Univ.Lyon, INSA-Lyon, UCBL1, UJM-Saint Etienne, CNRS, Inserm, CREATIS UMR 5220, U1206, Villeurbanne, France*, ²*Univ Lyon, INSA Lyon, Inria, CITI, Villeurbanne, France*

Background, Motivation, and Objective

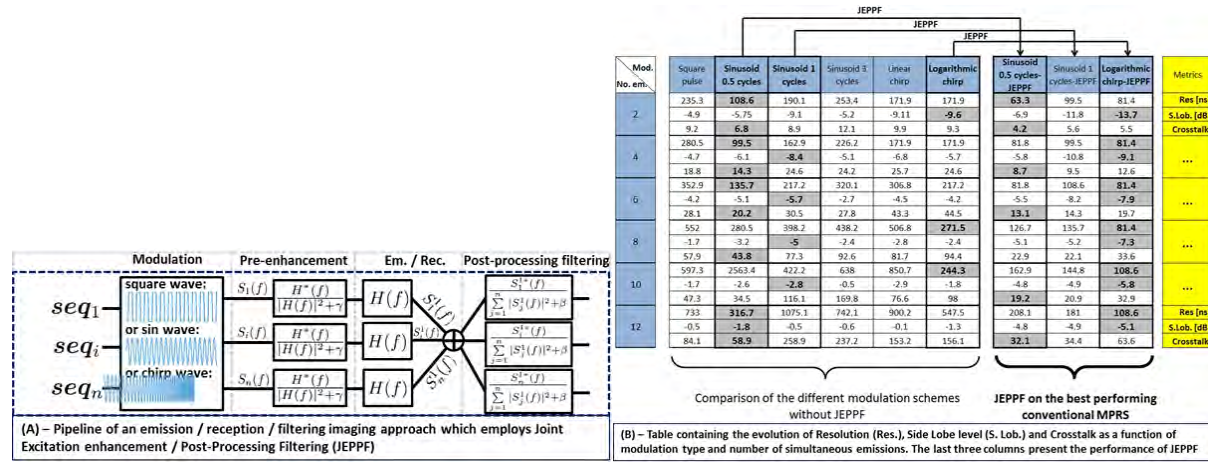
Modulated Pseudo-Random Sequences (MPRS) are often employed as coded excitations in imaging techniques, which use matched filters or inverse problem approaches for echo separation. However, the MPRS orthogonality is degraded by the effect of the bandlimited ultrasound probe, which results in lower image quality. To reduce this effect, a novel chirp based MPRS and a Joint Excitation enhancement / Post Processing Filtering (JEPPF) are proposed.

Statement of Contribution/Methods

The pipeline of the proposed approach is shown in (A). After the binary sequence (seq_i) modulation using different carrier waves (Modulation), the signals $S_i(f)$ are de-convolved with the probe pulse-echo transfer function $H(f)$ (Pre-enhancement). The simultaneous emission / reception, simulated by the convolution with $H(f)$ and by the addition (Em. / Rec.), generates a sum of echoes $S^1_i(f)$ (of waveform similar to $S_i(f)$). Thus, the influence of $H(f)$ is compensated. Optimal filtering is performed in reception (Post-processing filtering).

Results/Discussion

The Resolution (Res.), the Side Lobe level (S. Lob.) and the Crosstalk were used to evaluate the orthogonality of the MPRS. Binary sequences were modulated using six techniques in order to obtain MPRSSs of same duration (15 μ s). 2, 4, 6, 8, 10 and 12 simultaneous emissions were studied. Without JEPPF, the best Crosstalk (Res. and S. Lob.) is obtained by half (one) cycle sinusoid (see (B)) modulation. JEPPF improves the orthogonality of the MPRS, by providing improvements for all the studied modulations (for the three metrics). In (B), we show the impact of JEPPF on the best performing MPRS cited previously. JEPPF applied to Logarithmic MPRS provides the best Res. and S. Lob. Concerning the Crosstalk, the half cycle sinusoid combined with JEPPF provides the best values.



P1-C9 - Musculoskeletal System

Kairaku (posters 1)

Thursday, October 25, 9:30 AM - 4:00 PM

Chair: **Tadashi Yamaguchi** Chiba University

P1-C9-1

Ultrasound radiation from bovine cortical bone

Taiki Makino¹, Masaki Kuraoka¹, Daisuke Koyama¹, Shinji Takayanagi², Mami Matsukawa¹

¹Doshisha university, Japan, ²Nagoya Institute of Technology, Japan

Background, Motivation, and Objective

Fukada and Yasuda have reported piezoelectricity in bone by low frequency mechanical studies [1]. To confirm the piezoelectricity in the MHz range, we have fabricated ultrasound receivers using bone as piezoelectric devices and found very small induced potentials. [2]. In this study, we have fabricated ultrasonic transducers using cortical bone samples extracted from various directions of bovine femur and evaluated anisotropic inverse piezoelectric effects in the MHz range.

Statement of Contribution/Methods

Five different circular plates of cortical bone samples (diameter; 10.5-11.0 mm, thickness; 1.00 ± 0.01 mm) were extracted from the mid-femoral shaft of a 34 month-old bovine as shown in Fig. 1 (a). Using these plate samples as piezoelectric materials, we fabricated bone ultrasound transducers. The handmade bone or two PVDF transducers were used as a transmitter or a receiver. A burst wave with 10 sinusoidal cycles of 70 V_{peak-peak} in the frequency range from 0.8 to 2.4 MHz was applied to a transmitter and irradiated to the surface of a receiver in water. The transmitting sensitivities of bone transducers were obtained by the reciprocity method.

Results/Discussion

Fig. 1 (b) shows the observed waveforms at 2.0 MHz by a PVDF transducer and we could observe ultrasound radiation from bone transducers. The sound pressure of ultrasound radiation from bone transducer was about 15 Pa_{peak-peak}. Fig. 1 (c) shows the transmitting sensitivities of all bone transducers. The sensitivities were around 1/2000 of that of the PVDF transducer. The transmitting sensitivities of all bone transducers showed a peak around 2.0 MHz. Considering the ultrasound velocity in bovine femoral cortical bone (around 4000 m/s) [2], these peaks seem to result from the fundamental thickness resonance. The transmitting sensitivities of off axis bone transducers were higher than those of on axis bone transducers. In this study, we confirmed the ultrasound radiation from bone and the anisotropic piezoelectric character of the cortical bone.

[1] E. Fukada and I. Yasuda, J.Phys. Soc. Jpn, **12**, p.1158 (1957).

[2] S. Matsukawa et al., Appl. Phys. Lett. **110**, 143701 (2017).

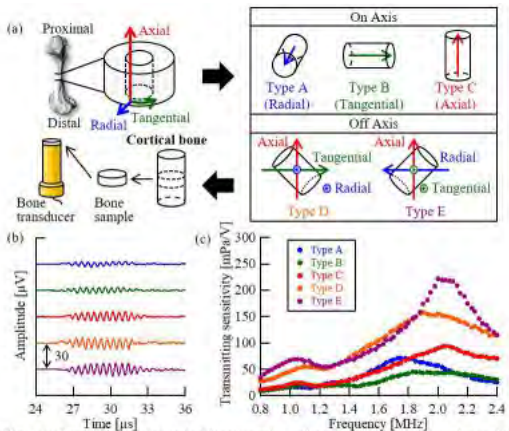


Fig. 1 (a) Preparation of the cortical bone samples and transducers (on axis samples; radial (A), tangential (B) or axial (C) directions, off axis samples; 45° directions from axial-tangential plane (D) or axial-radial plane (E)).
(b) Observed waveforms (transmitter: bone transducers, receiver: PVDF transducer).
(c) Transmitting sensitivities of bone transducers.

Ex vivo radius fracture discrimination from cortical thickness and porosity obtained by axial transmission

Jean-Gabriel Minonzio¹, Edison Zapata^{2,3}, Nicolas Bochud¹, Quentin Vallet¹, Frederic Rongieras^{2,4}, Jean-Baptiste Pialat^{3,5}, Helene Follet³, David Mitton², Pascal Laugier¹

¹CNRS, INSERM, Laboratoire d'Imagerie Biomédicale (LIB), Sorbonne Université, France, ²Univ Lyon, Université Claude Bernard Lyon 1, IFSTTAR, LBMC UMR_T9406, Lyon, France, ³Univ Lyon, Université Claude Bernard Lyon 1, INSERM, Lyon UMR1033, Lyon, France, ⁴Service de chirurgie orthopédique et traumatologique, Hôpital d'instruction des armées Desgenettes, Lyon, France, ⁵Service de Radiologie, Centre Hospitalier Lyon Sud, Pierre-Bénite, France

Background, Motivation, and Objective

Structural decay of bone is not fully assessed by the current X-ray gold standard, Dual X-Ray absorptiometry (DXA). Furthermore, there is an unmet need in identifying women at risk of fracture who should receive a treatment. Recent Axial Transmission (AT) techniques exploit the multimode waveguide response of long bones such as the radius [Q. Vallet *et al* IEEE UFFC 63:1361-1371, 2016]. The objective of this *ex vivo* study was to evaluate the performance of a prototype AT device to discriminate between fractured and non-fractured specimens under realistic fall loading conditions.

Statement of Contribution/Methods

Thirty radii from elderly donors (79 y.o. \pm 12 y.o., 15 males, 15 females) underwent AT measurements at one-third distal location, using a 1-MHz multi element prototype (Azalée, Paris, France). A singular value decomposition combined with a 2-D spatio-temporal Fourier transform were applied to the responses of all possible transmitter-receiver pairs to extract the dispersion curves. A model-based sparse inverse problem was used to estimate cortical thickness (Ct.Th) and porosity (Ct.Po) by fitting a 2-D transverse isotropic free plate waveguide model to the experimental dispersion curves. The radii were loaded at 2 m.s⁻¹ using a servo-hydraulic testing machine to mimic impact that corresponds to a fall [E. Zapata *et al* J Biomech. 63:174-178, 2017]. The specimens were also measured by DXA to obtain bone mineral density (BMD) values (g.cm⁻²) at radius distal end.

Results/Discussion

Among the 30 radii, 14 had a fracture after the impact, leading to two groups (fractured F and non-fractured NF). The AT measurement failed for one fractured case. Fracture discrimination was significant with Ct.Th mean values equal to 2.5 mm (NF) and 1.8 mm (F). Likewise Ct.Po mean values were equal to 4.3 % (NF) and 7.9 % (F). The odds ratios [ORs] of Ct.Th and Ct.Po were equals to 2.6 and 2.1. The areas under the receiver operating characteristic (ROC) curve [AUCs] were equal 0.76 in both cases lower than DXA (0.81). When adjusted on age and radius diameter, AUC were equal to 0.82, 0.81 and 0.83 for ultrasonic parameters and DXA, respectively. These results suggest that the multimode AT has the potential to yield cortical bone parameters to predict fracture risk, using a portable and non ionizing device.

| Table 1. Descriptive characteristics (means and standard deviations), Odds ratios (OR) and areas under the ROC curve (AUC) | | | | | | |
|--|------------------------|----------------------|---------------------------|--------------------|----------------------|--------------|
| | non fractured (N = 16) | | | fractured (N = 13) | | |
| Age (years) | 78.1 (12.8) | | | 79.6 (11.9) | | |
| Diameter (mm) | 7.41 (1.82) | | | 6.27 (1.33) | | |
| Ct.Th (mm) | 2.49 (0.69) | | | 1.84 (0.68) * | | |
| Ct.Po (%) | 4.31 (1.87) | | | 7.85 (4.26) * | | |
| BMD (g.cm ⁻²) | 0.416 (0.061) | | | 0.296 (0.101) ** | | |
| | unadjusted | | age and diameter adjusted | | | |
| | AUC [95% CI] | OR [95% CI] | p | AUC [95% CI] | OR [95% CI] | p |
| <i>Ultrasonic one-third distal measurements</i> | | | | | | |
| Ct.Th (mm) | 0.76 [0.55 - 0.90] | 2.61 [1.10 - 6.23]* | 0.027 | 0.81 [0.56 - 0.93] | 3.42 [1.12 - 10.45]* | 0.028 |
| Ct.Po (%) | 0.76 [0.48 - 0.92] | 2.08 [1.08 - 4.00]* | 0.025 | 0.82 [0.61 - 0.93] | 2.04 [1.03 - 4.04]* | 0.036 |
| <i>DXA distal measurements</i> | | | | | | |
| BMD (g.cm ⁻²) | 0.81 [0.57 - 0.96] | 2.75 [1.33 - 5.67]** | 0.005 | 0.83 [0.55 - 0.97] | 2.78 [1.21 - 6.39]* | 0.014 |

Reference category is non fractured, CI confidence interval, ROC receiver operating characteristic, *p < 0.05, **p < 0.01

adjustment on age and one-third distal diameter

Interpretation of Physical Meaning of Speed of Sound in Cartilage Tissue: Through Comparison with Elasticity and Magnetic Resonance Parameters

Naotaka Nitta¹, Masaki Misawa¹, Tomokazu Numano²

¹National Institute of Advanced Industrial Science and Technology (AIST), Tsukuba, Japan, ²Tokyo Metropolitan University, Japan

Background, Motivation, and Objective

To detect the disease and degeneration of cartilage early, evaluations of speed of sound (SOS) are prospective, but its physical meaning should be clarified. On the other hand, we have proposed a multimodal method using ultrasound (US) and magnetic resonance (MR) images for in vivo SOS measurement. In this study, with the aim of interpreting the physical meaning of SOS, the method was applied for the measurement of tissue-engineered cartilage, and the SOS was compared with T1, T2, apparent diffusion coefficient (ADC), attenuation coefficient (ATT), Young's modulus (YM) and bending modulus (BM).

Statement of Contribution/Methods

All procedures were approved by the Animal Care and Use Committee of our institution. 12-week-old male rats were used, and five different type (#1 to 5) of tissue-engineered cartilage was subcutaneously implanted in the back of rat ($n = 30$). Here, #1 and 5 consist of homogeneous cartilage tissue and #2, 3 and 4 include stiff particle-like scaffolds. In other words, #2 to 4 have inhomogeneous tissue structures. Under anesthesia, MR and US images including same cross-sections were acquired separately, by using a MR imager of 2 Tesla and a US device of 13 MHz. At this time, T1, T2, ADC were also measured. The SOS was determined by the thickness measurement in the MR image and the time of flight (TOF) measurement in the US image by using previously-proposed automatic detection by us. After that, the ATT, YM and BM were measured by using the extracted samples of tissue-engineered cartilage.

Results/Discussion

As the results, the SOS exhibited negative correlations with T1, T2 and ADC ($R^2 = 0.30, 0.94, 0.82$) as shown in Fig. 1. Among them, correlation between SOS and T2 was the highest, and T2 exhibited a high and positive correlation with sGAG, which quantifies the proteoglycan (PG) content. On the other hand, the SOS exhibited positive correlations with ATT and YM ($R^2 = 0.98, 0.87$) and negative correlation with BM ($R^2 = 0.58$) as shown in Fig. 1. Since not only the measured SOS but also other parameters are the macroscopic values (that is, average values), partial volume effect reflecting the ratio of non-cartilage area (scaffold area) to entire area including cartilage area may occur. Consequently, high SOS in the inhomogeneous cartilage tissue may indicate that the YM is high and the sGAG or water content is low, due to the existence of scaffold area.

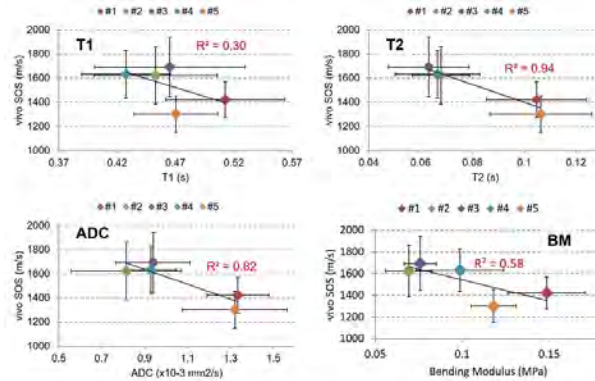


Fig. 1

A three-parameter empirical model of the angular dependence of the speed of sound in cortical bone**Quentin Grimal¹, Guillaume Renaud¹, Pascal Laugier¹**¹*Sorbonne Université, UPMC Univ Paris 06, INSERM, CNRS, Laboratoire Imagerie Biomédicale, Paris, France***Background, Motivation, and Objective**

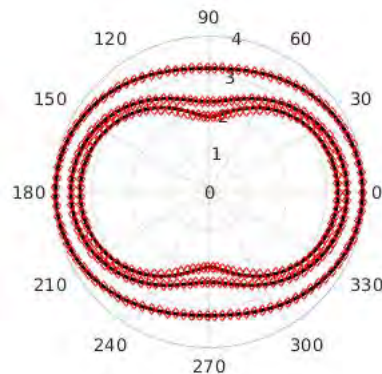
Bone quantitative ultrasound methods are developed to monitor bone health. The interpretation of signals from ultrasound waves propagating in cortical bone requires accounting for elastic anisotropy (i.e., transverse isotropy defined by 5 parameters). Recently, a characterization of all the coefficients of the stiffness tensor of cortical bone and their relationships with mass density was reported using resonant ultrasound spectroscopy (S Bernard et al Biomech Model Mechanobiol 2016). We used this database to investigate the angular variation of the phase velocity $V(\theta)$ of the compressional wave in a plane including the radial and axial directions of the bone diaphysis. Our objective was to validate an empirical model of $V(\theta)$ assuming a weak elastic anisotropy.

Statement of Contribution/Methods

We used a model of weak anisotropy based on (L Thomsen, Geophysics 51(10) 1986). Velocity is modeled as $V_{\text{model}}(\theta) = V_{\text{axial}} - (V_{\text{axial}} - V_{\text{radial}}) \times [\beta \sin^2(\theta) \cos^2(\theta) + \cos^4(\theta)]$, where V_{axial} and V_{radial} are velocities along the long bone axis and in the radial direction, and β is a shape parameter. The stiffness tensors of 55 bone samples from human tibia of 19 donors were used to calculate $V(\theta)$ for each sample. Then, $V(\theta)$ was fitted with $V_{\text{model}}(\theta)$ by determining the optimal β . The quality of the fits and the values of β were analyzed with respect to mass density, which is related to the mechanical quality of the bone sample.

Results/Discussion

The model of weak anisotropy provided an excellent fit of $V(\theta)$ (unit: mm/ μ s) (average RMSE=0.005). The range of β values was [0.35-1.37]. The figure is a polar plot of the angular dependence (0° =axial direction) of velocity with fits (red diamonds) of $V(\theta)$ (black line) for three samples of axial velocities 3.9 mm/ μ s ($\beta=0.77$, RMSE = 0.003), 3.6 mm/ μ s ($\beta=0.57$, RMSE=0.017), and 3.3 mm/ μ s ($\beta=0.35$, RMSE=0.038) corresponding to densities 2.0, 1.7, and 1.6 g/cm³. We found a positive correlation between density and β ($r=0.70$) and a shift to a more complex angular variation $V(\theta)$ as density decreases. The results suggest that angular variations of the compressional wave velocity in cortical bone can be reasonably predicted using only three parameters including velocities in two anatomical directions and a shape parameter. This is of practical interest for bone imaging and to solve inverse problems aiming at characterizing bone material and structural properties.



Study on the wave convergence in bone for the effective ultrasound radiation
Masaya Saeki¹, Yoshiki Nagatani², Ko Chiba³, Isao Mano¹, Mami Matsukawa¹
¹Doshisha university, Japan, ²Kobe City college of technology, Japan, ³Nagasaki University, Japan

Background, Motivation, and Objective

Clinical studies tell us that the healing time of the bone fracture can be reduced by using Low Intensity Pulsed Ultrasound (LIPUS) [1]. However, most LIPUS systems radiate ultrasound from the skin near the bone fracture. More effective ultrasound radiation to the bone fracture part is necessary without removing the cast, considering the complicated wave propagation in human body. Then, we have to develop an appropriate technique to converge the ultrasound to the fracture part wearing the cast. In this study, a 3D simulation was performed by using 3D human bone model. Here, ultrasound was transmitted from a virtual fracture part and received by two virtual transducer arrays, from which sound waves were re-radiated to converge at the part.

Statement of Contribution/Methods

The 3D human radius bone model was made from HR-pQCT data of a 66 years old female. A 3D elastic Finite-Difference Time-Domain (FDTD) method was used for simulation. Spatial and time resolutions were 61 mm and 8.3 ns, respectively. The input signal was one cycle of sinusoidal wave at 1 MHz with Hanning window. In the simulation, the model was immersed in water. A virtual emitter was set at the virtual fracture part (0.4×0.4 mm) and two virtual receiver arrays (8 elements) were set around the bone model as shown in Fig.1 (a). The propagation time and amplitude of the received wave at each transducer was analyzed and the modified sinusoidal ultrasound wave was virtually emitted from each transducer in the arrays. The propagation and distribution of ultrasound in bone was then investigated at the cross section of the virtual fracture part.

Results/Discussion

Peak to peak amplitude values of the observed waves at one array and emitted ultrasound waves from the arrays are shown in Figs.1 (b) and (c). Considering the propagation time and amplitudes, re-radiated waves were created. As can be seen in the Fig.1 (d), the re-radiated waves successfully converged to the area of initial virtual fracture. In the future studies, appropriate array conditions for arbitrary fracture parts should be considered. For clinical application, creation of a simple personal bone model from the X-ray radiography image should also be investigated.

[1] L.R. Duarte, Archives of Orthopaedic and Trauma Surgery, **101**, p.153 (1983).

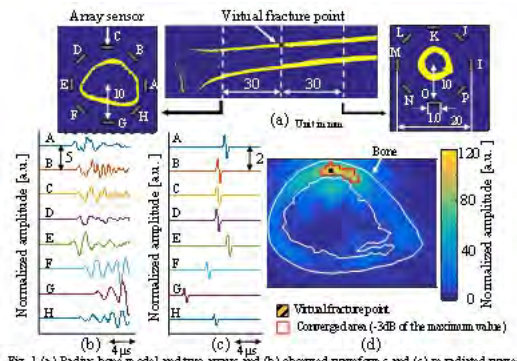


Fig. 1 (a) Radii bone model and two arrays (b) observed waveforms and (c) re-radiated waves and (d) intensity distribution of the cross section of the initial bone fracture point. Amplitude of waves were normalized by that of the initially transmitted wave from the fracture point.

In-bioreactor ultrasonic monitoring of human engineered cartilage

Guillermo Rus¹, Juan Melchor¹, Elena Lopez-Ruiz¹, Juan Manuel Soto¹, Gema Jimenez¹, Cristina Antich¹, Macarena Peran¹, Juan Antonio Marchal¹

¹*Structural Mechanics, University of Granada, Granada, Spain*

Background, Motivation, and Objective

Engineered cartilage tissue is one of the most promising treatments for a wide range of articular cartilage pathologies [1,2]. In this study, a bioreactor is designed to monitor non-invasively and in real-time the neo-cartilage tissue formation processes through ultrasonic signal analysis based in inversion and wave-tissue propagation models.

Statement of Contribution/Methods

Polylactic acid (PLA) scaffolds were bioprinted and seeded with human chondrocytes. Then, they were cultured in an ultrasound (US)-integrated bioreactor. The readings from the ultrasonic sensors were analyzed by numerical models of the ultrasound-tissue interaction embedded in a stochastic framework to infer the extracellular matrix (ECM) evolution in a probabilistic way, thus including uncertainty bounds. To reconstruct the velocity and attenuation from the recorded signals, a genetic-algorithm based inverse problem (IP) was combined with an iterative computational propagation [3,4]. The ultrasonic data were validated against destructive evolution measurements of the in vitro 3D chondrocyte cultures assessed by proliferation, morphological and ultrastructural observations, qualitative and quantitative biochemical parameters and gene expression analysis.

Results/Discussion

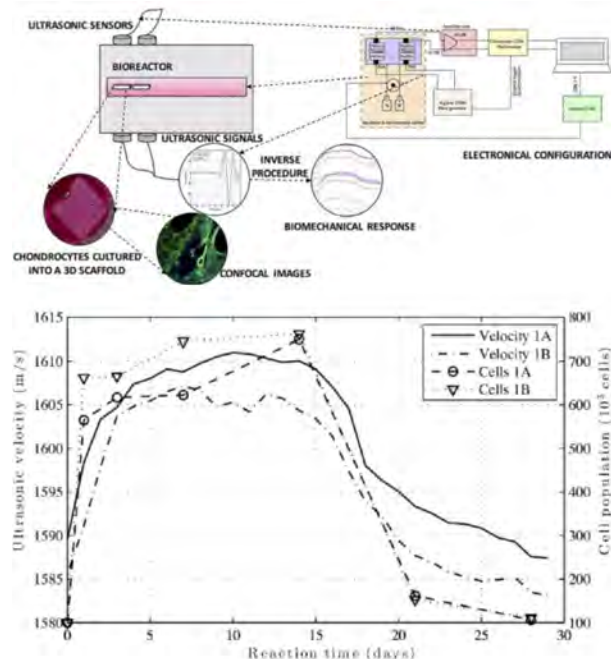
Overall, Parameters reconstructed from the ultrasonic monitoring (p-wave velocity, attenuation, density changes in the culture layer) were proved useful to indirectly determine cell culture proliferation parameters in a non-invasive manner. The significant correlation shown between glycosaminoglycans (GAG) and collagen II (Col II) expression with the elastic damping evolution of the novo ECM ($R=0.78$; $p<0.001$) and ($R=0.57$; $p<0.01$), respectively, reinforces the feasibility of using ultrasound to evaluate chondrocyte functionality.

References:

- [1] Jimnez G, et al. (2014) Sci Rep; 5 p16400.
- [2] Lopez-Ruiz E, et al. (2016) Expert Opin Ther Pat; 26:p877.
- [3] Bochud N, Rus G. (2012) IEEE T Ultrason Ferr. 59(7).
- [4] Rus G, et al. (2012) AIP Conf Proc, 1433 p375.

Acknowledgements:

Spanish govt. is acknowledged for projects DPI2017-85359-R, DPI2014-51870-R, TEC2014-57394-P, UNGR15-CE-3664, DTS15/00093, PI16/00339, PI-0107-2017, PIN-0030-2017, CTS-6568 and P11-CTS-8089.



Monitoring of Tetanic Contractions of Skeletal Muscle Using Wearable Ultrasonic Sensors**Ibrahim AlMohimeed^{1,2}, Yuu Ono¹**¹*Department of System and Computer Engineering, Carleton University, Ottawa, ON, Canada*, ²*Department of Medical Equipment Technology, Majmaah University, Majmaah 11952, Saudi Arabia***Background, Motivation, and Objective**

Ultrasound monitoring of skeletal muscle activities could provide useful information regarding mechanical characteristics and state of the muscle non-invasively and in real-time. However, one of the challenges for continuous and real-time monitoring of the muscle contractions is the motion artifacts due to inconsistent movement of a conventional handheld ultrasonic probe employed, which could deteriorate the monitoring accuracy. In addition, the probe pressed against a subject's skin surface may limit underlying muscle activities. A wearable ultrasonic sensor (WUS) made of piezoelectric polyvinylidene fluoride (PVDF) film could address these issues, due to its mechanical flexibility and lightweight. In this study, muscle contractions evoked by an electrical muscle stimulator (EMS) were monitored using the wearable ultrasonic sensors developed.

Statement of Contribution/Methods

Double-layer PVDF ultrasonic sensors (WUSs) were constructed with two 52- μm thick PVDF films. The size of the active sensing area was 20 mm by 20 mm, and the total thickness of the sensor was 350 μm . The center frequency and the bandwidth were 4.2 MHz and 4.6 MHz, respectively. The muscle contractions were monitored for the gastrocnemius (GC) muscle of a healthy subject in the ultrasonic through-transmission mode. The transmitter WUS was attached to the medial side of the GC muscle at the back of the tibia and fibula bones whereas the receiver WUS was placed on the opposite side. The pulsed ultrasound generated by the transmitter WUS propagated through the tissues toward the receiver WUS. The involuntary contractions of the GC muscle were evoked by an EMS at the stimulation frequencies of 2, 4, 6, 8, 10, 12, and 30 Hz. The total tissue thickness changes due to the muscle contraction were obtained using an ultrasound time-of-flight method.

Results/Discussion

The total tissue thickness was obtained 116.2 mm at the fully relaxed state of GC muscle, and it increased by 3.0 mm ± 0.42 mm (2.6% ± 0.36 %) at the contracted state. The fusion index (FI), defined by the ratio of a/b where a and b are the minimum and the maximum thickness changes from the thickness of full relaxation, was calculated from the measured thicknesses at each stimulation frequency in order to investigate the degree of the muscle relaxation during the stimulation. At the stimulation frequencies of 2 and 4 Hz, the muscle relaxed completely between the stimuli. The FI values became 4%, 11%, 84% and 98.7 % at 6, 8, 10 and 12 Hz, respectively. With our experimental conditions employed, the FI values were close to 100% above 12 Hz. The FI of 100% indicates the fused tetanus state that has no muscular relaxation between successive stimulation. The flexibility, small size and lightweight of the WUS could allow accurate muscle monitoring during physical activities, which may be challenging using a conventional handheld ultrasonic probe.

Inferring porosity from frequency dependent attenuation in bone mimicking porous materials
Marie Muller¹, H.T. Bank², Omid Yousefian³, Rebekah White⁴
¹*Mechanical and Aerospace Engineering, North Carolina State University, NC, United States*, ²*Mathematics, North Carolina State University, United States*, ³*Mechanical and Aerospace Engineering, North Carolina State University, United States*, ⁴*Mathematics, North Carolina State University, Raleigh, NC, United States*
Background, Motivation, and Objective

Osteoporosis affects both pore size and density in cortical bone. Quantifying levels of osteoporosis by inferring these micro-architectural properties from ultrasonic wave attenuation in cortical bone has yet to be done. Here, we propose a power law model to describe the frequency dependent attenuation in non-absorbing porous media mimicking a simplified cortical bone structure, with full control over pore diameter and pore size independently. We fit this model to attenuation values obtained using Finite Difference Time Domain (FDTD) simulations. By solving an inverse problem, we establish that information regarding the micro-architectural parameters of the heterogeneous media can be inferred from attenuation data.

Statement of Contribution/Methods

We generate porous media with the elastic properties of cortical bone, with various combinations of pore diameters (ranging from 20-100 μm) and pore densities (ranging from 3-10 pore/ mm^2) using a 2D FDTD package (Simsonic), which simulates the attenuation of elastic waves at frequencies of 1-8MHz. We use a phenomenological model that captures the frequency dependent attenuation in cortical bone. This model is optimized to fit the simulated attenuation data by solving an inverse problem under an Ordinary Least Squares (OLS) framework. With this we establish linear, functional relationships between the optimized power law model parameters and the micro-architectural parameters.

Results/Discussion

We first demonstrate that, although it is frequency dependent, absorption does not depend upon pore density and pore concentration, which justifies the use of non-absorbing media for the simulations. We show that a power law model can be used to describe the frequency-dependent attenuation in cortical bone-like samples. By solving an inverse problem, we find that the power law model parameters can accurately and confidently be estimated from attenuation data. Furthermore, we are able to establish underlying linear relationships between the optimized model parameters and the micro-architectural ones of the simplified cortical bone structures. These relationships showed that ranges of porosity could be inferred from attenuation data. Applying these techniques to attenuation data from cortical bone samples could allow one to characterize the micro-architectural properties of bone porosity.

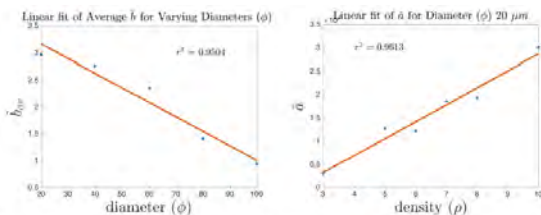


Figure 1: Left: Linear fit of average power law model parameter estimate, \bar{b} , as a function of pore diameter.
Right: Linear fit of model parameter estimate, \bar{a} , as a function of pore density for $\phi = 20 \mu\text{m}$.

Effects of Microstructure on Ultrasonic Attenuation in Skull BoneJinjin Liu¹, Shusheng Liao¹, Zhenzhang Wang¹, Qian Chen¹, Xiaoyu Chen¹, Yunjun Yang¹¹The First Affiliated Hospital of Wenzhou Medical University, Wenzhou, China, People's Republic of**Background, Motivation, and Objective**

Transcranial ultrasound has been widely used in both diagnostic and therapeutic applications. However, high ultrasonic attenuation of skull bone limits these applications; ultrasonic attenuation is strongly associated with the complex internal microstructure of skull bone.

Currently, attenuation mechanism considering both scattering and absorption in human skull cancellous bone has been rarely reported. The objective of this study was to investigate the influence of the microstructure of human skull cancellous bone on ultrasonic attenuation using a theoretical approach.

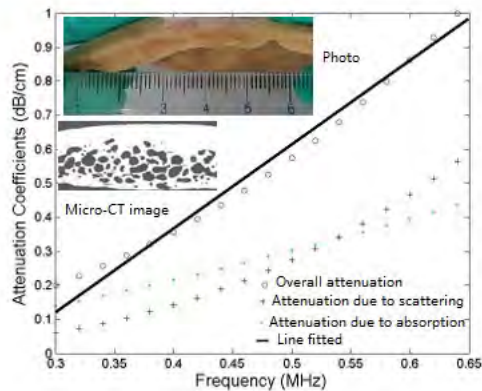
Statement of Contribution/Methods

In the theoretical model, human skull cancellous bone was considered as a two-phase composite composed of a matrix of marrow and the inclusions of trabecular. This theory models the independent scattering and takes into consideration the attenuation property of the matrix and the scattering cross-sections of a single inclusion. As a specific example, a skull bone was scanned using micro computed tomography (micro-CT) to acquire its microstructure information (see figure).

Results/Discussion

The influence of scattering and absorption at different frequency range was studied. Incorporating the microstructure information of the scanned skull bone into the theoretical prediction, it was found that the attenuation coefficients due to scattering and absorption were comparable below the frequency of approximately 0.6 MHz and the overall attenuation coefficient approximately linearly increased with frequency in this frequency region (see figure). Although the scattering portion of the intensity is frequency-cubed dependent, the absorption portion is comparable to the scattering part and more linear in trend at low frequency, which cause the overall attenuation approximately linearly depends on the ultrasonic frequency. Our finding validates the assumption of quantitative ultrasound, i.e., attenuation is a linear function over a typical frequency range of 0.3-0.65 MHz. As frequency increased to more than 1 MHz, however, attenuation coefficient due to scattering was dominant and strong non-linear behavior was apparent.

Dependencies of the overall attenuation coefficients on scatter size and bone volume fraction were also predicted. Predicted attenuation was comparable to reported experimental data.



Influence of porosity on apparent absorption coefficient in porous structures mimicking cortical bone

Yasamin Karbalaeisadegh¹, Omid Yousefian ², Marie Muller³

¹*North Carolina State University, NC, United States*, ²*Mechanical and Aerospace Engineering, North Carolina State University, United States*, ³*Mechanical and Aerospace Engineering, North Carolina State University, NC, United States*

Background, Motivation, and Objective

Ultrasound wave propagation in porous media is associated with energy loss and attenuation. The attenuation is caused by scattering and absorption and is influenced by size and distribution of the scatterers, and by frequency. In the present simulation study, we calculate the attenuation coefficient in porous geometries mimicking cortical bone both in presence and absence of absorption to isolate the effect of scattering. Results suggest that as pores get larger, the scattering regime changes and attenuation due to absorption becomes more dominant.

Statement of Contribution/Methods

Pore distributions with various pore sizes (40-120 μm) and concentrations (5-25pore/mm²) with assigned material properties of bone and water are generated. The propagation of 8 MHz plane waves is modeled using 2D FDTD simulations. The attenuation coefficient is measured by fitting the exponential decay of the received signal amplitude during propagation in absence or presence of absorption (coefficient of 10dB/(cm.MHz) to mimic bone tissue), for different pore diameters and concentrations. In absence of absorption, the attenuation coefficient is equal to the scattering coefficient. The difference between the total attenuation coefficient and scattering coefficient is considered to be the apparent absorption coefficient in the medium ($\alpha_{app.abs.}$).

Results/Discussion

The scattering attenuation (without absorption) and apparent absorption coefficient are shown on Fig1. For smaller ka (k:wave number; a:scatterer size) values (Fig.1-a; ka=0.754<1), the effect of absorption does not change with increase in porosity. However, for larger ka values (Fig.1-b; ka=1.2566>1), increasing the porosities leads to a higher apparent absorption coefficient, indicating a higher impact of absorption, although the absorption coefficient was kept constant for all simulations. This can also be observed in figures 1-c and 1-d which indicate, that an increased porosity, when the pore diameter is large enough (80 μm ; ka=1), leads to an increased apparent absorption. This could be attributed to the fact that longer paths in the solid phase of the medium lead to higher absorption of the wave.

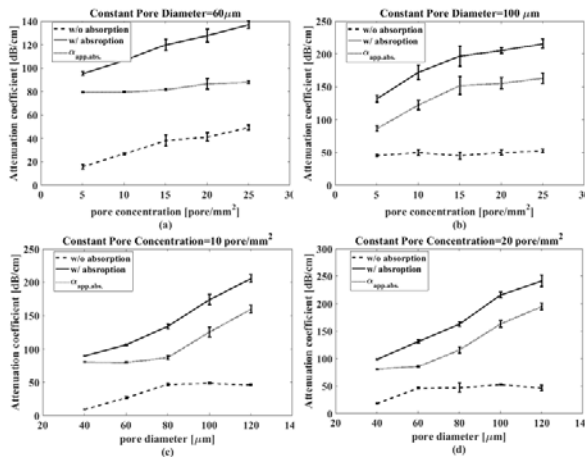


Figure 1. Attenuation coefficient in presence and absence of absorption is obtained for geometries with various pore sizes and concentrations. $\alpha_{app.abs.}$ is the difference between total attenuation and scattering coefficient.

Neural Network based Bone Density Estimation from the Ultrasound Waveforms inside Cancellous Bone derived by FDTD simulations

Yoshiki Nagatani¹, Shigeaki Okumura², Shuqiong Wu²

¹Kobe City College of Technology, Japan, ²Graduate School of Informatics, Kyoto University, Kyoto, Japan, Japan

Background, Motivation, and Objective

Quantitative ultrasound techniques for bone assessment now attract strong research attentions because of their non-invasiveness, portability, and the low diagnosis expense. However, since the cancellous bone has complexed porous structure, it is difficult to analytically understand the behavior of the ultrasound propagating inside it. Thus, the neural network (NN) based approaches are expected to derive more information potentially contained in the received waveforms.

Statement of Contribution/Methods

Three cuboidal specimens (specimen A, B, and C) are independently derived from bovine femoral necks and their X-ray CT images were taken. Firstly, each specimen was separated to nine parts. Then, these grayscale images of the 27 parts are binarized to separate into solid part and liquid part by deciding certain thresholds. As a result, the distribution of the BV/TV (bone volume fraction) of the specimen A was 0.05–0.47, B was 0.08–0.31, and C was 0.06–0.26, respectively. Next, the physical parameters for these 27 geometry data were decided: the density of trabecular material was varied from 1600 to 2200 kg/m³ and the longitudinal wave speed was varied from 3200 to 4400 m/s. Finally, 17199 simulation models were prepared.

We designed the NN with the waveform as an input and the BV/TV as an output. 10 neurons were used in the hidden layer. The NN is trained with the waveforms created by three-dimensional elastic FDTD method using pulse ultrasound at 1 MHz. Then, the BV/TV of the individual specimen that is not used in the training and validation process is estimated by using the NN.

Results/Discussion

The results are shown in the figure. Each plot corresponds a waveform. Figure (a) and (b) shows the estimation results of case 1 (the BV/TV of specimen C based on the NN trained using the data from A and B) and case 2 (specimen A using B and C), respectively. Thus, these figures indicate that the NN based estimation is specimen independent. The correlation coefficients R were higher than 0.9 in all conditions. In contrast, the correlation coefficients between BV/TV and the fast wave speed, which is the conventional index for the bone assessment, was 0.7. These results tell us that the NN works better than the traditional method especially in case 1.

The possibility of estimating several physical parameters, such as density, elasticity, and Poisson's ratio, might be checked in the future work.

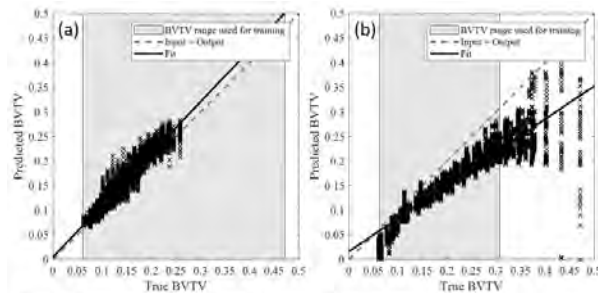


Fig. 1: Estimation results of the proposed NN based method, (a) case 1 and (b) case 2. The black solid and gray dotted lines show the estimated regression line and ideal regression line, respectively. Black cross marks show the output of the NN. Gray areas represents the range of the BV/TV used for the training and validation. These figures show that the NN works properly within the areas of the training. In other words, NN does not work well outside the area of the training.

P2-C1 - PGP & PNL: General Physical and Non-Linear Acoustics

Waraku (posters 2)

Thursday, October 25, 9:30 AM - 4:00 PM

Chair: **Yun Jing** North Carolina State University

P2-C1-1

Ultrasound radiation force to remotely control implanted medical devices

Samuel Callé¹, Guillaume Ferin², Marie-Coline Dumoux², Jean-Pierre Remenieras³

¹*GREMAN UMR 7347, Université de Tours, CNRS, INSA Centre Val de Loire, Tours, France*, ²*Vermon SA, France*, ³*UMR 1253, iBrain, Université de Tours, Inserm, France, Metropolitan*

Background, Motivation, and Objective

Remotely powering, triggering or operating deep implanted medical devices is increasingly investigated and even incorporated into coming products to perform both sensing and therapeutic tasks. Such approaches offer a significant gain in miniaturization and device complexity and would pave the way of new applications where integration is a key. Several techniques using Acoustic Energy Transfer (AET) have been presented since it allows a safe and directional energy beam which is capable to reach deep tissues but these technics mostly rely on the performances of a piezoelectric receiver connected to a custom (ASIC) power management IC (low voltage DC/DC converter and battery) to power up the medical device.

Another strategy would be to operate directly a passive medical device, like a micro pump, using the ultrasound radiation force. In this paper, we report numerical investigation in using such approach for in-situ drug delivery.

Statement of Contribution/Methods

Reflection of the incident acoustic beam at the interface (surface force) and attenuation of the US beam along the wave path (body force) both contribute to this US radiation force. The contributions of these forces were calculated for an example of device implanted 3 mm under the skin. First, a heterogeneous axisymmetric pseudo-spectral time-domain method was used to estimate the ultrasound particle velocity and acoustic pressure (amplitude, spatial repartition) inside the device and at the interface. These acoustic-field parameters were then inserted into analytical expressions obtained from a second-order nonlinear model to calculate the force applied to the implantable device. The contributions of the surface and body forces were analyzed, and the overall force was estimated for two configurations of a 5 MHz transducer (plane and focused) and two types of device mechanical characteristics (semi-rigid and rigid). Acoustic intensity and temperature increase were also computed for three different temporal conditions that are classically used in localized drug delivery applications.

Results/Discussion

The overall radiation force was found to be significant: approximately 6 mN with a rigid membrane (silicon nitride) and 3.5 mN with a semi-rigid (rubber) membrane. The results were quite similar for the geometry of the two transducers. The high amplitude of the radiation pressure (surface force) for the focused beam was counterbalanced by the narrowness of the active surface. Moreover, the force due to the beam attenuation integrated over the rubber membrane volume was very small (around 0.3 mN) compared to the force due to the interface.

Scattering cross-section estimation using passive imaging in reverberating elastic plates : case study of rigid isotropic inclusion

Lynda chehami¹, Julien de Rosny², Emmanuel Moulin¹, Jamal Assaad¹, Claire Prada²

¹Univ. Valenciennes, CNRS, Univ. Lille, YNCREA, Centrale Lille, UMR 8520 - IEMN, DOAE, F-59313 Valenciennes, France,

²ESPCI ParisTech, CNRS, Institut Langevin - 1 rue Jussieu, F-75005, Paris, France

Background, Motivation, and Objective

More than 10 years ago, it has been shown that the impulse response between two sensors called Green's function (GF) can be passively estimated by ambient noise correlation (NC). In recent works, Chehami et al., demonstrated the applicability of this approach in the case of a highly reverberating elastic plates, when a diffuse flexural wave field is approximately generated. When the noise is non uniformly distributed over the plate surface, the authors take benefit from reverberations to accelerate the convergence towards the GF. In the context of structural health monitoring, the authors show experimentally and numerically that NC is an efficient way to detect and localize defects in thin plates. In this work, we propose an original method to estimate the scattering cross-section which characterizes the strength of a defect to scatter the flexural incident waves.

Statement of Contribution/Methods

We discuss here from theoretical and numerical point of view the passive characterization of a rigid isotropic inclusion in a reverberating plate by estimating its scattering cross-section noted by σ . It is shown in previous works that by combining the approach of ambient noise correlation and imaging using ultrasound sensors array, we can localize correctly a defect in a thin reverberating plate. The imaging algorithm is based on the numerical backpropagation of the signals on all probed positions. The backpropagated function in the point location (x,y) at the angular frequency ω is given by Eq.1. We show here, through a numerical example realized using finite element method in the time domain, that the intensity of the focal spot on the defect location, can be directly linked to its scattering cross-section given by Eq.2.

Results/Discussion

The numerical configuration consists of 1 m x 0.7 m x 3 mm aluminum plate. 30 impulse noise sources are randomly distributed over the plate surface to generate the diffuse flexural field. An array of 8 receivers with known positions is considered. The simulated defect consists of a rigid inclusion of 5 mm diameter which represents a local modification of the plate properties (10 x (E, ρ)Aluminum). Fig.(a) shows the result obtained for a small area around the defect. By using Eq. 2, an estimate of σ is obtained and plotted (red curve) in Fig.(b). This result is compared to the works done by Norris and Vemula on the scattering of flexural waves from inclusions (black curve).

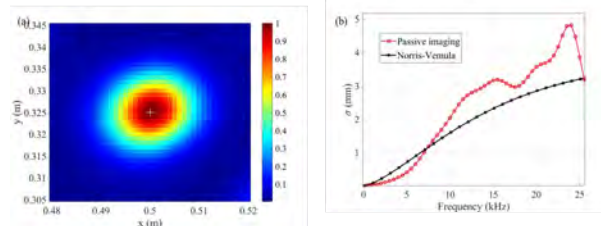
$$bpf_{j(x,y)}(k\omega) = \sum_{i=1}^{N_p N_p} \Delta C_{ij}(k\omega) \exp[i(d_i(x,y) + d_j(x,y))k\omega]. \quad (1)$$

where $d_i(x,y)$ is the distance between the i^{th} receiver and the pixel location (x,y) , k is the wave number, $\Delta C_{ij}(k\omega)$ is an element of the differential correlation matrix in Fourier domain.

We show here, through a numerical example realized using finite element method in the time domain (ELMER software), that the intensity of the focal spot on the defect location, can be directly linked to its scattering cross-section given by

$$\sigma(k\omega) = \frac{4\pi^2}{\left[\sum_{i=1}^{N_p N_p} \frac{1}{d_i^2(x,y)} \right]^2} \frac{k\omega |bpf_{j(x,y)}(k\omega)|^2}{|C_0(x,y)|^2}. \quad (2)$$

C_0 is the autocorrelation averaged over all the receiver positions, $bpf_{j(x,y)}$ is the windowed version of bpf on the defect location in time domain (only the first bpf wavepackets used to calculate the intensity), and r_{def} is the distance receiver-to-defect.



Effects of Ultrasonication on Gold Nanowire Arrays

Hannah Johnston¹, Antony Murphy¹, Yongqiang Qiu², Rachael McPhillips², Jae Hee Song², Paul Prentice², Sandy Cochran², Robert Pollard¹

¹*School of Mathematics and Physics, Queen's University Belfast, Belfast, United Kingdom*, ²*Medical and Industrial Ultrasonics, University of Glasgow, Glasgow, United Kingdom*

Background, Motivation, and Objective

Due to their biocompatibility and ability to yield a localised surface plasmon resonance, nanoparticles have gained popularity in various biosensing applications. Here, an array of gold nanowires is used as a sensing surface in a cuvette-based biosensing system into which solutions of proteins are injected.

Without sonication, the injected fluid remains static, so the rate of the biological material binding is diffusion limited. As a consequence, mixing is slow, particularly for large molecules. Acoustic streaming can be used to overcome the limitation of mixing in biosensing devices, e.g. many lab-on-a-chip devices have integrated acoustic streaming to promote mixing and pumping of fluids inside microchannels [1].

Statement of Contribution/Methods

In our work, we have evaluated the feasibility of a mechanical stimulus, provided by a miniature PZ54 (Meggitt Sensing Systems, Denmark) single-element ultrasonic transducer driven at 2.2MHz, to affect the behaviour of biomolecules in proximity to gold nanowire arrays, with particular interest in the change of rate of biomolecular adhesion to the gold nanowires. Sensorgram results, biological adsorption curves, show faster adsorption of proteins to the sensing surface with sonication, compared to non-sonicated samples.

Nanowire tips may also act as nucleation sites where cavitation events can occur. Substrate-bound gold nanowire arrays with differing aspect ratio and inter-wire spacing were grown by electrochemical deposition into a nano-porous alumina template. By varying the nanowire geometries, it is possible to evaluate the likelihood of nucleation on exposure to high intensity focused ultrasound (HIFU) generated by a single element piezoelectric transducer with an outer diameter of 110mm, driven at natural fundamental frequency of the transducer, 200kHz. High speed shadowgraphic imaging at 5×10^6 frames per second, 10ns temporal resolution and 256 frames per sequence shows the bubble expansion and collapse near the nanowire surface.

Results/Discussion

Preliminary results from high-speed imaging and SEM analysis show that every sample yielded cavitation and the size of the nanowire has an effect on the bubbles produced and the subsequent destruction of nanowires following bubble collapse.

[1] V. Cardosa et al, Lab-on-a-chip with b-PVDF based acoustic microagitation. IEEE Trans on Biom Eng. Vol 57 (2010), pp 1184-1190

Electrification of sonoluminescing bubble in water**Hyang-Bok Lee¹, Pak-Kon Choi¹**¹*Department of Physics, Meiji University, Kawasaki, Japan***Background, Motivation, and Objective**

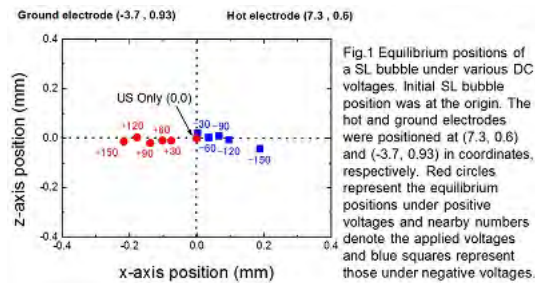
Microbubbles in water are considered to be negatively charged at the liquid–bubble interface. However, it has not been studied on the electrification of sonoluminescing (SL) bubble. It is useful to clarify electrical property of SL bubble interface for understanding the microstructure on the bubble interface and the medical application of bubble. We investigated, for the first time within our knowledge, the electrification of a SL bubble in water by measuring the translation of bubble when electric field was applied.

Statement of Contribution/Methods

A single bubble, which expands and contracts periodically, was spatially trapped at an antinode of acoustic standing waves via primary Bjerknes force in a cylindrical glass container which was sonicated at 28.5 kHz. The single bubble emits pulsed light with broadband spectrum called single-bubble sonoluminescence (SBSL). For investigating the electrification of a SL bubble, direct-current (DC) voltage up to 150 V was applied to SL bubble. Platinum needles were used as electrodes which were located on both sides of SL bubble. If the SL bubble is electrically charged, the single bubble will shift to the equilibrium position balancing Bjerknes and electrostatic forces. We captured SBSL images and observed the movement of bubble under various DC voltages using a digital camera.

Results/Discussion

Fig.1 shows equilibrium positions of SL bubble under various DC voltages, which were measured from SBSL images. Red circles represent the positions under positive voltages and nearby numbers denote the applied voltages and blue squares represent those under negative voltages. The hot and ground electrodes were positioned at (7.3, 0.6) and (-3.7, 0.93) in coordinates, respectively. When positive voltage was applied to SL bubble, the equilibrium position of SL bubble shifted toward ground electrode side as if the bubble received repulsive force from the hot electrode. In contrast, when negative voltage was applied, the equilibrium position of SL bubble shifted toward hot electrode side as if the bubble received attractive force from the hot electrode. If SL bubble was electrically charged by the water-dipoles orientation induced by electric field in the vicinity of the interface, the bubble would shift to the same direction regardless of positive or negative voltage. The present results suggest that the SL bubble is positively charged.



Looking at the skull in a new light: Rayleigh-Lamb waves in cranial bone.

Hector Estrada¹, Sven Gottschalk¹, Michael Reiss¹, Volker Neuschmelting^{1,2}, Roland Goldbrunner², Daniel Razansky^{1,3}

¹Institute of Biological and Medical Imaging, Helmholtz Center Munich, Munich, Germany, ²Department of Neurosurgery, University Hospital Cologne, Germany, ³School of Medicine, Technical University of Munich, Munich, Germany

Background, Motivation, and Objective

Current knowledge on the ultrasound wave propagation in the cranial bone is restricted to far-field observations. In order to extend our understanding on how ultrasound waves propagate in the skull, we use short laser pulses to excite ultrasound waves in water-immersed *ex vivo* mouse and human skulls and explored their near-field.

Statement of Contribution/Methods

The laser pulses (~10 ns duration) of 532 nm are absorbed by a small layer of black burnish deposited on the skull's inner surface and generate ultrasound waves due to the optoacoustic effect. The acoustic near-field is mapped using a needle hydrophone close to the skull surface, following a three-dimensional scanning path derived from a previous pulse-echo scan of the skull with a spherically focused ultrasound transducer.

Light fluence is optimized to generate detectable signals away from the source position but well below the non-linear regime to avoid the generation of cavitation and bleaching of the absorber, which would compromise the success of the experiment.

Numerical simulations are performed using a simple multilayered flat plate model.

Results/Discussion

The results for mouse and human skulls show different wave propagation regimes according to their differences in size, thickness, and internal structure. Leaky and non-leaky waves have been observed for both skull samples. Zero order Lamb modes were observed in the mouse skull, whereas Rayleigh-Lamb higher order modes can be observed in the human skull sample, presumably propagating in the outer cortical bone layer.

Good agreement is found between the experiments and the multilayered flat plate model.

Our results might be relevant for cranial bone assessment using non-ionizing imaging methods, non-invasive ultrasound and optoacoustic brain imaging as well as monitoring of surgical and therapeutic interventions. It may also open the door for novel detection or actuation methods using near-field skull excitation.

More work is needed to attain a better understanding of the properties of skull-guided waves and find excitation strategies suitable for *in vivo* applications.

Effect of Electrode Configurations on the Q-factor and Spurious modes for a Doubly Rotated Contoured Quartz Resonator

Mihir Patel¹, Bikash Sinha¹, **Yook-Kong Yong²**

¹Schlumberger Tech Corp, United States, ²Rutgers University, United States

Background, Motivation, and Objective

High Q thickness-shear mode (TS) quartz resonator with high spectral purity and suppression of unwanted harmonic and anharmonic modes is one of the key requirements for the development of high precision frequency control devices and sensors. The energy trapping of the TS modes helps to reduce the effect of mounting losses and possible reflections of anharmonics from the electrode or plate boundaries. This is achieved by the selection of an appropriate aspect ratio of the plate, contouring and beveling of the plate surfaces and optimal electrode geometry. The effects of these parameters on energy trapping and resonator performance depends on both the crystalline orientation and the selected TS mode of vibration. Earlier analytical work on the analysis of trapped energy mode quartz resonators by Tiersten, Sinha, Stevens, Lewis and Detiant et. al. helps to determine the optimal contouring of a single and doubly rotated quartz resonator and electrode shape for all the three thickness modes – thickness-extensional (A-), fast thickness-shear (B-) and slow thickness-shear (C-) modes to achieve high Q-factor.

The objective of this paper was to develop an accurate 3D-FEA model based on the existing analytical method to accurately characterize the effect of electrode configurations on the B-, C- and the spurious mode frequencies and their Q-factor for a doubly rotated contoured quartz resonator.

Statement of Contribution/Methods

In this paper, we develop an accurate 3-D FEA model based on the method developed by Patel & Yong, for the doubly rotated contoured thickness-shear quartz cut resonators that incorporates the material losses attributed to the acoustic viscosity tensor and the mounting losses using the Perfectly Matched Layer (PML's) concept. The Q-factors obtained from the free vibration analysis using the dissipation theory help in understanding the energy loss mechanisms for the B- and the C-mode in the SBTC-cut (Stress compensated B-mode, Temperature compensated C-mode) contoured quartz resonators.

Results/Discussion

The developed 3D-FEA model shows an excellent agreement for all the modal frequencies of interest with the existing analytical methods and experimental data. 3D-FEA results show a good agreement with the measured Q-factor of both the C- and the B-modes. One of the important parameters affecting the B-mode Q-value is the presence of Spurious-mode (S1) in the vicinity of B-mode. It is observed from FEM results that when $(F_b - S1) = +/- 0.03$ kHz, the B-mode Q-value drops with an increase in R_m . It is shown that the separation between S1-mode and B-mode can be controlled by "energy trapping" effect, and hence an improvement in the B-mode Q-value can be achieved. A new electrode configuration was proposed based on 3D-FEA results and the measured results for this design show an improvement in the B-mode Q-factor and the suppression of the anharmonic modes.

The use of airborne ultrasound for Varroa destructor mite control in beehives

Brendan Barry¹, Lindy Verstraten², Fidelma Butler², Padraig Whelan², William Wright¹

¹Electrical and Electronic Engineering, University College Cork, Cork, Ireland, ²School of Biological, Earth and Environmental Sciences, University College Cork, Cork, Ireland

Background, Motivation, and Objective

The declining health of honey bee (*Apis mellifera*) populations is of global concern, as they are arguably the most important pollinator insect with approximately 90 million bee hives worldwide [1]. At least 76% of European food production and 84% of cultivated vegetable species are dependent on bees for pollination [2]. The *Varroa destructor* mite weakens bees by sucking their haemolymph and spread debilitating illnesses such as Deformed Wing Virus. Current methods of *Varroa* mite control are usually pesticide-based with potential side effects for the bees or the beekeeper, and can leave residues in the honey or wax. The mites can also develop resistance to these pesticides. The objective of the current work is to investigate the use of high-frequency, high-intensity airborne ultrasound to control the *Varroa* mite populations using a chemical-free technology.

Statement of Contribution/Methods

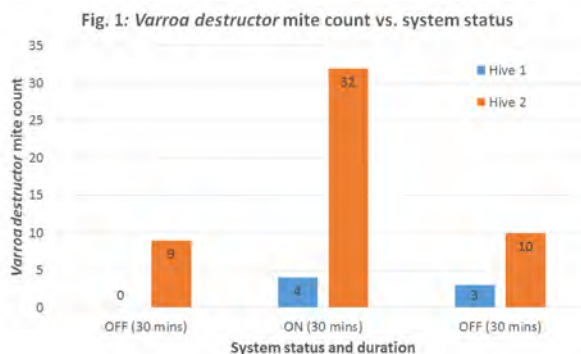
A prototype ultrasonic system that generates airborne ultrasonic waves at different frequencies and intensities was constructed and tested. In initial studies, small transparent enclosures were used to observe directly the effects of the ultrasound on the bees and the mites. Preliminary in-hive tests were then conducted. Bee hives with varying levels of *Varroa* mite infestation were temporarily sealed to prevent bee traffic and then the bees inside were exposed to the ultrasound. The mite drop from the hive was recorded for (i) 30 minutes before, (ii) during 30 minutes of ultrasound exposure, and (iii) 30 minutes after ultrasonic treatment.

Results/Discussion

The bees in the transparent enclosures exhibited normal behavior and appeared to be unaffected by the ultrasound. In some cases, *Varroa* mites dropped off their bee hosts. Preliminary results from the in-hive experiments indicate a significant increase in the rate of *Varroa* mite drop after only 30 minutes of exposure to the airborne ultrasound inside the hive, with the effect continuing after the ultrasonic system was switched off, as can be seen in Fig. 1. Further results and analysis from ongoing field trials in additional hives will be presented in more detail.

[1] <https://www.statista.com/statistics/818286/number-of-beehives-worldwide/>

[2] European Parliament, Resolution T6-0579/2008. Available at www.europarl.europa.eu/oeil/file.jsp?id=5695902¬iceType=null&language=en.



Localization of fatigue cracks using low-frequency nonlinear Lamb waves in numerical perspective
Xu Jichao¹, Wei Nuoke¹, Zhu Wujun¹, Xiang Yanxun¹
¹*East China University of Science and Technology, China, People's Republic of*
Background, Motivation, and Objective

Nonlinear Lamb waves had emerged as a promising technique for small-scale damage characterization in nondestructive evaluation(NDE) and structural health monitoring(SHM).

Recent studies had mainly investigated the generation of the higher harmonic by low-frequency guided wave. However, there were limited studies focused on low-frequency nonlinear Lamb waves interacting with fatigue cracks, and used its temporal features to locate damage. In this work, an imaging algorithm was carried out to locate a fatigue crack using nonlinear S0 mode Lamb waves,which was modeled by Three-dimensional(3D) Finite Element(FE) Simulation.

Statement of Contribution/Methods

The Lamb wave propagation and interaction with the fatigue crack in an aluminum plate was modeled by ABAQUS/CAE. The plate dimensions were $200*100*1\text{mm}^3$, and a non-reflecting boundary condition was setted on the plate's periphery. A fatigue crack was modeled as a through-thickness seam, and a contact pair with interaction properties was defined on the seam interfaces to model the contact acoustic nonlinearity(CAN).The benchmark state of a hole and the current state of a hole with a fatigue crack were studied respectively.

Short-time Fourier transform(STFT) was performed on the time-domain signal from FE model. The window size of STFT was carefully chosen such that the time of flight(ToF) of second harmonics of S0 Lamb wave could be recognized precisely. Then, an ellipse-like locus was formed on the sensing path, indicating all the possible damage points. A damage index(DI) was defined at each spatial point using a probabilistic imaging algorithm(PIA).

Results/Discussion

As a representative result, Fig.1(a) showed the time-domain signals acquired by path A-D in both benchmark and current states, and there were no apparent damage-scattered waves in the current state. As showed in Fig.1(e), the location of the fatigue crack was identified and distinguished from the hole,while the fatigue crack was diagnosed by mistake in Fig.1(d). It was noted that approximate group velocity matching based nonlinear S0 mode Lamb waves would affect severely the accuracy of damage location. This result verified that the proposed imaging algorithm would be a feasible and effective approach to locate fatigue crack by nonlinear S0 mode Lamb waves.

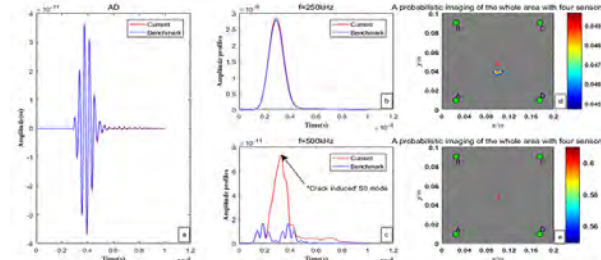


Fig.1. (a) the time-domain signals acquired by path A-D in both benchmark and current states; two slices of amplitude profiles obtained from the spectrogram of the signals via A-D were at 250kHz(b) and 500kHz(c); the ultimate diagnostic images with a threshold value of 90% using linear(d) and nonlinear damage index(e).^[1]

What Information about High-Pressure Thermophysical Properties of Liquids Can be Provided by Low-Intensity Ultrasonic Waves?**Piotr Kielczynski¹, Stanislaw Ptasznik², Marek Szalewski¹, Andrzej Balcerzak¹, Krzysztof Wiejka¹, Aleksander Rostocki³**¹*Polish Academy of Sciences, Poland*, ²*INSTITUTE OF AGRICULTURAL AND FOOD BIOTECHNOLOGY, Poland*, ³*Warsaw University of Technology, Poland***Background, Motivation, and Objective**

In many technological processes liquids are subjected to high pressures (up to 800 MPa), e.g., in high pressure preservation of liquid foodstuffs. Similarly, in modern fuel injection systems for diesel engines, biofuels are subjected to pressures up to 300 MPa. In such extreme conditions, thermophysical properties of liquid change considerably. Conventional methods for measuring thermophysical properties of liquids completely fail at high pressure conditions. Hence, these methods are of no use in real industrial conditions, during on-line monitoring of industrial processes. Thus, there exist a strong demand for industrial grade measurements methods, which can be used to monitor on-line the actual parameters of liquids. A very promising solution is offered by ultrasonic techniques which are particularly suitable for measurements of thermophysical properties of liquids at high pressures. In addition, the ultrasonic methods are totally non-destructive and can be fully automated in real time.

Statement of Contribution/Methods

The aim of this work was to evaluate the impact of temperature and high pressure on thermophysical properties of liquids, exemplified by a *Camelina sativa* (false flax) oil. *Camelina sativa* oil has gained recently a growing interest due to its health-promoting effect as well as for its potential use in biodiesel production. To achieve the above objective, we measured the speed of sound and density in the selected oil. The speed of sound is directly associated to many thermophysical parameters of liquids. Hence, measurements of ultrasonic longitudinal wave velocity ($f = 5$ MHz) and liquid density, as a function of pressure and temperature, allowed determination of several important thermophysical parameters of the investigated liquid. The speed of sound in the liquid was determined from the time of flight measured with the cross-correlation method. To perform numerical calculations, it was helpful to introduce a Tamman–Tait type equation of state to approximate the measured density isotherms of the investigated *Camelina sativa* oil.

Results/Discussion

Isotherms of adiabatic and isothermal compressibility, thermal expansion coefficient, thermal pressure coefficient, thermal conductivity, surface tension, and specific heat capacity versus pressure were evaluated, from measurements of the speed of sound and density of the *Camelina sativa* oil at high pressures (up to 660 MPa) and at various temperatures (3, 10, 20, and 30 °C). These data will be helpful in engineering practice to evaluate the optimum parameters of high-pressure technological processes in the food and chemical industries. In addition, they can be used to determine high-pressure thermophysical properties of biofuels, without the necessity for complex and time consuming off-line experimental investigations. Direct measurement of these parameters, at high pressure conditions, is virtually impossible using the conventional measurement methods.

P2-C10 - SAW Sensor & Actuator II

Waraku (posters 2)

Thursday, October 25, 9:30 AM - 4:00 PM

Chair: **Hagen Schmidt** IFW Dresden

P2-C10-1

AlN/Si based SAW resonators for very high sensitivity temperature sensors

Alexandra Nicoloiu¹, Alexandru Muller¹, Ioana Zdru¹, Dan Vasilache¹, George Stan², Claudia Nastase¹, Viorel Dumitru², Adrian Dinescu¹

¹IMT-Bucharest, Bucharest, Romania, ²National Institute of Material Physics, Magurele, Romania

Background, Motivation, and Objective

Wide bandgap thin AlN and GaN semiconductor layers grown or deposited on different substrates are reliable solutions for high sensitivity sensors based on GHz operating surface acoustic wave (SAW) resonators. AlN technology is compatible with CMOS and SiGe technology and the integrability in CMOS is possible since this material can be deposited at low temperatures (< 200°C). In this work single AlN/Si based SAW structures are used for temperature measurements and values of the sensitivities beyond state of the art are obtained.

Statement of Contribution/Methods

The AlN films (1 μm thick) were produced by reactive radio-frequency (13.56 MHz) magnetron sputtering using an AJA Phase II J deposition system (USA), equipped with a 3 inch-diameter planar magnetron gun. Different single SAW resonators having the IDTs with different finger and interdigit spacing widths (170, 200, 250 nm) and thicknesses (25, 50, 100 nm) were manufactured on AlN/Si wafers using advanced nanolithography. The IDTs have 150 digits and interdigit spacings, 50 μm long. The entire structure, including the measuring pads (conventional photolithography, e-gun metallization and lift-off technique), is presented in Fig 1a.

Results/Discussion

Fig.1b presents the reflection coefficient (S_{11}) measured at room temperature for three test structures having $w = 200$ nm and different metallization thicknesses. A monotonous decrease of the resonance frequency was noticed when the thickness of the Au metallization is increased, due to the mass loading effect of Au. The effective coupling coefficient at room temperature is extracted between 1.1 – 2%, higher than what the authors obtained for similar SAW resonators on GaN/Si [1]. The S parameters vs. T measurements were performed in a cryostat in the range 5–423K. The sensitivity, s, and the temperature coefficient of frequency, TCF, have been analyzed between 23–150 °C (Fig.1c). The sensitivities are higher than what was reported in literature for other SAW sensors developed on AlN on different substrates [2, 3] as well as for similar GaN based SAW T sensors recently reported by the authors [4].

[1] A. Muller et. al., IEEE Electron Device Letters, 36, 12, 1299, 2015

[2] T. Aubert, et. al., IEEE Trans. on Ultrasonics, Ferroelectrics and Freq. Control, 59, 5, 2012

[3] C. Li, et. al., Mater. Express, Vol. 5, No. 4, 367, 2015

[4] A. Muller et. al., Sens. and Actuators A 209, 115, 2014

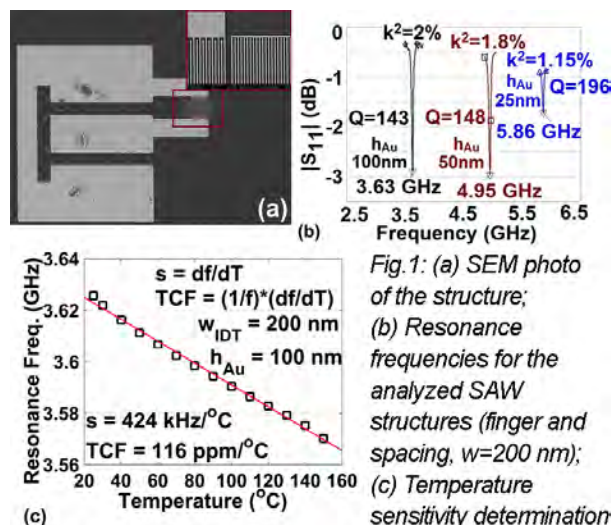


Fig. 1: (a) SEM photo of the structure;
(b) Resonance frequencies for the analyzed SAW structures (finger and spacing, $w=200$ nm);
(c) Temperature sensitivity determination

Displacement of Microparticles on Surface Acoustic Wave Delay Line Using High RF Power

Melvin Paquit¹, Lyes Djoumi², Meddy Vanotti², Valérie Soumann², Gilles Martin², Virginie Blondeau-Patissier², Thomas Baron²

¹*AR-Electronique, Besançon, France*, ²*Time & Frequency, FEMTO-ST Institute, Besançon, France*

Background, Motivation, and Objective

The measurement of microparticle concentration usually requires both large and expensive instruments. Recently, surface acoustic wave (SAW) delay lines based on Love wave have been successfully used as sensors for the detection of microparticles with diameters smaller than 10 μm and 2.5 μm (PM10 and PM2.5). This detection is performed by measuring a phase variation of the wave; PM10 and PM2.5 are first selected based on their aerodynamic diameter using a filtering system. However, the sensor saturates after about 20 hours of use when the damping reduces the wave magnitude until it cannot be probed.

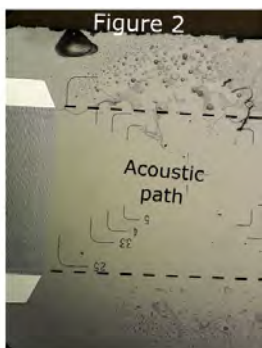
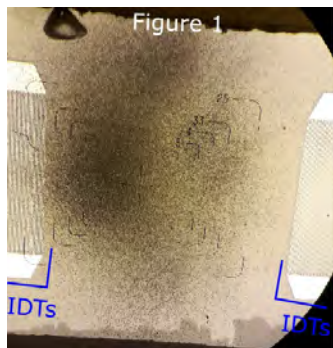
SAW delay lines based on Rayleigh waves have already been successfully used for moving drops of liquid. In this study, we investigate the possibility of using this type of SAW delay lines in order to remove microparticles from the sensor's surface.

Statement of Contribution/Methods

SAW delay line based on Rayleigh waves working at 100 MHz have been designed and built on lithium niobate (YX)/128° and quartz (YX)/36° substrates. The split finger pairs configuration has been chosen in order to reduce triple transit phenomena. Moreover, impedance matching has been taken into account during the design process so that no additional electronics is required for transmitting the high power RF signal which is comprised between 0dBm and 40 dBm. Components have been diced and wire bonded onto ceramic packages. Fume of burning candle has been used in order to saturate the sensor with particles smaller than 2.5 μm . High power RF signal has been applied at a single frequency point to the saturated device.

Results/Discussion

SAW delay line can sustain RF power levels higher than 36 dBm during hundreds of hours. Figure 1 shows a delay line on a lithium niobate substrate and covered with PM2.5 microparticles. Figure 2 exhibits the same surface after applying a 33 dBm RF signal during 2 minutes. The microparticles have been successfully moved out of the acoustic path. The same process has been applied to quartz based delay lines and, in this case, no microparticles moved even at 39 dBm for a few minutes. This behavior is due to the difference of electromechanical coupling between the two piezoelectric substrates. Additional experiments still need to be made with different microparticle types, nevertheless these results have a particular relevance to reduce the saturation of particles in SAW sensors.



PbS colloidal quantum dots coated SAW-based sensor for nitrogen dioxide room temperature detectionChen Fu¹, Min Li², Chong Li², Hui Li³, Hao Kan², Xueli Liu⁴, Wen Wang⁵, Jingting Luo²¹*Shenzhen University, Shenzhen, China, People's Republic of*, ²*Shenzhen University, China, People's Republic of*.³*1847087378@qq.com, China, People's Republic of*, ⁴*Institute of Acoustics, Chinese Academy of Sciences, China, People's Republic of*, ⁵*University of Chinese Academy of Sciences. Institute of Acoustics, Beijing, China, People's Republic of***Background, Motivation, and Objective**

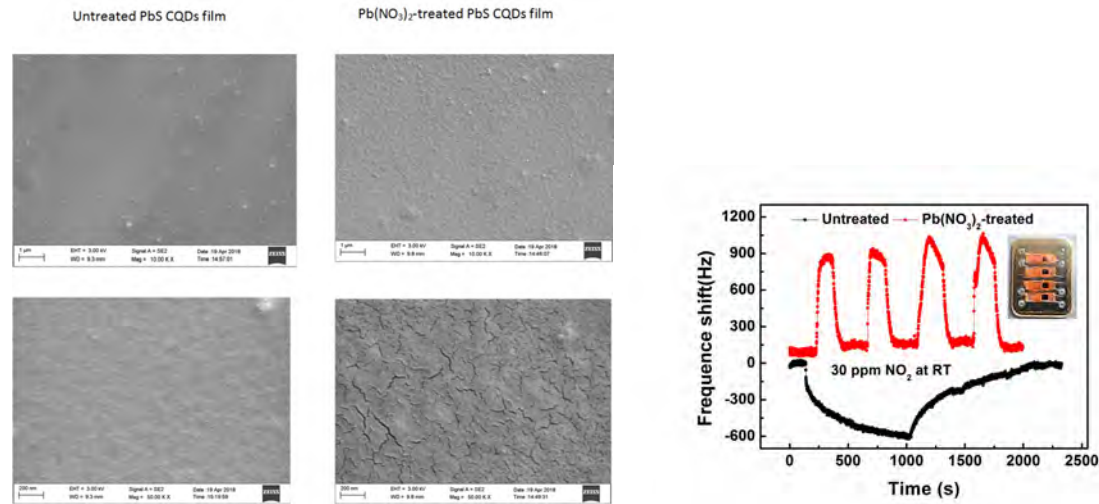
Colloidal quantum dot (CQD) is emerging as new substitution gas sensing materials due to the excellent accessibility of gas molecules to CQD surfaces realized via surface ligand removal. Surface acoustic wave (SAW) gas sensors are very attractive because of their miniature, low cost, and remarkable sensitivity. Therefore, the aim of this work is to develop a PbS colloidal quantum dots film and then use it to fabricate a highly sensitive NO₂ sensor with SAW technology.

Statement of Contribution/Methods

Firstly, we have demonstrated PbS CQD synthesis through a room-temperature route in ambient air. Then, a 200MHz SAW low insertion loss delay line with single phase unidirectional transducer (EWC/SPUDT) was optimally designed by FEM/BEM. Finally, the PbS CQDs was deposited via layer-by-layer (LBL) spin-coating onto the surface of the delay line. To conduct the ligand exchange treatment, PbS CQD film was spray-coated with the NaNO₂ to remove the oleate ligands capping on the CQDs surface for its excellent access of gas molecules. The response of the sensor was measured by a network analyzer upon exposure to NO₂ gas.

Results/Discussion

The average crystal size estimated from HRTEM results was ~4.0nm, indicating the PbS nanocrystals promising performance in the strong quantum confinement regime. The morphology of the PbS CQDs film was observed in Fig.1 using SEM. Cracks were observed on the surface of the Pb(NO₃)₂ treated CQDs film due to the ligand exchange process. The treated PbS film becomes more porous, thereby enables the PbS CQDs to be gas-sensitive. As is shown in Fig. 2, the Pb(NO₃)₂ treated sensor shows 33Hz/ppm sensitivity which is almost twice of the untreated one. Besides, the treated sensor exhibits much faster and more recoverable response upon exposure/release cycles at room temperature.



Towards an AlScN-based packageless acoustic wave sensor with RFID capabilities, for applications above 350°C.

Pascal Nicolay¹, Natalya Naumenko², Thierry Aubert³, Hugo Chambon⁴

¹CTR AG, Villach, Austria, ²National University of Science and Technology MISIS, Russian Federation, ³CentraleSupélec, France, ⁴CTR AG, Austria

Background, Motivation, and Objective

Housing failure is a blocking point, for the development of high-temperature SAW sensors. Packageless sensors constitute therefore a promising solution. Here, guided acoustic waves propagating in a protective multilayered stack are used instead of surface acoustic waves. The waves are usually guided in a low- Z_A (acoustic impedance) layer, sandwiched between two high- Z_A layers. An alternative solution was suggested in 2017, based on the AlN/Pt/LNY128 structure [1]. Here, the waves are guided at the AlN/LN interface, due to specific properties of the LNY128 cut and to the mass-loading effect of the Pt IDTs. This solution is the most promising, for applications above 350°C, up to 600°C. However, 2.45GHz Reflective Delay Lines (R-DL) cannot be implemented using this structure, as the guided waves do not exist in the absence of the Pt grating. Only resonators are possible. Guiding Pt patches in the R-DL gaps wouldn't solve the issue, as they would generate massive propagation losses. Another structure is therefore required.

Statement of Contribution/Methods

The use of a thin layer with a slightly lower acoustic velocity might solve the issue, as it would reduce the magnitude of the mass-loading effect required to guide the waves. Then, Cu (or even Al) could be used instead of Pt. We found that AlScN with %Sc>15% would have the right properties, to achieve a 2.45GHz R-DL based on an AlScN/Cu-IDT/LNY128 stack. The (electro-)acoustic properties of the stack were computed in a wide %Sc range, using a proprietary SDA/FEM/SDA software (see Fig. 1). COM parameters extraction and Design optimization were performed using classical fitting methods and P-Matrix models, respectively.

Results/Discussion

Optimal Design parameters were defined, to operate at 2.45GHz, using a 15%Sc-AlN/Cu-IDT/LNY128 structure. With $\lambda=1.842\mu\text{m}$ and $h_{\text{Cu}}/\lambda=12.5\%$, a guided mode is expected to propagate at the AlScN/LN interface, with velocity $V=4514\text{ m/s}$ and $k^2=5.03\%$. The COM parameters were computed for this configuration. A test R-DL design with two reflectors located on each side of the IDT was developed and simulated. Here, Cu patches are used to guide the wave, in the gaps between the IDT and reflectors. Computations show that the same Cu thickness can be used for the metal fingers and patches. The fabrication of the first demonstrator is in progress.

[1] N. Naumenko, P. Nicolay, <https://doi.org/10.1063/1.4985582>

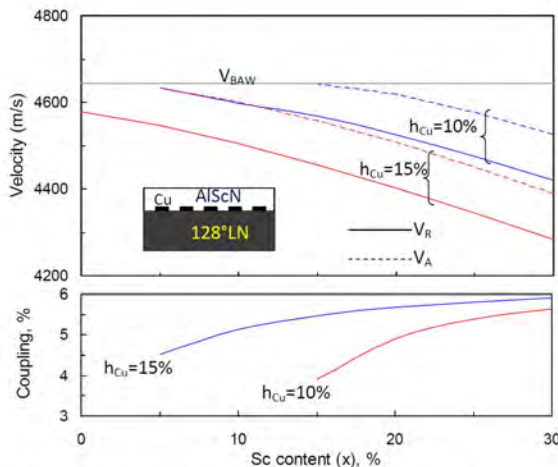


Fig. 1. Velocity (V_R , V_A) and k^2 of a guided acoustic mode propagating in AlScN/Cu/128°LN. Velocities and k^2 are plotted vs. % Sc, for two Cu thicknesses.

Development of surface acoustic wave magnetic field sensor incorporating with FeCo dot array

Yana Jia¹, Wen Wang², Xufeng Xue², Yong Liang²

¹Institute of Acoustics, Chinese Academy of Sciences, Beijing, China, People's Republic of, ²Institute of Acoustics, Chinese Academy of Sciences, Beijing, China, People's Republic of

Background, Motivation, and Objective

The hysteresis caused by the internal coercive force in magnetostrictive film results in significantly hysteresis error of the magnetic sensor. To suppress the hysteresis of the magnetostrictive thin-film coated surface acoustic wave (SAW) magnetic field sensor, dotted-design is proposed for magnetostrictive thin-film in this contribution to fully release the magnetostrictive effect and reduce the internal inhibition in the magnetostrictive thin-film.

Statement of Contribution/Methods

As shown in Fig.1, the developed sensor was composed of a sensor chip made by differential delay line-oscillators consist of two oscillation loops, the differential oscillation frequency is collected to evaluate the applied magnetic field. A FeCo dot array was deposited along the SAW propagation path of the sensing device by photolithography and overlay technologies. The size of the FeCo dots is set to $3\lambda \times 4\lambda$ (λ : wavelength). The patterned FeCo film produces magnetostrictive effect and ΔE effect generated by the applied magnetic field, resulting in changes in the SAW phase velocity and the corresponding oscillation frequency.

Results/Discussion

Using the Helmholtz coil system, the developed SAW magnetic field sensor (pictured in Fig. 1) with 500 nm FeCo dot array were evaluated. The measured results indicate the dotted pattern design on the FeCo thin-film improve effectively the sensitivity (21.4 KHz/A) and linearity, and also the hysteresis error was reduced significantly up to 0.85%. The comparison to 500nm FeCo thin-film coated sensor was also conducted in Fig. 2.

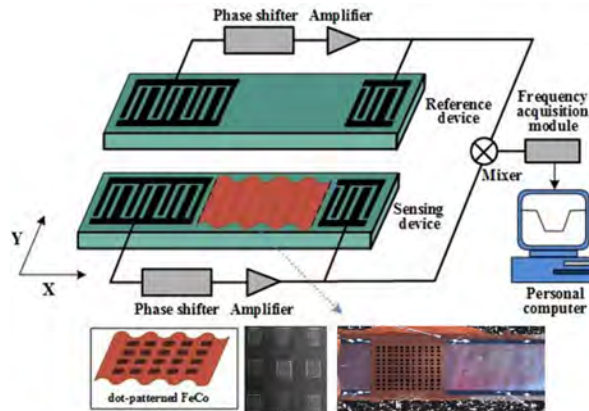


Fig. 1 The proposed SAW magnetic field sensor incorporating FeCo dot array

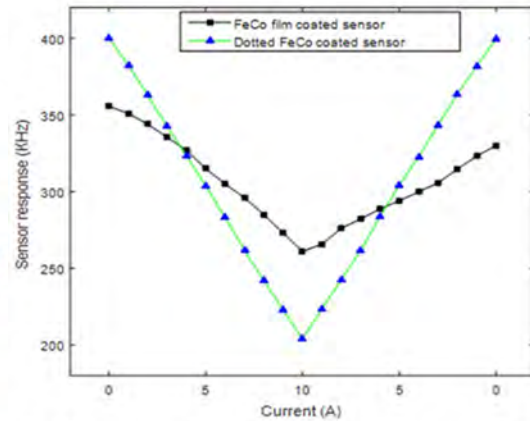


Fig. 2 The measured sensor response from the sensor with FeCo dot array, and in comparison with FeCo thin-film coated sensor

Pd-Cu nanowires coated SAW sensor for fast Hydrogen gas sensingWen Wang¹, Shenchao Mei², Xueli Liu², Yana Jia², Xufeng Xue², Yong Liang²¹*Institute of Acoustics, Chinese Academy of Sciences, Beijing, China, People's Republic of*, ²*Institute of Acoustics, Chinese Academy of Sciences, China, People's Republic of***Background, Motivation, and Objective**

Fast monitoring for hydrogen gas is essential in hydrogen energy utilization. The properties of fast response, high sensitivity, low power consumption, and small size of the surface acoustic wave (SAW) based gas sensor makes it be a very promising candidate for sensing hydrogen. Pd-Cu nanowires coated SAW sensor was conducted in this contribution for sensing hydrogen gas, fast response was realized thanking for the larger surface volume-surface ratio and porous structure of the Pd-Cu nanowires.

Statement of Contribution/Methods

The configuration of the proposed SAW sensor was composed of a differential oscillator, and a Pd-Cu nanowires depositing along the SAW propagation path of the sensing device. Using the standard photolithographic technique, the SAW delay lines with operation frequency of 150MHz were fabricated, and then, the Pd-Cu nanowires synthesized by using the wet chemical method was prepared onto the sensing device surface by drop-coating. The sensing device and a naked reference device were connected into the oscillation loop made by amplifier, phase shifter, mixer and so on. The adsorption towards hydrogen gas in Pd-Cu nanowires modulates the SAW propagation, and corresponding oscillation frequency signal was collected to evaluate the hydrogen gas.

Results/Discussion

The developed SAW sensor was pictured in Fig. 1. Figure 2 provides the sensor response towards 4% (v/v) hydrogen gas in 300 mL/min air flow at room temperature. Excellent repeatability and fast response were observed, and achieved response and recovery time are 2s and 3s, respectively. Corresponding sensitivity was evaluated as 650Hz/%.

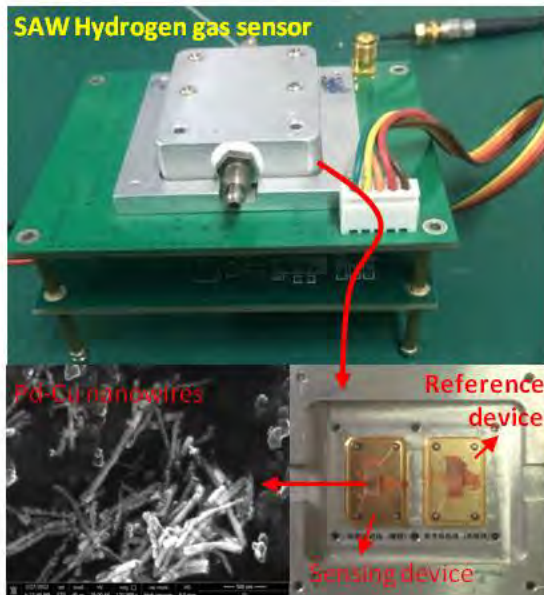


Fig. 1 The developed Pd-Cu nanowires coated SAW sensor for Hydrogen gas sensing

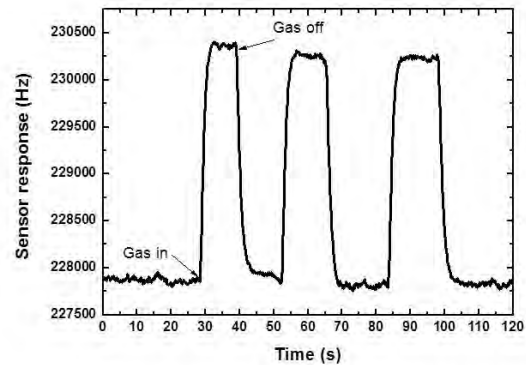


Fig. 2 The sensor response to 4% Hydrogen gas

P2-C11 - MEMS & Application II

Waraku (posters 2)

Thursday, October 25, 9:30 AM - 4:00 PM

Chair: **Jan Kuypers** Blickfeld GmbH

P2-C11-1

Micromachined Aluminum Scandium Nitride Lamb Wave Resonators Utilizing Low Order Symmetric Modes

Fazel Parsapour¹, Vladimir Pashchenko¹, Hugo Chambon², Pascal Nicolay², **Paul Muralt**³

¹*Electroceramic Thin Films, EPFL, Switzerland*, ²*CTR AG, Austria*, ³*Electroceramic Thin Films, EPFL, Lausanne, Switzerland*

Background, Motivation, and Objective

In recent years, more and more frequency bands were assigned for mobile phone communication. The totality of bands is now ranging from 0.3 to 3.8 GHz. The currently dominating electroacoustic technologies are based on surface acoustic waves (SAW) and thin film bulk acoustic waves (BAW). SAW devices are more suitable for the lower frequency range, and BAW devices with their thin film thickness mode resonance (TFBAR technology) are more suited for the higher frequency range. It is of high interest to dispose of an electroacoustic technology based on thin films for accessing the lower frequency range as well. In this context, the lamb wave resonator concept attracted much attention. The frequency is depending not only on the layer thickness, but also on the period of the interdigitated electrodes. The lowest order symmetric mode (S0) in AlN lamb wave resonators was widely explored since 2002. Such devices excel with a high phase velocity close to 10000 m/s, a weak phase velocity dispersion, a small temperature coefficient of frequency, and a high quality factor (Q). However, only moderate electromechanical coupling factors were achieved. Recently, it was shown that the piezoelectric coefficients of the AlN wurtzite can be strongly increased by the partial substitution of Al by Sc. In this work, we investigated Lamb wave devices by theory and experiment using thin films of Al0.84Sc0.16N.

Statement of Contribution/Methods

The device design contained a floating bottom electrode and interdigitated top electrodes. The active regions were thus those below the electrode fingers and mainly coupled through the e_{31} coefficient. Finite element modeling was employed to find an optimal coupling coefficient matching film thickness and IDT pitch. For 1.2 μm thick AlScN films, an optimal pitch ($\lambda/2$) equal to 2.5 to 3 μm was derived.

Results/Discussion

The best performance of S0 modes was found with a λ equal to 6 μm at resonance frequency close to 1.4GHz. The electromechanical coupling factor and quality factor were measured as 2.7% and 235, respectively. While the coupling factors were quite high and in excellent agreement with simulation results based on the DFT materials constants from Caro et al., the quality factors were not satisfactory. SEM and XRD investigation show that the film surface is covered with ab-normal grains and the texture is not entirely of (0002) symmetry. Patterning of Pt bottom electrode (BE) is the main reason for bad film quality in comparison to a wafer with full BE coverage, which yields an excellent c-textured fibrous film. This challenge was addressed by a number of measures involving electrode lay-out and deposition conditions. These modifications resulted in reduction of the density of ab-normal grains, and an almost fully c-textured film. Consequently, the coupling coefficient k^2 increased up to 2.5 %. The reduction in abnormal grains also led to an increase in the quality factor Q reaching up to 2700, probably due to a reduction in surface roughness.

ACTIVE AND INACTIVE FRAMES IMPROVE FIGURE OF MERIT OF TWO DIMENSIONAL MODE RESONATORS
Jeronimo Segovia-Fernandez¹, Cristian Cassella²
¹*Texas Instruments Kilby Labs, Santa Clara, CA, United States*, ²*Electrical and Computer Engineering, Northeastern University, Boston, MA, United States*
Background, Motivation, and Objective

The proliferation of *IoT* networks require that next-generation RF filters can be monolithically integrated and operate in a less crowded spectrum. FBARs have led the market of mid-band filters thanks to their high k_t^2 , Q and power handling. Two dimensional mode resonators (2DMRs) are promising candidates to implement 5G filters since they exhibit a dispersive S_0 mode in a fully-anchored interdigitated electrode scheme that allows significant lithographic tunability and high power handling. In terms of *FoM*, 2DMRs are still not comparable to FBARs.

Statement of Contribution/Methods

This paper introduces a technique to enhance the 2DMR *FoM* by using acoustic frames. Frames have been proved to suppress spurious modes and improve Q in FBARs. In this work, we thicken the edge of the electrodes (active frame) and place a metal strip between each resonator finger (inactive frame) (Fig. 1.a). As a result, the z-axis displacement (u_z) is approximated to a quasi-square waveform in the active region, boosting k_t^2 , and the x-axis displacement (u_x) is confined in the center and reduced at the edges of the inactive region, boosting Q . To prove our hypothesis we run 2D FEA on a framed 1-finger 2DMR operating at 2.5GHz that is based on a 1μm-thick AlN plate sandwiched between 0.1μm-thick bottom and top Pt electrodes.

Results/Discussion

To increase k_t^2 our framed 2DMR intends to replicate a continuous u_z across the W_e , resulting in more piezoelectric charge collected under the electrodes. In standard 2DMRs, $u_z = U_0 \sin(k_z z) \cos(k_x x)$, where k_z and k_x represent the z and x wave vectors, respectively (Fig. 1.b). Since U_0 depends on the electromechanical transduction, u_z can be reshaped by varying the equivalent stiffness across the finger. To do that, we soften the edge of electrodes by stepping-up the Pt thickness. By properly scaling the active frame a quasi-square wave can be generated under the electrodes (Fig. 1.c). To increase Q we place a metal frame between the electrodes and outer regions. Thus, this part of the inactive region becomes more compliant, confining most of the propagating acoustic energy. To simulate Q we add the Si substrate and apply PML. Fig. 1.d compares two framed 1-finger 2DMRs with and without inactive frames demonstrating that the inclusion of the latter clearly improves Q . Assuming only acoustic losses, $k_t^2=7\%$ when $W_{af}=0.4\mu\text{m}$ and $T_{af}=0.16\mu\text{m}$, and $Q=1300$ when $W_{if}=0.5\mu\text{m}$ and $T_{if}=0.1\mu\text{m}$.

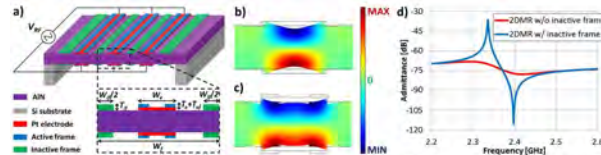


Figure 1: a) 3D schematics of a framed multi-finger 2DMR. b) FEA of the vertical displacement in a standard 1-finger 2DMR. c) FEA of the vertical displacement in a framed 1-finger 2DMR, and d) admittance responses of 1-finger 2DMRs with and without inactive frames.

Flexible Lamb wave resonators based on lithium niobate thin film

Xin Sun¹, Bohua Liu¹, Chuanhai Gao¹, Yuan Jiang¹, Wei Pang¹, **Menglun Zhang¹**

¹*State Key Laboratory of Precision Measuring Technology and Instruments, Tianjin University, Tianjin, China, People's Republic of*

Background, Motivation, and Objective

In recent years, Lamb wave resonators (LWRs) based on single-crystal lithium niobate (LN) thin films have become a research hotspot. The LWRs can meet high electromechanical coupling coefficient (K_t^2) and high quality factor (Q) requirements simultaneously for the next-generation reconfigurable and multi-frequency wideband filtering. Meanwhile, the recent advancements in flexible electronics allow us to envision a new era for micro-acoustics based electronics, which has both unique electrical performance and mechanical flexibility. By leveraging new technologies, our group has demonstrated flexible micro-acoustic resonators based on polycrystalline AlN thin film[1]. Nevertheless, with single-crystal LN as the piezoelectric thin film, it is supposed to build flexible resonators with much better key performance (i.e. K_t^2 and Q), and therefore high performance electronics (e.g. filters, oscillators) and transducers.

Statement of Contribution/Methods

The flexible resonators are modeled and designed by FEM, fabricated, and characterized in both electric and mechanical domains. The devices were fabricated by FlexMEMS technology originated from our group. It should be noted that the fabrication process has been re-developed in this work to better fit the unique features of the flexible resonators based on LN thin film. The details on fabrication will be fully disclosed in the full paper.

Results/Discussion

Figure 1(a) shows a photo of the flexible resonator, with schematics as the inset. The flexible LWR is driven by lateral field excitation (LFE). Figure 1(b) illustrates the electrical response of the flexible LWRs, with resonant frequency of 378.2 MHz, Q of 966, K_t^2 of 4.0%, and parallel-to-series resonance impedance ratio of 729. According to the simulation, we confirm that the device vibrates in S0 mode; however, the theoretical K_t^2 should be much higher than the experimental value. Nevertheless, compared with our earlier results on flexible AlN LWR driven by LFE[1], the experimental $Q \cdot K_t^2$ value of the flexible LN LWR improves by ~100 times. Test results of the bending performance and reliability of the flexible resonator will be included in the full paper.

[1] Xing Yang, Menglun Zhang, Wei Pang, et al. AlN Lamb Wave Resonators on a Flexible Substrate[J]. IEEE ELECTRON DEVICE LETTERS, 2017, VOL. 38, NO. 8.

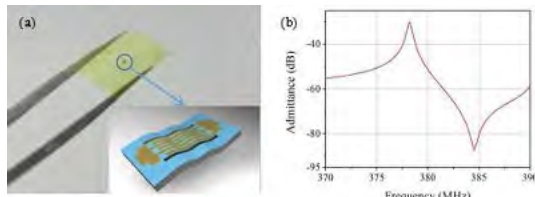


Fig. 1. (a) Photo and (b) electrical response of the flexible LWR based on LN.

An Improved Design for 2D Arrays of Capacitive Micromachined Ultrasound Transducers: Modeling, Fabrication, and Characterization

Mario Baum¹, Nooshin Saeidi¹, Klaus Vogel¹, Tim Schroeder¹, Karman G. M. Selvam¹, Maik Wiemer¹, Thomas Otto^{1,2}

¹Fraunhofer ENAS, Chemnitz, Germany, ²Chair Microtechnology, TU Chemnitz, Chemnitz, Germany

Background, Motivation, and Objective

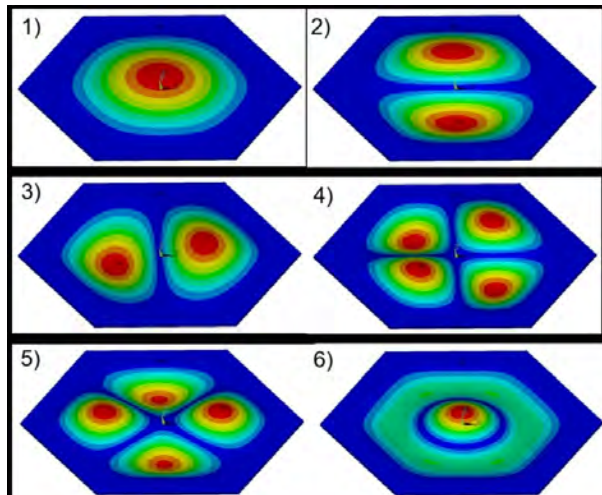
Capacitive Micromachined Ultrasonic Transducers (CMUTs) technologies utilize well established silicon fabrication processes to manufacture highly miniaturized ultrasound transducers in diverse shapes, sizes, arrangements and materials. Superior performance of these transducers such as large bandwidth and no self-heating have made them promising alternatives to their piezo based counterparts. In this work, an improved CMUT fabrication process based on wafer bonding is presented and modeling, implementation, and characterization results were discussed.

Statement of Contribution/Methods

Comprehensive Finite Element Analysis (FEA) simulations were carried out using ANSYS and COMSOL software tools to study CMUTs in a variety of functional aspects such as, mechanics, electrostatics and acoustics (see figure below: Simulation result of the first 6 Eigenfrequencies of a hexagonal shaped membrane). Models of different CMUT cell geometries, shapes and materials compromising their vibrating membranes were analyzed to examine CMUTs with center frequencies ranging between 1 to 15 MHz. The process flow to realize CMUTs used in this work is based on wafer bonding, a suitable way for creating free standing membranes over cavities. In-process wafer characterizations were performed to obtain residual stress within membrane materials, as this has profound effect on resonance frequency of a CMUT.

Results/Discussion

CMUTs with various cell designs were fabricated and characterizations are conducted to establish a valid correlation between simulation and characterization results of fabricated devices. In addition, the impact of encapsulation on CMUTs was investigated and analytically compared with different polymers as well as the acoustics pressure levels at an effective distance from the device could be assessed. Finally, the preliminary characterizations of 2D arrays of CMUT cells using a custom-made test setup will be described within the paper.



Apodization technique for significant spurious mode suppression of AlN plate mode resonators

Yao Zhu¹, Nan Wang¹, Geng Li Chua¹, Bangtao Chen¹, Srinivas Merugu¹, Navab Singh¹, Yuandong Gu¹

¹Institutes of Microelectronics, A*STAR, Singapore

Background, Motivation, and Objective

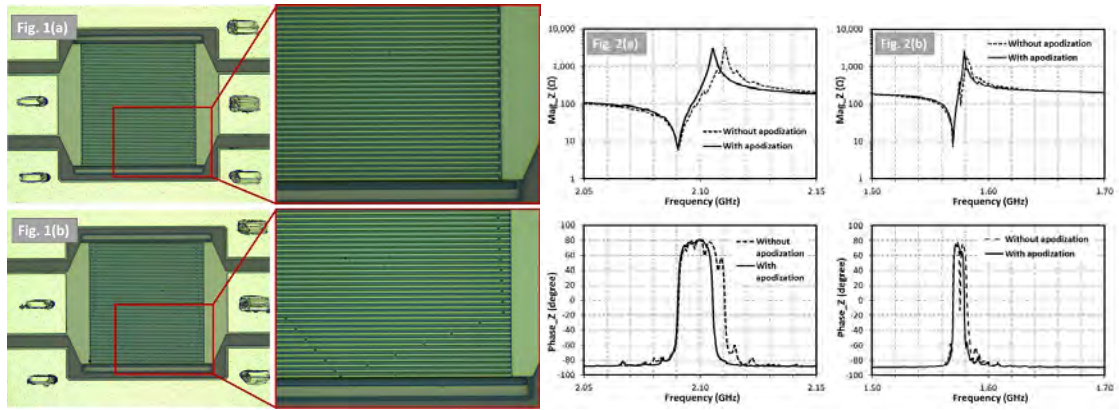
In order to suppress the spurious modes of the piezoelectric MEMS plate mode (PM) resonators, researchers have explored different optimization techniques such as micro phonics, resonator shape, anchor design, electrode apodization, bus bar design, etc. This paper presents a new apodization concept which can be easily applied to various resonators for effective spurious mode suppression.

Statement of Contribution/Methods

Spurious modes can arise from both longitudinal and transverse waves. The existing apodization shapes for PM resonator in literature are all symmetrical along the direction of electrode fingers, which is effective in suppressing transverse spurious modes. A new concept of apodization shape design which is inspired by BAW resonator is proposed in this work. Applying polygon shapes with no parallel sides to apodize the top electrodes of PM resonators is proven to be effective in spurious mode suppression.

Results/Discussion

Irregular pentagon shapes are applied to apodize the top electrodes of two AlN based PM resonators operating around 1.5GHz and 2GHz, respectively. Reference resonators with same dimensions but no apodization have been fabricated for comparison. The microphoto of 1.5GHz resonators is shown in Fig. 1 and the impedance of the two sets of resonators are plotted in Fig. 2. It can be observed that in both sets, the magnitude and phase of the resonators are significantly smoother throughout the wide measurement range for the resonators with apodization. The slight reduction in the coupling coefficient is caused by the parasitic capacitance introduced by the dummy electrodes, which can be avoided by design optimization.



Quality Factor Improvement of a 2.4GHz AlN Checker Mode Resonator by Novel Distributed Anchor Design

Yao Zhu¹, Nan Wang¹, Geng Li Chua¹, Bangtao Chen¹, Srinivas Merugu¹, Navab Singh¹, Yuandong Gu¹

¹Institutes of Microelectronics, A*STAR, Singapore

Background, Motivation, and Objective

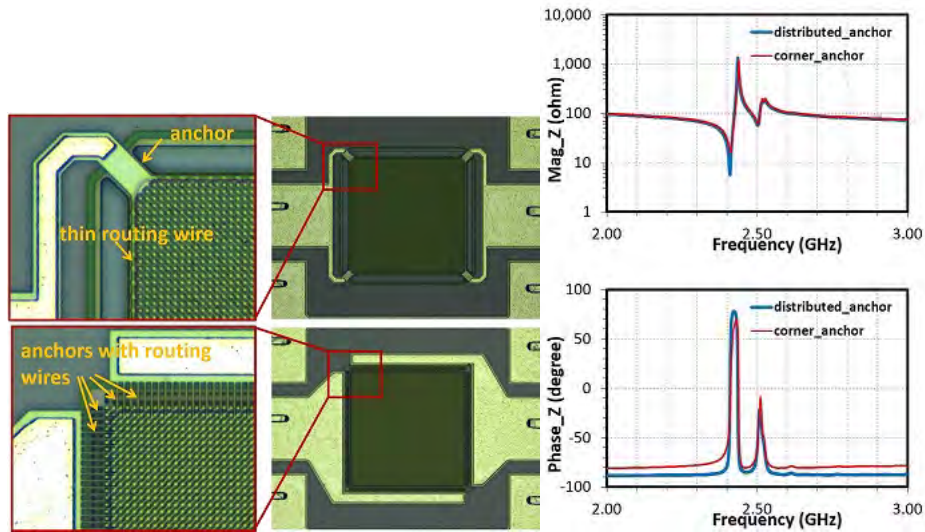
Anchor loss is one of the major mechanical losses in AlN MEMS resonators. For checker patterned resonator [C. Sun, et al., *Appl. Phys. Lett.*, 106, 253502, 2015], the anchor design impacts not only the mechanical aspects, but also the signal routing which is crucial to the electrical loss of the resonator. In this paper, distributed anchor design is used to improve the quality factor of a 2.4GHz AlN checker mode resonator.

Statement of Contribution/Methods

When anchoring at the resonator corners as shown in Fig. 1, checker electrodes far from the anchor need to go through a long and thin routing wire at the resonator border before reaching the anchor, which introduces high resistive loss. Distributed anchor design to shorten the electrical routing paths is proposed in this work to improve the quality factor. The anchoring positions are carefully chosen to minimize the mechanical loss through the array of anchors.

Results/Discussion

Measurement results depicted in Fig. 2 shows that both the resonators with distributed anchors and corner anchors resonate at around 2.4GHz, with a coupling coefficient of 2.6%. Same parallel resistance obtained for both designs implies that the distributed anchors do not introduce additional mechanical losses. The series resistance is 5.6Ω for the distributed anchor design compared to 16Ω for the corner anchor design, which corresponds to bode quality factor improvement from 370 to 475 contributed by the distributed anchor design.



P2-C12 - Material for Acoustic Wave Device II

Waraku (posters 2)

Thursday, October 25, 9:30 AM - 4:00 PM

Chair: **Sylvain Ballandras** frec[n]sys SASU

P2-C12-1

The dielectric loss of wurtzite Al_{0.67}Sc_{0.33}N thin films for mass production of piezoelectric MEMS

Andrea Mazzalai¹, Bernd Heinz¹

¹BU Semiconductor, Evatec AG, Trübbach, Switzerland

Background, Motivation, and Objective

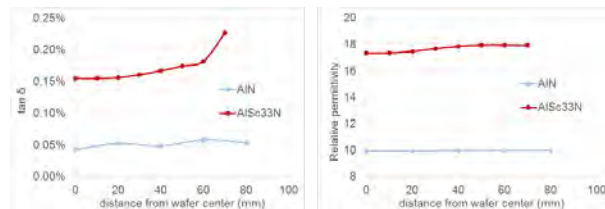
We see nowadays a large interest in Al_{1-x}Sc_xN alloy thin films for piezoelectric MEMS applications, due to the enhancement of piezoelectric properties with respect to undoped AlN [Akiyama et al., APL 95, 2009]. The resulting improved electromechanical coupling coefficient can indeed be exploited for a performance boost of resonators and microphones, but only if the dielectric loss remains confined to very low values. They indeed affect negatively the quality factor of resonators and lower the signal to noise ratio of microphones [Muralt, Int. Ferroel. 17, 1997]. While the piezoelectric properties for films with high Sc concentration are well understood, the dielectric loss for films with a Sc concentration larger than 25at% are still undefined. A detailed characterization of the dielectric losses for scandium doped wurtzite films is therefore essential.

Statement of Contribution/Methods

For this reason, we investigated the dielectric properties of AlN and Al_{0.67}Sc_{0.33}N thin films deposited onto metallized 200mm substrates with an Evatec CLUSTERLINE® 200-II tool. The films have been sputtered from a single 304mm target, which represents the preferred deposition solution for mass production as it allows for high deposition rates. We then deposited and patterned the top electrodes thus forming parallel-plate capacitors, which have been probed to map permittivity and tan δ along the wafer radius at different frequencies in the range of 1 kHz to 10 kHz.

Results/Discussion

Excellent (002) orientation with a narrow rocking curve of 1.1° (FWHM) and a good within wafer distribution for the 1000nm thick films was confirmed by XRD measurements on the 1000nm thick Al_{0.67}Sc_{0.33}N films. The dielectric permittivity ε_r of these films has been measured with about 17.5. The dielectric losses increase significantly with respect to the pure AlN reference sample. An increase of a factor of 3 has been measured in the center part of the substrate while the film on the outer part of the substrate shows even higher loss values. Based on results for the permittivity, the dielectric losses and the enhancement of the piezoelectric activity, the figures of merit (FOM) for different applications will be discussed.



Study of Cr₅Si₃ Electrodes on Langasite Surface Acoustic Wave Resonators for High Temperature Sensing

Jérémie Streque¹, Mohamed-Akram Soussou², Florian Bartoli^{1,3}, Sami Hage-Ali¹, Thierry Aubert³, Thomas Mazingue², Marc Lomello², Omar Elmazria¹

¹Institut Jean Lamour, Université de Lorraine, CNRS, Nancy, France, ²SYMME, Université Savoie Mont Blanc, Annecy-le-Vieux, France, ³LMOPS, CentraleSupélec - Université de Lorraine, Metz, France

Background, Motivation, and Objective

Many piezoelectric materials are viewed as potential candidates for high temperature SAW applications, including langasite (LGS) and AlN. Only a few metals or alloys can withstand such temperatures, among them platinum and iridium based alloys or nanocomposites. These materials cannot be considered when high quality factors are required, due to their higher resistivity and density. The (Cr, V)-Si system was previously studied [1], but has never been proposed as a solution for SAW electrodes, in spite of its high thermal stability, lower density (about 6 g/cm³) and decent resistivity. This study focuses on the development of Cr₅Si₃ alloy deposition for its use in LGS-based resonators, aiming at wireless applications.

Statement of Contribution/Methods

A preliminary study was conducted at high temperatures on bulk materials candidates with high corrosion resistance and low density.

Thermogravimetric investigations on (Cr, V)-Si arc-melted ingots showed an excellent stability to oxidation in air at temperatures, up to 1000°C for Cr₅Si₃. Then, a magnetron sputtering process was developed for Cr-Si thin film synthesis and the operational parameters were optimized in order to obtain 200 nm thick layers with the Cr₅Si₃ stoichiometry.

Synchronous resonators were then fabricated on (0°, 90°, 0°) LGS substrates along X-axis using Cr₅Si₃ electrodes, for various wavelengths. They were subsequently tested on a high-temperature prober compatible with temperatures up to 600°C. The Cr₅Si₃ thin film resistivity was first tested on electrode-shaped patterns, in order to assess the thermal behavior of the alloy.

Results/Discussion

The room temperature resistivity of Cr₅Si₃ was first measured at 187 μΩ.cm, then dropped to 132 μΩ.cm after an annealing process at 600°C performed in order to improve its crystallinity. This value is comparable to those of state-of-the-art Pt-based high-temperature thin films [2]. The temperature dependence of the resistivity was then measured and proved to be quasilinear up to 600°C (Fig. 1.a). The temperature coefficient of resistance was measured at a very low 0.05 %/°C, which remains an asset for sensor design on large temperature ranges. Resonators with wavelengths of 5 and 8 μm were characterized up to 550°C (Fig. 1.b).

[1] E. Mazzega et al., J. of Phys. F: Metal Phys., 17 1135, 1987.

[2] M. Pereira da Cunha et al., Proc. IEEE Ultrason. Symp., 2015.

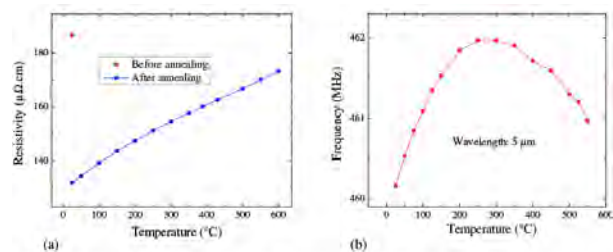


Fig.1. Resistivity variation with temperature measured on 200 nm thick Cr₅Si₃ electrodes vs temperature (a)
Evolution of operation frequency with temperature for LGS resonators based on Cr₅Si₃ electrodes (b).

Evaluation of Piezoelectric Ta₂O₅ Thin Films Using Line-Focus-Beam Ultrasonic Material Characterization SystemRyota Suenaga¹, Masashi Suzuki¹, Shoji Kakio¹, Yuji Ohashi², Mototaka Arakawa^{3,4}, Jun-ichi Kushibiki⁴¹*Integrated Graduate School of Medicine, Engineering, and Agricultural Sciences, University of Yamanashi, Kofu, Japan*, ²*New Industry Creation Hatchery Center (NICHe), Tohoku University, Sendai, Japan*, ³*Graduate School of Biomedical Engineering, Tohoku University, Sendai, Japan*, ⁴*Graduate School of Engineering, Tohoku University, Sendai, Japan***Background, Motivation, and Objective**

A line-focus-beam ultrasonic material characterization (LFB-UMC) system is suitable for the highly accurate, nondestructive, and noncontact measurement of the elastic properties of materials. It provides the velocities and normalized attenuation factor of leaky surface acoustic waves (LSAWs) excited on a water-loaded material surface. The normalized attenuation factor measured by the LFB-UMC system includes leakage loss into water because LSAWs propagate at the boundary between the water and the material while the acoustic energy of the waves leaks into water. Therefore, to evaluate acoustical loss using the LFB-UMC system, it is necessary to subtract the calculated leakage loss from the measured attenuation. We previously reported the possibility of evaluating acoustical loss by subtracting the calculated attenuation from the propagation loss of LSAWs using an amorphous Ta₂O₅ thin film deposited on 128°YX-LiNbO₃ with interdigital transducers (IDTs). In this study, we measured the phase velocity and normalized attenuation of LSAWs for a piezoelectric Ta₂O₅ thin film using the LFB-UMC system, and compared the measured values with calculated values.

Statement of Contribution/Methods

X-axis-oriented piezoelectric Ta₂O₅ thin films were deposited on synthetic fused silica glass substrates using an RF magnetron sputtering system with a long-throw sputter cathode and a metal Ta target. The deposition conditions used to obtain the films were gas flow rates (Ar:O₂) of 30:10 sccm, a gas pressure of 0.75 Pa, a substrate temperature T_S of 750 °C, and an RF power (Ta target and O₂ radicals) of 150 W. Ta₂O₅ thin films with thickness H of 1.8–7.0 μm were fabricated. The dependences of fH , which is the product of the thickness of the Ta₂O₅ thin film and the frequency of the phase velocity, and the normalized attenuation factor of LSAWs were measured using the LFB-UMC system in the frequency range from 100 to 300 MHz.

Results/Discussion

The measured phase velocity and normalized attenuation of LSAWs in the fH range from 180 to 2,100 Hz·m were in good agreement with the calculated results in the velocity range from approximately 2,340 to 2,920 m/s and in the normalized attenuation range from 0.015 to 0.052, respectively. On the other hand, for the high-order mode of LSAWs, the measured values were larger than those calculated using the reported constants. The difference between the measured and calculated values is considered to be due to the differences in the sputtering conditions because the elastic properties of the thin film strongly depend on the fabrication conditions. Thus, it is necessary to recalculate the material constants of the piezoelectric Ta₂O₅ thin film to evaluate the acoustical loss accurately.

The influence of negative ions generation on the arc-melted and hot press sintered ScAl alloy targets to the crystalline orientation and k_t^2 of the ScAlN films

Yuka Endo^{1,2}, Rei Karasawa^{1,2}, Shinji Takayanagi³, Makoto Imakawa⁴, Keisuke Morisaka⁴, Yu Suzuki⁴, Takahiko Yanagitani^{1,2,5}

¹Waseda University, Japan, ²ZAIKEN, Japan, ³Nagoya Institute of Technology, Japan, ⁴FURUYA METAL Co., Ltd., Japan, ⁵IST PRESTO, Japan

Background, Motivation, and Objective

ScAlN films have attracted much attention as FBAR material because of their high piezoelectricity. In previous studies, we reported degradation of the crystallinity due to the ion bombardment on ScAlN films during the sputtering growth [1]. Large amount of O⁻ and CN⁻ ions generation at sputtering target were observed. In this study, we compared the energy distributions of negative ions of arc-melted ScAl alloy target (oxygen: 900 ppm, carbon: 50 ppm) and hot press sintered ScAl alloy target (oxygen: 8000 ppm, carbon: 300 ppm) which have different oxygen and carbon concentration. The c-axis orientation and electromechanical coupling coefficient k_t^2 of ScAlN films fabricated with these different targets were also compared.

[1] S. Takayanagi and T. Yanagitani, 2016 IUS., (2016).

Statement of Contribution/Methods

The O⁻ and CN⁻ negative ion bombardment was measured during RF magnetron sputtering using an energy analyzer with Q-mass after the 70-90 min presputtering. Next, ScAlN thin films were prepared using these targets. The c-axis orientation of the films was determined by XRD rocking curve. The k_t^2 were determined by comparing the experimental and theoretical conversion losses of HBAR. The experimental conversion loss curves were measured by a network analyzer.

Results/Discussion

Fig. 1(a) and Fig. 1(b) show the ion energy distribution of O⁻ and CN⁻ during the sputtering growth, respectively. The O⁻ ion flux generated at sintered ScAl alloy target were much larger than that in the arc-melted ScAl alloy target probably because the oxygen concentration in the hot press sintered target (O: 8000 ppm) is higher than that of arc-melted target (O: 900 ppm). CN⁻ ion flux from arc-melted target was slightly larger than the sintered target despite of low carbon concentration compared to the arc-melted target. Although rocking curve FWHM of the ScAlN films grown by using two targets is almost similar, the peak intensity for sintered target was about 20 times higher than that for the arc-melted target. This shows that degree of crystallization of ScAlN films decreases with increasing of negative ion bombardments. No apparent differences were found in the k_t^2 between the two targets as shown Fig. 1(d). In conclusion, although oxygen concentration in the target affects the degree of crystallization, that in the does not significantly affect the resulting k_t^2 of the ScAlN films.

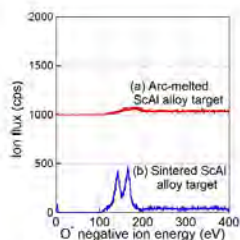


Fig. 1(a) Energy of O⁻ negative ion generated on the ScAl alloy target

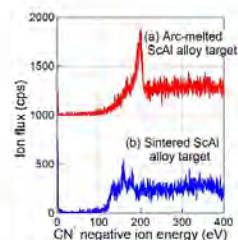


Fig. 1(b) Energy of CN⁻ negative ion generated on the ScAl alloy target

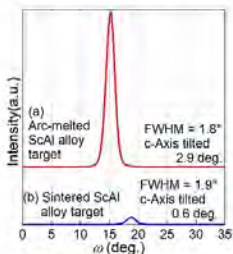


Fig. 1(c) X-ray rocking curves of ScAlN films

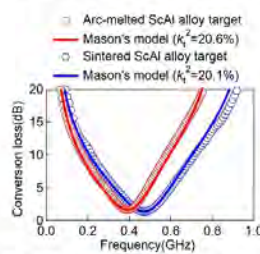


Fig. 1(d) Experimental conversion loss curves of ScAlN films

P2-C2 - PUM & PNR: Ultrasonic Devices and Non-Reciprocal Acoustics

Waraku (posters 2)

Thursday, October 25, 9:30 AM - 4:00 PM

Chair: **Yun Jing** North Carolina State University

P2-C2-1

High-power non-metal ultrasonic motor with an alumina vibrator

Jiang Wu¹, Yosuke Mizuno¹, Kentaro Nakamura¹

¹Tokyo Institute of Technology, Yokohama, Japan

Background, Motivation, and Objective

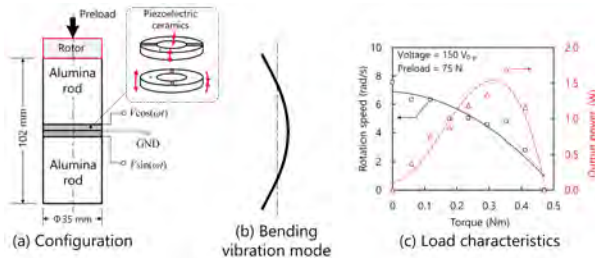
Recently, high-power actuators capable of working in acid/alkaline environment have become demanded in chemical industry and other use under severe atmosphere. Though ultrasonic motor (USM) is a possible candidate owing to high torque, good response, and simple structure, current USMs are inapplicable since their vibrators are made of metals. In this study, we attempt to substitute the metal part of USM with functional ceramics, and assessed their performance. In addition to the chemical resistance, functional ceramics have higher Young's modulus. Thus, ceramic/PZT vibrators are expected to provide higher force factors, which may lead to higher output powers as motors than metal/PZT ones.

Statement of Contribution/Methods

We employed a well-established bending rod structure. Two pieces of piezoelectric ceramic disks were sandwiched by two cylindrical alumina vibrating bodies with a bolt. When two sinusoidal voltages with a 90° phase shift were applied, two orthogonal bending vibration modes were excited on the vibrator. All points on the end vibrate elliptically, and drive the rotor via frictional force.

Results/Discussion

The load characteristics of the developed motor were measured under a voltage of 150 V and a preload of 75 N. The prototype motor yielded a maximum torque of 0.46 Nm and a maximum output power of 1.65 W, which were respectively 1.2 and 1.5 times the values of the metal-based motor operated in the same vibration mode. In addition, the motor prototype exhibited a maximum efficiency of approximately 15%, twice the value of the metal-based one since the alumina/PZT motor provided lower frictional loss.



A cylindrical ultrasonic vibration mixer for continuous flow chemical process

Kazuki Harita¹, Seren Miyake¹, Takefumi Kanda¹, Shuichi Wakimoto¹, Norihisa Seno¹, Shin-ichiro Kawasaki²

¹Graduate School of Natural Science and Technology, Okayama University, okayama, Japan, ²National Institute of Advanced Industrial Science and Technology, Japan

Background, Motivation, and Objective

A microreactor process that utilizes a microspace including a microchannel has various advantages such as energy efficiency and heat transfer efficiency improvement by carrying out chemical reaction in microspace. A micromixer is one of key components for the process. In such a mixer, blocking of the flow path and deterioration of the mixing performance become a problem depending on mixing conditions. We have fabricated a cylindrical type ultrasonic vibration mixer for high pressure fluid application and evaluated mixing performance.

Statement of Contribution/Methods

The designed and fabricated mixer is for a continuous flow process using supercritical fluid. Figure 1 shows a schema of the cylindrical ultrasonic vibration mixer. The mixer consists of two transducer blocks, four insulating plates and a housing. By using the housing, it is possible to mix fluids under a high temperature and high pressure environment. The mixer imparts ultrasonic vibration to the micro flow channel and generate a sound pressure distribution near the micro flow channel. It is possible to promote mixing by the sound pressure distribution and to prevent blocking of the flow path. We performed Villermaux-Dushman reaction to evaluate the mixing performance of the prototype ultrasonic mixer quantitatively.

Results/Discussion

Figure 2 shows the relationship between estimated absorbance and flow rate of solutions. The applied voltage and driving frequency were 100 V_{p-p} and 52.3 kHz. At the flow rate of 100 ml/min, the influence of the ultrasonic vibration on the optical absorbance is small. However, at the flow rate of 150 and 200 ml/min, the absorbance decreases. The result shows that we have succeed in obtaining the effective mixing performance in the higher flow rate condition by the ultrasonic vibration.

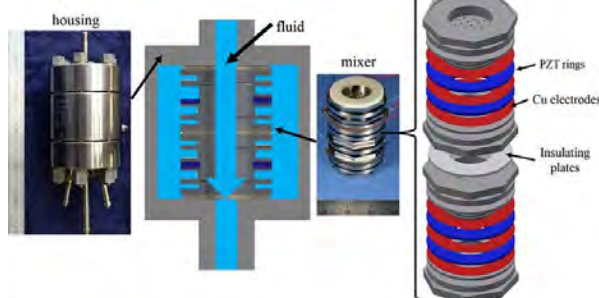


Figure 1 Schematic of the proposed mixer for a continuous flow chemical process

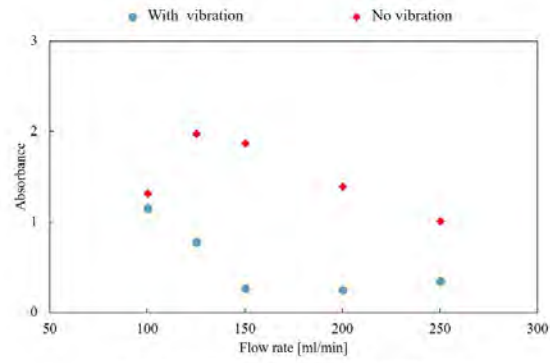


Figure 2 Relationship between estimated absorbance and flow rate for solutions when the applied voltage for the micromixer was 100V_{p-p}

A cryogenic rotary valve using bolt-clamped type transducerTakefumi Kanda¹, Taiki Yamada¹, Shuichi Wakimoto¹, Daisuke Yamaguchi²¹Okayama University, Okayama, Japan, ²Saitama University, Saitama, Japan**Background, Motivation, and Objective**

Recently, there is a demand for a flow rate control of low temperature fluid such as liquid hydrogen for hydrogen-fueled systems. In this study, a small rotary valve for a cryogenic fluid has been fabricated and evaluated. In past IUS conferences, we reported ultrasonic motors for cryogenic condition. In those studies, we succeeded in designing and driving the motor in cryogenic environment although a piezoelectricity of piezoelectric material decreases in cryogenic condition. In this study, we have applied the driving principle of the cryogenic ultrasonic motor to the flow rate control valve.

Statement of Contribution/Methods

Figure 1 shows the proposed rotary spool valve. A cylindrical spool is rotated by a deflection type transducer using PZT plates. The transducer is a bolt-clamped type, which has been designed and adjusted for cryogenic condition. The transducer and other parts are mainly made of SUS to avoid the thermal stress by temperature condition. The valve has a length and a diameter of 21 mm and 22 mm. By controlling the rotation speed, the flow rate can be controlled. To avoid the non-linear relation between applied voltage and rotation speed, the burst wave was used for the drive. In addition, to obtain precise positioning of rotation, the driving signal of burst wave was also switched periodically.

Results/Discussion

The valve has been successfully driven under the condition from 4.5 K to 300 K. The result of flow rate control experiment at 80 K is shown in Fig. 2. Liquid nitrogen was supplied at 20 kPa. The driving frequency and voltage were 79.0 kHz and 80 V. The switching duty ratio was changed from 1 to 3 %. The number of driving means the repetition time of drive for 0.1 s. By controlling the applied time of the burst wave, the flow rate has been successfully controlled using the proposed valve.

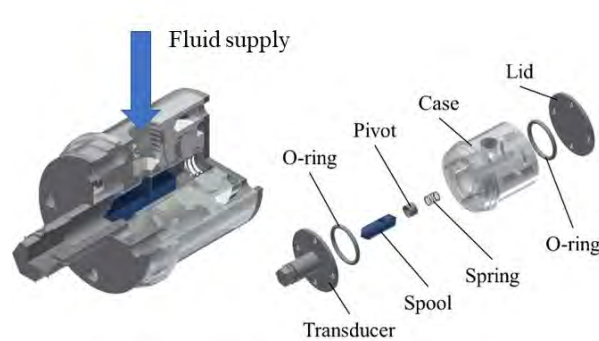


Fig. 1 Structure of the proposed cryogenic valve driven by bolt-clamped type transducer

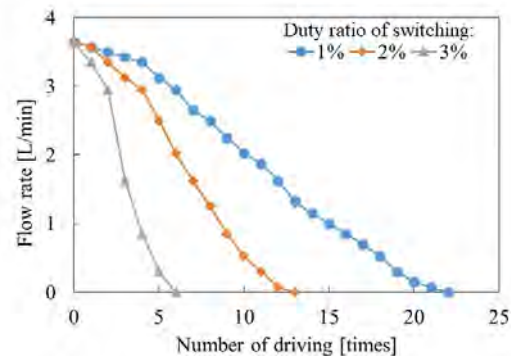


Fig. 2 Relationship between flow rate and driving number when the valve was intermittently driven at 80 K

Vibration Amplitude Modulation for Roughness Sensation Rendering with Ultrasound Vibration
Masaya Takasaki¹, Itaru Shimizu¹, Masayuki Hara¹, Daisuke Yamaguchi¹, Yuji Ishino¹, Takeshi Mizuno¹
¹*Dept. Mechanical Eng., Saitama University, Saitama, Japan*
Background, Motivation, and Objective

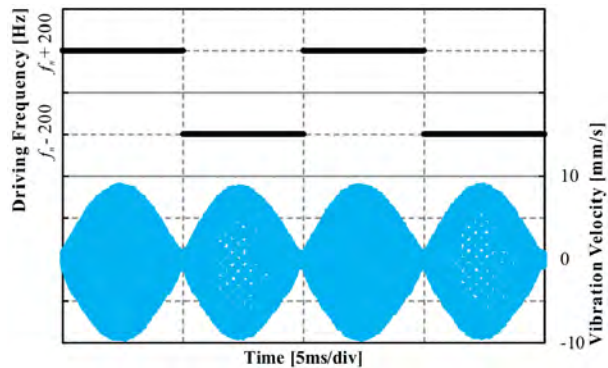
Presentation of human haptic sensation has lately attracted attentions for various fields, such as remote control of robots, tablet type terminals and so on. We focused on reproduction of roughness sensation. Previously, a method to provide human tactile sensation with friction reduction caused by ultrasonic vibration was proposed. During rubbing motion on the vibrating surface, friction between the fingertip and the surface can be reduced. Amplitude-modulated ultrasonic waves cause periodic friction fluctuations and can be recognized as a roughness sensation. When modulation depth and frequency are changed, the roughness sensation can also be changed. On the other hand, it is difficult to realize the modulation with high quality factor ultrasonic transducers like a Langevin type transducer, because settling time of vibration amplitude is longer in case of high quality factor. To solve the long settling time problem, we have proposed a novel method to maintain the modulation and its frequency even with high mechanical quality factor of the ultrasonic transducer.

Statement of Contribution/Methods

Driving the transducer at an off-resonance frequency, a beat can be induced in the transducer during transient response. The ultrasonic transducer can be modeled as a damped spring-mass model. Just after start of driving at the off-resonance frequency, impulse response vibration at the natural frequency of the model and transient response of forced oscillation at the driving frequency are induced in the transducer simultaneously. As a result, their beat is observed during the impulse response remains, then no beat is found as the impulse response is damped. To keep the beat, it is needed to repeat the beat at the transient response. For the repeat, the frequency of the driving voltage was switched (frequency modulation) at certain intervals.

Results/Discussion

The driving frequency was modulated as $f_n + f_b$ or $f_n - f_b$, where f_n and f_b are natural frequency of the transducer and beat frequency, respectively. These frequencies were modulated at the interval of $T_b = 1/f_b$. A sample ultrasonic transducer was prepared as a coupling of a Langevin type transducer and a horn to enhance the quality factor of the coupled transducer. Vibration amplitude was observed by a laser Doppler velocity meter. Vibration velocity, namely amplitude, modulated at 200 Hz was successfully observed.



An ultrasonic motor with 2 mm in rotor diameter using transmission line and a spring washer driven by a Langevin transducer.

Keishu Hosokawa¹, Takaaki Ishii¹, Tsuyoshi Shimizu¹

¹University of Yamanashi, Kofu, Japan

Background, Motivation, and Objective

In our conventional research, the outer diameter of the rotor using transmission line was 5 mm. Since the diameter of the endoscope forceps is around 2 mm, small sized rotor is needed for that applications. Also, if the diameter of the transmission line is reduced, the flexibility can be improved. In this research, we are aiming at manufacturing an ultrasonic motor with 2 mm in rotor diameter using transmission line, and measuring basic characteristics of the proposed motor.

Statement of Contribution/Methods

The driving vibration excited by the Langevin transducer is amplified by the stepped horn and travelled through the thin transmission line of 1 mm in diameter (figure 1). A spiral structure is used to convert the vibration mode as shown in figure 2. A spring washer is used for mode conversion and preload is provided by this spring washer at the same time. The outer diameter of the spring washer is 2.1 mm. The preload by the spring washer is about 10 N.

Results/Discussion

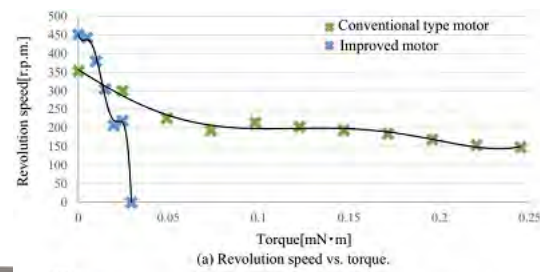
Voltage of 50 Vp-p was applied to the Langevin transducer. When using a transmission line with 1 mm in diameter, the maximum revolution speed and the maximum efficiency were 451.3 r.p.m. and 0.064 %, respectively. And, when using a transmission line with 0.5 mm in diameter, the maximum revolution speed and the maximum efficiency were 109.1 r.p.m. and 0.586 %, respectively.



Fig. 1 Picture of the ultrasonic micro-motor with a spring washer.



Fig. 2 Picture of comparing tip structures.



(a) Revolution speed vs. torque.

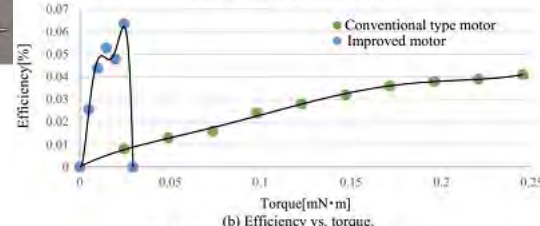


Fig. 3 Load characteristics of the proposed motor.

Modeling and Experimental Study on the Current Harmonics of a High Power Ultrasonic Motor
Xiaoniu Li¹, Zhiyuan Yao¹, Dawei Wu¹
¹*State Key Laboratory of Mechanics and Control of Mechanical Structures, Nanjing University of Aeronautics and Astronautics, China, People's Republic of*
Background, Motivation, and Objective

The high power ultrasonic motors have been widely used in micro-positioning, semiconductor manufacturing and biomedical applications. However, they tend to appear nonlinear behaviors under the high voltage and the high stress working condition. In particular, the current harmonics of the motors pose challenges to efficiency improvement, temperature control, and the development of the driving circuit. Therefore, it is necessary to study their current harmonics and to develop an efficient model to predict their nonlinear behaviors.

Statement of Contribution/Methods

To measure steady-state current of a high power ultrasonic motor, an experimental setup was developed. The setup was composed of a signal generator, a power amplifier, an oscilloscope, a current sensor, and a V-shape high power ultrasonic motor. The voltage current of the motor were collected for spectrum analysis. The relation between the motor driving voltage and its corresponding current harmonics was investigated. A novel equivalent circuit model, which consists of a nonlinear capacitance, was proposed to simulate the nonlinear behavior of the ultrasonic motor. Parameters of the proposed model were identified by the least square method.

Results/Discussion

The experimental results show that the major contents of the current are the first, the second harmonics and the DC component, and the third and higher harmonics can be negligible. The first current harmonic increases with the raising of the voltage until saturated while the second harmonic current continues to increase rapidly, as shown in Fig. 1(a). The simulation results based on the proposed model agree well with experimental results, as shown in Fig. 1(b). The proposed model is capable to predict the current harmonics of high power ultrasonic motors, and is helpful in the driving circuits design of high power ultrasonic motors. Furthermore, this model is also capable to simulate the current harmonics of the piezoelectric transducers, transformers and actuators driven under high power.

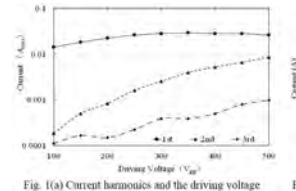


Fig. 1(a) Current harmonics and the driving voltage

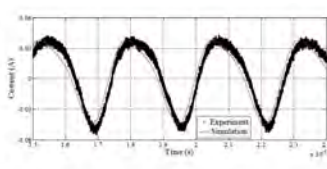


Fig. 1(b) Simulated and experimental currents of an ultrasonic motor

Numerical Simulation of Non-reciprocal Acoustic Waveguide based on Indirect Interband Transitions**Junyi Ge¹, Atsushi Ishikawa¹, Kenji Tsuruta¹**¹*Electrical and Electronic Engineering, Okayama University, Okayama, Japan***Background, Motivation, and Objective**

Recently non-reciprocity in acoustic-wave propagation has been extensively studied. Although practical levels of one-way acoustic isolation were achieved in those systems, they still suffer from several drawbacks including high input energy and limited bandwidth. To improve those, we designed a non-reciprocal acoustic waveguide using indirect interband transition between two guided modes. By applying spatio-temporal density modulation, the mirror symmetry of the dispersion relations will achieve the one-way mode conversion. Since our approach is based on a linear dynamic system, high efficiency can be achieved with wide-band tunability. Practical device implementation for wide-band tunable operation can be proposed via the tolerance analyses for the phase matching condition.

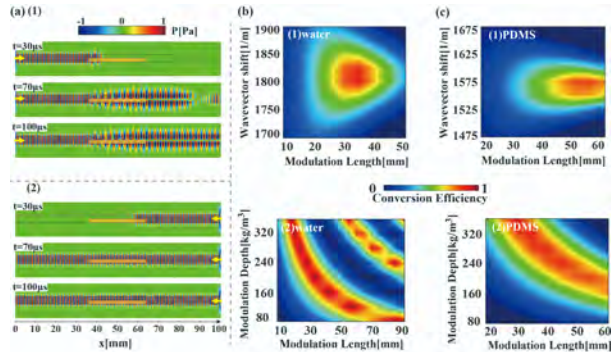
Statement of Contribution/Methods

We have recently proposed a non-reciprocal acoustic device based on an indirect interband transition by applying space-time density modulation in a two-dimensional acoustic waveguide formed by a water core sandwiched by metal claddings [1]. By performing a series of the Finite Difference Time Domain (FDTD) simulations, we demonstrated the non-reciprocity of wave propagation and obtained optimum parameter sets of the modulation length and the wavevector shift. To further optimize the present model toward practical applications, we extend the model to the waveguide with the core filled with a solid medium and search for its optimum matching conditions for the mode transition.

Results/Discussion

Figure (a) shows the time evolutions of the acoustic wave propagation in the waveguide with water core for the forward and backward incident wave of $m=0$ mode. In the calculation, modulation frequency $\Delta f = f_1 - f_0 = 0.1$ MHz and wavevector $\Delta\beta = \beta_0 - \beta_1 = 1810 \text{ m}^{-1}$ were used for the transition from the $m=0$ to $m=1$ mode. Figure (b) shows the mode conversion efficiency as functions of the modulation length, wavevector shift, and modulation depth. Figure (c) depicts the mode conversion achieved in the system with a Poly Dimethyl Siloxane (PDMS) core using the same modulation frequency as the water core. The optimum parameter sets are obtained from the figures, and they thus prove that the present design principle is applicable to the solid-state devices.

[1]A. Ishikawa and K. Tsuruta, Jpn. J. Appl. Phys. **57**, 07JB01, 2017.



Design of Non-reciprocal Lamb Wave Filter by Heterojunction Phononic Crystals
Kenji Tsuruta¹, Shota Asada¹, Yuhei Iwasaki¹, Atsushi Ishikawa¹
¹*Electrical and Electronic Engineering, Okayama University, Okayama, Japan*
Background, Motivation, and Objective

Acoustic diode has been attracting much attention recently as a means of achieving high efficiency for noise insulation and/or as an energy harvester which transforms vibrational energy in environment to electricity. Various types of rectification mechanisms have been proposed; a method for rectification by using phononic band gap and second harmonic wave generated by nonlinear medium, and a method for realizing theory of topological insulator (in which edge states propagate only in one direction) by using the acoustic structure including circulating fluid. Most of the models realize the rectification via asymmetry in time and space given by applying external fields such as fluid flow in the media and external biases in the system. However, these models require complex structures which hamper miniaturization of the device for further applications.

Statement of Contribution/Methods

In the present study, we design a new acoustic diode model, based on a one-dimensional structure consisting of piezoelectric ceramic films placed periodically in an epoxy plate. Specifically, the model is designed to exhibit an efficient rectification effect in the audible and ultrasonic range. Our model includes no artificial forces to generate the asymmetry in the system but utilizes a mode conversion of elastic-wave propagation at an interface.

Results/Discussion

We have previously proposed a non-reciprocal phononic model and demonstrated numerically that the model can achieve efficient rectification at a particular frequency range for both S-mode and A-mode incidence of the Lamb wave (Fig.1) [1]. We further attempt to develop an additional model that can suppress unwanted backward propagation due to a large mismatch at the heterjunction interface.

[1] Y. Iwasaki, K. Tsuruta, and A. Ishikawa, Jpn. J. Appl. Phys. 55, 07KB02 (2016).

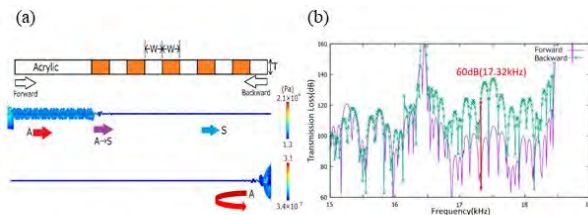


Fig. 1 (a) A-mode non-reciprocal transmission model and (b) its transmission property.

P2-C3 - Volume and 2D/3D Flow Imaging

Waraku (posters 2)

Thursday, October 25, 9:30 AM - 4:00 PM

Chair: Charlie Demené INSERM

P2-C3-1

4D Ultrasensitive Doppler monitoring of in situ thromboembolic stroke and reperfusion using tissue-type plasminogen activator in mouse model

Vincent Hingot¹, Camille Brodin², Cyrille Orset², Denis Vivien², Mickaël Tanter¹, Olivier Couture¹, Thomas Deffieux¹

¹Institut Langevin, ESPCI Paris, PSL Research University, CNRS UMR 7587, INSERM U979, PARIS, France, ²Université de CAEN, UMR CNRS 6551, Bd H. Becquerel, Cycles, BP 5229, F-14074 CAEN, Cedex, France, France

Background, Motivation, and Objective

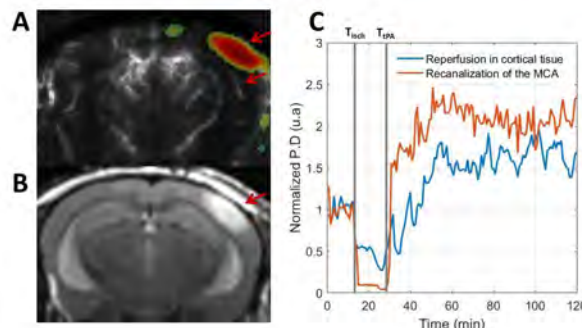
Early reperfusion using tissue-type plasminogen activator (tPA) is the only therapeutic agent to treat focal cerebral ischemia with proven efficacy in humans. Although transcranial Doppler sonography is already used to assess stroke in patients, the gold standard for cerebro-vascular pathologies for both preclinical and clinical cases remains MRI imaging. Preclinical Ultrafast Doppler may offer similar or better spatial and temporal resolution and we wish to demonstrate its application to monitor thromboembolic stroke and reperfusion in mouse model and its ability to perform hour long acquisitions through an intact skull, while imaging the whole brain every 20s, with a spatial resolution of 100 mm.

Statement of Contribution/Methods

Injection of thrombin was used to trigger a local clot formation in anesthetized mice. Ultrafast Doppler of the whole brain was done using 2D scanning over 15 coronal planes distant of 0.4 mm every 20 second. Scanning was performed for 20 minutes before and for 2 hours following the thrombin injection. 20 minutes after the formation of the clot, 200 mL of tPA were injected intravenously over 40 min. Mice were allowed to wake up and another 20 minute scanning was performed after 24 hours. Ischemia was segmented on ultrasensitive Doppler images as the difference in Doppler intensity on images before and after the focal ischemia (**A**) and on high resolution T2 MRI images after 24 hours (**B**). Seed based methods enabled the differentiation between recanalization of descending branches of the middle cerebral artery and reperfusion of the cortical tissue (**C**). Acquisitions performed at a fast frame rate enabled the observation of fast transitory phenomenon.

Results/Discussion

Volume of lesion was estimated around 12 mm³. Estimations of reperfusion and recanalization times were performed as well as a comparative study between spontaneous reperfusion and reperfusion following the injection of tPA. Ultrafast Doppler is a reliable preclinical imaging method to image fast hemodynamic changes in the whole rodent brain and could be a very useful tool for preclinical studies of various cerebro-vascular disorders both to understand recovery mechanisms and to quantify the efficiency of treatments.



3D Flow Reconstruction and Wall Shear Stress Evaluation with 2D Ultrafast Ultrasound Particle Imaging Velocimetry

Xinhan Zhou¹, Xiaowei Zhou², Chee Hau Leow², Peter Vincent², Mengxing Tang²

¹Department of Bioengineering, Imperial College London, London, United Kingdom, ²Imperial College London, London, United Kingdom

Background, Motivation, and Objective

3D full field intravascular flow quantification is challenging and valuable for atherosclerosis study but currently there is a lack of effective clinical tools for this purpose. Ultrafast Ultrasound Imaging Velocimetry (UIV) with microbubbles is a minimally invasive technique capable of characterising 2D intravascular flow with high accuracy (error <10%) and high frame rate (HFR, >1000 fps). However ultrafast UIV is limited to estimating 2D velocity field.

In this study, a new algorithm for fast/accurate 3D flow and wall shear stress (WSS) reconstruction was proposed by divergence free interpolation based on sparse 2D velocity obtained by UIV at different planes/angles of the flow domain.

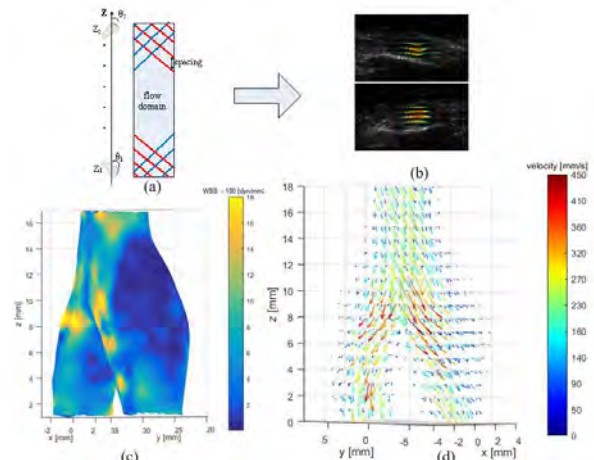
Statement of Contribution/Methods

Microbubble contrast enhanced HFR ultrasound plane wave B-mode data, acquired by a L12-3v linear array probe, was used for 2D in-plane UIV velocity mapping of a carotid artery bifurcation phantom with a steady flow. An automatically motorized stage was chosen to control the transducer to scan multiple planes (two sets of parallel equal-interval scanning planes with 90° rotation and 3 mm spacing, shown in Fig. 1a) for the UIV estimations. After 2D acquisition 3D flow velocity of the flow domain is reconstructed by a sum of weighted divergence free basis which captures the incompressible physics of fluids. The weight coefficient of the divergence free basis is found by minimizing error between 2D UIV velocity and projection of 3D velocity and suppressing the effect of measurement error.

Comparing to previous methods which require 3D data samples to reconstruct the flow field, the new approach only requires 2D data, making this applicable for currently available clinical probes. The method is compared with Computational Fluid Dynamics (CFD) on the same flow phantom.

Results/Discussion

In plane velocity acquired by UIV is shown in Fig. 1 (b). The reconstructed velocity field and WSS are shown in Fig. 1 (c) and (d). The method is mesh-free, does not require fluid properties such as viscosity or even the full geometry to be known. It is computationally efficient, typically an order of magnitude faster than CFD in a range of problems (< 10 minutes including UIV acquisition), and can achieve high accuracy (relative error < 15% compared with CFD). *In vitro* results from the flow phantom demonstrate its applicability to fast and accurate physiological flow reconstruction.



3D coronary blood flow imaging: A comparison of automatic adaptive clutter filter algorithmsCristiana Gofetto^{1,2}, Jørgen Avdal^{1,2}, Hans Torp^{1,2}, Ingvild Kinn Ekroll^{1,2,3}¹*Department of Circulation and Medical Imaging, NTNU, Norway*, ²*Centre for Innovative Ultrasound Solutions (CIUS), Norway*,³*St Olavs Hospital, Norway***Background, Motivation, and Objective**

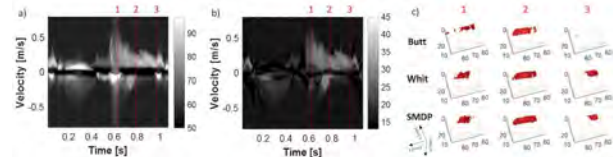
Ultrasound imaging may be used to assess blood flow in the coronary arteries, which supply the heart muscle with oxygen and nutrients. However, Doppler measurements are challenging due to the presence of strong tissue signal overlapping with the blood flow signal. In this work, we aim to improve detection of coronary artery blood flow by using a combination of 3D high frame rate ultrasound imaging and adaptive eigen-based clutter filtering. Two automatic methods are suggested: whitening filter and similarity matrix diagonal projection (SMDP).

Statement of Contribution/Methods

A locally modified commercial scanner (GE-Vingmed Vivid E95, GE 4V-D matrix array probe) was used for continuous high frame rate acquisition of 3D channel data from left anterior descending coronary artery (LAD, 8383 fps) and left circumflex artery (LCX, 6074 fps) of healthy volunteers. When using the whitening filter, the original signal is multiplied by the square root of the reciprocal of the signal covariance matrix estimated from the whole region of interest, resulting in suppression and whitening of the clutter signal. The SMDP filter is based on the assumption that blood and clutter have different spatial distributions. The elements of the similarity matrix described in Baranger et al. (2018) were weighted and projected onto the diagonal, yielding the SMDP curve. The last peak of the SMDP corresponds to a blood eigenvector, and three eigenvectors around this peak were used. A standard Butterworth filter with cut-off velocity 0.08 m/s was used for comparison.

Results/Discussion

Figure 1 a) shows a sonogram from the LCX after applying the Butterworth filter. In parts of the cardiac cycle, rapid tissue motion results in clutter sidelobes interfering with the blood signal. In the sonogram after whitening filter in Figure 1 b) the spectral leakage of clutter is reduced significantly. Figure 1 c) displays 3D power Doppler images in early (1), middle (2), and late diastole (3). In (1) and (3) the coronary is not visible using Butterworth filter, whereas detection is possible after whitening filtering and SMDP. Using specificity of 99%, blood sensitivity at (1) is equal to 55%, 99%, and 98%, while at (3) it is 45%, 76%, and 75% after Butterworth, whitening and SMDP filter respectively.



3D velocity and volume flow measurement using speckle decorrelation and high frame rate contrast-enhanced ultrasound

Xiaowei Zhou¹, Chee Hau Leow¹, Ethan Rowland¹, Kai Riemer¹, Jonathan Rubin², Peter D. Weinberg¹, Mengxing Tang¹

¹Department of Bioengineering, Imperial College London, London, United Kingdom, ²Department of Radiology, University of Michigan, United States

Background, Motivation, and Objective

Being able to measure 3D flow velocity and volumetric flow rate in the cardiovascular system is valuable but remains a significant challenge. Currently there has not been an effective and practical solution to volume flow measurement with ultrasound imaging systems due to challenges in existing 3D imaging techniques and high system cost. In this study, a new technique for quantifying volumetric flow rate was developed with a standard 1D linear array transducer, by employing speckle decorrelation, 2D plane wave high frame rate contrast-enhanced ultrasound imaging and ultrasound imaging velocimetry(UIV).

Statement of Contribution/Methods

Through decorrelation analysis of 2D non-compounded B-mode images, the overall flow velocity magnitude can be estimated and resolved temporally and spatially; then by using UIV to estimate two in-plane velocity components, the out-of-plane velocity component can be obtained and integrated to estimate volume flow. The proposed technique was evaluated on a wall-less flow phantom (steady flow) by scanning the cross-section of the vessel with a L12-3 probe (centered at 8 MHz) and the research platform from Verasonics VantageTM. UIV in the longitudinal direction was conducted to obtain a velocity reference, and timed-collection was used to obtain a flow rate reference. The influences of frame rate (FR) and mechanical index (MI) on velocity estimation were also studied. In addition, an *in vivo* trial of the proposed method was conducted on the abdominal aorta of a rabbit; experiments complied with national and local regulations. Both the UIV technique and an invasive catheter were used to measure the velocities at the same site in the rabbit's aorta for comparison.

Results/Discussion

The proposed method can estimate volume flow with an averaged error of about 5% under physiological flow rates, and an imaging frame rate of 6000 Hz. The corresponding velocity estimates are shown in Figure 1a. A lower frame rate (2000 Hz) was found to significantly underestimate the flow rate, while a high MI (about 0.40) produced significant errors in flow estimation due to the destruction of bubbles. In conclusion, the proposed method can generate accurate estimates of volumetric flow, using a standard 1D linear imaging probe. *In vivo* flow velocities up to 1 m/s were correctly measured (Fig 1b), demonstrated the potential of the technique in clinical applications.

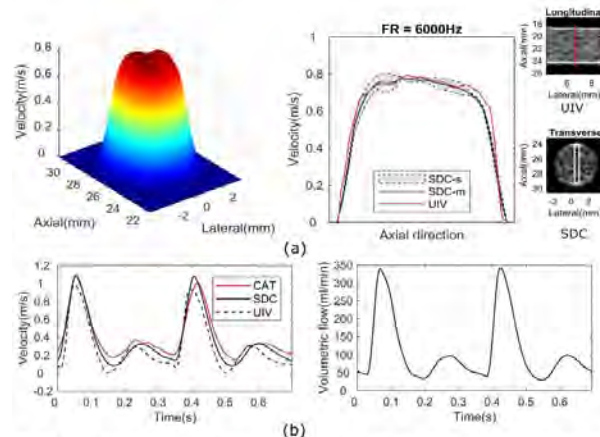


Figure 1. In vitro and in vivo results: (a) in vitro. On the left, the 2D velocity profile in the out-of-plane direction. In the middle, velocity profile along a line across the center of the vessel from UIV and SDC where SDC-m curve is mean profile obtained from a 1-mm wide white box shown in the lower-right picture, and SDC-s area is the standard deviation, and UIV curve is from the red line shown in the upper-right picture. (b) in vivo. On the left, maximum velocities measured from abdominal aorta with different methods. SDC curve is the mean value located within a 1-mm square area in the center of the aorta in transverse view, and UIV curve is the mean value within a 1-mm square area crossing the center of the aorta in the longitudinal view, and CAT curve is from the invasive catheter. On the right, the volumetric flow rate over the aorta calculated from the SDC method. SDC represents speckle decorrelation; UIV represents ultrasound imaging velocimetry; CAT represents catheter.

Volumetric Color Flow Mapping using a Row-Column Array**Jørgen Jensen¹, Lasse Thurmann Jørgensen¹, Kseniya Chetverikova¹, Matthias B. Stuart¹**¹*Technical University of Denmark, Lyngby, Denmark***Background, Motivation, and Objective**

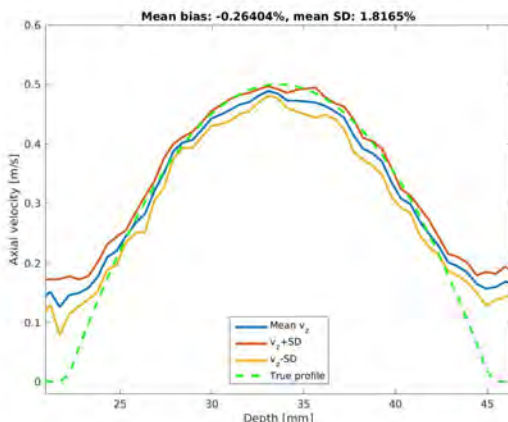
Volumetric color flow mapping (CFM) is currently performed using matrix probes with up to 9,000 elements. ECG gating is employed to cover a large region of e.g. the heart, and this lowers the volume rate. The many elements necessitate use of highly specialized and expensive probes with dedicated electronics. This paper demonstrates that row-column (RC) arrays can provide volumetric CFM with 23 times lower number of elements without ECG gating.

Statement of Contribution/Methods

Volumetric imaging is conducted by emitting a focused field using the column elements and receiving with all row elements in parallel. The imaging lines in the selected slice are then beamformed in parallel. This is repeated N times and velocities are estimated for all the beam directions in the slice. The next slice is excited and the processing is repeated. A 192 + 192 linear RC array with $\lambda/2$ pitch and a center frequency of 3 MHz was simulated in Field II for a vessel with radius 6 mm and parabolic flow with peak velocity 1 m/s at a beam-to-flow angle of 60° and placed at a depth of 65 λ . Sixty-four elements for an F-number of 2 were used in transmit and all 192 transducer elements were active in receive. Beamformation using a sliding aperture with 64 elements yielded 129 imaging lines for one slice, where the axial velocity was estimated in parallel for all lines using $N=8$ emissions and a cross-correlation estimator. Thirty-two imaging planes with a pitch of 2 λ was used for covering the full rectilinear volume equal to 33 x 33 x 100 mm for a pulse repetition frequency of 7.7 kHz. This yields a volume rate of 30 Hz.

Results/Discussion

The lateral Full Width Half Max resolutions obtained were 2.34 λ (1.20 mm) in the transmit plane and 2.12 λ (1.09 mm) in the receive plane when beamforming at the center of the aperture. Beamforming at a position of $(x, y) = (30\lambda, 30\lambda)$ gave resolutions of 2.08 λ (1.07 mm) in y and 2.15 λ (1.10 mm) in x demonstrating that a uniform resolution is obtained in the full volume. The velocities were estimated for 10 profiles at the center of the aperture. Fig. 1 shows the measured mean velocity profile ± 1 standard deviation (SD) along with the theoretical profile. The relative bias compared to the peak velocity was -0.26% and the mean SD was 1.81% for the central 90% of the profile to exclude edge effects from echo canceling. This demonstrate that full volumetric CFM can be attained with RC arrays at 30 volumes/s down to 10 cm.



Relative blood volume estimation from clinical super-resolution US imaging in breast cancer

Stefanie Dencks¹, Marion Piepenbrock¹, Tatjana Opacic², Barbara Krauspe³, Elmar Stickeler³, Fabian Kiessling², Georg Schmitz¹

¹*Department of Electrical Engineering and Information Technology, Ruhr-Universität Bochum, Bochum, Germany*, ²*Institute for Experimental Molecular Imaging, RWTH University Clinic Aachen, Aachen, Germany*, ³*Department of Obstetrics and Gynecology, RWTH University Clinic Aachen, Aachen, Germany*

Background, Motivation, and Objective

In [1] we demonstrated the feasibility of applying super-resolution US imaging in a clinical set-up. However, pronounced motion and a non-optimized microbubble (MB) injection scheme reduced the length of evaluable sequences for the estimation of the clinically relevant *relative blood volume* (rBV). To estimate the degree of reconstruction of the microvasculature for these sequences and to predict the rBV, we apply the saturation model proposed in [2] to the clinical data. It assumes, that the reconstruction of new vessels saturates to the full vessel tree over measurement time. This model is also used to assess the measurement times needed for a reliable rBV prediction and to define objective criteria for the quality of measurements.

Statement of Contribution/Methods

Examinations (2 measurements for each timepoint) were performed before, and after the 1st, 2nd, and 3rd cycle of a breast carcinoma chemotherapy. CEUS measurements were acquired with a Toshiba Aplio 500 (Canon Medical Systems, Otawara, Japan) equipped with a 10 MHz PLT 1005BT linear transducer. After the slow injection of 0.5 ml of SonoVue (Bracco, Milan, Italy), in each measurement 1350 B-mode and contrast mode images were recorded with a frame rate of 15 Hz. An affine image registration [3] was applied to the B-mode images for the motion estimation. The MB positions were detected in the contrast mode images and corrected by the estimated motion. The tracking was carried out with a probabilistic tracking algorithm [4]. Furthermore, the established *maximum-intensity-over-time (MIOT)* images were calculated. Then, the saturation model successfully applied in preclinical experiments [2] was fitted to the tracking and to the MIOT data, and the saturation value rBV_{final} , the *percentage of reconstruction pR*, and the *quality of fit R²* were calculated.

Results/Discussion

After 90 s acquisition time, the filling was between $pR = 29\%$ and 50%. A reliable prediction of rBV_{final} would have been already possible after 20 s to 75 s. To reconstruct 90% of the microvasculature, between 180 s and 350 s would have been necessary. However, these times could be substantially reduced with an optimized MB injection scheme. The correlation between the rBV derived from MIOT and from tracking was high ($r^2 = 0.85$), although MIOT strongly overestimated the rBV. We further found $25\% \leq pR, R^2 \geq 0.98$ and a stabilization of the rBV_{final} for increasing acquisition times, to be suitable criteria for the assessment of the measurements. Generally, the vessel maps derived from MB tracking give a much better impression of the organization and the complexity of the vascularization.

[1] Opacic et al., Nat. Commun., 2018.

[2] Dencks et al., IUS 2017.

[3] Rueckert et al., IEEE Trans. Med. Imag., 1999.

[4] Ackermann and Schmitz, IEEE TUFFC, 2016.

The use of ultrasound Doppler in Dentistry: pulpal blood flow measurement and its clinical advantage over electric pulp tester.Dohyun Kim¹, Sungho Park¹¹*Conservative Dentistry, Yonsei University, Dept. of Conservative Dentistry, Seoul, Korea, Republic of***Background, Motivation, and Objective**

The assessment of pulp vitality and evaluation of the necessity for root canal treatment are among the most important procedures in treating traumatized teeth.

The most common pulp testing methods are thermal tests and the electrical pulp test (EPT). However, these are indirect testing methods that rely on the subjective sensibility of patients. The precise status of the pulp cannot be determined based on these sensibility tests alone, particularly in immature teeth, traumatized teeth, teeth with a chronically inflamed pulp, and teeth in patients who have lost sensory function after orthognathic surgery. Temporary loss of sensory response in teeth is caused by injury, inflammation, pressure, or tension on the nerve fibers in the apical area. Therefore, it is preferable to use a method to directly measure the pulpal blood flow.

Ultrasound Doppler (UDF) is a noninvasive and radiation-free technique used to assess blood flow by transmitting ultrasound to the tissues (6). However, its application to dentistry has been restricted due to high impedance, hard and slippery small nature of teeth. However, Our team has reported the successful application of UDF in measuring the blood flow in teeth *in vivo*. Recently, UDF was demonstrated to be an effective tool in measuring pulpal blood flow velocity by means of a microfluidic-based pulpal arteriole blood flow phantom. The first purpose of this presentation is to share our ideas on UDF application in dentistry. The second purpose is present our recent research to compare the ability of EPT and UDF in determining pulp vitality of traumatized teeth, and to evaluate the influence of these 2 methods on the decision-making for root canal treatment in traumatized teeth.

Statement of Contribution/Methods

A total of 246 teeth in 78 patients who visited our hospital with histories of dental trauma between February 2012 and May 2015 were included. Patients were divided into 2 groups based on the diagnostic methods used to determine pulp vitality during follow-ups. In Group 1, EPT alone was used to assess pulp vitality, whereas in Group 2, both UDF and EPT were used. Kaplan-Meier survival analysis was performed following propensity score matching. Survival was defined as the tooth not having to undergo root canal treatment. Differences between the survival graphs were tested using the log-rank test. Additionally, the McNemar test was used to compare the results of UDF with those of EPT in Group 2.

Results/Discussion

After propensity score matching, 69 teeth were included in each group. The survival rate of Group 1 was 74% at 1 year. The survival rate of Group 2 was 90% at 1 year. The survival rates of Group 1 and 2 were significantly different ($p=0.005$). In Group 2, there was a significant difference between the UDF and EPT results at all follow-up periods.

Acknowledgements This work was supported by the National Research Foundation of Korea (NRF) grant funded by the Korea government (MSIP) (NRF-2017R1A2B2003751).

Functional ultrasound imaging in the non-human primate posterior parietal cortex during a memory-guided saccade task

David Maresca¹, Vasileios Christopoulos¹, Sumner Norman¹, Charlie Demené², Thomas Deffieux², Richard Andersen¹, Mickaël Tanter², Mikhail Shapiro¹

¹*California Institute of Technology, United States, ²Institut Langevin, ESPCI Paris, PSL Research University, CNRS UMR 7587, INSERM U979, France*

Background, Motivation, and Objective

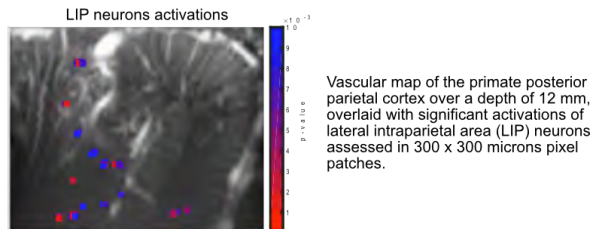
Functional ultrasound imaging (fUS) is a recent technology that provides a unique combination of spatial coverage (several cm), spatiotemporal resolution (< 100 µm and 10 ms) and compatibility with freely moving animals. However, most of the previous fUS studies have focused predominantly on small animals (e.g., rodents) leaving open the question of whether fUS is capable of monitoring brain activity in larger organisms such as non-human primates (NHPs). Here, we examined the capabilities of fUS in a NHP by imaging the left intraparietal sulcus in which patches of neurons are responsible for planning eye movements to memorized target locations.

Statement of Contribution/Methods

fUS imaging (750 Hz framerate after coherent compounding, 1 Hz fUS framerate) was performed with a programmable ultrasound system connected to a 15 MHz linear array probe inserted in a custom-designed square chamber (24 mm width) over the left intraparietal sulcus (IPS). The animal was trained to perform memory-guided saccades to a single target presented either in the left or in the right visual field. Each trial started with the animal fixating at a central cue for 6 s before a single target was presented in the peripheral visual field for 300 ms. The animal had to memorize the location of the briefly flashed target for 10 s while maintaining eye fixation. When the central fixation cue was extinguished, the animal had to perform an eye movement to the remembered target location to receive a liquid reward.

Results/Discussion

By acquiring fUS images with a 1 s temporal resolution over the IPS, we found that the Doppler signal in the lateral intraparietal area (LIP) – an area that is involved in planning of eye movements – was higher during the memory-period for contralateral than for ipsilateral eye movements. No changes on the Doppler signal were found during the eye-fixation period prior to the target flash. This result suggests that fUS is capable of capturing the preparatory motor signal in LIP that precedes the motor response (i.e., eye movement) in a memory-guided saccade task (see figure). Our findings provide direct evidence that fUS is capable of measuring an accurate readout of regional brain activity in cortical regions in awake and behaving NHPs, opening a new avenue in non-invasive functional neural imaging.



3D Printed Flow Phantoms with Fiducial Markers for Super-Resolution Ultrasound Imaging

Martin Lind Ommen¹, Mikkel Schou², Rujing Zhang¹, Carlos Villagomez-Hoyos³, Jørgen Arendt Jensen², Niels Bent Larsen¹, Erik Vilain Thomsen¹

¹Nanotech, Technical University of Denmark, Kgs. Lyngby, Denmark, ²Center for Fast Ultrasound Imaging, DTU Elektro, Technical University of Denmark, Lyngby, Denmark, ³BK Ultrasound, Herlev, Denmark

Background, Motivation, and Objective

Super-resolution ultrasound imaging (SRI) has provided an order of magnitude increase in the imaging resolution. This improvement sets new demands for the fabrication of phantoms. To properly resemble tissue, phantoms should replicate the 3D nature of tissue vasculature. This can be attained through 3D printing of polymers.

As phantom features become smaller, proper alignment of the ultrasound probe to the phantom becomes increasingly more difficult. Figure a) shows an SRI image of micro-bubble flow through the channel of a 3D printed phantom. The inserted color wheel indicates the flow direction. Fewer detected bubbles are observed through the top channel. This may be due to channel misalignment. The objective of our work is to 3D print phantoms for SRI with integrated fiducial markers, which can be used for accurate positioning of the probe to the phantom.

Statement of Contribution/Methods

We present a method for 3D printing phantoms for SRI using a custom built stereolithographic printer assembled at DTU Nanotech, which uses a 365 nm LED light source. Projected light of the desired patterns converts an aqueous PEGDA polymer solution into a hydrogel, a material which acoustically resembles tissue. Within this polymer, fiducial markers can for instance be printed as cavities or as local areas of increased density of polymer.

The markers are characterized in terms of their size, relative image contrast, and the precision of the printed pitch.

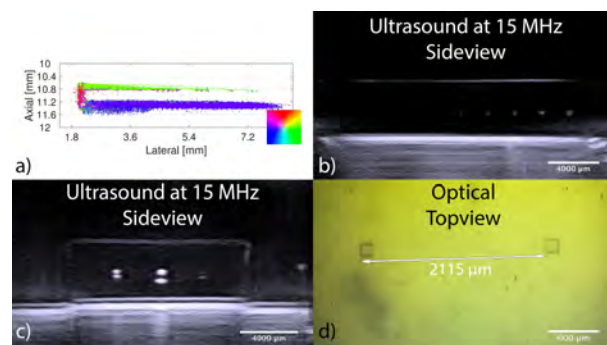
Results/Discussion

Figure b) shows an ultrasound image (@15 MHz) of a row of cavity fiducial markers. The design includes markers from (60 μm)³ to (140 μm)³, increasing by 10 μm in all dimensions from left to right. The smallest visible marker is (100 μm)³ at the shown dynamic range.

Figure c) shows a comparison of cavity markers (left and middle) and a high density marker (right) (@15 MHz). The cavity markers have a larger change in acoustical impedance, resulting in brighter intensity values.

The designed pitch between the fiducial markers was 2074 μm . Figure d) shows an optical microscope image of two cavities. The printed pitch was measured from microscope and ultrasound images to be $2115 \pm 9 \mu\text{m}$ and $2133 \pm 23 \mu\text{m}$ on average respectively, corresponding to a mean difference of 41 μm and 59 μm .

In conclusion, we have demonstrated a 3D printed flow phantom for SRI. Fiducial markers can be printed as small as (100 μm)³, and be used for alignment of structures.



P2-C4 - Multimodal Systems

Waraku (posters 2)

Thursday, October 25, 9:30 AM - 4:00 PM

Chair: **Mohammad Mehrmohammadi** Wayne State University

P2-C4-1

An open real-time photoacoustic imaging scanner

Aneline Dolet^{1,2}, Alessandro Ramalli^{2,3}, Enrico Boni², Alessandro Dallai², Piero Tortoli², Didier Vray¹, François Varay¹

¹Univ.Lyon, INSA-Lyon, Université Claude Bernard Lyon 1, UJM-Saint Etienne, CNRS, Inserm, CREATIS UMR 5220, U1206, F-69621, CREATIS, Lyon, France, Metropolitan, ²Department of Information Engineering, University of Florence, Florence, Italy,

³Lab. on Cardiovascular Imaging & Dynamics, Dept. of Cardiovascular Sciences, KU Leuven, Leuven, Belgium

Background, Motivation, and Objective

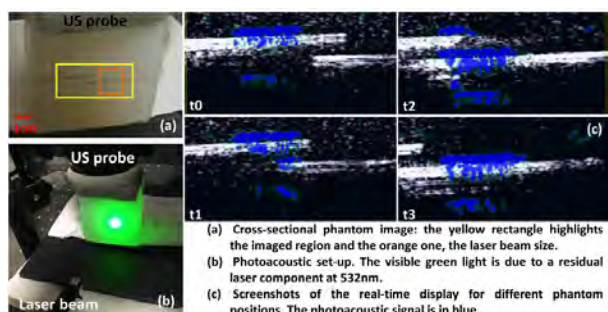
Multispectral photoacoustic imaging is an emerging technique to assess functional imaging of biological tissues by exploiting their wavelength-dependent optical absorption. In particular, the use of wavelengths in the range 600-900 nm allows distinguishing between oxygenated and deoxygenated blood, which is of interest for applications like the follow-up of diseases involving atherosoma plaques or carcinoma. Some systems produce photoacoustic images in real-time but provide limited access to raw data, or vice-versa. However, both characteristics are important, to correctly position the sample and to improve the processing methods. This study reports on the development and preliminary tests of a continuous real-time photoacoustic imaging system based on the ULA-OP256 research scanner, which allows full raw data accessibility.

Statement of Contribution/Methods

The ULA-OP256 system was connected to a 192-element linear array (7.8 MHz center frequency and 92% bandwidth) and programmed to produce interleaved standard and passive B-Mode images. For each laser pulse, transmitted at 10 Hz repetition frequency, a custom electronic circuit triggers the passive data acquisition and processing. The multi-line parallel beamformer of ULA-OP 256 reconstructs one passive image of 128 lines in real-time (0.4 ms). The time available between two consecutive laser pulses is exploited to produce standard B-Mode images (each reconstructed in 1 ms) that are overlapped to the passive one on the same real-time display. The preliminary validation was done on graphite mines included in 4% agar phantom (a), and using a laser beam at 1064nm (b). The phantom was translated from right to left by maintaining the plane of the graphite mines aligned with the imaged region.

Results/Discussion

The synchronization of an external laser source with ULA-OP256 allowed exploiting the parallel beamforming capability of such system to continuously produce photoacoustic images at 10Hz. The sample frames (c) extracted from the real-time movie highlight the correct synchronization of the optical illumination and passive acquisition, as well as the accurate display of passive and active images. In addition to the continuous real-time display modality, ULA-OP256 makes also all the raw data available for possible quantification processing improvements, which are currently under development.



A configurable module-based ultrasound imaging system: all-in-one ultrasound, photoacoustics, and elasticity imaging**Heechul Yoon¹, Yiyi I. Zhu¹, Donald VanderLaan¹, Vadakkancheril S. Jisha¹, Andrei Karpouk¹, Stanislav Emelianov^{1,2}**¹*School of Electrical and Computer Engineering, Georgia Institute of Technology, Atlanta, GA, United States*, ²*Wallace H. Coulter Department of Biomedical Engineering, Georgia Institute of Technology and Emory University School of Medicine, Atlanta, GA, United States***Background, Motivation, and Objective**

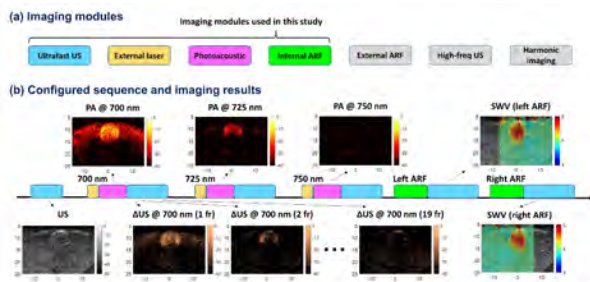
The sensitivity and specificity of widely used clinical ultrasound (US) imaging systems are relatively low compared to other imaging modalities. To address this limitation, shear wave elasticity imaging (SWEI) and spectroscopic photoacoustic (sPA) imaging were developed to provide additional diagnostic information based on mechanical or optical contrast. Furthermore, contrast agents such as optically triggered/respondive nanoagents have been developed for molecular and cellular imaging. This study introduces a configurable system combining these synergistic imaging technologies to further enhance ultrasound-based diagnosis of cancer and other diseases based on simultaneous anatomical, functional, and molecular imaging of tissue.

Statement of Contribution/Methods

Based on a programmable US system (Vantage 256) and a tunable pulsed laser (Phocus Mobile), we developed a configurable imaging system capable of supporting unconstrained allocation of imaging modules that allows users to create customizable imaging sequences (**Fig. 1a**). As an example, an imaging sequence acquiring pre-laser US images, three sPA images each followed by post-laser ultrafast US images, and two shear-wave velocity (SWV) images was implemented (**Fig. 1b**). This sequence was used to image a tissue mimicking gel phantom with a stiff gel inclusion containing perfluorohexane nanodroplets (PFHnDs) loaded with a squaraine dye (650 nm peak absorption).

Results/Discussion

The inclusion was barely visible in the pre-laser US image. In response to pulsed laser irradiation, PFHnDs vaporized and generated contrast in PA images. The PA signals were largest at 700 nm and decreased as wavelength increased. The vaporized PFHnDs temporarily persisted as gas bubbles, providing contrast in US images. As expected, the differential US (Δ US) signals from PFHnDs were strongest immediately after the 700 nm laser pulse, and then decreased in subsequent US frames as the PFHnDs recondensed. Finally, two SWV maps successfully identified the inclusion based on quantitative stiffness assessment. This study introduces a module-based, configurable ultrasound-laser imaging system that demonstrates simultaneous support of ultrafast US, sPA, and SWEI with imaging contrast mechanisms related to acoustic, optical, and mechanical properties of tissue for comprehensive diagnosis.



Design, Development and Cadaveric Validation of a Minimally Invasive Theranostic Device for Ablative Neuro-OncologyNao Gamo¹, Rajiv Iyer², Stephen Restaino³, Kyle Morrison⁴, Alan Cohen², Henry Brem², Mari Groves², Amir Manbachi⁵¹Biomedical Engineering, Johns Hopkins University, Baltimore, MD, United States, ²Department of Neurological Surgery, Johns Hopkins Medicine, MD, United States, ³Maryland Development Center, MD, United States, ⁴Sonic Concepts Inc., Bothell, WA, United States, ⁵Johns Hopkins University, Baltimore, MD, United States**Background, Motivation, and Objective**

Most brain surgeries to resect deep tumors / cysts are performed using craniotomies, which involve removing part of the skull bone to expose the brain. These invasive surgeries entail hours of blood loss. Most brain surgeries to resect deep tumors/cysts are performed using craniotomies, which involve removing part of the skull bone to expose the brain. These invasive surgeries entail hours of blood loss, potential infections, and long recovery. While several non-invasive devices using high-intensity focused ultrasound (HIFU) are in various phases of development, they are limited by the attenuation of ultrasound while passing through the skull, and inability to reach targets deep in the brain. The use of excessive power is also undesirable from a regulatory standpoint. Here, we report the design, development, and cadaveric testing of a novel HIFU device for brain tumor ablation. This device is designed to access the ventricular space via a minimally invasive burr hole in the skull (Fig. 1a), allowing ultrasound to reach targets deep in the brain, while eliminating the need for high power to penetrate the skull (Manbachi et al. 2018, PCT/US18/20159).

Statement of Contribution/Methods

A custom HIFU transducer with a hybrid imaging/therapeutic tip was designed and manufactured (Fig. 1b), based on prior simulation studies (Zhang et al. 2017, AAPM; Gamo et al. 2018, AANS). Once the transducer was verified to be functional in a phantom model, a cadaver trial was performed to demonstrate proof-of-concept in ablating a predetermined region of interest, according to the criteria listed in Fig. 1c. Following ablation, the brain was sectioned to verify that the transducer ablated the predicted location.

Results/Discussion

The transducer was successfully inserted into the ventricular space through a burr hole in the skull of a cadaver to create single-point ablations in a region of interest. These data showed similar accuracy relative to that of non-invasive approaches, but with considerably less power (12-35 W vs. 800 W with the non-invasive approach). Our solution presents a compromise between quality of care (treatment of lesions) and patient safety (amount of power applied). Based on these findings, a beta prototype will be developed to ablate medium to large-sized tumors.

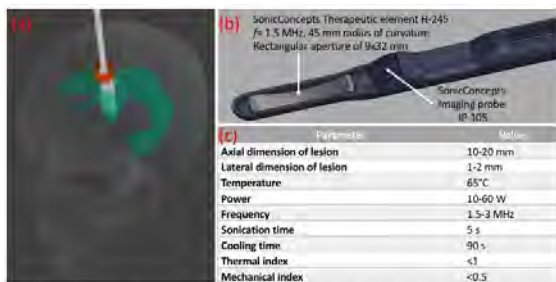


Figure 1 – (a) A burr hole (red) is placed on the skull for device (white) access into the lateral ventricle (green); (b) Isometric 3D view of the custom-designed manufactured transducer; (c) Cadaveric validation was conducted to evaluate whether the intraventricular probe can ablate with the specified criteria.

Design, Modeling, and characterization of a subject specific acoustic collimator for multi-index ultrasound neuron modulation system
Chih-Hsien Huang¹, Rachid Haouari¹, Veronique Rochus¹, Xavier Rottenberg¹
¹*STS, imec, Leuven, Belgium*
Background, Motivation, and Objective

The feasibility of ultrasound neuron modulation (UNMOD) has been generally observed and discussed for years. The mechanism and behavior model are deeply analysis based on both *in vivo* and *in vitro* experiments. However, most of the existing ultrasound delivery methodologies either using ultrasound transducer array with complex driving units or bulky transmission medium with restricted applying location. Therefore, to further discover the mechanism behind UNMOD, a reliable, easy fabricate, and flexible UNMOD system is required to conduct large quantity of experiments and integrate with more different sensors.

Statement of Contribution/Methods

The need to get a higher-pressure wave at the desired focus through specific medium inspire the development of an acoustic collimator. The purpose was to collect and direct soundwaves towards a certain region of neurons in ambient environment. In this study, a novel acoustic collimator was proposed and the efficiency was compared with an ordinary cone shape structure with straight wall. To maximize the pressure intensity at the volume of interest (VOI), a shape optimization of the collimator inner wall was performed by using COMSOL® Multiphysics (Fig. (a)) and showed 50% gain of signal intensity at VOI. Thereafter, the 3D-printed collimator was sealed and filled with water to make the acoustic adaptation with tissue. Eventually, acoustic measurement was made to compare between a straight and optimized shaped collimator by using a hydrophone as shown in Fig. (b).

Results/Discussion

The measured acoustic fields along axial direction were not only compared between different collimators, but also with the simulation results as shown in Fig. (c). It showed the collimator successfully modified the focal point and acoustic field distribution as simulation predicted. The collimator could deliver 2.5 MPa when apply 10Vp-p to a 1MHz transducer, which is adequate for UNMOD based on literature review. A multiple indexes UNMOD system has been built based on the collimator as Fig. (d) to allow synchronizing the injection of configurable ultrasound signals to animals and the monitoring of multiple physiological responses. The system is expected to execute numerous experiments in a short period since it is low cost, high productivity, and consistent.

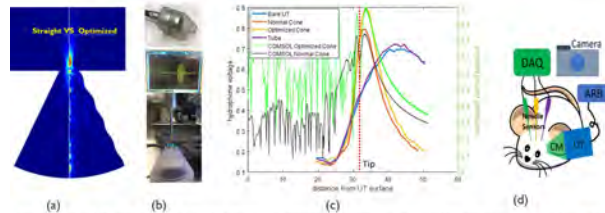


Fig. 1(a) Simulated 2D acoustic field of straight vs. optimized collimator. (b) Toy assembled acoustic collimator with a single element transducer. Middle: measured voltage. Bottom: acoustic pressure measured by a hydrophone on the tip of acoustic collimator with acoustic gel. (c) Measured axial pressure with no (blue), straight cone shape (red), optimized cone shape (yellow), and cylinder tube (purple) collimators as well as simulated acoustic field with optimized cone shape (green) and straight cone shape (black). Red dotted line indicates the location of the tip of collimator. (d) Schematic of a multi-index UNMOD system synchronized and controlled by LabView. DAQ: Data acquisition, CM: Collimator, UT: Ultrasonic transducer, ARB: Arbitrary waveform generator.

Design and Implementation of a Dual-Transmit/ Receive-Mode Therapeutic Ultrasound Phased Array System for Brain Therapy

Hao-Li Liu¹, Chih-Hung Tsai¹, Chen-Kai Jan¹, Sheng-Min Huang², Meng-Lin Li², Weibao Qiu³, Hairong Zheng³

¹Department of Electrical Engineering, Chang Gung University, Taoyuan, Taiwan, ²Department of Electrical Engineering, National Tsing-Hua University, Taiwan, ³Paul C. Lauterbur Research Center for Biomedical Imaging, Institute of Biomedical and Health Engineering, Shenzhen Institutes of Advanced Technology, China, People's Republic of

Background, Motivation, and Objective

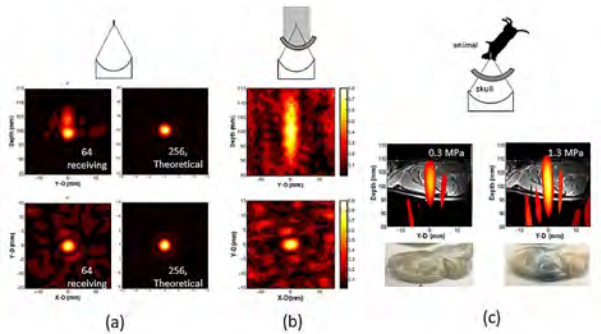
Focused ultrasound phased array systems have attracted increased attention for brain therapy applications. However, such systems currently lack a direct and real-time method to intraoperatively monitor ultrasound pressure distribution for securing the treatment. This study proposes a dual-mode ultrasound phased array system design to support transmit/receive operations for concurrent ultrasound exposure and backscattered focal-beam reconstruction through a hemispherical ultrasound array.

Statement of Contribution/Methods

The proposed system may have potential for real-time guidance of ultrasound brain intervention, and may facilitate the design of a dual-model ultrasound phased array for brain therapeutic applications. In brief, a 256-channel ultrasound transmission system was employed to transmit focused ultrasonic energy (full 256 channels), with an extended implementation of multiple-channel receiving function (64 channels) using the same spherically focused 256-channel ultrasound phased array. A coherent backscatter-received beam formation algorithm was implemented to map the point spread function (PSF) and focal beam distribution under a free-field/ transcranial environment setup, with the backscatter generated from a strong scatterer (point reflector) or a weakly scattered tissue-mimicking graphite phantom.

Results/Discussion

Our results showed that PSF and focal beam can be successfully reconstructed and visualized in free-field conditions (see Fig. 1a; compared with full 256 channel receiving effect), and can also be transcranially reconstructed following skull-induced aberration correction (see Fig. 1b; energy deposited in graphite phantom). Experimental results successfully demonstrate concept feasibility via sparsely-arranged element reception, showing that the reconstructed point spread function can be successfully built with a spatial resolution close to that theoretically predicted. In addition, we showed that the focal beam distribution can be transcranially reconstructed in a tissue mimicking phantom with sufficiently high sensitivity through the application of an additional phase aberration correction procedure In-vivo experiments were conducted to demonstrate its capability to pre-operatively and semi-quantitatively map a focal beam to guide blood-brain barrier (BBB)-opening (see Fig. 1c).



Precise Transcranial Ultrasound Imaging/HIFU by Adaptive Beamforming via a Dual-Mode Hand-Held Probe**Kiyanoosh Shapoori¹, Eugene Malyarenko², Jeffrey Sadler³, Adam Waspe^{4,5}, James Drake^{4,6}, Roman Maev^{1,3}**¹*Institute for Diagnostic Imaging Research (IDIR), Windsor, ON, Canada*, ²*Tessonics Corp., Birmingham, MI, United States*,³*University of Windsor, Windsor, ON, Canada*, ⁴*Neurosurgery, Hospital for Sick Children (SickKids), Toronto, ON, Canada*,⁵*Medical Imaging, University of Toronto, Toronto, ON, Canada*, ⁶*Surgery, University of Toronto, Toronto, ON, Canada***Background, Motivation, and Objective**

Precise transcranial brain diagnosis and treatment can be performed noninvasively with an ultrasound-guided HIFU (USgHIFU) system that employs a handheld dual-mode imaging/HIFU probe. Such probe offers a unique advantage of beamforming in both imaging and HIFU modes, allowing to expand the treatment envelope from a single focus to a sizable volume. Adding a skull-induced phase aberration correction technique into the beamforming process makes transcranial imaging and precise HIFU targeting possible. Development and evaluation of a prototype USgHIFU system with simultaneous transcranial imaging and HIFU capabilities are the main objectives of the presented study. The dual-mode USgHIFU system can be used both in brain diagnosis applications, such as intra-ventricular hemorrhage (IVH) of prematurity, and in treatment applications, such as tissue ablation and clot lysis.

Statement of Contribution/Methods

We have recently tested a state-of-the-art prototype handheld dual-mode probe that can perform imaging at 3-6MHz and HIFU at 3MHz. Previously, we had also developed an adaptive beamforming algorithm for transcranial imaging via small-aperture ultrasonic phased arrays. In the present study, we have extended the application of our adaptive beamforming algorithm to the HIFU mode, and tested it with the dual-mode probe. The operation is a four-stage process: (1) the probe is placed in contact with the scalp, and the sound speed and local thickness profile of the skull are extracted; (2) the measured profile is used to adaptively focus the ultrasound beam through the skull in the imaging mode, and a live sonogram is maintained on the screen for defining the HIFU target; (3) the same extracted profile is used to focus the high-intensity ultrasound beam to treat/obliterate the tissue; (4) live sonogram is used to monitor the HIFU process and observe the treatment results. Steps (1)-(4) are accomplished with the probe in the same position and within seconds or minutes, depending on the complexity of the medium and size of the treatment volume, which is a major improvement compared to long preparation and processing time (up to several hours) of a typical MRI-guided HIFU treatment.

Results/Discussion

We have conducted a comprehensive phantom study to assess the applicability of the dual-mode imaging/HIFU technique to pediatric brain diagnosis and treatment. The experiments on bovine serum albumin (BSA) gel phantoms confirmed the ability to precisely steer and focus high intensity ultrasound (up to 30° and 8cm) in a confined focal spot of ~1x1x3mm³, while simultaneously providing a sonogram of the sonicated area. Focal temperature rise up to 83°C was recorded in HIFU-mode at various depths and angles, creating lesions in BSA phantoms with denaturing temperature of ~61°C. The presented preliminary results show a promising future for application of this technique in many brain HIFU treatment scenarios, especially in pediatric and neonate populations.

Imaging-guided dual-target brain stimulation on mouse using array ultrasound

Guofeng Li¹, Jiehan Hong¹, Qiuju Jiang¹, Peitian Mu¹, Ge Yang¹, Congzhi Wang¹, Weibao Qiu¹, Hairong Zheng¹

¹Shenzhen Institutes of Advanced Technology, Chinese Academy of Sciences, China, People's Republic of

Background, Motivation, and Objective

Ultrasonic neurostimulation has become a promising approach for neural science with its non-invasive feature. Currently single element focused ultrasound transducers have been widely used for performing ultrasonic neurostimulation. However, such transducers need to be adjusted mechanically using a stereotaxic frame, which makes implementing multiple-target neurostimulation difficult. Moreover, the accuracy of stimulation is influenced by the accuracy of the original coordinates in a brain atlas and how much the acoustic focus deviates from the original pathway after penetrating through the skull. This study investigates the feasibility of using linear array ultrasound transducer for imaging-guided dual-target ultrasound brain stimulation on mouse.

Statement of Contribution/Methods

Figure (a) shows a block diagram of the proposed multifunction ultrasound system, which consists of four parts: a computer, a pulse generator, an imaging receiver, and a dual-mode transducer. The stimulation position was controlled by beamformer achieved by a field programmable gate array (FPGA) device. Brain imaging was done first and followed by imaging-guided stimulation. Three male C57BL/6 mice, 10-12 weeks old, 21g (+/-5%) in weight were used. Mouse was anesthetized and with its head gently immobilized using stereotaxic frame. Different positions in the brain were selected to evaluate the stimulation effect. Electromyography signals were recorded and the motion responses of mouse were captured in real-time.

Results/Discussion

Figure (b) demonstrates a B-mode image of a mouse brain for predetermining two different stimulation targets. Figure (c, d) show the video snapshot of the mouse forelimbs during ultrasound stimulation to target A and B, respectively. The upper waveform in Figure (e) plots the EMG signal acquired from the left forelimb of a mouse receiving ultrasonic neurostimulation applied alternately to target A and B. The bottom waveform shows the synchronous trigger signal. The EMG waveform illustrates that the EMG amplitudes were much higher during stimulation of target A than that of target B. Our results show that imaging-guided dual-target brain stimulation by array ultrasound can evoke different motion responses on mouse. This novel method provides a new tool for precise and flexible ultrasonic neurostimulation.

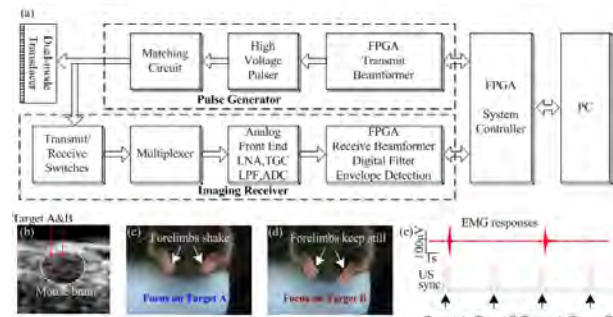


Figure (a) shows the block diagram of the proposed imaging-guided dual-target ultrasound brain stimulation system. (b) demonstrates a B-mode image of a mouse brain for predetermining two different stimulation targets. The exact positions of the targets can be adjusted electronically. (c, d) show the video snapshot of the mouse forelimbs during ultrasound stimulation to target A and B. (e) indicates the different effects of the EMG responses evoked by the ultrasound stimuli on the target A and B.

Revolving Permanent Magnet for Magnetomotive Ultrasound

Sandra Sjöstrand¹, Maria Evertsson¹, Ulrika Lindqvist¹, Rebecka Lindquist¹, Roger Andresson², Anders Wahlström³, Göran Nybom⁴, Ingrid Svensson¹, Magnus Cinthio¹, Tomas Jansson^{5,6}

¹Biomedical Engineering, Lund University, Sweden, ²Lund University, Sweden, ³Lundinova AB, Sweden, ⁴JOIN Business & Technology AB, Sweden, ⁵Department of Clinical Sciences, Lund University, Sweden, ⁶Clinical Engineering Skåne, Medical Services, Sweden

Background, Motivation, and Objective

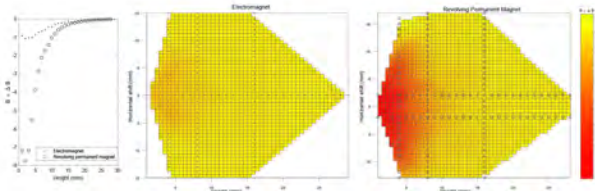
Magnetomotive ultrasound, MMUS, is a new imaging technique that utilizes superparamagnetic nanoparticles as a contrast agent. A time-varying magnetic field acts to move the particles, and the resulting tissue motion is detected with ultrasound. So far, electromagnets have almost exclusively been proposed for generating the field, either for pulsed or continuous excitation. Permanent magnets offer a higher field strength at a much lower volume. In order to produce a time varying magnetic field in the imaging plane, we propose the use of a permanent magnet that revolves around its axis to produce a time varying field in the imaging plane. In this paper, we present measurements that compare our hitherto most powerful electromagnet to the proposed design.

Statement of Contribution/Methods

The magnetic field of the electromagnet as well as the new design was measured using a Gaussmeter (FW Bell 9200) with a probe (HTB92-0608). Data from a measurement volume covering 30x30x30 mm was collected. Within the volume, a plane extending orthogonally from the surface of the magnet, was carefully measured together with external points to span the major properties of the field. For the revolving magnet, the field was covered in a similar manner, with the main plane extending radially outwards from the housing covering the revolving magnet. The electromagnet was operating at 5 Hz, with maximum current and voltage set to 60 A and 20 V respectively, due to saturation effects of the iron core beyond this point. The permanent magnet was rotated at 150 rpm to replicate the magnetic force frequency. Since the force on a magnetic particle depends (partly) on the field as well as its gradient, the results are presented as the product of the measured field component and its derivative (calculated from a spline interpolation of the data).

Results/Discussion

As shown in the figure, the permanent magnet gives rise to a field and gradient product greatly exceeding that of the powerful electromagnet. At a distance of 10 mm from the permanent magnets housing, the resulting force on a magnetic particle would exceed that exerted at the surface of the electromagnet. Since the main limitation to penetration depth of MMUS is the magnetic field, the proposed design may improve this significantly.



Sources of 2nd harmonic generation in a medical ultrasound probe
Thong Huynh¹, Lars Hoff¹, Trym Eggen²
¹*University College in Southeastern Norway, Borre, Norway*, ²*GE Vingmed, Horten, Norway*
Background, Motivation, and Objective

Tissue harmonic imaging is often the preferred ultrasound imaging modality due to its ability to suppress reverberations [1]. The method requires good control of the transmit stage of the ultrasound scanner, as harmonics in the transmitted ultrasound pulses will interfere with the harmonics generated in the tissue. The transmit stage consists of high-voltage output electronics, cable, tuning network, and the acoustic stack. The aim of this study was to get better insight into the sources of harmonics in transmitted ultrasound pulses, by measuring ultrasound pulses and electric signals at different stages in the scanner transmit chain.

Statement of Contribution/Methods

In the study, one element in a medical ultrasound array was excited using the 3-level pulser in the scanner. To test the system, voltages well above what is used in clinical imaging were also tested. Pulses were measured as close as possible to the probe, using an Onda HGL-0200 Hydrophone. Harmonic distortion of the received ultrasound pulses may have several sources: Transmit electronics, tuning networks, the transducer stack, and nonlinear propagation in water. To separate contribution of the electronics from that of the transducer, measurements were done with the transducer replaced by a passive load of similar impedance. The contribution from propagation through water was estimated by simulating nonlinear pulse propagation in the k-Wave acoustics toolbox for MATLAB.

Results/Discussion

In the received pulses, 2nd harmonic levels up to -20 dB relative to the fundamental frequency level were observed for the highest transmit voltages, giving 0.5 MPa acoustic pressure at distance 3 mm. Under these conditions, k-Wave simulations predict 2nd harmonic levels of -35 dB from propagation in water. Measurements on the electrical excitation voltages across the element showed a 2nd harmonic level of -22 dB. When the element was replaced by the passive load, the 2nd harmonic level was much lower, -50 dB. We conclude that the input driving voltage gets distorted in this setup, causing some 2nd harmonic in the transmitted sound pulse, but the true source of this distortion remains to be determined. Note that the drive voltages and pulse amplitudes were selected to investigate the phenomenon and push the system to the limit, and are well above what is used in a clinical scanner.

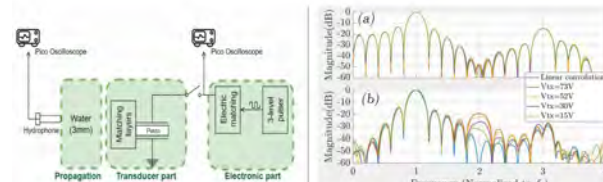


Fig.1. Diagram of the measurement setup and 3 main sources of the 2nd harmonic.

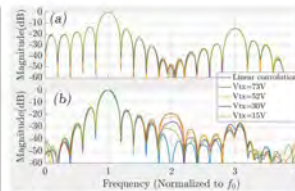


Fig.2. Spectrum of the output voltage of the electronic part on a passive load(a) and the transmit pressure measured by the hydrophone(b), at different transmit voltage. There is no 2nd harmonic generated in the electronic part with passive load but it is relative high (-20dB) in the pressure.

P2-C5 - Transducers

Waraku (posters 2)

Thursday, October 25, 9:30 AM - 4:00 PM

Chair: **Jiromaru Tsujino** Kanagawa University

P2-C5-1

Design, realization and characterization of a differential charge amplifier for ultrasonic piezopolymer transducers

Pietro Giannelli¹, Alessandra Martini¹, Giacomo Calabrese², Maurizio Granato³, Giovanni Frattini³, **Lorenzo Capineri¹**

¹Dept. of Information Engineering, University of Florence, Florence, Italy, ²Texas Instruments Deutschland GmbH, Freising, Germany, ³Texas Instruments Italia S.r.l., Vimercate (MB), Italy

Background, Motivation, and Objective

Piezopolymer (PVDF) film has been used for fabricating interdigital transducers (IDT) for NDT of plate structures [1]. The design of an IDT with independent fingers implicates smaller element capacitance like 10pF. The cabling of installed IDTs deteriorates the signal to noise ratio due to voltage partition between the small transducer's capacitance and the higher cable capacitance, when voltage mode preamplifiers are employed. The design of a low impedance charge preamplifier can solve this problem. This research work deals with the design of a new topology of charge amplifier: fully differential and symmetric, with the main gain stage made of a fully differential voltage amplifier, for interfacing high impedance piezo-polymer ultrasonic transducers. The -3dB band of interest for this design is 100 kHz-1MHz.

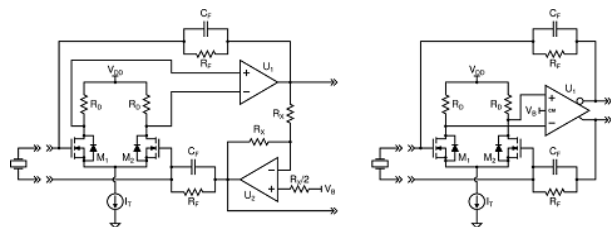
[1] P. Giannelli, A. Bulletti and L. Capineri, "Charge-mode interfacing of piezoelectric interdigital Lamb wave transducers", IEEE Electronics Letter, 2016, vol. 52, no. 11, pp.894-896.

Statement of Contribution/Methods

The novel proposed charge amplifier includes a Mosfet differential pair, placed before the fully differential voltage amplifier, used not only as a bias stage for the fully differential voltage amplifier, but also as an additional gain stage (see figure on the right). Two equivalent versions of the amplifier have been designed: one with the differential pair made of active loads and the other one with the differential pair made of resistive loads. A PCB-prototype has been realized for the two versions. The comparison of the performance with a previous version of the charge amplifier (see figure on the left) are reported.

Results/Discussion

Both the variants exhibit a 245dB[V/C] measured conversion gain, thus they are particularly suitable for preamplifying very small amount of charge (\sim FC) and have a theoretical differential input impedance lower than 140Ω on the whole band. A common mode rejection ratio of 60dB has been measured for the variant with active loads, while 50dB has been obtained for the variant with resistive loads. Measurements of noise and total harmonic distortion have also been performed and compared with simulations. The amplifiers have been tested with a pitch-catch set-up, to prove the detection of S0 and A0 Lamb waves over an aluminum plate with a cable of about 1m length.



Performance prediction of ultrasonic sensor for automotive application
Youngsoo Choi¹, Youngsoo Seo¹, Younghoon Kim¹
¹*Hyundai Mobis, APS Control Engineering Team, Korea, Republic of*
Background, Motivation, and Objective

An ultrasonic sensor in automotive system has been widely used in many kinds of application such as an automatic parking, an emergency rear breaking and parking assistance. The ultrasonic sensor has several strengths to be applied into those systems due to including lower price compared with other types of sensor and a high spatial resolution to measure a long distance from obstacles. In this study, we optimized sensitivity, a beam pattern and a mounting position of sensors according to vehicle designs. In addition, we also have applied novel methods for optimizing the location of ultrasonic sensors around the vehicle and predicting the system performance depending on an environment.

Statement of Contribution/Methods

We constructed a simulation model which is consisted of three parts, acoustical properties, and electrical characteristics of sensor and application logic to predict system performance using ultrasonic sensors. In the acoustical properties, we considered transmission, propagation and reflection, reception, and the TX, RX beam pattern have been applied by the 3D acoustic analysis results using the real bumper model. In electrical characteristics of sensor, the received acoustic pressure has been converted into voltage by using a signal processing of an internal ASIC model. Finally, for the application logic, we constructed mesh models using a global coordinate system and a sensitivity (sound pressure) map has been calculated according to the mounting position of the sensors. All simulation and analysis have been conducted by using Matlab (R2015b) which could be compatible with other commercial development packages.

Results/Discussion

In this study, our simulation model including the acoustic characteristics showed good prediction performances in the actual ultrasonic sensor system (Figure 1). The automotive ultrasonic application could be improved by correcting reference which is threshold, and predicting the performance depending on the temperature and humidity of the air medium. In addition, the development time for the maximum performance of the long distance (~ 3m) system was shortened by analyzing the mounting position and the beam pattern of sensors by our simulation. Our method can provide a theoretical basis to understand further developments of ultrasonic system.

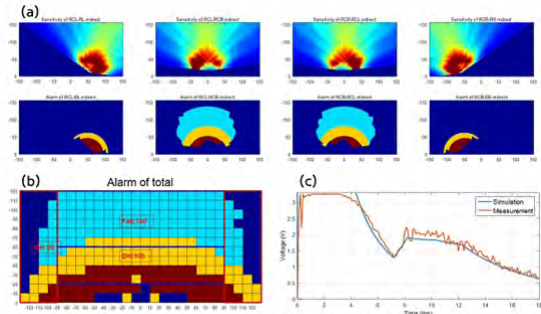


Figure 1. (a)Acoustic pressure map (b)Warning zone (c) Sensitivity results

Multielement Interdigital Transducers for Structural Health MonitoringAndrea Bulletti¹, Pietro Giannelli¹, Marco Calzolai¹, **Lorenzo Capineri¹**¹*Dipartimento Ingengeria Informazione, Università degli Studi di Firenze, Firenze, Italy***Background, Motivation, and Objective**

Many fiber-reinforced composite structures used in the automotive, aerospace, and transportation industries present a plate-like geometry. Plate-like structures support the guided propagation of ultrasound waves (like Lamb waves) over long distance with little attenuation: this has made guided-wave inspection of composites a thriving research field, with a large amount of literature covering the generation and reception of guided-waves, the interaction of those waves with material damages, and the extraction of diagnostic information.

This work presents an improved interdigital transducer (IDT) for ultrasonic guided-wave generation and reception in structural health monitoring systems, where each finger constitutes an independent electrode that can be driven and sensed with a multichannel system. The new design aims at improving the versatility in wavelength selectivity of the classical IDT.

Statement of Contribution/Methods

IDTs made with metal-coated piezopolymer film (polyvinylidene fluoride, PVDF) have already proven to be suitable to build SHM systems for aerospace applications. The manufacturing technology uses a laser to etch an electrode pattern on the film's metal coatings.

In [1], the authors presented a multifunctional transducer built by exploiting the possibility to pattern the metal coating of a PVDF film with arbitrary geometries.

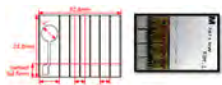
In this work an IDT variant was designed with each finger having an independent electrical connection to the front-end electronics: The new multielement interdigital transducer (MIDT) constitutes an actual periodic array (see Fig. 1).

Results/Discussion

Preliminary tests in aluminium plates have shown that each finger can be operated in reception with little attenuation. The time delay between each finger will be characterized for S_0 and A_0 propagation modes at frequencies of 450kHz and 250kHz respectively. The separation of fingers allows arbitrary wavelength selectivity but requires the multiplication of electronic front-end channels both in transmission and reception. For this purpose, a multichannel front-end is currently being developed by the authors to take full advantage of the proposed transducer design.

References

- [1] P. Giannelli et al., "Multifunctional piezopolymer film transducer for structural health monitoring applications," IEEE Sensors J., pp. 4583-4586, 2017.



Detection effect of resonance frequency of both laser Doppler vibrometer and internal defect of concrete structure by spatial spectral entropy

Kazuko Sugimoto¹, Tsuneyoshi Sugimoto¹, Noriyuki Utagawa², Chitose Kuroda²

¹Graduate School of Engineering, Toin University of Yokohama, Japan, ²Technical Research Institute, SatoKogyo Co., Ltd., Japan

Background, Motivation, and Objective

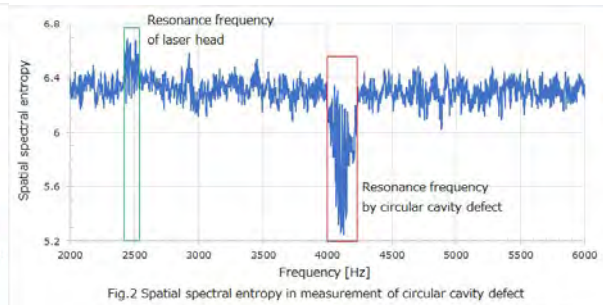
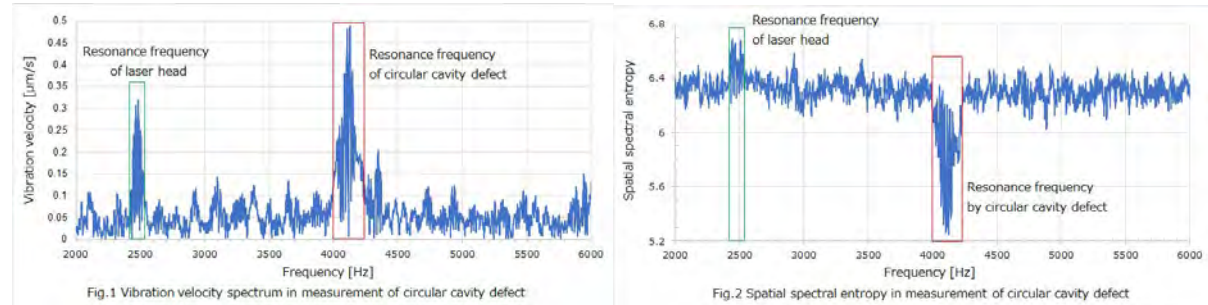
Noncontact acoustic inspection method using acoustic irradiation induced vibration and laser Doppler vibrometer (LDV) has made it possible to detect defects of concrete at a long distance in the same manner as a hammering test. However, in closed space such as underground large cavity, LDV head resonance due to strong reverberation becomes a problem. At plane scanning, in case that LDV head resonance occurs, vibration velocity was observed to increase at that resonance frequency in all measured points. When the specific frequency is viewed in the spatial direction, the whiteness is extremely high. Therefore, a spatial spectral entropy (SSE) is proposed. Here, spectral entropy, which detects the whiteness of a signal, is applied in the spatial direction at a specific frequency. We investigated whether SSE can detect an internal defect of concrete, in addition to the detection of LDV head resonance.

Statement of Contribution/Methods

An example of vibration velocity spectrum of a circular cavity defect is shown in Fig.1. From the vibration velocity distribution measured at all measurement points, it has been found that the peak at 2.5 kHz is a LDV head resonance frequency, and the peak at 4.2 kHz is a flexural resonance frequency of a cavity defect. It is usually difficult to distinguish whether it is a LDV head resonance or a resonance of internal defect, merely by looking at a peak that exists in vibration velocity spectrum.

Results/Discussion

The result using SSE is shown in Fig.2. As expected, it shows a high value at LDV head resonance frequency, on the other hand, it shows a low value at defect part. From this fact, the two can be distinguished at a glance. By introducing SSE, LDV head resonance and resonance of defect part can be clearly distinguished. In addition, their resonance frequencies were identified.



Autonomous Ultrasonic Inspection for Complex Geometry Using Unmanned Aerial Vehicle**Dayi Zhang¹, Gordon Dobie¹, Charles MacLeod¹, Gareth Pierce¹**¹*Electronic & Electrical Engineering, University of Strathclyde, Glasgow, United Kingdom***Background, Motivation, and Objective**

Ultrasonic inspection is a conventional non-destructive testing (NDT) method corrosion mapping. Large-scale facilities, such as vessels are difficult to access and have complex geometries. Hence, for safety, convenience and legal requirements, an Unmanned Aerial Vehicle (UAV) offers significant potential benefits. Traditionally, UAV remote inspections rely on high-resolution cameras, providing a general photogrammetry surface overview. The photogrammetry inspection cannot distinguish the miniature discontinues and displacements underneath the surface coating. Surface contacting ultrasonic transducers offer the potential for internal inspection of an asset or component, providing true integrity information. However, for safety reasons, it is highly challenging for the operator/inspector to perform a detailed and contact examination as the UAV requires to be flown over a significant distance away from the surface.

Statement of Contribution/Methods

This paper presents an autonomous UAV system for inspection of large steel storage vessels. The UAV is autonomously guided into position using the customised control systems. Distance to the surface and alignment are measured using a planar laser range scanner. Ultrasonic coupling is provided through a dry membrane. A spring-loaded transducer ensures appropriate contact force. Results are presented for a 2-meter-high vessel in a laboratory setting. The UAV autonomously takes 10 thickness samples at predefined locations on the surface using a 5MHz dual crystal probe.

Results/Discussion

The UAV with ultrasonic transducer payload can position the probe to within 7.5cm of the desired location and can quantity thickness to errors of less than 0.1mm. The system can provide the thickness measurements for an asset with complex geometry and detect the discontinues under the coating. Compared with the traditional photogrammetry inspection results, the ultrasonic measurements provide quantitative measurements of corrosion. This approach also illustrates the potential of autonomous remote ultrasonic testing for the large-scale infrastructures in the future. In addition, the dual crystal probe can be replaced by an ultrasonic array to cover more area in a limited battery lifecycle and increase the inspection efficiency.

Estimating Rheological Properties of Non-Newtonian Drilling Fluids using Ultrasonic-Through-Transmission combined with Machine Learning Methods**Morten Hansen Jondahl¹, Håkon Viumdal¹**¹*University College of Southeast Norway, Norway***Background, Motivation, and Objective**

Drilling an oil well and developing an oil/gas field involve great costs and economical risks. Situations where the pressure integrity of the well is lost during drilling are a great risk to assets, humans, and the environment, and represents a high cost of the drilling operation. The non-Newtonian drilling fluid that is circulated while drilling serves several purposes, and its properties are essential to fulfill them. The density (ρ) enables the drilling mud to maintain pressure integrity during drilling operations. The plastic viscosity (μ_p) enables the fluid to transport cuttings, while the gel strength (S) keeps the cuttings suspended when circulation is stopped. The industry standard today is to perform manual drilling fluid checks every six hours to measure these three important rheological properties. To increase safety, efficiency and enable more automated drilling operations sensor technology to perform these measurements in real-time is in high demand. Non-invasive ultrasonic measurement techniques in combination with machine learning represents one promising and easily implementable solution to meet these demands.

Statement of Contribution/Methods

In the presented work acoustic properties of different drilling fluids are studied. Three different pairs of ultrasonic transducers were utilized to evaluate the propagational properties of 22 different samples of water-based drilling fluids. The parameters measured in the ultrasonic experimental setup is received signal amplitude, time of flight (ToF) and the lateral distance between receiver and transmitter. In addition lab analysis of the drilling fluids were carried out to determine the fluid rheological properties. For a given frequency three machine learning models were trained, one to estimate density, a second to estimate plastic viscosity and a third to estimate gel strength.

Results/Discussion

New experimental results, along with the results from our earlier published study were used as training and validation data in machine learning (ML) models. Artificial neural networks with varying numbers of hidden neurons in one single layer were trained. The models with density as output had a mean absolute percentage error (MAPE) of between 0.8% and 0.9%, and the viscosity models ranged from 4.2% to 5.45%. The models for gel strength were not as promising with MAPE from 11.7% to 13.7%. These results show that the potential for relating ultrasonic measurements to density and viscosity in non-Newtonian drilling fluids are good. The accuracies are within acceptable ranges for the simple setup of the experiment. For high density fluids the acoustic attenuation might be critical in an industrial application. However, these models and sensor system represent a promising approach for estimating density and plastic viscosity of drilling fluids, and is considered the first step in developing a real-time non-invasive measurement system.

P2-C6 - Underwater Acoustics

Waraku (posters 2)

Thursday, October 25, 9:30 AM - 4:00 PM

Chair: **Jafar Saniie** Illinois Institute of Technology

P2-C6-1

Design of an Acoustic Modular Projector for Active Sonobuoys

Hayeong Shim¹, Seonghun Pyo¹, Yongrae Roh¹

¹*Kyungpook National University, Daegu, Korea, Republic of*

Background, Motivation, and Objective

Sonar tracking systems using remote sensors such as sonobuoys are mainly classified into active and passive systems. Recent underwater vehicles including submarines can operate with a much lower level of noise, thus the desire for active systems is increasing rapidly. An acoustic modular projector system (MPS) using bender transducers is a promising candidate for the transmitter in the active sonobuoy. However, modern underwater detection system requires the MPS to have superior acoustic performance than conventional monitoring systems. Hence, in this work, the optimal structure of the MPS is designed to meet the stringent performance requirement for modern active sonobuoys.

Statement of Contribution/Methods

Fig. 1(a) is the schematic structure of the MPS. The individual bender transducer is required to have the highest transmitting voltage response (TVR) while having the widest possible frequency bandwidth. The MPS consists of four bender transducers and is required to have the narrowest beam width and the lowest level of sidelobes. For the design of the MPS to meet the requirements, the effect of various structural parameters on the performance was analyzed first through finite element analysis. The parameters include diameters and thicknesses of the PZT disc and aluminum base, diameter and height of the cavity inside the base, location and dimension of the ribs inside the cavity, and different material of PZT ceramics. Subsequently, the effect of the separation between bender transducers was analyzed to determine the optimal separation to satisfy the beam width and sidelobe level specifications.

Results/Discussion

Expansion of the separation between bender transducers increased the sidelobe level and decreased the beam width. Hence, the separation was expanded up to the distance at which grating lobes began to appear. Further, the optimal combination of all the structural parameters have been determined to maximize the performance of the MPS. Fig. 1(b) compares the TVR spectra of the initial and optimized structures of the MPS. The TVR shows significant improvement as much as 7.1 dB, which verifies the efficacy of the optimal design conducted in this work. The validity of the TVR spectrum has been confirmed with an experimental MPS prototype. The modular projector designed in this work can allow more efficient and accurate detection of silent underwater targets.

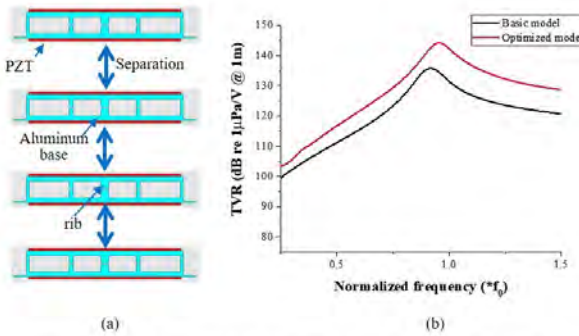


Fig. 1. (a) MPS composed of four bender transducers and (b) its TVR spectrum.

Preparation and sonocatalytic performance of a hierarchical structures Bi₂WO₆ microsphere for degradation of Methylene blue

Apeng Sun¹, Runyang Mo¹

¹Shaanxi Normal University, Xi'an, China, People's Republic of

Background, Motivation, and Objective

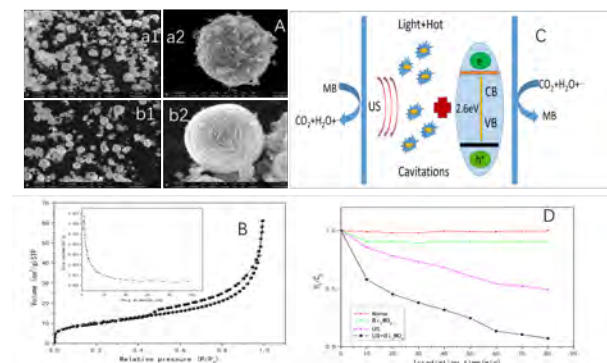
Methylene blue (MB) is widely used in industrial processes as a chemical indicators and industrial dyes, which is not easily biodegradable and is toxic to human health and aquatic life. In recent years, ultrasonic degradation as one of the advanced oxidation process (AOP) has been studied and extensively used to degrade MB, but it takes long reaction time and has limited efficiency, so the methods of sonocatalytic degradation are developed in this study.

Statement of Contribution/Methods

In this work, hierarchical structure Bi₂WO₆ microsphere with high surface area was prepared in the presence of polyvinylpyrrolidone(PVP) via an optimized hydrothermal method. The morphology and structures properties of the samples were characterized by means of X-ray diffraction(XRD), field emission scanning electron microscopy (FESEM) and N₂ adsorption- desorption technique. In order to evaluate the sonocatalytic activity of the as-prepared hierarchical structures Bi₂WO₆ microsphere, the Bi₂WO₆-assisted degradation of MB in aqueous solution was investigated under ultrasound irradiation as various experimental conditions. The surface area of prepared Bi₂WO₆ microsphere is 36 m²/g .The degradation efficiency was studied in three cases(adsorptions only, ultrasound only and Bi₂WO₆-assisted sonocatalytic). The degradation efficiency was found to be in the following order: adsorptions < ultrasounds<sonocatalysis. The order revealing that Bi₂WO₆ microsphere exhibit a good sonocatalytic activity. In addition, the effects of various experimental factors including ultrasonic power (*P*), ultrasonic pulse mode (*UPM*), catalyst dosage (*C_{catalyst}*) and *pH* of MB aqueous solutionon on the sonocatalysis efficiency were investigated. The degradation ratio achieved about 93.5% at 80 min under the optimum condition (*P*=500 W, *UPM* =9 s on/1 s off, *C_{catalyst}* =1.2 g/L, *pH*=11).

Results/Discussion

Results indicated that the kinetics of sonochemical reactions of MB were consistent with the pseudo first-order kinetics and Bi₂WO₆ had excellent reusability and stability during the sonochemical degradation processes. The degradation of MB in the presence of Bi₂WO₆ under ultrasonic irradiation is related to the generation of reactive oxygen species (ROS), in which both hydrogen peroxide (H₂O₂) and hydroxyl radical (- OH) play important roles in the sonochemical degradation of MB.



Degradation of Rhodamine B in seawater using ultrasonic combined with periodateDongdong Du¹, Chenghui Wang¹, Apeng Sun¹, Qingsong Deng¹, **Yongjie Sun¹**, Yanpeng Li¹¹*Applied Acoustics Institute, Shaanxi Normal University, Xi'an, China, People's Republic of***Background, Motivation, and Objective**

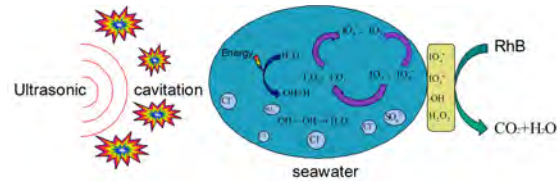
Sea has historically been subject to high anthropogenic pressures of direct and indirect loads of organic pollutants from intensive industrial and agricultural activities. Various families of organic pollutants were found in the ocean, most of the wastewaters are generated from soda ash, chloro-alkali, dye manufacturing, textile, pulp and paper, chemical, paint, food and beverage. Ultrasonic combined with periodate (US/IO₄⁻) is an innovative oxidation technique that was never tested in seawater as pollutants matrix.

Statement of Contribution/Methods

In this work, we attempted to investigate the treatment of seawater (salinity ~35.7 g/L, distributed as Na⁺=11 g/L, Mg²⁺=1.3 g/L, Ca²⁺=0.4 g/L, Cl⁻=20 g/L, SO₄²⁻=3 g/L) contaminated with Rhodamine B (RhB) dye, as a model of organic pollutants, using ultrasonic combined with periodate process. Aqueous samples were taken periodically from the solution and the concentrations of the dye were determined using a UV-visible spectrophotometer at 552 nm (the maximum absorption wavelength of the dye in the visible region).

Results/Discussion

It was found that periodate (0.2mM) assisted-ultrasound treatment of RhB (10 mg/L) in seawater resulted in 10.36-fold increase in the initial degradation rate, compared to periodate alone, and 65.6% of RhB was removed after 90 min face to 6.3% under periodate alone. The central role of hydroxyl radicals (-OH) in the degradation process was determined. The beneficial effect of US/IO₄⁻ treatment strongly dependent on operational parameters, such as initial solution pH, seawater-salts, initial RhB concentration, initial periodate concentration and ultrasound pulse mode. Based on the obtained results (initial solution pH, seawater-salts, initial RhB concentration, initial periodate concentration and ultrasound pulse mode), the reaction mechanism of US/IO₄⁻ degradation of RhB was proposed. More interestingly, the degradation rate increased with the increase in periodate but an optimal does was regarded for the best degradation rate, and the degradation efficiency of RhB can be increased under the condition of strong acid, making US/IO₄⁻ a promising technique for treating seawater contaminated with organic pollutants.



Design of an Underwater Vector Hydrophone using a Shear Mode Accelerometer made of Piezoelectric Single Crystals
Seonghun Pyo¹, Jungsuk Kim², Hoeyong Kim², Yongrae Roh¹
¹*Kyungpook National University, Daegu, Korea, Republic of*, ²*Hanwha Corporation, Korea, Republic of*
Background, Motivation, and Objective

A typical towed array sonar system, representative acoustic detection equipment to track underwater targets, is a line array of omnidirectional ring hydrophones, i.e. scalar hydrophones. The array consisting of scalar hydrophones is widely used due to the advantage of easy target detection but has difficulty in distinguishing the direction of the target. Therefore, researches regarding a vector hydrophone need to be conducted to address this problem. The vector hydrophone measures both the magnitude and direction of a sound pressure at a time. In this work, an underwater vector hydrophone has been designed using a thickness-shear mode accelerometer and an omnidirectional hydrophone. The performance of the vector hydrophone has been maximized through structural optimization of the accelerometer.

Statement of Contribution/Methods

The accelerometer is composed of seismic masses, piezoelectric elements, and a metallic base as illustrated in Fig. 1(a). The outer circular base works as the omnidirectional hydrophone. The piezoelectric single crystals PIN-PMN-PT are used for the piezoelectric elements. The acoustic characteristics of the hydrophone was analyzed in relation to its structural parameters by means of the finite element method using PZFlex®. Major parameters were the dimensions of the piezoelectric crystal and seismic mass. Based on the analysis, the optimal structure of the accelerometer has been optimized with OQ-NLP algorithm to achieve the highest receiving voltage sensitivity (RVS) of the vector hydrophone. Next, the receiving beam pattern of the hydrophone of the optimized structure was analyzed to check the possibility of achieving a cardioid pattern.

Results/Discussion

The validity of the optimal design was verified by fabricating a prototype hydrophone to have the designed geometry and comparing its measured performance with the design results. The RVS was measured to be -199.4 dB, which was higher than given requirement. Fig. 1(b) is the comparison of the estimated and measured beam patterns of the hydrophone at 24 kHz, which shows a clear dipole pattern. Hence, by combining the dipole response with the omnidirectional response of the outer circular base, a cardioid beam pattern could be obtained which estimates the direction of a sound wave. The agreement confirmed the validity and efficacy of the new vector hydrophone design in this work.

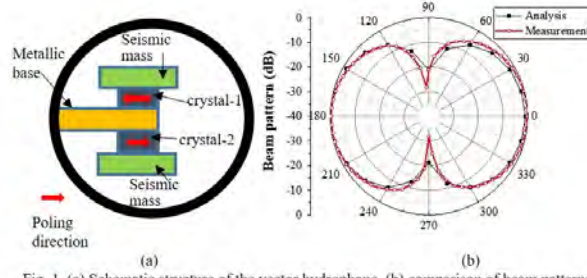


Fig. 1. (a) Schematic structure of the vector hydrophone, (b) comparison of beam patterns

Experimental Evaluation of High Intensity Ultrasound Source System using Acoustic Waveguide and Concave Transducer with 100 mm Diameter for Calibration of Hydrophone

Shigeru Igarashi¹, Takeshi Morishita², Shinichi Takeuchi²

¹Polytechnic University, Japan, ²Toin University of Yokohama, Japan

Background, Motivation, and Objective

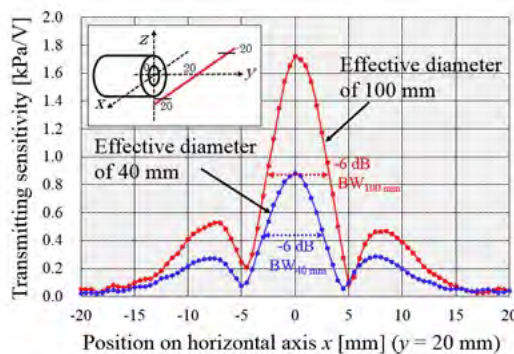
Recently, the equipment used a high intensity ultrasound have been increasing in the medical and the industrial field. A high intensity ultrasound source for calibrating a hydrophone for evaluating a high intensity ultrasound field is required. To calibrate the receiving sensitivity of the membrane type hydrophone as the primary standard, it is necessary to vibrate the area of receiving element on the hydrophone uniformly. Therefore, it is not a narrow beam form generated by a focused type transducer, but a beam form generated by a flat type transducer and a high acoustic pressure is required. We proposed and developed the high intensity ultrasound source system using a cylindrical acoustic waveguide and a concave type transducer. In this system, the focused ultrasound wave is emitted from the concave type transducer to one end aperture of the cylindrical acoustic waveguide, propagates while being reflected by the inner wall of that, and the output ultrasound wave from the other end aperture forms main beam similar to that formed by a flat type transducer and a high intensity. This system is expected to increase the ultrasound power acoustically by expanding the diameter of the concave transducer. We have fabricated the experimental source system using the concave transducer with the effective diameter of 40 mm, and confirmed the peak acoustic pressure of 670 kPa at the position of 10 mm from the transmitting aperture.

Statement of Contribution/Methods

The experimental source system was constructed with an acoustic waveguide in which a closed cell sponge was processed into a cylindrical shape with inner diameter of 7 mm, outer diameter of 16 mm and length of 15 mm by water jet method, and a 1 MHz concave type transducer with an effective diameter of 100 mm and a curvature of 100 mm. The aperture on the input side of the acoustic waveguide is arranged at the focal point of the concave type transducer. Using the experimental source system, the acoustic pressure distribution on the central axis, the horizontal axis and the vertical axis at the distances of 10, 20 and 30 mm from the transmitting aperture of the acoustic waveguide and transmitting sensitivity are measured, and it was compared with the previous source.

Results/Discussion

As the result, it was confirmed that the -6 dB beam width become almost equal with the previous source, and the transmitting sensitivity increase about 2-fold with that.



P2-C7 - Material and Defect Characterization

Waraku (posters 2)

Thursday, October 25, 9:30 AM - 4:00 PM

Chair: **Patrick Johnston** NASA Langley Research Center

P2-C7-1

Ultrasonic detection of stress corrosion cracks in pipe samples using guided waves

Petter Norli¹, Martijn Frijlink^{1,2}, Øyvind Krøvel-Velle Standal^{1,2}, Tore Grüner Bjåstad^{1,2}, Fabrice Prieur^{1,3}, Emilie Vallée¹

¹*Halfwave, Høvik, Norway*, ²*InPhase Solutions, Trondheim, Norway*, ³*Department of Informatics, University of Oslo, Oslo, Norway*

Background, Motivation, and Objective

Stress corrosion cracking (SCC) is a serious threat to gas pipeline integrity. To mitigate this, pipeline operators perform numerous annual crack detection inspections of onshore pipelines. The current tools, however, are reported to have issues with sensitivity and sizing of small cracks. Recent advances in gas-coupled broadband ultrasound facilitate new methods based on guided plate waves. Previously, the potential to detect SCC using Halfwave's ART Scan tool was successfully demonstrated on test plates with machined crack-like defects [1].

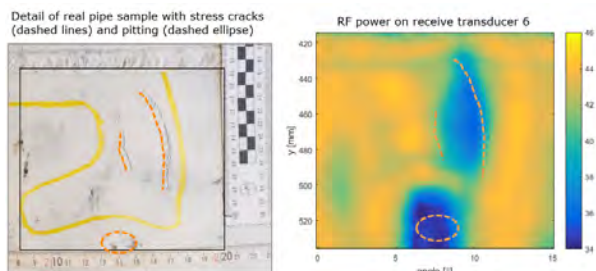
Statement of Contribution/Methods

The objective of this work is to experimentally demonstrate crack detection capability on a real pipe sample with SCC, submerged in water. The 36-inch outer diameter pipe sample (wall thickness of 12.7 mm) contains cracks, corrosion pitting and a girth weld. The maximum crack depths, measured by ultrasonic time-of-flight diffraction (TOFD), were 4.3 and 4.2 mm, respectively, for two cracks in the scan area (Fig. 1, left). The scanner head consisted of one transmit (Tx) transducer surrounded by eight receive (Rx) transducers, all oriented perpendicularly with respect to the pipe wall, with 80 mm standoff. Broadband chirped pulses were transmitted towards the target. Rx signals from all cylindrical scan positions (2 mm x 0.25° resolution) were processed, and several parameters (e.g. thickness estimate, RF power, spectral power) were calculated and plotted. Scans were performed on both an undamaged reference area and a part with cracks and pitting.

Results/Discussion

Amplitudes and features of the displayed parameters were dependent on the orientation of Tx-Rx transducer pairs. Rx signals from opposite sides of the Tx transducer were similar. The parameter plots displayed different features, such as the girth weld, corrosion pitting, and the crack area. The RF power was up to 6 dB lower in signal levels for the crack area (Fig. 1, right). Spectral power analysis suggested the use of different frequency bands to discriminate between cracks and other irregularities, such as welds and pitting corrosion. The results show that this new detection method, using guided waves, has the potential to detect real SCC using an ART Scan based tool.

[1] Norli, Petter, et al. "Ultrasonic detection of spark eroded notches in steel plates." Ultrasonics Symposium (IUS), 2017 IEEE International. IEEE, 2017.



Forward and inverse researches on scattering of ultrasonic surface waves by near-surface cavities
Bin Wang¹, Sohichi Hirose², Zhenghua Qian¹
¹*College of Aerospace Engineering, Nanjing University of Aeronautics and Astronautics, Nanjing, China, People's Republic of*
²*Department of Civil Engineering, Tokyo Institute of Technology, Tokyo, Japan*
Background, Motivation, and Objective

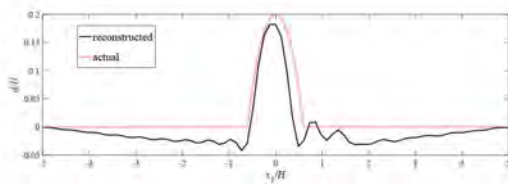
The ultrasonic surface waves have great potential in geological inspection and ultrasonic non-destructive testing for near-surface underground characteristics. A thorough and effective utilization of surface waves requires a better understanding of their scattering phenomenon. The paper studies the problem of Rayleigh and Love wave scattering by cavities near surface or on the interface between the upper layer and the lower half-space. For the forward analysis, a modified boundary element method (BEM) combined with method of fundamental solutions (MFS) is introduced, which can effectively eliminate fictitious reflections introduced by model truncation. For inverse analysis, we propose a quantitative reconstruction procedure for the flaw shape using reflection coefficients of the 1st order Rayleigh and Love wave.

Statement of Contribution/Methods

For the scattering problem concerning a half-space, one may encounter the problem of spurious reflection because of the artificial model truncation. In the paper, we suggest a modification where far-field displacement patterns with unknown coefficients were introduced onto the boundaries far from the scatterer, and then substituted into the basic BEM equation set. Our results show that the modified BEM is effective for suppress artificial reflections and shed light on its future extension to more complex waveguide configurations. Moreover, the modified BEM can be strengthened by expressing the source item with a series of virtual sources by MFS methods, which can considerably reduce the modelling and computation time. For the inverse analysis, we work on to derive an inverse reconstruction procedure to plot the location, size and shape of the near-surface cavity flaws, using the reflection coefficients obtained in the forward analysis as the input data. Take Love wave for example, we show in certain cases, the reflection coefficients in wavenumber domain and the objective function of flaw's geometrical properties have a Fourier relation. Thus, by performing a spatial Fourier transform pair we can fully reconstruct the cavity flaws' information.

Results/Discussion

For Love wave cases, the inversion results are shown in Fig 1, where the red curve representing actual flaw shape, while the black one the reconstructed result.



Characterization of ferroelastic martensites by resonant ultrasound spectroscopy.

Hanus Seiner¹, Petr Sedlák¹, Lucie Bodnarova¹, Martina Thomasova¹, Petr Sittner², Ladislav Straka², Oleg Heczko²

¹Institute of Thermomechanics, Czech Academy of Sciences, Prague, Czech Republic, ²Institute of Physics, Czech Academy of Sciences, Prague, Czech Republic

Background, Motivation, and Objective

Resonant ultrasound spectroscopy is a method capable of very accurate determination of elastic constants of anisotropic solids. The method is based on measuring a resonant spectrum of free elastic vibrations of a small sample with exactly known geometry and density. The elastic constants are then obtained by solving an inverse problem, i.e. by minimizing the misfit between the measured resonant spectrum and the spectrum calculated for the same sample with iteratively refined guesses of the elastic constants.

For most of the conventional materials, the orientation of the anisotropy axes with respect to the sample is fixed, and so the measurements on just one sample can provide only a limited information on the elastic constants. However, for a specific class of materials, called ferroelastic martensites (i.e., low-temperature phases of shape memory alloys), this limitation does not hold, and the crystallographic reorientation can be induced by external forces. This contribution will summarize the specific features of application of resonant ultrasound spectroscopy to this class of materials.

Statement of Contribution/Methods

Laser-based resonant ultrasound spectroscopy was applied for characterization of various samples ferroelastic martensites, in particular single crystals of Ni-Mn-Ga and Ni-Mn-Ga-based alloys and polycrystalline Ni-Ti and Ni-Ti-Cu alloys. For all these materials, the resonant ultrasound spectroscopy requires specific modifications, not only as far as the experimental arrangement is concerned, but also regarding the inverse problem for the determination of the elastic constants.

Results/Discussion

It was observed that while for the single crystals the reorientation mechanism enables full switching between two different crystallographic orientation, and, consequently, full characterization of elastic anisotropy, for polycrystalline materials the reorientation is affected by the crystallographic texture and by the loading history, and is also dependent on the particular crystallographic class of the studied alloy. In addition, the ferroelastic ordering in the examined materials leads to several interesting phenomena detectable by resonant ultrasound spectroscopy: i) strong elastic anisotropy with pronounced phonon softening; ii) high damping due to motion of twin interfaces in polycrystals; iii) non-linear vibrational response due to motion of twin interfaces in single crystals.

Study on The Effect of Fiber Weaving on Properties of Composite Materials by Acoustic Emission
Yuan Mi¹, Dawei Wu¹
¹*State Key Lab of Mechanics and Control of Mechanical Structures, Nanjing University of Aeronautics and Astronautics, Nanjing, China, People's Republic of*
Background, Motivation, and Objective

Compared with traditional structures, composite structures have more complex damage patterns. For glass fiber resin laminated composites, different fiber weaving can result in considerable strength differences. Although acoustic emission (AE) monitoring has been extensively applied to composite materials, e.g. failure modes classifications based on the frequency content, the effect of fiber weaving has not been well studied. This paper mainly focuses on analyzing the strength changes of glass fiber-resin composite materials (GF-EP) resulting from different weaving methods by using AE technique.

Statement of Contribution/Methods

Quasi-static tension tests were carried out in three types of GF-EP specimen (UD, 2AX, and 3AX) under the same conditions (Figure 1). During tests, mechanical parameters such as stress and strain data were recorded; AE features including peak amplitude, duration, and count numbers along with statistical features like AE energy, root mean square (RMS) were extracted. With the wavelet analysis of acquired data, we obtained a five-layer decomposition of the waveform and the corresponding frequency domain details ranging from high frequency to low frequency. High-frequency band (450 kHz to 750 kHz) containing fiber breakage information was clustered by means of pattern recognition.

Results/Discussion

The mechanical properties of specimen can be determined by quasi-static tension tests. The comparison of three types of specimen sufficiently shows that the strength of the biaxial (2AX) braided material is the lowest, and spoiled 2AX produces the lowest acoustic signal intensity (0.0075V) and the minimum count numbers (Figure 2). With the wavelet analysis and the fuzzy k-means identification clustering, we found that the AE parameters of the biaxial braided specimen are lower than the others in high-frequency range. This study reveals that the breakages of different braided fibers generate diverse strain energy and distinct AE signals.

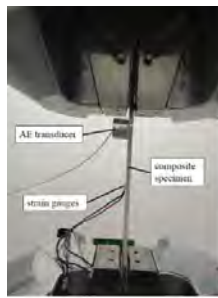


Figure 1: Experimental set-up

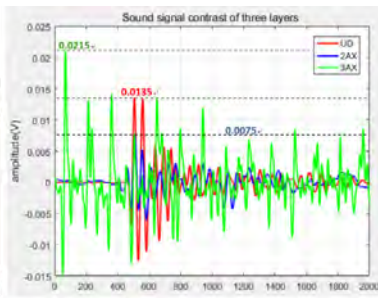


Figure 2: Waveform contrast

Defect Imaging Using Sub-Sampled Array Data with Least-Squares Migration
Katherine Tant¹, Carlos da Costa Filho², Andrew Curtis²
¹*Mathematics and Statistics, University of Strathclyde, Glasgow, United Kingdom*, ²*University of Edinburgh, United Kingdom*
Background, Motivation, and Objective

In ultrasonic phased array imaging, if the array pitch is greater than half the wavelength λ , unwanted artefacts known as grating lobes can become prevalent and obscure signals arising from the defect. This is problematic in the development of arrays for volumetric imaging, since the production of dense, periodic 2D arrays is currently inhibited by manufacturing limitations. Thus, imaging algorithms which act on sparsely collected data and retain good image quality are highly desirable. Here we apply, for the first time, Least-Squares Migration (LSM), an imaging methodology originating within the seismology community, to sub-sampled ultrasonic array data, which results in the attenuation of unwanted grating lobes. LSM can also be used to achieve an improvement in lateral resolution compared to that achieved by the Total Focussing Method, the current standard in ultrasonic NDT imaging.

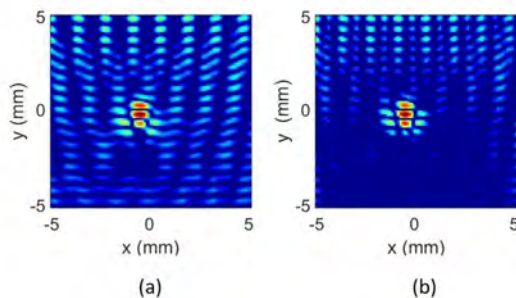
Statement of Contribution/Methods

Given the reflectivity map \mathbf{m} of the component under inspection, the ultrasonic phased array data can be written $\mathbf{d}=L(\mathbf{m})$, where L is some linear operator which models the reflected data from each point in the imaging domain. We can thus write $\mathbf{m}_\# = L^T(\mathbf{d})$, where L^T is the transpose of the operator L and is analogous to the operator employed by the Total Focussing Method to create an image representative of the material's reflectivity, denoted here $\mathbf{m}_\#$. However, if we have incomplete data (as the case where array element spacing is greater than $\lambda/2$) then some acquisition artefacts in the data fail to be cancelled out, and $\mathbf{m}_\#$ exhibits grating lobes. Least-squares migration searches for the map which minimises $\Psi(\mathbf{m}) = \|L(\mathbf{m}) - \mathbf{d}\|^2 - \eta(\mathbf{m})$, where $\eta(\mathbf{m})$ is some regularisation term, providing a pseudo-inverse solution to the forward problem.

Results/Discussion

The data examined here arises from the simulated ultrasonic phased array inspection of a stainless steel block at 3MHz where the array pitch is greater than $\lambda/2$. A 2mm diameter side drilled hole was embedded 20mm below the array. Figure 1 (a) shows the reconstruction arising from application of the Total Focussing Method (TFM) and Figure 1 (b) demonstrates the significant attenuation of grating lobes achieved when unregularised LSM is used (when $\eta(\mathbf{m})=0$).

Figure 1. Reconstruction of a 2mm diameter side-drilled hole embedded in stainless steel by (a) TFM and (b) LSM. Both images are plotted over a 20dB dynamic range.



Effect of Spot Weld Indentation on Spot Weld Nugget Characterization**Xiaoli Han¹, Wentao Wu¹, Fucheng Xiao¹, Ling Xiao¹**¹*Institute of Acoustics, Chinese Academy of Sciences, Beijing, China, People's Republic of***Background, Motivation, and Objective**

There is an average of 5,000 spot welds on the car body. Spot welding quality directly affects the robustness of the car and it is necessary to perform quality inspection on spot welding. The strength of the spot weld depends largely on the size and the shape of the nugget in the internal center of spot weld. Ultrasonic testing can be used for quantitative evaluation of spot welding nugget. When using the ultrasonic attenuation to size the nugget in the C scanning, the contribution of indentation to ultrasonic wave attenuation will affect the accuracy of sizing the nugget. This paper studies the effect of spot welding indentation on ultrasonic scattering and aims to explore the effect of attenuation due to scattering on the ultrasonic quantification of spot weld nugget. If the tilt angle and scattering coefficient of the spot weld indentation are extracted based on the collected raw ultrasonic echoes, reasonable attenuation compensation can be given in the spot-welded C-scan image based on the extracted indentation information in order to get a more accurate size of the nugget, thus the strength of spot weld can be assessed more accurately.

Statement of Contribution/Methods

First, the impact of indentation is analyzed from a theoretical perspective, based on scattering and refraction theory in multi-layer media. The simulation data set with specific spot weld surface conditions are obtained based on the finite difference method in SimSonic2D. Using simulation data sets, the effects of different indentation shapes and tilt angles on ultrasonic attenuation and the specific influence of indentation on sizing of nugget in C-scan image are studied. Finally, the C-scan imaging and sizing of the spot weld are performed using actual two-dimensional scan data set and the estimated size of the nugget after the indentation attenuation compensation is given. The estimated nugget size before and after compensation are compared with the results shown in 1:1 X-ray photographs.

Results/Discussion

The results show that the existence of indentation does affect the accuracy of the nugget size estimation. In general, when the size of the nugget is estimated by ultrasonic attenuation in the C-scan image, indentation may result in smaller nugget quantification. By pre-estimating the indentation characteristics and then giving appropriate compensation in nugget sizing, the accuracy of the nugget quantification by the C-scan image can be improved. The indentation depth and tilt angle are different at different locations, and the accurate estimation of the tilt angle depends on the accuracy of the scan. This has become a key factor in determining the actual degree of improvement of attenuation compensation.

Numerical investigations on localization of material degradation using guided mixing wave**Tang Bo¹, Sun Maoxun¹, Zhu Wujun¹, Xiang Yanxun¹**¹*School of Mechanical and Power Engineering, East China University of Science and technology, China, People's Republic of***Background, Motivation, and Objective**

Nonlinear ultrasonic guided wave has been comprehensively explored because of their extremely sensitivity to material microdefects such as micro-cracks and micro-voids. Nevertheless, some critical shortcomings still restrict the progression of second harmonic generation. For instance, material hyperelastic property will confuse defect's recognition. Guided waves mixing approach is an excellent workaround for these problems. Whereas theoretically research about the conditions of guided wave mixing has been investigated for a long time, the interaction between mixing wave and material defects were rarely reported. In this article, application of guided wave mixing on localizing material degradation is studied using a numerical method.

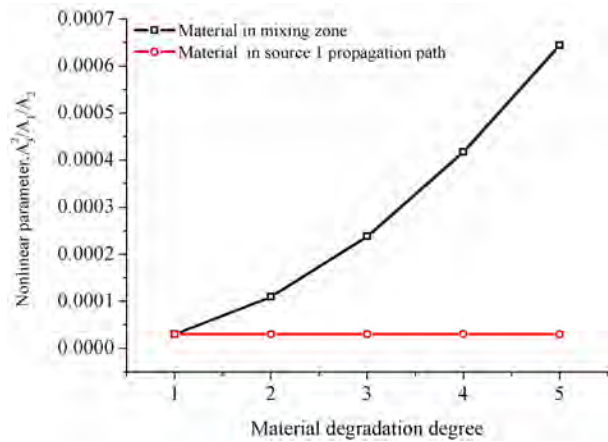
Statement of Contribution/Methods

A counter-propagating mixing in a 1 mm thickness aluminum plate was simulated using commercial CAE software ABAQUS/Explicit. Two sources selected based on nonzero power flux and phase matching were S0 mode at 1.13MHz and S0 mode at 1.82MHz. Material degradation was approximated through adjusting aluminum's third-order elastic constants. A nonlinear parameter $A_3^2/A_1/A_2$ was established to evaluate the degree of material degradation.

Results/Discussion

A 2.95 MHz sum frequency signal was observed at mixing zone, which was consistent with theoretical analysis. By calculating the group velocity, the mixing wave was determined to be S1 mode.

Two degradation regions were considered. One was in the center of mixing zone and the other was in the path of source waves propagation. The change of nonlinear parameter versus the degradation of material at different zones was shown in the figure below. A significant increase of nonlinear parameter was observed when material in mixing zone deteriorated, which validated mixing wave was sensitive to slight local material degradation. The nonlinear parameter kept stationary as material in source wave's propagation path deteriorated. The result demonstrated that defects in source wave's propagation path didn't impact the identification of defects at mixing zone.



P2-C8 - Flow Measurement and Microfluidics

Waraku (posters 2)

Thursday, October 25, 9:30 AM - 4:00 PM

Chair: **Nishal Ramadas** Elster Instromet

P2-C8-1

Surface Acoustic Wave Based Acoustofluidic Device for Particle Size Filtering

Jin-Chen Hsu¹, Yi-Jui Lin¹

¹*Department of Mechanical Engineering, National Yunlin University of Science and Technology, Douliou, Yunlin, Taiwan*

Background, Motivation, and Objective

Recently, acoustophoresis has gained increasing attention as an effective and gentle non-contact method for manipulating microparticles and cells in microfluidic systems. It combines microfluidics and acoustic-wave technology to offer means to move and localize particles and cells. According to desired functions, various analytical processes can be integrated in a small system to conduct transmission, separation, classification, and mixing of samples based on bulk acoustic waves (BAWs) and surface acoustic waves (SAWs) which enable fast analysis, less sample dosage, and performing a large number of sample operations. However, the function to achieve the size filtration of mixing particles by acoustophoretic devices is less developed.

Statement of Contribution/Methods

In this study, SAWs of 30–40 MHz are used as the driving force of the filtration system. It involves injecting the standing SAWs into the microfluid formed by interference of two SAW beams, which generate acoustic pressure and acoustic radiation force fields inside the microfluid to drive specific particles to be captured at the pressure nodes. To achieve size filtering, a square filter area is added in the microfluidic channel, and the standing SAWs travel at an angle of 45° towards the channel. This allows the particles to slow down while passing through the filter area. A comparison is made on the particle capturing effect with the numerical analysis with the SAW actuated acoustofluidic perturbation theory for a proper design of the interdigitated electrode (IDT), power under different frequencies, and relevant dimensions to achieve the goal of particle filtration. Then, the SAW acoustofluidic devices for particle size filtering based on the design simulation are fabricated using MEMS technology. Experiments are conducted to observe the performance of the devices on the control of particle movement and filtering.

Results/Discussion

The fabricated devices are used to test the capturing effect for single particle sizes from 2–8 μm and filtering effect for mixing particles of two different sizes, respectively. The experimental results show that the standing SAWs generated by the IDTs setting at an angle towards the microfluidic channel on the 128°YX LiNbO₃ is able to achieve the filtering effect in a solution of mixing particles of two different sizes through effectively capturing the targets of the larger size. It is achieved through the square-shaped filter area in the channel and with proper acoustic energy generated by the IDTs given with suitable frequencies. The flowing particles slow down in the filter area, and the acoustic pressure field captures the particles of specific size at its pressure nodes and drains them from the main flow in the filter area while particle of other sizes go through the filter area to the channel outlet. The present study enabled integration of size filtering function in SAW-based microfluidic devices for acoustophoretic applications.

Analysis of Influence of Inconsistent Performances of Array Elements on Flexural Ultrasonic Phased Array for Measurement of Ultrasonic Generation and Reception in Fluids

Lei Kang¹, Andrew Feeney¹, Steve Dixon¹

¹*University of Warwick, United Kingdom*

Background, Motivation, and Objective

The accuracy and the range of the transit-time ultrasonic flow measurement method are undermined by the sound beam drift effect. To compensate for it, two-dimensional flexural ultrasonic phased arrays have been designed and fabricated for a gas flow meter. The performances, such as centre frequencies and bandwidth of a flexural ultrasonic array element are primarily determined by the resonant vibration of its edge-clamped diaphragm. Inconsistent performances have been found in the flexural ultrasonic array elements as well as in commercial single element flexural transducers, which can cause measurement inaccuracy when working as a phased array in applications such as flow measurement or NDE. Consequently, the causes, the influences and the solutions to this problem are investigated.

Statement of Contribution/Methods

The structure and the fabrication process of a flexural ultrasonic phased array with 4×4 flexural elements are presented. An impedance analyzer and a laser vibrometer are utilized to characterize impedance, centre frequency and bandwidth of array elements at different fabrication stages. The final centre frequency of array elements approximately ranges from 46.5 kHz to 50.5 kHz and the bandwidth ranges from 1 kHz to 3 kHz. The sound pressure level (SPL) of the array, driven by 20 V_{pp} 8-cycle tone burst signals at frequencies from 46 kHz to 51 kHz is measured by a calibrated microphone, indicating that 48.5 kHz is the working frequency for the whole array with the maximum SPL. A flow meter, accommodating a single flexural transducer as a transmitter, facing 30° to the array as a receiver, is tested in a pipe with zero flow. The time-of-arrivals (ToAs) of the 16 ultrasonic beams are recorded and measured using interpolation and zero-crossing methods. To determine the influence of the inconsistent performance on the ToAs, differences of the ToAs between neighbouring rows of array elements are calculated, indicating that the optimum steering angle of the array is 26.3° , rather than 30° . Further analysis and investigation is carried out based on our established analog model to explain the reasons for this phenomenon, and methods for suppressing the influence of inconsistency are discussed.

Results/Discussion

The analog model demonstrates that the vibration of a flexural transducer driven by a tone burst signal consists of three stages. The first stage is a superposition of a signal with the driving frequency and a signal with the centre frequency of the transducer, and the zero-crossing times of the ultrasonic signal are largely affected by the results of the superposition, leading to an error in the measurement of ToAs. Methods for improving the consistency of the array elements are discussed, and signal processing algorithms including deconvolution and matched-filter methods are found effective to suppress the influence of the inconsistencies, enabling an improved accuracy of the flow measurement based on flexural ultrasonic phased arrays.

Selective killing of tumor cells based on patterned gold nanoparticles via surface acoustic wave device
Wei Zhou¹, Mian Chen², Lili Niu¹, Long Meng¹, Hairong Zheng¹
¹*Paul C. Lauterbur Research Center for Biomedical Imaging, Shenzhen Institutes of Advanced Technology, Chinese Academy of Sciences, China, People's Republic of*, ²*Shenzhen university, China, People's Republic of*
Background, Motivation, and Objective

Tumor hyperthermia has been recognized as a promising treatment modality. Thermal sensitive nanostructures absorbing energy from the external laser source is capable of increasing local temperature for the treatment of tumor tissue. However, the selective killing of tumor cell based on targeted enrichment of nanoparticles remains a great challenge. Ultrasound, as a mechanical wave, exerts radiation force on the particles in a non-invasive manner and could be used to trap nanoparticles at a designated location. Therefore, in this paper, surface acoustic wave was used to manipulate the nanoparticles at the designed pattern for selective killing of tumor cell with the assistance of laser irradiation.

Statement of Contribution/Methods

The surface acoustic wave (SAW) device includes three parts: interdigital transducers (IDTs), a Polydimethylsiloxane (PDMS) channel and a printed circuit board (PCB). The cancer cells were cultured in the micro-channel. The nanoparticles with hollow nanostructures was fabricated by the material of Ag nanocrystals and heated by laser irradiation. The fluorescent dye of propidium Iodide (PI) and Calcein-AM was used to monitor cellular activity.

Results/Discussion

Fig. 1 shows that the cells were cultured in the micro-channel and nanoparticles were aligned into a line by the acoustic radiation force. Cells at the position, where the patterned nanoparticles were located, were dead after two minutes of laser irradiation. On the other hands, the other cells remained viability. In summary, we have demonstrated that the nanoparticles can be manipulated and enriched in the targeted region by ultrasound. Moreover, with the assistance of laser irradiation, selective cell death could be achieved based on the patterned nanoparticles by surface acoustic wave.

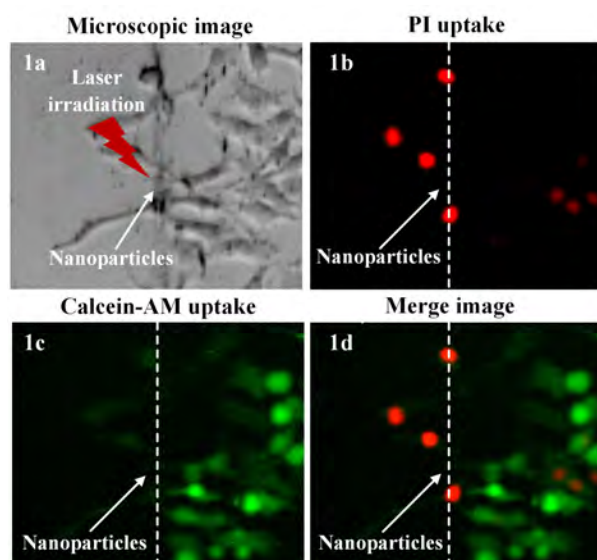


Fig. 1(a) one dimensional pattern of nano cages before laser irradiation. The (b) PI uptake (c) Calcein-AM uptake (d) Merge image represent that cells at the position, where the patterned nanoparticles were located, were dead after two minutes of laser irradiation and the other cells remained viability.

Minimizing the zero-flow error in transit time ultrasonic flow meters

Douwe van Willigen¹, Paul van Neer², Jack Massaad², Nicolaas de Jong², Martin D. Verweij², Michiel Pertijs¹

¹*Electronic Instrumentation Laboratory, Delft University of Technology, Delft, Netherlands*, ²*Laboratory of Acoustical Wavefield Imaging, Delft University of Technology, Delft, Netherlands*

Background, Motivation, and Objective

Transit-time ultrasonic flow meters are used to measure liquid flow in a range of industrial applications. The arrival-time difference between the upstream and downstream signals is a measure of the flow velocity. Practical flow meters usually show an offset in zero-flow conditions. Commonly this zero-flow offset is calibrated out before installation of the meter. However, due to process changes (temperature/liquid type), the zero-flow offset can change in operation.

Prior work has shown that the zero-flow error increases if transducers are operated in a non-reciprocal manner. Here we investigate the cause of the zero-flow error and apply circuit theory to reduce the effect.

Statement of Contribution/Methods

Two par-axially aligned transducers with a resonance frequency of 2 MHz were placed in a water tank to perform measurements with varying TX source and RX load impedances. The transducers were stimulated with a single-cycle sine wave and the received signal recorded by an acquisition card and processed in a PC. The circuit impedance was varied by using a high-impedance transmit and receive circuit and adding a parallel resistor, or by using a low-impedance transmit and readout circuit and adding a series resistor. In this work, we look at the difference in frequency instead of the commonly-used difference in phase, which reveals additional information about the zero-flow error. With an estimation of the mismatch between the two transducers, an expected zero-flow frequency difference can be calculated, from which an equivalent zero-flow error can be calculated.

Results/Discussion

Simulation results show that the zero-flow error is minimized by using the same electrical impedance for TX and RX (see figure) when using a simulated mismatch between the upstream and downstream transducer. Moreover, by taking circuit impedances significantly higher or lower than the impedance of the transducers at resonance, a larger variance in the piezo material can be tolerated. It is often not desirable to use 50 Ohm circuit impedance as this is close to the typical impedance of practical transducers.

Measurements show that for a pair of transducers where the circuit impedance for TX and RX differ significantly, the measured zero-flow error is in the range of 4 ns. Whereas the zero-flow error can be reduced to less than 10 ps when equal circuit impedances are used in TX and RX.

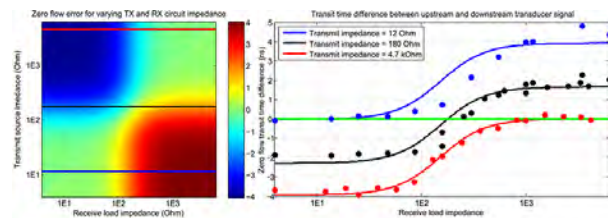


Figure 1: Zero-flow error for different combinations of transmit and receive circuit impedances, measured for three fixed transmit circuit impedances, as highlighted with a colored line on the left. On the right the simulated (continuous) zero-flow errors are shown that correspond to the three lines in the plot on the left, along with measured errors (dots). The measured zero-flow errors are an average value of 50 measurements each.

Viscosity Dependence of Harmonics and Ultra-harmonics of Acoustic Cavitation Noise**Takanobu Kuroyama¹**¹*Department of Electronic Control Engineering, National Institute of Technology, Gifu College, Motosu, Gifu, Japan***Background, Motivation, and Objective**

The viscosity is an important parameter of liquids and the measurement method of the viscosity is continually developed. However, a simple and easy measurement method which requires no probe insertion is still not achieved. This study focuses on acoustic cavitation noise generated by a high-intensity ultrasound to realize a novel viscosity measurement method. In this report, a relationship between harmonics / ultra-harmonics of the acoustic cavitation noise, which are susceptible to liquids property, and viscosity is shown and the feasibility of the viscosity measurement based on the acoustic cavitation noise is discussed.

Statement of Contribution/Methods

Figure 1(a) shows the experimental setup for measurement of acoustic cavitation noise. Acoustic cavitation bubbles are generated in water-glycerol mixture by driving a bolt-clamped Langevin-type transducer (BLT) with sinusoidal voltage, whose frequency f_0 is 19.25 kHz. The viscosity of the mixture is adjusted by changing the glycerol concentration. Acoustic cavitation noise is picked up with a piezoelectric transducer. The obtained signal is amplified by a 1 MHz band-limited amplifier and recorded by an analog-to-digital converter with a sampling frequency of 5 MHz. Power spectral densities of recorded signals are estimated with Welch's method.

Results/Discussion

Figures 1(b) and 1(c) show power spectral densities of acoustic cavitation noise for viscosity μ of 1.00 mPa·s and 13.7 mPa·s. Ultra-harmonic components, whose frequencies are multiple of $f_0 / 2$, increase with increasing driving voltage of the BLT V in both conditions. In the condition of $V = 35$ V, magnitude of ultra-harmonic components is close to magnitude of harmonic components, whose frequencies are multiple of f_0 , for $\mu = 1.00$ mPa·s, meanwhile the ultra-harmonic level is low for $\mu = 13.7$ mPa·s. This difference may originate from the suppression of the bubble coalescence, breakup, and non-spherical vibration caused by high viscous resistance. Thus, the magnitude of ultra-harmonic components can be an index of the viscosity. Figure 1(d) shows the ratio between frequency averaged harmonic components and ultra-harmonic components. The maximum value of the ratio increases with increasing viscosity. Therefore, the viscosity can be determined from the maximum ratio between frequency averaged harmonic and ultra-harmonic components.

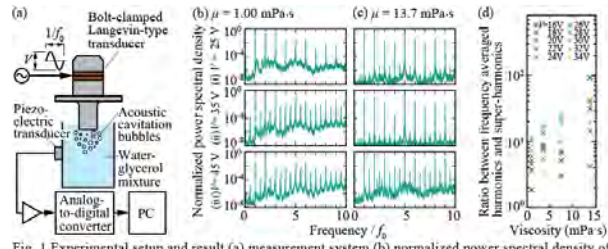


Fig. 1 Experimental setup and result (a) measurement system (b) normalized power spectral density of acoustic cavitation noise for viscosity $\mu = 1.00$ mPa·s and (c) $\mu = 13.7$ mPa·s (d) ratio between harmonic components averaged from $10f_0$ to $50f_0$ and super-harmonic components averaged from $10.5f_0$ to $50.5f_0$.

Acoustic field characterisation of an ultrasonic phased array for a novel flow sensor using an optical microphone.**Reinhard Klambauer¹, Alexander Bergmann¹**¹*Institute of Electronic Sensorsystems, Graz University of Technology, Graz, Austria***Background, Motivation, and Objective**

Various applications in science and industry demand a precise measurement of the flow rate of fluids. The industry standard are ultrasonic time of flight or hot wire flow sensors. Both have to deal with severe drawbacks in harsh environments like the determination of exhaust mass flow to estimate the mass emissions of combustion sources. Sensors in such an environment have to face high temperatures of the measured gas, turbulent flow fields and pulsations of the pressure.

To resolve this, we are researching on a novel flow sensor principle based on ultrasonic beamforming. This new sensor uses an ultrasonic beam which is created with a phased array consisting of piezo transmitters and acoustic wave guides. The beam can be steered to compensate the deflection from the flowing fluid. The counteraction necessary to steer the beam back to its predefined position is used as measured parameter.

To achieve this, precise knowledge of the acoustic field emitted from the acoustic wave guide as well as the created interference pattern from the phased array is key. The acoustic simulations which we have done with comsol have to be validated by experiment.

Statement of Contribution/Methods

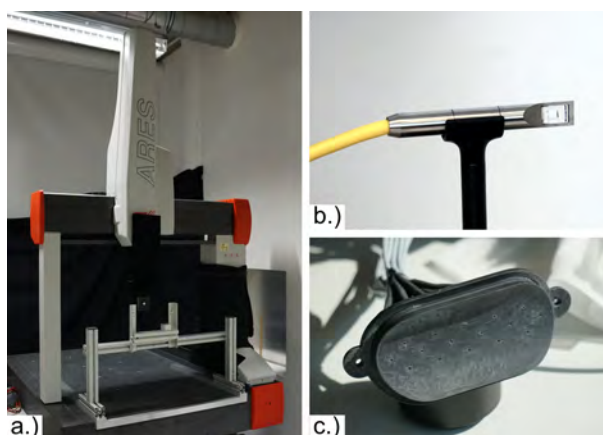
The use of acoustic wave guides causes a significant drop of the emitted sound pressure level compared to a piezo transmitter without it. The microphone used to characterize the field has to have a high sensitivity. The wavelength is roughly 1.1 mm which means that the features of the interference pattern are in this size region. The geometry of the microphone itself should make as little impact as possible on the acoustic field.

These considerations are the reason to use an optical membrane free microphone to characterise the acoustic field. Such a microphone works similar to a Fabry-Pérot-Interferometer to detect the changes of the refractive index caused by the local pressure changes of sound waves passing a sensor cavity, fig. 1b.

This microphone is mounted on a coordinate measuring machine (CMM), fig. 1a, to get a spatial resolution of 0.1 mm in all dimensions. The usage of a CMM also enables the automation of the measurement and scanning the region of interest also multiple times.

Results/Discussion

The results of our simulations look promising and a prototype, fig. 1c, was built to test the phased array setup. Experiments to validate the simulated acoustic field with the experimental setup are currently ongoing.



P2-C9 - SAW Device & Application II

Waraku (posters 2)

Thursday, October 25, 9:30 AM - 4:00 PM

Chair: **Shogo Inoue** Qorvo, Inc.

P2-C9-1

Programmable Low Loss Orthogonal Frequency Coded SAW Correlator Filters

Marshall Smith¹, Arthur Weeks¹, Donald Malocha²

¹University of Central Florida, Orlando, FL, United States, ²Pegasense, LLC, Winter Springs, FL, United States

Background, Motivation, and Objective

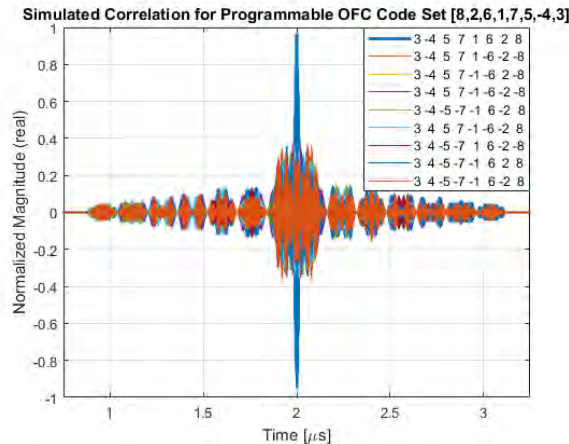
Emerging simultaneous transmit and receive (STAR) systems allow an increase in spectral efficiency up to double that of time or frequency duplexed systems, but face significant self-interference due to the presence of the transmission signal at the receiver. Correlators can reduce self-interference by using pseudo-orthogonal codes while also providing complex signal processing in real time at full radio frequency (RF). Surface Acoustic Wave (SAW) correlators can meet these needs, however, previous work has shown too high insertion loss for use in an RF front end and in most cases the code is fixed. This work is funded by the Defense Advanced Research Projects Agency (DARPA) Signal Processing at RF (SPAR) program, and further details can be found in the program's BAA.

Statement of Contribution/Methods

This work seeks to achieve low loss SAW correlators using orthogonal frequency coding (OFC) with an additional layer of programmable binary phase-shift keying (BPSK) coding. Insertion loss was reduced through a number of parallel approaches, and both fundamental and 3rd harmonic operation is considered. Single-phase unidirectional transducers (SPUDTs) are incorporated using balanced-unbalanced operation, delay is reduced, pad and electrode material and film thicknesses are tested, and transducer beamwidth is optimized empirically. A method for achieving real-time programmability within a single SAW correlator is presented and evaluated through simulation, results will be presented on the programmable filters.

Results/Discussion

This work has demonstrated low loss OFC SAW correlators, and demonstrates and evaluates a method for achieving programmability driven by the DARPA SPAR program specifications. Insertion loss has been reduced to approximately 5.5dB, and sidelobe levels approximately 11dB below the correlation peak have been achieved using a 4-chip OFC code operating at approximately 1GHz with 25MHz bandwidth. Programmability is simulated by generating the device responses for an OFC code with all possible programmable BPSK codes and choosing a set of codes with good characteristics. The correlation and cross-correlations for chosen programmable BPSK codes using OFC code [8 2 6 1 7 5 -4 3] is shown in the figure, giving a set of 9 programmable codes with 8.5dB rejection between mismatched codes.



Surface acoustic wave velocity anomaly in thin piezoelectric film detected by Picosecond Acoustics: application to extraction of piezoelectric coefficients

Arnaud DEVOS^{1,2}

¹IEMN CNRS, lille, France, ²MENAPiC, lille, France

Background, Motivation, and Objective

Piezoelectric thin-films are good candidates for actuator applications such as RF MEMS, loudspeakers or haptic interfaces; this is especially the case of PZT or AlN [1]. For a predictive design, the accurate knowledge of the mechanical properties of the materials at the submicronic scale is required especially because thin films behavior can exhibit significant changes with respect to bulk.

Statement of Contribution/Methods

The Picosecond Acoustic (PA) technique is able to measure accurately the Young modulus and the Poisson ratio on thin-film from acoustic velocity measurement. This is a full optical setup that offers the opportunity to implement a sonar at the nanoscale [2]. Acoustic pulses with frequency up to several 100 GHz result from the optical absorption of femtosecond laser pulses.

In its original configuration PA is only concerned with longitudinal waves that propagate perpendicular to the thin-film plane. To reach in-plane properties, we need to detect other waves with different polarization.

Previously we have shown that it is possible to excite and detect GHz surface acoustic waves (SAW) using the same technique if one adds some artificial crystals made of metal nanocubes on top of the sample [3]. Here we use such a technique to investigate both out-of-plane and in-plane properties of thin piezoelectric layers.

Results/Discussion

We apply the technique to a thin AlN and a thin PZT layer. For each, we detect several acoustic frequencies that correspond to a surface acoustic wave excited at various wavelectors. By building the corresponding dispersion curve, we are able to extract the Rayleigh wave velocity in the piezoelectric film itself. If no anomaly is detected in the AlN case, an unexpected high value of sound velocity is obtained for PZT. Such a result cannot be explained by adjusting the elastic moduli (Young modulus and Poisson ratio) of the thin film. Here we show that it's very well described if one takes into account the ferroelectric and the piezoelectric nature of the PZT layer. This work opens a new application of Picosecond acoustics to extract the e15 piezoelectric coefficient.

REFERENCES

- [1]. M. Cueff et al. Proc. IEEE Ultrasonics Symposium, 1948 (2011).
- [2]. A. Devos, Ultrasonics 2014, DOI 10.1016/j.ultras.2014.02.009.
- [3]. P.-A. Mante, A. Devos and A. Le Louarn, Phys. Rev. B. 81, 11, 113305 (2010).

SH-type Spurious Response Free TC-SAW Resonators Using Low Acoustic Velocity Rayleigh SAW on LiNbO₃ SubstrateMasakazu Mimura¹, Daisuke Ajima¹, Chihiro Konomo¹¹Murata Manufacturing Co., Ltd., Japan**Background, Motivation, and Objective**

Temperature compensated surface acoustic wave (TC-SAW) devices using LiNbO₃ (LN) substrates with SiO₂ overcoat are widely used. In this structure, an SH or SV-type spurious response appears near the main response and causes various undesired effects on the device characteristics. These effects can be removed by two means, minimization of its electromechanical coupling factor (K^2) and expulsion of the response from the filter passband. However, the effects are often non-negligible in practical use.

In order to explore a solution of this problem, we investigated the behavior of the SH-type spurious response on the low acoustic velocity Rayleigh SAW, which we presented last year [1].

Statement of Contribution/Methods

The K^2 and frequency of Rayleigh SAW (main response) and SH-type SAW (spurious response) were calculated by FEM changing various parameters such as electrode thickness, cut angle of LN, and so on, and robustness against variation of these parameters were evaluated.

To confirm the validity of the calculation results, we fabricated several one port resonators.

Results/Discussion

Figure 1 shows the calculated dependency of the K^2 of the SH-type SAW on normalized thickness of Pt electrode. Results of 128° Y-X LN and 120° Y-X LN, which are used for conventional Rayleigh SAW and low acoustic velocity Rayleigh SAW respectively, are shown. In the case of 120° Y-X LN, the K^2 is almost zero when Pt thickness is larger than 0.07 λ , and the thickness range where the SH-type SAW is not excited is much wider than that of 128° Y-X LN. Additional calculations indicated that the variation of K^2 is very small even when other parameters are changed. The validity of the calculation results was confirmed by experimental results of one port resonators.

Moreover, it is both theoretically and experimentally revealed that the frequency difference between the main and spurious responses can be large enough to place the spurious response outside the filter passband by employing the low acoustic velocity Rayleigh SAW.

Therefore, the developed technology can be an effective solution of the problem because of the stably small K^2 and the expulsion of the spurious response from the passband.

[1] M. Mimura, *et al.*, Proc. IEEE Ultrason. Symp. (2017), 7H-1.

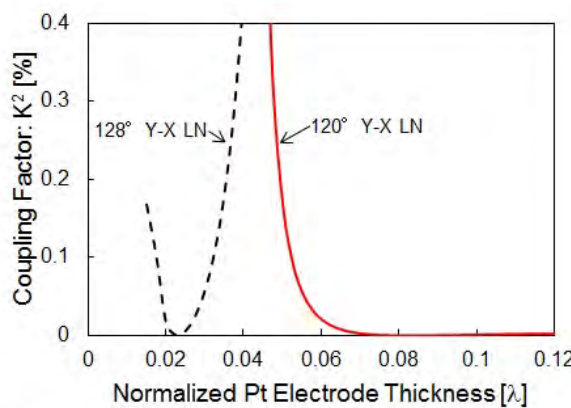


Fig. 1. Dependency of K^2 of the SH-type SAW on Pt electrode thickness.

Diamond SAW resonators made by Minimal-Fab process

Satoshi Fujii^{1,2}, Sommawan Khumpuang³, Shiro Hara³, Haruki Toonoe⁴, Yasunari Shiba⁴

¹National Institute of Technology, Okinawa College, Nago, Japan, ²Tokyo Institute of Technology, Tokyo, Japan, ³Minimal System Group, AIST, Tsukuba, Japan, ⁴Yokogawa Solution Service Corporation, Tachikawa, Japan

Background, Motivation, and Objective

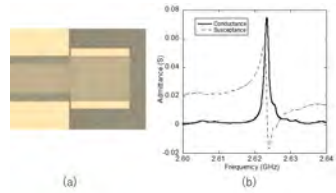
Diamond has the highest sound velocity among all materials and has been applied in high frequency surface acoustic wave (SAW) devices in the gigahertz range. To date, numerous researches have reported that the SAW devices built on a diamond wafer can work in the frequency range from 2 GHz to 10 GHz. S. Fujii et al. reported that the one-port resonator with an interdigital transducer (IDT)/AlN/single crystal diamond structure has an excellent quality factor Q of 8346 at 5.2 GHz. Hashimoto et al. also reported that an SAW resonator based on the ScAlN/single crystal diamond structure exhibited resonance Q , anti-resonance Q , and K^2 values of 520, 130, and 6.1%, respectively, at 3.6 GHz. In both reports, a small size single type Ib crystal diamond with a $3 \times 3 \text{ mm}^2$ area was employed as a substrate. However, these devices are far from becoming commercial devices because of the small substrate. Many researchers are still making an effort to realize a large diamond wafer. AIST has developed a large size single crystal diamond having a $10 \times 10 \text{ mm}^2$ area using plasma CVD method for application in power transistors and acoustic devices. Hara et al. has now developed a CMOS fabrication system known as the Minimal-Fab process. The Minimal-Fab process employs a half-inch size wafer and proceeds with the device process using a half-micron fine pattern lithograph without a clean room.

Statement of Contribution/Methods

We employed a half inch single-crystal diamond wafer made by EDP corp. and fabricated one-port SAW resonators with the interdigital transducer(IDT)/AlN/diamond structure using Minimal-Fab process except deposition of AlN thin film. The AlN thin film was deposited on the single-crystal wafer by the ECR sputtering machine.

Results/Discussion

Fig. 1 (a) shows the optical microscope image of IDT with $1\mu\text{m}$ line & space of the aluminum electrode on AlN thin film. Fig. 1 (b) shows the admittance of the best performing one-port SAW resonator in this time. The resonator exhibited a resonance frequency f of 2.6 GHz, and a quality factor Q of 2000. These values show sufficient performance even though the Q-value of this resonator is lower than the top data. Now, we try to improve diamond wafer, device design, and Minimal-fab process to obtain the highest performance of SAW resonator.



Suppression of Propagation Losses in TC SAW Resonators Using Thin Plates of LiTaO₃ Bonded to Quartz Substrates
Natalya Naumenko¹
¹*National University of Science and Technology 'MISIS', Moscow, Russian Federation*
Background, Motivation, and Objective

A thin plate of LiTaO₃ (LT) bonded to anisotropic quartz substrate was recently reported as a promising substrate material for temperature compensated (TC) SAW resonators with potentially high Q-factors [1, 2]. Quartz is attractive as a supporting substrate, due to positive temperature coefficients of some elastic constants. The existence of shear horizontally polarized (SH) waves with electromechanical coupling $k^2 > 11\%$ and TCF close to zero was verified experimentally in LT plates bonded to ST, X+90° quartz [1]. Due to very strong acoustic anisotropy of quartz, an attractive combination of properties can be also obtained for high velocity waves propagating in LT/quartz if LT and quartz orientations are optimized properly, but in general such waves leak into the substrate. In this paper, propagation losses are numerically investigated in LT plates bonded to different quartz orientations to find the optimal structures characterized by low propagation losses, low TCF, high k^2 and/or high velocity.

Statement of Contribution/Methods

Propagation losses caused by leakage and other wave characteristics, including k^2 and TCF, were extracted from the simulated admittances of Cu grating on LT plates bonded to (0, 0, 0), (0, 0, 90) and (0, 0, ψ) cuts of quartz. In LT/(0, 0, 90)-quartz, losses are zero due to quartz symmetry, but they can also vanish in some other bonded structures, e.g. in 30°LT/ST,X -quartz. For ST quartz as a substrate, velocities and k^2 change continuously with propagation direction rotated from 0 to 90°, as shown in Fig. 1, while TCF improves. Other bonded LT/quartz wafers with promising characteristics will be also reported.

Results/Discussion

Numerical investigation of acoustic waves propagating in thin LT plates bonded to quartz was performed to suppress generally nonzero propagation losses and revealed some promising combinations of quartz cut, LT and Cu electrode thicknesses for application in TC SAW resonators.

[1] M. Kadota and S. Tanaka, Proc. 2017 IEEE Ultrason. Symp., paper 5F-5, 2017.

[2] J. Hayashi, M. Gomi, M. Suzuki, S. Kakio, H. Suzuki, T. Yonai, K. Kishida, and J. Mizuno, Proc. 2017 IEEE Ultrasonics Symp., paper P4-C1-1.

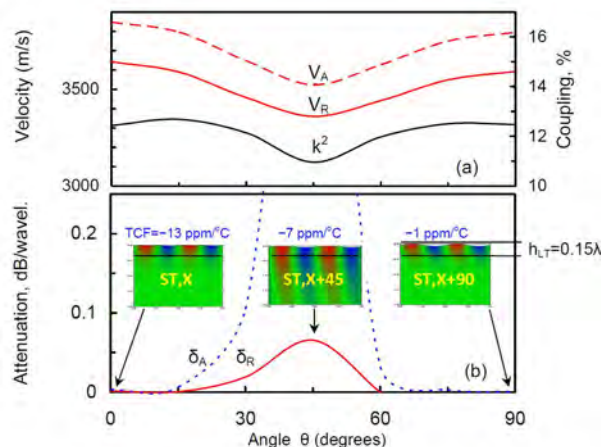


Fig. 1. Simulated velocities, coupling k^2 (a), propagation losses at f_R and f_A and TCF at f_R (b), as functions of angle θ , in resonators built on LT plate ($h_{LT}=0.15\lambda$) bonded to ST quartz, X+90° substrate. Wave structure is shown for $\theta=0^\circ$, 45° and 90° .